CODEN: JASMAN

The Journal of the Acoustical Society of America

ISSN: 0001-4966

Vol. 116, No. 2, August 2004

(Continued)

THE JOURNAL OF THE ACOUSTICAL SOCIETY OF AMERICA VOL. 116, NO. 2, AUGUST 2004

CONTENTS—*Continued from preceding page*

(Continued)

THE JOURNAL OF THE ACOUSTICAL SOCIETY OF AMERICA VOL. 116, NO. 2, AUGUST 2004

CONTENTS—*Continued from preceding page*

(Continued)

THE JOURNAL OF THE ACOUSTICAL SOCIETY OF AMERICA VOL. 116, NO. 2, AUGUST 2004

CONTENTS—*Continued from preceding page*

ACOUSTICAL NEWS—USA

Elaine Moran
Acoustical Society of America, Suite 1NO1, 2 Huntington Quadrangle, Melville, NY 11747-4502

Editor's Note: *Readers of this Journal are encouraged to submit news items on awards, appointments, and other activities about themselves or their colleagues. Deadline dates for news items and notices are 2 months prior to publication.*

Preliminary Notice: 148th Meeting of the Acoustical Society of America

The 148th Meeting of the Acoustical Society of America will be held Monday through Friday, 15–19 November 2004, at the Town and Country Hotel, San Diego, California, USA. A block of rooms has been reserved at the Town and Country Hotel.

Information about the meeting appears on the ASA Home Page at ⟨http://asa.aip.org/meetings.html⟩. Online registration is now available.

Technical Program

The technical program will consist of lecture and poster sessions. Technical sessions will be scheduled Monday through Friday, 15–19 November. The special sessions described below will be organized by the ASA Technical Committees.

Special Sessions

Acoustical Oceanography (AO)
Acoustic characterization of the benthic habitat
Acoustic methods provide powerful means for characterizing the habitat of benthic organisms. Methods and applications are presented

Acoustic sensing of internal waves
(Joint with Underwater Acoustics)
Forward propagation through internal waves including 3-D effects, and inversion for properties of internal waves using acoustic and oceanographic sensors

Animal Bioacoustics (AB)
Acoustic monitoring of large whales—The legacy of Paul Thompson
Use of acoustic monitoring to study the relative abundance, seasonality, and behavior of whales

Marine mammal acoustics: Session in honor of Ron Schusterman
Honoring the contributions of Ron Schusterman to studies of pinniped hearing and dolphin echolocation

Architectural Acoustics (AA)
Acoustics of libraries
Acoustic design of libraries, including music libraries and music archives

Coupled volume systems: Design processes and implications
Current research and design strategies in coupled volume systems

Implementation of classroom acoustics, I, II
(Joint with Noise, Psychological and Physiological Acoustics, Speech Communication, Committee on Standards)
Experience of practitioners implementing good classroom acoustics under ANSI S12.60-2002

Integration of synthesis techniques and ''acoustic'' music
(Joint with Musical Acoustics)
Various aspects of synthesis and acoustics, especially for music, will be considered

Spatial and binaural evaluation of performing arts spaces
(Joint with Signal Processing in Acoustics)
Measurement techniques of binaural and/or spatial information, evaluation and analysis methods, and physical and psychoacoustical aspects

Speech in architectural spaces—both intelligibility and privacy
(Joint with Speech and Committee on Standards)
Test methods, metrics, and the evaluation of architectural design on the resultant intelligibility or privacy of speech

Workshop on Classroom Acoustics
(Joint with Committee on Standards, Psychological and Physiological Acoustics, Speech Communication)
For teachers and other interested parties

Biomedical Ultrasound/Bioresponse to Vibration (BB)
Light and sound for imaging in the body
(Joint with Physical Acoustics)
Modalities that combine the interaction of light and sound for diagnostic imaging

Topical meeting on ultrasound characterization of cancellous and cortical bone
A one-day colloquium and discussion on the topic ''Ultrasound Characterization of Cancellous and Cortical Bone'' will be held. Subtopics will focus on the following areas: Propagation and Scattering Models, Experimental Measurement Techniques, Comparison with Other Characterization Modalities, and Clinical Impact. Each subtopic session will consist of invited and contributed papers and will be followed by a panel discussion.

Education in Acoustics (ED)
Hands-on demonstrations for high school students
Twenty demonstrations will be set up for experimentation by high school students.

Take ''5's''
Bring your short teaching tips—no abstract required

Engineering Acoustics (EA)
Hearing aids
(Joint with Signal Processing in Acoustics, Psychological and Physiological Acoustics, Committee on Standards)
State-of-the-art level presentations on hearing aid development

MEMS microphones: Fabrication, calibration, and application to high density
(Joint with Committee on Standards)
State-of-the-art experiences about aspects of MEMS microphones

Musical Acoustics (MU)
Computer music: Lecture presentations
Various aspects of acoustics in computer music. In some cases speakers may include demonstrations in the companion poster session

Computer music: Posters and demonstrations
Various aspects of computer music, including computer music related demonstrations

Musical instruments of the Asia-Pacific region
Acoustical studies of musical instruments from Asia, the Pacific Islands, Australia, and New Zealand

Performance session: A concert by Christopher Adler featuring instruments of Thailand and other parts of southeast Asia
Christopher Adler of the University of San Diego Music Department will perform with assisting musicians

Pipe organs
Innovations in pipe organ design will be highlighted

 0001-4966/2004/116(2)/609/5/$20.00

Noise (NS)
Active noise reduction for hearing protection: Technology opportunities and assessment of effectiveness
(Joint with Committee on Standards)
The application of active noise reduction techniques to the improvement of attenuation characteristics of hearing protection devices. Papers that provide insight into attenuation assessment, speech intelligibility, and techniques for improving the active noise reduction algorithms are solicited

Propulsion airframe aeroacoustics
Aircraft engines are typically mounted in isolation on test stands for preliminary noise measurements, but installation effects, especially for unconventional airframes, can modify source mechanisms and radically change radiation directivity

Soundscape sound quality
Interior noise and performance designing environments for aging populations

Special session to honor the contributions of Robert W. Young
(Joint with Architectural Acoustics, Musical Acoustics, Physical Acoustics, Committee on Standards, Underwater Acoustics, Engineering Acoustics)
Robert W. Young's contributions to acoustics cover the span from the 1930s to 1990s. This session will highlight some of these contributions

Physical Acoustics (PA)
Applications of acoustic radiation pressure
Acoustic radiation pressure applied to separation, transport, and micromanipulation of particles

Sonoluminescence, sonochemistry, and sonofusion
(Joint with Biomedical Ultrasound/Bioresponse to Vibration)
The physics, chemistry, and biology of intense cavitation

Signal Processing in Acoustics (SP)
Signal processing for arrays with many elements in novel configurations or novel environments
(Joint with Underwater Acoustics)
Special signal processing is required for efficiently overcoming specific problems in audio and underwater applications

Time delay estimation, localization, and tracking in acoustics
(Joint with Underwater Acoustics, Animal Bioacoustics, Noise, Acoustical Oceanography, Engineering Acoustics)
Techniques for using animal time information from any number of acoustics sensors to estimate a source location

Speech Communication (SC)
Fifty years of progress in speech communication: Honoring the contributions of James L. Flanagan
(Joint with Signal Processing in Acoustics)
Invited and contributed papers in honor of the contributions of James L. Flanagan in various areas of speech communication (speech analysis, synthesis, coding, perception, etc.)

Foreign-accented speech: Production, perception, and applications
Invited and contributed papers on theoretical and practical issues concerning foreign-accentedness: Theory, second-language learning variables in production and perception, training programs, etc.

Structural Acoustics and Vibration (SA)
Structural acoustics in MEMS
The generation, transmission, and effects of vibration in MEMS

Vibration of sports equipment
The mechanisms of vibration generation and the effects of vibration on the performance of sports equipment

Surface ship vibration and noise
The generation and transmission of vibration through ship structures, and the radiation of noise from ship structures into living spaces

Underwater Acoustics (UW)
Long range acoustic propagation
(Joint with Signal Processing in Acoustics and Acoustical Oceanography)
Recent experimental and theoretical results related to acoustic fluctuations from small scale oceanic variability over long ranges in the deep-water ocean

Very high frequency [0 (100) kHz] boundary interaction
Acoustic interaction with ocean boundaries at frequencies in 0 (100) kHz frequency range

Other Technical Events

Hot Topics Session

A ''Hot Topics'' session sponsored by the Tutorials Committee is scheduled covering the fields of Animal Bioacoustics, Architectural Acoustics, and Structural Acoustics, and Vibration.

Paper Copying Service

The ASA has replaced its traditional at-meeting ''Paper Copying Service'' with a new online site which can be found at http://scitation.aip.org/asameetingpapers/. Authors of papers to be presented at meetings will be able to post their full papers or presentation materials for others who are interested in obtaining detailed information about meeting presentations. The online site will be open for author submissions in September. Submission procedures and password information will be mailed to authors with the acceptance notices.

Those interested in obtaining copies of submitted papers for this meeting and the immediate past meeting may access the service at anytime. No password is needed.

Exhibit

The instrument and equipment exposition, which will be conveniently located near the registration and meeting rooms, will open at the Town and Country Hotel with a reception on Monday evening, 15 November, and will close on Wednesday afternoon, 17 November. The exposition will include computer-based instrumentation, sound level meters, sound intensity systems, signal processing systems, devices for noise control and acoustical materials, active noise control systems, and other exhibits on acoustics. For further information, please contact the Exhibit Manager, Robert Finnegan, Advertising and Exhibits Div., AIP, Suite 1NO1, 2 Huntington Quadrangle, Melville, NY 11747-4502, Tel: 516-576-2433; Fax: 516-576-2481; E-mail: rfinneg@aip.org.

Meeting Program

An advance meeting program summary will be published in the September issue of JASA and a complete meeting program will be mailed as Part 2 of the October issue. Abstracts will be available on the ASA Home Page (http://asa.aip.org) in September.

Tutorial Lecture

A tutorial presentation on Ocean Noise and Marine Mammals will be given by Gerald D'Spain and Doug Wartzok on Monday, 15 November, at 7:00 p.m.

Lecture notes will be available at the meeting in limited supply. Those who register by 18 October are guaranteed receipt of a set of notes.

To partially defray the cost of the lecture a registration fee is charged. The fee is $15 for registration received by 4 October and $25 thereafter including on-site registration at the meeting. The fee for students with current ID cards is $7.00 for registration received by 4 October and $12.00 thereafter, including on-site registration at the meeting. Use the registration form in the call for papers or register online at http://asa.aip.org to register for the Tutorial Lecture.

Short Course

A short course on Acoustical Oceanography in Shallow Water will be held on Sunday and Monday, 14 and 15 November, at the Town and Country Hotel.

In recent years, there has been considerable research activity on sound propagation and scattering in shallow water and in the use of acoustics to infer oceanographic properties of the shallow-water environment. This interest in the littoral zone has been motivated by practical considerations including antisubmarine warfare, mine countermeasures, underwater communication, homeland security, and geophysical exploration. Acoustical oceanography in shallow water is particularly challenging due to the heterogeneous nature of the seabed, the complexities associated with bubbles and roughness at the air–sea interface, and the lateral variability in the water column arising from oceanographic features such as internal waves. Nevertheless, significant theoretical and experimental advances have been made in our understanding of the complex interaction between sound waves and the littoral environment.

The objective of this course is to provide a foundation for understanding the major current scientific issues arising in shallow-water acoustical oceanography. A review of classical, range-independent, shallow-water acoustics will lead into discussions of key contemporary research topics and recent advances in those areas. Emphasis will be placed on the fundamental physical principles underlying both the acoustics and the oceanography. Relevant experimental results will be highlighted, and signal processing issues that are unique to the shallow-water environment will also be discussed.

The instructors will be George Frisk (Course Coordinator), Florida Atlantic University; Grant Deane, Marine Physical Laboratory, Scripps Institution of Oceanography; James Preisig, Woods Hole Oceanographic Institution; Dajun Tang, Applied Physics Laboratory, University of Washington.

The registration fee is $300.00 and covers attendance, instructional materials, and coffee breaks. The number of attendees will be limited so please register early to avoid disappointment. Only those who have registered by 18 October will be guaranteed receipt of instructional materials. There will be a $50 discount for registration made prior to 4 October. Full refunds will be made for cancellations prior to 4 October. Any cancellation after 4 October will be charged a $75 processing fee. Use the form in the call for papers or online at http://asa.aip.org to register for this short course.

Special Meeting Features

Student Transportation Subsidies

A student transportation subsidies fund has been established to provide limited funds to students to partially defray transportation expenses to meetings. Students presenting papers who propose to travel in groups using economical ground transportation will be given first priority to receive subsidies, although these conditions are not mandatory. No reimbursement is intended for the cost of food or housing. The amount granted each student depends on the number of requests received. To apply for a subsidy, submit a proposal (e-mail preferred) to be received by 4 October to Jolene Ehl, ASA, Suite 1NO1, 2 Huntington Quadrangle, Melville, NY 11747-4502, Tel: 516-576-2359, Fax: 516-576-2377, E-mail: jehl@aip.org. The proposal should include your status as a student; whether you have submitted an abstract; whether you are a member of ASA; method of travel; if traveling by auto, whether you will travel alone or with other students; names of those traveling with you; and approximate cost of transportation.

Young Investigator Travel Grant

The Committee on Women in Acoustics is sponsoring a Young Investigator Travel Grant to help with travel costs associated with presenting a paper at the San Diego meeting. This award is designed for young professionals who have completed the doctorate in the past five years (not currently enrolled as a student), who plan to present a paper at the San Diego meeting. Each award will be of the order of $300. It is anticipated that the Committee will grant a maximum of three awards. Applicants should submit a request for support, a copy of the abstract they have submitted for the meeting, and a current resume/vita which provides information on their involvement in the field of acoustics and to the ASA to Dr. Peggy Nelson, Department of Speech-Language-Hearing Sciences, University of Minnesota, 164 Pillsbury Drive SE, Minneapolis MN 55455; Fax: 612-624-7586; E-mail: nelso477@umn.edu. Deadline for receipt of applications is 1 October.

Students Meet Members for Lunch

The Education Committee has established a program for students to meet one on one with members of the Acoustical Society over lunch. The purpose is to make it easier for students to meet and interact with members at meetings. Each lunch pairing is arranged separately. Students who wish to participate may sign up by contacting David Blackstock, University of Texas at Austin, Mechanical Engineering Dept., 1 University Station C2200, Austin TX 78712-0292; Tel.: 512-471-3145; Fax: 512-471-1045; E-mail: dtb@mail.utexas.edu. The information needed in order to arrange each pairing is the student's name, university, department, status (graduate student or undergraduate), research field, interests in acoustics, and days that are free for lunch. The sign-up deadline is one week before the start of the meeting, but an earlier sign-up is strongly encouraged. The cost of the meal is the responsibility of each participant.

Plenary Session, Awards Ceremony, Fellows Suite, Fellows' Lunch and Social Events

Buffet socials with cash bar will be held on Tuesday and Thursday evenings, 16 and 18 November, at the Town and Country Hotel.

The Plenary session will be held on Wednesday afternoon, 17 November, at the Town and Country Hotel where Society awards will be presented and recognition of newly elected Fellows will be announced.

A Fellows' Hospitality Suite will be open on Tuesday afternoon, 16 November. Refreshments will be provided. A Fellows' Luncheon will be held on Thursday, 18 November, at 12:00 noon. Professor Walter Munk of The Scripps Institution of Oceanography will present a talk titled "'IVY-MIKE'—An account of the first thermonuclear explosion, through the eyes of a participating Scripps oceanographer.'' Each Fellow may bring one guest to the luncheon. Fellows should use the form in the call for papers or online at http://asa.aip.org to purchase tickets for themselves and their guests.

Women in Acoustics Luncheon

The Women in Acoustics luncheon will be held on Wednesday, 17 November. Those who wish to attend this luncheon must register using the form in the call for papers or online at http://asa.aip.org. The fee is $15 (students $5) for preregistration by 4 October and $20 (students $5) thereafter including on-site registration at the meeting.

Transportation and Hotel Accommodations

Air Transportation

San Diego is served by the San Diego International Airport (Airport Code SAN). A number of airlines fly in and out of San Diego. For flight information, visit ⟨http://www.san.org/⟩; for other information of interest, visit ⟨http://www.sandiego.org/index.asp⟩.

Ground Transportation

Transportation from the San Diego International Airport to the Town and Country Hotel:

Major car rental companies: Rental car counters are located adjacent to the airport's baggage claim areas or in Terminals 1 and 2. You can use the courtesy phones provided to request shuttle transport to the car rental company of your choice ⟨http://www.sandiego.org/gettingaround.asp⟩.

SuperShuttle shared-ride, door to door service: Shuttle cars and buses operated by off-airport companies are a popular and convenient transportation option. Shuttle service is available at the Transportation Plazas across from Terminals 1 and 2, and curbside at the Commuter Terminal.

From Terminal 1 you must cross the skybridge, and take either the escalators or the elevators to street level. From Terminal 2, cross the Terminal 2 skybridge and take either the escalators or the elevators to street level, or use the pedestrian crosswalk conveniently located outside the Terminal 2 Baggage Claim Area to access the Transportation Plaza. A Transportation Coordinator will place you with the first available shuttle, unless you specify a particular shuttle company. For a complete list of shuttle companies, visit ⟨http://www.sandiego.org/gettingaround.asp⟩.

Taxicabs and limousines: Many companies provide taxicab service at San Diego International Airport. If you need a taxi, simply follow the signs leading to the Transportation Plazas. A Transportation Coordinator will

place you with the first available taxi unless you specify a particular taxicab company. For more information visit ⟨http://www.sandiego.org/gettingaround.asp⟩. Taxi fares are metered and should cost approximately $30 from the airport to the Town and Country Hotel. Several companies offer chauffeur-driven limousine service from San Diego International Airport. Typically, you must make a reservation for a pick-up prior to your arrival.

Hotel Reservation Information

The meeting and all functions will be held at the Town and Country Hotel.

A block of guest rooms at discounted rates has been reserved for meeting participants at the Town and Country Hotel. Early reservations are strongly recommended. Please make your reservations directly with the hotel. Note that the special ASA meeting rates are not guaranteed after 22 October 2004. You must mention the Acoustical Society of America when making your reservations to obtain the special ASA meeting rates. You may book a room at this rate for the period November 13 through November 19, and possibly longer, if desired (depending on availability).

The Town and Country Hotel is located not too far from San Diego's sun-splashed coast. Located in the heart of San Diego—Mission Valley—The Town and Country is convenient to all the city's sights and famous attractions. The hotel offers four outdoor swimming pools and whirlpool, as well as a new world-class spa and fitness program, concierge and travel services, rental car services, five restaurants and lounges, and a gift shop. Guest services include complimentary in-room coffee and newspaper, business center, pay-per-view in-room movies, room service (6 a.m.–midnight), laundry and valet services, and data-port telephones with voice mail. Adjacent to the Town and Country is the Riverwalk Golf Course, one of San Diego's 27-hole championship courses. In addition, access to San Diego's newly expanded light rail trolley system provides visitors with convenient transportation to Downtown and the historic Gaslamp Quarter, east to Qualcomm Stadium, and south to the border at Tijuana, Mexico and, of course, Old Town. For additional information about the hotel, visit ⟨http://www.towncountry.com⟩.

For attendees who will be driving, complimentary self-parking is available. To obtain driving directions to the Town and Country Hotel, visit ⟨http://www.mapquest.com⟩.

Please make your reservation directly with the Town and Country Hotel. When making your reservation, you must mention the Acoustical Society of America to obtain the special ASA meeting rates.

Town and Country Hotel
500 Hotel Circle North
San Diego, CA 92108
Tel: 619-291-7131; Reservations: 1-800-772-8527
Fax: 619-291-3584

Rates
Single: $125.00
Double: $135.00
Govt. Rate Single/Double (limited quantity): $110.00

Room Sharing

ASA will compile a list of those who wish to share a hotel room and its cost. To be listed, send your name, telephone number, e-mail address, gender, and smoker or nonsmoker preference by 4 October to the Acoustical Society of America, preferably by E-mail, asa@aip.org, or by postal mail to Acoustical Society of America, Attn.: Room Sharing, Suite 1NO1, 2 Huntington Quadrangle, Melville, NY 11747-4502. The responsibility for completing any arrangements for room sharing rests solely with the participating individuals.

Weather

San Diego enjoys beautiful weather year round with an average daily temperature of 70.5 °F (21.4 °C). A marked feature of the climate is the wide variation in temperature within short distances due to the topography of the land. You can enjoy coastal, mountain, and desert environments all in the space of one day. For additional information on weather, visit ⟨http://www.sandiego.org/weather.asp⟩.

General Information

Assistive Listening Devices

Anyone planning to attend the meeting who will require the use of an assistive listening device is requested to advise the Society in advance of the meeting: Acoustical Society of America, Suite 1NO1, 2 Huntington Quadrangle, Melville, NY 11747-4502, asa@aip.org.

Accompanying Persons Program

Spouses and other visitors are welcome at the San Diego meeting. The registration fee for accompanying persons is $35/$45. A hospitality room for accompanying persons will be open at the Town and Country Hotel from 8:00 a.m. to 11:00 a.m. each morning throughout the meeting where information about activities in and around San Diego will be provided.

San Diego is fast making a name for itself as an important diverse cultural center, offering a kaleidoscope of opera, ballet, museums, and world-class, Tony Award-winning theater. Whether you want to go deep-sea fishing and boating along the coastline, ballooning or golfing in North County, shopping in Mission Valley, exploring East County's mountains and deserts, or ''doing it up'' downtown, San Diego has attractions all over San Diego County to fill your days and nights.

The **Gaslamp Quarter** is Southern California's premier dining, shopping, and entertainment district, where you'll find a truly eclectic blend of food, fun, and culture all within one of San Diego's most historic areas. Browse the area's fine art galleries, boutiques, bazaars, and specialty stores. As the sun sets, the streets come alive in the Gaslamp Quarter. The old-fashioned gaslamps glow along the wide brick walkways, illuminating many charming sidewalk cafes. You can stroll past the Victorian-style commercial buildings constructed between 1873 and 1930.

At the world-famous **San Diego Zoo**, you will see some of the world's rarest wildlife including giant pandas (and Hua Mei, the only panda cub in the U.S.) and koalas. Other exhibits include the Ituri Forest, Gorilla Tropics, Polar Bear Plunge, Children's Zoo, Rain Forest Aviary, Tiger River, and many more attractions worth visiting.

A visit to the **San Diego Wild Animal Park** is like a safari to many of the world's most exotic places. The 1800 acre wildlife preserve allows visitors to view herds of exotic animals as they might be seen in their native Asian and African countries. Today the park has over 3500 animals representing 260 species, and is also an accredited botanical garden.

World-renowned **Balboa Park** is home to 15 museums, various arts and international cultural associations, as well as the San Diego Zoo, making it one of the nation's largest cultural and entertainment complexes.

Sea World San Diego has hosted more than 100 million guests since opening in 1964. The park's land mass is 189.5 acres and has many exciting adventures, amazing animals, and wondrous shows.

Birch Aquarium at Scripps Institution of Oceanography opened on 16 September 1962 at a new location situated on a hillside overlooking the Pacific Ocean and Scripps Pier. Four times larger than its predecessor, the new complex contains more than 60 tanks, a demonstration tide pool, and an interactive museum. For a panoramic view of the La Jolla coast and the world-renowned Scripps Institution of Oceanography, this is a must to visit.

The Reuben H. Fleet Science Center is an educational, entertaining experience for visitors of all ages and has exhibits to touch, virtual reality experience films to see, and fun to be had. Their 76-foot IMAX domed theater presents the biggest films on the planet, plus planetarium shows and more. Its unique configuration wraps the audience in images and provides the illusion of being suspended in space. Ride **DEEP SEA**, the motion simulator ride, and plunge into the unexplored world at the bottom of the ocean. There are two virtual reality experiences that employ cutting-edge technology that puts you in the action. Plus, the Nierman Challenger Learning Center offers the experience of living and working in space.

Old Town San Diego State Historic Park recreates life in the Mexican and early American periods of 1821 to 1872. San Diego became California's first Spanish settlement when a mission and fort were established in 1769. Five original adobes are part of the complex, which includes shops, restaurants, and a museum. La Casa de Estudillo is a mansion built around a garden courtyard. La Casa de Machado y Stewart is full of artifacts that reflect ordinary life of the period. Other historic buildings include a schoolhouse, a blacksmith shop, San Diego's first newspaper office, and a stable with a carriage collection.

Registration Information

The registration desk at the meeting will open on Monday, 15 November, at the Town and Country Hotel. To register use the form in the call for papers or register online at ⟨asa.aip.org⟩. If your registration is not received at the ASA headquarters by 18 October, you must register on-site.

Registration fees are as follows:

Category	Preregistration by 4 October	Registration after 4 October
Acoustical Society Members	$300	$350
Acoustical Society Members One-Day	$150	$175
Nonmembers	$350	$400
Nonmembers One-Day	$175	$200
Nonmember Invited Speakers	Fee waived	Fee waived
Students (with current ID cards)	Fee waived	Fee waived
Emeritus members of ASA (Emeritus status preapproved by ASA)	$35	$45
Accompanying Persons (Spouses and other registrants who will not participate in the technical sessions)	$35	$45

Nonmembers who simultaneously apply for Associate Membership in the Acoustical Society of America will be given a $50 discount off their dues payment for the first year (2005) of membership. Invited speakers who are members of the Acoustical Society of America are expected to pay the registration fee, but **nonmember invited speakers** may register without charge.

NOTE: A $25 processing fee will be charged to those who wish to cancel their registration after 4 October.

Online Registration

Online registration is now available at ⟨asa.aip.org⟩.

Members of the Local Committee for the Meeting

General Chair—William A. Kuperman; Technical Program Chair—Michael J. Buckingham; Food Service/Social Events—Pat Jordan; Audio–Visual—Paul A. Baxley; Accompanying Persons Program—Gail Smith; Signs—Carolyn Ebrahimi; Student Coordinator—Matthew A. Dzieciuch; Poster Sessions—Aaron M. Thode

USA Meetings Calendar

Listed below is a summary of meetings related to acoustics to be held in the U.S. in the near future. The month/year notation refers to the issue in which a complete meeting announcement appeared.

2004

16–18 Sept. Twelfth Annual Conference on the Management of the Tinnitus Patient. For professionals and tinnitus patients. The University of Iowa, Iowa City, IA [Contact Rich Tyler, 319-356-2471, E-mail: rich-tyler@uiowa.edu, WWW: www.uihealthcare.com/depts/med/otolaryngology/conferences/index.html]

20–24 Sept. ACTIVE 2004—The 2004 International Symposium on Active Control of Sound and Vibration, Williamsburg, VA [INCE Business Office, Iowa State Univ., 212 Marston Hall, IA 50011-2153; Fax: 515-294-3528; E-mail: ibo@ince.org; WWW: inceusa.org].

15–19 Nov. 148th Meeting of the Acoustical Society of America, San Diego, CA [Acoustical Society of America, Suite 1NO1, 2 Huntington Quadrangle, Melville, NY 11747-4502; Tel.: 516-576-2360; Fax: 516-576-2377; E-mail: asa@aip.org; WWW: http://asa.aip.org].

2005

16–19 May Society of Automotive Engineering Noise & Vibration Conference, Traverse City, MI [Patti Kreh, SAE International, 755 W. Big Beaver Rd., Ste. 1600, Troy, MI 48084, Tel.: 248-273-2474; E-mail: pkreh@sae.org].

Cumulative Indexes to the *Journal of the Acoustical Society of America*

Ordering information: Orders must be paid by check or money order in U.S. funds drawn on a U.S. bank or by Mastercard, Visa, or American Express credit cards. Send orders to Circulation and Fulfillment Division, American Institute of Physics, Suite 1NO1, 2 Huntington Quadrangle, Melville, NY 11747-4502; Tel.: 516-576-2270. Non-U.S. orders add $11 per index.

Some indexes are out of print as noted below.

Volumes 1–10, 1929–1938: JASA and Contemporary Literature, 1937–1939. Classified by subject and indexed by author. Pp. 131. Price: ASA members $5; Nonmembers $10.

Volumes 11–20, 1939–1948: JASA, Contemporary Literature, and Patents. Classified by subject and indexed by author and inventor. Pp. 395. Out of Print.

Volumes 21–30, 1949–1958: JASA, Contemporary Literature, and Patents. Classified by subject and indexed by author and inventor. Pp. 952. Price: ASA members $20; Nonmembers $75.

Volumes 31–35, 1959–1963: JASA, Contemporary Literature, and Patents. Classified by subject and indexed by author and inventor. Pp. 1140. Price: ASA members $20; Nonmembers $90.

Volumes 36–44, 1964–1968: JASA and Patents. Classified by subject and indexed by author and inventor. Pp. 485. Out of Print.

Volumes 36–44, 1964–1968: Contemporary Literature. Classified by subject and indexed by author. Pp. 1060. Out of Print.

Volumes 45–54, 1969–1973: JASA and Patents. Classified by subject and indexed by author and inventor. Pp. 540. Price: $20 (paperbound); ASA members $25 (clothbound); Nonmembers $60 (clothbound).

Volumes 55–64, 1974–1978: JASA and Patents. Classified by subject and indexed by author and inventor. Pp. 816. Price: $20 (paperbound); ASA members $25 (clothbound); Nonmembers $60 (clothbound).

Volumes 65–74, 1979–1983: JASA and Patents. Classified by subject and indexed by author and inventor. Pp. 624. Price: ASA members $25 (paperbound); Nonmembers $75 (clothbound).

Volumes 75–84, 1984–1988: JASA and Patents. Classified by subject and indexed by author and inventor. Pp. 625. Price: ASA members $30 (paperbound); Nonmembers $80 (clothbound).

Volumes 85–94, 1989–1993: JASA and Patents. Classified by subject and indexed by author and inventor. Pp. 736. Price: ASA members $30 (paperbound); Nonmembers $80 (clothbound).

Volumes 95–104, 1994–1998: JASA and Patents. Classified by subject and indexed by author and inventor. Pp. 632. Price: ASA members $40 (paperbound); Nonmembers $90 (clothbound).

Volumes 105–114, 1999–2003: JASA and Patents. Classified by subject and indexed by author and inventor. Pp. 616. Price: ASA members $50 Nonmembers $90 (paperbound).

ACOUSTICAL NEWS—INTERNATIONAL

Walter G. Mayer
Physics Department, Georgetown University, Washington, DC 20057

New Presidents of societies

Canada: It was announced last December that Stan Dosso will be the next President of the Canadian Acoustical Association (CAA/ACA). Stan Dosso is a Professor at the University of Victoria. He is a Fellow of the Acoustical Society of America.

Europe: A new board of officers was elected by the European Acoustics Association (EAA) with Michael Vorländer of the Technical University Aachen, Germany, as President. Michael Vorländer is a Member of the Acoustical Society of America. J.-D. Polack (France) and E. Kozaczka (Poland) were elected Vice-Presidents.

Germany: The German Acoustical Society (DEGA) has elected Hugo Fastl to be the next President. He will begin his two-year term in the fall of 2004. Fastl is a Professor at the Technical University of Munich; he is a Fellow of the Acoustical Society of America.

United Kingdom: The new President of the Institute of Acoustics (IoA) will be Tony Jones who will take over from President Kerry. Jones is with AIRO Ltd.; he is a Fellow of the Institute of Acoustics and a Member of the Acoustical Society of America.

International Meetings Calendar

Below are announcements of meetings and conferences to be held abroad. Entries preceded by an ∗ are new or updated listings.

August 2004

23–27 **2004 IEEE International Ultrasonics, Ferroelectrics, and Frequency Control 50th Anniversary Conference**, Montréal, Canada (Fax: +1 978 927 4099; Web: www.ieee-uffc.org/index2-asp).

22–25 **Inter-noise 2004**, Prague, Czech Republic (Web: www.internoise2004.cz).

30–1 **Low Frequency 2004**, Maastricht, The Netherlands (G. Leventhall, 150 Craddlocks Avenue, Ashtead, Surrey KT 21 1NL, UK; Web: www.lowfrequency2004.org.uk).

September 2004

1–3 **Subjective and Objective Assessment of Sound**, Poznań, Poland (Institute of Acoustics, Adam Mankiewicz University, Poznań, Poland; Fax: +48 61 8295 123; Web: www.soas.amu.edu.pl/soas.html).

6–10 **51st Open Seminar on Acoustics; 9th School on Acoustooptics and Applications; Ultrasound in Biomeasurements**, Gdańsk, Poland (University of Gdańsk, Institute of Experimental Physics, 80-952 Gdańsk, Poland; Fax: +48 58 341 31 75; Web: univ.gda.pl/∼osa).

13–17 **4th Iberoamerican Congress on Acoustics, 4th Iberian Congress on Acoustics, 35th Spanish Congress on Acoustics**, Guimarães, Portugal (Fax: +351 21 844 3028; Web: www.spacustica.pt/novidades.htm).

14–16 **International Conference on Sonar Signal Processing and Symposium on Bio-Sonar Systems and Bioacoustics**, Loughboro, UK (Fax: +44 1509 22 7053 [c/o D. Gordon]; Web: ioa2004.lboro.ac.uk).

15–17 **26th European Conference on Acoustic Emission Testing**, Berlin, Germany (DGZIP, Max-Planck-Str. 26, 12489 Berlin, Germany; Web: www.ewgae2004.de).

20–22 **International Conference on Noise and Vibration Engineering (ISMA2004)**, Leuven, Belgium (Fax: +32 16 32 29 87; Web: www.isma-isaac.be/fut_conf/default_en.phtml).

20–22 **9th International Workshop "Speech and Computer" (SPECOM'2004)**, St. Petersburg, Russia (Web: www.spiiras.nw.ru/speech).

27–29 ∗**Hellenic National Conference on Acoustics 2004**, Thessaloniki, Greece (Web: www.wcl.ee.upatras/helina/ac2004.htm).

28–30 **Autumn Meeting of the Acoustical Society of Japan**, Naha, Japan (Fax: +81 3 5256 1022; Web: wwwsoc.nii.ac.jp/asj/index-e.html).

October 2004

4–8 **8th Conference on Spoken Language Processing (INTERSPEECH)**, Jeju Island, Korea (Web: www.icslp2004.org).

6–8 **Acoustics Week in Canada**, Ottawa, ON, Canada (J. Bradley, NRC Institute for Research on Construction [Acoustics Section], Ottawa, Ontario, K1A 0R6; Fax: +1 613 954 1495; Web: caa-aca.ca/ottawa-2004.html).

6–7 **Institute of Acoustics Autumn Conference**, Oxford, UK (Web: www.ioa.org.uk).

8–9 **Reproduced Sound 20**, Oxford, UK (Web: www.ioa.org.uk).

27–29 ∗**25th Symposium on Ultrasonic Electronics**, Sapporo, Japan (Web: www.use-jp.org/USEframepage_E.html).

November 2004

3–5 **Australian Acoustical Society Conference—Transportation Noise & Vibration**, Surfers Paradise, Queensland, Australia (Fax: +61 7 6217 0066; Web: www.acoustics.asn.au/conference/index.htm).

4–5 **Autumn Meeting of the Swiss Acoustical Society**, Rapperswil, Switzerland (Fax: +41 419 62 13; Web: www.sga-ssa.ch).

8–9 ∗**17th Biennial Conference of the New Zealand Acoustical Society**, Wellington, New Zealand (E-mail: miklin@marshallday.co.nz).

15–18 **15th Meeting of the Russian Acoustical Society**, Nizhny Novgorod, Russia (Fax: +7 95 126 0100; Web: www.akin.ru).

17–19 **7th National Congress of the Turkish Acoustical Society**, Nevsehir-Cappadocia, Turkey (Web: www.tak.der.org).

March 2005

14–17 ∗**31st Annual Meeting of the German Acoustical Society (DAGA'05)**, Munich, Germany (Web: daga2005.de).

April 2005

18–21 **International Conference on Emerging Technologies of Noise and Vibration Analysis and Control**, Saint Raphaël, France (Fax: +33 4 72 43 87 12; E-mail: goran.pavic@insa-lyon.fr).

May 2005

16–20 **149th Meeting of the Acoustical Society of America**, Vancouver, British Columbia, Canada (ASA, Suite 1NO1, 2 Huntington Quadrangle, Melville, NY 11747-4502 USA; Fax: +1 516 576 2377; Web: asa.aip.org).

 0001-4966/2004/116(2)/615/2/$20.00

June 2005

20–23 *__IEEE Oceans05 Europe__, Brest, France (ENST Bretagne—Technopôle Brest Iroise, 29238 Brest Cedex, France; Fax: +33 229 00 1098; Web: www.oceans05europe.org).

23–24 *__2nd Congress of the Alps-Adria Acoustical Association (AAAA2005)__, Opatija, Croatia (Web: had.zea.fer.hr).

28–1 __International Conference on Underwater Acoustic Measurements: Technologies and Results__, Heraklion, Crete, Greece (Web: UAmeasurements2005.iacm.forth.gr).

July 2005

11–14 __12th International Congress on Sound and Vibration__, Lisbon, Portugal (Web: www.iiav.org).

August 2005

6–10 __Inter-Noise__, Rio de Janeiro, Brazil (Web: www.internoise2005.ufsc.br).

28–2 __EAA Forum Acusticum Budapest 2005__, Budapest, Hungary (I. Bába, OPAKFI, Fö u. 68, Budapest 1027, Hungary; Fax: +36 1 202 0452; Web: www.fa2005.org).

September 2005

4–8 __9th Eurospeech Conference (EUROSPEECH'2005)__, Lisbon, Portugal (Fax: +351 213145843; Web: www.interspeech2005.org).

5–9 __Boundary Influences in High Frequency, Shallow Water Acoustics__, Bath, UK (Web: acoustics2005.ac.uk).

11–15 __6th World Congress on Ultrasonics__, Beijing, China (Secretariat of WCU 2005, Institute of Acoustics, Chinese Academy of Sciences, P.O. Box 2712, Beijing 100080, China; Fax: +86 10 62553898; Web: www.ioa.ac.cn/wcu2005).

14–16 *__Autumn Meeting of the Acoustical Society of Japan__, Sendai, Japan (Acoustical Society of Japan, Nakaura 5th-Bldg., 2-18-20 Sotokanda, Chiyoda-ku, Tokyo 101-0021, Japan; Fax: +81 3 5256 1022; Web: www.asj.gr.jp/index-en.html).

18–21 *__IEEE International Ultrasonics Symposium__, Rotterdam, The Netherlands (Web: ieee-uffc.org).

October 2005

19–21 __36th Spanish Congress on Acoustics Joint with 2005 Iberian Meeting on Acoustics__, Terrassa (Barcelona), Spain (Sociedad Española de Acústica, Serrano 114, 28006 Madrid, Spain; Fax: +34 914 117 651; Web: www.ia.csic.es/sea/index.html).

June 2006

26–28 __9th Western Pacific Acoustics Conference (WESPAC 9)__, Seoul, Korea (Web: www.wespac8.com/WespacIX.html).

July 2007

9–12 __14th International Congress on Sound and Vibration (ICSV14)__, Cairns, Australia (E-mail: n.kessissoglou@unsw.edu.au).

September 2007

2–7 __19th International Congress on Acoustics (ICA2007)__, Madrid, Spain (SEA, Serrano 144, 28006 Madrid, Spain; Web: www.ica2007madrid.org).

June 2008

23–27 *__Joint Meeting of European Acoustical Association (EAA), Acoustical Society of America (ASA), and Acoustical Society of France (SFA)__, Paris, France (E-mail: phillipe.blanc-benon@ae-lyon.fr).

BOOK REVIEWS

P. L. Marston
Physics Department, Washington State University, Pullman, Washington 99164

These reviews of books and other forms of information express the opinions of the individual reviewers and are not necessarily endorsed by the Editorial Board of this Journal.

Editorial Policy: *If there is a negative review, the author of the book will be given a chance to respond to the review in this section of the Journal and the reviewer will be allowed to respond to the author's comments. [See "Book Reviews Editor's Note," J. Acoust. Soc. Am.* ***81****, 1651 (May 1987).]*

Acoustic Interactions with Submerged Elastic Structures

Part I: Acoustic Scattering and Resonances

A. Guran, J. Ripoche, and F. Ziegler

World Scientific, River Edge, New Jersey, 1996.
368 pp. Price: $75 (hardcover), ISBN: 981-02-2964-X.

Part II: Propagation, Ocean Acoustics and Scattering

A. Guran, G. Maugin, J. Engelbrecht, and M. Werby

World Scientific, River Edge, New Jersey, 2001.
388 pp. Price: $90 (hardcover), ISBN: 981-02-2965-8.

Part III: Acoustic Propagation and Scattering, Wavelets and Time Frequency Analysis

A. Guran, A. de Hoop, D. Guicking, and F. Mainardi

World Scientific, River Edge, New Jersey, 2001.
444 pp. Price: $90 (hardcover), ISBN: 981-02-2950-X.

Part IV: Nondestructive Testing, Acoustic Wave Propagation and Scattering

A. Guran, A. Boström, O. Leroy, and G. Maze

World Scientific, River Edge, New Jersey, 2002.
508 pp. Price: $120 (hardcover), ISBN: 981-02-4271-9.

This is a four-volume *Festschrift* honoring Herbert Überall. The emphasis is on areas of acoustics that overlap Überall's research on propagation and scattering, dating from the late 1960s through the present time. This is an impressive collection of 45 research and review chapters involving 78 authors or co-authors. (In this tally authors contributing to more than one chapter have not been double counted.) Taking into account the nature and quality of chapters and the topics considered, this set of books is recommended for purchase by libraries that serve research programs involved with acoustic scattering related to underwater acoustics and ultrasonics. All parts of this set have a helpful subject index and Parts 1, 3, and 4 include a name index of cited authors. Part 4 contains useful appendices listing chronologically Überall's publications in acoustics and related work on electromagnetic scattering, and a list of 50 M.S. and Ph.D. students who graduated under Professor Überall.

This is the third time a book (or set of books) has been published that contains collections of chapters that significantly overlap Überall's research on acoustic scattering. The present set does not appear to be weighted as much towards introductory and review material as the previous volumes.[1,2] Part 4 is a noteworthy exception which contains, for example, reviews of elastodynamic scattering (by A. Boström), computational modeling of transient wave fields (by A. de Hoop), linear viscoelasticity (by F. Mainardi), ocean-seismoacoustic modeling (by J. E. Murphy and S. A. Chin-Bing), and nearfield acoustic holography (by A. Sarkissian). Other exceptions, for example, in Part 2, are the chapters on matched field processing (by A. Tolstoy) and underwater acoustic modeling (by P. C. Etter). Several chapters in Parts 1 and 2 concern applications of the experimental "method of isolation and identification of resonances" (MIIR) for targets in water. MIIR is one of the methods used to detect the resonances predicted by the theoretical work of Professor Überall and other researchers.

The present reviewer is of the opinion that collections of chapters are of greatest value when they are weighted towards introductory and review material and they are written in a more relaxed style than may be permitted in some journals. Such chapters are potentially helpful for introducing graduate students to research fields or for "catching up" on areas of interest. Some chapters in these volumes, however, omit references needed to place the research reported in the broader context of acoustic scattering research. For example, the chapter in Part 3 concerning "...Scattering Theory for Strongly Overlapping Resonances" correctly notes that (for targets having certain symmetries) the unimodular S function may be expressed in a product expansion of unimodular complex functions of a specified form. The authors neglect to mention, however, that this correction to some early acoustic research was previously discussed. (See, for example, Refs. 1 and 3.) In one of the discussions of ray methods for scattering by elastic targets in Part 1, the principal confirmation of the formulation is comparison with the observed location of acoustic spectral peaks. Some readers may fail to realize that there has been considerable success in using quantitative ray methods to predict measured and computed *scattering amplitudes* (including cases that involve targets with truncations). Examples include research reviewed by Hackman[3] and various papers in the *Journal of the Acoustical Society of America*. Most of the chapters are valuable provided the reader keeps the limitations in perspective. Although many of the chapters on scattering emphasize targets having smooth external features, there are several chapters that consider the effects of *internal structure* on the scattering by shells. Phenomena associated with shells having a high degree of internal complexity are not examined in a significant way.

The very fact that such a wide range of authors participated in this *Festschrift* says a great deal about Professor Überall's contributions to acoustics, his charisma, and his helpful nature. While all of the volumes have an international flavor, Parts 1 and 2 are particularly well represented by groups based in France. The recommendation for purchase by certain libraries (noted earlier) reflects the perspective of the present reviewer concerning the overall educational and research value of this set of books.

[1] *Acoustic Resonance Scattering*, edited by H. Überall (Taylor and Francis, London, 1992). [Reviewed by K. L. Williams, J. Acoust. Soc. Am. **95**, 2786 (1994).]
[2] *Acoustic Propagation and Scattering, Electromagnetic Scattering*, edited by P. P. Delsanto and A. W. Saenz (Taylor and Francis, London, 1998).
[3] R. H. Hackman, "Acoustic scattering from elastic solids," Phys. Acoust. **22**, 1–194 (1993).

PHILIP L. MARSTON
Department of Physics
Washington State University
Pullman, Washington 99164-2814

 0001-4966/2004/116(2)/619/1/$20.00

REVIEWS OF ACOUSTICAL PATENTS

Lloyd Rice
11222 Flatiron Drive, Lafayette, Colorado 80026

The purpose of these acoustical patent reviews is to provide enough information for a Journal reader to decide whether to seek more information from the patent itself. Any opinions expressed here are those of reviewers as individuals and are not legal opinions. Printed copies of United States Patents may be ordered at $3.00 each from the Commissioner of Patents and Trademarks, Washington, DC 20231. Patents are available via the Internet at http://www.uspto.gov.

Reviewers for this issue:

GEORGE L. AUGSPURGER, *Perception, Incorporated, Box 39536, Los Angeles, California 90039*
JOHN ERDREICH, *Ostergaard Acoustical Associates, 200 Executive Drive, West Orange, New Jersey 07052*
DAVID PREVES, *Starkey Laboratories, 6600 Washington Ave. S., Eden Prarie, Minnesota 55344*
DANIEL R. RAICHEL, *2727 Moore Lane, Fort Collins, Colorado 80526*
CARL J. ROSENBERG, *Acentech Incorporated, 33 Moulton Street, Cambridge, Massachusetts 02138*
WILLIAM THOMPSON, JR., *Pennsylvania State University, University Park, Pennsylvania 16802*
ERIC E. UNGAR, *Acentech, Incorporated, 33 Moulton Street, Cambridge, Massachusetts 02138*
ROBERT C. WAAG, *Univ. of Rochester, Department of Electrical and Computer Engineering, Rochester, New York 14627*

6,704,247

43.25.Lj HIGH EFFICIENCY PARAMETRIC SONAR

Anthony A. Ruffa, assignor to The United States of America as represented by the Secretary of the Navy
9 March 2004 (Class 367/92); filed 24 March 2003

Items **44** and **46** are two conventional high power projectors that radiate signals at two slightly different frequencies. Tag **60** indicates the overlap region of these two signals **56** and **58** where nonlinear interactions occur, thereby generating, in particular, the low-frequency difference frequency signal **61**. It is proposed to increase the low amplitude of this difference frequency signal by increasing the nonlinearity of the medium in the overlap

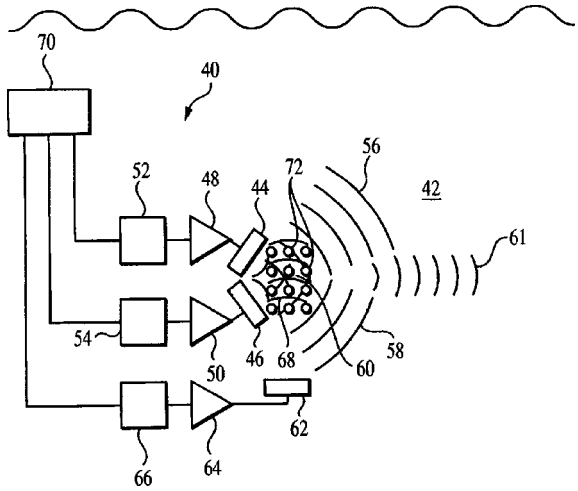

region **60**. This is accomplished by introducing a third transducer **62**, whose radiated signal, at an entirely different frequency, is oriented transverse to the signals radiated by the primary projectors, and whose purpose is to cause cavitation and hence the generation of vapor bubbles **72** within the signal overlap region. This should result in more efficient generation of the subharmonic difference frequency and hence an increased source level at that low frequency.—WT

6,700,833

43.30.Gv ACOUSTICAL IMAGING INTERFEROMETER FOR DETECTION OF BURIED UNDERWATER OBJECTS

Kenneth R. Erikson, assignor to BAE Systems Information and Electronic Systems Integration Incorporated
2 March 2004 (Class 367/88); filed 14 August 2002

A system for the detection of fully or partially buried underwater objects such as mines or cables consists of a remotely controlled underwater vehicle that houses a real-time, 3-D, downward looking acoustical camera and a high-intensity, low-frequency projector, also oriented downward. A tone burst or pulse radiated by the projector causes the loose particulate matter on the seafloor to move a detectable amount but has no effect on objects with higher elasticity or density than the seafloor material. Hence images recorded by the acoustical camera before and after the radiated sound can be compared for evidence of movement, or not, thus yielding a profile of any buried object. A memory bank of data helps the operator or a computer to discriminate between manmade and natural objects.—WT

6,707,760

43.30.Nb PROJECTILE SONAR

Andrew C. Coon *et al.*, assignors to BBNT Solutions LLC
16 March 2004 (Class 367/118); filed 22 November 2002

Shells fired from the gun of a surface ship, in the direction of a suspected target, create underwater explosions that are the sources of broadband sound for an active sonar system. The receivers may be a set of sonobuoys or a ship-towed array. Onboard signal processing equipment analyzes the return signals to locate submerged objects and to control the locations at which to fire the shells.—WT

 0001-4966/2004/116(2)/623/18/$20.00

6,697,301

43.30.Wi ACOUSTIC ARRAY DEPLOYMENT SYSTEM AND METHOD

Anthony A. Ruffa, assignor to The United States of America as represented by the Secretary of the Navy
24 February 2004 (Class 367/131); filed 11 September 2002

To obviate the problem of mounting a sensor suite on a supercavitating, noisy torpedo it is proposed to deploy a fiber optic line array in a direction substantially perpendicular to the torpedo axis. Housed within the torpedo body **10** is a small weighted projectile **20** that can be ejected from launch tube **14** via on board mechanism **40** or projectile motor **42**. Motor

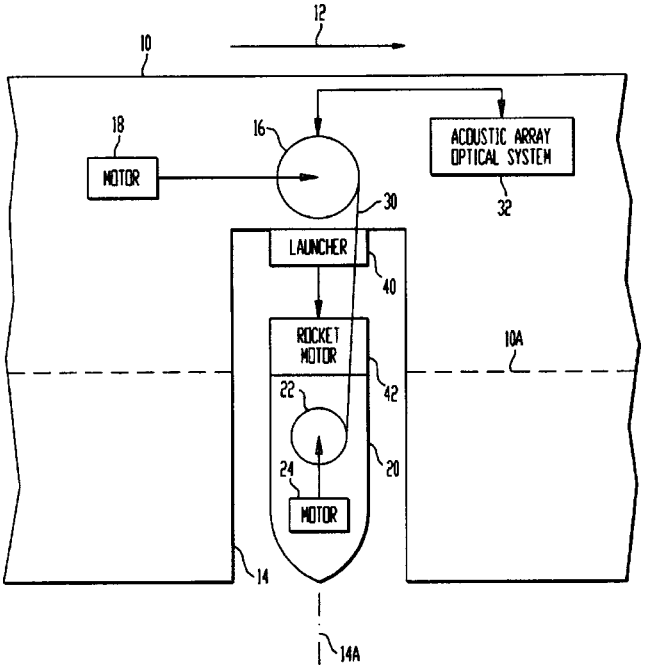

driven pulleys **16** and **22** play out a fiber optic cable **30** as the projectile sinks towards the ocean bottom. The broadside beam of acoustic array **30** should then not be affected by cavitation noise near the torpedo and should have sufficient vertical directivity to resolve both the torpedo and its intended target, thus providing relative target angle information to the onboard guidance system.—WT

6,697,302

43.30.Yj HIGHLY DIRECTIVE UNDERWATER ACOUSTIC RECEIVER

Benjamin A. Cray and Victor F. Evora, assignors to The United States of America as represented by the Secretary of the Navy
24 February 2004 (Class 367/141); filed 1 April 2003

A sensor package comprises a small pressure sensor and three orthogonally oriented pairs of conventional accelerometers, the two accelerometers within each pair separated by a small fraction of a wavelength. The ensemble is embedded in an acoustically transparent polymer such as polyurethane within a neutrally buoyant housing. The seven outputs, i.e., pressure, three components of acceleration, and three components of the spatial gradient of acceleration, are combined in a weighted fashion to produce a directional response pattern with a DI far greater than expected from such a small sensor.—WT

6,691,575

43.35.Zc MATERIAL EVALUATION METHOD BY ACOUSTIC VELOCITY MEASUREMENT

Jun-ichi Kushibiki *et al.*, assignors to Jun–Ichi Kushibiki
17 February 2004 (Class 73/597); filed in Japan 12 March 2001

Efficient evaluation of materials, particularly of crystals used in electronic device industries, is accomplished by measurement of the phase velocities of surface or bulk acoustic waves. A series of initial calibration measurements are used to relate these velocities to chemical composition and some physical parameters. The physical constants of interest (elastic, piezoelectric, and dielectric constants, and the density) are functions of the chemical composition. Thus, one may calculate numerically the acoustic velocities for desired combinations of the crystal cut plane and propagation directions.—EEU

6,711,096

43.38.Fx SHAPED PIEZOELECTRIC COMPOSITE ARRAY

Kim C. Benjamin, assignor to The United States of America as represented by the Secretary of the Navy
23 March 2004 (Class 367/162); filed 11 September 2002

An underwater electroacoustic transducer is realized by bonding precut and preelectroded piezoelectric pieces, machined from a solid block of piezoelectric polymer composite material, to suitable backing material. This backing material and the exposed faces of the piezoelectric pieces can be shaped as desired so that singly or doubly curved, conformal, active areas

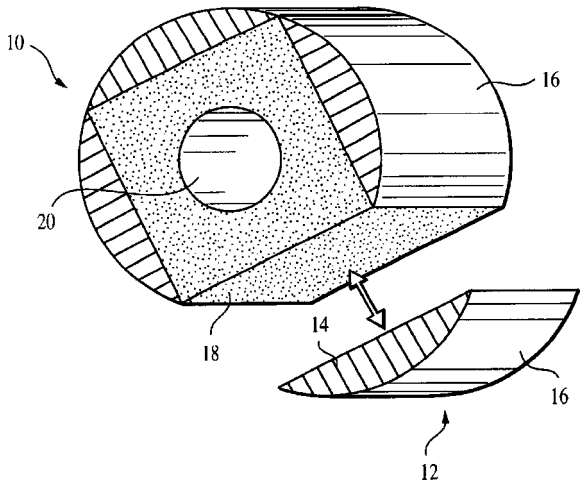

can be created. The figure illustrates a simple cylindrical transducer consisting of four transducer elements **12** whose outer faces are machined to create the cylindrical shape. These outer faces, as well as the inner flat faces of the pieces, are electroded. The pieces are bonded to the appropriately machined backing material **18** which includes the tunnel **20** for electrical leads. Other transducer shapes are discussed.—WT

6,694,028

43.38.Hz MICROPHONE ARRAY SYSTEM

Naoshi Matsuo, assignor to Fujitsu Limited
17 February 2004 (Class 381/92); filed in Japan 2 July 1999

Consider a simple array of two, closely spaced omnidirectional microphones. Simple electronic signal processing can be used to derive dipole, cardioid, or reverse-cardioid pickup patterns, or anything in between. An

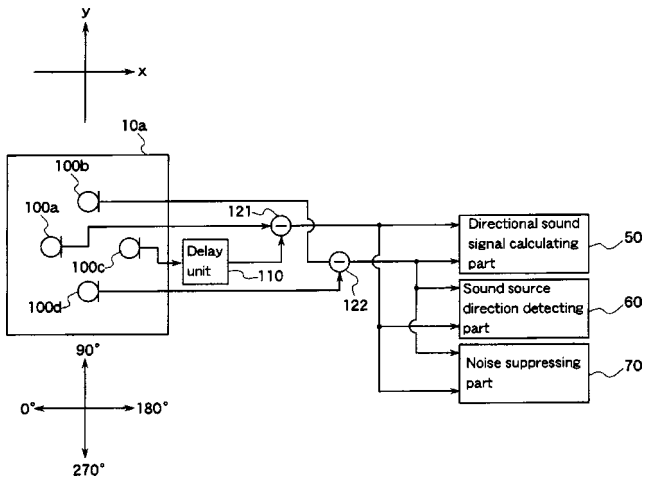

array of four microphones allows the patterns to be steered through a full 360°. With a little additional logic circuitry, the pickup pattern can be controlled and steered to achieve optimum pickup of a desired sound source while discriminating against unwanted sources.—GLA

6,695,783

43.38.Hz MULTILINE ULTRASOUND BEAMFORMERS

Derek Henderson *et al.*, assignors to Koninklijke Philips Electronics N.V.
24 February 2004 (Class 600/443); filed 22 December 2000

Ultrasonic beamformers receive signals produced by the elements of an ultrasonic array transducer and delay and combine these signals to produce, steer, and focus ultrasonic beams. In this embodiment, a digital multilane beamformer produces multiple receive beams in response to a single transmit event. An embodiment of the device incorporates a bulk delay that

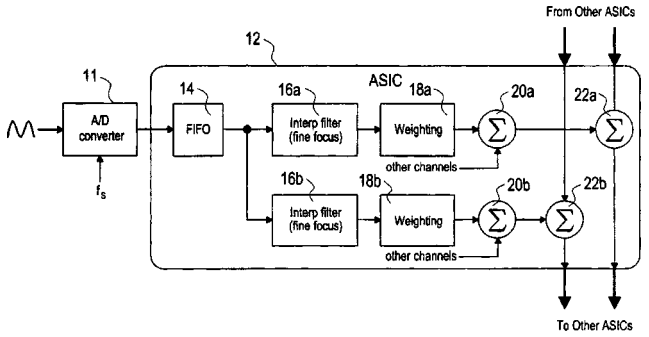

provides a common steering delay applicable to all of the beams received at one time. The bulk delay is followed by parallel filter processing paths which produce finely focused multiple beams simultaneously. The filter processing paths are capable of producing output samples of each beam at a fixed output data rate, regardless of the number of beams currently being processed.—DRR

6,687,381

43.38.Ja PLANAR LOUDSPEAKER

Mayuki Yanagawa, Burbank and Muto Keiko, North Hollywood, both of California
3 February 2004 (Class 381/423); filed 7 March 2002

One way to make a stiff, lightweight panel is to stretch thin skins over a cellular core. This kind of panel can be found in packing boxes and some

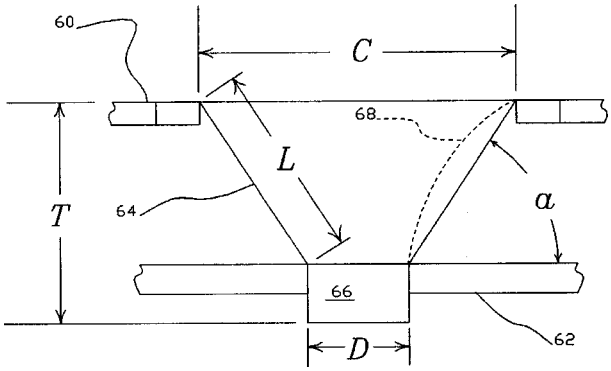

planar loudspeakers. The novel feature of this planar loudspeaker is a horn-shaped "radiator" **64** that couples motor voice coil **66** to honeycomb panel **60**.—GLA

6,694,037

43.38.Ja SPIDER-LESS LOUDSPEAKER WITH ACTIVE RESTORING APPARATUS

Robert Steven Robinson, Angleton, Texas *et al.*
17 February 2004 (Class 381/398); filed 10 December 1999

Motional feedback loudspeaker schemes require a sensor to track the true motion of the cone and provide a corresponding signal that can be compared with the electrical input signal. Prior art even includes an error signal that extends down to 0 Hz to counteract the offset produced by a

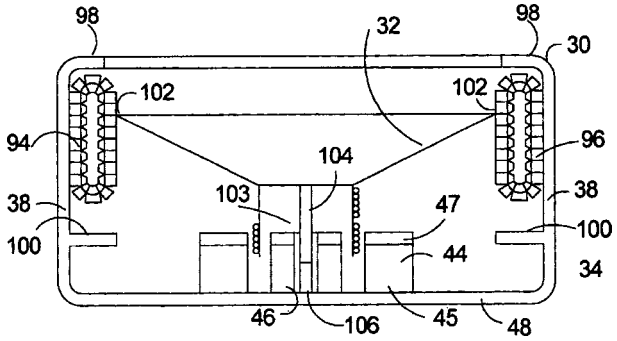

negative spring suspension. Well, suppose we eliminate elastic suspensions altogether and simply use the error signal to control the required restoring force. The patent describes several more or less practical embodiments of this idea.—GLA

6,694,038

43.38.Ja ACOUSTIC DEVICE

Henry Azima, assignor to New Transducers Limited
17 February 2004 (Class 381/423); filed in the United Kingdom 2 September 1998

For those interested in the design of panel form loudspeakers, this patent contains interesting and useful information. If the panel is appropriately shaped, then bending wave velocity can be varied in the region of coincidence, resulting in more uniform coupling. The patent includes numerous charts and graphs showing experimental results.—GLA

6,694,039

43.38.Ja LOUDSPEAKER

Wei-Chung Wu, assignor to Meiloon Industrial Company, Limited
17 February 2004 (Class 381/426); filed 24 January 2003

Commercial loudspeaker cones have been made of materials ranging from silk fabric to machined magnesium. This patent describes an interesting method of producing loudspeaker cones from a magnesium-lithium alloy.—GLA

6,687,379

43.38.Lc SYSTEM AND METHOD FOR ADJUSTING THE LOW-FREQUENCY RESPONSE OF A CROSSOVER THAT SUPPLIES SIGNAL TO SUBWOOFERS IN RESPONSE TO MAIN-SPEAKER LOW-FREQUENCY CHARACTERISTICS

James Thiel, assignor to Thiel Audio Products
3 February 2004 (Class 381/99); filed 4 May 2001

Setting up a subwoofer so that it blends seamlessly with existing loudspeakers can be time consuming and frustrating. Presumably, the characteristics of the subwoofer itself are known, at least by the manufacturer. If the characteristics of the main speakers were also known, then crossover filter frequencies and slopes could be optimized by an embedded computer chip. Since the characteristics of the main speakers often are not known, it still might be possible to fall back on a series of educated guesses. The patent describes a system and circuitry for doing just that.—GLA

6,636,750

43.38.Si SPEAKERPHONE ACCESSORY FOR A PORTABLE TELEPHONE

Robert A. Zurek *et al.*, assignors to Motorola, Incorporated
21 October 2003 (Class 455/569.1); filed 15 October 1999

This device is a desktop accessory having a cradle which accepts a cell phone or other portable phone and provides a speakerphone capability for the smaller phone device. Most of the short patent addresses the frequency

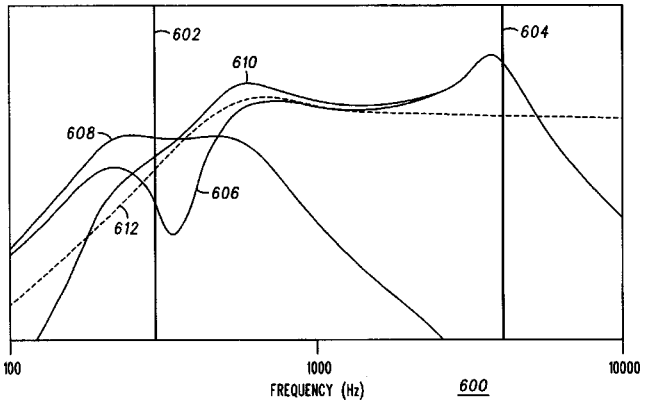

response of the speaker unit, which includes two resonating bodies with differing frequency characteristics. The figure indicates a response ranging from **602** at roughly 300 Hz to **604** at about 4 KHz.—DLR

6,611,596

43.38.Si SPEAKERPHONE INDICATOR

Joseph M. Cannon and James A. Johanson, assignors to Agere Systems Incorporated
26 August 2003 (Class 379/420.01); filed 20 July 1999

A caller-ID system tells the person on the other end who's calling. The legally required beep tells that person that their voice is being recorded. The single idea protected by this patent is that a speakerphone would periodically transmit a code indicating when the speaker/mic system is active. With various ways of making it work, the idea is covered by 25 claims. When will the Internet be able to tell us exactly and correctly who's sending us emails?—DLR

6,683,961

43.38.Si PROCESS AND APPARATUS FOR ELIMINATING LOUDSPEAKER INTERFERENCE FROM MICROPHONE SIGNALS

Dietmar Ruwisch, Berlin, Germany
27 January 2004 (Class 381/93); filed in Germany 1 September 2000

Consider one terminal of a two-way, hands-free telecommunication link. Ideally, the microphone should pick up only the voice of the talker and reject any sound from the loudspeaker. This problem has already been dealt with extensively, both acoustically and electronically. The electronic echo cancelling scheme described in this patent is said to be faster, more robust, and more effective than prior art. An inverse Fourier transform is first used

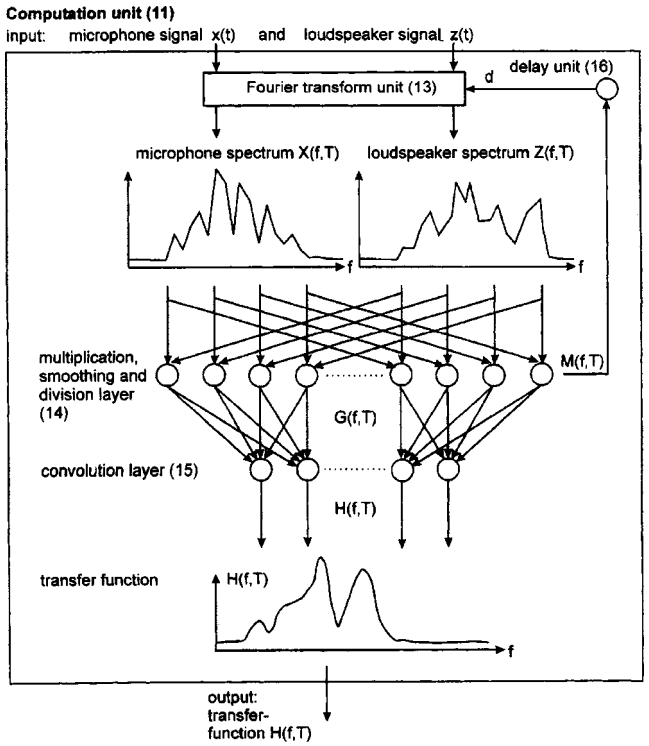

to calculate air path delay and synchronize the microphone output with the loudspeaker input. A computation unit then calculates the transfer function between the loudspeaker and the microphone and this information is used to create the desired digital filter. The process is repeated for each frame of sampled data. One might argue that several unstated assumptions are required for the system to work, but the invention is interesting and the patent is easy to follow.—GLA

6,683,959

43.38.Vk STEREOPHONIC DEVICE AND STEREOPHONIC METHOD

Koji Kuwano *et al.*, assignors to Kawai Musical Instruments Manufacturing Company, Limited
27 January 2004 (Class 381/17); filed in Japan 16 September 1999

A sophisticated electronic panning system is described that provides means for moving a virtual sound source left/right, near/far, and up/down. The system makes extensive use of digital filtering to include delay and

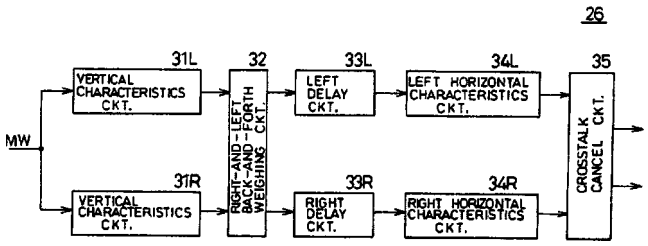

generalized head-related transfer functions as well as relative levels. The process can be adapted to two-channel loudspeaker or headphone listening.—GLA

6,683,962

43.38.Vk METHOD AND SYSTEM FOR DRIVING SPEAKERS WITH A 90 DEGREE PHASE SHIFT

David H. Griesinger, assignor to Harman International Industries, Incorporated
27 January 2004 (Class 381/97); filed 21 December 1998

The first seven pages of text in this patent summarize the inventor's experiments and theories concerning two-channel stereo reproduction in small rooms. The ''ideal'' installation of two symmetrically placed loudspeakers in a bilaterally symmetric listening room is shown to be much less than ideal at frequencies below 400 Hz or so. The patent asserts that in such a situation, driving the speakers in quadrature at low frequencies enables each speaker to excite all room modes, and produces an increased sense of spaciousness.—GLA

6,694,033

43.38.Vk REPRODUCTION OF SPATIALIZED AUDIO

Andrew Rimell and Michael Peter Hollier, assignors to British Telecommunications public limited company
17 February 2004 (Class 381/307); filed in the European Patent Office 17 June 1997

Sound recording and reproducing methods intended to immerse the listener in a virtual environment make use of elaborate filtering to cancel interaural crosstalk and simulate typical (or in some cases, individual) pinnae functions. The virtual sound sources thus created can be quite convincing, but only at the designated listening location. Multichannel cinema sound, on the other hand, is usually mixed using simple intensity panning, and sources that must be localized are panned to specific loudspeakers. The resulting sound field is stable over a large audience area. Now suppose that you have material recorded as spatialized audio but want to convert it to the second format for playback. Somehow you must derive the locations of virtual sources, convert the encoded signals to monophonic sources, and then pan these to appropriate loudspeakers. This patent sets forth in considerable detail a method for achieving this goal.—GLA

6,694,026

43.38.WI DIGITAL STEREO RECOVERY CIRCUITRY AND METHOD FOR RADIO RECEIVERS

Brian D. Green, assignor to Cirrus Logic, Incorporated
17 February 2004 (Class 381/3); filed 10 March 1999

In FM stereo reception, a pilot tone (typically 19 kHz) must be accurately recovered to properly demodulate the stereo information. This patent describes a digitally controlled oscillator that is used to recover the pilot

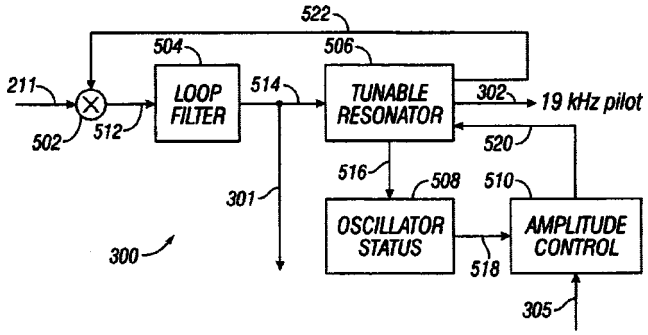

tone. ''By processing demodulated stereo signals on the digital side and digitally controlling the oscillator, the stereo decoder has increased efficiency and accuracy.''—GLA

6,684,168

43.40.At BODY DISPLACEMENT AND VIBRATION ANALYSIS METHOD

Atsushi Kawamoto *et al.*, assignors to Kabushiki Kaisha Toyota Chuo Kenkyusho
27 January 2004 (Class 702/56); filed in Japan 20 April 1999

This patent pertains to a technique for analyzing the rigid body motions and the elastic vibrations of a mechanical system on a global coordinate system. The patent asserts that the technique is able to take account of the interaction of multiple machine elements. A moving local observer reference frame that moves with a rigid body is used as a basis for analysis of the elastic vibrations, independent of the global coordinate system, and the motions of the reference frames are related to the rigid body motions.—EEU

6,702,761

43.40.Ng VIBRATION ASSISTED NEEDLE DEVICE

Jevan Damadian *et al.*, assignors to Fonar Corporation
9 March 2004 (Class 600/576); filed 6 March 2001

This is a biopsy needle that is driven to vibrate in a direction along the axis of the needle in order to ease passage of the needle through tissue and facilitate collection of a sample at the site of interest. The device consists of a chamber, a needle holder mounted externally to the chamber, and a mecha-

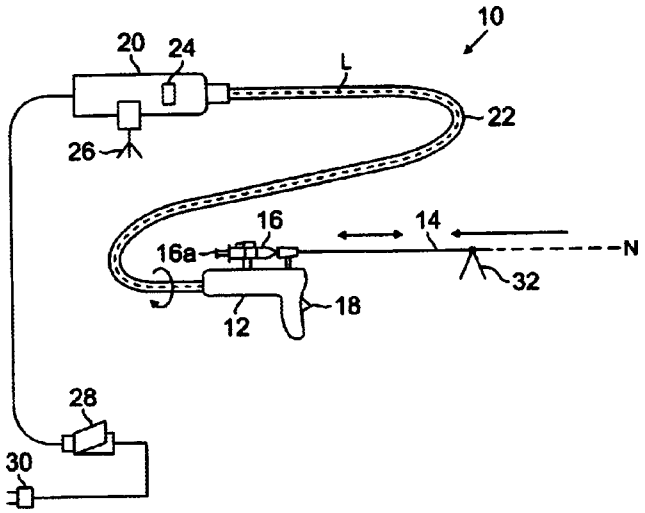

nism within the chamber for generating reciprocating motion of the needle support. A syringe support may also be mounted on the housing. The reciprocating mechanism may contain means of converting rotary motion into reciprocating action or it may consist of a stationary solenoid and a movable solenoid coupled to the needle holder.—DRR

6,666,108

43.40.Tm VIBRATION CONTROL BY CONFINEMENT OF VIBRATION ENERGY

Daryoush Alleai, assignor to Quality Research, Development & Consulting, Incorporated
23 December 2003 (Class 74/574); filed 9 June 1999

This patent deals with protecting some portions of a structure from vibrations present in other portions. Confinement of vibrations to a selected structural region is achieved by means of devices with suitable effective stiffnesses and effective masses that are installed on the boundaries of this region. These devices, of which some passive and active embodiments are described in the patent, are configured to produce translational, torsional, and inertia forces that block the transmission of vibrations.—EEU

6,681,755

43.40.Tm VIBRATION DAMPENING DEVICE

Pierre Pujos, Traverse City, Michigan
27 January 2004 (Class 124/89); filed 7 March 2001

This damper is intended for hand-held implements and particularly for archery bows. It consists of an essentially cylindrical container that is filled with a gelatinous material in which there is suspended a concentrated mass.—EEU

6,685,569

43.40.Tm VIBRATION ABSORBING UNIVERSAL JOINT

Patrick Kurzeja *et al.*, assignors to Meritor Heavy Vehicle Technology, LLC
3 February 2004 (Class 464/70); filed 14 February 2001

As stated in the patent's abstract, ''an elastomeric material, such as a polyurethane, is introduced between the bores of the yokes of the joint and the respective adjacent bearing cups that are mounted on the shafts of the cross bar.'' The purpose of these resilient inserts is to dissipate shocks and reduce torsional vibrations.—EEU

6,688,439

43.40.Tm VIBRATION DAMPING SYSTEM AND A METHOD OF DAMPING VIBRATIONS

Bishakh Bhattacharya *et al.*, assignors to Rolls–Royce plc
10 February 2004 (Class 188/267); filed in the United Kingdom 16 August 2000

This patent pertains to means for the control of structural vibrations, particularly in machining operations. A means for generating magnetic energy, such as an element including magnetostrictive material, is attached to the item that is to be damped. A means for dissipating magnetic energy, such as another element that includes magnetostrictive material, is affixed to a secondary structure located near the item of concern. Vibrations of that item thus generate magnetic energy, which is dissipated in the second element.—EEU

6,705,440

43.40.Tm CABLE STAY DAMPER BAND AND METHOD OF USE FOR REDUCTION OF FLUID INDUCED CABLE VIBRATIONS

R. Scott Phelan *et al.*, assignors to Texas Tech University
16 March 2004 (Class 188/378); filed 30 April 2002

This patent discusses the use of various kinds of damper bands sequentially positioned along cables to reduce fluid current flow induced vibrations, either in air or in water.—WT

6,681,883

43.40.Vn METHOD AND APPARATUS FOR SUPPRESSING VIBRATION IN VEHICLE A STEERING SYSTEM

Wei-Yi Loh *et al.*, assignors to Ford Global Technologies, LLC
27 January 2004 (Class 180/417); filed 12 March 2002

Reduction of vibrations in power-assisted steering systems is accomplished by means of a friction device, whose actuating force is controlled electronically. This force is maintained at a relatively large value when the power steering boost system applies little steering force to the steering actuator, but is reduced when the boost system applies larger steering forces.—EEU

6,698,543

43.55.Ev ACOUSTICAL WALL PANELS

Herb Golterman, assignor to Golterman & Sabo, Incorporated
2 March 2004 (Class 181/291); filed 1 July 2002

The patent describes what looks like a rather standard acoustical wall panel formed from a base of a sound absorbing core (like glass fiber) and a sound transparent face (like perforated plastic or metal or fabric). The panel has structural integrity so that it can either be applied to a wall or it can form a partition in an office cubicle.—CJR

6,700,304

43.55.Ti ACTIVE/PASSIVE DISTRIBUTED ABSORBER FOR VIBRATION AND SOUND RADIATION CONTROL

Christopher R. Fuller and Pierre E. Cambou, assignors to Virginia Tech Intellectual Properties, Incorporated
2 March 2004 (Class 310/321); filed 20 April 1999

This device is both an active tunable vibration absorber and a passive absorber. It has two layers. The first layer is corrugated and has a low stiffness. The second layer is principally a mass layer. Depending on the

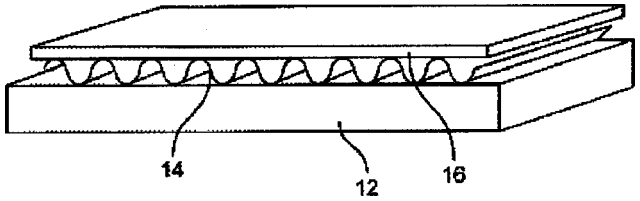

response of a sensor, the first layer can be induced to move in the direction perpendicular to its main plane (i.e., up and down), and this in turn changes the motion of the mass layer.—CJR

6,625,568

43.58.Kr SOUND-BASED VESSEL CLEANER INSPECTION

James Tyson, Pennsauken, New Jersey
23 September 2003 (Class 702/183); filed 23 October 2001

Many large processing tanks in the food, beverage, and drug industries must be cleaned thoroughly, typically after each use. However, there is frequently no direct means of monitoring the cleaning operation. Even a severe fault, such as a blocked nozzle or a damaged sprayer, may not be detected until the cleaning cycle is complete. This device would monitor an audio signal picked up during the cleaning and check properties such as sound energy, amplitude variations, and spectral content. Various patterns would be compared with reference signatures collected during successful cleaning operations. Several widely used signal processing techniques are described.—DLR

6,691,000

43.60.Lq ROBOT-ARM TELEMANIPULATING SYSTEM PRESENTING AUDITORY INFORMATION

Yasufumi Nagai *et al.*, assignors to Communications Research Laboratory, Independent Administrative Institution
10 February 2004 (Class 700/245); filed in Japan 26 October 2001

This patent, applicable for use in space stations, etc., presents auditory information to the manipulating system's operator so as to reduce his/her information processing burden. The audio signal here is converted from some of the robot arm's telemetered operating status information.—EEU

6,705,997

43.60.Lq SIGNAL PROCESSING CIRCUIT AND ULTRASOUND DOPPLER APPARATUS

Shinichi Amemiya, assignor to GE Medical Systems Global Technology Company, LLC
16 March 2004 (Class 600/467); filed in Japan 15 March 2001

This is a signal processing circuit for processing multiple continuous wave (CW) signals and an ultrasound Doppler apparatus for executing diagnosis through the use of a CW Doppler method. This is achieved through a signal processing circuit to amplify a number of CW input signals and to

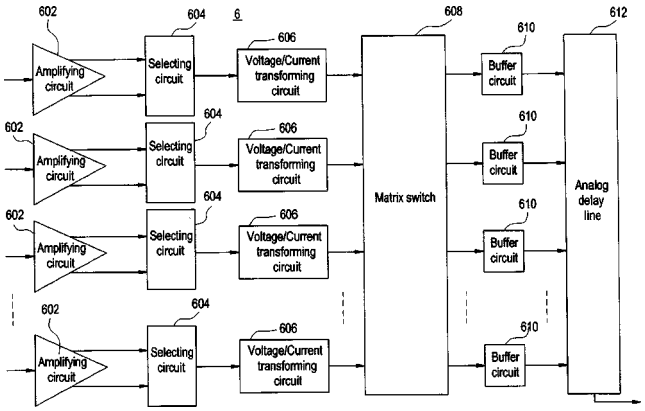

produce respective pairs of amplified signals with mutually opposite phases for each CW input signal. This is followed by a set of selector circuits, each of which selects one signal of each opposite-phase pair and a matrix switch which uses the output signals from the selector circuits.—DRR

6,711,267

43.60.Qv METHOD AND APPARATUS FOR PROCESSING SOUND

Kari Kirjavainen, assignor to Panphonics Oy
23 March 2004 (Class 381/71.1); filed in Finland 27 November 1996

In this method, the sound field of an ambient sound is measured and an actuator produces a sound field of opposite polarity. A desired value signal **I** is applied to the actuator to be reproduced. A sensor attached to the actuator measures the sound pressure level and the difference between the sensor

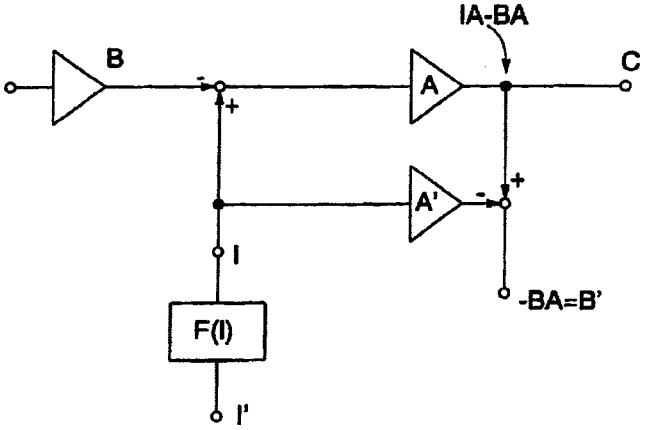

signal **B** and desired value signal **I** is applied as a high-gain feedback to the actuator. The result is that sound not pertaining to signal **I** may be attenuated in a simple manner and sound, in accordance with signal **I**, can be reproduced simultaneously with the same equipment.—DRR

6,709,407

43.64.Ri METHOD AND APPARATUS FOR FETAL AUDIO STIMULATION

Mostafa Fatemi, assignor to Mayo Foundation for Medical Education and Research
23 March 2004 (Class 600/559); filed 30 October 2001

The aim of this method and the associated apparatus is to apply a focused, directed audio beam at a fetus to stimulate the fetus *in utero*. An ultrasound signal, amplitude modulated with an audio range signal, is directed to an ultrasound transducer **20** positioned on the abdomen of the expectant mother. A focused beam from the ultrasound aims at the head of

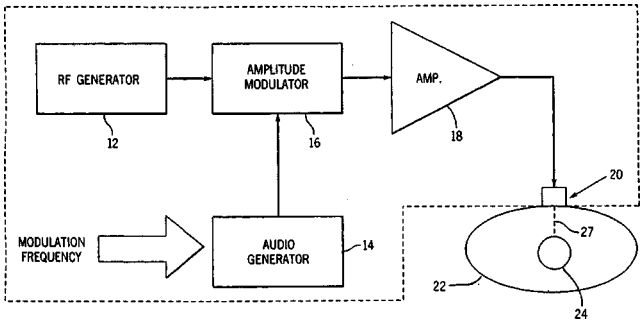

the fetus, and the resultant audio signal stimulates the middle ear, causing the fetus to move. The motion of the fetus can be tracked to test hearing in individual ears or to assess the general health of the fetus. Moreover, the focused beam can be directed at the fetus to cause the fetus to move to a selected location within the womb for the purpose of clinical evaluation or delivery.—DRR

6,697,494

43.66.Ts METHOD TO GENERATE A PREDETERMINED OR PREDETERMINABLE RECEIVING CHARACTERISTIC OF A DIGITAL HEARING AID, AND A DIGITAL HEARING AID

Ronald Klootsema and Gerard van Oerle, assignors to Phonak AG
24 February 2004 (Class 381/312); filed 15 December 1999

A two-microphone digital hearing aid is made directional via oversampling and precisely delaying one of the two microphone outputs and summing the resultant with the first microphone output. For best directional

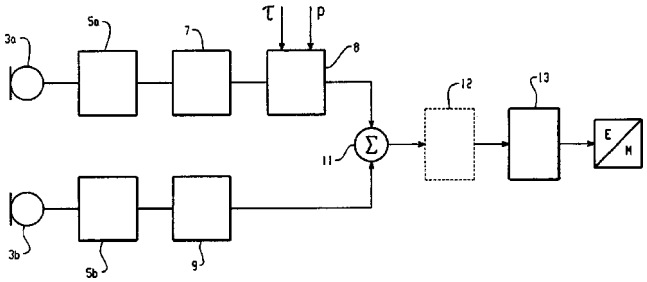

performance, the two signals must also be level matched. A method is described to implement both the level matching and the signal delay with the same circuitry, e.g., a shift register.—DAP

6,700,982

43.66.Ts HEARING INSTRUMENT WITH ONSET EMPHASIS

Luc J. R. Geurts *et al.*, assignors to Cochlear Limited
2 March 2004 (Class 381/312); filed in the European Patent Office 8 June 1998

The object of this hearing instrument is to transform an audio signal into an output signal that is more readily discernible by the hearing-impaired patient. The device is based on the supposition that the neural activity in a person's hearing system at the onset of sound stimulus is much higher than the neural activity after the onset. The more suddenly the stimulus intensity increases, the higher the activity will be. The duration of this so-called short-term adaptation is of the order of magnitude of 10 ms. It is assumed that the origin of the adaptation effect is at the inner hair cell auditory nerve synapse. The patent asserts that this hearing instrument will provide an improved perception of sounds for persons whose hearing system is damaged in such a manner that this adaptation effect is not fully present. Experiments have reportedly shown that when this instrument emphasizes the onset of the typical intensity increase of speech, the speech intelligibility for users improves considerably. Accordingly, an embodiment contains a filtering device that is coupled to an emphasizer circuit that outputs a signal that stresses the onsets.—DRR

6,700,983

43.66.Ts HEARING AID

Tom Bøgeskov-Jensen *et al.*, assignors to Oticon A/S
2 March 2004 (Class 381/322); filed in Denmark 7 October 1998

Contruction techniques are described to allow at least partial automatic

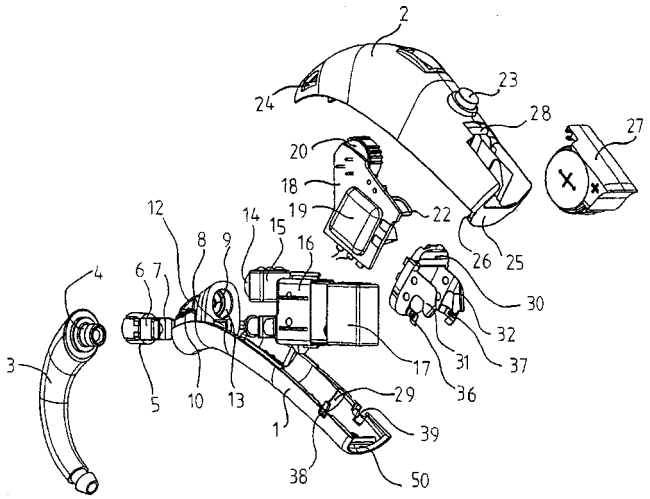

assembly and easier repairs of behind-the ear hearing aids.—DAP

6,701,162

43.66.Ts PORTABLE ELECTRONIC TELECOMMUNICATION DEVICE HAVING CAPABILITIES FOR THE HEARING-IMPAIRED

Brandon Christopher Everett, assignor to Motorola, Incorporated
2 March 2004 (Class 455/556.1); filed 31 August 2000

The patent relates to portable electronic telecommunication devices, such as cellular telephones and other portable telecommunications computers that include displays and have computer platforms that can execute programs for speech-to-text translation. A device of this sort includes a computer platform incorporating storage for one or more programs, a display for alphanumeric text, and at least a speech recognition program residing and selectively executable in the computer platform. Upon connection with a communicating party, the speech recognition program converts the words of the party into text that is presented on the display. The device may also include a text-to-speech program that translates input by the user into synthetic speech for transmission to the communicating party. The preferred embodiment of the device is a cellular telephone with an electronic organizer serving as the computer platform.—DRR

6,704,422

43.66.Ts METHOD FOR CONTROLLING THE DIRECTIONALITY OF THE SOUND RECEIVING CHARACTERISTIC OF A HEARING AID A HEARING AID FOR CARRYING OUT THE METHOD

Lars Baekgaard Jensen, assignor to Widex A/S
9 March 2004 (Class 381/313); filed 26 October 2000

The directionality of a two-microphone hearing aid is adjustable between omnidirectional and directional modes by varying attenuation and

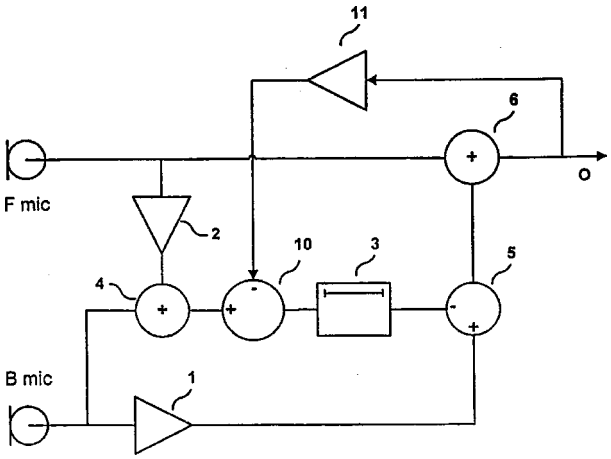

time delay of the microphone outputs before they are combined. Using the method described, the frequency response and time delay of the output signal from the hearing aid do not change as the direction is changed. This helps to ensure that the two signals in a binaural fitting always arrive at the ears in the same relative phase regardless of the directional mode.—DAP

6,704,423

43.66.Ts HEARING AID ASSEMBLY HAVING EXTERNAL DIRECTIONAL MICROPHONE

C. Roger Anderson *et al.*, assignors to Etymotic Research, Incorporated
9 March 2004 (Class 381/313); filed 20 December 2000

Directional microphones are one of the few methods available to increase signal-to-noise ratio for hearing aids. Because of limited space available and poorer performance due to deeper positioning in the ear canal,

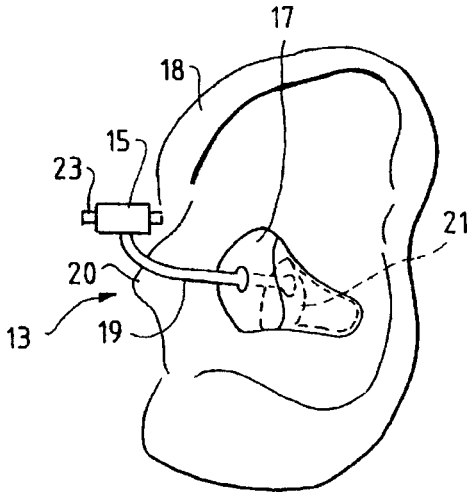

directional microphones are not routinely incorporated inside the smallest hearing aids. A mounting arm extending from in-the-canal or completely in-the-canal hearing aids allows incorporating directional microphones into small hearing aid models.—DAP

6,710,744

43.66.Ts INTEGRATED CIRCUIT FRACTAL ANTENNA IN A HEARING AID DEVICE

Steve Morris and Steve Pollard, assignors to Zarlink Semiconductor (U.S.) Incorporated
23 March 2004 (Class 343/700 MS); filed 28 February 2002

To enable wireless capabilities in a programmable hearing aid, a fractal antenna may be incorporated as a conductive trace on a semiconductor

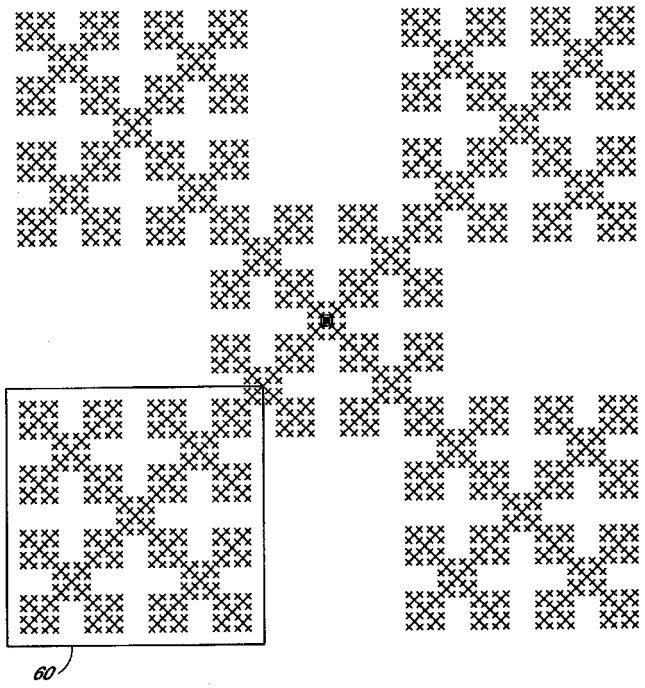

substrate and implemented as an integrated circuit in the hearing aid.—DAP

6,711,271

43.66.Ts POWER MANAGEMENT FOR HEARING AID DEVICE

Zezhang Hou, assignor to Apherma Corporation
23 March 2004 (Class 381/323); filed 3 July 2001

A power saving mode puts a hearing aid to sleep when no stimuli are present. Intelligent switching between modes is said to reduce power consumption. After a sound identification is performed, the signal processing

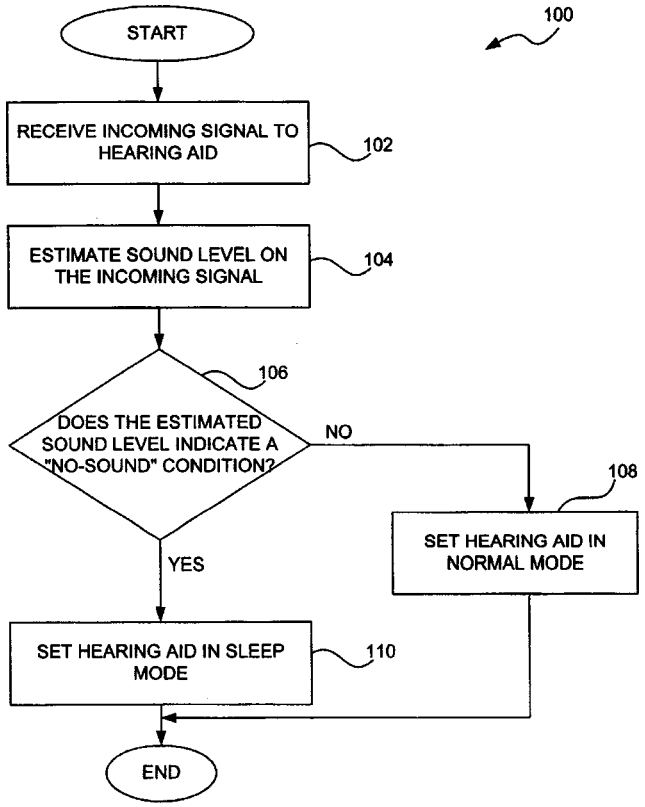

circuitry in a hearing aid is placed in reduced power mode when it deter-

mines that no significant sound or desired sound characteristic is present.—DAP

6,704,424

43.66.Ts HEARING AID WITH AUDIBLE ALARM

Mead C. Killion, assignor to Etymotic Research, Incorporated
9 March 2004 (Class 381/323); filed 20 June 2002

A low battery detection alarm is provided for hearing aids and other battery operated devices. The detection circuitry is said to not increase overall battery drain or component count significantly. The amplitude and frequency of the alarm signal increase as battery voltage decreases below a preset threshold.—DAP

6,567,524

43.66.Vt NOISE PROTECTION VERIFICATION DEVICE

Jarle Svean *et al.*, assignors to Nacre AS
20 May 2003 (Class 381/71.1); filed 1 September 2000

This device is an active hearing protector that combines active noise cancellation with passive attenuation of the insert protector. The device uses external microphone **M1** and internal microphone **M2** to sense acoustic pressure at the pinna and inside the meatus. An acoustic signal is produced

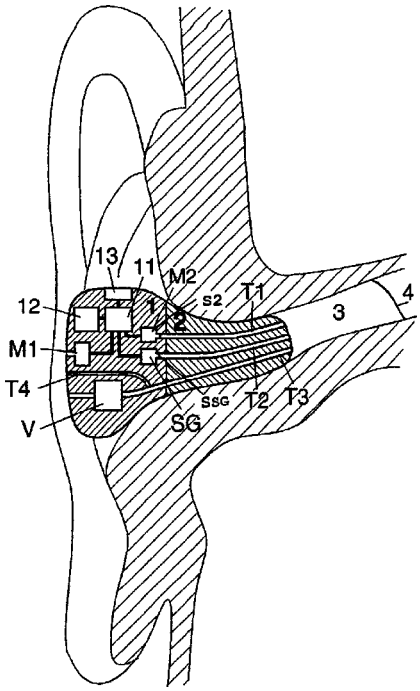

inside the meatus by included sound generator **SG**. By various digital signal processing algorithms the device can verify the attenuation provided by the protector *in situ*, provide controlled feedback of the speaker's voice sensed by the internal microphone, or provide wireless communication through the internal microphone and a wireless communication link.—JE

6,699,178

43.66.Yw ENDOSCOPIC AUDITORY CANAL CLEANING APPARATUS

Yoshiharu Koda, assignor to Coden Company Limited
2 March 2004 (Class 600/104); filed in Japan 15 November 1999

This device is essentially an endoscopic auditory canal cleaning apparatus. An ear-pick main body has a scraping part at its distal end, to which light is introduced by an included light source. A fiber scope captures images

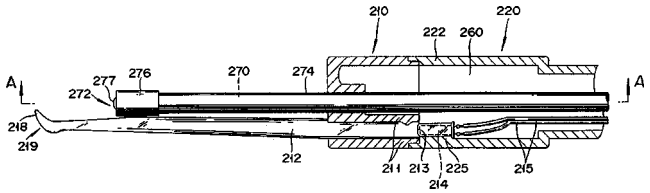

of the inside of the ear canal and presents these images for display. A retainer holds the ear-pick main body and allows the fiber scope to pass through a hollow opening in the retainer. The retainer can rotate freely about the fiber scope.—DRR

6,702,758

43.66.Yw HAND-HELD HEARING SCREENER APPARATUS

Steven J. Iseberg, assignor to Etymotic Research, Incorporated
9 March 2004 (Class 600/559); filed 9 October 2001

This device is a hearing screener that applies distortion-product otoacoustic emissions (DPOAEs) to determine the function of the outer hair cells within the middle ear structure. The functional viability of the outer hair cells indicates the effectiveness of the middle ear. The absence of DPOAE indicates a probable hearing loss. In one embodiment, the screener is a hand-held device that couples to an infant's ear to perform DPOAE testing. The device generates tones and relays them to the ear canal through two receivers. The emissions are then picked up by a low-noise microphone and analyzed via a built-in digital signal processor. The result is displayed on a liquid crystal display and can be printed out through an infrared link to a separate hand printer.—DRR

6,599,129

43.71.Gv METHOD FOR ADAPTIVE TRAINING OF SHORT TERM MEMORY AND AUDITORY/ VISUAL DISCRIMINATION WITHIN A COMPUTER GAME

William M. Jenkins *et al.*, assignors to Scientific Learning Corporation
29 July 2003 (Class 434/169); filed 24 September 2001

This patent joins a long list assigned to the same company and covering computer-based speech perception training methods. Here, a group of words or other clues are presented on a screen. Clicking each item causes the presentation of a phonetic sound. The game is to match pairs of items

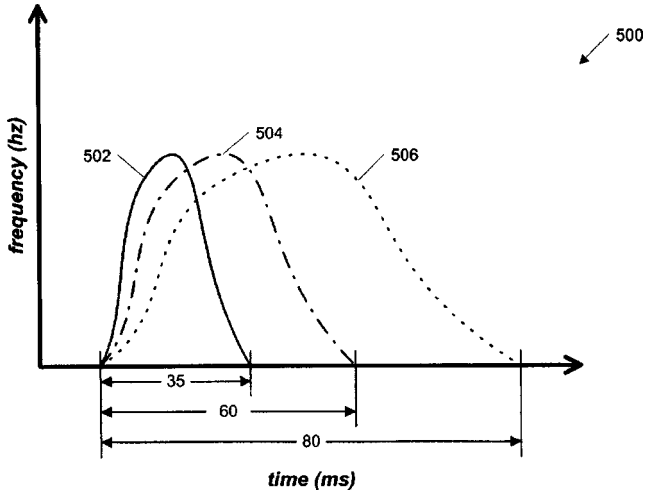

which produce similar sounds. As the game proceeds, there are two ways to make it harder. Either more test items may be presented or the sounds played for each can be distorted. This game mostly does the latter, following the patterns of adjusting transitionn rates which have been described in many previous reviews of these patents.—DLR

6,604,947

43.71.Hw ALPHABET IMAGE READING METHOD

Shogen Rai, Meguro-ku, Tokyo, Japan
12 August 2003 (Class 434/170); filed 21 June 2000

Presented by a Japanese author and intended for a non-English-speaking audience, this software system for teaching English sounds and spelling relies on a graphic display of word cues, combining a picture and an English word. Some special visual cues are included, such as the use of pastel (''soft'') colors for weak vowels and grayed-out display of silent letters in a word. There is surprisingly little mention of whether the program

Root color vowels and their relative sounding chart.

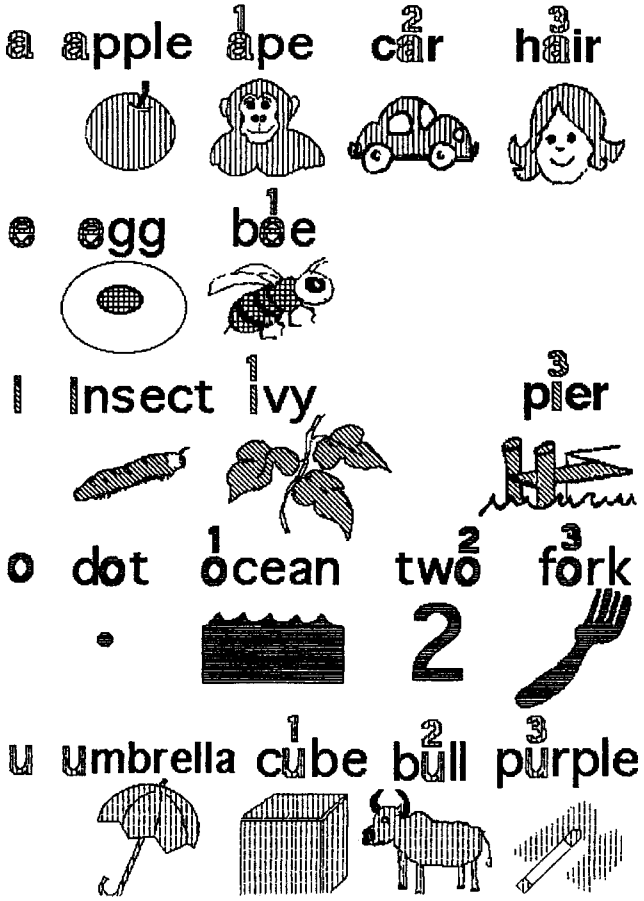

uses audio output. There is some mention of a movie, but it is not clear how it is related to this system. Some of the questionable associations include the assertions that the ''i'' in ''insect'' and in ''pier'' sound different, that the vowels in ''oar,'' ''for,'' and ''all'' sound the same, and the use of the word ''picture'' to illustrate one of the sounds of ''t.'' The latter perhaps makes sense to a native speaker of Japanese in that the English cluster ''ksh'' would likely be perceived as a single phoneme.—DLR

6,629,844

43.71.Ky METHOD AND APPARATUS FOR TRAINING OF COGNITIVE AND MEMORY SYSTEMS IN HUMANS

William M. Jenkins *et al.*, assignors to Scientific Learning Corporation
7 October 2003 (Class 434/169); filed 8 October 1999

In yet another application of the assignee's often-patented speech modification technology, this system emphasizes the teaching of higher-level linguistic constructs through the usual modification of onset and offset

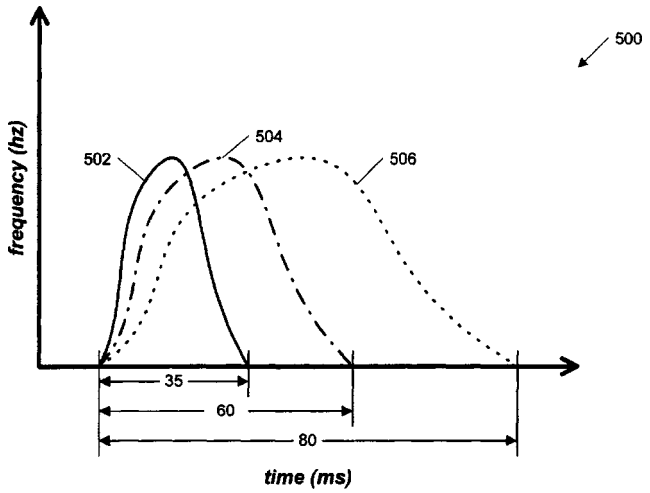

times, transition rates, frequency shifts, etc. The presentation is, as usual, a computer game environment.—DLR

6,615,174

43.72.Ar VOICE CONVERSION SYSTEM AND METHODOLOGY

Levent Mustafa Arslan and David Thieme Talkin, assignors to Microsoft Corporation
2 September 2003 (Class 704/270); filed 22 February 2000

This voice changer uses codebook mapping methods to modify the speaker characteristics of a speech signal from those of the source speaker to those of a target speaker. All speech qualities, including vocal tract patterns, excitation patterns, the linear prediction residual, duration, and amplitude patterns are represented as weighted codebook entries. By adjusting the weights, which are based on perceptual distance measures, using a gradient descent approach, different speakers' voices can be reproduced.—DLR

6,614,466

43.72.Gy TELESCOPIC RECONSTRUCTION OF FACIAL FEATURES FROM A SPEECH PATTERN

David R. Thomas, assignors to Texas Instruments Incorporated
2 September 2003 (Class 348/14.13); filed 22 February 2001

This speech coding system would combine video features with audio features in the optimization to reduce the bit rate for a talking head display.

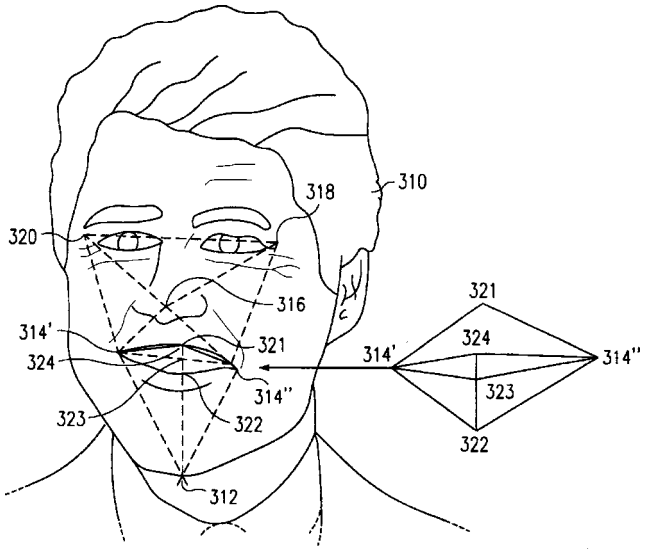

Predictors are applied to both visemes in the video domain and allophones in the speech domain to allow the transmission of only the novel information. The patent suggests that, in some cases, after adaptation, the complete video image can be produced using only the audio signal.—DLR

6,598,021

43.72.Ja METHOD OF MODIFYING SPEECH TO PROVIDE A USER SELECTABLE DIALECT

Craig R. Shambaugh, Wheaton, Illinois *et al.*
22 July 2003 (Class 704/270); filed 13 July 2000

The premise of this patent is that the operation of an automated call center or a telemarketing operation would be enhanced if a computer-synthesized voice could embody a specific chosen dialect for the interaction with called or calling individuals. Like so many disappointing patents which appear to be of a technical nature, this one does not attempt to describe or propose specific methods or technology by which its goals could be met. The entire text speculates on situations and scenarios which might be encountered in the use of such a system and possible ways that such scenarios might be handled.—DLR

6,598,022

43.72.Ja DETERMINING PROMOTING SYNTAX AND PARAMETERS FOR LANGUAGE-ORIENTED USER INTERFACES FOR VOICE ACTIVATED SERVICES

Matthew John Yuschik, assignor to Comverse Incorporated
22 July 2003 (Class 704/275); filed 13 August 2002

The ''Summary of the Invention'' section of this patent begins with the assertion that a voice interaction system will be more acceptable to and more useable by its intended user group if it speaks the language of the group. Not only the phonetic dialect, but also word usage, syntactic structure, and all other linguistic characteristics are included in the premise. In an attempt to achieve this goal, the first step is to pursue a preliminary interaction using general estimates of the appropriate settings. Based on the responses and speech collected through these early tests, more definitive measures are adaptively learned. During all tests and subsequent usage, additional vocabulary items and modes of expression are incorporated into the linguistic architecture, converging toward an acceptable level of speech fluency. Details are a bit sketchy as to just how this is all to be done, but, as far as they go, the general directions given seem appropriate. The claims cover various aspects of the process of ''defining a (temporal) prompting system.''—DLR

6,600,814

43.72.Ja METHOD, APPARATUS, AND COMPUTER PROGRAM PRODUCT FOR REDUCING THE LOAD ON A TEXT-TO-SPEECH CONVERTER IN A MESSAGING SYSTEM CAPABLE OF TEXT-TO-SPEECH CONVERSION OF E-MAIL DOCUMENTS

Paul L. Carter and Sachin Shangarpawar, assignors to Unisys Corporation
29 July 2003 (Class 379/88.16); filed 27 September 1999

Some applications for text-to-speech playback, such as the cell phone voice email system described here, may involve frequent repetition of identical phrases or other fragments of sentences. In addition to storing the text from a large number of previous email messages, the system would also include storage for the corresponding converted speech output. Phrases used in a new email message are used to search the past messages. When an identical phrase occurs, the corresponding speech segment is retrieved, avoiding the computational load of recomputing the speech signal for that phrase. Methods proposed for searching the old material are somewhat blunt. An obvious case is the content of the ''To:,'' ''From:,'' ''CC:,'' and ''Re:'' lines. Text within the message body is indexed solely by sentence length.—DLR

6,625,575

43.72.Ja INTONATION CONTROL METHOD FOR TEXT-TO-SPEECH CONVERSION

Keiichi Chihara, assignor to Oki Electric Industry Company, Limited
23 September 2003 (Class 704/260); filed in Japan 3 March 2000

This patent presents a new model for describing the pitch structure of the mora, as used in synthesizing Japanese speech. The general criticism of previous pitch models seems to be that many different parameters were too

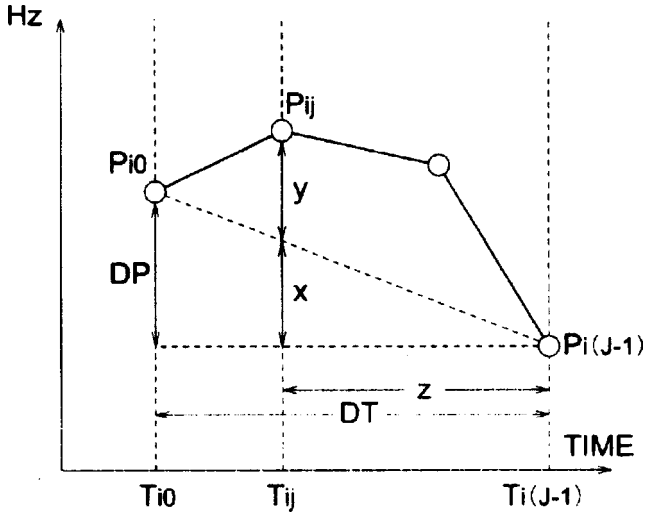

closely interrelated. Here, it is possible to alter a number of the details without changing the effects of other parameter settings. Here, for example, the pitch of each word can be specified without regard to the accent type and without changing the overall average pitch.—DLR

6,625,576

43.72.Ja METHOD AND APPARATUS FOR PERFORMING TEXT-TO-SPEECH CONVERSION IN A CLIENT/SERVER ENVIRONMENT

Gregory P. Kochanski *et al.*, assignors to Lucent Technologies Incorporated
23 September 2003 (Class 704/260); filed 29 January 2001

To allow more efficient operation in a network environment, this speech synthesis system is separated into two parts, the conversion of text to an intermediate phonetic representation, and the conversion of the phonetic text to speech audio data. This division allows a server to be used for the first portion of the task, which may involve access to large databases. A relatively low rate transmission to a client device, such as a cell phone, allows completion of the process at the point where the audio speech samples will be immediately converted to sound using a process which requires access to relatively smaller databases. Various embodiments allow certain exceptions to this simple model which result in better quality output.—DLR

6,647,363

43.72.Ja METHOD AND SYSTEM FOR AUTOMATICALLY VERBALLY RESPONDING TO USER INQUIRIES ABOUT INFORMATION

Antonius M. W. Claassen, assignor to ScanSoft, Incorporated
11 November 2003 (Class 704/1); filed in the European Patent Office 9 October 1998

This automated voice response system includes a dialogue manager and a presentation manager, which work together to provide a more natural interaction with the human inquirer. Based on the inquiry and database information, the dialogue manager constructs the basic response phrases. The presentation manager then takes into consideration the phrasing used in present and past inquiries, among other details, to reorganize the dialogue. It determines which aspects of the response will be of greatest interest to the inquirer and restructures the response accordingly.—DLR

6,615,173

43.72.Kb REAL TIME AUDIO TRANSMISSION SYSTEM SUPPORTING ASYNCHRONOUS INPUT FROM A TEXT-TO-SPEECH (TTS) ENGINE

Joseph Celi, Jr., assignor to International Business Machines Corporation
2 September 2003 (Class 704/260); filed 28 August 2000

This is a collection of network servers of various types, which work together to implement a network-based text-to-speech capability. The synthesis server passes the synthesized audio packets to an audio server, which manages the real-time aspects of transmitting the speech signal. Most of the short patent, in fact, deals with real-time issues; how to manage time-critical data in an environment where packet arrival times cannot be guaranteed.—DLR

6,606,597

43.72.Ne AUGMENTED-WORD LANGUAGE MODEL

Eric K. Ringger and Lucian Galescu, assignors to Microsoft Corporation
12 August 2003 (Class 704/270); filed 8 September 2000

The essence of this speech recognition system is a lexicon built up of ''augmented'' words. By this is meant simply that each word is attached to additional information fields, including a phonetic representation, a spelled form, syntactic information where applicable, and various forms of semantic information. Such fields might include *n*-gram information, including the probability that the word occurs in various combinations with other words. Most of the brief patent deals with methods for efficiently storing useful amounts of word-oriented *n*-gram information. Surely, this is all completely obvious to anyone who needs to build a lexicon. Fifteen claims outline the possible contents and arrangements of computer memory storage.—DLR

6,615,178

43.72.Ne SPEECH TRANSLATOR, SPEECH TRANSLATING METHOD, AND RECORDED MEDIUM ON WHICH SPEECH TRANSLATION CONTROL PROGRAM IS RECORDED

Kazuhiko Tajima, assignor to Sony Corporation
2 September 2003 (Class 704/277); filed in Japan 19 February 1999

This device would recognize an input speech signal and display a translation of the message in a different language. Frame-by-frame analysis, noise reduction based on a second signal, and HMM fitting are all traditional. Syntactic/semantic analysis would use two databases, a statistical model and a head-and-complement grammar model, although little further detail is disclosed in the patent. Phonetic patterns, statistical patterns, and repeatedly used grammatical structures would be tracked with a history mechanism and used to guide further analysis.—DLR

6,622,121

43.72.Ne TESTING SPEECH RECOGNITION SYSTEMS USING TEST DATA GENERATED BY TEXT-TO-SPEECH CONVERSION

Hubert Crepy *et al.*, assignors to International Business Machines Corporation
16 September 2003 (Class 704/243); filed in the European Patent Office 20 August 1999

This system would use a large body of audio material based on a text source and spoken by a speech synthesizer for testing a speech recognition system. The brief patent concentrates on the advantages of such an approach, primarily the repeatability of test conditions. There is no mention of possible issues that could arise because of the synthetic qualities of the testing materials.—DLR

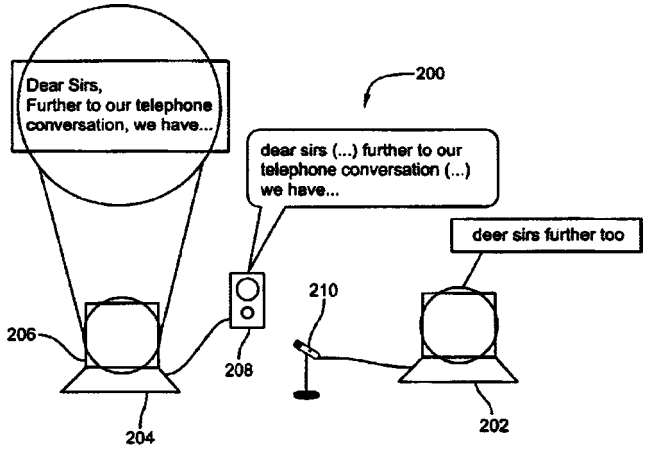

6,633,844

43.72.Ne LATE INTEGRATION IN AUDIO-VISUAL CONTINUOUS SPEECH RECOGNITION

Ashish Verma *et al.*, assignors to International Business Machines Corporation
14 October 2003 (Class 704/251); filed 2 December 1999

Reminscent of Hal's performance in the movie ''2001, A Space Odyssey,'' this system would make use of features extracted from a video signal to assist in the recognition of speech from an associated audio signal. The patent makes reference to the McGurk effect and extensive prior work in automated lip reading. Visemes are extracted from the video signal and an initial classification is performed. Most of the short patent deals with the way these visual features are integrated with the corresponding audio-based features to reconstruct a phoneme sequence.—DLR

6,701,293

43.72.Ne COMBINING N-BEST LISTS FROM MULTIPLE SPEECH RECOGNIZERS

Steven M. Bennett and Andrew V. Anderson, assignors to Intel Corporation
2 March 2004 (Class 704/251); filed 13 June 2001

An audio input stream is routed to at least two speech recognizers. Each recognizer produces an *n*-best list of possible results. The quality of the *n*-best lists may vary with different recognizers due to different algo-

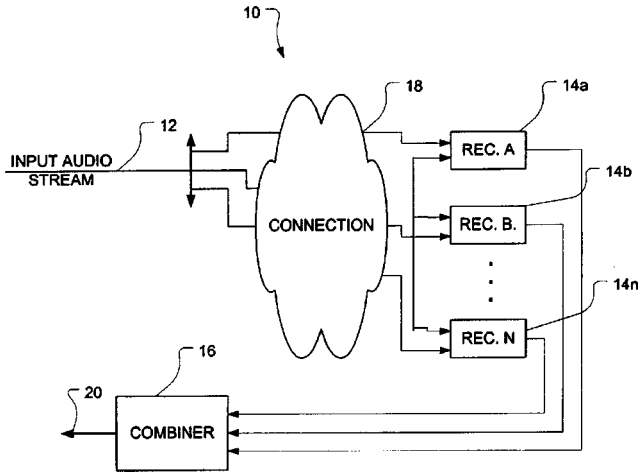

rithms used. A method is described for selecting among the lists of best possible results from several recognizers and combining them into an overall sorted *n*-best list. A subset of entries is then generated and sent to the application.—DAP

6,704,707

43.72.Ne METHOD FOR AUTOMATICALLY AND DYNAMICALLY SWITCHING BETWEEN SPEECH TECHNOLOGIES

Andrew V. Anderson and Steven M. Bennett, assignors to Intel Corporation
9 March 2004 (Class 704/231); filed 14 March 2001

A method is described to improve efficiency and cost effectiveness by switching between different speech recognizers depending on the requirements for recognition of the audio input stream. Desired applications range

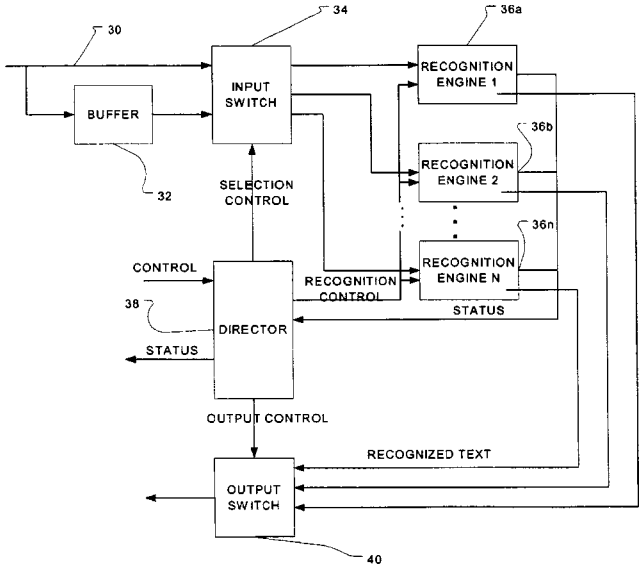

from inexpensive, high accuracy, dedicated capability systems for recognizing numerical choices within a closed set to computationally expensive, speaker-independent systems for recognizing dictation.—DAP

6,694,920

43.80.Lb METHOD OF USING SOUND FOR ATTRACTING AND GRADING FISH

Wendell Harold Noe, Lake City, Arkansas
24 February 2004 (Class 119/712); filed 18 March 2003

This is a rather oddly written patent that refers in its title to a method of attracting and grading fish in fish farming but seems to concentrate on the setup of a duck shooting resort layout. The semi-circular layout of the duck hunting blinds appears to be sure to precipitate quite a few human casualties. Also, a rather preposterous method is proposed to use sound for attracting and grading fish in an auxiliary fish farming operation. A certain sound, such as a bell or other noise, is made during a ''training period'' during which fish supposedly learn to associate feeding with that sound and they learn to congregate in a certain location so that they can receive food (and medication when needed). During harvesting, the sound is used to attract the fish into grading areas so that grading screens can be used to segregate fish of different sizes for harvesting. The patent was granted on 24 February 2004, precisely 35 days ahead of a more appropriate date (April 1).—DRR

6,695,785

43.80.Qf CATHETER INCLUDING ULTRASOUND TRANSDUCER WITH EMISSIONS ATTENUATION

Axel F. Brisken and N. Parker Willis, assignors to Cardiac Pathways Corporation
24 February 2004 (Class 600/459); filed 21 August 2001

This catheter incorporates an ultrasound transducer situated on an elongated body member and a damping region adjacent to a portion of the transducer. The transducer is configured to emit or receive an ultrasonic signal. The purpose of the ultrasonic damping region is to improve uniformity of the signal in three-dimensional space. Either air or a material containing air constitutes the means of damping.—DRR

6,699,191

43.80.Qf ULTRASOUND DEVICE TO DETECT CAISSON'S DISEASE

George A. Brock-Fisher, assignor to Koninklijke Philips Electronics N.V.
2 March 2004 (Class 600/437); filed 18 June 2002

This is a device designed to detect decompression disease (more popularly known as ''the bends'') that occurs when gas bubbles are released in body tissues and fluids due to an overly rapid decrease in surrounding pressure after prolonged exposure of the body to a compressed atmosphere. The device consists of an ultrasonic transducer that sends and receives sound signals to/from a blood vessel of a patient being examined for the occurrence of the bends and an analyzer that processes the received sound signals to establish the presence or nonpresence of bubbles in the blood vessel.—DRR

6,699,201

43.80.Qf ACOUSTIC WINDOW IDENTIFICATION

Scott Donaldson Stearns, assignor to MedAcoustics, Incorporated
2 March 2004 (Class 600/528); filed 29 November 2001

This patent describes a method for determining an acoustic window suitable for passive-acoustic coronary artery disease evaluation. A multichannel acoustic sensor array (having at least four and preferably more sensors) is positioned onto the chest of a subject. A weighting value is calculated for each of the sensor channels in the sensor array. The location of each sensor in the array is determined. The sensor channels which meet predetermined test criteria (*viz.*, those entailing the highest weighting values) are identified and a perimeter is defined which extends about and sub-

stantially encloses the identified sensor channels, thereby establishing an acoustic window suitable for acoustic listening diagnostics procedures. In the preferred embodiment, the calculation is done by assigning signal-to-noise ratio based weighting values to each of the sensor channels. The predetermined test criteria include identifying the sensors manifesting the three highest calculated weighting values or identifying at least three sensors exhibiting one or more high weighting values.—DRR

6,699,204

43.80.Qf DEVICE FOR ANALYZING AUSCULTATION SOUNDS, IN PARTICULAR RESPIRATORY SOUNDS

Georges Kehyayan *et al.*, assignors to Georges Kehyayan; Ivan Kehayoff
2 March 2004 (Class 600/533); filed in France 24 March 1999

This device for analyzing respiratory sounds consists of a set of acoustic sensors that relay the intensity of sound signals sampled at selected times at specific points on the body to a data storage module. A processing module

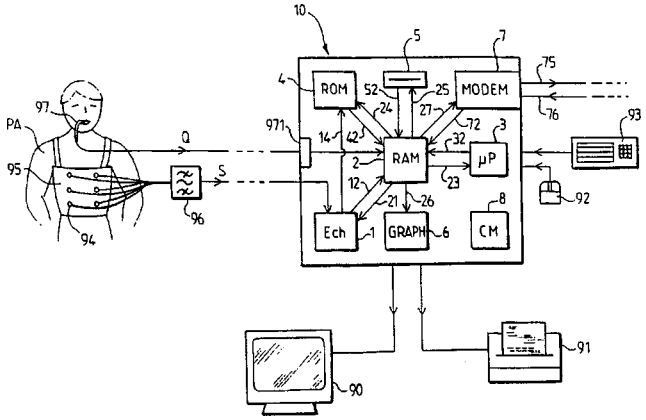

evaluates the set of transformed intensity levels to provide a three-dimensional presentation of the sound in the time and frequency domains.—DRR

6,699,711

43.80.Qf DEVICE AND METHOD FOR SELECTIVE EXPOSURE OF A BIOLOGICAL SAMPLE TO SOUND WAVES

Thomas Hahn *et al.*, assignors to Fraunhofer-Gesellschaft zur Forderung der angewandten Forschung e.V.
2 March 2004 (Class 435/283.1); filed in Germany 7 May 1998

This is an apparatus for selective exposure of a biological sample, e.g., cell materials or tissue samples, to sound waves. It consists of a receptacle into which the biological sample is introduced in suspended form and an electroacoustic transducer that generates the sound waves. The transducer is located outside the receptacle in such a manner that the sound wave coupling occurs through the receptacle wall into the sample.—DRR

6,702,743

43.80.Qf ULTRASOUND APPARATUS AND METHOD FOR TISSUE RESONANCE ANALYSIS

David Michaeli, assignor to Inta–Medics, Limited
9 March 2004 (Class 600/438); filed 24 June 2002

This patent, a derivative of United States Patent 5,840,018 by the same discloser, covers an ultrasonic probe that is placed on the head of a patient and is used to generate an ultrasonic pulse that propagates through the skull and the brain. The pulse is reflected off the skull and off of tissue lying in a

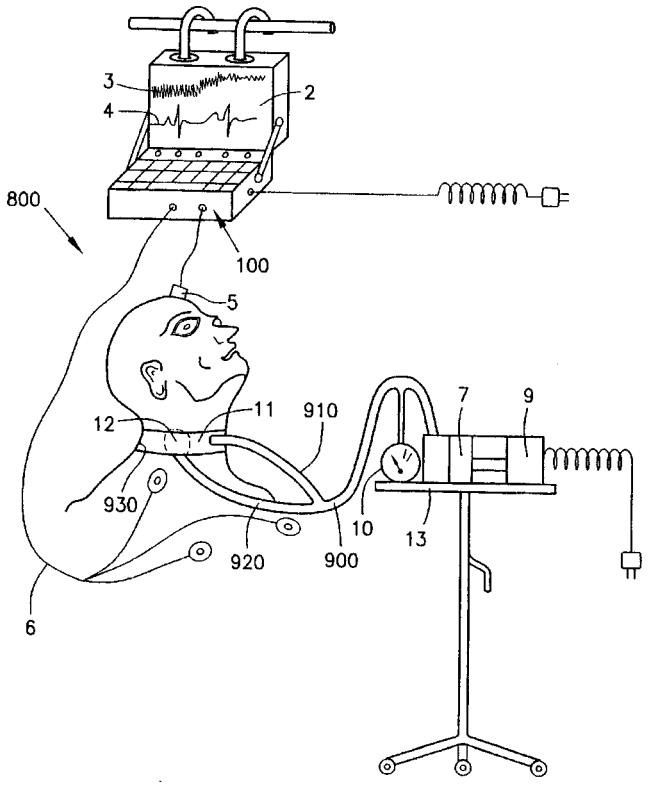

path normal to the probe. A portion of the echo-generated (EG) signal is selected and that signal is integrated over the selected portion to generate an echo pulsograph (EPG) signal. The EPG signal provides information regarding the physiological state of the tissue at a depth from the ultrasonic pulse corresponding to the selected portion of the EG signal.—DRR

6,702,746

43.80.Qf ALVEOLAR BONE MEASUREMENT SYSTEM

Samer M. Srouji, assignor to Dentosonic Limited
9 March 2004 (Class 600/449); filed in Israel 23 June 1999

An ultrasound system is provided for assessment of distance between an area of interest and a known location of a nonbone canal for use in drilling an implant-receiving cavity in the alveolar bone of a human patient's posterior mandible or posterior maxilla. The system includes an ultrasonic probe that can be inserted into the area of interest and transceives pulse-echo ultrasound to the alveolar bone. An electronic circuit processes the ultrasound signal and provides an indication of the remaining alveolar bone distance between the ultrasound probe and a canal within the alveolar bone.—DRR

6,705,319

43.80.Qf MINIATURE ACOUSTICAL GUIDANCE AND MONITORING SYSTEM FOR TUBE OR CATHETER PLACEMENT

George R. Wodicka *et al.*, assignors to Purdue Research Foundation
16 March 2004 (Class 128/207.14); filed 26 May 2000

This patent refers to an apparatus and method for acoustically guiding, positioning, and monitoring a tube or catheter within a body conduit or cavity in order to ensure the patency of the tube or catheter. An incident sound pulse is generated and propagated down the tube into the body. Multiple microphones are located within the tube and positioned to detect pulses traveling through the tube. A discriminator distinguishes between the inci-

dent sound pulse and the reflections from within the body. The detected sound pulses are processed to yield an indication of the location of the distal end of the tube within the body, to provide guidance of the insertion into the body, to estimate dimensions of the body adjacent to the distal end of the tube, and to indicate if the tube is obstructed.—DRR

6,709,396

43.80.Qf ULTRASOUND ARRAY TRANSDUCER FOR CATHETER USE

Aimé Flesch *et al.*, assignors to Vermon
23 March 2004 (Class 600/459); filed 17 July 2002

This patent describes an ultrasonic linear array transducer to be used in catheter instruments and the methods of fabricating this type of array to meet the requirements of surgical procedures. The array consists of a piezoelectric member sandwiched between matching layers and a backing member. A flexible stiffening element or elements are embedded in the backing member—opaque to radio frequencies and integrated along the azimuthal axis of the array so as to allow a user to view the element on a display and determine the angular position of the array. A flexible interconnect assembly connects the electrodes of the piezoelectric member and the external cabling. Various methods for adding a surrounding protective cover to the array are also described.—DRR

6,709,397

43.80.Qf SCANNING PROBE

James D. Taylor, assignor to Envisioneering, LLC
23 March 2004 (Class 600/459); filed 16 October 2002

This ultrasound cavital probe suitable for transrectal or other usage features a pair of motors within one end of its housing and consists of two shafts—a shaft connected to one motor to provide longitudinal movement of the ultrasound transducer and another shaft extending through the hollow

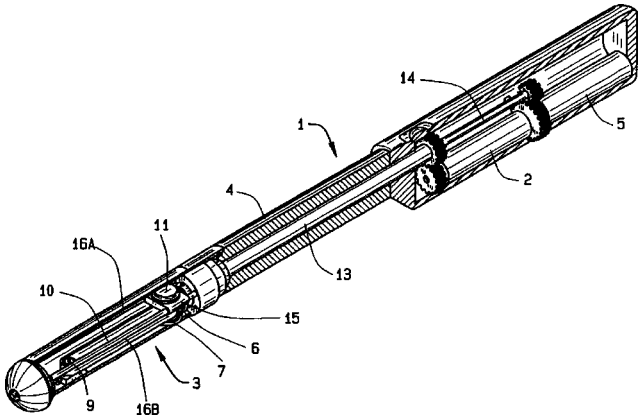

interior of the first shaft and connected to the second motor to provide rotary or pivotal movement to the transducer/probe. This probe can provide a two-dimensional view of the surrounding anatomy and, because of the longitudinal movement of the first shaft, can also provide a three-dimensional volumetric scan of the surrounding anatomy.—DRR

6,695,781

43.80.Sh ULTRASONIC MEDICAL DEVICE FOR TISSUE REMODELING

Robert A. Rabiner and Bradley A. Hare, assignors to OmniSonics Medical Technologies, Incorporated
24 February 2004 (Class 600/439); filed 27 July 2001

This is a device intended for use by plastic surgeons. The cylindrical ultrasonic probe provides transverse mode ultrasonic waves to fragment tissue by emulsification. The probe can be utilized with acoustic and/or aspiration sheaths to enhance destruction and removal of an occlusion. Armed with an imaging device, the probe can, in effect, remodel human tissue in medical and cosmetic surgical procedures.—DRR

6,695,782

43.80.Sh ULTRASONIC PROBE DEVICE WITH RAPID ATTACHMENT AND DETACHMENT MEANS

Kevin Ranucci *et al.*, assignors to OmniSonics Medical Technologies, Incorporated
24 February 2004 (Class 600/439); filed 11 October 2001

This is another version of the probe described in Patent 6,695,781, reviewed above. It is also an ultrasonic tissue ablation device incorporating a transversely vibrating elongated probe, but it features a coupling assembly for probe attachment/detachment so that it can be used in combination with a flexible catheter wire, whereby the probe can be rapidly attachable to and detachable from its ultrasonic energy source.—DRR

6,702,775

43.80.Sh ULTRASOUND METHOD FOR REVASCULARIZATION AND DRUG DELIVERY

Lauri J. DeVore, assignor to SciMed Life Systems, Incorporated
9 March 2004 (Class 604/22); filed 15 January 2003

The described method entails an intravascular ultrasound percutaneous myocardial revascularization (PMR) device that features a needle for supplying the heart with an angiogenic material or contrasting agent. In one embodiment, a needle is attached to the ultrasound PMR device adjacent to the catheter along the catheter's longitudinal axis. The needle delivers angiogenic materials or a contrasting agent to an area of interest. The patent maintains that by combining ultrasound myocardial revascularization with an additional lumen for delivery materials, advantage is gained over the prior art by the fact that virtually no myocardial tissue is destroyed and seepage of angiogenic materials is minimized.—DRR

6,695,778

43.80.Vj METHODS AND SYSTEMS FOR CONSTRUCTION OF ULTRASOUND IMAGES

Polina Golland and Stacy Ho, assignors to AITech, Incorporated
24 February 2004 (Class 600/437); filed 3 July 2002

Echoes from a single unfocused transmission by a number of elements are processed to produce an image so that high frame rates are possible for volumetric imaging.—RCW

6,695,779

43.80.Vj METHOD AND APPARATUS FOR SPATIOTEMPORAL FREEZING OF ULTRASOUND IMAGES IN AUGMENTED REALITY VISUALIZATION

Frank Sauer *et al.*, assignors to Siemens Corporate Research, Incorporated
24 February 2004 (Class 600/437); filed 16 August 2002

A sequence of ultrasound images is stored. Images selected using time are displayed as a set. Additional selected images can be added or removed from the set.—RCW

6,695,784

43.80.Vj ULTRASOUND PULSATILITY IMAGING

David Michaell, assignor to Inta–Medics, Limited
24 February 2004 (Class 600/453); filed in Israel 9 March 1999

A three-dimensional image of pulsatile activity in a selected volume of tissue is formed by processing ultrasound echo signals as the ultrasonic focus is varied along a line. The processing is repeated for additional lines within a plane. The line-by-line processing is then repeated in additional planes within the volume.—RCW

6,699,189

43.80.Vj ULTRASOUND DISTORTION COMPENSATION USING BLIND SYSTEM IDENTIFICATION

Feng Lin and Robert C. Waag, assignors to University of Rochester
2 March 2004 (Class 600/437); filed 26 December 2001

Aberration in ultrasonic imaging is modeled by using a linear filter bank. The response of each filter is determined by a so-called blind system

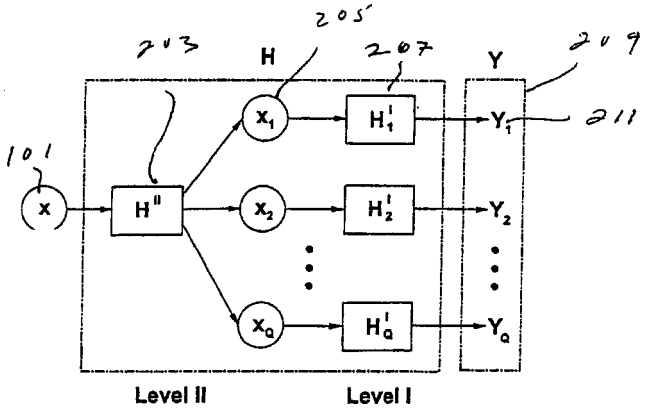

identification method that assumes the signals arise from a common origin and uses only signals from an array of receiving elements. Computation is reduced by grouping receiver array elements into subapertures.—RCW

6,702,745

43.80.Vj 3D/4D ULTRASOUND IMAGING SYSTEM

David Smythe, Glasgow, the United Kingdom
9 March 2004 (Class 600/443); filed in the United Kingdom 21 January 1999

An array of transducers is used to emit omnidirectional ultrasonic waves. Echoes are detected, sampled, and processed to obtain reflection amplitude in a volume. Arbitrary planes in the volume may be imaged.—RCW

6,702,747

43.80.Vj ACOUSTICALLY GENERATED IMAGES HAVING SELECTED COMPONENTS

George F. Garlick, assignor to Advanced Imaging Technologies II LLC
9 March 2004 (Class 600/459); filed 17 October 2001

Diffracted and undiffracted components of signals in a through-transmission system are received. Images are produced from either the diffracted component or the undiffracted component. Alternatively, selected frequencies from the diffracted component may be used to produce images.—RCW

6,704,438

43.80.Vj APPARATUS AND METHOD FOR IMPROVING THE SIGNAL TO NOISE RATIO ON ULTRASOUND IMAGES USING CODED WAVEFORMS

Radu Alexandru, assignor to Aloka Company, Limited
9 March 2004 (Class 382/128); filed 8 May 2000

Real-valued ultrasound signals are filtered in parallel in the frequency domain by using fast forward and inverse Fourier transforms. Filter characteristics are selected from stored sets of characteristics by using factors such as depth of focus. This allows the use of coded waveforms to improve the signal-to-noise ratio in ultrasonic images.—RCW

6,705,992

43.80.Vj ULTRASOUND IMAGING ENHANCEMENT TO CLINICAL PATIENT MONITORING FUNCTIONS

Ronald D. Gatzke, assignor to Koninklijke Philips Electronics N.V.
16 March 2004 (Class 600/437); filed 28 February 2002

An ultrasonic imaging capability is integrated in a patient monitoring

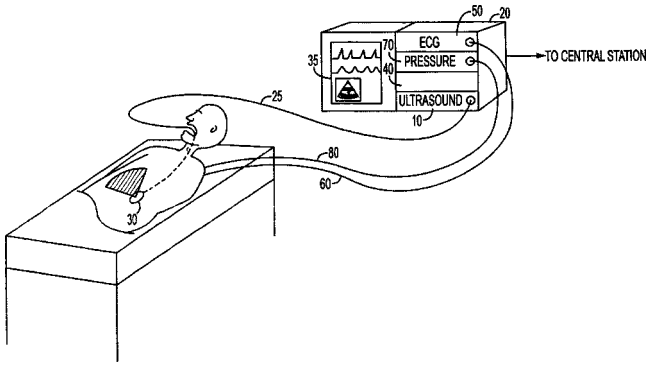

system to display ultrasonic images continuously as well as to provide diagnostic data continuously from the images.—RCW

6,705,993

43.80.Vj ULTRASOUND IMAGING SYSTEM AND METHOD USING NON-LINEAR POST-BEAMFORMING FILTER

Emad S. Ebbini and Pornchai Phukpattaranont, assignors to Regents of the University of Minnesota
16 March 2004 (Class 600/443); filed 10 May 2002

Linear and nonlinear components of ultrasonic beamformed signals are

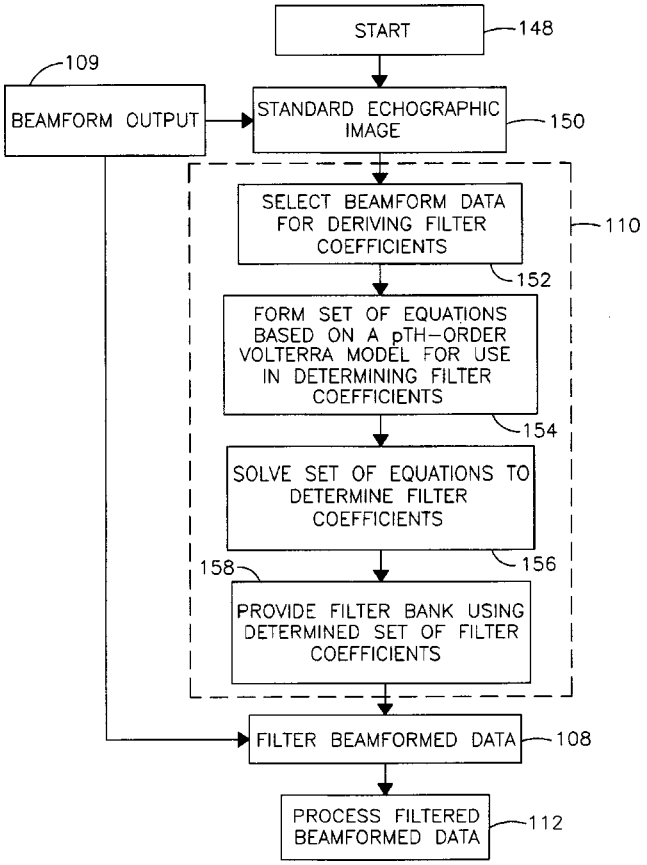

separated using filter coefficients based on a Volterra filter model.—RCW

6,705,994

43.80.Vj TISSUE INHOMOGENEITY CORRECTION IN ULTRASOUND IMAGING

Kobi Vortman and Shuki Vitek, assignors to Insightec–Image Guided Treatment Limited
16 March 2004 (Class 600/443); filed 8 July 2002

Focusing delay times are computed for transducer array elements by using the speed of sound in a selected region of tissue and the boundaries of the region. The selected regions may be fat or other tissues. The site of interest is imaged using the computed delay times.—RCW

6,709,392

43.80.Vj IMAGING ULTRASOUND TRANSDUCER TEMPERATURE CONTROL SYSTEM AND METHOD USING FEEDBACK

Ivan Salgo *et al.*, assignors to Koninklijke Philips Electronics N.V.
23 March 2004 (Class 600/439); filed 10 October 2002

The temperature of an ultrasonic transducer is controlled by changing operating system parameters. The changes are based on feedback from temperature sensing elements in the transducer. The system parameters that are changed may be preset, determined by the system user, or a combination of the two. Alteration of the parameters may be based on the imaging mode being used, the difference between the current temperature and a preferred temperature, or a threshold temperature being reached.—RCW

6,709,394

43.80.Vj BIPLANE ULTRASONIC IMAGING

Janice Frisa *et al.*, assignors to Koninklijke Philips Electronics N.V.
23 March 2004 (Class 600/445); filed 29 August 2002

The plane of one image has a fixed orientation relative to the transducer. The plane of the other image can be rotated and tilted relative to the fixed plane. An image orientation icon is displayed together with the biplane images to depict the relative orientation of the two images.—RCW

6,709,395

43.80.Vj SYSTEM AND METHOD FOR ELECTRONICALLY ALTERING ULTRASOUND SCAN LINE ORIGIN FOR A THREE-DIMENSIONAL ULTRASOUND SYSTEM

McKee Poland, assignor to Koninklijke Philips Electronics N.V.
23 March 2004 (Class 600/447); filed 25 June 2002

The orientation of ultrasonic scan lines in two or more dimensions is altered to produce scan lines apparently emanating from a location other than the center of the ultrasound transducer used to acquire the scan lines.—RCW

A closed-form solution for reflection and transmission of transient waves in multilayers

G. Caviglia
Dipartimento di Matematica, Università, Via Dodecaneso 35, 16146 Genova, Italy

A. Morro[a)]
Università, DIBE, Via Opera Pia 11 a, 16145 Genova, Italy

(Received 4 October 2002; accepted for publication 4 May 2004)

The reflection–transmission problem for a multilayer is examined in the time domain. The layers are linearly elastic, possibly anisotropic, but homogeneous. The multilayer is sandwiched between two homogeneous half-spaces and the incident wave propagates along the normal to the layers. By applying repeatedly the continuity of displacement and traction, the outgoing waves at each interface are evaluated in terms of the incoming ones. As a result, a system of equations is established which eventually determines the reflected and transmitted waves and the waves inside the layers, in terms of the incident wave. A few simple cases are examined in detail to show, e.g., the distortion of a rectangular incident pulse, originated by multiple reflections, and the occurrence of resonance effects. © *2004 Acoustical Society of America.* [DOI: 10.1121/1.1765193]

PACS numbers: 43.20.Bi, 43.20.El, 46.40.Cd [ADP] Pages: 643–654

I. INTRODUCTION

The wide extent of applicability, besides the conceptual interest *per se*, motivates the large body of literature on reflection–transmission processes generated by multilayers. References 1–4 and references therein provide a wide set of applications and mathematical approaches to solve the associated problems.

Quite often, the reflection–transmission processes are investigated in the frequency domain. This scheme is natural in connection with wave propagation generated by time-harmonic incident waves and sources. Further, if the governing equations are linear, the application of the Fourier transform allows us to study a time dependent process in the frequency domain. The frequency domain seems to be convenient if the material is inhomogeneous or the incidence is oblique.[4,5] However, a time domain description is often the most direct and natural representation of a material behavior and can be expected to provide results and insights which may be hard to arrive at in the frequency domain through the eventual inverse Fourier transform. Also an analysis in the time domain overcomes the difficulties of accurate computations associated with nonanalytical functions.[6]

In this paper we examine the reflection–transmission problem for a multilayer in the time domain. The layers are homogeneous and linearly elastic, possibly anisotropic. The multilayer is sandwiched between two homogeneous half-spaces. The incident wave propagates in the direction of inhomogeneity (normal incidence). This simplifies somewhat the reflection–transmission problem. In fact, the problem is three-dimensional as far as the polarization is concerned but is geometrically one-dimensional. The existence and uniqueness of the solution is proved in Ref. 7; here we look for an operative procedure to establish the solution.

The formulation of the reflection–transmission process is set up for n layers. At any interface between adjacent layers, the continuity of displacement and traction is required and this results in a set of boundary conditions. A careful analysis of the equations provided by the boundary conditions allows us to write, at any interface, the functions representing the outgoing waves in terms of the incoming ones. Appropriate developments and repeated use of D'Alembert's formula give the solution to the reflection–transmission problem, at a time t, through a finite number of terms involving incoming waves since the initial time. In addition, an efficient algorithm is provided for the evaluation of the (exact) solution.

In essence, in this paper we provide the reflected and transmitted waves $\mathbf{u}^R, \mathbf{u}^T$ generated by a given incident wave $\mathbf{u}^I$, through n layers in the time-domain. In general $\mathbf{u}^R$ and $\mathbf{u}^T$ are given by a system of equations to be solved through an algorithm with a finite number of steps. In addition, the results hold for anisotropic layers between anisotropic half-spaces. In simple cases $\mathbf{u}^R$ and $\mathbf{u}^T$ are given in closed form. Both the closed form and the algorithm show how the reflected and transmitted waves are affected by the superposition, at different times, of waves propagating forward and backward in the layers. Consistent with the main advantage of the time-domain, $\mathbf{u}^R$ and $\mathbf{u}^T$ are found explicitly in space-time variables, in a more direct and immediate form (see Figs. 1–8). To our knowledge similar results are found only in the context of electromagnetism in undeformable isotropic solids.[8–10] The originality of the present results is also due to the efficient form obtained, through integration in time, for the boundary condition on the traction.

II. WAVES IN UNIAXIAL ELASTIC SOLIDS

Consider a body occupying the whole space domain $\mathbb{R}^3$. Each position in the body is associated with the Cartesian coordinates x,y,z or x_1,x_2,x_3. Denote by $\mathbf{x}=(x,y,z)$ the

[a)]Corresponding author: A. Morro. Electronic mail: morro@dibe.unige.it

position vector. Let $\mathbf{u}(\mathbf{x},t)$ be the displacement at time t. Body forces are disregarded and hence the equation of motion is expressed by

$$\rho\partial_t^2\mathbf{u}=\boldsymbol{\nabla}\cdot\mathbf{T},$$

where ρ is the mass density and $\mathbf{T}$ is the Cauchy stress tensor. Since we have in mind linear models, ∂_t denotes the (partial) time derivative.

The body is taken to be anisotropic and elastic. We then write $\mathbf{T}$ in terms of the gradient of displacement, $\boldsymbol{\nabla}\mathbf{u}$, in the form

$$\mathbf{T}=\mathbf{C}\boldsymbol{\nabla}\mathbf{u},$$

where $\mathbf{C}$ is the fourth-order elastic tensor. In indicial form,

$$T_{ij}=C_{ijhk}\partial u_k/\partial x_h.$$

The tensor $\mathbf{C}$ is required to satisfy the minor and major symmetries,

$$C_{ijhk}=C_{jihk}=C_{ijkh}=C_{hkij}.$$

We now look for uniaxial solutions $\mathbf{u}(z,t)$ in homogeneous layers namely when $\mathbf{C}$ is piecewise constant in z and constant in x,y. Letting $\mathbf{n}$ be the unit vector of z and $\partial_z=\partial/\partial z$ we have

$$\boldsymbol{\nabla}\mathbf{u}=\mathbf{n}\otimes\partial_z\mathbf{u},$$

whence

$$\mathbf{T}=\mathbf{C}[\mathbf{n}\otimes\partial_z\mathbf{u}].$$

Hence the traction,

$$\mathbf{t}=\mathbf{T}\mathbf{n},$$

at the surfaces $z=$ constant, is given by

$$\mathbf{t}=\mathbf{Q}\partial_z\mathbf{u}, \tag{1}$$

where

$$\mathbf{Q}=\mathbf{n}\mathbf{C}\mathbf{n} \quad \text{or} \quad Q_{ik}=C_{i33k}$$

is the acoustic tensor. By the major symmetry it follows that $\mathbf{Q}$ is symmetric. Further, we assume that $\mathbf{Q}$ is positive definite.

Because

$$\boldsymbol{\nabla}\cdot\mathbf{T}=\mathbf{Q}\partial_z^2\mathbf{u},$$

the equation of motion becomes

$$\rho\partial_t^2\mathbf{u}=\mathbf{Q}\partial_z^2\mathbf{u}. \tag{2}$$

Let q_1,q_2,q_3 be the (positive) eigenvalues of the matrix $\mathbf{Q}$ and let $\mathbf{a}_1,\mathbf{a}_2,\mathbf{a}_3$ be the associated eigenvectors,

$$\mathbf{Q}\mathbf{a}_r=q_r\mathbf{a}_r, \quad r=1,2,3.$$

Irrespective of the multiplicity of the eigenvalues, we can always regard $\mathbf{a}_1,\mathbf{a}_2,\mathbf{a}_3$ as orthonormal. Hence we can write

$$\sum_r \mathbf{a}_r\otimes\mathbf{a}_r=\mathbf{1}, \quad \mathbf{Q}=\sum_r q_r\mathbf{a}_r\otimes\mathbf{a}_r; \tag{3}$$

hereafter, if not otherwise indicated, it is understood that the summation is over 1 to 3. By using the eigenvectors $\{\mathbf{a}_k\}$ as a basis we can express $\mathbf{u}(z,t)$ in the form

$$\mathbf{u}(z,t)=\sum_r u_r(z,t)\mathbf{a}_r. \tag{4}$$

Within a homogeneous region $\mathbf{Q}$ and $\{\mathbf{a}_k\}$ are constant and, upon substitution of (4) in (2), we find that

$$\rho\sum_r \partial_t^2u_r\mathbf{a}_r=\sum_r q_r\partial_z^2u_r\mathbf{a}_r.$$

Hence it follows that the component functions u_r satisfy a decoupled system of wave equations,

$$\frac{\rho}{q_r}\partial_t^2u_r-\partial_z^2u_r=0, \quad r=1,2,3.$$

This implies that $c_r=\sqrt{q_r/\rho}$ is the speed of propagation of the wave u_r. Also,

$$u_r(z,t)=\hat{u}_r^f(z-c_rt)+\hat{u}_r^b(z+c_rt),$$

where $\hat{u}_r^f$ and $\hat{u}_r^b$ represent forward(-propagating) and backward(-propagating) waves in the z-direction.

In view of the representation (4) we can say that any uniaxial solution $\mathbf{u}(z,t)$ can be expressed by

$$\mathbf{u}=\sum_r \hat{u}_r^f(z-c_rt)\mathbf{a}_r+\sum_r \hat{u}_r^b(z+c_rt)\mathbf{a}_r. \tag{5}$$

The first sum involves three forward waves, the second one three backward waves. The eigenvectors $\{\mathbf{a}_r\}$ are the directions of polarization and $\{\hat{u}_r^f\},\{\hat{u}_r^b\}$ are the corresponding components. Also, $\hat{u}_r^f\mathbf{a}_r$ ($\hat{u}_r^b\mathbf{a}_r$) is the r-th mode of forward-(backward-) propagation.

If the material is isotropic then

$$\mathbf{Q}=\mu\mathbf{1}+(\mu+\lambda)\mathbf{n}\otimes\mathbf{n},$$

where μ and λ are the Lamé elastic moduli. Hence if, e.g.,

$$\mathbf{a}_3=\mathbf{n}, \quad \mathbf{a}_1,\mathbf{a}_2\perp\mathbf{n},$$

we have

$$c_3=\sqrt{(2\mu+\lambda)/\rho}, \quad c_1=c_2=\sqrt{\mu/\rho}.$$

III. REFLECTION–TRANSMISSION PROBLEM FOR A MULTILAYER

Let $z<0$ and $z>L$ be homogeneous half-spaces. The interval $0<z<L$ consists of n adjacent homogeneous layers separated by interfaces at $z=z_1,\ldots,z_{n-1}$. At $z=z_0=0$ and $z=z_n=L$ an interface separates the multilayer from the adjacent half-space. The α-th layer, $\alpha=1,2,\ldots,n$ occupies the interval $z\in(z_{\alpha-1},z_\alpha)$. As is quite a common practice we let the displacement $\mathbf{u}$ and the traction $\mathbf{t}$ be continuous across any interface, namely

$$\mathbf{u}(z_{\alpha-},t)=\mathbf{u}(z_{\alpha+},t), \quad \mathbf{t}(z_{\alpha-},t)=\mathbf{t}(z_{\alpha+},t),$$

$$\alpha=0,1,\ldots,n.$$

The reflection–transmission process can be framed as follows. The incident transient wave $\mathbf{u}^I$ is coming from $z=-\infty$ and impinges on the multilayer at $z=0$. The reflected wave $\mathbf{u}^R$ propagates in the half-space $z<0$, the transmitted wave $\mathbf{u}^T$ in $z>L$. Both half-spaces are homogeneous. Denote

by a superscript $-$ or $+$ the parameters pertaining to $z<0$ or $z>L$. Hence we can represent $\mathbf{u}^I,\mathbf{u}^R,\mathbf{u}^T$ as

$$\mathbf{u}^I(z,t)=\sum_s \hat{u}_s^I(z-c_s^- t)\mathbf{a}_s^-, \tag{6}$$

$$\mathbf{u}^R(z,t)=\sum_s \hat{u}_s^R(z+c_s^- t)\mathbf{a}_s^-,$$

$$\mathbf{u}^T(z,t)=\sum_s \hat{u}_s^T(z-c_s^+ t)\mathbf{a}_s^+. \tag{7}$$

The displacement $\mathbf{u}$ is then expressed by

$$\mathbf{u}(z,t)=\begin{cases}\mathbf{u}^I(z,t)+\mathbf{u}^R(z,t), & z<0,\\ \mathbf{u}^\alpha(z,t), & z\in(z_{\alpha-1},z_\alpha),\quad \alpha=1,2,\ldots,n,\\ \mathbf{u}^T(z,t), & z>L.\end{cases} \tag{8}$$

The function $\mathbf{u}^\alpha$, $\alpha=1,2,\ldots,n$, denotes the solution in the α-th layer $z\in(z_{\alpha-1},z_\alpha)$. The continuity of $\mathbf{u}$ and $\mathbf{t}$ at each interface implies that, for each time $t\in\mathbb{R}$,

$$\begin{aligned}&\mathbf{u}^I(0_-,t)+\mathbf{u}^R(0_-,t)=\mathbf{u}^1(0_+,t),\\ &\mathbf{u}^\alpha(z_{\alpha-},t)=\mathbf{u}^{\alpha+1}(z_{\alpha+},t),\quad \alpha=1,2,\ldots,n-1,\\ &\mathbf{u}^n(L_-,t)=\mathbf{u}^T(L_+,t),\end{aligned} \tag{9}$$

and, by means of (1) and (8),

$$\begin{aligned}&\mathbf{Q}(0_-)[\partial_z\mathbf{u}^I(0_-,t)+\partial_z\mathbf{u}^R(0_-,t)]=\mathbf{Q}(0_+)\partial_z\mathbf{u}^1(0_+,t),\\ &\mathbf{Q}(z_{\alpha-})\partial_z\mathbf{u}^\alpha(z_{\alpha-},t)=\mathbf{Q}(z_{\alpha+})\partial_z\mathbf{u}^{\alpha+1}(z_{\alpha+},t),\\ &\qquad\qquad \alpha=1,2,\ldots,n-1,\\ &\mathbf{Q}(L_-)\partial_z\mathbf{u}^n(L_-,t)=\mathbf{Q}(L_+)\partial_z\mathbf{u}^T(L_+,t).\end{aligned} \tag{10}$$

For definiteness we let $\mathbf{u}^I$ be nonzero, at $z=0_-$, only after $t=0$. It is then assumed that $\mathbf{u}^R,\mathbf{u}^\alpha,\mathbf{u}^T$ are nonzero after $t=0$. This is made precise by writing the initial conditions

$$\begin{aligned}&\mathbf{u}^I(0_-,0)=0,\quad \mathbf{u}^R(z,0)=0,\quad \partial_t\mathbf{u}^R(z,0)=0,\quad z<0,\\ &\mathbf{u}^\alpha(z,0)=0,\quad \partial_t\mathbf{u}^\alpha(z,0)=0,\quad z\in(z_{\alpha-1},z_\alpha),\\ &\alpha=1,2,\ldots,n,\\ &\mathbf{u}^T(z,0)=0,\quad \partial_t\mathbf{u}^T(z,0)=0,\quad z>L.\end{aligned} \tag{11}$$

We can then state the problem as follows.

Reflection–transmission problem. Given $\mathbf{u}^I$, in the form (6), while $\mathbf{u}^R,\mathbf{u}^T$ possess the outgoing character as in (7), find the function (8) in $\mathbb{R}\times\mathbb{R}^+$ such that the equation of motion (2) holds as $z\in(0,z_1)\cup(z_1,z_2)\cup\cdots\cup(z_{n-1},L)$ subject to the boundary conditions (9)–(10) and the initial conditions (11).

Based on existence and uniqueness results[7] we now look for the representation of the solution.

IV. CONSEQUENCES OF THE CONTINUITY CONDITIONS

The multilayer occupies the interval $0<z<L$ and is comprised of n homogeneous layers. As before, we denote by the superscripts $-$ or $+$ the values pertaining to $z<0$ or $z>L$ and by the superscript or subscript α, $\alpha=1,\ldots,n$, the values pertaining to the α-th layer, $z\in(z_{\alpha-1},z_\alpha)$. The representations (6) and (7) remain valid.

Also by analogy with (6), (7), we find it convenient to represent the solution $\mathbf{u}^\alpha$ in the α-th layer as a superposition of the forward waves $u_p^{\alpha f}$ and the backward waves $u_p^{\alpha b}$ such that

$$\mathbf{u}^\alpha=\sum_p (u_p^{\alpha f}+u_p^{\alpha b})\mathbf{a}_p^\alpha.$$

They are functions on $(z_{\alpha-1},z_\alpha)\times\mathbb{R}$ of the form

$$\begin{aligned}&u_p^{\alpha f}(z,t)=\hat{u}_p^{\alpha f}(z-c_p t),\quad u_p^{\alpha b}(z,t)=\hat{u}_p^{\alpha b}(z+c_p t),\\ &p=1,2,3,\quad \alpha=1,\ldots,n.\end{aligned} \tag{12}$$

Hence we can replace (8) with

$$\mathbf{u}(z,t)=\begin{cases}\sum_p [u_p^I(z,t)+u_p^R(z,t)]\mathbf{a}_p^-, & z<0,\\ \sum_p [u_p^{\alpha f}(z,t)+u_p^{\alpha b}(z,t)]\mathbf{a}_p^\alpha, & z\in(z_{\alpha-1},z_\alpha),\\ \sum_p u_p^T(z,t)\mathbf{a}_p^+, & z>L.\end{cases} \tag{13}$$

The initial conditions (11) take the form

$$\begin{aligned}&u_p^I(0_-,0)=0,\quad u_p^R(z,0)=0,\quad \partial_t u_p^R(z,0)=0,\quad z<0,\\ &u_p^{\alpha f}(z,0)=0,\quad \partial_t u_p^{\alpha f}(z,0)=0,\quad u_p^{\alpha b}(z,0)=0,\\ &\partial_t u_p^{\alpha b}(z,0)=0,\quad z\in(z_{\alpha-1},z_\alpha),\\ &u_p^T(z,0)=0,\quad \partial_t u_p^T(z,0)=0,\quad z>L,\end{aligned} \tag{14}$$

where $p=1,2,3$. Next we apply (14) also at the limit $z\to 0_-,0_+,L_-,L_+$.

Owing to the form (12) of the functions $\hat{u}_p$ it follows that the same value occurs at different places provided appropriate times are considered. Of course this is obvious and well known for any single function $g(z\pm ct)$. Here we have to account for $n+2$ different sets of speeds c_p, $p=1,2,3$, according as $z<0$, $z\in(z_{\alpha-1},z_\alpha)$, $z>L$. In particular we find the relations

$$\begin{aligned}&u_p^R(z,t)=u_p^R(0,t+z/c_p^-),\quad z<0,\\ &u_p^T(z,t)=u_p^T(L,t-(z-L)/c_p^+),\quad z>L,\end{aligned}$$

which allow us to find the solution at any point, in the half-spaces, once the functions $u_p^R(0,\cdot)$ and $u_p^T(L,\cdot)$ are determined. It is understood that the value of u_p^I and u_p^R, at $z=0$, or u_p^T at $z=L$, is meant as the limit as $z\to 0_-$ or $z\to L_+$. Analogous relations hold for $u_p^{\alpha f}(z_\alpha,t)$ and $u_p^{\alpha b}(z_{\alpha-1},t)$. The values at $z_0=0,z_1,\ldots,z_n=L$ are meant as the limit when $z\to 0,z_1,\ldots,z_n$ from within the appropriate interval.

We now evaluate $\mathbf{t}$ and then require that $\mathbf{u}$ and $\mathbf{t}$ be continuous at the interfaces $z=0=z_0,z_1,\ldots,z_n=L$. Since $\mathbf{t}=\mathbf{Q}\partial_z\mathbf{u}$, by (13) and (3) we have

$$\mathbf{t}(z,t)=\begin{cases}\sum_p \rho^-(c_p^-)^2[(\hat{u}_p^I)'(z-c_p^-t)+(\hat{u}_p^R)'(z+c_p^-t)]\mathbf{a}_p^-, & z<0,\\ \sum_p \rho^\alpha(c_p^\alpha)^2[(\hat{u}_p^{\alpha f})'(z-c_p t)+(\hat{u}_p^{\alpha b})'(z+c_p t)]\mathbf{a}_p^\alpha, & z\in(z_{\alpha-1},z_\alpha),\\ \sum_p \rho^+(c_p^+)^2(u_p^T)'(z-c_p^+t)\mathbf{a}_p^+, & z>L.\end{cases}$$

It is convenient to express the derivatives $(\hat{u}_p^I)',(\hat{u}_p^R)',\ldots,(\hat{u}_p^T)'$ in terms of $\partial_t\hat{u}_p^I,\partial_t\hat{u}_p^R,\ldots,\partial_t\hat{u}_p^T$ to obtain

$$\mathbf{t}(z,t)=\begin{cases}\partial_t\sum_p \rho^- c_p^-[-\hat{u}_p^I(z-c_p^-t)+\hat{u}_p^R(z+c_p^-t)]\mathbf{a}_p^-, & z<0,\\ \partial_t\sum_p \rho^\alpha c_p^\alpha[-\hat{u}_p^{\alpha f}(z-c_p t)+\hat{u}_p^{\alpha b}(z+c_p t)]\mathbf{a}_p^\alpha, & z\in(z_{\alpha-1},z_\alpha),\\ \partial_t\sum_p -\rho^+c_p^+\hat{u}_p^T(z-c_p^+t)\mathbf{a}_p^+, & z>L.\end{cases}$$

The continuity of $\mathbf{u}$ at $z=0=z_0,z_1,\ldots,z_n=L$ results in

$$\sum_p [u_p^I(0,t)+u_p^R(0,t)]\mathbf{a}_p^-=\sum_p [u_p^{1f}(0,t)+u_p^{1b}(0,t)]\mathbf{a}_p^1, \tag{15}$$

$$\sum_p [u_p^{\alpha f}(z_\alpha,t)+u_p^{\alpha b}(z_\alpha,t)]\mathbf{a}_p^\alpha = \sum_p [u_p^{\alpha+1,f}(z_\alpha,t)+u_p^{\alpha+1,b}(z_\alpha,t)]\mathbf{a}_p^{\alpha+1}, \quad \alpha=1,2,\ldots,n-1, \tag{16}$$

$$\sum_p [u_p^{nf}(L,t)+u_p^{nb}(L,t)]\mathbf{a}_p=\sum_p u_p^T(L,t)\mathbf{a}_p^+. \tag{17}$$

Meanwhile the continuity of $\mathbf{t}$ results in

$$\partial_t\sum_p \rho^- c_p^-[-\hat{u}_p^I(-c_p^-t)+\hat{u}_p^R(c_p^-t)]\mathbf{a}_p^- = \partial_t\sum_p \rho c_p^1[-\hat{u}_p^{1f}(-c_p t)+\hat{u}_p^{1b}(c_p t)]\mathbf{a}_p^1,$$

$$\partial_t\sum_p \rho c_p^\alpha[-\hat{u}_p^{\alpha f}(z_\alpha-c_p^\alpha t)+\hat{u}_p^{\alpha b}(z_\alpha+c_p^\alpha t)]\mathbf{a}_p^\alpha = \partial_t\sum_p \rho c_p^{\alpha+1}[-\hat{u}_p^{\alpha+1,f}(z_\alpha-c_p^{\alpha+1}t)+\hat{u}_p^{\alpha+1,b}(z_\alpha+c_p^{\alpha+1}t)]\mathbf{a}_p^{\alpha+1},$$

$$\partial_t\sum_p \rho^n c_p^n[-\hat{u}_p^{nf}(L-c_p^n t)+\hat{u}_p^{nb}(L+c_p^n t)]\mathbf{a}_p^n = \partial_t\sum_p -\rho^+c_p^+\hat{u}_p^T(L-c_p^+t)\mathbf{a}_p^+.$$

Upon integration over $[0,t]$ and use of (14), we can express the continuity of $\mathbf{t}$ in terms of the functions u_p^α in the form

$$\sum_p \rho^- c_p^-[u_p^I(0,t)-u_p^R(0,t)]\mathbf{a}_p^- = \sum_p \rho^1 c_p^1[u_p^{1f}(0,t)-u_p^{1b}(0,t)]\mathbf{a}_p^1, \tag{18}$$

$$\sum_p \rho^\alpha c_p^\alpha[u_p^{\alpha f}(z_\alpha,t)-u_p^{\alpha b}(z_\alpha,t)]\mathbf{a}_p^\alpha = \sum_p \rho^{\alpha+1}c_p^{\alpha+1}[u_p^{\alpha+1,f}(z_\alpha,t)-u_p^{\alpha+1,b}(z_\alpha,t)]\mathbf{a}_p^{\alpha+1}, \tag{19}$$

$$\sum_p \rho^n c_p^n[u_p^{nf}(L,t)-u_p^{nb}(L,t)]\mathbf{a}_p^n = \sum_p \rho^+c_p^+u_p^T(L,t)\mathbf{a}_p^+. \tag{20}$$

Henceforth we regard (15) to (20) as the set of continuity conditions for $\mathbf{u}$ and $\mathbf{t}$.

The boundary (here continuity) conditions on $\mathbf{u}$ and $\mathbf{t}$ are essential for solving the reflection–transmission problem.

V. EQUATIONS FOR *n* ANISOTROPIC LAYERS

The vector equations (15) to (20) are now given the form of a system of scalar equations. Inner multiply (15) and (18) by $\mathbf{a}_j^-$, (16) and (19) by $\mathbf{a}_j^\alpha$, and (17) and (20) by $\mathbf{a}_j^n$. We find that

$$u_j^I(0,t)+u_j^R(0,t)=\sum_p \mathbf{a}_j^-\cdot\mathbf{a}_p^1[u_p^{1f}(0,t)+u_p^{1b}(0,t)], \tag{21}$$

$$u_j^{\alpha f}(z_\alpha,t)+u_j^{\alpha b}(z_\alpha,t) = \sum_p \mathbf{a}_j^\alpha\cdot\mathbf{a}_p^{\alpha+1}[u_p^{\alpha+1,f}(z_\alpha,t)+u_p^{\alpha+1,b}(z_\alpha,t)], \tag{22}$$

$$u_j^{nf}(L,t)+u_j^{nb}(L,t)=\sum_p \mathbf{a}_j^n\cdot\mathbf{a}_p^+u_p^T(L,t), \tag{23}$$

$$\rho^- c_j^- [u_j^I(0,t) - u_j^R(0,t)]$$

$$= \sum_p \mathbf{a}_j^- \cdot \mathbf{a}_p^1 \rho^1 c_p^1 [u_p^{1f}(0,t) - u_p^{1b}(0,t)], \quad (24)$$

$$\rho^\alpha c_j^\alpha [u_j^{\alpha f}(z_\alpha,t) - u_p^{\alpha b}(z_\alpha,t)]$$

$$= \sum_p \mathbf{a}_j^\alpha \cdot \mathbf{a}_p^{\alpha+1} \rho^{\alpha+1} c_p^{\alpha+1} [u_p^{\alpha+1,f}(z_\alpha,t) - u_p^{\alpha+1,b}(z_\alpha,t)], \quad (25)$$

$$\rho^n c_j^n [u_j^{nf}(L,t) - u_j^{nb}(L,t)]$$

$$= \sum_p \mathbf{a}_j^n \cdot \mathbf{a}_p^+ \rho^+ c_p^+ u_p^T(L,t), \quad (26)$$

where $\alpha = 1,2,\ldots,n-1$. The inner products $\mathbf{a}_j^- \cdot \mathbf{a}_p^1, \ldots, \mathbf{a}_j^n \cdot \mathbf{a}_p^+$ are entries of appropriate rotation matrices. Let

$$\mathcal{R}_{jp}^\alpha = \mathbf{a}_j^\alpha \cdot \mathbf{a}_p^{\alpha+1}, \quad \alpha = 0,1,\ldots,n,$$

where $\mathbf{a}_j^0 = \mathbf{a}_j^-$ and $\mathbf{a}_j^{n+1} = \mathbf{a}_j^+$. To determine the outgoing waves at each interface, in terms of the ingoing ones, we then compare the pair of equations (21)–(24), (22)–(25), (23)–(26). Specifically, we evaluate $\rho^- c_j^-$ times (21) plus (24) to find $u_p^{1f}(0,t)$, and use (21) to determine $u_j^R(0,t)$. Similarly, $\rho^\alpha c_j^-$ times (22) plus (25) provides $u_p^{\alpha+1,f}(z_\alpha,t)$ whereas use of (22) determines $u_j^{\alpha b}(z_\alpha,t)$. Finally, $\rho^n c_j^n$ times (23) plus (26) gives $u_p^T(L,t)$ whereas use of (23) determines $u_j^{nb}(L,t)$. We find that

$$\sum_p A_{jp}^0 u_p^{1f}(0,t) = 2\rho^- c_j^- u_j^I(0,t) - \sum_p B_{jp}^0 u_p^{1b}(0,t), \quad (27)$$

$$u_j^R(0,t) = -u_j^I(0,t) + \sum_p \mathcal{R}_{jp}^- [u_p^{1f}(0,t) + u_p^{1b}(0,t)], \quad (28)$$

$$\sum_p A_{jp}^\alpha u_p^{\alpha+1,f}(z_\alpha,t) = 2\rho^\alpha c_j^\alpha u_j^{\alpha f}(z_\alpha,t) - \sum_p B_{jp}^\alpha u_p^{\alpha+1,b}(z_\alpha,t), \quad (29)$$

$$u_j^{\alpha b}(z_\alpha,t) = -u_j^{\alpha f}(z_\alpha,t) + \sum_p \mathcal{R}_{jp}^\alpha [u_p^{\alpha+1,f}(z_\alpha,t) + u_p^{\alpha+1,b}(z_\alpha,t)], \quad (30)$$

$$\sum_p A_{jp}^n u_p^T(L,t) = 2\rho^n c_j^n u_j^{nf}(L,t), \quad (31)$$

$$u_j^{nb}(L,t) = -u_j^{nf}(L,t) + \sum_p \mathcal{R}_{jp}^n u_p^T(L,t) \quad (32)$$

where

$$A_{jp}^\alpha = \mathcal{R}_{jp}^\alpha (\rho^\alpha c_j^\alpha + \rho^{\alpha+1} c_p^{\alpha+1}),$$

$$B_{jp}^\alpha = \mathcal{R}_{jp}^\alpha (\rho^\alpha c_j^\alpha - \rho^{\alpha+1} c_p^{\alpha+1}), \quad \alpha = 0,1,\ldots,n,$$

and

$$\rho^0 = \rho^-, \quad c_p^0 = c_p^-, \quad \rho^{n+1} = \rho^+, \quad c_p^{n+1} = c_p^+.$$

Moreover, $u_p^{1f}(0,t), u_p^{\alpha+1,f}(z_\alpha,t), u_p^T(L,t)$ on the right-hand-side of (28), (30) and (32) have to be replaced with the corresponding expressions given by (27), (29) and (31). The function $u^I(0,t)$ is known; the other ones are unknown.

Any matrix A^α turns out to be invertible.[7] Hence, for any interface, we can express the outgoing waves in terms of the incoming ones. Specifically we have

$$u_k^{1f}(0,t) = 2\sum_j (A^0)_{kj}^{-1} \rho^- c_j^- u_j^I(0,t) - [(A^0)^{-1} B^0]_{kj} u_j^{1b}(0,t), \quad (33)$$

$$u_j^R(0,t) = -u_j^I(0,t) + \sum_p \mathcal{R}_{jp}^- [u_p^{1f}(0,t) + u_p^{1b}(0,t), \quad (34)$$

. . . . . .

$$u_j^T(L,t) = 2\sum_k (A^n)_{jk}^{-1} \rho^n c_k^n u_k^{nf}(L,t), \quad (35)$$

$$u_j^{nb}(L,t) = -u_j^{nf} + \sum_p \mathcal{R}_{jp}^n u_p^T(L,t). \quad (36)$$

Next we observe that, because of the homogeneity of the layers and of D'Alembert's formula, the incoming waves at an interface may be expressed through the values, at the opposite side of the layer, at suitable previous times. This is a central property in deriving the solution in terms of the incident function $u^I(0,t)$ only.

We now examine the procedure by considering in detail the solution in particular, simple cases of interest.

VI. CLOSED-FORM SOLUTION FOR A SINGLE ANISOTROPIC LAYER

To give evidence to the effects of anisotropy and to the construction of the solution we preliminarily consider the reflection and transmission originated by a single homogeneous anisotropic layer. Because of the single layer, we can determine easily the closed-form, explicit, solution for the reflected and transmitted waves.

Consider Eqs. (33) to (36) with $n=1$. In a more compact form, (33) reads as

$$u_q^f(0,t) = \sum_p [T_{qp}^- u_p^I(0,t) + R_{qp}^b u_p^b(0,t)], \quad (37)$$

where

$$T_{qp}^- = 2(A^-)_{qp}^{-1} \rho^- c_p^-, \quad R_{qp}^b = -[(A^-)^{-1} B^-]_{qp},$$

and $A^- = A^0$, $B^- = B^0$. The substitution of (37) in (34) gives u_p^R in the form

$$u_p^R(0,t) = \sum_q [R_{pq}^- u_q^I(0,t) + T_{pq}^b u_q^b(0,t)], \quad (38)$$

where

$$R_{pq}^- = (\mathcal{R}^- T^-)_{pq} - \delta_{pq}, \quad T_{pq}^b = \mathcal{R}_{pq}^- + (\mathcal{R}^- R^b)_{kq}.$$

Also, letting

$$T_{qp}^+ = 2\rho c_p (A^-)_{qp}^{-1}, \quad R_{qp}^f = (\mathcal{R} T^+)_{qp} - \delta_{qp},$$

we write (35) and (36) as

$$u_p^T(L,t)=\sum_q T_{pq}^+ u_q^f(L,t), \tag{39}$$

$$u_p^b(L,t)=\sum_q R_{pq}^f u_q^f(L,t). \tag{40}$$

Let $t_q=L/c_q$, the travel time, in the layer, of the q-th mode. The functions u_q^f, u_q^b satisfy the conditions

$$u_q^f(L,t)=u_q^f(0,t-t_q), \quad u_q^b(0,t)=u_q^b(L,t-t_q), \tag{41}$$

for any time t. Consequently, by (40) and (41) we have

$$u_p^b(0,t)=u_p^b(L,t-t_p)=\sum_q R_{pq}^f u_q^f(L,t-t_p)$$

$$=\sum_q R_{pq}^f u_q^f(0,t-t_p-t_q),$$

and likewise for $u_p^f(0,t)$ by means of (37) and (41). Hence we obtain

$$u_p^b(0,t)=\sum_q R_{pq}^f u_q^f(0,t-t_p-t_q),$$

$$u_p^f(0,t)=\sum_q T_{pq}^- u_q^I(0,t)+\sum_{q,s} R_{pq}^b R_{qs}^f u_s^f(0,t-t_q-t_s).$$

Substitution for $u_s^f(0,t-t_q-t_s)$ on the right-hand side and iteration give

$$u_j^b(0,t)=\sum_{p,q} R_{jp}^f T_{pq}^- u_q^I(0,t-t_j-t_p)$$
$$+\sum_{p,r}\left[R_{jp}^f \sum_{m=1}^{\infty} \sum_{q_1,\ldots,q_{2m}} R_{pq_1}^b R_{q_1q_2}^f \right.$$
$$\times R_{q_2q_3}^b R_{q_3q_4}^f \cdots R_{q_{2m-2}q_{2m-1}}^b R_{q_{2m-1}q_{2m}}^f T_{q_{2m}r}^-$$
$$\left.\times u_r^I\left(0,t-t_j-t_p-\sum_{k=1}^{2m} t_{q_k}\right)\right]$$

and

$$u_p^f(0,t)=\sum_q T_{pq}^- u_q^I(0,t)+\sum_r \sum_{m=1}^{\infty} \sum_{q_1,\ldots,q_{2m}} R_{pq_1}^b R_{q_1q_2}^f$$
$$\times R_{q_2q_3}^b R_{q_3q_4}^f \cdots R_{q_{2m-2}q_{2m-1}}^b R_{q_{2m-1}q_{2m}}^f T_{q_{2m}r}^- u_r^I$$
$$\times\left(0,t-\sum_{k=1}^{2m} t_{q_k}\right),$$

namely the wave field inside the layer. Consequently, by (38), (39) and (41) we have

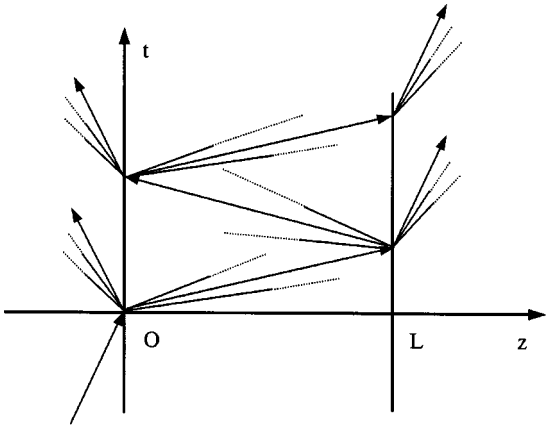

FIG. 1. A schematic diagram of the reflection–transmission process for a single layer. The t-axis is vertical and the layer occupies the interval $z \in [0,L]$.

$$u_j^R(0,t)=\sum_q R_{jq}^- u_q^I(0,t)+\sum_{p,q,r} T_{jp}^b R_{pq}^f T_{qr}^- u_r^I(t-t_p-t_q)$$
$$+\sum_{k,p,r}\left[T_{jk}^b R_{kp}^f \sum_{m=1}^{\infty} \sum_{q_1,\ldots,q_{2m}} R_{pq_1}^b R_{q_1q_2}^f R_{q_2q_3}^b \right.$$
$$\times R_{q_3q_4}^f \cdots R_{q_{2m-2}q_{2m-1}}^b R_{q_{2m-1}q_{2m}}^f T_{q_{2m}r}^-$$
$$\left.\times u_r^I\left(0,t-t_k-t_p-\sum_{k=1}^{2m} t_{q_k}\right)\right], \tag{42}$$

$$u_j^T(L,t)=\sum_{p,q} T_{jp}^+ T_{pq}^- u_q^I(0,t-t_p)$$
$$+\sum_{p,r}\left[T_{jp}^+ \sum_{m=1}^{\infty} \sum_{q_1,\ldots,q_{2m}} R_{pq_1}^b R_{q_1q_2}^f R_{q_2q_3}^b \right.$$
$$\times R_{q_3q_4}^f \cdots R_{p_{2m-2}q_{2m-1}}^b R_{q_{2m-1}q_{2m}}^f T_{q_{2m}r}^-$$
$$\left.\times u_r^I\left(0,t-t_p-\sum_{k=1}^{2m} t_{q_k}\right)\right], \tag{43}$$

namely the reflected and transmitted waves.

Since the reflection–transmission process is viewed as an initial-value problem and $u_r^I(t)=0$ as $t<0$, the series on m in fact reduces to a finite number of terms.

At any interface, an incident mode produces three reflected and three transmitted modes. This is roughly represented in Fig. 1 for a single layer. The slope of the segments is the inverse of the speed of propagation of the pertinent mode. In (42) and (43) each term accounts for the pertinent contribution. For instance, in (42), $\Sigma_q R_{jq}^- u_q^I(0,t)$ provides the contribution of the waves reflected instantaneously at the interface from the incident wave, $\Sigma_{pqr} T_{jp}^b R_{pq}^f T_{qr}^- u_r^I(t-t_p-t_q)$ is the result of $\mathbf{u}^I$ through the transmission at $z=0$, forward propagation, reflection at $z=L$, back transmission at $z=0$. Each sum accounts for the generation of three modes at the appropriate interface.

It is worth applying (42) and (43) to evaluate the effect of a particular case. Let the layer be made of beryllium, which is transversally isotropic, where

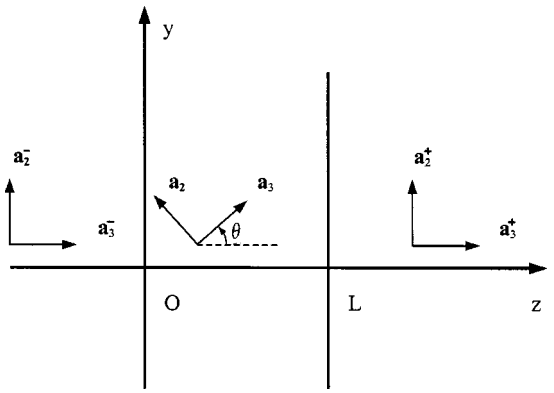

FIG. 2. Geometry of the problem and orientation of the eigenvectors of the polarization.

$$c_1 = c_2 = 9362 \text{ m/s}, \quad c_3 = 13483 \text{ m/s},$$

$$\rho = 1848 \text{ Kg/m}^3, \quad L = 0.2 \text{ m}.$$

Moreover let the axis of rotational symmetry, $\mathbf{a}_3$, form an angle θ with the direction of propagation $\mathbf{n}$. The half-spaces are made of aluminum and then are regarded as isotropic media with

$$c_1 = 3100 \text{ m/s}, \quad c_3 = 6300 \text{ m/s}, \quad \rho = 2700 \text{ Kg/m}^3.$$

For formal convenience the $\mathbf{a}_1$-axes, of half-spaces and layer, are taken to coincide. In the half-spaces, $\mathbf{a}_3 = \mathbf{n}$. The geometry of the problem is then represented as in Fig. 2.

For definiteness we let $\theta = \pi/6$ and take the incident wave to be longitudinal and to have a rectangular shape in the form

$$u_3^I(0,t) = \begin{cases} 0, & t<0, \\ 1, & t\in(0,t_3), \\ 0, & t>t_3, \end{cases}$$

where $t_3 = L/c_3$, c_3 being the value for the layer ($t_3 = 1.48 \times 10^{-5}$ s). By applying (42) we find that the reflected longitudinal component $u_3^R(0,t)$, in the time interval $[0,10t_3]$, is given as in Fig. 3. Since the incident wave is longitudinal, no horizontally-polarized wave arises.

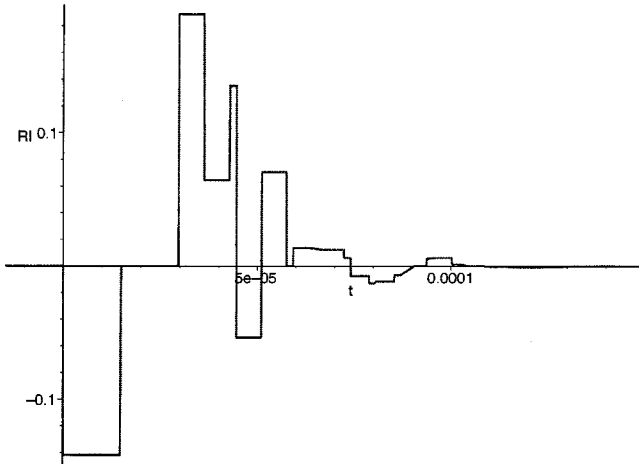

FIG. 3. Reflected longitudinal wave ($Rl = u_3^R$) at $z=0$ as $t\in[0,10t_3]$ produced by a rectangular incident longitudinal wave.

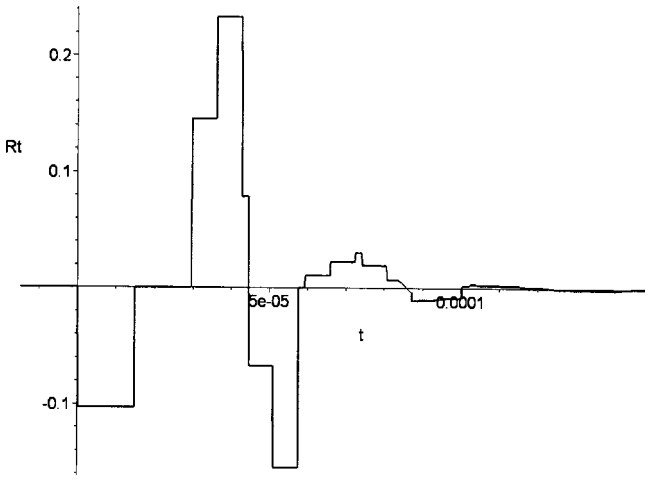

FIG. 4. Reflected transverse wave ($Rt = u_2^R$) at $z=0$ as $t\in[0,10t_3]$ produced by a rectangular incident longitudinal wave.

Meanwhile the reflected transverse wave is directed along $\mathbf{a}_2$ and has the form given in Fig. 4.

Figures 3 and 4 show the reflected longitudinal and transverse waves produced by a rectangular incident longitudinal wave. The loss or distortion of the rectangular shape is due to the superposition, with different travel times, of the longitudinal and transverse waves in the layer. The details exhibited in the figures are examples of the advantage obtained by proceeding in the time domain rather than deriving the results by Fourier inverting from the frequency domain.

Since the incident wave is longitudinal, no wave arises which is polarized horizontally (along $\mathbf{a}_1$).

VII. REFLECTION–TRANSMISSION BY *n* ISOTROPIC LAYERS

In connection with homogeneous, isotropic solids we consider the representation (13) with a common basis for the layers, namely $\mathbf{a}_3 = \mathbf{n}$ and $\mathbf{a}_1, \mathbf{a}_2$ perpendicular to $\mathbf{n}$. The incident wave travels in the $+z$ direction in the half-space $z<0$. For formal convenience let $\alpha = 0,1,\ldots,n$. The superscript $\alpha = 0$ denotes the values—e.g., ρ^0, c_p^0—at the half-space $z<0$. The superscripts $\alpha = 1,2,\ldots,n$ denote the values in the pertinent layer, $z\in(z_\alpha, z_{\alpha+1})$. Also, the superscript $\alpha = n+1$ denotes the values at the half-space $z>L$. With this in mind we see that Eqs. (15) to (20) simplify to

$$u_p^{\alpha f}(z_\alpha,t) + u_p^{\alpha b}(z_\alpha,t) = u_p^{\alpha+1,f}(z_\alpha,t) + u_p^{\alpha+1,b}(z_\alpha,t),$$

$$\rho^\alpha c_p^\alpha [u_p^{\alpha f}(z_\alpha,t) - u_p^{\alpha b}(z_\alpha,t)] = \rho^{\alpha+1} c_p^{\alpha+1} [u_p^{\alpha+1,f}(z_\alpha,t) - u_p^{\alpha+1,b}(z_\alpha,t)],$$

where $p = 1,2,3$ and $\alpha = 0,1,\ldots,n$. Of course the scalars

$$u_p^{0f}, \quad u_p^{0b}, \quad u_p^{n+1,f}$$

stand for the p-th component of the incident, reflected and transmitted displacements $\mathbf{u}^I$, $\mathbf{u}^R$ and $\mathbf{u}^T$. The simplicity is due to the conservation of the polarization across any interface. A further formal simplification is obtained by letting the subscript $p = 1,2,3$ be understood and not written. Hence, in essence, the continuity conditions (15) to (20) amount to requiring that

$$u^{\alpha f}(z_\alpha,t)+u^{\alpha b}(z_\alpha,t)=u^{\alpha+1,f}(z_\alpha,t)+u^{\alpha+1,b}(z_\alpha,t), \tag{44}$$

$$\rho^\alpha c^\alpha[u^{\alpha f}(z_\alpha,t)-u^{\alpha b}(z_\alpha,t)]=\rho^{\alpha+1}c^{\alpha+1}[u^{\alpha+1,f}(z_\alpha,t) - u^{\alpha+1,b}(z_\alpha,t)], \tag{45}$$

for any layer ($\alpha=0,1,\ldots,n$) and any component u_p (mode) of the displacement.

Multiply Eq. (44) by $\rho^\alpha c^\alpha$ and compare with (45) to obtain

$$u^{\alpha+1,f}(z_\alpha,t)=T^{\alpha f}u^{\alpha f}(z_\alpha,t)+R^{\alpha b}u^{\alpha+1,b}(z_\alpha,t), \tag{46}$$

whereas the substitution for $u^{\alpha+1,f}$ in (46) gives

$$u^{\alpha b}(z_\alpha,t)=R^{\alpha f}u^{\alpha f}(z_\alpha,t)+T^{\alpha b}u^{\alpha+1,b}(z_\alpha,t), \tag{47}$$

where

$$T^{\alpha f}=\frac{2\rho^\alpha c^\alpha}{\rho^\alpha c^\alpha+\rho^{\alpha+1}c^{\alpha+1}}, \quad T^{\alpha b}=\frac{2\rho^{\alpha+1}c^{\alpha+1}}{\rho^\alpha c^\alpha+\rho^{\alpha+1}c^{\alpha+1}}, \tag{48}$$

$$R^{\alpha f}=\frac{\rho^\alpha c^\alpha-\rho^{\alpha+1}c^{\alpha+1}}{\rho^\alpha c^\alpha+\rho^{\alpha+1}c^{\alpha+1}}=-R^{\alpha b}. \tag{49}$$

The quantities $T^{\alpha f},T^{\alpha b},R^{\alpha f},R^{\alpha b}$ coincide with the forward and backward transmission and reflection coefficients at the interface between two half-spaces with mass density and speed ρ^α,c^α and $\rho^{\alpha+1},c^{\alpha+1}$, respectively.

To obtain the reflected and transmitted waves in terms of the incident one we proceed as follows. Let

$$t_\alpha=\frac{1}{c^\alpha}(z_\alpha-z_{\alpha-1}).$$

Since $u^{\alpha f}(z,t)=\hat{u}^{\alpha f}(z-c^\alpha t)$ we have

$$u^{\alpha f}(z_\alpha,t)=u^{\alpha f}(z_{\alpha-1},t-t_\alpha), \quad \alpha=1,\ldots,n. \tag{50}$$

Likewise,

$$u^{\alpha b}(z_{\alpha-1},t)=u^{\alpha b}(z_\alpha,t-t_\alpha), \quad \alpha=1,\ldots,n. \tag{51}$$

For any layer we can express the forward waves in terms of the backward ones. If $\alpha=0$ then (46) provides

$$u^{1f}(z_0,t)=T^{0f}u^I(z_0,t)+R^{0b}u^{1b}(z_0,t). \tag{52}$$

Meanwhile, by (46), (50) and (51) we have

$$u^{\alpha+1,f}(z_\alpha,t)=T^{\alpha f}u^{\alpha f}(z_{\alpha-1},t-t_\alpha) + R^{\alpha b}u^{\alpha+1,b}(z_{\alpha+1},t-t_{\alpha+1}),\ \alpha=1,\ldots,n. \tag{53}$$

For any $\beta=1,\ldots,n$ apply (53) with $\alpha=\beta$ to have

$$u^{\beta+1,f}(z_\beta,t)=T^{\beta f}u^{\beta f}(z_{\beta-1},t-t_\beta) + R^{\beta b}u^{\beta+1,b}(z_{\beta+1},t-t_{\beta+1}). \tag{54}$$

Let $\alpha=\beta-1$ and evaluate $u^{\beta f}(z_{\beta-1},t-t_\beta)$ via (53). Substitution gives

$$u^{\beta+1,f}(z_\beta,t)=T^{\beta f}[T^{\beta-1,f}u^{\beta-1,f}(z_{\beta-2},t-t_\beta-t_{\beta-1}) + R^{\beta-1,b}u^{\beta b}(z_\beta,t-2t_\beta)] + R^{\beta b}u^{\beta+1,b}(z_{\beta+1},t-t_{\beta+1}).$$

We now let $\alpha=\beta-2$, evaluate $u^{\beta-1,f}(z_{\beta-2},t-t_\beta-t_{\beta-1})$ via (53) and replace to get

$$u^{\beta+1,f}(z_\beta,t)=T^{\beta f}\{T^{\beta-1,f}[T^{\beta-2,f}u^{\beta-2,f} \times(z_{\beta-3},t-t_\beta-t_{\beta-1}-t_{\beta-2}) + R^{\beta-2,b}u^{\beta-1,b}(z_{\beta-1},t-t_\beta-2t_{\beta-1})] + T^{\beta f}R^{\beta-1,b}u^{\beta b}(z_\beta,t-2t_\beta)\} + R^{\beta b}u^{\beta+1,b}(z_{\beta+1},t-t_{\beta+1}).$$

By iterating the procedure we see that, at the following steps, the forward wave is $u^{\beta-3,f}$, $u^{\beta-4,f},\ldots$. The iteration stops after β steps in which case the forward wave is u^I at $z=0_-$. Ultimately we find that, for any $\alpha=0,\ldots,n$,

$$u^{\alpha+1,f}(z_\alpha,t)=\left(\prod_{h=0}^{\alpha}T^{\alpha-h,f}\right)u^I\left(0,t-\sum_{h=1}^{\alpha}t_h\right) + R^{\alpha b}u^{\alpha+1,b}(z_{\alpha+1},t-t_{\alpha+1}) + \sum_{k=1}^{\alpha}\left(\prod_{h=0}^{k-1}T^{\alpha-h,f}\right)R^{\alpha-k,b}u^{\alpha-k+1,b} \times(z_{\alpha-k+1},t-t_{\alpha-k+1}-\tau_{\alpha k}), \tag{55}$$

where

$$\tau_{\alpha 0}=0, \quad \tau_{\alpha k}=\sum_{h=0}^{k-1}t_{\alpha-h}, \quad k=1,2,\ldots.$$

Equation (55) provides the forward wave at the interval $\alpha+1$, namely $z\in(z_\alpha,z_{\alpha+1})$, in terms of the incident wave, at $z=0_-$, and of the backward waves in the intervals $1,\ldots,\alpha,\alpha+1$.

We then need a similar procedure to determine the backward waves. By (47), (50) and (51) we have

$$u^{\alpha b}(z_\alpha,t)=R^{\alpha f}u^{\alpha f}(z_{\alpha-1},t-t_\alpha)+T^{\alpha b}u^{\alpha+1,b} \times(z_{\alpha+1},t-t_{\alpha+1}), \ \alpha=0,1,\ldots,n-1, \tag{56}$$

and, because $u^{n+1,b}=0$,

$$u^{nb}(z_n,t)=R^{nf}u^{nf}(z_n,t). \tag{57}$$

Apply (56) for $\alpha=n-1$ to obtain

$$u^{n-1,b}(z_{n-1},t)=R^{n-1,f}u^{n-1,f}(z_{n-2},t-t_{n-1}) + T^{n-1,b}R^{nf}u^{nf}(z_{n-1},t-2t_n).$$

Letting $\alpha=n-2$ in (56) and substituting for $u^{n-1,b}$ we have

$$u^{n-2,b}(z_{n-2},t)=R^{n-2,f}u^{n-2,f}(z_{n-3},t-t_{n-2}) + T^{n-2,b}R^{n-1,f}u^{n-1,f}(z_{n-2},t-2t_{n-1}) + T^{n-2,b}T^{n-1,b}R^{nf}u^{nf} \times(z_{n-1},t-t_{n-1}-2t_n).$$

The backward wave, at the right end of the $(n-2)$-th interval, is determined by a reflection of the $(n-2)$-th forward wave at the same time and by the forward waves at the subsequent $(n-1)$-th and n-th intervals at previous times. By repeating the procedure we see that the backward wave at the α-th interval is an analogous combination of the forward

waves at the $n+1$ intervals $\alpha=0$ to $\alpha=n$. By (56) and (57) we find that

$$u^R(0,t)=R^{0f}u^I(0,t)+\sum_{l=1}^{n}\left(\prod_{j=0}^{l-1}T^{jb}\right)\times R^{lf}u^{lf}(z_{l-1},t-t_l-\tilde{\tau}_{0l}), \tag{58}$$

$$u^{\alpha b}(z_\alpha,t)=R^{\alpha f}u^{\alpha f}(z_{\alpha-1},t-t_\alpha)+\sum_{l=1}^{n-\alpha}\left(\prod_{j=0}^{l-1}T^{\alpha+j,b}\right)\times R^{\alpha+l,f}u^{\alpha+l,f}(z_{\alpha+l-1},t-t_{\alpha+l}-\tilde{\tau}_{\alpha l}), \tag{59}$$

as $\alpha=1,\ldots,n-1$, and

$$u^{nb}(z_n,t)=R^{nf}u^{nf}(z_{n-1},t-t_n), \tag{60}$$

where

$$\tilde{\tau}_{\alpha l}=\sum_{j=1}^{l}t_{\alpha+j},\quad l\geqslant 1.$$

Evaluate (59)–(60) with the replacements

$$\alpha\to\alpha+1,\quad t\to t-t_{\alpha+1},$$

$$\alpha\to\alpha-k+1,\quad t\to t-t_{\alpha-k+1}-\tau_{\alpha k}.$$

Upon substitution in (55) we obtain

$$\begin{aligned}u^{\alpha+1,f}(z_\alpha,t)=&\left(\prod_{h=0}^{\alpha}T^{\alpha-h,f}\right)u^I\left(0,t-\sum_{h=1}^{\alpha}t_h\right)+R^{\alpha b}R^{\alpha+1,f}u^{\alpha+1,f}(z_\alpha,t-2t_{\alpha+1})+R^{\alpha b}\sum_{l=1}^{n-\alpha-1}\\&\times\left(\prod_{j=0}^{l-1}T^{\alpha+j+1,b}\right)R^{\alpha+l+1,f}u^{\alpha+l+1,f}(z_{\alpha+l},t-t_{\alpha+1}-t_{\alpha+l+1}-\tilde{\tau}_{\alpha+1,l})+\sum_{k=1}^{\alpha}\left(\prod_{h=0}^{k-1}T^{\alpha-h,f}\right)\\&\times R^{\alpha-k,b}\Bigg[R^{\alpha-k+1,f}u^{\alpha-k+1,f}(z_{\alpha-k},t-2t_{\alpha-k+1}-\tau_{\alpha k})+\sum_{l=1}^{n-\alpha+k-1}\left(\prod_{j=0}^{l-1}T^{\alpha-k+1+j,b}\right)\\&\times R^{\alpha+l-k+1,f}u^{\alpha+l-k+1,f}(z_{\alpha+l-k},t-t_{\alpha-k+1}-\tau_{\alpha k}-t_{\alpha+l-k+1}-\tilde{\tau}_{\alpha-k+1,l})\Bigg],\end{aligned} \tag{61}$$

as $\alpha=0,\ldots,n-1$ and

$$\begin{aligned}u^T(z_n,t)=&\left(\prod_{h=0}^{n}T^{n-h,f}\right)u^I\left(0,t-\sum_{h=1}^{n}t_h\right)+\sum_{k=1}^{n}\left(\prod_{h=0}^{k-1}T^{n-h,f}\right)R^{n-k,b}\Bigg[R^{n-k+1,f}u^{n-k+1,f}(z_{n-k},t-2t_{n-k+1}-\tau_{nk})\\&+\sum_{l=1}^{k-1}\left(\prod_{j=0}^{l-1}T^{n-k+1+j,b}\right)R^{n+l-k+1,f}u^{n+l-k+1,f}(z_{n+l-k},t-t_{n-k+1}-\tau_{nk}-t_{n+l-k+1}-\tilde{\tau}_{n-k+1,l})\Bigg].\end{aligned} \tag{62}$$

By means of (58)–(60) and (61)–(62) we can solve any reflection–transmission process generated by a multilayer. By (61) we determine the forward (internal) waves $u^{\alpha+1,f}$ at any time t in terms of the incident wave u^I and of the forward waves at appropriate previous times. Equation (61) provides the internal forward waves while (62) yields the transmitted wave $u^T=u^{n+1,f}$. Likewise, once the forward waves have been determined, Eqs. (59)–(60) provide the backward waves and, in particular, the reflected wave $u^R=u^{0b}$.

It is worth remarking that Eqs. (61) constitute a closed system of n equations in the n unknown functions $u^{1f}(z_0,\cdot),\ldots,u^{nf}(z_{n-1},\cdot)$ in terms of the known incident function $u^I(0,\cdot)$. Once $u^{1f}(z_0,\cdot),\ldots,u^{nf}(z_{n-1},\cdot)$ are determined we can substitute in (58) and (62) to derive the reflected wave function $u^R(0,\cdot)$ and the transmitted wave function $u^T(z_n,\cdot)$. This allows us to find u^R and u^T without solving for $u^{1b},\ldots,u^{nb}$ via (59) and (60).

The system (58)–(62), as well as the system (61), involves the values of the unknown functions at different times. This calls for an operative procedure to solve the system. In the next sections we provide such a procedure and show, through particular cases, how it works.

VIII. RESONANCE EFFECT BY AN ISOTROPIC LAYER

It is of interest now to consider the particular case of a single layer between two half-spaces (Fig. 5).

Consider a single mode with travel time $\tau=L/c$. By Eqs. (58), (61) and (62) we find that

$$u^R(0,t)=R^-u^I(0,t)+T^bR^fu^f(0,t-2\tau),$$

$$u^f(0,t)=T^-u^I(0,t)+R^bR^fu^f(0,t-2\tau),$$

$$u^T(L,t)=T^+u^f(L,t),$$

where

$$T^-=T^{0f},\quad T^+=T^{1f},$$

$$R^-=R^{0f},\quad R^f=R^{1f},\quad R^b=R^{0b}.$$

Substitution for u^f in the expression of u^R and u^T and iteration provide the explicit closed-form solution

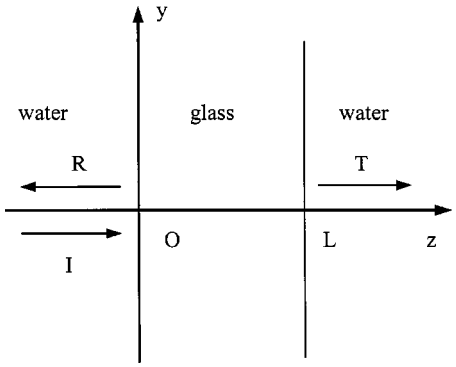

FIG. 5. Reflection–transmission through a layer (glass) immersed in water.

$$u^R(0,t)=R^- u^I(0,t)+\sum_{m=1}^{\infty} T^b R^f (R^b R^f)^{m-1} T^- u^I \times(0,t-2m\tau), \tag{63}$$

$$u^T(L,t)=\sum_{m=0}^{\infty} T^+ (R^b R^f)^m T^- u^I(0,t-(2m+1)\tau). \tag{64}$$

As a simple interesting case we consider an incident wave with a sawtooth form given by

$$u^I(0,t)=\begin{cases} 0, & t<0, \\ t/2\tau & t\in(0,2\tau), \end{cases}$$

and then repeated by periodicity as $t\in(2\tau,4\tau)$, $t\in(4\tau,6\tau)$, and so on.

For definiteness we consider a layer of glass immersed in water. The parameters for glass are

$$\rho=2500 \ \text{Kg/m}^3, \quad c=5800 \ t\text{m/s}, \quad L=0.2 \ \text{m},$$

$$\tau=3.45 \ 10^{-5} \ \text{s}$$

Hence, by (48) and (49) we have

$$T^-=\frac{2\rho^- c^-}{\rho^- c^- +\rho c}=0.185, \quad T^+=\frac{2\rho c}{\rho^- c^- +\rho c}=1.815, \tag{65}$$

$$R^b=R^f=-R^-=\frac{\rho c-\rho^- c^-}{\rho^- c^- +\rho c}=0.815. \tag{66}$$

Figure 6 shows the transmitted wave $u^T(L,t)$ as $t\in[0,10\tau]$. While $u^I(0,t)$ repeats unchanged every period 2τ, $u^T(0,t)$ shows a sawtooth form with a growing amplitude. The growth is due to the fact that a forward and backward travel in the layer takes a period of the incident wave and hence each contribution of the internal waves is in phase with the incident one. Moreover, since $u^I(0,t)$ is periodic as $t>0$ then by (64) and (65)–(66) we see that, asymptotically,

$$u^T(L,t)=\frac{T^+ T^-}{1-R^b R^f} u^I(0,t)=u^I(0,t),$$

which is consistent with the behavior in Fig. 6. Because of the periodicity of the incident wave, asymptotically the layer becomes transparent in that $u^T(L,t)=u^I(0,t)$ and the reflected wave vanishes. This is a remarkable effect of the resonance (period=twice the travel time).

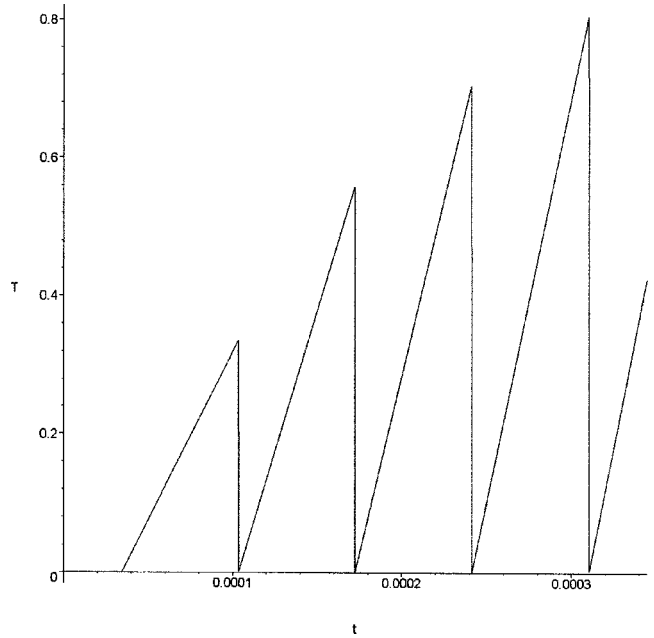

FIG. 6. Transmitted wave ($T=u^T$) produced by a sawtooth-like incident wave through a layer; the period of the wave equals twice the travel time.

IX. STEP-BY-STEP PROCEDURE

Let the travel times $t_1,t_2,\ldots,t_n$ of the layers be commensurable; at least this is true numerically. We can then set up a systematic procedure which avoids the successive substitutions applied in the previous section. We illustrate the general procedure for the system (58)–(62) in the simple case of a multilayer with two isotropic layers. Since $n=2$ we have

$$u^R(0,t)=R^{0f}u^I(0,t)+T^{0b}R^{1f}u^{1f}(0,t-2t_1) + T^{0b}T^{1b}R^{2f}u^{2f}(z_1,t-t_1-2t_2), \tag{67}$$

$$u^{1b}(z_1,t)=R^{1f}u^{1f}(0,t-t_1)+T^{1b}R^{2f}u^{2f}(z_1,t-2t_2), \tag{68}$$

$$u^{2b}(z_2,t)=R^{2f}u^{2f}(z_1,t-t_2), \tag{69}$$

$$u^{1f}(0,t)=T^{0f}u^I(0,t)+R^{0b}R^{1f}u^{1f}(0,t-2t_1) + R^{0b}T^{1b}R^{2f}u^{2f}(z_1,t-t_1-2t_2), \tag{70}$$

$$u^{2f}(z_1,t)=T^{1f}T^{0f}u^I(0,t-t_1)+R^{1b}R^{2f}u^{2f}(z_1,t-2t_2) + T^{1f}R^{0b}[R^{1f}u^{1f}(0,t-3t_1) + T^{1b}R^{2f}u^{2f}(z_1,t-2t_1-2t_2)], \tag{71}$$

$$u^T(z_2,t)=T^{2f}T^{1f}T^{0f}u^I(0,t-t_1-t_2) + T^{2f}R^{1b}R^{2f}u^{2f}(z_1,t-3t_2) + T^{2f}T^{1f}R^{0b}[R^{1f}u^{1f}(0,t-3t_1-t_2) + T^{1b}R^{2f}u^{2f}(z_1,t-2t_1-3t_2)]. \tag{72}$$

As with (58)–(62), the right-hand sides involve only forward-propagating waves.

The system of equations (67)–(72), provides explicitly the solution $U=(u^R,u^{1b},u^{2b},u^{1f},\ u^{2f},u^T)$ in terms of the

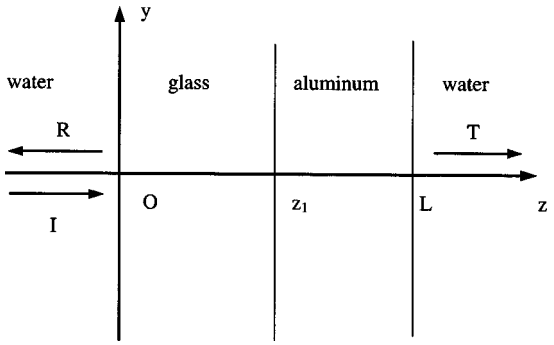

FIG. 7. Two layers (glass, aluminum) immersed in water.

given function $u^I(0,t)$. Indeed, U is the 6-tuple of values given by the left-hand side of (67)–(72). Owing to the initial conditions (14) we have

$$U(t)=0, \quad t\leqslant 0. \tag{73}$$

Let δ be a proper submultiple of t_1, t_2 and proceed as follows. First we evaluate $u^R, u^{1b}, u^{2b}, u^{1f}, u^{2f}, u^T$ at $t=\delta$; we have

$$u^R(0,\delta)=R^{0f}u^I(0,\delta), \quad u^{1f}(0,\delta)=T^{0f}u^I(0,\delta),$$

and zero otherwise. Next we evaluate U at 2δ, 3δ, ..., and so on. For some $m\in\mathbb{N}$ we have $m\delta>t_1$ or t_2; to fix ideas let $t_2>m\delta>t_1$. Hence

$$u^R(0,m\delta)=R^{0f}u^I(0,m\delta),$$

$$u^{1f}(0,m\delta)=T^{0f}u^I(0,m\delta)+R^{0b}R^{1f}u^{1f}(0,m\delta-t_1),$$

$$u^{2f}(z_1,m\delta)=T^{1f}T^{0f}u^I(0,m\delta-t_1),$$

and zero otherwise. We then continue by increasing the value of $t=k\delta$ and determine the discrete values of the solution,

$$U(k\delta), \quad k\in\mathbb{N}.$$

Remark: If t_1, t_2, or $t_1, \ldots, t_n$, are not commensurable then, as a first step, we write U at a chosen time t. The right-hand sides of (67)–(72) involve the components of U at appropriate, different, previous times. At the second step, we determine such values, namely $u^{1f}(0,t-2t_2), u^{2f}(z_1, t-t_1-2t_2), \ldots$, by applying again Eqs. (70) and (71) at the pertinent times $(t\to t-2t_2, t-t_1-2t_2, \ldots)$. We obtain u^{1f} and u^{2f} in terms of u^I and of their previous values. At the third step we determine such values by applying again Eqs. (70) and (71). The steps continue until, due to the initial conditions (73), $U(t)$ involves only values of the u^I.

By way of example we consider two layers immersed in water (Fig. 7). The first layer, $z\in(0,z_1)$, is made of glass, the second one, $z\in(z_1,z_2)$, $z_2=L$, is made of aluminum. Of course we consider longitudinal waves and adopt the following values for the half-spaces and the layers:

$$\rho^0=\rho^3=1000 \ \text{kg/m}^3, \quad c^0=c^3=1480 \ \text{m/s},$$

$$\rho^1=2500 \ \text{kg/m}^3, \quad c^1=5800 \ \text{m/sec},$$

$$t_1=1.2\ 10^{-5} \ \text{s};$$

$$\rho^2=2700 \ \text{kg/m}^3, \quad c^2=6300 \ \text{m/sec},$$

$$t_2=0.6\ 10^{-5} \ \text{s}.$$

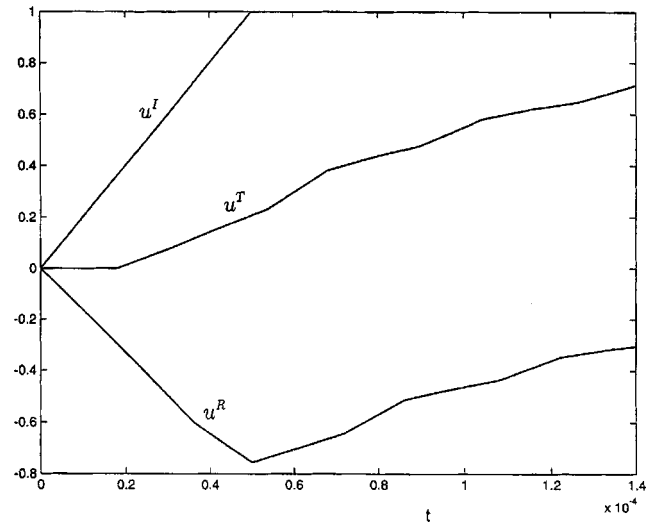

FIG. 8. Reflected and transmitted amplitudes $R=u^R, T=u^T$ generated by u^I as functions of time $t\in[0,1.4\ 10^{-4}]$ s.

The values of t_1 and t_2 correspond to $z_1=6.96$ cm and $z_2-z_1=3.78$ cm.

We find that

$$R^{0f}=-0.81=-R^{0b}, \quad R^{1f}=-0.08=-R^{1b},$$

$$R^{2f}=0.84;$$

$$T^{0b}=1.81, \quad T^{0f}=0.19, \quad T^{1b}=1.08,$$

$$T^{1f}=0.92, \quad T^{2f}=1.84.$$

We let $\delta=10^{-6}$ s and evaluate the solution U in terms of u^I as $t=k\delta$, $k=0,1,\ldots,100$.

Figure 8 shows the reflected and transmitted amplitudes $u^R(0,t)$, $u^T(z_2,t)$ generated by the incident amplitude

$$u^I(0,t)=\begin{cases} 0, & t<0, \\ 2\ 10^4 t, & t\in[0,5\ 10^{-5}], \\ 1, & t>5\ 10^{-5}. \end{cases}$$

As $0\leqslant t<2t_1=0.24\times10^{-4}$ the reflected amplitude u^R is merely $R^{0f}u^I$, the next additional contributions arise from reflected waves (u^{1b}) within the multilayer. Really, because of the smallness of $R^{1f}=-0.08$, u^R is unaffected by u^{1f} and u^{1b} up to $2(t_1+t_2)=0.36\times10^{-4}$. Since $t=2(t_1+t_2)$ the reflected wave u^R is affected by the wave reflected at $z=z_2$. Also, the transmitted amplitude is zero up to t_1+t_2. Next the transmitted wave results from the transmission of u^{2f}.

X. CONCLUSIONS

In this paper we provide the solution to the reflection–transmission problem, in the time domain, for normal incidence. As is done with a single isotropic or anisotropic layer, for a few layers the pertinent waves (reflected, transmitted and within the layers) can be determined explicitly, in closed form, in terms of the incident wave $\mathbf{u}^I$ at suitable previous times—see (42)–(43) and (63)–(64). Figure 1 shows a qualitative behavior in time for a single layer. For a large number of possibly-anisotropic layers the waves are given by a system for reflected, transmitted and forward-propagating waves

within the layers. In such a case to express $\mathbf{u}^R$ and $\mathbf{u}^T$ in terms of $\mathbf{u}^I$ only is an unpracticable task. We then solve the system at discrete times. We can do this by successive substitutions or at the discrete times $t=\delta,2\delta,\ldots,m\delta$ for a properly chosen δ (Sec. VIII). In any case, anisotropy results in a further complexity due to the fact that, at each interface, any incoming wave (or mode) produces three reflected and three transmitted waves. The procedure, though, provides the solution to the reflection–transmission problem, viewed as an initial-value problem, for any multilayer.

It is an advantage of the time-domain that the results are immediate and direct. Hence, for instance, as shown in Figs. 3, 4 we can see the effects of the successive reflections and transmissions of waves within the layer, with different travel times for different modes. Likewise, Fig. 6 shows a resonance effect. When the period of the incident wave is 2τ, twice the travel time in the layer, then the amplitude of the transmitted wave jumps after every period 2τ and eventually approaches that of the incident wave. Figure 8 deals with two layers and shows the effects, on the reflected and transmitted waves, of the waves within the layers after the appropriate travel times t_1, t_2.

The linear elastic model adopted for the homogeneous multilayer and half-spaces makes the results of practical interest. The anisotropy, the generic number of slabs and the direct procedure in the time domain ascribe a remarkable generality to the results for the initial-value, reflection–transmission problem.

ACKNOWLEDGMENTS

The research leading to this paper has been supported by the Italian MIUR through the Research Project COFIN 2002 ''Mathematical Models for Materials Science.''

[1] D. E. Chimenti, ''Guided waves in plates and their use in materials characterization,'' Appl. Mech. Rev. **50**, 247–284 (1977).
[2] B. A. Auld, *Acoustic Fields and Waves in Solids* (Krieger, Malabar, FL, 1990), Vols. 1 and 2.
[3] A. H. Nayfeh, *Wave Propagation in Layered Anisotropic Media with Applications to Composites* (Elsevier, Amsterdam, 1995).
[4] A. J. Niklasson, S. K. Datta, and M. L. Dunn, ''On ultrasonic guided waves in a thin anisotropic layer lying between two isotropic layers,'' J. Acoust. Soc. Am. **108**, 2005–2011 (2000).
[5] G. Caviglia and A. Morro, ''Existence and uniqueness of the solution in the frequency domain for the reflection–transmission problem in a viscoelastic layer,'' Arch. Mech. **56**, 59–82 (2004).
[6] Z. E. A. Fellah, C. Depollier, S. Berger, W. Lauriks, P. Trompette, and J. Y. Chapelon, ''Determination of transport parameters in air-saturated porous materials via reflected ultrasonic waves,'' J. Acoust. Soc. Am. **114**, 2561–2569 (2003).
[7] G. Caviglia and A. Morro, ''Reflection and transmission of transient waves in anisotropic elastic multilayers,'' Q. J. Mech. Appl. Math. **56**, 571–587 (2003).
[8] H. E. Moser and R. T. Prosser, ''Propagation of an electromagnetic field through a planar slab,'' SIAM Rev. **35**, 610–620 (1993).
[9] P. Bassanini, ''Wave reflection from a system of plane layers,'' Wave Motion **8**, 311–319 (1986).
[10] P. Nardone, F. Fortuny, and A. Sieber, ''Initial conditions, reflection and transmission coefficients revisited,'' J. Electromagn. Waves Appl. **10**, 1527–1541 (1996).

On formulation of a transition matrix for poroelastic medium and application to analysis of scattering problem

Chau-Shioung Yeh[a)]
Department of Civil Engineering, and Institute of Applied Mechanics, National Taiwan University, Taipei, Taiwan

Tsung-Jen Teng
National Center for Research on Earthquake Engineering, Taipei, Taiwan

Po-Jen Shih
Department of Civil Engineering, National Taiwan University, Taipei, Taiwan

(Received 13 June 2003; accepted for publication 5 April 2004)

Based on the approach of Pao (1978) for elastic medium, we propose a set of the basis functions and an associated relationship of the material properties of the dilatational wave in the poroelastic medium. A transition matrix, which relates the coefficients of scattered waves to those of incident waves, is then derived through the application of Betti's third identity and the associated orthogonality conditions for the poroelastic medium. To illustrate the application, we consider a simple case of the scattering problem of a spherical inclusion, either elastic or poroelastic, embedded within the surrounding poroelastic medium subjected to an incident plane compressional wave. [DOI: 10.1121/1.1755240]

PACS numbers: 43.20.Bi, 43.20.Fn, 43.20.Gp, 43.30.Ma [JJM] Pages: 655–676

I. INTRODUCTION

In a poroelastic medium, Biot (1956a,b) predicted first the existence of an additional propagating dilatational wave and then Plona (1980,1982) reported experimental observation of this wave. Berryman (1980) analyzed Plona's data and then confirmed Biot's theory. Since then the wave propagation in such a medium has become an attractive topic for physical fields.

Deresiewicz and Skalak (1963) derived a set of boundary conditions that are sufficient to guarantee a unique solution to Biot's equations when an interface separates a poroelastic medium from the others. Many studies have applied these conditions to the reflection and transmission of incident waves at a planar interface separating infinite half-spaces. While the reflection of a wave from a planar interface is essentially a scattering phenomenon, little work has been done on the scattering from three-dimensional-bounded inclusion embedded within a poroelastic medium. Berryman (1985) derived the multipole expansion of a field scattered by a spherical inhomogeneity within poroelastic media. Zimmerman and Stern (1993a,b) also treated the scattering of a plane compressional wave by a spherical inclusion embedded in an infinite poroelastic medium. However, their solutions are obtained only for the spherical inclusion composed of elastic solid, fixed rigid, or fluid. Morochnik *et al.* (1996) proposed an approximate method based on the definition of equivalent-viscoelastic materials to study the scattering of plane dilatational waves by a spherical poroelastic inhomogeneity. All the preceding studies are only for spherical inclusion. The transition matrix first proposed by Waterman (1976) is a convincing method to treat an elastic obstacle of arbitrary shape. Kargl and Lim (1993) developed the transition matrix for poroelastic medium. They followed Pao's approach for elastic medium to prove the orthogonality conditions of the basis functions for the poroelastic medium using Betti's identity and the far-field asymptotic formulations. Then Lim (1994) combined their previous paper (Kargl and Lim, 1993) with a generalization of existing acoustic waveguide solutions to solve a more complicated problem: an obstacle buried in a plane porous medium. It should be noted that Kargl and Lim (1993) did not prove the relationships between two dilatational waves in the third orthogonal condition (regular-singular relationship) throughout; moreover, the far-field asymptotic formulation (which with S_∞) or the Wronskian formula is inadequate to prove the orthogonality conditions, we have to consider other conditions from the material properties as well [i.e., Eqs. (A8) and (A14)].

In this paper, we adopt Pao's (1978) approach to develop the transition matrix for a poroelastic medium. We reduce the coupled equations of motion to two parts: the dilatational part and the rotational one. The latter part is easily shown to satisfy the vector Helmholtz equation with a complex shear wave number, and the associated basis functions are expressed in terms of the vector spherical wave functions. On the other hand, the decomposition of the dilatational waves, the fast and the slow ones, are governed by two scalar Helmholtz equations. In order to obtain the independent and orthogonal sets of these two basis functions, we reconstruct these functions by normalizing with characteristic vectors elaborately. Although Halpern and Christiano (1986) have reported the normalizing procedure by the numerical method, the result has not been expressed in an analytical form in their study. In our formulation, we present the basis functions in an analytical form and preserve their indispensable features for the orthogonality relationships as well. In-

[a)]Author to whom all correspondence should be addressed; electronic mail: csyeh@iam.ntu.edu.tw

stead of the asymptotic method, we apply the Wronskian formula to prove the orthogonality conditions. To illustrate the application of the transition matrix formulation in our study, we present the solutions for the scattering of the incident plane waves by a spherical inclusion, either poroelastic or elastic, embedded within a poroelastic medium.

The numerical results for the elastic spherical inclusion are presented such that the comparison can be made with those obtained by Zimmerman and Stern (1993a). We also present the results of the amplitude of radial displacement and the normal traction at the surface of the inclusion. Some illustrative numerical results show that the regions near the interface have stronger interference which is caused by the coupling effects of the dilatational and rotational waves. The difference between the elastic and poroelastic inclusions shows that the amplitude of normal traction for elastic case has more obvious patterns with larger values.

II. THE BASIS FUNCTIONS AND THE ORTHOGONALITY CONDITIONS

A. Betti's third identity for the poroelasticity

Let $\mathbf{u}^{(A)}$ and $\mathbf{u}^{(B)}$ be two admissible displacement fields in a poroelastic medium, and $\boldsymbol{\sigma}^{(A)}$ and $\boldsymbol{\sigma}^{(B)}$ be the corresponding stress tensors. The superscripts (A) and (B) denote two different fields in the controlled system. At a surface with a unit outward normal vector $\mathbf{n}$, the traction vector is given by

$$\mathbf{t}(\mathbf{u}) = \mathbf{n}\cdot\boldsymbol{\sigma}(\mathbf{u}). \tag{1}$$

For a poroelastic material with material constants λ_c, μ, α, and M (Biot, 1962, 1963), the stress–strain relations are

$$\begin{aligned} \sigma_{ij} &= 2\mu e_{ij} + \delta_{ij}(\lambda_c e - \alpha M \varsigma), \\ p_f &= -\alpha M e + M\varsigma. \end{aligned} \tag{2}$$

The physical quantities in the preceding equations are defined as follows: $\mathbf{u}$ is the displacement vector of solid with components u_i, $e_{ij} = \frac{1}{2}(\partial u_i/\partial x_j + \partial u_j/\partial x_i)$, $e = \nabla\cdot\mathbf{u}$, $\varsigma = -\nabla\cdot\mathbf{w}$, $\mathbf{w}$ is the displacement vector of fluid relative to solid with components w_i, p_f is the fluid pressure in the pores, σ_{ij} is the total stress in the medium, δ_{ij} denotes Kronecker symbol. For the harmonic wave with circular frequency, ω, the time factor, $\exp(i\omega t)$, is suppressed in all the following expressions. Then the equations of motion are reduced to

$$\begin{aligned} \sigma_{ji,j} &= -\rho\omega^2 u_i - \rho_f \omega^2 w_i, \\ p_{f,i} &= \rho_f \omega^2 u_i + \rho_m \omega^2 w_i, \end{aligned} \tag{3}$$

where ρ is the mass density of the mixed medium, and ρ_f is that of the fluid. $\rho_m = m^* - ib^*/\omega$ represents the complex (frequency dependent) mass density of viscous fluid in a rigid framed medium where m^* and b^* denote the inertia parameter and the viscous dissipation parameter, respectively.

Applying Eq. (3) for a controlled volume V bounded by a closed surface S_v, the following identity can be obtained easily:

$$\begin{aligned} &\iiint_V \{[u_i^{(B)}\sigma_{ji,j}^{(A)} + w_i^{(B)}(-p_{f,i}^{(A)})] \\ &\quad -[u_i^{(A)}\sigma_{ji,j}^{(B)} + w_i^{(A)}(-p_{f,i}^{(B)})]\}dV = 0. \end{aligned} \tag{4}$$

On the basis of the assumption that $u_i^{(A)}$, $u_i^{(B)}$, and their first and second derivatives are continuous inside the volume V, we obtain the following equation by applying the divergence theorem:

$$\begin{aligned} &\iiint_V \{[u_i^{(B)}\sigma_{ji,j}^{(A)} + w_i^{(B)}(-p_{f,i}^{(A)})] \\ &\quad -[u_i^{(A)}\sigma_{ji,j}^{(B)} + w_i^{(A)}(-p_{f,i}^{(B)})]\}dV \\ &= \oiint_{S_v} \{[\sigma_{ji}^{(A)}u_i^{(B)}n_j + (-p_f^{(A)}w_i^{(B)}n_i)] \\ &\quad -[(\sigma_{ji}^{(B)}u_i^{(A)}n_j) + (-p_f^{(B)}w_i^{(A)}n_i)]\}dS_V \\ &\quad -\iiint_V \{[\sigma_{ji}^{(A)}e_{ij}^{(B)} + p_f^{(A)}\varsigma^{(B)}] \\ &\quad -[\sigma_{ji}^{(B)}e_{ij}^{(A)} + p_f^{(B)}\varsigma^{(A)}]\}dV. \end{aligned} \tag{5}$$

With the aid of Eqs. (2) and (4), Eq. (5) can be reduced to a surface integral referred to as the poroelastic reciprocal theorem,

$$\begin{aligned} &\oiint_{S_V} [\mathbf{t}^{(A)}\cdot\mathbf{u}^{(B)} - p_f^{(A)}\mathbf{n}\cdot\mathbf{w}^{(B)}] \\ &\quad -[\mathbf{t}^{(B)}\cdot\mathbf{u}^{(A)} - p_f^{(B)}\mathbf{n}\cdot\mathbf{w}^{(A)}]dS_V = 0. \end{aligned} \tag{6}$$

Furthermore, the closed surface S_V may be deformed into another closed surface without encompassing any discontinuities during the deformation.

B. Decomposition and normalization of equations of motion

Substitution of Eq. (2) into Eq. (3) yields the coupled governing equations:

$$\begin{aligned} &\mu\nabla^2\mathbf{u} + (\lambda_c + \mu)\nabla e - \alpha M\nabla\varsigma = -\rho\omega^2\mathbf{u} - \rho_f\omega^2\mathbf{w}, \\ &\nabla(-\alpha M e + M\varsigma) = \rho_f\omega^2\mathbf{u} + \rho_m\omega^2\mathbf{w}. \end{aligned} \tag{7}$$

The displacements $\mathbf{u}$ and $\mathbf{w}$ are decomposed into two scalar potentials φ_s, φ_f, one vector potential $\boldsymbol{\psi}_s$, and one factor μ_3,

$$\begin{aligned} \mathbf{u} &= \nabla\varphi_s + \nabla\times\boldsymbol{\psi}_s, \\ \mathbf{w} &= \nabla\varphi_f + \nabla\times(\mu_3\boldsymbol{\psi}_s), \\ \nabla\cdot\boldsymbol{\psi}_s &= 0. \end{aligned} \tag{8}$$

The subscripts s and f represent the solid and the relative fluid, respectively. Substitution of Eq. (8) into the coupled equations (7) yields two parts: the rotational part and the dilatational one. The rotational part is written as

$$\begin{aligned} &\nabla^2\boldsymbol{\psi}_s + k_s^2\boldsymbol{\psi}_s = 0, \\ &\mu_3 = -\rho_f/\rho_m, \end{aligned} \tag{9}$$

where $k_s = \omega\sqrt{[\rho - (\rho_f^2/\rho_m)]/\mu}$ is the rotational wave number. The dilatational part is written in a matrix form,

$$\begin{bmatrix} (\lambda_c+2\mu) & \alpha M \\ \alpha M & M \end{bmatrix}\begin{Bmatrix} \nabla^2\varphi_s \\ \nabla^2\varphi_f \end{Bmatrix}+\omega^2\begin{bmatrix} \rho & \rho_f \\ \rho_f & \rho_m \end{bmatrix}\begin{Bmatrix} \varphi_s \\ \varphi_f \end{Bmatrix}=\begin{Bmatrix} 0 \\ 0 \end{Bmatrix}. \tag{10}$$

Two characteristic values in Eq. (10) are obtained as follows:

$$(k/\omega)^2=(B\pm\sqrt{B^2-4AC})/2A, \tag{11}$$

where

$$\begin{aligned} A&=[(\lambda_c+2\mu)-\alpha^2 M]M,\\ B&=[\rho_m(\lambda_c+2\mu)+M(\rho-2\alpha\rho_f)],\\ C&=[\rho\rho_m-\rho_f^2]. \end{aligned} \tag{12}$$

Two corresponding characteristic vectors associated with the characteristic values in Eq. (11) are obtained as shown in the following:

$$\langle\mu_1,1\rangle^T=\langle -d/2c,1\rangle^T,\quad \langle 1,\mu_2\rangle^T=\langle 1,d/2a\rangle^T, \tag{13}$$

where

$$\begin{aligned} a&=(\alpha\rho_m-\rho_f)M,\\ b&=\rho M-\rho_m(\lambda_c+2\mu),\\ c&=\alpha\rho M-\rho_f(\lambda_c+2\mu),\\ d&=b-\sqrt{b^2+4ac}, \end{aligned} \tag{14}$$

and

$$\begin{aligned} \mu_1&=-d/2c,\\ \mu_2&=d/2a. \end{aligned} \tag{15}$$

After certain elaborative manipulations, we obtain a set of characteristic vectors,

$$\mathbf{\Phi}=\begin{bmatrix} \mu_1 & 1 \\ 1 & \mu_2 \end{bmatrix}. \tag{16}$$

Then Eq. (10) can be normalized to the diagonal matrix form:

$$\begin{bmatrix} (\lambda_c+2\mu)^* & 0 \\ 0 & M^* \end{bmatrix}\begin{Bmatrix} \nabla^2\varphi_1 \\ \nabla^2\varphi_2 \end{Bmatrix}+\omega^2\begin{bmatrix} \rho^* & 0 \\ 0 & \rho_m^* \end{bmatrix}\begin{Bmatrix} \varphi_1 \\ \varphi_2 \end{Bmatrix}=\begin{Bmatrix} 0 \\ 0 \end{Bmatrix}, \tag{17}$$

where

$$\begin{aligned} \varphi_1&=\frac{1}{\mu_1\mu_2-1}(\mu_2\varphi_s-\varphi_f),\\ \varphi_2&=\frac{1}{\mu_1\mu_2-1}(\mu_1\varphi_f-\varphi_s), \end{aligned} \tag{18}$$

and

$$\begin{aligned} (\lambda_c+2\mu)^*&=(\lambda_c+2\mu)\mu_1^2+2\alpha M\mu_1+M,\\ M^*&=(\lambda_c+2\mu)+2\alpha M\mu_2+M\mu_2^2,\\ \rho^*&=\rho\mu_1^2+2\rho_f\mu_1+\rho_m,\\ \rho_m^*&=\rho+2\rho_f\mu_2+\rho_m\mu_2^2. \end{aligned} \tag{19}$$

The details in the derivation of Eq. (17) are discussed in Appendix A. From Eq. (17), we readily obtain two uncoupled scalar Helmholtz equations,

$$\begin{aligned} \nabla^2\varphi_1+k_{p1}^2\varphi_1&=0,\\ \nabla^2\varphi_2+k_{p2}^2\varphi_2&=0, \end{aligned} \tag{20}$$

where $(k_{p1}^2/\omega^2)\equiv\rho^*/(2\mu+\lambda_c)^*$ and $(k_{p2}^2/\omega^2)=\rho_m^*/M^*$. k_{p1} and k_{p2} denote the fast and slow dilatational wave numbers, respectively.

C. The basis functions in the spherical coordinates

For waves in a three-dimensional poroelastic medium, the total motions may be decomposed into four parts: $\mathbf{L}_1$, $\mathbf{L}_2$, $\mathbf{M}$, and $\mathbf{N}$. $\mathbf{L}_1$ and $\mathbf{L}_2$ represent the dilatational motions propagating with speeds c_{p1} and c_{p2}, and wave numbers $k_{p1}=\omega/c_{p1}$ and $k_{p2}=\omega/c_{p2}$; $\mathbf{M}$ and $\mathbf{N}$ are the rotational ones propagating with speed c_s and wave number $k_s=\omega/c_s$. The three wave speeds are given by $c_{p1}=\sqrt{(2\mu+\lambda_c)^*/\rho^*}$, $c_{p2}=\sqrt{M^*/\rho_m^*}$, and $c_s=\sqrt{\mu/(\rho-\rho_f^2/\rho_m)}$, respectively.

In spherical coordinates (R,θ,ϕ), similar to the expression for elastic media (Morse and Feshbach, 1953), we propose four wave functions for the vector displacements of solid for a poroelastic medium as follows:

$$\begin{aligned} \mathbf{u}_{\sigma mn}^{(1)}&=\mathbf{L}_{1\sigma mn}=\frac{\mu_1}{k_p}\nabla[h_n^{(2)}(k_{p1}R)Y_{\sigma mn}(\theta,\phi)]\\ &=\frac{\mu_1 k_{p1}}{k_p}\left\{h_n^{(2)\prime}(k_{p1}R)\mathbf{A}_{\sigma mn}+(n^2+n)^{1/2}\frac{h_n^{(2)}(k_{p1}R)}{k_{p1}R}\mathbf{B}_{\sigma mn}\right\}, \end{aligned} \tag{21}$$

$$\begin{aligned} \mathbf{u}_{\sigma mn}^{(2)}&=\mathbf{L}_{2\sigma mn}=\frac{1}{k_p}\nabla[h_n^{(2)}(k_{p2}R)Y_{\sigma mn}(\theta,\phi)]\\ &=\frac{k_{p2}}{k_p}\left\{h_n^{(2)\prime}(k_{p2}R)\mathbf{A}_{\sigma mn}+(n^2+n)^{1/2}\frac{h_n^{(2)}(k_{p2}R)}{k_{p2}R}\mathbf{B}_{\sigma mn}\right\}, \end{aligned} \tag{22}$$

$$\begin{aligned} \mathbf{u}_{\sigma mn}^{(3)}&=\mathbf{M}_{\sigma mn}=\nabla\times[h_n^{(2)}(k_sR)Y_{\sigma mn}(\theta,\phi)R\mathbf{e}_R]\\ &=(n^2+n)^{1/2}h_n^{(2)}(k_sR)\mathbf{C}_{\sigma mn}, \end{aligned} \tag{23}$$

$$\begin{aligned} \mathbf{u}_{\sigma mn}^{(4)}&=\mathbf{N}_{\sigma mn}=\frac{1}{k_s}\nabla\times\mathbf{M}_{\sigma mn}=(n^2+n)\left(\frac{h_n^{(2)}(k_sR)}{k_sR}\right)\mathbf{A}_{\sigma mn}\\ &\quad+(n^2+n)^{1/2}\frac{[k_sRh_n^{(2)}(k_sR)]'}{k_sR}\mathbf{B}_{\sigma mn}, \end{aligned} \tag{24}$$

where $k_p\equiv\sqrt{\omega^2\rho/(\lambda_c+2\mu)}$ is a convenient common wave number used to make the basis function dimensionless. The symbol σmn is an abbreviation for three integers: σ from 1 (even) to 2 (odd), m from 0 to n, and n from 0 to ∞. The function $h_n^{(2)}(x)$ is the second kind of the spherical Hankel function, and $[xh_n^{(2)}(x)]'=xh_n^{(2)\prime}(x)+h_n^{(2)}(x)$ and $h_n^{(2)\prime}(x)$

$=dh_n^{(2)}(x)/dx$. The spherical surface harmonics $Y_{\sigma mn}(\theta,\phi)$ consists of an even part ($\sigma=1$) and an odd one ($\sigma=2$),

$$Y_{1mn}(\theta,\phi)=P_n^m(\cos\theta)\cos m\phi,$$
$$Y_{2mn}(\theta,\phi)=P_n^m(\cos\theta)\sin m\phi, \tag{25}$$

where $P_n^m(\cos\theta)$ are the associated Legendre polynomials, $m=0,1,...,n$ and $n=0,1,...,\infty$. The three mutually perpendicular vectors $\mathbf{A}_{\sigma mn}$, $\mathbf{B}_{\sigma mn}$, and $\mathbf{C}_{\sigma mn}$ are related to the three unit vectors $\mathbf{e}_R$, $\mathbf{e}_\theta$, and $\mathbf{e}_\phi$ in the spherical coordinates,

$$\mathbf{A}_{\sigma mn}=\mathbf{e}_R Y_{\sigma mn},$$
$$\mathbf{B}_{\sigma mn}=(n^2+n)^{-1/2}\left[\mathbf{e}_\theta\frac{\partial}{\partial\theta}+\mathbf{e}_\phi\frac{\partial}{\sin\theta\partial\phi}\right]Y_{\sigma mn}, \tag{26}$$
$$\mathbf{C}_{\sigma mn}=(n^2+n)^{-1/2}\left[\mathbf{e}_\theta\frac{\partial}{\sin\theta\partial\phi}-\frac{\partial}{\partial\theta}\mathbf{e}_\phi\right]Y_{\sigma mn}.$$

According to Eqs. (8) and (18), the vector operators of relative displacements of fluid are obtained as follows:

$$\mathbf{w}(\mathbf{u}_{\sigma mn}^{(1)})=\frac{k_{p1}}{k_p}\left[h_n^{(2)\prime}(k_{p1}R)\mathbf{A}_{\sigma mn}+(n^2+n)^{1/2}\frac{h_n^{(2)}(k_{p1}R)}{k_{p1}R}\mathbf{B}_{\sigma mn}\right],$$
$$\mathbf{w}(\mathbf{u}_{\sigma mn}^{(2)})=\frac{\mu_2 k_{p2}}{k_p}\left[h_n^{(2)\prime}(k_{p2}R)\mathbf{A}_{\sigma mn}+(n^2+n)^{1/2}\frac{h_n^{(2)}(k_{p2}R)}{k_{p2}R}\mathbf{B}_{\sigma mn}\right], \tag{27}$$
$$\mathbf{w}(\mathbf{u}_{\sigma mn}^{(3)})=\mu_3[(n^2+n)^{1/2}h_n^{(2)}(k_sR)\mathbf{C}_{\sigma mn}],$$
$$\mathbf{w}(\mathbf{u}_{\sigma mn}^{(4)})=\mu_3\left[(n^2+n)\left(\frac{h_n^{(2)}(k_sR)}{k_sR}\right)\mathbf{A}_{\sigma mn}+(n^2+n)^{1/2}\left(\frac{[k_sRh_n^{(2)}(k_sR)]'}{k_sR}\right)\mathbf{B}_{\sigma mn}\right].$$

Whereas according to the constitutive relation Eq. (2), the scalar operators of fluid pressures are shown as follows:

$$p_f(\mathbf{u}_{\sigma mn}^{(1)})=M(\alpha\mu_1+1)\frac{k_{p1}^2}{k_p}h_n^{(2)}(k_{p1}R)Y_{\sigma mn},$$
$$p_f(\mathbf{u}_{\sigma mn}^{(2)})=M(\alpha+\mu_2)\frac{k_{p2}^2}{k_p}h_n^{(2)}(k_{p2}R)Y_{\sigma mn}, \tag{28}$$
$$p_f(\mathbf{u}_{\sigma mn}^{(3)})=0,$$
$$p_f(\mathbf{u}_{\sigma mn}^{(4)})=0.$$

The vector operators for the tractions at a surface with a unit outward normal $\mathbf{n}$ can be calculated from Eq. (2), and are shown as follows:

$$\mathbf{t}(\mathbf{u}_{\sigma mn}^{(1)})=(\lambda_c+\alpha M/\mu_1)(\nabla\cdot\mathbf{L}_{1\sigma mn})\mathbf{n}+\mu\mathbf{n}\cdot(\nabla\mathbf{L}_{1\sigma mn}+\mathbf{L}_{1\sigma mn}\nabla),$$
$$\mathbf{t}(\mathbf{u}_{\sigma mn}^{(2)})=(\lambda_c+\alpha M\mu_2)(\nabla\cdot\mathbf{L}_{2\sigma mn})\mathbf{n}+\mu\mathbf{n}\cdot(\nabla\mathbf{L}_{2\sigma mn}+\mathbf{L}_{2\sigma mn}\nabla), \tag{29}$$
$$\mathbf{t}(\mathbf{u}_{\sigma mn}^{(3)})=\mu\mathbf{n}\cdot(\nabla\mathbf{M}_{\sigma mn}+\mathbf{M}_{\sigma mn}\nabla),$$
$$\mathbf{t}(\mathbf{u}_{\sigma mn}^{(4)})=\mu\mathbf{n}\cdot(\nabla\mathbf{N}_{\sigma mn}+\mathbf{N}_{\sigma mn}\nabla).$$

If we consider a special case of a spherical surface $\mathbf{n}=\mathbf{e}_R$, the four traction operators are reduced to the following simpler forms:

$$\mathbf{t}^r(\mathbf{u}_{\sigma mn}^{(1)})=\left\{-\frac{k_{p1}^2}{k_p}(\lambda_c\mu_1+\alpha M)h_n^{(2)}(k_{p1}R)+\mu\times\left[-2\mu_1\frac{k_{p1}^2}{k_p}h_n^{(2)}(k_{p1}R)+\frac{2\mu_1(n^2+n)}{k_pR^2}h_n^{(2)}\times(k_{p1}R)-\frac{4\mu_1k_{p1}}{k_pR}h_n^{(2)\prime}(k_{p1}R)\right]\right\}\mathbf{A}_{\sigma mn}+2\mu\frac{\mu_1k_{p1}}{k_p}(n^2+n)^{1/2}\left[\frac{h_n^{(2)\prime}(k_{p1}R)}{R}-\frac{h_n^{(2)}(k_{p1}R)}{k_{p1}R^2}\right]\mathbf{B}_{\sigma mn}, \tag{30}$$

$$\mathbf{t}^r(\mathbf{u}_{\sigma mn}^{(2)})=\left\{-\frac{k_{p2}^2}{k_p}(\lambda_c+\alpha M\mu_2)h_n^{(2)}(k_{p2}R)+\mu\times\left[-2\frac{k_{p2}^2}{k_p}h_n^{(2)}(k_{p2}R)+\frac{2(n^2+n)}{k_pR^2}h_n^{(2)}\times(k_{p2}R)-\frac{4k_{p2}}{k_pR}h_n^{(2)\prime}(k_{p2}R)\right]\right\}\mathbf{A}_{\sigma mn}+2\mu\frac{k_{p2}}{k_p}(n^2+n)^{1/2}\left[\frac{h_n^{(2)\prime}(k_{p2}R)}{R}-\frac{h_n^{(2)}(k_{p2}R)}{k_{p2}R^2}\right]\mathbf{B}_{\sigma mn}, \tag{31}$$

$$\mathbf{t}^r(\mathbf{u}_{\sigma mn}^{(3)})=\mu\left[k_sh_n^{(2)\prime}(k_sR)-\frac{h_n^{(2)}(k_sR)}{R}\right]\times(n^2+n)^{1/2}\mathbf{C}_{\sigma mn}, \tag{32}$$

$$\mathbf{t}^r(\mathbf{u}^{(4)}_{\sigma mn}) = 2\mu k_s \Bigg\{ (n^2+n)\left[\frac{h_n^{(2)}(k_sR)}{k_sR}\right]' \mathbf{A}_{\sigma mn} + \left[\left(n^2+n-1-\frac{(k_sR)^2}{2}\right)\frac{h_n^{(2)}(k_sR)}{(k_sR)^2} - \frac{h_n^{(2)\prime}(k_sR)}{k_sR}\right](n^2+n)^{1/2}\mathbf{B}_{\sigma mn}\Bigg\}. \tag{33}$$

D. Orthogonality conditions of the spherical basis functions

The three vector functions $\mathbf{A}_{\sigma mn}$, $\mathbf{B}_{\sigma mn}$, and $\mathbf{C}_{\sigma mn}$ satisfy the following orthogonal relations (Morse and Feshbach, 1953):

$$\begin{aligned} &\mathbf{A}_{\sigma mn}\cdot\mathbf{B}_{\sigma mn}=0,\\ &\mathbf{A}_{\sigma mn}\cdot\mathbf{C}_{\sigma mn}=0,\\ &\mathbf{B}_{\sigma mn}\cdot\mathbf{C}_{\sigma mn}=0, \end{aligned} \tag{34}$$

and integrations over a spherical surface yield the following:

$$\begin{aligned} &\int_0^{2\pi}\int_0^{\pi}\mathbf{A}_{\sigma mn}\cdot\mathbf{A}_{\sigma' m' n'}\sin\theta\, d\theta\, d\phi\\ &\quad=(1/\gamma_{mn})\,\delta_{mm'}\delta_{nn'}\delta_{\sigma\sigma'},\\ &\int_0^{2\pi}\int_0^{\pi}\mathbf{B}_{\sigma mn}\cdot\mathbf{B}_{\sigma' m' n'}\sin\theta\, d\theta\, d\phi\\ &\quad=(1/\gamma_{mn})\,\delta_{mm'}\delta_{nn'}\delta_{\sigma\sigma'},\\ &\int_0^{2\pi}\int_0^{\pi}\mathbf{C}_{\sigma mn}\cdot\mathbf{C}_{\sigma' m' n'}\sin\theta\, d\theta\, d\phi\\ &\quad=(1/\gamma_{mn})\,\delta_{mm'}\delta_{nn'}\delta_{\sigma\sigma'}. \end{aligned} \tag{35}$$

The normalization constant is defined as follows:

$$\gamma_{mn}=\epsilon_m(2n+1)(n-m)!/4\pi(n+m)!, \tag{36}$$

where $\epsilon_m=1$ when $m=0$, and $\epsilon_m=2$ when $m>0$.

For the wave fields which are regular in the region enclosing the origin of the coordinate system, we use four regular basis functions $\hat{\mathbf{u}}^{(\alpha)}_{\sigma mn}$ (α=1, 2, 3, or 4) which are obtained from $\mathbf{u}^{(\alpha)}_{\sigma mn}$ by replacing the spherical Hankel function $h_n^{(2)}$, in $\mathbf{L}_{1\sigma mn}$, $\mathbf{L}_{2\sigma mn}$, $\mathbf{M}_{\sigma mn}$, and $\mathbf{N}_{\sigma mn}$, with the spherical Bessel function j_n.

Considering an infinite region divided by a surface S of an arbitrary shape as shown in Fig. 1, we add an artificial spherical surface S_+ exterior to S with radius R_+. Let V in Eq. (5) be the region inside S_+ first, and then let set (A) be one of a regular set and (B) be another regular set inside the region S_+. Thus Eq. (6) reduces to a special case referred to as the first orthogonality condition,

$$\oiint_{S+}\{\mathbf{t}(\hat{\mathbf{u}}^{(\alpha)}_{\sigma mn})\cdot\hat{\mathbf{u}}^{(\beta)}_{\sigma' m' n'}-\mathbf{t}(\hat{\mathbf{u}}^{(\beta)}_{\sigma' m' n'})\cdot\hat{\mathbf{u}}^{(\alpha)}_{\sigma mn} - p_f(\hat{\mathbf{u}}^{(\alpha)}_{\sigma mn})\mathbf{n}\cdot\mathbf{w}(\hat{\mathbf{u}}^{(\beta)}_{\sigma' m' n'}) + p_f(\hat{\mathbf{u}}^{(\beta)}_{\sigma' m' n'})\mathbf{n}\cdot\mathbf{w}(\hat{\mathbf{u}}^{(\alpha)}_{\sigma mn})\}dS=0, \tag{37}$$

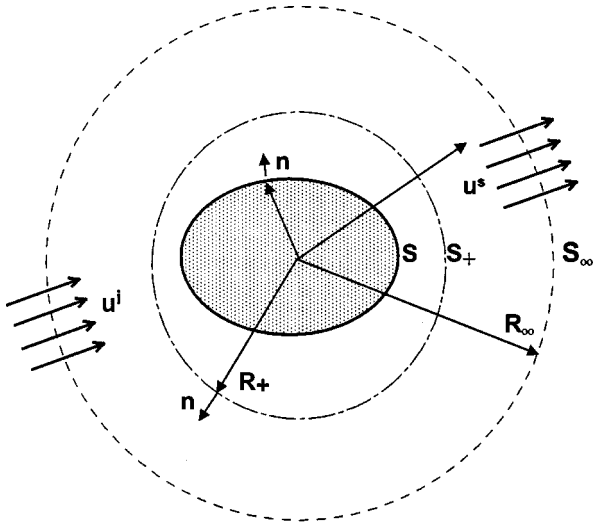

FIG. 1. Waves scattered by an inclusion bounded by the surfaces S.

where α, β=1, 2, 3, or 4. Next, let set (A) be one of a singular set and (B) be another singular one. Choose control volume to be the region bounded internally by S_+ and externally by S_∞. Since all $\mathbf{u}^{(\alpha)}_{\sigma mn}$ are regular outside the region S_+, we can obtain the second orthogonality condition,

$$\left(\iint_{S_\infty}-\iint_{S+}\right)\{\mathbf{t}(\mathbf{u}^{(\alpha)}_{\sigma mn})\cdot\mathbf{u}^{(\beta)}_{\sigma' m' n'}-\mathbf{t}(\mathbf{u}^{(\beta)}_{\sigma' m' n'})\cdot\mathbf{u}^{(\alpha)}_{\sigma mn} - p_f(\mathbf{u}^{(\alpha)}_{\sigma mn})\mathbf{n}\cdot\mathbf{w}(\mathbf{u}^{(\beta)}_{\sigma' m' n'}) + p_f(\mathbf{u}^{(\beta)}_{\sigma' m' n'})\mathbf{n}\cdot\mathbf{w}(\mathbf{u}^{(\alpha)}_{\sigma mn})\}dS=0. \tag{38}$$

The minus sign of the second integral is used because the outer normal at S_+ in this case is $-\mathbf{e}_R$. Through the zero value of Wronskian formula in Eq. (B13) (i.e., both are Bessel functions) and the relationship of material properties in Eqs. (A8) and (A14), we can prove the integrals on both surfaces S_∞ and S_+ vanish. Finally, let set (A) be one of a regular set and (B) be a singular one outside the surface S_+ and inside the surface S_∞. Through Eq. (35) and the application of the Wronskian formula (Abramowitz and Stegun, 1964), we obtain the third orthogonality condition,

$$\iint_{S+}\{\mathbf{t}(\mathbf{u}^{(\alpha)}_{\sigma mn})\cdot\hat{\mathbf{u}}^{(\beta)}_{\sigma' m' n'}-\mathbf{t}(\hat{\mathbf{u}}^{(\beta)}_{\sigma' m' n'})\cdot\mathbf{u}^{(\alpha)}_{\sigma mn} - p_f(\mathbf{u}^{(\alpha)}_{\sigma mn})\mathbf{n}\cdot\mathbf{w}(\hat{\mathbf{u}}^{(\beta)}_{\sigma' m' n'}) + p_f(\hat{\mathbf{u}}^{(\beta)}_{\sigma' m' n'})\mathbf{n}\cdot\mathbf{w}(\mathbf{u}^{(\alpha)}_{\sigma mn})\}dS = (-i\mu/k_s)D^{(\alpha)}_{\sigma mn}\delta_{\sigma\sigma'}\delta_{mm'}\delta_{nn'}\delta_{\alpha\beta}, \tag{39}$$

where

$$D^{(\alpha)}_{\sigma mn}=\begin{cases}\gamma_{(\alpha)}\cdot 4\pi(n+m)!/[\,\epsilon_m\cdot(2n+1)(n-m)!\,],\\ 0 \quad \text{if } \sigma=\text{odd}, \quad \text{and } m=0,\end{cases} \tag{40}$$

and

$$\gamma_{(\alpha)}=\begin{cases}(\lambda_c+2\mu)^*(k_s k_{p1}/\mu k_p^2) & \text{if } \alpha=1,\\ M^*(k_s k_{p2}/\mu k_p^2) & \text{if } \alpha=2,\\ n^2+n & \text{if } \alpha=3, \text{ or } 4.\end{cases} \tag{41}$$

Equations (37)–(39) are the desired orthogonality conditions among the basis functions that are the key step in the derivation of the transition matrix. In particular, the derivation of Eq. (39) is different from that obtained by Kargl and Lim (1993) (shown in Appendix B). Notice that the surface integrals in Eqs. (37)–(39) are independent of radius R_+. These invariant properties imply a conservation law and mean that the shape of S_+ may be deformed to S, and the surface integral over S_+ can be replaced with the one over S. The details of the derivation of Eqs. (37)–(39) are discussed in Appendix B.

III. THE TRANSITION MATRIX FOR AN INCLUSION

A. Series expansions of the incident, refracted, and scattered waves

Let a region inside S as shown in Fig. 1 be filled with a material different from that of the surrounding medium, and all material constants inside S are designated by a subscript (0): $\lambda_{c(0)}$, $\mu_{(0)}$, $\alpha_{(0)}$, and $M_{(0)}$. An incident wave $\mathbf{u}^i(R)$ impinging on the inclusion is refracted into the inclusion with the displacement $\mathbf{u}_-(R)$ and scattered into the surrounding medium as $\mathbf{u}^s(R)$. Each of these three kinds of waves can be represented by a series representation of the basis functions within a specific region,

$$\mathbf{u}^i(R)=\sum_{\sigma' m' n'}\sum_{\beta=1}^{4} a^{(\beta)}_{\sigma' m' n'}\hat{\mathbf{u}}^{(\beta)}_{\sigma' m' n'}, \tag{42}$$

$$\mathbf{u}^s(R)=\sum_{\sigma' m' n'}\sum_{\beta=1}^{4} c^{(\beta)}_{\sigma' m' n'}\mathbf{u}^{(\beta)}_{\sigma' m' n'}, \tag{43}$$

$$\mathbf{u}_-(R)=\sum_{\sigma' m' n'}\sum_{\beta=1}^{4} f^{(\beta)}_{\sigma' m' n'}\hat{\mathbf{u}}^{(\beta)}_{\sigma' m' n'(0)}. \tag{44}$$

The symbol $\Sigma_{\sigma' m' n'}$ is an abbreviation for three summations over the indexes. The quantities $a^{(\beta)}_{\sigma' m' n'}$, $c^{(\beta)}_{\sigma' m' n'}$, and $f^{(\beta)}_{\sigma' m' n'}$ denote the incident, scattered, and refracted coefficients, respectively. The incident wave in Eq. (42) is uniformly convergent for $R<R_\infty$. The basis functions for $\mathbf{u}^s(R)$ are regular outside and at the interface of the inclusion. Similarly, the series for $\mathbf{u}_-(R)$ is uniformly convergent inside and at the interface of the inclusion. The total displacement fields in the exterior region can be represented by the series in Eqs. (42) and (43),

$$\mathbf{u}=\mathbf{u}^i(R)+\mathbf{u}^s(R)=\sum_{\sigma' m' n'}\sum_{\beta=1}^{4} a^{(\beta)}_{\sigma m' n'},\hat{\mathbf{u}}^{(\beta)}_{\sigma' m' n'} + \sum_{\sigma' m' n'}\sum_{\beta=1}^{4} c^{(\beta)}_{\sigma' m' n'}\mathbf{u}^{(\beta)}_{\sigma' m' n'}. \tag{45}$$

Since both series are uniformly convergent, we can apply the associated operators $\mathbf{t}$, $\mathbf{w}$, and p_f to Eq. (45), such as the following,

$$\mathbf{t}(\mathbf{u})=\sum_{\sigma m' n'}\sum_{\beta=1}^{4} a^{(\beta)}_{\sigma' m' n'}\mathbf{t}(\hat{\mathbf{u}}^{(\beta)}_{\sigma' m' n'}) + \sum_{\sigma' m' n'}\sum_{\beta=1}^{4} c^{(\beta)}_{\sigma' m' n'}\mathbf{t}(\mathbf{u}^{(\beta)}_{\sigma' m' n'}),$$

$$\mathbf{w}(\mathbf{u})=\sum_{\sigma' m' n'}\sum_{\beta=1}^{4} a^{(\beta)}_{\sigma' m' n'}\mathbf{w}(\hat{\mathbf{u}}^{(\beta)}_{\sigma' m' n'}) + \sum_{\sigma' m' n'}\sum_{\beta=1}^{4} c^{(\beta)}_{\sigma' m' n'}\mathbf{w}(\mathbf{u}^{(\beta)}_{\sigma' m' n'}), \tag{46}$$

$$p_f(\mathbf{u})=\sum_{\sigma' m' n'}\sum_{\beta=1}^{4} a^{(\beta)}_{\sigma' m' n'}p_f(\hat{\mathbf{u}}^{(\beta)}_{\sigma' m' n'}) + \sum_{\sigma' m' n'}\sum_{\beta=1}^{4} c^{(\beta)}_{\sigma' m' n'}p_f(\mathbf{u}^{(\beta)}_{\sigma' m' n'}).$$

Analogous to the exterior region, the same operators can also be applied to the refracted fields as follows:

$$\mathbf{t}(\mathbf{u}_-)=\sum_{\sigma' m' n'}\sum_{\beta=1}^{4} f^{(\beta)}_{\sigma' m' n'}\mathbf{t}(\hat{\mathbf{u}}^{(\beta)}_{\sigma' m' n'(0)}),$$

$$\mathbf{w}(\mathbf{u}_-)=\sum_{\sigma' m' n'}\sum_{\beta=1}^{4} f^{(\beta)}_{\sigma' m' n'}\mathbf{w}(\hat{\mathbf{u}}^{(\beta)}_{\sigma' m' n'(0)}), \tag{47}$$

$$p_f(\mathbf{u}_-)=\sum_{\sigma' m' n'}\sum_{\beta=1}^{4} f^{(\beta)}_{\sigma' m' n'}p_f(\hat{\mathbf{u}}^{(\beta)}_{\sigma' m' n'(0)}).$$

B. The transition matrix for a poroelastic inclusion with an arbitrary shape

Consider the region V in Eq. (6) to be bounded by S_+ and S, and let $\mathbf{u}^{(A)}=\mathbf{u}^{(\alpha)}_{\sigma mn}$ and $\mathbf{u}^{(B)}=\mathbf{u}$ at the surface S_+, and $\mathbf{u}^{(B)}=\mathbf{u}_+$, $\mathbf{w}^{(B)}=\mathbf{w}_+$, $\mathbf{t}^{(B)}=\mathbf{t}_+$, and $p_f^{(B)}=p_{f+}$ at the surface S. Then Eq. (6) yields

$$\begin{aligned}&\int\int_S [\mathbf{t}(\mathbf{u}^{(\alpha)}_{\sigma mn})\cdot\mathbf{u}_+ - p_f(\mathbf{u}^{(\alpha)}_{\sigma mn})\mathbf{n}\cdot\mathbf{w}_+]\\ &\quad -[\mathbf{t}_+\cdot\mathbf{u}(\mathbf{u}^{(\alpha)}_{\sigma mn}) - p_{f+}\mathbf{n}\cdot\mathbf{w}(\mathbf{u}^{(\alpha)}_{\sigma mn})]dS\\ &= \iint_{S+} [\mathbf{t}(\mathbf{u}^{(\alpha)}_{\sigma mn})\cdot\mathbf{u} - p_f(\mathbf{u}^{(\alpha)}_{\sigma mn})\mathbf{n}\cdot\mathbf{w}]\\ &\quad -[\mathbf{t}\cdot\mathbf{u}^{(\alpha)}_{\sigma mn} - p_f\mathbf{n}\cdot\mathbf{w}(\mathbf{u}^{(\alpha)}_{\sigma mn})]dS,\\ &\alpha=1,\ 2,\ 3,\ \text{or}\ 4,\end{aligned} \tag{48}$$

where the normal vector $\mathbf{n}$ for $\mathbf{t}$ at S_+ is in the direction $\mathbf{e}_R$. Substitution of Eqs. (45) and (46) into Eq. (48) yields the following relationship:

$$\int\int_S [\mathbf{t}(\mathbf{u}^{(\alpha)}_{\sigma mn})\cdot\mathbf{u}_+ - p_f(\mathbf{u}^{(\alpha)}_{\sigma mn})\mathbf{n}\cdot\mathbf{w}_+] - [\mathbf{t}_+\cdot\mathbf{u}^{(\alpha)}_{\sigma mn} - p_{f+}\mathbf{n}\cdot\mathbf{w}(\mathbf{u}^{(\alpha)}_{\sigma mn})]dS$$

$$= \sum_{\sigma' m' n'} \sum_{\beta=1}^{4} a^{(\beta)}_{\sigma' m' n} \iint_{S+} \{\mathbf{t}(\mathbf{u}^{(\alpha)}_{\sigma mn})\cdot\hat{\mathbf{u}}^{(\beta)}_{\sigma' m' n'} - p_f(\mathbf{u}^{(\alpha)}_{\sigma mn})\mathbf{n}\cdot\mathbf{w}(\hat{\mathbf{u}}^{(\beta)}_{\sigma' m' n'}) - \mathbf{t}(\hat{\mathbf{u}}^{(\beta)}_{\sigma' m' n'})\cdot\mathbf{u}^{(\alpha)}_{\sigma mn} + p_f(\hat{\mathbf{u}}^{(\beta)}_{\sigma' m' n'})\mathbf{n}\cdot\mathbf{w}(\mathbf{u}^{(\alpha)}_{\sigma mn})\} dS$$

$$+ \sum_{\sigma' m' n'} \sum_{\beta=1}^{4} c^{(\beta)}_{\sigma' m' n'} \iint_{S+} \{\mathbf{t}(\mathbf{u}^{(\alpha)}_{\sigma mn})\cdot\mathbf{u}^{(\beta)}_{\sigma' m' n'} - p_f(\mathbf{u}^{(\alpha)}_{\sigma mn})\mathbf{n}\cdot\mathbf{w}(\mathbf{u}^{(\beta)}_{\sigma' m' n'}) - \mathbf{t}(\mathbf{u}^{(\beta)}_{\sigma' m' n'})\cdot\mathbf{u}^{(\alpha)}_{\sigma mn}$$

$$+ p_f(\mathbf{u}^{(\beta)}_{\sigma' m' n'})\mathbf{n}\cdot\mathbf{w}(\mathbf{u}^{(\alpha)}_{\sigma mn})\} dS,$$

$$\alpha = 1,\ 2,\ 3,\ \text{or}\ 4. \tag{49}$$

The surface integral associated with $c^{(\beta)}_{\sigma' m' n}$ vanishes because of Eq. (38), and the remaining surface integral on the right-hand side of Eq. (49) is equal to $(-i\mu/k_s)D^{(\alpha)}_{\sigma mn}\delta_{\sigma\sigma'}\delta_{mm'}\delta_{nn'}\delta_{\alpha\beta}$ because of Eq. (39). Hence, we obtain the incident coefficient,

$$a^{(\alpha)}_{\sigma mn} = \frac{ik_s}{\mu D^{(\alpha)}_{\sigma mn}} \iint_S [\mathbf{t}(\mathbf{u}^{(\alpha)}_{\sigma mn})\cdot\mathbf{u}_+ - p_f(\mathbf{u}^{(\alpha)}_{\sigma mn})\mathbf{n}\cdot\mathbf{w}_+ - \mathbf{t}_+\cdot\mathbf{u}^{(\alpha)}_{\sigma mn} + p_{f+}\mathbf{n}\cdot\mathbf{w}(\mathbf{u}^{(\alpha)}_{\sigma mn})] dS. \tag{50}$$

The subscript "+" denotes the field on S approaching from the $+\mathbf{n}$ side. Similarly, assigning $\mathbf{u}^{(A)} = \hat{\mathbf{u}}^{(\alpha)}_{\sigma mn}$ in Eq. (6) and making use of the procedure for obtaining $a^{(\alpha)}_{\sigma mn}$, we obtain the scattered coefficient,

$$c^{(\alpha)}_{\sigma mn} = \frac{-ik_s}{\mu D^{(\alpha)}_{\sigma mn}} \iint_S [\mathbf{t}(\hat{\mathbf{u}}^{(\alpha)}_{\sigma mn})\cdot\mathbf{u}_+ - p_f(\hat{\mathbf{u}}^{(\alpha)}_{\sigma mn})\mathbf{n}\cdot\mathbf{w}_+ - \mathbf{t}_+\cdot\hat{\mathbf{u}}^{(\alpha)}_{\sigma mn} + p_{f+}\mathbf{n}\cdot\mathbf{w}(\hat{\mathbf{u}}^{(\alpha)}_{\sigma mn})] dS. \tag{51}$$

Equation (51) shows clearly that the coefficient of the scattered waves is determined by the dynamic sources $\mathbf{u}_+$, $\mathbf{w}_+$, $\mathbf{t}_+$, and p_{f+} at the surface S. Equations (50) and (51) manifest the Huygens' principle for poroelastic waves. If a poroelastic inclusion is perfectly welded to the surrounding medium, the following fields must be continuous at the interface S (Deresiewicz and Skalak, 1963):

$$\mathbf{u}_+ = \mathbf{u}_-, \quad \mathbf{t}_+ = \mathbf{t}_-, \quad \mathbf{w}_+\cdot\mathbf{n} = \mathbf{w}_-\cdot\mathbf{n},$$

$$p_{f+} = p_{f-} \quad \text{on } S. \tag{52}$$

Thus $\mathbf{u}_+$, $\mathbf{w}_+\cdot\mathbf{n}$, $\mathbf{t}_+$, and p_{f+}, defined in Eqs. (50) and (51), can be replaced by $\mathbf{u}_-$, $\mathbf{w}_-\cdot\mathbf{n}$, $\mathbf{t}_-$, and p_{f-}, respectively. Therefore, we can extend the series representation for $\mathbf{u}_-$ of Eq. (44) to interface S. Substitution of this series of $\mathbf{u}_-$, $\mathbf{w}_-\cdot\mathbf{n}$, $\mathbf{t}_-$, and p_{f-} into Eq. (50) for the notations $\mathbf{u}_+$, $\mathbf{w}_+\cdot\mathbf{n}$, $\mathbf{t}_+$, and p_{f+} yields the relationship between the incident and refracted coefficients,

$$a^{(\alpha)}_{\sigma mn} = i \sum_{\sigma' m' n'} \sum_{\beta=1}^{4} Q^{(\alpha,\beta)}_{\sigma mn,\sigma' m' n'} f^{(\beta)}_{\sigma' m' n'}, \tag{53}$$

where

$$\mathbf{Q}^{(\alpha,\beta)}_{\sigma mn,\sigma m' n'} = \frac{k_s}{\mu D^{(\alpha)}_{\sigma mn}} \iint_S [\mathbf{t}(\mathbf{u}^{(\alpha)}_{\sigma mn})\cdot\hat{\mathbf{u}}^{(\beta)}_{\sigma' m' n'(0)} - p_f(\mathbf{u}^{(\alpha)}_{\sigma mn})\mathbf{n}\cdot\mathbf{w}(\hat{\mathbf{u}}^{(\beta)}_{\sigma' m' n'(0)}) - \mathbf{t}(\hat{\mathbf{u}}^{(\beta)}_{\sigma' m' n'(0)})\cdot\mathbf{u}^{(\alpha)}_{\sigma mn} + p_f(\hat{\mathbf{u}}^{(\beta)}_{\sigma' m' n'(0)})\mathbf{n}\cdot\mathbf{w}(\mathbf{u}^{(\alpha)}_{\sigma mn})] dS. \tag{54}$$

Similarly, we substitute the series representation of $\mathbf{u}_-$ into Eq. (51) and then obtain the relationship between the scattered and refracted coefficients,

$$c^{(\alpha)}_{\sigma mn} = -i \sum_{\sigma' m' n'} \sum_{\beta=1}^{4} \hat{\mathbf{Q}}^{(\alpha,\beta)}_{\sigma mn,\sigma' m' n'} f^{(\beta)}_{\sigma' m' n'}, \tag{55}$$

in which

$$\hat{\mathbf{Q}}^{(\alpha,\beta)}_{\sigma mn,\sigma' m' n'} = \frac{k_s}{\mu D^{(\alpha)}_{\sigma mn}} \iint_S [\mathbf{t}(\hat{\mathbf{u}}^{(\alpha)}_{\sigma mn})\cdot\hat{\mathbf{u}}^{(\beta)}_{\sigma' m' n'(0)} - p_f(\hat{\mathbf{u}}^{(\alpha)}_{\sigma mn})\mathbf{n}\cdot\mathbf{w}(\hat{\mathbf{u}}^{(\beta)}_{\sigma' m' n'(0)}) - \mathbf{t}(\hat{\mathbf{u}}^{(\beta)}_{\sigma' m' n'(0)})\cdot\hat{\mathbf{u}}^{(\alpha)}_{\sigma mn} + p_{f+}(\hat{\mathbf{u}}^{(\beta)}_{\sigma' m' n'(0)})\mathbf{n}\cdot\hat{\mathbf{w}}^{(\alpha)}_{\sigma mn}] dS. \tag{56}$$

In matrix notation, we can write Eqs. (53) and (55) as follows:

$$\mathbf{a} = i\mathbf{Q}\mathbf{f}, \qquad \mathbf{c} = -i\hat{\mathbf{Q}}\mathbf{f}, \tag{57}$$

where $\mathbf{a}$, $\mathbf{c}$, and $\mathbf{f}$ are column matrices for fixed σ, m, and n; and $\mathbf{Q}$ and $\hat{\mathbf{Q}}$ are square matrices with the indexes (α,β) and infinite matrices with indexes $m = 0,...,n$ and $n = 0,...,\infty$. Denoting the inverse of the matrix $\mathbf{Q}$ by $\mathbf{Q}^{-1}$, we have the results,

$$\mathbf{f} = -i\mathbf{Q}^{-1}\mathbf{a}, \qquad \mathbf{c} = -(\hat{\mathbf{Q}}\mathbf{Q}^{-1})\mathbf{a} = \mathbf{T}\mathbf{a}. \tag{58}$$

The product $-\hat{\mathbf{Q}}\mathbf{Q}^{-1}$ is called the transition matrix,

$$\mathbf{T} \equiv -\hat{\mathbf{Q}}\mathbf{Q}^{-1}, \tag{59}$$

for the porous medium. The transition matrix relates directly the unknown scattered coefficient **c** to the given incident coefficient **a**. The refracted coefficient **f** is related to **a** through $\mathbf{Q}^{-1}$ matrix. Since we choose the spherical wave functions for the basis functions, the surface integrals can be evaluated analytically if S is spherical. For the surface of an arbitrary shape, $\hat{\mathbf{Q}}$, $\mathbf{Q}$ can only be evaluated numerically.

C. The transition matrix for a spherical porous inclusion

When S turns out to be a spherical surface with radius a, the traction $\mathbf{t}(\mathbf{u}^{(\beta)}_{\sigma mn})$ in the surface integrals for $\mathbf{Q}^{(\alpha,\beta)}_{\sigma mn,\sigma' m' n'}$ and $\hat{\mathbf{Q}}^{(\alpha,\beta)}_{\sigma mn,\sigma' m' n'}$ is replaced by $\mathbf{t}^r(\mathbf{u}^{(\beta)}_{\sigma mn})$ defined in Eqs. (30)–(33). The resulting integrals can be evaluated in a closed form by using Eqs. (34) and (35). The corresponding elements of $\mathbf{Q}^{(\alpha,\beta)}_{\sigma mn,\sigma' m' n'}$ obtained from Eq. (54) are listed in Appendix B, and those of $\hat{\mathbf{Q}}^{(\alpha,\beta)}_{\sigma mn,\sigma' m' n'}$ can be obtained from $\mathbf{Q}^{(\alpha,\beta)}_{\sigma mn,\sigma' m' n'}$ by replacing the spherical Hankel function $h^{(2)}_n$ with the spherical Bessel function j_n. Notice that Q matrix for the spherical poroelastic inclusion is a diagonal matrix with the indexes $(\sigma mn,\sigma' m' n')$,

$$\mathbf{Q}^{(\alpha,\beta)}_{\sigma mn,\sigma' m' n'} \begin{cases} \neq 0 & \text{when } \sigma=\sigma', m=m', n=n', \\ =0 & \text{otherwise.} \end{cases} \tag{60}$$

Furthermore, the associated transition matrix is also diagonal with the same indexes,

$$[\mathbf{T}^{(\alpha,\beta)}]_{\sigma mn,\sigma' m' n'} \begin{cases} \neq 0 & \text{when } \sigma=\sigma', m=m', n=n', \\ =0 & \text{otherwise.} \end{cases} \tag{61}$$

On the other hand, concerning the indexes (α,β), the transition matrix is not a diagonal form. Omitting the subscripts indexes "σmn, σmn" and the brackets enclosing the superscripts, we can write the nonzero elements of the transition matrix listed as follows:

$$\begin{aligned}
T^{11}&=[\hat{Q}^{11}(Q^{24}Q^{42}-Q^{22}Q^{44})+\hat{Q}^{12}(-Q^{24}Q^{41}\\
&\quad +Q^{21}Q^{44})+\hat{Q}^{14}(Q^{22}Q^{41}-Q^{21}Q^{42})]/\Delta,\\
T^{21}&=[\hat{Q}^{21}(Q^{24}Q^{42}-Q^{22}Q^{44})+\hat{Q}^{22}(-Q^{24}Q^{41}\\
&\quad +Q^{21}Q^{44})+\hat{Q}^{24}(Q^{22}Q^{41}-Q^{21}Q^{42})]/\Delta,\\
T^{41}&=[\hat{Q}^{41}(Q^{24}Q^{42}-Q^{22}Q^{44})+\hat{Q}^{42}(-Q^{24}Q^{41}\\
&\quad +Q^{21}Q^{44})+\hat{Q}^{44}(Q^{22}Q^{41}-Q^{21}Q^{42})]/\Delta,\\
T^{12}&=[\hat{Q}^{11}(-Q^{14}Q^{42}+Q^{12}Q^{44})+\hat{Q}^{12}(Q^{14}Q^{41}\\
&\quad -Q^{11}Q^{44})+\hat{Q}^{14}(-Q^{12}Q^{41}+Q^{11}Q^{42})]/\Delta,\\
T^{22}&=[\hat{Q}^{21}(-Q^{14}Q^{42}+Q^{12}Q^{44})+\hat{Q}^{22}(Q^{14}Q^{41}\\
&\quad -Q^{11}Q^{44})+\hat{Q}^{24}(-Q^{12}Q^{41}+Q^{11}Q^{42})]/\Delta,\\
T^{42}&=[\hat{Q}^{41}(-Q^{14}Q^{42}+Q^{12}Q^{44})+\hat{Q}^{42}(Q^{14}Q^{41}\\
&\quad -Q^{11}Q^{44})+\hat{Q}^{44}(-Q^{12}Q^{41}+Q^{11}Q^{42})]/\Delta,\\
T^{14}&=[\hat{Q}^{11}(Q^{14}Q^{22}-Q^{12}Q^{24})+\hat{Q}^{12}(-Q^{14}Q^{21}\\
&\quad +Q^{11}Q^{24})+\hat{Q}^{14}(Q^{12}Q^{21}-Q^{11}Q^{22})]/\Delta,\\
T^{24}&=[\hat{Q}^{21}(Q^{14}Q^{22}-Q^{12}Q^{24})+\hat{Q}^{22}(-Q^{14}Q^{21}\\
&\quad +Q^{11}Q^{24})+\hat{Q}^{24}(Q^{12}Q^{21}-Q^{11}Q^{22})]/\Delta,\\
T^{44}&=[\hat{Q}^{41}(Q^{14}Q^{22}-Q^{12}Q^{24})+\hat{Q}^{42}(-Q^{14}Q^{21}\\
&\quad +Q^{11}Q^{24})+\hat{Q}^{44}(Q^{12}Q^{21}-Q^{11}Q^{22})]/\Delta,\\
T^{33}&=-\hat{Q}^{33}/Q^{33},
\end{aligned}$$

and

$$T^{31}=T^{32}=T^{13}=T^{23}=T^{34}=T^{43}=0, \tag{62}$$

where

$$\begin{aligned}
\Delta=(&-Q^{14}Q^{22}Q^{41}+Q^{12}Q^{24}Q^{41}+Q^{14}Q^{21}Q^{42}\\
&-Q^{11}Q^{24}Q^{42}-Q^{12}Q^{21}Q^{44}+Q^{11}Q^{22}Q^{44}).
\end{aligned} \tag{63}$$

Substituting the above mentioned results into Eq. (58), we can determine the solutions for the waves scattered by a spherical poroelastic inclusion. The relationships between the incident coefficients and scattered coefficients for the case of the spherical poroelastic inclusion are obtained as follows:

$$\begin{aligned}
c^1&=T^{11}a^1+T^{12}a^2+T^{14}a^4,\\
c^2&=T^{21}a^1+T^{22}a^2+T^{24}a^4,\\
c^3&=T^{33}a^3,\\
c^4&=T^{41}a^1+T^{42}a^2+T^{44}a^4.
\end{aligned} \tag{64}$$

D. The transition matrix for a spherical elastic inclusion

Now, let us consider a degenerated case where a spherical elastic inclusion is perfectly welded to the poroelastic surrounding. The continuity conditions now are rewritten as follows:

$$\mathbf{u}_+=\mathbf{u}_-, \quad \mathbf{t}_+=\mathbf{t}_-, \quad \mathbf{w}_+\cdot\mathbf{e}_R=0 \quad \text{on } S. \tag{65}$$

Similarly, we use an alternative series expansion of $\mathbf{u}_-$ in Eq. (44) to represent the field inside the interface S. For an elastic medium, the regular basis functions are expressed as (Pao, 1978)

$$\begin{aligned}
\hat{\mathbf{u}}^{(1)}_{\sigma' m' n' (0)}&=\hat{\mathbf{L}}_{\sigma' m' n' (0)}=j_n'(k_{p(0)}R)\mathbf{A}_{\sigma' m' n'}\\
&\quad +(n^2+n)^{1/2}\frac{j_n(k_{p(0)}R)}{k_{p(0)}R}\mathbf{B}_{\sigma' m' n'},\\
\hat{\mathbf{u}}^{(3)}_{\sigma' m' n' (0)}&=\hat{\mathbf{M}}_{\sigma' m' n' (0)}=(n^2+n)^{1/2}j_n(k_{s(0)}R)\mathbf{C}_{\sigma' m' n'},
\end{aligned} \tag{66}$$

$$\begin{aligned}
\hat{\mathbf{u}}^{(4)}_{\sigma' m' n' (0)}&=\hat{\mathbf{N}}_{\sigma' m' n' (0)}=(n^2+n)\left(\frac{j_n(k_{s(0)}R)}{k_{s(0)}R}\right)\mathbf{A}_{\sigma' m' n'}\\
&\quad +(n^2+n)^{1/2}\frac{[k_{s(0)}Rj_n(k_{s(0)}R)]'}{k_{s(0)}R}\mathbf{B}_{\sigma' m' n'},
\end{aligned}$$

in which we skip the superscript (2) deliberately to avoid the unmatching order when we degenerate from the poroelastic case. The associated wave numbers for the dilatational and rotational waves of the elastic inclusion are $k_{p(0)}=\omega\sqrt{\rho_{(0)}/(\lambda_{(0)}+2\mu_{(0)})}$ and $k_{s(0)}=\omega\sqrt{\rho_{(0)}/\mu_{(0)}}$, respectively. The associated traction operators for the elasticity are written as follows:

$$\begin{aligned}\mathbf{t}(\hat{\mathbf{u}}^{(1)}_{\sigma' m' n'(0)})&=\lambda_{(0)}\nabla\cdot\hat{\mathbf{L}}_{\sigma' m' n'(0)}\mathbf{n}+\mu_{(0)}\mathbf{n}\cdot(\nabla\hat{\mathbf{L}}_{\sigma' m' n'(0)}\\&\quad+\hat{\mathbf{L}}_{\sigma' m' n'(0)}\nabla),\\ \mathbf{t}(\hat{\mathbf{u}}^{(3)}_{\sigma' m' n'(0)})&=\mu_{(0)}\mathbf{n}\cdot(\nabla\hat{\mathbf{M}}_{\sigma' m' n'(0)}+\hat{\mathbf{M}}_{\sigma' m' n'(0)}\nabla),\\ \mathbf{t}(\hat{\mathbf{u}}^{(4)}_{\sigma' m' n'(0)})&=\mu_{(0)}\mathbf{n}\cdot(\nabla\hat{\mathbf{N}}_{\sigma' m' n'(0)}+\hat{\mathbf{N}}_{\sigma' m' n'(0)}\nabla).\end{aligned}\tag{67}$$

The series representations of the displacement vector and the traction vector for elastic inclusion can be written through Eq. (47),

$$\begin{aligned}\mathbf{u}_-(R)&=\sum_{\sigma' m' n'}\sum_{\beta=1,3,4}f^{(\beta)}_{\sigma' m' n}\hat{\mathbf{u}}^{(\beta)}_{\sigma' m' n'(0)},\\ \mathbf{t}(\mathbf{u}_-)&=\sum_{\sigma' m' n'}\sum_{\beta=1,3,4}f^{(\beta)}_{\sigma' m' n}\mathbf{t}(\hat{\mathbf{u}}^{(\beta)}_{\sigma' m' n'(0)}),\end{aligned}\tag{68}$$

in which we also skip the superscript, $\beta=2$. Under the continuity conditions for the elastic inclusion, the incident coefficient in Eq. (50) is reduced to the solution,

$$\begin{aligned}a^{(\alpha)}_{\sigma mn}=\frac{ik_s}{\mu D^{(\alpha)}_{\sigma mn}}\iint_S[&\mathbf{t}(\mathbf{u}^{(\alpha)}_{\sigma mn})\cdot\mathbf{u}_+-\mathbf{t}_+\cdot\mathbf{u}^{(\alpha)}_{\sigma mn}\\&+p_{f+}\mathbf{n}\cdot\mathbf{w}(\mathbf{u}^{(\alpha)}_{\sigma mn})]dS,\quad \alpha=1,\ 2,\ 3,\ \text{or}\ 4.\end{aligned}\tag{69}$$

The interface pressure p_{f+} is considered as the pressure approaching to interface from the outside of the inclusion. Therefore, it can be constructed through the regular part expansions,

$$\begin{aligned}p_{f+}=\sum_{\sigma' m' n'}[&f^{*(1)}_{\sigma' m' n'}p_f(\hat{\mathbf{u}}^{(1)}_{\sigma' m' n'})|_{R=a}\\&+f^{(2)}_{\sigma' m' n'}p_f(\hat{\mathbf{u}}^{(2)}_{\sigma' m' n'})|_{R=a}],\end{aligned}\tag{70}$$

where $f^{*(1)}_{\sigma' m' n'}$ and $f^{(2)}_{\sigma' m' n'}$ are the undetermined coefficients, and the scalar regular pressures are defined by the exterior material properties,

$$\begin{aligned}p_f(\hat{\mathbf{u}}^{(1)}_{\sigma' m' n'})|_{R=a}&=M(\alpha\mu_1+1)\frac{k_{p1}^2}{k_p}j_{n'}(k_{p1}a)Y_{\sigma' m' n'},\\ p_f(\hat{\mathbf{u}}^{(2)}_{\sigma' m' n'})|_{R=a}&=M(\alpha+\mu_2)\frac{k_{p2}^2}{k_p}j_{n'}(k_{p2}a)Y_{\sigma' m' n'}.\end{aligned}\tag{71}$$

Then substituting Eq. (68) into Eq. (69) and replacing $\mathbf{u}_+$ and $\mathbf{t}_+$ through the continuity conditions in Eq. (65), we obtain the incident coefficient,

$$\begin{aligned}a^{(\alpha)}_{\sigma mn}=i\sum_{\sigma' m' n'}\Bigg[&\sum_{\beta=1}^{4}\mathbf{Q}'^{(\alpha,\beta)}_{\sigma mn,\sigma' m' n'}f^{(\beta)}_{\sigma' m' n'}\\&+\mathbf{R}^{(\alpha)}_{\sigma mn,\sigma' m' n'}f^{*(1)}_{\sigma' m' n'}\Bigg],\quad \alpha=1,\ 2,\ 3,\ \text{or}\ 4.\end{aligned}\tag{72}$$

For this special case of spherical elastic inclusion, $\mathbf{Q}'^{(\alpha,\beta)}_{\sigma mn,\sigma' m' n'}$ and $\mathbf{R}^{(\alpha)}_{\sigma mn,\sigma' m' n'}$ are diagonal with the indexes $(\sigma mn,\sigma' m' n')$ and the off-diagonal elements vanish. Thus

$$\mathbf{Q}'^{(\alpha,\beta)}_{\sigma mn,\sigma mn}=\frac{k_s}{\mu D^{(\alpha)}_{\sigma mn}}\begin{cases}\displaystyle\iint_S[\mathbf{t}(\mathbf{u}^{(\alpha)}_{\sigma mn})\cdot\hat{\mathbf{u}}^{(\beta)}_{\sigma mn(0)}-\mathbf{t}(\hat{\mathbf{u}}^{(\beta)}_{\sigma mn(0)})\cdot\mathbf{u}^{(\alpha)}_{\sigma mn}]dS & \text{for } \beta=1,3,4,\\ \displaystyle\iint_S p_f(\hat{\mathbf{u}}^{(2)}_{\sigma mn})\mathbf{n}\cdot\mathbf{w}(\mathbf{u}^{(\alpha)}_{\sigma mn})dS & \text{for } \beta=2,\end{cases}\tag{73}$$

and

$$\mathbf{R}^{(\alpha)}_{\sigma mn,\sigma mn}=\frac{k_s}{\mu D^{(\alpha)}_{\sigma mn}}\iint_S p_f(\hat{\mathbf{u}}^{(1)}_{\sigma mn})\mathbf{n}\cdot\mathbf{w}(\mathbf{u}^{(\alpha)}_{\sigma mn})dS.\tag{74}$$

Similarly, the scattered coefficient in Eq. (51) can be deduced through the continuity conditions for the elastic inclusion,

$$\begin{aligned}c^{(\alpha)}_{\sigma mn}=\frac{-ik_s}{\mu D^{(\alpha)}_{\sigma mn}}\int_S[&\mathbf{t}(\hat{\mathbf{u}}^{(\alpha)}_{\sigma mn})\cdot\mathbf{u}_+-\mathbf{t}_+\cdot\hat{\mathbf{u}}^{(\alpha)}_{\sigma mn}\\&+p_{f+}\mathbf{n}\cdot\mathbf{w}(\hat{\mathbf{u}}^{(\alpha)}_{\sigma mn})]dS,\quad \alpha=1,\ 2,\ 3,\ \text{or}\ 4.\end{aligned}\tag{75}$$

Substitution of Eqs. (66) and (67) into Eq. (75) yields,

$$\begin{aligned}c^{(\alpha)}_{\sigma mn}=-i\sum_{\sigma' m' n'}\Bigg[&\sum_{\beta=1}^{4}\hat{\mathbf{Q}}'^{(\alpha,\beta)}_{\sigma mn,\sigma' m' n'}f^{(\beta)}_{\sigma' m' n'}\\&+\hat{\mathbf{R}}^{(\alpha)}_{\sigma mn,\sigma' m' n'}f^{*(1)}_{\sigma' m' n'}\Bigg],\quad \alpha=1,\ 2,\ 3,\ \text{or}\ 4,\end{aligned}\tag{76}$$

where for the diagonal elements with index $(\sigma mn,\sigma' m' n')$,

$$\hat{\mathbf{Q}}'^{(\alpha,\beta)}_{\sigma mn,\sigma mn}=\frac{k_s}{\mu D^{(\alpha)}_{\sigma mn}}\begin{cases}\iint_S[\mathbf{t}(\hat{\mathbf{u}}^{(\alpha)}_{\sigma mn})\cdot\hat{\mathbf{u}}^{(\beta)}_{\sigma mn(0)}-\mathbf{t}(\hat{\mathbf{u}}^{(\beta)}_{\sigma mn(0)})\cdot\hat{\mathbf{u}}^{(\alpha)}_{\sigma mn}]dS & \text{for } \beta=1,3,4,\\ \iint_S p_f(\hat{\mathbf{u}}^{(2)}_{\sigma mn})\mathbf{n}\cdot\mathbf{w}(\hat{\mathbf{u}}^{(\alpha)}_{\sigma mn})dS & \text{for } \beta=2,\end{cases} \tag{77}$$

and

$$\hat{\mathbf{R}}^{(\alpha)}_{\sigma mn,\sigma mn}=\frac{k_s}{\mu D^{(\alpha)}_{\sigma mn}}\iint_S p_f(\hat{\mathbf{u}}^{(1)}_{\sigma mn})\mathbf{n}\cdot\mathbf{w}(\hat{\mathbf{u}}^{(\alpha)}_{\sigma mn})dS, \tag{78}$$

and the off-diagonal elements of $\hat{\mathbf{Q}}'^{(\alpha,\beta)}_{\sigma mn,\sigma' m' n'}$ and $\hat{\mathbf{R}}^{(\alpha)}_{\sigma mn,\sigma' m' n'}$ also vanish. In order to obtain the undetermined coefficient $f^{*(1)}_{\sigma' m' n'}$, we have to make use of the impervious boundary condition at the interface $\mathbf{w}_+\cdot\mathbf{e}_R=0$. The vector operator $\mathbf{w}_+$ is obtained by substitution of Eqs. (72) and (76) into the operator $\mathbf{w}$ of Eq. (46) for the exterior region. The condition, $\mathbf{w}_+\cdot\mathbf{e}_R=0$, requires

$$\sum_{\gamma=1}^{4}\left\{[J^{(\gamma)}\mathbf{R}^{(\gamma)}_{\sigma mn,\sigma mn}-H^{(\gamma)}\hat{\mathbf{R}}^{(\gamma)}_{\sigma mn,\sigma mn}]f^{*(1)}_{\sigma mn}+\sum_{\beta=1}^{4}[J^{(\gamma)}\mathbf{Q}'^{(\gamma,\beta)}_{\sigma mn,\sigma mn}-H^{(\gamma)}\hat{\mathbf{Q}}'^{(\gamma,\beta)}_{\sigma mn,\sigma mn}]f^{(\beta)}_{\sigma mn}\right\}=0, \tag{79}$$

for each spherical surface harmonics $Y_{\sigma mn}(\theta,\phi)$ where $J^{(\gamma)}$ and $H^{(\gamma)}$ are radial parts of $\mathbf{w}(\hat{\mathbf{u}}^{(\gamma)}_{\sigma mn})|_{R=a}\cdot\mathbf{n}$ and $\mathbf{w}(\mathbf{u}^{(\gamma)}_{\sigma mn})|_{R=a}\cdot\mathbf{n}$ at the interface S, respectively.

Since the inclusion is spherical with radius a, $J^{(\gamma)}$ is reduced by the normal vector $\mathbf{n}=\mathbf{e}_R$,

$$J^{(\gamma)}=\begin{cases}k_{p1}j_n'(k_{p1}a)/k_p & \text{for } \gamma=1,\\ \mu_2 k_{p2}j_n'(k_{p2}a)/k_p & \text{for } \gamma=2,\\ 0 & \text{for } \gamma=3,\\ \mu_3(n^2+n)j_n(k_s a)/k_s a & \text{for } \gamma=4,\end{cases} \tag{80}$$

and $H^{(\gamma)}$ is obtained by replacing the spherical Bessel function j_n in Eq. (80) with the spherical Hankel function $h^{(2)}_n$. Hence, we find the undetermined coefficient $f^{*(1)}_{\sigma mn}$ in terms of the refracted coefficients,

$$f^{*(1)}_{\sigma mn}=-\sum_{\beta=1}^{4}\mathbf{P}^{(\beta)}_{\sigma mn,\sigma mn}f^{(\beta)}_{\sigma mn}, \tag{81}$$

where

$$\mathbf{P}^{(\beta)}_{\sigma mn,\sigma mn}=\frac{\sum_{\gamma=1}^{4}[J^{(\gamma)}\mathbf{Q}'^{(\gamma,\beta)}_{\sigma mn,\sigma mn}-H^{(\gamma)}\hat{\mathbf{Q}}'^{(\gamma,\beta)}_{\sigma mn,\sigma mn}]}{\sum_{\gamma=1}^{4}[J^{(\gamma)}\mathbf{R}^{(\gamma)}_{\sigma mn,\sigma mn}-H^{(\gamma)}\hat{\mathbf{R}}^{(\gamma)}_{\sigma mn,\sigma mn}]}. \tag{82}$$

Finally, substitution of Eq. (81) into Eqs. (72) and (76) gives the following relationships:

$$a^{(\alpha)}_{\sigma mn}=i\sum_{\beta=1}^{4}\mathbf{Q}^{(\alpha,\beta)}_{\sigma mn,\sigma mn}f^{(\beta)}_{\sigma mn},$$
$$c^{(\alpha)}_{\sigma mn}=-i\sum_{\beta=1}^{4}\hat{\mathbf{Q}}^{(\alpha,\beta)}_{\sigma mn,\sigma mn}f^{(\beta)}_{\sigma mn}, \tag{83}$$

where

$$\mathbf{Q}^{(\alpha,\beta)}_{\sigma mn,\sigma mn}=\mathbf{Q}'^{(\alpha,\beta)}_{\sigma mn,\sigma mn}-\mathbf{R}^{(\alpha)}_{\sigma mn,\sigma mn}\mathbf{P}^{(\beta)}_{\sigma mn,\sigma mn},$$
$$\hat{\mathbf{Q}}^{(\alpha,\beta)}_{\sigma mn,\sigma mn}=\hat{\mathbf{Q}}'^{(\alpha,\beta)}_{\sigma mn,\sigma mn}-\hat{\mathbf{R}}^{(\alpha)}_{\sigma mn,\sigma mn}\mathbf{P}^{(\beta)}_{\sigma mn,\sigma mn}. \tag{84}$$

Similar to Eq. (57), we obtain the transition matrix for the case of the elastic spherical inclusion as

$$\mathbf{c}=\mathbf{T}\mathbf{a}. \tag{85}$$

The nonzero elements of $\mathbf{Q}'$ matrix as well as $\mathbf{R}_{\sigma mn,\sigma mn}$ for a spherical elastic inclusion are listed in Appendix C.

IV. NUMERICAL RESULTS

In order to illustrate the validity and the accuracy of the transition matrix method, we present some typical numerical examples in the following.

A. Verification of the numerical implementation

To validate the numerical implementation presented in this study, we verify the continuity conditions at the interface by considering first a special example of the spherical inclusion subjected to an artificial incident wave. Let an artificial and arbitrary choice of the incident coefficients be given by

$$\langle a^{(1)}_{\sigma mn},a^{(2)}_{\sigma mn},a^{(3)}_{\sigma mn},a^{(4)}_{\sigma mn}\rangle^T=\begin{cases}\langle 1.0,2.0,3.0,4.0\rangle^T & \text{when } (\sigma,m,n)=(1,3,5),\\ \langle 0,0,0,0\rangle^T & \text{otherwise.}\end{cases} \tag{86}$$

The material properties in the exterior and interior media are converted from Zimmerman and Stern (1993a) and Yew and Jogi (1978), respectively. The corresponding material constants are listed in Table I. Since we adopt a special type of the incident wave defined in Eq. (86), the series representation of the field associated with the indexes σmn is reduced merely to a single one $(\sigma,m,n)=(1,3,5)$. With the aid of Eqs. (53) and (55), we can get the simpler forms,

TABLE I. Material properties for the cases studied.

	Exterior surrounding	Interior inclusion	
	Coarse sand (poroelasticity)	Alundum (poroelasticity)	Iron (elasticity)
λ_c (Pa)	4.3316×10^9	1.6759×10^{10}	$\lambda=9.938\times10^{10}$
μ (Pa)	2.610×10^7	2.533×10^{10}	7.81×10^{10}
α	0.987 334 1	0.60	⋯
M (Pa)	$4.014\,228\,6\times10^9$	$6.349\,206\,3\times10^9$	⋯
ρ (kg/m^3)	1874	2618	7870
ρ_f (kg/m^3)	1000	1000	⋯
m^* (kg/m^3)	2129.924 85	3174.603 17	⋯
b^* (N s/m^4)	$1.001\,064\,6\times10^7$	$3.749\,055\,2\times10^8$	⋯

TABLE II. The comparison with the coefficients obtained from the exterior and the interior regions.

	Component		Exterior region	Interior region
Surface displacement **u**	$\mathbf{A}_{\sigma mn}$	Real	3.149 836 582 067 977$E-002$	3.149 836 582 020 882$E-002$
		Image	−2.278 746 278 743 160$E-002$	−2.278 746 278 576 360$E-002$
	$\mathbf{B}_{\sigma mn}$	Real	−1.069 388 568 430 973$E-002$	−1.069 388 568 635 610$E-002$
		Image	1.530 721 666 871 404$E-003$	1.530 721 668 937 751$E-003$
	$\mathbf{C}_{\sigma mn}$	Real	−2.814 212 411 037 520$E-003$	−2.814 212 411 037 555$E-003$
		Image	−4.426 656 392 015 449$E-003$	−4.426 656 392 015 722$E-003$
Surface relative fluid displacement **w**(**u**)	$\mathbf{A}_{\sigma mn}$	Real	−5.021 354 976 511 661$E-002$	−5.021 354 976 521 485$E-002$
		Image	0.389 292 743 033 368	0.389 292 743 032 655
	$\mathbf{B}_{\sigma mn}$	Real	6.608 854 149 965 06	0.131 148 687 499 589
		Image	6.682 124 300 918 16	0.224 211 345 631 806
	$\mathbf{C}_{\sigma mn}$	Real	−4.304 536 227 428 268$E-004$	−1.473 556 357 287 508$E-005$
		Image	4.683 584 516 659 844$E-004$	9.589 692 286 739 554$E-006$
Surface traction $\mathbf{t}^r(\mathbf{u})$	$\mathbf{A}_{\sigma mn}$	Real	2 428 314 018.991 16	2 428 314 018.989 99
		Image	−1 054 103 839.385 82	−1 054 103 839.384 77
	$\mathbf{B}_{\sigma mn}$	Real	1 399 305 709.137 16	1 399 305 709.136 72
		Image	−2 995 786 997.034 60	−2 995 786 997.034 18
	$\mathbf{C}_{\sigma mn}$	Real	−284 238 498.416 907	−284 238 498.416 907
		Image	−447 101 072.216 521	−447 101 072.216 522
Surface pressure $p_f(\mathbf{u})$	$Y_{\sigma mn}$	Real	19 402 353 258.420 7	19 402 353 258.421 5
		Image	−11 075 018 273.124 7	−11 075 018 273.124 2

$$a_{135}^{(\alpha)} = i\sum_{\beta=1}^{4} \mathbf{Q}_{135,135}^{(\alpha,\beta)} f_{135}^{(\beta)},$$
$$c_{135}^{(\alpha)} = -i\sum_{\beta=1}^{4} \hat{\mathbf{Q}}_{135,135}^{(\alpha,\beta)} f_{135}^{(\beta)}. \tag{87}$$

Let the radius of the spherical inclusion be $a=1.0$ m, and the excitation circular frequency be $\omega=400\pi$ rad/s. Based on the series representations in Eqs. (45) and (46), we obtain the surface displacement, traction, and pore pressure fields in the exterior surrounding. In the same way, we use Eq. (47) to obtain those in the interior region. These results are represented through the composition of three mutually perpendicular vectors $\mathbf{A}_{\sigma mn}$, $\mathbf{B}_{\sigma mn}$, and $\mathbf{C}_{\sigma mn}$ in Table II. For example: the exterior surface displacements can be written as follows:

$$\begin{aligned}\mathbf{u}_+(a,\theta,\phi) = {} & (3.149\,836\,582\,067\,977\times 10^{-2} \\ & - 2.278\,746\,278\,743\,160\times 10^{-2} i)\mathbf{A}_{\sigma mn} \\ & + (-1.069\,388\,568\,430\,973\times 10^{-2} \\ & + 1.530\,721\,666\,871\,404\times 10^{-3} i)\mathbf{B}_{\sigma mn} \\ & + (-2.814\,212\,411\,037\,520\times 10^{-3} \\ & - 4.426\,656\,392\,015\,449\times 10^{-3} i)\mathbf{C}_{\sigma mn},\end{aligned} \tag{88}$$

and the exterior pressure as

$$\begin{aligned}p_{f+}(a,\theta,\phi) = {} & (19\,402\,353\,258.4207 \\ & - 11\,075\,018\,273.1247 i) Y_{\sigma mn}.\end{aligned} \tag{89}$$

The final value of the displacements at any point (a,θ,ϕ) on the interface may be calculated by assigning the associated coordinates θ and ϕ to the vectors $\mathbf{A}_{\sigma mn}$, $\mathbf{B}_{\sigma mn}$, and $\mathbf{C}_{\sigma mn}$. On the other hand, we also tested the continuity condition at the interface for the elastic inclusion case subjected to the same incident wave. The material properties of this elastic inclusion are listed in Table I. The displacement and traction fields approaching from inside or outside are shown in Table III. Notice that the tangential relative fluid displacement and the pressure at the interface are not equal to zero. From Tables II and III, we can observe that the data for the displacements, tractions, and pressure at the interface indeed satisfy the conditions of the continuity with high accuracy.

B. A spherical inclusion subjected to a plane compressional wave

Here, we compare our results with those obtained by Zimmerman and Stern (1993a) for the case of an elastic inclusion embedded within a poroelastic medium. In another case, we consider a poroelastic inclusion instead. The normal tractions at the interface and the displacements along the z axis were calculated for both cases.

For an incident plane compressional wave impinging on the inclusion, the incident coefficients for the transition matrix can be obtained by Eq. (50). Let the incident wave be a fast dilatational plane wave with a wave number k_{p1} and the incident wave travel along the negative z direction. Therefore, the incident wave with unit amplitude travels from top to bottom to the inclusion as shown in Fig. 2. The potential of this plane wave can be represented as

TABLE III. The comparison with the coefficients obtained from the exterior surrounding and the elastic inclusion.

	Component		Exterior region	Interior region
Surface displacement **u**	$\mathbf{A}_{\sigma mn}$	Real	4.071 286 613 427 816$E-003$	4.071 286 611 782 576$E-003$
		Image	$-1.685\,221\,590\,015\,828E-003$	$-1.685\,221\,592\,749\,420E-003$
	$\mathbf{B}_{\sigma mn}$	Real	2.035 293 559 519 147$E-003$	2.035 293 565 217 255$E-003$
		Image	$-5.012\,095\,768\,116\,342E-003$	$-5.012\,095\,766\,713\,687E-003$
	$\mathbf{C}_{\sigma mn}$	Real	$-9.107\,823\,272\,134\,219E-004$	$-9.107\,823\,272\,139\,289E-004$
		Image	$-1.437\,668\,292\,634\,142E-003$	$-1.437\,668\,292\,634\,112E-003$
Surface relative fluid displacement **w**(**u**)	$\mathbf{A}_{\sigma mn}$	Real	$-3.006\,039\,861\,475\,074E-012\approx 0$	
		Image	$8.982\,370\,403\,032\,292E-012\approx 0$	
	$\mathbf{B}_{\sigma mn}$	Real	6.680 955 005 514 02	
		Image	6.959 414 289 793 27	
	$\mathbf{C}_{\sigma mn}$	Real	$-1.399\,010\,338\,725\,970E-004$	
		Image	1.517 358 390 854 540$E-004$	
Surface traction $\mathbf{t}^r(\mathbf{u})$	$\mathbf{A}_{\sigma mn}$	Real	2 434 871 386.974 41	2 434 871 386.975 46
		Image	−1 182 345 039.949 28	−1 182 345 039.950 07
	$\mathbf{B}_{\sigma mn}$	Real	1 363 138 977.279 15	1 363 138 977.279 54
		Image	−3 007 829 193.450 28	−3 007 829 193.448 97
	$\mathbf{C}_{\sigma mn}$	Real	−283 656 981.051 847	−283 656 981.051 846
		Image	−447 752 042.894 842	−447 752 042.894 843
Surface pressure $p_f(\mathbf{u})$	$Y_{\sigma mn}$	Real	20 087 161 071.830 8[a]	20 087 161 071.890 7[b]
		Image	−11 072 223 754.063 4[a]	−11 072 223 754.018 2[b]

[a]This result is calculated from Eq. (46).
[b]This result is calculated from Eq. (70).

$$\varphi_1^i = \frac{\varphi_0}{\mu_1} e^{ik_{p1}(z-a)}. \tag{90}$$

With the series expansion, the exponential term can be expanded into the series of the spherical Bessel function and the Legendre polynomials (Ying and Truell, 1956) as

$$\varphi_1^i = \frac{\varphi_0}{\mu_1} e^{ik_{p1}z} e^{-ik_{p1}a} = \frac{\varphi_0}{\mu_1} e^{-ik_{p1}a} \sum_{n=0}^{\infty} (2n+1) i^n j_n(k_{p1}R) P_n(\cos\theta), \tag{91}$$

where $P_n(\cos\theta)$ is the Legendre polynomials [i.e., $P_n^m(\cos\theta)$ with $m=0$]. At the same time, we set $\sigma=1$ (even) through comparing Eq. (91) with the spherical surface harmonics in Eq. (25). Thus the associated displacement fields are obtained from Eqs. (8) and (18),

$$\mathbf{u}^i = \nabla(\varphi_0 e^{ik_{p1}z}) e^{-ik_{p1}a} = \frac{k_p}{\mu_1} \varphi_0 e^{-ik_{p1}a} \sum_{n=0}^{\infty} (2n+1) i^n \hat{\mathbf{u}}_{10n}^{(1)}. \tag{92}$$

Substituting Eq. (92) into Eq. (50), we obtain the incident coefficients,

$$a_{\sigma mn}^{(\alpha)} = \begin{cases} \varphi_0 e^{-ik_{p1}a}(2n+1) i^n k_p/\mu_1 & \alpha=1, \sigma=1, m=0, \quad \text{and} \quad n \in N, \\ 0 \quad \text{otherwise.} \end{cases} \tag{93}$$

All results pertain to a spherical inclusion with $a=1.0$ m. Figure 3 shows the surface normal tractions on the elastic inclusion at a low frequency 200 Hz and at a high frequency 2000 Hz, respectively. Figure 4 shows the amplitudes of the scattered wave along the z axis at the two frequencies. The results obtained by Zimmerman and Stern (1993a) are also plotted by an asterisk (*) in Figs. 3 and 4. The differences are negligible except those in the region near the interface at 2000 Hz. In fact, the amplitude obtained from Eq. (43) consists of four parts: $\mathbf{u}^{(1)}$, $\mathbf{u}^{(2)}$, $\mathbf{u}^{(3)}$, and $\mathbf{u}^{(4)}$. Under the incidence of the fast dilatational plane wave, the contribution of the mode conversion for the third part $\mathbf{u}^{(3)}$ is zero. The details of the second and fourth parts in the region near the interface plotted in Fig. 5 show that the curves sway stronger and their phases change faster. As a result of the constructive and destructive phase interference, the curve for the radial amplitude in the region near the interface seems to be rough and irregular as shown in Fig. 4. Figure 6 presents the results for the surface normal tractions for the poroelastic inclusion at a low frequency 200 Hz and at a high frequency 2000 Hz. The patterns in this case are more obscure than those in the elastic case. The results shown in Fig. 7 display

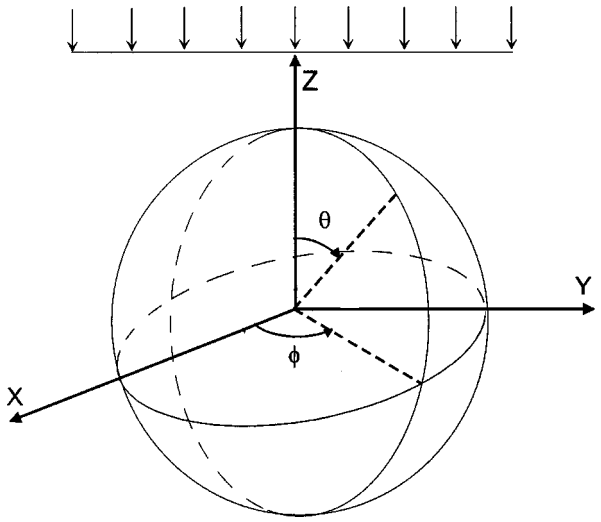

FIG. 2. A plane harmonic wave impinges on an inclusion embedded in an infinite medium.

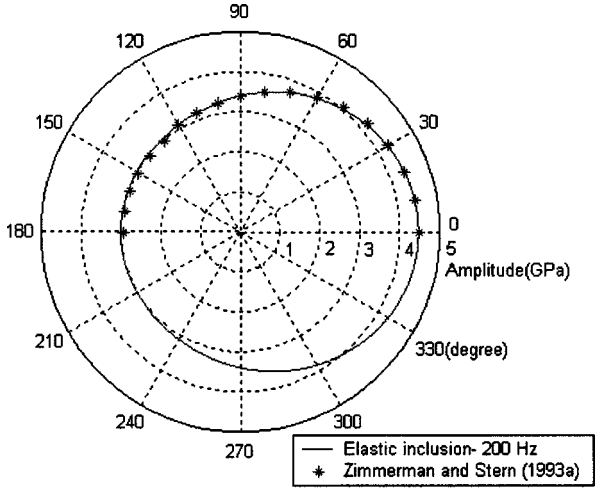

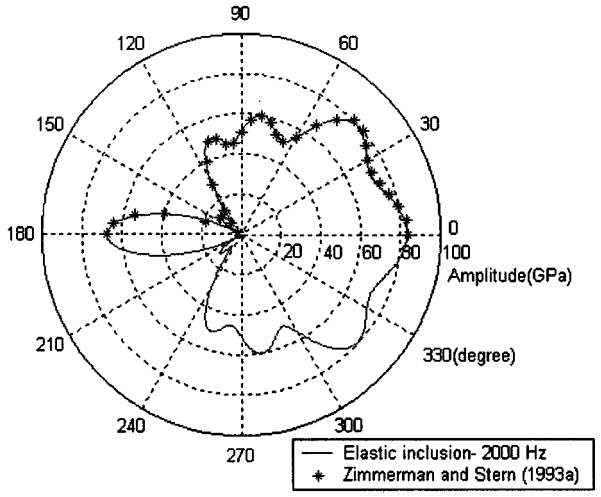

FIG. 3. Amplitude of normal traction at surface (elastic inclusion).

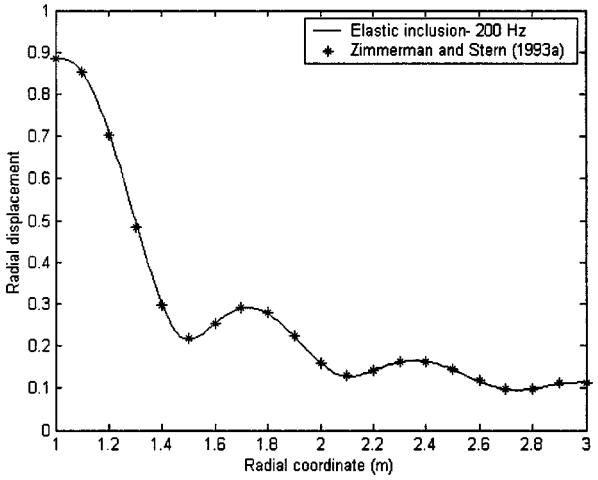

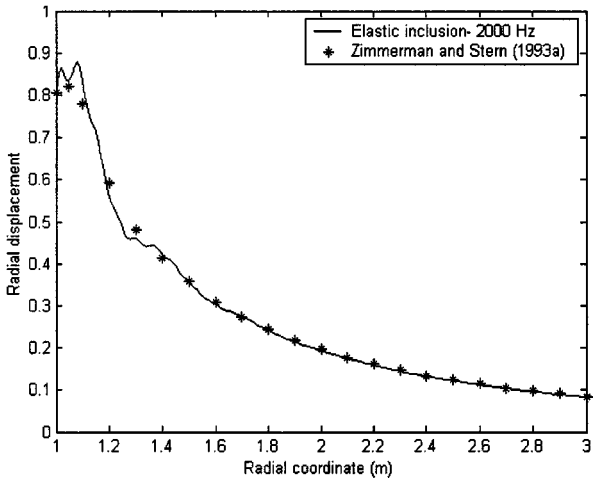

FIG. 4. Amplitude of radial displacement along *z* axis (elastic inclusion).

the amplitudes of the radial displacements for the scattered waves along the *z* axis at the two frequencies. The swaying region for the curve at 2000 Hz is due to the interference which has been discussed in the elastic inclusion case.

V. CONCLUDING REMARKS

A solution based on the transition matrix for the scattered wave has several advantages especially for scatterers

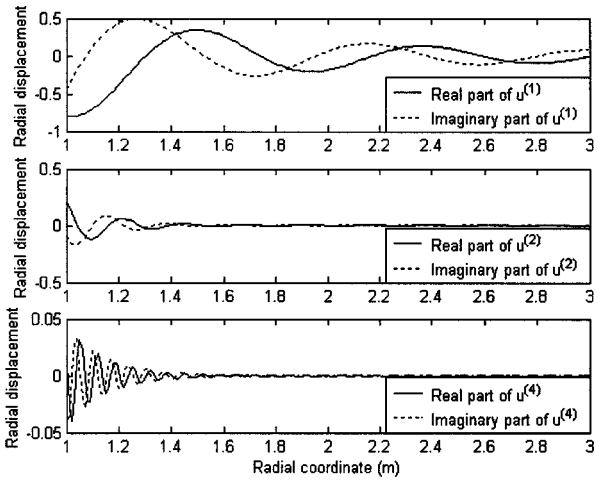

FIG. 5. Radial displacement for each coupling part along *z* axis at 2000 Hz (elastic inclusion).

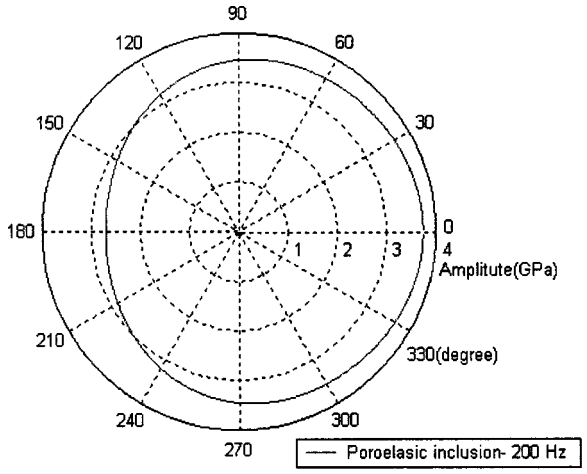

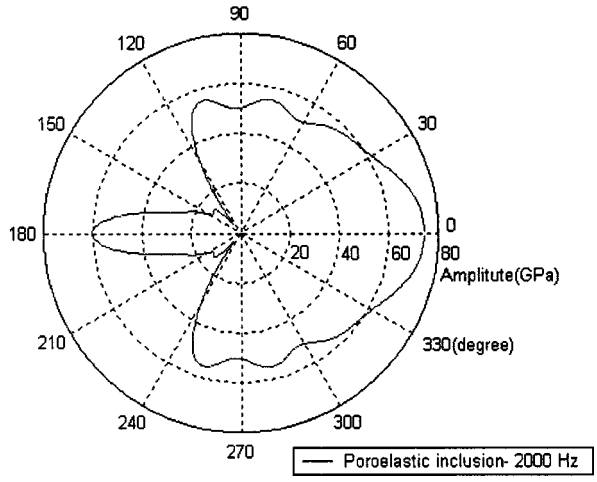

FIG. 6. Amplitude of normal traction at surface (poroelastic inclusion).

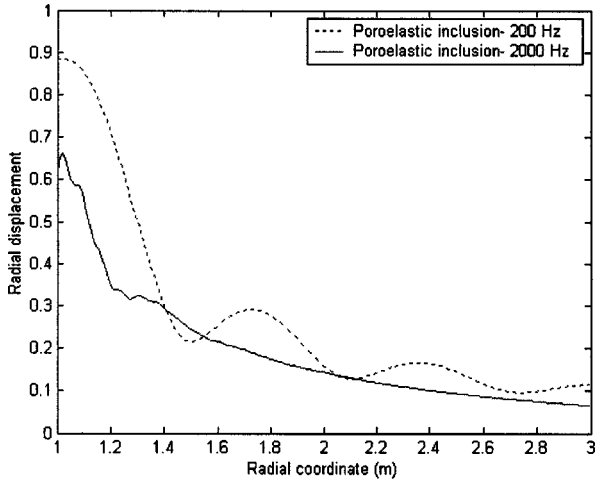

FIG. 7. Amplitude of radial displacement along z axis (poroelastic inclusion).

with an arbitrary shape because this approach can match the surface boundary conditions geometrically. However, to apply the transition matrix method, it is necessary to construct a set of complete and orthogonal basis functions satisfying the three orthogonality conditions.

In this paper we adopt the approach introduced by Pao (1978) for elastic scattering problem to develop the transition matrix for the analysis of the scattering problem in poroelastic medium. A set of basis functions for a poroelastic medium are presented. The related orthogonality conditions are obtained by applying Betti's third identity generalized for the poroelasticity and the transition matrix is derived accordingly. In order to show its validity and accuracy, this transition matrix is employed to analyze the wave scattered by an elastic spherical inclusion embedded in a poroelastic medium.

It appears that solving the scattering problem for a poroelastic inclusion is more complex than that for the elastic one. However, in our opinion, the analysis of the poroelastic inclusion problem by applying the transition matrix approach is actually easier than the elastic inclusion case because the conditions at the interface of the latter are the degenerated case of the former.

Some illustrative numerical results show that the regions near the interface present strong interferences which are caused by the coupling effect of the dilatational and rotational waves. This phenomenon can be explained by the reflection of the coupling waves. In addition, the amplitude of the radial displacement increases rapidly when the receiver approaches to the interface. The difference between the elastic and poroelastic inclusion shows that the amplitudes of normal traction for the elastic case are larger with more definite patterns.

ACKNOWLEDGMENTS

The authors gratefully acknowledge the financial support granted by the National Science Council, R.O.C., (NSC-091-2211-E-002-080). The facility of calculation provided by National Taiwan University is also highly appreciated.

APPENDIX A: NORMALIZING TO THE DILATATIONAL WAVES

This appendix presents the normalizing procedure for the dilatational waves. The determinant of the coefficients from the characteristic equation in Eq. (10) is set to zero as

$$\begin{vmatrix} \rho-(2\mu+\lambda_c)\dfrac{k^2}{\omega^2} & \rho_f-\alpha M\dfrac{k^2}{\omega^2} \\ \rho_f-\alpha M\dfrac{k^2}{\omega^2} & \rho_m-M\dfrac{k^2}{\omega^2} \end{vmatrix}=0. \tag{A1}$$

Equation (A1) provides the characteristic values as

$$k_{p1}^2/\omega^2=(B-\sqrt{B^2-4AC})/2A,$$
$$k_{p2}^2/\omega^2=(B+\sqrt{B^2-4AC})/2A. \tag{A2}$$

where A, B, and C are defined in Eq. (12). Substitution of Eq. (A2) into Eq. (A1) gives two corresponding characteristic vectors,

$$\langle \mu_1,1\rangle^T=\left\langle -\left(\rho_m-M\frac{k_{p1}^2}{\omega^2}\right)\Big/\left(\rho_f-\alpha M\frac{k_{p1}^2}{\omega^2}\right),1\right\rangle^T,$$
$$\langle 1,\mu_2\rangle^T=\left\langle 1,-\left[\rho-(\lambda_c+2\mu)\frac{k_{p2}^2}{\omega^2}\right]\Big/\left(\rho_f-\alpha M\frac{k_{p2}^2}{\omega^2}\right)\right\rangle^T. \tag{A3}$$

In order to normalize Eq. (10), we rewrite the parameters μ_1 and μ_2 shown in the preceding equations in a common denominator form,

$$\mu_1=-\left(\rho_m-M\frac{k_{p1}^2}{\omega^2}\right)\left(\rho_f-\alpha M\frac{k_{p2}^2}{\omega^2}\right)\Big/\left[\left(\rho_f-\alpha M\frac{k_{p1}^2}{\omega^2}\right)\left(\rho_f-\alpha M\frac{k_{p2}^2}{\omega^2}\right)\right],$$
$$\mu_2=-\left[\rho-(\lambda_c+2\mu)\frac{k_{p2}^2}{\omega^2}\right]\left(\rho_f-\alpha M\frac{k_{p1}^2}{\omega^2}\right)\Big/\left[\left(\rho_f-\alpha M\frac{k_{p1}^2}{\omega^2}\right)\left(\rho_f-\alpha M\frac{k_{p2}^2}{\omega^2}\right)\right], \tag{A4}$$

where Eq. (A4) can be further simplified to the equations presented in Eq. (15). The normalized matrices corresponding to Eq. (10) are expressed as

$$\begin{bmatrix}(\lambda_c+2\mu)^* & 0\\ 0 & M^*\end{bmatrix}\equiv\begin{bmatrix}\mu_1 & 1\\ 1 & \mu_2\end{bmatrix}^T\begin{bmatrix}(\lambda_c+2\mu) & \alpha M\\ \alpha M & M\end{bmatrix}\begin{bmatrix}\mu_1 & 1\\ 1 & \mu_2\end{bmatrix}$$
$$=\begin{bmatrix}(\lambda_c+2\mu)\mu_1^2+2\alpha M\mu_1+M & (\lambda_c+2\mu)\mu_1+\alpha M\mu_1\mu_2+\alpha M+M\mu_2\\ (\lambda_c+2\mu)\mu_1+\alpha M\mu_1\mu_2+\alpha M+M\mu_2 & (\lambda_c+2\mu)+2\alpha M\mu_2+M\mu_2^2\end{bmatrix}, \tag{A5}$$

and

$$\begin{bmatrix}\rho^* & 0\\ 0 & \rho_m^*\end{bmatrix}\equiv\begin{bmatrix}\mu_1 & 1\\ 1 & \mu_2\end{bmatrix}^T\begin{bmatrix}\rho & \rho_f\\ \rho_f & \rho_m\end{bmatrix}\begin{bmatrix}\mu_1 & 1\\ 1 & \mu_2\end{bmatrix}=\begin{bmatrix}\rho\mu_1^2+2\rho_f\mu_1+\rho_m & \rho\mu_1+\rho_f\mu_1\mu_2+\rho_f+\rho_m\mu_2\\ \rho\mu_1+\rho_f\mu_1\mu_2+\rho_f+\rho_m\mu_2 & \rho+2\rho_f\mu_2+\rho_m\mu_2^2\end{bmatrix}. \tag{A6}$$

With the aid of

$$4ac-d^2=-2b^2+2b\sqrt{b^2+4ac}, \tag{A7}$$

the symmetric off-diagonal elements of Eq. (A5) vanish,

$$(\lambda_c+2\mu)\mu_1+\alpha M\mu_1\mu_2+\alpha M+M\mu_2=0, \tag{A8}$$

in which the analogous condition has not been presented in Kargl and Lim's paper. Through the aid of

$$b^2+4ac=B^2-4AC, \tag{A9}$$

the element (1,1) of Eq. (A5) is given by

$$(\lambda_c+2\mu)^*=\frac{1}{c^2}[-A\sqrt{B^2-4AC}]\left[\rho-(\lambda_c+2\mu)\frac{k_{p2}^2}{\omega^2}\right], \tag{A10}$$

and the element (2,2) of Eq. (A5) is given by

$$M^*=\frac{1}{a^2}A\sqrt{B^2-4AC}\left(\rho_m-M\frac{k_{p1}^2}{\omega^2}\right). \tag{A11}$$

Based on the definitions of Eqs. (12) and (14), we have the diagonal elements of Eq. (A6),

$$\rho^*=-\frac{A}{c^2}\frac{k_{p1}^2}{\omega^2}\sqrt{B^2-4AC}\left[\rho-(\lambda_c+2\mu)\frac{k_{p2}^2}{\omega^2}\right], \tag{A12}$$

$$\rho_m^* = \frac{A}{a^2}\frac{k_{p2}^2}{\omega^2}\sqrt{B^2-4AC}\left(\rho_m - M\frac{k_{p1}^2}{\omega^2}\right), \tag{A13}$$

and show that the symmetric off-diagonal elements of Eq. (A6) are zero. Furthermore, we also use some algebraic techniques to obtain the following identities among the factors μ_1, μ_2, and μ_3:

$$\mu_1(\lambda_c+2\mu)+\alpha M-\mu\mu_1(k_s^2/k_{p1}^2)+\mu_3 M(\alpha\mu_1+1)=0, \tag{A14}$$

$$\lambda_c+2\mu+\mu_2\alpha M-\mu(k_s^2/k_{p2}^2)+\mu_3 M(\alpha+\mu_2)=0.$$

These results will be useful in the evaluation of Eq. (B17) and the analogous conditions have not been presented in Kargl and Lim's paper.

APPENDIX B: ELEMENTS IN Q MATRIX FOR A POROELASTIC SPHERICAL INCLUSION AND THE DERIVATION OF ORTHOGONALITY CONDITIONS

This appendix lists the elements of **Q** for a poroelastic spherical inclusion with radius a. In addition, we apply the $\mathbf{Q}^*$ matrix to derive the orthogonality conditions defined in Eqs. (37)–(39). An opening interface condition is assumed between the sphere inclusion and the surrounding medium. To take the advantage of the spherical symmetry in evaluation $\mathbf{Q}^{(\alpha,\beta)}_{\sigma mn,\sigma' m' n'}$, it is convenient to choose the origin of the coordinate system to be located at the center of the sphere and designate the outward unit surface-normal vector $\mathbf{n}=\mathbf{e}_R$. Making use of Eqs. (30)–(35), we can evaluate the surface integral in Eq. (54). The Q matrix is written as

$$\mathbf{Q}^{(\alpha,\beta)}_{\sigma mn,\sigma mn} = \frac{k_s}{\mu D^{(\alpha)}_{\sigma mn}}\begin{bmatrix} \mathbf{Q}^{*(1,1)} & \mathbf{Q}^{*(1,2)} & \mathbf{Q}^{*(1,3)} & \mathbf{Q}^{*(1,4)} \\ \mathbf{Q}^{*(2,1)} & \mathbf{Q}^{*(2,2)} & \mathbf{Q}^{*(2,3)} & \mathbf{Q}^{*(2,4)} \\ \mathbf{Q}^{*(3,1)} & \mathbf{Q}^{*(3,2)} & \mathbf{Q}^{*(3,3)} & \mathbf{Q}^{*(3,4)} \\ \mathbf{Q}^{*(4,1)} & \mathbf{Q}^{*(4,2)} & \mathbf{Q}^{*(4,3)} & \mathbf{Q}^{*(4,4)} \end{bmatrix}_{\sigma mn,\sigma mn}, \tag{B1}$$

where Q matrix is diagonal with the indexes $(\sigma mn,\sigma' m' n')$. The elements are shown as follows:

$$\begin{aligned}\mathbf{Q}^{*(1,1)}_{\sigma mn,\sigma mn} = {} & \frac{4\pi(n+m)!a^2}{\epsilon_m(2n+1)(n-m)!}\left\{ h_n^{(2)}(k_{p1}a)j_n(k_{p1(0)}a)\left(\frac{-2\mu_1\mu_{1(0)}n(n+1)}{k_p k_{p(0)}a^3}\right)(\mu-\mu_{(0)}) + h_n^{(2)}(k_{p1}a)j_n'(k_{p1(0)}a)\right. \\ & \times\left(\frac{k_{p1}^2 k_{p1(0)}}{k_p k_{p(0)}}\right)\left[-\lambda_c\mu_1\mu_{1(0)}-\alpha\mu_{1(0)}M-\mu_1\alpha M-M+\left(\frac{2\mu_1\mu_{1(0)}n(n+1)}{k_{p1}^2a^2}\right)(\mu-\mu_{(0)})-2\mu\mu_1\mu_{1(0)}\right] \\ & + h_n^{(2)'}(k_{p1}a)j_n(k_{p1(0)}a)\left(\frac{k_{p1}k_{p1(0)}^2}{k_p k_{p(0)}}\right)\left[\lambda_{c(0)}\mu_1\mu_{1(0)}+\mu_1\alpha_{(0)}M_{(0)}+\alpha_{(0)}\mu_{1(0)}M_{(0)}+M_{(0)}\right. \\ & \left.+\left(\frac{2\mu_1\mu_{1(0)}n(n+1)}{k_{p1(0)}^2a^2}\right)(\mu-\mu_{(0)})+2\mu_{(0)}\mu_1\mu_{1(0)}\right] + h_n^{(2)'}(k_{p1}a)j_n'(k_{p1(0)}a)\left(\frac{-4\mu_1\mu_{1(0)}k_{p1}k_{p1(0)}}{k_p k_{p(0)}a}\right) \\ & \left.\times(\mu-\mu_{(0)})\right\}, \end{aligned} \tag{B2}$$

$$\begin{aligned}\mathbf{Q}^{*(1,2)}_{\sigma mn,\sigma mn} = {} & \frac{4\pi(n+m)!a^2}{\epsilon_m(2n+1)(n-m)!}\left\{ h_n^{(2)}(k_{p1}a)j_n(k_{p2(0)}a)\left(\frac{-2\mu_1 n(n+1)}{k_p k_{p(0)}a^3}\right)(\mu-\mu_{(0)}) + h_n^{(2)}(k_{p1}a)j_n'(k_{p2(0)}a)\left(\frac{k_{p1}^2k_{p2(0)}}{k_p k_{p(0)}}\right)\right. \\ & \times\left[-\mu_1\lambda_c-2\mu\mu_1-\mu_1\mu_{2(0)}\alpha M-\alpha M-\mu_{2(0)}M+\left(\frac{2\mu_1 n(n+1)}{k_{p1}^2a^2}\right)(\mu-\mu_{(0)})\right] + h_n^{(2)'}(k_{p1}a)j_n(k_{p2(0)}a) \\ & \times\left(\frac{k_{p1}k_{p2(0)}^2}{k_p k_{p(0)}}\right)\left[\mu_1\lambda_{c(0)}+2\mu_{(0)}\mu_1+\mu_1\mu_{2(0)}\alpha_{(0)}M_{(0)}+\alpha_{(0)}M_{(0)}+\mu_{2(0)}M_{(0)}+\left(\frac{2\mu_1 n(n+1)}{k_{p2(0)}^2a^2}\right)(\mu-\mu_{(0)})\right] \\ & \left.+ h_n^{(2)'}(k_{p1}a)j_n'(k_{p2(0)}a)\left(\frac{-4\mu_1 k_{p1}k_{p2(0)}}{k_p k_{p(0)}a}\right)(\mu-\mu_{(0)})\right\}, \end{aligned} \tag{B3}$$

$$\mathbf{Q}^{*(1,4)}_{\sigma mn,\sigma mn}=n(n+1)\frac{4\pi(n+m)!a^2}{\epsilon_m(2n+1)(n-m)!}\left\{h_n^{(2)}(k_{p1}a)j_n(k_{s(0)}a)\left(\frac{k_{p1}^2}{k_pk_{s(0)}a}\right)\left[-\lambda_c\mu_1-2\mu\mu_1-\alpha M+2\mu_1\left(\frac{n^2+n-1}{k_{p1}^2a^2}\right)\right.\right.$$
$$\left.\times(\mu-\mu_{(0)})+\mu_1\mu_{(0)}\frac{k_{s(0)}^2}{k_{p1}^2}-\mu_{3(0)}M(\alpha\mu_1+1)\right]+h_n^{(2)}(k_{p1}a)j_n'(k_{s(0)}a)\left(\frac{-2\mu_1}{k_pa^2}\right)(\mu-\mu_{(0)})$$
$$\left.+h_n^{(2)'}(k_{p1}a)j_n(k_{s(0)}a)\left(\frac{-2\mu_1k_{p1}}{k_pk_{s(0)}a^2}\right)(\mu-\mu_{(0)})+h_n^{(2)'}(k_{p1}a)j_n'(k_{s(0)}a)\left(\frac{2\mu_1k_{p1}}{k_pa}\right)(\mu-\mu_{(0)})\right\},\tag{B4}$$

$$\mathbf{Q}^{*(2,1)}_{\sigma mn,\sigma mn}=\frac{4\pi(n+m)!a^2}{\epsilon_m(2n+1)(n-m)!}\left\{h_n^{(2)}(k_{p2}a)j_n(k_{p1(0)}a)\left(\frac{-2\mu_{1(0)}n(n+1)}{k_pk_{p(0)}a^3}\right)(\mu-\mu_{(0)})+h_n^{(2)}(k_{p2}a)j_n'(k_{p1(0)}a)\right.$$
$$\times\left(\frac{k_{p2}^2k_{p1(0)}}{k_pk_{p(0)}}\right)\left[-\mu_{1(0)}\lambda_c-2\mu\mu_{1(0)}-\mu_{1(0)}\mu_2\alpha M-\alpha M-\mu_2M+\left(\frac{2\mu_{1(0)}n(n+1)}{k_{p2}^2a^2}\right)(\mu-\mu_{(0)})\right]$$
$$+h_n^{(2)'}(k_{p2}a)j_n(k_{p1(0)}a)\left(\frac{k_{p2}k_{p1(0)}^2}{k_pk_{p(0)}}\right)\left[\mu_{1(0)}\lambda_{c(0)}+2\mu_{(0)}\mu_{1(0)}+\mu_{1(0)}\mu_2\alpha_{(0)}M_{(0)}+\alpha_{(0)}M_{(0)}+\mu_2M_{(0)}\right.$$
$$\left.\left.+\left(\frac{2\mu_{1(0)}n(n+1)}{k_{p1(0)}^2a^2}\right)(\mu-\mu_{(0)})\right]+h_n^{(2)'}(k_{p2}a)j_n'(k_{p1(0)}a)\left(\frac{-4\mu_{1(0)}k_{p1(0)}k_{p2}}{k_pk_{p(0)}a}\right)(\mu-\mu_{(0)})\right\},\tag{B5}$$

$$\mathbf{Q}^{*(2,2)}_{\sigma mn,\sigma mn}=\frac{4\pi(n+m)!a^2}{\epsilon_m(2n+1)(n-m)!}\left\{h_n^{(2)}(k_{p2}a)j_n(k_{p2(0)}a)\left(\frac{-2n(n+1)}{k_pk_{p(0)}a^3}\right)(\mu-\mu_{(0)})+h_n^{(2)}(k_{p2}a)j_n'(k_{p2(0)}a)\left(\frac{k_{p2}^2k_{p2(0)}}{k_pk_{p(0)}}\right)\right.$$
$$\times\left[-\lambda_c-\mu_2\alpha M-\mu_{2(0)}\alpha M-\mu_2\mu_{2(0)}M+\left(\frac{2n(n+1)}{k_{p2}^2a^2}\right)(\mu-\mu_{(0)})-2\mu\right]+h_n^{(2)'}(k_{p2}a)j_n(k_{p2(0)}a)$$
$$\times\left(\frac{k_{p2}k_{p2(0)}^2}{k_pk_{p(0)}}\right)\left[\lambda_{c(0)}+\mu_{2(0)}\alpha_{(0)}M_{(0)}+\mu_2\alpha_{(0)}M_{(0)}+\mu_2\mu_{2(0)}M_{(0)}+\left(\frac{2n(n+1)}{k_{p2(0)}^2a^2}\right)(\mu-\mu_{(0)})+2\mu_{(0)}\right]$$
$$\left.+h_n^{(2)'}(k_{p2}a)j_n'(k_{p2(0)}a)\left(\frac{-4k_{p2}k_{p2(0)}}{k_pk_{p(0)}a}\right)(\mu-\mu_{(0)})\right\},\tag{B6}$$

$$\mathbf{Q}^{*(2,4)}_{\sigma mn,\sigma mn}=n(n+1)\frac{4\pi(n+m)!a^2}{\epsilon_m(2n+1)(n-m)!}\left\{h_n^{(2)}(k_{p2}a)j_n(k_{s(0)}a)\left(\frac{k_{p2}^2}{k_pk_{s(0)}a}\right)\left[-\lambda_c-2\mu-\mu_2\alpha M+2\left(\frac{n^2+n-1}{k_{p2}^2a^2}\right)\right.\right.$$
$$\left.\times(\mu-\mu_{(0)})+\frac{\mu_{(0)}k_{s(0)}^2}{k_{p2}^2}-\mu_{3(0)}M(\alpha+\mu_2)\right]+h_n^{(2)}(k_{p2}a)j_n'(k_{s(0)}a)\left(\frac{-2}{k_pa^2}\right)(\mu-\mu_{(0)})$$
$$\left.\times+h_n^{(2)'}(k_{p2}a)j_n(k_{s(0)}a)\left(\frac{-2k_{p2}}{k_pk_{s(0)}a^2}\right)(\mu-\mu_{(0)})+h_n^{(2)'}(k_{p2}a)j_n'(k_{s(0)}a)\left(\frac{2k_{p2}}{k_pa}\right)(\mu-\mu_{(0)})\right\},\tag{B7}$$

$$\mathbf{Q}^{*(3,3)}_{\sigma mn,\sigma mn}=n(n+1)\frac{4\pi(n+m)!a^2}{\epsilon_m(2n+1)(n-m)!}\left\{h_n^{(2)}(k_sa)j_n(k_{s(0)}a)\left(\frac{-1}{a}\right)(\mu-\mu_{(0)})+h_n^{(2)}(k_sa)j_n'(k_{s(0)}a)(-\mu_{(0)}k_{s(0)})\right.$$
$$\left.+h_n^{(2)'}(k_sa)j_n(k_{s(0)}a)(\mu k_s)\right\},\tag{B8}$$

$$\mathbf{Q}^{*(4,1)}_{\sigma mn,\sigma mn}=n(n+1)\frac{4\pi(n+m)!a^2}{\epsilon_m(2n+1)(n-m)!}\left\{h_n^{(2)}(k_sa)j_n(k_{p1(0)}a)\left(\frac{k_{p1(0)}^2}{k_{p(0)}k_sa}\right)\left[\mu_{1(0)}\lambda_{c(0)}+2\mu_{(0)}\mu_{1(0)}+\alpha_{(0)}M_{(0)}\right.\right.$$
$$\left.+2\mu_{1(0)}\frac{n^2+n-1}{k_{p1(0)}^2a^2}(\mu-\mu_{(0)})-\frac{\mu\mu_{1(0)}k_s^2}{k_{p1(0)}^2}+\mu_3M_{(0)}(\alpha_{(0)}\mu_{1(0)}+1)\right]+h_n^{(2)}(k_sa)j_n'(k_{p1(0)}a)$$
$$\times\left(\frac{-2\mu_{1(0)}k_{p1(0)}}{k_{p(0)}k_sa^2}\right)(\mu-\mu_{(0)})+h_n^{(2)'}(k_sa)j_n(k_{p1(0)}a)\left(\frac{-2\mu_{1(0)}}{k_{p(0)}a^2}\right)(\mu-\mu_{(0)})+h_n^{(2)'}(k_sa)j_n'(k_{p1(0)}a)$$
$$\left.\times\left(\frac{2\mu_{1(0)}k_{p1(0)}}{k_{p(0)}a}\right)(\mu-\mu_{(0)})\right\},\tag{B9}$$

$$\mathbf{Q}^{*(4,2)}_{\sigma mn,\sigma mn}=n(n+1)\frac{4\pi(n+m)!a^2}{\epsilon_m(2n+1)(n-m)!}\left\{h_n^{(2)}(k_sa)j_n(k_{p2(0)}a)\left(\frac{k_{p2(0)}^2}{k_{p(0)}k_sa}\right)\left[\lambda_{c(0)}+2\mu_{(0)}+\mu_{2(0)}\alpha_{(0)}M_{(0)}\right.\right.$$
$$\left.+2\frac{(n^2+n-1)}{k_{p2(0)}^2a^2}(\mu-\mu_{(0)})-\frac{\mu k_s^2}{k_{p2(0)}^2}+\mu_3M_{(0)}(\alpha_{(0)}+\mu_{2(0)})\right]+h_n^{(2)}(k_sa)j_n'(k_{p2(0)}a)\left(\frac{-2k_{p2(0)}}{k_{p(0)}k_sa^2}\right)(\mu-\mu_{(0)})$$
$$\left.+h_n^{(2)'}(k_sa)j_n(k_{p2(0)}a)\left(\frac{-2}{k_{p(0)}a^2}\right)(\mu-\mu_{(0)})+h_n^{(2)'}(k_sa)j_n'(k_{p2(0)}a)\left(\frac{2k_{p2(0)}}{k_{p(0)}a}\right)(\mu-\mu_{(0)})\right\},\tag{B10}$$

$$\mathbf{Q}^{*(4,4)}_{\sigma mn,\sigma mn}=n(n+1)\frac{2[4\pi(n+m)!]a^2}{\epsilon_m(2n+1)(n-m)!}\left\{h_n^{(2)}(k_sa)j_n(k_{s(0)}a)\left(\frac{-1}{k_sk_{s(0)}a^3}\right)\left[(\mu-\mu_{(0)})+\frac{1}{2}a^2(\mu k_s^2-\mu_{(0)}k_{s(0)}^2)\right]+h_n^{(2)}\right.$$
$$\times(k_sa)j_n'(k_{s(0)}a)\left(\frac{1}{k_sa^2}\right)\left[(n^2+n-1)(\mu-\mu_{(0)})-\frac{1}{2}a^2\mu k_s^2\right]+h_n^{(2)'}(k_sa)j_n(k_{s(0)}a)\left(\frac{1}{k_{s(0)}a^2}\right)\left[(n^2+n-1)\right.$$
$$\left.\left.\times(\mu-\mu_{(0)})+\frac{1}{2}a^2\mu_{(0)}k_{s(0)}^2\right]+h_n^{(2)'}(k_sa)j_n'(k_{s(0)}a)\left(\frac{-1}{a}\right)(\mu-\mu_{(0)})\right\},\tag{B11}$$

and $\mathbf{Q}^{*(1,3)}_{\sigma mn,\sigma mn}=\mathbf{Q}^{*(2,3)}_{\sigma mn,\sigma mn}=\mathbf{Q}^{*(3,1)}_{\sigma mn,\sigma mn}=\mathbf{Q}^{*(3,2)}_{\sigma mn,\sigma mn}=\mathbf{Q}^{*(3,4)}_{\sigma mn,\sigma mn}=\mathbf{Q}^{*(4,3)}_{\sigma mn,\sigma mn}=0$. Recall that a subscript (0) is used to indicate the parameters of the interior material. Also, remember that there are no zero-order rotational basis functions. The elements of $\hat{\mathbf{Q}}$ are obtained from those of $\mathbf{Q}$ by replacing the spherical Hankel function $h_n^{(2)}$ with the spherical Bessel function j_n.

If the interior medium is identical with the exterior one, the subscript (0) is directly removed. Consider on a specific surface S_+ with radius a, the elements of $\mathbf{Q}^*$ matrix reduce to the third orthogonality condition presented in Eq. (39). They are

$$\mathbf{Q}^{*(1,1)}_{\sigma mn,\sigma mn}=\frac{4\pi(n+m)!a^2}{\epsilon_m(2n+1)(n-m)!}\left(\frac{-k_{p1}^3}{k_p^2}\right)W\{h_n^{(2)}(k_{p1}a),j_n(k_{p1}a)\}[(\lambda_c+2\mu)\mu_1^2+2\mu_1\alpha M+M]$$
$$=\left(\frac{-i\mu}{k_s}\right)\frac{4\pi(n+m)!}{\epsilon_m(2n+1)(n-m)!}\left[(\lambda_c+2\mu)^*\frac{k_sk_{p1}}{\mu k_p^2}\right],\tag{B12}$$

where the Wronskian formula (Abramowitz and Stegun, 1964) is defined as

$$W\{h_n^{(2)}(ka),j_n(ka)\}=h_n^{(2)}(ka)j_n'(ka)-h_n^{(2)'}(ka)j_n(ka)$$
$$=i/(ka)^2,\tag{B13}$$

and $(\lambda_c+2\mu)^*$ has been defined in Eq. (19):

$$\mathbf{Q}^{*(2,2)}_{\sigma mn,\sigma mn}=\frac{4\pi(n+m)!a^2}{\epsilon_m(2n+1)(n-m)!}\left(\frac{-k_{p2}^3}{k_p^2}\right)W\{h_n^{(2)}(k_{p2}a),j_n(k_{p2}a)\}\times[\lambda_c+2\mu+2\mu_2\alpha M+\mu_2^2M]$$
$$=\left(\frac{-i\mu}{k_s}\right)\frac{4\pi(n+m)!}{\epsilon_m(2n+1)(n-m)!}\left[M^*\frac{k_sk_{p2}}{\mu k_p^2}\right],\tag{B14}$$

where M^* has also been defined in Eq. (19),

$$\mathbf{Q}^{*(1,2)}_{\sigma mn,\sigma mn}=\frac{4\pi(n+m)!a^2}{\epsilon_m(2n+1)(n-m)!}\left(\frac{-k_{p1}k_{p2}}{k_p^2}\right)[k_{p1}h_n^{(2)}(k_{p1}a)j_n'(k_{p2}a)-k_{p2}h_n^{(2)'}(k_{p1}a)j_n(k_{p2}a)]$$
$$\times[\mu_1\lambda_c+2\mu\mu_1+\mu_1\mu_2\alpha M+\alpha M+\mu_2 M]=0, \tag{B15}$$

and

$$\mathbf{Q}^{*(2,1)}_{\sigma mn,\sigma mn}=\frac{4\pi(n+m)!a^2}{\epsilon_m(2n+1)(n-m)!}\left(\frac{-k_{p1}k_{p2}}{k_p^2}\right)[k_{p2}h_n^{(2)}(k_{p2}a)j_n'(k_{p1}a)-k_{p1}h_n^{(2)'}(k_{p2}a)j_n(k_{p1}a)]$$
$$\times[\mu_1\lambda_c+2\mu\mu_1+\mu_1\mu_2\alpha M+\alpha M+\mu_2 M]=0, \tag{B16}$$

where the zero value is given from Eq. (A8). In addition,

$$\begin{aligned}&\mathbf{Q}^{*(1,4)}_{\sigma mn,\sigma mn}=0,\\&\mathbf{Q}^{*(4,1)}_{\sigma mn,\sigma mn}=0,\\&\mathbf{Q}^{*(2,4)}_{\sigma mn,\sigma mn}=0,\\&\mathbf{Q}^{*(4,2)}_{\sigma mn,\sigma mn}=0,\end{aligned} \tag{B17}$$

where we have made use of the relations in Eq. (A14). Finally, we evaluate the last two elements:

$$\mathbf{Q}^{*(3,3)}_{\sigma mn,\sigma mn}=\left(\frac{-i\mu}{k_s}\right)\frac{4\pi(n+m)!}{\epsilon_m(2n+1)(n-m)!}[n(n+1)], \tag{B18}$$

$$\mathbf{Q}^{*(4,4)}_{\sigma mn,\sigma mn}=\left(\frac{-i\mu}{k_s}\right)\frac{4\pi(n+m)!}{\epsilon_m(2n+1)(n-m)!}[n(n+1)]. \tag{B19}$$

When the spherical Bessel function is replaced by the spherical Hankel function from the Wronskian formulation of Eqs. (B2)–(B11), we obtain the zero value identically on any arbitrary surface S (outside S_+ and inside S_∞) and this result leads the second orthogonality condition. While the spherical Hankel function is replaced by the spherical Bessel function in Eqs. (B2)–(B11) on a specific surface inside S_+, we derive the first orthogonality condition.

APPENDIX C: ELEMENTS IN Q′ MATRIX FOR AN ELASTIC SPHERICAL INCLUSION

For the case of an elastic spherical inclusion, the traction operators for a spherical surface of the inclusion are obtained as follows (Pao, 1978):

$$\mathbf{t}^r(\hat{\mathbf{u}}^{(1)}_{\sigma mn(0)})=2\mu_{(0)}k_{p(0)}\left\{\left[\left(n^2+n-\frac{1}{2}k_{s(0)}^2R^2\right)\frac{j_n(k_{p(0)}R)}{(k_{p(0)}R)^2}-\frac{2j_n'(k_{p(0)}R)}{k_{p(0)}R}\right]\mathbf{A}_{\sigma mn}\right.$$
$$\left.+(n^2+n)^{1/2}\left[\frac{j_n'(k_{p(0)}R)}{k_{p(0)}R}-\frac{j_n(k_{p(0)}R)}{(k_{p(0)}R)^2}\right]\mathbf{B}_{\sigma mn}\right\}, \tag{C1}$$

$$\mathbf{t}^r(\hat{\mathbf{u}}^{(3)}_{\sigma mn(0)})=\mu_{(0)}\left[k_{s(0)}j_n'(k_{s(0)}R)-\frac{j_n(k_{s(0)}R)}{R}\right](n^2+n)^{1/2}\mathbf{C}_{\sigma mn}, \tag{C2}$$

$$\mathbf{t}^r(\hat{\mathbf{u}}^{(4)}_{\sigma mn(0)})=2\mu_{(0)}k_{s(0)}\left\{(n^2+n)\left[\frac{j_n(k_{s(0)}R)}{k_{s(0)}R}\right]'\mathbf{A}_{\sigma mn}\right.$$
$$\left.+\left[\left(n^2+n-1-\frac{(k_{s(0)}R)^2}{2}\right)\frac{j_n(k_{s(0)}R)}{(k_{s(0)}R)^2}-\frac{j_n'(k_{s(0)}R)}{k_{s(0)}R}\right](n^2+n)^{1/2}\mathbf{B}_{\sigma mn}\right\}. \tag{C3}$$

Then the elements of $\mathbf{Q}'$ matrix defined in Eq. (73) are

$$\mathbf{Q}'^{(\alpha,\beta)}_{\sigma mn,\sigma mn}=\frac{k_s}{\mu D^{(\alpha)}_{\sigma mn}}\begin{bmatrix}\mathbf{Q}^{*(1,1)} & \mathbf{Q}^{*(1,2)} & \mathbf{Q}^{*(1,3)} & \mathbf{Q}^{*(1,4)}\\ \mathbf{Q}^{*(2,1)} & \mathbf{Q}^{*(2,2)} & \mathbf{Q}^{*(2,3)} & \mathbf{Q}^{*(2,4)}\\ \mathbf{Q}^{*(3,1)} & \mathbf{Q}^{*(3,2)} & \mathbf{Q}^{*(3,3)} & \mathbf{Q}^{*(3,4)}\\ \mathbf{Q}^{*(4,1)} & \mathbf{Q}^{*(4,2)} & \mathbf{Q}^{*(4,3)} & \mathbf{Q}^{*(4,4)}\end{bmatrix}_{\sigma mn,\sigma mn}. \tag{C4}$$

The nonzero elements are listed as follows:

$$\mathbf{Q}^{*(1,1)}_{\sigma mn,\sigma mn}=\frac{4\pi(n+m)!a^2}{\epsilon_m(2n+1)(n-m)!}\left\{h_n^{(2)}(k_{p1}a)j_n(k_{p(0)}a)\left(\frac{-2\mu_1 n(n+1)}{k_pk_{p(0)}a^3}\right)(\mu-\mu_{(0)})+h_n^{(2)}(k_{p1}a)j_n'(k_{p(0)}a)\left(\frac{k_{p1}^2}{k_p}\right)\right.$$
$$\times\left[-\lambda_c\mu_1-\alpha M-2\mu\mu_1+2\mu_1\frac{n(n+1)}{k_{p1}^2a^2}(\mu-\mu_{(0)})\right]+h_n^{(2)'}(k_{p1}a)j_n(k_{p(0)}a)\left(\frac{2\mu_1k_{p1}}{k_pk_{p(0)}a^2}\right)$$
$$\left.\times\left[n(n+1)(\mu-\mu_{(0)})+\frac{1}{2}\mu_{(0)}k_{s(0)}^2a^2\right]+h_n^{(2)'}(k_{p1}a)j_n'(k_{p(0)}a)\left(\frac{-4\mu_1k_{p1}}{k_pa}\right)(\mu-\mu_{(0)})\right\},\tag{C5}$$

$$\mathbf{Q}^{*(1,2)}_{\sigma mn,\sigma mn}=\frac{4\pi(n+m)!a^2}{\epsilon_m(2n+1)(n-m)!}h_n^{(2)'}(k_{p1}a)j_n(k_{p2}a)\left\{M(\alpha+\mu_2)\left(\frac{k_{p1}k_{p2}^2}{k_p^2}\right)\right\},\tag{C6}$$

$$\mathbf{Q}^{*(1,4)}_{\sigma mn,\sigma mn}=n(n+1)\frac{4\pi(n+m)!a^2}{\epsilon_m(2n+1)(n-m)!}\left\{h_n^{(2)}(k_{p1}a)j_n(k_{s(0)}a)\left(\frac{k_{p1}^2}{k_pk_{s(0)}a}\right)\right[(-\lambda_c\mu_1-2\mu\mu_1-\alpha M)$$
$$+\left(\frac{2\mu_1}{k_{p1}^2a^2}\right)(n^2+n-1)(\mu-\mu_{(0)})+\frac{\mu_1\mu_{(0)}k_{s(0)}^2}{k_{p1}^2}\left]+h_n^{(2)}(k_{p1}a)j_n'(k_{s(0)}a)\left(\frac{-2\mu_1}{k_pa^2}\right)(\mu-\mu_{(0)})\right.$$
$$\left.+h_n^{(2)'}(k_{p1}a)j_n(k_{s(0)}a)\left(\frac{-2\mu_1k_{p1}}{k_pk_{s(0)}a^2}\right)(\mu-\mu_{(0)})+h_n^{(2)'}(k_{p1}a)j_n'(k_{s(0)}a)\left(\frac{2\mu_1k_{p1}}{k_pa}\right)(\mu-\mu_{(0)})\right\},\tag{C7}$$

$$\mathbf{Q}^{*(2,1)}_{\sigma mn,\sigma mn}=\frac{4\pi(n+m)!a^2}{\epsilon_m(2n+1)(n-m)!}\left\{h_n^{(2)}(k_{p2}a)j_n(k_{p(0)}a)\left(\frac{-2n(n+1)}{k_pk_{p(0)}a^3}\right)(\mu-\mu_{(0)})+h_n^{(2)}(k_{p2}a)j_n'(k_{p(0)}a)\left(\frac{k_{p2}^2}{k_p}\right)\right.$$
$$\times\left[-\lambda_c-\alpha M\mu_2-2\mu+\frac{2n(n+1)}{k_{p2}^2a^2}(\mu-\mu_{(0)})\right]+h_n^{(2)'}(k_{p2}a)j_n(k_{p(0)}a)\left(\frac{2k_{p2}}{k_pk_{p(0)}a^2}\right)\left[(n^2+n)(\mu-\mu_{(0)})\right.$$
$$\left.\left.+\frac{1}{2}\mu_{(0)}k_{s(0)}^2a^2\right]+h_n^{(2)'}(k_{p2}a)j_n'(k_{p(0)}a)\left(\frac{-4k_{p2}}{k_pa}\right)(\mu-\mu_{(0)})\right\},\tag{C8}$$

$$\mathbf{Q}^{*(2,2)}_{\sigma mn,\sigma mn}=\frac{4\pi(n+m)!a^2}{\epsilon_m(2n+1)(n-m)!}h_n^{(2)'}(k_{p2}a)j_n(k_{p2}a)\left[M(\alpha+\mu_2)\left(\frac{\mu_2k_{p2}^3}{k_p^2}\right)\right],\tag{C9}$$

$$\mathbf{Q}^{*(2,4)}_{\sigma mn,\sigma mn}=n(n+1)\frac{4\pi(n+m)!a^2}{\epsilon_m(2n+1)(n-m)!}\left\{h_n^{(2)}(k_{p2}a)j_n(k_{s(0)}a)\left(\frac{k_{p2}^2}{k_pk_{s(0)}a}\right)\right[(-\lambda_c-2\mu-\alpha M\mu_2)$$
$$+\frac{2}{k_{p2}^2a^2}(n^2+n-1)(\mu-\mu_{(0)})+\frac{\mu_{(0)}k_{s(0)}^2}{k_{p2}^2}\left]+h_n^{(2)}(k_{p2}a)j_n'(k_{s(0)}a)\left(\frac{-2}{k_pa^2}\right)(\mu-\mu_{(0)})\right.$$
$$\left.+h_n^{(2)'}(k_{p2}a)j_n(k_{s(0)}a)\left(\frac{-2k_{p2}}{k_pk_{s(0)}a^2}\right)(\mu-\mu_{(0)})+h_n^{(2)'}(k_{p2}a)j_n'(k_{s(0)}a)\left(\frac{2k_{p2}}{k_pa}\right)(\mu-\mu_{(0)})\right\},\tag{C10}$$

$$\mathbf{Q}^{*(3,3)}_{\sigma mn,\sigma mn}=n(n+1)\frac{4\pi(n+m)!a^2}{\epsilon_m(2n+1)(n-m)!}\left\{h_n^{(2)}(k_sa)j_n(k_{s(0)}a)\left(\frac{-1}{a}\right)(\mu-\mu_{(0)})+h_n^{(2)}(k_sa)j_n'(k_{s(0)}a)(-\mu_{(0)}k_{s(0)})\right.$$
$$\left.+h_n^{(2)'}(k_sa)j_n(k_{s(0)}a)(\mu k_s)\right\},\tag{C11}$$

$$\mathbf{Q}^{*(4,1)}_{\sigma mn,\sigma mn}=n(n+1)\frac{4\pi(n+m)!a^2}{\epsilon_m(2n+1)(n-m)!}\left\{h_n^{(2)}(k_sa)j_n(k_{p(0)}a)\left(\frac{2}{k_{p(0)}k_sa^3}\right)\left[(n^2+n-1)(\mu-\mu_{(0)})\right.\right.$$
$$\left.-\frac{1}{2}a^2(\mu k_s^2-\mu_{(0)}k_{s(0)}^2)\right]+h_n^{(2)}(k_sa)j_n'(k_{p(0)}a)\left(\frac{-2}{k_sa^2}\right)(\mu-\mu_{(0)})+h_n^{(2)'}(k_sa)j_n(k_{p(0)}a)\left(\frac{-2}{k_{p(0)}a^2}\right)(\mu-\mu_{(0)})$$
$$\left.+h_n^{(2)'}(k_sa)j_n'(k_{p(0)}a)\left(\frac{2}{a}\right)(\mu-\mu_{(0)})\right\}, \tag{C12}$$

$$\mathbf{Q}^{*(4,2)}_{\sigma mn,\sigma mn}=\frac{4\pi(n+m)!a^2}{\epsilon_m(2n+1)(n-m)!}h_n^{(2)}(k_sa)j_n(k_{p2}a)\left[M(\alpha+\mu_2)\left(\frac{\mu_3k_{p2}^2(n^2+n)}{k_pk_sa}\right)\right], \tag{C13}$$

$$\mathbf{Q}^{*(4,4)}_{\sigma mn,\sigma mn}=2n(n+1)\frac{4\pi(n+m)!a^2}{\epsilon_m(2n+1)(n-m)!}\left\{h_n^{(2)}(k_sa)j_n(k_{s(0)}a)\left(\frac{-1}{k_sk_{s(0)}a^3}\right)\left[(\mu-\mu_{(0)})+\frac{1}{2}a^2(\mu k_s^2-\mu_{(0)}k_{s(0)}^2)\right]\right.$$
$$+h_n^{(2)}(k_sa)j_n'(k_{s(0)}a)\left(\frac{1}{k_sa^2}\right)\left[(n^2+n-1)(\mu-\mu_{(0)})-\frac{1}{2}a^2\mu k_s^2\right]+h_n'^{(2)}(k_sa)j_n(k_{s(0)}a)$$
$$\left.\times\left(\frac{1}{k_{s(0)}a^2}\right)\left[(n^2+n-1)(\mu-\mu_{(0)})+\frac{1}{2}a^2\mu_{(0)}k_{s(0)}^2\right]+h_n'^{(2)}(k_sa)j_n'(k_{s(0)}a)\left(\frac{-1}{a}\right)(\mu-\mu_{(0)})\right\}, \tag{C14}$$

and $\mathbf{Q}^{*(1,3)}_{\sigma mn,\sigma mn}=\mathbf{Q}^{*(2,3)}_{\sigma mn,\sigma mn}=\mathbf{Q}^{*(3,1)}_{\sigma mn,\sigma mn}=\mathbf{Q}^{*(3,2)}_{\sigma mn,\sigma mn}=\mathbf{Q}^{*(3,4)}_{\sigma mn,\sigma mn}=\mathbf{Q}^{*(4,3)}_{\sigma mn,\sigma mn}=0$. In the preceding equations, the elements $Q^{*(1,2)}$, $Q^{*(2,2)}$, and $Q^{*(4,2)}$ are attributed from the pore pressure part. The elements of $\hat{\mathbf{Q}}'$ can be obtained from those of $\mathbf{Q}'$ by replacing the spherical Hankel function $h_n^{(2)}$ with the spherical Bessel function j_n. Similarly, the nonzero $\mathbf{R}$ vector defined in Eq. (74) can be evaluated analytically,

$$\mathbf{R}^{(1)}_{\sigma mn,\sigma mn}=\left(\frac{k_s}{\mu D^{(1)}_{\sigma mn}}\right)\frac{4\pi(n+m)!a^2}{\epsilon_m(2n+1)(n-m)!}j_n(k_{p1}a)h_n^{(2)'}(k_{p1}a)M(\alpha\mu_1+1)\left(\frac{k_{p1}^3}{k_p^2}\right), \tag{C15}$$

$$\mathbf{R}^{(2)}_{\sigma mn,\sigma mn}=\left(\frac{k_s}{\mu D^{(2)}_{\sigma mn}}\right)\frac{4\pi(n+m)!a^2}{\epsilon_m(2n+1)(n-m)!}j_n(k_{p1}a)h_n^{(2)'}(k_{p2}a)M(\alpha\mu_1+1)\left(\frac{\mu_2k_{p1}^2k_{p2}}{k_p^2}\right), \tag{C16}$$

$$\mathbf{R}^{(4)}_{\sigma mn,\sigma mn}=n(n+1)\left(\frac{k_s}{\mu D^{(4)}_{\sigma mn}}\right)\frac{4\pi(n+m)!a^2}{\epsilon_m(2n+1)(n-m)!}j_n(k_{p1}a)h_n^{(2)}(k_sa)M(\alpha\mu_1+1)\left(\frac{\mu_3k_{p1}^2}{k_pk_sa}\right). \tag{C17}$$

The elements of $\hat{\mathbf{R}}$ can be obtained from those of $\mathbf{R}$ by replacing the spherical Hankel function $h_n^{(2)}$ with the spherical Bessel function j_n.

Abramowitz, M., and Stegun, I. A. (**1964**). *Handbook of Mathematical Functions With Formulas, Graphs, and Mathematical Tables*, National Bureau of Standards Applied Mathematics Series Vol. 55 (National Bureau of Standards, Washington, DC), Eq. (10.17), 437 pp.

Berryman, J. G. (**1985**). "Scattering by a spherical inhomogeneity in a fluid-saturated porous medium," J. Math. Phys. **26**, 1408–1419.

Biot, M. A. (**1956a**). "Theory of propagation of elastic waves in a fluid-saturated porous solid. I. Low-frequency range," J. Acoust. Soc. Am. **28**, 168–178.

Biot, M. A. (**1956b**). "Theory of propagation of elastic waves in a fluid-saturated porous solid. II. Higher frequency range," J. Acoust. Soc. Am. **28**, 179–191.

Biot, M. A. (**1962**). "Mechanics of deformation and acoustic propagation in porous media," J. Appl. Phys. **33**, 1482–1498.

Biot, M. A. (**1963**). "Generalized theory of acoustic propagation in porous dissipative media," J. Acoust. Soc. Am. **34**, 1254–1264.

Deresiewicz, H., and Skalak, R. (**1963**). "On uniqueness in dynamic poroelasticity," Bull. Seismol. Soc. Am. **53**, 783–788.

Halpern, M. R., and Christiano, P. (**1986**). "Response of poroelastic halfspace to steady-state harmonic surface tractions," Int. J. Numer. Analyt. Meth. Geomech. **10**, 609–632.

Kargl, S. G., and Lim, R. (**1993**). "A transition-matrix formulation of scattering in homogeneous, saturated, porous media," J. Acoust. Soc. Am. **94**, 1527–1550.

Lim, R., Lopes, J. L., Hackman, R. H., and Todoroff, D. G. (**1993**). "Scattering by objects buried in underwater sediments: theory and experiment," J. Acoust. Soc. Am. **93**, 1762–1783.

Lim, R. (**1994**). "Scattering by an obstacle in a plane-stratified poroelastic medium: Application to an obstacle in ocean sediments," J. Acoust. Soc. Am. **95**, 1223–1244.

Morochnik, V., Bardet, J. P., and Trifunac, M. D. (**1996**). "Viscoelastic approximation of poroelastic media for wave scattering problems," Soil Dyn. Earthquake Eng. **15**, 337–346.

Morse, P. M., and Feshbach, H. (**1953**). *Methods of Theoretical Physics* (McGraw–Hill, New York), Eq. (9), 1865 pp.

Pao, Y. H. (**1978**). "Betti's identity and transition matrix for elastic waves," J. Acoust. Soc. Am. **64**, 302–310.

Plona, T. J. (**1980**). "Observation of a second bulk compressional wave in a

porous medium at ultrasonic frequencies,'' Appl. Phys. Lett. **36**, 259–261.
Plona, T. J. (**1982**). ''Acoustics of fluid-saturated porous media,'' Ultrason. Symp. Proc. **2**, 1044–1048.
Waterman, P. C. (**1976**). ''Matrix theory of elastic wave scattering,'' J. Acoust. Soc. Am. **60**, 567–587.
Yew, C. H., and Jogi, P. N. (**1978**). ''The determination of Biot's parameters for sandstones. 1. Static tests,'' Exp. Mech. **18**, 167–172.
Ying, C. F., and Truell, R. (**1956**). ''Scattering of a plane longitudinal wave by a spherical obstacle in an isotropically elastic solid,'' J. Appl. Phys. **27**, 1086–1097.
Zimmerman, C., and Stern, M. (**1993a**). ''Scattering of plane compressional waves by spherical inclusions in a poroelastic medium,'' J. Acoust. Soc. Am. **94**, 527–536.
Zimmerman, C., and Stern, M. (**1993b**). ''Boundary element solution of 3-D wave scatter problems in a poroelastic medium,'' Eng. Anal. Boundary Elem. **12**, 223–240.

Impulsive sound reflection from an absorptive and dispersive planar boundary

Chee-Heun Lam, Bert Jan Kooij,[a] and Adrianus T. De Hoop
Laboratory of Electromagnetic Research, Faculty of Electrical Engineering, Mathematics and Computer Science, Delft University of Technology, 4 Mekelweg, 2628 CD Delft, The Netherlands

(Received 17 July 2003; revised 9 April 2004; accepted 6 May 2004)

The impulsive sound reflection from a planar boundary with absorptive and dispersive properties is investigated. The acoustic properties of the boundary are modeled via a local impedance transfer function whose complex frequency domain representation is taken to be a Padé (2,2) expression. The coefficients in this representation are matched to frequency domain acoustic wave reflection measurements. With the aid of the Cagniard–De Hoop method, a closed-form space-time expression is derived for the acoustic pressure of the reflected wave arising from the incidence of a point-source monopole excited spherical pulse. Depending on the acoustic impedance properties of the boundary, large-amplitude oscillating surface effects can occur. These surface phenomena differ in nature from the true surface waves like the Rayleigh, Scholte, and Stoneley waves in elastodynamics. Illustrative numerical results are presented.
[DOI: 10.1121/1.1766023]

PACS numbers: 43.20.El, 43.20.Bi, 43.20.Px, 43.55.Ev [JJM] Pages: 677–685

I. INTRODUCTION

For a variety of applications, the analysis of the reflection of sound waves, generated by a localized source, from a boundary surface with certain reflection and absorption properties is of importance. In outdoor sound propagation, the boundary can be a natural ground surface. In noise control, it can be a sound-absorbing layer covering a machine part. In architectural acoustics, the boundary can be a part of the sound reflecting and/or scattering structure that serves to realize a particular distribution of sound in, for example, a concert hall. In all these cases, it is of importance to have certain design parameters at one's disposition. This need can, at least partly, be satisfied through the study of certain canonical problems, in which category the analytically solvable ones have the advantage of revealing rather explicitly how the different configurational and material parameters influence the acoustic behavior of a particular structure as a whole.

The present paper performs a study in this category. It discusses the reflection of sound waves generated by an impulsive monopole point source, from a planar boundary with absorptive and dispersive properties. The latter are modeled as a local acoustic impedance relation, i.e., a local relation between the acoustic pressure and the normal component of the particle velocity of the sound wave.[1,2] The absorptive and dispersive properties are expressed via a complex-frequency domain Padé-type expression that guarantees passivity and causality, and in which the parameters can be adjusted to fit measured material reflection data. With the aid of the Cagniard–De Hoop (CdH) method,[3,4] closed-form analytic space-time expressions are obtained for the acoustic pressure in its dependence on the mutual position of a (monopole) source and a (monopole) receiver with respect to the boundary. In the literature,[5–8] much attention is paid to surface effects that show up when source and receiver are close to the boundary and that manifest themselves as large amplitudes in the acoustic pressure (in excess even of the ones associated with the reflection from a rigid boundary) occurring after the arrival of the wave front of the impulsive reflected wave. This phenomenon also shows up in acoustic experiments[9] as well as in the pertaining Finite-Difference Time-Domain method (FDTD) and field emission microscopy Finite Element Method (FEM) studies.[10,11] A careful analysis of the structure of our reflection function shows, however, that this phenomenon is not in the same category as the Rayleigh wave[12] along the planar boundary of a traction free elastic solid, the Scholte wave[3] along the planar fluid/solid interface, or the Stoneley waves[13] along the interface of two different solids. The analytic CdH method employed, further provides the changes in wave shape that the reflected wave undergoes, in their dependence on the parameters[14] occurring in the expression for the boundary's acoustic impedance.

One can argue whether a local impedance-type reaction sufficiently accurately models the presence of the second medium. As the analysis of the two-media problem with point-source excitation shows, the relation between acoustic pressure and normal component of the particle velocity is a nonlocal one of the type of a Dirichlet-to-Neumann map.[15] On the other hand, many studies in the acoustic literature use the local impedance concept. In particular, this holds for the numerical FDTD and FEM studies, where the discretization of a nonlocal Dirichlet-to-Neumann map would destroy the sparsity of the matrix representing the discretized acoustic pressure, while the incorporation of dispersive effects would also imply the incorporation of (noninstantaneous) time-relaxation effects via the relevant temporal convolution integrals. At least the latter phenomena are fully and exactly handled in an approach.

[a]Electronic mail: b.j.kooij@ewi.tudelft.nl

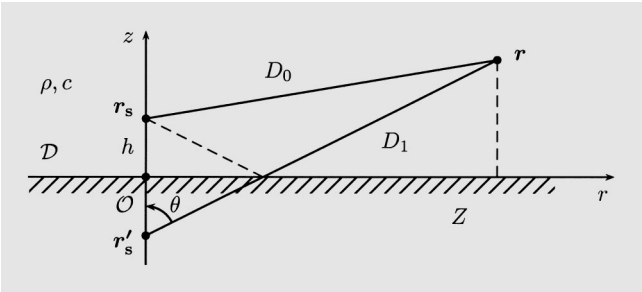

FIG. 1. Half-space configuration where h is the source height. Z is the normalized acoustic impedance transfer function of the planar boundary.

Finally, the analytic expressions obtained can serve as benchmarks in further computational studies based on the discretization of the acoustic wave equations.

II. FORMULATION OF THE PROBLEM

Position in the configuration is specified by the coordinates $\{x,y,z\}$ with respect to an orthogonal, Cartesian reference frame with the origin $\mathcal{O}$. Its base vectors $\{\mathbf{i}_x,\mathbf{i}_y,\mathbf{i}_z\}$ are mutually perpendicular, of unit length each, and they form, in the indicated order, a right-handed system. The position vector is $\mathbf{r}=x\mathbf{i}_x+y\mathbf{i}_y+z\mathbf{i}_z$. The vectorial spatial differentiation operator is $\boldsymbol{\nabla}=\mathbf{i}_x\partial_x+\mathbf{i}_y\partial_y+\mathbf{i}_z\partial_z$. The time coordinate is t; differentiation with respect to time is denoted by ∂_t.

The acoustic wave motion is studied in the half-space $\mathcal{D}=\{-\infty<x<\infty,-\infty<y<\infty,0<z<\infty\}$, which is filled with a fluid with volume density of mass ρ and compressibility κ. The speed of sound waves in it is given by $c=(\rho\kappa)^{-1/2}$. The acoustic pressure $p(\mathbf{r},t)$ and the particle velocity $\mathbf{v}(\mathbf{r},t)$ satisfy the first-order acoustic wave equations

$$\boldsymbol{\nabla}p+\rho\partial_t\mathbf{v}=0, \tag{1}$$

$$\boldsymbol{\nabla}\cdot\mathbf{v}+\kappa\partial_t p=Q(t)\,\delta(\mathbf{r}-\mathbf{r}_s). \tag{2}$$

Here, $Q(t)$ is the volume source density of injection rate (model for the action of a monopole transducer), and $\mathbf{r}_s=\{0,0,h\}$ is the location of the point source. The source starts to act at $t=0$ and prior to this instant the configuration is at rest. Figure 1 shows the configuration. The acoustical properties of the planar boundary are modeled via the linear, time-invariant, local acoustic impedance relation

$$p(x,y,0,t)=-(\rho c)^{-1}Z(t)\overset{(t)}{*}v_z(x,y,0,t), \tag{3}$$

where $\overset{(t)}{*}$ denotes temporal convolution and $Z(t)$ is the acoustic time-domain impedance function of the wall, normalized with respect to the acoustic wave impedance ρc of the fluid. A detailed discussion of the properties of the acoustic impedance is given in Sec. V. The acoustic wave field in the half space is written as the superposition of the incident wave field $\{p^i,\mathbf{v}^i\}$, which is the wave field in the fluid in the absence of the boundary, and the reflected wave field $\{p^r,\mathbf{v}^r\}$, that expresses the action of the reflecting wall, i.e.:

$$\{p,\mathbf{v}\}=\{p^i,\mathbf{v}^i\}+\{p^r,\mathbf{v}^r\}\quad\text{in }\mathcal{D}. \tag{4}$$

III. THE COMPLEX SLOWNESS REPRESENTATION FOR THE ACOUSTIC WAVE FIELDS

The time invariance and the causality of the sound waves are taken into account by the use of the unilateral Laplace transform

$$\{\hat{p},\hat{\mathbf{v}}\}(\mathbf{r},s)=\mathcal{L}[\{p,\mathbf{v}\}(\mathbf{r},t)]$$
$$=\int_{t=0}^{\infty}\exp(-st)\{p,\mathbf{v}\}(\mathbf{r},t)dt. \tag{5}$$

The Laplace transform parameter s is taken positive and real. Then, according to Lerch's theorem,[16] a one-to-one mapping exists between $\{p,\mathbf{v}\}(\mathbf{r},t)$ and their time-Laplace transformed counterparts $\{\hat{p},\hat{\mathbf{v}}\}(\mathbf{r},s)$. The configuration is initially at rest with the consequence that the transformation property $\partial_t\rightarrow s$ holds. Next, the complex slowness representations for $\{\hat{p},\hat{\mathbf{v}}\}(\mathbf{r},s)$ are introduced as

$$\{\hat{p},\hat{\mathbf{v}}\}(\mathbf{r},s)=\frac{s^2}{4\pi^2}\int_{\alpha=-\infty}^{\infty}d\alpha\int_{\beta=-\infty}^{\infty}\{\tilde{p},\tilde{\mathbf{v}}\}$$
$$\times(\alpha,\beta,z,s)\exp[-is(\alpha x+\beta y)]d\beta, \tag{6}$$

where α and β are the wave slownesses in the x and y directions, respectively. This representation entails the properties $\partial_x\rightarrow-is\alpha$, $\partial_y\rightarrow-is\beta$. Use of the transforms in Eqs. (1) and (2) yields

$$\begin{bmatrix}\tilde{p}^i\\ \tilde{p}^r\end{bmatrix}(\gamma,z,s)=\frac{\rho\hat{Q}(s)}{2\gamma}\begin{bmatrix}\exp(-s\gamma|z-h|)\\ \tilde{R}(\gamma,s)\exp(-s\gamma D_z)\end{bmatrix}, \tag{7}$$

in which

$$\gamma(\alpha,\beta)=(c^{-2}+\alpha^2+\beta^2)^{1/2} \tag{8}$$

is the wave slowness normal to the boundary with $\mathrm{Re}\{\gamma\}>0$, $D_z=z+h$, and $\tilde{R}$ denotes the slowness-domain reflection coefficient. Using the property, $\tilde{v}_z=-(s\rho)^{-1}\partial_z\tilde{p}$, the impedance boundary condition in the complex slowness domain can be written as

$$\lim_{z\downarrow0}\partial_z\tilde{p}=\frac{s}{c\hat{Z}(s)}\lim_{z\downarrow0}\tilde{p}. \tag{9}$$

From Eqs. (7) and (9), it follows that

$$\tilde{R}(\gamma,s)=\frac{c\gamma-1/\hat{Z}(s)}{c\gamma+1/\hat{Z}(s)}. \tag{10}$$

IV. SPACE-TIME EXPRESSIONS FOR THE ACOUSTIC WAVE FIELD CONSTITUENTS

A. Space-time incident wave fields

The expressions for the space-time incident sound waves can be found in De Hoop[17] and are given by

$$p^i(\mathbf{r},t)=\rho\partial_t^2Q(t)\overset{(t)}{*}G^i(\mathbf{r},t), \tag{11}$$

$$\mathbf{v}^i(\mathbf{r},t)=-\partial_tQ(t)\overset{(t)}{*}\boldsymbol{\nabla}G^i(\mathbf{r},t), \tag{12}$$

where

$$G^i(\mathbf{r},t)=\frac{1}{4\pi D_0}H(t-T_0) \tag{13}$$

denotes the incident-wave Green's function for the acoustic pressure. Here, $D_0=(x^2+y^2+|z-h|^2)^{1/2}>0$ is the distance between source and receiver, $T_0=D_0/c$ is the arrival time of the incident wave and $H(t)$ denotes the Heaviside unit step function.

B. Space-time reflected wave fields

The expressions for the reflected acoustic wave fields in the space-time domain are now constructed. With the aid of Eqs. (6) and (7), we first write the expressions for $\hat{p}^r$ and $\hat{v}_z^r$ as

$$\hat{p}^r(\mathbf{r},s)=\rho s^2\hat{Q}(s)\hat{G}^r(\mathbf{r},s), \tag{14}$$

$$\hat{\mathbf{v}}^r(\mathbf{r},s)=-s\hat{Q}(s)\boldsymbol{\nabla}\hat{G}^r(\mathbf{r},s), \tag{15}$$

where

$$\hat{G}^r(\mathbf{r},s)=\frac{1}{4\pi^2}\int_{\alpha=-\infty}^{\infty}d\alpha\int_{\beta=-\infty}^{\infty}\frac{\tilde{R}(\gamma,s)}{2\gamma}\times\exp\{-s[i(\alpha x+\beta y)+\gamma D_z]\}d\beta \tag{16}$$

denotes the reflected-wave Green's function for the acoustic pressure. From Eqs. (14)–(16), it is clear that the determination of the space-time reflected acoustic wave fields has been reduced to finding the space-time domain counterpart of Eq. (16). To this end, we employ the standard procedures in the CdH method.[3,4] The following transformation is carried out first

$$\begin{aligned}\alpha&=-ip\cos(\theta)-q\sin(\theta),\\ \beta&=-ip\sin(\theta)+q\cos(\theta),\end{aligned} \tag{17}$$

which for the vertical slowness leads to $\gamma(q,p)=[\Omega(q)^2-p^2]^{1/2}$, with $\Omega(q)=(c^{-2}+q^2)^{1/2}$. Next, the integration along the imaginary p axis in the complex p plane is replaced by one along the hyperbolic path $pr+\gamma(q,p)D_z=\tau$ with $T_1(q)<\tau<\infty$ where $T_1(q)=D_1\Omega(q)$. Here, $D_1=(x^2+y^2+D_z^2)^{1/2}>0$ is the distance from the image source to the receiver. Subsequently, the transformation

$$q=(\tau^2/D_1^2-c^{-2})^{1/2}\sin(\psi) \tag{18}$$

leads to

$$\hat{G}^r(\mathbf{r},s)=\frac{1}{4\pi D_1}\int_{\tau=T_1}^{\infty}\hat{K}^r(\mathbf{r},\tau,s)\exp(-s\tau)d\tau. \tag{19}$$

Here

$$\hat{K}^r(\mathbf{r},\tau,s)=\frac{2}{\pi}\int_{\psi=0}^{\pi/2}\mathrm{Re}[\tilde{R}(\overline{\gamma},s)]d\psi \tag{20}$$

denotes the reflected-wave kernel function, $T_1=T_1(0)=D_1/c$ is the arrival time of the reflected wave and $\overline{\gamma}(\mathbf{r},\tau,\psi)$ is the slowness after carrying out the indicated transformations. Assuming that $\hat{K}^r(\mathbf{r},\tau,s)$ has a causal time-domain counterpart $K^r(\mathbf{r},\tau,t)$, the space-time reflected-wave Green's function is found as

$$G^r(\mathbf{r},t)=\frac{1}{4\pi D_1}\times\int_{\tau=T_1}^{t}K^r(\mathbf{r},\tau,t-\tau)d\tau H(t-T_1). \tag{21}$$

Finally, the space-time reflected acoustic wave field quantities are obtained as

$$p^r(\mathbf{r},t)=\rho\partial_t^2Q(t)\overset{(t)}{*}G^r(\mathbf{r},t), \tag{22}$$

$$\mathbf{v}^r(\mathbf{r},t)=-\partial_tQ(t)\overset{(t)}{*}\boldsymbol{\nabla}G^r(\mathbf{r},t). \tag{23}$$

The determination of the reflected-wave kernel function, which depends on the impedance of the acoustic wall is discussed in the next section.

V. THE ACOUSTIC IMPEDANCE MODEL AND THE CORRESPONDING REFLECTED-WAVE KERNEL FUNCTION

The acoustic impedance transfer function must satisfy the conditions of linearity, time invariance, causality, and passivity. Accordingly, its complex frequency-domain counterpart must, together with its inverse, be an analytic function of s in $\{\mathrm{Re}(s)>0\}$ and it must take on real values for $\{\mathrm{Re}(s)>0,\mathrm{Im}(s)=0\}$. To meet the condition of partly instantaneous impulse response, $\hat{Z}(s)$ must attain a finite, real, positive limit as $|s|\to\infty$ in $\{\mathrm{Re}(s)\geqslant 0\}$. As in standard linear, time-invariant, causal, passive system theory, we take for $\hat{Z}(s)$ the Padé (2,2) expression

$$\hat{Z}_{(2,2)}(s)=Z_\infty\frac{(s+\alpha_z)(s+\beta_z)}{(s+\alpha_p)(s+\beta_p)}, \tag{24}$$

in which Z_∞, α_z, β_z, α_p, and β_p are adjustable parameters, subject to the conditions $Z_\infty>0$, $\{\alpha_z,\beta_z\}$ either both real and positive or each other's complex conjugate with a positive real part, and $\{\alpha_p,\beta_p\}$ either both real and positive or each other's complex conjugate with a positive real part. In an illustrative numerical result, the values of these coefficients will be matched to frequency-domain ($s=i2\pi f$) reflection measurements applying to the impedance boundary at hand. The time-domain impedance transfer function follows from Eq. (24) as

$$Z_{(2,2)}(t)=Z_\infty[\delta(t)+C_1\exp(-\alpha_pt)H(t)+C_2\exp(-\beta_pt)H(t)], \tag{25}$$

in which

$$\begin{aligned}C_1&=(\alpha_z\beta_z-\alpha_z\beta_p-\beta_z\beta_p+\beta_p^2)/(\alpha_p-\beta_p),\\ C_2&=(\alpha_z\beta_z-\alpha_z\alpha_p-\beta_z\alpha_p+\alpha_p^2)/(\beta_p-\alpha_p).\end{aligned} \tag{26}$$

To proceed with the determination of the reflected wave, $\tilde{R}(\overline{\gamma},s)$ is written as a partial-fraction expression of the type

$$\tilde{R}(\overline{\gamma},s)=\tilde{R}_0(\overline{\gamma})+\frac{\tilde{R}_1(\overline{\gamma})}{s+\tilde{p}_1(\overline{\gamma})}+\frac{\tilde{R}_2(\overline{\gamma})}{s+\tilde{p}_2(\overline{\gamma})}. \tag{27}$$

From Eqs. (10) and (24), the coefficients in this expression are found as

$$\tilde{R}_0(\overline{\gamma})=a_2/b_2,\quad \tilde{R}_1(\overline{\gamma})=d_1/2+D^{-1}(d_1e_1/2-d_0),$$

$$\tilde{R}_2(\overline{\gamma}) = d_1/2 + D^{-1}(d_0 - d_1 e_1/2), \tag{28}$$
$$\tilde{p}_1(\overline{\gamma}) = (e_1 + D)/2, \quad \tilde{p}_2(\overline{\gamma}) = (e_1 - D)/2,$$

where

$$D(\overline{\gamma}) = (e_1^2 - 4e_0)^{1/2}, \quad d_0(\overline{\gamma}) = a_0/b_2 - b_0 a_2/b_2^2,$$
$$d_1(\overline{\gamma}) = a_1/b_2 - b_1 a_2/b_2^2, \quad e_0(\overline{\gamma}) = b_0/b_2,$$
$$e_1(\overline{\gamma}) = b_1/b_2, \quad a_0(\overline{\gamma}) = c\overline{\gamma} Z_\infty \alpha_z \beta_z - \alpha_p \beta_p,$$
$$a_1(\overline{\gamma}) = c\overline{\gamma} Z_\infty (\alpha_z + \beta_z) - (\alpha_p + \beta_p), \tag{29}$$
$$a_2(\overline{\gamma}) = c\overline{\gamma} Z_\infty - 1, \quad b_0(\overline{\gamma}) = c\overline{\gamma} Z_\infty \alpha_z \beta_z + \alpha_p \beta_p,$$
$$b_1(\overline{\gamma}) = c\overline{\gamma} Z_\infty (\alpha_z + \beta_z) + (\alpha_p + \beta_p),$$
$$b_2(\overline{\gamma}) = c\overline{\gamma} Z_\infty + 1.$$

Use of Eq. (27) in Eq. (20) yields

$$\hat{K}^r(\mathbf{r},\tau,s) = \frac{2}{\pi} \int_{\psi=0}^{\pi/2} \mathrm{Re}\left[\tilde{R}_0 + \frac{\tilde{R}_1}{(s+\tilde{p}_1)} + \frac{\tilde{R}_2}{(s+\tilde{p}_2)}\right] d\psi, \tag{30}$$

from which the space-time counterpart follows as:

$$K^r(\mathbf{r},\tau,t) = \frac{2}{\pi} \int_{\psi=0}^{\pi/2} \mathrm{Re}[\tilde{R}_0 \delta(t) + \tilde{R}_1 \exp(-\tilde{p}_1 t) H(t) + \tilde{R}_2 \exp(-\tilde{p}_2 t) H(t)] d\psi. \tag{31}$$

If in the integration on the right-hand side values of ψ are met where $D(\overline{\gamma}) = 0$, the last two terms do blow up, but their sum attains a finite limit, as inspection of Eqs. (28) and (29) learns. This difficulty is circumvented by keeping, in the numerical procedure, always the last two terms together.

The solution for the kernel function is now complete and the space-time Green's function for the reflected acoustic pressure is found with Eq. (21). The delta function in Eq. (31) yields an instantaneous response in the reflected-wave Green's function, while the remaining terms, containing the exponential functions, start with zero values at the arrival time, and lead to the occurrence of a dispersive tail.

VI. SPECIAL CASES

In this section, we present expressions for the Green's function in some special cases. These are A: the arrival-time value, B: the case of source and receiver both placed on the boundary, C: the case of source and receiver aligned normal to the boundary.

A. Green's function at the arrival time

At the arrival time, $t = T_1$, the τ integral in Eq. (21) vanishes and only the delta function in Eq. (31) with $\tilde{R}_0$ as coefficient contributes to the reflected wave field value. $\tilde{R}_0$ depends on Z_∞ only and, hence, the relaxation properties of the boundary material do not influence the reflected wave at the early time. In terms of the angle θ, which is indicated in Fig. 1, the space-time reflected-wave Green's function for the acoustic pressure at the arrival time is

$$G^r(\theta(\mathbf{r}), t = T_1) = \frac{1}{4\pi D_1} R(\theta), \tag{32}$$

where

$$R(\theta) = \frac{\cos(\theta) - 1/Z_\infty}{\cos(\theta) + 1/Z_\infty}. \tag{33}$$

At normal incidence, we have $R(0) = (Z_\infty - 1)/(Z_\infty + 1)$, while at grazing incidence $R(\pi/2) = -1$. Another observation is that the numerator in Eq. (33) becomes zero when $\tan(\theta_B) = (Z_\infty^2 - 1)^{1/2}$. This occurs only for $Z_\infty \geqslant 1$, in which case θ_B is the Brewster angle, known from optics.

B. Source and receiver both on the boundary

For the case where both source and receiver are placed on the boundary, $D_z = 0$, we can not treat the incident and reflected wave fields separately. Therefore, we consider the total-wave Green's function for the acoustic pressure, whose complex slowness representation is given by (cf. Eqs. (16) and (17)):

$$\hat{G}(\mathbf{r},s)|_{D_z=0} = \frac{1}{4\pi^2 i} \int_{q=0}^{\infty} dq \int_{p=-i\infty}^{i\infty} \frac{1 + \tilde{R}(\gamma,s)}{\gamma} \times \exp(-spr) dp. \tag{34}$$

Replacing the integration along the imaginary p axis by a loop integral along the branch cut on the positive real p axis, which procedure is admissible since Jordan's lemma and Cauchy's theorem apply, the total-wave Green's function for the acoustic pressure is obtained as

$$\hat{G}(\mathbf{r},s)|_{D_z=0} = \frac{1}{2\pi r} \int_{\tau=T_1}^{\infty} \hat{K}(r,\tau,s) \exp(-s\tau) d\tau, \tag{35}$$

where

$$\hat{K}(\mathbf{r},\tau,s)|_{D_z=0} = \frac{2}{\pi} \int_{\psi=0}^{\pi/2} \frac{|\overline{\gamma}|^2}{|\overline{\gamma}|^2 + [\hat{Z}(s)c]^{-2}} d\psi \tag{36}$$

denotes the kernel function and $T_1 = r/c$ is the arrival time in this special case. After some elaboration the kernel function can be written in the form

$$\hat{K}(\mathbf{r},\tau,s)|_{D_z=0} = 1 - [1 + \hat{Z}(s)^2(\tau^2/T_1^2 - 1)]^{-1/2}. \tag{37}$$

For two special cases of this configuration, the transformation back to the time domain can be carried out analytically rather than numerically. The first one occurs when the acoustic impedance can be modeled as a Padé (0,0) expression, $\hat{Z}_{(0,0)}(s) = Z_\infty$, i.e., when no boundary relaxation effects occur. Then

$$G(\mathbf{r},t)|_{D_z=0} = \frac{1}{2\pi r}[1 - (1 + u^2)^{-1/2}] H(t - T_1), \tag{38}$$

where $u(r,t) = Z_\infty(t^2/T_1^2 - 1)^{1/2}$. This function decreases monotonically with increasing r and t and, hence, no peaked surface effects do occur. The second case amounts to a (1,1) Padé representation of the acoustic impedance

$$\hat{Z}_{(1,1)}(s)=Z_\infty\frac{(s+\alpha_z)}{(s+\alpha_p)}, \tag{39}$$

which case covers a large class of wool felts and grass grounds.[10] With the aid of Eqs. (35), (37), and (39), the space-time total-wave Green's function becomes

$$G(\mathbf{r},t)|_{D_z=0}=\frac{1}{2\pi r}H(t-T_1) - \frac{1}{\pi}\int_{\tau=T_1}^{\infty}\mathcal{L}^{-1}\left[\frac{(s+\alpha_p)\exp(-s\tau)}{(a_2s^2+a_1s+a_0)^{1/2}}\right]d\tau, \tag{40}$$

with

$$a_0(r,\tau)=\alpha_p^2+\alpha_z^2u^2,\quad a_1(r,\tau)=2(\alpha_p+\alpha_zu^2),\quad a_2(r,\tau)=1+u^2, \tag{41}$$

where $u=u(r,\tau)$. Using

$$\mathcal{L}^{-1}\left[\frac{\exp(-s\tau)}{\sqrt{s^2+a^2}}\right]=J_0[a(t-\tau)]H(t-\tau),\quad a\geqslant 0, \tag{42}$$

where $J_0(t)$ is the Bessel function of the first kind and order zero, the space-time total-wave Green's function for the acoustic pressure is obtained as

$$G(\mathbf{r},t)|_{D_z=0} =\frac{1}{2\pi r}\left[1-\frac{1}{\sqrt{a_2(r,t)}}-\int_{\tau=T_1}^{t}\frac{\exp[-v(t-\tau)]}{\sqrt{a_2(r,\tau)}} \times L\{J_0[w(t-\tau)]\}d\tau\right]H(t-T_1), \tag{43}$$

where

$$v(r,\tau)=a_1/(2a_2),\quad w(r,\tau)=|\alpha_z-\alpha_p|u/a_2\geqslant 0, \tag{44}$$

and L given by $L(r,t,\tau)=\partial_t+\alpha_p-v$. The time derivative acting on the Bessel function can be circumvented by using the Bessel functions property: $J_1(t)=-\partial_tJ_0(t)$. The argument of this Bessel function in Eq. (43) is always nonnegative and real. As a result, the part of the total-wave Green's function containing the Bessel function shows an oscillating behavior.

Equation (43) is in agreement with the result obtained by Donato[8] through a different procedure. In his paper, Donato used the Padé (0,1) representation for this special case.

C. Source and receiver aligned normal to the boundary

For the case of source and receiver aligned normal to the impedance boundary, we proceed differently and first introduce new variables of integration in Eq. (16), *viz.* $\alpha=\nu\cos(\phi)$ and $\beta=\nu\sin(\phi)$. Using the rotational symmetry, the reflected-wave Green's function for the acoustic pressure now becomes

$$\hat{G}^r(\mathbf{r},s)|_{r=0}=\frac{1}{4\pi}\int_{\nu=0}^{\infty}\frac{\nu\tilde{R}(\gamma,s)}{\gamma}\exp(-s\gamma D_z)d\nu, \tag{45}$$

where $\gamma=(c^{-2}+\nu^2)^{1/2}$. After introducing $\tau=\gamma D_z$, the result is

$$\hat{G}^r(\mathbf{r},s)|_{r=0}=\frac{1}{4\pi D_z}\int_{\tau=T_1}^{\infty}\tilde{R}(\tau/D_z,s)\exp(-s\tau)d\tau, \tag{46}$$

where $T_1=D_z/c$ is the arrival time. The space-time reflected-wave Green's function for the acoustic pressure then follows as:

$$G^r(\mathbf{r},t)|_{r=0}=\frac{1}{4\pi D_z}\int_{\tau=T_1}^{t}\tilde{R}(\tau/D_z,t-\tau)d\tau H(t-T_1). \tag{47}$$

VII. SURFACE EFFECTS

As a result of the conditions laid upon γ and $\hat{Z}(s)$ (positive real parts for real, positive s), the denominator of $\tilde{R}(\gamma,s)$ as it occurs in Eq. (16) is free from zeros. This implies that no true surface waves like the Rayleigh wave,[12] Scholte wave,[3] and Stoneley waves[13] in elastodynamics, where such zeroes do occur in the pertaining complex slowness domain reflection coefficients, exist. However, large surface effects in the acoustic pressure have been reported if both source and receiver are close to the boundary, depending on the values of the parameters determining $\hat{Z}(s)$. In the frequency domain, an impedance showing this behavior is found to have a resistive part that is small compared with a (negative) reactance part.[6–8] Such a type of impedance can be modeled as a Padé (1,1) representation of the kind in Eq. (39). For source and receiver on the boundary, Eqs. (43) and (44) provide the Green's function. The Bessel function in it shows an oscillating behavior. Its argument is proportional to $|\alpha_z-\alpha_p|$ which is large as $\alpha_z\gg\alpha_p$ (the other possibility, $\alpha_z\ll\alpha_p$, has not been encountered in the literature). To what degree the oscillations in the Bessel function finally show up in the Green's function is, due to the integration with respect to τ, difficult to say.

The acoustic pressure is mathematically the temporal convolution of the time signature of the source with the Green's function. Convolution is, however, a smoothing process whose final result may mask many interesting details in the Green's function, the latter being determined by the configurational and material parameters only. Therefore, we discuss and do show in the next section the Green's functions for three types of physical impedances and we will reveal interesting features in the reflected sound waves that are only mentioned qualitatively in the experimental literature.

VIII. NUMERICAL RESULTS

For three acoustic impedance models, the space-time reflected-wave Green's function for the acoustic pressure will be presented. The results for the three impedance models are discussed separately later.

A. Instantaneously reacting impedance boundary (Padé (0,0) complex frequency domain representation)

For the instantaneously reacting impedance boundary, we have the Padé (0,0) representation: $\hat{Z}_{(0,0)}(s)=Z_\infty$. For

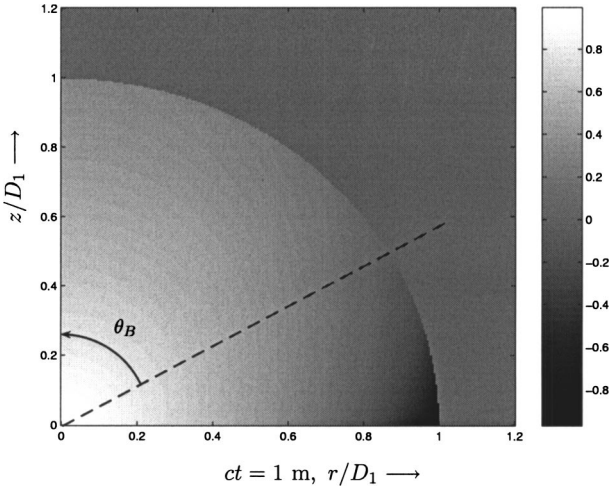

FIG. 2. Normalized density plot of G^r at $ct/h=330$, where $h>0$, for an instantaneously reacting wall impedance: $Z=2$. The Brewster angle is $\theta_B=60°$. No surface phenomenon appears at large offsets parallel to the boundary.

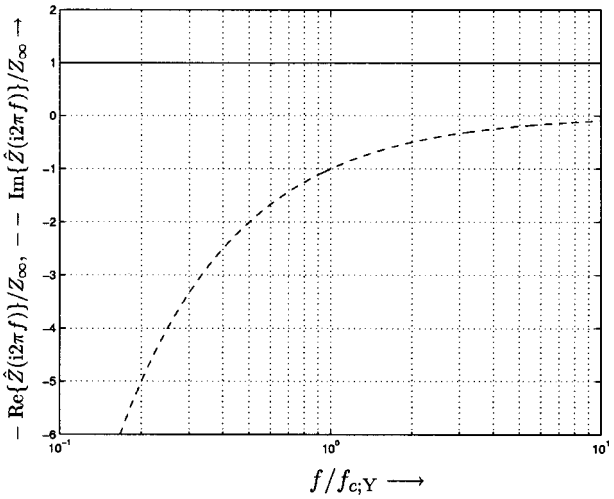

FIG. 3. Frequency response of the mineral wool acoustic impedance model. The acoustic admittance corner frequency is $f_{c;Y}=1.06$ kHz.

this type of boundary, no large amplitude oscillating surface effects are expected, a result confirmed by the literature.[6–8] For $Z=2$, Fig. 2 shows a density plot of the normalized reflected-wave Green's function, $4\pi D_1 \times G^r$ (normalization with respect to the reflected-wave Green's function in the rigid boundary case, $Z\rightarrow\infty$), at $ct/h=330$ where $ct=1$ m and $h>0$. Note that the arrival-time response of G^r vanishes at the Brewster angle $\theta_B=60°$. The plot is in agreement with the results of Ingard.[2] It is observed that the reflected-wave Green's function is less than unity everywhere in the configuration.

B. Mineral wool acoustic impedance boundary (Padé (1,1) complex frequency domain representation)

A 50 mm mineral wool with hard backing can be modeled as a Padé (1,1) representation (Eq. (39)). From the literature,[18] the following values are taken $Z_\infty=1$, $\alpha_z=6700\,\mathrm{s}^{-1}$, $\alpha_p=0$. The corresponding acoustic admittance relaxation time is $\tau_{\mathrm{rel}}=940\,\mu$s and the spectral diagram acoustic admittance corner frequency is $f_{c,Y}=1.06$ kHz. Figure 3 shows the real and imaginary parts of the frequency-domain mineral wool acoustic impedance model, $\hat{Z}_{(1,1)}(i2\pi f)$. Figures 4(a)–(c) show density plots for the normalized reflected-wave Green's function at $ct/h=330$ where

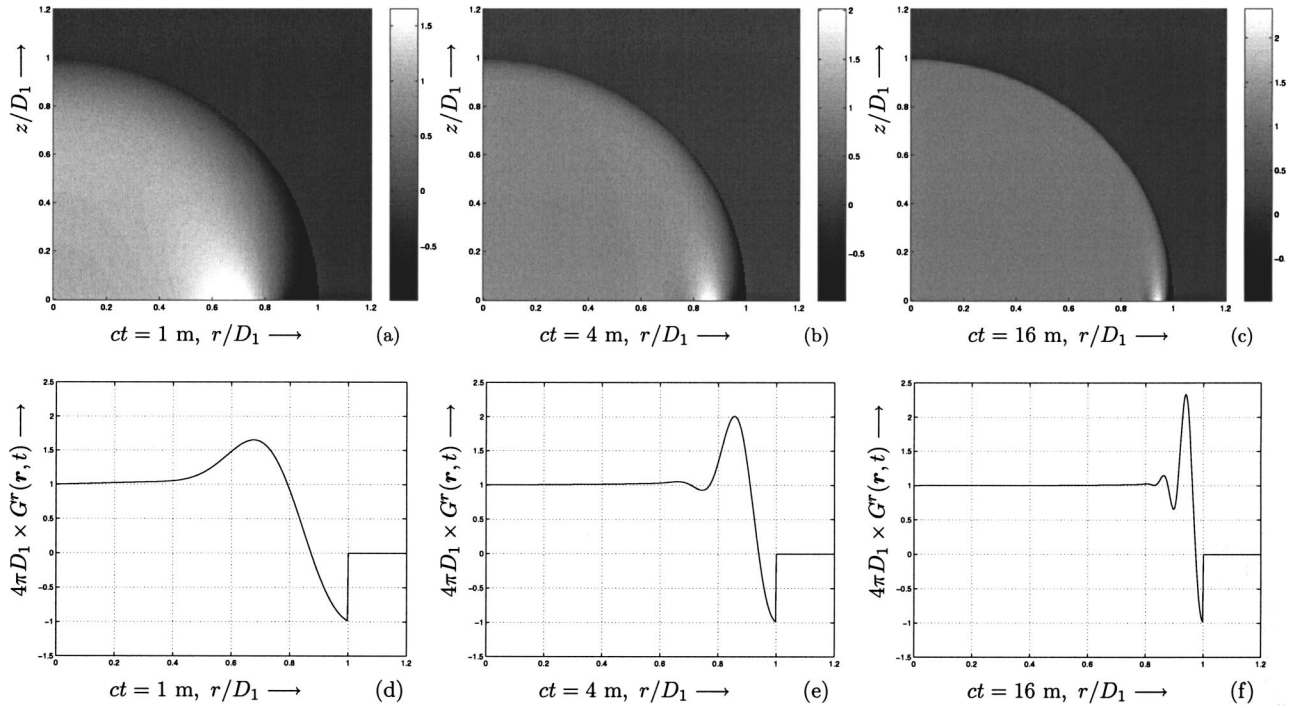

FIG. 4. (a)–(c) Normalized density plot of G^r in the mineral wool acoustic impedance model with $ct/h=330$ where $ct=\{1,4,16\}$ m. Oscillating surface effects occur at large offsets parallel to the boundary. The maximum value exceeds the value of the Green's function in the rigid boundary case. (d)–(f) The corresponding time snaps at source height h.

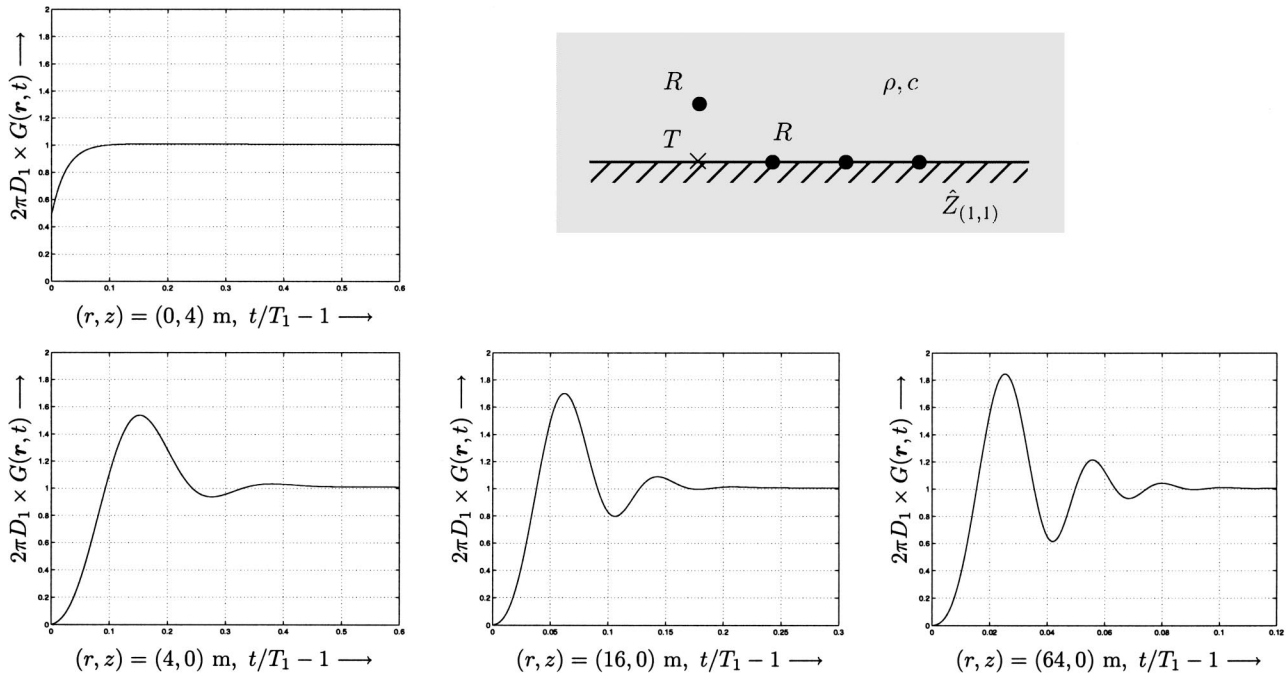

FIG. 5. Time traces of the normalized total-wave Green's function in the mineral wool acoustic impedance model. Time oscillations occur at large offsets parallel to the boundary. The Green's function $G \rightarrow 1/2\pi D_1$ as $t \rightarrow \infty$.

$ct = \{1,4,16\}$ m, respectively. The relevant amplitude at source height h are depicted in Figs. 4(d)–(f). Large amplitude oscillatory surface effects are observed at large offsets parallel to the boundary. The maximum value of the Green's function exceeds the value of the rigid boundary case Green's function, a phenomenon which has also been reported by Diagle *et al.*[7] It is noted that this phenomenon is entirely due to the absorptive and dispersive behavior of the boundary impedance. Furthermore, its magnitude depends on the actual values of the parameters employed. Finally, some time traces are shown in Fig. 5.

C. NASA Langley CT73 acoustic impedance (Padé (2,2) complex frequency domain representation)

The NASA Langley CT73 flow impedance tube with a constant depth ceramic tubular liner is considered and modeled as a Padé (2,2) expression. The data from frequency-response measurements are taken from Özyörük *et al.*[19] The first parameter to be estimated is the arrival time acoustic impedance, which is taken as $Z_\infty = 2$. The relaxation parameters in Eq. (24) are found by fitting the acoustic impedance model to the measured data spectrum in the frequency interval $f \in (0.5,3.0)$ kHz. The obtained values in the $\hat{Z}_{(2,2)}(s)$ impedance model are: $Z_\infty = 2$, $\alpha_z = 1000\pi\ \mathrm{s}^{-1}$, $\beta_z = 5200\pi\ \mathrm{s}^{-1}$, $\alpha_p = 1300\pi + i3400\pi\ \mathrm{s}^{-1}$ and $\beta_p = 1300\pi - i3400\pi\ \mathrm{s}^{-1}$. The acoustic impedance damped natural frequency is $f_{d;Z} = 1.7$ kHz. Figure 6 shows the real and imaginary parts of the frequency-domain Langley CT73 acoustic impedance model, $\hat{Z}_{(2,2)}(i2\pi f)$. Figures 7(a)–(c) show density plots for the normalized reflected-wave Green's function at $ct/h = 330$ where $ct = \{1,4,16\}$ m, respectively. The relevant amplitude at source height h are depicted in Figs. 7(d)–(f). Small amplitude oscillatory surface effects occur in the Green's function, which are, however, hardly detectable in the (measured) acoustic pressure. It is noted that the Green's function is less than unity in all space. In Fig. 8, finally, some time traces at source height and different horizontal offsets are depicted to show the small amplitude transient oscillations in the reflected-wave Green's function.

IX. DISCUSSION OF THE RESULTS

In Sec. VIII B, we used the same impedance model as in the Refs. 6–8 where it can lead to large amplitude surface effects. In the present analysis, oscillations in the reflected-wave Green's function do occur in space and time. The maximum amplitude of the oscillations exceeds the value of the rigid boundary Green's function for the situations where source and receiver are close to the impedance boundary.

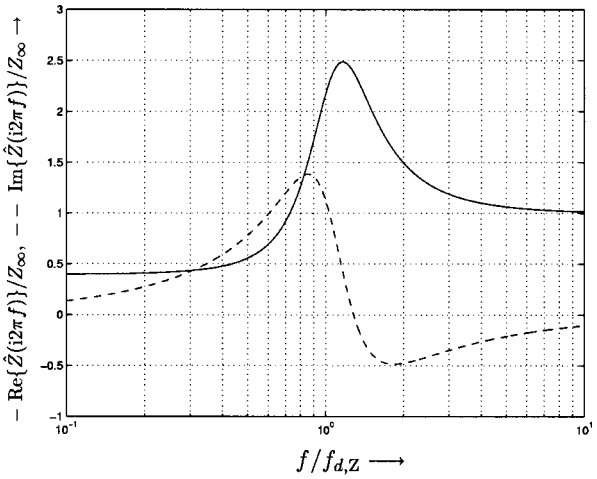

FIG. 6. Frequency response of the Langley CT73 acoustic impedance model. The acoustic impedance damped natural frequency is $f_{d;Z} = 1.7$ kHz.

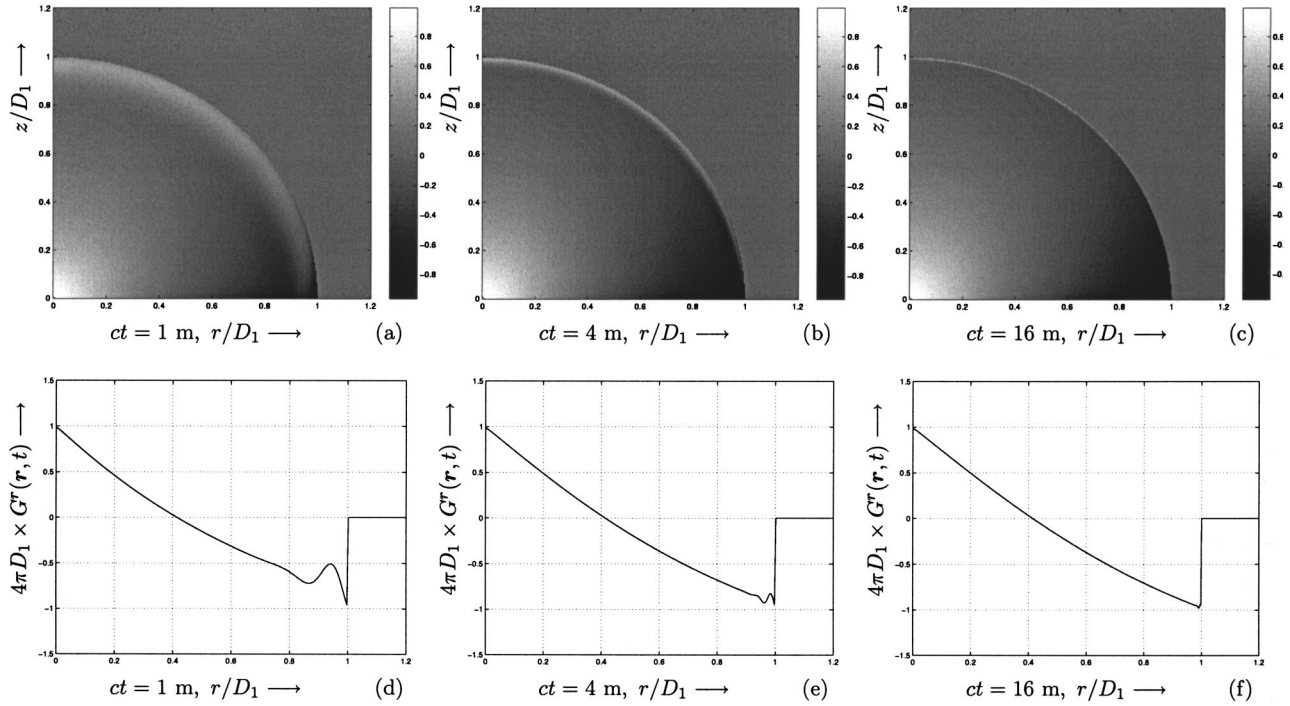

FIG. 7. (a)–(c) Normalized density plots of G^r in the Langley CT73 acoustic impedance model with $ct/h = 330$, where $ct = \{1,4,16\}$ m. No oscillations with large amplitudes in the Green's function occur at large horizontal offsets parallel to the boundary. (d)–(f) The corresponding time snaps at source height.

When the source and receiver are placed away from the boundary, the magnitude of the oscillations decreases gradually.

In Sec. VIII C, we modeled the Langley CT73 acoustic impedance with a Padé (2,2) expression. Small amplitude oscillations do occur in the reflected-wave Green's function, but they are hardly detectable in measurements.

As far as the agreement with the literature is concerned, surface effects in the form of oscillatory features do occur. The magnitude of the oscillations depends on the parameters in the impedance model. Other experiments with the mineral wool impedance model, where only Z_∞ is increased, i.e., increasing the resisitive part of the frequency-domain acoustic impedance, while retaining the magnitude of the reactance part, show that the amplitude of the oscillations decreases. This experimental finding, together with the remarks in Sec. VII are indicative for the presence of large amplitude oscillatory surface effects in the cases where the frequency-domain acoustic impedance has a large negative reactance part as compared with its positive resistive part. This spectral property holds for the mineral wool impedance model, but not for the Langley CT73 impedance model as observed from Figs. 3 and 6.

X. CONCLUSIONS

Closed-form time-domain expressions are derived for the reflected sound waves above an absorptive and dispersive planar boundary. A Padé type expression has been used to model the acoustic impedance. This choice makes the partial-fraction decomposition of the reflection coefficient possible with the consequence that the transformation back to the time domain can be carried out analytically.

The surface wave phenomenon above the impedance boundary has been discussed in Sec. VII. No surface waves like the Rayleigh wave, the Scholte wave, and the Stoneley waves in elastodynamics, are argued to exist. However, oscillatory surface effects do occur due to the absorptive and

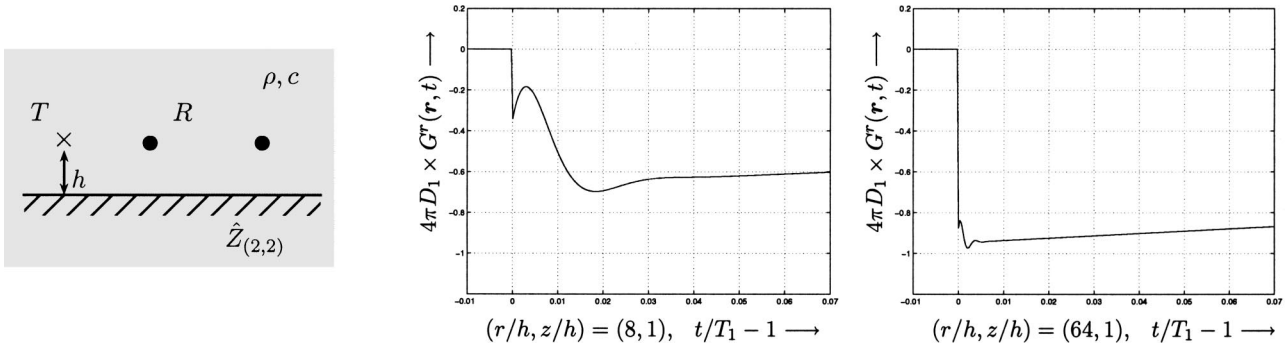

FIG. 8. Time traces of the normalized reflected-wave Green's function in the Langley CT73 acoustic impedance model at source height and different horizontal offsets. The Green's function $G^r \to 1/4\pi D_1$ as $t \to \infty$.

dispersive properties of the boundary material. These oscillatory features are large in magnitude only if the frequency-domain acoustic impedance possesses the property of a large negative reactance part as compared with its positive resistive part.

[1] P. M. Morse and K. U. Ingard, *Theoretical Acoustics* (McGraw Hill, New York, 1968), pp. 259–266.
[2] K. U. Ingard, ''On the reflection of a spherical sound wave from an infinite plane,'' J. Acoust. Soc. Am. **23**, 329–335 (1951).
[3] A. T. De Hoop and J. H. M. T. van der Hijden, ''Generation of acoustic waves by an impulsive point source in a fluid/solid configuration with a plane boundary,'' J. Acoust. Soc. Am. **75**, 1709–1715 (1984).
[4] A. T. de Hoop, ''Reflection and transmission of a transient, elastic line-source excited SH-wave by a planar, elastic bounding surface in a solid,'' Int. J. Solids Struct. **39**, 5379–5391 (2002).
[5] S. R. Wenzel, ''Propagation of waves along an impedance boundary,'' J. Acoust. Soc. Am. **55**, 956–963 (1974).
[6] S. I. Thomasson, ''Reflection of waves from a point source by an impedance boundary,'' J. Acoust. Soc. Am. **59**, 780–785 (1976).
[7] R. J. Donato, ''Propagation of a spherical wave near a plane boundary with a complex impedance,'' J. Acoust. Soc. Am. **60**, 34–39 (1976).
[8] R. J. Donato, ''Spherical-wave reflection from a boundary of reactive impedance using a modification of Cagniard's method,'' J. Acoust. Soc. Am. **60**, 999–1002 (1976).
[9] G. A. Daigle, M. R. Stinson, and D. I. Havelock, ''Experiments on surface waves over a model impedance plane using acoustical pulses,'' J. Acoust. Soc. Am. **99**, 1993–2005 (1996).
[10] H. B. Ju and K. Y. Fung, ''Time-domain simulation of acoustic sources over an impedance plane,'' J. Comput. Acoust. **10**, 311–329 (2002).
[11] B. Van den Nieuwenhof and J. P. Coyette, ''Treatment of frequency-dependent admittance boundary conditions in transient acoustic finite/infinite-element models,'' J. Acoust. Soc. Am. **110**, 1743–1751 (2001).
[12] J. D. Achenbach, *Wave Propagation in Elastic Solids* (Elsevier Science, New York, 1999).
[13] L. Cagniard, *Reflection and Refraction of Progressive Seismic Waves* (McGraw-Hill, New York, 1962), pp. 47–50, 244. E. A. Flinn and C. H. Dix, *Réflexion et Réfraction des Ondes Séismiques Progressives* (Gauthier-Villars, Paris, 1939), translation and revision of L. Cagniard.
[14] K. Attenborough, ''Ground parameter information for propagation modeling,'' J. Acoust. Soc. Am. **92**, 418–427 (1992).
[15] M. Lassas, M. Cheney, and G. Uhlmann, ''Uniqueness for a wave propagation inverse problem in a half space,'' Inverse Probl. **14**, 679–684 (1998).
[16] D. V. Widder, *The Laplace Transform* (Princeton University Press, Princeton, NJ, 1946), pp. 63–65.
[17] A. T. de Hoop, *Handbook of Radiation and Scattering of Waves* (Academic, San Diego, 1995).
[18] L. C. Sutherland and G. A. Daigle, ''Atmospheric sound propagation,'' in *Handbook of Acoustics*, edited by M. J. Crocker (Wiley, New York, 1998), pp. 305–329.
[19] Y. Özyörük and L. N. Long, ''Time-domain impedance boundary conditions for computational aeroacoustics,'' J. Comput. Acoust. **5**, 277–296 (1997).

Modal theory applied to the acoustic scattering by elastic cylinders of arbitrary cross section

Fernand Léon,[a] Farid Chati, and Jean-Marc Conoir
Laboratoire d'Acoustique Ultrasonore et d'Electronique, UMR CNRS 6068, Université du Havre, Place Robert Schuman, BP 4006, 76610, Le Havre, France

(Received 24 September 2003; revised 15 April 2004; accepted 21 May 2004)

A modal theory is developed for investigating the acoustic scattering by elastic cylinders of arbitrary cross section immersed in a fluid. Numerical results are presented for a plane wave incidence normal to the axis of an elliptical cylinder but arbitrary with respect to the noncircular cross section. Experimental results are obtained for an aluminum elliptical cylinder with the use of an impulse method. Comparisons between theoretical and experimental data are performed in the broad frequency range $8.5 \leqslant ka \leqslant 30$ (k is the wave number in the fluid and a the major axis radius of the elliptic cylinder). The experimental observations are in good agreement with the theoretical predictions. © *2004 Acoustical Society of America.* [DOI: 10.1121/1.1771592]

PACS numbers: 43.20.Fn, 43.20.Ks, 43.20.Bi [MO] Pages: 686–692

I. INTRODUCTION

Considerable work has been done on the scattering by cylindrical objects having a circular cross section. A large amount of literature devoted to this topic can be found in Ref. 1. Comparatively, little attention has been given to the more general case of the noncircular cylindrical cylinders. Experimental results are even fewer for this type of scatterers.[2,3] The aim of our paper is first to calculate the acoustic scattering by noncircular elastic cylinders with the use of a modal formalism and then to compare theoretical and experimental results in the case of elliptical elastic cylinders immersed in water.

Generally speaking, the theoretical studies can be classified into three groups: Those concerned with elliptical cylinders based on expansions in Mathieu functions,[4–7] those based on the T-matrix (or null field) method for which any noncircular cylindrical geometries can be considered,[8–14] and those using the Green's function approach to obtain a governing Fredholm integral equation.[15,16] Another method referred to as the Fourier Matching Method (FFM) which involves a conformal change of variables has also been developed by DiPerna and Stanton.[17] As discussed by Simon and Radlinski,[10] since the angular Mathieu function depends on the wave speeds, the wave functions for shear waves are not necessarily orthogonal to any of those for dilatation over a coordinate surface of constant radius. This results in a greatly increased difficulty which has led to the exploration of alternate methods. The more efficient method, on a computational point of view, for elastic scatterers in which both compressional (P) and shear (SV) waves propagate, is the T-matrix method. Goal and Jain have considered the simpler case of scattering of SH waves[15] and the FFM has only been applied to fluid scatterers even if the extension to elastic cylinders would be direct. The T-matrix formalism based on the full elasticity theory solutions has been first applied to elliptic cylinders.[8,11] In this case, numerical results are limited to the low frequency range $0.1 \leqslant ka \leqslant 5$, where k is the corresponding wave number and a the major axis radius of the elliptic cylinder. It has been observed that at $ka = 5$ one cannot really distinguish between a rigid cylinder and an elastic one.[12] Then, the T-matrix has been coupled with different thin shell theories.[10,13] The use of thin shell theories has allowed to calculate the scattering by elliptical shells at higher frequencies ($0.1 \leqslant ka \leqslant 15$).[13] It can be noted here that the Fredholm integral equation coupled with the boundary element method has also provided excellent results for thin elliptical shells, even at high frequency.[16] Resonances of thin elliptical shells are most of the time analyzed in terms of bending waves at low frequency and in terms of flexural waves at higher frequency.[14,16] The limitations of the thin shell theory has been discussed by Baskar *et al.*[13] according to the ratio $\tilde{b}/\tilde{a}$ (a is the shell external radius and b the inner one) and were shown to be material dependent by Radlinski and Simon.[14] Special attention has also been given to the resonances of water-filled cylindrical shells of elliptical cross section.[2] As the symmetry of the circular shell is broken by deforming it to the more general ellipse, the resonance spectrum changes. Mode splittings and level crossings are observed as the eccentricity increases.[2] In connection with that, it would be of interest to study resonances from the T-matrix approach in the scope of the multichannel resonant acoustic scattering.[18–20]

The modal formalism developed in this paper can be considered as being rather similar to the T-matrix approach. The procedure consists first in expanding the incident field in a complete, orthogonal basis set with known coefficients a_n, and the scattered field in terms of the unknown coefficients A_n. Let (r, θ) be polar coordinates, the basis set is $J_n(kr)e^{in\theta}$ for the incident field and $H_n^{(1)}(kr)e^{in\theta}$ for the scattered field, where J_n are the Bessel functions and $H_n^{(1)}$ the Hankel functions of the first kind [the time dependence $\exp(-i\omega t)$ is omitted throughout the text]. As for the T-matrix, the goal is finally to calculate the unknown coefficients A_n.[9] However, the modal formalism differs here from

[a]Author to whom correspondence should be addressed. Electronic mail: fernand.leon@univ-lehavre.fr

 0001-4966/2004/116(2)/686/7/$20.00

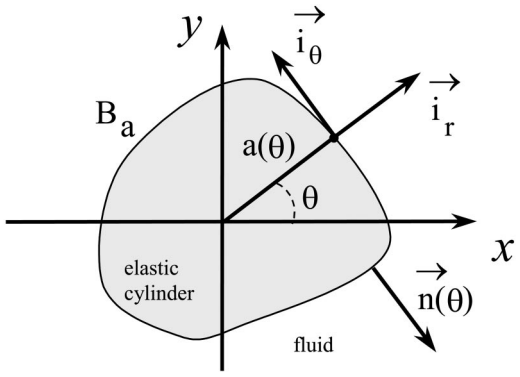

FIG. 1. Geometry of the problem.

the T-matrix because the unknown coefficients A_n are not directly expressed in terms of the known coefficients a_n. Instead of using the Helmholtz integral formula as required by the T-matrix method, displacement and stress fields in the noncircular cylinder are directly expressed in terms of modal series as for the incident and scattered fields. Of course, the difficulty then consists in writing the boundary conditions. The way of circumventing this difficulty is to expand all the fields in trigonometric series. This procedure has already been discussed by Varadan[21] (cf. the comment on pp. 38–39) in another context dealing with elliptical cavities and the angular Mathieu functions. Theoretically, the extension of the modal formalism to the elastic scattering case is direct. However, the real difficulty stands in the computations.

As previously mentioned, the aim of our paper is to calculate the acoustic scattering by noncircular elastic cylinders immersed in a fluid. The formulation of the problem is presented in Sec. II. The elliptical elastic cylinder case is considered in Sec. III. In this section, the validity of the modal method is established by comparing our results with those of Pillai *et al.*[11] in the $0.1 \leqslant ka \leqslant 5$ frequency range. Section IV gives a description of the experimental setup. Experimental results are obtained for an elliptical aluminum cylinder with the use of an impulse method.[22] Comparisons between theoretical and experimental results are performed in Sec. V in the broad frequency range $8.5 \leqslant ka \leqslant 30$ (100–350 kHz).

II. FORMULATION OF THE PROBLEM

Consider a homogeneous fluid of density ρ_f and sound velocity c_f. An elastic infinite cylinder of arbitrary cross section is immersed in the fluid. It is characterized by the density ρ_s and the longitudinal and transverse velocities c_L and c_T, respectively. The wave numbers involved in the problem are defined by $k=\omega/c_f$, $k_L=\omega/c_L$, and $k_T=\omega/c_T$, where ω is the circular frequency. As previously indicated, the time dependence $\exp(-i\omega t)$ is suppressed throughout in the paper. The *z*-axis is taken parallel to the axis of the cylinder and (r,θ) are the polar coordinates in a plane perpendicular to *z*. The boundary B_a of the cylindrical cross section is assumed to be a closed curve $a(\theta)$ (Fig. 1) with a continuously turning outward normal $n(\theta)$. This normal can be written as follows:

$$n(\theta)=n_r i_r+n_\theta i_\theta, \tag{1}$$

where

$$n_r=\frac{a(\theta)}{\sqrt{a(\theta)^2+\left(\frac{da(\theta)}{d\theta}\right)^2}}$$

$$\text{and}\quad n_\theta=\frac{-\frac{da(\theta)}{d\theta}}{\sqrt{a(\theta)^2+\left(\frac{da(\theta)}{d\theta}\right)^2}}. \tag{2}$$

A plane acoustic wave of unit amplitude and wave number *k* is assumed to be incident on the scatterer with a direction of propagation normal to the *z*-axis. Consequently, the problem reduces to two dimensions. The incident plane wave is taken as

$$p_{\text{inc}}=e^{ik(x\cos\theta_{\text{inc}}+y\sin\theta_{\text{inc}})}, \tag{3}$$

it makes an angle θ_{inc} with the *x*-axis.

As indicated in the Introduction, the incident and scattered fields are expanded in cylindrical wave functions. Since the incident wave has no singularity in the neighborhood of the origin, it can be expanded in regular wave functions

$$p_{\text{inc}}=\sum_{-\infty}^{+\infty} a_n J_n(kr)e^{in\theta} \tag{4}$$

with

$$a_n=i^n e^{-in\theta_{\text{inc}}}. \tag{5}$$

The scattered field must satisfy the Sommerfeld's radiation conditions at infinity and hence it is expanded in outgoing wave functions

$$p_s=\sum_{-\infty}^{+\infty} a_n A_n H_n^{(1)}(kr)e^{in\theta}, \tag{6}$$

where A_n are the unknown coefficients to be determined. In other words, incident and scattered waves are expanded in modal series or Rayleigh's series.[23] Using the Helmholtz decomposition[23] the elastic displacement *u* within the cylinder is given by

$$u=-\nabla\phi+\nabla\times\psi, \tag{7}$$

where ϕ and ψ are the scalar and vector potentials associated to the longitudinal and transverse fields. We have $\psi=\psi i_z$ because of the invariance of the problem with regard to the *z*-axis, and the scalar potentials ϕ and ψ verify the Helmholtz equations $\nabla^2\phi+k_L^2\phi=0$ and $\nabla^2\psi+k_T^2\psi=0$. Since the longitudinal and transverse fields in the elastic cylinder have no singularity in the neighborhood of the origin, they can also be expanded in regular wave functions

$$\phi=\frac{1}{\rho_s\omega^2}\sum_{-\infty}^{+\infty} a_n A_n^L J_n(k_L r)e^{in\theta}, \tag{8}$$

$$\psi=\frac{1}{i\rho_s\omega^2}\sum_{-\infty}^{+\infty} a_n A_n^T J_n(k_T r)e^{in\theta}, \tag{9}$$

where $A_n^{(L)}$ and $A_n^{(T)}$ are the unknowns of the problem associated to the longitudinal and transverse displacements

within the elastic cylinder. As usual, the unknown coefficients A_n, $A_n^{(L)}$, and $A_n^{(T)}$ are calculated by applying the boundary conditions at the surface B_a of the cylinder. These boundary conditions are the following ($u=(u_r,u_\theta)$):

(a) Continuity of the normal displacement

$$u_r n_r+u_\theta n_\theta=\frac{1}{\rho_f\omega^2}\left[\frac{\partial(p_{\rm inc}+p_s)}{\partial r}n_r+\frac{1}{r}\frac{\partial(p_{\rm inc}+p_s)}{\partial\theta}n_\theta\right]; \tag{10}$$

(b) continuity of the stress

$$\sigma_{rr}n_r+\sigma_{r\theta}n_\theta=-(p_{\rm inc}+p_s)n_r, \tag{11}$$

$$\sigma_{r\theta}n_r+\sigma_{\theta\theta}n_\theta=-(p_{\rm inc}+p_s)n_\theta. \tag{12}$$

The expression of the stress tensor σ is given by Morse and Feshbach.[24] In the case of the circular cylindrical cylinder ($n_r=1$ and $n_\theta=0$) Eq. (11) and Eq. (12) reduce to the well known boundary conditions[1,23]

$$u_r=\frac{1}{\rho_f\omega^2}\frac{\partial(p_{\rm inc}+p_s)}{\partial r}, \tag{13}$$

$$\sigma_{rr}=-(p_{\rm inc}+p_s), \quad \text{and} \quad \sigma_{r\theta}=0. \tag{14}$$

Inserting Eqs. (4), (6), (8), and (9) into the boundary conditions leads us to write the system of equations

$$\begin{aligned}&\sum_{n=-\infty}^{+\infty}a_n[a_n^s n_r+ib_n^s n_\theta]A_n e^{in\theta}\\&\quad+\sum_{n=-\infty}^{+\infty}a_n[a_n^L n_r+ib_n^L n_\theta]A_n^L e^{in\theta}\\&\quad+\sum_{n=-\infty}^{+\infty}a_n[a_n^T n_r+ib_n^T n_\theta]A_n^T e^{in\theta}\\&=\sum_{n=-\infty}^{+\infty}a_n[a_n^{\rm inc}n_r+ib_n^{\rm inc}n_\theta]e^{in\theta},\end{aligned} \tag{15}$$

$$\begin{aligned}&\sum_{n=-\infty}^{+\infty}a_n c_n^s n_r A_n e^{in\theta}+\sum_{n=-\infty}^{+\infty}a_n[c_{nn}^L n_r-id_n^L n_\theta]A_n^L e^{in\theta}\\&\quad+\sum_{n=-\infty}^{+\infty}a_n[c_n^T n_r-id_n^T n_\theta]A_n^T e^{in\theta}=\sum_{n=-\infty}^{+\infty}a_n c_n^{\rm inc}n_r e^{in\theta},\end{aligned} \tag{16}$$

$$\begin{aligned}&i\sum_{n=-\infty}^{+\infty}a_n e_n^s n_\theta A_n e^{in\theta}+\sum_{n=-\infty}^{+\infty}a_n[e_n^L n_r-if_n^L n_\theta]A_n^L e^{in\theta}\\&\quad+\sum_{n=-\infty}^{+\infty}a_n[e_n^T n_r-if_n^T n_\theta]A_n^T e^{in\theta}=i\sum_{n=-\infty}^{+\infty}a_n e_n^{\rm inc}n_\theta e^{in\theta},\end{aligned} \tag{17}$$

where the structural functions a_n^τ, b_n^τ, c_n^τ, e_n^τ ($\tau=$inc, s, L, T) and d_n^τ, f_n^τ ($\tau=L$, T) are given in Appendix A. For circular cylindrical cylinders the structural functions are independent of angle θ so that Eqs. (15), (16), and (17) reduce to the linear system of equations[1,23]

$$\begin{pmatrix}a_n^s & a_n^L & a_n^T\\ c_n^s & c_n^L & c_n^T\\ 0 & e_n^L & e_n^T\end{pmatrix}\begin{pmatrix}A_n\\A_n^L\\A_n^T\end{pmatrix}=\begin{pmatrix}a_n^{\rm inc}\\c_n^{\rm inc}\\0\end{pmatrix}. \tag{18}$$

In such a case, the modes of vibration are uncoupled. As the structural functions are 2π-periodic with regard to θ, the only way of solving the system of Eqs. (15), (16), and (17) is to expand it in trigonometric series. The following convention is used:

$$F(\theta)=\sum_{q=-\infty}^{+\infty}F_q e^{iq\theta}$$

$$\text{with}\quad F_q=\frac{1}{2\pi}\int_{-\pi}^{+\pi}F(\theta)e^{-iq\theta}d\theta. \tag{19}$$

In order to circumvent the numerical problems related to the convergence of trigonometric series, it is preferable to introduce a number of expansions as little as possible. From this ''implicit rule,'' the system of equations composed of Eqs. (15), (16), and (17) is rewritten as follows:

$$\begin{aligned}&\sum_{p=-\infty}^{+\infty}\left(\sum_{n=-\infty}^{+\infty}a_n[\alpha_{n,p-n}^s A_n+\alpha_{n,p-n}^L A_n^L+\alpha_{n,p-n}^T A_n^T]\right)e^{ip\theta}\\&=\sum_{p=-\infty}^{+\infty}\left(\sum_{n=-\infty}^{+\infty}\alpha_{n,p-n}^{\rm inc}a_n\right)e^{ip\theta},\end{aligned} \tag{20}$$

$$\begin{aligned}&\sum_{p=-\infty}^{+\infty}\left(\sum_{n=-\infty}^{+\infty}a_n[\beta_{n,p-n}^s A_n+\beta_{n,p-n}^L A_n^L+\beta_{n,p-n}^T A_n^T]\right)e^{ip\theta}\\&=\sum_{p=-\infty}^{+\infty}\left(\sum_{n=-\infty}^{+\infty}\beta_{n,p-n}^{\rm inc}a_n\right)e^{ip\theta},\end{aligned} \tag{21}$$

$$\begin{aligned}&\sum_{p=-\infty}^{+\infty}\left(\sum_{n=-\infty}^{+\infty}a_n[\gamma_{n,p-n}^s A_n+\gamma_{n,p-n}^L A_n^L+\gamma_{n,p-n}^T A_n^T]\right)e^{ip\theta}\\&=\sum_{p=-\infty}^{+\infty}\left(\sum_{n=-\infty}^{+\infty}\gamma_{n,p-n}^{\rm inc}a_n\right)e^{ip\theta},\end{aligned} \tag{22}$$

where the Fourier coefficients $\alpha_{n,q}^\tau$, $\beta_{n,q}^\tau$, $\gamma_{n,q}^\tau$ ($\tau=$inc,s, L, T) are given in Appendix B.

In order to obtain compact expressions for the system of equations made of Eqs. (15), (16), and (17), we are led to define the following matrices: $A^{(\tau)}$, the matrices whose components $A_{pn}^{(\tau)}$ are $a_n\alpha_{n,p-n}^\tau$ ($\tau=s,L,T$); $B^{(\tau)}$, the matrices whose components $B_{pn}^{(\tau)}$ are $a_n\beta_{n,p-n}^\tau$ ($\tau=s,L,T$); $C^{(\tau)}$ the matrices whose components $C_{pn}^{(\tau)}$ are $a_n\gamma_{n,p-n}^\tau$ ($\tau=s,L,T$); and the following vectors: a_s, the vector whose components are A_n; a_L, the vector whose components are A_n^L; a_T the vector whose components are A_n^T; $a_{\rm inc}$ the vector whose components are

$$\sum_{n=-\infty}^{+\infty}\alpha_{n,p-n}^{\rm inc}a_n;$$

$b_{\rm inc}$ the vector whose components are

$$\sum_{n=-\infty}^{+\infty}\beta_{n,p-n}^{\rm inc}a_n;$$

c_{inc} the vector whose components are

$$\sum_{n=-\infty}^{+\infty} \gamma_{n,p-n}^{\text{inc}} a_n,$$

where the unknown vector a_s is related to the scattered field and the unknown vectors a_L and a_T are related to the longitudinal and transverse fields in the cylinder. The use of these vectors and matrices allows us to write

$$\begin{pmatrix} A^{(s)} & A^{(L)} & A^{(T)} \\ B^{(s)} & B^{(L)} & B^{(T)} \\ C^{(s)} & C^{(L)} & C^{(T)} \end{pmatrix} \begin{pmatrix} a_s \\ a_L \\ a_T \end{pmatrix} = \begin{pmatrix} a_{\text{inc}} \\ b_{\text{inc}} \\ c_{\text{inc}} \end{pmatrix} \tag{23}$$

which is the linear system of equations used for computations.

It must be noted here that Eq. (23) do not provide an explicit relation between the unknown vector a_s and the known vector a whose components are a_n, as required by the T-matrix formalism.[9] However, with the building of the T-matrix in view, we can introduce the matrices: $A^{(\text{inc})}$, the matrix whose components $A_{pn}^{(\text{inc})}$ are $\alpha_{n,p-n}^{\text{inc}}$; $B^{(\text{inc})}$, the matrix whose components $B_{pn}^{(\text{inc})}$ are $\beta_{n,p-n}^{\text{inc}}$; $C^{(\text{inc})}$, the matrix whose components $C_{pn}^{(\text{inc})}$ are $\gamma_{n,p-n}^{\text{inc}}$, and rewrite the system of Eq. (23) as follows:

$$\begin{pmatrix} A^{(s)} & A^{(L)} & A^{(T)} \\ B^{(s)} & B^{(L)} & B^{(T)} \\ C^{(s)} & C^{(L)} & C^{(T)} \end{pmatrix} \begin{pmatrix} a_s \\ a_L \\ a_T \end{pmatrix} = \begin{pmatrix} A^{(\text{inc})} & 0 & 0 \\ 0 & B^{(\text{inc})} & 0 \\ 0 & 0 & C^{(\text{inc})} \end{pmatrix} \begin{pmatrix} a \\ a \\ a \end{pmatrix}. \tag{24}$$

Then, the matrix Eq. (24) can be formally inverted to solve a_s, a_L, and a_T in terms of a. Consequently, we can write

$$a_s = Ta, \tag{25}$$

where the matrix T in Eq. (25) is, by definition,[9] the T-matrix. Its expression is given in Appendix C.

As a conclusion, the modal formalism allows to build the T-matrix but we are dealing with Eq. (23) instead of Eq. (25) for computations.

III. ELLIPTICAL ELASTIC CYLINDERS AT LOW FREQUENCY

This section deals with the acoustic scattering by an elliptical aluminum cylinder immersed in a fluid. The geometry of the scatterer is shown in Fig. 2. The aspect ratio b/a of the ellipse is equal to 1/2 as in Ref. 11. Aluminum is characterized by a density $\rho_s = 2695\ \text{kg/m}^3$, a longitudinal velocity $c_L = 6296$ m/s, and a transverse velocity $c_T = 3016$ m/s. The density and the sound velocity in the surrounding fluid are $\rho_f = 1000\ \text{kg/m}^3$ and $c_f = 1480$ m/s. The close curve $a(\theta)$ describing the boundary B_a of the elliptical cylinder can be written as follows:

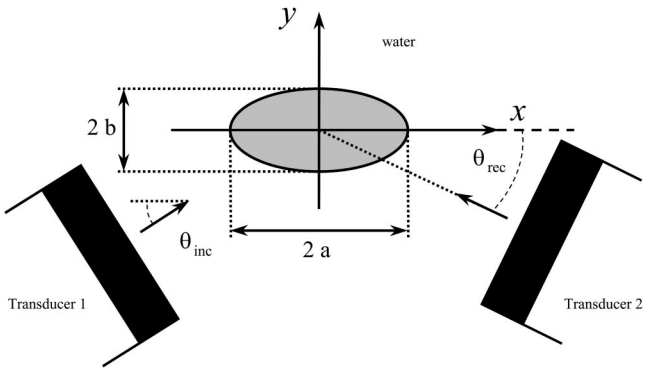

FIG. 2. Sketch of the experimental set-up (top view not drawn to scale).

$$a(\theta) = \frac{a}{\left[\cos^2\theta + \left(\frac{a}{b}\right)^2 \sin^2\theta\right]^{1/2}}. \tag{26}$$

In order to verify the accuracy of the results obtained with the use of the modal formalism, they have been compared to those of Pillai *et al.*[11] for ka ranging from 0.1 to 5. To this end, the following form function f_∞ is considered:

$$f_\infty = \sqrt{\frac{a_{\text{eff}}}{a}} \sqrt{\frac{2r}{a}} \left|\frac{p_s}{p_{\text{inc}}}\right|, \tag{27}$$

with an effective radius a_{eff} defined by

$$a_{\text{eff}} = \sqrt{\frac{a^2+b^2}{2}}. \tag{28}$$

The adjustment factor $\sqrt{a_{\text{eff}}/a}$ is equal to 1 for circular cylinders and the form function in Eq. (27) is reduced to the one usually considered in that case.[1]

As the linear systems to invert are infinite [cf. Eq. (23)], a truncation has to be performed at some order $N_{\max}$. The truncation order $N_{\max}$ has been fixed according to a criterion adapted from the one used for circular cylinders.[28] In this case, the number of terms of the modal series is given by $2N+1$ with $N = ka + 10$. In a similar way, the vectors a_s, a_L, and a_T are truncated in order to keep $2N+1$ components with $N = ka + 10$. As the matrix in Eq. (23) must be a square one, the number of terms of the trigonometric series is also equal to $2N+1$ with $N = ka + 10$. Consequently, the truncation order $N_{\max}$ has been defined for the studied cylinders by

$$N_{\max} = 3(2(ka+10)+1). \tag{29}$$

Of course, the flatter the ellipse is, the higher the truncation order of the trigonometric series is; the outward normal turns quickly around the sharp ends of the flat ellipse. In such a case, $N_{\max}$ increases and computations are more difficult to manage.

The comparison between our results and those obtained by Pillai *et al.*[11] shows a very good agreement for the form functions and the bistatic scattering patterns as well. Two examples are presented in Fig. 3. So, the modal method has been validated in the frequency range $0.1 \leqslant ka \leqslant 5$.

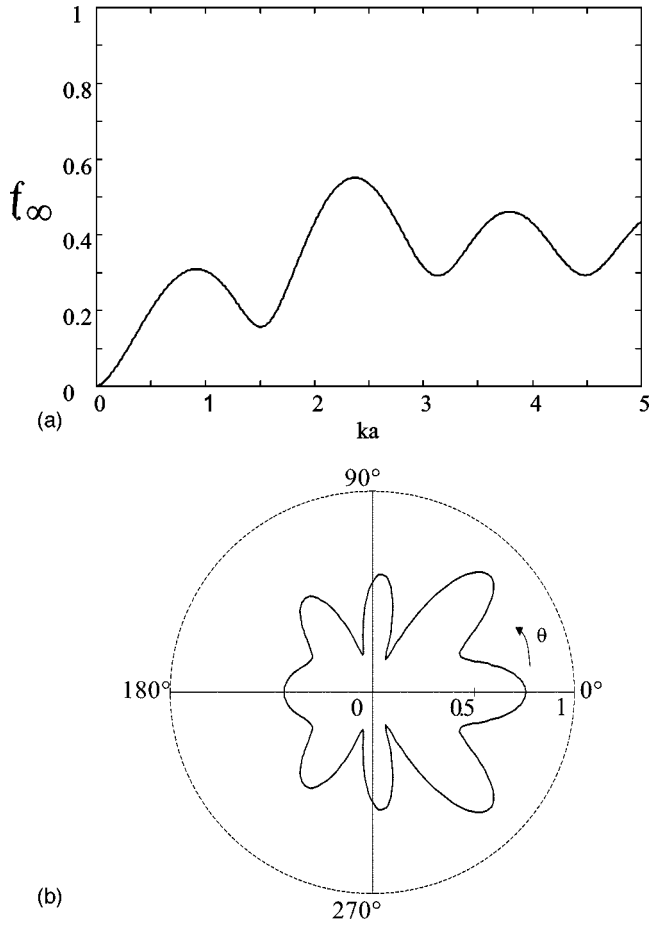

FIG. 3. (a) Far field form function ($\theta_{inc}=\theta_{rec}=0$) of the elliptical elastic cylinder considered by Pillai *et al.* (Ref. 11) (cf. Fig. 2). (b) Angular diagram of the elliptical elastic cylinder considered by Pillai *et al.* (Ref. 11) (cf. Fig. 9).

IV. EXPERIMENTAL SET-UP

The sketch of the experimental set-up is presented in Fig. 2. The elliptical aluminum cylinder is vertically immersed in a water-filled tank, 3 m in diameter and 2 m deep. The aspect ratio b/a of the elliptical cylinder is equal to 3/4, its length is 20 cm and the major axis radius a is equal to 2 cm. The aluminum alloy used in our experiments is different from that used by Pillai *et al.*[11] Consequently, the material properties are not the same ones. Aluminum is characterized by a density $\rho_s=2765\ \mathrm{kg/m^3}$, a longitudinal velocity $c_L=6440$ m/s, and a transverse velocity $c_T=3113$ m/s. The density and the sound velocity in the surrounding fluid are $\rho_f=1000\ \mathrm{kg/m^3}$ and $c_f=1470$ m/s. The transducers we used are Panametric V3507 broad band transducers with central frequency 200 kHz. The central frequency corresponds to $ka=17.1$ in reduced frequency. These transducers allow us to analyze the acoustic scattering in the 100–350 kHz frequency range ($8.5\leqslant ka\leqslant 30$). The distance between the transducer and the elliptical cylinder is equal to 0.76 m so that the experiments are conducted in the far field of the transducers. As the diameter of the radiating surface of the transducers is 5 cm, this distance is large enough to be sure that the cylinder is fully insonified.

An impulse method detailed in Ref. 22 is used. The incident signal is a wide-band short pulse and the scattered signal is the response of the elliptical cylinder obtained for a given azimuth angle. The received signals were recorded on a computer for further signal processing. This one is based on an algorithm of Fast Fourier Transform. Two types of measurement are performed:

(a) Monostatic set-up: Only one transducer (transducer 1 in Fig. 2), acting alternatively as an emitter and as a receiver, enables us to obtain the form function in backscattering. The incident angle θ_{inc} is fixed.
(b) Bistatic set-up: Two transducers, one acting as an emitter (transducer 1 in Fig. 2), and the other one as a receiver (transducer 2 in Fig. 2), enable us to obtain the bistatic scattering patterns. The incident angle θ_{inc} is fixed, while the recording angle θ_{rec} varies.

V. RESULTS AND ANALYSIS

In order to test the validity of the modal formalism at higher frequency, numerical and experimental results are compared for the elliptical aluminum cylinder. To this end, a correction of the bandwidth of the transducers is carried out. Figures 4 show both the experimental backscattered signal (solid line) and the theoretical form function in backscattering (dotted line), plotted for the incidence angles $\theta=0°$, 45°, and 90°.

Figure 4(a) ($\theta=0°$) shows a good agreement between the calculated and measured curves. Nevertheless, some differences pointed out by asterisks can be observed in the low frequency part of the backscattering spectrum. Sharp variations on the experimental curve are not visible on the theoretical one. The sharp variations, which are regularly spaced, are very certainly due to the resonances of guided waves. This interpretation of sharp variations can be suggested according to what happens for the acoustic scattering by elastic circular cylinders.[25] The guided waves are SH-polarized helical surface waves excited at oblique incidence only (the wave vector of the incident wave is not perpendicular to the z-axis). This is the reason why the sharp variations are not observed on the theoretical curve calculated for a normally incident wave. However, they can be experimentally observed because of the directivity of the transducers. So, if we omit the differences due to guided waves, we can consider that the experimental observations are in good agreement with the theoretical computations. This analysis is still valid for the other angles of excitation [cf. Figs. 4(b) and 4(c)].

It is clear that the backscattering spectra can be analyzed in terms of resonances. As for the elliptical elastic shells, for which resonances are analyzed in terms of bending and flexural waves,[2,14,16] the elliptical elastic cylinder resonances can be associated to surface waves. Without performing a complete study, it is rather obvious that Rayleigh and Wispering–Gallery-type waves propagate around the elliptical elastic cylinders. These waves reduce to the usual Rayleigh and Wispering–Gallery waves circumnavigating circular elastic cylinders[26,27] when the aspect ration b/a tends towards 1.

It can also be observed that there are more detectable resonances for the incidence angle $\theta=45°$ than for the incidence angle $\theta=0°$. This result is in agreement with the observations of Radlinski and Simon[14] for elliptical thin elastic

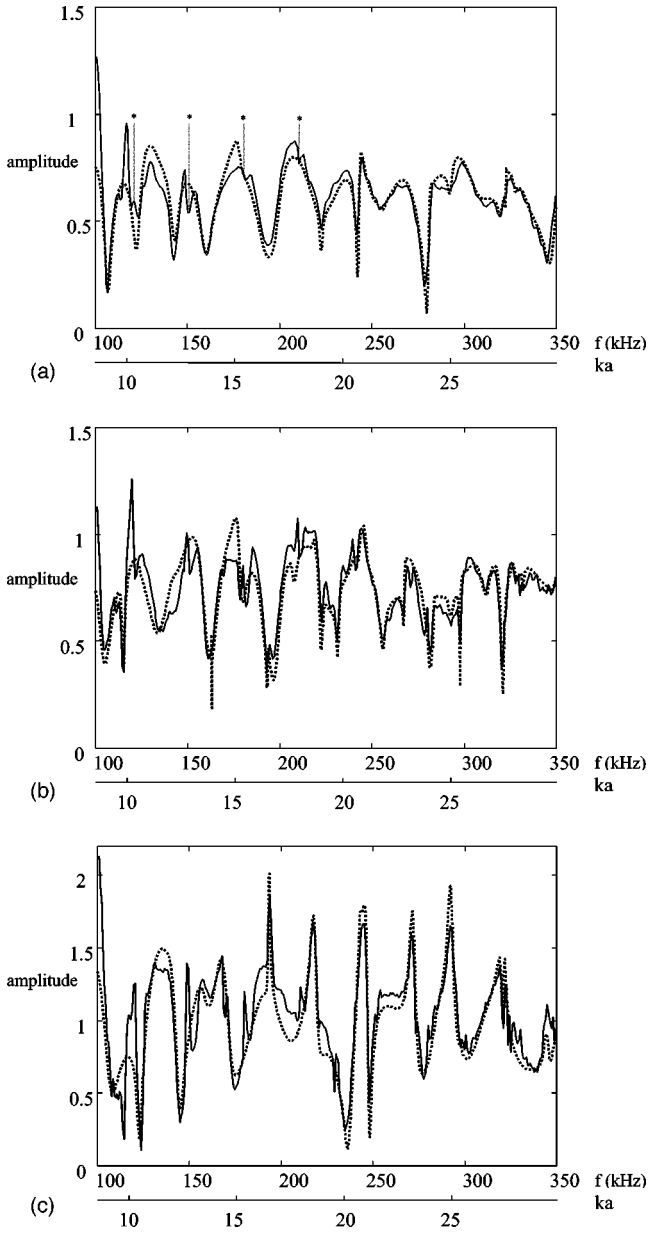

FIG. 4. (a) Far field form function of the elliptical aluminum cylinder $\theta_{inc} = \theta_{rec} = 0$: Theoretical (dotted line) experimental (solid line); (b) Far field form function of the elliptical aluminum cylinder $\theta_{inc} = \theta_{rec} = 45$: Theoretical (dotted line) experimental (solid line); (c) Far field form function of the elliptical aluminum cylinder $\theta_{inc} = \theta_{rec} = 90$: Theoretical (dotted line) experimental (solid line).

shells. This behavior can be explained by studying the symmetry of the displacement field of the surface waves (Rayleigh and Whispering–Gallery-type waves) which are responsible of the resonances. Finally, bistatic scattering patterns have also been investigated. Two of them are plotted in Figs. 5. They correspond to frequencies $f_1 = 207.5$ kHz ($ka = 17.8$) and $f_2 = 222.5$ kHz ($ka = 19.02$). These frequencies were chosen in the vicinity of the central frequency of the transducers and correspond in the backscattering spectrum to either a peak or a deep. The frequency at a deep is a resonance frequency, contrary to the one at a peak. The feature of these two angular diagrams is rather similar. The resonance influence is not obvious on the bistatic scattering patterns. We can also observe the presence of a large lobe in

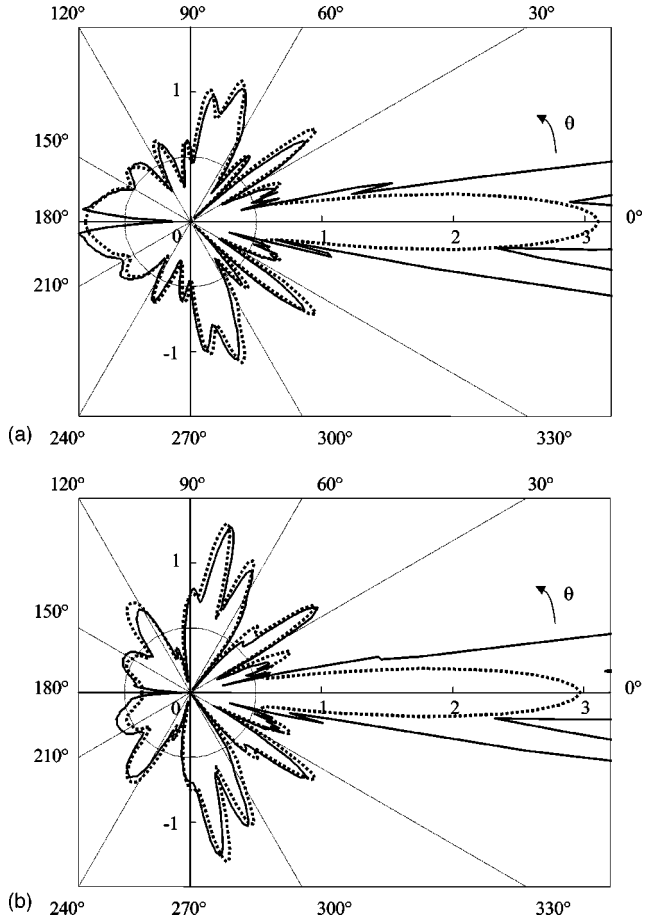

FIG. 5. (a) Angular diagram of the elliptical aluminum cylinder at the frequency $f_1 = 207.5$ kHz: theoretical (dotted line) experimental (solid line). (b) Angular diagram of the elliptical aluminum cylinder at the frequency $f_2 = 222.5$ kHz: theoretical (dotted line) experimental (solid line).

forwardscattering due to the Franz (creeping) waves.[1] As in the case of the backscattering spectra, a good agreement is noted between theoretical and experimental angular diagrams. Of course, a significant variation is observed in the vicinity of the recording angle $\theta_{rec} = 180$. This one is due to the passage of the receiver transducer in front of the emitter one.

VI. CONCLUSION

A modal formalism based on the theory of elasticity has been developed for studying the acoustic scattering by elastic cylinders of arbitrary cross section. It has been validated in the elliptical aluminum cylinder case by comparing the theoretical predictions with the experimental results. The computation of the acoustic scattering in a large frequency range is the major result of our study.

APPENDIX A

The structural functions involved in the problem are 2π-periodic. Let

$$x = ka(\theta), \quad x_L = k_L a(\theta), \quad \text{and} \quad x_T = k_T a(\theta)$$

be terms which can be interpreted at fixed angle as reduced frequencies, we have (the ''prim'' indicates the derivative with regard to the argument of the considered function):

$$a_n^s=\frac{\rho_s}{\rho_f}xH_n^{(1)\prime}(x),\quad b_n^s=\frac{\rho_s}{\rho_f}nH_n^{(1)}(x),$$

$$a_n^L=x_LJ_n'(x_L),\quad b_n^L=nJ_n(x_L),$$

$$a_n^T=-nJ_n(x_T),\quad b_n^T=-x_TJ_n'(x_T),$$

$$a_n^{\text{inc}}=-\frac{\rho_s}{\rho_f}xJ_n'(x),\quad b_n^{\text{inc}}=-\frac{\rho_s}{\rho_f}nJ_n(x),$$

$$c_n^s=x_T^2H_n^{(1)}(x),\quad c_n^{\text{inc}}=-x_T^2J_n(x),$$

$$c_n^L=(x_T^2-2n^2)J_n(x_L)+2x_LJ_n'(x_L),$$

$$d_n^L=2n(x_LJ_n'(x_L)-J_n(x_L)),$$

$$c_n^T=2n(x_TJ_n'(x_T)-J_n(x_T)),$$

$$d_n^T=(x_T^2-2n^2)J_n(x_T)+2x_TJ_n'(x_T),$$

$$e_n^s=x_T^2H_n^{(1)}(x),\quad e_n^{\text{inc}}=c_n^{\text{inc}},$$

$$e_n^L=d_n^L,\quad f_n^L=(2x_L^2-x_T^2-2n^2)J_n(x_L)+2x_LJ_n'(x_L),$$

$$e_n^T=d_n^T,\quad f_n^T=c_n^T.$$

APPENDIX B

$$a_n^\tau n_r+ib_n^\tau n_\theta=\sum_{q=-\infty}^{+\infty}\alpha_{n,q}^\tau e^{iq\theta}(\tau=\text{inc},s,L,T),$$

$$c_n^\tau n_r-id_n^\tau n_\theta=\sum_{q=-\infty}^{+\infty}\beta_{n,q}^\tau e^{iq\theta}(\tau=L,T),$$

$$c_n^\tau n_r=\sum_{q=-\infty}^{+\infty}\beta_{n,q}^\tau e^{iq\theta}(\tau=\text{inc},s),$$

$$e_n^\tau n_r-if_n^\tau n_\theta=\sum_{q=-\infty}^{+\infty}\gamma_{n,q}^\tau e^{iq\theta}(\tau=L,T),$$

$$ie_n^\tau n_\theta=\sum_{q=-\infty}^{+\infty}\gamma_{n,q}^\tau e^{iq\theta}(\tau=\text{inc},s).$$

APPENDIX C

The expression of the T-matrix is given by

$$T=[I-G_LB^{(s)}-G_TC^{(s)}]A^{(s)^{-1}}A^{(\text{inc})}+G_LB^{(\text{inc})}+G_TC^{(\text{inc})}$$

with

$$G_L=-[A^{(s)^{-1}}+G_TU_{CL}]U_{BL}^{-1},$$

$$G_T=-A^{(s)^{-1}}[U_{BT}^{-1}-U_{BL}^{-1}][U_{CT}U_{BT}^{-1}-U_{CL}U_{BL}^{-1}]^{-1},$$

and

$$U_{BL}=B^{(L)}A^{(L)^{-1}}-B^{(s)}A^{(s)^{-1}},$$

$$U_{BT}=B^{(T)}A^{(T)^{-1}}-B^{(s)}A^{(s)^{-1}},$$

$$U_{CL}=C^{(L)}A^{(L)^{-1}}-C^{(s)}A^{(s)^{-1}},$$

$$U_{CT}=C^{(T)}A^{(T)^{-1}}-C^{(s)}A^{(s)^{-1}}.$$

[1] N. D. Veksler, *Resonant Acoustic Spectroscopy* (Springer-Verlag, Berlin, 1993).
[2] P. A. Chinnery and V. F. Humphrey, "Fluid column resonances of water-filled cylindrical shells of elliptical cross section," J. Acoust. Soc. Am. **103**, 1296–1305 (1997).
[3] A. Pereira, A. Tadeu, and J. Antonio, "Influence of the cross section geometry of a cylindrical solid submerged in an acoustic medium on wave propagation," Wave Motion **36**, 23–39 (2002).
[4] R. Barakat, "Diffraction of plane waves by an elliptic cylinder," J. Acoust. Soc. Am. **35**, 1990–1996 (1963).
[5] J. E. Burke and V. Twersky, "On scattering of waves by an elliptic cylinder and by a semielliptic protuberance on a ground plane," J. Opt. Soc. Am. **54**, 732–744 (1964).
[6] J. E. Burke, "Low-frequency approximations for scattering by penetrable elliptic cylinders," J. Acoust. Soc. Am. **36**, 2059–2070 (1964).
[7] K. Sato, "Free flexural vibrations of an elliptical ring in its plane," J. Acoust. Soc. Am. **57**, 113–115 (1975).
[8] V. V. Varadan, "Scattering matrix for elastic waves. II. Application to elliptic cylinders," J. Acoust. Soc. Am. **63**, 1014–1024 (1978).
[9] *Acoustic, Electromagnetic, and Elastic Waves Scattering-Focused on the T-Matrix Approach*, edited by V. K. Varadan and V. V. Varadan (Pergamon, New York, 1980).
[10] M. M. Simon and R. P. Raddlinski, "Elastic wave scattering from elliptical shells," J. Acoust. Soc. Am. **71**, 273–281 (1982).
[11] T. A. Pillai, V. V. Varadan, and V. K. Varadan, "Sound scattering by rigid and elastic infinite elliptical cylinders in water," J. Acoust. Soc. Am. **72**, 1032–1037 (1982).
[12] T. A. Pillai, V. K. Varadan, V. V. Varadan, and R. P. Raddlinski, "Acoustic wave scattering by elastic cylindrical shells in water," J. Acoust. Soc. Am. **74**, 619–624 (1983).
[13] S. Baskar, V. V. Varadan, and V. K. Varadan, "Thin shell theories and acoustic wave scattering by infinitely long cylindrical shells of arbitrary cross section," J. Acoust. Soc. Am. **75**, 1673–1679 (1984).
[14] R. P. Raddlinski and M. M. Simon, "Acoustic and elastic scattering from elliptic-cylindrical shells," J. Acoust. Soc. Am. **93**, 2443–2453 (1993).
[15] G. C. Goel and D. L. Jain, "Scattering of plane waves by a penetrable elliptic cylinder," J. Acoust. Soc. Am. **69**, 371–379 (1981).
[16] N. D. Veksler, B. Dubus, and A. Lavie, "Acoustic wave scattering by an ellipsoidal shell," Acoust. Phys. **45**, 46–51 (1999).
[17] P. T. DiPerna and T. K. Stanton, "Sound scattering by cylinders of noncircular cross section: A conformal mapping approach," J. Acoust. Soc. Am. **96**, 3064–3079 (1994).
[18] R. G. Newton, *Scattering Theory of Waves and Particles* (Springer, New York, 1982).
[19] A. Bohm, *Quantum Mechanics, Foundations and Applications* (Springer, Berlin, 1993).
[20] E. B. Danila, J. M. Conoir, P. Pareige, and J. L. Izbicki, "Multichannel resonant scattering theory applied to the acoustic scattering by eccentric cylindrical shell immersed in a fluid," Wave Motion **28**, 297–318 (1998).
[21] V. V. Varadan, "Elastic wave scattering," in *Acoustic, Electromagnetic and Elastic Waves Scattering-Focused on the T-Matrix Approach*, edited by V. K. Varadan and V. V. Varadan (Pergamon, New York, 1980).
[22] P. Pareige, P. Rembert, J. L. Izbicki, G. Maze, and J. Ripoche, "Méthode impulsionnelle numérisée (MIN) pour l'isolement et l'identification des résonances de tubes immergés," (Digitized Impulse Method (DIM) applied to the isolation and the identification of immersed cylindrical shell resonances) Phys. Lett. A **135**, 143–146 (1989).
[23] J. J. Faran, "Sound scattering by solid cylinders and spheres," J. Acoust. Soc. Am. **23**, 405–418 (1951).
[24] P. M. Morse and H. Feshbach, *Methods of Mathematical Physics* (McGraw–Hill, New York, 1953).
[25] J. M. Conoir, P. Rembert, O. Lenoir, and J. L. Izbicki, "Relation between surface helical waves and elastic cylinder resonances," J. Acoust. Soc. Am. **93**, 1300–1307 (1993).
[26] G. V. Frisk, J. W. Dickey, and H. Überall, "Surface wave modes on elastic cylinders," J. Acoust. Soc. Am. **58**, 996–1008 (1975).
[27] G. V. Frisk and H. Überall, "Creeping waves and lateral waves in acoustic scattering by large elastic cylinders," J. Acoust. Soc. Am. **59**, 46–54 (1976).
[28] J.-L. Rousselot, "Méthode numérique en diffusion acoustique" (Numerical method in acoustic scattering) in La diffusion acoustique par des cibles élastiques de forme géométrique simple, edited by N. Gespa (1987).

Shock-induced borehole waves in porous formations: Theory and experiments

G. Chao and D. M. J. Smeulders[a)]
Delft University of Technology, Department of Applied Earth Sciences, P.O. Box 5028, 2600 GA, Delft, The Netherlands

M. E. H. van Dongen
Eindhoven University of Technology, Department of Applied Physics, Fluid Dynamics Laboratory, P.O. Box 513, 5600 MB, Eindhoven, The Netherlands

(Received 30 January 2004; revised 29 April 2004; accepted 4 May 2004)

The characteristics of the pseudo-Stoneley wave along boreholes in porous formations are studied in a broad band of frequencies (100 Hz–200 kHz). Experiments are performed using a shock tube technique to excite the pseudo-Stoneley wave in a water saturated confined reservoir. The formation is a natural Berea sandstone. Frequency-dependent phase velocities and damping coefficients are measured using this technique. Quantitative agreement between the experimental results and the theoretical predictions is found for the phase velocity in the frequency range from 10 to 50 kHz. Theoretically, the influence of the permeability on the phase velocity, attenuation, radial displacement, and pore pressure is studied on the basis of the Biot theory and the contribution of the different bulk modes to the average radial displacement is analyzed in the frequency domain. The numerical results indicate that the permeability dependence at low frequencies is caused by the Biot slow wave. © *2004 Acoustical Society of America.* [DOI: 10.1121/1.1765197]

PACS numbers: 43.20.Jr, 43.20.Hq [RR] Pages: 693–702

I. INTRODUCTION

The study of surface acoustic waves provides a useful tool in the characterization of elastic materials in a wide range of applications. Several techniques in geophysics for example, make use of surface acoustic waves in order to characterize water and hydrocarbon reservoirs. In these situations, the effects of the presence of the fluid on wave propagation cannot be neglected. Therefore, a realistic approach must consider both the porous medium and the saturating fluid separately rather than a single elastic material with averaged fluid–solid properties.

Acoustic wave propagation in a fully saturated porous medium can be described in terms of Biot's theory.[1] This theory assumes a frequency-dependent coupling between the solid matrix and the saturating fluid. An extra longitudinal wave, usually called slow *P* wave, is predicted in addition to the usual *P* and *S* waves. This wave is strongly frequency-dependent, it shows a diffusive behavior at low frequencies and a propagative behavior at high frequencies.

The influence of the slow Biot wave in the phase velocity and attenuation of the surface waves that propagate along the interface between a fluid and a fully saturated porous medium has been subject of study in the past. Feng and Johnson[2] applied Biot's theory to the study of surface acoustic waves in flat interfaces. They considered the high-frequency limit of the Biot theory for which the bulk waves become nonattenuated and a lossless medium is obtained. They found that there are three types of surface waves that can propagate in these configurations: The Stoneley wave, the pseudo-Stoneley wave and the pseudo-Rayleigh wave. For lower frequencies the phase velocities and the attenuation coefficients of the surface waves are predominantly influenced by the permeability of the formation, since the fluid inflow and outflow in the interface region is the main dissipative mechanism. Experimental data regarding flat interfaces have been reported by Mayes *et al.*,[3] Nagy,[4] and recently by Allard *et al.*[5,6] who studied surface waves in air-saturated porous media.

Also in the case of a cylindrical porous medium-fluid interface, the behavior of the surface waves has been discussed. Rosenbaum[7] applied Biot's theory to solve the high-frequency modes of a fluid-filled borehole surrounded by a porous formation. The low-frequency limit, where the predominant surface wave is referred as the tube wave, was derived by Chang *et al.*[8] Norris[9] extended White's formulation[10] for tube waves to take into account the compressibility of the solid matrix. Schmitt *et al.*[11] studied the wave response to a point source in both the time and frequency domain using Biot's theory modified according to homogenization theory. They presented results for the Stoneley mode and the pseudo-Rayleigh mode. Cheng *et al.*[12] applied Biot's theory to interpret the permeability dependence of the properties of the Stoneley wave observed in field data. Liu and Johnson[13] simulated the effect of a mudcake in the wall of the borehole with an elastic membrane. The influence of a thin impairment layer in the wall of the borehole on the dispersion relation of the surface waves was analyzed by Tichelaar *et al.*[14] Liu[15] studied borehole modes in a cylindrical water-saturated permeable medium.

Laboratory data for surface waves along boreholes in porous formations are scarce. Winkler *et al.*[16] measured phase velocities and damping coefficients of Stoneley waves in porous samples saturated with silicone oil. Hsu *et al.*[17]

a)Electronic mail: d.m.j.smeulders@citg.tudelft.nl

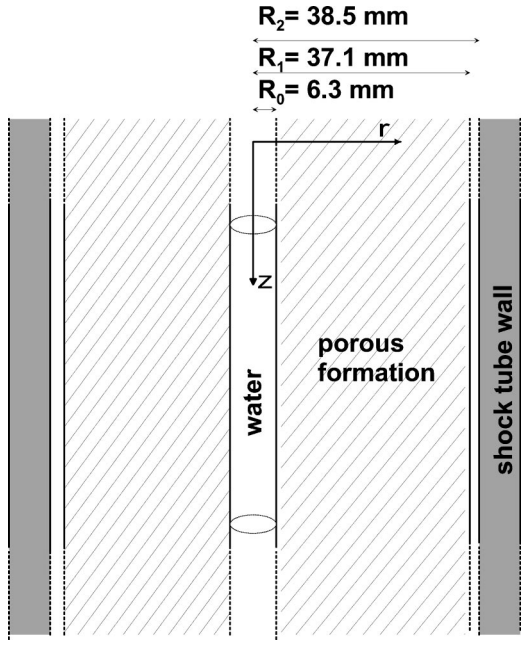

FIG. 1. Scaled borehole configuration in a confined reservoir.

studied the influence of a cylindrical permeable mandrel on the tube wave in an elastic formation. They performed measurements using stainless steel and polyethylene as formations.

In this work we study the frequency-dependent behavior of the pseudo-Stoneley wave along boreholes in a fully saturated porous formation. We investigate the use of shock waves to generate surface waves in a borehole. The Biot theory is applied to calculate the phase velocity, attenuation coefficient and radial penetration in the porous formation of the pseudo-Stoneley wave. The experiments are performed using a water-saturated natural rock sample placed in a vertical shock tube. This shock tube has already been used to study diverse aspects of wave propagation in porous media. Van der Grinten *et al.*[18,19] performed experiments in air and water-saturated porous columns consisting of agglutinated sand particles. Wave propagation in partially saturated porous media was studied by Smeulders and van Dongen.[20] Wisse *et al.*[21] presented data for shock-induced guided waves along the outer surface of porous cylinders.

The organization of this paper is as follows. The theoretical considerations that lead to the dispersion relation are summarized in Sec. II. The numerical results in terms of the permeability effects on the phase velocity, damping, radial displacement and pore pressure are discussed in Sec. III. The contribution of the slow *P* wave to the radial displacement induced by the pseudo-Stoneley wave is analyzed too. The experimental setup is described in Sec. IV, followed by the experimental results in terms of the frequency-dependent wave speeds and attenuation coefficients. The conclusions are summarized in Sec. V.

II. THEORY FORMULATION

Figure 1 shows the borehole configuration. It consists of a porous cylinder with a radius $R_1=37.1$ mm placed in the test section of a shock tube. In this cylindrically confined reservoir, a borehole with a radius $R_0=6.3$ mm was drilled. The borehole and the pores are fully filled with water. The inner shock tube radius R_2 is 38.5 mm. Between the external radius of the cylinder and the wall of the shock tube there is a small annulus filled with water. Our aim is to study the behavior of the pseudo-Stoneley wave which can be observed in our experimental setup (as we will see). All possible wave solutions that may exist in our borehole configuration can be written as a linear combination of the bulk modes in the borehole, the porous medium, and the fluid annulus. The bulk modes are described as wave potentials. In the borehole fluid only compressional waves can propagate and the wave potential for the fluid displacement can be written as

$$\Phi_0(k_z,\omega,r)=A_0(k_z,\omega)J_0(k_f r), \tag{1}$$

where k_z refers to the wavenumber in the *z*-direction, k_f to the radial wavenumber, ω is the angular frequency, and r the radial coordinate. In the formation both fast and slow compressional waves, and shear waves can propagate. We introduce for the wave potentials Φ_{c1}, Φ_{c2}, and Ψ_{sh} the following expressions (Ψ_{sh} is the component of Ψ_{sh} in the θ-direction):

$$\Phi_{c1}(k_z,\omega,r)=A_{c1}(k_z,\omega)J_0(k_{c1}r) + B_{c1}(k_z,\omega)H_0(k_{c1}r), \tag{2}$$

$$\Phi_{c2}(k_z,\omega,r)=A_{c2}(k_z,\omega)J_0(k_{c2}r) + B_{c2}(k_z,\omega)H_0(k_{c2}r), \tag{3}$$

$$\Psi_{\mathrm{sh}}(k_z,\omega,r)=A_{\mathrm{sh}}(k_z,\omega)J_1(k_{\mathrm{sh}}r) + B_{\mathrm{sh}}(k_z,\omega)H_1(k_{\mathrm{sh}}r), \tag{4}$$

where J_0 and J_1 are Bessel functions and H_0 and H_1 are Hankel functions of the first kind. The subscript $c1$ refers to the fast compressional wave, $c2$ to the slow compressional wave and sh to the shear wave. The above potentials describe axially symmetric wave modes that propagate in the *z*-direction, where the exponential dependence, $e^{i(k_z z-\omega t)}$, is implicitly assumed. The relation between the radial wavenumbers k_j and k_z is given by:

$$k_j^2=\frac{\omega^2}{c_j(\omega)^2}-k_z^2, \quad j=c1,c2,\mathrm{sh},f, \tag{5}$$

where c_j denotes the free-field velocity of the corresponding body wave. In the water annulus the following expression holds

$$\Phi_2(k_z,\omega,r)=A_2(k_z,\omega)J_0(k_f r)+B_2(k_z,\omega)H_0(k_f r). \tag{6}$$

The acoustic modes are determined by the boundary conditions. In this case there are four boundary conditions that must be satisfied both at the borehole wall and at the outer cylinder wall. The first boundary condition represents the continuity of volume flux:

$$U_0=(1-\phi)u_1+\phi U_1 \quad \text{at } r=R_0 \tag{7}$$

and

$$(1-\phi)u_1+\phi U_1=U_2 \quad \text{at } r=R_1. \tag{8}$$

In Eqs. (7) and (8) U refers to the radial component of the fluid displacement and u to the radial component of the solid displacement. The porosity is denoted by ϕ. The subscript 0 refers to the bore-fluid, 1 to the porous formation, and 2 to the water annulus. The continuity of the average stress in terms of the stress in the solid τ_{ij}, and the pressure in the fluid p, yields that

$$-p_0=\tau_{rr1}-\phi p_1 \quad \text{at } r=R_0, \tag{9}$$

$$\tau_{rr1}-\phi p_1=-p_2 \quad \text{at } r=R_1, \tag{10}$$

$$\tau_{rz1}=0, \quad \text{at } r=R_0,\ R_1. \tag{11}$$

We also have that

$$p_0=p_1-i\omega Z\phi(U_1-u_1). \tag{12}$$

This last boundary condition defines the surface impedance Z, which can be used to model permeability discontinuity effects such as the mudcake and impairment layers.[13,14,22] In this work we only consider the case $Z=0$, which corresponds to open-pore conditions and leads to the continuity of pressure:

$$p_0=p_1 \quad \text{at } r=R_0 \tag{13}$$

and

$$p_1=p_2 \quad \text{at } r=R_1. \tag{14}$$

The shock tube sections are made out of steel and have a wall thickness of 24 mm in order to minimize compliance effects. Therefore it is reasonable to consider the shock tube wall as rigid. Then, at the inner shock tube wall, the radial displacement must be equal to zero:

$$U_2=0 \quad \text{at } r=R_2. \tag{15}$$

The boundary conditions are expressed in terms of displacements, pressures and stresses. These quantities are obtained using the wave potentials according to Biot's theory (see Appendix A). Substitution of the wave potentials (1)–(4) and (6) into the boundary conditions leads to a linear system of 9 equations and 9 unknowns,

$$\mathbf{M}(k_z,\omega)\cdot\mathbf{a}=\mathbf{b}, \tag{16}$$

where the matrix $\mathbf{M}$ contains information about the fluid and the porous formation, $\mathbf{a}$ is a vector containing the amplitudes of the wave potentials, $\mathbf{a}^T=(A_0,A_{c1},B_{c1},A_{c2},B_{c2},A_{\rm sh},B_{\rm sh},A_2,B_2)$ and $\mathbf{b}$ is a source term. In order to find the dispersion relation of the borehole modes, $\mathbf{b}=0$ is considered. The matrix elements are shown in Appendix B.

The guided wave modes are obtained by solving the complex equation

$$\det[\mathbf{M}(k_z,\omega)]=0. \tag{17}$$

At a fixed frequency ω, the equation is numerically solved for complex k_z using a Newton–Raphson algorithm. In this way, frequency-dependent phase velocities, $V(\omega)=\omega\mathrm{Re}^{-1}(k_z)$, and damping coefficients, $D(\omega)=\mathrm{Im}(k_z)$, are obtained. There are an infinite number of wavemodes satisfying the boundary conditions. One of these is the so-called pseudo-Stoneley wave which is generated in our experimental set-up (as we will show). Following Feng and Johnson,[2] we define the pseudo-Stoneley wave as the surface wave that propagates at a speed that is higher than the slow wave and lower than that of the rest of the bulk modes. The main difference with the true surface Stoneley wave is that the pseudo-Stoneley wave is strongly attenuated in the direction of propagation. We will compare the results for the pseudo-Stoneley wave in our configuration, when the reservoir has a finite lateral dimension R_1 (confined reservoir) with a more realistic situation where $R_1\to\infty$ (laterally infinite reservoir). In this case, $A_{c1}=A_{c2}=A_{\rm sh}=A_2=B_2=0$, and the dimension of the matrix reduces to 4×4. The matrix elements for this case are given in Appendix C.

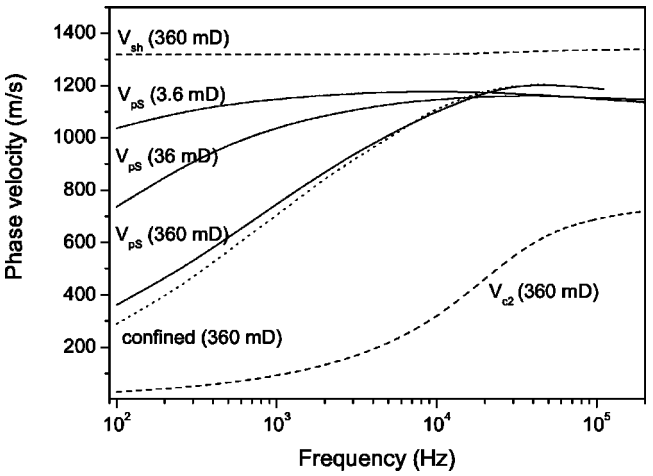

FIG. 2. Frequency-dependent phase velocity for the p-Stoneley wave for different permeability values. The solid lines correspond to the infinite reservoir configuration. The results for the confined reservoir configuration for $k_0=360$ mD are shown in dotted line. The slow wave and shear wave velocities are also displayed for this case ($k_0=360$ mD).

III. PERMEABILITY EFFECTS ON THE PSEUDO-STONELEY WAVE

In this section we investigate the permeability dependence of the properties of the pseudo-Stoneley wave for laterally infinite reservoirs. We also examine how good this condition of lateral infinity is approached by our shock tube configuration which has a confined reservoir at $r=R_1$.

In Figs. 2 and 3 we compute the phase velocities and damping coefficients as a function of frequency for different permeability values. We generally assumed laterally unbounded media, except for the case $k_0=360$ mD where also the bounded reservoir is considered (dotted line). For comparison, the bulk slow and shear waves are also shown for this case (dashed lines, $k_0=360$ mD). The parameter values for the porous reservoir and the saturating fluid are given in Table I. It can be seen that the pseudo-Stoneley wave is always faster than the slow wave and slower than the rest of the bulk modes. Its attenuation is in between the damping coefficients of both bulk modes. For frequencies over 30 kHz for the $k_0=360$ mD case, the damping decreases, but we found that a f^1 behavior is reached for $f\to\infty$ (not shown in the figure). It is also noticed that the shock tube configuration is a good approximation for the radially infinite reservoir,

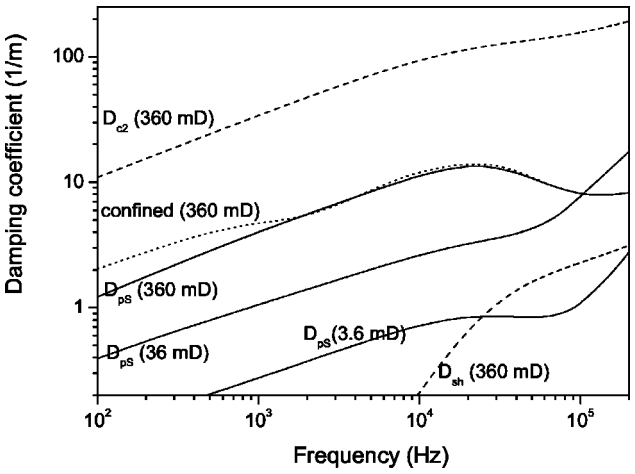

FIG. 3. Frequency-dependent damping coefficient for the p-Stoneley wave for different permeability values. The solid lines correspond to the infinite reservoir configuration. The results for the confined reservoir configuration for $k_0=360$ mD are shown in dotted line. The slow wave and shear wave damping are also displayed for this case ($k_0=360$ mD).

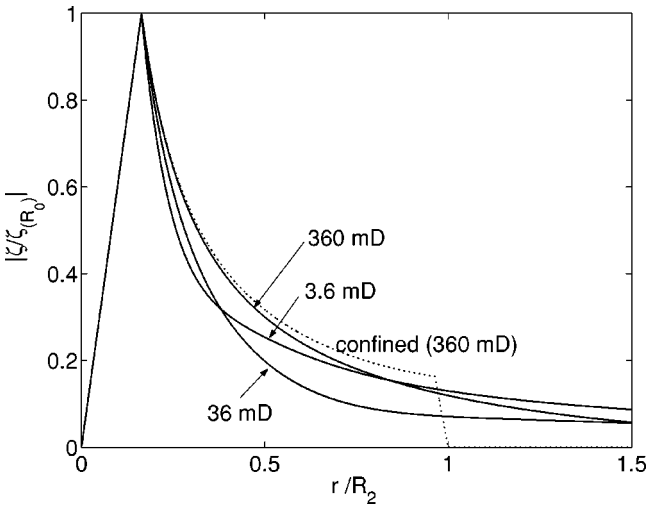

FIG. 4. Radial and permeability dependence of the average radial displacement at $f=500$ Hz. The results for the confined reservoir are shown in dotted line.

especially at high frequencies. As this agreement is expected to become better for lower permeability values (less influence of the shock tube structure as will be explained below), all other permeability curves are computed for the laterally infinite reservoir only.

A clear dependence on permeability was found for both the phase velocities and damping coefficients. The increase of the attenuation with permeability can be explained by the fact that a larger permeability implies a larger flow rate between the pores and the borehole. This constitutes the main dissipative mechanism for the surface waves and it is present in the complete range of studied frequencies (100 Hz–200 kHz). The dependence of the phase velocities on permeability is basically restricted to the low-frequency range (100 Hz–10 kHz).

We also study the radial distribution of the pore pressure and the weighted radial displacement $\zeta=\phi U_1+(1-\phi)u_1$ which is continuous across the fluid–porous solid interfaces. This provides yet another way to compare radially bounded and infinite reservoirs and helps to assess the validity of shock tube data for infinitely extended reservoirs. Also the permeability dependence of the radial distributions of p and ζ is studied (for the laterally infinite configuration).

Figures 4 and 5 show the radial distribution of ζ as a function of the permeability. The results are normalized with respect to the value at the borehole wall ($r=R_0$). In the borehole ($r<R_0$) the weighted radial displacement linearly increases with radius until the maximum value is reached at $r=R_0$. In the porous material, ζ decreases which is typical for nonradiating surface waves. The decrease is displaying $1/r$ dependence (incompressibility condition at low frequencies). For the confined reservoir, the weighted radial displacement in the annulus linearly decreases until it reaches zero at the rigid wall. Also here, a good agreement between the results for confined and infinite reservoirs is obtained. This agreement is even better for $f=5$ kHz (Fig. 5). Here the wavelengths involved are much smaller than the radius of the borehole and the shock tube, so less influence of the shock tube wall is to be expected.

Similar conclusions can be drawn for the radial distributions of the pore pressure (Figs. 6 and 7). The dependence on the permeability, however, is more prominent in this case and it is more clear that the radial decay increases when the per-

TABLE I. Physical properties of the Berea sandstone and the saturating fluid (water).

Inner radius R_0 (mm)	6.3
External radius R_1 (mm)	37.1
Density of the solid ρ_s (kg/m^3)	2644
Porosity ϕ	0.20
Permeability k_0 (mD)	360
Tortuosity α_∞	2.4
Bulk modulus of the solid K_b (GPa)	10.37
Shear modulus N (GPa)	4.02
Bulk modulus of the solid grains K_s (GPa)	36.5
Density of the fluid ρ_f (kg/m^3)	1000
Bulk modulus of the fluid K_f (GPa)	2.25
Viscosity of the fluid η (mPa s)	1.0

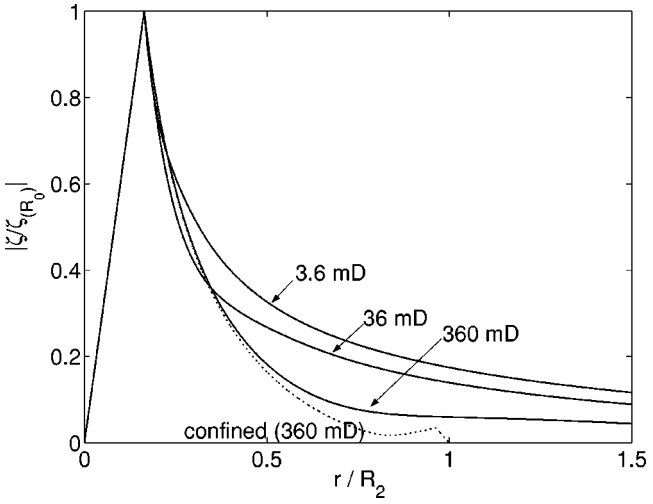

FIG. 5. Radial and permeability dependence of the average radial displacement at $f=5$ kHz. The results for the confined reservoir are shown in dotted line.

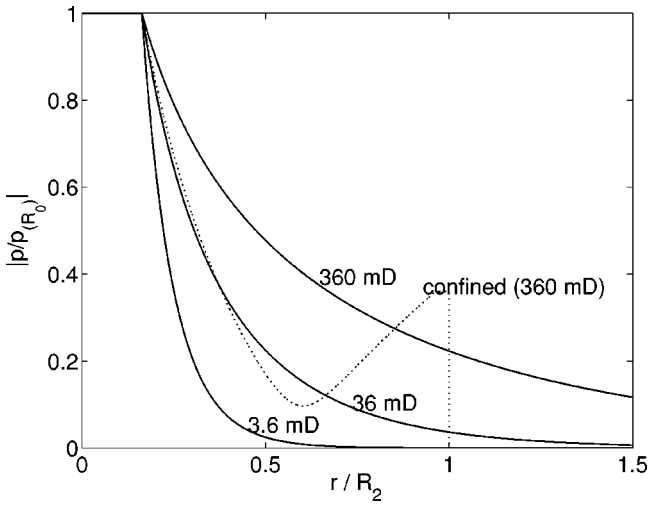

FIG. 6. Radial and permeability dependence of the pore pressure at $f=500$ Hz. The results for the confined reservoir are shown in dotted line.

meability is decreased. This implies that the use of lower permeability samples will improve the agreement between the results corresponding to the radially bounded and unbounded reservoirs. For $f=500$ Hz (Fig. 6) there is still discrepancy between the results for bounded and unbounded reservoirs but it has disappeared at 5 kHz (Fig. 7). These results correspond to the low-frequency deviations between the bounded and unbounded configurations that are found in the phase velocities and damping coefficients (Figs. 2 and 3).

Next, we examine the relative contributions of the different bulk modes to the weighted radial displacement caused by the pseudo-Stoneley wave (Fig. 8). We limit our analysis to the laterally infinite reservoir. Following the theoretical considerations explained in Appendix A, the weighted radial displacement $\zeta^{(pS)}$ induced by the pseudo-Stoneley wave can be written as:

$$\zeta^{(pS)} = \gamma_{c1}^{(pS)} B_{c1}^{(pS)}(k_z,\omega) H_1(k_{c1} r) + \gamma_{c2}^{(pS)} B_{c2}^{(pS)}(k_z,\omega) H_1(k_{c2} r) + \gamma_{\mathrm{sh}}^{(pS)} B_{\mathrm{sh}}^{(pS)}(k_z,\omega) H_1(k_{\mathrm{sh}} r), \tag{18}$$

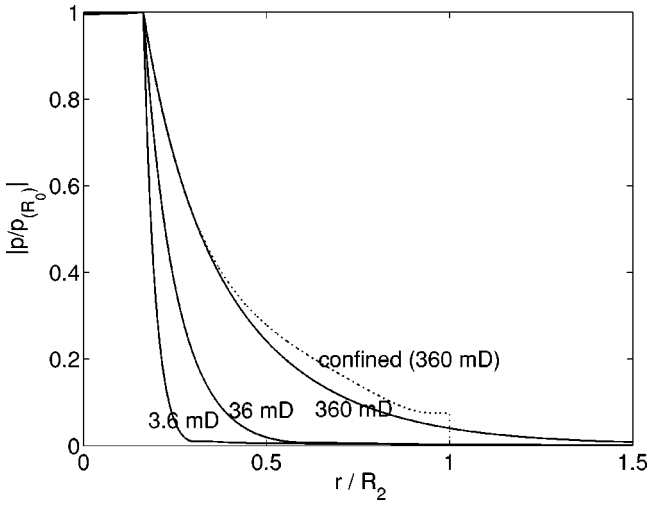

FIG. 7. Radial and permeability dependence of the pore pressure at $f=5$ kHz. The results for the confined reservoir are shown in dotted line.

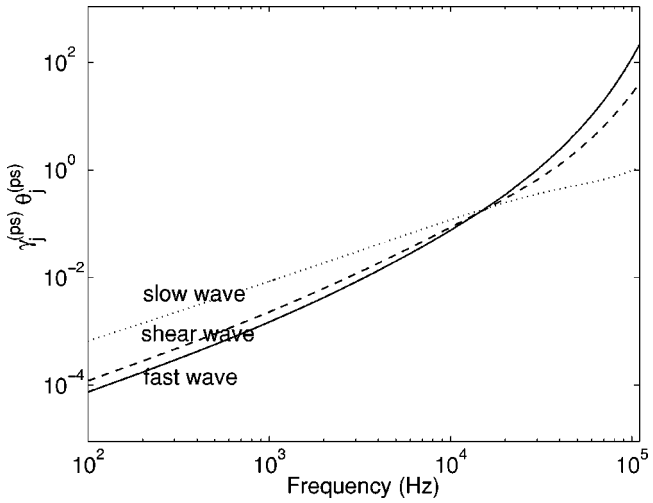

FIG. 8. Bulk modes weight for the pseudo-Stoneley wave. The results are expressed in terms of the frequency-dependent contribution of each bulk mode to the weighted radial displacement.

where the frequency-dependent coefficients $\gamma_{c1}^{(pS)}$, $\gamma_{c2}^{(pS)}$, and $\gamma_{\mathrm{sh}}^{(pS)}$ are given in Appendix B. Furthermore, the potential amplitudes $B_{c1}^{(pS)}$, $B_{c2}^{(pS)}$, and $B_{\mathrm{sh}}^{(pS)}$ are at each frequency linearly related to the potential amplitude of the fluid wave in the borehole, $A_0^{(pS)}$, by frequency-dependent coefficients $\theta_j^{(pS)}(\omega)$ [this follows from the fact that the pseudo-Stoneley wave mode satisfies Eq. (17)]. Then, the contribution of each bulk mode to the average radial displacement of the pseudo-Stoneley wave is defined as follows:

$$\zeta_j^{(pS)}(\omega) = \gamma_j^{(pS)}(\omega)\,\theta_j^{(pS)}(\omega) A_0^{(pS)}(\omega), \quad j = c1, c2, \mathrm{sh}. \tag{19}$$

In Fig. 8 the normalized mode contributions ($\gamma_j^{(pS)}\theta_j^{(pS)}$) are displayed representing the relative effect of the different bulk modes $c1$, $c2$, and sh upon the radial displacement $\zeta^{(pS)}$ associated with the pseudo-Stoneley wave. The dependence of the pseudo-Stoneley wave on the permeability can now be explained by considering the contribution $\gamma_{c2}^{(pS)}\theta_{c2}^{(pS)}$ of the slow wave. By nature, the slow wave is highly permeability-dependent. We notice that it plays an important role at low frequencies and thus also the phase velocity and damping of the pseudo-Stoneley wave are strongly dependent on permeability at those low frequencies (see Figs. 2 and 3). At higher frequencies the contributions of the fast and shear waves become more important and consequently the dependence on permeability of the properties of the pseudo-Stoneley wave diminishes.

IV. EXPERIMENTAL SETUP AND RESULTS

The vertical shock tube is shown in Fig. 9. It consists of a high-pressure section and a low-pressure section, separated by a diaphragm which is ruptured by an electric pulse. The dimensions of the sections are indicated in the figure.

A porous Berea cylinder with a concentric borehole is mounted in the test section of the shock tube and carefully saturated with water. The water level is approximately 70 cm above the top of the sample. The properties of the sample used are given in Table I. A miniature pressure transducer is mounted in a mobile probe, P2, that can be displaced along

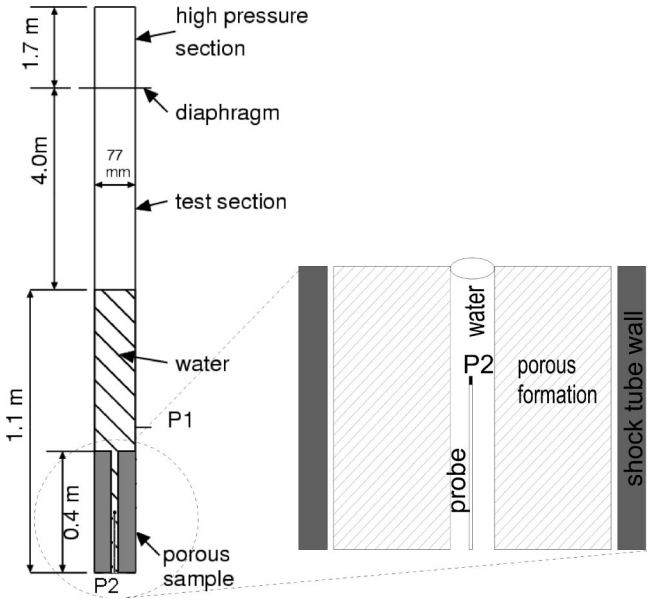

FIG. 9. Vertical shock tube. The measuring probe P2 is shown in detail.

the axial direction of the borehole. In practice, the position of the transducer is changed 0.5 cm after each shock tube run; then a new shock wave experiment is carried out. Due to the excellent repeatability of the wave experiments, these measurements can be combined in one single record. Combining 25 measurements, a record of 25 equidistant pressure signals is obtained. The pressure transducer P1 mounted in the shock tube wall is used to trigger the data acquisition system. Figure 10 shows a typical FFT conversion of the signal registered by P1.

Figure 11 shows the combined record of four pressure measurements. Distances are measured with respect to the water–porous medium interface. Knowing their approximate velocities, two arrivals can be distinguished. The first one corresponds to the fast bulk wave followed by an arrival with a larger amplitude corresponding to the pseudo-Stoneley wave. It can be observed how these two arrivals separate in time when the depth increases. In order to find the dispersion relation and consequently $V(\omega)$ and $D(\omega)$, the complete

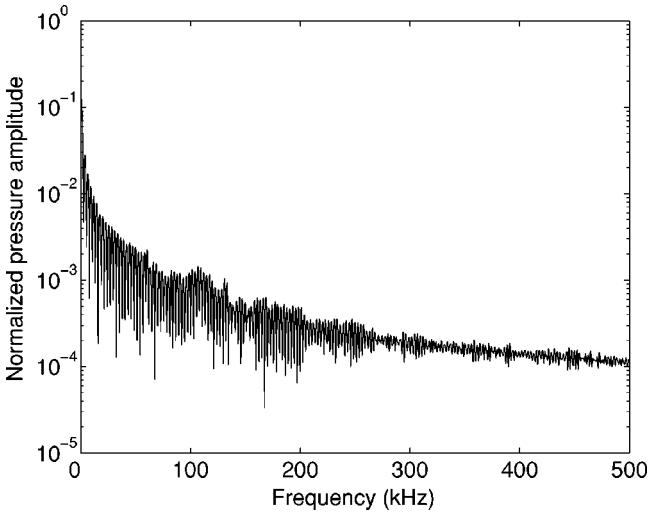

FIG. 10. Normalized absolute pressure values of the incident wave.

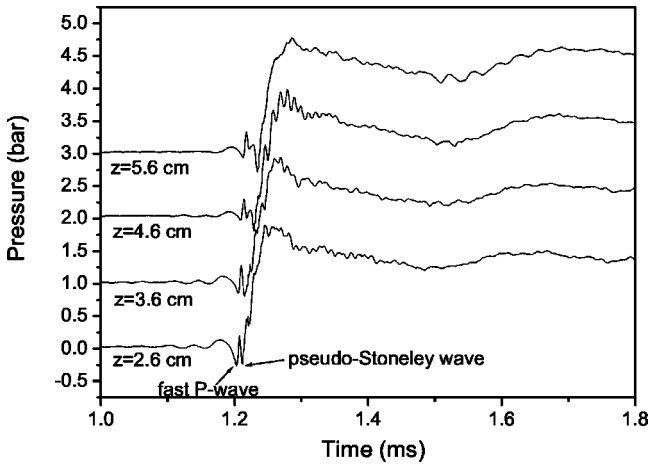

FIG. 11. Pressure recordings at different depths. For readability, traces have been shifted upwards.

record of 25 measurements is transformed from the time-space domain to the frequency-wave number domain applying a combined FFT-Prony method.[21] For further details about Prony's method we refer to Marple[23] and Wisse.[24] The results are shown in Figs. 12 and 13, together with the theoretical computations. Good agreement is obtained for the phase velocity in a broad band of frequencies (10–50 kHz). At lower frequencies there are deviations from the theoretical values. The resolution for low frequencies is limited by the length of the sample and diminishes when the wavelength is comparable with that length. The experimentally determined damping coefficients present large oscillations. Similar problems were reported by Hsu *et al.*[17] and Wisse *et al.*[21] Ellefsen *et al.*[25] have pointed out that the combined FFT-Prony method has inherent limitations in the determination of the attenuation coefficients. Moreover, Wisse *et al.*[21] indicate that the accuracy of the determination of the damping coefficient is very sensitive to the signal-to-noise ratio. We note that all input parameters for the numerical computations (Table I) were obtained from independent laboratory measurements without any adjustable parameters. Our results are in agreement with those reported by Winkler *et al.*,[16] who

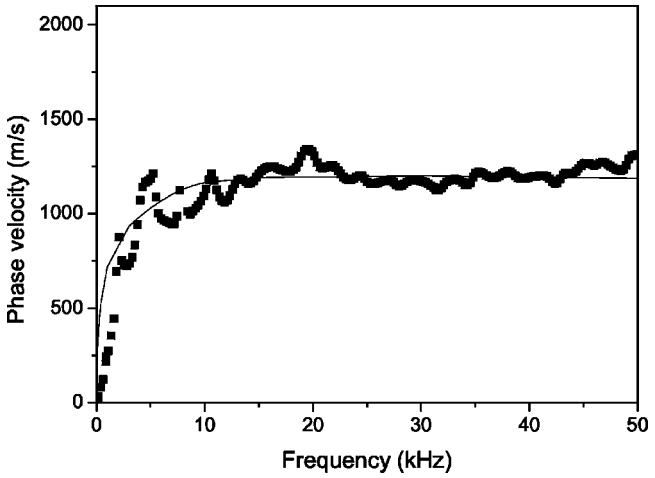

FIG. 12. Comparison between experiment and theory for the phase velocity of the pseudo-Stoneley wave. The formation is a Berea sandstone. Dots: experimental data, solid line: theoretical computations.

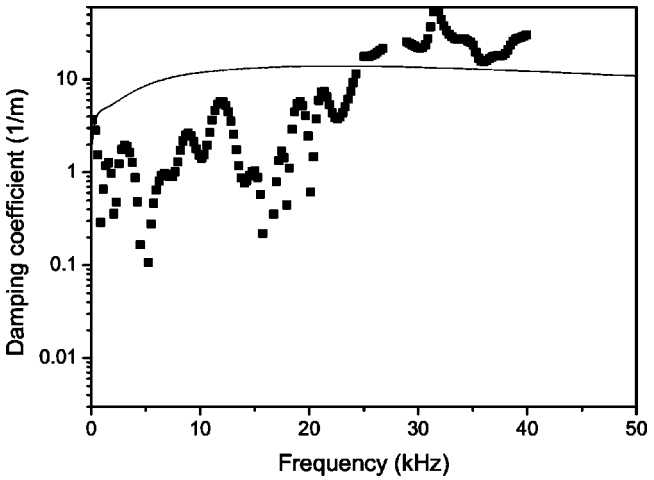

FIG. 13. Experimental (dots) and theoretical (solid lines) damping coefficients of the pseudo-Stoneley wave. The formation is a Berea sandstone.

performed similar measurements using an acoustic source located in the borehole. In their technique, however, considerably less oscillations in the damping were observed.

V. CONCLUSIONS AND DISCUSSION

Using a shock tube technique, accurate measurements of the phase velocity of the pseudo-Stoneley wave along boreholes in a water-saturated porous reservoir were performed. The frequency band involved ranges from 1 to 50 kHz. Good agreement with the computations based on Biot's theory is observed. The quality of the attenuation data is less good; intense scattering is observed and only qualitative agreement with the theoretical calculations is possible.

Permeability effects were studied numerically. The damping of the pseudo-Stoneley wave shows a strong dependence on permeability over the entire frequency range. The phase velocity shows strong dependence on permeability for low frequencies only (below 10 kHz). The contribution of the slow wave in comparison with the other bulk modes has been calculated for the weighted radial displacement. The slow wave contribution to the weighted radial displacement is one order of magnitude larger than that of the fast compressional and shear waves in the porous reservoir. The outcome of these calculations explains the strong dependence of the properties of the pseudo-Stoneley wave on permeability for low frequencies.

Finally, we point out that the results obtain so far indicate that the shock tube technique can be successfully implemented in order to study the propagation of surface waves in porous infinite reservoirs. The agreement will improve when samples with low permeability values are used, since the radial penetration of the weighted radial displacement and pore pressure in the formation decreases with permeability.

ACKNOWLEDGMENTS

This research is supported by the ISES (Integrated Solid Earth Sciences) program. The authors thank A. Holten, H. Koolmees, and J. Willems for technical support during the experiments. The Berea sample was provided by M. Peeters from the Colorado School of Mines, USA, in the framework of a cooperation project.

APPENDIX A: POTENTIAL FORMULATION OF BIOT'S THEORY IN CYLINDRICAL COORDINATES

Biot's equation of poroelasticity can be written in terms of the displacements as follows:

$$\rho_{11}\frac{\partial^2 \boldsymbol{u}}{\partial t^2}+\rho_{12}\frac{\partial^2 \boldsymbol{U}}{\partial t^2}=P\nabla(\nabla\cdot\boldsymbol{u})+Q\nabla(\nabla\cdot\boldsymbol{U})-N\nabla\times\nabla\times\boldsymbol{u}+\frac{\eta\phi^2}{\kappa_0}F(\omega)\left(\frac{\partial \boldsymbol{U}}{\partial t}-\frac{\partial \boldsymbol{u}}{\partial t}\right) \tag{A1}$$

and

$$\rho_{12}\frac{\partial^2 \boldsymbol{u}}{\partial t^2}+\rho_{22}\frac{\partial^2 \boldsymbol{U}}{\partial t^2}=R\nabla(\nabla\cdot\boldsymbol{U})+Q\nabla(\nabla\cdot\boldsymbol{u})-\frac{\eta\phi^2}{\kappa_0}F(\omega)\left(\frac{\partial \boldsymbol{U}}{\partial t}-\frac{\partial \boldsymbol{u}}{\partial t}\right), \tag{A2}$$

where $\boldsymbol{u}$ is the solid displacement, $\boldsymbol{U}$ is the fluid displacement. N is the shear modulus of the composite material, P, Q, and R are the so called generalized elastic coefficients. They are related to the porosity ϕ, the solid frame bulk modulus K_b, the solid grain bulk modulus K_s, the pore fluid modulus, K_f and N according to the following expressions:

$$P=\frac{(1-\phi)\left(1-\phi-\frac{K_b}{K_s}\right)K_s+\phi\frac{K_s}{K_f}K_b}{1-\phi-\frac{K_b}{K_s}+\phi\frac{K_s}{K_f}}+\frac{4}{3}N, \tag{A3}$$

$$Q=\frac{\left(1-\phi-\frac{K_b}{K_s}\right)\phi K_s}{1-\phi-\frac{K_b}{K_s}+\phi\frac{K_s}{K_f}}, \tag{A4}$$

$$R=\frac{\phi^2 K_s}{1-\phi-\phi\frac{K_b}{K_s}+\phi\frac{K_s}{K_f}}. \tag{A5}$$

The density terms are given by:

$$\rho_{11}=(\alpha_\infty-1)\phi\rho_f+(1-\phi)\rho_s, \tag{A6}$$

$$\rho_{12}=(1-\alpha_\infty)\phi\rho_f, \tag{A7}$$

$$\rho_{22}=\alpha_\infty\phi\rho_f, \tag{A8}$$

where ρ_s is the density of the constitutive material (quartz in our case), ρ_f is the density of the saturating pore fluid and α_∞ is the tortuosity. The frequency-dependent formation factor $F(\omega)$ is given below according to the formulation of Johnson *et al.*[26]

$$F(\omega)=\left(1-\frac{i\omega\rho_f\alpha_\infty\kappa_0}{2\eta\phi}\right)^{1/2}, \tag{A9}$$

where η is the viscosity of the pore fluid and κ_0 is the steady-state permeability.

Introducing the displacements wave potentials associated with each of the three different body waves that can propagate in the porous medium, Φ_{c1}, Φ_{c2}, Ψ_{sh}, the solid and fluid displacement can be expressed as follows ($\mathbf{e}_\theta$ is the unit vector in the θ-direction):

$$\boldsymbol{u}=\nabla\Phi_{c1}+\nabla\Phi_{c2}+\nabla\times(\Psi_{\mathrm{sh}}\mathbf{e}_\theta), \tag{A10}$$

and

$$\boldsymbol{U}=G_{c1}\nabla\Phi_{c1}+G_{c2}\nabla\Phi_{c2}+G_{\mathrm{sh}}\nabla\times(\Psi_{\mathrm{sh}}\mathbf{e}_\theta), \tag{A11}$$

where

$$G_{c1}=\frac{P-v_{c1}^2\tilde{\rho}_{11}}{v_{c1}^2\tilde{\rho}_{12}-Q}, \tag{A12}$$

$$G_{c2}=\frac{P-v_{c2}^2\tilde{\rho}_{11}}{v_{c2}^2\tilde{\rho}_{12}-Q} \tag{A13}$$

and

$$G_{\mathrm{sh}}=\frac{\tilde{\alpha}-1}{\tilde{\alpha}}. \tag{A14}$$

In the above equations v_{c1}, v_{c2}, and v_{sh} refer to the frequency-dependent wave velocities of the fast, the slow and the shear wave, respectively, and $\tilde{\alpha}$ to the frequency-dependent tortuosity given by[26]

$$\tilde{\alpha}=\alpha_\infty+\frac{i\eta\phi^2F(\omega)}{k_0\phi\omega\rho_f}. \tag{A15}$$

The density terms $\tilde{\rho}_{11}$, $\tilde{\rho}_{12}$, and $\tilde{\rho}_{22}$ in Eqs. (A12) and (A13) are frequency dependent and are calculated using $\tilde{\alpha}$:

$$\tilde{\rho}_{11}=(\tilde{\alpha}-1)\phi\rho_f+(1-\phi)\rho_s, \tag{A16}$$

$$\tilde{\rho}_{12}=(1-\tilde{\alpha})\phi\rho_f, \tag{A17}$$

$$\tilde{\rho}_{22}=\tilde{\alpha}\phi\rho_f. \tag{37}$$

The stress in the solid and the pore pressure in the porous reservoir can be obtained using the Biot stress–strain relations given by:

$$\tau_{ij}=(P-2N)u_{kk}\delta_{ij}+2Nu_{ij}+QU_{kk}\delta_{ij} \tag{A18}$$

and

$$p=\frac{-1}{\phi}(Qu_{kk}+RU_{kk}), \tag{A19}$$

where summation over repeated indexes is assumed, $u_{ij}=1/2(\partial u_i/\partial x_j+\partial u_j/\partial x_i)$ and δ_{ij} is the Kronecker delta. In the bore fluid the following expressions hold for the radial displacement and pressure:

$$U=\frac{\partial\Phi_0}{\partial r} \tag{A20}$$

and

$$p=\rho_f\omega^2\Phi_0. \tag{A21}$$

APPENDIX B: MATRIX COEFFICIENTS FOR THE CONFINED RESERVOIR

In this Appendix we give the matrix elements for the confined reservoir. In order to simplify the notation, we introduce the following variables:

$$\gamma_{c1}=(1-\phi+\phi G_{c1})k_{c1}, \tag{B1}$$

$$\gamma_{c2}=(1-\phi+\phi G_{c2})k_{c2}, \tag{B2}$$

and

$$\gamma_{\mathrm{sh}}=(1-\phi+\phi G_{sh})ik_z. \tag{B3}$$

$$m_{11}=-k_fJ_1(k_fR_0),\quad m_{12}=\gamma_{c1}J_1(k_{c1}R_0),$$

$$m_{13}=\gamma_{c1}H_1(k_{c1}R_0),\quad m_{14}=\gamma_{c2}J_1(k_{c2}R_0),$$

$$m_{15}=\gamma_{c2}H_1(k_{c2}R_0),\quad m_{16}=\gamma_{\mathrm{sh}}J_1(k_{\mathrm{sh}}R_0),$$

$$m_{17}=\gamma_{sh}H_1(k_{sh}R_0),\quad m_{21}=-\rho_0\omega^2J_0(k_fR_0),$$

$$m_{22}=\frac{\omega^2}{v_{c1}^2}J_0(k_{c1}R_0)C_{c1}+2Nk_{c1}^2\left[J_0(k_{c1}R_0)-\frac{J_1(k_{c1}R_0)}{k_{c1}R_0}\right],$$

$$m_{23}=\frac{\omega^2}{v_{c1}^2}H_0(k_{c1}R_0)C_{c1}+2Nk_{c1}^2\left[H_0(k_{c1}R_0)-\frac{H_1(k_{c1}R_0)}{k_{c1}R_0}\right],$$

$$m_{24}=\frac{\omega^2}{v_{c2}^2}J_0(k_{c2}R_0)C_{c2}+2Nk_{c2}^2\left[J_0(k_{c2}R_0)-\frac{J_1(k_{c2}R_0)}{k_{c2}R_0}\right],$$

$$m_{25}=\frac{\omega^2}{v_{c2}^2}H_0(k_{c2}R_0)C_{c2}+2Nk_{c2}^2\left[H_0(k_{c2}R_0)-\frac{H_1(k_{c2}R_0)}{k_{c2}R_0}\right],$$

$$m_{26}=2Nik_zk_{\mathrm{sh}}\left[J_0(k_{\mathrm{sh}}R_0)-\frac{J_1(k_{\mathrm{sh}}R_0)}{k_{\mathrm{sh}}R_0}\right],$$

$$m_{27}=2Nik_zk_{\mathrm{sh}}\left[H_0(k_{\mathrm{sh}}R_0)-\frac{H_1(k_{\mathrm{sh}}R_0)}{k_{\mathrm{sh}}R_0}\right],$$

$$m_{32}=-2ik_zk_{c1}NJ_1(k_{c1}R_0),$$

$$m_{33}=-2ik_zk_{c1}NH_1(k_{c1}R_0),$$

$$m_{34}=-2ik_zk_{c2}NJ_1(k_{c2}R_0),$$

$$m_{35}=-2ik_zk_{c2}NH_1(k_{c2}R_0),$$

$$m_{36}=\left[2k_z^2-\frac{\omega^2}{v_{\mathrm{sh}}^2}\right]NJ_1(k_{\mathrm{sh}}R_0),$$

$$m_{37}=\left[2k_z^2-\frac{\omega^2}{v_{\mathrm{sh}}^2}\right]NH_1(k_{\mathrm{sh}}R_0),\quad m_{41}=\rho_0\omega^2J_0(k_fR_0),$$

$$m_{42}=\frac{\omega^2}{v_{c1}^2}\frac{J_0(k_{c1}R_0)}{\phi}[-RG_{c1}-Q],$$

$$m_{43}=\frac{\omega^2}{v_{c1}^2}\frac{H_0(k_{c1}R_0)}{\phi}[-RG_{c1}-Q],$$

$$m_{44}=\frac{\omega^2}{v_{c2}^2}\frac{J_0(k_{c2}R_0)}{\phi}[-RG_{c2}-Q],$$

$$m_{45}=\frac{\omega^2}{v_{c2}^2}\frac{H_0(k_{c2}R_0)}{\phi}[-RG_{c2}-Q],$$

$$m_{52}=\gamma_{c1}J_1(k_{c1}R_1),$$

$$m_{53}=\gamma_{c1}H_1(k_{c1}R_1),\quad m_{54}=\gamma_{c2}J_1(k_{c2}R_1),$$

$$m_{55}=\gamma_{c2}H_1(k_{c2}R_1),\quad m_{56}=\gamma_{\mathrm{sh}}J_1(k_{\mathrm{sh}}R_1),$$

$$m_{57}=\gamma_{sh}H_1(k_{sh}R_1),\quad m_{58}=-k_fJ_1(k_fR_1),$$

$$m_{59}=-k_fH_1(k_fR_1),$$

$$m_{62}=\frac{\omega^2}{v_{c1}^2}J_0(k_{c1}R_1)C_{c1}+2Nk_{c1}^2\left[J_0(k_{c1}R_1)-\frac{J_1(k_{c1}R_1)}{k_{c1}R_1}\right],$$

$$m_{63}=\frac{\omega^2}{v_{c1}^2}H_0(k_{c1}R_1)C_{c1}+2Nk_{c1}^2\left[H_0(k_{c1}R_1)-\frac{H_1(k_{c1}R_1)}{k_{c1}R_1}\right],$$

$$m_{64}=\frac{\omega^2}{v_{c2}^2}J_0(k_{c2}R_1)C_{c2}+2Nk_{c2}^2\left[J_0(k_{c2}R_1)-\frac{J_1(k_{c2}R_1)}{k_{c2}R_1}\right],$$

$$m_{65}=\frac{\omega^2}{v_{c2}^2}H_0(k_{c2}R_1)C_{c2}+2Nk_{c2}^2\left[H_0(k_{c2}R_1)-\frac{H_1(k_{c2}R_1)}{k_{c2}R_1}\right],$$

$$m_{66}=2Nik_zk_{sh}\left[J_0(k_{\mathrm{sh}}R_1)-\frac{J_1(k_{\mathrm{sh}}R_1)}{k_{\mathrm{sh}}R_1}\right],$$

$$m_{67}=2Nik_zk_{sh}\left[H_0(k_{\mathrm{sh}}R_1)-\frac{H_1(k_{\mathrm{sh}}R_1)}{k_{\mathrm{sh}}R_1}\right],$$

$$m_{68}=-\rho_0\omega^2J_0(k_fR_1),\quad m_{69}=-\rho_0\omega^2H_0(k_fR_1),$$

$$m_{72}=-2ik_zk_{c1}NJ_1(k_{c1}R_1),$$

$$m_{73}=-2ik_zk_{c1}NH_1(k_{c1}R_1),$$

$$m_{74}=-2ik_zk_{c2}NJ_1(k_{c2}R_1),$$

$$m_{75}=-2ik_zk_{c2}NH_1(k_{c2}R_1),$$

$$m_{76}=\left[2k_z^2-\frac{\omega^2}{v_{\mathrm{sh}}^2}\right]NJ_1(k_{\mathrm{sh}}R_1),$$

$$m_{77}=\left[2k_z^2-\frac{\omega^2}{v_{\mathrm{sh}}^2}\right]NH_1(k_{\mathrm{sh}}R_1),$$

$$m_{82}=\frac{\omega^2}{v_{c1}^2}\frac{J_0(k_{c1}R_1)}{\phi}[-RG_{c1}-Q],$$

$$m_{83}=\frac{\omega^2}{v_{c1}^2}\frac{H_0(k_{c1}R_1)}{\phi}[-RG_{c1}-Q],$$

$$m_{84}=\frac{\omega^2}{v_{c2}^2}\frac{J_0(k_{c2}R_1)}{\phi}[-RG_{c2}-Q],$$

$$m_{85}=\frac{\omega^2}{v_{c2}^2}\frac{H_0(k_{c2}R_1)}{\phi}[-RG_{c2}-Q],$$

$$m_{88}=\rho_0\omega^2J_0(k_fR_1),\quad m_{89}=\rho_0\omega^2H_0(k_fR_1),$$

$$m_{98}=-k_fJ_1(k_fR_2),\quad m_{99}=-k_fH_1(k_fR_2),$$

and,

$$m_{18}=m_{19}=m_{28}=m_{29}=m_{31}=m_{38}=m_{39}=m_{46}=m_{47}=m_{48}=m_{49}=m_{51}=m_{61}=m_{71}=m_{78}=m_{79}=m_{81}=m_{86}=m_{87}=m_{91}=m_{92}=m_{93}=m_{94}=m_{95}=m_{96}=m_{97}=0,$$

where $C_{c1}=(P-2N)+G_{c1}Q+RG_{c1}+Q$ and $C_{c2}=(P-2N)+G_{c2}Q+RG_{c2}+Q$.

APPENDIX C: MATRIX COEFFICIENTS FOR THE RADIALLY INFINITE POROUS FORMATION

$$m_{11}=-k_fJ_1(k_fR_0),\quad m_{12}=\gamma_{c1}H_1(k_{c1}R_0),$$

$$m_{13}=\gamma_{c2}H_1(k_{c2}R_0),\quad m_{14}=\gamma_{sh}H_1(k_{sh}R_0),$$

$$m_{21}=-\rho_0\omega^2J_0(k_fR_0),$$

$$m_{22}=\frac{\omega^2}{v_{c1}^2}H_0(k_{c1}R_0)C_{c1}+2Nk_{c1}^2\left[H_0(k_{c1}R_0)-\frac{H_1(k_{c1}R_0)}{k_{c1}R_0}\right],$$

$$m_{23}=\frac{\omega^2}{v_{c2}^2}H_0(k_{c2}R_0)C_{c2}+2Nk_{c2}^2\left[H_0(k_{c2}R_0)-\frac{H_1(k_{c2}R_0)}{k_{c2}R_0}\right],$$

$$m_{24}=2Nik_zk_{\mathrm{sh}}\left[H_0(k_{\mathrm{sh}}R_0)-\frac{H_1(k_{\mathrm{sh}}R_0)}{k_{\mathrm{sh}}R_0}\right],$$

$$m_{32}=-2ik_zk_{c1}NH_1(k_{c1}R_0),$$

$$m_{33} = -2ik_z k_{c2} N H_1(k_{c2} R_0),$$

$$m_{34} = \left[2k_z^2 - \frac{\omega^2}{v_{sh}^2} \right] N H_1(k_{\mathrm{sh}} R_0), \quad m_{41} = \rho_0 \omega^2 J_0(k_f R_0),$$

$$m_{42} = \frac{\omega^2}{v_{c1}^2} \frac{H_0(k_{c1} R_0)}{\phi} [-RG_{c1} - Q],$$

$$m_{43} = \frac{\omega^2}{v_{c2}^2} \frac{H_0(k_{c2} R_0)}{\phi} [-RG_{c2} - Q],$$

$$m_{31} = m_{44} = 0.$$

[1] M. A. Biot, ''Theory of propagation of elastic waves in a fluid-saturated porous solid i. low-frequency range ii. higher frequency range,'' J. Acoust. Soc. Am. **28**, 168–191 (1956).

[2] S. Feng and D. L. Johnson, ''High-frequency acoustic properties of a fluid–porous solid interface,'' J. Acoust. Soc. Am. **74**, 906–924 (1983).

[3] Michael J. Mayes, Peter B. Nagy, and Laszlo Adler, ''Excitation of surface waves of different modes at fluid-porous solid interface,'' J. Acoust. Soc. Am. **79**(2), 249–252 (1986).

[4] Peter B. Nagy, ''Observation of a new surface mode on a fluid-saturated permeable solid,'' Appl. Phys. Lett. **60**(22), 2735–2737 (1986).

[5] J. F. Allard, G. Jansens, G. Vermeir, and W. Lauriks, ''Frame-borne surface waves in air-saturated porous media,'' J. Acoust. Soc. Am. **111**(2), 690–696 (2002).

[6] J. F. Allard, M. Henry, C. Glorieux, S. Petillon, and W. Lauriks, ''Laser-induced surface modes at an air-porous medium interface,'' J. Appl. Phys. **93**(2), 1298–1304 (2003).

[7] J. H. Rosenbaum, ''Synthetic microseismograms: Logging in porous formations,'' Geophysics **39**, 14–32 (1974).

[8] S. K. Chang, H. L. Liu, and D. L. Johnson, ''Low-frequency tube waves in permeable rocks,'' Geophysics **53**, 519–527 (1988).

[9] Andrew N. Norris, ''Stoneley-wave attenuation in permeable formations,'' Geophysics **54**(3), 330–341 (1989).

[10] J. E. White, *Underground sound-application of seismic waves* (Elsevier Science, New York, 1983).

[11] D. P. Schmitt, M. Bouchon, and G. Bonnet, ''Full-wave synthetic acoustic logs in radially semi-infinite saturated porous media,'' Geophysics **53**, 807–823 (1988).

[12] C. H. Cheng, Z. Jinzhong, and D. R. Burns, ''Effects of *in situ* permeability on the propagation of stoneley (tube) waves in a borehole,'' Geophysics **52**, 1279–1289 (1987).

[13] H. L. Liu and D. L. Johnson, ''Effects of an elastic membrane on tube waves in permeable formations,'' J. Acoust. Soc. Am. **101**, 3322–3329 (1997).

[14] Bart W. Tichelaar, Hsui-Lin Liu, and David L. Johnson, ''Modeling of borehole Stoneley waves in the presence of skin effects,'' J. Acoust. Soc. Am. **105**(2), 601–609 (1999).

[15] H. L. Liu, ''Borehole modes in a cylindrical fluid-saturated permeable medium,'' J. Acoust. Soc. Am. **84**, 424–431 (1988).

[16] K. W. Winkler, H.-S. Liu, and D. L. Johnson, ''Permeability and borehole Stoneley waves: Comparison between experiment and theory,'' Geophysics **54**, 66–75 (1989).

[17] C.-J. Hsu, S. Kostek, and D. L. Johnson, ''Tube waves and mandrel modes: Experiment and theory,'' J. Acoust. Soc. Am. **102**, 3277–3289 (1997).

[18] J. G. van der Grinten, M. E. H. van Dongen, and H. van der Kogel, ''A shock tube technique for studying pore-pressure propagation in a dry and water-saturated porous medium,'' J. Appl. Phys. **58**, 2937–2942 (1985).

[19] J. G. van der Grinten, M. E. H. van Dongen, and H. van der Kogel, ''Strain and pore pressure propagation in a water-saturated porous medium,'' J. Appl. Phys. **62**, 4682–4687 (1987).

[20] D. M. J. Smeulders and M. E. H. van Dongen, ''Wave propagation in porous media containing a dilute gas-liquid mixture: Theory and experiments,'' J. Fluid Mech. **343**, 351–373 (1997).

[21] C. J. Wisse, D. M. J. Smeulders, M. E. H. van Dongen, and G. Chao, ''Guided wave modes in porous cylinders: Experimental results,'' J. Acoust. Soc. Am. **112**(3), 890–895 (2002).

[22] H. Deresiewicz and R. Skalak, ''On uniqueness in dynamic poroelasticity,'' Bull. Seismol. Soc. Am. **53**, 783–788 (1963).

[23] S. L. Marple, *Digital spectral analysis: With applications* (Prentice-Hall, Englewood Cliffs, NJ, 1987).

[24] C. J. Wisse, ''On frequency dependence of acoustic waves in porous cylinders,'' PhD thesis, Delft University of Technology, 1999.

[25] K. J. Ellefsen, D. R. Burns, and C. H. Cheng, ''Homomorphic processing of the tube wave generated during acoustic logging,'' Geophysics **58**, 1400–1407 (1993).

[26] D. L. Johnson, J. Koplik, and R. Dashen, ''Theory of dynamic permeability and tortuosity in fluid-saturated porous media,'' J. Fluid Mech. **176**, 379–402 (1987).

Response of multiple rigid porous layers to high levels of continuous acoustic excitation

Olga Umnova, Keith Attenborough,[a] Ho-Chul Shin, and Alan Cummings
Department of Engineering, The University of Hull, Cottingham Road, Hull, HU6 7RX, United Kingdom

(Received 12 November 2003; revised 2 March 2004; accepted 6 May 2004)

A model has been developed for the response of a rigid-porous hard-backed medium containing an arbitrary number of layers to high amplitude sound. Nonlinearity is introduced by means of a velocity-dependent flow resistivity in Johnson's equivalent fluid model for the complex tortuosity of each layer. Numerical solution of the resulting system of algebraic equations allows prediction of the dependence of surface impedance and reflection coefficient on the incident pressure amplitude. Measurements have been made of the surface impedance of various triple layers, made from different diameters of spherical lead shot and double layers consisting of gravel with different mean particle size, subject to high-intensity continuous sound. Good agreement between the model predictions and data for these multiple-granular layers is demonstrated. Moreover it is shown both theoretically and experimentally that the layer configuration giving optimum performance at low sound intensities may not continue to do so as the incident sound level is increased and the response becomes increasingly nonlinear. It is shown also that the nonlinear behavior depends strongly on layering and that, in some cases, the behavior is changed simply by changing the top layer thickness. © *2004 Acoustical Society of America.* [DOI: 10.1121/1.1766051]

PACS numbers: 43.25.Ed, 43.25.Jh, 43.25.Ba, 43.58.Bh [RR] Pages: 703–712

I. INTRODUCTION

Multilayered porous absorbers are used widely in various acoustical applications.[1] In addition to geometrical parameters, including layer thickness, number of layers, and overall thickness, their performance depends on the porosity-related parameters in each layer.[2] By suitable manipulation of the properties of the layers, for example by having a flow resistivity that increases away from the insonified surface, it is possible to adjust the parameters to achieve maximum absorption in the required frequency range. The possibility of using a layered absorber with density gradually increasing from layer to layer for military noise mitigation purposes has been discussed.[3] In the linear domain, the use of the transfer matrix formalism based on the Biot theory[4] is the most convenient way to describe acoustic properties of multilayered absorbers. However at high intensities, the linear transfer matrix formalism cannot be used if the porous material response becomes dependent on the incident sound amplitude.[5] Consequently it is of interest to the study of nonlinear acoustic properties of rigid-porous absorbers with multiple layers.

The key role in the nonlinear behavior of rigid-porous materials is played by the variation of flow resistivity with flow velocity. Particular attention has been paid to Forchheimer's nonlinearity, i.e., a linear variation of flow resistivity with flow velocity,[6–8] which is valid in the range of moderate flow velocities. Forchheimer's nonlinearity has been combined with the Johnson/Allard equivalent fluid model for rigid porous materials[9–11] in previous publications.[12,13] The latter paper[13] allowed for non-constant flow through the porous material and paid particular attention to the reflection coefficient behavior near the resonance of a hard-backed porous layer for incident pressure levels up to 1 kPa. Either growth or decrease of reflection coefficient with pressure amplitude was predicted and measured depending on material parameters and layer thickness. There is an indirect evidence[14] that for much higher levels of incident sound (tens of kPa) Forchheimer's correction is no longer valid and has to be replaced by a more complicated dependence of flow resistivity on flow velocity. Here the previously published approach[13] is extended to predict acoustic properties of multiple rigid porous layers at high levels of incident sound.

In Sec. II the problem of sound reflection from a hard-backed multilayered absorber with arbitrary number of layers is treated theoretically. The resulting system of nonlinear algebraic equations describes the dependence of the reflection coefficient and surface impedance spectra on the incident pressure amplitude. Section III describes impedance tube experiments on three triple-layer configurations formed with different sizes of spherical lead shot and three double-layer configurations of gravel with different particle sizes in each layer. The resulting data are compared with predictions and good agreement is demonstrated. The acoustical characteristics of multiple-layer absorbers are shown to have a strong dependence on pressure amplitude especially near the system resonance. Section IV gives the conclusions.

II. NONLINEAR MODEL FOR MULTIPLE RIGID-POROUS LAYERS

A schematic representation of a multilayered absorber is shown in Fig. 1. The sound wave propagation in the nth layer ($n=1,...,N$, where N is the total number of layers and numbering starts with a top layer) is described by the complex tortuosity[9] $\alpha^{(n)}(\omega)$ and complex compressibility[10,11] $C^{(n)}(\omega)$ of the fluid contained in of the pores of the layer. These may be written[13]

[a]Author to whom correspondence should be addressed.

$$\alpha^{(n)}(\omega)=\alpha_\infty^{(n)}+\frac{\sigma^{(n)}\phi^{(n)}}{-i\omega\rho_0}\sqrt{1+(-i\omega)\frac{4\alpha_\infty^{(n)^2}\rho_0\eta}{\sigma^{(n)^2}\phi^{(n)^2}\Lambda^{(n)^2}}}, \tag{1}$$

$$C^{(n)}(\omega)=\gamma-\frac{\gamma-1}{\left(1+\frac{\eta\phi^{(n)}}{-i\omega\rho_0 k_0'^{(n)}N_{\mathrm{pr}}}\sqrt{1+(-i\omega)\frac{\rho_0 4k_0'^{(n)^2}N_{\mathrm{pr}}}{\eta\Lambda'^{(n)^2}\phi^{(n)^2}}}\right)}, \tag{2}$$

where ω is the angular frequency, c_0 is the adiabatic sound speed in air, ρ_0 is the air density, η is the coefficient of dynamic viscosity for air, γ is the adiabatic constant, and N_{pr} is the Prandtl number.

This approach requires knowledge of 6 parameters for the material in each layer. The tortuosity, $\alpha_\infty^{(n)}$, is a measure of pore or streamline curvature. The flow resistivity, $\sigma^{(n)}$, is the ratio of the static pressure gradient along the sample to the resulting flow velocity through the sample. The characteristic viscous length, $\Lambda^{(n)}$, is a geometrical parameter determined by the viscous interactions between fluid and structure and indicative of the narrowest pore dimensions. The thermal permeability, $k_0'^{(n)}$, is related to diffusion and trapping of air molecules at pore walls. The characteristic thermal length $\Lambda'^{(n)}$ is a geometrical parameter similar to hydraulic radius that can be determined from the internal surface area per unit volume. The volume porosity of the layer n material, $\phi^{(n)}$, is the ratio of the volume occupied by the connected pores to the total volume of the material. The number of parameters necessary to model sound propagation in granular materials with spherical grains can be reduced by using a similarity relationship between the complex density and complex compressibility functions[15]

$$C^{(n)}(\omega)=\gamma-\frac{\gamma-1}{\left(\frac{2}{3}(1-\Theta^{(n)})(\alpha^{(n)}(\omega N_{\mathrm{pr}})-\alpha_\infty^{(n)})+1\right)}, \tag{3}$$

where $\Theta^{(n)}\approx 0.675(1-\phi^{(n)})$.

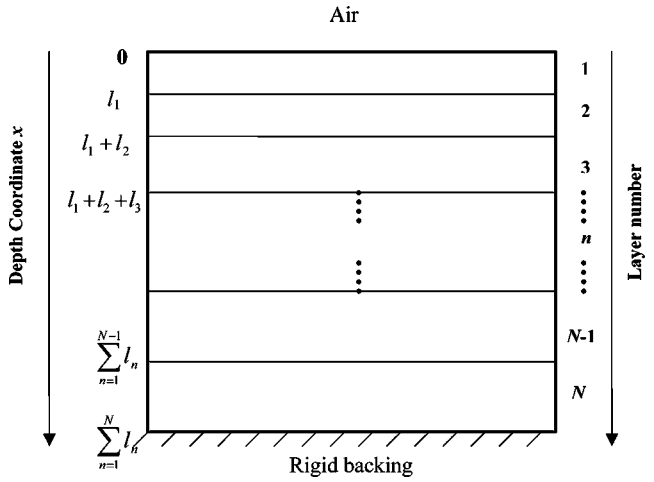

FIG. 1. Representation of a multiple-layer configuration of rigid-porous materials.

It is assumed that the flow resistivity of the material in the nth layer grows linearly with the particle velocity amplitude $|v^{(n)}|$ associated with the sound wave in this layer

$$\sigma^{(n)}(v^{(n)})=\sigma_0^{(n)}(1+\xi^{(n)}\phi^{(n)}|v^{(n)}|), \tag{4}$$

where $\xi^{(n)}$ is the Forchheimer's nonlinearity parameter which can be measured by standard flow resistivity tests. The factor of porosity in Eq. (4) allows for the difference between the velocity in the pores and the flow velocity measured outside the material in flow resistivity tests. As in the previously published approach,[13] $\sigma^{(n)}(v^{(n)})$ is substituted into (1) to get the velocity dependent complex tortuosity function $\alpha^{(n)}(\omega,v^{(n)})$. It is assumed that the complex compressibility does not depend on the particle velocity. The resulting equations for particle velocity variations in the nth layer are solved by the method of slowly varying amplitudes,[16] i.e., the solution for particle velocity associated with the sound wave is sought in the form

$$\begin{aligned} v^{(n)}&=V_+^{(n)}(x)+V_-^{(n)}(x)\\ &=v_+^{(n)}(x)e^{ik^{(n)}(\omega)x}+v_-^{(n)}(x)e^{-ik^{(n)}(\omega)x}, \end{aligned}$$

where $v_\pm^{(n)}$ are the slowly varying amplitudes of particle velocity in the forward and backward propagating waves in layer n.

The following pair of first order nonlinear differential equations describes spatial changes in $v_\pm^{(n)}$:

$$\begin{aligned} \frac{dv_+^{(n)}}{dx}&=-M^{(n)}(\omega)\left(\sqrt{1+i\frac{\omega_c^{(n)}}{\omega}(1+\xi^{(n)}\phi^{(n)}|v^{(n)}|)^2}\right.\\ &\quad\left.-\sqrt{1+i\frac{\omega_c^{(n)}}{\omega}}\right)v_+^{(n)},\\ \frac{dv_-^{(n)}}{dx}&=M^{(n)}(\omega)\left(\sqrt{1+i\frac{\omega_c^{(n)}}{\omega}(1+\xi^{(n)}\phi^{(n)}|v^{(n)}|)^2}\right.\\ &\quad\left.-\sqrt{1+i\frac{\omega_c^{(n)}}{\omega}}\right)v_-^{(n)}, \end{aligned} \tag{5}$$

where x is the vertical axis with $x=0$ being the top surface of the material,

$$M^{(n)}(\omega)=(1-i)\frac{\alpha_\infty^{(n)}\omega^2 C^{(n)}(\omega)}{c_0^2 k^{(n)}(\omega)}\frac{\delta(\omega)}{2\Lambda^{(n)}},$$

$$\omega_c^{(n)}=\left(\frac{\sigma_0^{(n)}\phi^{(n)}\Lambda^{(n)}}{2\alpha_\infty^{(n)}}\right)^2\frac{1}{\rho_0\eta},$$

and $\delta(\omega)=\sqrt{2\eta/\omega\rho_0}$ is the viscous layer thickness, $k^{(n)}(\omega)=(\omega/c_0)\sqrt{\alpha^{(n)}(\omega)C^{(n)}(\omega)}$.

If the velocities at the upper and lower surface of the nth layer are $V_{\pm}^{(n)}$ and $\tilde{V}_{\pm}^{(n)}$, respectively, the boundary condition of zero velocity on the impervious hard backing yields

$$\tilde{V}_{+}^{(N)}+\tilde{V}_{-}^{(N)}=0.$$

Another $2N-2$ equation results from continuity of the flux and pressure at the boundaries between layers and have the following form:

$$\phi^{(m)}(V_{+}^{(m)}+V_{-}^{(m)})=\phi^{(m-1)}(\tilde{V}_{+}^{(m-1)}+\tilde{V}_{-}^{(m-1)}), \tag{6}$$

$$\frac{1}{C^{(m)}(\omega)}\frac{d}{dx}(V_{+}^{(m)}+V_{-}^{(m)})=\frac{1}{C^{(m-1)}(\omega)}\frac{d}{dx}(\tilde{V}_{+}^{(m-1)}+\tilde{V}_{-}^{(m-1)}), \tag{7}$$

where $m=2,...,N$. At the insonified boundary, the air pressure and flux continuity equations can be written by introducing reflection coefficient R (defined as the ratio of particle velocities in the reflected and incident waves, $R=v_r/v_i$):

$$\phi^{(1)}(V_{+}^{(1)}+V_{-}^{(1)})=v_i+v_r=v_i(1+R), \tag{8}$$

$$\frac{1}{C^{(1)}(\omega)}\frac{d}{dx}(V_{+}^{(1)}+V_{-}^{(1)})=\frac{i\omega}{c_0}v_i(1-R). \tag{9}$$

A relationship between $V_{\pm}^{(n)}$ and $\tilde{V}_{\pm}^{(n)}$ can be found by approximate solution of (5) using the mean field approximation[13] and is defined by the following transcendental equation:

$$\tilde{V}_{\pm}^{(n)}=V_{\pm}^{(n)}\exp\{\pm s^{(n)}[\phi^{(n)}(V_{+}^{(n)}+V_{-}^{(n)}),\phi^{(n)}(\tilde{V}_{+}^{(n)}+\tilde{V}_{-}^{(n)})]l^{(n)}\}, \tag{10}$$

where

$$s^{(n)}(a,b)=\frac{G^{(n)}(a)+G^{(n)}(b)}{2}, \tag{11}$$

$$G^{(n)}(a)=ik^{(n)}-M^{(n)}\left(\sqrt{1+i\frac{\omega_c^{(n)}}{\omega}(1+\xi^{(n)}|a|)^2}-\sqrt{1+i\frac{\omega_c^{(n)}}{\omega}}\right), \tag{12}$$

and $l^{(n)}$ is the nth layer thickness.

The system of $2N+1$ equations can be simplified by introducing new unknown functions: $y^{(n)}=\phi^{(n)}(V_{+}^{(n)}+V_{-}^{(n)})$, $\tilde{y}^{(n)}=\phi^{(n)}(\tilde{V}_{+}^{(n)}+\tilde{V}_{-}^{(n)})$ and the plane wave reflection coefficient R:

$$\frac{c_0}{i\omega C^{(1)}(\omega)\phi^{(1)}}G^{(1)}(y^{(1)})[\tilde{y}^{(1)}Q^{(1)}(y^{(1)},\tilde{y}^{(1)})-y^{(1)}P^{(1)}(y^{(1)},\tilde{y}^{(1)})]=v_i(1-R), \tag{13}$$

$$y^{(1)}=v_i(1+R),$$

$$\frac{G^{(m)}(y^{(m)})}{C^{(m)}(\omega)\phi^{(m)}}[\tilde{y}^{(m)}Q^{(m)}(y^{(m)},\tilde{y}^{(m)})-y^{(m)}P^{(m)}(y^{(m)},\tilde{y}^{(m)})]=\frac{G^{(m-1)}(\tilde{y}^{(m-1)})}{C^{(m-1)}(\omega)\phi^{(m-1)}}[\tilde{y}^{(m-1)}P^{(m-1)}(y^{(m-1)},\tilde{y}^{(m-1)})-y^{(m-1)}Q^{(m-1)}(y^{(m-1)},\tilde{y}^{(m-1)})],$$

$$y^{(m)}=\tilde{y}^{(m-1)},$$

$$\tilde{y}^{(N)}=0,$$

where

$$Q^{(n)}(a,b)=2\frac{\exp(s^{(n)}(a,b)l^{(n)})}{\exp(2s^{(n)}(a,b)l^{(n)})-1}, \tag{14}$$

$$P^{(n)}(a,b)=\frac{\exp(2s^{(n)}(a,b)l^{(n)})+1}{\exp(2s^{(n)}(a,b)l^{(n)})-1}. \tag{15}$$

After some algebra (13) can be reduced to a system of $N+1$ transcendental equations for the unknown functions $x_0=(1+R)$, $x_n=\tilde{y}^{(n)}/v_i$:

$$x_0A_1(v_ix_0,v_ix_1)+x_1B_1(v_ix_0,v_ix_1)=2,$$

$$x_{m-2}A_m(v_ix_{m-2},v_ix_{m-1})+x_{m-1}B_m(v_ix_{m-2},v_ix_{m-1},v_ix_m)+x_mC_m(v_ix_{m-1},v_ix_m)=0, \tag{16}$$

$$x_N=0,$$

where

$$A_1(a,b)=-\frac{c_0G^{(1)}(a)}{i\omega C^{(1)}(\omega)\phi^{(1)}}P^{(1)}(a,b)+1, \tag{17}$$

$$B_1(a,b)=\frac{c_0G^{(1)}(a)}{i\omega C^{(1)}(\omega)\phi^{(1)}}Q^{(1)}(a,b), \tag{18}$$

$$A_m(a,b)=Q^{(m-1)}(a,b), \tag{19}$$

$$B_m(a,b,c)=\frac{G^{(m)}(b)}{G^{(m-1)}(b)}\frac{\phi^{(m-1)}}{\phi^{(m)}}\frac{C^{(m-1)}(\omega)}{C^{(m)}(\omega)}P^{(m)}(b,c)+P^{(m-1)}(a,b), \tag{20}$$

$$C_m(a,b)=-\frac{G^{(m)}(a)}{G^{(m-1)}(a)}\frac{\phi^{(m-1)}}{\phi^{(m)}}\times\frac{C^{(m-1)}(\omega)}{C^{(m)}(\omega)}Q^{(m)}(a,b). \tag{21}$$

To determine the reflection coefficient of a multilayered medium for different values v_i of particle velocity in the incident wave, Eqs. (16) must be solved numerically. By using the free-field relationship between v_i and pressure amplitude p_i, $v_i=p_i/\rho_0c_0$, the dependence on incident pressure amplitude can be obtained also. The nonlinear (pressure-dependent) normalized surface impedance Z of the multilayered medium can be calculated from the reflection coefficient using $Z=(1-R)/(1+R)$.

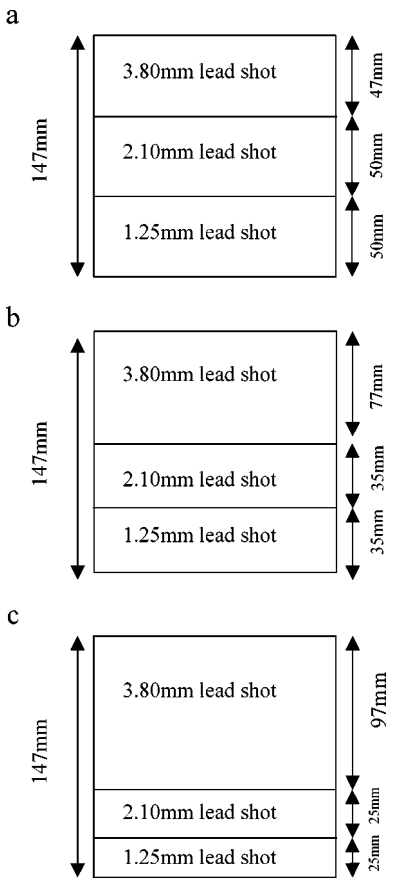

FIG. 2. The three triple-layer configurations of lead shot used in the experiments.

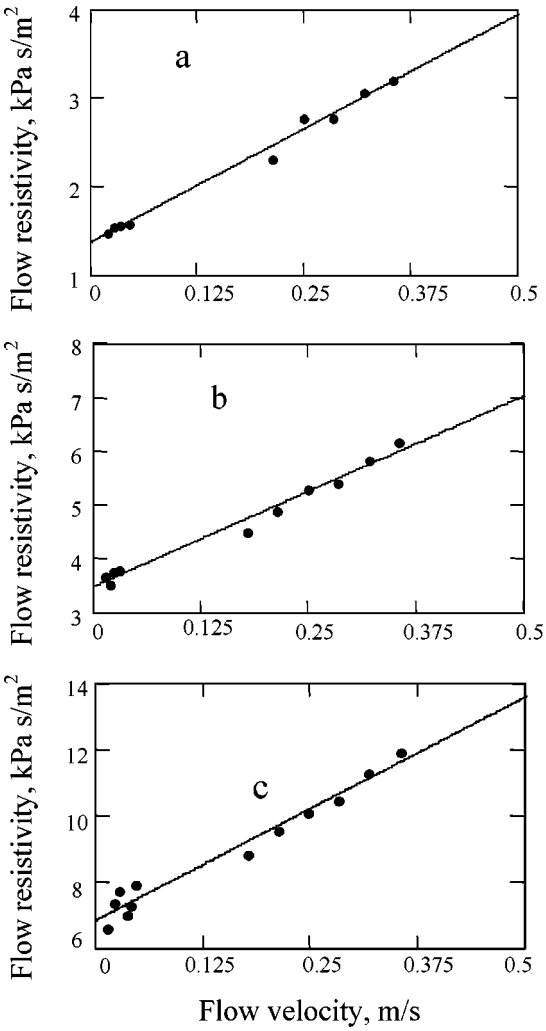

FIG. 3. Measured flow resistivity as a function of flow velocity for lead shot and best-fit straight lines, (a) $d=3.8$ mm, (b) $d=2.1$ mm, (c) $d=1.25$ mm.

III. EXPERIMENTS AND COMPARISON OF PREDICTIONS WITH DATA

A. Triple-layers of lead shot

The model has been tested against data for the acoustical properties of three triple-layer configurations formed from lead shot with three different particle sizes (Fig. 2). There are four reasons for using lead shot in such experiments. First, it is relatively easy to change the thickness of layers composed of unconsolidated particles. Secondly, particles of lead shot are approximately spherical and identical so the drag parameters required can be estimated using a cell model.[17] Thirdly, layers with different acoustic properties are obtained simply by changing particle size. This follows since the parameters controlling the acoustical behavior (σ_0, Λ, k', and Λ') depend on the particle radius.[17] Finally, lead shot packings exhibit strong Forchheimer-type nonlinearity.

Three triple-layer configurations were prepared in a cylindrical container with a hard backing and acoustically-transparent mesh lid. The container was designed to fit a vertically installed impedance tube. The length of the container was approximately 15 cm and the total length of all of the configurations was close to 14.7 cm. The top layer always consisted of 3.8 mm diameter lead shot, the middle layer was 2.1 mm diameter lead shot and bottom layer was formed from 1.25 mm diameter lead shot. The decreasing particle size from top to bottom results in layers with increasing flow resistivity. In the three tested configurations, the top layer thickness was 4.7 cm, 7.7 cm, and 9.7 cm, respectively. The middle and bottom layer thicknesses were made equal to each other. The smallest layer thickness was chosen to be at least ten times bigger than the particle size so that it should be representative of the bulk material.

The impedance measurements on the multiple layers were similar to those described elsewhere.[13] First the transfer function between the two transducers in a tube with a rigid termination was measured using pure tones of different intensity in the frequency range between 200 and 800 Hz and was shown to be independent of amplitude. This suggests that it is possible to exclude the influence of hydrodynamic nonlinearity inside the impedance tube. Linear reflection coefficient and impedance of single and multiple-layers were measured using the transfer function method for low intensity pure tones of different frequencies or by using low intensity white noise. The sound pressure levels in the impedance tube for these low intensity tests were between 60 and 90 dB. Subsequently high-intensity measurements were performed on the multiple layer configurations. As remarked in the previous study,[13] the high intensity measurements were

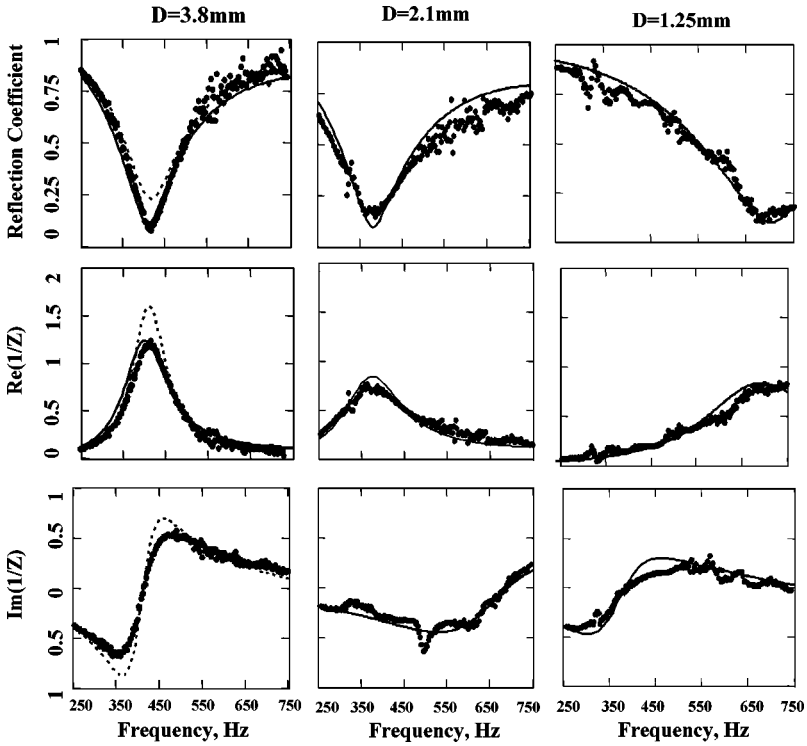

FIG. 4. The frequency dependence of the reflection coefficient amplitude and surface admittance for low amplitude sound incident on a single 14.7 cm thick layers of 3.8 mm, 2.1 mm, and 1.25 mm diameter lead shot (left to right respectively). For the 3.8 mm shot, the points represent data, the dashed line represents equivalent fluid model predictions using cell model values of Λ and α_∞, and the solid line represents predictions using fitted values of Λ and α_∞. For the smaller diameters of lead shot, the points represent data and the solid lines represent predictions using cell model values of Λ and α_∞.

made with pure tones to enable generation of sufficiently high pressures.

The porosity of a random packing of identical spheres does not depend on the particle radius. For all three types of lead shot it was obtained by weighing and was close to 0.385. The flow resistivity and Forchheimer's parameter for each type of lead shot were obtained experimentally [Figs. 3(a), 3(b), 3(c)]. The materials show strong dependence of flow resistivity on flow velocity, i.e., are highly nonlinear. The lead shot with the largest particles exhibits the strongest Forchheimer's nonlinearity. The tortuosity and the characteristic viscous length of lead shot can be estimated assuming identical spherical particles. Relationship (3) between the complex density and the complex compressibility for a packing of spheres was used for the predictions. Figure 4 shows good agreement between the predictions of the linear equivalent fluid model[9–11] and low intensity reflection coefficient and admittance data for single hard-backed layers of the two smaller types of lead shot, using measured values of flow resistivity and cell model values of tortuosity and characteristic viscous length. However, as a result of the larger discrepancy between impedance data and predictions near the layer resonance frequencies, it was found necessary to adjust the tortuosity and characteristic viscous length values for the lead shot with the largest particles for best fit. The parameter values and the methods used to determine them are summarized in Table I.

Figure 5 shows that the linear predictions for multiple layers of lead shot (with the layer parameters given in Table I) agree well with reflection coefficient data for all three

TABLE I. Parameters for lead shot and their method of determination.

Particle diameter/ parameter	$d=3.8$ mm	$d=2.1$ mm	$d=1.25$ mm	Method of parameter determination
Porosity ϕ	0.385	0.385	0.385	Measured
Flow resistivity σ_0, Pa s m^{-2}	1373	3496	6818	Measured
Characteristic viscous length Λ, m	5.5×10^{-4}	2.8×10^{-4}	2.1×10^{-4}	Cell model[a]
	3.7×10^{-4}			Adjusted to fit low amplitude impedance data
Tortuosity α_∞	1.6	1.6	1.6	Empirical formula[b]
	1.5			Adjusted to fit white noise impedance data
Forchheimer's parameter ξ, s m^{-1}	3.7	2.3	2.0	Measured

[a]Reference 17.
[b]Reference 18.

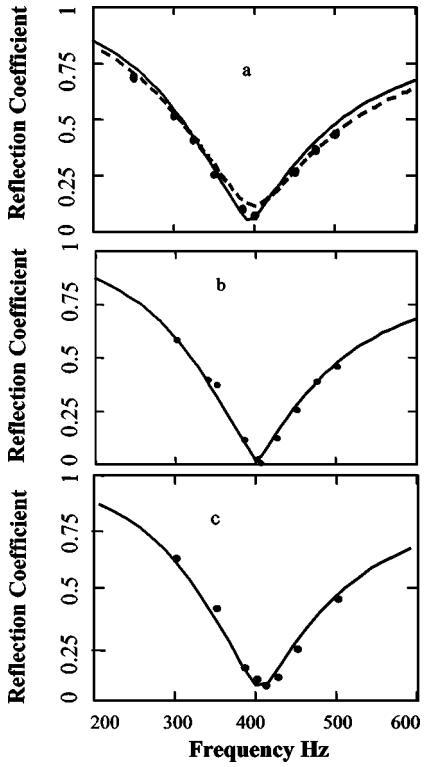

FIG. 5. Measurements and predictions of the reflection coefficient amplitude of the triple-layer lead shot configurations subject to low amplitude sound. Solid lines represent linear model results and points represent data. (a) $l_1 = 4.7$ cm, $l_2 = 5$ cm, $l_3 = 5$ cm. Dashed line represents predictions with the second layer flow resistivity increased by 100% compared with the measured value; (b) $l_1 = 7.7$ cm, $l_2 = 3.5$ cm, $l_3 = 3.5$ cm; (c) $l_1 = 9.7$ cm, $l_2 = 2.5$ cm, $l_3 = 2.5$ cm.

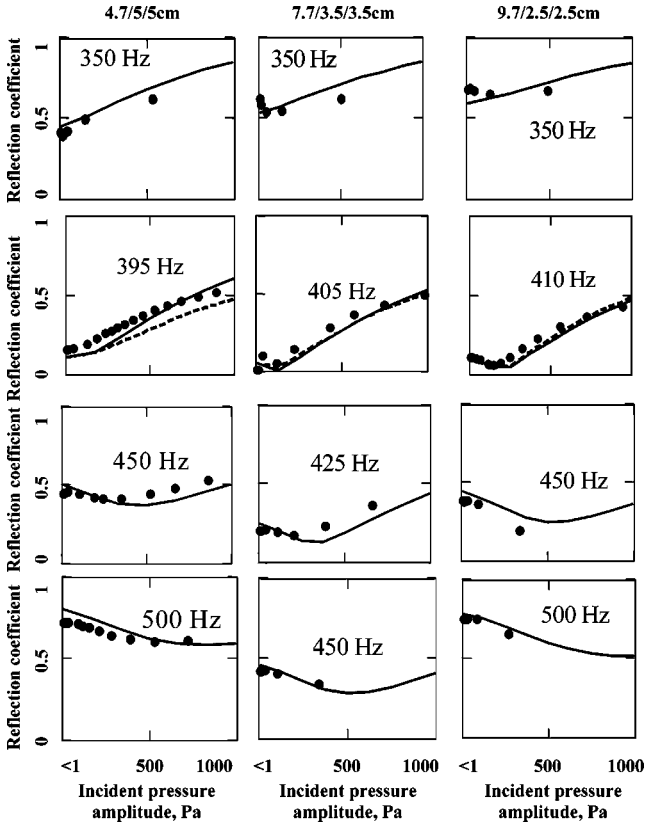

FIG. 6. The reflection coefficient of three configurations of triple-layers of lead shot as a function of incident wave pressure amplitude at four different frequencies. Respectively from left to right: $l_1 = 4.7$ cm, $l_2 = 5$ cm, $l_3 = 5$ cm, $l_1 = 7.7$ cm, $l_2 = 3.5$ cm, $l_3 = 3.5$ cm, and $l_1 = 9.7$ cm, $l_2 = 2.5$ cm, $l_3 = 2.5$ cm. Dashed lines represent predictions assuming nonlinearity only in the first layer.

configurations. Note that the resonant frequency of the configurations increases slightly as the top layer thickness is increased (the approximate values are 395 Hz, 405 Hz, and 410 Hz, respectively). The dashed line in Fig. 5(a) illustrates the effect of doubling the measured flow resistivity of second layer to 6992 Pa s/m^2. The resonant frequency of the absorber is not affected much by this change. However, after doubling the flow resistivity of the second layer, the predicted value of the reflection coefficient of the multilayer configuration at resonance frequency exceeds that predicted using the measured value of flow resistivity in the second layer by almost 100%.

The predictions of the nonlinear model have been tested against data for high amplitude sound in the frequency range between 300 Hz and 600 Hz and the results are shown in Fig. 6. It has been established elsewhere[13] that, as the incident pressure amplitude increases, two types of reflection coefficient behavior at layer resonance are possible depending on the material parameters. The typical result for high flow resistivity materials is that the reflection coefficient with incident pressure. For a single hard-backed rigid-porous layer, a criterion has been established for a different type of behavior in which the reflection coefficient decreases and then increases as the incident amplitude increases. The complexity of calculations precludes analytical derivation of a similar criterion in the case of a multilayered medium. However the data and predictions shown in Fig. 6 confirm that both types of nonlinear behavior are possible with multiple layered absorbers. Moreover it is apparent that the nonlinear behavior can be changed, simply, by increasing the top layer thickness. The pressure level at which the reflection coefficient at resonance is changed by 30% of its linear value decreases as the linear reflection coefficient decreases. It is approximately 180 Pa (139 dB re 2×10^{-5} Pa) for the 4.7/5/5 cm configuration, 65 Pa (130 dB re 2×10^{-5} Pa) for the 7.7/3.5/3.5 cm configuration, and 100 Pa (134 dB re 2×10^{-5} Pa) for the 9.7/2.5/2.5 cm configuration. In the first case there is an increase in the reflection coefficient value at the 30% ''threshold'' level. In the latter two cases the reflection coefficient is decreased by nonlinearity. At the resonant frequencies of all three triple-layer configurations, predictions have been made also with nonlinearity assumed in the first layer only ($\xi^{(2)} = \xi^{(3)} = 0$). The results are indicated by the dashed lines in the second row of Fig. 6. Not surprisingly, the nonlinearity of the inner layers has most effect for the configuration with the thinnest upper layer. As the thickness of the upper layer is increased, the attenuation of sound within this layer increases. This means a decrease in the amplitude of the sound entering the second layer and a weakening of the nonlinear effects in the inner layers. It seems that the top layer thickness used in the second and third configurations is too large for nonlinear effects beyond the top layer.

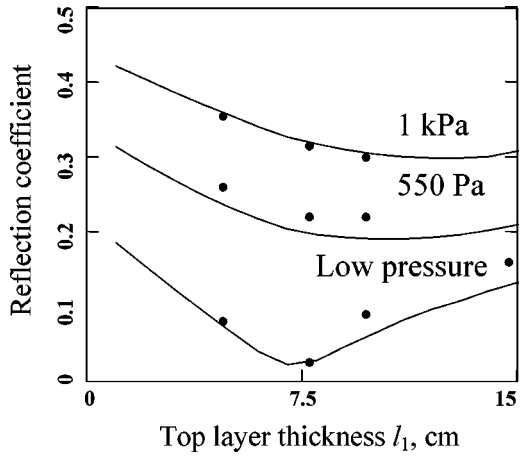

FIG. 7. Measured and predicted reflection coefficient at 400 Hz as a function of the top layer thickness l_1 at different levels of incident sound amplitude, $l_1+l_2+l_3=14.7$ cm, $l_2=l_3$. Points represent data and lines represent predictions: 1, low intensity sound (linear model); 2, $P_i=580$ Pa, 3, $P_i=1$ kPa.

In the linear regime for sound pressure, the best absorption in the chosen range of frequencies and for a given total thickness can be achieved by changing the relative thickness of the component layers. According to Fig. 5, at low amplitudes of the incident sound, the configuration with a 7.7 cm thick top layer has the lowest value of the reflection coefficient at 400 Hz. The dependence of predicted and measured reflection coefficient at 400 Hz on the first layer thickness at different amplitudes of incident sound is shown in Fig. 7. It is apparent that, as a result of nonlinearity, the optimum configuration depends on the incident pressure amplitude. The optimum configuration based on the linear assumption is not the most efficient when the incident sound amplitude is 1 kPa. In this case a single layer consisting exclusively of the largest diameter lead shot is predicted to perform equally well.

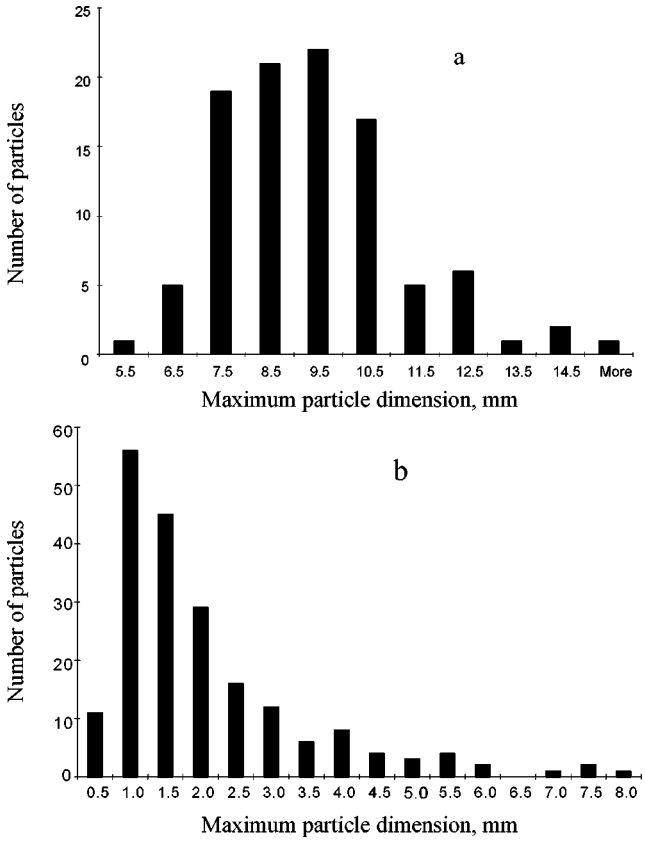

FIG. 8. Measured distributions of the maximum dimension in 103 particles of two types of gravel: (a) coarse gravel, mean maximum dimension $=9.02$ mm, standard deviation$=1.81$ mm; (b) fine gravel, mean maximum dimension$=1.81$ mm, standard deviation$=1.41$ mm.

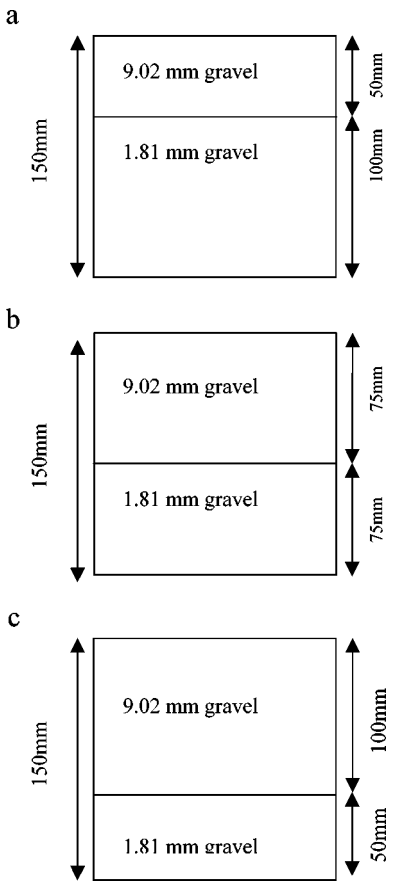

FIG. 9. The three double-layer gravel configurations used in the experiments.

B. Double-layers of gravel

Three double-layer configurations using two types of gravel were prepared in turn in the same cylindrical container as for the lead shot samples. Particle size distributions for these types of gravel are shown in Fig. 8. The mean maximum dimension of the coarse gravel is 9.02 mm and that of the fine gravel is 1.81 mm. As with the configurations of lead shot, the top layer was formed by gravel with bigger particles so that the flow resistivity of the bottom layer was greater than that of the top layer. Three configurations with overall thickness of approximately 15 cm were tested, the top layer thickness being 5 cm, 7.5 cm, and 10 cm, respectively [Figs. 9(a), (b), and (c)]. The acoustical properties of gravel are very sensitive to the degree of compaction. Moreover, since the degree of compaction could be changed by the action of high amplitude sound, each of the layers was compacted prior to any measurements. The porosity of the compacted layers was measured by weighing and was close

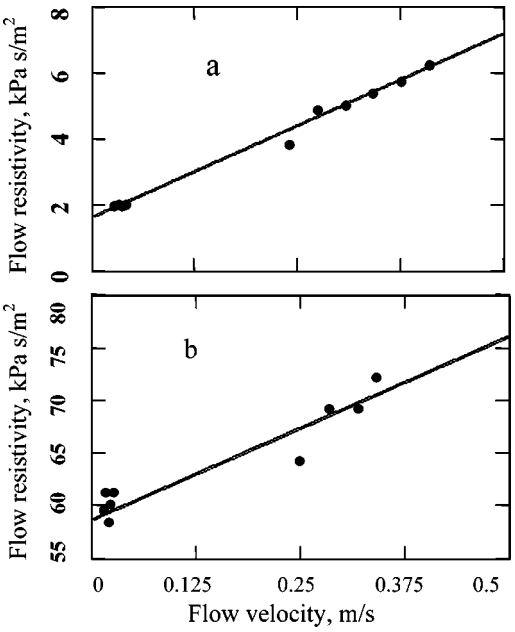

FIG. 10. Measured flow resistivity as a function of flow velocity for gravel and best-fit straight lines, (a) 9.02 mm gravel, (b) 1.81 mm gravel.

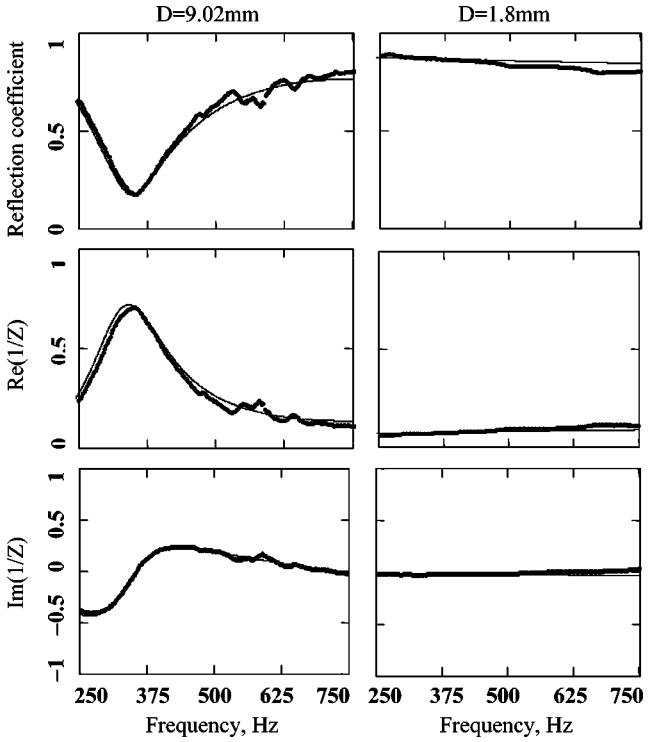

FIG. 11. The frequency dependence of the reflection coefficient amplitude and the surface admittance for low amplitude sound incident on a single 15 cm thick layer of gravel. The left-hand graphs correspond to 9.02 mm gravel and the right-hand graphs to 1.81 mm gravel. Points represent data and the solid line represents equivalent fluid model predictions using fitted values of Λ and α.

to 0.38 for both types of gravel. Results of flow resistivity and Forchhheimer's parameter measurements are shown in Fig. 10. There is a much bigger difference between the flow resistivities of the gravel layers than between those of the lead shot layers. The flow resistivity of the bottom gravel layer is more than thirty times higher than that of the top layer. A significant contrast is observed between the values of the Forchheimer's parameter also. The value for the top layer value is over ten times bigger than that for the bottom layer. Since gravel particles are irregularly shaped, estimations of tortuosity and characteristic viscous length assuming spherical particles are not possible. Instead their values have been deduced by fitting the linear model to the low intensity (linear) surface impedance data shown in Figs. 11 but assuming the relationship between complex density and complex compressibility [Eq. (3)] valid for identical spherical particles. The parameters of gravel layers used in the predictions are summarized in Table II.

In the linear regime the resonant frequency of the double layer is observed to decrease from approximately 750 Hz to 500 Hz, as the top layer thickness is increased from 5 to 10 cm, in reasonable agreement with the predictions (Fig. 12). Despite the fact that gravel parameters have been adjusted to fit single layer data the agreement between model and theory for double layers is not that good as in the case of lead shot triple-layers. The randomness in particle size and shapes means that their properties depend more strongly on the packing configuration and it is impossible to replicate gravel samples as well as lead shot samples. Moreover the wider distribution on particle size and shape leads to mixing at the boundary between the gravel layers. The behavior shown in Fig. 12 is different to that observed for the lead shot and results from the greater contrast between the properties of the top and bottom layers. For all three configurations, growth of the reflection coefficient at resonance with incident pressure

TABLE II. Parameters for gravel and their method of determination.

Maximum particle dimension/parameter	$d=9.02$ mm	$d=1.81$ mm	Method of parameter determination
Porosity ϕ	0.38	0.38	Measured
Flow resistivity σ_0, Pa s m^{-2}	1648	58710	Measured
Characteristic viscous length Λ m	1.9×10^{-4}	9.0×10^{-4}	Deduced by fitting (linear) surface impedance data
Tortuosity α_∞	1.55	1.8	Deduced by fitting (linear) surface impedance data
Forchheimer's parameter ξ, s m^{-1}	8.23	0.63	Measured

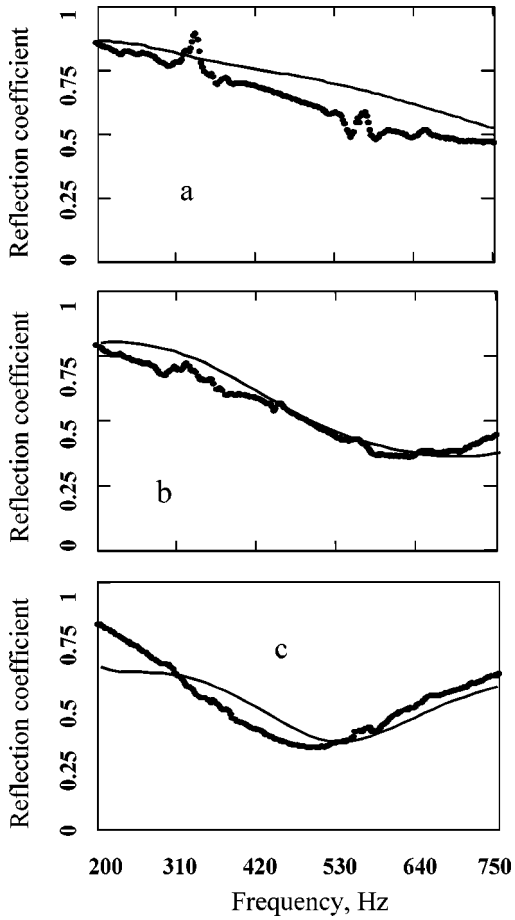

FIG. 12. Measurements and predictions of the reflection coefficient amplitude of two layered absorbers subject to low amplitude sound. Lines represent linear model prediction results, points represent data: (a) $l_1=5$ cm, $l_2=10$ cm; (b) $l_1=7.5$ cm, $l_2=7.5$ cm, (c) $l_1=10$ cm, $l_2=5$ cm.

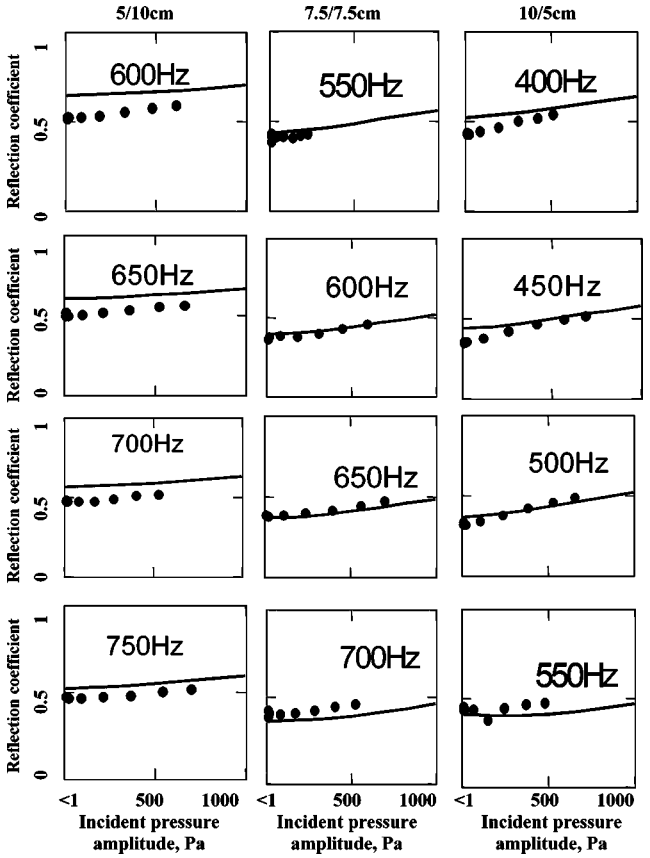

FIG. 13. The reflection coefficient of two double layer configurations of gravel as a function of incident wave pressure amplitude at four different frequencies. Lines represent nonlinear model predictions and points represent data. Respectively from left to right: $l_1=5$ cm, $l_2=10$ cm; $l_1=7.5$ cm, $l_2=7.5$ cm and $l_1=10$ cm, $l_2=5$ cm.

amplitude is observed and predicted (Fig. 13).

Despite the facts (a) that the Forchheimer's parameter of the larger gravel is higher than that of the lead shot and (b) that the flow resistivity values are comparable, the measured nonlinear variations in reflection coefficient are less pronounced with the gravel configurations than with the lead shot configurations. Indeed the incident sound pressure level required for a 30% increase in reflection coefficient at resonance is 1 kPa (154 dB re 2×10^{-5} Pa) for the configurations with 5 cm and 7.5 cm top layer thickness and is 375 Pa (145 dB re 2×10^{-5} Pa) when the top layer thickness is 10 cm. These threshold values are much higher than similar ones for lead shot layers. It should be noted that the pressure in the wave which penetrates a material configuration with low values of the reflection coefficient amplitude, is higher than in layers with higher values of reflection coefficient amplitude. The values of the reflection coefficient at layer resonance for the triple-layers of lead shot (between 0.02 and 0.09 according to Fig. 5) are much lower than the corresponding values for double layers of gravel (between 0.35 and 0.5 according to Fig. 12). This means that, at a given value of incident sound pressure, the amplitude of the sound penetrating the gravel is at least 4 times lower than that penetrating the lead shot layer. According to Eq. (4) the effect of nonlinearity is proportional to the product of Forchheimer's parameter, the particle velocity amplitude in the pores of the material (proportional to pressure) and porosity. Consequently, despite the fact that Forchheimer's parameter of the top layer gravel (8.32 s/m) is 2.25 times higher than that for top layer lead shot (3.7 s/m) and the porosity values are comparable, the four times smaller pressure and hence velocity associated with the penetrating sound means that the value of this product is still lower for gravel. Consequently nonlinear effects are predicted to be less pronounced in the gravel configurations. This is confirmed by Fig. 14 where reflection coefficients at 500 Hz, 650 Hz and 750 Hz for both layered gravel configurations are plotted as a function of the top layer thickness for different amplitudes of incident sound. The predicted dependence changes only slightly with sound amplitude and this is in agreement with data.

IV. CONCLUSION

A model which combines Forchheimer's nonlinearity with an equivalent fluid model[13] has been extended to predict acoustical properties of layered rigid-porous media with an arbitrary number of layers. It has been tested against data for three configurations of 3-layer and 2-layer absorbers and is shown to give valid predictions for the reflection coefficient behavior at sound amplitudes up to 1 kPa (154 dB re 2×10^{-5} Pa) over a wide range of frequencies. It has been shown that nonlinear effects are stronger with a multilayer

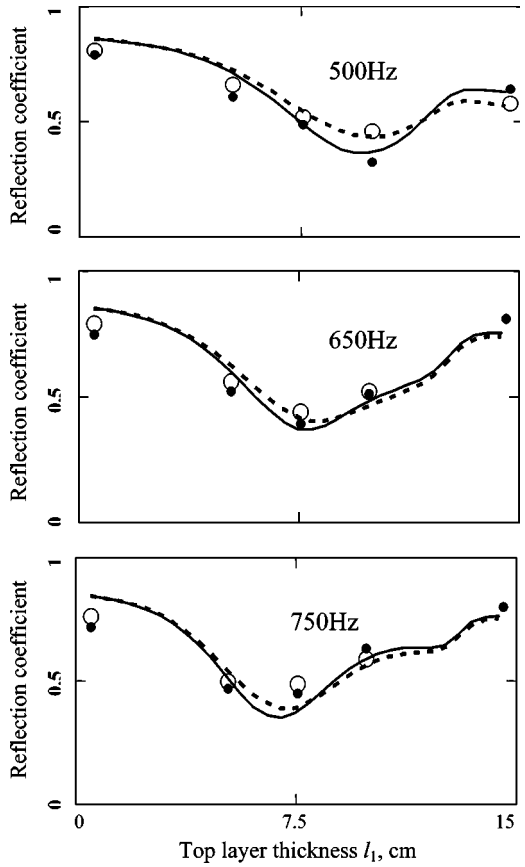

FIG. 14. Reflection coefficient of the double layer configurations of gravel at three frequencies (500 Hz, 650 Hz, and 750 Hz) as a function of the top layer thickness l_1 at different levels of incident sound amplitude. Lines represent predictions and points represent data (for the same configurations as in Fig. 13 and for single layers): $l_1+l_2=0.15$m, solid line, low intensity sound (linear model); dashed line, $P_i=540$ Pa; filled circles, low intensity data; open circles, data for $P_i=540$ Pa.

configuration having a relatively small contrast in layer properties. The transition between two types of the reflection coefficient behavior at resonance, (monotonic growth or decrease growth as the incident amplitude increases) observed with single hard-backed layers,[13] can be achieved with multiple layersby changing the relative thickness of the component layers while keeping the overall thickness constant. Finally, it has been shown both theoretically and experimentally that absorbers designed to perform optimally at low sound intensities may not have the optimum configuration as the sound level increases. These results suggest that both sound amplitude and Forchheimer's nonlinearity in component layers should be taken into account in the design of multilayered rigid-porous absorbers for high-intensity sound.

ACKNOWLEDGMENTS

The work is supported in part by USARSDG (UK), Contract No. R7D 8901-EN-01 with funds from the U.S. Army ERDC BT-25 Program. The authors are grateful to Edwin Standley for many of the acoustic measurements, to Tom Law for the measurements of gravel particle size, to A. Hereman for supplying lead shot, and to the reviewers for comments leading to significant improvements in the paper.

[1] J.F. Allard, *Propagation of Sound in Porous Media: Modelling of Sound Absorbing Materials* (Elsevier, New York, 1993).
[2] F.P. Mechel, ''Design charts for sound absorber layers,'' J. Acoust. Soc. Am. **83**, 1002–1013 (1988).
[3] K.W. Hirsch and E. Buchta, ''Absorption of blast sound close to the source,'' Noise Control Eng. J. **50**, 190–199 (2002).
[4] J.F. Allard, Y. Champoux, and C. Depolier, ''Modelization of layered sound absorbing materials with transfer matrices,'' J. Acoust. Soc. Am. **82**, 1792–1796 (1987).
[5] H.L. Kuntz and D.T. Blackstock, ''Attenuation of intense sinusoidal waves in air saturated, bulk porous materials,'' J. Acoust. Soc. Am. **81**, 1723–1731 (1987).
[6] D.K. Wilson, J.D. McIntosh, and R.F. Lambert, ''Forchheimer-type nonlinearity for high intensity propagation of pure tones in air: Saturated porous media,'' J. Acoust. Soc. Am. **84**, 350–359 (1988).
[7] J.D. McIntosh and R.F. Lambert, ''Nonlinear wave propagation through rigid porous materials. I: Nonlinear parametrization and numerical solutions,'' J. Acoust. Soc. Am. **88**, 1939–1949 (1990).
[8] R.F. Lambert and J.D. McIntosh, ''Nonlinear wave propagation through rigid porous materials. II: Approximate analytical solutions,'' J. Acoust. Soc. Am. **88**, 1950–1959 (1990).
[9] D.L. Johnson, J. Koplik, and R. Dashen, ''Theory of dynamic permeability and tortuosity in fluid-saturated porous media,'' J. Fluid Mech. **176**, 379–402 (1987).
[10] Y. Champoux and J.-F. Allard, ''Dynamic tortuosity and bulk modulus in air: Saturated porous media,'' J. Appl. Phys. **70**, 1975–1979 (1991).
[11] D. Lafarge, P. Lemariner, J.-F. Allard, and V. Tarnow, ''Dynamic compressibility of air in porous structures at audible frequencies,'' J. Acoust. Soc. Am. **102**, 1995–2006 (1997).
[12] Y. Auregan and M. Pachebat, ''Measurement of the nonlinear behavior of acoustical rigid porous materials,'' Phys. Fluids **11**, 1342–1345 (1999).
[13] O. Umnova, K. Attenborough, E. Standley, and A. Cummings, ''Behavior of rigid-porous layers at high levels of continuous acoustic excitation: theory and experiment,'' J. Acoust. Soc. Am. **114**, 1346–1356 (2003).
[14] O. Umnova, K. Attenborough, and A. Cummings, ''High amplitude pulse propagation and reflection from a rigid porous layer,'' Noise Control Eng. J. **50**, 204–210 (2002).
[15] O. Umnova, K. Attenborough, and K.M. Li, ''A cell model for the acoustical properties of packings of spheres,'' Acta Acust. **87**, 226–235 (2001).
[16] P.M. Morse and K.U. Ingard, *Theoretical Acoustics* (McGraw–Hill, New York, 1968), p. 838.
[17] O. Umnova, K. Attenborough, and K.M. Li, ''Cell model calculations of the dynamic drag parameters in packings of spheres,'' J. Acoust. Soc. Am. **107**, 3113–3119 (2000).
[18] K. Attenborough, ''Models for the acoustical characteristics of air filled granular materials,'' Acta Acust. **1**, 213–226 (1993).

Power spectrum of shear waves in finite one-dimensional granular medium

M. de Billy[a)]
Laboratoire Environnement et Développement, Université Paris 7, 2 place Jussieu, BP 7087, 75251 Paris cedex 05, France

(Received 28 August 2003; revised 8 May 2004; accepted 9 May 2004)

In this paper, we consider the propagation of shear acoustic waves in a single spherical bead and in linear one-dimensional periodic chains of identical spheres. In both cases, normal force of interaction compresses the sphere(s) and obeys the nonlinear Hertz' law. In the low-frequency domain, the spectroscopy of the transmitted impulses gives rise to peaks the existence and the origin of which are discussed. © *2004 Acoustical Society of America.* [DOI: 10.1121/1.1768251]

PACS numbers: 43.25.Gf, 43.25.Rq [MFH] Pages: 713–716

I. INTRODUCTION

The propagation of elastic waves in compressed granular media was thoroughly studied in the recent past and in many domains (physics, biology, geophysics, etc.). If most of the studies are concerned with the propagation of compressional waves in compact and linear media,[1–9] few theoretical papers are concentrated on the propagation of shear waves in periodic structures.[10–12] In the case of the linear limitation, it was shown that the system, describes two types of wave process characterized by dispersion laws of acoustic and optic type: The first one (low-frequency case) represents shear waves whose motion of spheres is reduced to a transverse deflection from the direction of propagation and a small rotation. The second one (high-frequency case) describes oscillations of the spheres and a small transverse displacement. These theoretical results are based on the periodicity of the specimen and on the nonlinear Hertz' law[13] which predicts that the relative distance of approach between two adjacent spheres submitted to a compressing force F_0 is not linear: $F_0 = C\delta^{3/2}$, where the constant C depends on the material properties and the radius of the sphere.

The purpose of this paper is to investigate the frequency response of finite one-dimensional chains (including the single sphere) made up of free spherical beads submitted to shear acoustic pulses and compressed by a static force applied to one of the extremities of the chain. In the low-frequency region, the experimental power spectra of the detected pulses point out peaks whose frequency positions vary with the radius of the sphere, the compressive force, and the material properties. These dependencies are experimentally recorded and the data are compared with the theoretical approaches which are available at the present time. To our knowledge, it is the first time that such a spectroscopy analysis is achieved on linear granular media submitted to a shear excitation.

II. EXPERIMENTAL RESULTS

The experimental procedure is described in Ref. 14. It includes a pair of shear broadband transmitters excited by short ultrasonic pulses. The transducers compress the investigated samples by a static force (F_0) applied in the direction of the line joining the centers of the spheres of the chain. The specimen are monodisperse chains of spheres the radius of which is designated by R.

A typical time signal recorded in the case of a linear chain made up of 13 spheres (diameter=8 mm) compressed by a force $F_0(=45\,\mathrm{N})$ is plotted in Fig. 1(a). The associated frequency spectrum is given in Fig. 1(b). We notice that this power spectrum (the vertical scale is in dB and the frequency resolution is 1 kHz) may be divided into two parts: The first one ($f>300\,\mathrm{kHz}$) reveals the excitation of free torsional and spheroidal modes;[14] the second one ($f<200\,\mathrm{kHz}$) points out the existence of a peak (64 kHz) the origin of which is not yet well established and needs additional experiments to elucidate its existence. Notice that this peak is much larger than the other maximum of the spectrum.

Now the question we try to answer is: How does one modify the structure of this peak when the number of the spheres of the chain diminishes up to a single sphere? A qualitative response can be obtained from Figs. 2–4 which display the power spectra obtained with chains made up of different numbers of steel beads: 19, 9, 4, 3, 2, and 1, respectively. The fast Fourier transforms are calculated over a time signal of 1 ms length and 6 μs after the beginning of the excitation.

Let us designate by n the number of spheres in the finite chain that corresponds to $(n+1)$ contact points which includes the contact points between the transmitters and the spheres located at the two extremities of the chain. One of the main experimental observations is the existence of $(n+1)$ peaks in the frequency power spectrum as is clearly illustrated in Figs. 3 and 4. For large values of n (Fig. 2), the frequency resolution of our experimental equipment does not let us isolate the $(n+1)$ peaks, and then the maximum shows small oscillations at the top. For very high values of n, the detected peak presents a frequency distribution which appears to be ''continuous'' and whose maximum can be identified as a resonance corresponding to the propagation of a ''stationary shear chain wave''. Notice that in the case of a chain, the spheres are driven in a cardboard cylinder. It was experimentally verified that for materials of high acoustic

a)Electronic mail: mdebilly@ccr.jussieu.fr

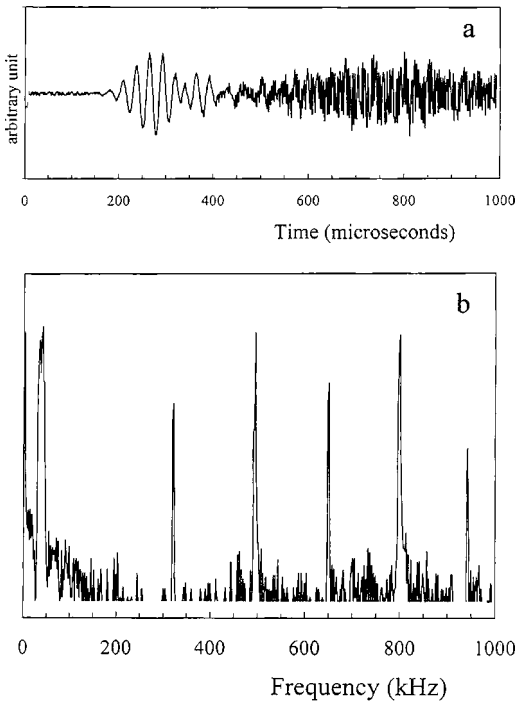

FIG. 1. (a) Temporal signal recorded with a one-dimensional chain of 13 steel spheres (diameter=8 mm); transverse excitation. (b) Frequency power spectrum of the time signal given in the (a).

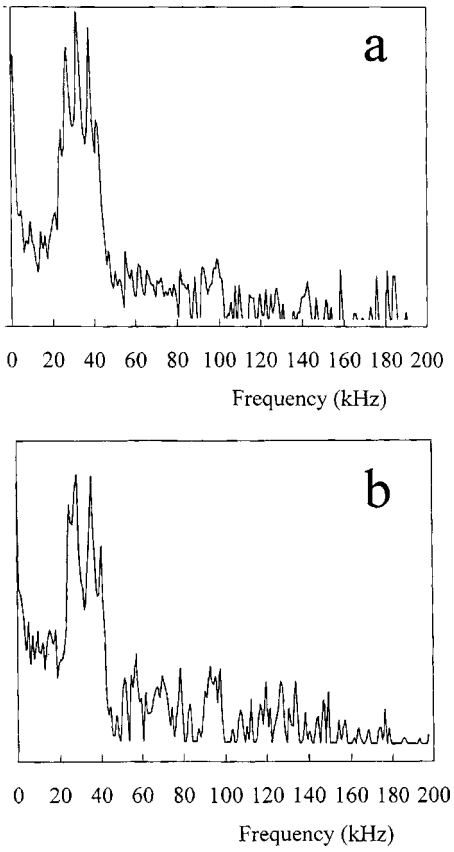

FIG. 3. Low-frequency range of the power spectra obtained in the case of a shear polarization of the initial pulse: (a) Case of four free steel spheres and (b) Case of three free steel spheres.

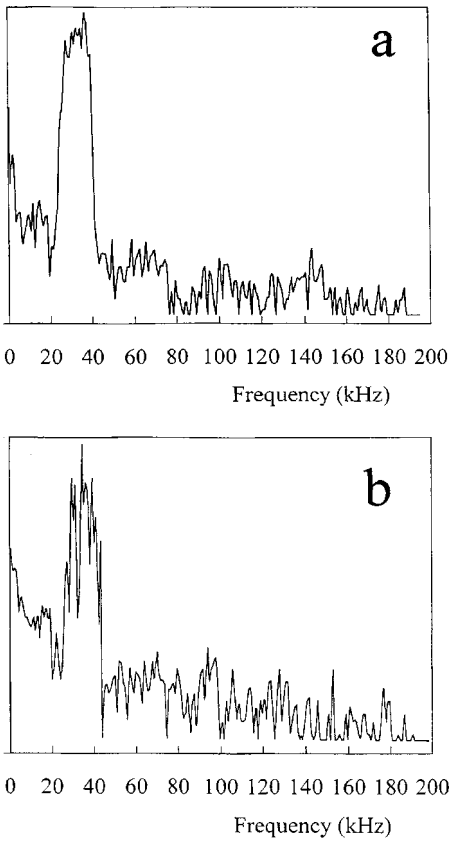

FIG. 2. Low-frequency range of the power spectra obtained in the case of a shear polarization of the initial pulse: (a) Case of 19 free steel spheres and (b) Case of nine free steel spheres.

impedance (steel, aluminum, brass, etc.), the presence of the cardboard tube modifies the amplitude of the time signal but does not affect the frequency. In the case of nylon material ($\rho=1.1\times10^3$ kg/m^3 and $C_1=2620$ m/s), the cardboard cylinder significantly modifies the frequency power spectrum. This is illustrated in Fig. 5 in which compared the frequency spectra obtained with two nylon beads of 7.9 mm in diameter without [Fig. 5(a)] and with [Fig. 5(b)] a cardboard tube, respectively. Incidentally, this behavior is typically characteristic of a surface wave.

In the case of a finite chain of few beads (typically less than five), the fine structure varies from one material to an other. In addition, it is observed that for a given material, the low-frequency resonance f depends on the static force (F_0) and on the radius (R) of the sphere as is expected for torsional and spheroidal modes.

The variations of the frequency of the two peaks of the multiplet observed in the case of a single steel bead were recorded as a function of the diameter. The experimental curves are plotted in Fig. 6(a). It is interesting to notice that, for each maximum, the best fitting of the curves by a power law (X^α) is obtained for $\alpha=-1.27$ and -1.34. These values are different from the unity encountered for torsional and spheroidal modes as is shown in Fig. 6(b) which represents the variations $f(2R)$ measured for the free modes T_{20} ($\alpha=-0.99$) and S_{11} ($\alpha=-1.01$).

The experimental variations of the frequency positions of each component of the lowest-frequency multiplet as a

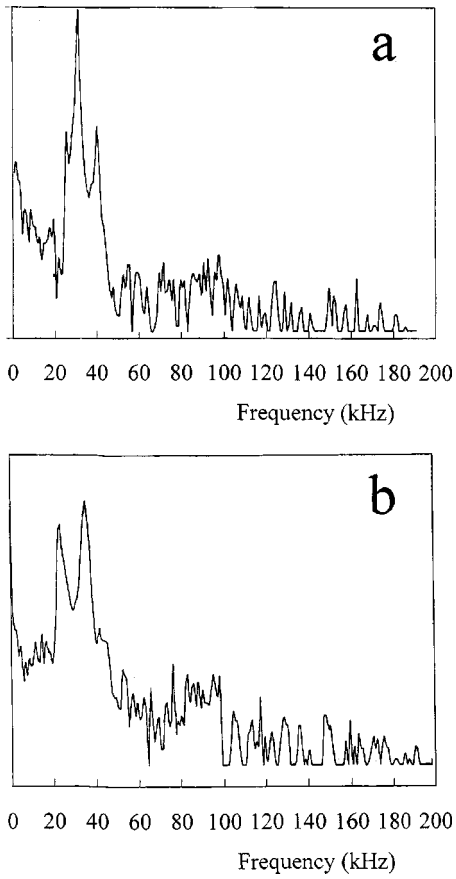

FIG. 4. Low-frequency range of the power spectra obtained in the case of a shear polarization of the initial pulse: (a) Case of two free steel spheres and (b) Case of a single free steel spheres.

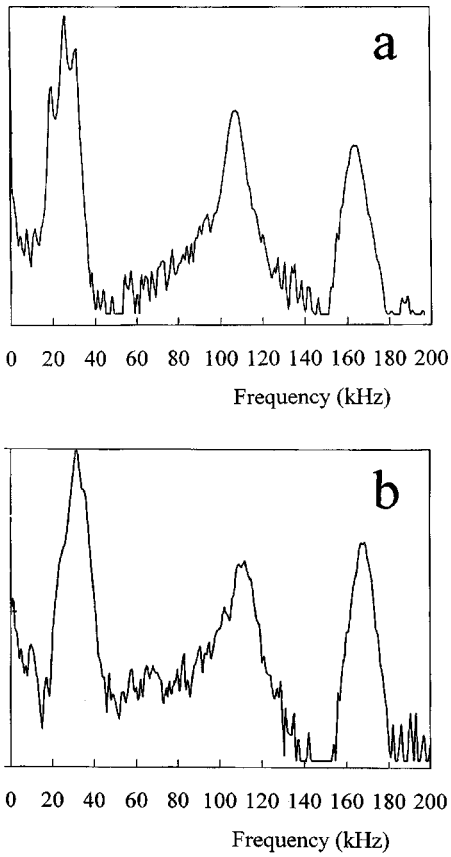

FIG. 5. Low-frequency range of the power spectra obtained with a nylon sphere (diameter=7.9 mm) in the case of a shear polarization of the initial pulse: (a) Case of two free spheres and (b) Case of two free spheres coupled with a cardboard cylinder.

function of the strength F_0 for samples of two and three steel spheres, respectively (diameter=8 mm), are plotted in Figs. 7 and 8. We can compare the experimental data obtained with a finite chain of 23 identical spheres of the same material plotted in Fig. 8 (open circular marks).

III. ANALYSIS OF THE RESULTS

The experimental results reported above suggest that low-frequency surface waves type propagate in the one granular medium (chain) made up of spherical beads excited by shear acoustic impulses. The multiplets observed in the frequency power spectra underline the discrete character of the investigated samples. At the present time, the difficulty seems to be the identification of the peaks which could be interpreted either as ''stationary nonlinear chain waves'' or solitary waves depending on the validity of the linear approximation.

It is interesting to notice that the experimental data confirm the $(R)^{-4/3}$ and the $(F_0)^{1/6}$ dependence of the frequency positions of the singlets [see Figs. 6(a), 7, and 8, respectively]. We may notice that these dependences are in agreement with the expression of the cutoff frequency f_c obtained in the case of the linear approximation for a one-dimensional chain of spheres under Hertz' law contact and compressed by a constant normal force F_0 applied along the line of the centers of the spherical beads. This particular frequency is given by the expression:

$$f_c = A(\nu, E, \rho) R^{-4/3} F_0^{1/6},$$

where A is a function of the material properties. So, the resonance observed in the low-frequency peak seems to verify a law similar to the one described in literature[1–3,7] and devoted to compressional excitation impulses. Each component of the multiplet verifying the same dependence versus R and F_0, it is not surprising to observe that in the case of a chain of a large number of beads, the R and F_0 dependences on of the peak are the same (see in the Fig. 8 the open circular marks).

It is also interesting to verify experimentally that the width of the low-frequency peak does not increase continuously with the number of beads in the chain; this behavior indicates the existence of permitted and forbidden bands in the process of the generation of this kind of waves as was predicted by Boganov and Skorvtsov[10,12] when a linear system is considered. However in that case the ''acoustic dispersion law'' seems to be only described.

IV. CONCLUSION

In this paper, we focused on the spectroscopy of a low-frequency component observed experimentally in a monodisperse finite chain of elastic spheres submitted to a static longitudinal force and impacted by a shear dynamic perturbation. In the case of a finite chain, our studies made up of n spherical beads revealed the existence of low-frequency peaks resulting from the superposition of $n+1$

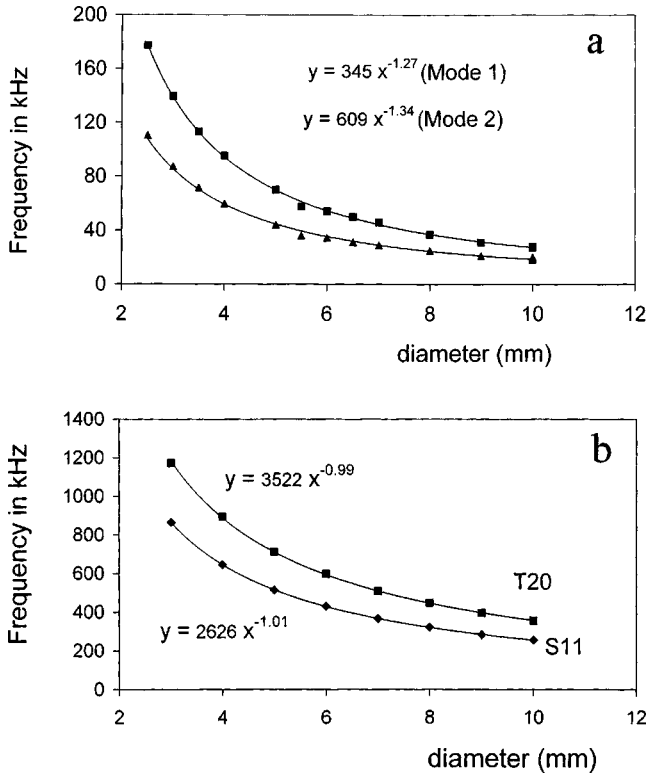

FIG. 6. Experimental variations of the frequencies as a function of the diameter ($F_0 = 45$ N) recorded in the case of a single steel sphere: (a) Case of the two low-frequency peaks and (b) Case of the modes T_{20} and S_{11}.

maximum or waves whose frequencies seem to belong to a ''permitted acoustic band'' and whose F_0 and R dependence are very similar to the one observed with limited periodic samples excited with compressional waves. We did not succeed in solving the difficulty to interpret these standing waves as ''shear chain waves'' or ''solitary type waves''. The influence of the cardboard tube was investigated and the results suggest that we have to consider the low-frequency waves as surface wave type. In this study, we hope to contribute to the interpretation of the low-frequency component observed in the power spectrum and simultaneously due to the nonlinear contact between the adjacent spheres and the dispersion provided by the periodicity of the sample. In the future, our objective is to apprehend how it would be possible to get information on the coupling at each contact surface of a finite one-dimensional chain by using the ultrasonic spectroscopy method which has been illustrated in this paper.

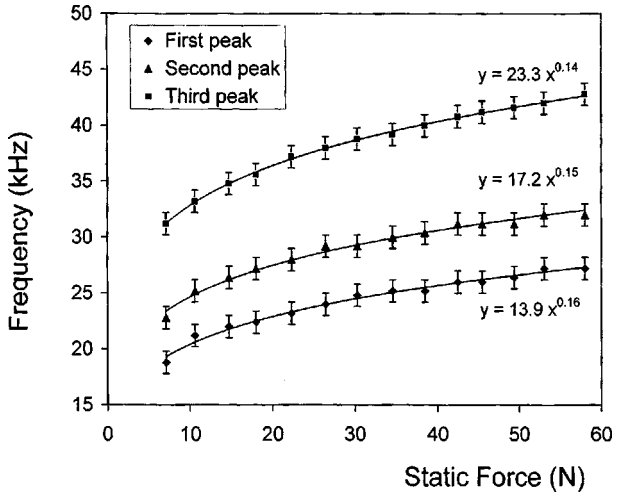

FIG. 7. Experimental variations of the low-frequency resonance as a function of the axial force F_0 (in N) recorded for the three low-frequency peaks observed with two steel beads.

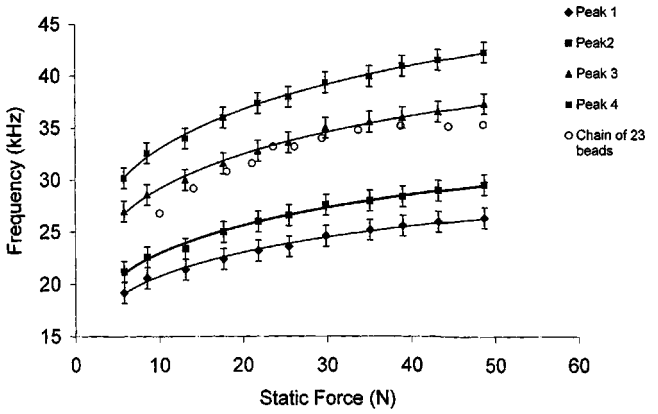

FIG. 8. Experimental variations of the low-frequency resonance as a function of the axial force (in N) recorded for the four low-frequency peaks observed with three steel beads. The open circular marks represent the experimental data obtained with a chain of 23 steel spheres.

[1] A. N. Lazaridi and V. F. Nesterenko, ''Observation of a new type of solitary waves in a one dimensional granular medium,'' J. Appl. Mech. Tech. Phys. **26**, 405–408 (1985).

[2] J. M. Bretell, ''Elastic wave propagation in powders,'' Acustica **65**, 49–51 (1987).

[3] C. Coste, E. Falcon, and S. Faure, ''Propagation d'ondes non-linéaires dans une chaîne de billes en contact de Hertz'' (Propagation of nonlinear waves in a chain of beads under Hertz contact), in *Des Géomatériaux aux Ouvrages*, edited by C. Petit, G. Pijandier-Cabot, and J. M. Reynouard (Hermès, Paris, 1995), pp. 33–52.

[4] M. Peyrard, ''Introduction to solitons and their applications in physics and biology,'' in *Nonlinear excitation in biomolecules*, Les Editions de Physique, edited by M. Peyrard (Springer, Berlin, 1995), Lecture 2.

[5] M. Remoissenet, *Waves Called Solitons: Concepts and Experiments*, 2nd ed. (Springer, Berlin, 1996).

[6] J. Anfosso, L. Forest, and V. Gibiat, ''Acoustical propagation in glass beads under uniaxial compression,'' 17th ICA Proceedings (2001), Vol. I.

[7] C. Coste, E. Falcon, and S. Fauve, ''Solitary waves in a chain of beads under Hertz contact,'' Phys. Rev. B **56**, 6104–6117 (1997).

[8] R. S. MacKay, ''Solitary waves in a chain of beads under Hertz contact,'' Phys. Lett. A **251**, 191–192 (1999).

[9] S. Sen and M. Manciu, ''Discrete Hertzian chains and solitons,'' Physica A **268**, 644–649 (1999).

[10] A. N. Bogdanov and A. T. Skvortsov, ''Nonlinear wave process in granular media,'' in *Research Trends in Physics: Nonlinear Acoustics*, edited by K. A. Naugol'nykh and L. A. Ostrovsky (La Jolla International School of Physics, 1994).

[11] R. D. Mindlin, ''Compliance of elastic bodies in contact,'' J. Appl. Mech., Trans. ASME **71**, A259–268 (1949).

[12] A. N. Bogdanov and A. T. Skvortsov, ''Nonlinear shear waves in granular medium,'' Sov. Phys. Acoust. **38**, 224–226 (1992).

[13] L. D. Landau and E. M. Lifchitz, *Theory of Elasticity* (Pergamon, Oxford, 1986).

[14] M. de Billy, ''Experimental study of sound propagation in a chain of spherical beads,'' J. Acoust. Soc. Am. **108**, 1486–1495 (2000).

Acoustic Casimir pressure for arbitrary media

J. Bárcenas, L. Reyes, and R. Esquivel-Sirvent[a)]
Instituto de Física, Universidad Nacional Autónoma de México, Apartado Postal 20-364, Ciudad Universitaria, México, 01000, México

(Received 12 March 2004; revised 8 May 2004; accepted 11 May 2004)

In this paper we derive a general expression for the acoustic Casimir pressure between two parallel slabs made of arbitrary materials and whose acoustic reflection coefficients are not equal. The formalism is based on the calculation of the local density of modes using a Green's function approach. The results for the Casimir acoustic pressure are generalized to a sphere/plate configuration using the proximity theorem. © *2004 Acoustical Society of America.*
[DOI: 10.1121/1.1768253]

PACS numbers: 43.25.Qp [RR] Pages: 717–720

I. INTRODUCTION

Due to quantum vacuum fluctuations, two parallel neutral plates will attract each other. This phenomenon is known as the Casimir force.[1] Although a small force, it has been measured accurately using torsion balances, atomic force microscopes, and micromechanical oscillators.[2–5] An acoustic analog to the Casimir effect was reported in 1996 by Larraza and collaborators,[6–8] where two parallel plates, placed at a distance L, were subjected to a broadband noise background. The plates were observed both to attract and to repel each other, depending on the separation distance and the broadband noise cutoff frequencies. Following Casimir's method,[1] a theory for the acoustic Casimir force was developed assuming perfectly reflective plates with approximations that turned out to be valid for the frequency range, material, and plate thickness that were used in the experiment. In this work we derive a general expression for the acoustic Casimir pressure for materials with arbitrary impedances by calculating the density of modes between the plates using the Green's function formalism borrowed from the electromagnetic case. We also present an acoustic analog to the proximity theorem to calculate the Casimir pressure between a sphere and a plate.

II. THEORY

Consider two different parallel slabs labeled $i=1,2$ of thickness $d_{1,2}$, separated by a distance L along the z axis. The slabs are parallel to the $x-y$ plane and have an arbitrary acoustic reflectivity $r_{1,2}$ [Fig. 1(a)].

For a perfect acoustic reflector, the radiation pressure of a wave of intensity I and speed c impinging on the slab is given by[6,9]

$$P=\frac{2I}{c}\cos^2(\theta), \tag{1}$$

where θ is the angle of incidence.

As in Refs. 6–8 we consider broadband acoustic noise of constant spectral intensity I_ω in the frequency interval $[\omega_1,\omega_2]$, and its spectral representation in the wave vector space

$$I_k=\frac{cI_\omega}{4\pi k^2}, \tag{2}$$

where $k^2=(\omega/c)^2=k_x^2+k_y^2+k_z^2$.

The total radiation pressure on a plate for perfect reflectors, using Eq. (1), is

$$P_0=\frac{I_\omega}{2\pi^2}\int dk_x dk_y dk_z \frac{k_z^2}{k^4}. \tag{3}$$

Between the plates, the total radiation pressure P_{in} is determined by the allowed modes that satisfy the boundary conditions at the plate surfaces. If the plates are large enough, k_x and k_y take on continuous values. For perfect reflectors the normal component of the wave vector takes the values $k_z=n\pi/L$, where n is an integer. Thus, the calculation of the energy density is reduced to integration over k_x and k_y and summation over n. The Casimir pressure results from the difference $P_{\text{in}}-P_0$.

For arbitrary materials the mode summation is no longer direct, since we are no longer allowed to specify Dirichlet boundary conditions that restrict the allowed modes, and it becomes necessary to calculate the total density of modes $\mathcal{D}(k_z)$ and integrate over all wave vector space. To do this we use a Green's function approach.

The wave equation for the velocity potential can be written as the eigenvalue equation $-\partial_z^2\phi=k_z^2\phi$, with eigenvalues k_z^2. Let λ_n be an eigenvalue for the eigenfunction ϕ_n. In terms of the velocity potential ϕ, the particle velocity v_z, the fluid density ρ and with the definitions $v_z=\partial_z\phi_n$ and $p=-\rho\partial_t\phi_n$ we can write the normal component of the wave stress tensor[10] as

$$w_n=\frac{\rho}{2}((\partial_z\phi_n)^2+k_z^2\phi_n^2). \tag{4}$$

The total contribution to the stress tensor is obtained by adding up all modes and integrating over all possible values of k_z^2.

a)Electronic mail: raul@fisica.unam.mx

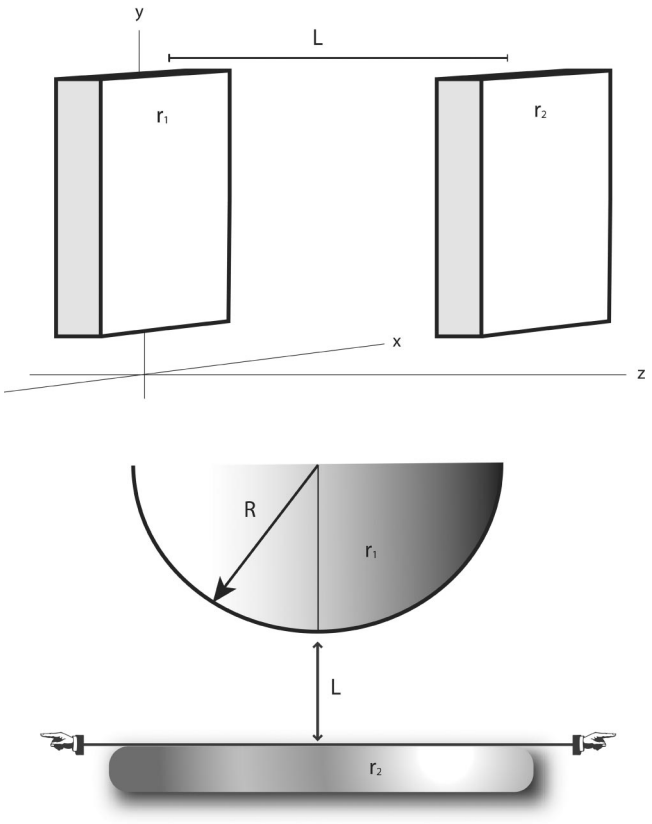

FIG. 1. (a) Geometry and coordinate system for the two parallel plate configuration and (b) for the sphere-plane configuration.

$$w=\frac{\rho}{2}\int dk_z^2\sum_n \delta(k_z^2-\lambda_n)((\partial_z\phi_n)^2+k_z^2\phi_n^2), \tag{5}$$

where we have assumed an harmonic behavior of the potential ϕ and the Dirac's delta function is introduced since only the eigenmodes contribute to w. Now, using the identity

$$\frac{1}{k_z^{+2}-\lambda_n}=P\frac{1}{k_z^2-\lambda_n}-i\pi\delta(k_z^2-\lambda_n), \tag{6}$$

with $k_z^{+2}=\lim_{\eta\to 0}(k^2+i\eta)$ we can write Eq. (5) as

$$w=\frac{\rho}{2}\int dk_z^2\left(-\frac{1}{\pi}\right)\mathrm{Im}\sum_n \frac{1}{k_z^{+2}-\lambda_n}((\partial_z\phi_n)^2+k_z^2\phi_n^2). \tag{7}$$

In this equation, we can identify the spectral representation (or eigenfunction expansion) of the Green's function and its derivative,[11] and we interpret the quantity

$$\mathcal{D}_{k_z^2}=-\frac{1}{\pi}\mathrm{Im}(G(z,z)+\partial_z\partial_z G(z,z)), \tag{8}$$

as the density of modes. Another way of understanding the result is as follows. The basic definition of denisty of modes in terms of the Green's funtion is obtained from Eq. (6) as $-\mathrm{Im}\,G(z,z)/\pi$. The acoustic pressure obeys the wave equation and with the appropriate boundary conditions, we can obtain the Green's function G_p and thus the density of modes. From the acoustic stress tensor component [Eq. (4)], besides the pressure field, there is a contribution from the velocity field. Let this field have an associated Green's function G_v. The total density of modes of the system is $-\mathrm{Im}(G_p+G_v)/\pi$. Writing the pressure and velocity in terms of the scalar potential yields Eq. (8). This is equivalent to what happens in zero point Casimir effect where the density of modes comes from adding the contribution of the electric field plus that due to the magnetic fields, and both fields are related through a constitutive equation (Maxwell's equations).

To construct the Green's function for the velocity potential we can use the standard definition

$$G_{k^2}(z,z')=\frac{\phi^<(z_<)\phi^>(z_>)}{W}, \tag{9}$$

where W is the Wronskian and

$$\begin{aligned}\phi^<(z)&=e^{-ik_z z}+r_1e^{ik_z z},\\ \phi^>(z)&=e^{ik_z(z-L)}+r_2e^{-ik_z(z-L)},\end{aligned} \tag{10}$$

are the solutions to the one-dimenional wave equation where the superscript $(<,>)$ represents the smaller and larger of z and z', respectively.

Substitution of the potentials [Eq. (10)] into Eqs. (9) and (8) yields the local density of modes

$$\mathcal{D}_{k_z^2}=\frac{1}{2k_z\pi}\mathrm{Re}\left[\frac{1+r_1r_2e^{2ik_zL}}{1-r_1r_2e^{2ik_zL}}\right], \tag{11}$$

where we have obviated the dependence of the reflectivities with wave vector. The density of states Eq. (11) was obtained from the Green's function for the Helmholtz equation with eigenvalues k_z^2. However, we are interested in the density of states for k_z. This is simply obtained from $\mathcal{D}_{k_z^2}=d(k_z^2)\mathcal{D}_{k_z}=2k_z\mathcal{D}_{k_z^2}$, or

$$\mathcal{D}_{k_z}=\frac{1}{\pi}\mathrm{Re}\left[\frac{1+r_1r_2e^{2ik_zL}}{1-r_1r_2e^{2ik_zL}}\right]. \tag{12}$$

The radiation pressure due to the inside modes can now be written as

$$P_{\mathrm{in}}=\frac{I_\omega}{4\pi}\int dk_x dk_y dk_z \mathcal{D}_{k_z}\frac{k_z^2}{k^4}. \tag{13}$$

In the limit of perfect reflectors $r\to 1$ the density of states becomes $(k_0/\pi)\,\delta(k_z-nk_0)$ where $k_0=\pi/L$. Thus, from Eq. (13) the pressure due to all the modes is

$$P_{\mathrm{in}}=\frac{k_0I_\omega}{2\pi^2}\int dk_x dk_y dk_z\sum_n \delta(k_z-nk_0)\frac{k_z^2}{k^4}, \tag{14}$$

or

$$P_{\mathrm{in}}=\frac{k_0^3I_\omega}{2\pi}\int dk_x dk_y\sum_n \frac{n^2}{(k_x^2+k_y^2+n^2k_0^2)^2}, \tag{15}$$

which is the same as that obtained by Larraza and collaborators.[6–8] Finally, the acoustic Casimir force per unit area $f=P_{\mathrm{in}}-P_{\mathrm{out}}$ takes the form

$$f=\frac{I_\omega}{2\pi^2}\mathrm{Re}\left(\int dk_x dk_y dk_z\frac{k_z^2}{k^4}\left(\frac{1}{\xi-1}\right)\right), \tag{16}$$

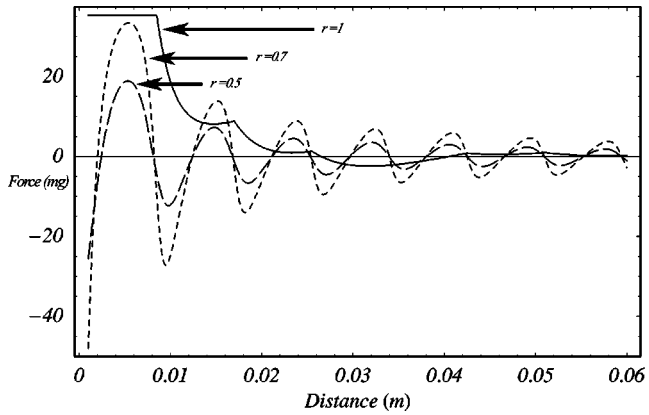

FIG. 2. Acoustic Casimir force between two parallel plates for different values of the reflectivity r assuming both plates are equal. The values of r are indicated. The intensity and bandwidth are the same as in the experiments of Laraza (Ref. 6).

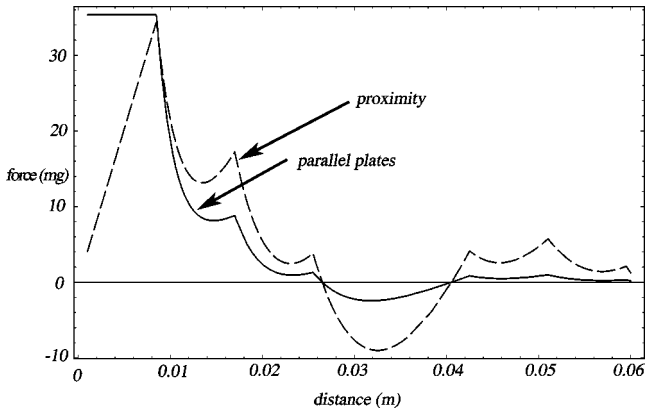

FIG. 3. Acoustic Casimir force between a sphere ($R=0.2$ m) and a plane for reflectivity $r=1$ (dashed line). For comparison the force between two parallel plates is also shown (solid line).

where $\xi=(r_1 r_2 \exp(2ik_z L))^{-1}$. Notice that it is enough to know the separation between the slabs and the reflectivities to determine the acoustic Casimir force.

To illustrate the application of Eq. (16), in Fig. 2 we plot the force *versus* separation for two identical slabs with constant reflectivities $r=1$, 0.8, 0.7. In all cases the force goes from attractive to repulsive as the separation increases. The magnitude of the force is not only related to the reflectivity but also to the finite bandwidth being used. If the bandwidth extends from zero to infinity, the acoustic Casimir pressure for a perfect reflector $-\pi I_\omega/4L$ is always attractive. If we integrate Eq. (16) over all frequencies the force is also always attractive and as the reflectivity decreases the force does too[12] in all cases. Without loss of generality we have assumed a constant value of r within the bandwidth under consideration. However, the formalism is valid even when the reflectivity shows a strong dependence with frequency. The bandwidth and intensity used in these calculations are the same as in Laraza.[6] Even if we consider a finite frequency bandwidth it is possible to obtain a purely attractive force if we consider the force between a surface with reflectivity $r_1=1$ and a pressure release surface $r_2=-1$. In this limit the force is constant and always attractive since $D_{k_z}\to 0$, as can be seen from Eq. (12) and the external pressure field pushes the plates together.

III. THE PROXIMITY THEOREM IN ACOUSTICS

Practical measurements of the Casimir force due to zero point energy fluctuations are done between a large sphere and a plane due to the difficulty of keeping two plates parallel at the submicron scale.[2–5] The force between a large sphere and a plane [see Fig. 1(b)] is calculated using the proximity theorem[13] or Derjaguin approximation,[14] which states that

> *the force between two smooth surfaces as a function of the separation degree of freedom is proportional to the interaction potential per unit area $\mathcal{E}$ between two flat surfaces, the proportionality factor being 2π times the reciprocal of the square root of the Gasussian cuadrature of the gap width function at the point of closest approach.*

For a sphere-plane system, the force F_{sp} is obtained from the Casimir free energy per unit area between two parallel plates $\mathcal{E}$ as

$$f_{sp}=2\pi R\mathcal{E}, \tag{17}$$

where R is the radius of the sphere. The proximity theorem is valid provided $L/R<1$, L being the closest distance between the surface, although the limit of $L\to 0$ can at be described by the proximity theorem. A current problem[15] is that there are no bounds on how big L/R has to be in order to obtain the correct result. Experimentally this becomes difficult at the submicron scale. The acoustic analog of the Casimir force provides a simpler (not necessarily easier) way of solving this problem, since as shown by Larraza[6] the scale of the acoustic experiments allows a more precise control of the involved parameters. Furthermore, the proximity theorem is valid for any interaction. In the acoustic case, the free energy per unit area for parallel plates is

$$\mathcal{E}=\frac{I_\omega}{4\pi^2}\int dk_x dk_y dk_z \frac{k_z}{k^4}\mathrm{Re}(\ln(1-r_1 r_2 e^{2ik_z L}))). \tag{18}$$

This expression for $\mathcal{E}$ is such that the force [Eq. (16)] is given by $f=-\partial\mathcal{E}/\partial L$. Thus, the force between a sphere and a plane is

$$f_{ps}=\frac{RI_\omega}{2\pi}\int dk_x dk_y dk_z \frac{k_z}{k^4}\mathrm{Re}(\ln(1-r_1 r_2 e^{2ik_z L}))). \tag{19}$$

To show the application of this approximation, in Fig. 3 we have plotted the force between two parallel plates and the force between a 20 cm sphere and a plate. We observe that although the proximity theorem gives a correct behavior and overall order of magnitude for the force, the region in the limit of L approaching zero is not well described.

IV. CONCLUSIONS

We have derived a general expression for the acoustic Casimir force between two parallel slabs with arbitrary acoustic properties characterized by the reflection coefficients of the material. We also extended our results to include

the force between a sphere and a plane. The expression we obtain for the Casimir force is convenient for calculations since it depends mainly on the reflection coefficients that can be obtained straightforwardly in theoretical computations or through experimental work. Our approach is analogous to the electromagnetic dielectric case, so this formalism is equivalent to the Liftshitz formula.[16,17] In the limit of a perfectly reflective plate our results agree with those of Larraza.[6] This formalism can be extended to the case of highly porous materials or viscous propagation media, although the calculations involved can be of increasing difficulty. It must be pointed out that for the case when the material is deformed by the wave, this density of states approach is no longer valid: the reflection coefficient is angular dependent, and since the angle itself is time dependent the use of a static density of states would be incorrect. Also, we have excluded the possible effects of roughness.

The crucial difference between the system we consider and the original treatment[6] is the inclusion of the density of states through the Green's function method. The analytical interpretation of the density function gives a deeper insight into what really happens in a nonperfect reflector. For a perfect reflector the density of modes consists of a series of Dirac's deltas. As the reflectivity decreases from unity, the resonance bands increase in width, which is heuristically equivalent to a spatial diffusion of the nodes that appear inside the resonant cavities.

Although the use of perfectly reflectiving plates is a good approximation in some experimental situations, this is not the case for other bodies (such as rubber, as an extreme example) hence our efforts to broaden the horizon of application. As an example, we have considered the possibility of using acoustic experiments to prove the validity of the proximity theorem. Additionally, this treatment could allow for a larger range of experimental versus theoretical comparison in this field where, as noted by Larraza *et al.*, the possibility of direct technological application of the acoustic Casimir effect is considerable.

ACKNOWLEDGMENT

Partial support provided by DGAPA-UNAM Project No. IN116002-2.

[1] H. B. G. Casimir, ''On the attraction between two perfectly conducting plates,'' Proc. K. Ned. Akad. Wet. **51**, 793 (1948).
[2] S. K. Lamoreaux, ''Demonstration of the Casimir force in the 0.6 to 6 μm range,'' Phys. Rev. Lett. **78**, 5 (1997).
[3] U. Mohideen and A. Roy, ''Precision measurement of the Casimir force from 0.1 to 0.9 μm,'' Phys. Rev. Lett. **81**, 4549 (1998).
[4] B. W. Harris, F. Chen, and U. Mohideen, ''Precision measurement of the Casimir force using gold surfaces,'' Phys. Rev. A **62**, 052109 (2000).
[5] H. B. Chan, V. A. Aksyuk, R. N. Kliman, D. J. Bishop, and F. Capasso, ''Quantum mechanical actuation of microelectromechanical systems by the Casimir force,'' Science **291**, 1942 (2001).
[6] A. Larraza, C. D. Holmes, R. T. Susbilla, and B. Denardo, ''The force between two parallel rigid plates due to the radiation pressure of broadband noise: An acoustic Casimir effect,'' J. Acoust. Soc. Am. **103**, 2267 (1998).
[7] A. Larraza and B. Denardo, ''An acoustic Casimir effect,'' Phys. Lett. A **248**, 151 (1998).
[8] A. Larraza, ''A demonstration apparatus for an acoustic analog to the Casimir effect,'' Am. J. Phys. **67**, 1028 (1999).
[9] L. D. Landau and E. M. Lifshitz, *Fluid Mechanics* (Pergamon, New York, 1987).
[10] C. P. Lee and T. G. Wang, ''Acoustic radiation pressure,'' J. Acoust. Soc. Am. **94**, 1099–1109 (1993).
[11] A. Gonis, *Theoretical Materials Science* (Materials Research Society, Warrendale, PA 2000).
[12] When the bandwidth extends from zero to infinity it is possible to evaluate the force by mapping the real frequency axis ω to $i\omega$, making the integral numerically stable. See, for example, Ref. 17.
[13] L. R. White, ''On the Deryaguin approximation for the interaction of macrobodies,'' J. Colloid Interface Sci. **95**, 286 (1983).
[14] J. Blocki, J. Randrup, W. J. Swiatecki, and C. F. Tsang, ''Proximity forces,'' Ann. Phys. (N.Y.) **105**, 427 (1977).
[15] C. Roman-Velazquez, C. Noguez, C. Villarreal, and R. Esquivel-Sirvent, ''Spectral representation of the nonretarded dispersive force between a sphere and a substrate,'' Phys. Rev. A (to be published).
[16] W. L. Mochán, C. Villarreal, and R. Esquivel-Sirvent, ''On Casimir forces for media with arbitrary dielectric properties,'' Rev. Mex. Fis. **48**, 339 (2002).
[17] R. Esquivel-Sirvent, C. Villarreal, and W. M. Mochan, ''Exact surface impedance formulation of the Casimir force: Application to spatially dispersive metals,'' Phys. Rev. A **68**, 052103 (2000).

Effect of polymer surface activity on cavitation nuclei stability against dissolution

Tyrone M. Porter[a] and Lawrence A. Crum
Center for Industrial and Medical Ultrasound, Applied Physics Laboratory, University of Washington, Seattle, Washington 98105
and Department of Bioengineering, University of Washington, Seattle, Washington 98195

Patrick S. Stayton and Allan S. Hoffman
Department of Bioengineering, University of Washington, Seattle, Washington 98195

(Received 27 January 2004; revised 3 May 2004; accepted 5 May 2004)

The persistence of acoustic cavitation in a pulsed wave ultrasound regime depends upon the ability of cavitation nuclei, i.e., bubbles, to survive the off time between pulses. Due to the dependence of bubble dissolution on surface tension, surface-active agents may affect the stability of bubbles against dissolution. In this study, measurements of bubble dissolution rates in solutions of the surface-active polymer poly(propyl acrylic acid) (PPAA) were conducted to test this premise. The surface activity of PPAA varies with solution *p*H and concentration of dissolved polymer molecules. The surface tension of PPAA solutions (55–72 dynes/cm) that associated with the polymer surface activity was measured using the Wilhelmy plate technique. Samples of these polymer solutions then were exposed to 1.1 MHz high intensity focused ultrasound, and the dissolution of bubbles created by inertial cavitation was monitored using an active cavitation detection scheme. Analysis of the pulse echo data demonstrated that bubble dissolution time was inversely proportional to the surface tension of the solution. Finally, comparison of the experimental results with dissolution times computed from the Epstein–Plesset equation suggests that the radii of residual bubbles from inertial cavitation increase as the surface tension decreases.
[DOI: 10.1121/1.1765198]

PACS numbers: 43.25.Yw, 43.35.Ei, 43.20.Fn [AJS] Pages: 721–728

I. INTRODUCTION

Several studies have demonstrated the therapeutic potential of the synergistic effect of ultrasound and chemical compounds. Ultrasound has been used to enhance the cytotoxicity of chemotherapeutic drugs (Harrison *et al.*, 1996; Saad and Hahn, 1989; Yu *et al.*, 2001), photodynamic agents (Tachibana *et al.*, 1993, 1994; Uchida *et al.*, 1997), and organic solvents (Jeffers *et al.*, 1995). In many of these studies, acoustic cavitation was proposed as a primary mechanism for cellular damage resulting in cell death or transport of the additive across the cell membrane. Unlike ultrasound contrast agents, these additives are not gas-based, and a relationship between these agents, cavitation, and cells has not been clearly identified.

In a study conducted by Mourad *et al.* (2001), high-intensity focused ultrasound (HIFU) was combined with a *p*H-responsive, membrane-destabilizing polymer, poly(ethyl acrylic acid) (PEAA) to hemolyse red blood cells synergistically. A passive cavitation detection system was used to monitor inertial cavitation during HIFU exposure. Inertial cavitation was detected only from red blood cell suspensions that were mixed with PEAA in mildly acidic conditions before insonation, and these samples had the highest percentage of lysed cells. The results suggested that the inception and dose of inertial cavitation was dependent on the presence and activity of the polymer, and that hemolysis was caused by cavitation activity. In order to elucidate the mechanism for the reported bioeffect, an understanding of the relationship between the polymer and inertial cavitation must be achieved. PEAA is a member of a poly(alkyl acrylic acid) family designed to become more surface active in mildly acidic conditions and adsorb to intracellular membranes, resulting in the destabilization of membranes and the release of internalized genetic material from endosomes (Cheung *et al.*, 2001; Murthy *et al.*, 1999; Thomas *et al.*, 1994). Given its *p*H-dependent hydrophobicity, PEAA may adsorb to bubble walls and enhance inertial cavitation in mildly acidic conditions.

There is evidence from theoretical and experimental work demonstrating that the presence of impurities, microparticles, or stabilized gas bodies in a liquid lowers the pressure threshold for inertial cavitation (Apfel, 1970, 1984; Chang *et al.*, 2001; Holland and Apfel, 1989, 1990; Miller and Thomas, 1995). Impurities or microparticles may contain crevices with stabilized gas pockets that serve as nucleation points for cavitation (Apfel, 1970, 1984; Holland and Apfel, 1990). Ultrasound contrast agents (UCA) such as Albunex® and Optison® can adequately serve as stabilized bubbles for cavitation nucleation (Chang *et al.*, 2001; Chen *et al.*, 2002, 2003; Holland and Apfel, 1990; Miller and Thomas, 1995; Poliachik *et al.*, 1999). The common characteristic of these endogenous (e.g., dust) and exogenous (e.g., UCA) nuclei is that they either stabilize or delay the dissolution of a gas

[a]Current address of corresponding author: Department of Biomedical Engineering, University of Cincinnati, 231 Albert Sabin Way, ML 0586, Cincinnati, OH 45267. Electronic mail: tyrone.porter@uc.edu

body until the arrival of a tensile stress (i.e., negative pressure wave) with a magnitude sufficient to drive the formation and/or oscillation of a bubble.

Unlike dust or UCAs, a poly(alkyl acrylic acid) has not been proven to carry trapped gas into a fluid. However, a poly(alkyl acrylic acid) has variable surface activity, and therefore may stabilize preexisting bubbles against dissolution. For example, PEAA is amphipathic and will dissolve in a neutral solution. Upon acidification, PEAA becomes more hydrophobic and migrates to air/liquid interfaces, lowering the surface tension (Thomas *et al.*, 1994). Because the dissolution of a gas microbubble depends on the surface tension (Epstein and Plesset, 1950; Leighton, 1994), the adsorption of PEAA onto the bubble wall may decrease the surface tension and, consequently, the dissolution rate. In the case of pulsed ultrasound, increasing the lifetime of a bubble created by a single pulse increases the probability that it will serve as a nucleation site for inertial cavitation in subsequent pulses (Flynn and Church, 1984). Understanding how surface-active molecules affect the nuclei population may allow for better control of cavitation in applications in medicine and industry. Therefore, the objective of this study was to investigate the relationship between the surface activity of poly(propyl acrylic acid) (PPAA) and the dissolution of bubbles created by acoustic cavitation.

A comparative study of the hemolytic activity of PEAA and PPAA concluded that PPAA is a more effective molecule for disrupting cell membranes (Murthy *et al.*, 1999). However, the surface activity of PPAA has not been well characterized. In this study, surface tension measurements of PPAA solutions at varying concentrations and *p*H's were made to evaluate the surface activity of the polymer. These measurements were used to calculate the surface excess concentration, which is a measure of the amount of polymer that migrates from the bulk media to the air/liquid interface. Measurements of the dissolution rate of air bubbles in these polymer solutions at varying surface tensions were made acoustically, and the results were compared with numerical simulations.

II. MATERIALS AND METHODS

A. Theory

The dissolution of an air bubble in fluid is dependent on the initial bubble radius (R_0) and the concentration of gas in solution. Additionally, as bubbles dissolve, the Laplace pressure due to surface tension begins to dominate, increasing the rate of dissolution. Because PPAA is a surface-active molecule, variations in surface tension were included in the theoretical treatment of bubbles dissolving in solution.

The stability of an air bubble in liquid-gas solutions was modeled by the following equation (Epstein and Plesset, 1950):

$$\frac{dR}{dt} = -D\frac{1-c_i/c_s+\tau/R\rho_g}{1+2\tau/3R\rho_g}\left\{\frac{1}{R}+\frac{1}{(\pi Dt)^{1/2}}\right\},$$
$$\tau = \frac{2M\sigma}{R_G T}. \tag{1}$$

TABLE I. Definition of variables used in the Epstein–Plesset equation and solution.

Variable	Description	Value
c_i	Initial concentration of dissolved gas in solution (kg/m^3)	
c_s	Saturation concentration of dissolved gas in solution (kg/m^3)	0.023
D	Diffusion coefficient of air (m^2/s)	2.42×10^{-9}
M	Molecular weight of air (kg/mol)	0.029
R_G	Gas constant (J/mol °K)	8.314
R	Radius of bubble (m)	
T	Temperature (°K)	293
t	Time (s)	
σ	Surface tension (N/m)	
ρ_g	Density of air (kg/m^3)	1.16

Definitions and values for variables used in the equation are listed in Table I.

For the special case when the gas concentration in polymer solution has reached saturation ($c_i = c_s$), the solution of the Epstein–Plesset equation is

$$1-\varepsilon^3+\delta(1-\varepsilon^2)=(3\delta/2)x'^2, \tag{2}$$

where $\delta=\tau/(R_0\rho_g)$, and ε and x are dimensionless variables proportional to bubble radius and time, respectively, as defined by

$$\varepsilon = R/R_0, \quad x'^2=(2Dd/R_0^2)t. \tag{3}$$

Given that $d=c_s/\rho_g$ and setting $\varepsilon=0$, the dissolution time for a free air bubble in solution can be solved while varying the surface tension.

B. Synthesis of poly(propyl acrylic acid)

The propyl acrylic acid monomer was synthesized according to the previously described method for ethyl acrylic acid (Ferrito and Tirrell, 1992). The propyl acrylic acid monomer was polymerized in bulk at 60 °C for 24 h using 2,2′-azobisisobutyronitrile (AIBN) as the initiator and cystamine as a chain transfer agent. The PPAA was purified by dissolving the reaction product in methanol and precipitating in diethyl ether three times. The weight-averaged molecular weight of PPAA was determined by gel permeation chromatography with PEG standards using Ultrahydrogel 250 and 1000 columns connected in series (Waters Corporation, Milford, MA), with the polydispersity index calculated by manual integration of the GPC curve (Rosen, 1993).

C. Surface tension measurements

The Wilhelmy plate technique was used to measure the surface tension of PPAA solutions (Thomas *et al.*, 1994). Solutions of PPAA (MW=83 kDa) were made at concentrations ranging from 1 to 10 mg/L in 100 mM phosphate buffered saline solutions made with water filtered by a nanofiltration system (Barnstead, Dubuque, IA). The measuring system consisted of a 1 cm W×1.5 cm L rectangular piece of Whatman hardened filter paper, force transducer, and computer. The filter paper was first boiled to remove surface-active agents before being suspended from the force transducer. Measurements for each polymer concentration

were made at *p*H 6.2, 6.6, 7.0, and 7.4, and the data were used for calculating the surface excess concentration for each *p*H.

D. Preparation of PPAA solutions for HIFU exposure

Solutions of PPAA (MW=83 kDa) were made at *p*H 6.2, 6.6, and 7. The volume of each sample was 0.5 ml and three polymer concentrations were used ([PPAA]=2, 5, and 10 μg/ml). Samples were treated in cylindrical sample chambers constructed with acoustically transparent 0.03-mm-thick biocompatible polyester heat shrink tubing (Advanced Polymers, Salem, NH) attached to a reusable delrin tube and plug. These sample chambers were durable, reusable, and allowed for easy deposition and recovery of the polymer solutions.

E. Acoustic arrangement

1. Cavitation inception

All experiments were conducted in a 16.5 cm L×12.5 cm W×12.5 cm H acrylic tank containing degassed water. HIFU provided by a source transducer (aperture=69.9 mm, focal length=62.6 mm) with a center frequency of 1.1 MHz was used for cavitation inception in the polymer solutions. The source transducer was mounted so that its beam axis was parallel to the long axis of the tank. An acoustic absorber made of Sylgard (Dow Corning, Midland, MI), nickel powder (Cerac, Inc., Milwaukee, WI), and microballoons (The PQ Corporation, Valley Forge, PA) was mounted to the opposing wall to minimize standing waves in the tank. The sample chambers were suspended vertically at the focus of the HIFU transducer with a delrin sample chamber carrier.

Waveforms for the HIFU transducer were created by a function generator (HP33120A, Hewlett Packard, Palo Alto, CA) and amplified by a power amplifier (ENI A150, Rochester, NY, Gain=55 dB) and matching network (Sonic Concepts). For this study, acoustic pulses (pulse length=0.1 ms, pulse repetition period=0.4 s) were used for bubble production in PPAA solutions.

2. Observation of bubble dissolution

An active cavitation detection (ACD) system was assembled to monitor bubble production and dissolution (Fig. 1). The system consisted of a 5 MHz transducer (aperture=12 mm, focal length=46 mm, Sonic Concepts, Woodinville, WA), a Transmit/Receive (T/R) switch (5072, Panametrics, Waltham, MA), an oscilloscope (LC334AM, Lecroy, Chestnut Ridge, NY), and a computer for data storage and processing. The 5-MHz transducer was mounted in the side wall adjacent to the wall with the HIFU transducer so that the focal volumes of the transducers overlapped. The T/R switch allowed for transmission and reception of interrogation pulses with the 5-MHz transducer. The focal volume of the 5-MHz transducer was comparable to the sample volume; therefore, the ACD scheme was sufficient to monitor for the existence and dissolution of bubbles. The peak pressure of the interrogation pulse was approximately 90 kPa, which is not sufficient to excite explosive bubble growth since it does not overcome atmospheric pressure. The pulses may retard bubble dissolution; therefore, a low duty cycle (~0.1%) was selected to limit the affect of the pulses on the dissolution rate (Chen *et al.*, 2002).

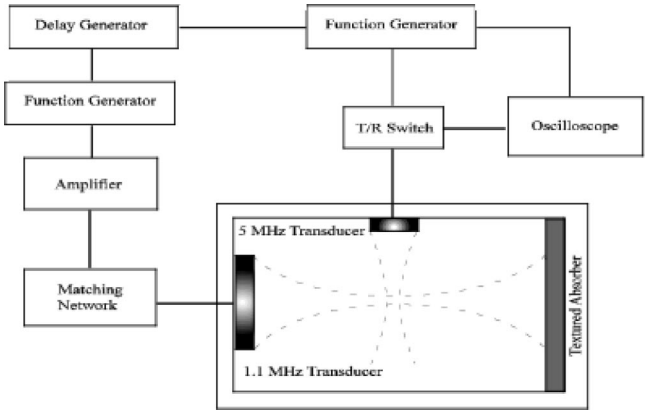

FIG. 1. Experimental setup for evaluating the effect of PPAA on dissolution rate of air bubbles. A central function generator controls the timing for the source transducer pulses and the active cavitation detection system.

The timing between the HIFU transducer and the ACD system was controlled by a series of function generators (HP33120A) and a time delay generator (Stanford Research Systems, DG535). The primary function generator delivered synchronized trigger signals to the T/R switch and time delay generator. The time delay generator, which was connected to the HIFU signal generator, offset the timing of the 1.1-MHz transducer and 5-MHz transducer by 0.4 s. A total of 1000 interrogation pulses with a PRF of 1 kHz were used for bubble detection, limiting the number of HIFU pulses to two.

F. Data acquisition and signal processing

The dissolution time of bubbles was determined by analyzing the acoustic data generated by the ACD. Acoustic signals received from sample volume interrogation were compared to predetermined baseline values. Signals with amplitudes greater than baseline were indicative of echoes from bubbles. Bubble dissolution times were determined by tracking the decay of these signals over time until baseline was reached.

The oscilloscope in the ACD system was operated in sequence acquisition mode, which allowed for digitization and storage of consecutive interrogation pulses in one data set. Each data packet was composed of 1000 segments, and each segment represented approximately 5 μs of acoustic data. The data packets were digitized (rate=5×10^7 samples/segment) and stored on a desktop computer (Dell, Austin, TX).

Each data packet was loaded into Matlab as a vector, but was restructured to allow for easier analysis of the 1000 segments for scattering. Each vector was transformed into an array in which each row contained 250 data points that were captured once every millisecond. This data array was condensed into a vector by taking the absolute value of each point and recording the maximum positive value for each row. A second vector was generated by taking the FFT of the original array and integrating the values in each row. The

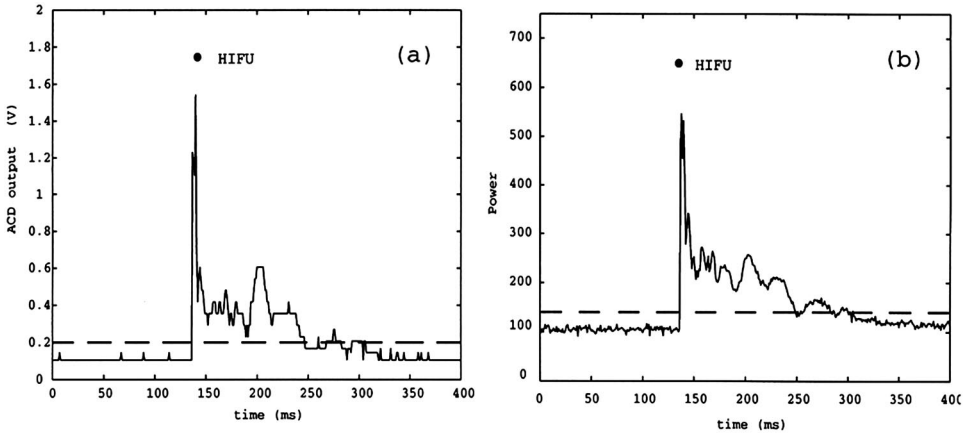

FIG. 2. Analysis of the pulse-echo data for determination of bubble dissolution time. (a) The maximum values collected every millisecond during interrogation of PPAA solution. (b) The values produced by taking the integral of spectral data calculated for each millisecond of pulse-echo data. In each plot, values above the established baselines (---) were inferred as scattering from bubbles.

resulting temporal and frequency data vectors (TDV, FDV) each contained 1000 points and each point represented 1 ms in time.

Baseline in the temporal and frequency domains was established by analyzing the voltages of the interrogation data that was captured from PPAA solutions prior to HIFU exposure (Fig. 2). Each sample of PPAA solution was carefully handled during preparation for HIFU exposure so that bubbles did not form. This was as close to a bubble-free solution that was achievable with the available instruments. Because the first HIFU pulse did not arrive until at least 400 ms after acoustic interrogation of the sample began, baseline was defined as the lowest voltage that was greater than 99% of the first 300 data points. Values that were greater than 10% above baseline were interpreted as evidence of bubbles in the polymer solution. For each vector, the timepoints for the arrival of the HIFU pulse (production of bubbles) and for the last integer greater than 10% above baseline were recorded. The difference between the two timepoints was calculated and recorded as the bubble dissolution time.

III. RESULTS

A. Simulation of bubble dissolution

The Epstein–Plesset equation [Eq. (1)] is a well-established model for the stability of a gas bubble in a liquid-gas solution. The solution given in Eq. (2) is for an air bubble that exists in a liquid saturated with air. In this case, the bubble dissolves primarily due to the pressure generated by the surface tension. This force is known as the Laplace pressure, p_σ, and is given by

$$p_\sigma = 2\sigma/R \tag{4}$$

where σ is the surface tension and R is the radius of the bubble. The simulations in Fig. 3 demonstrate how changes in bubble radius or surface tension affect the Laplace pressure, and ultimately the bubble dissolution time. It is difficult to resolve the size of bubbles generated from acoustic cavitation experimentally. However, by providing the surface tension and dissolution times, this model may be used to ascertain how a molecule like PPAA with varying surface activity may affect the size range of bubbles created with HIFU.

B. Polymer surface activity

The surface activity of PPAA was characterized by measuring the surface tension of PPAA solutions. The activity of this polymer varies, depending on the concentration of dissolved polymer and the *p*H of the solvent. Upon acidification, the polymer becomes more nonpolar and surface-active. The surface tension of several PPAA solutions (MW=83 kDa) was measured using the Wilhelmy plate technique, and the results are shown in Fig. 4.

The plot illustrates an inverse linear relationship between the surface tension of PPAA solutions and the logarithm of the concentration at all *p*H levels. Similar activity was reported by Thomas *et al.* (1994) for poly(ethyl acrylic acid) (PEAA), another member of the membrane-disruptive polycarboxylate family. Because measurements were made with dilute polymer solutions, this observation can be explained thermodynamically with the Gibbs equation:

$$\Gamma_i = -\frac{d\gamma}{d\mu_i} = -\frac{1}{R_G T}\frac{d\gamma}{d\ln c_i}, \tag{5}$$

where Γ_i is the surface excess of the polymer at the air/liquid interface, γ is the surface tension of the solution, μ_i is the chemical potential, and c_i is the polymer concentration.

The Gibbs equation states that for a dilute solution, a

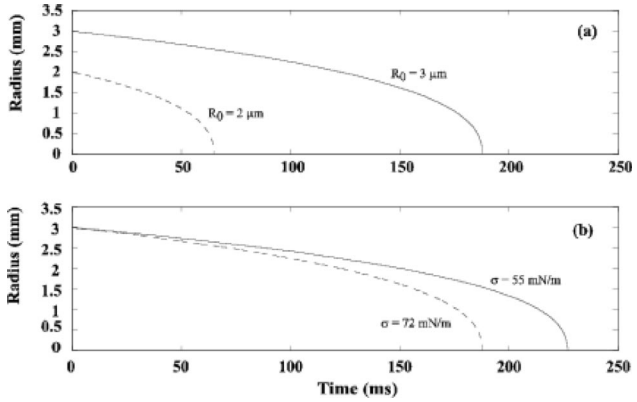

FIG. 3. Theoretical predictions for bubble dissolution times. (a) Predicted dissolution curves of air bubbles (R_0=2- and 3-μm; σ=72-mN/m) in PPAA solutions saturated with air. (b) Predicted dissolution curves of air bubbles (R_0=3-mm; σ=55- and 72-mN/m) in PPAA solutions saturated with air.

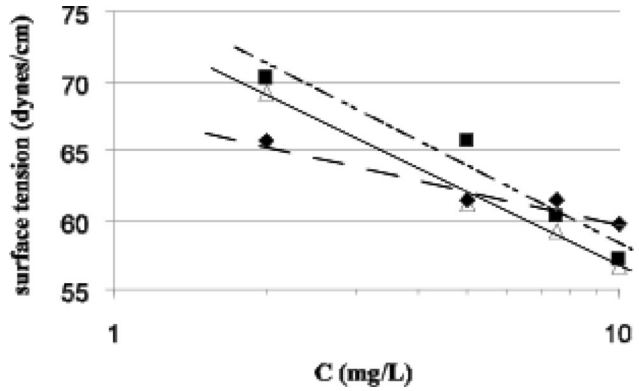

FIG. 4. Surface tension measurements of dilute PPAA solutions (MW=83 kDa) at *p*H 7 (♦), *p*H 6.6 (■), and *p*H 6.2 (△). A linear inverse relationship exists between surface tension and the logarithm of the polymer concentration, indicating surface excess of the polymer at the air/liquid interface.

reduction in surface tension is caused by the adsorption of the solute to the surface (Adamson, 1976).

Using the surface tension measurements, the surface excess of PPAA (MW=83 kDa) at *p*H 6.2, 6.6, and 7.0 was calculated (Table II). The increase in surface excess from *p*H 7.0 to *p*H 6.6 demonstrates the migration of PPAA to the air/water interface. Additionally, there is a change in the secondary structure of the polymer, which is illustrated by the reduction in area per molecule (Table II). In mildly acidic conditions, the carboxyl groups along the polymer chain are protonated, and the polymer undergoes a conformational change from an extended, hydrophilic state to a hydrophobic, more compact form (Borden *et al.*, 1987; Eum *et al.*, 1989). Thus, the energetic cost for keeping the polymer hydrated increases, forcing its migration to the air/liquid interface.

C. Acoustic interrogation of bubble dissolution

The recorded pulse-echo data was a collection of individual signal acquisitions or pulse-echo data packets. Each data packet contained 250 points, and was acquired every millisecond. The plots in Fig. 5 are typical recordings of pulse-echo data obtained from interrogation of polymer solutions. The main plot and insets represent three key events in time: pre-HIFU, arrival of HIFU, and post-HIFU. Before the arrival of the HIFU pulse, the signal recorded by the ACD system was primarily noise with no sinusoidal waveforms. We inferred from this data that bubbles of a detectable size were not present. The spike in the plot corresponded with the arrival of the HIFU pulse, followed by multiple sinusoidal waves with increased amplitude. This signal suggests that bubbles were created by the HIFU pulse, and that these bubbles survived for hundreds of milliseconds before

TABLE II. Surface excess concentrations for PPAA (MW=83 kDa).

*p*H	Γ_i, surface excess (molecules/nm^2)	area/molecule (nm^2/molecule)
7.0	0.380	2.63
6.6	0.859	1.16
6.2	0.823	1.22

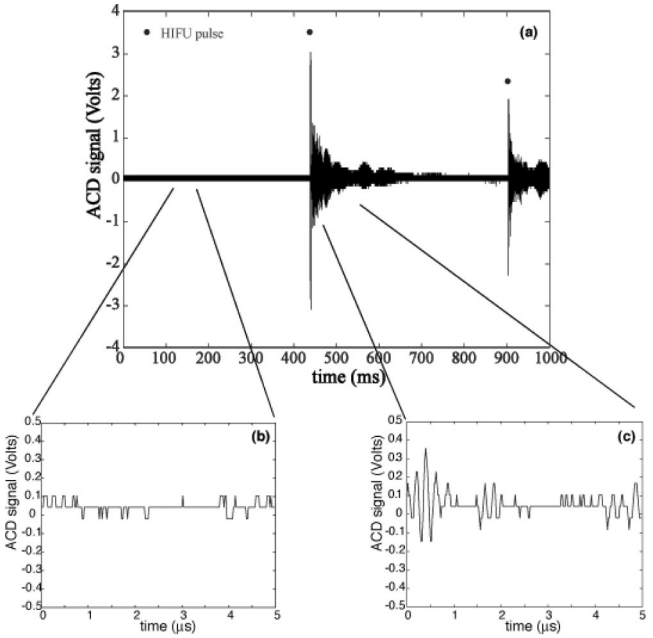

FIG. 5. Interrogation of PPAA solution for bubbles. (a) Bubbles generated by a HIFU pulse (●) dissolve before the arrival of the second HIFU pulse. (b) Before the arrival of the HIFU pulse, the amplitude of the signal was low and uneventful. (c) After the HIFU pulse, the amplitude of the acquired signal was heightened and contained multiple sinusoidal waves, characteristic of scattering from bubbles. The signal returned to baseline before the arrival of the second HIFU pulse, indicating bubble dissolution.

final dissolution. Dissolution of bubbles was represented by a slow decay in signal amplitude, eventually returning to baseline upon bubble extinction.

Each pulse-echo data packet was analyzed for bubble dissolution time using temporal- and frequency-analysis techniques. After signal processing, each data packet was represented by the maximum positive voltage in the temporal-domain and the integral of the power spectrum in the frequency domain. These values were compared against baseline values that were representative of signals acquired from interrogation of bubble-free media. The bubble dissolution times for PPAA solutions (MW=83 kDa) at varying *p*H's are presented in Fig. 6.

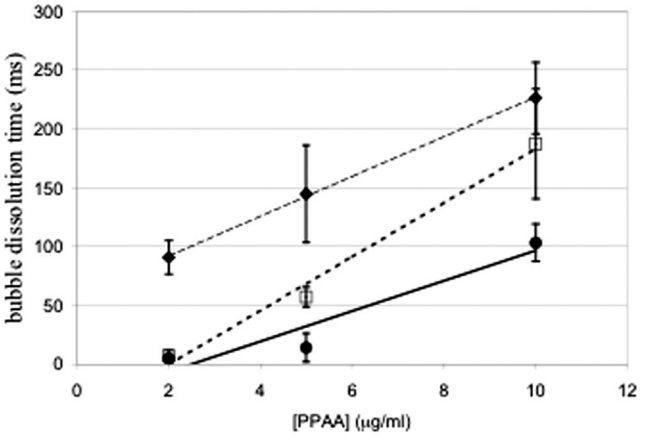

FIG. 6. Total time for bubble to dissolve in PPAA (MW=83 kDa) solutions as a function of polymer concentration for three *p*Hs (pH 7.0=●; pH 6.6=□; pH 6.2=♦).

The data demonstrate that decreasing the solution *p*H or increasing the polymer concentration enhanced the stability of bubbles formed in PPAA solutions. For example, in solutions where [PPAA]=5 μg/ml, the dissolution time was increased significantly by reducing the solution *p*H from 7.0 to 6.6 ($p<0.05$) or 6.2 ($p<0.01$). Increasing the polymer concentration from 2 to 10 μg/ml was also effective for increasing bubble lifetime significantly independent of the solution *p*H ($p<0.01$).

The fact that the lifetime of bubbles in PPAA solutions responded to variations in solution *p*H or polymer concentration implies that polymer surface activity was an important factor. Results in Fig. 4 demonstrate that polymer surface activity directly affects the tension at an air/liquid interface. PPAA may also affect other rate-determining factors of bubble dissolution, such as the radius of ''daughter nuclei'' resulting from bubble fragmentation. Simulations of bubble dissolution demonstrated that initial bubble radius has a significantly greater effect on the bubble dissolution rate than surface tension (Fig. 3). Therefore, a comparison between the experimental data and numerical solutions to the Epstein–Plesset equation was made to determine the relationship between the polymer, surface tension, bubble size, and bubble dissolution time. The bubble radii selected for the simulation were within a factor of 2 for the resonance size of a bubble at a frequency of 1.1 MHz ($R_{\text{res}} = 1.64–1.87\,\mu$m). The theoretical and experimental data support the hypothesis that the surface tension of the PPAA solution was a rate-determining factor for bubble dissolution. The data also suggest that larger bubbles were more likely formed at lower surface tensions. Explanations for this observation are given in the following section.

IV. DISCUSSION AND CONCLUSIONS

PPAA is a synthesized *p*H-sensitive polymer designed to disrupt intracellular membranes, resulting in the release of drugs from endosomes (Cheung *et al.*, 2001; Murthy *et al.*, 1999). It was hypothesized that PPAA would associate with bubbles upon acidification and influence the bubble dissolution rate. Data collected in this study revealed that the dissolution rate of bubbles in PPAA solutions was dependent on the chemical properties of the solution. There are several possible explanations for this observation.

First, the surface excess concentration data (Table II) show that PPAA will associate with air/liquid interfaces as its hydrophobicity increases, including a bubble wall, resulting in a decrease in the surface tension. Epstein and Plesset (1950) derived an equation to model the stability of gas bubbles in liquid/gas solutions as a function of gas concentration, initial bubble radius, and surface tension. In this study, the equation was solved for the case where the dissolved gas concentration in solution approaches saturation to predict bubble dissolution times in the polymer solution. Using the surface tension measurements from polymer solutions as the independent variable, good agreement between the numerical simulation and the experimental data was achieved for a bubble size distribution of 1.5–3.0 μm (Fig. 7). However, the analysis demonstrated that the dissolution time of a bubble was more dependent on the bubble radius

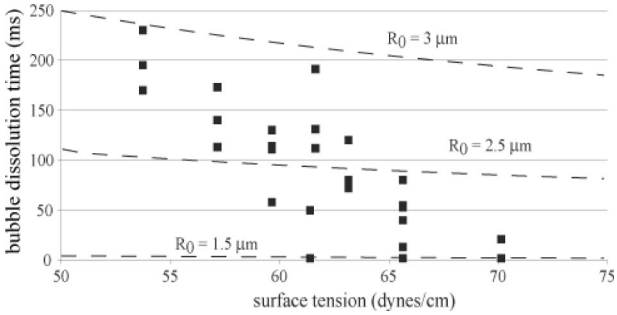

FIG. 7. Comparison between theory (———) and experimental data (■) of the relationship between surface tension and bubble dissolution for three radii.

rather than surface tension. A significant observation is that both surface tension and bubble radius can be controlled by the hydrophobicity of PPAA, which is dependent on the acidity of the solution.

When a bubble collapses, it will rebound or fragment and form residual bubbles. The factors that affect the number and size of these residual bubbles are not well understood. However, it can be postulated that the number, size, and surface characteristics of the collapsing bubbles play a role. Increasing the size of bubbles driven to oscillate, or the maximum radius attained during growth, may generate larger residual bubbles. Due to the hydrophobicity of PPAA, the polymer may increase the size range of activated cavitation nuclei to include larger gas bodies. It is unlikely that PPAA migrates to the surface of oscillating bubbles over the period of oscillation; the diffusion of PPAA is much too slow for this to occur. It is more likely that the polymer forms aggregates or associates with preexisting gas bodies found on dust or other floating particles. By reducing the surface tension of the host fluid, PPAA decreases a force that opposes explosive bubble growth. Therefore, bubbles that are released by cavitation nuclei into a solution of PPAA may grow to a larger maximum radius before collapse. These bubbles contain more gas and, upon collapse, may form larger residual bubbles.

Studies conducted by Ashokkumar *et al.* (1997, 1999, 2000) provide valuable information and insight into how surface-active solutes may affect the dynamics of bubbles forced into growth, collapse, and rebound. These studies have shown that quenching of sonoluminescence (SL) by surface-active agents could be directly related to the surface excess of the solutes at the bubble wall and not the bulk concentration (Ashokkumar *et al.*, 1997, 1999, 2000). Studies using simple organic acids and bases demonstrated that this quenching effect was dependent on the *p*H of the solution (Ashokkumar *et al.*, 1999). Similar to PPAA, the polarity and surface activity of these solutes can be altered by varying the solution *p*H. Ashokkumar *et al.* (1999) proposed that these solutes, when adsorbed to oscillating bubbles, eventually evaporate into the bubble and serve as an energy sink, resulting in a decline in bubble core temperature and a decrease in photon emissions.

The hydrodynamic radius of PPAA, R_H, has not been measured, but R_H for PEAA is approximately 6 nm in ionic form and collapses to ~4.4 nm at *p*H 5.9 (Eum *et al.*, 1989).

Therefore, the R_H for PPAA was assumed to be less than 10 nm. Assuming the volume occupied by the globular form of PPAA is spherical, then the volume of a bubble with $R_0 = 1\ \mu$m will be approximately nine orders of magnitude larger than the volume occupied by the polymer. Consequently, it is possible for PPAA to evaporate into the bubble core and affect the dynamics of bubble collapse and rebound. The bubbles that survive collapse may then grow upon rebound to an equilibrium size larger than the initial radius. There is evidence in experiments conducted by Ashokkumar *et al.* (2000) that supports this premise. Plotting the radius versus time profile of a single bubble undergoing sonoluminescence in an alcohol solution, an increase in equilibrium radius after collapse from 3.2 to 4.1 μm was measured. Similar to the analysis performed in the current study, a reduction in surface tension was not sufficient to explain this observation.

Viscosity and elasticity are factors that influence bubble dynamics; therefore, any changes in these properties due to the presence of PPAA may influence equilibrium bubble size and, accordingly, the time for the bubble to dissolve. It has been shown theoretically that a single layer of surface-active molecules possessing viscosity and elasticity will impart damping (Church, 1995; Hoff, 2001) and reduce the rate of diffusion of gas across the bubble wall upon collapse (Yount, 1979, 1982). Viscous damping of the radial oscillations of a bubble is dependent upon bulk and surface viscosity (Leighton, 1994, Hoff, 2001). The low concentrations of PPAA used in this study resulted in negligible changes in bulk viscosity. It is also unlikely that the association of PPAA with the bubble wall significantly changed the surface viscosity. Ashokkumar *et al.* (2000) demonstrated that the dynamics of a single bubble undergoing sonoluminescence was not significantly affected by the presence of solutes having surface activity similar to PPAA. In fact, the maximum radial displacement measured was increased by the presence of propanol, suggesting that the surface viscosity was not decreased. Therefore, a surface layer of PPAA probably does not change the surface viscosity, but it might increase the elasticity. Yount (1979, 1982) proposed that an elastic surface layer will counteract surface tension and will form an impermeable barrier to gas diffusion as the bubble radius decreases due to applied pressure. The increase in internal gas pressure and elasticity provides sufficient force to increase the displacement of the bubble wall during rebound, resulting in larger bubbles that require more time to dissolve.

Understanding how long bubbles will survive in PPAA solutions may provide some insight into the synergistic activity of the polymer PEAA and HIFU, which resulted in hemolysis (Mourad *et al.*, 2001). Because an increase in cavitation activity was seen in mixtures of red blood cells and PEAA exposed to bursts of HIFU at *p*H 6.2, inertial cavitation was proposed as a possible mechanism for the increase in measured hemolysis. The data collected in this study demonstrates that the presence of polymers such as PEAA and PPAA during insonation of a liquid can influence the persistence of bubbles that are generated by inertial cavitation events. Bubbles that survive can then serve as cavitation nuclei for additional acoustic pulses, and the energy and forces generated by cavitating bubbles can directly or indirectly cause hemolysis.

In conclusion, the results obtained in this study demonstrate that the dissolution rate of a bubble can be reduced by the presence of surface-active agents. Evidence was presented to support the idea that the adsorption of PPAA to bubbles at the gas/liquid interface precedes the changes in time of dissolution. The affinity for PPAA to the surface of the bubble is dependent on its surface activity, which is a function of the solution *p*H and concentration of dissolved polymer. Arguments were presented to explain how adsorbed PPAA could affect the dissolution of bubbles in solution. Information gathered in this study will prove helpful in elucidating the mechanisms for the synergy between HIFU and surface-active polymers. Using these polymers or similar agents, scientists can adjust chemical as well as acoustic parameters to control cavitation for scientific, medical, or industrial applications.

ACKNOWLEDGMENTS

The authors would like to thank Fiona Black for preparation of the polymers used in this work. The authors would also like to thank Andy Brayman, Wen-Shiang Chen, and Tom Matula for fruitful discussions on cavitation nucleation and acoustic interrogation of a sample volume. This work was supported by a UNCF/Merck Predoctoral Fellowship and funds from National Institute of Health Grant Nos. 5 RO1 EB000350-03 and EB000252.

Adamson, A. W. (**1976**). *Physical Chemistry of Surfaces* (Wiley, New York).
Apfel, R. E. (**1970**). ''The role of impurities in cavitation-threshold determination,'' J. Acoust. Soc. Am. **43**, 1179–1186.
Apfel, R. E. (**1984**). ''Acoustic cavitation inception,'' Ultrasonics **22**, 167–173.
Ashokkumar, M., Mulvaney, P., and Grieser, F. (**1999**). ''The effect of pH on multibubble sonoluminescence from aqueous solutions containing simple organic weak acids and bases,'' J. Am. Chem. Soc. **121**, 7355–7359.
Ashokkumar, M., Hall, R., Mulvaney, P., and Grieser, F. (**1997**). ''Sonoluminescence from aqueous alcohol and surfactant solutions,'' J. Phys. Chem. B **101**, 10845–10850.
Ashokkumar, M., Crum, L. A., Frensley, C. A., Greiser, F., Matula, T. J., McNamara, III, W. B., and Suslick, K. S. (**2000**). ''Effect of solutes on single-bubble sonoluminescence in water,'' J. Phys. Chem. A **104**, 8462–8765.
Borden, K. A., Eum, K. M., Langley, K. H., and Tirrell, D. H. (**1987**). ''On the mechanism of polyelectrolyte-induced structural reorganization in thin molecular films,'' Macromolecules **20**, 454–456.
Chang, P. P., Chen, W. S., Mourad, P. D., Poliachik, S. L., and Crum, L. A. (**2001**). ''Thresholds for inertial cavitation in Albunex suspensions under pulsed ultrasound conditions,'' IEEE Trans. Ultrason. Ferroelectr. Freq. Control **48**, 161–170.
Chen, W. S., Matula, T. J., and Crum, L. A. (**2002**). ''The disappearance of ultrasound contrast bubbles: Observations of bubble dissolution and cavitation nucleation,'' Ultrasound Med. Biol. **28**, 793–803.
Chen, W. S., Matula, T. J., Brayman, A. A. and Crum, L. A. (**2003**). ''A comparison of the fragmentation threshold and inertial cavitation doses of different ultrasound contrast agentsm,'' J. Acoust. Soc. Am. **113**, 643–651.
Cheung, C. Y., Murthy, N., Stayton, P. S., and Hoffman, A. S. (**2001**). ''A pH-sensitive polymer that enhances cationic lipid-mediated gene transfer,'' Bioconjugate Chem. **12**, 906–910.
Church, C. C. (**1995**). ''The effects of an elastic solid surface layer on the radial pulsations of gas bubbles,'' J. Acoust. Soc. Am. **112**, 906–915.
Epstein, P. S., and Plesset, M. S. (**1950**). ''On the stability of gas bubbles in liquid-gas solutions,'' J. Chem. Phys. **18**, 1505–1509.

Eum, K. M., Langley, K. H., and Tirrell, D. A. (**1989**). ''Quasi-elastic and electrophoretic light scattering studies of the reorganization of dioleoylphosphatidylcholine vesicle membranes by poly(2-ethylacrylic acid),'' Macromolecules **22**, 2755–2760.
Ferrito, M., and Tirrell, D. A. (**1992**). ''Poly(2-ethylacrylic acid),'' Macromol. Synth. **11**, 59–62.
Flynn, H. G., and Church, C. C. (**1984**). ''A mechanism for the generation of cavitation maxima by pulsed ultrasound,'' J. Acoust. Soc. Am. **76**, 505–512.
Harrison, G. H., Balcer-Kubiczek, E. K., and Gutierrez, P. L. (**1996**). ''*In vitro* mechanisms of chemopotentiation by tone-burst ultrasound,'' Ultrasound Med. Biol. **22**, 355–362.
Hoff, L. *Acoustic Characterization of Contrast Agents for Medical Ultrasound Imaging* (Kluwer, Boston).
Holland, C. K., and Apfel, R. E. (**1989**). ''An improved theory for the prediction of microcavitation thresholds,'' IEEE Trans. Ultrason. Ferroelectr. Freq. Control **36**, 204–208.
Holland, C. K., and Apfel, R. E. (**1990**). ''Thresholds for transient cavitation produced by pulsed ultrasound in a controlled nuclei environment,'' J. Acoust. Soc. Am. **88**, 2059–2069.
Jeffers, R. J., Feng, R. Q., Fowlkes, J. B., Hunt, J. W., Kessel, D., and Cain, C. A. (**1995**). ''Dimethylformamide as an enhancer of cavitation-induced cell lysis *in vitro*,'' J. Acoust. Soc. Am. **97**, 669–676.
Leighton, T. G. (**1994**). *The Acoustic Bubble* (Academic, London).
Miller, D. L., and Thomas, R. M. (**1995**). ''Ultrasound contrast agents nucleate inertial cavitation *in vitro*,'' Ultrasound Med. Biol. **21**, 1059–1065.
Mourad, P. D., Murthy, N., Porter, T., Poliachik, S. L., Crum, L. A., Hoffman, A. S., and Stayton, P. S. (**2001**). ''Focused ultrasound and poly(2-ethylacrylic acid) act synergistically to disrupt lipid bilayers *in vitro*,'' Macromolecules **34**, 2400–2401.
Murthy, N., Robichaud, J. R., Tirrell, D. A., Stayton, P. S., and Hoffman, A. S. (**1999**). ''The design and synthesis of polymers for eukaryotic membrane disruption,'' J. Controlled Release **61**, 137–143.
Poliachik, S. L., Chandler, W. L., Mourad, P. D., Bailey, M. R., Bloch, S., Cleveland, R. O., Kaczkowski, P., Keilman, G., Porter, T., and Crum, L. A. (**1999**). ''Effect of high-intensity focused ultrasound on whole blood with and without microbubble contrast agent,'' Ultrasound Med. Biol. **25**, 991–998.
Rosen, S. L. (**1993**). *Fundamental Principles of Polymeric Materials* (Wiley, New York).
Saad, A. H., and Hahn, G. M. (**1989**). ''Ultrasound enhanced drug toxicity on Chinese Hamster Ovary cells *in vitro*,'' Cancer Res. **49**, 5931–5934.
Tachibana, K., Kimura, N., Okumura, M., Eguchi, H., and Tachibana, S. (**1993**). ''Enhancement of cell killing of HL-60 cells by ultrasound in the presence of the photosensitizing drug Photofrin II,'' Cancer Lett. **72**, 195–199.
Tachibana, K., Sugata, K., Meng, J., Okumura, M., and Tachibana, S. (**1994**). ''Liver tissue damage by ultrasound in combination with the photosensitizing drug, Photofrin II,'' Cancer Lett. **78**, 177–181.
Thomas, J. L., Barton, S. W., and Tirrell, D. A. (**1994**). ''Membrane solubilization by a hydrophobic polyelectrolyte: Surface activity and membrane binding,'' Biophys. J. **67**, 1101–1106.
Uchida, T., Tachibana, K., Isano, S., and Morioka, E. (**1997**). ''Elimination of adult T cell leukemia cells by ultrasound in the presence of porfimer sodium,'' Anti-Cancer Drugs **8**, 329–335.
Yount, D. E. (**1979**). ''Skins of varying permeability: A stabilization mechanism for gas cavitation nuclei,'' J. Acoust. Soc. Am. **65**, 1429–1439.
Yount, D. E. (**1982**). ''On the evolution, generation, and regeneration of gas cavitation nuclei,'' J. Acoust. Soc. Am. **71**, 1473–1481.
Yu, T., Wang, Z., and Jiang, S. (**2001**). ''Potentiation of cytotoxicity of adriamycin on human ovarian carcinoma cell line 3AO by low-level ultrasound,'' Ultrasonics **39**, 307–309.

Acoustic scattering by axisymmetric finite-length bodies: An extension of a two-dimensional conformal mapping method

D. Benjamin Reeder[a] and Timothy K. Stanton
Department of Applied Ocean Physics and Engineering, Woods Hole Oceanographic Institution, Woods Hole, Massachusetts 02543

(Received 24 May 2002; revised 11 December 2003; accepted 30 December 2003)

A general scattering formulation is presented for predicting the far-field scattered pressure from irregular, axisymmetric, finite-length bodies for three boundary conditions—soft, rigid, and fluid. The formulation is an extension of a two-dimensional conformal mapping approach [D. T. DiPerna and T. K. Stanton, J. Acoust. Soc. Am. **96**, 3064–3079 (1994)] to scattering by finite-length bodies. This extended formulation, which is inherently numerically efficient, involves conformally mapping the surface of an irregular, finite-length body to a new, orthogonal coordinate system in which the separation of variables method may be used to solve the Helmholtz equation and satisfy the boundary conditions. Extensive comparisons with previously published results using other formulations are presented. This formulation is shown to be accurate in the prediction of scattering from smooth, symmetric bodies for a wide range of frequencies (Rayleigh through geometric scattering region), scattering angles (monostatic and bistatic), aspect ratios, and for each of the three boundary conditions listed above. Reasonable agreement has also been demonstrated for irregular, realistic shapes with soft boundary conditions.
[DOI: 10.1121/1.1648681]

PACS numbers: 43.30.Ft, 43.20.Fn [WMC] Pages: 729–746

I. INTRODUCTION

The prediction of acoustic scattering from finite and infinitely long bodies has been pursued for many years, starting with Lord Rayleigh's work on scattering from a sphere (Rayleigh, 1945). Exact analytical solutions to the acoustic wave equation require the scatterer's surface to exactly match the locus of all points for which the radial coordinate is a constant. Such exact analytical solutions exist only for a limited number of cases for which the separation of variables is possible (Morse and Feshbach, 1953, Vol. I, Chap. 5; Bowman *et al.*, 1987). In all of these cases, the boundary is simple; e.g., a sphere, infinitely long cylinder, and prolate spheroid.

For complex shapes, approximate analytical solutions, including the perturbation method, and approximate asymptotic formulations, such as physical optics (Gaunaurd, 1985) and the geometric theory of diffraction (Levy and Keller, 1959; Yamashita, 1990), have been developed. Numerical solutions have also been developed, including the boundary element method (Tobacman, 1984; Francis, 1993), T-matrix (Waterman, 1968; Varadan *et al.*, 1982; Lakhtakia *et al.*, 1984; Hackman and Todoroff, 1985), and the mode matching methods (Yamashita, 1990). All of these approaches are limited in one or more of the following: frequency range, class of surfaces, types of boundary conditions, eccentricity of shape and/or computational implementation, and numerical efficiency.

DiPerna and Stanton (1994) introduced a conformal mapping approach to predicting far-field sound scattering by infinitely long cylinders of noncircular cross section. The approach, termed the Fourier matching method (FMM), involves a conformal mapping of variables to a new coordinate system in which the constant radial coordinate exactly matches the scatterer surface. The method makes use of the Newton–Raphson algorithm to execute the mapping. The boundary conditions are satisfied by requiring the Fourier coefficients in the new angular variable of the total field to be zero, and then the resultant scattered field is expressed in terms of circular eigenfunctions. This method is particularly attractive because the conformal mapping produces a solvable transformed Helmholtz equation (Laura, 1994).

The FMM proved to be accurate over a wide range of frequencies, shapes of cross section, and penetrable (fluid) as well as impenetrable boundary conditions. Furthermore, the approach is inherently numerically efficient due to the nature of its formulation. For example, the FMM was shown by DiPerna and Stanton (1994) to be more efficient than the T-matrix method for the case of the high-aspect-ratio elliptic cylinder because fewer terms were needed for the numerical integrations. Even after incorporating the FMM basis functions into the T-matrix calculations, the FMM required 85% fewer integration points.

A major limitation of the two-dimensional FMM was the fact that it was formulated for the case of an infinitely long cylinder—a two-dimensional scattering solution. Many practical scattering problems involve scattering from finite bodies and cannot be accurately modeled by the two-dimensional solution. In order to address this need, the FMM is extended in this paper to predict the scattering from finite-length bodies. In order for this particular approach to be used for finite bodies, the outer boundary of the bodies must be described by a function rotated about the length-wise axis. Hence, al-

[a]Current address: Department of Oceanography, Naval Postgraduate School, Monterey, CA.

though the function is arbitrary and these bodies are three-dimensional, they are restricted to axisymmetric shapes. As with the two-dimensional formulation, this approach is intrinsically numerically efficient and is valid over a wide range of frequencies and shapes as well as both monostatic and bistatic scattering geometries. The extension has been formulated for three boundary conditions—Dirichlet (soft or pressure-release), Neumann (rigid), and Cauchy (fluid). In all three cases, the surrounding material is fluid.

In Sec. II, the theoretical basis for the formulation is presented, which includes the development of the new orthogonal coordinate system to which the body is mapped, the conformal mapping procedure, modal series solutions to the transformed Helmholtz equation, and resulting equations for the modal series coefficients after satisfying the three boundary conditions. In Sec. III, a description of the numerical implementation of the FMM is presented, as well as several practical numerical issues that arise in the solution of the scattering problem. In Sec. IV, the numerical results are presented for various shapes (spheres, smooth prolate spheroids, and two finite bodies with irregular surfaces), boundary conditions (soft, rigid, and fluid), and over a wide range of frequencies and scattering angles. The results are compared with various previously published results using other approaches. Section V contains a summary and concluding remarks.

II. THEORY

The derivation of the extended formulation for scattering by an axisymmetric finite-length body is conceptually very similar to the corresponding derivation of the two-dimensional solution for an irregularly shaped, infinitely long body described by DiPerna and Stanton (1994); in fact, some of the elements are identical. Both solutions begin with the wave equation in a known coordinate system and conformally map the coordinate variables to a new, orthogonal coordinate system in which the locus of all points for which the new radial coordinate is a constant exactly coincides with the scatterer surface. The difference in the coordinate systems between the two cases concerns the fact that one involves two-dimensional coordinates while the other involves an additional coordinate dimension with a new geometry defined for the finite body. Both solutions use mapping functions that are identical in form, transform the Helmholtz equation to the new coordinate system, and satisfy the boundary conditions using identical techniques to arrive at differing, yet structurally similar, expressions for the scattered pressure. The two-dimensional solution includes a mapping function that corresponds to the shape of the irregular boundary of a cross-sectional slice of the infinitely long body, while the three-dimensional solution uses a mapping function that corresponds to the shape of the boundary of a *length-wise* slice of the body (specifically, the function that is rotated about the longitudinal axis). Furthermore, the two-dimensional solution includes circular eigenfunctions while the three-dimensional solution for the scattered pressure is expressed in terms of spherical wave functions; i.e., spherical Bessel and Hankel functions and associated Legendre functions. Due to these similarities, the original work will be referred to quite regularly in the development that follows.

Consider the scalar wave equation,

$$\nabla^2 P = \frac{1}{c^2}\frac{\partial^2 P}{\partial t^2}, \tag{1}$$

where P is the acoustic pressure in three dimensions, ∇^2 is the Laplacian operator, c is the speed of sound, and t is time. Assuming a harmonic time dependence, $e^{-i\omega t}$, where ω is the angular frequency, the wave equation becomes the scalar Helmholtz differential equation in Cartesian coordinates:

$$\nabla^2 P(x,y,z) + k^2 P(x,y,z) = 0. \tag{2}$$

Here, $k = \omega/c = 2\pi/\lambda$ is the spatially independent acoustic wave number, and λ is the acoustic wavelength. In all cases considered here, a fluid medium surrounds the body, which supports some circumferential waves (i.e., Franz waves) but does not support shear waves. By a conformal (angle- and orientation-preserving) transformation of coordinates, the transformed Helmholtz equation in the new coordinate system becomes

$$\nabla^2 P(u,w,v) + k^2 F(u,w) P(u,w,v) = 0, \tag{3}$$

where (u,w,v) are the new coordinates, and $F(u,w)$ is a function which depends on the specific transformation (Morse and Feshbach, 1953, Vol. I, Chap. 5; DiPerna and Stanton, 1994). With the exception that the wave number is now a function of position, the new Helmholtz equation is formally identical to the Helmholtz equation in Cartesian coordinates.

A. Conformal mapping

Since x, y, and z are mutually orthogonal in the Cartesian coordinate system, conformally mapping them into a new coordinate system guarantees that the new coordinates (u,w,v) will be mutually orthogonal, which eases the computation of the normal particle velocity on the boundary. Additionally, the conformal mapping generates a new set of angular functions which fit the scatterer surface more naturally; that is, points along the surface that change rapidly in (x,y,z) are plotted at a higher spatial rate yet are equally spaced in (u,w,v). A new coordinate system must first be established, and then the conformal mapping function is defined and expanded to provide a method by which the body may be mapped to the new coordinate system.

1. Orthogonal coordinate system

An orthogonal coordinate system can be generated for a three-dimensional body of revolution from a two-dimensional conformal mapping. Consider the geometry in Fig. 1, in which ϕ is the azimuthal angular coordinate ranging from 0 to 2π (measured from the positive x-axis in the xy-plane), θ is the polar angular coordinate ranging from 0 to π (measured from the positive z-axis), and r is the radial coordinate ranging from 0 to ∞. This body is one of revolution that is formed by rotating the contour of the body about the z axis, in the same way that the prolate spheroidal coordinate system is created from an ellipse rotated about the major axis (Flammer, 1957). Consider a new coordinate sys-

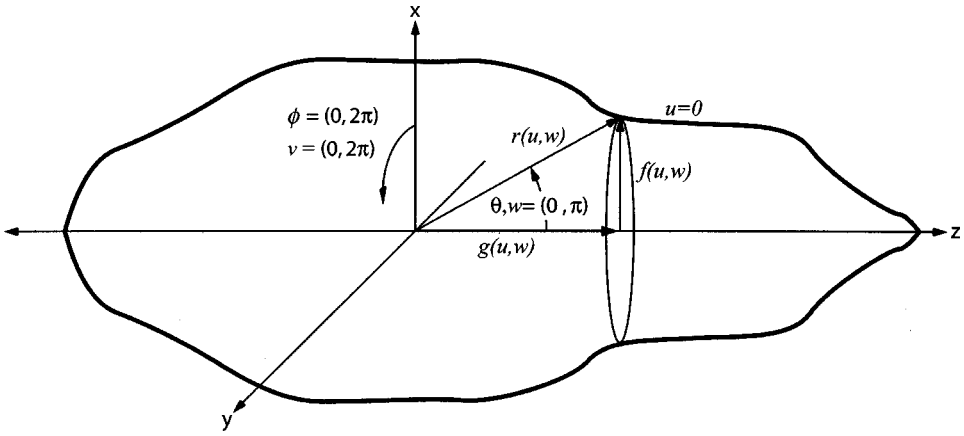

FIG. 1. Scattering geometry for an irregular, axisymmetric finite-length body. The body is symmetric about the z-axis. The azimuthal angular coordinates, ϕ and v, range from 0 to 2π in the xy-plane, and the polar angular coordinates, θ and w, range from 0 to π, measured from the z-axis. The radial coordinate in the (u,w,v) coordinate system equals zero on the surface. Broadside incidence corresponds to $\theta = \pi/2$. End-on incidence corresponds to $\theta = 0$ and π. In the new coordinate system, $g(u,w)$ is the length along the z-axis, and $f(u,w)$ is the projection in the xy-plane.

tem whose azimuthal angular coordinate, v, corresponds to ϕ in the original coordinate system. The new polar angular coordinate, w, is measured from the polar axis, z, and ranges from 0 to π, as does the original polar angular coordinate, θ. The scatterer surface in the original coordinate system is defined by the vector, $\mathbf{r}$, but in the new coordinate system the scatterer surface is defined by the locus of all points for which the new radial coordinate is a constant; specifically, $u=0$. Defining the functions, $f(u,w)$ and $g(u,w)$, of the new coordinate system as shown in Fig. 1, trigonometry prescribes dimensions of the body in the x, y and z directions to be

$$x(u,w,v) = f(u,w)\cos(v), \tag{4}$$

$$y(u,w,v) = f(u,w)\sin(v), \tag{5}$$

$$z(u,w,v) = g(u,w). \tag{6}$$

The position vector, $\mathbf{r}$, is defined in the new coordinate system by

$$\mathbf{r}(u,w,v) = x(u,w,v)\hat{i} + y(u,w,v)\hat{j} + z(u,w,v)\hat{k}, \tag{7}$$

where $\hat{i}$, $\hat{j}$, and $\hat{k}$ are unit vectors along the coordinate axes. The position vector can be alternatively expressed by substituting Eqs. (4)–(6) into Eq. (7):

$$\mathbf{r} = f(u,w)\cos(v)\hat{i} + f(u,w)\sin(v)\hat{j} + g(u,w)\hat{k}. \tag{8}$$

The local projection of $\mathbf{r}$ in each of the coordinate directions is given by the partial derivative of $\mathbf{r}$ with respect to each of the variables:

$$\mathbf{r}_u = f_u(u,w)\cos(v)\hat{i} + f_u(u,w)\sin(v)\hat{j} + g_u(u,w)\hat{k}, \tag{9}$$

$$\mathbf{r}_w = f_w(u,w)\cos(v)\hat{i} + f_w(u,w)\sin(v)\hat{j} + g_w(u,w)\hat{k}, \tag{10}$$

$$\mathbf{r}_v = -f(u,w)\sin(v)\hat{i} + f(u,w)\cos(v)\hat{j}, \tag{11}$$

where the subscript denotes the variable with respect to which the partial derivative is taken.

As mentioned earlier, an orthogonal coordinate system is desirable since it facilitates the computation of the normal particle velocity on the boundary necessary for satisfying the boundary conditions. An orthogonal coordinate system requires the following condition to be satisfied:

$$\mathbf{r}_u \cdot \mathbf{r}_v = 0, \tag{12}$$

$$\mathbf{r}_w \cdot \mathbf{r}_v = 0, \tag{13}$$

$$\mathbf{r}_u \cdot \mathbf{r}_w = 0, \tag{14}$$

which can be expanded as

$$f_u(u,w)f(u,w)\cos(v)\sin(v)(-1+1) = 0, \tag{15}$$

$$f_w(u,w)f(u,w)\cos(v)\sin(v)(-1+1) = 0, \tag{16}$$

$$f_u(u,w)f_w(u,w)(\cos^2(v)+\sin^2(v)) + g_u(u,w)g_w(u,w) = 0. \tag{17}$$

The first two conditions are automatically satisfied. The third condition simplifies to

$$f_u(u,w)f_w(u,w) + g_u(u,w)g_w(u,w) = 0, \tag{18}$$

which will be satisfied if

$$f_u(u,w) = g_w(u,w) \tag{19}$$

and

$$f_w(u,w) = -g_u(u,w). \tag{20}$$

These are precisely the Cauchy–Riemann equations for an analytic function (Hildebrand, 1964). Therefore, if $f(u,v)$ and $g(u,v)$ are chosen to be harmonic, then the Cauchy–Riemann conditions will be satisfied, making them analytic functions which represent a conformal transformation. A shape initially plotted in the (x,y,z) coordinate system will be transformed into a shape in the (u,w,v) coordinate system with changes in position and size while preserving angles and proportions (Morse and Feshbach, 1953). Orthogonality of the coordinate system as well as the form of the Helmholtz equation will be preserved (Strang, 1986).

2. Mapping function

As discussed above, a conformal mapping function must be developed to map the scatterer from the old coordinate system to the new orthogonal, axisymmetric coordinate system just developed. It must be noted at this point that, to the authors' knowledge, a general three-dimensional mapping does not exist in the field of mathematics. Due to the fact that conformal mappings are currently limited to two dimensions, the geometry for the finite body must be axisymmetric about one of the axes. The particular mapping used herein is a two-dimensional mapping developed by DiPerna and Stanton (1994) extended to a finite body of revolution which is

axisymmetric about the longitudinal axis. The infinitely long cylindrical geometry in DiPerna and Stanton (1994) was described in circular cylindrical coordinates with the radial coordinate, r, being a function of θ, the azimuthal angular coordinate ranging from 0 to 2π. The conformal mapping in that case applied to the function, $r(\theta)$, which corresponded to the shape of the boundary of a cross-sectional slice. In this work, θ is now the *polar* angular coordinate ranging from 0 to π, and ϕ is the azimuthal angular coordinate ranging from 0 to 2π. The function, $r(\theta)$, and associated conformal mapping is now associated with the shape of the boundary of a *length-wise* slice.

The category of surfaces described by Eqs. (4)–(6) has the additional limitation that r be single-valued; i.e., there can be only one value of r for each w. Following DiPerna and Stanton (1994), the mapping procedure for the axisymmetric finite body is commenced by expanding r in a Fourier series relative to the polar angle, θ, shown in Fig. 1:

$$r(\theta)=a+\sum_{n=1}^{\infty}\left[r_n^c\cos(n\theta)+r_n^s\sin(n\theta)\right], \tag{21}$$

where a is the average radius of the body, and r_n^c and r_n^s are the usual Fourier series coefficients that in this case correspond to the deviation of the surface from the shape of a circle. Note that the series requires more terms to converge for a high aspect ratio (ratio of length to width) prolate spheroid compared to the Fourier series for a shape that varies little from the shape of a circle. Rewriting the $\cos(n\theta)$ and $\sin(n\theta)$ functions in terms of exponentials and using the expression

$$R_n\equiv\tfrac{1}{2}[r_n^c+ir_n^s] \tag{22}$$

gives

$$r(\theta)=ae^{i\theta}+\sum_{n=1}^{\infty}\left[R_n^*e^{i(1+n)\theta}+R_ne^{i(1-n)\theta}\right]. \tag{23}$$

For a conformal mapping from the (x,y,z) coordinate system to the new coordinate system in (u,w,v),

$$M(\rho)=M(u+iw), \tag{24}$$

where $M(\rho)$ is the analytic mapping function in terms of u, the radial variable, and w, the polar angular variable, and $\rho\equiv u+iw$. It is desirable to make scattering predictions using this model without inversely mapping the results of this model back to the original coordinate system. The potentially difficult inverse mapping is avoided by choosing $M(\rho)$ such that the coordinate system becomes spherical as the radial coordinate is increased. While the choice of such a mapping function allows predictions of this model to be easily compared to existing solutions, it restricts direct comparisons to the far-field only. The general approach can certainly be used in the near-field, but comparisons of near-field scattering between this formulation and other solutions would require an inverse mapping. Note also that there will be two different mapping functions: $G(\rho)$ for the exterior problem and $T(\rho)$ for the interior problem. For the interior problem, $T(\rho)$ is chosen such that the coordinate system becomes spherical as the radial coordinate is decreased.

For the exterior problem, $G(\rho)$ must be chosen such that

(1) as $u\to\infty$, the coordinate system becomes spherical,
(2) the transformed Helmholtz equation is solvable, and
(3) $u=0$ is the scatterer surface.

The first two conditions can be satisfied by choosing the form of the exterior mapping function (DiPerna and Stanton, 1994) to be

$$G(\rho)=c_{-1}e^{\rho}+\sum_{n=0}^{\infty}c_ne^{-n\rho}, \tag{25}$$

which can be decomposed into the complex components

$$g(u,w)\equiv\mathrm{Re}(G(\rho))=c_{-1}e^{u}\cos(w)+\sum_{n=0}^{\infty}c_ne^{-nu}\cos(nw) \tag{26}$$

and

$$f(u,w)\equiv\mathrm{Im}(G(\rho))=c_{-1}e^{u}\sin(w)+\sum_{n=0}^{\infty}c_ne^{-nu}\sin(nw). \tag{27}$$

The coefficients of the mapping function must be chosen such that $u=0$ defines the scatterer surface in the new coordinate system. Equating the functions in Eqs. (23) and (25) (with $u=0$) that represent the surface in the two coordinate systems gives

$$ae^{i\theta}+\sum_{n=1}^{\infty}\left[R_n^*e^{i(1+n)\theta}+R_ne^{i(1-n)\theta}\right]=c_{-1}e^{iw}+\sum_{n=0}^{\infty}c_ne^{-inw}. \tag{28}$$

Since the left-hand side contains positive and negative angular components while the right-hand side contains only negative angular components (with the exception of $c_{-1}e^{iw}$), θ and w are not equal (for the irregular boundary); therefore, it is necessary to determine the extent to which θ depends on w. Since it was assumed earlier that the surface is periodic and can be represented as a Fourier series, the deviation of θ from w will be periodic and can be represented as a Fourier series. Specifically, assume

$$\theta(w)=w+\sum_{l=1}^{\infty}\left[\delta_l^c\cos(lw)+\delta_l^s\sin(lw)\right]. \tag{29}$$

Note that δ_l^c and δ_l^s represent the deviation of the surface from a smooth circular shape. Hence, θ and w are equal only for a smooth, circular length-wise cross section for which $\delta_l^c=\delta_l^s=0$. The conformal mapping relies on the choice of δ_l^c and δ_l^s such that Eq. (28) is satisfied. Using the orthogonality relationships of complex exponential functions, multiplying both sides by $(1/2\pi)e^{-ijw}$ and integrating over w from 0 to 2π gives

$$\frac{1}{2\pi}\int_0^{2\pi} e^{-ijw}\left(ae^{i\theta(w)} + \sum_{n=1}^{\infty} [R_n^* e^{i(1+n)\theta(w)} + R_n e^{i(1-n)\theta(w)}]\right) dw = \left\{ \begin{array}{ll} 0, & j>1 \\ c_j, & j\leqslant 1 \end{array} \right\}, \tag{30}$$

where j is an integer. This set of nonlinear constraints is identical in form to that of DiPerna and Stanton (1994) and is solved by use of an extension of the Newton–Raphson method, the details of which are laid out in Appendix A of DiPerna and Stanton (1994). Note, however, that even though the integral in Eq. (30) is performed from 0 to 2π, w is defined in the scattering geometry from 0 to π only (not 2π). Consequently, the mapping coefficients are computed based on the periodic extension from 0 to 2π, but only half of them are used. The upper result on the right-hand side of Eq. (30) is used to solve for the values of δ_l^c and δ_l^s, which are then used to solve for the mapping coefficients, c_n, through use of the lower result on the right-hand side of Eq. (30).

The uniqueness of the transformation is tested by verifying that the Jacobian of the transformation is nonzero. This ensures that there exists only one (x,z) for each (u,w). Specifically,

$$|G'(\rho)|^2 \neq 0, \quad u \geqslant 0. \tag{31}$$

The interior mapping procedure is identical to the exterior mapping procedure with the exception that the interior mapping function, $T(\rho)$, is different from $G(\rho)$; specifically, $T(\rho)$ is chosen such that the coordinate system becomes spherical as the radial coordinate is decreased. The remaining two conditions mentioned above in the choice of $G(\rho)$ remain the same for the interior problem. These conditions are satisfied by

$$T(\rho) = \sum_{n=0}^{\infty} t_n e^{n\rho}. \tag{32}$$

To summarize, the procedure described above to conformally map the scatterer shape from the original coordinate system to a new coordinate system is identical in form to the procedure presented in DiPerna and Stanton (1994). In this study, the same mapping procedure is extended to a different (finite-length, axisymmetric) scattering geometry; specifically, it is extended to the shape of the boundary in the length-wise slice. The results of this mapping will be used in solving the Helmholtz equation in three dimensions in the next section.

B. Solutions to the Helmholtz equation

The three-dimensional Helmholtz equation from Eq. (2) in the original coordinate system is expressed in spherical coordinates as

$$\nabla^2 P(r,\theta,\phi) + k^2 P(r,\theta,\phi) = 0, \tag{33}$$

the general solution to which is

$$P^{ext}(r,\theta,\phi) = \sum_{n=-\infty}^{\infty}\sum_{m=-\infty}^{\infty} a_{nm} j_n(kr) P_n^m(\cos(\theta)) e^{im\phi} + \sum_{n=-\infty}^{\infty}\sum_{m=-\infty}^{\infty} b_{nm} h_n^{(1)}(kr) \times P_n^m(\cos(\theta)) e^{im\phi}, \tag{34}$$

where $j_n(kr)$ is the spherical Bessel function of the first kind of order n, $h_n^{(1)}(kr)$ is the spherical Hankel function of the first kind of order n, and $P_n^m(\cos(\theta))$ is the associated Legendre function of degree n and order m. The radial coordinate is r, the polar angular coordinate is θ, and the azimuthal angular coordinate is ϕ. The scattered field coefficients, b_{nm}, are determined by satisfying the boundary conditions using the known coefficients, a_{nm}, of the incident plane wave field traveling from the θ_0 direction relative to the z axis:

$$a_{nm} = i^n \epsilon_m (2n+1) \frac{\Gamma(n-m+1)}{\Gamma(n+m+1)} P_n^m(\cos(\theta_0)), \tag{35}$$

where ϵ_m is the Neumann factor and Γ is the gamma function.

$P^{ext}(r,\theta,\phi)$ is the total pressure external to the scatterer in the original coordinate system (i.e., before transformation): the first term in Eq. (34) represents the incident pressure, and the second term represents the scattered pressure. Quantities in the original coordinate system can be expressed in terms of the new coordinate system defined in Sec. II A 1 and Fig. 1:

$$\phi = v, \tag{36}$$

$$r(u,w) = \sqrt{f^2(u,w) + g^2(u,w)}, \tag{37}$$

$$\cos(\theta(u,w)) = \frac{g(u,w)}{r(u,w)}. \tag{38}$$

Using these relations, the conformal mapping transforms the Helmholtz equation [Eq. (33)] into

$$\nabla^2 P(u,w,v) + k^2 F(u,w) P(u,w,v) = 0, \tag{39}$$

the solution to which is

$$P^{ext}(u,w,v) = \sum_{n=-\infty}^{\infty}\sum_{m=-\infty}^{\infty} a_{nm} j_n(kr(u,w)) \times P_n^m\left(\frac{g(u,w)}{r(u,w)}\right) e^{imv} + \sum_{n=-\infty}^{\infty}\sum_{m=-\infty}^{\infty} b_{nm} h_n^{(1)}(kr(r,w)) \times P_n^m\left(\frac{g(u,w)}{r(u,w)}\right) e^{imv}, \tag{40}$$

which is now the expression for the total far-field pressure in the new coordinate system as the sum of the incident and scattered pressure fields, respectively.

The procedure to determine the pressure field inside the scatterer is identical in nature to the exterior problem, but the mapping function is different for the interior problem; therefore, the new Helmholtz equation is identical in form, but

incorporates a different wave number, k_1, to accurately characterize the material properties of the scatterer's interior. The expression for the interior pressure field becomes

$$P^{int}(u,w,v)=\sum_{n=-\infty}^{\infty}\sum_{m=-\infty}^{\infty} l_{nm} j_n(k_1 r(u,w)) \times P_n^m\left(\frac{g(u,w)}{r(u,w)}\right) e^{imv}, \tag{41}$$

where l_{nm} are the internal field coefficients. Only the spherical Bessel function is included in the expression for the internal field since the spherical Hankel function becomes infinite at the origin.

In the limit of great distances from the scatterer, the coordinate system becomes spherical, and the asymptotic form of the Hankel function varies inversely with distance. The scattered pressure [the second term in Eq. (40)] in this far-field limit has the form:

$$P^{scat} \xrightarrow[u\to\infty]{} P^{inc}\frac{e^{ikr}}{r} f_s, \tag{42}$$

where the scattering amplitude, f_s, having units of length, is a measure of the efficiency with which an object scatters sound and is a function of the object's size, shape, orientation, material properties, and the wavelength of the incident wave. The scattering amplitude is given in general form as

$$f_s=\sum_{n=-\infty}^{\infty}\sum_{m=-\infty}^{\infty} b_{nm} i^{-n-1} P_n^m\left(\frac{g(u,w)}{r(u,w)}\right) e^{imv}. \tag{43}$$

The far-field scattered energy evaluated in the backscatter direction is often expressed in terms of the target strength (TS) with units of decibels (dB) relative to 1 m (Urick, 1983), which is given by

$$\mathrm{TS}=10\log\sigma_{bs}, \tag{44}$$

where σ_{bs} is the differential backscattering cross section, which differs from the often-used backscattering cross section, σ, by a factor of 4π ($\sigma=4\pi\sigma_{bs}$). Also, $\sigma_{bs}=|f_{bs}|^2$, where f_{bs} is the scattering amplitude evaluated in the backscattering direction. In order to compare scattering from objects of different sizes but similar proportions, target strength is often normalized by the square of some typical dimension. Using the length (L) of the elongated scatterer as the normalization constant, the ''reduced'' target strength (RTS) is

$$\mathrm{RTS}=10\log\left(\frac{\sigma_{bs}}{L^2}\right) =10\log|f_{bs}|^2-10\log(L^2)=10\log\left|\frac{f_{bs}}{L}\right|^2. \tag{45}$$

In the case of a sphere, the target strength is normalized by πa^2 instead of L^2. An alternative expression often used to represent the energy scattered in three dimensions is the normalized, steady-state form function (Neubauer, 1986):

$$f_\infty=\frac{2}{a} f_s, \tag{46}$$

where a is the radius of a sphere or the semi-minor axis of a prolate spheroid.

To summarize, a new orthogonal coordinate system has been established to which the original coordinate system is mapped via a conformal mapping function. The scatterer surface in the new coordinate system is defined by the locus of all points for which the radial coordinate is a constant. The solution to the Helmholtz equation in the new coordinate system will have the same form as the original solution, but with new coordinates using the realizations of Eqs. (36)–(38). This can be confirmed by inspecting the case of the exterior field for the spherical scatterer: $r(u,w)=c_{-1}e^u$, $\theta(u,w)=w$, and $\phi=v$, resulting in the same solution as in spherical coordinates using separation of variables. Also, for the case far ($u\to\infty$) from the nonspherical scatterer, $r(u,w)\to c_{-1}e^u$, $\theta(u,w)\to w$, and $\phi=v$, resulting in the same solution as in spherical coordinates in the far-field. Equations (40) and (41) are a general solution for the total pressure in the case of acoustic scattering from a finite-length, axisymmetric body for all frequencies, all angles (bistatic scattering), and for impenetrable (soft and rigid) and penetrable (fluid) boundary conditions. All the quantities needed to satisfy soft, hard, and fluid boundary conditions have now been established. Each boundary condition generates a different set of modal series coefficients, b_{nm}, which are used in Eq. (43) to compute the scattering amplitude. These coefficients will be determined for three boundary conditions in the following section.

C. Boundary conditions

The solution for the scattered field in Eqs. (40) and (43) depends on the boundary conditions. For each boundary condition, there is a different set of scattered field coefficients, b_{nm}, which needs to be evaluated. These coefficients are determined in the normal approach in which the pressures and/or velocities are matched at the boundaries. This matching is specific to the material properties on each side of the boundary. For each of the different boundary conditions, expressions are derived in the following sections for b_{nm}, all of which are in terms of the parameters of the new coordinate system.

The challenge presented by an irregular body is finding a solution to a system of equations in order to satisfy the boundary conditions; specifically, a set of functions, ψ, must be determined by which the basis functions are multiplied to generate the system of equations. For a separable geometry, ψ is chosen to be the angular eigenfunction to yield a closed-form solution based on the orthogonality of the eigenfunctions. In the case of irregular surfaces that do not conform to coordinate surfaces, a set of functions, ψ, must be chosen to solve the system of equations. DiPerna and Stanton (1994) chose the eigenfunctions in the new (cylindrical) coordinate system, $\psi_m=e^{-imv}$. It is in this choice of eigenfunctions that the FMM derives its name. Without the conformal change of variables to (u,w,v), this choice of functions would not be possible. For the three-dimensional case, the eigenfunctions in the spherical coordinate system are chosen; specifically (Morse and Feshbach, 1953),

$$\psi_n^m = P_n^m(\cos(w))\sin(w)e^{-imv}. \tag{47}$$

Using this choice for ψ, a system of equations is generated to satisfy each of the boundary conditions discussed herein (soft, rigid, and fluid). The system of equations is solved for the scattered field coefficients, b_{nm}, which are then used in Eq. (43) to determine the scattering amplitude.

1. Dirichlet boundary conditions

For soft (pressure release or Dirichlet) boundary conditions, the total pressure vanishes on the surface of the scatterer; i.e., $P^{ext}(u_0,w,v)=0$. Using Eq. (40), the series solution for the total exterior pressure field evaluated at the boundary with pressure release boundary conditions is set equal to zero:

$$\sum_{n=-\infty}^{\infty}\sum_{m=-\infty}^{\infty} a_{nm} j_n(kr(u_0,w))P_n^m\left(\frac{g(u_0,w)}{r(u_0,w)}\right)e^{imv} + \sum_{n=-\infty}^{\infty}\sum_{m=-\infty}^{\infty} b_{nm}h_n^{(1)}(kr(u_0,w)) \times P_n^m\left(\frac{g(u_0,w)}{r(u_0,w)}\right)e^{imv}=0. \tag{48}$$

The system of equations necessary to satisfy this boundary condition is generated by multiplying both sides of this equation by ψ_n^m from Eq. (47) and integrating over the range of w and v (Morse and Feshbach, 1953):

$$\int_0^{\pi}\int_0^{2\pi}\left\{\left(\sum_{n=-\infty}^{\infty}\sum_{m=-\infty}^{\infty} a_{nm} j_n(kr(u_0,w)) \times P_n^m\left(\frac{g(u_0,w)}{r(u_0,w)}\right)e^{imv} + \sum_{n=-\infty}^{\infty}\sum_{m=-\infty}^{\infty} b_{nm}h_n^{(1)}(kr(u_0,w))P_n^m\left(\frac{g(u_0,w)}{r(u_0,w)}\right)e^{imv}\right) \times P_n^m(\cos(w))\sin(w)e^{-imv}\right\}dv\,dw=0. \tag{49}$$

Performing the integration on v gives

$$\sum_{n=-\infty}^{\infty} a_{nm}\int_0^{\pi}\left(j_n(kr(u_0,w))P_n^m\left(\frac{g(u_0,w)}{r(u_0,w)}\right) \times P_n^m(\cos(w))\sin(w)\right)dw + \sum_{n=-\infty}^{\infty} b_{nm}\int_0^{\pi}\left(h_n^{(1)}(kr(u_0,w))P_n^m\left(\frac{g(u_0,w)}{r(u_0,w)}\right) \times P_n^m(\cos(w))\sin(w)\right)dw=0, \tag{50}$$

for each azimuthal order m. This system of equations for pressure release boundary conditions can be written in compact form:

$$\sum_{n=-\infty}^{\infty} a_{nm}R_n^m + \sum_{n=-\infty}^{\infty} b_{nm}Q_n^m = 0, \tag{51}$$

where a_{nm} is given in Eq. (35), and R_n^m and Q_n^m are defined, using Eq. (50), as

$$R_n^m \equiv \int_0^{\pi}\left(j_n(kr(u_0,w))P_n^m\left(\frac{g(u_0,w)}{r(u_0,w)}\right) \times P_n^m(\cos(w))\sin(w)\right)dw, \tag{52}$$

$$Q_n^m \equiv \int_0^{\pi}\left(h_n^{(1)}(kr(u_0,w))P_n^m\left(\frac{g(u_0,w)}{r(u_0,w)}\right) \times P_n^m(\cos(w))\sin(w)\right)dw. \tag{53}$$

Using Eq. (51), the series coefficients, b_{nm}, for the scattered field due to a soft boundary are

$$b_{nm} = -(Q_n^m)^{-1}R_n^m a_{nm}, \tag{54}$$

where $(\,)^{-1}$ denotes a matrix inversion.

2. Neumann boundary conditions

With rigid, or Neumann, boundary conditions, the normal particle velocity vanishes on the scatterer surface; i.e., $\hat{n}\cdot\nabla P^{ext}(u_0,w,v)=0$, where $\hat{n}$ is the unit vector normal to the surface and ∇ is the gradient operator. The method to solve for b_{nm} is broadly similar to the previous case, although several new terms are necessary to satisfy this particular boundary condition. The unit vectors in the u, w, and v directions are (Hildebrand, 1964)

$$\hat{a}_u = \frac{\mathbf{r}_u}{|\mathbf{r}_u|}, \tag{55}$$

$$\hat{a}_w = \frac{\mathbf{r}_w}{|\mathbf{r}_w|}, \tag{56}$$

$$\hat{a}_v = \frac{\mathbf{r}_v}{|\mathbf{r}_v|}. \tag{57}$$

Using Eqs. (9)–(11), the scale factors of each of the new coordinates (Morse and Feshbach, 1953) can be rewritten using the new coordinates:

$$h_u = |\mathbf{r}_u| = \sqrt{f_u^2(u,w)+g_u^2(u,w)} = \sqrt{f_u^2(u,w)+f_w^2(u,w)}, \tag{58}$$

$$h_w = |\mathbf{r}_w| = \sqrt{f_w^2(u,w)+g_w^2(u,w)} = \sqrt{f_w^2(u,w)+f_u^2(u,w)}, \tag{59}$$

$$h_v = |\mathbf{r}_v| = f(u,w). \tag{60}$$

Note that

$$h_u(u,w) = h_w(u,w) = h(u,w). \tag{61}$$

In the new coordinate system, the unit vectors become

$$\hat{a}_u = \frac{f_u(u,w)}{h(u,w)}\cos(v)\hat{i} + \frac{f_u(u,w)}{h(u,w)}\sin(v)\hat{j} + \frac{g_u(u,w)}{h(u,w)}\hat{k}, \tag{62}$$

$$\hat{a}_w = \frac{f_w(u,w)}{h(u,w)}\cos(v)\hat{i} + \frac{f_w(u,w)}{h(u,w)}\sin(v)\hat{j} + \frac{g_w(u,w)}{h(u,w)}\hat{k}, \tag{63}$$

$$\hat{a}_v = -\sin(v)\hat{i} + \cos(v)\hat{j}. \tag{64}$$

The scatterer surface has been defined by $u = u_0$; therefore, $\hat{n} = \hat{a}_u$. The gradient of the pressure P is

$$\nabla P(u,w,v) = \frac{1}{h_u(u,w)}\frac{\partial P}{\partial u}\hat{a}_u + \frac{1}{h_w(u,w)}\frac{\partial P}{\partial w}\hat{a}_w + \frac{1}{h_v(u,w)}\frac{\partial P}{\partial v}\hat{a}_v. \tag{65}$$

Using $\hat{n} = \hat{a}_u$ and $h_u(u,w) = \sqrt{f_w^2(u,w) + f_u^2(u,w)}$,

$$\hat{n}\cdot\nabla P(u,w,v) = \frac{1}{\sqrt{f_w^2(u,w) + f_u^2(u,w)}}\frac{\partial P}{\partial u}. \tag{66}$$

Using Eq. (40), the series solution for the normal particle velocity of the total external field for rigid boundary conditions evaluated at the boundary is set equal to zero:

$$\hat{n}\cdot\nabla\left(\sum_{n=-\infty}^{\infty}\sum_{m=-\infty}^{\infty} a_{nm} j_n(kr(u_0,w)) P_n^m\left(\frac{g(u_0,w)}{r(u_0,w)}\right)e^{imv}\right) + \hat{n}\cdot\nabla\left(\sum_{n=-\infty}^{\infty}\sum_{m=-\infty}^{\infty} b_{nm} h_n^{(1)}(kr(u_0,w)) P_n^m\left(\frac{g(u_0,w)}{r(u_0,w)}\right)e^{imv}\right) = 0. \tag{67}$$

The system of equations necessary to satisfy this boundary condition is generated by multiplying both sides of the equation by ψ_n^m in Eq. (47) and integrating over the range of w and v:

$$\int_0^{\pi}\int_0^{2\pi}\left\{\left(\hat{n}\cdot\nabla\left(\sum_{n=-\infty}^{\infty}\sum_{m=-\infty}^{\infty} a_{nm} j_n(kr(u_0,w)) P_n^m\left(\frac{g(u_0,w)}{r(u_0,w)}\right)e^{imv}\right) + \hat{n}\cdot\nabla\left(\sum_{n=-\infty}^{\infty}\sum_{m=-\infty}^{\infty} b_{nm} h_n^{(1)}(kr(u_0,w)) P_n^m\left(\frac{g(u_0,w)}{r(u_0,w)}\right)e^{imv}\right)\right) \times P_n^m(\cos(w))\sin(w)e^{-imv}\right\} dv\,dw = 0. \tag{68}$$

Using Eq. (66) and performing the integration on v gives

$$\sum_{n=-\infty}^{\infty} a_{nm}\int_0^{\pi}\left(j_n(kr(u_0,w)) P_{n,u}^m\left(\frac{g(u_0,w)}{r(u_0,w)}\right)\frac{r(u_0,w)g_u(u_0,w) - g(u_0,w)r_u(u_0,w)}{r^2(u_0,w)} + j_{n,u}(kr(u_0,w)) P_n^m\left(\frac{g(u_0,w)}{r(u_0,w)}\right)kr_u(u_0,w)\right)\frac{P_n^m(\cos(w))}{\sqrt{f_w^2(u_0,w) + f_u^2(u_0,w)}}\sin(w)dw + \sum_{n=-\infty}^{\infty} b_{nm}\int_0^{\pi}\left(h_n^{(1)}(kr(u_0,w)) P_{n,u}^m\left(\frac{g(u_0,w)}{r(u_0,w)}\right)\frac{r(u_0,w)g_u(u_0,w) - g(u_0,w)r_u(u_0,w)}{r^2(u_0,w)} + h_{n,u}^{(1)}(kr(u_0,w)) P_n^m\left(\frac{g(u_0,w)}{r(u_0,w)}\right)kr_u(u_0,w)\right)\frac{P_n^m(\cos(w))}{\sqrt{f_w^2(u_0,w) + f_u^2(u_0,w)}}\sin(w)dw = 0, \tag{69}$$

where, as with the other terms, the subscript, u, also indicates the partial derivative with respect to u.

As in the previous section, the system of equations for rigid boundary conditions can be written in compact form:

$$\sum_{n=-\infty}^{\infty} a_{nm} R_n'^m + \sum_{n=-\infty}^{\infty} b_{nm} Q_n'^m = 0, \tag{70}$$

where a_{nm} is given in Eq. (35), $R_n'^m$ is the integral in the first

half of Eq. (69), and $Q_n'^m$ is the integral in the second half of Eq. (69). Using Eq. (70), the series coefficients, b_{nm}, for the far-field scattered field due to a rigid boundary are

$$b_{nm} = -(Q_n'^m)^{-1} R_n'^m a_{nm}. \tag{71}$$

3. Cauchy boundary conditions

Fluid (Cauchy) boundary conditions is the case in which the body consists of a fluid with material properties other than that of the surrounding fluid and does not support a shear wave. In this case, the exterior and interior pressure fields and normal components of particle velocity are required to be equal on the surface. The fluid boundary conditions take the following form:

Pressure:

$$\begin{aligned}&\sum_{n=-\infty}^{\infty}\sum_{m=-\infty}^{\infty} a_{nm} j_n(kr(u_0,w)) P_n^m\left(\frac{g(u_0,w)}{r(u_0,w)}\right) e^{imv} \\ &\quad + \sum_{n=-\infty}^{\infty}\sum_{m=-\infty}^{\infty} b_{nm} h_n^{(1)}(kr(u_0,w)) P_n^m\left(\frac{g(u_0,w)}{r(u_0,w)}\right) e^{imv} \\ &\quad = \sum_{n=-\infty}^{\infty}\sum_{m=-\infty}^{\infty} l_{nm} j_n(k_1 r(u_0,w)) P_n^m\left(\frac{g(u_0,w)}{r(u_0,w)}\right) e^{imv},\end{aligned} \tag{72}$$

Particle velocity:

$$\begin{aligned}&\hat{n}\cdot\nabla\left(\sum_{n=-\infty}^{\infty}\sum_{m=-\infty}^{\infty} a_{nm} j_n(kr(u_0,w)) P_n^m\left(\frac{g(u_0,w)}{r(u_0,w)}\right) e^{imv}\right) + \hat{n}\cdot\nabla\left(\sum_{n=-\infty}^{\infty}\sum_{m=-\infty}^{\infty} b_{nm} h_n^{(1)}(kr(u_0,w)) P_n^m\left(\frac{g(u_0,w)}{r(u_0,w)}\right) e^{imv}\right) \\ &\quad = \hat{n}\cdot\nabla\left(\sum_{n=-\infty}^{\infty}\sum_{m=-\infty}^{\infty} l_{nm} j_n(k_1 r(u_0,w)) P_n^m\left(\frac{g(u_0,w)}{r(u_0,w)}\right) e^{imv}\right),\end{aligned} \tag{73}$$

where l_{nm} are the interior field coefficients. The system of equations necessary to satisfy this boundary condition is generated by multiplying both sides of the equation by ψ_n^m in Eq. (47) and integrating over the range of w and v:

Pressure:

$$\begin{aligned}&\int_0^{\pi}\int_0^{2\pi}\left\{\left(\sum_{n=-\infty}^{\infty}\sum_{m=-\infty}^{\infty} a_{nm} j_n(kr(u_0,w)) P_n^m\left(\frac{g(u_0,w)}{r(u_0,w)}\right) e^{imv}\right.\right. \\ &\quad \left.\left. + \sum_{n=-\infty}^{\infty}\sum_{m=-\infty}^{\infty} b_{nm} h_n^{(1)}(kr(u_0,w)) P_n^m\left(\frac{g(u_0,w)}{r(u_0,w)}\right) e^{imv}\right) P_n^m(\cos(w))\sin(w) e^{-imv}\right\} dv\,dw \\ &\quad = \int_0^{\pi}\int_0^{2\pi}\left\{\left(\sum_{n=-\infty}^{\infty}\sum_{m=-\infty}^{\infty} l_{nm} j_n(k_1 r(u_0,w)) P_n^m\left(\frac{g(u_0,w)}{r(u_0,w)}\right) e^{imv}\right) P_n^m(\cos(w))\sin(w) e^{-imv}\right\} dv\,dw,\end{aligned} \tag{74}$$

Particle velocity:

$$\begin{aligned}&\int_0^{\pi}\int_0^{2\pi}\left\{\left(\hat{n}\cdot\nabla\left(\sum_{n=-\infty}^{\infty}\sum_{m=-\infty}^{\infty} a_{nm} j_n(kr(u_0,w)) P_n^m\left(\frac{g(u_0,w)}{r(u_0,w)}\right) e^{imv}\right)\right.\right. \\ &\quad \left.\left. + \hat{n}\cdot\nabla\left(\sum_{n=-\infty}^{\infty}\sum_{m=-\infty}^{\infty} b_{nm} h_n^{(1)}(kr(u_0,w)) P_n^m\left(\frac{g(u_0,w)}{r(u_0,w)}\right) e^{imv}\right)\right) P_n^m(\cos(w))\sin(w) e^{-imv}\right\} dv\,dw \\ &\quad = \int_0^{\pi}\int_0^{2\pi}\left\{\hat{n}\cdot\nabla\left(\sum_{n=-\infty}^{\infty}\sum_{m=-\infty}^{\infty} l_{nm} j_n(k_1 r(u_0,w)) P_n^m\left(\frac{g(u_0,w)}{r(u_0,w)}\right) e^{imv}\right) P_n^m(\cos(w))\sin(w) e^{-imv}\right\} dv\,dw.\end{aligned} \tag{75}$$

Using Eq. (66) and performing the integration on v for both Eqs. (74) and (75) gives

Pressure:

$$\begin{aligned}&\sum_{n=-\infty}^{\infty} a_{nm}\int_0^{\pi} j_n(kr(u_0,w)) P_n^m\left(\frac{g(u_0,w)}{r(u_0,w)}\right) P_n^m(\cos(w))\sin(w)\,dw \\ &\quad + \sum_{n=-\infty}^{\infty} b_{nm}\int_0^{\pi} h_n^{(1)}(kr(u_0,w)) P_n^m\left(\frac{g(u_0,w)}{r(u_0,w)}\right) P_n^m(\cos(w))\sin(w)\,dw \\ &\quad = \sum_{n=-\infty}^{\infty} l_{nm}\int_0^{\pi} j_n(k_1 r(u_0,w)) P_n^m\left(\frac{g(u_0,w)}{r(u_0,w)}\right) P_n^m(\cos(w))\sin(w)\,dw,\end{aligned} \tag{76}$$

Particle velocity:

$$\sum_{n=-\infty}^{\infty} a_{nm}\int_0^{\pi}\Bigg(j_n(kr(u_0,w))P_{n,u}^m\left(\frac{g(u_0,w)}{r(u_0,w)}\right)\frac{r(u_0,w)g_u(u_0,w)-g(u_0,w)r_u(u_0,w)}{r^2(u_0,w)}$$

$$+j_{n,u}(kr(u_0,w))P_n^m\left(\frac{g(u_0,w)}{r(u_0,w)}\right)kr_u(u_0,w)\Bigg)\frac{P_n^m(\cos(w))}{\sqrt{f_w^2(u_0,w)+f_u^2(u_0,w)}}\sin(w)dw$$

$$+\sum_{n=-\infty}^{\infty} b_{nm}\int_0^{\pi}\Bigg(h_n^{(1)}(kr(u_0,w))P_{n,u}^m\left(\frac{g(u_0,w)}{r(u_0,w)}\right)\frac{r(u_0,w)g_u(u_0,w)-g(u_0,w)r_u(u_0,w)}{r^2(u_0,w)}$$

$$+h_{n,u}^{(1)}(kr(u_0,w))P_n^m\left(\frac{g(u_0,w)}{r(u_0,w)}\right)kr_u(u_0,w)\Bigg)\frac{P_n^m(\cos(w))}{\sqrt{f_w^2(u_0,w)+f_u^2(u_0,w)}}\sin(w)dw$$

$$=\sum_{n=-\infty}^{\infty} l_{nm}\int_0^{\pi}\Bigg(j_n(k_1r(u_0,w))P_{n,u}^m\left(\frac{g(u_0,w)}{r(u_0,w)}\right)\frac{r(u_0,w)g_u(u_0,w)-g(u_0,w)r_u(u_0,w)}{r^2(u_0,w)}$$

$$+j_{n,u}(k_1r(u_0,w))P_n^m\left(\frac{g(u_0,w)}{r(u_0,w)}\right)k_1r_u(u_0,w)\Bigg)\frac{P_n^m(\cos(w))}{\sqrt{f_w^2(u_0,w)+f_u^2(u_0,w)}}\sin(w)dw. \tag{77}$$

Writing Eqs. (76) and (77) in compact form,

$$\sum_{n=-\infty}^{\infty} a_{nm}R_n^m+\sum_{n=-\infty}^{\infty} b_{nm}Q_n^m=\sum_{n=-\infty}^{\infty} l_{nm}S_n^m, \tag{78}$$

$$\sum_{n=-\infty}^{\infty} a_{nm}R_n'^m+\sum_{n=-\infty}^{\infty} b_{nm}Q_n'^m=\sum_{n=-\infty}^{\infty} l_{nm}S_n'^m, \tag{79}$$

where a_{nm} is given in Eq. (35); R_n^m, Q_n^m, and S_n^m are now the first, second, and third integrals in Eq. (76); and $R_n'^m$, $Q_n'^m$, and $S_n'^m$ are now the first, second, and third integrals in Eq. (77). In contrast to the above two cases of impenetrable boundary conditions, b_{nm} must be solved for in two simultaneous equations. Solving for b_{nm} in Eqs. (78) and (79),

$$b_{nm}=-(Q_n'^mS_n^m-Q_n^mS_n'^m)^{-1}(R_n^mS_n'^m-R_n'^mS_n^m)a_{nm}. \tag{80}$$

In summary, the scattering amplitude [Eq. (43)] of a particular body is determined by conformally mapping the scatterer surface to a new coordinate system by solving Eq. (30), then solving for the scattering coefficients, b_{nm}, for the appropriate boundary condition as specified in the equations of this section.

III. NUMERICAL IMPLEMENTATION

A. General approach

Prediction of the scattering by an axisymmetric finite-length body using the above formulation requires a series of steps involving numerical methods. Given the complexity of the procedure, it is summarized briefly in this section, with some of the challenges elaborated upon in the next section. The shape of the scatterer is first described by the array of points, $(r,\ \theta)$, in polar coordinates in the xz plane (Fig. 1). The terms r and θ are then expanded in a Fourier series using Eqs. (21) and (29). The conformal mapping is based upon determining the values of δ_l^c and δ_l^s, which are determined by solving the upper result in the right-hand side of Eq. (30). This is a set of nonlinear constraints which are solved in an iterative, numerical manner by an extension of the Newton–Raphson method. The details of the Newton–Raphson method can be found in the Appendix of DiPerna and Stanton (1994) or in many math texts. Once the values of δ_l^c and δ_l^s are determined, the lower result on the right-hand side of Eq. (30) is used to determine the mapping coefficients, c_n, which are then used to compute functions, $g(u,w)$ and $f(u,w)$, of the new coordinate system [Eqs. (26) and (27)]. After the values of $g(u,w)$ and $f(u,w)$ are determined, the conformal mapping is complete, and the solution to the Helmholtz equation in the new coordinate system can be determined. The number of terms included in the summations in Eqs. (21), (29), and (30) are chosen in an iterative manner—predictions are made at first with a small number of terms, and then the number is increased for subsequent predictions until the scatterer is accurately mapped to the new coordinate system. The mapping can be verified visually by using $g(u,w)$ and $f(u,w)$ to plot on top of the shape in the original coordinate system (Fig. 1). For some shapes, the conformal mapping method can be avoided by using a function to describe the boundary. In the case of a smooth prolate spheroid, the functions $f=a\sin(w)$ and $g=b\cos(w)$ can be used in Eqs. (26) and (27), where a and b are the semi-minor and semi-major axes of the prolate spheroid, respectively. In the new coordinate system, the external far-field pressure [Eq. (40)] is solved by use of Eqs. (36)–(38). For soft boundary conditions, solve Eq. (54) by numerical integration of Eqs. (52) and (53). The numerical integration can be performed by use of one of numerous integration techniques, many of which are described in Press *et al.* (1992). In this work, simple matrix summation was used. Likewise for rigid and fluid boundary conditions, solve Eqs. (71) and (80) by performing the numerical integrations in Eq. (69) and Eqs. (76) and (77), respectively. With the scattered field coeffi-

cients, b_{nm}, the scattering amplitude is finally computed Eq. (43). The point at which the summations in Eq. (43) are truncated is determined in an iterative manner. The issues and challenges involved in truncation and performing the matrix inversions in Eqs. (54), (71), and (80) are discussed in the next section.

B. Numerical issues

In general, there exist significant inherent difficulties in the numerical implementation of infinite series solutions. For series solutions for simple geometries such as a sphere or cylinder, and with currently available computers, the series converges relatively rapidly. However, as the shape deviates from a simple geometry, higher modes are required for a converged solution. The problem is particularly complicated for objects of high aspect ratio and irregularity (roughness) on the boundary. The accuracy of the solution must be balanced with accounting for the degree of roughness and elongation of the boundary.

1. Precision

Some of the difficulty in the numerical calculation of the wave functions is merely the time required for the computer to compute the wave functions. Beyond this issue of time, the limiting factors in the numerical implementation are machine precision and matrix manipulation.

The FMM generates a transition matrix, much like the T-matrix model (Waterman, 1968), that relates the incident field coefficients to the scattered field coefficients. For a spherical scatterer, the transition matrix is diagonal and each nonzero term on the main diagonal is an eigenvalue for each mode computed. If the scatterer shape deviates from spherical, the matrix contains off-diagonal terms. The additional higher modal terms required to represent the scattering become extremely small, sometimes falling below the value that can be accurately represented numerically, resulting in a singular matrix in which the true values of its elements are below the precision of the machine. Thus, machine roundoff error is introduced into the solution and quickly dominates the results as it propagates through the solution via repetitive matrix manipulation.

The fundamental problem is finite machine precision. The number of modes required to accurately represent the scattering involves matrix elements that are sometimes numerically smaller than the machine can accurately compute. Little can be done to improve precision since it is a hardware limitation. Future technology may afford greater precision, but the extent to which it improves the solution is difficult to estimate. The relationship between greater precision and increased accuracy in the solution is not necessarily linear, but could be a rapidly decaying one instead.

Besides hardware limitations, numerical accuracy is very dependent upon accurate and efficient numerical implementation of the theory. There are a number of numerical algorithms that improve matrix manipulation and handling of roundoff error that have been investigated in this work, including orthogonal triangular decomposition, LU factorization, balancing of matrices, and scaling strategies (Press *et al.*, 1992). The single most important algorithm investigated and used in the implementation of this formulation is the well-known singular value decomposition (SVD) algorithm (Press *et al.*, 1992).

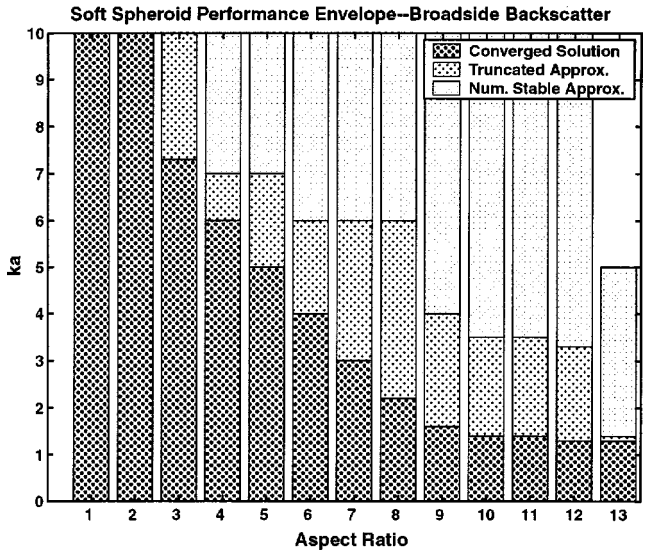

FIG. 2. Performance envelope for broadside backscatter for a smooth prolate spheroid with soft boundary conditions as a function of *ka* and aspect ratio. A converged solution is defined in this paper as one in which the computation of additional modes changed the scattering amplitude by less than 0.1% for a given value of *ka*. As the aspect ratio or value of *ka* is increased, converged solutions are more difficult to obtain. Aspect ratio (AR) is the ratio of length to width of the prolate spheroid (AR=1 for a sphere). The semi-minor axis of the prolate spheroid is designated as *a*.

For an ill-conditioned matrix in which some elements are below machine precision, the SVD algorithm sets those numerically indiscernible elements to zero. Eliminating one or more linear combinations of the set of equations that is to be solved is justified because those subspaces are dominated by roundoff error and contribute negligible energy to the solution and contribute principally to error; indeed, the error can be amplified. Singular values whose ratio to the largest singular value is less than *N* times the machine precision are

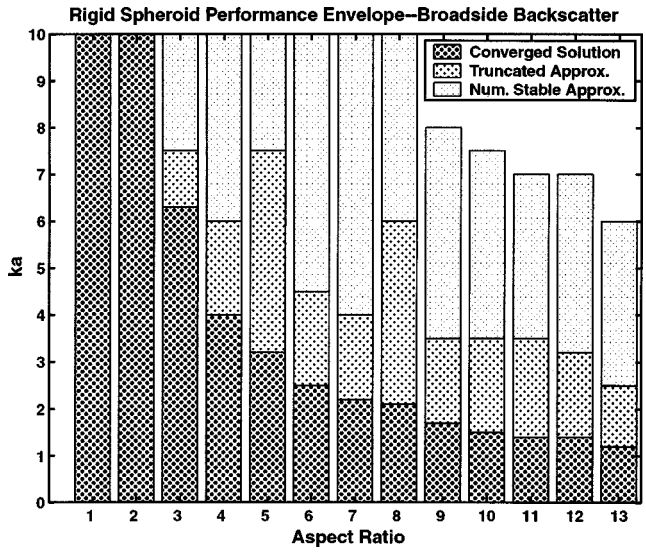

FIG. 3. Performance envelope for broadside backscatter by a smooth prolate spheroid with rigid boundary conditions as a function of *ka* and aspect ratio. Converged solutions are defined in the caption of Fig. 2.

set to zero (Press *et al.,* 1992). This threshold value is equivalent to the rank of the matrix, which is an estimate of the number of linearly independent rows or columns of a matrix. Eliminating erroneous subspaces yields a more stable numerical result and a convergent solution at higher frequencies; however, a disadvantage of the method is the potential of removing some energy that contributes to the solution, thereby diminishing the amplitude and structure of the results at higher frequencies. Therefore, the threshold used for SVD must be set with care.

2. Truncation

Regardless of whether the wave functions are difficult to compute and are susceptible to limitations of machine precision, numerical computation of an infinite series, such as in Eqs. (40) and (43), cannot be performed exactly due to the fact that there are an infinite number of terms in the series. Furthermore, the point at which the series must be truncated is not necessarily obvious. For lower frequencies and smooth spherical or smooth low-aspect-ratio spheroids (i.e., low eccentricity), reaching a converged solution before the onset of singularity is typically not a problem using currently available personal computers. As the frequency, aspect ratios, or degree of irregularity are increased, roundoff error begins to increase as a factor in preventing the solution from converging.

Given the importance of these numerical issues, a study was conducted to explore the conditions under which the solution would be reliable once numerically evaluated. The ''performance envelope'' of the FMM for broadside backscattering by smooth prolate spheroids of varying aspect ratios for soft and rigid boundary conditions was investigated (Figs. 2 and 3).

In this study, a ''converged'' solution is defined as one in which the computation of additional modes does not significantly change the result for a given value of *ka*. Specifically, the scattering amplitude for a converged solution (although strictly a truncated form of the exact solution) changed by less than 0.1% (an amount chosen arbitrarily in this study) with the computation of additional modes, which correlated very well with visual inspection. ''Truncated'' and ''numerically stable'' approximations are less objective and are a relative indication of the degree of reliability. Truncated approximations, as defined in this paper, employ a sufficient number of modes to represent the scattering to a lesser degree of accuracy than the above-defined converged solution, but still generally predicts the overall scattering levels and finer structure. Numerically stable approximations use a sufficient number of modes to adequately represent the overall amplitude, if not the finer structure, of the majority of the scattering. For both the soft (Fig. 2) and rigid (Fig. 3) cases, the solution was obtained for prolate spheroids with aspect ratios ranging from 1:1 (i.e., a sphere) to 13:1, and *ka* ranging from 0 to 10. Note that *a* is the semi-minor axis of the prolate spheroid, *b* is the semi-major axis, and the aspect ratio is b/a. This assignment of notation (*a* and *b*) differs from that in some literature, as *a* in this paper is intended to correspond to a cylindrical radius for the elongated bodies. For each of the two boundary conditions, a converged solution is

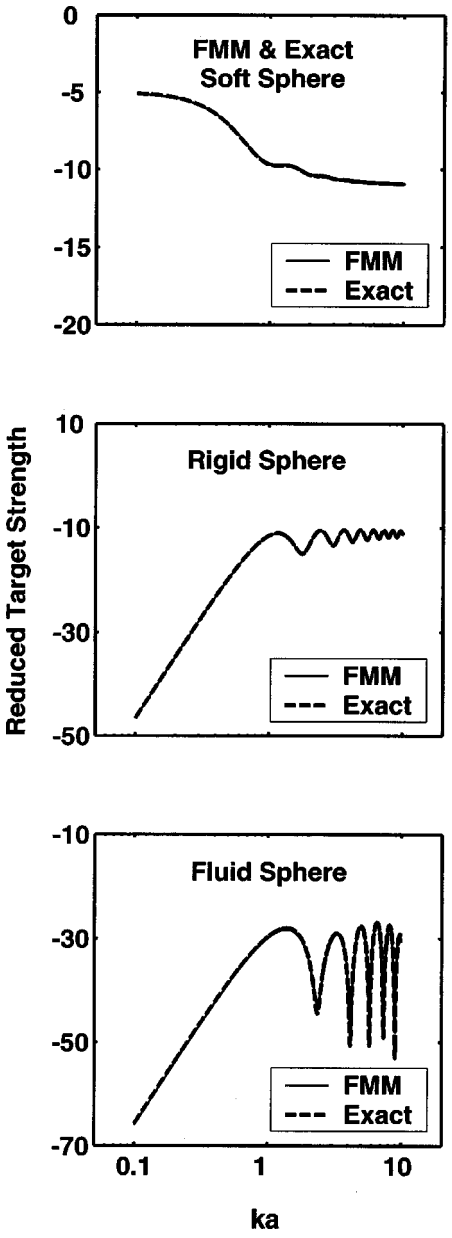

FIG. 4. FMM and exact solutions: Reduced target strength (in dB) as a function of *ka* for soft, rigid and fluid spheres. Mass and sound speed contrasts for the (weakly scattering) fluid case are $g=1.043$ and $h=1.052$, respectively. Exact solution calculation based on formulation from Anderson (1950).

reached for the sphere and 2:1 aspect ratio prolate spheroid for values of *ka* up to 10. As the aspect ratio is increased beyond 2:1, the value of *ka* at which the solution is converged falls off rapidly down to levels of 1.3 (soft) and 1.2 (rigid) at an aspect ratio of 13:1. The truncated approximation and numerically stable approximation behave less predictably as a function of *ka* and aspect ratio, but indicate generally decreasing convergence values of *ka* with increasing aspect ratio. The value of *ka* at which a converged solution is reached in the soft case is generally higher than that of the rigid case, particularly for aspect ratios of 8:1 or less. This is consistent with the fact that the soft case does not include an expression for the derivative of pressure as in the rigid case [Eq. (66)], thus requiring fewer matrix manipulations that would propagate roundoff error.

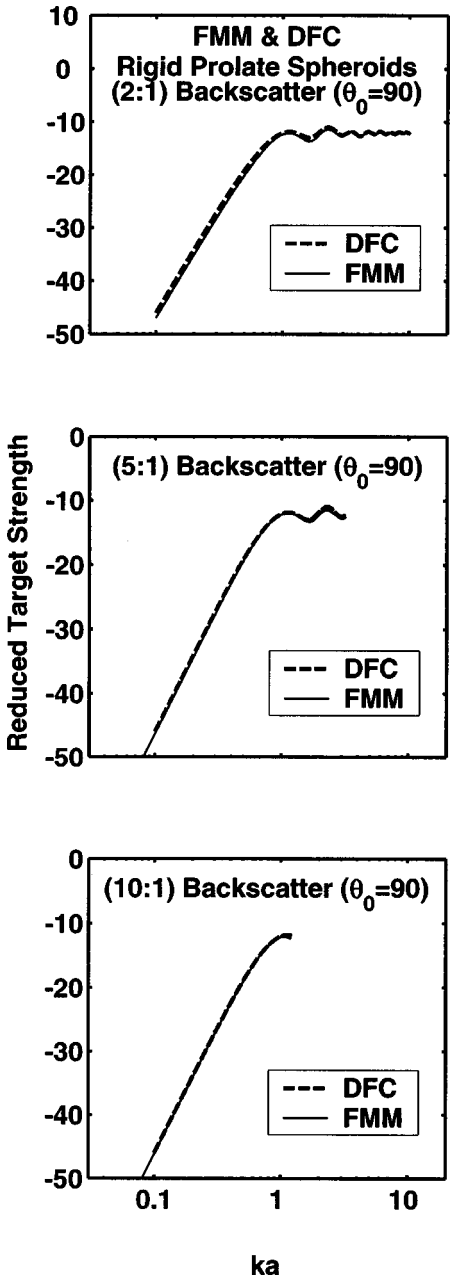

FIG. 5. FMM and DFC: Reduced target strength (in dB) of rigid prolate spheroids at broadside incidence as a function of *ka* for aspect ratios of 2:1, 5:1 and 10:1. DFC calculations are based on the formulation from Stanton (1989). The agreement between the FMM and DFC improves as the aspect ratio increases, which is consistent with the fact that the DFC is valid in the limit of high aspect ratio geometries.

IV. NUMERICAL RESULTS

All of the results plotted in Sec. IV were generated using Eqs. (43)–(46), (54), (71), and (80) to illustrate predictions as well as demonstrate the accuracy of the FMM in a wide variety of applications. Predictions using the FMM are first compared to those using the exact solution for soft, rigid, and fluid spheres. Predictions are then compared between the FMM and various formulations for smooth prolate spheroids for a variety of aspect ratios, frequencies, and incidence and scattering angles. Third, computations are presented for scattering from a realistic, irregular body. Lastly, predictions are presented for scattering by gaseous smooth prolate spheroids in the region of resonance for various aspect ratios.

A. Spheres: Comparison with exact solution

Computing the scattering from the sphere is an essential benchmark for the FMM since the exact solutions exist. The results for the soft, rigid, and fluid spheres produced by the FMM are identical to the exact solutions (Anderson, 1950) in all three cases (Fig. 4). In the case of fluid boundary conditions, material properties for a weak scatterer (i.e., one having properties resembling that of the surrounding fluid) were used. The specific values were chosen to resemble zooplankton tissue.

B. Prolate spheroids: Comparison with various solutions

As mentioned earlier, accurately computing the scattering from a prolate spheroid is a difficult task, particularly at high aspect ratios and high frequencies. Every scattering model has its strengths and weaknesses, so to thoroughly test the scope of applicability for the FMM, it is compared to a variety of models within their ranges of performance. The approaches used for comparison are the deformed finite cylinder (DFC) model, the T-matrix formulation, the boundary element method (BEM), the exact prolate spheroidal solution, and the Kirchhoff approximation. Note that a is the semi-minor axis of the prolate spheroid, b is the semi-major axis, and the aspect ratio is b/a.

1. Deformed finite cylinder model (DFC)

Stanton adapted his formulation for the finite cylinder (Stanton, 1988a, b) to finite cylinders of deformation; e.g., prolate spheroids and uniformly bent finite cylinders (Stanton, 1989). The model, which is based on the modal series solution for an infinitely long cylinder, has proven to be accurate at broadside and near-broadside orientations to the prolate spheroid for aspect ratios of 5:1 and higher (Partridge and Smith, 1995). The FMM compares well to the DFC for the case of broadside backscatter from a rigid prolate spheroid of aspect ratios 2:1, 5:1, and 10:1 (Fig. 5). As the aspect ratio is increased, results for the FMM are limited to lower frequencies to maintain a converged solution. In the Rayleigh region ($ka \leqslant 1$), the TS increases as expected, proportional to $(ka)^4$. Note also that the agreement between the FMM and the DFC in the Rayleigh region improves as the aspect ratio increases, reflecting the fact that the accuracy of the DFC improves with aspect ratio, eventually coinciding with the FMM results.

2. T-matrix method

The T-matrix method is a formally exact, numerical solution that has been the focus of much research to date and has proven to be an accurate model for numerous scattering problems. In two earlier studies, the T-matrix approach has been applied to backscatter and bistatic scattering by rigid prolate spheroids with an aspect ratio of 2:1 (Varadan *et al.*, 1982) and 10:1 (Hackman, 1993) and will be compared with FMM predictions. There is excellent agreement between the

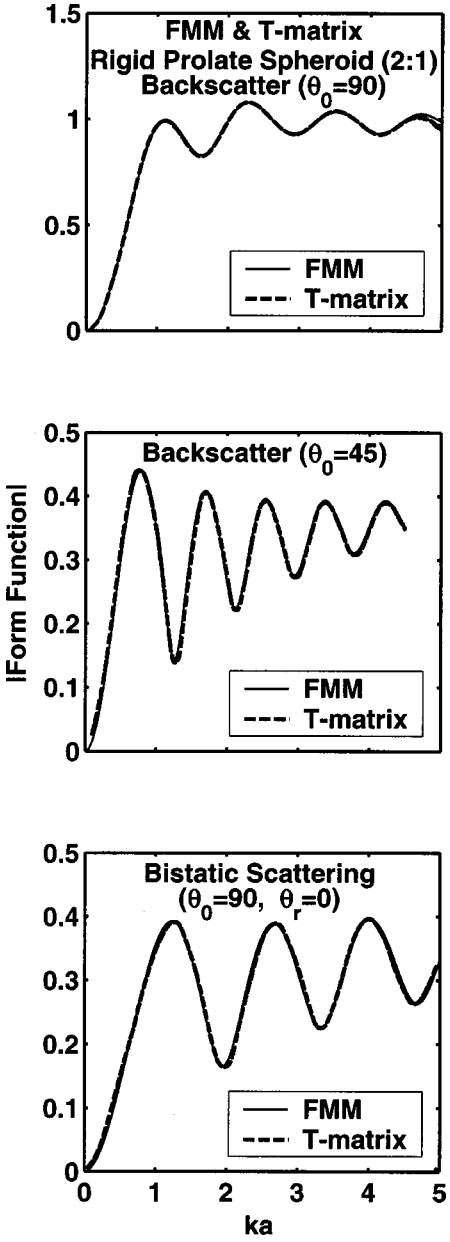

FIG. 6. FMM and T-matrix: Magnitude of backscattered and bistatic form function of a 2:1 rigid prolate spheroid as a function of *ka* for the cases of broadside backscatter, backscatter at oblique incidence, and bistatic scattering. T-matrix results are from Figs. 3–5 of Varadan *et al.* (1982). The form function is given in Eq. (46).

FMM and the T-matrix method in the cases of backscatter for a 2:1 aspect ratio prolate spheroid at broadside ($\theta_0 = 90°$) and oblique ($\theta_0 = 45°$) angles of incidence, as well as in the bistatic geometry of broadside incidence ($\theta_0 = 90°$) and end-on reception ($\theta_r = 0°$) (Fig. 6). There is also excellent agreement between the T-matrix and the FMM after increasing the aspect ratio from 2:1 to 10:1 for the rigid prolate spheroid in the case of broadside and end-on backscatter (Fig. 7). All of the cases in Figs. 6 and 7 illustrate the interference between the specular reflection and a Franz, or creeping, wave, and the associated shifts in the peaks and nulls for the different angles of incidence and reception (Uberall *et al.*, 1966).

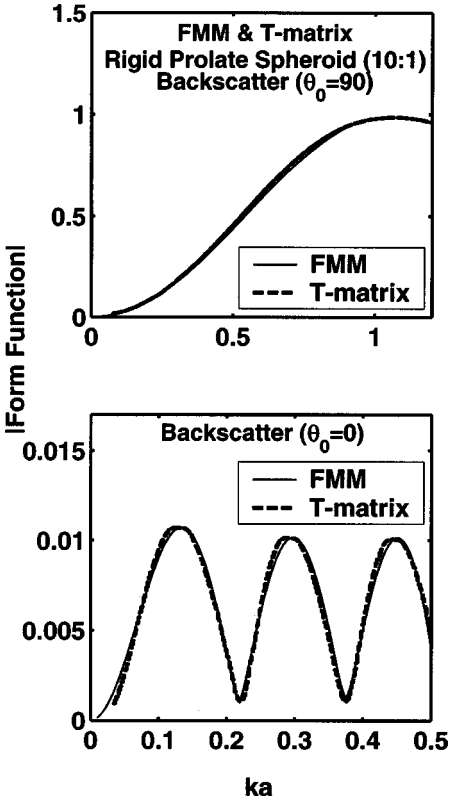

FIG. 7. FMM and T-matrix: Magnitude of backscattered form function for a 10:1 rigid prolate spheroid as a function of *ka* for the case of broadside incidence and end-on incidence. T-matrix results are from Fig. 37(a) of Hackman (1993). The form function is given in Eq. (46).

3. Boundary element method (BEM)

Francis (1993) developed a numerical method of computing the scattering by a finite body using a boundary element method based on a partial application of a Helmholtz gradient formulation. The FMM and BEM agree perfectly to high frequencies ($ka = 10$) in the case of end-on backscatter for a 2:1 aspect ratio rigid prolate spheroid (Fig. 8).

4. Exact prolate spheroidal solution

The exact solution for a prolate spheroid in prolate spheroidal coordinates has been used by various investigators

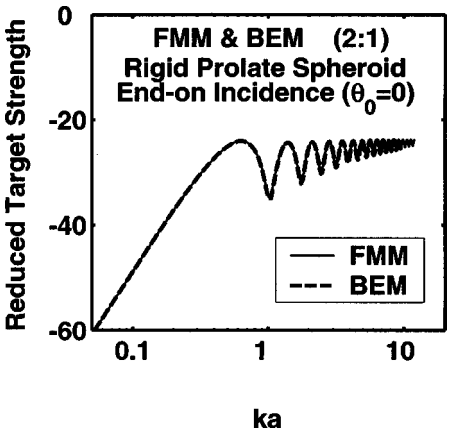

FIG. 8. FMM and BEM: Reduced target strength (in dB) as a function of *ka* for a 2:1 rigid prolate spheroid at end-on incidence. The agreement continues well past $ka = 10$. BEM results are from Francis (2001).

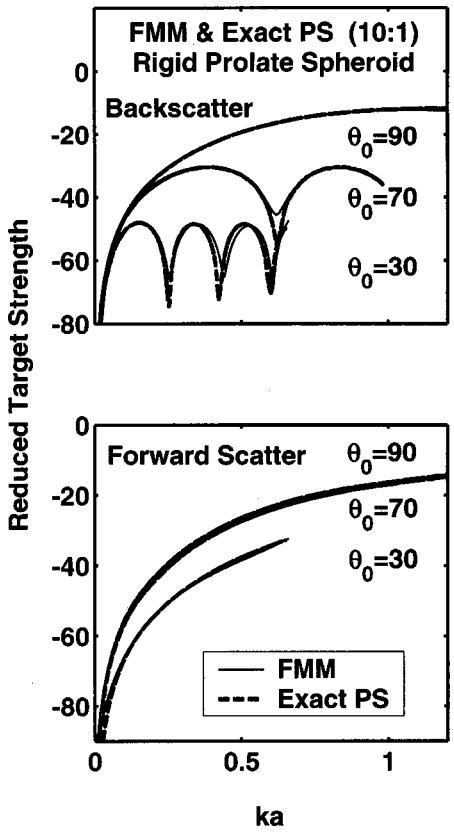

FIG. 9. FMM and exact prolate spheroidal solution: Reduced target strength (in dB) as a function of *ka* for a 10:1 rigid prolate spheroid at incidence angles of 30°, 70°, and 90° for backscatter and forward scatter. There are six lines plotted in each panel: three solid lines for the FMM and three dashed lines for the exact prolate spheroidal solution for each of the angles specified. Exact prolate spheroidal solutions are from Fig. 7 of Ye *et al.* (1997).

(Yeh, 1967; Furusawa, 1988; Ye *et al.*, 1997). While this is formally an exact solution, it encounters the same numerical challenges mentioned in Sec. III. Comparisons of the FMM to the exact solution in the case of backscatter and forward scatter for a range of incidence angles ($\theta_0 = 30°, 70°, 90°$) demonstrate good to excellent agreement in all cases (Fig. 9).

5. Kirchhoff approximation

The Kirchhoff approximation is a frequently used approximation for backscattering; however, it is generally limited to the geometric scattering region ($ka \gg 1$), perfectly reflecting boundary conditions (soft and rigid), and near-broadside incidence (Born and Wolf, 1999). It is a convenient approximation for the amplitude of the backscatter, but does not accurately represent the oscillations in the amplitude due to the interaction between the specular reflections and Franz waves. Comparisons of the FMM to this approximation within the range of reliability of the Kirchhoff approximation further establish the consistency of the FMM. Specifically, the reduced target strengths for broadside backscattering generally agree well for the single frequencies presented, with improved agreement as the frequency increases (Fig. 10). At $ka = 1$, the Kirchhoff approximation is near the limit of its range of validity and underestimates the amplitude. Additionally, it can be seen that the Kirchhoff approximation falls off much more rapidly than the FMM for all *ka* as the incidence angle moves away from broadside.

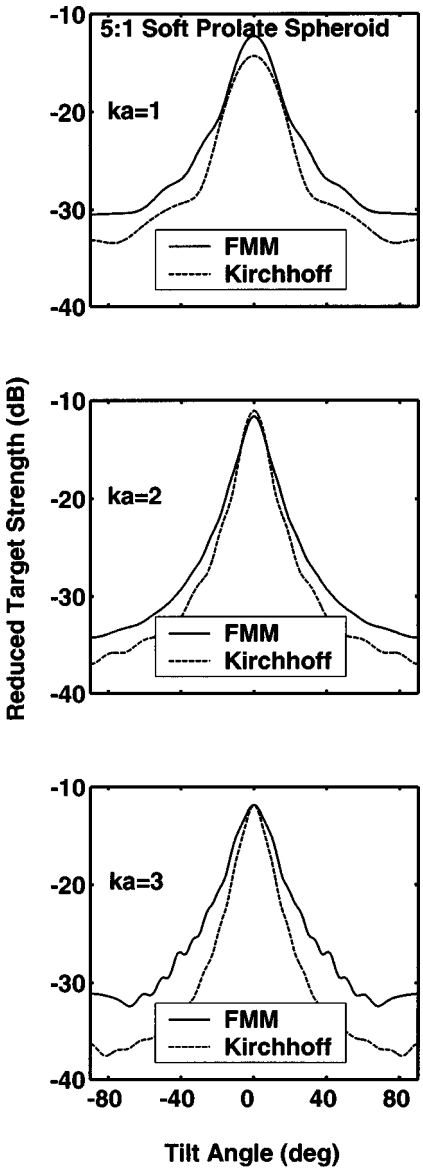

FIG. 10. FMM and Kirchhoff approximation: Reduced target strength as a function of tilt angle for a 5:1 soft prolate spheroid at $ka = 1$, $ka = 2$, and $ka = 3$. Kirchhoff approximation results are based on the formulation from Born and Wolf (1999). The largest differences occur well off broadside, where the Kirchhoff approximation characteristically underpredicts the scattering. Tilt angle, a coordinate commonly used with fish, corresponds in this case to angular deviation from normal incidence (0 deg).

C. Irregular bodies: Comparison with Kirchhoff approximation

As emphasized earlier, accurate computation of the scattering by smooth elongated bodies is not a simple task, particularly as the aspect ratio and frequencies increase. The additional complexity of an irregular surface further complicates an already difficult problem. A key distinction of the FMM is its ability to conformally map an irregular axisymmetric surface to an orthogonal coordinate system that better fits the scatterer surface. To demonstrate the practical application of the FMM to a realistic, asymmetrical, irregular body with non-Gaussian roughness, the acoustic scattering

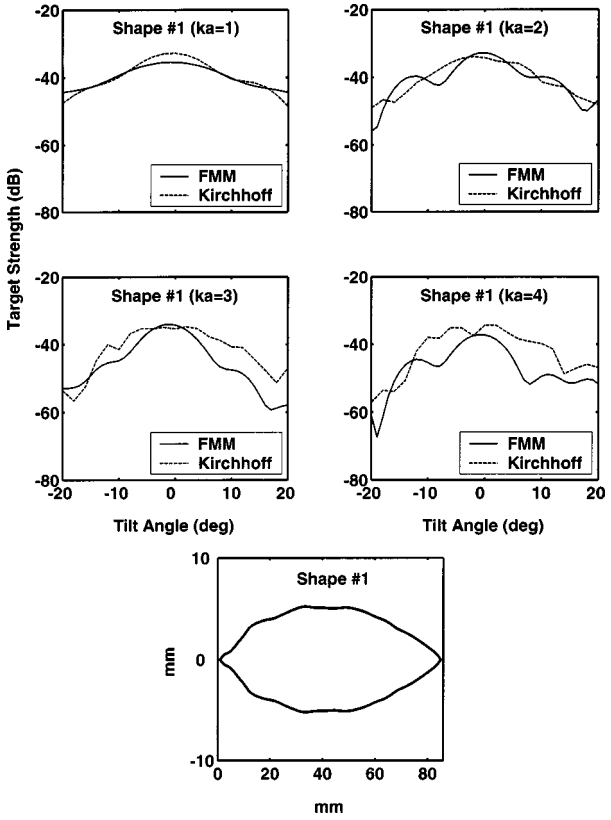

FIG. 11. FMM and Kirchhoff approximation: Target strength as a function of tilt angle for irregular shape 1 at $ka=1$, $ka=2$, $ka=3$ and $ka=4$. Kirchhoff approximation results are based on the formulation from Clay and Horne (1994). Shape 1 is shown in the bottom frame. The vertical axis is exaggerated to better illustrate the irregularity of the surface. Normal incidence corresponds to 0°. Positive tilt angle corresponds to the 0-mm end of target being closer to transducer.

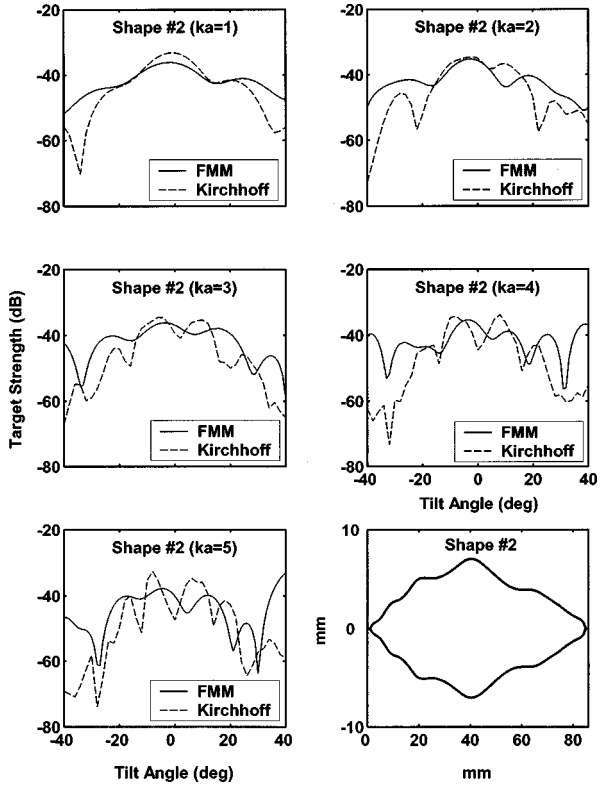

FIG. 12. FMM and Kirchhoff approximation: Target strength as a function of tilt angle for irregular shape 2 at $ka=1$, $ka=2$, $ka=3$, $ka=4$, and $ka=5$. Kirchhoff approximation results are based on formulation from Clay and Horne (1994). Shape 2 is shown in the bottom frame. The vertical axis is exaggerated to better illustrate the irregularity of the surface. Plotting convention for tilt angle described in caption to Fig. 11.

by a gas-filled swimbladder from an alewife fish (*Alosa pseudoharengus*) has been modeled and compared with the Kirchhoff approximation for two representative shapes corresponding to the dorsal and ventral aspects of the swimbladder (Figs. 11 and 12, respectively). This particular problem was chosen as fish are a significant scatterer of sound in the ocean, and the swimbladder is the organ in the fish that generally dominates the scattering. A more extensive treatment of this application is given in [Reeder *et al.* (J. Acoust. Am. **116**, 747–761 (2004)]. At these values of *ka*, soft boundary conditions were used, given the high contrast in material properties between the gas and surrounding tissue. There is generally reasonable agreement between FMM and Kirchhoff for most values of *ka* for shape 1 in Fig. 11, but for shape 2 in Fig. 12, the Kirchhoff predictions generally underestimate the scattering relative to the FMM at angles well off broadside.

D. Low *ka* resonance scattering for gaseous bodies: Comparison with T-matrix and exact prolate spheroidal solutions

In contrast to the cases of rigid and weakly scattering objects described above whose scattering levels decrease dramatically in the $ka \ll 1$ region, gaseous bodies have a strong resonance in that region and have been the subject of many earlier studies. Although in the low *ka* region there are fewer restrictions in the calculations, challenges still remain in the prediction of scattering from gaseous bodies with high aspect ratios. In this study, the FMM is directly compared with the T-matrix method and the exact prolate spheroidal solution over a range of aspect ratios up to 20:1 for constant volume prolate spheroids. Predictions from the T-matrix method and FMM are compared in Fig. 13 for aspect ratios up to 16:1. Results for aspect ratios up to 20:1 were presented by Feuillade and Werby (1994) using the T-matrix method, as well as Ye and Hoskinson (1998) using the exact prolate spheroidal solution. In addition, low *ka* resonance scattering by gaseous bodies of higher aspect ratio (up to 100:1) was calculated using the FMM with no difficulties relative to the numerical issues cited earlier. These ratios are much higher than what has previously appeared in the literature (Strasberg, 1953; Weston, 1967; Feuillade and Werby, 1994; Ye and Hoskinson, 1998). The FMM accurately predicts the scattering in the resonance region—the increase in the resonance frequency, the decrease in the resonance amplitude, and the broadening of the resonance peaks for prolate spheroids of constant volume and increasing aspect ratio within the verifiable range of aspect ratios presented in the literature (up to 20:1 aspect ratios). The FMM also predicts these same trends well beyond the aspect ratio of 20:1.

V. SUMMARY AND CONCLUSIONS

An extension of a two-dimensional conformal mapping approach to scattering by irregular, finite-length bodies of

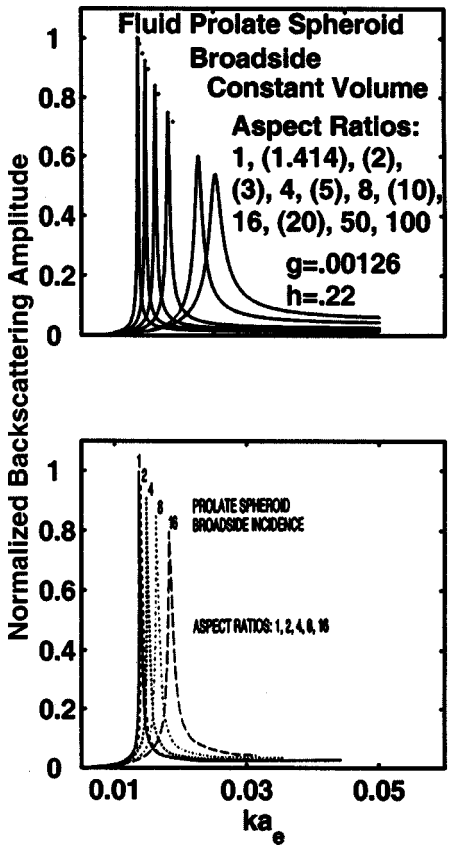

FIG. 13. FMM and T-matrix: Magnitude of normalized backscattering amplitude as a function of ka_e for a gaseous ($g=0.00126, h=0.22$) prolate spheroid at broadside incidence. Results from the FMM (top panel) are compared to results from the T-matrix method (bottom panel) from Fig. 4(a) of Feuillade and Werbe (1994). The single dots in the top panel are peak amplitudes for aspect ratios listed in parentheses. The scattering amplitude on the vertical axis is normalized to the peak amplitude of the sphere. As the aspect ratio of the spheroid is increased beyond 1:1, the dimensions of the spheroid are changed to maintain a volume equal to that of the original sphere. Thus, the a_e in ka_e is the equivalent spherical radius of the object, corresponding to the radius of the sphere (the 1:1 case shown) that has the same volume as the prolate spheroid. Results for aspect ratios up to 20:1 were tabulated by Feuillade and Werby (1994) using the T-matrix method, as well as Ye and Hoskinson (1998) using the exact prolate spheroidal solution. There is excellent agreement among predictions from all three formulations for aspect ratios up to 20:1.

revolution has been presented for three boundary conditions. The model conformally maps the coordinate variables of the original coordinate system to a new orthogonal coordinate system in which the locus of all points for which the new radial coordinate is a constant exactly coincides with the scatterer surface. The solutions to the transformed Helmholtz equation are a general solution for the total pressure in the case of far-field scattering from a finite body of revolution. This model has been shown to be very accurate in the prediction of scattering from smooth, symmetric bodies for a wide range of frequencies (Rayleigh through geometric scattering region), scattering angles (monostatic and bistatic), aspect ratios, and boundary conditions. Reasonable agreement has also been demonstrated for irregular, realistic shapes when compared to the Kirchhoff approximation. This work represents a significant advancement by providing a numerically efficient formulation that is applicable over a wide range of frequencies, scattering angles, and geometries for soft, rigid, and fluid boundary conditions.

There is great potential for further development of this model, including application to acoustic scattering by elastic solids and shells. The implementation of better numerical integration techniques, the use of extended precision format of floating point arithmetic, or various smoothing techniques (Yamashita, 1990) could delay the onset of ill-conditioned matrices, accelerating convergence. New scaling techniques based upon the physical scattering mechanisms could also increase accuracy (Schmidt, 1993).

ACKNOWLEDGMENTS

The authors would like to thank Dr. Daniel T. DiPerna (Signatures Directorate, Naval Surface Warfare Center, Carderock Division, Bethesda, MD) who derived an early form of the general solution and provided much guidance during the course of this work. The authors would also like to thank Dr. Trevor Francis of the University of Birmingham, UK, for generously providing the BEM calculation for Fig. 8 and Dr. J. Michael Jech of the NOAA/NMFS Northeast Fisheries Science Center, Woods Hole, MA, for computing the Kirchhoff approximations for Figs. 11 and 12. This work was supported by the U.S. Navy, the U.S. Office of Naval Research, and the Massachusetts Institute of Technology/Woods Hole Oceanographic Institution Joint Program in Oceanographic Engineering. This is Woods Hole Oceanographic Institution Contribution No. 10701.

Anderson, V. C. (**1950**). "Sound scattering from a fluid sphere," J. Acoust. Soc. Am. **22**, 426–431.

Born, M., and Wolf, E. (**1999**). *Principles of Optics*, 7th ed. (Cambridge U. P., Cambridge).

Bowman, J. J., Senior, T. B. A., and Uslenghi, P. L. E. (**1987**). *Electromagnetic and Acoustic Scattering by Simple Shapes* (Hemisphere, New York).

Clay, C. S., and Horne, J. K. (**1994**). "Acoustic models of fish: The Atlantic cod (*Gadus morhua*)," J. Acoust. Soc. Am. **96**, 1661–1668.

DiPerna, D. T., and Stanton, T. K. (**1994**). "Sound scattering by cylinders of noncircular cross section: A conformal mapping approach," J. Acoust. Soc. Am. **96**, 3064–3079.

Feuillade, C., and Werby, M. F. (**1994**). "Resonances of deformed gas bubbles in liquids," J. Acoust. Soc. Am. **96**, 3684–3692.

Flammer, C. (**1957**). *Spheroidal Wave Functions* (Stanford U. P., Stanford).

Francis, D. T. (**1993**). "A gradient formulation of the Helmholtz integral equation for acoustic radiation and scattering," J. Acoust. Soc. Am. **93**, 1700–1709.

Francis, D. T. I. (**2001**). Personal communication.

Furusawa, M. (**1988**). "Prolate spheroidal models for predicting general trends of fish target strength," J. Acoust. Soc. Jpn. (E) **9**, 13–24.

Gaunaurd, G. C. (**1985**). "Sonar cross sections of bodies partially insonified by finite sound beams," IEEE J. Ocean. Eng. **10**, 213–230.

Hackman, R. H. (**1993**). "Underwater Scattering and Radiation," in *Physical Acoustics*, Vol. XXII, edited by A. D. Pierce and R. N. Thurston (Academic, San Diego).

Hackman, R. H., and Todoroff, D. G. (**1985**). "An application of the spheroidal-coordinate-based transition matrix: The acoustic scattering from high aspect ratio solids," J. Acoust. Soc. Am. **78**, 1058–1071.

Hildebrand, F. B. (**1964**). *Advanced Calculus for Applications* (Prentice-Hall, Englewood Cliffs, NJ).

Lakhtakia, A., Varadan, V. K., and Varadan, V. V. (**1984**). "Iterative extended boundary condition method for scattering by objects of high aspect ratios," J. Acoust. Soc. Am. **76**, 906–912.

Laura, P. A. A. (**1994**). "Comments on sound scattering by cylinders of noncircular cross section: A conformal mapping approach" [J. Acoust. Soc. Am. **96**, 3064–3079 (1994)]" J. Acoust. Soc. Am. **98**, 3534–3535.

Levy, B. R., and Keller, J. B. (**1959**). "Diffraction by a smooth object," Commun. Pure Appl. Math. **12**, 159–209.

Morse, P. M., and Feshbach, H. (**1953**). *Methods of Theoretical Physics* (McGraw–Hill, Boston).

Neubauer, W. G. (**1986**). *Acoustic Reflection from Surfaces and Shapes* (Naval Research Laboratory, Washington, D.C.).
Partridge, C., and Smith, E. R. (**1995**). ''Acoustic scattering from bodies: Range of validity of the deformed cylinder method,'' J. Acoust. Soc. Am. **97**, 784–795.
Press, W. H., Teukolsky, S. A., Vetterling, W. T., and Flannery, B. P., (**1992**). *Numerical Recipes in Fortran: The Art of Scientific Computing*, 2nd ed. (Cambridge U. P., Australia).
Rayleigh, Lord (J. H. Strutt) (**1945**). *The Theory of Sound* (Dover, New York).
Reeder, D. B., Jech, J. M., and Stanton, T. K., (**2004**). ''Broadband acoustic backscatter and high resolution morphology of fish: Measurement and modeling,'' J. Acoust. Soc. Am. **116**, 747–761.
Schmidt, H. (**1993**). ''Numerically stable global matrix approach to radiation and scattering from spherically stratified shells,'' J. Acoust. Soc. Am. **94**, 2420–2430.
Stanton, T. K. (**1988a**). ''Sound scattering by cylinders of finite length. I. Fluid cylinders,'' J. Acoust. Soc. Am. **83**, 55–63.
Stanton, T. K. (**1988b**). ''Sound scattering by cylinders of finite length. II. Elastic cylinders,'' J. Acoust. Soc. Am. **83**, 64–67.
Stanton, T. K. (**1989**). ''Sound scattering by cylinders of finite length. III. Deformed cylinders,'' J. Acoust. Soc. Am. **86**, 691–705.
Strang, G. (**1986**). *Introduction to Applied Mathematics* (Wellesley-Cambridge, Wellesley, MA).
Strasberg, M. (**1953**). ''The pulsation frequency of nonspherical gas bubbles in liquids,'' J. Acoust. Soc. Am. **25**, 536–537.
Tobacman, W. (**1984**). ''Calculation of acoustic wave scattering by means of the Helmholtz integral equation,'' J. Acoust. Soc. Am. **76**, 599–607.
Uberall, H., Doolittle, R. D., and McNicholas, J. V. (**1966**). ''Use of sound pulses for a study of circumferential waves,'' J. Acoust. Soc. Am. **39**, 564–578.
Urick, R. J. (**1983**). *Principles of Underwater Sound* (McGraw-Hill, New York).
Varadan, V. K., Varadan, V. V., Dragonette, L. R., and Flax, L. (**1982**). ''Computation of rigid body scattering by prolate spheroids using the T-matrix approach,'' J. Acoust. Soc. Am. **71**, 22–25.
Waterman, P. C. (**1968**). ''New formulation of acoustic scattering,'' J. Acoust. Soc. Am. **45**, 1417–1429.
Weston, D. E. (**1967**). ''Sound propagation in the presence of bladder fish,'' in *Underwater Acoustics*, edited by V. M. Albers (Plenum, New York).
Yamashita, E. (**1990**). *Analysis Methods for Electromagnetic Wave Problems* (Artech House, Norwood, MA).
Ye, Z., and Hoskinson, E. (**1998**). ''Low-frequency acoustic scattering by gas-filled prolate spheroids in liquids. II. Comparison with the exact solution,'' J. Acoust. Soc. Am. **103**, 822–826.
Ye, Z., Hoskinson, E., Ding, L., and Farmer, D. M. (**1997**). ''A method for acoustic scattering by slender bodies. I. Theory and verification,'' J. Acoust. Soc. Am. **102**, 1964–1976.
Yeh, C. (**1967**). ''Scattering of acoustic waves by a penetrable prolate spheroid. I. Liquid prolate spheroid,'' J. Acoust. Soc. Am. **42**, 518–521.

Broadband acoustic backscatter and high-resolution morphology of fish: Measurement and modeling[a)]

D. Benjamin Reeder[b)]
Department of Applied Ocean Physics and Engineering, Woods Hole Oceanographic Institution, Woods Hole, Massachusetts 02543-1053

J. Michael Jech
NOAA/NMFS Northeast Fisheries Science Center, Woods Hole, Massachusetts 02543

Timothy K. Stanton
Department of Applied Ocean Physics and Engineering, Woods Hole Oceanographic Institution, Woods Hole, Massachusetts 02543-1053

(Received 28 May 2002; revised 31 October 2003; accepted 11 December 2003)

Broadband acoustic backscattering measurements, advanced high-resolution imaging of fish morphology using CT scans and phase-contrast x rays (in addition to traditional x rays), and associated scattering modeling using the images have been conducted involving alewife (*Alosa pseudoharengus*), a swimbladder-bearing fish. A greater-than-octave bandwidth (40–95 kHz) signal was used to insonify live, individual, adult alewife that were tethered while being rotated in 1-deg increments over all angles in two planes of rotation (lateral and dorsal/ventral). These data, in addition to providing the orientation dependence of the scattering over a continuous band of frequencies, were also used (after pulse compression) to identify dominant scattering features of the fish (including the skull and swimbladder). The x-ray and CT scan images of the swimbladder were digitized and incorporated into two scattering models: (1) Kirchhoff-ray mode (KRM) model [Clay and Horne, J. Acoust. Soc. Am. **96**, 1661–1668 (1994)] and (2) conformal-mapping-based Fourier matching method (FMM), which has recently been extended to finite-length bodies [Reeder and Stanton, J. Acoust. Soc. Am. **116**. 729–746 (2004)]. Comparisons between the scattering predictions and data demonstrate the utility of the CT scan imagery for use in scattering models, as it provided a means for rapidly and noninvasively measuring the fish morphology in three dimensions and at high resolution. In addition to further validation of the KRM model, the potential of the new FMM formulation was demonstrated, which is a versatile approach, valid over a wide range of shapes, all frequencies and all angles of orientation.
[DOI: 10.1121/1.1648318]

PACS numbers: 43.30.Sf, 43.30.Ft, 43.30.Xm [WMC] Pages: 747–761

I. INTRODUCTION

Acoustic methods have long been used to rapidly and synoptically survey marine organisms of ecological and economic importance. These methods complement traditional methods such as direct sampling with nets. Direct sampling furnishes biological data such as abundance, biomass, direct measurements of organism size and species identification, but encounters problems such as net avoidance, small sampling volumes, and catch destruction of delicate specimens. Acoustically surveying the organisms could avoid these problems, particularly in the case of large-scale synoptic surveys that require high-resolution data (Gunderson, 1993; Medwin and Clay, 1998). Since acoustic sampling does not directly produce biological data, inference of biological information from acoustic scattering by marine organisms requires an understanding of the process by which those organisms scatter sound.

Understanding the scattering mechanisms of fish is a challenge due to the fact that fish anatomy is complex and the acoustic scattering characteristics are correspondingly complex. For example, Nash *et al.* (1987) qualitatively illustrated the influence of the various anatomical components of fish on scattering by performing length-wise acoustic scans of whole fish, dissected swimbladders, and heads and vertebrae (Fig. 1). Given the complexities of the scattering characteristics of marine organisms as illustrated in that and a variety of other studies, detailed investigations must be made into the scattering mechanisms of the animals in order to determine and decipher the extent to which the various anatomical features contribute to the overall scattering characteristics. Studies must consist of careful, accurate measure-

[a)]Parts of this work were first presented at the Fall 2000 meeting of the Acoustical Society of America, 2001 Institute of Acoustics Conference on Acoustical Oceanography, and 2002 6th ICES Symposium on Acoustics in Fisheries and Aquatic Ecology. Certain results were summarized in the symposium proceedings papers: Stanton *et al.* (**2001**). ''Broadband acoustic classification of individual zooplankton and fish: A review of recent work,'' in Proceedings of the Institute of Acoustics Conference on Acoustical Oceanography (April), 181–188. Reeder, D. B., Jech, J. M., and Stanton, T. K. (**2002**). ''Broadband acoustic backscatter and high resolution morphology of fish: Measurements and scattering models,'' in Proceedings of the 6th ICES symposium on Acoustics in Fisheries and Aquatic Ecology (June). Paper #101 (3 pages).

[b)]Current address: Department of Oceanography, Naval Postgraduate School, Monterey, CA.

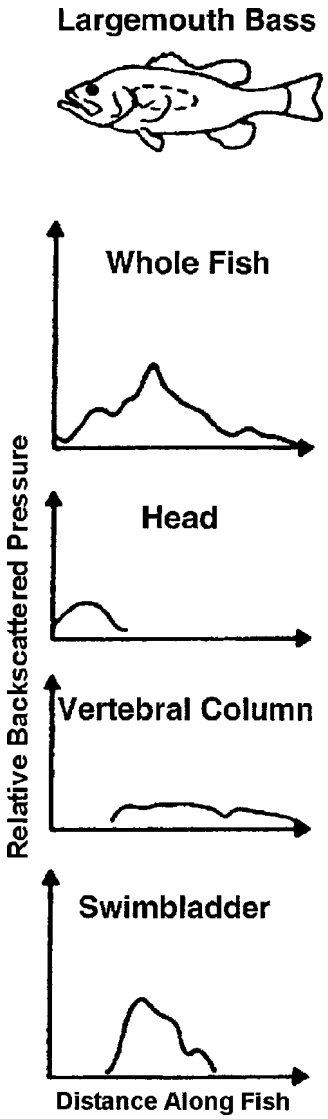

FIG. 1. Relative acoustic pressure as recorded along the length for a largemouth bass showing relative scattering contributions by the whole fish, head, vertebral column, and swimbladder. This qualitative illustration of the dependence of fish target strength on changes in morphology was generated through the use, in a laboratory, of a focused array transducer system that scanned the length of the fish at 220 kHz in the near field. Adapted from Nash *et al.* (1987).

ment of the acoustic scattering and associated modeling to effectively elucidate these mechanisms. Due to the large number of organisms that exist in the ocean, it is not possible to study scattering by all species; however, organisms can generally be categorized according to morphological groups. For example, fish can be categorized by morphological characteristics, such as size, shape, and the presence or absence of swimbladders (Foote, 2001). Regarding zooplankton, Stanton *et al.* (1994, 1998a, 1998b) identified three major categories: fluid-like (e.g., euphausiids, shrimp, copepods), gas inclusions (e.g., siphonophores), and elastic shells (e.g., pteropods).

A significant amount of research has been directed to date toward measurements and modeling of acoustic scattering by fish. The reader is referred to reviews in Foote (1997) and Medwin and Clay (1998) for a summary of the work. Most of the measurements performed have involved backscattering at single frequencies (or more precisely, frequencies within a narrow band). Much of the quantitative descriptions of the scattering has been through empirical target-strength/length relationships determined from the experiments. Although these have proven to be successful in many survey operations involving common fish species, the relationships are not predictive—that is, they cannot be applied directly to other types of fish. Various analytical and numerical models of the scattering have also been developed that are predictive. Each model is limited with respect to frequency range, class of surfaces, types of boundary conditions, eccentricity of shape, and/or numerical efficiency. These models generally include only the swimbladder as the dominant scatterer. While exclusion of all other body parts generally works well for angles of incidence near the main lobe of scattering (i.e., angles near normal incidence to the surface of the swimbladder), there is a potential for the models to underpredict the scattering for angles well away from the main lobe where the other organs may contribute significantly to the echo. Finally, model parameters of the swimbladder have normally been determined directly (through dissection and measurement) or through traditional x rays. The methods of dissection are normally quite tedious and time consuming, while the x-ray method only provides information in a single plane of projection.

As shown in the above studies, successful use of acoustics in ocean observations requires accurate scattering models for each category of animal, testing and refinement of the models through accurate, extensive measurements of scattering from fish, and reliable algorithms for numerical implementation of the models. Very importantly, advanced scattering models must include scatterer shapes that closely resemble the dominant scattering features within the fish. This information requires high-resolution morphological measurements of the fish to be made. Another important requirement is that the acoustic scattering measurements be conducted over a wide range of frequencies, preferably with continuous coverage over the frequency band.

In spite of the need for broad spectral coverage, the majority of acoustic measurements on fish is in terms of target strengths at single frequencies. Although this level of information has been proven to be very useful for certain applications, such as fishery population estimates, traditional target strength measurements lack spectral coverage for rigorous model development. Specifically, narrow-band measurements are limited to discrete frequencies which restrict the ability to measure frequency-dependent scattering mechanisms, although this has been addressed, in part, by the use of multiple discrete frequencies. Since an animal's scattering properties vary considerably with the frequency of the transmitted signal, the use of broadband transducers offers continuous coverage over a significant range of frequencies, thus increasing the amount of information contained in the signal. Furthermore, the broadband signals inherently have high temporal resolution (which varies with inverse bandwidth of the transmitted signal) which can be realized through the use of an impulse signal or pulse compression of

a longer signal (Chu and Stanton, 1998). With high temporal resolution, scattering features can possibly be resolved in time and identified. In spite of the great advantages of broadband signals, relatively few studies have investigated and/or exploited the animal's spectral characteristics (Holliday, 1972; Kjaergaard *et al.*, 1990; Simmonds and Armstrong, 1990; Zakharia, 1990; Bondarenko *et al.*, 1990; Simmonds *et al.*, 1996; Zakharia *et al.*, 1996; Au and Benoit-Bird, 2003).

The need for broadband acoustic measurements and advanced scattering models that incorporate high-resolution morphology is addressed in this study. Extensive broadband acoustic measurements were conducted on live, adult alewife (*Alosa pseudoharengus*), which were tethered while being rotated in 1-deg increments of orientation angle over all angles in two planes of rotation (lateral and dorsal/ventral). Spectral and time-domain analyses identify dominant scattering features and demonstrate the extent to which the scattering depends on size, shape, acoustic frequency, and orientation angle. Traditional x rays and advanced techniques involving computerized tomography (CT) scans were used to rapidly and noninvasively image the anatomy of the fish so that digitizations of swimbladder shape could be incorporated into two scattering models—the KRM (Kirchhoff-ray-mode) model using traditional x rays (Clay and Horne, 1994), as well as a newly developed scattering formulation, the Fourier matching method (FMM) for axisymmetric finite-length bodies [Reeder and Stanton, J. Acoust. Soc. Am. **116**, 729–746 (2004)]. The KRM model was chosen principally because it is based on the Kirchhoff-based modeling of the swimbladder, which has been quite successful in previous investigations. This approach has the additional capability of accounting, to some degree, the scattering by the fish flesh. The FMM formulation, which incorporated the CT scan images, is a versatile, numerically efficient model applicable over a wide range of shapes, all angles, and all frequencies. It was chosen in this study as a first test against experimental data and for intercomparison with the Kirchhoff calculations. Predictions by the two scattering models, using the morphological information, are compared to the acoustical backscattering laboratory measurements of the alewife. This study represents both a first use of CT-scan technology for comparisons between models and data as well as a first experimental investigation of the FMM model for use in predicting scattering by fish.

This paper is organized as follows. In Sec. II, basic descriptions of target strength and pulse compression (PC) processing of broadband signals are given, followed by a synopsis of the Kirchhoff-ray mode and Fourier matching method models. In Sec. III, the laboratory setup, methods used for data collection, and measurements of animal morphology are presented. Acoustic scattering results are presented in Sec. IV. Comparisons between model predictions and measurements are made in Sec. V, followed by a discussion and conclusions in Sec. VI.

II. THEORY

A. Definitions

The far-field scattered sound wave is expressed as

$$P^{\text{scat}} \underset{r\to\infty}{\longrightarrow} P^{\text{inc}} \frac{e^{ikr}}{r} f, \tag{1}$$

where P^{inc} is the pressure amplitude of the acoustic wave incident upon the object, r is the distance between the object and receiver, k ($=2\pi/\lambda$, where λ=wavelength) is the acoustic wave number of the incident field, and f is the scattering amplitude. The far-field scattering characteristics of the object are fully described by the scattering amplitude. Given the sometimes large dynamic range of the scattering amplitude, it is often expressed in logarithmic terms for the case of backscatter as target strength (TS), expressed in units of decibels (dB) relative to 1 m (Urick, 1983)

$$\text{TS} = 10\log_{10}|f_{\text{bs}}|^2 = 10\log_{10}\sigma_{\text{bs}}, \tag{2}$$

where $\sigma_{\text{bs}} \equiv |f_{\text{bs}}|^2$ is the differential backscattering cross section and differs from the often-used backscattering cross section, σ, by a factor of 4π ($\sigma = 4\pi\sigma_{\text{bs}}$). The term, f_{bs}, is the scattering amplitude evaluated in the backscatter direction. Target strength is often normalized by the square of some typical dimension to give the somewhat arbitrarily defined reduced target strength (RTS)

$$\text{RTS} = 10\log_{10}\left|\frac{\sigma_{\text{bs}}}{L^2}\right| = 10\log_{10}|f_{\text{bs}}|^2 - 10\log_{10}L^2, \tag{3}$$

where L is, in the case of elongated scatterers, the length of the scattering object. In the case of a sphere, the target strength is often normalized by πa^2 instead of L^2, where a is the radius of the sphere. The average target strength is expressed in terms of the value of the average backscattering cross section

$$\langle \text{TS} \rangle = 10\log_{10}\langle \sigma_{\text{bs}} \rangle, \tag{4}$$

where the average in this study, denoted $\langle ... \rangle$, is performed over the frequency band and before the logarithm operation is performed.

B. Pulse compression

In order to resolve major scattering features such as the skull and swimbladder of the fish, the received signal is compressed in time by cross correlating the echo with the received calibration signal. The result is a short, high-amplitude signal with increased signal-to-noise ratio (SNR). This type of process is particularly effective for long, wideband signals such as those used in this study. This approach is similar to the commonly used matched filter that involves cross correlating the received signal plus noise with the original signal without the noise (Turin, 1960). In the case of scattering from marine organisms, however, the exact scattering characteristics of the animal are not known; therefore, the ''replicate'' signal (corresponding to the signal without the noise) used in the correlation process for a true matched

filter, is not known. Chu and Stanton (1998) suggested using a different signal in the cross correlation: the received signal obtained during calibration. This modified matched-filter process is referred to as pulse compression and its output is referred to as the compressed pulse output (CPO). The resultant output is a series of echoes, corresponding to the dominant scattering features of the target.

C. Models

Two scattering models that are valid for elongated scatterers and for a wide range of frequencies and orientations are used to compare with the experimental data: the Kirchhoff-ray mode (KRM) model which has previously been applied to fish and the newly developed Fourier matching method (FMM).

1. KRM

The Kirchhoff-ray mode (KRM) model has been used to compute the scattering from fish with a hybrid approach by predicting the scattering by the swimbladder in the low-ka region (where a is the cylindrical radius of the swimbladder) with a monopole ($m=0$) mode to a cylinder solution and predicting the scattering by the swimbladder and fish body in the high-ka region with the Kirchhoff, or ''ray,'' approximation (Clay, 1991, 1992; Clay and Horne, 1994). For both components of the solution, the scattering object is approximated by a series of 1-mm-long cylindrical elements constructed from the digitized shape of the body and swimbladder using traditional x-ray images. The cross-sectional radius, a, is half of the width of each cylindrical element.

For the swimbladder scattering in the low-ka region ($ka \leqslant 0.15$), the cylindrical monopole solution is written as the sum of the scatter from N_e elements

$$f_{\mathrm{bs}}^{(\mathrm{sb})} = \frac{-i}{\pi} \sum_{j=1}^{N_e} b_0 e^{-i2kv(j)} dx(j), \quad (ka \leqslant 0.15), \tag{5}$$

where $f_{\mathrm{bs}}^{(\mathrm{sb})}$ is the backscattering amplitude as a function of frequency [notation of S_A in Clay (1991) is replaced by $f_{\mathrm{bs}}^{(\mathrm{sb})}$], b_0 is the zero-order mode scattering coefficient, $v(j)$ is the displacement of the central axis of the fish from a straight line, and dx is the incremental distance along the length of the object. The term b_0 accounts for the swimbladder resonance, although absorption is not included (Clay, 1991).

For the swimbladder scattering in the high-ka region ($ka > 0.15$), the Kirchhoff ray approximation is used. An equation similar in form to the above equation is used to sum the backscattered rays from N_e swimbladder elements

$$f_{\mathrm{bs}}^{(\mathrm{sb})} = -i \frac{R_{\mathrm{fs}}(1-R_{\mathrm{wf}}^2)}{2\sqrt{\pi}} \sum_{j=0}^{N_e-1} A_{\mathrm{sb}} (k_{\mathrm{fb}} a(j)+1)^{1/2} \times e^{-i(2k_{\mathrm{fb}} v_U(j)+\Psi_{\mathrm{sb}})} dx(j), \quad (ka > 0.15), \tag{6}$$

where R is a reflection coefficient, U and L indicate the upper and lower surfaces, wf refers to the water–fish interface, fs denotes the swimbladder–fish body interface, fb denotes the fish body, sb refers to the swimbladder, and A_{sb} and Ψ are previously determined empirical amplitude and phase adjustments for small ka (Clay and Horne, 1994).

A similar expression using the Kirchhoff approximation describes the scattering for the fish body in the high-ka region ($ka > 0.15$)

$$f_{\mathrm{bs}}^{(\mathrm{fb})} = -i \frac{R_{\mathrm{wf}}}{2\sqrt{\pi}} \sum_{j=0}^{N_e-1} \{(ka(j))^{1/2} [e^{-i2kv_U(j)} - (1-R_{\mathrm{wf}}^2) e^{i(-2kv_U(j)+2k_{\mathrm{fb}}(v_U(j)-v_L(j))+\Psi_{\mathrm{fb}})}] \times dx(j)\}, \quad (ka > 0.15), \tag{7}$$

where a is now one-half the width of the fish body. The water-body density contrast and sound-speed contrast are 1.08 and 1.075, respectively [modified from Clay and Horne (1994) for freshwater].

The total scattering from the fish is given as

$$f_{\mathrm{bs}}^{(\mathrm{tot})} = f_{\mathrm{bs}}^{(\mathrm{sb})}, \quad (ka \leqslant 0.15), \tag{8}$$

$$= f_{\mathrm{bs}}^{(\mathrm{sb})} + f_{\mathrm{bs}}^{(\mathrm{fb})}, \quad (ka > 0.15), \tag{9}$$

where the choice of expressions using either Eq. (5) or (6) for $f_{\mathrm{bs}}^{(\mathrm{sb})}$ is implicit in Eqs. (8) and (9) and depends on the particular value of ka.

2. FMM

The Fourier matching method (FMM) used herein to describe the scattering by the swimbladder involves the use of a two-dimensional conformal mapping approach to describe scattering by axisymmetric, irregular, finite-length bodies of revolution [Reeder and Stanton, J. Acoust. Soc. Am. **116**, 729–746)]. The model conformally maps the coordinate variables of the original coordinate system to a new orthogonal coordinate system in which the new radial coordinate being a constant exactly coincides with the scatterer surface. The solutions to the transformed Helmholtz equation are a general solution for the total pressure in the case of far-field scattering by a finite body of revolution. This model has been shown to be very accurate (i.e., generally well within 1 dB of the exact solution) in the prediction of scattering by smooth, symmetric bodies for a wide range of frequencies (resonance in the Rayleigh region through the geometric scattering region), scattering angles (monostatic and bistatic), aspect ratios, and boundary conditions. In the case of irregular, realistic shapes, there is consistency between the trends as well as some of the values predicted by the Kirchhoff approximation and the FMM-based calculations [Reeder and Stanton, J. Acoust. Soc. Am. **116**, 729–746 (2004)].

Using a conformal mapping function of the form

$$G(\rho) = c_{-1} e^{\rho} + \sum_{n=0}^{\infty} c_n e^{-np}, \tag{10}$$

where c_n are the conformal mapping coefficients determined by solving a system of nonlinear constraints using the Newton–Raphson method, the coordinate system is mapped to a new, orthogonal coordinate system in which the constant radial coordinate exactly coincides with the scatterer surface (in this case, an approximation to the swimbladder outer boundary). The scattering amplitude in the new coordinate system is

$$f = \sum_{n=-\infty}^{\infty} \sum_{m=-\infty}^{\infty} b_{nm} i^{-n-1} P_n^m \left(\frac{g(u,w)}{r(u,w)} \right) e^{im v}, \qquad (11)$$

where b_{nm} are the far-field scattering coefficients that depend on the shape and material properties of the scatterer, P_n^m is the associated Legendre function, $r(u,w)$ is the new radial coordinate, and $g(u,w)$ is a function of the new system. The far-field scattering coefficients, b_{nm}, are determined after solving the transformed Helmholtz equation and satisfying the boundary conditions at the surface of the scatterer. Details and definitions of the parameters are in Reeder and Stanton, J. Acoust. Soc. Am. **116**, 729–746 (2004).

The FMM results presented here are based upon the scattering by the swimbladder alone—they do not include the computation of scattering from the fish body. As a consequence, the FMM will expectedly underpredict the scattering. Furthermore, given the complex shape of the swimbladder, approximations had to be made in order to use the FMM model to predict the scattering. The challenge lies in the fact that the outer boundary of the swimbladder cannot be described in terms of a body of rotation. The problem was then broken up into three parts, concerning the dorsal, ventral, and side aspects separately using data from the CT scan. Details of the procedure are given in Sec. III B.

III. EXPERIMENTAL METHODS

Seventeen adult alewife were used in the acoustic backscattering measurements during May, 2000. The morphology of the fish was characterized through a combination of dissection and three radiographic technologies. The scattering measurements were performed on individual fish secured in a tether in a laboratory tank.

A. Animals

Alewife were chosen because they are readily caught and are similar to the commercially and ecologically important fish, Atlantic herring (*Clupea harengus*), in their body size, shape, and swimbladder construction (Fig. 2). Both alewife and Atlantic herring expand and contract their swimbladders primarily by transferring air via a pneumatic duct between their esophagus and swimbladder.

The fish were collected as they were migrating upstream to spawn in the freshwater ponds of Cape Cod, MA. The standard (caudal) lengths (measured from the nose to the end of the flesh near the tail) of these fish were quite uniform, averaging 22 cm. Their body weights averaged 144 grams. Since these fish were ready to spawn, their gonads were enlarged [Fig. 2(b)]. The males' gonads were approximately 10% of their body weight, while the females' gonads equaled as much as 15% of their body weight. The animals' physical dimensions and weights are summarized in Table I.

B. Morphometry of animal shapes: PCX and CT scans

In addition to visual inspection of the fish (both whole and in dissected form), the morphology was investigated through quantitative use of various radiograph technologies—traditional x rays, phase-contrast x rays (PCX), and computerized tomography (CT) scans. This study represents the first use of PCX and CT technologies in the comparison of model predictions with measured scattering data from fish (although note, CT scans have been used in the modeling of acoustic propagation within the head of a dolphin (Aroyan, 2001) and the modeling of acoustic scattering by fish (Macaulay, 2002)). Given the novelty of the approach, a progression of images will be shown for intercomparison, beginning with traditional photographic images and ending with images derived from a CT scan.

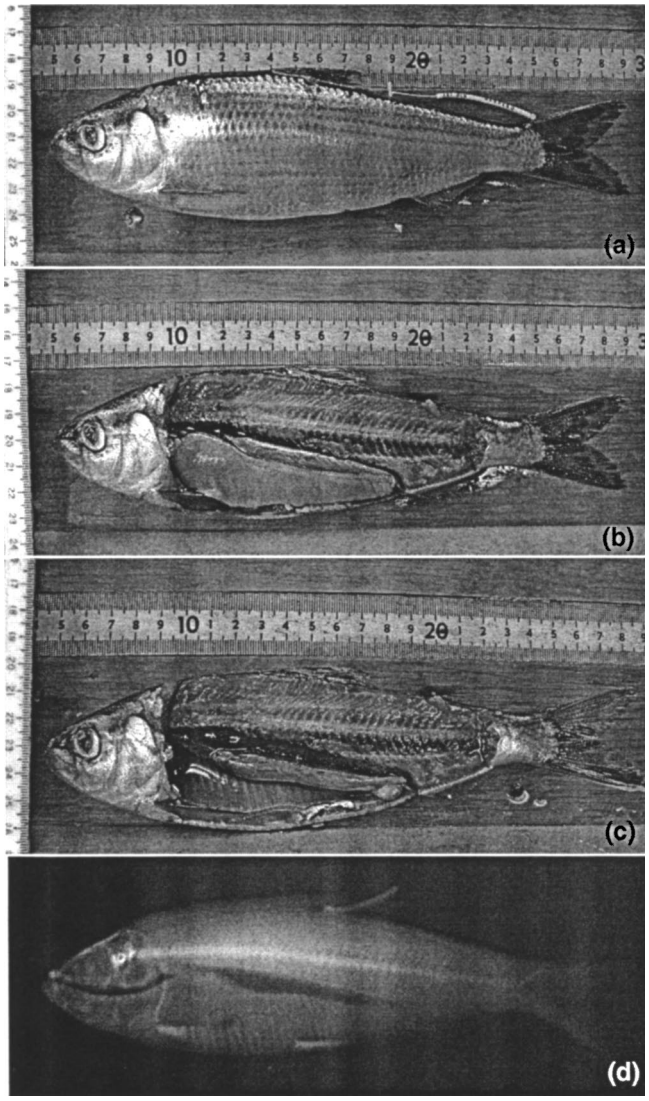

FIG. 2. Images of Alewife #18 used in the acoustic scattering experiments: (a) whole fish; (b) dissected fish showing enlarged gonads (large organ immediately below swimbladder); (c) dissected fish with gonads removed to expose the swimbladder; and (d) traditional x ray of whole fish showing (dark) outline of swimbladder. The fish were collected as they swam upstream to spawn in the freshwater ponds of Cape Cod, MA; consequently, their gonads were enlarged as seen in the images. All of the fish were adults with an average caudal length of 22 cm and an average body weight of 144 grams.

After the acoustic measurements were recorded, traditional x rays [Fig. 2(d)] of the fish were performed at the Falmouth Animal Hospital in N. Falmouth, Massachusetts. The (live) fish were anesthetized and in air during the procedure. These x-ray images, measured in both the dorsal/ventral and lateral planes, were later used to generate hand-

TABLE I. Dimensions, weights, and use (yes/no) of acoustic, (traditional) x-ray, and dissection techniques for each of the alewife used in the acoustic scattering measurements. Total length (TL) is the distance from the nose to the tip of the tail. Caudal (standard) length (CL) is the distance from the nose to the end of the flesh near the tail. PCX imaging was performed on Alewife #25. CT scans were performed on Alewife #3 (not listed). Asterisks indicate cases in which gender was not determined.

Animal desig	Animal tag #	Gender	TL (mm)	CL (mm)	Height (mm)	Width (mm)	Weight (g)	Acoustic:X-ray:Dissection
10	152	F	259	215	59.7	25.2	159	Yes:No:Yes
11	153	M	255	217	52.4	21.3	120	Yes:No:Yes
12	154	M	255	225	54.3	23.8	133	Yes:Yes:Yes
13	155	F	268	225	60.8	27.3	172	Yes:Yes:Yes
14	156	M	258	220	59.0	26.0	151	Yes:Yes:Yes
15	157	F	256	216	54.7	23.0	135	Yes:Yes:Yes
16	158	M	260	220	62.8	25.8	168	Yes:Yes:Yes
17	159	F	244	215	59.4	22.8	120	Yes:Yes:Yes
18	160	M	241	200	59.7	23.7	121	Yes:Yes:Yes
19	161	M	257	217	56.7	24.5	141	Yes:Yes:Yes
20	162	F	259	216	63.5	26.1	165	Yes:Yes:Yes
21	163	M	254	217	59.6	24.0	147	Yes:Yes:Yes
22	164	*	254	223	56.6	24.7	148	Yes:Yes:No
23	165	F	277	235	56.4	23.3	150	Yes:Yes:Yes
24	166	F	255	217	57.0	23.8	139	Yes:Yes:Yes
25	167	*	250	213	50.9	22.2	116	Yes:Yes:No
26	168	*	265	225	56.5	26.0	157	Yes:Yes:No

traced digitized objects of the swimbladder and fish body for use in the KRM model as described in Jech and Horne (2002).

Traditional x rays are gray-scale images produced on a film that is sensitive to the amplitude of energy absorbed by an object. However, x rays change not only in amplitude, but also in phase as the material distorts the wave as it passes through the material. Traditional x-ray imagery ignores this distortion, yet the newly developed PCX process captures these phase changes, resulting in a high-resolution image that contains much finer detail than traditional x-ray images (Wilkins *et al.*, 1996; Davis and Stevenson, 1996; Gureyev *et al.*, 2000). PCX imaging, performed on an alewife at the Commonwealth Scientific and Industrial Research Organization (CSIRO) in Melbourne, Australia, is sensitive to, and illustrates well, the small-scale anatomical features of alewife such as fins, ribs, striations in muscle tissue, gills, and weakly scattering soft tissue (Fig. 3). Such high-resolution imagery dramatically aids the determination of the scattering features in fish.

Additionally, high-resolution computerized tomography (CT) scans were performed on an alewife at the Falmouth Hospital in Falmouth, Massachusetts (Fig. 4). The (live) alewife was anesthetized and in air during the procedure. The CT scans are an efficient and noninvasive method of producing high-resolution three-dimensional images of fish. This method is in contrast to the direct, but time-consuming, method of microtoming (Foote, 1985; Ona, 1990). The images produced by the scans were used to generate a three-dimensional digital object of the swimbladder to be incorporated into the FMM scattering model. These data especially helped in determining the radius of curvature of each cross-sectional slice—an important element of the FMM model. The alewife was scanned along the longitudinal axis of the animal, producing 112 images 2 mm apart. ''Slices'' of the fish were created to examine the morphology of the animal

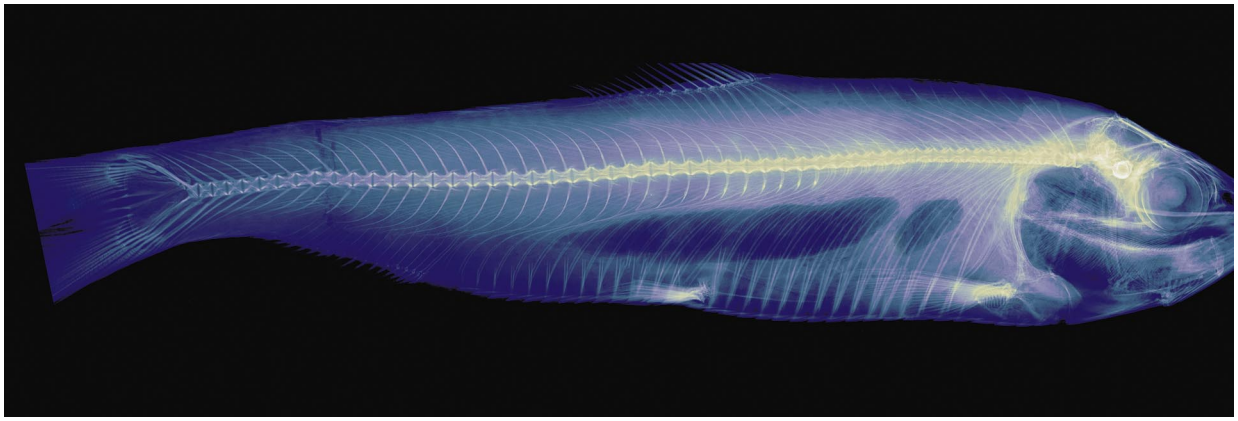

FIG. 3. Phase-contrast x ray (PCX) of Alewife #25. Imaging was performed at the Commonwealth Scientific and Industrial Research Organization (CSIRO) in Melbourne, Australia. The PCX process is an extremely high-resolution imaging technique which is sensitive to weakly scattering body tissue. Slight morphological details can be detected, such as the gills, fins, ribs, striations in the muscle tissue, gonads, and gut (Andrew Stevenson, personal communication, 2002).

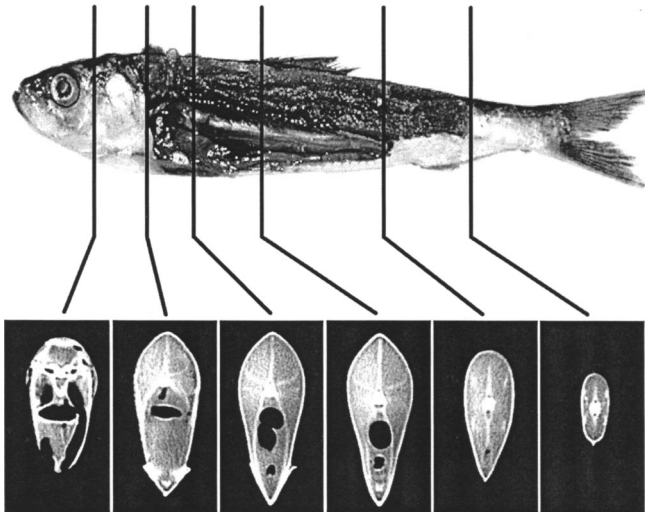

FIG. 4. High-resolution computerized tomography (CT) scan images of Alewife #3 (length of 24.2 cm; not listed in Table I) with their placement indicated along the fish body. The black areas within the cross-sectional slices include the swimbladder and gas inclusions in the gut, which is connected to the esophagus near the head. The vertebral column and muscle tissue can also be seen in the images.

in each cross section. The original CT images contained 500 ×900 pixels, but were then cropped (referenced to a common pixel to maintain accurate physical proportions) for ease of numerical manipulation. The CT images were then converted to a three-dimensional binary matrix, each element of which contained a "1" for each element of the original matrix whose value was above a certain threshold. Using this approach, a three-dimensional digital object of the fish was produced (Fig. 5, upper panel). A wire-cage diagram of the fish body was then created to better illustrate the exact physical morphology of the fish and its swimbladder (Fig. 5, lower panel). Coordinate points were then extracted from the top, bottom, and side boundaries of the digital object of the swimbladder.

Each of the three boundaries was rotated about an axis to form three bodies of revolution to separately model the scattering in the two planes—dorsal/ventral and lateral. There are two models associated with the dorsal/ventral plane—one for the dorsal aspect and the other for the ventral aspect. For the ventral and lateral models, the axis of rotation was simply the straight line between the two outermost points at the (front and back) ends of the swimbladder. However, given the straight profile of the dorsal side of the swimbladder (Fig. 5, lower panel), this approach produced unrealistically small cross-sectional slices which significantly underpredicted the scattering. This difficulty was remedied by choosing an axis that passes through the center of the middle section of the swimbladder, resulting in realistic values of cross-sectional radii. Once the surfaces were constructed, the points were used by the FMM to conformally map each of the three swimbladder shapes into a new coordinate system in which the new radial coordinate exactly matches the surface of the body.

C. Acoustic data acquisition

The acoustic backscattering measurements were conducted in a large freshwater tank at Benthos, Inc. in North

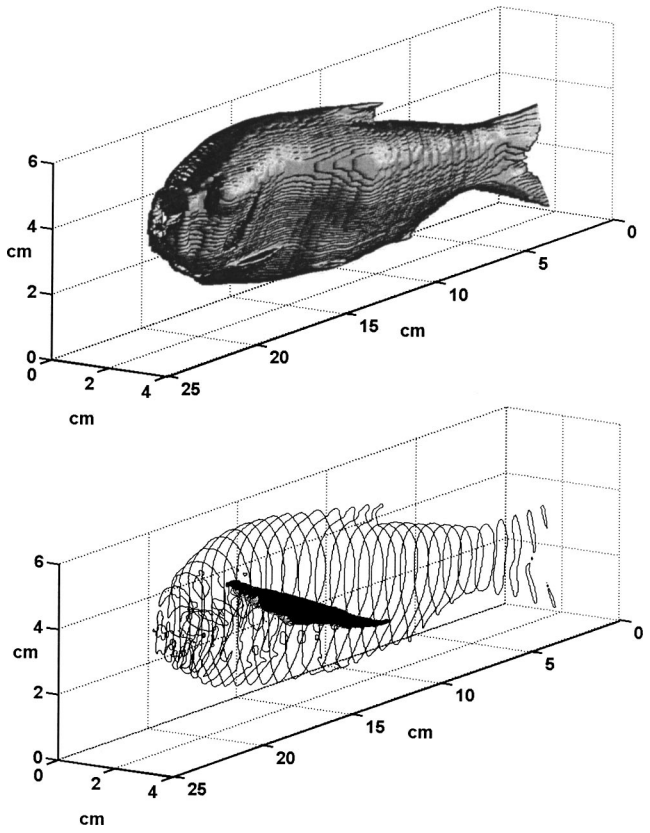

FIG. 5. Three-dimensional digital objects generated from CT scan imagery: whole fish (upper panel) and wire-cage diagram of fish body with swimbladder object inside (lower panel). The 112 images generated during the CT scan were processed by a digital image processing algorithm to generate the exact shapes to incorporate into the FMM for scattering predictions. The swimbladder image from the CT scan was quite distinct, and there were no issues in detecting and digitizing its outer boundary.

Falmouth, MA (Fig. 6). The experimental setup, similar in concept to that described in Stanton *et al.* (2000), included the use of a power amplifier, signal generator, a pair of transducers, preamplifier, bandpass filter, digital oscilloscope, and personal computer. The oscilloscope acquired all data at a 4-MHz sampling rate. All of these components, except for these particular transducers, were used in the experiment described in Stanton *et al.* (2000). During the measurements, the individual fish were secured in an acoustically transparent harness in the center of the acoustic beam and rotated. Although all animals were alive and in good condition at the beginning of each measurement, some died partway into the measurement. The data presented here are from nine data sets on three animals (15, 17, and 26), all of which remained alive for the entire measurement.

A pair of Reson TC2116 broadband acoustic transducers was mounted horizontally in the tank facing the fish in the tethering system, the center of which was attached to a computer-controlled stepper motor which rotated the assembly in 1° increments through two full rotations (720 pings per data set). The two transducers were identical and closely spaced, one used as the transmitter and one as the receiver, approximating a monostatic configuration. The use of two transducers allows closer scattering ranges, minimizes the effect of transmitter ringing, and makes the system easier to calibrate. The fish were insonified with a shaped chirp signal

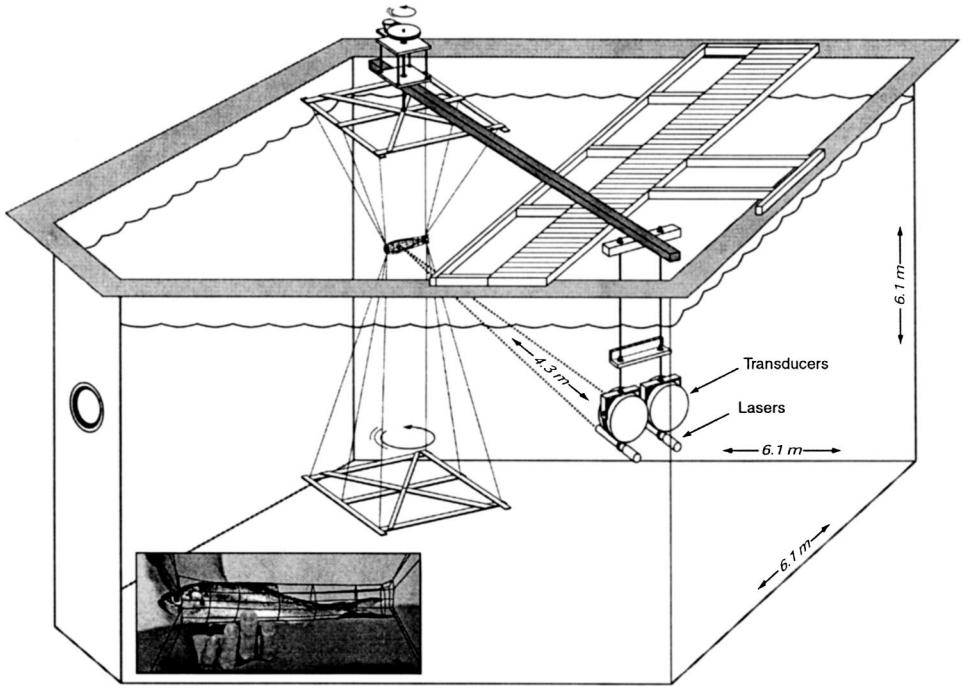

FIG. 6. Schematic of the laboratory system used for measuring acoustic backscattering by live, individual fish as a function of angle of orientation and frequency: tank, transducers, lasers used for alignment, stepper motor to rotate the animal in the acoustic beam, and acoustically transparent tether system. The transducers and rotation frame were drawn disproportionately larger than the tank to highlight them. Also, the photograph of the harness, shown in the inset, was enhanced so the thin monofilament could be illustrated.

with a usable frequency spectrum ranging from 40 to 95 kHz (Fig. 7). The transmitted signal was shaped to make the composite response of the transducer pair approximately uniform over the usable bandwidth. The transmitted voltage time series, $v_{\mathrm{bs}}^{T}(t)$, and the received voltage time series (the backscattered return echo from the animal), $v_{\mathrm{bs}}^{R}(t)$, were stored on a personal computer for later analysis. The beamwidth of each transducer at the intermediate frequencies was approximately 14°.

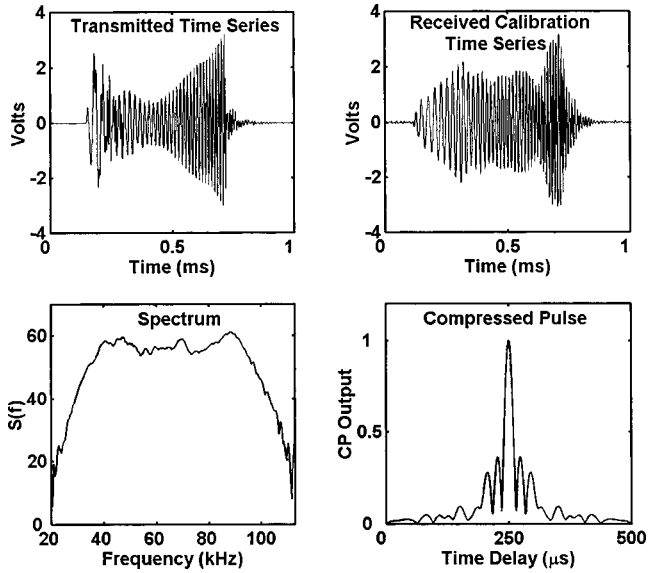

FIG. 7. Broadband chirp signals: (upper left panel) shaped chirp signal as applied to the transmitting transducer and used during both the scattering experiment and calibration; (upper right panel) signal as measured at the output of receiving transducer in the calibration setup with the transmitting transducer facing the receiving transducer; (lower left panel) frequency spectrum of received calibration signal; and (lower right panel) envelope of autocorrelation function (compressed pulse) of the received calibration signal which corresponds to matched filter output. The transmitted signal was shaped to flatten the composite response of the transducer pair across the frequency band of 40–95 kHz. The received calibration signal was stored for later use in the analysis to generate absolute target strengths on a ping-by-ping basis. The normalized compressed pulse output has sidelobes which are numerical processing artifacts with maximum peaks of 0.365. These sidelobes can introduce spurious artificial echoes in the analysis which must be taken into account during interpretation of scattering features.

The tethering system consisted of a specially designed, handmade harness (Fig. 6, inset) made of 4-lb. test fishing line suspended in the tank by six lines to a frame mounted just above the surface of the water and by six lines to a frame near the bottom of the tank. The harness was designed to hold the fish in the center of the acoustic beam and at a constant range ($r_{\mathrm{bs}}=4.3\,\mathrm{m}$) from the transducers as the fish was rotated. The harness uses the least amount of material possible so as to minimize any echoes that might interfere with the experiment. The echoes from the harness could not be detected above the background noise level. The harness was also designed to provide just enough restriction to prevent escape while allowing the fish to move as freely as possible to minimize stress. The harness has six longitudinal lines, one on the top, one on the bottom, and two along each side. The vertical members of the harness are spaced more closely together near the head of the fish to prevent escape, and spaced farther apart toward the rear of the fish to allow for freedom of movement. The vertical members near the gills are spaced so as not to restrict the gills. The harness has a cinch at the front that is tightened before the fish is slipped head-first into the harness. Once the experiment is complete, the cinch is loosened and the fish can be removed by slipping it forward through the front of the harness, avoiding damage to the fins and scales of the fish. The lines to each of the points on the top and bottom frames can be used to adjust the precise position of the harness in the tank. The bottom frame is suspended just above the bottom of the tank by the six bottom lines so that it is outside of the acoustic beam but does not drag on the bottom of the tank.

Before each fish was placed in the tether, much attention was given to ensuring that the harness was located in the

center of the acoustic beam and was free of bubbles. Underwater lasers were mounted and aligned on the bottom of the transducers to aid in the alignment of the transducers (Fig. 6). Because of the narrow transducer beamwidths involved (averaging 14°), these lasers proved to be indispensable in the process of alignment. The tether system was adjusted so that when the fish was placed in the harness for measurement, the system would pivot about the approximate center of its swimbladder. To eliminate bubbles coalescing on the harness, all of the lines on the tethering system were thoroughly wetted and rubbed with a soap solution prior to measurement. This process was done each time the tethering system was taken out of the water for any reason. Additionally, a small amount of soap was applied to each transducer face before calibration and measurement to ensure good contact with the water and to minimize adherence of bubbles that could contaminate the acoustic signals.

The background reverberation of the tank was taken into account for the scattering measurements. The background reverberation signals (with no fish in the harness) were first summed over approximately 500 pings and the resultant (unwanted) coherent echo was then stored in the digital oscilloscope. While collecting backscattering signals from the fish, the stored background reverberation signal was subtracted from the echo in real time by the oscilloscope. The difference signal that was stored, $v_{\mathrm{bs}}^{R}(t)$, during the experiment consisted of the (time-gated) echo from the fish and random noise of the entire system. Given the scattering geometry and directionality of the transducers, echoes received from indirect paths (i.e., fish–boundary–transducer) were not a factor.

The system was carefully calibrated prior to each set of backscattering measurements following the pseudo-self-reciprocity calibration procedure referred to by Urick (1983) and given in detail by Stanton *et al.* (1998a). The system was calibrated by mounting the transducers such that they faced each other and were separated by a range of $r_{\mathrm{cal}}=4.3\,\mathrm{m}$. The shaped chirp, transmitted calibration $[v_{\mathrm{cal}}^{T}(t)]$ voltage signal and the average of hundreds of received $[v_{\mathrm{cal}}^{R}(t)]$ calibration voltages were stored on a computer and used later in order to calculate fish target strengths. The received calibration signal was also used in the pulse compression analysis discussed in Sec. II.

The calibration signal waveform was also used as the transmitter waveform in the scattering measurements. Through the above procedure, performing pulse-compression processing and relating the scattered echoes to absolute measures of target strength is straightforward. Only the composite response of the system is needed, and it appears in terms of transmit and receive voltages in the calibration equations as described below. That is, the absolute source level, receive sensitivity, and phase characteristics of the transducers are not required to be known separately in this approach.

Taking into account the calibration data, the magnitude of the scattering amplitude of the fish was computed for each ping

$$|f_{\mathrm{bs}}|=\frac{V_{\mathrm{bs}}^{R}}{V_{\mathrm{cal}}^{R}}\frac{V_{\mathrm{cal}}^{T}}{V_{\mathrm{bs}}^{T}}\frac{r_{\mathrm{bs}}^{2}}{r_{\mathrm{cal}}}, \tag{12}$$

where V_{bs}^{R}, V_{bs}^{T}, V_{cal}^{R}, and V_{cal}^{T} are the absolute values of the Fourier transforms of the bandpass filtered voltage signals v_{bs}^{R}, v_{bs}^{T}, v_{cal}^{R}, and v_{cal}^{T} (Fig. 7).

IV. EXPERIMENTAL RESULTS

The broadband signals have been analyzed in both the frequency and time domains. The orientation dependence of the scattering has been examined for each Fourier component of the signal, and the spectral and temporal patterns have been examined for every orientation angle. Given the great difference in shape of the swimbladder in the dorsal/ventral and lateral planes, the results from these different planes are analyzed.

A. Spectral domain

Acoustic backscattering strength was observed to be strongly dependent upon acoustic frequency and animal orientation (Figs. 8–11). These relationships are demonstrated in both planes of scattering—dorsal/ventral and lateral. Generally, the target strength is maximum near normal incidence to the swimbladder. Also, at fixed angles of orientation, the target strength varies with frequency, represented by a series of peaks and nulls (Fig. 11). All plots in this paper either at fixed frequency or versus frequency were a result of a Fourier transform of the broadband echo with a 488-Hz bandwidth.

The beamwidth of the main scattering lobes from the fish generally becomes more narrow with increasing frequency (Figs. 8–10). Ventral aspect scattering is generally less directional than corresponding dorsal aspects (Figs. 9 and 10).

B. Time domain

The compressed pulse output (CPO) shows separation of the echo into multiple highlights, apparently due to different dominant scattering features in the fish (Figs. 12–14). In order to analyze this in terms of the scattering, time of arrival has been converted into separation distances along the length of the fish. The overall separation and structure of the highlights in the CPO are a strong function of orientation angle. At normal incidence, there is generally a single, dominant peak. At oblique angles of incidence, multiple significant peaks are present in the received signal. The separation between the first and last arrivals tends to increase for angles away from normal incidence.

The concept of partial wave target strength (PWTS) was introduced by Chu and Stanton (1998) to characterize the contributions by various individual highlights or partial waves that make up the total backscattered signal from the animal. PWTS is achieved by partitioning, or time gating, the CPO to isolate scattering highlights of interest. The spectral characteristics of the PWTS features of these echoes are significantly different than that of the total signal (Figs. 15 and 16).

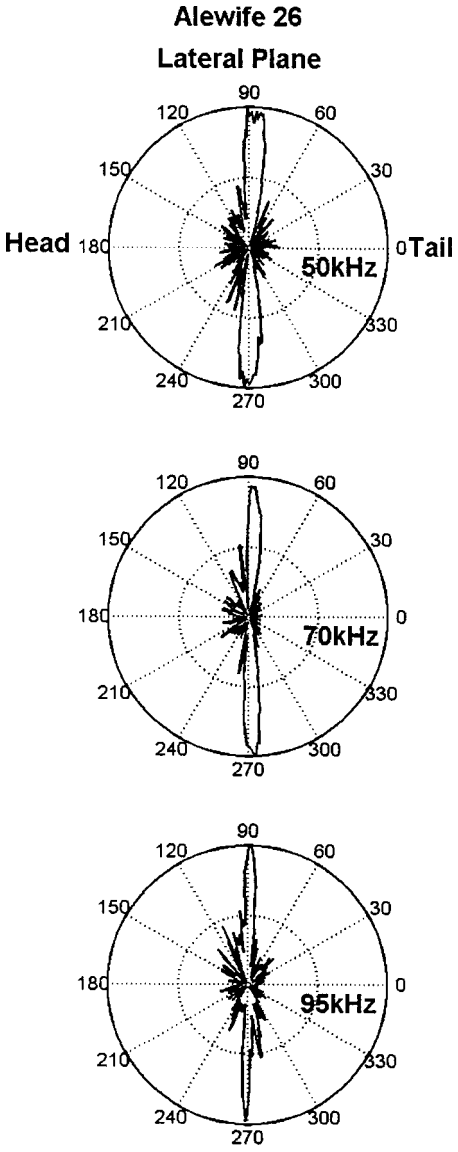

FIG. 8. Magnitude of backscattering amplitude as a function of angle as measured for Alewife 26 in the lateral plane at 50, 70, and 95 kHz. Each point plotted is from a single ping. Tail-on orientation corresponds to 0°. Each plot is on a linear scale, normalized to unity and based on a one-ping recording for each 1° increment of rotation. For example, the center circle represents scattering amplitudes with one-half the magnitude as those at the outer circle.

V. MODELING AND COMPARISON WITH DATA

A. Relating scattering features to fish anatomy

The dependencies of acoustic backscattering strength of the alewife on orientation, frequency, and morphology are clearly seen in the data. The narrow width of the main lobes indicated in Fig. 8 correlates to scattering from the relatively long, narrow swimbladder and body. The difference between dorsal and ventral scattering directivity in Figs. 9 and 10 is also consistent with an elongated shape that also possesses a difference in the curvature between the two sides [i.e., as illustrated in Figs. 2(d), 3, and 5, the ventral side of the swimbladder is more rounded in the length-wise direction than the dorsal side]. The pattern of peaks and nulls in Fig. 11 is consistent with constructive and destructive interference between multiple rays scattering from different parts of

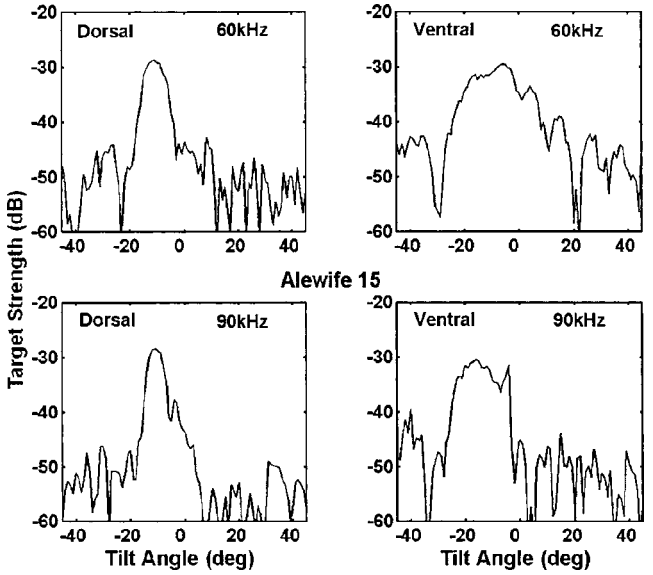

FIG. 9. Target strength as a function of angle of orientation as measured for Alewife 15 in the dorsal/ventral plane at 60 and 90 kHz. These data are single-ping realizations as described in the caption to Fig. 8. This coordinate system is different than that for Fig. 8, as it is in terms of the commonly used "tilt" angle of the fish body, relative to the horizontal plane. Zero degrees corresponds to normal incidence relative to the lengthwise body axis for the dorsal or ventral sides (left and right panels, respectively). For a free-swimming horizontally oriented fish, 0° dorsal and 0° ventral angles would correspond to a downward- and upward-looking acoustic transducer, respectively. The negative and positive tilt angles would correspond to head down and head up, respectively.

the body. The rays add constructively or destructively depending upon the location of the part of the body from which it is scattered, the frequency of the signal, and the angle of orientation in relation to the source/receiver transducer pair. Maximum target strength occurs near normal incidence, as these multiple arrivals are in phase (or nearly so) and add coherently to the total target strength. As the orientation moves away from normal incidence, the arrivals become

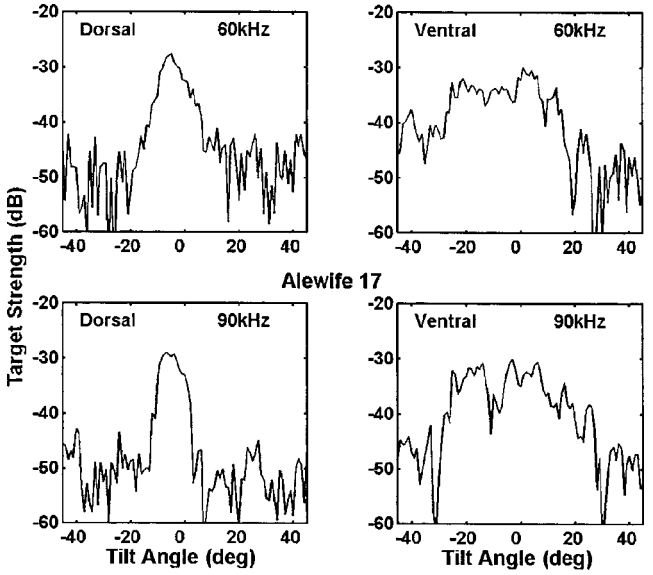

FIG. 10. Target strength as a function of angle of orientation as measured for Alewife 17 in the dorsal/ventral plane at 60 and 90 kHz. The plotting convention is the same as in Fig. 9.

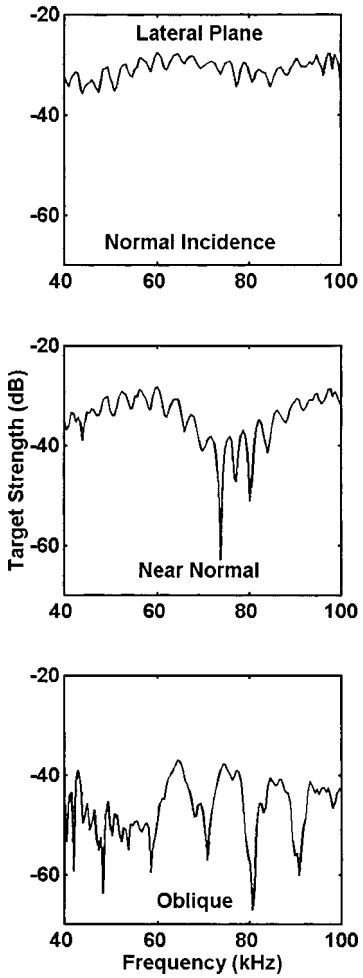

FIG. 11. Target strength as a function of frequency in the lateral plane as measured for Alewife 15 at broadside, near broadside, and oblique angles of incidence. These data are single-ping realizations. In this case, the oblique angle was 30° from end-on, or 60° from normal incidence. The near-normal incidence angle is 5° off normal.

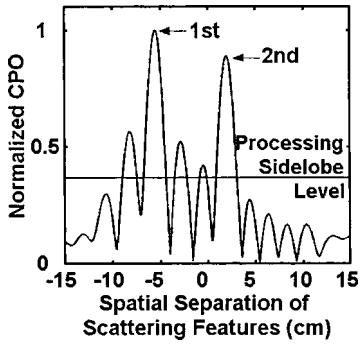

FIG. 12. Envelope of normalized compressed pulse output (CPO) for Alewife 15 at approximately 30° from tail-on orientation in the lateral plane (single-ping realization). The time delay on the horizontal axis has been converted to distance (cm) to represent the spatial separation between the scattering features of the fish, using the equation: separation $=$(time delay)$*c/(2\cos(\beta))$, where β is the angle of orientation relative to the transducer beam (as per polar plot in Fig. 8), and c is the speed of sound. The processing sidelobe is an artifact of the pulse compression process, as illustrated in Fig. 7; therefore, any peak significantly higher than the processing sidelobe level represents a physical arrival from the fish.

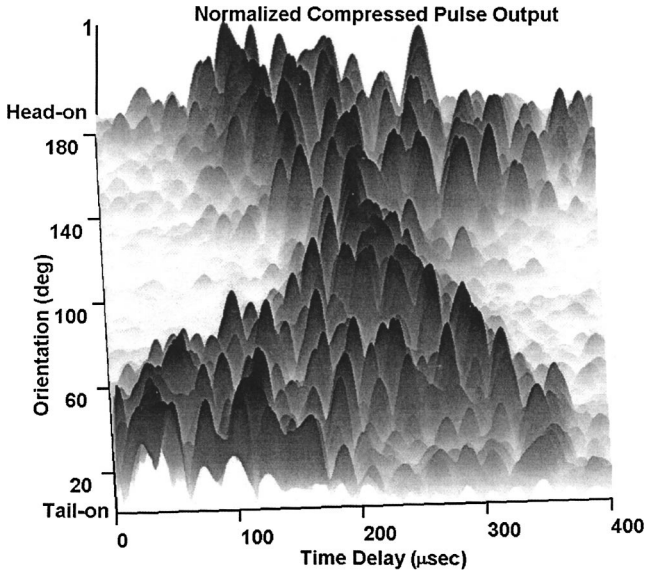

FIG. 13. Envelope of normalized CPO (contour plot) for Alewife 17 as a function of angle of orientation and time delay, depicting the changing CPO as the fish is rotated from tail-on through normal incidence to head-on orientation in the dorsal/ventral plane. Tail-on and head-on, in this case, correspond to scattering geometries when the direction of the incident acoustic signal is parallel to the lengthwise axis of the fish body, and incident upon the tail or head first, respectively (these directions also correspond to the 0° and 180° angles illustrated in Fig. 8). Each segment of the plot corresponding to each degree of rotation is the CPO from a single realization at that particular angle of orientation. Each segment is normalized to unity, so that the maximum value shown within each orientation value is unity. At angles near end-on, the individual arrivals are spread out in time, whereas at angles near normal incidence (approximately 90°), the individual rays return nearly simultaneously. In this latter case, the overall duration is at a minimum (again, near 90°), although an illusion from this plot is that the minimum occurs at a higher angle. Reduced echoes due to shadowing are evident for angles near end-on incidence toward the end of each time series (right side of upper and lower portions of plot). This pattern of extended duration of echoes away from normal incidence indicates the importance of the scattering by the various features of the fish along its entire length for angles well away from normal incidence.

well out of phase and add destructively at certain frequencies as evidenced by the one null and two broad peaks near normal incidence. At more oblique angles, the peaks and nulls are more closely spaced as constructive and destructive interferences occur at more frequencies within the band.

Through pulse-compression processing, the individual arrivals from different parts of the body (which apparently cause the interference patterns in the spectral plots) are resolved, resulting in several significant scattering features being extracted from the received signal (Fig. 12). The separation of the largest peaks correlates with the physical separation between the skull and swimbladder of the alewife used in the experiment.

The separation in time of the arrivals from individual scattering features in the fish as it rotated in the acoustic beam is illustrated in Fig. 13. At tail-on orientation, the scattering features nearest the tail scatter the incident wave first, followed by scattering from other features as the incident wave travels from tail to head. As the orientation moves toward normal incidence, the time separation between the partial waves decreases as the physical separation of the scattering features along the line between the transducers and fish decreases. As the orientation moves toward head-on, the

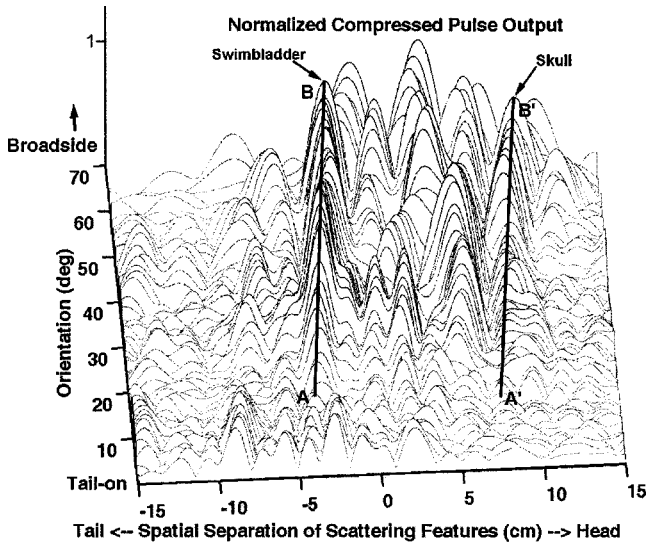

FIG. 14. Envelope of normalized CPO (''waterfall plot'') for Alewife 15 as a function of angle of orientation (single ping per orientation) and time delay converted to distance (along fish), depicting the changing CPO as the fish is rotated from tail-on to broadside orientation in the lateral plane. This figure is similar to Fig. 13, except that the conversion of time delay to distance allows better visualization of the scattering features and their changes as a function of angle of orientation. The conversion changes the appearance of the plot by making features parallel (or nearly so, as indicated by the two lines) instead of crossing as in Fig. 13. Lines AB and A′B′ correspond to echoes from the swimbladder and skull, respectively. Also, in contrast to Fig. 13, *all* values of the CPO are normalized by the same value (global maximum of data) so that directional effects can be better illustrated.

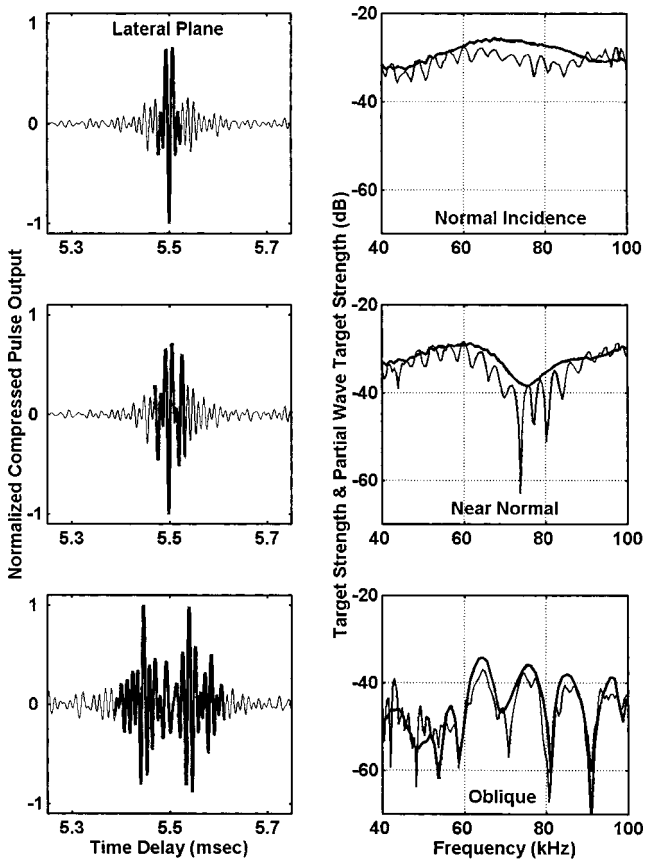

FIG. 15. Normalized CPO, target strength, and partial wave target strength (PWTS) of Alewife 15 at three different orientations (one ping per orientation) in the lateral plane. The plots on the right are TS (thin lines, taken directly from Fig. 11) computed from the whole time series and PWTS (thick lines) computed from the thick-lined (time-gated) portions of the time series on the left.

time separation increases again. The temporal distribution of the arrivals from different significant scatterers in the fish in Fig. 13 is apparent and is consistent with the physical separation of the anatomical features in the fish. In order to further elucidate the contributions of individual scatterers in the fish as a function of orientation, temporal separation is converted to spatial separation along the length-wise axis of the fish (Fig. 14). The arrivals nearest the beginning of the time series (line AB) and apparently from the swimbladder, are generally the most significant contributors to the overall scattering throughout the 90-deg rotation. The scattering near the end of the time series (line A′B′), is apparently from the skull. These two features (line AB and A′B′) correspond to a separation of approximately 12 cm, which is consistent with the distance between the back sides of the skull and swimbladder. The echo from the skull is initially shadowed by the body of the fish and cannot be detected acoustically (near point A′). As the fish is rotated toward normal incidence, the skull exits the acoustic shadow, and the amplitude of the arrival from the skull increases (near point B′). The arrivals that occur between the skull and swimbladder demonstrate complicated variable scattering features that are orientation dependent.

Partial wave target strength (PWTS) highlights the characteristics of selected portions of the backscattered signal and the interactions between multiple arrivals within the portion (Fig. 15). The constructive and destructive interferences between the multiple arrivals vary as the animal's orientation changes according to the separation (relative to the transducers) of the scattering features with respect to the wavelength of the sound. At normal incidence, the multiple arrivals are in phase (or nearly so) and add coherently, resulting in a relatively flat response over the band. As the orientation moves away from normal incidence, the arrivals add less coherently, causing the individual waves to add destructively at certain frequencies, which results in a series of peaks and nulls in the target strength over the frequency band. If the multiple arrivals are analyzed separately, the interference mechanism can be further elucidated (Fig. 16). The partial wave target strengths of the individual first and second major arrivals at oblique angles exhibit frequency responses that were smooth and relatively slowly varying compared with that of a combination of the two arrivals. This further illustrates the hypothesis that these resolved echoes are due to multiple singular scattering features which make significant contributions to the overall scattering.

B. Modeling the scattering

For all animals, it has been demonstrated experimentally that the acoustic backscattering is strongly dependent upon morphology, angle of orientation, and frequency. In an effort to quantify these dependencies, the FMM and KRM models were used for predictions of target strength vs angle to compare to the acoustic measurements of the alewife. Although, as shown above, there are several scattering features in the fish, the FMM predictions are based upon scattering from

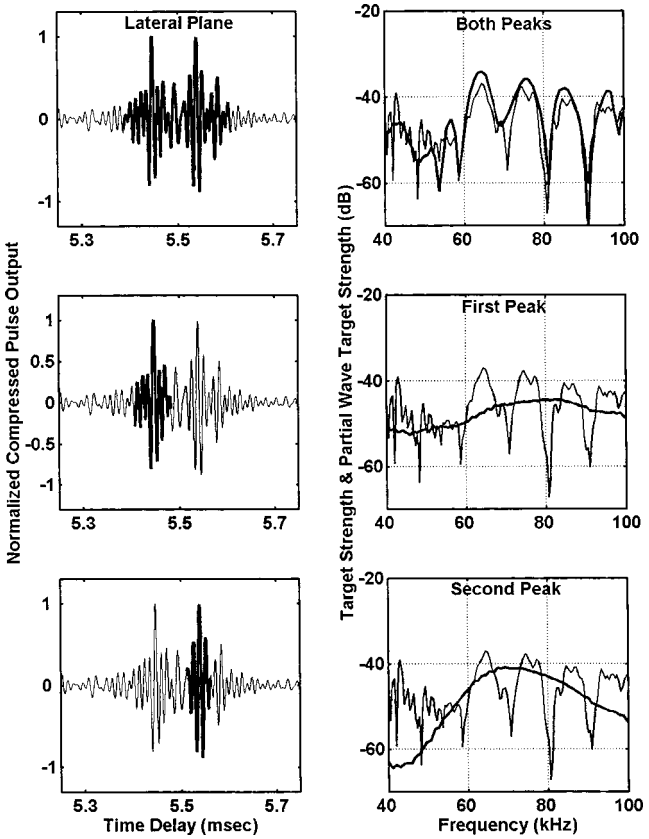

FIG. 16. Normalized CPO, target strength, and partial wave target strength (PWTS) for Alewife 15 in the lateral plane. All three pairs of panels are for the same oblique angle of orientation, but represent processing of different segments of the CPO. The top pair of plots is identical to the bottom pair of plots of Fig. 15 for reference, while the lower two rows illustrate the characteristics of the separate arrivals.

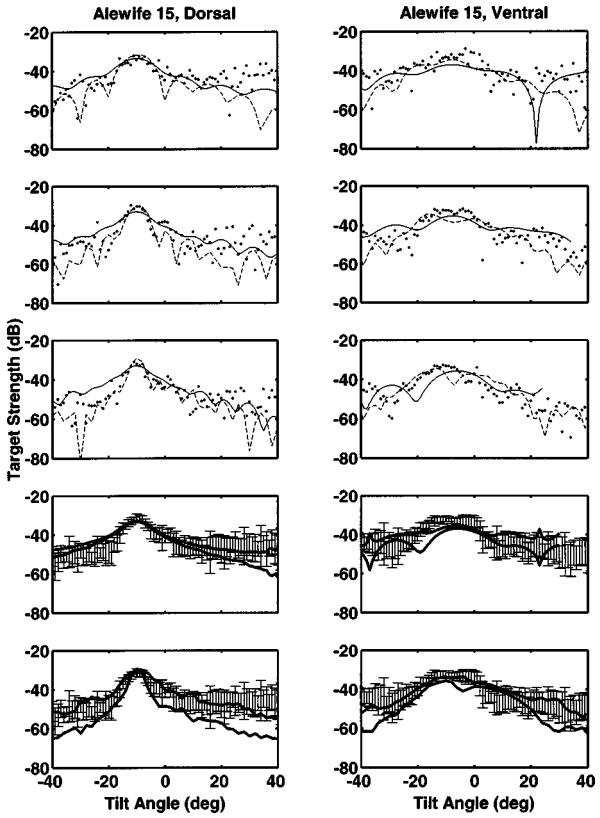

FIG. 17. Target strength as a function of angle of orientation for Alewife 15 in the dorsal/ventral plane at 45 (top row), 65 (second row), and 85 kHz (third row), and band-wide statistics of target strength as a function of angle of orientation (bottom two rows). The three frequencies in the top three rows are representative of the measurements and predictions across the 40–95 kHz frequency band. FMM (solid lines), KRM (dashed lines), and acoustic scattering data (dots) are plotted in the top three rows. In the bottom two rows, the average target strengths were computed by averaging the backscattering cross sections across the band before taking the logarithm. The vertical lines in the bottom two rows depict the standard deviation about the averaged measured values within the band, and the solid lines depict the corresponding standard deviation about the averaged FMM (fourth row) and KRM (bottom row) predictions. The tilt angles are defined in caption to Fig. 9. Portions of the FMM predictions for the ventral aspect are not shown due to numerical difficulties. The difficulties are due to the particularly irregular interface of the ventral side of the swimbladder.

high-resolution representations of the swimbladder alone, which is the dominant scatterer near normal incidence, modeled with soft, or pressure-release, boundary conditions. The KRM results are based upon the coherent addition of the scattering from the swimbladder with soft boundary conditions and the scattering from the fish body with fluid boundary conditions.

Experimental data and accompanying model calculations are presented for two different fish (#15 and #17) at dorsal and ventral aspects at three different frequencies (Figs. 17 and 18). There is generally reasonable agreement between the models and data in the general structure of the target strength as a function of orientation. Both models and data demonstrate well the narrower acoustic beam pattern at dorsal aspect compared to that of the ventral aspect, which is consistent with morphology. Also consistent with morphology is the position of the center of the main lobe near normal incidence.

Both models compared best with the data within 20° of the center (i.e., peak) of the main lobe of the scattering for the case of dorsal aspect (Figs. 17 and 18, left columns). In those cases, the KRM predictions were either very close to or slightly lower than the data. The FMM consistently predicts target strengths lower than the data by about 3–5 dB. Underpredictions in both cases can be explained, at least in part, by the fact that only the swimbladder is taken into account with the FMM and only the swimbladder plus body with the KRM. Also, as discussed earlier, although the swimbladder and body shapes were modeled at very high resolution, the process still involved a series of approximations, which is a source of error in the modeling both for dorsal and ventral aspects.

For angles well away from the main lobe [such as beyond 20° off the center of the lobe (dorsal aspect case)], the KRM consistently predicts lower target strengths, sometimes by up to 15 dB below the measurements. In contrast, the FMM predicts target strengths that are much closer to the data and, for some ranges of angles, the FMM predictions were within the range of values of data collected while the KRM predictions were below the range (Figs. 17 and 18, left columns, bottom two rows).

These differences between KRM and FMM predictions for angles well away from the main lobe are expected. The KRM, which is based on the Kirchhoff approximation at these frequencies, is inherently inaccurate at angles well

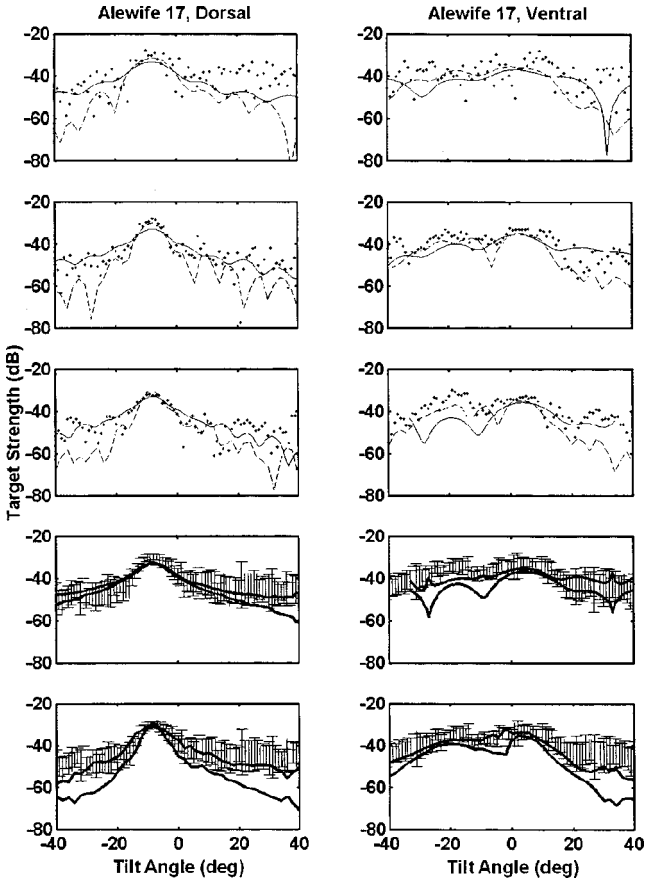

FIG. 18. Comparison of model predictions with data for Alewife 17. The plotting convention is the same as Fig. 17.

away from the main lobe (which is associated with normal incidence scattering by the swimbladder), and expectedly underpredicts the scattering levels in that region. The FMM, as demonstrated in Reeder and Stanton, J. Acoust. Soc. Am. **116**, 729–746 (2004), is valid for all angles of orientation. Deviations between the FMM predictions and data in this region are expected to be due to the approximations in the modeling of the shape of the swimbladder (scattering well off normal incidence is especially sensitive to precise shape of target) and exclusion of other parts of the fish anatomy.

For the cases involving ventral aspect (Figs. 17 and 18, right columns), both models predicted the broadening and shift (toward positive tilt angle) of the main lobe from Alewife 15 to Alewife 17. However, both models underpredicted near the main lobe by a larger degree than with the dorsal aspect cases. For angles more than 20° away from the main lobe, the FMM predictions were generally closer to the data than those from the KRM model (similar to the dorsal aspect cases). The biggest difference between the dorsal and ventral aspect cases is the fact that the large gonads are directly beneath the swimbladder [Fig. 2(b)]. One plausible explanation for the larger discrepancy between predictions and data in the ventral aspect case may be the added scattering by the gonad.

VI. DISCUSSION AND CONCLUSIONS

There are several important advancements made in this study involving use of advanced imagery of fish morphology, broadband acoustical measurements, and the modeling: (1) The CT-scan imagery, used for the first time in the comparison of measured scattering data and model predictions, proved to be a useful tool in synoptically and noninvasively mapping major morphological features of the fish. As suggested above, this approach appears to be a viable alternative to, or at least a method complementary to, the tedious process of microtoming. In addition to the insight that this method and the phase-contrast x ray provided in qualitatively understanding the morphology of the fish without dissection, the CT-scan data were useful in the modeling. The digitally constructed 3D image of the swimbladder was used in this case to provide the lengthwise profiles of the swimbladder shape for the FMM model, as well as to aid in the determination of the location of the axis of rotation for that model. (2) The broadband measurements provided information across a continuous range of frequencies (simultaneously) that was useful for the modeling. Furthermore, through pulse compression of the broadband echoes, the data provided insight into the dominant scattering mechanisms. For angles well off normal incidence, the compressed pulse output provided quantitative data on the relative contribution of various scattering features of the fish. For example, the importance of the scattering by the skull for these angles was demonstrated. (3) The comparison of model predictions with the data provided further validation of the range of accuracy of the KRM model, as well as providing a first test of the applicability of the FMM model with the fish scattering problem. Clearly, the Kirchhoff-based KRM model is valid for angles of orientation near the main lobe of the scattering (i.e., angles near normal to the swimbladder surface). However, well away from those angles, the KRM approach greatly underpredicts the scattering levels. The utility of the FMM approach in this latter case is apparent, where the model is valid for all angles of orientation (at least with objects with simple shapes) [Reeder and Stanton, J. Acoust. Soc. Am. **116**, 729–746 (2004)]. Specifically, the FMM can potentially provide accurate predictions of scattering by swimbladder-bearing fish over a wider range of angles than the KRM approach.

The above results yield potential for future advances. For example, as the push for advanced, reliable, 3D models of acoustic scattering by fish continues, there is a corresponding need for high-resolution 3D information on the morphology. The CT-scan imagery here provided valuable 3D morphological information for the fish-scattering models and visualization of potential scattering features. In addition, this information can be collected rapidly, as it already has for the zooplankton acoustics problem (Lavery *et al.*, 2002). The utility of broadband acoustics has already been demonstrated in the ocean where incoherent processing of the broadband echoes has allowed for discrimination of fish species (Simmonds *et al.*, 1996; Zakharia *et al.*, 1996). Through (coherent) pulse-compression processing of the broadband echoes, the scattering (at least in the laboratory) can be investigated at high resolution and, as a result, scattering models can be further advanced by allowing inclusion of parts of the anatomy beyond the swimbladder. This advancement would be especially important for angles well off normal incidence

where the contribution of the swimbladder does not necessarily dominate the scattering. Finally, advanced scattering models are needed to be accurate over a wide range of conditions. New models such as the FMM and BEM (Foote and Francis, 2002) have potential for modeling the scattering over a much larger range of orientation angles and frequencies than is currently possible, including near the resonance frequency of the swimbladder. Carefully taking into account high-resolution morphology as well as comparisons with data over a wide range of frequencies and orientations will help further advance the development of new models.

ACKNOWLEDGMENTS

The authors would like to thank Falmouth Hospital for performing the CT scans of the alewife, Falmouth Animal Hospital for the use of their x-ray machine, and Benthos, Inc. for the use of their test tank for the acoustic measurement portion of the study. Andrew Stevenson, D. Gao, and Steve Wilkins at Australia's Commonwealth Scientific and Industrial Research Organization (CSIRO) have been very generous in their PCX imaging of the fish. The help of Hanu Singh, Andone Lavery, and the Graphics Department at the Woods Hole Oceanographic Institution with image processing was much appreciated. This work was supported by the U.S. Navy, the U.S. Office of Naval Research, the National Oceanographic and Atmospheric Administration, and the Massachusetts Institute of Technology/Woods Hole Oceanographic Institution Joint Program in Oceanographic Engineering. This is Woods Hole Oceanographic Institution Contribution Number 10722.

Aroyan, J. L. (**2001**). "Three-dimensional modeling of hearing in *Delphinus delphis*," J. Acoust. Soc. Am. **110**, 3305–3318.

Au, W. W. L., and Benoit-Bird, K. J. (**2003**). "Acoustic backscattering by Hawaiian Lutjanid snappers. II. Broadband temporal and spectral structure," J. Acoust. Soc. Am. **114**, 2767–2774.

Bondarenko, V. M., Gavrilov, E. N., and Tarasov, S. P. (**1990**). "Use of parametric transducers for wideband measurements of fish target strength," Rapp. P.-V. Reun.-Cons. Int. Explor. Mer **189**, 366–369.

Chu, D., and Stanton, T. K. (**1998**). "Application of pulse compression techniques to broadband acoustic scattering by live individual zooplankton," J. Acoust. Soc. Am. **104**, 39–55.

Clay, C. S. (**1991**). "Low-resolution acoustic scattering models: Fluid-filled cylinders and fish with swimbladders," J. Acoust. Soc. Am. **89**, 2168–2179.

Clay, C. S. (**1992**). "Composite ray-mode approximations for backscattered sound from gas-filled cylinders and swimbladders," J. Acoust. Soc. Am. **92**, 2173–2180.

Clay, C. S., and Horne, J. K. (**1994**). "Acoustic models of fish: The Atlantic cod (*Gadus morhua*)," J. Acoust. Soc. Am. **96**, 1661–1668.

Davis, T. J., and Stevenson, A. W. (**1996**). "Direct measure of the phase shift of an x-ray beam," J. Opt. Soc. Am. A **13**, 1193–1198.

Foote, K. G. (**1985**). "Rather-high-frequency sound scattering by swimbladdered fish," J. Acoust. Soc. Am. **78**, 688–700.

Foote, K. G. (**1997**). "Target strength of fish," in *Encyclopedia of Acoustics*, edited by M. J. Crocker (Wiley, New York).

Foote, K. G. (**2001**). "Acoustic scattering by marine organisms," in *Encyclopedia of Ocean Sciences*, edited by J. H. Steele, K. K. Turekian, and S. A. Thorpe (Academic, London).

Foote, K. G., and Francis, D. T. I. (**2002**). "Comparing Kirchhoff-approximation and boundary-element models for computing gadoid target strengths," J. Acoust. Soc. Am. **111**, 1644–1654.

Gunderson, D. R. (**1993**). *Surveys of Fisheries Resources* (Wiley, New York).

Gureyev, T. E., Stevenson, A. W., Paganin, D., Mayo, S. C., Pogany, A., Gao, D., and Wilkins, S. W. (**2000**). "Quantitative methods in phase-contrast x-ray imaging," J. Digit Imaging **13**, 121–126.

Holliday, D. V. (**1972**). "Resonance structure in echoes from schooled pelagic fish," J. Acoust. Soc. Am. **51**, 1322–1332.

Jech, J. M., and Horne, J. K. (**2002**). "Three dimensional visualization of fish morphometry and acoustic backscattering," ARLO **3**(1), 35–40 (ojps.aip.org/ARLO).

Kjaergaard, L., Bjorno, L., Kirkegaard, E., and Lassen, H. (**1990**). "Broadband analysis of acoustical scattering by individual fish," Rapp. P.-V. Reun.-Cons. Int. Explor. Mer **189**, 370–380.

Lavery, A. C., Stanton, T. K., McGehee, D. E., and Chu, D. (**2002**). "Three-dimensional modeling of acoustic backscattering from fluid-like zooplankton," J. Acoust. Soc. Am. **111**, 1197–1210.

Macaulay, G. J. (**2002**). "Anatomically detailed acoustic scattering models of fish," in Bioacoustics, The International Journal of Animal Sound and its Recording, **12**, 275–277.

Medwin, H., and Clay, C. S. (**1998**). *Fundamentals of Acoustical Oceanography* (Academic, Boston).

Nash, D. M., Sun, Y., and Clay, C. S. (**1987**). "High resolution acoustic structure of fish," J. Cons., Cons. Int. Explor. Mer **43**, 23–31.

Ona, E. (**1990**). "Physiological factors causing natural variations in acoustic target strength of fish," J. Mar. Biol. Assoc. U.K. **70**, 107–127.

Reeder, D. B., and Stanton, T. K. (**2004**). "Acoustic scattering by axisymmetric finite bodies: An extension of a 2-dimensional conformal mapping method," J. Acoust. Soc. Am. **116**, 729–746.

Simmonds, E. J., and Armstrong, F. (**1990**). "A wideband echo sounder: Measurements on cod, saithe, herring, and mackerel from 27 to 54 kHz," Rapp. P.-V. Reun.-Cons. Int. Explor. Mer **189**, 381–387.

Simmonds, J. E., Armstrong, F., and Copland, P. J. (**1996**). "Species identification using wideband backscatter with neural network and discriminant analysis," ICES J. Mar. Sci. **53**, 189–195.

Stanton, T. K., Wiebe, P. H., Chu, D., Benfield, M. C., Scanlon, L., Martin, L., and Eastwood, R. L. (**1994**). "On acoustic estimates of zooplankton biomass," ICES J. Mar. Sci. **51**, 505–512.

Stanton, T. K., Chu, D., Wiebe, P. H., Martin, L. V., and Eastwood, R. L. (**1998a**). "Sound scattering by several zooplankton groups. I. Experimental determination of dominant scattering mechanisms," J. Acoust. Soc. Am. **103**, 225–235.

Stanton, T. K., Chu, D., and Wiebe, P. H. (**1998b**). "Sound scattering by several zooplankton groups. II. Scattering models," J. Acoust. Soc. Am. **103**, 236–253.

Stanton, T. K., Chu, D., Wiebe, P. H., Eastwood, R. L., and Warren, J. D. (**2000**). "Acoustic scattering by benthic and pelagic shelled animals," J. Acoust. Soc. Am. **108**, 535–550.

Turin, G. L. (**1960**). "An introduction to matched filters," IRE Trans. Inf. Theory **IT-6**, 311–329.

Urick, R. J. (**1983**). *Principles of Underwater Sound* (McGraw-Hill, New York).

Wilkins, S. W., Gureyev, T. E., Gao, D., Pogany, A., and Stevenson, A. W. (**1996**). "Phase-contrast imaging using polychromatic hard x rays," Nature (London) **384**, 335–338.

Zakharia, M. E. (**1990**). "Variations in fish target strength induced by movement: A wideband-impulse experiment," Rapp. P.-V. Reun.-Cons. Int. Explor. Mer **189**, 398–404.

Zakharia, M. E., Magand, F., Hetroit, F., and Diner, N. (**1996**). "Wideband sounder for fish species identification at sea," ICES J. Mar. Sci. **53**, 203–208.

Environmentally adaptive reverberation nulling using a time reversal mirror

H. C. Song, S. Kim,[a] W. S. Hodgkiss, and W. A. Kuperman
Marine Physical Laboratory, Scripps Institution of Oceanography, La Jolla, California 92093-0238

(Received 2 December 2003; revised 23 April 2004; accepted 4 May 2004)

Backscattering from the rough water-bottom interface can serve as a surrogate probe source in time reversal. A time-gated portion of the reverberation then is refocused to the bottom interface at the corresponding range [Lingevitch *et al.*, J. Acoust. Soc. Am. **111**, 2609–2614 (2002)]. In this paper, reverberation nulling is investigated to enhance active target detection without a priori knowledge of the environment. The basic idea is to minimize the acoustic energy incident on the corresponding scattering interface by applying an excitation weight vector on the time reversal mirror which is in the complementary subspace orthogonal to the focusing vector. Numerical simulations illustrate the potential of reverberation nulling using a time reversal mirror. © *2004 Acoustical Society of America.* [DOI: 10.1121/1.1765194]

PACS numbers: 43.30.Gv, 43.30.Hw [DRD] Pages: 762–768

I. INTRODUCTION

Assuming that the environment does not change significantly over the two-way travel time, an acoustic time reversal mirror (TRM) refocuses an incident acoustic field to the position of the original probe source (PS) regardless of the complexity of the medium between the PS and TRM.[1] Recent time reversal experiments have demonstrated the robustness of TRM in an oceanic waveguide at 450 and 3500 Hz.[1–3] The focusing capability suggests potential applications of TRMs to sonar system concepts including reverberation minimization without a priori environmental knowledge. For example, echo-to-reverberation enhancement recently has been demonstrated experimentally in the 3 to 4 kHz band in shallow water.[4] A drawback to the practical use of TRMs in sonar systems, however, is the apparent requirement of a cooperating probe source.

Seafloor focusing was investigated in a recent time reversal experiment by placing a PS on the boundary (i.e., 1 m off the seafloor) at 3 km range from the TRM resulting in the peak at the focal range about 3 dB higher than the background.[5,6] Backscattering from the rough water–bottom interface also can serve as a surrogate PS as described by Lingevitch *et al.*[7] The concept is based on the fact that a time-gated portion of reverberation provides a transfer function vector between a TRM array and the range cell along the bottom, which then is refocused to the corresponding bottom interface.

In this paper, we are concerned with reverberation nulling in order to enhance active target detection recognizing that focusing and nulling are complementary. The basic idea is to minimize the acoustic energy incident on a specific range cell on the boundary while more energy is projected into the water column possibly illuminating targets. Although interface roughness is not the only possible contributor to the bottom backscattering, in this paper we neglect sediment volume scattering which could be dominant in soft sediments.[8]

Section II briefly reviews the scattering model implemented to simulate reverberation from a rough interface in an oceanic waveguide. Section III describes the concept of reverberation nulling using time reversal techniques *vis-a-vis* array processing. Numerical simulations to demonstrate the proposed method are presented in Sec. IV.

II. REVERBERATION MODEL

Reference 7 describes the scattering model implemented in terms of normal modes based on the perturbation method[9] to simulate reverberation from a rough surface in a two-dimensional (x,z) Pekeris waveguide. In this paper, the reverberation model is extended to a general range-independent waveguide environment. For simulation purposes, it is assumed that the bottom roughness is the dominant contributor to the backscattering. However, we can include contributions from surface scattering, internal waves or volume scattering. We also assume that both the environment and bottom roughness are axisymmetric [i.e., (r,z)] so there is no out-of-plane scattering.

Based on the boundary perturbation method,[10–12] the modal representation of the backscattered field at a single frequency is derived by Tracey and Schmidt[9]

$$s(z;z_s)=\frac{-1}{8\pi}\sum_n\sum_m \frac{\phi_m(z_s)\phi_m(z_{\mathrm{int}})b_{mn}\phi_n(z_{\mathrm{int}})\phi_n(z)}{\sqrt{k_m k_n}} \times\int_0^\infty \gamma(r)e^{-i(k_m+k_n)r}dr, \quad (1)$$

where $\{\phi_m,k_m\}$ are the sets of propagating modes and horizontal wavenumbers, γ is the deformation from the unperturbed flat interface z_{int}, and z_s and z are the depths of source and receiver, respectively. The modal backscattering strength b_{mn} between mode m and n is

$$b_{mn}=\left(1-\frac{\rho_b}{\rho_w}\right)q_m q_n+k_w^2-\frac{\rho_w}{\rho_b}k_b^2+k_m k_n\left(1-\frac{\rho_w}{\rho_b}\right), \quad (2)$$

[a]Present address: Agency for Defense Development, Chinhae, 645-600, Seoul Korea.

 0001-4966/2004/116(2)/762/7/$20.00

$$q_n = \frac{\phi_n'(z_{\text{int}})}{\phi_n(z_{\text{int}})} = \left(\frac{\rho_w}{\rho_b}\right)\sqrt{k_n^2 - k_b^2}, \tag{3}$$

where the subscripts w and b denote the water and bottom at the interface $z = z_{\text{int}}$, respectively, and the prime $'$ indicates a derivative with respect to depth z. The b_{mn} can be interpreted as a mode-coupling matrix where the incident mode m is converted into the scattered mode n since the scattering process redistributes the acoustic energy among the scattered modes.

The backscattered field due to multiple sources can be obtained by a linear superposition and broadband pulses are modeled with Fourier synthesis. In this paper, we confine our interest to narrowband pulses.

III. REVERBERATION NULLING

A. Processing of reverberation data

This section describes how to process reverberation data measured on the source-receiver array (SRA) or TRM. The data are recorded on a N element SRA which is configured to transmit an incident pulse of length τ starting at $t = t_0$ (transmit mode). The resulting reverberation time series is then recorded on each element (receive mode). Neglecting multiple scattering, roughness in the vicinity of a range r will contribute to the received reverberation over a time window

$$w(t,r,\Delta) = \begin{cases} 1, & |t - t_c - t_0| \leqslant \Delta/2 \\ 0, & |t - t_c - t_0| > \Delta/2 \end{cases}, \tag{4}$$

where $t_c = 2r/c_0$ is the approximate round-trip travel time and c_0 is an average modal group speed. Δ is the width of the temporal window used for processing which depends on the source pulse length τ, the dispersive properties of the waveguide, and the range resolution cell size Δr. In an acoustic waveguide, the range resolution Δr for a single frequency point source is related to the mode interference distance between the lowest and highest modes involved,[13] i.e., $\Delta r = 2\pi/(k_{\min} - k_{\max})$. As will be shown in Sec. IV B, the range cell size for rough interface reverberation is larger than that for a point source due to the extended (diffusive) nature of the distributed sources.

For a narrowband signal, typically we choose $\Delta = \tau$ as the time window and evaluate the Fourier component at the center frequency to obtain an N-dimensional data vector $\mathbf{d}$. The basic idea of reverberation focusing or nulling comes from the fact that the data vector $\mathbf{d}$ contains a transfer function vector between the SRA and the scatterers clustered around range r acting as a single (extended) probe source. The reverberation then can be treated simply as a single source problem in array processing and the data vector $\mathbf{d}$ corresponds to a single snapshot. This suggests that a single snapshot would allow us to obtain the transfer function to the seafloor when there is a strong reverberation return, i.e., the high reverberation-to-noise case.

In the next section we revisit the time reversal operator (TRO) of the DORT method developed by Prada *et al.*[14–16] for selective focusing in multi-target media in the context of reverberation and array processing. The method is generalized in beam space to enhance the backscattered reverberation level by ensonifying the water column with the full source array rather than a single element as employed in the original DORT method.[7]

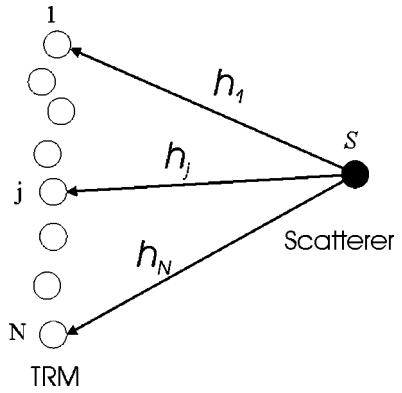

FIG. 1. The transfer function between a TRM and a scatterer with target strength s.

B. Reverberation: Array processing

Assume that a TRM array consists of N elements and the medium contains a single pointlike scatterer with a target strength s (see Fig. 1). We easily can extend it to the case with multiple scatterers neglecting multiple scattering. We also assume a high echo-to-noise ratio excluding the noise component in the derivation. Let $\mathbf{K}$ denote a noise-free, two-way data transfer matrix

$$\mathbf{K} = [\mathbf{h}]s[\mathbf{h}^T\mathbf{E}] = [\tilde{\mathbf{h}}][\tilde{\mathbf{h}}^T\mathbf{E}], \tag{5}$$

where $\mathbf{h} = [h_1, h_2, \ldots, h_N]^T$ is the array transfer function vector (multichannel Green's function) between the scatterer and the TRM array, and a superscript T indicates a transpose. The target strength s can be absorbed into $\tilde{\mathbf{h}}$ as $\tilde{\mathbf{h}} = \sqrt{s}\mathbf{h}$. $\mathbf{E} = [\mathbf{e}_1, \mathbf{e}_2, \ldots, \mathbf{e}_M]$ is an excitation matrix whose column vectors $\mathbf{e}_i$ represent M forms of excitation (or realizations) of the array. For example, $\mathbf{e} = [1,1,\ldots,1]^T$ means simultaneous excitation of the array elements (i.e., a broadside transmission),

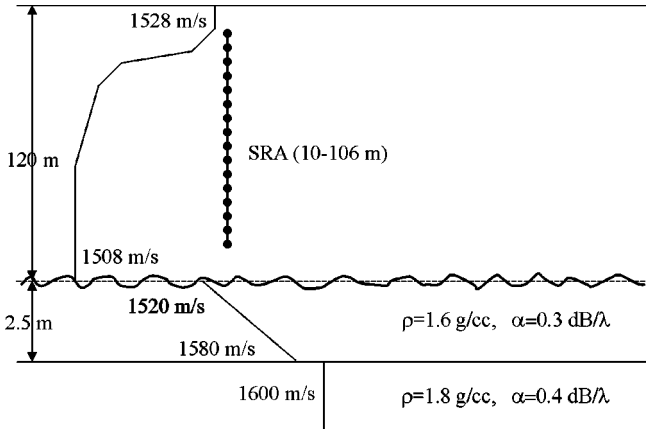

FIG. 2. Ocean environmental model used for the backscattered field simulations. The SRA spans the water column from 10 to 106 m with 3 m element spacing in 120 m water depth. The bottom roughness has 0.1 m rms height and 15 m correlation length with a Goff–Jordan power law spectrum. The sound-speed profile shows a typical downward refracting environment with the thermocline spanning 20–50 m. The sound speeds are 1528 m/s at the surface and 1508 m/s at the ocean bottom.

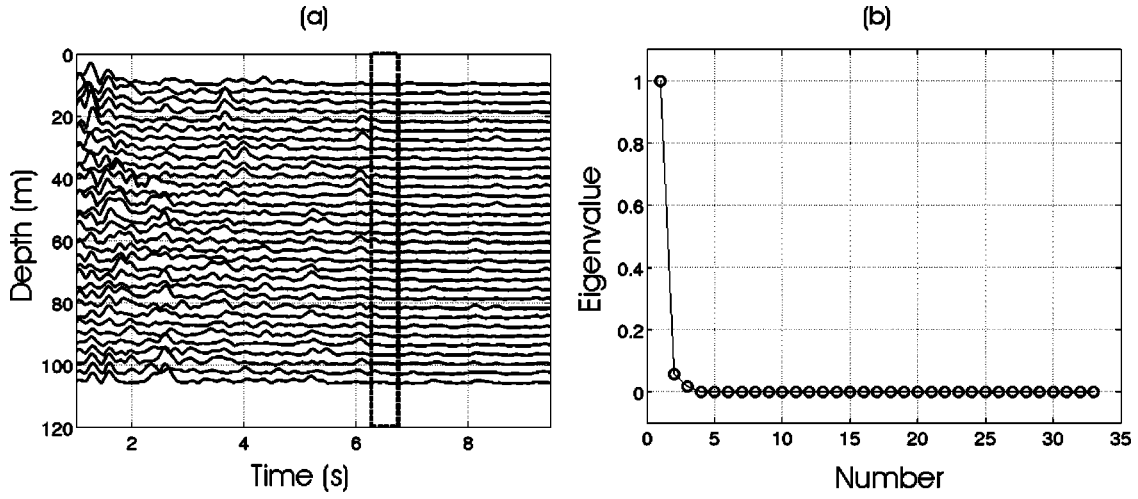

FIG. 3. Extraction of a transfer function from reverberation data for focusing or nulling. (a) The time series shows the monostatic reverberation at the SRA due to a broadside transmission. We construct a covariance matrix **R** using time-gated reverberation (6.25–6.35 s) excited by 5 different beams (excitation vectors $\mathbf{e}_i$). (b) Eigenvalue distribution of the covariance matrix **R** from 5 snapshots. The first eigenvector is used for bottom focusing in Fig. 4 while the linear combination of the nondominant eigenvectors (20–26) in the subspace orthogonal to the focusing vector is used for nulling.

whereas $\mathbf{e}=[1,0,...,0]^T$ indicates excitation of the first element only. For simplicity, we have not included explicitly the transducer characteristics (transmitting and receiving sensitivities) but have normalized them to unity. It is interesting to observe that the apparent two-way data matrix **K** represents simply the one-way transfer vector **h** with various amplitudes of $\mathbf{h}^T\mathbf{e}_i$ at the scatterer.

Typically, a single transducer does not have sufficient source level to yield significant backscatter so that simultaneous excitation (i.e., a beam) with maximum power is desirable. Although we can use arbitrary beams, in practice it will be difficult to excite high-angle beams efficiently (which corresponds to the higher order modes) since this requires both a dense sampling and long aperture of the TRM array. Reference 7 proposed that the beams should be orthogonal to each other and the processing be done in beam space by projecting the data vector in element space onto beam space. Here we use beams for excitation only and process the received data in element space. Therefore, orthogonality of the beams is not required. The advantage of using multiple beams is to illuminate the boundary more uniformly.

Note that M measurements correspond to the number of snapshots in array processing and **K** is not a square matrix in general. However, when the excitation matrix **E** is chosen to be an identity matrix **I** with size N, the square transfer matrix **K** reduces to the transfer matrix defined in the DORT method.[16] Note that **K** is a rank 1 matrix for a single scatterer and ideally a single snapshot allows for extraction of the transfer function vector **h**.

Now construct a covariance matrix $\mathbf{R}=\mathbf{K}\mathbf{K}^\dagger$ where † denotes a conjugate transpose (Hermitian) operation. Then the time reversal operator (TRO) is related to **R** as

$$\mathrm{TRO}\equiv\mathbf{K}^*\mathbf{K}^T=(\mathbf{K}\mathbf{K}^\dagger)^*=\mathbf{R}^*, \tag{6}$$

where * denotes a conjugate operation. The above relationship is valid even when **K** is not a square matrix although the original TRO derivation assumed **K** was square. Since $\mathbf{R}=\mathbf{K}\mathbf{K}^\dagger$ is a rank 1 matrix for a single scatterer, the first eigenvector is proportional to the transfer function vector **h**.

C. Reverberation: Focusing and nulling

In this section, we estimate the transfer function by the eigendecomposition of the covariance matrix **R** for either focusing or nulling. An alternative to first forming the measurement covariance matrix and then performing an eigendecomposition is to operate directly on the data transfer matrix **K** using singular value decomposition (SVD).

Consider the eigendecomposition of the $N\times N$ covariance matrix **R**

$$\mathbf{R}=\sum_{i=1}^{N}\lambda_i\mathbf{v}_i\mathbf{v}_i^\dagger, \tag{7}$$

where $\mathbf{v}_i$ is the eigenvector corresponding to the ith eigenvalue λ_i. We can break the sum into two parts: One for the d largest eigenvalues and one for the $N-d$ smallest eigenvalues

$$\mathbf{R}=\sum_{i=1}^{d}\lambda_i\mathbf{v}_i\mathbf{v}_i^\dagger+\sum_{i=d+1}^{N}\lambda_i\mathbf{v}_i\mathbf{v}_i^\dagger. \tag{8}$$

Note that most of the small eigenvalues are zero since **R** is less than a full rank matrix (rank-deficient). The number of significant eigenvalues d will be equal to the number of scatterers q assuming orthogonality of the transfer functions between them.[16] We refer to the d-dimensional subspace as a signal subspace and the $(N-d)$ dimensional subspace as a noise subspace.

Since focusing and nulling are complementary problems, the success of reverberation nulling depends entirely on obtaining a transfer (focusing) vector representing the reverberation which leads to a single spatial degree of freedom (DOF). This can be done by selecting a time window less than the corresponding reverberation range resolution which will be discussed in Sec. IV B. The time-gated reverberation then can reduce to a single source problem such that the first

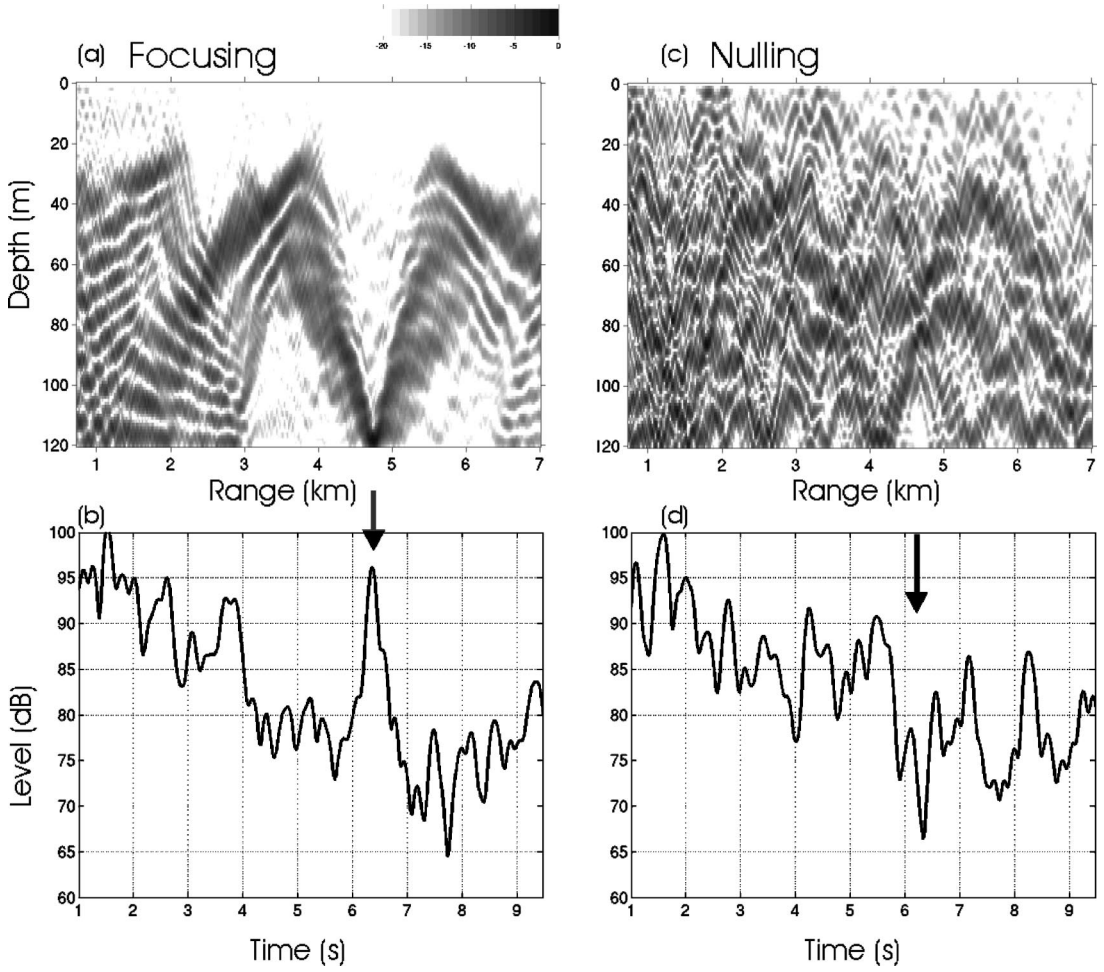

FIG. 4. Simulation results for bottom focusing and nulling from reverberation excited by a 100 ms Gaussian shaped probe source pulse at 1 kHz. (a) The focused field at 4.7 km and (b) resulting enhanced reverberation at the corresponding time (6.3 s). (c) A null placed at the same position and (d) reduced reverberation at the corresponding time. The colorbar level in (a) and (c) is normalized with respect to the maximum (0 dB) in the range-depth surface showing the relative strength of the field. The geometric spreading term $(1/r)$ has been removed in (a) and (c).

eigenvector is dominant, i.e., $d=1$. The conjugate of the first eigenvector is used as a new excitation weight vector $\mathbf{w}$ on the TRM for retransmission to focus the energy onto the range cell, i.e., $\mathbf{w}_{\text{focus}}=\mathbf{v}_1^*$. The resulting reverberation should yield a strong return at the corresponding time window.

Once we have a focusing vector, nulling can be achieved by choosing an arbitrary vector in the $(N-1)$-dimensional noise subspace orthogonal to the focusing vector in the one-dimensional signal subspace. One example of a nulling weight vector $\mathbf{w}_{\text{null}}$ is

$$\mathbf{w}_{\text{null}}=\left(\sum_{i=2}^{N}\mathbf{v}_i\right)^*. \tag{9}$$

Note that we have a single weight vectors in the N-dimensional space for focusing whereas there are many choices of nulling weight vectors. The question then is then how to select a nulling weight vector optimally in the sense that maximum energy is projected into the water column. Unfortunately, we cannot further optimize $\mathbf{w}_{\text{null}}$ since we have no other information available from the reverberation return except the transfer function between the array and the corresponding range cell. It should be mentioned that the proposed approach is similar to the eigenstructure approach (e.g., MUSIC algorithm) in obtaining vectors spanning the null subspace from a data covariance matrix.[17]

We easily can extend the approach to multiple point nulling by selecting several different time windows. Unlike a general multiple target problem, however, we can obtain the covariance matrix for each range cell separately without worrying about the cross terms between scatterers in different range cells and build a new covariance matrix by combining them i.e., $\mathbf{R}=\Sigma\mathbf{R}_i$. The nondominant eigenvectors then are used to construct a new excitation weight vector $\mathbf{w}_{\text{null}}$ for simultaneous multiple point nulling. In the next section, we will test the proposed method.

IV. SIMULATIONS

A. Environmental model

Figure 2 shows the waveguide environment model used for backscattered field simulations. The SRA consists of 33 elements spanning the water column from 10 to 106 m with 3 m inter-element spacing in the 120 m deep water. The sound-speed profile indicates a typical downward refracting environment with the thermocline spanning 20–50 m result-

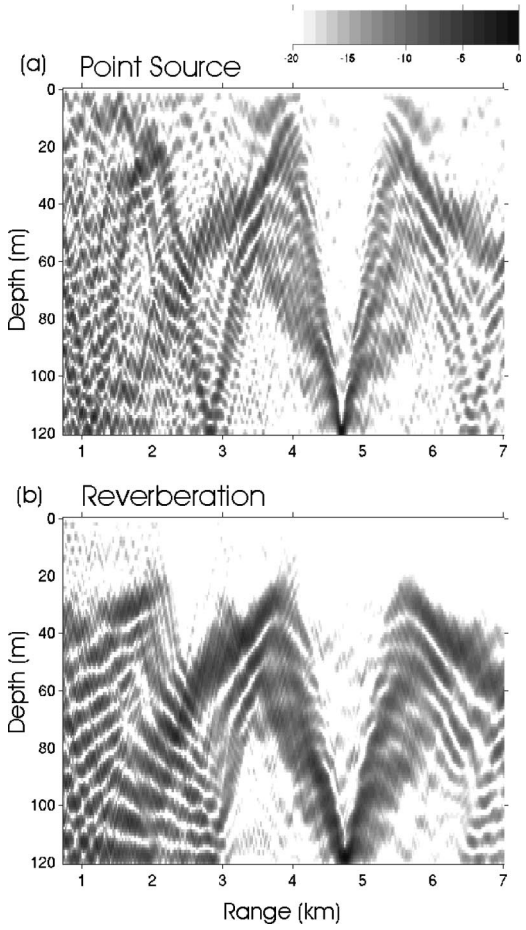

FIG. 5. Simulation results for focusing with: (a) A point source and (b) time-gated reverberation shown in Fig. 4(a). Note that reverberation focusing in (b) shows a diffusive nature due to the extended reverberation source as compared to a point source in (a), resulting in a larger range cell size in reverberation.

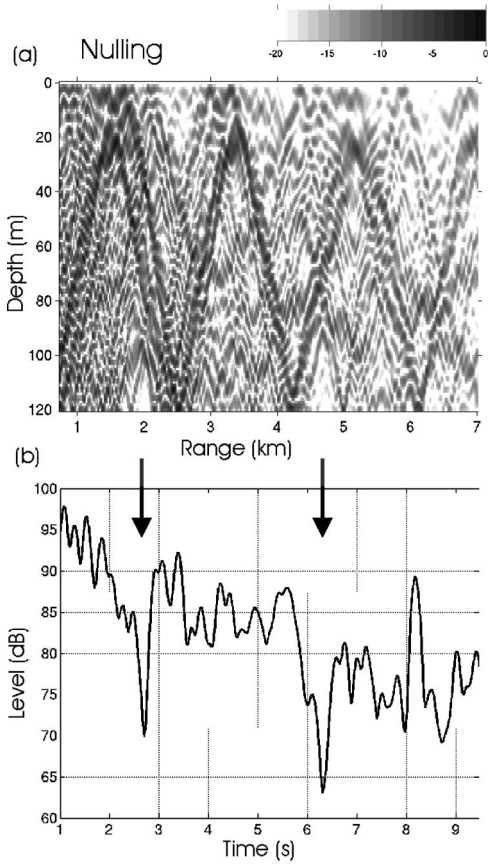

FIG. 6. Simulation result for two point (2 and 4.7 km) nulling. Two covariance matrices corresponding to each range ($\mathbf{R}_1$ and $\mathbf{R}_2$) are combined and eigendecomposed at the center frequency of 1 kHz. (a) The backpropagation with nondominant eigenvectors (25–30) at the center frequency and (b) resulting reverberation showing two notches corresponding to each range. The geometric spreading term ($1/r$) has been removed in (a).

ing in substantial sound interactions with ocean bottom. This profile justifies the neglect of surface scattering in the simulations. The ocean-sediment interface has a roughness of 0.1 m rms and 15 m correlation length generated using a Goff–Jordan power-law spectrum.[18] These parameters were deduced from sub-bottom profiler data collected during a previous TRM experiment.[4] The ocean bottom has a 2.5 m thick sediment layer with a sound speed of 1520 m/s at the top interface which also is similar to the environment discussed in Ref. 4. Since the water column sound speed at this depth is 1508 m/s, acoustic waves propagating above the critical angle of 7.2° are highly attenuated. We use a $\tau = 100$ ms Gaussian shaped pulse with a center frequency of 1 kHz. The vector time series transmitted by the SRA is normalized such that the maximum values across all elements and time is equal to the maximum source level of 174 dB re 1 μPa at 1 m.[4]

B. Reverberation nulling

The following is a summary of the reverberation nulling procedure based on the approach described in Sec. III. We assume that we observe a strong reverberation return in the absence of targets.

(1) Generate reverberation time series corresponding to a pulse length τ by exciting the SRA (TRM) array with M different beams thus obtaining M reverberation realizations (snapshots).
(2) Select a time window Δ corresponding to the range of interest and apply a Fourier Transform to each snapshot at the center frequency to obtain a data transfer matrix $\mathbf{K} = [\mathbf{d}_1, \mathbf{d}_2, \ldots, \mathbf{d}_M]$.
(3) Construct a data covariance matrix $\mathbf{R} = \mathbf{K}\mathbf{K}^{\dagger}$.
(4) Perform the eigendecomposition of $\mathbf{R}$ to obtain a set of eigenvectors spanning the signal and noise subspaces, respectively.
(5) Generate a vector time series based on a new excitation weight vector $\mathbf{w}$ for either focusing or nulling, broadcast the generated time series and measure the reverberation return.

Figure 3(a) shows an example reverberation time series received by the SRA after exciting all of the SRA elements simultaneously (i.e., a broadside transmission). We collect five different reverberation realizations or snapshots ($M = 5$) from excitation with various beams (i.e., excitation vectors $\mathbf{e}_i$). A reverberation signal spanning 6.25–6.35 s (i.e., time window of $\Delta = 100$ ms) from each data set was selected [denoted by the box in Fig. 3(a)] which corresponds to a

range around 4.7 km with $c_0 = 1500$ m/s. The selected time windows are Fourier-transformed and used to construct the covariance matrix **R** at center frequency 1 kHz. Figure 3(b) displays the normalized eigenvalue distribution showing three significant eigenvalues. The first eigenvalue contains more than 90% of the energy and the values decrease rapidly with increasing number. We will use the first eigenvector for focusing on the ocean bottom.

For nulling we have freedom to choose any of the eigenvectors in the noise subspace which excludes the first two or three in this example or arbitrary combinations of them as discussed in Sec. III C. It should be pointed out that some of the eigenvectors are more effective than others in terms of the distribution of energy within the water column and nulling patch size in range. However, this selection requires a priori knowledge of the environment which is not available in the proposed time reversal approach. Here a collection of eigenvectors (20–26) with equal weighting is employed for nulling.

Figure 4 shows the simulation results. The upper panels display the backpropagated field at the center frequency to demonstrate that the energy is either focused [Fig. 4(a)] or nulled [Fig. 4(c)] at the intended range cell (4.7 km). The field strength is normalized with respect to the maximum (0 dB) in the range-depth surface and the geometrical spreading term $(1/r)$ has been removed in Figs. 4(a) and (c). As expected, the reverberation return after backpropagation is enhanced [Fig. 4(b)] or reduced [Fig. 4(d)] at the corresponding time $t = 6.3$ s. In the lower plots of Fig. 4, the reverberation is averaged incoherently across the SRA channels. It is shown in Fig. 4(c) that the backpropagated field creates a null on the bottom area around $r = 4.7$ km. Figure 4(d) shows a notch of about 20 dB depth from the average reverberation level around 6.3 s. This nulling process implies that we can improve target detectability at this range by reducing the returning reverberation while maintaining ensonification of the water column.

It is appropriate here to discuss the relationship between the source pulse length τ, the time window Δ, and the range cell Δr. Given the environment and frequency, the natural waveguide range resolution Δr for a point source is about $2\pi/(k_{\min} - k_{\max}) \approx 30$ m as shown in Fig. 5(a). In the reverberation return, each sample is already integrated over a range corresponding to half the pulse length $(c_0\tau/2 = 75$ m) which is larger than the waveguide range resolution of 30 m. Selecting a time window of $\Delta = \tau$ increases the range by $c_0\Delta = 150$ m so that the total range interval represented by the time window of reverberation is 225 m. As expected, the resulting backpropagation in Fig. 5(b) shows the diffusive nature of the extended reverberation as opposed to Fig. 5(a) when a point source is placed at 4.7 km range and 120 m depth. Opening up the time window too wide prohibits capturing the transfer function properly. Empirical results from our simulations indicate that a time window $\Delta < 2\tau$ results in reasonable reverberation focusing and nulling.

Finally, we present simulation results with multiple range nulling. Two covariance matrices are constructed separately by taking $\Delta = 100$ ms time-gated reverberation time series corresponding to 2 and 4.7 km, respectively. The combined covariance matrix is decomposed into signal-and noise-subspace eigenvectors. A linear combination of the noise eigenvectors (25–30) then is used to generate two nulls in the backpropagated field shown in Fig. 6(a). Clearly, we observe the nulls on the ocean bottom at 2 km and 4.6 range simultaneously. The returning reverberation also shows two notches at $t = 2.7$ s and $t = 6.3$ s in Fig. 6(b).

V. CONCLUSIONS

Bottom backscattering potentially can be used as a surrogate probe source in a time reversal mirror. A time-gated portion of reverberation can be processed to provide the transfer function between a TRM array and the corresponding range cell of an extended source. Reverberation nulling is achieved by backpropagating an excitation weight vector that is in the complementary subspace orthogonal to the focusing vector. As part of the derivation of the reverberation nulling approach, it was shown that time reversal operator (TRO) is a special case of the general data covariance matrix. Numerical simulations were used to illustrate both focusing and nulling observed with the proposed method.

ACKNOWLEDGMENT

This research was supported by the Office of Naval Research under Grant No. N00014-94-1-0458 and contract N00014-01-D-0043-D06.

[1] W. A. Kuperman, W. S. Hodgkiss, H. C. Song, T. Akal, C. Ferla, and D. Jackson, ''Phase conjugation in the ocean: Experimental demonstration of an acoustic time-reversal mirror,'' J. Acoust. Soc. Am. **102**, 25–40 (1998).
[2] W. S. Hodgkiss, H. C. Song, W. A. Kuperman, T. Akal, C. Ferla, and D. R. Jackson, ''A long range and variable focus phase conjugation experiment in shallow water,'' J. Acoust. Soc. Am. **105**, 1597–1604 (1999).
[3] S. Kim, G. F. Edelmann, W. A. Kuperman, W. S. Hodgkiss, H. C. Song, and T. Akal, ''Spatial resolution of time-reversal arrays in shallow water,'' J. Acoust. Soc. Am. **110**, 820–829 (2001).
[4] S. Kim, W. A. Kuperman, W. S. Hodgkiss, H. C. Song, G. F. Edelmann, and T. Akal, ''Echo-to-reverberation enhancement using a time reversal mirror,'' J. Acoust. Soc. Am. **115**, 1525–1531 (2004).
[5] Charles W. Holland and B. Edward McDonald, ''Shallow water reverberation from a time reversed mirror,'' Technical report, SR-326, SACLANT Undersea Research Centre, La Spezia, Italy, 2000.
[6] B. Edward McDonald and Charles Holland, ''Shallow-water reverberation from a time reversed mirror: Data-model comparison,'' J. Acoust. Soc. Am. **109**, 2495 (2001).
[7] J. F. Lingevitch, H. C. Song, and W. A. Kuperman, ''Time reversed reverberation focusing in a waveguide,'' J. Acoust. Soc. Am. **111**, 2609–2614 (2002).
[8] D. R. Jackson, ''Application of the composite roughness model to high-frequency bottom backscattering,'' J. Acoust. Soc. Am. **79**, 1410–1422 (1986).
[9] B. H. Tracey and H. Schmidt, ''Seismo-acoustic field statistics in shallow water,'' IEEE J. Ocean. Eng. **22**, 317–331 (1997).
[10] W. A. Kuperman and F. Ingenito, ''Attenuation of the coherent component of sound propagating in shallow water with rough boundaries,'' J. Acoust. Soc. Am. **61**, 1178–1187 (1977).
[11] W. A. Kuperman and H. Schmidt, ''Self-consistent perturbation approach to rough surface scattering in stratified elastic media,'' J. Acoust. Soc. Am. **86**, 1511–1522 (1989).
[12] H. Schmidt and W. A. Kuperman, ''Spectral representations of rough interface reverberation in stratified ocean waveguide,'' J. Acoust. Soc. Am. **97**, 2199–2209 (1995).
[13] R. A. Koch, G. R. Wilson, and P. J. Vidmar, ''Matched mode localization,'' J. Acoust. Soc. Am. **84**, 310–320 (1988).

[14] C. Prada and M. Fink, ''Eigenmodes of the time reversal operator: A solution to selective focusing in multiple-target media,'' Wave Motion **20**, 151–163 (1994).
[15] C. Prada, J. L. Thomas, and M. Fink, ''The iterative time reversal process: Analysis of the convergence,'' J. Acoust. Soc. Am. **97**, 62–71 (1995).
[16] C. Prada, S. Manneville, D. Spoliansky, and M. Fink, ''Decomposition of the time reversal operator: Detection and selective focusing on two scatteres,'' J. Acoust. Soc. Am. **99**, 2067–2076 (1996).
[17] D. H. Johnson and D. E. Dudgeon, *Array signal processing: concepts and techniques* (Prentice Hall, Englecliffs, NJ, 1993).
[18] J. A. Goff and T. Jordan, ''Stochastic modeling of seafloor morphology: Inversion of sea beam data for second-order statistics,'' J. Geophys. Res. **93**, 13589–13608 (1988).

A three-parameter dispersion relationship for Biot's fast compressional wave in a marine sediment

Michael J. Buckingham[a)]
Marine Physical Laboratory, Scripps Institution of Oceanography, University of California, San Diego, 9500 Gilman Drive, La Jolla, California 92093-0238

(Received 18 November 2002; accepted for publication 15 December 2003)

When the bulk and shear moduli of the mineral frame are set to zero, the full Biot theory of wave propagation in a porous medium such as a marine sediment reduces to Williams' ''effective density fluid'' (EDF) model [J. Acoust. Soc. Am. **110**, 2276–2281 (2001)]. Although eight material variables appear in the EDF model, it is in fact tightly constrained, possessing just three degrees of freedom: the phase speeds in the limits of low and high frequency, c_0 and c_∞, respectively, and a transition frequency, f_T, separating the low- and high-frequency regimes. In this paper, an algebraic approximation to the EDF model is formulated, which is termed the ''modified viscous fluid'' (MVF) model, involving only the three parameters (c_0, c_∞, f_T). Expressions are developed for (c_0, c_∞, f_T) in terms of the eight material properties; and a comparison of the MVF and EDF dispersion curves is performed, showing that they are essentially identical at all frequencies. Apart from its computational simplicity, the MVF model provides insight into the effect of each material parameter on the shape of the dispersion curves. For instance, the transition frequency scales as the ratio of the pore–fluid viscosity to the permeability, but neither the viscosity nor the permeability affects the limiting phase speeds c_0 and c_∞.
[DOI: 10.1121/1.1646672]

PACS numbers: 43.30.Ma, 43.20.Jr. [WMS] Pages: 769–776

I. INTRODUCTION

In a recent article, Williams[1] developed an ''effective density fluid'' (EDF) model of acoustic wave propagation in an unconsolidated, saturated porous medium such as a marine sediment. Based on the classical theory of Biot[2,3] for wave propagation in a two-phase, porous medium, the EDF model is a reduced version of Biot's original formulation in which the (complex) frame bulk modulus and the (complex) frame shear modulus have been set to zero. Neglect of the elastic frame (in the context of Biot's theory) amounts to treating the porous medium as a homogeneous fluid, capable of supporting Biot's ''fast'' compressional wave but not the ''slow'' wave nor the shear wave of the full Biot theory.

Experimentally, the shear wave is observed to be weak[4] and the slow wave is negligible, if present at all,[5–10] in saturated, unconsolidated granular materials. For such materials, the ''effective fluid'' representation is probably reasonable. Indeed, in an alternative to the Biot theory, developed recently by Buckingham,[11] in which the internal stresses arise from intergranular traction rather than pore–fluid viscosity, the absence of a mineral frame has been taken as a defining feature of an unconsolidated sediment. Two types of wave emerge from Buckingham's model, a fast compressional wave and a shear wave (even though there is no elastic frame), the latter arising naturally from the rigidity introduced into the medium by the intergranular interactions.

Although the number of parameters involved in the EDF model is four less than in the full Biot theory, the final result for the complex sound speed [Eqs. (13) and (14), in Williams[1]] still involves eight variables, as listed in Table I, which describe material properties. At first sight, so many variables would seem to suggest that the EDF dispersion curves are highly adjustable, but this is not the case. As may be seen in Figs. 2 and 3 of Williams[1] showing the frequency dependence of the phase speed and attenuation, the EDF dispersion curves exhibit just three characteristic features: (1) a low-frequency limit to the phase speed, c_0; (2) a high-frequency limit to the phase speed, c_∞; and (3) a transition frequency, f_T, separating the low- and high-frequency regimes in the phase speed and attenuation curves. As frequency increases through f_T, the attenuation switches from a low-frequency power-law scaling of f^2 to a high-frequency scaling of $f^{1/2}$ and the phase speed begins to increase above the low-frequency value, c_0, to approach asymptotically the limiting high-frequency value, c_∞. If the complex sound speed can be represented by just the three parameters (c_0, c_∞, f_T), it follows that the eight material variables shown in Table I do not affect the predictions of the EDF model independently, but instead these eight variables must collapse into the three parameters (c_0, c_∞, f_T).

The phase speed and attenuation curves in Figs. 2 and 3 of Williams[1] are reminiscent of the complex sound speed in a purely viscous fluid[12] or, equivalently, a Voigt solid.[13] The only difference is that, in a viscous fluid, the phase speed diverges at high frequencies as $f^{1/2}$, which is tantamount to saying that c_∞ is infinite, as opposed to the EDF model where c_∞ is finite. Otherwise, the EDF model yields dispersion curves exhibiting the familiar characteristics of viscous dissipation. This is perhaps not surprising, since the only loss mechanism in the EDF model, and indeed in the full Biot

a)Also affiliated with the Institute of Sound and Vibration Research, The University, Southampton SO 17 1BJ, United Kingdom. Electronic mail: mjb@mpl.ucsd.edu

TABLE I. Nomenclature and values [after Williams (Ref. 1)] for the eight material properties relevant to the EDF model.

Material property	Symbol	Value
Porosity	β	0.4
Density of mineral grains	ρ_s	2650 kg/m^3
Bulk modulus of mineral grains	K_r	3.6×10^{10} Pa
Density of pore fluid	ρ_f	1000 kg/m^3
Bulk modulus of pore fluid	K_f	2.25×10^{9} Pa
Viscosity of pore fluid	η	0.001 kg/m s
Permeability	κ	1.0×10^{-10} m^2
Tortuosity	α	1.25

theory, is viscosity of the pore fluid. As discussed below, after introducing a minor modification, the expression for the complex sound speed in a viscous fluid is found to match accurately the phase speed and attenuation from the EDF model at all frequencies.

In this article, the predictions of the EDF model are summarized and compared with those of the modified viscous fluid (MVF) model,[14] the latter involving only the three parameters (c_0, c_∞, f_T). Explicit expressions are derived for these three parameters in terms of the eight material variables listed in Table I. It turns out that the MVF model is, for practical purposes, indistinguishable from the EDF model and, being purely algebraic, is easier to compute. The principal advantage of the MVF model, however, is that it provides an elementary means of identifying the effects of the material variables on the main features of the EDF dispersion curves. For example, the limiting low- and high-frequency phase speeds, c_0 and c_∞, respectively, are independent of both the permeability, κ, and the pore–fluid viscosity, η; these two material variables affect the dispersion curves *only* as the ratio (η/κ), which appears *only* as a linear scaling factor in the expression for the transition frequency, f_T. Obviously, it follows that if the permeability and viscosity are scaled by the same factor, the dispersion curves from the EDF model remain invariant.

Before proceeding with the development of the MVF model, it is as well to point out that many authors have applied the full Biot theory to the interpretation of wave propagation data obtained from a wide variety of porous media, including consolidated and unconsolidated marine sediments (for a bibliography covering much of the relevant material that had been published up until 1989, see the monograph by Stoll[15]). In other applications, the Biot model has been incorporated into a parabolic equation for the purpose of estimating acoustic propagation loss in ocean channels overlying poroelastic layers;[16] and, in a rather different arena, the Biot theory has been applied in the interpretation of medical-acoustics data, particularly on ultrasonic wave propagation in water-saturated cancellous and cortical bone.[17] Several authors have investigated the sensitivity of the Biot dispersion curves to variations in the material parameters of sediments, a recent example being the paper by Mu *et al.*,[18] which includes references to earlier work on a similar theme. Apart from the paper by Williams,[1] however, little has been done in the way of reducing the Biot theory to a form that provides simple physical insights into the predicted dispersion relationships for unconsolidated marine sediments. This is the aim of the following discussion.

II. SUMMARY OF THE EDF MODEL

In the following account of the EDF model, the nomenclature adopted is similar to that used by Williams.[1] As the symbols representing the eight material variables are identified in Table I, not all of their definitions are repeated in the text.

According to Eq. (13) in Williams,[1] the complex sound speed, c, in the two-phase, EDF medium is given by

$$\frac{1}{c}=\sqrt{\frac{\rho_{\mathrm{eff}}}{H}}, \tag{1}$$

where

$$H=\left[\frac{(1-\beta)}{K_r}+\frac{\beta}{K_f}\right]^{-1} \tag{2}$$

is the bulk modulus (i.e., the reciprocal of the compressibility) of the composite material. From an inspection of Williams' Eq. (14), it is clear that the complex effective density, ρ_{eff}, can be expressed in the form

$$\rho_{\mathrm{eff}}(\omega\tau_0)=\rho_f\left\{\frac{\rho_1+i\beta\rho\dfrac{F(\omega\tau_0)}{\omega\tau_0}}{\rho_2+i\beta\rho_f\dfrac{F(\omega\tau_0)}{\omega\tau_0}}\right\}, \tag{3}$$

where ω is angular frequency and ρ is the bulk density of the two-phase medium, as given by the following linear combination of the densities of the mineral grains and pore fluid:

$$\rho=\beta\rho_f+(1-\beta)\rho_s. \tag{4}$$

The two parameters $\rho_{1,2}$ in Eq. (3) have units of density and are given by the expressions

$$\rho_1=\alpha(1-\beta)\rho_s+\beta(\alpha-1)\rho_f, \tag{5a}$$

$$\rho_2=\beta(1-\beta)\rho_s+(\alpha-2\beta+\beta^2)\rho_f. \tag{5b}$$

Clearly, the tortuosity, α, affects ρ_1 and ρ_2 but appears nowhere else in the EDF model. Note that, in Eq. (3), the frequency dependence of ρ_{eff} is contained exclusively in the term $(\omega\tau_0)^{-1}F(\omega\tau_0)$, where $\omega\tau_0$ is a dimensionless frequency, and the normalizing time is

$$\tau_0=\frac{\kappa\rho_f}{\eta}. \tag{6}$$

It is to be emphasized that the permeability, κ, and pore–fluid viscosity, η, appear in the EDF model only through τ_0, and hence, as mentioned earlier, they affect the dispersion curves only as the ratio κ/η. Moreover, τ_0 appears only as the normalizing factor in the dimensionless frequency $(\omega\tau_0)$. A similar but not identical normalization was used by Biot[2,3] in the form of a "characteristic frequency" $f_c=\beta/(2\pi\tau_0)$, which he used when plotting compressional wave speeds as a function of frequency.

The function F in Eq. (3) was introduced by Biot[3] to account for the departure from Poiseuille flow through the pores of the mineral frame as frequency increases. He derived the expression

$$F(\varepsilon)=\frac{(\varepsilon/4)T(\varepsilon)}{1-(2i/\varepsilon)T(\varepsilon)}, \tag{7}$$

in which

$$T(\varepsilon)=\frac{-\sqrt{i}J_1(\varepsilon\sqrt{i})}{J_0(\varepsilon\sqrt{i})}, \tag{8a}$$

where J_n are Bessel functions of the first kind of order $n=0$, 1. The argument of F is

$$\varepsilon=a\sqrt{\frac{\omega\rho_f}{\eta}}, \tag{8b}$$

where a is the pore size parameter, an expression for which has been derived by Johnson, Koplik, and Dashen:[19]

$$a=\sqrt{\frac{8\alpha\kappa}{\beta}}. \tag{9}$$

On combining Eqs. (8b) and (9), it is evident that

$$\varepsilon=\varepsilon(\omega\tau_0)=\sqrt{\frac{8\alpha}{\beta}\omega\tau_0}, \tag{10}$$

thus confirming that frequency always appears in the EDF dispersion relationship as the dimensionless product $\omega\tau_0$.

Equations (1)–(10) constitute the complete ''fluid'' Biot, or EDF, model, although Eq. (3) for the effective density is formulated slightly differently from the version in Williams[1] in order to make explicit the dependence on the normalized frequency $\omega\tau_0$. Later, it will become clear that the transition frequency, f_T, is proportional to $(\tau_0)^{-1}$, from which it follows that the only role of the permeability and the pore–fluid viscosity is to scale f_T by the factor η/κ. This scaling amounts to a simple translation of the EDF dispersion curves along the (logarithmic) frequency axis, leaving their shapes unchanged.

To express f_T in terms of the material properties, it will be necessary to compare the MVF and EDF models, a procedure that will require the Taylor expansion of Eq. (1) to first order in the normalized frequency, $\omega\tau_0$. The series is straightforward to derive, although care must be taken to expand the function T in Eq. (8) to fourth order in ε, which then yields the function F to second order in ε:

$$F(\varepsilon)=1+\frac{i\varepsilon^2}{4}-\cdots. \tag{11}$$

When Eq. (11) is combined with Eq. (1), and after a little more algebra, the following expansion, to first order in $\omega\tau_0$, for the reciprocal of the complex sound speed is obtained:

$$\frac{1}{c}=\sqrt{\frac{\rho}{H}}\left\{1+\frac{i\omega\tau_0}{2\beta}\left(\frac{\rho_2}{\rho_f}-\frac{\rho_1}{\rho}\right)+\cdots\right\}. \tag{12}$$

This expression, and hence also Eq. (3), can be seen to correspond to a time dependence of the form $\exp(-i\omega t)$. It is obvious from Eq. (12) that, in the limit of low frequency, the complex sound speed becomes real and is given by

$$c_0=\sqrt{\frac{H}{\rho}}, \tag{13}$$

which is identical to Wood's equation[20] for a suspension of noninteracting particles in a fluid. In his original papers, Biot[2,3] used c_0 as a normalizing factor in plots of the phase speed of the dilatational waves of the first and second kind (i.e., the fast and slow compressional waves).

III. THE MVF MODEL

Wave propagation in a viscous fluid or a Voigt solid is governed by a linear, second-order, partial differential equation of the form[12,13]

$$\nabla^2\psi-\frac{1}{c_0^2}\ddot{\psi}+\tau\nabla^2\dot{\psi}=0, \tag{14}$$

where ∇^2 is the Laplacian, ψ is the velocity potential, the coefficient τ is a viscous dissipation time, and c_0 is still the phase speed in the medium in the limit of low frequency. From the solution of this equation, the reciprocal of the complex sound speed, $\overline{c}$, in a viscous fluid may be expressed as

$$\frac{1}{\overline{c}}=\frac{1}{c_0}\frac{\sqrt{1+i\omega\tau}}{[1+\omega^2\tau^2]^{1/2}}, \tag{15}$$

where, for consistency with the EDF model, the time-dependence has been chosen as $\exp(-i\omega t)$, as may be deduced from the plus (+) sign preceding the imaginary term under the radical in the numerator. Equation (15) is a well-known expression, which shows a frequency dependence that exhibits two regimes, high and low, separated by a transition frequency $f_T=(2\pi\tau)^{-1}$.

By taking its real and imaginary parts, Eq. (15) yields the following expressions for phase speed, $\overline{c_p}$, and attenuation, $\overline{\alpha_p}$, in a viscous fluid:

$$\overline{c_p}=[\Re(\overline{c}^{-1})]^{-1}=\frac{\sqrt{2}c_0\sqrt{1+\omega^2\tau^2}}{[1+\sqrt{1+\omega^2\tau^2}]^{1/2}} \rightarrow\begin{cases} c_0, & \text{for } \omega\tau\ll 1,\\ c_0\sqrt{2\omega\tau}, & \text{for } \omega\tau\gg 1,\end{cases} \tag{16}$$

and

$$\overline{\alpha_p}=[\omega\Im(\overline{c}^{-1})]=\frac{\omega}{\sqrt{2}c_0}\frac{[\sqrt{1+\omega^2\tau^2}-1]^{1/2}}{\sqrt{1+\omega^2\tau^2}} \rightarrow\begin{cases} \dfrac{\omega^2\tau}{2c_0}, & \text{for } \omega\tau\ll 1,\\ \dfrac{1}{c_0}\sqrt{\dfrac{\omega}{2\tau}}, & \text{for } \omega\tau\gg 1.\end{cases} \tag{17}$$

Clearly, the high- and low-frequency limiting forms of the attenuation in Eq. (17) are identical to those of the EFD model, as exemplified in Fig. 3 of Williams.[1] The low-frequency limit of the phase speed in Eq. (16) also conforms with the EDF model, but at high frequencies $\overline{c_p}$ in Eq. (16) scales as $\omega^{1/2}$, unlike the phase speed from the EDF model, which, as illustrated in Williams' Fig. 2, asymptotes to a finite limiting value, c_∞.

The full frequency dependence of the EDF model, including the high-frequency limiting behavior of the phase speed, may be reproduced by making Eq. (15) a little more general:[14]

$$\frac{1}{\overline{c}}=\left(\frac{1}{c_0}-\frac{1}{c_\infty}\right)\frac{\sqrt{1+i\omega\tau}}{[1+\omega^2\tau^2]^{1/2}}+\frac{1}{c_\infty}, \tag{18}$$

which is the form referred to earlier as the modified viscous fluid (MVF) model. [*N.B.*: As in Eq. (15), the plus (+) sign preceding the imaginary term under the radical in Eq. (18) corresponds to an implied time dependence of the form $\exp(-i\omega t)$, consistent with the convention used in the EDF model. This accounts for the difference between Eq. (18) and its counterpart, Eq. (25), in Ref. 14, where the imaginary term is preceded by a minus (−) sign, corresponding to a time dependence of the form $\exp(+i\omega t)$]. By an extension of Eqs. (16) and (17), the phase speed and attenuation from the MVF model may be expressed as follows:

$$\overline{c}_p=\left[\frac{1}{\sqrt{2}}\left(\frac{1}{c_0}-\frac{1}{c_\infty}\right)\left\{\frac{\sqrt{1+\omega^2\tau^2}+1}{1+\omega^2\tau^2}\right\}^{1/2}+\frac{1}{c_\infty}\right]^{-1}$$
$$\rightarrow\begin{cases}c_0, & \text{for } \omega\tau\ll 1,\\ c_\infty, & \text{for } \omega\tau\gg 1,\end{cases} \tag{19}$$

and

$$\overline{\alpha}_p=\frac{\omega}{\sqrt{2}}\left(\frac{1}{c_0}-\frac{1}{c_\infty}\right)\left\{\frac{\sqrt{1+\omega^2\tau^2}-1}{1+\omega^2\tau^2}\right\}^{1/2}$$
$$\rightarrow\begin{cases}\dfrac{\omega^2\tau}{2}\left(\dfrac{1}{c_0}-\dfrac{1}{c_\infty}\right) & \text{for } \omega\tau\ll 1,\\ \sqrt{\dfrac{\omega}{2\tau}}\left(\dfrac{1}{c_0}-\dfrac{1}{c_\infty}\right), & \text{for } \omega\tau\gg 1.\end{cases} \tag{20}$$

The value of the attenuation, $\overline{\alpha}_{pT}$, at the transition frequency, that is, when $\omega=2\pi f_T=1/\tau$, will be useful later as a normalizing factor. From Eq. (20),

$$\overline{\alpha}_{pT}=\frac{\sqrt{\sqrt{2}-1}}{2\tau}\left(\frac{1}{c_0}-\frac{1}{c_\infty}\right), \tag{21}$$

where, it should be noted, the term on the right is inversely proportional to τ.

Obviously, if c_∞ were infinite, Eq. (18) would reduce to the expression in Eq. (15) for a true viscous fluid. When c_∞ is finite, however, the MVF dispersion curves are almost identical in shape to those from the EDF model. In particular, the high-frequency phase speed from Eq. (19) asymptotes to c_∞, in accord with the EDF model.

For a quantitative comparison of the two models, it is necessary to express the three parameters (c_0, c_∞, f_T) in terms of the eight material variables of the EDF model. This has already been done for c_0 in Eq. (13). From the asymptotic expansions of the Bessel functions in Eq. (8), it can be shown that the function F in Eq. (7) scales as $\sqrt{\omega\tau_0}$ in the limit of high frequency, and hence it follows from Eqs. (1) and (3) that

$$c_\infty=c_0\sqrt{\frac{\rho_2\rho}{\rho_1\rho_f}}. \tag{22}$$

Unlike c_0, the high-frequency phase speed, c_∞, depends on the tortuosity, α, through the presence of the ratio ρ_2/ρ_1 under the radical in Eq. (22). Expressions equivalent to those in Eqs. (13) and (22) have been given by Williams,[1] although not in the context of the MVF model in Eq. (18).

The one remaining parameter to be identified in Eq. (18) is the transition frequency, $f_T=(2\pi\tau)^{-1}$. This is readily derived by expanding the MVF model [Eq. (18)] in a Taylor series to first order in $\omega\tau$:

$$\frac{1}{\overline{c}}=\frac{1}{c_0}\left[1+\frac{i\omega\tau}{2}\frac{(c_\infty-c_0)}{c_\infty}-\cdots\right]. \tag{23}$$

On equating the first-order term here to that in the Taylor series for the complex wave speed [Eq. (12)] from the EDF model, it is found that

$$\tau=\frac{\tau_0}{\beta}\left(\frac{\rho_2}{\rho_f}-\frac{\rho_1}{\rho}\right)\left(\frac{c_\infty}{c_\infty-c_0}\right). \tag{24}$$

Thus, the transition frequency, $f_T=(2\pi\tau)^{-1}$, scales as $(1/\tau_0)$, which, as has been shown in Eq. (6), is proportional to the ratio η/κ. It is also evident that τ depends on the porosity, β, and the tortuosity, α. Note that the transition frequency, f_T, differs from Biot's[2,3] characteristic frequency, f_c, through the presence of the terms in round brackets in Eq. (24).

IV. COMPARISON OF THE EDF AND MVF MODELS

To compare the EDF and MVF models, it is convenient to plot the dispersion curves as functions of the dimensionless frequency, $\omega\tau_0/2\pi$. Then the phase speed and attenuation (normalized to $\overline{\alpha}_{pT}$) from both models are invariant to changes in the permeability and the pore–fluid viscosity. As for the remaining six material variables, we shall adopt the values shown in Table I, which are the same as in Williams.[1] With these material properties, the values of the three parameters characterizing the MVF model are $c_0=1607.6$ m/s, from Eq. (13), $c_\infty=1752.1$ m/s, from Eq. (22), and $f_T=266.46$ Hz ($\tau=0.5973$ ms), from Eq. (24). The normalizing attenuation, from Eq. (21), is $\overline{\alpha}_{pT}=0.24$ dB/m.

Figure 1 shows the phase speed normalized to c_0 and the attenuation normalized to $\overline{\alpha}_{pT}$ as functions of the normalized frequency, $\omega\tau_0$. The curves in Figs. 1(a) and 1(b) have been evaluated from the EDF model [Eq. (1)] and the MVF model [Eq. (18)]. As noted above, the shapes of these curves are universally valid for all values of permeability and pore–fluid viscosity. To convert the normalized frequencies along the abscissa to Hz, it is necessary only to multiply by the factor $\tau_0^{-1}=10^4$ Hz for the particular values of the material variables in Table I. When the normalizing factors on the ordinates are backed out, the EDF curves in Fig. 1 are seen to be identical to those in Figs. 2 and 3 in Williams.[1]

The normalized transition frequency in Fig. 1 takes the value $f_T\tau_0=0.026\,65$, which falls toward the lower end of the low- to high-frequency transition region of the EDF sound speed and attenuation curves (unlike Biot's normaliz-

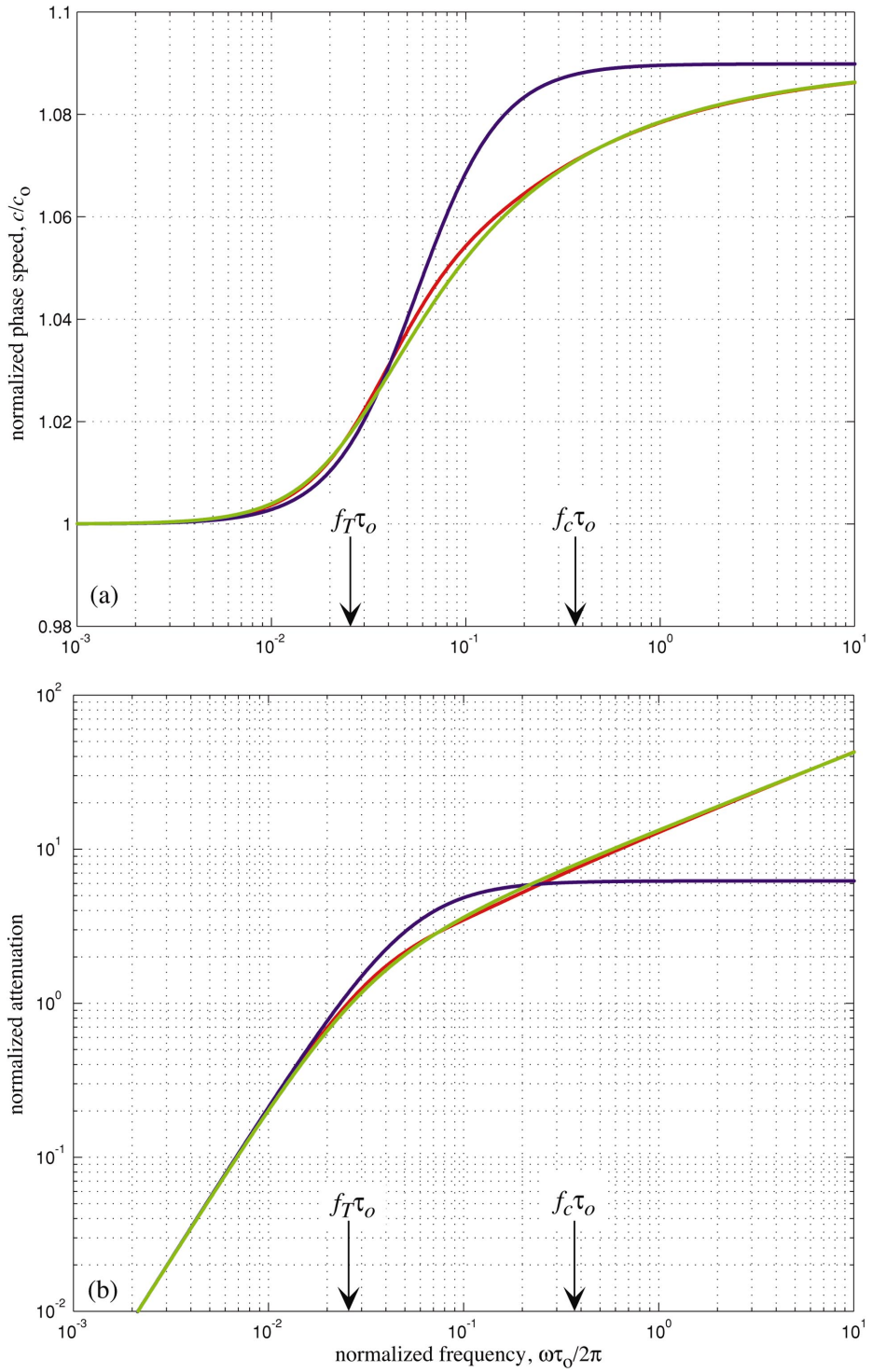

FIG. 1. Dispersion curves from the EDF model (red) and the MVF model (green) plotted as functions of normalized frequency $\omega\tau_0/2\pi$. (a) Phase speed normalized to c_0 and (b) attenuation normalized to $\overline{\alpha}_{pT}$. The blue curves are from the EDF model but with Biot's function F set to unity. The transition frequency, $f_T\tau_0$, and Biot's normalizing frequency, $f_c\tau_0=\beta$, are indicated on the frequency axes by the vertical arrows.

ing frequency, $f_c=\beta/\tau_0$, which falls well above the transition region). Thus, f_T provides a useful measure of the frequency at which the transition from low- to high-frequency behavior begins.

It is clear from Fig. 1 that the EDF and MVF models are indistinguishable at high and low frequencies, and are almost so at mid-frequencies, where the curves separate slightly but by little more than the thickness of the lines themselves. The natural conclusion is that, at all frequencies, the algebraic, three-parameter MVF model provides a very good approximation to Biot's "fluid" theory, as expressed through the EDF model developed by Williams.[1]

V. POROSITY AND TORTUOSITY

The normalizations in Fig. 1 are useful for making the comparison between the EDF and MVF models. For a me-

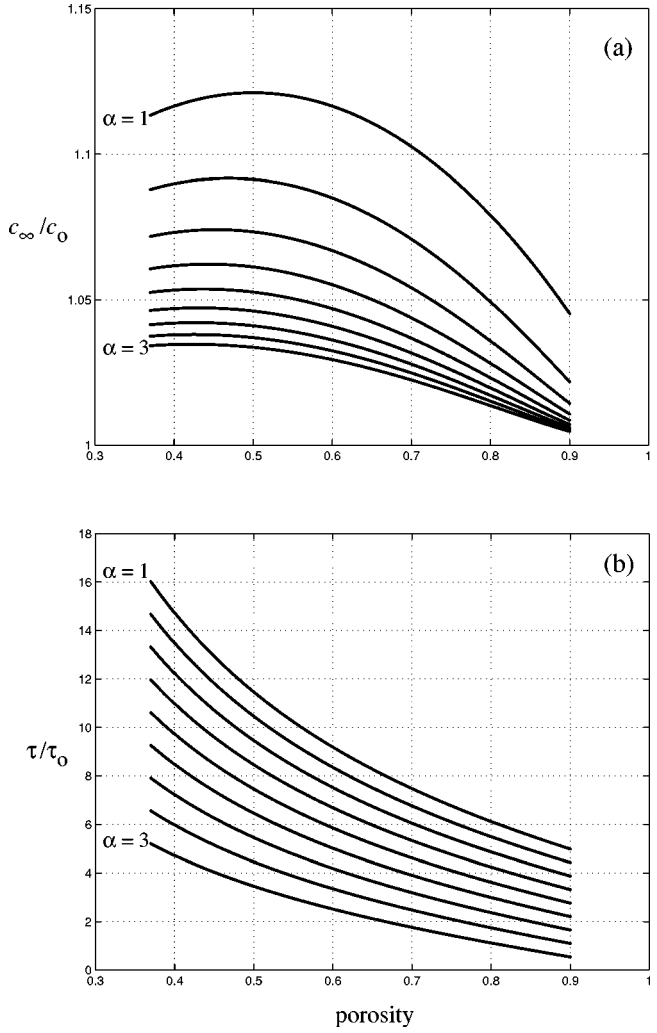

FIG. 2. The normalized variables a) c_∞/c_0 from Eq. (22) and b) τ/τ_0 from Eq. (24) as functions of porosity, with tortuosity, $\alpha = 1,1.25,1.5,...,2.75,3$, treated as a parameter.

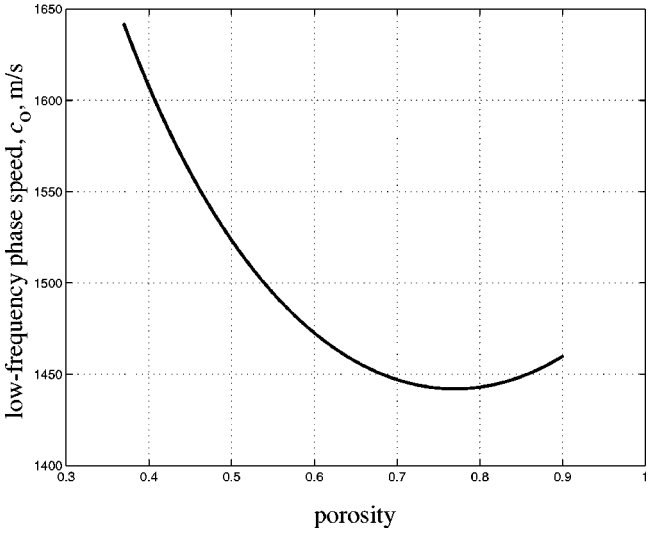

FIG. 3. Low-frequency (Wood's) phase speed, c_0, as a function of porosity, from Eqs. (13), (2), and (4).

dium described by the material properties in Table I, the absolute values of phase speed and attenuation are readily obtained from Fig. 1 by multiplying the normalized ordinates by the respective normalizing factors, $c_0 = 1607.6$ m/s and $\overline{\alpha}_{pT} = 0.24$ dB/m. In the following discussion, a simple scheme is outlined for evaluating the three parameters (c_0, c_∞, f_T) of the MVF model, and hence the normalizing factors, for a more general set of values for the material parameters.

Since the material constituents of many marine sediments are much the same, namely quartz–sand and seawater, the surficial densities, ρ_s and ρ_f, and bulk moduli, K_r and K_f, of the solid and fluid phases are more or less invariant (if minor temperature dependencies are neglected) from one sediment to another, with representative values as given in Table I. In contrast, the ratio of the permeability to the pore–fluid viscosity, κ/η, may vary by several orders of magnitude between sediments, primarily due to differences in the permeability[15] and perhaps a weak temperature dependence exhibited by the viscosity of seawater. However, the effects of such variations on the wave properties predicted by the EDF model have already been taken into account by plotting the dispersion curves (phase speed and normalized attenuation) in Fig. 1 as functions of the normalized frequency $\omega\tau_0$. Absolute frequency may be recovered once τ_0 has been determined from Eq. (6). This leaves only two variables still to be to dealt with in Table I, the porosity, β, and tortuosity, α, of the granular medium, both of which may vary significantly from one sediment to another.

According to Stoll,[15] the tortuosity (also known as the structure factor) may theoretically take values between 1 and 3; and, as summarized in Figs. 5, 6, and 9 of Buckingham,[21] observations by Hamilton[22,23] and Richardson[24–26] indicate that the fractional porosity may lie anywhere between 0.37 and 0.85, with the larger-grained sediments tending toward lower porosities. The lower limiting value of the porosity is exhibited by the coarser sands and, at 0.37, is consistent with a random packing of smooth, uniform spheres.[27,28] In the finer sediments, the rms roughness of the grains may be comparable with the grain diameter, thus permitting enhanced percolation of seawater between grains, which, according to a geometrical, random-packing model by Buckingham,[21] could account for the higher values of porosity observed in the fine-grained materials.

Be that as it may, the normalized parameters (c_∞/c_0) and (τ/τ_0) vary with the porosity and the tortuosity (but not with the permeability or pore–fluid viscosity). The functional dependence of these parameters on porosity is plotted in Fig. 2, where each curve is associated with a fixed value of the tortuosity. The families of curves in Figs. 2(a) and 2(b) were computed from Eqs. (22) and (24), respectively. The low-frequency phase speed, c_0, given by Wood's equation[20] [Eq. (13)], is independent of the tortuosity but varies with the porosity, as shown in Fig. 3.

Once the porosity and tortuosity of a sediment have been specified, the corresponding values of (c_∞/c_0), (τ/τ_0) and c_0 may be read from the curves in Figs. 2 and 3. Dispersion pairs (phase speed and absolute attenuation versus frequency) may then be computed directly from the MVF model in Eq. (18) for any set of values (representing sandy sediments) for the eight material variables. Alternatively,

since Figs. 2 and 3 yield the necessary normalizing factors, the absolute values of phase speed and attenuation at a spot frequency may be determined directly from the green curves in Fig. 1.

In the case of muds, silts and clays, where the density and bulk modulus of the mineral grains may vary significantly from one material to another, it is probably easier to abandon the graphical approach in favor of direct evaluation of the three parameters (c_0, c_∞, f_T) from Eqs. (13), (22), and (24). The phase speed and attenuation may then be computed directly from Eq. (18) or Eqs. (19) and (20).

VI. BIOT'S FLOW FUNCTION, *F*

It could be argued that the function F, introduced by Biot to account for the high-frequency departure from Poiseuille flow through the pores, is the most complicated part of the EDF model. As specified by Eqs. (7)–(10), F exhibits a frequency dependence that is not immediately apparent, since it involves the ratio of two Bessel functions of complex argument. Hence the effects of F on the dispersion curves are obscure, although it is fairly evident that the flow function has little influence at low frequencies, where it takes a value very close to unity.

To illustrate how F modifies the dispersion curves, the EDF model [Eq. (1)] has been evaluated with F set to unity at all frequencies. The result for the normalized phase speed and attenuation is illustrated by the blue curves in Fig. 1. Below the transition frequency (i.e., $f_T\tau_0 = 0.026\,65$ on the abscissa in Fig. 1), it is clear that F has a negligible effect on the phase speed and attenuation. At mid-frequencies, with $F=1$, the phase speed is overestimated, as is the attenuation, but in both cases by no more than about 2%; and at high frequencies, the phase speed asymptotes to c_∞, just as it does when using the full expression for F, but the attenuation becomes constant, independent of frequency, rather than diverging as $\omega^{1/2}$, as predicted by the complete EDF model.

Clearly, the effects of F on the dispersion curves are rather minor. Principally, the frequency dependence of F [Eqs. (7)–(10)] serves to ensure that the form of the attenuation predicted by the EDF model is, ironically, no different from that of a simple viscous fluid.

VII. CONCLUDING REMARKS

It is clear from the comparison of the EDF and MVF models that the dispersion curves predicted by the "fluid" Biot theory are constrained to take simple shapes that are governed by just three parameters, (c_0, c_∞, f_T). Two of these parameters, c_0 and c_∞, are the phase speeds in the limit of low and high frequency, respectively, and the third, f_T, is a transition frequency that separates the high- and low-frequency regimes in the phase speed and attenuation curves. Embedded in these three parameters are the eight variables, listed in Table I, that describe the material properties of the saturated porous medium. Explicit, algebraic expressions have been derived for all three parameters [Eqs. (13), (22), and (24)], allowing the MVF model to be evaluated for any set of the material properties.

The transition frequency, f_T, scales inversely with a normalizing time, τ_0, which itself is proportional to the ratio of the permeability to the pore–fluid viscosity (κ/ν). These two material properties appear nowhere in the "fluid" Biot theory outside τ_0. In particular, the limiting low- and high-frequency phase speeds, c_0 and c_∞, respectively, are independent of permeability and pore–fluid viscosity.

Taking as an example a typical sandy sediment represented by the values of the material properties in Table I, the normalizing time, τ_0, from Eq. (6), is 0.1 ms and, from Eq. (24), the transition frequency is $f_T = (2\pi\tau)^{-1} = 266.5$ Hz. Much below this frequency, the EDF model predicts a sound speed close to c_0 and an attenuation scaling as f^2; and much above the sound speed asymptotes to c_∞ and the attenuation scales as $f^{1/2}$. It is, however, still an open question as to whether the measured dispersion curves of sandy marine sediments show a pronounced transition from low- to high-frequency behavior somewhere around several hundred Hertz. This is an issue that has recently been the subject of debate within ONR's SAX99 research initiative on the interaction of sound with marine sediments.[14,29]

An alternative possibility, and one that is consistent with a grain-shearing argument,[11] is that no such transition occurs, and instead the phase speed and attenuation curves show more or less constant (log–log) gradients at all frequencies, including the band between 0.1 and 1 kHz. It is not easy, however, to measure the dispersion at frequencies below 1 kHz with sufficient precision to distinguish between the two theoretical predictions. New techniques that are currently under development,[30,31] involving a high-Doppler, airborne sound source (a propeller-driven aircraft) and acoustic sensors buried in the sediment, may yield sufficiently precise estimates of the phase speed and attenuation in the frequency band 0.1–1 kHz to resolve the issue.

ACKNOWLEDGMENTS

This work was supported by Dr. J. Simmen and Dr. E. Livingston, Ocean Acoustics Code, the Office of Naval Research, under Grants No. N00014-93-1-0054 and No. N00014-04-1-0063.

[1] K. L. Williams, "An effective density fluid model for acoustic propagation in sediments derived from Biot theory," J. Acoust. Soc. Am. **110**, 2276–2281 (2001).
[2] M. A. Biot, "Theory of propagation of elastic waves in a fluid-saturated porous solid: I. Low-frequency range," J. Acoust. Soc. Am. **28**, 168–178 (1956).
[3] M. A. Biot, "Theory of propagation of elastic waves in a fluid-saturated porous solid: II. Higher frequency range," J. Acoust. Soc. Am. **28**, 179–191 (1956).
[4] M. D. Richardson *et al.*, "Overview of SAX99: environmental considerations," IEEE J. Ocean. Eng. **26**, 26–53 (2001).
[5] H. J. Simpson and B. H. Houston, "A synthetic array measurement of a fast compressional and a slower wave in an unconsolidated water-saturated porous medium," J. Acoust. Soc. Am. **102**, 3210 (1997).
[6] H. J. Simpson and B. H. Houston, "Analysis of laboratory measurements of sound propagating into an unconsolidated water-saturated porous media," J. Acoust. Soc. Am. **103**, 3095–3096 (1998).
[7] H. J. Simpson, B. H. Houston, and L. S. Couchman, "Measurements and modeling of sound propagating into unconsolidated water-saturated porous media in a laboratory environment," J. Acoust. Soc. Am. **104**, 1787 (1998).
[8] H. J. Simpson and B. H. Houston, "Synthetic array measurements of

acoustical waves propagating into a water-saturated sandy bottom for a smoothed and a roughened interface,'' J. Acoust. Soc. Am. **107**, 2329–2337 (2000).
[9] T. J. Plona, ''Observation of a second bulk compressional wave in a porous medium at ultrasonic frequencies,'' Appl. Phys. Lett. **36**, 259–261 (1980).
[10] D. L. Johnson and T. J. Plona, ''Acoustic slow waves and the consolidation transition,'' J. Acoust. Soc. Am. **72**, 556–565 (1982).
[11] M. J. Buckingham, ''Wave propagation, stress relaxation, and grain-to-grain shearing in saturated, unconsolidated marine sediments,'' J. Acoust. Soc. Am. **108**, 2796–2815 (2000).
[12] M. J. Buckingham, ''Acoustic pulse propagation in dispersive media,'' in *New Perspectives on Problems in Classical and Quantum Physics. Part II. Acoustic Propagation and Scattering—Electromagnetic Scattering*, edited by P. P. Delsanto and A. W. Sáenz (Gordon and Breach, Amsterdam, 1998), Vol. 2, pp. 19–34.
[13] J. E. White, *Underground Sound: Application of Seismic Waves* (Elsevier, Amsterdam, 1983).
[14] M. J. Buckingham and M. D. Richardson, ''On tone-burst measurements of sound speed and attenuation in sandy marine sediments,'' IEEE J. Ocean. Eng. **27**, 429–453 (2002).
[15] R. D. Stoll, *Sediment Acoustics* (Springer-Verlag, Berlin, 1989).
[16] M. D. Collins, W. A. Kuperman, and W. L. Siegmann, ''A parabolic equation for poro-elastic media,'' J. Acoust. Soc. Am. **98**, 1645–1656 (1995).
[17] J. L. Williams, ''Ultrasonic wave propagation in cancellous and cortical bone: Prediction of some experimental results by Biot's theory,'' J. Acoust. Soc. Am. **91**, 1106–1112 (1992).
[18] Y. Mu, M. Badiey, and A. H.-D. Cheng, ''Parameter uncertainty analysis on acoustic response in fluid filled poroelastic media,'' J. Acoust. Soc. Am. **106**, 151–163 (1999).
[19] D. L. Johnson, J. Koplik, and R. Dashen, ''Theory of dynamic permeability and tortuosity in fluid-saturated porous media,'' J. Fluid Mech. **176**, 379–402 (1987).
[20] A. B. Wood, *A Textbook of Sound*, 3rd ed., p. 361, Eq. (3) (Bell and Sons, London, 1964).
[21] M. J. Buckingham, ''Theory of acoustic attenuation, dispersion, and pulse propagation in unconsolidated granular materials including marine sediments,'' J. Acoust. Soc. Am. **102**, 2579–2596 (1997).
[22] E. L. Hamilton, ''Sound velocity and related properties of marine sediments, North Pacific,'' J. Geophys. Res. **75**, 4423–4446 (1970).
[23] E. L. Hamilton, ''Compressional-wave attenuation in marine sediments,'' Geophysics **37**, 620–646 (1972).
[24] M. D. Richardson, ''Spatial variability of surficial shallow water sediment geoacoustic properties,'' in *Ocean-Seismo Acoustics: Low-Frequency Underwater Acoustics*, edited by T. Akal and J. M. Berkson (Plenum, New York, 1986), pp. 527–536.
[25] M. D. Richardson and K. B. Briggs, ''On the use of acoustic impedance values to determine sediment properties,'' in *Acoustic Classification and Mapping of the Seabed*, edited by N. G. Pace and D. N. Langhorne (University of Bath, Bath, 1993), Vol. 15, pp. 15–24.
[26] M. D. Richardson and K. B. Briggs, ''In situ and laboratory geoacoustic measurements in soft mud and hard-packed sand sediments: Implications for high-frequency acoustic propagation and scattering,'' Geo-Mar. Lett. **16**, 196–203 (1996).
[27] O. K. Rice, ''On the statistical mechanics of liquids, and the gas of hard elastic spheres,'' J. Chem. Phys. **12**, 1–18 (1944).
[28] M. R. Wyllie, A. R. Gregory, and L. W. Gardner, ''Elastic wave velocities in heterogeneous and porous media,'' Geophysics **21**, 41–70 (1956).
[29] K. L. Williams, D. R. Jackson, E. I. Thorsos, D. Tang, and S. G. Schock, ''Comparison of sound speed and attenuation measured in a sandy sediment to predictions based on the Biot theory of porous media,'' IEEE J. Ocean. Eng. **27**, 413–428 (2002).
[30] M. J. Buckingham, E. M. Giddens, J. B. Pompa, F. Simonet, and T. R. Hahn, ''Sound from a light aircraft for underwater acoustics experiments?,'' Acta Acustica united with Acustica **88**, 752–755 (2002).
[31] M. J. Buckingham, E. M. Giddens, F. Simonet, and T. R. Hahn, ''Propeller noise from a light aircraft for low-frequency measurements of the speed of sound in a marine sediment,'' J. Comput. Acoust. **10**, 445–464 (2002).

Space–time variations of the acoustic field scattered from a penetrable isovelocity wedge

C. Feuillade[a)]
Naval Research Laboratory, Stennis Space Center, Mississippi 39529

D. Chu
Department of Ocean Physics and Engineering, Woods Hole Oceanographic Institution, Woods Hole, Massachusetts 02543

C. S. Clay
Geophysical and Polar Research Center, University of Wisconsin—Madison, Madison, Wisconsin 53706

(Received 25 June 2003; revised 31 March 2004; accepted 20 May 2004)

The formalism of D. Chu [J. Acoust. Soc. Am. **86**, 1883–1896 (1989)] is used to detail the spatial and time domain variations of the scattered field of a penetrable isovelocity wedge. The direct, reflected, and diffracted field components, and their relationships, are investigated. Since diffractions often dominate rough surface scattering, these waves are carefully studied, with particular emphasis on the wave phenomena and transition behavior around the forward scattering shadow boundary, where the causal relationship between the direct and diffracted fields is specifically examined. The wave processes here, and above and below the geometrical shadow zone, lead to complicated temporal and azimuthal variations of the field. The phenomenon of diffractions associated with specular reflections of the source in the wedge faces is also studied. Among the conclusions reached are (*i*) direct/reflected impulses arrive first, followed by and separated from their associated diffractions; (*ii*) the direct/reflected impulse is a delta function, with arrival predicted by the source-receiver raypath travel time, and amplitude determined by spherical spreading and reflection/transmission coefficients at the wedge faces; and (*iii*) diffractions are causally associated with direct/reflected impulses interacting with the wedge apex, and their amplitude depends on the degree of acoustic shadowing at the apex. [DOI: 10.1121/1.1772394]

PACS numbers: 43.30.Hw, 43.20.Fn, 43.20.Px [RAS] Pages: 777–789

I. INTRODUCTION

The motivation for the research presented here derives from the need to develop practical acoustical methods for imaging rough seafloors and finding objects lying on it or embedded within it. Measurements of seafloor roughness have shown that much of the seafloor has a power law spectrum, and thus a fractal character.[1–3] Optical and sonar pictures of the seafloor often show ensembles of wedges or fractals. In this complicated environment the classical ''sonar equation'' approach is inadequate, and scattering models that assume the seafloor has a Gaussian PDF are wrong or misleading. Our intention is to develop a ''visualization'' paradigm for seafloor investigations, by creating accurate images of the seafloor, its subsurface structure, and objects on the seafloor, using time domain/multiple receiver techniques.

In order to even consider the inverse-imaging problem, we need firm analytical and computational bases in forward calculations, i.e., it is first necessary to be able to accurately compute the scattered and reflected sound pressures in the time domain, as observed by many receivers. A promising and powerful approach to the forward problem is offered by the use of a ''wedge assemblage'' method, in which the rough surface is modeled as a network of many concatenated wedge facets.[4,5] The total scattered field is calculated as the aggregate of contributions from the individual wedges, each one of which can be calculated using a time domain wedge scattering theory.

The impulse response is critically important in the construction of a useful theory for study of the sound scattered by rough interfaces, and especially the seafloor. In 1957, Biot and Tolstoy[6–8] introduced an exact closed form solution for the acoustic impulse response of an infinite rigid wedge. Their theory, which uses the method of normal coordinates, gives a complete time domain description of the total acoustic field, incorporating direct, reflected, and diffracted wave components. The normal coordinate method was subsequently extended to free (i.e., pressure-release) wedges[9] and free-rigid wedges.[12] The accuracy and reliability of the approach has been established by comparison with experimental results. In particular, it has been shown that the normal coordinate method exactly predicts both the amplitude and phase of the time domain field, which is of critical importance in rough surface scattering and seafloor investigation applications. For a general overview of the Biot–Tolstoy theory and its extensions, experimental investigations, and a comprehensive list of references, the reader is referred to a recent textbook (Ref. 10, Chaps. 11 and 12, and references therein).

In the rigid, free, and free-rigid wedge theories, the

a)Electronic mail: cf@nrlssc.navy.mil

boundary conditions at the wedge surfaces correspond to a reflectivity $R=\pm 1$, which means that the wedge faces are impenetrable, and thus limits applicability in many cases of practical interest. A significant step towards removing this restriction was taken in 1989, when Chu[11] used the normal coordinates to determine the impulse response of an infinite penetrable wedge, where acoustic transmission through the surfaces may occur. He showed that, while the wave equation for the wedge problem is nonseparable for a general penetrable wedge (i.e., when $c\neq c'$ and $\rho\neq\rho'$, where $c,c'/\rho,\rho'$ are the sound speeds/densities of the two media), the assumption of an isovelocity and density contrast wedge ($c=c',\rho\neq\rho'$) renders the problem solvable in cylindrical coordinates. The solution Chu obtained is exact and complete. His theory accurately describes the direct, reflected, and diffracted components of the time domain field, in both the exterior and interior wedge regions.

Chu's development is important, since it greatly increases the time domain functionality offered by the normal coordinate method. It also facilitates the extension of the wedge-assemblage method for rough surface scattering[4,5] to a broader range of seafloor environments. Shallow sediments at the water–seafloor interface commonly have sound speeds that are almost the same as the water, while their densities are typically greater. The density contrast surface appears to be a reasonable model for many features at the water–seafloor interface, and isovelocity density contrast boundary conditions are indicated in a surprisingly large proportion of environments (Ref. 11, Introduction). Chu subsequently adapted his theory for application to a shallow-water wedge environment and showed that it achieved good agreement with experimental data in cases where c/c' differed from unity by up to 20%.[12]

Rigorous solutions for the general penetrable wedge problem (i.e., where both the sound speed and density in the two media are different) have been reported by Davis[13] and Budaev and Bogy.[14] Both methods lead to CW, rather than time domain, descriptions. The work of Davis requires the solution of two simultaneous integral equations, while that of Budaev and Bogy involves the iterative solution of a pair of integral equations of the second kind. While these two types of solution are exact, the requirement to solve integral equations makes it difficult to gain physical insight into the problem.

More recently, Davis and Scharstein[15] and Davis[16] described an alternative time domain formulation of the density contrast wedge problem, using integral transform techniques. In cases where the wedge angle is a rational fraction of π, they were able to determine closed form expressions for the time domain field. Novarini and Keiffer[17] described a numerical technique for implementing the formalism of Davis and Scharstein for arbitrary wedge angles. We have used Chu's formalism to verify the calculations of Novarini and Keiffer, and those presented by Davis and Scharstein using their rational fraction expressions. Our analysis strongly indicates that Davis and Scharstein's formalism provides an alternative, but equivalent, route to the results presented by Chu in his original paper.

In the work described here we use Chu's formalism to perform a detailed investigation of the spatial and time domain variations of the scattered field of a penetrable wedge, in order to better understand their implications for boundary scattering applications. In this case we look at the field scattered back into the medium where the source is located. The direct, reflected, and diffracted field components are considered, and the relationship between them is investigated. Since diffractions comprise the dominant component in many rough surface scattering applications, it is critically important to provide an exact qualitative and quantitative description of these waves. In the case of a density contrast wedge, the behavior of the diffracted field is significantly complicated by the fact that the incident field is able to penetrate, and (for exterior wedge geometries) may traverse completely through, the wedge. For this reason, particular emphasis is placed on a detailed study of the wave phenomena and transition behavior around the forward scattering shadow boundary. Exactly at this boundary, the direct incident field infinitesimally precedes the diffracted field and complicated temporal and azimuthal variations of the field are observed. The behavior of diffractions associated with reflections in the faces of the wedge, particularly with reference to the reflectivity of the wedge surfaces, is also studied for both exterior and interior wedge geometries.

The most important conclusions regarding the acoustic scattering properties of penetrable wedges which result from the work may be summarized as follows: (*i*) The direct/reflected arrivals, and the diffracted arrivals associated with them, are separated in the time domain, with the direct/reflected impulse arriving first. (*ii*) The impulse response for the direct/reflected field is a delta function, and scattering computations may be facilitated by substituting a formal delta function [e.g., $\delta(t-\tau_{sr})$, where τ_{sr} is the travel time from source to receiver] multiplied by the spherical spreading reduction and the appropriate reflection and transmission coefficients, as the pulse interacts with the faces of the wedge. (*iii*) Diffraction arrivals are causally associated with direct/reflected impulses which interact with the wedge apex, and the diffraction amplitude is dependent on the degree of acoustic shadowing at the apex. (*iv*) For an exterior wedge, if the source creates an acoustic shadow, the azimuthal diffraction pattern forms a lobe where the field amplitude changes from negative to positive upon entering the geometric shadow zone, and other diffraction lobes may appear which are associated with reflections in the wedge faces of the wedge and whose amplitude depends on the reflectivity of the faces. (*v*) For an interior wedge, acoustic shadows cannot be formed, but diffractions associated with reflections in the wedge faces can still occur whose amplitude depends on the reflectivity.

In Sec. II of this paper we give a brief summary of Chu's penetrable wedge theory. Section III presents and describes the computational results. Section IV contains a discussion of conclusions.

II. CHU'S NORMAL COORDINATE PENETRABLE WEDGE THEORY

To determine the impulse response of a penetrable wedge (see Ref. 11 for a full discussion), two cylindrical

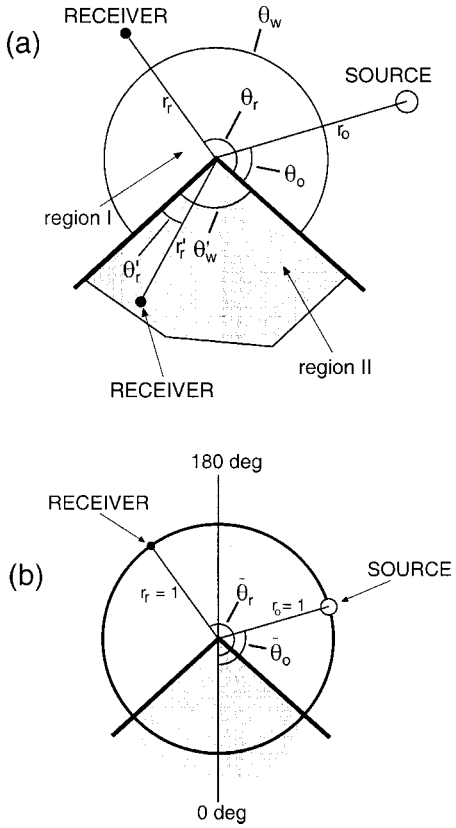

FIG. 1. The wedge geometry. (a) The coordinate systems used in Chu's theory. Equation (1) indicates that the azimuthal angle for a receiver placed in region II, as expressed in the *unprimed* coordinate system, would be given by $\theta_r = \theta'_r + \theta_w$, where θ'_r is the angle in the *primed* system. (b) Geometry and notation used for the computations discussed in the paper. The source and receiver(s) are placed on the circumference of a circle of unit radius whose center is located at the wedge apex. The z axis lies along the apex. Both $\tilde{\theta}_o$ and $\tilde{\theta}_r$ are measured counter-clockwise from a line drawn vertically downwards from the apex.

coordinate systems are used to represent the field in the two regions of the wedge [Fig. 1(a)], an unprimed system (region I) and a primed system (region II), which are related by

$$\theta' = \theta - \theta_w, \quad r' = r, \quad z' = z, \tag{1}$$

where θ_w is the wedge angle in the unprimed system, and $\theta'_w = 2\pi - \theta_w$ [see Fig. 1(a) for details of the coordinate systems used in Ref. 11]. The z axis is taken to lie along the wedge apex. The velocity potential of the acoustic field in region I, $\Phi(r,\theta,z,t)$, satisfies the wave equation:

$$\frac{1}{r}\frac{\partial}{\partial r}\left(r\frac{\partial \Phi}{\partial r}\right) + \frac{1}{r^2}\frac{\partial^2 \Phi}{\partial \theta^2} + \frac{\partial^2 \Phi}{\partial z^2} - \frac{1}{c^2}\frac{\partial^2 \Phi}{\partial t^2} = 0, \tag{2}$$

where c is the sound speed in region I. This equation has solutions:

$$\phi_n = \psi_n q_n, \tag{3}$$

where

$$\psi_n = J_{\nu_n}(\kappa r)\sin(\gamma z)[a_n \cos(\nu_n \theta) + b_n \sin(\nu_n \theta)]. \tag{4}$$

In (4), $\kappa^2 + \gamma^2 = \omega^2/c^2$, where ω is the angular frequency, and a_n, b_n are determined by satisfying boundary conditions at the wedge interfaces. Corresponding expressions for the solution in region II can be found using the primed quantities. The term q_n in Eq. (3) is the normal coordinate. It describes the time variation of the nth spatial normal coordinate, and satisfies the simple harmonic equation: $\ddot{q}_n + \omega^2 q_n = Q_n/\mu_n$, where $Q_n = -\lambda S H(-t)$, λ is the bulk modulus, S is the source strength (dimensions of volume per unit time), H is Heaviside's step function, and μ_n is an orthonormality factor determined through a spatial integration of the corresponding wave function over regions I and II. Chu[11] follows the method of normal coordinates[6–8] to determine the pressure field at time t, which is given by

$$\begin{aligned} p_r(r_r,\theta_r,z_r,t) = {} & \frac{2\rho_o \rho_r c^2 S}{\pi} \\ & \times \sum_{n=0}^{\infty} (a_o a_r \cos \nu_n \theta_o \cos \nu_n \theta_r \\ & + b_o b_r \sin \nu_n \theta_o \sin \nu_n \theta_r \\ & + a_o b_r \cos \nu_n \theta_o \sin \nu_n \theta_r \\ & + b_o a_r \sin \nu_n \theta_o \cos \nu_n \theta_r) \left(\frac{I_n}{D_n}\right), \end{aligned} \tag{5}$$

where

$$\begin{aligned} I_n &= 0 \quad (t < t_0) \\ &= (1/2c r_r r_o \sin \xi)\cos \nu_n \xi \quad (t_0 < t < \tau_0) \\ &= (-1/2c r_r r_o \sinh \eta)\sin \nu_n \pi e^{-\nu_n \eta} \quad (t \geqslant \tau_0) \end{aligned} \tag{6}$$

and

$$\begin{aligned} &\xi = \arccos[(r_r^2 + r_o^2 + z^2 - c^2 t^2)/2 r_r r_0], \quad |\xi| \leqslant \pi, \\ &\eta = \operatorname{arccosh}[(c^2 t^2 - (r_r^2 + r_o^2 + z^2))/2 r_r r_0], \\ &t_0 = (1/c)[(r_r - r_o)^2 + z^2]^{1/2}, \\ &\tau_0 = (1/c)[(r_r + r_o)^2 + z^2]^{1/2}. \end{aligned} \tag{7}$$

In these expressions, r_o is the radial distance from the source to the wedge apex, r_r is the radial distance from the receiver to the apex, θ_o is the source angle, θ_r is the receiver angle, z is the distance along the apex from source to receiver, t_0 is equivalent to the transmission time for the shortest possible direct ray path between the source and the receiver for a given r_r, r_o, and z (which actually occurs when $\theta_o = \theta_r$, for any given θ_o), and τ_0 is the earliest time of arrival for a transmission from the source to the apex, and then to the receiver. The quantity D_n is given by

$$\begin{aligned} D_n = {} & \rho \theta_w (a_n^2 D_n^+ + b_n^2 D_n^- + 2 a_n b_n D_n^\circ) + \rho' \theta'_w (a_n'^2 D_n'^+ \\ & + b_n'^2 D_n'^- + 2 a'_n b'_n D_n'^\circ), \end{aligned} \tag{8}$$

where $D_n^\pm = 1 \pm \operatorname{sinc}(2\nu_n \theta_w)$ and $D_n^\circ = \nu_n \theta_w \operatorname{sinc}^2(\nu_n \theta_w)$, with equivalent definitions for the primed quantities. In Eq. (5), the subscripts of a_o, b_o, and ρ_o, refer to the source location. If the source is in region I, then these are written a_n, b_n, and ρ, otherwise they are a'_n, b'_n, and ρ'. Similarly, if the receiver is in region I, then the subscripts "r" are replaced by "n" (and ρ_r by ρ), otherwise the primed quantities are used.

The pressure field p_r in Eq. (5) is directly related to the source strength S. The coefficients a_n, b_n, a'_n, b'_n are related to each other through a system of homogeneous equations, which necessitates the choice of a normalization scheme for their solution. However, since these quantities always appear as double products (i.e., a_n^2, $a_n b_n$, $b_n'^2$, etc.) in both the numerator and denominator of Eq. (5), the specific normalization scheme chosen is immaterial, since the proportionality factor cancels, and does not affect the field calculations. Also, the homogeneous equations have a nontrivial solution only if the determinant of coefficients is zero, when it yields the characteristic equation

$$(\rho^2+\rho'^2)\sin\nu_n\theta_w \sin\nu_n\theta'_w - 2\rho\rho' \cos\nu_n\theta_w \cos\nu_n\theta'_w + 2\rho\rho' = 0. \tag{9}$$

The roots of this equation provide discrete eigenvalues ν_n, which appear in the series expansion in Eq. (5) for the total acoustic field.

Equation (6) indicates that the field solution falls into three time regions. When $t < t_0$, none of the direct, reflected, and diffracted waves are present, and the field is zero. When $t_0 \leqslant t < \tau_0$, direct and/or reflected arrivals may occur, depending on the particular wedge geometry and the source and receiver locations. Both Chu[11,12] and Davis and Scharstein[15] have shown that these arrivals are delta functions corresponding to transmissions directly from the source, or from images of the source reflected in the faces of the wedge. When $t \geqslant \tau_0$, a diffracted arrival may occur. The time domain calculations presented here show the time separation between these two types of arrivals, with the direct/reflected component always preceding a diffracted field which is associated with it. We study both the time domain behavior and azimuthal variation of these waves for several geometric configurations of wedges with different density contrasts.

III. RESULTS OF COMPUTATIONS

All of the field calculations discussed here are based upon the geometry shown in Fig. 1(b). The acoustic (point) source and the receiver(s) are placed on the circumference of a circle of unit radius (i.e., $r_r = r_o = 1$) whose center is placed at the wedge apex, with the z axis of the cylindrical coordinates along the apex. We let $z=0$ and $c=1$. These parameter choices are used to ''normalize'' the calculations for the purposes of comparison. For the geometry depicted in Fig. 1(b), $\tau_0 = 2$. A value of $\tau_0 = 2$ s would apply in an underwater acoustics experiment, for example, if $r_r = r_o = 1500$ m, $z = 0$ m, and $c = 1500$ m/s.

The source/receiver angles are measured counterclockwise from a line drawn vertically downwards from the apex, and the wedges are located symmetrically athwart this line. This convention for referencing the source ($\tilde{\theta}_o = \theta_o + \theta'_w/2$) and receiver ($\tilde{\theta}_r = \theta_r + \theta'_w/2$) angles is that of Davis and Scharstein.[15] While it differs from the convention used by Chu,[11] the transformation between the two is algebraically straightforward, and does not adversely complicate the implementation of Chu's formalism, which is used to perform all of the computations shown here. The source (strength $S=1$) is located in region I, so that θ_w is the upper wedge angle [shown as an exterior angle in the particular case depicted in Fig. 1(b)], and θ'_w is the lower wedge angle.

A. Computational implementation of the penetrable wedge theory

Chu's theory provides an efficient general approach for determining the acoustic field throughout the penetrable wedge system, on both sides of the wedge boundary, for all wedge angles, and for all times following the original source emission, by using computations to determine the field solutions. The process is straightforward, requiring solution of Eq. (9) to find the eigenvalues ν_n of the characteristic equation, and then evaluation of the series in Eq. (5) by substituting these values of ν_n to calculate the pressure field.

The acoustic reflectivity at the density contrast boundary of the wedge, on passing from region I to region II, is given by $R = (\rho' - \rho)/(\rho' + \rho)$, and substitution of R in Eq. (9) leads to an alternative formulation of the characteristic equation, as noted by Davis and Scharstein,[15] i.e.,

$$\sin\nu_n\pi = \pm R \sin\nu_n(\pi - \theta_w). \tag{10}$$

The roots ν_n of this equation may be most easily determined by solving the two equations for $+R$ and $-R$ independently, and then collating the two sets of results.

While both the direct/reflected and diffracted field components may be calculated via Chu's formalism, there is an important difference in the computational implementation of Eq. (5) for the two cases. In practice, in order to compute the summation in Eq. (5), it is necessary to impose an upper limit on the range of ν_n. In the case of the diffracted component, inspection of Eq. (6), for $t \geqslant \tau_0$, shows that I_n contains a decaying exponential factor $e^{-\nu_n \eta}$, which causes higher order terms in the summation to decrease in amplitude. To calculate the diffracted field, therefore, it is necessary simply to choose an upper value of ν_n large enough to ensure that the summation converges to within a predetermined error tolerance. However, when $t_0 < t < \tau_0$, Eq. (6) shows that I_n does not incorporate this exponential factor. In this case, the series in Eq. (5) is analagous to a discrete Fourier cosine transform for the time domain field, and the need to truncate the series at some value of n leads to a band-limited representation of the impulse response for the direct/reflected field component. As a result, the computed impulse response typically varies in peak amplitude and exhibits Gibbs oscillations. In the following simulations, steps are taken to reduce these effects in order to clearly demonstrate the behavior of the direct/reflected component.

B. Time domain solutions in the forward scatter region ($\theta_w > 180°$)

Figures 2(a)–(d) show time domain impulse response solutions derived from Eq. (5), for a wedge angle $\theta_w = 281°$, and a source placed at $\tilde{\theta}_o = 90°$. The value of $\rho = 1$, and ρ' is adjusted so that the reflectivity of the wedge boundary is $R = -0.5$. The time interval between computed data points in these figures is $\Delta t = 4 \times 10^{-5}$. The field is calculated for a sequence of four receivers placed in the forward

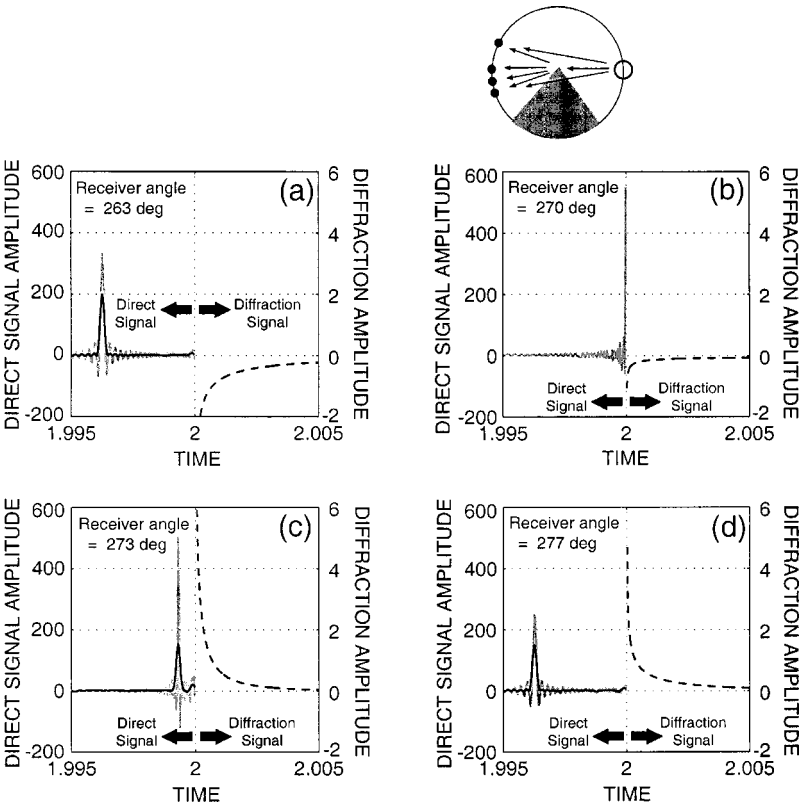

FIG. 2. Time domain solutions in the forward scatter region. Complete time domain impulse response solutions are shown for $\theta_w = 281°$, $\tilde{\theta}_o = 90°$, $\tilde{\theta}_r = 263°$, 270°, 273°, 277°, $R = -0.5$. Both the direct delta function arrival (solid lines) and the diffracted field (dashed line) are shown. Note the two vertical scales on the lhs and rhs of each figure. The solid gray lines depict the raw direct signals calculated using Eq. (5). The solid black lines show the direct signals after smoothing, time-shifted to compensate for the delay introduced by the filter. Filtering is not performed for the 270° case. Note that the arrival times for the delta functions vary with the receiver location, but the diffraction field always begins at $t = 2$.

scattering direction (with $\tilde{\theta}_r$ increasing from 263° to 277°), spanning the boundary region of the shadow cast by the source at the wedge apex. Complete solutions are presented, comprising both the direct transmission (not a reflection in this case) from the source to the receivers when $t_0 < t < \tau_0 = 2$, and the diffracted field when $t \geqslant \tau_0 = 2$. Since the peak amplitudes of the direct transmissions calculated here are typically much greater than the diffraction values, different scales have been used on the lhs and rhs of Fig. 2 (also in Fig. 3 below).

Look first at the direct signal components (i.e., the gray and black solid lines) in Figs. 2(a)–(d). The direct transmission is a delta function, and the gray lines in Figs. 2(a)–(d) show band-limited representations of the delta function arrivals for the four receiver angles, obtained by evaluating the summation in Eq. (5). The peak amplitudes of these features depend on the computational bandwidth and exhibit Gibbs oscillations, as discussed above. Further calculations were performed (not shown) which indicated that increasing the bandwidth leads to a narrower impulse with a higher peak amplitude. Independently of the bandwidth, close examination of the figures shows that the peak amplitude and oscillations of the direct arrivals also vary with the source angle, which is a characteristic arising directly from the evaluation of Eq. (5) [e.g., compare the gray curves in Figs. 2(c) and (d)]. However, the bandwidth power is preserved, such that the total area under the oscillating curves is unchanged. This is demonstrated by the black lines superimposed over the gray curves (except $\tilde{\theta}_r = 270°$) in Fig. 2, which show the corresponding results, for each receiver angle, when the direct wave train is smoothed in the time domain by convolving it with a minimum delay wavelet filter.[18,19] The filter also integrates the area under the oscillating curves, resulting in arrivals whose peak values depend on the bandwidth, but do not change with the receiver angle [compare the solid black lines in Figs. 2(c) and (d)]. Filtering is not performed when $\tilde{\theta}_r = 270°$, since Eq. (5) does not allow the direct field to be calculated when $t \geqslant \tau_0 = 2$, and this makes the time domain filtering operation problematical at this point. Due to the limited bandwidth, the peak values of the filtered delta function arrivals cannot be meaningfully compared with the peak values of the diffraction arrivals (which are also displayed in the figures—see the dashed lines), but can be compared with each other. A difference is seen between the delta function amplitudes for a receiver located above the shadow boundary ($\tilde{\theta}_r = 263°$), and one located below the geometric shadow by the same angular increment ($\tilde{\theta}_r = 277°$). This difference is determined by the reflectivity R. Below the shadow boundary, the amplitude is modified by a transmittivity factor $T = (1-R)(1+R) = 1-R^2$, as the waves pass sequentially through the wedge faces (i.e., in through one face and out through the other—see the thumbnail sketch at the top of Fig. 2). Since $R = -0.5$ in this case, then $T = 0.75$. Careful calculation and comparison of the peak values of the filtered direct arrivals in Figs. 2(a) and (d) shows that these differ by a ratio of 0.75.

Although the amplitudes of the direct and diffracted arrivals in Figs. 2(a)–(d) are not directly comparable, their arrival times are. For each receiver angle, the direct delta function signal arrives at a time determined by the source–receiver separation divided by the sound speed (which, we recall, is the same in both regions of the wedge). For example, the arrival time for $\tilde{\theta}_r = 263°$ [Fig. 2(a)] is calculated

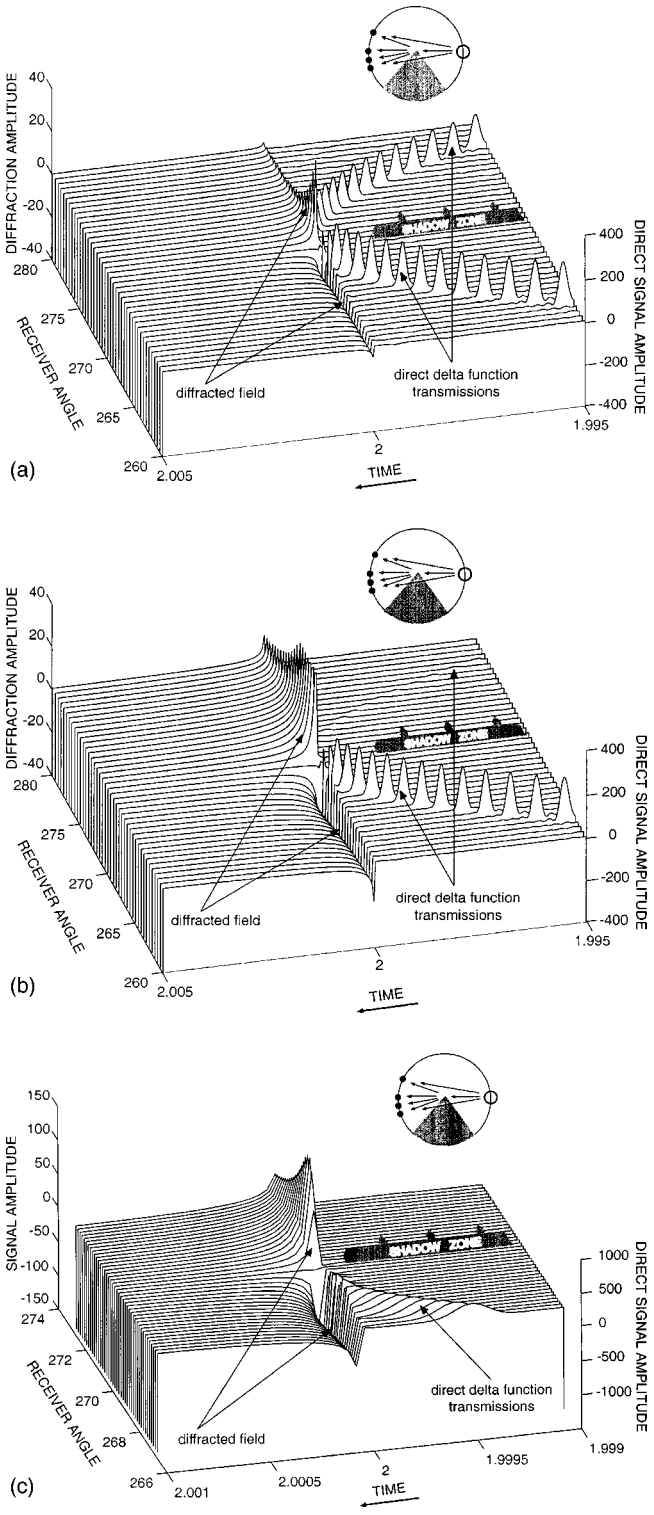

FIG. 3. The total field in the forward scatter region. The relationship is shown between the direct delta function signals [smoothed by filtering (cf. Fig. 2)], and the diffraction field. The amplitudes of the direct signals have been divided by 10, and also slightly time-shifted, for display purposes. Note the two vertical scales at the upper lhs and lower rhs of each figure. $\theta_w = 281°$ and $\tilde{\theta}_o = 90°$. When $\tilde{\theta}_r \neq 270°$, the two arrivals are separate from each other, and the delta function precedes the diffraction. When $\tilde{\theta}_r = 270°$, the delta function arrives at $t = 2^-$, infinitesimally preceding the beginning of the diffracted field. (a) $R = -0.5$, $\tilde{\theta}_r = 260 - 280°$. (b) $R = -0.99$, $\tilde{\theta}_r = 260 - 280°$. (c) $R = -0.99$, $\tilde{\theta}_r = 267 - 273°$, this is a close-up of the apex region in 3(b). Note the continuous change in the sign of the diffraction field as $\tilde{\theta}_r$ passes through 270°.

(using ray path arguments) as $t = 1.9963$. This is exactly the value predicted by the field expansion Eq. (5), as depicted in Fig. 2(a) (the gray line) where the delta function is clearly seen to arrive before the diffraction. When $\tilde{\theta}_r = 270°$ [Fig. 2(b)], such that the receiver is located directly opposite the source on the other side of the wedge apex, the expansion predicts a delta function arrival at $t \to 2^-$ (where the "$-$" superscript is intended to signify a point in time infinitesimally preceding $t = 2$ when, as we shall see, the diffracted field is initiated). This is expected from the geometry (see again the thumbnail sketch at the top of Fig. 2). When $\tilde{\theta}_r = 273°$ [Fig. 2(c)], $t = 1.9993$, again agreeing with ray path calculations, and when $\tilde{\theta}_r = 277°$ [Fig. 2(d)], $t = 1.9963$, exactly the same as in Fig. 2(a).

While the arrival times for the direct signals vary with the receiver location, the initial time of arrival of the diffracted signals is the same for every receiver. This is because the diffracted wave always arises from a wave propagating from the source to the wedge apex, and then from the apex to a receiver, i.e., the distance is the same in every case. Since $r_r = r_0 = 1$, $z = 0$, and $c = 1$, the initial arrival time for a diffraction detected by any receiver on the circumference of the circle shown in Fig. 1(b) is $t = \tau_0 = 2$. This is seen clearly in Figs. 2(a)–(d), which also exhibit another notable feature of the diffracted fields, i.e., the variation in sign and amplitude as a function of receiver angle. When $\tilde{\theta}_r = 263°$, 270°, the diffraction field is negative, while when $\tilde{\theta}_r = 273°$, 277°, it is positive. We will be looking in greater detail at this aspect of the diffractions below, but here we will concentrate specifically on their physical relationship to the direct delta function transmissions.

Figures 3(a)–(c) present computations for the same basic source/receiver configuration, and wedge angle, as Fig. 2. Waterfall plots are used here to show the complete acoustic field (the direct and diffraction arrivals) for a range of receiver angles spanning the shadow boundary region. The time interval between computed data points is again $\Delta t = 4 \times 10^{-5}$. The direct delta functions were calculated using the same range of ν_n as Fig. 2, and smoothed using the same filtering procedure. The resultant delta function signals were then concatenated (at $t = \tau_0 = 2$) with the corresponding computed diffraction signals for each receiver angle.

Figure 3(a) shows the time signals when the boundary reflectivity $R = -0.5$. The receiver angles range from $\tilde{\theta}_r = 260°$ to 280°. Consider first the direct transmissions. When $\tilde{\theta}_r = 270°$, the delta function arrives at $t \to 2^-$, and infinitesimally precedes the beginning of the diffracted field, as in Fig. 2(b). When $\tilde{\theta}_r \neq 270°$, either above or below the shadow boundary, the separation of the two arrivals, and the precedence of the direct delta function (seen previously in Fig. 2), is more clearly discernible. When $\tilde{\theta}_r < 270°$, the filtered direct arrivals for the several receiver angles all have about the same peak value, which we discussed above for Fig. 2. (This breaks down when $\tilde{\theta}_r \approx 270°$, due to the previously described difficulty of performing the filtering operation on the direct signal when it arrives at times approaching $\tau_0 = 2$.) The uniformity of the delta function peak values predicted for the closely grouped receiver locations used in Figs. 3(a)–

(c) is expected from simple physical reasoning, for there are only very slight differences in the spherical spreading reduction for the various source–receiver pairs. Since $R=-0.5$, the wedge represents a partially transmitting screen to the incident field, and propagation can occur through region II of the wedge [as seen in Figs. 2(c) and (d)]. This is evidenced in Fig. 3(a), where we clearly see direct delta function transmissions at receiver angles below the shadow boundary [note the ''shadow zone'' marked in Fig. 3(a)]. While they cannot be easily measured from this figure, the peak amplitudes of the pulses within the shadow zone are about 0.75 of the value of their counterparts at the same angles above the shadow boundary, as seen previously in Fig. 2.

If we now consider the diffraction field, we see that it is initiated at $t=\tau_0=2$ for all receiver angles, as expected. Above the shadow boundary, the initial amplitude of the diffractions is negative, while below the boundary, and inside the shadow region, it is positive, in agreement with the predictions of the classical theory of diffraction (Ref. 20, p. 575, see Fig. 11.11 and discussion). The figure indicates that the amplitude reversal occurs at, or very close to, the instant both when the direct field reaches the wedge apex and when the diffraction is initiated. Figure 3(a) demonstrates the causal association between the arrival of the direct field at the apex and the initiation of the diffracted field.

To investigate this issue further, Fig. 3(b) shows the time signals for the same wedge configuration when the boundary reflectivity is $R=-0.99$ (i.e., thus representing an almost perfect pressure release boundary). The overall phenomena are very similar to those shown in Fig. 3(a). Delta function arrivals are seen at receivers located below and above the shadow boundary although, since $|R|$ is close to unity and transmission through region II of the wedge consequently reduced, the peak amplitudes of the arrivals below the boundary are much smaller. Also, the amplitude of the diffraction field is much greater than for the $R=-0.5$ case [note that the vertical amplitude scales in Figs. 3(a) and (b) are identical, and that the positive diffraction peaks in Fig. 3(b) have been clipped]. This is due to the increased value of the boundary reflectivity. The deeper acoustic shadow behind the wedge indicates reduced transmission through region II, which implies a more pronounced shadowing effect imposed on the incident field at the apex.

Figure 3(c) again shows time signals for the $R=-0.99$ case, but zooms in closer to the apex (note the expanded time and receiver angle scales, and the condensed vertical amplitude scale) to display in greater detail the association between the direct and diffracted fields. Delta function arrivals are seen at receivers located above the shadow boundary, but appear smaller and broader than in Fig. 3(b) because of the altered scales. For the same reason, the delta functions seen previously below the shadow boundary in Fig. 3(b) are now no longer discernible. Overall, Fig. 3(c) shows the arrival of the direct field at the apex, and the subsequent initiation of the diffracted field. Also, a smooth (and quite symmetric) variation from negative ($\tilde{\theta}_r < 270°$) to positive ($\tilde{\theta}_r > 270°$) diffraction amplitudes at $t=2$, passing through zero close to $\tilde{\theta}_r=270°$, is clearly visible.

Figures 2 and 3 demonstrate a number of important features of the direct time domain field. Computational evaluations of Eq. (5) lead to band-limited delta functions, while increasing the bandwidth results in narrower impulses and higher peak amplitudes. This represents classic delta function behavior as consistent with spectral formulations for these functions (Ref. 20, Appendix IV, pp. 755–759). Biot and Tolstoy[6] showed, in the case of a rigid wedge, that the summation expression for the direct field reduces to a time delayed delta impulse $\delta(t-\tau_{sr})/R_{sr}$, where τ_{sr} is the travel time from source to receiver, and the division by R_{sr} (i.e., the distance between source and receiver) represents the spherical spreading reduction. Here the mathematics is more complicated, and we have not reduced these arrivals to impulse functions analytically. However, the implication of the results seen in Figs. 2 and 3 is that the impulse response for the direct field for a density contrast wedge, for general wedge angles, is again a delta function. Also, the delta function amplitude is modified by the appropriate reflection coefficient (as shown previously by Ref. 12), or transmission coefficient, as the pulse reflects from, or propagates through, the faces of the wedge.

Since the direct (or reflected) impulse responses are delta functions, these results show that tedious computational evaluations of these signal components may be avoided, in scattering calculations, by simply substituting $\delta(t-\tau_{sr})/R_{sr}$ (multiplied by appropriate values of S and R, etc., for the specific wedge and source-receiver configuration). These results substantiate Chu's original paper,[11] and also correspond to his later work in which convolutions of the complete computed impulse response with the source function were successfully used to analyze experimental data.[12] They also agree with the closed form delta function expressions of Davis and Scharstein[15] for the direct/reflected field components in cases where the wedge angle is a rational fraction of π. Since we have a simple understanding of these components, we will not discuss them any further in this work, but concentrate attention from this point on the diffracted field.

C. Angular/time domain variations of the diffracted field ($\theta_w > 180°$)

Using the same wedge angle and source location, Fig. 4 displays some examples of time domain diffraction solutions from Eq. (5) related to the cases shown in Figs. 2 and 3. A sequence of eight receivers are placed in the forward scattering direction, with $\tilde{\theta}_r$ increasing from 270° to 273°. The time signals in Figs. 4(a)–(h), which begin at $t=2.0006$, show diffractions for $R=-0.99$, $R=-0.5$, and $R=-0.1$. The primary feature of these signals which we want to exhibit is the variation in sign and amplitude of the field as a function of receiver angle and time. For a receiver angle $\tilde{\theta}_r=270°$, the first value calculated for the diffracted field (for all three values of R) is strongly negative. Then, as t increases, the field amplitude decays, but remains negative. However, when the receiver location is moved into the geometrical shadow zone, we see that the initial calculated values turn, and become positive. As time increases beyond $t=2.0006$, the amplitude rapidly falls, again becomes negative, and then decays away. This phenomenon is seen for all three values of

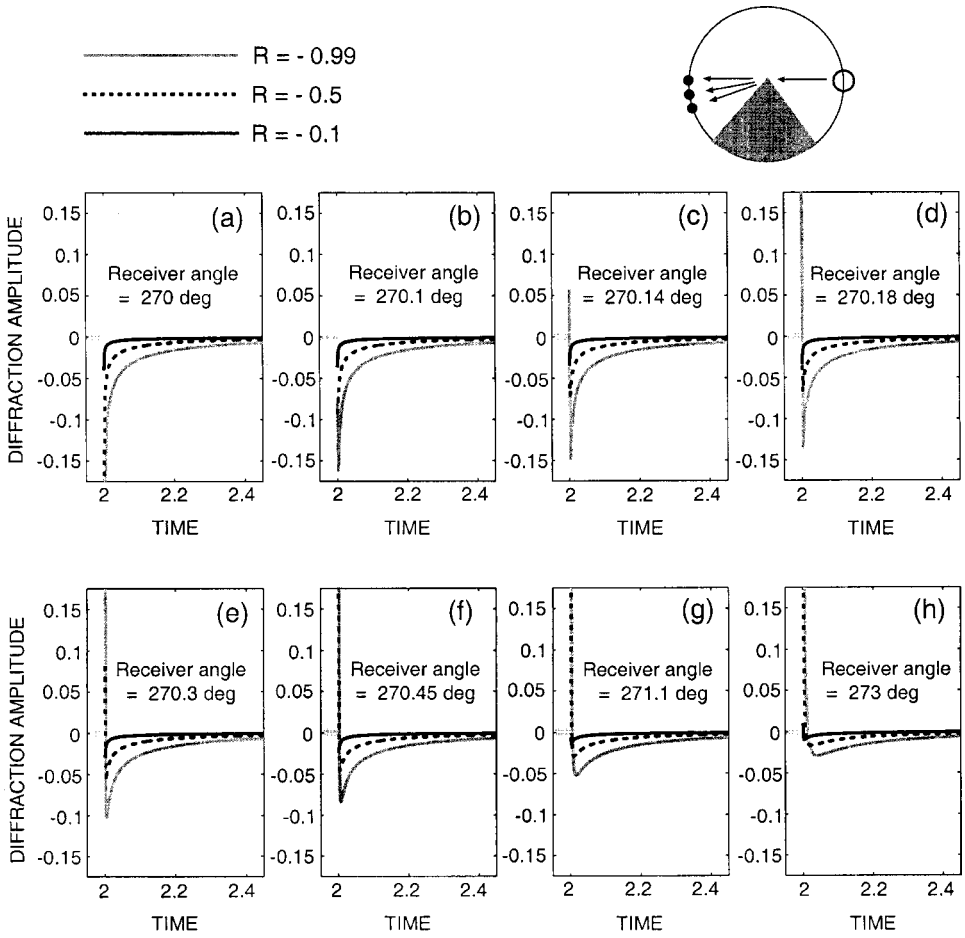

FIG. 4. Time domain diffraction signals in the forward scatter region. $\theta_w = 281°$ and $\tilde{\theta}_o = 90°$. Eight receivers are placed in the forward scattering direction. The time signals are plotted from $t = 2.0006$ (the short horizontal gray bars indicate that the diffraction field is zero for $t < 2$). Note the complicated variations in sign and amplitude of the field as a function of receiver angle and time near the zero in the shadow boundary diffraction lobe. This demonstrates the minute shift in the zero point of the shadow boundary diffraction lobe with time, which can be observed in the sequence of Figs. 5(a)–(c).

R, except that as R changes to -0.5, and then to -0.1, the receiver angle at which the turning behavior occurs increases, and the overall amplitude of the diffraction is reduced. Eventually, for $\tilde{\theta}_r = 273°$, the initial values of the diffracted field are positive for all three values of R. These figures indicate the complicated forms that the diffraction field can take in the time domain, especially near the shadow boundary.

Again using the same wedge angle and source location, Fig. 5(a) shows the angular distribution of the diffracted field amplitude in region I (the axial plot format used here displays both positive and negative variations), calculated for the initial time point ($t = 2.000\,02$) from which the diffracted field is plotted in Figs. 2 and 3, and for $R = -0.5$ and $R = -0.99$. The broad dashed lines superimposed on the plot represent the position of the wedge surfaces, and the large arrow indicates the direction of the incident field. Also plotted in Fig. 5(a) is the diffracted field predicted by the pressure release wedge theory of Kinney *et al.*[9] (a formal development of the Biot-Tolstoy theory) for the same wedge geometry. Note first the almost identical predictions of the pressure release theory and Chu's density contrast wedge theory for $R = -0.99$, showing that Chu's solution asymptotically approaches the pressure release solution when $R \rightarrow -1$ (previously demonstrated by Chu for a different case[11]). Look next at the behavior of the diffracted field at and around a receiver angle of 270°, i.e., in the shadow boundary region. For angles $\tilde{\theta}_r$ slightly less than 270°, the diffracted field amplitude is negative for both values of R. Then, as $\tilde{\theta}_r$ increases through 270°, the amplitudes pass through zero and become positive, exactly corresponding to the behavior seen in Figs. 3(a)–(c). We also see the increased amplitude of the diffracted wave for greater $|R|$, due to more pronounced shadowing of the incident field, as previously observed by contrasting Figs. 3(a) and (b). The azimuthal variations of the field in the forward scattering direction constitute a diffraction "lobe" due to the shadowing effect of the wedge apex. The basic form of this lobe, and the negative to positive change in the diffraction amplitude as the receiver passes into the geometric shadow, have been experimentally observed (Ref. 21, Fig. 4). Further examination of Fig. 5(a) shows that there is another diffraction lobe centered at a receiver angle $\tilde{\theta}_r \approx 169°$. This feature is associated with reflections from the wedge face closest to the source, since 169° is the angle at which the specular reflection occurs from this face at the apex. Waterfall time domain plots (not shown here) for the reflected field and diffracted field, similar to Fig. 3, have been made for receivers placed between $\tilde{\theta}_r = 159°-179°$ (i.e., straddling this "reflection" boundary). These demonstrate delta functions reflected from the wedge face at the apex which precede diffractions causally associated with them [similar to the phenomena seen in Figs. 3(a)–(c)]. If $R = -0.5$, they show that the delta function reflections have negative peaks, and the sign of the diffracted field around $\tilde{\theta}_r \approx 169°$ changes from $+ \rightarrow -$ [cf. Fig. 5(a)] as the

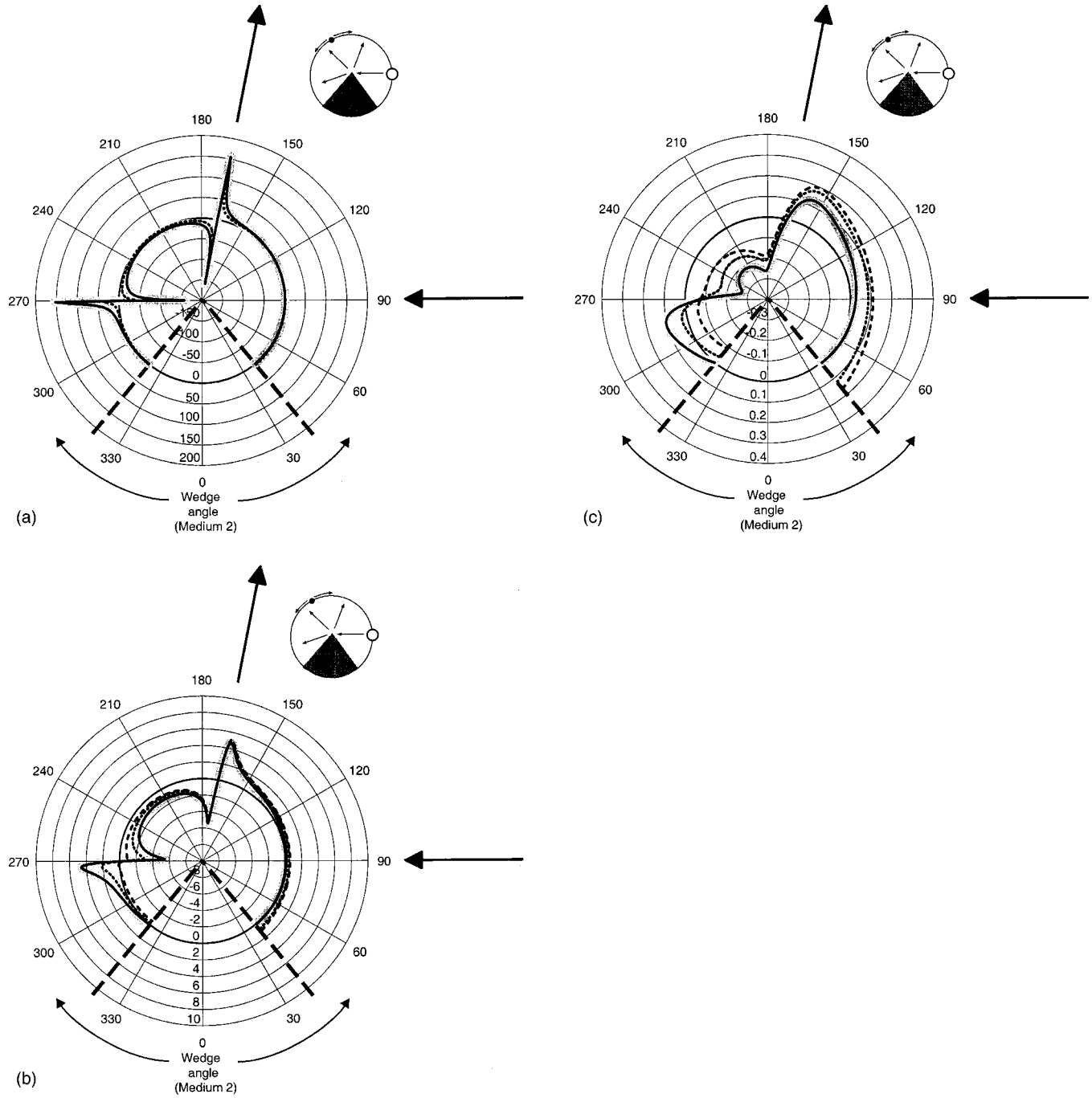

FIG. 5. Azimuthal distribution of the diffraction field. The angular variation of the diffracted field amplitude in region I is calculated for $\theta_w = 281°$ and $\tilde{\theta}_o = 90°$. The broad dashed lines represent the position of the wedge surfaces. The inward-pointing arrow shows the direction of the incident field. The outward-pointing arrow shows the limit of specular reflections from the near face. This axial plot shows both positive and negative variations. The darker annular grid line denotes the zero level. (a) $t = 2.000\,02$, $R = -0.99$ (solid line), $R = -0.5$ (dotted line), pressure release (broad gray line). (b) $t = 2.0006$, $R = -0.99$ (solid), $R = -0.5$ (dotted), $R = -0.1$ (dashed), pressure release (gray). (c) $t = 2.0168$, $R = -0.99$ (solid), $R = -0.5$ (dotted), $R = -0.1$ (dashed), pressure release (gray).

receiver angle is increased (cf. the $- \rightarrow +$ change for the shadow boundary diffractions shown in Fig. 3). If, on the other hand, R is given a positive value (e.g., $+0.5$), the delta function reflections are positive and the sign of the diffraction changes from $- \rightarrow +$. All of this strongly indicates that diffractions from the apex are always associated with either a direct transmission or a reflection as a causal agent, and is consistent with the statement of Davis and Scharstein[15] that the diffracted wave is physically generated to ''smooth out'' a geometrical shadow.

Figure 5(b) shows the angular distribution of the diffracted field, for the same wedge angle and source location, when $t = 2.0006$. In this case, three values of the boundary reflectivity are used, i.e., $R = -0.99$, $R = -0.5$, and $R = -0.1$. The pressure release solution is again included. In this figure, the amplitude values for the three diffraction curves have been scaled by dividing them by the corresponding value of $|R|$. This results in the three curves being practically superimposed over each other in the $\tilde{\theta}_r = 169°$ region,

strengthening the implication that the lobe in this direction is causally related to reflections at the wedge boundary. Comparison with Fig. 5(a) shows that the overall diffraction patterns for $R=-0.99$ are very similar in the two figures, although the amplitude is greatly reduced in Fig. 5(b) and the angular distribution has changed, particularly the exact locations of the zeros of the two diffraction lobes. The turning behavior of the diffraction field seen previously in Fig. 4 reflects the minute shift in the zero point of the shadow boundary diffraction lobe with time, which can be observed in the sequence of Figs. 5(a)–(c) (below).

Figure 5(c) shows the angular distribution of the diffracted field when $t=2.0168$. The same three values of R are used, and the pressure release solution is again included. The first point to note is that, while a further reduction in amplitude has occurred [compare the amplitude scales in Figs. 5(b) and (c)], Chu's theory for $R=-0.99$ remains asymptotically close to the pressure release solution. Second, even though the angular distribution is reduced in overall amplitude, the shape still broadly resembles that seen in Figs. 5(a) and (b), with both ''shadow boundary'' and ''reflection boundary'' diffraction lobes, and their accompanying zeros near 270° and 169°, respectively. Note, however, that the amplitudes of the 169° lobes for the different R cases no longer remain superimposed when scaled by division by $|R|$, indicating that the time decay constants for these cases, which enter through the exponential term in the third line of Eq. (6), are not identical. While we have not displayed them here, calculations of the angular distribution of the field at later times show that the same basic geometrical form persists and changes only slowly as t increases.

Taking Figs. 4 and 5 together suggests that it would be instructive to investigate the overall amplitude and sign of the diffracted impulse signal in region I, by integrating the sound pressure over time for receiver locations spanning the whole of this azimuthal range. This type of integration procedure is a standard technique in geophysics for producing a single quantitative measure of a time varying impulse signal. In this case, the area under the curves representing time signals detected at receivers located throughout region I (exemplified in Fig. 4) have been numerically integrated from $t=2$ to $t=2.9848$, for the three values of R used in Figs. 4 and 5, and then plotted azimuthally. The results are displayed in Fig. 6, and are similar to those seen in Fig. 5(c). In the backscattering direction (i.e., $\tilde{\theta}_r \sim 39.5°-169°$) and the shadow zone ($\tilde{\theta}_r=270°-320.5°$), the impulse is predominantly positive. Between the reflection and shadow boundary lobes ($\tilde{\theta}_r=169°-270°$), the impulse is generally negative. Figure 6 also shows that the amplitudes of the diffraction impulses in the angular region between 39.5° and 169°, for the different R cases, do not scale when divided by $|R|$. The integrated time behavior agrees, therefore, with that seen in Fig. 5(c), in tending to show that the overall impulse behavior is predominantly determined by longer term processes.

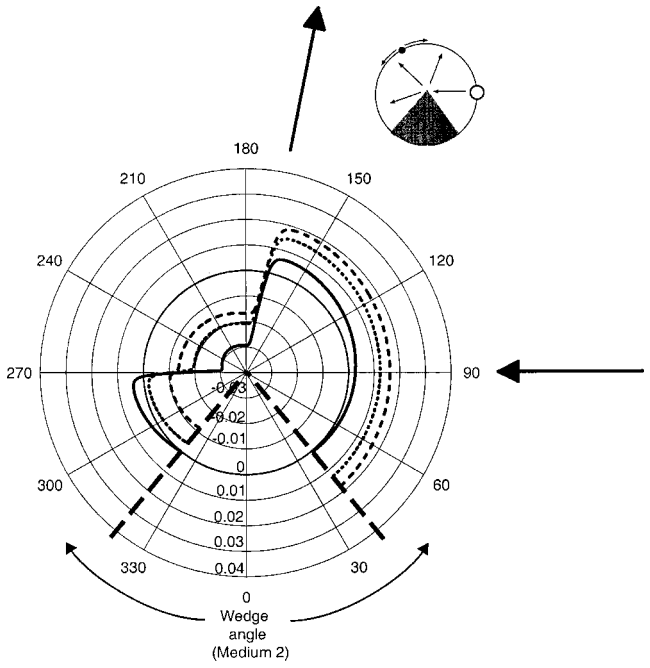

FIG. 6. Time-integrated azimuthal distribution of the diffraction field. Time signals detected at receivers located throughout region I have been numerically integrated from $t=\tau_0=2$ to $t=2.9848$, for $R=-0.99$ (solid), $R=-0.5$ (dotted), $R=-0.1$ (dashed). $\theta_w=281°$ and $\tilde{\theta}_o=90°$. The broad dashed lines represent the position of the wedge surfaces. The inward-pointing arrow shows the direction of the incident field. The outward-pointing arrow shows the limit of specular reflections from the near face. Note the similarity to Fig. 5(c), and that the amplitudes of the diffraction impulses in the region of the 169° lobe do not scale when divided by $|R|$.

D. Angular variations of the diffracted field ($\theta_w < 180°$)

Figure 7(a) shows the angular distribution of the diffracted field amplitude in region I for $\theta_w=79°$, $t=2.0006$, and $R=-0.99$, $R=-0.5$, and $R=-0.1$, together with the pressure release solution. The source is placed at $\tilde{\theta}_o=145°$. In this case there is no possibility of the apex casting a shadow with an associated diffraction lobe. Since multiple reflections of the source are possible between the two faces of the wedge in this case, the diffraction phenomenon is associated with a more complicated process than simple reflection by one face. It results here in a distribution with a deep trough at a receiver angle of 162.5°, and scaling the cases by division by $|R|$ does not lead to the superposition of curves as seen in Fig. 5(b).

One of the most interesting features of scattering from a rigid wedge,[6] or from a pressure release wedge,[9] is the prediction that when the wedge angle is a rational fraction of π (i.e., $\theta_w=\pi/m$, where $m=1,2,...$), the diffracted field is identically zero. This occurs because, for these cases, the eigenvalues $\nu_n=n\pi/\theta_w$. When substitution is then made in Eq. (6) (viz., the third line), we see that $\sin(\nu_n\pi)=0$, so that the diffracted field is zero at all times. It is of interest to investigate how this phenomenon is modified in the density contrast wedge case, i.e., when $|R|<1$. Figure 7(b) shows the angular distribution of the diffracted field amplitude in region I for a wedge angle $\theta_w=90°$, for $t=2.0006$, and again for the same three values of R and the pressure release case. The source is placed at $\tilde{\theta}_o=180°$. As expected from the theory, this figure shows that the diffracted field amplitude for the pressure release case is identically zero throughout the range plotted. It also shows that the corresponding result for Chu's theory when $R=-0.99$ again, as in previous ex-

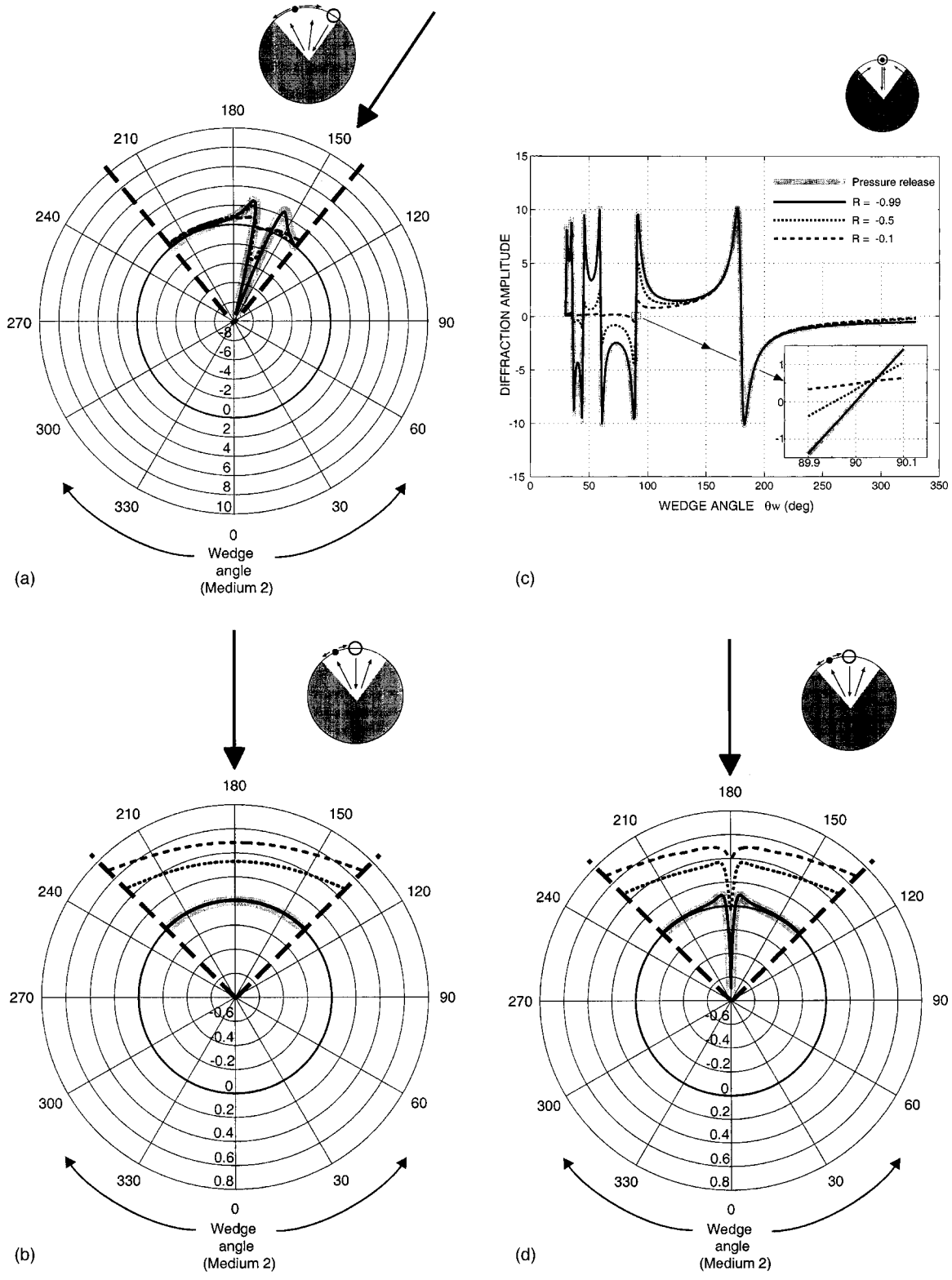

FIG. 7. Diffraction phenomena for interior wedges. (a) The azimuthal variation of the diffracted field amplitude in region I is calculated for $\theta_w = 79°$ and $\tilde{\theta}_o = 145°$. The broad dashed lines represent the position of the wedge surfaces and the inward-pointing arrow shows the direction of the incident field [also in (b) and (d)]. $t = 2.0006$, $R = -0.99$ (solid line), $R = -0.5$ (dotted line), $R = -0.1$ (dashed line), pressure release (broad gray line). (b) The azimuthal variation of the diffracted field for $\theta_w = 90°$ and $\tilde{\theta}_o = 180°$. $t = 2.0006$, $R = -0.99$ (solid), $R = -0.5$ (dotted), $R = -0.1$ (dashed), pressure release (gray). The field is zero throughout the angular range plotted for the pressure release case, and almost zero when $R = -0.99$. It is nonzero when $R = -0.5$ and $R = -0.1$. (c) Variation of the diffracted field for $\tilde{\theta}_o = \tilde{\theta}_r = 180°$, and $\theta_w = 30–330°$. $t = 2.0006$, $R = -0.99$ (solid), $R = -0.5$ (dotted), $R = -0.1$ (dashed), pressure release (gray). For the pressure release case the field amplitude passes through zero whenever θ_w is a rational fraction of π. (d) The azimuthal variation of the diffracted field for $\theta_w = 89.95°$ and $\tilde{\theta}_o = 180°$. $t = 2.0006$, $R = -0.99$ (solid), $R = -0.5$ (dotted), $R = -0.1$ (dashed), pressure release (gray). The field is zero for $R = -0.5$ for the single receiver angle $\tilde{\theta}_r = 180°$, but not throughout wedge as seen for the pressure release case when $\theta_w = 90°$.

amples, asymptotically approaches the pressure release result. However, changing the reflectivity to $R=-0.5$, and then $R=-0.1$, leads to a nonzero diffracted field. In his original paper [Ref. 11, see Eq. (19) and discussion], Chu showed how this may be explained by reference to the characteristic equation, i.e., Eq. (9) or (10). When $|R|=1$, the roots yield eigenvalues $\nu_n=n\pi/\theta_w$, as in the Biot–Tolstoy theory, and thus diffractions do not occur for wedge angles $\theta_w=\pi/m$, as explained above. However, when $|R|<1$, the eigenvalues generally do not take this form. In this case, typically, $\sin(\nu_n\pi)\neq 0$, leading to a nonzero diffracted field as computed via Eqs. (5) and (6).

Figure 7(c) plots the variation in the diffracted field amplitude for a source and receiver colocated at $\tilde{\theta}_o=\tilde{\theta}_r=180°$, as the wedge angle is incrementally increased from $\theta_w=30°$ to $\theta_w=330°$. The different line types represent the same cases as in Fig. 7(b). Look first at the pressure release solution. We see that the amplitude cycles between positive and negative values, passing through zero at wedge angles which are rational fractions of π (i.e., $\theta_w=30°, 36°, 45°, 60°, 90°, 180°$), as predicted by theory. Chu's solution for $R=-0.99$ closely follows the pressure release curve throughout the range plotted. What is somewhat surprising, however, is that the $R=-0.5$ and $R=-0.1$ lines also appear to pass through zero at points very close to those observed for the pressure release case. Does this indicate that the acoustic penetration into the lower region allowed in Chu's theory leads to a modified wedge angle where there is also zero diffraction? Further insight can be gained by looking more closely at the behavior near one of the angles where the field amplitudes pass through zero. Note the insert box in Fig. 7(c), which is a close-up of the curves near $\theta_w=90°$. Here, we see that the pressure release and the $R=-0.99$ curves indeed pass through zero at $\theta_w=90°$, or asymptotically close to $\theta_w=90°$, respectively. The $R=-0.5$ curve, conversely, passes through zero at about $\theta_w=89.95°$, while the $R=-0.1$ curve passes through zero for an even smaller angle (not shown). What is the general diffraction behavior for a wedge angle $\theta_w=89.95°$? Figure 7(d) plots the angular distribution of the diffracted field amplitude for all the same conditions as Fig. 7(b), except that $\theta_w=89.95°$. The behavior of the diffracted field now resembles that seen for the $\theta_w=79°$ wedge case of Fig. 7(a). The pressure release and $R=-0.99$ curves are zero, or almost zero, throughout much of the wedge angle, but also show deep troughs at $\tilde{\theta}_r=180°$, indicating a large negative diffracted field. In addition, throughout much of the wedge angle, the $R=-0.5$ and $R=-0.1$ cases display values close to those seen in Fig. 7(b), but again display deep troughs at $\tilde{\theta}_r=180°$. In particular, the $R=-0.5$ curve dips down and approaches zero at $\tilde{\theta}_r=180°$. This is indicative of the general behavior observed when $|R|<1$. The zero-crossings seen in Fig. 7(c) for the $R=-0.5$ and $R=-0.1$ cases do not indicate wedge angles where the diffracted field is generally zero for all locations of the source and receiver (as is the case when $\theta_w=\pi/m$ for rigid and pressure release wedges), but simply that the diffracted amplitude may be zero for specific combinations of the source and receiver angles, depending on the particular density contrast conditions and the wedge angle.

IV. CONCLUSIONS

Chu's normal coordinate theory for the acoustic impulse response of a density contrast isovelocity wedge gives an exact and complete description for the direct, reflected, and diffracted components of the time domain field in the medium where the source is located, and the field transmitted into and through the second wedge medium.

The direct/reflected arrivals, and the diffracted arrivals associated with them, are clearly separated in the time domain. The direct/reflected impulse always arrives first, followed by the associated diffraction. The two components do not interact with each other. In the exact forward scatter direction, the direct impulse precedes the diffraction arrival, but by an infinitesimally small period of time.

The impulse response for the direct/reflected field is a delta function. In scattering calculations computational evaluations of these signal components may be avoided by substituting a formal delta function [e.g., $\delta(t-\tau_{sr})$, where τ_{sr} is the travel time from source to receiver] multiplied by the spherical spreading reduction and the appropriate reflection coefficient, or transmission coefficient, as the pulse reflects from, or propagates through, the faces of the wedge. In the case of reflected paths, τ_{sr} would be calculated as the travel time from an image of the source, formed in the faces of the wedge, to the receiver. Transmissions into or through the second medium of the isovelocity wedge experience no time delay or refraction effects.

Diffraction waves are causally associated with direct/reflected impulses which interact with, and are wholly or partially screened by, the wedge apex. The diffraction arrival time depends upon the source and receiver locations, and upon the travel time from source to apex, and then from apex to receiver. The amplitude of the diffraction is dependent on the degree of acoustic shadowing at the apex.

In the case of an exterior wedge, if the source is placed to create an acoustic shadow boundary, the azimuthal diffraction pattern forms a lobe where the field amplitude changes from negative to positive upon entering the geometric shadow zone. The exact angle where the field passes through zero is close to the shadow boundary, but changes with time. This causes the behavior of the diffraction field, observed by receivers placed close to the shadow boundary, to exhibit complicated time varying forms. Other diffraction lobes may be seen which are associated with reflections in the faces of the wedge. In this case, for small t, the amplitude of the diffraction field is scaled by the reflectivity of the wedge boundary.

In the case of an interior wedge, acoustic shadows cannot be formed. However, diffractions associated with reflections in the wedge faces can still occur. Since the field may be determined by multiple reflections, the diffraction amplitude in this case may not depend simply on the reflectivity of a single wedge face. When $|R|\to 1$, Chu's theory asymptotically approaches the behavior, predicted by the rigid and pressure release wedge theories, of prescribing a zero diffraction field when the wedge angle $\theta_w=\pi/m$. However,

when $|R|<1$, Chu's theory indicates that the diffraction field is generally nonzero in these cases, but may be zero for specific combinations of the source and receiver angles.

ACKNOWLEDGMENTS

CF was supported by the Office of Naval Research with technical management provided by the Naval Research Laboratory, PE 61153N. DC was supported by the National Science Foundation, Grant No. OPP-0125629. CSC was supported by a grant from the Department of Geology and Geophysics, University of Wisconsin—Madison, Madison, Wisconsin.

[1] B. C. Heezen and C. D. Hollister, *Face of the Deep* (Oxford U.P., New York, 1971). Gives photographs of the seafloor and describes the processes that shape it. Figure 9.13 shows a power law spectrum for sediment ripples.

[2] J. M. Berkson and J. E. Matthews, ''Statistical properties of seafloor roughness,'' in *Acoustics of the Sea-Bed*, edited by N. G. Pace (Bath U.P., Bath, UK, 1983), pp. 215–223. An early path-breaking study of the nature of seafloor roughness.

[3] C. G. Fox and D. E. Hayes, ''Quantitative methods for analyzing the roughness of the seafloor,'' Rev. Geophys. **23**, 1–48 (1985). An excellent review of the background which also explains how to estimate sea spectra.

[4] M. R. Daneshvar and C. S. Clay, ''Imaging of rough surfaces for impulsive and continuously radiating sources,'' J. Acoust. Soc. Am. **82**, 360–369 (1987). Compares the seismic profile over a rough seafloor to Biot-Tolstoy wedge diffractions and reflections from facets. Also see Fig. 12.4.6 in Ref. 10.

[5] R. S. Keiffer and J. C. Novarini, ''A wedge assemblage method for 3-D acoustic scattering from sea surfaces: Comparison with a Helmholtz-Kirchhoff method,'' Comput. Acoust. **1**, 67–81 (1990).

[6] M. A. Biot and I. Tolstoy, ''Formulation of wave propagation in infinite media by normal coordinates with an application to diffraction,'' J. Acoust. Soc. Am. **29**, 381–391 (1957). Gives the time-dependent solution for an impulsive source. The solution is the displacement potential for the direct, image, and diffraction arrivals from a rigid wedge.

[7] I. Tolstoy and C. S. Clay, *Ocean Acoustics* (American Institute of Physics, New York, 1987). Appendix 5 is a corrected reprint of the Biot–Tolstoy 1957 paper.

[8] I. Tolstoy, *Wave Propagation* (McGraw–Hill, New York, 1973). Chapter 8 is a comprehensive exposition of the normal coordinate method and applications. Includes the time-dependent solution for the displacement potentials of the rigid wedge problem.

[9] W. A. Kinney, C. S. Clay, and G. A. Sandness, ''Scattering from a corrugated surface: Comparison between experiment, Helmholtz–Kirchhoff theory and the facet-ensemble method,'' J. Acoust. Soc. Am. **73**, 183–194 (1983). Also extends the Biot–Tolstoy solution to a wedge bounded by pressure release surfaces.

[10] H. Medwin and C. S. Clay, *Fundamentals of Acoustical Oceanography* (Academic, San Diego, 1998). Section 11.8 is a heuristic development of the normal coordinate solution of the rigid wedge problem that uses sound pressures. Comparisons of theory to acoustic experiments (spark sources) are in Secs. 11.8 and 12.2–12.4.

[11] D. Chu, ''Impulse response of density contrast wedge using normal coordinates,'' J. Acoust. Soc. Am. **86**, 1883–1896 (1989). Gives the complete development for the velocity potential solution for direct, reflection, and diffraction arrivals due to an impulsive source. All wedge angles are allowed.

[12] D. Chu, ''Exact solution for a density contrast shallow-water wedge using normal coordinates,'' J. Acoust. Soc. Am. **87**, 2442–2450 (1990). Extends Chu (1989), compares theory and experiment, and gives the wedge bounded by free and rigid interfaces.

[13] A. M. J. Davis, ''Two-dimensional acoustical diffraction by a penetrable wedge,'' J. Acoust. Soc. Am. **100**, 1316–1324 (1996).

[14] B. V. Budaev and D. B. Bogy, ''Rigorous solutions of acoustic wave diffraction by penetrable wedges,'' J. Acoust. Soc. Am. **105**, 74–83 (1999).

[15] A. M. J. Davis and R. W. Scharstein, ''The complete extension of the Biot–Tolstoy solution to the density contrast wedge with sample calculations,'' J. Acoust. Soc. Am. **101**, 1821–1835 (1997).

[16] A. M. J. Davis, ''Point-source excitation of the density contrast wedge: perturbation for nearly equal sound speeds,'' Q. J. Mech. Appl. Math. **54**, 613–630 (2001).

[17] J. C. Novarini and R. S. Keiffer, ''Impulse response of a density contrast wedge: practical implementation and some aspects of its diffracted component,'' Appl. Acoust. **58**, 195–210 (1999).

[18] E. A. Robinson and S. Treitel, *Geophysical Signal Analysis* (Prentice–Hall, Englewood Cliffs, NJ, 1980), pp. 112–118.

[19] C. Feuillade, R. W. Meredith, N. P. Chotiros, and C. S. Clay, ''Time domain investigation of transceiver functions using a known reference target,'' J. Acoust. Soc. Am. **112**, 2702–2712 (2002). This paper gives an explanation of how to construct a filter as the product of minimum delay wavelets, using vectorized notation. The wavelets used are simple low distortion filters that do not advance any of the signal components ahead of the actual arrival time.

[20] M. Born and E. Wolf, *Principles of Optics*, corrected 6th ed. (Pergamon, Oxford, 1991).

[21] H. Medwin, ''Shadowing by finite noise barriers,'' J. Acoust. Soc. Am. **69**, 1060–1064 (1981). Important experimental verification of the Biot-Tolstoy theory for semi-infinite wedges and screens.

Acoustic thermometry of the western Mediterranean basin

E. K. Skarsoulis[a)]
Institute of Applied and Computational Mathematics, Foundation for Research and Technology Hellas, P.O. Box 1527, 711 10 Heraklion, Crete, Greece

U. Send
Leibuiz-Institut für Meereswissenschaften an der Universität Kiel, Düsternbrooker Weg 20, 24105, Kiel, Germany

G. Piperakis
Institute of Applied and Computational Mathematics, Foundation for Research and Technology Hellas, P.O. Box 1527 711 10 Heraklion, Crete, Greece

P. Testor
Leibuiz-Institut für Meereswissenschaften an der Universitat Kiel, Dusternbrooker Weg 20, 24105, Kiel, Germany

(Received 3 December 2003; revised 14 May 2004; accepted 15 May 2004)

Ocean acoustic tomography is used to obtain heat-content estimates for the western Mediterranean basin. Travel-time data from 13 tomography sections of the Thetis-2 experiment (January–October 1994) are analyzed with a matched-peak inversion approach. The underlying analysis involves the use of peak arrivals and nonlinear model relations between travel-time and sound-speed variations. Slice inversion results are combined with temperature covariance functions for the western Mediterranean to obtain heat-content estimates for the basin. These estimates compare favorably with ECMWF data over the nine-month period of the Thetis-2 experiment. Furthermore, estimates for the basin-average temperature of the western Mediterranean deep water are obtained. [DOI: 10.1121/1.1771616]

PACS numbers: 43.30.Pc [AT] Pages: 790–798

I. INTRODUCTION

The ability to monitor the heat content of ocean basins is important for understanding the role of the oceans in climate change, as well as for studying ocean variability and large-scale ocean processes. Although the upper ocean is routinely monitored on large scales by the existing operational ocean observing systems, such as satellite remote sensing and ARGO floats, there is a significant observational gap concerning the deep ocean. Moreover, there are shortcomings related with the resolution and coverage of the existing observing systems, such as the lack of vertical resolution of altimetry data and the low horizontal coverage by the ARGO system.[1,2] These shortcomings/gaps can be resolved/filled by using acoustic monitoring techniques.

Ocean acoustic tomography was introduced by Munk and Wunsch[3,4] as a remote-sensing technique for large-scale monitoring of the ocean interior using low-frequency sound. Measuring the travel/arrival times of pulsed acoustic signals propagating from a source to a distant receiver through the water mass over a multitude of different paths, and exploiting the knowledge about how travel times are affected by the sound-speed distribution in the water, the latter can be obtained by inversion. Further, sound speed is related to temperature,[4,5] and, thus, ocean acoustic tomography can be used for the study of gyre- and basin-scale temperature and heat-content variability (acoustic thermometry).[6,7]

An ocean acoustic tomography experiment called Thetis-2 was conducted in the western Mediterranean from January to October 1994.[8] The 9-month long experiment involved seven acoustic transceivers at a nominal depth of 150 m operating at 250/400 Hz, with a geometric configuration shown in Fig. 1. Acoustic travel-time data were collected along 13 tomographic sections with ranges between 220 and 610 km. The seasonal variability in the area gives rise to nonlinear relations between arrival-time and sound-speed variations.[8] Furthermore, the lack of navigation data for one transceiver (W4) hampered the analysis of 4 tomographic sections originating at the particular transceiver. Preliminary heat-content results based on ray analysis of a single early arrival from 3 tomography sections were presented in a previous work.[9] Due to the above mentioned factors the complete analysis of the full dataset (all arrivals, all sections) became feasible only after the development of improved modeling and analysis methods.

The application of an adaptive scheme[10] based on the use of variable discrete background states, to be estimated from the tomography data rather than set *a priori*, enabled the efficient handling of nonlinear model relations. Further, the use of the peak-arrival approach[11,12] for modeling travel-time observables enabled the exploitation of the latter independently of their identification as ray or modal arrivals. The introduction of a matched-peak inversion approach[13] enabled the automatic analysis of travel-time data, bypassing the peak tracking and identification problem inherent in conventional analysis. Finally, an extended matched-peak approach made possible the analysis of the sections originating at W4,

a)Electronic mail: eskars@iacm.forth.gr

by addressing the inversion problem along those sections simultaneously with the navigation problem for W4.[14]

In this paper we present results from the integrated analysis of the Thetis-2 dataset, and we combine tomographic sections to provide average temperature and heat-content estimates for the western Mediterranean sea. The heat-content estimates based on the analysis of the full acoustic dataset (13 sections, multiple arrivals) are a significant improvement to previous estimates based on inversions of a single early arrival along three sections[9] in terms of both estimation accuracy (smaller errors) and agreement with estimates from independent heat-flux data. Furthermore, the exploitation of multiple arrivals adds vertical resolution to the inversion results.[3,4] This allows estimates for the evolution of the deep-water temperature.

The contents of this work are organized as follows. In Sec. II we give a brief description of the matched-peak approach for slice inversions, along with the adaptive scheme for the treatment of nonlinear model relations. In Sec. III a minimum-variance linear estimator for the basin average temperature is derived in terms of temperature averages along sections. In Section IV presents the analysis results from the application of these methods to the acoustic dataset from the Thetis-2 tomography experiment. The main conclusions from this work are presented and discussed in Sec. V.

II. MATCHED-PEAK SLICE INVERSION

The solution of the forward problem in ocean acoustic travel-time tomography leads to a set of model relations,

$$\tau_i = g_i(\vec{\vartheta}), \quad i=1,...,I, \quad \vec{\vartheta} \in \Theta, \tag{1}$$

nonlinear in general, between the arrival times τ_i, $i=1,...,I$ (I is the number of arrivals) and the sound-speed parameter vector $\vec{\vartheta}=(\vartheta_1,\ldots,\vartheta_L)$, made, e.g., of the amplitudes of the modes parametrizing the sound-speed profile; Θ denotes the parameter domain. Arrival times can be defined/modeled in various ways using, e.g., the notions of ray, modal, or peak arrivals.[4,11] Linearizing the relations (1) about a set of background states $\vec{\vartheta}^{(b)}$, $b \in B$, with corresponding arrival times $\tau_i^{(b)}=g_i(\vec{\vartheta}^{(b)})$, and, further, discretizing the local parameter space, about each background state, into a local grid with index $k \in K$, the following relations can be obtained:

$$\tilde{\tau}_i(b,k) = \tau_i^{(b)} + \sum_{l=1}^{L} \frac{\partial g_i(\vec{\vartheta}^{(b)})}{\partial \vartheta_l} [\tilde{\vartheta}_l(b,k) - \vartheta_l^{(b)}],$$

$$i=1,...,I, \quad b \in B, \quad k \in K, \tag{2}$$

where $\{\tilde{\vartheta}_1(b,k)\}$ represent the discrete model states, and $\{\tilde{\tau}_i(b,k)\}$ the corresponding arrival times. Using the relations (2), the arrival times corresponding to a set of discrete model states spanning the parameter space Θ can be calculated rapidly, since the full arrival-pattern calculations need to be carried out at a limited number of background model states $\vec{\vartheta}^{(b)}$, $b \in B$. The derivatives $\partial g_i(\vec{\vartheta}^{(b)})/\partial \vartheta_l$, called influence coefficients, can be expressed and calculated in terms of background quantities and sound-speed modes.[4,11] Depending on the background state b and the discretization steps $\delta\vec{\vartheta}$, an estimate for the upper bound of the prediction error ϵ_i can be obtained[13] as a sum of a discretization error and an observation/modeling error n_i,

$$\epsilon_i(b,\delta\vec{\vartheta}) = \frac{1}{2}\sum_{l=1}^{L} \left| \frac{\partial g_i(\vec{\vartheta}^{(b)})}{\partial \vartheta_l} \delta\vartheta_l \right| + n_i,$$

$$i=1,...,I, \quad b \in B, \tag{3}$$

The observed arrival times $\tau_j^{(o)}$, $j=1,...,J$ are allowed to associate with the model arrival times $\tilde{\tau}_i(b,k)$ if their time difference is smaller than the tolerance $\epsilon_i(b,\delta\vec{\vartheta})$. Finally, those model states are selected that maximize the number of associations between observed and model peaks.

Besides the ocean variability, represented by the model state $\{\tilde{\vartheta}_l(b,k)\}$, there are also other sources of variability, such as mooring motion. In this case the model relations can be written in the following linearized form:

$$\tilde{\tau}_i(b,k;\delta r) = \tau_i^{(b)} + \sum_{l=1}^{L} \frac{\partial g_i(\vec{\vartheta}^{(b)})}{\partial \vartheta_l} [\tilde{\vartheta}_l(b,k) - \vartheta_l^{(b)}] + \frac{\partial \tau_i}{\partial r}\delta r, \tag{4}$$

where r is the source–receiver range and δr represents the range variation due to mooring motion, which is a function of time. The mooring motion is usually estimated from additional navigation data, and its effect is removed from the observed travel times prior to the analysis. However, in the case of missing navigation data, as in the case of W4, the correction cannot be calculated/applied *a priori*.

The matched-peak approach can be extended to estimate δr together with the ocean state, by maximizing the number of peak associations as a function of the model state (b,k) and the range variation δr. In the case of the four Thetis-2 sections involving W4 the simultaneous transmissions along the four sections can be exploited to obtain better estimates; in that case the quantity to maximize is the joint number of peak associations along all sections.[14]

III. HORIZONTAL AVERAGE

For heat-budget studies it is desirable to obtain estimates for the average temperature (heat content) over a sea area, in order to balance its evolution with the surface heat fluxes and fluxes through the side boundaries.[15] Tomography provides estimates for the range-average temperature along a number of transmission lines defined by the geometry of the tomographic array for different layers in depth. Considering a temperature field $T(x,y)$ over an area A of size $|A|$, an optimal estimator is sought for the horizontally average temperature H,

$$H = \frac{1}{|A|}\int_A T(x,y)\,dx\,dy, \tag{5}$$

in terms of the temperature averages D_m along a number of lines S_m (of length L_m), $m=1,...,M$, representing tomography sections,

$$D_m = \frac{1}{L_m}\int_{S_m} T(x(s),y(s))\,ds. \tag{6}$$

The vertical dependence is omitted here for simplicity, but one can consider T as the vertically averaged temperature over a certain layer. The range-average temperature along a tomography section at a particular depth is directly related with the corresponding average sound speed, which, in turn, is related through the parameter vector $\vec{\vartheta}$ and the model relations (2) with the tomographic travel-time observables.

Taking the simplest case of a linear estimator of the horizontal average,

$$\hat{H}=\sum_{m=1}^{M} a_m D_m, \tag{7}$$

where a_m are unknown weights, and assuming it to be a minimum-variance estimator the following system of equations can be obtained by setting the derivatives of the variance $\langle(\hat{H}-H)^2\rangle$, with respect to a_m, equal to zero:

$$\sum_{k=1}^{M} a_k\langle D_m D_k\rangle=\langle HD_m\rangle, \quad m=1,...,M. \tag{8}$$

This system can be solved for the weights $\mathbf{a}=\{a_m\}$, which can be thus expressed in terms of $\mathbf{C_{DD}}=\{\langle D_m D_k\rangle\}$, the covariance matrix between the line averages (data), and $\mathbf{c_{HD}}=\{\langle HD_m\rangle\}$, the covariance vector between the horizontal and the line averages,

$$\mathbf{a}=\mathbf{C_{DD}^{-1}c_{HD}}. \tag{9}$$

The mean square error (error variance) then becomes

$$\langle(\hat{H}-H)^2\rangle=\langle H^2\rangle-\mathbf{c'_{HD}C_{DD}^{-1}c_{HD}}, \tag{10}$$

where a prime denotes transposition. The covariance matrix $\mathbf{C_{DD}}$ and covariance vector $\mathbf{c_{HD}}$ can be calculated from the temperature covariance function $\langle T(x',y')T(x,y)\rangle$,

$$\langle D_m D_k\rangle=\frac{1}{L_m L_k}\int_{S_m}\int_{S_k}\langle T(x(s_m),y(s_m))T(x(s_k),y(s_k))\rangle \times ds_m\, ds_k, \tag{11}$$

$$\langle HD_m\rangle=\frac{1}{|A|L_m}\int\int_{A}\int_{S_m}\langle T(x',y')T(x(s_m),y(s_m))\rangle \times dx'\, dy'\, ds_m. \tag{12}$$

The variance $\langle H^2\rangle$ can be calculated similarly. By assuming the temperature field to be homogeneous, i.e., by considering the temperature covariance to be a function of the distance between the points (x',y') and (x,y), the above expressions can be further simplified.

IV. ANALYSIS OF THETIS-2 DATA

Analysis of historical temperature data for the area covered by the Thetis-2 experiment (1°–9° E) resulted in a set of empirical orthogonal functions (EOFs). The first three EOFs, shown in Fig. 1, with rms amplitudes 18.48, 2.88, and 0.96, respectively, explain 99.6% of the anticipated variance concentrated mostly in the upper layers. Two systematic CTD surveys conducted in January and October 1994 (R/V Poseidon and R/V Suroit cruises) revealed significant deviations

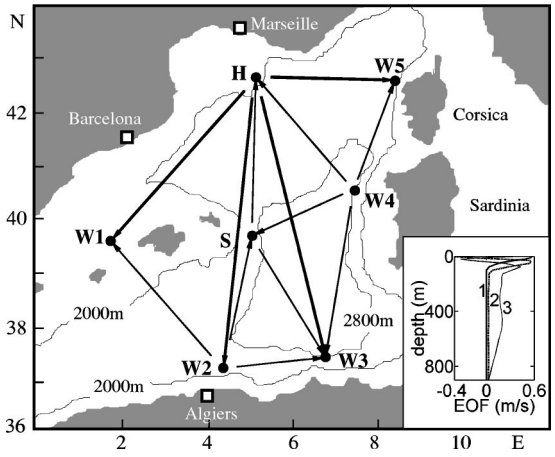

FIG. 1. The geometry of the Thetis-2 tomography experiment in the western Mediterranean sea and the first 3 EOFs for the area of interest (bottom right).

from the climatological mean conditions at large depths: the average 1994 temperatures below 600 m were about 0.05 °C higher than the 40-year historical mean. Because of that the reference sound-speed profile for the inversions in the deep layers was calculated from the CTD data rather than from the climatology. While the variability in the upper layers can be sufficiently described by the first three EOFs shown in Fig. 1, the description of the deep layers would require a larger number (>15) of higher-order EOFs. In order to keep the number of parameters low, the deep-water variability is described here by two additional box-shaped modes covering the 600–1000 and 1000–2000 m layer, respectively—the depth of 1000 m separates two main water masses: the Levantine intermediate water (LIW) and the western Mediterranean deep water (WMDW).[16] The three EOFs shown above are truncated below 600 m, such that the parametric description of the upper and the deeper layers is uncoupled. The variability of the CTD data along the tomography sections in the 600–1000 and 1000–2000 m layer is 0.14 and 0.02 m/s rms, respectively, on average.

It is known from previous works[8,13,14] that the seasonal variability associated with EOF-1 variations, confined in the upper 100 m, gives rise to a significant nonlinearity of the model relations, due to the passage from surface-reflected propagation conditions in winter to refracted propagation in the summer. The extent of the nonlinearity is such that the use of a single background state (annual mean) would give rise to linearization errors as large as 300 ms for intermediate arrivals of longer sections over the EOF-1 variability interval. By using a set of discrete background states with respect to ϑ_1 this error can be drastically reduced: taking the discretization step $\delta\vartheta_1=2$, the error becomes less than 2 ms, better than the travel-time measurement accuracy (8 ms). The background state appropriate for each tomographic reception is estimated from the inversion, as described in Sec. II, rather than set *a priori*, e.g., from the monthly climatology.[17] Still, the monthly climatology is useful for defining appropriate search intervals for the background state estimation, thus reducing the computational burden significantly.[13] The parameter domain Θ is taken as the Cartesian product of the parameter intervals for the amplitudes

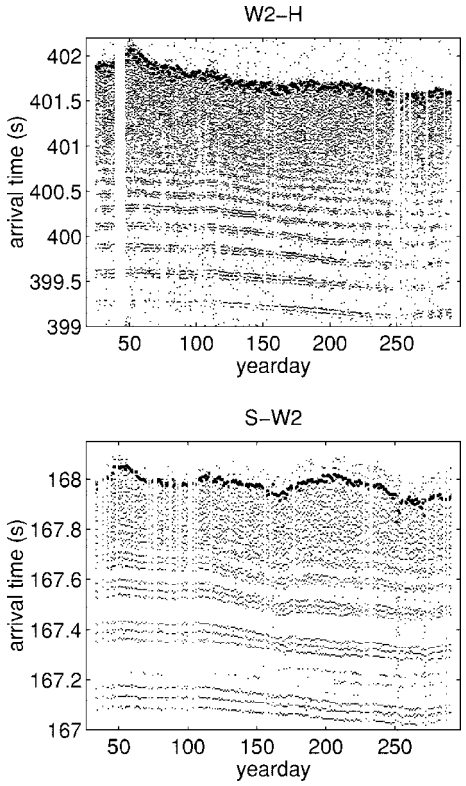

FIG. 2. Measured travel-time data along the sections W2-H and S-W2 over the nine-month duration of the experiment. The heavier dots denote cut-off peaks.

of the sound-speed modes, each one covering ± 2.5 standard deviations (rms values) of the EOF amplitudes and sound-speed anomalies.

A. Slice inversions

Figure 2 shows the travel-time data from two characteristic sections of the Thetis-2 experiment, a long section from H to W2 (605 km) and a short one from W2 to S (253 km), after correlation (matched-filter) processing, clock-drift correction, mooring-motion correction, offset calibration and incoherent one-day averaging of arrival patterns.[8] The horizontal axes represent yeardays of 1994 and span the nine-month period of the experiment, whereas the vertical axes measure the arrival time in seconds. Early arrivals corresponding to steep propagation angles arrive in groups of three (arrival triplets). Later groups of arrivals get closer and overlap with each other such that their identification, e.g., in terms of ray arrivals, becomes a problem. The most characteristic feature of the late arrival pattern is the abrupt end of the reception following the typical crescendo in the intensity of late arrivals.[4] The cut-off peaks, defined as the last of the five highest peaks in each reception, are shown in Fig. 2 through the heavier dots. Additional peaks in Fig. 2 are due to noise or due to bottom-interacting acoustic energy. Further, it is seen from Fig. 2 that there are periods of poor data quality or absence of data; these are periods of low signal/noise ratio (SNR).

The geometry of eigenrays sampling the sections W2-H and S-W2, calculated for the annual mean sound-speed profile, is shown in Fig. 3, to highlight the effectiveness of the

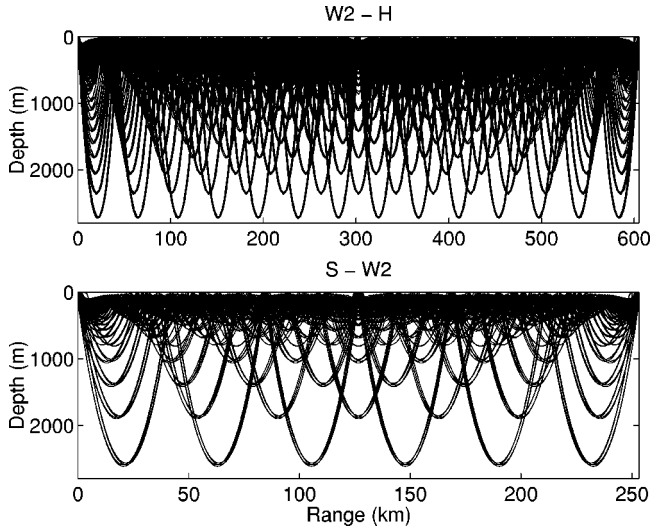

FIG. 3. Geometry of eigenrays along the sections W2-H and S-W2 (calculation based on the annual mean sound-speed profile).

horizontal averaging implicit in the tomography sampling. Above 2000 m, which is the maximum depth analyzed in this paper, the largest horizontal gaps (unsampled regions) are of the order of 30 km, but more typically approximately 10 km. Most of the ocean variability is in mesoscale and large-scale fields, with scales of 100 km and higher, as presented in the next subsection, so good horizontal averages are expected from the tomography travel-time data. The steep rays penetrating the deep layers in Fig. 3 correspond to the early arrivals in Fig. 2 and the shallow rays to the late arrivals. The eigenrays are grouped in bundles of four characterized by similar arrival times (two of which are identical[4]) and corresponding to the arrival triplets in Fig. 2.

For every tomography section influence coefficients were calculated for all arrivals (relative maxima) at the various background states using the peak-arrival approach.[13] The arrivals that could be continuously traced over the entire range of anticipated variability (over the different background states) were used as the model arrivals to be associated with the observed ones in the matched-peak inversion. Those contain the distinguishable groups of early arrivals followed by a number of intermediate arrivals and finally the cut-off peak. The observation errors for the early and intermediate arrivals were set equal to 10 ms, close to the travel-time measurement accuracy. Late arrivals and, in particular, the cut-off peak are subject to range-dependence effects.[18] The reason is that these arrivals sample the shallow water layers where range dependence is strongest. From the study of large-scale range-dependence effects on travel times along the Thetis-2 sections bias and variability estimates were obtained for the cut-off arrival times; the effects on the early and intermediate arrivals were small compared to the observation accuracy, whereas for the cut-off travel-times biases between 50 and 200 ms (delay bias) and residual variability between 50 and 100 ms rms were observed.[18] These effects on the cut-off arrival times are taken into account in the following range-independent inversions by correcting for the bias and increasing the observation error for the cut-off peak to 50–100 ms, depending on the section.

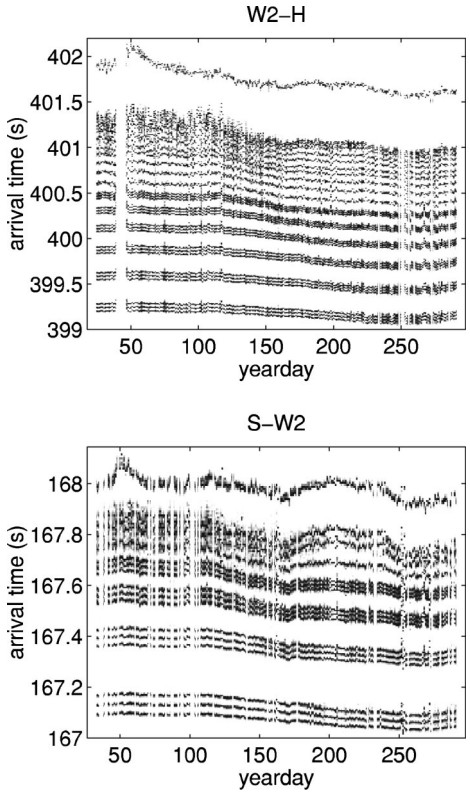

FIG. 4. The *a posteriori* probability density functions (pdfs) of peak arrival times (theoretical arrival times) for the sections W2-H and S-W2, corresponding to the population of selected model states for each reception. A gray scale is used for the representation of each pdf, with white representing zero density and black representing the density maximum.

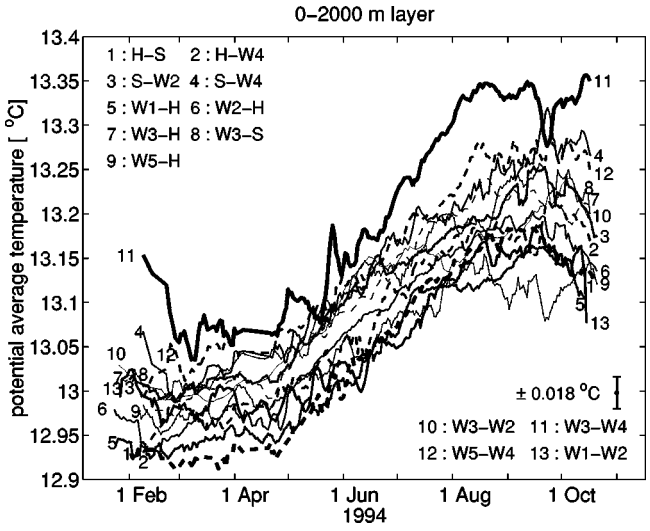

FIG. 5. Inversion results from individual sections for the 0–2000 m layer. The different sections are identified by numbers (1–13) and different line types. The average rms inversion error for all sections (0.018 °C) is plotted (bottom right), whereas the individual inversion error for each section is given in Table I (rightmost column).

Figure 4 shows the *a posteriori* probability density functions (pdfs) of peak arrival times for the sections W2-H and S-W2 after the application of the matched-peak inversion approach. The analysis of each reception leads to a population of model states (background states and perturbations). For each model state the corresponding arrival times can be calculated from the model relations, and, thus, a population of travel times can be obtained for each arrival. Figure 4 shows the pdfs for the travel-time populations for the theoretical arrivals used in the W2-H and S-W2 inversions. It is seen that the travel-time data (Fig. 2) are well reproduced by the model results (Fig. 4), even though in a weak (distribution) sense. The quality of the inversion depends on the quality of the data; low SNR data lead to poor inversion quality. The identification of the individual intermediate arrivals following the distinct arrival triplets are associated with larger ambiguity, depending on the separability of adjacent peaks in the measured travel-time data. In this connection, the inclusion of additional peaks with small separability in the inversions will have no substantial contribution to the information content. An important feature of the matched-peak approach is that it applies to any reception, independently of previous inversion results or initial conditions. This enables the analysis of data even in the presence of large gaps. On the other hand, a problematic reception/inversion will not at all affect the analysis of subsequent receptions.

Figure 5 shows the slice inversion results for the individual sections in the form of potential temperatures averaged over the 0–2000 layer. The inversion errors for the various sections/layers are summarized in Table I; in Fig. 5 only the average rms error for all 13 sections (0.018 °C rms) is plotted. A typical seasonal trend is observed in the inversion results of Fig. 5 along all sections. The seasonal cycle though confined in the upper water layer has a significant

TABLE I. Average rms inversion errors (°C) for the 13 Thetis-2 sections in various depth layers.

Layer (m):	0–50	50–100	100–200	200–400	400–600	600–1000	1000–2000	0–2000
H-S	0.5810	0.2874	0.0515	0.0475	0.0574	0.0468	0.0124	0.0168
H-W4	0.5278	0.3158	0.0808	0.0626	0.0649	0.0487	0.0116	0.0219
S-W2	0.5689	0.3209	0.0683	0.0496	0.0505	0.0462	0.0122	0.0169
S-W4	0.5834	0.3461	0.0867	0.0620	0.0597	0.0502	0.0125	0.0244
W1-H	0.5810	0.2356	0.0533	0.0456	0.0512	0.0414	0.0127	0.0162
W1-W2	0.6634	0.3609	0.0710	0.0494	0.0509	–	–	0.0337
W2-H	0.5854	0.3327	0.0493	0.0420	0.0508	0.0471	0.0117	0.0130
W3-H	0.5053	0.2870	0.0646	0.0504	0.0541	0.0436	0.0102	0.0100
W3-S	0.5784	0.3699	0.0833	0.0563	0.0505	0.0541	0.0116	0.0156
W3–W2	0.5850	0.3318	0.0779	0.0566	0.0562	0.0522	0.0126	0.0157
W3–W4	0.4950	0.2983	0.0716	0.0533	0.0541	0.0458	0.0079	0.0190
W5-H	0.5708	0.2816	0.0681	0.0547	0.0581	0.0488	0.0116	0.0155
W5–W4	0.5264	0.3485	0.0646	0.0484	0.0525	0.0454	0.0098	0.0187

signature in the average over the whole water column. Apart from the seasonal signal the spatial spread, i.e., the variability between the various sections, is also significant and nearly as large as the seasonal signal. The inversion results from two sections, W3–W4 and H-S, are highlighted in Fig. 5, through heavy solid and dashed lines, respectively. The section W3–W4 in the southeast is by far the warmest, as far as the whole water column is concerned. This is due to the inflow of warm water masses from the eastern Mediterranean, in particular, of the Levantine intermediate water. On the other hand, the section H-S is among the coldest. This section partly covers the Gulf of Lions, where deep convection takes place in winter.[19]

Table I presents the average inversion errors for the various layers along the Thetis-2 sections. The errors are larger for the shallow layers and smaller for the deep layers, in agreement with the larger variability anticipated at shallow depths. The temperature anomalies in the various depth layers are not statistically independent. Therefore, the variance of the average temperature in the 0–2000 m layer is not simply a sum of variances of the contributing layers scaled by the layer thicknesses; cross-terms are important and have to be accounted for. In general, the inversion errors decrease with an increasing source–receiver range but they also depend on data quality. The largest errors are observed along the section W1–W2. This section samples depths up to 600 m due to energy stripping taking place at the Balearic sill between Mallorca and Ibiza. As a result, the receptions lack the clear identifiable groups of early arrivals and this has an impact on the inversion errors. The error estimate for the 0–2000 m layer in this case was obtained, assuming zero variability for depths larger than 600 m. Further, large errors, especially for the deep layers, are observed along the sections H-W4 and S-W4 for which the inversion problem is solved together with the navigation problem of W4. The other two sections involving W4 (W3–W4 and W5–W4) have significantly smaller errors; the reason is that these two sections have about the same orientation such that the W4-mooring-motion effects on arrival times are strongly correlated in the two datasets.

B. Horizontal averages

By combining inversion results from the 13 sections, three-dimensional temperature averages for the area covered by the Thetis-2 tomographic array (1°–9° E) are presented in this section. To obtain the optimal (minimum-variance) linear estimator, covariance functions from temperature data were calculated. The temperature anomalies were assumed to be spatially homogeneous, i.e., the covariance of temperature anomalies was treated as a one-dimensional function of the horizontal distance between any two locations.

For the 0–2000 m layer, a superposition of two Gaussian models was used to represent the one-dimensional temperature covariance function covering large- and mesoscale structures. The covariance function of the large-scale seasonal temperature fluctuations was obtained from historical seasonal data for the area of interest after subtraction of the local time-mean values. This one-dimensional covariance function reveals dominant large-scale structures of 300 km scale dominated by the seasonal variability. Then the departures from the seasonal means at different locations were calculated and grouped according to their horizontal distance to calculate a mesoscale covariance function. This covariance function of the mesoscale temperature fluctuations has a scale of 100 km. These values were also found to be consistent with data from a high-resolution numerical model of the western Mediterranean.[20] Table II (mid-column) presents the weights of the resulting minimum-variance linear estimator for the horizontal average temperature in the 0–2000 m layer. The estimation error of the three-dimensional average for this layer is 0.0025 °C rms.

TABLE II. Weights for the minimum-variance estimator of the horizontal average temperature in the 0–2000 and 600–2000 m layers.

Layer (m):	0–2000	600–2000
H-S	−0.0128	0.0349
H-W4	0.0182	0.0265
S-W2	−0.0110	0.0567
S-W4	0.0514	0.0316
W1-H	0.1858	0.1083
W1–W2	0.1544	0
W2-H	0.1355	0.0077
W3-H	0.0384	0.0442
W3-S	0.0503	0.0239
W3–W2	0.0667	0.0429
W3–W4	0.1275	0.0665
W5-H	0.1031	0.0526
W5–W4	0.0906	0.0514

Figure 6 shows the evolution of the average temperature over the area 1°–9° E in the layer 0–2000 m (heavy solid line) estimated from the inversion results along the 13 Thetis-2 sections shown in Fig. 5. The rms error (shaded

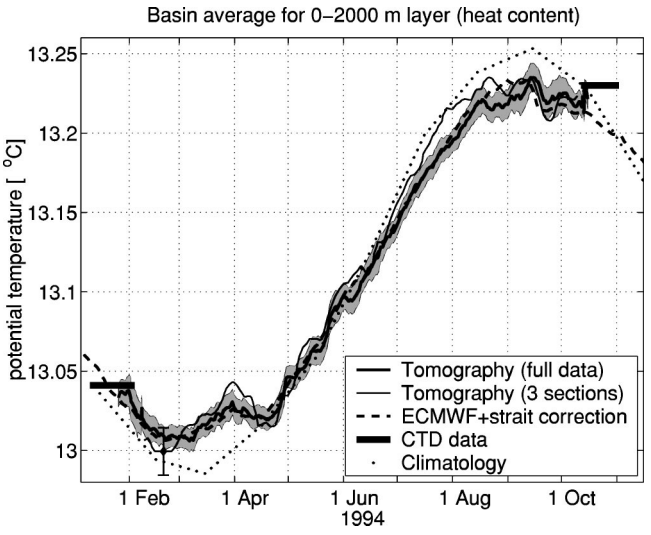

FIG. 6. Evolution of the average temperature of the upper 2000 m of water in the western Mediterranean (1°–9° E) estimated from tomography (solid lines) and ECMWF heat-flux data (dashed line), and compared with the seasonal cycle from the climatology (dotted line). The CTD data from the Poseidon/Suroit cruises in January/October are also shown (horizontal bars). The heavy solid line and the shaded area represent the mean tomography estimate and rms error from the complete analysis of the 13 Thetis-2 sections. The light solid line and vertical error bar represent earlier tomography results based on the analysis of a single early arrival along three sections (W1-H, W3-H, and W5-H).

area), integrating the inversion error and the error of the averaging process, is variable depending on the quality of data; its average value is 0.0081 °C. The heavy horizontal bars in January and October represent the average temperatures from the Poseidon and Suroit CTD data, respectively; the horizontal extent of the bars represents the time spread of these data. The dashed line in Fig. 6 shows the integral of independent heat-flux data, i.e., the total input of heat into the basin through the surface converted to volume-average temperature, for the western Mediterranean basin, obtained from the European Center for Medium-range Weather Forecasts (ECMWF). The ECMWF heat-flux data for the entire western basin were corrected by 5.7 W/m^2 to account for heat transport through the Sicily/Gibraltar straits—there is a net heat influx through the straits—and the resulting temperature amplitude was adjusted (scaled by 92.5%) to a smaller seasonal amplitude for the 1°–9 °E subregion.[9] The agreement of the tomography results and the ECMWF data is surprisingly good, not only on annual time scale but also seasonally and reproducing many short term events, such as a warming interruption in April and a strong cooling in mid September. The deviations of the ECMWF data are in most cases within the error bars of the tomography results.

The dotted line in Fig. 6 represents the seasonal cycle in the 1°–9° E area for the 0–2000 m layer resulting from the monthly mean climatology, up to a constant. The seasonal amplitude from the climatology is about 20% higher than the ECMWF flux integral and the tomography results. This indicates that the *a priori* setting of a time-variable background state for tomographic inversions based on the climatology could have led to significant biases. Earlier tomography estimates, based on inversions of a single early arrival along three sections (W1-H, W3-H, and W5-H)[9] are also plotted in Fig. 6 for comparison. The corresponding rms error is 0.015 °C, about twice as large as the error from the latest estimates; the error remains constant in this case. In connection with the larger errors, the deviation from the ECMWF heat-flux integral is also significantly larger than in the latest results.

Average temperature estimates for the 600–2000 m layer, i.e., for the western Mediterranean deep water, are presented in the following. Due to the sparseness of historical data for this layer the temperature covariance function was calculated using data from a large number of profiling floats deployed by IfM Kiel in the western Mediterranean from 1997 to 2002. Again a two-scale Gaussian model was fitted to the one-dimensional covariance function, revealing dominant structures of 100 and 12 km scales, respectively, i.e., the correlation lengths are significantly smaller than for the 0–2000 m layer. The reason is the absence of the seasonal signal at depth. The mesoscale is the same in both layers, but in addition here submesoscale features are captured (e.g., submesoscale coherent vortices, so-called SCV's, fronts, filaments, etc.). Probably the additional very short scales become more visible here since at depth they are not dominated by the large seasonal variability. Table II (rightmost column) presents the weights of the minimum-variance linear estimator for the horizontal average temperature in the 600–2000 m layer. The estimation error of the 3-D average for this layer is

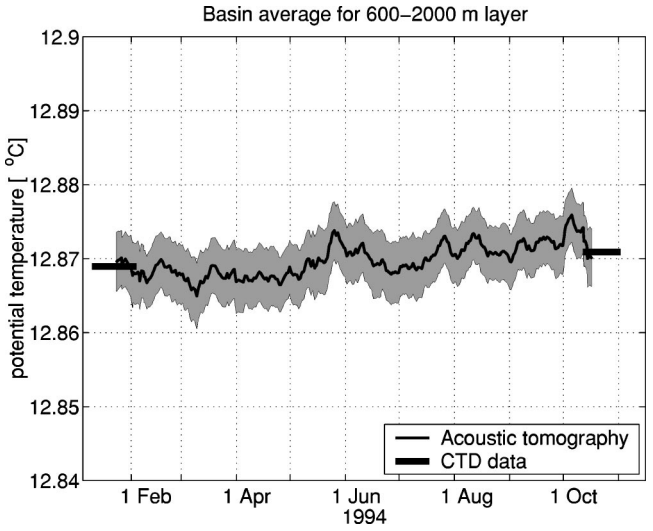

FIG. 7. Evolution of the average temperature in the deep water (600–2000 m layer) of the western Mediterranean basin (1°–9° E) estimated from acoustic tomography; the solid line represents the mean and the shaded area the rms error. CTD data from the Poseidon/Suroit cruises in January/October are shown as horizontal bars.

0.0024 °C rms. Figure 7 shows the average temperatures over the area 1°–9° E for the deep layer (600–2000 m). The rms error, represented by the shaded area, has an average value of 0.0038 °C; this is the accuracy of the Thetis-2 configuration for the deep-water temperature measurement. The average temperatures from the Poseidon and Suroit CTD data in January and October are also shown in Fig. 7 and they agree with the tomography results.

A previous analysis of long-term historical *in situ* observations in some parts of the western Mediterranean basin revealed a long-term warming trend of the deep water by ~0.003 °C/year.[21] However, it was not clear from these studies how widespread this signal was. Over a period of nine months, such a trend would give a temperature increase of 0.0022 °C. The difference of the basin-average temperatures in the CTD data from January (Poseidon) to October (Suroit) in Fig. 7 is about 0.0019 °C, which is very close to the above estimate. Some of this agreement may be spurious, but it is not inconsistent with the hypothesis of a basin-wide warming trend for the western Mediterranean deep water. Further, as mentioned before, the average 1994 temperatures below 600 m, estimated from the Poseidon/Suroit CTD data, were about 0.05 °C higher than the 40-year historical mean; this is also compatible with a basin-wide warming trend of 0.003 °C/year. An indication of a basin-wide warming trend can be seen in the tomography results as well. Nevertheless, the anticipated temperature difference (0.0022 °C) over the nine months is smaller than the tomography error (0.0038 °C), and, in this connection, longer-term (≥two-year) tomography measurements would be necessary to draw more reliable conclusions.

V. DISCUSSION AND CONCLUSIONS

Results from an integrated analysis of the complete set of travel-time data from the Thetis-2 tomography experiment were presented. In the first place the 13 tomographic sections

of the Thetis-2 experiment were analyzed individually. Travel-time observables were modeled using the peak-arrival approach and inverted using the matched-peak inversion approach. An adaptive scheme was used for treating the nonlinearity of the model relations, in which the background state (linearization reference) was treated as an unknown of the problem. As an alternative, one could think of using a time-variable background state, set *a priori* from the climatology;[17] this approach would be sufficient for small deviations of the actual state from the climatology. However, for the case of the Thetis-2 experiment the deviations are significant, as shown in Fig. 6, and the use of climatologically constrained background states could bias the inversion results.

By combining slice inversion results from the 13 sections and exploiting the knowledge of the temperature covariance structure for the western Mediterranean basin, estimates for the evolution of the three-dimensional average temperature for the western Mediterranean sub-basin from 1° E to 9° E for the layers 0–2000 m (heat content) and 600–2000 m (deep-water temperature) were obtained. The accuracy of ocean acoustic tomography (Thetis-2 configuration) for temperature measurement was larger for the deep layer (rms error 0.0038 °C) than for the heat content (rms error 0.0081 °C). While the reduced ocean variability at large depths improves the accuracy of temperature measurements, the smaller horizontal scales of the dominating temperature structures plays a deteriorating role as regards the ability to infer horizontal temperature averages from a given tomographic configuration.

A remarkable agreement between tomography heat-content estimates and the ECMWF heat-flux integral was obtained. In this respect, the results presented here are a significant improvement to previous heat-content results, based on simple analyses of a subset of the Thetis-2 data,[9] in terms of accuracy (~50% error reduction) and also in terms of agreement with the independent heat-flux data. Heat-flux data describe the transfer of heat through the ocean surface, whereas tomographic data can be used to obtain estimates for the total heat content and, in general, horizontal temperature averages over particular depth layers. Surface heat fluxes and heat content are two terms of the heat-budget equation,[15] which also includes advection as a third term. If the advection term can be estimated (as was the case here), then the other two can be compared to verify their accuracy and consistency, on the basis of the heat-budget equation. In open-ocean applications, however, it is never enough to have only one of these, and, in general, heat-flux, heat-content, and advection data are needed to carry out heat-budget analyses.

Ocean acoustic tomography is depth resolving and can be used for the study of temperature evolution of certain depth layers, and hence the transfer of heat between layers (overturning circulation). Of particular interest is the behavior of the western Mediterranean deep water in the light of previous studies reporting the existence of a warming trend in some parts of the basin.[21] The CTD data and tomography results are consistent with the hypothesis that the warming trend is widespread over the whole basin. Nevertheless, given the size of the tomography error for the 600–2000 m layer (0.0038 °C), longer term (≥2-year) measurements would be required to draw reliable conclusions. The error of the tomography estimates for the horizontal average deep-water temperature is ~20% of the rms variability of the temperature measurements conducted during the Poseidon and Suroit cruises (0.02 °C). This means that a transmission across the Thetis-2 tomography array offers an accuracy for the deep-water temperature measurement equivalent to that of the average of 25 independent point samples.

The Thetis-2 tomography experiment was conducted as a pilot experiment for long-term monitoring of the western Mediterranean basin with acoustics. For this reason the locations of most of the moorings were selected to make a cable connection of the instruments to shore feasible. The results presented here demonstrate that tomography has the potential to monitor across the extents of the basin with sufficient temporal resolution as well as resolution in depth.

ACKNOWLEDGMENTS

The Thetis-2 project was supported by the EU MAST-2 program (CT91-0006). The authors would like to thank the anonymous reviewers for helpful comments and suggestions.

[1] GCOS-82 (WMO/TD No. 1143), The 2nd report on the adequacy of the global observing systems for climate in support of the UNFCC, April 2003.
[2] N. R. Smith and C. Koblinsky, in *The Ocean Observing System for Climate*, Conference Proceedings, St. Raphael, France, 1999.
[3] W. H. Munk and C. Wunsch, ''Ocean acoustic tomography: A scheme for large scale monitoring,'' Deep-Sea Res. **26A**, 123–161 (1979).
[4] W. H. Munk, P. F. Worcester, and C. Wunsch, *Ocean Acoustic Tomography* (Cambridge University Press, New York, 1995).
[5] V. A. Del Grosso, ''New equation for the speed of sound in natural waters (with comparisons to other equations),'' J. Acoust. Soc. Am. **56**, 1084–1091 (1974).
[6] P. F. Worcester, B. D. Cornuelle, M. A. Dzieciuch, W. H. Munk, B. M. Howe, J. A. Mercer, R. C. Spindel, J. A. Colosi, K. Metzger, T. G. Birdsall, and A. B. Baggeroer, ''A test of basin-scale acoustic thermometry using a large-aperture vertical array at 3250-km range in the eastern North Pacific Ocean,'' J. Acoust. Soc. Am. **105**, 3185–3201 (1999).
[7] B. D. Dushaw, ''Inversion of multimegameter-range acoustic data for ocean temperature,'' IEEE J. Ocean. Eng. **24**, 215–223 (1999).
[8] U. Send, in ''Thetis-2: A pilot tomography system for monitoring the western Mediterranean basin,'' Final Report, EU MAST-2 project CT91-0006, March 1996.
[9] U. Send, G. Krahmann, D. Mauuary, Y. Desaubies, F. Gaillard, T. Terre, J. Papadakis, M. Taroudakis, E. Skarsoulis, and C. Millot, ''Acoustic observations of heat content across the Mediterranean sea,'' Nature (London) **385**, 615–617 (1997).
[10] E. K. Skarsoulis, ''An adaptive scheme for ocean acoustic tomography of large sound-speed variations,'' *Proceedings of the 3rd European Conference on Underwater Acoustics*, edited by J. S. Papadakis (Crete University, Press, Herakion, 1996), pp. 803–808.
[11] G. A. Athanassoulis and E. K. Skarsoulis, ''Arrival-time perturbations of broadband tomographic signals due to sound-speed disturbances. A wave theoretic approach,'' J. Acoust. Soc. Am. **97**, 3575–3588 (1995).
[12] E. K. Skarsoulis, G. A. Athanassoulis, and U. Send, ''Ocean acoustic tomography based on peak arrivals,'' J. Acoust. Soc. Am. **100**, 797–813 (1996).
[13] E. K. Skarsoulis, ''A matched-peak inversion approach for ocean acoustic travel-time tomography,'' J. Acoust. Soc. Am. **107**, 1324–1332 (2000).
[14] E. K. Skarsoulis, ''Multi-section matched-peak tomographic inversion with a moving source,'' J. Acoust. Soc. Am. **110**, 786–797 (2001).
[15] G. L. Pickard and W. J. Emery, *Descriptive Physical Oceanography*, 5th ed. (Pergamon, Oxford, 1990).
[16] H. Lacombe and C. Tchernia, ''Caractères hydrologiques et circulation des eaux en Méditerranée,'' in *The Mediterranean Sea*, edited by D. J. Stanley (Dowden, Hutcinson & Ross, Stroudsburg, 1972), pp. 26–36.

[17] B. D. Dushaw, P. F. Worcester, B. D. Cornuelle, and B. M. Howe, ''Variability of heat content in the central north Pacific in summer 1987 determined from long-range acoustic transmissions,'' J. Phys. Oceanogr. **23**, 2650–2666 (1993).
[18] E. K. Skarsoulis and U. Send, ''One-step analysis of non-linear travel-time data in ocean acoustic tomography,'' J. Atmos. Ocean. Technol. **17**, 240–254 (2000).
[19] K. D. Leaman and F. Schott, ''Hydrographic structure of the convection regime in the Gulf of Lions: Winter 1987,'' J. Phys. Oceanogr. **21**, 573–596 (1991).
[20] G. Madec, M. Crepon, and M. Chartier, ''The effect of thermohaline forcing variability on deep water formation in the western Mediterranean Sea: a high-resolution three-dimensional numeric study,'' Dyn. Atmos. Oceans **15**, 301–332 (1991).
[21] J. P. Bethoux, B. Gentili, J. Raunet, and D. Tailliez, ''Warming trend in the western Mediterranean deep water,'' Nature (London) **347**, 660–662 (1990).

Directional frequency and recording (DIFAR) sensors in seafloor recorders to locate calling bowhead whales during their fall migration[a)]

Charles R. Greene, Jr.,[b)] Miles Wm. McLennan, and Robert G. Norman
Greeneridge Sciences, Inc., 1411 Firestone Road, Goleta, California 93117

Trent L. McDonald
Western EcoSystems Technology, Inc., 2003 Central Ave., Cheyenne, Wyoming 82001

Ray S. Jakubczak
BP Exploration (Alaska) Inc., 900 East Benson Boulevard, Anchorage, Alaska 99519-6612

W. John Richardson
LGL Ltd., environmental research associates, 22 Fisher Street, POB 280, King City, Ontario L7B 1A6, Canada

(Received 7 November 2003; revised 1 May 2004; accepted 3 May 2004)

Bowhead whales, *Balaena mysticetus*, migrate west during fall ~10–75 km off the north coast of Alaska, passing the petroleum developments around Prudhoe Bay. Oil production operations on an artificial island 5 km offshore create sounds heard by some whales. As part of an effort to assess whether migrating whales deflect farther offshore at times with high industrial noise, an acoustical approach was selected for localizing calling whales. The technique incorporated DIFAR (directional frequency and recording) sonobuoy techniques. An array of 11 DASARs (directional autonomous seafloor acoustic recorders) was built and installed with unit-to-unit separation of 5 km. When two or more DASARs detected the same call, the whale location was determined from the bearing intersections. This article describes the acoustic methods used to determine the locations of the calling bowhead whales and shows the types and precision of the data acquired. Calibration transmissions at GPS-measured times and locations provided measures of the individual DASAR clock drift and directional orientation. The standard error of the bearing measurements at distances of 3–4 km was ~1.35° after corrections for gain imbalance in the two directional sensors. During 23 days in 2002, 10 587 bowhead calls were detected and 8383 were localized. [DOI: 10.1121/1.1765191]

PACS numbers: 43.30.Sf, 43.30.Yj, 43.80.Nd [WWA] Pages: 799–813

I. INTRODUCTION

Whales use sound to communicate and to acquire information about their environment. Also, they often react to man-made sounds by changing their behavior and swimming away, or occasionally toward, the sound source (Richardson *et al.*, 1995, 1999). Beginning in late August and continuing past mid-October, bowhead whales (*Balaena mysticetus*) migrate west across the Beaufort Sea, swimming parallel to the north coast of Alaska (Moore and Reeves, 1993). The majority of the whales travel along a corridor 5–40 n.mi. (10–75 km) offshore, with the southern part of that corridor being through water <25 m deep. Alaska Eskimos have traditionally hunted these whales for subsistence (Stoker and Krupnik, 1993). The whalers are concerned about any industrial activity that might result in the bowheads swimming farther offshore and therefore being more difficult to hunt and retrieve.

In early 2000, BP Exploration (Alaska), Inc., began constructing its Northstar oil development, the first oil production facility seaward of the barrier islands in the Beaufort Sea. The development is centered on Northstar Island, an artificial gravel island 5 km seaward of the coastal barrier islands (Fig. 1). Oil production and gas injection began in late 2001, powered by gas-turbine engines, and drilling of additional wells continued through 2002. Northstar is 27 km west of a natural island (Cross Island) from which migrating bowhead whales are hunted in fall. Thus, the possible effects of the industrial operations on the whales, and on their accessibility to subsistence hunters, were of concern.

Because of both BP corporate policy and regulatory requirements, BP decided to study any possible effects of island sound on the path of migrating bowheads. The primary question was whether the whales passing Northstar were farther offshore during times when more sound was emitted from the island and its associated vessels. The approach taken was based on use of a passive acoustic method to determine the locations of calling whales. An acoustical method was selected, in preference to aerial surveys, because acoustics works 24 hours/day, during good weather and bad, night and day, and allows simultaneous monitoring of a large

[a)]Portions of this work were presented at a workshop on acoustic detection and localization of marine mammals. The workshop sponsor was DRDC Atlantic, Dartmouth, Nova Scotia; the dates were 19–21 November 2003. An abstract is to appear in the *Canadian Journal of Acoustics*.

[b)]Electronic mail: cgreene@greeneridge.com

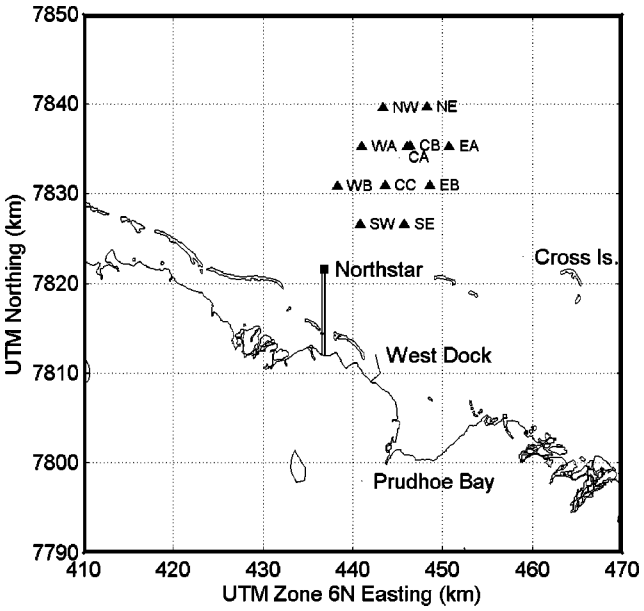

FIG. 1. Map of the central Alaskan North Slope including Prudhoe Bay and Northstar Island.

area. Previous experience showed that thousands of bowhead whale calls would be detected during one autumn season of monitoring, providing a far larger sample size than could be obtained from aerial surveys. To compare whale locations with sound emissions, continuous data on sounds from the island were needed. These were obtained with a hydrophone near the island, connected by cable to a digital recording system on the island. Statistical analyses were essential to assess whether any ''displacement'' effect was evident at times of high sound emission and, if so, to determine the magnitude of displacement. To date, field work has been done during the early autumn of 2000, 2001, and 2002, with equipment development and a pilot study in 2000, and effective data collection in 2001 and 2002. The study is continuing in 2003.

This paper describes the acoustical methodology developed to detect bowhead whale calls and to locate their source positions. Although the approach was the same in 2001 and 2002, some improvements were made from 2001 to 2002, and the following specific description concerns the 2002 techniques. Some results from 2002 are included to illustrate the approach and the nature and precision of the resulting data. Another paper (McDonald and Richardson, 2003) describes the statistical approach that has been developed for analysis of the whale locations versus sound emission data.

II. METHODS

There are two basic methods by which passive acoustic (hydrophone) data can be used to locate the sources of underwater sounds: hyperbolic fixing and triangulation (McLennan and Greene, 1996). Hyperbolic fixing involves measuring differences in the times when a given sound arrives at pairs of hydrophones, usually with cross-correlation. This method has been used extensively in previous studies of bowhead whales (e.g., Greene, 1987; Clark *et al.*, 1996). Triangulation involves measuring bearings to sound sources from two or more known locations, and then computing the intersections of the bearings.

Hyperbolic fixing with cross-correlation generally performs very well, but it requires synchronized timing of all the hydrophone signals. This is possible if the hydrophone signals are cabled or radioed to a common recording or processing point with a single clock. However, it is difficult to have precise timing with autonomous, asynchronous recorders, each with its own clock, as required here. Surface buoys were undesirable because of hazards from drifting ice, and interconnection by bottom cables was impractical.

Triangulation was chosen for this study because synchronized timing of autonomous units would be difficult to achieve, but autonomous bearing measurements could be obtained. Directional frequency and recording (DIFAR) sonobuoys (AN/SSQ-53) use a three-channel sensor from which azimuthal bearings to sound sources can be computed. Standard DIFAR sonobuoys have been used previously to obtain bearings to calling bowhead whales (Ljungblad, 1986; Greeneridge Sciences unpublished data) and to other baleen whales (e.g., Swartz *et al.* 2003). We incorporated DIFAR sensors from Sparton Electronics (De Leon Springs, FL) into seafloor recorders called DASARs, for directional autonomous seafloor acoustic recorders. A DASAR records the three DIFAR channels directly to disk in the seafloor recorder. An array of 11 DASARs deployed in the southern part of the whale migration corridor offshore of Northstar provided the needed intersecting bearings to the calling whales.

A. DIFAR principles

The concept of DIFAR is to use two horizontal, orthogonal directional sensors and an omnidirectional pressure sensor to sense an acoustic field. The directional sensors are particle velocity hydrophones with dipole patterns. A DIFAR sonobuoy uses a magnetic compass to provide a geographic reference. However, the DASARs (unlike drifting sonobuoys) sit firmly on the bottom and normally do not move after installation. Their locations are measured during installation with GPS. Thereafter, acoustic calibration transmissions from known locations around each DASAR can provide information on its reference direction with respect to grid north. As shown in Sec. III (later), this can provide more precise bearing data than could be obtained by reference to the compass built into a standard DIFAR sensor, especially during operation at high latitudes where magnetic compasses are less accurate and less stable.

Figure 2 shows the DIFAR sensor pattern. The orthogonal directional sensor patterns are circular, corresponding to a dipole response. A sound from a given direction results in received levels determined by the dipole response patterns. The angle to the source, relative to the reference axis, is determined from the arctangent of the ratio of the two response magnitudes. The phases of the dipole signals relative to the omnidirectional signal resolve the bearing ambiguities that would otherwise result from the arctangent.

The DIFAR sensor functions as if it were a three-channel analog device, including the following outputs:

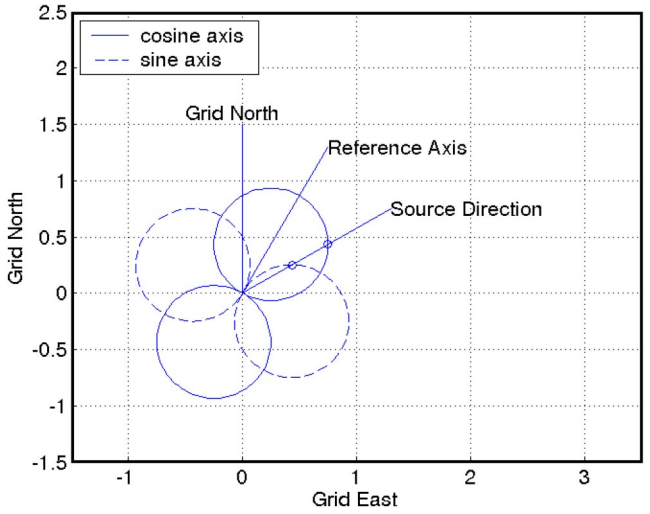

FIG. 2. DIFAR sensor omni and dipole patterns and reference angle. The angle between the reference axis and the source direction is the angle b used in the section on DIFAR principles.

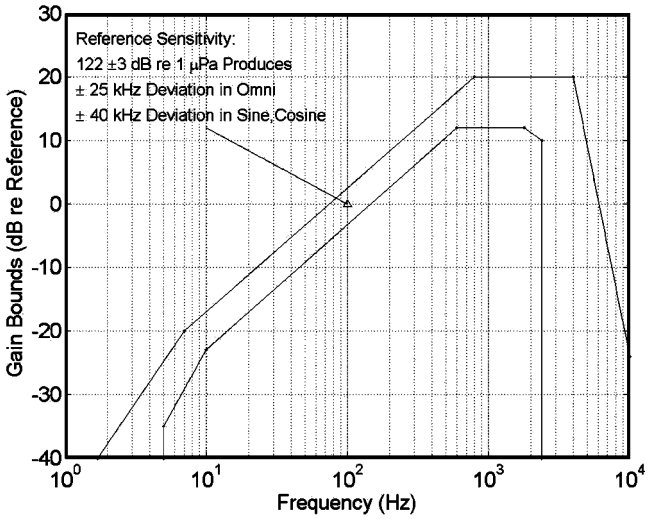

FIG. 3. DIFAR frequency response envelope. The response is specified to be within ±3 dB at 100 Hz.

(i) omnidirectional pressure sensitive hydrophone, and
(ii) two horizontal, orthogonal particle motion sensors whose outputs are proportional to the cosine and sine of the direction to the source. One is the ''cosine channel'' and the other is the ''sine channel.''

The DIFAR sensor reference axis is aligned with the cosine channel maximum (Fig. 2).

Assume the DIFAR sensor is mounted in the water away from any reflecting surfaces and interfering sound sources. Assume there is a source emitting sinusoidal waves so the instantaneous pressure at the omnidirectional sensor is

$$P_o(t) = A\sin(\omega t),$$

where A is the peak amplitude, ω is the radian frequency, and t is time. If the source direction is at bearing angle b from the reference axis, the instantaneous outputs of the cosine and sine channels will be

$$P_c(t) = \cos(b)\cdot A\sin(\omega t),$$

$$P_s(t) = \sin(b)\cdot A\sin(\omega t).$$

These two channels, plus the omnidirectional pressure channel, are recorded in the DASAR for offline processing. The direction can be found by forming the instantaneous products

$$Qoc(t) = Po(t)\cdot Pc(t) = \cos(b)\cdot A^2\sin^2(\omega t),$$

$$Qos(t) = Po(t)\cdot Ps(t) = \sin(b)\cdot A^2\sin^2(\omega t).$$

Taking the time average of the two products results in the bearing b in degrees as

$$b = 57.2957\cdot \text{arctangent}(\text{mean}(Qos)/\text{mean}(Qoc)),$$

where the arctangent is defined for four quadrants.

If other sound sources are audible simultaneously, their signals add to the above expressions and distort the process. Thus it is important to exclude other sources as much as possible. In our processing of the DASAR data, the time and frequency extents of each whale call are first determined by inspection of a spectrogram. Then the signal is time-gated and bandpass filtered tightly before computing the products. These products are derived separately for every 1-ms time sample within the duration of a given bowhead call (typically 1–3 s), and then averaged across the call duration. The resulting averages are used to derive the estimated bearing to that whale call relative to the reference axis.

Alternatively, the bearing can be computed from the magnitude and phase of the discrete Fourier transforms of the three sensor channels. For a signal whose frequency changes or spans a range of frequencies, the bearings for every frequency component in the call can be computed and averaged to improve the bearing estimate. In our experience, the time domain and the frequency domain approaches yield very close to the same result. After initially deriving a bearing to each call via both approaches and finding little difference in the results, we now rely on the time-domain method. However, in Sec. III we present an example of the frequency-domain method.

The DIFAR specification for sonobuoy bearing accuracy calls for angles with respect to magnetic north to be within ±10°. Much better accuracy has been achieved with the DIFAR sensors incorporated into DASARs as described below, with the DASARs firmly on the bottom, calibrated externally, and not reliant on a magnetic compass (see Sec. III).

Figure 3 graphs the frequency response of DIFAR sonobuoys. It is specified to be from 10 to 2400 Hz, but there is some sensitivity at both higher and lower frequencies. The response is deliberately not flat; it rises with increasing frequency up to ~1000 Hz. This rise is to counter the natural drop in ocean ambient noise with increasing frequency, providing improved dynamic range and noise performance, especially at low frequencies. Most bowhead calls occur in the frequency range from 50 to 400–500 Hz (Clark and Johnson, 1984; Würsig and Clark, 1993), so the DIFAR coverage is an excellent match.

B. Directional autonomous seafloor acoustic recorder (DASAR)

The DASAR was conceived to incorporate DIFAR technology in an autonomous recorder that would operate for at

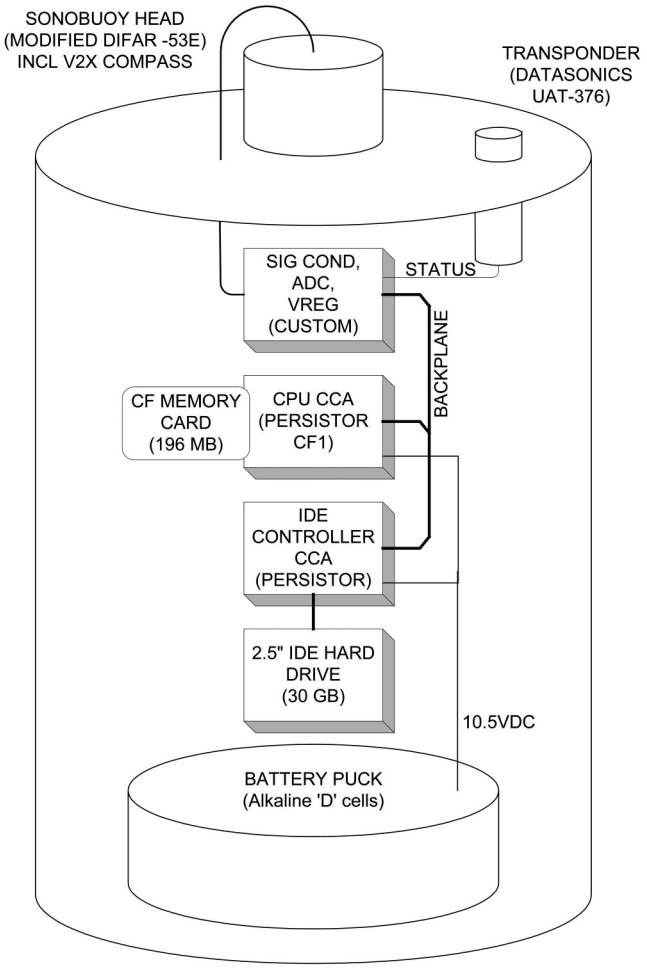

FIG. 4. Block diagram of the DASAR recording system.

least 30 days in the water north-northeast of Northstar Island, at depths up to 30 m. To achieve frequency coverage from 50 to almost 500 Hz, a sample frequency of 1000 samples/second was selected. For anti-aliasing, the three acoustic channels were lowpass filtered at 400 Hz. With three acoustic channels, 3000 samples/second had to be written to a computer disk storage unit.

Although DASAR orientation on the bottom was determined by calibration (see below), a compass was still desired in the DASAR as a check on any possible changes in orientation during a deployment. The compass in the standard DIFAR sensor used excessive battery power because of the high effective sample rate needed for the acoustic data. However, we did not require frequent compass readings. A substitute flux-gate compass, small in size and low in power drain (Model V2X from PNI Corp., Santa Rosa, CA), was installed in the sensor. Its output was recorded once for every disk write, which occurred at intervals of 46.6 min. Compass bearings were stored in the compact flash memory in the DASAR, independent of the disk storing the acoustic data.

1. Digital recording

Figure 4 is a block diagram of a DASAR. A Persistor Instruments Inc. (Bourne, MA) single-board computer, model CF1, serves as the central processor unit and controls the sampling, buffer storage, and disk recording from the buffer. The instrument uses a 196-MByte compact flash memory for double buffering so no data are lost during the disk write operation. However, in practice, the sounds of the disk drive increased the local acoustic noise for about 30 s each time disk writing occurred, once every 46.6 min. A disk of 30-GByte capacity (IBM Travelstar 2.5″) provides continuous storage for over 45 days' recording. The disk is controlled by Persistor Instruments' ''BigIdea'' IDE controller. A custom circuit card handles signal conditioning, analog-to-digital conversion for the three DIFAR channels, compass I/O, and various switching and linear regulators to power the CF1, compass, and sensor head.

2. Transponder for health checks

An acoustic transponder (Benthos model UAT-376, North Falmouth, MA) was built into each DASAR to permit checks on operational health during a deployment. This was essentially a check on the digital recording. If a sensor quit working, it was not likely to be reported as ''bad health.'' The transponder was powered by its own 9-V cells so it would continue operating if the main DASAR batteries failed. Upon interrogation at 26 kHz by a topside unit, each transponder transmitted on one of seven frequencies: 25, 27, 28, 29, 30, 31 or 32 kHz. In the DASAR application, the transponders were modified so that the frequency selection could be altered from the embedded controller. In this manner, one of two codes corresponding to ''OK'' or ''failed'' could be asserted.

The topside unit was a Benthos model DRI-267A, built as a diver-operated transponder/interrogator and deployed on a hand-held pole over the side of a boat. Upon receipt of transponder signals, it read out distance as well as the operational code. It operated over distances of at least 200 m, but GPS always brought the boat to within about 40 m of the DASAR being interrogated. In this project, the ''health'' of each deployed DASAR was checked about once per week. No failures were detected in 2002, but in 2001 some reports of ''bad health'' were received, and in these cases it was possible to retrieve and replace the failed DASAR.

3. Physical construction and batteries

The pressure housing is a cylinder 12 in. in diameter and 14 in. high (30×36 cm). The recording electronics and the transponder are mounted on the underside of the lid, which incorporates double O-ring seals. Three packs (Nexergy model SMP-7S4P, Escondido, CA) of 28 D-cell alkaline batteries are wired in series and parallel to provide 10.5 V. They are secured by a plate and threaded rods anchored in the cylinder bottom. Diodes protect the packs from internal shorts.

On the top of the DASAR are two plastic posts 8.75 in. (22 cm) tall, extending upward from opposite sides of the top plate. Between them is a rubber band 1 in. (2.5 cm) wide from which the DIFAR sensor is suspended. The top of the sensor is secured to a plastic block with a double O-ring seal. The wires from the compass and three acoustic sensors pass from the sensor through the block and into a plastic tube and

FIG. 5. DASAR on deck with anchor and tag line, ready for deployment. Also on deck are other DASARs without their protective socks.

thence to a waterproof access in the main body of the DASAR. The rubber suspension permits the sensor to ''float'' relatively freely in the water for sensing the particle motion essential to the directional sensing, while at the same time minimizing twisting.

As deployed in 2002, a latex ''sock'' secured over an aluminum cage shielded the sensor from motion induced by water currents. Figure 5 portrays a DASAR in its sock on the deck ready for deployment with the small anchor and tag line. (In 2001, a different frame and a self-supported thin plastic dome were used.) Each DASAR was installed on the bottom with a tag line between the DASAR and an anchor, both of whose positions were measured by GPS during deployment. No surface buoys were used because of hazards from drifting ice floes. The DASARs were retrieved from depths of 16–24 m by grappling for the tag line based on the GPS coordinates.

C. The DASAR array

The basic array configuration is a series of equilateral triangles. Bearing measurements from pairs of elements in a triangle provide good resolution of source location for sources at any angle around the triangle. Six triangles sharing a center unit formed a hexagon (Fig. 6). Two overlapping hexagons completed the array of ten locations oriented roughly north-northeast from Northstar Island, toward the path of migrating bowheads. The basic spacing between adjacent DASARs was 5 km (2.7 n.mi.), selected based on known bowhead call detection distances of 15–20 km and experience with 2-km spacing in a 1986 application of passive localization (Greene, 1987). The closest and farthest units were, respectively, 7 and 22 km (4 and 12 n.mi.) northeast of Northstar, with the most offshore unit being about $\frac{1}{3}$ of the distance from Northstar to the shelf-break.

Twelve DASARs were constructed and tested. Two were intended to be spares, but it made sense to deploy one of the spares as a redundant element at a central location in the ten-position array. Thus, two DASARs were used at the center of the northern hexagon, spaced about 200 m apart at locations CA and CB (Fig. 6).

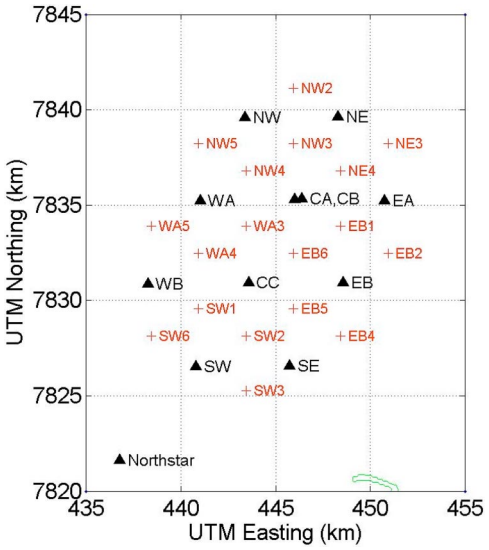

FIG. 6. Map of DASAR locations with respect to Northstar Island. The stations from which calibration signals were transmitted are also shown.

D. Time and reference axis calibration

Calibrations were very important to the success of the triangulation approach to whale call localization. The times had to be known within 1–2 s to permit associating calls received on two or more independent DASARs, as necessary to localize based on bearings from two or more DASARs to the same call. With 5 km between adjacent DASARs, the maximum difference in acoustic travel time to an adjacent pair of DASARs is 3.3 s. The travel time across the longest separation of DASARs (units NE and SW in Fig. 6) is 10 s.

Reference axis calibration was very important to minimizing localization errors. Clearly, the smaller the uncertainty in the bearing measurements, the smaller the uncertainty in the whale call location. A detailed description of localization errors is contained in Appendix B.

The approach taken to calibration for both time and reference axis direction was to transmit a signal from a boat at known locations around and within the DASAR array. The equipment included a U.S. Navy model J-9 underwater sound projector (U.S. Navy Sound Reference Laboratory, Newport, RI), a 400-W Mackie FR series M-800 amplifier (Woodinville, WA), a notebook computer, and a Trimble Lassen Model 39261-10 (Sunnyvale, CA) GPS receiver with a pulse time signal output precisely at every UTC (Universal Time Coordinated) second. The notebook computer contained the waveform file and reproduced it for amplification and transmission on receipt of the timing signal from the GPS. Although the J-9 is not rated for source levels greater than ~150 dB *re* 1 μPa·m, its efficiency is very low and a high-powered amplifier is required to achieve such a source level.

The waveform of the calibration signal required a clear start time for clock timing and wide bandwidth for determining the reference axis bearing. The sound waveform used in 2002 began with a 400-Hz tone for 5 s, followed by a 2-s gap, a downsweep from 400 to 200 Hz, another 2-s gap, an upsweep from 200 to 400 Hz, a 2-s gap, and a final downsweep from 400 to 200 Hz. (In future applications, the 2-s

TABLE I. DASAR calibration results for 2002, including corrections for gain imbalance in the two directional channels and clock drift coefficients.

DASAR location	Total Pings	Original ref. bearing (deg)	Corrected ref. bearing (deg)	Gain factor	Original std. dev. (deg)	Corrected std. dev. (deg)	Clock drift (s/day)	Scatter after fit (s)
NW	126	89.9	89.5	1.0607	1.50	0.87	−0.4836	0.19
CC	198	248.9	248.8	1.0270	1.70	1.60	−1.3582	0.16
WB	138	34.3	34.0	1.0286	1.30	1.20	−1.7558	0.22
CB	194	157.0	157.0	1.0883	2.30	1.50	−1.1756	0.28
CA	192	186.9	187.0	1.1337	2.60	0.99	0.3827	0.21
EA	139	58.6	57.6	1.1594	2.90	0.93	−1.1898	0.34
WA	165	192.9	192.3	0.8661	3.30	1.30	−1.3838	0.19
SE	127	26.7	26.7	1.0038	0.80	0.80	−1.9505	0.54
SW	33	59.0	59.5	1.0781	3.60	3.30	−0.2753	0.30
NE	135	96.0	95.7	0.9294	2.50	0.80	−1.1723	0.21
EB	154	190.5	190.8	1.0529	1.90	1.60	−0.7723	0.19
					Avg: 2.22	Avg: 1.35		

gaps will be omitted.) The total duration of one transmission was 22 s. For each calibration location, two full transmissions occurred at sound projector depth 9 m followed by two more at depth 6 m. All transmissions were analyzed as received at the closest two or three DASARs, generally within distance 3–4 km.

Calibration stations were selected in and around the array such that each DASAR received calibration signals from at least four (and often six) nearby stations on different bearings. Figure 6 shows the 18 calibration stations used in 2002 in relation to the 11 DASARs. Obtaining bearings to several known sites around each DASAR permitted searching for possible systematic bearing errors. One such error was found and attributed to ''gain imbalance'' between the two directional channels.

E. Gain imbalance between the directional sensors

The DIFAR sensor manufacturer, Sparton Electronics, employs careful calibration techniques to equalize the sensitivities of the sensors for the two directional channels. However, the manufacturing specification is for bearing accuracies of $\pm 10°$ and we desired better performance. There was evidence in our data that, as installed in the Beaufort Sea, the gains (sensitivities) of the DIFAR sensors were slightly unbalanced, resulting in systematic bearing errors. A gain-correction procedure has been developed. It is described in Appendix A.

F. Localization process and its accuracy

The locations of the calling whales were estimated based on triangulation. However, when more than two bearings to a given call were available, the 2+ intersections of bearings usually did not coincide exactly. A maximum-likelihood approach was developed to estimate the most likely location, taking account of the variability in bearings from each DASAR as determined during calibration. Also, an estimate of the precision of each whale call location was used as a weighting factor in subsequent statistical analyses (McDonald and Richardson, 2003). Appendix B describes the localization process and the derivation of the localization accuracy measures.

G. High background noise cutoff distance

The objective of the project was to evaluate whether offshore distances of whales were related to the level of industrial sound measured near the island (400 m away). Early data indicated that, during higher background noise conditions (>96 dB *re* 1 μPa broadband) at the DASAR array, fewer whale calls were detected. Further analysis confirmed that, at such times, proportionally fewer calls were detected at longer distances. To minimize the influence of variations in background noise on the observed distribution of whale call locations, it was necessary to limit the study area to the region within which whale calls were likely to be detected even during high noise conditions. The appropriate distance was determined by comparing the distribution of distances from the array-center to the detected whale calls during times with high and low background noise (see Sec. III).

III. RESULTS

Examples of the results of the calibration process and the localization of whale calls for 2002 are presented here. McDonald and Richardson (2003) show how these results can be analyzed statistically to assess whether bowhead whales are displaced offshore at times when much industrial sound emanates from the Northstar area. In 2002, the DASARs were deployed on 30–31 August and recovered on 3 October. One DASAR apparently physically tipped over on 4 September, but the other ten functioned well until 23 September when all apparently tipped over during an unusually strong storm. Thus, the effective study period was from 31 August to 23 September. Health checks were done about once per week, and there were no reports of ''bad health.'' (In 2001, some such reports were received, and this allowed us to replace failed units with functional ones.)

A. Calibration of DASAR clock times and reference axis bearings

The calibration results for each DASAR are presented in Table I. Calibration data were collected on 2, 7, 13 and 21 September 2002. For 10 of 11 DASARs, the calibration was based on 126–198 calibration pings. For the DASAR at location ''SW,'' only 33 pings (all from 2 September) were useable; SW was the unit that upset in high storm surge on 4 September.

The benefit of correcting for the gain imbalance between the two directional sensors of each DASAR is evident by comparing the standard deviations of the ''original'' (uncorrected) bearings, which averaged 2.22°, with those of the ''corrected'' bearings (average 1.35°). Corresponding average values for 2001 were, respectively, 6.60° and 6.28°. The higher values in 2001 resulted primarily from using tones as calibration sounds, in contrast to the frequency sweeps used in 2002. The year-to-year differences in the DASAR housings may have been a minor factor.

Based on the DIFAR sonobuoy specification that bearing errors should be within ±10°, standard deviations on the order of 3° had been expected. The improvement over the specification (in 2002) is partly from the broadband calibration signals used, partly from the gain-correction procedure, and partly because the orientations of the bottom-mounted DASARs were fixed and externally calibrated. In contrast, a DIFAR sonobuoy is designed to drift, with bearings being determined in relation to an internal magnetic compass.

The time-drift calibrations showed that the clocks in the DASARs drifted by as much as 2 s per day (Table I). However, the drift-rate was quite stable over time, a result expected given the frequency/temperature sensitivity of the crystal oscillator time base and the fact that the ambient temperature varies only slightly once deployed. After compensation for the measured drift, the times of events recorded between calibrations generally could be determined to an accuracy of 1 or 2 s. This was adequate for assessing whether a whale call received at several DASARs represented a single call from one whale. The residual measurement scatter is mostly due to imprecision in determining the time of the received signal during data analysis. This precision can be improved, as described in Sec. IV.

B. Whale call localization

During the period from mid-day on 31 August until mid-day on 23 September 2002, 10 587 whale calls were detected. Of these, 2022 (19%) were detected by only one DASAR and thus could not be localized. Also, 182 (2%) of the remaining 8565 calls did not yield a location because the maximum likelihood procedure (Appendix B) did not converge, and 461 (5%) of the remaining 8383 calls yielded a location but the variance-covariance matrix of the solution was not positive definite. Overall, 7922 (75%) of the 10 587 calls yielded useable locations in 2002.

Figure 7 presents an example of a whale call bearing measurement, in this case from DASAR unit EB. The bearings of all the 1-ms time samples spanning the duration of the call are plotted as vectors from the DASAR location. The bearing estimate comes from the arctangent of the average of the north-south components divided by the average of the east-west components.

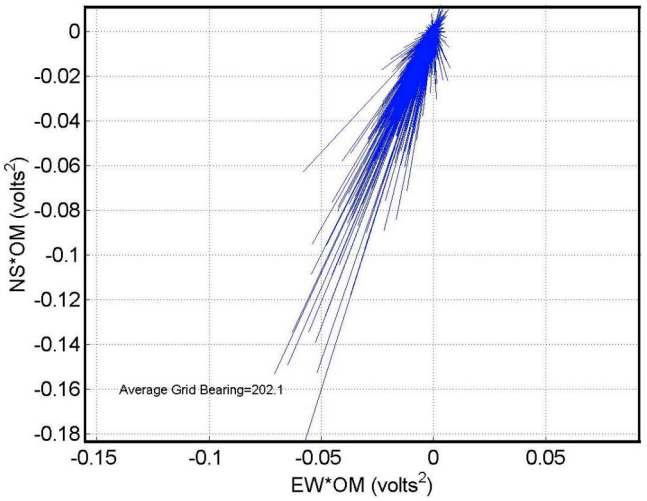

FIG. 7. Example of a time-domain bearing display illustrating the spread of the bearings computed for each 1-ms time sample. From the DASAR at location EB in 2002.

The same call as received at the same DASAR was also processed by the frequency domain method. Figure 8 presents the magnitude of the sound pressure density spectrum computed over the duration of the call as delimited by the analyst. The relatively high spectrum levels at 190–320 Hz represent the whale call. Figure 9 presents the bearing-frequency result for the same call, with the bearing selected from the time-domain solution superimposed across the frequencies selected by the analyst.

The specific call illustrated above was detected via six DASARs, and Fig. 10 shows the intersections of those bearings, including the bearing from Fig. 10 (unit EB). Of the 7922 useable call locations during the 23-day study period in 2002, the numbers based on 2, 3, 4, and 5+ bearings were 2085, 1429, 1129, and 3279, respectively.

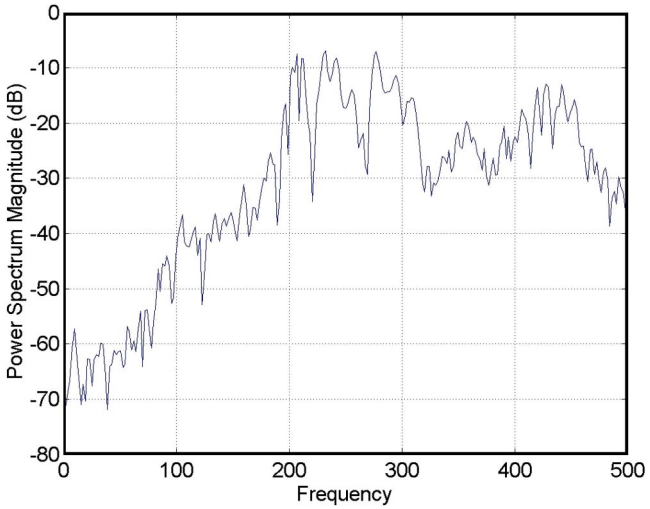

FIG. 8. Sound pressure spectral density for the whale call in Fig. 7. The peak at about 200–320 Hz represents the whale call. The increasing slope in the background noise is a result of the sloped sensitivity of the DIFAR sensor as shown in Fig. 3.

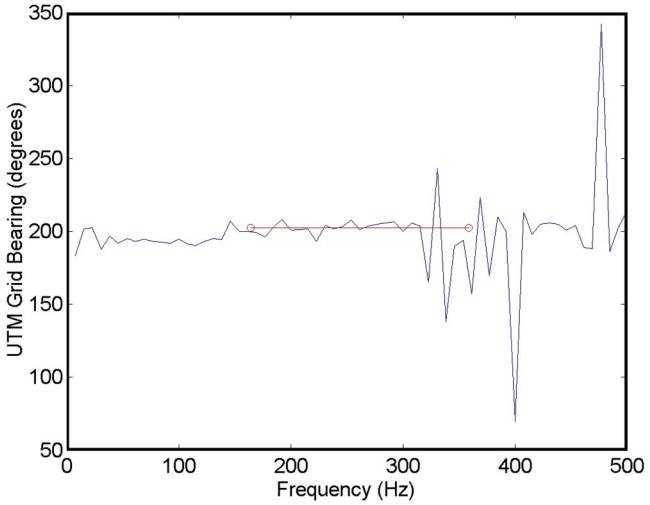

FIG. 9. The directional spectrum for the whale call in Figs. 7 and 8. The bearing from the time domain analysis (Fig. 7) is drawn for the frequency band selected by the analyst.

The numbers of bowhead whale calls detected per hour varied widely through the operational period (Fig. 11). Call detection rates depended not only on the number of whale calls, but also on the background noise level. High background noise (>90th percentile, 101 dB *re* 1 μPa broadband) tended to mask the more distant calls (see below). The best estimates of the locations of the 350 localizable bowhead whale calls detected on 14 September 2002 are mapped in Fig. 12.

C. Localization accuracy

Figure 13 maps one measure of the accuracy of whale call localizations for locations around the DASAR array, based on all 7922 of the useable call locations from 2002. The calculations were based on the estimated accuracy of individual locations, which in part depended upon error in the calibration bearings (see Appendix B). As expected, accuracy tended to deteriorate with increasing distance from the center of the array of DASARs. For most locations within the perimeter of the array, the length of the major axis of the 90% confidence ellipse based on asymptotic intervals averaged between 0.25 and 1 km. For most locations 10 km

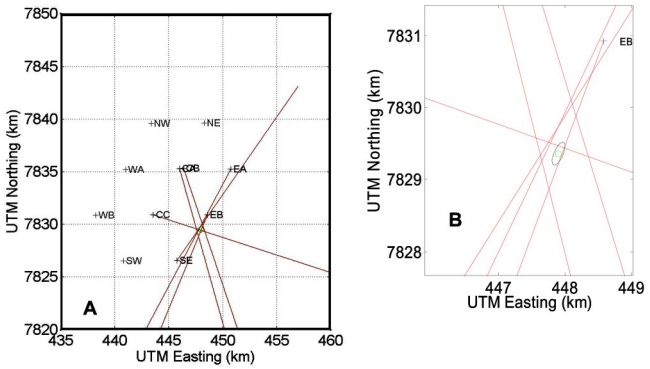

FIG. 10. Map of an example of intersecting bearings to a whale call. The bearing is included from unit EB for the call shown in Figs. 7–9. (a) Large area view. (b) Exploded view of the intersection area showing the 90% confidence ellipse and best estimate of calling whale's location.

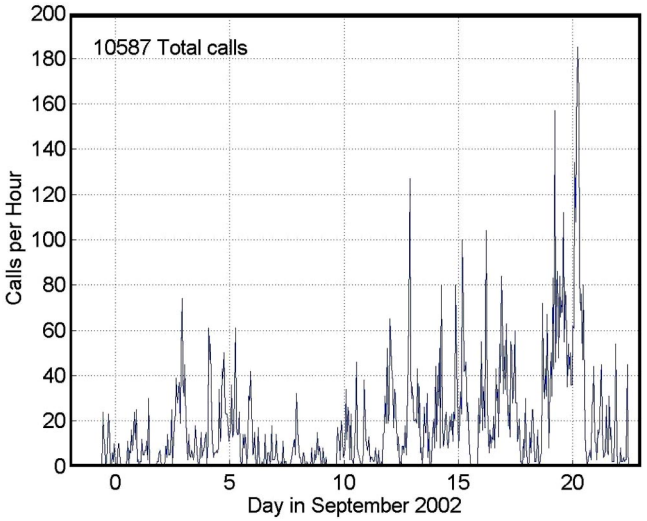

FIG. 11. Numbers of bowhead whale calls detected per hour over the period 31 August–23 September 2002. A total of 10 587 calls were received at one or more of the DASARs.

from the center of the array (~6 km outside the perimeter), the corresponding average was ~1 km. Average localization accuracy was apparently poorer in an area southwest of the DASARs (and northwest of Northstar), but very few calling whales were detected there. Beyond about 10 km from the center of the array, localization accuracy deteriorated rapidly (Fig. 13).

D. High background noise cutoff distance

Distances were determined from "center" DASAR CB to all whale calls detected during times of very high (>90th

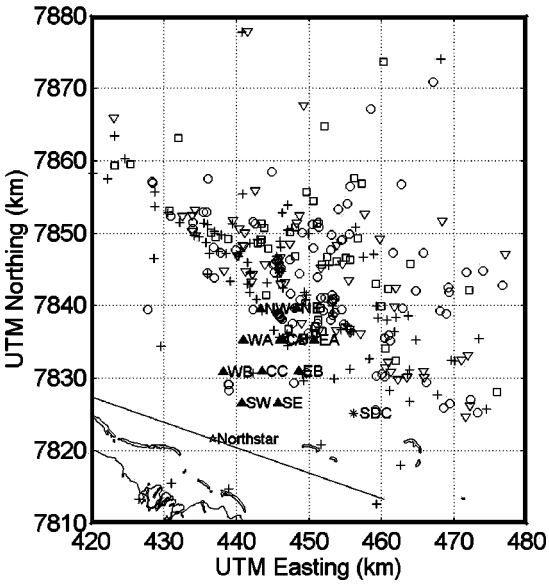

FIG. 12. Whale call localizations for 14 September 2002. Filled upright triangles represent DASAR locations. Symbol types discriminate calls whose locations were estimated based on bearings from two (+), three (▽), four (□), or more (○) DASARs. On this date, 42 calls (not localizable) were detected on only one DASAR, 115 calls on two DASARs, 65 with three DASARs, 55 with four DASARs, and 115 with five or more DASARs. The WNW-ESE line through Northstar Island shows the general trend of the coastline; the autumn bowhead migration is to the WNW, parallel to shore.

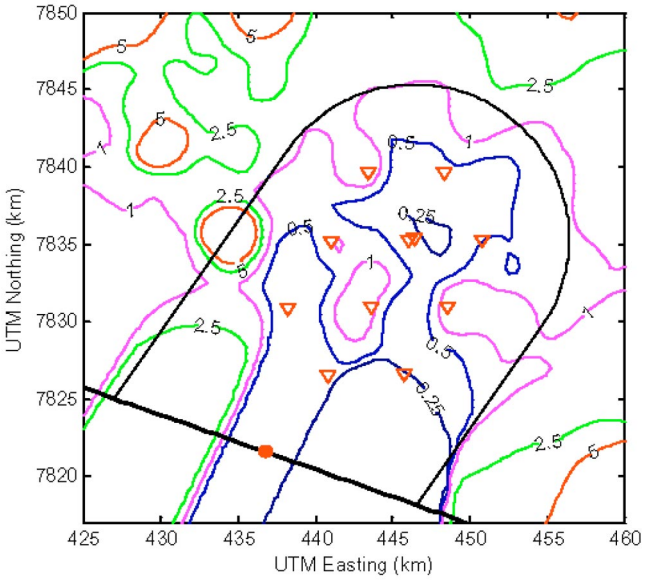

FIG. 13. Mean length (in meters) of major axis of 90% confidence ellipses around estimated call locations shown as a contour plot. Filled circle represents Northstar Island, open triangles represent DASARs, and the solid black line through Northstar is parallel to the (idealized) coastline. The horseshoe pattern oriented northeastward represents the area within which bowhead calls were retained for the displacement study.

percentile, 101 dB *re* 1 μPa broadband), moderately high (>75th percentile, 96 dB), and low (<25th percentile, 87 dB background noise) (Fig. 14). Background noise was measured at the DASAR farthest from Northstar (DASAR NE). The proportion of the detected calls that were at distances >10 km was lower during the very high and moderately high background noise conditions. To minimize potential biases, calls >10 km from the ''central axis'' of the DASAR array were not used in statistical analyses of call locations relative to Northstar noise. That central axis extended from CB to Northstar. Thus, the study area for those statistical analyses was a ''silo-shaped'' area (Fig. 13) that was 20 km wide extending offshore to DASAR CB, capped by a semi-circle of radius 10 km centered at CB.

IV. DISCUSSION AND CONCLUSIONS

Background noise has a strong influence on the detectability of whale calls. At times with high background noise (>101 dB *re* 1 μPa broadband), calls with low source levels, and other calls whose received levels at the DASARs are low because of propagation from long distances, are less likely to be detected. [See Blackwell and Greene (2004) for data on sounds, noise, and propagation at Northstar.] The variability in background noise is one reason why simple counts of whale calls (e.g., calls detected per hour) are not a reliable index of the number of whales in the area. (The potentially variable calling rate of individual whales is another reason.) In using the data from this project, it has been important to limit the size of the study area to a region where calling bowhead whales are generally detectable even when the background noise is high. In 2002, the ''high background

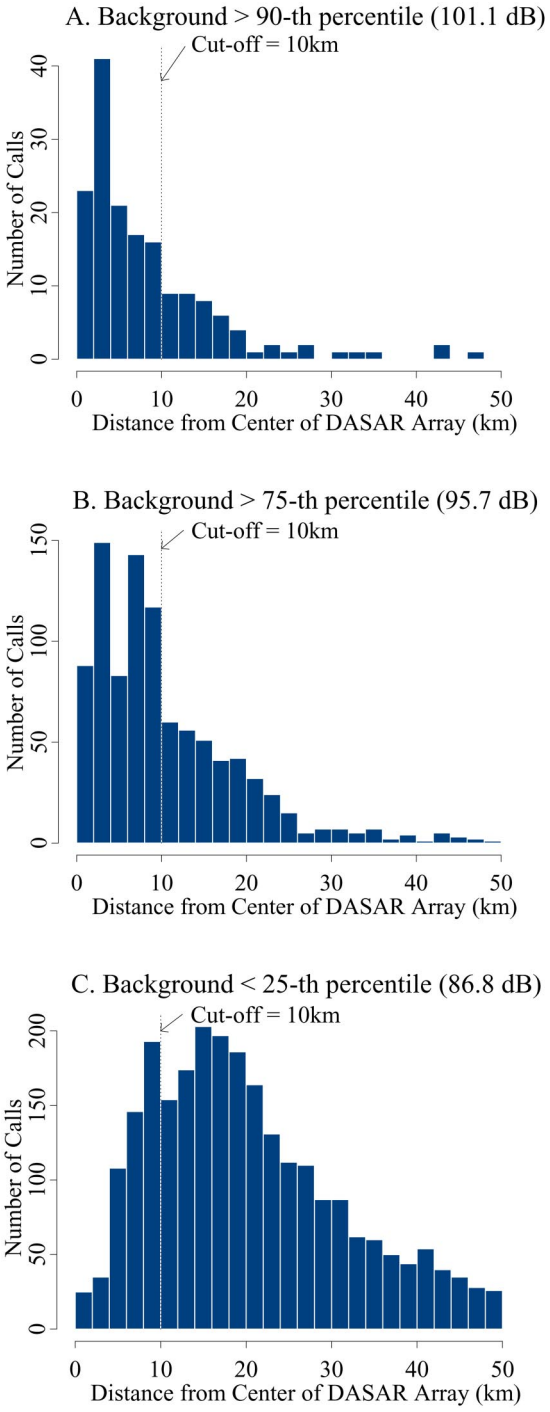

FIG. 14. Histograms of distance from estimated locations of calling whales to the center DASAR (CB) during very high (a), moderately high (b), and low (c) background sound conditions in 2002. A cutoff distance of 10 km was established at the ''shoulder'' evident in (a) and (b). Background sound was measured at the NE DASAR in the 5–500-Hz band.

cutoff distance'' was determined to be 10 km (Fig. 14). A corresponding analysis for 2001 showed it to be 12 km in that year (Greene *et al.*, 2002).

A. Comparison with hyperbolic localization

A well-known and widely used technique for passive acoustic localization is hyperbolic fixing based on arrival time differences at widely spaced sound pressure sensors. (A symposium on this method, as applied to the localization of

calling marine mammals, was held at Halifax in November 2003. The papers are to be published in the *Canadian Journal of Acoustics* during summer 2004.) The technique requires an accurate time base (~1 ms for sounds like bowhead whale calls) and involves crosscorrelating sensor pairs. Clark and Ellison (2000) reported a calibration experiment conducted during spring at Barrow, Alaska, to verify the accuracy of their analysis of bowhead call locations as determined via arrival-time differences. Their three sensors were roughly in line, spaced 670 and 946 m apart. Two theodolites spaced 482 m apart provided ''ground truth.'' Their acoustic bearing errors for angles not far from the normal to their baseline were on the order of 0.1° compared to about 1° for our DIFAR bearings at all azimuths. Multipaths frequently create significant uncertainties and biases in hyperbolic fixes, but propagation in the Barrow environment during spring was reported to be basically plane waves without reflections.

B. Potential improvements to DASAR performance

The controlling software will be revised to permit entering a sleep mode after initialization, with startup programmed for a time after the units are on the bottom and stable. In the past, when DASARs have been writing to disk while being handled, write failures have sometimes occurred.

In future applications, the sound transmitted for calibration of times and reference bearings will be frequency sweeps or a pseudo random noise waveform of at least 200-Hz bandwidth. Wideband sounds have been shown to produce less bearing scatter than tones. There will be no gaps in the sound transmissions. Also, 14 more calibration stations will be added to the 18 used in 2002 (Fig. 6), providing better azimuthal calibration data for the peripheral DASARs and hence better gain imbalance corrections.

Data analysis will be enhanced to permit more accurate measurements of the arrival times of the calibration transmissions. Also, more automation in detecting whale calls will be investigated. At present, whale calls are detected based on simultaneous visual inspection of spectrograms of the data from all active DASARs, one minute at a time. The computer might be programmed to detect whale calls by using their frequency characteristics and the fact that they are stronger than the background sounds (Mellinger and Clark, 1997, 2000).

C. Utility of DASARs in localizing sound sources

This application of DIFAR techniques, as incorporated into autonomous bottom-mounted recording units, has been successful in monitoring the locations of calling bowhead whales over extended periods in a remote region. This approach allows distributed data acquisition and requires only moderately accurate synchronization (e.g., ± 1 or 2 s) of the time bases of the various recording units. This approach is suitable in situations where it would be difficult or impossible to acquire all the data with a single recording system and time base, as needed for localization by time-of-arrival methods.

Experience from two years' use of DASARs to localize bowhead whale calls reinforces the concept of applying DIFAR sensor technology to sound source localization. The frequency range of 10–500 Hz, as presently recorded by the DASARs, suits the frequency ranges of most bowhead calls, and may also be suitable for most other baleen whales (Richardson *et al.*, 1995). However, the DIFAR sensors are useful at frequencies >2 kHz and could conceivably be used to detect and localize clicks from sperm whales and some other marine species. A higher frequency range would require a higher sampling rate, which would affect recording life depending on disk space.

The present DASAR units are designed for deployment in relatively shallow water and retrieval by a simple grappling technique. The physical configuration of the units would need to be revised if deeper deployments were required. However, the DIFAR-based approach should be useable in deeper water.

ACKNOWLEDGMENTS

Dave Iddings, Quy Nguyen, Bob Early, and Patrick Dexter designed the DASAR pressure housing, sensor suspension, and sensor wire routing (including waterproofing). Mark Cavalier, Nautronix-MariPro, fabricated the aluminum frames and cages. Kent Reinhardt of Sparton Electronics was very helpful with engineering details of the DIFAR sensors, permitting us to disable the built-in compass and extract the sensor signals before they were multiplexed. David Christian made the cable harness from the sensor to the recording electronics, and he wired the DASAR electronics and batteries, making battery installation simple and foolproof. During deployment, calibrations, and retrieval, crews of Alaska Clean Seas provided excellent navigation and seamanship consistent with safe operations. Jonah Leavitt of Barrow, Alaska, helped with mobilization at Deadhorse, Alaska, as well as deployment and retrieval at sea. Mike Williams of LGL helped in innumerable ways. Wilson Cullor and Allison Erickson of OASIS Environmental, on behalf of BP, helped with logistics planning for the fieldwork. Dr. Bill Streever of BP and Dave Trudgen of OASIS, also on behalf of BP, guided the project. BP Exploration (Alaska) Inc. supported the work. Two anonymous reviewers made helpful remarks. We thank them all.

APPENDIX A: GAIN IMBALANCE BETWEEN DIRECTIONAL SENSORS AND ITS EFFECT ON BEARING ACCURACY

Summary: This Appendix investigates gain imbalance between the two DIFAR directional sensors. A method is developed to quantify and correct for this factor, thereby improving the accuracy of measured bearings to whale calls. Calibration ping data taken for time and bearing calibration are analyzed to determine the imbalance.

1. Introduction

DIFAR hydrophones are the acoustic sensors in the DASARs. These small units were installed in water 20–25 m deep with an unknown orientation. To measure the orientation on the bottom and calibrate the clock time drift, acoustic pings were transmitted in the water from known locations.

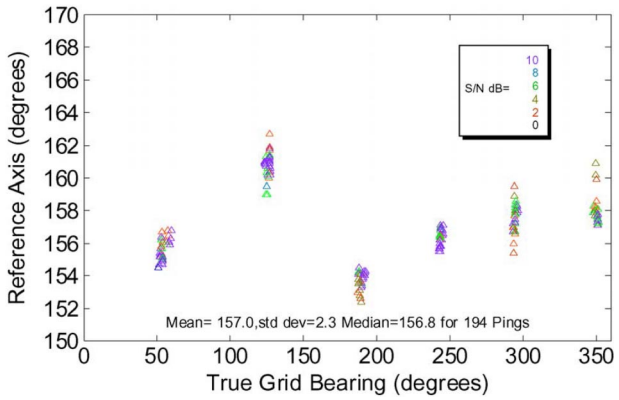

FIG. 15. Measured reference axis direction versus true grid bearing for DASAR CBa. From each location of the ping projector, 4–8 pings were transmitted. For each DASAR, bearings were determined to the pings projected from 4–6 positions at different azimuths. The vertical axis is the calculated bearing of the reference axis of the DIFAR hydrophone.

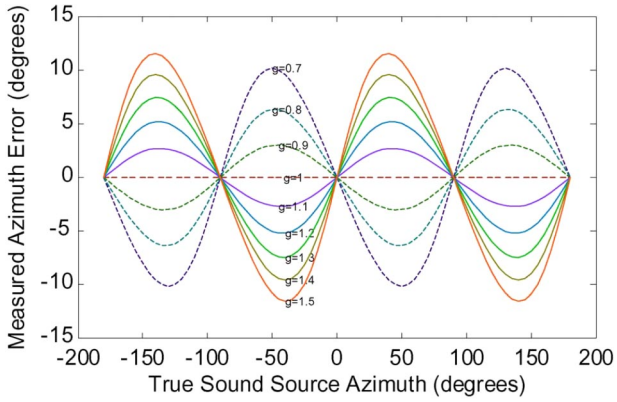

FIG. 16. Azimuthal bearing error due to DIFAR gain imbalance.

By measuring the bearing of each ping with the DIFAR logic and comparing it to the known bearing from the DASAR to the projector position, it was possible to measure the reference axis direction on the bottom.

The reference axis direction is given by

$$b_{\mathrm{ref}} = b_{\mathrm{true}} - b_d\,, \tag{A1}$$

where b_{true} is the known true bearing of the ping, and b_d is the measured DIFAR bearing relative to the reference axis direction.

Figure 15 presents the measured reference bearing for DASAR CB data plotted versus true bearing. The overall scatter is ~10° peak-to-peak. This meets the bearing accuracy specified for DIFAR, but is larger than desired. At any given true bearing, the scatter is on the order of 3°–5°, but the variation across bearing appears to follow an orderly pattern, suggesting that improvement would be possible if the cause of the variation could be determined and modeled.

Reflecting objects near the DASAR could explain some bearing error; however, the installation area is uniform and relatively flat. Vertical multipaths (which do exist) would not introduce azimuthal bearing errors. We were led to investigate the effects of a gain imbalance in the DIFAR directional channels and to find a means of correcting for it.

2. The effects of a gain imbalance

The DIFAR sensor includes three acoustic channels, one omni and two directional. The bearing measurement process requires that the acoustic sensitivity of the two directional channels be equal. The DIFAR sensor is complex and includes many adjustments by the manufacturer to match the outputs, including temperature compensation. However, the manufacturing specification permits bearing errors of ±10° and it appeared better performance was possible. Gain imbalance seemed a possibility. We first investigate what the effect would be of such a gain imbalance.

We introduce three new variables:

g gain factor of sine channel relative to cosine channel ($g=1$ means no imbalance)

b_{err} error angle introduced by the gain imbalance

b_{meas} measured bearing including the error, such that

$$b_{\mathrm{meas}} = b_d + b_{\mathrm{err}} \tag{A2}$$

Assume there is an acoustic signal of amplitude A arriving from bearing b_d relative to the DIFAR reference axis. The x and y components of that signal will be

$$\begin{aligned} vx &= A\sin b_d\,,\\ vy &= A\cos b_d\,. \end{aligned} \tag{A3}$$

However, if there is a relative gain error g, these will be measured as

$$\begin{aligned} vx_{\mathrm{meas}} &= g\cdot A\sin b_d\,,\\ vy_{\mathrm{meas}} &= A\cos b_d\,, \end{aligned} \tag{A4}$$

and the measured bearing will be

$$b_{\mathrm{meas}} = \arctan(vx_{\mathrm{meas}}/vy_{\mathrm{meas}}) = \arctan(g\cdot vx/vy), \tag{A5}$$

where arctan is the form of the arctangent that accounts for all four quadrants. This measured bearing can be converted to the error b_{err} by subtracting the known b_d. Figure 16 shows the bearing error resulting from values of g ranging from 0.7 to 1.5.

When the error is plotted versus the true azimuth, it very closely resembles a sine wave with two cycles in the 360° of azimuth, with amplitudes ranging up to about 10° for the extreme values of gain shown. In fact, it is NOT a sinusoid. In such a two-cycle sinusoid the maximum value would be at exactly 45° (northeast) off the main axis. In this function, the maximum is lower or higher, depending on the value of g.

Manipulation of (A5) shows the DIFAR bearing of the maximum is

$$b_{d\,\max} = \arcsin\left(\frac{1}{\sqrt{1+g}}\right). \tag{A6}$$

This is graphed in Fig. 17.

Note that this is just the principal bearing value. There will be similar maxima and minima near the corresponding points on the (almost) sine wave; a positive peak at 180° plus $b_{d\,\max}$, and negative peaks at minus $b_{d\,\max}$ and 180 minus $b_{d\,\max}$. The magnitude of the error at that maximum is

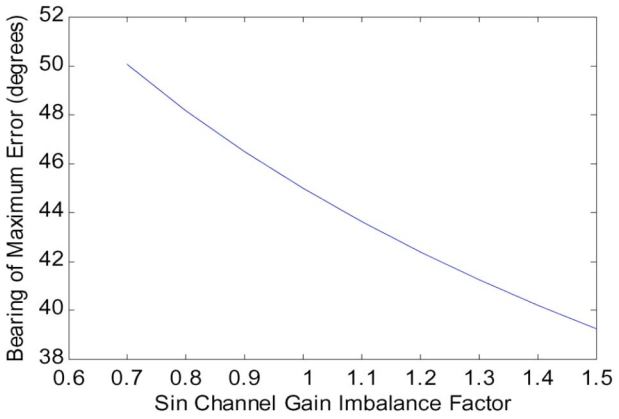

FIG. 17. Bearing of maximum bearing error versus gain imbalance.

$$b_{\text{err max}} = \arctan\left(0.5\left(\sqrt{g} - \frac{1}{\sqrt{g}} \right) \right), \tag{A7}$$

This is plotted in Fig. 18, which presents the magnitude of the maxima and minima of the near-sinusoidal waves.

3. Measuring the actual error and gain factor

The relations above give a feeling for the error behavior as a function of possible gain factors, and the errors observed in Fig. 15 are in the same range. The actual data include random errors from other sources, so we must use a statistical approach to characterize the actual errors while measuring the reference bearing. We do so by fitting a curve similar to Fig. 17 to the distribution in Fig. 16.

The basic equation we use is

$$b_{\text{true}} = b_{\text{ref}} + b_{\text{meas}} - b_{\text{err}}, \tag{A8}$$

where, to review,

b_{true} is the actual true bearing determined by GPS coordinates of the sound projector and the DASAR

b_{ref} is the true bearing of the reference (cosine) channel axis

b_{meas} is the measured bearing of the target from the reference axis

$b_{\text{meas}} = b_d + b_{\text{err}}$

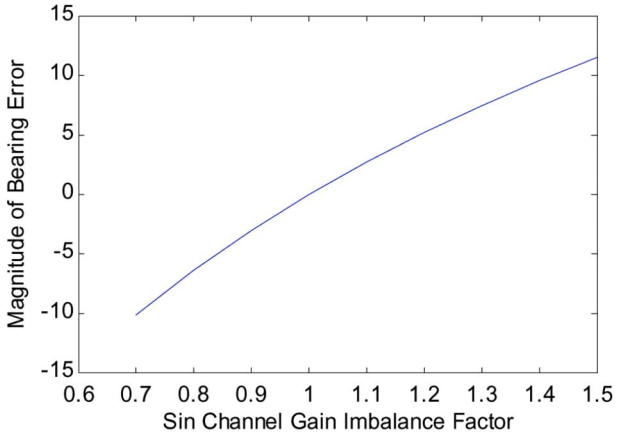

FIG. 18. Maximum magnitude of bearing error versus gain imbalance.

b_d bearing of sound source relative to DASAR reference

b_{err} is the small error due to gain imbalance

We assume b_{err} can be calculated as

$$\begin{aligned} b_{\text{errcalc}} &= a \cdot f(g, b_d) \\ &= a \cdot (\arctan(g \cdot \sin(b_d), \cos(b_d)) - b_d), \end{aligned} \tag{A9}$$

where a is an unknown amplitude and f is a function giving the shape of the error as shown in Fig. 17. The maximum value of this will be $a \cdot f_{\max}$, where $f_{\max}$ is given by Eq. (A7).

We also have a body of measurements allowing us to measure the error for a single trial. From Eq. (A8) we can say

$$b_{\text{errmeas}} = b_{\text{ref}} + b_{\text{meas}} - b_{\text{true}}. \tag{A10}$$

We wish to compare the calculated form and the measured data, and solve for the values of b_{ref} and gain factor g. We do this by a least-squares fit of the function f to the measured data, then solving for the gain and b_{ref}. Because of the nonlinearity of the equations, it is necessary to use a starting guess for g (for instance 1.2), then solve iteratively for new values.

We start with the ith measurement giving $b_{\text{true}}(i)$ and $b_{\text{meas}}(i)$. We assume a starting value for g and calculate $b_d(i)$ as

$$b_d(i) = \arctan(\sin(b_{\text{meas}}(i))/g, \cos(b_{\text{meas}}(i))). \tag{A11}$$

This can be inserted into Eq. (A9) to give a calculated value of the error $b_{\text{calc}}(i)$. The difference of these is the measurement error:

$$\begin{aligned} \text{error}(i) &= b_{\text{errmeas}}(i) - b_{\text{eercalc}}(i) \\ &= b_{\text{ref}}(i) + b_{\text{meas}}(i) - b_{\text{true}}(i) - a^* f(g, b_d(i)). \end{aligned} \tag{A12}$$

One measure of the goodness of a fit is the sum of the squares of all measurements:

$$S = \sum_i \text{error}(i)^2. \tag{A13}$$

We wish to select the parameters b_{ref} and a such that S is a minimum. There will be two simultaneous equations. One is

$$\frac{\partial S}{\partial b_{\text{ref}}} = \sum 2\text{error}(i) \frac{\partial \text{error}(i)}{\partial b_{\text{ref}}} = 0. \tag{A14}$$

Observing from (A12) that

$$\frac{\partial \text{error}(i)}{\partial b_{\text{ref}}} = 1, \tag{A15}$$

Eq. (A14) may be manipulated to the form

$$b^*_{\text{ref}} \sum_i 1 - a^* \sum_i f(i) = \sum_i [b_{\text{true}}(i) - b_{\text{meas}}(i)]. \tag{A16}$$

The second of the two equations is

$$\frac{\partial S}{\partial a} = \sum_i 2\text{error}(i) \frac{\partial \text{error}(i)}{\partial a} = 0. \tag{A17}$$

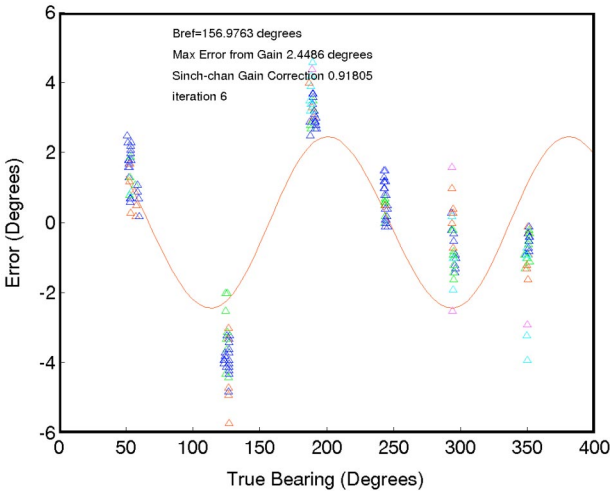

FIG. 19. Measured and computed errors for the ping calibrations for DASAR CBa.

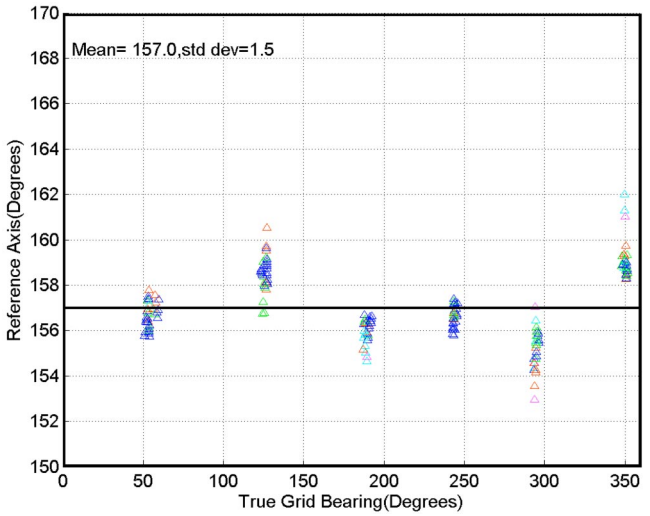

FIG. 20. Reference bearing measurements for DASAR CBa after correcting for gain imbalance.

From (A12)

$$\frac{\partial \text{error}(i)}{\partial a} = -f(i). \tag{A18}$$

Thus Eq. (A17) may be manipulated to give

$$b_{\text{ref}} \sum_i f(i) - a \cdot \sum_i f^2(i) = \sum_i f(i) \cdot (b_{true}(i) - b_{meas}(i)). \tag{A19}$$

Equations (A16) and (A19) are two linear equations for the unknowns b_{ref} and a. In matrix form they are

$$\begin{bmatrix} nm & -\sum f \\ \sum f & -\sum f^2 \end{bmatrix} \begin{bmatrix} b_{\text{ref}} \\ a \end{bmatrix} = \begin{bmatrix} \sum (b_{true} - b_{meas}) \\ \sum f \cdot (b_{true} - b_{meas}) \end{bmatrix}, \tag{A20}$$

where nm is the total number of measurements and all summations are over all measurements. This system can then be solved for b_{ref} and a. b_{ref} is used as is. The value of a is used to improve the estimate of the gain factor as follows: the maximum value of the calculated error is found as $a \cdot f_{\max}$ where $f_{\max}$ is found from Equation (A7) using the old value of g. Then a new value of a is computed by inverting (A7):

$$tbe = \tan(a \cdot f_{\max}), \tag{A21}$$

$$r_g = tbe \pm \sqrt{1 + tbe^2}, \tag{A22}$$

$$g = r_g^2, \tag{A23}$$

where tbe and r_g are just intermediate variables for computing g. Equation (A22) gives two possible values of g that are inverse to each other. If tbe is greater than zero, use the smaller value; if tbe is negative, use the larger.

The entire calculation is then iterated from Eq. (A11) until a approaches a value of 1.000. This implies that g has attained its final value. In typical cases this took around five iterations.

4. Results

Figure 19 shows the measured and calculated values from one such set of measurements. It appears that a substantial proportion of the deviations in Fig. 19 is due to some mechanism such as the gain imbalance. However, there are also other measurement errors.

Once the gain correction factor and reference bearing have been determined for a given DASAR, the correction may be applied in either of two ways:

(1) by calculating the correction factor in degrees for each measurement or
(2) by multiplying the digitized output of the sine channel by the inverse of g before measuring bearings.

The first of these methods is used if the digitized time series has already been used to calculate bearings. The correction is applied to the calculated bearings. The second method is applied if the digitized time series is available but has not already been used for the bearing measurement.

The data plotted in Fig. 15 were processed according to the previous section. b_{ref} was measured as 156.97° with $g = 1.0883$. The error (the difference between measured and true bearings) when plotted against true bearing was (approximately) two cycles of a sine wave with amplitude 2.45°. The data were remeasured after dividing the sine channel by g. The results are in Fig. 20.

The gain imbalance correction reduced the scatter for DASAR CBa from 2.3° to 1.3°. This second data set measured with gain correction was run through the same analysis. The results showed that there was no remaining two-cycle sine wave contribution. Out of curiosity, the data were run again looking for three- and four-cycle sine waves. This showed peak errors of −0.88° and +0.18°, respectively. However, we are not aware of any physical explanation for the apparent three-cycle dependence.

APPENDIX B: LOCALIZATION ACCURACY

The precision of whale call locations, in the form of error (or, more accurately, ''confidence'') ellipses, was esti-

mated following the methods of Lenth (1981) under which individual bearings from a DASAR to a received whale call were assumed to follow a Von Mises distribution (Mardia, 1972). The Von Mises distribution is analogous to the normal distribution, but applies to directional data in which angles x and $x+360°$ are the same. The Von Mises distribution has probability density function

$$f(\theta;\mu,\kappa)=[2\pi I_0(\kappa)]^{-1}\exp[\kappa\cos(\theta-\mu)],$$

where μ is the mean bearing, κ is the concentration parameter, and I_0 is a modified Bessel function. Assuming s is the standard deviation of bearings calculated in the usual way from a random sample of bearings, the concentration parameter can be calculated approximately as

$$\hat{\kappa}^{-1}\approx 2(1-A)+\frac{(1-A)^2(0.48794-0.82905A-1.3915A^2)}{A},$$

$$A=\exp\left[\frac{-1}{2}\left(\frac{s\pi}{180}\right)^2\right].$$

Estimates of s for each DASAR were computed from the gain-corrected calibration data (presented in Sec. III).

Histograms of the differences between gain-corrected bearings and true bearings (known during calibration) confirmed that it was reasonable to assume bearings followed a Von Mises distribution.

When two or more DASARs received the same call, the (x,y) location with maximum statistical likelihood, according to the Von Mises distribution, was used as the estimate of the call's location. Random errors in bearings (observed bearing—true bearing) from each DASAR to a given call were assumed to be independent. The statistical likelihood of the bearings was constructed and maximized as described in footnote 1. An estimate of the variance-covariance matrix of (x,y),

$$Q=\begin{bmatrix}\mathrm{Var}(x) & \mathrm{Cov}(x,y)\\ \mathrm{Cov}(x,y) & \mathrm{Var}(y)\end{bmatrix},$$

was obtained using formulas given in Lenth (1981) and White and Garrott (1990). Relying on the fact that maximum likelihood estimates are asymptotically normally distributed, the area of a 90% confidence ellipse for the true call position was calculated as

$$a=\pi|Q|^{1/2}\cdot\chi^2_{2,0.10},$$

where $\chi^2_{2,0.10}$ was the 10th quantile of a Chi-square distribution having 2 degrees of freedom and $|Q|=\mathrm{Var}(x)\mathrm{Var}(y)-\mathrm{Cov}(x,y)^2$ (White and Garrott, 1990). The length of the major axis of the error ellipse was calculated as

$$l_1=2(\lambda_1\chi^2_{2,0.10})^{1/2},$$

where λ_1 was the largest eigenvalue of Q. Similarly, the angle of the major axis was obtained from the eigenvector corresponding to the largest eigenvalue as

$$\phi_1=\tan^{-1}\left(\frac{\nu_{1,2}}{\nu_{1,1}}\right),$$

where $\nu_{1,1}$ was the first element of the first eigenvector of Q (Mardia *et al.*, 1979).

Not all calls received by 2+ DASARs were localizable or suitable for inclusion in subsequent analyses. Calls were discarded for one of three reasons. (1) A location could not always be computed because the maximum likelihood procedure occasionally failed to converge on a maximum. Generally, this happened when the geometry of the estimated bearings was unfavorable, i.e., when bearings did not intersect, or when multiple bearings intersected at widely separated locations. Convergence failure meant that neither the location nor its covariance could be calculated. (2) In some cases, the maximum likelihood procedure converged on a location estimate, but the variance-covariance matrix, Q, was not positive definite. Positive definite variance-covariance matrices were required for the corresponding error ellipse to have positive area. Nonpositive definite Q tended to occur when bearings were nearly parallel. This typically occurred at locations far from the DASAR array or near lines connecting pairs of DASARs. (3) In a few cases, the maximum likelihood solution was ''behind'' one of the DASARs. This occurred if the angle reported by the DASAR and the angle to the estimated location differed by 180°. For example, if a DASAR reported a bearing to a call of 45°, and the maximum likelihood procedure converged on a location 225° from the DASAR, the solution was ''behind'' the DASAR and was discarded. This situation generally occurred when only two bearings were available and when those two bearings were divergent and did not intersect (except if one or both bearings were changed by 180°).

To map the typical precision of the estimated call locations near the DASAR array, values of a (error ellipse size), l_1 (long axis length), and ϕ_1 (angle of long axis) were calculated for each call and smoothed using a kernel density estimator modified for continuous data. The usual Gaussian kernel density estimator for point location data (Wand and Jones, 1995) was modified for continuous data by multiplying values of the continuous variable by the usual kernel weights and computing a weighted average, i.e.,

$$\hat{\mu}(y|x)=\frac{\Sigma_{i=1}^n w(x,X_i,h)y_i}{\Sigma_{i=1}^n w(x,X_i,h)},$$

where $\hat{\mu}(y|x)$ was the estimated mean of variable y at location x (e.g., $y=$ area of 90% confidence ellipse), X_i was the coordinates of the ith observed location, y_i was the value of the continuous variable at the ith observed location, h was the smoothing parameter, and

$$w(x,X_i,h)=\exp\left[\frac{1}{2h^2}(x-X_i)^T(x-X_i)\right]$$

(Bailey and Gatrell, 1995). The smoothing parameter h dictated the degree of smoothing and for this analysis h was set to 1000 m. The weighted average, $\hat{\mu}(y|x)$, was computed at every intersection of a 500×500 m grid. The resulting surface of $\hat{\mu}(y|x)$ was then plotted for inspection.

[1]The statistical likelihood was a function of the unknown parameters κ and μ_i, where $i=1,2,...$ indexed the various DASARs receiving the call. The statistical likelihood represented the probability of observing the entire set

of bearings given hypothetical values of μ_i and κ. To assure that all μ_i intersected at a common point, the statistical likelihood was reparametrized by setting $\mu_i = \arctan((y-y_i)/(x-x_i))$, where (x_i, y_i) was the location of the ith DASAR and (x,y) was the point where all μ_i intersected. After reparametrization, the statistical likelihood was a function of the unknown parameters x, y, and κ. Given estimates of κ from the calibration data, estimates of x and y (the call's location) were obtained by repeatedly evaluating the statistical likelihood over a range of values until the probability of the observed bearings was maximized. The (x,y) point that maximized the statistical likelihood was used as the estimate of the call's location.

Bailey, T. C., and Gatrell, A. C. (**1995**). *Interactive Spatial Data Analysis* (Longman Scientific & Technical, Essex, UK).

Blackwell, S. B., and Greene, Jr., C. R. (**2004**). ''Sounds from an oil production island in the Beaufort Sea in summer: characteristics and contribution of vessels,'' to be submitted to J. Acoust. Soc. Am. Available from Greeneridge Sciences, 1411 Firestone Road, Goleta, CA 93117; info@greeneridge.com.

Clark, C. W., and Ellison, W. T. (**2000**). ''Calibration and comparison of the acoustic location methods used during the spring migration of the bowhead whale, *Balaena mysticetus*, off Pt. Barrow, Alaska, 1984–1993,'' J. Acoust. Soc. Am. **107**, 3509–3517.

Clark, C. W., and Johnson, J. H. (**1984**). ''The sounds of the bowhead whale, *Balaena mysticetus*, during the spring migrations of 1979 and 1980,'' Can. J. Zool. **62**(7), 1436–1441.

Clark, C. W., Charif, R., Mitchell, S., and Colby, J. (**1996**). ''Distribution and behavior of the bowhead whale, *Balaena mysticetus*, based on analysis of acoustic data collected during the 1993 spring migration off Point Barrow, Alaska,'' Rep. Int. Whal. Comm. **46**, 541–552.

Greene, C. R. (**1987**). ''Acoustic studies of underwater noise and localization of whale calls,'' Chap. 2, in ''Responses of bowhead whales to an offshore drilling operation in the Alaskan Beaufort Sea, autumn 1986,'' Report from LGL Ltd., King City, Ontario, and Greeneridge Sciences Inc., Santa Barbara, CA, for Shell Western E & P Inc., Anchorage, AK. Available from Greeneridge Sciences, 1411 Firestone Road, Goleta, CA; info@greeneridge.com.

Greene, C. R., Jr., McLennan, M. W., McDonald, T. L., and Richardson, W. J. (**2002**). ''Acoustic monitoring of bowhead whale migration, autumn 2001,'' in ''Monitoring of industrial sounds, seals, and whale calls during construction of BP's Northstar oil development, Alaskan Beaufort Sea, 2001, Draft, October 2002 ed.,'' edited by W. J. Richardson and M. T. Williams. LGL Rep. TA2573-2. Report from LGL Ltd., King City, Ontario, and Greeneridge Sciences Inc., Santa Barbara, CA, for BP Exploration (Alaska) Inc., Anchorage, AK, and Nat. Mar. Fish. Serv., Anchorage, AK, and Silver Spring, MD. pp. 8-1 to 8–79. Available from Greeneridge Sciences, Inc., 1411 Firestone Road, Goleta, CA 93117; info@greeneridge.com

Lenth, R. V. (**1981**). ''On finding the source of a signal,'' Technometrics **23**, 149–154.

Ljungblad, D. K. (**1986**). ''Endangered whale aerial surveys in the Navarin Basin and St. Matthew Hall planning areas, Alaska,'' in ''Aerial surveys of endangered whales in the northern Bering, eastern Chukchi, and Alaskan Beaufort Seas, 1985: with a seven year review, 1979–85,'' Appendix E in NOSC Tech. Rep. 1111; OCS Study MMS 86-0002. Report from Naval Ocean Systems Center, San Diego, CA, for U.S. Minerals Manage. Serv., Anchorage, AK. NTIS AD-A172 753/6.

Mardia, K. V. (**1972**). *Statistics of Direction Data* (Academic, New York).

Mardia, K. V., Kent, J. T., and Bibby, J. M. (**1979**). *Multivariate Analysis* (Academic, London).

McDonald, T. L., and Richardson, W. J. (**2003**). ''A statistical approach for assessing displacement of bowhead whale locations associated with elevated sound levels,'' LGL Rep. TA2706-4. Chap. 9, in ''Monitoring of industrial sounds, seals, and bowhead whales near BP's Northstar oil development, Alaskan Beaufort Sea, 1999–2002,'' edited by W. J. Richardson and M. T. Williams. Report from LGL Ltd., King City, Ontario, and Greeneridge Sciences Inc., Santa Barbara, CA, for BP Exploration (Alaska) Inc., Anchorage, AK, and Nat. Mar. Fish. Serv., Anchorage, AK, and Silver Spring, MD. pp 9–1 to 9–26. Available from Greeneridge Sciences Inc., 1411 Firestond Road, Goleta, CA 93117; info@greeneridge.com.

McLennan, M. W., and Greene, C. R., Jr. (**1996**). ''Passive acoustic localization and tracking of vocalizing marine mammals using buoy and line arrays,'' Appendix in ''Report of the cetacean acoustic assessment workshop,'' report by Australian Nature Conservation Agency (now Biodiversity Group of Environment Australia), Hobart, Tas.

Mellinger, D. K., and Clark, C. W. (**1997**). ''Methods for automatic detection of mysticete sounds.'' Mar. Freshwater Behav. Physiol. **29**(1–4), 163–181.

Mellinger, D. K., and Clark, C. W. (**2000**). ''Recognizing transient low-frequency whale sounds by spectrogram correlation,'' J. Acoust. Soc. Am. **107**, 3518–3529.

Moore, S. E., and Reeves, R. R. (**1993**). ''Distribution and movement,'' in *The Bowhead Whale*, edited by J. J. Burns, J. J. Montague, and C. J. Cowles. (Spec. Publ. 2. Soc. Mar. Mammal., Lawrence, KS), pp. 313–386.

Richardson, W. J., Miller, G. W., and Greene, Jr., C. R. (**1999**). ''Displacement of migrating bowhead whales by sounds from seismic surveys in shallow waters of the Beaufort Sea,'' J. Acoust. Soc. Am. **106**(4 Pt 2), 2281(A).

Richardson, W. J., Greene, C. R., Jr., Malme, C. I., and Thomson, D. H. (**1995**). *Marine Mammals and Noise* (Academic, San Diego).

Stoker, S. W., and Krupnik, I. I. (**1993**). ''Subsistence whaling,'' in *The Bowhead Whale* edited by J. J. Burns, J. J. Montague, and C. J. Cowles (Spec. Publ. 2, Soc. Mar. Mammal., Lawrence, KS), pp. 579–629.

Swartz, S. L., Cole, T., McDonald, M. A., Hildebrand, J. A., Oleson, E. M., Martinez, A., Clapham, P. J., Barlow, J., and Jones, M. L. (**2003**). ''Acoustic and visual survey of humpback whale (*Megaptera novaeangliae*) distribution in the eastern and southern Caribbean Sea,'' Carib. J. Sci. **39**, 195–208.

Wand, M. P., and Jones, M. D. (**1995**). *Kernel Smoothing* (Chapman & Hall/CRC, Boca Raton, FL).

White, G. C., and Garrott, R. A. (**1990**). *Analysis of Wildlife Radio-tracking Data* (Academic, New York).

Würsig, B., and Clark, C. (**1993**). ''Behavior,'' in *The Bowhead Whale*, edited by J. J. Burns, J. J. Montague, and C. J. Cowles (Spec. Publ. 2. Soc. Mar. Mammal., Lawrence, KS), pp. 157–199.

Acoustic waves generated by a laser point source in an isotropic cylinder

Yongdong Pan[a)]
Institute of Acoustics, Tongji University, 200092, Shanghai, People's Republic of China

Clément Rossignol and Bertrand Audoin
Laboratoire de Mécanique Physique, UMR CNRS 8469, Université Bordeaux 1, 33405 Talence, France

(Received 1 January 2004; revised 19 May 2004; accepted 20 May 2004)

The acoustic field of a homogeneous and isotropic cylinder generated by a laser point source in either ablation or thermoelastic regime is obtained theoretically. A three-dimensional Fourier transform is used to calculate the acoustic displacement at the cylinder surface. Experimental waveforms were measured and analyzed for both regimes. Theoretical normal displacements under either regime are calculated and compared to the experimental signals for aluminum cylinders. Very good agreements are observed in the arrival time, shape, and relative amplitude (i) of the cylindrical Rayleigh waves with different round trips, and (ii) of the various longitudinal and transverse bulk waves propagating through the cylinder or reflected at the free circular surface. © *2004 Acoustical Society of America.* [DOI: 10.1121/1.1771618]

PACS numbers: 43.35.Cg, 43.20.Px, 43.20.Bi [YHB] Pages: 814–820

I. INTRODUCTION

There is an increasing demand of nondestructively evaluating cylindrical parts. However, the understanding of wave propagation in cylinders is a necessary step before considering any possible application to nondestructive purposes. Moreover, a cylinder with its unique geometry is a basic target for the acoustic wave propagation.

Surface acoustic or Rayleigh wave propagating on an isotropic and homogenous cylinder was considered in 1927 by Sezawa,[1] who obtained its characteristic equation and calculated the dependence of its velocity on the radius of the cylinder. More detailed studies were reported in 1967 by Viktorov,[2] who calculated the dispersive curve and made a comparison to experimental data detected by conventional piezoelectric transducers. Higher Rayleigh-type waves were termed as ''Whispering-gallery modes'' by Uberall in 1973.[3] Due to the coupling difficulty of such transducers, few experimental reports on the wave propagation for such a curved medium had been published until the development of the laser ultrasonic technique,[4] in which ultrasonic waves are both generated and detected by lasers. With the remarkable features of noncontact, high spatial and temporal resolutions introduced by this technique, various studies on materials of curved surfaces have been carried out. For instance, the Rayleigh wave propagating on a sphere was observed experimentally in 1988,[5] and a further detailed study has been reported later.[6] The Rayleigh wave propagating on a cylinder was also studied by this technique.[7,8] The finite element method has been used to predict the bulk and surface wave propagation when the laser beam was focused by a cylindrical lens.[9]

Very recently, authors have published a model[10] to predict the bulk and surface wave propagations in a transversely isotropic cylinder under either ablation or thermoelastic generation. As the laser pulse was focused by a cylindrical lens, the laser was represented by a transient line source. But the model can only predict the wave propagation within the isotropic plane perpendicular to the z axis, and the propagation along the z axis was still not studied. In this paper, a novel physical model is presented to predict the acoustic field generated by a laser point source in either ablation or thermoelastic regime for a homogenous and isotropic cylinder. The wave propagation along the z axis is now considered. Experimental normal displacements generated under either regime were measured by the laser ultrasonic technique. Theoretical normal displacements are calculated and compared with the corresponding experimental waveforms.

II. STATEMENT OF THE PROBLEM

Let us consider a homogenous and isotropic cylinder of infinite length, radius a, and density ρ. As shown in Fig. 1, the symmetrical axis of the cylinder is assumed to coincide with the z axis of its cylindrical coordinates (r,θ,z). A pulsed laser is used to generate acoustic waves in this material. Here, ''detection'' is to denote an experimental technique, generally an optical detection technique,[4] which is applied to measure these acoustic waves. If a spherical lens is used to focus the laser beam, this laser can be modeled as a point-like acoustic source, which impacts at the boundary of the cylinder, $r=a$. To denote the detection position on the cylinder, cylindrical coordinates (a,θ,z) are chosen, considering $\theta=0$ and $z=0$ for the source position.

Let λ and μ denote the Lamé coefficients. The components of the displacement vector depend on three spatial variables r, θ, z and on time t. These components, denoted as u_r, u_θ, and u_z can be written as[11]

$$u_r(r,\theta,z,t)=\frac{\partial\varphi}{\partial r}+a\frac{\partial^2\psi}{\partial r\,\partial z}+\frac{1}{r}\frac{\partial\chi}{\partial\theta},$$

[a)]Electronic mail: y.pan@lmp.u-bordeaux1.fr

 0001-4966/2004/116(2)/814/7/$20.00

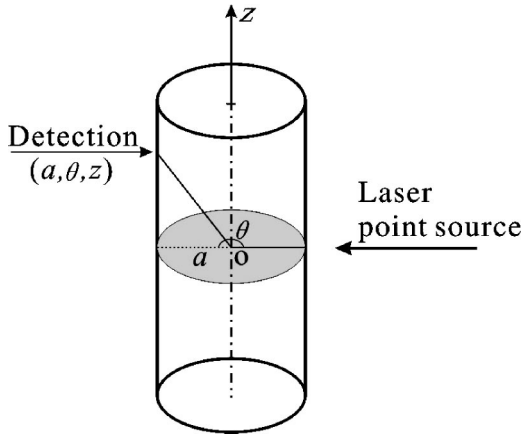

FIG. 1. Problem geometry.

$$u_\theta(r,\theta,z,t)=\frac{1}{r}\frac{\partial\varphi}{\partial\theta}+\frac{a}{r}\frac{\partial^2\psi}{\partial\theta\,\partial z}-\frac{\partial\chi}{\partial r},\tag{1}$$

$$u_z(r,\theta,z,t)=\frac{\partial\varphi}{\partial z}-a\left(\frac{\partial^2\psi}{\partial r^2}+\frac{\partial\psi}{r\partial r}+\frac{\partial^2\psi}{r^2\,\partial\theta^2}\right),$$

where the three scalar potentials φ, ψ, and χ are governed by the waves motion equations

$$\nabla^2\varphi=\frac{\rho}{\lambda+2\mu}\frac{\partial^2\varphi}{\partial t^2},\quad \nabla^2\psi=\frac{\rho}{\mu}\frac{\partial^2\psi}{\partial t^2},\quad \nabla^2\chi=\frac{\rho}{\mu}\frac{\partial^2\chi}{\partial t^2},\tag{2}$$

and by either of the following boundary conditions: for a source at position $\theta=0°$, components σ_{rr}, $\sigma_{r\theta}$, and σ_{rz} of the stress tensor at any point of the surface are determined by either

$$\sigma_{rr}|_{r=a}=-F_0\delta(t)\delta(z)\sum_{n=-\infty}^{+\infty}\delta(\theta-2n\pi),$$

$$\sigma_{r\theta}|_{r=a}=0,\quad \sigma_{rz}|_{r=a}=0,\tag{3}$$

for the ablation generation,[12] or

$$\sigma_{rr}|_{r=a}=0,$$

$$\sigma_{r\theta}|_{r=a}=-F_0h(t)\delta(z)\sum_{n=-\infty}^{+\infty}\delta'(\theta-2n\pi),\tag{4}$$

$$\sigma_{rz}|_{r=a}=-F_0ah(t)\delta'(z)\sum_{n=-\infty}^{+\infty}\delta(\theta-2n\pi),$$

for the thermoelastic generation.[13] In Eqs. (3) and (4), F_0 is a certain loading in $\mathrm{N}\cdot\mu\mathrm{s}\cdot\mathrm{m}^{-2}$ related to the laser pulse, and n stands for the number of clockwise ($n>0$) or anticlockwise ($n<0$) round trips of the generated acoustic waves. Here a delta function of time $\delta(t)$ and a Heaviside step function of time $h(t)$ are used for the ablation and thermoelastic generations, respectively; $\delta'(\theta-2n\pi)$ denotes the derivative of the delta function $\delta(\theta-2n\pi)$, and $\delta'(z)$ denotes the derivative of the delta function $\delta(z)$. In Eq. (3), a delta force is postulated in time and space to represent the sudden normal loading in the ablation regime. A Heaviside step function in time is considered in the thermoelastic regime, Eq. (4), since thermal diffusion is neglected. Owing to the interface, a dipolar force is considered in Eq. (4) for the source shape.[14]

III. TRANSFORMED SOLUTIONS AND NUMERICAL INVERSE SCHEME

The three-dimensional Fourier transform of the displacement field over the coordinate θ, z, and time t is now considered, and it is noted as U_i $i=r$, θ or z. On noting $\nu=k_\theta a$, where k_θ is the component of the wave vector $\mathbf{k}$ along the θ direction, three components of the displacement at a given surface position and time are then as follows:

$$u_i(a,\theta,z,t)=(2\pi)^{-3}\int\int\int_{-\infty}^{+\infty}U_i(a,\nu,k,\omega)\times e^{-j(\nu\theta+kz-\omega t)}\,d\nu\,dk\,d\omega.\tag{5}$$

Here k is the component of the wave vector $\mathbf{k}$ along the z direction. Doing so, the wave motion equations and the boundary equations can be linearized, providing explicit forms for the potentials φ, ψ, and χ under either generation regime. Components of the displacement at the boundary are then obtained for the ablation regime,

$$U_r(a,\nu,k,\omega)=-\frac{F_0a}{2\mu D(\nu,k,\omega)}\{A_1B_L-jkaA_2B_T-j\upsilon A_3\}\times\sum_{n=-\infty}^{+\infty}e^{j\nu 2n\pi},$$

$$U_\theta(a,\nu,k,\omega)=-\frac{F_0a}{2\mu D(\nu,k,\omega)}\{-j\upsilon A_1-\upsilon kaA_2-A_3B_T\}\times\sum_{n=-\infty}^{+\infty}e^{j\nu 2n\pi},\tag{6}$$

$$U_z(a,\nu,k,\omega)=-\frac{F_0a}{2\mu D(\nu,k,\omega)}\{-jkaA_1-\gamma^2a^2A_2\}\times\sum_{n=-\infty}^{+\infty}e^{j\nu 2n\pi},$$

and for the thermoelastic regime,

$$U_r(a,\nu,k,\omega)=\frac{F_0aH(w)}{2\mu D(\nu,k,\omega)}\{T_1B_L-jkaT_2B_T-j\upsilon T_3\}\times\sum_{n=-\infty}^{+\infty}e^{j\nu 2n\pi},$$

$$U_\theta(a,\nu,k,\omega)=\frac{F_0aH(w)}{2\mu D(\nu,k,\omega)}\{-j\upsilon T_1-\upsilon kaT_2-T_3B_T\}\times\sum_{n=-\infty}^{+\infty}e^{j\nu 2n\pi},\tag{7}$$

$$U_z(a,\nu,k,\omega)=\frac{F_0aH(w)}{2\mu D(\nu,k,\omega)}\{-jkaT_1-\gamma^2a^2T_2\}\times\sum_{n=-\infty}^{+\infty}e^{j\nu 2n\pi},$$

where

$$B_L=\beta a J'_\nu(\beta a)/J_\nu(\beta a), \quad B_T=\gamma a J'_\nu(\gamma a)/J_\nu(\gamma a),$$
$$\beta=\sqrt{k_L^2-k^2}, \quad \gamma=\sqrt{k_T^2-k^2}, \tag{8}$$
$$A_1=(m_{22}m_{33}-m_{23}m_{32}), \quad A_2=(m_{23}m_{31}-m_{21}m_{33}),$$
$$A_3=(m_{21}m_{32}-m_{22}m_{31}), \tag{9}$$

$$T_1=j\nu(m_{13}m_{32}-m_{33}m_{12})+jka(m_{12}m_{23}-m_{22}m_{13}),$$
$$T_2=j\nu(m_{11}m_{33}-m_{31}m_{13})+jka(m_{21}m_{13}-m_{11}m_{23}), \tag{10}$$
$$T_3=j\nu(m_{31}m_{12}-m_{11}m_{32})+jka(m_{11}m_{22}-m_{21}m_{12}),$$

$$m_{ij}=\begin{pmatrix} \nu^2-k_T^2a^2/2+k^2a^2-B_L & -jka(\nu^2-\gamma^2a^2-B_T) & j\nu(1-B_T) \\ j\nu(1-B_L) & \nu ka(1-B_T) & \gamma^2a^2/2-\nu^2+B_T \\ -jkaB_L & (k_T^2/2-k^2)a^2B_T & -\nu ka/2 \end{pmatrix}. \tag{11}$$

Note that in these Eqs. (8) and (11), $k_L=\omega\sqrt{\rho/(\lambda+2\mu)}$ and $k_T=\omega\sqrt{\rho/\mu}$ are the scalar wave vector of the longitudinal and transverse waves, respectively. In Eqs. (6) and (7), $D(\nu,k,\omega)=\det(m_{ij})$ is the determinate of the matrix m_{ij} of Eq. (11). Additionally, $H(\omega)$ is the Fourier transform of $h(t)$, and $J'_\nu(x)$ is the derivative of the Bessel function $J_\nu(x)$.

Now, let us focus on the calculation of the three-dimensional integral in Eq. (5). When dealing with an elastic material, this integrand shows discontinuities for a particular set of ω, ν, and k values. They correspond to poles associated with the zeros of the dispersion equation,

$$D(\nu,k,\omega)=0. \tag{12}$$

Note that for $k=0$, Eq. (9) yields to

$$(\nu^2-k_T^2a^2/2)^2-\nu^2+k_T^2a^2(B_L+B_T)/2+(1-\nu^2)B_LB_T=0, \tag{13}$$

which is identical to the dispersion equation for the line source; see Eq. (8) in Ref. 10. These poles describe the cylindrical Rayleigh waves[2] and Whispering Gallery waves.[3] The integration thus appears to be inconsistent with the Fourier transformation. A suited numerical integration method should, therefore, be applied. For each value of the angular frequency ω, the two-dimensional integral on the real axes of the variable ν and k is calculated by means of the method suggested by Weaver *et al.*[15] In this scheme, the Fourier transform is generalized by replacing ω by a complex variable $\omega-j\delta$ with a small, constant, and imaginary part δ. With this change of variable, Eq. (5) becomes

$$u_i(a,\theta,z,t)=\frac{e^{\delta t}}{8\pi^3}\int\int\int_{-\infty}^{+\infty} U_i(a,\nu,k,\omega-j\delta) \times e^{-j(\nu\theta+kz-\omega t)}\,d\nu\,dk\,d\omega. \tag{14}$$

The benefit of this method is twofold: (i) it preserves the application of the fast Fourier transform algorithms for the final inversion, and (ii) the two-dimensional integrand is a nonsingular function that may now be integrated numerically. To perform the numerical integration, the value $\delta=0.01$ rad$\cdot\mu$s^{-1} has been chosen for the auxiliary parameter in the following numerical calculations.

IV. ACOUSTIC WAVES GENERATED BY A LASER LINE SOURCE

Signals measured by the laser ultrasonic technique[4] for a cylinder impacted by an impulsive point source, contain a large amount of information that may be difficult to interpret. However, there is much less difficulties once signals generated by an impulsive line source have been understood. Therefore, in this section, the calculated normal displacements are compared to the experimental signals for aluminum cylinders under line source generations.

An Nd:YAG laser is used for ultrasonic wave generation in either ablation or thermoelastic regime. The pulse duration is 20 ns and infrared light emission is obtained at 1064 nm with a maximum burst energy output of 340 mJ. The collimated optical beam is focused by means of a cylindrical lens (the focus length is 150 mm). The line length and width are about 4 cm and 0.1 mm, respectively. Using an optical heterodyne probe with a power output of 100 mW and with a sensitivity[5] of $10^{-14}\,\mathrm{m}/\sqrt{\mathrm{Hz}}$, the normal displacement is measured at the surface. See Ref. 16 for the detailed experimental setup.

The experimental and calculated normal displacements generated by a laser line source under ablation generation ($a=4.99$ mm) and thermoelastic generation ($a=2.06$ mm) are shown in Fig. 2 and Fig. 3, respectively. The observation angle is 180°. In this paper, the observation angle is the difference between angular coordinates of the line source and point receiver in the cylindrical reference frame. The aluminum density considered for calculations is $\rho=2690$ Kg m^{-3}, and the Lamé coefficients are $\lambda=59.1$ GPa and $\mu=31.1$ GPa.[17] The calculated wave forms have been scaled vertically by a constant corresponding to the source strength to bring the amplitudes of the two signals into the same scale. As shown in Figs. 2–3, calculated and experimental waveforms are in very good agreement for both generation regimes. The arrival time, shape, and relative amplitude of each wave are identical. Especially, the arrivals of the first (R_1) and the second (R_2) round trip of the cylindrical Rayleigh waves and their dispersive behavior (the component of the low-frequency part travels relatively fast) are clearly observed in the four waveforms. The arrival of the third (R_3)

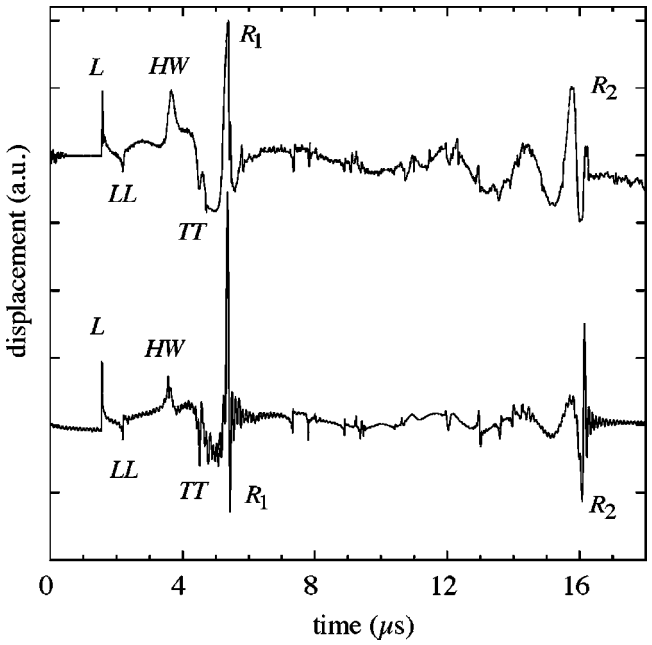

FIG. 2. Experimental (top) and calculated (below) normal displacements at an observation angle of 180° for an aluminum cylinder ($2a=9.97$ mm) and for a laser line source under ablation generation.

round trip cylindrical Rayleigh wave is also calculated and measured in the thermoelastic generation. It is clear that such a cylindrical Rayleigh wave has the similar shape and dispersive property as the spherical Rayleigh wave studied by Royer *et al.*[5] The experimental and calculated direct longitudinal wave (L) and the reflected transverse wave (TT) are observed under the ablation generation, whereas they are not observable under the thermoelastic generation. This phenomenon can be explained by the different directivities of the two generations.[4] Moreover, this difference of the directivity between ablation and thermoelastic generation can also explain the relative amplitude difference of the reflected longitudinal waves (LL) and the head waves (HW), which are observed for both regimes. The ray trajectories of L, LL, TT, and HW waves are shown in Fig. 4. Following arrivals (not marked in Figs. 2–3) with small amplitude are bulk wave modes resulting from the multiple reflections of the longitudinal and transverse waves within the cylinder.[8] A comparison of relative arrival times and amplitudes of these bulk waves emphasize the very good agreement between experiment and theory.

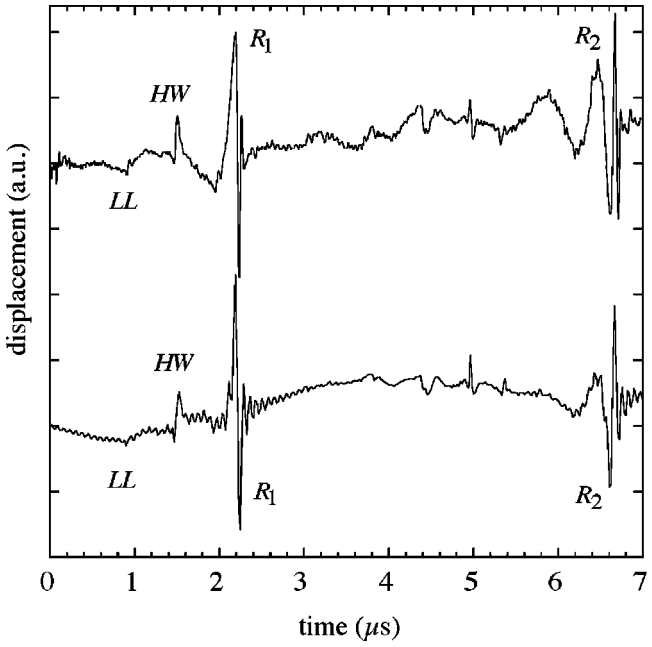

FIG. 3. Experimental (top) and calculated (below) normal displacements at an observation angle of 180° for an aluminum cylinder ($2a=4.12$ mm) and for a laser line source under thermoelastic generation.

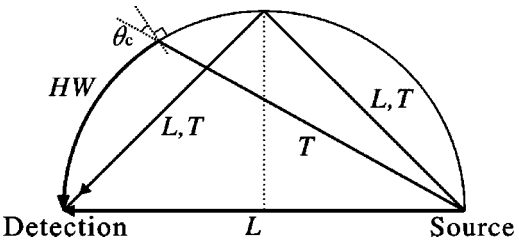

FIG. 4. Ray trajectories of bulk waves (L,LL,TT), and a head wave (HW) observed in Figs. 2–3. Here θ_c is the critical angle for aluminum rods.

V. ACOUSTIC WAVES GENERATED BY A LASER POINT SOURCE

In this section, the calculated normal displacements are compared to the experimental signals for two aluminum cylinders under point source generations. The Nd:YAG laser is used for ultrasonic wave generation in either the ablation or thermoelastic regime. The collimated optical beam is focused by means of a spherical lens (the focus length is 150 mm). The diameter of the laser spot size is about 0.2 mm. The normal displacement is still measured at the surface by using the same optical heterodyne probe.

A. Ablation regime

First let us look at the acoustic waves under ablation generation. The experimental signals generated by the laser point source were detected at $z=0,1,...,$ and 12 mm for an aluminum rod with a diameter $2a=9.62$ mm. Here the observation angle is also 180°. As shown in Fig. 5, the waterfall plot of these waveforms reveals various wave modes (see marked symbols). The direct longitudinal wave (L) and the once reflected longitudinal wave (LL) are clearly observable. The direct transverse wave (T) and the once reflected transverse wave (TT) are also observable. The arrival times (displayed as dashed lines in Fig. 5) are calculated along the ray trajectories shown in Fig. 6(a). The first round trip of the cylindrical Rayleigh wave (R_1) is clearly observable. Its arrival time is in agreement with that calculated along the ray trajectory shown in Fig. 6(b). Moreover, the twice reflected longitudinal wave ($3L$) is observed, and its ray trajectory is found in Fig. 6(c). A head wave (H_1) is observed, and its arrival time is also identical to that calculated along the corresponding ray trajectory in Fig. 6(b). Another head wave (H_2) is also observed; its ray trajectory is shown in Fig. 6(d).

To illustrate the pertinence of the modeling, calculated normal displacements are obtained and compared to the experimental signals at the epicenter ($z=0$) and at a nonepi-

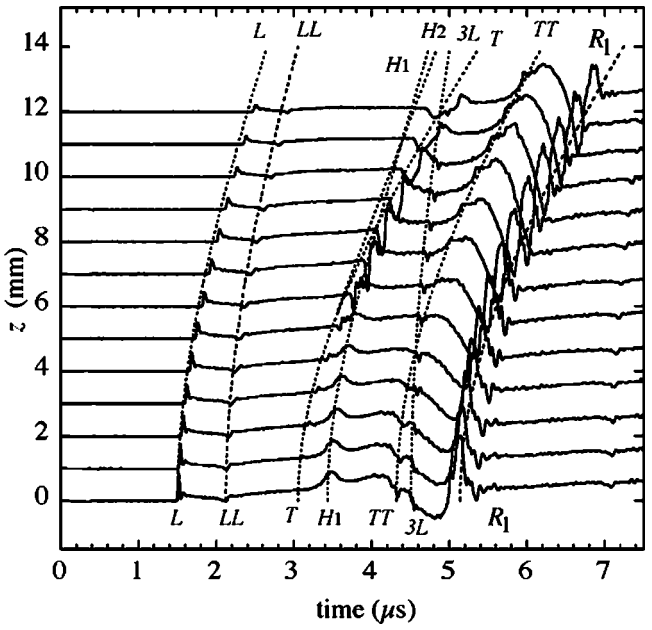

FIG. 5. Waterfall plots of experimental displacements generated by a laser point source under ablation generation at $z=0,1,...,$ and 12 mm for an aluminum cylinder ($2a=9.62$ mm).

center ($z=6$ mm) position of the laser point detection, for an aluminum cylinder ($2a=9.62$ mm). Comparisons are shown in Figs. 7(a) and 7(b), where the two calculated waveforms are vertically scaled to account for the source magnitude. The experimental and theoretical waveforms are in very good agreement. The time, shape, and relative amplitude of each wave arrival are identical. The arrivals of R_1 and R_2 waves and their dispersive behavior (the component of the low-frequency part travels relatively fast) are clearly observed. The arrival time of the R_2 wave is in agreement with that predicted by the time of flight calculations along the ray trajectory shown in Fig. 6(c). These Rayleigh waves have the same shapes and dispersive properties as those generated by the laser line source (see Fig. 2). Moreover, the bulk waves

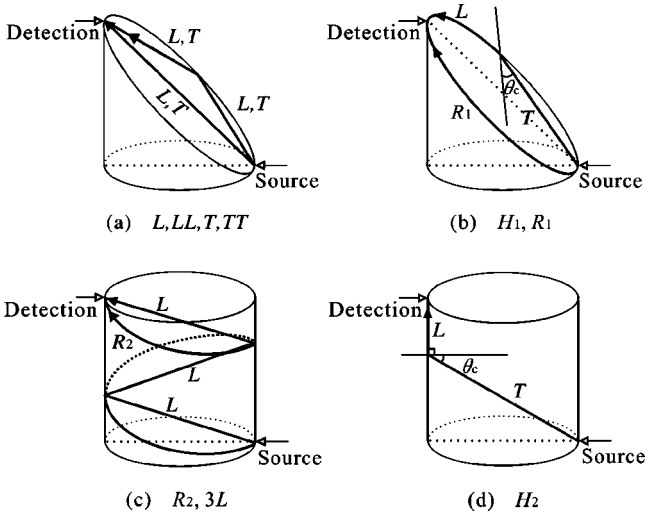

FIG. 6. Ray trajectories of bulk waves ($L,LL,T,TT,3L$), head waves (H_1,H_2), and Rayleigh waves (R_1,R_2) observed in Fig. 5 and Fig. 8. Here θ_c is the critical angle for aluminum.

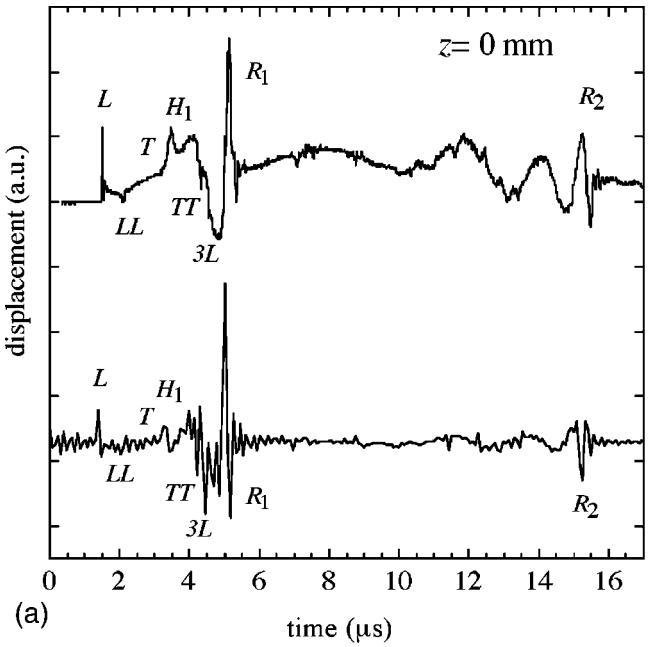

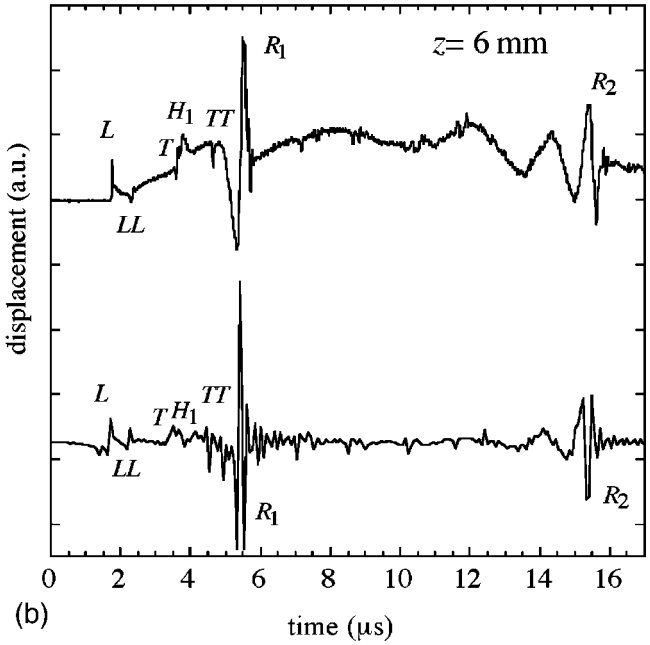

FIG. 7. Experimental (top) and calculated (below) normal displacements of an aluminum cylinder ($2a=9.62$ mm) at (a) the epicenter $z=0$ and (b) nonepicenter $z=6$ mm positions of the laser point detection under ablation generation for a laser point source.

(L,LL,T,TT), and the head wave (H_1) are observable. Their propagations can be explained by the corresponding ray trajectories for the point source in Fig. 6. For the epicenter, these trajectories are identical to those for the laser line source in Fig. 4. Following arrivals (not marked) with small amplitude are bulk wave modes resulting from the multiple reflections of the longitudinal and transverse waves within the cylinder.

B. Thermoelastic regime

Now let us look at the acoustic waves under thermoelastic generation. The experimental signals generated by the

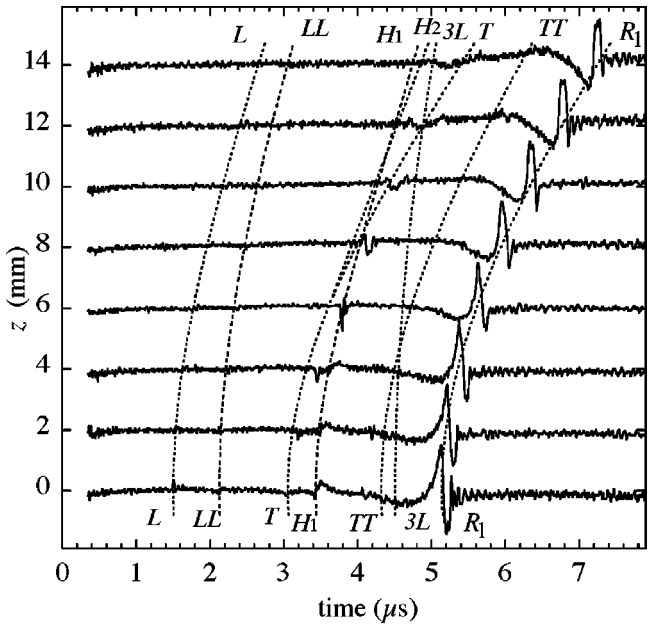

FIG. 8. Waterfall plots of experimental displacements generated by a laser point source under thermoelastic generation at $z=0,2,...,$ and 14 mm for an aluminum cylinder ($2a=9.62$ mm).

laser point source are detected at $z=0,2,...,$ and 14 mm for the aluminum rod with a diameter $2a=9.62$ mm. The observation angle is still 180°. As shown in Fig. 8, the waterfall plot of these waveforms also clearly reveals various wave modes. Note that the L, $3L$, and TT waves were observed under the ablation generation (Fig. 5), whereas they are not observable under the thermoelastic generation (Fig. 8). As already mentioned for the line source, this can be explained by the different directivities of the two generation regimes.[4] The arrival times of LL, H_1, and R_1 waves are identical to those (displayed as dashed lines in Fig. 8) calculated according to their corresponding ray trajectories in Fig. 6.

To further illustrate the accuracy of the modeling, calculated normal displacements are obtained and compared to the experimental signals at the epicenter ($z=0$) and at a nonepicenter ($z=6$ mm) position of the laser point source for the same sample. The two calculated waveforms are again vertically scaled to account for the source magnitude. As shown in Figs. 9(a) and 9(b), the experimental and theoretical waveforms are in good agreement. The time, shape, and relative amplitude of each wave arrival are identical. The arrivals of the R_1 and R_2 Rayleigh waves are clearly observed. Their ray trajectories are shown in Figs. 6(b) and 6(c), respectively. Moreover, they have the same shapes and dispersive properties as the Rayleigh waves generated by the laser line source for this regime (see Fig. 3). Moreover, the LL and the HW waves are observable. Their propagations can also be explained by the corresponding ray trajectories for the point source in Fig. 6. Following arrivals (not marked) with small amplitude are also bulk wave modes resulting from the multiple reflections of the longitudinal and transverse waves within the cylinder. Again, good agreement of the experimental and calculated arrival times is observed in the waterfall plots for a set of detection points located at $z=0,2,4,...,$ and 14 mm (see Fig. 9).

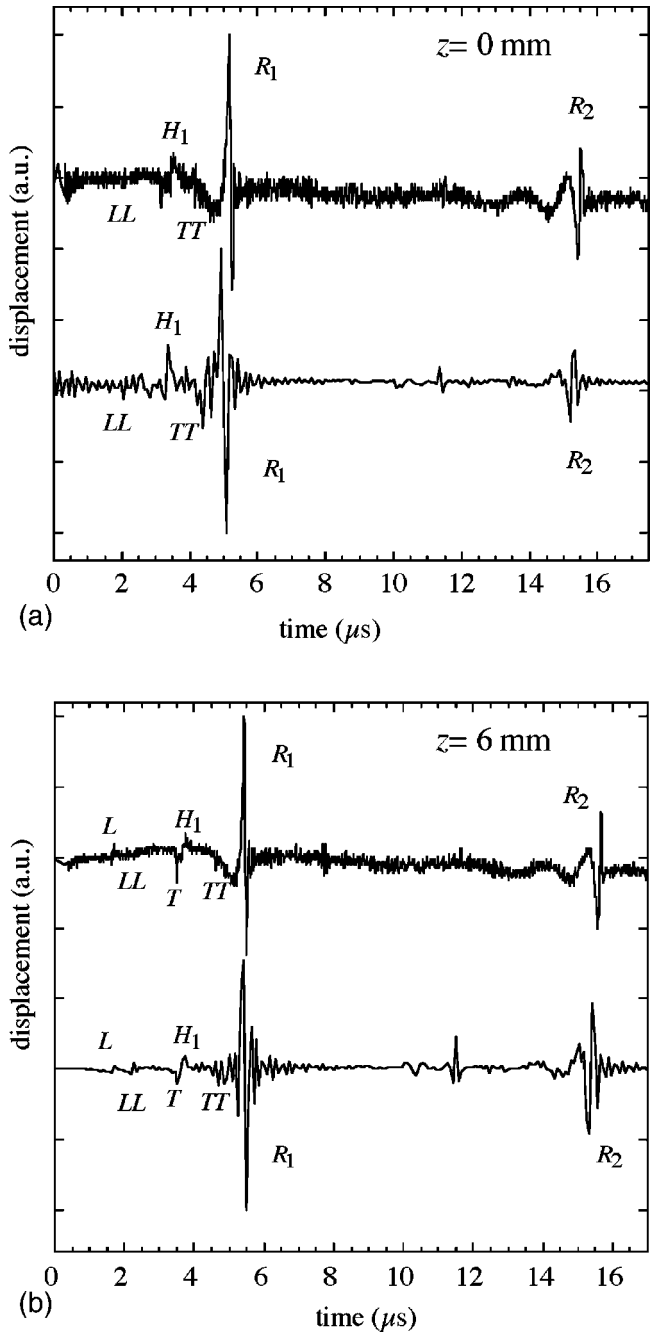

FIG. 9. Experimental (top) and calculated (below) normal displacements of an aluminum cylinder ($2a=9.62$ mm) at (a) the epicenter $z=0$ and (b) nonepicenter $z=6$ mm positions of the laser point detection under thermoelastic generation for a laser point source.

At the epicenter detection, for the point source generation, the experimental and calculated L and TT waves are observed under the ablation generation, Fig. 7(a), whereas they are not observable under the thermoelastic generation, Fig. 9(a). This phenomenon can be explained by the different directivities of the two generations.[4] Moreover, this difference of the directivities between ablation and thermoelastic generations also explains the relative amplitude differences for the LL and H_1 waves, which are observed for both regimes. Additionally, owing to the directivity of the thermoelastic generation, the L wave is observable at the nonepicenter detection position, Fig. 9(b), whereas it is not visible at the epicenter, Fig. 9(a).

VI. CONCLUSION

A theoretical solution has been presented to predict the acoustic field generated by a laser point source in either the ablation or thermoelastic regime at any point of a homogeneous and isotropic cylinder. Experimental and theoretical normal displacements under either regime are obtained and compared for aluminum cylinders. Very good agreements are observed in the time, shape and relative amplitude (i) of the cylindrical Rayleigh waves with different round trips, and (ii) of the various longitudinal and transverse bulk waves propagating through the cylinder or reflected at the free circular surface. These results will be helpful in identifying the useful wave modes when dealing with the inverse problem of the nondestructive evaluation of cylindrical parts.

ACKNOWLEDGMENTS

This work was done at the Laboratoire de Mécanique Physique, Université Bordeaux 1. One of the authors (Y. P.) was supported by the National Center for Scientific Research of France (CNRS) and China Scholarship Council.

[1] K. Sezawa, ''Dispersion of elastic waves propagated on the surface of stratified bodies and on curved surfaces,'' Bull. Earthquake Res. Inst., Univ. Tokyo **3**, 1–18 (1927).
[2] A. Viktorov, *Rayleigh and Lamb Waves* (Plenum, New York, 1967).
[3] H. Uberall, *Physical Acoustics* (Academic, New York, 1973), Vol. 10, pp. 1–60.
[4] C. B. Scruby and L. E. Drain, *Laser Ultrasonics: Techniques and Applications* (Adam Hilger, New York, 1990).
[5] D. Royer, E. Dieulesaint, X. Jia, and Y. Shui, ''Optical generation and detection of surface acoustic waves on a sphere,'' Appl. Phys. Lett. **52**, 706–708 (1988).
[6] S. Ishikawa, H. Cho, Y. Tsukahara, N. Nakaso, and K. Yamanaka, ''Analysis of spurious bulk waves in ball surface wave device,'' Ultrasonics **41**, 1–8 (2003).
[7] M. Qian and X. Wu, ''Studies of cylindrical Rayleigh waves with laser ultrasonics,'' Prog. Nat. Sci. **11**, s258–s264 (2001).
[8] D. Clorennec and D. Royer, ''Analysis of surface acoustic wave propagation on a cylinder using laser ultrasonics,'' Appl. Phys. Lett. **82**, 4608–4610 (2003).
[9] X. Wu and M. Qian, ''Simulation of the finite element method on wave propagation in cylinders,'' Prog. Nat. Sci. **11**, s265–s268 (2001).
[10] Y. Pan, C. Rossignol, and B. Audoin, ''Acoustic waves generated by a laser line pulse in a transversely isotropic cylinder,'' Appl. Phys. Lett. **82**, 4379–4381 (2003).
[11] F. Honarvar and A. N. Sinclair, ''Acoustic wave scattering from transversely isotropic cylinders,'' J. Acoust. Soc. Am. **100**, 57–63 (1996).
[12] D. A. Hutchins, *Physical Acoustics* (Academic, New York, 1988), Vol. 18, pp. 21–123.
[13] L. R. F. Rose, ''Point-source representation for laser-generated ultrasound,'' J. Acoust. Soc. Am. **75**, 723–732 (1984).
[14] Y. H. Berthelot and I. J. Busch-Vishniac, ''Thermoacoustic radiation of sound by a moving laser source,'' J. Acoust. Soc. Am. **81**, 317–327 (1987).
[15] R. L. Weaver, W. Sachse, and K. Y. Kim, ''Transient elastic waves in a transversely isotropic plate,'' J. Appl. Mech. **63**, 337–346 (1996).
[16] F. Reverdy and B. Audoin, ''Elastic constants determination of anisotropic materials from phase velocities of acoustic waves generated and detected by lasers,'' J. Acoust. Soc. Am. **109**, 1965–1972 (2001).
[17] O. L. Anderson, *Physical Acoustics* (Academic, New York, 1965), Vol. 3, pp. 43–95.

Mathematical model for collective bubble dynamics in strong ultrasound fields

Alexander A. Doinikov
Institute of Nuclear Problems, Belarus State University, 11 Bobruiskaya Street, Minsk 220050, Belarus

(Received 6 January 2004; revised 3 April 2004; accepted 13 May 2004)

Using the Lagrangian formalism, coupled equations are derived that describe radial and translational motions of an arbitrary bubble in a three-dimensional cluster subject to an ultrasound field. The obtained equations incorporate the nonlinear coupling of the volume and the translational modes of bubbles as well as interactions between all bubbles in the cluster up to terms of third order in the inverse separation distances. Solving these equations for each bubble in a multibubble structure, consisting of *N* bubbles with arbitrary spatial arrangement, the collective dynamics of this structure can be simulated. The potentialities of the proposed model in simulating the bubble dynamics in strong ultrasound fields are illustrated by numerical examples. © *2004 Acoustical Society of America.* [DOI: 10.1121/1.1768255]

PACS numbers: 43.35.Ei, 43.25.Yw [AS] Pages: 821–827

I. INTRODUCTION

The mainstream of modern ultrasound applications is the use of increasingly stronger fields with pressure amplitudes exceeding 1 bar. In strong fields, the bubble behavior is shown by experiments to differ markedly from what classical theory, developed for weak fields, suggests. Examples, such as acoustic streamers and dancing motion, are the subject of an extensive literature.[1–10] Another recently detected phenomenon in this line is microbubble precession about the pressure node plane in an intense ultrasound standing wave.[11] Investigations of these effects pose respective problems to theory.

Since the driving field is strong and the ultimate aim is to investigate its impact on a multibubble structure rather than a single bubble, there is no way of efficiently using conventional analytical techniques. The only line of attack on the problem is evidently to use numerical simulations. The most natural and accurate way of simulating the dynamics of a bubble cluster would be to trace the motion of every bubble in the cluster, taking proper account of its interactions with all other bubbles. Not very long ago this way was considered to be unrealizable, even if an adequate mathematical model were available, because of extreme time consumption required. Therefore studies on the dynamics of bubble structures in strong acoustic fields were reduced either to an examination of the motion of a single bubble, fully ignoring its interaction with neighboring bubbles,[12–16] or to an examination of pairwise bubble interactions, assuming that two interacting bubbles move along their center line alone.[6,7,17–21] Another approach was to average the properties of a bubble–liquid mixture over space and thus obtain a continuous medium with new values of density, sound speed, etc.[2–4] Today, due to progress of computer performance, the view on this problem is rapidly changed and attempts of modeling the paths of many interacting bubbles are already making their appearance. The most progress in numerical simulations of collective bubble motion in strong acoustic fields has been made by Mettin *et al.*[5,22] (see also Ref. 4). Their purpose was to gain an insight into processes of formation of cavitation bubble structures such as acoustic streamers in standing-wave resonators, and they achieved considerable success in this area. Their numerical simulations provide bubble patterns that are in good qualitative agreement with experimental observations. However, they used a rather simple model, which may be inadequate for other situations. Their radial equations of motion neglect the effect of translation on the volume oscillation and the interactions between bubbles are accounted for by only secondary Bjerknes forces. Furthermore, utilizing the assumption that translation occurs at a much slower time scale than the radial motion, they average the translational equations of motion over the radial oscillation period. As was shown recently,[6,14,16] such assumptions are not generally valid at strong forcing.

The purpose of this paper is to propose more accurate equations describing coupled radial and translational motions of an arbitrary bubble in a three-dimensional cluster subject to an ultrasound field of high intensity. The equations are derived by using the Lagrangian formalism and allow for the nonlinear coupling of the volume and the translational modes of bubbles as well as interactions between all bubbles in the cluster up to terms of third order in the inverse separation distances.

One further important comment should be made. As mentioned above, there are papers where the coupled equations of the radial and translational motions of two interacting bubbles are derived up to third,[6,17] and even fourth,[21] order in the inverse separation distance between the bubbles. However, it is assumed in those papers that the bubbles only translate along their line of centers and therefore it is unclear how the equations obtained there can be extended to more than two bubbles, the translational velocities of which do not coincide with their lines of centers. The approach used in the present paper solves this problem. As regards its accuracy, although the present paper is restricted to terms of third order in the inverse separation distances, it will be seen below that the derivation can be extended to terms of any order, the only problem being the unwieldiness of the resulting expressions.

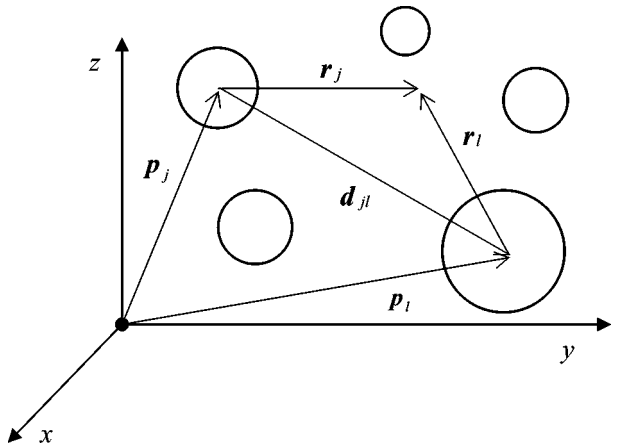

FIG. 1. Geometry of the bubble cluster.

This can only be necessary at rather small separation distances, though.

II. MATHEMATICAL FORMULATION

Let N gas bubbles undergo radial and translational motions in an ideal incompressible liquid. The geometry of the bubble cluster is shown in Fig. 1. The motion of the bubbles is observed with reference to the global Cartesian coordinates (x,y,z) with the unit vectors $\mathbf{e}_x$, $\mathbf{e}_y$, $\mathbf{e}_z$. Each bubble has also its own local spherical coordinate system $(r_l,\theta_l,\varepsilon_l)$, $l=1,2,...,N$, the origin of which is at its moving center. Assume that the distances between the bubbles are large compared with their sizes so that the bubbles remain spherical at all times. Then the total velocity potential of the bubble cluster, satisfying the Laplace equation $\Delta\varphi=0$, can be represented as

$$\varphi=\sum_{l=1}^{N}\varphi_l, \tag{1}$$

where φ_l, the velocity potential generated by the lth bubble, is given by

$$\varphi_l=\sum_{n=0}^{\infty}\sum_{m=-n}^{n}A_{nm}^{(l)}(t)r_l^{-n-1}Y_{nm}(\theta_l,\varepsilon_l) \tag{2a}$$

$$=\sum_{n=0}^{\infty}\sum_{m=-n}^{n}B_{nm}^{(lj)}(t)r_j^{n}Y_{nm}(\theta_j,\varepsilon_j). \tag{2b}$$

Equation (2a) gives φ_l in the proper coordinates of the lth bubble and Eq. (2b) in the coordinates of the jth (different) bubble. The spherical harmonics $Y_{nm}(\theta,\varepsilon)$ are defined as in Ref. 23. The time-dependent coefficients $B_{nm}^{(lj)}(t)$ can be expressed in terms of the coefficients $A_{nm}^{(l)}(t)$ using the following identity, which is a particular case of the so-called Clebsch–Gordan expansion,[23]

$$\frac{Y_{nm}(\theta_l,\varepsilon_l)}{r_l^{n+1}}=\frac{(-1)^n}{d_{jl}^{n+1}}\sqrt{\frac{4\pi}{(2n)!}}\sum_{\nu=0}^{\infty}\sum_{\mu=-\nu}^{\nu}\sum_{\mu'=-\nu'}^{\nu'}(-1)^{\nu}\times\sqrt{\frac{(2\nu+2n)!}{(2\nu+1)!}}\left(\frac{r_j}{d_{jl}}\right)^{\nu}(\nu\nu'\mu\mu'|\nu\nu'nm)\times Y_{\nu\mu}(\theta_j,\varepsilon_j)Y_{\nu'\mu'}(\theta_{jl},\varepsilon_{jl}). \tag{3}$$

Here $\nu'=\nu+n$, $d_{jl}=|\mathbf{d}_{jl}|$, $\mathbf{d}_{jl}=\mathbf{p}_l-\mathbf{p}_j$, $\mathbf{p}_l$ and $\mathbf{p}_j$ are the position vectors of the lth and jth bubbles with respect to the global coordinates (see Fig. 1), the angles θ_{jl} and ε_{jl} specify the direction of the vector $\mathbf{d}_{jl}$ in the global coordinates, and $(\nu\nu'\mu\mu'|\nu\nu'nm)$ denotes the Clebsch–Gordan coefficients.[24] Note also that $\mathbf{d}_{jl}$, $\mathbf{p}_l$, and $\mathbf{p}_j$ are time-dependent quantities. Substituting Eq. (3) into Eq. (2a) and comparing with Eq. (2b), one finds

$$B_{nm}^{(lj)}(t)=\frac{(-1)^n}{d_{jl}^{n+1}}\sqrt{\frac{4\pi}{(2n+1)!}}\sum_{\nu=0}^{\infty}\sum_{\mu=-\nu}^{\nu}\sum_{\mu'=-\nu'}^{\nu'}\frac{(-1)^{\nu}}{d_{jl}^{\nu}}\times\sqrt{\frac{(2\nu+2n)!}{(2\nu)!}}(n\nu'm\mu'|n\nu'\nu\mu)\times Y_{\nu'\mu'}(\theta_{jl},\varepsilon_{jl})A_{\nu\mu}^{(l)}(t), \tag{4}$$

where $\nu'=\nu+n$ as before. Other equations relating the coefficients $A_{nm}^{(l)}(t)$ and $B_{nm}^{(lj)}(t)$ are obtained using the boundary conditions at the bubble surfaces. For the jth bubble, this condition takes the form

$$\frac{\partial\varphi}{\partial r_j}=\dot{R}_j(t)+\dot{\mathbf{p}}_j\cdot\mathbf{n}_j \quad \text{at } r_j=R_j(t), \tag{5}$$

where $R_j(t)$ is the time-varying radius of the jth bubble, the overdot denotes the time derivative, and $\mathbf{n}_j$ is the outward unit normal to the surface of the jth bubble. Utilizing Eqs. (2a) and (2b), the total velocity potential in the vicinity of the jth bubble is written as

$$\varphi=\sum_{n=0}^{\infty}\sum_{m=-n}^{n}\left[A_{nm}^{(j)}(t)r_j^{-n-1}+\sum_{\substack{l=1\\l\neq j}}^{N}B_{nm}^{(lj)}(t)r_j^{n}\right]Y_{nm}(\theta_j,\varepsilon_j). \tag{6}$$

Substitution of this equation into Eq. (5) yields

$$A_{00}^{(j)}=-2\sqrt{\pi}R_j^2\dot{R}_j, \tag{7}$$

$$A_{10}^{(j)}=-\sqrt{\frac{\pi}{3}}R_j^3\dot{p}_{jz}+\frac{R_j^3}{2}\sum_{\substack{l=1\\l\neq j}}^{N}B_{10}^{(lj)}, \tag{8}$$

$$A_{11}^{(j)}=\sqrt{\frac{2\pi}{3}}\frac{R_j^3}{2}(\dot{p}_{jx}-i\dot{p}_{jy})+\frac{R_j^3}{2}\sum_{\substack{l=1\\l\neq j}}^{N}B_{11}^{(lj)}, \tag{9}$$

$$A_{1-1}^{(j)}=-\sqrt{\frac{2\pi}{3}}\frac{R_j^3}{2}(\dot{p}_{jx}+i\dot{p}_{jy})+\frac{R_j^3}{2}\sum_{\substack{l=1\\l\neq j}}^{N}B_{1-1}^{(lj)}, \tag{10}$$

$$A_{nm}^{(j)}=\frac{nR_j^{2n+1}}{n+1}\sum_{\substack{l=1\\l\neq j}}^{N}B_{nm}^{(lj)} \quad \text{for } n\geqslant 2. \tag{11}$$

For the sake of simplicity the time dependence will be omitted from this point on.

There is now all that is needed to get the Lagrangian function of the bubble cluster. The kinetic energy T of the cluster is determined by the kinetic energy of the host liquid,

$$T=\frac{\rho}{2}\int_V |\nabla\Phi|^2\,dV, \tag{12}$$

where ρ is the liquid density, $\Phi=\mathrm{Re}\{\varphi\}$ is the real part of φ, and V denotes the volume occupied by the liquid. Using the fact that $\Delta\Phi=0$ along with Eq. (5), Eq. (12) can be transformed as follows:

$$\begin{aligned}T&=\frac{\rho}{2}\int_V \nabla\cdot(\Phi\nabla\Phi)dV\\&=-\frac{\rho}{2}\sum_{j=1}^{N}\int_{S_j}\mathbf{n}_j\cdot\Phi\nabla\Phi\,dS_j\\&=-\frac{\rho}{2}\sum_{j=1}^{N}\int_{S_j}\Phi(\dot R_j+\dot{\mathbf{p}}_j\cdot\mathbf{n}_j)dS_j,\end{aligned} \tag{13}$$

where S_j designates the surface of the jth bubble. Substituting Eq. (6), integrating, and then using Eqs. (7)–(10), one obtains

$$\begin{aligned}T=2\pi\rho\sum_{j=1}^{N}R_j^3(\dot R_j^2+\dot{\mathbf{p}}_j^2/6)-\sqrt{\pi}\rho\,\mathrm{Re}\sum_{\substack{j,l=1\\ j\neq l}}^{N}\Bigg\{&R_j^2\dot R_j B_{00}^{(lj)}\\&+\frac{\sqrt{3}R_j^3}{2\sqrt{2}}[\sqrt{2}\dot p_{jz}B_{10}^{(lj)}-\dot p_{jx}(B_{11}^{(lj)}-B_{1-1}^{(lj)})\\&-i\dot p_{jy}(B_{11}^{(lj)}+B_{1-1}^{(lj)})]\Bigg\}.\end{aligned} \tag{14}$$

All the equations obtained up to this point impose no restriction on the order of scattering between the bubbles. In other words, they contain terms of all powers in the inverse separation distances d_{jl}. However, to go on with analytical calculations and to avoid superfluous complexity, further derivation will be carried out with accuracy up to terms of third order in d_{jl}^{-1}.

From Eqs. (4) and (7)–(11), one finds

$$B_{00}^{(lj)}\approx-2\sqrt{\pi}R_l^2\dot R_l/d_{jl}+\sqrt{\pi}R_l^3\dot{\mathbf{p}}_l\cdot(\mathbf{p}_l-\mathbf{p}_j)/d_{jl}^3, \tag{15}$$

$$\begin{aligned}B_{10}^{(lj)}\approx\sqrt{\pi/3}(R_l^2/d_{jl}^3)[&2\dot R_l(p_{jz}-p_{lz})-R_l\dot p_{lz}\\&+3R_l(p_{lz}-p_{jz})\dot{\mathbf{p}}_l\cdot(\mathbf{p}_l-\mathbf{p}_j)/d_{jl}^2],\end{aligned} \tag{16}$$

$$\begin{aligned}B_{11}^{(lj)}-B_{1-1}^{(lj)}\approx\sqrt{2\pi/3}(R_l^2/d_{jl}^3)[&2\dot R_l(p_{lx}-p_{jx})+R_l\dot p_{lx}\\&-3R_l(p_{lx}-p_{jx})\dot{\mathbf{p}}_l\cdot(\mathbf{p}_l-\mathbf{p}_j)/d_{jl}^2],\end{aligned} \tag{17}$$

$$\begin{aligned}i(B_{11}^{(lj)}+B_{1-1}^{(lj)})\approx\sqrt{2\pi/3}(R_l^2/d_{jl}^3)[&2\dot R_l(p_{ly}-p_{jy})+R_l\dot p_{ly}\\&-3R_l(p_{ly}-p_{jy})\dot{\mathbf{p}}_l\cdot(\mathbf{p}_l-\mathbf{p}_j)/d_{jl}^2].\end{aligned} \tag{18}$$

Substitution of these equations into Eq. (14) yields finally

$$\begin{aligned}T=2\pi\rho\sum_{j=1}^{N}R_j^3(\dot R_j^2+\dot{\mathbf{p}}_j^2/6)+\pi\rho\sum_{\substack{j,l=1\\ j\neq l}}^{N}R_j^2R_l^2\{&2\dot R_j\dot R_l/d_{jl}\\&-2R_j\dot R_l\dot{\mathbf{p}}_j\cdot(\mathbf{p}_j-\mathbf{p}_l)/d_{jl}^3+R_jR_l(\dot{\mathbf{p}}_j\cdot\dot{\mathbf{p}}_l)/2d_{jl}^3\\&+3R_jR_l[\dot{\mathbf{p}}_j\cdot(\mathbf{p}_j-\mathbf{p}_l)][\dot{\mathbf{p}}_l\cdot(\mathbf{p}_l-\mathbf{p}_j)]/2d_{jl}^5\}.\end{aligned} \tag{19}$$

The potential energy U of the bubble cluster can be written as

$$U=-\sum_{j=1}^{N}(4\pi R_j^3P_j/3+\mathbf{p}_j\cdot\mathbf{F}_j), \tag{20}$$

where P_j is the liquid pressure at the surface of the jth bubble and $\mathbf{F}_j$ denotes external forces on the jth bubble, such as viscous drag and the primary Bjerknes force.

The Lagrangian function of the bubble cluster can now be obtained by $L=T-U$. The equations of radial and translational motions of the nth bubble can then be derived by the use of the Lagrangian equations,

$$\frac{d}{dt}\frac{\partial L}{\partial\dot q_n}-\frac{\partial L}{\partial q_n}=0, \tag{21}$$

considering R_n and $\mathbf{p}_n$ as generalized coordinates. This yields

$$\begin{aligned}R_n\ddot R_n+\frac{3}{2}\dot R_n^2-\frac{P_n}{\rho}&=\frac{\dot{\mathbf{p}}_n^2}{4}-\sum_{\substack{l=1\\ l\neq n}}^{N}\Bigg\{\frac{R_l^2\ddot R_l+2R_l\dot R_l^2}{d_{nl}}+\frac{R_l^2}{2d_{nl}^3}(\mathbf{p}_n-\mathbf{p}_l)\cdot(R_l\ddot{\mathbf{p}}_l\\&+\dot R_l\dot{\mathbf{p}}_n+5\dot R_l\dot{\mathbf{p}}_l)-\frac{R_l^3}{4d_{nl}^3}\Bigg[\dot{\mathbf{p}}_l\cdot(\dot{\mathbf{p}}_n+2\dot{\mathbf{p}}_l)\\&+\frac{3}{d_{nl}^2}[\dot{\mathbf{p}}_l\cdot(\mathbf{p}_l-\mathbf{p}_n)][(\mathbf{p}_n-\mathbf{p}_l)\cdot(\dot{\mathbf{p}}_n+2\dot{\mathbf{p}}_l)]\Bigg]\Bigg\},\end{aligned} \tag{22}$$

$$\begin{aligned}\frac{1}{3}R_n\ddot{\mathbf{p}}_n+\dot R_n\dot{\mathbf{p}}_n&=\frac{\mathbf{F}_n}{2\pi\rho R_n^2}+\sum_{\substack{l=1\\ l\neq n}}^{N}\Bigg\{\frac{\mathbf{p}_n-\mathbf{p}_l}{d_{nl}^3}(R_nR_l^2\ddot R_l+2R_nR_l\dot R_l^2+\dot R_nR_l\dot R_l^2)\\&-\frac{R_l^2}{2d_{nl}^3}[R_nR_l\ddot{\mathbf{p}}_l+(\dot R_nR_l+5R_n\dot R_l)\dot{\mathbf{p}}_l]\\&+\frac{3R_l^2(\mathbf{p}_n-\mathbf{p}_l)}{2d_{nl}^5}[(\mathbf{p}_n-\mathbf{p}_l)\cdot[R_nR_l\ddot{\mathbf{p}}_l\\&+(\dot R_nR_l+5R_n\dot R_l)\dot{\mathbf{p}}_l]]\Bigg\}.\end{aligned} \tag{23}$$

Equation (22) governs the volume pulsation of the nth bubble in the cluster and Eq. (23) its translational motion. It is easy to check that for $N=2$ Eqs. (22) and (23) reduce to the equations of motion which were obtained in Refs. 6, 17, and 21 for two interacting bubbles undergoing radial and

translational motions; note also that in Refs. 17 and 21 approaches different from the Lagrangian formulation were applied.

The pressure P_n can be taken in the form

$$P_n=\left(P_0+\frac{2\sigma}{R_{n0}}\right)\left(\frac{R_{n0}}{R_n}\right)^{3\gamma}-\frac{2\sigma}{R_n}-\frac{4\eta\dot{R}_n}{R_n}-P_0-P_{ex}(\mathbf{p}_n), \tag{24}$$

where P_0 is the hydrostatic pressure, R_{n0} is the equilibrium radius of the nth bubble, σ is the surface tension, γ is the polytropic exponent of the gas within the bubbles, η is the liquid viscosity, and $P_{ex}(\mathbf{p}_n)$ is the external (driving) acoustic pressure at the location of the nth bubble. The external forces $\mathbf{F}_n$ are set equal to the primary Bjerknes force, given by

$$\mathbf{F}_{Bn}=-(4\pi/3)R_n^3\nabla P_{ex}(\mathbf{p}_n), \tag{25}$$

and the Levich viscous drag, given by[25]

$$\mathbf{F}_{dn}=-12\pi\eta R_n\left(\dot{\mathbf{p}}_n-\mathbf{v}_{ex}(\mathbf{p}_n)-\sum_{\substack{l=1\\ l\neq n}}^{N}\mathbf{v}_{ln}\right), \tag{26}$$

where $\mathbf{v}_{ex}(\mathbf{p}_n)$ is the liquid velocity generated by the imposed acoustic field at the center of the nth bubble and $\mathbf{v}_{ln}$ is the liquid velocity generated by the lth bubble at the center of the nth bubble. Using Eqs. (2a) and (7)–(10), with accuracy up to order d_{jl}^{-3}, the velocity $\mathbf{v}_{ln}$ is given by

$$\mathbf{v}_{ln}=\frac{R_l^2\dot{R}_l(\mathbf{p}_n-\mathbf{p}_l)}{d_{nl}^3}+\frac{R_l^3}{2d_{nl}^3}\times\left\{\frac{3(\mathbf{p}_n-\mathbf{p}_l)}{d_{nl}^2}[\dot{\mathbf{p}}_l\cdot(\mathbf{p}_n-\mathbf{p}_l)]-\dot{\mathbf{p}}_l\right\}. \tag{27}$$

One can readily see that the left-hand side of Eq. (22) is simply the Rayleigh–Plesset equation. It is known that for large forcing amplitudes the Keller–Miksis equation[26] is a more suitable model than the Rayleigh–Plesset equation since the former, unlike the latter, allows for the fact that in strong fields the velocity of the bubble wall is no longer small compared with the speed of sound in the liquid. Therefore, in order to make Eq. (22) more adequate for large forcing amplitudes, it is worthwhile replacing its left-hand side with the Keller–Miksis equation, keeping the right-hand side intact. This results in

$$\left(1-\frac{\dot{R}_n}{c}\right)R_n\ddot{R}_n+\left(\frac{3}{2}-\frac{\dot{R}_n}{2c}\right)\dot{R}_n^2-\frac{P_n}{\rho}\left(1+\frac{\dot{R}_n}{c}\right)-\frac{R_n}{\rho c}\frac{dP_n}{dt}$$
$$=\frac{\dot{\mathbf{p}}_n^2}{4}-\sum_{\substack{l=1\\ l\neq n}}^{N}\left\{\frac{R_l^2\ddot{R}_l+2R_l\dot{R}_l^2}{d_{nl}}+\frac{R_l^2}{2d_{nl}^3}(\mathbf{p}_n-\mathbf{p}_l)\cdot(R_l\ddot{\mathbf{p}}_l+\dot{R}_l\dot{\mathbf{p}}_n+5\dot{R}_l\dot{\mathbf{p}}_l)-\frac{R_l^3}{4d_{nl}^3}\left[\dot{\mathbf{p}}_l\cdot(\dot{\mathbf{p}}_n+2\dot{\mathbf{p}}_l)+\frac{3}{d_{nl}^2}[\dot{\mathbf{p}}_l\cdot(\mathbf{p}_l-\mathbf{p}_n)][(\mathbf{p}_n-\mathbf{p}_l)\cdot(\dot{\mathbf{p}}_n+2\dot{\mathbf{p}}_l)]\right]\right\}, \tag{28}$$

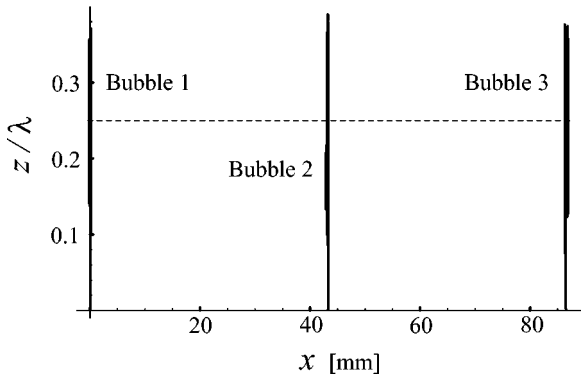

FIG. 2. Paths of three interacting bubbles in a high-intensity plane standing wave at large separation distances. The equilibrium bubble radii are $R_{10}=93\,\mu$m, $R_{20}=60\,\mu$m, and $R_{30}=80\,\mu$m. The sound wave, with $f=25$ kHz and $P_a=1.35$ bar, propagates along the z axis; the dashed line denotes the pressure node.

where c is the speed of sound in the liquid. Equation (23) can be left untouched since in most cases of interest the translational velocities of bubbles are small compared with their radial velocities. Explanation of why Eq. (28) cannot be derived directly using the Lagrangian formalism is given in Ref. 14.

III. NUMERICAL EXAMPLES

The purpose of this section is to demonstrate the potential of the obtained equations in modeling the collective bubble dynamics in strong ultrasound fields. As a basis for the present simulation, data from Refs. 11 and 14 were taken. The physical parameters were set to $P_0=1$ bar, $\rho=998$ kg/m^3, $\sigma=0.0725$ N/m, $\eta=0.001$ kg/(m s), $c=1500$ m/s, and $\gamma=1.4$. These values correspond to air bubbles in water. Calculations were made for three-bubble structures.

The first example, Figs. 2 and 3, is concerned with Ref. 14, where it is shown that in a high-intensity plane standing wave, a bubble driven below resonance can reciprocate about the pressure node plane instead of moving to the pressure antinode as it does in a weak wave. According to Fig. 2 of Ref. 14, this effect should occur for bubbles with radii 93 μm ($\omega/\omega_0=0.7$), 80 μm ($\omega/\omega_0=0.6$), and 60 μm ($\omega/\omega_0=0.45$), when they are driven at $f=25$ kHz and $P_a=1.35$ bar, where $f=\omega/2\pi$ and P_a are the frequency and the pressure amplitude of the imposed plane standing wave, and ω_0 denotes the linear resonance frequency of the respective bubble. Let us apply Eqs. (23)–(28) to the same three bubbles. Recall once again that this simulation allows for interactions between the bubbles, in contrast to Ref. 14 where each of the bubbles is considered separately. Figure 2 shows bubble paths for the case where the equilibrium radii of the bubbles and the initial coordinates of their centroids are set as follows: $R_{10}=93\,\mu$m$(0,0,0.001\lambda)$; $R_{20}=60\,\mu$m$(250(R_{10}+R_{30}),0,0.001\lambda)$; $R_{30}=80\,\mu$m$(500(R_{10}+R_{30}),0,0.001\lambda)$, λ denoting the wavelength of sound in the liquid. In other words, the bubbles are aligned in the direction of the x axis slightly off the pressure antinode plane. It is assumed that the plane standing wave, with $f=25$ kHz and $P_a=1.35$ bar, propagates along the z axis so that the position 0 of the z axis corresponds to the pressure antinode, 0.25 to

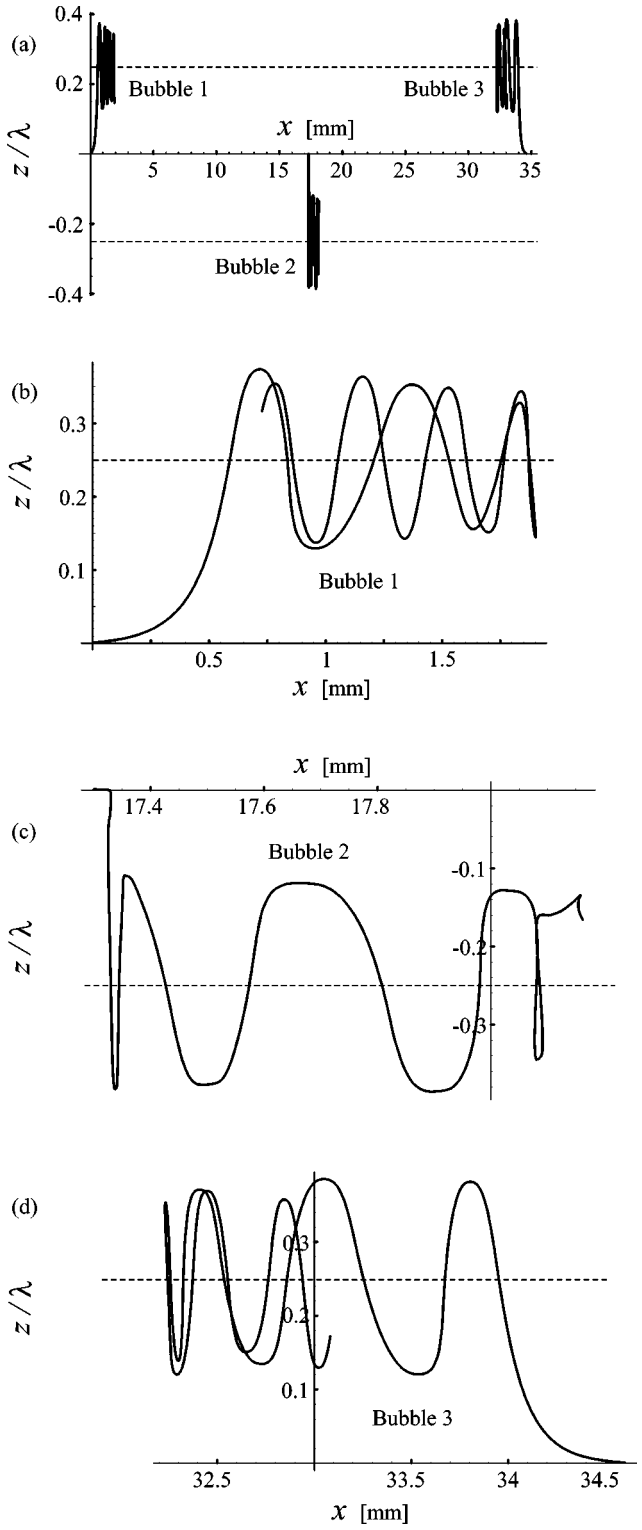

FIG. 3. Bubble paths for separation distances smaller than in Fig. 2 by a factor of 2.5, all other parameters being the same. (b)–(d) show the paths on an enlarged scale.

the pressure node, 0.5 to the next antinode, and so forth. The computation time is 500 acoustic cycles. Since the separations between the bubbles are very large, their interaction is weak and the behavior of the bubbles is practically identical to that described in Ref. 14, i.e., the bubbles move to the upper pressure node (dashed line) and reciprocate there (thick vertical lines). In Fig. 3, the separation distances are

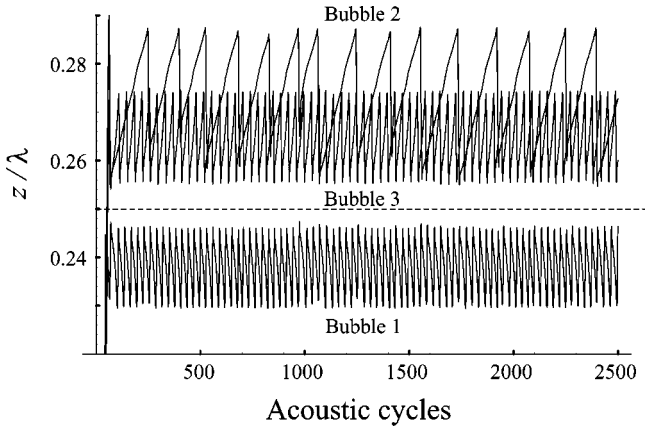

FIG. 4. Precession of three interacting microbubbles about the pressure node plane (dashed line) in an intense MHz standing wave: $R_{10}=2\ \mu$m, $R_{20}=1.6\ \mu$m, $R_{30}=1.9\ \mu$m, $f=1.5$ MHz, $P_a=0.98$ MPa.

smaller by a factor of 2.5, all other parameters being equal. Although the distances are still quite large, the bubbles are seen to feel one another strongly enough. As a result, bubble 2 turns to the lower pressure node, Fig. 3(a). It is also of interest to look at the path of each bubble separately, Figs. 3(b)–(d). One can see that the bubbles execute rather intricate motions which include attraction and repulsion due to the interaction of the bubbles. Figure 3 is evidence that strong fields, in contrast to weak fields, cause interactions between bubbles that cannot be ignored even though inter-bubble separations may be fairly large.

The example considered above is of academic rather than practical interest. Because, under the given conditions, for bubbles of rather big size in a strong field of relatively slow frequency, a fast growth of shape modes should be expected, which are neglected in the proposed model. Hence the model may be adequate for the initial stage of motion at most. From this point of view, it is of greater interest to apply Eqs. (23)–(28) to the experiments described in Ref. 11, where micron-sized bubbles and megahertz wave fields were dealt with. Under such conditions bubbles are able to keep the spherical shape even for very strong pressures. In Ref.

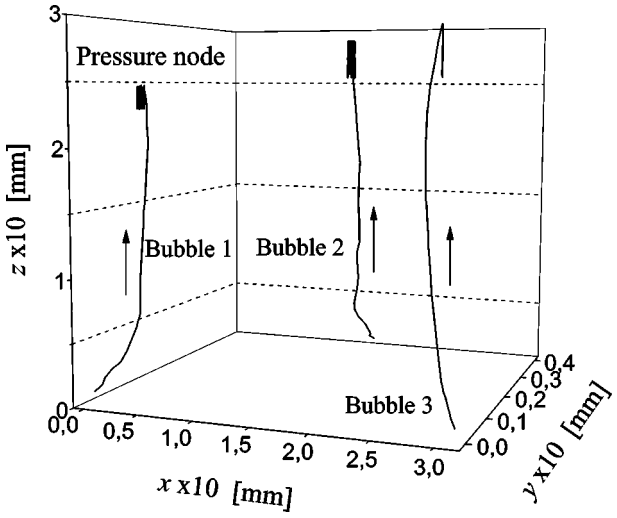

FIG. 5. Three-dimensional paths of the three microbubbles shown in Fig. 4.

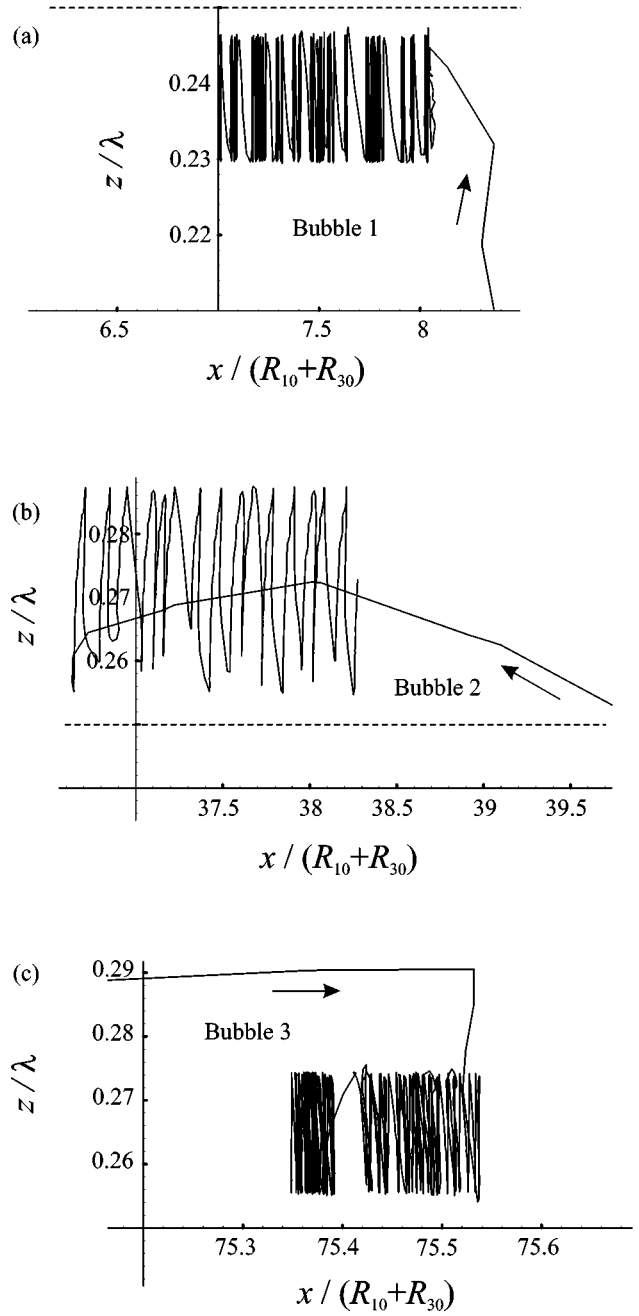

FIG. 6. Projections of the bubble paths shown in Fig. 5 on the xz plane.

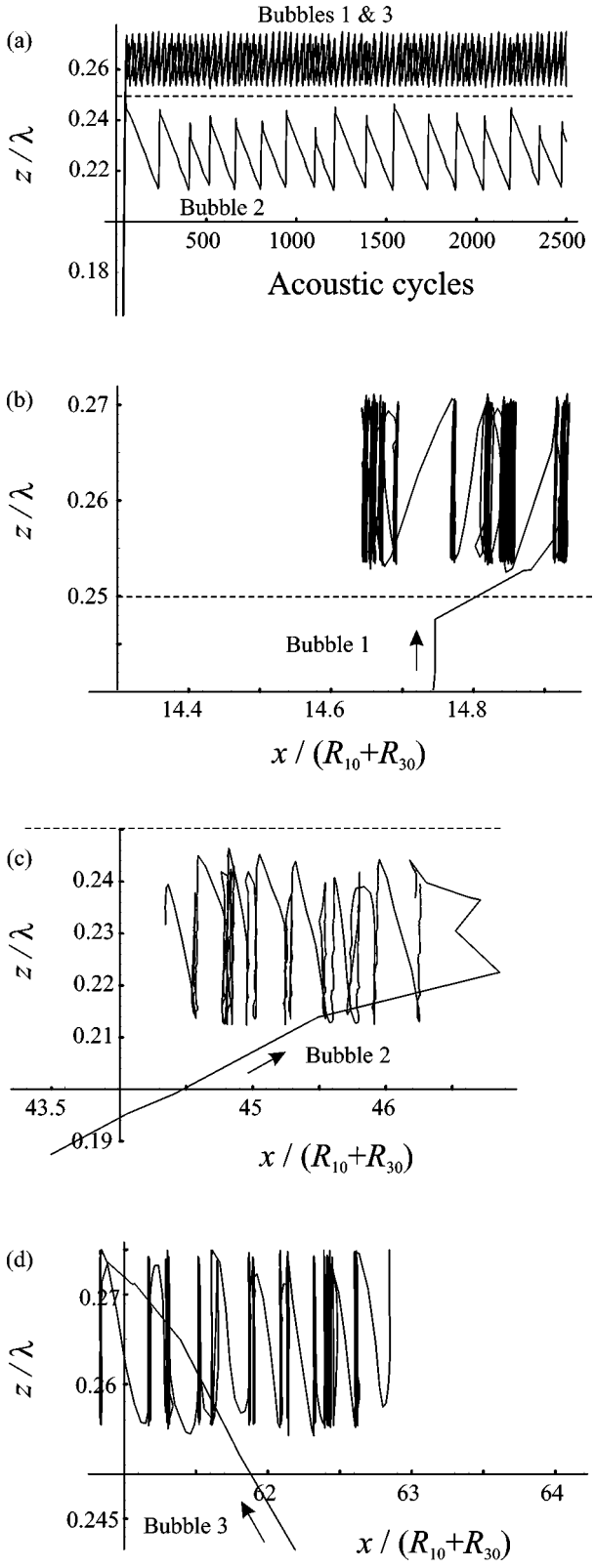

FIG. 7. The same bubble paths as in Figs. 4 and 6 but calculated using the reduced equations of motion, which include only the leading coupling terms: the $1/d_{nl}$ terms in Eq. (28) and the $1/d_{nl}^2$ terms in Eqs. (23) and (27).

11, suspensions of human blood cells and contrast agent (artificial encapsulated bubbles) were exposed to ultrasound in a standing wave chamber driven at its resonance frequency of 1.5 MHz and a pressure amplitude of 0.98 MPa. It was observed that the cells precessed about the pressure node plane. Since this phenomenon did not occur in the absence of contrast agent and since contrast agent bubbles were observed to disappear at the very outset of insonation, it was conjectured that the cell precession arose from their entrainment in the hydrodynamic drag of rapidly precessing free microbubbles that ensued from fragmentation of contrast agent. To check this hypothesis, let us apply Eqs. (23)–(28) to three bubbles with radii of 2, 1.6, and 1.9 μm, driven by a plane standing wave with $f=1.5$ MHz and $P_a=0.98$ MPa, which propagates along the z axis, as in Figs. 2 and 3. The initial coordinates of the bubble centers are set equal to $(0,0,0.01\lambda)$, $(40(R_{10}+R_{30}),10(R_{10}+R_{30}),0.01\lambda)$, and $(80(R_{10}+R_{30}),0,0.01\lambda)$. It is seen that the bubbles are now not arranged in a line and hence we deal with a true 3D case. Figure 4 depicts the calculated z coordinates of the bubble

centers versus time measured in acoustic cycles. It is seen that the simulation does predict that the bubbles should move to the pressure node plane and precess there. This result indicates that the proposed model correlates well with the observations made in Ref. 11 and is able to describe such phenomena. Figure 4 also allows us to disclose the fact that the bigger the bubble, the higher the precession frequency. The paths traversed by the bubbles during 2500 acoustic cycles are shown in Fig. 5 and their projections on the xz plane, for each bubble individually, in Fig. 6. The arrows next to the curves indicate the direction of bubble motion. One can see that, although the initial separations were set large enough, the bubbles actively interact so that their moving directions with respect to one another are repeatedly changed.

Figure 7 shows the same bubble paths as in Figs. 4 and 6 but calculated using the reduced equations of motion, which include only the leading coupling terms, namely, the $1/d_{nl}$ terms in Eq. (28) and the $1/d_{nl}^2$ terms in Eqs. (23) and (27). Similar calculations were also made for Figs. 2 and 3 but changes in these figures were found to be insignificant, as one would expect, since the separation distances are too large for the higher order coupling terms to show themselves. In Figs. 4 and 6, the separation distances are considerably smaller (besides the driving pressure is much higher) and therefore a noticeable disagreement is observed between these figures and Fig. 7. As can be seen in Fig. 4, bubble 1 is oscillating below the pressure node and bubble 2 above the pressure node, while in Fig. 7(a) the reverse takes place. There is also a significant discrepancy in the form of the bubble paths in Figs. 6 and 7(b)–(d). This comparison demonstrates that the higher order coupling terms may be important even for rather large separations.

IV. CONCLUSIONS

Applying Eqs. (23)–(28) to each bubble in a multibubble structure, which is composed of N bubbles with arbitrary spatial arrangement, we can simulate the collective dynamics of this structure in a strong acoustic field, allowing for the nonlinear coupling of the radial and translational motions of the bubbles as well as the interaction between all the bubbles in the structure up to terms of third order in the inverse separation distances. The potentialities of the obtained equations in modeling the bubble dynamics have been illustrated by numerical examples. It has been shown that the proposed model is able to describe the phenomenon of precession of microbubbles about the pressure node plane in an intense megahertz standing wave, which was recently detected in experiment. The weakness of the model is that it ignores shape modes of bubbles. It also needs a certain procedure that would allow for bubble coalescence.

ACKNOWLEDGMENT

This research was supported by the Ministry of Education of Belarus.

[1] T. G. Leighton, *The Acoustic Bubble* (Academic, London, 1994).
[2] I. Akhatov, U. Parlitz, and W. Lauterborn, ''Pattern formation in acoustic cavitation,'' J. Acoust. Soc. Am. **96**, 3627–3635 (1994).
[3] I. Akhatov, U. Parlitz, and W. Lauterborn, ''Towards a theory of self-organization phenomena in bubble-liquid mixtures,'' Phys. Rev. E **54**, 4990–5005 (1996).
[4] U. Parlitz, R. Mettin, S. Luther, I. Akhatov, M. Voss, and W. Lauterborn, ''Spatio-temporal dynamics of acoustic cavitation bubble clouds,'' Philos. Trans. R. Soc. London, Ser. A **357**, 313–334 (1999).
[5] R. Mettin, S. Luther, C.-D. Ohl, and W. Lauterborn, ''Acoustic cavitation structures and simulations by a particle model,'' Ultrason. Sonochem. **6**, 25–29 (1999).
[6] A. A. Doinikov, ''Translational motion of two interacting bubbles in a strong acoustic field,'' Phys. Rev. E **64**, 026301 (2001).
[7] N. A. Pelekasis, A. Gaki, A. Doinikov, and J. A. Tsamopoulos, ''Secondary Bjerknes forces between two bubbles and the phenomenon of acoustic streamers,'' J. Fluid Mech. **500**, 313–347 (2004).
[8] A. I. Eller and L. A. Crum, ''Instability of the motion of a pulsating bubble in a sound field,'' J. Acoust. Soc. Am. **47**, 762–767 (1970).
[9] Z. C. Feng and L. G. Leal, ''Nonlinear bubble dynamics,'' Annu. Rev. Fluid Mech. **29**, 201–243 (1997).
[10] A. A. Doinikov, ''Translational motion of a bubble undergoing shape oscillations,'' J. Fluid Mech. **501**, 1–24 (2004).
[11] S. Khanna, N. N. Amso, S. J. Paynter, and W. T. Coakley, ''Contrast agent bubble and erythrocyte behavior in a 1.5-MHz standing ultrasound wave,'' Ultrasound Med. Biol. **29**, 1463–1470 (2003).
[12] T. Watanabe and Y. Kukita, ''Translational and radial motions of a bubble in an acoustic standing wave field,'' Phys. Fluids A **5**, 2682–2688 (1993).
[13] I. Akhatov, R. Mettin, C. D. Ohl, U. Parlitz, and W. Lauterborn, ''Bjerknes force threshold for stable single bubble sonoluminescence,'' Phys. Rev. E **55**, 3747–3750 (1997).
[14] A. A. Doinikov, ''Translational motion of a spherical bubble in an acoustic standing wave of high intensity,'' Phys. Fluids **14**, 1420–1425 (2002).
[15] P. A. Dayton, J. S. Allen, and K. W. Ferrara, ''The magnitude of radiation force on ultrasound contrast agents,'' J. Acoust. Soc. Am. **112**, 2183–2192 (2002).
[16] A. J. Reddy and A. J. Szeri, ''Coupled dynamics of translation and collapse of acoustically driven microbubbles,'' J. Acoust. Soc. Am. **112**, 1346–1352 (2002).
[17] G. N. Kuznetsov and I. E. Shchekin, ''Interaction of pulsating bubbles in a viscous fluid,'' Sov. Phys. Acoust. **18**, 466–469 (1973).
[18] H. N. Oguz and A. Prosperetti, ''A generalization of the impulse and virial theorems with an application to bubble oscillations,'' J. Fluid Mech. **218**, 143–162 (1990).
[19] N. A. Pelekasis and J. A. Tsamopoulos, ''Bjerknes forces between two bubbles. Part 2. Response to an oscillatory pressure field,'' J. Fluid Mech. **254**, 501–527 (1993).
[20] R. Mettin, I. Akhatov, U. Parlitz, C. D. Ohl, and W. Lauterborn, ''Bjerknes forces between small cavitation bubbles in a strong acoustic field,'' Phys. Rev. E **56**, 2924–2931 (1997).
[21] A. Harkin, T. J. Kaper, and A. Nadim, ''Coupled pulsation and translation of two gas bubbles in a liquid,'' J. Fluid Mech. **445**, 377–411 (2001).
[22] R. Mettin, C.-D. Ohl, and W. Lauterborn, ''Particle approach to structure formation in acoustic cavitation,'' in *Proc. NATO ASI Sonochemistry and Sonoluminescence*, edited by L. A. Crum *et al.* (Kluwer Academic, Amsterdam, 1999), pp. 139–144.
[23] D. A. Varshalovich, A. N. Moskalev, and V. K. Khersonskii, *Quantum Theory of Angular Momentum* (in Russian) (Nauka, Moscow, 1975).
[24] M. Abramowitz and I. A. Stegun, *Handbook of Mathematical Functions* (Dover, New York, 1972).
[25] B. V. Levich, *Physicochemical Hydrodynamics* (Prentice-Hall, Englewood Cliffs, NJ, 1962).
[26] J. B. Keller and M. Miksis, ''Bubble oscillations of large amplitude,'' J. Acoust. Soc. Am. **68**, 628–633 (1980).

Wideband micromachined capacitive microphones with radio frequency detection

Sean T. Hansen,[a] A. Sanli Ergun, William Liou, Bertram A. Auld, and Butrus T. Khuri-Yakub
Edward L. Ginzton Laboratory, Stanford University, Stanford, California 94305-4088

(Received 19 December 2003; revised 2 April 2004; accepted 21 May 2004)

Silicon microphones based on capacitive micromachined ultrasonic transducer membranes and radio frequency detection overcome many of the limitations in bandwidth, uniformity of response, and durability associated with micromachined condenser microphones. These membranes are vacuum-sealed to withstand submersion in water and have a flat mechanical response from dc up to ultrasonic frequencies. However, a sensitive radio frequency detection scheme is necessary to detect the small changes in membrane displacement that result from utilizing small membranes. In this paper we develop a mathematical model for calculating the expected output signal and noise level and verifies the model with measurements on a fabricated microphone. Measurements on a sensor with 1.3 mm^2 area demonstrate less than 0.5 dB variation in the output response between 0.1 Hz to 100 kHz under electrostatic actuation and an A-weighted equivalent noise level of 63.6 dB(A) SPL in the audio band. Because the vacuum-sealed membrane structure has a low mechanical noise floor, there is the potential for improved sensitivity using higher carrier frequencies and more sophisticated detection circuitry.
[DOI: 10.1121/1.1771617]

PACS numbers: 43.38.Gy, 43.38.Kb [AJZ] Pages: 828–842

I. INTRODUCTION

The demand for inexpensive microphones, coupled with advancements in silicon micromachining technology, has led to the development of many miniature acoustic pressure sensors.[1] The development of miniature microphones primarily has focused on hearing aid applications, and therefore concentrates on acoustic detection only in a limited audio range.[2] However, some scientific, industrial, and military applications require acoustic data collection over a broader bandwidth for proper signal identification. Frequencies above 25 kHz contain useful information for condition-monitoring applications, particularly for machining and welding processes.[3] Acoustic sensing below the audio range is useful for target tracking and monitoring of heavy equipment and engines,[4,5] as well as for studying infrasonic geophysical phenomena.[6,7] In addition, unattended operation in harsh outdoor environments requires sensors that are impervious to dust and moisture. While certain measurement microphones have the necessary bandwidth and durability for such applications, the high cost of precision instruments can be a barrier to their widespread use. A micromachined silicon sensor is therefore desirable, as micromachining and lithography techniques offer the prospect of inexpensive, mass-produced acoustic sensors and sensor arrays.

A durable, wideband micromachined microphone is possible using ultrasonic membranes that are vacuum-sealed. To maintain sensitivity, a radio frequency (rf) detection technique senses the changes in membrane capacitance in order to recover the acoustic signal. Applying rf techniques to measure changes in microphone capacitance is not new. Zuckerwar[8] and Hibbings[9] describe several rf techniques that have been applied to microphones. Most of these systems incorporate a condenser cartridge in a resonator and measure the resulting amplitude, frequency, or phase modulation of an oscillator signal. Ergun *et al.*[10,11] recently proposed an acoustic sensor using an alternative rf technique, in which capacitance variations were detected through the phase modulation of a rf carrier signal along a capacitively loaded transmission line. This technique, henceforth referred to as rf detection, elegantly applies to a capacitive transducer consisting of multiple small cells. Following a general description of the microphone's mechanical structure and the rf detection technique, we develop a mathematical model for simulating its performance using rf detection. A comparison of the predictions and experimental measurements is followed by a discussion of the model and the potential capabilities of the microphone. To highlight the differences between this sensor and other common microphone approaches, we begin with an overview of micromachined condenser microphones.

II. MICROMACHINED CONDENSER MICROPHONES

A. Conventional microphone membranes

Many micromachined condenser microphones use a similar membrane structure to that of large measurement microphones and studio recording microphones. One common structure for omnidirectional pressure microphones, shown in Fig. 1, consists of a conductive membrane suspended over a conductive backplate that is perforated with holes for acoustic damping. Sound detection is possible when the impinging pressure wave vibrates the membrane, thus changing the capacitance of the transducer. Under normal operation,

[a]Electronic mail: sthansen@piezo.stanford.edu

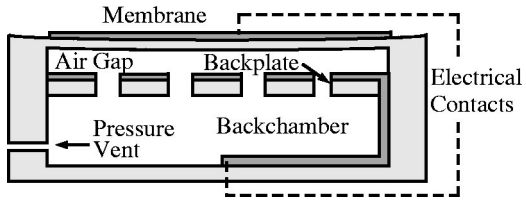

FIG. 1. Cross-sectional structure of a condenser microphone.

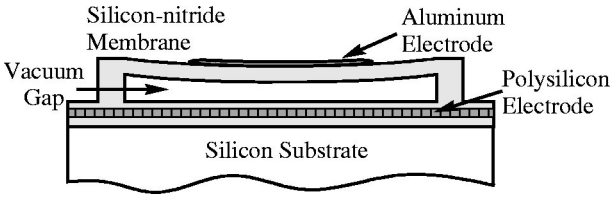

FIG. 3. Cross-sectional structure of a single CMUT membrane.

the electrodes of the capacitor are charged using an external voltage bias through a large resistor. The changes in capacitance of the membrane are translated into changes in voltage, which can be sensed using a high-impedance preamplifier. A pressure equalization vent in the backchamber prevents fluctuations in atmospheric pressure from collapsing the membrane against the backplate.

A precision condenser microphone for measurement or calibration applications is capable of a uniform frequency response due to its relatively large air gap, on the order of 20 μm, behind the membrane.[2] Silicon micromachined microphones, with membrane dimensions of 1–2 mm, require air gaps on the order of a few microns to maintain adequate sensitivity due to the reduced motion that results from a smaller membrane. However, the reduced dimensions of the air gap magnify the effects of squeeze-film damping, introducing frequency-dependent stiffness and loss.[1] This creates undesirable variations in the mechanical response with acoustic frequency. Furthermore, achieving a large dynamic range and a high sensitivity can be conflicting goals, since large sound pressures may cause the membrane to collapse under its voltage bias.[12]

Beranek[13] derives a small-signal acoustic equivalent circuit model for condenser microphones that can be applied to micromachined microphones of a similar structure. This model, shown in Fig. 2, includes additional elements to model the effects of the pressure equalization vent, discussed by Scheeper.[14] Due to the difficulty of fabricating a vent with high acoustic impedance using silicon micromachining technology, low-frequency acoustic signals at the membrane are partially equalized. This reduces the net pressure differential between the two sides of the membrane and results in a low-frequency mechanical roll-off in the membrane response.[8] The vent not only influences the directionality of the microphone, but also prevents many micromachined microphones from sensing below 100 Hz, an important range for military acoustic applications. Finally, miniature condenser microphones can be susceptible to condensation in the narrow air gaps when exposed to humid environments or sudden temperature changes.[2] Moisture in the air gap can hinder membrane movement and may require regular cleaning to remove.

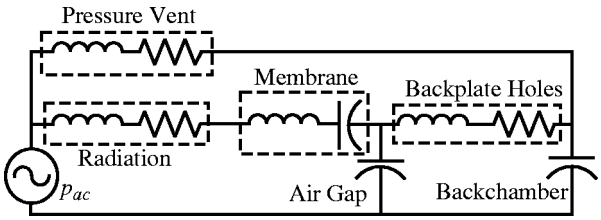

FIG. 2. Acoustic small-signal equivalent circuit representation of the microphone structure in Fig. 1. The harmonic pressure amplitude p_{ac} is that at the membrane surface when it is restrained from moving.

B. The sealed CMUT membrane

An alternative membrane structure that overcomes many of the drawbacks of conventional capacitive micromachined microphone designs incorporates many smaller vacuum-sealed membranes. Capacitive micromachined ultrasonic transducers (CMUTs), which have been developed for the generation and reception of ultrasound in air and water,[15,16] can be used in microphones. The structure of a single CMUT membrane, shown in Fig. 3, consists of a metallized circular or rectangular silicon nitride membrane suspended over a silicon substrate. A typical membrane thickness is less than 1 μm, while lateral dimensions range from tens of microns to 100 μm. Because the individual membranes are small, tens or hundreds of them are electrically connected to form a transducer for the generation or reception of acoustic waves.

A CMUT membrane is smaller and stiffer than a conventional condenser microphone membrane, which permits vacuum sealing of the volume behind the membrane. The vacuum-sealed membrane structure has many important implications for microphone performance. First, the absence of air and a perforated backplate in the CMUT structure simplifies its equivalent circuit model, which is shown in Fig. 4. This model can be derived from that of the condenser microphone by noting that the stiffness of the air behind the membrane is zero in vacuum, thereby shorting the capacitors that represent the air gap and backchamber in the equivalent circuit of Fig. 2. In addition, the resistors that model the air flow through the backplate holes and pressure vent become open circuits, as there is no pathway for the flow of air behind the membrane. Therefore, squeeze-film damping, which is usually the dominant source of noise in condenser microphones over most of the audio range,[17] is eliminated. The absence of frequency-dependent circuit elements of the backchamber and pressure equalization vents in the circuit model suggests that the uniformity of the frequency response is also improved. Unlike standard unsealed microphones, the sealed CMUT structure does not have a low-frequency acoustic

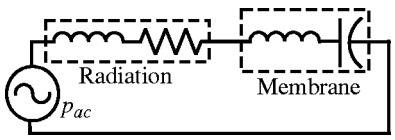

FIG. 4. Acoustic small-signal equivalent circuit representation of one or more CMUT membranes.

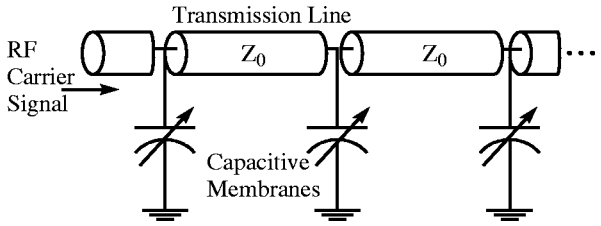

FIG. 5. In rf detection, the capacitive membranes periodically load a transmission line. A rf carrier signal experiences a phase shift with the changing capacitance.

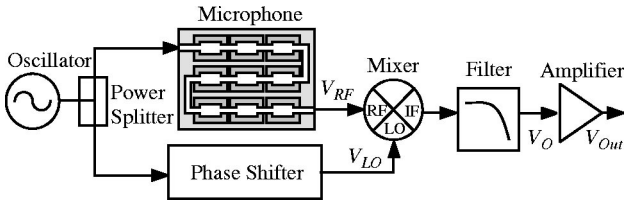

FIG. 6. Block diagram showing the microphone as part of a phase detection circuit that recovers the acoustic signal incident on the microphone.

roll-off and responds to excitations at arbitrarily low frequencies, including atmospheric pressure fluctuations.

Because small CMUT membranes resonate at frequencies greater than several hundred kilohertz, the spring compliance of the membrane, represented by a capacitor in the equivalent circuit, dominates its response for the frequencies of interest. Therefore, the displacement response of the membrane is flat below its resonant frequency. Finally, the durability of the microphone is improved because the hermetic structure prevents condensation and particle contamination from getting inside the narrow capacitor gaps and hindering membrane motion. Experimental measurements in air confirm that such microphones are not affected by prior submersion in water. In fact, we confirm that the sensor can operate as a hydrophone in a liquid medium.

Condenser microphone systems measure capacitance changes, which are approximately a linear function of the membrane displacement due to acoustic pressure. For a circular membrane, the low-frequency displacement response is roughly proportional to its area.[8] Therefore, the use of N small CMUT membranes, rather than a single membrane of the same total area, reduces the displacement and the expected change in capacitance by a factor of N. This illustrates the primary tradeoff for the uniform, durable response provided by small CMUT membranes. Fortunately, the expected mechanical noise level of the sealed CMUT structure is extremely low, which suggests that a sensitive microphone remains possible. A rf detection technique compensates for the small displacement response of the membranes with a sensitive method for detecting slight capacitance changes.

III. RADIO FREQUENCY DETECTION WITH CAPACITIVE MEMBRANES

A. Description

In rf detection, tens or hundreds of capacitive membranes are periodically spaced along a rf transmission line, creating a capacitively loaded transmission line, as shown in Fig. 5. This structure acts as a filter for millimeter-wave microwave signals, but still behaves as a transmission line for rf signals within its passband.[18] As the capacitive membranes in the line vibrate due to sound pressure, the transmission line's propagation constant, or equivalently, the phase velocity of the rf signal, also changes. Thus, a rf carrier signal that is launched down the loaded transmission line is phase modulated by the acoustic signal that impinges on the capacitive membranes. Subsequent demodulation using a phase detection circuit recovers the acoustic signal.

B. Circuitry

The phase modulation of the rf carrier can be sensed when the microphone is included as part of a phase detection circuit, such as the one shown in Fig. 6, commonly used to detect phase variations in electrical devices.[19] The circuit first splits the rf signal from an oscillator into two branches. One branch passes through the microphone, which phase modulates the rf signal by the acoustic signal on the CMUT membranes. Mathematically, this signal takes the form

$$V_{\mathrm{rf}} = V_1 \cos(2\pi f_c t + \Phi(t)), \tag{1}$$

where V_1 and f_c are the amplitude and frequency of the rf carrier, respectively, and $\Phi(t)$ represents some time-varying phase modulation due to an acoustic signal. The second branch transfers a reference signal to the local oscillator (LO) port of the mixer,

$$V_{\mathrm{LO}} = V_2 \cos(2\pi f_c t + \phi), \tag{2}$$

where V_2 is the amplitude of the voltage signal and ϕ represents some fixed phase relative to the signal V_{rf}. Ideally, the mixer performs multiplication of the signals at its input ports, resulting in output components at the sum and difference of the input frequencies:

$$V_{\mathrm{rf}} \times V_{\mathrm{LO}} = K_d[\cos(\Phi(t) - \phi) + \underbrace{\cos(4\pi f_c t + \Phi(t) + \phi)}_{\text{removed by low-pass filter}}]. \tag{3}$$

These signals have a new voltage amplitude K_d due to losses during mixing. A low-pass filter at the mixer output removes the component of the signal at twice the carrier frequency, $2f_c$, as well as any additional higher-order harmonics that may be generated. The demodulated (or baseband) signal,

$$V_O = K_d \cos(\Phi(t) - \phi), \tag{4}$$

consists of a phase varying term $\Phi(t)$ and a fixed phase reference ϕ. If ϕ is adjusted to $\pi/2$ rad so that the two signals at the mixer inputs are in quadrature, the demodulated signal V_O is proportional to the small phase variations of $\Phi(t)$:

$$V_O = K_d \sin(\Phi(t)) \approx K_d \Phi(t). \tag{5}$$

Because $\Phi(t)$ is proportional to the change in capacitance, recovering $\Phi(t)$ recovers the acoustic pressure signal on the membranes. The scaling term K_d, with units of V/rad, acts as a phase detection constant for the mixer that converts radian phase shifts of the rf carrier into a baseband voltage signal. Additional amplification increases the signal to the desired level.

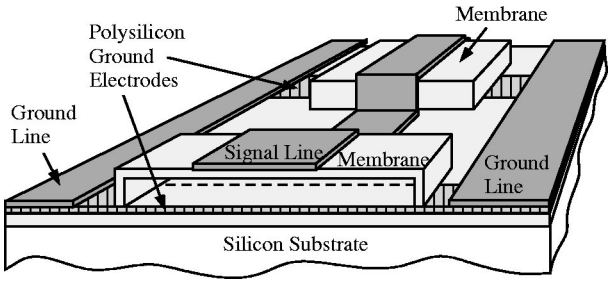

FIG. 7. The signal line of a coplanar waveguide transmission line traverses the rectangular CMUT membranes. Doped polysilicon electrodes extend underneath a portion of the membrane and connect to the ground conductors of the transmission line.

Although more complicated than the constant voltage detection systems usually applied to condenser microphones, the rf detection system has some distinct advantages. First, the parasitic capacitance between membrane cells due to interconnects is incorporated into the rf transmission line structure. This is particularly relevant for a microphone composed of many small capacitors such as CMUTs, because parasitic capacitance degrades the sensitivity of the microphone in constant voltage detection.[8] A dc voltage bias is not required for operation, although a voltage can be applied to the membranes to adjust their deflection with changes in atmospheric pressure and to alter the microphone's sensitivity or calibration. In addition, the output impedance of the mixer in rf detection is low, typically around 50 Ω, so an amplifier with a high-impedance input is unnecessary. Because the output is independent of acoustic frequency variations in $\Phi(t)$, the low-frequency response of the CMUT structure is preserved for a broadband microphone. As a consequence, the circuit in Fig. 6 responds to shifts in atmospheric pressure or slow drifts in the electrical components. Therefore, a practical implementation uses feedback, applied through a voltage-controlled phase shifter or a variable voltage bias on the membranes, to nullify such offsets over the long term. Thus, the minimum detectable acoustic frequency of the system becomes selectable through the time constant of the feedback signal.

C. Sensor fabrication

The transmission line structure of Fig. 5 is implemented using a coplanar waveguide transmission line over CMUT membranes. Similar capacitively loaded structures with a coplanar waveguide have been fabricated for microwave phase shifters using voltage-actuated metal bridges[20] instead of enclosed membranes. The final structure of the microphone for rf detection, shown in Fig. 7, consists of a series of surface-micromachined membranes covered by a coplanar waveguide transmission line, which consists of three conductors: a center signal line that traverses the membranes and one ground line on either side of a row of membranes. The lower electrode of each capacitive membrane is formed by a locally doped polysilicon layer that extends underneath the center portion of the membrane to the ground lines. Polysilicon is used for this conductor instead of metal because the high deposition temperature of silicon nitride for the membrane exceeds the melting temperatures of common metals.

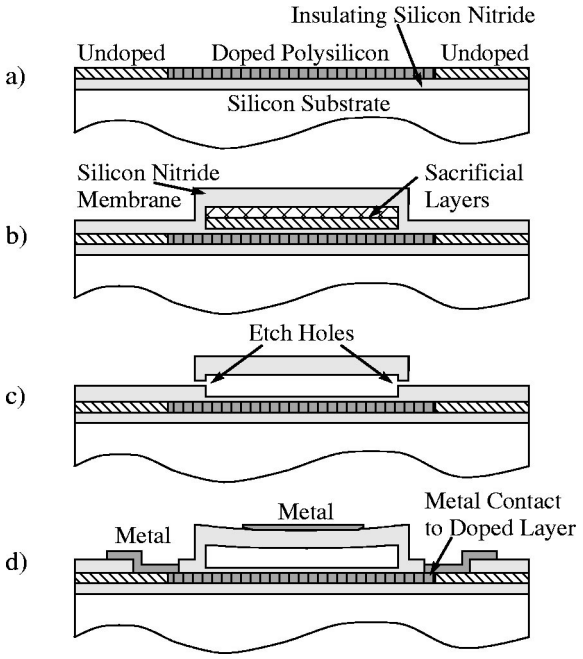

FIG. 8. Cross-sections showing selected fabrication steps of CMUT membranes for use in rf detection. The relevant dimensions of the fabricated microphone are presented in subsequent sections.

The absence of the perforated backplate and capillary tube for pressure equalization, which are usually found in other micromachined condenser structures, simplifies the fabrication of the membranes. The processing steps for the sealed CMUT membrane are similar to those described by Jin,[21] with a few differences for rf detection. We start with an insulating, high-resistivity (2000 Ω cm) silicon substrate, which is suitable for low-loss coplanar transmission lines at several gigahertz.[22] The silicon substrate is coated with insulating films of silicon nitride and polysilicon, both deposited using low-pressure chemical vapor deposition (LPCVD). Sections of the polysilicon layer under the membranes are doped in a high-temperature furnace with phosphorous oxychloride using silicon dioxide to mask areas of the polysilicon that should act as electrical insulators. Figure 8(a) shows the structure after removing the silicon dioxide mask in hydrofluoric acid. Following a thin silicon nitride deposition, which serves as an etch stop, the membrane structure is formed by depositing silicon nitride over patterned sacrificial layers of polysilicon and low-temperature silicon dioxide, as shown in Fig. 8(b). Small via holes are plasma etched at the side of the silicon nitride membrane, which permit the subsequent wet etch of the sacrifical layers to release the membrane. The etch is accomplished with a solution of potassium hydroxide followed by hydrofluoric acid, producing the membrane structure of Fig. 8(c). A second deposition of silicon nitride seals the etch holes, and because the deposition occurs in a vacuum furnace, the membrane structure is vacuum-sealed. The sealed silicon nitride membrane is etched to its final thickness to obtain the desired stiffness and deflection under atmospheric pressure. A plasma-etch opens contacts to the doped polysilicon electrode that extends underneath the membrane. Finally, Fig. 8(d) shows the complete structure after patterning the metal transmission lines of sputtered alu-

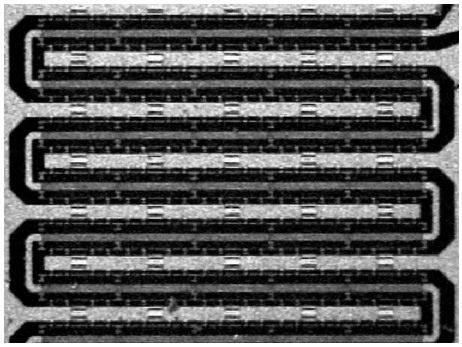

FIG. 9. Microscope photograph showing a portion of the fabricated 1.3 mm^2 microphone, formed by snaking a transmission line over an array of 45 rectangular CMUT membranes, each 70 μm by 190 μm in size.

minum. The fabricated microphone die is mounted and wire bonded to a printed circuit board that has connectors to interface with the detection electronics. An optional coating of parylene can provide electrical insulation between the transmission line conductors if the microphone is operated in water.

IV. A MATHEMATICAL MODEL

The development of a mathematical model of a microphone using CMUTs and rf detection is essential to explore the potential capabilities and design tradeoffs of the sensor. Microphone sensitivity, one of the most important specifications for a microphone, is traditionally described in terms of the output voltage for an incident pressure. While this figure is useful for describing a condenser cartridge with or without a preamplifier, it is not straightforward to apply this measure to rf detection since the microphone and detection circuitry are interdependent. Furthermore, the use of voltage per pressure to describe the sensitivity of a rf detection system is misleading since subsequent amplification increases the output voltage without any apparent tradeoffs. A measure of sensitivity also should provide information about the minimum detectable sound pressure of the microphone, and, therefore, should incorporate both electrical and mechanical noise sources. Thus, the output signal-to-noise ratio (SNR) is a convenient measure of microphone sensitivity, and it is not limited to any particular frequency range. This ratio compares the rms signal voltage and rms noise voltage at the system output for a given frequency, noise bandwidth, and incident pressure.

The following sections develop a model to calculate the signal and noise levels necessary to predict microphone sensitivity. Sample calculations using the parameters for the fabricated microphone, shown in Fig. 9, are compared to experimental results in Sec. V. In both the simulation and the experimental measurements, the phase detection circuit of Fig. 6 consists of the following components: a free-running dielectric resonator oscillator (EMF Systems model 52747-512086) with 20 dBm of output power at 2.8 GHz, a reactive power splitter (Minicircuits model ZAPDQ-4), a mechanical phase shifter (ARRA model L9428A), a double-balanced mixer (Marki Microwave model M1-0204NA), a low-pass filter (Minicircuits model SLP-1.9), and a baseband amplifier using an operational amplifier (Analog Devices model AD797). Values for the relevant parameters associated with the fabricated microphone and its phase detection circuit are presented as needed in the model development. For parameters that are measured directly from the fabricated microphone, the number of significant digits indicates the estimated precision of the measurement.

A. Membrane response

The first step in modeling the output signal of the microphone in a phase detection circuit involves the calculation of the membrane movement in response to the pressure at its surface. As the acoustic equivalent circuit for the vacuum-sealed CMUT does not contain any acoustic elements behind the membrane that influences its motion, the analysis is simpler than for unsealed microphones. However, the microphone's size and packaging can influence its response at high frequencies, where the wavelength of sound in air approaches the size of the microphone.[23] To separate the effects of packaging from the analysis, the starting point for analyzing membrane motion is the pressure at the membrane surface. For frequencies at which the sensor and its packaging are much smaller than the wavelength of sound in fluid, diffraction effects are negligible and the pressure signal at the diaphragm surface is approximately the same as would exist in free-field conditions.[23]

Both the membrane deflection under static (dc) pressure and the movement of the membrane under harmonic (ac) pressures are considered. Although a CMUT membrane is a compound structure consisting of partially metalized silicon nitride, measurements of membrane deflection under atmospheric pressure before and after metallization usually differ by less than 2%. Therefore, the silicon nitride membrane dominates the stiffness of the structure, and the effects of the metal are neglected in the model.

Mason[24] derives a general equation of motion for a uniform stretched diaphragm, shown with slight modifications to the notation:

$$D\nabla^4 u - l_m \sigma \nabla^2 u - p + l_m \rho \frac{\partial^2 u}{\partial t^2} = 0. \tag{6}$$

Here, u is the vertical or transverse displacement, l_m is the membrane thickness, p is either the static or acoustic pressure, σ is the residual stress, and ρ is the density of the membrane material. Although we continue to use the common term *membrane* throughout the following analysis, the precise structure modeled by Eq. (6) is a *stretched diaphragm* since both the bending stiffness of a finite-thickness plate and the residual tensile stress of the material are included. The flexural rigidity D in Eq. (6) is given by

$$D = \frac{E l_m^3}{12(1-\upsilon^2)}, \tag{7}$$

where E is the Young's modulus, and υ is the Poisson's ratio of the material.[24]

A rectangular membrane geometry is used in the fabricated microphone because its peak displacement is greater than that of the inscribed circular membrane of the same

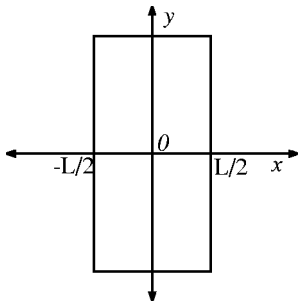

FIG. 10. Coordinate system and top view of the membrane orientation for a mathematical analysis.

thickness. For rectangular membranes, it is convenient to analyze the equation in Cartesian spatial coordinates (x,y), so the ∇^2 and ∇^4 operators are

$$\nabla^2=\left(\frac{\partial^2}{\partial x^2}+\frac{\partial^2}{\partial y^2}\right)$$

and

$$\nabla^4=\left(\frac{\partial^2}{\partial x^2}+\frac{\partial^2}{\partial y^2}\right)\left(\frac{\partial^2}{\partial x^2}+\frac{\partial^2}{\partial y^2}\right).$$

Following the approach of Badi *et al.*,[25] the complexity of the partial differential equation is reduced considerably by treating the rectangular membrane as very long in one dimension and taking the other dimension to be length L. Treating the displacement u only as a function of time and the x coordinate in Fig. 10, Eq. (6) becomes

$$Du''''(x,t)-l_m\sigma u''(x,t)-p+l_m\rho\ddot{u}(x,t)=0, \tag{8}$$

where $u'(x,t)$ denotes a spatial derivative, and $\dot{u}(x,t)$ denotes a time derivative of $u(x,t)$.

For the case of dc deflection under atmospheric pressure p_{dc}, the time variations in u are negligible, reducing Eq. (8) to a fourth-order ordinary differential equation for $u(x)$:

$$Du''''(x)-l_m\sigma u''(x)=p_{\mathrm{dc}}. \tag{9}$$

The general solution of the equation for the static displacement $u_{\mathrm{dc}}(x)$ is

$$u_{\mathrm{dc}}(x)=c_1+c_2x+c_3e^{\sqrt{l_m\sigma/D}x}+c_4e^{-\sqrt{l_m\sigma/D}x}-\frac{p_{\mathrm{dc}}}{2l_m\sigma}x^2. \tag{10}$$

The four unknown constants are found by applying the boundary conditions for a clamped plate, specifically that $u_{\mathrm{dc}}(x)$ and $u'_{\mathrm{dc}}(x)$ are zero at the edges of the diaphragm, where $x=\pm L/2$. Due to the symmetry of the coordinate system of Fig. 10, c_3 and c_4 are identical and c_2 is zero in Eq. (10). Redefining the constants and applying the boundary conditions yields the solution for the static deflection under pressure p_{dc}:

$$u_{\mathrm{dc}}(x)=\frac{p_{\mathrm{dc}}}{2l_m\sigma}\left[c'_1-x^2+c'_{3,4}\cosh\left(\sqrt{\frac{l_m\sigma}{D}}x\right)\right], \tag{11}$$

where

TABLE I. Dimensions and parameters of the CMUT membranes in the fabricated microphone.

Parameter	Symbol	Value
Length	L	70 μm
Width	W	190 μm
Thickness[a]	l_m	0.40 μm
Residual stress[a]	σ	1.1×10^8 Pa
Young's modulus[b]	E	3.2×10^{11} Pa
Density[b]	ρ	3270 kg/m^3
Poisson's ratio[b]	v	0.26
Atmospheric (dc) pressure	p_{dc}	1.01×10^5 Pa
Pressure (ac) amplitude	p_{ac}	1.41 Pa (=1 Pa rms)

[a]Measured from the fabricated microphone.
[b]Taken from Appendix B of Kino (Ref. 41) for silicon nitride.

$$c'_1=\frac{L^2}{4}-L\sqrt{\frac{D}{l_m\sigma}}\coth\left(\frac{L}{2}\sqrt{\frac{l_m\sigma}{D}}\right)$$

and

$$c'_{3,4}=L\sqrt{\frac{D}{l_m\sigma}}\operatorname{csch}\left(\frac{L}{2}\sqrt{\frac{l_m\sigma}{D}}\right).$$

This result is used later to calculate the static capacitance of the vacuum-sealed capacitive membranes under atmospheric pressure. Using the parameters from the fabricated microphone membranes, shown in Table I, Eq. (11) predicts 0.895 μm deflection at the membrane center $(x=0)$ under standard atmospheric pressure.

The response of the membrane to time-varying pressure is similarly calculated from Eq. (8). For a time-harmonic pressure amplitude of p_{ac} at angular acoustic frequency ω_a, the second-order time derivative scales u by $-\omega_a^2$. Thus, at a fixed excitation frequency, Eq. (8) reduces to an ordinary differential equation in a single variable:

$$Du''''(x)-l_m\sigma u''(x)-l_m\rho\omega_a^2u(x)=p_{\mathrm{ac}}. \tag{12}$$

The solution for harmonic excitation is obtained by finding a general solution and then applying the same clamped boundary conditions as in the static case to solve for the unknown constants. Following this procedure, the solution for amplitude of the ac displacement $u_{\mathrm{ac}}(x)$ is

$$u_{\mathrm{ac}}(x)=\frac{p_{\mathrm{ac}}}{\rho l_m\omega_a^2}[c_{1,2}\cosh(k_1x)+c_3\cos(k_3x)-1], \tag{13}$$

where

$$k_1=\sqrt{\frac{l_m\sigma+\sqrt{l_m^2\sigma^2+4Dl_m\rho\omega_a^2}}{2D}},$$

$$k_3=\sqrt{\frac{-l_m\sigma+\sqrt{l_m^2\sigma^2+4Dl_m\rho\omega_a^2}}{2D}},$$

$$c_{1,2}=\frac{k_3\sin(k_3L/2)}{k_1\sinh(k_1L/2)\cos(k_3L/2)+k_3\cosh(k_1L/2)\sin(k_3L/2)},$$

and

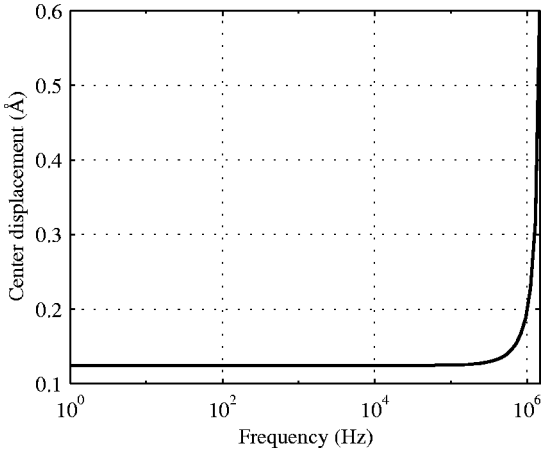

FIG. 11. The simulated displacement amplitude u_{ac} at the membrane center using Eq. (13) and the values given in Table I.

$$c_3 = \frac{k_1 \sinh(k_1 L/2)}{k_1 \sinh(k_1 L/2)\cos(k_3 L/2) + k_3 \cosh(k_1 L/2)\sin(k_3 L/2)}.$$

The ac motion at the center of a membrane with the dimensions and parameters of Table I is simulated in Fig. 11. As suggested earlier, the predicted displacement amplitude of 0.124 Å for 1.41 Pa amplitude ac pressure (or equivalently, 1 Pa rms) is extremely small, due to the miniature lateral dimensions of the membrane. Below 1 MHz, the membrane response does not vary appreciably from its low-frequency value. Because the membrane resonance is significantly greater than the usable frequency range of the microphone, the solution for the static deflection can be used to calculate the low-frequency harmonic excitation in most cases. Indeed, the static and dynamic solutions shown in Eq. (11) and Eq. (13) converge below the membrane resonant frequency for the same pressure input. Because the equations and solutions presented here for membrane displacement are linear with applied pressure, the previous analysis implicitly assumes that the dc deflection of the membrane under atmospheric pressure does not influence the ac response of the membrane to acoustic pressure signals. This assumption is a potential source of error in the model, as large deformations of the membrane likely stiffen the structure, reducing its ac response.

B. Capacitance calculations

Once the membrane response is characterized, it is straightforward to calculate the capacitances that load the transmission line in rf detection. The capacitance C_m between the top metal electrode and the ground electrode beneath the membrane, neglecting fringing fields near the conductor edges, is calculated by integrating the parallel-plate capacitance formula with two dielectrics over the area of overlap of the electrodes:

$$C_m = \int\int_{Area} \frac{\epsilon_m \epsilon_0}{l_m + l_i + \epsilon_m l_g(x,y)}\, dx\, dy. \tag{14}$$

Here, l_g is the effective vacuum gap between the membrane and substrate with free-space permittivity ϵ_0, and l_m is the thickness of the membrane material with relative permittivity ϵ_m. The small insulation thickness l_i of silicon nitride, shown in Fig. 12 over the ground electrode, adds directly to the membrane dielectric thickness in the capacitance formula. The vacuum gap l_g is shown as a function of position to indicate that the size of the gap changes with coordinate position because of the membrane's deflection under atmospheric pressure. Since the expression for u_{dc} is a function of x position only, the integration over area can be simplified to a single integral by neglecting the y-coordinate variations. Based on the geometries shown in Figs. 12 and 13, the capacitance of a membrane with metal electrode width w_m and ground electrode width w_g is

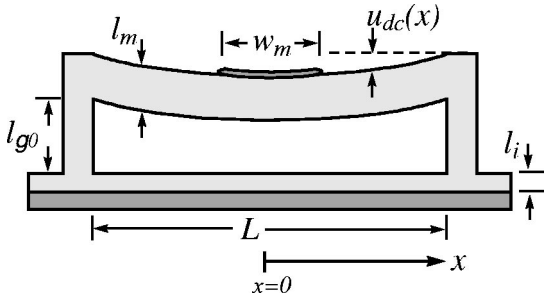

FIG. 12. Labeled schematic cross-section of a membrane, taken along the x coordinate axis of Fig. 10.

$$C_m = \int_{-w_m/2}^{w_m/2} \frac{w_g \epsilon_m \epsilon_0}{l_m + l_i + \epsilon_m (l_{g0} - u_{dc}(x))}\, dx, \tag{15}$$

where the gap l_g is replaced by the difference between the initial zero-deflection gap l_{g0} and the membrane static deflection $u_{dc}(x)$. Following the calculation of $u_{dc}(x)$ using Eq. (11), the integral of Eq. (15) can be evaluated numerically to calculate the static membrane capacitance.

The capacitance due to an incremental acoustic pressure is found by superimposing the membrane's ac displacement $u_{ac}(x)$ onto its static deflection in the capacitance formula:

$$C_{dc+ac} = \int_{-w_m/2}^{w_m/2} \frac{w_g \epsilon_m \epsilon_0}{l_m + l_i + \epsilon_m (l_{g0} - u_{dc}(x) - u_{ac}(x))}\, dx. \tag{16}$$

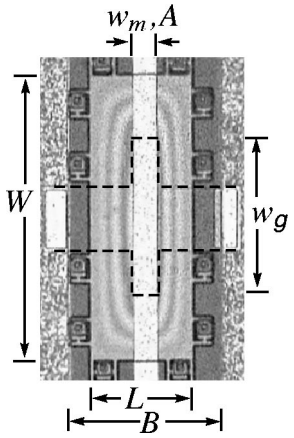

FIG. 13. Labeled photograph (top view) of a single membrane from the fabricated microphone. The dashed lines indicate the shape and extent of the polysilicon ground electrode under the membrane.

TABLE II. Additional parameters and dimensions of the fabricated CMUT membrane for capacitance calculations.

Parameter	Symbol	Value
Metal electrode width	w_m	20 μm
Ground electrode width	w_g	100 μm
Initial vacuum gap[a]	l_{g0}	1.00 μm
Insulation thickness[a]	l_i	0.10 μm
Membrane relative permittivity[a]	ϵ_m	5.7
Free-space permittivity	ϵ_0	8.854×10^{-12} F/m

[a]Measured from the fabricated microphone.

Finally, the change in membrane capacitance ΔC_m due to the ac pressure is calculated by subtracting the static membrane capacitance C_m from the capacitance under both static and acoustic pressures $C_{\mathrm{dc+ac}}$:

$$\Delta C_m = C_{\mathrm{dc+ac}} - C_m . \tag{17}$$

Using the parameters in Table II, the predicted static capacitance of a membrane from the fabricated microphone is 79 fF using the calculated static deflection under atmospheric pressure. The amplitude of the changing capacitance ΔC_m of a single membrane is 4.3 aF for the calculated displacement amplitude of 0.124 Å associated with a 1 Pa rms pressure signal. These values are used in the following section to calculate the phase shift of the microphone transmission line in rf detection.

C. Transmission line with capacitive loading

As previously described, rf detection senses the phase shift of a carrier signal at frequency f_c through a transmission line loaded with capacitive membranes. Before modeling the effects of capacitive loading, the characterization of the unloaded transmission line is necessary. Wen[26] derives an expression for the capacitance per unit length C_t of a coplanar waveguide transmission line:

$$C_t = 4\epsilon_{\mathrm{eff}}\epsilon_0 \frac{K(k)}{K(k')}, \tag{18}$$

where

$$\epsilon_{\mathrm{eff}} = (\epsilon_{\mathrm{sub}}+1)/2, \quad k = A/B,$$

and

$$k' = \sqrt{1-k^2}.$$

Equation (18) models a line with center conductor width A and separation between ground lines B, as shown in Fig. 13. The lines are modeled on a silicon half-plane with relative permittivity ϵ_{sub}. The effective relative permittivity ϵ_{eff} of the transmission line is treated as the average of the free-space and substrate relative permittivities, and the function K represents the complete elliptic integral of the first kind. The transmission line can be treated as being immersed in a single dielectric of relative permittivity ϵ_{eff} with characteristic impedance $Z_0 = \sqrt{\epsilon_{\mathrm{eff}}}/(cC_t)$, where c is the speed of light in free space.[26] Because the characteristic impedance of a low-loss transmission line also is $Z_0 = \sqrt{L_t/C_t}$, the inductance per unit length L_t can be calculated using the previous expressions for C_t and Z_0. Using the parameters in Table III and Eq. (18), the predicted capacitance and inductance per unit length are 118 pF/m and 596 nH/m, respectively. The predicted characteristic impedance Z_0 of the unloaded line is 71 Ω.

TABLE III. Additional parameters and dimensions for the calculation of unloaded coplanar waveguide impedance Z_0.

Parameter	Symbol	Value
Center conductor width	A	20 μm
Ground conductor separation	B	100 μm
Silicon substrate relative permittivity	ϵ_{sub}	11.7
Speed of light	c	3.0×10^8 m/s

The propagation constant in rad/m of an unloaded rf transmission line is $2\pi f_c\sqrt{L_tC_t}$. To determine the effects of the capacitive loading by the membranes, the total length of the unloaded transmission line can be viewed as a composite of N sections of line, each of length d. The phase length of the capacitively loaded transmission line is calculated by incorporating a single membrane capacitor into each section of the lumped, reactive transmission line model shown in Fig. 14. Thus, the total radian phase length of the loaded line becomes

$$\Phi = 2\pi f_c N\sqrt{L_t d(C_t d + C_m)}. \tag{19}$$

To calculate the phase shift $\Delta\Phi$ due to changes in membrane capacitance, the phase length of the line, loaded with capacitance C_m, is subtracted from that loaded with $C_m+\Delta C_m$, as shown below:

$$\Delta\Phi = 2\pi f_c N[\sqrt{L_t d(C_t d + C_m + \Delta C_m)} - \sqrt{L_t d(C_t d + C_m)}]. \tag{20}$$

However, a simpler approximate expression for $\Delta\Phi$ can be obtained in terms of the characteristic impedance of the loaded transmission line impedance Z_L. Differentiating Eq. (19) with respect to C_m and linearizing the expression for small changes in capacitance yields

$$\Delta\Phi \approx \frac{\pi f_c N\sqrt{L_t d}}{\sqrt{C_t d + C_m}}\Delta C_m . \tag{21}$$

Because the characteristic impedance of the low-loss, capacitively loaded transmission line is given by

$$Z_L = \sqrt{\frac{L_t d}{C_t d + C_m}}, \tag{22}$$

Eq. (21) simplifies to

$$\Delta\Phi \approx \pi f_c N Z_L \Delta C_m . \tag{23}$$

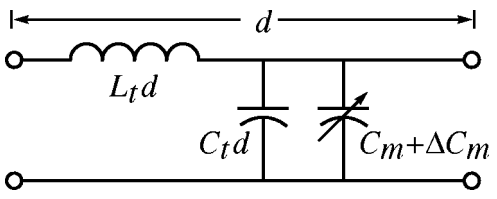

FIG. 14. The lumped-element, lossless model of a single section of loaded transmission line, including the capacitive membrane.

TABLE IV. Simulated and measured parameters for the phase shift calculations.

Parameter	Symbol	Value
Capacitance of unloaded line[a]	C_t	118 pF/m
Inductance of unloaded line[a]	L_t	596 nH/m
Membrane static capacitance[a]	C_m	79 fF
Change in membrane capacitance[a]	ΔC_m	4.3 aF
Number of sections	N	45
Length of each section	d	206 μm
Carrier frequency	f_c	2.8 GHz

[a]Calculated from previous formulas.

This expression can be used to compute the phase shift due to a fluctuation in membrane capacitance ΔC_m and predicts that the phase shift is proportional to ΔC_m, the loaded transmission line impedance Z_L, the number of membranes N, and the rf carrier frequency f_c.

Using either Eqs. (20) or (23) and the fabricated microphone parameters and previously calculated values given in Table IV, the expected phase shift amplitude is 58.6 μrad for 1 Pa rms acoustic pressure. The calculated loaded line impedance from Eq. (22) is 34.5 Ω. This impedance is sufficiently similar to the typical 50-Ω impedances of other rf circuit components to obviate the need for impedance-matching networks in the phase detection circuit.

D. Phase detection

The mixer in the phase detection circuit converts the phase shift to a voltage, assuming the input signals are in quadrature. The detection constant K_d of the mixer, first introduced in Eq. (3), is a function of the mixer loss, the rf frequency, the terminating impedance, and the rf power level at the mixer inputs.[19] Although K_d can be measured directly in the phase detection circuit, an estimate of K_d is useful for the simulation model.

The voltage amplitude of a rf signal on a transmission line with impedance Z_L is $\sqrt{2Z_L P_c}$, where P_c is the rf carrier power at the output of the microphone or at the input to the mixer. Assuming perfect impedance matching and taking L_m as the mixer conversion loss, defined as the ratio of power available from the rf port to the power delivered to the output, the voltage at the rf port is reduced by a factor of $\sqrt{L_m}$ at the mixer output. Therefore, the detection constant K_d in V/rad is approximately

$$K_d \approx \sqrt{\frac{2Z_L P_c}{L_m}}. \tag{24}$$

This expression assumes that sufficient drive power is available at the mixer LO port to fully switch the mixer diodes. Furthermore, it does not account for any impedance mismatch at the mixer ports nor does it account for saturation or compression of the output signal for large rf powers. Therefore, for a low-loss microphone transmission line, as is the case here, the input rf power that saturates the mixer should be substituted for P_c. This sets the upper limit for K_d. Using experimentally determined values for the mixer of 7 dB for conversion loss and 7 dB m for the input power compression, as shown in Table V, the estimated mixer detection constant is 0.263 V/rad.

TABLE V. Simulated and measured parameters for the mixer phase detection constant K_d.

Parameter	Symbol	Value
Loaded line impedance[a]	Z_L	34.5 Ω
rf power (saturation)[b]	P_c	5.0 mW (7 dBm)
Conversion loss[b]	L_m	5.0 (7 dB)

[a]Calculated from the previous formulas.
[b]Experimentally measured in the phase detection circuit.

E. Baseband amplification

The output voltage amplitude from the mixer is 15.4 μV, using a calculated phase shift amplitude of 58.6 μrad for 1 Pa rms. Because this demodulated voltage signal is small, a baseband amplifier is necessary to increase the magnitude of the voltage signal before further signal processing or digitization. An amplifier providing 60.0 dB of gain brings the signal level to 15.4 mV, or 10.9 mV rms. Fortunately, the low output impedance of the rf mixer in the phase detection circuit allows for such an amplification with only a slight degradation to the SNR. The noise considerations of the amplifier and of the entire system are considered in the following sections.

F. Mechanical noise

Acoustic transducers are subject to thermal mechanical noise from the acoustic medium. This mechanical noise is often referred to as acoustic self-noise,[23] since it is a property of the microphone's structural design and is unrelated to the electrical detection system. In many microphones, the squeeze-film damping due to air flow through the acoustic holes in the backplate and through the pressure equalization vent is the dominant noise mechanism for the entire system over most of the audio frequency range.[27,28] Furthermore, experiments by Zuckerwar and Ngo[29] suggest that the mechanical $1/f$ noise of an unsealed microphone structure also correlates with the air gap resistance. As there is no acoustic flow behind a vacuum-sealed CMUT membrane, the structure has a much lower mechanical noise floor than that of an unsealed structure. This is evident in the equivalent circuit model of the CMUT by the absence of many acoustical resistances, which represent dissipation mechanisms in the structure. As seen in Fig. 4, the remaining dissipation mechanism in a sealed membrane structure is represented by the radiation resistance. This thermal noise due to acoustic radiation of the moving membranes is experienced by all microphones that are exposed to the air.

A common approach to calculating the pressure noise of small sensors, originally undertaken by Sivian and White,[30] is to calculate the pressure noise from the radiation of a piston in an infinite baffle. Fellgett,[31] however, notes that the infinite-baffle assumption leads to a factor-of-2 discrepancy and is not the usual configuration for a miniature microphone. A more general approach examines the intrinsic ther-

mal noise of the medium, derived by Hunt.[32] The resulting mean-square pressure fluctuation noise in a 1-Hz band is

$$\overline{p^2} = \frac{4\pi k_B T_0 \rho_a f_a^2}{c_a}, \tag{25}$$

where k_B is Boltzmann's constant (1.38×10^{-23} J/K), T_0 is the absolute temperature of the system, ρ_a is the density of air, c_a is the speed of sound in air, and f_a is the acoustic frequency. Taking the square root of Eq. (25) yields the rms pressure fluctuations per $\sqrt{\text{Hz}}$, valid for a sensor that is smaller than the wavelength of sound at the frequencies of interest. Integrating the A-weighted rms pressure noise yields an equivalent self-noise of -9.3 dB(A) SPL at standard pressure and room temperature. As the mechanical noise due to radiation is small, it does not impose practical limits on the sensitivity of a miniature microphone composed of otherwise lossless, vacuum-sealed CMUT membranes. Therefore, mechanical noise can be neglected in simulations since the electrical noise dominates.

G. Electrical noise

There are several sources of electrical noise in the phase detection electronics that must be considered. First, the oscillator, which serves as the rf signal source in Fig. 6, contributes phase noise to the circuit. This phase noise is present in both the microphone and the reference branches of the detection circuit. For similar time delays in the two circuit branches, it is largely correlated at the rf and LO inputs of the mixer. Therefore, most of the oscillator phase noise cancels at the mixer output for a low-noise signal source, such as a dielectric resonator oscillator, and the phase noise of the signal source can be neglected in this model. For acoustic frequencies below 100 kHz, we have experimentally confirmed that the noise floor of the detection circuit does not change with high-quality oscillators of varying spectral purities.

The dominant source of noise in rf detection is due to thermal noise, shot noise in the mixer diodes, and $1/f$ noise.[19] The white noise floor of the mixer is modeled using the mixer's single sideband noise figure F_m and the mixer's conversion loss L_m. The available noise power in W/Hz at the mixer output is given by

$$N_m = \frac{k_B T_0 F_m}{L_m}, \tag{26}$$

which has a flat acoustic spectrum. Assuming a matched termination of R_0 at the mixer output, the expected rms output voltage per $\sqrt{\text{Hz}}$ is

$$v_{m,N} = \sqrt{\frac{k_B T_0 F_m R_0}{L_m}}. \tag{27}$$

In addition to white noise with a flat spectral density, realistic mixers also have a component that varies approximately as $1/f$. Equation (27) can be modified to account for this noise by defining a corner frequency $f_{1/f}$ as the baseband or acoustic frequency f_a at which the $1/f$ component of the noise equals the mixer's white noise floor:

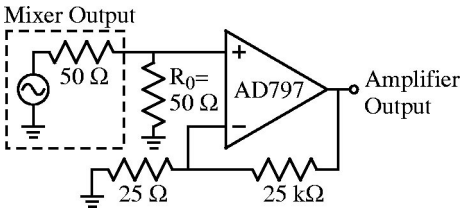

FIG. 15. Schematic of the baseband amplifier, along with the 50-Ω source resistance of the mixer, seen through the low-pass filter of the previous stage.

$$v_{m,N} = \sqrt{\frac{k_B T_0 F_m R_0 (1 + f_{1/f}/f_a)}{L_m}}. \tag{28}$$

The $1/f$ noise corner frequency depends on the rf frequency, the power levels in the circuit, and the cleanliness of the semiconductor fabrication facility for the Schottky diodes in the mixer.[33,34] This makes estimation of the $1/f$ corner frequency difficult without specific information about the mixer diodes and how the mixer's $1/f$ noise is influenced by external circuit components. Thus, the noise performance of a specific mixer in the phase detection circuit is best determined experimentally. Although lower noise performance is possible, a typical value for the corner frequency $f_{1/f}$ in rf double-balanced mixers is 100 kHz.[35] In the absence of further information, a value of 100 kHz is assumed for $f_{1/f}$ in sample noise calculations to illustrate the effects of mixer $1/f$ noise on system performance.

The baseband amplifier contributes thermal electrical noise and, below 100 Hz, excess $1/f$ noise, which is neglected in the model. Because the output impedance of the mixer and low-pass filter combination is low, near 50 Ω, the effects of the current noise contributed by the baseband amplifier are usually negligible. Therefore, an amplifier with high current noise may be used as long as the voltage noise is very low. Figure 15 shows the schematic of the baseband amplifier with feedback resistors, set for a voltage gain of 1001 or 60.0 dB. The 50 Ω resistor at the positive terminal serves as the terminating load for the mixer, R_0, which itself has an output impedance near 50 Ω. Although the matched termination reduces the signal level at the input of the amplifier, experimental measurements show that it also reduces the noise floor and the dc offsets from the mixer for an overall improvement in the SNR.

For the resistor values of Fig. 15 and the parameters in Table VI, the baseband amplifier noise figure is 3 dB, or a factor of 2.0, calculated using a source resistance of 50 Ω from the previous stage. Figure 16 shows the calculated electrical noise at the output of the baseband amplifier that is due to the mixer and the amplifier. The simulation suggests that the mixer's $1/f$ noise dominates the total output noise of the detection circuit over the audio range.

H. Calculating sensitivity

An estimate of the sensitivity can be obtained with the models developed for calculating the signal and noise levels of the microphone and its phase detection circuit. The predicted signal after amplification is -39.2 dB relative to 1 V rms for a 1 Pa rms acoustic signal and is independent of the

TABLE VI. Additional parameters for simulating the electrical noise from the mixer and amplifier at the amplifier output.

Parameter	Symbol	Value
Terminating resistance	R_0	50 Ω
Mixer noise figure[a]	F_m	5.0 (7 dB)
Mixer 1/f corner frequency[b]	$f_{1/f}$	100 kHz
Op-amp input voltage noise[c]		0.9 nV/Hz
Op-amp input current noise[c]		2.0 pA/Hz
Boltzmann's constant	k_B	1.38×10^{-23} J/K
System temperature	T_0	293 K

[a]Typical manufacturer's specifications for Marki Microwave M1-0204 NA mixer.
[b]A typical value for rf mixers (Ref. 35).
[c]Typical manufacturer's specifications for the Analog Devices AD797 operational amplifier.

acoustic frequency below 100 kHz. The predicted noise level at 1 kHz is -106.7 dB V rms per $\sqrt{\text{Hz}}$ from the simulation shown in Fig. 16. Therefore, the predicted SNR in a 1 Hz noise bandwidth at 1 kHz is 67.5 dB for 1 Pa rms of pressure. Referring the integrated, A-weighted output noise to the pressure input of the microphone yields a predicted equivalent noise level of 61.9 dB(A) SPL over the audio band.

The model's prediction of the signal level is most sensitive to the membrane thickness l_m, as this determines the membrane's static deflection and the effective capacitor gap spacing. Due to nonuniformities across the wafer, the estimated uncertainty in the measurement membrane film thickness is ±5 nm. Recalculating the signal level using the maximum range of 0.395 to 0.405 μm for l_m, the predicted output signal ranges from -38.0 to -40.4 dB V rms for an uncertainty of up to 2.4 dB in the model's prediction for a signal level.

V. EXPERIMENTAL RESULTS

Acoustic characterization of the CMUT microphone with rf detection is performed in an anechoic chamber, using a Brüel & Kjær Type 4135 1/4 in. free-field microphone as the reference microphone. The reference microphone is positioned 1 cm above the microphone under test, both oriented toward the speaker for normal incidence. The reference microphone is calibrated at 1 kHz using an ACO Pacific 511E Sound Level Calibrator for 94 dB SPL, or 1 Pa rms. Following the calibration of the reference microphone, both microphones are exposed to the same 1 kHz sound field. A comparison of the relative output signals between the reference and test microphones determines the response of the CMUT microphone with rf detection, which is -42.7 dB V rms for 1 Pa rms of pressure.

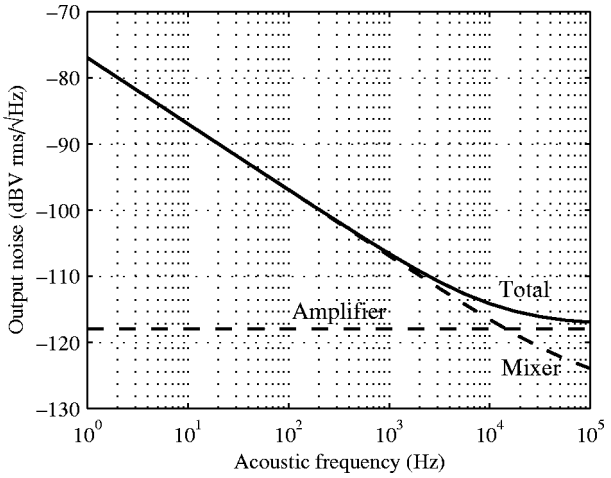

FIG. 16. Simulated total voltage noise (solid line) at amplifier output as a function of acoustic frequency, separated into components (dashed lines) due to the mixer and amplifier.

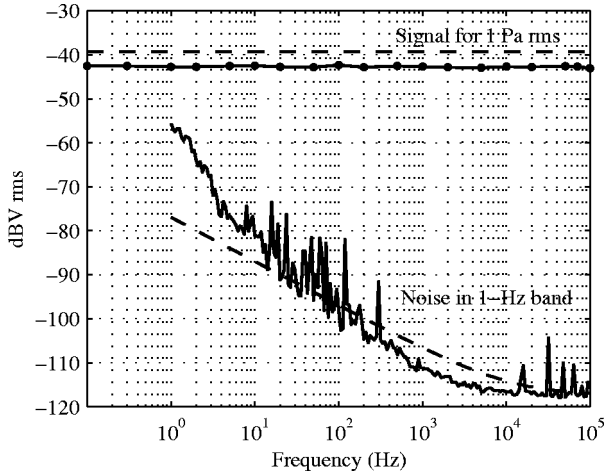

FIG. 17. Measured (solid) and simulated (dashed) output signal for 1 Pa rms and output noise voltage in a 1 Hz band. The signal response is measured using voltage actuation and correlated to the acoustic measurement at 1 kHz.

Acoustic testing over many decades of frequency is difficult without specialized low- and high-frequency microphones and sound sources. An alternative method of testing the frequency response uses electrostatic actuation of the CMUT membranes at infrasonic through ultrasonic frequencies. This method captures the response of the microphone and rf detection system to the force or pressure at the surface of the membranes, but does not account for acoustic diffraction effects of the microphone. The application of voltage actuation signal and dc bias is accomplished by inserting a bias T before and after the microphone in the circuit in Fig. 6. To compensate for the variations in response of the bias T with frequency, the actuation voltage applied to the input of the bias T is adjusted at each frequency to maintain a constant ac voltage on the capacitive membranes of the microphone.

The frequency of voltage actuation is varied from 0.1 Hz to 100 kHz, while maintaining a 5.8-V dc bias and a 68-mV amplitude excitation on the membrane capacitors. This voltage bias and excitation are both small enough to prevent an electrostatic collapse of the membrane while producing an output signal, -11.0 dB V rms, that is much larger than the noise floor. The output signal of the microphone and detection circuitry varies less than 0.5 dB over six decades of frequency, from 0.1 Hz to 100 kHz. The previous acoustic measurement at 1 kHz correlates the output under voltage actuation with that from pressure excitation, generating the frequency response plot in Fig. 17. The predicted response curves use the simulation models developed in Sec. IV with the parameters for the fabricated microphone and phase detection circuit.

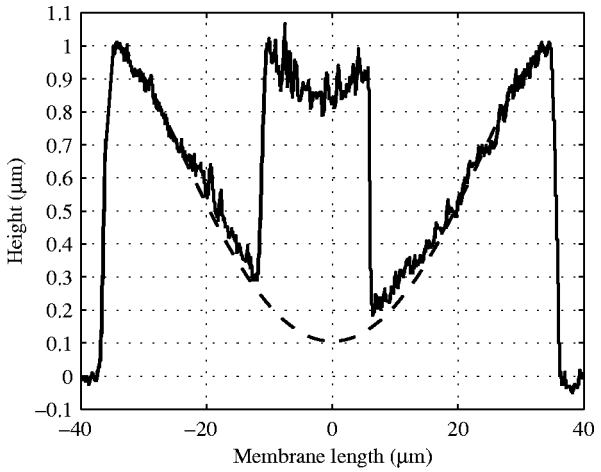

FIG. 18. Measured (solid line) AFM profile of a membrane from the fabricated microphone, compared to the calculated profile (dashed line) from Eq. (11). The patterned metal transmission line causes the step in the measured profile. The 70-μm scan path along the membrane length corresponds to the x coordinate axis of Fig. 10.

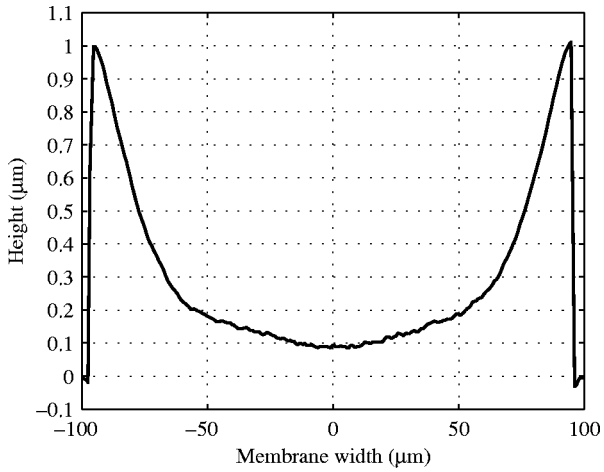

FIG. 19. Measured optical interferometer profile of a membrane from the fabricated device along the metal transmission line. The 190-μm profile of membrane width corresponds to the y-coordinate axis of Fig. 10.

The output voltage noise of the microphone in the phase detection circuit is measured with a fast Fourier transform (FFT) spectrum analyzer (Stanford Research Systems model SR760). Figure 17 shows the measured output noise floor of the microphone with its detection circuitry measured in a laboratory environment. At 1 kHz, the measured noise is $-111.1\,\mathrm{dB}/\sqrt{\mathrm{Hz}}$ relative to 1 V rms. Therefore, the measured SNR at 1 kHz is 68.4 dB/Pa rms in a 1-Hz noise band. The measured signal and noise plots of Fig. 17 correspond to an A-weighted equivalent noise level of 63.6 dB(A) SPL for the microphone.

VI. DISCUSSION

A. Model verification and comparison

The measured acoustic response of the microphone at 1 kHz is 3.5 dB lower than that predicted by the model, and the measured noise level at 1 kHz is 4.4 dB lower than predicted. Both of the measurements are slightly out of the range of expected error based on uncertainties in thickness and $1/f$ corner frequency. However, some additional measurements of membrane deflection, the rf transmission line, and the mixer lend insight as to the probable sources of error in the simulation model.

Accurate modeling of the membrane deflection under atmospheric pressure is important because the capacitance calculations are sensitive to the electrode spacing. Fortunately, u_{dc} can be verified on the fabricated microphone. An atomic force microscope (AFM; Digital Instruments Dimension 3000), scanning along the membrane's length, generates the profile shown in Fig. 18. Subtracting the 0.71-μm metal line thickness yields a peak membrane deflection of approximately 0.89 μm, which is similar to the predicted peak deflection of 0.895 μm. The profile along the membrane width, shown in Fig. 19, is measured optically since the metal signal line is reflective over the entire scan. An optical interferometer (Zygo White-Light 3D Surface Profiler) measures a peak static deflection of 0.91 μm, slightly greater than predicted. Both measurements verify the initial gap height of 1.00 μm. Since both the AFM and optical interferometer measurements of u_{dc} are very similar to the predicted deflection, no adjustments to this part of the model are necessary. Although the static deflection of the membrane is easily verified, the ac displacement amplitude u_{ac} is too small for us to accurately determine, even when using voltage excitation of the membranes to increase the measurable movement. Therefore, an error in the prediction of u_{ac} by Eq. (13) could account for the larger predicted signal level than measured.

Although the output signal is not particularly sensitive to the impedance or loss of the microphone transmission line structure, rf measurements provide another verification of the transmission line aspects of the model. Measurements at 2.8 GHz using a network analyzer (Hewlett-Packard model 8510C with 8517A S-parameter test set) indicate the characteristic impedance of the transmission line structures. An unloaded coplanar waveguide with the same dimensions as those of the fabricated microphone has a characteristic impedance Z_0 of 78 Ω, similar to the predicted value of 71 Ω for the dimensions shown in Table III. The higher measured impedance of the line is likely due to the finite extent of the ground conductors of the unloaded coplanar waveguide, as expected from more elaborate transmission line models.[36] The measured impedance of the loaded transmission line of the fabricated microphone is 37 Ω, only slightly larger than the predicted loaded impedance of 34.5 Ω. The measured transmission line loss on the microphone device is 4.1 dB at 2.8 GHz. The loss is higher than that of other published coplanar lines on silicon,[22] but this is likely due to the capacitive loading as well as the thin, 0.71 μm aluminum metalization and step coverage over the membranes. Nonetheless, this loss still is small enough to be neglected in the calculation of the mixer detection constant K_d, as there still is sufficient rf power at mixer to saturate it.

The model for mixer detection constant K_d is verified experimentally for the specific mixer in our phase detection circuit at 2.8 GHz. A 50-Ω step attenuator replaces the microphone in the phase detection circuit of Fig. 6 to vary the amount of rf power P_c at the mixer. The detection constant is measured by recording and scaling the output voltage for

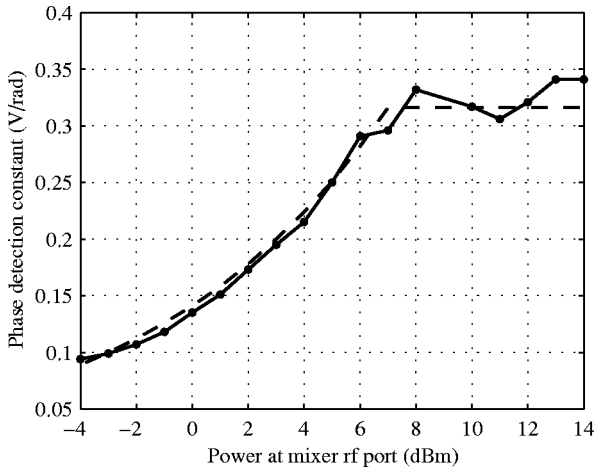

FIG. 20. Mixer phase detection constant K_d measurement (solid line) and model (dashed line). The model assumes 7 dBm of conversion loss, 7 dBm of saturation power, and 50 Ω for the line impedance.

small departures in phase from quadrature, using a micrometer-drive phase shifter. As shown in Fig. 20, the measured K_d conforms to that predicted by Eq. (24) if one assumes 7 dB for the conversion loss L_m, 7 dBm saturation power for P_c, and 50 Ω for the line impedance Z_L. Replacing the step attenuator with the fabricated microphone permits direct measurement of 0.27 V/rad for K_d for this microphone. As the measurement is similar to the simulation value of 0.263, the calculation of K_d is not a cause of the observed discrepancy between the measurement and the model.

One likely cause for the overestimate of the signal level in the simulation model is evident from the deflection profile along membrane width in Fig. 19. The one-dimensional membrane and capacitance models assume that the dc and ac deflections along the membrane width W remain constant over the ground electrode width w_g. For the device tested, w_g extends between ± 50 μm along the width in the profile of Fig. 19. Since the membrane deflection decreases over this region of W, the one-dimensional simplification to model diaphragm motion overestimates the capacitances C_m and ΔC_m in the model. The larger calculated value for C_m also explains why the predicted impedance of the loaded transmission line is lower than measured, since a larger loading capacitance decreases the line impedance. A second possible source of error in the prediction for signal level arises from nonlinear stress-stiffening effects in the membranes, which are neglected in the equations for dc and ac membrane response. As the membrane deflects under atmospheric pressure, the tensile stress of the structure increases, thereby increasing the stiffness of the structure and reducing the incremental ac motion of the membrane. A more accurate model might use finite element simulations to calculate the two-dimensional membrane deflection profile and capacitance, including stress-stiffening effects. This method potentially reduces both of the likely sources of error in the simulation model, although the model complexity and necessary computation time increase with finite element simulations. For analyzing tradeoffs or for developing optimal microphone designs, the closed-form, one-dimensional solution to the membrane response may be preferable if some error can be tolerated.

TABLE VII. A summary of measured parameters for the fabricated microphone and its detection circuitry, compared to those predicted by the model for a 1 Pa rms signal.

Parameter	Predicted	Measured
Static deflection (μm)	0.895	0.89–0.91
Unloaded line impedance (Ω)	71	78
Loaded line impedance (Ω)	34.5	37
Detection constant (V/rad)	0.263	0.27
Output signal (dB V rms)	−39.2	−42.7
Equivalent noise level [dB(A) SPL]	61.9	63.6

The measured noise floor of Fig. 17 indicates the presence of ambient acoustic noise in the audio band. In addition, there are several peaks in the noise floor at multiples of 16 kHz. The high-frequency peaks could be due to electromagnetic interference with the rf detection circuitry, with regular multiples created by mixing products. The simple $1/f$ noise model of the mixer overestimates the noise at higher frequencies and underestimates the noise at very low frequencies. Below 10 Hz, the measured noise varies almost as $1/f^2$. Other measurements of $1/f$ noise in diodes suggest that the noise exhibits a dependence of $1/f^{\alpha}$, where α is slightly greater than unity.[37] As previously discussed, $1/f$ noise is difficult to predict because its dependence on several factors, internal and external to the mixer, is unknown. Table VII summarizes and compares selected measurements with the model predictions.

B. Improving sensitivity

The use of sealed CMUT membranes in the microphone provides a uniform, wideband response to pressure while sealing out particle contamination and moisture. Improving the SNR of the microphone is a remaining design challenge, as the use of relatively small, stiff membranes reduces the sensor's mechanical response to pressure. Some possible approaches for reducing the stiffness of the membranes include corrugated structures or a reduction of the membrane material's residual stress through doping and annealing.[38] The use of larger, unsealed membranes that are not fully supported along their perimeters also may increase the membrane motion though some of the advantages in bandwidth, frequency response, and durability may be forfeited.

Some unique opportunities for improvement exist with the described rf detection technique, without necessarily modifying the sealed membrane structure. Since the loaded transmission line translates the capacitance variations of the membranes into phase variations, methods that increase the phase modulation of the rf carrier or reduce the noise of the phase detection electronics also have the potential to improve the sensing capability of the microphone. For example, the use of higher rf frequencies increases the phase shift of the rf carrier that travels along the microphone transmission line. Because the phase shift is proportional to f_c, as shown in Eq. (23), each doubling of frequency increases the signal level by up to 6 dB if K_d remains unchanged. However, the optimum rf frequency balances the increase in phase shift

with the increases in rf loss through the transmission line structure and any increase in the noise floor of the detection electronics at higher operating frequencies.

In addition to increasing the phase shift of the rf carrier, the resolution of the phase detection circuitry also can be improved. More sophisticated circuit topologies suppress the carrier through an rf interferometer, as demonstrated by Sann.[39] Because the suppressed carrier prevents saturation of the mixer, it is possible to amplify the phase modulation signal at rf frequencies prior to the mixer, which introduces most of the electrical noise. Since low-noise, narrowband amplifiers are available at rf frequencies, the effects of the mixer $1/f$ noise and baseband amplifier noise are mitigated, and the system noise floor can approach that of fundamental electrical thermal noise limits. Ivanov *et al.*[40] demonstrate such a phase detection system capable of measuring rms phase variations at 1 kHz of $0.3\,\mathrm{nrad}/\sqrt{\mathrm{Hz}}$, using a carrier frequency of 9 GHz and the same rf power level as our circuit. For comparison, the phase detection circuit presented here is capable of measuring rms phase variations of $17\,\mathrm{nrad}/\sqrt{\mathrm{Hz}}$ at 1 kHz, based on the measured SNR of Fig. 17 using a calculated rms phase variation of 41.4 μrad. This suggests that up to 35 dB improvement in SNR at 1 kHz may be possible through carrier-suppressed phase detection topologies. The potential improvement is greater at lower audio and infrasonic frequencies.

VII. CONCLUSIONS

The use of the sealed CMUT membrane as the mechanical structure for a microphone provides a uniform, wideband response while sealing out moisture. In rf detection, the small capacitance variations of the membranes along a transmission line are sensed through the phase variations of a rf carrier. The mathematical model presented here predicts a SNR of 67.5 dB/Pa rms at 1 kHz in a 1-Hz band, compared to a measured SNR of 68.4 dB for the fabricated microphone. Over the audio bandwidth, the measured sensitivity corresponds to an equivalent noise level of 63.6 dB(A) SPL. Electrostatic actuation of the membrane demonstrates the potential bandwidth of the microphone, which exhibits less than 0.5 dB of variation in the output response of the system from 0.1 Hz to 100 kHz.

While various rf or carrier-based methods have been applied to other microphones, to the authors' knowledge such techniques previously have not been applied to sealed membrane structures such as the CMUT. As the mechanical noise of the condenser structure ultimately limits the minimum detectable pressure that can be sensed, applying a sensitive electrical detection technique to a conventional micromachined microphone may offer little or no improvement to the microphone's sensing capability. However, the combination of a sensitive rf technique and a sealed membrane structure extends the range of possible sensitivities for micromachined microphones. The rf detection technique presented here translates variations in membrane capacitance into phase variations of a rf signal, which can be measured extremely accurately. Therefore, the use of sealed CMUTs in conjunction with rf detection offers the potential to surpass the sensitivity of other micromachined microphones, which often are limited by their structural mechanical noise, while retaining advantages such as a uniform, wideband response and protection from moisture.

ACKNOWLEDGMENTS

This work is supported by the Defense Advanced Research Projects Agency's Microsystems Technology Office. The microphone was fabricated at the Stanford Nanofabrication Facility, which is supported in part by the National Science Foundation. The authors also wish to thank Nino Srour, Michael Scanlon, and their colleagues at the Army Research Laboratory for their assistance in testing the microphone.

[1] P. Scheeper, A. van der Donk, W. Olthuis, and P. Bergveld, "A review of silicon microphones," Sens. Actuators, A **44**, 1–11 (1994).
[2] S. Bouwstra, T. Storgaard-Larsen, P. Scheeper, J. O. Gulløv, J. Bay, M. Müllenborg, and P. Rombach, "Silicon microphones—a Danish perspective," J. Micromech. Microeng. **8**, 64–68 (1998).
[3] N. Masuzawa and E. Ohdaira, "Information contained in the radiating ultrasound during ultrasonic welding," Ultrasonics **38**, 609–613 (2000).
[4] N. Versfeld and J. Vos, "Annoyance caused by sounds of wheeled and tracked vehicles," J. Acoust. Soc. Am. **101**, 2677–2685 (1997).
[5] C. Birkett, E. Shalis, N. Vlahopoulos, and Z. Wu, "Numerical load generation, vibration analysis, and acoustic signature prediction of a ground vehicle," in *Proceedings of the National Conference on Noise Control Engineering* (Inst. of Noise Control Engineering, University Park, PA, 1997), Vol. 1, pp. 123–128.
[6] A. Bedard, Jr. and T. Georges, "Atmospheric infrasound," Phys. Today **53**, 32–37 (2000).
[7] R. K. Cook and A. Bedard, Jr., "On the measurement of infrasound," Geophys. J. R. Astron. Soc. **26**, 5–11 (1971).
[8] A. J. Zuckerwar, "Principles of operation of condenser microphones," in *AIP Handbook of Condenser Microphones: Theory, Calibration, and Measurements*, edited by G. S. K. Wong and T. F. W. Embleton (AIP Press, New York, 1995), Chap. 3, pp. 37–69.
[9] M. Hibbing, "High-quality RF condenser microphones," in *Microphone Engineering Handbook*, edited by M. L. Gayford (Focal Press, Oxford, 1994), Chap. 4, pp. 158–186.
[10] A. S. Ergun, A. Atalar, B. Temelkuran, and E. Özbay, "A new detection method for capacitive micromachined ultrasonic transducers," Appl. Phys. Lett. **72**, 2957–2959 (1998).
[11] A. S. Ergun, B. Temelkuran, E. Özbay, and A. Atalar, "A new detection method for capacitive micromachined ultrasonic transducers," IEEE Trans. Ultrason. Ferroelectr. Freq. Control **48**, 932–942 (2001).
[12] A. van der Donk, P. Scheeper, W. Olthuis, and P. Bergveld, "Modelling of silicon condenser microphones," Sens. Actuators, A **40**, 203–216 (1994).
[13] L. L. Beranek, *Acoustics* (Acoustical Society of America, Woodbury, NY, 1996), Chap. 6, pp. 144–182.
[14] P. R. Scheeper, "A silicon condenser microphone: Materials and technology," Ph.D. thesis, University of Twente, 1993, pp. 23–25.
[15] M. I. Haller and B. T. Khuri-Yakub, "A surface micromachined electrostatic ultrasonic air transducer," IEEE Trans. Ultrason. Ferroelectr. Freq. Control **43**, 1–6 (1996).
[16] I. Ladabaum, X. C. Jin, H. T. Soh, A. Atalar, and B. T. Khuri-Yakub, "Surface micromachined capacitive ultrasonic transducers," IEEE Trans. Ultrason. Ferroelectr. Freq. Control **45**, 678–690 (1998).
[17] V. Tarnow, "Thermal noise in microphones and preamplifiers," Brüel & Kjær Tech. Rev. **3**, 3–14 (1972).
[18] D. M. Pozar, *Microwave Engineering*, 2nd ed. (Wiley, New York, 1998), Chap. 8, pp. 422–493.
[19] F. Walls, A. Clements, C. Felton, M. Lombardi, and M. Vanek, "Extending the range and accuracy of phase noise measurements," in *Proceedings of the 42nd Annual Symposium on Frequency Control* (IEEE, Baltimore, MD, 1988), pp. 432–441.
[20] N. S. Barker and G. M. Rebeiz, "Distributed MEMS true-time delay phase shifters and wide-band switches," IEEE Trans. Microwave Theory Tech. **46**, 1881–1890 (1998).

[21] X. Jin, ''Micromachined capacitive ultrasonic immersion transducer array,'' Ph.D. thesis, Stanford University, 2002, Chap. 4, pp. 51–71.
[22] A. C. Reyes, S. M. El-Ghazaly, S. J. Dorn, M. Dydyk, D. K. Schroder, and H. Patterson, ''Coplanar waveguides and microwave inductors on silicon substrates,'' IEEE Trans. Microwave Theory Tech. **43**, 2016–2022 (1995).
[23] L. L. Beranek, *Acoustical Measurements*, revised ed. (American Institute of Physics, Cambridge, MA, 1993), Chap. 5, pp. 177–265.
[24] W. P. Mason, in *Electromechanical Transducers and Wave Filters* (Van Nostrand, New York, 1948), Chap. 5, pp. 158–184.
[25] M. H. Badi, G. G. Yaralioglu, A. S. Ergun, S. T. Hansen, E. J. Wong, and B. T. Khuri-Yakub, ''Capacitive micromachined ultrasonic lamb wave transducers using rectangular membranes,'' IEEE Trans. Ultrason. Ferroelectr. Freq. Control **50**, 1191–1203 (2003).
[26] C. P. Wen, ''Coplanar waveguide: A surface strip transmission line suitable for nonreciprocal gyromagnetic device application,'' IEEE Trans. Microwave Theory Tech. **17**, 1087–1090 (1969).
[27] S. C. Thompson, J. L. LoPresti, E. M. Ring, H. G. Nepomuceno, J. J. Beard, W. J. Ballad, and E. V. Carlson, ''Noise in miniature microphones,'' J. Acoust. Soc. Am. **111**, 861–866 (2002).
[28] T. B. Gabrielson, ''Mechanical-thermal noise in micromachined acoustic and vibration sensors,'' IEEE Trans. Electron Devices **40**, 903–909 (1993).
[29] A. J. Zuckerwar and K. C. T. Ngo, ''Measured $1/f$ noise in the membrane motion of condenser microphones,'' J. Acoust. Soc. Am. **95**, 1419–1425 (1994).
[30] L. J. Sivian and S. D. White, ''On minimum audible sound fields,'' J. Acoust. Soc. Am. **4**, 288–321 (1933).
[31] P. B. Fellgett, ''Thermal noise limits of microphones,'' J. Inst. Electron. Radio Eng. (UK) **57**, 161–166 (1987).
[32] F. V. Hunt, ''Propagation of sounds in fluids,'' in *American Institute of Physics Handbook*, edited by D. E. Gray, 3rd ed. (McGraw-Hill, New York, 1972), Sec. 3c-11, pp. 65–68.
[33] A. Yoginder and W. J. Moroney, ''Microwave mixer and detector diodes,'' Proc. IEEE **59**, 1182–1190 (1971).
[34] S. Marki (*private communication*, Marki Microwave, Morgan Hill, CA, 2002).
[35] S. Spohrer (*private communication*, Miteq, Hauppauge, NY, 2001).
[36] G. Ghione and C. U. Naldi, ''Coplanar waveguides for MMIC applications: Effect of upper shielding, conductor backing, finite-extent ground planes, and line-to-line coupling,'' IEEE Trans. Microwave Theory Tech. **35**, 260–267 (1987).
[37] R. J. King, *Microwave Homodyne Systems* (Peter Peregrinus, Stevenage, England, 1978), Chap. 4, pp. 78–105.
[38] J. Miao, R. Lin, L. Chen, Q. Zou, S. Y. Lim, and S. H. Seah, ''Design considerations in micromachined silicon microphones,'' Microelectron. J. **33**, 21–28 (2002).
[39] K. H. Sann, ''The measurement of near-carrier noise in microwave amplifiers,'' IEEE Trans. Microwave Theory Tech. **16**, 761–766 (1968).
[40] E. N. Ivanov, M. E. Tobar, and R. A. Woode, ''Microwave interferometry: Application to precision measurements and noise reduction techniques,'' IEEE Trans. Ultrason. Ferroelectr. Freq. Control **45**, 1526–1536 (1998).
[41] G. S. Kino, *Acoustic Waves: Devices, Imaging, and Analog Signal Processing* (Prentice–Hall, Englewood Cliffs, NJ, 1987), pp. 548–562.

Manipulation of sound intensity within a selected region using multiple sources

Joung-Woo Choi and Yang-Hann Kim[a)]
Center for Noise and Vibration Control, Department of Mechanical Engineering, Korea Advanced Institute of Science and Technology, Science Town, Daejon 305-701, Korea

(Received 2 August 2003; revised 6 May 2004; accepted 12 May 2004)

In this paper, the authors propose a method of enhancing sound in a selected region by controlling multiple sources. The physical variables of enhancing sound have not been well defined, but we may consider basic acoustic variables such as acoustic potential energy, sound power or intensity. A method of maximizing sound potential energy was found to be very straightforward [J.-W. Choi and Y.-H. Kim, J. Acoust. Soc. Am. **111**, 1695 (2002)]. In this paper, the authors attempt to control the sound power or intensity of a zone in a desired direction. It is noteworthy that control of the direction and magnitude is needed to enhance the sound intensity. This control requires a new definition of the direction and magnitude of spatially distributed intensity. For this purpose, the authors introduce two different kinds of cost functions, and the theoretical formulation based on the new definitions show the possibility of maximizing the sound intensity of a selected zone in a desired direction. © *2004 Acoustical Society of America.* [DOI: 10.1121/1.1768945]

PACS numbers: 43.38.Hz, 43.38.-p [AJZ] Pages: 843–852

I. INTRODUCTION

Multiple sources are essential for controlling the sound field over a wide area beyond a particular point. The main issue is how we can selectively enhance a desired acoustic variable in a zone of interest. This kind of problem can be regarded as an optimization problem, in which we seek the optimal control signals of multiple sources that maximize the selected acoustic variable within a zone. As a matter of course, many possible choices exist in the control method, depending on the acoustic variable we wish to enhance. For example, in previous papers,[1,2] the acoustic potential energy of a selected region is controlled to generate an acoustically bright and dark zone.[1]

On the other hand, sound intensity or sound power is a major factor in evaluating the performance of an acoustic source. Most conventional acoustic sources consist of a single actuator, and their performances are measured by how well they radiate sound power. From the listener's point of view, however, the important factor is the sound power transmitted to the region where the listener is located. The main objective of this research is to enhance acoustic intensity by controlling multiple sources. This control makes it possible for a speaker array to radiate maximum sound power to the listener, or to create a virtual power source by changing the direction of the sound power in a region where the listener is located.

With respect to sound intensity or power control, several methods that use multiple sources have been proposed.[3–6] However, these works were developed exclusively for noise control and they concentrated on minimizing the sound power radiated by the sources. In contrast, we aim to enhance sound intensity or, in a stricter sense, to increase the magnitude of sound intensity only in a desired direction within a zone of interest. This problem also requires that both the magnitude and the direction of the spatially distributed intensity be controlled. To achieve this goal, two kinds of cost functions that can evaluate both the magnitude and direction of acoustic intensity are defined. The first cost function maximizes the magnitude of the sound intensity in a desired direction, and the second one distributes more weight in the direction of the intensity field.

We then use eigenvalue analysis to determine the optimal solutions that maximize the defined cost functions. Before solving the optimization problem, however, we consider a practical constraint: the limitation of the input power that can be supplied to the control sources. We therefore determine the optimal solution within a finite input power range.

II. PROBLEM FORMULATION

A. Definition of variables

We consider a system with an arbitrary boundary condition, as depicted in Fig. 1. Each control source is fixed at position $\vec{r}_s^{(i)}\,(i=1,...,K)$ and driven by input signal $\hat{s}(\vec{r}_s^{(i)},\omega)$. Control zone V_0 represents a zone (volume or surface) of interest.

The objective of this research is to maximize the intensity of zone V_0 in a desired direction by controlling source input signals. The desired direction at field position $\vec{r}$ is defined as control direction $\vec{n}_0(\vec{r})$.

To describe the acoustic intensity of a zone, we first express the pressure and velocity in terms of control signals. The total pressure and velocity field can be written in the following manner as a superposition of the fields generated by multiple control sources:

$$\hat{p}(\vec{r},\omega)=\sum_{i=1}^{K}\hat{H}(\vec{r}|\vec{r}_s^{(i)},\omega)\hat{s}(\vec{r}_s^{(i)},\omega), \tag{1}$$

a)Electronic mail: yanghannkim@kaist.ac.kr

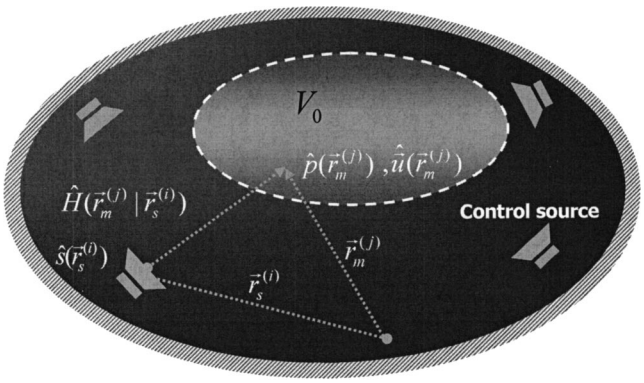

FIG. 1. Definitions of acoustic variables. V_0, control zone; $\vec{r}_s^{(i)}$, position of ith control source; $\hat{s}(\vec{r}_s^{(i)},\omega)$, source strength of the ith source; $\hat{H}(\vec{r}|\vec{r}_s^{(i)},\omega)$, transfer function between source and measurement point.

$$\hat{\vec{u}}(\vec{r},\omega)=\frac{\nabla\hat{p}(\vec{r},\omega)}{j\rho_0\omega}=\frac{1}{j\rho_0\omega}\sum_i \nabla\hat{H}(\vec{r}|\vec{r}_s^{(i)},\omega)\hat{s}(\vec{r}_s^{(i)},\omega), \tag{2}$$

where $\hat{H}(\vec{r}|\vec{r}_s^{(i)},\omega)$ is a transfer function between the ith source and field position $\vec{r}$. We assume that the control zone is sampled by discrete positions and denote these positions as $\vec{\mathbf{r}}_m=[\vec{r}_m^{(1)},\ldots,\vec{r}_m^{(M)}]^T$. The pressure and velocity at the sampled positions is then written in the following vector form:

$$\hat{p}(\vec{\mathbf{r}}_m)=H(\vec{\mathbf{r}}_m|\vec{\mathbf{r}}_s)\hat{s}(\vec{\mathbf{r}}_s), \tag{3}$$

$$\hat{\vec{u}}(\vec{\mathbf{r}}_m)=\nabla\hat{H}(\vec{\mathbf{r}}_m|\vec{\mathbf{r}}_s)\hat{s}(\vec{\mathbf{r}}_s), \tag{4}$$

where $\hat{s}(\vec{\mathbf{r}}_s)=[\hat{s}(\vec{r}_s^{(1)}),\ldots,\hat{s}(\vec{r}_s^{(K)})]^T$ is a source signal vector, and matrix $\hat{H}(\vec{\mathbf{r}}_m|\vec{\mathbf{r}}_s)$ represents transfer functions between the sources and field positions. In this paper, all the equations are expressed in frequency domain, and the frequency description ω is omitted.

B. Formulation of acoustic intensity

Our major problem is to define a measure that can represent the performance of the intensity control. Because we are considering a zone control, we have to define a physical quantity that can represent the zone's overall intensity. Moreover, the quantity has to represent both the magnitude and the direction of the intensity field. In our first attempt, we introduce a space-averaged active intensity, which is the mean value of instantaneous intensity with respect to time and space. To include the characteristics of magnitude and direction, the active intensity projected to the control direction $\vec{n}_0(\vec{r})$ is averaged throughout the zone as follows:

$$\overline{I}_{V_0}\equiv\langle\vec{I}_a(\vec{r})\cdot\vec{n}_0(\vec{r})\rangle_{V_0}$$
$$=\frac{1}{2}\mathrm{Re}\left[\frac{1}{V_0}\int\hat{p}(\vec{r})(\vec{n}_0(\vec{r})\cdot\hat{\vec{u}}(\vec{r})^*)dV(\vec{r})\right], \tag{5}$$

where $\vec{I}_a(\vec{r})$ represents the active (mean) intensity.

Using Eqs. (3) and (4), the integrand of Eq. (5) is rewritten as

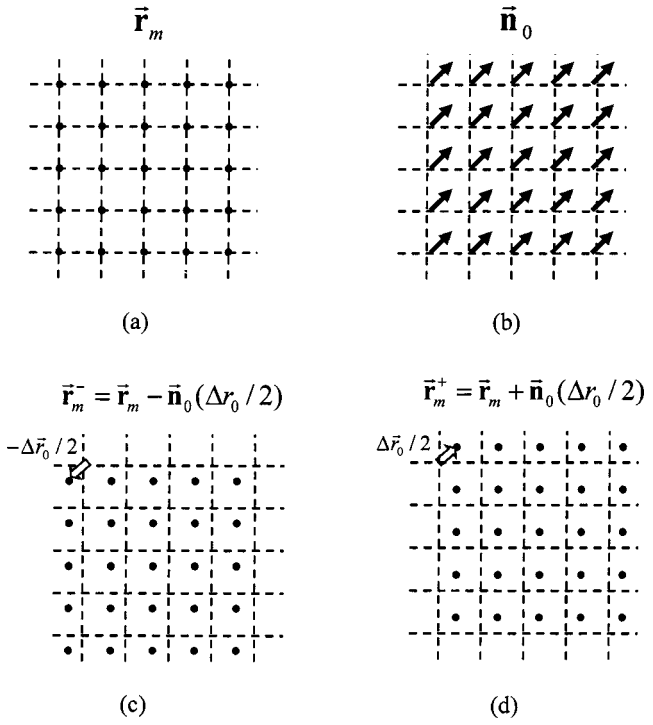

FIG. 2. Matrix definitions for multiple measurement points. (a) $\vec{\mathbf{r}}_m$, original points where intensity should be calculated; (b) $\vec{\mathbf{n}}_0$, control direction; (c)–(d) $\vec{\mathbf{r}}_m^-$, $\vec{\mathbf{r}}_m^+$, shifted measurement points for $p-p$ technique.

$$\overline{I}_{V_0}=\frac{1}{2M}\mathrm{Re}[\vec{\mathbf{n}}_0\cdot\hat{\vec{u}}(\vec{\mathbf{r}}_m)^H\hat{p}(\vec{\mathbf{r}}_m)]$$
$$=-\frac{1}{2\rho_0\omega M}\hat{s}(\vec{\mathbf{r}}_s)^H$$
$$\times\mathrm{Im}[\vec{\mathbf{n}}_0\cdot\nabla\hat{H}(\vec{\mathbf{r}}_m|\vec{\mathbf{r}}_s)^H\hat{H}(\vec{\mathbf{r}}_m|\vec{\mathbf{r}}_s)]\hat{s}(\vec{\mathbf{r}}_s), \tag{6}$$

where $\vec{\mathbf{n}}_0=\mathrm{diag}[\vec{n}_0(\vec{r}_m^{(1)}),\ldots,\vec{n}_0(\vec{r}_m^{(M)})]$.

In practice, we have to measure the transfer function $\hat{H}(\vec{\mathbf{r}}_m|\vec{\mathbf{r}}_s)$ and its gradient $\nabla\hat{H}(\vec{\mathbf{r}}_m|\vec{\mathbf{r}}_s)$. Several methods of measurement exist such as those of Mollo *et al.*[4] and Cunefare *et al.*[5] These methods demonstrated that the sound power radiating through an enclosed surface can be expressed by using a boundary element method though this method is only applicable when the control zone is a volume enclosed by a surface. We therefore used a more general formulation based on the $p-p$ measurement technique[7,8] which has been widely used for intensity measurement.

The essential aspect of the $p-p$ measurement technique is simply that the pressure and particle velocity at a point $\vec{r}_m$ can be approximated to the first order by measuring the pressure at two positions. To express the space-averaged active intensity using this approximation, we consider two measurement sets that have slightly shifted from $\vec{\mathbf{r}}_m$ to the $\vec{\mathbf{n}}_0$ direction by a small distance of $\pm\Delta r_0/2$, and we denote these parameters as $\vec{\mathbf{r}}_m^+$ and $\vec{\mathbf{r}}_m^-$ (Fig. 2). By measuring the transfer functions at these two measurement sets, the transfer function and its gradient at the original measurement position $\vec{\mathbf{r}}_m$ can be approximated. We denote the transfer functions measured at these two measurement sets as $\hat{H}(\vec{\mathbf{r}}_m^+|\vec{\mathbf{r}}_s)$

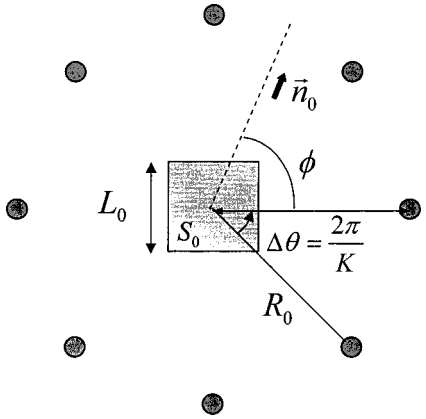

FIG. 3. Configuration for numerical simulation. K, number of sources; $\Delta\theta$, angle between the control sources; $\vec{n}_0$, control direction; ϕ, angle of control direction; L_0, aperture size of control zone (S_0); R_0, distance between the source and origin.

and $\hat{H}(\vec{\mathbf{r}}_m^-|\vec{\mathbf{r}}_s)$. Then the transfer function and its gradient to the control direction can be approximated as

$$\hat{H}(\vec{\mathbf{r}}_m|\vec{\mathbf{r}}_s) \simeq \frac{\hat{H}(\vec{\mathbf{r}}_m^+|\vec{\mathbf{r}}_s)+\hat{H}(\vec{\mathbf{r}}_m^-|\vec{\mathbf{r}}_s)}{2}, \tag{7}$$

$$\vec{\mathbf{n}}_0 \cdot \nabla \hat{H}(\vec{\mathbf{r}}_m|\vec{\mathbf{r}}_s) \simeq \frac{\hat{H}(\vec{\mathbf{r}}_m^+|\vec{\mathbf{r}}_s)-\hat{H}(\vec{\mathbf{r}}_m^-|\vec{\mathbf{r}}_s)}{\Delta r_0}. \tag{8}$$

Finally, the space-averaged active intensity of Eq. (6) is written as follows:

$$\begin{aligned}\overline{I}_{V_0} &\cong -\frac{1}{2\rho_0\omega M}\,\mathrm{Im}\left[\mathbf{s}^H \frac{(\mathbf{H}_+-\mathbf{H}_-)^H}{\Delta r_0}\,\frac{(\mathbf{H}_++\mathbf{H}_-)}{2}\mathbf{s}\right] \\ &= \frac{1}{2\rho_0 c}\mathbf{s}^H\,\mathrm{Im}\left[\frac{\mathbf{H}_-^H\mathbf{H}_+}{(k\Delta r_0)M}\right]\mathbf{s} = \frac{\mathbf{s}^H\mathbf{C}_{V_0}\mathbf{s}}{2\rho_0 c},\end{aligned} \tag{9}$$

where $\mathbf{H}^+$, $\mathbf{H}^-$, $\mathbf{s}$ are the abbreviations of $\hat{H}(\vec{\mathbf{r}}_m^+|\vec{\mathbf{r}}_s)$, $\hat{H}(\vec{\mathbf{r}}_m^-|\vec{\mathbf{r}}_s)$, $\hat{s}(\vec{\mathbf{r}}_s)$.

III. SOLUTION METHOD

A. Cost function of the first kind

This section addresses a way to determine control signal $\mathbf{s}$, which maximizes the space-averaged active intensity. However, we cannot increase the intensity infinitely; that is, in practice, the available input power is limited. With regard to the input power limitation, we attempt to find the most energy-efficient solution. The total input power of the control sources is written as a vector norm of the source signal vector

$$J_0 = \frac{|\hat{H}_0|^2}{2\rho_0 c}\mathbf{s}^H\mathbf{s}, \tag{10}$$

where $\hat{H}_0$ is a constant introduced to normalize the transfer function. Using Eqs. (9) and (10), we define the optimization problem of maximizing $\overline{I}_{V_0}$ with finite J_0. The solution is found by determining control signal $\mathbf{s}$, which maximizes the following cost function:

TABLE I. Parameters of numerical simulation. ϕ, control angle; K, number of sources; R_0, distance between source and origin; L_0, aperture size of the control zone; Δr_m, measurement interval; $\alpha_{\max}$, value of cost function after optimization.

Expt. No.	K	R_0/λ	L_0/λ	$\Delta r_m/\lambda$	ϕ (Deg.)	$\alpha_{\max}$
1	3	20	0.175	1/40	90	1.011
2	3	20	0.175	1/40	120	0.976
3	3	20	0.175	1/40	150	1.011
4	3	20	0.175	1/40	180	1.043
5	3	20	0.7	1/10	90	0.864
6	5	20	0.7	1/10	90	1.034
7	5	[1,1.4,1.8,2.2,2.6]	0.7	1/10	90	Fig. 11
8	5	[1,1.4,1.8,2.2,2.6]	0.7	1/10	90	
9	5	[0.5,0.7,0.9,1.1,1.3]	0.7	1/10	0~360	Fig. 12(b)

$$\alpha = \frac{\overline{I}_{V_0}}{J_0} = \frac{\mathbf{s}^H\mathbf{C}_{V_0}\mathbf{s}}{|\hat{H}_0|^2\mathbf{s}^H\mathbf{s}}. \tag{11}$$

This ratio, known as the Rayleigh coefficient,[9] has a maxi-

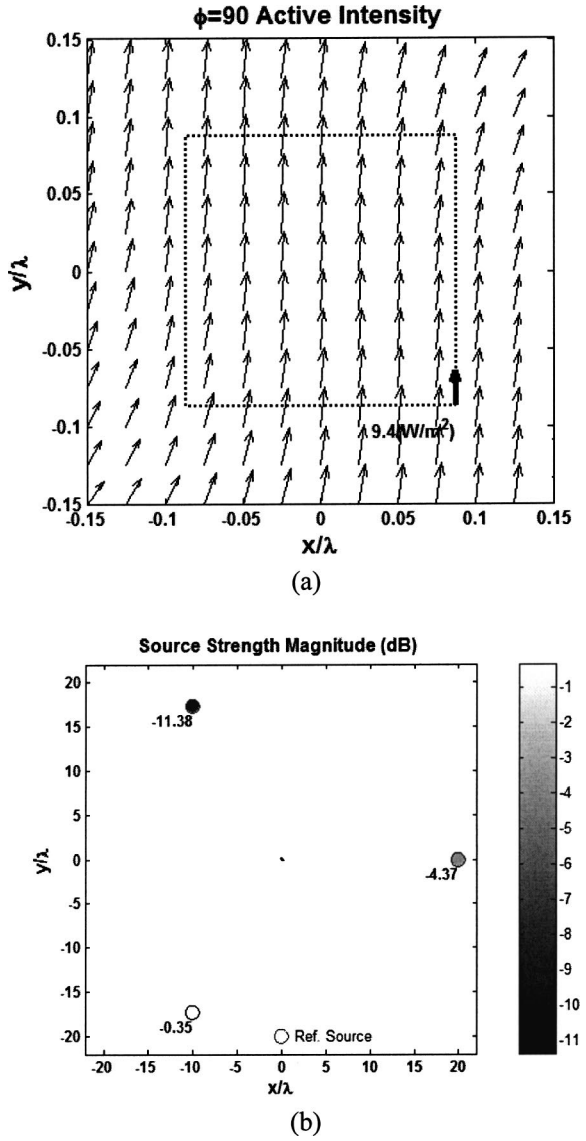

FIG. 4. (Expt. 1) (a) Active intensity field after optimization. (b) Control source position and its magnitude.

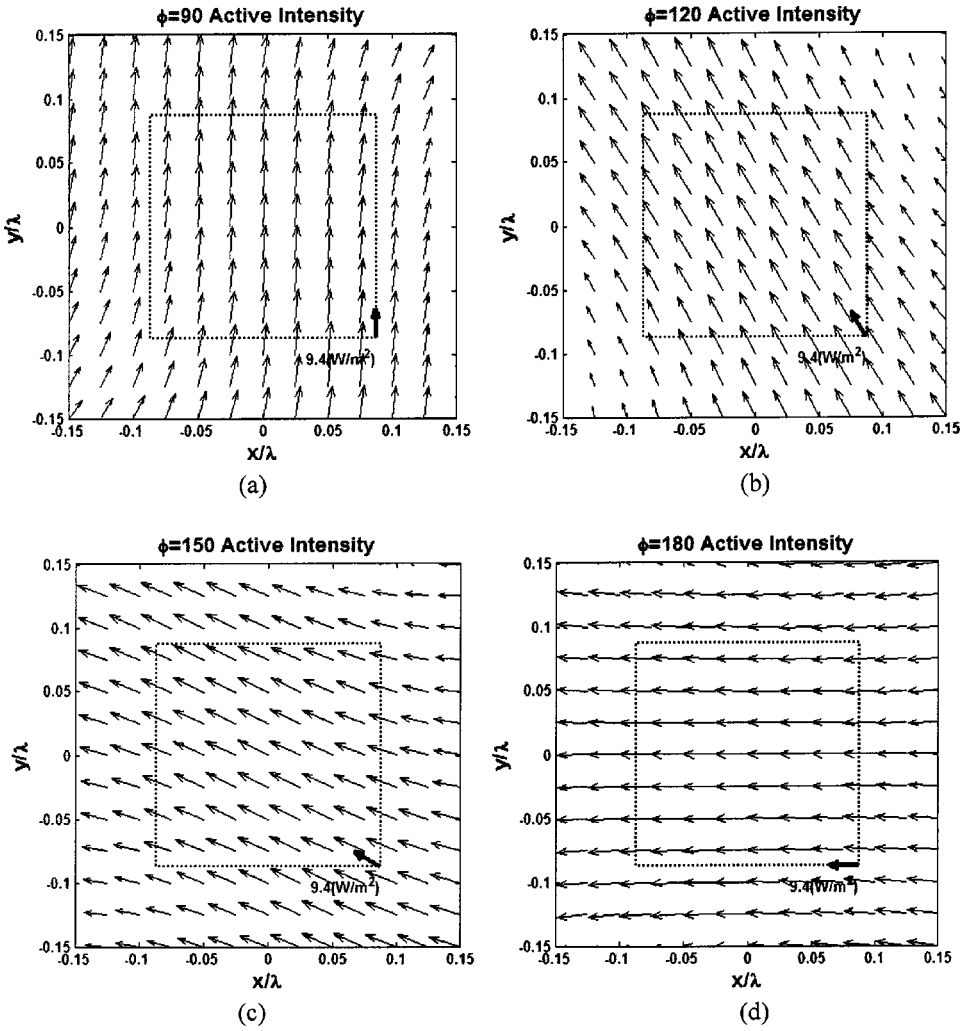

FIG. 5. Active intensity distribution after optimization for various control direction. (a) (Expt. 1) $\phi=90°$; (b) (Expt. 2) $\phi=120°$; (c) (Expt. 3) $\phi=150°$; (d) (Expt. 4) $\phi=180°$.

mum when **s** is the eigenvector that corresponds to the maximum eigenvalue of $\mathbf{C}_{V_0}$,

$$\frac{\mathbf{C}_{V_0}}{|\hat{H}_0|^2}\mathbf{s}_{\text{opt}}=\alpha_{\max}\mathbf{s}_{\text{opt}}. \tag{12}$$

Although this mathematical procedure can be applied to an arbitrary boundary condition and source, the control performance might vary according to the boundary condition of the room and type of source. To examine the performance of the proposed method and the effect of the variables involved with the control, we performed numerical simulations.

We started with a simple case in which we assumed a free field condition and regarded the control zone as a two-dimensional area (S_0) of aperture size L_0 (Fig. 3). The control sources, which were arranged on the same lateral plane as S_0, were positioned at an equal distance (R_0) from the point of origin. Among the many possible source types, we started with simple plane wave sources. Monopole sources located at a very distinct distance from the control zone might satisfy the plane wave model ($L_0^2/2R_0 \ll \lambda$). Each source was distributed to have the same angular distance $\Delta\theta$.

1. Control direction change

The first simulation was performed using a zone that was small in comparison to the wavelength ($L_0 \ll \lambda$). The zone was optimized by three control sources, and simulation parameters are presented in Table I. All parameters were normalized by wavelength. For the comparison of the control performance, we introduced a reference source, which directly generated a plane wave in the control direction [Fig. 4(b)]. The normalization constant of Eq. (10) was $\hat{H}_0 = j\rho_0\omega/4\pi R_0$, which is the pressure magnitude generated by the reference source with the unit input power. Then the cost function of Eq. (11) represents the ratio of I_{V_0} generated by the optimally controlled multiple sources to that generated by the reference source.

Figure 4(a) illustrates the resultant active intensity field. The lined box in Fig. 4(a) represents control zone S_0, and the thick arrow in the right corner is the control direction $\vec{n}_0$. The space-averaged active intensity was calculated using Eq. (9) with a finite distance of $\Delta r_0=\lambda/40$. The resultant intensity field was scaled so that its spatial average throughout the control zone was equal to the spatial averaged active intensity generated by the reference monopole source. All the intensity was controlled to head in the same direction ($\vec{\mathbf{n}}_0$

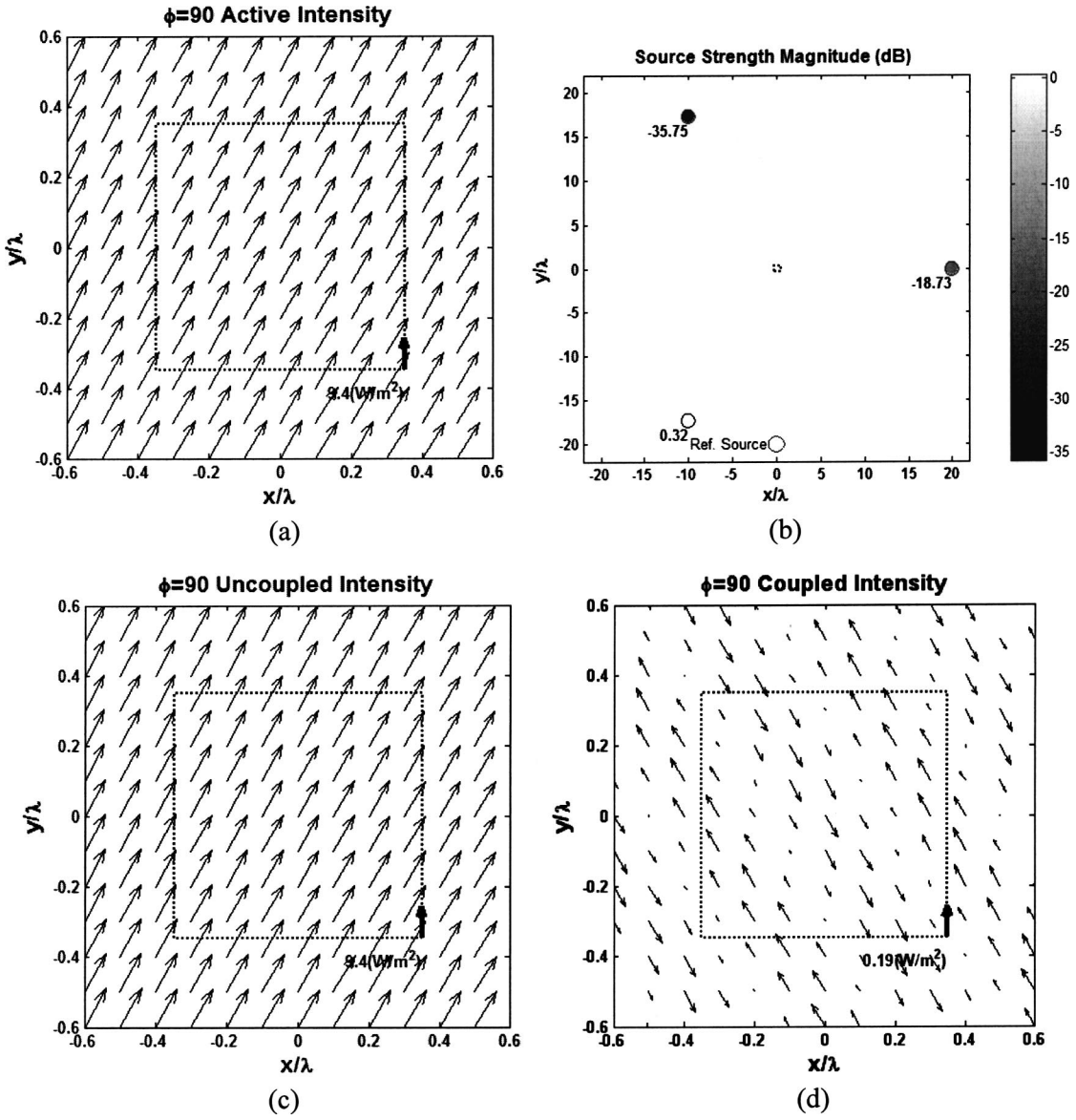

FIG. 6. (Expt. 5) (a) Active intensity field after optimization. (b) Control source position and its strength. (c) Uncoupled intensity component. (d) Coupled intensity component [note that different intensity scale was used for (c) and (d)].

$=\vec{n}_0\mathbf{I}$) throughout the entire zone. The result shows that active intensity vectors are well arranged for the control direction. The magnitude of the source strength of Fig. 4(b) represents the consumed control effort of each source compared to the unit input power.

To check the effect of the control direction, additional simulations with different $\vec{n}_0$ were performed (Expt. 2–4). The results are presented in Fig. 5. In the case of the small zone case, the control direction clearly has little effect on optimization performance. For every direction presented here, the cost functions are close to unity, which means we can obtain space-averaged active intensity as if the reference source exists using the same input power.

2. Effect of the control zone size

The next experiment (Expt. 5) shows the performance change with respect to the zone size. As the size of the zone increases, the intensity less accurately follows the desired direction [Fig. 6(a)]. In this case, only one source dominates [Fig. 6(b)], and the cost function decreases to 0.86.

To understand the relation between the size of the zone and the control performance, the interference characteristics of multiple sources should be investigated. The interference of acoustic intensity has been studied for various kinds of sources.[10–13] We follow the work of Pascal,[11] which presented the interference characteristics of two plane wave sources. For plane wave sources, the complex magnitude of pressure and velocity can be written as follows:

$$\hat{p}(\vec{r}) = \sum_{n=1}^{N} \hat{P}^{(n)} e^{j\vec{k}^{(n)}\cdot\vec{r}},$$

$$\vec{\hat{u}}(\vec{r}) = \frac{1}{\rho_0 \omega} \sum_{n=1}^{N} \vec{k}^{(n)} \hat{P}^{(n)} e^{j\vec{k}^{(n)}\cdot\vec{r}}, \tag{13}$$

where $\hat{P}(\vec{k}^{(n)})$ represents the complex pressure magnitude, and $\vec{k}^{(n)}$ represents the wave number of each plane wave source. The active intensity at position $\vec{r}$ is then given by

$$\vec{I}_a(\vec{r})=\vec{I}_{uc}+\vec{I}_c(\vec{r})=\frac{1}{2\rho_0\omega}\left\{\left(\sum_n \vec{k}^{(n)}|\hat{P}^{(n)}|^2\right)+\left(\frac{1}{2}\sum_{m\neq l}\sum_l (\vec{k}^{(m)}+\vec{k}^{(l)})|\hat{P}^{(m)}||\hat{P}^{(l)}|\cos((\vec{k}^{(m)}-\vec{k}^{(l)})\cdot\vec{r}+\psi^{(m)}-\psi^{(l)}\right)\right\}, \quad (14)$$

where $\hat{P}^{(n)}=|\hat{P}^{(n)}|e^{j\psi^{(n)}}$.

The first term $\vec{I}_{uc}$ of Eq. (14) represents the summation of the intensity field separately generated by each plane wave. The second term $\vec{I}_c(\vec{r})$ represents the intensity components generated by the pressure and velocity coupling between different plane waves. It is noteworthy that no spatial variation exist in the uncoupled intensity component $\vec{I}_{uc}$. The uncoupled intensity term therefore determines the overall direction of the sound intensity field.[11] The coupled intensity, on the other hand, is a spatially varying function, and the amount of spatial variation is determined by the wave number difference as follows:

$$\Delta\vec{k}^{(m,l)}\cdot\vec{r}=(\vec{k}^{(m)}-\vec{k}^{(l)})\cdot\vec{r}. \quad (15)$$

Using these representations, we can describe Eq. (9) in a different form. By introducing the plane wave matrix $\mathbf{E}^{[i,m]}=e^{j\vec{k}^{(m)}\cdot(\vec{r}_m^{(i)}-\vec{r}_s^{(m)})}$ and the wave number matrix $\mathbf{N}^{[i,i]}=\vec{n}_0\cdot\vec{k}^{(i)}$, the transfer function $\mathbf{H}=\hat{H}(\vec{\mathbf{r}}_m|\vec{\mathbf{r}}_s)$ and the space-averaged active intensity can be rewritten as

$$\mathbf{H}=\hat{H}_0\mathbf{E}, \quad \vec{n}_0\cdot\nabla\mathbf{H}=j\hat{H}_0\mathbf{NE}, \quad (16)$$

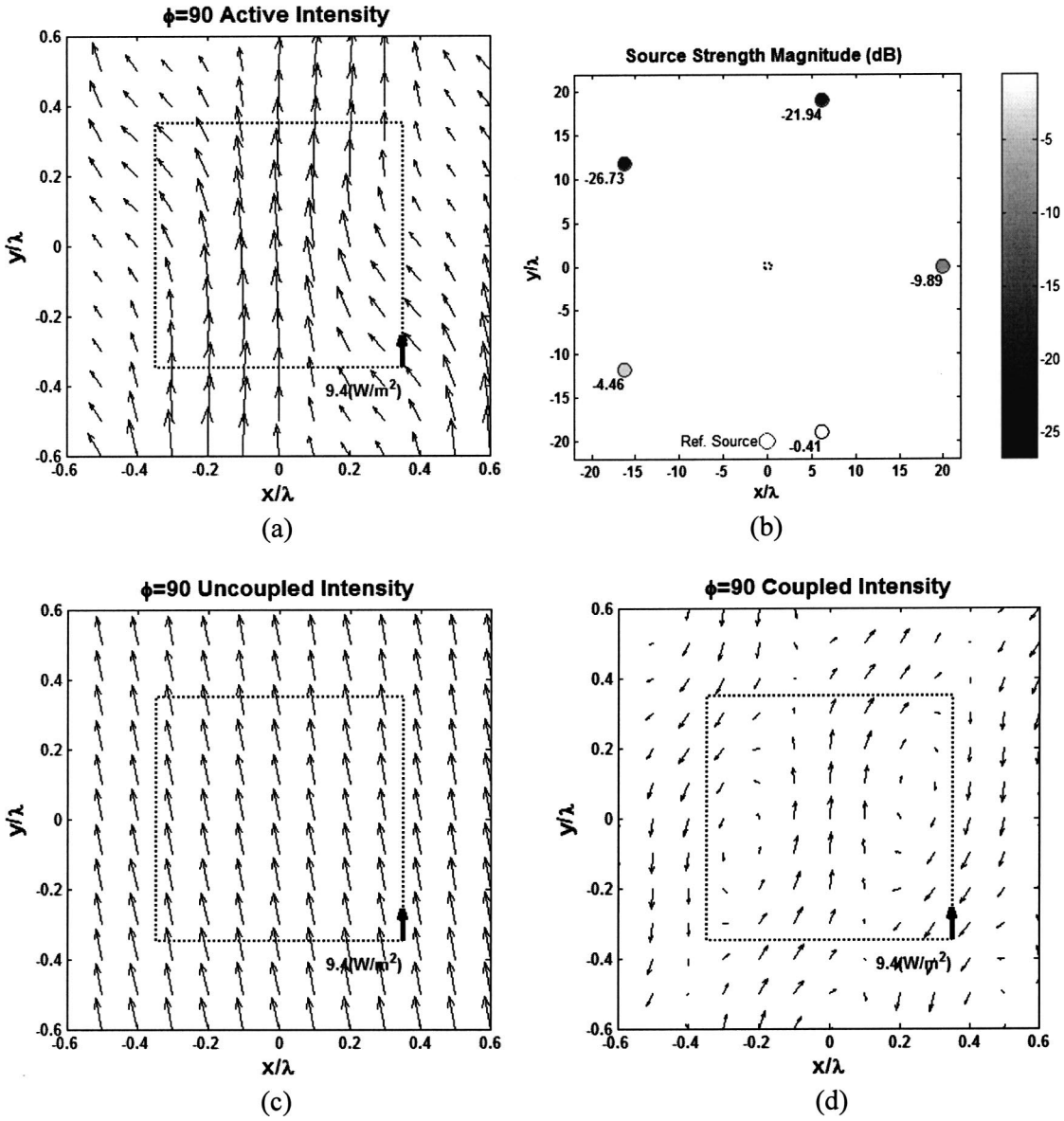

FIG. 7. (Expt. 6) (a) Active intensity field after optimization. (b) Control source position and its strength. (c) Uncoupled intensity component. (d) Coupled intensity component.

$$\overline{I}_{V_0} = \frac{1}{2M}\mathrm{Re}[\hat{u}_{\vec{n}_0}(\vec{\mathbf{r}}_m)^H \hat{p}(\vec{\mathbf{r}}_m)]$$

$$= \frac{|\hat{H}_0|^2}{2\rho_0 \omega M}\mathbf{s}^H \mathrm{Re}[\mathbf{N}\mathbf{E}^H\mathbf{E}]\mathbf{s}. \quad (17)$$

The diagonal terms of matrix $\mathrm{Re}[\mathbf{N}\mathbf{E}^H\mathbf{E}]$ are the uncoupled intensity components, and the off-diagonal terms are the coupled intensity components averaged throughout the control zone. As the zone size of V_0 increases, the spatial correlation of different plane waves decreases, and only the diagonal terms of $\mathbf{E}^H\mathbf{E}$ dominate. As a result, the space-averaged active intensity and the optimal solution approach to

$$\overline{I}_{V_0} \approx \frac{|\hat{H}_0|^2}{2\rho_0 \omega}\mathbf{s}^H\mathbf{N}\mathbf{s}, \quad \alpha_{\max} \approx \max(\vec{n}_0 \cdot \vec{k}^{(i)}). \quad (18)$$

This result means that the coupled intensity has little effect on the cost function, and the optimized sound field is mainly dominated by a single plane wave source whose propagating direction is mostly similar to $\vec{n}_0$. Thus, for a large zone, we observed that the coupled intensity made little contribution to the intensity field, as presented in Fig. 6(d).

From this understanding, the possible size of the control zone is restricted by the spatial variation of the coupled intensity. Because the spatial variation is proportional to the wave number difference between the sources [Eq. (15)], we can increase the size of the zone by decreasing the wave number difference, that is, the angle difference $\Delta\theta$ between the sources. The results shown in Fig. 7 (Expt. 6) present the enhanced control performance by decreasing the angle between the sources. Actually, the number of sources increases as the angle decreases. As shown in Fig. 7(a), the spatial variation of the total intensity field is insignificant, and the coupled intensity field [Fig. 7(c)] cooperates with the uncoupled intensity [Fig. 7(d)] to control the intensity field.

B. Cost function of the second kind

1. Effect of source locations

In the example presented in Fig. 8(b), the source locations are changed so that their distances from the origin are unequal ($R_0 = [1, 1.4, 1.8, 2.2, 2.6]\lambda$). In this case, the active intensity does not flow in the desired direction [Fig. 8(a)]. This phenomenon can be explained as follows: because the given cost function only concerns the magnitude of the intensity projected to the desired direction, the cost function tends to determine the solution with regard to the magnitude of intensity. For example, as presented in Fig. 9, if a solution exists that has a greater intensity magnitude with a less similar direction ($\vec{I}_A$) than another solution $\vec{I}_B$, the first kind of cost function determines $\vec{I}_A$ as the optimal solution. In the case of Fig. 8, the nearest source (source No. 1) generates a greater intensity magnitude than the other sources, and the optimal intensity field therefore tends to shift to the left-hand side [Fig. 8(a)].

Consequently, when the direction of the power flow is more important than the magnitude, the cost function should be modified so that the intensity direction has greater priority than the magnitude. Next illustrates the idea to improve directional characteristics of intensity field.

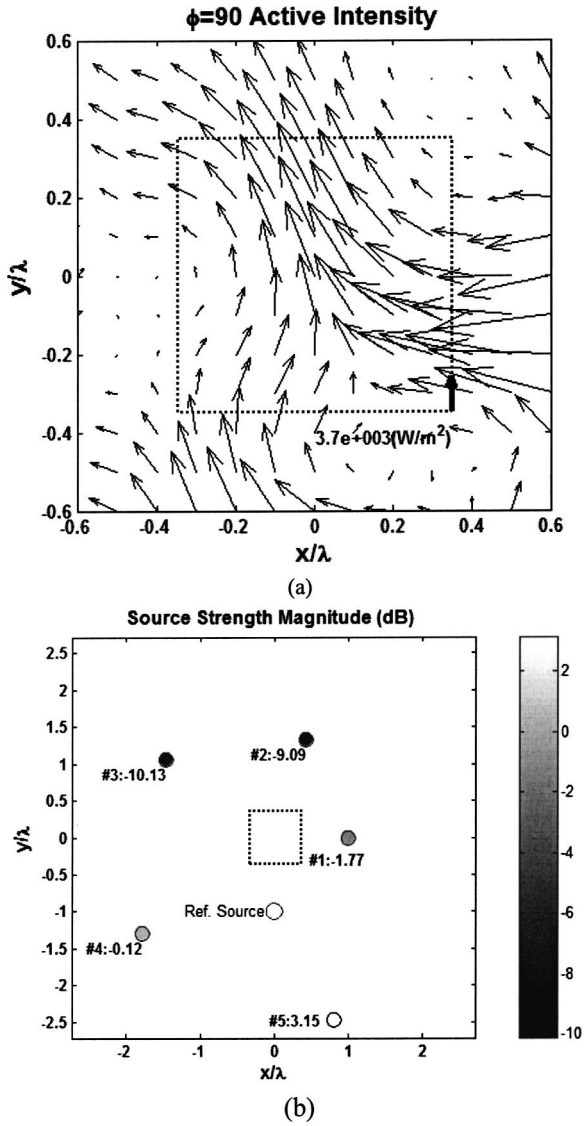

FIG. 8. (Expt. 7) Irregular source distances. (a) Active intensity field after the first kind of optimization. (b) Source locations and their strength magnitude.

2. Modification on the cost function

As noted elsewhere,[8] the acoustic intensity can be interpreted as a product of the acoustic potential energy and the rate of spatial phase change,

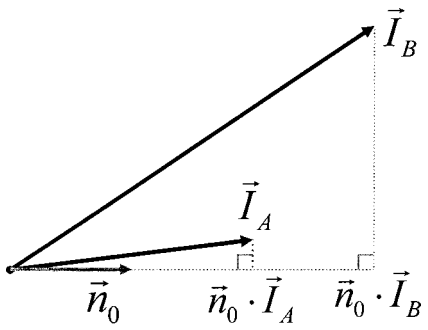

FIG. 9. Problem case of the first kind of optimization.

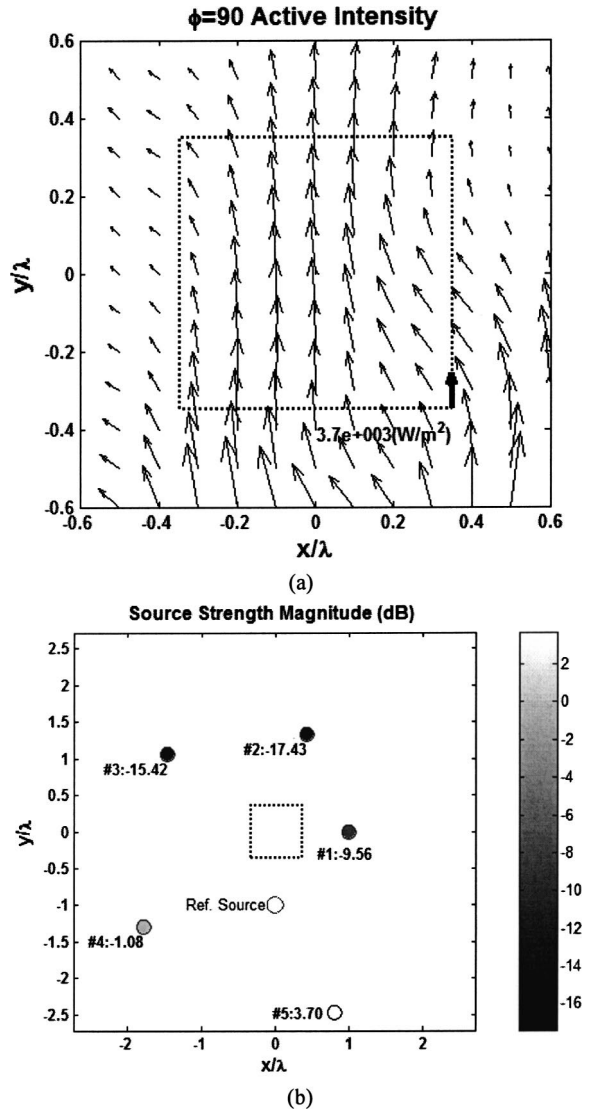

FIG. 10. (Expt. 8) (a) Active intensity field after the second kind of optimization. (b) Source locations and their strength magnitude.

$$\vec{I}_a(\vec{r}) = \frac{1}{2\rho_0\omega}|\hat{p}(\vec{r})|^2 \nabla\psi(\vec{r}), \tag{19}$$

where $\hat{p}(\vec{r}) = |\hat{p}(\vec{r})|e^{j\psi(\vec{r})}$. It is noteworthy that the direction of sound power depends solely on the spatial phase change. Therefore, by decreasing the effect of the acoustic potential energy, we can give greater priority to the spatial phase change $\nabla\psi(\vec{r})$. Our basic idea is normalizing the transfer function of each source, so that every source has the same ability to generate the potential energy in the control zone. In this regard, the first kind of cost function can be modified as follows:

$$\beta = \frac{\mathbf{s}^H \mathbf{C}_{V_0} \mathbf{s}}{(\mathbf{s}^H \,\mathrm{Diag}[\mathbf{H}^H\mathbf{H}/2\rho_0 cM]\mathbf{s})} = \frac{\mathbf{s}^H \mathbf{C}_{V_0} \mathbf{s}}{\mathbf{s}^H \mathbf{E}_{V_0} \mathbf{s}}. \tag{20}$$

Note that each diagonal element of $\mathbf{E}_{V_0}$ is proportional to the space-averaged potential energy generated by each source. Because Eq. (20) is mathematically equivalent to

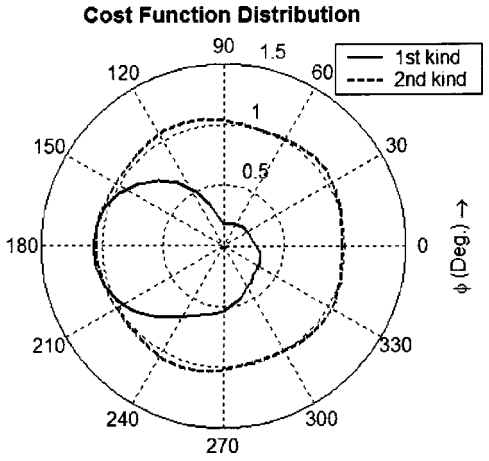

FIG. 11. Comparison of the first and second kind of optimization. Distribution of each cost function with respect to the control angle.

$$\beta = \frac{\mathbf{s}^H(\mathbf{E}_{V_0}^{-1/2}\mathbf{C}_{V_0}\mathbf{E}_{V_0}^{-1/2})\mathbf{s}}{\mathbf{s}^H\mathbf{s}} = \frac{\mathbf{s}^H\mathbf{C}'_{V_0}\mathbf{s}}{\mathbf{s}^H\mathbf{s}}, \tag{21}$$

the modified cost function differs from Eq. (11) in that it uses the transfer function normalized by the root mean value of

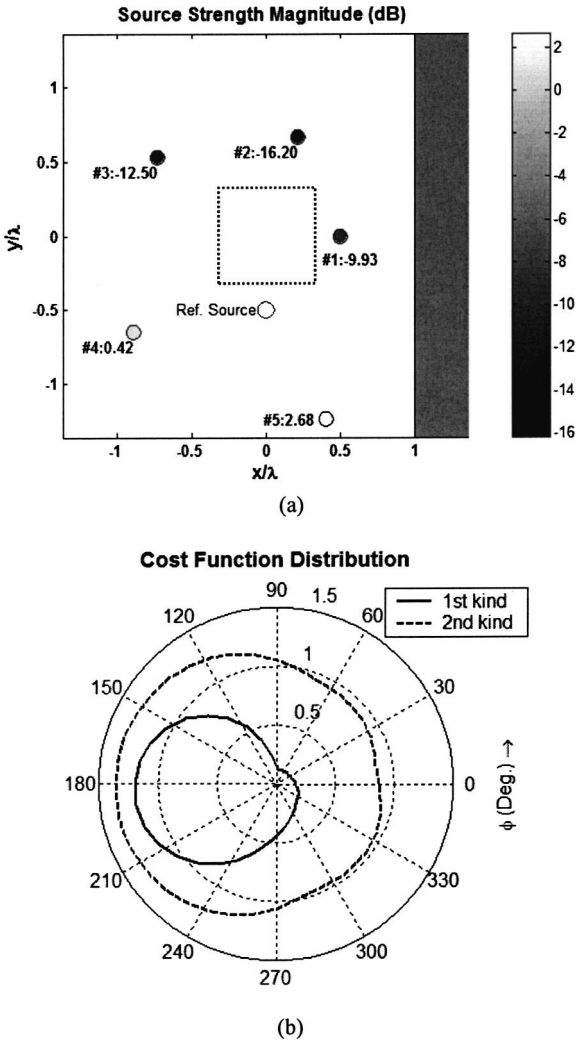

FIG. 12. (Expt. 9) Wall reflection case. (a) Source locations and their strength magnitude. (b) Cost function distribution.

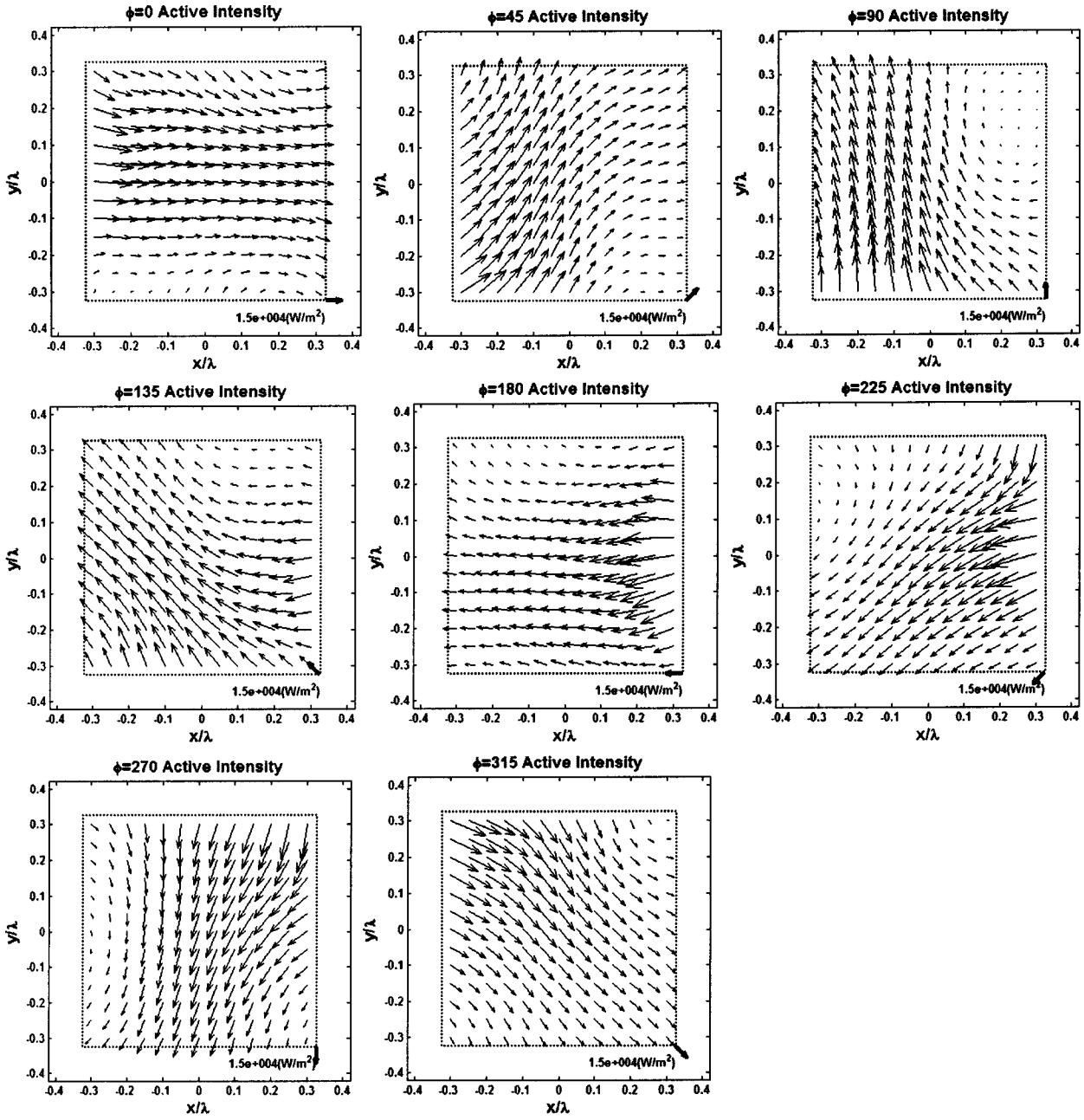

FIG. 13. Resultant intensity fields of Expt. 9 for various control angles.

the acoustic potential energy ($\mathbf{E}_{V_0}^{1/2}$) instead of the normalization constant $|\hat{H}_0|$. The optimal solution of this cost function can be obtained by calculating the eigenvector of matrix $\mathbf{C}'_{V_0}$.

Figure 10 shows improved directional characteristic of intensity field after the second kind of cost function is applied. In contrast to Fig. 8(b), the input power is concentrated on the source No. 5, which radiates sound power in the most similar direction to $\vec{n}_0$. We also examined the control performances for different control directions. The change in both the cost functions with respect to the control direction is presented in Fig. 11, which shows that the first kind of cost function is heavily affected by the control direction though the second kind has a uniform distribution for all directions.

A more complex case is represented in Fig. 12(a). In this simulated case, a rigid boundary was added at position $x=\lambda$, and some sources were brought to near field from the control area ($R=[0.5\,0.7\,0.9\,1.1\,1.3]\lambda$). We also observed that the first kind of cost function is very sensitive to the control direction, whereas the second cost function is relatively unaffected by the presence of a wall [Fig. 12(b)]. Figure 13 shows the resultant intensity fields controlled by the second kind of cost function for various control angles. The intensity fields are slightly affected by the presence of the wall, but they still follow the control direction.

C. Concluding remarks

In general, many factors can influence the optimization performance, such as reflections from the room boundary and directional characteristics of control sources. In addition,

the low modal density of an enclosed sound field and rigid boundary condition decrease the controllability of the intensity field. Although we cannot deal with every possible case, we can predict from our sample cases that the free field results might still hold if the control zone is within the range of direct field dominance. For example, let us consider a reverberant room where the reflected or reverberant field is modeled as diffuse field. If the control sources are not so close to each other, the spatial average of diffuse intensity field converges to zero by the definition of the diffuse sound field. As a result, only direct field contributes to the cost function, and the cost function that involves spatial averaging of intensity field [the numerator of Eqs. (11) and (20)] converges to the value obtained in the free field case. Therefore, the optimal solution might not be changed significantly. However, in the resultant intensity field generated by the optimal solution, random variations might occur due to the existence of reverberant intensity field. To be able to neglect these random variations, the control zone should be in the region where the direct field dominates; that is, at least closer than the radius of reverberation. Other work in this field has shown that the radius of reverberation defined in terms of intensity is three to eight times larger than the classical definition that uses an energy density ratio.[14] This result means that there is more area where the direct field dominates.

IV. CONCLUSION

In proposing a method of maximizing the active intensity of a zone, we defined the space-averaged active intensity to represent the intensity distribution of a zone. To express the space-averaged active intensity in terms of the source signal, we developed a quadratic formulation based on the $p-p$ measurement technique and formulated an optimization problem with an input power constraint.

As an extreme example, a simple free-field condition was examined. We inspected the coupled and uncoupled components of active intensity and found that the possible size of the control zone can be enlarged by decreasing the angle between the sources. From the original method of maximizing sound power using finite control effort, we proposed a modified cost function that is more focused on the direction of the intensity field. Numerical simulations under various circumstances showed that the modified approach has a better directional characteristic and is more robust with respect to the control direction.

ACKNOWLEDGMENTS

This study was partly supported by the NRL (National Research Laboratory) project of KISTEP (Korea Institute Of Science and Technology Evaluation and Planning) and the BK21 (Brain Korea 21) project initiated by Ministry of Education and Human Resources Development of Korea.

[1] J. W. Choi and Y. H. Kim, ''Generation of an acoustically bright zone within an illuminated region,'' J. Acoust. Soc. Am. **111**, 1695–1700 (2002).
[2] J. W. Choi and Y. H. Kim, ''Generation of acoustically bright and dark zone using multiple sources,'' on the CD-ROM: in Proceedings of Inter-Noise 2002, the 2002 International congress and exposition on noise control engineering, Held in Dearborn, Michigan on 2002 August 19–21, edited by A. Selamet, R. Singh and G. C. Maling, International Institute of noise control enginering, 2002, paper N202.
[3] P. A. Nelson and S. J. Elliot, ''The minimum power output of a pair of free field monopole sources,'' J. Sound Vib. **105**, 173–178 (1986).
[4] C. G. Mollo and R. J. Bernhard, ''Numerical evaluation of the performance of active noise control systems,'' ASME J. Vibr. Acoust. **112**, 230–236 (1990).
[5] K. A. Cunefare and G. H. Koopmann, ''A boundary element approach to optimization of active noise control sources on three-dimensional structures,'' ASME J. Vibr. Acoust. **113**, 387–394 (1990).
[6] S. W. Kang and Y. H. Kim, ''Causally constrained active sound power control in an enclosed space,'' J. Sound Vib. **204**, 807–822 (1997).
[7] R. H. Bolt and A. A. Petrauskas, ''An acoustic impedance meter for rapid field measurements,'' J. Acoust. Soc. Am. **13**, 124–136 (1941).
[8] F. J. Fahy, *Sound Intensity* (Elsevier Applied Science, London, 1989), Chap. 5, pp. 91 and 92.
[9] P. Lancaster and M. Tismenetsky, *The Theory of Matrices*, 2nd ed. (Academic, San Diego, CA, 1985), pp. 282–294.
[10] G. Krishnappa, ''Acoustic intensity in the nearfield of two interfering monopoles,'' J. Acoust. Soc. Am. **74**, 1291–1294 (1983).
[11] J. C. Pascal, ''Structure and patterns of acoustic intensity fields,'' in Proceedings of the Second International Congress on Acoustic Intensity, Held in Senlis, France on 1985 September 23–26, published by Centre technique des industries maecaniques (CETIM), 1985, pp. 97–104.
[12] S. Y. Ham, W. S. Kim, and M. G. Prasad, ''Interference studies of acoustic pressure and intensity fields of two simple sources,'' J. Acoust. Soc. Am. **90**, 1149–1154 (1991).
[13] M. G. Prasad, S. Y. Ham, and W. Kim, ''A generalized interference study of acoustic intensity and pressure fields of sources,'' in Proceedings of Noise-Con 87, Held at The Pennsylvania State University, Pennsylvania on 1987, June 08–10, edited by Jiri Tichy and Sabih Hayek, Institute of noise control engineering of the USA, 1987, pp. 573–578.
[14] F. Jacobsen, ''Active and reactive sound intensity in a reverberant sound field,'' J. Sound Vib. **143**, 231–240 (1990).

The stability of multichannel sound systems with frequency shifting

Mark A. Poletti
Industrial Research Ltd., P.O. Box 31-310, Lower Hutt, New Zealand

(Received 21 September 2003; revised 4 April 2004; accepted 2 May 2004)

Time-varying components are used in some multichannel sound systems designed for the enhancement of room acoustics. Time-variation can usefully reduce the risk of producing ringing tones and improve stability margins, provided that any modulation artefacts are inaudible. Frequency-shifting is one form of time-variation which provides the best case improvement in loop gain, and for which the single channel stability limit has been derived. This paper determines the stability limit for multiple channel systems with frequency-shifting by generalizing the previous single-channel analysis. It is shown that the improvement in stability due to frequency-shifting reduces with the number of channels. Simulations are presented to verify the theory. The stability limits are also compared with those of time-invariant systems, and preliminary subjective assessments are carried out to indicate useable loop gains with frequency-shifting. © *2004 Acoustical Society of America.* [DOI: 10.1121/1.1763972]

PACS numbers: 43.38.Tj, 43.55.Jz [MK] Pages: 853–871

I. INTRODUCTION

Sound systems are limited in the maximum amplification they can provide by regenerative feedback of sound from the loudspeakers to the microphones, which causes instability at high loop gains. For single channel systems with flat transfer functions in their electronic processors, the mean loop gain μ must be kept below -12 dB to avoid ringing tones or instability.[1,2] For systems with N broadband independent channels the total mean loop power gain $\mu^2 N$ rises with the number of channels, allowing a greater enhancement of early energy and reverberation time (RT).[3]

A common application of multichannel sound systems is in room acoustic enhancement systems.[1,4–7] For systems without electronic reverberation devices, the room reverberation time gain is approximately equal to the steady state sound intensity gain Γ,[1]

$$\Gamma = \frac{1}{1-\mu^2 N}. \tag{1}$$

Multichannel acoustic enhancement systems aim to provide sound quality which is indistinguishable from a natural room with enhanced acoustic properties. Therefore, they must provide a more subtle sound enhancement than that produced by typical sound systems, and with a lower risk of unnatural artefacts. For example, the tolerance of ringing tones from a sound system is lower in a classical music concert than it would be at a rock concert. For this reason, eliminating ringing tones, and other more subtle colouration effects that might occur at lower loop gains, is of primary importance. The use of multiple channels allows increased power gains with a reduced risk of colouration artefacts. Nevertheless, unnatural artefacts can still occur at high loop gains.

Aside from multiple channels, there are three other methods available for achieving increased loop gains and reducing unnatural artefacts. The first is the use of equalization.[8–13] Broadband equalization allows the loop gain to be maximized across all frequencies. Narrowband equalization allows individual ringing tones to be eliminated, but has the risk that the ringing frequency can change with small changes in microphone positions or room characteristics. A more stable approach is the use of adaptive filters which lock onto and null ringing tones.[14–16] These systems must distinguish between musical tones and ringing tones, but several commercial devices are available which suggest that this is feasible. A more comprehensive adaptive strategy is to have a filter adapt to the inverse of the loop transfer function, which renders the loop transfer function a simple delay. Alternatively, echo cancellation methods can in principle allow the cancellation of the loudspeaker to microphone signal, eliminating feedback.[17] These adaptive filter strategies rely on the robustness of an adaptive algorithm to allow the sound system to operate well above the naturally occurring stability limit.

For multichannel systems, both inverse and echo-cancellation methods require the measurement of the loop transfer function matrix which is problematic due to the large amount of memory and processing required. In addition the inverse equalization method requires calculation of the inverse of the matrix, which imposes a further large processing burden.

The second method for increasing loop gains is to employ artificial reverberation devices to provide greater reverberation gain for a given loop gain.[7,18–21] Most of these applications are in in-line systems, where the microphones are close to the sound sources. In Ref. 7 it is shown that a reverberator in a non-in-line system is the electroacoustic equivalent of a coupled room and that high reverberation gains are possible at moderate loop gains, provided that the loop gain is high enough to prevent double-sloping effects. It has also been shown that sound system stability may be improved by using unitary reverberators which produce a constant power gain with frequency, further reducing colouration effects.[22]

The third approach to controlling colouration is the use

of time-varying systems, which slowly change their transfer functions with time to prevent the build-up of ringing tones.[23–29] These systems are not as sensitive to changes in the room acoustics as narrowband equalization and are inherently more robust, and simpler, than adaptive systems.

There are several methods of producing time variation, such as delay modulation, phase- and frequency-modulation and frequency-shifting. Delay modulation provides a frequency shift which rises linearly with frequency. Therefore, it produces a reduced risk of coloration at high frequencies, but may not improve performance at low frequencies.[30] In some cases time-varying delays are incorporated into a digital reverberation device which produces a more complicated phase and amplitude variation with frequency.

Phase-modulation alters the signal phase at each frequency without affecting the amplitude. It can be carried out using time-varying allpass filters, but these produce a phase deviation that varies with frequency. A more precise method of phase modulation is achieved by taking the analytic signal and modulating it with a complex modulation of the form $\exp[j\phi(t)]$. This provides the same phase variation at all frequencies and a more consistent control of feedback across the signal bandwidth. If the complex phase function is analytic, then all components of the signal are shifted by positive frequency shifts.[31]

Frequency-shifting (FS) is a special case of analytic phase-modulation using a linear phase sinusoid. The input signal is made analytic by eliminating the negative frequencies and the frequency shifted output is the real part of the modulated signal. This single sideband technique shifts the positive frequencies in the signal by ω_0 and the negative frequencies by $-\omega_0$.[32]

The stability of sound systems with frequency-shifting has been investigated by Schroeder.[23] He developed methods for determining the maximum loop gain possible in a single channel system with and without frequency-shifting. Without frequency-shifting, his loop gain for a 50% risk of instability was -8 dB for a reverberation time, bandwidth product of 10 000. With frequency-shifting the loop gain could theoretically be increased to 2.5 dB, an increase of 10.5 dB. However, at this value the sound quality was found to be strongly affected by modulation artefacts. In practice, Schroeder determined that a 2 dB stability margin was required without FS, and a 6 dB margin was required with FS in order to avoid audible beating effects. The net benefit due to FS was then about 6 dB.

Nielsen and Svensson have recently considered the performance of periodic phase, frequency and delay modulation in single channel systems.[29] They review the theory of frequency-shifting and show that it is the most efficient method for controlling regenerative feedback since it completely smooths the loop gain and provides infinite carrier suppression.

While frequency-shifting provides the maximum possible loop gain increase, it may not produce subjectively acceptable performance for music applications. There are two reasons. First, the frequency shift is a significant fraction of a semitone at low frequencies. For example a 5 Hz shift is about a semitone at 82 Hz (low E on a guitar). Delay modulation avoids this issue but has poor stability control at low frequencies.[29] Secondly, the frequency shift is strictly positive each time the signal goes around the feedback loop (for positive modulation frequencies). The subjective effect at high loop gains is that the signal frequency rises with time which is subjectively unacceptable. However, other time-variation components which produce both positive and negative frequency shifts exhibit other problems.[29] Systems which have nonzero carrier suppression (a nonshifted component) provide a reduced stability improvement, and those which produce both positive and negative sidebands produce a net shift of zero after two or more times through the feedback loop, which also limits stability.

Nielsen and Svensson suggest that time-variation may be more successful in room enhancement systems where the sound enhancement is more subtle than that provided by sound reinforcement systems.[29] For example, frequency-shifting may offer useful control of ringing and improve the loop gain provided that the shift is small enough to avoid low-frequency problems and the loop gain increase is not too great.

The analysis of time-varying systems has to date concentrated on single channel systems, although some experiments on a four-channel time-varying system are reported in Ref. 30. However, no analysis of the theoretical performance gains that can be achieved using time-variation in multichannel systems has been carried out.

In this paper, an analysis of frequency-shifting in multichannel systems is undertaken. Frequency-shifting is the simplest form of time-variation to analyze and, as discussed above, it provides the best-case increase in loop gain. The analysis of the multichannel case follows that in Schroeder's paper and Ref. 29. The multichannel extension of this work is based on a norm approximation for the total power gain of the loop transfer function matrix.

Two forms of simulations are carried out to verify the theory. Monte Carlo stability simulations are used first to verify the theoretical loop gain limits, and then a time-varying system simulator based on digital reverberators is used to allow a more detailed investigation of the behavior of sound systems with frequency-shifting.

Finally, the frequency-shifting stability limits are compared with the stability limits for time-invariant systems and subjective tests are carried out in order to estimate the practically useable loop gain for both cases. The practical increase in loop gain brought about by frequency-shifting is then estimated.

II. THEORETICAL STABILITY LIMITS

A. Review of power gains

The analysis of multichannel frequency-shifting is based on the power gain of the loop transfer function matrix. The power gain is therefore briefly reviewed here.

Consider a room containing N loudspeakers and microphones. Assume that the distances between loudspeakers and microphones are large enough so that the reverberant sound transmission dominates the direct sound. Each transfer function $H_{nm}(\omega)$ then has real and imaginary parts which are

normally distributed (with transducer positions) with zero mean and equal variances $\sigma_I^2=\sigma_R^2$.[23] The magnitude $|H_{nm}(\omega)|$ is Rayleigh distributed.

If a signal with power spectral density (psd) $S_{uu}(\omega)$ is input to $H_{nm}(\omega)$, the output psd is[33]

$$S_{vv}(\omega)=|H_{nm}(\omega)|^2 S_{uu}(\omega). \tag{2}$$

The power gain at each frequency is then $|H_{nm}(\omega)|^2$.

The mean power gain may be found as the expected value of $|H_{nm}(\omega)|^2$ over the ensemble of all possible microphone and loudspeaker positions. $|H_{nm}(\omega)|^2=H_{nmR}^2(\omega)+H_{nmI}^2(\omega)$ is χ-squared distributed with two degrees of freedom and so[34]

$$E\{|H_{nm}(\omega)|^2\}=2\sigma_R^2. \tag{3}$$

Assume further without loss of generality that the mean power gain of each transfer function is unity ($\sigma_R^2=1/2$), and that the output of each microphone preamplifier is attenuated by a factor μ to control stability.

Consider now the matrix of all transfer functions, **H**. Assume that N uncorrelated signals with the same power spectrum $S_{uu}(\omega)$ are applied to the N inputs of **H**. (This is realistic if the microphones receive predominantly reverberant energy and have the same sensitivities and preamplifier gains.) The power at each output of **H** is then the sum of the powers arriving from each input

$$S_{vvn}(\omega)=\sum_{m=1}^{N}|H_{nm}|^2 S_{uu}(\omega) \tag{4}$$

and the total output power is

$$S_{vv}(\omega)=\sum_{m=1}^{N}\sum_{n=1}^{N}|H_{nm}|^2 S_{uu}(\omega)=\|\mathbf{H}\|^2 S_{uu}(\omega), \tag{5}$$

where $\|\,\|$ denotes the Frobenius norm of **H**. The total input power is $NS_{uu}(\omega)$. Therefore the total power gain is

$$\Gamma_H=\frac{1}{N}\|\mathbf{H}\|^2. \tag{6}$$

The expected value of the power gain is, with the assumptions above

$$E\{\Gamma_H\}=\frac{1}{N}N^2=N. \tag{7}$$

This is scaled by μ^2 to control stability.

B. Frequency-shifting and analytic signal analysis

In frequency-shifting a real signal $s(t)$ is made complex by deriving an imaginary part $\hat{s}(t)$ which is the Hilbert transform of $s(t)$,[33]

$$s_a(t)=s(t)+j\hat{s}(t). \tag{8}$$

This analytic signal has no negative frequency components. Frequency-shifting is carried out by multiplying the analytic signal by $\exp(j\omega_0 t)$ and taking the real part of the result

$$\mathrm{Re}\{s_a(t)e^{j\omega_0 t}\}=s(t)\cos(\omega_0 t)-\hat{s}(t)\sin(\omega_0 t), \tag{9}$$

which reintroduces negative frequency components such that the spectrum is Hermitian.[33]

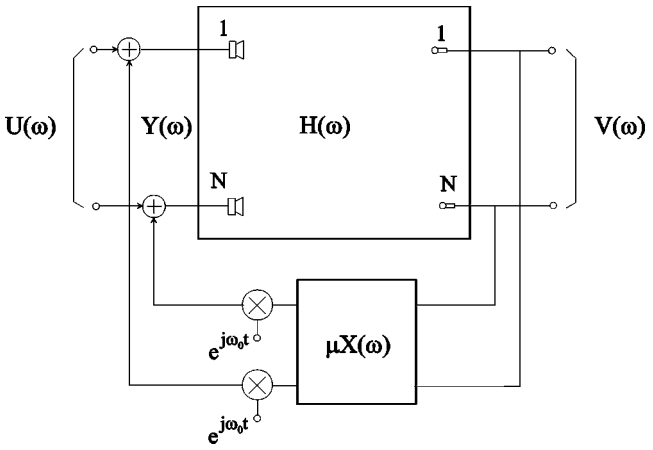

FIG. 1. Multichannel sound system with frequency-shifting, assuming an analytic input signal.

The analytic signal is often used in the analysis of time-invariant physical systems, because any real, physical signal is simply the real part of the associated analytic signal. The same approach is followed here. However, in the case of time-varying systems, the analytic signal is modulated and this modulation may produce negative frequency components. In frequency-shifting, this occurs for large, negative frequency shifts. In the application of interest here the frequency shift is small, and the room transfer functions have magnitudes that reduce to zero at zero Hz (since the loudspeaker responses are zero at dc). Therefore the modulated analytic signal will also remain analytic for negative frequency shifts. Hence, the analysis of stability with frequency-shifting may be carried out using analytic signals, and the spectrum of the output signal for the associated real signal is simply the Hermitian part of the analytic signal output.

C. Multichannel systems with frequency-shifting

Consider the regenerative system shown in Fig. 1. The transfer function matrix from the N loudspeaker inputs to the N microphone outputs is $\mathbf{H}(\omega)$. For simplicity, we have omitted the use of separate input and output transfer functions as in Ref. 2, since this has no effect on the stability. The input signals are applied directly to the N system loudspeakers. The stability of the system will be examined by considering the vector of spectra at the input to the room, Y. In the time invariant case, this is given by

$$Y=[\mathbf{I}-\mu\mathbf{XH}]^{-1}U=\mathbf{H}^{-1}[\mathbf{I}-\mu\mathbf{HX}]^{-1}\mathbf{H}U. \tag{10}$$

The stability of the time-invariant system is governed by the scaled eigenvalues of **XH**, which are the same as those of **HX**.[35] The output vector is $V=\mathbf{H}Y$ which has the same stability criteria as Y.

For the time-variant case, we assume for simplicity of analysis that all microphones signals are frequency shifted by the same modulation function $\exp[j\omega_0 t]$. As discussed above, we assume an input signal $U(\omega)$ which is analytic. The vector of spectra $Y(\omega)$ at the inputs to the room with frequency-shifting may then be written

$$Y(\omega)=U(\omega)+\mu\mathbf{X}(\omega-\omega_0)\mathbf{H}(\omega-\omega_0)Y(\omega-\omega_0) \tag{11}$$

Substituting for $Y(\omega-\omega_0)$ from the same equation

$$\begin{aligned}Y(\omega)&=U(\omega)+\mu\mathbf{X}(\omega-\omega_0)\mathbf{H}(\omega-\omega_0)[U(\omega-\omega_0)\\&\quad+\mu\mathbf{X}(\omega-2\omega_0)\mathbf{H}(\omega-2\omega_0)Y(\omega-2\omega_0)]\\&=U(\omega)+\mu\mathbf{X}(\omega-\omega_0)\mathbf{H}(\omega-\omega_0)U(\omega-\omega_0)\\&\quad+\mu^2\mathbf{X}(\omega-\omega_0)\mathbf{H}(\omega-\omega_0)\mathbf{X}(\omega-2\omega_0)\\&\quad\times\mathbf{H}(\omega-2\omega_0)Y(\omega-2\omega_0).\end{aligned}\tag{12}$$

This procedure may be continued, and the vector of spectra is given by the infinite series

$$\begin{aligned}Y(\omega)&=U(\omega)+\mu\mathbf{X}(\omega-\omega_0)\mathbf{H}(\omega-\omega_0)U(\omega-\omega_0)\\&\quad+\mu^2\mathbf{X}(\omega-\omega_0)\mathbf{H}(\omega-\omega_0)\mathbf{X}(\omega-2\omega_0)\mathbf{H}(\omega-2\omega_0)\\&\quad\times U(\omega-2\omega_0)\cdots+\mu^M\left[\prod_{m=1}^{M}\mathbf{X}(\omega-m\omega_0)\right.\\&\quad\left.\times\mathbf{H}(\omega-m\omega_0)\right]U(\omega-M\omega_0)+\cdots.\end{aligned}\tag{13}$$

If the system is to be stable the output power must be finite for a finite input power. The total power in all channels that contributes to Y after M iterations through the feedback loop is the total input power multiplied by the power gain

$$\Gamma_M=\frac{\mu^{2M}}{N}\left\|\prod_{m=1}^{M}\mathbf{X}(\omega-m\omega_0)\mathbf{H}(\omega-m\omega_0)\right\|^2.\tag{14}$$

D. Stability analysis for unitary systems

We consider first the case where there is no second transfer function matrix $\mathbf{X}$, and each output is connected directly via a frequency-shifter and loop gain to the corresponding input. The power gain becomes

$$\Gamma_M=\frac{\mu^{2M}}{N}\left\|\prod_{m=1}^{M}\mathbf{H}(\omega-m\omega_0)\right\|^2.\tag{15}$$

This expression is more problematic than the single channel case, because the squared norm of the product of matrices is not equal to the product of the squared norms unless $N=1$. It is known that for products of matrices, the following inequality holds:[35]

$$\left\|\prod_{m=1}^{M}\mathbf{H}(\omega-m\omega_0)\right\|^2<\prod_{m=1}^{M}\|\mathbf{H}(\omega-m\omega_0)\|^2,\tag{16}$$

but this does not provide a tight enough bound to allow the stability to be accurately determined. However, for the case where the frequency shifted matrices are uncorrelated, consisting of entries which are complex, zero-mean, and whose real and imaginary parts are normally distributed, it can be shown (Appendix A) that

$$\left\|\prod_{m=1}^{M}\mathbf{H}(\omega-m\omega_0)\right\|^2\approx\frac{1}{N^{[M-1]}}\prod_{m=1}^{M}\|\mathbf{H}(\omega-m\omega_0)\|^2.\tag{17}$$

This approximation is good for large N, but is less accurate for small N, becoming least accurate for $N=2$.

The transfer functions in $\mathbf{H}$ have identical real part and squared-magnitude covariances of [36]

$$\rho(\omega_0)=\frac{1}{1+\left(\frac{\omega_0 T}{13.8}\right)^2},\tag{18}$$

where T is the reverberation time. The covariance is 0.2 for $\omega_0=27.6/T$ and the norm approximation should be reasonably accurate (up to the accuracy governed by N) for frequency shifts greater than this value. For a reverberation time of 1 s this requires a frequency shift of 4.4 Hz.

Using the norm approximation, the power gain

$$\Gamma_M\approx\frac{\mu^{2M}}{N^M}\prod_{m=1}^{M}\|\mathbf{H}(\omega-m\omega_0)\|^2\tag{19}$$

must reduce to zero as M tends to infinity. Writing the approximation in dB

$$\begin{aligned}10\log(\Gamma_M)&=M\mu_{\mathrm{dB}}-M10\log(N)\\&\quad+\sum_{m=1}^{M}10\log[\|\mathbf{H}(\omega-m\omega_0)\|^2]\rightarrow-\infty\end{aligned}\tag{20}$$

as M tends to infinity. For large M, the summation tends to the scaled mean of the norm in dB,

$$\begin{aligned}10\log(\Gamma_M)&=M[\mu_{\mathrm{dB}}-10\log(N)+\overline{10\log[\|\mathbf{H}(\omega)\|^2]}]\\&\rightarrow-\infty,M\rightarrow\infty\end{aligned}\tag{21}$$

the stability requirement then becomes

$$\mu_{\mathrm{dB}}<10\log(N)-\overline{10\log[\|\mathbf{H}(\omega)\|^2]}.\tag{22}$$

In Appendices B and C it is shown that

$$\begin{aligned}\overline{10\log[\|\mathbf{H}(\omega)\|^2]}&=\frac{10}{\ln(10)}\Psi(N^2)\\&=\frac{10}{\ln(10)}\left[\sum_{k=1}^{N^2-1}\frac{1}{k}-C\right],\end{aligned}\tag{23}$$

where Ψ (.) is the psi function,[37] and so the stability limit is

$$\mu_{\mathrm{dB}}<10\log(N)-\frac{10}{\ln(10)}\Psi(N^2).\tag{24}$$

This is the stability requirement for an N channel system with identical frequency-shifting in each channel, assuming that the norm approximation is accurate. For $N=1$ it yields $\mu_{\mathrm{dB}}<2.5$ as in the original analysis.[23] The maximum loop gain with frequency-shifting reduces with N. For example, it is -12 dB for a 16 channel system. This is in keeping with the maximum loop gain per channel without frequency-shifting, which also decreases with N.

The stability limit also applies to multichannel systems with unitary processors in their feedback loops, since a unitary matrix does not alter the loop power gain. Specifically, if $\mathbf{X}$ is a unitary matrix, then

$$\|\mathbf{XH}\|^2=\mathrm{Tr}\{(\mathbf{XH})^\dagger(\mathbf{XH})\}=\mathrm{Tr}\{\mathbf{H}^\dagger\mathbf{X}^\dagger\mathbf{XH}\}=\|\mathbf{H}\|^2,\tag{25}$$

where † denotes the conjugate transpose and Tr the trace function.

E. Stability analysis with finite *M*

The analysis in the previous section requires that the sound regenerate through the feedback loop a large number of times. This requirement is satisfied in wideband systems with small frequency shifts. However for bandlimited systems, and high-frequency input signals, the number of iterations M will be smaller than for low frequency signals. It is therefore instructive to consider the stability analysis for a finite M. The analysis will also be useful for verification of the stability equation using Monte Carlo simulations.

Consider Eq. (20). The stability condition is obtained by assuming that the summation tends to the average of the norm in dB, scaled by M. An alternative viewpoint is that the summation is a random variable (with microphone and loudspeaker position) which tends to a normal variable as M increases. Provided that ω_0 is large enough each term in the sum is independent of the others, and has the form $10\log(y_m)$, where $y_m=\|H(\omega-m\omega_0)\|^2$. The squared norm y_m is χ-squared distributed with $n=2N^2$ degrees of freedom. The mean of the squared norm in dB is given by Eq. (23) and the variance is (Appendix B)

$$\sigma_y^2=\mathrm{var}\{10\log(y)\}=\left(\frac{10}{\ln(10)}\right)^2\zeta(2,N^2)=\left(\frac{10}{\ln(10)}\right)^2\left[K-\sum_{k=1}^{N^2-1}\frac{1}{k^2}\right], \tag{26}$$

where $K=1.644924$ and $\zeta(2,N^2)$ is the Riemann zeta function (Appendix C).

The sum of M terms, by the Central limit theorem, tends to a normal density with mean $M\overline{y}$ and variance $M\sigma_y^2$. If y is scaled by a loop gain μ^2 the probability of instability is then

$$\Pr\{\mathrm{inst},\mathbf{H}\}(\mu_{\mathrm{dB}},N,M)=\Pr\left\{\sum_{m=0}^{M-1}10\log(\mu^2 y_m)>10M\log(N)\right\} \tag{27}$$

[this is equivalent to saying that the power gain of the Mth term in Eq. (13) is greater than one]. Hence

$$\Pr\{\mathrm{inst},\mathbf{H}\}(\mu_{\mathrm{dB}},N,M)=\frac{1}{2}-\frac{1}{2}\mathrm{erf}\left(\sqrt{\frac{M}{2}}\frac{10\log(N)-\mu_{\mathrm{dB}}-\frac{10}{\ln(10)}\Psi(N^2)}{\frac{10}{\ln(10)}\sqrt{\zeta(2,N^2)}}\right), \tag{28}$$

where erf is the error function. The 50% risk of instability occurs when the argument of the erf function is zero, which yields the stability limit in Eq. (24). As M increases, the transition from 0 to 1 through the 50% value as μ increases becomes increasingly rapid, and for large M the stability limit is sufficient to characterize the stability of the system.

F. Stability analysis for systems including reverberators

We now consider the case where the second transfer function matrix $\mathbf{X}$ represents a nonunitary reverberator. Many sound systems include reverberators to enhance the sound transmitted into the room. This increases the variance of the power gain of the feedback loop. In time-invariant systems this means that the loop gain must be reduced to maintain stability. With frequency-shifting, it has been shown that for single channel systems this increased variance allows a higher loop gain to be achieved than that without a reverberator present.[29]

We will assume that the reverberator has the same statistical norm properties as the room matrix $\mathbf{H}$ but is scaled by $1/\sqrt{N}$ to have unit power gain, which allows comparison with the unitary case. Equivalently, $\mathbf{X}$ is statistically identical to $\mathbf{H}$ and the loop gain is scaled by $1/\sqrt{N}$.

The stability requirement is given by Eq. (22), but the matrix $\mathbf{H}$ is replaced by $\mathbf{XH}$, and the division by $\sqrt{N}$ introduces an additional $10\log(N)$ to the loop gain

$$[\mu_{\mathrm{dB}}-10\log(N)]<10\log(N)-\overline{10\log[\|\mathbf{X}(\omega)\mathbf{H}(\omega)\|^2]}. \tag{29}$$

Treating $\mathbf{H}$ and $\mathbf{X}$ as independent, identically distributed matrix random variables, and using the norm approximation

$$\overline{10\log[\|\mathbf{XH}\|^2]}\approx\overline{10\log\left[\frac{1}{N}\|\mathbf{X}\|^2\|\mathbf{H}\|^2\right]}=20\,\overline{\log[\|\mathbf{H}\|^2]}-10\log(N) \tag{30}$$

the stability requirement is

$$\mu_{\mathrm{dB}}+20\,\overline{\log[\|\mathbf{H}(\omega)\|^2]}<30\log(N). \tag{31}$$

Substituting for $20\,\overline{\log[\|\mathbf{H}(\omega)\|^2]}$ from Appendix B yields the stability criterion

$$\mu_{\mathrm{dB}}<30\log(N)-\frac{20}{\ln(10)}\Psi(N^2). \tag{32}$$

The analysis for a finite number of iterations through the feedback loop may be carried out in a similar manner to the previous case. Applying the norm equality to $\mathbf{XH}$ it may be shown that the mean with normalized $\mathbf{X}$ is

$$10\log\left\|\frac{1}{\sqrt{N}}\mathbf{XH}\right\|^2=-20\log(N)+\frac{20}{\ln(10)}\Psi(N^2). \tag{33}$$

The variance of the norm in dB is unaffected by the $1/\sqrt{N}$ scaling, and is twice that without a reverberator [see Eqs. (30) and (26)]

$$\mathrm{var}\left\{10\log\left\|\frac{1}{\sqrt{N}}\mathbf{XH}\right\|^2\right\}=2\left(\frac{10}{\ln(10)}\right)^2\zeta(2,N^2). \tag{34}$$

The stability for M iterations is then

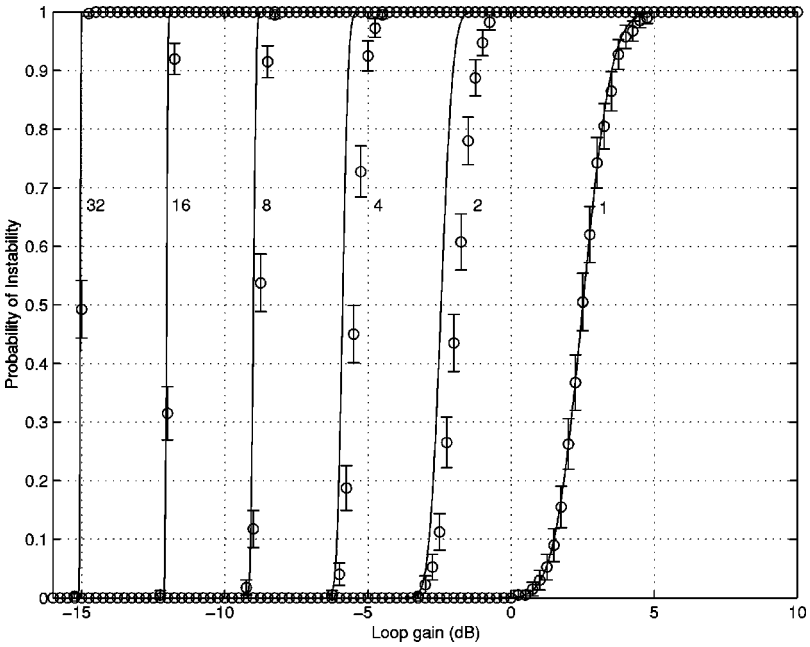

FIG. 2. Monte Carlo Simulation results for sound system with unitary feedback for $N=1-32$.

$$\Pr\{\text{inst},\mathbf{XH}\}(\mu_{\text{dB}},N,M) = \frac{1}{2}-\frac{1}{2}\text{erf}\left(\frac{\sqrt{M}}{2}\frac{30\log(N)-\mu_{\text{dB}}-\frac{20}{\ln(10)}\Psi(N^2)}{\frac{10}{\ln(10)}\sqrt{\zeta(2,N^2)}}\right). \quad (35)$$

The 50% risk loop gain is then given by the right-hand side of Eq. (32).

III. STABILITY SIMULATIONS

A. Introduction

The validity of the theoretical stability limits were investigated using two forms of simulation. In the first, Monte Carlo simulations were carried out to assess Eqs. (28) and (35) for a finite value of M. The 50% risk values of these simulations should match the stability limits in Eqs. (24) and (32). In the second approach a digital reverberator was used to represent a room and feedback was applied from N outputs to N inputs via frequency shifters. A second reverberator could be optionally included in the feedback loop to simulate the inclusion of a reverberator in a sound system.

B. Monte Carlo simulations

The transfer function matrix between a loudspeaker and microphone in a room has real and imaginary parts which are normally distributed, provided that the direct sound level is small compared to the reverberant sound level. The correlation functions of the real and imaginary parts are as given in Eq. (18). Therefore, complex random processes may be generated using an autoregressive (AR) process which produce the same statistical and correlation properties as the transfer functions in rooms.[2,38]

If an N channel sound system is used, and the microphones and loudspeakers are further away from each other than the spatial correlation distance,[39] then independent autoregressive processes with the same statistics and correlation properties may be used to model the transfer function matrix.

Hence, to determine the stability of multichannel sound systems with frequency-shifting, an AR process is used to produce a set of transfer function matrices at equally spaced frequencies. The set of transfer function matrices are scaled by the loop gain. The values of the scaled transfer function matrices at M frequencies spaced at f_0, where f_0 is the frequency shift, are multiplied together. The squared norm of the product is then found and the power gain calculated. If the power gain exceeds one, the system is assumed to be unstable. The simulation is then repeated with a new AR process. The probability of instability at the given loop gain may be determined from K such simulations, and the variance calculated.[2] For systems including reverberators, a second AR process is used to simulate the reverberator.

Monte Carlo simulations are shown in Fig. 2 for a room with a reverberation time of 1 second, for numbers of channels in powers of 2 from 1 to 32 and for $M=50$. The number of trials was 400. The frequency shift was 10 Hz, for which the correlation between samples is 0.05. The predicted stability risk is closely matched by theory for $N=1$, where the norm approximation is exact. For $N=2$ the theoretical 50% value is 0.5 dB too low. For $N=4$ and 8 the error is 0.4 and 0.25 dB, respectively. For $N=16$ and 32 the error is negligible. Hence, the norm approximation produces a worst-case error of half a dB for $N=2$ and the error reduces with N.

For smaller frequency shifts, the assumption of independent variables in the summation of Eq. (20) becomes less correct. The slope of the resulting stability curve reduces slightly, diverging from the theoretical curve predicted by Eq. (28) for small and large probabilities, and particularly for small N where the slope is lower. However, the deviation is small for probabilities near 50% and the 50% stability limit

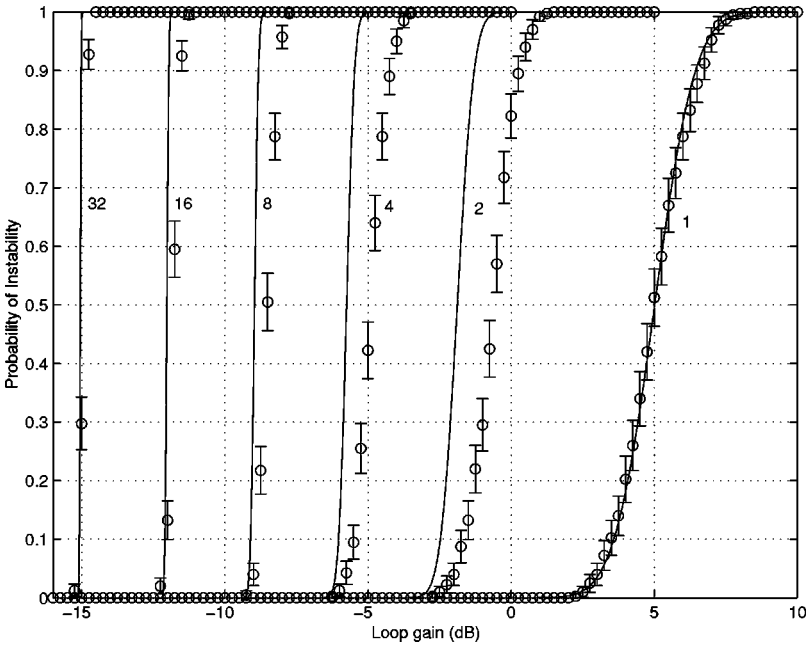

FIG. 3. Monte Carlo Simulation results for sound system with a reverberator in the feedback path for $N=1-32$.

remains close to the theoretical stability limit predicted by Eq. (28).

The equivalent simulations for a sound system including a multichannel reverberator with natural statistics are shown in Fig. 3. The $N=1$ results are again accurate. The errors for $N=2$, 4, 8, and 16 are 1.3, 0.9, 0.5, and 0.25 dB, respectively. These are larger than the results without a reverberator, because the norm approximation was applied twice to produce the probability of instability.

C. Reverberator-based simulations

In order to further investigate the accuracy of the stability limits derived above, a second simulator was developed. The transfer function matrix of a room was simulated as a time-invariant, 24-channel reverberator using 24 delay lines cross-coupled via an orthonormal matrix.[7] This provided a fully cross-coupled 24×24 matrix of transfer functions with Rayleigh magnitude statistics. Feedback was then applied around $N<24$ channels of the reverberator and frequency-shifting was implemented in the feedback loop. A second reverberator was implemented in the feedback loops as required. This second reverberator could either simulate the Rayleigh statistics of rooms, or could be of a unitary design. The majority of simulations were carried out with no secondary reverberator, or with a standard nonunitary reverberator. Some unitary reverberator simulations were later run to check that the stability limits were the same as the no-reverberator case.

A block diagram of the simulator is shown in Fig. 4. As discussed, this simulator uses an analytic input signal, and so the analytic filter $A(\omega)$ is placed at the input to eliminate the negative frequencies in any applied real signal. The signals in the reverberator are thus complex. The envelope of a given output is obtained from its low-pass filtered magnitude, and the real part of two adjacent channels written to a stereo wave file for subjective assessments, discussed in Sec. IV.

The continuous-time analytic filter $A(\omega)$ has the theoretical complex impulse response

$$h_a(t)=\delta(t)+j\frac{1}{\pi t}. \tag{36}$$

In practice, a discrete, finite response, bandlimited form of the analytic filter is required. The finite response means that

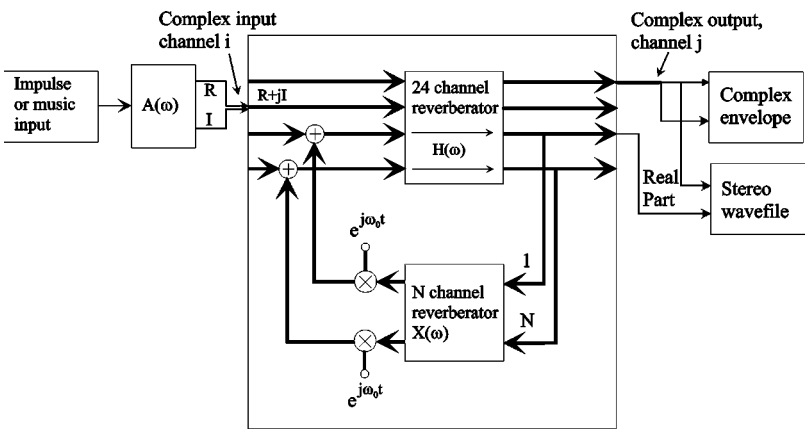

FIG. 4. Reverberator-based frequency shifting simulator. $X(\omega)$ is bypassed for simulations without a secondary reverberator.

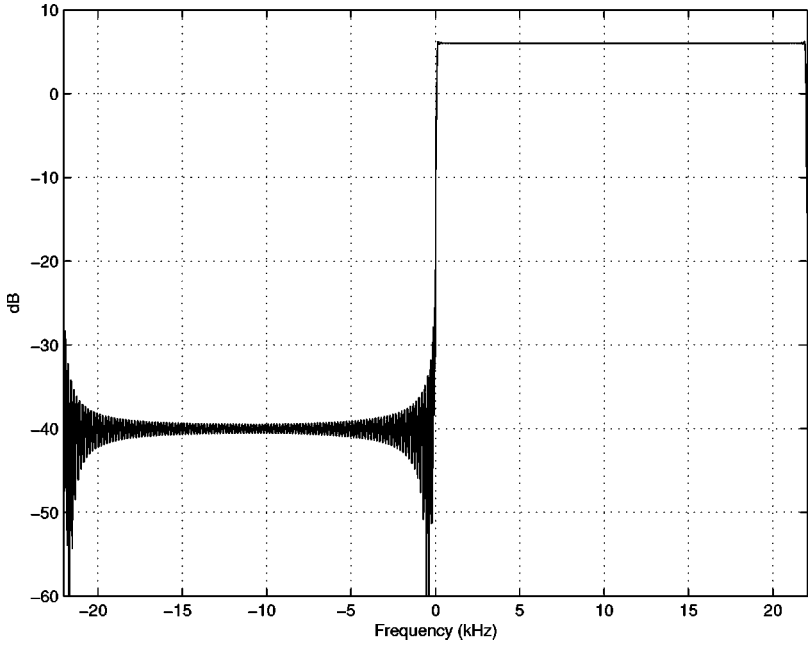

FIG. 5. Magnitude of the analytic filter response.

the analytic filter has a low frequency cutoff below which the magnitude of the response reduces. A 512 tap finite impulse response filter was designed by specifying a desired complex filter response with a gain of two for positive frequencies and a linear transition from a transition frequency of 100 Hz to an attenuation of -40 dB at zero frequency. The filter taps were then obtained from a least squares fit to the desired response. The resulting magnitude response is shown in Fig. 5.

The ''naturalness'' of the reverberators may be verified by showing that they produce ideal statistics in the frequency domain, and that they have a high echo density in time with an absence of flutter effects. The squared norm of the reverberator transfer function matrices were close to the theoretical probability densities for all N. For example, the measured probability density of the squared norm of the transfer function matrix for 8 channels is shown in Fig. 6 together with the theoretical χ-squared density. The measured density is closely similar to the theoretical.

The echo density was evaluated by listening to the impulse response. The response sounded smooth without any noticeable flutter effects. The envelope of the decay was exponential and matched the required RT. No damping was applied to the reverberator, so that its reverberation time was constant with frequency. A reverberation time of 1.0 s was used in both the main and the secondary reverberator. The theoretical stability limit is not affected by the RT, and the RT of the reverberators was controlled by altering their internal delay times which did not affect their norm statistics. A frequency shift of 5 Hz was used, producing a correlation between adjacent samples of 0.16. The sample rate was 44.1 kHz, and first-order 20 Hz high pass and 20 kHz low pass

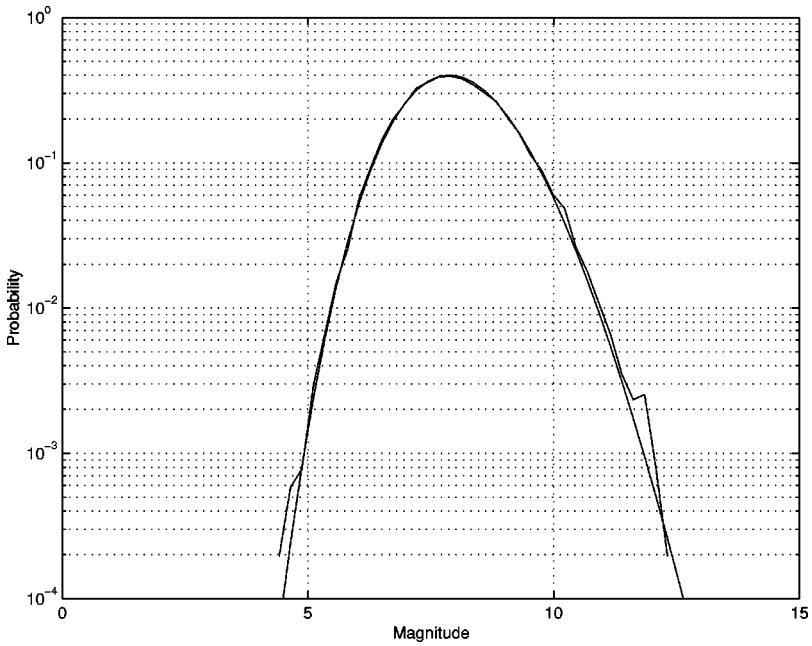

FIG. 6. Theoretical and measured probability density of the power gain of an 8 channel reverberator transfer function matrix.

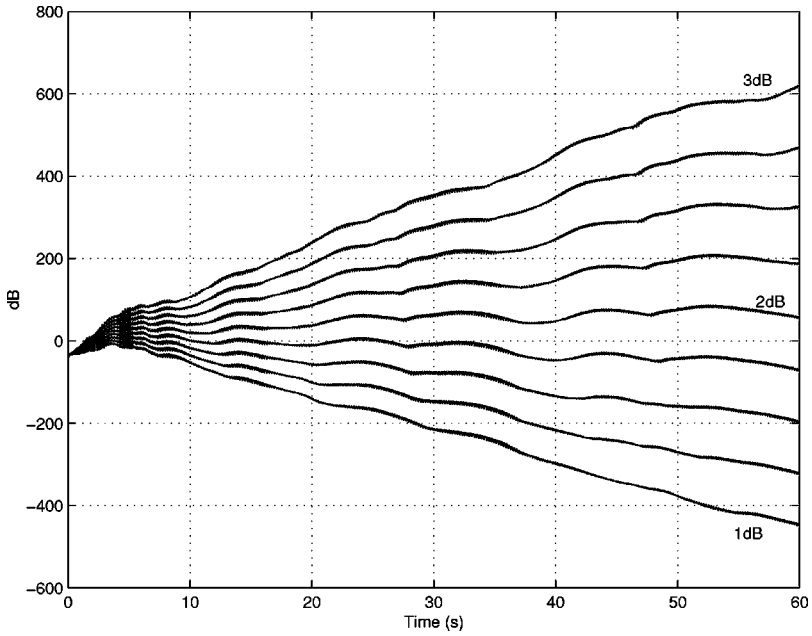

FIG. 7. Set of output envelopes for a single channel system without reverberator and with loop gains from 1 dB to 3 dB in 0.25 dB steps.

filters were implemented in each channel to prevent the appearance of negative frequency components.

Simulations were run for $N=1$, and for even channels from 2 to 16, and for a number of loop gains from below to above the relevant theoretical stability limits in Eqs. (24) and (32). A duration of 60 s was used to allow the envelope to be observed for a considerable time. For high numbers of channels the decays were linear and 30 s were sufficient to establish stability. In all cases the input was a unit delta function which, upon being filtered by the analytic filter, produces the analytic filter impulse response.

For low channel numbers the loop gain was incremented in 0.25 dB steps, but for some of the higher channel numbers more closely spaced increments of 0.1 and 0.05 dB were possible. For each simulation the squared magnitude of the analytic output signal was found. This was low-pass filtered and then decimated by a factor of 128 to reduce the data size. The set of power envelopes for the range of loop gains was then plotted. The stability limit was estimated as the loop gain which produced the envelope with slope closest to zero.

A set of power envelopes obtained for $N=1$ are shown in Fig. 7, for loop gains from 1 to 3 dB in 0.25 dB steps. The envelope initially rises for all loop gains, but then reduces with time for loop gains below 2 dB, suggesting that 2 dB is the stability limit. This is close to the theoretical limit of 2.5 dB. Nielsen and Svensson produce a maximum loop gain of 0 dB from measurements.[29] However, they noted that large temporary level increases occurred which saturated their equipment, particularly for low frequency shifts. Figure 7 verifies that these large increases occur even for the relatively large shift of 5 Hz (and larger level increases were found for simulations with lower frequency shifts). This suggests that, in practice, the 2.5 dB limit is not achievable because any sound system will have insufficient dynamic range to handle the signal amplitude at such loop gains. It is also highly likely that the sound quality will be unacceptable at loop gains approaching the stability limit in any case.

A second simulation for $N=1$ is shown in Fig. 8, using lower loop gains ranging from -1 to $+1$ dB, and looking at the first 2 s of the response. The output envelope slope is zero or negative for loop gains of 0 dB and lower, and so saturation of audio systems is unlikely. Hence 0 dB is a practical stability limit, and is consistent with the results measured by Nielsen and Svensson.

The output envelopes for a 16 channel system with no secondary reverberator are shown in Fig. 9, for loop gains ranging from -12.15 to -11.85 dB in 0.05 dB steps. In this case, there is no large initial buildup of level. The envelopes are approximately linear with time, and the stability limit is in the vicinity of -11.95 dB, which is 0.08 dB from the theoretical value of -12.03 dB. The simulations in this case produce a stability limit very close to the theoretical prediction.

The complete set of simulation-derived and theoretical stability limits without a reverberator are shown in Fig. 10. Also included are Monte Carlo results for the 50% risk loop gain. The $N=1$ simulator result is 0.5 dB lower than theory, whereas the Monte Carlo result is closer. Since both simulations include the correlations between samples of the transfer function matrix, finite correlations between adjacent products does not explain this discrepancy. It may be explained by the approximation of the sum in Eq. (20) by the exact mean. For $N=2$ both simulations are about 0.5 dB higher than theory and the error tends to reduce with N. Also included in Fig. 10 is the 50% risk of instability limit without time variation found using the methods in Ref. 2. This allows the theoretical improvement in loop gain produced by frequency-shifting to be determined. For $N=1$ the theoretical increase is about 11 dB and as N increases the improvement reduces to around 3 dB for the 16 channel case. Thus, it may be concluded that time-variation produces a reducing benefit with the number of channels. The reason for this is that for large N, the statistics of the loop power gain become increasingly ideal. From Eqs. (B3) and (B4), the mean of the squared norm of H is N^2 (for $2\sigma_R^2=1$) and the variance is

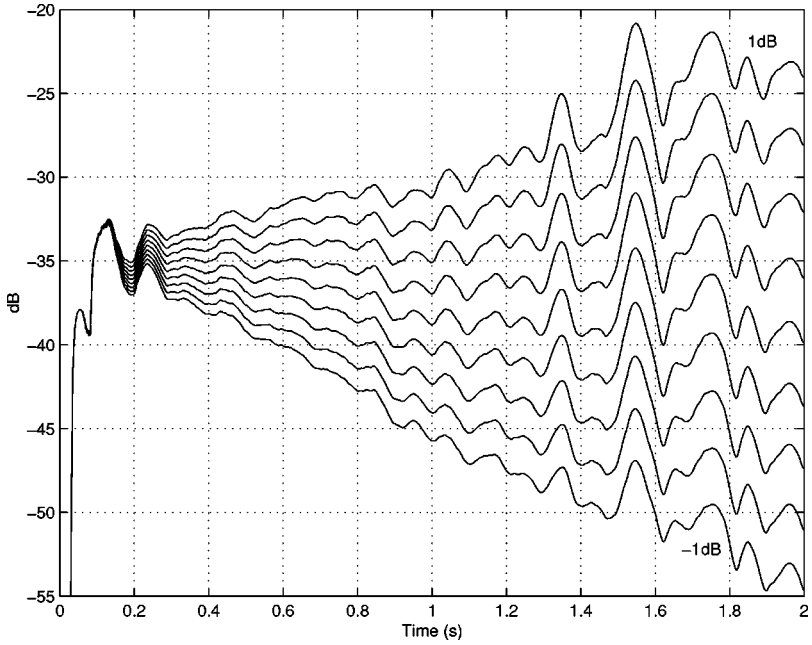

FIG. 8. Set of output envelopes for a single channel system without reverberator and with loop gains from −1 dB to 1 dB in 0.25 dB steps.

$N^2/4$. The relative deviation of the squared norm may be quantified by the ratio of the standard deviation to the mean, which is

$$\varepsilon = \frac{1}{2N}. \tag{37}$$

The deviation of the loop power gain thus reduces with N, and there is a reducing variation for time variation to exploit.

Simulations were also carried out which included a nonunitary reverberator with the same statistics as those of a room. The output envelopes showed a reduced slope variation with loop gain compared to the no-reverberator case. An example for $N=16$ is shown in Fig. 11 for loop gains varying in 0.1 dB steps (twice the stepsize of that in Fig. 9). The envelope slopes have about half the variation with loop gain of those in Fig. 9. This is explained by Fig. 3, which shows a slower transition from stability to instability compared to Fig. 2. The stability limit is about −11.8 dB. Because of the slower transition from instability to stability, time varying systems with nonunitary reverberators will require a larger stability margin than systems without reverberators.

The complete set of stability limits for systems with nonunitary reverberators is shown in Fig. 12. For $N=1$ the Monte Carlo result is closer to theory than the reverberator simulation, but the remaining results follow a similar trend, with around 1 dB error for $N=2$ and a reducing error with N. However, the closeness of theory and measurement is not as good as the previous case, due to the additional norm approximation required in the derivation of the theoretical stability limit.

The stability limits for the case of no time variation are also included in Fig. 12. (These values are discussed more

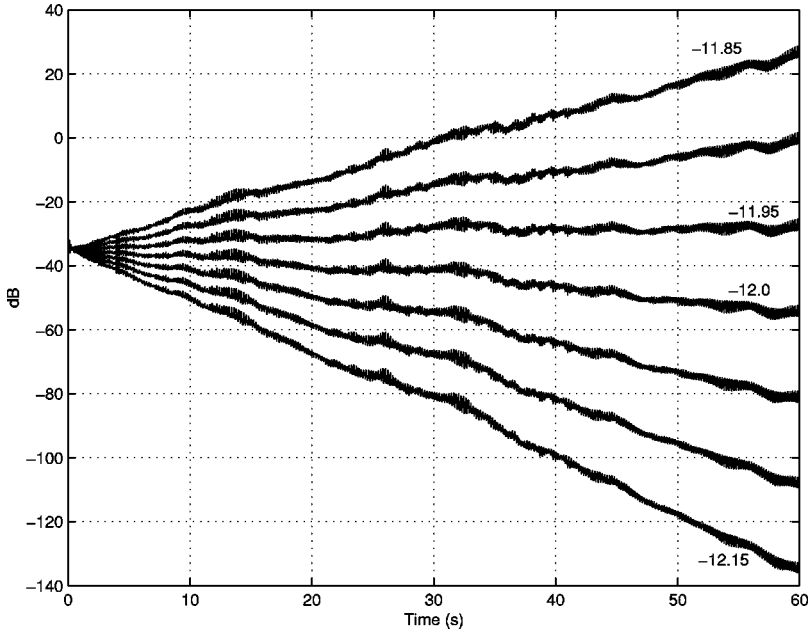

FIG. 9. Set of output envelopes for a sixteen channel system without reverberator and with loop gains from −12.15 dB to −11.85 dB in 0.05 dB steps.

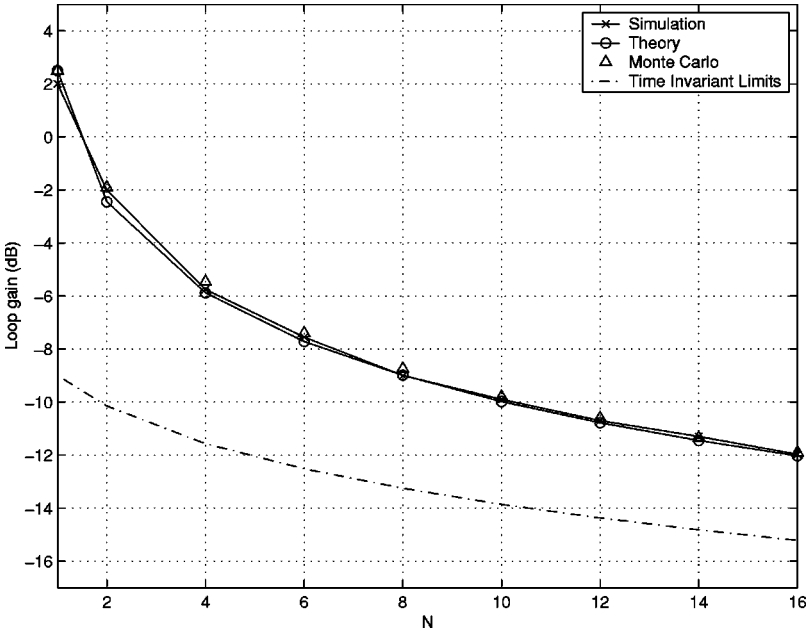

FIG. 10. Stability limits for multichannel sound systems without reverberators, including Monte Carlo results and theoretical time-invariant loop gain limits for 50% risk of instability.

fully in Sec. III D.) The results show that frequency-shifting allows the mean loop gain to be increased by 18 dB for the single channel case, which is 7 dB larger than the case with no reverberator.

For $N>1$ the maximum loop gain limits are approximately the same for systems with and without reverberators, and the two limits become closer as N increases. The increased loop gain enhancement for systems with reverberators at low channel numbers occurs because these systems have an inherently poorer performance without frequency-shifting, due to the greater variance of their loop transfer functions. Time-variance allows these systems to bring their loop gains up to the same levels as unitary systems, and to exceed them at low channel numbers.

The calculation of the theoretical loop gain limits in Sec. II requires that the same frequency shift is used in all channels. In practice, different frequency shifts could be used. To investigate this case a simulation was run for a 16 channel system with the same parameters as in Fig. 9, but with normally distributed frequency shifts varying from 3.27 Hz to 6.31 Hz, with a nominal mean of 5 Hz. The power envelopes are shown in Fig. 13, which may be compared to the envelopes in Fig. 9. Each decay curve has a slightly increased slope, and this is probably due to the fact that the frequency shift in some channels is lower than 5 Hz. However the stability limit of about -12.02 dB is only slightly higher than the -11.95 dB limit in Fig. 9. Hence the stability limit does not appear to be significantly affected by using different frequency shifts per channel. However, if too many channels have low frequency shifts, it is likely that the stability performance will degrade more significantly. Furthermore, high frequency shifts will produce more noticeable modulation artefacts.

In practical multichannel sound systems, variable rever-

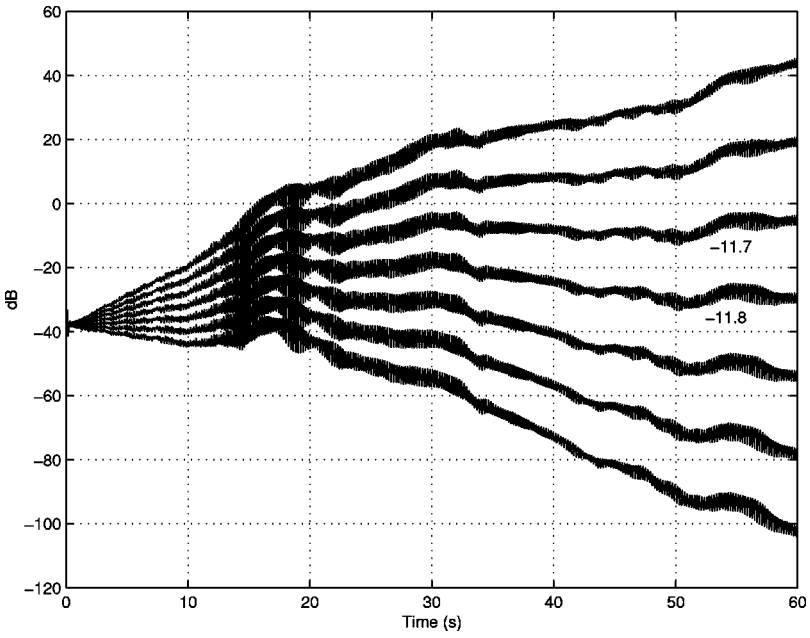

FIG. 11. Set of output envelopes for a sixteen channel system with reverberator and with loop gains from -12.1 dB to -11.5 dB in 0.1 dB steps.

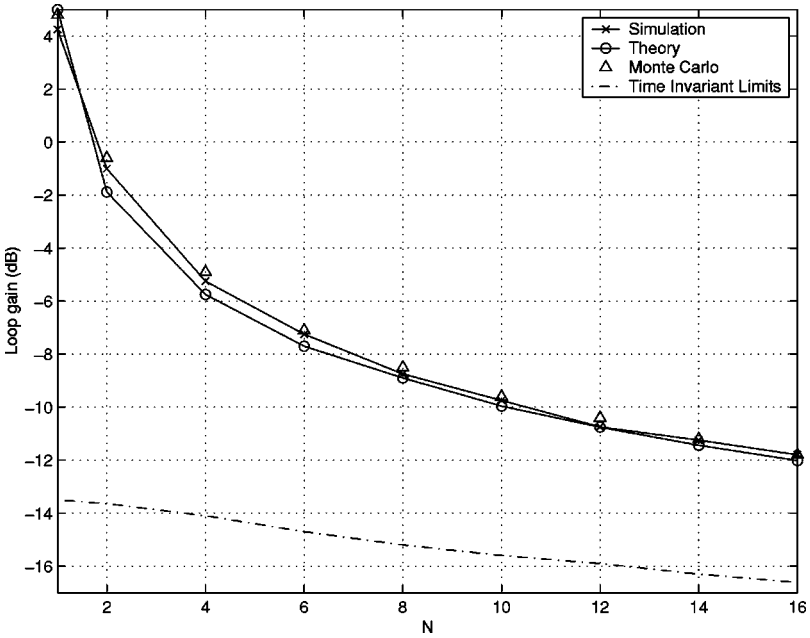

FIG. 12. Stability limits for multichannel sound systems including nonunitary reverberators, including Monte Carlo results and theoretical time-invariant loop gain limits for 50% risk of instability.

beration levels with distance mean that the loop gain in each channel may not be the same.[42] In the time-invariant case, this increases the variance of the characteristic functions,[2] and leads to a reduction in stability margin. Simulations were therefore undertaken in which the loop gains varied uniformly from $-\sigma_{\mathrm{dB}}$ to σ_{dB} dB about the chosen value. The loop gains were then normalized so that the linear mean equalled the chosen value. Figure 14 shows the output decays for a sixteen channel system with -3 to 3 dB variation in loop gain for each case. The stability limit is close to -12.05 dB, which is only 0.1 dB higher than the -11.95 dB limit in Fig. 9. This shows that frequency-shifting allows the stability limit with moderate loop gain variations to approach that for the mean loop gain across channels. However, the stability is likely to be more significantly affected for larger loop gain variations. For example, if one loop gain is set to zero the system has $N-1$ channels and Fig. 10 shows that in this case the mean loop gain limit will increase.

Finally, simulations were also undertaken in which the secondary reverberator was unitary, for $N=16$ and $N=8$ channels. A set of output envelopes for $N=16$ are shown in Fig. 15. The limit is closely similar to the decays in Fig. 9, with a stability limit of -12 dB. This is to be expected since for $N=16$ both unitary and nonunitary reverberators produce the same stability limit. The variation in the decay slopes with loop gain is slightly reduced compared to the no-reverberator case but is not as low as the standard reverberator case, however the variation in each unitary envelope is smaller than those of the no-reverberator case. This may be due to the fact that the unitary reverberator is diffusing the feedback signals from the primary reverberator, which reduces the effect of dominant feedback paths that occur with no reverberator. The envelope fluctuations are also smaller than those of the nonunitary reverberator which is probably a

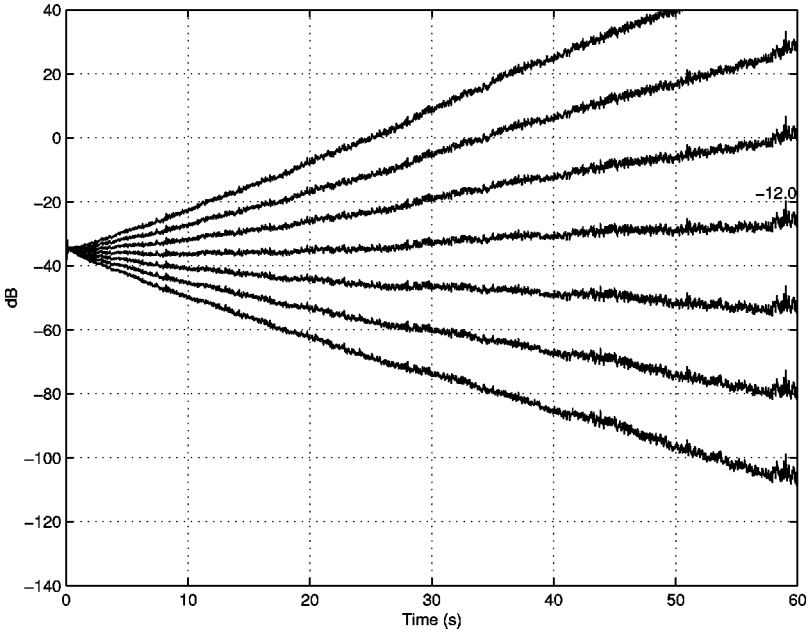

FIG. 13. Set of output envelopes for a sixteen channel system without reverberator, with loop gains -12.15 dB to -11.85 dB in 0.05 dB steps and with different frequency shifts in each channel.

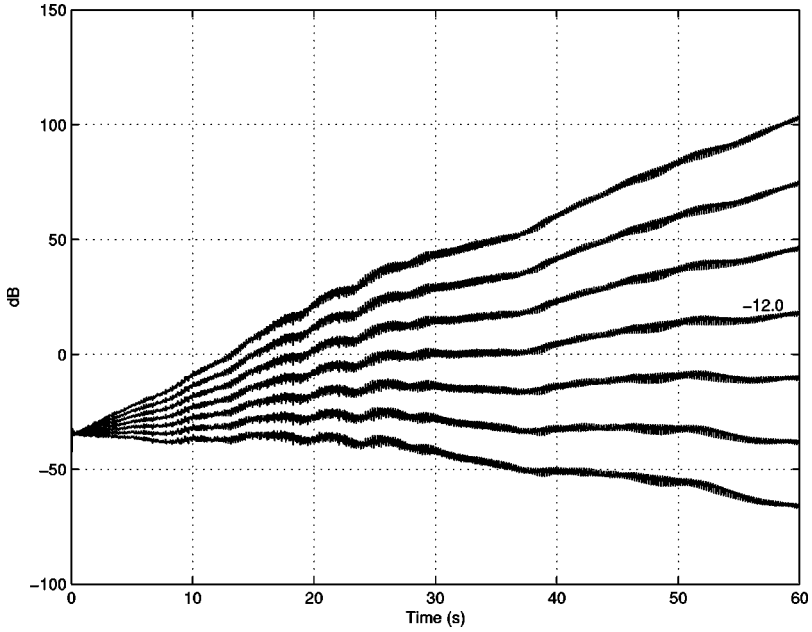

FIG. 14. Set of output envelopes for a sixteen channel system without reverberator, with loop gains −12.15 dB to −11.85 dB in 0.05 dB steps and with loop gain variation −3 to +3 dB across channels for each case.

result of the reduced variance in the unitary case.

The $N=8$ channel results were also similar to the no-reverberator case with an estimated stability limit of between −8.8 and −9 dB in both cases, close to the −9 dB theoretical limit.

D. Stability of time-invariant multichannel systems with reverberators

In order to assess the effectiveness of frequency-shifting, the stability limits must be compared to those obtained for multichannel time-invariant systems.[23] The stability limits for unitary systems have been derived in Ref. 2, and included in Fig. 10. However, the stability results for multichannel sound systems with a reverberator in the feedback loop—which require knowledge of the statistics of the eigenvalues of the product of two complex normal matrices—are unknown. The risk of instability (and the 50% limits used in Fig. 12) are determined empirically here using Monte Carlo simulations.

The loop transfer function matrix in systems including reverberators is the product of the room transfer function matrix and the reverberator matrix. Therefore, the stability of these systems may be estimated by generating a separate multichannel autoregressive process representing each matrix. The eigenvalues of the matrix product at each frequency are determined, and if the real part of any eigenvalue exceeds one, the system is assumed to be unstable.

For the single channel case, the calculation of eigenvalues is not required and a theoretical stability limit can be calculated. In Ref. 2 the stability of a single channel system with secondary reverberator was determined using a magnitude analysis. In Appendix D the real part analysis is carried

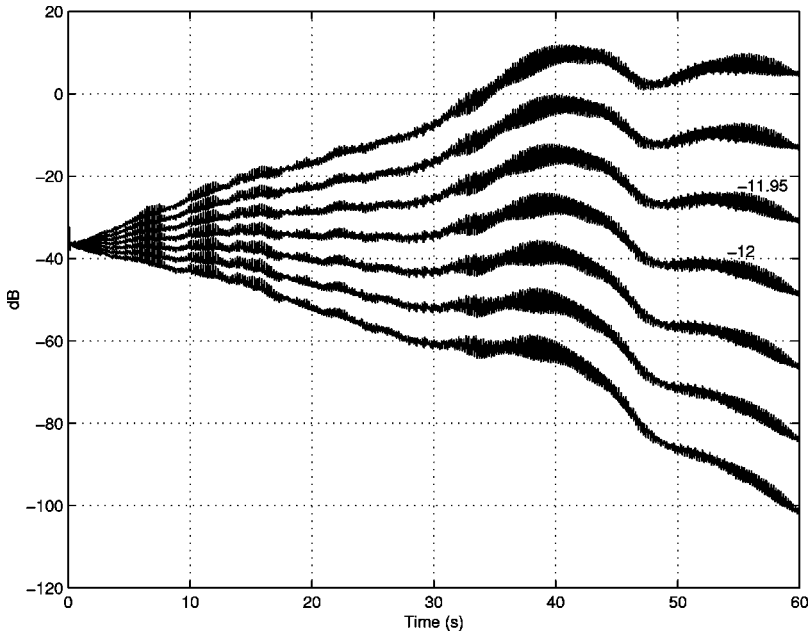

FIG. 15. Set of output envelopes for a sixteen channel system with a unitary reverberator and with loop gains from −12.15 dB to −11.85 dB in 0.05 dB steps.

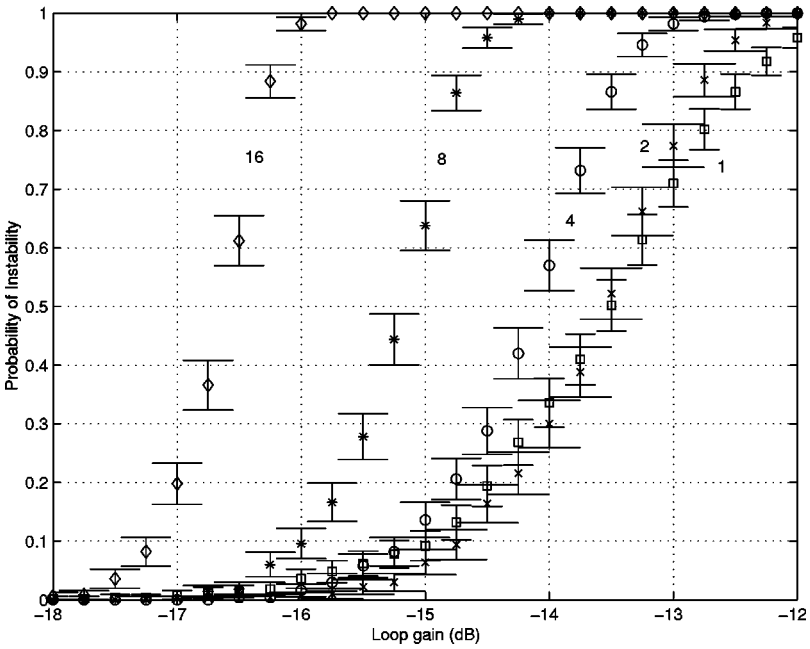

FIG. 16. Monte Carlo simulations of the probability of instability for time-invariant systems with nonunitary reverberator feedback: $N=1(\square)$, $N=2(\times)$, $N=4(\bigcirc)$, $N=8(*)$, and $N=16(\diamond)$.

out, which is more accurate. The resulting theoretical limit of -13.6 dB was closely matched by the Monte Carlo simulation result of -13.5 dB.

The probability of instability for channels in powers of two up to 16 is shown in Fig. 16, and—for comparison—the Monte Carlo results for the unitary case are shown in Fig. 17.

Note first that the unitary 50% stability limits have a 6 dB range from -9 dB ($N=1$) to -15.2 dB ($N=16$), whereas the nonunitary results have a reduced range of 3 dB from -13.5 dB to -16.6 dB. The two results become increasingly similar for increasing N, but at low channel numbers, unitary systems show an increasing 50% stability limit over the nonunitary case of up to 4.5 dB for $N=1$. (This 4.5 dB difference using the real part analysis is more accurate than the magnitude-based analysis in Ref. 2, which predicted a 5 dB difference between unitary and nonunitary cases.) The reduced performance of nonunitary systems is due to the larger variance in the eigenvalues of these systems, particularly at low channel numbers.

Secondly, the nonunitary results have a reduced slope with loop gain, showing a higher risk of instability for a given number of dB below the 50% limit than the unitary case. In other words, nonunitary time-invariant systems are likely to require a larger stability margin than unitary systems. This is again due to the increased variance of the eigenvalues, and is similar to the FS results in Figs. 2 and 3.

Thirdly, the stability limits for the non-unitary case are approximately the same for $N=1$ and $N=2$ channels. This is due to the fact that the real part of the eigenvalues of the $N=2$ system have similar statistics to the real part of the $N=1$ case.

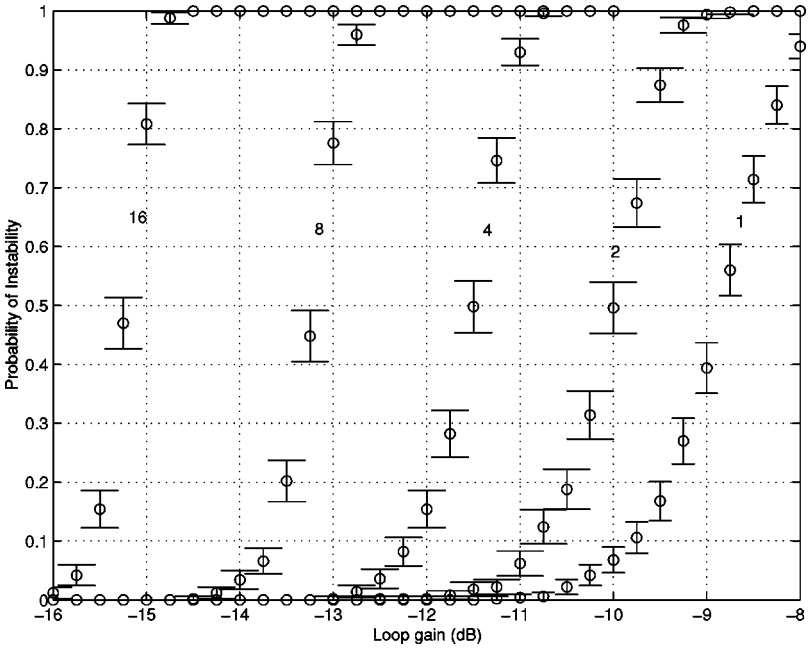

FIG. 17. Monte Carlo simulations of the probability of instability for time-invariant systems with unitary reverberator feedback.

TABLE I. Time-invariant, unitary feedback.

N	50% Limit	Impulse	Music	Minimum	Margin
1	−9.0	−15 (2.5)	−14 (5)	−15	6
2	−10.2	−15 (2)	−15 (3)	−15	5
4	−11.6	−17 (1)	−17 (4)	−17	6
8	−13.3	−19 (2.5)	−20 (3)	−20	7
16	−15.2	−21 (1.5)	−21 (3)	−21	6

TABLE III. Frequency-shifting, unitary feedback.

N	50% Limit	Impulse	Music	Minimum	Margin
1	2.5	−8 (2)	−12 (8)	−12	15
2	−2.4	−10 (1)	−14 (4)	−14	12
4	−5.9	−11 (1)	−15 (1)	−15	9
8	−9.0	−13 (1)	−18 (2)	−18	9
16	−12.0	−16 (2)	−21 (1)	−21	9

IV. PRELIMINARY ASSESSMENT OF SUBJECTIVE LOOP GAIN LIMITS

Sound systems must always be operated at some margin below the absolute stability limit to sound acceptable. The theoretical limits derived above do not provide sufficient information to determine these loop gain limits. Subjective tests were therefore carried out to estimate them. Both impulse response and music sound sources were used, to allow the assessment of both running music and transient decays. For the frequency-shifting simulations a 5 Hz shift was used. The same simulator was used for the time-invariant case with a frequency shift of 0 Hz.

The reverberation times in both reverberators were kept constant with frequency. This simplification allowed the subjective results to be compared directly with the stability limits, which also assume constant reverberation time with frequency. Three researchers made assessments of the acceptable loop gains with impulse responses, and four researchers assessed the music simulations. The results were averaged and rounded to the nearest decibel. The number of subjects is relatively small, and the results are therefore indicative only. A more rigorous subjective analysis would be required to produce more accurate results, but such tests are beyond the scope of this paper.

Stereo impulse responses were generated from adjacent outputs from the reverberator for $N=1$ to 16 channels in powers of 2. For each N, five sets of simulations were carried out for the time-invariant case, with different randomly generated matrices in the reverberators to produce a range of ringing conditions. One of these impulse responses was used to filter the music excerpt to produce a set of music samples. For the time-varying case three simulations were done, with the assumption that the results would be more homogeneous due to the averaging of the transfer functions. For each simulation, the impulse response was generated for a range of loop gains from near the stability limit to several dB below.

For the music simulations, a 10 s excerpt from Handel's water music was used as the source.[40] This includes a bass note of close to 82 Hz (E2) which allows the low frequency performance to be heard.

TABLE II. Time-invariant, nonunitary feedback.

N	50% Limit	Impulse	Music	Minimum	Margin
1	−13.5	−21 (2)	−18 (6)	−21	8
2	−13.6	−21 (2)	−20 (7)	−21	8
4	−14.1	−21 (2)	−20 (5)	−21	7
8	−15.2	−23 (1)	−22 (4)	−23	8
16	−16.6	−23 (2)	−23 (3)	−23	6

The time-invariant stereo impulse responses had cross-correlation coefficients less than 0.5 and so were reasonably binaurally dis-similar. The stereo wave files were evaluated using headphones.

A. Results

The subjective loop gain limits determined from the impulse responses and music are shown in Tables I–IV and the estimated increases in loop gain due to frequency-shifting are shown in Table V. Also given in Tables I–IV are the range of the subjective loop gain estimates in parentheses. The ranges are typically greater for the music samples, showing that artefacts are more difficult to discern with a continuous and complex music signal.

The subjective loop gain limit for the time-invariant unitary $N=1$ case with music is -14 dB, whereas the limit with impulses was -15 dB. These results are, respectively, 2 and 3 dB lower than the -12 dB often quoted for single channel systems.[1] One reason for this is that these results are from simulations with flat loop gains and reverberation times with frequency, whereas the results in Ref. 1 are based on listening tests with actual sound systems, where the loop gain tends to reduce with frequency due to loudspeaker power responses and air absorption. In a simulation with damped reverberation times in both reverberators, but with the same low frequency loop gain, the ringing was subjectively reduced. Hence loop gains closer to -12 dB are more likely to be achieved in practical installations.

For the time-invariant unitary case the minimum subjective loop gain limit for $N=1$ is -15 dB and with frequency-shifting it is -12 dB. This 3 dB improvement is smaller than Schroeder's value of 6 dB.[23] However, the loop gain increase for the impulse case is 7 dB which is closer to Schroeder's value. This suggests that music signals offer a more stringent test for the quality of sound with frequency-shifting and that smaller loop gain improvements are possible with music than for signals with fewer continuous tones or less low frequency content, such as impulsive or speech signals.

For increasing numbers of channels, the available increase in loop gain tends to be reduced for both unitary and nonunitary cases, aside from the anomalous reduction to 1

TABLE IV. Frequency-shifting, nonunitary feedback.

N	50% Limit	Impulse	Music	Minimum	Margin
1	5	−14 (4)	−13 (8)	−14	19
2	−1.9	−15 (3)	−14 (5)	−15	13
4	−5.8	−15 (2)	−15 (2)	−15	9
8	−8.9	−17 (1)	−18 (1)	−18	9
16	−12.0	−18 (2)	−21 (1)	−21	9

TABLE V. Loop gain improvement due to frequency-shifting.

N	Unitary loop gain increase	Nonunitary loop gain increase
1	3	7
2	1	6
4	2	6
8	2	5
16	0	2

dB for the $N=2$ unitary case, which is attributed to the range of subjective estimates for the music samples and the relatively small number of subjects used.

B. Discussion

The subjective limits determined here show that—while frequency-shifting provides significant increases in theoretical loop gain—the gain increases that can be achieved without introducing artefacts are smaller. This is consistent with the results in Ref. 23. Furthermore, in keeping with the theoretical stability limits, the subjective potential gain due to frequency-shifting reduces with the number of channels. For example, for unitary systems with 16 channels, the time-invariant loop gain and frequency-shifting limits are both about -21 dB and no benefit is produced by FS. For the nonunitary 16 channel case the benefit is only 2 dB. This lack of loop gain improvement is due to the pitch-shifting of low frequencies that occurs in music which limits the loop gain to well below the theoretical value. If the frequency shift was reduced at low frequencies, the loop gain could be increased, producing some possible benefit.

Low frequency pitch-shifting artefacts may be reduced by using other time-variation methods such as delay-modulation, which produces lower pitch shifts at low frequencies. However, this also means that the low frequencies are not shifted sufficiently to produce the stability limits that frequency-shifting produces. In essence, at low frequencies, the requirement for low pitch-shifting means that the system becomes quasi-time-invariant, leading to low frequency instability, as has been reported by Nielsen and Svensson.[29] Such systems could be viewed as a low frequency time-invariant part and a high frequency time-varying part. The stability limits then become a complicated function of the two contributing parts.

Other time-variation systems may introduce both amplitude and phase modulation. Amplitude modulation has the effect of modulating the loop gain at each frequency, whereas phase modulation shifts each frequency by (in general) a varying amount with time. The subjective effect of such time variation will undoubtedly differ from that produced by frequency-shifting.

Therefore, while the theoretical maximum loop gains derived here provide an upper bound for any time-varying system, the subjective stability limits determined apply specifically to frequency-shifting, and it is expected that different subjective limits would be obtained for other forms of time-variation.

V. CONCLUSIONS

This paper has determined the theoretical stability limits of multichannel sound systems which employ frequency-shifting and compared the results with the time-invariant case. Frequency-shifting produces the best-case stability for time-varying systems since it produces infinite carrier suppression and one-sided sidebands which avoids shifting frequencies back to the carrier. It therefore provides an upper limit to the loop gain increase that may be expected from the application of time-variation methods in sound systems.

The derived stability limits show that the improvement in loop gain produced by frequency-shifting reduces with the number of channels, N, since the power gain statistics become increasingly ideal with N. Multichannel sound systems with additional nonunitary reverberation systems have an inherently lower stability limit without time-variation, and therefore time-variation provides a greater improvement in loop gain for these systems, particularly at low channel numbers.

Preliminary estimates of the subjective loop gain limits have also been made, based on both impulse responses and a music sample. The results show a reducing benefit of frequency-shifting with channel numbers, and are consistent with the theoretical limits.

Simulations have been included for the case of different frequency shifts and loop gains in each channel. These show that the theoretical stability limit is robust to such variations, although wide variations of frequency shift or loop gain can be expected to produce a degradation in performance. The subjective assessment of these variations has not been investigated.

The theoretical stability limits have been derived assuming ideal room transfer functions with zero-mean complex normal statistics (Rayleigh magnitudes), for the case of both unitary and nonunitary (Rayleigh) feedback. The analysis could be extended to include the case where one of the room transfer function matrices has nonzero means (Ricean magnitudes), producing a squared matrix norm which is noncentral χ-squared distributed.[41] This case has not been considered here, but the normalized Ricean case will produce a stability limit between the unitary and Rayleigh cases,[2] and at high channel numbers, the two stability limits become identical.

Practical sound systems have frequency-dependent loop gains due to factors such as air absorption and loudspeaker power responses. Since frequency-shifting produces a stability limit governed by the mean loop gain, it is possible that time-variation will produce greater benefits in practical systems due to the increased loop gain variance. However, the peak loop gains will also be higher, which may produce increased subjective artefacts at frequencies near the peaks. Furthermore, if the loop gain has wide variations with frequency, equalization would be more appropriate than the use of time-variance.

Frequency-shifting—while it produces the maximum possible loop gain increase—may not be subjectively optimum, since it produces significant pitch-shifting artefacts at low frequencies which limit the loop gain increase. Other time-variance techniques, while producing lower theoretical

stability limits, may be able to operate with smaller loop gain margins and sound more natural, although it remains unclear to what extent low frequency stability may be controlled with any time-varying system. However, since the maximum loop gain increase due to time-variance reduces with the number of channels, the potential increase for any time-varying system is limited for systems with large numbers of channels.

APPENDIX A: NORM EQUALITY

Consider an $N\times N$ matrix $\mathbf{H}$ with entries which are complex random variables which are zero-mean, normally distributed with identical variances σ_R^2 in the real and imaginary parts. The total variance for each complex r.v. is $\sigma^2=2\sigma_R^2$. The expected value of the Frobenius norm of $\mathbf{H}$ is

$$E\{\|\mathbf{H}\|^2\}=E\left\{\sum_{n=1}^{N}\sum_{m=1}^{N}|H_{nm}|^2\right\}=\sum_{n=1}^{N}\sum_{m=1}^{N}E\{|H_{nm}|^2\}=N^2\sigma^2. \tag{A1}$$

Consider now a product of M independent, identically distributed matrices

$$\mathbf{H}_M=\prod_{m=1}^{M}\mathbf{H}_m. \tag{A2}$$

The elements of $\mathbf{H}_M$ each consist of a sum of N^{M-1} terms, and each term is a product of M terms. The variance of a product of M zero mean terms has a variance which is the product of the individual variances, or σ^{2M}. The sum of N^{M-1} of these terms has a variance of $N^{M-1}\sigma^{2M}$. Therefore the norm of $\mathbf{H}_M$ is

$$E\{\|\mathbf{H}_M\|^2\}=N^{M+1}\sigma^{2M}. \tag{A3}$$

The norm of a single matrix raised to the power of M is

$$E\{\|\mathbf{H}\|^2\}^M=N^{2M}\sigma^{2M}. \tag{A4}$$

Hence

$$E\{\|\mathbf{H}_M\|^2\}=\frac{1}{N^{M-1}}E\{\|\mathbf{H}\|^2\}^M. \tag{A5}$$

The norm approximation is obtained by removing the expectation

$$\|\mathbf{H}_M\|^2\approx\frac{1}{N^{M-1}}\prod_{m=1}^{M}\|\mathbf{H}_m\|^2 \tag{A6}$$

since taking the expected values of both sides produces Eq. (A5).

APPENDIX B: RELATIONSHIP BETWEEN THE MEAN OF THE LOG AND LOG OF THE MEAN OF χ-SQUARED VARIABLES

Let $\mathbf{H}$ be an $N\times N$ matrix with elements which are zero-mean, normally distributed, with real and imaginary part variances $\sigma_I^2=\sigma_R^2$. The squared Frobenius norm of $\mathbf{H}$ is

$$y=\|\mathbf{H}\|^2=\sum_{n=1}^{N}\sum_{m=1}^{N}(H_{nmR}^2+H_{nmI}^2), \tag{B1}$$

where H_{nmR} is the real part of H_{nm} and H_{nmI} the imaginary part. The norm thus consists of a sum of $2N^2$ normal random variables squared. The probability density of the sum is χ squared with $2N^2$ degrees of freedom[41]

$$p(y)=\frac{1}{2^{N^2}\sigma_R^{2N^2}\Gamma(N^2)}y^{N^2-1}e^{-y/2\sigma_R^2}. \tag{B2}$$

The mean of y is

$$E\{y\}=2\sigma_R^2N^2. \tag{B3}$$

The variance of y is

$$\mathrm{var}\{y\}=(2\sigma_R^2)^2N^2. \tag{B4}$$

Consider now the mean and variance of $z=\ln(y)$. The mean of z can be calculated using the formula[34]

$$E\{g(y)\}=\int_0^\infty g(y)p(y)dy, \tag{B5}$$

where $g(y)=\ln(y)$. Substituting for $g(y)$ and $p(y)$,

$$E\{\ln(y)\}=\frac{1}{2^{N^2}\sigma_R^{2N^2}\Gamma(N^2)}\int_0^\infty \ln(y)y^{N^2-1}e^{-(y/2\sigma_R^2)}dy. \tag{B6}$$

Using the integral from Ref. 37 [4.352]

$$\int_0^\infty y^n e^{-\mu y}\ln(y)dy=\frac{n!}{\mu^{n+1}}\left[1+\frac{1}{2}+\frac{1}{3}+\cdots+\frac{1}{n}-C-\ln(\mu)\right], \tag{B7}$$

where $C=0.577215$ is Euler's constant, this may be simplified to

$$E\{\ln(y)\}=\left[\sum_{k=1}^{N^2-1}\frac{1}{k}-C\right]+\ln(2\sigma_R^2)=\Psi(N^2)+\ln(2\sigma_R^2), \tag{B8}$$

where Ψ (.) is the psi function (Appendix C). For unit power gain transfer functions $2\sigma_R^2=1$ and $E\{\ln(y)\}=\Psi(N^2)$.

The variance of $z=\ln(y)$ requires the expected value of z^2, which may be found by substituting $(\ln(y))^2$ in Eq. (B6) Using Ref. 37 [4.352]

$$\int_0^\infty x^{\nu-1}e^{-\mu x}(\ln(x))^2dx=\frac{\Gamma(\nu)}{\mu^\nu}\{[\Psi(\nu)-\ln(\mu)]^2+\zeta(2,\nu)\}, \tag{B9}$$

where ζ is the zeta function (Appendix C), yields

$$E\{(\ln(y))^2\}=\zeta(2,N^2)+(\Psi(N^2))^2. \tag{B10}$$

Hence the variance for unit power gain is

$$\mathrm{var}\{\ln(y)\}=\zeta(2,N^2). \tag{B11a}$$

The difference between $\ln(E(y))$ and $E(\ln(y))$ is

$$\ln(E(y)) - E(\ln(y)) = 2\ln(N) - \Psi(N^2)$$
$$= 2\ln(N) - \left[K - \sum_{k=1}^{N^2-1} \frac{1}{k^2} \right]. \quad \text{(B11b)}$$

In dB, $10\log(E\{y\}) = 20\log(N)$ for unit power gain, and so the difference between $\overline{10\log[\|\mathbf{H}(\omega)\|^2]}$ and $10\log[\overline{\|\mathbf{H}(\omega)\|^2}]$ is

$$\Delta(N) = 20\log(N) - \frac{10}{\ln(10)}\Psi(N^2)$$
$$= 20\log(N) - \frac{10}{\ln(10)}\left[\sum_{k=1}^{N^2-1} \frac{1}{k} - C \right]. \quad \text{(B12)}$$

APPENDIX C: PSI AND ZETA FUNCTIONS

The psi function has the series definition[37]

$$\Psi(x) = -C - \sum_{k=0}^{\infty} \left[\frac{1}{x+k} - \frac{1}{k+1} \right], \quad \text{(C1)}$$

where $C = 0.577215$ is Euler's constant. For integers $x = n$ this becomes

$$\Psi(n) = -C + \sum_{k=1}^{n-1} \frac{1}{k}. \quad \text{(C2)}$$

The Riemann Zeta function has the series definition[37]

$$\zeta(z,q) = \sum_{k=0}^{\infty} \frac{1}{(q+k)^z}. \quad \text{(C3)}$$

For integers $z = n$ and $q = m$ this can be written

$$\zeta(n,m) = \sum_{k=1}^{\infty} \frac{1}{k^n} - \sum_{k=1}^{m-1} \frac{1}{k^n}. \quad \text{(C4)}$$

For $n = 2$ the infinite sum is approximately

$$K = \sum_{k=1}^{\infty} \frac{1}{k^2} = 1.644924 \quad \text{(C5)}$$

and

$$\zeta(2,m) = K - \sum_{k=1}^{m-1} \frac{1}{k^2}. \quad \text{(C6)}$$

APPENDIX D: STABILITY OF A SINGLE CHANNEL SOUND SYSTEM WITH REVERBERATOR

Consider a single channel sound system with a room transfer function between the power amplifier input and microphone preamplifier output $H(\omega)$ and a reverberator with transfer function $X(\omega)$. We assume that both of these have real and imaginary parts with are zero-mean normal with the same variances $\sigma_R^2 = 0.5$, so that they have unit power gain. The preamplifier output is then scaled by μ to control stability. The loop gain transfer function (excluding μ) is HX. For stability, the Nyquist theorem requires that the locus of HX does not encircle the point $1 + j0$. For a statistical analysis we assume this is equivalent to saying that the real part of HX does not exceed 1.

The real part of the loop transfer function is

$$\mathrm{Re}\{HX\} = H_R X_R - H_I X_I, \quad \text{(D1)}$$

where the subscripts R and I denote real part and imaginary part, respectively. This term is the sum of two products of normals. It may be shown that the pdf of a product of normal random variables $z = xy$ each with the same variance σ_R^2 has the form[41]

$$p(z) = \frac{1}{\pi\sigma_R^2} K_0\left(\frac{|z|}{\sigma_R^2} \right) \quad \text{(D2)}$$

and the characteristic function is

$$\phi_1(\omega) = \frac{1}{\sqrt{1 + (\omega\,\sigma_R)^2}}. \quad \text{(D3)}$$

The sum of two products of normal random variables $v = x_1 y_2 + x_2 y_2$ therefore has the characteristic function

$$\phi_2(\omega) = \frac{1}{1 + (\omega\,\sigma_R)^2} \quad \text{(D4)}$$

and the resulting pdf is

$$p(v) = \frac{1}{2\sigma_R^2} e^{-|v|/\sigma_R^2}. \quad \text{(D5)}$$

The cumulative distribution is

$$C(v) = \begin{cases} \frac{1}{2} e^{v/\sigma_R^2}, & v < 0 \\ 1 - \frac{1}{2} e^{-v/\sigma_R^2}, & v \geq 0 \end{cases}. \quad \text{(D6)}$$

Assuming that the transfer function is sampled with spacing Δf sufficient to produce uncorrelated samples, across a bandwidth B, the total number of uncorrelated samples is $B/\Delta f$, and the risk of instability with loop gain μ is[2]

$$\Pr\{\text{inst}\} = 1 - \left[C\left(\frac{1}{\mu} \right) \right]^{B/\Delta f} = 1 - \left[1 - \frac{1}{2} e^{-2/\mu} \right]^{B/\Delta f}. \quad \text{(D7)}$$

[1] A. Krokstad, "Electroacoustic means of controlling auditorium acoustics," Appl. Acoust. **24**, 275–288 (1988).
[2] M. A. Poletti, "The stability of single and multichannel sound systems," Acust. Acta Acust. **86**, 163–178 (2000).
[3] M. A. Poletti, "Direct and reverberant power analysis of multichannel sound systems," Acta Acust. (Beijing) **87**, 531–541 (2001).
[4] P. H. Parkin, W. A. Allen, and T. E. Bean, "A special report on the experimental, 'Assisted Resonance' system in the Royal Festival Hall," J. Sound Vib. **1**, 335–342 (1964).
[5] S. H. De Koning, "The MCR system-multiple-channel amplification of reverberation," Philips Tech. Rev. **41**, 12–23 (1983/84).
[6] A. J. Berkhout, D. D. Vries, and P. Vogel, "Acoustic control by wave field synthesis," J. Acoust. Soc. Am. **93**, 2764–2778 (1993).
[7] M. A. Poletti, "The performance of a new assisted reverberation system," Acta Acust. (Beijing) **2**, 511–524 (1994).
[8] C. P. Boner and C. R. Boner, "A procedure for controlling room-ring modes and feedback modes in sound systems with narrow-band filters," J. Audio Eng. Soc. **13**, 297–299 (1965).
[9] C. P. Boner and C. R. Boner, "Behaviour of sound system response immediately below feedback," J. Audio Eng. Soc. **14**, 200–203 (1966).
[10] C. P. Boner and C. R. Boner, "Problems of sound reinforcement in large halls," J. Audio Eng. Soc. **19**, 138–140 (1971).
[11] W. Rudmose, "Equalisation of sound systems," Noise Control **24**, 24–29 (1958).
[12] W. K. Connor, "Theoretical and practical considerations in the equalisation of sound systems," J. Audio Eng. Soc. **15**, 194–198 (1967).

[13] W. K. Connor, ''Experimental investigation of sound-system-room feedback,'' J. Audio Eng. Soc. **21**, 27–32 (1973).
[14] J. A. S. Angus, ''Howl-round detection and control using adaptive filtering techniques,'' in Proceedings of the Institute for Acoustics, (Institute of Acoustics Ltd, St Albans, Herts, UK, 1988), Vol. 9, Part 6, pp. 63–68.
[15] Y. Ikegami and T. Stephenson, ''Automatic feedback processing,'' *Sound and Video Contractor*, (Primedia, Inc., New York 1995), pp. 76–79.
[16] T. Umeda and K. Ozeki, ''Suppression of howling between microphones and monitoring speakers: An application of an adaptive filter,'' *11th International Congress on Acoustics* (ICA '83), Revue d'acoustique, hors'série, tome5 (1983) Acoustic, Paris, pp. 103–106.
[17] A. Goertz, ''An adaptive subtraction filter for feedback cancellation in public address sound systems,'' in *15th International Congress on Acoustics*, 1995, pp. 69–72.
[18] H. F. Olson, ''Acoustoelectronic auditorium,'' J. Acoust. Soc. Am. **31**, 872–879 (1959).
[19] P. S. Veneklasen, ''Method for synthesising auditorium sound,'' U.S. patent 3 535 453 (1970).
[20] H. Kuttruff, *Room Acoustics* (Applied Science, New York, 1973).
[21] D. Griesinger, ''Design and performance of multichannel time variant reverberation enhancement systems,'' *International Symposium on Active Control of Sound and Vibration* (Active 95) (Newport Beach, California, 1995), pp. 1203–1212.
[22] M. A. Poletti, ''A unitary reverberator for reduced colouration in assisted reverberation systems,'' in *International Symposium on Active Control of Sound and Vibration*, (Active 95) (Newport Beach, California, 1995), pp. 1223–1232.
[23] M. R. Schroeder, ''Improvement of acoustic-feedback stability by frequency shifting,'' J. Acoust. Soc. Am. **36**, 1718–1724 (1964).
[24] T. A. C. M. Claasen and W. F. G. Mecklenbrauker, ''On stationary linear time-varying systems,'' IEEE Trans. Circuits Syst. **29**, 169–184 (1982).
[25] D. Griesinger, ''Improving room acoustics through time-variant synthetic reverberation,'' in Audio Engineering Society 90th Convention, Preprint 3014 (B-2), 1991.
[26] J. L. Nielsen, ''Control of stability and colouration in electroacoustic systems in rooms,'' Ph.D. thesis, Norwegian University of Science and Technology, Trondheim, Norway, 1996.
[27] M. K. P. Svensson and B. Dalenback, ''A study of periodically time-variant electroacoustic reverberation enhancement and public address systems,'' 93rd Convention of the Audio Engineering Society, 3378 (F-1), 1992 (Preprint).
[28] P. U. Svensson, ''Computer simulations of periodically time-varying filters for acoustic feedback control,'' J. Audio Eng. Soc. **43**, 667–677 (1995).
[29] J. L. Nielsen and U. P. Svensson, ''Performance of some linear time-varying systems in control of acoustic feedback,'' J. Acoust. Soc. Am. **106**, 240–254 (1999).
[30] U. P. Svensson, ''On reverberation enhancement in auditoria,'' Ph.D. thesis, Department of Applied Acoustics, Chalmers University of Technology, Sweden, 1994.
[31] B. Picinbono, *Time and Frequency Representations of Signals and Systems* (Springer, New York, 1989).
[32] S. Haykin, *An Introduction to Analog and Digital Communications* (Wiley, New York, 1989).
[33] A. Papoulis, *Signal Analysis* (McGraw–Hill, New York, 1977).
[34] A. Papoulis, *Probability, Random Variables, and Stochastic Processes*, 3rd ed. (McGraw–Hill, New York, 1991).
[35] R. A. Horn and C. R. Johnson, *Matrix Analysis* (Cambridge University Press, Cambridge, 1985).
[36] M. R. Schroeder, ''Frequency correlation functions of frequency responses in rooms,'' J. Acoust. Soc. Am. **34**, 1819–1823 (1962).
[37] I. S. Gradshteyn and I. M. Ryzhik, *Table of Integrals, Series, and Products* (Academic, New York, 1965).
[38] S. Haykin, *Adaptive Filter Theory* (Prentice–Hall, Englewood Cliffs, 1991).
[39] H. Nelisse and J. Nicolas, ''Characterisation of a diffuse field in a reverberant room,'' J. Acoust. Soc. Am. **101**, 3517–3524 (1997).
[40] Denon, Anechoic Orchestral Music Recording, 1988.
[41] M. K. Simon, *Probability Distributions Involving Gaussian Random Variables: A Handbook for Scientists* (Kluwer Academic, Dordrecht, 2002).
[42] M. Barron, Auditorium Acoustics and Architectural Design E and FN Spon (Routledge, New York, 1993).

Analysis of the acoustical edge flexural mode in a plate using refined asymptotics[a)]

Dmitry D. Zakharov[b)]
Institute for Problems in Mechanics, Russian Academy of Sciences, 101-1 Vernadsky Avenue, 117529 Moscow, Russia

(Received 12 December 2003; accepted for publication 2 May 2004)

The dispersion properties of bending wave, localized near the stress-free edge of a thin isotropic plate, are investigated for relatively high frequency. In order to clarify the nature of the wave, attention is focused to the sensibility to the improved boundary conditions and to the iterations of the main differential operator when describing by two-dimensional (2-D) approximate plate theories. As shown, the boundary conditions of next asymptotic order do not change too much the leading part of the desired wave, but the corrections of the main operator lead to dramatical changes. Finally, beginning with its simplest Kirchooff's plate model only the leading part of wave may be subjected to asymptotic correction. For applications the wave speed calculation is reduced to two simple analytical formulas. The results agree well with experiments and finite element testing. The alternative approach related to the Timoshenko–Reissner–Mindlin theory is discussed. © *2004 Acoustical Society of America.* [DOI: 10.1121/1.1763957]

PACS numbers: 43.40.Dx, 43.20.Hq [ADP] Pages: 872–878

I. INTRODUCTION

This paper is devoted to the properties of the elastic bending wave propagating along the stress-free edge. As known, since the first paper by Konenkov[1] in 1960, many authors investigated this type of waves on the basis of the classical Kirchhoff's plate theory. Thurston, McKenna,[2] and Sinha[3] rediscovered them in 1974 and Thurston, Boyd, McKenna,[4] and Krylov[5] considered flexural waves guided by the wedge tip with a transition to the limit cases of the infinitely thin wedge (i.e., to the bending wave of the thin plate). Then further progress has been focused on the interface bending waves, which represent an analog of the Stonely waves at the edge-by-edge junction of the semi-infinite plates. Such waves have been studied by Zilbergleit and Suslova[6] and Kouzov *et al.*[7] for different configurations of nodal contact.

The edge bending wave in structures, immersed in a relatively light fluid, has been described by Krylov[8] (a fluid-loaded wedge), and by Abrahams and Norris.[9] The latter has shown that in the immersed plate the edge waves exist in the limited frequency band and may propagate without energy loss.

As far as anisotropic materials in vacuum are concerned, Norris[10] and Belubekyan and Engibaryan[11] treated a simplest case of the orthotropic plate with the principal axis directed along the edge. The more general case of anisotropy has been studied by Thompson, Abrahams, and Norris[12] and by Zakharov and Becker,[13,14] with the relevant analysis of the possible reverse power flow direction. Y. B. Fu[15] has recently investigated formal aspects of the edge wave existence and uniqueness.

For what follows we also have to mention results of 3-D finite element analysis of the ridge surface waves, obtained by Lagasse[16] and by Burridge and Sabina.[17,18] The wave speed, experimentally measured by Lagasse and Oliner,[19] is in a good agreement with the FEM calculation.[19] A comparison of their results with those of the classical Kirchhoff's theory demonstrates a satisfactory prediction at low frequencies only.

As shown by Norris, Krylov, and Abrahams[20] at the higher frequencies, the wave speed can be also predicted using the Timoshenko–Reissner–Mindlin (TRM) theory. Based on the rotation inertia assumption with respective shear correction of the plate equations and boundary conditions, this theory is not asymptotically justified, but is widespread in engineering practice. The consistent procedure we refer to below is to consider an asymptotic series with respect to the small relative thickness, and to deduce the high-order solving equation using recurrent formulas resulting from 3-D dynamic elasticity. Boundary conditions are refined on analyzing the boundary layer behavior. Among the first researchers who developed such methods of asymptotic integration were Friedrichs and Dresller,[21] Reissner,[22] Green,[23] and Goldenweiser.[24] In what follows we use this asymptotic method to clarify the nature of the edge bending wave in the isotropic plate and its sensibility to the perturbations of the boundary conditions and of the main differential operator.

To begin with we consider the Kirchhoff equation, which has an asymptotic error of second order. The respective classical boundary conditions have the error of the first order and require an additional term when improving. The desired solution of the boundary value problem with uniform asymptotic error is obtained and analyzed at the initial step. As in the classical case this solution contains a partial wave mostly responsible for the localization. Since it is low sensible to the perturbed boundary condition, the influence of the iteration of the main differential operator is investigated

[a)]Dedicated to the memory of Professor Alexei Goldenweizer, 1910–2003.

[b)]Present address: FESBE, London South Bank University, 103 Borough Road, London SE1 0AA, United Kingdom. Electronic mail: dd_zakh@mail.ru

 0001-4966/2004/116(2)/872/7/$20.00

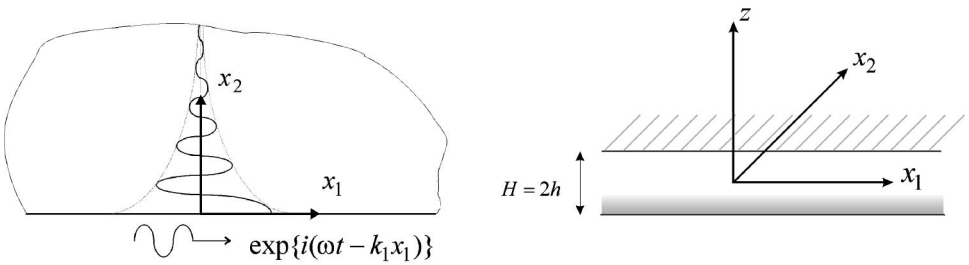

FIG. 1. The geometry of the problem.

at the next step. The trick of the suggested approach is in the asymptotic correction of this main part of wave only. Finally, we arrive at the wave speed formula valid for high frequencies or a relatively thick plate. These results are compared with experimental data and with those obtained using the Timoshenko–Reissner–Mindlin theory, and discussed.

II. FOUNDATIONS

Consider a semi-infinite thin elastic plate of total thickness $H=2h$, made of isotropic material with Young modulus E, Poisson's ratio ν, and mass density ρ, and occupying a region $x_2 \geqslant 0$, $\infty < x_1 < \infty$ in its middle plane (plate geometry is shown in Fig. 1). According to the classical Kirchhoff theory, introduce the normal deflection $w=w(\mathbf{x},t)$, slopes $\theta_\alpha = -\partial_\alpha w$ $(\alpha=1,2)$ and longitudinal displacements $u_\alpha = z\theta_\alpha$, where z is a transversal coordinate. Assuming that the plate faces $z=\mp h$ are stress-free, the respective stress couples $M_{\alpha\beta}$ and the transverse shear stress resultants $N_{\alpha z}$ acquire the form

$$M_{11} = -d(\partial_1^2 + \nu\partial_2^2)w, \quad M_{12} = -(1-\nu)d\partial_{12}^2 w,$$

$$M_{22} = -d(\partial_2^2 + \nu\partial_1^2)w, \quad N_{\alpha z} \equiv \partial_\beta M_{\alpha\beta} = -d\partial_\alpha \Delta w,$$

where $d = 2Eh^3/3(1-\nu^2)$ is the bending stiffness. The normal deflection satisfies the equation of motion (t denotes time),

$$\{d\Delta^2 + 2\rho h\partial_t^2\}w = 0 \quad (\Delta \equiv \partial_1^2 + \partial_2^2). \tag{1}$$

To set the boundary conditions of the plate edge, the effective transverse shear force is introduced,

$$P_{\alpha z} = N_{\alpha z} + \partial_\beta M_{12} \quad (\alpha \neq \beta; \alpha, \beta = 1,2),$$

and the stress-free edge $x_2=0$ is described by two requirements:

$$M_{22} = 0, \tag{2}$$

$$P_{2z} = 0. \tag{3}$$

Thus, in Kirchhoff's plate theory the edge bending waves is sought in the form

$$w = Ae^{i(\omega t - k_1 x_1) - k_2 x_2}, \quad k_1 > 0, \tag{4}$$

where ω is the frequency and k_1 is the wave number, with further deducing the dispersion relations from Eqs. (1)–(3). Following the approach of Konenkov,[1] let us introduce the dimensionless quantities

$$\xi \equiv \frac{k_2}{k_1} \geqslant 0, \quad s \equiv \sqrt[4]{\frac{2\rho h\omega^2}{dk_1^4}} = \frac{V_K}{V_B},$$

where the phase speeds of the edge wave V_K and of the usual bending wave V_B are

$$V_K \equiv \frac{\omega}{k_1}, \quad V_B = \sqrt[4]{\frac{d\omega^2}{2\rho h}},$$

respectively. Classical plate theory results in the following frequency independent value $s=s_*$ given by Konenkov:[1]

$$s_* = \sqrt[4]{(1-\nu)(-1+3\nu+2\sqrt{1-2\nu+2\nu^2})}$$
$$= 1 - \frac{\nu^4}{16} - \frac{\nu^5}{8} - \frac{5\nu^6}{32} + O(\nu^7). \tag{5}$$

III. SENSIBILITY TO THE IMPROVED BOUNDARY CONDITIONS

Now let us overview the above from the asymptotical viewpoint. For this purpose consider a longitudinal scale L (minimal wavelength), natural small parameter $\epsilon = h/L \ll 1$ and time scale $T = O(\epsilon^{-1})$. As it follows from 3-D elasticity consideration under such assumptions,[21,22,24] the displacement field can be subdivided into two components: an internal stress and strain state (at the distance of a few thickness apart from the edge) and a boundary layer (near the edge). The internal components can be represented in the form of asymptotic series

$$w = L\epsilon^{-3}(w^0 + \epsilon w^1 + \cdots),$$
$$u_\alpha = L\epsilon^{-2}(u_\alpha^0 + \epsilon u_\alpha^1 + \cdots), \tag{6}$$

where displacements and stresses of different orders satisfy the chain of recurrent relations. All the relations of Sec. II for the displacements and stress couples, and Eq. (1), hold for the leading terms of the internal stress and strain state, which is necessarily long wave within the relative truncation error $O(\epsilon^2)$ to be neglected. Conditions (2), (3) coincide with the so-called *natural* or *variational* boundary conditions in accordance with presented stress couples and resultants, and displacements as given linear functions of z. But the error of the boundary conditions (2) and (3) is $O(\epsilon)$ and exceeds that of the equation of motion, i.e., the asymptotic of the respective total boundary value problem is formally not uniform. It is remarkable that the first-order boundary condition (3) operates with the modified shear stress couple. The refinement requires incorporating the second order terms associated with the out of plane boundary layer localized in the vicinity of the plate edge (e.g., see Friedrichs and Dresller[21]) in formula (3) as well.

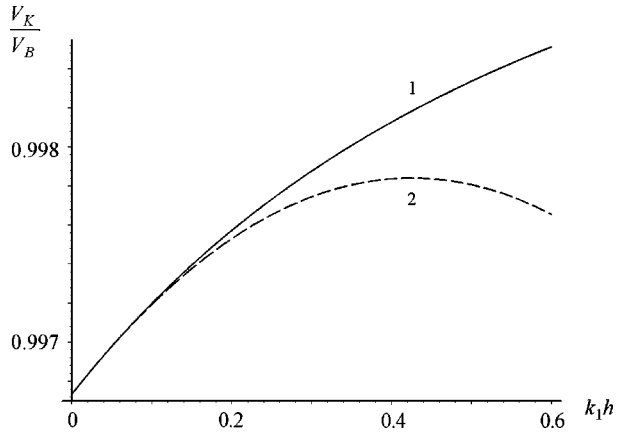

FIG. 2. The asymptotic behavior of $s=V_K/V_B$ for small k_1h (curve 2).

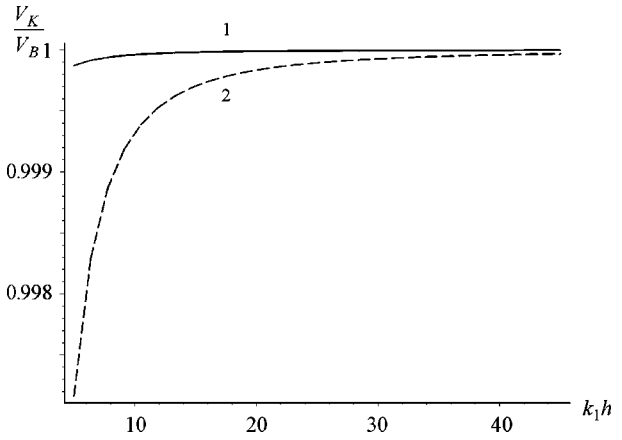

FIG. 3. The asymptotic behavior of $s=V_K/V_B$ for large k_1h (curve 2).

As it follows from the boundary layer analysis[24–26] when increasing the asymptotic accuracy up to the error $O(\epsilon^2)$, the *refined boundary conditions* [i.e., the modified equations (2), (3)] look as follows:

$$M_{22}+\chi h\,\partial_1 M_{12}=0, \quad P_{2z}=0, \tag{7}$$

where the value $\chi=\Sigma_{n=1}^{\infty}(2n-1)^{-5}\approx 1.260\,497\,75$ is found by Kolos.[25]

Hence, in the correct asymptotic formulation within the square relative error, the edge wave (4) satisfies Eqs. (1), (3) and (7). Let us now represent the results for the obtained wave properties in this consistent model.

Substitution of the expression (4) into Eq. (1) yields

$$(1-\xi^2)^2-s^4=0,$$

with two non-negative roots $\xi_{1,2}$,

$$\xi_{1,2}=\sqrt{1\mp s^2}, \quad s\leqslant 1.$$

The refined boundary conditions lead to the matrix equation with respect to two corresponding magnitudes $A_{1,2}$,

$$\begin{bmatrix} \xi_1^2-\nu+\sigma\xi_1 & \xi_2^2-\nu+\sigma\xi_2 \\ \xi_1(\xi_1^2-2+\nu) & \xi_2(\xi_2^2-2+\nu) \end{bmatrix}\begin{bmatrix} A_1 \\ A_2 \end{bmatrix}=0,$$

where $\sigma=\chi k_1 h\geqslant 0$. Its determinant is a function

$$F(s^2)=\sqrt{1+s^2}(1-\nu-s^2)(1-\nu-s^2+\sigma\sqrt{1-s^2}) - \sqrt{1-s^2}(1-\nu+s^2)(1-\nu+s^2+\sigma\sqrt{1+s^2}).$$

Since $F(1)=\sqrt{2}\,\nu^2>0$ and

$$F(0)=0,$$

$$F'(0)=-(1-\nu)(3+\nu)-2\sigma<0$$

(the derivative is taken with respect to s^2), the dispersion equation

$$F(s^2)=0, \tag{8}$$

always has at least one root $s^2\in(0,1)$. At $\sigma=0$, this root $s=s_*$. Expanding the root of Eq. (8) into power series with respect to σ, the following approximate formula, valid at $k_1h\ll 1/\chi$, is easily obtained,

$$s=s_*+s_1\sigma+s_2\sigma^2+O(\sigma^3),$$

$$s_1=\frac{\nu^4}{8\sqrt{2}}\left(1+\frac{\nu}{2}+\frac{9\nu^2}{4}+\frac{3\nu^3}{4}-\frac{87\nu^4}{32}+O(\nu^5)\right), \tag{9}$$

$$s_2=-\frac{3\nu^4}{32}\left(1+2\nu+2\nu^2-\frac{2\nu^3}{3}-\frac{77\nu^4}{12}+O(\nu^5)\right).$$

To illustrate this the plot of root s against k_1h for the Poisson's ratio, $\nu=0.39$ is shown in Fig. 2 by a solid curve together with the approximation (9) by a dashed line. Similarly, the root expansion into power series with respect to σ^{-1} gives at $\chi k_1 h\gg 1$ another approximation:

$$s=1-\frac{\nu^2}{4(1-\nu)^2}\sigma^{-2}-\frac{\nu^4(2-\nu^2)^2}{4(1-\nu)^3}\sigma^{-3}+O(\sigma^{-4}),$$

shown in Fig. 3 by a dashed line. However, this approximation is more formal since the cited 2-D plate theory remains in force at low frequencies only, when they are less than the first cutoff frequency.

Numerical analysis of roots has been carried out using the standard code MAPLE7 at different values of Poisson's ratio, $\nu=0$, 0.8(3), 0.1(6), 0.25, 0.3(3), 0.41(6), 0.5. Roots of Eq. (8) are plotted against k_1h in Fig. 4. For zero Poisson's ratio, the respective curve coincides with line $s=1$ and does not cause any attenuation of the edge bending wave; other curves are numbered from 1 to 6, respectively. As seen, there is a weak dependence on the frequency (or on the wave number) and the deviation of each root from the initial val-

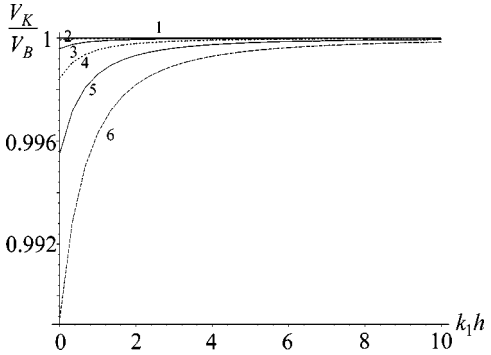

FIG. 4. The values of s for the Poisson's ratios $\nu=0$, 0.8(3), 0.1(6), 0.25, 0.3(3), 0.41(6), 0.5 (curves 1, 2,...,6, respectively).

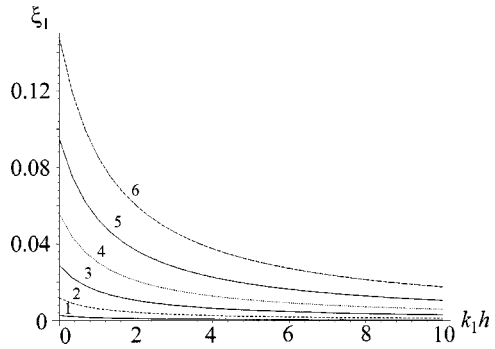

FIG. 5. The attenuation ξ_1 for the Poisson's ratios ν=0, 0.8(3), 0.1(6), 0.25, 0.3(3), 0.41(6), 0.5 (curves 1, 2,...,6, respectively).

ues $s=s_*$ is no more than 1%. The respective attenuation ξ_1 is shown in Fig. 5. Figure 6, representing the ratio of magnitudes

$$\frac{A_2}{A_1}=-\frac{\sqrt{1-s^2}(1-\nu+s^2)}{\sqrt{1+s^2}(1-\nu-s^2)},$$

shows that the magnitude A_1 cannot be neglected and the branch ξ_1 defines the slowest attenuation and responsible for the wave localization near the edge.

Thus, the behavior of variable s as well as of branches $\xi_{1,2}$ *is low sensible* to the perturbation of the boundary conditions.

IV. HIGH-ORDER EQUATIONS OF PLATE BENDING

Further improvement in the plate modeling meet considerable technical obstacles caused by taking into account both the out-of-plane boundary layer and the in-plane one for the boundary conditions of high-order iterations. In the meantime, the refinement of the homogeneous Kichhoff equation may be easily done.

The equation of plate bending within the error $O(\epsilon^8)$ is deduced[26] using 3-D elasticity and recurrent formulas for next terms of asymptotic expansions (6), and reduced to a final form in terms of the middle plane deflection w,

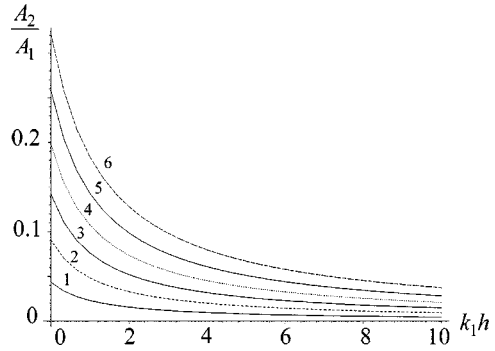

FIG. 6. The ratio A_2/A_1 for Poisson's ratios ν=0, 0.8(3), 0.1(6), 0.25, 0.3(3), 0.41(6), 0.5 (curves 1, 2,...,6, respectively).

$$d\Delta^2 w+2\rho h\left\{1+a_0(\nu)h^2\Delta+a_1(\nu)\frac{h^2}{c_2^2}\partial_t^2+a_2(\nu)\frac{h^4}{c_2^2}\partial_t^2\Delta\right\}\partial_t^2 w=0,$$

$$a_0=\frac{7\nu-17}{15(1-\nu)},\quad a_1=\frac{422-424\nu-33\nu^2}{1050(1-\nu)},\quad a_2=\frac{32-96\nu+261\nu^2-197\nu^3}{15750(1-\nu)}, \tag{10}$$

where c_2 is a shear wave speed. The evident analog with Eq. (1) consists in the replacement

$$2\rho h\,\partial_t^2 w\to 2\rho h\left\{1+a_0(\nu)h^2\Delta+a_1(\nu)\frac{h^2}{c_2^2}\partial_t^2+a_2(\nu)\frac{h^4}{c_2^2}\partial_t^2\Delta\right\}\partial_t^2 w.$$

For a free plate vibration mode, which satisfies the condition $\Delta w<0$, expressing Δw upon this analog from Eq. (10),

$$\Delta w=-\frac{\omega}{hc_2}\sqrt{\frac{3(1-\nu)}{2}}\left\{1+b_1(\nu)\frac{\omega h}{c_2}+b_2(\nu)\left(\frac{\omega h}{c_2}\right)^2+O(\epsilon^6)\right\},$$

and substituting into (10), we arrive at the high-order equation of a plate in terms of *effective inertia*,[26]

$$\{d\Delta^2-2\rho h\omega_n^2\}w=0, \tag{11}$$

$$\omega_n^2=\omega^2\sum_{k=0}^{n}B_k(\nu)\left(\frac{\omega h}{c_2}\right)^k, \tag{12}$$

where coefficients B_k are

$$B_0=1,\quad B_1=\sqrt{\frac{3(1-\nu)}{2}}\frac{17-7\nu}{15(1-\nu)},\quad B_2=\frac{1179-818\nu+409\nu^2}{2100(1-\nu)},$$

$$B_3=\sqrt{\frac{3(1-\nu)}{2}}\frac{5951-2603\nu+9953\nu^2-4901\nu^3}{126\,000(1-\nu)^2}.$$

For indices $n=0$, 1, 2, 3 the relative truncation error of the respective high-order operator is $O(\epsilon^{2n+2})$.

Of course, in the high-order model the displacements are polynomial with respect to the transversal coordinate z.

The *assumption* $\Delta w<0$ corresponds to many practically important cases. In particular, it holds for the propagation vibration modes. For the latter, a correction of the equation of motion appears to be more important than that of bound-

ary conditions.[26] As we show later, the last feature may also be characteristic of the most important components of the sought-for edge wave since they obey the same inequality.

V. EDGE MODE SENSIBILITY TO THE IMPROVED MAIN DIFFERENTIAL OPERATOR

Numerical results for the wave speed are obtained using formulas (11) and (12) for the high-order operator. Let us now proceed to the verification of our results in the same manner as they are presented in Refs. 19 and 20. The procedure looks as follows. Introduce a dimensionless frequency (c_R is a speed of the Rayleigh wave),

$$\Omega = \frac{\omega H}{c_R},$$

just to be in the same scale as our precessors.[19,20] After calculating the root of Eq. (8), express the frequency Ω via s and $k_1 h$,

$$\Omega \equiv \frac{\omega H}{c_R} = \sqrt{\frac{8}{3(1-\nu)}}\frac{(sk_1h)^2}{\psi}, \quad \psi = \frac{c_R}{c_2},$$

together with the normalized speed

$$\frac{V_K}{c_R} = \sqrt[4]{\frac{4}{9(1-\nu)^2}}\frac{s^2 k_1 h}{\psi}. \tag{13}$$

Excluding $k_1 h$ we finally plot V_K/c_R against Ω and this is absolutely correct for $n=0$.

When index $n>1$, one arrives at the same characteristic equation (8), but the meaning of parameter s differs, namely

$$s^4 \equiv \frac{2\rho h \omega_n^2}{d k_1^4} = \left(\frac{V_K}{V_B}\right)^4 \sum_{k=0}^{n} B_k \left(\frac{\omega h}{c_2}\right)^k.$$

Hence, the respective frequency $\Omega \equiv \Omega_n$ satisfies the equation

$$\Omega \sqrt{\sum_{k=0}^{n} B_k \left(\frac{\Omega\psi}{2}\right)^k} = \sqrt{\frac{8}{3(1-\nu)}}\frac{(sk_1h)^2}{\psi} = \sqrt{6(1-\nu)}\frac{\psi}{s^2}\left(\frac{V_K}{c_R}\right)^2. \tag{14}$$

Obviously, this is the only difference caused by the operator itself.

In Fig. 7, the relative speed V_K/c_R is shown as function of Ω at Poisson's ratio $\nu=0.39$. The letter K marks the curve for classical Kirchhoff's theory, K_R denotes the case of refined boundary conditions (7) ($n=0$), and numbers 1, 2, 3 correspond to the iteration indices in formulas (10) and (11). Balls represent the experimental measurement of the wave speed[19] also tested by the finite element calculation. As seen, there is only a slight difference between the curves K and K_R (practical coincidence), i.e., the results are now asymptotically justified within the second-order asymptotic error. Iteration $n=1$ gives the intermediate results, but when using two steps of iterations ($n=2$) wave speed matches well to the experimental data. The use of the third-order iteration ($n=3$) agrees with experiment quite well. The additional

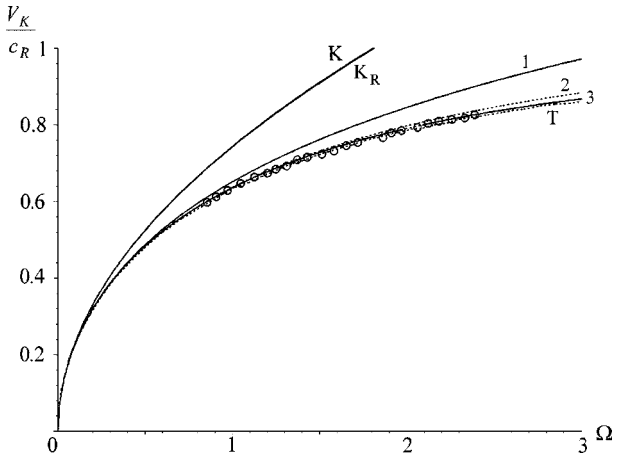

FIG. 7. A comparison with results by the Timoshenko–Reissner–Mindlin (curve *T*) theory, results by iteration of the main operator (curves 1–3), and by measurement (balls).

curve, marked by *T*, is obtained using the TRM theory of plate.[20] It slightly deviates from our curve 3, especially at large frequencies, where we hope to deal with a better approximation. Let us discuss this fact in the next section. To be complete, the dimensionless absolute attenuation $k_2 H$ is plotted in Fig. 8. For the practical viewpoint it should be noted that the absolute attenuation obtained for high frequency is about 40% less than predicted by classical Kirchhoff's theory.

To sum up, the dispersion curve is *high sensible* to the order of the main operator. Everything done is correct for the leading component of the edge wave corresponding to the root s and branch ξ_1, i.e., for the main partial wave, responsible for the localization.

VI. DISCUSSION

First, let us make some observations concerning the TRM[20,27] theory. As known, the assumed displacement field may be represented as follows:

$$w = w(\mathbf{x},t), \quad u_\alpha = z(\theta_\alpha + \varphi_\alpha),$$

where φ_α is an additional component causing *the rotation inertia* of the plate cross section. The respective expressions for the torques and transverse shear stress resultants may be reduced to a form:

$$M_{11} = d\lfloor -(\partial_1^2 + \nu\partial_2^2)w + \partial_1\varphi_1 + \nu\partial_2\varphi_2 \rfloor,$$

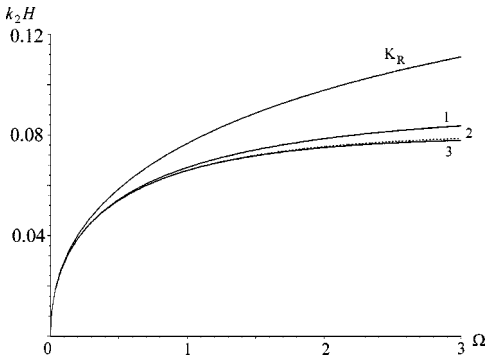

FIG. 8. The attenuation $k_2 H$ for a different approximation order.

$$M_{12}=d\left[-(1-\nu)\partial_{12}^2 w+\frac{1-\nu}{2}(\partial_2\varphi_1+\partial_2\varphi_1)\right],$$

$$M_{22}=d[-(\partial_2^2+\nu\partial_1^2)w+\partial_2\varphi_2+\nu\partial_1\varphi_1],$$

$$N_{\alpha z}=2\rho h a^2 c_2^2\varphi_\alpha=d\left\{-\partial_\alpha\Delta w+\frac{1-\nu}{2}\Delta\varphi_\alpha+\frac{1+\nu}{2}\partial_{\alpha\beta}^2\varphi_\beta\right\},$$

The factor a is a so-called ''shear correction,'' which, in principle, may be chosen according to different principles, but normally $a^2\leqslant 1$. Here it is chosen as $a=c_R/c_2$ for a better description of the high-frequency asymptote of the fundamental antisymmetric mode of a plate. Thus, the boundary conditions at the stress-free edge can be rewritten in terms of Sec. II using the same notations as in formulas (7):

$$M_{12}=0,$$

$$M_{22}+\chi h\,\partial_1 M_{12}=0,$$

$$P_{2z}\equiv N_{2z}+\partial_1 M_{12}=0.$$

They differ only by the additional requirement imposed to the shear stress couple. By the way, Reissner has shown[28] that in the long-wave and low-frequency limit of his theory these three boundary conditions are reduced to two:

$$M_{22}+\chi_* h\,\partial_1 M_{12}=0,\quad P_{2z}=0,$$

and $\chi_*\approx 1.264$, which differs from χ in (7) just by the third digit.

It is easily to derive that the rotation angles φ_α and the normal deflection are related by the equation

$$\partial_t^2 w=c_R^2\,\partial_\alpha\varphi_\alpha,$$

and after simplifications w satisfies the main resolving equation in the form

$$d\Delta^2 w+2\rho h\left\{1+m_0(\nu)h^2\Delta+m_1(\nu)\frac{h^2}{c_2^2}\partial_t^2\right\}\partial_t^2 w=0,$$
$$m_0=-\frac{1}{3}-\frac{2}{3(1-\nu)\psi^2},\quad m_1=\frac{1}{3\psi^2}. \tag{15}$$

The structure of the operator in Eq. (15) is similar to that in Eq. (10) at $n=2$, but coefficients differ. Despite the absence of the correct asymptotical justification of this theory, it catches the dynamics of the plate with practical accuracy since being constructed by combining the components of the low-frequency Kirchhoff plate theory and those of the high-frequency terms for the fundamental flexural mode.

Generally, when increasing the order of the operator, the set of roots ξ increases necessarily and contains two roots coming from the Kirchhoff model and a few ''parasitic'' roots, which correspond to the partial waves of *high variation* near the edge and *high attenuation* when going far from the edge. By the way, the situation is a bit contradictive, since the initial long wave asymptotic assumption demands a *slow variation* and a large longitudinal scale L. However, besides the satisfactory description of low-frequency phenomena, as well as high-frequency behavior of Rayleigh asymptotics of plate modes, the fortune of TRM theory is in its happy interaction of ''parasitic'' terms with a physically meaningful Kirchhoff's contribution. Due to the asymptotic hierarchy of the equations and boundary conditions, the root branches possess a different sensibility to the changes involved. In contrast to the low sensible Kirchoff's root, the new roots must be very sensible to the modification of boundary conditions.

Thus, the good correspondence with the T curve in Fig. 7 is a consequence of this temptation to improve the total description of the mode.

Now let us discuss why the simplified description from Secs. II–IV is so accurate as to predict the speed of the edge flexural mode. Above we improve exactly this partial wave ξ_1, whose behavior is *stable*. It defines the smallest attenuation and is responsible to the effect of localization near the stress-free edge. It is also physically meaningful and corresponds to the initial asymptotic assumption about scaling. As shown in Sec. II, this branch is rather sensible to the iteration of the equation, but has a small sensibility to the boundary condition improvement, and even at first correction $s-s_*$ is $O(\nu^4)$ (numerically this is less than 1%). As it turned out, the information about the leading term is sufficient to describe the edge wave propagation.

VII. CONCLUSION

The performed analysis exhibits some essential properties of the edge bending waves in a thin isotropic plate. *First*, it concerns the possibility to describe this wave at relatively high frequencies, where 2-D plate theories are used very seldom. *Second*, it clarifies the nature of this wave. The leading part ξ_1 mostly responsible for the wave localization can be singled out. Its behavior is determined by the differential equation of plate bending and by its improved versions of the highest orders. The sensibility to the improvement of the boundary condition can be neglected, since even first correction has the order $O(\nu^4)$ and is numerically small. Other partial waves arising in this representation must be very sensible to the perturbation of boundary conditions, but the description of ξ_1 is a key, quite sufficient to simulate the edge wave propagation. *Third*, such an important acoustic characteristic as wave speed may be predicted very easy with high accuracy. To this end the root of Eq. (8) and frequency correction (14) are used. In addition, the root s of Eq. (8) may be replaced by its approximation $s\approx s_*$ and, finally, just one simple formula,

$$\frac{\omega H}{c_2}\sqrt{\sum_{k=0}^{3}B_k\left(\frac{\omega H}{2c_2}\right)^k}\approx\sqrt{\frac{6}{-1+3\nu+2\sqrt{1-2\nu+2\nu^2}}}\left(\frac{V_K}{c_2}\right)^2,$$

describes the wave dispersion in a closed form. Results are in a good agreement with experimental measurement and with those obtained using the Timoshenko–Reissner–Mindlin theory. The latter is not justified from the asymptotical viewpoint but the remarks given above explain why it is also

efficient. It should be noted that the suggested procedure of the speed calculation is more precise and much more simple the any of previous.[19,20]

ACKNOWLEDGMENTS

This work has been carried out under partial support from the Russian Foundation for Basic Research (Grant No. 02-01-00843), which is gratefully acknowledged. The author also would like to thank Dr. J. D. Kaplunov for many fruitful discussions.

[1] Yu. K. Konenkov, ''A Rayleigh-type flexural wave,'' Sov. Phys. Acoust. **6**, 122–123 (1960).
[2] R. N. Thurston and J. McKenna, ''Flexural acoustic waves along the edge of a plate,'' IEEE Trans. Sonics Ultrason. **21**, 296–297 (1974).
[3] B. K. Sinha, ''Some remarks on propagation characteristics of ridge guide for acoustic waves at low frequencies,'' J. Acoust. Soc. Am. **56**, 16–18 (1974).
[4] R. N. Thurston, G. D. Boyd, and J. McKenna, ''Plate theory solution for guided flexural acoustic waves along the tip of the wedge,'' IEEE Trans. Sonics Ultrason. **21**, 178–186 (1974).
[5] V. V. Krylov, ''Geometrical-acoustic approach to the description of localized modes of an elastic solid wedge,'' Sov. Phys. Tech. Phys. **35**, 137–140 (1990).
[6] A. S. Zilbergleit and I. B. Suslova, ''Contact flexural waves in thin plates,'' Sov. Phys. Acoust. **29**, 108–111 (1983).
[7] D. P. Kouzov, T. S. Kravtsova, and V. G. Yakovleva, ''On the scattering of the vibrational waves on a knot contact of plates,'' Sov. Phys. Acoust. **35**, 392–394 (1989).
[8] V. V. Krylov, ''On the velocities of localized vibration modes in immersed solid wedges,'' J. Acoust. Soc. Am. **103**, 767–770 (1998).
[9] I. D. Abrahams and A. N. Norris, ''On the existence of flexural edge waves on submerged elastic plates,'' Proc. R. Soc. London, Ser. A **456**, 1559–1582 (2000).
[10] A. N. Norris, ''Flexural edge waves,'' J. Sound Vib. **174**, 571–573 (1994).
[11] M. V. Belubekyan and I. A. Engibaryan, ''Waves, localized along the stress-free edge of a plate with cubic symmetry,'' Mech. Solids **6**, 139–143 (1994) (in Russian).
[12] I. Thompson, I. D. Abrahams, and A. N. Norris, ''On the existence of flexural edge waves on thin orthotropic plates,'' J. Acoust. Soc. Am. **112**, 1756–1765 (2002).
[13] D. D. Zakharov, ''Konenkov's waves in anisotropic layered plates,'' Acoust. Phys. **48**, 171–175 (2002).
[14] D. D. Zakharov and W. Becker, ''Rayleigh type bending waves in anisotropic media,'' J. Sound Vib. **261**, 805–818 (2003).
[15] Y. B. Fu, ''Existence and uniqueness of edge waves in a generally anisotropic elastic plate'' (unpublished).
[16] P. E. Lagasse, ''High-order finite-element analysis of topographic guides supporting elastic surface waves,'' J. Acoust. Soc. Am. **53**, 1116–1122 (1973).
[17] R. Burridge and F. J. Sabina, ''Theoretical computations on ridge acoustic surface waves using the finite element method,'' Electron. Lett. **7**, 720–722 (1971).
[18] R. Burridge and F. J. Sabina, ''The propagation of elastic surface waves guided by ridges,'' Proc. R. Soc. London, Ser. A **330**, 417–441 (1972).
[19] P. E. Lagasse and A. A. Oliner, ''Acoustic flexural mode on a ridge of semi-infinite height,'' Electron. Lett. **12**, 11–13 (1976).
[20] A. N. Norris, V. V. Krylov, and I. D. Abrahams, ''Flexural edge waves and Comments on 'A new bending wave solution for the classical plate equation,''' J. Acoust. Soc. Am. **107**, 1781–1784 (2000).
[21] K. O. Friedrichs and R. F. Dressler, ''A boundary-layer theory for elastic plates,'' Commun. Pure Appl. Math. **14**, 1–33 (1961).
[22] E. Reissner, ''On the derivation of the theory of thin elastic shells,'' J. Math. Phys. **43**, 263–277 (1964).
[23] A. E. Green, ''On the linear theory of thin elastic shells,'' Proc. R. Soc. London, Ser. A **266**, 143–160 (1962).
[24] A. L. Goldenveiser, ''Derivation of the approximate theory of plate bending by asymptotic integration method,'' J. Appl. Math. Mech. **26**, 668–686 (1962).
[25] A. V. Kolos, ''Methods of refining the classical theory of bending and extension of plates,'' J. Appl. Math. Mech. **29**, 771–781 (1965).
[26] A. L. Goldenveizer, J. D. Kaplunov, and E. V. Nolde, ''On Timoshenko–Reissner type theories of plates and shells,'' Int. J. Solids Struct. **30**, 675–694 (1993).
[27] A. N. Norris, ''Flexural waves on narrow plates,'' J. Acoust. Soc. Am. **113**, 2647–2658 (2003).
[28] E. Reissner, ''On the analysis of first and second order shear deformation effects for isotropic elastic plates,'' ASME J. Appl. Mech. **47**, 959–961 (1980).

Local/global homogenization of fluid-loaded periodic structures

Pavel Danilov and Donald Bliss[a)]
Department of Mechanical Engineering and Materials Science, Duke University, Durham, North Carolina 27708

(Received 11 August 2003; revised 31 March 2004; accepted 5 May 2004)

A novel homogenization method for periodic structures that utilizes a local/global separation of the high and low wavenumber spectrum is presented. The low-wavenumber global problem has an infinite-order operator. The global problem is self-contained; local solutions can be reconstructed after the fact if desired. Global problems are constructed for a membrane and a plate *in vacuo*, each with periodic impedance discontinuities. A fluid-loading approximation is introduced in order to homogenize problems of interaction between fluid and structure. Radiating acoustic modes are contained in the smooth global problem, and the global structural operator accounts for an influence of evanescent acoustic modes. As an example, oblique sound reflection from a flexible barrier with impedance discontinuities is analyzed. Accurate results are obtained from the method. [DOI: 10.1121/1.1766022]

PACS numbers: 43.40.Dx, 43.40.Rj [ANN] Pages: 879–890

I. INTRODUCTION

Many important structures have discontinuities such as ribs, stringers, braces, and/or attachments placed at regular intervals. Ribbed hulls, aircraft fuselages, and truss structures are examples. These structures may be periodic, or quasi-periodic, depending on whether the discontinuities are identical and equally spaced. When forced at a single frequency, the response occurs in a broad spectrum of spatial wavenumbers due to the discontinuities. Furthermore, structures such as fuselages and hulls are fluid loaded, which alters their response. The structural motion and the acoustic radiation, scattering, and/or interior sound field may be of interest.[1–3]

Calculating the motion of such structures is a complex and computationally expensive task.[4] The disparity of scales requires high numerical resolution. The forcing may be a series of locally applied forces or continuously distributed forces having a spectrum of wavenumbers. If the structure is spatially periodic, the response will exhibit stop- and pass-bands and the wavenumber spectrum will be discrete.[5,6]

The low wavenumber (long wavelength) portion of the response is often of primary interest, since it models the gross vibratory motion of the structure. Also, for fluid-loaded structures, the low-wavenumber part of the response corresponds to supersonic phase speeds, which are most efficiently coupled to the acoustic field. This paper presents results of ongoing research[7] to formulate *self-contained governing equations* that describe *directly* the low-wavenumber response of spatially periodic structures. It is important to emphasize that this method leads to *direct* formulations of the low-wavenumber problem. In particular, it is not a matter of solving the full problem and subsequently isolating the low-wavenumber part of the solution. This formulation for the low-wavenumber part of the solution is self-contained, and indeed, the high-wavenumber content can be reconstructed after the fact using information from the low-wavenumber solution. The present work shows that it is possible to include fluid-loading effects in a convenient manner.

Because the low-wavenumber problem is smooth and contains transfer function information from the high-wavenumber part of the problem, the approach is a type of homogenization method. However, it differs from classical homogenization,[8] and in many cases it is valid for the full frequency range. The low-wavenumber problem is smooth and *global*, namely, it spans the structure. The high-wavenumber problem involves waves typically shorter than the discontinuity spacing, and it can be thought of as a series of contiguous *local* solutions between the discontinuities. Therefore the method is called *local-global homogenization*. Since the global problem has a known degree of smoothness, there are potential advantages in accuracy and efficiency if the approach can be extended to numerical methods. The approach is an analytical reformulation method for complex problems, prior to solution, to allow the calculation of the important aspects directly and efficiently.

II. TECHNICAL APPROACH

In this section, the approach is developed in general for a periodic structure. Later it is applied to the problem of acoustic scattering from a fluid-loaded membrane, as illustrated in Fig. 1. Due to the periodic discontinuities, excitation by even one wavenumber β leads to a broad spectrum response. As shown in Fig. 2, the response wavenumbers are shifted from the excitation wavenumber by multiples of $2\pi/L$.

The goal is to divide the original problem into a *global* problem and a *local* problem distinguished by their low- and high-wavenumber content, respectively. As illustrated in Fig. 3, the global problem is smooth and has only low-wavenumber content. In the first scattering problem to be solved later, the global problem contains a single wavenumber falling in the interval $-\pi/2<\alpha_0 L<\pi/2$, which corresponds to the wavenumber range that produces acoustic radiation for sufficiently low frequencies. However, the

[a)]Author to whom correspondence should be addressed. Electronic mail: dbb@duke.edu

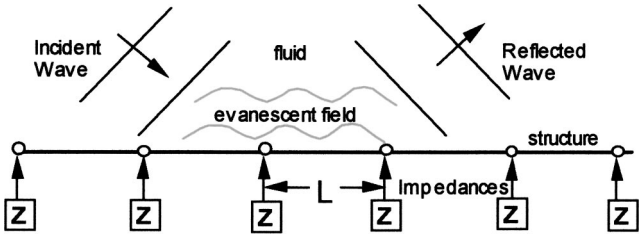

FIG. 1. The problem of acoustic scattering from a fluid-loaded membrane.

approach can be readily generalized to include more wavenumber intervals in the global solution, and thereby be extended to higher frequencies, as will also be shown later in the paper. The local problem, as shown in Fig. 3, is seen to have rapid spatial variation and to contain the remainder of the wavenumbers, which excite only evanescent (nonradiating) fluid modes.

A. General theory

First, consider harmonic motion of a continuous structure, such as a membrane or plate with no fluid, having displacement $\eta(x)e^{i\omega t}$ governed by a linear differential operator $D(x)$ and subjected to applied forcing $F(x)$. Assuming harmonic motion removes the time dependence. Identical discontinuities having impedance $Z(\omega)$ are attached at intervals $x_n = nL$. Then, the governing equation is given by,

$$D(x)\,\eta(x) = i\omega Z \sum_n \eta(x)\,\delta(x - x_n) + F(x). \tag{1}$$

This equation will be used to illustrate the general approach to local/global decomposition. The Fourier transform in the following form is used to rewrite Eq. (1) in the wavenumber space:

$$\overline{f}(\alpha) = \int_{-\infty}^{\infty} f(x) e^{i\alpha x}\, dx;$$

$$f(x) = \frac{1}{2\pi} \int_{-\infty}^{\infty} \overline{f}(\alpha) e^{-i\alpha x}\, d\alpha. \tag{2}$$

Using Fourier transform properties[9] one yields

$$\eta(x) \sum_n \delta(x - x_n) \equiv \frac{\eta(x)}{L} \sum_n \exp\left[i \frac{2\pi n}{L} x \right]$$

$$\rightarrow \frac{1}{L} \sum_n \overline{\eta}(\alpha - 2\pi n/L). \tag{3}$$

Thus, the Fourier transform of Eq. (1) is

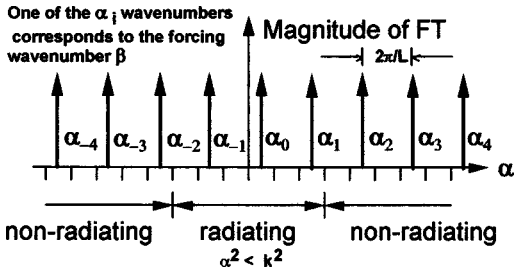

FIG. 2. Solution spectrum.

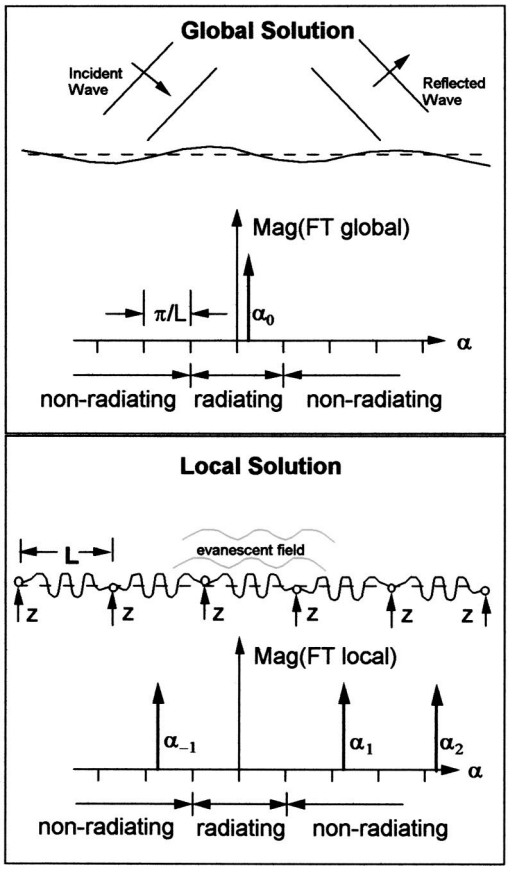

FIG. 3. Global and local solutions contain radiating and nonradiating wavenumbers, respectively.

$$D(\alpha)\,\overline{\eta}(\alpha) = \frac{i\omega Z}{L} \sum_n \overline{\eta}(\alpha - 2\pi n/L) + \overline{F}(\alpha) \tag{4}$$

The global and local parts of displacement are defined in terms of wavenumber domains:

$$\overline{\eta} = \overline{\eta}_{\text{global}} + \overline{\eta}_{\text{local}};$$

$$\overline{\eta}_{\text{global}}(\alpha) = 0, for \quad \alpha \notin [-\pi/L; \pi/L];$$

$$\overline{\eta}_{\text{local}}(\alpha) = 0, \quad for \quad \alpha \in [-\pi/L; \pi/L]. \tag{5}$$

Considering Eq. (4) separately in the global and local intervals gives the expressions

$\alpha \in [-\pi/L; \pi/L]$:

$$D(\alpha)\,\overline{\eta}_{\text{global}}(\alpha) = \frac{i\omega Z}{L} \sum_{n \neq 0} \overline{\eta}_{\text{local}}(\alpha - 2\pi n/L)$$

$$+ \frac{i\omega Z}{L} \overline{\eta}_{\text{global}}(\alpha) + \overline{F}(\alpha), \tag{6a}$$

$\alpha \notin [-\pi/L; \pi/L]$:

$$D(\alpha)\,\overline{\eta}_{\text{local}}(\alpha) = \frac{i\omega Z}{L} \sum_{n \neq n^*} \overline{\eta}_{\text{local}}(\alpha - 2\pi n/L)$$

$$+ \frac{i\omega Z}{L} \overline{\eta}_{\text{global}}(\alpha - 2\pi n^*/L) + \overline{F}(\alpha), \tag{6b}$$

where in Eq. (6b) n^* is an integer, such that $-\pi/L<\alpha-2\pi n^*/L<\pi/L$. Subtracting Eq. (6a) taken at $\alpha^*=\alpha-2\pi n^*/L$ from Eq. (6b) and using the definitions of local and global displacements yields

$$\alpha\notin[-\pi/L;\pi/L]:$$

$$\overline{\eta}_{\text{local}}(\alpha)=\frac{1}{D(\alpha)}[D(\alpha^*)\overline{\eta}_{\text{global}}(\alpha^*)+\overline{F}(\alpha)-\overline{F}(\alpha^*)]. \tag{7}$$

Equation (7) is the *local-global relationship*. It allows the local displacement η_{local} to be eliminated to obtain a new governing equation involving only the global displacement η_{global}. The local short-wave solution can be reconstructed once the global long-wave solution is known. Equation (7) can also be rewritten as

$$\alpha\in[-\pi/L;\pi/L];n\neq 0:$$

$$\overline{\eta}_{\text{local}}(\alpha-2\pi n/L)=\frac{D(\alpha)\overline{\eta}_{\text{global}}(\alpha)+\overline{F}(\alpha-2\pi n/L)-\overline{F}(\alpha)}{D(\alpha-2\pi n/L)}. \tag{8}$$

Then, using Eq. (8), the governing equation for the global displacement Eq. (4) in the wavenumber space becomes

$$D(\alpha)\left[1-\frac{i\omega Z}{L}\sum_n\frac{1}{D(\alpha-2\pi n/L)}\right]\overline{\eta}_{\text{global}}(\alpha)=\overline{F}(\alpha)+\frac{i\omega Z}{L}\sum_{n\neq 0}\frac{\overline{F}(\alpha-2\pi n/L)-\overline{F}(\alpha)}{D(\alpha-2\pi n/L)}. \tag{9}$$

Since the global solution is defined only in the narrow wavenumber interval $-\pi/L<\alpha<\pi/L$, the right-hand side of Eq. (9) can be considered as a modified forcing (MF) in that interval only, i.e., multiplied by a filter function $S(\alpha)$, which is 1 in the global interval and 0 outside. Nevertheless, this modified forcing depends on the original excitation through the whole range of wavenumbers. The left-hand side of Eq. (9) contains the transform of a new differential operator, called the global operator.

B. A membrane with discontinuities

The procedure is best illustrated by the specific example of a 1-D membrane with attached impedances, namely, described by the following structural operator (sum can be found, e.g., in tables by Jolley[10]):

$$D(\alpha)=k_s^2-\alpha^2\Rightarrow\sum_n\frac{1}{D(\alpha-2\pi n/L)}=\sum_n\frac{1}{k_s^2-(\alpha-2\pi n/L)^2}=\frac{L}{2k_s}\frac{\sin k_sL}{\cos\alpha L-\cos k_sL}, \tag{10}$$

where $k_s=\omega/c_s$ is the wavenumber for free motion, and c_s is the membrane (structure) phase speed. Thus, in this case, Eq. (9) becomes

$$\left(\cos\alpha L-\cos k_sL-\frac{i\omega Z}{2k_s}\sin k_sL\right)\overline{\eta}_{\text{global}}(\alpha)=\overline{\text{MF}}, \tag{11}$$

$$\overline{\text{MF}}=S(\alpha)\frac{\cos\alpha L-\cos k_sL}{k_s^2-\alpha^2}\times\left(\overline{F}(\alpha)+\frac{i\omega Z}{L}\sum_{n\neq 0}\frac{\overline{F}(\alpha-2\pi n/L)-\overline{F}(\alpha)}{D(\alpha-2\pi n/L)}\right).$$

Without forcing, the wavenumber operator on the left side of Eq. (11) yields the dispersion relation for Bloch waves on the structure. After a series expansion of the cosines, Eq. (11) can be written as a power series in wavenumber α with frequency-dependent coefficients. Using the inverse Fourier transform to return to physical space leads to a governing equation with an infinite-order differential operator acting on the unknown $\eta_{\text{global}}(x)$:

$$\left(1-\cos k_sL-\frac{i\omega Z}{2k_s}\sin k_sL+\frac{L^2\partial^2}{2!\,\partial x^2}+\frac{L^4\partial^4}{4!\,\partial x^4}+\mathsf{K}\right)\times\eta_{\text{global}}(x)=\text{MF}(x). \tag{12}$$

The "modified forcing" term on the right side of Eq. (12) is a filtered version of the original forcing. For a given forcing wavenumber β, corresponding to the original forcing $F(x)=F_0e^{i\beta x}$, one can write: $\text{MF}(x)=F_0H(\beta)e^{i\tilde{\beta}x}$, where $\tilde{\beta}=\beta-2\pi n/L\in[-\pi/L,\pi/L]$ is the original wavenumber shifted into the global interval, and the filter function $H(\beta)$ has the following form:

$$H(\beta)=\begin{cases}\dfrac{\cos\tilde{\beta}L-\cos k_sL}{k_s^2-\tilde{\beta}^2}\left[1-\dfrac{i\omega Z}{L}\left(\dfrac{L}{2k_s}\dfrac{\sin k_sL}{\cos\beta L-\cos k_sL}-\dfrac{1}{k_s^2-\beta^2}\right)\right], & if\ \ \beta\in[-\pi/L,\pi/L],\\ \dfrac{i\omega Z}{L}\dfrac{\cos\tilde{\beta}L-\cos k_sL}{k_s^2-\tilde{\beta}^2}\dfrac{1}{k_s^2-\beta^2}, & if\ \ \beta\notin[-\pi/L,\pi/L].\end{cases} \tag{13}$$

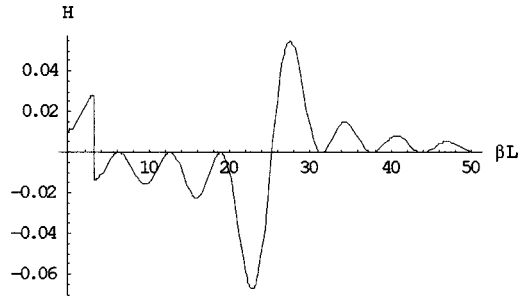

FIG. 4. Modified forcing filter function. Mass impedance case. $c_s/c=0.6$; $m/\rho_s L=1.5$; $kL=25$.

Modified forcing wavenumber $\tilde{\beta}$ lies within the global interval; however, modified forcing amplitude, given by the filter function $H(\beta)$, depends on exact location of the original forcing wavenumber β. A typical filter function is shown in Fig. 4. Qualitatively it shows how much the given forcing wavenumber contributes to the global excitation. The case of arbitrary forcing is considered in the Appendix in detail.

The same global equation, Eq. (11), was derived earlier by Bliss and Franzoni[11,12] using a *smooth force* method. The present *wavenumber filtering* approach has advantages for fluid loading cases.

C. A plate or beam with discontinuities

As mentioned above, the global operator can be used to determine the free vibrations of a structure in the global wavenumber interval. Another such example is 1-D waves on a plate or beam with discontinuities, in general described by a fourth-order differential operator:

$$
\begin{aligned}
D(\alpha) &= -\frac{\omega^2}{a^2}+\alpha^4 \Rightarrow \sum_n \frac{1}{D(\alpha-2\pi n/L)} \\
&= \sum_n \frac{1}{(\alpha-2\pi n/L)^4-\omega^2/a^2} \\
&= \frac{a^2}{2\omega^2}\left[\sum_n \frac{1}{(\alpha-2\pi n/L)^2-\omega/a}\right. \\
&\quad \left.+\sum_n \frac{1}{(\alpha-2\pi n/L)^2+\omega/a}\right] \\
&= \frac{L^3}{4}\left(\frac{a}{\omega}\right)^{3/2}\left[\frac{\sin L\sqrt{\omega/a}}{\cos L\sqrt{\omega/a}-\cos \alpha L}\right. \\
&\quad \left.+\frac{\sinh L\sqrt{\omega/a}}{\cosh L\sqrt{\omega/a}-\cos \alpha L}\right],
\end{aligned}
\tag{14}
$$

where $a=\sqrt{EI/\rho_s}$ in the case of beam, or $a=\sqrt{D_s/\rho_s h}$ in the case of plate, where D_s is the bending stiffness of the structure and h is the plate thickness.

Then, after algebraic manipulation, the global equation in the wavenumber space can be derived from Eq. (9) with Eq. (14) used for the operator. In this case, denoting $k_s=\sqrt{\omega/a}$,

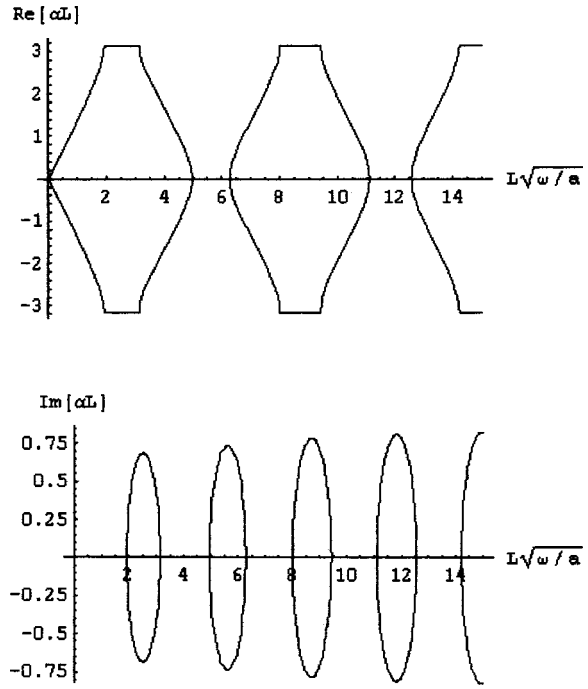

FIG. 5. Dispersion curve for plate with mass discontinuities, $m/\rho_p Lh=3$.

$$
\begin{aligned}
&\left(\cos^2 \alpha L-\left(\cos k_s L+\cosh k_s L-\frac{iZa}{4k_s}\right.\right. \\
&\quad \left.\left.\times[\sin k_s L-\sinh k_s L]\right)\cos \alpha L+\cos k_s L\cosh k_s L\right. \\
&\quad \left.-\frac{iZa}{4k_s}[\sin k_s L-\sinh k_s L]\right)\overline{\eta}_{\text{global}}(\alpha) \\
&\quad =\overline{\text{MF}}_{\text{plate}}(\alpha).
\end{aligned}
\tag{15}
$$

Modified forcing in this case will be similar to the membrane case, given in Eq. (11), taking into account that structural operator $D(\alpha)$ is now different. The dispersion relation can be derived by setting the right-hand side of Eq. (15) to zero. Thus, in the plate case, the dispersion relation is a quadratic equation with respect to $\cos \alpha L$. It can be solved for αL and then one set of the roots corresponds to a nonpropagating mode, and the other set exhibits stop-pass band behavior, shown in Fig. 5. Equation (15) is a 1-D dispersion relation, which can also be derived from its 2-D counterpart, given by Mace.[13] The left-hand side can be recast in powers of α; the inverse transform then leads again to an infinite order operator.

D. Other issues

In order to solve the global problem, in general, it may be necessary to truncate the global operator in physical space, for example, in cases when forcing is too complicated to use its Fourier transform. The effect of truncation was investigated in the wavenumber space for the model problems described later. In the case of membrane several terms of the Taylor series of $\cos \alpha L$ in Eq. (11) were used. Four

terms in series were enough to get a solution practically indistinguishable from the exact solution in the wavenumber space.

The extension of the global interval is straightforward in the "dry" cases. Any interval of length $2\pi/L$ can be treated as global, repeating the derivation of Eq. (11). Hence, on the wider global interval, consisting of several subintervals of this length, the global operator stays the same, but the modified forcing is now calculated by Eq. (11) in each subinterval. This procedure will be different in the fluid-loaded case.

Modifications of the outlined approach are possible. Additional conditions can be imposed on the global or local parts of the solution. For example, it is possible to make the local solution vanish at the impedances, thereby making the global solution coincide with the total solution at these important locations on the structure. However, to satisfy this additional condition, a part of the previously local solution must be transferred to the global solution, or vice versa.

III. A FLUID-LOADED MEMBRANE WITH DISCONTINUITIES

A fluid-loaded membrane with attached impedances is described by the preceding membrane equation with the addition of pressure forcing. This equation is coupled to the acoustic wave equation through the boundary condition that matches normal velocities at the interface:

$$\begin{aligned}&\frac{\partial^2\eta}{\partial x^2}+k_s^2\eta=i\omega Z\sum_n \eta\,\delta(x-x_n)+F(x)+\frac{1}{T}p|_{z=0},\\&\frac{\partial^2 p}{\partial x^2}+\frac{\partial^2 p}{\partial z^2}+k^2p=0,\quad w|_{z=0}=\frac{i}{\rho\omega}\frac{\partial p}{\partial z}\bigg|_{z=0}=i\omega\eta,\end{aligned}\tag{16}$$

where c and c_s are wave speeds, and $k=\omega/c$ and $k_s=\omega/c_s$ are wavenumbers, in the fluid and on the structure, respectively; T is the membrane tension. In wavenumber-frequency space Eq. (16) can be written as

$$\begin{aligned}&(k_s^2-\alpha^2)\overline{\eta}=\frac{i\omega Z}{L}\sum_n \overline{\eta}(\alpha-2\pi n/L)+\overline{F}+\frac{1}{T}\overline{P}|_{z=0},\\&\frac{\partial^2\overline{P}}{\partial z^2}+(k^2-\alpha^2)\overline{P}=0;\quad \frac{\partial\overline{P}}{\partial z}\bigg|_{z=0}=\rho\omega^2\overline{\eta}.\end{aligned}\tag{17}$$

A. Local/global separation with fluid loading

Introducing the global displacement as in Eq. (5) and also the global and local pressures,

$$\begin{aligned}&\overline{P}=\overline{P}_{\text{global}}+\overline{P}_{\text{local}};\\&\overline{P}_{\text{global}}(\alpha)=0, for\quad \alpha\notin[-\pi/L;\pi/L];\\&\overline{P}_{\text{local}}(\alpha)=0,\quad for\quad \alpha\in[-\pi/L;\pi/L].\end{aligned}\tag{18}$$

Since the acoustic equation and the velocity matching boundary condition both do not couple pressure and displacement at different wavenumbers α, they remain the same in both local and global regions. Assuming $P(x,z)=P(x)e^{\mu z}$, the acoustic solution is equivalent to the condition $\mu(\alpha)=-(\alpha^2-k^2)^{1/2}$, where the sign of the square root is chosen to guarantee the correct direction of reflected propagating waves and decay of evanescent modes. Using the boundary condition it is possible now to eliminate pressure completely, yielding the equation for displacement only. However, in order to derive a closed system on the global interval, it is useful to keep the global pressure in the equations. Also it is convenient to distinguish in this problem between two operators: the structural operator $D(\alpha)=k_s^2-\alpha^2$ and the structural operator with fluid loading $D_f(\alpha)=k_s^2-\alpha^2-k_s^2(\rho/\rho_s)/\mu(\alpha)$, which appears after eliminating pressure. Then the structural equations on the local and global intervals, counterparts to Eqs. (6a) and (6b), are

$$\begin{aligned}D(\alpha)\overline{\eta}_{\text{global}}(\alpha)=&\frac{i\omega Z}{L}\sum_{n\neq 0}\overline{\eta}_{\text{local}}(\alpha-2\pi n/L)\\&+\frac{i\omega Z}{L}\overline{\eta}_{\text{global}}(\alpha)+\overline{F}(\alpha)\\&+\frac{1}{T}\overline{P}_{\text{global}}(\alpha),\end{aligned}\tag{19a}$$

$$\begin{aligned}D_f(\alpha)\overline{\eta}_{\text{local}}(\alpha)=&\frac{i\omega Z}{L}\sum_{n\neq n^*}\overline{\eta}_{\text{local}}(\alpha-2\pi n/L)\\&+\frac{i\omega Z}{L}\overline{\eta}_{\text{global}}(\alpha-2\pi n^*/L)+\overline{F}(\alpha).\end{aligned}\tag{19b}$$

Analogous to previous work on fluid-loaded plates, one can introduce a nondimensional fluid-loading parameter[1,14] $\varepsilon=(\rho L/\rho_s)(c_s/\omega L)$. For evanescent fluid modes, physically this parameter scales the ratio of fluid apparent mass to structure mass. Comparing this parameter to unity, one can define light fluid loading as $\varepsilon\leqslant 1$, and, respectively, heavy loading as $\varepsilon\geqslant 1$. Unlike the plate case, there is no intrinsic fluid-loading parameter[14,15] independent of frequency. Thus, the higher the frequency, the lighter the membrane is loaded with fluid. Physically, the apparent mass is proportional to wavelength, which is reduced at higher frequency. Also the Mach number of free waves on the structure is defined as $M=c_s/c$, which is a constant less than unity, for the subsonic case.

B. Fluid-loading approximation for evanescent modes

From Eq. (19) a global equation similar to the "dry" case Eq. (9) can be derived:

$$\begin{aligned}&D_f(\alpha)\left[1-\frac{i\omega Z}{L}\sum_n\frac{1}{D_f(\alpha-2\pi n/L)}\right]\overline{\eta}_{\text{global}}(\alpha)\\&\quad=\overline{F}(\alpha)+\frac{i\omega Z}{L}\sum_{n\neq 0}\frac{\overline{F}(\alpha-2\pi n/L)-\overline{F}(\alpha)}{D_f(\alpha-2\pi n/L)}.\end{aligned}\tag{20}$$

A serious difficulty in the direct evaluation of the global operator arises from the fluid loading terms involving $\mu(\alpha)$. In particular, this term appears in the infinite summations $\Sigma_n 1/D_f(\alpha-2\pi n/L)$. To be able to sum them directly, one needs an approximation for the reciprocal operator $1/D_f(\alpha)$ in the form $1/(k_{\text{eff}}^2-\alpha^2)$. This particular form is chosen because, first, the global operator will be very similar to the

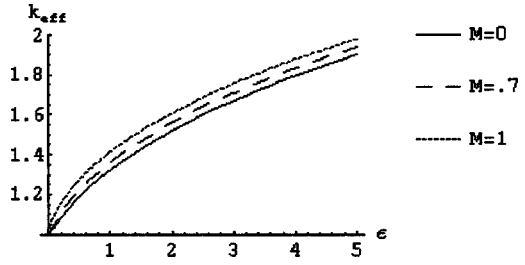

FIG. 6. Effective wavenumber k_{eff} versus fluid-loading parameter ε.

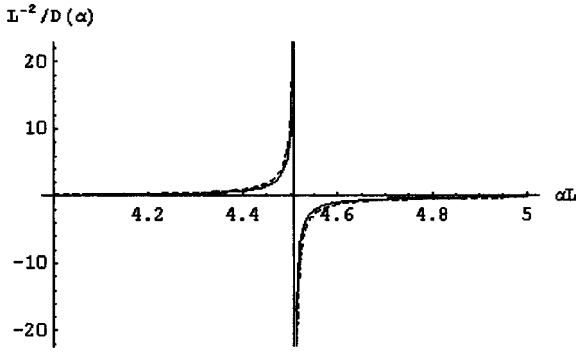

FIG. 7. Reciprocal fluid loading operator approximation. Vicinity of the real root. Solid line—exact; dashed—full approximation [Eq. (26)]. $M=c_s/c=0.8$; $kL=3$; $\varepsilon=0.5$.

"dry" case global operator, and, second, by introducing an "effective" wavenumber k_{eff} on the membrane the terms in the local intervals corresponding to the effect of the evanescent modes can be approximated. In the problem under consideration, there are discontinuities that produce a broad spectrum of wavenumbers on the membrane. However, between discontinuities the waves on the membrane will have a dominant wavelength associated with k_{eff}, to be approximated here as the wavenumber of free motion of a uniform fluid-loaded membrane. If the membrane waves were very subsonic, there would typically be many waves of small wavelengths between discontinuities. All of the wavenumbers on the membrane with discontinuities, none of which are typically k_{eff}, are simply adding up to make the membrane motion that looks approximately like k_{eff} between discontinuities. The approximate simplification of the sum of operators above embodies this effect.

Strictly speaking, this fluid-loading model would seem to apply only to lightly loaded waves that are very subsonic. However, this approximation is found to work remarkably well for heavy fluid loading and higher subsonic wave speeds. Subsequent examples utilize a structural Mach number $\mathrm{M}=0.8$ and a ratio of fluid and structure densities $\rho L/\rho_s=80$. For a 5-mm-thick aluminum plate $\rho_s=13.5\ \text{kg/m}^2$; in water, $\rho=1000\ \text{kg/m}^3$; with impedances attached at the distances $L=1$ m, this ratio would be 74.1. In fact, the proposed approximation yields good results even at higher values of fluid-structure density ratio.

To approximate the sum as described above, it is necessary to recover roots of the denominator, since the largest error comes from the region around the real root. Thus, the best choice for k_{eff} would be the free-wave propagation wavenumber of a coupled structure: $D_f(k_{\text{eff}})=0$. In the membrane case, using nondimensional parameters,

$$D_f(k_{\text{eff}})=k_s^2-k_{\text{eff}}^2+\frac{\varepsilon k_s^2}{\sqrt{k_{\text{eff}}^2/k_s^2-\mathrm{M}^2}}=0\Rightarrow\left(\frac{k_{\text{eff}}}{k_s}\right)^2$$

$$=1+\frac{\varepsilon}{\sqrt{(k_{\text{eff}}/k_s)^2-\mathrm{M}^2}}. \tag{21}$$

Introducing $\sigma=\sqrt{(k_{\text{eff}}/k_s)^2-\mathrm{M}^2}$ yields a reduced cubic equation governing the free-wave motion wavenumbers: $\sigma^3-(1-\mathrm{M}^2)\sigma-\varepsilon=0$. This cubic can be solved in closed form,[16] providing the appropriate root as

$$k_{\text{eff}}^2=k_s^2\left[\mathrm{M}^2+\left(u+\frac{1-\mathrm{M}^2}{3u}\right)\right],$$

$$where\ \ u=\left(\frac{\varepsilon}{2}+\sqrt{\frac{\varepsilon^2}{4}-\left(\frac{1-\mathrm{M}^2}{3}\right)^3}\right)^{2/3}. \tag{22}$$

A plot of effective wavenumber versus fluid-loading parameter ε for different Mach numbers of *in vacuo* structural waves $\mathrm{M}=c_s/c=k/k_s$ is shown in Fig. 6. Thus, k_{eff} is a function of Mach number and the fluid-loading parameter and does not depend on wavenumber α. In the global equation k_{eff} will be just a constant, not affecting the inverse of the transform. In Fig. 7 exact values of reciprocal operator are compared with approximate values. First, the approximation $k_{\text{eff}}=k_s$ is shown, which does not recover the correct root and fails to approximate the behavior; second, the approximation Eq. (22) is shown, which provides excellent agreement with the exact solution. In Fig. 8 exact and approximate operator sums from Eq. (20) are shown in the global interval.

Back in Eq. (19), in the intervals corresponding to evanescent modes, one can use Eq. (22) to approximate fluid loading. Then Eqs. (19a) and (19b) can be written in the following form:

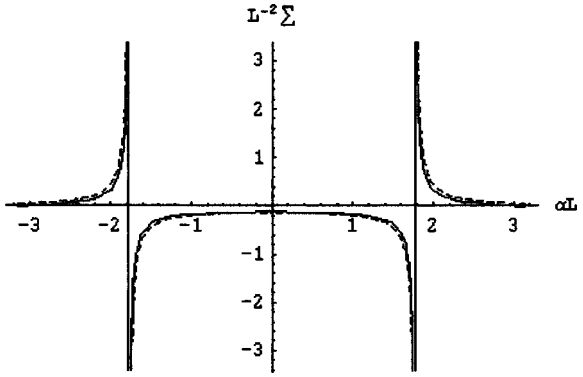

FIG. 8. Approximation of the infinite sum in the global operator. Solid line—exact; dashed—fluid loading approximation. $M=c_s/c=0.8$; $kL=3$; $\varepsilon=0.5$.

$$D_{\text{eff}}(\alpha)\,\overline{\eta}_{\text{global}}(\alpha)=\frac{i\omega Z}{L}\sum_{n\neq 0}\overline{\eta}_{\text{local}}(\alpha-2\pi n/L)+\frac{i\omega Z}{L}\overline{\eta}_{\text{global}}(\alpha)+\overline{F}(\alpha)+\frac{1}{T}\overline{P}_{\text{eff}}(\alpha), \tag{23a}$$

$$D_{\text{eff}}(\alpha)\,\overline{\eta}_{\text{local}}(\alpha)=\frac{i\omega Z}{L}\sum_{n\neq n^*}\overline{\eta}_{\text{local}}(\alpha-2\pi n/L)+\frac{i\omega Z}{L}\overline{\eta}_{\text{global}}(\alpha-2\pi n^*/L)+\overline{F}(\alpha), \tag{23b}$$

where ''effective'' operator and ''effective'' pressure are defined as

$$D_{\text{eff}}(\alpha)=k_{\text{eff}}^2-\alpha^2,\qquad \overline{P}_{\text{eff}}(\alpha)=\overline{P}_{\text{global}}(\alpha)+\rho_s c_s^2(k_{\text{eff}}^2-k_s^2)\,\overline{\eta}_{\text{global}}(\alpha). \tag{24}$$

Thus, the fluid-loading approximation is applied in the local intervals only. However, to keep the operators on the left-hand side the same both in the local and the global intervals, Eq. (24) introduces a correction to the propagating pressure field.

Equations (23a) and (23b) are similar to the ''dry case'' equations, Eqs. (6a) and (6b). Eliminating local components from these coupled equations in the same manner as before, the following global equation is derived:

$$D_{\text{eff}}(\alpha)\left[1-\frac{i\omega Z}{L}\sum_{n}\frac{1}{D_{\text{eff}}(\alpha-2\pi n/L)}\right]\overline{\eta}_{\text{global}}(\alpha)=\text{MF}+\text{MP}_{\text{eff}}, \tag{25}$$

where MF is the modified forcing and MP_{eff} is the modified effective pressure, defined as

$$\text{MF}=\overline{F}(\alpha)+\frac{i\omega Z}{L}\sum_{n\neq 0}\frac{\overline{F}(\alpha-2\pi n/L)-\overline{F}(\alpha)}{D_{\text{eff}}(\alpha-2\pi n/L)},\qquad \text{MF}_{\text{eff}}=\frac{\overline{P}_{\text{eff}}}{T}\left[1-\frac{i\omega Z}{L}\sum_{n\neq 0}\frac{1}{D_{\text{eff}}(\alpha-2\pi n/L)}\right]. \tag{26}$$

To close the system the boundary condition has to be used:

$$\mu(\alpha)\overline{P}_{\text{global}}=\rho\omega^2\overline{\eta}_{\text{global}}. \tag{27}$$

However, it must be written in terms of the ''effective'' pressure, using Eq. (24):

$$\mu(\alpha)\overline{P}_{\text{eff}}=(\rho\omega^2+\rho_s c_s^2\mu(\alpha)(k_{\text{eff}}^2-k_s^2))\,\overline{\eta}_{\text{global}}. \tag{28}$$

Equations (25) and (28) govern the long-wave content of membrane displacements and the pressure in the fluid. The local-global relationship can be used afterwards to reconstruct the short-wave content. After evaluation of the infinite sums, which is now possible due to the ''fluid loading approximation,'' Eqs. (25) and (28) constitute the global problem in the wavenumber space:

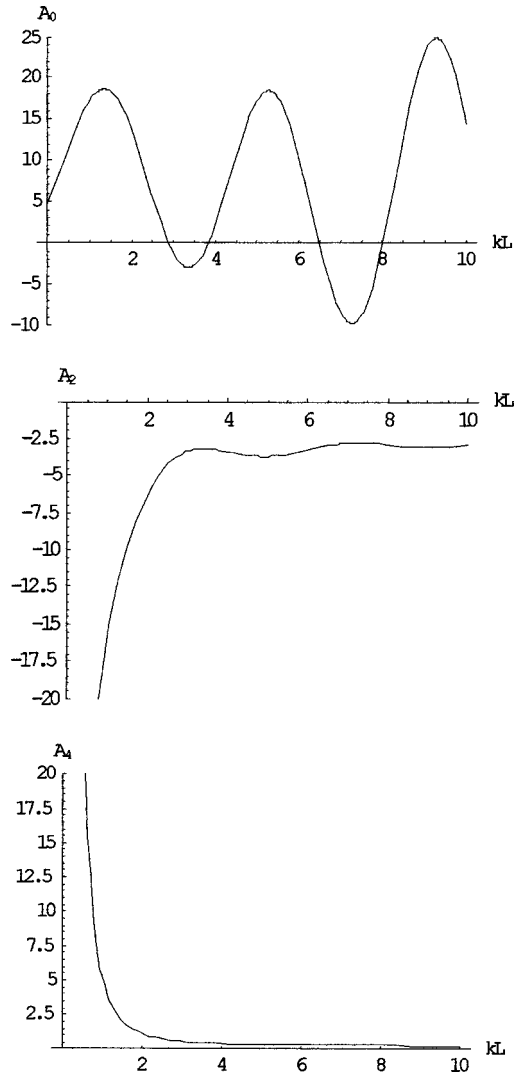

FIG. 9. First coefficients of the global differential operator versus frequency. Structural characteristics: $\rho L/\rho_s=0.83$; $c_s/c=0.67$; $m/\rho_s L=0.5$. Coefficients are normalized by $(kL)^4$.

$$\left(\cos\alpha L-\cos k_{\text{eff}}L-\frac{i\omega Z}{2k_{\text{eff}}}\sin k_{\text{eff}}L\right)\overline{\eta}_{\text{global}}(\alpha)=\frac{\cos\alpha L-\cos k_{\text{eff}}L}{k_{\text{eff}}^2-\alpha^2}(\text{MF}+\text{MP}_{\text{eff}}),\qquad \mu(\alpha)\overline{P}_{\text{eff}}=(\rho\omega^2+\rho_s c_s^2\mu(\alpha)(k_{\text{eff}}^2-k_s^2))\,\overline{\eta}_{\text{global}}. \tag{29}$$

The modified forcing and effective pressure are given in wavenumber space by Eq. (26). In general, they can be inverted in the physical space as a convolution with the filter functions, similar to a dry case. The forcing filter function is the same as for a dry structure as was discussed earlier [Eq. (13), Fig. 4]. The boundary condition Eq. (28) retains the square root term $\mu(\alpha)$ necessary to describe radiation effects. However, further approximations could be made[14,17] to invert this condition as well.

Note that the result Eq. (29) has a form similar to the original problem formulation Eq. (17) for the coupled fluid and structure, only now the operators are different and the response is smooth. A similar form also occurs upon return-

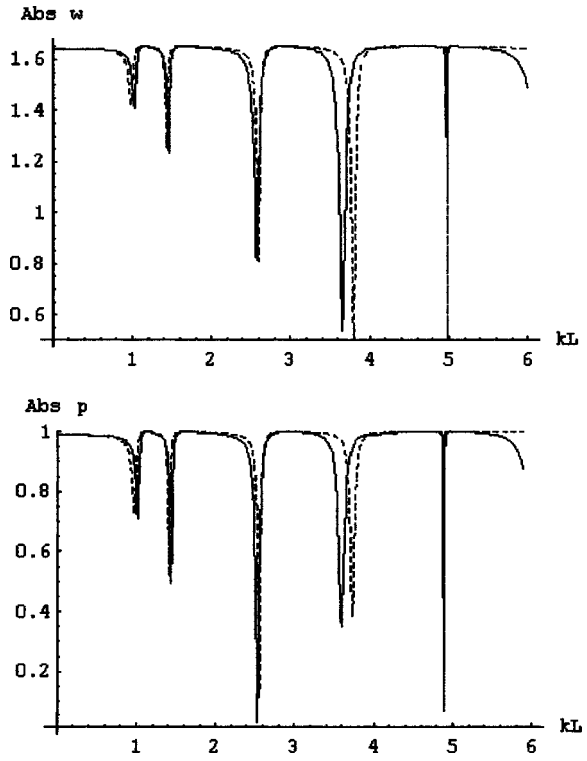

FIG. 10. Displacement magnitude $w=\rho c\omega\eta/P^+$ and global pressure magnitude $p=P^-/P^+$ versus frequency. Structural characteristics: $\rho L/\rho_s=80$; $c_s/c=0.8$; $\varphi=0.6$; $Z/\rho_s L=0.5+ikL$ 2.75. Second harmonic turns on at $kL=4.01$. Full—exact; dashed—approximation.

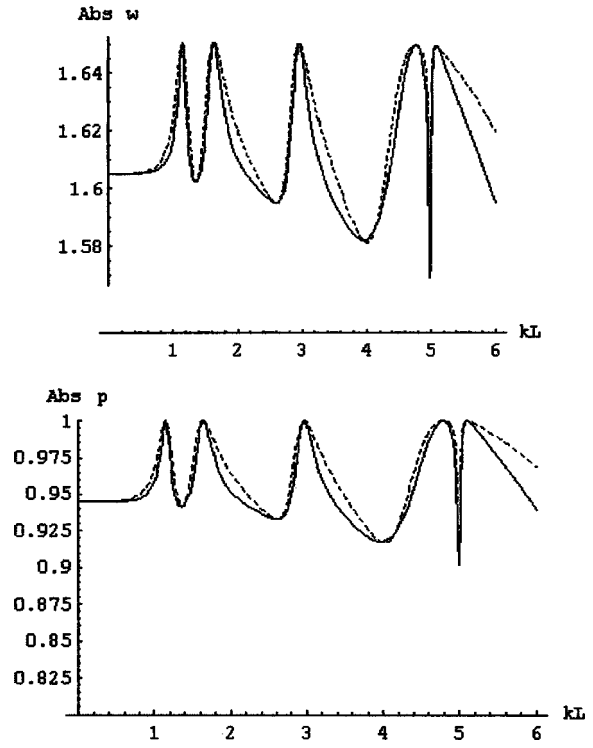

FIG. 11. Displacement magnitude $w=\rho c\omega\eta/P^+$ and global pressure magnitude $p=P^-/P^+$ versus frequency. Structural characteristics: $\rho L/\rho_s=80$; $c_s/c=0.8$; $\varphi=0.6$; $Z/\rho_s L=2.75+ikL$ 0.5. Second harmonic turns on at $kL=4.02$. Full—exact: dashed—full approximation.

ing to physical-space variables. After a series expansion in powers of α and a transform inversion, the structural equation (29) can be reexpressed in physical space variables in a form involving infinite order operators:

$$\sum_{n=0}^{\infty} A_{2n}\frac{\partial^{2n}\eta_{\text{global}}}{\partial x^{2n}}=\int_{-\infty}^{\infty}F(\xi)G(x,\xi)\,d\xi + \int_{-\infty}^{\infty}P_{\text{eff}}(\xi)g(x,\xi)\,d\xi. \tag{30}$$

Along with the inverted acoustic equation and boundary condition, this equation provides a closed system for the global displacement and pressure. When radiation occurs only in the global interval, this method accounts for propagating pressure waves in the fluid, with the effect of the evanescent modes contained in the operator. The summations can be truncated after a few terms (typically $n=4$) and accurate results are still obtained. Several coefficients A_{2n} are plotted versus frequency in Fig. 9.

C. Extension of the global interval

The case of radiation from a wider wavenumber interval can be treated similarly. As an example, consider the global system on the interval $[-3\pi/L,3\pi/L]$, i.e., two more intervals are added to the global interval. Now the global displacement and pressure also include wavenumber content from the left $[-3\pi/L,-\pi/L]$ and right $[\pi/L,3\pi/L]$ added intervals. Considering every subinterval of length $2\pi/L$ as global, one can repeat the derivation of local-global relationships, similar to Eq. (7), which now also include coupling between subintervals in the global region; afterwards they may be used to write an analog of equations (23) and (25) for pressure and displacement in the global region. Then the inverse Fourier transform can be applied to this system, using the fluid-loading approximation, discussed above.

In general, the extended version of Eqs. (25)–(28) for multiple global intervals is given by

$$D_{\text{eff}}(\alpha)\left[1-\frac{i\omega Z}{L}\sum_n\frac{1}{D_{\text{eff}}(\alpha-2\pi n/L)}\right]\overline{\eta}_{\text{global}}(\alpha) = \sum_m \text{MF}_m+\sum_m \text{MP}_m, \tag{31}$$

$$\text{MF}_m=\overline{F}(\alpha)+\frac{i\omega Z}{L}\sum_{(n\neq 0)}\frac{\overline{F}(\alpha-2\pi n/L)-\overline{F}(\alpha)}{D_{\text{eff}}(\alpha-2\pi n/L)},$$

$$\text{MP}_m=\frac{\overline{P}_m}{T}+\frac{i\omega Z}{LT}\sum_{\text{global}}\frac{\overline{P}_m(\alpha-2\pi n/L)-\overline{P}_m(\alpha)}{D_{\text{eff}}(\alpha-2\pi n/L)},$$

$$\mu(\alpha)\sum_m\overline{P}_m=(\rho\omega^2+\rho_s c_s^2\mu(\alpha)(k_{\text{eff}}^2-k_s^2))\,\overline{\eta}_{\text{global}},$$

where the modified forcing and pressure are composed of the modified forcing and pressure on all subintervals. Also the summation in pressure terms is fulfilled over global subintervals only. In the case of three intervals in the global region, as was sketched in Fig. 2, there are three separate terms on the right-hand side of the equation and three terms in the finite sum for modified pressure on each subinterval ($m=0,-1,1$).

Finally, Eq. (31) can be transformed back into the real space yielding the infinite order differential equation. Then various numerical methods can be applied to the smooth closed global system. However, as in the dry case, the modified forcing and pressure may be readily provided in the physical space only in limited cases. In general, one has to employ numerical procedures to invert the right-hand side of Eq. (31).

IV. APPLICATION TO SCATTERING PROBLEM

Acoustic scattering from the membrane with discontinuities is now considered. The forcing comes only from the global pressure field having a prescribed incident pressure wave of amplitude P^+. Suppose the incident pressure wavenumber is low enough to be in the global interval $[-\pi/L, \pi/L]$. Then

$$P_{\text{global}}(x,z,t) = P^+ e^{i\omega t} e^{-ik_x x} e^{ik_z z} + P^- e^{i\omega t} e^{-ik_x x} e^{-ik_z z}, \tag{32}$$

where $k_x = k \sin\varphi$ and $k_z = k\cos\varphi$, with incidence angle φ measured from the normal.

Other excited harmonics $P^{\text{local}n}(x,z,t) = P_n \exp(i\omega t - ik_x^{\text{local}n} x - ik_z^{\text{local}n} z)$ are characterized by the wavenumbers $k_x^{\text{local}n} = k_x + 2\pi n/L$ and, correspondingly, $(k_z^{\text{local}n})^2 = k^2 - (k_x^{\text{local}n})^2 = k^2 - (k\sin\varphi + 2\pi n/L)^2$. The last expression must be real for the nth harmonic to propagate. Thus, the first wave outside the global interval[18] (corresponding $n = -1$) starts to propagate at frequency $kL = 2\pi/(1+\sin\varphi)$. Then, including only one propagating mode in the fluid-loading approximation above, for the incidence angle $\varphi = 0.6$ a good approximation is expected for frequencies $kL < 4.0$, when all modes outside the global interval are evanescent.

Due to linearity, this problem can be divided into two parts: first, reflection from a rigid structure, providing reflected wave $P^+ e^{-ik_z z} e^{-ik_x x} e^{i\omega t}$ and forcing, exerted on the structure as $F(x,t) = (2P^+/T) e^{-ik_x x} e^{i\omega t}$, and second, radiation from the structure, due to the forcing just mentioned.

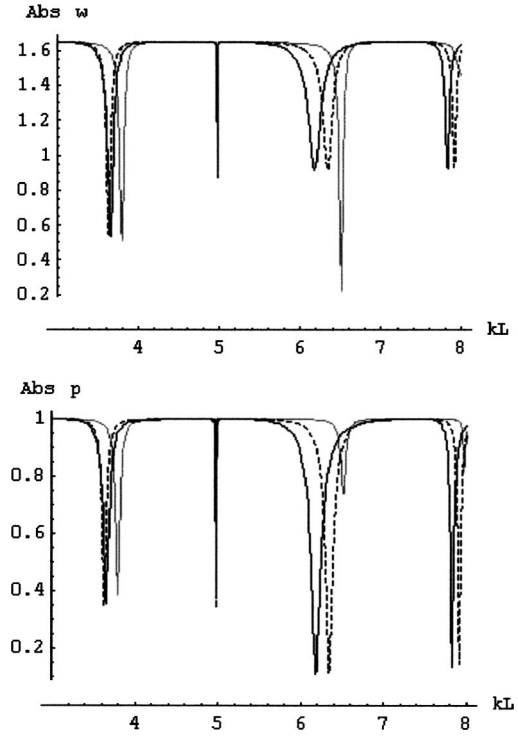

FIG. 12. Pressure and displacement magnitudes $p = P^-/P^+$, $w = \rho c \omega \eta / P^+$ of propagating harmonics versus frequency. Structural characteristics: $\rho L/\rho_s = 80$; $c_s/c = 0.8$; $\varphi = 0.6$; $Z/\rho_s L = 0.5 + ikL$ 2.75. Second harmonic turns on at $kL = 4.01$. Solid line—exact solution; gray—approximation by one global interval; dash—approximation by three global intervals.

The second part is to be solved using fluid-loading approximation. Then the pressure components are simply added to construct full pressure field. The fact that there is only one harmonic in the global interval greatly simplifies the homogenization procedure. The use of the fluid-loading approximation and operator truncation leads to a simple representation of homogenized system [Eq. (32)] for the scattering problem in the physical space:

$$\begin{cases} \left(1 - \cos k_{\text{eff}} L - \dfrac{i\omega Z}{2k_{\text{eff}}} \sin k_{\text{eff}} L + \dfrac{L^2 \partial^2}{2!\,\partial x^2} + \dfrac{L^4 \partial^4}{4!\,\partial x^4} + \cdots\right) \eta_{\text{global}}(x) \\ = \dfrac{2P^+}{T} H_{\text{MF}}(k_x) e^{-ik_x x} + \dfrac{P^-}{T} H_{\text{MP}}(k_x) e^{-ik_x x} + (k_{\text{eff}}^2 - k_s^2)\, \eta_{\text{global}}(x) H_{\text{MP}}(k_x); \\ \mu(k_x) P^- e^{-ik_x x} = \rho\omega^2 \eta_{\text{global}}(x), \end{cases} \tag{33}$$

where $H_{\text{MF}}(k_x)$ and $H_{\text{MP}}(k_x)$ are calculated using Eq. (13). The different subscripts are used to show which part in Eq. (29) these terms correspond to. For this scattering problem, numerical simulations showed an excellent convergence for truncation of the operator beyond the eighth derivative (five terms in the operators since only even derivatives are present). The truncated results are then indistinguishable from the approximate results shown below, within the appropriate range of validity ($kL < 4.0$).

The exact and approximate pressure fields and structural displacement were calculated and compared for relatively heavy fluid loading. The results shown in Figs. 10 and 11 are magnitudes of dimensionless displacements and reflected pressure versus frequency at the fixed angle. There is an excellent agreement between the exact and approximate results for frequencies below second mode cut-on. Equation (31) was used to include more propagating modes. On Figs. 12 and 13 an enhancement of the global solution harmonics

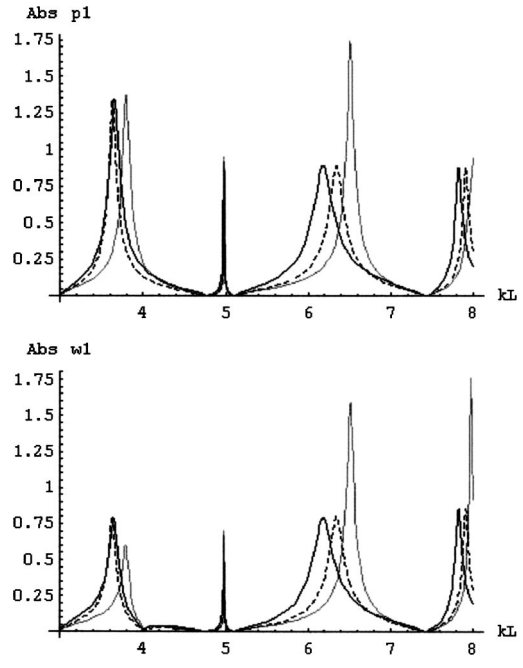

FIG. 13. Pressure and displacement magnitudes $pI=P^{\text{local1}}/P^{+}$, $wI=\rho c\omega\eta_{\text{local1}}/P^{+}$ of second propagating harmonic versus frequency. Structural characteristics: $\rho L/\rho_s=80$; $c_s/c=0.8$; $\varphi=0.6$; $Z/\rho_s L=0.5+ikL$ 2.75. Second harmonic turns on at $kL=4.01$. Solid line—exact solution; gray—approximation by one global interval; dash—approximation by three global intervals.

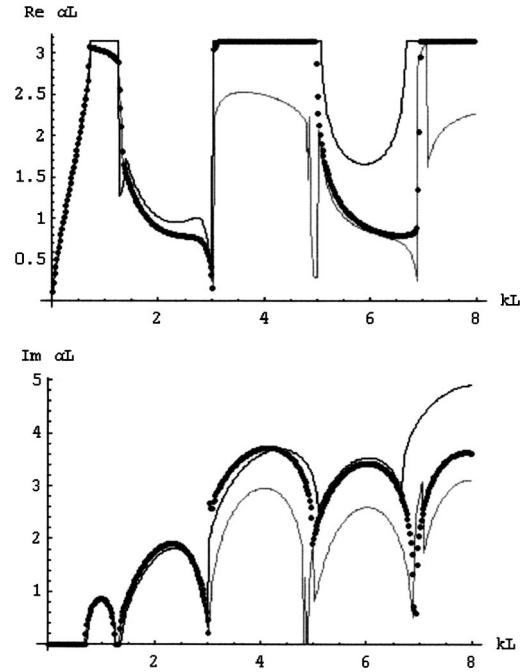

FIG. 14. Dispersion curves: real and imaginary part of global wavenumber versus frequency. Structural characteristics: $\rho L/\rho_s=5$; $c_s/c=0.67$; $m/\rho_s L=2.5$; Full—exact; gray—one propagating mode approximation; dots—three propagating modes approximation.

for higher frequencies can be observed.

Also free vibration (no incident waves or applied forcing) of the fluid-loaded membrane with impedance discontinuities is considered. The dispersion equation (structural equation with no forcing and pressure expressed through displacement via boundary condition) relating global wavenumber and frequency is solved numerically for the exact formulation Eq. (17), and for the approximate formulation Eqs. (29) and (31). The real and imaginary parts of the nondimensionalized global wavenumber αL, shown in Fig. 14, exhibit the expected stop-band and pass-band behavior; however, when the global wave speed is supersonic, there is a nonzero imaginary part in the pass bands due to damping from fluid radiation. Figures show that the fluid-loading approximation provides good results when number of propagating modes is less then accounted for in the approximation Eq. (31). As more propagating modes turn on, extension of the global interval enhances the approximation.

V. CONCLUSION

A self-contained problem was constructed which accounts for the exact global low-wavenumber content of vibrational problems and fluid-structure interaction problems. The high-wavenumber local part may be reconstructed afterwards. In the absence of a fluid, the homogenization technique provides the exact low-wavenumber content. In the case of fluid loading an approximation was introduced to make possible a Fourier inversion of the global differential operator. The approximation is relatively simple, but very accurate. The technique was applied to a problem of sound reflection from a membrane with discontinuities. The approximated pressure field and structural displacement were compared with exact values and found to be in excellent agreement, even for heavy fluid loading. Also, the free vibration dispersion curves were constructed using homogenization technique. Numerical experiments showed excellent accuracy of approximation in the model problems.

Future goals include extension of technique to higher-order systems, such as beams and plates, and 2-D problems.

APPENDIX

In the general case of arbitrary forcing, the functional form of the modified forcing can be derived from Eq. (11) using the inverse Fourier transform. Then in the physical space:

$$\mathrm{MF}(x)=F*H_2-\frac{i\omega z\sin k_s L}{2k}F*H_1+\frac{i\omega Z}{L}\sum_n Fe^{i2\pi nx/L}*G_n$$

where "*" denotes convolution, and the filter functions are

$$H_1(x)=\frac{1}{\pi}\int_0^{gp/L}\frac{\cos\alpha x}{k_s^2-\alpha^2}d\alpha\equiv\frac{1}{2\pi k_s}[(\mathrm{Ci}(k_s+\pi/L)x-\mathrm{Ci}(k_s-\pi/L)x)\cos k_s x+(\mathrm{Si}(k_s+\pi/L)x-\mathrm{Si}(k_s-\pi/L)x)\sin k_s x];$$

$$H_2(x)=\frac{1}{\pi}\int_0^{\pi/L}\frac{\cos\alpha L-\cos k_s L}{k_s^2-\alpha^2}\cos\alpha x\,d\alpha\equiv\frac{1}{2}(H_1(x+L)+H_1(x-L))-H_1(x)\cos k_s L;$$

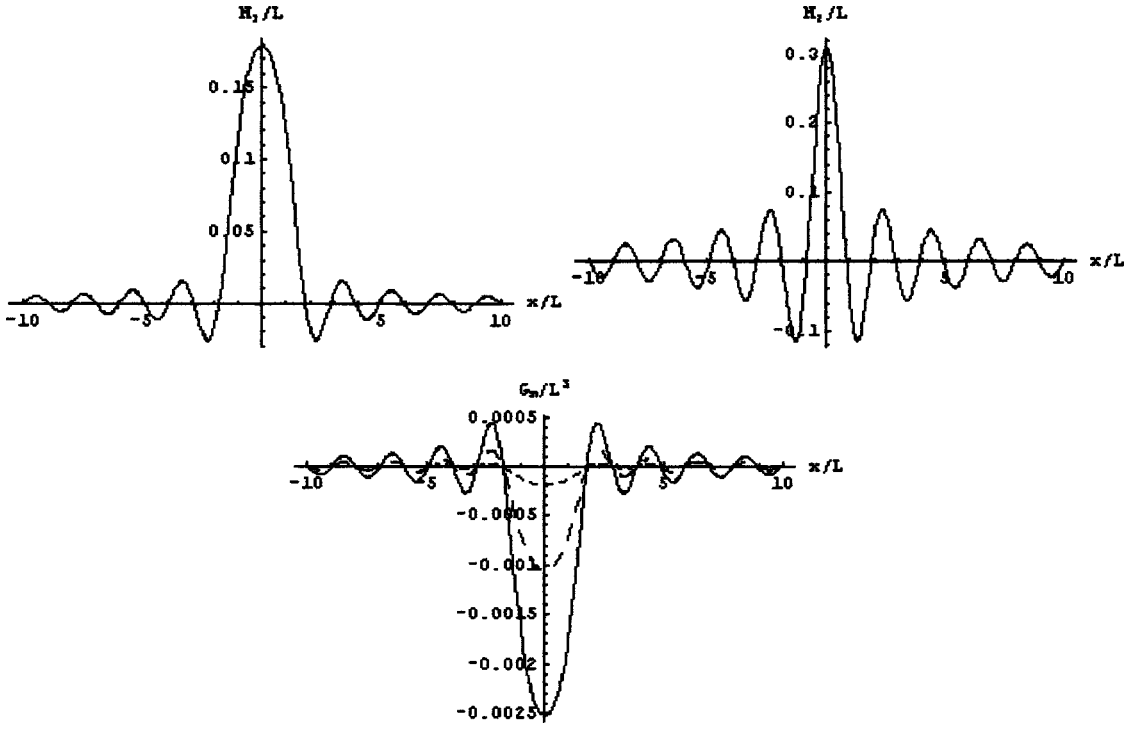

FIG. 15. Modified forcing filter functions in physical space, $kL=3.8$, $n=2,3,7$.

$$G_n(x)=\frac{1}{2\pi}\int_{-\pi/L}^{\pi/L}\frac{\cos\alpha L-\cos k_sL}{k_s^2-\alpha^2}\times\frac{e^{i\alpha x}}{k_s^2-(\alpha-2\pi n/L)^2}\,d\alpha.$$

All of the functions above can be written in closed form using sine and cosine integrals: $\mathrm{Si}(x)=\int_0^x[(\sin\xi)/\xi]\,d\xi$, $\mathrm{Ci}(x)=\int_x^\infty[(\cos\xi)/\xi]\,d\xi$ as shown for $H_1(x)$, $H_2(x)$. Filter functions do not depend on impedances. Typical graphs of filter functions $H_1(x)$, $H_2(x)$, $G_n(x)$ are shown in Fig. 15.

For some original forcings their modified counterpart can be directly found from Eq. (11). For instance, if the original forcing is a point force $F(x)=F_0\delta(x)$, then $\overline{F}(\alpha)=F_0$ and $\overline{\mathrm{MF}}(\alpha)=F_0S(\alpha)(\cos\alpha L-\cos k_sL)/(k_s^2-\alpha^2)$, where $S(\alpha)=1$ in the global interval and 0 outside. Inverting the right-hand side of Eq. (11) gives $\mathrm{MF}(x)=F_0H_2(x)$. Thus, Eq. (11) with this modified forcing yields the global part of the solution of the point force excitation problem. If the point force is applied at the arbitrary point ξ on the structure, the modified forcing can also be found:

$$G(0\leqslant\xi<L,x)=H_2(x-\xi)-\frac{i\omega Z\sin k_sL}{2k_s}H_1(x-\xi)+\frac{i\omega Z}{2k_s}(\sin k_s\xi H_1(x-L)-\sin k_s(\xi-L)H_1(x)),$$

$$G(mL\leqslant\xi<(m+1)L,x)=G(0\leqslant\xi<L,x-mL),\quad m=\pm1,\pm2,\ldots.$$

The function $G(\xi,x)$ is the Green's function of the modified forcing, which can be used for an arbitrary forcing instead of Eq. (13):

$$\mathrm{MF}(x)=\int_{-\infty}^{\infty}F(\xi)G(\xi,x)\,d\xi\equiv F*H_2-\frac{i\omega Z\sin k_sL}{2k_s}F*H_1+\frac{i\omega Z}{2k_s}\sum_m H_1(x-mL-L)\times\int_0^L F(\xi+mL)\sin k_s\xi\,d\xi-\frac{i\omega Z}{2k_s}\sum_m H_1(x-mL)\times\int_0^L F(\xi+mL)\sin k_s(\xi-L)\,d\xi.$$

Another example is spatial harmonic excitation, i.e., $F(x)=\cos(\pi x/A)$. Assuming $A>L$, the original transform has two harmonics inside the global interval. Then, from Eq. (13) one can find

$$\mathrm{MF}(x)=\cos(\pi x/A)\left[1-\frac{i\omega Z}{L}\left(\frac{L}{2k_s}\frac{\sin k_sL}{k_s^2-(\pi A/L)^2}-\frac{\cos\pi A/L-\cos k_sL}{(k_s^2-(\pi A/L)^2)^2}\right)\right].$$

This form can be used in Eq. (12) to find the global part of the solution of the cosine force excitation problem. Note that if $A=nL$, then at the impedance nodes, where the forcing is zero, the displacement is also zero. Thus the problem of periodic excitation on an infinite membrane can be employed to solve the problem of the excitation of a membrane of length A with fixed ends, using the method of images. The finite membrane has $n-1$ discontinuities. However, this can

be done only for simple boundary conditions, when it is possible to restate them in the global problem. In this case both the local and global parts vanish at the fixed ends, therefore, in the global problem the boundaries are also fixed.

The derivation of the modified forcing Green's function is outlined further. This is the modified forcing corresponding to the original point force $F(x)=\delta(x-\xi)$ with wavenumber content $\overline{F}(\alpha)=e^{i\alpha\xi}$. Then, from Eq. (11),

$$\overline{G}(\xi,\alpha)=\mathrm{MF}(\alpha)=e^{i\alpha\xi}S(\alpha)\frac{\cos\alpha L-\cos k_s L}{k_s^2-\alpha^2}\times\left[1+\frac{i\omega Z}{L}\sum_{n\neq 0}\frac{e^{-i\xi 2\pi n/L}-1}{k_s^2-(\alpha-2\pi n/L)^2}\right].$$

Summation can be performed using Poisson summation formula.[11] For any function $f(x)$ with Fourier transform $\overline{f}(\gamma)$ it is given by

$$\sum_n f(2\pi n/L)=\frac{L}{2\pi}\sum_n \overline{f}(nL).$$

Put $f(x)=e^{-i\xi x}/[k_s^2-(\alpha-x)^2]$; then by direct integration in the complex plane its Fourier transform can be found:

$$\overline{f}(\gamma)=\begin{cases} i\pi/k_s e^{i(\alpha+k_s)(\gamma-\xi)}, & \gamma>\xi,\\ i\pi/k_s e^{i(\alpha-k_s)(\gamma-\xi)}, & \gamma<\xi.\end{cases}$$

Hence, the summation becomes

$$\sum_n \frac{e^{i\xi 2\pi n/L}}{k_s^2-(\alpha-2\pi n/L)^2}=\sum_n f(2\pi n/L)=\frac{L}{2\pi}\sum_n \overline{f}(nL)=\frac{L}{2\pi}\left(\sum_{nL<\xi}\frac{i\pi}{k_s}e^{i(\alpha-k_s)(nL-\xi)}+\sum_{nL>\xi}\frac{i\pi}{k_s}e^{i(\alpha+k_s)(nL-\xi)}\right).$$

Both sums are now just geometric series and can be evaluated directly. After further considerable algebraic manipulation it can be shown that if original force is exerted in the first bay $0\leqslant\xi<L$,

$$\sum_n \frac{e^{i\xi 2\pi n/L}}{k_s^2-(\alpha-2\pi n/L)^2}=\frac{L}{2k_s}e^{-i\alpha\xi}\frac{\sin k_s L\cos k_s\xi+(\cos\alpha L-\cos k_s L+i\sin\alpha L)\sin k_s\xi}{\cos\alpha L-\cos k_s L}.$$

Substitution of this result back into the expression for the Green's function yields

$$\overline{G}(\xi,\alpha)=\frac{S(\alpha)}{k_s^2-\alpha^2}\left[e^{i\alpha\xi}\left(\cos\alpha L-\cos k_s L-\frac{i\omega Z}{2k_s}\sin k_s L\right)+\frac{i\omega Z}{2k_s}(\sin k_s(L-\xi)+e^{i\alpha L}\sin k_s\xi)\right].$$

Using functions $H_1(x)$, $H_2(x)$ this expression can be easily inverted and after the inversion it yields the Green's function in physical space, presented above.

The case of a point force in any other bay $mL\leqslant\xi<(m+1)L$ is identical to that considered above due to the periodicity of the system. Thus, using change of the spatial coordinate, $G(\xi,x)\equiv G(\xi-mL,x-mL)$.

[1] M. C. Junger and D. Feit, *Sound, Structures, and their Interaction*, 2nd ed. (MIT, Cambridge, 1986).
[2] E. A. Skelton and J. H. James, *Theoretical Acoustics of Underwater Structures* (Imperial College, London, 1997).
[3] F. J. Fahy, *Sound and Structural Vibration: Radiation, Transmission and Response* (Academic, London, 1985).
[4] J. M. Cuschieri and D. Feit, "Full numerical solution for the far field and near field scattering from a fluid loaded elastic plate with distributed mass and stiffness inhomogeneuity," J. Acoust. Soc. Am. **104**, 915–925 (1998).
[5] A. J. Cooper and D. G. Crighton, "Transmission of energy down periodically ribbed elastic structures under fluid loading: Algebraic decay in the stop bands," Proc. R. Soc. London, Ser. A **454**, 1337–1355 (1998).
[6] A. J. Cooper and D. G. Crighton, "Transmission of energy down periodically ribbed elastic structures under fluid loading: Spatial periodicity in the pass bands," Proc. R. Soc. London, Ser. A **454**, 2893–2909 (1998).
[7] D. B. Bliss and P. V. Danilov, "Sound reflection from a flexible structure with impedance discontinuities using Local/Global homogenization," *Proceedings of Forum Acousticum* (2002).
[8] B. Z. Steinberg and J. J. McCoy, "Toward local effective parameter theories using multiresolution decomposition," J. Acoust. Soc. Am. **96**, 1130–1143 (1994).
[9] R. N. Bracewell, *The Fourier Transform and its Application* (McGraw–Hill, Boston, 2000), pp. 246–248.
[10] L. B. W. Jolley, *Summation of Series*, 2nd ed. (Dover, New York, 1961), pp. 160–161.
[11] D. B. Bliss and L. P. Franzoni, "Reduction of ribbed plates to equivalent uniform structures for mid-to-high frequency structural acoustic analysis," *Proceedings of the Joint ICA/ASA Conference* (1998).
[12] D. B. Bliss and L. P. Franzoni, "The method of Local-Global homogenization for structural acoustics," *Proceedings of the 17th International Congress of Acoustics* (2001).
[13] B. R. Mace, "Periodically stiffened fluid-loaded plates, I: Response to convected harmonic pressure and free wave propagation," J. Sound Vib. **73**, 473–486 (1980).
[14] D. T. DiPerna and D. Feit, "An approximate analytic solution for the radiation from a line-driven fluid-loaded plate," J. Acoust. Soc. Am. **110**, 3018–3024 (2001).
[15] D. G. Crighton, A. P. Dowling, J. E. Ffowcs Williams, M. Heckl, and F. G. Leppington, *Modern Methods in Analytical Acoustics* (Springer-Verlag, London, 1992).
[16] M. R. Spiegel, *Mathematical Handbook of Formulas and Tables* (McGraw–Hill, Boston, 1995).
[17] D. T. DiPerna and D. Feit, "An approximate Green's function for a locally excited fluid-loaded thin elastic plate," J. Acoust. Soc. Am. **114**, 194–199 (2003).
[18] P. V. Danilov and D. B. Bliss, "Calculation of the radiated sound field from a fluid-loaded plate with periodic structural discontinuities," *Proceedings of Tenth International Congress on Sounds and Vibrations* (2003).

Response of force excited elastic solids with internal fluid loading

Scott E. Hassan[a)]
Naval Undersea Warfare Center Division, Newport, Rhode Island 02841

Peter R. Stepanishen
Department of Ocean Engineering, University of Rhode Island, Kingston, Rhode Island 02881

(Received 25 October 2003; revised 21 April 2004; accepted 6 May 2004)

A general approach to solving for the velocity response and associated pressure field of elastic solids loaded internally by a fluid is formulated. An *in vacuo* eigenvector expansion is used to describe the time dependent velocity field of the fluid loaded solid resulting from an arbitrary force excitation. The pressure field in the fluid is expressed using a Green's function and fluid loading on the structure is included via the use of the impulse responses of the modal acoustic radiation impedances. The time dependent modal velocity responses are obtained from the solution to a set of coupled convolution integral equations. A Fourier transform approach is used to develop the associated equations of motion for the harmonic response. The special case of a fluid filled axisymmetric elastic cylindrical shell with a base plate is considered. Transient and harmonic velocity and pressure responses due to a bandlimited axisymmetric point force excitation applied to the base plate are discussed and compared with experimental measurements. [DOI: 10.1121/1.1766052]

PACS numbers: 43.40.Ey, 43.40.Fz, 43.20.Tb [EGW] Pages: 891–899

I. INTRODUCTION

Predicting the response of elastic structures with internal fluid loading is of interest for applications such as noise and vibration control in piping systems and aircraft fuselages. Active noise and vibration control techniques applied to these systems are often implemented with adaptive algorithms where time domain methods are particularly well suited. In general, analytical time domain methods suitable for evaluating the response of fluid-filled elastic solids have received little attention. Furthermore, very few experimental measurements have been published for both the harmonic and time domain response of these structures.

Boone *et al.*[1] developed an approach, using modal superposition methods, to predict the time domain response of a rigid acoustic cavity. Acoustic propagation in a finite length cylinder was considered by El-Raheb[2] using an eigenfunction expansion approach. The harmonic response of a piping system section was determined by Everstine[3] using the FEM (finite element method) for the pipe and fluid. Cheng,[4] and Cheng and Nicolas[5] considered the pressure field and structural response of a finite length fluid loaded cylindrical shell coupled to two end plates with a spring system. Feng[6] conducted experimental studies of the acoustic properties associated with an elastic pipe filled with water and subjected to nonideal boundary conditions. Mauzch[7] computed normal modes and natural frequencies of partially filled elastic cylindrical shells with a rigid base plate using FEM and compared theory with experiments.

The present study addresses the transient and harmonic response of general force excited elastic solids with internal fluid loading. Mature numerical methods, such as FEM, are capable of solving this class of problem. Analytical and semianalytical methods, such as the present approach, enable the development of reduced-order parametric models and are, therefore, well suited for active noise and vibration control applications.

The theory is presented in Sec. II using a time domain formulation based on an eigenvector expansion using the *in vacuo* modes of the structure. Internal fluid loading is included via the use of modal radiation impedance impulse responses which couple the *in vacuo* modes of the structure. The unknown time dependent modal velocity coefficients are determined as the solution to a set of coupled convolution integral equations. Coupled convolution integral equations have been used previously for structures with external fluid loading. Membranes and plates were addressed by Stepanishen,[8] and an approach to solve for the transient acoustic radiation from shells of revolution was developed by Chen and Stepanishen.[9]

The special case of a force excited axisymmetric cylindrical shell and base plate with fluid loading is introduced at the end of Sec. II and details of the associated experiments are given in Sec. III. Both transient and harmonic velocity and pressure responses were obtained from the experiments and are compared with theory in Sec. IV.

II. THEORY

Consider the general fluid filled elastic solid shown in Fig. 1. The solid volume V_s contains a fluid volume V_f. A pressure release (zero-normal stress) boundary is denoted as surface S_a and the fluid boundary in contact with the elastic solid is denoted as S_b. A unit normal vector $\mathbf{n}$ is defined on the surface $S_a U S_b$ directed into the fluid volume. It is of interest to determine the transient and harmonic velocity re-

[a)]Electronic mail: hassanse@npt.nuwc.navy.mil

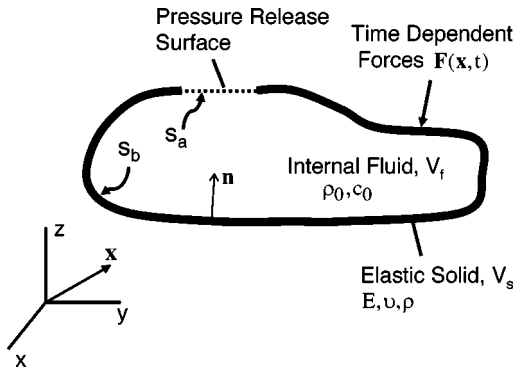

FIG. 1. Elastic solid with internal fluid loading and applied forces.

sponse of the solid and the associated pressure field in the fluid resulting from a general applied force excitation to the elastic solid.

A. Elastic solid transient response

The equations of motion for the linear elastic solid shown in Fig. 1 can be expressed as

$$[L]\mathbf{u}(\mathbf{x},t)+\rho(\mathbf{x})\frac{\partial^2\mathbf{u}(\mathbf{x},t)}{\partial t^2}=\mathbf{f}(\mathbf{x},t)+\mathbf{f}^a(\mathbf{x},t),\quad \mathbf{x}\in V_s \tag{1}$$

where the matrix L contains spatial derivatives that operate on the displacements $\mathbf{u}(\mathbf{x},t)$. The $\mathbf{f}(\mathbf{x},t)$ and $\mathbf{f}^a(\mathbf{x},t)$ are applied and acoustic force vectors per unit volume acting on the solid. It is noted that Eq. (1) assumes the Navier form for an isotropic elastic medium[10] and additional kinematic constraints can be imposed on Eq. (1) to arrive at various forms the of shell and plate equations.[11] The acoustic force per unit volume acting on the elastic solid is confined to the surface S_b and can be expressed as

$$\mathbf{f}^a(\mathbf{x},t)=-\int_{S_b}\mathbf{n}(\mathbf{x})p(\mathbf{x},t)\,\delta(\mathbf{x}-\mathbf{x}_0)dS_0, \tag{2}$$

where $p(\mathbf{x},t)$ is the acoustic pressure in the fluid and $\delta(\ )$ is the Dirac delta function.

Using a standard approach for *in vacuo* elastic solids,[12] the velocity field of the inhomogeneous transient problem in Eq. (1) is expressed using an eigenvector expansion with time dependent coefficients. It follows that

$$\mathbf{v}(\mathbf{x},t)=\sum_m v_m(t)\boldsymbol{\phi}_m(\mathbf{x}), \tag{3}$$

where $v_m(t)$ are the scalar time dependent modal velocity components and $\mathbf{v}(\mathbf{x},t)$ is the time derivative of the displacement $\mathbf{u}(\mathbf{x},t)$.

The eigenvectors of the *in vacuo* elastic solid form a basis for the solution to the inhomogeneous fluid loaded elastic solid vibration problem and satisfy the homogeneous equations of motion and kinematic boundary conditions. It follows from Eq. (1) that the eigenvectors $\boldsymbol{\phi}_m(\mathbf{x})$ and the associated natural frequencies ω_m satisfy the following

$$[L]\boldsymbol{\phi}_m(\mathbf{x})-\rho(\mathbf{x})\omega_m^2\boldsymbol{\phi}_m(\mathbf{x})=0. \tag{4}$$

The eigenvectors in Eq. (4) form a complete set of orthogonal functions such that

$$\int_{V_s}\rho(\mathbf{x})\boldsymbol{\phi}_m(\mathbf{x})\cdot\boldsymbol{\phi}_n(\mathbf{x})dV=M_m\delta_{mn}, \tag{5}$$

where δ_{mn} is the Kronecker delta and M_m is the normalization factor (modal mass). After substituting Eq. (3) into Eq. (1) and using Eqs. (4) and (5), the unknown modal velocity coefficients are found to satisfy

$$L'v_m(t)=f_m(t)-p_m(t), \tag{6}$$

where the operator L' is expressed as

$$L'=M_m\left(\frac{d}{dt}+\omega_m^2\int_t dt'\right). \tag{7}$$

The applied and acoustic modal forces in Eq. (6) are defined, respectively, as

$$f_m(t)=\int_{V_s}\mathbf{f}(\mathbf{x}_0,t)\cdot\boldsymbol{\phi}_m(\mathbf{x}_0)dV_0, \tag{8}$$

$$p_m(t)=\int_{S_b}p(\mathbf{x}_0,t)\psi_m(\mathbf{x}_0)dS_0, \tag{9}$$

and the component of the mth eigenvector normal to the surface S_b is defined as

$$\psi_m(\mathbf{x})=\boldsymbol{\phi}_m(\mathbf{x})\cdot\mathbf{n}(\mathbf{x}). \tag{10}$$

To obtain the general solution to Eq. (6), the impulse response of the modal admittance is first defined as the solution to

$$L'y_m(t)=\delta(t). \tag{11}$$

The solution to Eq. (11) can be expressed as

$$y_m(t)=\frac{1}{M_m}\cos(\omega_m t). \tag{12}$$

Using properties of the Dirac delta function and convolution operator, the time dependent modal velocity response can be expressed using Eqs. (6) and (11) as:

$$v_m(t)=y_m(t)\otimes f_m(t)-y_m(t)\otimes p_m(t), \tag{13}$$

where $\otimes$ denotes temporal convolution.

B. Fluid transient response

A general solution to the linear time dependent pressure field in the fluid is derived in this section. For later convenience, a Fourier transform pair is first introduced

$$\tilde{B}(\mathbf{x},\omega)=\int_{-\infty}^{\infty}b(\mathbf{x},t)e^{-j\omega t}dt, \tag{14a}$$

$$b(\mathbf{x},t)=\frac{1}{2\pi}\int_{-\infty}^{\infty}\tilde{B}(\mathbf{x},\omega)e^{j\omega t}d\omega, \tag{14b}$$

where $b(\mathbf{x},t)$ is a field variable of interest and the tilde denotes a complex quantity. The time harmonic pressure field, $\tilde{P}(\mathbf{x},\omega)$ in V_f, can be expressed as the solution to the Helmholtz equation

$$[\nabla^2+k^2]\tilde{P}(\mathbf{x},\omega)=0, \quad \mathbf{x}\in V_f \tag{15}$$

with the following mixed boundary conditions

$$\begin{aligned}&\mathbf{n}\cdot\nabla\tilde{P}(\mathbf{x},\omega)=-j\omega\rho_0\mathbf{n}\cdot\tilde{\mathbf{V}}(\mathbf{x},\omega), \quad \mathbf{x}\in S_b,\\ &\tilde{P}(\mathbf{x},\omega)=0, \quad \mathbf{x}\in S_a,\end{aligned} \tag{16}$$

where c_0 is the acoustic wave speed and $k=\omega/c_0$ is the acoustic wave number. A Green's function for the problem of interest is now introduced such that

$$[\nabla^2+k^2]G(\mathbf{x}|\mathbf{x}_0,\omega)=-\delta(\mathbf{x}-\mathbf{x}_0), \quad \mathbf{x}\in V_f \tag{17}$$

along with mixed homogeneous boundary conditions over the bounding surfaces

$$\begin{aligned}&\mathbf{n}\cdot\nabla G(\mathbf{x}|\mathbf{x}_0,\omega)=0, \quad \mathbf{x}\in S_b,\\ &G(\mathbf{x}|\mathbf{x}_0,\omega)=0, \quad \mathbf{x}\in S_a.\end{aligned} \tag{18}$$

Following a standard development,[13,14] it can be shown that the pressure in the fluid is expressed as

$$\tilde{P}(\mathbf{x},\omega)=j\omega\rho_0\int_{S_b}G(\mathbf{x}|\mathbf{x}_0,\omega)\mathbf{n}\cdot\tilde{\mathbf{V}}(\mathbf{x}_0,\omega)dS_0, \tag{19}$$

where the Green's function is expressed as

$$G(\mathbf{x}|\mathbf{x}_0,\omega)=\sum_i\frac{\Phi_i(\mathbf{x})\Phi_i(\mathbf{x}_0)}{VN_i(k^2-k_i^2)}. \tag{20}$$

The fluid spectral parameters Φ_i and k_i in Eq. (20) are the ith scalar eigenfunction and eigenvalue, respectively, of the mixed homogeneous boundary value problem in Eq. (17) that satisfy the boundary conditions in Eq. (18). The eigenfunctions form a complete set of orthogonal functions in V_f. It follows that

$$\int_{V_f}\Phi_n(\mathbf{x})\Phi_i(\mathbf{x})dV=VN_i\delta_{in}, \tag{21}$$

where N_i is the normalization constant and V is the fluid volume.

The time dependent field pressures and acoustic Green's function are found by applying Eq. (14b) to Eqs. (19) and (20). The final results are expressed, respectively, as

$$p(\mathbf{x},t)=\rho_0\frac{\partial}{\partial t}\int_{S_b}g(\mathbf{x},t|\mathbf{x}_0,0)\otimes\mathbf{n}\cdot\mathbf{v}(\mathbf{x}_0,t)dS_0, \tag{22}$$

and

$$g(\mathbf{x},t|\mathbf{x}_0,0)=c_0\sum_i\frac{\Phi_i(\mathbf{x})\Phi_i(\mathbf{x}_0)}{VN_ik_i}\sin(c_0k_it). \tag{23}$$

C. Coupled transient response

The acoustic modal force can now be simplified by substituting Eqs. (22) and (3) into Eq. (9). The final result is

$$p_m(t)=\sum_n z_{mn}(t)\otimes v_n(t), \tag{24}$$

where the modal radiation impulse responses, $z_{mn}(t)$, are expressed as

$$z_{mn}(t)=\rho_0\frac{\partial}{\partial t}\int_{S_b}\int_{S_b}\psi_m(\mathbf{x}_0)g(\mathbf{x},t|\mathbf{x}_0,0)\psi_n(\mathbf{x})dSdS_0. \tag{25}$$

It follows from substituting Eq. (24) into Eq. (13) that the following set of coupled convolution integral equations is obtained for the unknown modal velocity

$$v_m(t)=y_m(t)\otimes f_m(t)-y_m(t)\otimes\sum_n z_{mn}(t)\otimes v_n(t). \tag{26}$$

From Eq. (26), it is evident that the modal radiation impedances couple the mth and nth *in vacuo* modes of the elastic solid.

To develop an expression for the modal radiation impulse responses, the time dependent acoustic Green's function in Eq. (23) is substituted into Eq. (25) resulting in

$$z_{mn}(t)=\rho_0c_0^2\sum_i\frac{I_{im}I_{in}}{VN_i}\cos(c_0\mathbf{k}_it). \tag{27}$$

The I_{im} in Eq. (27) are surface integrals that couple the ith fluid mode and mth *in vacuo* mode of the elastic solid. These integrals are expressed as

$$I_{im}=\int_{S_b}\Phi_i(\mathbf{x}_0)\psi_m(\mathbf{x}_0)dS_0, \tag{28}$$

and are evaluated using standard quadrature techniques once the $\psi_m(\mathbf{x}_0)$ and $\Phi_i(\mathbf{x}_0)$ are determined using analytical or numerical methods.

Recalling the associative property of the convolution operator, Eq. (26) can also be expressed as:

$$v_m(t)=y_m(t)\otimes f_m(t)-\sum_n\alpha_{mn}(t)\otimes v_n(t), \tag{29}$$

where

$$\alpha_{mn}(t)=y_m(t)\otimes z_{mn}(t). \tag{30}$$

The $\alpha_{mn}(t)$ are found by substituting Eqs. (12) and (27) into Eq. (30) and evaluating the convolution integral resulting in

$$\alpha_{mn}(t)=\rho_0c_0^2\frac{1}{M_m}\times\sum_i\frac{I_{im}I_{in}}{VN_i}\frac{\omega_m\sin(\omega_mt)-c_0k_i\sin(c_0k_it)}{\omega_m^2-(c_0k_i)^2}. \tag{31}$$

The unknown $v_m(t)$ in Eq. (29) can now be solved by marching forward in time for a specified applied force excitation. The final solution for the velocity field of the elastic solid is then obtained from Eq. (3).

The transient pressure field in the fluid is determined by substituting Eqs. (23) and (3), and the solution for $v_m(t)$ from Eq. (29), into Eq. (22). The final result is expressed as

$$p(\mathbf{x},t)=\sum_m v_m(t)\otimes h_m(\mathbf{x},t), \tag{32}$$

where $h_m(t)$ is the modal impulse response of the pressure field, given as

$$h_m(\mathbf{x},t)=\rho_0 c_0^2 \sum_i \frac{\Phi_i(\mathbf{x})}{VN_i} I_{im} \cos(c_0 k_i t). \tag{33}$$

D. Coupled harmonic response

The coupled harmonic response is developed in this section using a Fourier transform approach. It is noted that the resulting equations of motion are similar to those derived by Fahy.[13] The time harmonic response of the elastic solid is obtained by applying Eq. (14a) to Eq. (3) resulting in

$$\tilde{\mathbf{V}}(\mathbf{x},\omega)=\sum_m \tilde{V}_m(\omega)\boldsymbol{\phi}_m(\mathbf{x}), \tag{34}$$

A set of linear algebraic equations for the unknown complex $\tilde{V}_m(\omega)$ is obtained by applying Eq. (14a) to Eq. (26) and rearranging. The final result is

$$\tilde{Z}_m^M(\omega)\tilde{V}_m(\omega)+\sum_n \tilde{Z}_{mn}(\omega)\tilde{V}_n(\omega)=\tilde{F}_m(\omega). \tag{35}$$

The complex modal mechanical impedance $\tilde{Z}_m^M(\omega)$ in Eq. (35) is defined for a conservative system as

$$\tilde{Z}_m^M(\omega)=\frac{M_m}{j\omega}(\omega_m^2-\omega^2). \tag{36}$$

The acoustic modal radiation impedances $\tilde{Z}_{mn}(\omega)$ in Eq. (35) are obtained by applying Eq. (14a) to Eq. (27) resulting in

$$\tilde{Z}_{mn}(\omega)=-j\omega\rho_0 \sum_i \frac{I_{im}I_{in}}{VN_i(k_i^2-k^2)}, \tag{37}$$

where the I_{im} are defined in Eq. (28). Similarly, the field pressure in the fluid is found by applying Eq. (14a) to Eqs. (32) and (33) resulting in

$$\tilde{P}(\mathbf{x},\omega)=-j\omega\rho_0 \sum_m \tilde{V}_m(\omega)\Phi_m(\mathbf{x}) \sum_i \frac{I_{im}}{VN_i(k_i^2-k^2)}. \tag{38}$$

E. Special case

Consider the fluid filled axisymmetric elastic cylindrical shell and base plate shown in Fig. 2. For convenience, a cylindrical coordinate system is used where $\mathbf{x}=(r,z)$. The fluid spectral parameters (Φ_i, N_i, and k_i) and elastic solid spectral parameters ($\boldsymbol{\phi}_m$, M_m, and ω_m) will be evaluated using analytical techniques and numerical methods (e.g., FEM) respectively. As an illustrative example, a point force acting normal to the base plate along the axis of symmetry in the $-$z direction will be considered. This applied force, with time dependence $q(t)$, excites only the axisymmetric response of the shell, base plate, and fluid. It follows that the applied force can be expressed as

$$f(\mathbf{x},t)=-q(t)\frac{\delta(r)\,\delta(z-L)}{2\pi r}. \tag{39}$$

Substituting Eq. (39) into Eq. (8) and using Eq. (10) results in the following expression for the applied modal force

$$f_m(t)=-q(t)\psi_m(0,L), \tag{40}$$

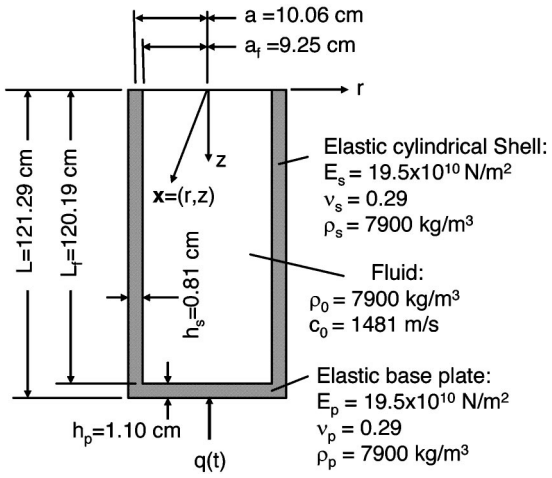

FIG. 2. Axisymmetric elastic cylindrical shell and base plate with internal fluid loading.

where the ψ_m is obtained from Eq. (10). The *in vacuo* modal response, denoted as $v_m^I(t)$ is obtained from substituting Eq. (40) into Eq. (13) with $p(t)=0$. The final result for a triangular pulse with peak amplitude of Q_0 and a duration of T_0 is

$$v_m^I(t)=\frac{-2Q_0\psi_m(0,L)}{M_m\omega_m^2 T_0}[g_1(t)+g_2(t)+g_3(t)], \tag{41}$$

where

$$\begin{aligned} g_1(t)&=[1-\cos(\omega_m t)]u(t),\\ g_2(t)&=2\{1-\cos[\omega_m(t-T_0/2)]\}u(t-T_0/2),\\ g_3(t)&=2\{1-\cos[\omega_m(t-T_0)]\}u(t-T_0), \end{aligned} \tag{42}$$

and $u(t)$ denotes the unit step function.

For this special case, the fluid boundary conditions enable separation of variables and it is common to replace the single index for the fluid spectral parameters with multiple indices; each associated with an axis of the orthogonal coordinate system. For the axisymmetric problem of interest, it follows that the scalar fluid eigenfunctions can be expressed as

$$\Phi_{ij}(r,z)=J_0(\chi_i r)\sin(\gamma_j z), \tag{43}$$

where

$$\gamma_j=\frac{(2j-1)\pi}{L_f}, \quad j=1,2,3,..., \tag{44}$$

and J_n is the Bessel function of the first kind, order n. The boundary conditions at $r=a_f$ result in

$$J_1(\chi_i a_f)=0, \tag{45}$$

and the eigenvalues are expressed as

$$k_{ij}^2=\chi_i^2+\gamma_j^2. \tag{46}$$

The fluid normalization factor is determined by substituting Eq. (43) into Eq. (21) resulting in

$$N_i=\frac{1}{2}J_0^2(\chi_i a_f). \tag{47}$$

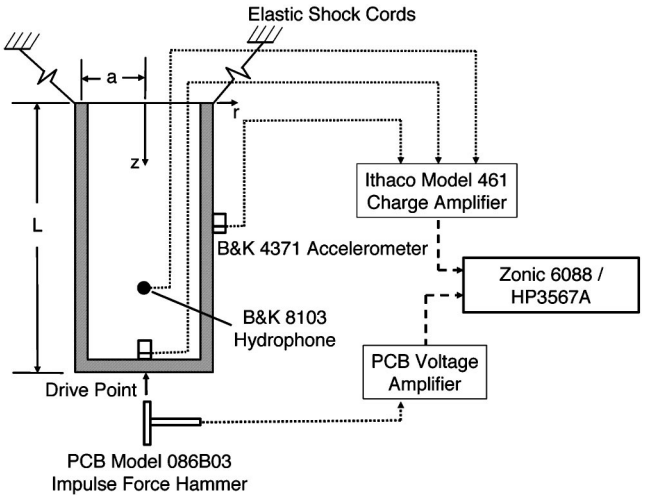

FIG. 3. Instrumentation and data acquisition configuration.

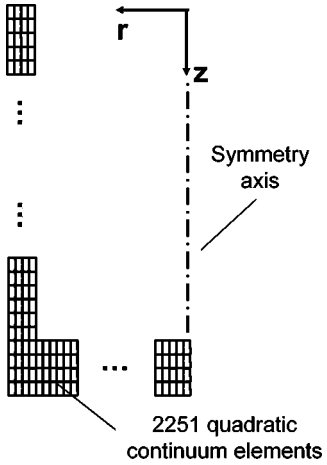

FIG. 4. Finite element model of the *in vacuo* axisymmetric cylindrical shell and base plate.

The α_{mn} in Eq. (31) may now be evaluated and the time dependent model velocity response is obtained from Eq. (29) by marching forward in time. The harmonic modal velocity response is obtained from Eq. (35) using the acoustic modal radiation impedances in Eq. (37).

III. EXPERIMENTS

To validate the theory presented in Sec. II, transient and harmonic response measurements were taken on the fluid loaded cylindrical shell shown in Fig. 2. Input force, acceleration response, and pressure response measurements were obtained using a force impact hammer, accelerometers, and a hydrophone respectively. Figure 3 shows the general configuration of the instrumentation and interface with the data acquisition systems. The cylinder and base plate were fabricated with stainless steel (type 304) and welded together resulting in an overall mass of 87.01 kg for the water-filled structure. A fixed drive point accelerometer and two roving accelerometers mounted to the shell and base plate, and one hydrophone was positioned in the fluid. During testing, elastic shock cords were attached to four small hooks (not shown) to support and isolate the structure.

Modal data were acquired using the Zonic 6088 system and Zonic Modal software.[15] Modes were first identified using an indicator function then the structure was re-excited with the force impact hammer and processed using a zoom fast Fourier transform about the resonant frequency of interest. Mode shapes were then determined using the circle fit single degree of freedom method detailed in Ewins.[16] Transient response measurements were taken using the Hewlett Packard HP3567A system. Velocity response was determined by numerical integration of the ensemble averaged accelerometer signals using ten sample functions.

TABLE I. Normalization factors.

Variable	Normalization factor
Length	a
Velocity	$c_p=(E/\rho_p(1-\nu^2))^{1/2}$
Density	ρ_p
Radian frequency	c_p/a
Time	a/c_p
Pressure	$\rho_p c_p^2$
Admittance (velocity/force)	$1/\rho_p c_p a^2$
Impedance (force/velocity)	$\rho_p c_p a^2$

IV. DISCUSSION OF NUMERICAL AND EXPERIMENTAL RESULTS

Numerical and experimental results are presented in this section for a fluid-filled cylindrical shell and base plate structure. The structure dimensions are given in Fig. 2 along with the associated physical and mechanical properties. All quantities are normalized in accordance with Table I and indicated by a hat. The parameters chosen for frequency normalization include: a (radius of cylindrical shell middle surface) and c_p (plate wave speed). These parameters result in the shell ring frequency (8260 Hz) occurring at a normalized frequency of $\hat{\omega}=1$. The following discussion of the shell and base plate response is based on global cylindrical coordinates where the coordinate system origin is located on the axis of symmetry at the air/water interface. Thus, axial motion is used to designate in-plane motion of the shell and normal motion of the base plate. For both harmonic and transient numerical results, the *in vacuo* spectral parameters of the shell and base plate are determined using the FEM code ABAQUS.[17] The finite element mesh is shown in Fig. 4 and consists of 2251 quadratic continuum elements and 7673 nodes. Numerical and experimental harmonic response results for the fluid loaded structure are presented first followed by time domain numerical results for the special case. Finally, a comparison of transient numerical and experimental results is presented.

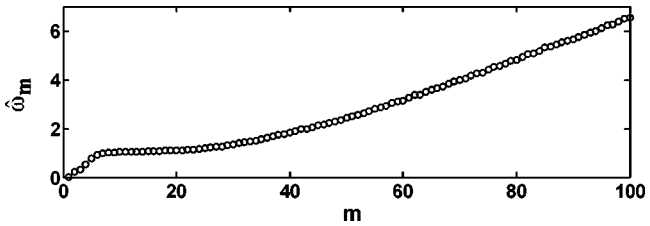

FIG. 5. Normalized *in vacuo* natural frequencies of cylindrical shell and base plate.

TABLE II. Natural frequencies of the fluid loaded cylindrical shell and base plate.

Mode	Num.	Exp.	% Error
1	0.0395	0.0390	1.28%
2	0.0947	0.0952	0.53%
3	0.1486	0.1491	0.34%
4	0.1952	0.1970	0.90%
5	0.2461	0.2429	1.32%
6	0.2622	0.2617	0.19%
7	0.3091	0.3079	0.39%
8	0.3690	0.3653	1.01%

A. Harmonic results

Numerical and experimental results for the fluid loaded axisymmetric harmonic response of the shell and base plate, due to an applied point force excitation acting in the $-z$ direction normal to the base plate and along the axis of symmetry, are considered. Measurements associated with the axial response (i.e., z direction) are presented.

Normalized *in vacuo* natural frequencies of the shell and base plate structure, predicted using FEM, are shown in Fig. 5 as a function of mode number. The *in vacuo* natural frequencies are distinct and well spaced in the frequency range of $\hat{\omega}<1$ and a single rigid body mode associated with uniform axisymmetric axial motion is evident at zero frequency. As $\hat{\omega}\rightarrow 1$, the modal density increases rapidly due to the large number of modes associated with the cylindrical shell near the ring frequency.

A comparison of numerical and experimental results for the fluid loaded natural frequencies is given in Table II. The results for the first eight modes are found to be in agreement within 1.32%. Figure 6 shows the fluid loaded axial displacement mode shapes of the cylindrical shell and base plate for modes 2, 4, and 7. These modes are normalized such that the maximum displacement magnitude is unity. For all modes presented, it is apparent that the base plate response is significantly greater than the response of the cylindrical shell.

Fluid loaded admittance at the drive point and on the external surface of the cylindrical shell at $z/L=0.5$ (midspan of the cylindrical shell) are presented in Fig. 7. Admittance is defined as the ratio of harmonic axial velocity response to applied force on the base plate, denoted as $\tilde{Y}(\omega)$. The fluid loaded resonances, indicated by a local maximum in admittance, are found to be approximately even spaced with frequency. This spacing does not directly correspond to the specific resonances associated with the fluid or the *in vacuo* structure. This general result exhibits one of the complicating effects of fluid loading on the shell where the interior fluid is reactive as either a mass or stiffness depending on frequency. The interior fluid loaded elastic solid resonant frequencies can therefore be shifted up or down from the *in vacuo* frequencies.

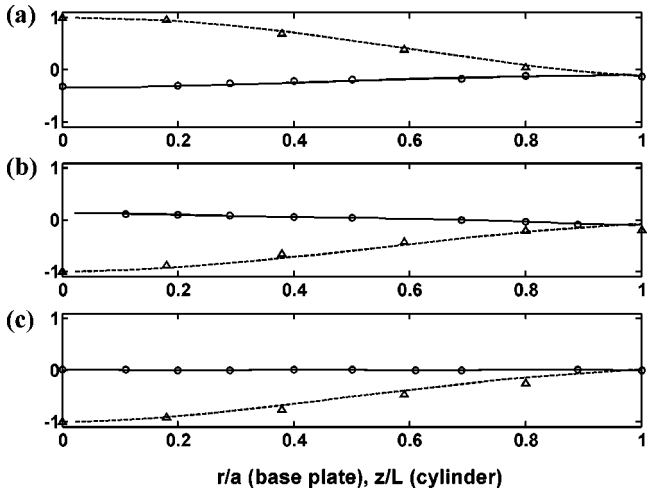

FIG. 6. Axial component of fluid loaded modal vectors. Cylinder numerical (solid line), base plate numerical (dashed line), cylinder experimental (○), base plate experimental (△): (a) mode 2, (b) mode 4, (c) mode 7.

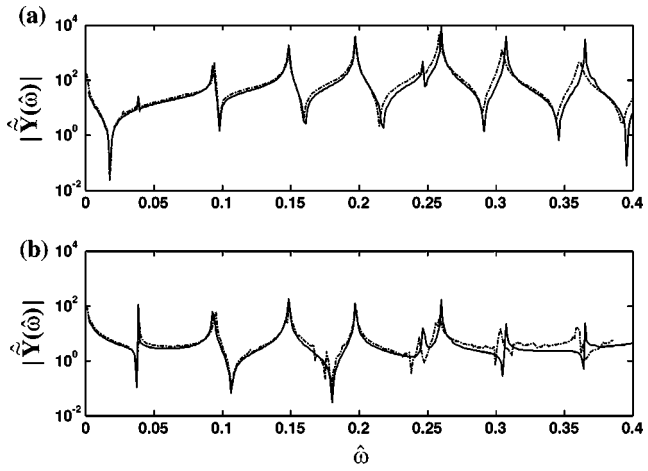

FIG. 7. Axial component of fluid loaded admittance at drive location and midpoint on cylinder: Numerical (solid line), experimental (dashed line).

B. Transient numerical results

The special case of a point force acting in the $-z$ direction along the axis of symmetry of the base plate with the time history shown in Fig. 8(a) is considered next. It is noted that the *in vacuo* time dependent modal velocity coefficients are obtained from Eq. (13) with $p_m(t)=0$. For the present case, the convolution integral can be evaluated analytically with the final result given in Eq. (41). The results from Eq. (41) for $m=1$ and 4 are shown in Fig. 8(b). The rigid body

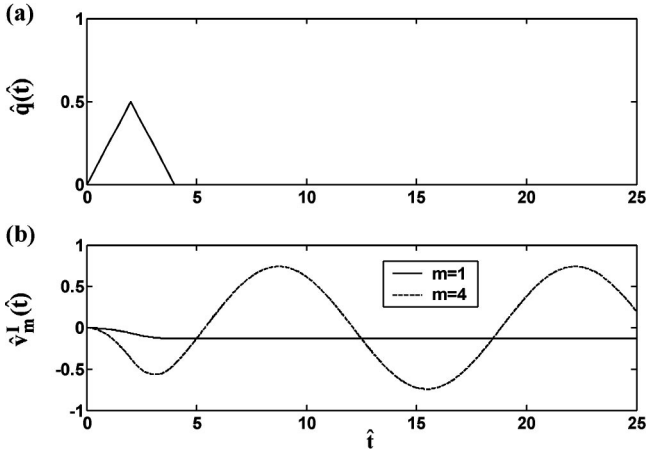

FIG. 8. (a) Input force to base plate and (b) *In vacuo* modal velocity.

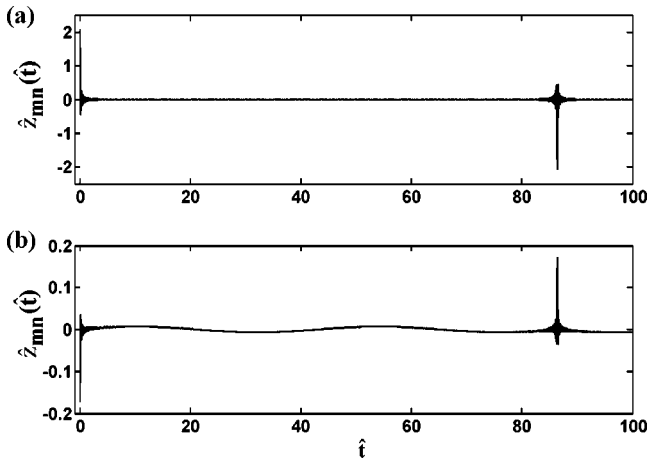

FIG. 9. Impulse response of modal impedance: (a) $(m,n)=(1,1)$ and (b) $(m,n)=(4,1)$.

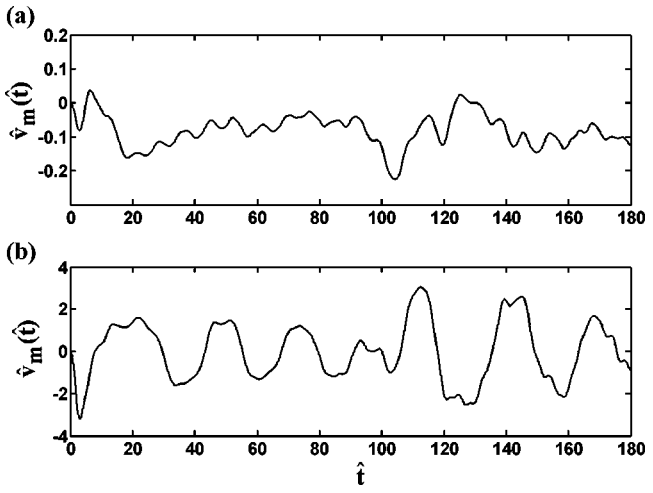

FIG. 11. Fluid loaded modal velocity: (a) $m=1$ and (b) $m=2$.

mode, $m=1$, reaches a constant velocity at $\hat{t}=4$. The small amplitude of the $m=1$ mode is a result of the large modal mass associated with the rigid body mode. Higher-order modes exhibit a forced response behavior which becomes sinusoidal with amplitude inversely proportional to the modal mass, natural frequency squared, and force duration T_0.

Numerical results for the fluid loaded modal velocity response and field pressures are evaluated using Eqs. (29) and (32), respectively. The fluid loading is known to couple the *in vacuo* modes of the structure through the impulse response of the modal radiation impedances given in Eq. (27). The impulse responses of the modal radiation impedance for selected modes are shown in Fig. 9. The case $(m,n)=(1,1)$ shown in Fig. 9(a) corresponds to the rigid body mode of the cylindrical shell and base plate where the motion is uniform in the axial (z) direction. For this mode, only the surface of the base plate contributes to the integrations in Eq. (25) as a result of the zero-normal (radial) displacement over the cylindrical shell. Furthermore, only the plane wave acoustic modes of the fluid contribute to the impulse response of the modal impedance for $(m,n)=(1,1)$. This situation is equivalent to a rigid one-dimensional duct of length L_f and radius a_f with a pressure release at $z=0$ and a rigid piston at $z=L_f$. For this particular case, the impulse response of the fluid impedance due to the piston can be expressed as: $z_p(t)=\rho_0 c_0 \pi a_f^2[\,\delta(t)-\delta(t-2L_f/c_0)+\delta(t-4L_f/c_0)-\ldots]$. The time delays in this expression are due to the acoustic propagation time associated with a plane wave propagating a distance of $2L_f$. The alternating sign of the impulse response of the fluid impedance is due to the phase change (π radians) associated with the pressure release boundary condition at $z=0$. These features are clearly evident in the normalized impulse response of the modal radiation impedance shown in Fig. 9(a). The higher-order $(m,n)=(4,1)$ mode is shown in Fig. 9(b) where it is evident that the response is nonzero between peaks. This is due to the $m=4$ mode contributing to the integration over the cylindrical shell surface of S_b in Eq. (25).

From a computational standpoint, the $\alpha_{mn}(t)$ from Eq. (31) are used during the numerical evaluation of the coupled convolution integral equations. Figure 10 shows the normalized $\alpha_{mn}(t)$ for two mode combinations. Oscillation at the natural frequency of the mth *in vacuo* mode is clearly evident in addition to the discontinuities associated with the Dirac delta function components of the $z_{mn}(t)$. Additionally, since the $\alpha_{mn}(t)$ are evaluated as the convolution of $y_m(t)$ with $z_{mn}(t)$, there is a filtering and corresponding smoothing of the resulting $\alpha_{mn}(t)$.

The normalized fluid loaded modal velocity response, computed from Eq. (29), for selected modes are shown in Fig. 11. In contrast to the *in vacuo* modal velocities obtained from Eq. (41), the fluid loaded modal velocity coefficients are not pure sinusoids as a result of the modal coupling.

The normalized fluid loaded axial velocity responses due

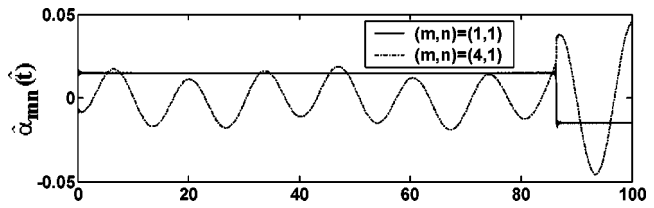

FIG. 10. $\hat{\alpha}_{mn}(\hat{t})$ from Eq. (31).

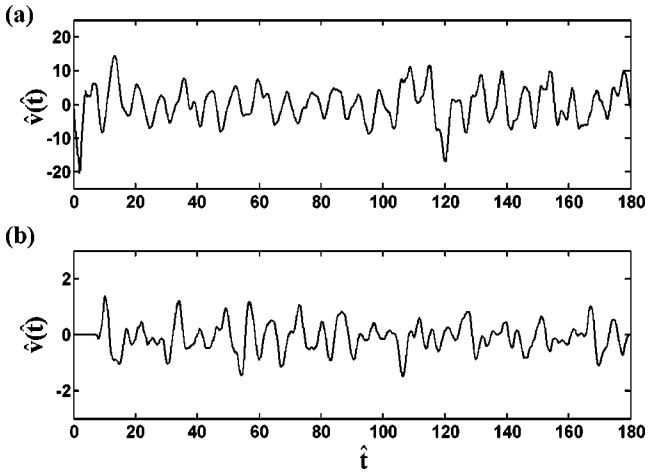

FIG. 12. Fluid loaded axial velocity response: (a) drive point and (b) external surface of cylinder at $z/L=0.5$.

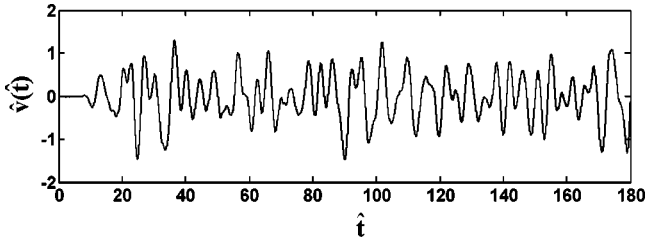

FIG. 13. Fluid loaded radial velocity on external surface of cylinder at $z/L=0.5$.

to the applied force are shown in Fig. 12. The delay in the initial axial response for the point along the cylindrical shell is in agreement with plate wave speed propagation times indicating that the initial axial response is due to the predominantly in-plane waves on the cylindrical shell.

The radial velocity response on the cylindrical shell at $z/L=0.5$ (midspan of the cylindrical shell) is shown in Fig. 13. The time delay is greater than the propagation time associated with waves traveling at the plate wave speed indicating an initial response predominantly due to waves with a phase speed slower than the plate wave speed.

Results for the normalized field pressure response at two locations are shown in Fig. 14. The field pressure response at the drive point, shown in Fig. 14(a), exhibit a separation in peaks at approximately the delay time associated with an acoustic wave propagating in the radial direction, reflecting from the cylindrical shell and returning to the axis of symmetry ($\Delta\hat{t}\approx 2c_p/c_0\approx 7.0$). Figure 14(b) shows the field pressure on axis for a point with increased distance from the drive point. It is clear that the response delay time increases with separation distance, however, the delay is greater than the minimum time associated with the plate wave speed propagation in the structure and the acoustic wave speed propagation in the fluid. This occurs because the fluid is coupled to the cylindrical shell via the normal motion of the shell and base plate. The waves with predominantly normal velocity are propagating with slower phase speed than waves associated with in-plane motion.

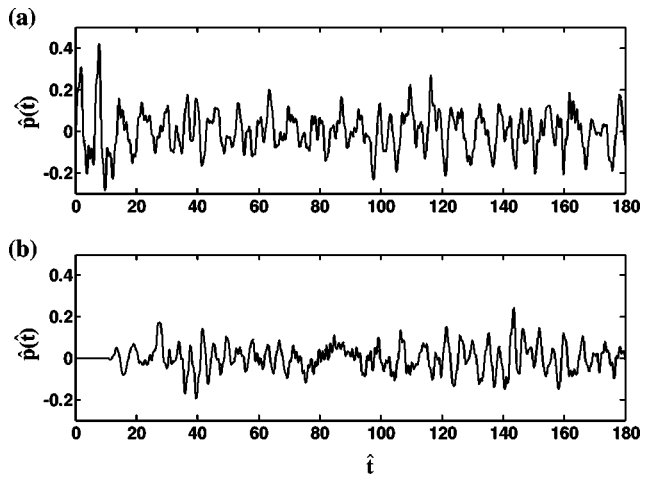

FIG. 14. Field pressure response: (a) drive point and (b) external surface of cylinder at $z/L=0.5$.

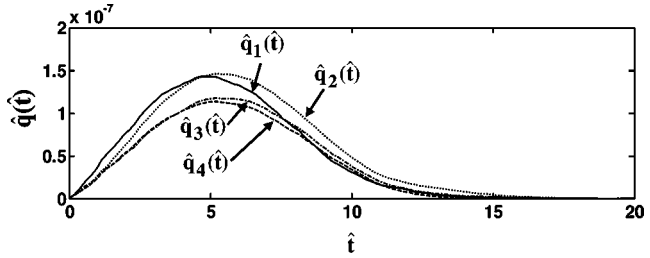

FIG. 15. Measured forces applied to base plate due to hammer strike.

C. Comparison of transient numerical and experimental results

Experimental data for the fluid loaded transient response of the shell, base plate, and fluid are presented and compared with numerical results. The numerical results presented in this section are computed from the series expansions with 80 terms in Eqs. (29) and (32), and 1400 terms in Eqs. (31) and (33). The excitation to the structure consists of a point force impulse applied normal to the base plate acting along the axis of symmetry. Four transient force input data sets are necessary to obtain response measurements at all locations. Figure 15 shows the normalized input forces applied to the base plate where each time history is the ensemble average of ten sample records. For direct comparison of experimental and numerical results, these time dependent forces are used as input to the numerical model.

The normalized fluid loaded axial velocity responses at the drive point and on the cylinder at $z/L=0.5$ are shown in Fig. 16. In general, the agreement is excellent with the difference between numerical results and experimental results increasing with time. This is primarily attributed to possible nonaxisymmetric reflections at the open end of the cylinder and dissipation which is not accounted for in the present model.

The on-axis pressure responses at two axial locations are shown in Fig. 17. The initial pressure response is due to the coupling of the fluid with elastic waves in the cylindrical shell traveling at approximately the plate wave speed. These elastic waves have a predominantly axial displacement and

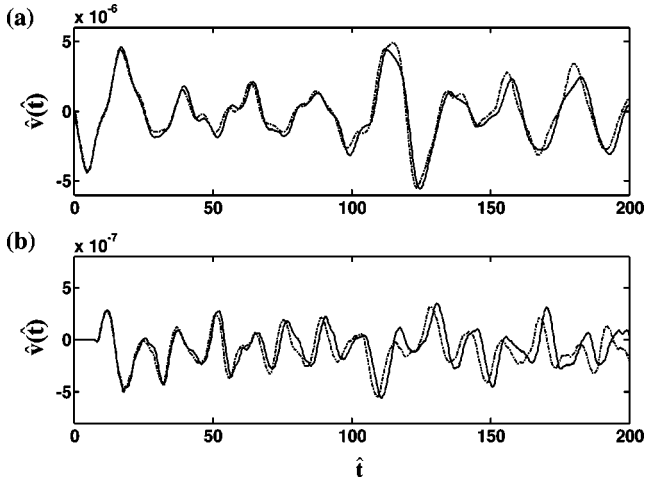

FIG. 16. Fluid loaded axial velocity response. Numerical (solid line) and experimental (dashed line) results at (a) drive point due to $\hat{q}_1(\hat{t})$ and (b) external surface of cylinder at $z/L=0.5$, due to $\hat{q}_2(\hat{t})$.

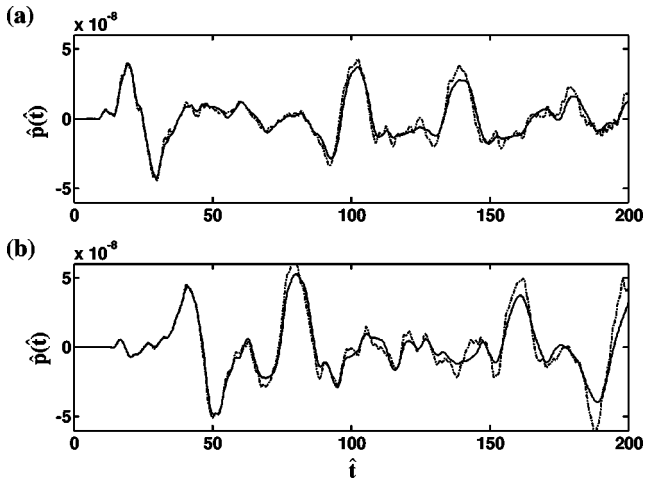

FIG. 17. Field pressure response on z axis ($r/a=0.0$). Numerical (solid line) and experimental (dashed line) results at (a) $z/L=.74$, due to $\hat{q}_3(\hat{t})$ and (b) $z/L=0.29$, due to $\hat{q}_4(\hat{t})$.

therefore are only weakly coupled to the fluid. Consequently, the initial pressure response is of small amplitude. The subsequent large amplitude acoustic response is due to waves generated at the base plate and propagating through the fluid, and bending waves traveling at phase speeds lower than the plate wave speed but strongly coupled to the fluid.

V. SUMMARY

A general approach to solve for the transient and harmonic velocity response and the associated pressure field of a fluid-filled elastic solid has been presented. The approach is based on an expansion of the spectral parameters associated with the fluid and *in vacuo* solid. The solid and fluid spectral parameters can be obtained independently and, therefore, enable convenient analytical or numerical methods, such as FEM, to be used. The resulting series containing these spectral parameters, may be truncated to provide reduced-order parametric models of the coupled response. This general approach has not been previously used for elastic solids with internal fluid loading and is also applicable to infinite and semi-infinite fluid loaded elastic ducts. The associated harmonic response is formulated using a Fourier transform approach applied to the time dependent equations of motion for the elastic solid. The special case of a fluid-filled axisymmetric cylindrical shell with a base plate was considered. For this configuration, the FEM was used to determine the spectral parameters of the elastic solid, and analytic techniques were implemented for the evaluating the spectral parameters of the fluid. The theory was validated by comparison with results from a series of experiments conducted for the special case.

[1] M. Boone, G. Janssen, and M. van Overbeek, ''Modal superposition in the time domain: Theory and experimental results,'' J. Acoust. Soc. Am. **97**, 92–97 (1995).
[2] M. El-Raheb, ''Acoustic propagation in finite length elastic cylinders. Part 1: Axisymmetric excitation,'' J. Acoust. Soc. Am. **71**, 296–306 (1982).
[3] G. C. Everstine, ''Dynamic analysis of fluid-filled piping systems using finite element techniques,'' J. Pressure Vessel Technol. **108**, 57–61 (1986).
[4] L. Cheng, ''Fluid-structural coupling of a plate-ended cylindrical shell: vibration and the internal sound field,'' J. Sound Vib. **174**, 641–654 (1994).
[5] L. Cheng and J. Nicolas, ''Free vibration analysis of a cylindrical shell–circular plate system with general coupling and various boundary conditions,'' J. Sound Vib. **155**, 231–247 (1992).
[6] L. Feng, ''Experimental studies of the acoustic properties of a finite elastic pipe filled with water/air,'' J. Sound Vib. **189**, 511–524 (1996).
[7] T. Mauzch, ''Natural modes of a thin clamped-free steel cylindrical storage tank partially filled with water: FEM and Measurement,'' J. Sound Vib. **193**, 669–690 (1996).
[8] P. Stepanishen, ''Transient radiation and scattering from fluid-loaded oscillators, membranes, and plates,'' J. Acoust. Soc. Am. **88**, 374–385 (1990).
[9] H. Chen and P. Stepanishen, ''Acoustic transient radiation from fluid-loaded shells of revolution using time-dependent *in-vacuo* eigenvector expansions,'' J. Acoust. Soc. Am. **95**, 601–816 (1994).
[10] I. S. Sokolnikoff, *Mathematical Theory of Elasticity*, 2nd ed. (McGraw–Hill, New York, 1956).
[11] A. Leissa, *Vibration of Shells* (AIP, Melville, N.Y., 1983).
[12] L. Meirovitch, *Computational Methods in Structural Dynamics* (Sijthoff and Noordhoff, Rockville, Maryland, 1980).
[13] F. Fahy, *Sound and Structural Vibration* (Academic, New York, 1985).
[14] P. Morse and K. Ingard, *Theoretical Acoustics* (McGraw–Hill, New York, 1968).
[15] Zonic Corporation, ZONIC MODAL *Users Manual (6088 Version)* (Milford, Ohio, July 1985).
[16] D. W. Ewins, *Modal Testing: Theory, Practice, and Applications* (Research Studies, Letchworth, England, 2000).
[17] Hibbet, Karlsson, and Sorensen, Incorporated, ABAQUS/*Standard User's Manual* Pawtucket, Rhode Island, 1994.

A linear least-squares version of the algorithm of mode isolation for identifying modal properties. Part I: Conceptual development

Jerry H. Ginsberg[a] and Matt Allen
G. W. Woodruff School of Mechanical Engineering, Georgia Institute of Technology, Atlanta, Georgia 30332-0405

(Received 28 October 2003; revised 23 April 2004; accepted 5 May 2004)

The Algorithm of Mode Isolation (AMI) is an iterative procedure for identifying the number of modes contributing to a frequency response function (FRF) concurrently with identifying the complex eigenvalues and eigenvectors of those modes. The latest modifications obtain these modal properties solely by using linear least squares fits of the FRF data to canonical forms. The algorithmic operations are explained in a detailed sequence of steps that are illustrated by some sample data. The computational efficiency of AMI relative to other modal identification algorithms that fit response data to multi-degree-of-freedom model equations is discussed. © *2004 Acoustical Society of America.* [DOI: 10.1121/1.1765195]

PACS numbers: 43.40.Le, 43.40.Cw, 43.40.Yq [JGM] Pages: 900–907

I. INTRODUCTION

Algorithms for experimental modal analysis of linear dynamic systems can be categorized as to whether they use frequency or time domain data. Another categorization addresses the analytical representation of a response to which the measured data is fit. Single-degree-of-freedom (SDOF) techniques consider modes to act independently, whereas multiple-degree-of-freedom (MDOF) techniques allow for the modal contributions to overlap. A third descriptor pertains to the number of locations for excitation and response measurement. Single input-single output (SISO) uses a single pair, while multiple input-single output (MISO) uses multiple excitations and measures response at one location. If the system is time invariant, so that the principle of reciprocity applies, then single input-multiple output (SIMO) is equivalent to MISO. Multiple input-multiple output (MIMO) uses the data obtained from a multitude of excitations and response measurements. The texts by Maia *et al.*[1] and Ewins[2] provide a good background for these concepts.

Modal properties to be identified are the natural frequencies and modal damping ratios, which are system properties that are independent of the selection of points at which the data is measured. Mode vectors also require determination, but their values are dependent on the locations of the measurement points. Underlying this need is the requirement to identify the number of modes active in a frequency band, or equivalently, the system order associated with a time domain response. MDOF algorithms, which seem to be most commonly employed, make an *a priori* guess for the number of modes. One approach for verifying the correctness of that guess is to examine a metric that indicates how well a reconstruction of the response using the identified modal properties fits the measured response. However, because the frequency response functions (FRFs) corresponding to a different excitation feature different weightings of the modal parameters, it does not follow that parameters giving a good metric for one set of FRFs are suitable for other excitations. An alternative for verifying the system order displays in stabilization charts the natural frequencies identified from a range of guesses, then discards modes that are not consistently obtained.[3] This practice often requires considerable expertise of the analyst, and increases the computational effort. Also, it is best to overestimate the number of modes, but doing so raises the computational effort; it can also lead to false estimations and split modes, as was shown by Doebling, Alvin, and Peterson.[4]

Even if the number of participatory modes were known, the presence of relatively large damping can give rise to identification difficulties for several reasons. Some algorithms implicitly assume that dissipation is viscous. Furthermore, if a system has a wide range of modal damping ratios, the more highly damped modes in any transient temporal responses are rapidly attenuated, thereby magnifying the contribution of noise to those modes. For frequency domain data, high damping lowers the resonant peak of a frequency response function (FRF). Both serve to make it more difficult to distinguish the response from ambient noise, especially for *in situ* applications such as health monitoring applications. A further complication of large damping arises when natural frequencies are close, which is a common situation for high-frequency modes in complex systems. In such situations, the modal bandwidth of adjacent resonant peaks might exceed the natural frequency difference, leading to a merger of the resonant peaks into one broader peak, which is known as mode coupling. This can make it difficult to distinguish the individual modes.

For any identification technique proper selection of the drive point(s) is a primary factor affecting the quality of the identification. If the drive point mobility in a mode is small, that mode will participate little in the measured response, making it difficult to extract the mode. This situation is exacerbated by the presence of substantial noise, where one

[a]Electronic mail: jerry.ginsberg@me.gatech.edu

would expect that it is necessary for the response to stand out from the ambient noise.

Previous papers have suggested that the Algorithm of Mode Isolation (AMI) has the potential to address these difficult issues. It recognizes that several modes might simultaneously contribute to a FRF at any frequency, but does so in an iterative manner, in the course of which one obtains the number of modes active in any frequency interval. The algorithm was initially described by Drexel and Ginsberg[5] for a classical, undamped, modal analysis, although the basic concept was previously mentioned by Joh and Lee.[6] It then was extended to modal analysis in the state space in order to account for arbitrary damping (Drexel and Ginsberg,[7] Drexel, Ginsberg, and Zaki[8]). In its original version AMI was a SISO algorithm, in that each FRF was processed individually. In order to improve the ability to identify modes that are poorly excited Zaki[10] modified AMI by deferring identification of the normal mode coefficients. In the modified approach the original AMI algorithm is solely used to extract the eigenvalues, after which a global SIMO/MISO approach using a linear least-squares procedure identifies normalized mode vectors.

The heart of the AMI algorithm is to fit iteratively a FRF to the canonical form of a single mode. The aforementioned investigations used a nonlinear least squares routine to fit the data, which was the best available approach. It required good starting values, and entailed significant computational effort. Even then, convergence could be slow in some situations, and the results less accurate than desired. Ginsberg *et al.*[11] presented a general SDOF fitting procedure, in which linear least squares is used to match a resonant peak in an FRF to the FRF of a complex mode. That technique is not iterative, and it yields an exact match for the analytical FRF of a SDOF system. Implementation of this fitting procedure in AMI substantially increases the reliability and computational efficiency of the individual iterative steps.

The complete elimination of nonlinear least squares routines within AMI, coupled with separate identification of eigenvalues and complex mode vectors, are significant alterations. In the present paper we provide a detailed description of the latest version. In Part II[1] we assess its performance in comparison to analytical results, as well as relative to a popular modal identification algorithm.

II. THE STANDARD MODE ISOLATION ALGORITHM

The data to be input to AMI are the FRFs $H_{jP}(\omega_m)$, which are defined as the complex amplitudes of a set of generalized displacements q_j when a specific generalized force Q_P has a unit amplitude over a discrete set of frequencies ω_m, and all other generalized forces are zero,

$$Q_j = \mathrm{Re}[\,\delta_{jP}\exp(i\omega_m t)] \Rightarrow q_j = \mathrm{Re}[H_{jP}(\omega_m)\exp(i\omega_m t)]. \quad (1)$$

By reciprocity, $H_{jP}(\omega_m) = H_{Pj}(\omega_m)$. Hence, regardless of whether measurements are taken according to a SIMO or MISO protocol, the input data for AMI can be considered to be a rectangular array of FRF values, in which column j holds the FRF values over a discrete set of frequencies ω_m associated with displacement j and specified drive point P.

A FRF may be expressed as a finite sum of contributions of complex modes associated with a state-space description. If N is the number of degrees of freedom, then there are $2N$ eigensolutions, consisting of an eigenvalue λ_k and eigenvector $\{\Phi_k\}$ that satisfy the symmetric eigenvalue problem,

$$\left[\begin{bmatrix}[0] & [K]\\ [K] & [C]\end{bmatrix} - \lambda_k \begin{bmatrix}[K] & [0]\\ [0] & -[M]\end{bmatrix}\right]\{\Phi_k\} = \{0\}. \quad (2)$$

The eigenvectors $\{\Phi_k\}$ are normalized according to

$$\{\Phi_k\}^T \begin{bmatrix}[K] & [0]\\ [0] & -[M]\end{bmatrix}\{\Phi_k\} = 1. \quad (3)$$

It is assumed that all eigenvalues occur as complex conjugate pairs. This corresponds to modes that are underdamped, meaning that their free response is oscillatory within an exponentially decaying window. By analogy with a SDOF system, an undamped natural frequency Ω_k and modal damping ratio ζ_k can be extracted from an eigenvalue according to

$$\Omega_k = |\lambda_k|, \quad \zeta_k = -\mathrm{Re}(\lambda_k)/|\lambda_k|. \quad (4)$$

If all eigenvalues are complex conjugates, the system may be considered to possess N underdamped modes, whose contribution to any response may be represented by evaluating the role of the N eigensolutions whose eigenvalues have positive imaginary parts, then using the conjugate property to account for the other N eigensolutions. It is convenient in that case to sequence the eigenvalues such that those having positive imaginary parts come first followed by the conjugate values in the matching sequence. When this is done, each eigenvector may be expressed in terms of one of a set of N column vectors $\{U_k\}$ whose N elements represent the (complex) modal proportions of the generalized coordinates, according to

$$\lambda_{k+N} = \lambda_k^* \Rightarrow \{\Phi_k\} = \begin{Bmatrix}\{U_k\}\\ \lambda_k\{U_k\}\end{Bmatrix}, \quad \{\Phi_{k+N}\} = \{\Phi_k\}^* \quad (5)$$

As a result of the conjugate properties of the complex modes, a FRF value may be expressed[12] as a superposition of modal contributions according to

$$H_{jP}(\omega) = \sum_{k=1}^{N}\left[\frac{A_{jP,k}}{i\omega - \lambda_k} + \frac{A_{jP,k}^*}{i\omega - \lambda_k^*}\right], \quad (6)$$

where $(\,)^*$ denotes a complex conjugate, and $A_{jP,k}$ are residue factors that depend solely on the eigensolution for mode k,

$$A_{jP,k} = \lambda_k U_{jk} U_{Pk} \quad (7)$$

The foregoing is the analytical perspective, whereas in experimental modal analysis one does not know the number of degrees of freedom. Henceforth, N_0 will denote the number of measurement points for which FRFs are available, and N will denote the number of modes whose natural frequency falls in the frequency interval covered by the FRF data. The determination of N is a key aspect of any modal identification.

AMI begins by sequentially processing each of the N_0 FRF datasets. Two processes are applied to this data, both of

which use current estimates of the eigenvalues and residue factors to subtract estimated modal contributions from the original data. The term ''subtraction residual,'' denoted as $Y_{j,k}(\omega)$, refers to the data obtained by subtracting from $H_{jP}(\omega)$ estimated contributions for modes 1 to k, where the modes are numbered in the sequence in which they are detected. This data may be evaluated incrementally, such that

$$Y_{j,0}(\omega_m)=H_{jP}(\omega_m),$$
$$Y_{j,k}(\omega_m)=Y_{j,(k-1)}(\omega_m)-\left[\frac{A_{jP,k}}{i\omega_m-\lambda_k}+\frac{A^*_{jP,k}}{i\omega_m-\lambda^*_k}\right]. \quad (8)$$

In the Subtraction Phase, modes are identified one at a time, and their contribution to the FRF is subtracted until all significant modes have been removed. These operations may be summarized by a sequence of algorithmic steps.

(S.1) Pick a generalized displacement j and initialize the subtraction residual $Y_{j,0}(\omega_m)$ to be the FRF values for this coordinate at a discrete set of frequencies. Initialize the mode number as $k=0$.

(S.2) Identify the frequency range of the most dominant mode in the subtraction residual by searching for $\max(Y_{j,k}(\omega_m))$. Use a SDOF fit of the data in this frequency range to estimate the most dominant mode's properties. (This step now uses the linear least-squares procedure presented by Ginsberg *et al.*[11] and summarized in a later section.) Increment k by one, and assign the identified modal parameters as λ_k and $A_{jP,k}$.

(S.3) Form subtraction residual data $Y_{j,k}(\omega_m)$ according to Eq. (8).

(S.4) Decide whether $Y_{j,k}(\omega_m)$ contains the contribution of another mode. (The criteria for this decision are discussed below.) If so, return to Step (S.2). If $Y_{j,k}(\omega_m)$ consists solely of noise, then set the initial estimate for the number of modes to be $N=k$, and proceed to the Isolation Phase.

A troublesome aspect of the residual in Step (S.3) was recognized recently. The modal parameters identified in Step (S.2), being initial estimates, might differ significantly from the true values. Depending on their quality and the noise level, the residual $Y_{j,k}(\omega_m)$ formed from them might still contain an identifiable peak. This would cause the peak search in Step (S.2) to eventually return to this mode, for which an initial guess has already been obtained. The consequence would be multiple distinct initial estimates of a single mode. A simple way to avoid having the subtraction phase ''chase its tail'' is to zero $Y_{j,k}(\omega_m)$ over a range of ω_m surrounding the natural frequency, $|\lambda_k|$, that was identified.

The range for this zeroing must be selected carefully. If it is too big, it will obliterate the FRF in the vicinity of adjacent modes, whereas zeroing over an interval that is too small might leave significant spikes at the shoulders of the resonance peak. The range that was found to be effective is suggested by trials of the linear least squares identification algorithm described later. It was found for two-degree-of-freedom systems that the two complex modes could be distinguished if the difference of their adjacent undamped natural frequencies significantly exceeds 40% of the average bandwidth. Modes that are not distinguished because of their proximity are essentially treated as one mode in any SIMO/MISO identification scheme. In view of this limitation, zeroing out the residual FRF over 80% of its bandwidth would only remove data containing modes that could not be distinguished from the one just found. This leads to the insertion of another operation after Step (S.3).

(S.3a) Set the subtraction residual data $Y_{j,k}(\omega_m)=0$ for $0.8\,\mathrm{Re}(\lambda_k)+|\lambda_k|<\omega_m<-0.8\,\mathrm{Re}(\lambda_k)+|\lambda_k|$.

The Isolation Phase has the primary purpose of accounting for the fact that more than one mode may contribute to a FRF. It uses current estimates for the modal parameters to isolate the contribution of a specific mode. This requires forming an ''isolation residual,'' denoted $X_{j,k}(\omega_m)$, in which the current estimated contributions of all modes other than number k are subtracted from $H_{jP}(\omega_m)$ according to

$$X_{j,k}(\omega_m)=H_{jP}(\omega_m)-\sum_{\substack{n=1\\ n\neq k}}^{N}\left[\frac{A_{jP,n}}{i\omega_m-\lambda_n}+\frac{A^*_{jP,n}}{i\omega_m-\lambda^*_n}\right]. \quad (9)$$

The estimated modal properties required to begin the isolation process are those at the end of the Subtraction Phase, and the sequence in which the modes are isolated matches that in which the modes were identified in the Subtraction Phase. The steps required to carry out these operations are as follows.

(I.1) Initialize the mode number $k=0$.

(I.2) Increment k by one, and form isolation residual data $X_{j,k}(\omega_m)$ according to Eq. (9). For this, use the latest values for λ_k and $A_{jP,k}$.

(I.3) Apply the linear least-squares SDOF fit to $X_{j,k}(\omega_m)$ in order to obtain refined estimates of λ_k and $A_{jP,k}$. Retain the previous values for convergence tests.

(I.4) If $k<N$, return to Step (I.2). If $k=N$, compare the new values and old values of all λ_k and $A_{jP,k}$. If these values have not converged, return to Step (I.1). (Iterating until the real and imaginary parts of λ_k and $A_{jP,k}$ change by less than 0.01% yields good results. For modes whose natural frequency differs from those of adjacent modes by more than the modal bandwidth, no more than five iterations are typically required.)

(I.5) Use the converged set of values of all λ_k and $A_{jP,k}$ to form subtraction residual $Y_{j,N}(\omega_m)$, which accounts for all modes identified thus far.

(I.6) Decide whether $Y_{j,N}(\omega_m)$ contains the contribution of a (previously unidentified) mode. If not, cease processing of the FRF for the jth displacement, and return to Step (S.1) to process another set of FRF data.

(I.7) This step is reached if there is evidence of an additional mode in $Y_{j,N}(\omega_m)$. Apply the linear least squares SDOF fit to this data in order to obtain initial estimates of λ_{N+1} and $A_{jP,(N+1)}$.

(I.8) Increment N by one, then set $k=N-1$ and return to Step (I.1).

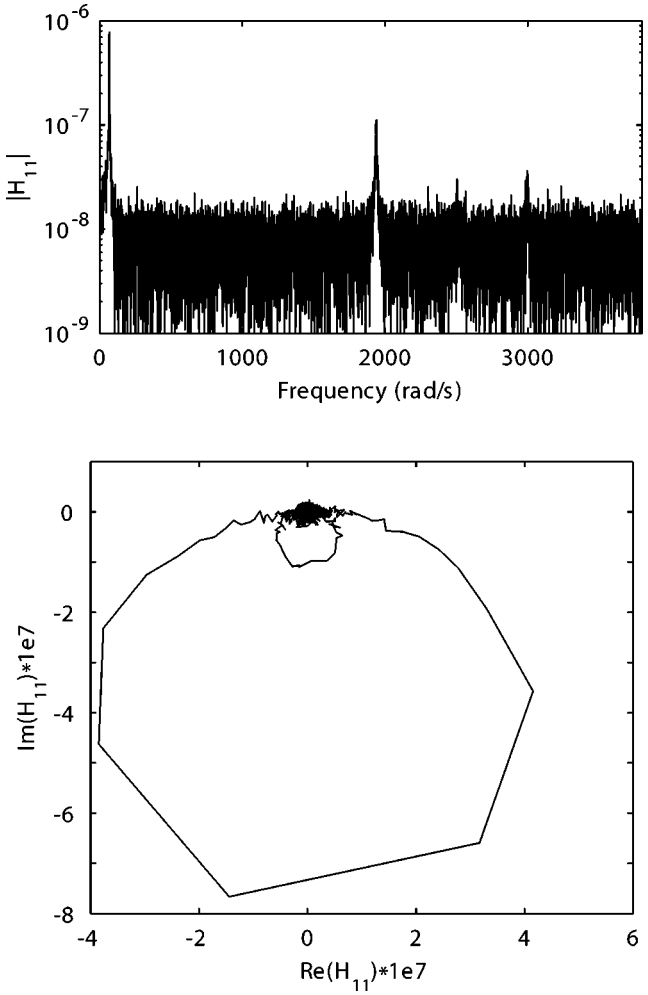

FIG. 1. Typical subtraction residual after removal of the first five modes.

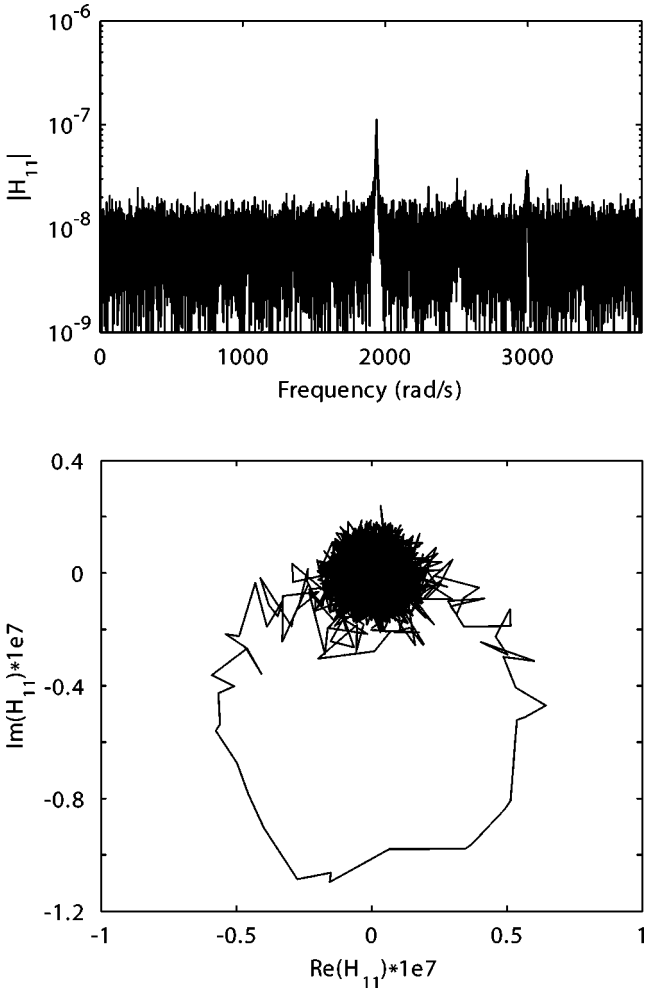

FIG. 2. Typical subtraction residual after removal of the first six modes.

All of the preceding operations are straightforward, except for Steps (S.4) and (I.6), which require a decision as to whether a residual FRF contains the contribution of a mode. If all of the modal contributions have been subtracted, the residual FRF should appear to be incoherent. The present procedure requires that the user visually search plots of the data to determine if there is some degree of coherence, e.g., several points form a noticeable peak in a Bode magnitude plot and a regular arc in a Nyquist plot. The identification of a quantitative measure on which to base this decision is a current area of investigation.

A useful perspective for the isolation stage is obtained by recognizing that because the isolation residual is formed by subtracting the current estimates for the contribution of known modes other than the one in focus, what remains consists of several parts: the actual contribution of the current mode, noise, measurement error, and errors associated with using parameters for the other modes that are not exact. Any of the latter that stand out above the noise will influence successive isolation steps until they are driven below the noise level. A corollary is that the noise floor defines the weakest modes that can be identified.

As an illustration of the Subtraction Phase, the latter stages of the processing of one of the FRFs described in Part II shall be followed here. The upper part of Fig. 1 shows the Bode magnitude plot of a residual FRF $|H_{11}(\omega)|$ after five modes have been identified and their contributions subtracted, that is, Step (S.4) with $k=5$. The lower part of Fig. 1 is a Nyquist plot of the same data. The irregularity of the data is a consequence of the white noise that was added to the data. Eleven modes have their natural frequency in the band covered by this figure, and five have been subtracted. The effect of the noise is to mask some of the six remaining modes. The Bode plot displays three peaks, but the Nyquist plot shows only two loops. (Each mode can be expected to produce a loop in a Nyquist plot.[2]) The presence of peaks in the Bode plot and coherent loops in the Nyquist plot indicates that the Subtraction Phase should continue, so the procedure passes to Step (S.2) with $k=6$. The peak below 100 rad/s is the highest. The linear least squares routine is used to fit the data in the vicinity of this peak, thereby identifying the sixth eigenvalue and residue. The subtraction residual is computed in Step (S.3), and plotting of this data in accord with Step (S.4) leads to Fig. 2. The low-frequency peak has been eliminated, and there is only one loop in the Nyquist plot. Because there is still evidence of the presence of a mode in the FRF data, the procedure returns to Step (S.2) with $k=7$. The highest peak in the plot of $|H_{11}(\omega)|$ versus ω now lies in the vicinity of 2000 rad/s, so the data in that region is used for the parameter identification, which yields

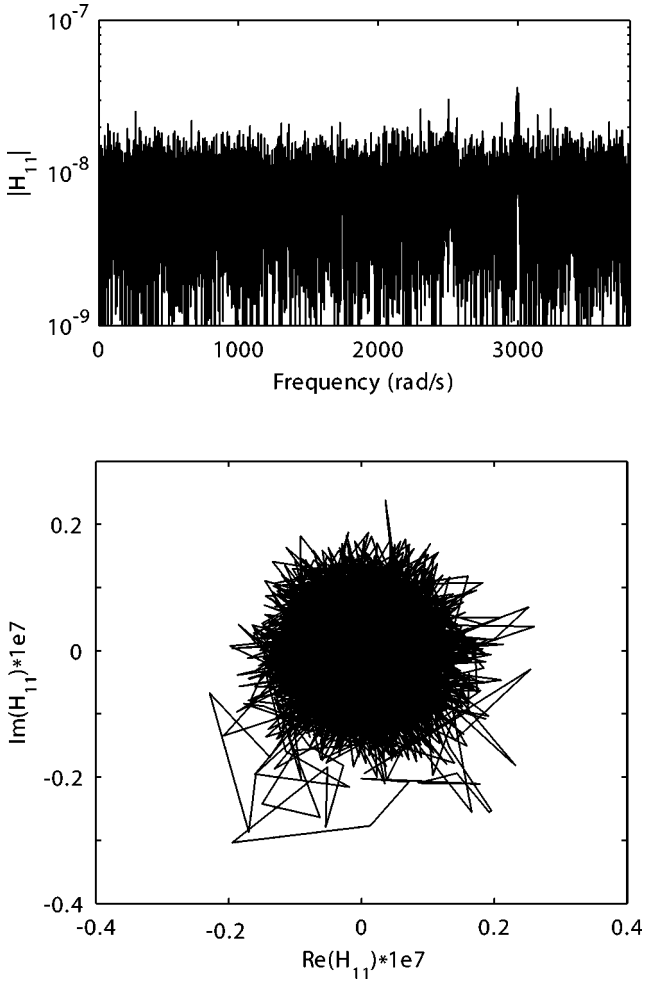

FIG. 3. Typical subtraction residual after removal of the first seven modes.

the seventh eigenvalue/residue estimate. Computing the subtraction residual FRF in Step (S.3) leads to the plots in Fig. 3, which are examined in Step (S.4). Although the Bode plot shows evidence of a small peak in the vicinity of 3000 rad/s, the Nyquist plot shows no evidence of a regular arc. This indicates that the data is incoherent, so even if the peak actually corresponds to a mode, the identification of its properties would be unreliable. Consequently, the search is discontinued, and processing proceeds to the Isolation Phase with $N=7$.

Under ideal circumstances, processing the FRF for the jth displacement coordinate as described in the preceding would give an estimate of λ_k and $A_{jP,k}$ for $k=1,...,N$. Subjecting each displacement dataset to the same processing then would lead to N_0 estimates of each of the λ_k values, and a single estimate of each $A_{jP,k}$ coefficient for $j=1,...,N_0$. In such ideal circumstances, each set of λ_k for fixed k would be averaged. However, as illustrated by Figs. 1–3, weakly excited modes or modes whose amplitude is small at the measurement location actually might not be identified in a specific FRF dataset. If such is the case, the missing values are merely omitted when average eigenvalues are computed.

There also might be noticeable discrepancies between corresponding eigenvalues obtained from different FRF sets. This leads to the question of whether the individual estimates

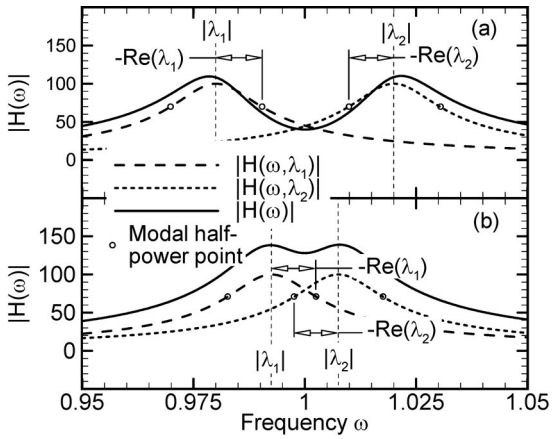

FIG. 4. Frequency response function formed by summing the FRFs of two modes having close natural frequencies. (a) $A_{1P,1}=A_{1P,2}=1$, $\lambda_1=-0.01+0.98i$, $\lambda_2=-0.01+1.02i$; (b) $A_{1P,1}=A_{1P,2}=1$, $\lambda_2=-0.01+0.9975i$, $\lambda_2=-0.01+1.0025i$.

should be merged by averaging, or whether differences of estimates are sufficiently large to consider the eigenvalues to be distinct. The criterion that was implemented compares the difference of adjacent natural frequencies, $|\lambda_{k+1}|-|\lambda_k|$, to the modal bandwidths. For a single mode, the bandwidth is $-2\,\mathrm{Re}(\lambda_k)$.[12] Subtracting from the frequency difference the half-bandwidth for each mode yields the frequency interval between the adjacent half-power points belonging to two peaks. This is illustrated in Fig. 4, where a FRF $H(\omega)$ is synthesized from the contributions $H(\omega,\lambda_1)$ and $H(\omega,\lambda_2)$ of two neighboring modes having equal residues. In Fig. 4(a), $|\lambda_2|-|\lambda_1|$ is greater than the sum of the half-bandwidths, and the peaks of the FRF are quite distinct. In Fig. 4(b) $|\lambda_2|-|\lambda_1|$ is less than the sum of the half-bandwidths, which means that the bandwidths overlap. The peak FRF is a merger of the individual peaks, with a flattened region that shows a dimple. The sum of the half-bandwidths is the average bandwidth. Modal overlap corresponds to an average bandwidth that substantially exceeds the frequency difference. Experience has shown that the linear least squares identification algorithm described later usually will distinguish between eigenvalues *in a single FRF* if the difference of adjacent undamped natural frequencies significantly exceeds 40% of the average bandwidth. Based on this observed behavior, eigenvalues obtained from different FRFs are considered to be distinct if they fit a similar specification, specifically,

$$|\lambda_{k+1}|-|\lambda_k|>0.4[-\mathrm{Re}(\lambda_k)-\mathrm{Re}(\lambda_{k+1})]. \tag{10}$$

Conversely, adjacent eigenvalues are averaged if they do not meet this specification. It should be noted that incorrectly merging modes having distinct eigenvalues results in their being treated as two (or more) modes that share the same eigenvalue. The full identification of such modes requires a MIMO algorithm; see Maia *et al.*[1]

III. SINGLE MODE PARAMETER IDENTIFICATION

Both the Subtraction and Isolation Phases require that one identify the properties of a single mode that best fit the FRF data in the vicinity of a resonance peak. Ginsberg

et al.[11] derived a linear least squares procedure for this purpose. The first step is to combine the two terms associated with a single mode in Eq. (6). This gives

$$H_{jP}(\omega)=2\,\frac{[i\omega-\mathrm{Re}(\lambda_k)]\mathrm{Re}(A_{jP,k})-\mathrm{Im}(\lambda_k)\mathrm{Im}(A_{jP,k})}{|\lambda_k|^2-\omega^2-2i\omega\,\mathrm{Re}(\lambda_k)}. \tag{11}$$

Clearing the denominator in Eq. (11) and breaking the result into real and imaginary parts then leads to

$$\mathrm{Re}[H_{jP}(\omega)](|\lambda_k|^2-\omega^2)+2\omega\,\mathrm{Im}[H_{jP}(\omega)]\mathrm{Re}(\lambda_k) = -2[\mathrm{Re}(\lambda_k)\mathrm{Re}(A_{jP,k})+\mathrm{Im}(\lambda_k)\mathrm{Im}(A_{jP,k})] \tag{12}$$

$$\mathrm{Im}[H_{jP}(\omega)](|\lambda_k|^2-\omega^2)-2\omega\,\mathrm{Re}[H_{jP}(\omega)]\mathrm{Re}(\lambda_k) = 2\omega\,\mathrm{Re}(A_{jP,k}). \tag{13}$$

Both equations are linear in four variables: $|\lambda_k|^2$, $\mathrm{Re}(\lambda_k)$, $\mathrm{Re}(A_{jP,k})$, and $[\mathrm{Re}(\lambda_k)\mathrm{Re}(A_{jP,k})+\mathrm{Im}(\lambda_k)\mathrm{Im}(A_{jk})]$. In principle, evaluating this pair of real equations at two arbitrary frequencies would yield four linear simultaneous equations that could be solved for the unknowns, from which the values of λ_k and $A_{jP,k}$ could be extracted. In practice, the evaluation of Eqs. (12) and (13) at two frequencies is not sufficient for a variety of reasons. Hence, the strategy is to evaluate the equations at a multitude of frequencies, from which the four combination variables are determined by a linear least-squares procedure.

Not all of the FRF data is used to obtain the least squares solution. Selecting values increasingly far from the vicinity of a resonance enhances the contribution of other modes to the FRF, thereby defeating the notion that a single mode can be fit. Also, for additive white noise the best signal-to-noise ratios are at the resonance peaks. However, there are not likely to be many FRF values at a resonance unless the frequency increment is very fine. Furthermore, raising the number of values to be matched by using FRF values away from a resonance affords a greater opportunity for distributing the error. This dilemma was explored by Ginsberg *et al.*[11] through a Monte Carlo study. They found that using all FRF points above the quarter-power points gave the best results for uniformly distributed random noise at several levels. This criterion is met by selecting for the least-squares fit only those values of $H_{jP}(\omega)$ that satisfy $|H_{jP}(\omega)|\geqslant\delta\max(|H_{jP}(\omega)|)$, where $\delta=0.5$ yields the quarter-power points.

IV. IMPROVEMENT FOR LOW MODAL MOBILITY

In the original conception of AMI the residue factors $A_{jP,k}$ obtained from a set of FRF data were used to calculate normal modes according to

$$U_{Pk}=\left(\frac{A_{PP,k}}{\lambda_k}\right)^{1/2},\quad U_{jk}=\left(\frac{A_{jP,k}}{\lambda_k U_{Pk}}\right),\quad j\neq P. \tag{14}$$

A problematic aspect of the preceding arises if a generalized displacement has a near nodal value in some mode. Let J denote the number of this generalized displacement and let K denote the mode at which this condition occurs. Because U_{JK} is very small, the signal-to-noise ratio for $H_{JP}(\omega)$ will be poor when $\omega\approx\Omega_K$.

Consequently, there will be no evidence of the Kth mode's contribution when the FRF dataset for displacement J is processed, resulting in a missing value of $A_{JP,k}$ and failure to estimate λ_K from that FRF. Two possibilities exist. The simpler situation corresponds to $J\neq P$, that is, the near-nodal measurement point is not the location where the system was driven. If the transfer functions for other displacements in the vicinity of $\omega=\Omega_K$ have reasonable signal-to-noise ratios, then processing the $H_{jP}(\omega)$ datasets for $j\neq J$ will lead to a reasonable estimate for λ_K and $A_{jP,K}$. As explained previously, averaging the estimates of λ_K will ignore the missing value. Also, the missing residue factor $A_{JP,K}$ may be considered to be zero, so the normal mode coefficients may be computed according to Eqs. (14).

The situation is much worse if the near-nodal measurement point is the location where the system was excited, $J=P$. If one were so unfortunate as to drive the system at a true modal node, so that $U_{PK}=0$, the Kth mode would not be excited. In that case, identifying mode K would require redoing the measurements with a different drive point. The more likely circumstance is that U_{PK} is very small, but nonzero. In that case smallness of the first denominator in Eq. (6) when $\omega_m\approx\Omega_K$ might lead to $H_{jP}(\omega)$ values for $j\neq P$ that have good signal-to-noise ratios in the vicinity of ω_K. This would make it possible for AMI to estimate λ_K and $A_{jP,K}$ for $j\neq P$ from those other displacements. However, the failure to identify mode K from the data for displacement P would leave the coefficient $A_{PP,K}$ undetermined. It therefore would not be possible to identify the normalized mode coefficients according to Eqs. (14).

In the last case, one could readily extract an estimate of a relative mode shape according to

$$U_{nK}/U_{jK}\equiv A_{nP,K}/A_{jP,K}. \tag{15}$$

Here $A_{jP,K}$ is a residue factor that has been identified as being nonzero, and $A_{nP,k}$ would be considered to be zero for any missing values. However, a simple change in the strategy for using AMI ensures that if an estimate of λ_K is obtained from *any* FRF dataset, then an estimate for *all* corresponding normal mode coefficients will be obtained. Some existing algorithms in their later stages use known eigenvalues to estimate eigenvectors through a global fit of all FRF data; see Richardson and Formenti,[9] for example. This notion is eminently suitable for the present situation. If the eigenvalues are taken to be known, then the only unknowns in Eq. (6) are the $A_{jP,k}$ coefficients, which occur there linearly. Many values of $H_{jP}(\omega)$ are available, corresponding to numerous frequencies and each of the displacements. Therefore, the right side of Eq. (6) can be matched to the measured values of $H_{jP}(\omega)$ in a linear least-squares procedure, which is relatively efficient, and not iterative. The result is that a value is obtained for every $A_{jP,k}$ coefficient for which a value of λ_k has been estimated, and consequently that an estimate for each mode vector will be obtained.

To implement the procedure in the current context, each FRF is broken into real and imaginary parts, which leads to an error function for each part. The squared errors to be

minimized are the inner products of the total error vector formed from the individual errors at each frequency,

$$R_j^{(1)} = \sum_{m=1}^{M} \left[\mathrm{Re}(H_{jP}(\omega_m)) - \mathrm{Re} \sum_{k=1}^{N} \left(\frac{A_{jP,k}}{i\omega_m - \lambda_n} + \frac{A_{jP,k}^*}{i\omega_m - \lambda_k^*} \right) \right]^2,$$
$$R_j^{(2)} = \sum_{m=1}^{M} \left[\mathrm{Im}(H_{jP}(\omega_m)) - \mathrm{Im} \sum_{k=1}^{N} \left(\frac{A_{jP,k}}{i\omega_m - \lambda_k} + \frac{A_{jP,k}^*}{i\omega_m - \lambda_k^*} \right) \right]^2. \quad (16)$$

As was done for the SDOF identification of the eigenvalues, the frequencies ω_m are selected to be close to each identified natural frequency, so that the $H_{jP}(\omega_m)$ used for the fit have the best signal-to-noise ratio. The presence of the residue factors and their complex conjugates in the preceding is most readily handled by considering the real and imaginary parts of each $A_{jP,k}$ to be distinct unknowns. Applying the linear least squares procedure to $R_j^{(1)}$ and $R_j^{(2)}$ individually for a specific j yields both parts of $A_{jP,k}$ for $k=1,...,N$. Hence, a full evaluation of the normal modes entails repeating the procedure for each FRF dataset, $j=1,...,N_0$. The normal mode coefficients are then calculated according to Eqs. (14).

V. DISCUSSION

The algorithm of mode isolation (AMI) is an iterative procedure for extracting modal properties from frequency response functions (FRFs). Each FRF is fit to the analytical form, which consist of a sequence of poles that define the natural frequencies and modal damping ratios, and residue factors, from which the mode vectors are extracted. Each step of the two iterative phases focuses on a single mode's contribution.

The latest version of AMI uses linear least-squares routines to identify that mode's eigenvalue and residue factors. Separate identifications are performed on each FRF, leading to multiple estimates. The eigenvalues obtained from each FRF are averaged using a specified merging criterion. Instead of using the residue factors obtained by processing the individual FRFs, the third phase of the procedure uses the average eigenvalues as inputs to a linear least-squares identification that yields a global estimate of all residue factors. These modifications improve the accuracy, as well as the computational efficiency of the identification, because linear least-squares is a not iterative, and it does not depend on having a good initial guess for the desired parameters.

The computational efficiency of AMI also is enhanced by the fact that only a subset of the FRF data is processed. The frequency increment for a FRF must be a fraction of the smallest modal bandwidth, in order to recognize the existence of all modes. Consequently, the number of frequency samples is inherently very large in comparison to the number of modes to be identified. MDOF identification algorithms in current use estimate the parameters by fitting all of the response data to the modal representation. As a result, the associated computational effort is scaled by the size of the dataset. In contrast, the effort entailed in AMI's identification processes is scaled by the relatively small number of FRF values that reside close to resonance peaks. In fact, the bulk of operations for AMI are devoted to forming the subtraction and isolation residuals.

Another aspect of the question of efficiency revolves around the need to identify as part of the overall process the number of modes whose natural frequency resides in the frequency interval of interest. Other MDOF techniques begin with an *a priori* guess for the number of modes, so that multiple such guesses are usually tried in order to identify which modes are computational artifacts. In AMI, the number of modes is obtained directly as part of the overall procedure. As a result, the FRF data is processed only once.

One overall limitation of AMI that was identified concerns modes that are very closely spaced. Trials using data for a two-degree-of-freedom system whose FRF are noise-free indicated that the two complex modes could not be identified if their natural frequencies differed by less than 40% of the average of their bandwidth. Recognition of this limitation was built into the general procedure. When AMI is applied to systems whose modes have this characteristic, the outcome is the identification of a single mode whose properties match the combined FRF contributions of the individual modes. In general, the robust identification of modes whose natural frequencies are extremely close requires a MIMO procedure. Work on such a version of AMI is presently underway.

ACKNOWLEDGMENT

This material is based on work supported under a National Science Foundation Graduate Research Fellowship.

[1] N. M. M. Maia, J. M. M. Silva, J. He, N. A. J. Lieven, R. M. Ling, G. W. Skingle, W.-T. To, and A. P. V. Urgueira, *Theoretical and Experimental Modal Analysis and Testing* (Research Studies Press, Ltd., Taunton, Somerset, England, 1997), Chap. 4.

[2] D. J. Ewins, *Modal Testing: Theory, Practice and Applications*, 2nd edition (Research Studies Press Ltd., Baldock, Hertfordshire, England, 2001), Chap. 4.

[3] R. J. Allemeng and D. L. Brown, "A unified matrix polynomial approach to modal identification," J. Sound Vib. **211**, 301–322 (1998).

[4] S. W. Doebling, K. F. Alvin, and L. D. Peterson, "Limitations of state-space system identification algorithms for structures with high modal density," *Proceedings of the 12th International Modal Analysis Conference*, Honolulu, HI, 1994, pp. 633–637.

[5] M. V. Drexel and J. H. Ginsberg, "Mode isolation: a new algorithm for modal parameter identification," J. Acoust. Soc. Am. **110**, 1371–1378 (2001).

[6] Y.-D. Joh and C.-W. Lee, "Excitation methods and modal parameter identification in complex modal testing of rotating machinery," Int. J. Anal. Exp. Modal Anal. **8**, 179–203 (1993).

[7] M. V. Drexel and J. H. Ginsberg, "Modal parameter identification using state space mode isolation," *Proceedings of the 19th International Modal Analysis Conference*, Orlando, FL, 2001.

[8] M. V. Drexel, J. H. Ginsberg, and B. R. Zaki, "State space implementation of the algorithm of mode isolation," Trans. ASME, J. Vib. Acoust. **125**, 205–213 (2003).

[9] M. H. Richardson and D. L. Formenti, "Global curve-fitting of frequency response measurements using the rational fraction polynomial method," *Proceedings of the 3rd International Modal Analysis Conference*, Orlando, FL, 1985.

[10] B. R. Zaki, *A Modified Approach to Improve the Robustness of the Algo-*

rithm of Mode Isolation, Ph.D. thesis, Georgia Institute of Technology, Atlanta, GA, 2002.
[11] J. H. Ginsberg, M. Allen, A. Ferri, and C. Moloney, ''A general linear least squares sdof algorithm for identifying eigenvalues and residues,'' *Proceedings of the 21st International Modal Analysis Conference*, Orlando, FL, 2003.
[12] J. H. Ginsberg, *Mechanical and Structural Vibrations: Theory and Applications* (Wiley, New York, 2001), Chap. 10.

A linear least-squares version of the algorithm of mode isolation for identifying modal properties. Part II: Application and assessment

Matt Allen and Jerry H. Ginsberg
G. W. Woodruff School of Mechanical Engineering, Georgia Institute of Technology, Atlanta, Georgia 30332-0405

(Received 28 October 2003; revised 23 April 2004; accepted 5 May 2004)

The latest modifications of the algorithm of mode isolation (AMI) for identification of modal properties from frequency response data are tested with synthetic data derived from an analytical model of an elastic frame in which flexure and torsion are coupled. The parameters of this model are selected to cause the occurrence of localized modal patterns in two modes having close natural frequencies. The response data is contaminated with white noise at a level sufficient to almost mask the two close modes. Results for the real and imaginary part of the eigenvalues are tabulated. The analytical modal patterns of displacement and torsional rotation are depicted graphically, accompanied by the discrete values obtained from AMI. Excellent agreement is found to occur for each mode, other than one of the pair of close modes. The poorer quality of that mode's identified properties is shown to be a consequence of its localized modal pattern. Results for the eigenvalues obtained by the rational fraction polynomial algorithm, which is an alternative modal identification technique, are found to be substantially less accurate as a consequence of difficulty in the presence of noise. [DOI: 10.1121/1.1765196]

PACS numbers: 43.40.Le, 43.40.Cw, 43.40.Yq [JGM] Pages: 908–915

I. INTRODUCTION

Part I[1] described an iterative procedure that extracts the modal properties of a vibratory system from measured frequency response data. The procedure is called the algorithm of mode isolation (AMI) because its primary feature entails isolating a single mode's contribution to each frequency response function (FRF). The first effort[2] was founded on a classical undamped modal representation of an FRF. A formulation fitting FRFs to a damped modal description was described subsequently.[3,4] The new features of AMI developed in Part I were its implementation of linear least squares for all aspects of parameter identification. The present paper examines AMI's performance under conditions where modal identification is known to encounter difficulty.

One faces a philosophical dilemma in deciding how to assess any algorithm for experimental modal analysis. Response data can be derived from an analytical model and then contaminated by a standard noise model. Using such data as the input to the algorithm leaves no ambiguity as to what the modal parameters should be, for they are available from the analytical model. However, such a line of investigation does not address how the algorithm would perform when applied to actual measured response data, where the noise might not fit a standard model, and where nonrandom errors may be present. The problem with using actual measured data is that there is no way of knowing exactly what the actual modal properties are, because ideal features, such as a clamped end condition for a beam, cannot be reproduced exactly, and prediction of dissipation effects from first principles is beyond present capabilities for built-up systems. It is for this reason that the present effort uses synthetic data derived from an analytical model.

Any modal analysis algorithm can be expected to have the most difficulty in systems that have close natural frequencies, weakly excited modes, and low signal-to-noise ratios in their measured data. Prior works have used relatively simple systems to examine the accuracy of AMI in the presence of these problematic features. The initial effort[2] used data derived from a four-degree-of-freedom system with substantial non-proportional damping. That system had previously been used by Roemer and Mook[5] to test a modification of Juang and Suzuki's frequency domain eigenvalue realization algorithm.[6]

The next model used to test AMI was a cantilevered beam with three suspended spring-mass-dashpot systems.[3,4] This system was a simplified version of one used by Strasberg and Feit[7] to examine energy transfer between structural components. In addition to permitting exploration of the role of noise, the small size of the suspended masses caused two modes to have natural frequencies that were closer than their bandwidths. This led to modal coupling, which refers to the merger in an FRF of resonance peaks that otherwise would be distinct. The small size of the suspended masses also led to a pair of modes that are weakly excited, and therefore readily masked by noise. (In fact, as will be evident here, high damping, close natural frequencies, and high noise levels mingle in their effect.) One consequence of tuning the subsystems to give the desired modal properties was that the first four modes were well separated from the high-frequency modes, which substantially simplified the identification task. The performance of AMI for this model was assessed solely by comparing its predictions to the analytical modal properties. It was found that AMI worked well at identifying the natural frequencies and modal damping ratios, even in the presence of substantial additive white noise. However, some

normalized mode vectors could not be found because they were weakly excited.

The need to improve the identification of weakly excited modes led to Zaki's modification of AMI,[8] in which identification of the normal mode coefficients was deferred until the natural frequencies and modal damping ratios had been determined. The data he used to test this revision was synthesized from an analytical model of a frame composed of two orthogonally welded cantilevered beams loaded out-of-plane, which couples flexure and torsion. One reason for using this model is that many modes are required to describe its response. Also, the system parameters were adjusted such that mode coupling occurred. Various levels of white noise were added to test the limits of AMI, but the sole assessment criterion for AMI's performance was how well it identified the analytical modal properties.

The exposition in Part I incorporated Zaki's modification, as well as a linear least squares routine for extracting the eigenvalues from the FRF data. The present objective is to assess the performance of this latest version of AMI. The data to be analyzed is obtained from Zaki's elastic frame model. An additional measure beyond comparison with the analytical modal properties will be a comparison of AMI's values to those obtained by the Rational Fraction Polynomial algorithm first proposed by Richardson and Formenti,[9] and then modified by many investigators, as detailed by Formenti and Richardson[10], in order to improve the algorithm's numerical stability and accuracy.

Zaki used Ritz series to formulate the system equations for the frame structure. Further examination of that analysis revealed that the series diverged because of a poor choice of the Ritz basis functions. The model development presented here corrects this. However, it should be noted that after Zaki reduced the model to a finite number of degrees of freedom, all subsequent work depended only on that reduced order model. Consequently, the modal identification was consistent with the erroneous analytical modal properties, and Zaki's findings regarding AMI were consistent.

The frame's parameters in the present work are adjusted such that two modes have close natural frequencies, and sufficient damping is introduced to cause modal coupling. Furthermore, these close modes display patterns of displacement and rotation that are localized to one span, and the degree to which flexure and torsion are coupled generally varies strongly between modes. Hence, there is a large variation in FRF magnitudes at various peaks.

II. ELASTIC FRAME PROTOTYPE

The parameters of an exercise offered by Ginsberg[11] are adjusted to obtain a system in which a pair of modes are coupled. It consists of two cantilevered beams that are oriented orthogonally and welded at their free ends, as depicted in Fig. 1. Their junction has the effect of coupling the out-of-plane flexural displacement w and torsional rotation θ. Each beam has a solid circular cross section with 100 mm radius, modulus of elasticity $E=70\times10^9$ Pa, modulus of rigidity $G=26.32\times10^9$ Pa, and 2700 kg/m^3 density. The span lengths are set at $L_1=4$ m, $L_2=3.85$ m. Two transverse dampers, $c_1=c_2=155.88$ N-s/m, oriented out-of-plane are

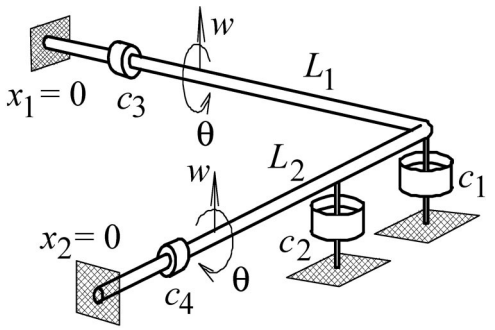

FIG. 1. L-shaped frame cantilevered at both ends with attached dashpots.

placed at $x_1=4$ m and $x_2=3$ m. In addition, two torsional dampers, $c_3=c_4=77.94$ N-s-m/rad, are placed at $x_1=x_2=1$ m.

The span lengths were selected because they lead to two modes having close natural frequencies and modal patterns that are localized to one span, as will be seen. This occurs because $L_2=L_1$ gives a symmetric system, so that setting L_2 slightly different from L_1 represents a small deviation from symmetry of a system consisting of weakly coupled components. As described by Pierre, Tang, and Dowell,[12] one cause of mode localization is weak coupling between two energy depositories that deviate slightly from perfect symmetry. In the present system, the energy depositories are the individual spans, and the coupling is provided by their welded connection. (An evaluation of the natural frequencies as a function of L_1 with L_1+L_2 held fixed would show veering of the eigenvalue loci, which often accompanies mode localization, as shown by Chen and Ginsberg.[13]) Because the modes having close natural frequencies also have regions of low modal response, the selected values of L_1 and L_2 lead to a strong test of AMI's capabilities.

To construct an analytical model of the system the transverse deflection and torsional rotation of each beam are represented by Ritz series, with the associated Ritz coefficients serving as generalized coordinates for the system. The expansions for beam $n=1$ or 2 are given by

$$w(x_n,t)=\sum_{j=1}^{N_R}(\Psi_w^{(n)})_j(q_w^{(n)})_j,$$
$$\theta(x_n,t)=\sum_{j=1}^{N_R}(\Psi_\theta^{(n)})_j(q_\theta^{(n)})_j. \tag{1}$$

A similar model was constructed by Zaki[8] using monomial functions, but they lead to numerical problems due to ill-conditioning when the series length is increased beyond $N_R=5$. For that reason, the eigenfunctions of a clamped-free beam are used as the basis functions for both beams. These are

$$(\Psi_w^{(n)})_j=\sin\left(\alpha_j\frac{x_n}{L_n}\right)-\sinh\left(\alpha_j\frac{x_n}{L_n}\right)-R_j\left[\cos\left(\alpha_j\frac{x_n}{L_n}\right)-\cosh\left(\alpha_j\frac{x_n}{L_n}\right)\right], \tag{2}$$

$$R_j=\frac{\sinh(\alpha_j)+\sin(\alpha_j)}{\cosh(\alpha_j)+\cos(\alpha_j)},\quad (\Psi_\theta^{(n)})_j=\sin\left[\frac{(2j-1)\pi x_n}{2L_n}\right]. \quad (3)$$

The response data presented here were obtained by truncating each series at $N_R=11$. Bernoulli–Euler beam theory gives functionals describing the kinetic and strain energy in terms of w and θ, while the Rayleigh dissipation function depends on w and θ at the dashpot locations. Substitution of Eqs. (1) into those expressions yields quadratic sums in the generalized coordinates or velocities. A similar operation applied to the virtual work yields the generalized forces. Lagrange's equations then leads to a set of $4N_R$ ordinary differential equations for the Ritz series coefficients.

The Lagrange equations do not couple the motion of the two beams. That effect is described by constraint conditions enforcing continuity of transverse displacement, and of rotation about the axis of each beam. It is required that

$$w(x_1=L_1)=w(x_2=L_2),$$
$$\left.\frac{\partial w}{\partial x_1}\right|_{x=L_1}=-\theta|_{x_2=L_2},\quad \left.\frac{\partial w}{\partial x_2}\right|_{x_2=L_2}=\theta|_{x_1=L_1}. \quad (4)$$

Substitution of the Ritz series into the preceding leads to three algebraic constraint equations that supplement the $4N_R$ Lagrange equations. The unknowns are the Ritz series coefficients and three Lagrange multipliers. An elimination process based on solving the constraint equations for three generalized coordinates reduces the system to a set of $4N_R-3$ differential equations. These equations may be solved through a state-space formulation for $8N_R-6$ eigenvalues. Heavy damping would lead to overdamped modes marked by pairs of real eigenvalues. The more usual case is underdamped modes, which correspond to pairs of complex conjugate eigenvalues. This is the situation for all modes of the present system, so there are $4N_R-3$ complex modes.

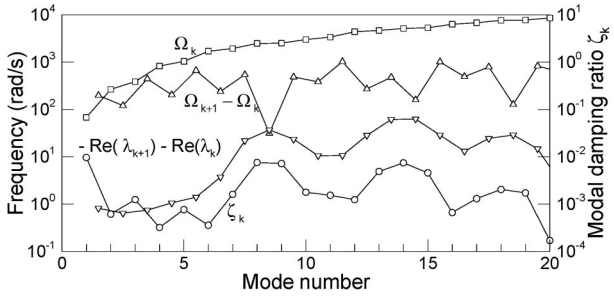

FIG. 2. Natural frequencies, modal damping ratios, frequency differences, and average modal bandwidths for the first twenty modes of the frame.

Figure 2 displays the eigenvalue properties. In addition to displaying the undamped natural frequencies, $\Omega_k=|\lambda_k|$, and modal damping ratios, $\zeta_k=-\mathrm{Re}(\lambda_k)/|\lambda_k|$, the frequency difference, $\Omega_{k+1}-\Omega_k$, and the average bandwidth, $-\mathrm{Re}(\lambda_{k+1})-\mathrm{Re}(\lambda_k)$ are plotted in order to assess the relative closeness of adjacent modes. As noted in the discussion in Part I, Eq. (10), one can anticipate that the FRFs will exhibit mode coupling whenever the frequency difference $\Omega_{k+1}-\Omega_k$ is less than $-\mathrm{Re}(\lambda_{k+1})-\mathrm{Re}(\lambda_k)$. This is the case for modes 8 and 9. Also notable is the wide range of damping ratios, which will be seen to significantly affect the data analysis.

The present work assesses AMI's performance when applied to synthetic FRF data describing the transverse displacement and torsional rotation at four locations on each beam: $x_1=1$, $x_2=2$, $x_3=3$, and $x_4=4$ m on beam 1 and $x_5=1$, $x_6=2$, $x_7=3$, and $x_8=3.85$ m on beam 2. Both beams have the same displacement at their junction. As a result, the data to be synthesized consists of fifteen impulse responses: Seven displacements and eight rotations, which are grouped to form a vector according to

$$\{y(t)\}=[w_1\ w_2\ w_3\ w_4\ \theta_1\ \theta_2\ \theta_3\ \theta_4\ w_5\ w_6\ w_7\ \theta_5\ \theta_6\ \theta_7\ \theta_8]^{\mathrm{T}}. \quad (5)$$

The FRF data will be a synthetic set mimicking an experiment in which a transverse impulsive force is applied at the first displacement point, so $P=1$. The impulse responses are obtained analytically by employing a modal transformation that leads to a set of uncoupled equations for the modal generalized coordinates. The impulse response of a modal coordinate has the general form $\xi_k=C_k\exp(\lambda_k t)$, where λ_k are the modal eigenvalues and the participation factors C_k depend on the modal coefficients for the drive point. The modal coordinates are evaluated at a uniform increment of time at a fixed sampling rate Δt within a window $0\leqslant t\leqslant t_{\max}$, based on sampling criteria discussed later. The state-space modal transformation then yields a data set describing the history of the unconstrained set of Ritz series coefficients. Values of the full set of Ritz series coefficients are then obtained from the solution of the constraint equations. Finally, the impulse responses of the $\{y\}$ variables are obtained by synthesizing the Ritz series, Eqs. (1). Replacing the series coefficients in Eqs. (1) with a state-space eigenvector leads to the corresponding modal displacement pattern. Details of each step of this analysis are provided by Ginsberg.[11]

The impulse response of each element of $\{y(t_n)\}$ is contaminated by white noise that is scaled relative to the peak magnitude of that variable, according to

$$y_j(t_n)_{\mathrm{corrupt}}=y_j(t_n)+\alpha\max_n\ (y_j(t_n))r_{jn}, \quad (6)$$

where $-1<r_{jn}<1$ is a uniformly distributed random number and α is a constant that scales the random value to the required fraction of signal amplitude (0.02 for the data analyzed here). Fast Fourier transform (FFT) processing of the contaminated impulse response data for each j yields the FRF $H_{jP}(\omega)$.

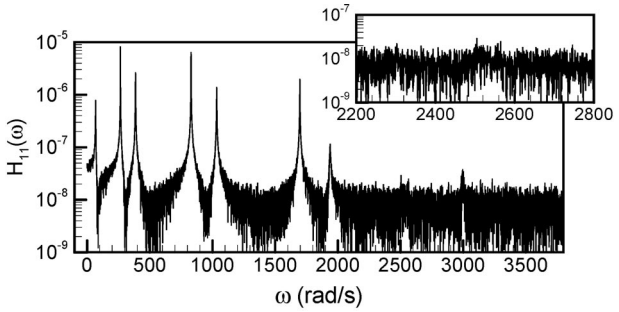

FIG. 3. Noise contaminated displacement FRF at $x=1$ m on beam 1.

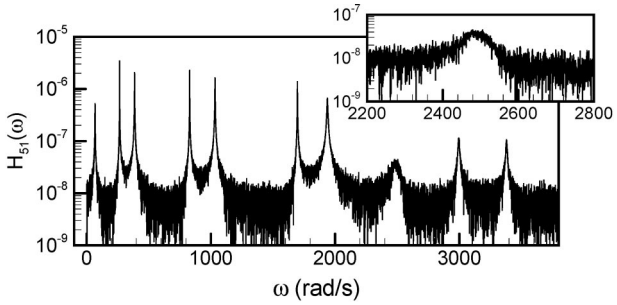

FIG. 5. Noise contaminated rotation FRF at $x=1$ m on beam 1.

III. RESULTS

The objective here is to assess the capability of AMI when the data has been sampled properly. Toward that end, the time window in which the impulse responses are sampled was set such that the slowest decaying complex modal coordinate reduced to an amplitude not exceeding 10^{-4} of its maximum. This is attained if $t_{\max}>\ln(10^4)/\min(|\mathrm{Re}(\lambda_k)|)$. The sampling rate was set by the Nyquist criterion for the highest natural frequency, which requires $\Delta t<\pi/\max(|\mathrm{Im}(\lambda_k)|)$. The values that were used are $t_{\max}=14.2$ s and $\Delta t=0.217$ ms, which corresponds to 2^{16} time values for each displacement variable. The frequency response data was truncated at $\omega=3800$ rad/s, so the length of a frequency data set processed by AMI was 8589 samples.

As previously described, the excitation index is $P=1$. Figure 3 shows $H_{11}(\omega)$, which is the noise-contaminated FRF at the drive point. Only seven resonant peaks are easily distinguished. For comparison, the noise-free analog in Fig. 4 shows ten peaks. However, eleven modes have natural frequencies in the plotted frequency band. The discrepancy of each figure between the number of peaks and the number of in-band modes is readily explained. In the case of the analytical data, the expanded window shows only one peak in the vicinity of modes 8 and 9. The missing peak is a combination of coupling of these modes, and poor excitation of one of them, as will be seen. Figure 3 corresponds to superposition of white noise onto Fig. 4. The level of this noise is comparable to the level of the resonant peaks above 2000 rad/s, resulting in masking of all high frequency peaks in the data to be processed by AMI.

To better understand the masking effect of noise consider the noise model invoked in Eq. (6), in which the noise amplitude in the time domain is constant and scaled by the peak impulse response. In the frequency domain this represents white noise whose level in an FRF also is scaled proportionately to the peak amplitude of the corresponding impulse response. Because the noise level is essentially flat in frequency, the signal-to-noise ratio of $H_{jP}(\omega)$ in the vicinity of a resonance peak is set by the magnitude of the corresponding noise-free data. When the damping is light, so that $|\mathrm{Re}(\lambda_k)|\ll\mathrm{Im}(\lambda_k)$, a resonance is well approximated as $\omega=\mathrm{Im}(\lambda_k)$. Combining Eqs. (4), (6), and (7) of Part I shows the peak FRF to be

$$(H_{jP})_{\mathrm{peak}}\approx i\frac{U_{jk}U_{Pk}}{\zeta_k}, \tag{7}$$

where U_{jk} is the kth modal coefficient for displacement j and ζ_k is the modal damping ratio. Thus, for a specified measurement point (fixed j) the modes k having the lowest peaks are those that are either the least responsive at the drive or measurement point, or most heavily damped. The normal mode functions for transverse displacement, which are presented later, decrease significantly with increasing frequency. Furthermore, Fig. 2 shows that modes 8 and 9 are the most heavily damped, other than mode 1. Thus, the FRF contributions of the high-frequency modes may be expected in general to be masked to a greater extent, with the effect especially noticeable for modes 8 and 9.

The FRF for the torsional rotation at the drive point, $H_{51}(\omega)$, is depicted in Fig. 5, while Fig. 6 is the noise-free version. These present a different picture, in that ten peaks are evident even in the noisy data. Modes 8 and 9 are still coupled, but the torsional modal responses at $x=1$ meter on the first beam is sufficient to exceed the added noise level. Careful examination of the enlarged view in Fig. 6 shows that there is a slight dimple in the coupled peak, which suggests the presence of multiple modes, but this feature is completely masked by the noise. Most of the other FRFs are like

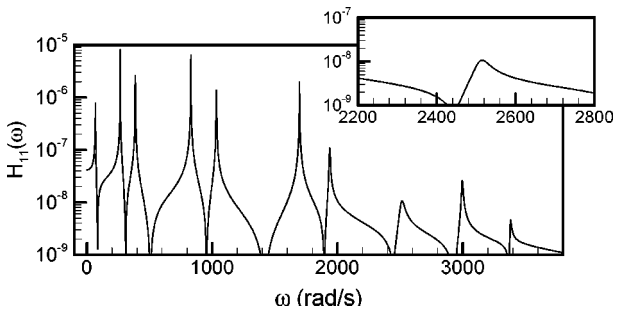

FIG. 4. Noise-free displacement FRF at $x=1$ m on beam 1.

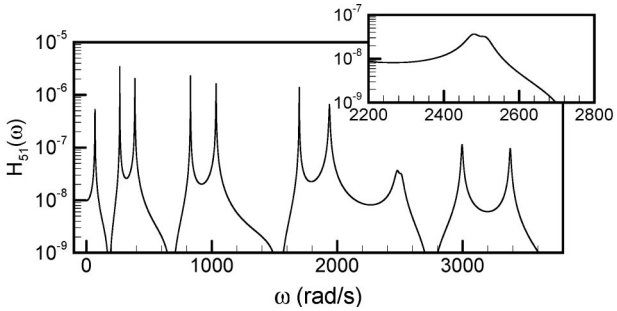

FIG. 6. Noise-free rotation FRF at $x=1$ m on beam 1.

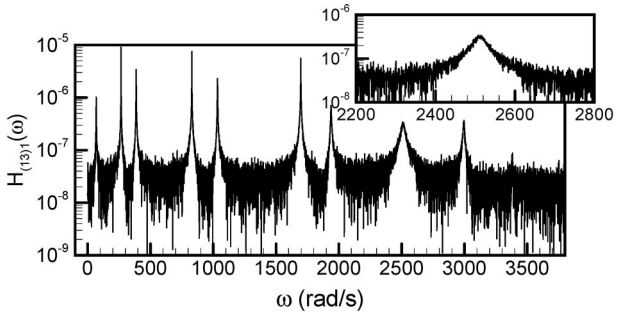

FIG. 7. Noise contaminated rotation FRF at $x=2$ m on beam 2.

Fig. 3, in that the resonances above 2000 rad/s are masked. However, a few show one or more peaks in the upper frequency range. Typical of the latter is Fig. 7, which depicts the torsional response at $x=2$ meter on beam 2. Overall, the first seven modal peaks occur in each FRF, but the number of higher frequency modes that appear ranges between zero and three.

Application of the first two stages of AMI to each FRF yields multiple estimates of the eigenvalues in the range below 3800 rad/s, at which the FRFs are truncated. Table I lists the number of eigenvalues and corresponding mode numbers obtained by processing each of the seven displacement FRFs and eight rotation FRFs. It is not surprising, given the fact that none of the FRFs display peaks at all eleven natural frequencies in this range, that in no case did processing an FRF give eleven eigenvalues. The first seven modes were identified in each FRF. For the closely spaced pair of modes, mode 8 was identified from a single FRF and mode 9 was identified in only three FRFs.

Except for modes 8 and 9, the magnitude of the analytical eigenvalues are quite distinct, as evidenced by Fig. 2. In those cases, averaging like eigenvalues identified in each FRF is straightforward. In contrast, because of their closeness, merging the eigenvalue results for modes 8 and 9 poses a dilemma, especially if one divorces themself from analytical knowledge of the eigenvalue structure. The difficulty arises because no single FRF yielded both eigenvalues. Thus,

TABLE I. Modes identified by processing each set of displacement data. (Maximum number of modes is 11.).

Displacement data set	Identified modes	
	#	Indices
(1) $w_1@x_1=1$	7	1–7
(2) $w_2@x_1=2$	7	1–7
(3) $w_3@x_1=3$	7	1–7
(4) $w_4@x_1=4$	7	1–7
(5) $\theta_1@x_1=1$	10	1–8, 10, 11
(6) $\theta_2@x_1=2$	9	1–7, 10, 11
(7) $\theta_3@x_1=3$	7	1–7
(8) $\theta_4@x_1=4$	9	1–7, 10, 11
(9) $w_5@x_2=1$	7	1–7
(10) $w_6@x=2$	7	1–7
(11) $w_7@x_2=3$	7	1–7
(12) $\theta_5@x_2=1$	10	1–7, 9, 10, 11
(13) $\theta_6@x_2=2$	9	1–7, 9, 10
(14) $\theta_7@x_2=3$	9	1–7, 9, 10
(15) $\theta_8@x_2=3.85$	8	1–7, 10

TABLE II. Identified eigenvalues for the 8th and 9th modes obtained by processing individual FRFs.

FRF #	Eigenvalue
5	$-22.876\pm2490.838i$
12	$-17.927\pm2510.592i$
13	$-17.153\pm2511.112i$
14	$-17.221\pm2510.661i$

these modes are a manifestation of the discussion in Part I as to whether eigenvalues obtained from different FRFs should be averaged or kept distinct. The results obtained from the four FRFs giving λ_8 or λ_9 are listed in Table II. One indication that the value obtained from FRF 5 does not belong to the values obtained from FRFs 12 to 14 is the fact that its real part deviates significantly from the other tabulated values. However, this difference might merely indicate that processing the eigenvalue obtained from FRF 5 has a much greater error than the other three. The question of whether to merge these eigenvalues is addressed by the distinctiveness criterion in Part I, Eq. (10). The values of $|\lambda|$ obtained from FRFs 12 to 14 are very close, with differences that are much less than either $-\mathrm{Re}(\lambda)$. Thus, the criterion is met by a large margin, leading to the conclusion that these three values of λ describe the same mode. In contrast, the largest average bandwidth using the tabulated λ from FRF 5 and any other FRF is 40.803 rad/s, while the smallest corresponding natural frequency difference 19.649 rad/s. The distinctiveness criterion is met (barely) in this case, so the eigenvalue obtained from FRF 5 is taken to be distinct from the others.

The statistics of the averaged imaginary parts of the eigenvalues are provided in Table III, while the corresponding information for the real parts appears in Table IV. The largest error in $|\mathrm{Im}(\lambda_k)|$ relative to the analytical value is 0.4% for mode 8, but the average error for all modes is 0.04%. Also note that the 21.7% error for $\mathrm{Re}(\lambda_8)$ is the largest, but the average error for all $\mathrm{Re}(\lambda_k)$ is 3.7%. For both parts the standard deviation is a small fraction of the corresponding mean value, especially for modes 1–7, which means that there was little scatter in the individual values. Equation (4) in Part I converts the eigenvalues to modal natural frequency and damping ratio. The average errors are found to be 0.04% for frequency and 3.7% for the damping ratios. (The fact that

TABLE III. Statistics of the identified natural frequencies.

Mode number	$\lvert\mathrm{Im}(\lambda)\rvert$		
	Analytical value	Mean	Standard deviation
1	68.008	68.005	0.0072
2	265.912	265.913	0.0022
3	386.325	386.332	0.0200
4	829.452	829.452	0.0008
5	1033.752	1033.754	0.0276
6	1697.012	1697.013	0.0047
7	1937.890	1937.912	0.0695
8	2479.743	2490.838	0.0000
9	2511.042	2510.788	0.2305
10	2995.661	2995.853	0.3833
11	3380.042	3380.367	0.4793

TABLE IV. Statistics of the identified modal decay rates.

Mode number	$-\mathrm{Re}(\lambda)$ Analytical value	Mean	Standard deviation
1	0.6565	0.6557	0.0080
2	0.1640	0.1641	0.0011
3	0.4826	0.4836	0.0040
4	0.2670	0.2670	0.0010
5	0.7935	0.7929	0.0146
6	0.6107	0.6115	0.0028
7	3.1205	3.0668	0.1123
8	18.7961	22.8759	0.0000
9	18.1254	17.4338	0.3496
10	5.3462	5.0665	0.5277
11	5.2109	4.7864	0.6445

these statistics are like those of the imaginary and real parts of each eigenvalue is a consequence of the former being much larger and more accurate than the latter.) This represents a substantial improvement over the previous AMI algorithm. Zaki[8] reported 1.73% average error in natural frequency and 12.68% in damping ratio. (As described in the Introduction, the system used by Zaki was slightly different, so this is not a perfect comparison.)

The transverse displacement and torsional rotation for the seven lowest frequency modes are depicted in Fig. 8; the abscissa is the distance along the centerline measured from the supported end of beam 1. Only the imaginary part of the mode function is displayed because the real parts of the mode functions are much smaller. For example, the most highly damped mode is the first, with a modal damping ratio of 0.0096. The ratio of the maximum imaginary part to the maximum real part of the displacement in this mode is 120. This ratio is substantially higher for the other modes. (It can be proven that damped modal analysis of an undamped system will lead to purely imaginary eigenvectors that match the undamped modes. The dominance of the imaginary part of

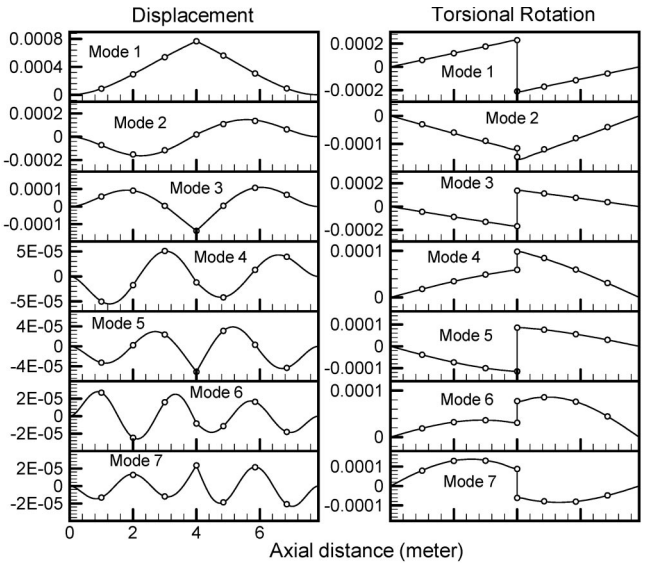

FIG. 8. Imaginary part of the modal amplitudes, modes 1–7; analytical value: ——, identified by AMI: ○.

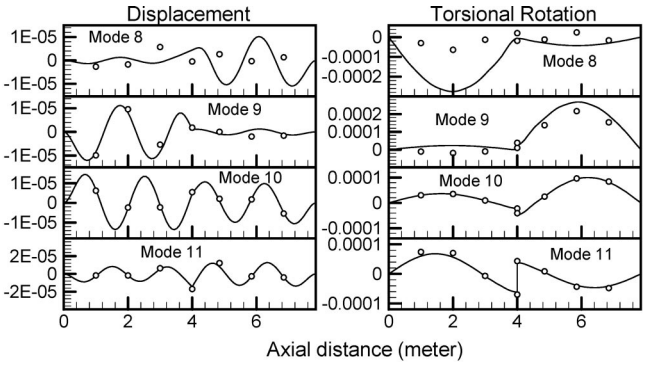

FIG. 9. Imaginary part of the modal amplitudes, modes 8–11; analytical value: ——, identified by AMI: ○.

the modal displacement here is a consequence of the smallness of the overall damping level.)

The two spans are nearly equal, but it is easier to interpret the analytical modes if one first considers the case of equal span lengths. The modes then would be either symmetric or antisymmetric. The definition of positive w and θ for each span is such that a symmetric pattern would consist of a function for w that is even with respect to the midspan, while the function for θ is odd. Thus, the odd numbered modes in Fig. 8 are comparable to the symmetric modes, and the even modes are like the antisymmetric modes. Increasing mode number is marked by an increase in the number of inflection points for w, but not for θ. This is a consequence of the fact that the beams are substantially stiffer in torsion than they are in flexure, so that the lower natural frequencies of the joined beams are well below the frequency at which either beam resonates in torsion.

It is evident that the first seven modes obtained from AMI are in close agreement with the analytical values. Even the jump in the torsional rotation at the juncture of the beams is captured. The seven displacement data points used to synthesize the data for AMI give a good picture of the torsional rotation for each mode in Fig. 8, and they adequately sample the displacement pattern in the first five modes.

Figure 9 indicates that there also is good agreement between AMI's identification and the analytical values of modes 10 and 11, although it is evident that the analytical modes have been undersampled. This figure also shows that the differences between the identified and analytical modal displacements are substantial for mode 8, while the discrepancies for mode 9 are less severe. Not shown is the fact that the AMI prediction for mode 8 has a real part that is not small compared to the imaginary part. Furthermore, the identified real part shows an irregular pattern for both displacement and torsional rotation. Modes 8 and 9 are the ones whose natural frequencies are close, with significant damping, but another factor also is responsible for the errors in the modes shapes. To recognize this consider the analytical mode functions. In mode 8 there is little displacement in the left span, $x<4$ m, and little torsional rotation in the right span. This pattern is reversed for mode 9. Situations like this are recognized as mode localization phenomena, described by Pierre, Tang, and Dowell.[12]

The significance of the occurrence of mode localization

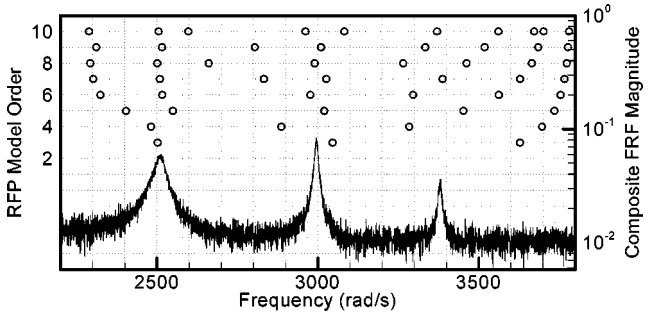

FIG. 10. Stabilization chart corresponding to results from the RFP algorithm for a range of model orders. Im(λ_k) obtained from RFP: ○, composite FRF: ——.

lies in Eq. (7). The excitation used to construct the present data set was a transverse force at $x=1$ m on the first span. Examination of the displacement functions in Fig. 9 shows that mode function 8 at $x=1$ m is an order of magnitude smaller than mode function 9. Hence, the lower frequency mode is much more weakly excited. At most locations, the 8th modal response is masked by the noise, which is scaled by the maximum displacement at that location, or else it is dominated by the 9th modal response because of mode coupling. The one FRF from which mode 8 was identified was the torsional response at $x=1$ m on the first span. Observe in Fig. 9 that because of mode localization, the 9th modal response is very weak along this span, thereby leaving an opportunity for mode 8 to appear.

For comparison purposes, the noise-contaminated FRF data sets were analyzed using the rational fraction polynomial (RFP) method. This is an MDOF method in which an FRF is represented as a ratio of polynomials in $(i\omega)$. Clearing the denominator leads to

$$H_{jP}(\omega)\sum_{k=1}^{2N} b_k(i\omega)^k = \sum_{k=1}^{2N-1} a_k(i\omega)^k, \tag{8}$$

where N is the system order for the data fit. When this expression is evaluated at many frequencies where the FRF value is known, the result is a set of linear equations for the a_k and b_k coefficients that are solved in a least-squares sense. The eigenvalues and residues are readily obtained from these coefficients. The RFP version that was implemented follows the development provided by Maia *et al.*,[14] including the application of orthogonal polynomials. This version concurrently processes all FRFs, thereby leading to a single global estimate of the eigenvalues. However, numerical ill-conditioning was found to occur when the full data set was processed at the higher system orders. For this reason the full frequency range was decomposed into three bands that contained modes 1–5, 6 to 7, and 8–11, and the system order was limited to be ten or less.

Because RFP requires an initial guess as to the number of participitory modes, computations within each frequency band were carried out with a range of guesses up to a maximum of ten. A stabilization chart[15] was constructed to identify which modes were consistently identified. Figure 10 shows the stabilization chart for the frequency band containing modes 8–11. Like AMI, this implementation of RFP had the greatest difficulty in this range. The marks in the chart indicate the frequencies, $|\lambda_k|$ identified by RFP for each model order from three to ten. The FRF that accompanies these values is a composite obtained by adding the absolute value of the fifteen individual FRFs at each frequency. It serves to pictorially indicate where natural frequencies might reside. At each peak no consistent pattern is observed, with the scatter at the second and third peaks being quite substantial. Also, the apparent convergence to an eigenvalue at 3800 rad/s should be ignored because it is at the limit of the frequency band. Note that there is no system order at which the stabilization chart indicates the presence of two modes in the vicinity of 2500 rad/s, where modes 8 and 9 are situated.

Because of the limitation on the system order, no consistent pattern was recognized. For this reason, the RFP results discussed here are for the model order that yielded estimated natural frequencies closest to the analytical values. For the lower and upper frequency bands the best results were obtained when the system order was set to nine, while a system order of six gave the best results for modes 6 and 7. For the first seven modes, RFP showed an average error in Im(λ_k) of 0.22%, with a worst case of 1.2% for mode 1. The corresponding errors for Re(λ_k) were 7.1% average, with a worst case error of 24.8% for mode 2. Mode 8 was not detected at all by RFP. For modes 9–11, the average error of Im(λ_k) was 0.68% with a worst case of 1.36% for mode 11. Mode 11 also had the largest error for Re(λ_k), at 60%, while the average error of Re(λ_k) for these modes was 24%. These statistics are substantially worse than those for AMI, as described by Tables III and IV. Also, AMI did succeed in identifying mode 8.

IV. SUMMARY AND CONCLUSIONS

The performance of the linear-least-squares version of AMI was tested with synthetic data derived from an analytical model of an elastic frame formed by joining two cantilever beams at right angles. The frame is loaded out-of-plane, so the welded connection couples flexure and torsion. The synthetic response data were derived by using Ritz series to represent the transverse displacement and torsional rotation. The temporal response to a transverse impulse force at the quarter-point of one span was obtained by applying state space modal analysis. The impulse responses of the Ritz coefficients were discretely sampled, and used to synthesize the transverse displacement and torsional rotation at eight cross-sectional locations. Each impulse response was contaminated be adding uniformly distributed random noise. The data then was FFT processed to produce FRFs that were input to the modified AMI. Generally, the best signal-to-ratios are obtained at resonance peaks, which are the regions from which AMI selects the data for its numerical fits. However, the manner in which the white noise was scaled resulted in masking the higher frequency resonance peaks in most FRFs.

The span lengths of the model were selected to be nearly equal, which resulted in the occurrence of a pair of modes, 8 and 9, having close natural frequency and modal patterns that are localized to one span. The damping of these modes was sufficient to cause the individual resonant peaks to merge, in the phenomenon known as modal coupling. The

role of noise was magnified by the localized nature of these modes, which weakened the modal excitation of one and the modal response of the other.

The frequency band that was processed contained eleven modes. AMI identified the first seven modes when each of the fifteen FRFs were processed, but the higher frequency modes were sparsely identified because their contribution to an FRF was masked by the added noise. The close localized modes 8 and 9 were the most difficult to identify. Mode 8 was identified from only one FRF, while mode 9 was found from three FRFs. The eigenvalue of mode 8 showed the greatest discrepancy with the analytical value. Its imaginary part, which is analogous to the damped natural frequency for proportionally damped systems, had an error of 0.4%, while its real part, which is the negative of the modal decay rate, was 21.7% in error. The corresponding average errors for all eleven modes were 0.04% for the imaginary part and 4% for the real part.

The analytical mode shapes were depicted by plotting the transverse displacement and torsional rotation dependence on the distance along the cross-section centerline. The discrete modal displacements and rotations extracted by AMI were overlaid onto the analytical graphs. The agreement was quite good, except for mode 8. The main features of the first five modes were clearly discernible from the discrete pattern identified by AMI. However, the higher frequency modal patterns were undersampled because the locations selected for the FRF data were too sparsely spaced. The error encountered in mode 8 was substantial, and indicated that the mode was not essentially imaginary, which is unlike the corresponding analytical mode function. The primary source of the lower quality of this mode's identification was shown to be a combination of relatively high damping and low modal response at the drive point.

An alternative identification of the eigenvalues was also carried out using a global version of the rational fraction polynomial (RFP) algorithm. RFP requires an *a priori* guess as to the number of participitory modes. A range of guesses was used to identify the system order giving the best results. The average and worst case errors for both parts of the eigenvalues were found to be substantially larger than the errors encountered with AMI. Also, RFP did not identify mode 8. In a separate computation, not reported here, RFP was applied to the noise-free FRFs. This yielded excellent agreement for all eigenvalues, including that for mode 8. This observation suggests that RFP is more sensitive to noise than is AMI.

The results presented here indicate that the current version of AMI algorithm is capable of accurate system identification in the presence of extreme noise and modal coupling. At the same time, modes that are weakly excited were found to be more difficult to identify, because they were barely discernible relative to the noise floor. In this sense, AMI is like other techniques that process response data derived from a single excitation. One can anticipate that extension of AMI to process simultaneously response data obtained from several excitations would address this shortcoming.

ACKNOWLEDGMENT

This material is based on work supported under a National Science Foundation Graduate Research Fellowship.

[1] J. H. Ginsberg and M. Allen, ''A linear least-squares version of the algorithm of mode isolation for identifying modal properties. Part I: Conceptual development,'' J. Acoust. Soc. Am. **116**, 900–907 (2004).
[2] M. V. Drexel and J. H. Ginsberg, ''Mode Isolation: A new algorithm for modal parameter identification,'' J. Acoust. Soc. Am. **110**, 1371–1378 (2001).
[3] M. V. Drexel and J. H. Ginsberg, ''Modal parameter identification using state space mode isolation,'' Proc. 19th International Modal Analysis Conference, Orlando, FL, 2001.
[4] M. V. Drexel, J. H. Ginsberg, and B. R. Zaki, ''State space implementation of the algorithm of mode isolation,'' J. Vibr. Acoust. **125**, 205–213 (2003).
[5] M. J. Roemer and D. J. Mook, ''Enhanced realization/identification of physical modes,'' J. Aero. Eng. **3**, 122–136 (1990).
[6] J. N. Juang and H. Suzuki, ''An eigensystem realization algorithm in frequency domain for modal parameter identification,'' J. Vib., Stress, Rel. in Design **110**, 24–29 (1988).
[7] M. Strasberg and D. Feit, ''Vibration damping of large structures induced by attached small resonant structures,'' J. Acoust. Soc. Am. **99**, 335–344 (1996).
[8] B. R. Zaki, *A Modified Approach to Improve the Robustness of the Algorithm of Mode Isolation*, Ph.D. thesis, Georgia Institute of Technology, Atlanta, GA (2002).
[9] M. H. Richardson and D. L. Formenti, ''Global curve-fitting of frequency response measurements using the rational fraction polynomial method,'' Proc. 3rd International Modal Analysis Conference, Orlando, FL, 1985.
[10] D. Formenti and M. H. Richardson, ''Parameter estimation from frequency response measurements using rational fraction polynomials (twenty years of progress),'' Proc. 20th International Modal Analysis Conference, Los Angeles, CA, 2002.
[11] J. H. Ginsberg, *Mechanical and Structural Vibrations: Theory and Applications* (Wiley, New York, 2001), Chap. 9.
[12] C. Pierre, D. M. Tang, and E. H. Dowell, ''Localized vibrations of disordered multi-span beams: theory and experiment,'' AIAA J. **25**, 1249–1257 (1987).
[13] P.-T. Chen and J. H. Ginsberg, ''On the relationship between veering of eigenvalue loci and parameter sensitivity of eigenfunctions,'' J. Vibr. Acoust. **114**, 141–148 (1992).
[14] N. M. M. Maia, J. M. M. Silva, J. He, N. A. J. Lieven, R. M. Ling, G. W. Skingle, W.-T. To, and A. P. V. Urgueira, *Theoretical and Experimental Modal Analysis and Testing* (Research Studies Press Ltd., Taunton, Somerset, England, 1997), Chap. 4.
[15] R. J. Allemeng and D. L. Brown, ''A unified matrix polynomial approach to modal identification,'' J. Sound Vib. **211**, 301–322 (1998).

The field of sound of a circular membrane

Berndt Zeitler[a)]
TU-Berlin, Institute of Technical Acoustics, Einsteinufer 25, 10587 Berlin, Germany

Elmar Zeitler[b)]
Fritz-Haber-Institut der Max-Planck-Gesellschaft, Faradayweg 4-6, 14195 Berlin, Germany

(Received 21 November 2003; revised 18 May 2004; accepted 21 May 2004)

In this note we give a simple straightforward method for obtaining, in closed form, the expansion coefficients in the solution of a basic acoustic problem with symmetry, the baffled vibrating membrane. © *2004 Acoustical Society of America.* [DOI: 10.1121/1.1771612]

PACS numbers: 43.40.Rj, 43.20.Rz [MO] Pages: 916–917

In his 1930 paper with like title based on Rayleigh's work[1] and on the symmetry of the problem Backhaus[2] makes the following ansatz in spherical coordinates for calculating the sound produced by a vibrating disk, that is embedded in an infinite rigid screen (see Fig. 1):

$$\Phi(r,\theta)=e^{i\omega t}\sum_{n=0}^{\infty} A_{2n}h_{2n}^{(2)}(kr)P_{2n}(\cos\theta) \tag{1}$$

(symbols have their customary meaning).

The absence of odd Legendre polynomials $P_{2n+1}(\cos\theta)$ and of any azimuthal dependence is dictated by symmetry while the appearance of the spherical Hankel functions of the second kind guaranties for the fulfillment of Sommerfeld's radiation condition. (We shall drop the harmonic time dependence.)

The main part of Backhaus' 35-page paper is dedicated to the determination of the unknown arbitrary expansion coefficients A_{2n}, which in turn render the solution of the problem. Again, symmetry is applied to this simple generator of sound, which is thought of as a circular disk of radius a uniformly loaded with point sources that produce spherical waves and thus deliver to the axis of the system the combined amplitude:

$$\Phi_0(r)=\frac{1}{a}\int_0^a \frac{e^{ikR}}{R}y\,dy, \tag{2}$$

the factor $1/a$ assuring the freedom of dimensions.

Setting the distance R from a source located at radius y on the disk to an axial point at r equal to $\sqrt{r^2+y^2}$ and observing that $R\,dR=y\,dy$, this integral can readily be performed, yielding

$$\Phi_0(r)=\frac{-i}{ak}(e^{-ik\sqrt{a^2+r^2}}-e^{-ikr}), \tag{3}$$

whereas Eq. (1) renders on axis ($\theta=\pi/2$) for the same amplitude the expression

$$\Phi_0(r)=\Phi\left(r,\frac{\pi}{2}\right)=\sum_{n=0}^{\infty} A_{2n}h_{2n}^{(2)}(kr)P_{2n}(0). \tag{4}$$

In a lengthy procedure Backhaus succeeds to extract the desired coefficients by comparing these two last equations.

It is our purpose in this note to show a simpler and swifter way toward this goal. The rendition of the coefficients in closed form has computational and didactic implications that justify, we trust, publication.

The essence of our procedure is the reversal of that of Bachhaus. We start by expanding first the integrand of Eq. (2) and performing the integration and comparison thereafter.

The well-known addition theorem, valid for $|ye^{i\theta}|<|r|$ (see, e.g., Watson[3]),

$$\frac{e^{-ikX}}{X}=-ik\sum_{m=0}^{\infty}(2m+1)j_m(ky)h_m^{(2)}(kr)P_m(\cos\theta), \tag{5}$$

with

$$X=\sqrt{r^2+y^2-2ry\cos\theta},$$

gives us the expanded integrand upon specifying $\cos\theta=0$, i.e., $\theta=\pi/2$, namely,

$$\frac{e^{-ikR}}{R}=-ik\sum_{m=0}^{\infty}(2m+1)j_m(ky)h_m^{(2)}(kr)P_m(0). \tag{6}$$

Integrating both sides of Eq. (6) with regard to y such that the left-hand side equals Eq. (3) while the right hand side yields

$$\sum_{n=0}^{\infty} A_n h_n^{(2)}(kr)P_n(0), \quad \text{with}$$

$$A_n=\frac{-i}{ak}(2n+1)\int_0^1 j_n(aky)y\,dy. \tag{7}$$

As mentioned before, odd Legendre polynomial are unsuited and, indeed, $P_{2n+1}(0)=0$, whereas $P_{2m}(0)=2^{2m}\binom{2m}{m}$ so that our final result is the integral in Eq. (7), which we shall discuss in a slightly changed and more convenient form:

$$Z_n(z)=\frac{iz}{2n+1}\times A_n=\int_0^1 j_n(zy)y\,dy. \tag{8}$$

[a)]Current address: Sekr. TA 7, Technical University of Berlin, Institute of Technical Acoustics, Einsteinufer 25, 10587 Berlin, Germany; Electronic mail: berndt.zeitler@tu-berlin.de

[b)]Current address: Fritz-Haber-Institut der Max-Planck-Gesellschaft, Faradayweg 4-6, 14195 Berlin, Germany; Electronic mail: zeitler@fhi-berlin.mpg.de

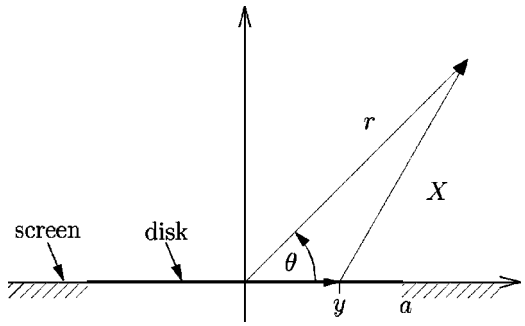

FIG. 1. Model of baffled vibrating disk of radius a, with $X=\sqrt{r^2+y^2-2ry\cos\theta}$ and $R=X$ for $\theta=\pi/2$.

The integral can be seen as a Mellin transform of the Bessel function and found as such in standard tables (e.g., Ref. 4) or can be gained by integrating memberwise the power series of the Bessel function, which again leads to the hypergeometric function

$$Z_n(z)=\frac{1}{(n+2)\left(\frac{3}{2}\right)_n}\left(\frac{z}{2}\right)^n {}_1F_2\left(\frac{n}{2}+1;\frac{n}{2}+2,n+\frac{3}{2};\frac{-z^2}{4}\right). \tag{9}$$

The hypergeometric function consists of one cosine term and of one sine term, both multiplied by finite algebraic expressions of negative powers of the argument, and one constant dc term. Finally, best of all, many symbolic math programs can handle this function as exemplified by the following table. It displays the MATHEMATICA output[5] of $Z_n(z)$ normalized such that the constant term is unity, which is in agreement with the corresponding list of Backhaus:[2]

$$Z_0(z)=1-\cos z,$$

$$Z_2(z)=1+\frac{1}{2}\cos z-\frac{3}{2}\frac{\sin z}{z},$$

$$Z_4(z)=1-\frac{3}{8}(1-35z^{-2})\cos z+\frac{15}{4}\left(1-\frac{7}{2}z^{-2}\right)\frac{\sin z}{z}$$

$$Z_6(z)=1+\frac{5}{16}(1-189z^{-2}+2079z^{-4})\cos z$$

$$+\frac{105}{16}(1-42z^{-2}+99z^{-4})\frac{\sin z}{z}.$$

ACKNOWLEDGMENTS

One of us (B. Z.) is indebted to Professor M. Möser for the introduction to the problem.

[1] J. W. S. Rayleigh, *Theory of Sound* (Dover, New York, NY, 1945), Vol. II.
[2] H. Backhaus, "The field of sound of a circlular membrane," Ann. Phys. (Leipzig) **30**, 1–35 (1930) (in German).
[3] G. N. Watson, *The Theory of Bessel Functions* (Cambridge University Press, Cambridge, 1958), p. 358.
[4] A. Erdélyi, M. F. Oberhettinger, and F. G. Tricomi, *Tables of Integral Transforms* (McGraw-Hill New York, 1955), Vol. I.
[5] Wolfram Research Inc.

Equal-loudness-level contours for pure tones[a)]

Yôiti Suzuki[b)]
Research Institute of Electrical Communication, Tohoku University, Katahira 2-1-1, Aoba-ku, Sendai 980-8577, Japan

Hisashi Takeshima[c)]
Sendai National College of Technology, Ayashi-chuo 4-16-1, Aoba-ku, Sendai 989-3128, Japan

(Received 5 February 2003; revised 19 April 2004; accepted 26 April 2004)

Equal-loudness-level contours provide the foundation for theoretical and practical analyses of intensity-frequency characteristics of auditory systems. Since 1956 equal-loudness-level contours based on the free-field measurements of Robinson and Dadson [Br. J. Appl. Phys. **7**, 166–181 (1956)] have been widely accepted. However, in 1987 some questions about the general applicability of these contours were published [H. Fastl and E. Zwicker, Fortschritte der Akustik, DAGA '87, pp. 189–193 (1987)]. As a result, a new international effort to measure equal-loudness-level contours was undertaken. The present paper brings together the results of 12 studies starting in the mid-1980s to arrive at a new set of contours. The new contours estimated in this study are compared with four sets of classic contours taken from the available literature. The contours described by Fletcher and Munson [J. Acoust. Soc. Am. **5**, 82–108 (1933)] exhibit some overall similarity to our proposed estimated contours in the mid-frequency range up to 60 phons. The contours described by Robinson and Dadson exhibit clear differences from the new contours. These differences are most pronounced below 500 Hz and the discrepancy is often as large as 14 dB.
 [DOI: 10.1121/1.1763601]

PACS numbers: 43.50.Ba, 43.50.Qp, 43.66.Cb [DKW] Pages: 918–933

I. INTRODUCTION

The loudness of a sound strongly depends on both the sound intensity and the frequency spectrum of a stimulus. For sounds such as a pure tone or a narrow-band noise, an equal-loudness-level contour can be defined. This contour represents the sound pressure levels of a sound that give rise to a sensation of equal-loudness magnitude as a function of sound frequency. The equal-loudness-level contours are so foundational that they are considered to reveal the frequency characteristics of the human auditory system.

Many attempts have been made to determine equal-loudness-level contours spanning the audible range of hearing. The earliest measurements of equal-loudness-level contours were reported by Kingsbury (1927). Those measurements were obtained under monaural listening conditions and were relatively limited. Although equal-loudness relations can be measured in a free field, in a diffuse field, and under earphone listening conditions, most of the published equal-loudness-level contours have been measured either under binaural listening conditions or under conditions relative to a free field. The first complete set of equal-loudness-level contours obtained under binaural listening conditions and given relative to free-field listening was made by Fletcher and Munson (1933). Their pioneering study was followed by studies measuring contours by Churcher and King (1937), Zwicker and Feldtkeller (1955), and Robinson and Dadson (1956). The contours measured by Robinson and Dadson (1956) were adopted as an international standard for pure tones heard under free-field listening conditions (ISO/R 226, 1961; ISO 226, 1987); they have been widely accepted.

In recent years there has been renewed interest in equal-loudness-level contours. This interest was triggered by a report from Fastl and Zwicker (1987) who noted marked departures from the contours specified by Robinson and Dadson (1956) in the region near 400 Hz. Subsequently, the deviations found by Fastl and Zwicker (1987) have been confirmed by many investigators (Betke and Mellert, 1989; Suzuki *et al.*, 1989; Fastl *et al.*, 1990; Watanabe and Møller, 1990; Poulsen and Thøgersen, 1994; Lydolf and Møller, 1997; Takeshima *et al.*, 1997; Bellmann *et al.*, 1999; Takeshima *et al.*, 2001, 2002). Specifically, all of the new data show that at frequencies below about 800 Hz equal-loudness levels are higher than the levels measured by Robinson and Dadson (1956); one example of this is the level differences of loudness levels of 40 phons which record differences from 12.7 to 20.6 dB at the frequency of 125 Hz. Figure 1 illustrates the extent of this discrepancy. Here the 40-phon contour measured by Robinson and Dadson (1956) is compared with data obtained from recent studies. Clearly, in the low-frequency region all the newer data deviate systematically from the equal-loudness-level contour based on Robinson and Dadson's data. Possible causes of the difference are discussed in Sec. IV. Such marked deviations are not only of theoretical importance, they also have practical implications. For example, the current A-weighting for sound level meters is based on the equal-loudness-level contour at 40 phons.

[a)]Portions of this article were presented at InterNoise 2000 in Nice, France, August 2000 [Suzuki *et al.*, Proc. InterNoise 2000, pp. 3664–3669 (2000)] and the 143rd Meeting of the Acoustical Society of America in Pittsburgh, PA, June 2002 [Y. Suzuki and H. Takeshima, J. Acoust. Soc. Am. **111**(5) Pt. 2, 2468 (2002)].

[b)]Electronic mail: yoh@riec.tohoku.ac.jp
[c)]Electronic mail: takesima@cc.sendai-ct.ac.jp

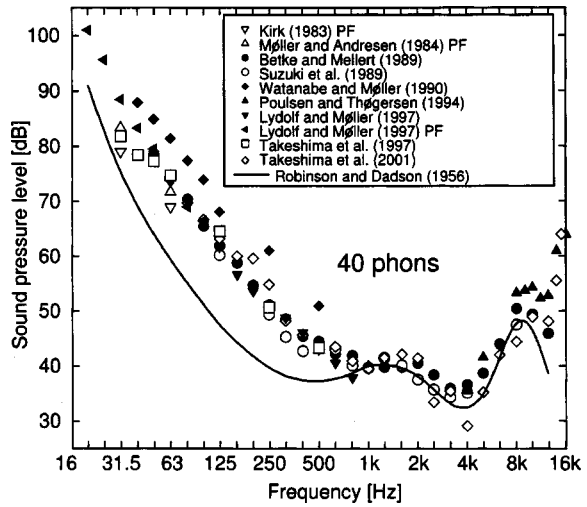

FIG. 1. Equal-loudness-level contour of 40 phons for pure tones. The solid lines represent the contour measured by Robinson and Dadson (1956), which were adapted as an international standard, ISO R/226 (1961) and ISO 226 (1987). Symbols show the experimental data collected since 1983.

Given the marked and consistent deviations obtained by the newer data, an attempt has been made to establish a new set of equal-loudness-level contours. Section II of this paper provides a brief review of equal-loudness relations measured for pure tones. Data from this overview are analyzed and evaluated to help establish new equal-loudness-level contours. The results are compared with those reported in four classic studies (Fletcher and Munson, 1933; Churcher and King, 1937; Zwicker and Feldtkeller, 1955; Robinson and Dadson, 1956). In Sec. III a new set of equal-loudness-level contours that span a wide range of frequencies and levels is introduced. A loudness function that provides a good account of the data (Takeshima *et al.*, 2003) is utilized. In this paper, we focus on contours for pure tones under free-field listening conditions that represent the average judgment of otologically normal persons.

II. A BRIEF REVIEW OF STUDIES OF EQUAL-LOUDNESS-LEVEL CONTOURS AND THRESHOLDS OF HEARING

A. Equal-loudness-level contours

This section gives an overview of all published studies of equal-loudness-level contours. Our analysis provides a basis for selecting basic data to use for constructing a new set of equal-loudness-level contours. Table I lists 19 studies in chronological order.

Although our aim is to establish new equal-loudness-level contours under free-field listening conditions, in several studies equal-loudness levels at low frequencies were measured in a pressure field obtained by using a small room installed with a number of loudspeakers on each of the walls and the ceiling. These loudspeakers are driven in phase so

TABLE I. Studies on the equal-loudness-level contours and their important experimental conditions. FF: free field, PF: pressure field, MA: method of adjustment, CS: method of constant stimuli, RMLSP: randomized maximum likelihood sequential procedure (Takeshima *et al.*, 2001), and CP: category partitioning procedure.

Year	Researchers	Listening condition	No. of subjects (age)	Method	Reference tone frequency (level)	Test tone frequency (Hz)
1927	Kingsbury	Earphone	22 (unspecified)	MA	700 Hz (fix)	60–4000
1933	Fletcher–Munson	Earphone with FF correction	11 (unspecified)	CS	1 kHz (variable)	62–16 000
1937	Churcher–King	FF	10 (unspedified)	CS	1 kHz (fix)	54–9000
1955	Zwicker–Feldtkeller	Earphone with FF equalizer	8 (unspecified)	Modified Békésy	1 kHz (fix)	50–16 000
1956	Robinson–Dadson	FF	90 (16–63)/ 30 (ave. 30)	CS	1 kHz (variable)	25–15 000
1972	Whittle *et al.*	PF	20 (ave. 20)	CS	higher freq. (fix)	3.15–50
1983	Kirk	PF	14 (18–25)	RMLSP	63 Hz (fix)	2–63
1984	Møller–Andresen	PF	20 (18–25)	RMLSP	63 Hz (fix)	2–63
1989	Betke–Mellert	FF	13–49 (17–25)	CS	1 kHz (fix)	50–12 500
1989	Suzuki *et al.*	FF	9–32 (19–25)	CS	1 kHz (fix)	31.5–16 000
1990	Fastl *et al.*	FF	12 (21–25)	CS	1 kHz (fix)	100–1000
1990	Watanabe–Møller	FF	10–12 (18–30)	Bracketing	1 kHz (fix)	25–1000
1994	Müller–Fichtl	Open headphones	8 (21–25)	CP	—	62.5–10 000
1994	Poulsen–Thøgersen	FF	29 (18–25)	Bracketing	1 kHz (fix)	1000–16 000
1997	Lydolf–Møller	FF	27 (19–25)	RMLSP	1 kHz (fix)	50–1000
		PF	27 (19–25)	RMLSP	100 Hz (fix)	20–100
1997	Takeshima *et al.*	FF	9–30 (19–25)	CS	1 kHz (fix)	31.5–12 500
1999	Bellmann *et al.*	FF	12 (unspecified)	Adaptive 1up–1down	1 kHz (fix)	100–1000
		PF	12 (unspecified)	Adaptive 1up–1down	100 Hz (fix)	16–160
2001	Takeshima *et al.*	FF	7–32 (18–25)	RMLSP	1 kHz (fix)	50–16 000
2002	Takeshima *et al.*	FF	21 (20–25)	RMLSP	1 kHz (fix)	1000–12 500

that no energy could flow in the room. They are Whittle *et al.* (1972), Kirk (1983), Møller and Andresen (1984), Lydolf and Møller (1997), and Bellmann *et al.* (1999). These studies are also included in Table I because at frequencies lower than a few hundred Hertz equal-loudness levels of pure tones measured in a free field are consistent with those measured in a pressure field (Lydolf and Møller, 1997).

Of the 19 studies listed in Table I, we suggest that three studies (Kingsbury, 1927; Whittle *et al.,* 1972; Müller and Fichtl, 1994) be excluded as candidates for the basic data. Kingsbury (1927) measured equal-loudness levels under monaural listening conditions with a telephone receiver. However, the levels measured were not calibrated relative to the levels in a free field. Although Whittle *et al.* (1972) made their measurements in a pressure field, equal-loudness levels at 3.15, 6.3, 12.5, and 25 Hz were obtained with reference tones set at 6.3, 12.5, 25, and 50 Hz. No comparison was made to a 1-kHz reference tone. As a result of this shortcoming, the equal-loudness levels they measured cannot be expressed directly in phons. Finally, in Müller and Fichtl (1994) the loudness of the pure tones was based on the category partitioning procedure. In this procedure, loudness was judged by two successive scalings. First, subjects judge loudness by choosing from seven categories ranging from ''nothing heard'' to ''painfully loud.'' Then when a subject chose one of the six categories other than ''nothing heard,'' the same stimulus was presented once more and the subject was asked to judge the loudness on a more finely subdivided scaling which consisted of five steps for the ''painfully loud'' category and ten steps for the other five ''middle'' categories from ranging ''very soft'' to ''very loud.'' Using this technique, the loudness of a pure tone is recorded as an integer ranging from 0 (nothing heard) to 55 (painfully loud). Equal-loudness-level contours are based on these categorized loudness-related values. Unfortunately, category-scaling procedures are easily influenced by context effects such as stimulus spacing, frequency of stimulus presentation, stimulus range, and stimulus distribution (Gescheider, 1997). The degree of these context effects cannot be assessed because no paired-comparison data were obtained.

Figure 2 shows the equal-loudness-level data from the studies listed in Table I excluding the results of Kingsbury (1927), Whittle *et al.* (1972), and Müller and Fichtl (1994). Four studies, Fletcher and Munson (1933), Churcher and King (1937), Zwicker and Feldtkeller (1955), and Robinson and Dadson (1956), proposed a complete set of equal-loudness-level contours whereas the remaining studies reported only measured equal-loudness levels. Results from the individual studies are given by the symbols; the curves represent the four sets of equal-loudness-level contours. Owing to their importance, these four sets of contours are referred to as *classic* equal-loudness-level contours, whereas the studies published since 1983 are referred to as *recent* experimental data.

In spite of some differences among the results of the various studies, Fig. 2 makes it clear that most of the *recent* data sets exhibit similar trends. By comparison, none of the four sets of *classic* contours coincide acceptably over the whole range of frequencies and levels with the recent data. The four sets of *classic* contours show both similarity and dissimilarity to these data sets. Thus the *recent* data are compared with the *classic* contours more in detail. It is notable that the three sets of *classic* contours apart from that of Robinson and Dadson (1956) agree remarkably well with the *recent* data at 20 phons. Moreover, the agreement between the *recent* data and the *classic* contours of Fletcher and Munson (1933) is quite good at 60 phons and below; at higher loudness levels the contours of Fletcher and Munson (1933) become progressively flatter than the *recent* data value. At the 100-phon level the difference at 25 Hz amounts to 30 dB. Between 60 and 90 phons the *classic* contours of Churcher and King (1937) and Zwicker and Feldtkeller (1955) also tend to be flatter in the low-frequency region than the *recent* data values. Another conflict between the *recent* data and the *classic* contours of Zwicker and Feldtkeller (1955) is evident at 4 kHz. In this frequency region, the contours of Zwicker and Feldtkeller (1955) are inconsistent with both the *recent* data and the other three *classic* contours. Unlike all the other studies, the contours reported by Zwicker and Feldtkeller (1955) do not exhibit a dip in the 4-kHz region. Finally, in the low-frequency region below 1 kHz almost all of the *recent* data are located well above the contours proposed by Robinson and Dadson (1956). Moreover, between 20 and 80 phons the differences are often greater than 14 dB. Based on these observations, it is clear that the discrepancies both among the *classic* contours and between the *classic* contours and the *recent* data can be considered non-negligible and systematic. Consequently, we decided to use the *recent* data to estimate a new set of equal-loudness-level contours. We would then be able to critically compare the classic and new equal-loudness levels as contours.

The *recent* data show certain variance among the studies. The most marked discrepancies can be seen in the data by Fastl *et al.* (1990). The deviations are most pronounced at the 30- and 50-phon levels (filled squares). A possible explanation for the deviation between these results and our estimated contours can be found in the results of Gabriel *et al.* (1997) and Takeshima *et al.* (2001). These latter studies showed that when the method of constant stimuli is used a strong range effect may bias the results toward the central level of the variable stimuli. In the study by Fastl *et al.* (1990) the central levels were set to the equal-loudness-level contours calculated by Zwicker (1958): At 125 Hz the central levels applied by Fastl *et al.* (1990) were 40.2 dB at 30 phons, 57.6 dB at 50 phons, and 76.5 dB at 70 phons. These levels are considerably lower than the loudness levels in the other *recent* studies. Another data set that requires closer scrutiny is the one obtained from the results of Watanabe and Møller (1990). According to Møller and Lydolf (1996) this data (filled diamonds) may have been biased towards higher sound pressure levels because, in the bracketing procedure used, the initial level was invariably set at 15 to 20 dB above the expected equal-loudness levels reported by Robinson and Dadson (1956). Despite these caveats, the data from the two studies do not show extreme variation from the other *recent* data. We therefore decided to include all of the *recent* data in the determination of a new set of equal-loudness-level contours.

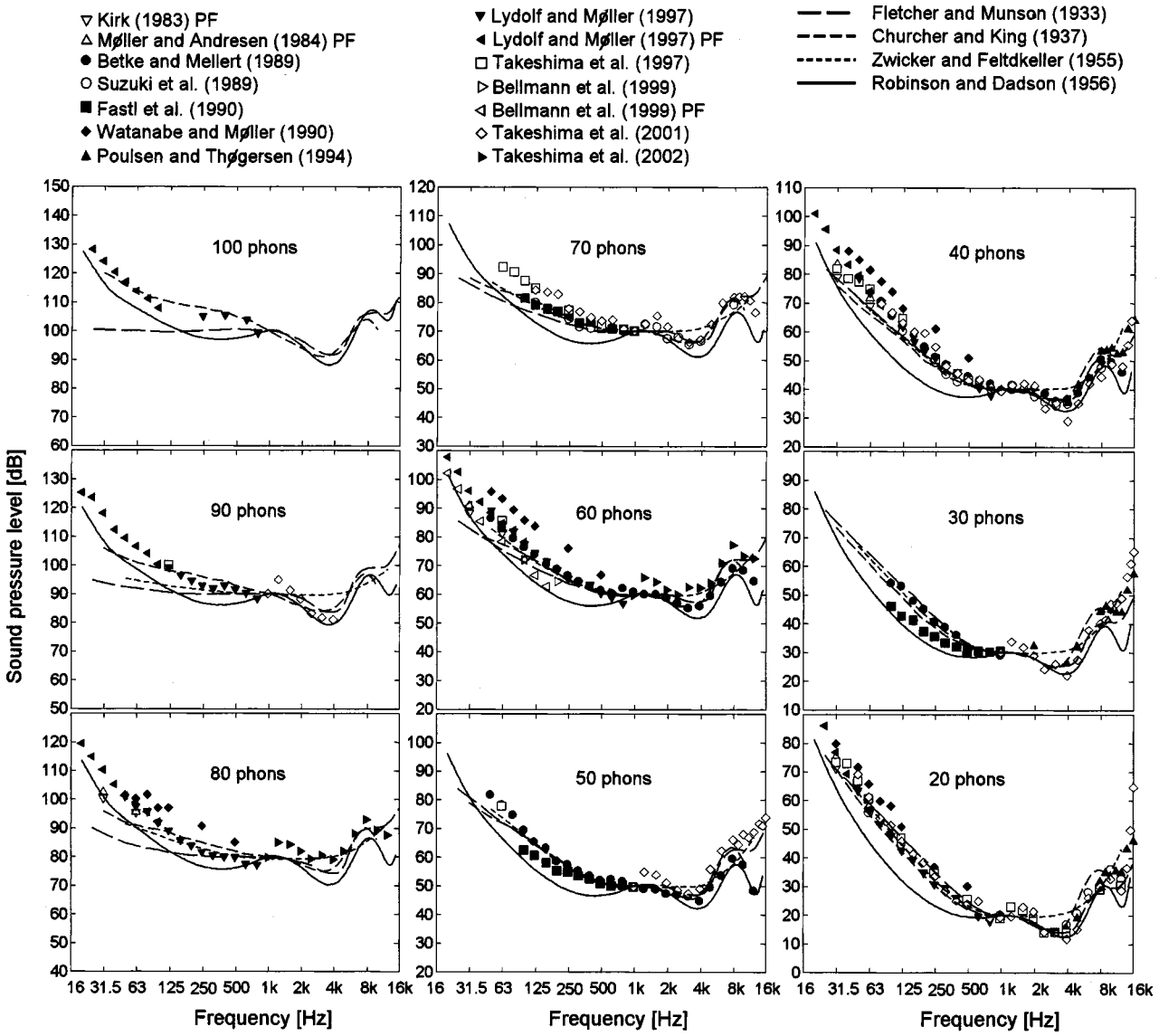

FIG. 2. Equal-loudness-level contours for pure tones. The four lines in each panel represent the contour reported by Fletcher and Munson (1933), by Churcher and King (1937), by Zwicker and Feldtkeller (1955), and by Robinson and Dadson (1956). The symbols are the experimental data of the *recent* studies reported since 1983. In the legend, PF means that the study was carried out under pressure-field listening condition.

B. Threshold of hearing

It is natural to draw a hearing threshold curve as a lower limit of audibility on a figure of equal-loudness-level contours; the threshold of hearing is also useful in estimating the new equal-loudness-level contours described in the following sections. Table II lists studies of the threshold of hearing for pure tones in chronological order. In most of the studies listed in Table II, equal-loudness relations were measured at the same time and are thus also listed in Table I. Studies other than those listed in Table I are Teranishi (1965), Brinkmann (1973), Vorländer (1991), Betke (1991), Takeshima *et al.* (1994), and Poulsen and Han (2000). The data concerning the threshold of hearing from all of the studies listed in Table II are shown in Fig. 3. In the figure, threshold curves reported with the four sets of *classic* equal-loudness-level contours are also drawn. It should be noted, however, that the curve of the threshold of hearing is not always regarded as an equal-loudness-level contour (Fletcher and Munson, 1933; Hellman and Zwislocki, 1968; Buus *et al.*, 1998).

As seen from Fig. 3, the data concerning the threshold of hearing are similar across the recent studies and fit well with the threshold curve of Robinson and Dadson (1956) while the other three curves, Fletcher and Munson (1933), Churcher and King (1937), and Zwicker and Feldtkeller (1955), deviate from the recent threshold data and the curve by Robinson and Dadson (1956) under 1 kHz.

III. DERIVATION OF A NEW SET OF EQUAL-LOUDNESS-LEVEL CONTOURS

The review carried out in Sec. II clearly indicates that a new set of equal-loudness-level contours needs to be drawn. The experimental measures of the equal-loudness relation reported in the 12 *recent* studies are given in Fig. 2 as discrete points along the frequency and sound pressure level axes. If the equal-loudness-level contours are drawn simply, by using a smoothing function across frequency at each loudness level, then the contours do not exhibit an acceptable pattern of parallel displacement. To achieve that goal, the smoothing

TABLE II. Studies on the threshold of hearing for pure tones under free-field listening condition and their important experimental conditions. (FF: free field, PF: pressure field)

Year	Researchers	Listening condition	No. of subjects (age)	Method	Frequency range (Hz)
1927	Kingsbury	Earphone	22 (unspecified)	unspecified	60–4000
1933	Fletcher–Munson	Earphone with FF correction	11 (unspecified)	Bracketing method	62–16 000
1937	Churcher–King	FF	10 (unspecified)	unspecified	54–6400
1955	Zwicker–Feldtkeller	Earphone with FF equalizer	8 (unspecified)	Békésy tracking	50–16 000
1956	Robinson–Dadson	FF	51 (ave. 20)[a]	Bracketing method	25–15 000
1965	Teranishi	FF	11 (18–24)[b]	Bracketing method	63–10 000
1973	Brinkmann	FF	9–56 (18–30)	Bracketing method	63–8000
1989	Suzuki *et al.*	FF	31 (19–25)	Bracketing method	63–12 500
1990	Fastl *et al.*	FF	12 (21–25)	Ascending method	100–1000
1990	Watanabe–Møller	FF	12 (18–30)	Bracketing method	25–1000
1991	Betke	FF	16–49 (18–25)	Bracketing method	40–15 000
1991	Vorländer	FF	31 (18–25)	Bracketing method	1000–16 000
1994	Poulsen–Thøgersen	FF	29 (18–25)	Bracketing method	1000–16 000
1994	Takeshima *et al.*	FF	10–30 (19–25)[c]	Bracketing method	31.5–16 000
1997	Lydolf–Møller	FF	27 (19–25)	Ascending method	50–8000
		PF	27 (19–25)	Ascending method	20–100
2000	Poulsen–Han	FF	31 (18–25)	Bracketing method	125–16 000
2001	Takeshima *et al.*	FF	7–32 (18–25)	Bracketing method	31.5–16 000
2002	Takeshima *et al.*	FF	21 (20–25)	Bracketing method	1000–12 500

[a]120 subjects below 2000 Hz.
[b]51 subjects with wide range of age (18–64 years old) participated in his experiments.
[c]Excluding the results of the experiments (EX1 and EX2) which have been reported in Suzuki *et al.* (1989).

process must be performed in a two-dimensional plane that takes into account both the frequency and sound pressure level axes. Fletcher and Munson (1933) produced functions for their discrete data values by first plotting the measured relation between loudness level and sound pressure level at each of their ten test frequencies and then fitting a smooth curve to each of the measured data sets. The ten data sets enabled a family of equal-loudness-level contours to be drawn. Based on the presumption that the equal-loudness-level contours were related to the underlying hearing mechanism, Fletcher and Munson (1933) hypothesized that these contours should be smooth and parallel. Robinson and Dadson (1956) applied a similar approach to the analysis of their data values. They used a second-order polynomial fit to obtain the relations between loudness level and sound pressure level at each of their 13 test frequencies.

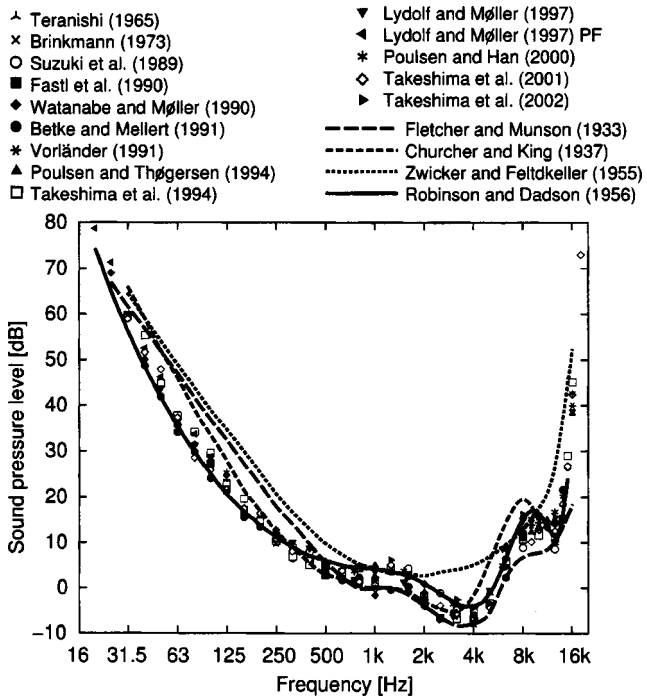

FIG. 3. Thresholds of hearing for pure tones. The four lines represent the threshold curve reported by Fletcher and Munson (1933), by Churcher and King (1937), by Zwicker and Feldtkeller (1955), and by Robinson and Dadson (1956). In the legend, PF means that the study was carried out under pressure-field listening condition.

In the present study, equal-loudness-level contours are obtained by making use of the established loudness-intensity relation, a compressive relation shown to be approximately compatible with recent measures of the nonlinear input–output response of the basilar membrane (Schlauch *et al.*, 1998; Yates, 1990; Florentine *et al.*, 1996; Buus and Florentine, 2001a,b). Our procedure makes it possible to parametrically derive a set of equal-loudness-level contours over the measured range of loudness levels from 20 to 100 phons.

A. Loudness functions suitable for representing the equal-loudness relation

At moderate to high sound pressure levels, the growth of loudness is well approximated by Stevens's (1953, 1957) power law in the form

$$S = ap^{2\alpha}, \tag{1}$$

where p is the sound pressure of a pure tone, a is a dimensional constant, α is the exponent, and S is the perceived loudness. However, Stevens's power law cannot describe the deviation of the loudness function from power-law behavior

below about 30 dB HL (see, e.g., Hellman and Zwislocki, 1961; Scharf and Stevens, 1961). As a result, several modifications of Stevens's power law have been proposed. In the late 1950s a number of authors (Ekman, 1959; Luce, 1959; Stevens, 1959) suggested that the power law could be rewritten in the form

$$S = a(p^2 - p_t^2)^{\alpha}, \tag{2}$$

where p_t is the threshold of hearing in terms of sound pressure. Later on, Zwislocki and Hellman (1960) and Lochner and Burger (1961) also proposed modifications. In these latter modifications, the relation between loudness and sound pressure is given by the equation

$$S = a(p^{2\alpha} - p_t^{2\alpha}). \tag{3}$$

The difference between Eqs. (2) and (3) lies in the domain where the subtraction is executed. In Eq. (2) a constant corresponding to the threshold is subtracted in the stimulus domain, whereas in Eq. (3) a constant corresponding to the threshold loudness is subtracted in loudness domain (Hellman, 1997). When $p = p_t$, both Eqs. (2) and (3) yield a threshold loudness of zero.

Zwicker (1958) considered that a power law stands between the sum of the excitation evoked by a sound and the internal noise and the sum of the specific loudness of the sound and the internal noise. By solving this equation, he derived the following specific loudness function:

$$S = a\{(p^2 + Cp_t^2)^{\alpha} - (Cp_t^2)^{\alpha}\}, \tag{4}$$

where C is the noise-to-tone energy ratio required for a just detectable tone embedded in the internal masking noise. In 1965 Zwislocki introduced the internal noise into Eq. (3), resulting in a function that predicts the total loudness of a pure tone in quiet and in noise. The form of Zwislocki's (1965) equation for loudness functions is similar to the one obtained for the specific loudness function in Eq. (4). Unlike Eqs. (2) and (3), the threshold loudness given by Eq. (4) is greater than zero.

Zwicker and Fastl (1990) further modified Eq. (4) to set the loudness at threshold to be zero, resulting in the following equation for specific loudness function:

$$S = a[\{p^2 + (C-1)p_t^2\}^{\alpha} - (Cp_t^2)^{\alpha}]. \tag{5}$$

Above 30 dB HL, the modifications in Eqs. (2)–(5) asymptotically approach Stevens's power law in Eq. (1). However, none of the equations describe the mid-level flattening claimed in recent studies of loudness growth (Allen and Neely, 1997; Neely and Allen, 1997; Buus and Florentine, 2001a,b), but they are probably sufficiently precise for present purposes and have the advantage of having few free parameters to fit.

Takeshima *et al.* (2003) examined which loudness function is the most appropriate to describe the equal-loudness relation between two pure tones with different frequencies. First, they measured equal-loudness levels of 125-Hz pure tone from 70 phons down to 5 phons. Then fitted the experimental data to the above-mentioned five loudness functions. Figure 4 shows the results (Takeshima *et al.*, 2003). Equations (1) and (2) clearly showed poorer performances. The other three were well able to explain the equal-loudness relation down to 5 phons. The goodness of fit for these three functions did not differ significantly. Takeshima *et al.* (2003) further concluded that the number of parameters of Eq. (3) is less than the other two and free from the estimation of the parameter C, which represents the level of the intrinsic noise which suggests Eq. (3) is the most appropriate for present purposes. Since estimation of C is often unstable in the fitting of the three parameters with the available data, estimation of equal-loudness contours with Eq. (4) or (5) would be extremely problematic.

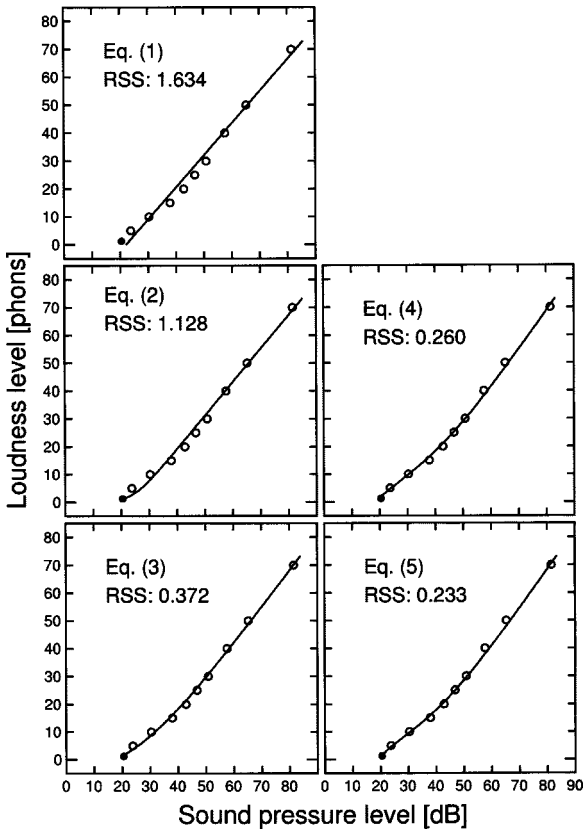

FIG. 4. Equal-loudness-relation curves derived from Eqs. (1) and (5), respectively. Open circles in each panel show equal-loudness levels of 125-Hz pure tones measured by the randomized maximum likelihood sequential procedure. The solid lines in each panel are the best fitting curves of each loudness function to the experimental data. RSS means the residual sum of squares in the fitting process of the nonlinear least squares method. This figure is a reprinting of Fig. 2 in Takeshima *et al.* (2003).

When loudness growth is expressed by use of Eq. (3), the following limitation should be noted. Equation (3) assumes the loudness at threshold of hearing to be zero. This is inconsistent with experimental data where the loudness at threshold of hearing is not zero (e.g., Hellman and Zwislocki, 1961, 1964; Hellman and Meiselman, 1990; Hellman, 1997; Buus *et al.*, 1998). Moreover, loudness at threshold is not zero but dependent on frequency as shown in the data of Hellman and Zwislocki (1968), Hellman (1994), and Buus and Florentine (2001a). Equation (4), and among the five only this equation, can account for these experimental results. However, as mentioned above, the fitting of this equation in our preliminary examination often resulted in unstable estimation. As seen from Fig. 4, Eqs. (3) and (4)

resemble each other and acceptably coincide at and above 10 phons and we are encouraged that the fitting to Eq. (3) was quite stable. Furthermore, experimental data for the equal-loudness levels are available only at and above 20 phons. Therefore, in the present study, we adopt Eq. (3) for further consideration.

B. Derivation of equations describing the equal-loudness relation

As noted above in Sec. III A, Eq. (3) is used for the loudness function. Here, the authors assume that a and α are dependent on frequency since this makes the residual sum of squares in the fitting process much less than with a constant a and α. Thus, over the loudness ranges of interest the terms a and α in Eq. (3) at frequency f are denoted as a_f and α_f. When the loudness of an f-Hz comparison tone is equal to the loudness of a reference tone at 1 kHz with a sound pressure of p_r, then the sound pressure of p_f at the frequency of f Hz is given by the following function:

$$p_f^2=\frac{1}{U_f^2}\{(p_r^{2\alpha_r}-p_{rt}^{2\alpha_r})+(U_f p_{ft})^{2\alpha_f}\}^{1/\alpha_f}, \tag{6}$$

where suffixes r and f indicate that the parameters denote the sound pressure for the 1-kHz reference tone and the f-Hz comparison tone, respectively. Moreover, $U_f=(a_f/a_r)^{1/2\alpha_f}$. Obviously, U_f is unity at the reference frequency (1 kHz).

An equal-loudness-level contour for a specific p_r can be drawn by connecting p_f as a function of frequency, if the frequency-dependent parameters, α_f and U_f, are given. To do this, the value of α_r, the exponent of the loudness function at 1 kHz, is a prerequisite. Many investigators have reported that for a 1-kHz tone the exponent in Stevens's power law has a value of about 0.3 for sound intensity (e.g., Fletcher and Munson, 1933; Stevens, 1957, 1959; Robinson, 1957; Feldtkeller *et al.*, 1959; Hellman and Zwislocki, 1961, 1963; Hellman, 1976; Humes and Jesteadt, 1991; Lochner and Burger, 1961; Rowley and Studebaker, 1969; Scharf and Stevens, 1961; Zwislocki, 1965). Fletcher (1995) examined results from several studies based on the doubling and halving of loudness, tenfold magnification and reduction, and the multi-tone method. As a result, a value of 0.33 was proposed. Stevens (1955) examined available data measured with various methods at that time and suggested 0.3 as the median of the data. Robinson (1953) measured this exponent based on doubling and halving loudness and tenfold magnification and reduction. He derived a value of 0.29 but later, in 1957, he adjusted the central tendency and order effect and obtained a slightly corrected value of 0.30 (Robinson, 1957). The typical exponent value obtained by the AME method is 0.27 (Hellman and Zwislocki, 1961, 1963; Lochner and Burger, 1961; Rowley and Studebaker, 1969; Hellman, 1976). In 1963, Hellman and Zwislocki reconfirmed this value by a combination of magnitude estimation and magnitude production (Hellman and Zwislocki, 1963). Zwicker denoted the value for the 1-kHz tone as 0.3 (Zwicker and Fastl, 1990) based on an experiment with doubling and halving loudness (Zwicker, 1963).

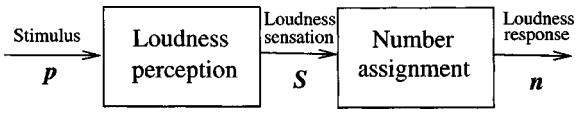

FIG. 5. A block diagram of a model for the loudness rating process.

The meaning behind this exponent derived from the method of magnitude estimation and production and exponents derived from other methods such as doubling and halving loudness based on the additivity of loudness may be different. Atteneave (1962) argued that there are two different processes used in absolute magnitude estimation (AME) for assessing the functional relation between assigned numbers and the corresponding perceived magnitudes (i.e., loudness) of a tone presented at a certain sound pressure level. One process was denoted as a "loudness perception process" and the other was as a "number assignment process" (Fig. 5). In addition, Atteneave (1962) proposed a two-stage model in which the outputs of both processes are described by separate power transformations. This idea is important in estimating the appropriate values for the exponent α in the loudness function. According to this model, the exponent observed in psychophysical experiments must be the product of the exponents of the two underlying processes. This two-stage model was used successfully by Zwislocki (1983) and by Collins and Gescheider (1989) to account for loudness growth measured by AME.

The loudness function based on a method of magnitude estimation and production is determined by the output of the "number assignment process." On the other hand, loudness functions based on other methods based on the additivity of loudness are determined by the output of the "loudness perception process." Since judgment of equal loudness between two sounds must be based on the comparison of the output of the "loudness perception process," the exponent value based on the loudness additivity may be used as it is (Allen, 1996). Values based on the method of magnitude estimation and production should be corrected to eliminate the effect of the number assignment process. The number assignment process can be expressed by Stevens's power law (Atteneave, 1962). We assume, in accordance with Zwislocki (1983), that the transformation in the number assigning process is independent of frequency and estimated as 1.08. By this account, the value of 0.27 based on the method of magnitude estimation and production is equivalent to 0.25 (0.27/1.08) for values from experiments based on the additivity of loudness.

The average of the above-mentioned values is 0.296. In the present paper, by rounding this, a value of 0.30 is used as the value of the exponent of the loudness function at 1 kHz, α_r. It is noteworthy that a preliminary examination showed that this value scarcely affects the resultant shape of the equal-loudness-level contours at least in the range of 0.20 and 0.33 so long as the ratio of the exponent components of the 1-kHz reference tone and the f-Hz comparison tone, α_r/α_f, is appropriately established (Takeshima *et al.*, 2003).

C. Derivation of equal-loudness-level contours

A set of equal-loudness-level contours was estimated by applying Eq. (6) to the data obtained from the 12 *recent*

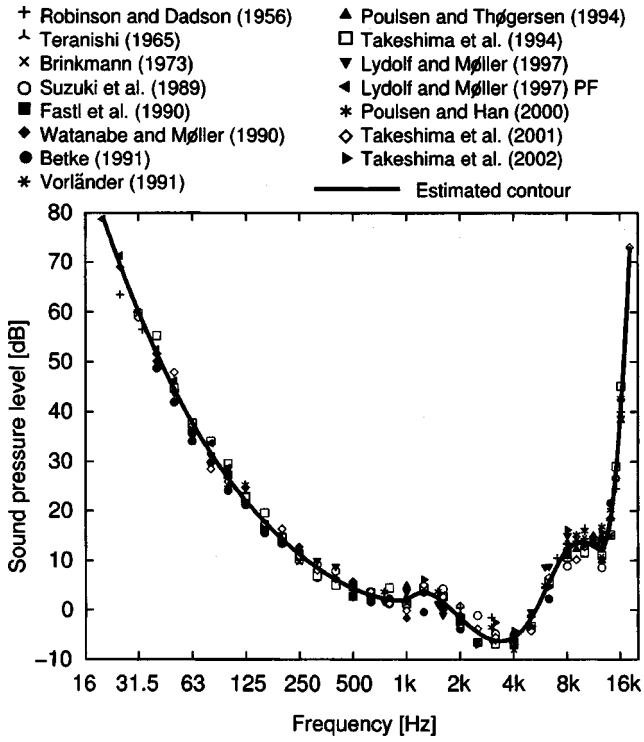

FIG. 6. Threshold of hearing for pure tones. The solid line represents a smoothed line of the averages of the experimental data, the symbols were generated by a cubic B-spline function for the frequency range from 20 Hz to 18 kHz.

studies plotted in Fig. 2. The estimation of the contours was carried out for the frequency range 20 Hz to 12.5 kHz. Above 12.5 kHz, equal-loudness-level data are relatively scarce and tend to be very variable.

As the exponent at 1 kHz was fixed as 0.30 in this study, the procedure outlined below was used to estimate the equal-loudness-level contours.

(1) To obtain the best-fitting threshold function, the experimental threshold data selected in Sec. II B were compiled and averaged at each frequency from 20 Hz to 18 kHz. The data reported by each study were median values except for Brinkmann (1973) in which only mean values were available. The data were averaged by arithmetic mean in terms of dB. Then, the averages were smoothed across frequency by a cubic B-spline function for the frequency range from 20 Hz to 18 kHz. No weighting was used for this procedure. The result is shown by the solid line in Fig. 6. The numerical values calculated for p_{ft} and p_{rt} were used in Eq. (6) to obtain the equal-loudness-level value for any given comparison-reference frequency pair.

(2) Equation (6) was then fitted to the experimental loudness-level data at each frequency by the nonlinear least-squares method. A computer program package for general-purpose least squares fittings called SALS (Nakagawa and Oyanagi, 1980) was used for estimating the values of α_f and U_f. The residual for the least-square method was calculated in terms of dB. The estimated values of α_f are shown by the symbols in Fig. 7; the curve shows the fit to these values. To obtain the curve in Fig. 7, the estimated α_f values were smoothed by the cubic B-spline function using the assumption that α_f does not change abruptly as a function of frequency.

(3) The third step in our process was to reestimate the values of U_f at each frequency. This was accomplished with the help of the smoothed curve in Fig. 7 together with Eq. (6). Using the values of α_f obtained from the smoothed curve in Fig. 7, reestimated values of U_f were obtained. The circles in Fig. 8 show the results in log-log coordinates. The ordinate shows U_f in dB, i.e., $20\log(U_f)$. The change in the values of U_f from the initial to the final estimation ranged from -3.0 to 2.5 dB. This third step was introduced to realize a smoother frequency characteristic than that available with the initial values. The solid line is the cubic B-spline function fitted to the reestimated U_f values. It relies on the assumption that U_f, like α_f, does not change abruptly with frequency.

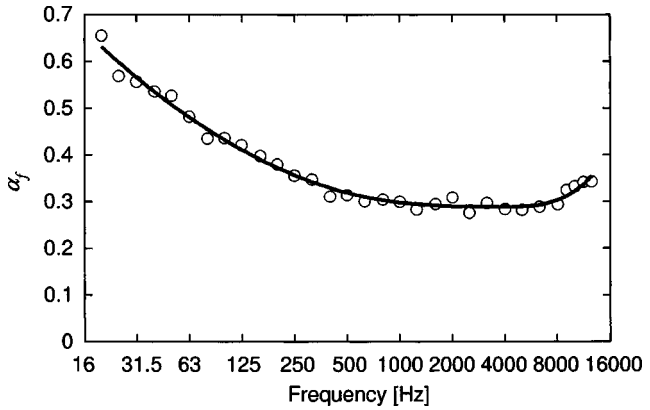

FIG. 7. Estimated α_f's from the nonlinear least squares method. Solid line shows a smoothed line generated by a cubic B-spline function.

Following these computations, equal-loudness relations were generated using the data reported in the 12 *recent* studies. For each comparison-reference frequency pair the values of p_{ft}, p_{rt}, α_f, and U_f entered in Eq. (6) were determined from the smoothed curves in Figs. 6–8. The results of these calculations are shown in Fig. 9 for 31 frequencies ranging from 20 to 12 500 Hz. The solid lines show the calculations

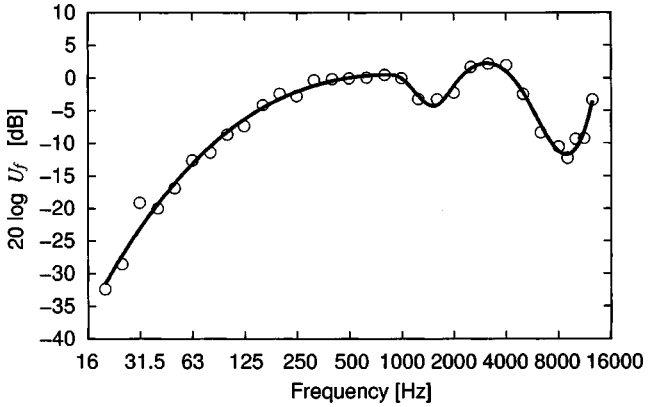

FIG. 8. U_f, a parameter in Eq. (6), reestimated using the interpolated α_f shown in Fig. 7 as a solid line. Values of U_f's are transformed into dB to show the plots in the figure. Solid line shows a smoothed line generated by a cubic B-spline function.

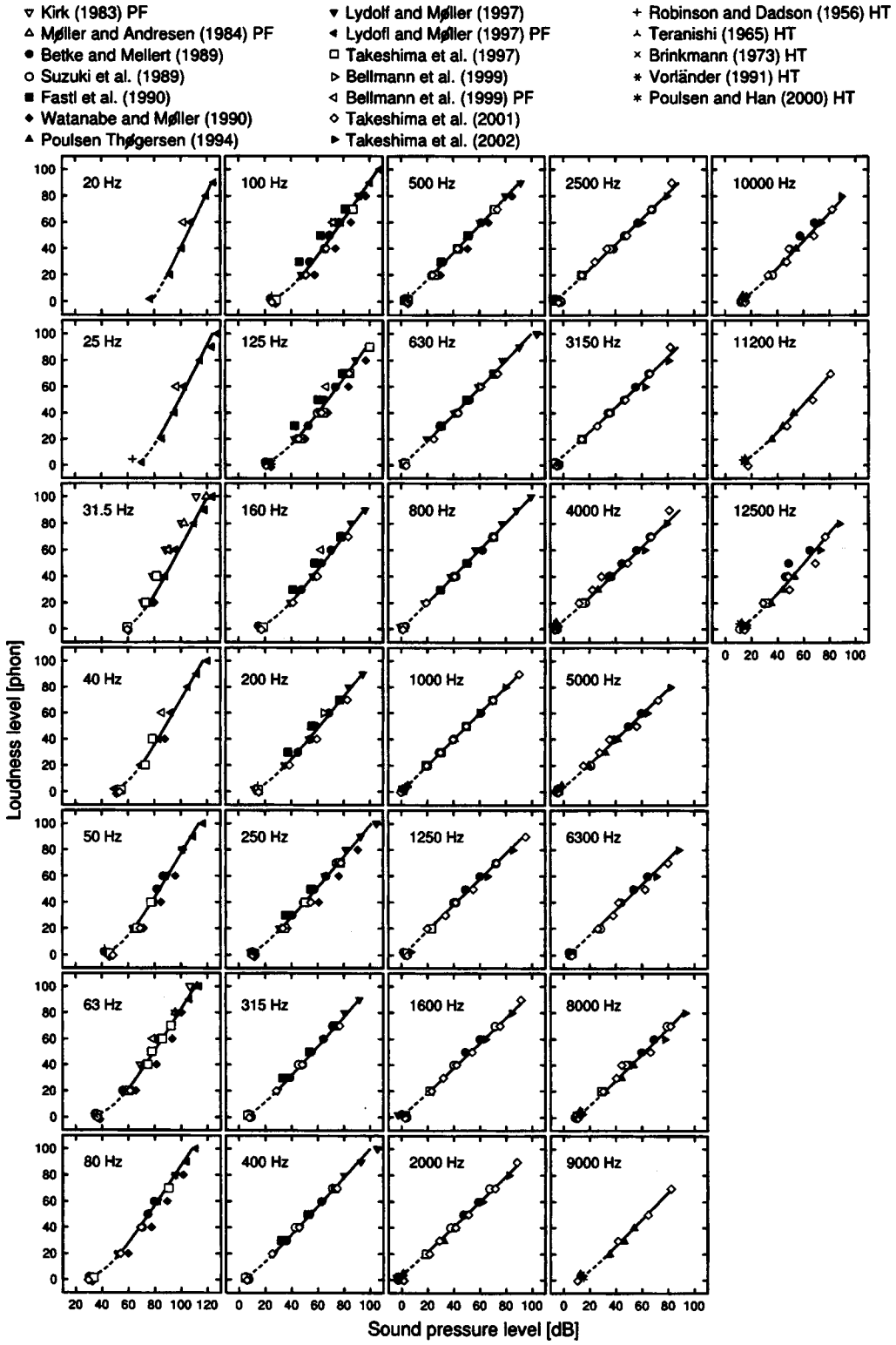

FIG. 9. Equal-loudness relations drawn by the model equation, Eq. (6), and the experimental data used for the estimation. In the legend, HT means that the study was only referenced in the panel of hearing threshold.

fit with the data values obtained for a loudness-level range from 20 to 100 phons; the dashed lines are extrapolations down to the threshold. Despite parametric drawing with smoothed values for the parameters, over the loudness-level range where equal-loudness-level data are available, the calculated functions provide good fits to the measured values.

Figure 10 compares directly the estimated contours to the equal-loudness levels obtained in the 12 *recent* studies. Overall, the equal-loudness-level contours estimated with the calculated functions provide a reasonable description of the experimental results. A family of equal-loudness-level contours obtained in this manner is shown in Fig. 11. The resultant contours exhibit a pattern of parallel displacement in accord with the contours of Fletcher and Munson (1933) and

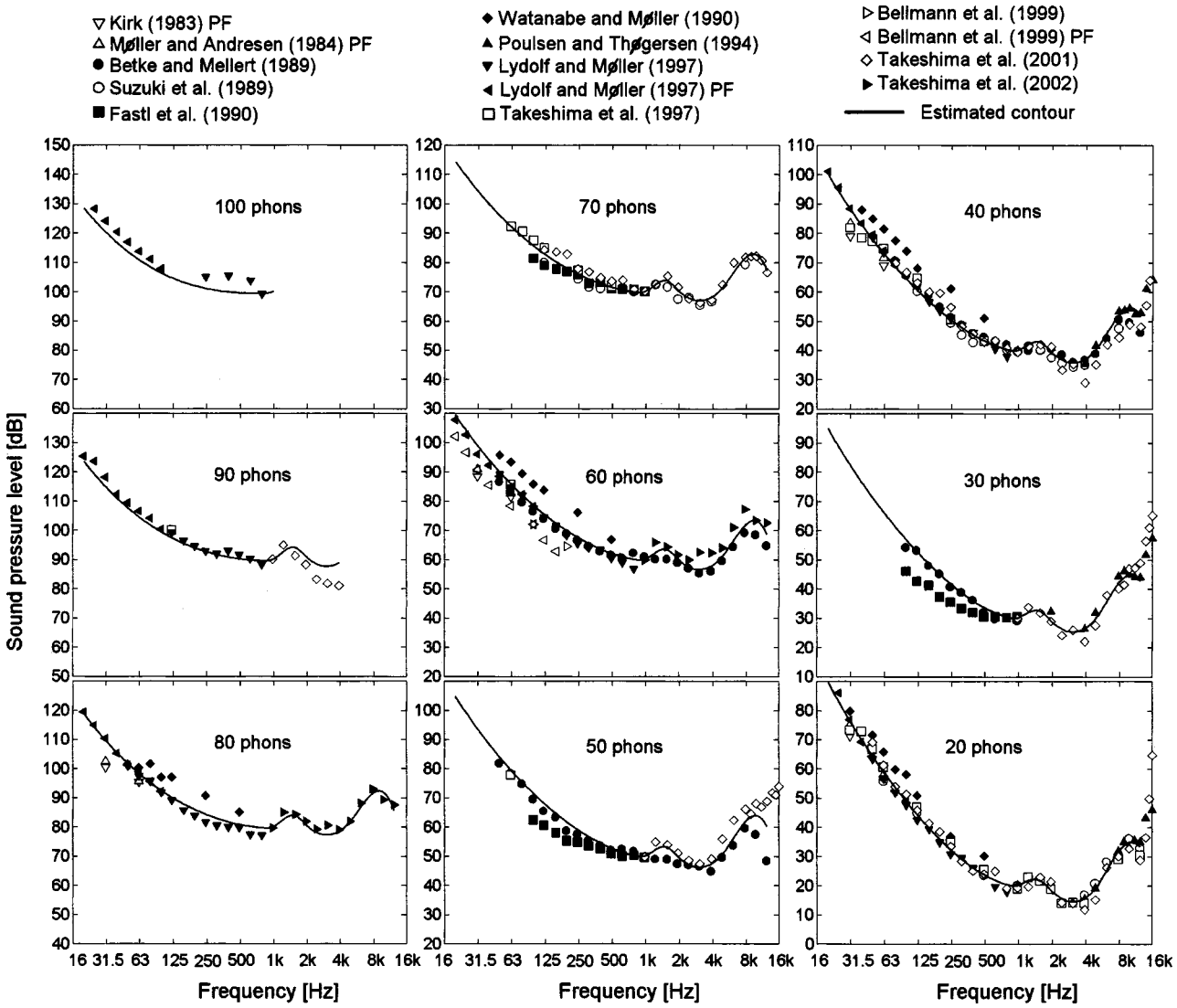

FIG. 10. Estimated equal-loudness-level contours drawn with the experimental data used for the estimations.

Robinson and Dadson (1956). If the contour for each loudness level had been estimated separately and independently of the other contours, then the pattern of parallel displacement may not have been as good.

The contours in Fig. 11 show several notable aspects. First, owing to the lack of experimental data at high loudness levels, the 90-phon contour does not extend beyond 4 kHz and the 100-phon contour does not extend beyond 1 kHz. Second, because data from only one institute are available, the 100-phon contour is drawn by a dotted line. Third, owing to the lack of experimental data between 20 phons and the hearing threshold curve, the 10-phon contour is also drawn with a dotted line. Finally, the hearing threshold curve is drawn with a dashed line just to show the ''lower boundary'' of the audible area.

IV. DISCUSSION

In this section the relation between the equal-loudness-level contours estimated from our calculations in Fig. 11 and the results of other studies are assessed and evaluated.

Individual panels in Fig. 12 compare the newly estimated contours with those published by Fletcher and Munson (1933; panel a), Churcher and King (1937; panel b), Zwicker and Feldtkeller (1955; panel c), and Robinson and Dadson (1956; panel d). The threshold contour from Fig. 11 is also shown. This contour is compared with the threshold contour measured in each of the four classic studies.

The contours in Fig. 12(a) reported by Fletcher and Munson (1933) were based on equal-loudness levels measured binaurally with earphones. The levels were calibrated relative to free-field listening conditions by means of loudness matching. To obtain the free-field levels, a sound source was placed in a free field 1 m in front of the listener. Fletcher and Munson (1933) did not measure the equal-loudness levels below 62 Hz, and their curves below 62 Hz represent extrapolations based on the available data. Taking this factor into consideration, their contours of 20 and 40 phons at 62 Hz and above are very similar to those estimated in the present study. However, at loudness levels above 40 phons their contours lie below the estimated contours at frequencies below 1 kHz. As the loudness level increases their contours

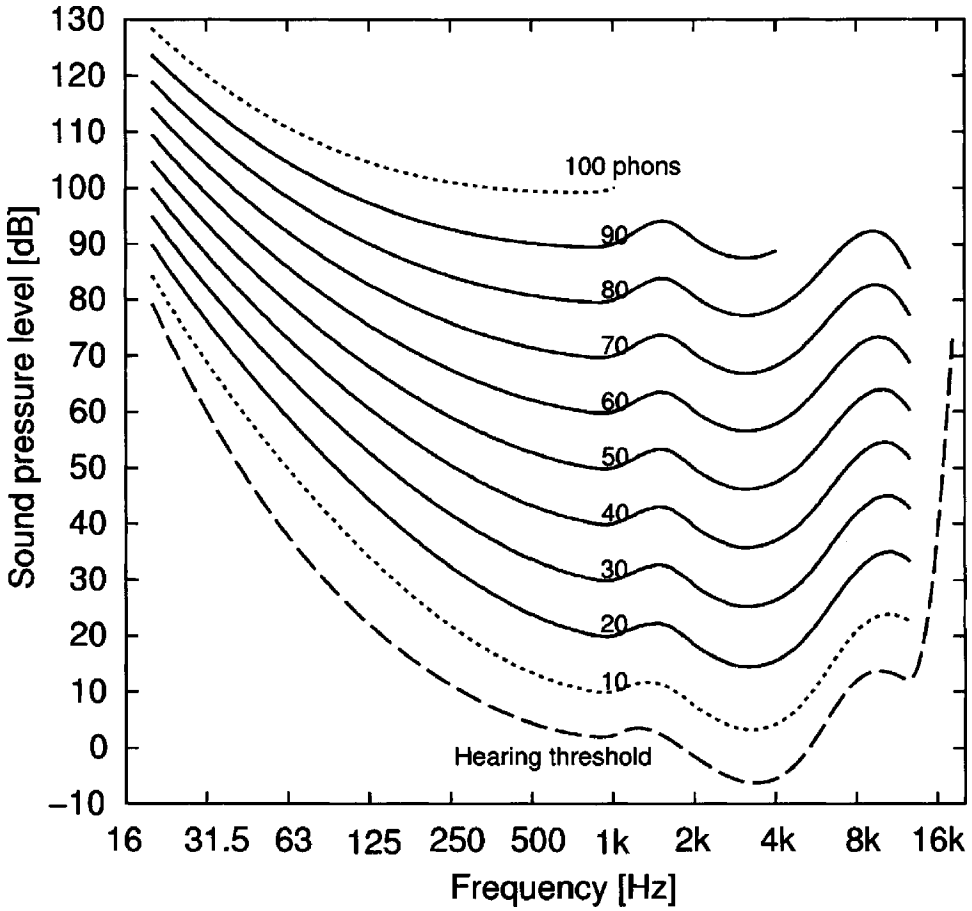

FIG. 11. Estimated equal-loudness-level contours drawn by the equation (6). The dashed line shows the threshold of hearing shown in Fig. 6. The contour at 100 phons is drawn by a dotted line because data from only one institute are available at 100 phons. The contour at 10 phons is also drawn by a dotted line because of the lack of experimental data between 20 phons and the hearing thresholds.

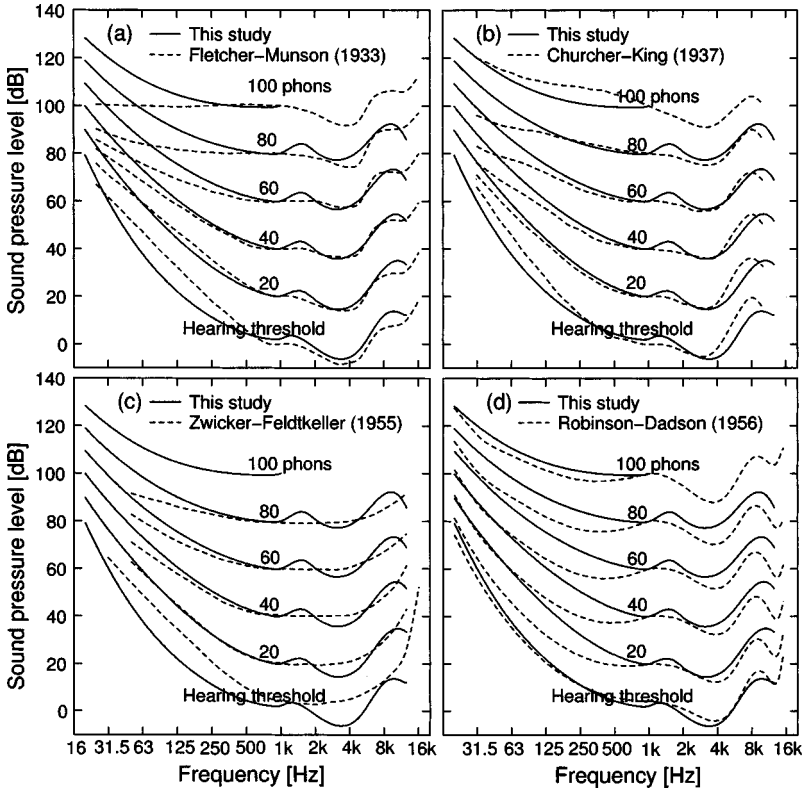

FIG. 12. Comparison of the estimated equal-loudness-level contours in this study with those reported (a) by Fletcher and Munson (1933), (b) by Churcher and King (1937), (c) by Zwicker and Feldtkeller (1955), and (d) by Robinson and Dadson (1956). Note that Fletcher and Munson (1933) did not measure equal-loudness levels below 62 Hz, and their curves below 62 Hz represent extrapolations based on the available data.

become much flatter across frequency than the estimated contours. Despite these differences, it is important to note that the two sets of contours in panel (a) closely agree across a wide range of frequencies at the 40-phon level. This contour, derived from Fletcher and Munson's (1933) pioneering work, is used as the basis of the A-weighting function. Below 1 kHz, the threshold curve measured by Fletcher and Munson (1933) lies above the threshold values reported in the present study. The elevation of their hearing-threshold curve may be attributed to masking caused by physiological noise transmitted by the earphone cushion (Killion, 1978; Rudmose, 1982).

Figure 12(b) shows that the 20-phon contour of Churcher and King (1937) closely resembles the 20-phon contour estimated in the present study. Between 20 and 80 phons their contours are also similar to the present estimated ones above about 250 Hz, whereas at 100 phons the overall shape of their contour below 1 kHz differs from both our estimated contour and the contour proposed by Fletcher and Munson (1933).

Figure 12(c) shows that the contours by Zwicker and Feldtkeller (1955) generally fit the estimated contours at the 20-phon level. Likewise, above 20 phons the overall shape of the contours of Zwicker and Feldtkeller (1955) is similar to the estimations above about 250 Hz. However, there are important differences in their micro-structure, i.e., the rise between 1 and 2 kHz and the dip between 3 and 4 kHz observed in our estimated contours do not appear in the smooth contours of Zwicker and Feldtkeller (1955). By comparison, the dip between 3 and 4 kHz appears in all the other sets of *classic* equal-loudness-level contours as well as in the threshold contours. Moreover, deviations also appear in their threshold curve. Except near 1 and 8 kHz, Zwicker and Feldtkeller's threshold curve lies above the proposed threshold curve and is generally smoother than the threshold contour estimated in this study. This smoothness might be attributable to the use of a free-field equalizer created by a passive filter (Zwicker and Feldtkeller, 1967). Because the passive filter was implemented with only two filter sections, the effect is unlikely to be reproduced in the details of the rather complicated frequency responses of HRTF, such as the peaks and valleys caused by an ear, head, and torso. At low frequencies, the threshold elevation may be explained by physiological noise transmitted by the earphone cushions as in the threshold curve measured by Fletcher and Munson (1933). Above 1 kHz, the detailed shape of their threshold contour may have been obscured by the averaging process inherent in Békésy tracking other than any effects that may come out of the use of the free-filed equalizer. Békésy tracking, unlike the classical method of adjustment, also increases variability in loudness matching (Hellman and Zwislocki, 1964). It is possible that this known increase in variability increased the smoothing observed in Zwicker and Feldtkeller's (1955) equal-loudness-level contours.

Finally, Fig. 12(d) compares the equal-loudness-level contours of Robinson and Dadson (1956) to the present estimated contours. It is notable that their threshold curve closely resembles the one estimated in the present study. Except for the threshold curve, however, the estimated equal-loudness-level curves lie distinctly above the contours recommended by Robinson and Dadson (1956). The deviation between the two sets of contours is especially evident in the frequency region below 1 kHz over the loudness-level range from 20 to 80 phons. A possible cause of this systematic discrepancy was examined by Suzuki *et al.* (1989). They focused on the manner in which the sound pressure levels of the test and reference stimuli were selected. In the 12 *recent* studies a 2AFC paradigm was consistently used. Within each session, the level of the reference tone, usually a 1-kHz pure tone, was fixed, whereas the level of the test tone was varied. This method enables the equal-loudness level of the test tones to be directly determined. In contrast, Robinson and Dadson (1956) fixed the level of the test tone and varied the level of the reference tone. Fletcher and Munson (1933) used a similar methodological approach. However, within each session they also presented the reference tones in a mixed order at three different levels. Suzuki *et al.* (1989) investigated the possible effects of these variations by using the following experimental procedures: (1) the level of the test tone was varied as in the recent studies, (2) only the level of the reference tones was varied as in the work of Robinson and Dadson (1956), and (3) the levels of both the test and reference tones were fully randomized with a range of 12 dB.

The latter method is a little different from the one used by Fletcher and Munson (1933), but the basic concept that the levels of both the test and reference tones are randomized within a session is the same. The results showed that procedures (1) and (3) gave almost identical loudness levels, whereas the results of procedure (2) were similar to those of Robinson and Dadson (1956). Although the difference between the results of procedures (1) and (3) and those of procedure (2) amounted to only 5 dB, the outcome suggests that the discrepancy between the contours of Robinson and Dadson (1956) and the proposed estimated contours may be ascribed, at least in part, to methodological factors.

There is one tendency commonly observed in all the sets of equal-loudness-level contours. The spacing of the contours generally becomes narrower as frequency goes down over the medium loudness levels. This means that the exponent of the loudness function, α, becomes large in the low frequency region as shown in Fig. 7. In other words, our hearing system is less compressive in lower frequency regions and this is qualitatively consistent with the experimental results on suppression by Delgutte (1990) suggesting that the cochlea would be close to linear at low frequencies.

Small differences are observable between the *classic* contours and the proposed estimated ones. In the frequency region between 1 and 2 kHz a small peak amounting to a few decibels is seen in the estimated contours but it does not appear in the *classic* contours. A peak between 1 and 2 kHz has been consistently observed in recent work (Suzuki *et al.*, 1989; Takeshima *et al.*, 1994, 2001, 2002; Lydolf and Møller, 1997; Poulsen and Han, 2000). This peak seems to correspond to a small dip in the HRTF near this frequency range (Shaw, 1965; Takeshima *et al.*, 1994). One possible reason to explain the lack of a peak between 1 and 2 kHz in the *classic* studies is that Fletcher and Munson (1933) did not measure any equal-loudness levels between 1 and 2 kHz

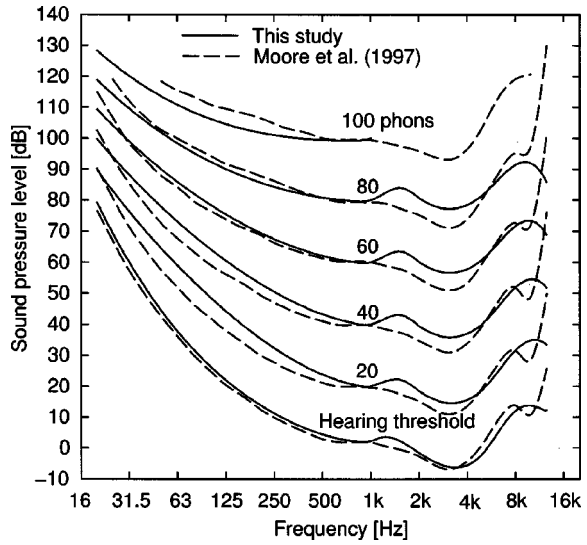

FIG. 13. Comparison of the estimated equal-loudness-level contours in this study with those derived from a loudness calculation method proposed by Moore *et al.* (1997).

whereas Churcher and King (1937) and Robinson and Dadson (1956) measured equal-loudness levels at only one point within this frequency region. As a result, this peak may have been overlooked. In the case of Zwicker and Feldtkeller (1955), they measured equal-loudness levels at several frequencies within the 1-to-2-kHz region, but the greater variability inherent in Békésy tracking as a tool for loudness matching (Hellman and Zwislocki, 1964) may have obscured the effect. Another possible explanation may be the use of the free-field equalizer in their measurements as anticipated in the earlier paragraph.

Another relevant issue is the fine structure of equal-loudness-level contours. It is well known that individual hearing thresholds often exhibit fine, but distinctive, peaks and valleys along the frequency continuum (e.g., Elliot, 1958). This fine structure in the threshold curve is closely related to the OAE (Schloth, 1983; Smurzynski and Probst, 1998). More recently, Mauermann *et al.* (2000a,b) reported that the fine structure observed in the threshold curve is reflected in observed equal-loudness levels up to around 40 phons. However, their data indicate that above 40 phons the influence of the fine structure of the threshold contour on the equal-loudness-level contours is less evident. Moreover, it decreases with level. Since the peaks and valleys in the fine structure are likely to be at different frequencies for different listeners, their effect ought to be strongly diminished when data are averaged across a number of listeners.

Figure 13 compares the equal-loudness-level contours derived from a loudness-calculation procedure suggested by Moore *et al.* (1997) to the ones estimated in this study. The work by Moore *et al.* (1997) in assessing the loudness of sounds at various frequencies is a revision of a previous proposal (Moore and Glasberg, 1996). This is given as a modification of the formulation by Zwicker (1958) based on the auditory excitation-pattern model (Fletcher and Munson, 1937). In their modification, Moore *et al.* (1997) assume that the loudness perception process is followed by a linear block with a transfer function. The specific loudness of a sound is given by an equation equivalent to Eq. (4), whereas an equation equivalent to Eq. (3) was used in the earlier proposal (Moore and Glasberg, 1996). Moreover, the linear block is expressed as the product of HRTF and the middle ear transfer function (Puria *et al.*, 1997). With a few more assumptions, a family of equal-loudness-level contours is predicted.

As shown in Fig. 13, the overall agreement between our estimated contours and those predicted by Moore *et al.* (1997) is much better than the agreement between our contours and those of Robinson and Dadson in Fig. 12(d). However, there are some discrepancies between the two data sets. First, at frequencies below 250 Hz and loudness levels below 60 phons their contours are somewhat lower than ours. However, the differences are small and may be within the error of measurement. Second, and most notable, in the frequency region between 1 and 2 kHz the peak observed in our estimated contours is absent in Moore *et al.* (1997). Third, at the 100-phon level the contour of Moore *et al.* (1997) is somewhat higher than our estimated contour. However, it is similar to the classic contour of Churcher and King (1937). A wider spacing between the contours at high levels is consistent with evidence that at high sound pressure levels the slope of the loudness function at low frequencies is shallower than it is over the middle range of levels (Hellman and Zwislocki, 1968). This level dependency could be consistent with the nonlinear input–output characteristic observed in the basilar-membrane mechanics. After all, recent studies show that the exponent of the loudness function shape may probably be dependent on sound level (Yates, 1990; Buus and Florentine, 2001b). This is supported by recent data, which indicate more compression at moderate levels than at low and high levels (e.g., Florentine *et al.*, 1996; Buus and Florentine, 2001a).

The middle ear acoustic reflex may also affect the shape of the contours, especially at high intensities in the low frequency range. If the loudness at low frequencies was attenuated, then the contours at high SPLs would be elevated relative to the contours estimated with a constant power-function slope α. Borg (1968) found that the transmission loss of the middle ear caused by activation of the reflex is largest at 500 Hz and smallest at 1450 Hz. His results showed that at 500 Hz the transmission of sound is reduced by 0.6 to 0.7 dB for each 1-dB increment in the stimulus level. This result means that at 20 dB above the threshold, the transmission loss at 500 Hz is about 13 dB, whereas at the same level, the loss at 1450 Hz is about 6 dB. According to Borg's measurements, the maximum frequency-dependent difference in the transmission loss amounts to 7 dB. However, Borg's data do not account for the decrease in the slope observed in the loudness function for 100- and 250-Hz tones at high SPLs (Hellman and Zwislocki, 1968).

Another factor to be considered is the latency of the reflex. This latency is estimated to be around 100 ms. This means that the initial 100 ms of a tone burst is not affected by the reflex. Since the time constant for loudness perception is around this value (e.g., Munson, 1947; Takeshima *et al.*, 1988), the loudness of a tone burst longer than 100 ms will be determined to a large extent by the initial part of the burst during which the reflex does not play a role. Thus, the effect

of the following attenuated portion of the tone burst would be at most a few decibels. As a result, we conclude that the influence of the reflex on the equal-loudness-level contours is limited. Nevertheless, in accordance with the analysis of the relation between loudness level and sound pressure level in Fig. 9, it is evident that the data at 400 and 630 Hz are all less steep at 80 and 100 phons than the estimated loudness-level curves predict. This reduction in loudness, which is attributable to the reflex activation (Hellman and Scharf, 1984), is compatible with some loudness measurements (e.g., Hellman and Zwislocki, 1968). Since data from only one institute at 100 phons is available, more data are needed to clarify this important issue. Nonetheless, despite the possibility that the acoustic reflex plays some role in the reduced high-level slope of the loudness function at low frequencies, it cannot also account for the reduced high-level slope observed in the loudness function at 12.5 kHz and higher (Hellman *et al.*, 2000). The evidence indicates that at low frequencies the loudness function tends to approach the high-level slope at 1 kHz, whereas at 12.5 kHz and higher, it becomes flatter than the 1-kHz function (Hellman and Zwislocki, 1968; Hellman *et al.*, 2001). In light of these limitations, the exponent α_f used in the estimation of the proposed contours in Fig. 9 can only be regarded as valid over the stimulus range of interest below high sound pressure levels. The slope (exponent) estimated in Fig. 7 does not provide an accurate account of the data above 80 phons for 630 Hz and below and above 60 phons for 12.5 kHz and above.

V. CONCLUSIONS

After reviewing all known published studies of equal-loudness-level contours for pure tones, a new family of equal-loudness-level contours was estimated from 12 *recent* studies. An equation was derived to express the equal-loudness relation between pure tones at different frequencies. The procedure using this equation made it possible to draw smooth contours from discrete sets of data values. Except in the vicinity of the threshold and at very high SPLs, the equation provides a good description of the experimental results. In general, the classic contours proposed by Fletcher and Munson (1933), Churcher and King (1937), and Zwicker and Feldtkeller (1955) exhibit some overall similarity to the proposed estimated contours up to 60 phons. However, at higher levels, they deviate from the proposed contours in the frequency region below about 500 Hz. By contrast, the estimated contours exhibit clear differences from those reported by Robinson and Dadson (1956). The differences are most pronounced below 1 kHz. The proposed threshold curve closely resembles the one reported by Robinson and Dadson (1956) whereas the thresholds given by Fletcher and Munson (1933), Churcher and King (1937), and Zwicker and Feldtkeller (1955) exhibit clear deviations from those obtained in the present study, especially in the frequency region below 1 kHz.

ACKNOWLEDGMENTS

The authors wish to thank Professor Rhona Hellman and Professor Jont B. Allen for their helpful comments as reviewers of an earlier version of this work in 1997 that substantially improved the manuscript. The authors thank Professor Hugo Fastl, Professor Jont B. Allen and an anonymous reviewer for instructive comments and advice as reviewers to substantially improve former versions of the manuscript. The authors wish to thank the members of ISO/TC 43/WG 1 for continuing discussions which have lasted more than 15 years. The authors especially single out the convener, Professor Henrik Møller, for intensive discussions including one on the effects of head related transfer function on the contours. The authors wish to thank Professor Birger Kollmeier for useful comments on an earlier model for loudness perception. The authors wish to thank Professor Toshio Sone for triggering and sustaining this study. The authors wish to thank the research team members for this study, Professor Hajime Miura, Takeshi Fujimori, Professor Masazumi Kumagai, Dr. Kaoru Ashihara, and Professor Kenji Ozawa, for their respective contributions. We also thank Professor Søren Buus and Professor Tetsuaki Kawase for discussions on the nonlinearity of loudness perception and Yusaku Sasaki for his technical support. The authors are grateful to Professor Jeremy Simmons for his comments and correction of English expressions. The last phase of this study was supported by a NEDO International Joint Research Grant Program. The authors wish to thank the members of the grant program for intensive discussions.

Allen, J. B. (**1996**). ''Harvey Fletcher's role in the creation of communication acoustics,'' J. Acoust. Soc. Am. **99**, 1825–1839.

Allen, J. B., and Neely, S. T. (**1997**). ''Modeling the relation between the intensity JND and loudness for pure tones and wide-band noise,'' J. Acoust. Soc. Am. **102**, 3628–3646.

Atteneave, F. (**1962**). ''Perception and related areas,'' in *Psychology: A Study of Science* Vol. 4, edited by S. Koch (McGraw–Hill, New York), pp. 619–659.

Bellmann, M. A., Mellert, V., Reckhardt, C., and Remmers, H. (**1999**). ''Perception of sound and vibration at low frequencies,'' Joint meeting of ASA and EAA: Forum Acusticum integrating German Acoustics DAGA Conference 1999, Berlin, Germany.

Betke, K. (**1991**). ''New hearing threshold measurements for pure tones under free-field listening conditions,'' J. Acoust. Soc. Am. **89**, 2400–2403.

Betke, K., and Mellert, V. (**1989**). ''New measurements of equal-loudness level contours,'' Proc. Inter-noise 89, pp. 793–796.

Borg, E. (**1968**). ''A quantitative study of the effect of the acoustic stapedius reflex on sound transmission through the middle ear of man,'' Acta Oto-Laryngol. **66**, 461–472.

Brinkmann, K. (**1973**). ''Audiometer-Bezugsschwelle und Freifeld-Hörschwelle (Audiometer reference threshold and free field hearing threshold),'' Acustica **28**, 147–154.

Buus, S., and Florentine, M. (**2001a**). ''Growth of loudness in listeners with cochlear hearing losses: Recruitment reconsidered,'' J. Asso. Res. Otolaryn. **3**, 120–139 (online publication: 2001, paper publication: 2002).

Buus, S., and Florentine, M. (**2001b**). ''Modifications to the power function for loudness,'' in *Fechner Day 2001*, edited by E. Sommerfeld, R. Kompass, and T. Lachmann (Pabst, Berlin), pp. 236–241.

Buus, S., Müsch, H., and Florentine, M. (**1998**). ''On loudness at threshold,'' J. Acoust. Soc. Am. **104**, 399–410.

Churcher, B. G., and King, A. J. (**1937**). ''The performance of noise meters in terms of the primary standard,'' J. Inst. Electr. Eng. **81**, 57–90.

Collins, A. A., and Gescheider, G. A. (**1989**). ''The measurement of loudness in individual children and adults by absolute magnitude estimation and cross-modality matching,'' J. Acoust. Soc. Am. **85**, 2012–2021.

Delgutte, B. (**1990**). ''Two-tone rate suppression in auditory-nerve fibers: Dependence on suppressor frequency and level,'' Hear. Res. **49**, 225–246.

Ekman, G. (**1959**). ''Weber's law and related functions,'' J. Psychol. **47**, 343–352.

Elliott, E. (**1958**). ''A ripple effect in the audiogram,'' Nature (London) **181**, 1079.
Fastl, H., and Zwicker, E. (**1987**). ''Lautstärkepegel bei 400 Hz; Psychoakustische Messung und Berechnung nach ISO 532B (Loudness level at 400 Hz: Psychoacoustical measurement and calculation by ISO 532B),'' Fortschritte der Akustik, DAGA '87, pp. 189–193.
Fastl, H., Jaroszewski, A., Schorer, E., and Zwicker, E. (**1990**). ''Equal loudness contours between 100 and 1000 Hz for 30, 50, and 70 phon,'' Acustica **70**, 197–201.
Feldtkeller, R., Zwicker, E., and Port, E. (**1959**). ''Lautstärke, Verhältnislautheit und Summenlautheit (Loudness, loudness ratio and summed loudness),'' Frequenz **4**, 108.
Fletcher, H. (**1995**). *Speech and Hearing in Communication*, edited by J. B. Allen (Acoustical Society of America, Woodbury, NY), Chap. 11, pp. 176–209 [original: (Krieger Huntington, NY, 1953)].
Fletcher, H., and Munson, W. A. (**1933**). ''Loudness, its definition, measurement and calculation,'' J. Acoust. Soc. Am. **5**, 82–108.
Fletcher, H., and Munson, W. A. (**1937**). ''Relation between loudness and masking,'' J. Acoust. Soc. Am. **9**, 1–10.
Florentine, M., Buus, S., and Poulsen, T. (**1996**). ''Temporal integration of loudness as a function of level,'' J. Acoust. Soc. Am. **99**, 1633–1644.
Gabriel, B., Kollmeier, B., and Mellert, V. (**1997**). ''Influence of individual listener, measurement room and choice of test-tone levels on the shape of equal-loudness level contours,'' Acustica **83**, 670–683.
Gescheider, G. A. (**1997**). *Psychophysics: The Fundamentals* (Erlbaum, Mahwah, NJ), Chap. 10, pp. 207–230.
Hellman, R. P. (**1976**). ''Growth of loudness at 1000 and 3000 Hz,'' J. Acoust. Soc. Am. **60**, 672–679.
Hellman, R. P. (**1994**). ''Relation between the growth of loudness and high-frequency excitation,'' J. Acoust. Soc. Am. **96**, 2655–2663.
Hellman, R. P. (**1997**). ''Growth of loudness in sensorineural impariment: Experimental results and modeling implications'' in *Modeling Sensorineural Hearing Loss*, edited by W. Jesteadt (Lawrence Erlbaum, Mahwah, NJ), Chap. 12, pp. 199–212.
Hellman, R. P., and Meiselman, C. H. (**1990**). ''Loudness relations for individuals and groups in normal and impaired hearing,'' J. Acoust. Soc. Am. **88**, 2596–2606.
Hellman, R. P., and Scharf, B. (**1984**). ''Acoustic reflex and loudness,'' in *The Acoustic Reflex: Basic Principles and Clinical Applications*, edited by S. Silman (Academic, New York), pp. 469–516.
Hellman, R. P., and Zwislocki, J. J. (**1961**). ''Some factors affecting the estimation of loudness,'' J. Acoust. Soc. Am. **33**, 687–694.
Hellman, R. P., and Zwislocki, J. J. (**1963**). ''Monaural loudness function at 1000 cps and interaural summation,'' J. Acoust. Soc. Am. **35**, 856–865.
Hellman, R. P., and Zwislocki, J. J. (**1964**). ''Loudness function of a 1000 cps tone in the presence of masking noise,'' J. Acoust. Soc. Am. **36**, 1618–1627.
Hellman, R. P., and Zwislocki, J. J. (**1968**). ''Loudness determination at low sound frequencies,'' J. Acoust. Soc. Am. **43**, 60–64.
Hellman, R. P., Takeshima, H., Suzuki, Y., Ozawa, K., and Sone, T. (**2000**). ''Equal-loudness contours at high frequencies,'' Proc. Inter-noise 2000, pp. 3653–3658.
Hellman, R. P., Takeshima, H., Suzuki, Y., Ozawa, K., and Sone, T. (**2001**). ''Determination of equal-loudness relations at high frequencies,'' in Proceedings of the 17th Annual Meeting of the International Society for Psychophysics, Leipzig, Germany, pp. 225–230.
Humes, L. E., and Jesteadt, W. (**1991**). ''Models of the effects of threshold on loudness growth and summation,'' J. Acoust. Soc. Am. **90**, 1933–1943.
International Organization for Standardization (**1961**). *Normal equal-loudness contours for pure tones and normal threshold of hearing under free field listening conditions* [ISO R/226:1961] (International Organization for Standardization, Geneva).
International Organization for Standardization (**1987**). *Acoustics—Normal Equal-Loudness Contours* [ISO 226:1987] (International Organization for Standardization, Geneva).
Killion, M. C. (**1978**). ''Revised estimate of minimum audible pressure: Where is the 'missing 6 dB?'" J. Acoust. Soc. Am. **63**, 1501–1508.
Kingsbury, B. A. (**1927**). ''A direct comparison of the loudness of pure tones,'' Phys. Rev. **29**, 588–600.
Kirk, B. (**1983**). ''Hørestyrke og genevirkning af infralyd (Loudness and annoyance from infrasound),'' Institute of Electronic Systems, Aalborg University, Aalborg, Denmark, pp. 1–111.
Lochner, J. P. A., and Burger, J. F. (**1961**). ''Form of the loudness function in the presence of masking noise,'' J. Acoust. Soc. Am. **33**, 1705–1707.
Luce, R. D. (**1959**). ''On the possible psychophysical laws,'' Psychol. Rev. **66**, 81–95.
Lydolf, M., and Møller, H. (**1997**). ''New measurements of the threshold of hearing and equal-loudness contours at low frequencies,'' in Proceedings of the 8th International Meeting on Low Frequency Noise and Vibration, Gothenburg, Sweden, pp. 76–84.
Mauermann, M., Long, G., and Kollmeier, B. (**2000a**). ''Comparison of fine structure in isophone contours, threshold in quiet and otoacoustic emissions,'' in Abstracts of the 23th ARO Midwinter Research Meeting #984, p. 284.
Mauermann, M., Long G., and Kollmeier, B. (**2000b**). ''Vergleich der Feinstruktur von Isophonen, Ruhehorschwelle und otoakustischen Emissionen (Comparison of the fine structure of the equal loudness level contours, absolute hearing threshold and otoacoustic emission),'' Fortschritte der Akustik—DAGA 2000, Oldenburg, Deutsche Gesellschaft für Akustik e.V., pp. 292–293.
Møller, H., and Andresen, J. (**1984**). ''Loudness at Pure Tones at Low and Infrasonic Frequencies,'' J. Low Freq. Noise. Vib. **3**, 78–87.
Møller, H., and Lydolf, M. (**1996**). ''Equal loudness contours, literature overview'' (Letter to ISO/TC 43/WG 1, Document N232).
Moore, B. C. J., and Glasberg, B. R. (**1996**). ''A revision of Zwicker's loudness model,'' Acust. Acta Acust. **82**, 335–345.
Moore, B. C. J., Glasberg, B. R., and Baer, T. (**1997**). ''A model for the prediction of thresholds, loudness, and partial loudness,'' J. Audio Eng. Soc. **45**, 224–240.
Müller, F., and Fichtl, E. (**1994**). ''The measurement of equal loudness contours using a direct scaling procedure and validation by equal time contours,'' Proc. Inter-noise 94, pp. 1069–1072.
Munson, W. A. (**1947**). ''The growth of auditory sensation,'' J. Acoust. Soc. Am. **19**, 584–591.
Nakagawa, T., and Oyanagi, Y. (**1980**). ''Program system SALS for nonlinear least-squares fitting in experimental sciences,'' in *Recent Developments in Statistical Inference and Data Analysis*, edited by K. Matusita (North Holland, Amsterdam), pp. 221–225.
Neely, S. T., and Allen, J. B. (**1997**). ''Relation between the rate of growth of loudness and the intensity DL,'' in *Modeling Sensorineural Hearing Loss*, edited by W. Jesteadt (Erlbaum, Mahwah, NJ), pp. 213–222.
Poulsen, T., and Han, L. A. (**2000**). ''The binaural free field hearing threshold for pure tones from 125 Hz to 16 kHz,'' Acust. Acta Acust. **86**, 333–337.
Poulsen, T., and Thøgersen, L. (**1994**). ''Hearing threshold and equal loudness level contours in a free sound field for pure tones from 1 kHz to 16 kHz,'' Proc. Nordic Acoust. Meeting, pp. 195–198.
Puria, S., Rosowski, J. J., and Peake, W. T. (**1997**). ''Sound-pressure measurements in the cochlear vestibule of human-cadaver ears,'' J. Acoust. Soc. Am. **101**, 2754–2770.
Robinson, D. W. (**1953**). ''The relation between the sone and phon scales of loudness,'' Acustica **3**, 344–358.
Robinson, D. W. (**1957**). ''The subjective loudness scale,'' Acustica **7**, 217–233.
Robinson, D. W., and Dadson, R. S. (**1956**). ''A re-determination of the equal-loudness relations for pure tones,'' Br. J. Appl. Phys. **7**, 166–181.
Rowley, R. R., and Studebaker, G. A. (**1969**). ''Monaural loudness-intensity relationships for a 1000-Hz tone,'' J. Acoust. Soc. Am. **45**, 1186–1192.
Rudmose, W. (**1982**). ''The case of the missing 6 dB,'' J. Acoust. Soc. Am. **71**, 650–659.
Scharf, B., and Stevens, J. C. (**1961**). ''The form of the loudness function near threshold,'' Proc. Int. Congress on Acoustics, 3rd, Stuttgard, 1959, edited by L. Cremer (Elsevier, Amsterdam), pp. 80–82.
Schlauch, R. S., DiGiovanni, J. J., and Ries, D. T. (**1998**). ''Basilar membrane nonlinearity and loudness,'' J. Acoust. Soc. Am. **103**, 2010–2020.
Schloth, E. (**1983**). ''Relation between spectral composition of spontaneous oto-acoustic emission and fine-structure of threshold in quiet,'' Acustica **53**, 251–256.
Shaw, E. A. G. (**1965**). ''Earcanal pressure generated by a free sound field,'' J. Acoust. Soc. Am. **39**, 465–470.
Smurzynski, J., and Probst, R. (**1998**). ''The influence of disappearing and reappearing spontaneous otoacoustic emition on one subject's threshold of hearing,'' Hear. Res. **115**, 197–205.
Stevens, S. S. (**1953**). ''On the brightness of lights and loudness of sounds,'' Science **118**, 576.
Stevens, S. S. (**1955**). ''The measurement of loudness,'' J. Acoust. Soc. Am. **27**, 815–829.

Stevens, S. S. (**1957**). ''On the psychophysical law,'' Psychol. Rev. **64**, 153–181.
Stevens, S. S. (**1959**). ''Tactile vibration: Dynamics of sensory intensity,'' J. Exp. Psychol. **59**, 210–218.
Suzuki, S., Suzuki, Y., Kono, S., Sone, T., Kumagai, M., Miura, H., and Kado, H. (**1989**). ''Equal-loudness level contours for pure tone under free field listening condition (I)—Some data and considerations on experimental conditions,'' J. Acoust. Soc. Jpn. (E) **10**, 329–338.
Takeshima, H., Suzuki, Y., Ozawa, K., Kumagai, M., and Sone, T. (**2003**). ''Comparison of loudness functions suitable for drawing equal-loudness-level contours,'' Acoust. Sci. Tech. **24**, 61–68.
Takeshima, H., Suzuki, Y., Ashihara, K., and Fujimori, T. (**2002**). ''Equal-loudness contours between 1 kHz and 12.5 kHz for 60 and 80 phons,'' Acoust. Sci. Tech. **23**, 106–109.
Takeshima, H., Suzuki, Y., Fujii, H., Kumagai, M., Ashihara, K., Fujimori, T., and Sone, T. (**2001**). ''Equal-loudness contours measured by the randomized maximum likelihood sequential procedure,'' Acust. Acta Acust. **87**, 389–399.
Takeshima, H., Suzuki, Y., Kumagai, M., Sone, T., Fujimori, T., and Miura, H. (**1997**). ''Equal-loudness level measured with the method of constant stimuli—Equal-loudness level contours for pure tone under free-field listening condition (II),'' J. Acoust. Soc. Jpn. (E) **18**, 337–340.
Takeshima, H., Suzuki, Y., Kumagai, M., Sone, T., Fujimori, T., and Miura, H. (**1994**). ''Threshold of hearing for pure tone under free-field listening conditions,'' J. Acoust. Soc. Jpn. (E) **15**, 159–169.
Takeshima, H., Suzuki, Y., Kono, S., and Sone, T. (**1988**). ''Growth of the loudness of a tone burst with a duration up to 10 seconds,'' J. Acoust. Soc. Jpn. (E) **9**, 295–300.
Teranishi, R. (**1965**). ''Oto no ôkisa Keiryô ni kansuru kenkyû—Saisyô Katyôti ni tuite;'' ''Study about measurement of loudness—On the problems of minimum audible sound,'' Researches of the Electrotechnical Laboratory, No. 658.
Vorländer, M. (**1991**). ''Freifeld-Horshwellen von 8 kHz–16 kHz, (Free field hearing threshold from 8 kHz to 16 kHz),'' Fortschritte der Akustik—DAGA '91, Bad Honnef, DPG-GmbH, pp. 533–536.
Watanabe, T., and Møller, H. (**1990**). ''Hearing threshold and equal loudness contours in free field at frequencies below 1 kHz,'' J. Low Freq. Noise Vib. **9**, 135–148.
Whittle, L. S., Collins, S. J., and Robinson, D. W. (**1972**). ''The audibility of low frequency sounds,'' J. Sound Vib. **21**, 431–448.
Yates, G. K. (**1990**). ''The basilar membrane input-output function,'' in *The Mechanics and Biophysics of Hearing*, edited by P. Dallos, C. D. Geisler, J. M. Matthews, M. A. Ruggero, and C. R. Steele (Springer-Verlag, New York), pp. 106–113.
Zwicker, E. (**1958**). ''Über Psychologische und Methodische Grundlagen der Lautheit (On psychological and methodological bases of loudness),'' Acustica **8**, 237–258.
Zwicker, E. (**1963**). ''Über die Lautheit von Ungedrosselten und Gedrosselthen Schallen,'' Acustica **13**, 194–211.
Zwicker, E., and Fastl, H. (**1990**). *Psychoacoustics—Facts and Models* (Springer-Verlag, Berlin), Chap. 8, pp. 181–214.
Zwicker, E., and Feldtkeller, R. (**1955**). ''Über die Lautstärke von Gleichförmigen Geräuschen (On the loudness of stationary noises),'' Acustica **5**, 303–316.
Zwicker, E., and Feldtkeller, R. (**1967**). *Das Ohr als Nachrichtenempfänger* (Hirzel-Verlag, Stuttgart, Germany). English translation by H. Müsch, S. Buus, and M. Florentine, *The Ear as a Communication Receiver* (Acoustical Society of America, Woodbury, NY, 1999).
Zwislocki, J. J. (**1965**). ''Analysis of some auditory characteristics,'' in *Handbook of Mathematical Psychology*, edited by R. D. Luce, R. R. Bush, and E. Galanter (Wiley, New York), pp. 1–97.
Zwislocki, J. J. (**1983**). ''Group and individual relations between sensation magnitudes and their numerical estimates,'' Percept. Psychophys. **33**, 460–468.
Zwislocki, J. J., and Hellman, R. P. (**1960**). ''On the psychophysical law,'' J. Acoust. Soc. Am. **32**, 924.

Virtual sensing for broadband noise control in a lightly damped enclosure

Jing Yuan[a)]
Department of Mechanical Engineering, The Hong Kong Polytechnic University, Hunghom, Kowloon, Hong Kong

(Received 17 July 2003; revised 6 March 2003; accepted 10 May 2004)

Available virtual sensing schemes either depend on assumptions that are valid for isolated frequencies, or require heavy online adaptations. A simple method is proposed here to predict the virtual signal exactly for broadband noise control in a lightly damped enclosure. The proposed method requires two physical sensors installed judiciously in a sound field to predict a virtual signal. The method is based on an exact mathematical relation between the virtual and physical sensors, which is valid for the entire frequency of interest. It is possible to use multiple sensor-pairs to reduce the sensitivity of the proposed method with respect to acoustic parameters, such as speed of sound or sensor mismatching. Experimental results are presented to verify the analytical results. © *2004 Acoustical Society of America.* [DOI: 10.1121/1.1768946]

PACS numbers: 43.50.Ki [KAC] Pages: 934–941

I. INTRODUCTION

In many active noise control (ANC) systems, secondary sources are employed to generate destructive interference and create local zones of quiet in sound fields.[1,2] Practical implementation of these systems requires the installation of error sensors in the quiet zones to monitor the ANC performance. In adaptive ANC systems, the adaptation of ANC transfer functions depends on the feedback of error signals.

In some applications, it may not be possible to install physical sensors in an area which is part of a quiet zone. Consequently sound signals in such an area have to be predicted with signals measured in other locations. The technique is known as virtual sensing, which was originated by Garcia-Bonito *et al.*[3,4] They make use of the fact that the spatial rate of pressure change of the primary field is small at low frequencies, and assumed that the primary field pressure is the same in both virtual and actual locations. They also observed that the pressure of the secondary source is different between the virtual and actual locations when both are close to the secondary source. The prior measurement of this difference makes it possible to estimate the signal at the virtual location. The method was applied to improve the performance of a pair of ANC ear defenders.[5] Another virtual sensing scheme is extrapolation of signals measured by physical sensors.[6] It was shown applicable to control tonal noise in the one-dimensional (1D) duct[7,8] and the three-dimensional (3D) free field.[9] For broadband applications, the extrapolation weights should be tuned by an adaptation algorithm.[10] Virtual sensors were also studied by Roure and Albarrazin,[11] assuming the existence of a transfer matrix $M(z)$ between the virtual signal vector $p_v(z)$ and the physical signal vector $p(z)$ via $p_v(z)=M(z)p(z)$.

Analytically, the relation between the virtual and physical signals is neither filtering nor extrapolating. Instead, it depends on both the primary and secondary sources. An exact way to predict the virtual signal is by means of an adaptive observer.[12] For virtual sensing of a tonal noise, an exact modal model of a sound field is required. If the model is truncated to the first m modes, then m online adaptive filters are required to adjust the observer state vector. If the noise contains multiple frequencies, the exact method[12] has an increased complexity proportional to the number of tonal frequencies.

For a noise field with a single broadband primary source, it is desired to have a simpler and exact virtual sensing method, which is proposed in this paper. This is an exact method based on the spatial distributions of the primary and secondary fields, and it is valid for the entire frequency range of interest. Only two physical sensors are required to predict a virtual signal exactly. Details of the proposed method are presented in the following text.

II. PRESSURE SIGNALS IN A DUCT

In most cases, available physical sensors are microphones measuring pressure signals. It is important to analyze the spatial distribution of pressure signals in a sound field, to design and implement an exact virtual sensing scheme. For this reason, a sound field in a lightly damped finite 1D duct is studied first.

A. A sound field in a finite 1D duct

Shown in Fig. 1(a) is a 1D ANC system, where the primary and secondary sources are placed at opposite ends of a duct. Let u_p, Z_p, u_s, and Z_s denote, respectively, the strengths and impedances of the sources where subscripts p and s refer to the primary and secondary sources. The strength of a mechanical-acoustic source is the volume velocity, and the strength of an electro-acoustic source is the driving current. Spatial distribution of sound signals may be described analytically by path transfer functions from the sources to a point x meters away from the primary source. The values of x are in the range $0 \leqslant x \leqslant l$ where l is the length of the duct.

[a)]Electronic mail: mmjyuan@polyu.edu.hk

 0001-4966/2004/116(2)/934/8/$20.00

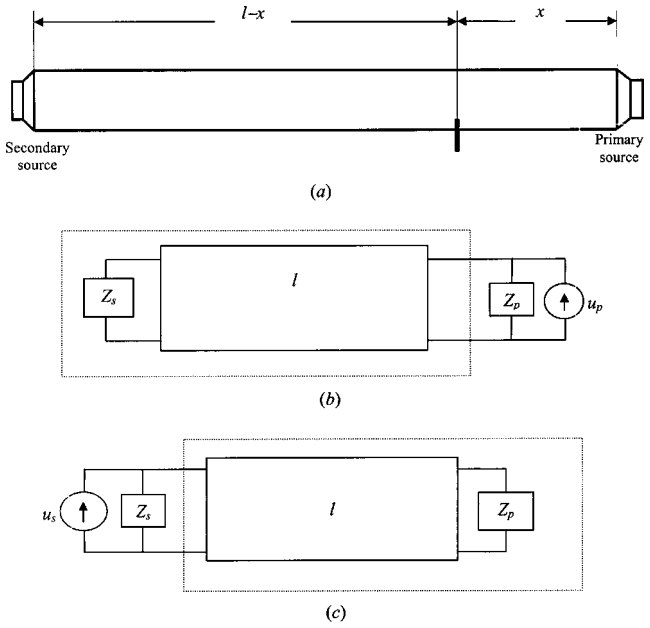

FIG. 1. (a) ANC configuration, (b) acoustic circuit of the primary field, and (c) acoustic circuit of the secondary field.

One way to obtain the path transfer functions is the use of transmission matrix, which is an exact model of 1D sound fields when the near field effects are negligible. The model is adopted here because the virtual sensor location can be assumed sufficiently away from noise sources. Let p_p and p_s denote, respectively, signals measured immediately in front of the two sources, when the secondary source is off ($u_s=0$), p_p and p_s, are related to each other by

$$\begin{bmatrix} p_p \\ v_p \end{bmatrix}_{u_s=0} = \begin{bmatrix} \cos(kl) & jZ_0\sin(kl) \\ j\dfrac{\sin(kl)}{Z_0} & \cos(kl) \end{bmatrix} \begin{bmatrix} p_s \\ \dfrac{p_s}{Z_s} \end{bmatrix}_{u_s=0}. \tag{1}$$

where Z_0 is the characteristic impedance of the duct; and v_p is the particle velocity caused by p_p. Equation (1) implies

$$\hat{Z}_s = Z_0 \frac{Z_s c_l + jZ_0 s_l}{Z_0 c_l + jZ_s s_l} = \left.\frac{p_p}{v_p}\right|_{u_s=0}, \tag{2}$$

where $c_l=\cos(kl)$, and $s_l=\sin(kl)$.

Impedance $\hat{Z}_s$ describes the acoustical effects of the dash-line box in Fig. 1(b), which acts as an acoustical load to the primary source when $u_s=0$. With the help of Eq. (2), one obtains

$$p_p|_{u_s=0} = \frac{\hat{Z}_s u_p}{Z_p+\hat{Z}_s} = \frac{Z_0(Z_s c_l + jZ_0 s_l)}{Z_0(Z_p+Z_s)c_l + j(Z_pZ_s+Z_0^2)s_l} u_p. \tag{3}$$

A microphone, placed x meters away from the primary source, measures signal p_x, which is related to p_p by

$$\begin{bmatrix} p_x \\ v_x \end{bmatrix}_{u_s=0} = \begin{bmatrix} c_x & -jZ_0 s_x \\ -j\dfrac{s_x}{Z_0} & c_x \end{bmatrix} \begin{bmatrix} p_p \\ \dfrac{p_p}{\hat{Z}_s} \end{bmatrix}_{u_s=0}, \tag{4}$$

where $c_x=\cos(kx)$ and $s_x=\sin(kx)$. Substituting Eq. (3) into Eq. (4), one obtains

$$p_x|_{u_s=0} = \frac{Z_0(Z_s c_{l-x} + jZ_0 s_{l-x})}{Z_0(Z_p+Z_s)c_l + j(Z_pZ_s+Z_0^2)s_l} u_p = H_{px}(j\omega)u_p, \tag{5}$$

where $c_{l-x}=\cos[k(l-x)]$, and $s_{l-x}=\sin[k(l-x)]$.

The derivation of secondary path $H_{sx}(j\omega)$ is very similar to that of $H_{px}(j\omega)$, due to the symmetric placement of the secondary source. Following a process similar to the derivation of Eq. (5), one can obtain

$$p_x|_{u_p=0} = \frac{Z_0(Z_p c_x + Z_0 s_x)}{Z_0(Z_p+Z_s)c_l + j(Z_pZ_s+Z_0^2)s_l} u_s = H_{sx}(j\omega)u_s. \tag{6}$$

One may combine Eqs. (5) and (6) to calculate the pressure at x from the primary source. The result is given by

$$p_x = Z_0 \frac{(Z_p c_x + jZ_0 s_x)u_s + (Z_s c_{l-x} + jZ_0 s_{l-x})u_p}{Z_0(Z_p+Z_s)c_l + j(Z_pZ_s+Z_0^2)s_l}, \tag{7}$$

which represents the spatial distribution of the field as a function of x, for the configuration of Fig. 1.

B. A novel virtual sensing scheme

Let p_1 and p_2 denote, respectively, signals measured by two physical sensors placed at x_1 and x_2. The objective is to predict p_v for a virtual sensor placed x_v meters away from the primary source. One may introduce a complex function

$$F(j\omega) = \frac{Z_0}{Z_0(Z_p+Z_s)c_l + j(Z_pZ_s+Z_0^2)s_l} \tag{8}$$

to represent the product of Z_0 with the denominator of Eq. (7). This makes it possible to rewrite Eq. (7) as

$$p_x = F(j\omega)[(Z_p c_x + jZ_0 s_x)u_s + (Z_s c_{l-x} + jZ_0 s_{l-x})u_p]. \tag{9}$$

Since $c_x=0.5(e^{jkx}+e^{-jkx})$ and $js_x=0.5(e^{jkx}-e^{-jkx})$, Eq. (9) is equivalent to

$$p_x = A(j\omega)e^{jkx} + B(j\omega)e^{-jkx}, \tag{10}$$

where

$$A(j\omega) = F(j\omega)\left[\frac{Z_p+Z_0}{2}u_s + \frac{Z_s-Z_0}{2}u_p e^{-jkl}\right] \tag{11a}$$

and

$$B(j\omega) = F(j\omega)\left[\frac{Z_p-Z_0}{2}u_s + \frac{Z_s+Z_0}{2}u_p e^{jkl}\right] \tag{11b}$$

are independent of x. These are the forward and backward waves traveling in the duct in opposite directions. For virtual sensing, Eq. (10) implies

$$\begin{bmatrix} p_1 \\ p_2 \end{bmatrix} = \begin{bmatrix} e^{jkx_1} & e^{-jkx_1} \\ e^{jkx_2} & e^{-jkx_2} \end{bmatrix} \begin{bmatrix} A(j\omega) \\ B(j\omega) \end{bmatrix} \tag{12}$$

and

$$\begin{bmatrix} A(j\omega) \\ B(j\omega) \end{bmatrix} = \frac{1}{e^{jx(x_1-x_2)} - e^{jk(x_2-x_1)}} \begin{bmatrix} e^{-jkx_2} & -e^{-jkx_1} \\ -e^{jkx_2} & e^{jkx_1} \end{bmatrix} \times \begin{bmatrix} p_1 \\ p_2 \end{bmatrix}. \quad (13)$$

The location of the virtual signal is in the range of $x_1 \geqslant x_v \geqslant x_2$. Once $A(j\omega)$ and $B(j\omega)$ are available, the virtual signal can be recovered exactly by $p_v = A(j\omega)e^{jkx_v} + B(j\omega)e^{-jkx_v}$.

C. Causality and accuracy

In a digital implementation, $\exp(-jkl) = \exp(-j\omega\tau)$ is equivalent to a delay time $\tau = l/c$, where c is the speed of sound. The implementation of $\exp(jkl) = \exp(j\omega\tau)$ is not causal, which is a practical problem if one wishes to predict a causal version of p_v. A possible solution is to rewrite Eq. (13) into

$$\begin{bmatrix} A(j\omega)e^{jkx_1} \\ B(j\omega)e^{-jkx_2} \end{bmatrix} = \frac{1}{1 - e^{2jk(x_2-x_1)}} \begin{bmatrix} 1 & -e^{jk(x_2-x_1)} \\ -e^{jk(x_2-x_1)} & 1 \end{bmatrix} \times \begin{bmatrix} p_1 \\ p_2 \end{bmatrix}, \quad (14)$$

where $A(j\omega)\exp(jkx_1)$ and $B(j\omega)\exp(-jkx_2)$ can be used to predict a causal version of $p_v = A(j\omega)e^{jkx_v} + B(j\omega)e^{-jkx_v}$ in the range of $x_1 \geqslant x_v \geqslant x_2$. It involves delay operations $\exp[jk(x_v - x_1)]$ and $\exp[jk(x_2 - x_v)]$, respectively. The implementation of Eq. (14) is causal because it contains a delay operator $\exp[jk(x_2 - x_1)]$. This method requires accurate knowledge of the speed of sound c.

Since the delay operator is equivalent to $\exp(-j\omega\tau_{12})$ with $\tau_{12} = (x_1 - x_2)/c$, an error δc in the speed of sound will cause an error in τ_{12}, denoted by $\delta\tau_{12} = (x_2 - x_1)\,\delta c/c^2$. One may reduce the distance between the two sensors to reduce the effect of $\delta\tau_{12} = (x_2 - x_1)\,\delta c/c^2$. A possible method is to place a pair of microphones in x_1 and $x_1' = x_1 - \Delta x$, respectively, to measure pressure signals p_1 and p_1'. A replacement of x_2 by $x_1' = x_1 - \Delta x$ in Eq. (14) leads to

$$\begin{bmatrix} A(j\omega)e^{jkx_1} \\ B(j\omega)e^{jk(\Delta x - x_1)} \end{bmatrix} = \frac{1}{1 - e^{-2jk\Delta x}} \begin{bmatrix} 1 & -e^{-jk\Delta x} \\ -e^{-jk\Delta x} & 1 \end{bmatrix} \times \begin{bmatrix} p_1 \\ p_1' \end{bmatrix}, \quad (15a)$$

where $A(j\omega)\exp(jkx_1)$ can be used to predict a causal version of p_v in the range of $x_1 \geqslant x_v \geqslant x_2$, by a simple delay operation $\exp[jk(x_v - x_1)]$. However, $B(j\omega)\exp[-jk(x_1 - \Delta x)]$ can only be used to predict p_v in the range of $x_1 \geqslant x_v \geqslant x_1 - \Delta x$. For this reason, another pair of sensors is placed in x_2 and $x_2 - \Delta x$, respectively, to measure pressure signals p_2 and p_2'. Replacing x_1 with x_2 in Eq. (15a), one obtains

$$\begin{bmatrix} A(j\omega)e^{jkx_2} \\ B(j\omega)e^{jk(\Delta x - x_x)} \end{bmatrix} = \frac{1}{1 - e^{-2jk\Delta x}} \begin{bmatrix} 1 & -e^{-jk\Delta x} \\ -e^{-jk\Delta x} & 1 \end{bmatrix} \times \begin{bmatrix} p_2 \\ p_2' \end{bmatrix}, \quad (15b)$$

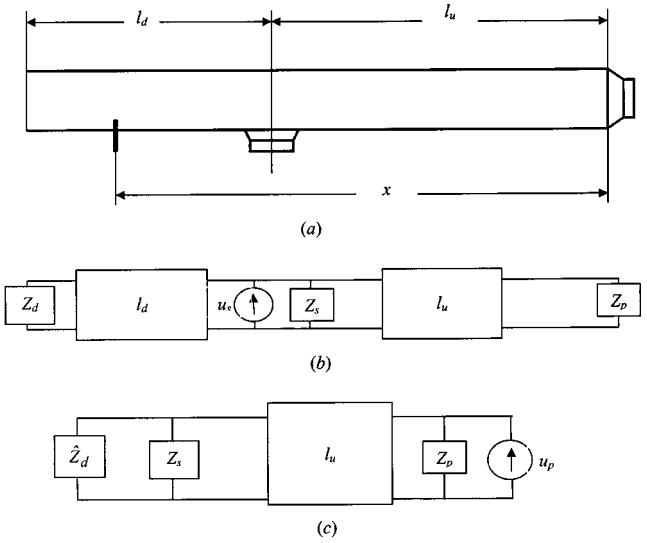

FIG. 2. (a) Another ANC configuration, (b) acoustic circuit of the secondary field, and (c) acoustic circuit of the primary field.

where $B(j\omega)\exp[jk(\Delta x - x_2)]$ can be used with $A(j\omega)\exp(jkx_1)$ to predict a causal version of $p_v = A(j\omega)e^{jkx_v} + B(j\omega)e^{-jkx_v}$ in the range of $x_1 \geqslant x_v \geqslant x_2$.

Theoretically, Eq. (14) is as exact as Eqs. (15a) and (15b). Both methods use delay operators equivalent to $\exp(-j\omega\tau_{12})$ and $\exp(-j\omega\Delta\tau)$, respectively, where $\tau_{12} = (x_1 - x_2)/c$ and $\Delta\tau = \Delta x/c$. If there is an error δc in the speed of sound, τ_{12} and $\Delta\tau$ contain errors $\delta\tau_{12}$ and $\delta\Delta\tau$, respectively. Since $\delta\tau_{12} = (x_2 - x_1)\,\delta c/c^2$ is significantly larger than $\delta\Delta\tau = \Delta x\,\delta c/c^2$ if $x_1 - x_2 \gg \Delta x$, the second method is less sensitive to errors in the speed of sound. Besides, the effect of possible sensor mismatch can be reduced by averaging the results obtained with multiple sensor-pairs.

III. A DIFFERENT CONFIGURATION

The ANC configuration in Fig. 1 is similar to those examined and tested by some researchers.[7,8,12] In many applications, the secondary source is placed between the primary source and the duct outlet as shown in Fig. 2. If virtual sensing is applied to such an ANC configuration, the proposed method must be modified.

A. Secondary path transfer function

The main difference between Figs. 1 and 2 is the location of the secondary source, which causes a different spatial distribution of the secondary field. The acoustical circuit for Fig. 2(a) is shown in Fig. 2(b) when the primary source is off. It is equivalent to a secondary source driving two parallel duct segments, though in reality this is a serial of up- and down-stream segments connected at the location of the secondary source.

The two segments of the duct are terminated by impedances Z_p and Z_d, respectively, where Z_p is the impedance of the primary source and Z_d is the impedance of the duct outlet. Similar to the derivation of Eq. (2), one can derive

$$\hat{Z}_p = Z_0 \frac{Z_p c_u + jZ_0 s_u}{Z_0 c_u + jZ_p s_u}, \quad \hat{Z}_d = Z_0 \frac{Z_d c_d + jZ_0 s_d}{Z_0 c_d + jZ_d s_d}, \quad (16)$$

where $c_u=\cos(kl_u)$, $s_u=\sin(kl_u)$, $c_d=\cos(kl_d)$, and $s_d=\sin(kl_d)$ respectively. Impedances $\hat{Z}_p$ and $\hat{Z}_d$ describe the loading effects of Z_p and Z_d to the secondary source. The parallel of $\hat{Z}_p$ and $\hat{Z}_d$ is $Z_1=\hat{Z}_d\hat{Z}_p/(\hat{Z}_d+\hat{Z}_p)$. The signal at the location of Z_1 is given by

$$p_s|_{u_p=0}=\frac{Z_1}{Z_s+Z_1}u_s=\frac{\hat{Z}_d\hat{Z}_p}{Z_s\hat{Z}_p+\hat{Z}_d(Z_s+\hat{Z}_p)}u_s. \tag{17}$$

Unlike the configuration of Fig. 1, a secondary path transfer function to a point x meters away from the primary source has two different expressions, depending on the values of x and l_u. For the case $x<l_u$, the secondary sound propagate upwards to reach x, which means

$$\begin{bmatrix} p_x \\ v_x \end{bmatrix}_{u_p=0}=\begin{bmatrix} \cos[k(l_u-x)] & -jZ_0\sin[k(l_u-x)] \\ -j\dfrac{\sin[k(l_u-x)]}{Z_0} & \cos[k(l_u-x)] \end{bmatrix} \times\begin{bmatrix} p_s \\ \dfrac{p_s}{\hat{Z}_p} \end{bmatrix}_{u_p=0}. \tag{18}$$

Let $c_{ux}=\cos[k(l_u-x)]$ and $s_{ux}=\sin[k(l_u-x)]$, then one can substitute Eq. (17) and write

$$\begin{aligned} p_x|_{u_p=0}&=\frac{\hat{Z}_d(\hat{Z}_pc_{ux}-jZ_0s_{ux})}{Z_s\hat{Z}_p+\hat{Z}_d(Z_s+\hat{Z}_p)}u_s \\ &=G_u(\hat{Z}_pc_{ux}-jZ_0s_{ux})u_s, \end{aligned} \tag{19}$$

where

$$G_u=\frac{\hat{Z}_d}{Z_s\hat{Z}_p+\hat{Z}_d(Z_s+\hat{Z}_p)}$$

is independent of x.

Similarly, for the case of $x\geqslant l_u$, the secondary sound propagate downwards to reach x, which means

$$\begin{bmatrix} p_x \\ v_x \end{bmatrix}_{u_p=0}=\begin{bmatrix} \cos[k(x-l_u)] & -jZ_0\sin[k(x-l_u)] \\ -j\dfrac{\sin[k(x-l_u)]}{Z_0} & \cos[k(x-l_u)] \end{bmatrix} \times\begin{bmatrix} p_s \\ \dfrac{p_s}{\hat{Z}_d} \end{bmatrix}_{u_p=0}. \tag{20}$$

Let $c_{xu}=\cos[k(x-l_u)]$ and $s_{xu}=\sin[k(x-l_u)]$, then one can use Eq. (17) again to write

$$\begin{aligned} p_x|_{u_p=0}&=\frac{\hat{Z}_p(\hat{Z}_dc_{xu}-jZ_0s_{xu})}{Z_s\hat{Z}_p+\hat{Z}_d(Z_s+\hat{Z}_p)}u_s \\ &=G_d(\hat{Z}_dc_{xu}-jZ_0s_{xu})u_s, \end{aligned} \tag{21}$$

where

$$G_d=\frac{\hat{Z}_p}{Z_s\hat{Z}_p+\hat{Z}_d(Z_s+\hat{Z}_p)}$$

is independent of x. Spatial distribution of the secondary field is now completely available as a function of x in Eq. (19) or Eq. (21), depending on the values of x and l_u.

B. Primary path transfer function

The transfer function of the primary path is derived by turning off the secondary source. As a result, the configuration of Fig. 2(a) is now represented by an acoustical circuit shown in Fig. 2(c). The down-stream segment, terminated by impedance Z_d, is equivalent to an impedance $\hat{Z}_d$ shown in the second equation of Eq. (16). The parallel of $\hat{Z}_d$ and Z_s is an impedance $Z_2=Z_s\hat{Z}_d/(Z_s+\hat{Z}_d)$, whose effects is an acoustical load to the primary source with an impedance

$$\hat{Z}_2=Z_0\frac{Z_2c_u+jZ_0s_u}{Z_0c_u+jZ_2s_u}. \tag{22}$$

Similar to the development of Sec. II, the pressure signal in front of the primary source is denoted by p_p, which is given by

$$p_p|_{u_s=0}=\frac{\hat{Z}_2u_p}{Z_p+\hat{Z}_2}, \tag{23}$$

when the secondary source is off.

The microphone sensor, placed x meters away from the primary source, measures pressure signal p_x, which is related to p_p by

$$\begin{bmatrix} p_x \\ v_x \end{bmatrix}_{u_s=0}=\begin{bmatrix} c_x & -jZ_0s_x \\ -j\dfrac{s_x}{Z_0} & c_x \end{bmatrix}\begin{bmatrix} p_p \\ \dfrac{p_p}{\hat{Z}_2} \end{bmatrix}, \tag{24}$$

where $c_x=\cos(kx)$ and $s_x=\sin(kx)$. Substituting Eq. (23) into the above equation, one obtains

$$p_x|_{u_s=0}=\frac{\hat{Z}_2c_x-jZ_0s_x}{Z_p+\hat{Z}_2}u_p=H_{px}(j\omega)u_p. \tag{25}$$

When both primary and secondary paths are available analytically, one can write

$$\begin{aligned} p_x&=p_x|_{u_s=0}+p_x|_{u_p=0}=H_{px}(j\omega)u_p+H_{sx}(j\omega)u_s \\ &=\alpha(j\omega)e^{jkx}+\beta(j\omega)e^{-jkx}, \end{aligned} \tag{26}$$

where

$$\alpha(j\omega)=\begin{cases} \dfrac{\hat{Z}_2-Z_0}{2(Z_p+\hat{Z}_2)}u_p+\dfrac{G_ue^{-jkl_u}}{2}(\hat{Z}_p+Z_0)u_s, & x<l_u \\ \dfrac{\hat{Z}_2-Z_0}{2(Z_p+\hat{Z}_2)}u_p+\dfrac{G_de^{-jkl_u}}{2}(\hat{Z}_d-Z_0)u_s, & x\geqslant l_u \end{cases} \tag{27a}$$

and

$$\beta(j\omega) = \begin{cases} \dfrac{\hat{Z}_2+Z_0}{2(Z_p+\hat{Z}_2)}u_p + \dfrac{G_u e^{jkl_u}}{2}(\hat{Z}_p - Z_0)u_s, & x<l_u \\ \dfrac{\hat{Z}_2+Z_0}{2(Z_p+\hat{Z}_2)}u_p + \dfrac{G_d e^{jkl_u}}{2}(\hat{Z}_d + Z_0)u_s, & x\geqslant l_u \end{cases} \tag{27b}$$

can be derived from Eqs. (19), (21), and (25). These two signals are independent of x, similar to $A(j\omega)$ and $B(j\omega)$ in Sec. II.

C. Modified scheme

Although $\alpha(j\omega)$ and $\beta(j\omega)$ look more complicated than $A(j\omega)$ and $B(j\omega)$ in Sec. II, the two signals need not be available analytically. Instead, they can be obtained from signals of the physical sensors. Since $\alpha(j\omega)$ and $\beta(j\omega)$ have different expressions in Eqs. (27a) and (27b), these signals need separate estimations for the case of $x<l_u$ and $x\geqslant l_u$, respectively. It means a double number of sensors and computation load.

One may reduce the number of sensors by separating the primary and secondary fields. In an ANC operation, the strength of the secondary source u_s is always available. It is also possible to identify a path transfer function $H_{sv}(j\omega)$ from offline data,[3–5,13,14] therefore $p_v|_{u_p=0}=H_{sv}(j\omega)u_s$ is available accurately. Only $p_v|_{u_s=0}$ needs prediction from signals p_1 and p_2. Before predicting $p_v|_{u_s=0}$, one may separate the primary field by

$$p_1|_{u_s=0}=p_1-H_{s1}(j\omega)u_s, \quad p_2|_{u_s=0}=p_2-H_{s2}(j\omega)u_s, \tag{28}$$

where $H_{s1}(j\omega)$ and $H_{s2}(j\omega)$ are transfer functions from the secondary source to the two physical sensors, available by offline identification.

Equation (25) describes the spatial distribution of the primary pressure field as a function of x. It may be expressed as

$$p_x|_{u_s=0}=\gamma(j\omega)e^{jkx}+\eta(j\omega)e^{-jkx}, \tag{29}$$

where

$$\gamma(j\omega)=\frac{\hat{Z}_2-Z_0}{2(Z_p+\hat{Z}_2)}u_p, \quad \eta(j\omega)=\frac{\hat{Z}_2+Z_0}{2(Z_p+\hat{Z}_2)}u_p$$

are valid in the entire duct. This implies

$$\begin{bmatrix} p_1 \\ p_2 \end{bmatrix}_{u_s=0} = \begin{bmatrix} p_1-H_{s1}u_s \\ p_2-H_{s2}u_s \end{bmatrix} = \begin{bmatrix} e^{jkx_1} & e^{-jkx_1} \\ e^{jkx_2} & e^{-jkx_2} \end{bmatrix} \begin{bmatrix} \gamma(j\omega) \\ \eta(j\omega) \end{bmatrix}, \tag{30}$$

and hence

$$\begin{bmatrix} \gamma(j\omega) \\ \eta(j\omega) \end{bmatrix} = \frac{1}{e^{jk(x_1-x_2)}-e^{jk(x_2-x_1)}} \begin{bmatrix} e^{-jkx_2} & -e^{jkx_1} \\ -e^{jkx_2} & e^{jkx_1} \end{bmatrix} \times \begin{bmatrix} p_1-H_{s1}u_s \\ p_2-H_{s2}u_s \end{bmatrix}, \tag{31}$$

which is very similar to Eq. (13). It can be re-written in a form similar to Eq. (14) for causal prediction of $p_v = \gamma(j\omega)e^{jkx_v}+\eta(j\omega)e^{-jkx_v}+H_{sv}(j\omega)u_s$, which requires the same number of sensors as Eq. (14) does.

IV. SOUND FIELD IN A 3D ENCLOSURE

Similar to the 1D case, locations of sources affect the spatial distributions of signals in a 3D sound field. Spatial relations between the virtual signal and physical signals may be descried analytically by path transfer functions between sources and sensors.

A. Path transfer functions

For a sound field in a lightly damped 3D enclosure, path transfer functions between sources and sensors may be modeled with the modal theory. The eigenfunctions of the sound field are denoted as $\phi_i(\mathbf{x})$ with spatial coordinate vector $\mathbf{x}$ and mode index $1\leqslant i\leqslant m$ for the first m modes. Let $\mathbf{x}_p$ and $\mathbf{x}_s$ represent spatial coordinates of the primary and secondary sources with strengths u_p and u_s, respectively. For a sensor placed at coordinate $\mathbf{x}$, the measured pressure signal is a linear superposition of two fields, with transfer functions given by

$$H_{px}(j\omega)=\left.\frac{p_x}{u_p}\right|_{u_s=0}=\sum_{i=1}^{m}\frac{\phi_i(\mathbf{x})\phi_i(\mathbf{x}_p)}{\omega_i^2-\omega^2+2j\xi_i\omega\omega_i} \tag{32}$$

and

$$H_{sx}(j\omega)=\left.\frac{p_x}{u_s}\right|_{u_p=0}=\sum_{i=1}^{m}\frac{\phi_i(\mathbf{x})\phi_i(\mathbf{x}_s)}{\omega_i^2-\omega^2+2j\xi_i\omega\omega_i}, \tag{33}$$

where ω_i and ξ_i are resonant frequency and damping ratio of the ith mode. In some applications, the primary source does not locate at a single spot $\mathbf{x}_p$. Let $w_p(\mathbf{x},t)$ model the primary source as a spatial and temporal function of $\mathbf{x}$ and t, then it may be expressed as $w_p(\mathbf{x},t)=f_p(\mathbf{x})u_p(t)$, where $f_p(\mathbf{x})$ describes the spatial distribution, $u_p(t)$ the temporal effect. One may rewrite Eq. (32) as

$$H_{px}(j\omega)=\left.\frac{p_x}{u_p}\right|_{u_s=0}=\sum_{i=1}^{m}\frac{\phi_i(\mathbf{x})f_i}{\omega_i^2-\omega^2+2j\xi_i\omega\omega_i}, \tag{34}$$

where $f_i=\int_X\phi_i(x)f_p(x)dx$ is the inner product of $f_p(\mathbf{x})$ with the ith eigenfunction of the noise field; and X represents the boundary of the sound field. Similar to the 1D fields, $H_{sx}(j\omega)$ and $H_{px}(j\omega)$ share the same denominator in a 3D resonant field. Their difference in the numerators is due to the different source locations $\mathbf{x}_p$ and $\mathbf{x}_s$, which vanishes if $\mathbf{x}_p=\mathbf{x}_s$.

In most ANC applications, digital controllers are implemented and path transfer functions are identified in the Z-transform domain as

$$H_{px}(z)=\left.\frac{p_x}{u_p}\right|_{u_s=0}=\frac{N_{px}(z)}{D(z)},$$

$$H_{sx}(z)=\left.\frac{p_x}{u_s}\right|_{u_p=0}=\frac{N_{sx}(z)}{D(z)}, \tag{35}$$

where all transfer functions share a same denominator $D(z)$; and they differ from each other in the numerators. The subscripts of the numerators indicate the source-destination of the paths.

B. Separation of primary and secondary signals

In this study, spatial coordinates of the two physical sensors and the virtual sensor are denoted as $\mathbf{x}_1$, $\mathbf{x}_2$, and $\mathbf{x}_v$, respectively. Transfer functions from the primary source to the two physical sensors and the virtual sensor are denoted, respectively, as $H_{p1}(z)$, $H_{p2}(z)$, and $H_{pv}(z)$; and transfer functions from the secondary source to the sensors are denoted as $H_{s1}(z)$, $H_{s2}(z)$, and $H_{sv}(z)$ respectively. These transfer functions are assumed available accurately by offline identification. Let p_1, p_2, and p_v denote, respectively, pressures of the two physical sensors and the virtual sensor, these signals are linear combinations of the primary and secondary fields, such as $p_1=H_{p1}(z)u_p+H_{s1}(z)u_s$. Due to the different spatial distributions of the primary and secondary fields, it is important to separate the two fields in predicting the virtual signal.

Since the strength of the secondary source is always available to the controller, it is relatively easy to predict the part of the virtual signal contributed by the secondary source. This part is simply $p_v|_{u_p=0}=H_{sv}(z)u_s$, where transfer function $H_{sv}(z)$ can be identified from offline measurement data. The focus is the prediction of the other part of the virtual signal, contributed by the primary source. For this reason, signals measured by the physical sensors should be processed first to remove the contributions of the secondary source by

$$p_1|_{u_s=0}=p_1-H_{s1}(z)u_s \tag{36}$$

before used to predict the virtual signal.

Some researchers used filters to recover a virtual signal from the signal of a physical sensor.[13,14] Let $F(z)$ denote the transfer function of such a filter, then broadband recovery of a virtual signal at location $\mathbf{x}_v$ is mathematically equivalent to

$$H_{pv}(z)=\frac{N_{pv}(z)}{D(z)}=H_{px}(z)F(z)=\frac{N_{px}(z)}{D(z)}F(z), \tag{37}$$

which requires

$$F(z)=\frac{N_{pv}(z)}{N_{px}(z)} \tag{38}$$

in a frequency range of interest.

In many ANC applications, path transfer functions are nonminimum phase, which means some roots of $N_{px}(z)$ are unstable and outside the unit circle in the Z plane. The filter in Eq. (38) is unstable in such a case, which is very likely to be true in an ANC application if the physical sensors do not collocate with the primary source.

C. The proposed method

The proposed method avoids Eq. (38) to avoid the instability of $N_{px}(z)$. It uses two physical sensors to predict a virtual signal. These sensors are installed judiciously in a noise field with coordinates $\mathbf{x}_1$ and $\mathbf{x}_2$, such that $N_{p1}(z)$ and $N_{p2}(z)$ do not share any zeros. This is ensured if the spectra of p_1 and p_2 do not have the same antiresonant frequencies, when both are measured in the absence of the secondary source.

When $N_{p1}(z)$ and $N_{p2}(z)$ do not share any zeros, there exist two polynomials $F_1(z)$ and $F_2(z)$, such that

$$N_{pv}(z)=N_{p1}(z)F_1(z)+N_{p2}(z)F_2(z), \tag{39}$$

which implies

$$H_{pv}(z)=H_{p1}(z)F_1(z)+H_{p2}(z)F_2(z). \tag{40}$$

Equation (39) is known as the Bezout equation,[15] which has a matrix-vector expression

$$\begin{bmatrix} n_{v0} \\ n_{v1} \\ \vdots \\ n_{vm} \end{bmatrix} = \begin{bmatrix} n_{10} & & & & n_{20} & & & \\ n_{11} & n_{10} & & n_{21} & n_{20} & & & \\ \vdots & n_{11} & \ddots & & \vdots & n_{21} & \ddots & \\ n_{1m} & & \ddots & n_{10} & n_{2m} & & \ddots & n_{20} \\ & n_{1m} & & n_{11} & & n_{2m} & & n_{21} \\ & & \ddots & \vdots & & & \ddots & \vdots \\ & & & n_{1m} & & & n_{2m} & \end{bmatrix} \times \begin{bmatrix} f_{10} \\ f_{11} \\ \vdots \\ f_{1m} \\ f_{20} \\ f_{21} \\ \vdots \\ f_{2m} \end{bmatrix}, \tag{41}$$

where $N_{pv}(z)=\Sigma_{i=0}^{m}n_{vi}z^{-i}$, $N_{p1}(z)=\Sigma_{i=0}^{m}n_{1i}z^{-i}$, $N_{p2}(z)=\Sigma_{i=0}^{m}n_{2i}z^{-i}$, $F_1(z)=\Sigma_{i=0}^{m}f_{1i}z^{-i}$, and $F_2(z)=\Sigma_{i=0}^{m}f_{2i}z^{-i}$, respectively. The matrix in Eq. (41) is known as the Sylvester resultant matrix, which is nonsingular if $N_{p1}(z)$ and $N_{p2}(z)$ do not share zeros.[15] This is ensured if the two physical sensors are installed judiciously.

The Bezout equation establishes the existence of the solutions in the entire frequency range of interest. It is valid when $N_{s1}(z)$ or $N_{s2}(z)$ is nonminimum phase. This is an important difference between the proposed method and those by Popovich[13] and Kammer.[14] Practically, $F_1(z)$ and $F_2(z)$ can be obtained adaptively, because the product of $u_p(z)$ to both sides of Eq. (40) leads to

$$\tilde{p}_v=F_1(z)\tilde{p}_1+F_2(z)\tilde{p}_2 \tag{42a}$$

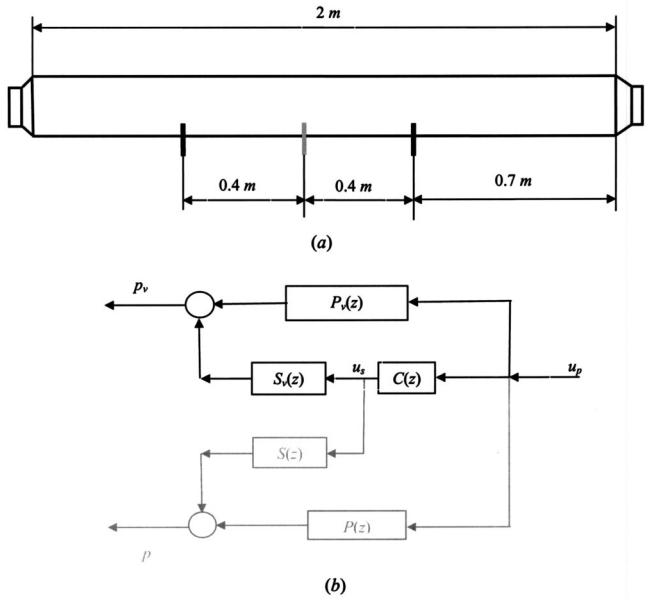

FIG. 3. (a) Experiment setup, (b) block diagram of the experiment system.

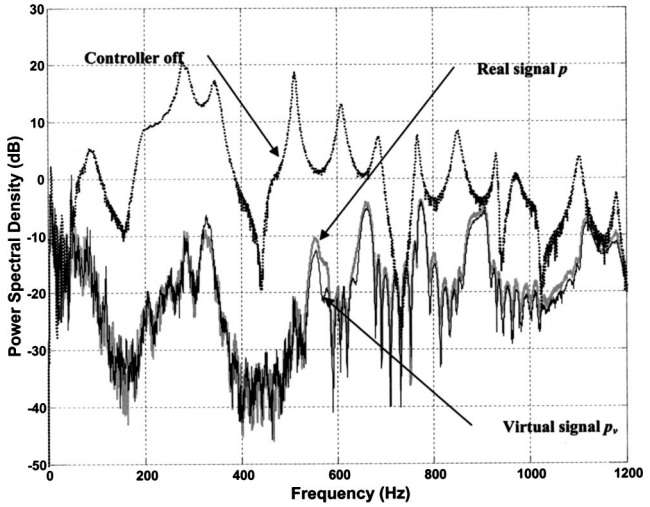

FIG. 4. Comparison of uncontrolled noise (dashed-black curve) with controlled real signal (thick-gray curve) and controlled virtual signal (thin-black curve).

where $\tilde{p}_v = H_{pv}(z)u_p$, $\tilde{p}_1 = H_{p1}(z)u_p$, and $\tilde{p}_2 = H_{p2}(z)u_p$ are measured when $u_s = 0$. The time domain version of Eq. (42a) is a regressive form

$$\tilde{p}_v(k) = \sum_{i=0}^{m} [f_{1i}\tilde{p}_1(k-i) + f_{2i}\tilde{p}_2(k-i)]. \tag{42b}$$

It may be used for the identification of $F_1(z)$ and $F_2(z)$ by a LMS algorithm when $u_s = 0$. Once $F_1(z)$ and $F_2(z)$ are available from Eq. (42b), the two polynomials are implemented as FIR filters to predict the virtual signal by

$$p_v = F_1(z)[p_1 - H_{s1}(z)u_s] + F_2(z)[p_2 - H_{s2}(z)u_s] + H_{sv}(z)u_s, \tag{43}$$

where $H_{s1}(z)$, $H_{s2}(z)$, and $H_{sv}(z)$ are available by offline identification.

V. EXPERIMENTAL VALIDATION

An experiment was conducted to verify the analytical results. A feedforward ANC was implemented in a duct with a cross-sectional area of $11 \times 14.5\ \text{cm}^2$ as depicted in Fig. 3(a). The primary and secondary actuators were 4 in loudspeakers placed at the opposite ends of the duct. Two physical sensors (represented by thick-black lines) were placed in the duct to predict the virtual sensor signal (represented by a thick-gray line). All sensor signals were low-pass filtered with a cutoff frequency 1 kHz.

A block diagram of the experimental system is shown in Fig. 3(b), where $P_v(z)$ and $S_v(z)$ represent the paths to the virtual sensor. The primary noise was a broadband pseudo-random signal. The virtual secondary path $S_v(z)$ was identified offline first, and then used by a filtered-x LMS ANC [not shown in Fig. 3(b) for brevity] to suppress virtual signal $p_v = A(j\omega)e^{jkx_v} + B(j\omega)e^{-jkx_v}$, where $A(j\omega)\exp(jkx_1)$ and $B(j\omega)\exp(-jkx_2)$ were calculated by substituting $x_1 = 1.5$ m and $x_2 = 0.7$ m into Eq. (14). The virtual signal p_v is supposed to predict the pressure signal p at $x_v = 1.1$ m with $x_1 \geqslant x_v \geqslant x_2$.

Since there may be implementation errors in the system, it is possible that the virtual signal p_v is well suppressed while the real signal p is not suppressed by the same amount. For this reason, a real sensor was placed at x_v to check the difference between p and p_v. The signal paths to the real sensor are depicted in Fig. 3(b) by the gray-lines, to show that these paths were not related to the control system.

The experimental results are plotted in Fig. 4 in three curves. The dashed-black curve, labeled "controller off," represents the normalized power spectral density (PSD) $|p(z)/u_p(z)|$ of the uncontrolled noise. The other curves were collected when the controller was active. The thick-gray curve, labeled "real signal p," plots the normalized PSD $|p(z)/u_p(z)|$. The thin-black curve, labeled "virtual signal p_v," represents the normalized PSD $|p_v(z)/u_p(z)|$. The difference between the two closely spaced curves are $|p(z)/u_p(z)|$ (real signal) versus $|p_v(z)/u_p(z)|$ (virtual signal).

The objective of the controller is to minimize $|p(z)/u_p(z)|$ without placing a real sensor at x_v. Since p was not available to the controller, the controller had to minimize $|p_v(z)/u_p(z)|$ without any information on p. The experiment verifies the effectiveness of the virtual sensor because the minimization of $|p_v(z)/u_p(z)|$ indeed leads to the minimization of $|p(z)/u_p(z)|$, though $|p_v(z)/u_p(z)|$ appears to be better than $|p(z)/u_p(z)|$ in some frequencies. Such a difference was due to implementation errors in the system.

Another way to verify the virtual sensing method is to compare p_v with either p_1 or p_2. For this reason, the primary and secondary sources were placed at the opposite ends of the duct. At convergence, the ANC created a quiet zone near x_v, which included neither x_1 nor x_2. Both p_1 and p_2 were collected in the experiment. Only p_1 is plotted in Fig. 5 to compare with p_v. Since p_1 was measured approximately halfway between the secondary source and x_v, its magnitude is significantly different from that of p_v, as shown in Fig. 5.

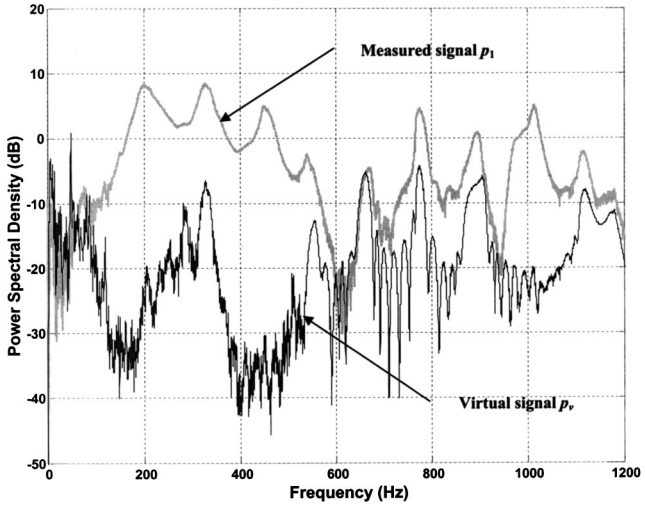

FIG. 5. Comparison of virtual signal p_v (thin-black curve) with a measured signal p_1 (thick-gray curve).

A similar difference exists between p_2 and p_v, since p_2 was measured between the primary source and x_v. That result is not plotted to avoid distractions due to the similar peak levels of p_1 and p_2 distributed in two sets of different frequencies.

VI. CONCLUSION

A novel virtual sensing scheme is developed for active control of broadband noise in lightly damped enclosures. It is based on path transfer functions derived analytically in sound fields. These transfer functions describe the analytical distribution of sound signals, on basis of which the proposed method is developed. Unlike available virtual sensing schemes, which work well for tonal signals, the proposed scheme enables exact prediction of the virtual signal in the entire frequency of interest. This method may be applied to an available ANC scheme for broadband noise control in a lightly damped field.

ACKNOWLEDGMENTS

The work described in this paper was substantially supported by a grant from the Research Grant Council of the Hong Kong Special Administration Region (Project No. PolyU 5175/01E).

[1] C. H. Hansen and S. D. Snyder, *Active Control of Noise and Vibration* (Spon, London, 1997).
[2] P. A. Nelson and S. J. Elliott, *Active Control of Sound* (Academic, London, 1992).
[3] J. Garcia-Bonito, S. J. Elliott, and C. C. Boucher, ''A virtual microphone arrangement in a practical active headrest,'' in Proceedings of Inter-noise, 96, pp. 1115–1120.
[4] J. Garcia-Bonito, S. J. Elliott, and C. C. Boucher, ''Generation of zones of quiet using a virtual microphone arrangement,'' J. Acoust. Soc. Am. **101**, 3498–3516 (1997).
[5] C. Carme and P. De Man, ''How to improve an ANC headset by using a virtual microphone,'' in Proceedings of Inter-noise, 98, Christchurch.
[6] B. S. Cazzolato, ''Sensing systems for active control of sound transmission into cavities,'' Ph.D. thesis, The University of Adelaide, Adelaide, South Australia, 1999.
[7] C. D. Kestell, B. S. Cazzolato, and C. H. Hansen, ''Active noise control with virtual sensors in a long narrow duct,'' Int. J. Acoust. Vibration **5**, 63–76 (2000).
[8] J. M. Munn, B. S. Cazzolato, C. D. Kestell, and C. H. Hansen, ''Virtual error sensing for active noise control in a one-dimensional waveguide: Performance prediction versus measurement,'' J. Acoust. Soc. Am. **113**, 35–38 (2003).
[9] C. D. Kestell, B. S. Cazzolato, and C. H. Hansen, ''Active noise control in a free field with virtual sensors,'' J. Acoust. Soc. Am. **109**, 232–243 (2001).
[10] B. S. Cazzolato, ''An adaptive LMS virtual microphone,'' in Proceedings of Active 2002, ISVR, Southampton, pp. 105–116.
[11] A. Roure and A. Albarrazin, ''The remote microphone technique for active noise control,'' in Proceedings of Active 1999, Ft. Lauderdale, FL, pp. 1233–1244.
[12] C. M. Tran and S. C. Southward, ''A virtual sensing method for tonal ANVC systems,'' ASME J. Dyn. Syst., Meas., Control **124**, 35–40 (2002).
[13] S. R. Popovich, ''Active acoustic control in remote regions,'' U.S. Patent, 5,701,350 (1997).
[14] D. C. Kammer, ''Estimation of structural response using remote sensor location,'' J. Guid. Control **20**, 501–508 (1997).
[15] G. C. Goodwin and K. S. Sin, *Adaptive Filtering, Prediction and Control* (Prentice–Hall, Englwood Cliffs, NJ. 1984).

Multimode shunt damping of piezoelectric smart panel for noise reduction

Jaehwan Kim[a] and Joon-Hyoung Kim
Department of Mechanical Engineering, Inha University, 253 Younghyun-Dong, Nam-Ku, Incheon 402-751, Korea

(Received 14 March 2003; revised 31 March 2004; accepted 17 May 2004)

Multimode shunt damping of piezoelectric smart panel is studied for noise reduction. Piezoelectric smart panel is a plate structure on which a piezoelectric patch is attached with an electrical shunt circuit. When an incidence sound is impinged on the panel structure, the structure vibrates and the attached piezoelectric patch produces an electrical energy, which can be effectively dissipated as heat via the electrical shunt circuit. Since the energy dissipation strongly depends on the vibration mode of the panel structure, many patches are required for multiple vibration modes. Instead of using multiple piezoelectric patches, a single piezoelectric patch is used in conjunction with a blocked shunt circuit for multimode shunt damping. Modeling, shunt parameter tuning, and implementation of the blocked shunt circuit along with an acoustic test of the panel are explained. A remarkable reduction of the transmitted noise was achieved for multiple modes of the panel. Since this technology has many merits in terms of compactness, low cost, robustness, and ease of installation, practical applications in many noise problems can be anticipated. © *2004 Acoustical Society of America.* [DOI: 10.1121/1.1768947]

PACS numbers: 43.50.Ki, 43.55.Rg [KAC] Pages: 942–948

I. INTRODUCTION

Noise reduction of panels is increasingly required in aircrafts, vehicles, ships, buildings, etc., to provide a comfortable living environment. There are two categories in reducing the noise of panels: active and passive methods. Active control uses sensors and actuators along with a proper control so as to minimize the noise at a certain frequency band. Successful noise reductions have been obtained by using piezoelectric sensors and actuators along with a controller.[1] However, this method becomes infeasible at high frequencies due to the increased complexity of the controller to take into account many radiating modes of the structure. In contrast, passive control does not bring any complexity and instability of the system brought out from active control.[2] Also, it is easy to set up with low cost. The most popular approach in passive control is the use of sound absorbing materials. However, since an increasing amount of material is required for the effective noise reduction at low frequencies, the passive approach is impractical for low frequency applications.

In order to get over such a limit, a new passive method has been proposed, which is based on piezoelectric shunt damping. Piezoelectric shunt damping has been discussed by Forward and experimentally demonstrated in an optical system.[3] This system is composed of piezoelectric elements and a simple electrical circuit. Briefly, the concept of piezoelectric shunt damping is energy conversion and energy dissipation, similar to a dynamic absorber of mechanical systems. Hagood and von Flotow have investigated the possibility of dissipating mechanical energy with passive electrical circuits.[4] They optimally tuned an electrical resonance of shunt circuit to structural resonance in a manner analogous to the mechanical vibration absorber for a selected model. Recently, an electrical impedance model of piezoelectric structures determined by the measured impedance data was proposed, and the optimal parameter tuning of the shunt circuit was performed based on the maximum energy dissipation near the target frequency.[5] A remarkable suppression of the transmitted noise was achieved for broadband frequencies by utilizing a hybrid concept that combines the use of sound absorbing materials for the midfrequency range and piezoelectric shunt damping for the low frequency range.[6] However, several piezoelectric patches were used to take into account the multiple vibration modes of the panel. Hollcamp has expanded the theory of piezoelectric shunting for single mode so that a single piezoelectric element can be used to suppress two modes by optimally designing the shunt parameters.[7] Wu has accomplished a multimode shunt damping with blocking circuit.[8] The blocking circuit consists of one parallel capacitor and inductor antiresonance circuit. This antiresonance circuit is designed to produce infinite electrical impedance at the natural frequencies of all other resonant shunt circuits.

In this paper, multimode shunt damping of the piezoelectric smart panel is studied for the noise reduction of the panel. On a single piezoelectric patch, a blocked shunt circuit is connected to implement the multimode shunt damping (Fig. 1). The tuning process for shunt parameters is based on the electrical impedance model and the maximum energy dissipation method. Implementation of the shunt circuit, the tuning process of the circuit, as well as the acoustic test of the panel for noise reduction are addressed.

II. PIEZOELECTRIC SHUNT DAMPING

The concept of piezoelectric shunt damping is the energy conversion by piezoelectric effect. Piezoelectric materi-

[a]Electronic mail: jaehwan@inha.ac.kr

 0001-4966/2004/116(2)/942/7/$20.00

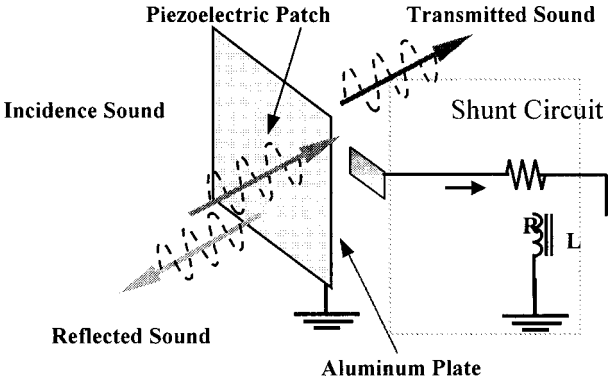

FIG. 1. Schematic diagram of piezoelectric smart panels.

als convert mechanical energy into electrical energy and vice versa. The converted energy can be dissipated as heat through a load resistor of the shunt circuit. Eventually, mechanical vibration level is reduced due to the energy dissipation. Usually, resonant shunt damping is used to effectively dissipate out the energy at the resonance. However to maximize the energy dissipation at the resonance frequency of the system, the choice of the optimal inductance and resistance of the shunt circuit is very important. An optimal tuning method for shunt parameters has been developed based on an electrical impedance model.[5] An electrical impedance model of piezoelectric structures has been derived to take into account the coupled structure in conjunction with the shunt circuit. The new shunt parameter tuning method based on the electrical impedance model and the maximum dissipation energy criterion has been applied. This method can be expanded to the problem of multimode shunt damping because the same tuning process can be applied for multimode in the presence of blocking circuit. Details of the modeling and tuning process for single-mode shunt damping are summarized, and they are subsequently expanded to the multimode shunt damping.

A. Modeling

Piezoelectric materials can be approximately represented as an equivalent electric circuit at a resonance frequency. Van Dyke's model is well known for the equivalent resonance model of piezoelectric materials. Figure 2 shows Van Dyke's equivalent model. Here, C_0 describes an inherent dielectric capacity of piezoelectric material, while L_1, R_1, and C_1 imply mass, damping, and compliance of the material, respectively. The model has five variables including the dielectric loss, R_0. However, since the dielectric loss is small, it is neglected in the model.

By invoking Van Dyke's model, the piezoelectric smart structure on which the piezoelectric patch is bonded along with a shunt circuit can be modeled as shown in Fig. 3. This is an equivalent circuit model for the piezoelectric smart panel. The impedance at each branch of the equivalent circuit is described as

$$Z_1(s)=m_1 s+\frac{k_1}{s}+c_1=j\omega L_1+\frac{1}{j\omega C_1}+R_1,$$

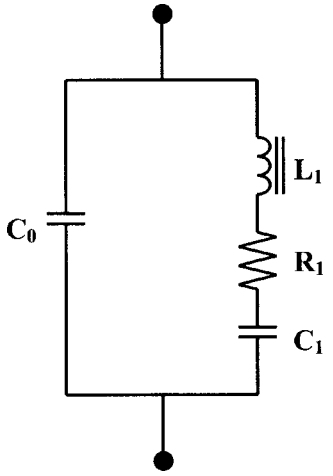

FIG. 2. Van Dyke's circuit model of piezoelectric materials.

$$Z_2(s)=\frac{k_2}{s}=\frac{1}{j\omega C_2},$$

$$Z_3(s)=Ls+R=j\omega L+R, \tag{1}$$

where Z_1 is the impedance of the first system, Z_2 and Z_3 express impedances of the secondary system. The total impedance of the equivalent circuit can be written as

$$Z=Z_1+\frac{Z_2 Z_3}{Z_2+Z_3}. \tag{2}$$

Also, the transfer function can be defined as the ratio of the velocity output to the applied force of the mechanical system. In other words, the transfer function, T_r, can be expressed in terms of electrical admittance of piezoelectric structure including shunt circuit,

$$T_r=\left|\frac{v}{F}\right|=\left|\frac{i}{V}\right|=\frac{1}{|Z|}=|Y|, \tag{3}$$

where v is the velocity, F the force, i the current, V the voltage, and Y the admittance. To use the electrical impedance model, coefficients of Van Dyke's model should be determined. To determine the parameters, the electrical impedance at the piezoelectric patch bonded on the structure is measured by using the impedance analyzer (HP4192A), and

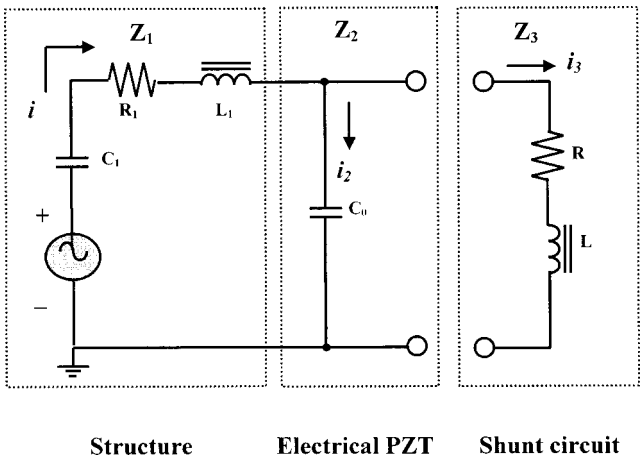

FIG. 3. Equivalent electrical circuit of piezoelectric structure.

the equivalent parameters are extracted from the impedance data by PRAP (Piezoelectric Resonance Analysis Program).[9]

B. Parameter tuning

It is essential to maximize the performance of piezoelectric shunt damping by adjusting parameters of the shunt circuit. The shunt circuit is composed of an inductor and a resistor for single-mode shunt damping. Therefore, values of each parameter should be optimized to achieve effective noise reduction, which is called the optimal parameter tuning. Instead of tuning the transfer function geometrically as used in the conventional tuning method for dynamic absorber,[4] a new parameter tuning method based on the maximum dissipated power at the shunt circuit is adopted.[5] From the equivalent impedance model shown in Fig. 2, the induced electrical power of the system associated with external excitation is

$$P_{\mathrm{IN}}=\tfrac{1}{2}|V\cdot i^{*}|=\tfrac{1}{2}|(Z\cdot i)\cdot i^{*}|=\tfrac{1}{2}|Z|\cdot|i|^{2}, \tag{4}$$

where i^{*} is the complex conjugate of the current i. This power can be referred to as input power for the shunt circuit. In Fig. 3, the current through the load resistor is

$$i_3=\frac{Z_2}{Z_2+Z_3}i, \tag{5}$$

where i is the input current generated by the excitation. The dissipated power at the shunt circuit can be described in terms of impedance and the current of the equivalent circuit,

$$\begin{aligned}P_D&=\tfrac{1}{2}|V_R\cdot i_3^{*}|=\tfrac{1}{2}|(\mathrm{Re}(Z_3)\cdot i_3)\cdot i_3^{*}|\\&=\tfrac{1}{2}\mathrm{Re}(Z_3)\cdot\left|\left(\frac{Z_2}{Z_2+Z_3}\right)\right|^{2}\cdot|i|^{2}.\end{aligned} \tag{6}$$

Also, the ratio of the dissipated power to the input power is

$$J=\frac{P_D}{P_{\mathrm{IN}}}=\frac{\mathrm{Re}(Z_3)\cdot\left|\left(\frac{Z_2}{Z_2+Z_3}\right)\right|^{2}}{|Z|}. \tag{7}$$

This ratio is given at a specific frequency near the resonance frequency. In the tuning process, however, this should be maximized by optimally changing the shunt circuit parameters. Thus, the objective function in the optimization is taken as the averaged J at a certain frequency band near the targeted resonance frequency. The optimal design variables, L^{*}, R^{*}, are found by maximizing the objective function:

$$[L^{*},R^{*}]=\underset{\substack{L\\R}}{\mathrm{Max}}\left[\frac{1}{n}\sum_{k=1}^{n}|J_k|\right], \tag{8}$$

where n is the number of single frequency points in the frequency band. Optimization is performed with optimization toolbox in MATLAB®.

III. MULTIMODE SHUNT DAMPING

In general, piezoelectric shunt damping includes a single piezoelectric patch and a shunt circuit for one target frequency. In order to deal with several strong-radiation modes of the panel, several piezoelectric patches should be attached on the structure as many as the number of modes. However, increasing the number of piezoelectric patches increases the weight of the system. Thus, the multimode shunt damping with single piezoelectric patch is very useful for lightweight structures. When multimode shunt circuit is connected to a piezoelectric element, the circuit can resonate at multiple frequencies. In this study, a blocking circuit is adopted to construct a multimode shunt circuit.[8] Figure 4 represents the concept of the multimode shunt circuit for two resonance modes. R_1^{*} and L_1^{*} are shunt circuit parameters for the first mode. A blocking circuit is connected to the second shunt circuit such that the blocking circuit blocks the current flow passing through the branch at the first mode. In other words, at the first mode the current $i_{\omega 1}$ flows through the first shunt circuit only since the blocking circuit protects the current at the first mode, and at the second mode the current $i_{\omega 2}$ flows through the second shunt circuit. Of course some current flows through the first shunt circuit at the second mode also.

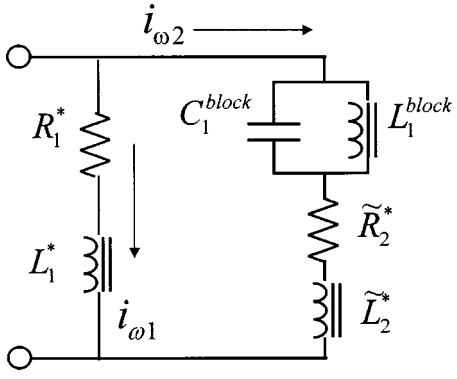

FIG. 4. Schematic of shunt circuit for multimode.

The tuning process for multimode shunt circuit has three steps. At first, optimal shunt parameters are found for a resonance mode by using the new tuning method based on the maximum dissipated power. Second, a blocking circuit is designed, which will block the current flow at the resonance mode. Third, other shunt circuit parameters are determined for an additional mode in the presence of the first shunt circuit and the blocking circuit.

As shown in Fig. 4, two resonance modes are investigated in this study. Before determining parameters for multimode shunt circuit, shunt parameters for a single mode are employed from the previous tuning process. Next the blocking circuit is designed for the first mode by satisfying the resonance equation,

$$\omega_1^{2}=\frac{1}{L_1^{\mathrm{block}}C_1^{\mathrm{block}}}. \tag{9}$$

While tuned parameters for the first mode and the blocking circuit are kept in the tuning process, optimal parameters for the next resonance mode are found according to the maximum dissipated power. According to Ref. 8, the reactance of the entire circuit can be calculated and the modified inductance, $\tilde{L}_2^{*}$, can be given as

$$\tilde{L}_2^{*}=\frac{L_1^{*}L_2^{*}+L_2^{*}L_1^{\mathrm{block}}-L_1^{*}L_1^{\mathrm{block}}-\omega_2^{2}L_1^{*}L_2^{*}L_1^{\mathrm{block}}C_1^{\mathrm{block}}}{(L_1^{*}-L_2^{*})(1-\omega_2^{2}L_1^{\mathrm{block}}C_1^{\mathrm{block}})}. \tag{10}$$

Also, the modified resistance, $\tilde{R}_2^*$, can be written in the same manner as

$$\tilde{R}_2^* = \frac{R_1^* R_2^*}{R_1^* - R_2^*}. \tag{11}$$

When the excitation frequency is near the first resonance frequency, the current only flows into the first branch such that two parameters, L_1^* and R_1^*, only work due to the operation of the blocking circuit. On the other hand, near the next resonance frequency, whole parameters of the circuit are related with the shunt damping at the frequency since the blocking circuit passes the current flow at this frequency.

When multimode shunt circuit is used, however, as the number of target modes (n) increases, the complexity of the circuit increases. This is due to the fact that $(n-1)$ blocking circuits are needed at each branch. Also the expression for optimal inductance and resistance becomes complicated. Fortunately, a single piezoelectric patch does not exhibit many modes of the host structure in dominant noise frequency band. Thus, two or three modes on a single piezoelectric patch are practical. In real applications, a couple of piezoelectric patches should be optimally located to take into account several modes that will radiate noise dominantly.

IV. EXPERIMENTS

A. Piezoelectric smart panel and shunt circuit

Piezoelectric smart panel is designed to reduce the transmitted noise at the low frequency range. A 300×300×1.5 mm aluminum plate is used as host structure for the panel. To implement the shunt damping, a piezoceramic patch (PZT-5H, 100×50×0.5 mm) is bonded on the plate with epoxy adhesives. Figure 1 is a schematic diagram of the piezoelectric smart panel. The location of piezoceramic patch is important for multimode shunt damping. Generally, strong radiation modes of rectangular plate are odd modes such as (1,1) and (1,3), which are the first and second symmetric modes. By locating the piezoceramic patch at the center of the panel, the first and second symmetric modes can be taken into account.

In order to build the shunt circuit, an inductor that has large inductance is necessary. So far, a synthetic inductor has been used to accomplish such a large inductance. However, the use of a synthetic inductor requires an external power to drive OP amps of the circuit, which is an obstacle for practical application. Furthermore, synthetic inductor circuits can interfere with each other. Thus, a coil inductor is used instead of the synthetic inductor. The use of coil inductor has many advantages—cheap, less interference with other components, no external power requirement, and easy to install. Also to implement an independent system of piezoelectric smart panel, the coil inductor can be integrated into the panel without any external power. However, when high inductance value is needed to suppress low modes of realistic large structure, the use of a synthetic inductor or the use of capacitance in conjunction with the piezoelectric patch can be required.

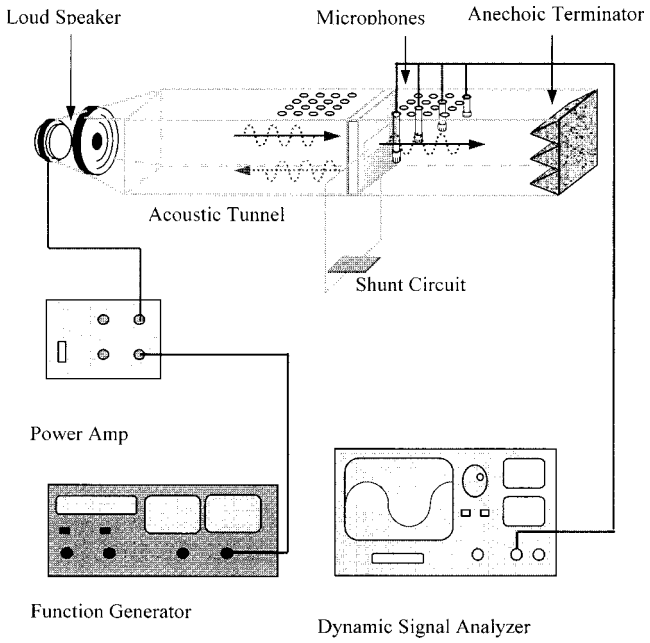

FIG. 5. A schematic diagram of experimental apparatus.

B. Acoustic test setup for piezoelectric smart panel

To test the noise reduction performance of piezoelectric smart panel, the transmission measurement from low to high frequencies should be available. For most panel materials the transmission loss has been measured under strict control.[10] Since this test facility is too expensive, a simple acoustic tunnel has been innovated (Fig. 5).[6] Figure 5 shows the diagram of the experimental apparatus for the acoustic panel test. The tunnel is a square tube of 300 mm × 300 mm and 4 m long. It is divided into two sections—upper and lower sections in equal length. A loudspeaker is set up at the end of the upper section and an anechoic terminator made with wedge is installed at the other end of the lower section. A specially designed flange is provided where two sections meet such that smart panels can be mounted in both. Four edges of the smart panel are clamped using bolts and two sections are tightly connected so as to secure pressure leak. The function generator (Wavetek178) generates a sine sweep signal and the signal is fed to the loudspeaker through the power amplifier. The loudspeaker produces an incident sound and when it excites the panel, the transmitted and reflected sounds occur. Sound pressure levels of the transmitted signal through the panel are measured using microphones and they are analyzed and displayed at the dynamic signal analyzer (HP35665A). Through the measurement of sound pressure level, plane wave is guaranteed below 800 Hz.[6]

Before conducting smart panel tests, modal analysis of the panel structure was performed numerically by using a finite element program, NASTRAN. Figure 6 shows the mode shapes of the panel structure. With these results, target modes are determined to be the first mode (133 Hz) and the fifth mode (513 Hz), and the location of piezoceramic patch is chosen at the center of panel. After bonding the piezoceramic patch at the center of the panel, the admittance at the patch was measured to tune the shunt circuit.

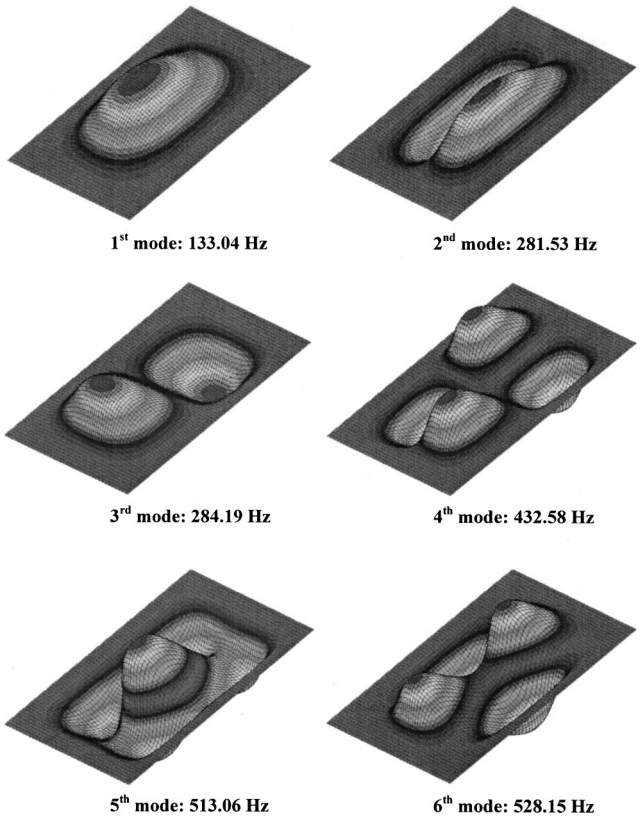

FIG. 6. Modal analysis for piezoelectric panel.

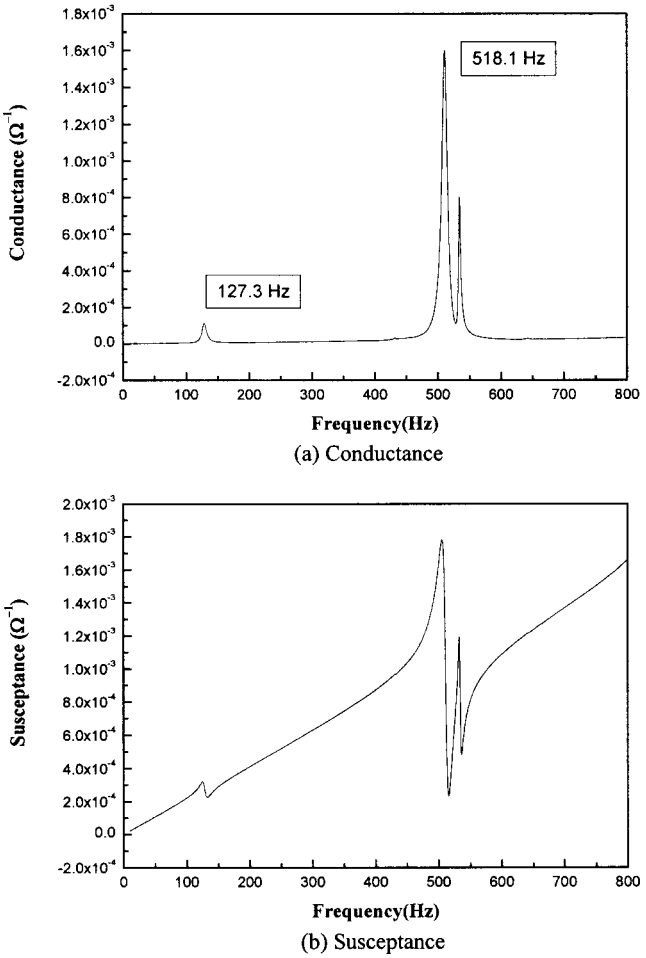

FIG. 7. Measured admittance of piezoelectric panel.

V. RESULTS AND DISCUSSION

Two experiments were accomplished for the transmitted noise reduction: first and fifth modes were tuned separately, and two modes were tuned simultaneously. Figure 7 shows the measured admittance of piezoelectric smart panel in terms of conductance (real part) and susceptance (imaginary part). From the measured admittance, the first and fifth resonance frequencies are found to be 127 and 518 Hz, respectively, which are somewhat different from the modal analysis results. This is due to the effect of bonded piezoelectric patch. From the measured admittance curves, the parameters for the equivalent impedance model (Van Dyke) were extracted using the piezoelectric resonance analysis program (PRAP), for the first and fifth modes, respectively. The second column in Table I shows these values.

At first, the piezoelectric shunt damping was tested for the first and fifth modes individually. The third column in Table I exhibits the shunt circuit parameters found by the optimization for each mode. The optimally searched values (Simul) are found according to Eq. (8). However, due to the presence of uncertainties in the system, the optimally found

TABLE I. Van Dyke's coefficients (C_0, C_1, L_1, R_1) are founded by analyzing the measured admittance, and the optimal parameters $(L_1^*, R_1^*, L_1^{\text{block}}, C_1^{\text{block}})$ for multimode shunt damping are determined in order to dissipate the maximum power through the load resistor.

	Parameters		Single Mode		Multimode	
Freq.	Coeff	Values	Simul	Expt.	Simul	Expt.
First mode (127.3 Hz)	C_0(F)	$3.3161E-7$	$L_1^*=4.42$	$L_1^*=3.98$	$L_1^*=4.42$	$L_1^*=3.98$
	C_1(F)	$9.413E-9$				
	L_1(H)	162.9	$R_1^*=511.02$	$R_1^*=600$	$R_1^*=511.02$	$R_1^*=150$
	R_1 (Ω)	9097				
Fifth mode (518.1 Hz)	C_0	$3.160E-7$	$L_2^*=0.30$	$L_2^*=0.30$	$\tilde{L}_2^*=0.458$	$\tilde{L}_2^*=0.446$
	C_1	$1.161E-8$				
	L_1	8.421	$R_2^*=125.25$	$R_2^*=100$	$\tilde{R}_2^*=165.9$	$\tilde{R}_2^*=120$
	R_1	644				
Blocking freq			Parameters			
First mode (127 Hz)			$L_1^{\text{block}}=1.07$		$C_1^{\text{block}}=1.647E-6$	

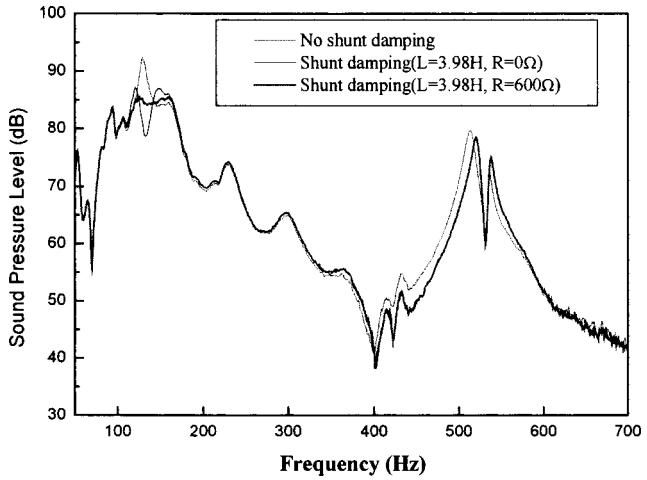

FIG. 8. Shunt damping for first mode.

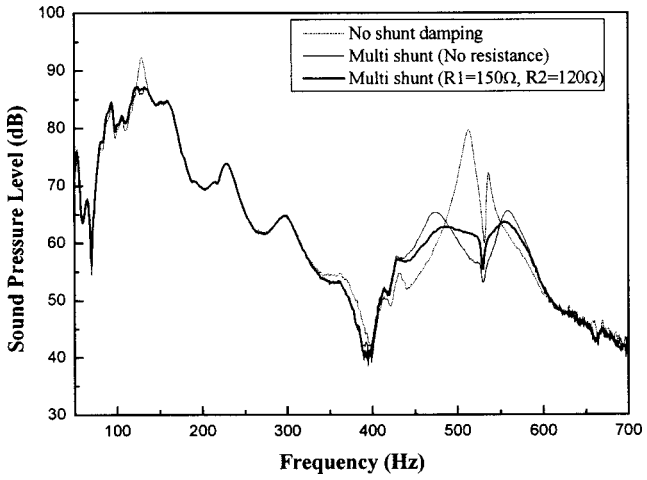

FIG. 10. Experimental result for multimodes shunt damping.

parameters are necessarily adjusted in the experiment. Thus, the inductance (L_1) and resistance (R_1) are adjusted from the optimal simulation results. The experimental values are also shown in Table I. The simulation and experimental values show a closer comparison. Figure 8 shows the sound pressure levels near the first resonance. $R=600\,\Omega$ is the optimal resistance experimentally found for the resonant shunt. When $R=0\,\Omega$ was plotted for a comparison, 7 dB reduction of the transmitted sound pressure level was obtained near the first resonance frequency. Figure 9 shows the sound pressure levels near the fifth resonance frequency. At the fifth mode, much more reduction is obtained by 20 dB down since there is much strain at the center of panel, which results in larger electrical energy generation from the piezoelectric patch.

Second, the experiment for multimode shunt damping was performed. By keeping the shunt circuit parameters for the first mode L_1^*, R_1^*, those for the fifth mode were tuned. During the tuning process, the impedance analyzer was employed to measure the inductance and resistance of the circuit directly. The last two columns in Table I show the simulation and experimental values. All values of the experiment parameters are almost identical with the simulation parameters, except R_1^*. This is due to the presence of internal resistance of coil inductors in the shunt circuits as well as the blocking circuit. Figure 10 shows the transmitted sound pressure levels when two modes were reduced simultaneously. The sound pressure levels in two resonance modes were reduced by 6 and 20 dB, respectively. The reduction level at the first mode is 1 dB less than the individual tuning result. This is due to a slight leakage of the current flowing into the blocking branch.

When this multimode shunt technology is combined with the use of several piezoelectric patches, the application for large-scale structures will be possible for broadband noise reduction. Also, the use of coil inductor for the circuit may be attractive for real application since coil inductor is compact and does not require any external power.

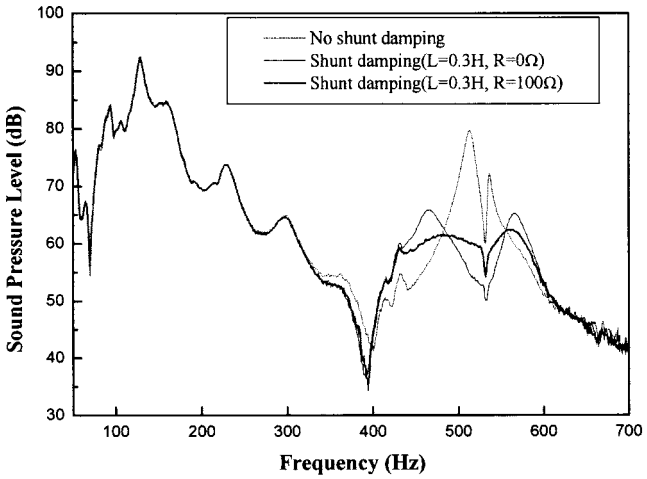

FIG. 9. Shunt damping for fifth mode.

VI. CONCLUSIONS

Multimode shunt damping of piezoelectric smart panel was studied for the noise reduction of the panel. Single piezoceramic patch was bonded on a host panel and shunt circuit was connected to the patch to accomplish multimode shunt damping. As tuning method, the maximum dissipated energy method in conjunction with the electrical impedance model was adopted. In implementing the shunt circuit, a coil inductor was used instead of a synthetic inductor, which does not require external power to drive the circuit. The optimal values of shunt parameters were verified by measuring these values of the shunt circuit.

Before testing the multimode shunt damping of the panel, single mode tests were individually performed, and 7 and 20 dB noise reduction obtained at the first and fifth resonance modes of the panel, respectively. By implementing the multimode shunt damping, 6 and 20 dB noise reductions were obtained simultaneously for each mode, which are almost same as the single-mode test results.

When this multimode shunt technology is combined with the use of several piezoelectric patches, the application for large-scale structures will be possible for broadband noise reduction.

ACKNOWLEDGMENTS

This work was supported by Korea Research Foundation Grant (No. KRF-2002-041-D00031) and the Creative Research Initiatives.

[1] C. R. Fuller, ''Active control of sound transmission/radiation from elastic plate by vibration input. I. Analysis,'' J. Sound Vib. **136**, 1–15 (1990).
[2] J. S. Bolton and N.-M. Shiau, ''Random incidence transmission loss of lined, finite double panel systems,'' 12th AIAA Aeroacoustics Conference, AIAA-89-1048, San Antonio, TX, 1989.
[3] R. L. Forward, ''Electric damping of vibrations in optical structures,'' J. Appl. Opt. **18**, 690–697 (1979).
[4] N. W. Hagood and A. von Flotow, ''Damping of structural vibrations with piezoelectric materials and passive electrical networks,'' J. Sound Vib. **146**, 243–268 (1991).
[5] J. Kim, Y.-H. Ryu, and S.-B. Choi, ''New shunting parameter tuning method for piezoelectric damping based on measured electrical impedance,'' Smart Mater. Struct. **9**, 868–877 (2000).
[6] J. Kim and J. K. Lee, ''Broadband transmission noise reduction of smart panels featuring piezoelectric shunt circuits and sound absorbing material,'' J. Acoust. Soc. Am. **112**, 990–1008 (2002).
[7] J. J. Hollkamp, ''Multimodal passive vibration suppression with piezoelectric materials and resonant shunts,'' J. Intell. Mater. Syst. Struct. **5**, 49–57 (1994).
[8] S. Y. Wu, ''Multiple PZT transducer implemented with multiple-mode piezoelectric shunt for passive vibration damping,'' Proc. SPIE **3672**, 112–122 (1999).
[9] PRAP (Piezoelectric Resonance Analysis Program), TASI Technical Software, 174 Montreal Street Kingston, Ontario K7K 3G4, Canada.
[10] L. H. Bell and D. H. Bell, *Industrial Noise Control* (Dekker, New York, 1994), pp. 215–218.

Relationship between exposure to multiple noise sources and noise annoyance

Henk M. E. Miedema[a)]
TNO Inro, Department Environment and Health, P.O. Box 6041, 2600 JA Delft, Netherlands

(Received 15 May 2003; revised 30 April 2004; accepted 6 May 2004)

Relationships between exposure to noise [metric: day-night level (DNL) or day-evening-night level (DENL)] from a single source (aircraft, road traffic, or railways) and annoyance based on a large international dataset have been published earlier. Also for stationary sources relationships have been assessed. Here the annoyance equivalents model concerning noise annoyance from combined sources and the underlying assumptions are presented. The model first translates the noise from the individual sources into the equally annoying sound levels of a reference source, road traffic, and then sums these levels giving total level L. The annoyance from the combined sources is found by substituting exposure L in the road traffic exposure-annoyance relationship. The most important assumption, independence of the contributions of the sources, is discussed. It appears that independence will be violated substantially only due to the effect of the presence or absence of a quiet side of a building, which is not incorporated in the model. For use in practice, the application of the model is broken down in five steps. The step by step procedure can be used for the assessment of the total noise level and the associated total annoyance on the basis of the DNL or DENL values of the individual sources. © *2004 Acoustical Society of America.* [DOI: 10.1121/1.1766305]

PACS numbers: 43.50.Sr, 43.50.Qp [DKW] Pages: 949–957

I. INTRODUCTION

Relationships between exposure to noise [metric: day-night level (DNL) or day-evening-night level (DENL)] from a single source (aircraft, road traffic, or railways) and annoyance based on a large international dataset have been published earlier. Also for stationary sources relationships have been assessed. However, it is not sufficient to have relationships for individual sources only, because in many cases people are not exposed to either aircraft, road traffic, railway noise, or noise from stationary sources, but to a combination of these types of noises. As a consequence, there is also a need for a model that predicts the annoyance caused by combinations of different types of noise sources. This article presents a method for quantifying the total annoyance caused by exposure of a dwelling to noise from multiple noise sources.

An overview of procedures that have been proposed for rating the total annoyance caused by multiple noise sources can be found in Schulte-Fortkamp *et al.* (1996). In Sec. III, we discuss the simplest approach (energy summation model), and the model that often has been found to give a better description of empirical data than other models (dominance model). Two elements can be distinguished in models for combined exposures: the definition of a noise metric for the combined exposure (L), which is often but not always defined in terms of the noise metrics for the individual sources (L_j), and the relationship between L and the total noise annoyance (A). The discussions of the energy summation model and the dominance model in Sec. III consist of the presentation of these two elements, and an evaluation of the model. The evaluations conclude that the energy summation and the dominance model are not consistent with empirical data in important respects.

Section IV takes a new, systematic approach to formulating a model of annoyance caused by multiple sources. Simple qualitative assumptions expressing what is thought to be known about the relationship between multiple exposures and annoyance are explicitly formulated. Then the model that predicts the annoyance caused by combinations of noise sources (annoyance equivalents model) follows from these assumptions. The theorem which implies that the annoyance equivalents model follows from the assumptions, is proven in the Appendix.

The assumptions on which the annoyance equivalents model is based, are in principle testable on the basis of comparisons of (combined) exposures with respect to the annoyance they cause. No measurement of the (absolute level of) total annoyance, which appears to have limited validity, is needed. Section V discusses the critical assumption of the annoyance equivalents model (independence), and possible violations are identified.

Section VI uses earlier published exposure-annoyance relationships for single transportation sources (aircraft, road traffic, railways) to estimate ''parameters'' of the annoyance equivalents model. Using the parameter estimates, a step by step procedure is presented that can be used for the assessment of the total noise level and the associated total annoyance on the basis of the DNL or DENL values of the individual sources.

In principle, industrial sources without substantial impulsive or tonal components can be included in the procedure for DENL using relationships that have been recently established for such sources. However, complications arise because a relatively high variance of the annoyance scores was found for stationary sources, and because it appears that de-

a)Electronic mail: hme.miedema@inro.tno.nl

viant relationships apply to certain specific sources (e.g., shunting yards and seasonal industry). This is discussed in Sec. VII.

In the final section, conclusions are formulated and further work needed is described. Preceding the earlier mentioned sections, the next section gives a description of noise metrics and annoyance measures used in this article.

II. NOISE METRICS AND ANNOYANCE MEASURES

The day-night level, DNL, is defined in terms of the L_{Aeq}'s (''average'' noise levels) during daytime and night-time, and applies a 10 dB penalty to noise in the night

$$\mathrm{DNL} = 10 \ \lg[(15/24)\times 10^{\mathrm{LD}/10} + (9/24)\times 10^{(\mathrm{LN}+10)/10}].$$

Here LD and LN are the L_{Aeq} as defined in ISO 1996-2 (2002) for the day (7–22 h) and the night (22–7 h), respectively.

A noise metric related to DNL is the DENL. It is defined in terms of the ''average'' levels during daytime, evening, and night-time, and applies a 5 dB penalty to noise in the evening and a 10 dB penalty to noise in the night. The definition is as follows:

$$\mathrm{DENL} = 10 \ \lg[(12/24)\times 10^{\mathrm{LD}/10} + (4/24)\times 10^{(\mathrm{LE}+5)/10} + (8/24)\times 10^{(\mathrm{LN}+10)/10}].$$

Here LD, LE, and LN are the *A*-weighted long term L_{Aeq} as defined in ISO 1996-2 (2002) for the day (7–19 h), evening (19–23 h), and night (23–7 h) determined over the year at the most exposed facade. DENL is the new uniform noise metric for the European Union (EC/DG Environment 2002a). For noise from one type of source, DNL and DENL are highly correlated.

The distribution of the annoyance scores at a given noise exposure level can be summarized in various ways, after transformation to a 0–100 scale. Often a cutoff point is chosen on the scale from 0 to 100 and the percentage of the responses exceeding the cutoff is reported. If the cutoff is 72 on a scale from 0 to 100, then the result is called the percentage ''highly annoyed'' persons (%HA), with a cutoff at 50 it is called the percentage ''annoyed'' (%*A*) and with a cutoff at 28 the percentage ''(at least) a little annoyed'' (%LA) (cf. Schultz, 1978; EC/DG Environment, 2002b). An alternative to the percentage measures is the mean or expected annoyance score (EA).

III. ENERGY SUMMATION AND DOMINANCE MODEL

The energy summation model (see, e.g., Taylor, 1982) simply applies the same metric used for individual sources (e.g., DNL or DENL) to the total noise exposure. According to the energy summation model, the DNL or DENL of the total exposure gives a consistent indication of the annoyance caused by this exposure. It can be calculated from the exposures to the individual sources by ''energetic summation''

$$L = 10 \ \lg \Sigma_j 10^{0.1\times L_j}.$$

The noise annoyance *A* then is given by an exposure-annoyance relationship (not specified by the energy summation model)

$$A = h(L).$$

In a single source situation, the above total noise metric *L* is equal to the noise level L_j of the single source. Since the model assumes that there is one single relation *h* between *L* and annoyance, this means that the energy summation model predicts that exposures to aircraft noise, to road traffic noise, and to railway noise cause equal annoyance if their DNLs or DENLs are equal. This, however, is not consistent with empirical findings [see, e.g., the early meta-analysis by Kryter (1982), and the later meta-analyses by Miedema and Vos (1998), and Miedema and Oudshoorn (2001)], which show that the DNLs or DENLs of two transportation sources that cause equal annoyance can differ 10 dB. Thus, the energy summation model does not describe empirical findings with sufficient accuracy because it does not take into account the differences among transportation noise sources in their potency to cause annoyance.

According to the dominance model (see, e.g., Rice and Izumi, 1986), the total annoyance is equal to the maximum of the single source annoyances

$$A = \max_j[h_j(L_j)].$$

Here h_j is the exposure-annoyance function for source *j*. The source causing the highest annoyance is called the dominant source. A total noise metric can be defined by translating the annoyance of the dominant source into the equally annoying exposure level of an arbitrary reference source

$$L = h^{-1} \circ \max_j[h_j(L_j)].$$

Here h^{-1} is the inverse of an exposure-annoyance function (not specified by the model).

It has been frequently observed that the total annoyance rating is equal or *lower* than the highest single source annoyance (see, e.g., Rice and Izumi, 1986). The dominance model implies that the total annoyance is always *equal* to the highest single source annoyance while alternative models, such as the above energy summation model, imply that the total annoyance is (equal or) *higher* than the highest single source annoyance. Consequently, the dominance model fits the data on total annoyance ratings better than the alternative models. Therefore, it has been regarded as the proper model for the prediction of annoyance caused by combined sources. However, as described earlier, there is a systematic discrepancy between the dominance model and the data showing lower total annoyance. This discrepancy may be related to difficulties people have with evaluating the total annoyance from various sources at once in a single judgment. This is discussed, e.g., by Job and Hatfield (2000), and a model for the underlying cognitive process has been recently proposed by Botteldooren and Verkeyn (2003).

Empirical findings also contradict the following implication of the dominance model. According to the dominance model, the total annoyance *A* is constant when the level of nondominant source changes, as long as it does not become the dominant source. This means that such situations with

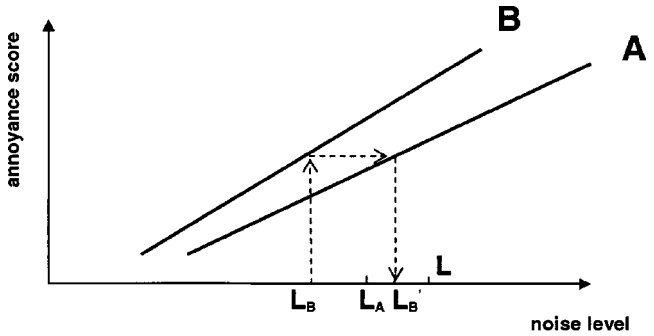

FIG. 1. Illustration of the annoyance equivalents model.

different levels of the nondominant source are predicted to cause equal annoyance. However, it has been found (see Miedema, 1987) that the total annoyance increases if the annoyance level of the nondominant source approaches the annoyance level of the dominant source. Thus, the dominance model does not describe the empirical data correctly for the important cases where the difference in annoyance between dominant and nondominant sources is limited.

IV. ANNOYANCE EQUIVALENTS MODEL

The annoyance equivalents model (cf. Vos, 1992; Miedema, 1996) resembles the toxic equivalents models used in toxicology to describe the toxicity of certain mixtures, e.g., mixtures of dioxins. Using so-called toxic equivalence factors, the concentrations of compounds are translated into the equally toxic concentrations of a reference compound which then are summed. The annoyance equivalents model can be seen as an elaboration of the energy summation model. Instead of summing the sound energy from the individual sources directly, it first translates the noise from the individual sources into the equally annoying sound energy levels of a reference source and then sums these levels. Figure 1 illustrates this for two different noise sources A and B. The noise levels from these sources are L_A and L_B, respectively. Source A is selected as the reference. In order to calculate the total noise annoyance, L_B is transformed into the equally annoying level of A, L_B', as shown in the figure. Then L_A and L_B' are added on an energy basis, giving L. The corresponding annoyance from the two combined sources is found by using the exposure-annoyance relationship of A, with exposure L.

The above description of the annoyance equivalents model means that the total noise level L is defined as follows:

$$L = 10 \ \lg \sum_j \ 10^{0.1 \times h_{\mathrm{ref}}^{-1} \circ h_j (L_j)}.$$

Here h_j is the exposure-annoyance function for source j, and h_{ref}^{-1} is the inverse of that function for the reference source. Thus, the composite function $h_{\mathrm{ref}}^{-1} \circ h_j$ transforms the noise level of source j into the equally annoying level of the reference source, as illustrated in Fig. 1. Furthermore, the total annoyance is the value of the exposure-annoyance function of the reference source at L:

$$A = h_{\mathrm{ref}}(L).$$

There is a theorem (see Appendix; also see: Krantz *et al.*, 1971; Miedema, 1996: theorem 6.1) which implies that the annoyance equivalents model is correct for combinations of aircraft, road traffic, railway noise, and noise from stationary sources, provided that the following five conditions hold. We call this application of the theorem to annoyance from multiple sources the total annoyance theorem. In the following description of the conditions, x, y, and z are each a combination of four noise levels from the four different types of sources (levels may be nihil so that the variables may also represent a quiet situation or an exposure to only a single source):

(1) *Transitivity*: If x is at least as annoying as y, and y is at least as annoying as z, then x is at least as annoying as z;
(2) *Restricted solvability*: If x is at least as annoying as y, then the exposure of any source in the combination y can be changed so that the combination becomes equally annoying as x.
(3) *Independence*: If x and y both are combinations of exposures such that (1) source j (say, aircraft) has in combination x a noise level that is at least equal as its noise level in combination y, and (2) the exposure levels of the other sources (e.g., road traffic, railway, and stationary sources) are equal in x and y, then x is at least as annoying as y.
(4) *Connected*: either x is at least as annoying as y or y is at least as annoying as x, or both, i.e., the annoyance level of a combination relative to another combination always is defined.
(5) *Representation of source specific annoyance*: for one type of source j, if noise level x_j is as least as high as noise level y_j, then x_j is as least as annoying as y_j.

V. EMPIRICAL BASIS AND LIMITATIONS

The earlier mentioned theorem is *not* an empirical theory, but a theorem that has been mathematically proven to be correct (see Appendix). The theorem means that the annoyance equivalents model is correct, if the five specified properties of annoyance hold. In principle, verification of the properties of noise annoyance requires empirical testing. The properties also may be accepted without testing if they are considered to be very plausible, or acceptable simplifications or useful idealizations. An important aspect of the properties is that only comparisons of the annoyance caused by (combined) exposures are needed for their testing and not total annoyance rating of which the validity is questionable (see the earlier discussion of the dominance model).

The critical property is independence. The following example illustrates one type of violation of independence. The ordering of (combined) exposures with respect to the noise annoyance they cause is called the annoyance ordering. Consider:

• the annoyance ordering of all situations with only road traffic noise; and

• the annoyance ordering of the situations obtained from the ''only road traffic noise'' situations by adding to each the same tonal sound (e.g., squeeling railway noise).

Then independence is violated if a tonal sound with little or no road traffic noise is more annoying than the same tonal sound with a higher level of road traffic noise. This may actually occur if the tonal sound is masked in the latter case. A similar phenomenon may be found with very low frequency noise, or impulsive noise instead of tonal noise. In these cases the annoyance reduction caused by the masking of the very irritating sound may outweigh the annoyance increase caused by the higher road traffic noise.

Although such situations do exist, they will be rather scarce because of the following reasons:

- The earlier-mentioned types of very irritating sounds are rather scarce compared to the widespread prevalence of noise without these specific aspects; and
- In general, if the earlier-mentioned types of very irritating sounds occur, it is unlikely that masking will occur to an extent that affects the reaction to this sound. The reason for this is that important binaural masking requires, in addition to a sufficiently high level of the masker, overlap in time, overlap in frequency spectrum, and spatial proximity of the source of the irritating sound and the masking noise.

Findings of Fields (1998) demonstrate that the influence of a second noise source on the evaluation of another source in general is not important. He found that ''residents' reactions to an audible environmental noise (...) are only slightly or not at all reduced by the presence of another noise source (...) in residential environments.'' This supports that in general the earlier discussed violations of independence are not important.

A more important violation of independence is related to variation in the spatial pattern of the exposures. The combined sources may all affect the same side of a dwelling but they may also affect different sides. This is likely to have consequences for the level of annoyance, which would mean a violation of independence. This is not discussed further here, because already for single sources the effect of having a quiet side or not, has been neglected. As will also be suggested in the conclusion and discussion, the effect of the number of exposed sides needs further attention both for the single and multiple source situations.

VI. TOTAL ANNOYANCE ASSESSMENT FOR TRANSPORTATION NOISE

For use of the annoyance equivalents model, the individual exposure-annoyance relationships h_j need to be known, and a reference source must be chosen (see the earlier equations for the model).

Except for relationships between DNL and the expected annoyance score (EA) and the choice of the reference source, all the information needed regarding relationships of annoyance with DNL or DENL is specified in Miedema and Oudshoorn (2001) and Miedema and Vos (2004). Because relationships with DNL as the noise metric are not available for the EA, it is not possible to assess total EA on the basis of DNL.

In principle, the choice of the reference source is not arbitrary. However, the choice of the reference source is not important when it can be assumed that one of the transportation sources can be taken as reference, because the relationships given in the earlier-mentioned references are linear and have nearly equal slopes for the transportation sources. The equally annoying level of the reference source can be approximated by adding a source dependent bonus (or penalty) to the level of the source considered. With the possible reference sources having linear relationships with equal slopes, the annoyance predicted by the annoyance equivalents model is independent of the choice of the reference source. Road traffic is chosen as the reference source, as has been done previously.

Then, using the individual exposure-annoyance relationships from the references, the assessment of the total noise level and the corresponding percentage annoyed can be broken down in the following steps when using DNL:

(1) Assess DNL for aircraft, road traffic, and railways (L_{air}, L_{road}, and L_{rail});
(2) Calculate the annoyance level for aircraft and for railways[1]
   - $A_{\text{air}} = 2.16\ L_{\text{air}} - 89.7$,
   - $A_{\text{rail}} = 2.06\ L_{\text{rail}} - 107.5$;
(3) Calculate the equally annoying road traffic levels for aircraft and for railways
   - $L'_{\text{air}} = (A_{\text{air}} + 105.7)/2.21$,
   - $L'_{\text{rail}} = (A_{\text{rail}} + 105.7)/2.21$;
(4) Calculate the total noise level
   $L = 10\ \lg(10^{0.1\times L'_{\text{air}}} + 10^{0.1\times L_{\text{road}}} + 10^{0.1\times L'_{\text{rail}}})$;
(5) Calculate the percentage a little annoyed, annoyed, or highly annoyed for the combined, multiple sources
   - $\%\text{LA} = -6.188\times 10^{-4}(L-32)^3 + 5.379 \times 10^{-2}(L-32)^2 + 0.723(L-32)$;
   - $\%A = 1.732\times 10^{-4}(L-37)^3 + 2.079 \times 10^{-2}(L-37)^2 + 0.566(L-37)$; and
   - $\%\text{HA} = 9.994\times 10^{-4}(L-42)^3 - 1.523 \times 10^{-2}(L-42)^2 + 0.538(L-42)$.

When using DENL, the steps are:

(1) Assess DENL for aircraft, road traffic, and railways (L_{air}, L_{road}, and L_{rail});
(2) Calculate the annoyance level for aircraft, and for railways[1]
   - $A_{\text{air}} = 2.17\ L_{\text{air}} - 91.4$,
   - $A_{\text{rail}} = 2.10\ L_{\text{rail}} - 110.1$;
(3) Calculate the equally annoying road traffic levels for aircraft, and for railways
   - $L'_{\text{air}} = (A_{\text{air}} + 107.0)/2.22$,
   - $L'_{\text{rail}} = (A_{\text{rail}} + 107.0)/2.22$;
(4) Calculate the total noise level
   $L = 10\ \lg(10^{0.1\times L'_{\text{air}}} + 10^{0.1\times L_{\text{road}}} + 10^{0.1\times L'_{\text{air}}})$; and

(5) Calculate the percentage a little annoyed, annoyed, highly annoyed, or the expected annoyance score for the combined, multiple sources

- $\%\mathrm{LA} = -6.235\times10^{-4}(L-32)^3 + 5.509\times10^{-2}(L-32)^2 + 0.6693(L-32)$,
- $\%A = 1.795\times10^{-4}(L-37)^3 + 2.110\times10^{-2}(L-37)^2 + 0.5353(L-37)$,
- $\%\mathrm{HA} = 9.868\times10^{-4}(L-42)^3 - 1.436\times10^{-2}(L-42)^2 + 0.5118(L-42)$; and
- $\mathrm{EA} = -9.154\times10^{-5}(L-32)^3 + 2.307\times10^{-2}(L-32)^2 + 0.537(L-32)$.

VII. STATIONARY SOURCES

In principle, industrial sources without substantial impulsive or tonal components can be included in the procedure for DENL described earlier by using $A_{\mathrm{ind}} = 2.49\,L_{\mathrm{ind}} - 126.5$ in step 2 (based on: Miedema and Vos, 2004) and $L'_{\mathrm{ind}} = (A_{\mathrm{ind}} + 107.0)/2.22$ in step 3, and by adding $10^{0.1\times L_{\mathrm{ind}}}$ in the addition in the argument of lg in step 4. In case of substantial impulsive or tonal components, corrections proposed for the extra annoying character of these aspects may be applied to DENL (see, e.g: ISO-1996-2, 2002; Delta Acoustics, 1997). However, complications arise because a relatively high variance of the annoyance scores was found for stationary sources. Moreover, it appears necessary to apply for shunting yards and seasonal industry in step 2 relations that are different from the earlier mentioned relation for other industry.

A. High variance of annoyance scores for stationary sources

The models used to assess the exposure-annoyance relationships for individual sources assume a constant variance of the (latent) annoyance scores at different exposures levels, but do not assume that this variance is the same for different types of sources. Nonetheless, for the transportation sources (aircraft, road traffic, and railway) nearly equal variances are found. With scores in the range 0–100, the variance of the normal distribution of the scores comes in the ranges 1100–1300. This means that for these types of sources the percentage of persons above a certain cutoff, such as the cutoff 72 which is used to determine %HA, is nearly equal if the mean annoyance is equal. In the preceding section, the mean annoyance score has been used to find the equally annoying road traffic level for the other transportation sources (in steps 2 and 3). Consequently, ''equally annoying'' means ''having equal mean annoyance.'' Because the variances are almost equal, for the three types of transportation sources the %HA (or the %*A*, the %LA, etc.) of the transportation sources are also equal if they have equal mean annoyance. This implies that for a single source, calculating the percentages directly with the source specific annoyance relationship, gives about the same result as calculation of the percentages with the procedure for combined sources from preceding section applied to that single source.

For stationary sources complications arise because a higher variance of the normally distributed annoyance (2054) has been found. A consequence of this higher variance is that for a single stationary source, calculating an annoyance percentage directly with the source specific annoyance relationship, gives a result that is somewhat different from the percentage calculated with the procedure for combined sources applied to that single source. Comparison of the %LA, of the %*A* and of the %HA obtained in the two different ways (directly and with the procedure for multiple sources), shows that the latter procedure underestimates the %*A* and the %HA especially at lower exposure levels. Until more research is done to clarify the cause of the higher variance in annoyance found for stationary sources, it is suggested that the following ad hoc step is added to the procedure from the previous section: the maximum is taken of the %HA (or %*A* or %LA or EA) resulting from step 5 and the %HA (or %*A* or %LA or EA) for the individual sources. If an industrial source is involved, the extra step prevents that the procedure underestimates the annoyance in situations dominated by the industrial source. The relationships needed to calculate %LA, %*A*, %HA or EA from DENL or DNL of the individual sources, can be found in Miedema and Oudshoorn (2001), and Miedema and Vos (2004).

B. Shunting yards and seasonal industry

Stationary sources are more heterogeneous than transportation sources of a single kind. In principle, different exposure-annoyance relationships could be established for different types of stationary sources, but the limited amount of data regarding stationary sources restricts the possibilities to do so. Miedema and Vos (2004) found that the relationships for shunting yards and for seasonal industry were significantly different from the single relationship that fitted the data for nine other, very different types of industry. The latter relationship is used in the introduction of Sec. VII A. On the basis of the best estimate for shunting yards, for this type of stationary source the constant -126.5 in step 2 must be replaced by -85.8. On the basis of the best estimate for a seasonal industry, with most of the activities concentrated in circa 3 months, the constant -126.5 must be replaced by -156.5.

VIII. CONCLUSION AND DISCUSSION

The annoyance equivalents model has been presented which describes the total annoyance caused by aircraft, road traffic, railway noise, and, in principle, stationary sources. This model has not been tested directly, but follows from five assumptions regarding noise annoyance, using a (mathematical) theorem. The theorem means that the annoyance equivalents model is correct, if the five specified properties hold. The properties may be accepted without testing if they are considered to be very plausible, or acceptable simplifications or useful idealizations. The critical property is independence. The violation of independence is discussed, and it is concluded that, apart from complications related to the number of exposed sides of a dwelling, important violations are expected only in a limited number of practical situations. The unspecified exposure-annoyance relationships of the indi-

vidual source types in the annoyance equivalents model are substituted on the basis of results for individual source types published earlier. For use in practice, the application of the model is broken down in five steps. This step by step procedure can be used for the assessment of the total noise level and the associated total annoyance.

At present, we consider the annoyance equivalents model to be the best available model for the prediction of total annoyance in practice, e.g., for monitoring, impact assessment, or policy making. As a model of the experience of annoyance it needs further evaluation in order to learn to what extent it is a simplification, or what may be limitations in addition to those discussed. One aspect which needs further attention, it the choice of the reference source, to which the noise levels of all other sources are translated.

Further insight in possible limitations of the annoyance equivalents model may be obtained when examples of violations of its underlying assumptions, in particularly independence, are put forward. For example, it may be possible to formulate examples based on specific temporal patterns of the individual sources. Also, there is a need for empirical studies testing either the tenability of the underlying assumptions (independence), or directly the adequacy of the annoyance equivalents model for predicting total annoyance from multiple noise sources. In these studies, the annoyance equivalents model can de evaluated on the basis of comparisons between multiple exposures; no absolute total annoyance judgments, of which the validity is questionable, are needed.

According to the present insight, the elaboration of the earlier approach that is most needed concerns the spatial distribution of the noise exposure of a dwelling. It is likely that there is a difference in total annoyance between the situation with two sources affecting the same side of a dwelling, and the situation with the same two sources affecting different sides of the dwelling. Taking this into account would require further elaboration of the exposure-annoyance relationships of the individual source types by including more (exposure) variables as predictors of annoyance, in addition to DNL or DENL (at the most exposed side of a dwelling), especially the presence of a relatively quiet side of the dwelling.

ACKNOWLEDGMENTS

We thank Truls Gjestland (SINTEF, Norway) and Martin van den Berg (Ministry of Environment, Netherlands) for their insightful comments regarding our work on the assessment of annoyance from combined noise sources. The work reported in this article has been made possible by financial support of the Netherlands' Ministry of Environment, also for the underlying theoretical work.

APPENDIX

A. Introduction

A theorem, from which the total annoyance theorem directly follows, is presented and proven in this Appendix. The theorem is phrased abstractly in terms of a binary relation (=annoyance ordering) on a (product) set (=possible multiple exposures). First some definitions are given, thereafter the theorem and its proof, and finally the correspondence with the total annoyance theorem is pointed out. In the total annoyance theorem there are more than two components in the domain, namely combined exposures to aircraft, road traffic, railways, and stationary sources, i.e., four components (each of them may be nihil). The theorem presented here is stated for any finite number of components. Because independence is a weaker property when there are two components instead of more than 2, for that case an additional property, the Thomsen condition, must be assumed.

The proof is adapted from Miedema (1996: Lemma A in the proof of theorem 6.1). The method of proof used is from Holman (1971), and has been used by Krantz *et al.* (1971: theorem 6.2) and Narens (1985: theorem 3.3) to proof similar theorems. The present proof is self-contained, except for the use of a result from functional equation theory (Aczél, 1987). Interpreted in terms of the annoyance ordering and noise exposures, the method of proof is closely related to the way in which the total annoyance theorem is introduced (see Fig. 1). First functions are defined that translate the noise levels of the individual sources in a combination into the equally annoying levels of a reference source. Then it is shown that combining these equally annoying levels in the same way as levels of the reference source usually are combined, gives consistent indications of the total annoyance of multiple exposures.

B. Definitions

The generalizations of the definitions of induced ordering, independence, and restricted solvability, given here for a domain with two components, to multiple components are straightforward, and can be found in Miedema (1996: Appendix B).

A binary relation R is *transitive* on X iff xRy and yRz implies xRz for all x, y, and z in X. A binary relation R is *connected* on X iff xRy or yRx (or both) for any x and y in X. A binary relation is a *weak ordering* iff it is transitive and connected. When "$\succcurlyeq$" is used as the sign for a weak ordering, then "$\sim$" is used as the sign for the corresponding equivalence relation, i.e., $x \sim y$ iff $x \succcurlyeq y$ and $y \succcurlyeq x$, and e is used to denote a minimal element, i.e., an element such that $x \succcurlyeq e$ for all x in the domain of $\succcurlyeq$.

A nonminimal element u with respect to the ordering $\succcurlyeq$ is an element for which there is an element v such that $u \succcurlyeq v$ while not $v \succcurlyeq u$. When $\succcurlyeq$ is a weak ordering on $X \times P$, then $\succcurlyeq_1$, defined as follows, is called the *ordering induced* on X by $\succcurlyeq$: for all x and y in X, $x \succcurlyeq_1 y$ iff there is a nonminimal zp in $X \times P$ such that $xp \succcurlyeq yp$. Similarly, $\succcurlyeq_2$, defined as follows, is said to be the ordering induced on P by $\succcurlyeq$: for all p and q in P, $p \succcurlyeq_2 q$ iff there is a nonminimal xr in $X \times P$ such that $xp \succcurlyeq xq$.

A *relational structure* $S = \langle V, R \rangle$ consists of relation R and its nonempty domain V. When V is the product of a finite number of sets, then S is called a *conjoint structure*. When $S = \langle \times_{j \in J} V_j, \succcurlyeq \rangle$ is a conjoint structure with $\succcurlyeq$ a weak ordering, then the relational structure $\langle V_j, \succcurlyeq_j \rangle$, where $\succcurlyeq_j$ is the ordering induced by $\succcurlyeq$ on V_j, is called a *substructure* of S. When $S = \langle V, \succcurlyeq \rangle$ is a relational structure with $\succcurlyeq$ a

weak ordering, then a function φ that maps V onto $[0,\infty)$ so that for all u and v in V, $u \succcurlyeq v$ iff $\varphi(u) \geqslant \varphi(v)$, is called a *quantification* of S.

A weak ordering $\succcurlyeq$ on $X \times P$ is *independent* iff: (1) for all x and y in X and p in P, $x \succcurlyeq_1 y$ implies that $xp \succcurlyeq yp$; and (2) for all x in X and p and q in P, $p \succcurlyeq_2 q$ implies that $xp \succcurlyeq xq$. A weak ordering $\succcurlyeq$ on $X \times P$ is said to be *restrictedly solvable* iff, for all x and y in X and p and q in P, $xp \succcurlyeq yq$ implies that there is r in P such that $xp \sim yr$, and z in X such that $xp \sim zq$. A weak ordering $\succcurlyeq$ on $X \times P$ satisfies the *Thomsen condition* iff, for all x,y,z in X and p,q,r in P, $xp \sim yq$ and $yr \sim zp$ implies that $xr \sim zq$.

Let $S = \langle \times_{j \in J} V_j, \succcurlyeq \rangle$ be a conjoint structure. Then S is said to be a *restrictedly solvable structure* iff:

(i) $\succcurlyeq$ is a weak ordering on $\times_{j \in J} V_j$;
(ii) $\succcurlyeq$ is independent and restrictedly solvable;
(iii) if $n(J) = 2$, then $\succcurlyeq$ satisfies the Thomsen condition; and
(iv) each substructure $\langle V_j, \succcurlyeq_j \rangle$ of S has a quantification.

C. Theorem

Let $S = \langle \times_{j \in J} V_j, \succcurlyeq \rangle$ be a restrictedly solvable structure with substructures $\langle V_j, \succcurlyeq_j \rangle$ having quantifications φ_j. Then there are strictly increasing functions f_j from $[0,\infty)$ onto itself such that $\Sigma_{j \in J} f_j \varphi_j$ is a quantification of S, i.e., for all $(\ldots,u_j,\ldots)$, $(\ldots,v_j,\ldots)$ in $\times_{j \in J} V_j$:

$$(\ldots,u_j,\ldots) \succcurlyeq (\ldots,v_j,\ldots) \quad \text{iff}$$
$$\Sigma_{j \in J} f_j \varphi_j(u_j) \geqslant \Sigma_{j \in J} f_j \varphi_j(v_j).$$

D. Proof

We adopt the two following conventions. Let f be a function and y an element from its range. Then $f^{-1}(y)$ denotes a particular choice from the set $\{x | y = f(x)\}$. Furthermore, minimal coordinates e_j are omitted, and, e.g., $u_j \sim v_i$ is written instead of $(e_1,\ldots,e_{j-1},u_j,e_{j+1},\ldots,e_{n(J)}) \sim (e_1,\ldots,e_{i-1},v_i,e_{i+1},\ldots,e_{n(J)})$.

The organization of this proof is as follows. First we define functions π_j on the components V_j, and show them to be quantifications of the substructures $\langle V_j, \succcurlyeq_j \rangle$. With these substructure quantifications, an operation $\oplus$ is defined and shown to have the properties which imply that its form is $x \oplus y = g^{-1}[g(x) + g(y)]$, and it is shown that $\oplus$ can be used to combine the substructure quantifications φ_j into a quantification of the entire structure S.

The functions π_j are defined to be real-valued functions on the substructure domains V_j such that for all u_j in V_j and v_1 in V_1:

$$\pi_j(u_j) = \varphi_1(v_1) \quad \text{iff} \quad u_j \sim v_1. \tag{1}$$

They are shown to be quantifications of substructures $\langle V_j, \succcurlyeq_j \rangle$. Note that $\pi_1 = \varphi_1$.

π_j is a function, because, if $\pi_j(u_j) = x$ and $\pi_j(u_j) = y$, then, by definition [1], $u_j \sim \varphi_1^{-1}(x)$ and $u_j \sim \varphi_1^{-1}(y)$. Consequently, $\varphi_1^{-1}(x) \sim \varphi_1^{-1}(y)$, and, by independence, $\varphi_1^{-1}(x) \sim_1 \varphi_1^{-1}(y)$, which implies, since φ_1 is an (order preserving) quantification, that $x = y$. π_j is defined on each u_j in V_j, because there is a minimal element $e_j = \varphi_j^{-1}(0)$ and for all u_j, $u_j \succcurlyeq e_j$, so that, by restricted solvability, there is a v_1 such that $u_j \sim v_1$ and, by definition [1], $\pi_j(u_j) = \varphi_1(v_1)$. π_j is onto $[0,\infty)$, because for each $x \in [0,\infty)$ there is a v_1 such that $\varphi_1(v_1) = x$, and by restricted solvability, there is a u_j in V_j such that $u_j \sim v_1$ so that by definition [1] $\pi_j(u_j) = x$.

Finally, we show with respect to π_j that it preserves the ordering $\succcurlyeq_j$. To simplify the notation we define $\psi_j = \pi_j^{-1}$. Note that it directly follows from definition [1] that $\psi_1(x) \sim \psi_j(y)$ iff $x = y$, which implies that, more generally

$$\psi_i(x) \sim \psi_j(y) \quad \text{iff} \quad x = y. \tag{2}$$

Using first $\psi_1 = \varphi_1^{-1}$, second independence, third $\psi_1(z) \sim \psi_j(z)$, and finally again independence, we find that

$$\begin{aligned} x \succcurlyeq y \quad &\text{iff} \quad \psi_1(x) \succcurlyeq_1 \psi_1(y), \\ &\text{iff} \quad \psi_1(x) \succcurlyeq \psi_1(y), \\ &\text{iff} \quad \psi_j(x) \succcurlyeq \psi_j(y), \\ &\text{iff} \quad \psi_j(x) \succcurlyeq_j \psi_j(y). \end{aligned}$$

Because $\psi_j = \pi_j^{-1}$ this result means that π_j translates ordering $\succcurlyeq_j$ into $\succcurlyeq$.

Thus, π_j is a function from V_j onto $[0,\infty)$ which translates ordering $\succcurlyeq_j$ into $\succcurlyeq$, which means that it is a quantification of substructure $\langle V_j, \succcurlyeq_j \rangle$.

The (partial) binary operation $\oplus$ on $[0,\infty)$, defined with the functions ψ_j by

$$\psi_1(x)\psi_2(y) \sim \psi_1(x \oplus y), \tag{3}$$

is shown to be closed, associative, cancellative, and continuous. $\oplus$ is a function, because if $x \oplus y = u$ and $x \oplus y = v$, then $\psi_1(x)\psi_2(y) \sim \psi_1(u)$ and $\psi_1(x)\psi_2(y) \sim \psi_1(v)$, so that $\psi_1(u) \sim \psi_1(v)$. Since $\psi_1 = \varphi_1^{-1}$, this means that $u = v$.

Because π_j is a function onto $[0,\infty)$, $\psi_j = \pi_j^{-1}$ is defined for each element in $[0,\infty)$, and, by restricted solvability, for all $x,y \in [0,\infty)$ there is a v_1 in V such that $\psi_1(x)\psi_2(y) \sim v_1$. Thus, there is $z \in [0,\infty)$ such that $\psi_1(z) \sim v_1$ and, by definition [3], $x \oplus y = z$. So $\oplus$ is *closed on* $[0,\infty)$.

Commutativity and *associativity* are first shown for the case $n(J) = 2$. Let $w,x,y,z \in [0,\infty)$. Since, by [2], for each w $\psi_1(w) \sim \psi_2(w)$, the following demonstrates that commutativity of $\oplus$ is implied by a true condition. In the first step the Thomsen condition is used and definition [3] is used in the second step

$$\begin{aligned} &\psi_1(x) \sim \psi_2(x) \quad \text{and} \quad \psi_2(y) \sim \psi_1(y) \\ &\quad \Rightarrow \psi_1(x)\psi_2(y) \sim \psi_1(y)\psi_2(x), \\ &\quad \Rightarrow \psi_1(x \oplus y) \sim \psi_1(y \oplus x), \\ &\quad \Rightarrow x \oplus y = y \oplus x. \end{aligned}$$

Using commutativity, and again the Thomsen condition and definition [3]:

$$\begin{aligned} &\psi_1(y)\psi_2(x) \sim \psi_1(y \oplus x) \sim \psi_1(x \oplus y) \quad \text{and} \\ &\quad \psi_1(y \oplus z) \sim \psi_1(y)\psi_2(z), \\ &\qquad \Rightarrow \psi_1(y \oplus z)\psi_2(x) \sim \psi_1(x \oplus y)\psi_2(z), \end{aligned}$$

$$\Rightarrow \psi_1([y\oplus z]\oplus x)\sim\psi_1([x\oplus y]\oplus z),$$

$$\Rightarrow (y\oplus z)\oplus x=(x\oplus y)\oplus z,$$

$$\Rightarrow x\oplus(y\oplus z)=(x\oplus y)\oplus z,$$

which demonstrates that associativity of $\oplus$ is implied by a true condition.

Next consider the case $n(J)>2$. Let $i,j,k\in J$ be such that $i\neq j$, $i\neq k$, and $j\neq k$. Then, since by [2], e.g., $\psi_j(y)\sim\psi_k(y)$ and by independence

$$\psi_i(x)\psi_j(y)\sim\psi_i(x)\psi_k(y)\sim\psi_j(x)\psi_k(y)\sim\psi_i(y)\psi_j(x).$$

That is, the arguments x and y may be interchanged in $\psi_i(x)\psi_j(y)$. By independence, these arguments may also be interchanged if the coordinates of the components other than i and j are not minimal. Because the arguments are interchangeable

$$\psi_1(x\oplus y)\sim\psi_1(x)\psi_2(y)\sim\psi_1(y)\psi_2(x)\sim\psi_1(y\oplus x),$$

so that $\oplus$ is commutative. Using in the fourth step the possibility to interchange arguments twice

$$\begin{aligned}\psi_1([x\oplus y]\oplus z)&\sim\psi_1(x\oplus y)\psi_2(z),\\&\sim\psi_1(x\oplus y)\psi_3(z),\\&\sim\psi_1(x)\psi_2(y)\psi_3(z),\\&\sim\psi_1(y)\psi_2(z)\psi_3(x),\\&\sim\psi_1(y\oplus z)\psi_3(x),\\&\sim\psi_1(y\oplus z)\psi_2(x),\\&\sim\psi_1([y\oplus z]\oplus x),\\&\sim\psi_1(x\oplus[y\oplus z]),\end{aligned}$$

so that $\oplus$ is associative.

Because, using independence

$$\begin{aligned}y\geqslant z\quad&\text{iff}\quad \psi_2(y)\geqslant_2\psi_2(z),\\&\text{iff}\quad \psi_2(y)\geqslant\psi_2(z),\\&\text{iff}\quad \psi_1(x)\psi_2(y)\geqslant\psi_1(x)\psi_2(z),\\&\text{iff}\quad \psi_1(x\oplus y)\geqslant\psi_1(x\oplus z),\\&\text{iff}\quad x\oplus y\geqslant x\oplus z,\end{aligned}$$

and because it could be similarly shown that $x\geqslant z$ iff $x\oplus y\geqslant z\oplus y$, $\oplus$ is strictly increasing in both arguments. Consequently, $\oplus$ is *cancellative*, i.e., for all $x,y,z\in[0,\infty)$:

$$(x\oplus y=x\oplus z)\vee(y\oplus x=z\oplus x)\rightarrow y=z.$$

Because $\oplus$ is closed, strictly increasing in both arguments, and $x\oplus 0=x$, with the left argument fixed at arbitrary $a\in[0,\infty)$, $\oplus$ is a strictly increasing function from $[0,\infty)$ onto $[a,\infty)$. Similarly, with the right argument fixed at arbitrary $b\in[0,\infty)$, $\oplus$ is a strictly increasing function from $[0,\infty)$ onto $[b,\infty)$. Hence, $\oplus$ is *continuous*.

Because $\oplus$ is a closed, associative, cancellative, and continuous operation on $[0,\infty)$, by Aczél [(1987): p. 107], a continuous, strictly monotone function g, mapping $[0,\infty)$ onto interval I exists such that

$$x\oplus y=g^{-1}[g(x)+g(y)]. \tag{4}$$

I is one of the intervals $(-\infty,a]$, $[b,\infty)$ or $\mathbb{R}$, with $b\geqslant 0\geqslant a$. Because $x\oplus 0=x$ and g is a continuous, strictly monotone function, it follows from [4] that $g(0)=0$ and that g is onto $[0,\infty)$ and strictly increasing, or onto $(-\infty,0]$ and strictly decreasing. Let $h=g$ if g is positive valued, and let $h=-g$ if g is negative valued. Clearly, in both cases $h^{-1}[h(x)+h(y)]=g^{-1}[g(x)+g(y)]$. Thus, a strictly increasing function h from $[0,\infty)$ onto itself exists such that

$$x\oplus y=h^{-1}[h(x)+h(y)]. \tag{5}$$

To arrive at a quantification of S which is defined in terms of $\oplus$, it is shown that

$$(\ldots,\psi_j(u_j),\ldots)\geqslant(\ldots,\psi_j(v_j),\ldots)\quad\text{iff}\quad\oplus_{j\in J}u_j\geqslant\oplus_{j\in J}v_j. \tag{6}$$

First the case $n(J)=2$ is considered. For each $u,v,x,y\in[0,\infty)$:

$$\begin{aligned}x\oplus y\geqslant u\oplus v\quad&\text{iff}\quad\psi_1(x\oplus y)\geqslant\psi_1(u\oplus v),\\&\text{iff}\quad\psi_1(x)\psi_2(y)\geqslant\psi_1(u)\psi_2(v).\end{aligned}$$

Next the case $n(J)=3$ is considered. For each $u,v,w,x,y,z\in[0,\infty)$:

$$\begin{aligned}&x\oplus y\oplus z\geqslant u\oplus v\oplus w\\&\quad\text{iff}\quad\psi_1(x\oplus y)\psi_2(z)\geqslant\psi_1(u\oplus v)\psi_2(w),\\&\quad\text{iff}\quad\psi_1(x\oplus y)\psi_3(z)\geqslant\psi_1(u\oplus v)\psi_3(w),\\&\quad\text{iff}\quad\psi_1(x)\psi_2(y)\psi_3(z)\geqslant\psi_1(u)\psi_2(v)\psi_3(w).\end{aligned}$$

The recursive argument for higher n is omitted since, apart from the recursion, nothing new is involved.

The theorem is shown by combining the results obtained earlier.

Because both φ_j and π_j are quantifications of $\langle V_j,\geqslant_j\rangle$ onto $[0,\infty)$, there is a strictly increasing function g_j from $[0,\infty)$ onto itself such that $\pi_j=g_j\varphi_j$. By definition $\psi_j=\pi_j^{-1}$, so that $\psi_j=\varphi_j^{-1}g_j^{-1}$. Using this, it follows from [6] that

$$\begin{aligned}&(\ldots,\varphi_j^{-1}(u_j),\ldots\geqslant(\ldots,\varphi_j^{-1}(v_j),\ldots)\\&\quad\text{iff}\quad\oplus_{j\in J}g_j(u_j)\geqslant\oplus_{j\in J}g_j(v_j).\end{aligned} \tag{7}$$

From [5] and [7] it follows that there is a strictly increasing function h from $[0,\infty)$ onto itself such that

$$\begin{aligned}&(\ldots,\varphi_j^{-1}(u_j),\ldots)\geqslant(\ldots,\varphi_j^{-1}(v_j),\ldots)\\&\quad\text{iff}\quad h^{-1}[\Sigma_{j\in J}hg_j(u_j)]\geqslant h^{-1}[\Sigma_{j\in J}hg_j(v_j)].\end{aligned}$$

Hence, $f_j=hg_j$ is a strictly increasing function from $[0,\infty)$ onto itself such that $\Sigma_{j\in J}f_j\varphi_j$ is a quantification of S onto $[0,\infty)$.

E. Total annoyance theorem

The general theorem in Sec. C directly implies the more specifically phrased total annoyance theorem. With the five assumptions presented in Sec. IV, structure $S=\langle\mathbb{R}^n,\geqslant\rangle$, with

$\succcurlyeq$ the total annoyance ordering on n tuples of noise levels from different sources, is a restrictedly solvable structure. With L_j the noise level of source j:

$$\varphi_j(L_j) = 10^{0.1 \times L_j},$$

with $0 = \varphi_j(-\infty)$, is a quantification of substructure $\langle \mathbb{R}, \succcurlyeq_j \rangle$, where $\succcurlyeq_j$ is the induced annoyance ordering on the noise levels of source j. By the general theorem, there are strictly increasing functions f_j from $[0,\infty)$ onto itself such that $\Sigma_{j \in J} f_j \varphi_j$ is a quantification of S.

With functions h_j^* defined as follows:

$$h_j^*(L_j) = 10 \ \lg f_j(10^{0.1 \times L_j}),$$

the quantification of S can be written as follows:

$$\sum_j \ 10^{0.1 \times h_j^*(L_j)}.$$

Since the functions h_j^* assign the same number to equally annoying noise levels of different individual noise sources, h_j^* is interpreted as being a composite function, $h_j^* = h_{\text{ref}}^{-1} h_j$, with h_j the exposure-annoyance function for source j, and h_{ref}^{-1} the inverse of the exposure-annoyance function for a reference source. Then

$$L = 10 \ \lg \sum_j \ 10^{0.1 \times h_{\text{ref}}^{-1} \circ h_j(L_j)}$$

is the noise level of the reference source that is equally annoying as the combined levels L_j, and $h_{\text{ref}}(L)$ is the annoyance level corresponding to L.

[1]Note that the linear relationships do not have the observed annoyance score as the dependent variable, but the corresponding (latent) variable with a normal distribution (see references in text regarding exposure-annoyance relationships). While the range of the observed annoyance score is 0–100 so that negative values do not occur, the corresponding normally distributed (latent) annoyance variable A may be negative.

Aczél, J. (**1987**). *A short course on functional equations* (D. Reidel, Dordrect).

Botteldooren, D., and Verkeyn, A. (**2003**). "Fuzzy models for accumulation of reported community noise annoyance from combined sources," J. Acoust. Soc. Am. **112**, 1496–1508.

Delta Acoustics. (**1997**). *Objective Measurement of Audible Tones in Noise* (Delta Acoustics, Copenhagen).

EC/DG Environment. (**2002a**). *Directive 2002/49/EC of the European Parliament and of the Council* (EC/DG Environment, Brussels).

EC/DG Environment. (**2002b**). *Position Paper on Dose Response Relationships between Transportation Noise and Annoyance* (EC/DG Environment, Brussels).

Fields, J. M. (**1998**). "Reactions to environmental noise in an ambient noise context in residential areas," J. Acoust. Soc. Am. **104**, 2245–2260.

Holman, E. W. (**1971**). "A note on conjoint measurement," J. Math. Psychol. **8**, 489–494.

ISO. (**2002**) "Acoustics—Description, measurement and assessment of environmental noise—Part 2: Determination of environmental noise levels," ISO/CD 1996-2 (International Standards Organization, Geneva).

Job, R. F. S., and Hatfield, J. (**2000**). "Factors contributing to reported reaction to combined noise sources," In: *Proceedings Internoise 2000*, edited by D. Cassereau (Société Française d'Acoustique Nice).

Krantz, D. H., Luce, R. D., Suppes, P., and Tversky, A. (**1971**). *Foundations of Measurements* (Academic, New York).

Kryter, K. D. (**1982**). "Community annoyance from aircraft and ground vehicle noise," J. Acoust. Soc. Am. **72**, 1222–1242.

Miedema, H. M. E. (**1987**). "Annoyance from combined noise sources," In: *Environmental Annoyance: Characterization, Measurement*, edited by H. S. Koelega (Elsevier, Amsterdam), pp. 313–320.

Miedema, H. M. E. (**1996**). "Quantification of annoyance caused by environmental noise and odour," PhD thesis (TNO-PG, Leiden).

Miedema, H. M. E., and Vos, H. (**1998**). "Exposure-response relationships for transportation noise," J. Acoust. Soc. Am. **104**, 3432–3445.

Miedema, H. M. E., and Oudshoorn, C. G. M. (**2001**). "Annoyance from transportation noise: Relationships with exposure metrics DNL and DENL and their confidence intervals," Environ. Health Perspect. **109**, 409–416.

Miedema, H. M. E., and Vos, H. (**2004**). "Noise annoyance from stationary sources: Relationships with exposure metric DENL and their confidence intervals," J. Acoust. Soc. Am. **116**, 334–343.

Narens, L. (**1985**). *Abstract Measurement Theory* (MIT Press, Cambridge, MA).

Rice, C. G., and Izumi, K. (**1986**). "Factors affecting the annoyance of combinations of noise sources," Proceedings of the Institute of Acoustics **8**, 325–332.

Schulte-Fortkamp, B., Weber, R., Ronnebaum, T., and Dönnges, T. (**1996**) *Literaturstudie zur Gesamtgeräuschbewertung* (Universität Oldenburg, Oldenburg).

Schultz, T. J. (**1978**). "Synthesis of social surveys on noise annoyance," J. Acoust. Soc. Am. **64**, 377–405.

Taylor, S. M. (**1982**). "A comparison of models to predict annoyance reactions to noise from mixed sources," J. Sound Vib. **81**, 123–138.

Vos, J. (**1992**). "Annoyance caused by simultaneous impulse, road traffic, and aircraft sounds: A quantitative model," J. Acoust. Soc. Am. **91**, 3330–3345.

Statistical-acoustics models of energy decay in systems of coupled rooms and their relation to geometrical acoustics[a)]

Jason E. Summers,[b),c)] Rendell R. Torres, and Yasushi Shimizu[d)]
Program in Architectural Acoustics, Rensselaer Polytechnic Institute, Troy, NY 12180

(Received 26 August 2003; revised 19 March 2004; accepted 2 May 2004)

An improved statistical-acoustics model of high-frequency sound fields in coupled rooms is developed by incorporating into prior models geometrical-acoustics corrections for both energy decay within subrooms and energy transfer between subrooms. The conditions under which statistical-acoustics models of coupled rooms are valid approximations to geometrical acoustics are examined by comparison of computational geometrical-acoustics predictions of decay curves in two- and three-room systems with those of both improved and prior statistical-acoustics models. The accuracy of the decay model used within subrooms is found to have a primary influence on the accuracy of predictions in coupled systems. Likewise, nondiffuse transfer of energy is shown to significantly affect decay of energy in systems of coupled rooms. The decrease in energy density of the reverberant field with distance from the source, which is predicted by geometrical acoustics, is found to result in spatial dependence of decay-curve shape for certain coupling geometries. Geometrical effects are shown to contribute to the failure of statistical-acoustics models in the case of strong coupling between subrooms; thus, previously proposed statistical-acoustics criteria cannot predict the point at which the models break down with consistent accuracy. [DOI: 10.1121/1.1763974]

PACS numbers: 43.55.Br, 43.55.Ka [MK] Pages: 958–969

I. INTRODUCTION

The high-frequency modeling techniques of statistical acoustics (SA) and geometrical acoustics (GA) are increasingly being applied to systems of large, coupled rooms as the use of auxiliary coupled volumes in the design of performance spaces becomes more frequent. SA models offer the advantages of speed and simplicity, but their accuracy in predicting the sound fields in systems of large, coupled rooms has not been established. The interrelationship of these two modeling techniques has been theoretically characterized[1–3] and studied in single-volume rooms both computationally[4–6] and experimentally.[7] Based on GA concepts, semiempirical refinements of Sabine's original SA model[8] have been developed.[9–12] In systems of coupled rooms SA models involve additional assumptions that further limit their agreement with GA models. Thus, the relationships established between SA and GA for single-volume rooms must be reevaluated for systems of coupled rooms. Many of the semiempirical corrections developed for SA models of single-volume rooms have not been applied to SA models of coupled rooms. Moreover, new corrections can be developed to address the additional assumptions required to model coupled rooms. This paper describes an improved SA model of coupled rooms, which comprises prior models while incorporating additional corrections, and examines the relationship of SA models to GA.

An SA model of two coupled rooms was first developed by Davis[13] based on a system of coupled ordinary differential equations (ODEs). Detailed expositions of this model have been given by Cremer and Müller[14] and Lyle.[15,16] Kuttruff[17] has generalized this model to systems of an arbitrary number of coupled rooms by expressing it in matrix formalism (though Peutz[18] earlier used an analog computer to solve the same system of ODEs). Eyring[19] modified Davis's derivation to incorporate an alternative decay model.[9]

II. STATISTICAL-ACOUSTICS MODEL

A. Models of single-volume rooms

The Sabine model[8] is a limiting case of GA in enclosures that are ergodic, sufficiently mixing, and weakly absorbing.[1,3] In conditions for which the assumptions of the Sabine model are not valid, additional information is required in order to yield a true first-order correction to the Sabine model.[20] Other decay models[9–11] can often, but not always, yield predictions that are more accurate than those of the Sabine model.[2] The Eyring model[9] considers only the first moment of the free-path distribution, and thus assumes energy is lost every time a phonon travels a distance of one mean-free path $\langle \bar{\ell} \rangle$. Defining η as the ratio of the Eyring absorption exponent α' to the geometrically averaged absorption coefficient $\bar{\alpha}$

$$\eta = \frac{\alpha'}{\bar{\alpha}}, \tag{1}$$

allows the Eyring decay constant δ' to be expressed in terms of the Sabine decay constant

[a)]Portions of this work have been presented at the 143rd meeting of the Acoustical Society of America [J. Acoust. Soc. Am. **111**, 2390 (A) (2002)].
[b)]Electronic mail: summers@abyss.nrl.navy.mil
[c)]Current address: Naval Research Laboratory, Washington, D.C. 20375-5350.
[d)]Current address: Yamaha Corporation, 10-1 Nakazawa-cho, Hamamatsu 430-8650 Japan.

$$\delta' = \frac{cS\alpha'}{8V} = \eta\delta, \tag{2}$$

where c is the speed of sound, S is the total surface area, and V is the volume of the room. Regardless of its merit in single-volume rooms, the similar Millington–Sette model[10] is not suitable for use in coupled rooms because it predicts that any surface with $\alpha=1$, such as a coupling aperture, causes decay rate to become infinite.[17]

Kuttruff[11] showed that accounting for the second moment of the free-path distribution leads to the absorption exponent

$$\alpha'' = -\ln(1-\overline{\alpha})\left[1+\frac{\gamma^2}{2}\ln(1-\overline{\alpha})\right], \tag{3}$$

where γ^2 is the normalized variance $(\langle\overline{\ell^2}\rangle-\langle\overline{\ell}\rangle^2)/\langle\overline{\ell}\rangle^2$. The decay constant δ'' can be expressed by defining η as before.

In the presence of strong nonuniform absorption the Sabine model fails. But, under these conditions, a room that is sufficiently mixing can decay exponentially.[7,21,22] The decay rate, however, may not be well predicted by SA models.[17] Embleton[12] has presented a Markov-process implementation of the radiosity method that specifically accounts for this effect. The model reduces to a simple form in the practical case of a room having only two distinct types of surface. Given an absorbent floor or aperture area S_1 with absorption coefficient α_1 and the remaining area S_0 having a uniform absorption coefficient α_0, the absorption exponent α''' is given by

$$\alpha''' = -\ln[1-(\overline{\alpha}+\Delta\overline{\alpha})], \tag{4}$$

where

$$\Delta\overline{\alpha} = \frac{(\alpha_1-\alpha_2)^2}{1-\overline{\alpha}}\left(\frac{S_1}{S}\right)^2. \tag{5}$$

As previously developed, this model only accounts for the mean of the free-path distribution. If the variance in the free-path distribution is addressed the absorption exponent is given by

$$\alpha'''' = -\ln[1-(\overline{\alpha}+\Delta\overline{\alpha})]\left\{1+\frac{\gamma^2}{2}\ln[1-(\overline{\alpha}+\Delta\overline{\alpha})]\right\}. \tag{6}$$

The resulting new decay model is here termed the Kuttruff–Embleton model. The correction term $\Delta\overline{\alpha}$ is positive; thus these models predict larger decay constants than the unmodified Eyring or Kuttruff expressions, respectively. This is correct only for some enclosure geometries. For example, predictions agree with GA in rectangular parallelepipeds with one absorptive surface only if the absorptive surface is one of the larger surfaces.[17] Further, if more than two types of surface exist in a room, applying the simplified form of these models can lead to substantial error.[12]

Propagation loss can be accounted for in any of the models discussed above by adding a factor of $4mV$ to the total absorption power, where m is the energy dissipation coefficient of air expressed in units of Nepers per meter.[23]

In coupled rooms the shapes of decay curves are functions of both decay constants and steady-state energy densities. For this reason, it is especially important that a SA model predict both behaviors accurately. The expression for steady-state energy density ε_0 in a single-volume room containing a source of power Π,

$$\varepsilon_0 = \frac{4\Pi\exp(-A/S)}{cA}, \tag{7}$$

proposed by Vorländer,[24] was found most accurate when compared to GA predictions. The total absorption power A is defined as the product of the surface area and the average absorption coefficient or absorption exponent. The Sabine form, $A=S\overline{\alpha}$, has been adopted for this work. While this model predicts a uniform level of the reverberant field, it is known[25,26] that the steady-state level of the reverberant sound decreases with distance from the source. If it is assumed that the energy density due to the reverberant field decays exponentially and the instantaneous level of the reverberant field is uniform throughout the space, ε_0 will be given by the sum of the energy density contributed by the direct sound and the integration of the reverberant field energy density arriving after the direct sound. Assuming spherical propagation from the source and a receiver located at a distance r from the source, the expression for energy density is[26]

$$\varepsilon_0(r) = \frac{\Pi}{4\pi r^2 c} + \varepsilon_0\exp\left(-2\delta\frac{r}{c}\right). \tag{8}$$

B. Prior models of coupled rooms

When two or more rooms are joined together in such a way that energy can be transmitted between them, the rooms constitute a coupled system. The reverberant field in a system of coupled rooms is not described by SA models that have been developed for single-volume rooms.

Knudsen[23] has suggested that, for a uniform distribution of absorption between the subrooms, single-slope decay curves will result that can be described by the Eyring model using the mean-free path of the total system $\langle\overline{\ell}\rangle$

$$\varepsilon(t) = \varepsilon_0\exp\left(\frac{-c}{\langle\overline{\ell}\rangle}\alpha'\right). \tag{9}$$

This expression can be refined by replacing α' with another absorption exponent [e.g., Eqs. (3), (4), or (6)]. In rooms of disparate size the conjecture is incorrect because the bimodality of the free-path distribution is pronounced and double-slope decay curves result.[27] But, even if the decay curves in the subrooms are dominated by a single rate, it may be inaccurate to treat the subrooms as a single room.[16]

To treat a more general case, an enclosure consisting of coupled rooms must be modeled as a system of independently decaying subrooms that interact through the exchange of energy between their diffuse fields. The expression of this by Kuttruff[17] is formally equivalent to all prior models of coupled rooms based on the Sabine model of energy decay within subrooms.

Such dynamic energy-balance approaches assume that (1) each subroom has a unique diffuse sound field and that at coupling aperture(s) there is an abrupt transition between

sound fields, (2) the subrooms of the system interact only by an exchange of diffuse energy, and (3) the decay properties of the subrooms are unaltered by the coupling other than the small shift in the decay constant of each room predicted by the SA model (see, e.g., Ref. 14). The validity of these assumptions is examined in Sec. II D 2.

C. Improved model of coupled rooms

Under the Sabine assumptions irradiation strength $B = \varepsilon c/4$. However, Eyring[19] observed that assuming any decay model other than Sabine's is tantamount to multiplying B by the factor η. Eyring applied this observation only to the case of two coupled rooms with the decay rates in the subrooms predicted by the Eyring decay model. In the improved model presented here, Eyring's observation is used to modify Kuttruff's matrix formulation. Thus, the new model described below can use any of the decay models discussed in Sec. II A—including the newly introduced Kuttruff–Embleton model—to solve for the decay rates in the subrooms of a coupled system containing an arbitrary number of subrooms. If the Sabine model is used within the subrooms $\eta=1$ and the improved model (excluding the additional corrections discussed further below) is identical to Kuttruff's.

The energy density in the ith room is described by

$$\frac{d\varepsilon_i(t)}{dt} = -2\eta_i\zeta_i\varepsilon_i(t) = \frac{\eta_i B_i(t) A_{i0}}{V_i}, \tag{10}$$

where ζ_i is the Sabine decay constant of the ith room when uncoupled, $B_i(t)$ is the irradiation strength in the ith room, and A_{i0} is the absorption power of the ith room exclusive of the coupling area. For a system of N rooms with apertures of area S_{ij} that allow energy to be transferred between the ith and jth rooms, the system of N coupled ODEs representing the dynamic energy balance is, following Kuttruff's derivation[17]

$$\frac{d\varepsilon_i(t)}{dt} = -\eta_i\left(2\zeta_i + \frac{c\sum_{\substack{j=1\\ j\neq i}}^{N} S_{ij}}{4V_i}\right)\varepsilon_i(t) + \sum_{\substack{j=1\\ j\neq i}}^{N} \eta_j \frac{cS_{ij}}{4V_i}\varepsilon_j(t) \quad (i=1...N). \tag{11}$$

The values $B_i(t)$, rather than the decay rates themselves, must be adjusted using the factors η_i to account for different decay models if Eq. (11) is to be self-consistent. Separating the decay terms in the ith room [the first term of the right-hand side of Eq. (11)] into decay due to absorption and decay due to transfer of energy through the aperture(s) essentially separates A_{i0} of Eq. (10) into two terms so that changing the decay rate of the subroom cannot be effected by altering A, since the terms would not add, but rather by altering their common multiplying factor.

Defining a set of constant coefficients ψ_{ij} in the manner of Ref. 17 allows the system to be written in matrix notation

$$\dot{\boldsymbol{\varepsilon}} = \boldsymbol{\Psi}\boldsymbol{\varepsilon} \tag{12}$$

and solved using conventional procedures for such systems of ODEs. The N eigenfunctions of this system are of the form

$$\boldsymbol{\varepsilon}^{(i)} = \boldsymbol{\varepsilon}_0^{(i)} \exp(-2\delta_i t) \quad (i=1...N), \tag{13}$$

with eigenvectors $\boldsymbol{\varepsilon}_0^{(i)}$ and eigenvalues δ_i. The general solution in the ith room is expressed as a linear combination of the eigenfunctions

$$\varepsilon_i(t) = C_1\varepsilon_{i0}^{(1)}\exp(-2\delta_1 t) + \ldots + C_N\varepsilon_{i0}^{(N)}\exp(-2\delta_N t) \quad (i=1...N), \tag{14}$$

where $\varepsilon_{i0}^{(j)}$ is the ith component of the jth eigenvector. By considering the steady-state solution of Eq. (11) the coefficients C_i are solved for in terms of the steady-state energy-density values. These are determined by solving the system of coupled energy-balance equations

$$\frac{\Pi_i}{V_i} = -\sum_{j=1}^{N} \psi_{ij}\varepsilon_j(0) \quad (i=1...N), \tag{15}$$

where Π_i is the power of the source located in the ith room. There is some ambiguity concerning which form of $\boldsymbol{\Psi}$ should be used to solve for steady-state values. Eyring[19] held that his formulation was not appropriate for the steady-state case and should only be used to determine decay rates; instead, the Sabine model should be used for steady-state processes. While use of either can be validated by formal derivation,[17] the Sabine form of $\boldsymbol{\Psi}$ is adopted in this paper. Further, Vorländer's correction is applied to the resulting values of $\varepsilon_j(0)$.

Unlike prior models, this improved model can treat multiple sources distributed throughout the subrooms or sources that simultaneously radiate into more than one subroom. The latter case is accommodated by finding $\Delta\Omega_{ij}$, the fraction of the total solid angle subtended by S_{ij} as viewed from the source (see the appendix A of Ref. 25). For example, given a source of power P located in the ith room of a two-room system two sources are modeled. In the jth room $\Pi_j = P\Delta\Omega_{ij}/4\pi$ and in the ith room $\Pi_i = P - \Pi_j$. For complex aperture configurations, a computational approach must be used. In many cases the ratio $\Delta\Omega_{ij}/4\pi$ can be estimated as the ratio of aperture area to total surface area of the room.

Barron and Lee's revised theory for steady-state energy density[26] explicitly assumes that the reverberant field in a room will decay at a single exponential rate. In a system of N coupled rooms, the reverberant field will, in general, decay as the linear combination of N exponential decays. In this case, the energy contained in the impulse response integrated from the arrival time of the direct sound to infinity summed with the energy density due to the direct sound is given in the ith room by the new expression

$$\varepsilon_0(r) = \frac{\Pi}{4\pi r^2 c} + \sum_{j=1}^{N} C_j\varepsilon_{i0}^{(j)}\exp\left(-2\delta_j\frac{r}{c}\right), \tag{16}$$

where r is the distance from the source to the receiver. It should be noted that r/c is typically much smaller than the reverberation time of the ith room T_i corresponding to δ_i of the subrooms. Therefore, it is the ability of the decay model

to accurately predict the early portion of the decay that is most critical to the accuracy of Eq. (16). Moreover, variation in energy level with position is governed almost entirely by δ_j for which $C_j\varepsilon_{i0}^{(j)}$ is largest, unless the knee of the decay curve occurs rather early. If the source and receiver are in the same room, Π and r in Eq. (16) have the conventional interpretations, but if they are in separate rooms both the source, if it is visible, and the coupling aperture behave as sources of the reverberant field in the room not containing the source. To address this requires greater revision of Eq. (8) than that given in Eq. (16).

D. Limitations of and corrections to the improved model

1. Strength of coupling

SA models of coupled rooms are most accurate when applied to systems that are not strongly coupled.[13–18] Strongly coupled systems are defined by equipartition of energy whereas weakly coupled systems are defined by subsystems that behave as though isolated.[28] The intermediate case is that of loosely coupled rooms. In such systems, the steady-state levels and decay processes can only be described by a theory that accounts for the exchange of energy between the spaces. Based on these definitions, Smith[28] has given the criterion for strong coupling in a two-room system as $\kappa>1$, where

$$\kappa=\frac{S_{ij}}{A_{i0}}+\frac{S_{ji}}{A_{j0}}, \tag{17}$$

(where $S_{ij}=S_{ji}$ for the two-room case). Cremer and Müller[14] presented a similar criterion for two-room systems described by the coupling factor

$$k_j=\frac{S_{ji}}{A_{j0}+S_{ji}}. \tag{18}$$

For a source in the ith room, strong coupling is defined by $k_j\sim 1$ and weak coupling is defined by $k_j\sim 0$. Note that, by Smith's definition, two rooms are strongly coupled if either k_i or $k_j>0.5$. This is a stricter formulation of Kuttruff's guideline that the SA model of coupled rooms is applicable to those cases where the energy lost via coupling is not substantially larger than the energy lost via absorption.[17]

Lyle[15] has proposed an empirically derived upper limit for the accurate application of the SA model based on the idea of coupling strength

$$\max S_{ij}=\min M(0.4-\overline{\alpha_i})S_i \quad \text{for } \forall i,j, \tag{19}$$

where $M\leqslant 1$ is the "mixing constant." In ideally diffuse rooms $M=1$ and, for apertures above the limit, the system can be treated as a single room. In rooms that are not ideally diffuse $M<1$ and no model can be certain to work for the strong-coupling condition. In such cases, equipartition of energy between the now unified subrooms may not occur even though the system is, geometrically, a single space.[15]

Each of these criteria is fallible. In comparisons with GA, Eq. (17), often predicts that the model should fail before it does. In contrast, Eqs. (18) and (19) often fail to predict that single-volume rooms should be treated as such.

2. Failure of statistical assumptions

Progressive discrepancy between predictions of GA and SA as rooms become more strongly coupled is partly due to violations of the additional assumptions made by the SA model of coupled rooms, as given in Sec. II B.

Coupling apertures on the boundaries of subrooms violate the assumption that decay properties of individual rooms are unaltered by coupling. Geometrical averaging of absorption coefficients can be understood to originate in the multinomial distribution describing the number of reflections that occur from each surface of an enclosure in the case of independent reflections.[17] Though this assumption is never fully correct,[2] especially for specular reflection,[6] it is further flawed if any portion of the surface, such as a coupling aperture, is perfectly absorptive. If a phonon travels out of an aperture, the next reflection will not occur in the original room and the two successive reflections are dependent. This leads to flaws in the averaging of the absorption coefficients because an aperture diminishes the probability that all room surfaces will be uniformly sampled, as Eyring first observed.[19]

Large apertures, because they act initially as perfect absorbers, cause anisotropy in the sound field due to the establishment of a net flow of energy (i.e., there are fewer phonons moving away from the aperture than toward it[2]). If the aperture area is not too large, SA models can still describe the behavior.[1,6] However, if the area is too large, SA models will fail as the preferential selection of trajectories by the aperture slows the mixing process.[6]

Locations and sizes of the apertures also affect free-path distribution. Unless conditions are such that the Sabine model is valid, the decay associated with the room will vary as a function of the location of apertures. Even if free-path distribution as modified by the apertures is known for each of the subrooms, distributions will differ when the rooms are coupled due to interaction of the subrooms. Certain free paths that are not available in either of the subrooms are made possible in the coupled system. Therefore, the eigenvalue decay rates will not be exactly those derived from the uncoupled decay rates because coupling the two rooms will shift the natural decay rates of the rooms by changing the shapes of the free-path distributions.

3. Nondiffuse transfer of energy

The first assumption of the SA model, that there is an abrupt transition at the coupling aperture between unique diffuse sound fields, is also not accurate. Sound radiates from the coupling aperture with energy density that is distinct from the energy density of the reverberant field of the room into which it radiates. Therefore, it behaves, initially, as a direct-sound component. Only after it has undergone reflection is it part of the reverberant field. This phenomenon has been observed for rooms coupled by partially transondent partitions[13] and for rooms coupled by apertures.[19] Assuming a diffuse field in the source room at a large distance r from the aperture the finite dimensions of the aperture can be neglected and the aperture is approximated by a Lambert

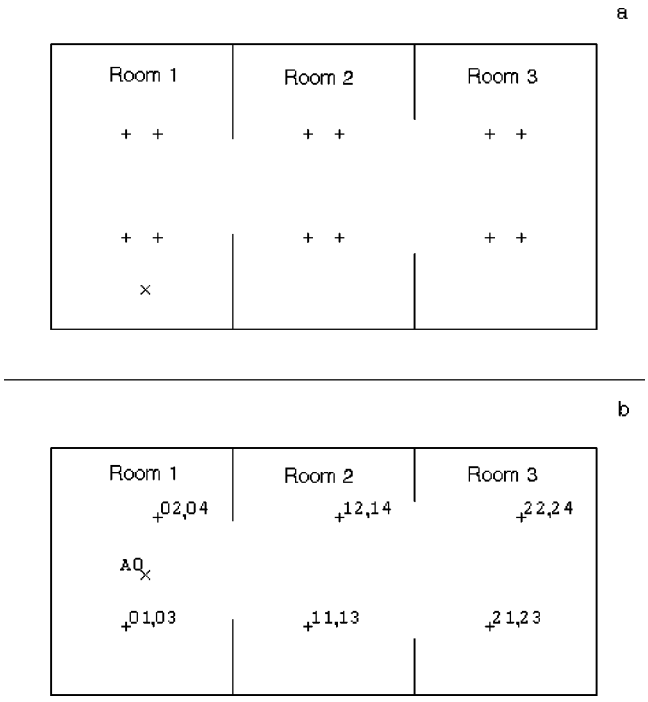

FIG. 1. Three-room coupled system first studied by Kuttruff. Transverse section (a) and plan (b) views are shown. Volumes V and areas S are the same for each subroom: $V=6270$ m^3 and $S=2066$ m^2 15 m$\times$19 m $\times$22 m); areas include coupling areas. Crosses (+) indicate receiver positions: 1–4 in Room 1, 11–14 in Room 2, and 21–24 in Room 3. The single source position in Room 1, A0, is indicated by an X.

source[17] of power $B_i S_{ij}$. If the locally planar assumption is met, the energy density in room j due to the direct contributions from an aperture, ε_j, is

$$\varepsilon_j(\mathbf{r},t)=\frac{\cos(\theta)S_{ij}\varepsilon_i(t)}{4\pi r^2} \tag{20}$$

for an aperture coupling the jth room to the ith room, where $\mathbf{r}$ is the position vector of the receiver in the jth room (with magnitude r), θ is the angle from the normal to the wall containing the aperture, and $\varepsilon_i(t)$ is the energy density of the ith room. This implies that, in regions near coupling apertures, direct radiation from adjacent rooms can dominate the sound fields of rooms with lower energy density than those adjacent rooms.

Because energy transmitted through coupling apertures is first radiated as a quasidirect component, reverberant energy can be transferred between rooms that are not adjacent. This is illustrated by considering the system of three coupled rooms shown in Fig. 1 that was first studied by Kuttruff.[17] Traditional analysis assumes $S_{13}=S_{31}=0$. However, a certain portion of the sound radiated from S_{12} will pass through S_{23} before undergoing a reflection in room 2. Likewise, a portion of the sound radiated from S_{32} passes directly through S_{21}. If the radiation from the aperture has an angular distribution given by Eq. (20), the fraction of the sound power radiated by S_{12} that passes directly through S_{23} (or vice versa), is given by the radiation shape factor between the two apertures

$$F_{13}=F_{31}=\frac{1}{\pi S_{12}}\int_{S_{12}}\int_{S_{23}}\frac{\cos\phi_{12}\cos\phi_{23}}{r^2}dS_{12}dS_{23}, \tag{21}$$

where r the magnitude of the vector between points on the aperture surfaces and ϕ_{ij} are the angles between the vector connecting the points and the normals of S_{ij}. Having determined the fraction of energy transmitted directly between the apertures, the corrected coupling areas are given by

$$\begin{aligned} S'_{12}&=(1-F_{13})S_{12},\\ S'_{32}&=(1-F_{13})S_{32},\\ S'_{13}&=F_{13}S_{12},\\ S'_{31}&=F_{13}S_{32}. \end{aligned} \tag{22}$$

This approach can be extended to more complex geometries. For example, a room with multiple apertures, which is not convex in the region containing the apertures, may have F_{ii} that is nonzero. Given simple configurations and aperture shapes, the radiation shape factors can be calculated directly (see the appendix A of Ref. 25). In more complex geometries, they must be determined computationally. In such cases it is possible to form rough estimates of the factors from ratios of surface areas of the apertures to the total surface areas of the rooms.

4. Spatial variation

Equation (16) suggests a correction to the basic theory as the level of the reverberant energy density at the coupling aperture may differ from the value used in Eq. (11). Thus B in the prior derivation should be modified if B is the irradiation strength in a room containing a source. Even in rooms that do not contain a source, the aperture itself acts as a source so that spatial variation may result. The spatial variation in the level of the reverberant energy suggests that spatial variation in decay shape may occur under certain conditions because the multiplier terms in Eq. (14) will be functions of position.

III. GEOMETRICAL-ACOUSTICS MODEL

The exact GA solution for the energy decay can be obtained through the solution of an integral equation.[4,17,29] In practice, GA solutions are obtained computationally using ray tracing or its variants, which can be viewed as Monte Carlo approximations to the exact solution.[30]

In this study, the geometrical-acoustics software CATT-Acoustic V. 8.0 is used.[31,32] Nonspecular reflection is modeled as Lambert diffuse reflection,[17] for which scattering coefficients s are defined as the fraction of energy that is not specularly reflected. While angular dependence of absorption coefficients is not accounted for, it can be safely neglected for large, reverberant enclosures having sufficiently large scattering coefficients.[33,34] The original algorithm assumes a constant, quadratic rate of growth of the reflection density, which is not true in certain coupled rooms.[35] To address this, a new version of the algorithm[35] (introduced in commercial versions 8.0b and above) is used.

IV. COMPARISON OF STATISTICAL AND GEOMETRICAL ACOUSTICS

In order to characterize the relationship between SA models and GA models of coupled-room systems, two- and three-room coupled systems are studied. In the two-room geometry, the volumes of the subrooms are based on averages of performance spaces which employ either a coupled stage house or an auxiliary coupled chamber. The predictions of decay curves and steady-state energy densities given by SA and GA are compared for each of the rooms under a series of different conditions of the room surfaces. The purpose of these simulations is to determine how the additional assumptions implicit in SA models of coupled rooms affect the relationship of their predictions with those of GA. By comparing predictions of energy decay and steady-state energy density, conditions for which the GA model is approximated by SA models are assessed in terms of degree of coupling and absorption and scattering coefficients of the surfaces of the subrooms. The three-room geometry is taken from previous work conducted by Kuttruff[17] and serves to evaluate elements of the new model that improve the accuracy of predictions in systems having more than two rooms. In both two- and three-room geometries the subrooms are modeled as rectangular parallelepipeds, which, though not ergodic given specular reflection,[3,29] are both ergodic and mixing for $s>0$.

A. Methodology

The GA computer model is used to generate energy echograms for each source-receiver combination. Time-ensemble-average decay curves $\langle s(t)\rangle$ for fixed source-receiver pairs are derived by Schroeder integration of energy echograms and steady-state energy-density values are taken from maxima of these integrated echograms. Steady-state energy-density values are plotted as a function of the distance of the receiver from the source, a so-called sound-propagation curve, and compared with predictions of the SA model. For comparison with SA predictions of decay rate, spatial averaging is used to more accurately describe global characteristics of the sound field within each subroom. Space-ensemble-average decay curves $\{\langle s(t)\rangle\}$ are calculated by synchronous averaging of $\langle s(t)\rangle$ over receiver and/or source positions.[36] The number of source and receiver positions is chosen in accordance with the recommendations given in Ref. 37.

The mean-free path $\langle\overline{\ell}\rangle$, averaged both over the time history of each cone/ray and over the ensemble average of all the cones/rays, is calculated from the trajectories of all the cones/rays emitted from a given source position according to

$$\langle\overline{\ell}\rangle=\frac{1}{M}\sum_i \langle\ell\rangle_i=\frac{1}{MN}\sum_{ij}\ell_{ij}, \tag{23}$$

where ℓ_{ij} is the length of the jth path taken by the ith cone/ray, M is the total number of cones/rays, and N is the total number of paths traced per cone/ray.

Fitting sums of decaying exponentials to decay curves by a least-square method is ill conditioned. Therefore, specifying the difference between two models in terms of rms error is not generally meaningful. Instead, decay curves are compared visually. In some cases, the decay parameters predicted by SA are compared with those extracted from the decay curve predicted by GA using Bayesian parameter estimation.[38]

B. Uncertainty analysis

In comparing SA predictions with GA predictions, there are two sources of uncertainty (1) u_a, uncertainty of the model outputs due fluctuations in the algorithm, which applies to the computational GA model only, and (2) u_i, uncertainty of the model outputs due to uncertainty in the inputs, which applies both to GA and SA models. Only u_a directly concerns the comparisons made here, because the input parameters for the models are known exactly. However, in practice both models will be evaluated on their ability to predict reality. In that case, the relative sensitivity of the GA and SA models to uncertainty in the input parameters determines whether one model is more accurate than the other.

1. Algorithmic uncertainty

As discussed in Sec. III, CATT-Acoustic yields Monte Carlo approximations to the exact GA solution which display stochastic run-to-run fluctuations. For simple algorithms, analytic estimates of u_a exist.[38] For CATT-Acoustic, no uncertainty estimate has been developed; therefore u_a in each case is estimated from the standard deviation of ten predictions. This uncertainty is larger at later times and smaller for larger numbers of cones/rays. Many cone/rays were used for the simulations such that, for $\{\langle s(t)\rangle\}$, $u_a\ll 1$ dB. Because of this, u_a is not plotted along with results and can be assumed negligible.

2. Input uncertainty

Real input parameters, including room geometry and surface parameters, are known to finite precision. Comparative merit of the modeling approaches can be practically assessed only in terms of u_i, uncertainties of predictions due to uncertainties of input parameters. Consideration here is limited to input parameters whose uncertainty is of most significance: absorption and scattering coefficients, which may have uncertainties of 10% or more.

For small numbers of subrooms, it is tractable to solve the SA model algebraically and therefore possible to develop analytical expressions for u_i.[39] In general, Eqs. (11) and (15) are solved numerically. Uncertainty in the final predictions is estimated (up to first-order terms in a Taylor-series expansion) by computing influence coefficients for each input parameter at the limits of its region of confidence.[39] While this is in error if the predictions are a nonlinear function of the input parameters,[40] this linear approximation, which also neglects interactions between the input parameters, is reasonable for small uncertainties.

A similar procedure is applied to estimate u_i in the GA model. Though the additional input parameter s makes the assumption of noninteraction less plausible, the alternative—Monte Carlo estimation of the distribution of the output data—is too time consuming. Variations in s for $s>0.5$ typi-

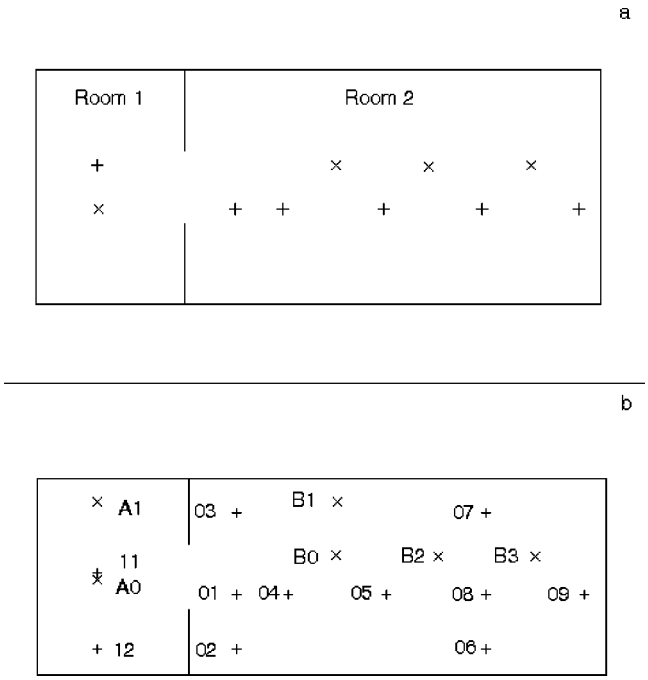

FIG. 2. Two-room coupled system. Transverse section (a) and plan (b) views are shown. The volumes V and areas S of the subrooms are $V_1 = 6270\ \mathrm{m}^3$, $S_1 = 2066\ \mathrm{m}^2$ (15 m×19 m×22 m) and $V_2 = 17\,556\ \mathrm{m}^3$, $S_2 = 4280\ \mathrm{m}^2$ (42 m×19 m×22 m) and; areas include coupling areas. Crosses (+) indicate receiver positions: 1–9 in Room 2, 11–14 in Room 1. Sources are indicated by X's: A0-A1 in Room 1 and B0-B3 in Room 2.

cally have little influence on decay curves.[7,21] Therefore, in many cases (and most of the cases of interest here) keeping only the linear term of the Taylor series is a reasonable approximation.

C. Two-room system

A simplified representation of a concert hall with an auxiliary coupled room is constructed by positioning the auxiliary volume, Room 1, along the short side of the audience chamber, Room 2, as shown in Fig. 2. Source positions in Room 1, A0-A1, and Room 2, B0-B3, are considered. A total of 11 receiver positions are simulated for each of the seven source positions. As shown in Fig. 2, nine of the receivers, labeled 1–9, are distributed within Room 2 and the remaining two receivers, labeled 11, 12, are located in Room 1. The rooms are coupled by a single aperture centered in the wall separating them. Four aperture sizes, 25, 50, 100, and 200 m^2 are used. The aspect ratio of each is one. For each geometrical condition three different absorption conditions are modeled: (1) uniform absorption ($\alpha = 0.10$) for all wall surfaces, (2) uniform α for wall surfaces within each subroom ($\alpha_1 = 0.10$, $\alpha_2 = 0.20$), such that the absorption power in Room 2 is equivalent to that presented by an audience, and (3) a similar condition in which the increase in the absorption of Room 2 is affected by increasing the absorption coefficient of the floor surface to 0.80 in order to simulate the nonuniform absorption presented by an audience and all other surfaces are assigned $\alpha = 0.10$. For each absorption condition there are three scattering conditions for which Lambert scattering coefficients $s = 0.10$, 0.60 and 0.99 are applied to all surfaces uniformly.

Coupling strengths are calculated according to the criteria described in Sec. II D 1. Equation (17) predicts that the coupling is strong in all cases for which $S_{12} \geqslant 100\ \mathrm{m}^2$. By contrast, Eqs. (18) and (19) predict that the system is never strongly coupled, even when configured as a single room.

For Condition 1, much of the relationship between SA and GA predictions is known from previous studies of single-volume rooms. Thus, comparison is made only between the improved SA model using the Kuttruff decay model ($\eta = \alpha''/\overline{\alpha}$) within the subrooms and GA. Predictions of Knudsen's conjecture using Eyring and Kuttruff models are then similarly compared with GA predictions. For Conditions 2 and 3, the improved-SA-model decay-curve predictions using Sabine ($\eta = 1$), Eyring ($\eta = \alpha'/\overline{\alpha}$), and Kuttruff ($\eta = \alpha''/\overline{\alpha}$) decay models within the subrooms are compared with GA predictions. Condition 3 also allows for the Kuttruff–Embleton decay model ($\eta = \alpha'''/\overline{\alpha}$) to be used in Room 2. For each condition, the predictions of Eq. (16) are compared with sound-propagation curves calculated by GA. In the case of Conditions 2 and 3 the influence of this on the spatial variation of decay-curve shape is shown.

1. Condition 1: Uniform absorption

Given uniform absorption, Room 1 is less reverberant than Room 2 and, thus, single-slope decay curves result in Room 2 if the source is located in that room, while in Room 1 the initial slope of the decay is zero and over time approaches the slope of the decay curve in Room 2, as shown in Fig. 3. Also shown in Fig. 3, as the size of the coupling aperture increases, initial levels of decay curves approach each other and the initial transition period of the decay in Room 1 becomes shorter. It is this condition of sources in Room 2 that is analyzed below.

As expected, the improved model using the Kuttruff decay model within the subrooms accurately predicts decay curves, as illustrated in Fig. 3 for $S_{12} = 25$ and 200 m^2. In comparison (though, for clarity, not shown in Fig. 3), the Sabine decay model slightly underpredicts the decay rates and the Eyring decay model slightly overpredicts the decay rates. For $S_{12} \leqslant 100\ \mathrm{m}^2$ there is little variation in the accuracy of the predictions of the SA model with aperture size. As shown in Fig. 3, the error increases markedly for $S_{12} = 200\ \mathrm{m}^2$. The reasons for this have been discussed in Sec. II D 2. As shown in Fig. 4, $\langle \overline{\ell} \rangle$ of the uncoupled subrooms decrease from $4V/S$ (Room 1:12.1 m, Room 2:16.4 m) as the size of the aperture is increased due to an increase in the relative frequency of short paths. Increasing the size of the aperture also allows increased access to long-length paths associated with the coupled system as a whole. The longest free path available in Room 2 is 51.08 m. Figure 4 shows that as the aperture size increases the relative frequency of path lengths in the coupled system greater than 51.08 m also increases. The net effect of these phenomena is an increase in γ^2 of the subrooms. Because increased γ^2 decreases the decay rate of a room, overprediction of the decay rates in the subrooms is made more severe as aperture size increases. Increase in γ^2 depends on the geometry of room. However, there is not a known relationship between γ^2 and aperture size for a fixed geometry or between geometry and rate in-

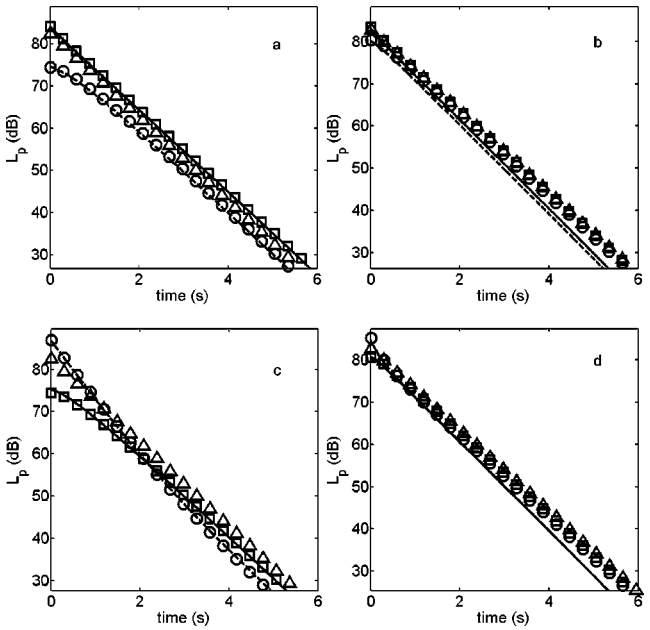

FIG. 3. For the two-room coupled system (Fig. 2) in Condition 1, spatial averages of GA-model predictions ($s=0.99$) for receivers in Room 1 (dashed line) and Room 2 (solid line) are compared with improved-SA-model predictions using Kuttruff's decay model within the subrooms [Eq. (11), $\eta=\alpha''/\overline{\alpha}$] for Room 1 (circles), Room 2 (squares), and the Kuttruff form of Knudsen's conjecture [Eq. (9) using α''] (triangles). Ensemble averages of all source positions in Room 2 with $S_{12}=25\ \mathrm{m}^2$ (a) and $200\ \mathrm{m}^2$ (b) and in Room 1 with $S_{12}=25\ \mathrm{m}^2$ (c) and $200\ \mathrm{m}^2$ (d) are shown.

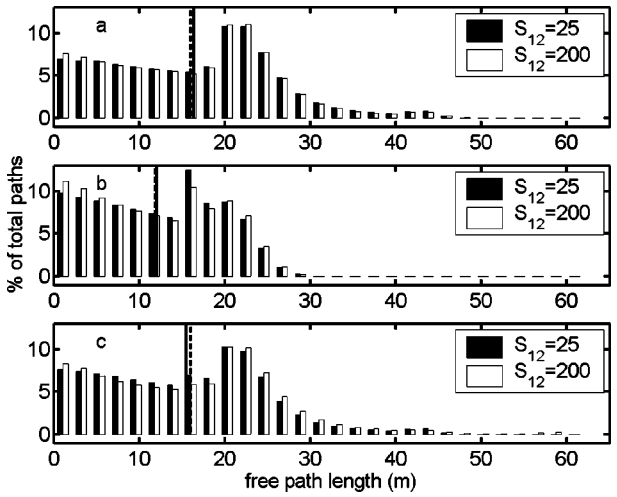

FIG. 4. For the two-room coupled system (Fig. 2), free-path distributions of cones/rays emitted (a) from source B2 in isolated Room 2 with $S_{12}=25\ \mathrm{m}^2$ (black bars) and $200\ \mathrm{m}^2$ (white bars) simulated by absorbing patches, (b) from source A0 in isolated Room 1 with $S_{12}=25\ \mathrm{m}^2$ (black bars) and $200\ \mathrm{m}^2$ (white bars) simulated by absorbing patches, and (c) from source B2 in the coupled system with $S_{12}=25\ \mathrm{m}^2$ (black bars) and $200\ \mathrm{m}^2$ (white bars) are shown. Mean-free paths are indicated by vertical lines for $S_{12}=25\ \mathrm{m}^2$ (solid lines) and $200\ \mathrm{m}^2$ (dashed lines).

crease in γ^2 with aperture size. Instead increase can be accounted for heuristically by multiplying γ^2 by a correction factor. Factors $\sim 1-2$ have been found to work well for this particular coupled system. These observations and corrections hold generally for this coupled system because absorption configurations with $\alpha<1$ do not alter the free-path distribution.

Bayesian analysis gives additional insight into phenomena observed. For $S_{12}\leqslant 100\ \mathrm{m}^2$ the two rates extracted from the decay curves computed by the GA computer model approximately agree with the decay rates predicted by the SA model. The differences between the rates predicted by the models increase as the aperture size increases. In the case of $S_{12}=200\ \mathrm{m}^2$, with the source in Room 1, Bayesian analysis supports three decay rates. The first rate is associated with Room 1 and is similar to the SA prediction. The other two rates, which correspond to reverberation times of 6.10 and 6.40 s, may correspond, respectively, to the decay rate associated with Room 2 or the decay rate associated with the entire coupled system. The rate associated with Room 2 has a platykurtic posterior probability distribution and is only weakly supported by the data. As the decay curves shown in Fig. 3 suggest, the system is at the point of transition between one- and two-room behaviors.

GA predictions are also compared with Knudsen's conjecture [Eq. (9)]. As determined by GA, $\langle\overline{\ell}\rangle$ of the coupled system differs little from $4V/S$ ($S_{12}=25\ \mathrm{m}^2$: $\langle\overline{\ell}\rangle=15.5$, $4V/S=15.1$; $S_{12}=200\ \mathrm{m}^2$: $\langle\overline{\ell}\rangle=16.0$, $4V/S=16.0$). Differences increase for small coupling apertures due, most likely, to increase in mixing time of the geometry such that $\langle\overline{\ell}\rangle=4V/S$ is not satisfied within the truncation time of the computation. Using the Eyring decay model, Knudsen's approach overpredicts the decay rate. But, by accounting for γ^2, the Kuttruff form of Knudsen's conjecture becomes rather accurate, as shown in Fig. 3. The remaining error is primarily the incorrect prediction of equipartition of energy. Therefore, Knudsen's conjecture becomes more accurate as S_{12} increases.

For sources and receivers both in Room 2, the steady-state energy density is well predicted by the modified form of Barron and Lee's revised theory using $\eta=\alpha''/\overline{\alpha}$ (errors <1 dB), as shown in Fig. 5 for Source B3. As expected, errors increase for higher s due to backscattering. Equation (16) suggests that the level of the reverberant field should decrease linearly with distance at a single rate determined by the dominant decay rate in Room 2. But, due to backscattering, there are two distinct rates; one associated with the receivers near the source (1–5) and a second associated with the receivers far from the source (6–9).

2. Condition 2: Uniform absorption within each subroom

When loosely coupled, the system displays for these absorption conditions the strongly nonlinear decay curves typically associated with coupled rooms.

The GA model predicts that the decay rate of the late portions of the decay curves decreases with time for $s=0.10$. This is especially notable for $S_{12}\geqslant 100\ \mathrm{m}^2$. In cases for which the late decay is not dominated by long-lived paths ($s=0.60,0.99$), using the Kuttruff decay model ($\eta=\alpha''/\overline{\alpha}$) in the improved SA model most accurately predicts the decay curves, as shown in Fig. 6, while Sabine ($\eta=1$) and Eyring ($\eta=\alpha'/\overline{\alpha}$) decay models used in the improved SA model underpredict or overpredict the decay rates, respectively. The Kuttruff decay model tends toward overprediction of these decay rates, which is greater for larger S_{12} and can be attrib-

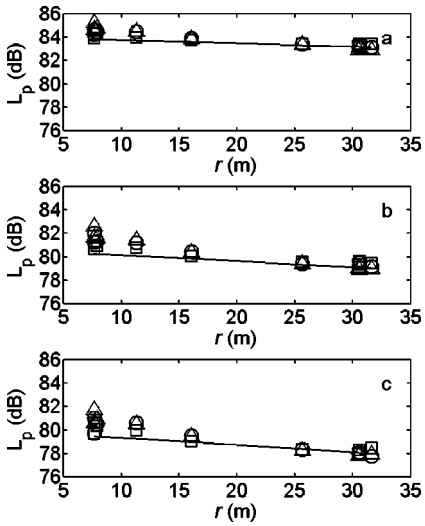

FIG. 5. Sound propagation curves (with direct sound subtracted) in Room 2 for Source B3 and $S_{12}=25\ \mathrm{m}^2$ in Conditions 1 (a), 2 (b), and 3 (c) computed by the GA model for $s=0.10$ (squares), 0.60 (circles), and 0.99 (triangles) are compared with the predictions of Eq. (16) (solid line).

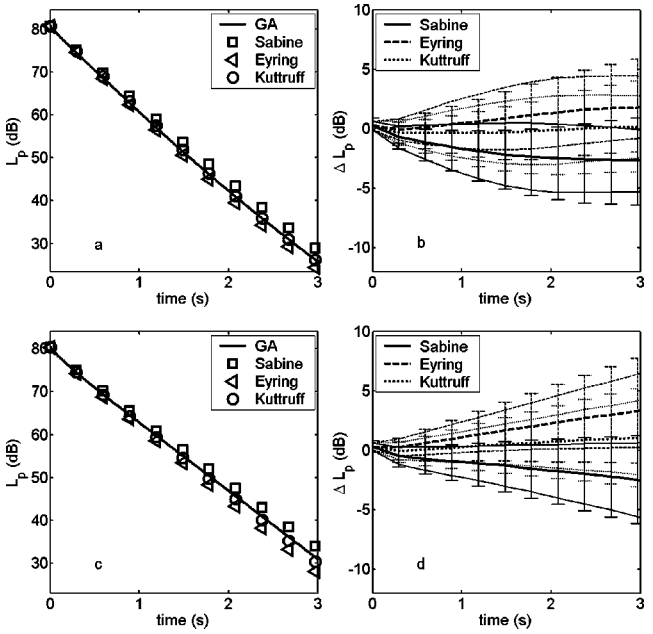

FIG. 6. For the two-room coupled system (Fig. 2) in Condition 2, ensemble averages of GA-model predictions ($s=0.99$) for all sources and receivers in Room 2 (solid line) are compared with improved-SA-model predictions using Sabine [Eq. (11), $\eta=1$] (squares), Eyring [Eq. (11), $\eta=\alpha'/\overline{\alpha}$] (circles) decay models within the subrooms for $S_{12}=25\ \mathrm{m}^2$ (a) and 200 m^2 (c). Differences between GA and SA predictions ($10\log_{10}\mathrm{GA}-10\log_{10}\mathrm{SA}$) [using Sabine (solid line), Eyring (dashed line), and Kuttruff (dotted line) decay models] are plotted for $S_{12}=25\ \mathrm{m}^2$ (b) and 200 m^2 (d). The regions of confidence defined by u_i are plotted as error bars for SA predictions and as fainter lines lying on either side of the primary lines for GA predictions. Confidence limit predictions assume α and s are known to $\pm 10\%$ at the same level of confidence.

uted to increased variance of the free-path distribution, as observed in Sec. IV C 1. Multiplying γ^2 by a correction factor can address this error. As shown in Fig. 6, the GA model is typically less sensitive to input uncertainty. For uncertainty in α and s of $\pm 10\%$, the confidence limits of the predictions are such that all of the models can be considered equally accurate.

Section II D 4 suggests that spatial variation in the shape of the decay curve may occur as a result of spatial variation in the energy density associated with each eigenfunction. Such variation should be most significant for Source B3, for which the difference in the distance between the source and a given receiver and the aperture and a given receiver is greatest. Instead, the GA model predicts little spatial variation. The level and rate of the late decay vary somewhat with position (as shown in Fig. 5), but the decay curve maintains the same basic shape, as shown in Fig. 7. As before, the level of the reverberant field decreases with distance from the source, as shown in Fig. 5. Because δ_1 is larger, the rate of decrease is greater, as Eq. (16) predicts. However, the increase in level near the source for large s, which is not predicted by the model, is also larger and steeper in slope. This variation is not due to the nonlinearity of the decay curve predicted by the SA model, because over the time range relevant here ($\leqslant$150 ms) the decay curve is essentially single sloped. Instead, it can be attributed to the additional absorption in Room 2.[25]

3. Condition 3: Simulated audience absorption

Because of nonuniform distribution of absorption in Room 2, for $s<0.40$ reasonable accuracy of SA models cannot be assured.[21] In Room 2 there is a balance between long-lived paths and anisotropy of the sound field.[35] For small s, long-lived paths and two-dimensional reverberation dominate, resulting in a nonlinear decay curve of the room when uncoupled. For higher scattering coefficients, the enclosure is more mixing, so the effects of anisotropy dominate.

Because of this, the improved SA model using Sabine model of decay in the subrooms ($\eta=1$) underpredicts the decay rate in Room 2 for all aperture conditions. The Embleton model suggests that the Eyring model should also underpredict the decay rate in Room 2. The combination of an increase in the decay constant due to anisotropy and a decrease in the decay constant due to variance in the free-path distribution tend to negate one another in this particular case, producing a decay curve in the primary room that agrees with the prediction of the improved SA model using the Eyring model of decay in the subrooms ($\eta=\alpha'/\overline{\alpha}$). This is confirmed by employing the Kuttruff–Embleton decay model ($\eta=\alpha'''/\overline{\alpha}$), which predicts the decay rate well in Room 2. Figure 8 illustrates the comparisons made above. In Room 1 the behavior is the same as in the previous cases and the Kuttruff model ($\eta=\alpha''/\overline{\alpha}$) gives the most accurate prediction of the decay rate. The GA model is seen in Fig. 8 to be less sensitive to input uncertainty, as observed for Condition 2. However, overall errors are greater than Condition 2 and the different decay models cannot be considered equally accurate for input uncertainties of $\pm 10\%$.

As in Condition 2, Eq. (16) predicts the propagation curves well, with larger errors for higher values of s, as shown in Fig. 5. While the energy propagation curve is similar to the previous case, the spatial variation of the decay curve shape is greater. As shown in Fig. 7, Receivers 1–5 start at lower levels than Receivers 6–9, because they are further from the source, but end at higher levels, because

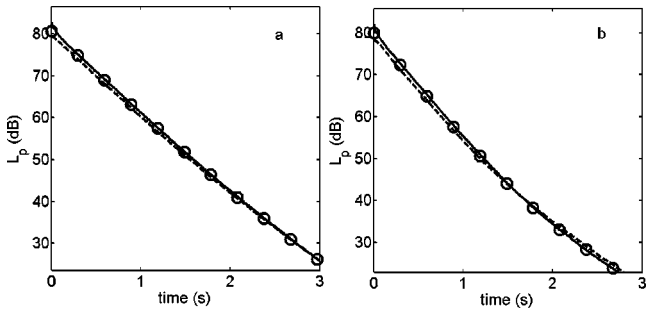

FIG. 7. For the two-room coupled system (Fig. 2) with $S_{12}=25\ \mathrm{m}^2$ and Source B3, spatial variation in decay shape is shown between ensemble-averaged decay curves of receivers 1–5 (dashed lines), far from the source, and 6–9 (solid lines), near the source, given absorption Condition 2, with $s=0.99$ (a), and absorption Condition 3, with $s=0.99$ (b). The predictions of the improved SA model [Eq. (11) with $\eta=\alpha''/\overline{\alpha}$, for Condition 2, and with $\eta=\alpha'''/\overline{\alpha}$ for Condition 3] are shown for reference (circles).

they are nearer to the coupling aperture. In an actual room the effect may be more marked due to grazing-incidence attenuation, which is not accounted for by the GA model.

D. Three-room system

SA calculations of the decay curves in a system of three coupled rooms have been discussed previously by Kuttruff.[17] Because the three-room model studied by Kuttruff was computed only by SA, all of the room parameters were not given explicitly. Taking the three rooms of equal volume to be geometrically identical, Kuttruff's specifications are $\alpha_2=\alpha_1/10$, $\alpha_3=\alpha_1/2$, $S_{12}=S\alpha_1/20$, and $S_{23}=S\alpha_1/10$, where S is the area of each room, inclusive of the aperture area. As shown in Fig. 1, the rooms are chosen to be of the size and shape of Room 1 of the previous geometry and are coupled through their largest wall with a square aperture centered in each interior dividing wall. The absorption coefficients are determined by specifying that $\alpha_1=0.50$, which results in a reverberation time of approximately one second in Room 1. Kuttruff's conceptual model of three rooms did not specify the distribution of absorption within the subrooms; thus, the absorption is uniformly distributed.

Four receivers are modeled in each room, as shown in Fig. 1. The decay curves computed for the four receivers in each room are ensemble averaged to give $\{\langle s(t)\rangle\}$ for that room. A single source position, located in Room 1, is modeled. The solid angle subtended by S_{12} as viewed from the source is computed in order to evaluate the initial power distribution.

The configuration shape factor of the two apertures S_{12} and S_{23} is determined according to Eq. (21). An adaptive Gaussian-quadrature routine is used to evaluate the four-dimensional integral. Note that Receivers 11 and 12 are in the direct path of the transmission between Room 1 and Room 3. Therefore, they are affected by the transmitted energy as it passes them. While this may appear problematic, removing the receivers from the ensemble average in Room 2 alters the decay-curve level only a small amount ($\sim$0.2 dB).

Comparing the predictions of the improved SA model [Eq. (11), $\eta=\alpha''/\overline{\alpha}$, with additional corrections discussed above] and Kuttruff's original model [Eq. (11), $\eta=1$, without additional corrections] with those of GA indicate that the improved model yields significantly more accurate predictions, as shown in Fig. 9. Conservative uncertainty estimates of $\pm 10\%$ for each α yield only slight overlap between the two SA models suggesting that their prediction will be significantly different in actual circumstances. The sensitivity of the GA model to input uncertainty is somewhat lower than the SA models, for this geometry. As a result, the predictions of the improved SA model and GA are identical given the 10% uncertainty in all the input parameters (α and s).

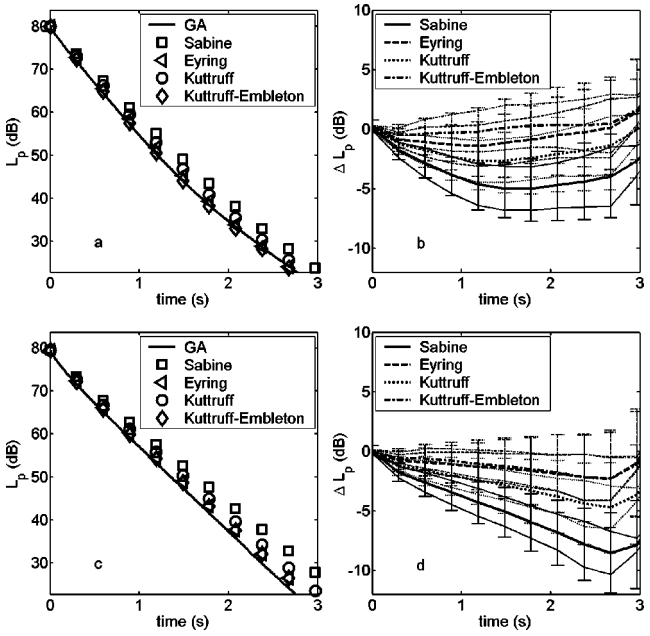

FIG. 8. For the two-room coupled system (Fig. 2) in Condition 3, ensemble averages of GA-model predictions ($s=0.99$) for all sources and receivers in Room 2 (solid line) are compared with improved-SA-model predictions using Sabine [Eq. (11), $\eta=1$] (squares), Eyring [Eq. (11), $\eta=\alpha'/\overline{\alpha}$] (triangles), and Kuttruff [Eq. (11), $\eta=\alpha''/\overline{\alpha}$] (circles) decay models within the subrooms for $S_{12}=25\ \mathrm{m}^2$ (a) and 200 m^2 (c). Differences between GA and SA predictions ($10\log_{10}\mathrm{GA}-10\log_{10}\mathrm{SA}$) [using Sabine (solid line), Eyring (dashed line), and Kuttruff (dotted line) decay models] are plotted for $S_{12}=25\ \mathrm{m}^2$ (b) and 200 m^2 (d). The regions of confidence defined by u_i are plotted as error bars for SA predictions and as fainter lines lying on either side of the primary lines for GA predictions. Confidence limit predictions assume a and s are known to $\pm 10\%$ at the same level of confidence.

The improvement over the prior model can be attributed to multiple factors. First, the improved model incorporates more accurate decay models. In this system the decay curves in all of the rooms are dominated by the rates associated with Rooms 1 and 2. Bayesian analysis of the decay curves computed by the GA model does not support the extraction of a decay rate associated with Room 3. Nevertheless, comparing the predictions of the statistical models with the extracted decay rates for various scattering coefficients indicates that using the Kuttruff decay model ($\eta=\alpha''/\overline{\alpha}$) within the improved SA model is most consistently accurate. Second, the improved model incorporates the Vorländer model of steady-state energy density [Eq. (7)], which is less prone to overestimation than the Sabine model used in prior work. Finally, the improved model accounts for the nondiffuse transfer of energy between Rooms 1 and 3. The impact of this correction is most notable in an improvement in the accuracy of the decay curve predicted in Room 3. Without this correction,

the improved model cannot accurately predict the early part of this decay curve.

In contrast with these findings, the solid-angle correction for the initial power distribution does not give a consistent improvement. While it does improve the fit of the SA model to the GA prediction in Room 1 (by decreasing the level of the decay associated with Room 1 and increasing the level of the decay associated with Room 2), it results in overprediction of the levels in Rooms 2 and 3.

A significant factor in this system of rooms is that the receivers are near the apertures. As such, the considerations described in Sec. II D 3 can be made for each receiver.

Finally, it should be noted that this geometry violates Eq. (19), because $\alpha_1 > 0.40$. However, repeating the previous work with $\alpha_1 = 0.30$ does not notably alter the conclusions drawn.

V. CONCLUDING REMARKS

A. Observations

The accuracy of SA models of coupled rooms is greatly influenced by the accuracy of the SA model used to estimate decay rates in the subrooms of the coupled system. Criteria required for SA models to be approximately correct in single-volume rooms must be met in each of the subrooms if SA models of coupled rooms are to be used. Surface scattering is neither necessary nor sufficient to ensure the agreement of SA predictions with those of GA. Increasing the amount of surface scattering in a room that does not otherwise satisfy the conditions of diffuse-field models tends to improve agreement with the predicted decay rate but, once a linear decay curve has been achieved, increases in surface scattering will not necessarily improve the agreement with a given statistical model.

Stronger coupling increases the disagreement between SA and GA. Previously introduced guidelines for the conditions under which SA models can be used conflict with one another and with comparisons to GA. The possible causes for the failure of SA models are sufficiently interconnected and diverse that a single criterion cannot predict the conditions for failure. Particularly, previous guidelines have been based purely on SA and therefore neglect causes of failure that are rooted in GA, as discussed in Sec. II D.

In systems of coupled rooms, the decrease in level of the reverberant field with distance can be predicted by a modified form of Barron and Lee's revised model. For such systems, this variation in the level of the reverberant field can result in spatial dependence in the shape of the decay curve. This effect is most significant when the coupling aperture and the source are in disparate locations. In contrast, decay curves vary spatially in level but not in shape if the source is located near the coupling aperture.

Unlike prior work, the improved SA model introduced here accounts for the nondiffuse transfer of energy due to (1) radiation of the source into adjacent subrooms and (2) radiation from apertures into adjacent apertures. Study of a previously investigated three-room geometry indicates that this phenomenon can notably affect the shape of decay curves in subrooms.

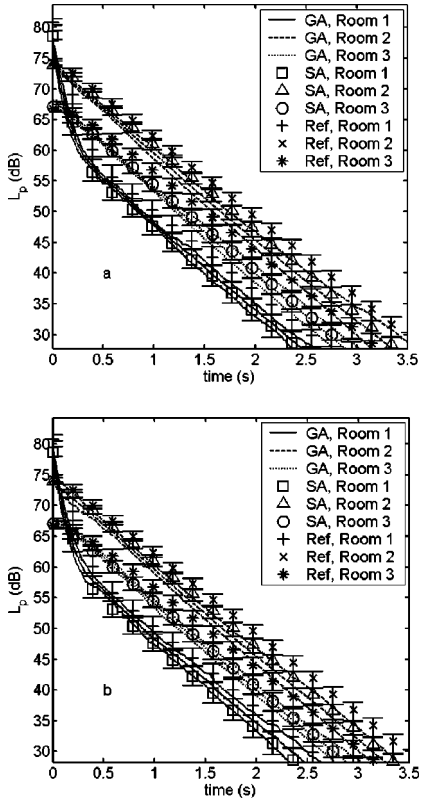

FIG. 9. For the three-room coupled system (Fig. 1), the GA model (ensemble averages of all receiver positions within each of the subrooms) (GA) is compared with the improved SA model [Eq. (11), $\eta = \alpha''/\overline{\alpha}$] (SA) and Kuttruff's original SA model [Eq. (11), $\eta = 1$] (Ref) for two different scattering coefficients $s = 0.40$ (a) and 0.99 (b). In the improved model the correction for nondiffuse transmission between the subrooms is used but the solid-angle correction for the initial power distribution is not. For each GA curve the lines on either side of the central curve represent the region of confidence defined by u_i, assuming α and s are known to $\pm 10\%$ at the same level of confidence. Error bars represent the regions of confidence for SA and reference curves assuming α is known to $\pm 10\%$ at the same level of confidence.

Uncertainty in the values of input parameters to the models (α and s) has a greater effect on predictions of the SA model than those of the GA model, such that GA and SA predictions can often be considered equivalent. For the $\pm 10\%$ input uncertainty used here, the resulting uncertainties in the predictions are large enough to obscure differences between different SA decay models. They are also large enough to be audibly significant, indicating the particular importance of accurate input parameters for modeling coupled rooms.[35]

B. Recommendations

Though developing a SA model that is consistently accurate in all circumstances is difficult, for many cases, the model presented here should prove applicable at high frequencies. Geometrical acoustics is an intrinsically high-frequency model and therefore can only assess the accuracy of the SA model in the limit of vanishing wavelength. However, in practice, the frequency range of validity can extend into the 1000 Hz octave band or below.[35] At lower frequencies, other methods, such as those described in Ref. 35, should be used.

ACKNOWLEDGMENTS

This work was supported by the Bass Foundation and the Rensselaer Polytechnic Institute School of Architecture. J.E.S. gratefully acknowledges B.-I. L. Dalenbäck, for development of a new algorithm in CATT-Acoustic, and N. Xiang, for discussions concerning Bayesian parameter estimation.

[1] W. B. Joyce, ''Sabine's reverberation time and ergodic auditoriums,'' J. Acoust. Soc. Am. **58**, 643–655 (1975).
[2] E. N. Gilbert, ''Ray statistics in reverberation,'' J. Acoust. Soc. Am. **83**, 1804–1808 (1988).
[3] J. D. Polack, ''Modifying chambers to play billiards: the foundations of reverberation theory,'' Acustica **76**, 257–272 (1992).
[4] H. Kuttruff, ''Simulierte Nachhallkurven in rechteckräumen mit diffuseen schallfeld,'' (''Simulated decay curves in rectangular rooms with diffuse sound fields'') Acustica **25**, 333–342 (1971).
[5] O. Legrand and D. Sornette, ''Test of Sabine's reverberation time in ergodic auditoriums within geometrical acoustics,'' J. Acoust. Soc. Am. **88**, 865–870 (1990).
[6] F. Mortessange, O. Legrand, and D. Sornette, ''Role of the absorption distribution and generalization of exponential reverberation law in chaotic rooms,'' J. Acoust. Soc. Am. **94**, 154–161 (1993).
[7] M. Hodgson, ''Evidence of diffuse surface reflection in rooms,'' J. Acoust. Soc. Am. **89**, 765–771 (1991).
[8] W. C. Sabine, *Collected Papers on Acoustics* (Dover, New York, 1964); see also W. S. Franklin, ''Derivation of equation of decaying sound in a room and definition of open window equivalent of absorption power,'' Phys. Rev. **16**, 372–374 (1903); G. Jäger, ''Zur theorie des nachhalls,'' (''On the theory of reverberation'') Sitzungsber. Akad. Wiss. Wien, Math.-Naturwiss. Kl., Abt. 2A **120**, 613–634 (1911).
[9] K. Schuster and W. Waetzmann, ''Nachhall in geschlossenen Räumen,'' (''Reverberation in closed rooms'') Ann. Phys. (Leipzig) **1**, 671–695 (1929); R. F. Norris, ''An instrumental method of reverberation measurement,'' presented at the 1st meeting of the Acoustical Society of America, New York, 10–11 May 1929, published in Ref. 23 Appendix II, pp. 603–605; C. F. Eyring, ''Reverberation time in 'dead' rooms,'' J. Acoust. Soc. Am. **1**, 217–241 (1930).
[10] G. Millington, ''A modified formula for reverberation,'' J. Acoust. Soc. Am. **4**, 69–82 (1932); W. J. Sette, ''A new reverberation time formula,'' *ibid.* **4**, 193–210 (1932).
[11] H. Kuttruff, ''Weglängverteilung und Nachhallverlauf in Räumen mit diffuse reflektierenden Wänden,'' (''Path-length distributions and reverberation processes in rooms with diffusely reflecting walls'') Acustica **23**, 238–239(L) (1970); see also Ref. 17 pp. 122–126.
[12] T. M. W. Embleton, ''Absorption coefficients of surfaces calculated from decaying sound fields,'' J. Acoust. Soc. Am. **50**, 801–811 (1971); see also A. D. Pierce, *Acoustics: An Introduction to Its Physical Principles and Applications* (Mc–Graw Hill, New York, 1981), pp. 265–267.
[13] A. H. Davis, ''Reverberation equations for two adjacent rooms connected by an incompletely sound-proof partition,'' Philos. Mag. **50**, 75–80 (1925).
[14] L. Cremer and H. A. Müller, *Principles and Applications of Room Acoustics*, trans. T. J. Schultz (Applied Science, New York, 1982), Vol. 1, pp. 261–283.
[15] C. D. Lyle, ''The prediction of steady state sound levels in naturally coupled enclosures,'' Acoust. Lett. **5**, 16–21 (1981).
[16] C. D. Lyle, ''Recommendation for estimating reverberation time in coupled spaces,'' Acoust. Lett. **5**, 35–38 (1981).
[17] H. Kuttruff, *Room Acoustics*, 4th ed. (Spon, New York, 2000), pp. 110–114, 126–129, 130, 133–137, 139–141, 142–145.
[18] V. M. A. Peutz, ''Electrical analog for studying acoustical coupled rooms,'' Fifth International Congress on Acoustics, Liége, Belgium, 7–14, Sept. 1965, paper G34.
[19] C. F. Eyring, ''Reverberation time measurement in coupled rooms,'' J. Acoust. Soc. Am. **3**, 181–206 (1931).
[20] W. B. Joyce, ''Power series for the reverberation time,'' J. Acoust. Soc. Am. **67**, 564–571 (1980).
[21] H. Kuttruff and Th. Straßen, ''Zur Abhängigkeit des Raumnachhalls von der Wanddiffusität und von der Raumform'' (''On the dependence of reverberation time on the 'wall diffusion' and on room shape''), Acustica **45**, 246–255 (1980).
[22] M. Hodgson, ''When is diffuse-field theory accurate?'' in Proc. Wallace Clement Sabine Centennial Symposium, Cambridge, MA, 1994, pp. 157–160 [also on the CD-ROM: *Proceedings of the Sabine Centennial Symposium on CD ROM* (available from the Acoustical Society of America), paper 1pAAe2].
[23] V. O. Knudsen, *Architectural Acoustics* (Wiley, New York, 1932) pp. 130–132, 141–143.
[24] M. Vorländer, ''Revised relation between the sound power and the average sound pressure level in rooms and consequence for acoustics measurements,'' Acustica **81**, 332–343 (1995).
[25] R. N. Miles, ''Sound field in a rectangular enclosure with diffusely reflecting boundaries,'' J. Sound Vib. **92**, 203–226 (1984).
[26] M. Barron and L.-J. Lee, ''Energy relations in concert auditoriums I,'' J. Acoust. Soc. Am. **84**, 618–628 (1988).
[27] M. Vorländer, ''Room acoustical simulation algorithm based on the free path distribution,'' J. Sound Vib. **232**, 129–137 (2000).
[28] P. W. Smith, Jr., ''Statistical models of coupled dynamical systems and the transition from weak to strong coupling,'' J. Acoust. Soc. Am. **65**, 695–698 (1979).
[29] W. B. Joyce, ''The exact effect of surface roughness on the reverberation time of a uniformly absorbing spherical enclosure,'' J. Acoust. Soc. Am. **64**, 1429–1436 (1978).
[30] A. Le Bot and A. Bocquillet, ''Comparison of an integral equation on energy and the ray-tracing technique in room acoustics,'' J. Acoust. Soc. Am. **108**, 1732–1740 (2000).
[31] B.-I. L. Dalenbäck, ''Room acoustic prediction based on a unified treatment of diffuse and specular reflection,'' J. Acoust. Soc. Am. **100**, 899–909 (1996).
[32] B.-I. L. Dalenbäck, ''Verification of prediction based on Randomized Tail-Corrected cone-tracing and array modeling,'' on the CD-ROM: *Collected Papers, 137th Meeting of the Acoustical Society of America and the Second Convention of the European Acoustical Association*, Berlin, 14–19 March 1999 (ISBN) 3-9804458-5-4, available from Deutsche Gesellschaft für Akustik, Fachbereich Physik, Universität Oldenburg, 26111 Oldenburg, Germany), paper 3pAAa1. [J. Acoust. Soc. Am. **105**, 1173(A) (1999)].
[33] H. Kuttruff, ''Zum Einfluß eines winkelabhängigen Schallabsorptionsgrades auf die Nachhallzeit'' (''On the influence of an angle-dependent sound absorption coefficient on reverberation time''), Acustica **42**, 187–188(L) (1979).
[34] G. Benedetto and R. Spagnolo, ''Reverberation time in enclosures: The surface reflection law and the dependence of absorption coefficient on the angle of incidence,'' J. Acoust. Soc. Am. **77**, 1447–1451 (1985).
[35] J. E. Summers, *Reverberant acoustic energy in auditoria that comprise systems of coupled rooms* (Ph.D. dissertation, Rensselaer Polytechnic Institute, Troy, NY, 2003).
[36] F. Kawakami and K. Yamaguchi, ''Space-ensemble average of reverberation decay curves,'' J. Acoust. Soc. Am. **70**, 1071–1082 (1981).
[37] ISO 3382, ''Acoustics—Measurement of the reverberation time of rooms with reference to other parameters,'' 1997.
[38] J. Giner, C. Militello, and A. García, ''Ascertaining confidence within the ray-tracing method,'' J. Acoust. Soc. Am. **106**, 816–823 (1999); ''The Monte Carlo method to determine the error in calculation of objective acoustic parameters within the ray tracing technique,'' *ibid.* **110**, 3081–3085 (2001).
[39] P. R. Bevington and D. K. Robinson, *Data Reduction and Error Analysis for the Physical Sciences*, 2nd ed. (McGraw–Hill, New York, 1992), pp. 41–50.
[40] S. G. Rabinovich, *Measurement Errors and Uncertainties: Theory and Practice*, 2nd ed., trans. M. E. Alferieff (Springer, New York, 2000), pp. 166–172.

Improved algorithms and methods for room sound-field prediction by acoustical radiosity in arbitrary polyhedral rooms

Eva-Marie Nosal[a)]
Department of Mathematics, University of British Columbia, Vancouver, BC, Canada V6T 1Z2

Murray Hodgson
School of Occupational and Environmental Hygiene and Department of Mechanical Engineering, University of British Columbia, Vancouver, BC, Canada V6T 1Z3

Ian Ashdown
by Heart Consultants Limited, West Vancouver, BC, Canada V7S 1W3

(Received 30 March 2003; revised 6 March 2004; accepted 20 May 2004)

This paper explores acoustical (or time-dependent) radiosity—a geometrical-acoustics sound-field prediction method that assumes diffuse surface reflection. The literature of acoustical radiosity is briefly reviewed and the advantages and disadvantages of the method are discussed. A discrete form of the integral equation that results from meshing the enclosure boundaries into patches is presented and used in a discrete-time algorithm. Furthermore, an averaging technique is used to reduce computational requirements. To generalize to nonrectangular rooms, a spherical-triangle method is proposed as a means of evaluating the integrals over solid angles that appear in the discrete form of the integral equation. The evaluation of form factors, which also appear in the numerical solution, is discussed for rectangular and nonrectangular rooms. This algorithm and associated methods are validated by comparison of the steady-state predictions for a spherical enclosure to analytical solutions. © *2004 Acoustical Society of America.* [DOI: 10.1121/1.1772400]

PACS numbers: 43.55.Ka, 43.55.Br [MK] Pages: 970–980

I. INTRODUCTION

Room acousticians have been attempting to understand and predict the behavior of sound in rooms for hundreds of years. The prediction of sound fields in enclosures is needed for design purposes, such as the optimization of classrooms and lecture halls for intelligibility, of concert halls, recording studios, and theatres for sound quality, of workrooms for minimized noise levels, of offices for privacy, and so on. Moreover, as computer simulations become increasingly popular for entertainment and training purposes, fast and accurate room-acoustical modeling techniques are required.

One approach to room acoustics is through geometrical-acoustics models, in which sound waves are replaced by sound rays.[1,2] As many important perceptual effects mainly involve middle to high frequencies (where geometrical-acoustics models are accurate) such models have been used extensively in room acoustics over the past 40 years. This paper explores a geometrical-acoustics method known as acoustical radiosity (AR). The method assumes perfectly lambertian-diffuse reflection from all surfaces of the enclosure. AR has been called various names, including the integral equation method,[2] radiant exchange,[3] and an intensity-based boundary element method.[4] The name ''acoustical radiosity'' is taken from a similar (time-independent) technique used in computer graphics, where it is simply called radiosity.[5–7]

Kuttruff derived the governing integral equation for AR in the early 1970s.[2,8,9] Analytical solutions for the integral equation exist for spheres[10–13] and for infinitely long, flat enclosures[2,14] (in which side walls are neglected). In general, however, the equation must be solved numerically.

Several papers outline and/or make use of a numerical solution to the integral equation. In 1984, Miles[15] gave a detailed account of his iterative solution for both steady-state and time-varying sources in rectangular enclosures. In 1993, Lewers[3] used AR to model the diffuse reverberant tail of the impulse response in a hybrid model. Shi, Zhang, Encarnação, and Göbel,[16] outlined an algorithm for AR, but few details or results were given. More recently, Le Bot and Bocquillet,[17] compared steady-state sound-level predictions from AR to predictions from ray tracing, and Kang[18] used AR to investigate the propagation of sound in long enclosures with diffusely reflecting boundaries.

Despite these developments and the potential of AR, relatively little attention has been given to the technique. Reasons for this likely include the limiting assumption of diffuse reflection and high computational costs. As discussed in this paper, neither assumption is unreasonably restrictive—AR deserves further attention. In particular, there is a need for a clear, complete exposition of the theory and assumptions behind the method. Moreover, algorithms and methods nonrectangular rooms need to be further developed for and incorporated into AR. These should include improvements for efficiency, and the numerical solution should be validated. These aspects are the objectives of the present paper.

[a)]Author to whom correspondence should be addressed. Current affiliation: School of Ocean and Earth Sciences and Technology, Department of Geology and Geophysics, University of Hawaii at Manoa, 1680 East-West Road POST 813, Honolulu, HI, 96822; Electronic mail: nosal@hawaii.edu

II. ASSUMPTIONS, DISADVANTAGES, AND BENEFITS OF ACOUSTICAL RADIOSITY

Since AR is an energy-based method, phase relationships between propagating waves are assumed incoherent.[13] This assumption is usually sufficient, and may be justified when the wavelengths are small compared to the dimensions of the room.[19] Further simplifications made in this work include reflection coefficients independent of their angle of incidence, empty convex enclosures, and omni-directional point sources.

The main assumption of AR is that all boundaries are diffusely reflecting—that is, reflection is governed by Lambert's law,

$$I(\theta,R)=I(0,R)\cos\theta, \tag{1}$$

where $I(\theta,R)$ is the intensity of the sound which is scattered by a surface element in direction θ ($0\leqslant\theta\leqslant\pi/2$) from the surface normal measured at distance R from the element (this formulation is different from in other fields, such as computer graphics, because of the differences in definition of intensity). This assumption allows for major simplifications in the development of the model because diffuse reflection is memoryless. In particular, the way that a ray is reflected is not dependent on the direction from whence it came.

It has been suggested[13,20] that the assumption of diffuse reflection is less restrictive than the commonly made assumption of specular reflection, and it is certainly less restrictive than the assumption of a diffuse field that is still popular among room acousticians. Further, some characteristics of the field may not be sensitive to a change from specular to diffuse reflection.[21,22] AR may be an effective predictor of such characteristics.

Certainly, it is likely that AR is highly effective in predicting the late part of a decay curve. It has been shown that the conversion of specular energy into diffuse energy is irreversible and that all walls produce some diffuse reflection.[23] Hence, though the initial reflections in a room may be more specular than diffuse, most of the energy in the sound decay of a room will involve higher-order, diffuse reflections. Indeed, after several reflections, nearly all energy becomes diffusely reflecting.[20]

The effectiveness of AR in predicting the late part of decay curves has been shown for spherical[12] and rectangular[23] enclosures by comparison of decay curves for rooms with and without diffusely reflecting walls. Thus, hybrid methods that account for the specular component by another method (such as ray-tracing or the method of images) and for the diffuse component by AR may be highly successful in predicting room sound fields. Such a model was suggested by Lewers[3] and, for rectangular enclosures, by Baines.[24]

It may be possible to extend AR methods to nondiffuse reflection. Such extensions have been made in computer graphics for time-independent cases[25–27] and for a few time-dependent cases.[28,29]

Time dependence in AR is one of its limitations, because of the high computational costs involved (in other fields, such as computer graphics, radiosity is time independent). Nevertheless, the method is promising, since the costs are incurred only in the initial rendering of a room. In particular, once a room has been rendered for a given source, the remaining computational costs are low enough to enable real-time sound-field simulation for moving receivers. This view independence is particularly advantageous for interactive simulations. Furthermore, there are methods to accelerate the initial rendering.[28,29]

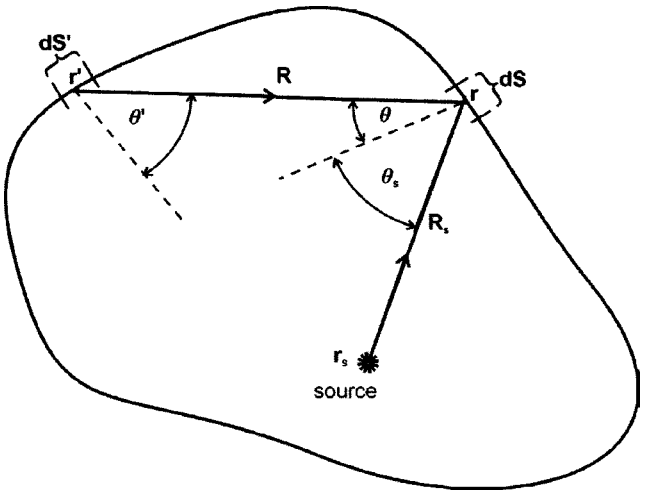

FIG. 1. Geometry relevant to the integral equation.

III. ANALYTICAL EQUATIONS

Define radiation density as the rate at which energy leaves a unit area of surface. (This definition is after Kuttruff[2]—other authors use different terms to mean the same thing. In computer graphics, the term would be exitance.) To find the radiation density of an infinitesimal wall element, dS, the individual contributions from all other wall elements of the enclosure are added up (integrated). Consider one such element, dS'. Characterize the locations of dS and dS' by the position vectors r and r'. Let R be the length of the line joining dS and dS', and let θ and θ' be the angles between the line and the normals of dS and dS', respectively (R, θ and θ' are functions of r and r'). Refer to Fig. 1 for the relevant geometry. Denote the radiation density at dS at time t by $B(r,t)$. Similarly define $B(r',t)$.

The first step is to find $I(\theta',R,t)$, the intensity at time t of the sound scattered by dS' in the direction θ' from the normal to dS' measured at distance R from dS'. Consider a hemisphere, H, of radius R centered over dS'. If no energy is lost in propagation, the rate of energy incident on this hemisphere at time t from dS' must equal $B(r',t-R/c)$, where c is the speed of sound. Thus

$$B(r',t-R/c)dS'=\int_H I(\theta',R,t)dS$$

$$=I(0,R,t)\int_H \cos\theta'\,dS, \tag{2}$$

where the surface integral is over H and the second equality follows from Eq. (1). Evaluation of Eq. (2) yields

$$B(r',t-R/c)dS' = I(0,R,t) \times \int_0^{2\pi}\int_0^{\pi/2} R^2 \sin\theta' \cos\theta' \, d\theta' \, d\phi = \pi I(0,R,t) R^2. \quad (3)$$

It follows that

$$I(\theta',R,t) = B(r',t-R/c)\frac{\cos\theta'}{\pi R^2} e^{-mR} dS', \quad (4)$$

where the term e^{-mR} accounts for air absorption and m is the air-absorption exponent. If dS has reflection coefficient $\rho(r)$, it follows that the radiation density of dS due to $B(r',t-R/c)$ is

$$B_{dS'}(r,t-R/c) = \rho(r) I(\theta',R,t)\cos\theta = \rho(r) B(r',t-R/c)\frac{\cos\theta\cos\theta'}{\pi R^2} \times e^{-mR} dS'. \quad (5)$$

To get $B(r,t)$, Eq. (5) is integrated over all wall elements dS' and the direct contribution from the source, $B_d(r,t)$ is added. This gives

$$B(r,t) = \frac{\rho(r)}{\pi}\int_S B(r',t-R/c) e^{-mR}\frac{\cos\theta\cos\theta'}{R^2} dS' + B_d(r,t), \quad (6)$$

where S is the surface of the enclosure. For an omnidirectional source with power $W(t)$, $B_d(r,t)$ is given by

$$B_d(r,t+R_s/c) = \frac{W(t)\cos\theta_s}{4\pi R_s^2}\rho(r) e^{(-mR_s)}. \quad (7)$$

Here, R_s is the distance between the source and wall element r, and the line between the source and dS makes angle θ_s with the normal to dS (refer once again to Fig. 1 for the geometry).

Equation (6) is the governing equation of AR. The integral equation is usually expressed for irradiation density—the rate at which energy is incident on a unit area of surface—instead of for radiation density. The difference lies in the incorporation of the surface-absorption term; when irradiation density is used, it lies inside the integral, and when radiation density is used, it lies outside the integral. The latter results in fewer operations in the final AR algorithm.

Once $B(r,t)$ is known for all r and $t \geqslant 0$, the intensity at the receiver is found by[2,15]

$$I(r_r,t) = \frac{1}{\pi}\int_S \frac{B(r,t-R_r/c)\cos\theta_r}{R_r^2} e^{(-mR_r)} dS + I_d(r_r,t) \quad (8)$$

with the direct contribution

$$I_d(r_r,t) = \frac{W(t-R_{sr}/c)}{4\pi R_{sr}^2} e^{(-mR_{sr})}, \quad (9)$$

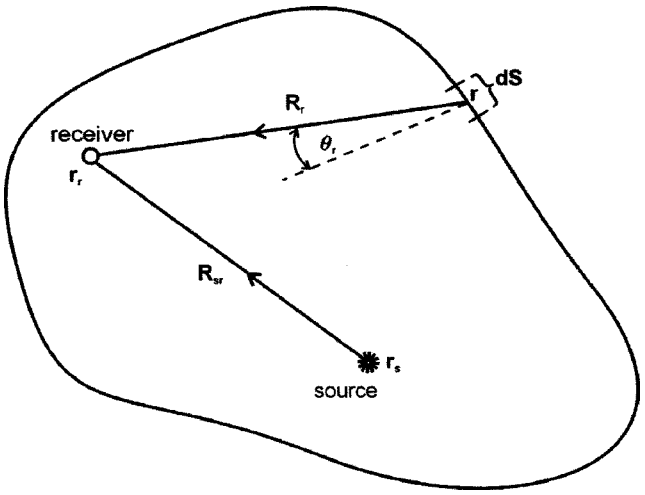

FIG. 2. Geometry relevant to the calculation of intensity at the receiver.

where r_r is the position of the receiver, R_{sr} is the distance between the source and the receiver, R_r is the distance between r and r_r, and θ_r is the angle between the line joining r and r_r, and the normal to dS. The relevant geometry is shown in Fig. 2.

Assuming an impulsive sound source simplifies the above equations by allowing air absorption to be neglected until the end. First, intensity is found at the receiver without air absorption, $I_0(r_r,t)$, where $t=0$ is the time of generation of the signal impulse. Then the intensity with air absorption, $I_m(r_r,t)$, is given by

$$I_m(r_r,t) = e^{-mtc} I_0(r_r,t). \quad (10)$$

The term e^{-mct} factors out because all energy in the system is introduced at time $t=0$, so it has traveled tc meters through the air at time t. A further simplification for impulsive sources is that $B_d(r,t)$ is zero except at a unique value of t for each wall element. This value of t is simply the distance between the source and the wall element, divided by the speed of sound. Finding the impulse response is of fundamental interest, since it can be convolved with the source signal to give the response for any source[2] (here, "impulse response" means the pressure-squared response to an impulse—as opposed to the usual pressure response—since radiosity traces energy).

Given $I(r_r,t)$, the energy density $E(r_r,t)$ and the square of the average sound pressure $p^2(r_r,t)$ are found as:[15]

$$E(r_r,t) = I(r_r,t)/c \quad \text{and} \quad p^2(r_r,t) = I(r_r,t)\rho_0 c, \quad (11)$$

where ρ_0 is the medium density. For air under usual room conditions, $\rho_0 c = 414\ \mathrm{kg\,m^{-2}\,s^{-1}}$.

From the equations above, it is clear why AR is view independent; $B(r,t)$ is defined by the enclosure and the source, and is independent of the receiver. Once $B(r,t)$ is known, the intensity at any receiver position is found relatively easily. This feature gives AR an advantage over more traditional room-acoustical models, such as ray tracing or the method of images in which the entire process must be repeated for different receiver positions. It is especially useful in walk-through simulations, where the environment is constant, and only the receiver position changes.

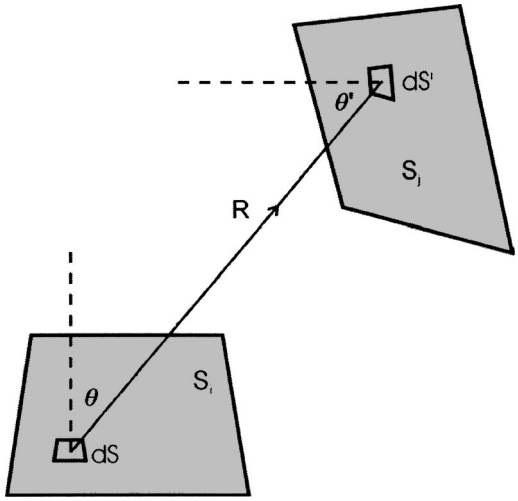

FIG. 3. Form-factor geometry.

IV. NUMERICAL SOLUTION

Analytical solutions to the integral equation exist for spherical[10–13] and long, flat[2,14] enclosures. In general, however, the inhomogeneous, time-dependent integral equation, Eq. (6), must be solved numerically.

In the numerical solution, the room interior is discretized into small planar patches, S_i. If the room has curved surfaces, then this discretization will be an approximation of the true surface. From Eq. (6) the average radiation density of the ith patch is given by[15]

$$B_i(t)=\rho_i\sum_{j=1}^{N} B_j(t-R_{ij}/c)e^{-mR_{ij}}F_{ij}+B_{di}(t). \tag{12}$$

In the above, N is the number of patches, the reflection coefficient is assumed constant over each patch, with ρ_i the reflection coefficient of patch i, R_{ij} is the distance between some central points on patches S_i and S_j. The form factor, F_{ij}, between patch i and patch j is given by

$$F_{ij}=\frac{1}{A_i}\int_{S_i}\int_{S_j} F(r,r')dS'\,dS$$

$$=\frac{1}{A_i}\int_{S_i}\int_{S_j}\frac{\cos\theta\cos\theta'}{\pi R^2}dS'\,dS, \tag{13}$$

where the integrals are taken over the patch areas S_i and S_j, A_i is the area of the ith patch, R is the distance between the points of integration on S_i and S_j, and θ and θ' are the angles between the line joining the points of integration and the normals to S_i and S_j, respectively. Physically, F_{ij} is the fraction of energy leaving patch i that is incident on patch j. See Fig. 3 for the relevant geometry. Form factors are discussed in Sec. V.

The discrete form for the direct contribution, Eq. (7), is given by[15]

$$B_{di}(t)=\frac{W(t-R_{si}/c)\rho_i}{4\pi A_i}e^{-mR_{si}}\int_{S_i}d\Omega_s, \tag{14}$$

where R_{si} is the distance between the source and the central point on S_i and

$$\int_{S_i}d\Omega_s=\int_{S_i}\frac{\cos\theta_s}{R_s^2}dS \tag{15}$$

is the integral over the solid angle subtended by S_i at the source. Here, R_s is the distance between the source and the point of integration on S_i, and θ_s is the angle between the line joining the source and the point of integration and the normal to S_i. Solid angles, and the evaluation of the integral over them, are discussed in Sec. VI.

Similarly, Eq. (8) can be discretized, to obtain[15]

$$I(r_r,t)=\frac{1}{\pi}\sum_{i=1}^{N}\int_{S_i}\frac{B_i(t-R_{ri}/c)\cos\theta_r}{R_r^2}e^{-mR_{ri}}dS+I_d(r_r,t)$$

$$=\frac{1}{\pi}\sum_{i=1}^{N}B_i(t-R_{ri}/c)e^{-mR_{ri}}\int_{S_i}d\Omega_r+I_d(r_r,t), \tag{16}$$

where $I_d(r_r,t)$ is as in Eq. (9), R_{ri} is the distance between the receiver and r, and

$$\int_{S_i}d\Omega_r=\int_{S_i}\frac{\cos\theta_r}{R_r^2}dS \tag{17}$$

is the integral over the solid angle subtended by S_i and the receiver. Here, R_r is the distance between the source and the point of integration on S_i, and θ_r is the angle between the line joining the source and the point of integration and the normal to S_i. As with Eq. (15), Eq. (17) is dealt with in Sec. VI.

V. FORM FACTORS

The evaluation of form factors, as in Eq. (13), is difficult since for most pairs of surfaces S_i and S_j there is no analytical solution to the form-factor equation. Form factors have been well researched in other fields where radiosity is used—in particular, in illumination engineering, thermal radiation heat transfer and, most notably, in computer graphics.[5,6] Form factors in acoustics are the same as form factors in these other fields; the many methods developed in these fields, applicable to. Howell's[30] catalog of radiation configuration factors (point-to-patch form factors), gives some useful references, although most of the configurations that are dealt with are not applicable to room acoustics (for example, that between a differential element and a cow).

A few properties of form factors of interest for reducing computation times are outlined here. Many other properties can be found in the thermal-engineering literature, in which the topic is called form-factor algebra.[6] Perhaps the most important property is that of reciprocity. Notice that F_{ji} can be found by simply reversing the patch subscripts, i and j, of F_{ij}. This gives the reciprocity relation

$$A_iF_{ij}=A_jF_{ji}. \tag{18}$$

Furthermore, a planar patch cannot irradiate itself, thus

$$F_{ii}=0. \tag{19}$$

Moreover, for a closed environment with N patches, no energy can escape the environment, so all energy leaving one patch must be received by the patches in the environment

(conservation of energy). This gives the summation relation

$$\sum_{j=1}^{N} F_{ij} = 1. \tag{20}$$

Researchers in AR have applied various approaches in the evaluation of form factors. For rectangular, perpendicular, and parallel patches, Miles[15] reduced the equation integrals to ones that may be calculated numerically by standard methods. Lewers[3] applied a discrete approximation. More recently, Tsingos[29] estimated form factors by point-to-polygon form factors (called configuration factors—see later in this section), which are estimated over a sampling of the receiver patch. The sampling method is very popular in the computer graphics community, and can be extended[6] to find area-to-area form factors using a technique known as Monte Carlo integration. This method can be highly effective, particularly in the case of occlusions, and has been extensively researched in computer graphics. In the present research, however, other methods were employed.

When only rectangular patches in rectangular rooms are being considered, form factors are found using the analytical formulas from Gross *et al.*[31] These formulas allow for very simple and fast computation of form factors for rectangular patches. Because of their lengths, the formulas are not reproduced here.

To generalize the algorithms to nonrectangular rooms discretized by nonrectangular patches, *HeliosFF*—software modified for this research from the commercial graphics radiosity renderer *Helios*32[32]—was used to find form factors. Given a room and the reflection coefficients of its surfaces, *HeliosFF* meshes the room, and outputs form factors along with other pertinent data, such as patch vertices, centers, areas, normals, and reflection coefficients. An ordered listing of the vertices for each of its surfaces specifies the room, and the user has basic control over the number of patches and elements (see the following paragraph) into which each room surface is meshed. *HeliosFF* uses a two-level hierarchical, cubic-tetrahedral algorithm to compute form factors. These methods are briefly discussed below.

In radiosity, the patches in a room have two functions: (1) receivers of energy from the source and from other patches; and (2) sources emitting towards other patches. The main idea behind a two-level hierarchy is that when the patches are behaving as sources, it is sufficient to have a coarser meshing than when the patches are behaving as receivers.[6] In a two-level hierarchy, the N patches are subdivided into M smaller elements ($N<M$), with each patch composed of the union of a subset of the elements. The patches act as sources and the elements act as receivers. The radiation density of a patch is then the weighted average of the radiation densities of the elements forming the patch.

To account for two-level hierarchy, Eq. (12) is modified to

$$B_{E_i}(t) = \rho_{E_i} \sum_{j=1}^{N} B_{P_j}(t - R_{E_iP_j}/c) e^{-mR_{E_iP_j}} F_{E_iP_j} + B_{dE_i} \tag{21}$$

with

$$B_{P_j}(t) = \frac{1}{A_{P_j}} \sum_{i \in E} A_{E_i} B_{E_i}(t), \tag{22}$$

where E_i and P_j denote element i and patch j, respectively, and E is the set of all i such that element i is contained in patch j—i.e., $E=\{i=1,2,...,M | E_i \subseteq P_j\}$.

The reason for a two-level hierarchy in computer graphics is intuitive.[6] When the patches are emitting energy to a distant receiver, the assumption of diffuse reflection effectively averages the energy arriving over a solid angle. Hence, the details of the energy leaving the patch are lost, and a coarser meshing is sufficient. When an image is rendered, however, the details of its surface are crucial, so a finer meshing is needed. Since the number of patches required is less than the number of elements, a two-level hierarchy may considerably improve computational efficiency. More on two-level hierarchies (as well as extended hierarchical representations) may be found in books dealing with radiosity in computer graphics.[5,6]

In acoustics, the benefit of a two-level hierarchy is questionable and remains to be explored. The goal is to reproduce the impulse response at some point in the room, so the details of the sound field at the surfaces are not as crucial. In particular, since the sound field may not depend significantly on the exact details of the surface, further subdivision of the patches into elements may not improve the model to the same extent as it does in graphics. Since *HeliosFF* uses a two-level hierarchy, since the approach can only make predictions more accurate, and since computing efficiency is not the main objective of this research, a two-level hierarchy was used.

The cubic-tetrahedral method is a Gaussian-quadrature method popular in computer science for its computational efficiency and accuracy. It is important to understand that the cubic-tetrahedral algorithm makes one underlying assumption that may affect predictions by the AR algorithm. This main assumption is that the form factor, F_{ij}, from patch i to j can be approximated by the configuration factor[5] between one point on patch i and patch j. Equation (13) becomes

$$F_{ij} \approx \int_{S_j} \frac{\cos\theta \cos\theta'}{\pi R^2} dS \tag{23}$$

at some sample point x_i on S_i. Fundamental to this approximation is an assumption that the integral over S_j is (nearly) constant over patch i. That assumption is reasonable if the distances between the patches are much greater than the size of patch i, but is questionable for large or near patches—what makes a patch large or near remains to be investigated. In illumination engineering, a five-times rule is used, which states that a patch can be modeled as a point source only when the distance to the receiver is at least five times the maximum projected dimension of the patch.[5] Researchers in illumination engineering and in computer graphics have investigated the errors introduced by the approximation. For sound sources, Rathe[33] has shown that, for a receiver located on the vertical line of symmetry of a rectangular source, the source can be modeled as a point source if the distance to the

receiver is at least the maximum dimension of the receiver divided by π.

For patches that are too large or too close, it is possible to reduce the error of this assumption by subdividing the patch areas (a two-level hierarchy may also be beneficial in this case). Criteria governing when to stop subdividing (i.e., when further subdivision has insignificant effect on the rendered image) are available in the literature on computer graphics.[6] Because details of the field are not as crucial in acoustics as they are in graphics, such criteria will likely be less stringent in acoustics than in graphics.

To find configuration factors, the cubic-tetrahedral method involves centering a tetrahedron over a differential element on patch *i*, meshing the tetrahedron into cells, and finding the configuration factors between the differential element and the cells. The configuration factors are stored in a look-up table. Patch *j* is then projected onto one or more of the cells of the tetrahedron. The sum of the configuration factors of the cells covered by the patch is approximately F_{ij}. For further details, the reader is referred to the computer graphics literature, where the method is well documented.[5,6,34,35]

Several tests were carried out to compare the form factors given by *HeliosFF* to analytical form factors for rectangular rooms and rectangular patches.[31] For all cases considered, the maximum difference between the analytical form factors and those predicted by *HeliosFF* was 15%. For example, for an $8\times4\times2$ room with 160 patches, the maximum difference between corresponding form factors was 14%; Helios gave a form factor of 0.073 when, analytically, it should have been 0.064. In general, finer subdivisions resulted in less error in the form factors predicted by *HeliosFF*.

VI. INTEGRALS OVER SOLID ANGLES—THE SPHERICAL-TRIANGLE METHOD

The problem of finding the integral over the solid angles subtended by a point r and a surface S_i appeared twice [Eqs. (15) and (17)] in the numerical form of the integral equation. The point was either the source or the receiver, and the planar surface was one of the patches used to mesh the enclosure. The following integral must be evaluated:

$$\int_{S_i} d\Omega = \int_{S_i} \frac{\cos\theta}{R^2} dS, \tag{24}$$

where θ is the angle between the surface normal and the line joining a point r and the surface element S_i, and R is the distance between r and the surface element.

Miles[15] gave simple, closed-form expressions for the evaluation of Eq. (24) for rectangular surfaces. To be able to work with nonrectangular patches, however, a more general approach to the evaluation of the integral must be found. To do so, the assumption of planar, convex surfaces with straight edges (convex polygons) is retained.

One obvious approach is to approximate the integral by the value of $A_i(\cos\theta_0/R_0^2)$, where A_i is the area of S_i, and θ_0 and R_0 are defined for some central point on the surface. Unfortunately, this is an unacceptable approximation, particularly for points that are close to the surface. Another approach that has been suggested[36,37] is to convert the integral to a contour integral using Stoke's theorem, but this is unnecessarily complicated.

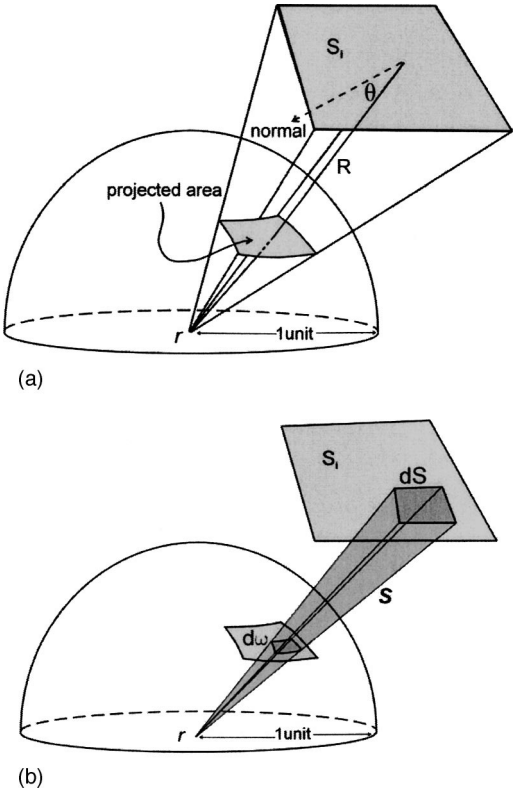

FIG. 4. Illustrations relevant to the spherical-triangle method.

The approach developed and taken here, which we call the spherical-triangle method, was not found elsewhere in the literature. It was developed to quickly and accurately determine integrals over solid angles subtended by polygonal planar patches. The idea is to recognize that the integral is simply the area of the unit-spherical polygon subtended by the planar polygon and r (the unit sphere is centered at r) [see Fig. 4(a)]. To understand this, consider an infinitesimally small differential element of S with area dS, at distance R from r. To find the area, $d\omega$, that it subtends on the unit sphere, consider the conical solid **S** with vertex at r and the differential element as its base [see Fig. 4(b)]. The area of the cross section of **S** at distance R from r is the area that the differential element projects in the direction θ—i.e., $\cos\theta\, dS$. Keeping the ratio of distance from r to cross-sectional area constant, the area of the cross section of **S** at unit distance from r must be $\cos\theta\, dS/R^2$ (since the cross-sectional area is proportional to the square of the distance from the vertex). Since dS is a differential area, $d\omega$ is precisely this cross-sectional area at unit distance from r—i.e.,

$$d\omega = \frac{\cos\theta}{R^2} dS. \tag{25}$$

Thus $\int_{S_i} d\Omega$ is just the integral over S_i of infinitesimally small areas on the unit sphere, so is itself the area of the unit-spherical polygon subtended by S_i and r, as required.

It follows that finding $\int_{S_i} d\Omega$ reduces to finding the surface area of a spherical polygon. To do this, the generaliza-

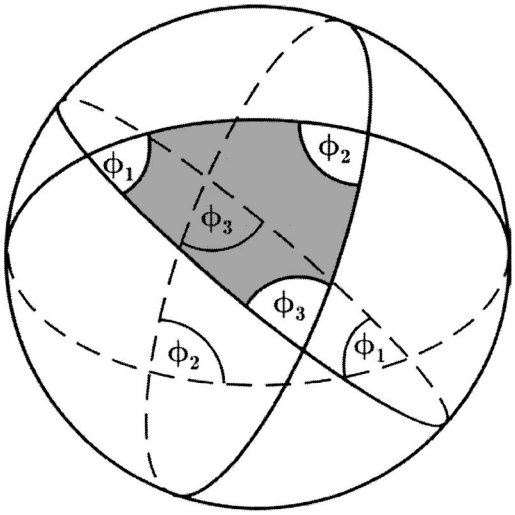

FIG. 5. Spherical triangle with angles ϕ_1, ϕ_2, and ϕ_3.

tion (to arbitrary spherical polygons) of Girard's theorem (for spherical triangles) can be applied. This theorem states that the surface area of an N-sided spherical convex polygon with angles ϕ_1, $\phi_2,\ldots,\phi_N$ (measured in radians) is

$$A=a^2\left(\sum_{i=1}^{N}\phi_i+(2-N)\pi\right), \tag{26}$$

where a is the radius of the sphere. See Fig. 5 for an illustration of a spherical triangle with angles ϕ_1, ϕ_2, and ϕ_3. A simple and elegant proof can be found in Weeks.[38]

By this theorem, finding the surface area of a spherical polygon reduces to finding the sum of all angles between adjacent edges of the polygon and the center (source/receiver). Call this sum Φ. Then, by Eq. (26) (with $a=1$):

$$\int_{S_i} d\Omega=\Phi+(2-N)\pi, \tag{27}$$

where N is the number of edges of the polygon. Φ is easily found, given the vertices of the polygon and the central point, by taking cross products and using the cosine law, as follows. Let v_1, $v_2,\ldots,v_N$ be the vertices of the polygon listed in clockwise (or counter-clockwise) order around the polygon and let p be the central point. Define $v_{N+1}=v_1$. Then, for $i=1,2,...,N$, the normal to the plane P_i passing through v_i, v_{i+1}, and p is

$$n_i=(v_{i+1}-p)\times(v_i-p). \tag{28}$$

Let ϕ_i be the angle between P_i and P_{i+1} where $P_{N+1}=P_1$. Then, by the cosine law

$$\cos\phi_i=\frac{-n_{i+1}\cdot n_i}{\|n_{i+1}\|\|n_i\|}, \tag{29}$$

where $-n_{i+1}$ is taken to get the interior angle. Then

$$\Phi=\sum_{i=1}^{N}\phi_i. \tag{30}$$

VII. TIME DISCRETIZATION

The final step in the numerical solution of the integral equation is to discretize time. The idea of discretizing time has been previously applied to AR by several authors,[12,16] although the present approach differs slightly in several respects. Time is split into equal steps,

$$t_0=0,\quad t_1=\Delta t,\quad t_2=2\Delta t,\ldots,\quad t_n=n\Delta t=t_{\max}, \tag{31}$$

where $n=t_{\max}/\Delta t$ is the number of time steps, and is dependent on the length of the time interval, Δt, and on the maximum time, $t_{\max}$, for which predictions are to be performed. The choice of Δt and $t_{\max}$ are affected by various considerations, such as the room dimensions, frequency of the sound source, absorption coefficients, desired accuracy and speed of predictions, and so forth. For notational purposes, note the following property:

$$t_a+t_b=a\Delta t+b\Delta t=(a+b)\Delta t=t_{a+b}. \tag{32}$$

Energy is followed as it propagates through the room from one time step to the next. The sound is generated at $t_0=0$ and is propagated through the room according to Eq. (12). Now, however, any energy that arrives at a patch between time steps is pushed forward and added to the later time step. In this way, the radiation densities of the patches, B_i, become discrete functions, with their domain being the set of all time steps. In a similar way, sound pressure at the receiver becomes a discrete function.

VIII. ALGORITHMS

Based on the numerical solutions, algorithms were developed to implement the numerical solution. The algorithm involves three steps. First, an outline is given for finding the numerical solution without further approximation. Second, an approximating (averaging) technique is introduced to find the later part of the decay more efficiently. Finally, the element radiation densities found using the first two algorithms are used to find the pressure-squared response at a receiver.

A. Basic algorithm

Define

$$T_{E_iP_j}=\left[\frac{R_{E_iP_j}}{c\Delta t}\right] \tag{33}$$

as the number of time steps (rounded up to the nearest integer) between element E_i and patch P_j, where Δt is the time interval between time steps, as in Sec. VII (recall that $R_{E_iP_j}$ is the distance between some central points on element E_i and patch P_j). The time, rounded to the nearest step, taken for sound to travel from element i to patch j is simply $t_{T_{E_iP_j}}=T_{E_iP_j}\Delta t$. Similarly define time steps for source-to-element, receiver-to-element, and source-to-receiver separations, T_{sE_i}, T_{rE_i}, and T_{sr}, respectively. To reduce the number of operations, also define

$$K_{E_iP_j}=\rho_{E_i}F_{E_iP_j}. \tag{34}$$

Now, consider an omni-directional, impulsive sound source of power W that emits energy at time t_0. Using the

Compute $T_{E_iP_j}, K_{E_iP_j}, B_{dE_i}(t_q)$ % Eqs. (33-35)

for $q=1$ to $q=n$
  for $i=1$ to $i=M$
    $B_{E_i}(t_q)=B_{E_i}(t_q)+B_{dE_i}(t_q)$
  end for
  for $j=1$ to $j=N$
    $B_{P_j}(t_q)=\frac{1}{A_{P_j}}\sum_{i\in \mathrm{E}} A_{E_i}B_{E_i}(t_q)$
    % Eq. (22), $\mathrm{E}=\{i|E_i\subseteq P_j\}$
    for $i=1$ to $i=M$
      $B_{E_i}(t_{q+T_{E_iP_j}})=B_{P_j}(t_q)K_{E_iP_j}+B_{E_i}(t_{q+T_{E_iP_j}})$
      % Eq. (21)
    end for
  end for
end for

FIG. 6. Algorithm 1: Calculation of element radiation densities.

simplification suggested in Sec. III for impulsive sources, air attenuation can be neglected until the end of the calculations, and added according to Eq. (10). By Eq. (14), the direct contribution to element E_i is given by

$$B_{dE_i}(t_{T_{rE_i}})=\frac{\rho_{E_i}W}{A_{E_i}4\pi}\int_{E_i} d\Omega_s, \tag{35}$$

where A_{E_i} is the area of element i. The integral is as in Eq. (15) and is evaluated by the spherical-triangle method (Sec. VI).

Algorithm 1 in Fig. 6 implements this time-discretized approach to AR. In the algorithm, n is the number of time steps, M is the number of elements, and N is the number of patches.

B. Averaging algorithm

Because the above process is very costly in the case of many time steps (i.e., large n), it may be desirable to estimate the late radiation densities rather than calculate them explicitly. A method for doing this, given by Rougeron *et al.*[28] for electromagnetic waves, is as follows.

Algorithm 1 traces element radiation densities beyond the maximum time-step, t_n. Indeed, $q+T_{E_iP_j}$, the subscript in the last "for" loop, may be greater than n (for $q=n$, for example). Let n' be the maximum such subscript. Then, for $n<q\leqslant n'$, $B_{E_i}(t_q)$ is the unshot instantaneous radiation density of element E_i at time t_q (where unshot means that it has not yet propagated to other elements). Define

$$B_{\mathrm{avg}}(t_q)=\frac{\Sigma_{i=1}^{M}A_{E_i}B_{E_i}(t_q)}{\Sigma_{i=1}^{M}A_{E_i}} \quad \text{for } n<q\leqslant n' \tag{36}$$

as the average unshot radiation density at time t_q. B_{avg} for other time steps is zero. Also define

$$\rho_{\mathrm{avg}}=\frac{\Sigma_{i=1}^{M}A_{E_i}\rho_{E_i}}{\Sigma_{i=1}^{M}A_{E_i}} \tag{37}$$

Calculate $B_{avg}(t_q)$ for $q=n+1$ to $q=n'$, ρ_{avg}, and q_{avg} % Eqs. (36-39)

Define $M_{est}(t_i)=0$ for $i\leq n+q_{avg}$

for $i=1$ to $i=q_{avg}$
  for $j\geq 1$
    while $n+i+jq_{avg}\leq n'+q_{avg}$
      $M_{est}(t_{n+i+jq_{avg}})=B_{avg}(t_{n+i+(j-1)q_{avg}})+\rho_{avg}M_{est}(t_{n+i+(j-1)q_{avg}})$
      % Eq. (41)
    end while
    while $n'+i+jq_{avg}\leq n_{\max}$
      $M_{est}(t_{n+i+jq_{avg}})=\rho_{avg}{}^{j}M_{est}(t_{n'+i})$ % Eq. (42)
    end while
  end for
end for

for $q=n+1+q_{avg}$ to $q=n_{\max}$
  $B_{E_i}(t_q)=B_{E_i}(t_q)+\rho_{E_i}M_{est}(t_q)$ % Eq. (43)
end for

FIG. 7. Algorithm 2: Averaging to estimate late element radiation densities.

as the average reflection coefficient. The mean free path length of sound in the room is

$$R_{\mathrm{avg}}=\frac{4V}{\Sigma_{i=1}^{M}A_{E_i}}, \tag{38}$$

where V is the volume of the enclosure (since $4V/S$ is the mean free path length in a room of arbitrary shape, with diffusely reflecting boundaries, where S is the surface area[2]). Note that Rougeron *et al.*[28] use the average distance between patches and elements rather than mean free path length. For sufficiently small patches, these methods should be equivalent. Then define

$$q_{\mathrm{avg}}=\left\lceil\frac{R_{\mathrm{avg}}}{c\Delta t}\right\rceil \tag{39}$$

Compute $\int_{E_i} d\Omega_r$, T_{rE_i} % Eqs.(17) and (33)

for $q=1$ to $q=n_{\max}$
  for $i=1$ to $i=M$
    $I_0(r_r,t_{q+T_{rE_i}})=I_0(r_r,t_{q+T_{rE_i}})+\frac{1}{\pi}B_{E_i}(t_q)\int_{E_i} d\Omega_r$
    % Eq. (16)
  end for
end for
$I_0(r_r,t_{T_{sr}})=I_0(r_r,t_{T_{sr}})+\frac{W}{4\pi R_{sr}^{2}}$ % Eq. (9)
for $q=1$ to $q=n_{\max}$
  $I_m(r_r,t_q)=e^{-mlq}I_0(r_r,t_q)$ % Eq. (10)
  $p^2(r_r,t_q)=I_m(r_r,t_q)\rho_0 c$ % Eq. (11)
end for

FIG. 8. Algorithm 3: Pressure-squared response at a receiver.

TABLE I. Numerical and analytical predictions for three spheres.

Case	a (m)	α	r (m)	B_{theory} (W/m^2)	$\overline{B_{\text{rad}}}$ (W/m^2)	B_{rad} (W/m^2)	RT_{theory} (s)	RT_{rad} (s)	$L_{p,\text{theory}}$ (dB)	$L_{p,\text{rad}}$ (dB)
1	1	0.05	1/2	0.0076	0.0076	0.0074	1.047	1.044	105.18	105.24
2	2	0.20	$\sqrt{2}$	3.98e-4	4.03e-4	4.11e-4	0.483	0.488	92.68	92.66
3	3	0.50	$\sqrt{2}$	4.42e-5	4.48e-5	4.52e-5	0.242	0.240	85.90	85.90

as (an approximation to) the average number of time steps between elements. From this, the estimated irradiation density at time t_q, for $n+1+q_{\text{avg}}<q\leqslant n'+q_{\text{avg}}$, is

$$M_{\text{est}}(t_q)=B_{\text{avg}}(t_q-t_{q_{\text{avg}}})+\rho_{\text{avg}}B_{\text{avg}}(t_q-2t_{q_{\text{avg}}})+\rho_{\text{avg}}^2B_{\text{avg}}(t_q-3t_{q_{\text{avg}}})+\cdots$$

$$=\sum_{i=1}\rho_{\text{avg}}^{i-1}B_{\text{avg}}(t_{q-iq_{\text{avg}}}), \tag{40}$$

where $B_{\text{avg}}(t_q)=0$ for $q>n'$ and the summation is taken to the maximum i such that $q-iq_{\text{avg}}>n$. Expressed recursively

$$M_{\text{est}}(t_q)=B_{\text{avg}}(t_{q-q_{\text{avg}}})+\rho_{\text{avg}}M_{\text{est}}(t_{q-q_{\text{avg}}}), \tag{41}$$

where $M_{\text{est}}(t_q)=0$ for q such that $n+1\leqslant q\leqslant n+q_{\text{avg}}$.

Now, let $n_{\max}$ be the maximum time step for which the predictions are to be made. $M_{\text{est}}(t_q)$ for $n'+q_{\text{avg}}<q\leqslant n_{\max}$ can be found by Eq. (41) but, since $B_{\text{avg}}(t_q)=0$ for $q>n'$, it is simpler to use

$$M_{\text{est}}(t_{n'+i+jq_{\text{avg}}})=\rho_{\text{avg}}^jM_{\text{est}}(t_{n'+i}) \tag{42}$$

for $i=1,2,...,q_{\text{avg}}$ and $j\geqslant 1$ such that $n'+i+jq_{\text{avg}}\leqslant n_{\max}$.

Once all irradiation densities, $M_{\text{est}}(t_q)$, have been found, the estimated radiation densities are simply $\rho_{E_i}M_{\text{est}}(t_q)$. They are added to the exact radiation densities to get the updated radiation densities

$$B'_{E_i}(t_q)=B_{E_i}(t_q)+\rho_{E_i}M_{\text{est}}(t_q) \tag{43}$$

for $n+1\leqslant q\leqslant n_{\max}$ [where $B_{E_i}(t_q)$ for $q>n'$ are zero]. Algorithm 2 in Fig. 7 implements this averaging technique.

C. Sound pressure at the receiver

Having found all $B_{E_i}(t_q)$ (where primes in the updated radiation densities are dropped for ease in notation), the sound intensity at the receiver (characterized by position r_r) is found using Eq. (16). It remains to account for air absorption, which is done according to Eq. (10). The squared pressure at the receiver is found using Eq. (11). These steps are implemented in Algorithm 3 in Fig. 8.

IX. NONIMPULSIVE SIGNAL RESPONSES

Once the (pressure-squared) impulse response at the receiver is known, convolving it with any signal will give the (pressure-squared) signal response.[2] For walk-through simulations, however, convolution increases the computational requirements for the final simulation. To reduce time lag in the walk-through, it is desirable to perform the convolution in the rendering phase of the algorithm rather than during walk-through. This can be done simply by convolving the signal with the (impulse) radiation densities of each of the patches. The impulse radiation densities are those found in Algorithm 2 multiplied by e^{-mct} to include air absorption. The resulting signal radiation densities can then be used in the first ''for'' loop of Algorithm 3 to find intensity responses, hence pressure-squared responses, with changing receiver positions. In doing so, the last part of the third algorithm must be modified slightly to include air absorption in the propagation of sound from the elements to the receiver. Also, the direct contribution must be modified to incorporate the time dependence of the signal and to include air absorption. These simple modifications are left to the reader.

X. VALIDATION

Algorithms 1–3 were realized in code written in *MATLAB*.[39] Validation of the numerical solution, the algorithm and methods, and the corresponding code was done by comparison of predictions made by the program with known analytical solutions. Analytical solutions for a spherical enclosure with a continuous sound source[10–13] are used in the present validation; they are compared to predictions by the *MATLAB* program run for a spherical enclosure with the curved walls approximated by a sufficiently fine mesh.

Data for a meshed sphere, ready for input into *HeliosFF*, was determined. The meshing consisted of 288 patches and 408 elements. Predictions were made for three spheres of varying sizes and absorption coefficients. In all cases, the source was an omni-directional point source with a continuous power of 0.005 W located at the center of the sphere. The sphere's surfaces had constant absorption coefficient, α, and air absorption was neglected. The results are given in Table I. In the table, a is the radius of the sphere and r is the distance between source and receiver, both in meters. The subscripts ''theory'' and ''rad'' denote predictions by the analytical solution based on analytical formulas[10–13] and numerical predictions, respectively. RT is reverberation time in seconds, and L_p is steady-state sound-pressure level in dB. The radiation densities listed (B in W/m^2) are for a steady-state source with power 0.005 W. For the numerical values, radiation densities, B, are found by summing radiation den-

TABLE II. Time and memory requirements for predictions for three spheres.

Case	Computer speed (MHz)	max. time (s)	CPU time (s)	Memory (MB)
1	1794	1.0	6.33e4	93
2	2193	0.6	4.20e2	63
3	2193	0.6	2.40e2	30

sities for an impulsive source of power 0.005 W over all time for each patch. This is the radiation-density signal response of the patch—that is, the radiation-density impulse response of the patch convolved with the signal. B_{rad} is the average over all patches, and B_{rad} is the value for the patch that differed most from B_{theory} (the worst case).

Simulations were run on Pentium III computers, with speeds indicated in the Table II. Run times and memory requirements are also given in the table. In each case, time is discretized at 24 000 samples per second, and the impulse response is found up to ''max. time'' seconds. Note that the long run times are for finding the radiation densities of the patches. Run times for finding the impulse response at the receiver, and making predictions, are always only a few seconds. Furthermore, *HeliosFF* found the form factors within a few seconds.

XI. CONCLUSIONS

The close agreement between the analytical solutions and numerical predictions for the spherical enclosures validates two aspects of the AR work presented here: (1) the numerical solution based on a discretization of the enclosure as presented by Miles;[15] and (2) the algorithm and methods incorporated and developed in this paper for nonrectangular enclosures—in particular, the averaging technique suggested to improve efficiency, the cubic-tetrahedral method used for finding form factors, and the spherical-triangle method developed for solid angles.

A relatively coarse meshing of the spherical enclosure, with 288 patches and 408 elements was sufficient for convergence of the numerical solution to the analytical solution. Time discretization of 24 000 samples per second was also sufficient. Although the rendering of the enclosure took a long time (up to 1055 minutes for trials in this research), impulse responses at varying receiver positions were found in a matter of seconds.

Further validation of AR might use analytical solutions for the flat enclosure. Other future research may explore the necessary and sufficient conditions (such as time and mesh resolution, or times limits for exact and approximate solutions) for convergence of the numerical solution to the (possibly unknown) analytical solution in various enclosures. Beyond this, comparisons of AR with other prediction methods (such as ray tracing) and to measurements in real rooms would be highly informative. Further improvements in efficiency could also be made, as could the incorporation of specular reflection into AR.

ACKNOWLEDGMENTS

This research was funded by the Natural Sciences and Engineering Research Council of Canada. Thanks also to the Institute of Applied Mathematics at UBC for facilitating collaboration between the authors.

Parts of this work were presented in ''Preliminary experimental validation of the radiosity technique for predicting room sound fields'' at the International Congress on Acoustics in Seville, Spain in September 2002.

[1] L. Cremer and H. A. Müller, *Principles and Applications of Room Acoustics*, translated by Theodore Schultz (Applied Science Publishers, London, 1982).
[2] H. Kuttruff, *Room Acoustics*, 4th ed. (Spon Press, London, 2000).
[3] T. Lewers, ''A combined beam tracing and radiant exchange computer model of room acoustics,'' Appl. Acoust. **38**, 161–178 (1993).
[4] L. P. Franzoni and J. W. Rouse, ''An intensity-based boundary element method for analyzing broadband high frequency sound fields in enclosures,'' in Proceedings of the Forum Acusticum Sevilla in Seville, Spain, September 16–20, 2002, by the Spanish Acoustical Society.
[5] I. Ashdown, *Radiosity: A Programmer's Perspective* (Wiley, New York, 1994).
[6] M. F. Cohen and J. R. Wallace, *Radiosity and Realistic Image Synthesis* (Academic, Boston, 1993).
[7] F. X. Sillion and C. Puech, *Radiosity and Global Illumination* (Morgan Kaufmann, San Fransisco, 1994).
[8] H. Kuttruff, ''Simulierte Nachhallkurven in Rechteckräumen mit diffusem Schallfeld,'' [Simulated reverberation curves in rectangular rooms with diffuse sound fields], Acustica **25**, 333–342 (1971).
[9] H. Kuttruff, ''Nachhall und effective Absorption in Räumen mit diffuser Wandreflexion,'' [Reverberation and effective absorption in rooms with diffuse wall reflections], Acustica **35**, 141–153 (1976).
[10] M. M. Carroll and C. F. Chien, ''Decay of reverberant sound in a spherical enclosure,'' J. Acoust. Soc. Am. **62**, 1442–1446 (1977).
[11] M. M. Carroll and R. N. Miles, ''Steady-state sound in an enclosure with diffusely reflecting boundary,'' J. Acoust. Soc. Am. **64**, 1424–1428 (1978).
[12] W. B. Joyce, ''Exact effect of surface roughness on the reverberation time of a uniformly absorbing spherical enclosure,'' J. Acoust. Soc. Am. **64**, 1429–1436 (1978).
[13] H. Kuttruff, ''Energetic sound propagation in rooms,'' Acust. Acta Acust. **83**, 622–628 (1997).
[14] H. Kuttruff, ''Stationäre Schallausbreitung in Flachräumen,'' [Stationary sound propagation in flat enclosures], Acustica **57**, 62–70 (1985).
[15] R. N. Miles, ''Sound field in a rectangular enclosure with diffusely reflecting boundaries,'' J. Sound Vib. **92**, 203–226 (1984).
[16] J. Shi, A. Zhang, J. Encarnação, and M. Göbel, ''A modified radiosity algorithm for integrated visual and auditory rendering,'' Comput. Graphics **17**, 633–642 (1993).
[17] A. LeBot and A. Bocquillet, ''Comparison of an integral equation on energy and the ray-tracing technique in room acoustics,'' J. Acoust. Soc. Am. **108**, 1732–1740 (2000).
[18] J. Kang, ''Reverberation in rectangular long enclosures with diffusely reflecting boundaries,'' Acust. Acta Acust. **88**, 77–87 (2002).
[19] M. R. Schroeder and H. Kuttruff, ''On frequency response curves in rooms,'' J. Acoust. Soc. Am. **34**, 76–80 (1962).
[20] H. Kuttruff, ''A simple iteration scheme for the computation of decay constants in enclosures with diffusely reflecting boundaries,'' J. Acoust. Soc. Am. **98**, 288–293 (1995).
[21] M. Hodgson, ''Measurements of the influence of fittings and roof pitch on the sound field in panel-roof factories,'' Appl. Acoust. **16**, 369–391 (1983).
[22] M. Hodgson, ''Evidence of diffuse surface reflections in rooms,'' J. Acoust. Soc. Am. **89**, 756–771 (1991).
[23] H. Kuttruff and T. Strassen, ''Zur Abhängigkeit des Raumnachhalls von der Wanddiffusität und von der Raumform,'' [On the dependence of reverberation time on the ''wall diffusion'' and on room shape], Acustica **45**, 246–255 (1980).
[24] N. C. Baines, ''An investigation of the factors which control non-diffuse sound fields in rooms,'' Ph.D. thesis, University of Southampton, 1983.
[25] H. Rushmeier, ''Extending the radiosity method to transmitting and specularly reflecting surfaces,'' Master's thesis, Cornell University, 1986.
[26] F. X. Sillion, J. R. Arvo, S. H. Westin, and D. P. Greenberg, ''A global illumination solution for general reflectance distributions,'' Comput. Graphics **25**, 187–196 (1991).
[27] F. Sillion and C. Puech, ''A general two-pass method integrating specular and diffuse reflection,'' Comput. Graphics **23**, 335–344 (1989).
[28] G. Rougeron, F. Gaudaire, Y. Gabillet, and K. Bouatouch, ''Simulation of the indoor propagation of a 60 GHz electromagnetic wave with a time-dependent radiosity algorithm,'' Comput. Graphics **26**, 125–141 (2002).
[29] N. Tsingos, ''Simulation de champs sonores de haute qualité pour des applications graphiques interactives,'' [Simulating high quality dynamic virtual sound fields for interactive graphics applications], Ph.D. thesis,

Universite Joseph Fourier-Grenoble 1, 1998 (www-sop.inria.fr/reves/personnel/Nicolas.Tsingos/).
[30] J. R. Howell, *A Catalog of Radiation Configuration-Factors* (McGraw-Hill, New York, 1982) (www.me.utexas.edu/~howell/tablecon.html).
[31] U. Gross, K. Spindler, and E. Hahne, ''Shape-factor equations for radiation heat transfer between plane rectangular surfaces of arbitrary position and size with rectangular surfaces of arbitrary position and size with rectangular boundaries,'' Lett. Heat Mass Transfer **8**, 219–227 (1981).
[32] *HeliosFF* and *Helios32* are trademarks of *byHeart Consultants Limited* (www.helios32.com).
[33] E. J. Rathe, ''Note on two common problems of sound propagation,'' J. Sound Vib. **10**, 472–479 (1969).
[34] J. Beran-Koehn and M. J. Pavicic, ''A cubic tetrahedral adaptation of the hemi-cube algorithm,'' in *Graphics Gems II*, edited by James Arvo (Academic, Boston, 1991), pp. 299–302.
[35] J. Beran-Koehn and M. J. Pavicic, ''Delta form-factor calculation for the cubic tetrahedral algorithm,'' in *Graphics Gems III*, edited by David Kirk (Academic, Boston, 1992), pp. 324–328.
[36] J. S. Asvestas and D. C. Englund, ''Computing the solid angle subtended by a planar figure,'' Opt. Eng. **33**, 4055–4056 (1994).
[37] R. A. Hermann, *Treatise of Geometric Optics* (Cambridge University Press, Cambridge, MA, 1910).
[38] J. R. Weeks, *The Shape of Space*, 2nd ed. (Marcel Dekker, New York, 2002).
[39] *MATLAB* is a registered trademark of *The Math Works, Inc.*

Statistical properties of acoustic emission signals from metal cutting processes[a)]

F. A. Farrelly, A. Petri, L. Pitolli, and G. Pontuale[b)]
Consiglio Nazionale delle Ricerche, Istituto di Acustica "O. M. Corbino," Via del Fosso del Cavaliere, 100-00133 Roma, Italy

A. Tagliani and P. L. Novi Inverardi
Faculty of Economics, Trento University, Via Vigilio Inama, 5-38100 Trento, Italy

(Received 14 June 2003; accepted for publication 3 May 2004)

Acoustic emission (AE) data from single point turning machining are analyzed in this paper in order to gain a greater insight of the signal statistical properties for tool condition monitoring applications. A statistical analysis of the time series data amplitude and root mean square (rms) value at various tool wear levels are performed, finding that aging features can be revealed in all cases from the observed experimental histograms. In particular, AE data amplitudes are shown to be distributed with a power-law behavior above a crossover value. An analytic model for the rms values probability density function is obtained resorting to the Jaynes' maximum entropy principle; novel technique of constraining the modeling function under few fractional moments, instead of a greater amount of ordinary moments, leads to well-tailored functions for experimental histograms. [DOI: 10.1121/1.1764831]

PACS numbers: 43.60.Cg, 43.40.Le, 43.60.Gf [EJS]

Pages: 981–986

I. INTRODUCTION

Due to global competition and rapidly changing customer requirements, enterprises are required to constantly redesign their products and continuously reconfigure their manufacturing processes in terms of increasing flexibility and complexity, in order to satisfy the international market's demands to reduce production costs and increase precision and quality. Design and development of on-line systems for monitoring the process parameters, parts and manufacturing environment, is becoming more and more important, as the actual Sixth Framework European Program FP6 efforts demonstrate. In this framework, main problems in the field of metal cutting are constituted by tool wear and tool breakage. These phenomena limit the cutting speed and feed rate, and consequently, the metal removal rates that can be used in machining various workpiece materials in an economic way. Also, this fact plays a negative role in the machine tool environment causing unexpected breakdowns, defective workpieces, overloads due to high cutting forces and machine tool damages, as well as other problems that reduce the productiveness of the machine tool. Usually, these problems are solved using a conservative limit for the tool useful life, this leading to a less optimum use of the tool. The complexity of such a problem has lead to an impressive amount of literature on this subject, and a variety of techniques have been proposed. An extended review of the state of the art, technological challenges, and future developments of these systems is described by Byrne *et al.*[1] This paper deals in great detail on describing the physical parameters to be analyzed for industrial control applications, together with their appropriate sensory systems. Among these, acoustic emission (AE) signal analysis has been demonstrated to be one of the most efficient tool condition monitoring (TCM) techniques which can be applied to machining processes control, as the impressive amount of literature on this subject shows; Li's article[2] is just an example of a brief review about AE methods for tool wear monitoring during turning machining. Also, AE source identification and modeling, for this particular application, is a subject in which, during the last years, a large number of studies have been conducted (see only as a few important examples Refs. 3–6); Heiple *et al.*[7] found that the primary source of AE from single point machining is the sliding friction between the nose and the flank of the tool and the machined surface. This kind of friction is related in a complex manner with tool wear and the material being machined; therefore, depending on machining conditions, the root mean square (rms) levels and other AE related values may increase or decrease as the tool wears, affecting the parameters of the experimental frequency distributions.

In this framework, our paper tackles the problem of gaining greater insight into the basic statistical properties of AE signals, whose better and deeper knowledge, besides shedding light upon this fundamental aspect of AE for this application, may greatly facilitate an appropriate implementation of AE sensor-based devices leading to efficient TCM systems. To do this, single-point turning machining conditions, that will be described in the next section, were held fixed throughout the experiment, so as to limit the number of varying parameters that might affect the behavior of the observed quantities. The experimental probability density functions (pdf) of AE time series amplitude and root mean squared values are shown for different levels of tool wear, both these approaches being capable of showing interesting and not yet completely exploited features. Furthermore, the effects of tool wear on such statistical properties are high-

[a)]Portions of this work were published in "A statistical analysis of acoustic emission signals for tool condition monitoring (TCM)," ARLO-Acoustic Research Letters Online, **4**, January 2003.

[b)]Electronic mail: pontuale@idac.rm.cnr.it

lighted, thus outlining possible further signal analysis scenarios.

An analytic model for the rms pdf reconstruction is presented here, resorting to the Jaynes' maximum entropy principle (MEp) principle; the technique, recently proposed by some of the authors, of constraining the modeling function under some fractional moments instead of a greater amount of ordinary integer moments, leads to well-tailored functions for the experimental pdf. These results are compared with previously considered models, showing a substantial improvement in the agreement with experimental histograms.

II. DETECTORS AND EXPERIMENTAL SETUP

To achieve the objectives of this work, simultaneous AE data acquisition has been conducted by means of two different AE sensors: a custom-built AE sensor, and a Brüel & Kjr 8312 AE sensor. The choice of using two different transducers for signal pickup not only allows a more reliable and intensive harvest of data, but also makes it possible to perform a compared analysis on signals gathered at the same time but at different locations and in different conditions. In fact, the propagation of AE signals in the range investigated is characterized by significant attenuation. Thus, in order to achieve a good signal to noise ratio, the sensor should be placed as close as possible to the machining point where the AE signal is generated;[8] as an added benefit, reduction of the signal distortion due to the number of interfaces and mechanical resonances is also achieved by avoiding a long measurement chain. This motivated the use of a custom-built sensor, made of a small rectangular shaped piezoelectric ceramic (PZT-5), $5.0\times1.5\times0.7$ mm in size, working as a resonant sensor with a resonance frequency near 370 kHz, housed inside a small cavity bored into the cutting tool holder so as to protect it from chip damages and liquid coolant effects, and placed about 2 cm from the AE signal sources. An electrically conductive adhesive is used to bond the ceramic to the internal face of the cavity. The commercial sensor is a 40 dB preamplified Brüel & Kjaer Type 8312 AE transducer, placed at the extremity of the tool holder by means of a special mounting, about 12 cm from the cutting area.

AE measurements were performed while machining stainless steel (AISI 303) bars on a SAG14 GRAZIANO lathe. Cutting speeds range from 0.5 to 1 m/s, while feed rates and cutting depths are kept constant at 0.0195 mm/turn and 2 mm, respectively. In all measurements, cutting tool inserts were ''IMPERO'' PCLNR with 2020/12-type tungsten carbide; the acquisitions were performed on inserts with various degrees of wear. Specifically, inserts were grouped into three different wear categories: new ones, those estimated to be halfway through their life cycle (50%), and those completely worn through (100%).

In the new and 100% worn cases, eight cutting edges were analyzed per wear level, while four edges were utilized in the 50% case. For each edge one acquisition run was conducted, collecting 15 banks of 40 960 AE time series point corresponding to 16.38 ms, for a total of 614 400 points each run. Hence, a total of 12 288 000 (4.9152s) AE time series points were collected over all 20 runs.

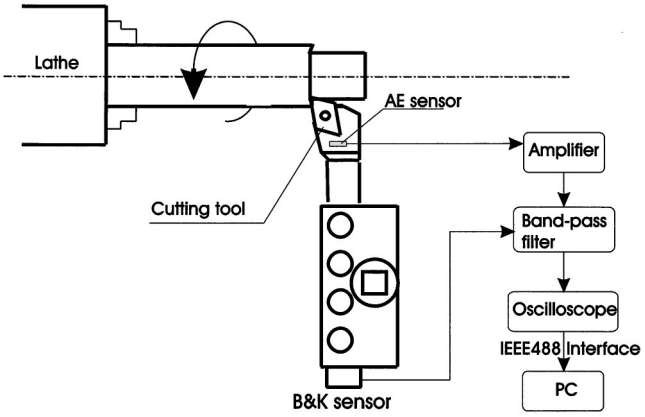

FIG. 1. The signals detected by the two transducers were amplified (by means of a 40 dB Analog Module preamplifier for the custom sensor, its own 40 dB preamplifier for the Brüel & Kjaer one), and filtered in the 200–1000 kHz range through a Krohn-Hite 3944 filter. The signals were then captured by a Tektronix digital oscilloscope (TDS420) using a 2.5 MHz sampling rate, and finally stored in a PC through an IEEE488 interface.

The experimental setup is roughly sketched in Fig. 1. The signals detected by the transducers were amplified (by means of a 40 dB Analog Module preamplifier for the custom sensor, its own 40 dB preamplifier for the Brüel & Kjaer one), and filtered in the 200–1000 kHz range through a Krohn-Hite 3944 filter. The signals were then captured by a Tektronix digital oscilloscope (TDS420) using a 2.5 MHz sampling rate, and finally stored in a PC through an IEEE488 interface. Blank measurements performed just prior to machining indicated no significant electrical noise. The data were analyzed both directly in their time series form and through root mean squared (rms) values.

III. EXPERIMENTAL RESULTS AND DISCUSSION

A. Time series analysis

Typical time splice series for the two sensors are shown in Fig. 2. In both cases two rather well distinct parts can be

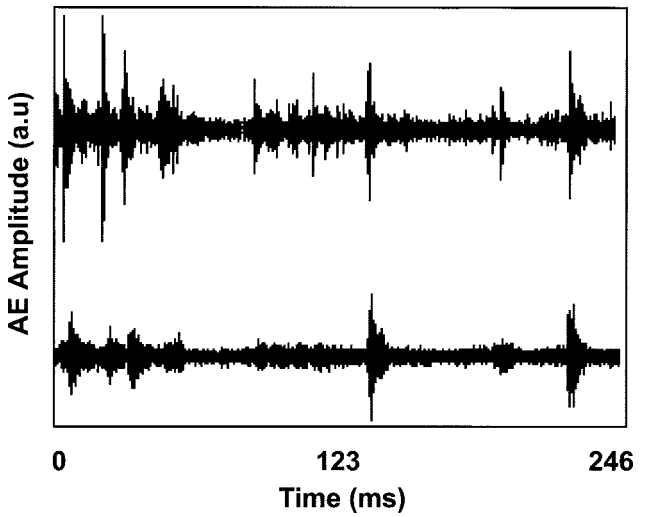

FIG. 2. Typical AE time splice series for the two sensors, in which two rather well distinct parts can be identified: a *continuous* part that is characterized by a relatively constant amplitude with small fluctuations, and a *burst emission* exhibiting strong intermittence and relatively high amplitudes.

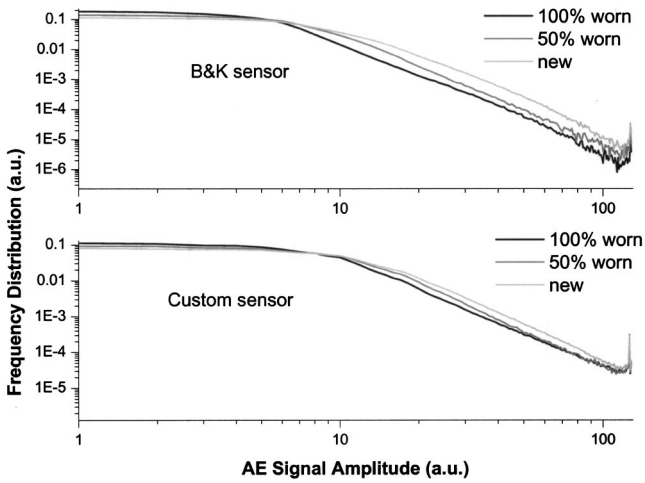

FIG. 3. For the two sensors, the histograms of the absolute value of AE time series amplitudes (a), taken from measurements performed using inserts in three stages of wear, show a power-law behavior, with a slope slightly dependent on the sensor.

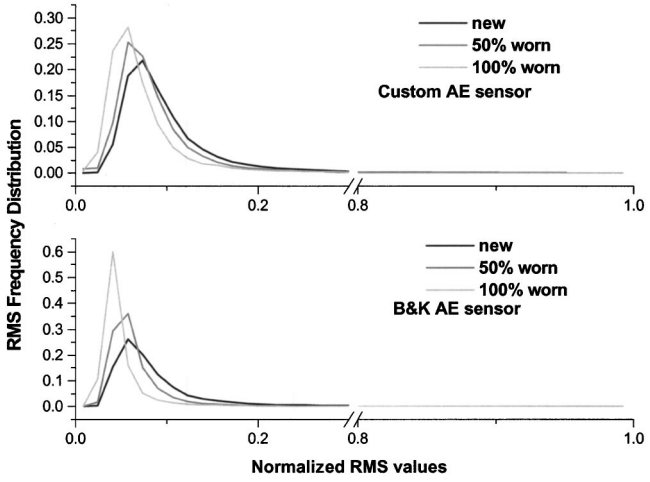

FIG. 4. For the two AE sensors, and for the three levels of wear, the average histograms of the rms values show a noticeable shift tending towards lower levels of the modal value of the frequency distribution, as well as a change in the skewness tending towards values compatible with a symmetrical shape.

identified: a *continuous part* that is characterized by a relatively constant amplitude with small fluctuations, and a *burst emission* exhibiting strong intermittence and relatively high amplitudes. The former is associated with plastic deformation and frictional processes during the cutting operations, the latest with chip breakage as well with microcracks and dislocation kinetics.[9,3]

For the two sensors, the histograms of the absolute value of time series amplitudes, a, taken from measurements performed using inserts in three stages of wear are portrayed in Fig. 3. All these experimental frequency distributions $p(a)$ are normalized over the related number of data and grouped into 126 classes. It is possible to observe how in all cases the curves exhibit a power-law behavior $p(a)=Aa^{-\alpha}+B$ above a crossover value from a nearly flat distribution, the value of the slope being slightly dependent on the sensor used ($\alpha=-3.7$ and $\alpha=-3.9$ for custom-built and Brüel & Kjaer sensors, respectively), but similar for all three stages of wear. The corresponding exponents for the energy E are $\alpha'=-2.35$ and $\alpha'=-2.45$, as they can be derived from the amplitude exponents assuming $E\propto a^2$.

For both sensors, data from tools with greater wear level show within the power-law range a slightly smaller frequency count for a given value in amplitude; this leads to the conclusion that, in this set of trials, the newer tools are the most active ones in terms of acoustic emission.

It is interesting to note that power-law behavior, strongly suggestive of a critical dynamics associated with this particular AE phenomena, has been observed in many studies on acoustic emission signals, e.g., those related to the formation of microfractures.[10–12] In general, power-law characteristics are associated with scale invariant properties underlying the physical phenomena under study, and in some cases this has been explained by self-organized criticality[13] models.

B. Root mean squared analysis

A substantial effort in the past has been dedicated towards analyzing the relationship between signal rms and tool wear level in various experimental situations, e.g., see Ref. 14 for identifying catastrophic tool failure conditions in carbide inserts. The analysis of the rms was conducted calculating values on the basis of 100 points, corresponding to 40 ms, this choice being effective in making the rms signal sensitive to the different contributions from burst and continuous events. In order to study the rms values' statistical properties, also as a function of aging, their experimental frequency distributions were analyzed by grouping the values into 60 bins, after their normalization over the largest values of the entire rms data set. For each wear level, and for both the sensors utilized, the average histograms are shown in Fig. 4. For increasing levels of wear the curves show a noticeable shift towards lower levels of the modal value of the frequency distribution, as well as a change in the skewness tending towards values compatible with a symmetrical shape, these features being particularly evident for Brüel & Kjaer sensor. In order to test the difference among these graphs, T-Test analyses regarding the sample means were performed, which indicate that the null hypothesis of equal means can be rejected with a confidence level of 95%. This approach appears to be effective in discriminating tool wear features, and could be used as the basis for implementing algorithms for TCM applications.

In literature, borrowing from a technique used in the description of surfaces roughness by Whitehouse,[15] various attempts have been made at determining tool condition relying on the hypothesis that a beta distribution $f(x)$ (see, for example, Refs. 14 and 16) properly describes the probability density function (pdf) of the rms values

$$f(x)=\frac{x^{r-1}(1-x)^{s-1}}{\beta(r,s)}, \tag{1}$$

where β is the complete beta function

$$\beta(r,s)=\int_0^1 x^{r-1}(1-x)^{s-1}dx. \tag{2}$$

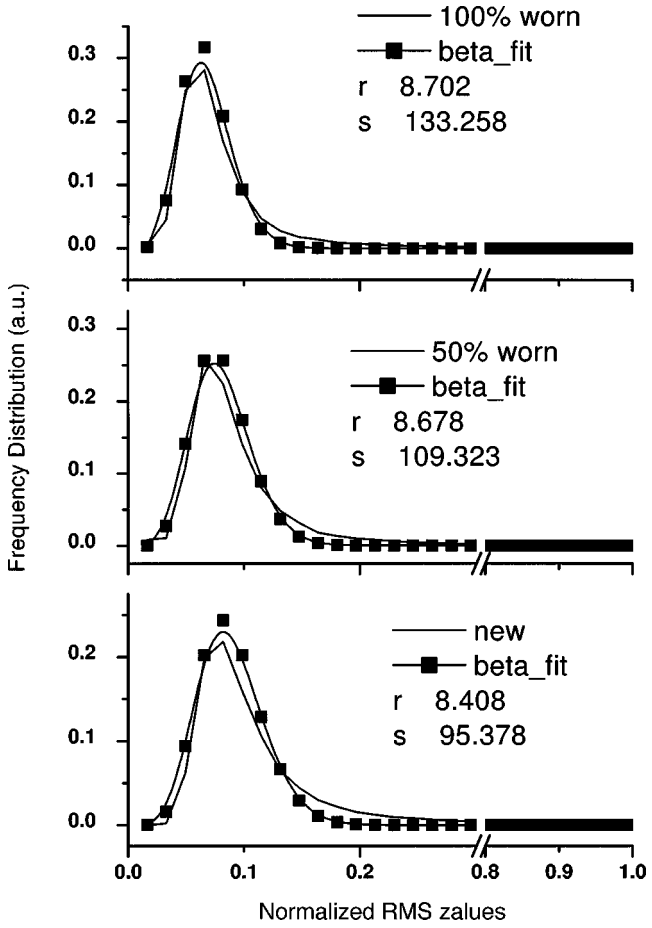

FIG. 5. The best fit of the rms histograms, for the custom-built sensor, with a beta function show that discrepancies are clearly visible between the fitting function and the experimental distributions, especially for values just above the peaks where the curves level off; this indicates that a better empirical fitting function may exist.

With this assumption it is possible to characterize the moments of the distribution in terms of the two parameters r and s, and vice versa. In particular, as far as mean (μ) and variance (σ^2) are concerned, we have

$$r = \frac{\mu}{\sigma^2}(\mu - \mu^2 - \sigma^2)$$
$$s = \frac{1-\mu}{\sigma^2}(\mu - \mu^2 - \sigma^2). \tag{3}$$

Thus, values for r and s can be estimated on the basis of the mean and variance of the data set. Past studies have shown that r, s pairs are scattered in different ways, depending on tool conditions.[16] One shortcoming of this method is that no estimate of the errors on the r and s parameters is directly available; this is particularly serious as real-life signals often contain outliers which can bring a noticeable shift in the actual values of both mean and variance. One possibility is to use more robust estimators (e.g., median instead of mean) although this still does not give an error estimate for the calculated parameters. A further choice is to perform a nonlinear best fit on the data set using the function given in Eq. (1).[17]

In Fig. 5 the best fit of the experimental frequency distributions from custom-built sensor data as in Fig. 4 are shown. From these graphs it is possible to see that while there is a good matching between the fitting function and the data sets in the neighborhood of the peaks, some discrepancies are visible in the residual for rms bin values just above the peak where the curves level off; this indicates that in this range, the data sets are richer in events than what Eq. (1) would indicate, and this suggests that a better empirical fitting function may exist. In Fig. 6 r, s estimates from Eqs. (3) are compared to the ones obtained by the best-fitting process. It is evident that the two groups greatly differ and that these discrepancies are not compatible considering the error estimates given on the fitted parameters. Furthermore, the scattering patterns of these two groups are entirely different; whereas both the best-fitted r, s parameters tend to increase with wear, the estimated ones show an essentially opposite behavior. One possible explanation for this difference is that while the best-fit process minimizes mean-square differences between the fitting function and the frequency distribution (so that heavily populated bins are weighted more), the estimate method relies on μ and σ^2. Variance, in particular, is highly sensitive to outliers, so values far from the mean weigh heavily on its determination.

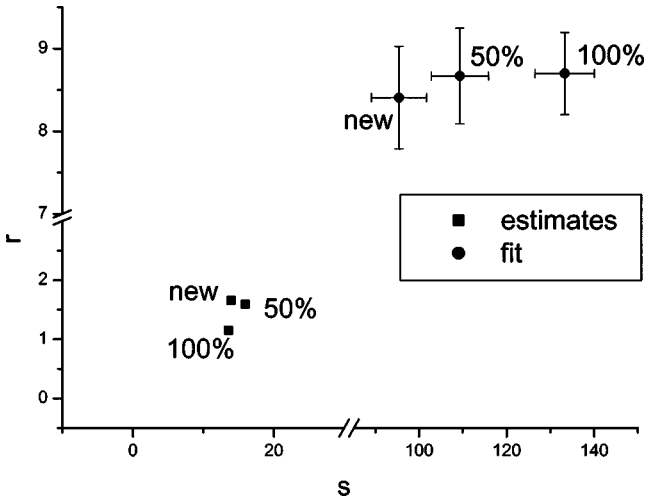

FIG. 6. The beta function r, s estimates from Eqs. (3) are compared to the ones obtained by the best fitting process, showing great differences between the two groups; these could be explained by the fact that while the best-fit process minimizes mean-square differences between the fitting function and the frequency distribution (so that heavily populated bins are weighted more), the estimate method relies on μ and σ^2. Variance, in particular, is highly sensitive to outliers, so values far from the mean weigh heavily on its determination.

In this framework, a method is proposed here to reconstruct the approximate rms's pdf by applying the ME technique, under the constraint of some fractional moments, the latter ones being explicitly obtained in terms of given ordinary moments. Such an approach allows one to obtain well-tailored fitting functions for the experimental curves.

C. Recovering rms's *pdf* from fractional moments

Jaynes' maximum entropy principle (MEp) says that "*the best (minimally prejudiced) assignment of probabilities is that one which minimizes the entropy subject to the satisfaction of the constraints imposed by the available*

information''.[18] Thus, taking the Kullback-Leibler information functional or differential entropy (KL, in the following) as the relevant information measure, the spirit of Jaynes' principle implies that the best probability assignment $f_M(x)$ is the solution of the following minimization problem:

$$\min \mathrm{KL}(f,f_0)=\min \int_D f(x)\ln\frac{f(x)}{f_0(x)}dx, \tag{4}$$

subject to the satisfaction of the following requirements:

(i) $f(x)\geqslant 0,\ \forall x\in D;$
(ii) $\int_D f(x)dx=1;$
(iii) $I_k(f(x))=0,\ k=1,2,...,M,$

where $f_0(x)$ is the ''prior distribution'' of X and $\{I_k(f(x))=0,\ k=1,2,...,M\}$ is a set of relations representing the information available on the distribution whose $f(x)$ is the density. In other words Jaynes' prescription is to take the best probability assignement $f_M(x)$ as close as possible to the prior distribution $f_0(x)$ without, however, contradicting the available physical information as summarized by the constraints I_k and the general requirements of any legitimate density function. Usually

$$I_k(f(x))=\mu_k-\int_D x^k f(x)dx,\quad k=1,2,...,M, \tag{5}$$

where μ_k represents the kth integral moment of the population having $f(x)$ as pdf. If the population moments are unknown, it is possible to replace them with their sample counterparts.[19] But, it should be clear that integral moments are not the unique choice. In fact, when the underlying random variable takes positive values, Novi Inverardi and Tagliani[20] proposed the use of fractional moments

$$\tilde{\mu}_{\alpha_k}=:E(X^{\alpha_k})=\int_D x^{\alpha_k}f(x)dx,\quad \alpha_k\in IR,$$

$$k=0,1,2,...,M,\quad \tilde{\mu}_0=1$$

to represent the available information in the set of constraints given in Eq. (5) to spend for recovering the unknown pdf. With this setup, the solution of Eq. (4) which gives back the Jaynes' MEp model

$$f_M(x;\alpha_k,\lambda_k)=\exp\left\{-\sum_{k=0}^{M}\lambda_k x^{\alpha_k}\right\}. \tag{6}$$

The parameter M, unknown when the available information consists only of a sample, represents the order of the model given by the Jaynes' MEp and the λ_k, $k=1,2,...,M$, are the Lagrangian multipliers associated with the physical constraints $I_k(f(x))$.

The main reason that asks for the choice of fractional moments rests on the fact that integral moments could be a very poor tool to extract information from a sample when the corresponding distribution exhibits fat tails or the characterizing moments are not integral. In the last case, giving the fractional moments a better approximation of the characterizing moments, the performance of the reconstruction density procedure based on them is expected to be reasonably better than that based on integral moments.

When the only information available consists of a sample, the Jaynes' MEp needs to be combined with the Akaike selection approach to obtain a complete procedure for the reconstruction of the underlying unknown pdf: in fact Jaynes' MEp produces an infinite hierarchy of ME models and Akaike's approach permits one to select the optimal member from the hierarchy of models given by MEp.

It is clear from Eq. (6) that when constraints involve fractional moments there is an additional problem to solve: being the exponents α_k of fractional moments new variables to take into account, it needs to decide not only *how many* but also *what* fractional moments to choose in such a way that the estimated density reflects properly the information contained in a given sample about the unknown probability distribution. Both of these choices rest on the exploiting of differential entropy contribution or in other terms choose the M α's exponents and the M λ's coefficients which minimize the KL distance between $f(x)$ and $f_M(x)$; it means the solution of the following optimization problem:

$$\min_M\left\{\min_\alpha\left\{\min_\lambda\left\{-\frac{1}{n}\sum_{i=1}^{n}\ln(f_M(x_i;\lambda,\alpha))+\frac{M}{n}\right\}\right\}\right\}, \tag{7}$$

where $-1/n\Sigma_{i=1}^{n}\ln(f_M(x_i;\lambda,\alpha))+M/n$ represents the sample differential M-order model entropy. The term M/n is proportional to the model order M, i.e., to the number of parameters which we try to estimate using a given sample, and inversely proportional to the size n of the sample and can be interpreted in the Akaike's philosophy as a ''penalty term'' which prevents us from establishing ''too elaborate'' models which cannot be justified by the given data. Consequently, the parsimony principle becomes an important criterion whereby we attempt to retain only relevant and useful information and discard the redundant part of it. More details on the estimation procedure can be found in Novi Inverardi and Tagliani.[20]

The above technique is applied here to recover from AE's values the analytic form of the rms's pdf that are the solution of Eq. (7) and that represent a well-tailored model for experimental data distributions. Figure 7 shows, for the three levels of tool wear previously considered, the results of rms values pdf recovering by the ME technique, using only five fractional moments. Curves are compared with the experimental histograms showing a good agreement, especially for newer tools curves, and the visual inspection of entropy values related to the approximating functions indicates it decreases with increasing tool wear level, this representing a possible further indicator for the phenomena evolution.

IV. CONCLUSIONS

Various ways of analyzing the basic statistical properties of AE signals in a TCM application have been illustrated, in which machining conditions were held fixed throughout the experiment, in order to limit the number of varying parameters that might affect the behavior of the observed quantities. The analysis has been performed on signals gathered at the same time using two different AE sensors, enabling a comparative analysis in which, for both sensors, some interesting features, till now not sufficiently underlined, have

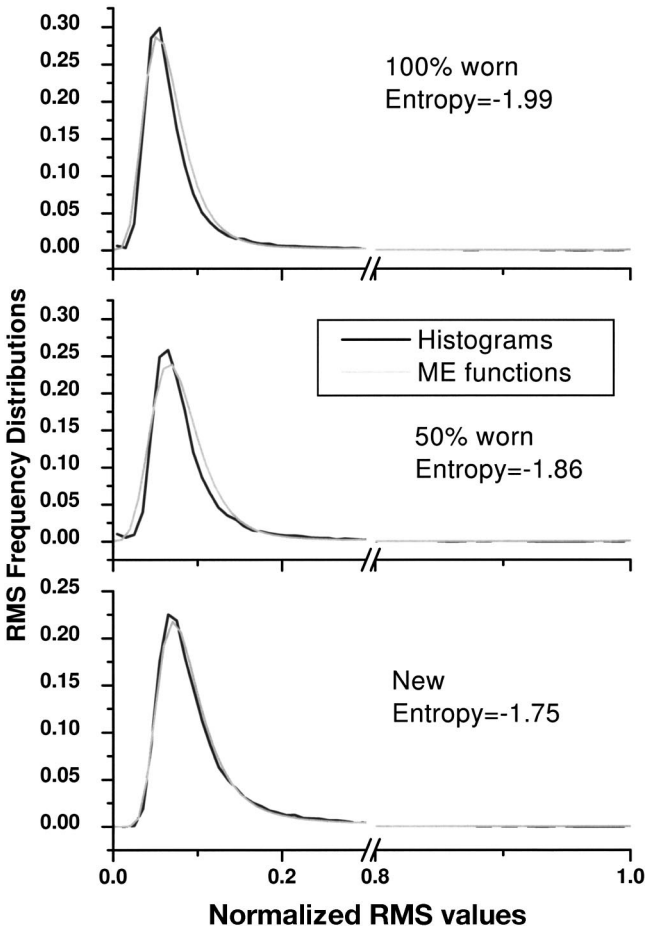

FIG. 7. For the custom-built sensor, the same experimental rms frequency distributions as in Fig. 4 are compared with the *pdf* recovered by the ME technique using only five fractional moments. This comparison shows a good agreement, especially for newer tool curves, and the visual inspection of entropy values related to the approximating functions indicates it decreases whit increasing tool wear level, this representing a possible further indicator for the phenomena evolution.

emerged. In particular, both AE time series and their associated rms values experimental frequency distributions have been derived, allowing one to analyze how tool wear affects such statistical features in the kind of situations investigated in our experiment. For what concerns the rms values, the shape of the curves indicates a noticeable shift towards lower levels of the modal value for increasing levels of wear, this indicating a reduced AE activity, together to with a reduction in the signal variability and a change in the skewness towards values compatible with a symmetrical shape.

A beta function model for describing the rms's *pdf* has been tested, and the residuals in the best-fitted function indicate that a more appropriate fitting model should be sought. A much better agreement has been reached by resorting to a ME technique by means of which the general Hausdorff moment problem has been tackled in an original way by using only few sampling fractional moments, this providing a better tailored analytic form for the rms's experimental distributions than previously proposed models. It has also been observed that the entropy of the functions monotonically changes for increasing wear. On the other hand, the physical meaning of the Lagrange multipliers λ_j obtained in this fitting function reconstruction (or the equivalent fractional moments order α_j) is not clear, and future efforts should be done to clarify this aspect.

Particularly interesting are the statistical properties of the time series, in which power laws in the frequency distributions have been identified, in accordance with what has been pointed out as a feature of acoustic emission phenomena in numerous other fields. In particular, the evidence of the non-Gaussianity of the process would make it reasonable to tackle the signal blind deconvolution problem by means of higher order statistics.[21] The recovering, only from the observed output, of the unknown original signal before it had been altered by the sensor response and the measurement chain, would be a fundamental step towards a deeper understanding of AE phenomena associated with TCM and more general applications as well.

[1] G. Byrne, D. A. Dornfeld, I. Inasaki, K. Ketteler, W. Konig, and R. Teti, "Tool condition monitoring (TCM)—The status of research and industrial application," Ann. CIRP **44**, 541–567 (1995).
[2] X. Li, "A brief review: acoustic emission method for tool wear monitoring during turning," Int. J. Mach. Tools Manuf. **42**, 157–165 (2002).
[3] H. Hatano, "Quantitative measurements of acoustic emission related to its microscopic mechanisms," J. Acoust. Soc. Am. **57**, 639–645 (1975).
[4] K. Ono, "Acoustic emission," in *Encyclopedia of Acoustics*, edited by Malcolm J. Crocker (Wiley, New York, 1997), Chap. 68, pp. 797–809.
[5] D. A. Dornfeld and E. Kannatey-Asibu, "Acoustic emission during orthogonal metal cutting," Int. J. Mech. Sci. **22**, 285–296 (1980).
[6] J. Chung and E. Kannatey-Asibu, "Acoustic emission from plastic deformation of a pure single cristal," J. Appl. Phys. **72**, 1812–1820 (1992).
[7] C. R. Heiple, S. H. Carpenter, D. L. Armentrout, and P. McManigle, "Acoustic emission from single point machining: source mechanisms and signal changes with tool wear," Mater. Eval. **52**, 590–596 (1994).
[8] K. Jemielniak, "Some aspects of AE application in tool condition monitoring," Ultrasonics **38**, 604–608 (2000).
[9] S. Y. Liang and D. A. Dornfeld, "Tool wear detection using time series analysis of acoustic emission," J. Eng. Ind. **111**, 199–205 (1989).
[10] A. Petri, "Acoustic emission and microcrack correlation," Philos. Mag. B **77**, 491–498 (1996).
[11] A. Garcimartin, A. Guarino, L. Bellon, and S. Ciliberto, "Statistical properties of fracture precursors," Phys. Rev. Lett. **79**, 3202–3205 (1997).
[12] G. Caldarelli, F. Di Tolla, and A. Petri, "Self-organization and annealed disorder in a fracturing process," Phys. Rev. Lett. **77**, 2503–2506 (1996).
[13] P. Bak, C. Tang, and K. Wiesenfeld, "Self-organized criticality: An explanation of 1/f noise," Phys. Rev. Lett. **59**, 381–384 (1997).
[14] K. Jemielniak and O. Otman, "Catastrophic tool failure detection based on acoustic emission signal analysis," Ann. CIRP **47**, 31–34 (1998).
[15] D. J. Whitehouse, "Beta functions for surface typologie?" Ann. CIRP **27**, 491–497 (1978).
[16] E. Kannatey-Asibu and D. A. Dornfeld, "Study of tool wear using statistical analysis of metal cutting acoustic emission," Wear **76**, 247–261 (1982).
[17] Fitting the function given in Eq. (1) requires a nontrivial effort, as this function cannot be linearized, so that the fitting process requires initial seed values; these might be obtained using the *r, s* estimation technique described above. Additionally, fully automating the fitting process requires appropriate handling of specific exceptions which can occur in nonlinear regressions (e.g., singular matrix conditions, reaching iteration limits without having satisfied tolerance criteria, etc.). In this paper no attempt at automating this process has been made.
[18] E. T. Jaynes, "On the rationale of maximum-entropy methods," Proc. IEEE **70**, 939–952 (1982).
[19] R. Baker, "Probability estimation and information principles," Struct. Safety **9**, 97–116 (1990).
[20] P. L. Novi Inverardi and A. Tagliani, "Maximum entropy density estimation from fractional moments," Commun. Stat: Theory Meth. **32**, 327–345 (2003).
[21] J. Cadzow and X. Li, "Blind deconvolution," Digit. Signal Process. **5**, 3–20 (1995).

Performance bounds for passive sensor arrays operating in a turbulent medium: Spherical-wave analysis

S. L. Collier[a)]
U.S. Army Research Laboratory, AMSRD-ARL-CI-EE, 2800 Powder Mill Road, Adelphi, Maryland 20783-1197

D. K. Wilson
U.S. Army Engineer Research and Development Center, 72 Lyme Rd., Hanover, New Hamphshire 03755-1290

(Received 2 October 2002; revised 23 March 2004; accepted 5 April 2004)

The Cramer–Rao lower bounds of the angle-of-arrival estimates for a spherical wave incident on a passive acoustic array are investigated for propagation through a turbulent medium with fluctuations described by a von Kármán spectrum. A single monochromatic source and a line-of-sight propagation path are assumed. The propagation distance, turbulence parameters (characteristic length scale and index-of-refraction variance), phase of the source, and signal-to-noise ratio are also included in the unknown parameter set. The Cramer–Rao lower bounds of the angle-of-arrival estimates are affected by the addition of the propagation distance and source phase as unknowns, and are not affected by the addition of the turbulence parameters and signal-to-noise ratio as unknowns. [DOI: 10.1121/1.1760111]

PACS numbers: 43.60.Cg, 43.28.Gq [LCS] Pages: 987–1001

I. INTRODUCTION

Acoustic sensor arrays are used for applications such as target detection, identification, and localization. Generally, these systems perform direction finding by determining the wave front angles of arrival (AOAs) from the phase differences across the array. Inhomogeneities in the atmosphere or ocean, such as turbulence and internal gravity waves, may strongly distort propagating wave fronts, resulting in fluctuations in the apparent bearing angles and intensity of the source. The error in estimating the wave front's AOAs will increase as the propagation distance increases and/or the intensity of the turbulence increases. Experiments have shown that random inhomogeneities can significantly affect the ability to perform direction finding in both the atmosphere[1,2] and the ocean.[3,4]

The performance of a sensor array may be quantified by calculating the error variance between the estimated parameter (such as the AOA) and its actual value. The minimum theoretically attainable error variance is the Cramer–Rao lower bound (CRLB), which is calculated from the Fisher information (FI). The CRLBs of the AOA estimates for a plane wave incident on a passive sensor array were investigated in Ref. 5. This latter study considered propagation through a random, inhomogeneous medium with fluctuations described by a von Kármán turbulence spectrum. Specifically, the authors addressed the case when a propagating acoustic wave is strongly diffracted by the medium and may be either strongly or weakly scattered by the medium. The received signal was modeled as a complex Gaussian random variable with a nonzero mean.[6,7] The technique was based on that of Wilson,[8] which followed the general framework of Song and Ritcey.[9] The advantage of the analyses of Refs. 5, 8, and 9 is that the statistical effects of the random medium on the propagating wave were directly incorporated into the calculation of the CRLBs. By comparison, there are many analyses that compute the CRLBs in the presence of noise only (see, e.g., Ref. 10 and references therein).

The analyses in Refs. 8 and 9, which were based on a *zero*-mean complex Gaussian signal model, with equal real and imaginary variances, strictly apply only to strong scattering and diffraction. In Ref. 5, this signal model was generalized to include a *nonzero* mean, thereby extending the applicability of the analysis to weak scattering but still in the presence of strong diffraction (the so-called *Rytov extension* region[6]). The nonzero-mean signal model has the advantage of tractability, since the FI for this case is a well-known result.[11,12] The main shortcoming is that it does not capture cases where phase variations are much stronger than amplitude variations (the so-called *geometric acoustics* region). Data for sound propagation through the atmosphere provide a mixed picture on the validity of the complex Gaussian, equal variance signal model. In the data of Norris *et al.*,[13] the model appeared to be reasonable for some frequencies, but other frequencies exhibited strong phase variations with comparatively little amplitude variation.

The present paper is a logical continuation of Ref. 5, but for an incident spherical wave. The theoretical model of Ref. 5 (herein referred to as the plane-wave paper) is adopted, with the appropriate changes made for a spherical wave. For simplicity, a single, monochromatic source and a line-of-sight propagation path are assumed. This paper investigates the effects of scattering from atmospheric turbulence on the ability to estimate the azimuthal and elevational angles of arrival. Other physical phenomena, such as ground reflections and refraction by atmospheric wind and temperature gradients, are not considered in this analysis and may have a considerable impact on the ability to estimate the elevation.

a)Electronic mail: scollier@arl.army.mil

Due to limitations of the theoretical model, this investigation is limited to near-normal incidence at a planar array. The primary focus is to calculate the CRLBs of the AOAs. However, there may exist other unknown parameters that will affect the ability to estimate the AOAs, and result in an increase in the CRLBs of the AOAs. The azimuth, elevation, phase of the source, propagation distance, signal-to-noise ratio (SNR), and turbulence parameters are considered in the unknown parameter set. As the estimates of the AOAs will degrade when they are simultaneously estimated with other parameters, the partial correlations between the estimates of the AOAs and the estimates of the other parameters are also calculated.

The paper is ordered as follows: The theoretical model is developed in Sec. II and properties of the resulting FI and CRLBs are discussed in Sec. III. The numerical results and concluding remarks are given in Secs. IV and V. For convenience, lists of all variables, symbols, and acronyms are given in the Appendix.

II. THEORY

Before proceeding to develop the theoretical model, let us first define notation that shall be used throughout: $[\cdot]^*$ denotes the complex conjugate; $[\cdot]^{\mathrm{T}}$ the transpose; $[\cdot]^{\dagger}$ the Hermitian adjoint (complex conjugate transpose); $\mathbf{I}_N$ is the identity matrix of order N; $\langle\cdot\rangle$ the ensemble average or expectation value; and $\mathbf{x}\sim\mathcal{CN}_N(\boldsymbol{\mu}, \mathbf{C})$ denotes that the $N\times 1$ complex random vector $\mathbf{x}$ is distributed as a complex Gaussian random variable with the $N\times 1$ mean vector (or first moment) $\boldsymbol{\mu}$ and the $N\times N$ covariance matrix $\mathbf{C}$.

The FI is determined from the probability likelihood function of the received signal, as discussed in Sec. II D. We model the total received signal as the sum of the signal of interest, which has propagated through atmospheric turbulence, and additive white Gaussian noise. For this analysis, we consider a sensor array with N elements.

A. Signal model

The total received complex signal $\mathbf{s}=[s_1, s_2, \ldots, s_N]^{\mathrm{T}}$ may be written as a column vector with N elements, one corresponding to each sensor. It is given by the sum

$$\mathbf{s}(\phi, \theta, t)=\mathbf{p}(\phi, \theta, t)+\mathbf{n}(t), \tag{1}$$

where t is time, $\mathbf{n}=[n_1, n_2, \ldots, n_N]^{\mathrm{T}}$ is the noise, and $\mathbf{p}=[p_1, p_2, \ldots, p_N]^{\mathrm{T}}$ is the signal that has propagated from the source and that arrives at the array center with azimuth ϕ and elevation θ. Both contributions are time dependent. It is assumed that the noise signals at the sensors are mutually uncorrelated with equal variance σ_n^2 and that $\mathbf{n}\sim\mathcal{CN}_N(0, \sigma_n^2\mathbf{I}_N)$. It is approximated that $\mathbf{p}\sim\mathcal{CN}_N(\boldsymbol{\mu}, \mathbf{C}_p)$, where $\boldsymbol{\mu}$ and $\mathbf{C}_p$ are calculated from the moments

$$\mu_i=\langle p_i\rangle \quad \text{and} \quad [\mathbf{C}_p]_{ij}=\langle p_i\, p_j^*\rangle-\mu_i\, \mu_j^*. \tag{2}$$

The theory of wave propagation in a random medium is used to calculate the first and second moments of the complex sound pressure field, $\langle p_i\rangle$ and $\langle p_i\, p_j^*\rangle$, respectively, as discussed in Sec. II B. We further assume that the source signal, $\mathbf{p}$, and noise, $\mathbf{n}$, are uncorrelated. Thus the total received signal, $\mathbf{s}$, is also a complex Gaussian random variable, $\mathbf{s}\sim\mathcal{CN}_N(\boldsymbol{\mu}, \mathbf{C}=\mathbf{C}_p+\sigma_n^2\mathbf{I}_N)$.

As noted in the Introduction, this signal model, in which the real and imaginary parts are Gaussian random variables with equal variances, is reasonable for strong scattering or the Rytov extension region. However, it is not suited to situations where both scattering and diffraction are weak (geometric acoustics), in which case the phase variance dominates the signal behavior.[6,7] The signal and noise models used here are admittedly idealized. But the FI should be affected primarily by the number of degrees of freedom in the signal and noise, rather than their detailed statistical behavior. More complicated signal and noise models are left to future study.

B. First and second moments

The statistical moments of the complex pressure field for a spherical wave propagating in a random medium have been derived in Refs. 7, 14, and 15. The analysis by Ostashev[15] includes fluctuations in the medium velocity, which is an extension of the works by Ishimaru[7] and Rytov *et al.*[14] In all of these analyses, the small-angle parabolic and Markov approximations were used to obtain closed form solutions for the moments. These approximations are valid in far field, for small scattering angles, and for $\mathcal{L}\gg\lambda>\ell$, where λ is the wavelength, and $\mathcal{L}$ and ℓ are the outer (integral) and inner (Kolmogorov) length scales of the turbulence, respectively.

1. Normal incidence

Consider a sound wave that is propagating with wave vector $\mathbf{k}=k\hat{\mathbf{e}}_r$, where $k=2\pi/\lambda$, λ is the wavelength of the source, and $\hat{\mathbf{e}}_r$ is the unit radial vector. Let the observation point be $\mathbf{r}_i=[x, y_i, z_i]$. For propagation in a *homogeneous* medium, the complex acoustic pressure field at $\mathbf{r}_i$ is

$$\begin{aligned} &p_{\mathrm{H}}(\mathbf{r}_i)=p_0(r_i)e^{\mathrm{i}\boldsymbol{\Phi}_i}, \quad \text{where} \\ &p_0(r_i)=\frac{\mathcal{A}r_0}{r_i} \quad \text{and} \quad \boldsymbol{\Phi}_i=kr_i+\chi. \end{aligned} \tag{3}$$

Here $p_0(r_i)$ is the pressure amplitude at r_i, $\mathcal{A}$ is the pressure amplitude at $r_i=r_0$, $\boldsymbol{\Phi}_i$ is the total phase of the signal at $\mathbf{r}_i$, and χ is the phase of the source. [The quantities $p_0(r_i)$, $\mathcal{A}$, r_i, r_0, and χ are all real valued.]

Suppose that $|x|\gg R_i=(y_i^2+z_i^2)^{1/2}$. The small-angle approximation (SAA) for a spherical wave propagating in free space is the Taylor series expansion up to first order in $1/|x|$ when $|x|\gg R_i$:

$$\begin{aligned} &\check{p}_{\mathrm{H}}(\mathbf{r}_i)=\check{p}_0(r_i)\ \exp\ (\mathrm{i}\check{\boldsymbol{\Phi}}_i), \quad \text{where} \\ &\check{p}_0(r_i)\approx\frac{\mathcal{A}r_0}{|x|} \quad \text{and} \quad \check{\boldsymbol{\Phi}}_i\approx k|x|+\frac{kR_i^2}{2|x|}+\chi. \end{aligned} \tag{4}$$

Here the breve, $\check{}$, is used to denote quantities taken in the SAA. When $|x|\gg R_i$, the component x is usually referred to as the longitudal component and $\mathbf{R}_i=[0, y_i, z_i]$ as the transverse component.

The first moment of the complex sound pressure field at $\mathbf{r}_i$ has been derived in Ref. 15 using the SAA for a spherical wave. The first moment for propagation in a *random, inho-*

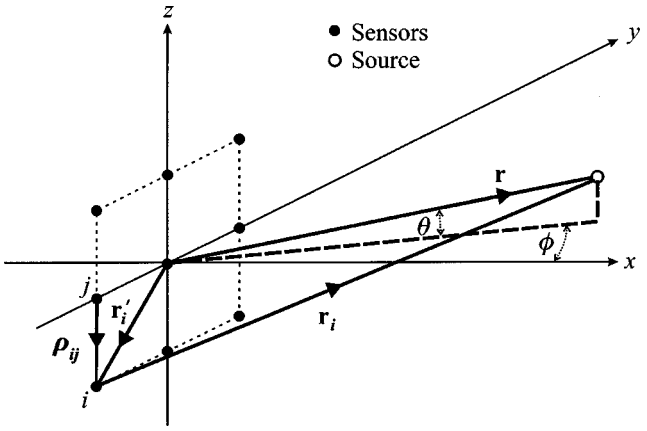

FIG. 1. Coordinate system. The closed circles represent the sensors and the open circle represents the source. The azimuth ϕ and elevation θ are defined with respect to $\hat{\mathbf{r}}$.

mogeneous medium is given by the product of the SAA of the complex sound field in a homogeneous medium and an extinction term due to fluctuations in the medium:

$$\mu_i = \breve{p}_{\mathrm{H}}(\mathbf{r}_i) e^{-\gamma|x|}, \tag{5}$$

where γ is the extinction coefficient for the first moment.

Consider now two observation points $\mathbf{r}_i = [x_i, y_i, z_i]$ and $\mathbf{r}_j = [x_j, y_j, z_j]$. Specifically, consider $x_i = x_j = x$ and $|x| \gg R_i, R_j$. From Ref. 15, the second moment of the complex pressure field in a *random, inhomogeneous* medium is

$$\langle p_i p_j^* \rangle = \breve{p}_{\mathrm{H}}(\mathbf{r}_i)\, \breve{p}_{\mathrm{H}}^*(\mathbf{r}_j) e^{-\alpha(\boldsymbol{\rho}_{ij})|x|}, \tag{6}$$

where $\boldsymbol{\rho}_{ij} = \mathbf{r}_i - \mathbf{r}_j$ is the sensor separation vector and α is the extinction coefficient for the second moment which is dependent upon the sensor separation ρ_{ij}. Here $\boldsymbol{\rho}_{ij}$ is transverse to propagation, as $x_i = x_j$ and hence $\boldsymbol{\rho}_{ij} = [0, y_i - y_j, z_i - z_j]$. We refer to Eq. (6) as the second moment for normal incidence, i.e., the second moment when the transverse components of $\mathbf{r}_i$ and $\mathbf{r}_j$ are equal. The exponential decay of the moments represents the decay of the coherent sound field due to scattering by the turbulent medium. The extinction coefficients for the first and second moments are related by

$$2\gamma = \alpha(\rho_{ij} = \infty). \tag{7}$$

Expressions for α and γ will be given in Sec. II C.

2. Oblique incidence

We are not aware of a general closed-form solution for the second moment at oblique incidence, i.e., when the transverse components of $\mathbf{r}_i$ and $\mathbf{r}_j$ are not equal, $x_i \neq x_j$. Therefore we consider an approximate formulation as follows. Let the vector from the center of the array to the source be $\mathbf{r} = r\hat{\mathbf{r}}$, so that r is the propagation distance of the sound wave to the array center and $\hat{\mathbf{r}}$ is the unit vector in the direction of $\mathbf{r}$. The azimuthal and elevational AOAs, ϕ and θ, respectively, are measured with respect to the array center, so that $\hat{\mathbf{r}} = [\cos\phi\cos\theta, \sin\phi\cos\theta, \sin\theta]$. Let $\mathbf{r}_i' = [x_i', y_i', z_i']$ be the vector from the center of the array to the ith sensor, $\mathbf{r}_i = \mathbf{r} - \mathbf{r}_i'$ be the vector from the ith sensor to the source, and $\boldsymbol{\rho}_{ij} = \mathbf{r}_i - \mathbf{r}_j = \mathbf{r}_j' - \mathbf{r}_i'$ be the vector between the jth and ith sensors. An illustration is given in Fig. 1.

For oblique incidence, we must take care in deriving approximations for the moments. A consistent treatment of both the phase terms and decay terms of the moments is necessary to ensure that the covariance matrix $\mathbf{C}_p$ is nonsingular. We consider the case when $r \gg r_i'$ for every i, i.e., when the propagation distance to the array center is much larger than the baseline of the array. For this case, we expand $p_{\mathrm{H}}(\mathbf{r}_i)$ about r up to first order in $1/r$. In doing so, we assume that the spherical spreading of the pressure amplitude across the array is nearly constant and may be approximated by its value at the array center. We refer to this approximation as the extended SAA, and use a tilde, $\sim$, to denote these quantities:

$$\tilde{p}_{\mathrm{H}}(\mathbf{r}_i) = \tilde{p}_0(r_i)\ \exp(\mathrm{i}\tilde{\Phi}_i), \quad \text{where}$$

$$\tilde{p}_0(r_i) \approx \frac{\mathcal{A} r_0}{r} \equiv p_0(r) \quad \text{and} \tag{8}$$

$$\tilde{\Phi}_i \approx k\left[r - \hat{\mathbf{r}}\cdot\mathbf{r}_i' + \frac{r_i'^2 - (\hat{\mathbf{r}}\cdot\mathbf{r}_i')^2}{2r} \right] + \chi.$$

For the first moment at the ith sensor, we approximate that the decay of the moment due to the random medium is also nearly constant across the array and may be approximated by its value at the array center. Thus for oblique incidence

$$\mu_i \approx p_0(r) e^{-\gamma r} e^{\mathrm{i}\tilde{\Phi}_i}. \tag{9}$$

Similarly, the second moment for oblique incidence is approximated to be

$$\langle p_i p_j^* \rangle \approx p_0^2(r) e^{-\alpha(\rho_{ij})r} e^{\mathrm{i}\tilde{\Phi}_{ij}}, \tag{10}$$

where $\tilde{\Phi}_{ij}$ is the difference in the total phase

$$\tilde{\Phi}_{ij} \equiv \tilde{\Phi}_i - \tilde{\Phi}_j. \tag{11}$$

We are thereby assuming that for every i and j, the extinction coefficient of the second moment satisfies

$$\alpha(\rho_{ij}^{\perp}) \approx \alpha(\rho_{ij}), \tag{12}$$

where $\rho_{ij}^{\perp}$ is the magnitude of the component of $\boldsymbol{\rho}_{ij}$ that is transverse to $\mathbf{r}$, $\rho_{ij}^{\perp} = |\boldsymbol{\rho}_{ij} \times \hat{\mathbf{r}}|$.

In Eqs. (9) and (10), the factors of r in the extinction terms are necessary to ensure consistency between the moments. That is, the covariance matrix is

$$[\mathbf{C}_p]_{ij} = \langle p_i p_j^* \rangle - \mu_i \mu_j^* = p_0^2(r)[e^{-\alpha(\rho_{ij})r} - e^{-2\gamma r}] e^{\mathrm{i}\tilde{\Phi}_{ij}}, \tag{13}$$

which becomes, in the limit $\rho_{ij} \to \infty$,

$$[\mathbf{C}_p]_{ij} \to p_0^2(r)[e^{-2\gamma r} - e^{-2\gamma r}] e^{\mathrm{i}\tilde{\Phi}_{ij}} = 0, \tag{14}$$

as it should. Because of the approximations made in deriving the moments for oblique incidence, we limit the investigation in this paper to near-normal incidence at a planar array. At normal incidence to a planar array, the wave front arrives normal to the array center (parallel to $\mathbf{r}$) and $x_i = x_j = r$ for every i and j. Therefore, at normal incidence, $\tilde{\Phi}_i = \breve{\Phi}_i$, $\tilde{p}_0(r_i) = \breve{p}_0(r_i)$, and the results for the moments derived by Ostashev [Eqs. (5) and (6)] are exactly recovered. The approximations for the moments derived in this section are equivalent to assuming that the largest variations in the moments from normal incidence to near-normal incidence are

due to the changes in phases, rather than to changes in magnitudes.

For the present treatment, the *i-j* element of the mutual coherence function (MCF) matrix is

$$\Gamma_{ij}=|\langle p_i p_j^*\rangle|/p_0^2(r)=e^{-\alpha(\rho_{ij})r}. \tag{15}$$

The minimum value of the MCF occurs when $\rho_{ij}=\infty$, and we denote this quantity by $\Gamma_{\min}$,

$$\Gamma_{\min}=\Gamma_{ij}(\rho_{ij}=\infty)=e^{-2\gamma r}. \tag{16}$$

If we define a vector of the phases

$$s=[e^{i\tilde{\Phi}_1},\ e^{i\tilde{\Phi}_2},\ \ldots,\ e^{i\tilde{\Phi}_N}]^{\mathrm{T}} \tag{17}$$

and the matrix

$$\boldsymbol{\mathcal{S}}=s\otimes s^{\dagger},\ \ \mathcal{S}_{ij}=\exp(i\tilde{\Phi}_{ij}), \tag{18}$$

where $\otimes$ is the (right) Kronecker product, we may then write

$$\boldsymbol{\mu}=p_0(r)\Gamma_{\min}^{1/2}s, \tag{19}$$

$$\mathbf{C}_p=p_0^2(r)\Gamma\odot\boldsymbol{\mathcal{S}}-p_0^2(r)\Gamma_{\min}\boldsymbol{\mathcal{S}}, \tag{20}$$

where $\odot$ is the Hadamard product[16] (element-by-element multiplication). This mathematical expression is useful for computational purposes. As we are approximating that the decay of the moments (due to both spherical spreading and extinction by the medium) is constant across the array, we may think of s and $\boldsymbol{\mathcal{S}}$ as a steering vector and a steering matrix that involve only the phases of the wave front.

C. Turbulence model

The extinction coefficients depend on the structure of the random medium. For an incident spherical wave, the extinction coefficient for the second moment[15,17,18]

$$\alpha(\rho)=2\pi k^2\int_0^1[f(0)-f(\rho u)]du, \tag{21}$$

where f is the two-dimensional (2D), or projected, correlation function for the sound-speed fluctuations. Since $f(\rho)\rightarrow 0$ as $\rho\rightarrow\infty$,

$$\alpha(\rho=\infty)=2\gamma=2\pi k^2 f(0). \tag{22}$$

Note that this limit [Eq. (22)] is the same for both an incident spherical wave [Eq. (21)] and an incident plane wave [Eq. (15) of Ref. 5]. Hence the minimum value of the mutual coherence function, $\Gamma_{\min}$ [Eq. (16)], is the same for both a plane wave and a spherical wave.

We use a von Kármán form for the 2D correlation functions. For a scalar field (such as sound-speed fluctuations induced in air by temperature and humidity fluctuations)

$$f_s(\rho,\varsigma^2,l)=\frac{2\varsigma^2 l}{\sqrt{\pi}\Gamma(\frac{1}{3})}\left(\frac{\rho}{2l}\right)^{5/6}K_{5/6}\left(\frac{\rho}{l}\right) \tag{23}$$

and for a vector field (such as fluctuations induced by wind velocity fluctuations)

$$f_v(\rho,\varsigma^2,l)=\frac{2\varsigma^2 l}{\sqrt{\pi}\Gamma(\frac{1}{3})}\left(\frac{\rho}{2l}\right)^{5/6}\left[K_{5/6}\left(\frac{\rho}{l}\right)-\frac{\rho}{2l}K_{1/6}\left(\frac{\rho}{l}\right)\right], \tag{24}$$

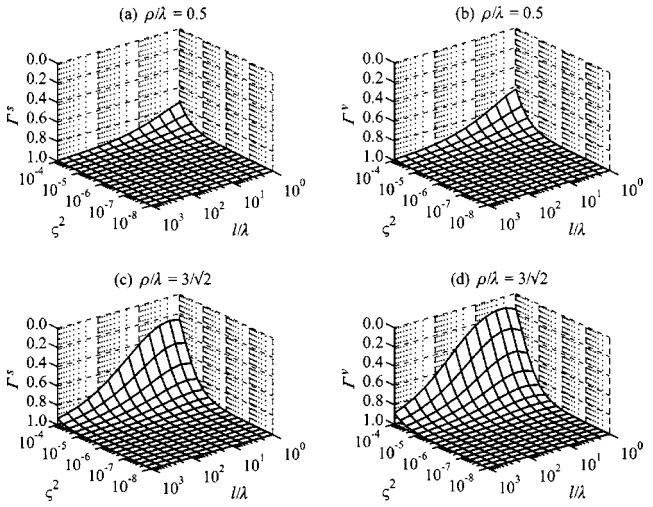

FIG. 2. Coherence for an incident spherical wave: (a) and (c) are for a scalar von Kármán spectrum; (b) and (d) are for a vector von Kármán spectrum. All calculations are for $r/\lambda=500$.

where $l=[\Gamma(1/3)\mathcal{L}]/[\sqrt{\pi}\Gamma(\frac{5}{6})]$ is a characteristic length scale of the turbulence, ς^2 is the index-of-refraction variance, $\Gamma(x)$ is the gamma function, and $K_\nu(x)$ is the modified Bessel function of order ν.[15,18]

In the limit that $\rho\rightarrow 0$, the 2D correlation functions for a scalar spectrum and a vector spectrum are equal. This limiting value is $f_{s,v}(\rho=0)=[\varsigma^2 l\Gamma(\frac{5}{6})]/[\sqrt{\pi}\Gamma(1/3)]$. Therefore the minimum value of the mutual coherence function, $\Gamma_{\min}$, is the same for both a scalar and a vector von Kármán spectrum, as well as for both plane- and spherical-wave propagation. $\Gamma_{\min}$ is plotted in Fig. 3 of Ref. 5 as a function of index-of-refraction variance, ς^2, and the characteristic length scale normalized by the wavelength, l/λ. Note the orientation of the axes: $\Gamma_{\min}$ decreases along the axis, l/λ decreases, and ς^2 increases. To avoid explicit wavelength dependence, normalized length scales are used throughout this paper.

The mutual coherence function (MCF) for an incident spherical wave is plotted in Fig. 2 as a function of ς^2 and l/λ, for both a scalar and a vector von Kármán spectrum. Again note the orientation of the axes. The MCFs are calculated for $r/\lambda=500$ and for $\rho/\lambda=0.5$ in Figs. 2(a) and 2(b) and for $\rho/\lambda=3/\sqrt{2}$ in Figs. 2(c) and 2(d). The behavior of the MCF for a spherical wave is similar to that of the plane wave (refer to Fig. 2 of Ref. 5): the coherence for both spectra decreases significantly when $\varsigma^2\sim 10^{-4}$ and $10<l/\lambda<1$; a larger sensor separation leads to a more rapid decrease in the MCFs; and for both sensor separations, the MCF for the vector spectrum is more sensitive to the changes in the turbulence parameters, and its minimum with respect to the turbulence parameters is smaller than that for the scalar spectrum. Therefore, based on the results from the plane-wave paper, we expect the behavior of the CRLBs of the AOAs for an incident spherical wave to be similar to that of the corresponding plane wave. However, as the MCF for the spherical wave is larger, the CRLBs for spherical-wave propagation should be smaller.

D. Cramer–Rao lower bound

Suppose that the $N\times 1$ random vector $\mathbf{s}$ is parametrized by the vector of *real* unknowns $\boldsymbol{\Theta}=[\Theta_1, \Theta_2, \ldots, \Theta_{\mathcal{N}}]^{\mathrm{T}}$. For an unbiased estimator $\hat{\boldsymbol{\Theta}}$, the Cramer-Rao theorem [11,12] gives

$$\langle(\Theta_\nu-\hat{\Theta}_\nu)^2\rangle \geqslant [\mathbf{J}^{-1}(\boldsymbol{\Theta})]_{\nu\nu}, \tag{25}$$

where $\mathbf{J}(\boldsymbol{\Theta})$ is the $\mathcal{N}\times\mathcal{N}$ Fisher information matrix (FIM). The CRLB of the νth parameter estimate is $[\mathbf{J}^{-1}(\boldsymbol{\Theta})]_{\nu\nu}$. If $\mathbf{s}\sim\mathcal{CN}_N(\boldsymbol{\mu}, \mathbf{C})$, the λ-ν element of the FIM is[11]

$$J_{\lambda\nu}=M\,\mathrm{tr}\left(\mathbf{C}^{-1}\frac{\partial\mathbf{C}}{\partial\Theta_\lambda}\mathbf{C}^{-1}\frac{\partial\mathbf{C}}{\partial\Theta_\nu}\right)+2M\,\mathrm{Re}\left(\frac{\partial\boldsymbol{\mu}^\dagger}{\partial\Theta_\lambda}\mathbf{C}^{-1}\frac{\partial\boldsymbol{\mu}}{\partial\Theta_\nu}\right), \tag{26}$$

for M independent and identically distributed data sets. Let us use the convention that $\lambda,\nu\in[1, 2, ..., \mathcal{N}]$ are the indices on the parameters and $i,j\in[1, 2, ..., N]$ are the indices on the sensors.

We define $\sigma_\nu=\sqrt{[\mathbf{J}^{-1}]_{\nu\nu}}$ and refer to either σ_ν (standard deviation) or σ_ν^2 (variance) as the CRLB of Θ_ν, as the meaning should be evident from the units involved. By definition, the partial correlation between the λth and νth parameter estimates is

$$\zeta_{\lambda\nu}\equiv\frac{J_{\lambda\nu}^2}{J_{\lambda\lambda}J_{\nu\nu}},\quad 0\leqslant\zeta_{\lambda\nu}\leqslant 1. \tag{27}$$

When $\zeta_{\lambda\nu}=1$, the estimates of Θ_λ and Θ_ν are fully correlated, the FIM is rank deficient, and hence neither parameter can be estimated. When $J_{\lambda\nu}=0$, the partial correlation is zero. (In some instances, $J_{\lambda\nu}\ll J_{\lambda\lambda}$, $J_{\nu\nu}$ so that $\zeta_{\lambda\nu}\ll 1$, and the partial correlation may be approximated as zero.) However, $J_{\lambda\nu}=0$ is not a sufficient condition for the estimates of Θ_λ and Θ_ν to decouple if there are additional unknown parameters. For example, consider

$$\mathbf{J}=\begin{bmatrix} J_{11} & J_{12} & 0 \\ J_{12} & J_{22} & J_{23} \\ 0 & J_{23} & J_{33}\end{bmatrix}. \tag{28}$$

For this case,

$$\sigma_1^2=\frac{1}{J_{11}}\frac{1-\zeta_{23}}{1-\zeta_{12}-\zeta_{23}}. \tag{29}$$

Therefore, even though $J_{13}=0$, as $J_{12}\neq 0$ and $J_{23}\neq 0$, the CRLBs of Θ_1 and Θ_3 are correlated.

Therefore, the CRLB of Θ_λ will decouple from the CRLBs of the remaining parameters if $J_{\lambda\nu}=0$ for every ν, $\nu\neq\lambda$. In this case the CRLB of Θ_λ attains its minimum value of $\sigma_{\lambda_0}^2=1/J_{\nu\nu}$, i.e., the CRLB when Θ_ν is the only unknown. As the number of unknowns increases, σ_ν^2 will increase. Ideally, we would like to determine conditions under which $J_{\lambda\nu}=0$ for every $\nu\neq\lambda$, so that the FIM is a diagonal matrix. This is seldom feasible. However, in some instances the FIM will be block diagonal, in which case only the subspace of interest need be calculated.

E. Fisher information of theoretical model

As discussed in Sec. II A, we are modeling the total received signal, $\mathbf{s}$, as a complex Gaussian random variable, $\mathbf{s}\sim\mathcal{CN}_N(\boldsymbol{\mu}, \mathbf{C})$. We write the elements of the mean vector, $\boldsymbol{\mu}$, as

$$\mu_i=p_0(r)e^{-\gamma r}e^{i\tilde{\Phi}_i}=p_0(r)\Gamma_{\min}^{1/2}e^{i\tilde{\Phi}_i} \tag{30}$$

and of the total covariance matrix, $\mathbf{C}$, as

$$\begin{aligned} C_{ij}&=p_0^2(r)\left\{[e^{-\alpha(\rho_{ij})r}-e^{-2\gamma r}]e^{i\tilde{\Phi}_{ij}}+\frac{\sigma_n^2}{p_0^2(r)}\delta_{ij}\right\} \\ &=p_0^2(r)\left[(\Gamma_{ij}-\Gamma_{\min})e^{i\tilde{\Phi}_{ij}}+\frac{\sigma_n^2}{p_0^2(r)}\delta_{ij}\right], \end{aligned} \tag{31}$$

where δ_{ij} is the Kronecker delta function. The FI of the theoretical model may then be determined by substituting Eqs. (30) and (31) into Eq. (26).

The signal-to-noise variance ratio is $\mathrm{L}=\langle p_{\mathrm{H}}(r_i)\, p_{\mathrm{H}}^*(r_i)\rangle/\langle n_i\, n_i^*\rangle$. It is related to the signal-to-noise ratio in decibels (SNR) by $L=10^{\mathrm{SNR}/10}$. For our signal model, $\mathrm{L}=p_0^2(r)/\sigma_n^2$. Since for a spherical wave $p_0(r)$ is dependent upon r, we consider L_0, the signal-to-noise variance ratio at a distance r_0, as the unknown. Then $\sigma_n^2=(\mathcal{A}r_0)^2/(\mathrm{L}_0 r_0^2)$. All of the terms of $\mathcal{A}r_0$ cancel in the FI, therefore the explicit value of $\mathcal{A}r_0$ is not needed.

The FI may be calculated from Eq. (26) for those parameters we wish to consider as unknowns: the azimuth (ϕ), elevation (θ), phase of the source (χ), propagation distance (r), turbulence length scale (l), index-of-refraction variance (s^2), and signal-to-noise variance ratio (L_0) evaluated at the reference point r_0. It was shown in the plane-wave paper that the source phase χ must be treated as an unknown parameter when a nonzero mean is considered; therefore, χ must be treated as an unknown for the spherical-wave case as well. For brevity, the derivatives of the covariance matrix and mean with respect to the unknown parameter set are not presented here.

III. THEORETICAL RESULTS

Let us write the covariance matrix and mean as

$$\mathbf{C}=\mathbf{X}\odot\boldsymbol{\mathcal{S}}\ \text{ and }\ \boldsymbol{\mu}=\mathbf{m}\odot s, \tag{32}$$

where $\boldsymbol{\mathcal{S}}$ and s are the steering matrix and steering vector previously defined, $\mathbf{X}$ is the real symmetric matrix given by $X_{ij}=C_{ij}/e^{i\tilde{\Phi}_{ij}}$, and $\mathbf{m}$ is the real column vector given by $m_i=\mu_i/e^{i\tilde{\Phi}_i}$. Physically, X_{ij} is the covariance amplitude between the i and jth sensors, and m_i is the amplitude of the mean at the ith sensor. Matrices and vectors that may be decomposed into these forms may also be written as

$$\mathbf{C}=\mathbf{S}\mathbf{X}\mathbf{S}^\dagger\ \text{ and }\ \boldsymbol{\mu}=\mathbf{S}\mathbf{m}, \tag{33}$$

where $\mathbf{S}$ is a diagonal matrix of the phases, $\mathbf{S}=\mathrm{diag}[e^{i\tilde{\Phi}_1}, e^{i\tilde{\Phi}_2}, \ldots, e^{i\tilde{\Phi}_N}]$. Note that $\mathbf{S}$ is unitary, $\mathbf{S}^{-1}=\mathbf{S}^\dagger$, and that

$$\frac{\partial \mathbf{S}}{\partial \Theta_\lambda} = i\mathbf{S}\mathbf{D}_\lambda \quad \text{where} \quad \mathbf{D}_\lambda = \text{diag}\left[\frac{\partial \tilde{\Phi}_1}{\partial \Theta_\lambda}, \frac{\partial \tilde{\Phi}_2}{\partial \Theta_\lambda}, \ldots, \frac{\partial \tilde{\Phi}_N}{\partial \Theta_\lambda}\right]. \tag{34}$$

Using these properties, the commutation of diagonal matrices, and the properties of the trace, it can be shown that

$$\begin{aligned} J_{\lambda\nu} &= 2M\,\text{tr}(\mathbf{D}_\lambda \mathbf{X}\mathbf{D}_\nu \mathbf{X}^{-1}) - 2M\,\text{tr}(\mathbf{D}_\lambda \mathbf{D}_\nu) \\ &\quad + M\,\text{tr}\left(\mathbf{X}^{-1}\frac{\partial \mathbf{X}}{\partial \Theta_\lambda}\mathbf{X}^{-1}\frac{\partial \mathbf{X}}{\partial \Theta_\nu}\right) + 2M\frac{\partial \mathbf{m}^{\mathrm{T}}}{\partial \Theta_\lambda}\mathbf{X}^{-1}\frac{\partial \mathbf{m}}{\partial \Theta_\nu} \\ &\quad + 2M\mathbf{m}^{\mathrm{T}}\mathbf{D}_\lambda \mathbf{X}^{-1}\mathbf{D}_\nu \mathbf{m}. \end{aligned} \tag{35}$$

There are three distinct contributions: (*i*) The first, second, and fifth terms only have derivatives of the phase terms, $\tilde{\Phi}_i$'s. (*ii*) The third term only has derivatives of the covariance amplitude, **X**. (*iii*) The fourth term only has derivatives of the mean amplitude, **m**. This observation provides insight into the partial correlations.

The CRLBs of parameters that appear only in the phase terms, $\tilde{\Phi}_i$'s, can only be correlated to the CRLBs of other parameters that also appear in the phase terms (i.e., in the steering vector). Similarly, the CRLBs of parameters that appear only in the covariance amplitude matrix, **X**, can only be correlated to the CRLBs of other parameters that also appear in **X**. Likewise for parameters that only appear in the mean amplitude vector, **m**. Hence, if the phase terms, $\tilde{\Phi}_i$'s, are dependent upon parameters upon which **X** and **m** are independent, then the FIM is block diagonal, and only the subspace of interest need be calculated.

For the problem at hand, $\tilde{\Phi}_i$ is dependent upon ϕ, θ, χ, and r; **X** is dependent upon r, ℓ, ς^2, and L_0; and **m** is dependent upon r, ℓ, and ς^2. If all of these parameters are unknown, the FIM takes the form

$$\mathbf{J} = \begin{bmatrix} J_{\phi\phi} & J_{\phi\theta} & J_{\phi\chi} & J_{\phi r} & 0 & 0 & 0 \\ J_{\phi\theta} & J_{\theta\theta} & J_{\theta\chi} & J_{\theta r} & 0 & 0 & 0 \\ J_{\phi\chi} & J_{\theta\chi} & J_{\chi\chi} & J_{\chi r} & 0 & 0 & 0 \\ J_{\phi r} & J_{\theta r} & J_{\chi r} & J_{rr} & J_{r\ell} & J_{r\varsigma^2} & J_{r\mathrm{L}_0} \\ 0 & 0 & 0 & J_{r\ell} & J_{\ell\ell} & J_{\ell\varsigma^2} & J_{\ell\mathrm{L}_0} \\ 0 & 0 & 0 & J_{r\varsigma^2} & J_{\ell\varsigma^2} & J_{\varsigma^2\varsigma^2} & J_{\varsigma^2\mathrm{L}_0} \\ 0 & 0 & 0 & J_{r\mathrm{L}_0} & J_{\ell\mathrm{L}_0} & J_{\varsigma^2\mathrm{L}_0} & J_{\mathrm{L}_0\mathrm{L}_0} \end{bmatrix}. \tag{36}$$

Therefore, for the spherical-wave case, the FIM is not block diagonal, and the FIM must be calculated for the entire unknown parameter set. However, if conditions can be determined for which the partial correlations $\zeta_{\phi r}$, $\zeta_{\theta r}$, $\zeta_{\theta\chi}$, and $\zeta_{\theta\chi}$ are zero, or $\ll 1$, then the FIM for the subspace generated by ϕ and θ need only be calculated.

Also notice that there is no explicit dependence on $\tilde{\Phi}_i$ in Eq. (35), only on its derivatives. Therefore, for $\Theta_\nu = \chi$, $\mathbf{D}_\nu = \mathbf{I}_N$, and hence **J** has no dependence on χ. This is an expected result, as the actual value of the phase of the source should not affect our ability to estimate the other parameters.

Equation (35) is valid for any complex Gaussian process in which the equations in (33) hold. Therefore, it is also applicable to the previous plane-wave study of Ref. 5. Equation (35) may also be applied to the study by Song and Ritcey[9] when considering a single source: In their analysis the only dependence on the AOA is in the phase terms; therefore for a single source, the estimate of the AOA is not correlated to the estimate of the noise variance.

A. No turbulence

Due to the complexity of Eq. (35), it is easiest to begin by examining the case of no turbulence.

1. Full spherical wave

In the absence of turbulence, not considering the SAA for the present, the mean and covariance of the total received signal **s** are

$$\begin{aligned} \boldsymbol{\mu} &= [p_0(r_1)e^{\mathrm{i}\Phi_1},\ p_0(r_2)e^{\mathrm{i}\Phi_2},\ \ldots,\ p_0(r_N)e^{\mathrm{i}\Phi_N}]^{\mathrm{T}}, \\ \mathbf{C} &= \sigma_n^2 \mathbf{I}_N. \end{aligned} \tag{37}$$

The elements of the FIM are

$$\begin{aligned} J_{\lambda\nu} &= \frac{MN}{\sigma_n^4}\frac{\partial \sigma_n^2}{\partial \Theta_\lambda}\frac{\partial \sigma_n^2}{\partial \Theta_\nu} + \frac{2M}{\sigma_n^2} \\ &\quad \times \sum_{i=1}^{N}\left[p_0^2(r_i)\frac{\partial \Phi_i}{\partial \Theta_\lambda}\frac{\partial \Phi_i}{\partial \Theta_\nu} + \frac{\partial p_0(r_i)}{\partial \Theta_\lambda}\frac{\partial p_0(r_i)}{\partial \Theta_\nu}\right]. \end{aligned} \tag{38}$$

If the azimuth, ϕ, elevation, θ, and phase of the source, χ, are the unknowns, then the elements of the FIM are

$$J_{\phi\phi} = \frac{2M}{\sigma_n^2}\sum_{i=1}^{N}\left(\frac{\mathcal{A}^2 k^2 r_0^2 r^2}{r_i^4} + \frac{\mathcal{A}^2 r_0^2 r^2}{r_i^6}\right)\left[\frac{\partial(\hat{\mathbf{r}}\cdot\mathbf{r}_i')}{\partial\phi}\right]^2, \tag{39}$$

$$J_{\theta\theta} = \frac{2M}{\sigma_n^2}\sum_{i=1}^{N}\left(\frac{\mathcal{A}^2 k^2 r_0^2 r^2}{r_i^4} + \frac{\mathcal{A}^2 r_0^2 r^2}{r_i^6}\right)\left[\frac{\partial(\hat{\mathbf{r}}\cdot\mathbf{r}_i')}{\partial\theta}\right]^2, \tag{40}$$

$$J_{\chi\chi} = \frac{2M}{\sigma_n^2}\sum_{i=1}^{N}\frac{\mathcal{A}^2 r_0^2}{r_i^2}, \tag{41}$$

$$J_{\phi\theta} = \frac{2M}{\sigma_n^2}\sum_{i=1}^{N}\left(\frac{\mathcal{A}^2 k^2 r_0^2 r^2}{r_i^4} + \frac{\mathcal{A}^2 r_0^2 r^2}{r_i^6}\right)\frac{\partial(\hat{\mathbf{r}}\cdot\mathbf{r}_i')}{\partial\phi}\frac{\partial(\hat{\mathbf{r}}\cdot\mathbf{r}_i')}{\partial\theta}, \tag{42}$$

$$J_{\phi\chi} = -\frac{2M}{\sigma_n^2}\sum_{i=1}^{N}\frac{\mathcal{A}^2 k r_0^2 r}{r_i^3}\frac{\partial(\hat{\mathbf{r}}\cdot\mathbf{r}_i')}{\partial\phi}, \tag{43}$$

$$J_{\theta\chi} = -\frac{2M}{\sigma_n^2}\sum_{i=1}^{N}\frac{\mathcal{A}^2 k r_0^2 r}{r_i^3}\frac{\partial(\hat{\mathbf{r}}\cdot\mathbf{r}_i')}{\partial\theta}, \tag{44}$$

where

$$\hat{\mathbf{r}}\cdot\mathbf{r}_i' = x_i'\cos\phi\cos\theta + y_i'\sin\phi\cos\theta + z_i'\sin\theta, \tag{45}$$

$$\frac{\partial(\hat{\mathbf{r}}\cdot\mathbf{r}_i')}{\partial\phi} = -x_i'\sin\phi\cos\theta + y_i'\cos\phi\cos\theta, \tag{46}$$

$$\frac{\partial(\hat{\mathbf{r}}\cdot\mathbf{r}_i')}{\partial\theta} = -x_i'\cos\phi\sin\theta - y_i'\sin\phi\sin\theta + z_i'\cos\theta. \tag{47}$$

For the estimates to decouple, the off-diagonal elements of the FIM must be zero. Thus in order for the estimates of ϕ

and θ to decouple from the estimate of χ, for every ϕ and θ, we must have

$$\sum_{i=1}^{N} \frac{x_i'}{r_i^3} = \sum_{i=1}^{N} \frac{y_i'}{r_i^3} = \sum_{i=1}^{N} \frac{z_i'}{r_i^3} = 0. \tag{48}$$

Therefore, unlike the plane-wave case, there is no simple array geometry that will result in the decoupling of the estimates of the AOAs from the estimate of the phase angle. The conditions for the estimates of ϕ and θ to decouple are also, in general, unattainable in practice:

$$\sum_{i=1}^{N} x_i'^2 \left(\frac{k^2}{r_i^4} + \frac{1}{r_i^6} \right) = \sum_{i=1}^{N} y_i'^2 \left(\frac{k^2}{r_i^4} + \frac{1}{r_i^6} \right) \tag{49}$$

and

$$\sum_{i=1}^{N} x_i' y_i' \left(\frac{k^2}{r_i^4} + \frac{1}{r_i^6} \right) = \sum_{i=1}^{N} x_i' z_i' \left(\frac{k^2}{r_i^4} + \frac{1}{r_i^6} \right) = \sum_{i=1}^{N} y_i' z_i' \left(\frac{k^2}{r_i^4} + \frac{1}{r_i^6} \right) = 0. \tag{50}$$

Suppose now that the propagation distance, r, is also unknown. Then

$$J_{rr} = \frac{2M}{\sigma_n^2} \sum_{i=1}^{N} \left(\frac{\mathcal{A}^2 k^2 r_0^2}{r_i^4} + \frac{\mathcal{A}^2 r_0^2}{r_i^6} \right) (r - \hat{\mathbf{r}} \cdot \mathbf{r}_i')^2, \tag{51}$$

$$J_{r\phi} = -\frac{2M}{\sigma_n^2} \sum_{i=1}^{N} \left(\frac{\mathcal{A}^2 k^2 r_0^2 r}{r_i^4} + \frac{\mathcal{A}^2 r_0^2 r}{r_i^6} \right) (r - \hat{\mathbf{r}} \cdot \mathbf{r}_i') \frac{\partial (\hat{\mathbf{r}} \cdot \mathbf{r}_i')}{\partial \phi}, \tag{52}$$

$$J_{r\theta} = -\frac{2M}{\sigma_n^2} \sum_{i=1}^{N} \left(\frac{\mathcal{A}^2 k^2 r_0^2 r}{r_i^4} + \frac{\mathcal{A}^2 r_0^2 r}{r_i^6} \right) (r - \hat{\mathbf{r}} \cdot \mathbf{r}_i') \frac{\partial (\hat{\mathbf{r}} \cdot \mathbf{r}_i')}{\partial \theta}, \tag{53}$$

$$J_{r\chi} = \frac{2M}{\sigma_n^2} \sum_{i=1}^{N} \frac{\mathcal{A}^2 k r_0^2}{r_i^3} (r - \hat{\mathbf{r}} \cdot \mathbf{r}_i'). \tag{54}$$

Because of the factor r in the second term in parentheses, we see that the estimate of r will always be correlated to the estimates of ϕ, θ, and χ, regardless of array geometry.

2. Extended small-angle approximation

Let us now consider results for the extended SAA, i.e., the approximations $\tilde{p}_0(r_i)$ and $\tilde{\Phi}_i$ given in Eq. (8). The elements of the FIM are now given by

$$J_{\lambda\nu} = \frac{MN}{\sigma_n^4} \frac{\partial \sigma_n^2}{\partial \Theta_\lambda} \frac{\partial \sigma_n^2}{\partial \Theta_\nu} + \frac{2MN}{\sigma_n^2} \frac{\partial p_0(r)}{\partial \Theta_\lambda} \frac{\partial p_0(r)}{\partial \Theta_\nu} + \frac{2Mp_0^2(r)}{\sigma_n^2} \sum_{i=1}^{N} \frac{\partial \tilde{\Phi}_i}{\partial \Theta_\lambda} \frac{\partial \tilde{\Phi}_i}{\partial \Theta_\nu}. \tag{55}$$

Specifically, when the unknown parameter vector is $\boldsymbol{\Theta} = [\phi, \theta, r, \chi]^{\mathrm{T}}$, the elements of the FIM are

$$J_{\phi\phi} = \frac{2Mk^2 p_0^2(r)}{\sigma_n^2} \sum_{i=1}^{N} \left[\left(1 + \frac{\hat{\mathbf{r}} \cdot \mathbf{r}_i'}{r} \right) \frac{\partial (\hat{\mathbf{r}} \cdot \mathbf{r}_i')}{\partial \phi} \right]^2, \tag{56}$$

$$J_{\theta\theta} = \frac{2Mk^2 p_0^2(r)}{\sigma_n^2} \sum_{i=1}^{N} \left[\left(1 + \frac{\hat{\mathbf{r}} \cdot \mathbf{r}_i'}{r} \right) \frac{\partial (\hat{\mathbf{r}} \cdot \mathbf{r}_i')}{\partial \theta} \right]^2, \tag{57}$$

$$J_{\chi\chi} = \frac{2MNp_0^2(r)}{\sigma_n^2}, \tag{58}$$

$$J_{rr} = \frac{2MNp_0^2(r)}{r^2 \sigma_n^2} + \frac{2Mk^2 p_0^2(r)}{\sigma_n^2} \sum_{i=1}^{N} \left[1 - \frac{r_i'^2 - (\hat{\mathbf{r}} \cdot \mathbf{r}_i')^2}{2r^2} \right]^2, \tag{59}$$

$$J_{\phi\theta} = \frac{2Mk^2 p_0^2(r)}{\sigma_n^2} \sum_{i=1}^{N} \left[\left(1 + \frac{\hat{\mathbf{r}} \cdot \mathbf{r}_i'}{r} \right) \frac{\partial (\hat{\mathbf{r}} \cdot \mathbf{r}_i')}{\partial \phi} \right] \times \left[\left(1 + \frac{\hat{\mathbf{r}} \cdot \mathbf{r}_i'}{r} \right) \frac{\partial (\hat{\mathbf{r}} \cdot \mathbf{r}_i')}{\partial \theta} \right], \tag{60}$$

$$J_{\phi\chi} = -\frac{2Mkp_0^2(r)}{\sigma_n^2} \sum_{i=1}^{N} \left[\left(1 + \frac{\hat{\mathbf{r}} \cdot \mathbf{r}_i'}{r} \right) \frac{\partial (\hat{\mathbf{r}} \cdot \mathbf{r}_i')}{\partial \phi} \right], \tag{61}$$

$$J_{\theta\chi} = -\frac{2Mkp_0^2(r)}{\sigma_n^2} \sum_{i=1}^{N} \left[\left(1 + \frac{\hat{\mathbf{r}} \cdot \mathbf{r}_i'}{r} \right) \frac{\partial (\hat{\mathbf{r}} \cdot \mathbf{r}_i')}{\partial \theta} \right], \tag{62}$$

$$J_{r\phi} = -\frac{2Mk^2 p_0^2(r)}{\sigma_n^2} \sum_{i=1}^{N} \left[\left(1 + \frac{\hat{\mathbf{r}} \cdot \mathbf{r}_i'}{r} \right) \frac{\partial (\hat{\mathbf{r}} \cdot \mathbf{r}_i')}{\partial \phi} \right] \times \left[1 - \frac{r_i'^2 - (\hat{\mathbf{r}} \cdot \mathbf{r}_i')^2}{2r^2} \right], \tag{63}$$

$$J_{r\theta} = -\frac{2Mk^2 p_0^2(r)}{\sigma_n^2} \sum_{i=1}^{N} \left[\left(1 + \frac{\hat{\mathbf{r}} \cdot \mathbf{r}_i'}{r} \right) \frac{\partial (\hat{\mathbf{r}} \cdot \mathbf{r}_i')}{\partial \theta} \right] \times \left[1 - \frac{r_i'^2 - (\hat{\mathbf{r}} \cdot \mathbf{r}_i')^2}{2r^2} \right], \tag{64}$$

$$J_{r\chi} = \frac{2Mkp_0^2(r)}{\sigma_n^2} \sum_{i=1}^{N} \left[1 - \frac{r_i'^2 - (\hat{\mathbf{r}} \cdot \mathbf{r}_i')^2}{2r^2} \right]. \tag{65}$$

Notice that the summations on the lowest order terms (zeroth order in $1/r$) are the same as those for the plane-wave case [compare to Eqs. (31)–(36) in Sec. III C of Ref. 5]. Consider first the partial correlation between the azimuth, ϕ, and the phase of the source, χ. From the plane-wave paper, we know that the zeroth-order terms in $J_{\phi\chi}$ will be zero for every value of ϕ and θ if the array center is located at the origin (i.e., $\Sigma_i x_i' = \Sigma_i y_i' = \Sigma_i z_i' = 0$). However, the conditions for the first order term to be zero for every value of ϕ and θ are $\Sigma_i y_i'^2 = \Sigma_i x_i'^2 = 0$ and $\Sigma_i x_i' y_i' = \Sigma_i x_i' z_i' = \Sigma_i y_i' z_i' = 0$. These are the same conditions that were found for the estimates of ϕ and θ to decouple in the plane-wave case. It was demonstrated in that paper that, if a planar array satisfies these conditions, then the CRLB of ϕ is infinite at normal incidence. Therefore, for the consideration in this paper (a spherical wave in the SAA arriving at near-normal incidence to a planar array) these conditions again cannot be satisfied. Therefore, $\zeta_{\phi\chi}$, and, analogously, $\zeta_{\theta\chi}$, $\zeta_{r\phi}$, and $\zeta_{r\theta}$, cannot be zero; however, these correlations may be minimized by satisfying the zeroth-order conditions. In other words, we can use the results from the plane-wave case to minimize these partial correlations so that they decay by $1/r$.

B. Turbulence

Let us now consider propagation through atmospheric turbulence. For multi-dimensional receiving arrays, a general, analytical treatment of Eq. (35) is beyond the scope of the present paper. However, we can derive an analytical solution for a simple, two-element array.

1. Two-element array

Let us consider a two-element array, with sensor separation d. In the plane-wave paper, a general solution for the FI was derived for a two-element array. That analysis is also valid here.

Let the unknown parameter set consist of the angle of arrival ϕ and the phase of the source χ. Let $a=C_{11}$, $b=|C_{12}|$, and $c^{1/2}=|\mu_1|=|\mu_2|$, where μ_i and C_{ij} are as defined in Eqs. (30) and (31). As $\partial\tilde{\Phi}_i/\partial\chi=1$ for every i, from Eqs. (45) and (46) of Ref. 5, we know

$$J_{\phi\phi}=\frac{2Mb^2}{a^2-b^2}\left(\frac{\partial\tilde{\Phi}_{12}}{\partial\phi}\right)^2+\frac{2Mc}{a^2-b^2}\times\left\{a\left[\left(\frac{\partial\tilde{\Phi}_1}{\partial\phi}\right)^2+\left(\frac{\partial\tilde{\Phi}_2}{\partial\phi}\right)^2\right]-2b\,\frac{\partial\tilde{\Phi}_1}{\partial\phi}\,\frac{\partial\tilde{\Phi}_2}{\partial\phi}\right\}, \quad (66)$$

$$J_{\phi\chi}=\frac{2Mc}{a+b}\left(\frac{\partial\tilde{\Phi}_1}{\partial\phi}+\frac{\partial\tilde{\Phi}_2}{\partial\phi}\right), \quad (67)$$

$$J_{\chi\chi}=\frac{4Mc}{a+b}. \quad (68)$$

Therefore, the CRLB of the angle of arrival ϕ is

$$\sigma_\phi^2=\frac{1}{J_{\phi\phi}-J_{\phi\chi}^2/J_{\chi\chi}} \quad (69)$$

$$=\frac{a^2-b^2}{M[2b^2+c(a+b)](\partial\tilde{\Phi}_{12}/\partial\phi)^2}. \quad (70)$$

From Eq. (67), we know that if $\partial\tilde{\Phi}_1/\partial\phi=-\partial\tilde{\Phi}_2/\partial\phi$, the estimates of ϕ and χ will decouple for any value of c. Now

$$J_{\phi\chi}=-\frac{2Mkc}{a+b}\left[\left(1+\frac{\hat{\mathbf{r}}\cdot\mathbf{r}_1'}{r}\right)\frac{\partial(\hat{\mathbf{r}}\cdot\mathbf{r}_1')}{\partial\phi}+\left(1+\frac{\hat{\mathbf{r}}\cdot\mathbf{r}_2'}{r}\right)\frac{\partial(\hat{\mathbf{r}}\cdot\mathbf{r}_2')}{\partial\phi}\right] \quad (71)$$

$$=\frac{2Mkc}{a+b}\left[(x_1'+x_2')\sin\phi-(y_1'+y_2')\cos\phi+\frac{x_1'^2+x_2'^2-y_1'^2-y_2'^2}{r}\cos\phi\sin\phi+\frac{x_1'y_1'+x_2'y_2'}{r}(\sin^2\phi-\cos^2\phi)\right]. \quad (72)$$

Therefore, in order for $J_{\phi\chi}$ to be zero for every value of ϕ and c, the following must hold

$$\text{zeroth order in } 1/r\text{:}\quad x_1'=-x_2' \text{ and } y_1'=-y_2', \quad (73)$$

$$\text{first order in } 1/r\text{:}\quad x_1'^2+x_2'^2=y_1'^2+y_2'^2 \text{ and } x_1'y_1'=-x_2'y_2'. \quad (74)$$

The zeroth order conditions are those found for the plane wave: the origin must be at the array center. However, only one of the two first order conditions in (74) can hold when (73) holds. Therefore, the estimates of ϕ and χ will always be correlated, but this correlation may be minimized by satisfying Eq. (73).

If $x_1'=x_2'=0$ and $y_1'=-y_2'=d/2$, then

$$J_{\phi\chi}=-\frac{Mkd^2c\cos\phi\sin\phi}{(a+b)r} \quad (75)$$

$$=-\frac{Mkd^2\Gamma_{\min}^2\sin 2\phi}{2(1+\Gamma-2\Gamma_{\min}^2+\sigma_n^2/p_0^2)r} \quad (76)$$

$$=-\frac{Mkd^2e^{-2\gamma r}\sin 2\phi}{2[1+e^{-\alpha(d/2)r}-2e^{-2\gamma r}+\sigma_n^2/p_0^2]r}. \quad (77)$$

At normal incidence, $\phi=0$, thus $J_{\phi\chi}$ is zero. Moreover, $J_{\phi\chi}$ decays by at least $e^{-2\gamma r}/r$; therefore at large values of r, $J_{\phi\chi}$ very rapidly approaches zero. And as

$$\left(\frac{\partial\tilde{\Phi}_{12}}{\partial\phi}\right)^2=k^2\left[\left(1+\frac{\hat{\mathbf{r}}\cdot\mathbf{r}_1'}{r}\right)\frac{\partial(\hat{\mathbf{r}}\cdot\mathbf{r}_1')}{\partial\phi}-\left(1+\frac{\hat{\mathbf{r}}\cdot\mathbf{r}_2'}{r}\right)\frac{\partial(\hat{\mathbf{r}}\cdot\mathbf{r}_2')}{\partial\phi}\right]^2=k^2d^2\cos^2\phi, \quad (78)$$

it follows that

$$\sigma_\phi^2=\frac{a^2-b^2}{Mk^2d^2\cos^2\phi\,[2b^2+c(a+b)]} \quad (79)$$

$$=\frac{1-\Gamma^2-2\Gamma_{\min}(1-\Gamma)+2(1-\Gamma_{\min})\sigma_n^2/p_0^2(r)+\sigma_n^4/p_0^4(r)}{Mk^2d^2\cos^2\phi\,\{2\Gamma^2-3\Gamma\Gamma_{\min}+\Gamma_{\min}[1+\sigma_n^2/p_0^2(r)]\}}. \quad (80)$$

This is the same as found for the plane wave, except that p_0 now has a $1/r$ dependence. Note that the first order corrections in the phase term cancelled.

IV. NUMERICAL RESULTS

In this section, we consider the numerical results for a planar array operating in turbulence. For the problem here, we assume that the wave is propagating near the x axis, take the array plane to be the yz plane, and take the origin to be at the center of the array. There are some caveats to the numerical analysis.

Numerical difficulties may arise when trying to invert the Fisher information matrix $\mathbf{J}$. There are several possible causes. First, $\mathbf{J}$ may be ill-conditioned due to scale discrepancies between the contributions to the FIM. As in the plane-wave case, this may be simply handled by constructing the diagonal matrix $\mathbf{D}$, whose elements are the inverse of the square-root of the diagonal elements of the FIM, $D_{\lambda\nu}=J_{\lambda\nu}^{-1/2}\delta_{\lambda\nu}$. The CRLBs are then determined from

$$\langle(\Theta_\nu-\hat{\Theta}_\nu)^2\rangle=[\mathbf{D}(\mathbf{DJD})^{-1}\mathbf{D}]_{\nu\nu}, \quad (81)$$

where the matrix **DJD** may usually be inverted by standard numerical techniques. Second, the matrix **DJD** may be still be ill-conditioned due to a high correlation between parameters; a singular value decomposition may then be used to invert **DJD**. Third, there may be a single parameter that cannot be estimated but whose estimate is not correlated to the estimates of other parameters; conditional testing may be used and the subspace of the FIM for the remaining parameters may be inverted. Lastly, the FIM may be ill-conditioned because there is not enough information to determine all the unknown parameters. These numerical issues are not difficult to address; however, the computation time may increase considerably.

Our primary interest is in determining the CRLBs of the angles of arrival ϕ and θ. Due to the large number of unknown parameters, it is easiest to understand the results by first examining some subspaces.

Consider first the unknown parameter vector $\mathbf{\Theta}_a = [\phi, \theta, r, \chi]^{\mathrm{T}}$. Numerically, we find that: the estimates of ϕ, θ, r, and χ are all correlated; the partial correlations $\zeta_{\phi\chi}$, $\zeta_{\theta\chi}$, $\zeta_{\phi r}$, and $\zeta_{\theta r}$ are always small ($\lesssim 10^{-3}$ for the cases considered in the following section), and under some conditions tend to zero. For example, at large values of r/λ, $J_{\chi\chi}$, $J_{\phi\chi}$, $J_{\theta\chi}$, $J_{r/\lambda\chi} \to 0$. Hence **J** becomes rank deficient. But **J** is also block diagonal and the subspace generated by ϕ, θ, and r is invertible. Hence the CRLBs of ϕ, θ, and r can be determined by inverting this submatrix of the FIM. Numerically, this case is handled by using conditional testing. These correlations will be discussed further in the remainder of this section.

Second, consider the unknown parameter vector $\mathbf{\Theta}_b = [r, \ell, \varsigma^2, \mathrm{L}_0]^{\mathrm{T}}$. Numerically, we find that the estimates of all of these parameters are correlated. There are many regions in which the FIM becomes ill-conditioned due to (a) the inability to estimate one or two of the unknowns, (b) highly correlated parameters, or (c) there is not enough information to estimate all parameters.

Consider now all seven unknown parameters: $\mathbf{\Theta} = [\phi, \theta, r, \chi, \ell, \varsigma^2, \mathrm{L}_0]^{\mathrm{T}}$. Numerically, we find that the CRLBs of ϕ and θ are not affected by the addition of ℓ, ς^2, and L_0 as unknowns. The largest percent difference on the CRLBs of the AOAs when considering $\mathbf{\Theta}$ versus $\mathbf{\Theta}_a$ is only $\sim 10^{-3}$ for the cases considered in the following section. This is well within the error tolerance of the problem. Conditional testing and singular value decomposition are almost always needed to determine the CRLBs of the AOAs when considering all seven unknowns.

The phase of the source, χ, cannot be estimated from this model, no matter what other parameters are considered as unknowns. This result is expected as this model utilizes phase differences across the array.

In the remainder of this section, we specifically calculate the CRLBs of the AOAs for a square array (Sec. IV A), the CRLBs of the AOAs for a rectangular array (Sec. IV B), and the CRLBs of other parameters for a square array (Sec. IV C). As the CRLB (σ, standard deviation) for M independent and identically distributed datasets is $1/\sqrt{M}$ times the CRLB for one dataset, all results presented in this section consider $M = 1$.

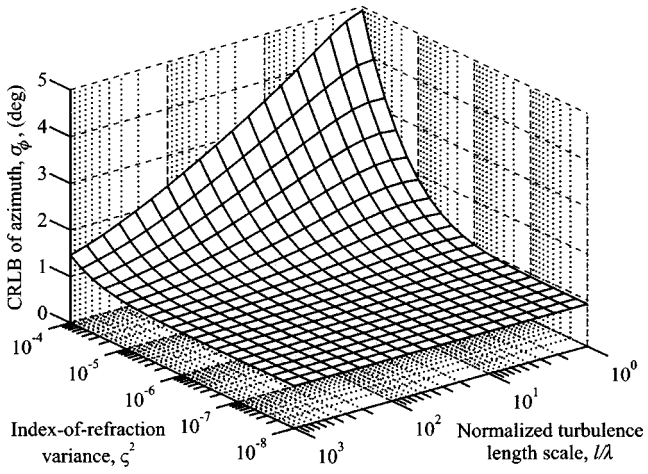

FIG. 3. CRLB of azimuth as a function of turbulence parameters: normal incidence, 4×4 square array with $d/\lambda = 0.5$, $r/\lambda = 500$, $\mathrm{SNR}_0 = 10$ dB evaluated at $r_0/\lambda = r/\lambda$, and a scalar von Kármán spectrum. Due to symmetry, $\sigma_\phi = \sigma_\theta = \sigma_{\phi_0} = \sigma_{\theta_0}$ at $\phi = \theta = 0$.

A. CRLBs of AOAs: Square array

The array geometry considered for this analysis is a 4×4 square grid with an adjacent sensor spacing of d. In all calculations to follow $d/\lambda = 0.5$. The azimuth, ϕ, elevation, θ, normalized propagation distance, r/λ, and phase of the source, χ, are considered as unknowns in this section.

Due to the symmetry of the array, the CRLBs of ϕ and θ, σ_ϕ and σ_θ, respectively, are the same at normal incidence. At $\phi = 0$, the partial correlations $\zeta_{\phi\theta}$, $\zeta_{\phi\chi}$, and $\zeta_{\phi\, r/\lambda}$ are all zero. And at $\theta = 0$, the partial correlations $\zeta_{\phi\theta}$, $\zeta_{\theta\chi}$, and $\zeta_{\theta\, r/\lambda}$ are all zero. Therefore, at $\phi = \theta = 0$, the CRLBs are equal and attain their minimum values: $\sigma_\phi = \sigma_\theta = \sigma_{\phi_0} = \sigma_{\theta_0}$. (Recall that σ_{ϕ_0} is the CRLB of ϕ when ϕ is the only unknown parameter and that $\sigma_\phi \geqslant \sigma_{\phi_0}$.) All the angular partial correlations increase with increasing ϕ and θ.

In Fig. 3 the CRLB of the azimuth, σ_ϕ, is plotted versus the normalized turbulence length scale, ℓ/λ, and index-of-refraction variance, ς^2. This plot is for normal incidence, $r/\lambda = 500$, and $\mathrm{SNR}_0 = 10$ dB at $r_0/\lambda = 500$. A scalar von Kármán spectrum is used. A peak in the CRLB occurs at larger values of ς^2 and smaller values of ℓ/λ. Referring to Fig. 2 in Sec. II C and Fig. 3 of Ref. 5, we see that this corresponds to the region where both Γ_{ij} and $\Gamma_{\min}$ are approaching their minimum values as functions of the turbulence parameters. (The location of the maximum value of the CRLB does not exactly correspond to the locations of the minimum values of the coherence functions due to the contributions to the covariance matrix and mean from every pair of sensors in the array.) The overall values of σ_ϕ are smaller than for the plane-wave case (see Fig. 11 of Ref. 5). This is expected as the values of the MCF for a plane wave are smaller than for a spherical wave. The ratio $\sigma_\phi^v/\sigma_\phi^s$, where the superscripts refer to the type of turbulence spectrum, is plotted in Fig. 4. As expected, σ_ϕ for the vector spectrum is larger than that for the scalar spectrum. As with the plane-wave case, the use of a nonzero mean reduces the CRLBs of the AOAs. The largest reduction occurs at the peak in Fig. 3. For other values of ϕ and θ, the behavior of CRLBs of the

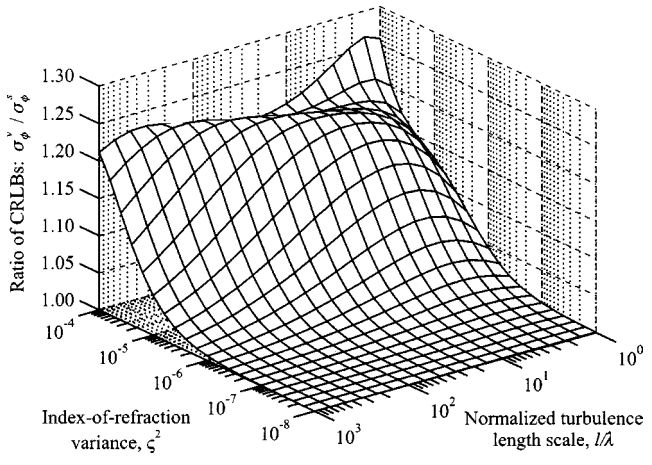

FIG. 4. Ratio of CRLB of azimuth for a vector turbulence spectrum to that for a scalar spectrum as a function of turbulence parameters. Parameters same as Fig. 3.

AOAs is similar, with σ_ϕ and σ_θ increasing with increasing ϕ and θ. And for other values of the SNR, the behavior is similar, provided that the SNR is not so low that the noise dominates the performance.

In Fig. 5 the CRLB of the azimuth, σ_ϕ, is plotted versus the normalized propagation distance, r/λ, for normal incidence and a scalar von Kármán spectrum. Two values of ς^2, ℓ/λ, and SNR_0 evaluated at $r_0/\lambda = 500$ are considered. In order to see the limiting behavior of the model, the graph is extended to include smaller values of r/λ than are valid for the propagation model. At small values of r/λ, we see that σ_ϕ is dependent upon the values of the turbulence parameters (particularly ς^2) and is independent of the value of SNR_0 (as it should be as SNR_0 is evaluated at $r_0/\lambda = 500$). Note the difference between the outward spherical-wave propagation and the plane-wave propagation (where p_0^2/σ_n^2 is constant) depicted in Fig. 13 of Ref. 5. The behavior for other values of ϕ and θ is the same; σ_ϕ increases slightly as ϕ and θ increase.

The partial correlation between ϕ and θ, $\zeta_{\phi\theta}$, is plotted in Fig. 6 as a function of the normalized propagation distance for $\phi = \theta = 15°$. All other parameters are the same as in Fig. 5. Notice the small variation along the y axis. For $r/\lambda = 10$, $\zeta_{\phi\theta}$ is dependent upon the values of the SNR and the turbulence parameters; however, this dependence rapidly vanishes and $\zeta_{\phi\theta}$ becomes constant for $r/\lambda > 100$. Therefore, for values of r/λ that are consistent with the SAA, $\zeta_{\phi\theta}$ is independent of ς^2, ℓ/λ, and SNR_0. Figure 7 depicts the partial correlation between ϕ and χ. For all values of ς^2, ℓ/λ, and SNR_0, $\zeta_{\phi\chi}$ diminishes exponentially with increasing r/λ. The partial correlation between ϕ and r/λ is plotted in Fig. 8. Again, for large values of r/λ, $\zeta_{\phi\, r/\lambda}$ diminishes exponentially. The analogous graphs of Figs. 5–8 for θ (instead of ϕ) have the same behavior.

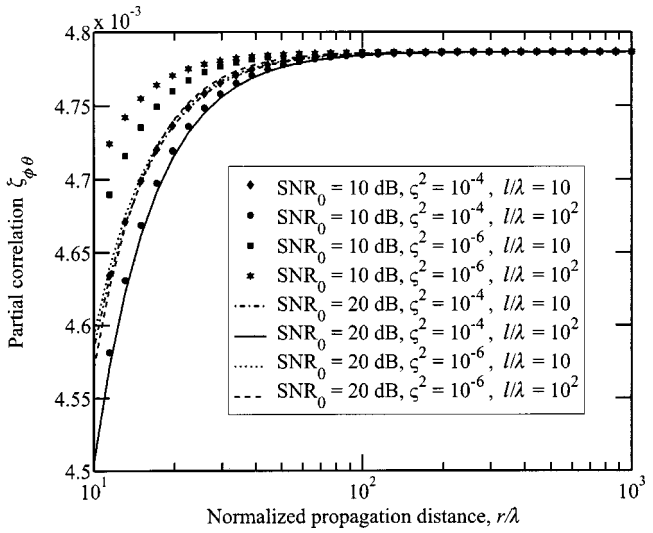

FIG. 6. Partial correlation between estimates of azimuth and elevation as a function of normalized propagation distance at $\phi = \theta = 15°$. All other parameters same as Fig. 5.

The behavior of σ_ϕ and σ_θ, as well as all the partial correlations, as a function of propagation distance is the same for a vector von Kármán spectrum. The values of σ_ϕ

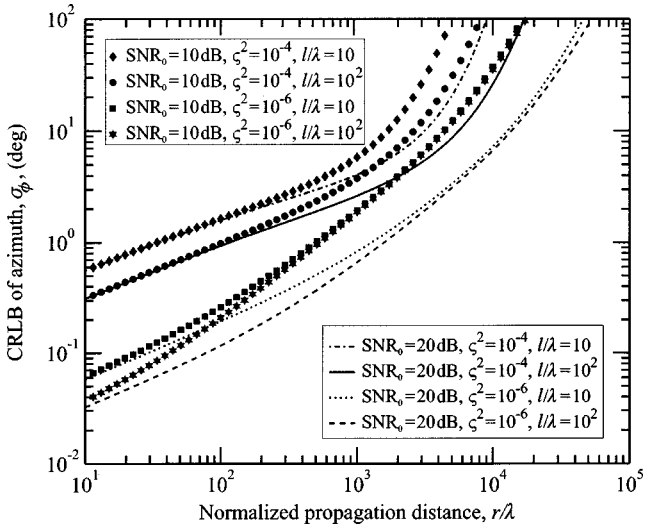

FIG. 5. CRLB of azimuth as a function of normalized propagation distance: normal incidence, 4×4 square array with $d/\lambda = 0.5$, SNR_0 evaluated at $r_0/\lambda = 500$, and a scalar von Kármán spectrum.

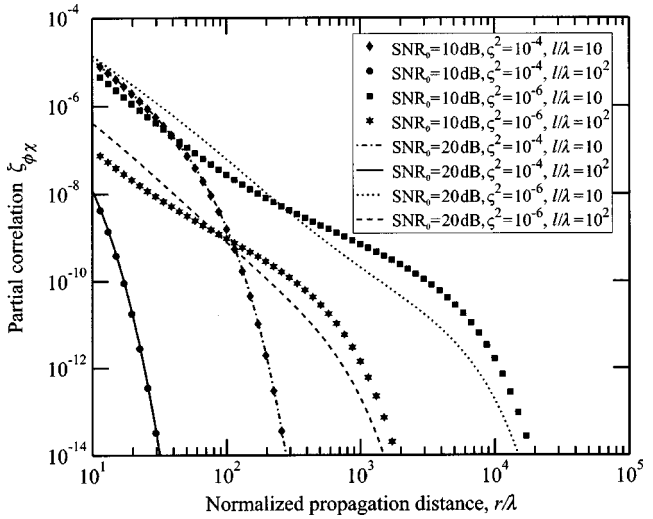

FIG. 7. Partial correlation between estimates of azimuth and source phase as a function of normalized propagation distance at $\phi = \theta = 15°$. All other parameters same as Fig. 5. (Analogous plots for $\zeta_{\theta\chi}$ have same behavior and almost same values.)

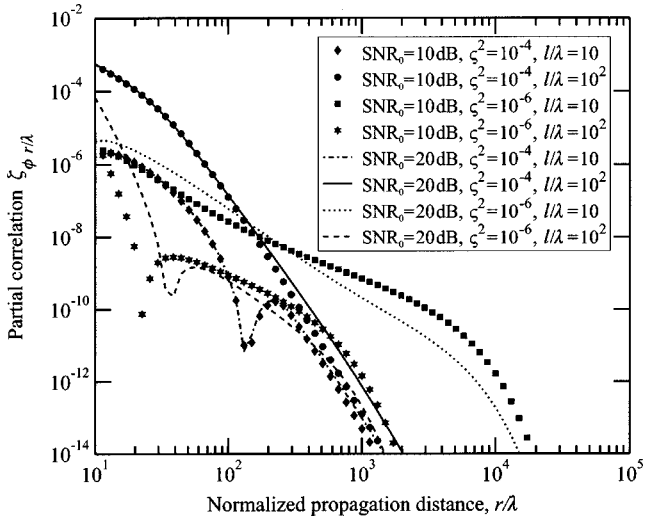

FIG. 8. Partial correlation between estimates of azimuth and normalized propagation distance as a function of normalized propagation distance at $\phi=\theta=15°$. All other parameters same as Fig. 5. (Analogous plots for $\zeta_{\theta r/\lambda}$ have same behavior and almost same values.)

and σ_θ are slightly higher. Referring back to Fig. 6, the partial correlation $\zeta_{\phi\theta}$ for a vector spectrum has similar values for $r/\lambda<100$ and approaches the same constant for $r/\lambda>100$.

The angular dependence of the CRLBs of the AOAs is shown in Fig. 9 for a scalar von Kármán spectrum. In Figs. 9(a)–9(c), $\varsigma^2=10^{-4}$, $\ell/\lambda=10$, $r/\lambda=500$, and $\mathrm{SNR}_0=10$ dB at $r_0/\lambda=r/\lambda$. We see the same symmetry in σ_ϕ as in the plane-wave case, and σ_θ is again independent of azimuth. (Refer to Figs. 15 and 16 in Ref. 5.) Not shown are the partial correlations $\zeta_{\phi\, r/\lambda}$ and $\zeta_{\theta\, r/\lambda}$, which are at most $\sim 10^{-12}$ at $\phi=\theta=15°$. To within the numerical accuracy of the calculation, the partial correlations $\zeta_{\phi\chi}$ and $\zeta_{\theta\chi}$ are both zero. In Figs. 9(d)–(f), all the parameters are the same except $\varsigma^2=10^{-6}$. The CRLBs have decreased, as expected. Here $\zeta_{\phi\, r/\lambda}$, $\zeta_{\theta\, r/\lambda}$, $\zeta_{\phi\chi}$, $\zeta_{\theta\chi}\sim 10^{-9}$ at $\phi=\theta=15°$. The partial correlation $\zeta_{\phi\theta}$ is the same for both cases. At $\phi=\theta=15°$, $\zeta_{\phi\theta}=4.8\times10^{-3}$. In fact, the partial correlation between ϕ and θ is the same (less than 0.02% difference) as for the plane-wave case for all parameters and both spectra when $r/\lambda\gtrsim 100$. See Fig. 16 in Ref. 5. The analogous results for a vector spectrum have the same behavior.

B. CRLBs of AOAs: Rectangular array

The analysis of the previous section considered optimal conditions: a square array with a sensor separation of $d/\lambda=0.5$. Obviously, these conditions cannot always be satisfied. In this section, we again consider a 4×4 array, but with a column separation of $d_y/\lambda=1.1$ and a row separation of $d_z/\lambda=2.1$. Again, at $\phi=0$, the partial correlations $\zeta_{\phi\theta}$, $\zeta_{\phi\chi}$, and $\zeta_{\phi\, r/\lambda}$ are all zero, and, at $\theta=0$, the partial correlations $\zeta_{\phi\theta}$, $\zeta_{\theta\chi}$, and $\zeta_{\theta\, r/\lambda}$ are all zero. Therefore, at $\phi=\theta=0$, $\sigma_\phi=\sigma_{\phi_0}$ and $\sigma_\theta=\sigma_{\theta_0}$, but $\sigma_{\phi_0}\neq\sigma_{\theta_0}$. In Fig. 2 it was illustrated that the coherence loss increased with increasing sensor separation; moreover, the coherence loss for a vector von Kármán spectrum is larger than for a scalar spectrum. Therefore, we expect the CRLBs of the AOAs to be

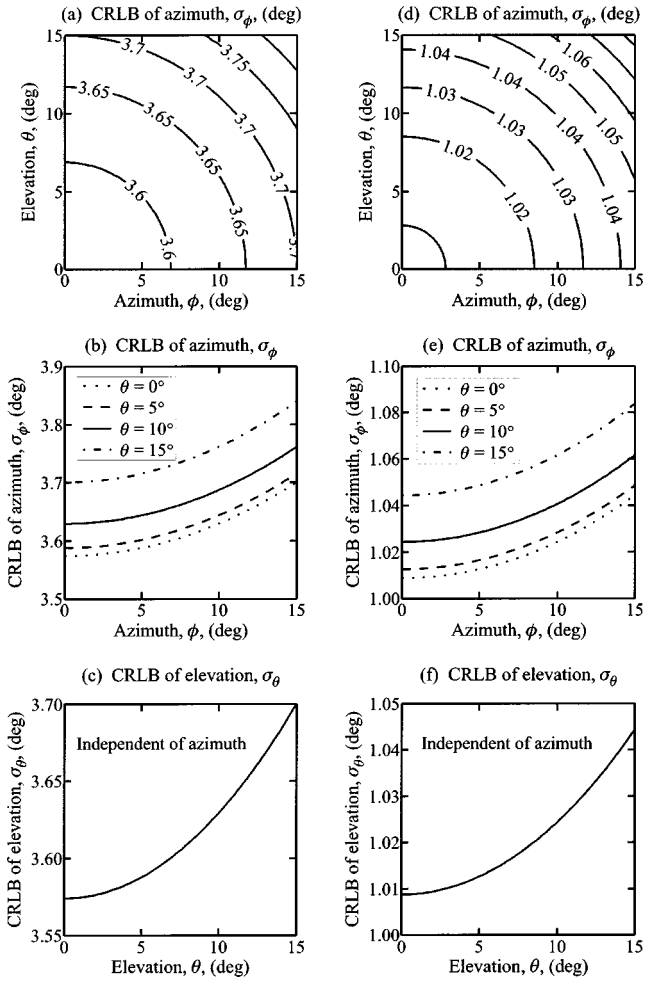

FIG. 9. Angular dependence of CRLBs of azimuth and elevation for a 4×4 square array with $d/\lambda=0.5$ and a scalar von Kármán spectrum. In (a)–(c): $\varsigma^2=10^{-4}$, $\ell/\lambda=10$, $r/\lambda=500$, $\mathrm{SNR}_0=10$ dB at $r_0/\lambda=500$. Same in (d)–(f), but $\varsigma^2=10^{-6}$.

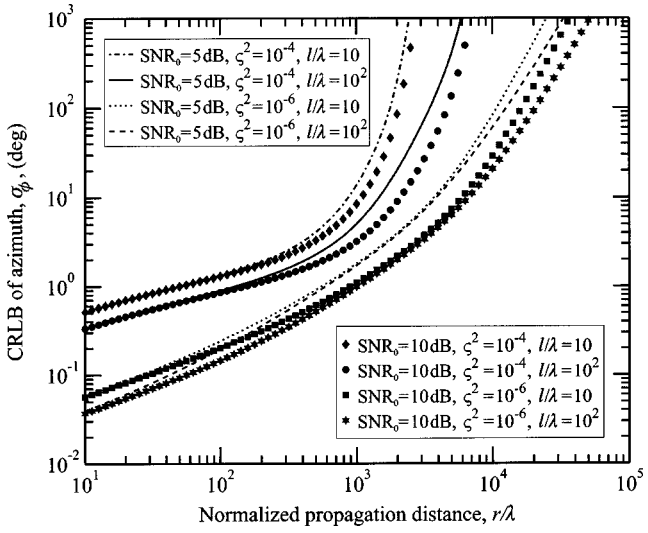

FIG. 10. CRLB of azimuth as a function of normalized propagation distance: $\phi=\theta=15°$, 4×4 rectangular array with $d_y/\lambda=1.1$ and $d_z/\lambda=2.1$, SNR_0 evaluated at $r_0/\lambda=500$, and a vector von Kármán spectrum.

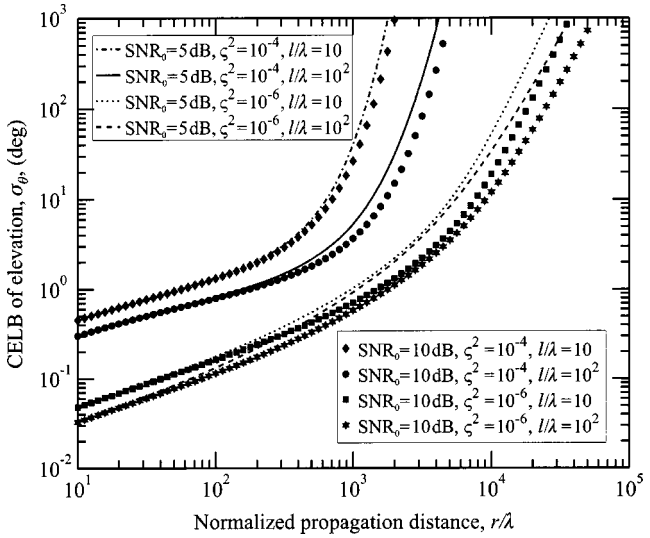

FIG. 11. CRLB of elevation as a function of normalized propagation distance. Parameters same as Fig. 10.

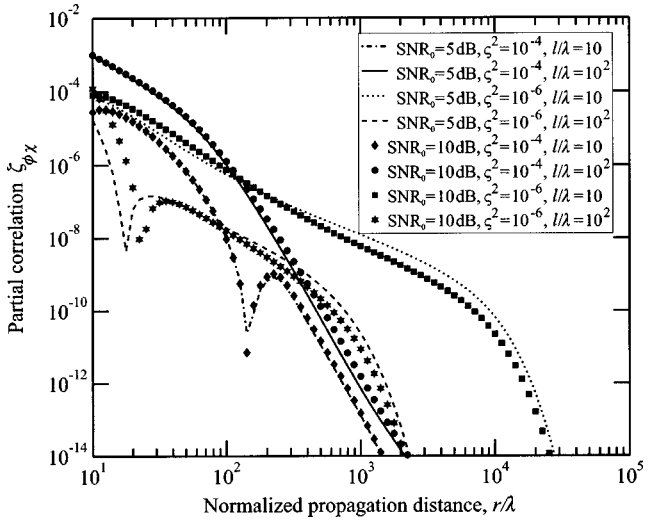

FIG. 13. Partial correlation between estimates of azimuth and source phase as a function of normalized propagation distance. Parameters same as Fig. 10.

larger for the sensor configuration considered in this section. Here the largest sensor separation is 7.11 λ, whereas for the array considered in the preceding section the largest sensor separation was 2.12 λ.

The CRLBs of the AOAs at $\phi=\theta=15°$ are shown in Figs. 10 and 11 and the partial correlations in Figs. 12–16. A vector von Kármán spectrum is considered. Notice the difference in behavior from the previous case, in particular that of the partial correlation $\zeta_{\phi\theta}$. All the angular partial correlations increase with increasing ϕ and θ.

C. CRLBs of other parameters

While the phase of the source χ and the signal-to-noise variance ratio L_0 are nuisance parameters that we do not wish to estimate, the propagation distance r and turbulence parameters ℓ and ς^2 are of interest. For the plane-wave case, it was found that for a large number of independent and identically distributed samples M, there may be sufficient information to obtain estimates of r/λ, ς^2, and ℓ/λ, but only at large values of ς^2 and small values of ℓ/λ. For the spherical-wave case, we find the same limitations on the ability to estimate ς^2 and ℓ/λ. However, the spherical-wave propagation model does provide more information about the propagation distance.

Figure 17 investigates the relative error of the CRLB of the normalized propagation distance, i.e., $\sigma_{r/\lambda}/(r/\lambda)$. All seven parameters are considered as unknowns: r, χ, ϕ, θ, ℓ, ς^2, and L_0. A 4×4 square array with $d/\lambda=0.5$ and a scalar von Kármán spectrum are considered. For a SNR of 10 dB at $r_0/\lambda=500$, we find that it may be possible to estimate the normalized propagation distance for $r/\lambda\lesssim10^3$ if a sufficient number of independent and identically distributed data sets can be obtained. While $\phi=\theta=15°$ is considered for this case, the dependence of $\sigma_{r/\lambda}$ on ϕ and θ is nominal. In Fig. 18 the relative error of the CRLB of r/λ is depicted as a function of turbulence parameters for $r/\lambda=500$ and SNR$_0$

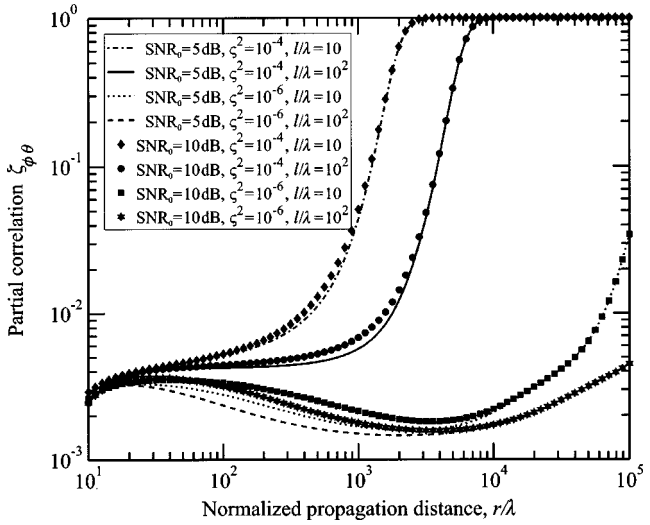

FIG. 12. Partial correlation between estimates of azimuth and elevation as a function of normalized propagation distance. Parameters same as Fig. 10.

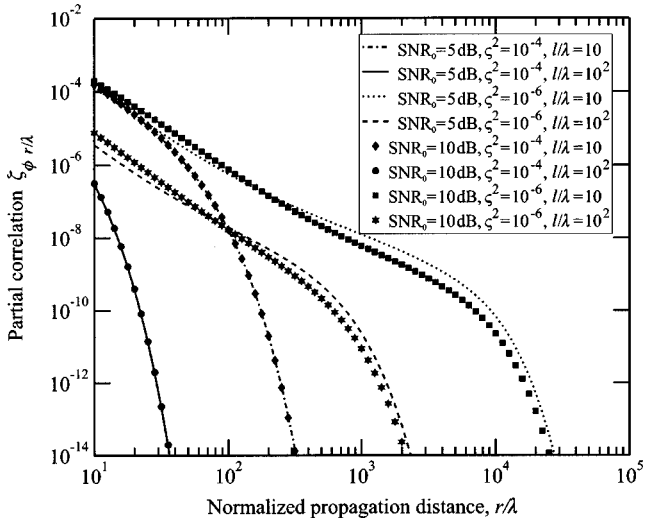

FIG. 14. Partial correlation between estimates of azimuth and normalized propagation distance as a function of normalized propagation distance. Parameters same as Fig. 10.

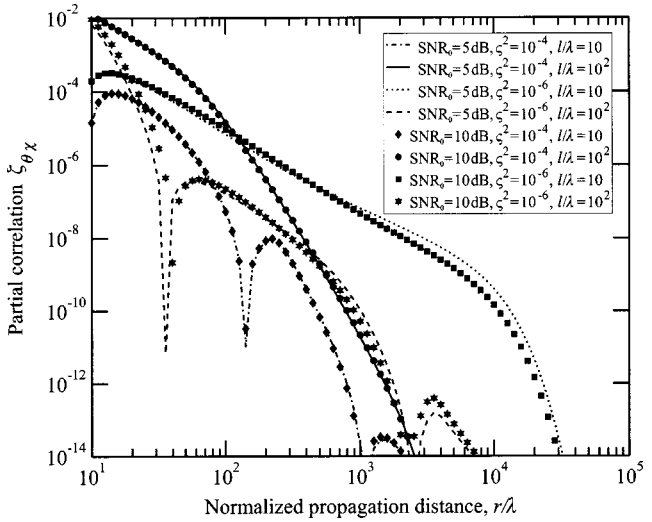

FIG. 15. Partial correlation between estimates of elevation and source phase as a function of normalized propagation distance. Parameters same as Fig. 10.

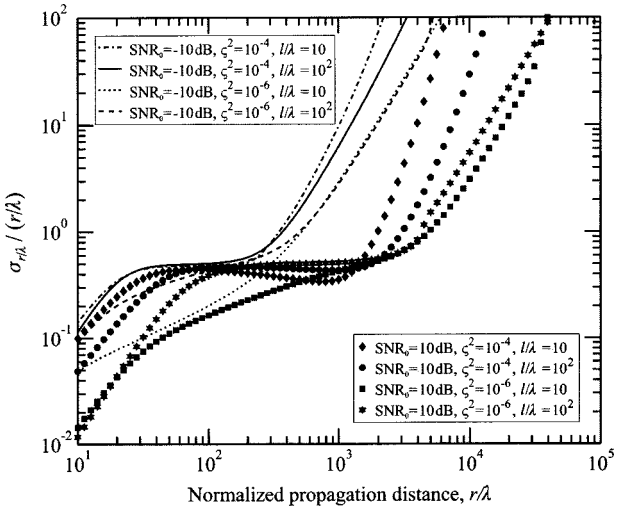

FIG. 17. CRLB of normalized propagation distance as a function of normalized propagation distance: $\phi=\theta=15°$, 4×4 square array with $d/\lambda=0.5$, SNR$_0$ evaluated at $r_0/\lambda=500$, and a scalar von Kármán spectrum.

$=10$ dB at r/λ. Again, all seven parameters are considered as unknowns. For illustration purposes, the orientation of the x axis is reversed from that in Fig. 2 and in Fig. 3 of Ref. 5. Notice that $\sigma_{r/\lambda}/(r/\lambda)$ reaches its smallest values for $\varsigma^2 \sim 10^{-8}$ and $\ell/\lambda \sim 10$. This corresponds to the region where the effects of the turbulence are minimal: Γ_{ij} is near one (strong coherence) and $\Gamma_{\min}$ is also near one (weak scattering). The largest values of the normalized CRLB occur when $\varsigma^2 \sim 10^{-4}$ and $\ell/\lambda \sim 10^3$. In this region, Γ_{ij} is near one (strong coherence) and $\Gamma_{\min}$ is near zero (strong scattering).

V. CONCLUSIONS

We have investigated the Cramer–Rao lower bounds (CRLBs) of the wave front angles of arrival (AOAs) for a spherical wave propagating through atmospheric turbulence with fluctuations described by a von Kármán spectrum. This investigation is the logical continuation of a previous investigation[5] for a plane-wave source. Both investigations consider a nonzero mean, two bearing angles, and multiple unknown parameters. As expected, the CRLBs of the AOAs for the spherical-wave model are smaller than those for the plane-wave model due to the change in the mutual coherence function. However, this reduction in the CRLBs of the AOAs comes at the expense that the estimates of the AOAs are correlated to the estimates of the normalized propagation distance and source phase. It has also been shown that the estimates of the AOAs are always uncorrelated from the estimates of the turbulence parameters and signal-to-noise ratio. Moreover, unlike the plane-wave case, it is found that it may be possible to estimate the normalized propagation distance if there are a sufficient number of independent and identically distributed data sets.

The significance of incorporating the scattering by atmospheric turbulence is evident from the results presented here. In particular, it is found that CRLBs of the AOAs increase substantially for large values of the normalized propagation

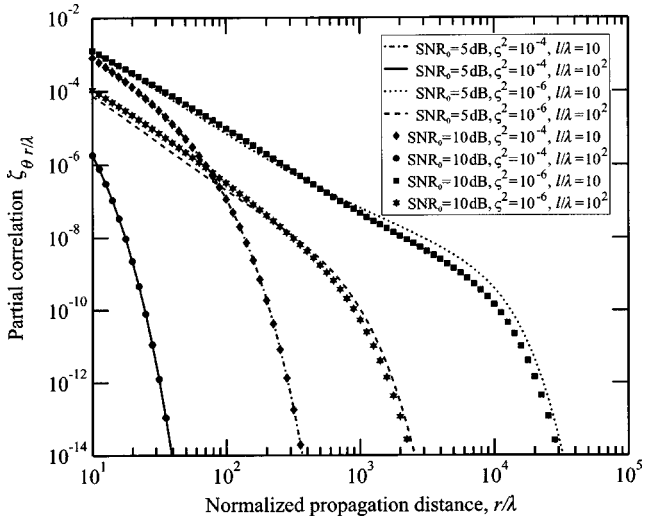

FIG. 16. Partial correlation between estimates of elevation and normalized propagation distance as a function of normalized propagation distance. Parameters same as Fig. 10.

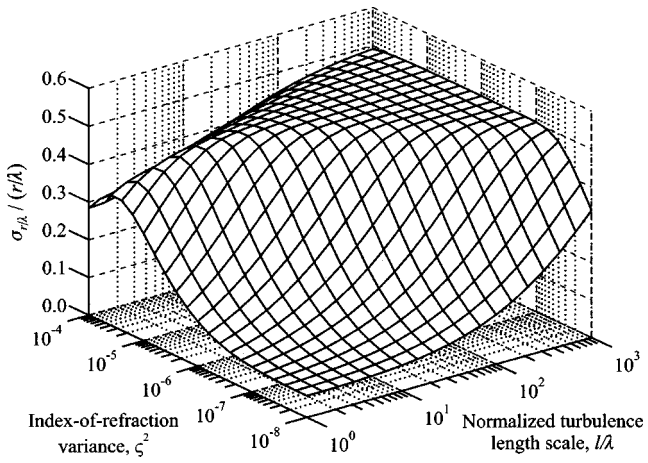

FIG. 18. CRLB of normalized propagation distance as a function of turbulence parameters for $r/\lambda=500$ and SNR$_0=10$ dB at r/λ. All other parameters same as Fig. 17.

distance and for values of the turbulence parameters that result in low values of the mutual coherence function (large values of the index-of-refraction variance and moderate to small values of the normalized characteristic length scale). This investigation is limited by the model of the moments of the pressure field, which considers that the decay of the moments is constant across the array. In addition other physical phenomena, such as ground reflections and refraction by atmospheric wind and temperature gradients, not included in this analysis, may have a considerable impact on the ability to estimate the elevation.

ACKNOWLEDGMENTS

The authors are grateful to V. E. Ostashev of NOAA/Environmental Technology Laboratory, B. M. Sadler of the U.S. Army Research Laboratory, and R. J. Kozick of Bucknell University for many helpful discussions.

APPENDIX: NOTATION

Symbols

$[\cdot]^*$	Complex conjugate
$[\cdot]^\dagger$	Hermitian adjoint (complex conjugate transpose)
$[\cdot]^{\mathrm{T}}$	Transpose
$[\cdot]^{\parallel}$	Component parallel to $\hat{\mathbf{r}}$
$[\cdot]^{\perp}$	Component perpendicular to $\hat{\mathbf{r}}$
$[\mathbf{A}]_{ij}, A_{ij}$	i-j element of the matrix $\mathbf{A}$
$\odot$	Hadamard product, element-wise product, $[\mathbf{A}\odot\mathbf{B}]_{ij}=A_{ij}B_{ij}$
$\otimes$	Kronecker product of matrices (direct or tensor product)
$\equiv$	Defined as
$\sim$	On the order of
$\sim\mathcal{CN}_N(\boldsymbol{\mu}, \mathbf{C})$	Distributed as a $N\times 1$ complex Gaussian random vector with mean $\boldsymbol{\mu}$ and covariance $\mathbf{C}$
$\langle\cdot\rangle$	Ensemble average or expectation value
$(\breve{\cdot})$	Quantity (accented with a breve) derived in SAA
$(\tilde{\cdot})$	Quantity (accented with a tilde) derived in extended SAA
$\mathrm{Im}(\cdot)$	Imaginary part
$\mathrm{Re}(\cdot)$	Real part
$\mathrm{diag}(a_1, ..., a_N)$	Diagonal matrix whose i-i element is a_i

Integers and subscripts

M	Number of independent and identically distributed data sets
N	Number of elements in the array
$\mathcal{N}$	Number of unknown parameters
i, j	Indices on elements of the array
λ, ν	Indices on unknown parameters

Matrices and vectors

$\mathbf{C}$	Covariance matrix for total pressure field, $C_{ij}=\langle s_i\ s_j^*\rangle-\langle s_i\rangle\langle s_j^*\rangle$; $[N\times N$, complex$]$
$\mathbf{C}_p$	Covariance matrix for source pressure field $[\mathbf{C}_p]_{ij}=\langle p_i p_j^*\rangle-\langle p_i\rangle\langle p_j^*\rangle$; $[N\times N$, complex$]$
$\mathbf{I}_N$	Identity matrix; $[N\times N$, real$]$
$\mathbf{J}$	Fisher informaiton matrix; $[\mathcal{N}\times\mathcal{N}$, real$]$
$\mathbf{k}$	Wavenumber vector
$\mathbf{m}$	Mean amplitude vector, $m_i\equiv\mu_i/e^{\mathrm{i}\tilde{\Phi}_i}$; $[N\times 1$, real$]$
$\mathbf{n}$	Noise pressure field; $[N\times 1$, complex$]$
$\mathbf{p}$	Source pressure field; $[N\times 1$, complex$]$
$\mathbf{r}$	Vector from center of array to source
$\hat{\mathbf{r}}$	Unit vector in direction of $\mathbf{r}$, $\hat{\mathbf{r}}=[\cos\phi\cos\theta, \sin\phi\cos\theta, \sin\theta]^{\mathrm{T}}$
$\mathbf{r}_i'$	Vector from center of array to ith sensor, $\mathbf{r}_i'=[x_i', y_i', z_i']^{\mathrm{T}}$
$\mathbf{r}_i$	Vector from ith sensor to source, $\mathbf{r}_i=\mathbf{r}-\mathbf{r}_i'$
$\mathbf{s}$	Total pressure field, $\mathbf{s}\equiv\mathbf{p}+\mathbf{n}$; $[N\times 1$, complex$]$
$\mathbf{S}$	Diagonal matrix of phases, $\mathbf{S}\equiv\mathrm{diag}[e^{\mathrm{i}\tilde{\Phi}_1}, \ldots, e^{\mathrm{i}\tilde{\Phi}_N}]^{\mathrm{T}}$; $[N\times N$, complex$]$
s	Steering vector, $s\equiv[e^{\mathrm{i}\tilde{\Phi}_1}, \ldots, e^{\mathrm{i}\tilde{\Phi}_N}]^{\mathrm{T}}$; $[N\times 1$, complex$]$
$\boldsymbol{\mathcal{S}}$	Steering matrix, $\mathcal{S}_{ij}\equiv e^{\mathrm{i}\tilde{\Phi}_{ij}}$; $[N\times N$, complex$]$
$\mathbf{X}$	Covariance amplitude matrix, $X_{ij}\equiv C_{ij}/e^{\mathrm{i}\tilde{\Phi}_{ij}}$; $[N\times N$, real$]$
Γ	Mutual coherence matrix; $[N\times N$, real$]$
$\boldsymbol{\mu}$	First moment (mean) of source pressure field; $\mu_i\equiv\langle p_i\rangle$; $[N\times 1$, complex$]$
$\boldsymbol{\rho}_{ij}$	Vector from jth to ith sensor, $\boldsymbol{\rho}_{ij}\equiv\mathbf{r}_i-\mathbf{r}_j=\mathbf{r}_j'-\mathbf{r}_i'$
$\boldsymbol{\Theta}$	Vector of unknown parameters; $[\mathcal{N}\times 1$, real$]$
$\hat{\boldsymbol{\Theta}}$	Unbiased estimator of $\boldsymbol{\Theta}$; $[\mathcal{N}\times 1$, real$]$

Functions and scalar quantities

d	Separation between adjacent sensors in a uniformly spaced array
$f_{s,v}(\rho_{ij})$	2D correlation function for a scalar or vector field, as a function of sensor separation
k	Wavenumber
$K_\nu(x)$	Modified Bessel function of order ν evaluated at x
L	Signal-to-noise variance ratio, $\mathrm{L}=p_0^2(r)/\sigma_n^2$
L_0	Signal-to-noise variance ratio evaluated at $r=r_0$
l	Characteristic length scale of turbulence, $l=\Gamma(\frac{1}{3})\mathcal{L}/[\sqrt{\pi}\Gamma(\frac{5}{6})]$
$\mathcal{L}$	Outer (integral) length scale of turbulence
ℓ	Inner (Kolmogorov) length scale of turbulence
$p_{\mathrm{H}}(\mathbf{r}_i)$	Pressure field in a *homogeneous* medium for a spherical wave at observation point $\mathbf{r}_i$; [complex]
$p_0(r_i)$	Amplitude of $p_{\mathrm{H}}(\mathbf{r}_i)$; [real]
$\langle p_i p_j^*\rangle$	Second moment of source pressure field between ith and jth sensor; [complex]
r	Propagation distance of wave front to the center of the array
$\alpha(\rho_{ij})$	Extinction coefficient for second moment, function of sensor separation
χ	Phase of the source
δ_{ij}	Kronecker delta function
γ	Extinction coefficient for first moment
$\Gamma(x)$	Gamma function evaluated at x
Γ_{ij}	Mutual coherence between ith and jth sensors, a function of sensor separation ρ_{ij}; [real]

$\Gamma_{\min}$	Minimum value of Γ_{ij}, $\Gamma_{\min} \equiv \Gamma_{ij}$ $(\rho_{ij}=\infty)$
λ	Wavelength (when symbol not used as subscript)
μ_i	First moment (mean) at ith sensor, $\mu_i \equiv \langle p_i \rangle$; [complex]
ϕ	Azimuthal angle of arrival
Φ_i	Total phase of signal received at the ith sensor
Φ_{ij}	Difference in total phase between ith and jth sensors, $\Phi_{ij} \equiv \Phi_i - \Phi_j$
ρ_{ij}	Separation between ith and jth sensors
σ_n^2	Noise variance
σ_ν^2	CRLB of Θ_ν, $\sigma_\nu^2 = [\mathbf{J}^{-1}]_{\nu\nu}$
$\sigma_{\nu_0}^2$	CRLB of Θ_ν when Θ_ν is the only unknown, $\sigma_{\nu_0}^2 = 1/J_{\nu\nu}$
ς^2	Index-of-refraction variance
θ	Elevational angle of arrival
$\zeta_{\lambda\nu}$	Partial correlation between the estimates of Θ_λ and Θ_ν

Acronyms

AOA	Angle of arrival
CRLB	Cramer–Rao lower bound
FI(M)	Fisher information (matrix)
MCF	Mutual coherence function
SAA	Small-angle approximation
SNR	Signal-to-noise ratio (in dB)
SNR_0	Signal-to-noise ratio evaluated at $r=r_0$ (in dB)
2D	Two-dimensional

[1] D. K. Wilson, C. R. Tate, D. C. Swanson, and D. M. Reichard, "Acoustic scintillations and angle-of-arrival fluctuations observed outdoors with a large planar vertical michrophone array," ARLO **106**, L24–L29 (1999).

[2] B. G. Ferguson, "Variability in the passive ranging of acoustic sources in air using a wavefront curvature technique," J. Acoust. Soc. Am. **108**, 1535–1544 (2000).

[3] B. J. Uscinski and D. E. Reeve, "The effect of ocean inhomogeneities on array output," J. Acoust. Soc. Am. **87**, 2527–2534 (1990).

[4] E. Y. Gorodetskaya, A. I. Malekhanov, A. G. Sazontov, and N. K. Vdovicheva, "Deep-water acoustic coherence at long ranges: Theoretical prediction and effects on large-array signal processing," IEEE J. Ocean. Eng. **24**, 156–171 (1999).

[5] S. L. Collier and D. K. Wilson, "Performance bounds for passive sensor arrays operating in a turbulent medium: Plane-wave analysis," J. Acoust. Soc. Am. **113**, 2704–2718 (2003).

[6] S. M. Flatté, editor, *Sound Transmission Through a Fluctuating Ocean* (Cambridge U.P., Cambridge, 1979).

[7] A. Ishimaru, *Wave Propagation and Scattering in Random Media* (IEEE, Piscataway, NJ, 1997).

[8] D. K. Wilson, "Performance bounds for acoustic direction-of-arrival arrays operating in atmospheric turbulence," J. Acoust. Soc. Am. **103**, 1306–1319 (1998).

[9] B.-G. Song and J. A. Ritcey, "Angle of arrival estimation of plane waves propagating in random media," J. Acoust. Soc. Am. **99**, 1370–1379 (1996).

[10] B. Ottersten, M. Viberg, P. Stoica, and A. Nehorai, "Exact and large sample maximum likelihood techniques for parameter estimation and detection in array processing," J. Acoust. Soc. Am. **99**, 1370–1379 (1996).

[11] S. M. Kay, *Fundamentals of Statistical Signal Processing: Estimation Theory* (PTR Prentice Hall, Englewood Cliffs, NJ, 1993).

[12] L. L. Scharf, *Statistical Signal Process: Detection, Estimation, and Time Series Analysis* (Addison–Wesley, Reading, MA, 1991).

[13] D. E. Norris, D. K. Wilson, and D. W. Thomson, "Correlations Between Acoustic Travel-Time Fluctuations and Turbulence in the Atmospheric Surface Layer," Acust. Acta Acust. **87**, 677–684 (2001).

[14] S. M. Rytov, Yu. A. Kravtsov, and V. I. Tatarskii, *Principles of Statistical Radiophysics 4: Wave Propagation Through Random Media* (Springer-Verlag, New York, 1989).

[15] V. E. Ostashev, *Acoustics in Moving Inhomogeneous Media* (E & FN Spon, London, 1997).

[16] R. A. Horn and C. R. Johnson, *Matrix Analysis* (Cambridge U.P., New York, 1993).

[17] V. E. Ostashev and D. K. Wilson, "Relative Contributions from Temperature and Wind Velocity Fluctuations to the Statistical Moments of a Sound Field in a Turbulent Atmosphere," Acustica **86**, 260–268 (2000).

[18] D. K. Wilson, "A turbulence spectral model for sound propagation in the atmosphere that incorporates shear and buoyancy forcings," J. Acoust. Soc. Am. **108**, 2021–2038 (2000).

Iterative algorithms for computing the shape of a hard scattering object: Computing the shape derivative

Stephen J. Norton[a)]
Oak Ridge National Laboratory, Oak Ridge, Tennessee 37831-6200

(Received 25 August 2003; revised 18 May 2004; accepted 20 May 2004)

The problem of determining the shape of an acoustically hard scattering object from remote scattering measurements is considered. An iterative approach is used to find the object shape that minimizes the mean-squared difference between a set of actual and predicted scattering observations. A crucial task in this minimization is the computation of the ''shape derivative,'' or functional gradient, of the mean-square error with respect to the object's shape or boundary. The shape derivative tells us how to update the object's shape to reduce the mean-square error at each iteration. If, for example, the object's boundary is parameterized with N variables, a brute-force approach to computing the shape derivative using finite-differences would require a minimum of $N+1$ forward solutions per iteration. We show how the shape derivative can be computed with just *two* forward solutions: one ordinary forward solution and a suitably constructed adjoint solution. This approach is independent of N and is not only far more efficient, but numerically less error prone, than finite-difference schemes for computing derivatives. © *2004 Acoustical Society of America.* [DOI: 10.1121/1.1771611]

PACS numbers: 43.60.Rw, 43.60.Pt [JS] Pages: 1002–1008

I. INTRODUCTION

We consider the problem of reconstructing the shape of an acoustically hard object from a set of remote scattering measurements. Since this inverse problem is nonlinear, an iterative approach is generally required. A convenient strategy is to find the object that best predicts a set of observations in the sense of minimizing a global error norm, such as the weighted mean-squared difference between the actual and predicted observations; the predicted observations are obtained by solving the forward problem on the basis of the current shape estimate. A crucial quantity in the minimization of the mean-square error is the functional derivative (or ''shape derivative'') of the mean-square error with respect to the shape, or boundary, of the object. This tells us how to update the current shape estimate to reduce the mean-square error at each iteration. Suppose, for example, that the surface of the object is parameterized using N variables. Many parameterization schemes are possible; the parameters might be the coefficients in the expansion of the surface of the object in a convenient basis set, such as spherical harmonics. Or the parameters might be the coordinates of the nodes of a spline interpolation of the surface, and so on. A brute force approach would be to perturb each of these parameters one by one and compute the resulting change in the error norm, but this would require a minimum of $N+1$ forward scattering solutions per iteration. In this paper, we show how all derivative information can be obtained with just two forward solutions: an ordinary solution and a forward adjoint solution, to be defined. Not only is this approach far more efficient than a finite-difference method, but is numerically more accurate since the adjoint method provides true derivatives (i.e., based on infinitesimal differences as opposed to finite differences). A discussion of the adjoint method for recovering a continuously-distributed scattering parameter was given by the author in a previous publication,[1] but that method does not apply to a hard scatterer in which the quantity sought is the shape of its boundary. This problem is addressed here. Dorn *et al.* devised another technique for reconstructing the boundary of a ''soft'' and homogeneous object (into which the fields penetrate) based on the iterative adjustment of level sets.[2,3] These authors also employ an adjoint calculation to update the boundary of the object. This method differs from the present approach and is unsuitable for hard scatterers.

We assume the object is embedded in a homogeneous medium with sound speed c and illuminated by an acoustic field from one or more directions; the wave can be steady-state or transient, although, for simplicity, we consider the former case first. For convenience, we let the steady-state field, $\phi(\mathbf{r})$, denote the acoustic velocity potential, which obeys the reduced wave equation in the domain Ω outside the scattering object

$$\nabla^2\phi(\mathbf{r})+k^2\phi(\mathbf{r})=0, \quad \mathbf{r}\in\Omega, \tag{1}$$

where $k=\omega/c$ is the wave number of the medium occupying Ω. We assume that the scatterer is spatially bounded and occupies the domain $\overline{\Omega}$ (the complement of Ω) with boundary Γ. The boundary condition for a ''hard scattering object'' is that the normal component of the particle velocity vanishes on the boundary Γ,

$$\nabla\phi\cdot\hat{n}|_{\mathbf{r}\in\Gamma}=0, \tag{2}$$

where $\hat{n}$ is the outward-pointing unit normal vector on Γ.

Our objective is to determine the shape of the scatterer from observations of the scattered field, $\phi(\mathbf{r})$, at M remote scattering locations, $\mathbf{r}_m$, $m=1,...,M$. Our approach is to find

[a)]Current address: Geophex, Ltd., Raleigh, North Carolina 27603. Electronic mail: norton@geophex.com

the shape that best predicts the set of M observations, $\phi_{\text{obs}}(\mathbf{r}_m)$, by minimizing the following weighted mean-square error:

$$\mathcal{E}=\frac{1}{2}\sum_{m=1}^{M} w_m|\phi(\mathbf{r}_m)-\phi_{\text{obs}}(\mathbf{r}_m)|^2, \tag{3}$$

where w_m is a positive weight that can be used to emphasize some measurements more than others, if desired.

Because the inverse-scattering problem is nonlinear, the minimization of $\mathcal{E}$ must proceed iteratively. This means, at each iteration, the forward problem, defined by (1) and (2), is numerically solved to compute the predicted measurements, $\phi(\mathbf{r}_m)$, on the basis of the current estimate of the scatterer's shape. To reduce $\mathcal{E}$ at each iteration, a crucial step is the calculation of the derivative of $\mathcal{E}$ with respect to the ''shape'' of the scatterer. Our aim in this paper is to demonstrate an elegant and efficient way of computing this shape derivative. To do this, we employ below the concept of the ''material derivative'' that has played a very useful role in the optimal shape design of engineering structures.[4,5] In computing the shape derivative, a question that we will examine is: what is the variation of $\mathcal{E}$ due to an arbitrary and infinitesimal variation in the shape of the scatterer given that the field obeys (1)?

Although we shall assume that the shape Γ is a continuous function, at some point this function needs to be represented by a finite number of parameters. That is, in practice, the shape of the object's surface must be defined in some convenient manner by a set of N parameters, p_n, $n=1,...,N$, where, for example, the p_n's might represent the coordinates of the nodes of a set of spline functions that approximate the object's boundary or the coefficients in a basis-set expansion of the object's surface (e.g., using spherical harmonics). For the moment, the details of the parameterization are not important, although we illustrate with specific examples later.

For the finite-dimensional problem, in which the surface is defined by N parameters, the functional gradient of the mean-square error, $\mathcal{E}$, reduces to an ordinary gradient, that is, to the set of N partial derivatives, $\partial\mathcal{E}/\partial p_n$. As noted, the derivatives could be numerically computed using finite-difference approximations, requiring $N+1$ forward calculations per iteration. The adjoint method, however, allows us to compute these partial derivatives using two forward solutions per iteration, independent of N. In the next section, we introduce the concept of the material derivative which leads to an explicit expression for $\partial\mathcal{E}/\partial p_n$. Once the derivatives are computed, a simple scheme that updates the j-th estimate, $p_n^{(j)}$, of the nth parameter is given by

$$p_n^{(j+1)}=p_n^{(j)}-\alpha_j\frac{\partial\mathcal{E}}{\partial p_n}, \tag{4}$$

where α_j is a suitably chosen step-size parameter that varies with the iteration. This is the simplest descent algorithm (steepest descent), but others, such as the conjugate gradient method or quasi-Newton methods, converge significantly more rapidly. The point is that any descent approach requires a computable shape derivative.

II. ADJOINT METHOD FOR COMPUTING THE SHAPE DERIVATIVE

Consider the domain, Ω, that occupies the volume outside the scatterer. Suppose the domain Ω is continuously deformed into the domain Ω_τ, where τ is a deformation parameter; we define $\Omega\equiv\Omega_{\tau=0}$. The boundary of the deformed domain is Γ_τ and $\Gamma\equiv\Gamma_{\tau=0}$. Let us define a mapping of the point $\mathbf{r}\in\Omega$ into the corresponding point $\mathbf{r}_\tau\in\Omega_\tau$, as follows:

$$\mathbf{r}_\tau=\mathbf{r}+\tau\mathbf{v}(\mathbf{r}). \tag{5}$$

Here $\mathbf{v}(\mathbf{r})$ is a vector field that defines the deformation of the domain Ω into Ω_τ. The quantity $\mathbf{v}(\mathbf{r})$ is analogous to a velocity field, in which case τ can be thought of as playing the role of a time variable. As τ increases from zero, (5) thus describes a continuous deformation of the domain Ω into Ω_τ and the object's surface Γ into Γ_τ.

In the domain Ω, the field ϕ obeys the reduced wave equation (1) subject to the boundary condition (2) on Γ. When the domain Ω is deformed into Ω_τ, the field $\phi(\mathbf{r})$ changes into the new field $\phi_\tau(\mathbf{r})$, obeying the equation

$$\nabla^2\phi_\tau(\mathbf{r})+k^2\phi_\tau(\mathbf{r})=0, \quad \mathbf{r}\in\Omega_\tau, \tag{6}$$

subject to the boundary condition on the deformed boundary Γ_τ:

$$\nabla\phi_\tau\cdot\hat{n}_\tau|_{\mathbf{r}\in\Gamma_\tau}=0. \tag{7}$$

Our goal is to compute the derivative of the mean-square error, $\mathcal{E}$, with respect to the deformation parameter, τ; the shape derivative will follow from this result. To accomplish this, we first compute the total derivative of ϕ_τ with respect to τ. The total derivative has two contributions: when the domain is deformed into Ω_τ, not only will the function value, ϕ_τ, change due to the new boundary condition (7), but also the location where the function is defined will change; the total derivative takes both changes into account. To be precise, the total derivative, denoted $\dot{\phi}$ (also called the ''material derivative''), is defined by

$$\dot{\phi}\equiv\frac{d}{d\tau}\phi_\tau(\mathbf{r}+\tau\mathbf{v}(\mathbf{r}))|_{\tau=0}=\lim_{\tau\to0}\left[\frac{\phi_\tau(\mathbf{r}+\tau\mathbf{v}(\mathbf{r}))-\phi(\mathbf{r})}{\tau}\right]$$

$$=\phi'(\mathbf{r})+\nabla\phi(\mathbf{r})\cdot\mathbf{v}(\mathbf{r}), \tag{8}$$

where

$$\phi'(\mathbf{r})\equiv\left.\frac{\partial\phi_\tau(\mathbf{r})}{\partial\tau}\right|_{\tau=0}=\lim_{\tau\to0}\left[\frac{\phi_\tau(\mathbf{r})-\phi(\mathbf{r})}{\tau}\right]. \tag{9}$$

Thus, the partial derivative, ϕ', of ϕ with respect to τ holds the location, $\mathbf{r}$, fixed, and accounts for the change in the functional value arising from the change in the domain only [i.e., through the change in the boundary condition (7)].

Now consider a general functional of the field ϕ_τ of the form

$$\Psi(\tau)=\int_{\Omega_\tau}G(\phi_\tau)d\Omega_\tau, \tag{10}$$

for $\tau\geqslant0$, where G is a known (differentiable) function of ϕ and possibly a function of the spatial derivatives of ϕ as

well. We wish to compute the total derivative of $\Psi(\tau)$ with respect to τ evaluated at $\tau=0$. There will be two contributions: one due to the change in G in the integrand, and one due to the change in the integration domain, Ω. Thus, we have

$$\dot{\Psi} \equiv \frac{d}{d\tau}\Psi(\tau)\big|_{\tau=0} = \lim_{\tau\to 0}\frac{1}{\tau}\left\{\int_{\Omega_\tau} G(\phi_\tau)d\Omega_\tau - \int_\Omega G(\phi)d\Omega\right\}. \tag{11}$$

In the Appendix, we show that this result can be evaluated to yield, under the mapping (5),

$$\dot{\Psi} = \int_\Omega \left.\frac{\partial G(\phi_\tau)}{\partial\tau}\right|_{\tau=0} d\Omega + \int_\Gamma G(\phi)\mathbf{v}\cdot\hat{n}d\Gamma. \tag{12}$$

This fundamental relation will be used below. The second integral in (12) over the surface, Γ, accounts for the infinitesimal change in Ψ due to the deformation of the domain Ω.

Our ultimate objective is to minimize the mean-square error (3) *subject to the constraint* that the field obeys the reduced wave equation (1) and the boundary condition (2). This constrained minimization problem can be transformed into an unconstrained problem with the aid of Lagrange multipliers. This is accomplished by minimizing the following unconstrained, but augmented, mean-square error functional:

$$\mathcal{E}_A = \frac{1}{2}\sum_{m=1}^{M} w_m|\phi(\mathbf{r}_m)-\phi_{\text{obs}}(\mathbf{r}_m)|^2 + \text{Re}\int_\Omega \lambda(\mathbf{r})[\nabla^2\phi(\mathbf{r})+k^2\phi(\mathbf{r})]d\Omega, \tag{13}$$

where $\lambda(\mathbf{r})$ is a continuous Lagrange multiplier to be determined and Re means real part. We allow the Lagrange multiplier, $\lambda(\mathbf{r})$, to be complex. One can show that the taking of the real part of the constraint term, as is done in (13), is sufficient to impose the constraint (that ϕ obeys the wave equation) because $\lambda(\mathbf{r})$ is allowed to be complex.[1]

For brevity, define the quantity

$$\Psi_\lambda \equiv \int_\Omega \lambda(\nabla^2\phi+k^2\phi)d\Omega, \tag{14}$$

so that (13) reads

$$\mathcal{E}_A = \frac{1}{2}\sum_{m=1}^{M} w_m|\phi(\mathbf{r}_m)-\phi_{\text{obs}}(\mathbf{r}_m)|^2 + \text{Re}\{\Psi_\lambda\}. \tag{15}$$

Now taking the total derivative of (15), we have

$$\dot{\mathcal{E}}_A = \text{Re}\sum_{m=1}^{M} w_m[\phi(\mathbf{r}_m)-\phi_{\text{obs}}(\mathbf{r}_m)]^*\phi'(\mathbf{r}_m) + \text{Re}\{\dot{\Psi}_\lambda\}, \tag{16}$$

where, in obtaining this result, we have used the fact that $\dot{\phi}(\mathbf{r}_m)=\phi'(\mathbf{r}_m)$. This follows because the observation points, $\mathbf{r}_m$, are fixed and are not allowed to move as the domain, Ω, is deformed.

Our objective now is to evaluate $\dot{\Psi}_\lambda$. When the domain is deformed, (14) becomes

$$\begin{aligned}\Psi_\lambda(\tau) &= \int_{\Omega_\tau}\lambda_\tau(\nabla^2\phi_\tau+k^2\phi_\tau)d\Omega_\tau \\ &= \int_{\Omega_\tau}[-\nabla\phi_\tau\cdot\nabla\lambda_\tau+k^2\lambda_\tau\phi_\tau]d\Omega_\tau \\ &\quad + \int_{\Gamma_\tau}\lambda_\tau\nabla\phi_\tau\cdot\hat{n}_\tau d\Gamma_\tau \\ &= \int_{\Omega_\tau}[-\nabla\phi_\tau\cdot\nabla\lambda_\tau+k^2\lambda_\tau\phi_\tau]d\Omega_\tau,\end{aligned} \tag{17}$$

where the second line results on integrating by parts and the third line results on noting that the surface integral in the second line vanished due to the boundary condition (7). For brevity, define

$$c(\phi,\lambda) \equiv -\nabla\phi\cdot\nabla\lambda+k^2\phi\lambda, \tag{18}$$

so that (17) may be written

$$\Psi_\lambda(\tau) = \int_{\Omega_\tau} c(\phi_\tau,\lambda_\tau)d\Omega_\tau, \tag{19}$$

which is of the form (10). Now using (12), the total derivative of Ψ_λ is

$$\dot{\Psi}_\lambda = \int_\Omega \frac{\partial c(\phi,\lambda)}{\partial\tau}d\Omega + \int_\Gamma c(\phi,\lambda)\mathbf{v}\cdot\hat{n}d\Gamma, \tag{20}$$

where it is understood that all partial derivatives with respect to τ are to be evaluated at $\tau=0$; we have thus dropped the subscript τ on ϕ and λ in (20). Now note that, from (18),

$$\frac{\partial c(\phi,\lambda)}{\partial\tau} = c(\phi',\lambda)+c(\phi,\lambda'), \tag{21}$$

so (20) becomes

$$\dot{\Psi}_\lambda = \int_\Omega [c(\phi',\lambda)+c(\phi,\lambda')]d\Omega + \int_\Gamma c(\phi,\lambda)\mathbf{v}\cdot\hat{n}d\Gamma. \tag{22}$$

The term involving $c(\phi,\lambda')$ in the first integral vanishes as we now show. Integrating by parts and using the divergence theorem, we have

$$\begin{aligned}\int_\Omega c(\phi,\lambda')d\Omega &= \int_\Omega[-\nabla\phi\cdot\nabla\lambda'+k^2\phi\lambda']d\Omega \\ &= \int_\Omega \lambda'[\nabla^2\phi+k^2\phi]d\Omega \\ &\quad + \int_\Gamma \lambda'\nabla\phi\cdot\hat{n}d\Gamma = 0,\end{aligned}$$

from (1) and (2). Thus (22) reduces to

$$\dot{\Psi}_\lambda = \int_\Omega c(\phi',\lambda)d\Omega + \int_\Gamma c(\phi,\lambda)\mathbf{v}\cdot\hat{n}d\Gamma. \tag{23}$$

Now define the adjoint source

$$\tilde{S} \equiv \sum_{m=1}^{M} w_m[\phi(\mathbf{r}_m)-\phi_{\text{obs}}(\mathbf{r}_m)]^*\delta(\mathbf{r}-\mathbf{r}_m), \tag{24}$$

where $\delta(\mathbf{r}-\mathbf{r}_m)$ is a 3D Dirac delta function. Then (16) can be written, on substituting (24) and (23),

$$\dot{\mathcal{E}}_A = \mathrm{Re}\left\{ \int_\Omega \tilde{S}(\mathbf{r})\phi'(\mathbf{r})d\Omega + \int_\Omega c(\phi',\lambda)d\Omega + \int_\Gamma c(\phi,\lambda)\mathbf{v}\cdot\hat{n}d\Gamma \right\}. \quad (25)$$

From the definition of $c(\phi,\lambda)$ given by (18), this may be written

$$\dot{\mathcal{E}}_A = \mathrm{Re}\left\{ \int_\Omega [\tilde{S}(\mathbf{r})\phi'(\mathbf{r}) - \nabla\phi'\cdot\nabla\lambda + k^2\phi'\lambda]d\Omega + \int_\Gamma c(\phi,\lambda)\mathbf{v}\cdot\hat{n}d\Gamma \right\}. \quad (26)$$

Integrating the $\nabla\phi'\cdot\nabla\lambda$ term by parts and using the divergence theorem, this becomes

$$\dot{\mathcal{E}}_A = \mathrm{Re}\left\{ \int_\Omega [\tilde{S} + \nabla^2\lambda + k^2\lambda]\phi' d\Omega + \int_\Gamma \phi'\nabla\lambda\cdot\hat{n}d\Gamma + \int_\Gamma c(\phi,\lambda)\mathbf{v}\cdot\hat{n}d\Gamma \right\}. \quad (27)$$

We wish to eliminate all terms multiplying the unknown derivative ϕ'. To accomplish this, we define the adjoint equation,

$$\nabla^2\lambda + k^2\lambda = -\tilde{S}, \quad (28)$$

subject to the boundary condition on Γ:

$$\nabla\lambda\cdot\hat{n}|_\Gamma = 0. \quad (29)$$

Thus, when (28) and (29) hold, (27) reduces to

$$\dot{\mathcal{E}}_A = \mathrm{Re}\int_\Gamma c(\phi,\lambda)\mathbf{v}\cdot\hat{n}d\Gamma. \quad (30)$$

This is our fundamental result. Equation (30) gives the change in the mean-square error due to a change in the deformation parameter, τ, in terms of the ''deformation field,'' $\mathbf{v}(\mathbf{r})$. Our next step is to relate $\mathbf{v}(\mathbf{r})$ to a set of parameters, p_n, $n=1,...,N$, which define the surface Γ.

III. SURFACE PARAMETERIZATION

Here we consider the problem of surface parameterization. Suppose the boundary is parameterized with N variables, p_n, $n=1,...,N$, which we assume represent the components of a vector, $\mathbf{p}$. We express this parameterization by writing the position vector of a point $\mathbf{r}$ on the surface Γ as a function of $\mathbf{p}$,

$$\mathbf{r} = \mathbf{r}(\mathbf{p}), \quad \mathbf{r}\in\Gamma. \quad (31)$$

Now when the domain Ω is deformed, each parameter will change as follows:

$$p_{n\tau} = p_n + \tau\delta p_n, \quad (32)$$

and the point $\mathbf{r}$ on the surface will change to $\mathbf{r}_\tau = \mathbf{r} + \tau\mathbf{v}(\mathbf{r})$. We then have

$$\mathbf{v}(\mathbf{r}) = \left.\frac{\partial\mathbf{r}_\tau}{\partial\tau}\right|_{\tau=0} = \sum_{n=1}^N \frac{\partial\mathbf{r}_\tau}{\partial p_{n\tau}}\left.\frac{\partial p_{n\tau}}{\partial\tau}\right|_{\tau=0} = \sum_{n=1}^N \frac{\partial\mathbf{r}}{\partial p_n}\delta p_n, \quad (33)$$

from (32). Now substituting this into (30), we obtain on interchanging orders of integration and summation,

$$\dot{\mathcal{E}}_A \equiv \frac{d\mathcal{E}_A}{d\tau} = \mathrm{Re}\sum_{n=1}^N \left\{ \int_\Gamma c(\phi,\lambda)\left[\hat{n}\cdot\frac{\partial\mathbf{r}}{\partial p_n}\right]d\Gamma \right\}\delta p_n. \quad (34)$$

But we also have

$$\frac{d\mathcal{E}_A}{d\tau} = \sum_{n=1}^N \frac{\partial\mathcal{E}_A}{\partial p_{n\tau}}\left.\frac{\partial p_{n\tau}}{\partial\tau}\right|_{\tau=0} = \sum_{n=1}^N \frac{\partial\mathcal{E}_A}{\partial p_n}\delta p_n. \quad (35)$$

Comparing (34) and (35), since δp_n is arbitrary, we have

$$\frac{\partial\mathcal{E}_A}{\partial p_n} = \mathrm{Re}\int_\Gamma c(\phi,\lambda)\left[\hat{n}\cdot\frac{\partial\mathbf{r}}{\partial p_n}\right]d\Gamma. \quad (36)$$

This is the fundamental result when the surface is defined by a set of discrete parameters. To evaluate (36), at each iteration of the algorithm, the solution to two forward problems are numerically solved to obtain ϕ and the adjoint field λ by numerically solving, respectively, the reduced wave equation (1) subject to the boundary condition (2), and the adjoint wave equation (28) subject to the same boundary condition (29). The adjoint equation is driven by the source given by (24). Once these field are computed, (36) then provides the derivatives of the mean-square error with respect to the shape parameters, p_n. We consider next an example of a finite-dimensional surface parameterization in two dimensions.

A. Circular harmonic surface expansion

Suppose scattering takes place from a cylinder whose boundary can be parameterized by a radial distance, $R(\theta)$, prescribed as a function of angle, θ, measured from some convenient origin inside the cylinder. We assume that $R(\theta)$ is single valued. Thus the 2D boundary curve is given by the vector

$$\mathbf{r} = \hat{r}R(\theta), \quad (37)$$

where $\hat{r}$ is the radial unit vector. Since the function $R(\theta)$ is periodic, we can expand it in a Fourier series. Suppose we keep the first N terms in the series; then

$$R(\theta) = \sum_{n=0}^N [a_n\cos(n\theta) + b_n\sin(n\theta)], \quad (38)$$

where the coefficients, a_n and b_n, are the parameters that we seek. Thus we have a total of $2N+1$ unknown parameters (since $b_0\equiv 0$). From (37) and (38), we note that

$$\frac{\partial\mathbf{r}}{\partial a_n} = \hat{r}\cos(n\theta) \quad \text{and} \quad \frac{\partial\mathbf{r}}{\partial b_n} = \hat{r}\sin(n\theta). \quad (39)$$

Now the unit normal vector, $\hat{n}$, can be expressed in terms of the radial unit vector, $\hat{r}$, and the angular unit vector, $\hat{\theta}$, as follows:

$$\hat{n} = \frac{R\hat{r} - R'\hat{\theta}}{\sqrt{R^2+R'^2}}, \quad (40)$$

where $R' \equiv dR/d\theta$. An element of arc length along the boundary curve, $d\Gamma$, can be rewritten in terms of $d\theta$ using

$$d\Gamma = \frac{d\Gamma}{d\theta} d\theta = \sqrt{R^2 + R'^2}\, d\theta,$$

so $\hat{r} \cdot \hat{n} d\Gamma = R(\theta) d\theta$, and (36) becomes in this case

$$\frac{\partial \mathcal{E}_A}{\partial a_n} = \mathrm{Re} \int_0^{2\pi} c(\phi, \lambda) R(\theta) \cos(n\theta) d\theta, \tag{41}$$

$$\frac{\partial \mathcal{E}_A}{\partial b_n} = \mathrm{Re} \int_0^{2\pi} c(\phi, \lambda) R(\theta) \sin(n\theta) d\theta. \tag{42}$$

B. Polygonal surface

Here we consider a 2D object having the shape of an N-sided polygon. The object boundary is thus comprised of N straight line segments each of unknown length and orientation. Denote by $\mathbf{p}_j$, $j = 1,...,N$, the coordinate vectors of the end points of each of these segments. We let the $2N$ components of these vectors [where we write $\mathbf{p}_j = (p_{xj}, p_{yj})$] represent our unknown shape parameters. Define the jth line segment as having end points $\mathbf{p}_{j-1}$ and $\mathbf{p}_j$. Let s denote arc length along the boundary segments. We can then define a vector from some fixed origin to a point on the jth segment as

$$\mathbf{r}_j(s) = \mathbf{p}_{j-1} + f_j(s)(\mathbf{p}_j - \mathbf{p}_{j-1}), \quad s_{j-1} \leqslant s \leqslant s_j, \tag{43}$$

where

$$f_j(s) \equiv \frac{s - s_{j-1}}{s_j - s_{j-1}}. \tag{44}$$

Thus, $f_j(s)$ ranges between 0 and 1 as s ranges between s_{j-1} and s_j. Replacing j by $j+1$ in (43) gives

$$\mathbf{r}_{j+1}(s) = \mathbf{p}_j + f_{j+1}(s)(\mathbf{p}_{j+1} - \mathbf{p}_j), \quad s_j \leqslant s \leqslant s_{j+1}. \tag{45}$$

Differentiating (43) and (45) with respect to the parameter p_{jx}, we obtain

$$\frac{\partial \mathbf{r}_j(s)}{\partial p_{jx}} = f_j(s)\hat{x}, \quad s_{j-1} \leqslant s \leqslant s_j, \tag{46}$$

$$\frac{\partial \mathbf{r}_{j+1}(s)}{\partial p_{jx}} = [1 - f_{j+1}(s)]\hat{x}, \quad s_j \leqslant s \leqslant s_{j+1}, \tag{47}$$

where $\hat{x}$ is the x unit vector. Similar equations hold for the derivative with respect to p_{jy} with $\hat{x}$ replaced with $\hat{y}$. Substituting into (36) and denoting by $\hat{n}_j$ the unit vector normal to the jth line segment, we then have

$$\begin{aligned}\frac{\partial \mathcal{E}_A}{\partial p_{jx}} = \mathrm{Re} &\int_{s_{j-1}}^{s_j} c(\phi, \lambda)|_{\mathbf{r}=\mathbf{r}_j(s)} f_j(s)\hat{x} \cdot \hat{n}_j ds \\ &+ \mathrm{Re} \int_{s_j}^{s_{j+1}} c(\phi, \lambda)|_{\mathbf{r}=\mathbf{r}_{j+1}(s)} \\ &\times [1 - f_{j+1}(s)]\hat{x} \cdot \hat{n}_{j+1} ds.\end{aligned} \tag{48}$$

A similar relation holds for $\partial \mathcal{E}_A / \partial p_{jy}$, with $\hat{x}$ replaced by $\hat{y}$ in (48).

IV. TIME-DEPENDENT CASE

Here we assume time-dependent fields and suppose that the scatterer is illuminated with the incident transient field, $\phi_i(\mathbf{r}, t)$. The total field (incident plus scattered) is $\phi(\mathbf{r}, t)$ and assumed to obey the time-dependent wave equation

$$\nabla^2 \phi(\mathbf{r}, t) - \frac{1}{c^2} \frac{\partial^2 \phi(\mathbf{r}, t)}{\partial t} = 0, \quad \mathbf{r} \in \Omega, \tag{49}$$

subject to the boundary condition on the surface

$$\nabla \phi(\mathbf{r}, t) \cdot \hat{n} = 0, \quad \mathbf{r} \in \Gamma, \tag{50}$$

and the initial conditions

$$\phi(\mathbf{r}, 0) = \left. \frac{\partial \phi(\mathbf{r}, t)}{\partial t} \right|_{t=0} = 0. \tag{51}$$

That is, we "turn on" the incident field after $t = 0$. We also assume that the field observations, $\phi_{\mathrm{obs}}(\mathbf{r}_m, t)$, are made over the time interval $[0, T]$ at the M points r_m. We modify the mean-square error to include a time integration over the observation interval

$$\mathcal{E} = \frac{1}{2} \sum_{m=1}^{M} \int_0^T w_m(t)[\phi(\mathbf{r}_m, t) - \phi_{\mathrm{obs}}(\mathbf{r}_m, t)]^2 dt, \tag{52}$$

where the positive weight function, $w_m(t)$, we allow to be time dependent for generality. The augmented mean-square error functional now becomes

$$\mathcal{E}_A = \frac{1}{2} \sum_{m=1}^{M} \int_0^T w_m(t)[\phi(\mathbf{r}_m, t) - \phi_{\mathrm{obs}}(\mathbf{r}_m, t)]^2 dt + \Psi_\lambda, \tag{53}$$

where the constraint term now reads

$$\Psi_\lambda \equiv \int_\Omega d\Omega \int_0^T dt \lambda(\mathbf{r}, t) \left[\nabla^2 \phi(\mathbf{r}, t) - \frac{1}{c^2} \frac{\partial^2 \phi(\mathbf{r}, t)}{\partial t} \right], \tag{54}$$

and the Lagrange multiplier, $\lambda(\mathbf{r}, t)$, is now time and space dependent. The total derivative of the augmented mean-square error, $\mathcal{E}_A$, is then

$$\begin{aligned}\dot{\mathcal{E}}_A = &\sum_{m=1}^{M} \int_0^T w_m(t)[\phi(\mathbf{r}_m, t) - \phi_{\mathrm{obs}}(\mathbf{r}_m, t)]\phi'(\mathbf{r}_m, t) dt \\ &+ \dot{\Psi}_\lambda.\end{aligned} \tag{55}$$

We wish to evaluate $\dot{\Psi}_\lambda$. Integrating (54) by parts with respect to both space and time, we have

$$\Psi_\lambda \equiv \int_\Omega d\Omega \int_0^T dt \left[-\nabla \phi \cdot \nabla \lambda + \frac{1}{c^2} \frac{\partial \phi}{\partial t} \frac{\partial \lambda}{\partial t} \right]. \tag{56}$$

In performing the integration by parts with respect to time, an integrated term results, but this term vanishes on account of the initial conditions (51) and the "terminal condition" $\lambda(\mathbf{r}, T) = 0$, which we shall assume. Defining

$$c(\phi, \lambda) \equiv \int_0^T \left[-\nabla \phi \cdot \nabla \lambda + \frac{1}{c^2} \frac{\partial \phi}{\partial t} \frac{\partial \lambda}{\partial t} \right] dt, \tag{57}$$

(56) may be written

$$\Psi_\lambda \equiv \int_\Omega c(\phi,\lambda)\, d\Omega. \tag{58}$$

The total derivative of this with respect to τ is, in view of (12),

$$\dot{\Psi}_\lambda = \int_\Omega c(\phi',\lambda)\, d\Omega + \int_\Gamma c(\phi,\lambda)\mathbf{v}\cdot\hat{n}\, d\Gamma. \tag{59}$$

Now define the time- and space-dependent adjoint source as follows:

$$\tilde{S}(\mathbf{r},t) \equiv \sum_{m=1}^{M} w_m(t)[\phi(\mathbf{r}_m,t) - \phi_{\text{obs}}(\mathbf{r}_m,t)]. \tag{60}$$

Thus (55) can be written

$$\dot{\mathcal{E}}_A = \int_\Omega d\Omega \int_0^T dt \tilde{S}\phi' + \int_\Omega d\Omega \int_0^T dt \left[-\nabla\phi'\cdot\nabla\lambda + \frac{1}{c^2}\frac{\partial\phi'}{\partial t}\frac{\partial\lambda}{\partial t}\right] + \int_\Gamma c(\phi,\lambda)\mathbf{v}\cdot\hat{n}\, d\Gamma. \tag{61}$$

This can be written again on integrating by parts

$$\dot{\mathcal{E}}_A = \int_\Omega d\Omega \int_0^T dt \left[\nabla^2\lambda - \frac{1}{c^2}\frac{\partial^2\lambda}{\partial t^2} + \tilde{S}\right]\phi' - \int_\Gamma d\Gamma \int_0^T dt\, \phi' \nabla\lambda\cdot\hat{n} + \int_\Omega d\Omega\, \phi' \left.\frac{\partial\lambda}{\partial t}\right|_0^T + \int_\Gamma c(\phi,\lambda)\mathbf{v}\cdot\hat{n}\, d\Gamma. \tag{62}$$

We now require that $\lambda(\mathbf{r},t)$ obey the following wave equation:

$$\nabla^2\lambda - \frac{1}{c^2}\frac{\partial^2\lambda}{\partial t^2} = -\tilde{S}, \tag{63}$$

subject to the boundary condition

$$\nabla\lambda\cdot\hat{n}|_{\mathbf{r}\in\Gamma}, \tag{64}$$

and the ''terminal conditions,''

$$\lambda(\mathbf{r},T) = \left.\frac{\partial\lambda(\mathbf{r},t)}{\partial t}\right|_{t=T} = 0. \tag{65}$$

The first two terms in (62) vanish on account of (63) and (64). For the third term to vanish we require the terminal conditions (65) and the initial condition $\phi'(\mathbf{r},0)=0$, which follows from (51). When these conditions are satisfied, (62) reduces to

$$\dot{\mathcal{E}} = \int_\Gamma c(\phi,\lambda)\mathbf{v}\cdot\hat{n}\, d\Gamma = \int_\Gamma d\Gamma \int_0^T dt \left[-\nabla\phi\cdot\nabla\lambda + \frac{1}{c^2}\frac{\partial\phi}{\partial t}\frac{\partial\lambda}{\partial t}\right]\mathbf{v}\cdot\hat{n}. \tag{66}$$

This is the time-domain analog of (30).

V. ANALYTICAL EXAMPLE

It is a useful exercise to verify the relation (36) using a very simple example that can be treated analytically. Although the power of the technique becomes apparent in more complex problems (in which the number of parameters, N, is large), this example shows that the adjoint method agrees with a direct differentiation of the mean-square error. Consider a plane wave of unit amplitude incident upon a cylinder of radius a. The wave obeys the Helmholtz equation (1) subject to the boundary condition (2). Denote the solution in cylindrical coordinates by $\phi(r,\theta)$. We wish to recover the radius, a, of the cylinder with a single observation at the point (r_0,θ_0). The total field (incident plus scattered) can be shown to be[7]

$$\phi(r,\theta) = \sum_{n=-\infty}^{\infty} i_n e^{in\theta}\left[J_n(kr) - \frac{J_n'(ka)}{H_n^{(1)'}(ka)} H_n^{(1)}(kr)\right], \tag{67}$$

where J_n and $H_n^{(1)}$ are Bessel and Hankel functions. The prime indicates differentiation with respect to the argument of the function. To obtain the radius of the cylinder, we wish to minimize the squared error

$$\mathcal{E} = \tfrac{1}{2}|\phi(r_0,\theta_0) - \phi_{\text{obs}}(r_0,\theta_0)|^2 \tag{68}$$

with respect to the radius, a. Here, $\phi_{\text{obs}}(r_0,\theta_0)$ is the observation at the point (r_0,θ_0). Our objective is to compute $\partial\mathcal{E}/\partial a$. Since we have an expression, given by (67), that gives the explicit functional dependence of the field on a, we can directly differentiate the squared error (68) to give

$$\frac{\partial\mathcal{E}}{\partial a} = \text{Re}\left\{ [\phi(r_0,\theta_0) - \phi_{\text{obs}}(r_0,\theta_0)]^* \frac{\partial\phi(r_0,\theta_0)}{\partial a}\right\}, \tag{69}$$

where $\partial\phi(r_0,\theta_0)/\partial a$ is obtained by differentiating (67) with respect to a. We should, however, get the same result using the adjoint formula (30), which in this case reads

$$\frac{\partial\mathcal{E}}{\partial a} = \text{Re}\int_0^{2\pi} [-\nabla\phi\cdot\nabla\lambda + k^2\phi\lambda]|_{r=a}\, a\, d\theta, \tag{70}$$

where the integration is around the surface of the cylinder and $\lambda(r,\theta)$ is the adjoint solution that obeys (28) and (29) with the adjoint source given by (24). In this case, $\lambda(r,\theta)$ is the solution to

$$\nabla^2\lambda + k^2\lambda = -[\phi(r_0,\theta_0) - \phi_{\text{obs}}(r_0,\theta_0)]^* \frac{1}{r} \times \delta(r-r_0)\,\delta(\theta-\theta_0), \tag{71}$$

subject to the boundary condition (29). For brevity, define the residual

$$R \equiv \phi(r_0,\theta_0) - \phi_{\text{obs}}(r_0,\theta_0). \tag{72}$$

Then the solution to (71) can be shown to be

$$\lambda(r,\theta)=\frac{iR^*}{4}\sum_{n=-\infty}^{\infty} i_n e^{in(\theta-\theta_0)}H_n^{(1)}(kr_0)$$
$$\times\left[J_n(kr)-\frac{J_n'(ka)}{H_n^{(1)'}(ka)}H_n^{(1)}(kr)\right]. \tag{73}$$

If we substitute $\phi(r,\theta)$ and $\lambda(r,\theta)$, given by (67) and (73), into (70) and integrate, we obtain the result

$$\frac{\partial \mathcal{E}}{\partial a}=\frac{2}{\pi a k^2}\mathrm{Re}\left\{iR^*\sum_{n=-\infty}^{\infty} i_n e^{in\theta_0}\frac{H_n^{(1)}(kr_0)}{H_n^{(1)'}(ka)^2}\right.$$
$$\left.\times\left[\frac{n^2}{a^2}-k^2\right]\right\}. \tag{74}$$

In obtaining this result, we have made use of the Wronskian

$$J_n(ka)H_n^{(1)'}(ka)-J_n'(ka)H_n^{(1)}(ka)=\frac{2i}{\pi ka}. \tag{75}$$

When we perform the direct differentiation (69) using (68) and setting $r=r_0$ and $\theta=\theta_0$, and again using (75), we obtain after some algebra the same result (74).

VI. CONCLUSION

In this paper, we consider the problem of reconstructing the shape or boundary of a hard acoustic scatterer. Explicit relations are derived for the derivatives of the mean-square error with respect to a set of parameters that defines the surface of the scattering object. Both steady-state and time-dependent problems are treated. In deriving the functional gradient of the mean-square error, we make use of the concept of the ''material derivative,'' used previously for computing design sensitivities in the analysis of engineering structures. The method works for very general parametric representations of the surface. As simple 2D examples, we considered circular harmonic and polygonal representations of the object's surface. From these examples, it should be clear how other representations can be derived, such as a spherical harmonic expansion of a 3D surface, or a spline approximation to a surface. In the latter case, the coordinates of the nodes of the spline functions could be taken as the parameters to be determined. We finally note that the adjoint approach can be extended to the case of determining the shape of a ''soft'' and homogeneous object into which the fields penetrate.

APPENDIX

Here we present a simple derivation of the key relation (12) borrowed from Ref. 6. A more rigorous derivation can also be found in the aforementioned reference. If

$$\Psi(\tau)=\int_{\Omega_\tau} G(\phi_\tau)d\Omega_\tau,$$

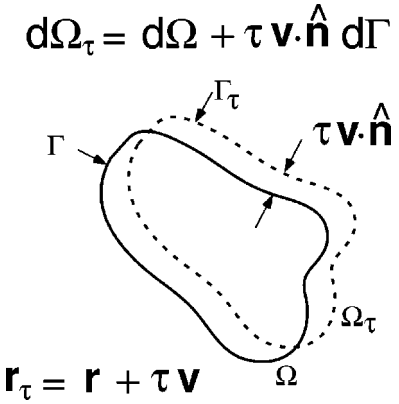

FIG. 1. Illustration of an infinitesimal variation of the domain Ω.

then

$$\dot{\Psi}\equiv\lim_{\tau\to 0}\frac{1}{\tau}\left\{\int_{\Omega_\tau} G(\phi_\tau)d\Omega_\tau-\int_{\Omega} G(\phi)d\Omega\right\}$$
$$=\lim_{\tau\to 0}\frac{1}{\tau}\int_{\Omega}[G(\phi_\tau)-G(\phi)]d\Omega_\tau$$
$$+\lim_{\tau\to 0}\frac{1}{\tau}\int_{\Omega} G(\phi)[d\Omega_\tau-d\Omega]$$
$$=\int_{\Omega}\left.\frac{\partial G(\phi_\tau)}{\partial\tau}\right|_{\tau=0}d\Omega+\int_{\Omega} G(\phi)\lim_{\tau\to 0}\frac{1}{\tau}[d\Omega_\tau-d\Omega]. \tag{A1}$$

From Fig. 1, we see that, for infinitesimally small τ,

$$d\Omega_\tau=d\Omega+\tau\mathbf{v}\cdot\hat{n}d\Gamma,$$

and substituting this into (A1) gives (12), as desired.

[1] S. J. Norton, ''Iterative inverse-scattering algorithms: Methods for computing the Frechet derivative,'' J. Acoust. Soc. Am. **106**, 2653–2660 (1999).
[2] O. Dorn, E. L. Miller, and C. M. Rappaport, ''A shape reconstruction method for electromagnetic tomography using adjoint fields and level sets,'' Inverse Probl. **16**, 1119–1156 (2000).
[3] O. Dorn, ''Shape reconstruction in scattering media with voids using a transport model and level sets,'' Can. Appl. Math. Quart. **10**, 239–275 (2002).
[4] E. J. Haug, K. K. Choi, J. W. Hou, and Y. M. Yoo, ''A variational method for shape optimal design of elastic structures,'' in *New Directions in Optimal Structure Design*, edited by E. Atrek (Wiley, New York, 1984), pp. 105–137.
[5] E. J. Haug, K. K. Choi, and V. Komkov, *Design Sensitivity Analysis of Structural Systems* (Academic, Orlando, 1986).
[6] In Ref. 5, Sec. 3.2.
[7] P. M. Morse and K. U. Ingard, *Theoretical Acoustics* (McGraw–Hill, New York, 1968).

A nonreciprocal implementation of time reversal in the ocean

Philippe Roux,[a] W. A. Kuperman, W. S. Hodgkiss, Hee Chun Song, and T. Akal
Marine Physical Laboratory, Scripps Institution of Oceanography, University of California, San Diego, La Jolla, California 92093-0238

Mark Stevenson
NATO Undersea Research Centre, La Spezia, Italy

(Received 24 November 2003; revised 20 February 2004; accepted 27 February 2004)

The performance of a time reversal mirror (TRM) in complex ocean scenarios can be evaluated without invoking spatial reciprocity in the experimental procedure. The experimental implementation requires connectivity between a source array and a receiver array but eliminates the requirement of actually having a probe source collocated with the receiver array. It is shown with data taken in a recent experiment that this streamlined, nonreciprocity-based time reversal procedure yields results potentially better than the classical time reversal method. Further, it provides a more versatile method to study a TRM in a fluctuating medium. © *2004 Acoustical Society of America.* [DOI: 10.1121/1.1707089]

PACS numbers: 43.60.Tj, 43.30.Pc. [DRD] Pages: 1009–1015

I. INTRODUCTION

Acoustic time reversal mirrors (TRMs) have been implemented in the laboratory[1,2] and at sea.[3–7] Classically, time reversal (TR) is based on spatial reciprocity and time symmetry of the wave equation. To avoid any confusion with earlier work,[8] we wish to distinguish between spatial reciprocity and the impact of temporal fluctuations in a medium. By definition,[9] spatial reciprocity (and thus time reversal[10]) is broken when a steady-state (time-invariant) flow or a vorticity field is present in the medium. In the presence of a flow, the Green's function between two points remains constant over time, but the forward and backward Green's functions are different. Based on this principle, reciprocity measurements have been used for a long time to measure steady-state currents at sea.[11] Temporal fluctuations in the medium cannot be considered the same way as steady-state currents because they also affect the one-way Green's function. Time-reversal requires spatial reciprocity because of the two-way propagation of the acoustic field (Fig. 1). Indeed, a successful time reversal requires both forward and backward Green's functions between a source and a TRM to be identical, i.e., spatial reciprocity. In the literature, temporal fluctuations and steady-state currents often are placed in the same category of effects inhibiting successful time-reversal experiments.[8] However, their acoustic consequences on time-reversal are different. For example, time-reversal can survive slowly varying ocean fluctuations but still suffer from reciprocity-breaking stationary currents.[12]

Throughout this paper, we present an experimental implementation of time reversal in the ocean without the need for spatial reciprocity in the propagation medium. This nonreciprocity-based time reversal (NR-TR) is built from the forward propagation between the TRM and the desired focal point. The results are compared with the classical procedure between a probe source and a TRM. Aside from obtaining equivalent results when appropriate, it is clear that the NR-TR procedure provides a method to study the time reversal physics in a complicated, time-varying medium to a detail that experimenters, until now, had not yet achieved.

The paper is structured as follows. In Sec. II, we describe the implementation of nonreciprocity-based TR (both active and passive) and we underline the differences with the classical TR procedure. In Sec. III, we compare at-sea experimental results between classical TR and NR-TR. Finally, we show that NR-TR provides research results that would either be impractical or not even possible to obtain by the classical procedure as constrained by the realities of an ocean experiment.

II. IMPLEMENTATION OF NONRECIPROCITY-BASED TIME REVERSAL

In the classical TR configuration, a probe source ensonifies a source-receiver array [Figs. 1(a) and (b)] that retransmits a time-reversed version of the received signals at each element [Fig. 1(c)]. The result is a focus at the original probe source position [Fig. 1(d)].

The procedure discussed in this paper combines the use of a source array (SA) and a receiver array (RA) with a new time-reversal procedure schematically shown in Fig. 2. Practically speaking, a pulsed signal is emitted sequentially (with a time delay T) by each element of the SA [Fig. 2(a)]. The refracted and/or reflected signals recorded at one point of the RA are sent back to the SA [Fig. 2(b)] via an external connection (for example, by means of radio telemetry in the ocean or more simply using a wired connection in ultrasonics). The signals then are synchronized, time-reversed, and loaded into the memory of the SA. Here, the synchronization consists in cutting the received successive signals into pieces of duration T and addressing each signal to the corresponding SA element [Fig. 2(c)]. After propagation, the time reversed field then will naturally focus at the desired point [Fig. 2(d)]. To be effective, note that the time delay T must be longer than the impulse response of the propagation me-

[a]Electronic mail: philippe@mpl.ucsd.edu

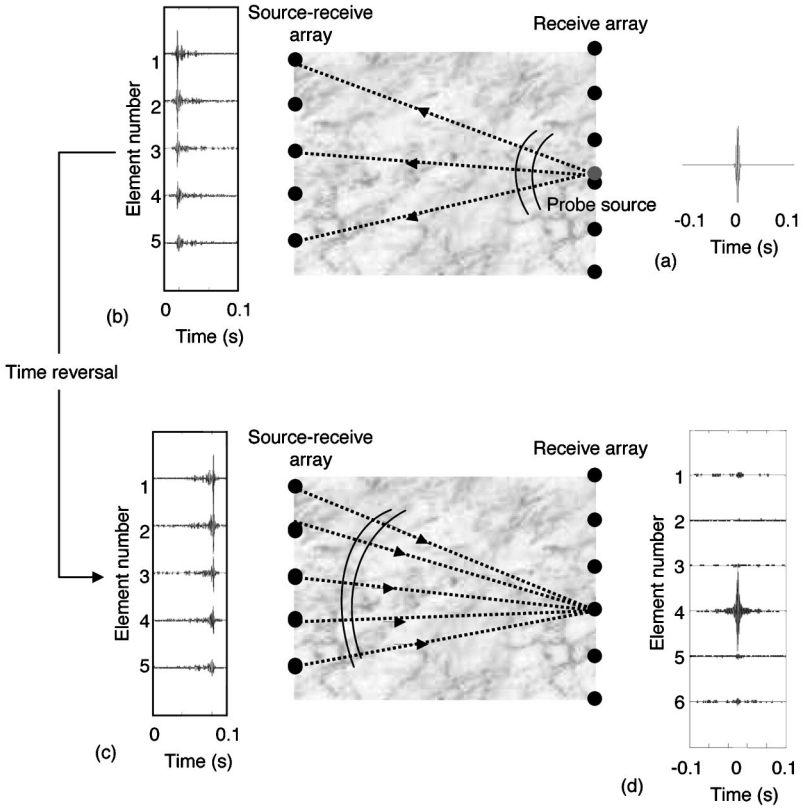

FIG. 1. Schematic of a classical TR implementation. The experimental data involved are discussed in Sec. III. A source-receiver array (SRA) is facing a receive array (RA). A probe source (PS) is collocated with one element of the RA. The propagation medium between the two arrays can be a complex reverberating/scattering medium. (a) The PS emits a pulsed signal. (b) The incident field is received on the RA. (c) The field is time reversed and transmitted back from the SRA. (d) The time-reversed field focuses back at the PS location and is recorded on the RA.

dium. An alternative to obtain the Green's function between the SA and the RA would be the use of N orthogonal signals sent simultaneously from the N-element SA. The correlation of the signal received on every RA element by the set of orthogonal signals yields the impulse responses between the two arrays without synchronization. In the configuration of Fig. 2, no probe source is required but an external connection is needed between the SA and the RA. The main difference with classical TR is that the acoustic field propagates twice from the SA to the focal point on the RA but never, as in classical TR, from the focal point to the TRM. As a consequence, the advantage of this implementation of time reversal is that it provides a good focus even when spatial reciprocity does not hold in the medium. However, as with classical TR, the medium must remain stationary enough during this time-reversal procedure to achieve a good focus. The medium stationarity may become dramatically important when the use of an external connection induces delays in the

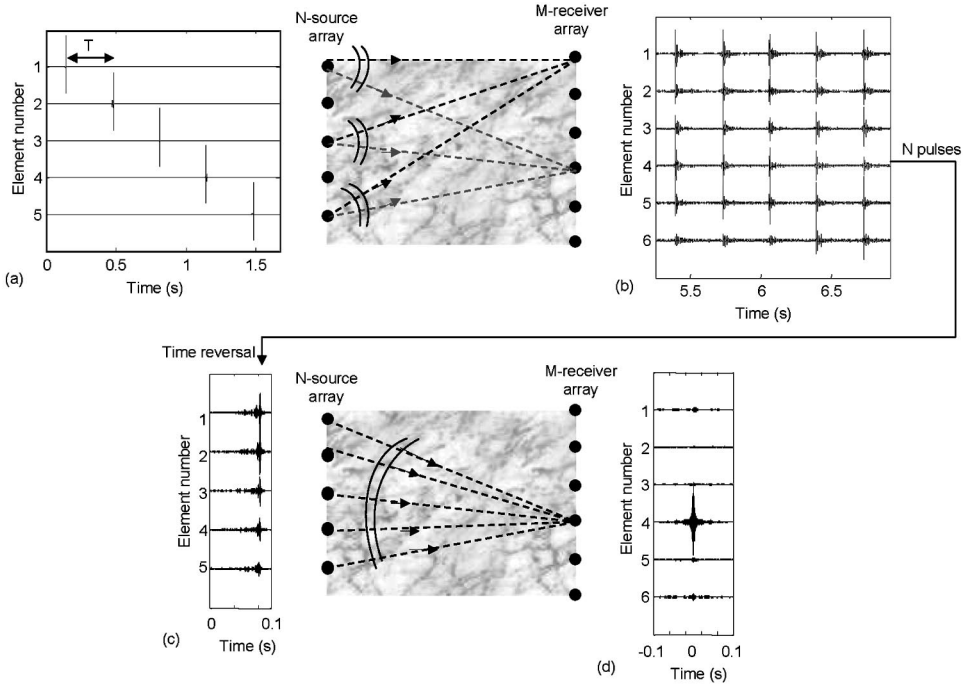

FIG. 2. Schematic of a NR-TR implementation. The experimental data involved are discussed in Sec. III. An N-element source array (SA) is facing an M-element receive array (RA). The propagation medium between the two arrays can be a complex reverberating/scattering medium. (a) The SA sequentially emits pulsed signals from each of its N elements. (b) After propagation, each RA element records N dispersed signals. (c) The N signals received on a selected RA element are sent back to the SA using an external connection (e.g., radio telemetry). The signals are time-reversed, time-aligned, and transmitted by the corresponding SA elements. (d) The time-reversed field focuses back at the chosen RA element.

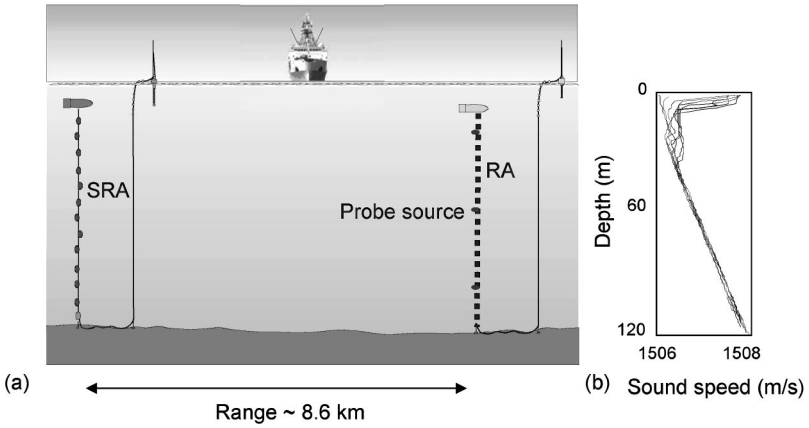

FIG. 3. Experimental setup at sea. (a) On the left, a bottom-moored source-receiver array (SRA) consisting of 29 transducers centered at 3.5 kHz that cover 78 m of the water column. On the right, a bottom-moored receiver array (RA) consisting of 32 hydrophones with 90 m aperture. The three large transducers on the RA correspond to probe sources at 40, 60, and 80 m. The two surface buoys contain batteries and rf telemetry hardware for data communication with ship. The water depth is 118 m and the distance between the SRA and the RA is 8.6 km. (b) Collection of sound speed profiles recorded in the area the same day the acoustic experiment was performed. The average temperature profile is nearly uniform leaving the sound speed profile with a constant pressure-related gradient.

transmission of the data back from the RA to the SA before active TR can be achieved. An alternative consists of performing passive TR without connection between the SA and the RA by cross-correlating the direct fields received on the RA at different times. To summarize, starting from the measurement of the impulse-response matrix between the SA and the RA [Fig. 2(b)], one has two options to finish the time-reversal implementation.

Procedure 1: As depicted in Fig. 2, construct from the received signal on the ith RA element the time-reversed field as input to the SA [Fig. 2(c)] and actually perform a physical transmission to focus on the ith RA position [Fig. 2(d)]. If spatial reciprocity holds in the medium, this active NR-TR procedure is equivalent to classical TR achieved with a probe source collocated with the ith RA element (Fig. 1).

Procedure 2: The waveguide impulse-response matrix being known from measurement, the full time reversal process can be obtained by simply cross-correlating the outgoing signals received at different times. The focal spot $f(t,z_{rk})$ on the ith element of the RA is implemented numerically using

$$f(t,z_{rk})=\sum_{j=1}^{N} h(r,z_{ri},t;0,z_{sj},0)\otimes h(r,z_{rk},t;0,z_{sj},0), \tag{1}$$

where $\otimes$ refers to correlation, defined as $h_1(t)\otimes h_2(t)=\int_{-\infty}^{+\infty} h_1(t+\tau)h_2(\tau)d\tau$. In Eq. (1), the notation of the impulse response $h(r,z_{ri},t;0,z_{sj},0)$ flows from right to left, meaning that it refers to the time-domain Green's function (limited to the transducer frequency bandwidth) between a source at range $r=0$, depth z_{sj}, emitting at time $t=0$ $(0,z_{sj},0)$ and a hydrophone at range r, depth z_{ri}, receiving at time t (r,z_{ri},t). More precisely, z_{sj} is the depth of each of the N-element SA, z_{ri} is the depth of focus on the RA, z_{rk} is the depth of any point on the RA and r is the SA–RA range. Note that when $z_{rk}=z_{ri}$, Eq. (1) corresponds to the autocorrelation of the Green's function averaged over the N-element SA, hence a Dirac function (in the diffration limit) around $t=0$. This passive NR-TR is described in the literature as passive phase conjugation.[13] However, passive phase conjugation is classically performed using multiple receivers while the correlation process in Eq. (1) is averaged over multiple sources. Actually, the acquisition of the impulse-response matrix between the SA and the RA allows us to perform passive phase conjugation on either array. Indeed, the following process:

$$\tilde{f}(t,z_{sk})=\sum_{j=1}^{M} h(r,z_{rj},t;0,z_{si},0)\otimes h(r,z_{rj},t;0,z_{sk},0), \tag{2}$$

now refers to a passive focus obtained from the M-element RA on the ith element of the SA. Once again, when spatial reciprocity holds in the medium, the correspondence between passive phase conjugation and active time reversal is straightforward (see, for example, the mathematical formulations in Refs. 13–15). In the presence of low Mach-number currents[16] and when the SA covers the whole water column, we can show that Eq. (1) still converges to a Dirac function (in the diffraction limit). However, as stated in Eq. (1), passive phase conjugation is a circular process since it results in the autocorrelation of data taken at the same time. If we cross-correlate impulse-response matrices obtained at different times, then one can study the properties of time reversal focus in a fluctuating ocean without the use of a probe source and despite the presence of reciprocity-breaking current.

Procedure 1 is very similar to classical TR but does not invoke reciprocity. Parvelescu[17] did the single-element implementation of this NR-TR method in the early 1960s. Its practical limitation relies in the necessary connection between the two arrays as well as the time needed to transfer the data back from the RA to the SA before active time-reversal can be achieved. Procedure 2 represents an efficient way to study the time evolution of time-reversal focal spots by recording the impulse-response matrix of the medium on the RA at different times. In this case, no connection between the two arrays is needed. Further, since in both procedures the data were taken from transmitting in one direction only, the effects of reciprocity breaking currents in the environment are eliminated.

Note also that matched field processing (MFP)[18] is the hybrid model/data version of NR-TR, and not classical time reversal (or phase conjugation in the frequency domain). That is, one models the replica as propagating from the same direction as the data we received (i.e., spatial reciprocity is not invoked). Therefore, the discussion in this paper also is relevant to the distinction between the backpropagation implementation of MFP[19] which formally invokes reciprocity and the usual replica-based MFP which does not.

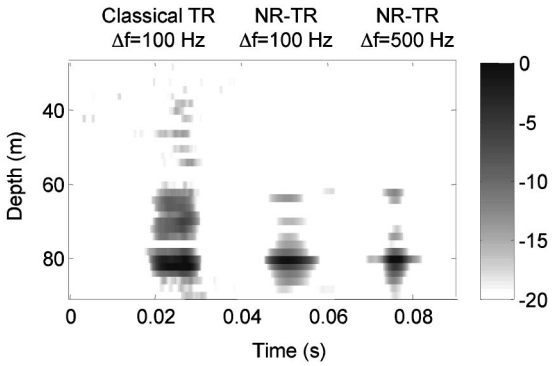

FIG. 4. Comparison between the depth–time focal spots obtained at 80 m with classical TR (left) and NR-TR using procedure 1 (center and right). The classical TR focal spot has been obtained with a $\Delta f = 100$ Hz bandwidth while a $\Delta f = 500$ Hz bandwidth has been used to create the NR-TR focal spot on the right. The central focal spot is a filtered version of the NR-TR one in a $\Delta f = 100$ Hz bandwidth. The gray scale is in decibels.

The next step is in two parts. First, we experimentally compare focal spots obtained at sea with both non-reciprocity-based and classical time reversal. Second, we investigate different applications for the two NR-TR procedures described earlier.

III. EXPERIMENTAL RESULTS

We have performed an at-sea experiment in April 2003 north of Elba Island, Italy with the same equipment, location, and basic setup as discussed previously.[6,7] As shown in Fig. 3, there were $N = 29$ equally spaced SRA transducers spanning 78 m in 115 m water depth and $M = 32$ equally spaced RA hydrophones covering 90 m. Three probe sources are collocated with the RA elements. The data were sent back from each array to the ship via radio frequency telemetry. The range between the two arrays was 8.6 km. The transducers had a central frequency of 3.5 kHz with a 1 kHz bandwidth.[20] The pulses transmitted during the experiment were 100 ms chirps that were compressed after reception to their pulse-like equivalent. This allowed us to obtain high signal-to-noise ratio signals with power-limited transmissions.

A. Simultaneous focal spots in depth

In Fig. 4, we compare depth-time dependent focal spots obtained with two different time-reversal procedures. On the left, classical TR has been achieved using an 80 m deep probe source transmitting an initial 10-ms-long pulse at 3.5 kHz ($\Delta f = 100$ Hz). On the right, active NR-TR has been implemented (Procedure 1) to focus on the 80-m-deep element of the RA. In this case, the acquisition of the impulse-response matrix has been performed with a $\Delta f = 500$-Hz pulse centered on 3.75 kHz [Figs. 2(a) and (b)]. Three reasons explain the better focus obtained with NR-TR. First, the main reason is the use of a larger frequency bandwidth. In Ref. 6, a classical TR focus performed in the same environment with a 2 ms initial pulse exhibits lower sidelobes. To achieve a fair comparison, the focal spot at the center of Fig. 4 is a filtered version of the NR-TR focal spot in a frequency bandwidth $\Delta f = 100$ Hz. When focal spots are compared in the same bandwidth, the sidelobes level still remains lower using NR-TR. The second reason may be the role played by reciprocity-breaking currents in the degradation of the focal spot obtained with classical time reversal.[12] In Ref. 12, it is shown that currents lead to a focus shift in range propor-

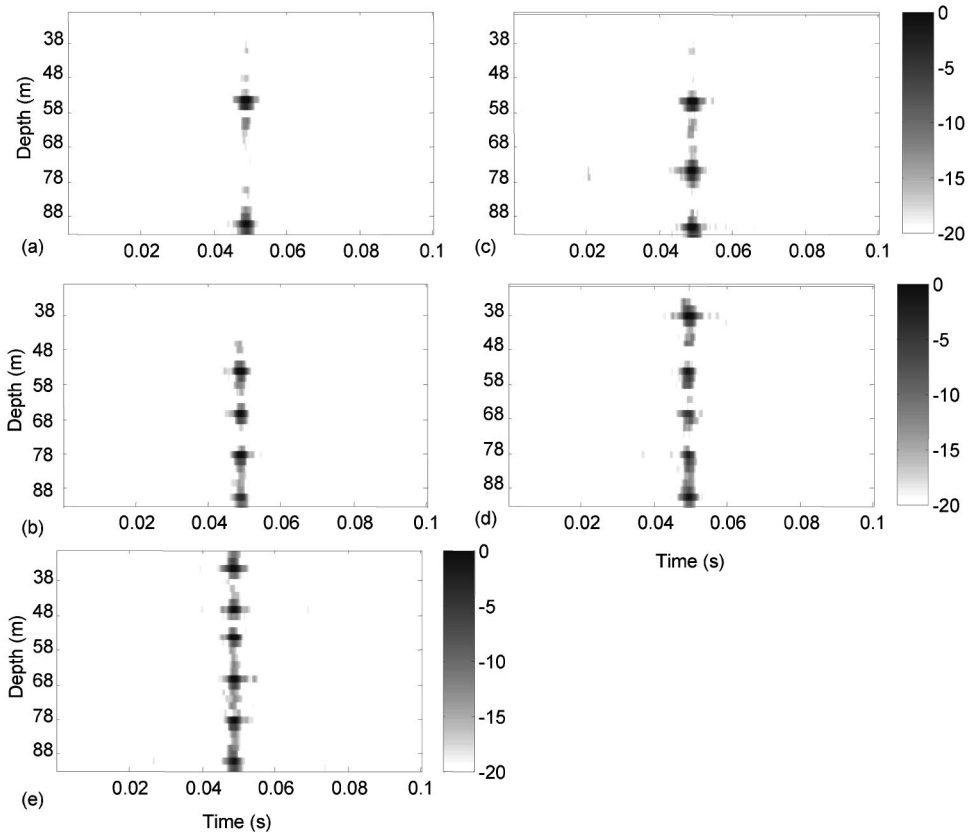

FIG. 5. Simultaneous depth–time focal spots obtained from NR-TR with active transmission (procedure 1) (a) two foci at depths 54 and 90 m, (b) three foci at 54, 76, and 90 m, (c) four foci at depths 54, 66, 78, and 90 m, (d) five foci at 38, 54, 66, 78, and 90 m, and (e) six foci at depths 34, 46, 54, 66, 78, and 90 m. The gray scales are in decibels.

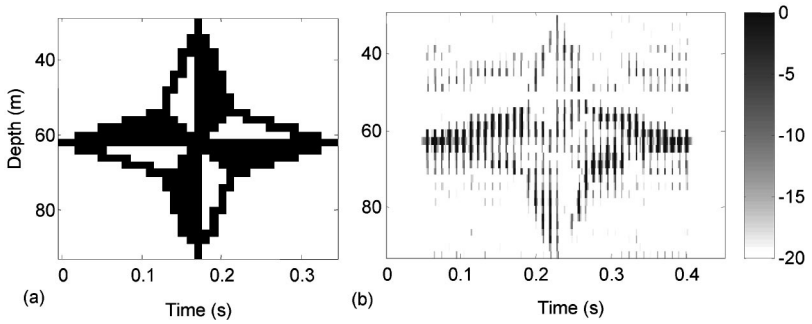

FIG. 6. Acoustic projection of the NATO symbol at 8.6 km in shallow water. (a) Depth–time representation of the digitized image to be transmitted through the waveguide. The image is made of 32×35 pixels encoded using a binary amplitude modulation (BAM) scheme with a 10 ms bit length for a 500 Hz bandwidth. (b) Depth–time representation of the field received on the RA after propagation. Despite the low quality of this space–time multiplexed image acoustic transmission over a significant distance in an ocean waveguide, the pattern of the NATO symbol is clearly recognizable. The gray scale is in decibels.

tional to the magnitude of the flow projected on the SA–RA axis. Current meter data recorded at the time the experiment was done exhibit current amplitudes on the SA–RA axis from 12 cm/s at 20 m to 2 cm/s at 60 m. Simulated results using environmental information show that classical TR will suffer a 5 dB loss in amplitude for the main lobe, which seems to confirm that current effects may be a good candidate to explain the different sidelobes level between classical TR and NR-TR. Finally, we already have pointed out that classical TR technically was more difficult to implement at sea than NR-TR because it requires an additional probe source collocated with the RA. This technical complexity also could result in a degraded focal spot.[20]

In our experimental configuration (Fig. 3), the big advantage of active nonreciprocity-based time reversal versus classical time-reversal resides in the multiple choices of the focal depth. Indeed, procedure 1 permits us to focus on any of the M receivers of the RA. Going one step further, we demonstrate in Fig. 5 that NR-TR enables us to focus simultaneously at different depths. Using the waveguide impulse-response matrix, the set of signals that would individually refocus at each depth are summed together before time reversal. In Fig. 5(e), we show that as many as six simultaneous focal spots can be obtained in the water column. This demonstration of simultaneous multiple foci in the ocean (space–time multiplexing) opens the way to multiple input–multiple output communications[21,22] in underwater acoustics.[23–25]

Finally, in Fig. 6, we show an example using procedure 1 where we projected the NATO symbol at 8.6 km. Each pixel of the transmitted image [Fig. 6(a)] has been encoded using a binary amplitude modulation (BAM) scheme with a 10 ms bit length for a 500 Hz bandwidth. Hence, the image of the logo essentially is a picture. Of course, the point here is not the actual image transmission but the focal position control that was not thought to be possible in ocean acoustics before this NR-TR implementation.

B. Waveguide fluctuations

Figure 7 shows a comparison of procedure 1 (upper panel) and procedure 2 (lower panel). Two data sets were taken 8 min apart by originally firing 500 Hz bandwidth pulses centered at 3.75 kHz following the acquisition procedure shown in Figs. 2(a) and (b). Our objective here was to focus back sequentially at every element of the RA. Compared to Fig. 5 where the foci were achieved simultaneously, a 20 ms delay is introduced here between each focal spot. Note in Fig. 7 that the 50-m-deep RA element is not working. The results are nearly identical for procedures 1 and 2, essentially demonstrating that one can study the TR process without using the final transmission step. That is, one can study medium-induced fluctuations in the TR process by continuously recording the waveguide impulse-response matrix as described in Figs. 2(a) and (b) and then invoking procedure 2. The advantage of using procedure 2 versus procedure 1 lies in its easier practical implementation and in the speed at which time reversal can be achieved. Indeed, procedure 1 requires the data recorded at the RA to be sent back to the SA (via an external connection), time reversed and then re-transmitted. Using our experimental setup, this could not be done in less than 8 min. On the other hand, procedure 2 only requires the acquisition of the waveguide impulse-response matrix between the SA and the RA, which experimentally was done every 30 s.

Physically speaking, the interest in Fig. 7 is that it gives an instantaneous picture of the focal spots versus depth. In our case, the depth-dependent sound speed profile was rather uniform [Fig. 3(b)] and the resulting time reversal foci look similar in depth. Figure 8, with four panels, shows the decay

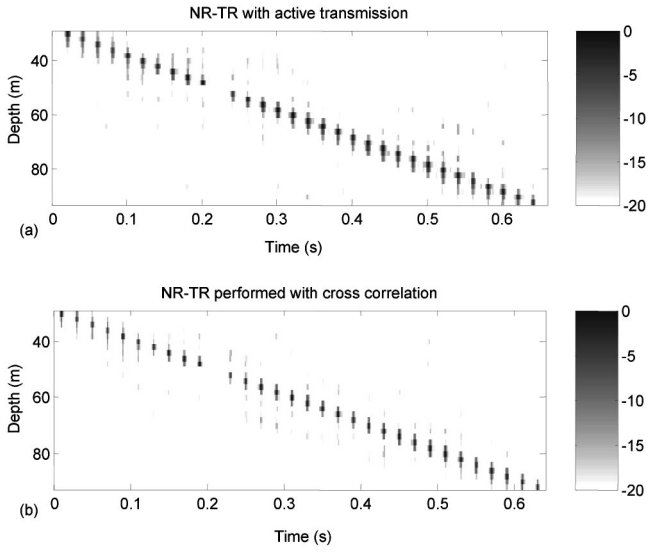

FIG. 7. Comparison between depth–time focal spots obtained with the two NR-TR procedures. The time-reversed field is focused sequentially at every element of the RA. The time delay between each focus is 20 ms. (a) Active NR-TR is achieved as fast as allowed by the acquisition system. There was an 8 min delay between acquisition of the waveguide impulse response matrix and retransmission. (b) Passive NR-TR is performed from two waveguide impulse-response matrices recorded 8 min apart. Note that the 50-m-deep RA element is not working. The gray scales are in decibels.

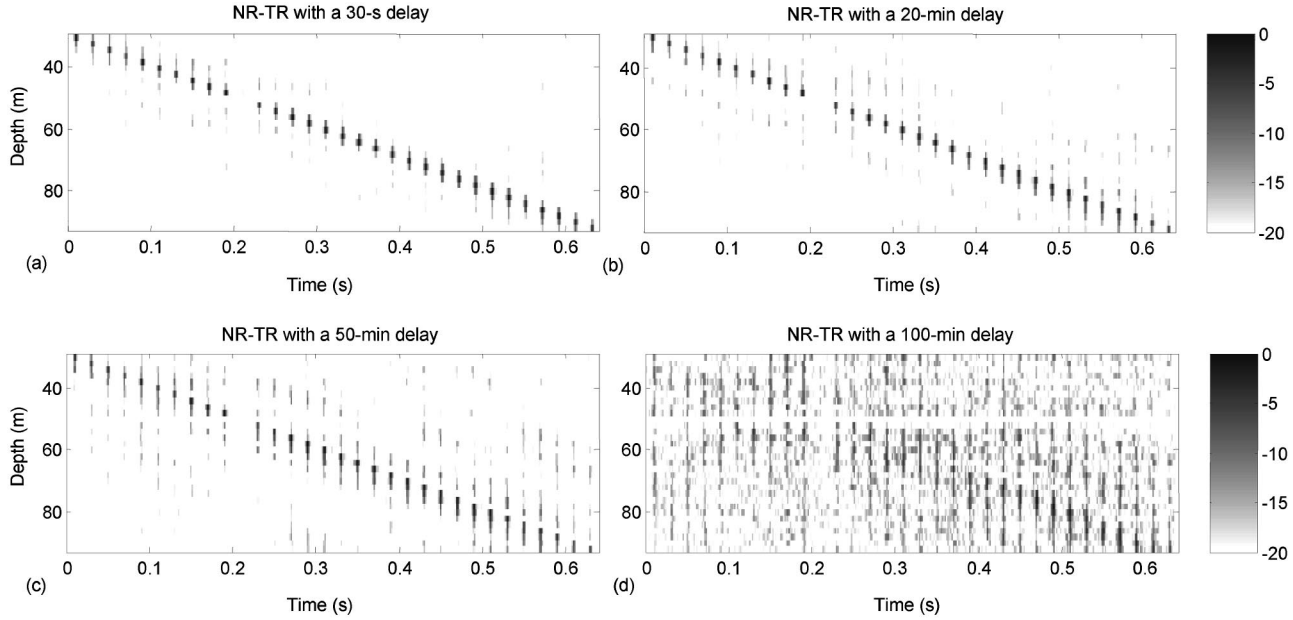

FIG. 8. Comparison between depth–time focal spots obtained from passive NR-TR as a function of time in a fluctuating shallow water ocean. The time-reversed field is focused sequentially at every element of the RA. The time delay between each focus is 20 ms. Passive NR-TR is performed from two waveguide impulse-response matrices recorded: (a) 30 s apart, (b) 20 min apart, (c) 50 min apart, and (d) 100 min apart. Note that the 50-m-deep RA element is not working. The gray scales are in decibels.

in the NR-TR focal properties after various delays. Here the data at the initial time were correlated (procedure 2) with subsequent data taken after 30 s, 20 min, 50 min, and 100 min delays, respectively. The degradation of the foci versus time is obvious. Figure 8(d) shows that the deeper focal spots are still visible after 100 min, confirming that the sound speed fluctuations are stronger near the ocean surface. According to Eq. (1), Figs. 7 and 8 result in the combination of a large number of point-to-point Green's functions recorded at different times (the SA and RA consist of 29 and 32 elements, respectively). In itself, each of these Green's function matrices is the oceanic equivalent of the data input in a CAT (computed axial tomography) scan in medicine. In a CAT scan, x rays are used to map a ''slice'' through the human body. Compared to ocean tomography which usually is performed on huge areas with sparsely distributed transducers, our CAT scan data are obtained with many elements on a short-range shallow water environment. We expect that a ray-based acoustic tomography performed on such data should reveal the space–time ocean fluctuations in the considered ocean ''slice'' to a high accuracy.

IV. CONCLUSION

In this paper we have demonstrated experimentally a way to greatly simplify the study of time reversal in a fluctuating medium without invoking reciprocity in the propagating medium. The method eliminates the effects of reciprocity breaking currents and requires minimum knowledge about the source/receive characteristics of the equipment typically used in classical time reversal experiments (in which an actual probe source is used). Conclusions of these NR-TR experiments are threefold. First, we showed that the underwater acoustic channel can support simultaneous foci in depth suggesting the feasibility of multiple-input multiple output (MIMO) acoustic communications. Second, our experimental setup enabled the real-time acquisition of the waveguide impulse-response matrix between a source array and a receive array, which is a first step toward a high-resolution measurement of the depth and time-dependent sound speed fluctuations in shallow water. Finally, the fact that reciprocity was not a requirement for this particular implementation of a TRM suggests that there may be alternative implementations that are robust to reciprocity violating media.

ACKNOWLEDGMENTS

The authors would like to thank Piero A. Boni, David Ensberg, Piero Guerrini, and Jeff Skinner for their contribution to this experiment. This research was supported by the Office of Naval Research, under Contract No. N00014-01-D-0043-D06.

[1] M. Fink, ''Time reversed acoustics,'' Phys. Today **50**, 34–40 (1997).
[2] P. Roux and M. Fink, ''Time reversal in a waveguide: Study of spatial and temporal focusing,'' J. Acoust. Soc. Am. **107**, 2418–2429 (2000).
[3] W.A. Kuperman, W.S. Hodgkiss, H.C. Song, T. Akal, C. Ferla, and D.R. Jackson, ''Phase conjugation in the ocean: Experimental demonstration of an acoustic time-reversal mirror,'' J. Acoust. Soc. Am. **103**, 25–40 (1998).
[4] W.S. Hodgkiss, H.C. Song, W.A. Kuperman, T. Akal, C. Ferla, and D.R. Jackson, ''A long range and variable focus phase-conjugation experiment in shallow water,'' J. Acoust. Soc. Am. **105**, 1597–1604 (1999).
[5] H.C. Song, W.A. Kuperman, and W.S. Hodgkiss, ''A time-reversal mirror with variable range focusing,'' J. Acoust. Soc. Am. **103**, 3234–3240 (1998).
[6] S. Kim, G.F. Edelmann, W.A. Kuperman, W.S. Hodgkiss, H.C. Song, and T. Akal, ''Spatial resolution of time-reversal arrays in shallow water,'' J. Acoust. Soc. Am. **110**, 820–829 (2001).
[7] S. Kim, W.A. Kuperman, W.S. Hodgkiss, H.C. Song, and G.F. Edelmann, ''Robust time reversal focusing in the ocean,'' J. Acoust. Soc. Am. **114**, 145–157 (2003).
[8] D.R. Dowling, ''Phase-conjugate array focusing in a moving medium,'' J. Acoust. Soc. Am. **94**, 1716–1718 (1993).

[9] P.M. Morse and K.U. Ingard, *Theoretical Acoustics* (Princeton University Press, Princeton, 1986), p. 320.
[10] P. Roux, J. De Rosny, and M. Fink, ''The Aharonov-Bohm effect revisited by an acoustic time-reversal mirror,'' Phys. Rev. Lett. **79**, 3637–3639 (1997).
[11] W.H. Munk, P.F. Worcester, and C. Wunsch, *Ocean Acoustic Tomography* (Cambridge University Press, New York, 1995).
[12] K.G. Sabra and D.R. Dowling, ''Effect of oceanic currents on the performance of a time-reversing array in shallow water,'' J. Acoust. Soc. Am. **114**, 3125–3135 (2003).
[13] D.R. Dowling, ''Acoustic pulse compression using passive phase-conjugate processing,'' J. Acoust. Soc. Am. **95**, 1450–1458 (1994).
[14] D.R. Jackson and D.R. Dowling, ''Phase conjugation in underwater acoustics,'' J. Acoust. Soc. Am. **89**, 171–181 (1991).
[15] D. Cassereau and M. Fink, ''Time-reversal of ultrasonic fields III. Theory of the closed time-reversal cavity,'' IEEE Trans. Ultrason. Ferroelectr. Freq. Control **39**, 579–592 (1992).
[16] J.S. Robertson, W.L. Siegmann, and M.J. Jacobson, ''Current and current shear effects in the parabolic equation for underwater sound channels,'' J. Acoust. Soc. Am. **77**, 1768–1780 (1985).
[17] A. Parvulescu, ''Matched-Signal ('MESS') processing by the ocean,'' J. Acoust. Soc. Am. **98**, 943–960 (1995).
[18] A.B. Baggeroer, W.A. Kuperman, and P.N. Mikhalevsky, ''An overview of matched field methods in ocean acoustics,'' IEEE J. Ocean. Eng. **18**, 401–424 (1993).
[19] F.D. Tappert and L. Nghiem-Phu, ''Localization of sources of acoustic transients using a broadband matched-field processing technique,'' J. Acoust. Soc. Am. **97**, 3368 (1985).
[20] W.S. Hodgkiss, J.S. Skinner, G.E. Edmonds, R.A. Harriss, and D.E. Ensberg, ''A high frequency phase conjugation array,'' Proceedings Oceans 2001, pp. 1581–1585.
[21] A. Derode, A. Tourin, J. de Rosny, M. Tanter, S. Yon, and M. Fink, ''Taking advantage of multiple scattering to communicate with time reversal antennas,'' Phys. Rev. Lett. **90**, 014301 (2003).
[22] S.H. Simon, A.L. Moustakas, M. Stoytchev, and H. Safar, ''Communication in a disordered world,'' Phys. Today **54**, 38–43 (2001).
[23] D. Rouseff, D.R. Jackson, W.L.J. Fox, C.D. Jones, J.A. Ritcey, and D.R. Dowling, ''Underwater acoustic communication by passive phase conjugation: Theory and experimental results,'' IEEE J. Ocean. Eng. **26**, 821–831 (2001).
[24] T.C. Yang, ''Temporal resolutions of time-reversal and phase conjugation for underwater acoustic communications,'' IEEE J. Ocean. Eng. **28**, 229–245 (2003).
[25] G.F. Edelmann, T. Akal, W.S. Hodgkiss, S. Kim, W.A. Kuperman, and H.C. Song, ''An initial demonstration of underwater acoustic communication using time reversal,'' IEEE J. Ocean. Eng. **27**, 229–245 (2003).

The cochlear amplifier as a standing wave: "Squirting" waves between rows of outer hair cells?

Andrew Bell[a)]
Research School of Biological Sciences, Australian National University, Canberra 0200, Australia

Neville H. Fletcher
Research School of Physical Sciences and Engineering, Australian National University, Canberra 0200, Australia

(Received 15 February 2004; revised 5 May 2004; accepted 7 May 2004)

This paper draws attention to symmetric Lloyd–Redwood (SLR) waves—known in ultrasonics as ''squirting'' waves—and points out that their distinctive properties make them well-suited for carrying positive feedback between rows of outer hair cells. This could result in standing-wave resonance—in essence a narrow-band cochlear amplifier. Based on known physical properties of the cochlea, such an amplifier can be readily tuned to match the full 10-octave range of human hearing. SLR waves propagate in a thin liquid layer enclosed between two thin compliant plates or a single such plate and a rigid wall, conditions found in the subtectorial space of the cochlea, and rely on the mass of the inter-plate fluid interacting with the stiffness of the plates to provide low phase velocity and high dispersion. The first property means SLR wavelengths can be as short as the distance between rows of outer hair cells, allowing standing wave formation; the second permits wide-range tuning using only an order-of-magnitude variation in cochlear physical properties, most importantly the inter-row spacing. Viscous drag at the two surfaces potentially limits SLR wave propagation at low frequencies, but this can perhaps be overcome by invoking hydrophobic effects. [DOI: 10.1121/1.1766053]

PACS numbers: 43.64.Bt, 43.64.Kc, 43.20.Ks, 87.18.Ed [BLM] Pages: 1016–1024

I. INTRODUCTION

A major unresolved problem in cochlear mechanics is a basic one: how is it physically possible to finely tune the human cochlea over three decades of frequency? The conventional model involving ''traveling'' waves propagating lengthwise along the basilar membrane (BM) certainly gives broad tuning, with the local resonance frequency being determined largely by the plate-stiffness and width of the BM, but a local-resonance theory, in some way involving the active outer hair cells (OHCs), appears necessary to provide the observed sharp tuning. The nature of this active tuning has been a matter for speculation and debate, since the identified material properties of the cochlear structures do not vary by the large factor required in order to cover the large frequency range involved.[1]

Here a solution is proposed involving standing-wave resonance between the rows of OHCs. The resulting wave direction is across the partition (radially) in a direction at right angles to the standard lengthwise (longitudinal) direction of propagation of the traveling wave. If the OHCs are excited by such a traveling wave, then their mechanical responses will deflect the membrane to which they are attached and launch a secondary wave from each cell. These secondary waves will interact with the other OHCs, causing them to respond with further waves, and so on. Because the phase change of the primary exciting wave along the rows is small, many OHCs will respond in unison. Furthermore, since the OHCs are arranged in three parallel rows, positive feedback at a resonance frequency related to the OHC spacing will occur and, as a result, will launch a ''radial'' wave in a direction normal to the rows. This mechanism would operate most efficiently if the central row, OHC2, responded in antiphase to the other two rows, and if response sensitivity of the individual cells were adjusted neurally to be just below the oscillation threshold.

A major difficulty confronting this radial wave hypothesis, however, is the extremely low wave velocity and high dispersion required in order to have the wavelength match the separation between OHC rows over the full frequency range of the human cochlea. In this paper a wave type is identified that meets these requirements: a symmetric Lloyd–Redwood (SLR) wave, known in ultrasonics as a ''squirting'' wave. This mechanism appears to provide the ''self-tuned critical oscillators'' whose existence has been proposed on general grounds by Duke and Jülicher.[2,3]

II. SLR "SQUIRTING" WAVES

SLR waves arise when a thin fluid layer is sandwiched between two deformable plates. They were predicted by Lloyd and Redwood[4] in 1965 and first experimentally verified in the ultrasonic regime by Hassan and Nagy[5] in 1997. Unlike normal flexural or shear waves in a plate,[6] the SLR wave relies primarily upon interaction between the inertia of the fluid and the elastic restoring force of the plates. While the original analysis of Lloyd and Redwood assumed that the plates deformed by shear, plates thinner than about one-sixth of the wavelength will deform by bending, the case considered by Coulouvrat *et al.*[7] and by Hassan and Nagy.[5] Both

a)Electronic mail: andrew.bell@anu.edu.au

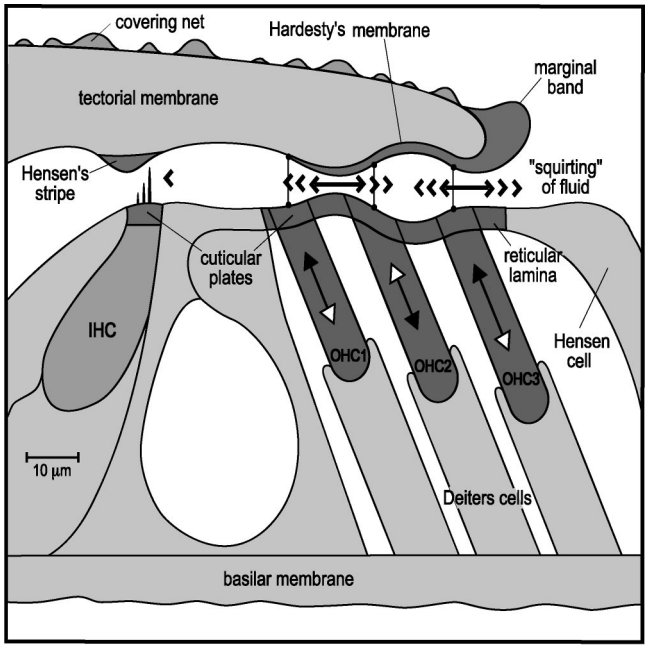

FIG. 1. Simplified diagram of the anatomy of the human cochlea in cross section. Radial SLR waves (''squirting'' waves) could be generated by cyclic length changes of OHCs. Symmetric undulations induced in the facing surfaces of the TM and the RL squeeze the intervening fluid and produce a squirting action (horizontal arrows). The wave will continue to the IHCs, where squirting will tilt the free-standing IHC stereocilia. Shorter OHC stereocilia (unattached to TM and also subject to squirting effects) are not shown. White areas are occupied by fluid.

these cases are treated in Appendix A and illustrated in Fig. 3, and certain other variations are also discussed.

To visualize liquid displacement patterns, Lloyd and Redwood solved the equations of motion numerically for two modes, one antisymmetric and the other symmetric with respect to a plane along the center of the fluid layer. In the antisymmetric mode, discussed in more detail in Appendix A, the upper and lower layers, and the fluid, move up and down together in a sinuous fashion, so that the width of the fluid layer is constant and no enhanced motion of fluid occurs. Applied to the cochlea, the lack of such fluid motion implies that the stereocilia would not be deflected. Moreover, this mode does not give appropriately low propagation speeds or such high dispersion [see (A13) in Appendix A], so we conclude it is not auditorily relevant.

The symmetric mode, however, in which the two facing solid layers vibrate in mirror symmetry to give a varicose wave, which we call the SLR mode, is of considerably greater interest. This mode involves squeezing of the intervening fluid backwards and forwards in the direction of propagation. Hassan and Nagy called it a ''squirting'' mode because horizontal displacements of the fluid become magnified when the gap is narrow relative to the wavelength, as is the case in the typical cochlear configuration shown in Fig. 1. Maximum horizontal velocity of fluid occurs one-quarter of a wavelength away from the place where the plates undergo maximum vertical displacement.

Hassan and Nagy studied the waves at ultrasonic frequencies (15–150 kHz) with a liquid film approaching 1 mm in thickness. At audio frequencies, however, the effect of viscosity becomes increasingly pronounced (see Appendices), a factor that, acting in the subtectorial space, would tend to damp the wave and prevent its propagation unless some other mechanism intervenes. As it happens, there appears to be just such a possibility deriving from the properties of hydrophobic surfaces, as will be discussed later.

Anatomically, the cochlea has a thin layer of fluid (aqueous endolymph) enclosed between the gelatinous tectorial membrane (TM) and the thin reticular lamina (RL), as shown in Fig. 1. The two surfaces are held apart by the stereocilia of the OHCs, with the tips of the tallest stereocilia embedded in the lower surface of the TM. From the analysis of Lloyd and Redwood[4] and of Hassan and Nagy,[5] the phase velocity c of the symmetric Lloyd–Redwood wave for two identical plates of half-thickness h, Young's modulus E, and Poisson's ratio σ, separated by a liquid layer of thickness d and density ρ, is given approximately by

$$c \approx \left[\frac{Eh^3 d\omega^4}{3(1-\sigma^2)\rho}\right]^{1/6}, \tag{1}$$

provided the plates are thin compared with the wavelength so that they deform by bending. The wavelength $\lambda = 2\pi c/\omega$ is then given by

$$\lambda \approx 2\pi\left[\frac{Eh^3 d}{3(1-\sigma^2)\rho}\right]^{1/6} \omega^{-1/3}, \tag{2}$$

which more readily illustrates the dispersive properties of the wave. A doubling of wavelength, for example, is accompanied by an eightfold change in frequency.

Plates thicker than about one-sixth of the wavelength undergo shear instead of bending, and the approximate result for the case where the plates are still thinner than the enclosed liquid layer is

$$c \approx \left[\frac{Ehd\omega^2}{(1+\sigma)\rho}\right]^{1/4}. \tag{3}$$

The corresponding expression for wavelength λ is

$$\lambda \approx 2\pi\left[\frac{Ehd}{(1+\sigma)\rho}\right]^{1/4} \omega^{-1/2}. \tag{4}$$

As shown in Appendix A, both (1) and (3) can be simply derived by neglecting the mass of the plates and equating the kinetic energy of the ''squirting'' liquid to the elastic strain energy of the plates. Inclusion of the mass of the plates is simple, but complicates the resulting expressions unnecessarily.

When one of the plates is much thicker, much stiffer, or much denser than the other, then it moves very little and the motion reduces essentially to that of the original model with the immobile plate located along the center-plane of the original fluid layer. Appendix A shows that this does not change the form of the dispersion relations (1) and (3), except that d is now equal to twice the thickness of the liquid layer. The wave of relevance is therefore that involving bending and with a dispersion relation of the form (1), provided at least one of the plates is sufficiently thin.

In the case of the cochlea, there is liquid on the outer side of each plate as well as between them, and the wave

motion extends some distance into this liquid. But again, Appendix A shows that the effect of this surrounding liquid is small in the case of a structure with dimensions typical of the cochlea.

An important property of Eqs. (1) and (3) is that the SLR wave velocity increases markedly with frequency, as $\omega^{2/3}$ in the first case and as $\omega^{1/2}$ in the second. The wave is thus highly dispersive and, as given by (2) or (4), the wavelength range for a given frequency range is greatly compressed, varying as $\omega^{-1/3}$ and $\omega^{-1/2}$, respectively, for the two cases discussed, rather than as ω^{-1} for nondispersive propagation. It is this feature that potentially allows SLR waves to provide a way of tuning an active cochlear amplifier over a 3-decade (10-octave) frequency range by requiring only an order of magnitude variation in other physical parameters.

III. SLR WAVE IN THE COCHLEA

As Appendix A makes clear, the primary requirement for generating SLR waves in accordance with (1) is that at least one of the two enclosing plates is thin enough to deform by bending. Given the extreme thinness of the RL (1–3 μm), this condition appears likely to be met in the cochlea, although no direct measurements of this structure's stiffness have been made. It is known, however, that this articulated mesh of interlocking plates appears more flexible than the basilar membrane[8] and there is some indication[9] that it is more compliant than the TM. In what follows, therefore, it is assumed that deformation is by bending of at least one of the plate structures involved, so that the dispersion relation is given by (1). A difficulty, however, is that no individual data set provides all required values, so it is necessary to use data compiled from measurements on several different species of mammal.

The most comprehensive data in the literature relates to the water buffalo;[10] here the thicknesses of the TM (3–8 μm) and RL (1.8–2.9 μm) are tabulated along the cochlea. It is immediately apparent that, in this case, both of these key structures are appreciably thinner than a wavelength, suggesting that both undergo bending. Since the RL appears to have an elastic modulus comparable to that of the TM,[9] it is appropriate to use RL dimensions and to combine these with a representative Young's modulus of 2 kPa, as derived from recent measurements[11] on the guinea pig TM in which figures of 0.7–3.9 kPa were reported. The gap width, d, reflects the height of the tallest stereocilia, and here there is no water buffalo data; instead, human data,[12] showing a gradation of 3–7 μm from base to apex, are used.

For the mid-region of the cochlea where frequencies near 1000 Hz ($\omega \approx 6000$ rad s^{-1}) are detected, the assumed values are thus, $E \approx 2$ kPa, $h \approx 1\ \mu$m, $d \approx 3\ \mu$m, and $\rho \approx 1000$ kg/m^3. Equation (1) then gives a wave speed $c \approx 40$ mm/s and a wavelength, c/f, of about 40 μm. A plot of wave speed against frequency over the length of the cochlea is shown as the full line in Fig. 2 and shows values ranging from 3 mm/s at the apex (20 Hz) to 300 mm/s at the base (20 kHz). Extremely slow wave speeds and short wavelengths thus appear possible in the cochlear structure. According to LePage,[13] the tonotopic mapping (for humans) of frequency f to fractional distance x from the apex is well-approximated by the function $f = 165.4(10^{2.1x} - 0.88)$, and this expression is used in the following calculations.

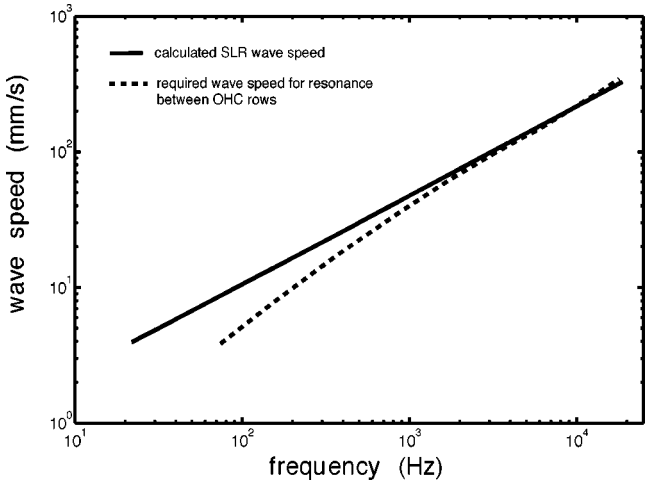

FIG. 2. Calculated speeds of SLR waves (full line) based on measured RL dimensions of the water buffalo (Ref. 10) and assuming that the RL has an elastic modulus similar to that of the TM (Ref. 11) (2 kPa). The gap width is that for human stereociliar height (Ref. 12) and a human frequency–place map (Ref. 13) is used. These speeds agree well with wave speeds inferred (dotted line) from assuming one wavelength of a standing wave to form between the experimentally determined (Ref. 17) spacing OHC1–OHC3 for humans.

Since Fig. 2 reflects a mixture of cochlear properties from water buffalo, guinea pig, and human, one may question the aptness of the values derived from (1) to human hearing. In general, micrographs show that the differences between these species are not major, and most cross sections appear similar. Although detailed measurements of human TM dimensions are lacking, it does seem, however, that the thickness of the human TM is, at least at the apex, appreciably greater than in the water buffalo, and its overall structure thus appears as in Fig. 1. The analysis in Appendix A then shows that SLR waves will propagate by bending of the RL with the TM remaining nearly inactive. Since the speed of an SLR wave varies only as the sixth root of the Young's modulus, errors introduced by assuming values of RL stiffness about equal to those of the TM (2 kPa) should not be serious.

As well as the subtectorial space in the cochlea being well-configured for propagation of SLR waves, it is important to note that OHCs appear strategically positioned to generate these waves, as shown in Fig. 1. A key property of OHCs is that they are electromotile, with the ability to change length, cycle by cycle, in response to variations in cell potential,[14] such as might be caused by stereocilia deflection. Thus, changes in length of OHCs could excite SLR waves.

OHCs are clamped at the bottom by Deiters cells, which rest on the basilar membrane, and are firmly connected at the top to the interlocking platelike network of the RL. When OHCs are electrically stimulated *in vivo*, the RL at the top moves 5–10 times more[8] than does the basilar membrane at the bottom, a key indicator that the RL is highly flexible and could readily respond to elongation and contraction of OHCs.

From this numerical analysis, supported by the theoret-

ical results in Appendix A, it can be concluded that audio-frequency SLR waves with speeds as low as tens to hundreds of millimeters per second and wavelengths of tens to hundreds of micrometers could occur in many, if not all, mammalian cochleas. The wave speed will be governed by the bending of the thinnest membrane, usually the RL, although deformation of the TM may also contribute in some cases.

The possible existence of such radial waves prompts the question of how they may interact with a longitudinal traveling wave. Some kind of direct coupling of excitation from the longitudinal direction to the radial would presumably help in funneling energy of a particular frequency to its appropriate location on the partition, at which point the OHCs could then begin actively fine-tuning the response via SLR waves. The precise micromechanics of this process is beyond the scope of this paper. It is reasonable, however, to treat the radial wave as an independent entity because its wavelength is generally very small—tens of micrometers—compared to that of a traveling wave, which is typically in the range of millimetres. In turn this means that the input stimulus to the OHCs is essentially in phase over reasonably large OHC aggregates. In the case of spontaneous emissions, of course, where the active process dominates, the situation could be rather different.

A simple interpretation, then, broadly in keeping with existing traveling wave theory, might be that the traveling wave is the primary filter and the SLR wave the second filter. However, the SLR mechanism proposed here does underscore the importance of clarifying the nature of the primary input to the OHCs, which is not certain. In particular, the possible role of the fast pressure wave in stimulating OHCs requires careful consideration.[15,16]

IV. DISPERSION AND TONOTOPIC TUNING

It was noted earlier that SLR waves are highly dispersive ($c \propto \omega^{2/3}$), so that in order to vary tuning 1000-fold, dispersion will provide a factor of 100, leaving only a factor of 10 to be contributed by other variables. This means that if inter-row spacing of OHCs were constant between base and apex, physical and geometrical characteristics of the cochlea would only be called on to alter wave speed by tenfold in order to maintain a full wavelength between OHC1 and OHC3. In reality, the spacing of OHC rows in humans[17] widens by a factor of 2.5 from base to apex, meaning that wave speed need only vary by a factor of 4 through the other parameters in (1).

The same equation indicates that elasticity E and gap thickness d are of little consequence in tuning, as phase velocity only varies as their sixth root. The most likely parameter leading to tuning is the membrane half-thickness h, since $c \propto h^{1/2}$. A systematic variation in h from base to apex might therefore be expected, with h smaller at the apex (low frequencies). The detailed water buffalo data[10] confirms this expectation. For this animal, the thickness of the TM decreases from 26 μm at the base to 10 μm at the apex (2.6-fold); similarly, the RL thins out from 2.9 μm to 1.8 μm (1.6-fold).

V. THE COCHLEAR AMPLIFIER AS A STANDING WAVE?

Distinctive features of SLR waves are their low speeds and correspondingly short wavelengths. At the same time, a system in which motile elements (OHC cell bodies) are in close proximity to sensory elements (OHC stereocilia) immediately raises the possibility of feedback. Over the span of a single SLR wavelength the phase of a propagating wave changes by 360°, a situation inviting positive feedback and, given a suitable two-way interaction, standing waves. It appears significant that OHCs typically lie in three well-defined rows and are graded in their separation along the cochlea so as to span a distance ranging from 20 to 50 μm, dimensions comparable to calculated SLR wavelengths. It is also of some reassurance for our previous pooling of data that the graded spacings of OHC rows for both human[17] and water buffalo[10] are nearly identical.

A real possibility, therefore, is that positive feedback may occur between OHC rows. In response to a sound stimulus, the OHCs will undergo movement, launching an SLR wave, and the distinctive squirting motion of the wave will then initiate positive feedback through bending of neighboring OHC stereocilia, creating a standing wave. Here we consider that it is the shorter OHC stereocilia, which are free-standing, that are bent and contribute most to feedback. At the same time, the tallest stereocilia, which are firmly attached to the TM may still contribute feedback as they must tilt with respect to their bases when the reticular lamina, on which they rest, undulates underneath. The important result is that in the end some of the oscillating fluid flow associated with the standing wave will escape the OHC region and propagate towards the IHCs, where the jetting fluid will bend stereocilia (which here are all free-standing) and greatly enhance the responses of the cells at the standing-wave resonance frequency.

A mention of nonradial propagation of SLR waves is also called for. Because OHCs are regularly arranged longitudinally as well as radially, cell interaction may launch lengthwise SLR waves, too. We note, however, that the longitudinal cell spacing is smaller than the radial spacing, so the corresponding resonance frequency would be much higher, perhaps making the initial tuned stimulus from a traveling wave ineffective. Moreover, these waves would travel in directions that would not strongly affect the IHCs. While subtle effects due to nonradial waves cannot therefore be immediately ruled out, they do not constitute the major mechanism investigated here.

The location of the maxima and minima of the standing wave relative to the OHC rows will depend upon the mechanical impedance of the OHCs relative to the wave impedance of the surrounding plate. Since the cells are large in diameter relative to the thickness of the plate, it is likely that their mechanical impedance (force divided by displacement velocity) is also relatively large, which means that the standing wave will be excited in such a way that the OHCs lie close to, but not coincident with, the displacement nodes of the plate. Furthermore, because these plate displacement nodes are also the regions of maximum squirting wave fluid velocity (and maximum tilt of stereocilia with respect to their

bases), this location also provides optimal feedback to the OHCs through displacement of their stereocilia. Although each OHC acts as a circular wave source, their linear arrangement effectively produces a nearly linear wavefront parallel to the OHC rows, and in this way an escaping wave propagates at right angles to the rows and towards the IHCs. Some experiments[18,19] have seen large phase variations across the partition (up to 180° between points 10 μm apart[18]), which can be interpreted as good evidence for short wavelength radial wave motion; however others[20] have seen no radial phase variability, so that more work is needed to clarify this behavior.

The dotted line in Fig. 2 shows the phase velocity required to create feedback resonance between rows of OHCs in the human cochlea, placed next to a line showing the wave velocities expected from an SLR wave based on composite cochlear data. To calculate the dotted line, the speed needed to make the OHC1–OHC3 distance a full-wavelength standing wave cavity was used; this distance is continuously graded[17] from base (20 μm) to apex (50 μm) in humans, and the same frequency–place map[13] was again used to convert location to frequency. The general trend and proximity of the lines support the possibility that resonance between OHC rows may occur via SLR waves. An SLR wave thus makes an ideal candidate for tuning standing waves between OHC rows. Modeling of this process is incomplete, and so further details are not given here. However, since OHC stereocilia are particularly sensitive to lateral jets of fluid,[21] the postulated reverberating activity between rows of OHCs could provide a physical realization of the cochlear amplifier, the device proposed by Davis[22] to explain the active nature of the cochlea at low sound pressures. It also has strong parallels with the ''regenerative receiver'' described by Gold[23] and with surface acoustic wave (SAW) resonator devices.[15,16] If SLR waves do operate in the cochlea as supposed here, it would confirm some long-standing conjectures that fluid flow in the subtectorial space was crucial for IHC stimulation[24,25] and would relate to a recent speculation[26] that the cochlear amplifier was a fluid pump.

There is, however, a major problem with the SLR wave hypothesis: the analysis in Appendix A indicates that propagation of SLR waves in the narrow subtectorial space might be expected to be strongly damped by viscous forces, particularly at low frequencies as indicated in Eq. (A15). But it is now known that the effects of viscosity in narrow channels can be greatly diminished when hydrophobic surfaces are involved, and it may well be that the cochlea makes use of this phenomenon. As described in more detail in Appendix B, slippage between a polar liquid and its bounding surfaces can be considerably enhanced if the surfaces are made hydrophobic by coating them with a thin layer of oil. The relevance here is that lipid droplets are secreted by Hensen cells, immediately next to the subtectorial space (see Fig. 1), and a natural supposition is that the function of these droplets is to coat both TM and RL surfaces (but presumably not the stereocilia) and so reduce their viscous drag upon the squirting fluid in the subtectorial space.

VI. CONCLUSIONS

This paper has constructed an attractively simple model for sharp tuning in the cochlea by assuming that SLR waves are generated by interaction between rows of motile outer hair cells, the reticular lamina, and the fluid lying between it and the tectorial membrane. In turn, these squirting waves create, through stereocilia-mediated positive feedback, a standing wave between the rows. The gain of the reverberating system—operating broadly like a solid-state surface acoustic wave device—is presumably neurally adjusted so as to be close to the oscillation threshold in order to provide high gain and narrow frequency response. Squirting waves generated in the OHC region could propagate radially across the space to the inner hair cells and there initiate a strong and sharply tuned neural response.

This model also displays other interesting features. For example, it assigns a role to Hensen cell lipids in overcoming limitations imposed by viscosity. It also points to a highly localized basis for the cochlear amplifier, suggesting for example that spontaneous otoacoustic emissions could arise from a small group of OHCs with positive feedback gain exceeding the oscillation threshold for SLR waves.

ACKNOWLEDGMENTS

The authors thank M. V. Srinivasan, A. W. Gummer, and T. Maddess for helpful comments. A.B. is supported by a Ph.D. scholarship from the Australian National University and received seed funding from the University of Tübingen. This research complies with the Declaration of Helsinki; a full statement of animal research ethics for A.B. is set out elsewhere (Ref. 27). Catherine Eadie helped in drawing the figures.

Note added in proof. Since acceptance of this article we have come across the papers ''Active control of waves in a cochlear model with subpartitions,'' by R. S. Chadwick, E. K. Dimitriadis, and K. H. Iwasa, Proc. Natl. Acad. Sci. U.S.A., **93**, 2564–2569 (1996) and ''Evidence of tectorial membrane radial mositon in a propagating mode of a comples cochlear model,'' by H. Cai, B. Shoelson, and R. S. Chadwick, Proc. Natl. Acad. Sci. U.S.A., **101**, 6243–6248 (2004). These papers considered radial fluid motion in the RL-TM gap, but rejected it because of viscosity considerations.

APPENDIX A: DERIVATION OF EQUATIONS GOVERNING SQUIRTING WAVES

Suppose that, to conform to the notation of previous investigators, the system consists of two identical parallel plates, each of thickness $2h$, density ρ_1, Young's modulus E, and Poisson's ratio σ, separated by a layer of liquid of thickness d, and density ρ, as shown in Fig. 3. The simplest way to determine the phase velocity c of a wave of angular frequency ω that is symmetric about the center plane AB, which we have called an SLR wave, is to equate the maximum values of the potential and kinetic energies of the wave. This procedure is clearly appropriate in the case of standing waves, where displacement and velocity are 90° out of phase with each other, but can also be shown to be correct for propagating waves. In the derivations below, some factors of

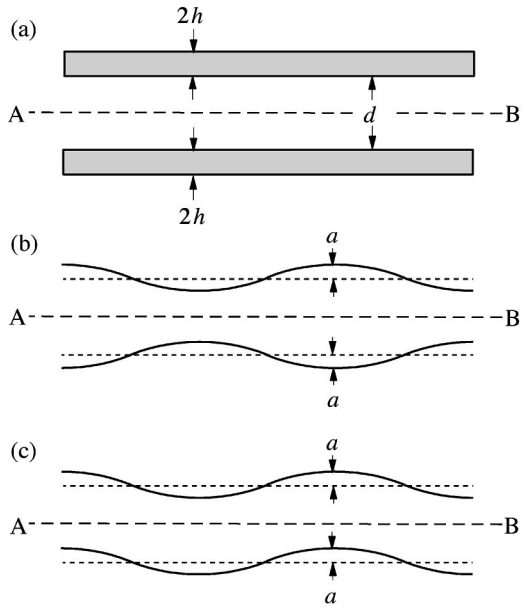

FIG. 3. (a) Section of two parallel plates surrounded by liquid. (b) Geometry of the symmetric Lloyd–Redwood (SLR) wave, the motion of which gives rise to the "squirting" of liquid between the plates. (c) The antisymmetric wave, displayed here for completeness. It is considered to play no functional role in the cochlea.

order unity are neglected in the interests of simplicity of presentation. The final results are therefore only approximate but, since fourth or sixth roots are involved, this is of little practical consequence.

In what follows, we consider the behavior on only one side of the symmetry plane AB, and assume a standing wave of the form

$$y(x,t)=a\cos kx\sin\omega t, \tag{A1}$$

where $k=\omega/c$. If λ is the wavelength at angular frequency ω, and the plates are sufficiently thin that $h\ll\lambda$, then their elastic distortion occurs through bending, and the peak elastic potential energy P_{bend} per unit area is

$$P_{\text{bend}}=\frac{Eh^3k^4a^2}{3(1-\sigma^2)}=\frac{Eh^3\omega^4a^2}{3(1-\sigma^2)c^4}. \tag{A2}$$

If, however, the plates are thicker so that h is greater than about λ/π, then the plates distort predominantly by shear rather than bending, and the corresponding result is

$$P_{\text{shear}}=\frac{Ehk^2a^2}{2(1+\sigma)}=\frac{Eh\omega^2a^2}{2(1+\sigma)c^2}. \tag{A3}$$

The difference in structure between (A2) and (A3) is accounted for partly by the fact that the bending modulus is involved in (A2) while the shear modulus is involved in (A3), and partly by the fact that the wave equation for a bending wave involves the operator $\partial^4z/\partial x^4$ while that for a shear wave involves only $\partial^2z/\partial x^2$.

The kinetic energy in the simple system considered involves two contributions, one from the moving mass of the plates, and one from that of the liquid between them. The kinetic energy K_{plate} per unit area of the single plate has the simple form

$$K_{\text{plate}}=\rho_1h\omega^2a^2, \tag{A4}$$

but the liquid motion requires more analysis.

From (A1), if it is assumed that the plates are close enough together that $d\ll1$, the fluid flow velocity in the space between the plates is essentially parallel to AB and has the form

$$v(x,z,t)=\frac{2f(z)}{d}\int_0^x\frac{\partial y}{\partial x}dx=\frac{2a\omega}{kd}f(z)\sin kx\cos\omega t, \tag{A5}$$

where z is the coordinate normal to the plates and the function $f(z)$ is approximately parabolic and becomes zero at the plane of contact with the plates, so that $\int_0^d f(z)dz=1$. Since $f(z)$ contributes a factor of order unity, it will be neglected in the following analysis. The mean square velocity amplitude averaged over the x-direction is

$$\langle v^2\rangle\approx\frac{2a^2\omega^2}{k^2d^2}=\frac{2a^2c^2}{d^2}, \tag{A6}$$

and the peak kinetic energy of the flow is

$$K_{\text{liq}}\approx\frac{\rho a^2c^2}{d}. \tag{A7}$$

Finally, because in the case of the cochlea the plates are immersed in a surrounding liquid, account must be taken of the kinetic energy associated with flow in this liquid. Consideration of the wave equation for a liquid with a standing or propagating wave disturbance imposed upon its surface shows that this wave is exponentially attenuated with distance y from the surface by a factor $\exp(-ky)$. To evaluate, to an adequate approximation, the kinetic energy associated with this motion, the quantity d in (A7) can simply be replaced by $k^{-1}=c/\omega$, giving a kinetic energy contribution

$$K_{\text{outer}}=\tfrac{1}{2}\rho a^2c\omega, \tag{A8}$$

and the total kinetic energy is

$$K_{\text{total}}=K_{\text{plate}}+K_{\text{liq}}+K_{\text{outer}}. \tag{A9}$$

The total symmetric propagation problem can now be solved by choosing either P_{bend} or P_{shear}, depending upon the thickness of the plates, and setting this equal to K_{total}. For the standard SLR-wave situation, the plates are taken to be thin enough that $h\ll\lambda/2\pi$ so that P_{bend} is the appropriate choice, and they are close enough together that $d\ll\lambda/2\pi$, so that K_{plate} and K_{outer} can be neglected relative to K_{liq}. Setting $P_{\text{bend}}=K_{\text{liq}}$ then leads to the Hassan–Nagy result

$$c\approx\left[\frac{Eh^3d\omega^4}{3(1-\sigma^2)\rho}\right]^{1/6}\propto\omega^{2/3}. \tag{A10}$$

If the thickness of the plates is comparable to or greater than the wavelength, however, then distortion is by shear and, provided the plates are close enough together that K_{liq} is still greater than K_{plate} and K_{outer}, the equation $P_{\text{shear}}=K_{\text{liq}}$ leads to the result

$$c\approx\left[\frac{Ehd\omega^2}{(1+\sigma)\rho}\right]^{1/4}\propto\omega^{1/2}. \tag{A11}$$

For intermediate cases, an appropriate interpolation between (A2) and (A3) for the potential energy must be used, and the full expression (A9) may be required for the kinetic energy.

One further important implication of the model is also worth noting. The squirting-wave motions considered above are mirror-symmetric about the central plane AB of Fig. 3. This means that exactly the same results will be obtained if a rigid plate is set along this plane, so that there is only a single thin plate separated from it by a liquid-filled space of width $d/2$. Indeed, the elastic stiffness of a thin plate increases so rapidly with its thickness, as indicated by (A2), that in most asymmetric situations an assumption that the thicker plate is essentially rigid will provide a good approximation, provided the thinner plate can distort by bending rather than shear. Of course, the relative elastic moduli of the two plates must also be taken into account.

A similar approach to that above can be applied to the antisymmetric case. Since there is no squirting motion, the enclosed fluid simply moves up and down with the enclosing plates, and its mass is added to the combined plate mass. For plates thinner than about $\lambda/6$, so that they deform by bending, the result is

$$c \approx \left[\frac{2Eh^3}{3(\rho d + 4\rho_1 h)(1-\sigma^2)} \right]^{1/4} \omega^{1/2}, \tag{A12}$$

where $2h$ is the thickness and ρ_1 the density of each of the plates. If the plate sandwich is taken to be much thinner than $\lambda/6$ and immersed in surrounding liquid, as discussed above for the symmetric case, then the loading effect of the surrounding evanescent waves must be taken into account. The result is a propagation law of the form

$$c \approx \left[\frac{Eh^3}{3(1-\sigma^2)\rho} \right]^{1/5} \omega^{3/5}. \tag{A13}$$

These equations imply much faster speed and rather less dispersion than in the symmetric case. Another point of interest is that, in the case discussed above in which one of the plates is essentially rigid and the other flexible, antisymmetric waves do not exist, as can be seen from simple symmetry considerations.

There is, however, an apparent major obstacle to this cochlear model, namely the viscosity of the liquid in the narrow region between the two plates. These viscous losses will generally exceed all other losses in the system and thus provide the primary wave damping. The viscosity η of water at body temperature is about 7×10^{-4} Pa s, so that the diffusion length $L \approx (\eta/\rho\omega)^{1/2}$ at a frequency of 1 kHz is about 10 μm and essentially all of the inter-plate liquid will be within the boundary layer. Viscosity will therefore provide a nearly frequency-independent damping force $\kappa v \approx (\eta/d)v$ per unit area, where v is the flow velocity. Inserting this viscous damping term, an equation describing the behavior of an SLR standing wave has the form

$$\rho d \frac{\partial^2 y}{\partial t^2} + \frac{\eta}{d} \frac{\partial y}{\partial t} + Ky = 0, \tag{A14}$$

where y measures the longitudinal displacement of the fluid between the plates and K is the elastic stiffness of these plates, expressed in terms of y. If a standing-wave resonance for this oscillation is considered, then the quality factor Q is given by

$$Q = \frac{\rho d^2 \omega}{\eta}, \tag{A15}$$

where ω is the frequency of the standing-wave resonance. Inserting numerical values for the human cochlea into (A14) gives $Q \approx 10^{-5}\omega$, so that at 1 kHz Q is only about 0.1 and about 1 at 10 kHz. Any such standing-wave resonance is therefore virtually nonexistent under these simple assumptions. While active resonant feedback between cells would contribute negative resistance that could help reduce the effect of this damping, this would not overcome the damping between OHC1 and the IHCs, so the waves could not then propagate effectively.

Propagating SLR waves of frequency ω in the system are attenuated in amplitude as $\exp(-\omega x/2cQ)$, which amounts to $\exp(-\pi/Q)$ per wavelength. Clearly we require that $Q > 1$ for propagating waves to have any significance. Since Q increases nearly linearly with frequency while the viscous barrier-layer thickness is greater than the liquid film thickness, as assumed above (and actually as the square root of frequency above this limit), this explains why SLR waves have been studied mainly at megahertz frequencies and for much thicker liquid layers than found in the cochlea.

As suggested in the main text, however, the existence of a hydrophobic film on each of the two surfaces involved could induce slip between the endolymph and its bounding surfaces in the subtectorial space, thereby overcoming this limitation. The basis of viscosity calculations is the classical ''no slip'' assumption, and for narrow channels and hydrophobic surfaces this is not always correct. Instead, the interface may give rise to relative slip,[28] and this will make the liquid more slippery than its bulk viscosity would predict. In laboratory experiments[29] the effective viscous drag was reduced by a measured factor of about 5 for films of the thickness found in the cochlea and a single treated surface, using simple laboratory chemicals to produce the film. Such a film applied to both surfaces might be expected to increase the resonant Q value by a factor of about 10, and thus to about 1 at 1 kHz and 10 at 10 kHz, which begins to allow significant propagation of SLR waves. Indeed, when more is known about the molecular and hydrodynamic mechanisms involved, the increase might prove to be larger than this.

APPENDIX B: VISCOSITY AND THE EFFECTS OF HYDROPHOBICITY

As outlined in the main text and calculated in Appendix A, the viscosity of the waterlike endolymph between the reticular lamina and the tectorial membrane appears at first to offer an insurmountable barrier to the propagation of SLR waves below about 10 kHz.

However, the classical ''no slip'' assumption underlying high viscous forces in narrow channels may be unwarranted. Helmholtz[30] in 1860 published an analysis of experiments

using a water–gold interface and concluded there was appreciable slip. More recent experiments using atomic force microscopy[31] have confirmed these long-held suspicions and shown that in some situations the solid surface and liquid may slip relative to each other, a phenomenon describable in terms of a ''slip length.''[28] The present focus of much surface physics is on understanding the unique properties of water, and it is now known that water near boundaries is more ''slippery'' than its bulk viscosity value would predict.

The physics underlying slippage is still uncertain, but it is clear that the effect is one involving surface tension and is greatest for hydrophobic surfaces.[32] It is therefore significant for the configuration of the cochlea that Hensen cells are located immediately adjacent to the subtectorial space and that these cells are characterized by abundant production of lipid droplets[33] which, at least in the case of guinea pigs, accumulate on their surface. The function of the droplets is puzzling, but one could suppose that this substance might be readily conveyed by capillary effects to the nearby reticular lamina and, via the marginal net, to the underside of the tectorial membrane. By coating the subtectorial space with an oily, hydrophobic film, the cochlea could overcome the limitations imposed by the bulk viscosity of water and be able to support a full range of audiofrequency SLR waves. Significantly, Hensen cells are larger and the lipid droplets more abundant at the low-frequency apex where, as (A15) indicates, viscosity reduction is most needed. At the same time, the height of the tallest OHC stereocilia (and hence the width of the subtectorial gap) increases from about 3 μm at the base to 7 μm at the apex, again helping to reduce viscous drag.

The evidence for hydrophobic surfaces reducing viscous forces is widespread, but it has been collected using varying apparatus under disparate conditions. Perhaps most relevant to the subtectorial space is the finding[29] that the force between a spherical surface vibrating underwater within several micrometers of a plane surface was reduced by a factor of about 5 when one of the surfaces was made hydrophobic (and suggesting a factor of 10 if both surfaces were treated). Another experiment[34] involving a sphere and a plane vibrating relative to each other underwater found a slip length of up to 2 μm under some conditions; in this case hydrodynamic forces were 2–4 orders of magnitude less than those expected from the no-slip condition. More indirectly, observations[35] of water droplets sandwiched between hydrophobically treated glass plates have measured flow resistances 95% less than when the plates were untreated.

Much current work in surface physics is aimed at enhancing slippage between water and adjacent surfaces, either to increase water repellency or reduce hydrodynamic drag. Of particular interest, one way of increasing a surface's hydrophobicity is to increase the surface roughness,[36] leading to ''superhydrophobic states'' with contact angles approaching 180°. Thus, counterintuitively, a rough surface with high surface area can exhibit appreciably less hydrodynamic drag. A standard method of increasing surface roughness is to create tiny fingerlike protrusions from a surface,[37] in this way making the surface resemble that of a lotus leaf, off which water droplets effortlessly roll. In the cochlea we note that the reticular lamina[38] (as well as Hensen cells[33]) is decorated with similarly shaped microvilli whose large surface area would act to increase the hydophobicity of the surfaces from which they protrude.

These considerations suggest that the ear may use hydrophobic properties to increase slippage and escape the standard limitations imposed by viscosity. Measurements of the contact angle of endolymph on the reticular lamina would be of great interest, as would modern assessments of the chemical make up and physical properties of the lipids secreted by Hensen cells, which, as far as now known, are made up of cholesterol esters, triglycerides, and phospholipids.[39] These substances may provide a more effective slip than the materials used so far in surface film experiments.

[1] R. C. Naidu and D. C. Mountain, ''Measurements of the stiffness map challenge a basic tenet of cochlear theories,'' Hear. Res. **124**, 124–131 (1998).
[2] T. Duke and F. Jülicher, ''Active traveling wave in the cochlea,'' Phys. Rev. Lett. **90**, 158101 (2003).
[3] S. Camalet, T. Duke, F. Jülicher, and J. Prost, ''Auditory sensitivity provided by self-tuned critical oscillations of hair cells,'' Proc. Natl. Acad. Sci. U.S.A. **97**, 3183–3188 (2000).
[4] P. Lloyd and M. Redwood, ''Wave propagation in a layered plate composed of two solids with perfect contact, slip, or a fluid layer at their interface,'' Acustica **16**, 224–232 (1965).
[5] W. Hassan and P. B. Nagy, ''On the low-frequency oscillation of a fluid layer between two elastic plates,'' J. Acoust. Soc. Am. **102**, 3343–3348 (1997).
[6] M. C. Junger and D. Feit, *Sound, Structures, and Their Interaction* (Acoustical Society of America, New York, 1993), pp. 236–239.
[7] F. Coulouvrat, M. Rousseau, O. Lenoir, and J.-L. Izbiki, ''Lamb-type waves in a symmetric solid-fluid-solid trilayer,'' Acust. Acta Acust. **84**, 12–20 (1998).
[8] F. Mammano and J. F. Ashmore, ''Reverse transduction measured in the isolated cochlea by laser Michelson interferometry,'' Nature (London) **365**, 838–841 (1993).
[9] R. C. Naidu, ''Mechanical properties of the organ of Corti and their significance in cochlear mechanics,'' Ph.D. thesis, Boston University, 2001, pp. 117–134.
[10] H. Tiedemann, ''A new approach to theory of hearing,'' Acta Otolaryngol. Suppl. (Stockh) **277**, 1–50 (1970).
[11] B. Shoelson, E. K. Dimitriadis, H. Cai, and R. S. Chadwick, ''Theoretical and experimental considerations for the study of anisotropic elastic moduli of the mammalian tectorial membrane,'' Midwinter Meeting, Association for Research in Otolaryngology, Florida, 2003, http://www.aro.org/archives/2003/2003_732.html
[12] A. Wright, ''Dimensions of the cochlear stereocilia in man and the guinea pig,'' Hear. Res. **13**, 89–98 (1984).
[13] E. L. LePage, ''The mammalian cochlear map is optimally warped,'' J. Acoust. Soc. Am. **114**, 896–906 (2003).
[14] B. N. Evans and P. Dallos, ''Stereocilia displacement induced somatic motility of cochlear outer hair cells,'' Proc. Natl. Acad. Sci. U.S.A. **90**, 8347–8351 (1993).
[15] A. Bell, ''Are outer hair cells pressure sensors? Basis of a SAW model of the cochlear amplifier,'' in *Biophysics of the Cochlea*, edited by A. W. Gummer (World Scientific, Singapore, 2003), pp. 429–431.
[16] A. Bell, ''Cochlear mechanics without the traveling wave: The cochlea as a surface acoustic wave resonator,'' preprint at http://eprints.anu.edu.au/archive/00001258/
[17] G. Bredberg, ''Cellular pattern and nerve supply of the human organ of Corti,'' Acta Oto-Laryngol., Suppl. **236**, 1–135 (1968), Fig. 92.
[18] K. E. Nilsen and I. J. Russell, ''Timing of cochlear feedback: Spatial and temporal representation of a tone across the basilar membrane,'' Nature Neurosci. **2**, 642–648 (1999).
[19] M. P. Scherer, M. Nowotny, E. Dalhoff, H.-P. Zenner, and A. W. Gummer, ''High-frequency vibration of the organ of Corti *in vitro*,'' in *Biophysics of the Cochlea*, edited by A. W. Gummer (World Scientific, Singapore, 2003), pp. 271–277.

[20] T. Y. Ren, Y. Zou, J. F. Zheng, A. L. Nutall, E. Porsov, and S. Matthews, ''Measurements of basilar membrane vibration using a scanning laser interferometer,'' in *Biophysics of the Cochlea*, edited by A. W. Gummer (World Scientific, Singapore, 2003), pp. 211–219.
[21] B. Canlon and L. Brundin, ''Mechanically induced length changes of isolated outer hair cells are metabolically dependent,'' Hear. Res. **53**, 7–16 (1991).
[22] H. Davis, ''An active process in cochlear mechanics,'' Hear. Res. **9**, 79–90 (1983).
[23] T. Gold, ''Hearing II. The physical basis of the cochlea,'' Proc. R. Soc. London, Ser. B **135**, 492–498 (1948).
[24] C. R. Steele, ''A possibility for subtectorial membrane fluid motion,'' in *Basic Mechanisms in Hearing*, edited by A. R. Møller (Academic, New York, 1973), pp. 69–93.
[25] G. H. Frommer and C. R. Steele, ''Permeability of fluid flow through hair cell cilia,'' J. Acoust. Soc. Am. **65**, 759–764 (1979).
[26] K. D. Karavitaki and D. C. Mountain, ''Is the cochlear amplifier a fluid pump?'' in *Biophysics of the Cochlea*, edited by A. W. Gummer (World Scientific, Singapore, 2003), pp. 310–311.
[27] http://eprints.anu.edu.au/archive/00001532/
[28] S. Granick, Y. Zhu, and H. Lee, ''Slippery questions about complex fluids flowing past solids,'' Nature Mater. **2**, 221–227 (2003).
[29] W. Hild, A. Opitz, J. A. Schaefer, and M. Scherge, ''The effect of wetting on the microhydrodynamics of surfaces lubricated with water and oil,'' Wear **254**, 871–875 (2003).
[30] S. Goldstein, ''Note on the conditions at the surface of contact of a fluid with a solid body,'' in *Modern Developments in Fluid Dynamics*, edited by S. Goldstein (Dover, New York, 1965), pp. 676–680.
[31] V. S. J. Craig, C. Neto, and D. R. M. Williams, ''Shear-dependent boundary slip in an aqueous Newtonian liquid,'' Phys. Rev. Lett. **87**, 054504 (2001).
[32] C. Cotton-Bizonne, J.-L. Barrat, L. Bocquet, and E. Charlaix, ''Low-friction flows of liquid at nanopatterned interfaces,'' Nature Mater. **2**, 237–240 (2003).
[33] M. A. Merchan, J. A. Merchan, and M. D. Ludena, ''Morphology of Hensen's cells,'' J. Anat. **131**, 519–523 (1980).
[34] Y. Zhu and S. Granick, ''Rate-dependent slip of Newtonian liquid at smooth surfaces,'' Phys. Rev. Lett. **87**, 096105 (2001).
[35] J. Kim and C.-J. Kim, ''Nanostructured surfaces for dramatic reduction of flow resistance in droplet-based microfluidics,'' Proc. 2002 IEEE Conference MEMS, Las Vegas, NV, pp. 479–482 (2002).
[36] A. Lafuma and D. Quéré, ''Superhydrophobic states,'' Nature Mater. **2**, 457–460 (2003).
[37] L. Feng, S. Li, Y. Li, H. Li, L. Zhang, J. Zhai, Y. Song, B. Liu, L. Jiang, and D. Zhu, ''Super-hydrophobic surfaces: from natural to artificial,'' Adv. Mater. (Weinheim, Ger.) **14**, 1857–1860 (2002).
[38] R. V. Krstic, *Ultrastructure of the Mammalian Cell: An Atlas* (Springer-Verlag, Berlin, 1979), pp. 220–221.
[39] M. Schiff and H. Christiansen-Lou, ''The nature of lipid globules in Hensen's cells,'' Ann. Otol. Rhinol. Laryngol. **76**, 624–637 (1967).

Mathematical modeling of the radial profile of basilar membrane vibrations in the inner ear

Martin Homer[a] and Alan Champneys
Department of Engineering Mathematics, University of Bristol, Bristol BS7 8EX, United Kingdom

Giles Hunt
Department of Mechanical Engineering, University of Bath, Bath BA2 7AY, United Kingdom

Nigel Cooper
The MacKay Institute of Communication and Neuroscience, Keele University, Keele ST5 5BG, United Kingdom

(Received 22 August 2003; revised 13 May 2004; accepted 18 May 2004)

Motivated by recent experimental results, an explanation is sought for the asymmetry in the radial profile of basilar membrane vibrations in the inner ear. A sequence of one-dimensional beam models is studied which take into account variations in the bending stiffness of the basilar membrane as well as the potential presence of structural hinges. The results suggest that the main cause of asymmetry is likely to be differences between the boundary conditions at the two extremes of the basilar membrane's width. This has fundamental implications for more detailed numerical simulations of the entire cochlea. © *2004 Acoustical Society of America.* [DOI: 10.1121/1.1771571]

PACS numbers: 43.64.Kc, 43.40.At, 43.40.Cw [WPS] Pages: 1025–1034

I. INTRODUCTION

In this report we consider a succession of simple mathematical models which are intended to describe the distribution of sound-evoked vibrations across the width of the inner-ear's basilar membrane. This distribution, which we will refer to as a ''radial profile,'' has been the subject of several recent experimental studies (e.g., Cooper, 1999; Nilsen and Russell, 1999, 2000; Rhode and Recio, 2000) and has fundamental implications for detailed numerical simulations of the entire cochlea (cf. Steele, 1974; Brass, 2000; Lim, 2000; Barker, 2000).

Figure 1 shows a schematic cross section through the cochlear partition. The basilar membrane (BM, at the bottom of the figure) is thought to be responsible for converting sound-evoked pressure differences between the two sides of the partition (SM and ST in Fig. 1) into ''transverse'' structural motion (vertical arrows in Fig. 1). The various support cells and accessory structures which ride on top of the BM convert the transverse motion into shearing motion in the subtectorial space (see horizontal arrows in Fig. 1), as is needed to excite the partition's mechano-sensitive inner and outer hair cells (IHC/OHCs) and give rise to the sensation of hearing (Dallos *et al.*, 1996, for reviews). The situation in the real cochlea may be far more complex than this, as has been suggested in various experimental investigations (e.g., Karavitaki *et al.*, 1998; Nilsen and Russell, 1999, 2000). On the other hand, it may not be, as suggested in other investigations (e.g., Richter and Dallos, 1999; Fridberger *et al.*, 2002). Unfortunately, the basic physical characteristics of the components of the cochlea, and the mechanics of their interactions, are not well understood. The only well-established facts are that the BM varies in stiffness between the arcuate and pectinate zones (Miller, 1985; Olson and Mountain, 1994), and that the hair cells and most of the support cells are at least an order of magnitude less stiff than the BM (Hallworth, 1995). The only structures which seem to have a pronounced effect on the local stiffness of the BM are the pillar cells (labeled PC in Fig. 1; cf. Olson and Mountain, 1994; Tolomeo and Holley, 1997). The purpose of the present paper is to investigate the consequences of this structural knowledge in terms of the mechanical processing of sound in the cochlea.

The experimental studies of the BM's radial profile which have been performed to date have had mixed results: Nilsen and Russell (1999, 2000) have reported relatively complex radial profiles, while Cooper (1999) and Rhode and Recio (2000) have reported much simpler profiles. The present report will focus on the simpler profiles. There are several reasons for this: first, the more complex findings of Russell and Nilsen have not been confirmed in independent investigations, while the simpler profiles have been observed by at least two groups. Second, the observations made by Cooper (1999, 2000) are the most extensive available; they map the BM's radial profile with unprecedented resolution and they apply across a wide range of stimulus frequencies, a wide range of intensities at the BM's characteristic frequency, and a number of longitudinal locations in guinea-pig, gerbil, and chinchilla cochleae. Cooper's measurements are also consistent with previous radial profile studies in the cat (e.g., Wilson and Evans, 1983; Cooper and Rhode, 1992), despite the differences in physical parameters (such as BM thickness) between species. From the point of view of our mathematical analyses, the most important features of the simple radial profiles are that, at least to a first approximation, the BM moves in phase across its entire width, and the amplitude distribution is asymmetric about the BM's midpoint (cf. Fig. 2).

[a]Electronic mail: martin.homer@bristol.ac.uk

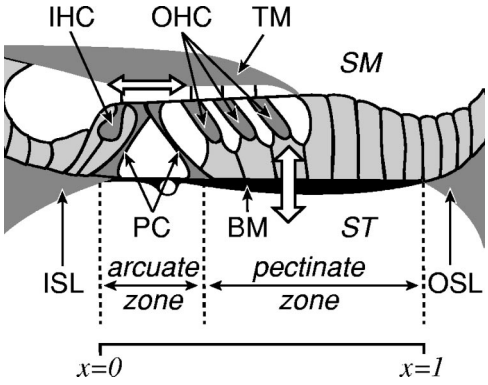

FIG. 1. Schematic diagram of the mammalian cochlear partition. BM denotes the basilar membrane, whose endpoints attach to the inner spiral lamina (ISL) and outer spiral ligament (OSL). TM denotes tectorial membrane; PC denotes pillar cells; OHC and IHC outer and inner hair cells, respectively; SM and ST scala media and tympani, respectively.

II. SIMPLE BEAM MODEL

Initially, we shall investigate whether a simple beam equation can provide a suitable model to describe the BM's radial profile. Our main aims are to consider what the appropriate boundary conditions might be, and to consider how variations in the stiffness of the arcuate and pectinate zones might affect the BM's radial profile. Throughout we shall consider only one-dimensional spatial variation of the BM, that is we assume the profile to be a function of radial position only (and not time). We justify this by the experimental observation that the BM vibrates in what appears, within experimental accuracy, to be its pure fundamental mode, across a wide range of frequencies, intensities, and longitudinal locations along the cochlear partition. Hence we can take a simple, second order in time, sinusoidally forced beam model, expand as a Fourier series, and keep only the term in the fundamental frequency. We discard nonlinear terms, as the displacement of the BM is extremely small, being less than 1% of the BM's width. Furthermore, over almost the entire range of measurement, the radial profile of the BM has the same shape, with a pronounced asymmetry.

We are left with a simple model of a one-dimensional beam, subject to a constant load representing the amplitude of forcing, whose static solutions describe the mode shape of the BM's vibration.

Initially, let us suppose that the beam has a constant bending stiffness EI (where E is the elastic modulus, with units Nm^{-2}, and I is the area moment of inertia, with units m^4), and is subject to a constant line pressure load q, with units Nm^{-1}. Then the equation governing the transverse displacement w as a function of position along the beam x, both with units m, is the Euler–Bernoulli beam equation

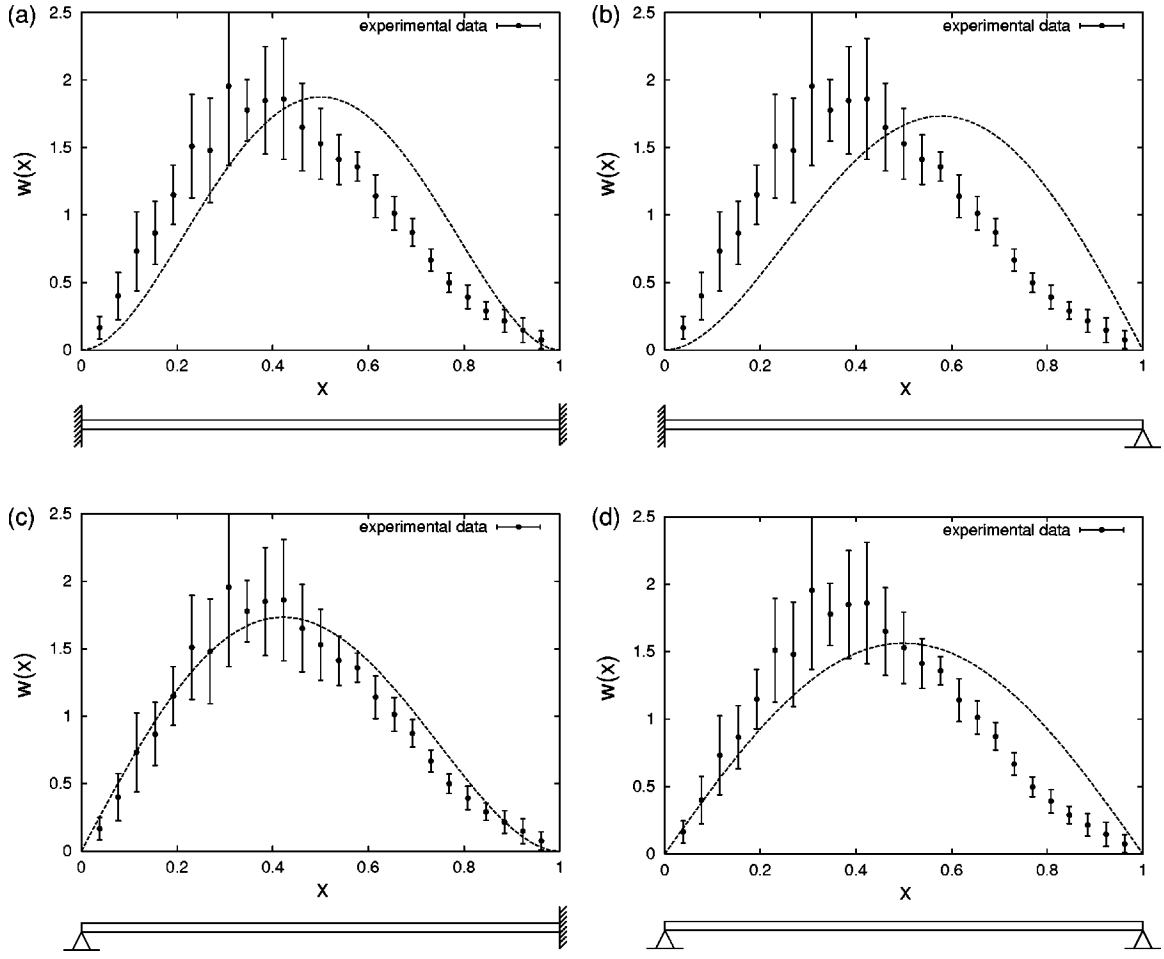

FIG. 2. Graphs of membrane deflection versus radial position, for the constant bending stiffness beam model, with boundary conditions indicated by schematics below (▨ denotes clamped, △ simply supported).

TABLE I. Constants of integration for simple beam model.

Boundary condition		Constants			
$x=0$	$x=1$	A	B	C	D
clamped	clamped	0	0	$\frac{1}{24}\frac{q}{EI}$	$-\frac{1}{12}\frac{q}{EI}$
clamped	simply supported	0	0	$\frac{1}{16}\frac{q}{EI}$	$-\frac{5}{48}\frac{q}{EI}$
simply supported	clamped	0	$\frac{1}{48}\frac{q}{EI}$	0	$-\frac{1}{16}\frac{q}{EI}$
simply supported	simply supported	0	$\frac{1}{24}\frac{q}{EI}$	0	$-\frac{1}{12}\frac{q}{EI}$

$$\frac{d^4w}{dx^4}=\frac{q}{EI}. \tag{1}$$

Therefore

$$w(x)=\frac{q}{4!EI}x^4+Dx^3+Cx^2+Bx+A, \tag{2}$$

where A, B, C, and D are constants determined from the boundary conditions. It is questionable which boundary conditions most accurately model the physiology. Therefore we shall consider the four possible combinations of clamped ($w=w'=0$) and simply supported ($w=w''=0$) boundary conditions at the two ends of the beam. Throughout this report we nondimensionalize all lengths by the width of the beam, so that $x=0$ corresponds to the left-hand end of the arcuate zone and $x=1$ to the right-hand end of the pectinate zone in the representation of the BM in Fig. 1, and the parameter q/EI is nondimensional.

The values of the constants given by the four combinations of boundary conditions are reported in Table I.

Figure 2 shows graphs of the solutions of Eq. (2), together with the experimental results we use throughout this study. Throughout this report we have normalized the deflection w, and the experimental data with which we compare our predictions, such that $\int w(x)dx=1$. The experimental results represent the means and standard deviations of 15 measurements made at various frequencies and intensities in a single guinea-pig cochlea (see Cooper, 1999, for details). Inspection of Fig. 2 shows that the uniform bending stiffness beam model with a simply supported boundary condition at $x=0$ and a clamped boundary at $x=1$ [as shown in Fig. 2(c)] provides the best agreement with experimental data. The closeness of this agreement between theoretical and experimental data motivates the beam equation as a suitable candidate to modify, in order to try and improve the fit.

III. NONUNIFORM BENDING STIFFNESS

Experimental measurements suggest that the bending stiffness of the BM varies across the width of the membrane. The nature of the variation is somewhat controversial: on the one hand, Miller (1985) has shown that the bending stiffness of the arcuate zone is, on average, around five times higher than that of the pectinate zone. On the other hand, however, Olson and Mountain (1994) have shown that the pectinate zone is around three times more stiff than the arcuate zone. In an attempt to refine our model, then, we shall now allow the bending stiffness (i.e., EI) of the model beam to vary across its width. The variations will first be allowed in a piecewise constant fashion. Our aim is not to derive a novel beam model, as achieved in earlier work (e.g., Allaire *et al.*, 1974; Miller, 1985), but rather to ask which simple modeling hypotheses are consistent with experimental data. As before, we shall consider the four combinations of clamped and simply supported boundary conditions at the endpoints. We initially choose a piecewise constant bending stiffness given by

$$EI(x)=\begin{cases} EI_1, & x\in[0,x_t), \\ EI_2, & x\in(x_t,1], \end{cases} \tag{3}$$

where EI_1 and EI_2 are the constant bending stiffnesses of the arcuate and pectinate zones (the regions $[0,x_t)$ and $(x_t,1]$, respectively). Experimental measurements by Cooper (1999) suggest a value $x_t=0.28$, though this value may vary slightly according to position along the cochlear partition, and so we shall also investigate the effect of varying x_t. For simplicity, we also define a stiffness ratio factor, Γ,

$$\Gamma=\frac{EI_2}{EI_1}. \tag{4}$$

As the bending stiffness is constant in each region, we may solve the beam equation Eq. (1) in each region to give

$$w(x)=\begin{cases} \frac{q}{4!EI_1}x^4+D_1x^3+C_1x^2+B_1x+A_1, & x\in[0,x_t), \\ \frac{q}{4!EI_2}x^4+D_2x^3+C_2x^2+B_2x+A_2, & x\in(x_t,1]. \end{cases} \tag{5}$$

Now to determine the eight constants of integration $A_{1,2}$, $B_{1,2}$, $C_{1,2}$, and $D_{1,2}$, we must pose boundary conditions at $x=0$, $x=1$, and $x=x_t$. The conditions at $x=0$ and $x=1$ (clamped or simply supported, for example) give four equations for the integration constants, as before, while those at $x=x_t$, the interface between the two zones, must provide another four equations. In the first instance we choose total continuity, that is, continuity of w, w', w'', and w''', at $x=x_t$. The values of the eight constants, for the four possible combinations of these boundary conditions, are given in Appendix A (note that each value is a function of x_t, Γ, q, and EI_2).

Figure 3 shows plots of beam displacement, with the four possible combinations of end boundary conditions, for various values of Γ.

Figure 3 clearly shows two plausible matches between the theoretical prediction of the piecewise constant beam model and the experimental data: clamped/clamped boundary conditions [Fig. 3(a)], with large Γ, and (arguably rather better) simply supported/clamped end conditions [Fig. 3(c)], with large or moderate Γ. Both of these models fit the data better than the simple constant stiffness beam model, in that they approximate the peak amplitude, and the decay near $x=1$, more accurately than the simplest model. In either case, we may reasonably hypothesize that the pectinate zone of the

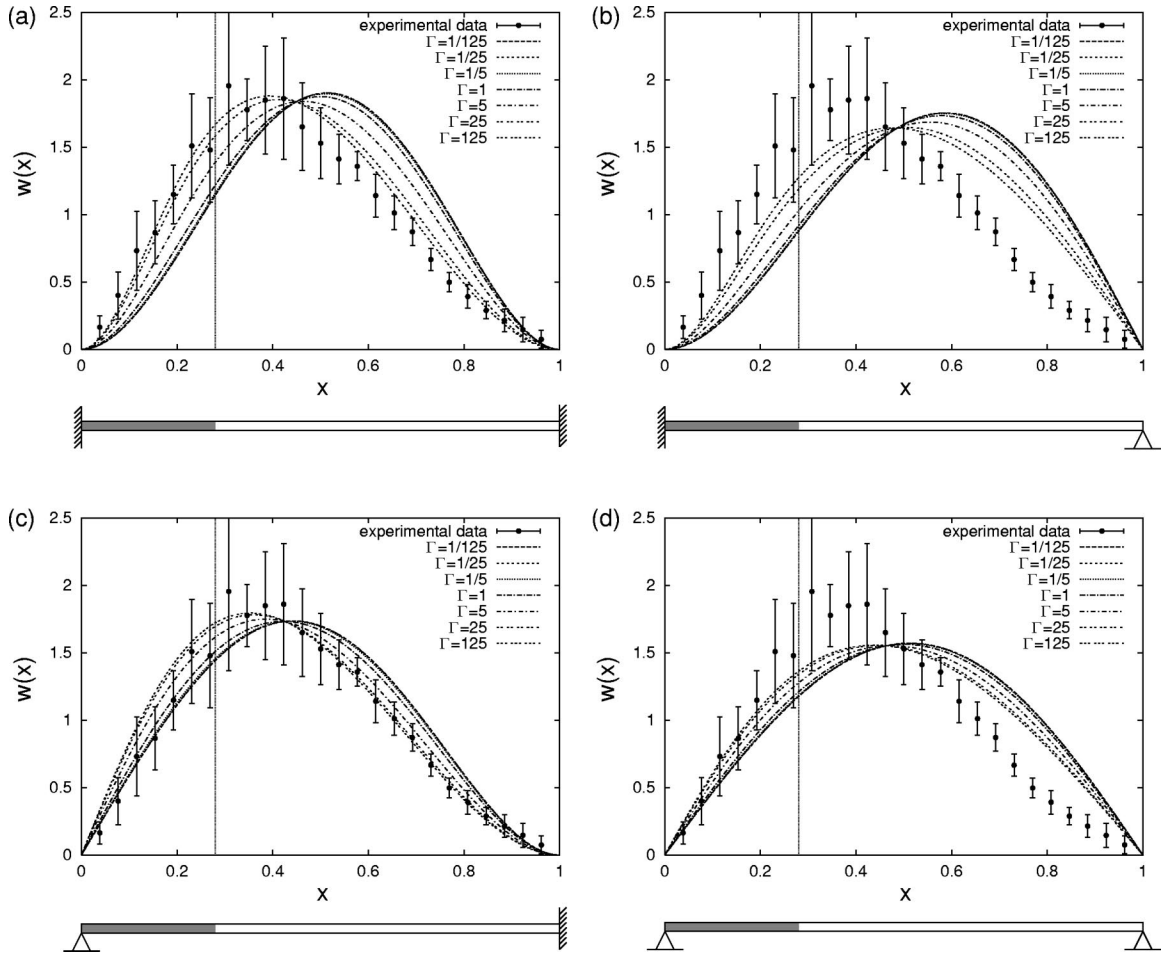

FIG. 3. Piecewise constant bending stiffness beam model, for fixed $x_t=0.28$ and varying bending stiffness ratio Γ, with boundary conditions indicated by schematics below (arcuate zone shaded).

basilar membrane is much stiffer than the arcuate zone, as in the measurements of Olson and Mountain (1994).

Figure 4 shows the effect of varying x_t for fixed Γ. We choose to vary x_t between 0.2 and 0.4; this could represent uncertainty in the position of the interface, or a variation with location in the cochlea. We fix $\Gamma=25$, as this provided the most plausible match between theoretical prediction and experimental data above.

Figure 4 shows that varying the interface position has a negligible effect on the shape of the model predictions. It seems that the boundary conditions have a far more important effect in governing the mode shape than the position of the junction between the arcuate and pectinate zones. This conclusion is supported by analyses at other values of Γ, including the limit $\Gamma\to\infty$.

IV. RIGID ROD AND HINGE MODEL

With reference to the physiology of the BM, it seems possible that the presence of the pillar cells might make an extremely rigid structure in the arcuate zone, while the joint between the arcuate and pectinate zones of the BM may be relatively weak. The conditions of total continuity proposed thus far may therefore be too strong. This prompts us to consider another simplified model for the basilar membrane, in which the arcuate zone is modeled by a rigid rod, and the pectinate zone as a flexible beam of constant bending stiffness EI. Thus the equations for the deflection $w(x)$ are

$$w(x)=\begin{cases} B_1 x, & x\in[0,x_t), \\ \dfrac{q}{4!EI}x^4+D_2x^3+C_2x^2+B_2x+A_2, & x\in(x_t,1]. \end{cases} \tag{6}$$

We suppose that there is a hinge, or rotational spring, at $x=0$, such that the slope of the BM there is proportional to the load applied q, so

$$B_1=\frac{\kappa q}{EI}, \tag{7}$$

where the factor EI is inserted to simplify the calculation. Note that small κ represents a relatively stiffer hinge. We now need four boundary conditions for the four unknowns A_2, B_2, C_2, D_2. As before, we allow the beam to be simply supported or clamped at $x=1$ so that, at $x=1$,

$$w=0, \quad \text{and either} \quad \frac{dw}{dx}=0 \quad \text{or} \quad \frac{d^2w}{dx^2}=0. \tag{8}$$

At the junction $x=x_t$, we suppose either that the beam and rod are ''clamped'' so that

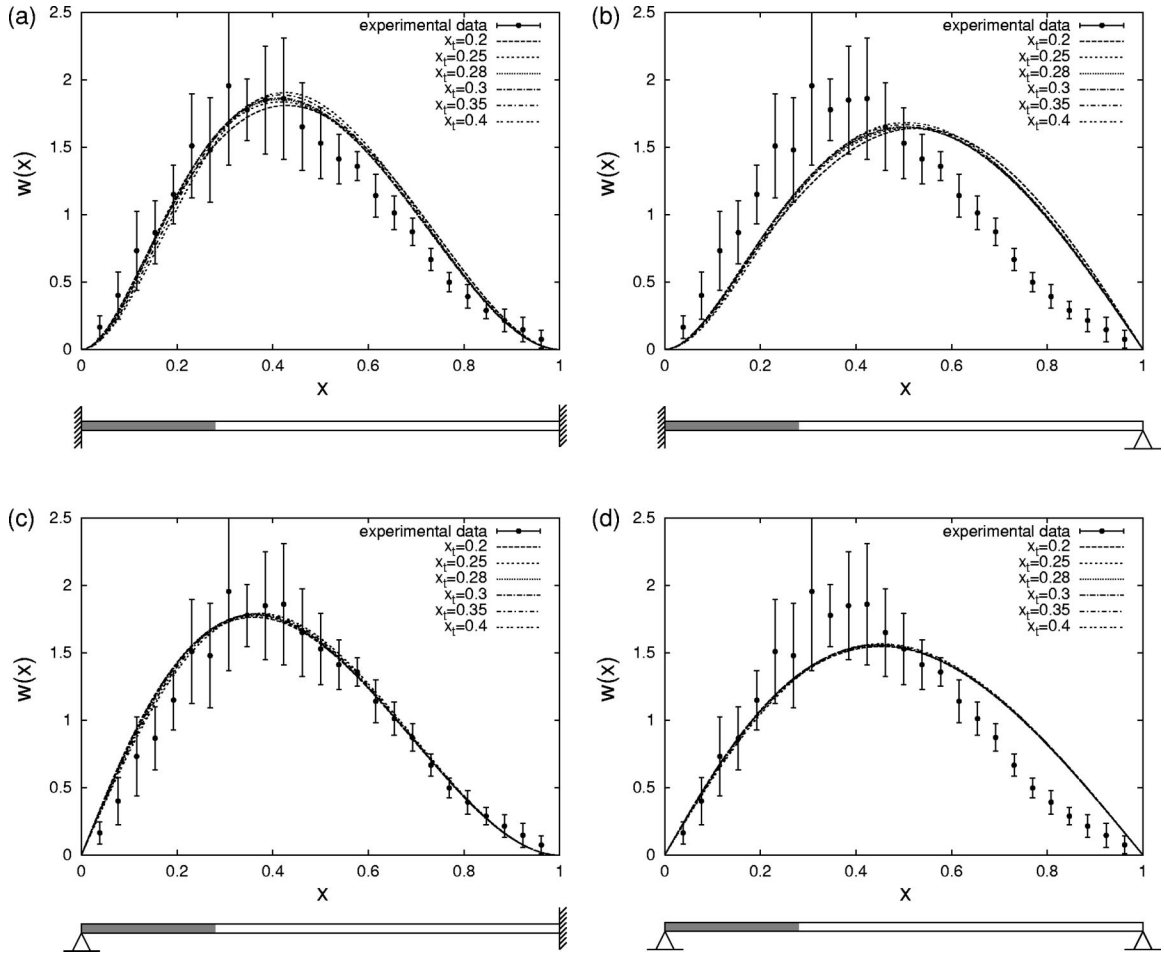

FIG. 4. Piecewise constant bending stiffness beam model, for varying x_t and fixed stiffness ratio $\Gamma=25$, with boundary conditions indicated by schematics below (arcuate zone shaded for a single x_t).

$$w(x) \text{ and } \frac{dw}{dx} \text{ are continuous} \tag{9}$$

at $x=x_t$, or "simply supported," so that

$$w(x) \text{ and } \frac{d^2w}{dx^2} \text{ are continuous} \tag{10}$$

at $x=x_t$.

Equations (8) together with either Eq. (9) or (10) give us four conditions for the four unknowns. As before, these conditions may be solved explicitly to find the four constants of integration A_2, B_2, C_2, D_2 (as functions of x, x_t, and κ), and hence give an analytic expression for the membrane displacement. The values of the constants are reported in Appendix B.

Figure 5 shows solutions of Eq. (6) for the four possible combinations of boundary conditions given in Eq. (8) and either Eq. (9) or (10). The most plausible match to the data in this case is where the membrane is pinned at $x=x_t$ and clamped at $x=1$ for $\kappa\approx 0.02$, as shown in Fig. 5(c). Varying x_t was again found not to have any significant effect, as shown for the case of two bending stiffness models above. Once again we see the importance of the boundary conditions.

V. CONTINUOUSLY VARIABLE BENDING STIFFNESS

Another possible refinement of our model is to allow the bending stiffness of the BM to vary continuously with position. While the arcuate zone of the real BM has a reasonably constant cross-sectional area and composition, and is therefore quite likely to have a constant bending stiffness, the pectinate zone certainly does not (cf. Iurato, 1962; Cabezudo, 1978). The individual fibrils of collagen which make up the BM are often arranged in such a way that the BM's pectinate zone has two distinct layers (cf. Fig. 6). The layers are separated by a ground substance with potential load-carrying ability, and the thickness of this ground substance varies across the width of the pectinate zone (Iurato, 1962; Cabezudo, 1978); the variation is particularly marked in the unfixed gerbil cochlea, as shown by Edge *et al.* (1998). In mechanical terms, the resultant variation in the cross-sectional area of the pectinate zone will lead to a nonconstant second moment of area, $I=I(x)$. In this case, we must solve a generalized beam equation:

$$\frac{d^2}{dx^2}\left(EI(x)\frac{d^2w}{dx^2}\right)=q. \tag{11}$$

We suppose that the BM has uniform cross section along the plane of the membrane; the approximation to the transverse

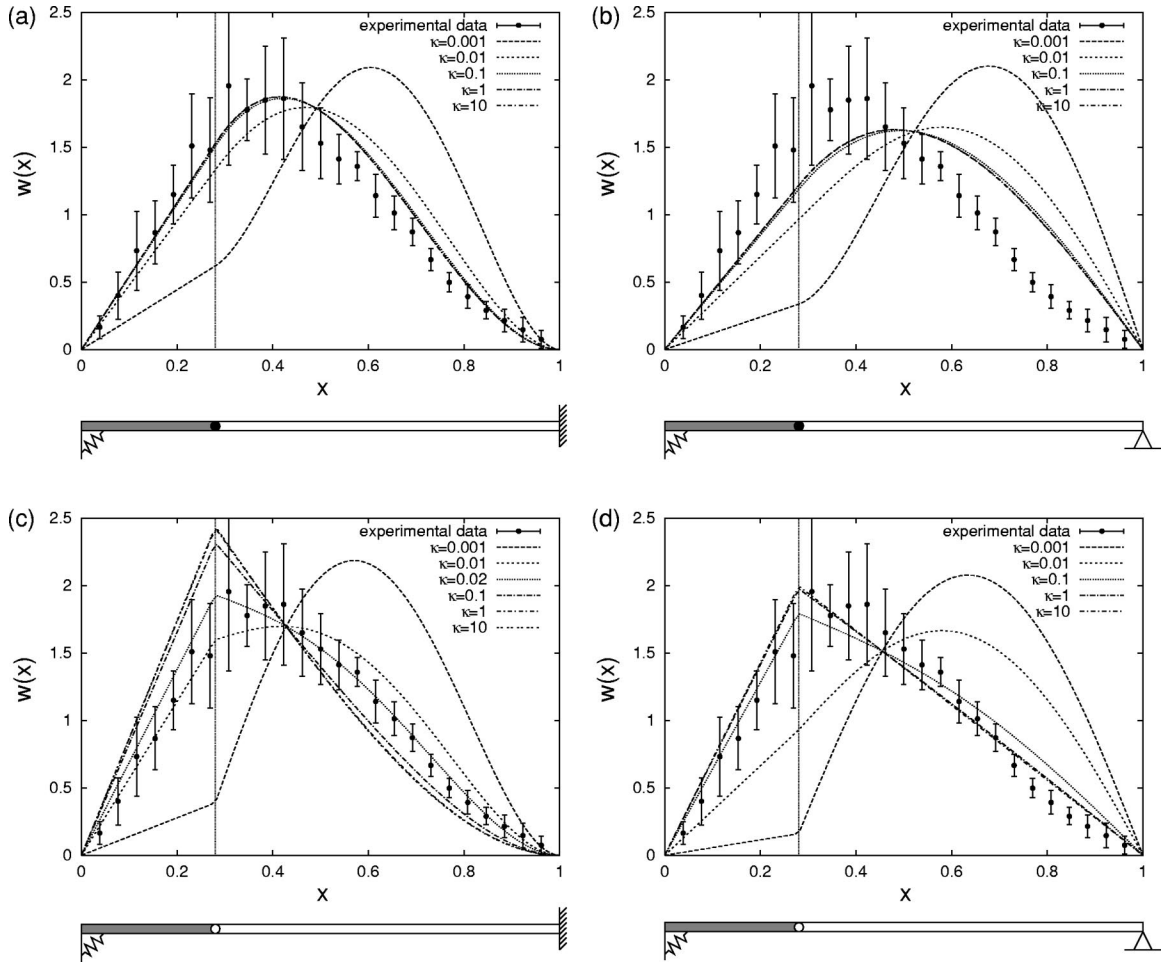

FIG. 5. Rigid rod and hinge models, for varying hinge stiffness κ and fixed $x_t = 0.28$. Boundary conditions at $x = 1$ indicated by schematics below. Continuity conditions at $x = x_t$: (a) and (b) w and w' are continuous; (c) and (d) w and w'' are continuous.

geometry of the cross section used in this study is shown in Fig. 6. We assume that the distance from the center line (the x axis) to each edge of the BM in the arcuate zone is a constant, r. In the pectinate zone, we assume that the BM is divided in two, each half having constant thickness r, and that the profile of the inner and outer edges is quadratic and symmetric about the x axis and the midpoint of the pectinate zone, $x = (1 + x_t)/2$, with maximum distance from the center line to the outer edge of the membrane R; thus the distances of the inner and outer edges from the center line, for $x \in [x_t, 1]$, are given by

$$r_{\text{inner}}(x) = \frac{4}{(1-x_t)^2}(R-r)(x-x_t)(1-x), \tag{12}$$

$$r_{\text{outer}}(x) = \frac{4}{(1-x_t)^2}(R-r)(x-x_t)(1-x) + r. \tag{13}$$

In reality, the upper and lower portions of the pectinate zone of the BM are tied together, both by exchange of fibers between the two portions, and via a ground substance. We shall suppose, for simplicity, that the two portions are joined by a light net of fibers with infinite shear stiffness, and so act together as a competent beam.

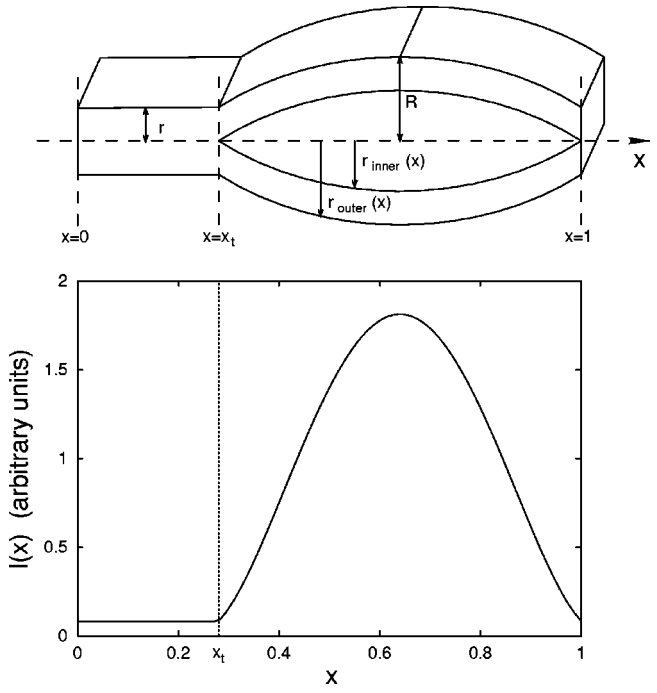

FIG. 6. (Above) Sketch profile of basilar membrane geometry. (Below) plot of second moment of area for the variable thickness membrane with realistic parameter values.

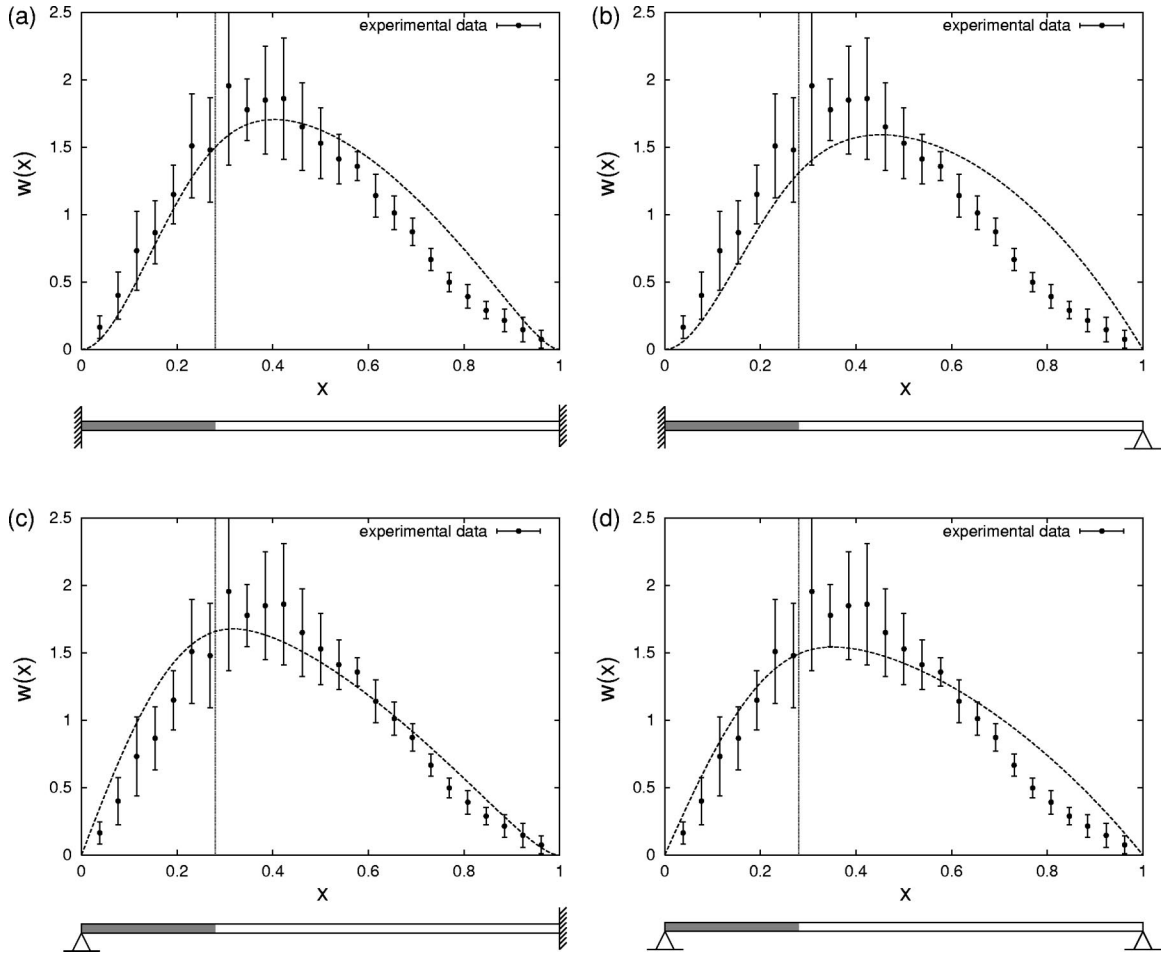

FIG. 7. Continuously variable bending stiffness model for fixed $x_t = 0.28$, with boundary conditions indicated by schematics below.

Since all lengths are nondimensionalized by the width of the beam, the second moment of area of a thin slice of membrane is given (cf. Gere and Timoshenko, 1991) by:

$$I(x) = \begin{cases} \frac{2}{3} r^3, & x \in [0, x_t), \\ \frac{2}{3} (r_{\text{outer}}(x)^3 - r_{\text{inner}}(x)^3), & x \in (x_t, 1]. \end{cases} \tag{14}$$

Direct measurement in the guinea-pig by Miller (1985) suggests values for the dimensional physical constants r and R of

$$r = 0.75 \ \mu\text{m}, \quad R = 2.15 \ \mu\text{m} \tag{15}$$

for a membrane of width 150 μm, so in our nondimensionalized variables we have that

$$r = \tfrac{1}{200}, \quad R = \tfrac{43}{3000}. \tag{16}$$

Figure 6 shows a plot of the variation of second moment of area in this case: the average bending stiffness of the pectinate zone is clearly much larger than that in the arcuate zone.

Once again, in order to solve Eq. (11), we must supply end boundary and junction conditions. We shall assume that the modulus of elasticity E is constant and equal in both zones. Figure 7 shows plots of the solution of Eq. (11) together with experimental data for the four possible combinations of clamped or simply supported boundary conditions at the two ends ($x = 0$ and $x = 1$) with total continuity at the junction. Given the values of the constants r and R and the boundary conditions, Eq. (11) can be integrated using Waterloo Maple Software (1996) to give explicit solutions, shown in Fig. 7. Once again we see reasonable agreement between theory and experiment, best of all when the beam is simply supported at $x = 0$ and clamped at $x = 1$ [cf. Fig. 7(c)]. However, the fit between experiment and data is not as close as that for the piecewise constant bending stiffness model of Figs. 3(a) and (c). It appears that the boundary conditions are much more important than the fine details of the model in determining the fundamental behavior of the membrane.

VI. CONCLUSIONS AND FURTHER WORK

In this report we have discussed simple beam equations as possible models to describe the radial profile of the basilar membrane's sound-evoked vibrations. Part of the benefit of using such simple models is that closed form solutions can be obtained, and so complete parametric studies can be made, a task that is much more difficult with finite element solution methods, for example.

It seems that solutions of the beam equation can fit experimental data well with certain combinations of boundary conditions and bending stiffness variations. The best fit to experimental data is obtained for a beam with piecewise constant bending stiffness, simply supported at the arcuate end

($x=0$), and clamped at the pectinate end ($x=1$), with the bending stiffness of the pectinate zone much larger than that of the arcuate zone. Good agreement is also obtained in the limit of this ratio of bending stiffnesses tending to infinity, with the membrane clamped at the pectinate end, and either simply supported or clamped at the arcuate end. More detailed modeling of the physiology, such as changing the location of the transition from arcuate to pectinate zone, or allowing the bending stiffness of the pectinate zone to vary with radial position, does not substantially improve the fit to experimental data. The more detailed models do support the conclusion, however, that the pectinate zone of the BM is substantially stiffer than the arcuate zone, and that the membrane is simply supported at the arcuate end and clamped at the pectinate end.

We may tentatively conclude, therefore, that the basilar membrane acts as if it is simply supported at the arcuate end, clamped at the pectinate end, and is substantially stiffer in the pectinate zone than the arcuate zone.

There are many possibilities for refinements and improvements to the types of model discussed here. Although a more detailed modeling of the physiology would perhaps be possible, not too much should be expected from a constant loading model; the fit is already reasonably good, given the large standard deviation in the data. Also, we have made no attempt to model the variation of BM properties with position in the cochlear partition, although experimental data suggests that such variation does not significantly affect the qualitative features of the radial profile. Perhaps more important would be to add a simple model of the dynamics of the hair cells, which seem to be largely responsible for enhancing the sensitivity of the BM at low stimulus levels, and try to understand their behavior in active and passive modes.

APPENDIX A: CONSTANTS OF INTEGRATION FOR THE PIECEWISE CONSTANT BENDING STIFFNESS MODEL

We record here the values of the eight constants of integration, $A_{1,2}$, $B_{1,2}$, $C_{1,2}$, and $D_{1,2}$, for the beam model with piecewise constant bending stiffness Eq. (3), and the four possible combinations of clamped and simply supported end boundary conditions.

Equations (A1)–(A4) show the values of the constants where the beam is clamped at $x=0$ and $x=1$; Eqs. (A5)–(A8) for clamped at $x=0$ and simply supported at $x=1$; Eqs. (A9)–(A12) for simply supported at $x=0$ and clamped at $x=1$; and Eqs. (A13)–(A16) for simply supported at $x=0$ and $x=1$:

$$A_1=0, \quad A_2=\frac{x_t^4}{24}(1-\Gamma)\frac{q}{EI_2}, \tag{A1}$$

$$B_1=0, \quad B_2=-\frac{x_t^3}{6}(1-\Gamma)\frac{q}{EI_2}, \tag{A2}$$

$$C_1=\left[\frac{-3x_t^4+8x_t^3-6x_t^2}{24}(1-\Gamma)+\frac{1}{24}\right]\frac{q}{EI_2},$$

$$C_2=\left[\frac{-3x_t^4+8x_t^3}{24}(1-\Gamma)+\frac{1}{24}\right]\frac{q}{EI_2}, \tag{A3}$$

$$D_1=\left[\frac{x_t^4-2x_t^3+2x_t}{12}(1-\Gamma)-\frac{1}{12}\right]\frac{q}{EI_2},$$

$$D_2=\left[\frac{x_t^4-2x_t^3}{12}(1-\Gamma)-\frac{1}{12}\right]\frac{q}{EI_2}; \tag{A4}$$

$$A_1=0, \quad A_2=\frac{x_t^4}{24}(1-\Gamma)\frac{q}{EI_2}, \tag{A5}$$

$$B_1=0, \quad B_2=-\frac{x_t^3}{6}(1-\Gamma)\frac{q}{EI_2}, \tag{A6}$$

$$C_1=\left[\frac{-x_t^4+4x_t^3-4x_t^2}{16}(1-\Gamma)+\frac{1}{16}\right]\frac{q}{EI_2},$$

$$C_2=\left[\frac{-x_t^4+4x_t^3}{16}(1-\Gamma)+\frac{1}{16}\right]\frac{q}{EI_2}, \tag{A7}$$

$$D_1=\left[\frac{x_t^4-4x_t^3+8x_t}{48}(1-\Gamma)-\frac{5}{48}\right]\frac{q}{EI_2},$$

$$D_2=\left[\frac{x_t^4-4x_t^3}{48}(1-\Gamma)-\frac{5}{48}\right]\frac{q}{EI_2}; \tag{A8}$$

$$A_1=0, \quad A_2=\frac{x_t^4}{24}(1-\Gamma)\frac{q}{EI_2}, \tag{A9}$$

$$B_1=\left[\frac{-3x_t^4+8x_t^3-6x_t^2}{48}(1-\Gamma)+\frac{1}{48}\right]\frac{q}{EI_2},$$

$$B_2=\left[\frac{-x_t^4-2x_t^2}{16}(1-\Gamma)+\frac{1}{48}\right]\frac{q}{EI_2}, \tag{A10}$$

$$C_1=0, \quad C_2=\frac{x_t^2}{4}(1-\Gamma)\frac{q}{EI_2}, \tag{A11}$$

$$D_1=\left[\frac{x_t^4-6x_t^2+8x_t}{48}(1-\Gamma)-\frac{1}{16}\right]\frac{q}{EI_2},$$

$$D_2=\left[\frac{x_t^4-6x_t^2}{48}(1-\Gamma)-\frac{1}{16}\right]\frac{q}{EI_2}; \tag{A12}$$

$$A_1=0, \quad A_2=\frac{x_t^4}{24}(1-\Gamma)\frac{q}{EI_2}, \tag{A13}$$

$$B_1=\left[\frac{-x_t^4+4x_t^3-4x_t^2}{24}(1-\Gamma)+\frac{1}{24}\right]\frac{q}{EI_2},$$

$$B_2=\left[\frac{-x_t^4-4x_t^2}{24}(1-\Gamma)+\frac{1}{24}\right]\frac{q}{EI_2}, \tag{A14}$$

$$C_1=0, \quad C_2=\frac{x_t^2}{4}(1-\Gamma)\frac{q}{EI_2}, \tag{A15}$$

$$D_1=\left[\frac{-x_t^2+2x_t}{12}(1-\Gamma)-\frac{1}{12}\right]\frac{q}{EI_2},$$

$$D_2=\left[-\frac{x_t^2}{12}(1-\Gamma)-\frac{1}{12}\right]\frac{q}{EI_2}. \quad \text{(A16)}$$

APPENDIX B: CONSTANTS OF INTEGRATION FOR THE RIGID ROD AND HINGE MODEL

We record here the values of the four constants of integration, A_2, B_2, C_2, and D_2, for the model described in Sec. IV, where the arcuate zone is modeled by a rigid rod, the pectinate zone as a flexible beam of constant bending stiffness, with a hinge, or rotational spring, at $x=0$, and the four possible combinations of clamped and simply supported boundary conditions.

Equations (B1)–(B4) show the values of the constants where the beam is clamped at $x=x_t$ and $x=1$; Eqs. (B5)–(B8) for clamped at $x=x_t$ and simply supported at $x=1$; Eqs. (B9)–(B12) for simply supported at $x=x_t$ and clamped at $x=1$; and Eqs. (B13)–(B16) for simply supported at $x=x_t$ and $x=1$:

$$A_2=\frac{((x_t-1)^3+48\kappa)x_t^2}{24(x_t-1)^3}\frac{q}{EI}, \quad \text{(B1)}$$

$$B_2=-\frac{x_t^5-2x_t^4+2(1+24\kappa)x_t^2+(12\kappa-1)x_t+12\kappa}{12(x_t-1)^3}\frac{q}{EI}, \quad \text{(B2)}$$

$$C_2=\frac{x_t^5+x_t^4-8x_t^3+8(1+6\kappa)x_t^2+(48\kappa-1)x_t-1+48\kappa}{24(x_t-1)^3}\frac{q}{EI}, \quad \text{(B3)}$$

$$D_2=-\frac{x_t^4-2x_t^3+2(1+6\kappa)x_t-1+12\kappa}{12(x_t-1)^3}\frac{q}{EI}, \quad \text{(B4)}$$

$$A_2=-\frac{x_t^6-6x_t^5+12x_t^4+(-10+48\kappa)x_t^3+(3-72\kappa)x_t^2}{48(x_t-1)^3}\frac{q}{EI}, \quad \text{(B5)}$$

$$B_2=\frac{x_t^6-6x_t^5+6x_t^4+(48\kappa+8)x_t^3-(72\kappa+15)x_t^2+6x_t-48\kappa}{48(x_t-1)^3}\times\frac{q}{EI}, \quad \text{(B6)}$$

$$C_2=\frac{3x_t^4-8x_t^3+6x_t^2-1+24\kappa}{16(x_t-1)^3}\frac{q}{EI}, \quad \text{(B7)}$$

$$D_2=-\frac{3x_t^4-4x_t^3-6x_t^2+12x_t+24\kappa-5}{48(x_t-1)^3}\frac{q}{EI}, \quad \text{(B8)}$$

$$A_2=\frac{3x_t^5-10x_t^4+12x_t^3-(6-72\kappa)x_t^2+(1-48\kappa)x_t}{48(x_t-1)^3}\frac{q}{EI}, \quad \text{(B9)}$$

$$B_2=-\frac{6x_t^5-15x_t^4+8x_t^3+(6+144\kappa)x_t^2-(6+72\kappa)x_t+1}{48(x_t-1)^3}\times\frac{q}{EI}, \quad \text{(B10)}$$

$$C_2=\frac{x_t^5-6x_t^3+(8+24\kappa)x_t^2-3x_t}{16(x_t-1)^3}\frac{q}{EI}, \quad \text{(B11)}$$

$$D_2=-\frac{5x_t^4-12x_t^3+6x_t^2+(24\kappa+4)x_t-3}{48(x_t-1)^3}\frac{q}{EI}, \quad \text{(B12)}$$

$$A_2=-\frac{x_t(-1+4x_t-4x_t^2+24\kappa+x_t^3)}{24(-1+x_t)}\frac{q}{EI}, \quad \text{(B13)}$$

$$B_2=\frac{(x_t^4-4x_t^3+(4+24\kappa)x_t-1)}{24(-1+x_t)}\frac{q}{EI}, \quad \text{(B14)}$$

$$C_2=\frac{x_t}{4}\frac{q}{EI}, \quad \text{(B15)}$$

$$D_2=-\frac{x_t+1}{12}\frac{q}{EI}. \quad \text{(B16)}$$

Allaire, P., Raynor, S., and Billone, M. (**1974**). "Cochlear partition stiffness-composite beam model," J. Acoust. Soc. Am. **55**, 1252–1258.

Barker, G. (**2000**). "Pressure-feedforward and piezoelectric amplification models for the cochlea," Ph.D. thesis, Department of Mechanical Engineering, Stanford University.

Brass, D. (**2000**). "A macro-mechanical model of the guinea pig cochlea with realistic parameters," J. Acoust. Soc. Am. **107**, 894–907.

Cabezudo, L. M. (**1978**). "The ultrastructure of the basilar membrane in the cat," Acta Otolaryngol (Stokh.) **86**(3-4), 160–175.

Cooper, N. P. (**1999**). "Radial variation in the vibrations of the cochlear partition," in *Recent Developments in Auditory Mechanics*, edited by H. Wada, T. Takasaka, K. Ikeda, K. Ohyama, and T. Koike (World Scientific, Singapore), pp. 109–115.

Cooper, N. P. (**2000**). "Radial variation in the sound-evoked vibrations of the cochlear partition," Assoc. Res. Otolaryngol **22**, 72, Abstract 254.

Cooper, N. P., and Rhode, W. S. (**1992**). "Basilar membrane mechanics in the hook region of cat and guinea-pig cochleae: sharp tuning and nonlinearity in the absence of baseline position shifts," Hear. Res. **63**(1-2), 163–190.

Dallos, P., Popper, A. N., and Fay, R. R. (**1996**). *The Cochlea* (Springer, New York).

Edge, R. M., Evans, B. N., Pearce, M., Richter, C. P., Hu, X., and Dallos, P. (**1998**). "Morphology of the unfixed cochlea," Hear. Res. **124**(1-2), 1–16.

Fridberger, A., de Monvel, J. B., and Ulfendahl, M. (**2002**). "Internal shearing within the hearing organ evoked by basilar membrane motion," J. Neurosci. **22**(22), 9850–9857.

Gere, J. M., and Timoshenko, S. P. (**1991**). *Mechanics of Materials* (Chapman & Hall, London).

Hallworth, R. (**1995**). "Passive compliance and active force generation in the guinea pig outer hair cell," J. Neurophysiol. **74**(6), 2319–2328.

Iurato, S. (**1962**). "Functional implications of the nature and submicroscopic structure of the tectorial and basilar membranes," J. Acoust. Soc. Am. **34**, 1386–1395.

Karavitaki, K. D., Mountain, D. C., and Cody, A. R. (**1998**). "Electrically evoked micromechanical movements from the apical turn of the gerbil cochlea," in *Diversity in Auditory Mechanics*, edited by E. R. Lewis (World Scientific, Singapore), pp. 392–398.

Lim, K.-M. (**2000**). ''Physical and mathematical cochlear models,'' Ph.D. thesis, Department of Mechanical Engineering, Stanford University.
Miller, C. E. (**1985**). ''Structural implications of basilar membrane compliance measurements,'' J. Acoust. Soc. Am. **77**, 1465–1474.
Nilsen, K. E., and Russell, I. (**1999**). ''Timing of cochlear feedback: spatial and temporal representation of a tone across the basilar membrane,'' Nat. Neurosci. **2**(7), 642–648.
Nilsen, K. E., and Russell, I. J. (**2000**). ''The spatial and temporal representation of a tone on the guinea-pig basilar membrane,'' Proc. Natl. Acad. Sci. U.S.A. **97**(22), 11751–11758.
Olson, E. S., and Mountain, D. C. (**1994**). ''Mapping the cochlear partition's stiffness to its cellular architecture,'' J. Acoust. Soc. Am. **95**, 395–400.
Rhode, W. S., and Recio, A. (**2000**). ''Study of mechanical motions in the basal region of the chinchilla cochlea,'' J. Acoust. Soc. Am. **107**, 3317–3332.
Richter, C., and Dallos, P. (**1999**). ''Vibrations of the inner hair cell stereocilia relative to the tectorial membrane and the reticular lamina,'' Assoc. Res. Otolaryngol. **21**, 211, Abstract 844.
Steele, C. R. (**1974**). ''Behavior of the basilar membrane with pure-tone excitation,'' J. Acoust. Soc. Am. **55**, 148–162.
Tolomeo, J. A., and Holley, M. C. (**1997**). ''Mechanics of microtubule bundles in pillar cells from the inner ear,'' Biophys. J. **73**(4), 2241–2247.
Waterloo Maple Software (**1996**). *Maple V Programming Guide* (Springer-Verlag, New York).
Wilson, J. P., and Evans, E. F. (**1983**). ''Some observations on the passive mechanics of cat basilar membrane,'' in *Mechanisms of Hearing*, edited by W. R. Webster and L. M. Aitkin (Monash U.P., Clayton), pp. 30–35.

Relationship of neural and otoacoustic emission thresholds during endocochlear potential development in the gerbil

David M. Mills[a)]
V. M. Bloedel Hearing Research Center, Dept. of Otolaryngology, Head & Neck Surgery, University of Washington, Seattle, Washington 98195-7923

(Received 5 April 2004; revised 12 May 2004; accepted 15 May 2004)

Distortion product otoacoustic emissions and auditory brainstem responses (ABRs) were measured in neonatal gerbils at three ages: at 15–16 days after birth (dab), near the onset of hearing when the endocochlear potential (EP) is known to be still immature; at 22 dab, when the EP first reaches mature levels; and at 30 dab. Comparing individual 15–16 dab animals to the 22 dab group, ABR threshold changes were typically larger than those for cubic distortion tone (CDT, $2f_1-f_2$) emission thresholds which were, in turn, larger than those for the simple difference tone (DT, f_2-f_1). In contrast, from 22 to 30 dab there were no important changes in CDT or DT emission thresholds. Observed threshold-change relationships were very similar to those found in differential diagnosis investigations, where the EP was experimentally decreased using a chronic furosemide application. Therefore, most of the change in cochlear function over the two week period studied could be attributed to the maturation of EP during the first week. Model calculations further show that relative changes in CDT and DT emission thresholds are compatible with a movement of the operating point of the cochlear amplifier toward its symmetrical ''central'' point as the EP reaches mature levels. [DOI: 10.1121/1.1771613]

PACS numbers: 43.64.Kc, 43.64.Jb, 43.64.Bt [BLM] Pages: 1035–1043

I. INTRODUCTION

The study of functional cochlear development involves the study of changes in cochlear mechanics as a result of natural changes in intrinsic and external parameters. As such, developmental studies have the potential to elucidate important aspects of cochlear function, particularly the function of the cochlear amplifier. The cochlear amplifier is the name given to the collection of active, vulnerable processes which act to physically amplify basilar membrane motion in mammals (Davis, 1983). The precise mechanisms that make up the cochlear amplifier have been difficult to identify and study, partly because of the extreme vulnerability of its function. Developmental studies in the gerbil neonate offer an opportunity in this regard. Cochlear amplifier function is clearly established in this animal near the onset of hearing (Mills and Rubel, 1996). However, the cochlea is still not completely mature at this point. In particular, the endocochlear potential (EP), believed to be the electrical source of energy for the cochlear amplifier, does not reach adult levels until a week later (Woolf *et al.*, 1986). This offers a window during which changes in cochlear amplifier function can be observed as a function of naturally occurring changes in parameters, especially the EP.

The present developmental study was also designed to further investigate the possibility of differential diagnosis of hearing dysfunction. This possibility has recently been demonstrated by the comparison of neural and emission threshold shifts in animal models of two of the major hearing dysfunctions. In adult gerbils that had permanent threshold shifts induced by acoustic damage, the emission threshold increase was typically observed to be about the same size as or larger than the neural threshold shift (Mills, 2003). However, in animals in which the endocochlear potential (EP) was chronically decreased by furosemide, the opposite relationship was true: the neural threshold shift was typically larger than the shift in the emission threshold (Mills and Schmiedt, 2004). In a plot comparing the two shifts, in fact, there was a complete separation of the responses to the two conditions for cases with significant dysfunction. That is, a diagnosis of the underlying condition in any individual could have been made by comparing only the relative thresholds in that individual. So far, such a result can only be claimed to be unequivocally established for the adult gerbil. The present investigation seeks to extend these results by investigating the threshold-shift relationships in the neonatal gerbil, by including ages over which there is a natural change in EP.

Figure 1 summarizes the development of EP with age in the gerbil, and the plan of the experiment. Emission responses can first be reliably measured in the neonatal gerbil at 15 days after birth (dab; Mills and Rubel, 1996). At that age, the EP is on average only 35 mV. The improvement in EP is rapid from that point, however, and by 22 dab the mean EP reaches 70 mV, nearly its mean adult value. The plan of the experiment is therefore to concentrate functional measurements at the dates indicated at the top of Fig. 1. Mean values established at 22 dab are used to compare with thresholds measured in individual animals that are up to one week younger, where there was a much lower EP. To compare changes in thresholds in the young animal over a similar period but without a major change of EP, another set of measurements are also obtained approximately one week later, at 30 dab. The interpretation of the results focuses on the hy-

[a)]Correspondence: David M. Mills, Ph.D., Box 357923, University of Washington, Seattle, Washington 98195. Telephone: (206) 616-7540; Fax: (206) 221-5685; Electronic mail: dmmills@u.washington.edu

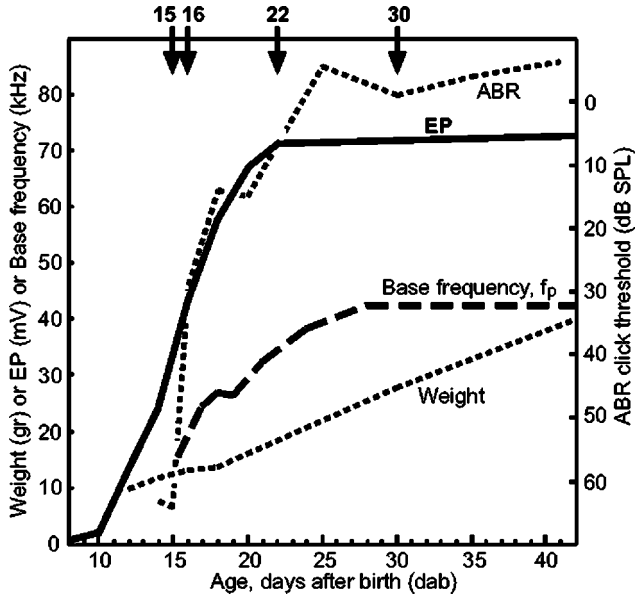

FIG. 1. Selected data for the neonatal Mongolian gerbil, and the plan of the present experiment. The animal's mean weight with age is given by the light dotted line along with the scale on the left axis (Woolf and Ryan, 1985). The same scale and the heavy solid line indicate the endocochlear potential (EP; Woolf *et al.*, 1986). The heavy dashed line summarizes the change in the "frequency limit," f_p, at the base of the cochlea due to the development of the place code in this species (see Sec. IV for details). The light dashed line and the right axis denote the threshold for the auditory brainstem response (ABR) for a click stimulus (Smith and Kraus, 1987). Note that this scale is inverted so that an improving threshold is plotted upward. The ages at which measurements were made in the present experiment are indicated at the top of the figure.

pothesis that most of the change in cochlear function over this two week period can be attributed to the maturation of the EP during the first week.

Neural responses in this study are estimated by measurement of the auditory brainstem response (ABR) using tone pips. Neural thresholds are compared to distortion product otoacoustic emission thresholds measured at similar stimulus frequencies in the same animals. The most important emission component is the cubic distortion tone (CDT) emission at $2f_1-f_2$ (stimulus frequencies f_1 and f_2). Thresholds for the difference tone (DT) component at f_2-f_1 are also reported, because relative changes in the strength of this component can be used to investigate changes in the operating point of the cochlear amplifier (e.g., Mills *et al.*, 1993; Frank and Kössl, 1996, 1997).

II. METHODS

Subjects for the study were young Mongolian gerbils (*Meriones unguiculates*) obtained from our colony, using breeding pairs originally obtained from Charles River Laboratories (Wilmington, MA). Births were recorded once a day, and litters culled to six total. All procedures were approved by the Animal Care Committee at the University of Washington.

Equipment and techniques for measurement of ABR and emissions were similar to those previously reported (Mills, 2003). Briefly, the anesthetized animal was attached to an adjustable surgical head holder (Kopf) employing a bite bar, and positioned on a heating pad. The pinna on the left side was removed, as was tissue over the ventral-posterior bulla. A small hole (about 0.5 to 1 mm diameter) was drilled into the bulla to provide static pressure relief to the middle ear. The positive ABR pin electrode was placed at the midline between the eyes, the negative electrode located at the top of the skull, and the reference electrode placed at the rear leg.

A custom coupler (Mills and Rubel, 1996) was sealed to the ear canal. This coupler contained a low-noise microphone (ER-10B, Etymotics), a probe tube reference microphone, and two ports for sound delivered through tubing from custom tweeters. Before beginning measurements, a wide-band noise signal was generated by one tweeter, and the output of the low-noise microphone was calibrated *in situ* by a comparison to the output of the probe tube microphone. The same coupler and calibration were used for both emission and ABR measurements.

For all animals, emission measurements were made first. These consisted primarily of input-output, or "growth," functions using two pure tone stimuli at frequencies f_1 and f_2. The stimulus frequency ratio was $f_2/f_1=1.21$ and stimulus levels were given by $L_1=L_2+10$ dB. The response to each stimulus presentation was synchronously averaged for 4–12 s, depending on the noise floor. For each growth function, stimulus levels were stepped together at 5 dB intervals up to levels of at least $L_1\times L_2=80\times 70$ dB SPL. Higher upper limits, up to 100 dB SPL maximum, were chosen in younger animals when emissions were weak, as illustrated by the example in Fig. 2. Each complete growth function was also repeated at least once at each f_2 frequency to verify reproducibility and to improve the accuracy of the threshold determinations. The f_2 frequencies were stepped at half octave intervals from 2 to 22.6 kHz, with $f_2=28$ kHz added for older animals. Instrumental distortion levels were estimated by repeating the measurements with the animal replaced by an "infinite" tube, 1/8″ ID by 25 ft length.

In all animals, ABR measurements were made using the same stimulus frequencies as the f_2 frequencies chosen for the emission measurements. Tone pips were generated with a 3 ms total duration, with 1 ms $\cos^2$ rise/fall times, and presented with alternating polarity. Typically, each measurement consisted of the average of the response to 400 pips presented at a rate of 12.5 Hz. Starting at a stimulus level of 80 dB SPL or more, stimulus levels were decreased at 10 dB intervals to find the approximate threshold, then the threshold was bracketed by repeating measurements at least twice at each stimulus level at 5 dB intervals. When thresholds were high, the maximum stimulus levels were increased up to 110 dB SPL. However, the highest levels were only used as the final measurements in each animal. The ABR responses were recorded and thresholds determined offline by visual inspection.

III. RESULTS

Typical emission growth functions are presented in Fig. 2, comparing measurements in a 15 dab animal (bold lines) with those for a 22 dab animal (lighter lines). As illustrated, the "emission threshold" for a given frequency component was defined to be the stimulus level that resulted in that

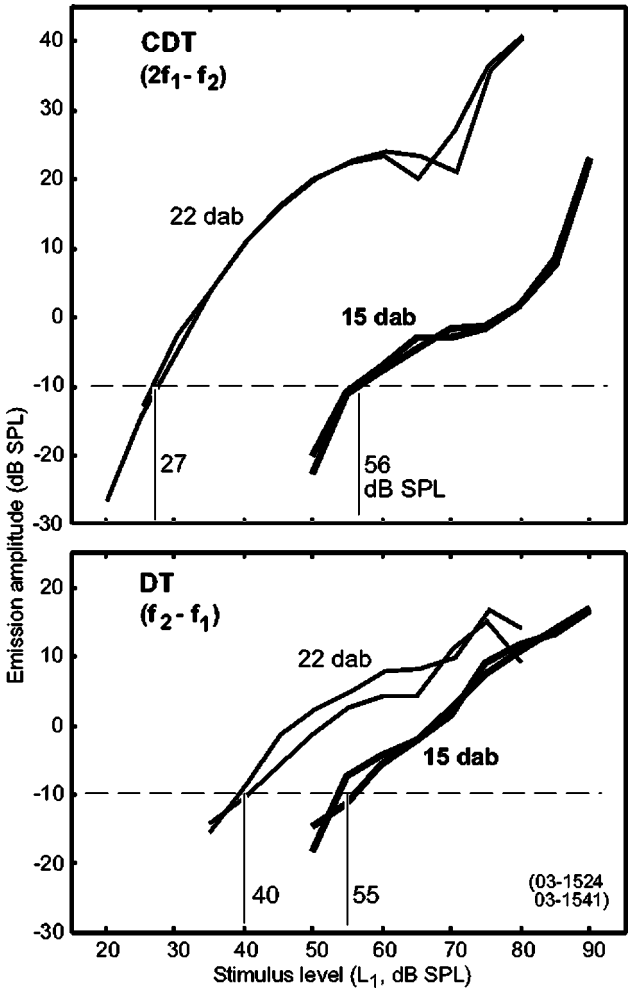

FIG. 2. Typical measured emission input–output, or "growth" functions, illustrating the definition of emission threshold. Bold lines indicate the response of a neonate gerbil 15 days after birth (dab), lighter lines indicate that of a 22 dab animal; both are for $f_2=8$ kHz. Spectral components in the emission at two frequencies are presented: the cubic distortion tone (CDT) emission at the frequency $2f_1-f_2$ (upper panel) and the simple difference tone (DT) emission at f_2-f_1 (lower panel). For each panel, the emission amplitude is on the vertical axis while plotted on the horizontal is the stimulus level, L_1. All growth functions were taken at least twice as shown. Typical threshold determinations are illustrated, using a criterion emission amplitude equal to −10 dB SPL for both components.

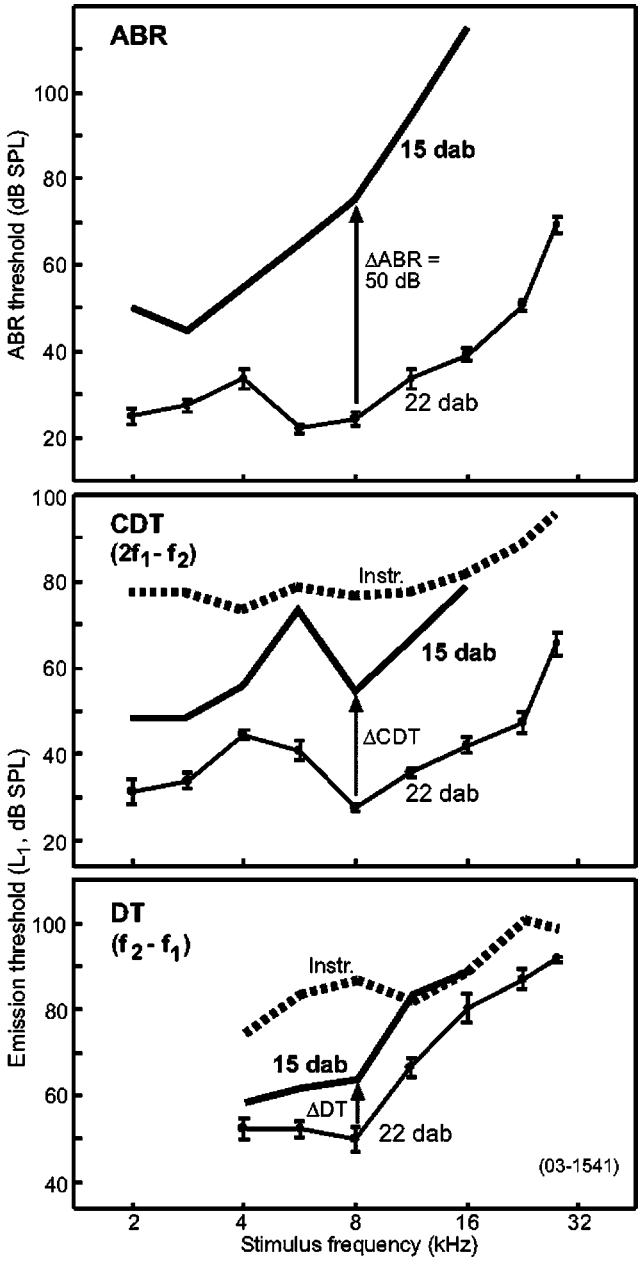

FIG. 3. Thresholds as a function of stimulus frequency, for the same 15 dab animal as in Fig. 2. For comparison, mean values for the 22 dab group are also shown, with error bars indicating the standard error of the mean ($N=7$). The top panel gives the auditory brainstem response (ABR) threshold, the middle panel the cubic distortion tone (CDT) emission threshold, and the lower panel the threshold for the difference tone (DT) emission. Due to the increase in noise floor at low frequencies, the DT emission component could not be reliably measured to −10 dB SPL for stimulus frequencies $f_2<4$ kHz, so thresholds are not shown for this frequency range. Estimated limits to emission threshold measurements due to instrumental distortion are indicated by the heavy dotted lines (see Sec. II). On the vertical axes, the ABR threshold indicates the peak stimulus level of the pip, while emission thresholds are indicated by the stimulus level, L_1. The frequency scale on the horizontal axis indicates the ABR pip stimulus frequency or the emission stimulus frequency, f_2. Each panel illustrates an example of the calculation of the threshold difference between the 15 dab neonate and the mean of the 22 dab group, in this case at 8 kHz. Note that this threshold "shift" as defined is positive for the usual case of a lowering of threshold with age, for animals under 22 dab.

component reaching criterion amplitude. For this study, the criterion amplitude was chosen to be −10 dB SPL for all components at all frequencies. For the 15 dab animal the calculated threshold for the CDT emission was $L_1=56$ dB SPL, compared to 27 dB SPL for the 22 dab animal. For the DT emission, the threshold for the younger animal was 55 dB SPL, compared to 40 dB SPL for the older animal.

Figure 3 presents observed thresholds as a function of frequency for the same 15 dab animal as in Fig. 2. For comparison, mean thresholds determined for the 22 dab group are also shown. The top panel illustrates ABR thresholds, and the calculation of the threshold difference between individual animals and the mean of the 22 dab group. This threshold "shift," denoted ΔABR, is defined to be positive in the usual case of a larger threshold for a younger animal compared to the average 22 dab animal. The lower panels similarly illustrate the definition of the emission threshold

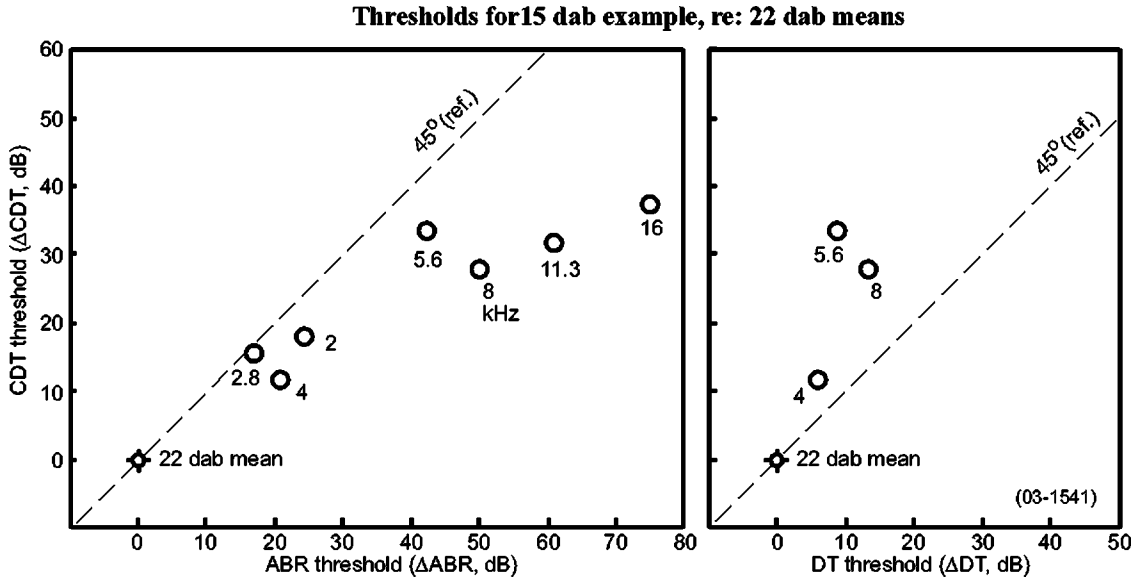

FIG. 4. Relationships between measured thresholds for the same 15 dab animal as in Figs. 2 and 3. These ''threshold-shift'' plots are formed by subtracting the mean thresholds for the 22 dab group at each frequency from the measured thresholds of the 15 dab example, as illustrated in Fig. 3. In the left panel, the horizontal axis indicates the shift in the ABR threshold, and the vertical axis indicates the shift in the cubic distortion tone (CDT) emission threshold. The right panel has the same vertical axis, but the horizontal axis is the shift in the difference tone (DT) emission threshold. Numbers next to points indicate the stimulus frequency in kHz. Responses were measured at half-octave intervals from 2 to 22.6 kHz, but points were omitted when a threshold could not actually be determined due to noise or instrumental distortion.

shifts, denoted ΔCDT and ΔDT for the $2f_1-f_2$ and f_2-f_1 components, respectively. For this individual, it can be seen that at most frequencies the ABR threshold shift was greater than the CDT threshold shift, which in turn was greater than the DT threshold shift. As shown below, these relationships were found to hold generally.

The threshold–shift relationships become more obvious when the shifts are plotted against each other, as illustrated in Fig. 4. This figure is in the same format as ''threshold–shift'' plots, which illustrated changes in relative thresholds following experimentally induced hearing dysfunction (Mills, 2003; Mills and Schmiedt, 2004). In those plots, a positive value for the threshold shift indicated an increase in threshold due to the experimental manipulation. In the present case, the plot is based on the 22 dab group being defined as the norm and is effectively ''looking back'' at the larger thresholds of the younger animals. That is, the ''hearing dysfunction'' underlying the threshold–shift relationships in Fig. 4 is comparative immaturity. Note that for animals younger than 22 dab, a positive value for a threshold shift as defined here is associated with a decrease, or improvement, in threshold with age.

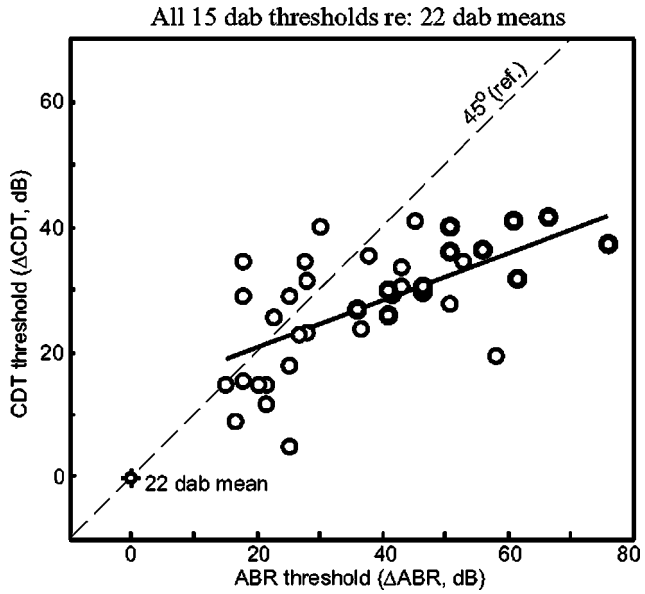

FIG. 5. Threshold shift plot for all 15 dab neonates; the same conventions as Fig. 4. Points for stimulus frequencies at 8 kHz and above are emphasized in bold. The line indicates the unconstrained least-squares linear regression for all 15 dab data, with a slope of 0.37 and $r^2=0.40$.

Next to the data points in Fig. 4 are noted the stimulus frequencies, i.e., the ABR pip frequency, equal to the emission f_2 frequency. At high frequencies, there were generally large threshold shifts, and the ABR shift was typically larger than the CDT shift (points were below the 45° line). In comparison, at lower frequencies the threshold shifts were generally moderate, with the shifts in ABR approximately equal to the shifts in the emission threshold. For the relatively few determinations of DT thresholds that were possible (right panel), the shift in DT threshold was found to be smaller than the shift in the CDT threshold.

There were a total of 7 animals measured at 15 dab, and the results are summarized in Fig. 5. As for Fig. 4, this plot was obtained by subtracting the mean thresholds at 22 dab from individual measurements at 15 dab on a frequency-specific basis. Stimulus frequencies at 8 kHz and above are indicated by bold symbols. The regression line shown is the best fit for all data in the plot, and accounts for 40% of the variance.

Clearly, the same trends noted in the individual animal in Fig. 4 are seen in the data for the whole 15 dab group in Fig. 5. At higher frequencies (bold symbols), the shift in ABR threshold tended to be significantly larger than the shift

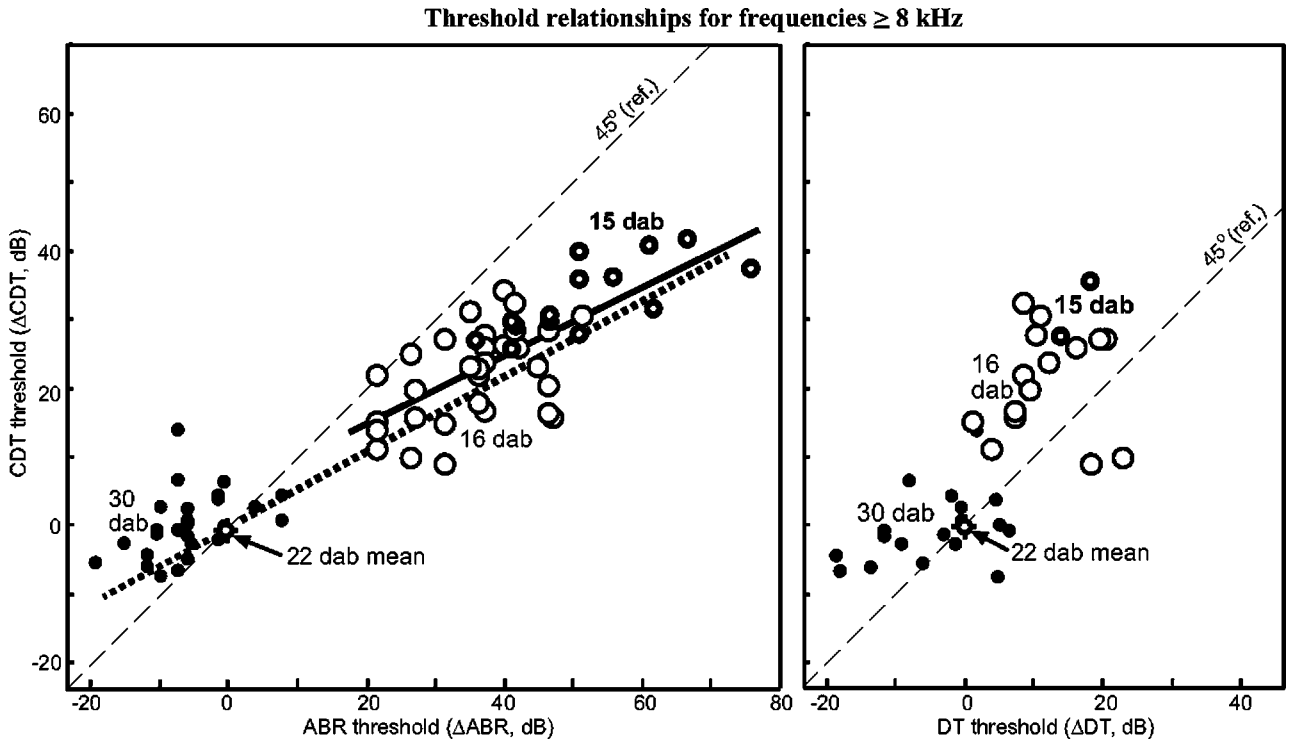

FIG. 6. Threshold-shift plots for all neonates; the same conventions as Fig. 4 except that only points for stimulus frequencies, f_2, at 8 kHz or above are included. The vertical axis for both panels is the shift in threshold for the cubic difference tone (CDT) emission, the horizontal axis in the left plot is the shift in auditory brainstem response (ABR) threshold, and the horizontal axis in the right plot is the change in threshold for the simple difference tone (DT) emission (see the definitions in Figs. 2 and 3). Results for the 15 dab animals are indicated by the smaller, bold unfilled circles, the 16 dab animals by the larger unfilled symbols, and the 30 dab animals by the solid dots. For the left panel, note that improving neural threshold moves from right to left along the ABR axis. All frequency-specific thresholds are given with reference to their mean values at 22 dab, indicated by the special cross symbol at the origin in each panel. An animal that had the same thresholds as the means of the 22 dab group at each frequency would therefore have its data points located at this cross. The bold line indicates the unconstrained regression line for the 15 and 16 dab ages treated as one group. This least-squares linear fit has a slope of 0.49, with $r^2=0.53$. For comparison, the heavy dashed line shows the threshold–shift relationship estimated from the responses for experimentally induced chronic low EP in the adult gerbil, derived as follows. The previous study (Mills and Schmiedt, 2004) had measured emission growth functions for two cases: $L_1=L_2$ and $L_1=L_2+20$ dB. The two cases gave very similar results for the comparison of CDT and ABR threshold shifts, the slopes of the regression lines being 0.51 and 0.59, respectively. In both cases, the regression accounted for about 60% of the variance and the best-fit lines approximately passed through the origin. From these observations, it was therefore estimated that a line with a slope of 0.55, passing through the origin, would be appropriate for the parameter choice $L_1=L_2+10$ dB as used in the present study. It is this relationship that is indicated by the heavy dashed line in the left panel.

in CDT emission threshold. At lower frequencies, the shifts were about equal.

Unfortunately, for the 15 dab animals, CDT emission measurements at higher frequencies tended to be limited by instrumental distortion. In addition, only a relatively few DT threshold measurements were possible due to the combination of weak emissions at this age and the relatively low threshold for instrumental distortion at f_2-f_1 (Fig. 3). A number of 16 dab animals were therefore added to make additional data available for the correlation analysis. Also, measurements in several 30 dab animals were added for a ''control'' comparison (Fig. 1).

Figure 6 compares threshold shifts for all animals in the study, for stimulus frequencies at 8 kHz and above. The left panel shows that the ABR threshold difference was typically larger than the CDT emission threshold shift. Considering the 15 and 16 dab animals together, the least-squares linear regression (solid line) accounts for over half of the variance and has a slope of about one-half. That is, a 50 dB shift in the ABR threshold was typically associated with a 25 dB shift in the CDT emission threshold for any animal, whether the animal happened to be 15 or 16 days old when measured. For comparison, the dashed line reproduces the regression estimated on the basis of experiments in which the EP was experimentally depressed in adult gerbils (Mills and Schmiedt, 2004). Clearly, observations of the relative change in thresholds of CDT emission compared to ABR, over the ages known to have a rapid change of EP, are compatible with the hypothesis that the major cause of the improvement can be attributed to the change in EP.

At 30 dab compared to 22 dab, there was typically found a slight improvement in ABR thresholds but little change in either CDT or DT emission thresholds (Fig. 6). Since the EP is known to be nearly constant during the period from 22 to 30 dab (Fig. 1), this finding also supports the main hypothesis.

The right panel of Fig. 6 shows that changes in the DT emission threshold for 15 and 16 dab animals were typically less than the changes in the CDT emission threshold at the same stimulus frequency. This is equivalent to saying that the amplitude of the DT emission component in the signal did not increase as fast as that of the CDT emission from 16 to 22 dab, or, in other words, that the *relative* amplitude of the DT emission decreased with maturation. In contrast, there was little change in the relationship observed between these two frequency components once a comparatively mature EP

was achieved, i.e., during the period from 22 to 30 dab. An interpretation of these results in terms of developmental changes in the cochlear operating point is discussed later.

IV. DISCUSSION

A. Emission threshold measures

The results presented here provide additional support for the usefulness of a ''threshold'' measure for distortion product otoacoustic emission measurements (e.g., Kössl, 1992, 1994; Puel *et al.*, 1995; Mills and Rubel, 1996, 1998; Mills, 1997, 2003; Mills and Schmiedt, 2004). This measure is simply defined, for a given emission frequency component, as the stimulus level required to obtain a criterion emission amplitude. The quotes, of course, indicate that it is not a true threshold measure, because the emission amplitude for any component tends to a finite slope as low stimulus levels are reached (Fig. 2). It is for this reason that a specific criterion level is desirable. If, for example, the threshold were instead to be defined in relationship to the noise floor (e.g., Horner *et al.*, 1985), the threshold would actually depend on the frequency characteristics of the measurement system as well as the integration time chosen for the particular measurement.

In general, a threshold definition has the effect of simplifying a function by characterizing it by a single number. For distortion product emissions, for example, this function is usually an input–output or ''growth'' function formed by holding the stimulus frequencies constant and varying the stimulus levels together (as in Fig. 2). If a number of such growth functions are obtained at different stimulus frequencies, the threshold characterization of each function leads to a frequency-threshold function applicable to each emission component (Fig. 3). It seems most natural to compare frequency-threshold functions from different emission components with each other and with other threshold measures useful for hearing function, such as the ABR. The usefulness of such a comparison is most evident in the threshold–shift plots such as Fig. 6.

Such threshold–shift comparisons can be especially useful in investigations where there are large individual differences in hearing function but where the main cause of the difference might be a single underlying factor. For example, one 15 dab gerbil might have a much higher EP than another simply because the EP is rising so quickly with age, whereas other differences might be comparatively minor (Fig. 1). In this case, the individual threshold–shift comparisons (Fig. 5) provide much more useful information than do the absolute frequency-threshold functions (Fig. 3). Similarly, for cases of experimentally-induced EP decline there was a large variation found in individual responses but a tight correlation in the relationship between the threshold shifts (compare Figs. 2 and 4 in Mills and Schmiedt, 2004).

There are other obvious advantages to emission threshold measurements as employed here. In young animals or in cases of dysfunction, emissions can be quite weak. It can be possible to estimate threshold, however, even when the lack of dynamic range makes suprathreshold measurements impossible. Even if threshold cannot be measured, at the least a lower limit can be obtained.

The results demonstrated here should be compared to some previous studies in which emission measures have been found to be relatively poor predictors of hearing threshold in humans (e.g., Gorga *et al.*, 1996; Stover *et al.*, 1996). In retrospect, it seems likely that the reason for the poor correlation is that there are a number of different underlying dysfunctions naturally present in the human population. Similarly poor correlations are obtained if, for example, one simply combines scatter plots containing two distinct dysfunctions such as acoustic damage and low EP [e.g., Fig. 9 in Mills, 2003; Fig. 5(b) in Mills and Schmiedt, 2004]. The point of view of the present work is that it is not useful to attempt to ''predict'' an audiometric status from emission measurements. Rather, it seems preferable to use emission measures as an additional dimension for the purpose of differential diagnosis.

The threshold approach advocated here should also be compared with other emission measures sometimes used to characterize the frequency response, such as the ''DP audiogram'' or ''DP gram.'' This is a plot of emission amplitude versus frequency with stimulus levels held constant and stimulus frequencies varied together (e.g., Lonsbury-Martin *et al.*, 1990; Schmiedt *et al.*, 2002). While it is an appealingly simple measurement and useful for some purposes, experiments in which DP grams or the equivalents have been measured in parallel with threshold measures clearly show that the threshold–shift relationship is superior in differentiating the underlying pathology (Mills, 2003; Mills and Schmiedt, 2004, data not shown.). The primary reason is that the stimulus levels for the DP gram cannot be chosen so that the emissions produced will be equally sensitive to cochlear function across frequencies and conditions. For example, if the stimulus level chosen turns out to be below the equivalent emission threshold at some frequency, the amplitude in the DP gram falls to the noise floor and little useful information is obtained beyond this fact. Even when the stimulus level is high enough that there is measurable amplitude in the emission, as frequency or condition are changed sooner or later a parameter range is encountered which brings a ''notch'' into the region of measurement (Mills 2002, 2003). Measurement near a notch (i.e., a relative minimum seen in a growth function) can produce a scatter in the emission amplitude that has nothing whatsoever to do with cochlear function. A good example is given by the two CDT growth functions sequentially measured for the 22 dab example (upper panel, Fig. 2). Overall, these considerations suggest that the DP gram is primarily useful for a quick determination of whether cochlear function is normal or not, while emission threshold measures are to be preferred for investigating the precise nature and degree of dysfunction.

B. Possible effect of place code shift on measurements

Possible effects of the known place code shift on the measurements reported here should be considered carefully. As noted in Fig. 1, in the neonatal gerbil the base ''cutoff'' frequency, f_p, increases from 16 kHz at 15 dab to about 35 kHz at 22 dab. This frequency is operationally defined as the highest frequency at which the cochlear amplifier gain can

reach its normal value at a given age (Mills and Rubel, 1998). That is, the estimated cochlear amplifier gain is observed to decrease rapidly as the stimulus frequency is increased above the frequency, f_p, tending to zero gain about a half octave above f_p. However, while measurements where the stimulus frequency was above the base frequency must have occurred for some of younger animals in the present study, it is easy to see that the contribution of such effects to the overall results would necessarily have been small. One reason is that, as the stimulus frequency goes above the base frequency, the emission amplitude decreases quickly and thresholds tend to move up out of the range of measurement. Further, the frequency range over which there would be expected any effect of the base cutoff is only a half octave, so relatively few measurements would fall into this range by chance. Finally, the ABR threshold appears to increase very rapidly at high frequencies when there is a low EP (Mills and Schmiedt, 2004). This would, of course, affect all responses from the base region in the younger animals, whether or not the stimulus frequency was above the base cutoff frequency in that animal. Overall, given the experimental design and these selection effects, the conclusion is that the effects of low EP should dominate those due to the place code shift in these observations of neonatal animals, as they appear to do.

C. Developmental changes in the operating point

There have been a number of investigations into the shape of the cochlear transfer function, usually made by monitoring a particular cochlear response as a function of the phase of a high-intensity, low-frequency bias tone (e.g., Patuzzi *et al.*, 1984; Chertoff *et al.*, 1996; Frank and Kössl, 1996, 1997; Lukashkin and Russell, 1998; Scholz *et al.*, 1999; Bian *et al.*, 2002). These observations generally agree that the cochlear transfer function is a saturating function that has approximately odd symmetry (e.g., Fig. 7). If the operating point (no-signal condition) is located at the symmetric point of such a function, then when there are pure tone inputs there will be only odd-order harmonics produced in the output (such as $2f_1-f_2$). The even-order harmonics, such as the emission at the f_2-f_1 frequency, will be produced only to the extent that the operating point is *offset* from the symmetric point.

To illustrate this, the results of a simple model calculation are summarized in Fig. 7. The upper panel displays the saturating transfer function assumed for the illustration. The stimulus level required to reach a criterion emission amplitude for each offset condition was calculated, and this relationship is displayed in the lower panel. It is seen that the threshold for the CDT emission component varies little with the amount of offset until the operating point moves quite far from the center position. In contrast, the threshold for the DT emission component changes by 10 dB for every factor of 10 change in the offset. (Note that decreasing threshold, or increasing emission amplitude, is plotted upward in the figure.) These two results together suggest that the threshold of the difference tone, *relative* to that of the cubic, can be used as a measure of the offset of the operating point from its center position. Further, these model calculations suggest that the relative offset can be estimated using only low-level signals and without determining the complete transfer function. Note also that the model result in Fig. 7, since it holds for small signal levels, cannot depend on the details of the saturation of the nonlinearity at the extremes of high signal levels. In comparison to simply measuring emission amplitudes at a fixed stimulus level, these calculations also suggest that an advantage of comparing thresholds for these emission components is that *relative* thresholds are likely to be more sensitive to offset and comparatively less sensitive to other changes, e.g., to changes in cochlear amplifier gain or middle ear.

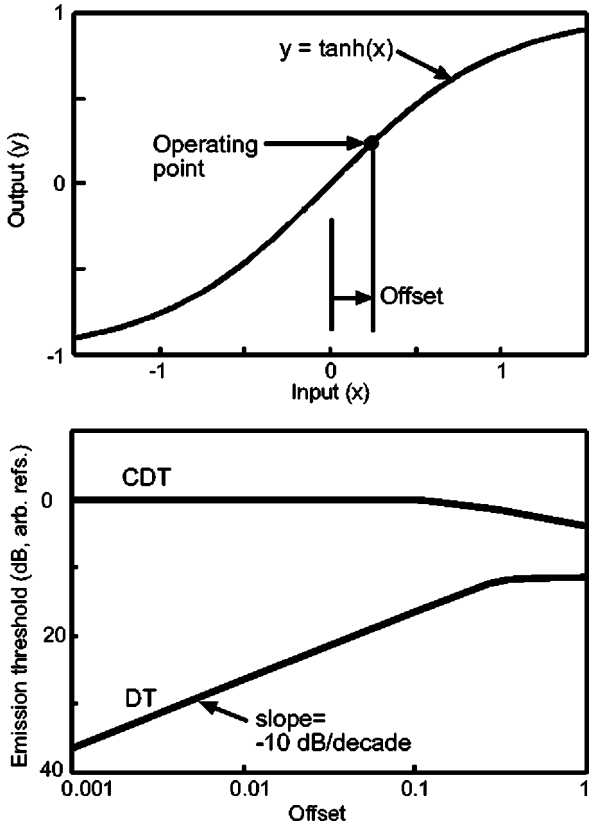

FIG. 7. Results of a simple model calculation. The cochlear transfer function and the source of distortion product otoacoustic emissions from the cochlea, was assumed to be a saturating nonlinearity, modeled by the hyperbolic tangent function illustrated in the top panel. The input signal present at the point of generation of the emissions was assumed to be the sum of two equal-level sinusoids, with a frequency ratio $f_2/f_1=1.25$, oscillating about an operating point offset from the symmetric point as illustrated. At each assumed offset, the stimulus level of the input signal was stepped from low to high levels and the amplitude of each emission component determined by Fourier analysis of the resulting output signal. The stimulus level required to obtain a criterion emission amplitude in each component was then calculated, and these thresholds are presented in the lower panel. Note that the zero dB reference levels are arbitrarily chosen for the display of these curves. For the calculation, the criterion emission amplitude was chosen to be small enough that only comparatively small signal amplitudes (x variations <0.1) were required to reach threshold over the range of offsets illustrated. The same threshold relationships are found for offsets to the left of the symmetric point, except that there is a change of sign (180° phase shift) in even-order components as the symmetric point is traversed (Mills *et al.*, 1993).

Data from the present observations applicable to these results have been summarized in the right panel of Fig. 6 (also see Figs. 2–4 for individual examples). The threshold

for the even-order difference tone (DT, f_2-f_1) is plotted on the horizontal axis against the threshold for the odd-order cubic difference tone component (CDT, $2f_1-f_2$) on the vertical. It can be seen that the magnitude of the CDT threshold change is typically larger than the DT threshold change during the age from 15 to 22 dab, when the EP is rapidly maturing. There is, however, almost no change in this relationship in the week-long period following this, during which the EP is nearly constant. These results suggest that, near the onset of hearing, the operating point starts out at a relatively large offset from its symmetric point, but that the operating point moves toward the symmetric point as the EP reaches mature levels. Further, the results suggest that the change in operating point only occurs during the time over which the EP is known to change. For this reason, the decrease in offset, or the ''improvement'' in the operating point during development, could potentially be a direct result of the maturation of the EP. It is known, for example, that the operating point changes dynamically when the EP is changed by acute furosemide intoxication (Mills *et al.*, 1993).

D. Interpretation of the relationship between CDT emission and neural thresholds during development

Obviously, there are a number of possible contributions to the development of hearing in the neonatal gerbil (review: Ryan and Woolf 1992). However, the gerbil cochlea is known to be of adult size by the onset of hearing and most of its cellular components, e.g., outer hair cell motility, are also known to be essentially mature by this age (Harris *et al.*, 1990; He *et al.*, 1994). There are cellular changes that do occur after the onset of hearing that appear to be related to the maturation of the frequency–place relationship in the base of the cochlea (Schweitzer *et al.*, 1996), and the possible effects of the place code shift on the present measurements are discussed above. However, the most obvious change that occurs during the week from 15 to 22 dab, and that does not occur during the following week, is the dramatic increase in EP to mature levels (Fig. 1). The simplest explanation for the results seen in this study is therefore that the major effect on cochlear function during the two-week period from 15 to 28 dab involves the change in EP during the first week. It is true that the observed simultaneous changes in neural and emission thresholds could be accomplished by fortuitous changes of several other aspects of cochlear function. However, in the absence of any evidence for this, it seems parsimonious to provisionally accept the simplest explanation compatible with the observations.

Support for this hypothesis is gained from studies of the effects of experimentally-induced EP decrease in the adult gerbil. In terms of its effects on frequency–threshold curves, for example, the most common result of the EP decrease was a ''sloping high-frequency loss'' pattern characterized by a rapid increase in the ABR threshold with frequency (Mills and Schmiedt, 2004). It has already been noted that a similar pattern was observed in the younger animals in the present study, e.g., as illustrated in Fig. 3 for a 15 dab animal.

For the experimentally manipulated EP, however, it was in the *relationship* between the threshold shifts that the most consistent responses were found. For cases in which there was substantial dysfunction, the shift in ABR threshold was almost always greater than that for the CDT emission (Mills and Schmiedt, 2004). The regression line estimated from that study is shown by the dashed line in the left panel of Fig. 6. Clearly, the shifts in the 15 and 16 dab animals are in agreement with the previous experiment where the EP was experimentally manipulated.

The results at 30 dab provide further evidence in favor of the main hypothesis. There is little change in the EP during the 22 to 30 dab period (Fig. 1), and there is almost no change observed in the emission characteristics, either in the CDT or DT threshold. The small improvement seen in the ABR threshold (Fig. 6) during this period can tentatively be attributed to minor improvements in the neural function in either the eighth nerve or the brainstem, rather than to changes in the cochlear function itself. Overall, therefore, the results of this study support the hypothesis that the major part of the improvement in cochlear function during the first two weeks of hearing in this animal can be attributed to the maturation of EP during the first week, and most of the observed effects are compatible with responses observed when the EP is experimentally manipulated.

ACKNOWLEDGMENTS

This research was supported by Grants No. DC 04077 and No. DC 04661 from the National Institute for Deafness and Other Communication Disorders, National Institutes of Health.

Bian, L., Chertoff, M. E., and Miller, E. (**2002**). ''Deriving a cochlear transfer function from low-frequency modulation of distortion product otoacoustic emissions,'' J. Acoust. Soc. Am. **112**, 198–210.

Chertoff, M. E., Steele, T., Ator, G. A., and Bian, L. (**1996**). ''Characterizing cochlear mechano-electric transduction using a nonlinear systems identification procedure,'' J. Acoust. Soc. Am. **100**, 3741–3753.

Davis, H. (**1983**). ''An active process in cochlear mechanics,'' Hear. Res. **9**, 79–90.

Frank, G., and Kössl, M. (**1996**). ''The acoustic two-tone distortions $2f_1-f_2$ and f_2-f_1 and their possible relation to changes in the operating point of the cochlear amplifier,'' Hear. Res. **98**, 104–115.

Frank, G., and Kössl, M. (**1997**). ''Acoustical and electrical biasing of the cochlea partition. Effects on the acoustic two tone distortions f_2-f_1 and $2f_1-f_2$,'' Hear. Res. **113**, 57–68.

Gorga, M. P., Stover, L., Neely, S. T., and Montoya, D. (**1996**). ''The use of cumulative distributions to determine critical values and levels of confidence for clinical distortion product otoacoustic emission measurements,'' J. Acoust. Soc. Am. **100**, 968–977.

Harris, D. M., Rotche, R., and Freedom, T. (**1990**). ''Postnatal growth of cochlear spiral in mongolian gerbil,'' Hear. Res. **50**, 1–6.

He, D. Z. Z., Evans, B. N., and Dallos, P. (**1994**). ''First appearance and development of electromotility in neonatal gerbil outer hair cells,'' Hear. Res. **78**, 77–90.

Horner, K. C., Lenoir, M., and Bock, G. R. (**1985**). ''Distortion product otoacoustic emissions in hearing-impaired mutant mice,'' J. Acoust. Soc. Am. **78**, 1603–1611.

Kössl, M. (**1992**). ''High frequency distortion products from the ears of two bat species, *Magaderma lyra and Corollia perspicillata*,'' Hear. Res. **60**, 156–164.

Kössl, M. (**1994**). ''Otoacoustic emissions from the cochlea of the 'constant frequency' bats, Pteronotus parnellii and Rhinolophus rouxi,'' Hear. Res. **72**, 59–72.

Lonsbury-Martin, B. L., Harris, F. P., Stagner, B. B., Hawkins, M. D., and Martin, G. K. (**1990**). ''Distortion product emissions in humans. I. Basic properties in normally hearing subjects,'' Ann. Otol. Rhinol. Laryngol. Suppl. **99**, 3–14.

Lukashkin, A. N., and Russell, I. J. (**1998**). ''A descriptive model of the receptor potential nonlinearities generated by the hair cell mechanoelectrical transducer,'' J. Acoust. Soc. Am. **103**, 973–980.
Mills, D. M. (**1997**). ''Interpretation of distortion product otoacoustic emission measurements. I. Two stimulus tones,'' J. Acoust. Soc. Am. **102**, 413–429.
Mills, D. M. (**2002**). ''Interpretation of standard distortion product otoacoustic emission measurements in light of the complete parametric response,'' J. Acoust. Soc. Am. **112**, 1545–1560.
Mills, D. M. (**2003**). ''Differential responses to acoustic damage and furosemide in auditory brainstem and otoacoustic emission measures,'' J. Acoust. Soc. Am. **113**, 914–924.
Mills, D. M., Norton, S. J., and Rubel, E. W. (**1993**). ''Vulnerability and adaptation of distortion product otoacoustic emissions to endocochlear potential variation,'' J. Acoust. Soc. Am. **94**, 2108–2122.
Mills, D. M., and Rubel, E. W. (**1996**). ''Development of the cochlear amplifier,'' J. Acoust. Soc. Am. **100**, 428–441.
Mills, D. M., and Rubel, E. W. (**1998**). ''Development of the base of the cochlea: Place code shift in the gerbil,'' Hear. Res. **122**, 82–96.
Mills, D. M., and Schmiedt, R. A. (**2004**). ''Metabolic presbycusis: Differential changes in auditory brainstem and otoacoustic emission responses with chronic furosemide application in the gerbil,'' J. Assoc. Res. Otolaryngol. **5**, 1–10.
Patuzzi, R., Sellick, P. M., and Johnstone, B. M. (**1984**). ''The modulation of the sensitivity of the mammalian cochlea by low frequency tones. III. Basilar membrane motion,'' Hear. Res. **13**, 19–27.
Puel, J. L., Durrieu, J. P., Rebillard, G., Vidal, D., Asie, R., and Uziel, A. (**1995**). ''Comparison between auditory brainstem responses and distortion products otoacoustic emissions after temporary threshold shift in guinea pig,'' Acta Acust. (Beijing) **3**, 75–82.
Ryan, A. F., and Woolf, N. K. (**1992**). ''Development of the lower auditory system in the gerbil,'' in *Development of Auditory and Vestibular Systems II*, edited by R. Romand (Elsevier, New York), pp. 243–271.
Schmiedt, R. A., Lang, H., Okamura, H., and Schulte, B. A. (**2002**). ''Effects of furosemide applied chronically to the round window: A model of metabolic presbyacusis,'' J. Neurosci. **22**, 9643–9650.
Schweitzer, L., Lutz, C., Hobbs, M., and Weaver, S. (**1996**). ''Anatomical correlates of the passive properties underlying the developmental shift in the frequency map of the mammalian cochlea,'' Hear. Res. **97**, 84–94.
Scholz, G., Hirschfelder, A., Marquardt, T., Hensel, J., and Mrowinski, D. (**1999**). ''Low-frequency modulation of the $2f_1-f_2$ distortion product otoacoustic emissions in the human ear,'' Hear. Res. **130**, 189–196.
Smith, D. I., and Kraus, N. (**1987**). ''Postnatal development of the auditory brainstem response (ABR) in the unanesthetized gerbil,'' Hear. Res. **27**, 157–164.
Stover, L., Gorga, M. P., and Neely, S. T. (**1996**). ''Toward optimizing the clinical utility of distortion product otoacoustic emission measurements,'' J. Acoust. Soc. Am. **100**, 956–967.
Woolf, N. K., and Ryan, A. F. (**1985**). ''Ontogeny of neural discharge patterns in the ventral cochlear nucleus of the mongolian gerbil,'' Dev. Brain Res. **17**, 131–147.
Woolf, N. K., Ryan, A. F., and Harris, J. P. (**1986**). ''Development of mammalian endocochlear potential: normal ontogeny and effects of anoxia,'' Am. J. Physiol. **250**, R493–R498.

Chronic excitotoxicity in the guinea pig cochlea induces temporary functional deficits without disrupting otoacoustic emissions[a)]

Colleen G. Le Prell,[b)] Masao Yagi,[c)] Kohei Kawamoto,[c)] Lisa A. Beyer, Graham Atkin, Yehoash Raphael, David F. Dolan, Sanford C. Bledsoe, Jr., and David B. Moody
Kresge Hearing Research Institute, Department of Otolaryngology, University of Michigan Medical School, 1301 East Ann Street, Ann Arbor, Michigan 48109-0506

(Received 8 May 2003; revised 30 April 2004; accepted 21 May 2004)

Brief cochlear excitotoxicity produces temporary neural swelling and transient deficits in auditory sensitivity; however, the consequences of long-lasting excitotoxic insult have not been tested. Chronic intra-cochlear infusion of the glutamate agonist AMPA (α-amino-3-hydroxy-5-methyl-4-isoxazolepropionic acid) resulted in functional deficits in the sound-evoked auditory brainstem response, as well as in behavioral measures of hearing. The electrophysiological deficits were similar to those observed following acute infusion of AMPA into the cochlea; however, the concentration-response curve was significantly shifted as a consequence of the slower infusion rate used with chronic cochlear administration. As observed following acute excitotoxic insult, complete functional recovery was evident within 7 days of discontinuing the AMPA infusion. Distortion product otoacoustic emissions were not affected by chronic AMPA infusion, suggesting that trauma to outer hair cells did not contribute to AMPA-induced deficits in acoustic sensitivity. Results from the current experiment address the permanence of deficits induced by chronic (14 day) excitotoxic insult as well as deficits in psychophysical detection of longer duration acoustic signals. © *2004 Acoustical Society of America.* [DOI: 10.1121/1.1772395]

PACS numbers: 43.64.Wn, 43.64.Ri, 43.66.Gf [WPS] Pages: 1044–1056

I. INTRODUCTION

A large body of evidence suggests the excitatory neurotransmitter released by cochlear inner hair cells (IHCs) is the amino acid glutamate (Glu: for reviews, see Eybalin, 1993; Puel, 1995; Le Prell *et al.*, 2001). In the central nervous system, glutamate is functionally active at three (or more) ionotropic receptor sub-types, including α-amino-3-hydroxy-5-methyl-4-isoxazolepropionic acid (AMPA), kainate (KA), and N-methyl-D-aspartate (NMDA). Most intracochlear effects of AMPA and KA are attributed to action at AMPA receptors (Ruel *et al.*, 1999; 2000), which were previously termed ionotropic quisqualate (QA) receptors (for discussion, see Puel, 1995; Le Prell *et al.*, 2001). AMPA and NMDA receptor sub-types (GluR2-3, NR-1) have been located in the cochlea whereas KA receptors (i.e., GluR5-7, KA1-2) have not (for reviews, see Parks, 2000; Le Prell *et al.*, 2001). It is unclear if the AMPA receptor sub-types GluR1 and GluR4 are present in the cochlea only during early developmental stages, or if they are expressed in adult cochlear tissues as well.

QA was initially found to be the most effective agonist at the auditory nerve fiber (ANF)/IHC synapse (Jenison and Bobbin, 1985; Jenison *et al.*, 1986). AMPA is as potent as QA at the ionotropic QA/AMPA receptor (Monaghan *et al.*, 1989; Watkins *et al.*, 1990). The consequences of intracochlear AMPA, KA, and QA are similar. In brief, intracochlear QA (Jenison and Bobbin, 1985) or KA (Bledsoe *et al.*, 1981) initially increases the spontaneous firing of ANFs, followed by suppression of ANF activity. Consequences of acutely perfusing the guinea pig cochlea with AMPA include elevated compound action potential (CAP) and auditory brainstem response (ABR) thresholds, depressed CAP amplitude, and swelling of auditory nerve dendrites (Puel *et al.*, 1991; 1994; 1997; Duan and Canlon, 2001). KA has similar effects when applied to the round window in chinchillas (Zheng *et al.*, 1996; 1998; 1999) or rats (Pujol *et al.*, 1985; Juiz *et al.*, 1989; Gil-Loyzaga and Pujol, 1990; Gil-Loyzaga *et al.*, 1993). Functional recovery following acute AMPA/KA infusion is generally complete in mammals; deficits may be more long-lasting in chickens (Sun *et al.*, 2000). Glutamate agonists do not disrupt outer hair cell function (assessed using cochlear microphonic or distortion product otoacoustic emissions).

The application of Glu (Janssen *et al.*, 1991) or Glu agonists (Puel *et al.*, 1991; 1994), noise exposure (Robertson, 1983), and oxygen-deprivation (i.e., ischemia, anoxia, see Rothman, 1984; Billett *et al.*, 1989) are excitotoxic events that result in functional deficits and swelling of auditory neurons; this pathology has been termed excitotoxic trauma. Although pathological changes have been evident during acute AMPA treatment in the cochlea, it is possible that chronic AMPA administration will not depress cochlear function throughout the duration of AMPA delivery. Synaptic modification of receptor properties, distribution, and/or composition of receptor subunits can compensate for chronic in-

[a)]Portions of this research were presented at the twenty-second midwinter meeting of the Association for Research in Otolaryngology (Le Prell *et al.*, 1999a; 1999b).

[b)]Electronic mail: colleeng@umich.edu
[c)]Current address: Department of Otolaryngology, Kansai Medical University, 10–15 Fumizonocho, Moriguchi, Osaka, 570-8506, Japan.

creases or decreases in excitatory input; these changes are termed homeostatic plasticity (Turrigiano, 1999). Down-regulation of AMPA receptors during chronic activity maintains excitatory output at a constant level in spinal cord neurons (O'Brien *et al.*, 1998; see also Turrigiano and Nelson, 1998; Turrigiano, 1999) and, perhaps, hippocampal slices (Jakobsen and Zimmer, 2001).

In contrast to the hypothesis that receptor changes can modulate neural responses to AMPA during chronic drug delivery is the speculation that vascular pathology associated with aging produces chronic anoxia, chronic glutamatergic excitotoxicity, and ultimately, loss of radial afferent fibers and type I ganglion cells (Pujol *et al.*, 1990). This investigation, therefore, tests the hypothesis that chronic excitotoxicity results in loss of afferent fibers and permanent functional deficits, in contrast to the reversible excitotoxic trauma induced by perfusing a Glu agonist through the cochlea for a relatively brief period of time. The permanence of deficits induced by longer-lasting excitotoxic insult has not been empirically tested previously.

In addition to typical electrophysiological and morphological assays, we used operant procedures to identify perceptual deficits. Behavioral thresholds and electrophysiological responses are typically well correlated (e.g., Borg and Engstrom, 1983; Miller *et al.*, 1995; Szymanski *et al.*, 1999; Wolski *et al.*, 2003). However, some audiology patients lack synchronous neural activity as measured using the ABR, but have intact otoacoustic emissions and only mild to moderate hearing loss (Worthington and Peters, 1980; Musiek, 1982; Starr *et al.*, 1996; Kraus *et al.*, 2000). This disorder is termed ''auditory neuropathy,'' and it can be produced by pathology of the auditory nerve (Starr *et al.*, 2000). Given that AMPA produces auditory nerve pathology, one prediction is AMPA-treated animals will exhibit normal psychophysical response thresholds. Responses to longer-duration signals during behavioral tests, in the absence of synchronous evoked potentials during electrophysiological tests, would reflect temporal integration of the longer-duration signals (for further discussion of temporal integration, see Green *et al.*, 1957; Watson and Gengel, 1969; Gerken *et al.*, 1990). The ABR is an electrophysiological response to the onset of a brief acoustic signal and thus does not depend on temporal integration (Gorga *et al.*, 1984). The current experiments thus provide the first examination of AMPA-induced disruption of longer duration signal detection.

II. METHODS

A. Subjects

Male and female pigmented guinea pigs from Murphy's Breeding Laboratory, Inc. (Plainfield, IN) and Elm Hill Breeding Labs (Chelmsford, MA) were individually housed with free access to water. Initial weights were 300–350 grams; weight gain was continual until each animal achieved a weight of approximately 900 grams. Food intake (Guinea Pig Chow, PMI Nutrition International Inc., Brentwood, MO) was moderately restricted to prevent additional weight gain. Treatments met or exceeded all guidelines in the Guide for the Care and Use of Laboratory Animals (National Research Council, 1996) and were approved by the University Committee on the Use and Care of Animals at the University of Michigan.

B. Experimental design

We implanted perfusion cannulas in 34 guinea pigs. Subject characteristics for animals included in the final data summary are described in Table I. Functional assays included sound-evoked auditory brainstem response (ABR), distortion product otoacoustic emission (DPOAE), and psychophysical testing. All animals underwent surgery during which a cannula used for chronic fluid delivery was implanted into scala tympani. In addition, a subset of animals were unilaterally deafened (for summary of individual animals, see Table I). Changes in each functional measure were assessed post-surgery and during intra-cochlear infusion of artificial perilymph solution (145 mM NaCl, 2.7 mM KCl, 2.0 mM $MgSO_4$, 1.2 mM $CaCl_2$, 5.0 mM HEPES; pH=7.40, osmolality=280–285 mOsm). Following infusion of artificial perilymph, a perilymph solution containing s-AMPA (Sigma Chemical, 1–20 mM, pH=7.40) was infused for 14 days at a rate of 0.5 μl/hr. Psychophysical testing was conducted daily. ABR thresholds were assessed at least once during AMPA infusion days 3–5 (''Week 1'') and again during infusion days 11–13 (''Week 2''). DPOAE was assessed only during Week 2.

Due to the time invested in training, several behavioral animals were tested with more than one AMPA concentration (see Table I). Lower concentrations were tested prior to higher concentrations, and a recovery period between concentrations was provided. To maintain cannula integrity, perilymph solution was infused during the recovery period. Testing of the higher concentration did not begin until complete functional recovery was observed in both operant and ABR measures of sensitivity. Some animals were euthanized following the final Week 2 ABR test (i.e., during AMPA infusion); other animals were used to examine the time course of functional and morphological recovery. At the conclusion of the test protocol, IHC/ANF synapses were examined using transmission electron microscopy. Each procedure is described below in greater detail.

All data are depicted as mean±standard error. The majority of the statistical analyses were two-way analyses of variance. When data were compared within the same animals, two-way repeated-measures analyses of variance were conducted. Pair wise multiple comparisons were conducted using the Tukey test. After excluding data from 14 animals with evidence of current or previous middle ear infections and animals in which the cannula was not fully inserted into scala tympani, a very small number of animals treated with 1 mM AMPA or 20 mM AMPA remained in the investigation. Given the small sample sizes, statistical comparisons were not possible for those subject groups and we therefore exclude those data from this report.

C. Electrophysiology

Anesthetized guinea pigs (20 mg/kg ketamine, 5 mg/kg xylazine) were placed on a warm heating pad in a double-

TABLE I. Subjects in this investigation were initially composed of multiple groups. Neither acoustic stimulation nor contralateral deafening influenced the effects of AMPA infusion. Subjects were therefore combined across these variables for the final data summary.

Animal ID and ear	Acoustic stimulation	Contralateral deafening	AMPA concentration	Recovery period[a]
P121-Right	None	No	3 mM	No
P123-Right	None	No	3 mM	No
P102-Left	Yes (Trained)	Yes	3 mM	Yes
CP64-Left	None	Yes	3 mM	Yes
CP66-Right	Yes (Trained)[b]	Yes	3 mM	Yes
CP88-Right	None	No	3 mM	Yes
CP90-Right	None	No	3 mM	Yes
P122-Right	None	No	10 mM	No
P125-Right	None	No	10 mM	No
P126-Right	None	No	10 mM	No
P103-Left	Yes (Trained)	Yes	10 mM	Yes
CP65-Right	Yes (Yoke)	Yes	3, 10 mM	Yes
CP67-Right	Yes (Trained)	Yes	3, 10 mM	Yes
P104-Left	Yes (Trained)	Yes	3, 20 mM	Yes
P111-Right	None	No	Unoperated, Age-Matched Control	
P111-Left	None	No	Unoperated, Age-Matched Control	
P119-Left	None	No	Unoperated, Age-Matched Control	
P127-Left	None	No	Unoperated, Age-Matched Control	

[a]Recovery period is defined as a period of time that the animal is allowed to recover from functional deficits observed during AMPA infusion. Recovery periods were of variable duration, and often extended well beyond the onset of recovery. During recovery periods, animals were infused with perilymph solution, or, the cannula was tied tightly and no additional substances were infused into the cochlea.

[b]Behavioral data from CP66 were excluded from the final analysis because baseline thresholds assessed behaviorally were substantially higher than the corresponding ABR thresholds.

walled sound-attenuated chamber (Industrial Acoustics Company, Bronx, New York). Tucker-Davis Technology (TDT; Alachua, FL) software was used for signal calibration (SigCal 3.2) and stimulus generation (SigGen 3.2). Signals were presented using TDT System II hardware and a 200 Ohm transducer (Beyer) coupled to the animals' ear canal via vinyl tubing. Sound-evoked brainstem responses were amplified (10 000×) and filtered (300–3000 Hz; Grass-Telefactor #P55, West Warwick, RI) then digitized (TDT, AD1) and averaged (1020x; TDT, BioSig 3.2).

Acoustic signals were 2, 4, 8, and 16 kHz tone bursts (10 ms duration, 0.5 ms rise/fall, 17/s). Stimulus levels were initially set at 80-decibels (dB) sound pressure level (SPL); levels were decreased in 10 dB increments until the evoked response disappeared. ABR at intermediate 5 dB increments was then assessed to more accurately assign threshold, which was defined as the lowest signal level that reliably elicited an electrophysiological response. Two independent observers scored all thresholds; at least one observer was blind to experimental condition. If threshold values differed by more than 5 dB, a third person blind to experimental condition evaluated the digitized waveforms. The amplitude of ABR wave III was assessed following Puel *et al.* (1995). Although ABR wave I is the most direct measure of auditory nerve activity, ABR wave III is the most robust component of the guinea pig ABR and as such, it was frequently the only identifiable component of the ABR during the AMPA infusion.

D. Psychophysical training and testing procedures

Guinea pigs were trained to depress a floor-mounted plastic response button in response to illumination of a cue light using positive reinforcement procedures (see Prosen *et al.*, 1978). The animals pressed the button during a quiet listening interval (1–9 s), and then released the button upon detecting an acoustic stimulus (0.25, 0.5, 1, 2, 4, 8, 16, or 22.4 kHz). Animals received food pellets [45 mg Dustless Precision Pellets (Bio-Serv, Frenchtown, NJ)] for correct releases. Acoustic stimuli were presented during 75% of the total trials (i.e., ''test trials''). During the remaining trials, release rates in the absence of the test signal (i.e., ''catch trials'') were monitored. Animals were punished with a 7 s time-out for any incorrect releases.

Animals were tested 5 days per week for approximately 45 minutes. Stimulus frequencies were randomly ordered; levels were varied using a transformed tracking algorithm (see Niemiec and Moody, 1995). At each frequency, animals were initially presented with a supra-threshold stimulus. After two consecutive correct release responses, tone level was decreased by 5 dB. If animals missed a tone (defined as failure to respond within 2.5 s of tone onset), the tone was turned off and a new trial was initiated with the tone level increased by 5 dB. After 6 transitions between supra- and sub-threshold stimulus levels were completed, threshold was defined as the average level of the final four transitions. Behavioral data from a single animal were excluded as behavioral thresholds were elevated by 20–30 dB relative to the corresponding ABR thresholds, suggesting the animal was not motivated to perform the detection task when tone levels were quieter and thus more challenging to detect.

Daily acoustic stimulation prior to loud sound reduces the extent of damage induced by later exposure to other loud sounds (Canlon and Fransson, 1995; McFadden *et al.*, 1997; Skellett *et al.*, 1998; Yoshida and Liberman, 2000). Because our acoustic stimuli were quieter and briefer than those used

for conditioning the ear, we did not expect group differences based on acoustic signals presented during behavioral tests. Nonetheless, we exposed a subset of the untrained animals to acoustic stimuli equivalent to those presented to the behavioral animals. We refer to these untrained animals as ''yoked control'' animals. There were no differences in ABR thresholds or AMPA-induced change in ABR thresholds when trained and yoked control animals were compared to other animals. Therefore, ABR data from trained animals, untrained yoked controls, and the other untrained animals were combined.

E. Surgical procedures

1. Cannulation of cochlea

As described by Brown *et al.* (1993), a perfusion cannula filled with artificial perilymph solution was inserted through the wall of the cochlea via a small fenestra. Following Prieskorn and Miller (2000), a ball of silastic was wrapped around the cannula to limit insertion depth to 0.5 mm and prevent perilymph leakage. An osmotic mini-pump (Durect Corporation, Cupertino, CA) was filled with artificial perilymph solution and attached to the opposite end of the cannula; this pump was inserted between the scapulae prior to suturing of the surgical wound. Perilymph was delivered at a constant rate of either 0.5 μl/hr (14 days, model 2002 pump) or 0.25 μl/hour (28 days, model 2004 pump). To further extend the duration of perilymph infusion, animals underwent brief ''pump change'' procedures during which the perilymph-dispensing pumps were removed, and a new pump (filled with perilymph solution) was inserted in its place. The total duration of perilymph infusion ranged from 14 to 56 days. There were no time-related changes in thresholds during perilymph infusion, and the pump change procedure did not affect thresholds.

2. Unilateral deafening

Prior to the implant procedure, a subset of subjects (including all behaviorally trained animals, see Table I) was unilaterally deafened. The monauralization procedure was required for behavioral assessment of functional changes when AMPA was delivered to the intact (not deafened) ear. If initial ABR screening revealed a threshold asymmetry, the ear selected for deafening was the less sensitive ear. To unilaterally deafen guinea pigs, neomycin sulfate (10% solution, 60 μl injection volume) was injected through the round window membrane of one ear (e.g., Miller *et al.*, 1995). Neomycin-induced deafening was verified by the elevation of ABR thresholds and morphological trauma. ABR responses at the highest stimulation levels (85-dB SPL) could reflect residual function of the neomycin-treated ear, or acoustic crossover due to stimulation of the intact contralateral ear (following Ozdamar and Stein, 1981). We verified that AMPA-induced deficits did not vary based on the functional status of the ear contralateral to the AMPA-treated ear using ABR.

F. Distortion product otoacoustic emission assessment

Threshold and amplitude of the cubic distortion product were assessed in anesthetized guinea pigs (40 mg/kg ketamine, 10 mg/kg xylazine) placed on a warm heating pad. The ear canal and the tympanic membrane were visually inspected (with magnification) prior to insertion and after removal of a microphone (gain=40 dB, ER-10B+Low Noise Microphone, Etymotic Research, Elk Grove Village, IL) from the ear canal. Two Beyer transducers were tightly coupled to sound delivery ports in the microphone assembly.

During DPOAE testing, the primary tones (F1, F2) were centered at 2, 4, 8, or 16 kHz and spaced such that F2=1.2*F1. The frequency of the distortion product was equal to 2F1-F2. Thus, when the primary tones were centered at 16 kHz, F1 was 14.5 kHz, F2 was 17.4 kHz, and the DPOAE was 11.6 kHz. Initially, the level of F1 was fixed at 80-dB SPL and the level of F2 was adjusted to be 10 dB quieter. The 10 dB difference in F1 and F2 sound levels was maintained as the level of F1 was decreased in 5–10 dB steps until the DPOAE disappeared into the noise floor. Threshold was defined as 10 dB above the noise floor.

G. Morphological procedures

1. AMPA-infused ears

Animals were deeply anesthetized and the thorax opened for vascular perfusion of the tissues by an individual blinded to animal treatment. After intracardiac perfusion of phosphate buffered saline, fixative (2% paraformaldehyde and 2.5% glutaraldehyde in phosphate buffer) was perfused. The temporal bones were harvested and the cochleae gently perfused with fixative. Placement of the cannula inside the cochlea was visually confirmed, and the middle and inner ear were carefully examined for infection or other pathology. The following day, the otic capsule and lateral wall were removed, and the bony modiolus was carefully detached at the base of the cochlea. Organ of Corti tissue was rinsed and decalcified in 3% EDTA with 0.25% glutaraldehyde and postfixed in 1% osmium tetroxide for 1 hour. The organ of Corti was separated to whole turn segments, which were embedded individually in plastic blocks (Embed 812, Electron Microscopy Sciences, Fort Washington, PA). The desired location for sectioning was designated to be in the 2nd segment from the base. Tissues from all but 5 animals were sectioned (80 nm) with a diamond knife on a Leica Ultracut R ultramicrotome. Sections were stained with uranyl acetate and lead citrate and analyzed in a Phillips 100 transmission electron microscope operated at 80 kV. Negatives were developed using a MOHR processor, scanned (ScanJet, Hewlett-Packard, Palo Alto, CA), and imaged (Photoshop 6, Adobe, San Jose, CA).

Sections were cut from upper-first/lower-second turn and upper-second/lower-third turn, corresponding to approximately 16 and 2 kHz regions of the guinea pig cochlea (Greenwood, 1961; 1990). At least six IHC/ANF synapses from each animal in each cochlear region were digitized and evaluated. Individuals responsible for imaging were blinded to both animal group and functional status. The number of

TABLE II. Quantification of neural swelling in the 16 kHz region of the cochlea (i.e., upper-first/lower-second turn).

Animal information[a]	Animal treatment	Hair cells sectioned[b]	Hair cells counted[c]	Swelling number[d]	Hair cells quantified[e]	Swelling size[f] (μm^2)	Swelling total[g] (μm^2)
P111-R	Unoperated	7	4	1.75	3	4.9	6.8
P111-L	Unoperated	7	7	4.7	1	2.6	20.6
P119-L	Unoperated	5	5	1.6	3	13.8	23.0
P127-L	Unoperated	6	4	2.8	3	23.2	69.7
P119-R	Operated	6	5	5	5	8.1	42.1
P127-R	Operated	6	6	5.7	6	12.4	70.5
Control Mean:				**3.6**		**10.8**	**38.8**
P125-R	10 mM	6	6	16.5	6	10.0	165.8
P126-R	10 mM	9	9	9.6	4	11.8	115.0
10 mM AMPA Mean:				**13.1**		**10.9**	**140.4**
CP98-L	20 mM	6	5	13.2	5	15.8	208.7
CP99-L	20 mM	6	6	4.7	4	36.6	182.8
20 mM AMPA Mean:				**9.0**		**26.2**	**195.8**
CP77-R	1 mM-R	6	6	1.8	4	2.3	4.0
P102-L	3 mM-R	5	4	8.0	4	17.0	132.0
CP66-R	3 mM-R	6	6	4.3	5	11.2	30.7
CP88-R	3 mM-R	6	6	2.3	3	9.8	29.5
CP90-R	3 mM-R	6	5	9.2	3	3.2	38.7
CP65-R	10 mM-R	7	7	6.4	2	28.6	186.1
CP67-R	10 mM-R	6	4	6.3	4	7.2	44.7
P104-L	20 mM-R	7	7	14.7	1	10.7	160.3
Post-AMPA Recovery Mean:				**6.6**		**11.3**	**78.3**

[a]Animal information includes identification number (as in Table I), ear (R: Right; L: Left), and treatment information (Controls: Unoperated, Operated; AMPA-treated: 10 mM, 20 mM; Recovered: 3 mM-R, 10 mM-R, 20 mM-R). This table includes information from all categories containing data from at least two animals. Hair cell images from two additional animals were excluded (P118-R, 1 mM; P123-R, 3 mM) based on this criteria. During vascular perfusion and tissue processing, individuals were blind to animal treatment.

[b]Hair cells sectioned: The number of inner hair cells that were sectioned in the upper-first/lower-second turn of the cochlea and imaged. Sectioning and imagining were conducted by an observer blinded to animal treatment.

[c]Hair cells counted: The number of hair cell images in which swellings were counted. Some images were excluded from the counting analysis based on inability to resolve sufficient image detail.

[d]Swelling number: Counts of neural swellings were conducted by an observer blinded to animal treatment. The average number of swellings per hair cell (for sample size, see ''Hair Cells Counted'') is reported.

[e]Hair cells quantified: The number of images in which swelling size could be quantified, based on inclusion of a scale bar within the photographic image. All images which included scale bars were quantified.

[f]Swelling size: The average size of individual neural swellings; swelling size was averaged across the image set for each animal.

[g]Swelling total: The size of individual neural swellings was summed, for each hair cell image, to estimate total neural swelling per hair cell. Average swollen area per hair cell is reported. Quantification of swelling size was conducted by an observer blinded to animal treatment.

swollen dendrites and the size of the swellings were qualitatively similar within each of the six samples from each animal/region. Quantification of the total area of the swellings was restricted to the subset of hair cell images containing scale bars within the digitized image set from each animal. Tables II and III summarize the number of IHCs evaluated for the number of and area of the swellings near each IHC, and the results of these analyses, for the upper-first/lower-second turn (Table II) and the upper-second/lower-third turn (Table III).

Individuals that identified swollen neurons and quantified swelling were blind to animal group and functional status. To quantify swelling, two measures of swelling diameter (i.e., length and width) were collected for each swollen neuron. Swelling area was then estimated as πr^2 where r=average diameter*0.5. The area of individual neural swellings surrounding the hair cell was summed to provide an estimate of total swelling. For most subjects, swelling could be quantified for several hair cell images. For these subjects, total swelling per hair cell was averaged to obtain a representative estimate of swelling.

2. Neomycin-injected ears

The temporal bones of the deafened ears were fixed and removed as described above. The following day, the otic capsule, lateral wall, and tectorial membrane were removed, and the bony modiolus was carefully detached at the base of the cochlea. Organ of Corti tissue, attached to the modiolus, was permeabilized with 0.3% Triton-X (Sigma Chemical) in phosphate buffered saline for 10 min and then incubated for 30 min with rhodamine phalloidin (Molecular Probes, Eugene, OR) diluted 1:100 in phosphate buffered saline (room temperature). After washing the tissues with phosphate buffered saline, individual turns from the organ of Corti were separated from the modiolus, mounted on microscope slides with GEL/Mount (Biomedia, Foster City, CA), and examined and photographed using a Leica (Eaton, PA) DMRB epifluorescence microscope.

TABLE III. Quantification of neural swelling in the 2 kHz region of the cochlea (i.e., the upper-second/lower third turn).

Animal information[a]	Animal treatment	Hair cells sectioned[b]	Hair cells counted[c]	Swelling number[d]	Hair cells quantified[e]	Swelling size[f] (μm^2)	Swelling total[g] (μm^2)
P111-R	Unoperated	6	6	2.8	1	1.2	1.2
P111-L	Unoperated	7	7	1.1	7	17.6	27.7
P119-L	Unoperated	6	6	2.3	6	10.7	26.9
P127-L	Unoperated	6	6	3.3	4	23.1	69.3
P119-R	Operated	6	6	2.8	5	24.6	63.9
P127-R	Operated	6	6	3.0	5	24.8	74.3
Control Mean:				**2.6**		**17.0**	**43.9**
P125-R	10 mM	6	6	5.2	1	31.3	187.7
P126-R	10 mM	6	6	7.7	2	26.0	220.9
10-mM AMPA Mean:				**6.5**		**28.7**	**204.3**
CP98-L	20 mM	6	6	7.0	5	27.0	194.3
CP99-L	20 mM	6	6	5.2	6	25.6	132.1
20-mM AMPA Mean:				**6.1**		**26.3**	**163.2**
CP77-R	1 mM-R	6	6	1.2	3	7.3	7.3
P102-L	3 mM-R	6	6	4.7	6	19.2	92.8
CP66-R	3 mM-R	6	6	2.8	5	8.6	22.4
CP88-R	3 mM-R	6	4	4.8	4	8.5	40.2
CP90-R	3 mM-R	6	6	9.2	6	13.8	126.1
CP65-R	10 mM-R	6	3	5.3	2	12.7	69.9
CP67-R	10 mM-R	6	5	3.2	4	31.2	101.5
P104-L	20 mM-R	4	4	4.0	4	20.7	82.8
Post-AMPA Recovery Mean:				**4.4**		**15.3**	**67.9**

[a]Animal Information includes identification number (as in Tables I and II), ear (R: Right; L: Left), and treatment information (Controls: Unoperated, Operated; AMPA-treated: 10 mM, 20 mM; Recovered: 3 mM-R, 10 mM-R, 20 mM-R). This table includes information from all categories containing data from at least two animals. Hair cell images from two additional animals were excluded (P118-R, 1 mM; P123-R, 3 mM) based on this criteria. During vascular perfusion and tissue processing, individuals were blind to animal treatment.

[b]Hair cells sectioned: The number of inner hair cells that were sectioned in the third turn of the cochlea and imaged. Sectioning and imagining were conducted by an observer blinded to animal treatment.

[c]Hair cells counted: The number of hair cell images in which swellings were counted. Some images were excluded from the counting analysis based on inability to resolve sufficient image detail.

[d]Swelling number: Counts of neural swellings were conducted by an observer blinded to animal treatment. The average number of swellings per hair cell (for sample size, see ''Hair cells counted'') is reported.

[e]Hair cells quantified: The number of images in which swelling size could be quantified, based on inclusion of a scale bar within the photographic image. All images which included scale bars were quantified.

[f]Swelling size: The average size of individual neural swellings; swelling size was averaged across the image set for each animal.

[g]Swelling total: The size of individual neural swellings was summed, for each hair cell image, to estimate total neural swelling per hair cell. Average swollen area per hair cell is reported. Quantification of swelling size was conducted by an observer blinded to animal treatment.

III. RESULTS

A. Electrophysiological and behavioral assays of function: Baseline sensitivity

ABR thresholds are depicted in Fig. 1(A). Thresholds assessed pre- and post-implant (i.e., during perilymph infusion) were not reliably different ($F=4.029$, $df=1, 110$: $p>0.05$). Pre- and post-implant thresholds were significantly lower than thresholds of neomycin-injected ears ($F=95.717$, $df=3, 61$: $p<0.001$). Thresholds assessed within 1-month of neomycin injection (''Neomycin-1'') and those assessed 6–13 months post-neomycin injection (''Neomycin 2'') were not reliably different (p's>0.05). Thresholds assessed using operant responses are depicted in Fig. 1(B). There were no statistically reliable differences between binaural, monaural, and monaural/implanted thresholds ($F=4.476$, $df=2, 95$: $p>0.05$). Operant response and ABR thresholds, assessed during perilymph infusion, are compared in Fig. 1(C). ABR thresholds were not reliably different from operant thresholds ($F=0.0439$, $df=1, 31$: $p>0.05$).

Taken together, post-implant acoustic sensitivity was normal in trained and untrained animals. In contrast to the implant procedure, which had little or no effect on sensitivity, neomycin injection induced significant hearing loss across a broad range of frequencies.

B. Electrophysiological and behavioral assays of function: AMPA-induced changes

Chronic intra-cochlear AMPA elevated ABR thresholds [Figs. 2(A) and 2(B)] and behavioral thresholds [Fig. 2(C)] and reduced the amplitude of ABR wave III (Fig. 3); these effects were reversible. ABR threshold increases were statistically reliable after treatment with either 3 mM ($F=5.814$, $df=2, 119$: $p<0.05$) or 10 mM ($F=4.960$, $df=2, 71$: $p<0.001$) s-AMPA. A significant concentration by frequency interaction was evident (3 mM: $F=4.966$, $df=6, 119$: $p<0.001$; 10 mM: $F=7.709$, $df=6, 71$: $p<0.001$). Pair wise comparisons revealed that 3 mM s-AMPA reliably elevated 16 kHz thresholds during the first week of infusion; both 8

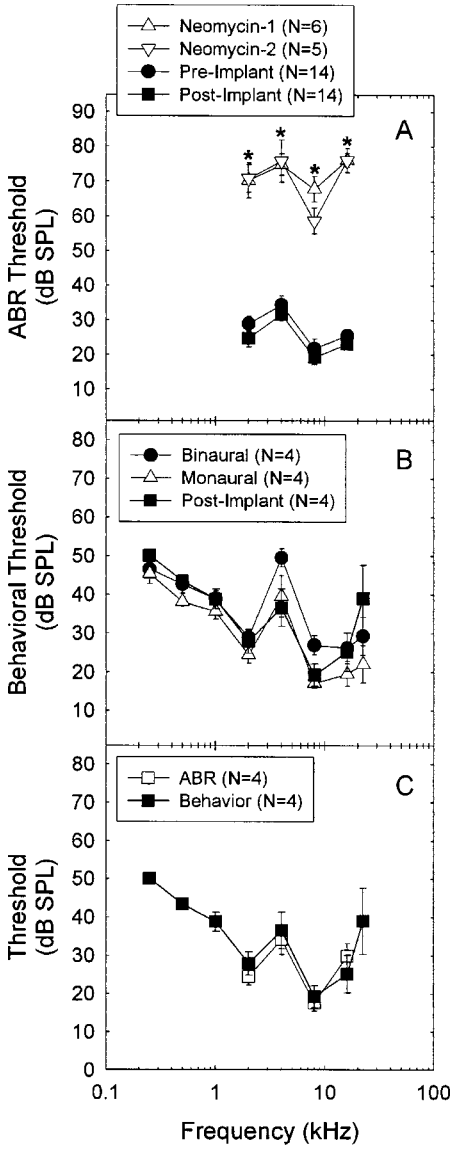

FIG. 1. (A) Threshold sensitivity of the auditory brainstem response (ABR), evoked using 2, 4, 8, and 16 kHz tone bursts, was normal before (''Pre-Implant'') and after (''Post-Implant'') insertion of a cannula into scala tympani. Post-implant thresholds were assessed during chronic infusion of artificial perilymph solution. Injecting 60 μl neomycin sulfate through the round window membrane of the contralateral ear elevated contralateral thresholds within the first month (''Neomycin-1'') and at longer time points (i.e., after 6–13 months, ''Neomycin-2''). Asterisks indicate statistically reliable threshold differences for comparisons of neomycin-injected ears and perilymph-infused ears. Figure (B) A subset of the animals was trained to report the detection of acoustic signals (0.25, 0.5, 1, 2, 4, 8, 16, and 22.4 kHz). Free-field thresholds were assessed with both ears intact (''Binaural''), following unilateral neomycin injection (''Monaural''), and after a perfusion cannula was implanted in the nondeafened ear (''Post-Implant''). There were no statistically reliable differences across conditions. Figure (C) Post-implant thresholds assessed behaviorally were not reliably different from thresholds assessed using ABR. The lack of statistically reliable differences between comparisons of pre- and post-implant ABR thresholds (A), binaural, monaural and post-implant behavioral thresholds (B), and ABR and behavioral thresholds (C) should be interpreted cautiously as the power of the performed tests was below the desired power of 0.800.

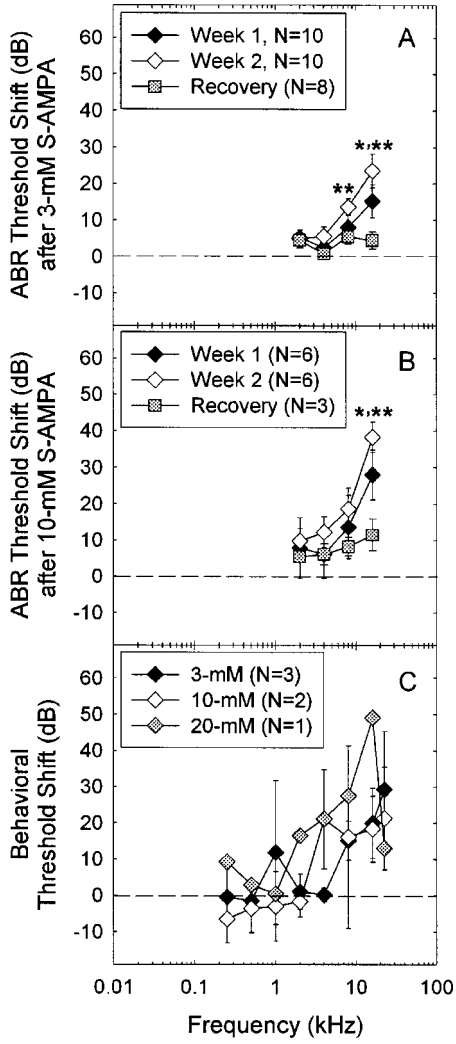

FIG. 2. Chronic AMPA elevated threshold sensitivity during AMPA infusion; an effect that was reversed post-AMPA. AMPA concentrations included 3 mM [Fig. (A)] and 10 mM [Fig. (B)]. Sensitivity was assessed using the sound-evoked auditory brainstem response (ABR) 3–5 days following the onset of AMPA infusion (''Week 1'') and 11–13 days following the onset of AMPA infusion (''Week 2''). A single asterisk indicates AMPA-induced threshold elevations were statistically reliable during the first week of AMPA infusion; double asterisks indicate threshold differences were statistically reliable during the second week of AMPA infusion. Recovery of function was assessed after AMPA infusion was discontinued (''Recovery''). Recovery sample size was smaller as some animals were euthanized immediately post-AMPA. Pre-AMPA baselines used to calculate AMPA-induced threshold shifts were perilymph-infused thresholds assessed a maximum of 1 week prior to the onset of AMPA infusion. Elevations in threshold sensitivity were similar in animals trained to report the detection of acoustic signals [Fig. (C)].

and 16 kHz thresholds were elevated during the second week of infusion. Following 10 mM s-AMPA, ABR thresholds at 16 kHz were elevated during both the first and second week of AMPA infusion (all p's<0.05). A second set of statistical comparisons, limited to the animals for which recovery data were available, revealed no significant differences between pre-AMPA perilymph-infused thresholds and post-3 mM AMPA recovery thresholds ($p>0.05$). The number of animals allowed to recover after 10 mM s-AMPA was not sufficient for statistical evaluation.

Chronic intra-cochlear AMPA depressed the amplitude of ABR wave III at all test frequencies. ABR amplitude was significantly reduced at 16 kHz [Fig. 3(A); $F=130.176$, $df=3$, 286: $p<0.001$), 8 kHz [Fig. 3(B); $F=51.956$, $df=3$, 274: $p<0.001$], 4 kHz [Fig. 3(C), $F=30.576$, $df=3$, 244: $p<0.001$], and 2 kHz [Fig. 3(D); $F=18.232$, $df=3$, 275: p

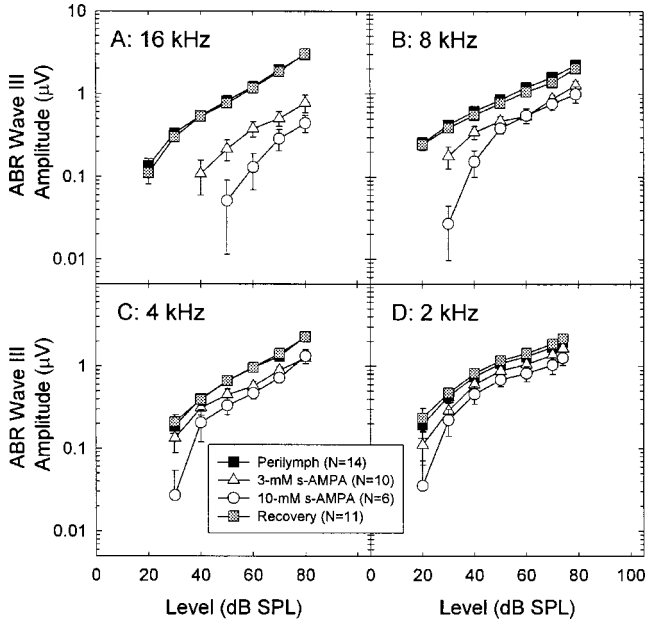

FIG. 3. AMPA infusion depressed the amplitude of wave III of the sound-evoked auditory brainstem response (ABR) at 16 kHz [Fig. (A)], 8 kHz [Fig. (B)], 4 kHz [Fig. (C)], and 2 kHz [Fig. (D)]. Perilymph data were assessed a maximum of 1 week prior to the onset of AMPA infusion. The AMPA data depicted here were collected 11–13 days following the onset of AMPA infusion. Recovery of function was assessed after AMPA infusion was discontinued.

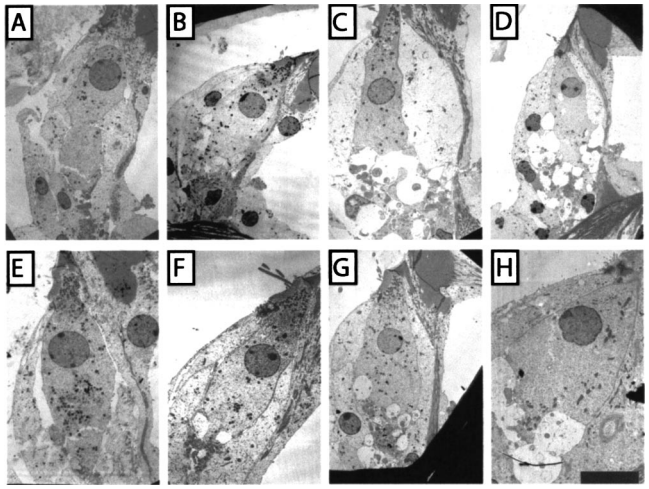

FIG. 4. Inner hair cells (IHCs) contacted by auditory nerve dendrites are depicted. Hair cells were sampled in the upper-first/lower-second turn of the cochlea (A, B, C, D) and the upper-second/lower-third turn of the cochlea (E, F, G, H). Images presented here are from control animals (A, E), post-AMPA recovery animals (B, F), and animals treated with 10 mM (C, G), or 20 mM (D, H) s-AMPA. AMPA treated animals shown here were euthanized during AMPA infusion. All images are depicted at the same scale; the scale bar in panel H is 10 μm.

<0.001]. Across frequencies, pair wise comparisons indicated that depression of ABR amplitude by AMPA was statistically reliable for comparisons between 3- or 10 mM AMPA and perilymph, as well as 3- or 10 mM AMPA and recovery (all p's<0.01). There were no reliable differences in ABR amplitude for comparisons between perilymph and recovery, or 3- and 10 mM AMPA (p's>0.05). Significant treatment by level interactions at 4 kHz ($F=3.461$, df$=15$, 244: $p<0.001$), 8 kHz ($F=2.273$, df$=18$, 274: $p<0.005$), and 16 kHz ($F=13.856$, df$=18$, 286: $p<0.001$) indicated the effect of AMPA treatment varied with level. The 10 mM dose produced a greater effect at low stimulus levels than at high stimulus levels, whereas the 3 mM dose produced equivalent depressions across levels. There was not a reliable interaction for concentration and level at 2 kHz ($F=0.678$, df$=18$, 268: $p>0.05$).

Deficits induced by 3 mM s-AMPA were reversible once AMPA infusion was discontinued (see Figs. 2 and 3, ''Recovery''). Deficits induced by 10 mM s-AMPA were also reversible, although recovery of ABR threshold sensitivity was incomplete in two of the three animals that were allowed a recovery period following infusion of 10 mM s-AMPA. One animal recovered to within 3 dB of baseline within 17 days; at the time of euthanasia, the other animals had deficits of 10 dB (day 36 post-AMPA) and 25 dB (day 44 post-AMPA).

C. AMPA-induced changes in morphology

Data from a small number of animals were available within each concentration. Therefore, for the morphological analysis, conditions for which data were available from at least two animals were included. Data from control animals, animals treated with 10- or 20 mM s-AMPA, and post-AMPA-recovery animals are included. Examples of IHC/ANF synapses in the upper-first/lower-second turn and the upper-second/lower-third turn are depicted in Fig. 4. The total number of hair cells evaluated, mean counts of neural swelling, and mean swollen area (per neuron as well as per hair cell) are listed in Tables II (upper-first/lower-second turn) and III (upper-second/lower-third turn).

Neural swelling was minimal in four unoperated ears harvested from three age-matched animals (i.e., control) as well as two animals in which the implant surgery was not successful (P119, P127). The small amount of swelling observed in control tissues is consistent with the slight anoxia sometimes associated with vascular perfusion procedures (following Duan and Canlon, 2001). However, these were large and relatively aged guinea pigs by the time of euthanasia and others have speculated that vascular pathology associated with aging may produce chronic anoxia and glutamatergic excitotoxicity (Pujol *et al.*, 1990). Thus, limited swelling in control tissues may be a consequence of animal age and individual variation in age-related deficits. Whatever the source of the limited swelling in control tissues, synapses in tissues from animals euthanized during AMPA infusion were clearly characterized by larger and more numerous neural swellings than were seen in tissues from control animals. Swellings in tissues from animals that were allowed a recovery period post-AMPA were intermediate to swelling observed in tissues from control and AMPA-treated animals.

Additional quantification of swollen area is presented in Fig. 5. Neural swelling in the upper-first/lower-second turn of the cochlea was comparable to that observed in the upper-second/lower-third turn of the cochlea [Fig. 5(A)]. The relationship between threshold shift and neural swelling varied with frequency [see Fig. 5(B): 16 kHz threshold shift versus

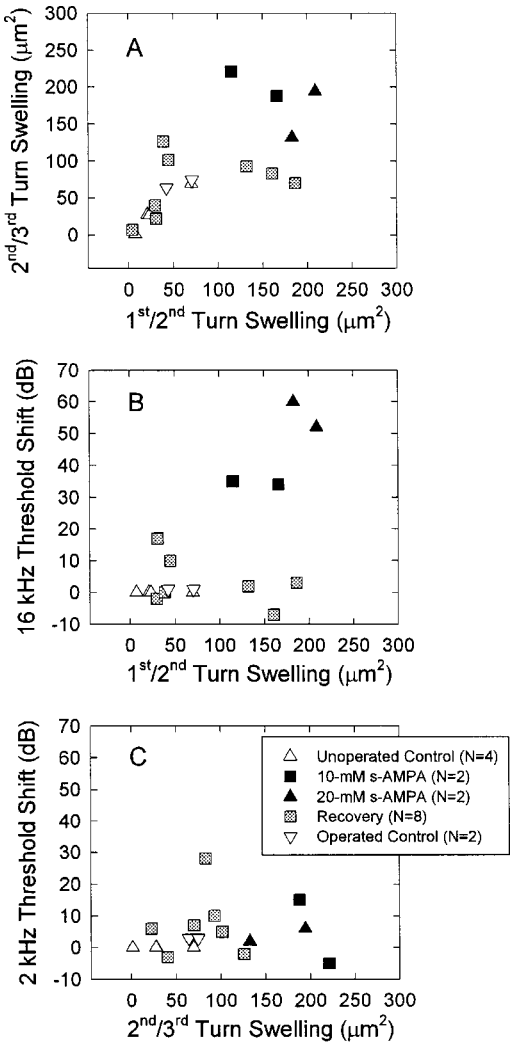

FIG. 5. (A). Neural swelling in the upper-first/lower-second turn of the cochlea was generally equivalent to swelling in the upper-second/lower-third turn of the cochlea. Figure (B). Animals euthanized while AMPA-induced 16 kHz threshold deficits were present had obvious neural swelling while control animals with normal thresholds did not. Tissues from the animals allowed a post-AMPA recovery period had variable swellings. Figure (C). Tissues from the upper-second/lower-third cochlear turn showed obvious neural swelling in some animals despite the lack of threshold deficits at the 2 kHz test frequency.

swelling in the first to second turn; Fig. 5(C): 2 kHz threshold shift versus neural swelling in the second to third turn). All animals with 16 kHz threshold deficits at the time of euthanasia had obvious neural swelling, but not all animals with neural swelling had threshold deficits. In contrast to the large AMPA-induced threshold deficits at 16 kHz, AMPA treatment did not reliably elevate 2 kHz thresholds (i.e., Fig. 2). Thus, there was no relationship between neural swelling in the upper-second/lower-third turn and 2 kHz threshold deficits.

D. AMPA does not affect distortion product otoacoustic emissions

There were no AMPA-induced changes in DPOAE threshold or amplitude at any test frequency (relative to perilymph baselines, see Fig. 6). As in Luebke *et al.* (2001), DPOAE threshold and amplitude were equivalent in unoperated ears and perilymph-infused ears (not depicted). In contrast, neomycin-treatment elevated DPOAE threshold and depressed DPOAE amplitude. In fact, DPOAE data from the neomycin-treated ears were equivalent to DPOAE data from ears assessed at 30-minute post-mortem time points. The DPOAE amplitudes assessed in neomycin-treated and post-mortem (''dead'') ears are consistent with the data of Frolenkov *et al.* (1998), who report DPOAE amplitudes that are approximately 25 dB above the noise floor, at least at higher sound pressure levels, in guinea pigs 75 min after lethal anoxia. Similar data are available from mutant (hyt/hyt) mice with OHC abnormalities (Li *et al.* 1999) and rats treated with kanamycin (Mills *et al.*, 1999).

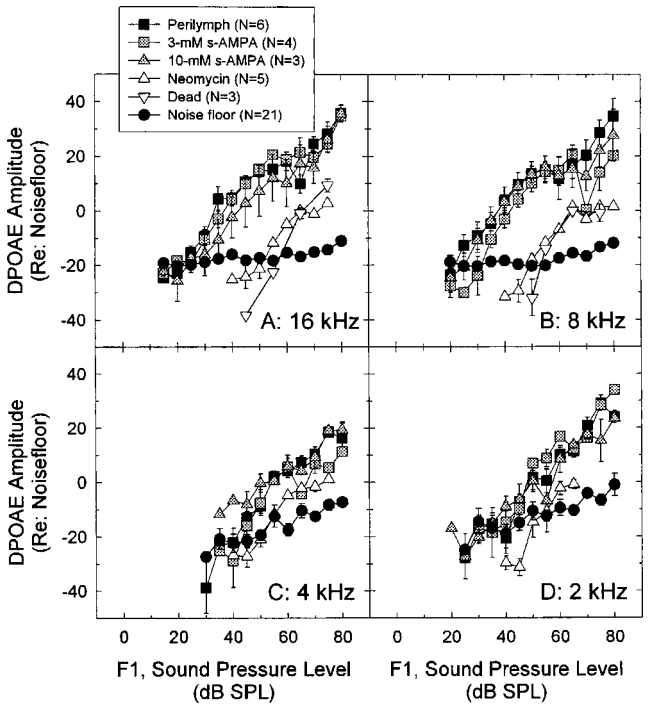

FIG. 6. The amplitude and threshold of distortion product otoacoustic emissions (DPOAEs) were not affected by AMPA infusion. In contrast, DPOAE threshold was elevated and DPOAE amplitude was depressed in neomycin-treated ears (''Neomcyin'') and ears in which DPOAEs were assessed 30 min post-mortem. Noise floor amplitude was measured in every test session and averaged across all sessions (i.e., perilymph, 3 mM s-AMPA, 10 mM s-AMPA, Neomycin, and Dead). Post-mortem testing was conducted only at the two higher test frequencies [Fig. (A), 16 kHz; Fig. (B), 8 kHz]. The total number of sessions contributing to the noise floor average is therefore N=18 for the 4 kHz [Fig. (C)] and 2 kHz [Fig. (D)] test frequencies.

IV. DISCUSSION

Chronic AMPA-induced deficits were evident in both electrophysiological and behavioral measures of function, indicating that temporal integration of long-duration signals was disrupted to a similar extent as were synchronous evoked potentials in response to short tone pips. In addition, functional deficits were found to be reversible even after long-lasting (14 day) excitotoxic insult, suggesting no long term consequences of chronic excitotoxicity of auditory neurons. Deficits in electrophysiological and operant measures of function were not accompanied by changes in DPOAE threshold or amplitude, suggesting that the temporary functional deficits were not a consequence of deficits in outer hair cell function.

A. AMPA disrupts temporal integration

The first animals tested behaviorally (chinchillas, see Garbe *et al.*, 1997) demonstrated little AMPA-induced elevation of behaviorally assessed thresholds. We speculated that AMPA-treated animals reliably integrated asynchronous auditory brainstem activity, and predicted that AMPA-treated animals would have normal operant thresholds in this investigation as stimuli used in behavioral test sessions are longer-duration signals (up to 2.5 s) for which temporal integration is possible (e.g., Green *et al.*, 1957; Watson and Gengel, 1969; Gerken *et al.*, 1990). Because behaviorally assessed deficits were equivalent to ABR-assessed deficits in the larger sample of guinea pigs described here, we conclude these animals could not reliably integrate asynchronous neural activity as a perceptual cue. The finding that behavioral measures of function were generally disrupted to the same extent as the electrophysiological measures is thus consistent with gross deficits in temporal processing during AMPA infusion.

B. Receptor homeostasis does not maintain normal function during chronic drug delivery

Because synaptic modification of receptor properties, distribution, and/or composition of receptor subunits can compensate for chronic increases or decreases in excitatory input and thus maintain homeostatic plasticity (see Turrigiano, 1999), we initially suggested the possibility that chronic AMPA administration would not depress cochlear function throughout the duration of AMPA delivery. Indeed, chronic AMPA-induced activity in spinal cord neurons decreases AMPA receptor numbers and thus maintains excitatory output at a constant level (O'Brien *et al.*, 1998; see also Turrigiano and Nelson, 1998; Turrigiano, 1999). While we cannot exclude subtle changes in AMPA receptor organization during the course of treatment, any homeostatic changes in receptor composition in the cochlea were not sufficient for restoring normal auditory function during the course of AMPA infusion.

C. Chronic AMPA does not induce permanent deficits

Recovery of threshold sensitivity was clearly observed after treatment with 3 mM AMPA, although we noted that functional recovery was incomplete in two of the three animals evaluated after 10 mM AMPA. Observations from a single animal allowed to recover following infusion of a higher concentration (20 mM) revealed no residual threshold deficits at day 6 post-AMPA. In addition, functional recovery typically occurred at a rate corresponding to that described after acute excitotoxic trauma (i.e., Puel *et al.*, 1995; Zheng *et al.*, 1998). Taken together, the data do not support the suggestion of Pujol (1990) that chronic glutamatergic excitotoxicity ultimately results in loss of radial afferent fibers and type I ganglion cells (Pujol *et al.*, 1990). These data contrast with reports of permanent damage to the adult rabbit optic nerve after chronic KA exposure, in the absence of long-term morphological deficits after brief KA exposure (Matute, 1998).

D. AMPA concentration and cochlear distribution

The AMPA concentrations chronically infused into the cochlea in this investigation were much greater than those in acute perfusion experiments conducted by others. Nonetheless, it seems unlikely that chronic infusion of AMPA at a very slow rate resulted in a high concentration of intracochlear AMPA. Longitudinal drug distribution is presumably quite rapid during perfusion between a drug delivery port and a drainage/pressure relief port (such as in the experiments conducted by Puel *et al.*, 1991; 1994). In contrast, during our very slow chronic infusion, there is probably very little increase in fluid pressure, and thus, drug diffusion depends on the slow cochlear fluid gradient (approximately 1.6 nl/min, see Ohyama *et al.*, 1988). Results from the work of Salt and Ma (2001) are consistent with the suggestion that diffusion of drugs in the cochlea depends on the slow cochlear fluid gradient.

We used the Washington University Cochlear Fluids Simulator (version 1.5, a public domain program available on the internet at http://oto.wustl.edu/cochlea/) to model diffusion of drugs delivered directly into the cochlear perilymph. Drugs reached the apex within the 120 min. maximum duration of the modeling program. However, apical concentrations remained low. The observation that AMPA-induced functional changes at low frequencies (i.e., 2 and 4 kHz) were more limited than effects at higher frequencies is thus consistent with the results of the modeling program. Experimental evidence consistent with this diffusion model comes from Lalwani *et al.* (1996), who delivered adeno-associated virus containing bacterial β-galactosidase using pumps that dispensed solutions at a rate of 0.5 μl/hr (8.3-day infusion duration). Cochlear staining, while evident throughout the entire cochlea, was strongest in the basal turn.

In addition to the limits imposed by a slow distribution gradient, long-term build-up of drugs delivered into scala tympani is limited by perilymph turnover. However, it seems unlikely that additional constraints are imposed by biological metabolism of the infused AMPA. AMPA does not undergo decarboxylation in mouse brain homogenates (Nielsen *et al.*, 1985) and is not thought to be taken up by glutamate transporters in the central nervous system (e.g., Minami *et al.*, 2001). Taken together, it seems unlikely that chronic infusion of AMPA at a very slow rate resulted in a high concentration of intra-cochlear AMPA, particularly within the apical turn of the cochlea. Thus, the more limited effects of AMPA on cochlear responses to low-frequency acoustic stimuli probably reflect uneven distribution of AMPA within the cochlea rather than a place-based difference in the sensitivity of neurons to AMPA-induced trauma. Unpublished observations from a single cochlear perfusion experiment in which threshold changes were examined across a broad range of frequencies are consistent with this interpretation (J.-L. Puel, personal communication).

E. Neural swelling: A cause of temporary threshold shifts?

Neural swelling induced by glutamate and its analogues (i.e., AMPA, KA) is an excitotoxic trauma. Observation of

neural swelling after exposure to loud sounds has led to the proposal that loud sounds induce release of excess glutamate which leads to neural swelling (Robertson, 1983). Temporary threshold shifts (TTS) have often been attributed to, or, at least, accompanied by, neural swelling (Spoendlin, 1971; Liberman and Mulroy, 1982; Robertson, 1983; Altschuler *et al.*, 1992; Puel *et al.*, 1998). However, a convincing argument that sound-induced neural swelling does not by itself account for TTS deficits was recently provided by Wang *et al.* (2002). Indeed, because acoustic overstimulation results in a number of morphological deficits, it has, to date, been difficult to determine the extent to which functional deficits depend on specific morphological changes. In the current investigation, although animals with large threshold shifts had obvious neural swelling, there were a number of animals that recovered normal threshold sensitivity despite significant morphological trauma (i.e., swelling). While considering the possibility that fixation and subsequent tissue processing may have contributed to artifactual neural swelling in some recovery animals, we note that this possibility seems unlikely given the minimal swelling in control tissues, and the concentration-dependent increase in swelling in animals euthanized during AMPA infusion. Taken together, these data support the argument of Wang *et al.* (2002) that there is not a simple relationship between neural swelling and TTS. Taken together, a causative relationship between neural swelling and temporary threshold deficits cannot be presumed at this time.

F. Auditory neuropathy: An animal model?

Auditory neuropathy is defined as disrupted ABR in the presence of intact DPOAEs. Chinchillas treated with carboplatin show deficits in CAP amplitude (Salvi *et al.*, 1999) and ABR thresholds are elevated (Harrison, 1998), but otoacoustic emissions are normal (Harrison, 1998; Salvi *et al.*, 1999), suggesting a carboplatin-induced model of auditory neuropathy. Treatment with AMPA similarly appears to induce a neuropathy-like condition. Application of KA depresses CAP (Zheng *et al.*, 1996; Zheng *et al.*, 1998) and auditory evoked potentials (measured in the inferior colliculus, Zheng *et al.*, 1997; Zheng *et al.*, 1998) in the absence of changes to DPOAEs (Zheng *et al.*, 1996; Zheng *et al.*, 1997; Zheng *et al.*, 1998). While Zheng *et al.*, (1996; 1997; 1998) did not explicitly argue this was an auditory neuropathy, KA clearly produces a neuropathy-like condition similar to that induced by AMPA in the current data set.

V. CONCLUSIONS

Chronic infusion of the glutamate agonist AMPA into the cochlea elevated behavioral detection thresholds as well as ABR thresholds, at least for the higher test frequencies. In addition, the amplitude of ABR Wave III was depressed across frequencies during AMPA infusion. Functional deficits at 16 kHz were accompanied by significant neural swelling in the base of the cochlea in animals euthanized during AMPA treatment. However, the relationship between neural swelling and threshold deficits remains unclear as animals with complete functional recovery often had significant neural swelling. Recovery of each of the functional measures, to pre-AMPA baselines, was observed in virtually all animals. In contrast to the AMPA-induced deficits in neural condition, ABR threshold and amplitude, and perceptual response measures, outer hair cell function (assessed via DPOAE integrity) was intact during AMPA treatment. The combination of impaired evoked potentials with intact DPOAEs suggests a reversible auditory-neuropathy-like condition.

ACKNOWLEDGMENTS

This research was supported by grants from the National Institutes of Health-National Institute of Deafness and Other Communication Disorders [NIH-NIDCD: P01-DC00078 (DBM, DFD, SCB, YR), R01-DC04194 (DFD), F32-DC00367 (CGL)]. The cochlear perfusion experiment (see discussion) was conducted at the Laboratoire de neurobiology de l'audition, plasticité synaptique, Université de Montpellier-I, France, under the supervision of J.-L. Puel and with the assistance of M. Guitton, R. Lloyd, R. Nouvian, and J. Wang. We thank R. P. Bobbin for comments on an earlier version of this article. In addition, we thank K. Abrashkin, J. Beals, D. Colesa, R. Diener, C. Ellinger, K. Hälsey, E. Labut, J. McLaren, D. Payer, L. Pierchala, D. Prieskorn, S. Shubert, and C. Thompson, who provided technical assistance.

Altschuler, R. A., Raphael, Y., Prosen, C. A., Dolan, D. F., and Moody, D. B. (**1992**). ''Acoustic stimulation and overstimulation in the cochlea: A comparison between basal and apical turns of the cochlea,'' in *Noise-Induced Hearing Loss*, edited by A. L. Dancer, D. Henderson, R. J. Salvi, and R. P. Hamernik (Mosby Year Book, St. Louis), pp. 60–72.

Billett, T. E., Thorne, P. R., and Gavin, J. B. (**1989**). ''The nature and progression of injury in the organ of Corti during ischemia,'' Hear. Res. **41**, 189–197.

Bledsoe, Jr., S. C., Bobbin, R. P., and Chihal, D. M. (**1981**). ''Kainic acid: an evaluation of its action on cochlear potentials,'' Hear. Res. **4**, 109–120.

Borg, E., and Engstrom, B. (**1983**). ''Hearing thresholds in the rabbit. A behavioral and electrophysiological study,'' Acta Otorhinolaryngol. (Stockh) **95**, 19–26.

Brown, J. N., Miller, J. M., Altschuler, R. A., and Nuttall, A. L. (**1993**). ''Osmotic pump implant for chronic infusion of drugs into the inner ear,'' Hear. Res. **70**, 167–172.

Canlon, B., and Fransson, A. (**1995**). ''Morphological and functional preservation of the outer hair cells from noise trauma by sound conditioning,'' Hear. Res. **84**, 112–124.

Duan, M. L., and Canlon, B. (**2001**). ''Short-term adaptation in the peripheral auditory system is related to the AMPA receptor,'' Acta Otorhinolaryngol. (Stockh) **121**, 21–27.

Eybalin, M. (**1993**). ''Neurotransmitters and neuromodulators of the mammalian cochlea,'' Physiol. Rev. **73**, 309–373.

Frolenkov, G. I., Belyantseva, I. A., Kurc, M., Mastroianni, M. A., and Kachar, B. (**1998**). ''Cochlear outer hair cell electromotility can provide force for both low and high intensity distortion product otoacoustic emissions,'' Hear. Res. **126**, 67–74.

Garbe, C. M., Prieskorn, D. M., Bledsoe, S. C., Jr., and Moody, D. B. (**1997**). ''Behavioral and electrophysiological assessment of changes in hearing following chronic AMPA-induced excitotoxicity,'' in *20th Midwinter Meeting of the Association for Research in Otolaryngology*, edited by G. R. Popelka (Association for Research in Otolaryngology, St. Petersburg Beach, FL), p. 109.

Gerken, G. M., Bhat, V. K., and Hutchison-Clutter, M. (**1990**). ''Auditory temporal integration and the power function model,'' J. Acoust. Soc. Am. **88**, 767–778.

Gil-Loyzaga, P., Hernandez-Ortiz, M. J., Rodriguez-Benito, T., and Lasso de la Vega, M. L. (**1993**). ''Diltiazem protects against neurotoxicity induced by excitotoxic amino acids on cochlear afferent fibers,'' ORL. J. Otorhinolaryngol. Relat. Spec. **55**(4), 211–215.

Gil-Loyzaga, P., and Pujol, R. (**1990**). ''Neurotoxicity of kainic acid in the rat cochlea during early developmental stages,'' Eur. Arch. Otorhinolaryngol. **248**, 40–48.
Gorga, M. P., Beauchaine, K. A., Reiland, J. K., Worthington, D. W., and Javel, E. (**1984**). ''The effects of stimulus duration on ABR and behavioral thresholds,'' J. Acoust. Soc. Am. **76**, 616–619.
Green, D. M., Birdsall, T. G., and Tanner, W. P. J. (**1957**). ''Signal detection as a function of signal intensity and duration,'' J. Acoust. Soc. Am. **29**, 523–531.
Greenwood, D. D. (**1961**). ''Critical bandwidth and the frequency coordinates of the basilar membrane,'' J. Acoust. Soc. Am. **33**, 1344–1356.
Greenwood, D. D. (**1990**). ''A cochlear frequency-position function for several species—29 years later,'' J. Acoust. Soc. Am. **87**, 2592–2605.
Harrison, R. V. (**1998**). ''An animal model of auditory neuropathy,'' Ear Hear. **19**, 355–361.
Jakobsen, B., and Zimmer, J. (**2001**). ''Chronic exposure of kainate and NBQX changes AMPA toxicity in hippocampal slice cultures,'' NeuroReport **12**, 3593–3597.
Janssen, R., Schweitzer, L., and Jensen, K. F. (**1991**). ''Glutamate neurotoxicity in the developing rat cochlea: physiological and morphological approaches,'' Brain Res. **552**, 255–264.
Jenison, G. L., and Bobbin, R. P. (**1985**). ''Quisqualate excites spiral ganglion neurons of the guinea pig,'' Hear. Res. **20**, 261–265.
Jenison, G. L., Winbery, S., and Bobbin, R. P. (**1986**). ''Comparative actions of quisqualate and N-methyl-D-aspartate, excitatory amino acid agonists, on guinea-pig cochlear potentials,'' Comp. Biochem. Physiol. C **84**, 385–389.
Juiz, J. M., Rueda, J., Merchan, J. A., and Sala, M. L. (**1989**). ''The effects of kainic acid on the cochlear ganglion of the rat,'' Hear. Res. **40**, 65–74.
Kraus, N., Bradlow, A. R., Cheatham, M. A., Cunningham, J., King, C. D., Koch, D. B., Nicol, T. G., McGee, T. J., Stein, L. K., and Wright, B. A. (**2000**). ''Consequences of neural asynchrony: a case of auditory neuropathy,'' J. Assoc. Res. Otolaryngol. **1**, 33–45.
Lalwani, A. K., Walsh, B. J., Reilly, P. G., Muzyczka, N., and Mhatre, A. N. (**1996**). ''Development of in vivo gene therapy for hearing disorders: introduction of adeno-associated virus into the cochlea of the guinea pig,'' Gene Ther. **3**, 588–592.
Le Prell, C. G., Bledsoe, S. C., Jr., Bobbin, R. P., and Puel, J. L. (**2001**). ''Neurotransmission in the inner ear: Functional and molecular analyses,'' in *Physiology of the Ear*, edited by J. Santos-Sacchi (Singular Publishing, New York), pp. 575–611.
Le Prell, C. G., Bledsoe, S. C., Jr., and Moody, D. B. (**1999a**). ''Deficits in tone-evoked operant and electrophysiological responses during chronic AMPA-induced excitotoxicity,'' in *22nd Midwinter Meeting of the Association for Research in Otolaryngology*, edited by G. R. Popelka (Association for Research in Otolaryngology, St. Petersburg Beach, FL), p. 164.
Le Prell, C. G., Yagi, M., Beyer, L. A., Bledsoe, S. C., Jr., Raphael, Y., and Moody, D. B. (**1999b**). ''Morphological trauma accompanying ABR-assessed deficits in hearing following chronic AMPA-induced excitotoxicity,'' in *22nd Midwinter Meeting of the Association for Research in Otolaryngology*, edited by G. R. Popelka (Association for Research in Otolaryngology, St. Petersburg Beach, FL), p. 164.
Li, D., Henley, C. M., and O'Malley, Jr., B. W. (**1999**). ''Distortion product otoacoustic emissions and outer hair cell defects in the hyt/hyt mutant mouse,'' Hear. Res. **138**, 65–72.
Liberman, M. C., and Mulroy, M. J. (**1982**). ''Acute and chronic effects of acoustic trauma: Cochlear pathology and auditory nerve pathophysiology,'' in *New Perspectives on Noise-Induced Hearing Loss*, edited by R. P. Hamernik, D. Henderson, and R. J. Salvi (Raven Press, New York).
Luebke, A. E., Steiger, J. D., Hodges, B. L., and Amalfitano, A. (**2001**). ''A modified adenovirus can transfect cochlear hair cells in vivo without compromising cochlear function,'' Gene Ther. **8**, 789–794.
Matute, C. (**1998**). ''Characteristics of acute and chronic kainate excitotoxic damage to the optic nerve,'' Proc. Natl. Acad. Sci. U.S.A. **95**, 10229–10234.
McFadden, S. L., Henderson, D., and Shen, Y. H. (**1997**). ''Low-frequency 'conditioning' provides long-term protection from noise-induced threshold shifts in chinchillas,'' Hear. Res. **103**, 142–150.
Miller, C. A., Woodruff, K. E., and Pfingst, B. E. (**1995**). ''Functional responses from guinea pigs with cochlear implants. I. Electrophysiological and psychophysical measures,'' Hear. Res. **92**, 85–99.
Mills, D. M., Loos, B. M., and Henley, C. M. (**1999**). ''Increased susceptibility of male rats to kanamycin-induced cochleotoxicity,'' Hear. Res. **128**, 75–79.
Minami, T., Matsumura, S., Okuda-Ashitaka, E., Shimamoto, K., Sakimura, K., Mishina, M., Mori, H., and Ito, S. (**2001**). ''Characterization of the glutamatergic system for induction and maintenance of allodynia,'' Brain Res. **895**, 178–185.
Monaghan, D. T., Bridges, R. J., and Cotman, C. W. (**1989**). ''The excitatory amino acid receptors: their classes, pharmacology, and distinct properties in the function of the central nervous system,'' Annu. Rev. Pharmacol. Toxicol. **29**, 365–402.
Musiek, F. E. (**1982**). ''ABR in eighth-nerve and brain-stem disorders,'' Am. J. Otol. **3**, 243–248.
National Research Council (**1996**). *Guide for the Care and Use of Laboratory Animals*, National Academy Press, Washington, D.C.
Nielsen, E. O., Schousboe, A., Hansen, S. H., and Krogsgaard-Larsen, P. (**1985**). ''Excitatory amino acids: studies on the biochemical and chemical stability of ibotenic acid and related compounds,'' J. Neurochem. **45**, 725–731.
Niemiec, A. J., and Moody, D. B. (**1995**). ''Constant Stimulus and Tracking Procedures for Measuring Sensitivity,'' in *Methods in Comparative Psychoacoustics, Vol. 6*, edited by G. M. Klump, R. J. Dooling, R. R. Fay, and W. C. Stebbins (Birkhauser Verlag, Basel, Switzerland), pp. 65–77.
O'Brien, R. J., Kamboj, S., Ehlers, M. D., Rosen, K. R., Fischbach, G. D., and Huganir, R. L. (**1998**). ''Activity-dependent modulation of synaptic AMPA receptor accumulation.'' Neuron **21**, 1067–1078.
Ohyama, K., Salt, A. N., and Thalmann, R. (**1988**). ''Volume flow rate of perilymph in the guinea-pig cochlea,'' Hear. Res. **35**, 119–129.
Ozdamar, O., and Stein, L. (**1981**). ''Auditory brain stem response (ABR) in unilateral hearing loss,'' Laryngoscope **91**, 565–574.
Parks, T. N. (**2000**). ''The AMPA receptors of auditory neurons,'' Hear. Res. **147**, 77–91.
Prieskorn, D. M., and Miller, J. M. (**2000**). ''Technical report: chronic and acute intracochlear infusion in rodents,'' Hear. Res. **140**, 212–215.
Prosen, C. A., Petersen, M. R., Moody, D. B., and Stebbins, W. C. (**1978**). ''Auditory thresholds and kanamycin-induced hearing loss in the guinea pig assessed by a positive reinforcement procedure,'' J. Acoust. Soc. Am. **63**, 559–566.
Puel, J. L. (**1995**). ''Chemical synaptic transmission in the cochlea,'' Prog. Neurobiol. **47**, 449–476.
Puel, J. L., d'Aldin, C., Ruel, J., Ladrech, S., and Pujol, R. (**1997**). ''Synaptic repair mechanisms responsible for functional recovery in various cochlear pathologies,'' Acta Otorhinolaryngol. Belg. **117**, 214–218.
Puel, J. L., Pujol, R., Ladrech, S., and Eybalin, M. (**1991**). ''Alpha-amino-3-hydroxy-5-methyl-4-isoxazole propionic acid electrophysiological and neurotoxic effects in the guinea-pig cochlea,'' Neuroscience **45**, 63–72.
Puel, J. L., Pujol, R., Tribillac, F., Ladrech, S., and Eybalin, M. (**1994**). ''Excitatory amino acid antagonists protect cochlear auditory neurons from excitotoxicity,'' J. Comp. Neurol. **341**, 241–256.
Puel, J. L., Ruel, J., Gervais d'Aldin, C., and Pujol, R. (**1998**). ''Excitotoxicity and repair of cochlear synapses after noise-trauma induced hearing loss,'' NeuroReport **9**, 2109–2114.
Puel, J. L., Saffiedine, S., Gervais d'Aldin, C., Eybalin, M., and Pujol, R. (**1995**). ''Synaptic regeneration and functional recovery after excitotoxic injury in the guinea pig cochlea,'' C. R. Acad. Sci. III **318**, 67–75.
Pujol, R., Lenoir, M., Robertson, D., Eybalin, M., and Johnstone, B. M. (**1985**). ''Kainic acid selectively alters auditory dendrites connected with cochlear inner hair cells,'' Hear. Res. **18**, 145–151.
Pujol, R., Rebillard, G., Puel, J. L., Lenoir, M., Eybalin, M., and Recasens, M. (**1990**). ''Glutamate neurotoxicity in the cochlea: a possible consequence of ischaemic or anoxic conditions occurring in ageing,'' Acta Otorhinolaryngol. Belg. **476**, 32–36.
Robertson, D. (**1983**). ''Functional significance of dendritic swelling after loud sounds in the guinea pig cochlea,'' Hear. Res. **9**, 263–278.
Rothman, S. (**1984**). ''Synaptic release of excitatory amino acid neurotransmitter mediates anoxic neuronal death,'' J. Neurosci. **4**, 1884–1891.
Ruel, J., Bobbin, R. P., Vidal, D., Pujol, R., and Puel, J. L. (**2000**). ''The selective AMPA receptor antagonist GYKI 53784 blocks action potential generation and excitotoxicity in the guinea pig cochlea,'' Neuropharmacology **39**, 1959–1973.
Ruel, J., Chen, C., Pujol, R., Bobbin, R. P., and Puel, J. L. (**1999**). ''AMPA-preferring glutamate receptors in cochlear physiology of adult guinea-pig,'' J. Physiol. (Paris) **518**, 667–680.
Salt, A. N., and Ma, Y. (**2001**). ''Quantification of solute entry into cochlear perilymph through the round window membrane,'' Hear. Res. **154**, 88–97.
Salvi, R. J., Wang, J., Ding, D., Stecker, N., and Arnold, S. (**1999**). ''Auditory deprivation of the central auditory system resulting from selective

inner hair cell loss: animal model of auditory neuropathy,'' Scand. Audiol. Suppl. **51**, 1–12.
Skellett, R. A., Cullen, Jr., J. K., Fallon, M., and Bobbin, R. P. (**1998**). ''Conditioning the auditory system with continuous vs. interrupted noise of equal acoustic energy: is either exposure more protective?,'' Hear. Res. **116**, 21–32.
Spoendlin, H. (**1971**). ''Primary structural changes in the organ of Corti after acoustic overstimulation,'' Acta Otorhinolaryngol. Belg. **71**, 166–176.
Starr, A., Picton, T. W., Sininger, Y., Hood, L. J., and Berlin, C. I. (**1996**). ''Auditory neuropathy,'' Brain **119**, 741–753.
Starr, A., Sininger, Y. S., and Pratt, H. (**2000**). ''The varieties of auditory neuropathy,'' J. Basic Clin. Physiol. Pharmacol. **11**, 215–230.
Sun, H., Salvi, R. J., Ding, D. L., Hashino, D. E., Shero, M., and Zheng, X. Y. (**2000**). ''Excitotoxic effect of kainic acid on chicken otoacoustic emissions and cochlear potentials,'' J. Acoust. Soc. Am. **107**, 2136–2142.
Szymanski, M. D., Bain, D. E., Kiehl, K., Pennington, S., Wong, S., and Henry, K. R. (**1999**). ''Killer whale (Orcinus orca) hearing: auditory brainstem response and behavioral audiograms,'' J. Acoust. Soc. Am. **106**, 1134–1141.
Turrigiano, G. G. (**1999**). ''Homeostatic plasticity in neuronal networks: the more things change, the more they stay the same,'' Trends Neurosci. **22**, 221–227.
Turrigiano, G. G., and Nelson, S. B. (**1998**). ''Thinking globally, acting locally: AMPA receptor turnover and synaptic strength [comment],'' Neuron **21**, 933–935.
Wang, Y., Hirose, K., and Liberman, M. C. (**2002**). ''Dynamics of noise-induced cellular injury and repair in the mouse cochlea,'' J. Assoc. Res. Otolaryngol. **3**, 248–268.
Watkins, J. C., Krogsgaard-Larsen, P., and Honore, T. (**1990**). ''Structure-activity relationships in the development of excitatory amino acid receptor agonists and competitive antagonists,'' Trends Pharmacol. Sci. **11**, 25–33.
Watson, C. S., and Gengel, R. W. (**1969**). ''Signal duration and signal frequency in relation to auditory sensitivity,'' J. Acoust. Soc. Am. **46**, 989–997.
Wolski, L. F., Anderson, R. C., Bowles, A. E., and Yochem, P. K. (**2003**). ''Measuring hearing in the harbor seal (Phoca vitulina): Comparison of behavioral and auditory brainstem response techniques,'' J. Acoust. Soc. Am. **113**, 629–637.
Worthington, D. W., and Peters, J. F. (**1980**). ''Quantifiable hearing and no ABR: paradox or error?,'' Ear Hear. **1**, 281–285.
Yoshida, N., and Liberman, M. C. (**2000**). ''Sound conditioning reduces noise-induced permanent threshold shift in mice,'' Hear. Res. **148**, 213–219.
Zheng, X. Y., Henderson, D., Hu, B. H., and McFadden, S. L. (**1997**). ''Recovery of structure and function of inner ear afferent synapses following kainic acid excitotoxicity,'' Hear. Res. **105**, 65–76.
Zheng, X. Y., McFadden, S. L., and Henderson, D. (**1998**). ''Faster recovery in central than in peripheral auditory system following a reversible cochlear deafferentation,'' Neuroscience **85**, 579–586.
Zheng, X. Y., Salvi, R. J., McFadden, S. L., Ding, D. L., and Henderson, D. (**1999**). ''Recovery of kainic acid excitotoxicity in chinchilla cochlea,'' Ann. N.Y. Acad. Sci. **884**, 255–269.
Zheng, X. Y., Wang, J., Salvi, R. J., and Henderson, D. (**1996**). ''Effects of kainic acid on the cochlear potentials and distortion product otoacoustic emissions in chinchilla,'' Hear. Res. **95**, 161–167.

The role of head-induced interaural time and level differences in the speech reception threshold for multiple interfering sound sources

John F. Culling[a)]
School of Psychology, Cardiff University, P.O. Box 901, Cardiff, CF10 3YG, United Kingdom

Monica L. Hawley[b)] and Ruth Y. Litovsky[c)]
Department of Biomedical Engineering, Boston University, 44 Cummington Street, Boston. Massachusetts 02215

(Received 11 July 2003; revised 13 May 2004; accepted 18 May 2004)

Three experiments investigated the roles of interaural time differences (ITDs) and level differences (ILDs) in spatial unmasking in multi-source environments. In experiment 1, speech reception thresholds (SRTs) were measured in virtual-acoustic simulations of an anechoic environment with three interfering sound sources of either speech or noise. The target source lay directly ahead, while three interfering sources were (1) all at the target's location (0°,0°,0°), (2) at locations distributed across both hemifields (−30°,60°,90°), (3) at locations in the same hemifield (30°,60°,90°), or (4) co-located in one hemifield (90°,90°,90°). Sounds were convolved with head-related impulse responses (HRIRs) that were manipulated to remove individual binaural cues. Three conditions used HRIRs with (1) both ILDs and ITDs, (2) only ILDs, and (3) only ITDs. The ITD-only condition produced the same pattern of results across spatial configurations as the combined cues, but with smaller differences between spatial configurations. The ILD-only condition yielded similar SRTs for the (−30°,60°,90°) and (0°,0°,0°) configurations, as expected for best-ear listening. In experiment 2, pure-tone BMLDs were measured at third-octave frequencies against the ITD-only, speech-shaped noise interferers of experiment 1. These BMLDs were 4–8 dB at low frequencies for all spatial configurations. In experiment 3, SRTs were measured for speech in diotic, speech-shaped noise. Noises were filtered to reduce the spectrum level at each frequency according to the BMLDs measured in experiment 2. SRTs were as low or lower than those of the corresponding ITD-only conditions from experiment 1. Thus, an explanation of speech understanding in complex listening environments based on the combination of best-ear listening and binaural unmasking (without involving sound-localization) cannot be excluded.
[DOI: 10.1121/1.1772396]

PACS numbers: 43.66.Ba, 43.66.Dc, 43.66.Pn [PFA] Pages: 1057–1065

I. INTRODUCTION

Listeners are often exposed to simultaneous sounds from many sources. The problem of extracting a single target voice from a competing milieu, so that it can be individually understood, has been termed ''the cocktail-party problem'' (Cherry, 1953). Most research on the cocktail-party problem has concentrated on listeners' ability to understand one voice in the presence of one other, or against an undifferentiated babble. In a recent study, Hawley *et al.* (2004) investigated listeners' ability to understand speech in a complex listening environment. They measured speech reception thresholds (SRTs) for up to three interfering sounds of different types and in different binaural configurations. Many, but not all,[1] aspects of their results were consistent with a model of binaural processing in complex listening environments that includes separate mechanisms to exploit interaural time delays (ITDs) and interaural level differences (ILDs). In such a model, the ITDs are exploited via the mechanism of binaural unmasking, while ILDs are exploited purely by best-ear listening. Hawley *et al.* measured monaural thresholds as a means of assessing best-ear listening, and subtracted these from the thresholds for binaural listening to derive a binaural interaction effect. The present study addresses two aspects of Hawley *et al.*'s results for which the individual roles of ILDs and ITDs were not completely clear.

First, Hawley *et al.* included two spatial configurations, (30°,60°,90°) and (90°,90°,90°), in which three interfering sound sources occupied the same hemifield. In one case, they occupied different locations in that hemifield (30°,60°,90°), while in the other, they occupied the same location (90°,90°,90°). No difference was observed between these configurations. This aspect of the data could be interpreted as contrary to expectation based on equalization-cancellation (E-C) theory (Durlach, 1963, 1972), undermining the notion that binaural unmasking effects are sufficient to explain the data. E-C theory suggests that a binaural processor first attempts to equalize (through various transformations) the sound input at the two ears and then subtracts one ear's input

[a)]Electronic mail: cullingj@cf.ac.uk
[b)]Current address: Department of Otolaryngology, University of Maryland Medical School, 16 S. Eutaw St., Suite 500, Baltimore, MD 21201.
[c)]Current address: University of Wisconsin Waisman Center, 1500 Highland Avenue, Madison, WI 53705.

from the other. This binaural processing only improves performance when the interfering source is more intense than the target; if the target is more intense, it is processed monaurally. When the interfering source has a different ITD from the target, the optimal equalization will compensate for the interferer's ITD (since it is more intense) and the cancellation stage will, in consequence, preferentially cancel the interferer. For three interfering sources in different locations, the three interferers will have different ITDs. Since the equalization stage can only equalize a single ITD,[2] one might expect the E-C mechanism to be rather ineffective compared to the case where the interferers share the same location and ITD. Although the data appear not to fit this expectation, Hawley *et al.*'s experiment used a combination of ILDs and ITDs. In both the (30°,60°,90°) and (90°,90°,90°) configurations, there was an advantageous signal-to-noise ratio at one ear produced by the ILDs and the resulting effects of ''best-ear'' listening may have obscured a difference between these configurations.

Second, Hawley *et al.* measured higher SRTs in the (−30°,60°,90°) configuration, in which interferers were present in both hemifields, than in the (30°,60°,90°) configuration, in which all sound sources were in the same hemifield. They interpreted this result as coming from a loss of best-ear listening in the (−30°,60°,90°) configuration, but the difference might in some way have been related to the differences in ITDs between these configurations.

Experiment 1 in the present series of experiments therefore set out to clarify the contributions of these cues using head-related impulse responses (HRIRs) that were manipulated to exclude one or other binaural cue. Experiments 2 and 3 were conducted in order to further clarify the interpretation, by analyzing the role of ITDs in each frequency band.

II. EXPERIMENT 1

A. Stimuli

The stimuli were similar to those of Hawley *et al.* except that the head-related impulse responses (HRIRs) were manipulated in the frequency domain to remove ITDs or ILDs, and only speech and speech-shaped-noise interferers were used. The target sentences were spoken by two male voices (''DA'' and ''CW'') from the MIT recordings of the Harvard Sentence lists (Rothauser *et al.*, 1969). The Harvard sentence lists are grammatically and semantically correct sentences with otherwise relatively low predictability; an example used in the present study (with keywords in capitals) was ''The SMALL PUP GNAWED a HOLE in the SOCK.'' These sentences were presented against either (1) a compound of three other sentences from the database and spoken by the same voice, but selected for greater length, or (2) a compound of three speech-shaped noises, each with the same mean long-term spectrum as the target voice.

In order to place the sounds in different virtual locations, they were convolved with anechoic HRIRs from the HMS III acoustic manikin, as published in the AUDIS catalog (Blauert *et al.*, 1998). The HRIRs were transformed into the frequency domain and processed in two different ways. First, in order to create HRIRs with no ITDs, the phase spectra of a HRIR pair were each replaced with identical phase spectra that linearly increased in phase with frequency (i.e., so that they had a zero ITD). HRIRs were then recreated by inverse Fourier transform. Second, in order to create HRIRs with no ILDs, the amplitude spectra of a HRIR pair were replaced with identical flat spectra. In conducting the latter alteration the scaling of the impulse responses was changed. These scale factors were therefore calculated and compensated for during the convolution process in order to reproduce the original rms.

Speech and speech-shaped-noise interferers were each convolved with the original HRIR and also with each of the manipulated HRIRs in order to produce stereo stimuli with both ILDs and ITDs, ILDs only, or ITDs only. These stimuli were then mixed to give interferers whose component sounds were distributed in virtual space[3] using the desired cues. The locations in virtual space were, as in Hawley *et al.*'s three-interferer conditions, all in front (0°,0°,0°), distributed in both hemifields (−30°,60°,90°), distributed in one hemifield (30°,60°,90°), or concentrated on one lateral location (90°,90°,90°).

With 3 sets of binaural cues ×4 spatial configurations there were 12 different interferer conditions. For the speech-interferer conditions, four versions of each interferer condition were created, two for each voice (''DA'' and ''CW'') using different sentence sets. There were, therefore, 2 voices ×2 sentence sets ×12 interferer conditions =48 interfering speech stimuli. An additional four interfering speech stimuli, one in each spatial configuration, were created for use in practice runs using both ILDs ands ITDs and voice ''DA.'' For the speech-shaped-noise conditions, there were 2 voice-spectra ×12 interferer conditions =24 interfering noise stimuli. In this case, the interferers with both ILDs and ITDs were also used in the practice.

The target sentences were also convolved with manipulated HRIRs, so that they possessed the same type or combination of binaural cues as the interferers against which they were to be presented (ITD, ILD or ITD+ILD). However, the targets were always convolved with HRIRs for directly in front (0°), so the binaural cues would be minimal. Ten target sentences were required for each SRT measurement. The target stimuli were created from 120 sources sentences in order to cover the 12 conditions, 60 from each voice. Once convolved with the 3 different HRIRs, there were 360. An additional 40 target stimuli were generated using voice ''DA'' for use in the practice stimuli.

B. Subjects

Thirty-six listeners with no reported hearing problems and English as a first language were recruited from among Cardiff University students in return for course credit.

C. Procedure

Each listener attended a single 2-h experimental session. For each listener, 16 SRTs were measured in all. The first 4 SRTs were a practice. The remaining 12 experimental SRTs covered each of the four spatial configurations using each of the three combinations of binaural cues. Twenty-four listen-

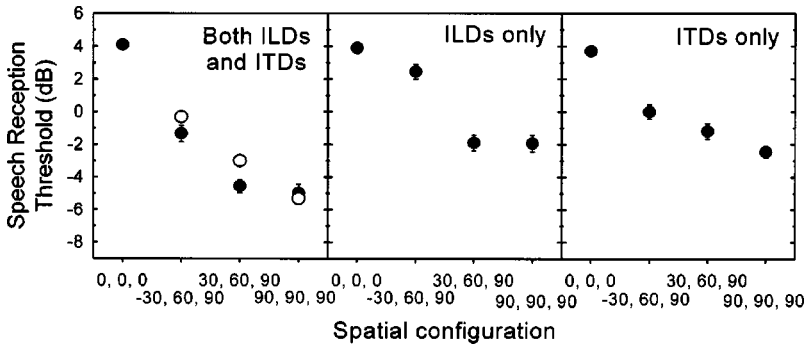

FIG. 1. Results of experiment 1 using speech interferers. Each panel shows speech reception thresholds for the four virtual listening situations for one combination of binaural cues (filled symbols). Error bars are one standard error of the mean. The leftmost panel also shows predicted thresholds based on Bronkhorst's (2000) formula (open symbols).

ers participated in the speech-interferer condition. Twelve listeners participated in the speech-shaped-noise condition.

For the speech interferer conditions, the interfering voice was the same as the target voice. Whether the interferer was the same voice, or a speech-shaped noise derived from that voice, each participant received 6 of the 12 conditions with a given target/interfering voice and 6 with the other. Each participant was paired with another who received the reciprocal allocation of voices to conditions, and experimental materials were rotated such that a given set of target sentences was heard by each listener in a different binaural condition.

Sounds were attenuated and mixed using a Tucker-Davis Technologies AP2 array processor and then presented to listeners via TDT System II hardware (DD1, FT6, PA4, HB6) and Sennheiser HD414 headphones in a single-walled IAC sound-attenuating chamber located in a sound-treated room. The listener made responses via a computer terminal, whose keyboard was placed within the booth and whose screen was visible through the booth window.

SRTs were measured using the method originally described by Culling and Colburn (2000) and based upon that of Plomp (1986). The listeners were instructed that the target sentence would initially be quieter than the interferers and that it would be heard from in front. The same interfering complex of three sounds was presented throughout a given SRT measurement at approximately 53 dB(A). In each run, the listener was informed using the computer terminal's screen of the transcripts of the interfering sentences. Initially, the first target sentence was presented against this interferer, both sentences beginning simultaneously, at a very adverse SNR, and the listener pressed the ''return'' key on the keyboard. The stimulus was repeated, each time at a 4-dB more favorable SNR until the listener judged that half the words of the targets sentence were audible. The listener then entered a transcript. When the listener's transcript was complete, the actual transcript was also displayed on the screen with five keywords in capitals. The listener self-marked his or her transcript and progressed to the next target sentence. The remaining nine sentences were presented at different SNRs according to a 1-up/1-down adaptive threshold algorithm, which increased SNR by 2 dB if fewer then three keywords were correctly transcribed and otherwise decreased SNR by 2 dB. The last eight SNRs derived in this way were averaged to yield a threshold value. The entire transaction was logged and displayed on the experimenter's computer monitor to ensure compliance with the instructions.

D. Results

The results of experiment 1 are shown in Figs. 1 and 2. Figure 1 shows the data for speech interferers, and Fig. 2 the data for speech-shaped-noise interferers. A three-way, mixed analysis of variance was conducted with the two types of interferer (speech and speech-shaped-noise) as a between-subject factor and the three sets of binaural cues (ILD+ITD, ILD-only, and ITD-only) and the four spatial configurations, (0°,0°,0°), (−30°,60°,90°), (30°,60°,90°), and (90°,90°,90°) as within-subjects factors. The patterns of data on these two figures are similar across both the available binaural cues and the spatial configurations. SRTs were significantly lower for speech than for speech shaped noise [$F(1,34)=57$, $p<0.0001$]. As in Hawley *et al.*'s results, the effects of different spatial configurations were smaller in magnitude for speech-shaped-noise interferers than for speech interferers. This effect was reflected by a significant interaction between interferer type and spatial configuration [$F(1,102)=13.8$, $p<0.0001$].

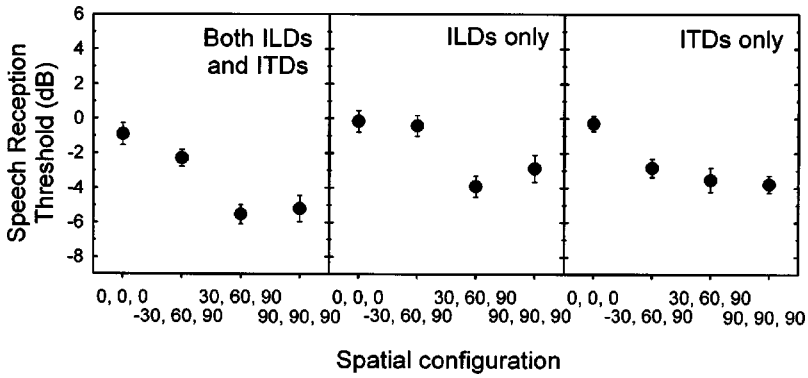

FIG. 2. As in Fig. 1, but for speech-shaped-noise interferers.

There was a significant effect of the available binaural cues [$F(1,68)=22.3$, $p<0.0001$], reflecting the fact that listeners derived more advantage from spatial separations between the target and interfering sources when both binaural cues were available than when either was available in isolation. Tukey pairwise comparisons showed that both binaural cues in combination (ILD+ITD) produced significantly lower SRTs than the ILD-only condition ($q=10.4$, $p<0.001$) and the ITD-only condition ($q=7.13$, $p<0.001$), but that the ILD-only and ITD-only conditions did not differ significantly.

There was a significant effect of spatial configuration [$F(1,102)=156$, $p<0.0001$] and the effect of the available binaural cues depended upon the spatial configuration [$F(1,6)=7.6$, $p<0.0001$]. There were significant differences between the different cue combinations in the (−30°,60°,90°), (30°,60°,90°), and (90°,90°,90°) configurations [in each case, $F(1,2)>20$, $p<0.0001$], but not in the (0°,0°,0°) configuration. The interaction was interrogated further using Tukey pairwise comparisons, which confirmed that there were no significant differences between effects of different binaural cues in the (0°,0°,0°) configuration, but showed further that the binaural advantage produced by the other spatial configurations displayed a different pattern across configuration. In the ITD+ILD and ITD-only configurations, all spatial configurations differed significantly from each other except the (30°,60°,90°) and (90°,90°,90°) configurations ($p<0.01$), whereas in the ILD-only condition the (0°,0°,0°) and (−30°,60°,90°) configurations did not differ either ($p>0.05$). In other words, in the ILD+ITD and ITD-only conditions, all forms of spatial separation between target and interferer produced a spatial advantage, but, in the ILD-only condition, this advantage did not occur when the interferers were distributed to both hemifields (−30°, 60°, 90°, configuration). The interaction between interferer type and binaural cues and the three-way interaction were both nonsignificant.

E. Discussion

1. The combination of ILDs and ITDs

The results obtained for the combination of ILDs and ITDs seem to be in agreement with previous studies. Bronkhorst (2000) derived a descriptive expression from several sets of published data (Bronkhorst and Plomp, 1992; Plomp and Mimpen, 1981; Peissig and Kollmeier, 1997), which allows us to predict binaural intelligibility level differences (BILDs) for SRTs measured against multiple speech interferers. In his expression, masking release, R, is predicted for a frontal target source for N interferers with azimuths, θ_i, as follows:

$$R=\left[\alpha\left(1-\frac{1}{N}\sum_{i=0}^{N}\cos\theta_i\right)+\beta\frac{1}{N}\left|\sum_{i=0}^{N}\sin\theta_i\right|\right]. \qquad (1)$$

The parameters α and β are constants, derived by Bronkhorst in a regression analysis. Their values (1.38 and 8.02) have not been altered to accommodate the present data set. Values of R produced by the formula were used to derive predicted differences between the measured (0°,0°,0°) data and the other three configurations. Figure 1 shows predictions based on his formula and parameters with open symbols. The fit appears to be quite good. The formula predicts that there is a substantial masking release in the (−30°,60°,90°) and (30°,60°,90°) configurations, although not quite as large as that observed in the experiment. In the equation, the cosine term evaluates the average angular disparity between the target and each of the interferers, while the sine term makes a symmetry-dependent contribution, which is lower when the arrangement is more symmetrical. It is the latter term, therefore, that introduces a difference between the predictions for (−30°,60°,90°) and (30°,60°,90°), while the former term introduces a difference between (30°,60°,90°) and (90°,90°,90°). It is also worth noting that there is nothing in this formula that would reduce predicted thresholds directly as a result of interferers having different locations and therefore different ITDs.

2. Effect of ITDs alone

Eliminating ILDs from the stimuli produced an effect of spatial configuration that was reduced in magnitude (Figs. 1 and 2, rightmost panels), but similar in form to that of the combination of ILDs and ITDs (leftmost panels). These results show that the binaural system is able to exploit ITDs not only when a single interferer is present (Bronkhorst and Plomp, 1992), but also when multiple interferers have multiple sources. At first sight, the result seems inconsistent with Durlach's (1963, 1972) E-C model, since the cancellation mechanism can only apply a single delay and cancel operation; in the current experiment one would expect this mechanism to eliminate only one of the three spatially distributed interferers and produce a rather small binaural advantage. In order to assess whether this interpretation is justified we evaluated this listening situation using a conceptual approach developed by Levitt and Rabiner (1967).

Levitt and Rabiner showed that it was possible to predict the effect of interaural temporal disparities in the BILD by assuming that the binaural advantage produced in each frequency band by the temporal differences is equivalent to an increase in SNR of the same magnitude. They divided the frequency spectrum into third-octave bands and used an expression for the size of the pure-tone BMLD at each center frequency to give the effective improvement in SNR for that band. They then used AI theory (Fletcher and Galt, 1950; Kryter, 1962) to predict improvement in speech recognition.

It is not straightforward to use Levitt and Rabiner's (1967) method to predict the BILD produced by ITDs for multiple interfering sources of the present experiment directly from the stimulus configuration. Experiments 2 and 3 therefore assessed empirically whether it is reasonable to suppose that the observed pattern of data can be predicted by improvements in this "effective" SNR in each frequency band. Further discussion of the effects of ITDs is deferred until after these experiments are described.

3. Effect of ILDs alone

The results of the ILDs-only condition are quite striking, in that they indicate quite clearly that listeners' use of ILDs

is overwhelmingly dominated by best-ear listening. The conclusion is mainly based upon the fact that SRTs were the same in the (−30°,60°,90°) configuration, where the interfering sources were spatially separated, as in the (0°,0°,0°) configuration, where they were coincident with the target source. This result is in marked contrast to what one would expect if listeners were using ILD as a sound-localization cue and attending to sound coming from directly in front. If that were so, one would expect that the (−30°,60°,90°) configuration would show some advantage over the (0°,0°,0°) configuration. This result is entirely consistent with best-ear listening, because in the (−30°,60°,90°) configuration interfering sources are located on both sides of the head, so that neither ear is shadowed from all the interferers by the head.

In addition, if listeners were attending to a particular location, one would also expect there to be little difference between the (−30°,60°,90°) and (30°,60°,90°) configurations, since in each case there are interfering sounds 30°, 60°, and 90° from the target source. In fact, there is a difference of about 4 dB between these configurations. Again, this result is entirely consistent with best-ear listening, because in the (30°,60°,90°) configuration, all three interfering sources are in the same hemifield leaving one ear in an acoustic shadow, while in the (−30°,60°,90°) configuration, neither ear is shadowed from all the interferers.

4. Effects of interferer type

Several recent studies have observed that spatial unmasking is greater for multiple speech interferers than for noise interferers (Peissig and Kollmeier, 1997; Noble and Perret, 2002; Hawley *et al.*, 2004). This effect was also observed for reversed-speech interferers (Hawley *et al.*, 2004). Comparing across Figs. 1 and 2, the present results replicate this effect. It is not obvious how these results can be interpreted in terms of simple binaural processing strategies. One possibility is that, for speech interferers, there is an additional effect of informational masking which makes the threshold particularly high in the (0°,0°,0°) configuration. A more detailed evaluation of the possible role of informational masking is presented in Hawley *et al.* (2004).

III. EXPERIMENT 2

Levitt and Rabiner (1967) showed that the effects of ITDs in the BILD can be predicted from pure-tone masking release data by (1) assuming that the effect of a given binaural configuration is, effectively, to reduce the spectrum level of the noise in accordance with magnitude of the pure-tone BMLD at each frequency, and (2) predicting intelligibility in the *effective* noise level using the articulation index (Kryter, 1962). In order to apply this model to the current data set, we first measured pure-tone BMLDs for the ITD-only, speech-shaped-noise maskers from experiment 1.

A. Method

Masked detection thresholds were measured for pure tones at 15 frequencies in $\frac{1}{3}$-oct intervals between 200 and 5080 Hz. The maskers were the ITD-only, speech-shaped-noise maskers employed in experiment 1. Four listeners each produced 120 thresholds (4 spatial configurations $\times$15 frequencies $\times$2 interfering voices). Recall that speech-shaped noises were modeled on two different voices. Thresholds were measured in 2I-FC, 2-down/1-up adaptive-threshold procedure with trial-by-trial feedback. The last 12 of 20 reversals contributed to each mean threshold. BMLDs for the (−30°,60°,90°), (30°,60°,90°), and (90°,90°,90°) configurations was determined by subtracting the equivalent thresholds in the (0°,0°,0°) configuration.

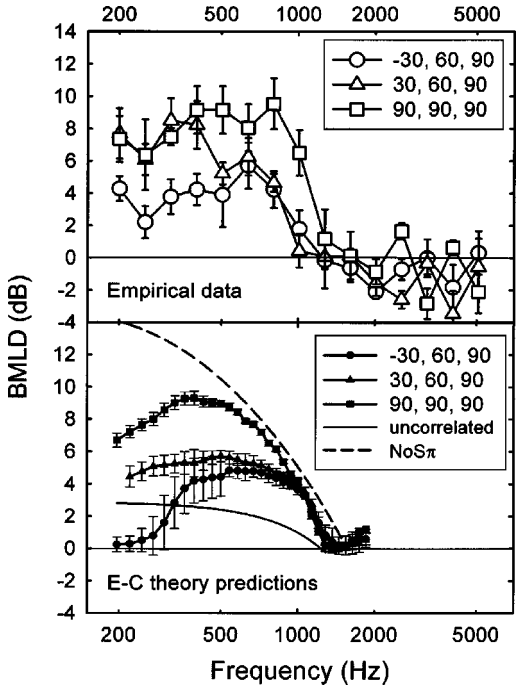

FIG. 3. Upper panel: pure-tone BMLDs for So tones measured at third-octave frequencies between 200 and 5008 Hz against three speech-shaped-noise interferer complexes with ITDs only. Error bars are one standard error of the mean. Lower panel: mean predictions for the same three conditions from E-C theory, implemented using Eq. (2) as well as for predicted thresholds in uncorrelated noise and for NoSπ. Error bars are one standard deviation.

B. Results

Eight of the 480 thresholds were rejected because they differed by more than 10 dB from the mean for frequency and spatial configuration. The remaining results, averaged across the four listeners, are plotted in the upper panel of Fig. 3. It is evident that all three spatial configurations produce a BMLD relative to the (0°,0°,0°) configuration at low frequencies; the differences in ITD between the three maskers in the (−30°,60°,90°) and (30°,60°,90°) configurations do not abolish masking release, although they do reduce it at some frequencies compared to the (90°,90°,90°) configuration. Masking release is smaller in magnitude in the (−30°,60°,90°) configuration than in the other two up to 400 Hz. From 504 Hz upwards, the release is larger in magnitude in the (90°,90°,90°) configuration than in the other two. From 1600 Hz upwards there was no masking release.

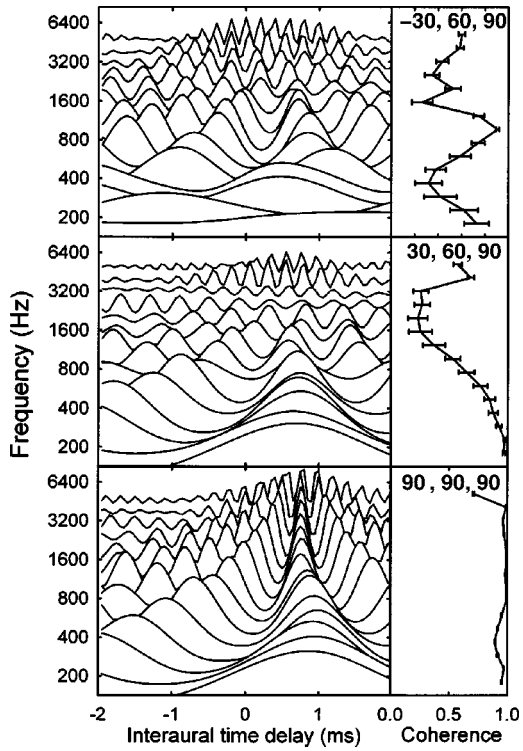

FIG. 4. The left-hand panels show a series of cross-correlations of corresponding left- and right-hand frequency channels from a gamma-tone filterbank (Patterson *et al.*, 1987, 1988) at third-octave frequencies between 200 and 5008 Hz within a 100-ms exponentially tapering temporal window. Separate panels show such cross-correlograms for the (−30°,60°,90°), (30°,60°,90°), and (90°,90°,90°) interferers (ITD-only, speech-shaped noise). The right-hand panels show the corresponding coherence (the maximum value of the cross-correlation function) averaged over a series of approximately 100-ms analysis windows. The duration and shape of these windows was measured by Culling and Summerfield (1998). Error bars are one standard deviation of this mean across the series of windows.

C. Discussion

Experiment 2 shows that the BMLD is a surprisingly robust effect in the (−30°,60°,90°) and (30°,60°,90°) configurations, where the interferers come from different directions. It is noteworthy that this was also the case in the (−30°,60°,90°), where the range of interferer ITDs encompasses that of the target. These results can be better understood with reference to the interaural statistics of the combined interference stimuli. Figure 4 shows cross-correlograms and channel-by-channel coherence measurements for the (−30°,60°,90°), (30°,60°,90°), and (90°,90°,90°) interference stimuli (ITD-only, speech-shaped noise). The cross-correlograms on the left-hand panels show the modulation of Pearson's *r* with interaural time delay at third-octave frequencies between 200 and 5000 Hz. The right-hand panels show the coherence (the maximum of the cross-correlation function) at the same frequencies. The error bars on the right-hand panels show the standard deviation of the coherence across a series of 100-ms temporal windows. The coherence values give some indication of the potential for binaural unmasking at each frequency.

The E-C model suggests that the binaural system detects a signal through the size of the residue after cancellation, but if the masker is incoherent, the masker will not cancel properly and will also be present in this residue. Detection will, therefore, be best with a coherent masker, but a second condition must also be met for binaural unmasking to be effective. In order to avoid being cancelled with the masker, the interaural phase of the signal must differ from that of the masker at the frequency in question. Durlach and Colburn (1978) pointed out that to a first approximation the pure-tone BMLD is dependent upon the phase difference between signal and masker. In principle, therefore, one can generate an approximate E-C prediction[4] for the BMLD at any frequency, ω, from the coherence, ρ, of the masker at that frequency and the phase difference $(\phi_s - \phi_m)$, between the signal and the masker at its maximum in the cross-correlation function.

Durlach (2003) has provided an expression that allows us to predict from E-C theory the binaural advantage, BMLD (in dB), from ω, c, and $(\phi_s - \phi_m)$:

$$\text{BMLD} = 10\log_{10}\left[\frac{1+\sigma_\epsilon^2-\cos(\omega(\phi_s-\phi_m))\exp(-\omega_s^2\sigma_\delta^2)}{c(1+\sigma_\epsilon^2-\exp(-\omega_s^2\sigma_\delta^2))+(1-c)(1+\sigma_\epsilon^2)}\right]. \quad (2)$$

In this formula, c is the proportion of noise that is common at both ears. It can be related to ρ using Eq. (3). σ_δ and σ_ϵ are taken from Durlach (1972) and have the fixed values of 0.000 105 and 0.25, respectively. Phase and frequency are in radians and radians/second:

$$c = \frac{\sqrt{\rho}}{\sqrt{\rho}+\sqrt{1-\rho}}. \quad (3)$$

The lower panel of Fig. 3 shows predictions that are based on these formulae combined with coherence and phase difference values measured from each type of ITD-only, speech-shaped-noise stimulus.[5] The plotted curves take account of Durlach's (1963) assumption that listeners' thresholds are never below their monaural thresholds, so where the formula returns a negative BMLD, the value has been set to zero. The predictions from E-C theory are broadly consistent with the observed thresholds in the upper panel of Fig. 3, although there is a marked deviation at low frequencies for the (−30°,60°,90°) condition. Also plotted is the theoretical prediction for uncorrelated noise, derived by setting ρ to zero and $(\phi_s - \phi_m)$ to π in Eq. (2) and for NoSπ. Comparing this curve with the others demonstrates that the (−30°,60°,90°) and (30°,60°,90°) maskers are not equivalent to uncorrelated noise from the standpoint of E-C theory. Clearly, E-C theory can predict a robust BMLD for multiple, spatially distributed interferers and more so than one might expect on the basis of being able to cancel just one of them. We set out below an explanation of how the E-C mechanism handles these multiple interfering sources.

In the (90°,90°,90°) configuration, Fig. 4 shows that the coherence is high at all frequencies. The target speech signal is not, however, out of phase with the complex of interferers at all frequencies. The phase of the target is always zero. The phase of the complex of interferers can be seen in the left panel in Fig. 4 from its cross-correlation function. At 504 Hz

the masker cross-correlation has a trough near zero ITD, indicating a phase difference of π radius between masker and signal, so a maximal masking release will occur at this frequency [i.e., the (90°,90°,90°) threshold is close to the NoSπ threshold]. However, at all other frequencies the phase difference is smaller. Whenever target and masker differ in ITD, there will always be frequencies at which the phase difference is less than π (or even zero). It is for this reason that different ITDs are never as effective in producing large BILDs as the NoSπ condition (e.g., Schubert, 1956), for which signal and masker are out of phase at all frequencies.

In the (30°,60°,90°) configuration, the coherence of the masker is lower at high frequencies than in the (90°,90°,90°) configuration, but is similar up to about 500 Hz where the pure-tone thresholds for these two configurations diverge (Fig. 3). E-C theory predicts some difference between (30°,60°,90°) and (90°,90°,90°) below 500 Hz, but not a very large one (~2 dB).

In the (−30°,60°,90°) configuration, there are few frequencies that show high coherence, reflected by the consistently small BMLD in Fig. 3. Predictions and observations show some similar features as a function of frequency. It is noteworthy, however, that both the observed and the predicted BMLDs tend to be above those predicted for uncorrelated noise.

IV. EXPERIMENT 3

Although Levitt and Rabiner (1967) used the articulation index to predict the BILD, we decided to employ an empirical approach by adopting their assumption that the effective spectrum level of the masker is reduced by its interaural configuration with respect to the signal. Culling and Summerfield (1995) postulated that, in the binaural system, each frequency band operates independently, such that the unmasking in each individual frequency band is unaffected by across-frequency differences in interaural configuration (note that peaks in cross-correlation functions in Fig. 4 do not all occur at the same delay). Here we combine these ideas to predict that the effective improvement in SNR at each frequency can be measured from pure tone BMLDs (like those from in experiment 2) without regard to the differences in equalization parameters required in different frequency channels. The size of the pure-tone BMLD predicts the effective reduction in the masker level. Therefore, an equivalent reduction in the actual level of the masker should yield the same thresholds. Experiment 3 tests this prediction.

A. Stimuli

The (0°,0°,0°) speech-shaped noise maskers were filtered in the frequency domain in order to attenuate each frequency by the magnitude of measured pure-tone BMLD at that frequency from experiment 2. BMLD was linearly interpolated between the frequencies measured in experiment 2. Attenuated stimuli of this sort were created to simulate the masking release of the (−30°,60°,90°), (30°,60°,90°), and (90°,90°,90°) configurations. SRTs were then measured in seven conditions using diotic target speech as in experiment 1. Four of these conditions were replications of the four ITD-only conditions from experiment 1. In addition, there were simulations of the (−30°,60°,90°), (30°,60°,90°), and (90°,90°,90°) configurations based on the filtered copies of the (0°,0°,0°) masker.

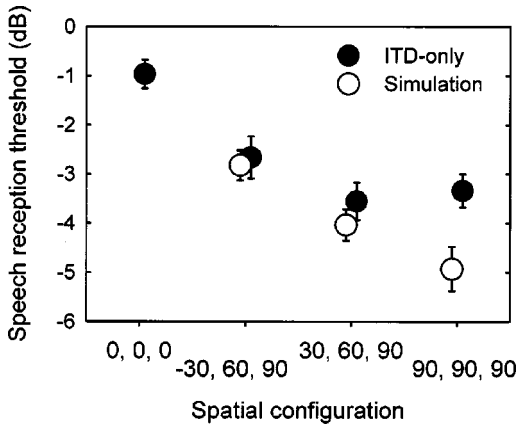

FIG. 5. Replicated SRTs for ITD-only stimuli (filled symbols) and SRTs for stimuli that simulate effects of the (−30°,60°,90°), (30°,60°,90°), and (90°,90°,90°) spatial configurations (open symbols). Simulation was achieved by filtering the (0°,0°,0°) interferers, so that each frequency is attenuated in accordance with the measured pure-tone BMLDs (see Fig. 3).

B. Procedure

Fourteen listeners each took part in a single 2-h session. During these sessions they completed a total 16 SRTs. The first two were practice runs, similar to those of experiment 1 and the following 14 were two SRTs in each of the seven conditions. As in experiment 1, the sentence materials were rotated round the different conditions from one participant to the next.

C. Results

The results are plotted in Fig. 5. Thresholds from the simulation condition were similar to, or lower than, those for the ITD-only condition. The results were analyzed using a 2×3 analysis of variance. This analysis covered the ITD-only versus simulation conditions and the three spatial configurations, (−30°,60°,90°), (30°,60°,90°), and (90°,90°,90°), that confer binaural advantage. The (0°,0°,0°) configuration could not be accommodated within this factorial analysis, since it was not replicated for the ITD-only and simulation conditions. The analysis revealed significant main effects of spatial configuration [$F(2,26)=11.9, p<0.0005$] and ITD-only versus simulation [$F(1,13)=7.8, p<0.02$]. There was also a significant interaction between the two [$F(2,26)=3.6, p<0.05$].

The interaction was interrogated using simple main effects: the simulation condition produced significantly lower thresholds than ITD-only condition in the (90°,90°,90°) configuration [$F(1)=17.7, p<0.005$], but did not differ significantly in the (−30°,60°,90°) and (30°,60°,90°) configurations.

D. Discussion

A significant difference was observed between the ITD-only and the simulation conditions only in the (90°,90°,90°) configuration. This result is therefore partially consistent

with Levitt and Rabiner's contention that the BILD results from an effective attenuation of the masker's spectrum in line with the pure-tone masking release at each frequency. If we assume that the pure-tone masking release reflects the action of an E-C mechanism, then such a mechanism can also explain the observed BILDs in the (−30°,60°,90°) and (30°,60°,90°) configurations.

The right-hand panels of Fig. 4 show a further noteworthy effect. The standard deviations of the coherence measurements are much larger in the (−30°,60°,90°) and (30°,60°,90°) configurations than in the (90°,90°,90°) configuration. In order to understand speech in noise, one would expect that the binaural system would need to extract information about the modulation of the residue from cancellation over time in each frequency channel. This modulation in this residue would mirror modulations in coherence of the signal +masker (Culling and Colburn, 2000). Figure 4 shows that in the (−30°,60°,90°) and (30°,60°,90°) configurations, where several maskers occupy different spatial positions, there is considerable modulation in coherence across time in the interferer complex itself. One might expect that this coherence-modulation noise would provide an additional source of high thresholds in the (−30°,60°,90°) and (30°,60°,90°) configurations. However, it appears on current evidence that consideration of this ''noise'' is not necessary to predict the observed performance.

The failure of experiment 3 to produce similar thresholds for the simulated effect of binaural unmasking to the ITD-only condition in the (90°,90°,90°) configuration is an outstanding puzzle. The main purpose of the experiment was to test whether the (−30°,60°,90°) and (30°,60°,90°) configurations could be simulated in this way, since it was difficult without a more detailed examination to see how an E-C mechanism would deal with these maskers. However, it is the (90°,90°,90°) configuration that was not well simulated by filtering the (0°,0°,0°) interferer. Levitt and Rabiner's assumption therefore appears to predict better performance for ITD-only stimuli than was observed. While we are not currently able to explain this result, it does, at least, help to refocus our inquiry into the lack of difference between (30°,60°,90°) and (90°,90°,90°). This lack of difference has been a consistent feature of all the experiments in this series. The current results suggest that, consistent with E-C theory, the (90°,90°,90°) configuration *should be* better than the (30°,60°,90°) configuration; the pure tone thresholds are lower and the simulation based on these thresholds did yield lower SRTs in (90°,90°,90°) than in (30°,60°,90°) (albeit nonsignificantly). It remains to find out why listeners seem to underperform (compared to the prediction) in the (90°,90°,90°) configuration.

V. CONCLUSIONS

Previous research has mostly examined the effect of one masking sound on speech intelligibility in noise. The present study and that of Hawley *et al.* (2004) have extended this research to cover the effects of multiple independent interfering sounds in common or distributed locations. The findings suggest that existing and well-documented mechanisms, best ear listening and binaural unmasking, are largely sufficient to explain performance in these circumstances. Two findings argue against a significant role for sound localization.

First, in experiment 1, SRTs in the ILD-only condition were lower only when the interfering sources were in one hemifield, allowing the contralateral ear an advantageous signal-to-noise ratio. If listeners used binaural cues to attend to the locations of target sources, one would expect improved intelligibility when the interfering sources were separate from the target source regardless of the effect at an individual ear. This result was observed for both speech and speech-shaped noise interferers.

Second, at least for the case of a speech-shaped noise, a combination of binaural unmasking and best-ear listening appear sufficient to explain listeners' performance with multiple, spatially separated interferers. Although one might expect both the BMLD and the BILD to be very poor for three spatially distributed interferers, we found that this intuition is neither predicted by conventional theories of binaural unmasking, nor observed experimentally. Experiment 1 found that, using ITDs alone, listeners were able to produce a spatial unmasking effect for spatially distributed interferers of both the speech and speech-shaped-noise types. Experiment 2 showed that the BMLD is quite robust to spatial distribution of speech-shaped noise interferers and E-C theory predicted the BMLD for these interferer complexes with reasonable accuracy. Experiment 3 showed that the BILD in the ITD-only condition was equal to or less than the effect of reducing the spectrum noise level at each frequency in accord with the size of the pure-tone BMLD at that frequency. Given that the pure-tone BMLDs were broadly predictable from E-C theory, such a mechanism (operating independently in each frequency channel) appears sufficient to explain the intelligibility data for these configurations.

Thus, simple binaural processing strategies, such as channel-independent equalization-cancellation, are quite robust in complex listening situations and can explain the data for speech-shaped-noise interferers quite adequately. However, larger effects of spatial unmasking are observed when multiple speech or reversed speech interferers are used (Hawley *et al.*, 2004). The pattern of thresholds is very similar, but the effects are larger. It is not obvious how these data can be explained by simple binaural processing strategies, but it is apparent from the present experiment that ILDs and ITDs make independent contributions to the spatial unmasking for speech, just as they do for speech-shaped-noise. The same arguments against a role for sound localization can therefore be applied.

ACKNOWLEDGMENTS

This work was supported by UK MRC and NIH-NIDCD Grant Nos. R01-DC00100 and R29-DC03083.

[1]The exceptional effect was an interaction between voicing of the interfering sounds and spatial distribution. If the interferers were speech or reversed speech, then the advantage of spatial separation attributable to binaural interaction was about twice as great as when the interferers were speech-shaped noise or speech-modulated, speech-shaped noise.

[2]The E-C model can also compensate for interaural differences in level. In this article, the time- and level-equalization processes will, until Sec. III C,

be assumed to operate efficiently, leaving the multiplicity of interfering sources at different ITDs as the main factor limiting performance. ILDs will mainly be considered for their effect on monaural performance at the ear with the most favorable signal-to-noise ratio.

[3]Although the stimuli contained realistic ILDs and ITDs for external virtual locations, the stimuli tended to be perceived as within the head, even when the full set of binaural cues was included.

[4]This application of E-C theory is only approximate because it assumes that the stimulus is composed of one noise that is identical at the two ears except for some interaural time delay and two that are independent and applied to different ears. The stimulus is not constructed that way, but by adding together three noises with different interaural time delays. The approximation relies on the assumption that within a given frequency channel, there is no effective difference between these two constructions, provided that the resulting coherence and time delay are identical. The advantage of making the approximation is that the same formula can be applied to practically any stimulus configuration.

[5]Interaural phase and coherence of the masker complex at each frequency were measured from the output of a gammatone filterbank using a cross-correlation with a 100-ms window. The phase of the target was always zero. Twenty samples were taken at 100-ms intervals and BMLDs calculated separately for each sample.

Blauert, J., Brueggen, M., Bronkhorst, A. W., Drullman, R., Reynaud, G., Pellieux, L., Krebber, W., and Sottek, R. (**1998**). ''The AUDIS catalog of human HRTFs,'' J. Acoust. Soc. Am. **103**, 3082.

Bronkhorst, A. W. (**2000**). ''The cocktail-party phemonenon: a review of research on speech intelligibility in multiple-talker conditions,'' Acustica **86**, 117–128.

Bronkhorst, A. W., and Plomp, R. (**1992**). ''Effect of multiple speechlike maskers on binaural speech recognition in normal and impaired hearing,'' J. Acoust. Soc. Am. **92**, 3132–3139.

Cherry, E. C. (**1953**). ''Some experiments on the recognition of speech with one and two ears,'' J. Acoust. Soc. Am. **25**, 975–979.

Culling, J. F., and Colburn, H. S. (**2000**). ''Binaural sluggishness in the perception of tone sequences and speech in noise,'' J. Acoust. Soc. Am. **107**, 517–527.

Culling, J. F., and Summerfield, Q. (**1995**). ''Perceptual separation of competing speech sounds: Absence of across-frequency grouping by common interaural delay,'' J. Acoust. Soc. Am. **98**, 785–797.

Culling, J. F., and Summerfield, Q. (**1998**). ''Measurements of the binaural temporal window using a detection task,'' J. Acoust. Soc. Am. **103**, 3540–3553.

Durlach, N. I. (**1963**). ''Equalization and cancellation theory of binaural masking-level differences,'' J. Acoust. Soc. Am. **35**, 1206–1218.

Durlach, N. I. (**1972**). ''Binaural signal detection: Equalization and cancellation theory,'' in *Foundations of Modern Auditory Theory Vol. II*, edited by J. V. Tobias (Academic, New York).

Durlach, N. I. (**2003**). Personal communication.

Durlach, N. I., and Colburn, H. S. (**1978**). ''Binaural Phenomena,'' in *The Handbook of Perception*, edited by E. C. Carterette and M. P. Friedman (Academic, New York).

Fletcher, H., and Galt, R. H. (**1950**). ''The perception of speech and its relation to telephony,'' J. Acoust. Soc. Am. **22**, 89–151.

Hawley, M. L., Litovsky, R. Y., and Culling, J. F. (**2004**). ''The benefit of binaural hearing in a cocktail party: Effect of location and type of masker,'' J. Acoust. Soc. Am. **115**, 833–843.

Kryter, K. D. (**1962**). ''Methods for calculation and use of the articulation index,'' J. Acoust. Soc. Am. **34**, 1689–1697.

Levitt, H., and Rabiner, L. R. (**1967**). ''Predicting binaural gain in intelligibility and release from masking for speech,'' J. Acoust. Soc. Am. **42**, 620–629.

Noble, W., and Perret, S. (**2002**). ''Hearing speech against spatially separate competing speech versus competing noise,'' Percept. Psychophys. **64**, 1325–1336.

Patterson, R. D., Nimmo-Smith, I., Holdsworth, J., and Rice, P. (**1987**). ''An efficient auditory filterbank based on the gammatone function'' paper presented to the IOC speech group on auditory modelling at the Royal Signal Research Establishment, 14–15 December.

Patterson, R. D., Nimmo-Smith, I., Holdsworth, J., and Rice, P. (**1988**). ''Spiral vos final report, Part A: The auditory filter bank,'' Cambridge Electronic Design, Contract Report (APU 2341).

Peissig, J., and Kollmeier, B. (**1997**). ''Directivity of binaural noise reduction in spatial multiple noise-source arrangements for normal and impaired listeners,'' J. Acoust. Soc. Am. **101**, 1660–1670.

Plomp, R. (**1986**). ''A signal-to-noise ratio method for the speech-reception SRT of the hearing impaired,'' J. Speech Hear. Res. **29**, 146–154.

Plomp, R., and Mimpen, A. M. (**1981**). ''Effect of the orientation of the speaker's head and the azimuth of a noise source on the speech reception threshold for sentences,'' Acustica **48**, 325–328.

Rothauser, E. H., Chapman, W. D., Guttman, N., Nordby, K. S., Silbiger, H. R., Urbanek, G. E., and Weinstock, M. (**1969**). ''I.E.E.E. recommended practice for speech quality measurements,'' IEEE Trans. Audio Electroacoust. **17**, 227–246.

Schubert, E. D. (**1956**). ''Some preliminary experiments on binaural time delay and intelligibility,'' J. Acoust. Soc. Am. **28**, 895–901.

Fine structure of hearing threshold and loudness perception[a)]

Manfred Mauermann[b)]
Medizinische Physik, Universität Oldenburg, D-26111 Oldenburg, Germany

Glenis R. Long[c)]
Hanse-Wissenschaftskolleg (HWK), 27753 Delmenhorst, Germany

Birger Kollmeier
Medizinische Physik, Universität Oldenburg, D-26111 Oldenburg, Germany

(Received 8 August 2003; revised 24 March 2004; accepted 19 April 2004)

Hearing thresholds measured with high-frequency resolution show a quasiperiodic change in level called threshold fine structure (or microstructure). The effect of this fine structure on loudness perception over a range of stimulus levels was investigated in 12 subjects. Three different approaches were used. Individual hearing thresholds and equal loudness contours were measured in eight subjects using loudness-matching paradigms. In addition, the loudness growth of sinusoids was observed at frequencies associated with individual minima or maxima in the hearing threshold from five subjects using a loudness-matching paradigm. At low levels, loudness growth depended on the position of the test- or reference-tone frequency within the threshold fine structure. The slope of loudness growth differs by 0.2 dB/dB when an identical test tone is compared with two different reference tones, i.e., a difference in loudness growth of 2 dB per 10-dB change in stimulus. Finally, loudness growth was measured for the same five subjects using categorical loudness scaling as a direct-scaling technique with no reference tone instead of the loudness-matching procedures. Overall, an influence of hearing-threshold fine structure on loudness perception of sinusoids was observable for stimulus levels up to 40 dB SPL—independent of the procedure used. Possible implications of fine structure for loudness measurements and other psychoacoustic experiments, such as different compression within threshold minima and maxima, are discussed. [DOI: 10.1121/1.1760106]

PACS numbers: 43.66.Cb [GK] Pages: 1066–1080

I. INTRODUCTION

When absolute hearing thresholds are evaluated with small frequency increments, consistent quasiperiodic patterns of threshold change with frequency (threshold fine structure or microstructure[1]) can be obtained. Regions of relatively stable poor sensitivity (hearing threshold maxima) are separated by narrow regions of greater sensitivity (threshold minima). In this study, we investigated in detail the relation between hearing-threshold fine structure and fine structure in loudness perception of sinusoidal signals for frequencies around 1800 Hz to receive a broader base for the understanding of loudness perception at low levels. Isolated investigations (Elliot, 1958; van den Brink, 1970; Thomas, 1975) of threshold fine structure were described in the literature prior to 1979, establishing that the frequency spacing of the threshold fine structure appeared to be a constant fraction of estimates of the frequency resolution capacity of the ear (the critical band). In 1979, Kemp noted that the capacity of the healthy ear to generate sounds (known as otoacoustic emissions—OAE) could be due to the same mechanisms as those responsible for the threshold fine structure (Kemp, 1979). These OAEs are generated by the processes responsible for the remarkable sensitivity of the human ear, and even small amounts of hearing loss correspond to significantly reduced levels of OAEs. All types of OAEs in humans are characterized by strikingly similar fine-structure patterns in the frequency domain with a frequency spacing between adjacent maxima or minima on the order of 0.4 bark (e.g., He and Schmiedt, 1993; Mauermann *et al.*, 1997; Zwicker and Peisl, 1990; Zweig and Shera, 1995). Threshold minima are associated with frequencies near spontaneous OAEs (SOAEs) or large evoked OAEs (EOAEs) (Zwicker and Schloth, 1984; Long and Tubis, 1988a, b; Horst and de Kleine, 1999). The depth of the minima is not simply related to the level because high-level emissions can interact with the stimuli and elevate thresholds (Long and Tubis, 1988a, b; Smurzynski and Probst, 1998). Changes in the emission frequency are associated with changes in the threshold-fine-structure frequency (Long and Tubis, 1988a; He, 1990; Furst *et al.*, 1992). Overall, the spacing of the threshold fine structure is very similar to that of otoacoustic emissions. Furthermore, it has been observed that normal-hearing subjects with weak otoacoustic emissions show a reduced ''audiogram ripple'' (Kapadia and Lutman, 1999).

[a)]Parts of this study were presented at the 23rd Midwinter Research Meeting of the Association for Research in Otolaryngology 2000 in St. Petersburg Beach, Florida [Mauermann *et al.*, Abstract No. 984, p. 284].

[b)]Electronic mail: manfred.mauermann@uni-oldenburg.de
[c)]Current affiliation: City University of New York; Graduate School and University Center, 365 Fifth Avenue, New York, N.Y. 10016-4309. Electronic mail: glong@gc.cuny.edu

Experimental evidence for a close link between OAE fine structure and threshold fine structure has been supported by different cochlear models. Any sound generated in the cochlea must be conducted through the middle ear if it is to be detected in the ear canal as an OAE. But, not all sound generated in the cochlea will be transmitted through the middle ear. Due to the impedance mismatch at the stapes, some sound will be reflected back into the cochlea (e.g., Shera and Zweig, 1993). The returning reflection will either enhance or partially cancel any energy at the original reflection site depending on the round-trip travel time. If the sound was initially reflected (and is not canceled by the returning echo), it will be reflected again unless the properties of the cochlea have changed. Multiple internal reflections of cochlear traveling waves will occur (Zweig and Shera, 1995), leading to the resonance behavior of the cochlea originally suggested by Kemp (1980) as an explanation for fine structure in stimulus frequency OAEs (SFOAE). This resonance will naturally enhance the response of the basilar membrane to sounds at some frequencies, and reduce its response to sounds at others. Frequencies at which the basilar-membrane response at CF is maximal will result in threshold fine-structure minima, and frequencies at which this basilar-membrane response is minimal will result in threshold fine-structure maxima. This same resonance behavior can be used to explain the origin of the pseudoperiodicity observed in all OAE fine structure with a single origin, and thus provides a common origin of the OAE fine structure and threshold (and other psychoacoustic) fine structures (see Talmadge *et al.*, 1998). Even though OAE and psychoacoustic fine structure are based on the same underlying mechanisms, and the periodicity is similar from the model point of view, the pattern of both does not necessarily match over all frequencies (Talmadge *et al.*, 1998).

In addition to the theoretical implications of cochlear fine structure, there are practical implications for psychoacoustic research. Except for the investigation of the relation between threshold fine structures and OAEs, there are only a small number of psychoacoustic studies investigating the dependence of suprathreshold psychoacoustic data on threshold fine structure. Variations of psychoacoustic observations related to threshold fine structures have been found in (a) the perceived loudness of low-sensation-level tones (Kemp, 1979); (b) temporal integration (Cohen, 1982); (c) masked thresholds (Long, 1984); (d) amplitude-modulation thresholds (Zwicker, 1986; Long, 1993); (e) monaural diplacusis (Kemp, 1979; Long, 1998); and (f) binaural diplacusis (van den Brink, 1970, 1980). The effects of cochlear fine structure get smaller as stimulus level is increased in most paradigms, and there is some indication that the spacing of the psychoacoustic fine structures can change at the highest levels tested (Long, 1984). In addition to screening of loudness maxima and minima at about 10 dB SL in 42 normal-hearing ears, Kemp (1979) showed equal-loudness contours for one subject around a pronounced threshold minimum, which flattens out with increasing levels at about 35 dB SPL. Van den Brink (1970) measured thresholds and isophons with a high-frequency resolution, using a 1-kHz reference tone at 40, 60, and 80 dB SPL, so they could be compared with patterns of diplacusis. He found ''some recruitment at low SPLs for the extreme peaks,'' i.e., a flattening of threshold fine structure at 40 dB. In the example shown (van den Brink 1970, Fig. 10), he linked maxima and minima in threshold with extrema in the isophons up to 80 dB SPL, which suggests a preservation of a reduced fine structure in isophons (with fluctuations of about 2–3 dB) for reference tones up to 80 dB SPL.

In studies taking the fine structure into account, the variance at each frequency is comparable to the within-subject variance seen in most other psychoacoustic research with well-trained subjects. The across-frequency variance is, however, much larger and comparable to the between-subject variance seen in many experiments. One interpretation of these results is that much of the between-subject variance seen might depend on the position of the stimuli within the cochlear fine structure. Hellman and Zwislocki (1961) found that presenting the stimuli at equal SL in comparison to equal SPL reduces the variability among listeners' loudness judgments, especially at low levels. Any effects of cochlear fine structure on psychoacoustic research will increase the variance and thus limit our ability to evaluate the underlying impact of some stimulus manipulations. Nevertheless, with a few exceptions, most psychoacoustic research with sinusoids is done at discrete, widely spaced frequencies chosen without any attempt to determine whether these tones lie in a minimum, a maximum, or a transition region within the cochlear fine structure. For studies interested in average effects over a sufficiently large number of subjects, it is certainly reasonable to ignore potential effects of cochlear fine structure. But, it might be necessary to strengthen the consideration of cochlear fine-structure effects on psychoacoustic measurements (a) to get a more detailed understanding of hearing mechanisms; (b) to investigate interindividual variations; and (c) to possibly increase the potential value of audiological tools for more precise and individual diagnoses, or for diagnoses at very early stages of cochlea injury. The aim of this study is to further examine the potential influences of the cochlear fine structure on perceived loudness of sinusoidal signals. Do the interference effects of cochlear mechanics most probably responsible for threshold fine structure, affect loudness perception? To get a broader base of detailed data on loudness perception taking the threshold fine structure into account, the following experiments were performed: Experiment 1 investigated the range of stimulus levels for which loudness fine structure is preserved in eight subjects. Thresholds and equal-loudness contours for different stimulus levels were measured with a high-frequency resolution. Experiment 2 observed loudness growth at low to moderate levels using test-tone frequencies associated with adjacent minima and maxima in individual thresholds in an attempt to describe the change in response with level for these different conditions. We also examined whether the position of the reference tone within threshold fine structure affected the measured loudness growth, to check whether threshold fine structure may influence loudness-matching procedures at low levels.

In experiment 3, loudness growth was again measured for different frequencies—matching either a minimum or a

maximum of threshold—but using a different paradigm. In this experiment, a categorical loudness scaling was used as a direct scaling technique in addition to the loudness-matching procedures used in experiments 1 and 2. By comparing across experiments, we can determine how the effects of fine structure depend on the measurement procedures.

II. GENERAL METHODS

A. Subjects

Ten normal-hearing subjects (GL, GM, JO, KW, MO, MW, RH, TB, RM, SU—six male, four female) with thresholds better than 15 dB HL at the standard audiometric frequencies from 125 Hz to 8 kHz, and two subjects with a slight hearing loss (MM—male, 25 dB HL at 8 kHz; DS—male, 25 dB HL at 3 and 4 kHz) participated in this study. The subjects TB, GL, JO, KW, MM, and MO had been scanned for spontaneous otoacoustic emissions (SOAE) in another study (Mauermann *et al.*, 1999). Three of these subjects (GL, TB, and MO) show weak SOAE within the frequency regions observed here. The frequencies of detectable SOAE are always indicated as asterisks in the first figure that shows a threshold fine structure of the respective subject (GL in Fig. 1(a) TB in Fig. 3(a), and for subject MO in Fig. 8). All frequencies of detected SOAE correspond to minima in threshold perception. The subjects were the authors, members of the medical physics group at the University of Oldenburg, and students getting paid for the measurements. For all subjects, the measurements were conducted on one ear. During the measurements, the subjects were seated in a double-walled sound-insulated booth (IAC).

B. Instrumentation and software

Adaptive loudness matches, and most of the threshold measurements, were controlled by the signal-processing software SI running on an Indy computer system (Silicon Graphics). The signals were generated digitally at a sampling rate of 44 100 Hz by the SI software, and converted by the 16-bit DA converters of the computer. They were attenuated by a computer-controlled audiometer and presented via an Etymotic Research ER2 insert ear phone. The presentation of each observation interval in one trial was marked optically by an LED, attached to the side of the computer display in the booth.

A PC/MATLAB-controlled setup was used for some of the interleaved adaptive threshold measurements, all of the adjustment measurements, and the categorical loudness scaling. The signals were generated digitally at a sampling rate of 44 100 Hz in the MATLAB programs and sent through an RME Digi96/8 PAD digital I/O card to a SEKD 2496 24-bit DA converter. After amplification (Behringer headphone amplifier Powerplay II) the signals were presented via an ER2 insert phone. Each observation interval was marked optically on the computer screen instead of using the LED marker. The ER2 were calibrated using an artificial ear for insert phones (Bruel & Kjaer type 4157).

III. EXPERIMENT 1: PRESERVATION OF THRESHOLD FINE STRUCTURE IN EQUAL-LOUDNESS CONTOURS

When Kemp (1979) investigated the equal-loudness contours around a pronounced sensitivity maximum in one subject, the threshold fine structure could be observed when the reference tone was about 35 dB SPL. To determine how, and up to what levels, loudness perception depends on threshold fine structure, data were gathered in detail from more subjects and a wider frequency region. Hearing thresholds were measured with a high-frequency resolution from 1600–2000 Hz and compared with equal-loudness contours. While Kemp (1979) used test tones fixed in level, we concentrated on a paradigm with the reference tone kept fixed in level.

A. Methods

1. Subjects

Subjects were GL, GM, JO, KW, MO, MW, RH, and TB (four male, four female). Subject GL (second author) performed measurements on hearing thresholds and extended measurements on equal-loudness contours using adaptive interleaved paradigms (see the procedures below). Hearing thresholds and equal-loudness contours using an adaptive-interleaved paradigm were also measured in subjects GM, MW, and to some extent in subject KW. Adjustment methods were used in subjects JO, KW, MM (first author), MO, TB, and partially in subject MW.

2. Procedures

a. Hearing thresholds (adaptive). Measurements of hearing thresholds were obtained from subjects GL, KW, MW, and GM using a 3 alternative forced choice (AFC) adaptive (1-up, 2-down) paradigm with feedback. Sinusoids of 250-ms duration were used as stimuli (including 25-ms Hanning-shaped ramps). The three observation intervals in each trial were marked optically and were separated by 500 ms of silence. The subject's task was to indicate the interval in which the tone was presented. The frequencies (1600–2000 Hz in 12.5-Hz steps) were divided into three blocks including 11 frequencies. Each of these blocks was measured in separate sessions.

Every track started with level steps of 8 dB. At each reversal, the step size was reduced to 4-, 2-, and finally 1-dB steps. The median of the final eight reversal points (at 1-dB steps) was taken as the preliminary estimate of the threshold. These measures were obtained in three sessions (exceptions are indicated in the figure captions). The mean of the three median values provided the final estimate of the threshold at each frequency.

b. Equal-loudness contours (interleaved adaptive). The instrumentation and signals were the same as those used for the loudness measurements. A frequency resolution of 25 Hz was used. During one session, all test-tone frequencies for one level were measured as 16 interleaved tracks (subject GL, GM) for the frequency range from 1600 to 2000 Hz. For

the subjects KW and MW, the measurements were divided in two sessions with eight interleaved tracks. The order of the 1000-Hz reference tone and the respective test tone were randomized in each trial. The subjects had to decide which of the two sinusoids presented in consecutive intervals was louder. The reference tone was held fixed in level while the test tones followed an adaptive 1-up, 1-down procedure converging to the 50% point of the psychometric function (this is the traditional isoloudness procedure). The measurements for each frequency started with level steps of 8 dB, which were decreased to 4 and finally to 2-dB steps at each reversal. The median from the final four reversals (with constant level changes of 2 dB) was taken as the preliminary estimate of equal loudness. Each session was repeated three times (exceptions are indicated in the figure captions) with different start levels of the test tones. In each session, the start levels for the stimuli were either the same as the reference tone level L_{ref} in dB SPL level or $L_{\mathrm{ref}} \pm 10$ dB (1/3 of the stimuli at each start level). In each session, a different start level was chosen for each frequency so that all the frequencies were tested with each start level. The order of test and reference tone in each trial was randomized. The mean of the resulting median values was taken as the final estimate for the level of equal loudness, referred to as the point of subjective equality (PSE).

For subject GL, the 1000-Hz reference tone was close to a threshold minimum. Additional equal-loudness contours were measured using a reference tone at 1800 Hz, which is close to a threshold maximum in this subject. A set of equal loudness contours was measured in comparison to a reference tone at 1000 Hz, as well as for a reference tone at 1800 Hz. All other parameters were the same as for the measurement of the equal-loudness contours. The position of the 1000-Hz reference tone within the fine structure was not evaluated in the other subjects.

c. Inverse loudness contours. In addition to the loudness matches using a reference tone with fixed level, subject GL provided ''inverse'' loudness contours with a variable reference tone level, while the test-tone level was kept fixed. In this procedure, the stimuli are not set to be equally loud. Instead, an estimate of the loudness in phons at each frequency and level is provided.

d. Equal loudness contours (adjustment). Due to the excessive measurement time and numerous critical remarks about the interleaved adaptive method from the majority of the subjects, we decided to find a quicker paradigm for the loudness measurements. This was done to avoid problems with massive reduction of subject motivation, and to permit higher frequency resolution with acceptable measurement effort. Consequently, a different setup was designed. The subjects' task was to adjust the test tone to be equally loud as the reference tone at 1 kHz. The subjects were allowed to hear a pair of reference and test tones (in fixed order—reference tone first) as often as they wanted by clicking on a ''play'' button. Each tone had a duration of 500 ms. They could change the level of the test tone by adjusting a slider on the computer screen. This permitted a maximum change in level of ± 6 dB during one step, not indicated to the subjects (minimal possible step size was 0.5 dB). When the subject clicked on the play button after a level adjustment, the tone pair was presented with the test tone at the new level. The slider control jumped back to the zero point when a new frequency was presented to avoid anchor effects stemming from the optical position of the slider. The two observation intervals in each trial were marked optically on the computer screen. When the subject was sure that both tones were equally loud, he/she was advised to press an ''is equal'' button to proceed to the next frequency. The order of frequencies was randomized. These measures were obtained in three sessions. The mean of three adjusted levels was taken as the estimate for the PSE. The same frequency range was measured as for the adaptive interleaved paradigm, but with a higher a frequency resolution of 12.5 Hz instead of 25 Hz.

e. Hearing thresholds (adjustment). Subjects who performed the adjustment method for loudness matching also used an adjustment paradigm to measure the hearing threshold in quiet. The subject could replay a single tone pressing the play button and change its level by adjusting the slider on the computer screen. The subject's task was to report a just-noticeable level. So, the subjects performed a kind of self-controlled audiogram with high-frequency resolution. The signals (sinusoids of 500-ms duration including 25-ms Hanning-shaped ramps) were identical to the ones used for the loudness matching used in the adjustment paradigm. Again, the order of frequencies was randomized. Each session, containing all frequencies, was repeated three times. The mean of the three adjusted levels was taken as the estimate of threshold.

B. Results

Most of the subjects participating in this study had threshold fine structure, i.e., maxima and minima in hearing thresholds with level differences of more than 5 dB. The only exception was subject RH (not shown here), who showed limited threshold and isophon variation (up to 65 dB SPL for the reference tone) for the frequencies investigated here. Subjects MO, KW, and JO showed reduced or no fine structure for frequencies between 1800 and 2000 Hz. The frequency range investigated in subject MO (data not shown here) was changed to 1400–1800 Hz, where he showed a more pronounced fine structure.[2] In frequency regions with fine structure, we mostly see a characteristic quasiperiodic pattern for the fine structure of hearing thresholds. The differences of the adjusted threshold levels for adjacent maxima and minima varied individually from about 5 dB up to about 15 dB.

The shape of the threshold fine structure was visible in the equal-loudness contours of all subjects up to a reference tone of at least 25 dB SPL (Figs. 1, 2, 3), and for subject GL (the one with most practice at the task) even up to 50 dB SPL (see Figs. 1, 4, 5). Overall, the pattern flattened out with increasing level. In some subjects, the patterns tended to shift or change shape at intermediate levels before becoming smooth (see, e.g., subject GL in Fig. 1 at 45 to 55 dB for the reference tone and subject GM in Fig. 2(b) for 35 and 45 dB). These observations hold for both paradigms used.

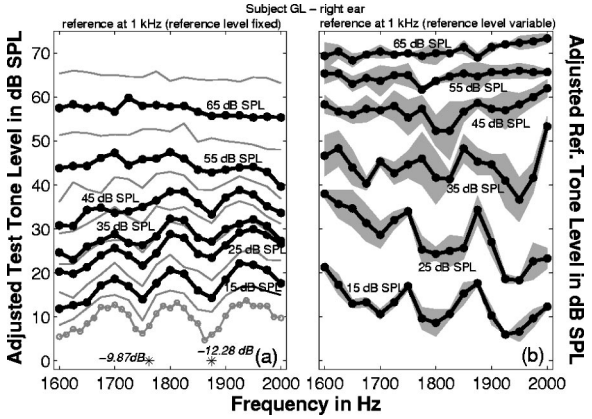

FIG. 1. (a) Hearing threshold and equal-loudness contours from subject GL—right ear, for a reference tone fixed at 1 kHz, measured with the interleaved adaptive paradigm (data are averages of 6 thresholds). From bottom to top: hearing threshold (gray line with open circles), equal loudness contours with reference level from 10 to 70 dB SPL in steps of 5 dB (alternating thin lines without symbols and thick lines with filled circles). The reference-tone levels of the thick lines are indicated by labels next to the lines. Two independent sets of thresholds showed similar patterns. (b) shows the results from ''inversed'' equal-loudness contour measurements keeping the test tone fixed in level while varying the level of the 1-kHz reference tone. In order to compare the difference in dynamic ranges for the two different paradigms, data with 10-dB step size are indicated with thick lines and symbols in both (a) and (b). Shaded areas give the standard deviation from one set of three repetitions of the loudness matches. While in (a) the most sensitive frequencies are represented by minima in the curves, in (b) the most sensitive frequencies are given by the maxima of the adjusted level; note, furthermore, the different dynamic range for the same reference-tone levels or test-tone levels, respectively (compare thick black lines with filled circles in the left and right panel). Within the observed frequency range subject GL has two SOAE at 1762 Hz (−9.9 dB SPL) and 1874 Hz (−12.3 dB SPL). The frequencies of the SOAE are indicated as black asterisks with labels that give the SOAE level in the sealed ear canal.

Figure 6 shows a comparison of threshold measurements and equal loudness contours (reference tone level at 15 dB SPL) from both paradigms, i.e., the interleaved adaptive and the adjustment paradigm. High consistency between the patterns from the two paradigms can be seen.

When the reference tone was fixed in level, the frequency regions with the lowest thresholds (most sensitive) presented as minima in the equal-loudness contours, while maxima line up with the maxima in the threshold fine structure. The level of the louder probe was reduced to match the loudness of the fixed-level reference. Varying the level of the reference tone while keeping the test tone fixed in level gave the reverse pattern with maxima in the loudness function associated with minima in the threshold fine structure. In this

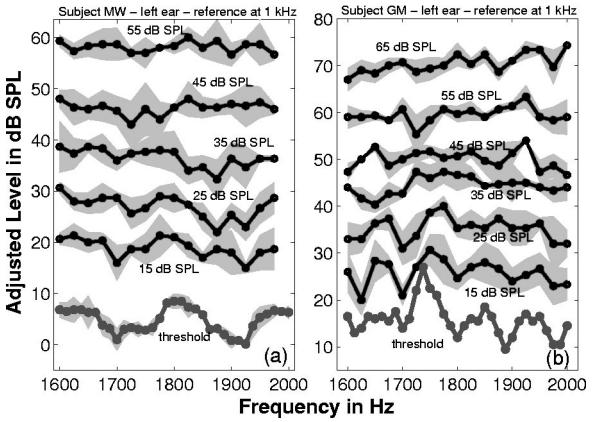

FIG. 2. Hearing threshold and equal-loudness contours from (a) subject MW—left ear and (b) subject GM—left ear, measured with the interleaved-adaptive paradigm. The curves are labeled with the reference levels used or ''threshold,'' respectively. The shaded areas give the standard deviation of three repetitions. The hearing threshold shown for subject GM is the result from only one measurement.

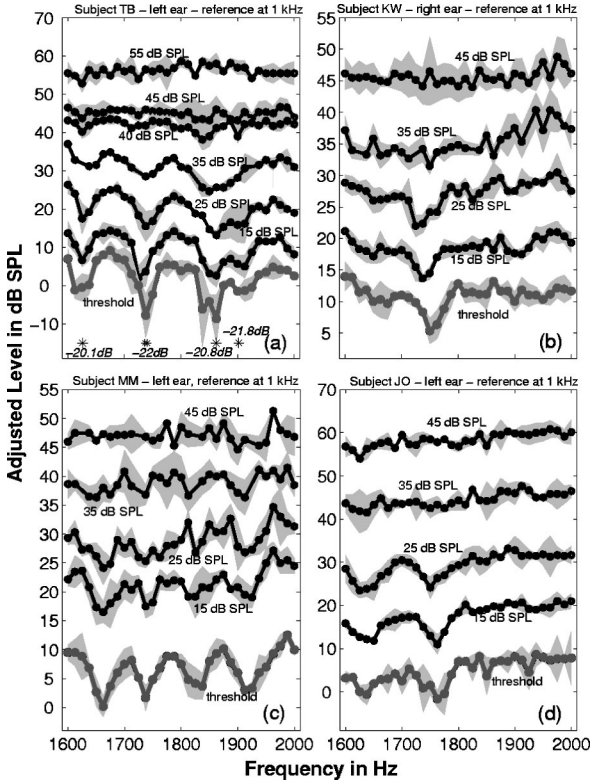

FIG. 3. Hearing threshold (gray) and equal-loudness contours (black) from (a) subject TB—left ear; (b) subject KM—right ear; (c) subject MM—left ear; and (d) subject JO—left ear measured with the adjustment paradigm. The curves are labeled with the reference levels used or ''threshold,'' respectively. The shaded areas give the standard deviations of three repetitions. The black asterisks in panel (a) indicate the SOAE frequencies found in subject TB—left ear. The levels of the SOAE are indicated as labels beside the asterisks. There were no SOAE detected in the other three subjects.

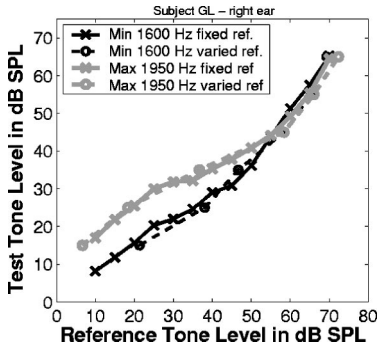

FIG. 4. Loudness growth functions from subject GL—right ear. The data are extracted from the data shown in Fig. 1 for reference tones fixed in level (solid lines, crosses) and (b) for the reference tone varied in level (dashed lines, open circles) both for two test-tone frequencies 1600 Hz (black lines) at a threshold minimum and 1950 Hz (gray lines) at a threshold maximum. While the data from the two paradigms are very consistent, a different position of the reference-tone frequency within fine structure results in different loudness slopes.

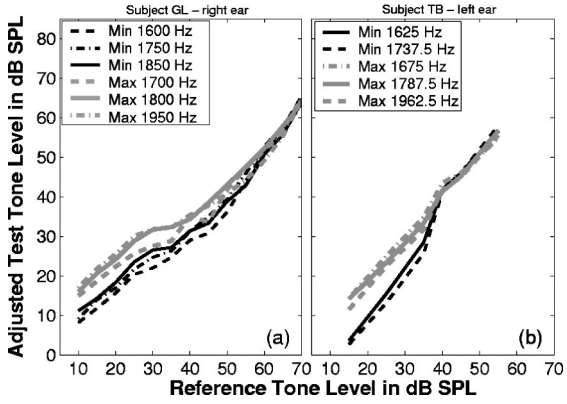

FIG. 5. Loudness growth functions (a) from subject GL—right ear (extracted from data shown in Fig. 1) and (b) TB—left ear [extracted from data shown in Fig. 3(a)] at different frequencies. While the data in (a) were collected using the adaptive interleaved paradigm, the data for (b) stem from measurements using the adjustment procedure. Both show similar loudness growth for stimuli from threshold maxima at three different frequencies (gray lines, for frequencies see the legend) that is different from the loudness growth from minima (black lines).

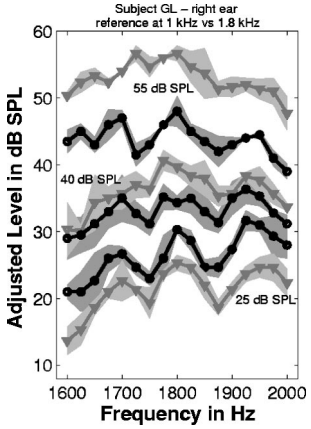

FIG. 7. Equal-loudness contours from subject GL—right ear for reference tone levels of 25, 40, 55 dB SPL (indicated by labels within the plot). The black lines with circles show data from measurements using a reference tone at 1 kHz; the gray lines with triangles show data for a reference tone at 1.8 kHz. While 1 kHz lies close to a local hearing threshold minimum, the reference at 1.8 kHz matches a threshold maximum. Note that the equal-loudness contours referenced to a tone near a threshold minimum (black lines) are closer together, i.e., indicate less loudness compression than the ones referenced to a tone near a maximum (gray lines).

paper, these are called inverse loudness contours. The level of the reference tone was increased to match the probes, which were loudest near threshold minima. Figure 1 compares results for these two strategies of loudness matching from the same subject. The pattern of the fine structure is reversed in Fig. 1(b). The level of the adjusted reference tone shows maxima at frequencies near threshold minima (the level of the reference tone is increased to match the louder probe and reduced near threshold maxima). However, the width of the fine structure is the same as for the equal-loudness contours [compare, e.g., Figs. 1(a) and (b)]. To illustrate the consistency of the data, Fig. 4 shows test-tone level as function of the reference tone level extracted from both the equal loudness contour data from Fig. 1(a) as well as from the inverse equal-loudness contours shown in Fig. 1(b) for one sensitive frequency at 1600 Hz and a more insensitive one at 1950 Hz. While the growth functions are

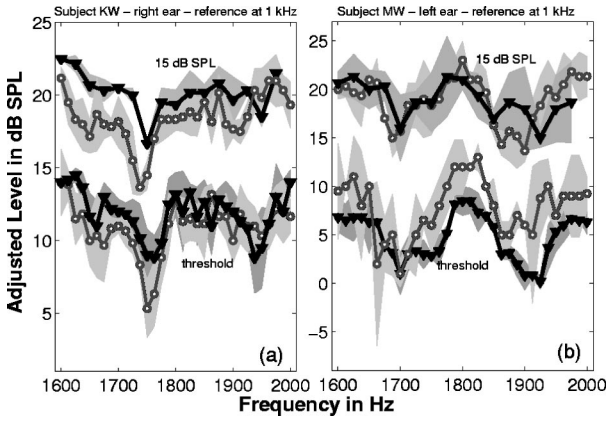

FIG. 6. Comparison of hearing threshold and equal-loudness contour measurements for two different paradigms. (a) From subject KW—right ear; (b) subject MW—left ear. The black lines with triangles show hearing thresholds and equal-loudness contours using the interleaved-adaptive paradigm, while the gray lines with open circles show results from adjustment measurements. The shaded areas give the standard deviation from three repetitions. Note the qualitative and quantitative correspondence between the two paradigms.

different for the two frequencies, the two matching strategies are identical within the limits of measurement error. The pronounced fine-structure pattern of thresholds flattens out towards equal-loudness contours at higher levels. This leads, obviously, to a difference in loudness compression of tones at frequencies of threshold maxima or minima, respectively (see also Fig. 5). At low to moderate levels, the growth of the level adjusted to sound equally loud as the reference tone has considerably (loudness-level-growth function) steeper slopes for tones at very sensitive frequencies (threshold minima) than for less responsive regions. This is equivalent to a higher loudness compression of the more sensitive frequencies for which a larger range of levels is mapped to the same range of loudness than for less sensitive frequencies. To illustrate the differences of loudness-level-growth functions from frequencies at threshold maxima and minima, Fig. 5 shows loudness-level-growth functions extracted for frequencies at three different threshold maxima and three minima for subject GL [Fig. 5(a)] and three different threshold maxima and two minima for subject TB [Fig. 5(b)].

In Fig. 7, equal-loudness contours for a reference tone at 1 kHz (fixed in level) are compared with equal-loudness contours obtained with a reference tone at 1.8 khz. While 1 kHz falls within a threshold minimum of the subject (GL—threshold at 1 kHz is 3.25 dB SPL), 1.8 kHz lies near a threshold maximum. The equal-loudness contours referenced to the tone near a threshold minimum (1 kHz) from the same subject and the same frequency range, are closer together,i.e., indicating less loudness compression than the ones referenced to a tone near a maximum (1.8 kHz). Due to the flattening of fine structure with increasing stimulus level, a reference tone at a threshold maximum needs a smaller range of stimulus levels for the same change in loudness (less loudness compression) than a reference tone at a threshold minimum. That means a tone near a threshold minimum shows a higher dynamic range, or larger amount of compression than

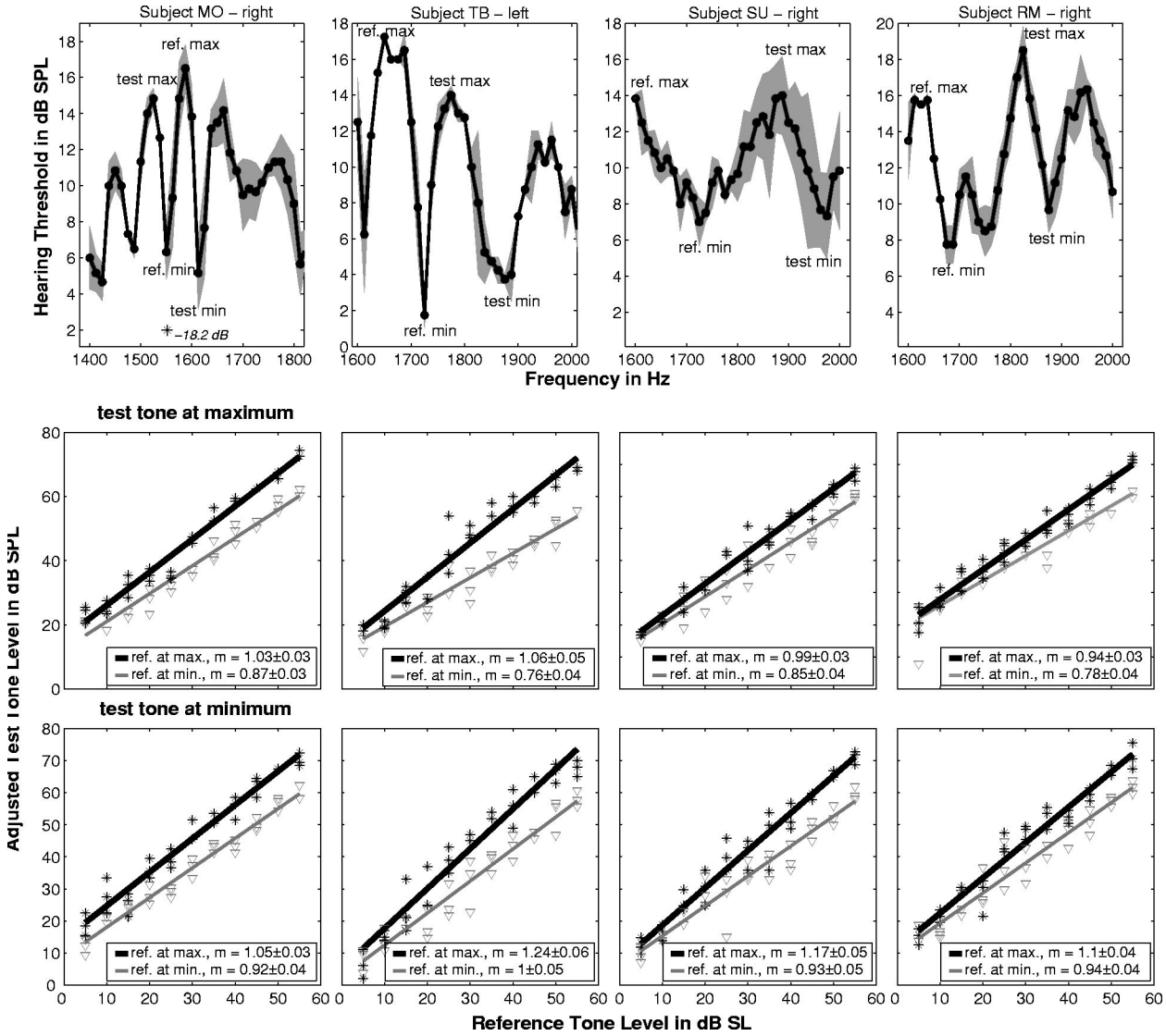

FIG. 8. Hearing-threshold fine structures (top row) for four subjects, from left to right: MO—right ear; TB—left ear; SU—right ear; and RM—right ear. The panels in the medium row show the associated loudness growth functions from a loudness-matching procedure for an individually selected test tone in a threshold maximum compared to a neighboring reference tone within a threshold maximum (black lines and asterisks) or minimum (gray lines and triangles), respectively. The lower panels show the loudness growth functions of a test tone at a threshold minimum in comparison to a reference frequency at a maximum (gray lines and asterisks) and a minimum (black lines and triangles). The symbols indicate each data point measured. Each loudness match was measured three times. A least-squares linear regression was computed for each data set. The slope *m* and its standard deviation for each fitted function is given in the legend of each panel as indicator for the different loudness growth behavior (compare Table I). The asterisk in the top left panel (subject MO) indicates the frequency of a SOAE in this subject.

a tone at an adjacent threshold maximum. Therefore, loudness matching of test signals with a reference tone near a threshold minimum (relatively high compression) will lead to a shallower loudness-level-growth function (indicating less compression), than loudness matching of the identical test tones matched with a reference tone at a frequency close to a threshold maximum (relative low compression), as can be seen in Fig. 7.

IV. EXPERIMENT 2: LOUDNESS GROWTH AT FREQUENCIES IN THRESHOLD MAXIMA AND MINIMA—LOUDNESS MATCHING

The results from the equal-loudness-contour measurements in experiment 1 indicate different loudness growth with increasing level depending on the position of the reference tone within the hearing-threshold fine structure. One may argue that the effect observed for different reference tones in subject GL might be mainly influenced by the different distance of the reference tones to the test tones or due to an overall difference in the dynamic characteristics of loudness growth around 1 kHz vs 1.8 kHz. Consequently, we investigated loudness growth functions for test-and reference tones from different maxima or minima in thresholds which are closer in frequency. The different character of loudness growth is clearly reflected in loudness growth functions at single frequencies, although some of the equal-loudness-contour patterns (experiment 1) show slight shifts in frequency with increases in level. This can be seen in Fig. 5 for two sets of representative growth functions for different test-tone frequencies extracted from the equal loudness contour

data of experiment 1. Consequently, loudness growth functions with level were measured directly in five subjects. An interleaved-adaptive loudness-matching procedure was used to investigate the different patterns of loudness growth (using a level resolution of 5 dB) for frequencies near threshold maxima and minima. The reference frequency was matched to two different positions on the individual's measured fine structure: (a) to a maximum and (b) to a minimum. This was done to investigate the influence of the different position of the reference-tone frequency on the measured loudness growth. The loudness growth was evaluated for reference conditions paired with test-tone frequencies from both a threshold maximum and minimum.

It is assumed that the loudness growth is almost the same for pure tones with adjacent frequencies and similar thresholds. Therefore, placing both reference and test-tone frequencies at either similar pronounced maxima or at similar minima in threshold should, ideally, give loudness matching (plotting the adjusted test-tone level as function of the reference tone level) which has an almost linear growth close to 1 dB/dB. When the reference tone is near a maximum but the test-tone frequency falls near a threshold minimum this should lead to an expansive growth >1 dB/dB. However, when a reference-tone frequency is within a minimum and the test tone near a threshold maximum we would expect a compressive growth with a slope <1 dB/dB. When probe tones are from both maxima and minima, the loudness growth function for a specific test-tone frequency is expected to be steeper for reference tones near threshold maximum than for reference tones at a threshold minimum.

A. Methods

1. Subjects

Four normal-hearing subjects (TB, MO, RM, SU) with thresholds of 15 dB HL or better in the clinical audiogram (125 Hz–8 KHz) and one subject (DS) with 25 dB HL at 3 and 4 kHz participated in this study. Subjects TB and MO also participated in experiment 1.[3]

2. Procedures

a. Hearing thresholds. The same adaptive paradigm described in experiment 1 was used for measuring hearing thresholds. Two frequency ranges from 1600–1800 and 1812.5–2012.5 Hz were each measured as 17 interleaved-frequency tracks with a frequency resolution of 12.5 Hz. Subjects MO and DS were also tested from 1387.5 to 1587.5 Hz to scan for regions with more pronounced fine structure.

b. Loudness growth functions. The stimuli were identical to the stimuli used in the interleaved-adaptive equal-loudness-contour experiments. The frequencies of individual threshold maxima and minima, as well as the appropriate SL conversion, were determined from the hearing threshold measurements. Loudness matching with a reference tone near a threshold maximum or a minimum was paired with a test tone close to a maximum and a test tone near a minimum. This gave four reference/test-tone conditions. Eleven different reference levels (5 to 55 dB SL in 5-dB steps) were presented using an interleaved-adaptive 2 AFC 1-up, 1-down procedure as previously described for experiment 1. The step size started at 8 dB and was halved at each reversal, ending with 2-dB steps. The median of the final four reversals with 2-dB steps was taken as an estimate of the PSE. The measurements were repeated three times with different test-tone start levels (in one session the start levels were the same as the reference tone level L_{ref} in dB SPL level, and in the two further sessions a start level of $L_{\mathrm{ref}} \pm 10$ dB was used). The order of test- and reference-tone presentation was randomized. A linear function was fitted to all estimates of the PSEs for each reference/test-tone condition. These slopes give indicators for the growth behavior for the different test-tone/reference-tone conditions.

B. Results

The slopes of the linear functions fitted to the data indicate the loudness growth for the different test-tone/reference-tone conditions. Figure 8 shows the results from four of the five subjects tested. The results for all five subjects are summarized in Table I. The slopes when two adjacent sinusoidal tones are compared vary around 1 dB/dB as expected. The comparison of either two minima (mean 0.96, standard deviation 0.04) or two maxima (mean 0.98, standard deviation 0.05) results in slopes quite close to 1 dB/dB, while the comparison of frequencies, one at a maximum and the other at a minimum, have slopes that depart from 1 dB/dB.

For all subjects, the slope of loudness growth at a test-tone frequency chosen to fall near a threshold maximum or minimum is steeper (indicating less loudness compression) when the reference tone is near a threshold maximum (mean slope 1.11, standard deviation 0.08) than when the reference tone is near a threshold minimum, i.e., a more sensitive place (mean 0.82, standard deviation 0.05). Thus, the results of loudness-matching paradigms using single sinusoids as reference stimuli are influenced by the position of this tone within threshold fine structure. The differences in loudness growth for a specific test frequency referenced to either a frequency within a threshold minimum or maximum, respectively, ranged from 0.13 to 0.30 dB/dB. Only subject DS (who has a slight hearing loss at 3 and 4 kHz) showed smaller slope differences but his data followed the same trend. The position of the reference tone within the fine structure and the position of the test tone are both important for the estimates of loudness growth as determined by loudness matching. For a fixed reference tone, the measured loudness growth of two adjacent test-tone frequencies is different if one is near a threshold minimum and the other around a maximum. That means results on loudness growth obtained with loudness-matching paradigms using sinusoidal test signals may be influenced by the position of the test tone in threshold fine structure. When the test tone is fixed in level, the observed dynamic in loudness growth, dependingon the reference or test tone frequencies, is reversed [compare Figs. 1(a) and (b)].

The cochlear fine structure is unique to each individual. This means that the same reference/test tone may fall near a minimum in one subject, while in another subject it will fall near a threshold maximum. This may—in part—explain the intersubject differences in loudness growth in similar psy-

TABLE I. Frequencies of test- and reference tones and individual hearing thresholds for frequencies used in experiment 2. The next to last column shows the slopes of loudness growth for each test-tone frequency when compared with a reference tone at a threshold minimum or maximum, respectively. The last column shows the difference of loudness growth for a test tone when compared either to a reference at a threshold minimum or maximum.

Subject side		Frequency of test tone in Hz	Hearing thres. of test tone in dB SPL		Frequency of ref. tone in Hz	Hearing thres. of ref. tone in dB SPL	Slope m in dB/dB	Difference of slopes
RM right	*test Min.*	1875	**9.67**	*ref. Min.*	1675	**7.75**	***0.94±0.04***	0.16±0.08
				ref. Max.	1625	**15.50**	***1.1±0.04***	
	test Max.	1825	**18.5**	*ref. Min.*	1675	**7.75**	***0.78±0.04***	0.16±0.07
				ref. Max.	1625	**15.50**	***0.94±0.03***	
TB left	*test Min.*	1875	**3.75**	*ref. Min.*	1725	**1.75**	***1±0.05***	0.24±0.11
				ref. Max.	1662.5	**16.00**	***1.24±0.06***	
	test Max.	1775	**14**	*ref. Min.*	1725	**1.75**	***0.76±0.04***	0.30±0.09
				ref. Max.	1662.5	**16.00**	***1.06±0.05***	
SU right	*test Min.*	1975	**7.33**	*ref. Min.*	1725	**7.00**	***0.93±0.05***	0.24±0.1
				ref. Max.	1600	**13.80**	***1.17±0.05***	
	test Max.	1887.5	**14**	*ref. Min.*	1725	**7.00**	***0.85±0.04***	0.14±0.07
				ref. Max.	1600	**13.80**	***0.99±0.03***	
MO right	*test Min.*	1612.5	**5.17**	*ref. Min.*	1550	**6.33**	***0.92±0.04***	0.13±0.07
				ref. Max.	1587.5	**16.50**	***1.05±0.03***	
	test Max.	1525	**14.83**	*ref. Min.*	1550	**6.33**	***0.87±0.03***	0.16±0.06
				ref. Max.	1587.5	**16.50**	***1.03±0.03***	
DS left	*test Min.*	1612.5	**4.33**	*ref. Min.*	1512.5	**3.33**	***1.01±0.05***	0.05±0.08
				ref. Max.	1462.5	**11.66**	***1.06±0.03***	
	test Max.	1650	**14.5**	*ref. Min.*	1512.5	**3.33**	***0.85±0.03***	0.09±0.07
				ref. Max.	1462.5	**11.66**	***0.94±0.04***	

choacoustical experiments done at levels near the absolute threshold.

V. EXPERIMENT 3: LOUDNESS GROWTH AT FREQUENCIES IN THRESHOLD MAXIMA AND MINIMA—CATEGORICAL LOUDNESS SCALING

Loudness growth functions were measured using a loudness-scaling paradigm to investigate the effects of cochlear fine structure when measured with a direct scaling technique in addition to the loudness matching procedures used in experiments 1 and 2.

A. Methods

1. Subjects

Same as in experiment 2.

2. Procedures

a. Categorical loudness scaling. A two-step loudness scaling procedure was implemented, which is similar to the one proposed by Heller (1985) and Hellbrück and Moser (1985). In the first step, the subject had to choose a response alternative out of the verbal categories ''very soft,'' ''soft,'' ''medium,'' ''loud,'' ''too loud,'' or ''inaudible'' after hearing the stimulus. In the second step, the subject had to refine his/her judgment using a finer scale by using numbers around the previously chosen category [very soft (1–10), soft (11–20), medium (21–30), loud (31–40), too loud (41–50)]. Using this procedure, loudness is mapped by the subjects to a numerical scale from 0 (inaudible) to 50. We refer to these numbers as categorical units (cu) (Brand and Hohmann, 2002).[4] The ''cu'' are directly used as loudness indicators for further analysis (i.e., in contrast to the loudness-level functions, a shallower slope indicates higher loudness compression). Stimuli were sinusoids of 500-ms duration including 50-ms Hanning-shaped ramps. The measurements from four individually selected frequencies, two from maxima and two from minima of the threshold fine structure (the same as for the loudness growth measurements from loudness matching described in experiment 2) were interleaved. Two different level ranges were used: (a) Stimuli from a subject independent SL range (in 2-dB steps) were presented randomly for each frequency investigated in a subject. To control for possible effects of stimulus range due to differences in thresholds (b) Stimuli with identical SPLs were presented randomly for all frequencies for each subject. Where appropriate, the specific ranges used were adjusted depending on the subject's thresholds at that frequency (the level ranges used are presented in Table II). Each measurement was repeated in three sessions in which all levels were shifted by ±0.5 dB from above levels to aid smoothing functions to the data.

Since categorical scaling is not necessarily expected to provide equal interval scales, the assumptions underlying a parametric fit to the data may be violated. Therefore, a robust locally weighted scatter plot smooth (robust lowess—

TABLE II. Individual level ranges used for the categorical loudness scaling in experiment 3.

Subject	SL range in dB SL	SPL range in dB SPL	SPL range in dB SL
MO	−4 to 56	−4.83 to 71.17	−10 to 66
RM	−8 to 72	−0.25 to 89.75	−8 to 82
SU	−8 to 72	−1.00 to 85.00	−8 to 78
TB	−6 to 74	−6.25 to 87.75	−8 to 86
DS	−8 to 72	−4.67 to 85.33	−8 to 82

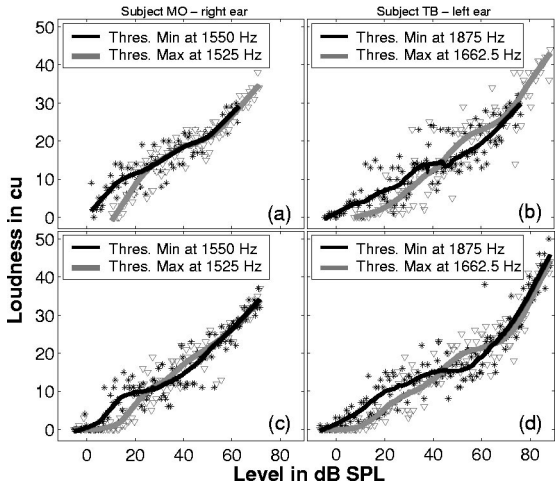

FIG. 9. Loudness growth functions from categorical loudness scaling measurements for two subjects MO—right ear, panel (a) and (c); TB—left ear (b) and (d). The upper panels (a) and (b) show the results when the stimuli covered the same SL range for each frequency, while the lower panels (c) and (d) give the results, from the same subjects, when the stimuli covered the identical SPL range for all frequencies. The symbols indicate the scaled points from three measurement sessions (asterisks for measurements within a threshold minimum, triangles at a frequency close to a threshold maximum). The lines are smoothed functions obtained from a robust ''lowess'' procedure. Note the different growth behavior at low stimulus levels for all subjects and level ranges depending on whether the frequency of the scaled tone lies near a threshold minimum (black lines) or maximum (gray lines). The asterisk in the top left panel (subject MO) indicates the frequency of a SOAE in this subject; the adjacent label indicates the level of this emission measured in the sealed ear canal.

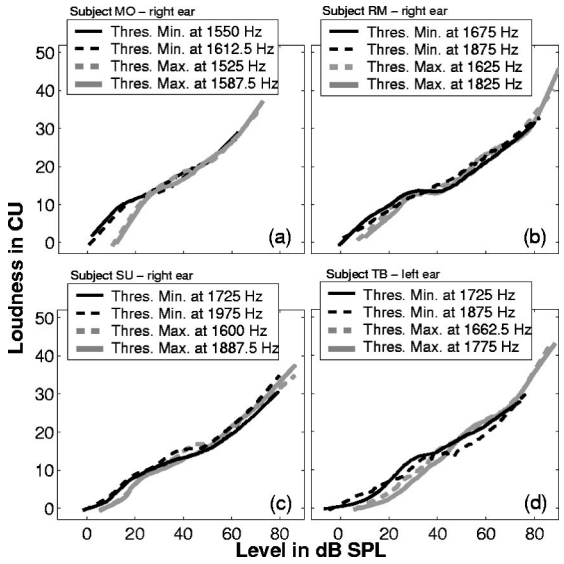

FIG. 10. Each panel shows the loudness growth functions obtained by a robust ''lowess'' procedure from the categorical loudness scaling data for frequencies at two individual fine-structure maxima (thick gray lines) and minima (thin black lines). From top to bottom: subject MO—right ear; subject RM—left ear; subject SU—right ear; and subject TB—left ear. Only the curves for the SL-range measurements are shown. The SPL-range measurements have very similar properties.

MATLAB 6.5, Curve Fitting Toolbox) was used to extract the trends from the categorical scaling data (e.g., Cleveland, 1979). This nonparametric locally weighted regression method computes linear least-squares regression of a first-degree polynomial to the locally weighted data points.[5] The whole range of presented levels was used in the smoothing procedure.

The presented levels were extended to negative SL to allow loudness judgments of 0 cu, i.e., ''not audible.'' Since a threshold estimated by a 3-AFC 1-up, 2-down procedure gives the level of a tone heard 70.7% of the time, occasionally tones below the threshold estimate will be heard and will have a loudness greater than 0 cu.

B. Results

Due to technical restrictions (maximum level of the ER2) the loudness could not be scaled over the whole dynamic range of each subject. This may bias the shape of the perceived loudness growth functions. However, a ''true'' loudness function was not the aim of this study; the aim was to investigate differences in adjacent frequencies falling either near a minimum or near a maximum of cochlear fine structure. There could have been range effects modifying the differences near threshold. If there was any major effect it should have been observable as a difference in the results from the two measured level ranges. We found no such difference.

Figure 9 shows typical scatter plots and fitted curves obtained by loudness scaling of tones from a threshold maximum and a threshold minimum for two subjects (MO, TB). The scaling data obtained from three measurements (slightly shifted in stimulus levels) are fitted by a robust locally weighted scatter plot smoothing procedure. The top panels in Fig. 9 show the data when the range of stimulus levels was based on SL, while the lower panels show the results for the SPL range. The data from the two level ranges show a very similar pattern.

All loudness functions show a more compressive region from about 30 to 60 dB SPL, and a steeper growth for higher levels. Although the loudness curves for adjacent frequencies tend to converge at higher levels (up to at least 20 dB SPL in subject SU, up to 40 dB SPL in subject TB), frequencies near threshold maxima had steeper loudness growth (see Fig. 10). Overall, the results are consistent with the results from experiments 1 and 2. The curves from threshold maxima and minima converge at levels which are similar to the levels at which the fine structure of the equal loudness contours flatten out. In almost all cases, a categorical loudness of 1 cu (which is always quite close to hearing threshold) for frequencies associated with threshold maxima or minima is clearly different. The curves for the different frequencies converge at around 30 dB SPL. Therefore, the loudness-scaling data also show different slopes of loudness growth at low levels for frequencies at threshold maxima or minima.

VI. DISCUSSION

Different paradigms were used to investigate how much cochlear fine structure typically affects loudness perception. Three consistent effects were found: (a) The fine structure of equal-loudness contours flattens out at reference-tone levels around 30–40 dB SPL; (b) the slope of loudness growth differs up to 0.3 dB/dB for reference tones in maxima versus adjacent threshold minimum; (c) loudness curves from categorical loudness scaling converge at levels of about 30 dB

SPL but show different slopes at lower levels. Overall, it can be concluded that cochlear fine structure affects loudness perception of sinusoids up to levels in the order of 40 dB SPL (for the frequency range investigated here). The aim of this study was not to obtain exact loudness functions but to evaluate differences in loudness perception stemming from cochlear fine structure. Consequently, we did not try to avoid all known bias effects, e.g., in the loudness-scaling measurements, we did not test the whole dynamic range of the subjects. However, the differences in loudness perception from minima and maxima in the fine structure were reliable. Bias effects, which may influence the differences with frequency, were avoided, e.g., range effects in the categorical loudness scaling due to different minimal levels for the different frequencies. One consequence of the loudness fine structure is that the slope of loudness growth at low levels depends on whether the reference tone lays within a threshold minimum or at a threshold maximum. Although this effect was only investigated for sinusoidal test tones, it is reasonable to assume that this is of relevance for all other kinds of test signals whenever a sinusoid is used as reference tone. The fine structure can influence the results of loudness matches between different reference frequencies (a) within one subject and (b) between subjects since the fine structure is unique to each individual.

Since the isophons, or equal-loudness contours, flatten out at about 40 phons, a larger dynamic range has to be mapped to the same loudness range for stimuli with frequencies near threshold minima than for stimuli with frequencies near threshold maxima. That means that loudness compression is greater for stimuli in threshold minima than stimuli related to threshold maxima. This is consistent with the results for low-level stimuli in both loudness matching (experiment 2) and categorical loudness scaling (experiment 3). Methodological differences between the two experiments mean that there are differences in the patterns of loudness growth. In the categorical loudness-scaling procedure, the subject is evaluating each tone in isolation, providing a direct estimate of subjective loudness. However, in the loudness-matching experiment, the subject is comparing the loudness of two sets of stimuli, and the slope of loudness growth depends on the position of both the test and reference tones within threshold fine structure. When the reference tone is fixed in frequency (e.g., at a threshold minimum) and the data are plotted as a function of the reference-tone level (loudness-growth function), the different compression for varying test-tone frequencies (e.g., one close to a threshold maximum while the other is close to threshold minimum) is indicated by distinct slopes of the matching functions. Compare the black lines (reference tone at a maximum) or gray lines (reference tone at a minimum), respectively, in the second and third rows of Fig. 8. The matching function is steeper, i.e., indicating more compression, if the same reference-tone frequency is matched with a test tone in a minimum than if it is matched with a test tone in a maximum (see also Table I). Similarly, the results from the categorical loudness scaling at low levels for frequencies close to threshold minima are more compressive than for frequencies close to threshold maxima (Figs. 9 and 10). In the loudness-matching experiment, the slopes for test tones from maxima differ on average by about 1.4 dB/dB from the slopes for tones from minima matched to the same reference tone. This indicates 6 dB less compression at threshold maxima compared to threshold minima over the range of 40 dB relevant for fine structure.

The absolute slopes of the loudness-matching functions depend on the position of the reference tone within the fine structure. If the reference tone is fixed to a frequency close to a minimum (more compressive site), loudness matching will lead to shallower slopes in the loudness-growth function ($L_{\text{test}}/L_{\text{ref}}$ representation) than matches to a reference tone at a threshold maximum (less compressive site). This means that differences in loudness-matching functions stemming from the choice of reference-tone position within threshold fine structure, most probably, depends on differences in compression at threshold maxima or minima. For example, Fig. 5 shows the loudness-growth function extracted from the fine-structure measurements of subjects GL [Fig. (5a)] and TB [Fig. (5b)]. Threshold measurements around 1 kHz from subject GL indicate that the reference tone at 1 kHz is located near a minimum leading to gradual slopes at low levels. The steeper slopes in subject TB indicate that the reference tone at 1 kHz is most probably placed close to a threshold maximum in this subject.

Several authors have suggested a link between basilar-membrane compression and loudness. Florentine *et al.* (1996), for instance, have derived a loudness function from loudness temporal integration data which shows similar characteristics to basilar-membrane measurements (e.g., Ruggero *et al.*, 1997). These functions are relatively linear near threshold and more compressive at moderate levels. The different loudness compression at low levels for frequencies related to threshold maxima or minima, respectively, is also most probably closely related to BM compression. A class of cochlea models, which explain a wide range of fine-structure effects of otoacoustic emissions, can also explain fine structure in hearing threshold (Talmadge *et al.*, 1998). In this kind of model, the threshold fine structure is obtained by a local enhancement or reduction of BM excitation due to constructive or destructive interference of the initial traveling wave and multiple reflections between the characteristic site of the stimulus frequency and the oval window. In the case of constructive interference, the BM excitation will be enhanced around the characteristic site for the stimulus frequency and so leads to a reduced threshold. The magnitude of the initial and subsequent reflections depends on local properties (roughness) on the basilar membrane. Therefore, the size of the reflection depends on the basilar-membrane input/output function. We assume that the BM compression is (a) a function of BM excitation amplitude and the same over a sufficiently wide frequency range and (b) close to linear at low BM excitation and compressive at moderate BM excitation (as suggested from physiological data, e.g., Ruggero *et al.*, 1997). Under these assumptions, there will be a difference in the magnitude of vibration for the same stimulus levels at BM sites with in-phase reflections and out-of-phase reflections. Consequently, sites with in-phase reflections will be affected by BM compression at lower stimulus levels than

BM sites with reduced BM excitation due to interference. BM sites with reduced excitation (threshold maxima) are kept in the more linear range of BM characteristics for a wider range of stimulus levels and, therefore, show less loudness compression. In this model, the different loudness compression for low to moderate levels at frequencies from threshold maxima and minima is closely, but not directly, linked to the BM compression. The locally different loudness compression is not the result of locally different BM compression but caused by a shift of the operating point due to internal cochlea reflections.

This kind of cochlea model also explains most of the properties of SOAE (Talmadge *et al.*, 1998; Shera, 2003) and their close relation to threshold fine structure (Talmadge *et al.*, 1998). This relation can also be seen from experimental comparisons of threshold fine structure and SOAE frequencies (e.g., Zwicker and Schloth, 1984; Long and Tubis, 1998a, b). Independent SOAE always occur at threshold minima (there are some SOAE that are distortion products of other SOAE, and there may be no minima at these frequencies). Large evoked OAE are seen at every threshold minimum. At frequencies where the multiple reflections between characteristic BM sites and the oval window interfere constructively and lead to an enhancement of BM excitation, the resulting standing wave in the cochlea is preserved by the amplification of the active cochlea mechanisms and stabilized by BM compression. When a fraction of the energy of the standing wave is transmitted through the middle ear, it can be detected as a SOAE. Consequently, frequencies of enhanced BM excitation are directly linked to SOAE frequencies (for a detailed description of SOAE mechanism see, e.g., Shera, 2003). Several studies investigating the relation of SOAE and fine structure showed that the interaction of a strong SOAE and an external tone can sometimes be perceived as beating (discussed, e.g., in Long, 1998), which may give additional cues for signal detection at threshold. When the external tone is close to the frequency of the emission, no beating is detected because the SOAE becomes entrained by the external tone and oscillates at the same frequency and phase (reviewed in Long, 1998). High-level emissions are only entrained by tones very close to the SOAE, while low-level emissions are more easily entrained. Under these conditions, the acoustic stimulation in the cochlea will be the in-phase sum of the external tone and the SOAE. Consequently, with fixed stimulus level, the stimulation on the basilar membrane will be greater at places near SOAE than at other places. We do not know how large the stimulus is in the cochlea, but previous research has shown that little beating is detected at the levels of SOAE observed in this study (Long, 1998). Consequently, we assume that effects of beating with SOAE have minimal effect on the threshold and loudness fine structure observed in this paper.

Psychoacoustic tasks other than loudness measurement are also influenced by fine structure. Cohen (1982) showed the temporal integration function at threshold to be considerably steeper for more sensitive frequencies, i.e., a fading out of threshold fine structure for shorter stimuli. The fine structure for short sinusoidal signals probably fades out for two reasons: (1) Spectral smearing for short stimuli and even more important (2) insufficient time to build up a stable interference pattern within the cochlea. Cohen questioned whether this effect of temporal integration at threshold holds for higher stimulus levels. Due to the preservation of fine structure in equal-loudness contours up to at least 40 dB SPL (see experiment 1), it is probable that the influence of cochlear fine structure on temporal integration will hold for levels up to 40 dB SPL, at least for sinusoidal signals.

Zwicker (1986) found a negative correlation between the level of hearing thresholds of the carrier frequency and the just-noticeable degree of amplitude modulation (JNDAM) using modulation frequencies of 1, 4, 16, and 64 Hz. These are two examples of the influence of cochlear fine structure on psychoacoustical measurements in addition to loudness measurements. However, the majority of psychoacoustical studies has not considered potential effects of cochlear fine structure even when measuring loudness at low levels and when using sinusoidal signals. There are only a few studies which partially regard possible effects. For example, Buus *et al.* (1998) measured loudness of tone complexes at low levels in comparison to a sinusoidal reference. Therefore, they selected complex components individually to avoid frequency components within a pronounced threshold maximum or minimum, respectively. All components were adjusted to individual sensation levels (SL). Reckhardt *et al.* (1999) measured loudness matches at low frequencies from 200 Hz up to 1 kHz in comparison to a 1-kHz reference tone at 30 and 50 dB SPL. They found nearly half the interindividual variation in equal-loudness matches when the individual hearing threshold was taken into account. Corrections to the SL may compensate for fine structure of low-level loudness perception. Based on Reckhardt *et al.* (1999), it is even possible that the fine structure below 1 kHz is preserved up to higher SPLs than in the frequency region observed in the current study. However, a simple SL correction will lead to an overcompensation for higher stimulus levels when fine structure in loudness perception flattens out (see experiment 1).

Sinusoids, such as those used in the current study, are a very special type of stimuli. However, they are well defined and for that reason often used for technical acoustic measurements, in audiology (e.g., tone audiogram), and in many psychoacoustic experiments. The question arises whether cochlear fine structure influences only the perception of this very special type of stimulus, or if it also affects the perception of a wider range of signals. Long and Tubis (1988a) found that narrow-band noise stimuli had little effect on threshold fine structure until the bandwidth reached the bandwidth of the fine structure (in their study, 100 Hz). They observed an overall flattening out of threshold fine structure for signals of increasing bandwidth, leading to increased thresholds near threshold fine-structure minima and decreased thresholds for stimuli near threshold maxima. In these circumstances, the threshold is probably due to integration of neural activity across the bandwidth of the stimuli and, thus, may provide an indication of growth of loudness uncontaminated by threshold fine structure. Using narrow-band noises, instead of sinusoids, as test and reference stimuli in the measurement of equal-loudness contours

would, most probably, decrease intersubject variability. There are multiple effects influencing the variability of equal-loudness contours between studies, such as measurement room and choice of test-tone levels (e.g., Gabriel, 1996; 1997). The individual fine structure most probably has only a small effect on the differences. Since most studies investigated about ten or more subjects (e.g., Betke and Mellert, 1989; Suzuki *et al.*, 1989; Fastl *et al.*, 1990; Poulsen and Thøgersen, 1994; Takeshima *et al.*, 1997), the individual fine structure should be averaged out in the mean data.[6] Since most studies on equal-loudness contours are performed in a free field, the individual head-related transfer functions (HRTF) will probably determine more of the across-subjects variability than threshold fine structure.

Fine structure is possibly only a side effect of cochlea mechanics, but the existence of more sensitive resonance points may even provide some gain for near-threshold signals with broader bandwidth. Fine structure might be useful as an indicator of a healthy cochlea whether or not it leads to any gain in hearing, influences our perception significantly, or is a minor side effect. The fine structure in the so-called ''normal''-hearing subjects in the current study is variable. While in some subjects it is pronounced, in others it was hard to measure. Therefore, the question arises whether the absence of fine structure may indicate the beginning of cochlear damage, or conversely, a pronounced fine structure may be an early sign of cochlea damage. There are some indications that cochlear fine structure is a property of a healthy ear. For example, fine structure is very sensitive to cochlea insult. DPOAE fine structure reappears at a very late stage of recovery after a sudden hearing loss (Mauermann *et al.*, 1999). Ototoxic aspirin consumption leads to a loss of fine structure in OAE as well as in threshold fine structure. Shortly after beginning aspirin consumption, there is an improvement of thresholds near threshold maxima while thresholds associated with threshold minima are only elevated following 3 or 4 days of aspirin consumption (Long and Tubis, 1988a, b). Although McFadden and Platsmier (1984) claimed that there was no consistent trend in thresholds with aspirin consumption, threshold shift due to aspirin consumption was negatively correlated with the initial thresholds (a rough estimate of the position of the tones in the cochlear fine structure). Similar effects can be observed for DPOAE fine structure in ears with noise-induced temporary threshold shift (Furst *et al.*, 1992; Engdahl and Kemp, 1996). Overall, these effects are in agreement with results from cochlea modeling (e.g., Talmadge *et al.*, 1998) which indicate that damage affecting the cochlear amplifier will cause a reduction in fine structure. On the other hand, they also say that the model predicts damage, which does not directly affect the cochlear amplifier but which causes an enhanced roughness in the mechanical parameters of the cochlea. Such damage would result in a more pronounced fine structure. The amount of fine structure differs between individuals, and the differences most probably depend on the health of the cochlea, the properties of the basilar membrane, and the condition of the middle ear. The high sensitivity of fine structure to cochlear damage may offer the opportunity to further categorize the group of the ''normal-hearing'' subjects and to find methods for early diagnosis of incipient cochlear damage. Such methods might be based on psychoacoustic experiments or on OAE measurements. Before the properties of cochlear fine structure can serve as an early indicator of hearing loss, further research on cochlear fine structure and its effects on perception is necessary.

VII. SUMMARY

Fine structure of hearing thresholds and loudness perception was investigated in detail for frequencies around 1800 Hz, using different measurement paradigms. The following experiments were carried out: measurements of isophons with a high-frequency resolution (experiment 1), measurement of loudness growth functions at frequencies either around a threshold maximum or minimum, using a loudness-matching paradigm (experiment 2), and categorical loudness scaling (experiment 3). In all experiments, the results are affected by the position of the frequency within threshold fine structure for levels up to 40 dB SPL. These fine-structure variations in threshold and loudness perception for adjacent frequencies are probably one reason that there is significant intersubject variability in several psychoacoustic experiments on loudness at low to moderate levels, e.g., this fine structure influences loudness-matching paradigms when using sinusoids either as reference or test signals.

Most probably, fine structure in hearing thresholds and loudness perception is caused by interference effects of incoming and reflected traveling waves within the cochlea closely linked to the mechanisms responsible for the fine structure observed in otoacoustic emissions.

While fine-structure effects are observable in most of the normal-hearing subjects, there are some listeners with no pathological findings who do not show noteworthy fine structure. Therefore, in future studies it might be valuable to investigate whether the presence of fine structure indicates a very healthy ear or, perhaps, initial damage already observable in most normal-hearing adults.

ACKNOWLEDGMENTS

This study was supported by Deutsche Forschungsgemeinschaft, DFG Ko 942/11-3.
A fellowship from Hanse-Wissenschaftskolleg, Delmenhorst partially supported the second author while on sabbatical in Germany. We gratefully acknowledge Stefan Uppenkamp, Gerald Kidd and two anonymous reviewers for the valuable comments on the manuscript. We want to thank Monica Wagner for proofreading the manuscript.

[1]In the literature, the term ''threshold microstructure'' is often used instead of fine structure. For reason of convenience, here we consistently use the term fine structure.
[2]This was done because subject MO also participated in a different study for which a frequency region with a sufficient pronounced fine structure was needed.
[3]The results for subject TB from study 1 are about 2 years older than from study 2/3, i.e., the thresholds measured with the simple adjustment paradigm in study 1 and the adaptive interleaved in study 2/3 are not necessarily identical.
[4]Brand and Hohmann used a one-step procedure with 11 categories mapped to the same range of numbers (0–50).
[5]The initial weights w_i for the adjacent data points within the span are given

by the tricube function $w_i=(1-|(x-x_i)/d(x)|^3)^3$, where x is the predictor value associated with the response value to be smoothed, the x_i are the adjacent points to x within the selected span of data points around x, $d(x)$ gives the distances between x and the most distant predictor value within the span. The data point to be smoothed has the largest weight, i.e., the most influence on the fit, while data points outside a selected span have zero weight, i.e., no influence on the fit. For the current data an empirically selected span of 31 data points was used to receive a smoothing function that keep details of the data while avoiding an oscillating curve. To reduce the influence of outliers for the robust lowess procedure, the residuals are computed from the initially obtained smooth function as described above. Then, the residuals are used to compute robust weights for each data point in the span. The robust weights are given by $w_i = \begin{cases} (1-(r_i/6\mathrm{MAD})^2)^2 & \text{if } |r_i|<6\mathrm{MAD} \\ 0 & \text{if } |r_i|\geqslant 6\mathrm{MAD} \end{cases}$, where r_i is the residual of the ith data point produced by the initial smoothing procedure, and $\mathrm{MAD}=\mathrm{median}(|r|)$ is the median absolute deviation. If r_i is greater than 6 MAD, the robust weight is 0; if the residual r_i is small compared to 6 MAD, the robust weight is close to 1. The data are smoothed again using both the local regression weight and the robust weight for computation. Again, the residuals from the smoothed function to the original data are calculated and new robust weights are derived. This procedure is repeated for a total of five iterations to obtain the final smoothed function.

[6]If we assume amplitude variations due to fine structure of ± 7 dB, and (as a raw guess) that the amplitude of averaged fine structures from different subjects goes down with $1/\sqrt{N}$ (similar to noise), and if we have a group of ten subjects, then the variation due to fine structure will be approximately ± 2 dB, i.e., on the order of intraindividual variation of equal-loudness contour measurements (see Gabriel, 1996)

Betke, K., and Mellert, V. (**1989**). ''New measurements of equal-loudness level contours,'' in Proceedings of Inter-noise 89, 793–796.

Brand, T., and Hohmann, V. (**2002**). ''An adaptive procedure for categorical loudness scaling,'' J. Acoust. Soc. Am. **112**, 1597–1604.

Buus, S., Musch, H., and Florentine, M. (**1998**). ''On loudness at threshold,'' J. Acoust. Soc. Am. **104**, 399–410.

Cleveland, W. S. (**1979**). ''Robust locally weighted regression and smoothing scatterplots,'' J. Am. Stat. Assoc. **74**, 829–836.

Cohen, M. F. (**1982**). ''Detection threshold microstructure and its effect on temporal integration data,'' J. Acoust. Soc. Am. **71**, 1719–1733.

Elliot, E. (**1958**). ''A ripple effect in the audiogram,'' Nature (London) **81**, 1076.

Engdahl, B., and Kemp, D. T. (**1996**). ''The effect of noise exposure on the details of distortion product otoacoustic emissions in humans,'' J. Acoust. Soc. Am. **99**, 1573–1587.

Fastl, H., Jaroszewski, A., and Zwicker, E. (**1990**). ''Equal loudness contours between 100 and 1000 Hz for 30, 50, and 70 phon,'' Acustica **70**, 197–201.

Florentine, M., Buus, S., and Poulsen, T. (**1996**). ''Temporal integration of loudness as a function of level,'' J. Acoust. Soc. Am. **99**, 1633–1644.

Furst, M., Reshef, I., and Attias, J. (**1992**). ''Manifestations of intense noise stimulation of spontaneous otoacoustic emissions and threshold microstructure: Experiment and model,'' J. Acoust. Soc. Am. **91**, 1003–1014.

Gabriel, B. (**1996**). ''Equal-loudness Level Contours: Procedures, Factors and Models,'' Ph.D. thesis, University of Oldenburg, Germany.

Gabriel, B., Kollmeier, B., and Mellert, V. (**1997**). ''Influence of individual listener, measurement room, and choice of test-tone levels on the shape of equal-loudness level contours,'' Acta Acust. (Beijing) **83**, 670–684.

He, N.-J. (**1990**). ''Frequency shift in spontaneous otoacoustic emission and threshold fine structure,'' Ph.D. thesis, University of Iowa.

He, N.-J., and Schmiedt, R. A. (**1993**). ''Fine structure of the 2 f_1-f_2 acoustic distortion product: Changes with primary level,'' J. Acoust. Soc. Am. **94**, 2659–2669.

Hellbruck, J., and Moser, L. M. (**1985**). ''Hörgeräte-Audiometrie: Ein computerunterstüztes psychologisches Verfabren zur Högeräteanpassung,'' Psychologische Beiträge **27**, 494–508.

Heller, O. (**1985**). ''Hörfeldaudiometrie mit dem Verfahren der Kategorienunterteilung (KU),'' Psychologische Beiträge **27**, 478–493.

Hellman, R. P., and Zwislocki, J. (**1961**). ''Some factors affecting the estimation of loudness,'' J. Acoust. Soc. Am. **33**, 687–694.

Horst, W. J., and de Kleine, E. (**1999**). ''Audiogram fine structure and spontaneous otoacoustic emissions in patients with Meniere's disease,'' Audiology **38**, 267–270.

Kapadia, S., and Lutman, M. E. (**1999**). ''Reduced-audiogram ripple in normally hearing subjects with weak otoacoustic emissions,'' Audiology **38**, 257–261.

Kemp, D. T. (**1979**). ''The evoked cochlear mechanical response and auditory microstructure—Evidence for a new element in cochlear mechanics,'' Scand. Audiol. Suppl. **9**, 35–47.

Kemp, D. T. (**1980**). ''Towards a model for the origin of cochlear echoes,'' Hear. Res. **2**, 533–548.

Long, G. R. (**1984**). ''The microstructure of quiet and masked thresholds,'' Hear. Res. **15**, 73–87.

Long, G. R. (**1993**). ''Perceptual consequences of otoacoustic emissions,'' in *Contributions to Psychological Acoustics: Results of the 6th Oldenburg Symposium on Psychological Acoustics*, edited by A. Schick (University of Oldenburg Press, Oldenburg, Germany), pp. 59–80.

Long, G. R. (**1998**). ''Perceptual consequences of the interactions between spontaneous otoacoustic emissions and external tones. I. Monaural diplacusis and aftertones,'' Hear. Res. **119**, 49–60.

Long, G. R., and Tubis, A. (**1988a**). ''Investigations into the nature of the association between threshold microstructure and otoacoustic emissions,'' Hear. Res. **36**, 125–138.

Long, G. R., and Tubis, A. (**1988b**). ''Modification of spontaneous and evoked otoacoustic emissions and associated psychoacoustic microstructure by aspirin consumption,'' J. Acoust. Soc. Am. **84**, 1343–1353.

Mauermann, M., Uppenkamp, S., van Hengel, P. W. J., and Kollmeier, B. (**1999**). ''Evidence for the distortion product frequency place as a source of distortion product otoacoustic emission (DPOAE) fine structure in humans. II. Fine structure for different shapes of cochlear hearing loss,'' J. Acoust. Soc. Am. **106**, 3484–3491.

Mauermann, M., Uppenkamp, S., and Kollmeier, B. (**1997**). ''Periodizität und Pegelabhängigkeit der spektralen Feinstruktur von Verzerrungsprodukt-Emissionen [Periodicity and dependence on level of the distortion product otoacoustic emission spectral fine-structure],'' Audiol. Akustik **36**, 92–104.

McFadden, D., and Plattsmier, H. S. (**1984**). ''Apirin abolishes spontaneous oto-acoustic emissions,'' J. Acoust. Soc. Am. **76**, 443–448.

Poulsen, T., and Thørgersen, L. (**1994**). ''Hearing threshold and equal loudness contours in a free sound field for pure tones from 1 kHz to 16 kHz,'' in Proc. Nordic Acoust. Meeting, 195–198.

Reckhardt, C., Mellert, V., and Kollmeier, B. (**1999**). ''Factors influencing equal-loudness contours,'' in *Psychophysics, Physiology and Models of Hearing*, edited by T. Dau, V. Hohmann, and B. Kollmeier (World Scientific, Singapore), pp. 113–116.

Ruggero, M. A., Rich, N. C., Recio, A., Narayan, S. S., and Robles, L. (**1997**). ''Basilar-membrane responses to tones at the base of the chinchilla cochlea,'' J. Acoust. Soc. Am. **101**, 2151–2163.

Shera, C. A. (**2003**). ''Mammalian spontaneous otoacoustic emissions are amplitude-stabilized cochlear standing waves,'' J. Acoust. Soc. Am. **114**, 244–262.

Shera, C. A., and Zweig, G. (**1993**). ''Order from chaos: Resolving the paradox of periodicity in evoked otoacoustic emissions,'' in *Biophysics of Hair Cell Sensory Systems*, edited by H. Duifhuis, J. W. Horst, P. van Dijk, and S. M. van Netten (World Scientific, Singapore), pp. 54–63.

Smurzynski, J., and Probst, R. (**1998**). ''The influence of disappearing and reappearing spontaneous otoacoustic emissions on one subject's threshold microstructure,'' Hear. Res. **115**, 197–205.

Suzuki, S., Suzuki, Y., Kono, S., Sone, T., Kumagai, M., Mirura, H., and Kado, H. (**1989**). ''Equal-loudness level contours for pure tone under free field listening condition (I)—Some data and considerations on experimental conditions,'' J. Acoust. Soc. Jpn. (E) **10**, 329–338.

Takeshima, H., Suzuki, Y., Kumagai, M., Sone, T., Fujimori, T., and Mirura, H. (**1997**). ''Equal loudness level measured with the method of constant stimuli—Equal loudness contours for pure tone under free-field listening condition (II),'' J. Acoust. Soc. Jpn. (E) **18**, 337–340.

Talmadge, C., Tubis, A., Long, G. R., and Piskorski, P. (**1998**). ''Modeling otoacoustic emission and hearing threshold fine structures in humans,'' J. Acoust. Soc. Am. **104**, 1517–1543.

Thomas, I. B. (**1975**). ''Microstructure of the pure-tone threshold,'' J. Acoust. Soc. Am. Suppl. 1 **57**, S26–27(abstract).

van den Brink, G. (**1970**). ''Experiments on binaural diplacusis and tone perception,'' in *Frequency Analysis and Periodicity Detection in Hearing*, edited by R. Plomp and G. F. Smoorenburg (Sijthoff, Leiden), pp. 362–374.

van den Brink, G. (**1980**). ''Cochlear mechanics as the possible cause of

binaural diplacusis,'' in *Psychological, Physiological and Behavioural Studies in Hearing*, edited by G. van den Brink and F. Bilsen (Delft University Press, Delft), pp. 64–67.
Zweig, G., and Shera, C. A. (**1995**). ''The origins of periodicity in the spectrum of evoked otoacoustic emissions,'' J. Acoust. Soc. Am. **98**, 2018–2047.
Zwicker, E. (**1986**). ''Spontaneous oto-acoustic emissions, threshold in quiet, and just noticeable amplitude modulation at low levels,'' in *Auditory Frequency Selectivity*, edited by B. C. J. Moore and R. D. Patterson (Plenum, New York), pp. 49–59.
Zwicker, E., and Peisl, W. (**1990**). ''Cochlear processing in analog models, in digital models, and in human inner ear,'' Hear. Res. **44**, 206–216.
Zwicker, E., and Schloth, E. (**1984**). ''Interrelation of different oto-acoustic emissions,'' J. Acoust. Soc. Am. **75**, 1148–1154.

Cochlear implant speech recognition with speech maskers[a)]

Ginger S. Stickney[b)] and Fan-Gang Zeng
University of California, Irvine, Department of Otolaryngology—Head and Neck Surgery, 364 Medical Surgery II, Irvine, California 92697-1275

Ruth Litovsky
University of Wisconsin, Department of Communicative Disorders, Madison, Wisconsin 53706

Peter Assmann
University of Texas at Dallas, School of Behavioral and Brain Sciences, Box 830688, Richardson, Texas 85083-0688

(Received 28 May 2003; revised 20 April 2004; accepted 16 May 2004)

Speech recognition performance was measured in normal-hearing and cochlear-implant listeners with maskers consisting of either steady-state speech-spectrum-shaped noise or a competing sentence. Target sentences from a male talker were presented in the presence of one of three competing talkers (same male, different male, or female) or speech-spectrum-shaped noise generated from this talker at several target-to-masker ratios. For the normal-hearing listeners, target-masker combinations were processed through a noise-excited vocoder designed to simulate a cochlear implant. With unprocessed stimuli, a normal-hearing control group maintained high levels of intelligibility down to target-to-masker ratios as low as 0 dB and showed a release from masking, producing better performance with single-talker maskers than with steady-state noise. In contrast, no masking release was observed in either implant or normal-hearing subjects listening through an implant simulation. The performance of the simulation and implant groups did not improve when the single-talker masker was a different talker compared to the same talker as the target speech, as was found in the normal-hearing control. These results are interpreted as evidence for a significant role of informational masking and modulation interference in cochlear implant speech recognition with fluctuating maskers. This informational masking may originate from increased target-masker similarity when spectral resolution is reduced. [DOI: 10.1121/1.1772399]

PACS numbers: 43.66.Dc, 43.66.Ts [KWG] Pages: 1081–1091

I. INTRODUCTION

Speech recognition by cochlear-implant users has improved significantly over the past decade as a result of advances in technology, with scores averaging 70%–80% for sentences in quiet. However, the ability of most implant users to understand speech in noisy environments remains quite poor. In general, cochlear-implant listeners require much higher target-to-masker ratios than normal-hearing listeners to achieve similar levels of performance on speech recognition tasks in noise (Kessler *et al.*, 1997; Dorman *et al.*, 1998; Zeng and Galvin, 1999). Poor performance in noise in cochlear-implant listeners is due, at least partially, to the limited number of electrodes that can be safely inserted into the cochlea and the spectral mismatch from the warped frequency-to-electrode allocation (Shannon *et al.*, 2001; Friesen *et al.*, 2001; Garnham *et al.*, 2002). When normal-hearing subjects listened to an eight-channel implant simulation, their speech recognition scores for sentences embedded in steady-state speech-shaped noise dropped from 100% correct in quiet to 55% correct at +2 dB signal-to-noise ratio, and to 16% correct at −2 dB signal-to-noise ratio (Dorman *et al.*, 1998). Compared to eight channels required to achieve maximum speech recognition in quiet, 12 or more channels were required to achieve maximum performance for speech in noise (Dorman *et al.*, 1998; Fu *et al.*, 1998). Potential masking effects and mechanisms contributing to the poor performance by cochlear-implant subjects in noise are described below.

Energetic masking is thought to be a peripheral masking phenomenon that occurs when energy from two or more sounds overlaps both spectrally and temporally, thereby reducing signal detection. Studies on speech intelligibility in noise with hearing impaired and cochlear-implant listeners have typically used energetic maskers. When steady-state speech-spectrum-shaped noise (SSN), one of the most effective energetic maskers of speech, is presented as a masker, the difference in the speech recognition threshold between normal-hearing and hearing-impaired listeners ranges from 2 to 5 dB (e.g., Glasberg and Moore, 1989; Plomp, 1994). Much larger differences of 7–15 dB can be found when the background fluctuates in intensity (Duquesnoy, 1983; Takahashi and Bacon, 1992; Eisenberg *et al.*, 1995). When the masking noise is speech, dips in intensity can occur during brief pauses between words or during the production of low-energy phonemes such as stop consonants. Spectral dips can occur in the valleys between formant peaks, or at low frequencies during the production of fricative sounds. Normal-

[a)]Portions of this work were presented at the 25th ARO Annual Midwinter Research Meeting, St. Petersburg Beach, FL, 2002.
[b)]Electronic mail: stickney@uci.edu

hearing listeners have the ability to take advantage of these brief intensity and/or spectral dips to produce improved speech intelligibility and release from masking. In contrast, hearing-impaired listeners show little or no masking release with fluctuating background sounds (Duquesnoy, 1983; Festen, 1987; Festen and Plomp, 1990; Hygge *et al.*, 1992). In addition to their higher thresholds in quiet and, consequently, poorer signal-to-noise ratios during the dips of the masker, the lack of masking release and the poorer performance of hearing-impaired listeners has been attributed to a loss of spectral and temporal resolution (Festen and Plomp, 1990).

More recent studies, however, have found that fluctuating maskers do not always allow masking release even in normal-hearing listeners. For example, some studies have found greater masking with a single competing talker than with SSN in normal-hearing individuals (Brungart, 2001; Hawley *et al.*, 2004). It is believed that the poorer performance with single-talker maskers is due to a combination of ''energetic masking'' (resulting from overlap of the target and masker in the auditory periphery) and a second type of masking called ''informational masking'' [resulting from competition between the target and masker at more central stages of auditory processing (e.g., Brungart, 2001)].

Traditionally, informational masking had been defined as a higher-level masking phenomenon that arises from masker uncertainty in detection tasks (Pollack, 1975; Watson *et al.*, 1976). In terms of speech perception, the temporal and spectral pattern in a competing voice is much less predictable than in a SSN masker. This variation might make it more difficult for the listener to develop certain knowledge about the competitor, and hence the listener may experience more difficulty segregating the target from competing sounds. Another component of informational masking with single-talker maskers can be attributed to the linguistic nature of the masker. Brungart (2001) observed that when listeners were asked to identify the closed-set number and color categories of a target phrase masked by a simultaneous phrase from the same corpus of materials, they often reported one of the words in the masker phrase, as opposed to a random response. Finally, informational masking is believed to occur when the listener is unable to segregate the target's components from those of the similar sounding masker. Thus temporal and spectral similarities between the masker and target appear to play a role in informational masking (Arbogast *et al.*, 2001; Brungart, 2001; Oh and Lufti, 2000; Kidd *et al.*, 2001).

Informational masking can be reduced by introducing a cue that reduces the similarity between the target and masker. For example, when two voices compete, it is easier to understand one voice if the competing voice has a different pitch, or occupies a different fundamental frequency (F0) range (Assmann and Summerfield, 1990; Bird and Darwin, 1998; Brokx and Nooteboom, 1982). Because cochlear-implant users do not receive a strong sensation of pitch through either the temporal or the place coding mechanism (Zeng, 2002), they would have great difficulty separating voices with similar F0's. In addition, due to the relatively small number of spectral channels in cochlear implants, the formants and their transitions are not well defined. Qin and Oxenham (2003) found that normal-hearing subjects listening to speech processed through a 4-, 8-, or 24-channel cochlear-implant simulation had difficulty segregating a target sentence from a competing voice. Normal-hearing subjects listening to simulated implant processing and cochlear-implant users may therefore experience more informational masking with a single-talker masker than has been found with normal-hearing subjects listening to natural, unprocessed speech.

Greater informational masking can also occur when the temporal modulation properties of competing sounds are similar. Support for this conclusion comes from psychophysical studies investigating modulation interference (Yost *et al.*, 1989). In two more recent studies, weaker masking effects have been observed with unmodulated maskers compared to modulated noise with modulation rates similar to those found in natural speech, but only when the target speech was band-limited (Kwon and Turner, 2001), presented to implant listeners, or presented as an implant simulation (Nelson *et al.*, 2003). Based on these results, it appears that when the noise was modulated at speechlike rates, it became perceptually indistinguishable from the spectrally limited, processed speech.

The present study investigated speech recognition in cochlear-implant and normal-hearing listeners using sentences masked by either SSN or one of three competing voices with varying degrees of temporal and spectral similarity to the target speech. It was hypothesized that cochlear-implant users would experience greater difficulties with competing single-talker speech than SSN because of the greater role of informational masking when spectral resolution is reduced. The masking effects were evaluated in normal-hearing listeners as a function of the number of noise bands in a cochlear-implant simulation (experiment 1) and in cochlear-implant listeners (experiment 2). The main objective was to determine if, and under what circumstances, listeners with reduced spectral information exploit temporal and/or spectral differences to segregate competing speech stimuli and thereby reduce informational masking.

II. EXPERIMENT 1: SPEECH RECOGNITION BY NORMAL-HEARING SUBJECTS WITH SINGLE-TALKER AND SSN MASKERS

A. Methods

1. Listeners

Three groups of 25 young native English speakers (five subjects for each of the five channel conditions) were recruited from the Undergraduate Social Sciences Subject Pool at the University of California, Irvine. All subjects reported normal hearing. Subjects received course credit for their participation.

2. Test materials

Subjects listened to IEEE sentences (Rothauser *et al.*, 1969) in two conditions: unprocessed and vocoder-processed. All sentences in this study consisted of a subset of the 72 phonetically balanced lists of ten sentences (five keywords each) that were recorded by Hawley *et al.* (1999). The target sentences were spoken by a male talker in the presence

of either steady-state, speech-spectrum-shaped noise (SSN), or a different sentence. Three different talkers and the SSN generated from that talker were used as the maskers for each of three groups of 25 listeners. The competing sentence could be spoken by the same male talker as the target sentence (mean F0=108 Hz), a different male talker (mean F0 =136 Hz), or a female talker (mean F0=219 Hz). The F0 values were estimated using a Matlab implementation of the TEMPO algorithm (Kawahara *et al.*, 1999). The same competing sentence (''Port is a strong wine with a smoky taste'') was used throughout testing to avoid confusion of the target and masker sentences when the same male was used as the masker. The SSN maskers were constructed by filtering white noise with the masker sentence's long-term spectral envelope derived via a 20-order autocorrelation LPC analysis. The LPC approach removed the harmonicity and periodicity associated with F0 while producing the same long-term spectrum as the masker sentence. The masker and target had the same onset, but the masker's duration was longer than all target sentences. The level of the masker was set to approximately 65 dB SPL (Brüel & Kjær 2260 Investigator sound level meter; Brüel & Kjær Type 4152 artificial ear) and the level of the target varied around 65 to 85 dB SPL depending on the target-to-masker ratio (TMR).

3. Signal processing

The unprocessed sentences and SSN were scaled to the same root-mean-square value prior to reducing the target sentence attenuation (TDT-II PA4) to allow the following TMR conditions: +20, +15, +10, +5, and 0 dB. The target sentence was then mixed with the masking signal (TDT-II SM3). In the cochlear-implant simulation, the combined target and masking signal was processed by a real-time noise-excited vocoder (DSP sound card: Turtle Beach FIJI; Motorola DSP chip: DSP56311EVM). The mixed signal was preemphasized using a first-order Bessel IIR filter with a cutoff frequency of 1200 Hz and processed into 1, 2, 4 or 8 frequency bands using sixth-order elliptical IIR filters based on the Greenwood map (Greenwood, 1990). The bandpass filter cutoff frequencies for the two-channel simulation were 300, 2009, and 10 000 Hz. For the four-channel simulation, the cutoff frequencies were 300, 840, 2009, 4536, and 10 000 Hz. Cutoff frequencies for the eight-channel processor were 300, 519, 840, 1314, 2009, 3032, 4536, 6748, and 10 000 Hz. The envelope from each band was extracted by half-wave rectification followed by low-pass filtering using second-order Bessel IIR filters at a 500-Hz cutoff frequency. The envelope was then used to modulate a white noise carrier processed by the same bandpass filter used for the original analysis band. The envelope-modulated noise from each band was then combined and delivered through headphones.

4. Procedure

The stimuli were presented monaurally to the right ear through headphones (Sennheiser HDA 200), with subjects seated in an IAC sound booth. Prior to testing, subjects were presented with three practice sessions of ten sentences each. The subjects typed their response using the computer keyboard and were encouraged to guess if unsure. Subjects were instructed to correct typos and avoid misspellings. Their responses were collected and automatically scored by the percentage of the keywords correctly identified. In the first practice session, subjects listened to unprocessed sentences in quiet at an average level of 65 dB SPL. Correct identification of at least 85% of the sentence key words was required to partake in the test session. Approximately 5% of the subjects were disqualified based on this performance criterion. The second and third practice sessions were used to familiarize listeners with the specific masking and channel condition that they were assigned to in the test session. Separate practice sessions were used for single-talker and noise maskers. In both of the latter practice sessions, two sentences were presented for each of the five TMR conditions used in the actual experiment: 0, 5, 10, 15, and 20 dB. No score was calculated for these two practice sets.

In the test session, each group of 25 subjects listened to one of the three competing talkers in one session, and the corresponding SSN in a separate session, with the order of sessions randomized. Each session took approximately 30 min to complete. Within each group of 25 listeners, there were five subjects for each of the randomly assigned speech processing conditions (one, two, four, or eight channels, or the unprocessed speech). Each subject was presented with one talker and speech processing combination, but received all five TMRs. There were ten randomized sentences (five keywords each) for each TMR, for a total of 50 sentences for the single-talker masker and another 50 sentences for the SSN masker. Results were scored in terms of the percentage of keywords correctly identified at each TMR. Results with one and two channels were close to 0% and were not included in the statistical analyses.

Because of the ceiling and floor effects for the natural and four-channel conditions, respectively, the TMR conditions were extended for a second group of ten subjects (five subjects each for the four-channel and natural speech conditions). For the four-channel condition, higher TMRs were added as well as a quiet condition, producing the following five conditions: 15, 20, 25, and 30 dB TMR and ''in quiet''. For natural speech, lower TMRs were added (−10 and −15 dB TMR), producing five conditions: 5, 0, −5, −10, and −15 dB TMR. Only the different male talker and the SSN generated from that talker were used as maskers, otherwise the previous procedures and sentences were retained.

B. Results

1. Speech recognition in noise as a function of the number of channels

Using HINT sentences, higher scores around 20% have been observed with a two-channel simulation (Friesen *et al.*, 2001). The lower performance with the IEEE sentences used here was most likely due to their reduced contextual information (Nittrouer and Boothroyd, 1990; Rabinowitz *et al.*, 1992).

Figure 1 shows speech recognition results as a function of the TMR for three types of maskers: same male talker as the target (top row), different male talker than the target (middle row), or a female talker (bottom row). These were

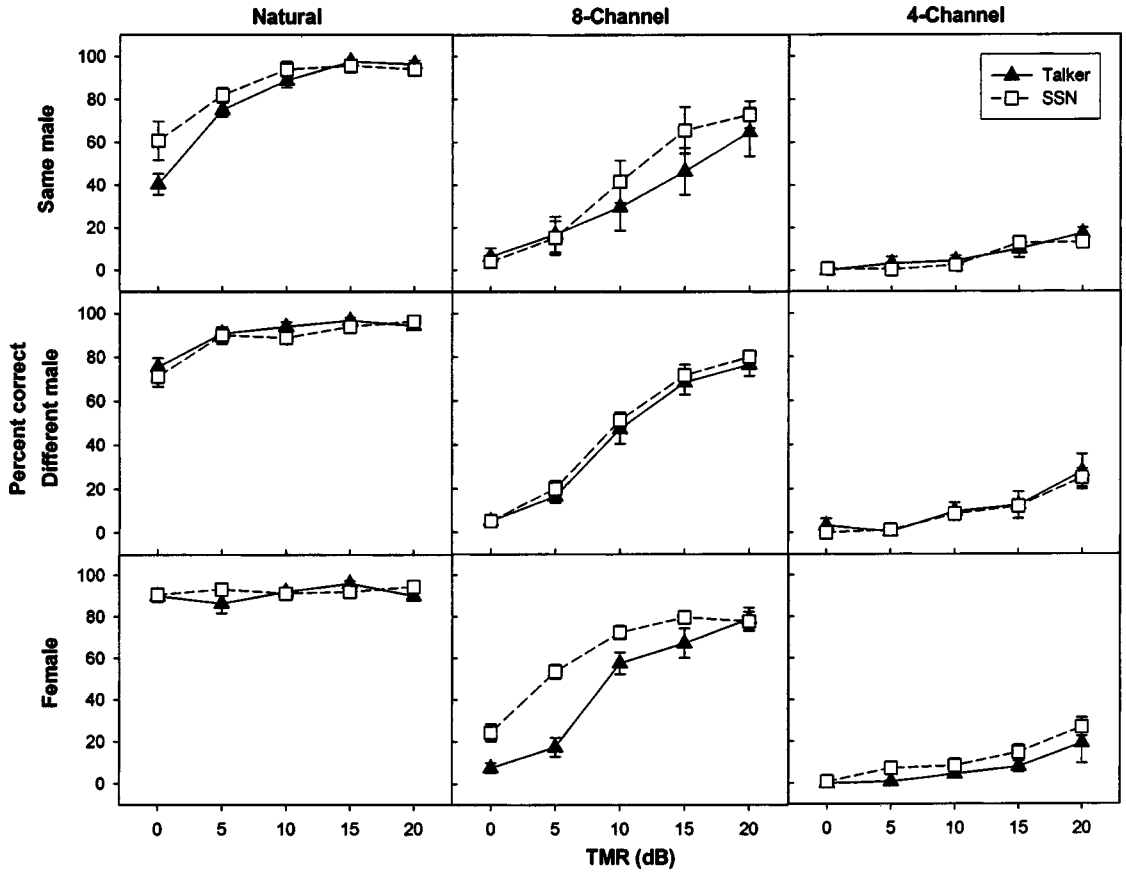

FIG. 1. Speech recognition performance of normal-hearing subjects listening to either a single-talker masker (filled triangles) or steady-state, speech-spectrum-shape noise, SSN (unfilled squares), as a function of the target-to-masker ratio (TMR). Separate panels show performance as a function of the number of channels (columns) and talker (rows) used for the masker. Error bars represent the standard error of the mean.

each presented either as natural speech (left column) or an eight-channel (middle column) or four-channel (right column) cochlear-implant simulation. Within each panel, results are compared for SSN (open squares) and single-talker (filled triangles) maskers. The SSN maskers had a constant intensity over time, whereas the single-talker masker was a sentence which varied in intensity and spectral content over time. Note that, similar to there being three single-talker maskers, there were three SSN maskers that were each generated from one of the three talkers. A mixed design ANOVA was performed with talker and channel as between-subjects variables and the TMR as a within-subjects variable. The general finding was that the cochlear-implant simulation produced significantly poorer performance than the natural condition [$F(2,36)=711.13$, $p<0.001$]. A *posthoc* Scheffé analysis (Scheffé, 1953), collapsed across masker type, showed significant differences among the three processing conditions ($p<0.001$). Higher performance was found with more channels, and natural speech produced the best performance. Performance generally increased as a function of the TMR [$F(4,33)=145.06$, $p<0.0001$], and there was a significant interaction between TMR and processing [$F(8,66)=27.42$, $p<0.001$]. Figure 1 demonstrates that natural speech maintained fairly high levels of intelligibility down to 0 dB TMR. Although performance with natural speech dropped to 40% at lower TMRs, it remained generally high compared with all other conditions. In the 8-channel condition, even the highest TMR of 20 dB resulted in less than 80% correct responses.

Of particular interest in the present findings was the significantly different performance between the SSN and the single-talker masker [$F(1,36)=36.00$, $p<0.001$] and the significant interaction between the masker type and the processing [$F(2,36)=5.21$, $p<0.01$]. A simple effects analysis revealed that single-talker maskers produced lower performance than noise maskers with natural speech [$F(1,12)=6.405$, $p<0.05$] and eight channels [$F(1,12)=8.404$, $p<0.05$], but not with four channels ($p=0.43$). For natural speech this occurred only when the masker was the same talker as the target. This was most apparent when the masker and target were at similar levels, suggesting that the same male masker produced some informational masking. Performance with the other two talkers was at or near ceiling and therefore failed to show an effect of masker. Likewise performance with four channels was so low for most TMR conditions that there was no masker effect. For the eight-channel condition, only the female talker showed a difference across masker types, with the single-talker masker producing lower performance than the noise masker. The combined results contributed to a main effect of talker [$F(2,36)=10.78$, $p<0.001$], a significant interaction of talker×masker [$F(2,36)=4.27$, $p<0.05$], and a significant four-way interaction of talker×masker×processing×TMR [$F(16,101)=2.65$, $p<0.01$].

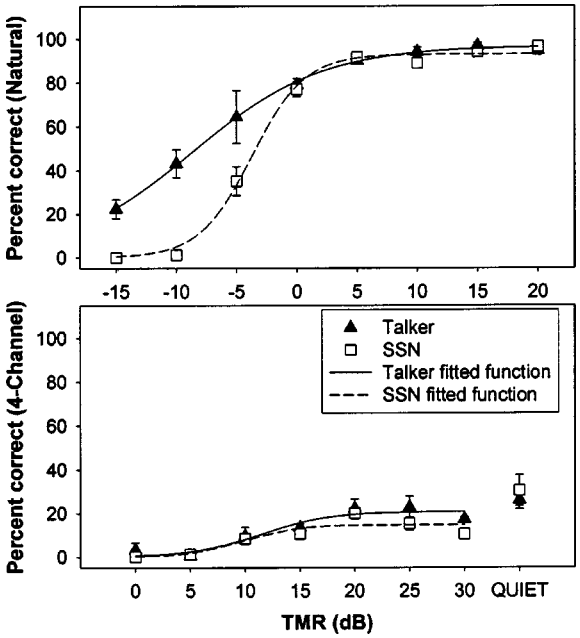

FIG. 2. Speech recognition performance with extended target-to-masker ratios (TMRs) for the natural speech (upper panel) and four-channel conditions (lower panel). Performance is shown for single-talker (filled triangles) and SSN maskers (unfilled squares). The data in this figure was for the "different male" masker condition only, since this was the only talker used for the "extended TMR" group.

The TMR conditions were subsequently extended in the four-channel and natural speech conditions to examine differential amounts of masking from single-talker and noise maskers without confounding floor and ceiling effects, respectively. Because independent sample *t*-tests showed no differences between standard and extended TMR subject groups with similar TMR conditions ($p \geqslant 0.06$), data from the two groups were averaged. Figure 2 shows pooled results with the different male masker for the natural speech (top) and the four-channel (bottom) processing conditions. A three-parameter sigmoid function was fitted with the solid line representing the fit to the single-talker masker data and the dashed line to the SSN data (Zeng and Galvin, 1999). The sigmoid function was well fit to the natural speech ($r^2 = 0.99$) and natural SSN ($r^2 = 0.99$) data, producing the estimated speech reception threshold (i.e., the TMR required to produce a score of 50%) of -9 dB for the single-talker masker and -4 dB for the SSN masker. The fit to the four-channel data was reasonable (single talker: $r^2 = 0.90$; SSN: $r^2 = 0.81$), producing the estimated speech reception threshold of 11 dB for the single talker masker and 10 dB for the SSN masker. For the natural speech data, note that from 0 to -10 dB TMR the difference in intelligibility between the single-talker and SSN masker increased. Although extending the TMRs below 0 dB produced significantly poorer performance for the SSN than for the single-talker masker [$F(1,4) = 21.92$, $p < 0.01$] in the natural speech condition, extending the TMRs above 20 dB in the four-channel condition produced no difference in performance between the two masker types ($p = 0.07$) and no further improvement in speech recognition scores. In the natural speech condition (for TMRs$<$0 dB), the better performance with the single-talker masker than with the noise masker indicated a release from masking, a phenomenon that was never observed in cochlear-implant simulations.

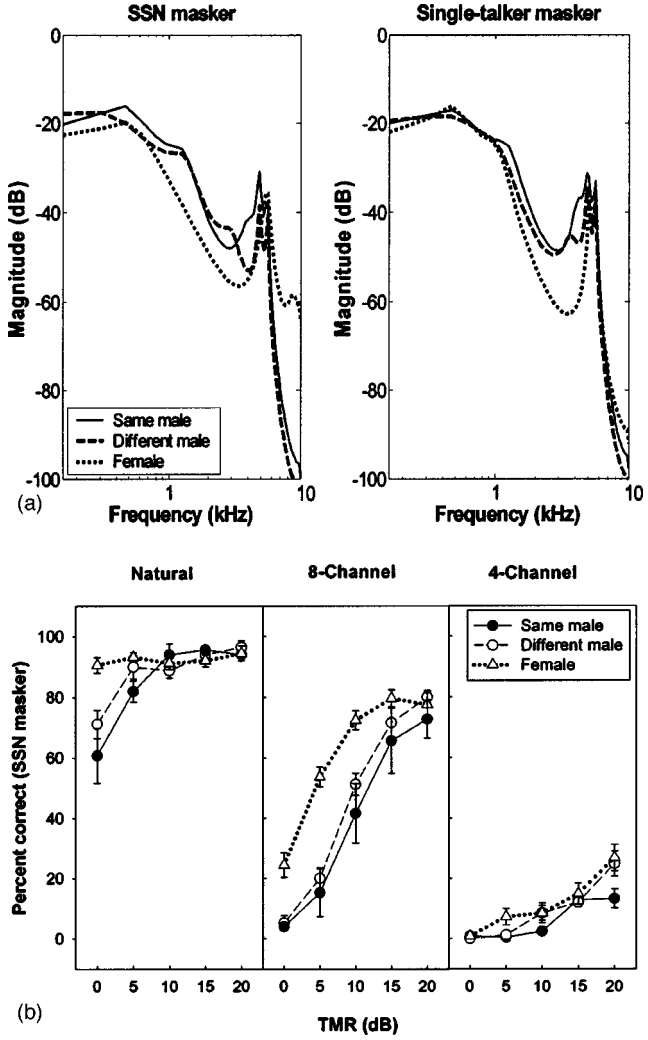

FIG. 3. (a) The long-term average spectral shape of the two male ("same male:" solid line; "different male:" dashed line) and female talkers (dotted line). Similar spectral shapes were found for the steady-state, speech-spectrum-shaped noise masker, SSN (left panel), and the single-talker masker (right panel). (b) Speech recognition performance with each steady-state, speech-spectrum-shaped noise masker (SSN) as a function of the target-to-masker ratio (TMR) and number of channels (columns). Results for the "same male" SSN as the masker are shown as filled circles with solid lines, unfilled circles and dashed lines are used for the "different male" SSN, and unfilled triangles with dotted lines are used for the "female" SSN.

2. Comparison of SSN maskers across talkers

For a closer inspection of the spectral energetic maskers, Fig. 3(a) shows the long-term SSN amplitude spectrum (left panel) and speech spectrum (right panel) for the same male (solid line), different male (dashed line), and female talkers (dotted line). The spectral shapes of the two male voices were fairly similar in comparison to the female voice, which had less energy at intermediate frequencies between 2 and 5 kHz but more energy at higher frequencies. To facilitate comparison, Fig. 3(b) replots the SSN data from Fig. 1 and contrasts speech recognition performance with different talkers in the same panel for both natural (left panel) and simu-

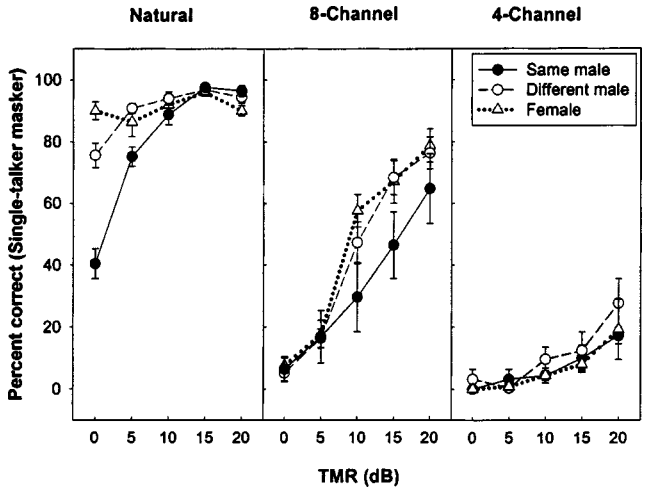

FIG. 4. Speech recognition performance with each competing talker as a function of the target-to-masker ratio (TMR) and number of channels (columns). Results for the ''same male'' talker as the masker are shown as filled circles with solid lines, unfilled circles and dashed lines are used for the ''different male'' talker, and unfilled triangles with dotted lines are used for the ''female'' talker.

lation conditions (two right panels). A simple effects analysis focusing on the three SSN maskers collapsed across channels revealed a significant effect of talker [$F(2,36)=16.58$, $p<0.001$]. A *posthoc* Scheffé analysis showed significant differences between male and female masker (same male: $p<0.001$; different male: $p<0.01$), but no differences between the two male maskers ($p=0.16$). These results are consistent with greater differences in the long-term average spectral shape for the female SSN relative to the male SSN maskers. Different from the female SSN, the two male SSN maskers provide similar amounts of spectral energetic masking.

For each channel condition, a Scheffé analysis along with an examination of the means showed that the natural speech condition did not exhibit any differences across SSN maskers [$F(2,12)=3.36$, $p=0.07$] due to the ceiling effect. For the eight-channel condition, the highest performance was obtained with female SSN (female versus same male: $p<0.01$; female versus different male: $p<0.05$) and no difference was found between the two male SSN maskers ($p=0.56$). For the four-channel condition, the highest scores were again obtained for the female SSN, but significant differences were only found between the most intelligible (i.e., the female SSN) and the least intelligible (i.e., the same male SSN) masker ($p<0.01$).

3. Comparison of single-talker maskers

Figure 4 shows speech recognition with single-talker maskers as a function of channel condition and talker. Simple effects analyses of single-talker maskers, averaged across processing conditions, revealed a significant effect of talker [$F(2,36)=5.17$, $p<0.05$]. A *posthoc* Scheffé analysis revealed that the lowest performance occurred with the same male single-talker masker ($p<0.05$), and no significant differences were found between the different male and female maskers ($p=0.99$).

An analysis of each channel condition showed that the differences across single-talker maskers stems exclusively from the natural speech condition [$F(2,12)=11.54$, $p<0.01$], which showed the lowest performance with the same male single-talker masker (Scheffé: $p<0.01$) and no difference between the other two single-talker maskers ($p=0.98$). In contrast, no significant talker differences were found across any of the single-talker maskers for the eight- and four-channel conditions. This interesting finding is unlike that found with each of the SSN maskers, and an explanation is offered in Sec. IV.

III. EXPERIMENT 2: SPEECH RECOGNITION BY COCHLEAR-IMPLANT SUBJECTS WITH SINGLE-TALKER AND SSN MASKERS

A. Methods

1. Listeners

Five postlinguistically deafened users of the Nucleus cochlear implant participated in this experiment (Table I). All cochlear-implant subjects were native English speakers with 5 to 13 years of experience with their device.

2. Test materials

The cochlear-implant subjects listened to only the unprocessed, natural sentences, which included the same target and masker sentences used for the normal-hearing listeners in experiment 1. As with the normal-hearing listeners, there was no repetition of the test material.

3. Procedure

The stimuli were passed through a Cochlear Corporation Audio Input Selector (AIS) connected to the subjects' speech processor. The AIS attenuates the analog output from the TDT or soundcard before it is delivered to the speech processor. Prior to testing, subjects listened to sentences and were asked to adjust the level of the AIS to a comfortable

TABLE I. Subject demographics.

Subject	Age	Implant	Speech strategy	Duration of hearing loss (years)	Duration of deafness (years)	Duration of implant use (years)
CI1	45	Nucleus-22	SPEAK	<1	<1	10
CI2	51	Nucleus-22	SPEAK	<1	5	12
CI3	60	Nucleus-22	SPEAK	51	13	11
CI4	69	Nucleus-22	SPEAK	43	5	13
CI5	68	Nucleus-24	SPEAK	<1	17	5

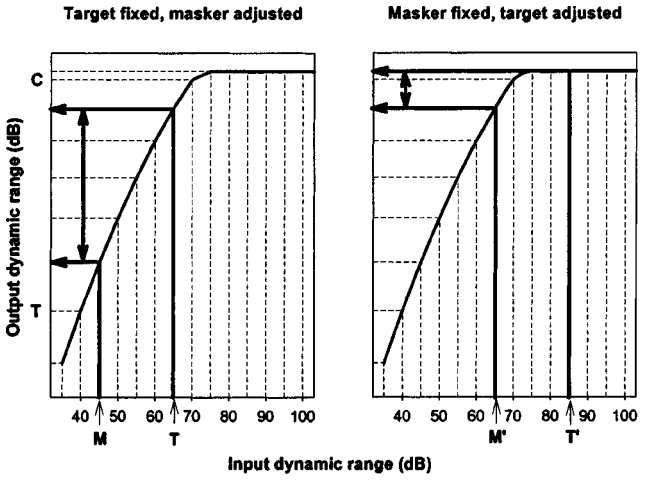

FIG. 5. Schematic of a compression input-output function. The input dynamic range (*x* axis) is shown as a function of the output dynamic range (*y* axis) for the two procedures used in experiment 2. The left panel shows the schematic for the procedure where the target (T) is fixed at a comfortable loudness and the masker (M) is adjusted from below that level to produce each target-to-masker ratio (TMR). The right panel shows the function for when the masker (M′) was fixed at the comfortable loudness level and the target (T′) was raised above that level to produce each TMR (right panel). Note the much greater range of TMRs (arrows along the *y* axis) available to the listener when both the masker and target are kept at or below the upper comfort level (C). Above the C-level the sound would be peak-clipped.

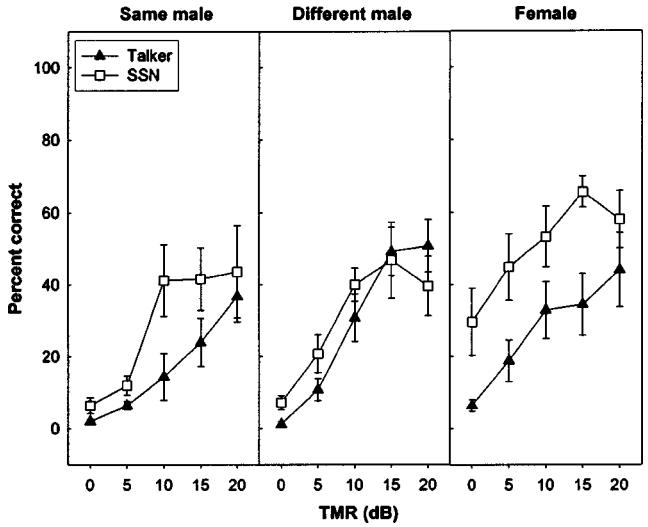

FIG. 6. Speech recognition performance for cochlear-implant subjects listening to a single-talker masker (filled triangles) or steady-state, speech-shaped noise masker, SSN, (unfilled squares). Results are shown as a function of the target-to-masker ratio (TMR) and talker (columns) used for the masker. The cochlear-implant data shown here (experiment 2) is with the ''fixed masker'' procedure (the same procedure used for the normal-hearing listeners) for a better comparison of implant and normal-hearing data. Error bars represent the standard error of the mean.

listening level. If the maximum setting was reached on the AIS, the subject then adjusted the sensitivity of their speech processor to reach a comfortable loudness.

One potential confound when testing subjects who use amplification devices is the possibility of presenting stimuli at intensities where compression occurs (Stone and Moore, 2003). This is particularly problematic for experiments that attempt to deliver a sound within the very narrow dynamic range of electric hearing. Figure 5 demonstrates the effect of compression using a schematic input–output function. In the Nucleus device, used by all five cochlear-implant subjects in this study, the input dynamic range is only 30 dB (User Manual, The Nucleus 22 Channel Cochlear Implant System, p. 4-SP). This means that compression will limit the sound input to a 30-dB range to fit within the cochlear-implant user's dynamic range, defined within the boundaries of the patient's threshold (T-level) and upper comfort level (C-level).

The right panel of Fig. 5 shows that when the masker level is fixed at 65 dB and the target level is adjusted above the level of the masker to produce each TMR, there would only be 5 dB of head room to effectively change the target-to-masker ratios. Thus, compression limits the intended 0–20 dB TMR range to 5 dB or less in cochlear-implant users, possibly producing a plateau or drop in performance (due to peak clipping) as the TMR is increased. On the other hand, when the target level is fixed at 65 dB and the masker level is adjusted from a lower intensity to produce the 0–20 dB TMR range (left panel), there would be about 25 dB of leg room which would minimize the compression effect. Both compressive (masker fixed; target increased above the most comfortable loudness level) and less-compressive techniques (target fixed; masker increased from below the comfortable loudness level) were used and compared in experiment 2, and all masker and talker conditions were performed with both techniques.

After establishing the appropriate level, cochlear-implant subjects were presented with a practice session in quiet. They were asked to type their response into the computer and were encouraged to guess if unsure. Because cochlear implant users typically have a wide range of performance variability, no formal minimum performance requirement was set other than that the subjects have some open-set, speech understanding with auditory cues alone. Scores for the cochlear implant subjects on the practice session ranged from 78% to 92%. For the test session, unlike the normal-hearing subjects, cochlear-implant listeners participated in all single-talker and SSN test sessions over a period of several days, with each session lasting between 1 and 2 h per day. All testing was performed with subjects seated in an IAC sound-booth. Results were scored in percent correct for the following TMRs: 0, 5, 10, 15, and 20 dB TMR.

B. Results

1. Speech recognition performance by cochlear-implant subjects

Figure 6 shows performance as a function of the TMR for single-talker and SSN maskers. The results in the figure are from the ''fixed masker'' data to provide an easier comparison with the normal-hearing listeners who used the same procedure. Average speech recognition performance in quiet was 83%, determined by the IEEE practice sentences. Consistent with previous studies, sentence recognition performance in noise by cochlear-implant subjects was between that obtained with a 4- to 8-channel simulation in normal-hearing listeners (Friesen *et al.*, 2001; Garnham *et al.*, 2002).

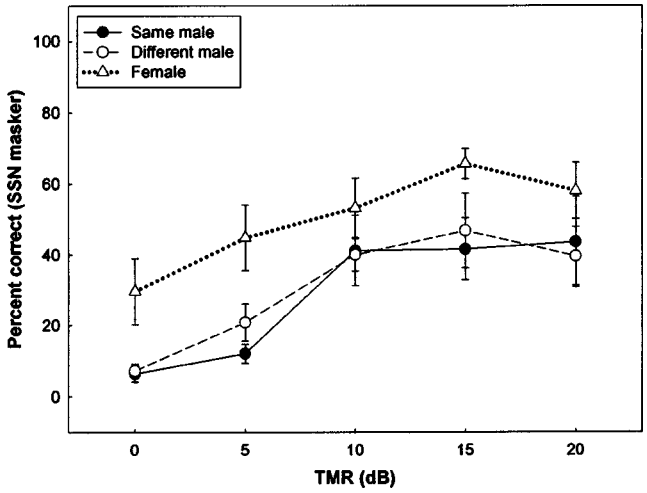

FIG. 7. Cochlear-implant data with the steady-state, speech-shaped noise (SSN) masker as a function of the TMR and talker used as the masker. Results for the ''same male'' SSN as the masker are shown as filled circles with solid lines, unfilled circles and dashed lines are used for the ''different male'' SSN, and unfilled triangles with dotted lines are used for the ''female'' SSN.

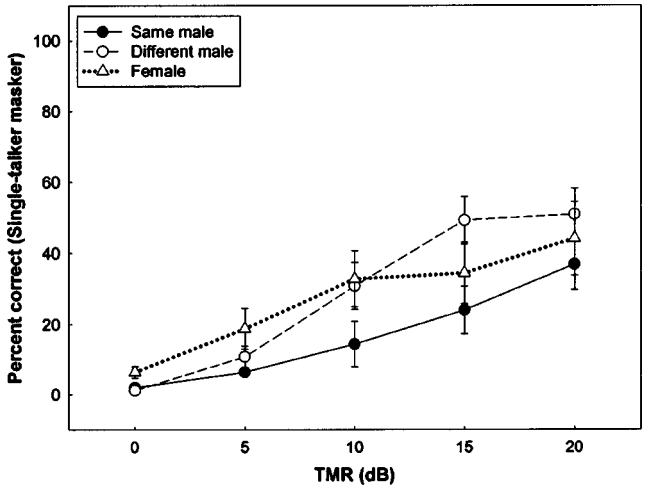

FIG. 8. Cochlear-implant data showing performance with single-talker maskers as a function of the TMR and competing talker. Results for the ''same male'' talker as the masker are shown as filled circles with solid lines, unfilled circles and dashed lines are used for the ''different male'' talker, and unfilled triangles with dotted lines are used for the ''female'' talker.

The average performance by cochlear-implant subjects was slightly better than normal-hearing subjects listening to a four-channel simulation, but only the highest performing cochlear-implant subjects were able to obtain similar levels of speech understanding as the normal-hearing subjects listening to an 8-channel simulation. Although Fig. 6 shows a trend for speech recognition performance in noise to improve with increasing TMRs, a repeated measures ANOVA failed to demonstrate a significant main effect of TMR for the cochlear-implant users ($p=0.19$). However, Bonferonni pairwise comparisons (Dunn, 1961) demonstrated a significant drop in performance from a 10 to 5 dB TMR ($p<0.01$), but no significant decrements in performance from a 5 to 0 dB TMR or improvements above a 10 dB TMR. As found in normal-hearing subjects listening to the eight-channel simulation, there was an effect of masker [$F(1,4)=11.92$, $p<0.05$], with single-talker maskers again producing lower performance (32.9%) than SSN maskers (41.8%). There was also a main effect of talker when collapsed across both masker types [$F(2,3)=10.77$, $p<0.05$]. This is discussed in more detail in the following two sections.

2. Comparison of SSN maskers across talkers

Figure 7 replots the SSN data from Fig. 6 to contrast performance with each of the three SSN maskers as a function of the TMR. Bonferonni pairwise comparisons confirmed significant differences between the female SSN masker and the different male SSN [$F(1,4)=29.92$, $p<0.01$], but no differences between the two male SSN maskers ($p=0.62$). These results are similar to those found with the 8-channel simulation in experiment 1, and closely follow the differences in the long-term average speech spectrum shown in Fig. 3(a).

3. Comparison of single-talker maskers

Figure 8 contrasts speech recognition performance with single-talker maskers as a function of the TMR and talker. No significant differences were found across single-talker maskers (Bonferonni pairwise comparisons: $p=0.26$). Thus, even though the cochlear-implant users were able to use gross spectral differences to segregate the steady-state female noise masker from the temporally fluctuating male speech target, the spectral differences were not sufficient for cochlear-implant users to segregate two fluctuating speech sounds. This result is similar to the normal-hearing subjects listening to the eight-channel simulation.

4. Effects of compression on performance in noise

Figure 9 compares the effect of compression on speech recognition in noise with either the masker fixed (filled triangles) or the target fixed (open triangles) at the most comfortable loudness for single-talker (upper panel) and SSN (lower panel) maskers. The ANOVA showed no main effect of method (i.e., masker fixed or target fixed), but there was a significant interaction between the method used and the TMR [$F(4,1)=1574.27$, $p<0.05$]. Paired *t*-tests confirmed significant differences between the two methods only at the highest TMRs for single-talker maskers (i.e., 15 and 20 dB) and at a 20 dB TMR for SSN maskers ($p<0.01$ for all three results). When the masker was fixed and the target was increased above the most comfortable loudness (Fig. 9: filled triangles), performance either reached a plateau or decreased at high TMRs. This effect was most evident for single-talker maskers whose peak amplitudes could exceed the upper comfort level and become peak-clipped. In contrast, performance generally improved with higher TMRs when the target was fixed and the masker was kept at or below the comfortable loudness level (open triangles). This pattern of results was consistent with the prediction shown in the schematic compression function (Fig. 5).

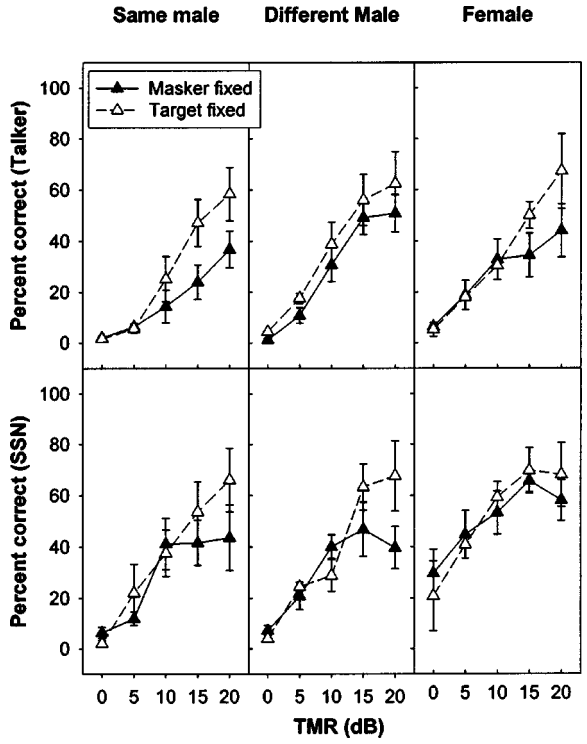

FIG. 9. Comparison of the two procedures (i.e., ''masker fixed'' or ''target fixed'') used to examine the effects of compression in cochlear-implant users. Performance (*y* axis) is shown as a function of the target-to-masker ratio (*x* axis). The data is plotted separately for single-talker (upper panels) and SSN maskers (lower panels). Data for each talker is shown in columns.

IV. GENERAL DISCUSSION

Although normal-hearing subjects listening to natural speech were able to maintain high levels of intelligibility for TMRs down to 0 dB, performance for cochlear-implant listeners and normal-hearing subjects listening to spectrally degraded speech declined sharply with the addition of noise. Even at high TMRs, performance was dramatically reduced from that obtained in quiet. Another difference among the subject groups was in their ability to take advantage of the temporal dips in the fluctuating masker to glimpse portions of the target sentence, allowing higher performance with a single-talker masker than SSN, and indicating a release from masking. As seen previously at low TMRs (Brungart, 2001; Peters *et al.*, 1998; Qin and Oxenham, 2003), normal-hearing subjects listening to natural speech at TMRs less than 0 dB showed a 20% improvement in score with the different male, single-talker masker over the steady-state noise masker. However, the higher performance with single-talker maskers relative to SSN maskers was not found in the simulation or cochlear-implant results presented here.

Regardless of whether sentences were presented in quiet or in noise, it was very difficult for normal-hearing listeners to recognize words from sentences with the four-channel simulation. It is likely that with only four coarse spectral channels, listeners found the low-context, processed IEEE target sentence too difficult to understand, in which case it was treated as ''noise'' in a similar manner as the SSN masker. In the study by Nelson *et al.* (2003), who also used IEEE target sentences, four-channel sentence recognition performance in noise showed very small differences between a steady and modulated noise masker at all of the gate frequencies tested. Only a very slight amount of masking release was found in the +16 and 0 dB TMR conditions, and none with the +8 dB TMR. These results suggest that with four or fewer functional channels, listeners may have more difficulty distinguishing between the target speech and the masker, regardless of whether the masker is steady-state noise or a modulating masker. It should be pointed out, however, that Qin and Oxenham (2003) found greater masking effects for single-talker than noise maskers with as few as four channels. One possible explanation for this result is that Qin and Oxenham used excerpts from a speech passage as a masker that varied from trial to trial whereas this study used a single sentence that was repeated each trial. Thus the fixed masker used here might have reduced the degree of informational masking.

In contrast with the four-channel simulation, greater masking was observed for single-talker than noise maskers with the eight-channel simulation and with cochlear-implant listeners. The most plausible explanation for these effects is that in addition to energetic masking, the single-talker masker contained meaningful information, thereby acting as a higher-level (informational) masker. Informational masking comprises at least three factors: stimulus uncertainty, target-masker similarity (which relates to modulation interference), and linguistic masking. Since the same masking sentence was used repeatedly, stimulus uncertainty most likely played a minor role. Linguistic masking, on the other hand, might have been an important factor with a single-talker masker. That is, informational masking is possible when the speech masker (e.g., reversed speech or a foreign language) is unintelligible (possesses no semantic content), but carries language-based context. This would parallel observations by Hawley *et al.* (2004) and Freyman *et al.* (2001) who found similar informational masking patterns with speech (content) and time-reversed speech (context). Although not intelligible, time-reversed speech maskers preserve some of the phonetic properties of natural speech which may become confused with those of the target sentence. Last, masking introduced by target-masker similarity might have contributed to the poorer performance found with competing speech compared to noise maskers. It is well known that the spectral and intensity variations in the speech masker are much more difficult for the listener to track and ignore when the target has similar variations (Arbogast *et al.*, 2002; Brungart, 2001; Kwon and Turner, 2001). The acoustic redundancy available to normal-hearing listeners provides a greater range for spectral-temporal discriminations. This makes auditory streaming (i.e., the process by which sound elements are grouped into auditory objects) an easier task by allowing the listener to first identify the masker separate from the target and then to use this information as an aid to glimpse unmasked portions of the target sentence. When the spectral detail is not available, the results presented here and elsewhere (Arbogast *et al.*, 2002; Kwon and Turner, 2001; Qin and Oxenham, 2003) suggest that it may be more difficult to perform the first step for auditory streaming, which is to identify which fluctuating sound is the target and which is the masker. As indicated in a recent study in our laboratory,

speaker identification is a very difficult task for cochlear-implant listeners, most likely because pitch and temporal fine structure cues are not adequately coded (Kong *et al.*, 2003). In support of this, the cochlear-implant users in the present study and the normal-hearing subjects listening to the simulations (both here and in the study by Qin and Oxenham) showed no greater benefit of one talker over another, even when the masker and target speech differed in gender.

With steady-state noise, the masker is more predictable, and obvious differences in temporal envelope between the masker and speech target make segregation a much easier task. Although the female single-talker masker failed to show a significant improvement over that obtained with the same male masker, there was a benefit from gross spectral differences when the masker was SSN (i.e., higher performance was observed with the ''female SSN'' over the ''same male SSN''). These results demonstrate that cochlear-implant users can segregate competing sounds much more easily if it is a simple, temporally based, ''steady vs. fluctuating'' distinction, but not when both masker and target are fluctuating and the listener is forced to rely on the coarse spectral information from their speech processor to segregate a female single-talker masker from a male speech target. This suggests that modulation interference may limit performance when spectral information is reduced.

V. SUMMARY AND CONCLUSIONS

Consistent with previous studies, these results demonstrate that most cochlear implant listeners can use the envelope information delivered through the speech processor to follow conversations in quiet environments, but their performance deteriorates substantially with background noise, particularly if the noise is also speech. Although not directly examined in the present study, the potential contributors to poor performance in noise include reduced spectral resolution and the lack of fine structure information in current cochlear implants. Additionally, the compression mechanism used in cochlear implants may often produce less than optimal TMRs and poorer speech recognition performance as demonstrated here. The cochlear-implant listener is therefore at a serious disadvantage for speech understanding in realistic listening environments, such as classrooms, restaurants, and other social gatherings that require more acoustic redundancy than current cochlear implants provide.

(i) Similar to the results of Qin and Oxenham (2003), the current study found poorer performance with a competing talker than SSN for normal-hearing subjects listening through an implant simulation, and the converse was observed when normal-hearing listeners heard natural, unprocessed speech stimuli.

(ii) The results presented here extend those of Qin and Oxenham by including data from actual cochlear-implant listeners who, like normal-hearing subjects listening to the 8-channel simulation, demonstrated lower scores with a competing talker than with SSN.

(iii) The combined effect of informational and energetic masking most likely contributed to the poorer performance with speech maskers. Informational masking appears to have a strong influence on spectrally impoverished speech since listeners have great difficulty distinguishing the components of the target speech from the masking speech. As a result, portions of the masker may become perceptually integrated with the target.

ACKNOWLEDGMENTS

We are very grateful for the time and dedication our cochlear-implant listeners have offered for this study. We also acknowledge Sheetal Desai, Michael Vongphoe, and Charlotte Guo for their assistance in data collection, Kaibao Nie and Sheng Liu for generating spectrograms [Figs. 3(a)], and John Wygonski for implementing the cochlear-implant simulation software. This work was supported in part by grants from the National Institutes of Health (F32 DC05900 to GSS and 2R01 DC02267 to FGZ).

Arbogast, T., Mason, C., and Kidd, G. (**2002**). ''The effect of spatial separation on informational and energetic masking of speech,'' J. Acoust. Soc. Am. **112**, 2086–2098.

Assmann, P. F., and Summerfield, Q. A. (**1990**). ''Modeling the perception of concurrent vowels: Vowels with different fundamental frequencies,'' J. Acoust. Soc. Am. **88**, 680–697.

Bird, J., and Darwin, C. J. (**1998**). ''Effects of a difference in fundamental frequency in separating two sentences,'' in *Psychophysical and Physiological Advances in Hearing*, edited by A. R. Palmer, A. Rees, A. Q. Summerfield, and R. Meddis (London, Whurr), pp. 263–269.

Brokx, J. P. L., and Nooteboom, S. G. (**1982**). ''Intonation and the perception of simultaneous voices,'' J. Phonetics **10**, 23–36.

Brungart, D. S. (**2001**). ''Informational and energetic masking effects in the perception of two simultaneous talkers,'' J. Acoust. Soc. Am. **109**, 1101–1109.

Dorman, M. F., Loizou, P. C., and Tu, Z. (**1998**). ''The recognition of sentences in noise by normal-hearing listeners using simulations of cochlear-implant signal processor with 6–20 channels,'' J. Acoust. Soc. Am. **104**, 3583–3585.

Dunn, O. (**1961**). ''Multiple comparisons among means,'' J. Am. Stat. Assoc. **56**, 52–64.

Duquesnoy, A. J. (**1983**). ''Effect of a single interfering noise or speech source on the binaural sentence intelligibility of aged persons,'' J. Acoust. Soc. Am. **74**, 739–743.

Eisenberg, L. S., Dirks, D. D., and Bell, T. S. (**1995**). ''Speech recognition in amplitude-modulated noise of listeners with normal and listeners with impaired hearing,'' J. Speech Hear. Res. **38**, 222–233.

Festen, J. M. (**1987**). ''Explorations on the difference in SRT between a stationary noise masker and an interfering speaker,'' J. Acoust. Soc. Am. **82**, S4.

Festen, J. M., and Plomp, R. (**1990**). ''Effects of fluctuating noise and interfering speech on the speech reception threshold for impaired and normal hearing,'' J. Acoust. Soc. Am. **88**, 1725–1736.

Freyman, R. L., Balakrishnan, U., and Helfer, K. S. (**2001**). ''Spatial release from informational masking in speech recognition,'' J. Acoust. Soc. Am. **109**, 2112–2122.

Friesen, L. M., Shannon, R. V., Baskent, D., and Wang, X. (**2001**). ''Speech recognition in noise as a function of the number of spectral channels: Comparison of acoustic hearing and cochlear implants,'' J. Acoust. Soc. Am. **110**, 1150–1163.

Fu, Q.-J., Shannon, R. V., and Wang, X. (**1998**). ''Effects of noise and spectral resolution on vowel and consonant recognition: Acoustic and electric hearing,'' J. Acoust. Soc. Am. **104**, 3586–3596.

Garnham, C., O'Driscoll, M., Ramsden, R., and Saeed, S. (**2002**). ''Speech understanding in noise with a Med-El COMBI 40+ cochlear implant using reduced channel sets,'' Ear Hear. **23**, 540–552.

Glasberg, B. R., and Moore, B. C. (**1989**). ''Psychoacoustic abilities of subjects with unilateral and bilateral cochlear impairments and their relationship to the ability to understand speech,'' Scand. Audiol. Suppl. **32**, 1–25.

Greenwood, D. (**1990**). ''A cochlear frequency-position function for several species—29 years later,'' J. Acoust. Soc. Am. **87**, 2592–2605.
Hawley, M. L., Litovsky, R. Y., and Colburn, S. H. (**1999**). ''Speech intelligibility and localization in a multi-source environment,'' J. Acoust. Soc. Am. **105**, 3436–3448.
Hawley, M. L., Litovsky, R. Y., and Culling, J. F. (**2004**). ''The benefit of binaural hearing in a cocktail party: Effect of location and type of interferer,'' J. Acoust. Soc. Am. **115**, 833–843.
Hygge, S., Ronnber, J., Larsby, B., and Arlinger, S. (**1992**). ''Normal-hearing and hearing-impaired subjects' ability to just follow conversation in competing speech, reversed speech, and noise backgrounds,'' J. Speech Hear. Res. **35**, 208–215.
Kawahara, K., Masuda-Katsuse, I., and de Cheveigne, A. (**1999**). ''Restructuring speech representations using a pitch-adaptive time-frequency smoothing and an instantaneous-frequency-based F0 extraction: Possible role of a repetitive structure in sounds,'' Speech Commun. **27**, 187–207.
Kessler, D. K., Osberger, M. J., and Boyle, P. (**1997**). ''CLARION patient performance: an update on the adult and children's clinical trials,'' Scand. Audiol. Suppl. **47**, 45–49.
Kidd, G., Arbogast, T. L., Mason, C. R., and Walsh, M. (**2001**). ''Informational masking in listeners with sensorineural hearing loss,'' J. Assoc. Res. Oto. **3**, 107–119.
Kong, Y.-Y., Vongphoe, M., and Zeng, F.-G. (**2003**). ''Independent contributions of amplitude and frequency modulations to auditory perception. II. Melody, tone, and speaker identification,'' abstract from the Twenty-sixth ARO Midwinter Meeting, Daytona, FL, p. 213.
Kwon, B.-J., and Turner, C. W. (**2001**). ''Consonant identification under maskers with sinusoidal modulation: Masking release or modulation interference?'' J. Acoust. Soc. Am. **110**, 1130–1140.
Nelson, P. B., Jin, S.-H., Carney, A. E., and Nelson, D. A. (**2003**). ''Understanding speech in modulated interference: Cochlear implant users and normal-hearing listeners,'' J. Acoust. Soc. Am. **113**, 961–968.
Nittrouer, S., and Boothroyd, A. (**1990**). ''Context effects in phoneme and word recognition by young children and older adults,'' J. Acoust. Soc. Am. **87**, 2705–2715.
Oh, E. L., and Lufti, R. A. (**2000**). ''Effect of masker harmonicity on informational masking,'' J. Acoust. Soc. Am. **108**, 706–709.
Peters, R. W., Moore, B. C., and Baer, T. (**1998**). ''Speech reception thresholds in noise with and without spectral and temporal dips for hearing impaired and normal hearing people,'' J. Acoust. Soc. Am. **103**, 577–587.
Plomp, R. (**1994**). ''Noise, amplification, and compression: Considerations of three main issues in hearing aid design,'' Ear Hear. **15**, 2–12.
Pollack, I. (**1975**). ''Auditory informational masking,'' J. Acoust. Soc. Am. **57**, S5.
Qin, M. K., and Oxenham, A. J. (**2003**). ''Effects of simulated cochlear-implant processing on speech reception in fluctuating maskers,'' J. Acoust. Soc. Am. **114**, 446–454.
Rabinowitz, W. M., Eddington, D. K., Delhorne, L. A., and Cuneo, P. A. (**1992**). ''Relations among different measures of speech reception in subjects using a cochlear implant,'' J. Acoust. Soc. Am. **92**(4 Pt. 1), 1869–1881.
Rothauser, E. H., Chapman, W. D., Guttman, N., Nordby, K. S., Silbiger, H. R., Urbanek, G. E., and Weinstock, M. (**1969**). ''I.E.E.E. recommended practice for speech quality measurements,'' IEEE Trans. Audio Electroacoust. **17**, 227–246.
Scheffé, H. (**1953**). ''A method for judging all contrasts in the analysis of variance,'' Biometrika **40**, 87–104.
Shannon, R. V., Galvin, III, J. J., and Baskent, D. (**2001**). ''Holes in Hearing,'' J. Assoc. Res. Oto. **3**, 185–199.
Stone, M. A., and Moore, B. C. J. (**2003**). ''Effect of the speed of a single-channel dynamic range compressor on intelligibility in a competing speech task,'' J. Acoust. Soc. Am. **114**, 1023–1034.
Takahashi, G. A., and Bacon, S. P. (**1992**). ''Modulation detection, modulation masking, and speech understanding in noise in the elderly,'' J. Acoust. Soc. Am. **35**, 1410–1421.
Watson, C., Kelly, W., and Wroton, H. (**1976**). ''Factors in the discrimination of tonal patterns. II. Selective attention and learning under various levels of stimulus uncertainty,'' J. Acoust. Soc. Am. **60**, 1176–1186.
Yost, W. A., Sheft, S., and Opie, J. (**1989**). ''Modulation interference in detection and discrimination of amplitude modulation,'' J. Acoust. Soc. Am. **86**, 2138–2147.
Zeng, F.-G., and Galvin, III, J. J. (**1999**). ''Amplitude compression and phoneme recognition in cochlear implant listeners,'' Ear Hear. **20**, 60–74.
Zeng, F.-G. (**2002**). ''Temporal pitch in electric hearing,'' Hear. Res. **174**, 101–106.

Across-frequency interference effects in fundamental frequency discrimination: Questioning evidence for two pitch mechanisms[a)]

Hedwig Gockel[b)] and Robert P. Carlyon
MRC Cognition and Brain Sciences Unit, 15 Chaucer Road, Cambridge CB2 2EF, United Kingdom

Christopher J. Plack
Department of Psychology, University of Essex, Wivenhoe Park, Colchester CO4 3SQ, United Kingdom

(Received 12 August 2003; revised 30 April 2004; accepted 6 May 2004)

Carlyon and Shackleton [J. Acoust. Soc. Am. **95**, 3541–3554 (1994)] presented an influential study supporting the existence of two pitch mechanisms, one for complex tones containing resolved and one for complex tones containing only unresolved components. The current experiments provide an alternative explanation for their finding, namely the existence of across-frequency interference in fundamental frequency (F0) discrimination. Sensitivity (d') was measured for F0 discrimination between two sequentially presented 400 ms complex (target) tones containing only unresolved components. In experiment 1, the target was filtered between 1375 and 15 000 Hz, had a nominal F0 of 88 Hz, and was presented either alone or with an additional complex tone (''interferer''). The interferer was filtered between 125–625 Hz, and its F0 varied between 88 and 114.4 Hz across blocks. Sensitivity was significantly reduced in the presence of the interferer, and this effect decreased as its F0 was moved progressively further from that of the target. Experiment 2 showed that increasing the level of a synchronously gated lowpass noise that spectrally overlapped with the interferer *reduced* this ''pitch discrimination interference (PDI)''. In experiment 3A, the target was filtered between 3900 and 5400 Hz and had an F0 of either 88 or 250 Hz. It was presented either alone or with an interferer, filtered between 1375 and 1875 Hz with an F0 corresponding to the nominal target F0. PDI was larger in the presence of the resolved (250 Hz F0) than in the presence of the unresolved (88 Hz F0) interferer, presumably because the pitch of the former was more salient than that of the latter. Experiments 4A and 4B showed that PDI was reduced but not eliminated when the interferer was gated on 200 ms before and off 200 ms after the target, and that some PDI was observed with a continuous interferer. The current findings provide an alternative interpretation of a study supposedly providing strong evidence for the existence of two pitch mechanisms. [DOI: 10.1121/1.1766021]

PACS numbers: 43.66.Fe, 43.66.Hg, 43.66.Ba [NFV] Pages: 1092–1104

I. INTRODUCTION

Many of the periodic sounds that we encounter in everyday life are broadband, and contain harmonics that differ widely in the extent to which they are resolved by the peripheral auditory system. A distinction that has informed much experiment and theory is that between the lower harmonics, which are resolved by the peripheral auditory system, and the higher harmonics, which are not (Plomp, 1964; Houtsma and Smurzynski, 1990; Fine and Moore, 1993; Moore and Ohgushi, 1993; Shackleton and Carlyon, 1994). The transition from resolved to unresolved harmonics appears to be around the 10th harmonic, but the exact locus seems to depend on the specific measure (e.g., fundamental frequency discrimination thresholds or the ability to hear out individual components) used to determine this transition (for a discussion see Bernstein and Oxenham, 2003b). The unresolved harmonics interact within auditory filters and, in the case of consecutive harmonics, produce a modulation at a rate equal to the fundamental frequency (F0). A wide body of evidence has shown that although this cue can give rise to a perception of pitch (Burns and Viemeister, 1976; Moore and Rosen, 1979), it is the resolved harmonics that dominate the pitch of broadband sounds (Plomp, 1967; Ritsma, 1967; Ritsma, 1970; Moore *et al.*, 1985). Furthermore, difference limens for F0 (F0DLs) are also lower for resolved than for unresolved harmonics (Houtsma and Smurzynski, 1990).

Early models, proposed to account for the pitch of complex tones, fall into two different classes. In the first, pitch is derived solely from the periodicity arising from the within-channel interaction of multiple harmonics (Schouten, 1940; Schouten, 1970). Such a mechanism would be effective for deriving the pitch of complex tones containing only unresolved components (referred to as ''unresolved complexes'' hereafter). In the second class of models, pitch is derived by a form of ''pattern recognition'' across resolved harmonics (Goldstein, 1973; Terhardt, 1974). This sort of mechanism would be effective for deriving the pitch of complex tones containing resolved components (referred to as ''resolved

[a)]Parts of this work were presented at the 145th meeting of the Acoustical Society of America, Nashville, Tennessee, 28 April–2 May 2003 [J. Acoust. Soc. Am. **113**, 2290 (2003)].

[b)]Author to whom correspondence should be addressed; electronic mail: hedwig.gockel@mrc-cbu.cam.ac.uk

complexes'' hereafter). A limitation of pattern recognition models is that they have difficulty in accounting for the weak but significant pitch percepts produced by unresolved harmonics (but see Houtsma and Smurzynski, 1990).

In contrast, a modern class of models, based loosely around the concept of autocorrelation, can produce a pitch estimate both from resolved and from unresolved harmonics (Slaney and Lyon, 1990; Meddis and Hewitt, 1991; Patterson *et al.*, 1992). Leaving aside, for the moment (but see Sec. VI), the question of whether the particular implementations of such a unitary model can account for all the findings in the pitch area, there is a more basic problem. This is the question of whether it is *necessary* to assume two separate mechanisms for extracting the pitch or whether one common mechanism would *in principle* be sufficient (Licklider, 1951; Meddis and Hewitt, 1991; Patterson *et al.*, 1992; Moore, 2003). This issue has been discussed repeatedly (Houtsma and Smurzynski, 1990; Carlyon and Shackleton, 1994; Meddis and O'Mard, 1997; Carlyon, 1998; Grimault *et al.*, 2002) and here we present findings which are relevant for this topic.

If there exists only one common pitch mechanism, then one would expect two complex tones with similar fundamental frequencies (F0s) which are presented simultaneously—one resolved and one unresolved—to be processed together, in the same way. The output of the single mechanism, the pitch estimate, would be expected to be dominated by whichever input gives the strongest output. Two pitches might be heard in the presence of strong segregation cues for the two tones, for example, an onset asynchrony. Two pitches might also be heard if the F0s of the two tones differ sufficiently. On the other hand, in the absence of strong segregation cues and large F0 differences, the single pitch perceived probably would be determined to a large extent by those components of the input that give the strongest pitch. Complex tones with resolved harmonics usually give a more salient pitch than complexes containing only unresolved harmonics (see, e.g., Moore and Glasberg, 1986); pitch salience has been determined by comparing subjects' ability to identify simple melodies or to identify musical intervals for high-pass filtered complex tones with various cutoff frequencies (Moore and Rosen, 1979; Houtsma and Smurzynski, 1990), and by comparing thresholds for F0 discrimination (Hoekstra and Ritsma, 1977; Moore and Glasberg, 1988; Houtsma and Smurzynski, 1990; Moore and Glasberg, 1990; Moore and Peters, 1992; Shackleton and Carlyon, 1994). Furthermore, the dominance region for pitch is concentrated around lower harmonic numbers (Plomp, 1967; Ritsma, 1967; Ritsma, 1970; Moore *et al.*, 1985; Dai, 2000). Therefore, one might expect the pitch of two simultaneously presented complex tones—one resolved and the other unresolved—to be dominated by the resolved complex. As a consequence, performance in a task requiring judgement of the pitch of the unresolved complex tone might be strongly impaired by the presence of a fixed-pitch resolved complex tone, even when presented in a different spectral region. In other words, one might see an interference in the pitch domain which is reminiscent of that seen in the modulation domain, i.e., modulation detection and modulation discrimination interference (MDI), (Yost and Sheft, 1989; Yost *et al.*, 1989). In contrast to MDI, which can occur when the interferer is lower in frequency than the target, or vice versa, the ''pitch discrimination interference'' (PDI) would be expected to be asymmetric; more interference would be expected from a resolved complex than from an unresolved complex when judging the pitch of an unresolved complex in a well separated spectral region. This direction of asymmetry would be expected because subjects would try to *ignore* the simultaneous interferer, as it carries no information for the task at hand. The contribution of a resolved interferer to the perceived pitch would be harder to ignore than that of an unresolved interferer, as the former evokes a more salient pitch (see earlier).

An asymmetric across-frequency interference effect somewhat similar to the one expected here, has been found for the discrimination of interaural time differences. Low-frequency interferers strongly impair the lateralization of high-frequency targets, while high-frequency interferers have little or no effect on the lateralization of low-frequency targets (McFadden and Pasanen, 1976; Bernstein and Trahiotis, 2001; for a short summary, see Moore, 2003).

The experiments presented here show that such PDI does indeed exist, and reveal some of the characteristics of PDI. Later on we will discuss data by Carlyon and Shackleton (1994), which have been interpreted as evidence for the existence of two separate pitch mechanisms, one for complex tones containing resolved and one for complex tones containing only unresolved components. We will argue that the current findings provide an alternative explanation for their results, and therefore question their evidence for the existence of two pitch mechanisms, which strongly influenced further research.

II. EXPERIMENT 1: THE INTERFERENCE EFFECT AND ITS TUNING IN F0

A. Stimuli

Listeners had to discriminate between the F0s of two sequentially presented complex tones (the targets) which had a nominal F0 of 88 Hz. Each target was bandpass filtered between 1375 and 15 000 Hz (3 dB down points) with a slope of 48 dB per octave; thus it contained a large number of only unresolved components (Carlyon and Shackleton, 1994; Shackleton and Carlyon, 1994). The pitch salience of such a wide-band unresolved complex would be increased relative to a narrow-band version, but it would nevertheless be considerably weaker than for a resolved complex (Kaernbach and Bering, 2001). The target was either presented alone (condition ''None''), or it was accompanied by another complex tone (the interferer). The interferer had an F0 of 88 Hz or higher, and was bandpass filtered between 125 and 625 Hz (3 dB down points) with a slope of 48 dB per octave; thus it contained resolved components only. Note that, as the target and the interferer were filtered into well-separated frequency regions, one would not expect them to interact in the auditory periphery; therefore any effect must be more central. When present, the interferer was gated synchronously with the target, and its F0 relative to the nominal target F0 was unchanged for a block of trials. The independent vari-

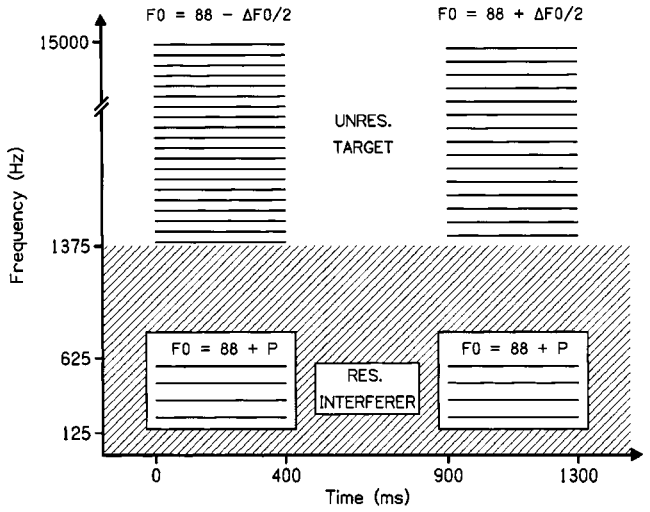

FIG. 1. Schematic spectrograms of stimuli presented over the course of one 2AFC trial in experiment 1.

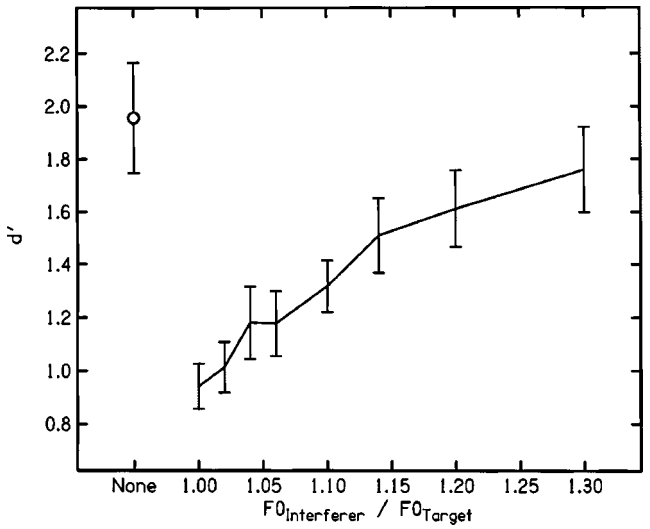

FIG. 2. The mean performance, and the associated standard errors (across subjects) obtained in experiment 1. The circle indicates d' in the absence of an interferer. The solid line indicates d' plotted as a function of the ratio between the F0 of the interferer and the nominal target F0.

able of the first experiment was the amount by which the F0 of the interferer was above that of the nominal target F0; possible values were: 0%, 2%, 4%, 6%, 10%, 14%, 20%, or 30%. The F0 difference between the low-F0 and the high-F0 targets (ΔF0) was fixed for each subject; it was determined in such a way that performance was below 100% correct in the easiest condition and was above 50% correct in the most difficult condition. The following values for ΔF0 were employed: 7.1% for one subject, 3.5% for four subjects, and 2% for the sixth subject.

The F0 of the digitally generated stimuli (see later) was randomly varied over the range ±10% between trials by varying the sample rate (also producing a slight variation in duration and in the filter cutoffs). This F0 randomization discouraged subjects from basing their decision on a long-term memory representation of the sound, and encouraged them to compare the pitch of the two targets presented in each trial. For both target and interferer, the level per component was 45 dB SPL, and components were always summed in sine phase. The nominal stimulus duration was 400 ms, including 5 ms raised-cosine onset and offset ramps. In order to mask possible distortion products, a continuous white background noise, lowpass filtered at the lower cutoff frequency of the target (nominally at 1375 Hz) with a slope of 96 dB per octave, was presented. The overall root-mean-square (rms) level of the noise in the region from 125 to 625 Hz, the nominal frequency band covered by the interferer, was 10 dB below that of the interferer. Schematic spectrograms of the stimuli are shown in Fig. 1.

The complex tones were generated and bandpass filtered digitally. They were played out using a 16-bit digital-to-analog converter (CED 1401 plus), with a sampling rate which was varied between trials over the range 40 kHz ±10%. This led to a variation of F0 and to a concomitant proportional change in the bandpass region of the tones. Stimuli were passed through an antialiasing filter (Kemo 21C30) with a cutoff frequency of 17.2 kHz (slope of 96 dB/oct), and presented monaurally, using Sennheiser HD250 headphones. Subjects were seated individually in an IAC double-walled sound attenuating booth.

B. Procedure

A two-interval two-alternative forced choice task was used to measure percent correct for the fixed values of ΔF0. The subjects were required to indicate the interval containing the target with the higher F0. The interferer was presented in both intervals in each trial. Its F0 was identical in both intervals and fixed at a certain percentage above the nominal target F0 throughout a block of 100 trials. The silent interval between presentations of the two stimulus intervals in a trial was fixed at 500 ms in all conditions (see Fig. 1). Each interval was marked by a light and visual feedback was provided following each response.

The total duration of a single session was about 2 h, including rest times. At least four (mostly five) blocks of 100 trials were run for each condition and subject. The order of the conditions was counterbalanced within and across subjects. One block was run for each condition in turn, before additional blocks were run in any other condition. To familiarize subjects with the procedure and equipment, they participated in at least three sessions, more if practice effects within conditions were seen, before data collection proper was started.

C. Subjects

In this and all following experiments, subjects ranged in age from 19 to 41 years, and their quiet thresholds at octave frequencies between 250 and 8000 Hz were within 15 dB of the 1969 ANSI standard. In all experiments, one of the subjects was the first author. In experiment 1, six subjects participated in all nine conditions. Four of the six subjects had considerable musical experience, and these were the ones with the lower values of ΔF0.

D. Results and discussion

Figure 2 shows the results averaged over all subjects and the corresponding standard errors. Performance in terms of

d' is plotted as a function of the ratio between the F0 of the interferer and the nominal F0 of the target. Performance was best, with a d' value of about 1.96, in the absence of an interferer (leftmost symbol, None). Performance was worst, at a d' value of about 0.94, when the interferer's F0 was at the nominal target F0 (ratio of one). With increasing difference between the interferer's F0 and the nominal target F0 performance recovered slowly. When the F0 of the interferer was 30% above the nominal target F0, performance was nearly, but not quite, back to that observed without any interferer (a d' value of 1.76).

To determine the statistical significance of the results, a repeated-measures one-way ANOVA (with nine levels for the factor condition) was calculated, using the mean d' value for each subject and condition as input. This showed a highly significant main effect of condition [$F(8,40)=21.6$, $p<0.001$].[1] Calculation of simple contrasts showed that all conditions with an interferer differed significantly from condition None. For the eight parameter values the following F values and significance levels were obtained. 0%: $F(1,5)=27.7$, $p=0.003$; 2%: $F(1,5)=34.1$, $p=0.002$; 4%: $F(1,5)=36.4$, $p=0.002$; 6%: $F(1,5)=29.4$, $p=0.003$; 10%: $F(1,5)=22.2$, $p=0.005$; 14%: $F(1,5)=23.1$, $p=0.005$; 20%: $F(1,5)=20.2$, $p=0.006$; 30%: $F(1,5)=13.6$, $p=0.014$.

In summary, F0 discrimination between two targets containing only unresolved components was clearly impaired in the presence of a tone complex with resolved components and an F0 similar to the nominal target F0. Importantly, this was true even though the target and interferer were filtered into well-separated spectral regions. Thus, peripheral interactions were unlikely to be responsible for this effect. The interference effect showed tuning between the F0s of target and interferer, which again suggests that the effect does not have a peripheral origin. Subjectively, the increase in F0 difference between target and interferer led to increased perceptual segregation of the two sounds. For interferers with an F0 within 10% of the nominal target F0, perceptual segregation was reported to be either absent or weak. When the interferer's F0 was 20% or 30% above that of the target, two sound sources were perceived. Nevertheless, a small impairment in F0 discrimination was still observed.

III. EXPERIMENT 2: EFFECT OF LEVEL OF SYNCHRONOUSLY GATED LOWPASS NOISE

The first experiment showed that the interference effect depended on the similarity between the interferer's F0 and the nominal F0 of the target. The second experiment provided a further test of whether the interference effect depends on the pitch characteristics of the added sound, or simply the presence of energy in the dominance region of pitch of the F0 of the target. The lowpass-filtered white noise—presented continuously in the first experiment—was now gated synchronously with the complex tone interferer and the target, in order to avoid them being segregated due to onset asynchrony. Thus, the added sound now consisted of a tonal and a noise component, and the level of the noise component was varied. Because the lowpass noise spectrally overlapped with the complex tone used as interferer in experiment 1, increasing the noise level would lead to a decrease in the tonality of the added sound, i.e., to a decrease in pitch strength and/or loudness of the tonal component of the added sound, due to the decrease of the tone-to-noise ratio in the spectral region containing the complex tone.

A. Stimuli and procedure

The basic stimuli and procedure were the same as in experiment 1, with the following exceptions. The level of the lowpass white noise was either the same as in experiment 1, i.e., 10 dB below that of the complex tone interferer in the frequency band covered by the tone (condition −10 dB), or it was 10 dB above that of the complex tone interferer in the frequency band covered by the tone (condition +10 dB). For the latter, the tone-to-noise ratio was around threshold. The noise was gated synchronously with the tones. In order to produce synchronously gated noise, we used digitally generated 400 ms bursts of white noise which were lowpass filtered digitally. Twenty different versions of noise bursts were pregenerated and stored on disk. One out of these 20 realizations of noise was chosen at random for each presentation in order to avoid masking effects that are specific to a particular ''frozen'' noise sample (Hanna and Robinson, 1985). The values for ΔF0 were 7.1% and 3.5% for all subjects.

Five blocks of 100 trials each were run for each condition and subject. The order of the conditions was counterbalanced within and across subjects. One block was run for each condition in turn, before additional blocks were run in any other condition. Subjects participated in at least one practice session before data collection proper was started.

Five subjects participated in all four conditions; three of them had considerable musical experience. Three of the five subjects were the same as in experiment 1, two of whom participated in experiment 2 before they ran in experiment 1.

B. Results and discussion

Figure 3 shows the mean results and the corresponding standard errors. The left and the right pairs of columns show d' values for F0 discrimination with ΔF0 equal to 3.5% and 7.1%, respectively. The white and black columns are for noise levels of −10 and +10 dB, respectively, re the level of the complex tone interferer in the band covered by the tone. As expected, overall performance was higher when the ΔF0 was 7.1% than when it was 3.5%. More importantly, in both cases performance *improved* when the level of the lowpass noise was increased by 20 dB. These results were confirmed by the outcome of a repeated-measures two-way ANOVA (with factors ΔF0 and level of noise). The main effects of ΔF0 [$F(1,4)=70.1$, $p<0.01$] and level of noise [$F(1,4)=26.9$, $p<0.01$] were highly significant, while the interaction between the two was not significant.

In summary, F0 discrimination performance in the presence of a complex tone interferer filtered into a spectrally remote region was improved by increasing the level of a lowpass noise which spectrally overlapped with and was gated synchronously with the interferer. This is one of the rare occasions where more noise helps (Warren, 1970; Carlyon, 1987; Plack and Viemeister, 1992; Plack and White, 2000a; Carlyon *et al.*, 2002a). More noise probably helped,

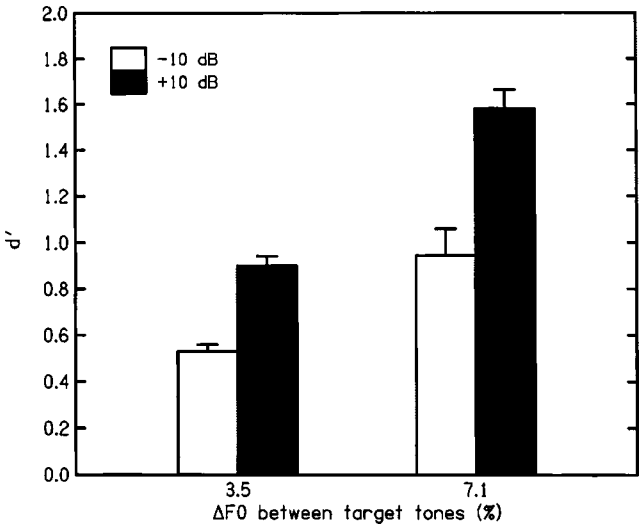

FIG. 3. The mean performance, and the associated standard errors (across subjects) obtained in experiment 2. d' for F0 discrimination is plotted as a function of ΔF0 (3.5% and 7.1%) between the two target tones. The white and black columns are for noise levels of −10 and +10 dB, respectively, re the level of the interferer in the band covered by the interferer.

because it reduced the perceived tonality of the added sound, i.e., the pitch strength and/or loudness of the tonal component of the added sound. This finding provides converging evidence that the interference effect does not primarily depend on the amount of energy present in the dominant region for pitch for the F0 used, and rules out an origin for the interference effect at a very peripheral stage of processing. Together with the findings from experiment 1, it suggests interference at the level of pitch processing itself.

IV. EXPERIMENT 3: PITCH SALIENCE VERSUS ENVELOPE MODULATION OF THE INTERFERER

The first two experiments showed that the tonality of the added sound and the similarity between the F0s of the target and interferer played a crucial role in PDI. In an attempt to further clarify the characteristics of the interference process, the next two experiments explored the role of two other aspects of a complex tone interferer, its resolvability and its degree of envelope modulation.

Resolved components are dominant in determining the pitch of a complex tone (Plomp, 1967; Ritsma, 1967; Ritsma, 1970; Moore *et al.*, 1985), and the pitch produced by complex tones containing resolved components is more salient than that produced by complexes containing only unresolved components (Houtsma and Smurzynski, 1990; Shackleton and Carlyon, 1994). As mentioned in the Introduction, if there exists only one common pitch mechanism, then one might expect the pitch estimate to be dominated by whatever components of the input give the strongest pitch. Therefore, one would predict more interference on F0 discrimination between two unresolved target tones by a resolved interferer than by an unresolved one. In contrast, if there exist two different *independent* pitch mechanisms whose outputs can be assessed independently, then one would not expect to see any PDI in the presence of a resolved interferer. However, PDI would be expected in the presence of an unresolved interferer, as this would feed into the same pitch mechanism for unresolved components as the target. If two *non*independent pitch mechanisms exist, then interference would be expected with both, resolved and unresolved interferers.

In the latter case, the relative amount of interference observed in the presence of a resolved or an unresolved interferer might depend on when the interference occurs. If the inteference across mechanisms occurs relatively early, then one might expect the unresolved interferer to be more disruptive than the resolved interferer. The reasoning for this is as follows. First, only an unresolved complex would feed directly into the putative pitch mechanism specific for unresolved components. Second, the unresolved interferer will produce a higher degree of envelope modulation at the outputs of the excited auditory filters than a resolved one. As the pitch of the unresolved target complex will partly or mainly be derived from envelope cues, one might expect more interference from an added complex with a strongly modulated internal envelope than from one with less modulation, i.e., an interference that is related to MDI *within* the putative specific pitch mechanism for unresolved complexes might be present. If the interference across mechanisms occurs at a late stage, i.e., after the pitch within each mechanisms has been estimated, then one might expect more interference in the presence of a resolved than an unresolved interferer, due to the more salient pitch evoked by the former. Experiments 3A and 3B investigated these possibilities.

A. Experiment 3A

1. Stimuli and procedure

The basic task and procedure were the same as in the first experiment. The stimuli differed in the following way: Listeners had to discriminate between the F0s of two sequentially presented target tones which had a nominal F0 of either 88 or 250 Hz. Each target was bandpass filtered between 3900 and 5400 Hz (3 dB down points, a slope of 48 dB/oct); thus, for both F0s it contained only unresolved components (Plomp, 1964; Carlyon and Shackleton, 1994). The target was either presented alone, or it was accompanied by an interferer with an F0 which was identical to that of the nominal target F0. The interferer was bandpass filtered between 1375 and 1875 Hz (3 dB down points, slope of 48 dB/oct). For the 88 Hz F0 this meant that the interferer's components were unresolved, while for the 250 Hz F0 they were resolved. As in the previous experiments, the level per component was 45 dB SPL for both target and interferer. For all subjects ΔF0 was equal to 3.5%.

To mask possible distortion products, a continuous pink background noise was presented with a spectrum level of 15 dB SPL at 1 kHz; this level was comparable to that of the lowpass-filtered white noise background used in experiment 1. Five blocks of 100 trials each were run for each condition and subject. The order of the conditions was counterbalanced within and across subjects. One block was run for each condition in turn, before additional blocks were run in any other condition. Subjects participated in at least one session, before data collection proper was started.

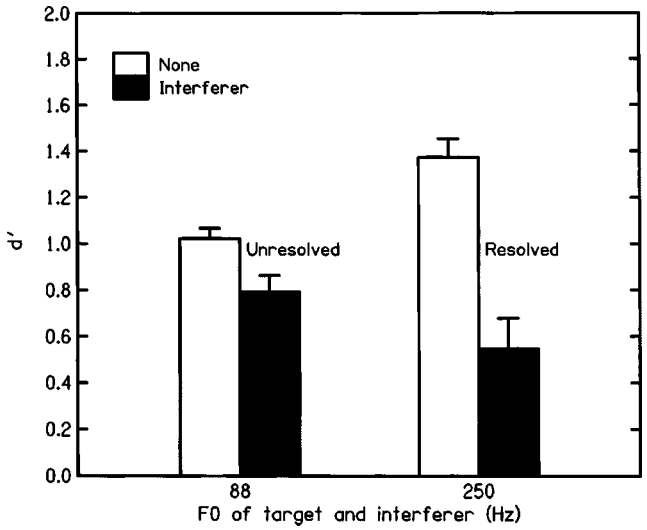

FIG. 4. The mean performance, and the associated standard errors (across subjects) obtained in experiment 3A. d' for F0 discrimination is plotted as a function of condition. The left two columns are for targets with a nominal F0 of 88 Hz, and the right two columns are for targets with a nominal F0 of 250 Hz. The white and black columns show performance in the absence and in the presence of an interferer with F0 corresponding to the nominal target F0, respectively.

Seven subjects participated in all four conditions. Five of them had considerable musical experience. Five of the seven subjects had also taken part in experiment 1, and five had also participated in experiment 2.

2. Results and discussion

Figure 4 shows the mean results and the corresponding standard errors across subjects. The left two columns are for targets with a nominal F0 of 88 Hz, and the right two columns are for targets with a nominal F0 of 250 Hz. The white and black columns show d' in the absence and in the presence of an interferer, respectively. The results show that adding an interferer with an F0 which is identical to the nominal F0 of the target always impaired performance. The important finding here is that performance was impaired more when the interferer was resolved than when it was unresolved. These results were confirmed by the outcome of a repeated-measures two-way ANOVA (with factors F0 and interferer), which showed that the main effect of the presence of the interferer [$F(1,6)=63.2$, $p<0.001$] and the interaction between F0 and presence of the interferer [$F(1,6)=23.2$, $p=0.003$] were both highly significant; the effect of the presence of the interferer was significant for the 88 Hz F0 [$F(1,6)=9.6$, $p=0.021$] and highly significant for the 250 Hz F0 [$F(1,6)=61.7$, $p<0.001$]. There was no main effect of F0.

In summary, performance was impaired most in the presence of the interferer which contained resolved components, i.e., dominant components with regard to pitch. This interferer had the more salient pitch, but a smaller degree of envelope modulation than the unresolved interferer. These results are not consistent with predictions based on the concept of two seperate pitch mechanisms, whose outputs can be assessed independently.

B. Experiment 3B

1. Stimuli and procedure

The basic task and procedure were the same as in experiment 3A. However, the stimuli differed. The characteristics of the interferer were manipulated in a different way from experiment 3A so that the pitch and the spectral region of the interferer stayed constant, even though the resolvability of the harmonics and the pitch strength were varied.

The nominal F0 of the target was 88 Hz and it was bandpass filtered between 1500 and 15 000 Hz (3 dB down points, a slope of 48 dB/oct); thus, it contained many components, all of which were unresolved. The target was either presented alone, or it was accompanied by an interferer, which was bandpass filtered between 250 and 750 Hz (3 dB down points, slope of 48 dB/oct). The interferer either had an F0 of 88 Hz, in which case its components were added in sine phase (condition 88-Sine), or it had an F0 of 44 Hz with components added in alternating phase (condition 44-Alt). In condition 88-Sine, the interferer's components were resolved, while they were expected to be unresolved in condition 44-Alt (Moore, 1993; Moore and Ohgushi, 1993). In the latter, the pitch of the interferer approximately corresponded to that of the 88 Hz F0 sine-phase complex (Flanagan and Guttman, 1960; Shackleton and Carlyon, 1994). Note, however, that the pitch of the alternating-phase complex was less salient than that of the sine-phase complex, while its degree of envelope modulation at the output of the auditory filters was greater. The latter follows from the fact that resolved components produce hardly any envelope modulation at the output of auditory filters centered on the frequency of the resolved components, while auditory filters centered at the frequency of unresolved components show an envelope modulation with a modulation rate corresponding to the repetition rate of the original waveform (see, e.g., Fig. 6.6 in Moore, 2003). For the 88 Hz F0 interferer, the level per component was 45 dB SPL (as in the experiments before), while for the 44 Hz F0 interferer the level per component was reduced to produce the same rms level for the two interferers.

For all subjects ΔF0 was equal to 3.5%. As in experiment 1, a continuous white background noise was presented with an overall rms level that—in the frequency region of the interferer—was 10 dB below that of the interferer. It was lowpass filtered at the lower cutoff frequency of the target (nominally 1500 Hz) with a slope of 96 dB per octave. Between four and five blocks with 100 trials each were run for each condition and subject. The order of the conditions was counterbalanced within and across subjects. One block was run for each condition in turn, before additional blocks were run in any other condition. Subjects participated in at least one session, before data collection proper was started.

Seven subjects participated in all three conditions. Four of them had considerable musical experience. All subjects took part in at least one of the earlier experiments before participating in this one.

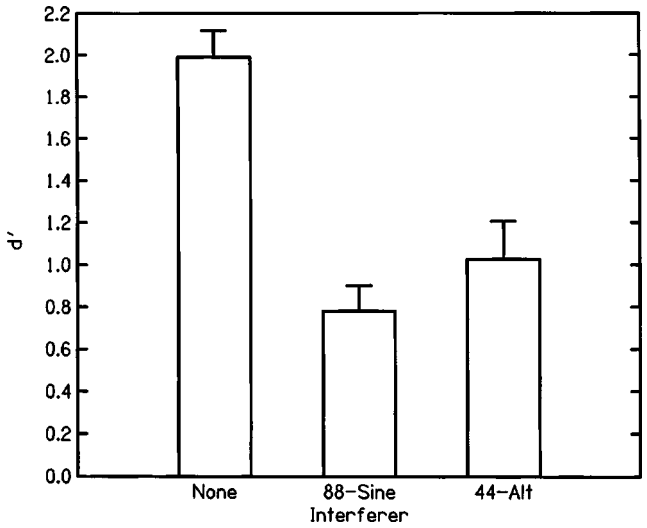

FIG. 5. The mean performance, and the associated standard errors (across subjects) obtained in experiment 3B. d' for F0 discrimination of a nominal 88 Hz target, bandpass-filtered into a frequency region between 1500 and 15 000 Hz, is plotted for each type of synchronously gated interferer (bandpass filtered between 250 and 750 Hz).

2. Results and discussion

Figure 5 shows the mean results and the corresponding standard errors across subjects. As was expected, both interferers reduced performance relative to that without an interferer [88-Sine: $F(1,6)=48.6$, $p<0.001$; 44-Alt: $F(1,6)=21.0$, $p<0.01$]. However, the question of interest here was whether condition 88-Sine would lead to worse performance than condition 44-Alt. Importantly, performance was significantly worse in condition 88-Sine than in condition 44-Alt. This was confirmed by the outcome of a repeated-measures one-way ANOVA [$F(1,6)=6.93$, $p<0.05$] in which only d' values from conditions 88-Sine and 44-Alt were used, in order to avoid getting a significant effect because of the difference between performance in the absence and in the presence of an interferer. Even though the size of the effect was small (the average difference between d' values in the two interferer conditions was 0.25), only one out of seven subjects showed a small difference (the smallest absolute difference of all subjects with a value of 0.04) in the opposite direction. In summary, performance was impaired most in the presence of the interferer which contained resolved components and had the more salient pitch. The higher degree of envelope modulation for the alternating-phase interferer did not produce more impairment than that observed for the interferer whose envelope was less modulated. Thus, the findings from experiment 3B are in agreement with those from experiment 3A.

Overall, the findings from experiments 3A and 3B indicate that the PDI observed with an unresolved target depends more on the pitch strength of the interferer than on the presence of unresolved components, which produce a higher degree of envelope modulation in the auditory periphery. These findings are not compatible with the existence of two independent pitch mechanisms whose outputs can be assessed independently. The current findings are consistent with either interaction in one common pitch mechanism, or, the existence of two pitch mechanisms whose outputs cannot be consciously assessed independently but instead are combined at a later stage. In the latter case, the outputs of the two pitch mechanisms would have to be combined at a *later* stage (after the individual pitch estimates have been derived), in order to explain that PDI is larger for a resolved interferer than for an unresolved interferer; the estimated pitch from the pitch mechanisms for resolved components would be more salient than the estimated pitch from the mechanism for unresolved components, and thus could dominate the consciously perceived pitch.

V. EXPERIMENT 4: EFFECT OF ONSET ASYNCHRONY OF INTERFERER

In all the experiments described so far, the interferer and the target were gated synchronously. This would have promoted perceptual grouping of the two. The last two experiments investigated the role of perceptual grouping in PDI. Onset asynchrony is one of the strongest cues for perceptual segregation (Darwin and Carlyon, 1995; Gockel, 2000). For example, Darwin and Ciocca (1992) showed that the influence of a mistuned fourth component on overall pitch of a complex tone was eliminated once the onset asynchrony between the mistuned component and the remaining harmonic complex was increased to 320 ms. As the remaining complex contained harmonics 1–12, this shows that *within* one pitch mechanism the contribution of part of the sound on the overall pitch can be reduced in the presence of a strong cue for perceptual segregation. Therefore, for the present experiments it was expected that introducing an onset asynchrony between interferer and target would reduce or even eliminate the interference effect.

A. Experiment 4A: Asynchronous interferer

1. Stimuli and procedure

The basic task and procedure were the same as in the first experiment. Five conditions were tested. The first condition (None), was a replication of condition None in experiment 1; the unresolved target with a nominal F0 of 88 Hz, bandpass filtered between 1375 and 15 000 Hz was presented together with a low-level continous lowpass-filtered white noise background. The second condition (CN−10), replicated the condition named ''0'' of the first experiment. It differed from condition None only through the presence of a synchronously gated resolved interferer with an F0 of 88 Hz (bandpass filtered between 125 and 625 Hz). The third condition (AsyInt) was new; while the target had the same 400 ms duration as before, the interferer started 200 ms before and stopped 200 ms after the target. Since the silent time between the two intervals within a trial was kept constant at 500 ms, this meant that the targets were now separated in time by 900 ms. To check whether the increased time between the two target stimuli might affect performance, a fourth condition (LongIsi) was run in which no interferer was presented and where the targets were separated by 900 ms. Finally, the fifth condition (CN+10) was similar to condition CN−10, except that the level of the continuous lowpass filtered noise was increased by 20 dB. This condition was included to check whether the lowpass noise could re-

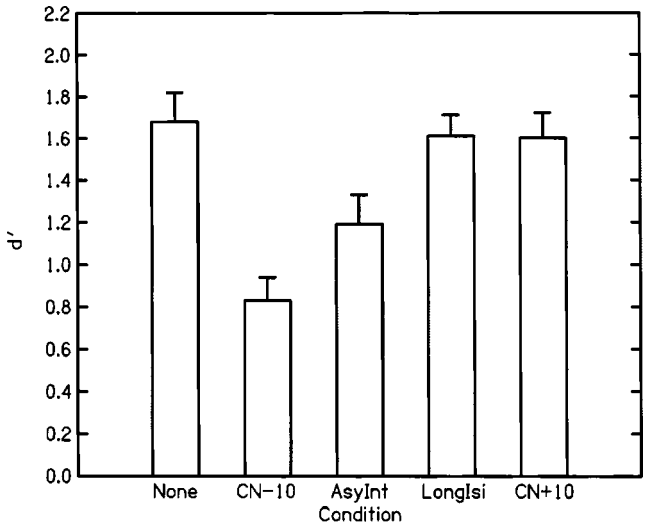

FIG. 6. The mean performance, and the associated standard errors (across subjects) obtained in experiment 4A. d' for F0 discrimination of a nominal 88 Hz target, bandpass filtered into a frequency region between 1500 and 15 000 Hz, is plotted for the five conditions used. See text for details of the conditions.

store performance back to that observed in the absence of an interferer, when presented at a high level so that it would nearly mask the interferer; and presented continuously, so that it would very likely be segregated from the target.

For five subjects, ΔF0 was 3.5% and for the sixth it was 2%. Four to five blocks of 100 trials were run for each condition and subject. The order of the conditions was counterbalanced over subjects. One block was run for each condition in turn, before additional blocks were run in any other condition.

Six subjects participated in all five conditions. Five of the six subjects had considerable musical experience, and five subjects took part in at least two of the previous experiments. Subjects participated in at least one practice session (three for the fresh subject), before data collection proper was started.

2. Results and discussion

Figure 6 shows the mean results and the corresponding standard errors across subjects. Performance in condition CN−10 was reduced by about $0.9\,d'$ units compared to that observed in the absence of an interferer (None). This reduction was very similar to that observed in experiment 1 for identical stimuli. When the interferer was gated asynchronously with the target (condition AsyInt), performance improved relative to that observed for synchronous gating (condition CN−10). However, performance in condition AsyInt was lower than in condition None. Performance in condition LongIsi was similar to that in condition None. This means that the increased time between the two target stimuli within a trial was not the reason for the impairment observed in condition AsyInt. Finally, performance in condition CN+10 was similar to that observed in condition None. This shows that a continous lowpass noise which spectrally overlaps with the interferer, and which is intense enough to nearly mask it, can bring performance back to that observed in the absence of an interferer. Note that one would not necessarily expect to see the same restoration effect with a *synchronously* gated lowpass noise of the same level. Remember that the results of experiment 2 showed improved performance with increased level of a synchronously gated lowpass noise. Performance in condition +10 dB for ΔF0 of 3.5% in experiment 2 was lower than that observed here with continous presentation of the same lowpass noise (condition None was not measured in experiment 2). Thus, it seems that gating the noise synchronously with the target might impair performance. However, the subjects were not all the same in experiment 2 and experiment 4A, and the subjects in common participated in experiment 4A after they ran in experiment 2. Therefore, this conclusion has to be treated with some caution.

To examine the statistical significance of the results, a repeated-measures one-way ANOVA (with five levels for the factor condition) was calculated, using the mean d' value for each subject and condition as input. This showed a highly significant main effect of condition [$F(4,20)=30.3$, $p<0.001$]. Calculation of simple contrasts, with condition None as the reference condition, showed that only condition CN−10 [$F(1,5)=67.2$, $p<0.001$] and condition AsyInt [$F(1,5)=14.4$, $p=0.01$] differed significantly from condition None. Performance in condition AsyInt was significantly better than that observed in condition CN−10 ($p=0.01$).

To summarize, asynchronous gating of the interferer and target reduced PDI relative to that caused by a synchronously gated interferer. Under the assumption that one single pitch mechanism exists, this would mean that perceptual segregation due to the 200 ms onset and offset asynchrony took place before the pitch estimate was derived and thus was able to influence the output of the pitch mechanism, at least to a certain degree. As mentioned earlier, Darwin and Ciocca (1992) reported that perceptual segregation due to onset asynchrony eliminated the contribution of a single mistuned harmonic to the overall pitch of a complex tone. As the mistuned harmonic was a low resolved harmonic and the harmonic complex contained resolved harmonics this gave evidence for the influence of perceptual segregation affecting the pitch of stimuli that would be processed *within* one pitch mechanism, i.e., either within the mechanism for the pitch of resolved components or within the common pitch mechanism. Hence, onset asynchrony can reduce across-frequency integration of information, even when that integration clearly occurs within a single pitch mechanism. This means that the observed reduction in PDI due to onset asynchrony cannot be used as an argument in favor of two pitch mechanisms.

In the present experiment, the imposed 200 ms asynchrony was not as effective in reducing the observed PDI as the continous higher-level lowpass noise. Therefore, we investigated in experiment 4B whether PDI could be eliminated by presenting the interferer continuously.

B. Experiment 4B: Continuous interferer

1. Stimuli and procedure

The task and procedure were the same as in experiment 4A. Three conditions were tested. The first two conditions, None and Syn.I. were replications of conditions None and

CN−10 in experiment 4A, respectively. The only difference from the corresponding conditions in experiment 4A was the absence of random variation of sample rate across trials in the present experiment (see later). In the third condition, the 88 Hz F0 interferer was presented continuously (condition Cont.I.); this was the only difference with respect to condition Syn.I. To produce a continuous interferer, the harmonic complex was generated and filtered in advance, and was then recorded on audio CD. During the experiment, it was played from audio CD and fed into a separate attenuator, whose output was then added via a headphone buffer to the target stimuli and the continuous low-level noise. This setup did not allow us to randomize the sample rate of the target and interferer together. Thus, there was no random variation of the sample rate of the stimuli in experiment 4B. Without random variation of the sample rate between trials, the task was easier. Thus, to avoid ceiling effects, ΔF0 was reduced to 2% for three subjects, and was kept at 3.5% for the fourth subject. Four to seven blocks of 100 trials were run for each condition and subject. The order of the conditions was counterbalanced over subjects. One block was run for each condition in turn, before additional blocks were run in any other condition.

Four subjects participated in all three conditions. All of them had participated in experiment 4A. Three of the four had considerable musical experience and were those who showed more impairment in condition AsyInt in experiment 4A than other subjects. The fourth subject had only shown a very slight impairment in performance in condition AsyInt. The other two subjects from experiment 4A, both with considerable musical experience, were no longer available. One of these had shown a medium impairment and the other had shown hardly any impairment in condition AsyInt. Subjects participated in at least one practice session before data collection proper was started.

2. Results and discussion

Figure 7 shows the mean results and the corresponding standard errors across subjects. Performance in condition Syn.I. was reduced by about $0.87\,d'$ units relative to that observed in the absence of an interferer (None). This reduction was very similar to that observed in experiment 4A for identical stimuli, except for the roving of the sample rate between trials. For the continuous interferer, performance was much improved relative to that observed in condition Syn.I.; however, it was still somewhat below that in condition None. The main interest of the present experiment was to test whether presenting the interferer continuously would restore performance to that observed in the absence of an interferer. To assess this, a related measures *t* test was calculated on the data from those two conditions. This showed that performance in condition None was significantly better than in condition Cont.I. [$T(3)=3.1$, $p_{\text{one-sided}}=0.027$]. For comparison, the same test, calculated for the same four subjects only on the data from conditions None and AsyInt in experiment 4A, resulted in $T(3)=3.8$ and $p_{\text{one-sided}}=0.016$.

In summary, presenting the interferer continously markedly reduced PDI relative to that caused by a synchronously gated interferer. The reduction was greater than found for an asynchronously presented interferer. However, performance was still slightly below that observed in the absence of an interferer.

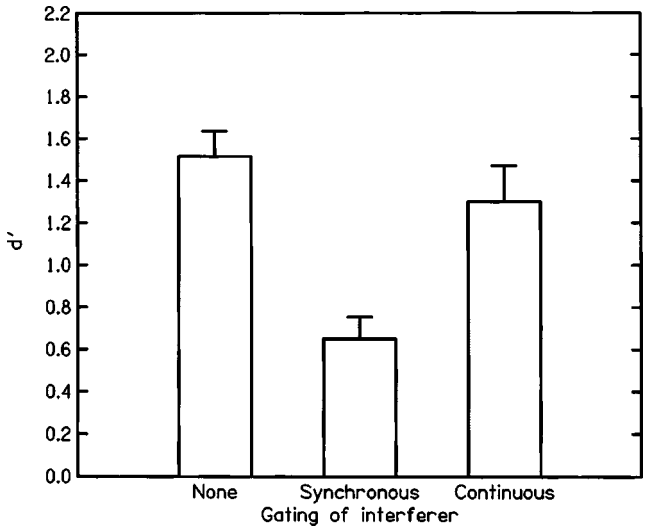

FIG. 7. The mean performance, and the associated standard errors (across subjects) obtained in experiment 4B. d' for F0 discrimination of a nominal 88 Hz target, bandpass filtered into a frequency region between 1500 and 15 000 Hz, is plotted for the three conditions used. See text for details of the conditions.

VI. GENERAL DISCUSSION

Evidence for a new type of interference in the pitch domain has been presented. F0 discrimination between sequentially presented complex tones containing only unresolved components was impaired in the presence of a simultaneous complex tone containing resolved harmonics, even though target and interferer were filtered into well separated spectral regions. The interference effect was tuned to the similarity between the F0s of target and interferer, indicating a central origin. A relatively broad tuning was observed; interferers with an F0 of 20%–30% above that of the target still produced a small impairment in F0 discrimination, even though interferer and target were clearly segregated. This tuning is much wider than that observed for the influence of a mistuned harmonic on the pitch of the overall harmonic complex; Moore *et al.* (1985) showed that pitch shifts caused by a mistuned harmonic approached zero at about 8% mistuning (with the maximum pitch shift arising at about 2%–3% mistuning). Also, Moore *et al.* (1986) found that a harmonic was sufficiently mistuned to be heard as a separate tone with mistunings between 1.3% and 2%, an amount of mistuning where the harmonic would still significantly contribute to overall pitch. Thus, a duplex region existed where sounds were perceptually segregated but nevertheless information from the two sounds was combined to some extent when determining the overall pitch. Subjective reports in experiment 1 of the present study support the existence of a duplex region in PDI too; even when target and interferer were perceptually segregated, a small interference effect was present. The generally broader tuning found in PDI than that found with a single mistuned harmonic might be a consequence of the fact that in the former paradigm the pitch investigated (via discrimination of F0) was that of an unre-

solved target complex while in the latter paradigm the investigated pitch was that of a complex tone containing resolved components. The former would have a less salient pitch than the latter even when presented alone. And of course, in the former the interferer was a complex tone containing several resolved components while in the latter the ''interference'' arose from one individual component only. These points might explain why PDI extends to greater F0 separations and might also explain why, even with a continuous interferer, some residual PDI was observed. Note that even though the influence of a mistuned component on overall pitch and its tuning characteristic has often been discussed in terms of a harmonic sieve (Moore *et al.*, 1985; Moore *et al.*, 1986; Darwin *et al.*, 1994) this does not imply that such an influence and tuning can *only* be represented within a class of models where pitch is derived by a pattern matching process across resolved harmonics (Goldstein, 1973; Terhardt, 1974).

The existence of PDI is compatible with the notion of one common pitch mechanism for resolved and unresolved components. The specific characteristics of the results are consistent with the dominant pitch produced by the resolved harmonics ''swamping'' the estimate of the F0 of the unresolved target, and with this interference occurring in a common pitch mechanism. Alternatively, if two different pitch mechanisms exist, then the existence of PDI indicates that they are not independent. Furthermore, the specific characteristics of PDI demonstrated in experiments 3A and 3B indicate that if two mechanisms exist, then the output of these two mechanism seems to be combined compulsorily at a relatively late stage, and the conscious pitch estimate is dominated by the more salient *output* of the resolved mechanism.

One of the most influential studies providing positive evidence for the existence of two pitch mechanisms was presented by Carlyon and Shackleton (1994). Their subjects had to compare the pitch of two simultaneously presented complex tones. The stimuli they used were quite similar to the ones employed here. The tones were bandpass filtered in either a LOW (125–625 Hz), MID (1375–1875 Hz), or HIGH (3900–5400 Hz) spectral region, and had an F0 of either 88 or 250 Hz. Depending on the combination of spectral region and F0, the complexes contained either mainly resolved harmonics (88-LOW, 250-LOW, 250-MID) or only unresolved harmonics (88-MID, 250-HIGH, 88-HIGH). The two complexes whose pitch had to be compared were always filtered into two different spectral regions.

Carlyon and Shackleton (1994) also measured performance for F0 discrimination of each of the complex tones alone (for each nominal F0 and spectral region) in the classical way, i.e., the tones were presented sequentially on their own. Performance in this sequential, within spectral region task was then used to estimate the noise associated with the encoding of F0. Within the framework of a model based on signal detection theory, those estimates were then used to derive predictions for F0 discrimination performance in experimental conditions where two complexes were presented *simultaneously*. The results showed that performance in the simultaneous task was worse than predicted when the two complexes differed in resolvability, but was not worse than predicted when they were both resolved. Note that the authors excluded from further analysis the simultaneous condition with two unresolved complexes because an additional cue was present in this specific condition. In order to explain why performance was worse than predicted when the simultaneous complexes differed in resolvability, but was not worse than predicted when they were both resolved, an additional ''translation noise'' was assumed; this was supposed to arise when the output from two different pitch mechanisms had to be compared. The need to assume an extra translation noise when predicting performance in the simultaneous F0 discrimination task from that observed in the sequential F0 discrimination task is the evidence Carlyon and Shackleton (1994) presented for the existence of two pitch mechanisms.[2]

The current experiments showed that the presence of an additional resolved complex tone significantly impaired F0 discrimination between two sequentially presented unresolved complexes. Thus, even though the two target tones had the *same* resolvability, performance was impaired simply due to the presence of another complex tone with similar F0. This means that Carlyon and Shackleton's (1994) performance predictions for F0 discrimination between two simultaneously presented complex tones probably were too high as they were based on performance measured in conditions were each stimulus was presented alone. Predicted performance would have been lower had predictions been derived from base line conditions where the sequentially presented target complex was accompanied by another complex tone.

A similar reasoning was used by Moore *et al.* (1984) with regard to the question of what constitutes the correct base line condition to determine the precision of the representation of individual components of a complex tone at the input to a central pitch processor (Goldstein, 1973). Moore *et al.* (1984) argued that the right measure was not the frequency DL of each component in isolation, but rather the frequency DL of each component when presented within the complex tone; they showed that, contrary to Goldstein's conclusion, no extra noise within channels conveying information from the periphery to the central processor was needed to account for precision of the estimate of the residue pitch, if the latter condition was used as base line. Similarly, the current study shows that probably no extra translation noise is necessary to explain the finding of Carlyon and Shackleton (1994) that performance was lower than predicted in conditions with two simultaneous tones differing in resolvability. Thus, the current findings question the basis of Carlyon and Shackleton's (1994) argument for two distinct pitch mechanisms.

Compatible with this, Micheyl and Oxenham (2003) did not find any evidence for translation noise when F0 discrimination was measured for two complex tones presented sequentially. In the study of Micheyl and Oxenham (2003) (see also Oxenham *et al.*, 2004) the sequentially presented complex tones were filtered into either the same or a different spectral region. Depending on the nominal F0 used in a given condition, this resulted in the two tones either having the same or different resolvability. Their results showed that

there was a large noise related to the comparison of F0 across spectal region, i.e., the timbre difference between the two sounds resulting from filtering into different spectral regions severely impaired performance. They did not need to assume an additional noise in order to successfully predict performance in conditions where the resolvability of the two tones differed based on performance observed in conditions where the two tones had the same resolvability.

In summary, the present results provide an alternative interpretation for the findings of Carlyon and Shackleton. The current findings are compatible with either the notion of one common pitch mechanism for resolved and unresolved components, or with the notion of two different mechanisms whose outputs at some higher stage cannot be accessed independently. Theoretically, one possible realization of such a higher stage interference could be an interference in memory. It has been shown that same/different judgements on pairs of complex tones separated by some time interval (around 4–5 s) was significantly impaired if other tones with similar pitch were presented during the retention interval (Semal and Demany, 1991; Semal and Demany, 1993). A similar interference in memory might have caused the PDI in the current experiments where two complex tones have been presented simultaneously. However, the fact that onset asynchrony significantly reduced PDI (experiment 4A) argues against an explanation of PDI mainly in terms of interference in memory. The onset asynchrony led subjects to perceive two sound sources instead of one (at least for small differences between the F0s of target and interferer where PDI was largest). In Semal and Demany's experiments several sound events were always heard, and introducing differences between the timbres of the target sounds and the interfering sounds hardly affected the observed pitch interference in auditory short-term memory. In contrast in the present experiment, PDI was substantially reduced when subjects heard two sound sources due to the onset asynchrony. Furthermore, the onset asynchrony in experiment 4A led to subjects hearing the interferer alone after presentation of the target in the first interval and before presentation of the target in the second interval. Thus, according to the ''interference in memory'' hypothesis one might even expect performance to be *worse* in the presence of onset asynchrony than with synchronous onsets of target and interferer. Therefore, it seems unlikely that PDI was mainly caused by a higher-stage interference in memory. Under the assumption that two pitch mechanisms exist, PDI rather seems to occur at the level where a conscious pitch estimate is derived.

A particularly influential example of a unitary model, termed the ''autocorrelogram'' model, can also account for the fact that, for a given F0, the lower harmonics give rise to a more salient pitch than do the unresolved harmonics (Meddis and Hewitt, 1991; Meddis and O'Mard, 1997). This latter prediction arises from a deterioration in phase locking with increasing frequency. However, this model has also been challenged (Carlyon and Shackleton, 1994; Shackleton and Carlyon, 1994; Carlyon, 1998; Kaernbach and Demany, 1998; Plack and White, 2000b; Kaernbach and Bering, 2001; Carlyon *et al.*, 2002b). One example comes from an experiment by Shackleton and Carlyon (1994), who showed that, when two complexes of different F0s are filtered into the same spectral region, the DLF0 still depends strongly on resolvability—even though the accuracy of phase locking is the same in the two cases, causing the model to predict no consistent effect of resolvability (Shackleton and Carlyon, 1994; Carlyon, 1998). This and other findings question the ability of the autocorrelogram model—in its current form—to account for all the data on the pitch of resolved and unresolved harmonics. Modifications like restricting and varying with center frequency the range of interspike intervals that can be analyzed as suggested by Moore (1997) and Bernstein and Oxenham (2003a) might improve on this. We conclude that, although existing models of pitch perception fail to capture the effects of resolvability on DLF0s, much of the experimental evidence is consistent with a unitary, but as yet unspecified, pitch mechanism.

VII. SUMMARY AND CONCLUSIONS

(1) Experiment 1 showed the existence of pitch duscrimination interference (PDI). F0 discrimination between two sequentially presented complex tones containing only unresolved components was severely impaired in the presence of another complex tone with similar F0 and resolved components, even though the target and interferer were filtered into well separated spectral regions. PDI decreased with increasing difference in F0 between the interferer and the target.

(2) Experiment 2 demonstrated further the crucial role of the tonality of the added sound in PDI. Increasing the level of a synchronously gated lowpass noise which spectrally overlapped with a complex tone interferer reduced PDI.

(3) Experiment 3A showed that PDI was larger when the interferer contained resolved components than when it contained only unresolved components. In experiment 3B, PDI was larger for a resolved interferer with components added in sine phase and F0 identical to the nominal target F0 than for an unresolved interferer with components added in alternating phase and F0 half that of the nominal target F0, but with a pitch equal to that of the target. This indicates that the pitch salience of the interferer plays a crucial role in PDI while its degree of envelope modulation after auditory filtering is less important.

(4) Experiment 4A showed that an interferer gated on 200 ms before and off 200 ms after the target produced less PDI than when gated synchronously with the target. Interference could be reduced further by presenting the interferer continuously; however, even then some residual impairment was observed (experiment 4B).

The current findings provide an alternative explanation for Carlyon and Shackleton's (1994) pattern of results; there might be no need to postulate additional translation noise when comparing F0 estimates for resolved and unresolved harmonics. The observed interference in the pitch domain between simultaneously presented complex tones that are well separated in spectral region might explain their pattern of results. The current results are consistent with the existence of one common pitch mechanism and question Carlyon and Shackleton's evidence for two pitch mechanisms.

ACKNOWLEDGMENTS

This work was supported by EPSRC Grant No. GR/R65794/01. The authors thank Brian Moore for helpful discussions and comments on an earlier version of this paper. They also thank Chris Darwin, Christophe Micheyl, Andy Oxenham, and Neil Viemeister for helpful comments.

[1]Throughout the paper, if appropriate, the Huynh–Feldt correction was applied to the degrees of freedom (Howell, 1997). In such cases, the corrected significance value is reported.

[2]The evidence is *not* their finding that in the simultaneous F0 discrimination task performance was better when the two complexes had the same resolvability status than when they differed in resolvability. This finding on its own does not provide an argument for the existence of two pitch mechanisms (even though it is sometimes used as if it would). The reason for this is that performance for F0 discrimination of unresolved complexes alone was worse than that of resolved complexes alone. Therefore, it had to be expected that in a task which requires the combination of the two, performance would be limited by the harder task. This logic explained why F0 discrimination of two simultaneously presented resolved complexes would be expected to be better than F0 discrimination of one resolved and one unresolved one. Thus, comparison between performance levels obtained in the various conditions with simultaneously presented pairs of complexes as such cannot and was not used by the authors when they argued in favor of two pitch mechanisms.

Bernstein, J., and Oxenham, A. (**2003a**). ''Effects of relative frequency, absolute frequency, and phase on fundamental frequency discrimination: Data and an autocorrelation model,'' J. Acoust. Soc. Am. **113**, 2290.

Bernstein, J. G., and Oxenham, A. J. (**2003b**). ''Pitch discrimination of diotic and dichotic tone complexes: Harmonic resolvability or harmonic number?'' J. Acoust. Soc. Am. **113**, 3323–3334.

Bernstein, L. R., and Trahiotis, C. (**2001**). ''Using transposed stimuli to reveal similar underlying sensitivity to interaural timing information at high and low frequencies: Support for the Colburn-Esquissaud hypothesis,'' in *Physiological and Psychophysical Bases of Auditory Function*, edited by D. J. Breebaart, A. J. M. Houtsma, A. Kohlrausch, V. F. Prijs, and R. Schoonhoven (Shaker, Maastricht).

Burns, E. M., and Viemeister, N. F. (**1976**). ''Nonspectral pitch,'' J. Acoust. Soc. Am. **60**, 863–869.

Carlyon, R. P. (**1987**). ''A release from masking by continuous, random, notched noise,'' J. Acoust. Soc. Am. **81**, 418–426.

Carlyon, R. P. (**1998**). ''Comments on ''A unitary model of pitch perception'' [J. Acoust. Soc. Am. **102**, 1811–1820 (1997)],'' J. Acoust. Soc. Am. **104**, 1118–1121.

Carlyon, R. P., Deeks, J., Norris, D., and Butterfield, S. (**2002a**). ''The continuity illusion and vowel identification,'' Acustica united with Acta Acustica **88**, 408–415.

Carlyon, R. P., and Shackleton, T. M. (**1994**). ''Comparing the fundamental frequencies of resolved and unresolved harmonics: Evidence for two pitch mechanisms?'' J. Acoust. Soc. Am. **95**, 3541–3554.

Carlyon, R. P., van Wieringen, A., Long, C. J., Deeks, J. M., and Wouters, J. (**2002b**). ''Temporal pitch mechanisms in acoustic and electric hearing,'' J. Acoust. Soc. Am. **112**, 621–633.

Dai, H. (**2000**). ''On the relative influence of individual harmonics on pitch judgment,'' J. Acoust. Soc. Am. **107**, 953–959.

Darwin, C. J., and Carlyon, R. P. (**1995**). ''Auditory grouping,'' in *Hearing*, edited by B. C. J. Moore (Academic, San Diego).

Darwin, C. J., and Ciocca, V. (**1992**). ''Grouping in pitch perception: Effects of onset asynchrony and ear of presentation of a mistuned component,'' J. Acoust. Soc. Am. **91**, 3381–3390.

Darwin, C. J., Ciocca, V., and Sandell, G. J. (**1994**). ''Effects of frequency and amplitude modulation on the pitch of a complex tone with a mistuned harmonic.,'' J. Acoust. Soc. Am. **95**, 2631–2636.

Fine, P. A., and Moore, B. C. J. (**1993**). ''Frequency analysis and musical ability,'' Music Percept. **11**, 39–53.

Flanagan, J. L., and Guttman, N. (**1960**). ''Pitch of periodic pulses without fundamental component,'' J. Acoust. Soc. Am. **32**, 1319–1328.

Gockel, H. (**2000**). ''Perceptual grouping and pitch perception,'' in *Results of the 8th Oldenburg Symposium on Psychological Acoustics*, edited by A. Schick, M. Meis, and C. Reckhardt (BIS, Oldenburg, Germany).

Goldstein, J. L. (**1973**). ''An optimum processor theory for the central formation of the pitch of complex tones,'' J. Acoust. Soc. Am. **54**, 1496–1516.

Grimault, N., Micheyl, C., Carlyon, R. P., and Collet, L. (**2002**). ''Evidence for two pitch encoding mechanisms using a selective auditory training paradigm,'' Percept. Psychophys. **64**, 189–197.

Hanna, T. E., and Robinson, D. E. (**1985**). ''Phase effects for a sine wave masked by reproducible noise,'' J. Acoust. Soc. Am. **77**, 1129–1140.

Hoekstra, A., and Ritsma, R. J. (**1977**). ''Perceptive hearing loss and frequency selectivity,'' in *Psychophysics and Physiology of Hearing*, edited by E. F. Evans and J. P. Wilson (Academic, London).

Houtsma, A. J. M., and Smurzynski, J. (**1990**). ''Pitch identification and discrimination for complex tones with many harmonics,'' J. Acoust. Soc. Am. **87**, 304–310.

Howell, D. C. (**1997**). *Statistical Methods for Psychology* (Duxbury, Belmont, CA).

Kaernbach, C., and Bering, C. (**2001**). ''Exploring the temporal mechanism involved in the pitch of unresolved harmonics,'' J. Acoust. Soc. Am. **110**, 1039–1048.

Kaernbach, C., and Demany, L. (**1998**). ''Psychophysical evidence against the autocorrelation theory of auditory temporal processing,'' J. Acoust. Soc. Am. **104**, 2298–2306.

Licklider, J. C. R. (**1951**). ''A duplex theory of pitch perception,'' Experientia **7**, 128–133.

McFadden, D., and Pasanen, E. G. (**1976**). ''Lateralization at high frequencies based on interaural time differences,'' J. Acoust. Soc. Am. **59**, 634–639.

Meddis, R., and Hewitt, M. (**1991**). ''Virtual pitch and phase sensitivity studied using a computer model of the auditory periphery. I: Pitch identification,'' J. Acoust. Soc. Am. **89**, 2866–2882.

Meddis, R., and O'Mard, L. (**1997**). ''A unitary model of pitch perception,'' J. Acoust. Soc. Am. **102**, 1811–1820.

Micheyl, C., and Oxenham, A. J. (**2003**). ''Further tests of the 'two pitch mechanisms' hypothesis,'' J. Acoust. Soc. Am. **113**, 2225.

Moore, B. C. J. (**1993**). ''Frequency analysis and pitch perception,'' in *Human Psychophysics*, edited by W. A. Yost, A. N. Popper, and R. R. Fay (Springer, New York).

Moore, B. C. J. (**1997**). *An Introduction to the Psychology of Hearing*, 4th ed. (Academic, San Diego).

Moore, B. C. J. (**2003**). *An Introduction to the Psychology of Hearing*, 5th ed. (Academic, San Diego).

Moore, B. C. J., and Glasberg, B. R. (**1986**). ''The role of frequency selectivity in the perception of loudness, pitch and time,'' in *Frequency Selectivity in Hearing*, edited by B. C. J. Moore (Academic, London).

Moore, B. C. J., and Glasberg, B. R. (**1988**). ''Effects of the relative phase of the components on the pitch discrimination of complex tones by subjects with unilateral and bilateral cochlear impairments,'' in *Basic Issues in Hearing*, edited by H. Duifhuis, H. Wit, and J. Horst (Academic, London).

Moore, B. C. J., and Glasberg, B. R. (**1990**). ''Frequency selectivity in subjects with cochlear hearing loss and its effects on pitch discrimination and phase sensitivity,'' in *Advances in Audiology*, edited by F. Grandori, G. Cianfrone, and D. T. Kemp (Karger, Basel).

Moore, B. C. J., Glasberg, B. R., and Peters, R. W. (**1985**). ''Relative dominance of individual partials in determining the pitch of complex tones,'' J. Acoust. Soc. Am. **77**, 1853–1860.

Moore, B. C. J., Glasberg, B. R., and Peters, R. W. (**1986**). ''Thresholds for hearing mistuned partials as separate tones in harmonic complexes,'' J. Acoust. Soc. Am. **80**, 479–483.

Moore, B. C. J., Glasberg, B. R., and Shailer, M. J. (**1984**). ''Frequency and intensity difference limens for harmonics within complex tones,'' J. Acoust. Soc. Am. **75**, 550–561.

Moore, B. C. J., and Ohgushi, K. (**1993**). ''Audibility of partials in inharmonic complex tones,'' J. Acoust. Soc. Am. **93**, 452–461.

Moore, B. C. J., and Peters, R. W. (**1992**). ''Pitch discrimination and phase sensitivity in young and elderly subjects and its relationship to frequency selectivity,'' J. Acoust. Soc. Am. **91**, 2881–2893.

Moore, B. C. J., and Rosen, S. M. (**1979**). ''Tune recognition with reduced pitch and interval information,'' Q. J. Exp. Psychol. **31**, 229–240.

Oxenham, A. J., Bernstein, J. G., and Micheyl, C. (**2004**). ''Pitch perception of complex tones within and across ears and frequency regions,'' in *Auditory Signal Processing: Physiology, Psychoacoustics, and Models*, edited by D. Pressnitzer, A. de Cheveigné, S. McAdams, and L. Collet (Springer, New York).

Patterson, R. D., Robinson, K., Holdsworth, J., McKeown, D., Zhang, C.,

and Allerhand, M. (**1992**). ''Complex sounds and auditory images,'' in *Auditory Physiology and Perception, Proceedings of the 9th International Symposium on Hearing*, edited by Y. Cazals, L. Demany, and K. Horner (Pergamon, Oxford).
Plack, C. J., and Viemeister, N. F. (**1992**). ''The effects of notched noise on intensity discrimination under forward masking,'' J. Acoust. Soc. Am. **92**, 1902–1910.
Plack, C. J., and White, L. J. (**2000a**). ''Perceived continuity and pitch perception,'' J. Acoust. Soc. Am. **108**, 1162–1169.
Plack, C. J., and White, L. J. (**2000b**). ''Pitch matches between unresolved complex tones differing by a single interpulse interval,'' J. Acoust. Soc. Am. **108**, 696–705.
Plomp, R. (**1964**). ''The ear as a frequency analyzer,'' J. Acoust. Soc. Am. **36**, 1628–1636.
Plomp, R. (**1967**). ''Pitch of complex tones,'' J. Acoust. Soc. Am. **41**, 1526–1533.
Ritsma, R. J. (**1967**). ''Frequencies dominant in the perception of the pitch of complex sounds,'' J. Acoust. Soc. Am. **42**, 191–198.
Ritsma, R. J. (**1970**). ''Periodicity detection,'' in *Frequency Analysis and Periodicity Detection in Hearing*, edited by R. Plomp and G. F. Smoorenburg (Sijthoff, Leiden).
Schouten, J. F. (**1940**). ''The residue and the mechanism of hearing,'' Proc. K. Ned. Akad. Wet. **43**, 991–999.
Schouten, J. F. (**1970**). ''The residue revisited,'' in *Frequency Analysis and Periodicity Detection in Hearing*, edited by R. Plomp and G. F. Smoorenburg (Sijthoff, Leiden).
Semal, C., and Demany, L. (**1991**). ''Dissociation of pitch from timbre in auditory short-term memory,'' J. Acoust. Soc. Am. **89**, 2404–2410.
Semal, C., and Demany, L. (**1993**). ''Further evidence for an autonomous processing of pitch in auditory short-term memory,'' J. Acoust. Soc. Am. **94**, 1315–1322.
Shackleton, T. M., and Carlyon, R. P. (**1994**). ''The role of resolved and unresolved harmonics in pitch perception and frequency modulation discrimination,'' J. Acoust. Soc. Am. **95**, 3529–3540.
Slaney, M., and Lyon, R. F. (**1990**). ''A perceptual pitch detector,'' Proceedings of the International Conference of Acoustics, Speech and Signal Processing, pp. 357–360.
Terhardt, E. (**1974**). ''Pitch, consonance, and harmony,'' J. Acoust. Soc. Am. **55**, 1061–1069.
Warren, R. M. (**1970**). ''Perceptual restoration of missing speech sounds,'' Science **167**, 392–393.
Yost, W. A., and Sheft, S. (**1989**). ''Across-critical-band processing of amplitude-modulated tones,'' J. Acoust. Soc. Am. **85**, 848–857.
Yost, W. A., Sheft, S., and Opie, J. (**1989**). ''Modulation interference in detection and discrimination of amplitude modulation,'' J. Acoust. Soc. Am. **86**, 2138–2147.

Perceptual evaluation of multi-dimensional spatial audio reproduction

Catherine Guastavino
McGill University, Department of Psychology, 1205 Dr. Penfield Avenue, Montreal, Quebec H3A 1B1, Canada

Brian F. G. Katz[a)]
LIMSI-CNRS, Perception Située, BP 133, F91403 Orsay France

(Received 2 September 2003; revised 13 April 2004; accepted 3 May 2004)

Perceptual differences between sound reproduction systems with multiple spatial dimensions have been investigated. Two blind studies were performed using system configurations involving 1-D, 2-D, and 3-D loudspeaker arrays. Various types of source material were used, ranging from urban soundscapes to musical passages. Experiment I consisted in collecting subjects' perceptions in a free-response format to identify relevant criteria for multi-dimensional spatial sound reproduction of complex auditory scenes by means of linguistic analysis. Experiment II utilized both free response and scale judgments for seven parameters derived form Experiment I. Results indicated a strong correlation between the source material (sound scene) and the subjective evaluation of the parameters, making the notion of an ''optimal'' reproduction method difficult for arbitrary source material. © *2004 Acoustical Society of America.* [DOI: 10.1121/1.1763973]

PACS numbers: 43.66.Lj, 43.66.Qp, 43.38.Md [MK] Pages: 1105–1115

I. INTRODUCTION

The use of multi-channel audio for the reproduction or simulation of multi-dimensional sound fields is becoming more common in research, artistic performances, home and commercial installations. In the field of psychoacoustic research, the ability to reproduce a multi-dimensional spatial sound field in laboratory conditions is advantageous for the study of auditory perception and cognition in complex sonic environments. A key question concerns the influence of the spatial presentation on a person's perception of various attributes of the reproduced sound field. In particular, how complete (spatially) must the information be for subjects to be ''convinced'' of the reproduction? In addition, are there potentially negative effects linked to providing ''too much'' information, and what if any is the balance? Is there a tradeoff between different perceptual aspects of the reproduced sound scene when more or less spatial information is included?

Sound quality assessment of reproduction methods have traditionally been concerned with non-spatial attributes, concentrating primarily on timbral and distortion issues when assessing the qualities of loudspeakers in monophonic reproductions (e.g., Eisler, 1966; Gabrielsson, Rosenberg, and Sjögren, 1974; Gabrielsson and Sjögren, 1979). Spatial attributes have however been investigated quite extensively in the field of room acoustics (e.g., Beranek, 1962; Schroeder, Gottlob, and Siebrasse, 1974; Kahle, 1995). More recently, the increasing use of multi-channel audio has led researchers to study spatial sound perception in the context of auditory displays (Rumsey, 1998, 2002; Berg and Rumsey, 1999, 2000, 2001, 2002; Zacharov and Koivuniemi, 2001), since spatial attributes are considered an important contributor to overall sound quality of multi-channel systems. The subjective evaluation of spatial features remains however at a very early stage in its development compared with other auditory attributes such as timber or loudness, and the need for a more accurate description of spatial attributes becomes clear to perceptually optimize multi-channel audio systems.

In the present work we examine the results of a set of listening tests in which several spatial loudspeaker configurations were compared, with a variety of source material. Subjects were presented with a reproduction of the same recorded sound scene over different systems. Subjects were asked to evaluate the different configurations using verbal descriptions and value scales. Perceptual evaluations of the different systems as a function of their dependence upon the source material are of particular interest, as the results highlight the fact that there is no single system that is optimal for all conditions.

II. EXPERIMENTAL SYSTEM

A. Recording and reproduction setup

There are various approaches for recording and reproducing spatially distributed audio. The recording industry has developed a wide range of methods over the years starting from 2-channel stereo, to 4-channel quadraphonic, and the current trend of 6-channel 5.1. Various other, often more complicated, systems have been developed for theatrical and performance situations using greater and greater numbers of channels in the recording and/or reproduction. Each system requires its own recording and reproduction technique, these being closely linked.

Our aim in the present work is to investigate the subjective differences regarding the spatial complexity of multi-dimensional audio reproduction. The interest of this work

a)Electronic mail: brian.katz@limsi.fr

concerns the perceptual effects of spatial presentation and is not intended to be an evaluation of different recording techniques. The method employed in this study was a versatile recording and playback method which consists in recording the sound field with a compact 3-D microphone, containing near-coincident elements. This method, termed Ambisonics (Gerzon, 1977), was chosen as the best suited method for this study, since an Ambisonics recording can be decoded onto a variety of speaker configurations. For each sound scene, a single recording was used and only the spatial presentation of the information varied. In this manner, the effects of recording techniques, multiple microphone placements, and other bias in the technical aspect were minimized.

Ambisonics is an approach to sound field recording and reproduction that decomposes the spatial sound field into spherical harmonics. Currently available 1st order microphones provide four signals: W (zeroth order omnidirectional) and XYZ (1st order components representing the Cartesian axis with figure of 8 directivity patterns). This output result, termed B-format, captures the spatial information of the sound field, resolved into a mono reference signal and left–right, front–back, and up–down information, thus enabling the reproduction of full 3-D information. Reproduction of the sound entails a decoding process from the B-format signal to the array of loudspeakers. The decoding process results in a signal to each loudspeaker being composed of a combination of the spherical harmonics dependent upon the location of the speaker. There are various parameters in the decoding process, but their discussion is beyond the scope of this paper (cf. Gerzon, 1977; Fellgett, 1974; Gaskell, 1979; Daniel, 2000). All recordings used were made with a B-format Soundfield model ST250 microphone and decoded without shelf filtering (Furse, 2003) on an array of Studer A1 speakers and included a JBL 4545C subwoofer.

B. Design of the listening room

A prototype listening room was created for this experiment to test different reproduction methods with the conceptual goal of easing the process of abstraction from the listening room to the original environment. The design of the room can be divided into three parts: the acoustics, the visual, and the reproduction system.

The acoustics of the room were designed to be as dry as possible, given architectural limitations, in order to allow for the reproduction of outdoor soundscapes. The room has a flat frequency response and a reverberation time of <0.05 seconds for frequencies above 200 Hz. Below 200 Hz the reverberation time increased gradually to 0.2 seconds at 40 Hz. The room is acoustically isolated (floated construction) with internal dimensions $2.77\times3.24\times3.62$ m.

The visual design of the room, the most strikingly different aspect as shown in Fig. 1, is based upon a hexagonal shape. The goals were to create a room with minimal reference to the sounds being reproduced or the subject's frame of reference, as well as to ensure that subjects are not visually aware of the test configuration. Other than the point of entrance, there is no Cartesian frame of reference. To further this effect, the room is hexagonal in the vertical plane as well as the horizontal plane, resulting in slanted walls tapering at the floor and ceiling. The visual boundaries of the room are defined using acoustically transparent panels having a neutral gray color, allowing for the structural and acoustic design of the room, as well as all of the loudspeakers, to be hidden from view.

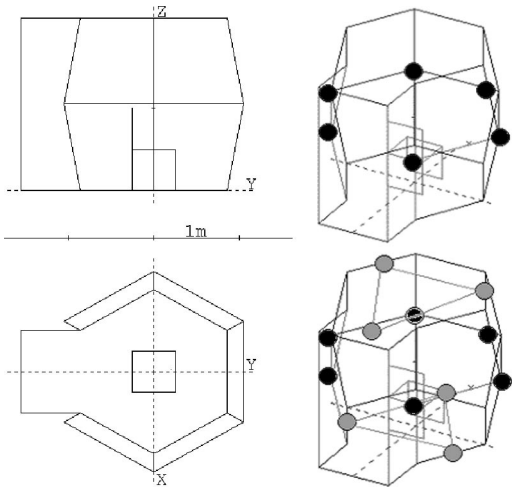

FIG. 1. Listening room visual surfaces indicating 3-D hexagonal structure. Locations for the 2-D and 3-D arrays are shown. The 1-D consists of solely the front pair of loudspeakers to generate a stereo pair. A chair is included for reference.

The reproduction system provides for 13 channels of discrete playback, including a low frequency subwoofer for frequencies below 100 Hz. Small high quality loudspeakers (low frequency roll-off at ~100 Hz) are suspended on a pipe grid that encircles the room and extends from floor to ceiling behind the visual screens. The subwoofer (flat response to 20 Hz) is placed in one corner of the room. Six speakers are located at seated listening level at the corners of the hexagon. The additional six are placed in two sets, three at ceiling level and three at floor level, corresponding to $\pm49°$ on alternating sides of the hexagon. This provides slightly reduced coverage for elevation sounds and full horizontal coverage in the listening plane. The level of the speakers was carefully adjusted to achieve a flat frequency response across the crossover frequency of 100 Hz. The 12 full range speakers were time and level aligned at the center of the listener position.

The result is a room far from the ''standard'' listening room, being in direct contrast to recommendation ITU-R BS.1116-1 for multi-channel sound systems (ITU-R, 1997). The area is one-third the minimum area, the reverberation time is one-half the prescribed value, and the room geometry contradicts the rectangle/trapezium prescription. However, the recommendation only prescribes for a multi-channel loudspeaker array conforming to the 5.1 format. While suitable for evaluating various audio processing techniques, it is not clear that the ''standard'' listing room is suitable for more specific situations such as psychoacoustic testing on individual subjects or more complex sound scenes such as outdoor material, where low reverberation times and abstraction from the listening room are necessary.

III. EXPERIMENT I: URBAN SOUNDSCAPES IN 2D AND 3D

A. Method

27 subjects with normal hearing, aged between 23 and 59 participated in the experiment. They were expert listeners, either studying or working in the field of acoustics. The participants served without pay.

The stimuli were five urban Parisian soundscapes selected from a list of places previously identified as representative of city noises by Maffiolo (1999). Live recordings were used rather than synthesized source material to fully capture complex spatial sound scenes and focus on the ''you are there'' approach to sound reproduction according to the concept of ecological validity, developed by Gibson (1979). Indeed, the familiarity of the sound material, together with the instructions given to ease the required process of abstraction, enabled the subjects to treat the stimuli with cognitive processes elaborated in real-life situation. The test samples were 45 to 60 seconds long. The B-format files were decoded using the full in-phase decoding scheme without shelf filtering (Furse, 2003). The test configurations were the 2-D (6-channel) and 3-D (12-channel) arrays with and without the subwoofer (x and x.1, following the familiar 5.1 convention). Configurations were equalized in level at the center of the listening position using a reverberant room recording of white noise decoded over each system. The subwoofer channel content was identical between 2-D.1 and 3-D.1 configurations and level matched to provide a flat frequency response over the crossover region.

B. Procedure

Subjects were presented with a reproduction of the same sound scene over four different systems, randomly ordered. Instructions were given to subjects to direct their response strategy towards everyday listening situations, so that they would react, to some extent, as if there were in the actual situation, i.e., in an ecological valid way (Gibson, 1979), rather than in the abstract situation of a laboratory experiment. For each sound example, a free verbalization task and a multiple comparison task were conducted: subjects listened to the four reproduction methods as many times as desired and were asked to freely describe the four versions, choose which one(s) sounded the most like their everyday experiences, and justify their choice. This elicitation method, used in previous studies to investigate the sound quality of complex auditory scenes (Maffiolo, 1999, Dubois, 2000, Guastavino and Cheminée, 2003), was chosen to identify perceptually relevant features without constraining the answers into predefined categories. More specifically, subjects were not instructed to focus on spatial attributes. The nature of the test and the details of the reproduction systems used were not disclosed to the subject prior to the test.

C. Analysis of the verbal data

A semantic analysis was conducted on the spontaneous descriptions of recreated acoustic environments. A total of 512 phrasings were classified in semantic categories emerging from free verbalizations. The verbal data was lemmatized, i.e., inflectional and variant forms of a word were reduced to their lemma: their base form. Synonyms were grouped together, as well as linguistic devices constructed on the same stem (e.g., ''bright,'' ''brightness''). Lexical devices belonging to the same semantic field as indicated in a French thesaurus (Péchoin, 1992), were grouped into semantic themes. Semantic themes with fewer than 3 occurrences were excluded from the analysis. Two coders independently combined semantic themes into larger semantic categories relating to presence/immersion, readability of the scene/sense of space, distance to the scene, timber, stability, localization, and hedonic judgments (e.g., ''annoying,'' ''pleasant''). Finally, all occurrences in each category were counted.

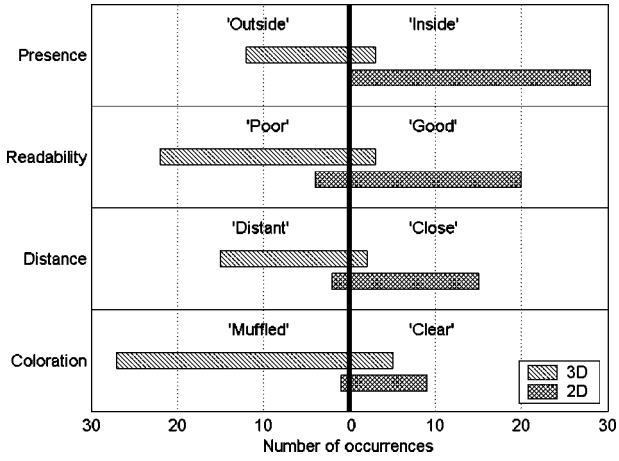

FIG. 2. The number of occurrences of spontaneous descriptions for the reproduction methods within different discriminating categories (2-D and 3-D). Opposing terms are represented on opposite sides of the graphs.

D. Results

The results of the comparison test show a strong preference for the 2-D configurations over other methods. Total results for the ''naturalness'' selection for the four reproduction setups were 62(2D), 45(2-D.1), 42(3-D), and 20(3-D.1). The number of occurrences for each reproduction method within discriminating semantic categories, namely presence, readability, distance, and coloration is presented in Fig. 2. It is interesting to note that nonspatial attributes were spontaneously evoked, although only the spatial presentation varied. The 2-D configurations (2-D and 2-D.1) were spontaneously described in the open questionnaires as very enveloping, spatially well defined, and providing a good sense of immersion in the scene, equating to a high degree of presence. Furthermore, subjects mentioned that the sound field reproduced by the 2-D systems sounded close to them. The 3-D configurations (3-D and 3-D.1) on the other hand were described as poorly enveloping and sounding farther away from the listener. Subjects indicated that space was poorly defined and indistinct. Regarding timber, the sound field recreated by the 3-D configurations was described as ''muffled.''

The 2-D.1 and 3-D.1 configurations were described as rich and too rich in low frequencies (31 and 39 occurrences, respectively), but were chosen for realism in the traffic noise

TABLE I. Details of the six soundscapes used in Experiment II.

Name	Description	Recording position
Train	Announcement on a train (small enveloping scene)	Seated within train car
Market	Walk in an open-air market (many sources at various distances)	Walking head height
Symphony	String orchestra (position close to conductor)	Above and behind conductor position
Organ	Organ music in a very large reverberant cathedral.	Well into the reverberant field
Traffic	Urban traffic noise (many sources at various distances and levels)	Corner of intersection
Improvised music	Modern improvisational music with organ, percussions, and wind instruments in a large reverberant cathedral (same as organ).	Well into the reverberant field

recordings. A further analysis of the comments suggested different ratings or different sound examples, depending on the relevance of the low frequency information in the scene (meaningful in traffic noise to recreate the rumbling of heavy vehicles, meaningless in pedestrian areas where no low frequency events are ''expected'' to occur regardless if it is actually present or not).

No distinction between the different configurations could be established on the basis of descriptions of stability of the image, localization, or hedonic judgments. The distinction between 2-D and 3-D configurations relies mainly on spatial attributes, but in an unexpected way. The 2-D systems provide a better feeling of presence and spatial definition and a closer image than the 3-D systems.

Relevant criteria for the perceptive evaluation of complex soundscapes were identified by considering semantic categories with the greatest number of occurrences. Six parameters were derived from the linguistic analysis: readability, presence, distance, localization, coloration and stability of the image. Experiment II was designed to evaluate multichannel spatial reproductions along these parameters on a wider range of auditory scenes.

IV. EXPERIMENT II: VARIOUS SOUNDSCAPES IN 1D, 2D, AND 3D

A. Method

26 subjects with normal hearing, aged between 23 and 62 participated in the experiment. They were expert listeners, either studying or working in the field of acoustics. All the participants served without pay.

The stimuli were recordings of six different soundscape excerpts as described in Table I, providing a wide variety of scenes. The decoding configuration was slightly altered, following observations and comments obtained from Experiment I, such that the B-format recordings were decoded using a 60% in-phase decoding scheme (comparable to a hyper-cardioid directivity pattern) without shelf filtering. This decoding option was seen as an improvement over the configuration in Experiment I as it provided the best compromise between localization of sources and sensitivity to listening position in preliminary listening tests. In addition, the low frequency level was adjusted to better compensate for the response of the microphone. The subwoofer channel content was identical between all three configurations. The test samples were 13 to 36 seconds long, and the subjects could listen to them as many times as desired.

The test configurations were 1-D (2.1), 2-D (6.1), and 3-D (12.1) arrays, all equalized in level at the center of the listening position. The subwoofer was included in all sound samples as it has been shown in Experiment I that the low frequency channel contributes to realism. Subjects were asked to compare perceptual differences between the three randomly ordered versions.

It should be noted that the 1-D, or stereo, configuration was not a simple 2.1 channel system. Due to the very low reverberation time in the listening room, the acoustics were deemed too dry for standard stereo. To present stereo in a more typical and favorable condition, a virtual listening room was utilized. The concept for this approach was to create a computer model of a good listening room (following a LEDE design with diffusion) using CATT-Acoustic, a geometric room acoustic simulation software. The virtual room had a mid-frequency reverberation time of 0.2 sec. The stereo speakers were placed in the model at the correct locations relative to the listener and 10 hyper-cardioid microphones were placed at the positions of the remaining speakers, pointing away from the listener. The predicted impulse responses from the virtual microphones were convolved with the

TABLE II. Perceptual parameters with extreme values as presented (translated from the original French) in Experiment II.

Parameter	Additional description	Left limit (−)	Right limit (+)
Readability ⟨Lisibilité⟩	Spatial definition, readability of the scene	Well defined	Poorly defined
Presence ⟨Présence⟩	Sense of ''being there,'' feeling of being	Inside	Outside
Distance ⟨Distance⟩	The auditory scene sounds ...	Close	Distant
Localization ⟨Localisation⟩	Localization of the sources/precision of the image	Precise	Indistinct
Coloration ⟨Coloration⟩	Spectral coloration/timber	Muffled	Clear
Stability ⟨Stabilité⟩	Stability/sensitivity to head movements	Stable	Unstable

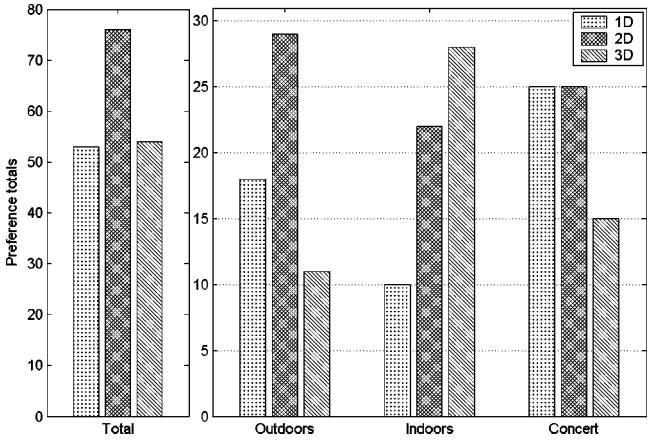

FIG. 3. Naturalness responses for the 3 types of soundscape.

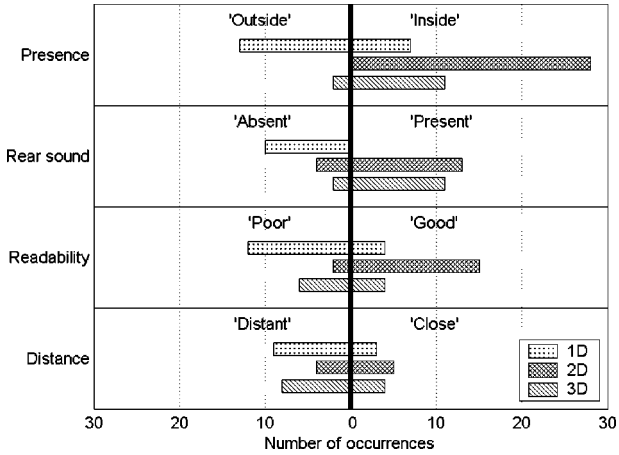

FIG. 4. The number of occurrences of spontaneous descriptions for the reproduction methods within different discriminating categories (1-D, 2-D, and 3-D). Opposing terms are represented on opposite sides of the graphs.

B-format 2-channel decoded signal, thus creating a 12.1 channel simulation of a 2.1 system reproduced in a good listening room. This method avoided the use of B-format synthesis for the room, maintaining the separation between systems. No negative effects were reported, and the system was described as a very natural stereo reproduction.

B. Procedure

For each sound example, subjects were asked to listen to the three reproduction methods, freely describe the three versions, choose which version(s) sounded the most like their everyday experiences and justify their choice, as in Experiment I. Following this, the six parameters (readability, presence, distance, localization, coloration, and stability of the image) were presented, in random order, with slider bars corresponding to each of the three samples for comparative judgments. An optional open questionnaire for each also existed for comments or explanations of perceptions. The semantic scales for this test, and their extreme values as presented on the slider scales, were derived from the spontaneous descriptions collected in Experiment I. These are listed in Table II.

C. Results

1. Naturalness

General results of Experiment II, as shown in Fig. 3, show a subjective impression of a more ''realistic'' or ''natural'' representation of the soundscape using the 2-D system versus the other systems. A more detailed analysis shows that the subjective ratings depend heavily on the soundscape.

For concert scenes, where clarity and precise localization of the instruments would be expected, the 1-D and 2-D systems were equally selected. We believe that modern listening habits also accounts for the choice of the 1-D system, as many subjects often listen to music on a stereo set-up and are thus inclined to choose this familiar configuration as seeming ''natural.'' For complex outdoor environments, where the sounds are expected to be surrounding at the level of the listener, but also with precise locations of the numerous sources, the 2-D system was selected, confirming the results of Experiment I on the reproduction of urban soundscapes. For indoor environments, where the sounds are expected to be surrounding and coming from above (announcement in the train, organ in the cathedral), the 3-D system was selected. For this grouping analysis, the Organ example was classified in the ''Indoors'' category rather than ''Concert'' due to the fact that the verbal data suggest that subjects paid greater attention to the room effect of the church than to the musical content. It should be stated that the Organ recording was made in the far reverberant field of the instrument, as noted in Table I.

2. Analysis of the verbal data

A total of 453 phrasings were classified in semantic categories emerging from free verbalizations using the same linguistic analysis as in Experiment I. Free descriptions were classified in semantic categories relating to the spatial distribution of the sound, presence, realism, readability, spectral balance, and localization. The number of occurrences for each reproduction method within discriminating categories, namely presence, readability, rear sound, and distance is presented in Fig. 4.

As regards perceptive evaluation, two major distinctions were established. The first one distinguishes the 1-D array from the 2-D and 3-D arrays on the basis of spatial distribution of sound. The 2-D and 3-D configurations were described as providing sound all around the listener, including behind and above the listener, as opposed to the 1-D configuration, which was spontaneously described as frontal. The second distinction, isolating the 2-D set-up, was observed on the basis of presence. The 2-D configuration was described as providing the most immersive environment.

3. Interaction between semantic scales

Cross-correlations were computed for every possible pair of variables over all ambiances. Results indicated a correlation between readability and localization for all three reproduction methods ($r^2=0.28$, $p=0.01$) as well as between presence and distance ($r^2=0.23$, $p=0.02$). The analysis of verbal comments confirmed these interactions: 14 comments indicated that an immersive scene sounds close, and 6 comments indicated that sources can easily be located in a spa-

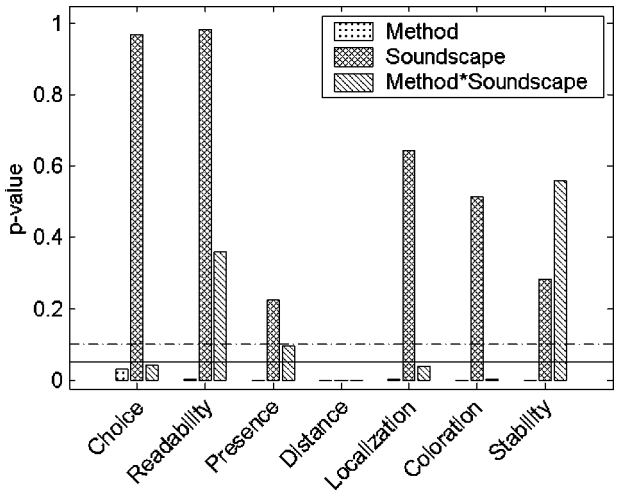

FIG. 5. ANOVA results (p-value) for a multivariate analysis of subjective parameters. Significant effects, evident from low p-values, of the method were observed for all variables : choice [$F(2,25)=3.58$], readability [$F(2,25)=6.0$], presence [$F(2,25)=162.7$], distance [$F(2,25)=43.6$], localization [$F(2,25)=6.5$], coloration [$F(2,25)=16.7$] and stability [$F(2,25)=41.67$]. A significant effect of soundscape was observed on distance ($F=6.5$). Significant effects of method*soundscape were observed for choice ($F=1.9$), distance ($F=8.2$), localization ($F=2.0$) and coloration ($F=3.2$).

tially well defined environment. The verbal data further suggested an interaction between distance and coloration, with 12 comments associating ''muffled'' with ''distant,'' or ''clear'' with ''close.''

4. ANOVA

A three (reproduction methods) by six (sound samples) by seven (variables) ANOVA on the ratings was calculated. The Green–Greenhouse correction was used for a violation of the sphericity assumption. The main effect of the reproduction method on the seven variables was significant ($p<0.05$) for all sound samples. Figure 5 presents the F and p values with regards to the relevance of method, soundscape, and the combination of method*soundscape for each variable.

The results show that the responses to all variables are strongly linked to the reproduction method. Aside from the distance parameter, all responses were invariant with regards to soundscape. Finally, there was an evident correlation between choice of the most ''natural'' method and the specific soundscape. This correlation was also seen for three other parameters: coloration, localization, and distance. To a lesser extent this correlation existed for presence. Significant effects of method and method*soundscape were observed on both spatial and timbral attributes. Gabrielsson, Rosenberg, and Sjögren (1974) also found a significant effect of both method and soundscape and a significant interaction between the most ''true-to-nature'' reproduction (monophonic reproduction on different loudspeakers) and sound samples (different music sections).

Post-hoc analyses for the present study were conducted using Bonferroni's comparison tests. Concerning the binary variable of choice, results indicated a strong tendency ($p=0.07$) for subjects to select the 2-D set-up rather than the other two configurations (1D and 3D). Similarly, the 2-D array was evaluated as providing a higher degree of readability, i.e., a more readable presentation of the sound scene, than the other two ($p=0.05$).

Results concerning the variables of presence and distance confirmed the counter-intuitive subjective judgments observed from the verbal data in the first experiment. Indeed, the 2-D set-up was again considered as more immersive and producing a closer auditory scene than the 3-D array ($p=0.01$ for presence and $p=0.05$ for distance). But the sound field recreated by the 1-D configuration was judged even less immersive and farther away ($p=0.01$ and $p=0.05$, respectively). Concerning localization and coloration, the 3-D reproduction was perceived as indistinct and muffled in comparison to the 1-D and 2-D reproductions, which were described as clearer and more precise ($p=0.05$ for localization and $p=0.01$ for coloration). Finally, the auditory recreation by the 1-D configuration was evaluated as more stable than the other two when the listeners moved away from the sweet spot ($p=0.01$).

The main effect of soundscape was significant for the perceived distance only. Along this variable, the three reproduction methods were ranked from ''close'' to ''far'' in the (2-D|3-D|1-D) order for all ambiances but the Organ, for which the order (1-D|2-D|3-D) was observed. An analysis of the verbal comments indicate that the 1-D set-up recreated a more direct frontal sound of the organ and less reverberated room effect than the 2-D and 3-D set-up, thus making the listener feel closer to the instrument.

5. Variations between sound scenes

To further examine the effect of soundscape on the various parameters, a statistical summary of the judgments is presented in Fig. 6, showing the responses for coloration, presence, and distance for each soundscape separately. While all recordings were made with the same microphone model (and all but the Symphony excerpt were made with the same physical microphone) and processed in an identical manner, there is a noticeable variation in coloration judgments between soundscapes. This indicates a potential bias in subjective evaluations of coloration as the responses are based upon the expectations of signal content, and not necessarily on the actual content. This effect is further complicated by the variations between method*soundscape which indicate that the spatial distribution of timbral information, and its expected distribution, is linked to coloration judgments.

The presence parameter judgments show the clear distinction between the methods, regardless of soundscape. Finally, the distance parameter shows the same general trend between soundscapes, but the distribution dependence on soundscape is interesting. For example, there is little variation for the Organ sample, while for the Improvised music excerpt there is a strong variation. This is most interesting as the microphone placement is identical and the Improvised music excerpt contains the same organ (with additional instruments at the same location), though playing a modern improvisational piece. For the Organ piece, verbal comments indicate that all subjects expected a large reverberant space, namely a church, whereas for the Improvised music excerpt,

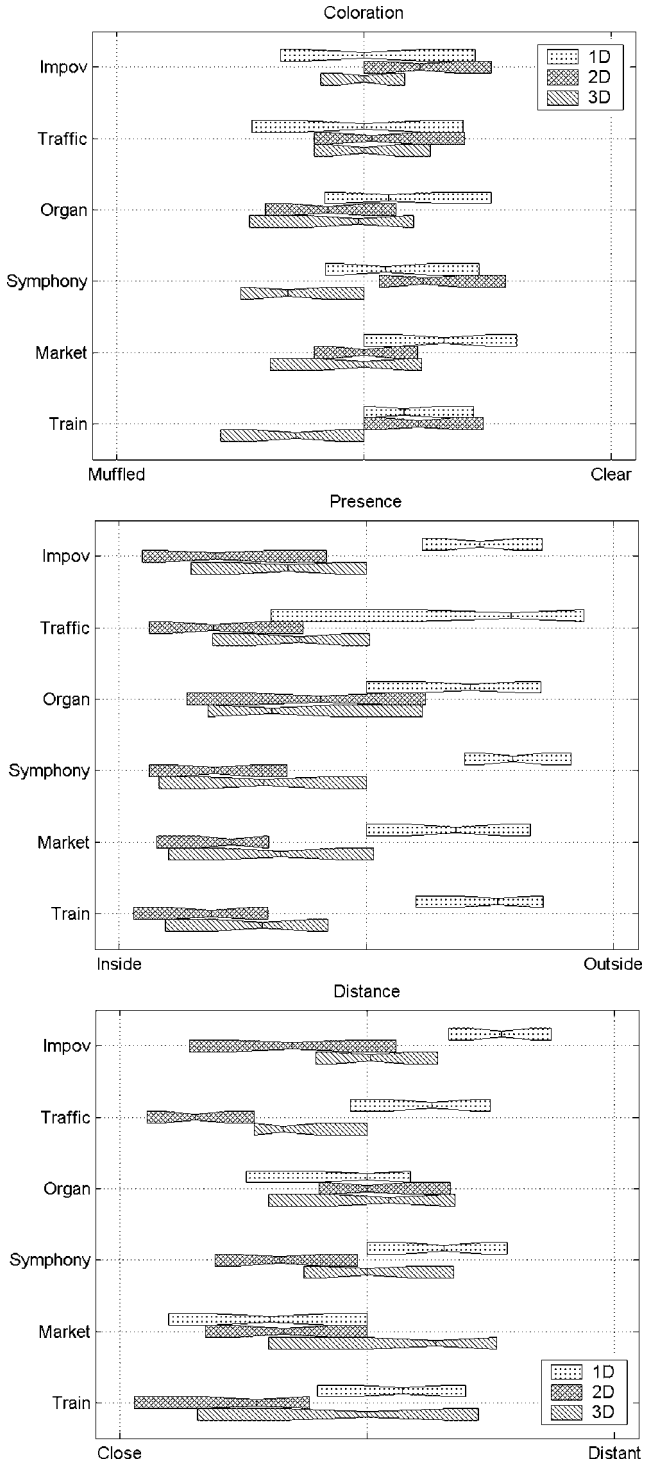

FIG. 6. A summary of slider parameter responses for the parameters ''Coloration,'' ''Distance,'' and ''Presence'' for each soundscape and the three different spatial presentation methods. Data shown as whisker plots spanning from the lower to upper quartiles, with the narrowest point identifying the median. The effect of soundscape on perceptive judgments is clear, as indicated in the ANOVA analysis.

no specific architectural configuration was expected, as it could have been recorded in different places (concert hall, studio), at various distances from the instruments. This indicates that a change in style and content of the audio information can affect the perceived distance of the events. Gabrielsson (1979) stated that interactions between parameters (and/or method) and sound material are due to ''physical interactions,'' i.e., differences in the physical properties of the sound samples. The present results suggest that such interactions can also be attributed to cognitive attributes, such as semantic content of the sound samples and subjects' expectations.

6. Principal component analysis

The subjective ratings obtained using the sliders provide information regarding the perceptual differences in the various methods according to the six parameter questions. In an attempt to reduce the complexity of the data space the Principal Component Analysis (PCA) reduction method is used. This technique is highly suitable for reducing the dimensions of a complex space into a smaller number of orthogonal dimensions, which are composed of a linear combination of the initial parameters. PCA analysis is commonly used in psychoacoustics to investigate sound quality attributes (Kahle, 1995; Susini, McAdams, and Winsberg, 1999), and has previously been used in particular to study the perceptual evaluation of sound reproduction systems (e.g., Eisler, 1966; Gabrielsson and Sjögren, 1979; Zacharov and Koivuniemi, 2001).

The PCA analysis on the slider dataset presents an orthogonal data space as described in Table III. Using the PCA projection, 74% of the variance of the responses can be explained using the first three components, and 84% with the first four. Projections of the subjective responses to the six parameters into the space defined by the first four components of the PCA are presented in Fig. 7 (see Table II for $+/-$ direction definitions of parameter vectors). From this analysis, it is possible to examine perceptual differences between the three spatial reproduction schemes.

The projection plane defined by PCA1$\times$PCA2 shows a clear separation between (1-D) and (2-D and 3-D) presentations. The 1-D is more ''distant'' and ''outside'' while being more ''stable,'' as shown by the apparent data clustering separations along the $+$distance, $+$presence, and $-$stability vectors. In addition, 1-D and 2-D are more ''clear'' in coloration than 3-D. Finally, 3-D is more ''indistinct'' and ''poorly defined'' in reference to the 1-D and 2-D presentations. The projection planes defined by PCA1$\times$PCA3 and PCA2$\times$PCA3 show similar tendencies. There is an evident correlation between ''localization'' and ''readability'' in both planes. The projection plane defined by PCA1$\times$PCA4 shows a separation of ''localization'' and ''readability'' with 1-D being more ''poorly defined'' than 2-D and 3-D, with localization becoming more precise when going from 1-D to 3-D to 2-D.

To summarize, there is a noticeable difference between 1-D and (2-D and 3-D) in terms of perceived distance, presence, and stability. The judgments for the 3-D representation fall between the 1-D and 2-D method values for all parameters but coloration.

Similar PCA analysis studies have been performed which showed correlations between Sense of space, Sense of depth, and Sense of movement, and with these three attributes loading positively Preference (Zacharov and Koivuniemi, 2001). It was also found that Penetration and timbral Emphasis were negatively correlated to Preference. It is un-

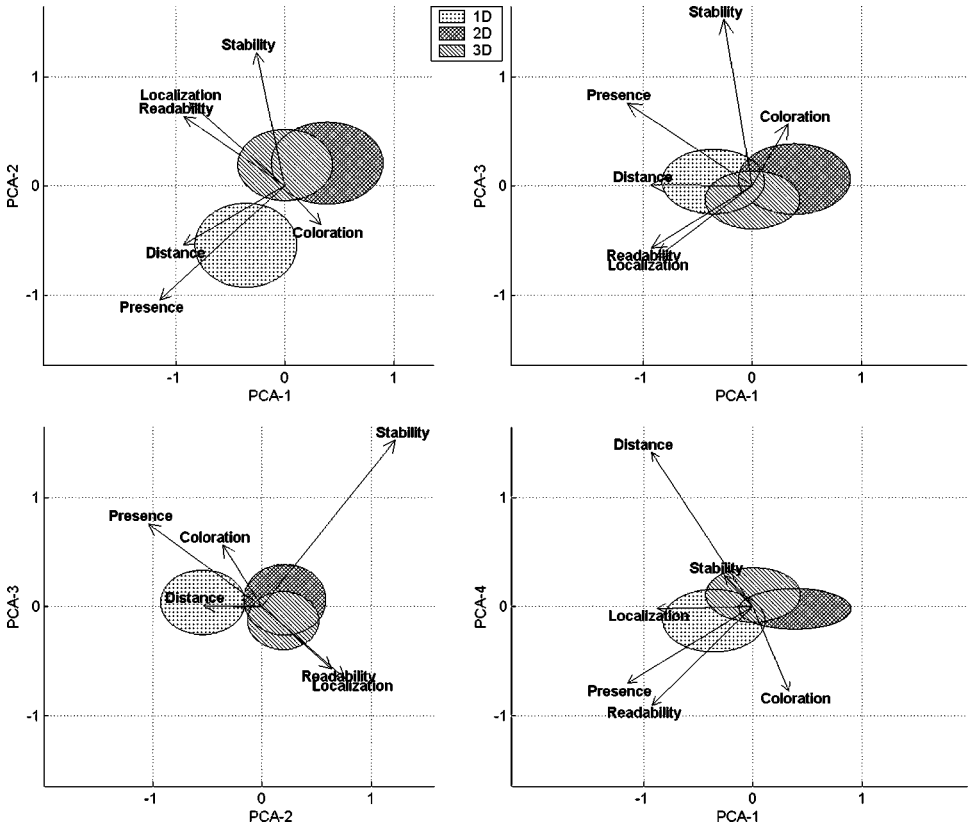

FIG. 7. Projection of subjective parameter judgments onto a PCA reduced space. Plates show the three orthogonal views for the space created by the first 3 PCA components and the projection of the space created by the 1st and 4th component. The projected data is represented by an ellipse spanning the spread of the data (using interquartile range to provide a robust estimate). The projections of the subjective parameters used in the construction of the PCA space are also presented (lengths multiplied by a factor of 2 to improve legibility). Arrows are in the direction of the *right*(+) limit of the slider scale, as presented in Table II.

clear from the citation the exact meanings of these parameters, but we have noted that the original term for Penetration (Pistävyys) can also be translated from the original Finnish as Piercing, and may therefore help explain the evaluation of this parameter toward a negative judgment.

D. Discussion

1. Spatial attributes

Traditionally, quantifying perceptual attributes involves rigorous subject training to minimize differences among subjects and to identify small differences between parametrized stimuli. However, in the absence of clearly identified subjective dimensions for spatial sound perception, a free exploratory approach was considered more appropriate to allow subjects to define their own attributes rather than impose predefined factors of interest. An experimental protocol was designed to elicit relevant features by analyzing spontaneous verbal descriptions without constraining the answers into categories predefined by the experimenter. Interestingly, most of the semantic scales derived from the analysis of spontaneous descriptions are similar to those tested in other spatial sound reproduction studies (Berg and Rumsey, 1999; Zacharov and Koivuniemi, 2001) although using different sound material, multi-channel configurations, and methodology.

Berg and Rumsey (1999) used the Repertory Grid Technique developed by Kelly (1955) to elicit a structure of perceptual features from free verbal descriptions of perceived similarity and dissimilarity between various spatial reproduction systems. Four perceptual attributes relating to spatial features were identified: naturalness (authenticity, feeling of presence), source localization (width and lateral positioning), envelopment (positioning of the sound field relative to the subjects), and depth (ability to perceive different distances to the sources). These attributes seem to be related to the parameters of naturalness, localization, presence, and readability derived from Experiment I. Berg and Rumsey (2001) further validated these attributes with a new group of subjects listening to new stimuli. These results were also extended from stimuli differing in modes of reproduction to stimuli recorded with different surround sound microphones tech-

TABLE III. Principal Component Analysis data reduction results for slider parameters. Data indicates the linear weighting components of each parameter in constructing the new orthogonal data space. Values are also presented indicating the percentage of variation in the data which can be explained by each principal component. The major contributions for each component are indicated with an*.

	Coloration	Presence	Readability	Localization	Stability	Distance	% Explained
PCA-1	0.16	−0.58*	−0.46*	−0.44*	−0.13	−0.47*	34.7
PCA-2	−0.18	−0.52*	0.32	0.38	0.61*	−0.27	26.7
PCA-3	0.28	0.38	−0.28	−0.33	0.76*	0.01	12.5
PCA-4	−0.39	−0.35	−0.45*	−0.01	0.14	0.71*	10.2
PCA-5	0.82*	−0.22	−0.11	0.44*	−0.05	0.28	9.1
PCA-6	0.21	−0.28	0.62*	−0.60*	0.03	0.36	6.8

niques (Berg and Rumsey, 2002). As regards interactions between attributes, the strongest correlation was observed between naturalness and presence (Berg and Rumsey, 2001), in agreement with our findings.

The parameters used in this study can also be compared to the 12 attributes elicited by Zacharov and Koivuniemi (2001) through guided discussion as follows: Sense of space, Sense of depth, Sense of directions, Sense of movement (all four similar to ''readability''), Penetration (or piercing, as a negative quality), Distance to events (''distance''), Broadness (similar to ''localization''), Naturalness (the ''choice'' parameter), and four timbral attributes (''coloration'') Richness, Emphasis, Tone color, and Hardness.

It is encouraging to note that a certain consensus begins to emerge in the field of spatial sound reproduction for perceptual attributes relating to spatial features, although the semantics of these terms vary across languages and may give rise to different interpretations (for a review of terminology and meanings of spatial attributes, cf. Rumsey, 2002). However, results suggest that these attributes are not independent dimensions as interactions between factors were observed in the present experiments as well as in other sound quality evaluation studies (Gabrielsson, 1979; Susini, McAdams, and Winsberg, 1999; Zacharov and Koivuniemi, 2001). The diversity of spontaneous descriptions of the systems and the interdependency between perceptual attributes suggest that sound quality is a complex concept aggregating various physical properties (spatial and spectral) and semantic features such as judgments of pleasantness.

2. Overall quality

Results of the linguistic exploration of free responses suggest that presence and readability play an important role in the evaluation of the overall sound quality of reproduction methods. Furthermore, the most frequently selected configuration was evaluated as providing a significantly stronger feeling of presence and better readability of the sound scene. However, a significant interaction was observed between choice of the reproduction method and soundscapes. Logistic regression procedures have been tried to model the choice as a function of the parameters, but the weights differ significantly between different methods and soundscapes, further suggesting that the selection of a universally optimal reproduction method remains difficult

V. CONCLUSION

The approach presented here brings together methodological tools derived from psycholinguistics and statistical analyses to investigate spatial quality for reproduced sound. In Experiment I, relevant criteria for sound quality were identified by means of linguistic analysis of spontaneous verbal descriptions. This exploratory study of verbal descriptors resulted in six parameters: presence, coloration, readability, timber, localization, and stability of the image. In Experiment II, three configurations (1-D, 2-D, and 3-D loudspeaker arrays) were evaluated using scale judgments and free responses along these parameters on a wider range of auditory scenes. These results of the statistical analysis are in agreement with the analysis of the verbal data and help provide a clear method for interpreting the perceptual variations of the reproduction systems.

Results of the perceptive evaluation can be summarized as follows. The 1-D (traditional 2-channel stereo) configuration was characterized as providing precise localization in a frontal image, stable with regards to head shifting, but distant from the listener and spatially poorly defined. The 2-D configuration (a periphonic horizontal 6-channel circular array), on the other hand, was judged as providing a very immersive and spatially well defined environment, but less stable relative to head shifting. The judgments for the 3-D configuration (a 12-channel spherical array) interestingly fell between the 1-D and 2-D method values for all parameters but coloration and localization. The 3-D configuration was characterized by a salient ''muffled'' coloration and a poor localization.

As regards sound quality, results suggest that presence and readability make a strong contribution to overall sound quality of reproduction methods. However, the selection of a universally optimal reproduction method remains difficult, as naturalness depends highly on the sound material. Indeed, the 3-D configuration appeared to be more adapted to indoor environments, the 2-D configuration to outdoor environments, and the 1-D configuration to frontal musical scenes, though the choice of the 1-D for musical scene can possibly be attributed to it resembling a home listening environment and not necessarily the live performance environment. Furthermore, interactions between parameters were observed, consistent with other perceptual evaluation studies.

In similar experiments, Guastavino (2003) observed that the choice of reproduction methods differed for different groups of subjects. Several recordings of indoor and outdoor material were carried out using simultaneously a Soundfield microphone, binaural microphones on a dummy head, and a set-up of five noncoincident microphones. A multiple comparison task was carried out on three groups of subjects: sound engineers, acousticians, and nonexperts. When asked to select which recording sounded more like their everyday experiences, audio engineers gave greater attention to the localization and precision of the sources, whereas the other two groups based their selection on presence and spatial distribution of sound. Similarly in the present study, a conflict was observed between precise localization (with the 1-D configuration) and presence (with the 2-D configuration), leading to different choice strategy among subjects. Similar differences were already observed by Gabrielsson (1979) for monophonic reproduction. When comparing various reproductions for similarity, experts based their judgment on ''brightness'' rather than ''loudness,'' while nonexperts tended to do the opposite. Furthermore, the reproduction method must be well suited for the tasks of the listening test. Guastavino, Katz, Polack, Levitin, and Dubois (submitted) showed that stereophonic reproduction was ecologically valid for source identification tasks, but not for processing complex auditory scenes in a global manner. It was further shown that a multichannel reproduction was necessary to enable subjects to process urban soundscapes in laboratory conditions as they would in real life situation.

Most relevant to the general notion of sound quality is the observed gap between ''objective'' physical accuracy and ''subjective'' perceived naturalness. Indeed for most auditory scenes, the 2-D configurations were judged by the participants as more natural and realistic than the 3-D configurations although spatially incomplete, thus indicating potentially negative effects linked to providing ''too much'' information. These findings underline the difference between illusion and accuracy pointed out by Rumsey (2002): the illusion of ''being there'' is not necessarily related to true spatial fidelity. This counter-intuitive observation, from a physical point of view, indicates the importance of considering subjective psychological attributes in the evaluation of perceived sound quality. Furthermore, the lack of preference for 3-D configurations could be explained by the unfamiliarity with 3-D audio reproduction, although the natural world is always present in 3D. As surround sound systems become more common, 2-D audio reproduction systems may sound more familiar and thus more ''natural'' than 3-D configurations, which are not widely used. The results reported here suggest a shift from physical descriptions to cognitive ones in exploratory studies, to identify relevant perceptual features and better understand how acoustic phenomena are perceived and cognitively processed before addressing physical parameters in more controlled experiments [for a further discussion on this point, see Dubois (2000) and Guastavino and Cheminée (2003)].

Together, these findings underline the fact that different applications give rise to different sound quality criteria. The appropriate choice of a reproduction method must take into account the type of sound samples (music, indoor, or outdoor material), the type of application (task, entertainment), and even the expertise of the audience.

ACKNOWLEDGMENTS

The authors would like to thank the following for contributing to the soundscape material: Jeff Silberman for providing the symphony recording; Christophe d'Alessandro and the Eglise Sainte-Elisabeth, Paris, for providing the material and location for the Organ and Improvisation Pieces; and IRCAM for providing the Soundfield microphone. Thanks also to Holger Strauss for the command line audio utility ASIOPLAY which allowed for the playing of multichannel audio from within MatLab. This work was funded by the French Ministries of Environment (equipment) and Research (funding for C. Guastavino's doctoral work conducted at the Université Paris 6) and a Chateaubriand Fellowship (B. Katz), Office for Science and Technology of the Embassy of France in the United States. The writing of this paper was supported by a CFI/VRQ grant attributed to Daniel Levitin (McGill University). The authors would like to thank Danièle Dubois and Jacques Poitevineau for fruitful discussions during the research and Daniel Levitin for helpful comments during revisions of this manuscript. Experimental work performed while at the Laboratoire d'Acoustique Musicale (Université Paris 6, CNRS, Ministère de la culture), 11 rue de Lourmel, 75015 Paris, France.

Beranek, L. L. (**1962**). *Music, Acoustics and Architecture* (Wiley, New York).

Berg, J., and Rumsey, F. (**1999**). ''Spatial attribute identification and scaling by repertory grid technique and other methods,'' *Proceedings of the 16th AES International Conference on Spatial Sound Reproduction*, Audio Eng. Soc.

Berg, J., and Rumsey, F. (**2000**). ''Correlation between emotive, descriptive and naturalness attributes in subjective data relating to spatial sound reproduction,'' *Proceedings of the 109th AES Convention*, Los Angeles, 22–25 September, preprint 5206, Audio Eng. Soc.

Berg, J., and Rumsey, F. (**2001**). ''Verification and correlation of attributes used for describing the spatial quality of reproduced sound,'' presented at the *AES 19th International Conference: Surround Sound Techniques, Technology and Perception*, 21-4 June, Schloss Elmau, Germany, Audio Eng. Soc.

Berg, J., and Rumsey, F. (**2002**). ''Validity of selected spatial attributes in the evaluation of 5-channel microphone techniques,'' presented at the *112th AES Convention*, Munich, Germany, 11–14 May, Paper 5593, Audio Eng. Soc.

Daniel, J. (**2000**). ''Représentation de champs acoustiques, application à la transmission et à la reproduction de scènes sonores complexes dans un contexte multimédia (Acoustic field representation, application to the transmission and the reproduction of complex sound environments in a multimedia context),'' Ph.D. dissertation, Université Paris 6.

Dubois, D. (**2000**). ''Categories as Acts of Meaning: The Case of Categories in Olfaction and Audition,'' Cogn. Sci. Qu. **1**, 35–68.

Eisler, H. (**1966**). ''Measurement of Perceived Acoustic Quality of Sound-Reproducing Systems by Means of Factor Analysis,'' J. Acoust. Soc. Am. **39**(**3**), 484–492.

Fellgett, P. B. (**1974**). ''Ambisonic reproduction of directionality in surround sound systems,'' Nature (London) **252**, 534–538.

Furse, Richard W. E. (**2003**). MN Audio Library, http://www.muse.demon.co.uk/ (site last visited 26-August-03).

Gabrielsson, A. (**1979**). ''Dimension analysis of perceived quality of sound reproduction systems,'' Scand. J. Psychol. **20**, 159–169.

Gabrielsson, A., and Sjögren, H. (**1979**). ''Perceived sound quality of sound-reproducing systems,'' J. Acoust. Soc. Am. **65**, 1019–1033.

Gabrielsson, A., Rosenberg, U., and Sjögren, H. (**1974**). ''Judgments and dimension analysis of perceived sound quality of sound-reproducing systems,'' J. Acoust. Soc. Am. **55**, 854–861.

Gabrielsson, A., Rosenberg, U., and Sjögren, H. (**1974**). ''Judgments and dimension analysis of perceived sound quality of sound-reproducing systems,'' J. Acoust. Soc. Am. **55**, 854–861.

Gaskell, P. S. (**1979**). ''Spherical harmonic analysis and some applications to surround sound,'' BBC Research Department Report No. BBC RD 1979/25.

Gerzon, M. A. (**1977**). ''Design of ambisonic decoders for multi speaker surround sound,'' presented at the 58th AES Convention, New York.

Gibson, J. J. (**1979**). *The Ecological Approach to Visual Perception* Houghton Mifflin, Boston, MA.

Guastavino, C. (**2003**). ''Étude sémantique et acoustique de la perception des basses fréquences dans l'environnemet sonore urbain (Semantic and acoustic approaches to low frequency perception),'' Ph.D., dissertation, Université Paris 6.

Guastavino, C., and Cheminée, P. (**2003**). ''Conceptualisations en langue, représentations cognitives et validité écologique: une approche psycholinguistique de la perception des basses fréquences (Cognitive and linguistic representations and ecological validity: A psycholinguistic approach to low frequency perception),'' Psychol. Française **48**(4), 91–101.

Guastavino, C., Katz, B., Polack, J-D., Levitin, D., and Dubois, D. (under review), ''Ecological validity of sound reproduction systems,'' Acustica.

ITU-R, Recommendation BS.1116-1 (**1997**). ''Methods for the subjective assessment of small impairments in audio systems including multichannel sound systems,'' International Telecommunications Union Radiocommunication Assembly.

Kahle, E. (**1995**). ''Validation d'un modèle objectif de caractérisation de la qualité acoustique dans un ensemble de salle de concerts et d'opéras (Validation of an objective model for characterizing the acoustic quality of a set of concerts hall and opera houses),'' Ph.D. dissertation, Université du Maine, Le Mans.

Kelly, G. (**1955**). *The Psychology of Personal Construct* (Norton, New York).

Maffiolo, V. (**1999**). ''De la caractérisation sémantique et acoustique de la qualité sonore de l'environnement sonore urbain (Acoustic and semantic

characterization of the sound quality of urban environments),'' Ph.D. dissertation, Université du Maine, Le Mans.
Péchoin, D. (**1992**). *Thésaurus Larousse; des Idées aux Mots, des Mots aux Idées* (Larousse, Paris).
Rumsey, F. (**1998**). ''Subjective assessment of the spatial attributes of reproduced sound,'' *Proceedings of the AES 15th International Conference on Audio, Acoustics and Small Space*, Audio Eng. Soc., pp. 122–135.
Rumsey, F. (**2002**). ''Spatial quality evaluation for reproduced sound: terminology, meaning and a scene-based paradigm,'' J. Audio Eng. Soc. **50**, 651–666.
Schroeder, M. R., Gottlob, D., and Siebrasse, K. F. (**1974**). ''Comparative study of European concert halls,'' J. Acoust. Soc. Am. **56**, 1195–1201.
Susini, P., McAdams, S., and Winsberg, S. (**1999**). ''A multidimensional technique for sound quality assessment,'' Acustica **85**, 650–656.
Zacharov, N., and Huopaniemi, J. (**1999**). ''Results of a round robin subjective evaluation of virtual home theatre sound systems,'' *Proceedings of the AES 107th International Convention*, New York, 24–27 September, Audio Eng. Soc.
Zacharov, N., and Koivuniemi, K. (**2001**). ''Audio descriptive analysis & mapping of spatial sound displays,'' *Proceedings of the 2001 International Conference on Auditory Display*, Espoo, Finland, July 29–August 1, 2001.

Quantifying the auditory saltation illusion: An objective psychophysical methodology

Joanna C. Kidd and John H. Hogben
School of Psychology, The University of Western Australia, 35 Stirling Highway, Nedlands, Western Australia, 6009

(Received 5 September 2003; revised 5 May 2004; accepted 7 May 2004)

Under conditions of rapid presentation, brief acoustic stimuli repeatedly delivered first at one location, then at another, are systematically mislocalized, with stimuli perceived as traveling smoothly between the two locations. This robust illusory motion percept is termed ''auditory saltation.'' Currently, the characteristics and mechanisms of auditory saltation are not well understood. The lack of objective methods capable of quantifying the illusion on an individual basis seems a limiting factor for this area of research. In this study, we outline an objective psychophysical task that estimates the interstimulus interval at which the saltation illusion is reliably distinguishable from simulated motion. Experiment 1 examined the psychophysical function relating task performance to ISI and addressed the suitability of the task for use with adaptive psychophysical procedures. Experiment 2 directly compared performance on the task with that of another quantification method. The results suggested that this objective approach to the study of auditory saltation overcomes difficulties associated with more subjective methods, and provides a reliable paradigm within which to quantify the temporal parameters of saltation on an individual basis. © *2004 Acoustical Society of America.* [DOI: 10.1121/1.1766054]

PACS numbers: 43.66.Mk, 43.66.Pn, 43.66.Qp, 43.66.Rq. [AK] Pages: 1116–1125

I. INTRODUCTION

The localization of acoustic signals in space is an important function of the human auditory system. Localization is facilitated by the integration of binaural cues, such as interaural time and intensity differences (Harris, 1960). Under normal environmental conditions, humans can derive location information from binaural cues with considerable precision (Middlebrooks and Green, 1991). However, this precision is greatly reduced under conditions in which multiple brief stimuli are presented first at one location, then at another, in regular and rapid succession. These conditions produce systematic mislocalization in which stimuli are perceived as traveling smoothly across the area between the two locations. This illusory motion percept is termed auditory ''saltation'' (Geldard, 1976a).

The saltation illusion differs from simple apparent motion illusions (such as phi-motion) because stimuli appearing later in the train systematically shift the perceived locations of those presented previous such that the area between the two locations is ''filled in'' (Kilgard and Merzenich, 1995; Phillips and Hall, 2001). Despite being recognized within three modalities (cutaneous, auditory, and visual) (Geldard, 1976a, 1976b; Geldard and Sherrick, 1972, 1983; Lockhead, Johnson and Gold, 1980), little is known about the characteristics and mechanisms of saltation. What is known is that the illusion is reliant on the brevity and constancy (identical intervals between stimuli) of the interstimulus interval (ISI) of the stimulus train. While veridical perception of individual stimuli within a train is possible at long ISIs (greater than 500 ms), short ISIs (typically less than 200 ms) produce the nonveridical localization that characterizes saltation (Geldard, 1976b; Kilgard and Merzenich, 1995; Hari, 1995; Shore, Hall, and Klein, 1998). Additionally, it is thought that the saltation illusion is reliant on binaural stimulus inputs: evidence suggests little illusory motion is apparent with monaural stimulus trains (Hari, 1995; Shore *et al.*, 1998).

Continued research on auditory saltation is warranted because varied speculations about its mechanisms have been offered, though not explicitly investigated. Shore *et al.* (1998) suggested that saltation arises as a result of Gestalt grouping processes that occur when localization cues cannot be easily individuated and integrated. Hari (1995) pointed to perceptual masking at rapid temporal intervals as a mechanism of saltation. According to this suggestion, because perception is not immediate, stimuli appearing early in a train might be masked by those subsequent, resulting in nonveridical localization percepts (see Gregory, 1995). In addition, Phillips and Hall (2001) proposed that ''binaural adaptation'' to the first localization cue within a rapidly presented stimulus train might also be explanatory. Experimental investigation of auditory saltation is important to evaluating these possibilities, and has the potential to provide insight into spatio-temporal information processing in the auditory system.

Given the potential usefulness of experimental investigations of saltation, it seems important that attention be paid to the development of appropriate quantification techniques. To date, a number of subtly different methods have been employed. Shore *et al.* (1998) developed a pictorial scale depicting a step function (representing veridical localization) and a linear function (representing saltation) as its two extremes. Listeners were asked to indicate the perceived pattern of stimulus locations that best matched their percept by selecting the corresponding pictorial function. Phillips and Hall (2001) and Phillips, Hall, Boehenke, and Rutherford (2002) used a rating scale system in which levels of the

 0001-4966/2004/116(2)/1116/10/$20.00

perceived ''smoothness'' of a stimulus sequence, which elicits either the saltation illusion or a veridical percept, were indicated by a number between 1 and 5. In a slightly different approach, Hari (1995) asked listeners to indicate on a scale of 0 (extreme left) to 20 (extreme right) the perceived location of the individual clicks within an eight-click sequence. In each of these types of tasks, estimates of the ISI at which perception changes from veridical to nonveridical are based on qualitative changes in responses as the ISI is altered. Because responses on such tasks are not classifiable as correct or incorrect, they are definitively subjective (Sekuler and Blake, 1994).

The use of subjective techniques to quantify perceptual phenomena is limiting for a number of reasons. First, the response criterion may be easily biased by explicit task instructions and suggested response patterns. Therefore, it is possible that listeners may respond not according to their percept per se, but rather to the available criterion. This point is of particular concern to the usefulness of data obtained from naive, inexperienced, listeners for whom interpretation of task instructions may vary. Second, these methods are open to the possibility that the listener's response criterion may alter within a block of trials in ways which are not quantifiable. This may well lead to poor test–retest reliability. Finally, accuracy in task performance will depend on the ability of the listener to relate his/her perceptual experience to the pictorial or numerical scale provided. Arguably, the accuracy of this translation remains to be established.

Recently, two studies have used the auditory saltation illusion to quantify auditory temporal processing in adults and children with dyslexia (Farmer and Klein, 1995; Tallal, 1980). Hari and Kiesilä (1996) employed the procedure outlined by Hari (1995) and found significant differences in the temporal onset of auditory saltation between Finnish adult dyslexics and controls. Using the same method with simplified instructions, Kronbichler, Hutzler, and Wimmer (2002) failed to replicate this finding in German grade 7 boys. It is difficult to account for these conflicting findings. In that auditory saltation is the product of a biological system for which temporal acuity is largely developed by the age of 10 (e.g., Irwin, Ball, Kay, Stillman, and Rosser, 1985), it is unlikely these conflicting findings are primarily the result of sampling differences. However, the participants of these studies were untrained in auditory psychophysics and undertook a subjective task under differing instructions. It is therefore likely that procedural issues related to the use of subjective tasks, such as differences in the interpretation of task instructions, response criterion, and the ability to adequately convey a percept, are important factors contributing to these differing results. The development of an objective task which eliminates such confounds therefore seems desirable to the study of saltation within samples of dyslexic and untrained listeners.

Given the potential for clinical application of the auditory saltation illusion, it is essential that a quantification technique derive precise threshold estimates on an individual basis. Because the available data on saltation in dyslexia presents only mean group trends, it is difficult to estimate between-subject variability in performance. Much research has indicated that dyslexia is a heterogeneous disorder (e.g., Castles and Coltheart, 1993; Wolf and Bowers, 1999). Thus, it is important that individual, rather than group, threshold estimates on any psychophysical task used in dyslexia be available so that between-subject variability can be accounted for and further investigated.

The present studies propose the use of an objective psychophysical saltation task that derives individual thresholds of saltation onset as an alternative to currently employed subjective techniques. Briefly described, this task delivers two binaural click trains, with interaural time difference (ITD) localization cues, via headphones. While one interval presents stimuli emulating a moving sound source, the other presents stimuli sufficient to elicit the saltation illusion. The ISI of the sequence is manipulated between trials, with thresholds defined as the ISI at which discrimination between the sequences is reliable. Experiment 1 examined the temporal parameters of performance on the task to assess its suitability for use with adaptive procedures. Experiment 2 compared the reliability and concurrent validity of saltation thresholds derived via this task with those derived via an alternative method outlined by Hari (1995).

II. EXPERIMENT 1

In developing a valid psychophysical task, it is important to establish that changes in the dependent and independent variables are related via a monotonic psychometric function. Therefore, it was necessary to examine performance on our psychophysical saltation task across a broad range of ISIs to ensure that increases in correct responses are concurrent only with increases in the length of the ISI presented, rather than with any extraneous cues. In addition, examining the shape of the psychometric function was important to assessing the suitability of the task for use with adaptive psychophysical methodology. Therefore, this study employed a Method of Constant Stimuli to examine performance on the proposed saltation task.

A. Methods

1. Listeners

Six adults (3 male and 3 female) with normal hearing participated in this study. Two (J.C.K. and N.W.R.) were experienced auditory psychophysical listeners.

2. Stimuli

Stimuli were created and delivered using MATLAB (version 6.1) on an Acer laptop computer, and presented via Sennheiser HD 25 headphones. Stimuli were trains of eight, 10 ms binaural clicks. The clicks were structurally identical, constructed from 10 ms white noise. All stimuli were presented at 81 dB SPL, a level deemed comfortable by all listeners.

A trial consisted of two stimulus trains that were separated by 1000 ms of silence. Each train comprised eight clicks. In order to generate the percept of a shift in the location of the stimuli, the clicks were delivered with an ITD. Under normal listening conditions, an external sound is localized to the left of the head if sound waves arrive at the left

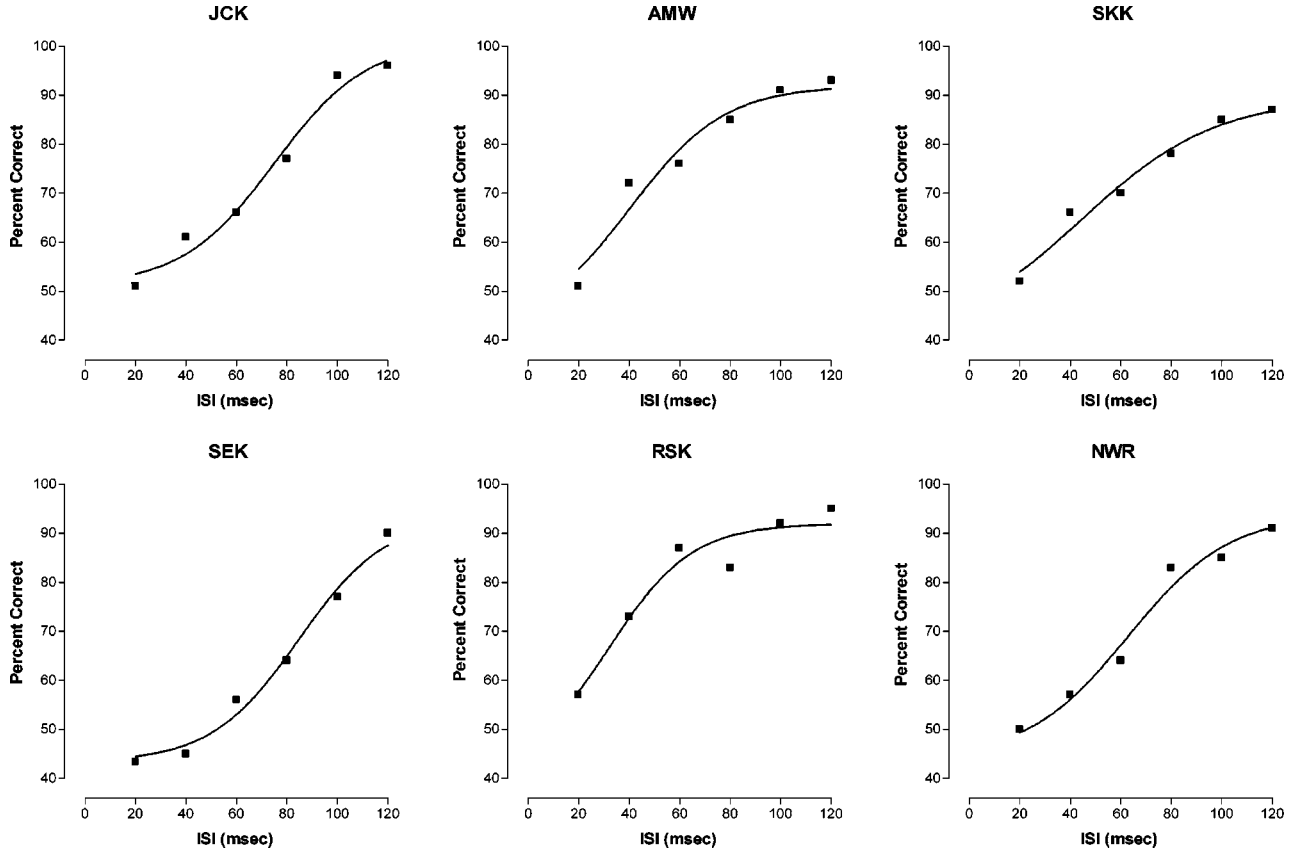

FIG. 1. Plots of individual data obtained using a method of constant stimuli procedure on the objective psychophysical saltation task.

ear before the right, and vice versa. Systematically altering the difference in the arrival time of stimuli to each ear systematically changes the perceived spatial location of stimuli along the horizontal plane (Moore, 1997). Therefore, one interval of the task contained a train of clicks manipulated with ITDs such that the first four clicks led in the left channel by 0.8 ms, and the second four clicks led in the right channel by 0.8 ms. This presentation was used to elicit the saltation illusion (and is similar to that described by Hari, 1995). In the other interval, each click in the train was manipulated such that the ITD applied to each successive click varied linearly from -0.8 ms (left leading) to 0.8 ms (right leading). This manipulation created the perception of a single sound source moving at equal intervals between the ears, regardless of the ISI of the sequence. The order of stimulus presentation was determined by random permutation. The ISI remained constant within the two stimulus intervals of a single trial.

3. Procedure

Using a Method of Constant Stimuli, six ISIs were examined (20, 40, 60, 80, 100, and 120 ms). An ISI was defined as the time between the offset of one stimulus and the onset of the following stimulus. Each listener completed 10 blocks of 60 trials, where one block comprised 10 trials per ISI. The task of the listener was to indicate, via a button press, the interval in which he/she perceived ''actual'' motion rather than the saltation illusion. Visual feedback was given following each trial to encourage prolonged motivation and concentration. Testing was conducted in an anechoic illuminated room. Listeners completed testing over at least two sessions, at their convenience.

B. Results and discussion

The percentage of correct discriminations of the ''moving'' stimulus from the saltation illusion as a function of ISI was of primary interest. The mean percent correct was calculated for each ISI and plotted for each participant. GraphPad Prism software was used to fit logistic curves to each data set. Thresholds were defined as the 75% correct point on the logistic curve. Individual data plots are given in Fig. 1.

Figure 1 reveals that for all listeners, performance on the psychophysical saltation task is characterized by monotonic logistic functions. This finding suggests that the ability to discriminate between the saltation illusion and simulated motion is solely facilitated by manipulation of the ISI of the sequence, rather than being modulated by any obvious cues inherent to the task. This reflects the construct validity of the task. Importantly, these data show that this psychophysical saltation task has the capacity to characterize task performance on an individual basis, generating precise individual thresholds. Therefore, the task seems well suited for use with adaptive psychophysical methodology, which operates on the premise that the relationship between the dependent and independent variable is monotonic.

III. EXPERIMENT 2

The results of Experiment 1 justified the use of adaptive psychophysical methods in further examination of this saltation task. Adaptive methods are useful, particularly in a clinical situation, because they allow for accurate estimation of individual thresholds with fewer trials. Experiment 2 employed an adaptive procedure to conduct the psychophysical saltation task, and directly compared the obtained thresholds from that task with those of the alternative task outlined by Hari (1995). The aim was to assess the concurrent validity of the two tasks, and compare the efficiency and reliability of both tasks in quantifying the temporal parameters of the saltation illusion.

A. Methods

1. Listeners

Thirty-seven adult volunteers (24 females, 13 males) participated in this study. Participants were recruited via word of mouth among the undergraduate and postgraduate population of The University of Western Australia. Thirty-two participants were students, while the remaining five participants were associates of the other participants.

2. Stimuli

Stimuli for both tasks were presented using MATLAB (version 6.1) on an Acer laptop computer and delivered via Sennheiser HD 25 headphones. All stimuli were presented at 81 dB SPL.

a. 8 Click lateralization task (Hari, 1995): Stimuli were trains of eight 10 ms binaural clicks, constructed from white noise. Each click within the train was delivered with a 0.8 ms ITD. In the first four clicks of each train, the left channel preceded the right by 0.8 ms while in the second four clicks, the right channel preceded the left by 0.8 ms. The ISI between clicks remained constant throughout the train. Each block comprised one stimulus train presented at each of 16 different ISIs (50, 60, 70, 80, 90, 100, 110, 120, 130, 140, 150, 200, 250, 300, 400, and 500 ms). The order of stimulus presentation was randomized both between and within blocks of trails.

b. Psychophysical saltation task: Stimuli for this task were identical to those described in Experiment 1.

3. Procedures

Listeners were seated comfortably in an anechoic illuminated room and were delivered standard instructions prior to the commencement of each task. The order of task presentation was randomized between listeners. Adequate rest breaks were given between tasks. Individual task procedures are described below.

a. 8 Click lateralization task (Hari, 1995): Listeners were instructed to listen to the stimulus sequence, and then use the computer mouse to adjust a series of 8 graphic sliders on the computer screen such that the position of each successive slider represented the perceived relative position of each click in the sequence. In accordance with the original task protocol, listeners were allowed to listen repeatedly to stimulus trains before making a response. Listeners completed two blocks of trials.

b. Psychophysical saltation task: The task was administered under identical conditions to those described in Experiment 1. An adaptive PEST procedure (Taylor and Creelman, 1967), set to converge on the 75% performance level was used to administer this task. Following each block of 60 trials, a threshold estimate was obtained by calculating the mean ISI following the third reversal. Listeners completed two blocks of trials on this task.

B. Results and discussion

1. 8 Click lateralization task (Hari, 1995)

Because Hari's (1995) participants completed only one trial at each ISI, we used responses from our first block of trials only in initial comparisons of the two tasks. Thus, it was assumed that practice-related differences between the results of the two procedures were largely eliminated. In accordance with the method of analysis adopted by Hari (1995), the data from each trial for all listeners were normalized so that the estimated click locations corresponded to the whole left–right (0–1) scale. Frequently, listeners' responses did not range across the whole scale. Of the total 592 responses (16 ISIs for 37 participants), 46 indicated clicks other than those presented first and last in a train as occupying the far left or far right positions on the response scale. The average position of the first click was 0.037, and the average position of the eighth click was 0.9233. That these patterns occurred is important to the validity of the task, and will be discussed further in the General Discussion.

In an identical manner to Hari (1995), the mean normalized estimated click location for the eight clicks was calculated for all 16 ISIs. Figure 2 presents the mean trend in estimated click location at each ISI. According to the group data presented in Fig. 2, as the ISI of the sequence is increased at steps between 50 and 500 ms, the estimated click location changes systematically from being linearlike (indicating the perception of saltation), to being steplike in function (indicating veridical perception). The most notable difference across ISIs is the systematic change in the estimated distance between the fourth and fifth click locations. This finding is consistent with that reported by Hari (1995).

Given our aim of examining individual rather than group estimates, the extent to which these group trends are characteristic of individual response patterns was investigated. To be described as ''similar'' to the mean pattern, the individual response patterns had to meet two criteria for monotonicity. First, a positive difference between the fourth and fifth estimated click locations was required. Second, the slopes of the regression lines calculated between the estimated locations of the first four clicks and the second four clicks had to be positive. Margin for error was granted such that negative slopes of $r \leqslant 0.1$ were included ensuring that clumsily estimated but essentially sensible data were not unnecessarily discarded. These criteria ensured that all data included in the analysis were sensible according to the predictions of the task. While the pooled group data in Fig. 2 indicated a sys-

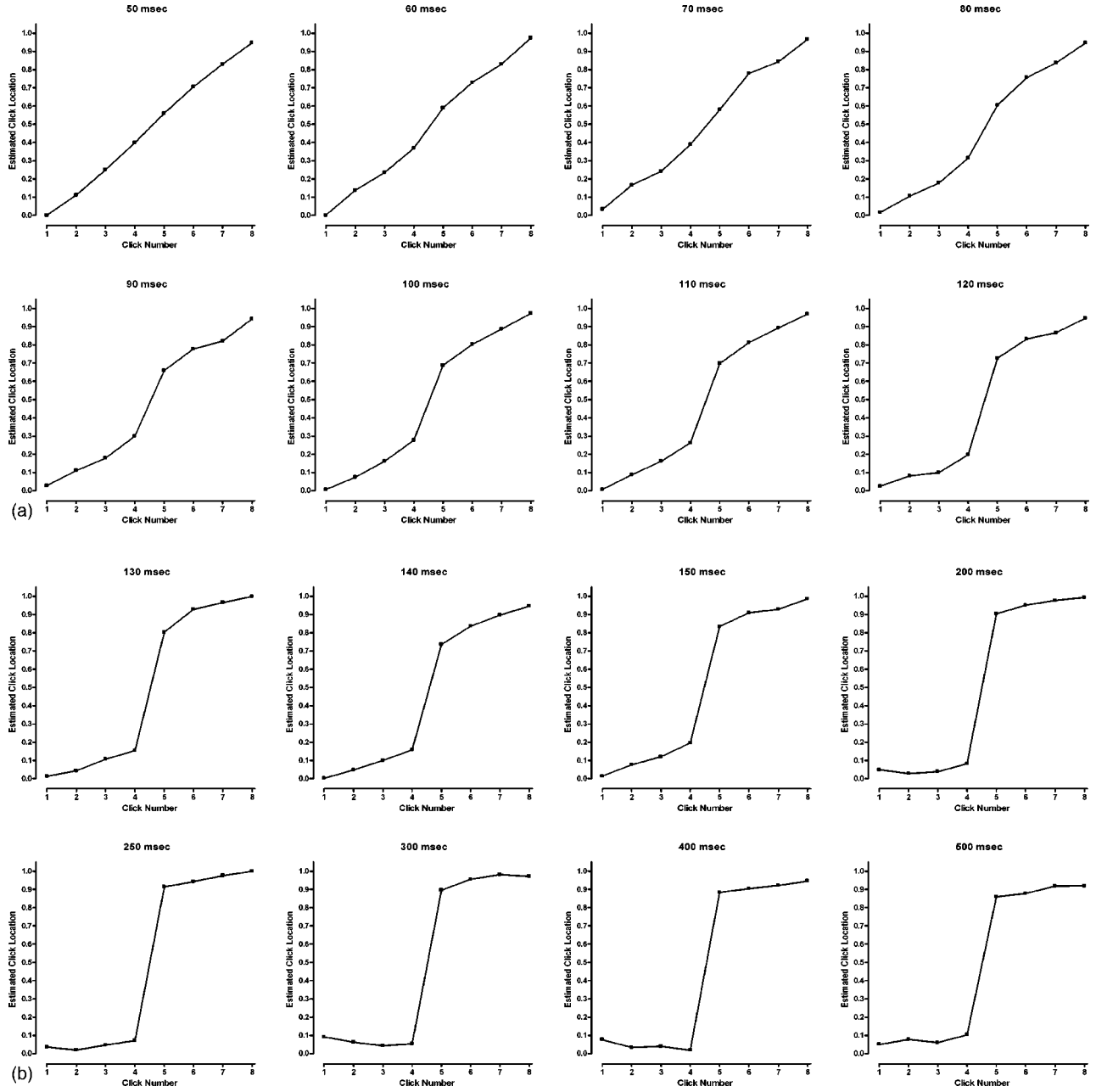

FIG. 2. Mean estimated click locations from 37 participants on the first block of the 8 click lateralization task (Hari, 1995).

tematic change from non-veridical to veridical perception as ISI is increased, 34 (approximately 5%) of response patterns were nonmonotonic, and therefore different from this mean pattern. These 34 nonmonotonic data sets were given by 11 different listeners, varying between 1 to 7 nonmonotonic responses for each listener. Although nonmonotonic response patterns were observed across a large range of ISIs, there was a trend towards greater numbers of these responses at longer ISIs, where the perception of saltation was diminishing or had diminished.

Figure 3 displays exemplars of four typical nonmonotonic responses. In these cases, listeners represented their percept of stimulus trains in ways which were unexpected given the predictions of the saltation illusion and veridical localization. It is difficult to know whether this finding is typical of the results obtained on such tasks in previous studies because group, rather than individual, data is reported for studies in which inexperienced listeners are used. However, the finding that monotonic data patterns can be obtained by averaging sometimes nonmonotonic data is an important one. The process of pooling data across participants on this task obviously obscures a great deal of individual variability in responses. As previously discussed, this individual variability is important to the study of dyslexia and should be acknowledged.

Hari and Kiesilä (1996) found large differences between controls and dyslexics when the difference between the fourth and fifth estimated click location was treated as the dependent variable. Because the validity of this dependent variable has not been examined in detail on an individual basis, it was thought necessary to do so here. GRAPHPAD PRISM software was used to fit exponential curves

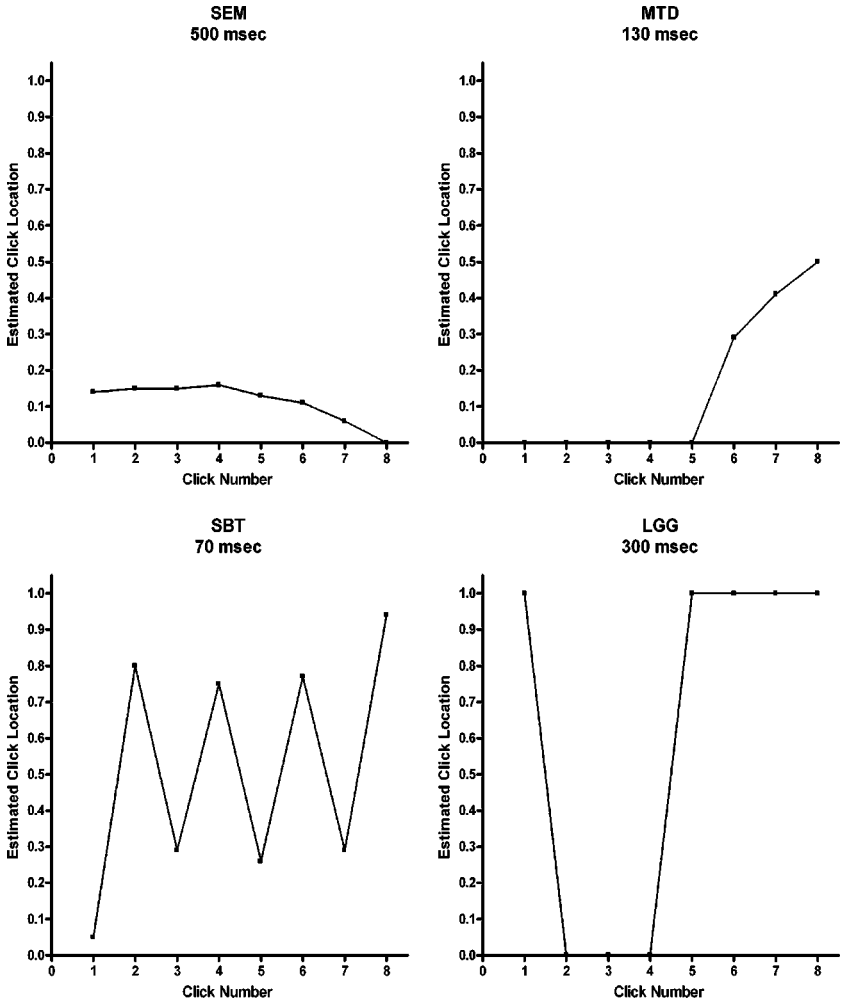

FIG. 3. Exemplars of typical non-monotonic responses on the 8 click lateralization task (Hari, 1995), by four observers (SEM, MTD, SBT, and LGG) at selected ISIs.

to the group mean difference between the fourth and fifth click locations across all ISIs. Figure 4 displays this trend. The exponential curve fits the mean data closely, with an R^2 value of 0.83.

As previously mentioned, 34 response patterns were removed from this analysis due to failure to fulfill the criteria for monotonicity. Following screening, GRAPHPAD PRISM software was used to fit exponential curves to the individual plots of the difference between the fourth and fifth click at each ISI for individual listeners. The R^2 of the curves for each individual data set were then calculated. Despite the initial screen for monotonicity, nonlinear regression analyses could not be performed on three data sets due to the unsuitability of the data for this analysis. The distribution of R^2 values for 34 participants is given in Fig. 5. As shown, the distribution of R^2 values is widely spread (mean $R^2=0.44$, SD$=0.26$) indicating large individual differences in the responses of individual listeners. Importantly, an $R^2 \leqslant 0.20$ was estimated for the data of approximately 30% of listeners, while only 12% of listeners yielded data with an $R^2 \geqslant 0.8$. The minimum R^2 was 0.001 while the maximum R^2 was 0.87. The results of this analysis indicate that, as a

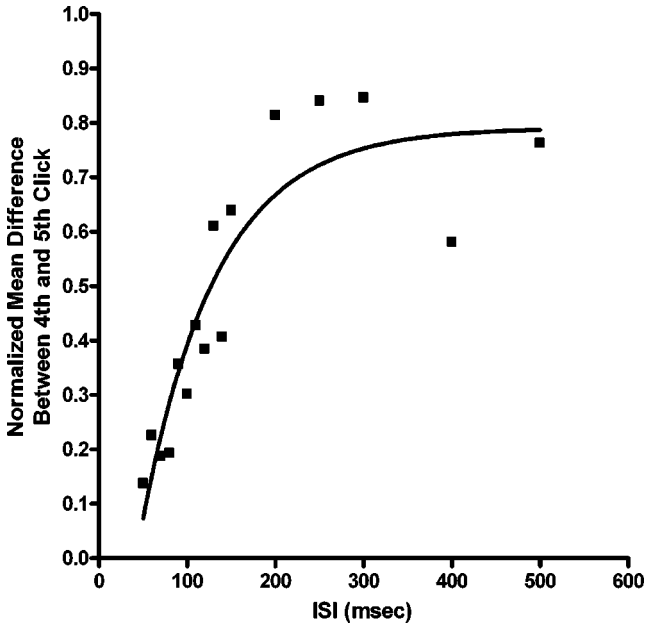

FIG. 4. The mean difference between the normalized estimated locations of the fourth and fifth clicks on the 8 click lateralization task (Hari, 1995).

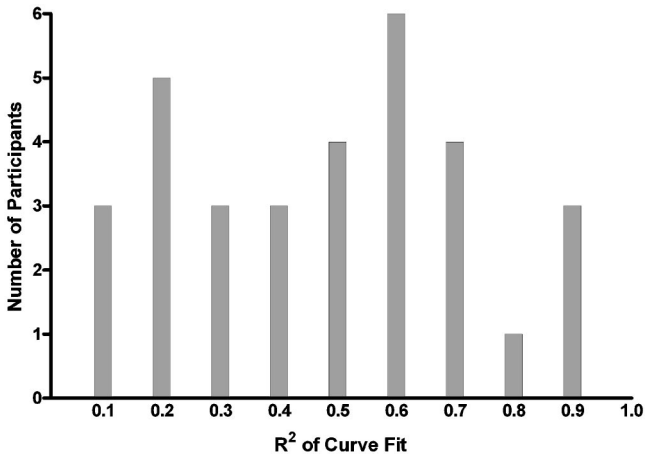

FIG. 5. Histogram representing the spread of R^2 values for the fit of an exponential curve on the difference in normalized estimated locations of the fourth and fifth clicks on the 8 click lateralization task (Hari, 1995) for 34 listeners.

dependent variable, the difference between the fourth and fifth click is somewhat inappropriate because accurate and sensible individual data cannot be derived for all participants. These results again demonstrate that monotonic data is obtainable by averaging sometimes nonmonotonic data.

An important criticism of the use of the difference between the fourth and fifth click to characterize performance on this task is that it merely examines two of the eight location estimates, therefore failing to take into account the full range of responses on the task. Given that saltation occurs across the entire stimulus train, this dependent variable falls short of quantifying the illusion fully. In an attempt to overcome this problem, the mean linear slope of the estimated click locations of the first four clicks, and the second four clicks, was calculated for each ISI. The data for all listeners for both blocks of trials were then standardized so that values of the dependent variable ranged between 0 and 1 in order that nonlinear curves could be fitted. GRAPHPAD PRISM software was used to fit logistic curves to each data set. It was therefore possible to define thresholds of saltation onset as the ISI corresponding to the 0.75 standardized regression coefficient point on the logistic function. While it is noted that this threshold definition is somewhat arbitrary, it was considered most appropriate given that a large number of data sets did not asymptote near the 0 standardized regression coefficient point and therefore did not have a centralized point of inflection. Of the 37 listeners who completed two blocks of trials on this task, thresholds for both blocks of trials could be calculated for only 19 listeners, 11 listeners had only one calculated threshold, and no threshold could be obtained on either block for the remaining 7 listeners (see Table I).

Correlation coefficients were calculated between log thresholds from the two blocks of trials to assess the test–retest reliability of this methodology (see Table II). The resultant relationship of $r=0.15$ (not significant) indicated the poor testretest reliability of thresholds on this task [see Fig. 6(a)]. This relationship is based only on the thresholds of the 19 listeners for whom two thresholds were obtainable.

2. Psychophysical saltation task

The test–retest reliability of the psychophysical saltation task was determined by calculating the correlation coefficient of log thresholds obtained from both blocks of trials. The correlation of $r=0.61$ ($p<0.05$) indicated the good test–retest reliability of the task. This relationship is evident in Fig. 6(b). Also evident from Figs. 6(a) and 6(b) is a difference in the variability of scores between thresholds of the two tasks. It was a possibility that this difference in variability, and difference in test–retest correlations, was the result of differences in the number of thresholds available for each task. Therefore, the test–retest reliability of the psychophysical saltation task was recalculated based only on the log thresholds of the 19 listeners for whom pairs of thresholds were calculable on Hari's (1995) procedure. A higher test–retest correlation of $r=0.73$ ($p<0.05$) was observed.

3. Comparison of the two saltation tasks

Overall performance on both blocks of trials on the two tasks is presented in Table I. As Table I indicates, the mean threshold values obtained from the two tasks are equivalent, with both tasks estimating the mean saltation threshold to be in the vicinity of 95–125 ms. It therefore appears that both tasks estimate roughly the same temporal parameters of the auditory saltation illusion, and obtain thresholds which are consistent with previously reported estimations (e.g., Shore *et al.*, 1998).

Correlation coefficients were calculated between log thresholds obtained from blocks 1 and 2 of both tasks to determine the concurrent validity of the tasks. Table II illustrates these results. The relationships between thresholds of block 1 of both tasks, and between block 2 of the 8 click lateralization task and block 1 of the psychophysical task, were found to be low and not significant. However, the relationship between block 2 of the psychophysical task and block 1 of the 8 click lateralization task was moderate and significant ($r=0.63$, $p<0.01$). This would seem to be further evidence of some degree of concurrent validity between the two tasks. However, given previously discussed findings of frequent failure to generate useful thresholds, and poor test–retest reliability of thresholds on the 8 click lateralization task, as well as the inherent differences between the methodologies of the two tasks, it is unsurprising that the interrelations of performances on these tasks are somewhat inconsistent.

IV. GENERAL DISCUSSION

In the present studies, we proposed the use of an objective psychophysical technique as a method of deriving individual thresholds of the onset of the auditory saltation illusion.

Experiment 1 employed a Method of Constant Stimuli to document the relationship between changes in task performance and ISI on this saltation task. The monotonic logistic functions which characterized this relationship were indicative of the validity of the task, as well as its suitability for use with efficient adaptive psychophysical methods.

TABLE I. Descriptive statistics of thresholds obtained from two blocks of trials on the 8 click lateralization task (Hari, 1995) and the objective psychophysical saltation task.

	8 Click Lateralization 1	8 Click Lateralization 2	Psychophysical Saltation 1	Psychophysical Saltation 2
N	23	26	37	37
Mean	97.34	102.0	122.2	101.3
Maximum	256.80	242.2	340	314.0
Minimum	56.80	54.8	46.67	32.76
Standard Deviation	42.00	37.19	75.27	68.56

Experiment 2 compared the validity and reliability of this and another saltation task outlined by Hari (1995). The results suggested that thresholds obtained via the proposed task were more reliable than those of Hari's (1995) procedure. Thresholds from the two tasks were also found to be roughly equivalent and, to some extent, concurrently valid. These findings suggested that, despite methodological differences, the proposed saltation task seemed to access the same saltation construct as a previously employed task. Thus, given that the proposed objective saltation task estimates the saltation illusion reliably and efficiently, the use of this task in further study of the characteristics and mechanisms of saltation seems justified.

The results of Experiment 2 indicated that analyzing the data obtained from a subjective saltation task is not straightforward. The theoretically appropriate method of fitting logistic curves to the mean linear slope across ISIs yielded thresholds for only a limited number of data sets. Similarly, the use of the difference between the fourth and fifth click as a dependent variable seemed inappropriate because this data was systematic only for a small number of participants. With regard to the latter, this finding is significant because the difference between fourth and fifth click locations has been used as a dependent variable in dyslexia research. Further examination of the saltation illusion in dyslexia using an alternative dependent variable therefore seems warranted. Thresholds of saltation onset derived via our task seem to provide an appropriate dependent variable because thresholds were obtained for all participants on both blocks of trials. The benefits of the proposed saltation task are therefore obvious: no data are discarded, therefore removing the need for reassessment or data averaging.

An important finding of Experiment 2 was that erratic, nonmonotonic responses were observed in a number of trials for Hari's (1995) task. For example, often participants indicated clicks other than those appearing first and last in the train as appearing in the left and rightmost positions. These responses were contrary to the predications of saltation perception and, therefore, contrary to expected performance on the task. Hari (1995) does not explicitly report similar patterns in her data, however she notes that in contrast to all other participants, one participant indicated hearing the clicks move in uneven steps. Similarly, Shore *et al.* (1998) reported that three participants indicated saltation across the full range of ISIs delivered (between 30 and 500 ms) on their task. Because of the subjective nature of the task, it is impossible to know whether these participants are experiencing a percept other than saltation, or whether their different response patterns reflect differences in interpretation of the instructions, response criterion, or the ability to use the given scale to translate their percept. Given that all participants in Experiment 2 derived sensible thresholds from our saltation task, it is unlikely that their responses on Hari's (1995) task reflect differences in their percept of the saltation illusion. Additionally, because listeners were mostly undergraduate and postgraduate students, it also seems unlikely that the nonmonotonic response patterns are the result of below average intelligence or of cognitive or behavioral problems

TABLE II. Pearson product moment correlation matrix of log thresholds of blocks 1 and 2 of the Hari (1995) 8 click lateralization saltation task and the objective psychophysical saltation task.

	8 Click Lateralization 1	8 Click Lateralization 2	Psychophysical Saltation 1	Psychophysical Saltation 2
8 Click Lateralization 1	⋯			
		0.15	0.44	0.63[a]
N		19	19	19
8 Click Lateralization 2		⋯		
			0.30	0.06
N			19	19
Psychophysical saltation 1			⋯	
				0.61[a]
N				37
Psychophysical saltation 2				⋯
N				

[a]Significant at $p<0.01$ level (2-tailed).

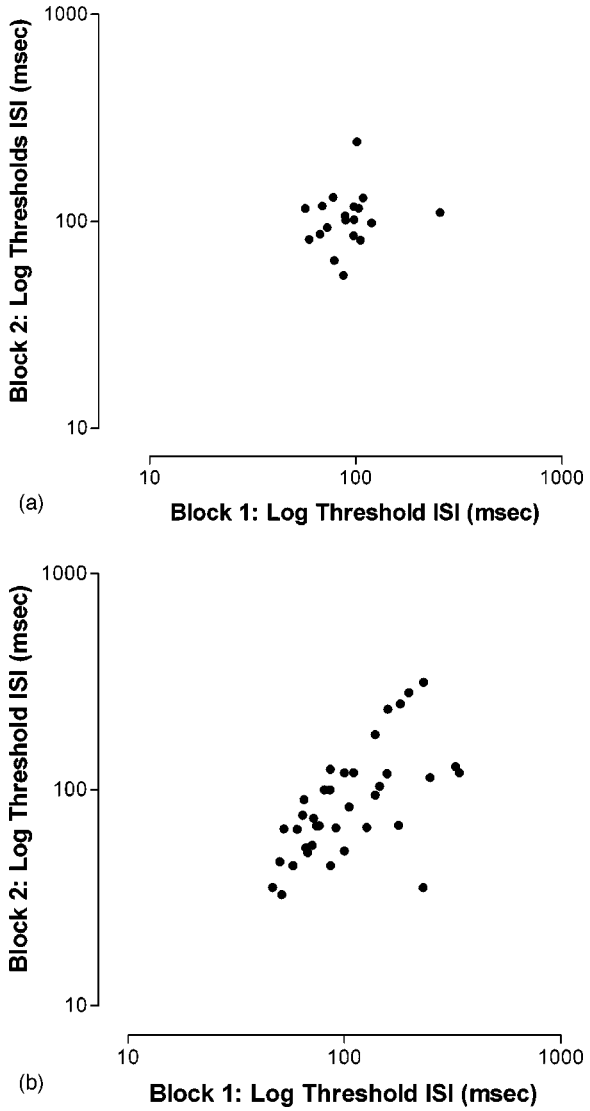

FIG. 6. (a) Log thresholds of block 1 plotted against log thresholds of block 2 for the 8 click lateralization task (Hari, 1995); (b) Log thresholds of block 1 plotted against log thresholds of block 2 for the objective psychophysical saltation task.

which might impede task performance. Thus, it remains possible that factors associated with the subjectivity inherent to such a task might account for these irregular response patterns.

In spite of the finding that some non-monotonic responses were given on the subjective saltation task, we do not suggest that subjective methods are always problematic when used to quantify saltation. Indeed, useful and systematic individual data have been reported using such methods (e.g., Phillips and Hall, 2001; Phillips *et al.* 2002). However, it is important to note that such studies have predominantly employed experienced psychophysical listeners, or have subjected naive participants to repeated testing. Undoubtedly, repeated practice on a subjective task would encourage the generation of meaningful systematic data. However, in a clinical situation such as the diagnostic testing of dyslexics, listeners are predominantly inexperienced in auditory psychophysics, and extended periods of practice are often not possible. Given that our objective psychophysical task estimates thresholds reliably and efficiently for inexperienced listeners, it seems a more appropriate task for use in a clinical setting.

The analyses of Experiment 2 also demonstrated that monotonic data can be obtained by averaging a combination of monotonic and nonmonotonic data. Thus, as previously mentioned, the process of averaging data such as these obscures a great deal of individual variability in task performance. A fundamental principle of data averaging is that within-group variance should be minimal. This is also a requirement of between-group statistics such as t-test and analysis of variance. If between-group comparisons are to be made on data from auditory saltation tasks, it is critical that individual variability in performance is first analyzed to ensure this requirement is met. In addition, as previously mentioned, dyslexia is thought to be a heterogeneous disorder. Therefore, careful inspection of individual data is necessary to investigation of the characteristics of dyslexia subtypes.

Sidman (1952) captured this issue in his statement ''the mean curve does not provide the information necessary to make statements concerning the function for the individual'' (p. 268). Estes (1956) added ''the fault lies, not in the averaged curves, but in our customary interpretations of them'' (p. 134). It is therefore important that future studies of the auditory saltation illusion using untrained and/or dyslexic participants report individual rather than group data in order that evaluations of between-subject differences in performance patterns can be made.

The present studies are indicative of the usefulness of our psychophysical saltation task in reliably estimating the temporal parameters of the saltation illusion. Usage of this task would enable careful examination of individual thresholds of saltation onset in dyslexia, thereby extending the work of Hari and Kiesilä (1996) and Tallal (1980) within an alternative paradigm. Investigation of the mechanisms of auditory saltation is also possible via this technique. Additionally, it may be possible to employ a variant of this task within other sensory modalities. This would allow thresholds of visual, cutaneous, and auditory saltation to be compared. Such a comparison might be an important first step in determining the commonalities of the mechanisms of saltation across modalities.

V. CONCLUSIONS

In conclusion, the results of the present studies have provided a firm empirical basis for the use of an objective psychophysical procedure in the study of the auditory saltation illusion. The psychophysical task we outline is efficient, reliable, and appropriate for use in deriving individual thresholds within samples of naive, inexperienced listeners. The use of this quantification paradigm could feasibly lead to important insights into the processes underlying the saltation illusion.

ACKNOWLEDGMENTS

We thank Sarah Kidd, Anna Ma-Wyatt, Robert Kidd, Neil Roach, and Sieu Khuu for their participation in Experiment 1. We also thank Veronica Edwards for very helpful

comments on a draft of this paper. This research was supported by a grant from the Australian Research Council.

Castles, A., and Coltheart, M. (**1993**). ''Varieties of developmental dyslexia,'' Cognition **47**, 149–180.
Estes, W. K. (**1956**). ''The problem of inference from curves based on group data,'' Psychol. Bull. **53**, 134–140.
Farmer, M., and Klein, R. (**1995**). ''The evidence for a temporal processing deficit linked to dyslexia:'' A review, Psychonomic, Bull. Rev. **2**, 460–493.
Geldard, F. (**1976a**). *Sensory Saltation: Metastability in the Perceptual World* (Lawrence Erlbaum Press, New Jersey).
Geldard, F. (**1976b**). ''The saltatory effect in vision,'' Sens Processes **1**, 77–86
Geldard, F., and Sherrick, C. E. (**1972**). ''The cutaneous rabbit: A perceptual illusion,'' Science **178**, 178–179.
Geldard, F., and Sherrick, C. E. (**1983**). ''The cutaneous saltatory area and its presumed neural basis,'' Percept. Psychophys. **33**, 299–304.
Gregory, R. (**1995**). ''Seeing backwards in time,'' Nature (London) **373**, 21–22.
Hari, R. (**1995**). ''Illusory directional hearing in humans,'' Neurosci. Lett. **189**, 29–30.
Hari, R., and Kiesilä, P. (**1996**). ''Deficit of auditory temporal processing in dyslexia,'' Neurosci. Lett. **205**, 138–140.
Harris, G. G. (**1960**). ''Binaural interactions of impulsive stimuli and pure tones,'' J. Acoust. Soc. Am. **32**, 685–692.
Irwin, R., Ball, A., Kay, N., Stillman, J., and Rosser, J. (**1985**). ''The development of auditory temporal acuity in children,'' Child Dev. **56**, 614–620.
Kilgard, M. P., and Merzenich, M. M. (**1995**). ''Anticipated stimuli across the skin,'' Nature (London) **373**, 663.
Kronbichler, M., Hutzler, F., and Wimmer, H. (**2002**). ''Dyslexia: Verbal impairments in the absence of magnocellular impairments,'' NeuroReport **13**, 617–620.
Lockhead, G. R., Johnson, R. C., and Gold, F. M. (**1980**). ''Saltation through the blind spot,'' Percept. Psychophys. **27**, 545–549.
Middlebrooks, J. C., and Green, D. M. (**1991**). ''Sound localization by human listeners,'' Annu. Rev. Psychol. **42**, 135–159.
Moore, B. J. C. (**1997**). *An Introduction to the Psychology of Hearing*, 4th ed. (Academic, New York).
Phillips, D. P., and Hall, S. E. (**2001**). ''Spatial and temporal factors in auditory saltation,'' J. Acoust. Soc. Am. **110**, 1539–1547.
Phillips, D. P., Hall, S. E., Boehenke, S. E., and Rutherford, L. E. D. (**2002**). ''Spatial stimulus cue information supplying auditory saltation,'' Perception **31**, 875–885.
Sekuler, R., and Blake, R. (**1994**). *Perception*, 3rd ed. (McGraw–Hill, New York).
Sidman, M. (**1952**). ''A note on the functional relations obtained from group data,'' Psychol. Bull. **49**, 263–269.
Shore, D. I., Hall, S. E., and Klein, R. M. (**1998**). ''Auditory saltation: A new measure for an old illusion,'' J. Acoust. Soc. Am. **103**, 3730–3733.
Tallal, P. (**1980**). ''Auditory temporal perception, phonics, and reading disabilities in children,'' Brain Lang **9**, 182–198.
Taylor, M. M., and Creelman, C. D. (**1967**). ''PEST: Efficient estimates on probability functions,'' J. Acoust. Soc. Am. **41**, 782–787.
Wolf, M., and Bowers, P. G. (**1999**). ''The double-deficit hypothesis for the developmental dyslexias,'' J. Educ. Psychol. **91**, 415–438.

Age effects on discrimination of timing in auditory sequences

Peter J. Fitzgibbons[a)]
Department of Hearing, Speech, and Language Sciences, Gallaudet University, Washington, DC 20002

Sandra Gordon-Salant
Department of Hearing and Speech Sciences, University of Maryland, College Park, Maryland 20742

(Received 26 November 2003; revised 16 April 2004; accepted 4 May 2004)

The experiments examined age-related changes in temporal sensitivity to increments in the interonset intervals (IOI) of components in tonal sequences. Discrimination was examined using reference sequences consisting of five 50-ms tones separated by silent intervals; tone frequencies were either fixed at 4 kHz or varied within a 2–4-kHz range to produce spectrally complex patterns. The tonal IOIs within the reference sequences were either equal (200 or 600 ms) or varied individually with an average value of 200 or 600 ms to produce temporally complex patterns. The difference limen (DL) for increments of IOI was measured. Comparison sequences featured either equal increments in all tonal IOIs or increments in a single target IOI, with the sequential location of the target changing randomly across trials. Four groups of younger and older adults with and without sensorineural hearing loss participated. Results indicated that DLs for uniform changes of sequence rate were smaller than DLs for single target intervals, with the largest DLs observed for single targets embedded within temporally complex sequences. Older listeners performed more poorly than younger listeners in all conditions, but the largest age-related differences were observed for temporally complex stimulus conditions. No systematic effects of hearing loss were observed. © *2004 Acoustical Society of America.* [DOI: 10.1121/1.1765192]

PACS numbers: 43.66.Mk, 43.66.Sr [GK] Pages: 1126–1134

I. INTRODUCTION

This paper describes results of some experiments that examined the ability of younger and older listeners to discriminate changes in the temporal characteristics of auditory sequences. The specific experiments are part of a larger project designed to explore the hypothesis that aging is accompanied by a general decline in auditory temporal processing that can affect listeners perception of both speech and nonspeech sequential sounds. Speech recognition studies have shown consistently that elderly listeners have difficulty understanding stimuli that have been time altered in some manner. This observation is most evident for listening tasks that utilize sentence-length speech samples presented at rapid presentation rates, produced either by fast talkers or time-compression techniques applied to speech waveforms (Wingfield *et al.*, 1985; Gordon-Salant and Fitzgibbons, 1993, 2001; Tun, 1998). By comparison to younger listeners, the diminished recognition performance exhibited by many elderly listeners with rapid speech can be quite pronounced. These speech results provide some general auditory support for a class of cognitive theories which stipulate that aging is accompanied by a generalized slowing of information processing for events throughout the nervous system (Birren, 1965; Salthouse, 1991).

Despite the prevalence of experimental observations, the specific sources of the speech understanding problems among elderly listeners are less certain. Part of the problem relates to the inherent temporal and spectral complexity of the speech signal itself. Additionally, a number of other factors, including the prevalence of sensorineural hearing loss among older listeners, as well as complex effects of speech semantic and syntactic factors, can each exert a significant influence on speech processing. However, in terms of acoustical changes, rapid speech is primarily characterized by a relative reduction in the duration of some or all of the component phoneme and pause intervals, together with consequent changes to overall speech tempo and rhythm. Therefore, it seems reasonable to assume that any loss of sensitivity to these component duration changes, or sequence timing characteristics, could be important factors underlying the age-related difficulties observed with rapid speech.

Additionally, psychophysical evidence lends some support to the conclusion that aging does appear to be a factor that contributes to diminished auditory temporal sensitivity. Some of the evidence relates to measured thresholds for the detection of brief temporal gaps between successive acoustic markers, either pairs of simple tone or noise bursts. Most of the gap thresholds measured for elderly listeners are reported to be about twice the magnitude of those observed for younger listeners (Schneider *et al.*, 1994, 1998; Snell, 1997). Older listeners are also observed to have difficulty discriminating changes in the duration of simple tones and noise bursts, or reference intervals defined by a silent interval inserted between a pair of acoustic markers (Abel *et al.*, 1990; Fitzgibbons and Gordon-Salant, 1994; Lister *et al.*, 2000; Grose *et al.*, 2001). Generally, the age-related deficits observed for duration discrimination are also found to be largely independent of sensorineural hearing loss, indicating that cochlear mechanisms are not the likely source of reduced temporal sensitivity among the elderly listeners.

Other evidence also indicates that measures of temporal

a)Electronic mail: peter.fitzgibbons@gallaudet.edu

sensitivity collected with simple stimuli do not always generalize to listening conditions that feature more complex extended sequences of sounds. For example, in one study (Fitzgibbons and Gordon-Salant, 1995), we compared the ability of younger and older listeners to discriminate duration changes for a simple tone presented in isolation and the same tone embedded as one component of a five-tone contiguous sequence that approximated the length of a simple spoken sentence. One notable finding of the study was that younger listeners were able to discriminate duration changes in the embedded target tone with about the same accuracy as they demonstrated for the target tone presented in isolation. However, this was not the case for older listeners. These listeners showed significant reductions in discrimination performance for tones within a sequential context versus the same targets presented in isolation. The performance of these older listeners was also reduced considerably if the sequence location of the embedded target tone changed randomly across a series of listening trials. By comparison, younger listeners were largely unaffected by uncertainty regarding sequential location of a target tone. These results indicate that relatively small age- related effects measured for simple isolated stimuli may become pronounced when examined within a more complex sequential stimulus context.

One possible explanation for the age effects seen with the sequential stimuli is that younger listeners are able to utilize overall timing cues related to changes of sequential rhythm or tempo to perform the duration discrimination tasks. By comparison, older listeners may not, or can not, process these overall timing cues as effectively. Recently, we conducted an initial investigation of this hypothesis by directly comparing the ability of younger and older listeners to discriminate changes in sequence tempo within relatively simple tonal patterns (Fitzgibbons and Gordon-Salant, 2001). The stimulus sequences consisted of five brief tones of equal frequency separated equally by silent intervals to create sequences with uniform tonal interonset intervals (IOIs) that corresponded to a given presentation rate. For each of several reference sequence rates, the intertone silent intervals were co-varied simultaneously in order to measure the relative DL for changes of tonal IOI corresponding to a slowing of the sequence rate. The results indicated that young listeners are generally quite sensitive to changes of sequence rate, with the relative DLs for IOI changes being about 3% over a broad range of presentation rates. The same results also revealed significant age-related performance differences, with the older listeners observed to be consistently less sensitive to changes of sequence rate than younger listeners. Additionally, the performance of older listeners was notably poor for discriminating localized changes in sequence timing, changes that were examined in some conditions by alterations of a single tonal interval within the otherwise equal-interval patterns. While the age differences in performance were evident across a range of stimulus sequence rates, many of the elderly listeners exhibited the greatest difficulty in tracking timing changes at the faster stimulus rates.

These results with simple tonal patterns suggest that older listeners may have specific problems processing the timing pattern within auditory sequences. However, the extent to which the results collected with the fixed-frequency uniform sequences is useful towards understanding the processing of more complex temporal patterns is unclear. We know, for example, that even simple sequences of speech sounds feature considerable spectral complexity as well as variation of timing within patterns. These stimulus factors may contribute to the speech recognition problems that are evident for many older listeners. Therefore, the focus of the present investigation is to examine the manner in which stimulus temporal and spectral complexity interact with the listeners age to influence sequential processing of nonspeech stimulus patterns. Additionally, because diminished speed of processing is hypothesized to be a consequence of aging, we anticipate that the specific effects of spectral and temporal stimulus factors will vary with sequence presentation rate. Finally, hearing loss is a well-established consequence of aging, one that is known to influence listeners' processing of both speech and non-speech sounds in a number of listening tasks (Dubno and Schaefer, 1992; Dubno and Ahlstrom, 1995). Thus, another purpose of the study is to examine the independent and interactive effects of listener age and hearing loss on all discrimination measures. This is accomplished by testing groups of younger and older listeners in the experiments who were matched by age and degree of sensorineural hearing loss.

II. METHODS

A. Subjects

Listeners in the study included 51 subjects assigned to four groups according to age and hearing status. One group included young normal-hearing subjects (YNH, $n=15$) ages 18–40 ($M=23.2$ years, s.d.$=5.3$) with pure-tone thresholds $\leqslant 15$ dB HL (*re*: ANSI, 1996) from 250 to 4000 Hz. Another group included young hearing-impaired listeners (YHI, $n=10$) of 18 to 40 years ($M=29.9$ years, s.d.$=10.2$) with mild-to-moderate sloping high-frequency sensorineural hearing losses of hereditary or unknown etiologies. A third group of subjects included normal-hearing elderly listeners (ENH, $n=11$) of 65–76 years ($M=70.8$, s.d.$=5.2$) who met the same audiometric criteria as the YNH listeners. Lastly, an elderly group of listeners with hearing impairment (EHI, $n=15$) were 65–76 years ($M=70.5$, s.d.$=3.9$) and also had mild-to-moderate sloping sensorineural hearing losses. The young and elderly listeners with hearing loss exhibited bilateral impairment of equivalent degree ($\pm 5-10$ dB) and configuration across the range of audiometric test frequencies. These subjects had a negative history of otologic disease, noise exposure, and family history of hearing loss. The probable etiology of hearing loss in the older listeners was presbycusis. All testing in the study was monaural, and Table I presents the mean audiograms for test ears of the four listener groups.

Additional criteria for subject selection included monosyllabic word recognition scores exceeding 80%, normal tympanograms, and acoustic reflex thresholds for contralateral pure tone stimuli (500–2000 Hz) elicited at levels below the 90th percentile for individuals with comparable hearing thresholds (Silman and Gelfand, 1981). None of the listeners

TABLE I. Thresholds (dB HL) (*re*: ANSI, 1996) and standard deviations (shown in parentheses) for test ears of young normal hearing (Yng Norm Hrg), elderly normal hearing (Eld Norm Hrg), young hearing-impaired (Yng Hrg Imp), and elderly hearing-impaired (Eld Hrg Imp) listeners for octave frequencies from 250 through 4000 Hz.

	Frequency (Hz)									
	250		500		1000		2000		4000	
Yng Norm Hrg	5.7	(4.6)	1.7	(3.1)	2.0	(3.2)	2.0	(5.6)	2.3	(5.3)
Eld Norm Hrg	12.7	(7.5)	7.7	(7.5)	7.3	(4.7)	5.45	(5.68)	11.82	(7.51)
Yng Hrg Imp	9.5	(17.4)	25.0	(19.7)	30.5	(18.6)	32.0	(17.5)	43.5	(14.9)
Eld Hrg Imp	19.0	(9.49)	19.3	(11.63)	25.3	(10.26)	36.0	(10.89)	50.67	(8.84)

had participated previously in listening experiments and each was paid for their services as subjects. Older listeners also passed a brief screening test for general cognitive awareness [the Mini-Mental Status Questionnaire (Pfeiffer, 1975)].

B. Stimuli

All stimulus sequences for the experiments were generated using an inverse fast Fourier transform (FFT) procedure with a digital signal processing board (Tucker-Davis Technologies, AP2) and a 16-bit D/A converter (DD1, 20-kHz sampling rate) that was followed by low-pass filtering (Frequency Devices 901F, 6000-Hz cutoff, 90 dB/oct). The sequences were constructed using five equal-duration tone bursts that were separated by silent intervals. Each tone burst of a sequence had a fixed duration of 50 ms that included 5-ms cosine squared rise/fall envelopes, with all tone and silent interval durations specified between zero-voltage points in the electrical waveforms. For each sequence the silent intervals between tones were adjusted to establish a desired tonal interonset interval (IOI), an interval that included both the tone and silent interval durations. The stimulus sequences used as reference patterns for discrimination testing were designed to feature spectral complexity, temporal complexity, or a combination of spectral and temporal complexity. Spectrally complex sequences (F) featured variable tone frequencies with fixed tonal IOIs, while temporally complex patterns (T) featured variable tonal IOIs with fixed tone frequencies. Sequences with combined spectral and temporal complexity (FT) featured variable frequencies and variable IOI values.

The stimulus sequences were used in different test conditions that were designed to examine listeners ability to discriminate either uniform changes in sequence presentation rate or localized changes of timing within a sequence. Uniform changes in sequence rate were introduced by covariation of all sequence IOIs (ALL), whereas localized timing changes were effected by variation of a single sequence IOI value (ONE). The experiments included four discrimination conditions, each of which was conducted with reference sequences that were presented at a faster and slower rate. One of the conditions (F_ALL) used the spectrally complex sequences in which all IOI values were varied equally to examine discrimination of uniform changes of sequence rate. The individual tones within the reference patterns were 2000, 2500, 3000, 3500, and 4000 Hz. This octave range was selected to allow a degree of spectral variability within sequences, while also restricting testing to a region that coincided with that of greatest sensitivity loss in the listeners with hearing impairment. For these reference patterns, the ordering of the five tone frequencies within a sequence was randomized across listening trials, but the sequence IOIs were equal, with values of 200 ms for the faster-rate sequences and 600 ms for the slower-rate sequences. Another condition (F_ONE) used these same spectrally complex reference sequences at the faster and slower rates to measure discrimination of changes in one sequence IOI. The sequence location of the selected target interval, an IOI of either 200 ms or 600 ms, also shifted randomly across the four possible tonal IOIs within a sequence on each listening trial.

The other two conditions also assessed discrimination of a single sequence interval, using reference stimulus patterns that featured temporal complexity. One of these (T_ONE) used fixed-frequency stimulus sequences, with all tones set to 4000 Hz. The tonal IOIs in these reference sequences were nonuniform in magnitude, with fixed values in the faster-rate sequences of 100, 150, 200, and 350 ms, with the 200-ms IOI representing the average interval magnitude that always served as the target interval for discrimination testing. Corresponding IOI values for the slower-rate reference sequences were 400, 500, 600, and 900 ms, with the 600-ms IOI being the average value that served as the target interval for discrimination testing. The selection of IOI values for these faster and slower reference sequences was in part arbitrary, but was intended to include intervals shorter and longer than that of the 200 or 600-ms target interval. Additionally, the fixed IOI values in these temporally complex reference patterns were selected to preserve overall sequence durations to match those of the corresponding equal-interval reference sequences of the F_ALL and F_ONE conditions. These sequence durations were 850 and 2450 ms, respectively, for the faster and slower patterns, which were intended to grossly mimic the durations of rapidly and slowly spoken sentences. The final condition (FT_ONE) used these same temporally complex reference sequences, but with the addition of tone frequencies that differed in the same manner as described for the spectrally complex patterns. These sequences with both frequency and temporal complexity were also used to assess discrimination of a single target IOI with reference values 200 or 600 ms, respectively, in the faster and slower stimulus patterns. For both conditions that utilized the temporally complex stimulus patterns, the ordering of the four tonal IOI values changed randomly across a series of discrimination trials. As such, the sequence location of the 200-ms, or 600-ms, target IOI for discrimination testing also changed ran-

domly across the four possible tone intervals of a sequence on each listening trial.

C. Procedures

The measurement of DLs for increments of tonal inter-onset intervals was obtained using an adaptive three-interval, two-alternative, forced-choice discrimination procedure. Each discrimination trial contained three observation intervals spaced 750 ms apart. The first listening interval of each trial contained a sample of the reference stimulus sequence, with the second and third intervals containing samples of the reference and comparison sequence in either order selected randomly across listening trials. For all conditions, reference and comparison sequences of a given listening trial differed only by the duration of one or more IOI values, which were always longer in the comparison sequence. In all cases, the lengthening of IOIs in the comparison sequence was accomplished by incrementing one or more intertone silent intervals, with no change of tonal durations, thus extending overall duration of the comparison sequence. In the F_ALL condition, measurements of sequence rate discrimination were collected with the spectrally complex reference sequences which featured uniform IOI values of 200 or 600 ms for the faster and slower patterns, respectively. Adjustments of sequence rate in the comparison sequences were implemented by co-varying all sequence IOIs equally to produce a slowing of presentation rate. The sequential ordering of tone frequencies changed randomly across trials, but was always the same for the reference and comparison sequences of a given listening trial. These same reference sequences were also used for the single-interval discrimination condition, F_ONE. For this condition, only one IOI in the comparison sequence, designated as the target interval, was lengthened, with other sequence IOI values remaining fixed and equal to their original reference values, either 200 or 600 ms. Within the comparison sequence, the location of the target IOI changed randomly across the four sequence intervals on each listening trial; the ordering of tone frequencies did not change across listening intervals within a trial but did change randomly across trials. In a similar manner, discrimination of a single target IOI was assessed in the two conditions that featured temporally complex reference sequences, that is, T_ONE, with the fixed-frequency patterns, and FT_ONE, with the variable-frequency patterns. In each condition, the variable target interval in the comparison sequences had a reference duration of 200 or 600 ms, respectively, for the faster and slower reference sequences. Again, the ordering of sequence tone frequencies, IOI values, and sequence location of the target interval changed randomly across discrimination trials, but not across listening intervals of a given trial.

Estimates of all duration DLs in each condition were obtained using an adaptive rule for varying the target IOI value(s), such that the target decreased in magnitude following two consecutive correct responses by the listener and increased following each incorrect response. Threshold estimates derived by this adaptive rule corresponded to values associated with 70.7% correct discrimination (Levitt, 1971). Testing was conducted in 50-trial blocks with an IOI starting value of 1.4 times its reference value, and step size for IOI changes that decreased logarithmically over trials to produce rapid convergence on threshold values. Following the first three reversals in direction of IOI change, a threshold estimate was calculated by averaging reversal-point IOI values associated with the remaining even-numbered reversals. An average of four threshold estimates was used to calculate a final DL for IOI with each listener in each condition. Prior to data collection, each listener received 2–3 h of practice for sequence discrimination, with all listeners showing performance stability after 3–4 trial blocks in each condition.

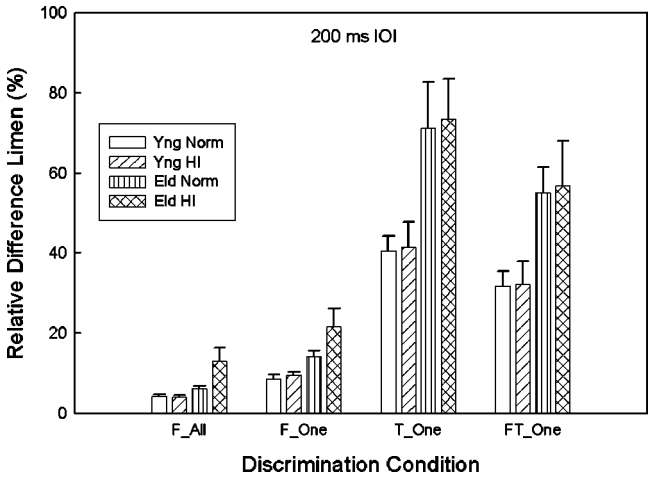

FIG. 1. Mean relative difference limen (DL) in percent for each listener group in the four stimulus sequence conditions with 200 ms as the reference tonal inter-onset interval (IOI). The four sequence conditions include equal increments of all IOIs in equal-interval patterns with variable frequencies (F_ALL), increments of a single IOI in equal-interval patterns with variable frequencies (F_ONE), increments of a single IOI in unequal-interval patterns with fixed frequencies (T_ONE), and increments of a single IOI in unequal-interval patterns with variable frequencies (FT_ONE). The four listener groups are young normal hearing (Yng Norm), young hearing-impaired (Yng HI), elderly normal hearing (Eld Norm), and elderly hearing-impaired (Eld HI). Error bars represent the standard error of the mean.

The listeners were tested individually in a sound-treated booth. The discrimination conditions were tested in a different random order for each listener. Stimulus levels were 85–90 dB SPL in order to provide adequate audibility and produce minimum sensation levels of 25–30 dB in the 2000–4000-Hz region for the listeners with hearing loss. Testing was monaural in the listener's preferred ear using an insert earphone (Etymotic ER-3A) that was calibrated in a 2-cm^3 coupler (B&K, DB0138). All listening was conducted in 2-h sessions over the course of several weeks. Total test time (not including practice) varied across listeners, but averaged about 8 h.

III. RESULTS

For the purpose of analysis and comparison with previous findings, all duration DLs collected in the experiments were converted to relative values expressed as a percentage of the reference IOI value. Results of the four experimental conditions for each of the four listener groups are displayed in Fig. 1, for the conditions with faster-rate sequences (200-ms IOI targets), and Fig. 2, for the conditions with slower-rate sequences (600-ms IOI targets). Each of the figures displays the mean relative DLs for each condition and

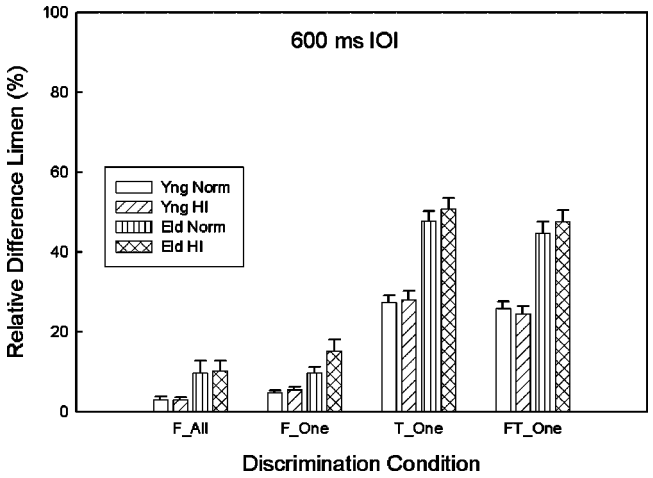

FIG. 2. Same as for Fig. 1, but for 600-ms reference IOIs.

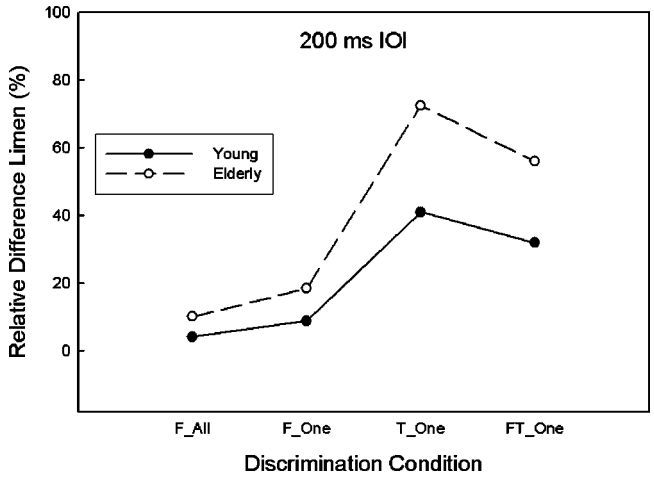

FIG. 3. Mean relative DLs in percent for 200-ms reference IOIs in the four sequence conditions for young and elderly listeners. The data are collapsed across the normal-hearing and hearing-impaired listener groups.

group of subjects, with vertical bars in the figures representing the standard error of the means. The relative DLs displayed in Fig. 1 are generally larger than those of Fig. 2, particularly for the three conditions that involved single-interval discrimination (F_ONE, T_ONE, FT_ONE). The F_ALL condition that involved discrimination of changes in sequence rate produced the smallest relative DLs, and these values were essentially equivalent for the sequences with the faster and slower reference rates. A separate analysis of variance (ANOVA) was conducted for the relative DLs shown in Figs. 1 and 2, using a split-plot factorial design with two between-subjects factors (age and hearing status) and one within-subjects factor (discrimination condition). Each analysis revealed significant main effects of listener age ($p<.001$), discrimination condition ($p<.001$), and significant interactions between age and condition ($p<0.01$). The analyses revealed no significant effects of hearing loss across conditions, for either the faster or slower sequence presentation rates.

Simple main effects analysis and multiple comparison tests were subsequently conducted to examine sources of the age×condition interactions that were evident in the data collected for both the faster and slower stimulus sequences. To examine the interaction effects, the mean relative DLs for the two age groups (collapsed across hearing status) are shown in Fig. 3, for the four conditions with 200-ms target intervals, and Fig. 4, for the four conditions with the 600- ms targets. As each figure shows, the relative DLs for both listener age groups were smaller for the conditions featuring only sequence spectral complexity (F_ALL and F_ONE), and significantly larger for the conditions featuring sequence temporal complexity (T_ONE and FT_ONE), ($p<0.01$). For both age groups, the mean performance differences were relatively small between the two conditions with spectral complexity (F_ALL and F_ONE), and were also not significantly different between the two conditions with temporal complexity (T_ONE and FT_ONE). The discrimination performance of the older listeners was poorer than that of the younger listeners in each of the four conditions, but the largest age-related performance differences were observed for the T_ONE and FT_ONE conditions at both sequence rates ($p<0.01$).

IV. DISCUSSION

The experiments compared the abilities of younger and older listeners to discriminate changes in the timing between successive components of tonal sequences that featured spectral complexity, temporal complexity, or a combination of the two. In some conditions, listeners were asked to respond to uniform changes in all tonal interonset intervals that altered the presentation rate of the sequential stimulus patterns. In other conditions, listeners responded to changes in the magnitude of a single sequence interval that produced a localized disruption of timing within the tonal patterns. The results showed that listeners sensitivity to changes of temporal intervals depends on both the number and magnitude of the temporal intervals that are subjected to change. Additionally, the spectral and temporal characteristics of the stimulus sequence can affect discrimination performance, with temporal complexity exerting the most pronounced effects. The results indicated that older listeners were less sensitive than younger listeners to changes of timing within the stimulus sequences.

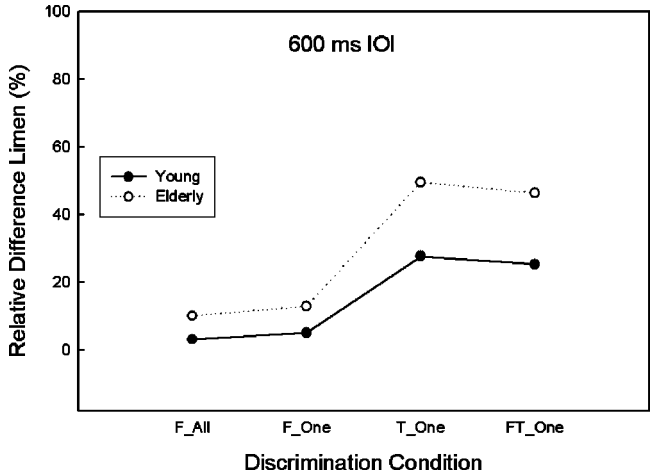

FIG. 4. Same as Fig. 3, but for 600-ms reference IOI values.

However, the magnitude of the age-related discrimination deficits varied across stimulus conditions, and depended largely upon the timing characteristics of the stimulus patterns.

A. Equal interval patterns

For the stimulus conditions that featured tonal IOIs of equal magnitude in the reference patterns (F_ALL and F_ONE), the younger listeners were able to discriminate interval changes with a relatively high degree of accuracy. The estimates of discrimination for overall changes of presentation rate with the equal-interval sequences revealed the best temporal sensitivity among the younger listeners. Thus, for the F_ALL condition, with all sequence IOIs co-varied equally, the relative DLs for rate change were 4.1% for the faster reference sequences and 3.1% for the slower sequences. The near equivalence of these DLs for rate discrimination with the faster and slower sequences agrees with earlier findings that were collected with fixed-frequency tone sequences that also featured uniform timing patterns (Drake and Botte, 1993; Fitzgibbons and Gordon-Salant, 2001). Collective findings from these earlier studies indicated that the relative DL for changes of sequence rate remains fairly constant over a broad range of reference tonal IOIs ranging from about 200 to 800 ms. This was not the case for the single-interval DLs, which generally reflected larger relative DL values for the shorter 200-ms interval compared to the longer 600-ms interval. For example, for the F_ONE condition that examined discrimination of a single embedded sequence interval, the younger listeners produced mean relative DLs of 8.9% and 5.2% for the target IOIs of 200 and 600 ms, respectively. These values are larger than the corresponding DLs for the F_ALL condition, indicating that localized changes of timing within sequences are more difficult to discern than uniform changes in presentation rate.

The discrimination performance of the older listeners with the equal-interval reference sequences was generally poorer than that of the younger listeners. For discrimination of sequence rate with the equal-interval patterns (F_ALL condition), the older listeners produced mean DLs of 9.6% for the faster sequences with 200-ms reference IOIs and 10.0% for the slower sequences with 600-ms IOIs. These values are larger than corresponding estimates for rate discrimination in the younger listeners. However, like the younger listeners, the mean DLs for rate discrimination among the older listeners were essentially equivalent for the faster and slower reference sequences, indicating a fairly constant Weber fraction for the two reference presentation rates. This outcome also agrees with observations from our previous experiment with fixed-frequency tone sequences (Fitzgibbons and Gordon-Salant, 2001), which revealed a relatively constant relative DL in elderly listeners for rate discrimination across a large range of reference sequence presentation rates.

For single-interval discrimination (F_ONE condition), the mean relative DLs of the older subjects was 17.9% and 12.4% for the 200- and 600-ms target IOIs, respectively. Each of these values is at least twice the corresponding DL values for the younger listeners. It should be noted, however, that the performance variability among the elderly listeners was sometimes large, especially among the DLs measured for the shorter 200-ms target interval. This outcome was primarily attributed to the poor discrimination performance of two elderly listeners, who produced abnormally large DLs for the 200-ms single target interval. However, even with the omission of the data for these two subjects, the mean relative DL for the elderly listeners was 14.6% for the 200-ms target, a value that remains considerably larger than that observed for the younger listeners.

B. Unequal interval patterns

The reference sequences with irregular timing featured unequal tonal intervals with an average value of 200 or 600 ms, values that served as the respective sequence targets for single-interval discrimination in the faster and slower reference sequences. For these temporally complex stimulus patterns, discrimination of changes in the single target interval proved to be difficult for both younger and older listeners, with performance being significantly poorer than that observed for the same target intervals embedded within the sequences with equal tone intervals. For the sequences with unequal intervals and fixed tone frequencies (T_ONE condition), the younger listeners produced mean relative DLs of 41.1% and 27.7% for the 200- and 600-ms single IOI targets, respectively. Similarly, for the same temporally complex sequences with variable tone frequencies (FT_ONE condition), the mean relative DLs of the younger listeners were 32.0% and 25.2% for the 200- and 600-ms single target intervals, respectively. For both conditions, discrimination performance among listeners was always poorer and more variable for the shorter 200-ms target than for the 600-ms target interval, a result that was also observed for the stimulus patterns with the equal tone intervals. Additionally, no significant differences in the discrimination performance of the younger listeners were observed between temporally complex sequence conditions that featured fixed-frequency and variable-frequency tonal patterns. Thus, the combined effects of spectral and temporal complexity in the stimulus sequences of the FT_ONE condition were about the same as those produced by temporal complexity alone with sequences of the T_ONE condition.

The older listeners exhibited pronounced difficulty discriminating changes in the target interval within the sequences with unequal timing. For the fixed-frequency patterns (T_ONE), these older listeners produced mean relative DLs of 72.4% and 49.3% for the 200- and 600-ms target IOIs, respectively. Corresponding mean DLs for the variable-frequency sequences (FT_ONE) were 56.0% and 46.2%, respectively, for the same 200- and 600-ms targets. These results also showed poorer and more variable discrimination performance for 200-ms targets relative to that for the longer 600-ms target intervals. This was particularly the case for the 200-ms targets in the T_ONE condition, in which two elderly listeners from each hearing status group exhibited abnormally poor discrimination. With the data from these subjects omitted, the mean DL value for the elderly listeners in the T_ONE condition with the 200-ms target interval would have shifted from 72.4% to 59.4%, a value equivalent to that

for the FT_ONE condition for the elderly listeners. In either case, the DL values of the older listeners with the unequal-interval patterns were at least three times larger than their corresponding DLs measured for the same reference target intervals embedded within the stimulus patterns with equal intervals. The performance of the elderly listeners was also significantly poorer than that of the younger listeners in both the T_ONE and FT_ONE sequence conditions. However, like the younger listeners, the discrimination performance of the older listeners with the temporally complex sequences was not significantly different for the conditions with fixed-frequency and variable-frequency tonal patterns.

C. Stimulus complexity effects

The experiments were designed to examine some effects of temporal and spectral complexity on listeners ability to discriminate changes of timing within tonal stimulus sequences. The results indicate that the temporal complexity associated with the unequal sequence intervals produced substantial performance decrements, relative to that observed for the patterns with equal intervals. This outcome was evident for all listeners, but the magnitude of the effects was significantly larger among the elderly subjects. It was anticipated, on the basis of earlier reports, that the introduction of irregular timing to stimulus patterns could influence listeners ability to discriminate one or more embedded target intervals. Some of the earlier studies (Bharucha and Pryor, 1986; Hirsh *et al.*, 1990; Monahan and Hirsh, 1990; Drake and Botte, 1993) reported that even small deviations from regularity in the timing patterns of tonal sequences could produce decrements in listeners temporal discrimination performance. In the present investigation, the temporally complex stimulus sequences featured a substantial degree of irregularity in the timing patterns, with each tonal IOI differing across a relatively wide range of values. This dispersion of interval values within the stimulus sequences undoubtedly contributed to the listeners difficulty in discriminating incremental changes to any single embedded target interval. Additionally, the procedure of randomizing the ordering of the unequal tonal IOIs within sequences across listening trials, as well as randomizing the sequential location of the target interval, introduced a large degree of stimulus uncertainty that further complicated the discrimination task. In all likelihood, this degree of stimulus uncertainty with the complex sequences precluded listeners from developing a memory trace for timing patterns within the reference sequences that was sufficiently strong to discern small deviations in the magnitude of a particular target interval. This would necessarily be the case for stimuli that required substantial memory resources to encode the pattern of temporal intervals within reference sequences, a task that was perhaps more taxing for the older listeners. Without the aid of stimulus context, it seems likely that even the younger listeners had to adopt the less efficient strategy of attempting to isolate and focus on the specific target interval that was subjected to duration changes. In this event, we might expect that the DLs measured for single target intervals within the temporally complex tonal patterns would more closely approximate those values reported for corresponding target intervals that are measured in isolation.

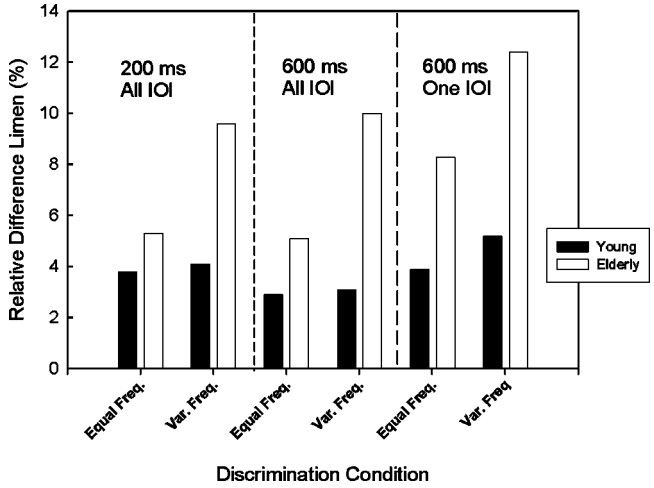

FIG. 5. Mean relative DLs in percent of young and elderly listeners for changes of IOI in three stimulus conditions with equal-interval tone sequences. The conditions include equal increments to all sequence IOIs with reference values of 200 ms (200 ms All IOI) or 600 ms (600 ms All IOI), and increments of a single 600 ms IOI (600 ms One IOI). The sequence tone frequencies were either fixed at 4 kHz (Equal Freq.), or variable in the 2–4-kHz range (Var. Freq.). The results are collapsed across normal-hearing and hearing-impaired listener groups. The DLs shown for Equal Freq. conditions are from Fitzgibbons and Gordon-Salant (2001).

Our results generally support this prediction, with the DLs of our younger listeners for both the 200- and 600-ms target intervals showing reasonably good agreement with the duration DLs reported previously for similar reference silent intervals bounded by a simple pair of stimulus markers presented in isolation (Abel, 1972b; Grose *et al.*, 2001).

The general equivalence of results observed for the T_ONE and FT_ONE single-interval discrimination conditions indicates that the effect of adding spectral complexity to the sequences with unequal intervals was minimal for both the younger and older listeners. This outcome was unexpected, primarily because we had previously observed substantial effects of sequential spectral variation on duration judgments in a different type of discrimination task. (Fitzgibbons and Gordon-Salant, 1995). However, the lack of spectral effects in the present results is most likely due to the high level of difficulty already associated with the temporally complex patterns, a situation that could have obscured observation of any potential additional spectral influences on temporal discrimination. We suspect this to be the case in part on the basis of a *post hoc* examination that compared the DLs measured here for the variable-frequency sequences with equal intervals (F_ALL and F_ONE conditions) to some corresponding results reported in our earlier study that utilized fixed-frequency tone sequences with the same uniform timing characteristics (Fitzgibbons and Gordon-Salant, 2001). Each of the studies examined groups of younger and older listeners that exhibited the same age and hearing characteristics. Some of these comparative data are displayed in Fig. 5, which shows the mean relative DLs of younger and older listeners for two corresponding conditions that measured discrimination of sequence rate changes, labeled All IOI for sequences with equal 200- or 600-ms tonal IOIs, and one condition that measured discrimination for a single sequence interval, labeled One IOI, for a 600-ms target inter-

val. Results in the figure from the earlier study are labeled Equal Frequency (Equal Freq.), while those from the present investigation are labeled Variable Frequency (Var. Freq.) As the figure shows, the sequence rate discrimination performance (All IOI conditions) of the younger listeners was virtually the same for the equal-frequency and variable-frequency tone sequences, while the single-interval DLs for the 600-ms target were slightly larger for the variable- frequency sequences. Thus, the discrimination performance of the younger listeners was largely unaffected by the addition of spectral variability to the stimulus patterns with uniform timing. By comparison, the data of elderly listeners show large effects of spectral complexity, with the relative DLs for the variable-frequency sequences (both All IOI, and the One IOI conditions) being considerably larger than those for the corresponding equal-frequency sequences, and also larger than those of the younger listeners in each condition.

The above comparison of data indicates that the independent effects of sequential spectral complexity on temporal discrimination performance may be substantial, at least for older listeners, and sequences with uniform timing characteristics. This outcome, in conjunction with the strong effects of temporal complexity seen in the present results, suggests that both of these stimulus factors could contribute to the age-related processing difficulties commonly associated with time-altered speech. While the importance of spectral cues in speech understanding is well documented, the role of variable timing within and across speech utterances is less well understood. However, the present findings with nonspeech sounds indicate that the processing of sequences with variable timing is difficult for all listeners, but especially for older listeners and faster sequence presentation rates. Of course, in addition to ongoing variations in frequency and timing, sequences of spoken speech also exhibit substantial variation in component intensity, a factor that undoubtedly contributes to the significant effects of listener hearing loss observed in many of the speech recognition studies. In the present experiments with nonspeech sequences, all testing was restricted to spectral regions of hearing loss, but stimulus intensity was fixed at a relatively high level to insure signal audibility. As a result, no systematic effects of hearing loss among either the young or elderly listeners were observed in the discrimination measures. This outcome agrees with conclusions previously reported for studies that examined effects of hearing loss on duration discrimination tasks (Fitzgibbons and Gordon-Salant, 1995, 2001; Grose *et al.*, 2001). These hearing- loss results regarding duration discrimination provide indirect support for the contention that the processing of stimulus duration is primarily controlled by central timing mechanisms (Creelman, 1962; Abel, 1972a; Divenyi and Danner, 1977). Given sufficient stimulus audibility, the postulated timing mechanisms are unlikely to be affected by peripheral hearing loss, but may exhibit diminished function with aging.

D. Summary

The temporal discrimination results collected from the young and elderly listeners for the sequential stimulus patterns used in the investigation can be summarized as follows:

(1) For equally timed tonal sequences, all listeners generally show better sensitivity for uniform changes of sequence rate than they do for localized changes of timing in a single sequence interval.
(2) The relative DLs for uniform changes of sequence rate were equivalent for the faster and slower sequences, but discrimination performance was generally poorer for single intervals within the faster, compared to slower, sequences.
(3) Discrimination of temporal intervals within sequences with unequal timing is considerably more difficult than discrimination of corresponding intervals within equally timed sequences.
(4) Older listeners exhibit larger relative DLs than younger listeners for all stimulus sequences, but the largest age-related differences were observed for stimulus patterns with unequal timing.
(5) There were no significant effects of hearing loss observed in any of the discrimination conditions for younger and older listeners.

The present findings confirm some of our previous observations that elderly listeners have difficulty discriminating temporal differences in tonal sequences. Whereas our earlier results were collected with fixed-frequency stimulus sequences with equal timing, the current results pertain to spectrally and temporally complex patterns that were intended to mimic some characteristics inherent to sequential speech patterns. The collective evidence indicates that spectral complexity within sequences may exert an important influence on the temporal discrimination performance of older listeners. The discrimination of temporal deviations in stimulus patterns with variable timing structure is relatively difficult for all subjects, but especially for older listeners. The combination of results lends further support to the hypothesis that aging is associated with significant difficulty processing the temporal characteristics of complex sequential stimuli.

ACKNOWLEDGMENTS

This research was supported by a grant form the National Institute of Aging of the NIH (R01AG09191). The authors are grateful to Jennifer Lantz, Claudia Pastorelli, and Saul Strieb for their assistance in data collection.

Abel, S. M. (**1972a**). ''Duration discrimination of noise and tone bursts,'' J. Acoust. Soc. Am. **51**, 1219–1223.
Abel, S. M. (**1972b**). ''Discrimination of temporal gaps,'' J. Acoust. Soc. Am. **52**, 519–524.
Abel, S. M., Krever, E. M., and Alberti, P. W. (**1990**). ''Auditory detection, discrimination, and speech processing in ageing, noise-sensitive and hearing-impaired listeners,'' Scand. Audiol. **19**, 43–54.
ANSI (**1996**). S3.6-1996. ''Specifications for audiometers'' (American National Standards Institute, New York).
Bharucha, J. J., and Pryor, J. H. (**1986**). ''Disrupting the isochrony underlying rhythm: An asymmetry in discrimination,'' Percept. Psychophys. **40**, 137–141.
Birren, J. E. (**1965**). ''Age changes in speed of behavior: Its central nature and physiological correlates,'' in *Behavior, Aging, and the Nervous System*, edited by A. T. Welford and J. E. Birren (Thomas, Springfield, IL), pp. 191–216.
Creelman, C. D. (**1962**). ''Human discrimination of auditory duration,'' J. Acoust. Soc. Am. **34**, 582–593.

Divenyi, P. L., and Danner, W. F. (**1977**). ''Discrimination of time intervals marked by brief acoustic pulses of various intensities and spectra,'' Percept. Psychophys. **21**, 125–142.
Drake, C., and Botte, M.-C. (**1993**). ''Tempo sensitivity in auditory seqeunces: Evidence for a multiple-look model,'' Percept. Psychophys. **54**, 277–286.
Dubno, J. R., and Ahstrom, J. (**1995**). ''Masked thresholds and consonant recognition in low-pass maskers for hearing-impaired and normal-hearing listeners,'' J. Acoust. Soc. Am. **97**, 2430–2441.
Dubno, J. R., and Schaefer, A. (**1992**). ''Comparison of frequency selectivity and consonant recognition among hearing-impaired and masked normal-hearing listeners,'' J. Acoust. Soc. Am. **91**, 2110–2121.
Fitzgibbons, P., and Gordon-Salant, S. (**1994**). ''Age effects on measures of auditory duration discrimination,'' J. Speech Hear. Res. **37**, 662–670.
Fitzgibbons, P., and Gordon-Salant, S. (**1995**). ''Age effects on duration discrimination with simple and complex stimuli,'' J. Acoust. Soc. Am. **98**, 3140–3145.
Fitzgibbons, P., and Gordon-Salant, S. (**2001**). ''Aging and temporal discrimination in auditory sequences,'' J. Acoust. Soc. Am. **109**, 2955–2963.
Gordon-Salant, S., and Fitzgibbons, P. (**1993**). ''Temporal factors and speech recognition performance in young and elderly listeners,'' J. Speech Hear. Res. **36**, 1276–1285.
Gordon-Salant, S., and Fitzgibbons, P. (**2001**). ''Sources of age-related recognition difficulty for time-compressed speech,'' J. Speech Hear. Res. **44**, 709–719.
Grose, J. H., Hall III, J. W., and Buss, E. (**2001**). ''Gap duration discrimination in listeners with cochlear hearing loss: effects of gap and marker duration, frequency separation, and mode of presentation,'' J. Assoc. Res. Otolaryn. **2**, 388–398.
Hirsh, I. J., Monahan, C. B., Grant, K. W., and Singh, P. G. (**1990**). ''Studies in auditory timing: I. Simple patterns,'' Percept. Psychophys. **47**, 215–226.
Levitt, H. (**1971**). ''Transformed up-down methods in psychoacoustics,'' J. Acoust. Soc. Am. **49**, 467–477.
Lister, J. J., Koehnke, J. D., and Besing, J. M. (**2000**). ''Binaural gap duration discrimination in listeners with impaired hearing and normal hearing,'' Ear Hear. **21**, 141–150.
Monahan, C. B., and Hirsh, I. J. (**1990**). ''Studies in auditory timing: 2. Rhythm patterns,'' Percept. Psychophys. **47**, 227–242.
Pfeiffer, E. (**1975**). ''A short portable mental status questionnaire for the assessment of organic brain deficit in elderly patients,'' J. Am. Geriatr. Soc. **23**, 433–441.
Salthouse, T. A. (**1991**). *Theoretical Perspectives on Cognitive Aging* (Erlbaum, Hillsdale, NJ).
Schneider, B. A., Pichora-Fuller, M. K., Kowalchuk, D., and Lamb, M. (**1994**). ''Gap detection and the precedence effect in young and old adults,'' J. Acoust. Soc. Am. **95**, 980–991.
Schneider, B. A., Speranza, F., and Pichora-Fuller, M. K. (**1998**). ''Age-related changes in temporal resolution: Envelope and intensity effects,'' Can. J. Psychol. **52**, 184–191.
Silman, S., and Gelfand, S. (**1981**). ''The relationship between magnitude of hearing loss and acoustic reflex thresholds,'' J. Speech Hear. Res. **46**, 312–316.
Snell, K. B. (**1997**). ''Age-related changes in temporal gap detection,'' J. Acoust. Soc. Am. **101**, 2214–2220.
Tun, P. A. (**1998**). ''Fast noisy speech: Age differences in processing rapid speech with background noise,'' Psychol. Aging **13**, 424–434.
Wingfield, A., Poon, L. W., Lombardi, L., and Lowe, D. (**1985**). ''Speed of processing normal aging: effects of speech rate, linguistic structure, and processing time,'' J. Gerontol. **40**, 579–585.

The across frequency independence of equalization of interaural time delay in the equalization-cancellation model of binaural unmasking

Michael A. Akeroyd[a)]
Laboratory of Experimental Psychology, University of Sussex, Brighton, BN1 9QG, United Kingdom

(Received 23 May 2004; revised 17 April 2004; accepted 3 May 2004)

The equalization stage in the equalization-cancellation model of binaural unmasking compensates for the interaural time delay (ITD) of a masking noise by introducing an opposite, internal delay [N. I. Durlach, in *Foundations of Modern Auditory Theory, Vol. II.*, edited by J. V. Tobias (Academic, New York, 1972)]. Culling and Summerfield [J. Acoust. Soc. Am. **98**, 785–797 (1995)] developed a multi-channel version of this model in which equalization was ''free'' to use the *optimal* delay in each channel. Two experiments were conducted to test if equalization was indeed free or if it was ''restricted'' to the same delay in all channels. One experiment measured binaural detection thresholds, using an adaptive procedure, for 1-, 5-, or 17-component tones against a broadband masking noise, in three binaural configurations (N_0S_{180}, $N_{180}S_0$, and $N_{90}S_{270}$). The thresholds for the 1-component stimuli were used to normalize the levels of each of the 5- and 17-component stimuli so that they were equally detectable. If equalization was restricted, then, for the 5- and 17-component stimuli, the $N_{90}S_{270}$ and $N_{180}S_0$ configurations would yield a greater threshold than the N_0S_{180} configurations. No such difference was found. A subsequent experiment measured binaural detection thresholds, via psychometric functions, for a 2-component complex tone in the same three binaural configurations. Again, no differential effect of configuration was observed. An analytic model of the detection of a complex tone showed that the results were more consistent with free equalization than restricted equalization, although the size of the differences was found to depend on the shape of the psychometric function for detection. © *2004 Acoustical Society of America.* [DOI: 10.1121/1.1768959]

PACS numbers: 43.66.Pn, 43.66.Ba, 43.66.Dc [AK] Pages: 1135–1148

I. INTRODUCTION

Licklider (1948) and Hirsh (1948) discovered that the threshold for detection of a signal masked by a noise could be dramatically reduced if the signal carried a different interaural temporal disparity from the noise. Since then, such ''binaural unmasking'' has been extensively studied [for reviews, see Durlach and Colburn (1978) and Blauert (1997)]. One of the most successful and influential models of binaural unmasking is Durlach's (1972) ''equalization-cancellation'' (EC) model. In that model the gain in the detectability of the signal results from the binaural auditory system first ''equalizing'' for the interaural configuration of the masking noise and then ''cancelling'' it, leaving, in the ideal case, just the signal. Figure 1 shows a schematic illustration of a multi-channel EC model. The left and right ears receive the waveforms of the signal and masking noise. These waveforms include any interaural phase differences (IPDs) or interaural time differences (ITDs) present naturally or introduced experimentally (for the purposes of this report, interaural intensity differences are not considered). The waveforms are then processed by a set of auditory filters that can be considered as a set of frequency channels. The equalization step introduces an internal time delay to compensate for, or equalize for, the external IPD or ITD of the masking noise. The cancellation step then subtracts the equalized waveforms, with the goal of reducing the level of the noise, so leaving the signal and enhancing its detectability. For a signal such as a pure tone, it would be expected that the system will use the ''optimal'' equalization delay: that which gives the maximum enhancement in the detectability of the signal. But, for a wider-frequency signal such as a complex tone, is equalization ''free'' to use the *optimal* delay at all frequencies, or is equalization ''restricted'' to the *same* delay at all? This question is addressed here.[1]

Free equalization was used in a recent modification of the EC model. Culling and Summerfield (1995) constructed stimuli from pairs of narrow-band noises placed at the frequencies of the first and second formants of selected vowels. Two such pairs were presented simultaneously. When one pair was diotic while the other was interaurally uncorrelated, listeners tended to hear the vowel defined by the interaurally uncorrelated pair of noise bands, yet when one pair had a different ITD from the other, listeners were unable to report the vowel corresponding to either pair. These results suggest that across-frequency grouping can make use of interaural correlation but not of ITD. Culling and Summerfield accounted for their results using an EC model in which, for each of a set of independent frequency channels, the post-cancellation residue was measured at each equalization delay between -5000 and $+5000$ μs.[2] The residues were averaged across the duration of the stimulus, using an exponential

[a)]Present address: MRC Institute of Hearing Research (Scottish Section), Glasgow Royal Infirmary, Alexandra Parade, Glasgow, G31 2ER, United Kingdom. Electronic mail: maa@ihr.gla.ac.uk

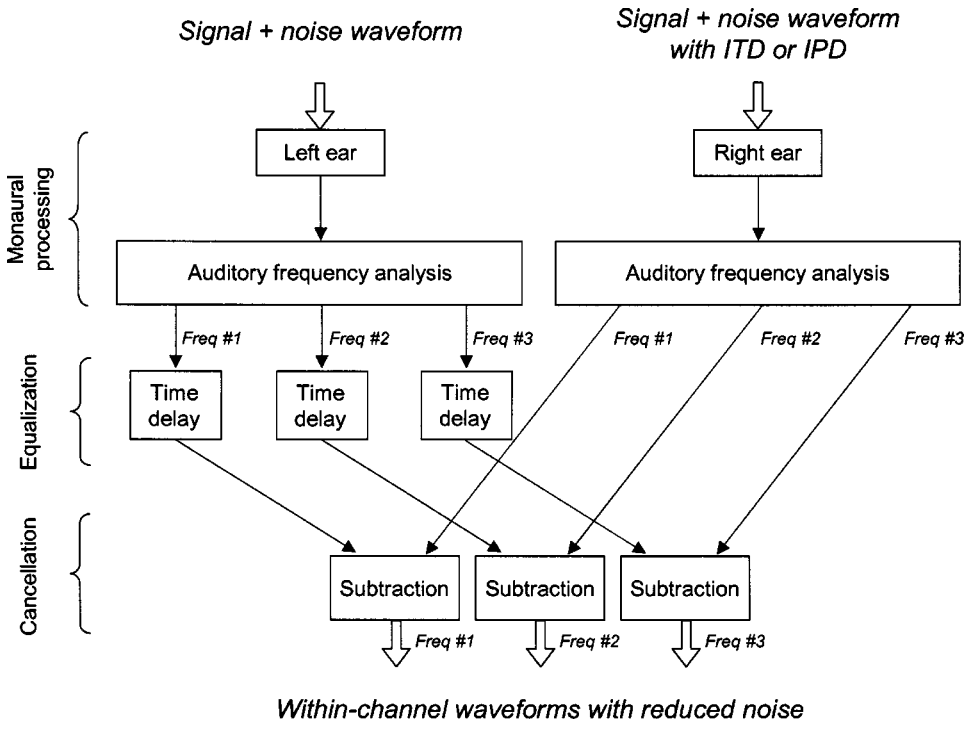

FIG. 1. A schematic outline of a three-channel EC model applied to a ITD- or IPD-shifted noise. The goal of the present experiments is to determine if the three equalization delays must be the same (''restricted'' equalization) or can be different (''free'' equalization).

window of 50-ms time constant, and then the *smallest* residue across delay was chosen and plotted against channel frequency as a ''recovered spectrum.'' The optimal equalization delay is that which gives the smallest post-cancellation residue, and, as that is found independently in each frequency channel, the strategy is a free-equalization one. Culling and others (Culling *et al.*, 1998a,b; Culling, 1999, 2000; Akeroyd *et al.*, 2001) subsequently applied their model to the phenomena of the dichotic pitches. It was unable to account for the existence of the ''dichotic repetition pitch'' (Bilsen and Goldstein, 1974), but it could predict the pitch values in all the other classes of dichotic pitch, namely the ''Huggins pitch'' (Cramer and Huggins, 1958), the ''Fourcin pitch'' (Fourcin, 1970), the ''binaural edge pitch'' (Frijns *et al.*, 1986), and the ''binaural coherence edge pitch'' (Hartmann and McMillon, 2001). Free equalization was particularly crucial in accounting for one data set on the binaural-edge pitch [Frijns *et al.*, 1986; an earlier set (Klein and Hartman, 1980) was instead consistent with restricted equalization], and for accounting for the data on the Fourcin pitch.

Equalization can be studied experimentally by measuring the thresholds of binaural detection for complex-tone stimuli against maskers of fixed or variable ITD. First, consider a complex tone masked by a *fixed*-ITD noise. Optimal cancellation at all frequencies will be achieved by equalizing at the same delay in all channels, for which both free and restricted equalization will serve. Signal-detection theory (Green and Swets, 1966) can be used to develop a quantitative prediction for an *N*-component complex tone. If it is assumed (1) that each of the *N* components of the complex tone is, individually, equally detectable, (2) that the detectability (d') of each is proportional to its energy, and (3) that the noises masking each are independent of one another, as though the components fell in separate critical bands, then the threshold of detection of the complex tone will be $10\log_{10}(\sqrt{N})$ dB less than that of any of the pure-tone components of the complex. Second, consider the same complex tone masked by a *variable*-ITD noise. Optimal cancellation will require an equalization delay that varies across frequency, for which only free equalization will serve. Provided equalization is indeed free, the threshold of detection of the complex tone will again be $10\log_{10}(\sqrt{N})$ dB less than that of the individual components. But if equalization is restricted, then optimal cancellation cannot be achieved at all frequencies, leading to a *greater* threshold. The variable-ITD configuration is the crucial condition distinguishing between free and restricted equalization. The fixed-ITD configuration acts as a check on the expected size of the change in threshold in going from a one-component to an *N*-component complex tone.

This design was used in the present research. Experiment 1 measured adaptively tracked thresholds for a set of 1-component pure tones in one fixed-ITD configuration (N_0S_{180}) and two variable-ITD configurations ($N_{180}S_0$ and $N_{90}S_{270}$).[3] The results were used to construct a set of 5- or 17-component complex tones, each of whose components were equally detectable. Experiment 2 measured adaptively tracked thresholds for these complex tones to test if equalization was free or restricted. Experiment 3 measured psychometric functions for 2-component complex tones to test the same question, and also served to check if the detectability of each signal was indeed proportional to its energy.

II. EXPERIMENT 1: ADAPTIVE THRESHOLDS FOR SINGLE COMPONENTS

A primary aspect of the design was that each of the pure tones making up the complexes used in experiments 2 and 3 offered equal amounts of detectability. As the binaural masked threshold of a pure tone depends on its frequency,

tones of equal SPL will be differentially detectable. Experiment 1 was conducted in order to correct for this effect by normalizing the levels. For example, Hirsh (1948, Table 1) reported thresholds of detection of 60, 64, and 67 dB SPL for pure tones of 200, 500, and 1000 Hz masked by a white noise of 59-dB spectrum level in the N_0S_{180} configuration. If a complex tone was synthesized using these three components, each at 60 dB, then the 200-Hz component would be at detection threshold ($d'=1$) but the 500- and 1000-Hz components would be considerably below threshold ($d' \ll 1$). Both the higher-frequency components would add little detectability to the complex. But if the complex tone was synthesized with the components at 60, 64, and 67 dB, then all three components would indeed contribute equal amounts of detectability.[4] Accordingly, this experiment measured the thresholds of detection of pure tones at 200, 400, 600, 800, and 1000 Hz in each of the binaural configurations of N_0S_{180}, $N_{180}S_0$, and $N_{90}S_{270}$.

A. Method

1. Stimuli synthesis and apparatus

The stimuli were constructed using MATLAB running on a Linux PC at a sampling rate of 32 000 samples per second. The signal was a pure tone of 200-, 400-, 600-, 800- or 1000-Hz frequency and of 0°, 180°, or 270° IPD. The masking noises were white noises, low-pass filtered at 2000 Hz. They were generated in the frequency domain using a 9600-point (3.33-Hz resolution) buffer: the real and imaginary parts of components below 2 kHz were taken from Gaussian distributions and those above 2 kHz were set to zero, then the inverse FFT of the buffer calculated and finally the real part taken. The IPDs of the noises were either 180°, 0°, or 90°, and were applied by appropriate phase shifts of the components of the buffer. Both signals and noises had 300-ms durations, including 20-ms raised-cosine onset and offset ramps. For each of the four intervals within a trial, a new masking noise was calculated. For the target intervals the signal's level was set according to the adaptive-tracking procedure (see below) and it was then added to the noise. The intervals were then concatenated, with 400 ms of silence separating each of them, and saved as a single 16-bit WAV-format file. This file was then converted to analog using a RME DIGI-96/8 PAD soundcard, and presented to listeners using Sennheiser HD-580 headphones, scaled so that the masking noise had a spectrum level of 30 dB SPL. The listeners sat in an individual single-walled, IAC booth installed in a larger single-walled IAC room.

2. Procedures

For each listener, individual thresholds were obtained from independent adaptive tests. The adaptive tests were divided into blocks of five, consisting of one of each of the signal frequencies (taken consecutively but chosen in a random order) for a fixed binaural configuration. Listeners typically completed about two blocks of adaptive tests in each session. The values of detection threshold reported below are the average of the thresholds from five adaptive tests, taken from a set of seven after the highest and lowest had been removed.

An adaptive tracking procedure, with four-interval, two-alternative forced-choice trials, was used to vary the level of the signal in order to find threshold (Bernstein and Trahiotis, 1982). All four intervals contained an independent masking noise, with the signal presented in either the second or third intervals. The listener's task was to determine which of those two intervals contained the signal. They made their response using a visual ''response box'' displayed on the PC monitor, which could be seen through a window in the botth, and which also gave correct/incorrect feedback. The adaptive test began at a signal level between 55 and 60 dB SPL. The first two trials were practice and the responses to them ignored. Then the signal level was varied adaptively, using a two-down, one-up rule asymptoting at the 70.7%-correct point on the psychometric function (Levitt, 1971). For the first five reversals the step size was 5 dB and for the next 12 reversals it was 2 dB. The threshold for the individual test was defined as the mean level (in dB) across those 12 reversals. The whole experiment was coded in MATLAB.

3. Listeners

Four listeners, aged 21–31 years, participated in the experiment. The author was listener A. The other listeners were paid for their participation. All had hearing levels less than 15 dB at octave frequencies from 250 to 4000 Hz (ISO, 1998) and had participated in earlier studies at the University of Sussex. All the listeners received extensive training in the task.

B. Results

The results are shown in Fig. 2. The symbols plot the detection thresholds from each of the three binaural configurations (triangles: N_0S_{180}; circles: $N_{180}S_0$; squares: $N_{90}S_{270}$). The lines mark smooth curves fitted to each set of results (see below). The error bars represent the 95% confidence intervals. As expected from many previous experiments (e.g., Hirsh, 1948; Kohlrausch, 1988; Breebaart *et al.*, 2001), the thresholds generally increased as frequency was increased. The thresholds from the $N_{180}S_0$ conditions were generally greater than those from the N_0S_{180} conditions, with the size of the difference reducing with increasing frequency (e.g., Hirsh, 1948; Durlach and Colburn, 1978; Breebaart *et al.*, 2001). This $N_0S_{180}-N_{180}S_0$ difference has been ascribed to a ''head-width constraint'' on the availability of equalization delays, with a substantially higher density around 0 μs compared to a relative paucity at the extremes (e.g., Durlach, 1972; Colburn, 1977; Breebaart *et al.*, 2001). The detection thresholds for the $N_{90}S_{270}$ configuration generally lay between those for the N_0S_{180} and $N_{180}S_0$ values. Such a result has been observed before (e.g., Durlach and Colburn, 1978), and Colburn (1977) again ascribed it to the distribution of equalization delays.

The purpose of this experiment was to obtain the data to allow a normalization of the levels of each of the components of the complex tones that would be used in experiment

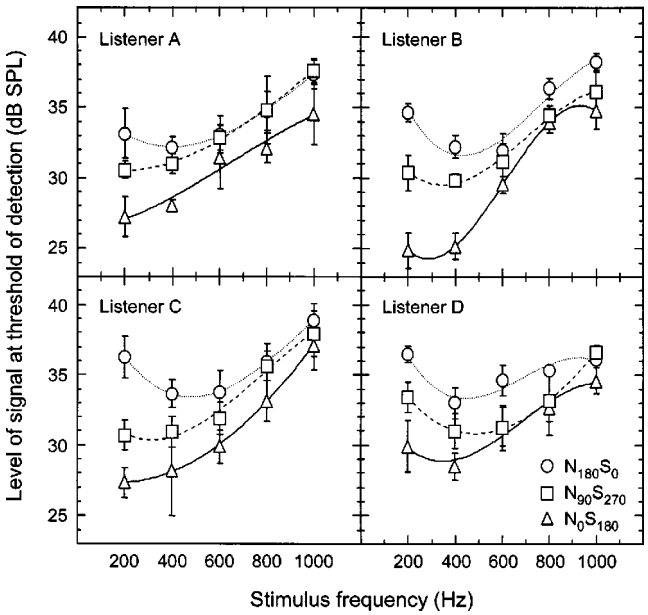

FIG. 2. Results from experiment 1. The four panels are for each listener, A, B, C, D. Within each panel, the symbols plot the thresholds from the three binaural configurations of N_0S_{180} (triangles), $N_{180}S_0$ (circles), and $N_{90}S_{270}$ (squares). The error bars plot the 95% confidence intervals. The lines plot cubic polynomials fitted to each set of results (see Table I).

2. To do so, first, a cubic polynomial was fitted to each set of data, so reducing any small-scale fluctuations resulting from experimental error; the goodness of fit (r^2) ranged between 0.91 and 1.00. These polynomials are represented by the lines in Fig. 2 (solid: N_0S_{180}; dotted: $N_{180}S_0$; dashed: $N_{90}S_{270}$) and their parameters are reported in Table I. Second, each individual pure tone was then synthesized with a level determined by the polynomial function. For example, for the 5-component N_0S_{180} condition of listener A, the components at 200, 400, 600, 800, and 1000 Hz were synthesized at 27.1, 28.6, 30.6, 32.7, and 34.4 dB SPL. The detection thresholds for the complex tones in experiment 2 were measured relative to these values; in the example, if the threshold of the 5-component N_0S_{180} complex tone had been found to be -10 dB, then the actual levels of the components in that signal, at threshold, would be 17.1, 18.6, 20.6, 22.7, and 24.4 dB SPL. A side effect of this normalization procedure is that it removed any differences across frequency or configuration. That is, were thresholds to be measured anew for the normalized pure tones, they would all be 0 dB. Such a check was included in the design of experiment 2.

III. EXPERIMENT 2: ADAPTIVE THRESHOLDS FOR 5- AND 17-COMPONENT COMPLEX TONES

In experiment 2 thresholds of detection were measured for two complex tones, one with 5 components from 200 to 1000 Hz at a fundamental frequency (F_0) of 200 Hz, and the other with 17 components from 200 to 1000 Hz at a F_0 of 50 Hz. The levels of the components were set by the normalization procedure described above. Detection thresholds were also measured for the normalized-level 600-Hz pure tones. These three signals were crossed with the three binaural configurations (N_0S_{180}, $N_{180}S_0$, $N_{90}S_{270}$) to give nine conditions in all.

If equalization was restricted, then the detection thresholds for the $N_{90}S_{270}$ and $N_{180}S_0$ complex tones (variable-ITD) would be greater than those for the N_0S_{180} complex tones (fixed-ITD). For free equalization, in which the thresholds should be determined by $10\log_{10}(\sqrt{N})$, it would be expected that the thresholds would be lowest for the 17-component complex tones, intermediate for the 5-component complex tones, and highest for the 1-component pure tones. Finally, if the normalization process was perfect, then the thresholds for the pure tones would all be 0 dB.

A. Method

The method and apparatus was the same as for experiment 1, except that (1) the starting phase of each component was chosen at random for each trial, (2) each block of tests consisted of nine adaptive tests (one of each of the nine conditions, taken consecutively in a random order), and (3) each session consisted of one block. The same four listeners participated after they had completed experiment 1.

B. Results

The results are shown in Fig. 3. The left panel is for the 1-component pure-tone stimuli, the middle panel is for the 5-component (200-Hz F_0) complex-tone stimuli, and the right panel is for the 17-component (50-Hz F_0) complex-tone stimuli. Within each panel, the left group of histogram bars (light dots) plots the thresholds from the N_0S_{180} conditions, the middle group (medium dots) from the $N_{180}S_0$ conditions, and the right group (dark dots) from the $N_{90}S_{270}$ conditions. Within each group, the histogram bars plot the detection thresholds from each listener: the plotted values are the levels, at threshold, relative to the normalized levels from experiment 1 (see Table I). The horizontal dashed line plots a relative level of 0 dB. The error bars represent the 95% confidence intervals.

TABLE I. The parameters of the polynomials fitted to the data of experiment 1 and plotted as solid lines in Fig. 2. In the equation f is in kHz and threshold is in dB. The equation is: threshold of detection $= c_3f^3 + c_2f^2 + c_1f + c_0$

	N_0S_{180}				$N_{180}S_0$				$N_{90}S_{270}$			
Parameter	A	B	C	D	A	B	C	D	A	B	C	D
c_3	−8.00	−78.79	−1.73	−37.48	−10.48	−48.89	−19.77	−52.71	−6.33	−36.03	−22.54	−12.15
c_2	15.30	143.83	16.99	76.76	33.03	111.70	59.05	108.34	19.85	76.34	52.89	45.85
c_1	0.68	−62.54	−6.03	−39.80	−21.40	−68.95	−43.05	−65.15	−7.22	−39.72	−26.47	−36.00
c_0	36.41	32.28	27.90	35.01	36.16	44.51	42.65	45.52	31.24	35.63	34.15	38.89

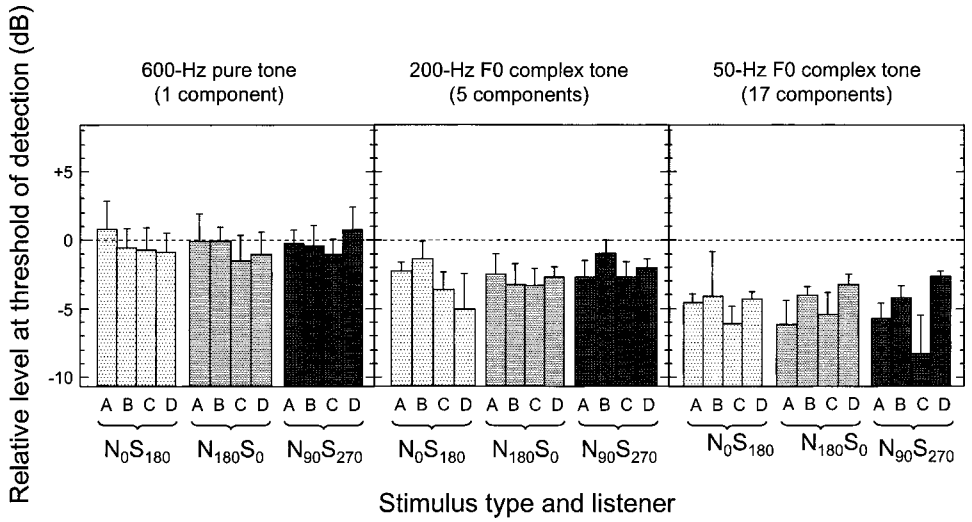

FIG. 3. Results from experiment 2. The three panels are for the three stimuli types of 1-component (600-Hz), 5-component (200-Hz F_0), or 17-component (50-Hz F_0) complex tones. Within each panel, the three groups of histogram bars are for the three configurations of N_0S_{180}, $N_{180}S_0$, and $N_{90}S_{270}$. Within each group, each histogram bar plots the threshold from each listener. The error bars plot the 95% confidence intervals. The horizontal dashed line marks a relative threshold of 0 dB. If the level-normalization procedure was perfect, each of the 1-component thresholds would be 0 dB, and all the complex-tone thresholds would be less than 0 dB. If equalization was restricted, the thresholds for the $N_{180}S_0$, and $N_{90}S_{270}$ complex tones would be greater than for the N_0S_{180} complex tone.

In general, the 1-component pure tones gave the greatest thresholds, the 5-component complex tones gave intermediate, and the 17-component complex tones gave the lowest. The mean values were, respectively, -0.4, -2.6, and -4.8 dB. A repeated-measure ANOVA, with binaural configuration (N_0S_{180} vs $N_{180}S_0$ vs $N_{90}S_{270}$), number-of-components (1 vs 5 vs 17), and threshold from each adaptive test (1–5) as within-subject factors, gave a significant F-ratio for the effect of number-of-components $[F(2,6)=27.52, p<0.001]$. The ordering of the thresholds is that predicted by $10\log_{10}(\sqrt{N})$, although not all the comparisons reached statistical significance: a Bonferroni-corrected multiple-comparison test showed that the mean threshold for the 1-component stimuli was significantly greater than the mean thresholds for both the 5- or 17-component stimuli, although the mean thresholds for the 5- and 17-component stimuli did not differ statistically.

The mean threshold for the 1-component pure tones, of -0.4 dB, was satisfyingly close to the expected value of 0 dB, so validating the method for level normalization. A second ANOVA, conducted on the 1-component data in isolation, supported this conclusion by finding no effect of binaural configuration $[F(2,6)=0.49, p>0.05]$.[5] That a further ANOVA, conducted on the earlier data of experiment 1 (see the 600-Hz data plotted in Fig. 2), *did* find such an effect $[F(2,6)=11.84, p=0.008]$ shows the success of the normalization procedure.

Crucially, the thresholds of detection for the complex tones did not depend upon binaural configuration. For the 5-component complex tones in the N_0S_{180}, $N_{180}S_0$, and $N_{90}S_{270}$ configurations, the mean thresholds were -3.0, -2.9, and -2.0 dB, respectively. For the 17-component complex-tones, the mean thresholds were -4.7, -4.6, and -5.2 dB. An additional ANOVA, limited to the data from all the complex-tone conditions, found an insignificant effect of configuration $[F(2,6)=0.07, p>0.05]$ and an insignificant interaction of configuration with number-of-components $[F(2,6)=2.29, p>0.05]$.

In summary, there was no evidence that the thresholds of detection of the complex tones in the two variable-ITD configurations of $N_{90}S_{270}$ and $N_{180}S_0$ were any greater than they were in the fixed-ITD configuration of N_0S_{180}.[6] This result is consistent with the idea that equalization was free to use the optimal delay at each frequency. The next section considers a quantitative model, in order to measure the degree to which this result is inconsistent with restricted equalization.

C. Quantitative predictions of binaural unmasking for complex tones

The presentation of the experiment so far has assumed that, when the masker is a variable-ITD noise, a free equalization will give an optimal reduction in threshold whereas any restriction on equalization will give some smaller, non-optimal reduction. This assumption results from the inability of any restricted equalization to use the *optimal* internal time delay at *each* of the frequencies, as, by definition, it can only choose the same delay for all frequencies. Nevertheless, it could still be the case that a single equalization delay, if not quite optimal, will be *near*-optimal for *all* frequencies. This section reports a set of quantitative predictions for just how near-optimal cancellation can be when it is determined by some near-optimal equalization.

The situation is illustrated in Fig. 4. The panels show a set of predictions for the 5-component (200-Hz F_0) stimuli for each of the three configurations. In the top panel (N_0S_{180}), the five dashed lines plot the expected detection threshold for each of the five component frequencies (200, 400, 600, 800, and 1000 Hz) if equalization used any delay between -3000 and $+3000$ μs. The lowest threshold for each component—that obtained at the optimal equalization delay—was assumed to be 0 dB. That all the other values are

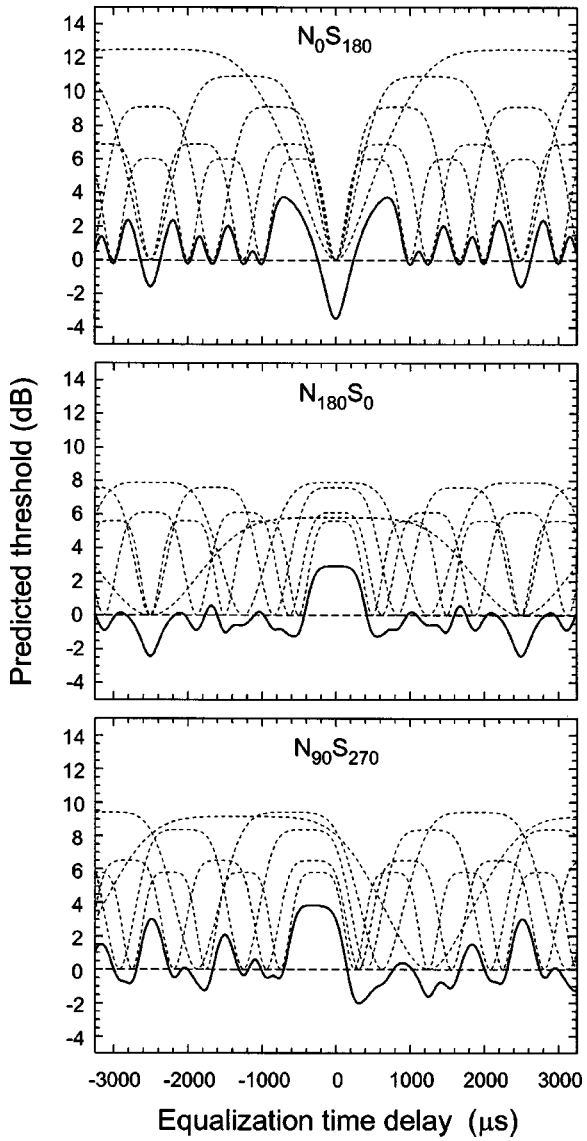

FIG. 4. An illustration of the effect of equalizing at nonoptimal delays for the 5-component complex tones used in experiment 2. The three panels are for the three configurations of N_0S_{180}, $N_{180}S_0$, and $N_{90}S_{270}$. The dashed lines show the threshold T_c (Sec. AII, step 3) for each of the five components if equalization had taken place at any delay between −3000 and +3000 μs. The "optimal" T_c was assumed to be 0 dB (step 1). The solid lines show the corresponding values of T_{Complex} (step 4). The predicted threshold for a restricted equalization operating at any delay is the value of T_{Complex} at that delay. The reason why restricted equalization predicts a greater threshold for $N_{180}S_0$ and $N_{90}S_{270}$ than N_0S_{180} is that the individual curves do not align at a single equalization delay for $N_{180}S_0$ or $N_{90}S_{270}$ but do for N_0S_{180}. The plots were computed using the model described in the Appendix and use a k of 1.0 [Eq. (A1)].

positive (apart from the optimal delay offset by 1, 2, 3,... periods) simply indicates that they are, by definition, *non*optimal. The solid line shows the expected detection threshold of the 5-component complex, if equalization used the *same* delay at all frequencies. It shows that the greatest change in threshold is for an equalization delay of 0 μs, predicting a change of −3.5 dB [$=10\log_{10}(\sqrt{N})$] compared to any of the individual components. Any other equalization delay will give a smaller change in threshold. This result occurs because the optimal delays for each frequency align at 0 μs. The middle panel shows the corresponding plots for the $N_{180}S_0$ configuration. Here, no single equalization delay is optimal for all frequencies—the optimal delays follow the phase track of the noise in each frequency channel—and so the predicted threshold of the 5-component complex is never as low as −3.5 dB. The lowest threshold that a restricted equalization could give would be −2.4 dB. The bottom panel shows the $N_{90}S_{270}$ configuration. Again, the optimal delays do not align, and the predicted threshold of a restricted equalization is −2 dB.

The result is that the distinction between free versus restricted equalization reduces to a distinction between optimal versus near-optimal equalization delays. In order to derive predictions from these two choices, an analytic model of the binaural unmasking of a complex tone was developed, allowing for any noise IPD, signal IPD, and, crucially for the present analyses, any equalization delay. The model was based on the N_0S_τ model developed by van der Heijden and Trahiotis (1999). It is described in the Appendix, and was also used to generate the plots in Fig. 4.

The predictions of the model are summarized in Table II. The values depend on the number of components in the complex tones and on whatever value for k—a parameter which describes the slope of the psychometric function [see Eq. (A1)]—is used. Nevertheless, in general the restricted-equalization model predicted that the fixed-ITD configuration (N_0S_{180}) will give a *lower* threshold than either of the variable-ITD configurations ($N_{180}S_0$ and $N_{90}S_{270}$), whereas the free-equalization model predicted that all three configurations will give the *same* threshold. The accuracy of each model was determined by measuring the rms error between the predictions and the experimental data across each of the six combinations of binaural configuration and fundamental frequency. The best-fitting model was found to be free equalization with a k of 1.3, which gave a rms error of 0.4 dB. This value of k results in a psychometric function that is slightly steeper than that for $k=1.0$—which represents detectability (d') being proportional to signal energy—and which gave slightly-larger rms errors (0.7 or 1.2 dB, depending if restricted-equalization or free-equalization is used).

It is clear that the predicted differences between free and restricted equalization are somewhat small. Their interpretation depends on the exact form of the psychometric function used for the detection of the signal. If the detectability is proportional to signal energy (e.g., van der Heijden and Trahiotis, 1999), then the results favor the restricted-equalization model. If instead the psychometric function is steeper than that (e.g., McFadden, 1968), then the results favor the free-equalization model. As will be reported below, the psychometric functions measured in experiment 3 gave a mean k of 1.4; if that value is applied here, then the results again favor the free-equalization model, giving a rms error of 0.5 dB (Table II). Overall, the results of experiment 1 are suggestive rather than conclusive, but edge towards free equalization instead of restricted equalization.

IV. EXPERIMENT 3: PSYCHOMETRIC FUNCTIONS FOR 2-COMPONENT COMPLEX TONES

For a second experimental test of free versus restricted equalization, psychometric functions were measured for the

TABLE II. The predictions of the analytic model described in the Appendix for the thresholds (in dB) of the complex-tone conditions of experiment 2. The models are either free-equalization or restricted-equalization with values of k of either 1.0 (d' proportional to signal energy), 1.3 (best overall fit), or 1.4 (experimentally observed, value from experiment 3). The rms error was computed across the six combinations of binaural configuration and fundamental frequency (F_0).

		200-Hz F_0			50-Hz F_0			rms error
k	Equalization	N_0S_{180}	$N_{180}S_0$	$N_{90}S_{270}$	N_0S_{180}	$N_{180}S_0$	$N_{90}S_{270}$	from data (dB)
⋯	Experimental data	−3.0	−2.9	−2.0	−4.7	−4.6	−5.2	⋯
1.0	Free	−3.5	−3.5	−3.5	−6.2	−6.2	−6.2	1.2
1.3	Free	−2.7	−2.7	−2.7	−4.7	−4.7	−4.7	0.4
1.4	Free	−2.5	−2.5	−2.5	−4.4	−4.4	−4.4	0.5
1.0	Restricted	−3.5	−2.4	−2.0	−6.2	−4.0	−4.8	0.7
1.3	Restricted	−2.7	−1.8	−1.4	−4.7	−2.8	−3.5	1.1
1.4	Restricted	−2.5	−1.7	−1.2	−4.4	−2.6	−3.2	1.3

detection of tonal stimuli at 400 or 800 Hz, presented either individually or together as a two-component complex. Once again the binaural configurations were N_0S_{180}, $N_{180}S_0$, and $N_{90}S_{270}$. If equalization can use the optimal delay at each component frequency, then there will be an equal gain in detectability—or a corresponding equal reduction of threshold—for all the complex tones in all three binaural configurations. The analytic model predicts a reduction of −1.5 dB ($k=1$) or −1.1 dB ($k=1.4$). If equalization is restricted, then there will be a smaller gain in the $N_{90}S_{270}$ and $N_{180}S_0$ configurations compared to the N_0S_{180} configuration. Figure 5 shows the corresponding plot to Fig. 4, generated using the analytic model for $k=1$; the changes in threshold will be, at most, 1.5 dB for the N_0S_{180} configuration, 0.1 dB for $N_{180}S_0$, and 0.3 dB for $N_{90}S_{270}$. For $k=1.4$, the predicted changes in threshold will be −1.1, −0.0, and −0.1 dB, respectively.

As in experiment 2, an attempt was made to equate the pure-tone stimuli for detectability. This was done by choosing a reference signal level for the 400- and 800-Hz conditions such that the psychometric functions, relative to the reference, were similar to each other. The reference levels used are reported in Table III. The choice of a two-component complex tone was made to reduce the number of psychometric functions that had to be measured, although it did mean that the size of the expected gain in detectability would be smaller than for the 5- or 17-component complex tones of experiment 2.

A. Method

1. Stimuli, procedures, and listeners

The stimuli were generated in the same way as in the previous experiments and presented to listeners using the same apparatus. Two-interval, two-alternative forced-choice trials were used (the change from the earlier four-interval design was made in order to speed-up the experiment). Both intervals contained an independent masking noise, with the signal presented in either. The listeners' task was to determine which interval contained the signal. They were given correct/incorrect feedback. Each block consisted of 180 trials, made up of 15 stimuli types (400 Hz, 800 Hz, and 400 +800 Hz, presented at each of five levels) repeated 12 times, presented in a random order (in contrast to experiments 1 and 2, therefore, the signal frequency could vary across successive trials). The binaural configuration was fixed within a block. Listeners typically completed four blocks in each ses-

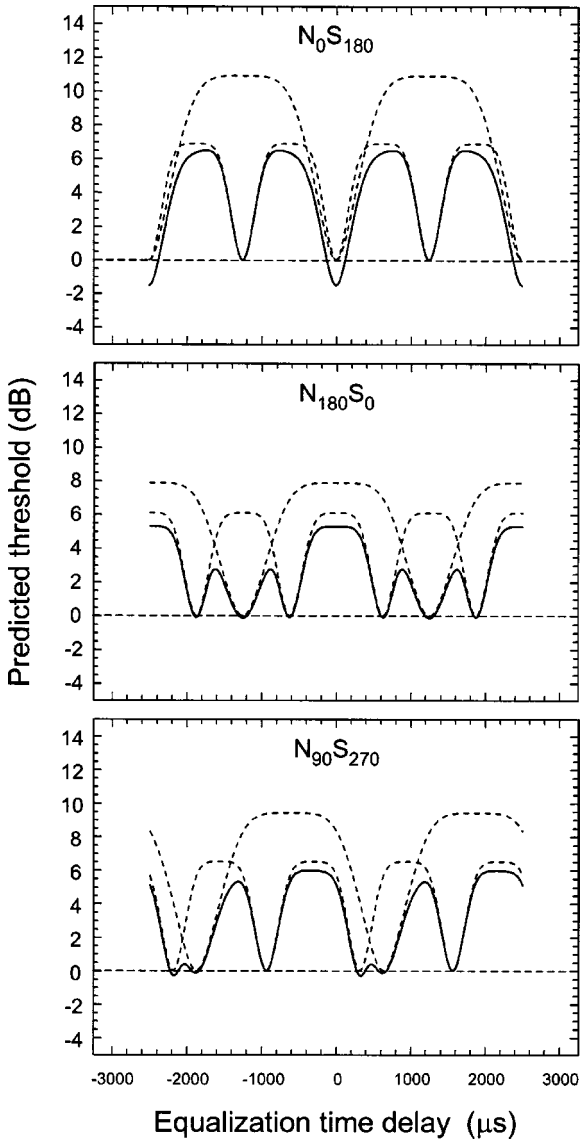

FIG. 5. As in Fig. 4 but for the two-component complex tones used in experiment 3.

TABLE III. The reference levels (in dB SPL) used to equate the detectabilty of the 400- and 800-Hz pure tones used in experiment 3. The abscissa in Fig. 6 is the level of the signal relative to these values, and corresponds to x (in decibels) from Eq. (1).

Frequency (Hz)	N_0S_{180}			$N_{180}S_0$			$N_{90}S_{270}$		
	B	C	D	B	C	D	B	C	D
400	26.2	27.1	29.0	31.7	33.1	34.4	28.7	30.6	32.0
800	34.0	33.6	35.1	35.8	36.9	36.8	36.2	36.0	36.7

sion. The four blocks in a session were one each of N_0S_{180}, $N_{180}S_0$, and $N_{90}S_{270}$, plus a second block of one of those. The choice of blocks and presentation order per session was counterbalanced across all sessions.

Three of the listeners participated. Listener B completed 22 blocks of trials for each configuration, giving 264 trials per point on the psychometric functions. Listeners C and D completed 24 blocks, giving 288 trials per point. The listeners received between 6 and 13 h of practice. The practice sessions also served to find a set of reference signal levels which gave psychometric functions that were similar and not limited by floor or ceiling effects. The experiment was conducted after experiment 2 was completed.

2. Fitting of psychometric functions

The data was fitted with a modified form of Egan's psychometric function [e.g., Egan, 1965; McFadden, 1966; Egan *et al.*, 1966; cf. Eq. (A1) in the Appendix]:

$$d'_{400}=m_{400}x^k, \quad d'_{800}=m_{800}x^k, \quad d'_{400+800}=m_{400+800}x^k, \tag{1}$$

where x is proportional to the energy of the signal, m and k are free parameters, and the subscripts refer to the frequency of the signal. It was assumed that k had the same value for both pure tones and the complex tone, but its value was allowed to vary across listener and binaural configuration. The value of m was allowed to vary across frequency as well as listener and binaural configuration. The best-fitting values of m and k were found separately for each combination of listener, frequency, and binaural configuration, using the ''Solver'' function of Microsoft Excel. Each fit was compared to the data by measuring the root-mean-squared difference in percent correct, not d' (Egan *et al.*, 1966); this method reduces errors resulting from d's near zero (50% correct) or infinity (100% correct). To simplify the conversion of percent correct to d' and vice versa, it was assumed that there was no bias in responding across the two intervals of the trials.

The signal level at threshold—corresponding to a d' of 1.0—was given by a simple rearrangement of Eq. (1), being equal to

$$\text{threshold (dB)} = -10\log_{10}(m) - 10\log_{10}(k), \tag{2}$$

for each of the three configurations. The change in threshold for the complex tones was given by the difference between the complex-tone threshold and the mean of the 400- and 800-Hz thresholds.

B. Results

The results for the three listeners are shown in Fig. 6. The symbols mark the experimental data, as percent correct as a function of x [cf. Eq. (1)] in decibels, from each of the three frequencies (asterisks: 400 Hz; circles: 800 Hz; solid diamonds: 400+800 Hz). The lines mark the best-fitting psychometric functions (dash: 400 Hz; dotted: 800 Hz; solid: 400+800 Hz). Each row of panels shows the results from one listener; each column shows the results from one binaural configuration.

The fitted psychometric functions accurately characterized the data: the root-mean-squared errors lay between 1.2% and 4.2%, with a mean of 2.8%. The form of the psychometric function did not depend upon the binaural configuration, as the values of k that were found by the fitting process did not differ statistically across configuration. The mean values were 1.3 (N_0S_{180}), 1.5 ($N_{180}S_0$), and 1.4 ($N_{90}S_{270}$), and a single-factor repeated-measures ANOVA failed to find a significant effect of configuration on k [$F(2,4)=2.46, p>0.05$].

In all the conditions, the complex tone yielded higher detectabilities than either of the two pure tones. An ANOVA showed a significant main effect of stimulus type (400 vs 800 vs 400+800) on the thresholds [$F(2,4)=35$; $p=0.003$], for which a Bonferroni-corrected multiple-comparisons test showed that the thresholds for 400- and 800-Hz pure-tones did not differ from each other but that the thresholds for the 400+800-Hz complex tone differed from both. There was no statistical effect of configuration [$F(2,4)=2.83, p>0.05$] or interaction of configuration with stimulus type [$F(4,8)=0.29, p>0.05$].

The mean changes in threshold [see Eq. (2)] were −1.8 dB (N_0S_{180}), −2.1 dB ($N_{180}S_0$), and −1.7 dB ($N_{90}S_{270}$). An ANOVA showed a nonsignificant trend of binaural configuration [$F(2,4)=6.23$, $p=0.06$].

Overall, there was no evidence that the threshold changes in the $N_{90}S_{270}$ and $N_{180}S_0$ conditions were any less than the threshold change in the N_0S_{180} condition. The results were, therefore, in favor of a free-equalization model.

C. Discussion

Although the data again supports the predictions of the free-equalization model, there are two concerns with the results that prevent it from being conclusive. First, the mean changes in threshold were −1.8, −2.1, and −1.7 dB, for, respectively, N_0S_{180}, $N_{180}S_0$, and $N_{90}S_{270}$. For the experimentally observed k of 1.4, the analytic model developed earlier predicts −1.1, −1.1, and −1.1 dB [$=10\log_{10}(\sqrt{N})/k$] for the free-equalization model, and −1.1, −0.1, and −0.0 dB for the restricted-equalization model. The free-equalization model gave the better fit, yet the predicted improvements in threshold were exceeded by almost 1 dB. The fits can be improved if a smaller k is used—the best free-equalization fit is with a k of just 0.8, giving −1.9 dB for all three configurations—yet that is an unsatisfactory solution, as such a low value of k would give a particularly poor fit to the data from experiment 2.

Second, the thresholds of the pure tones in this experi-

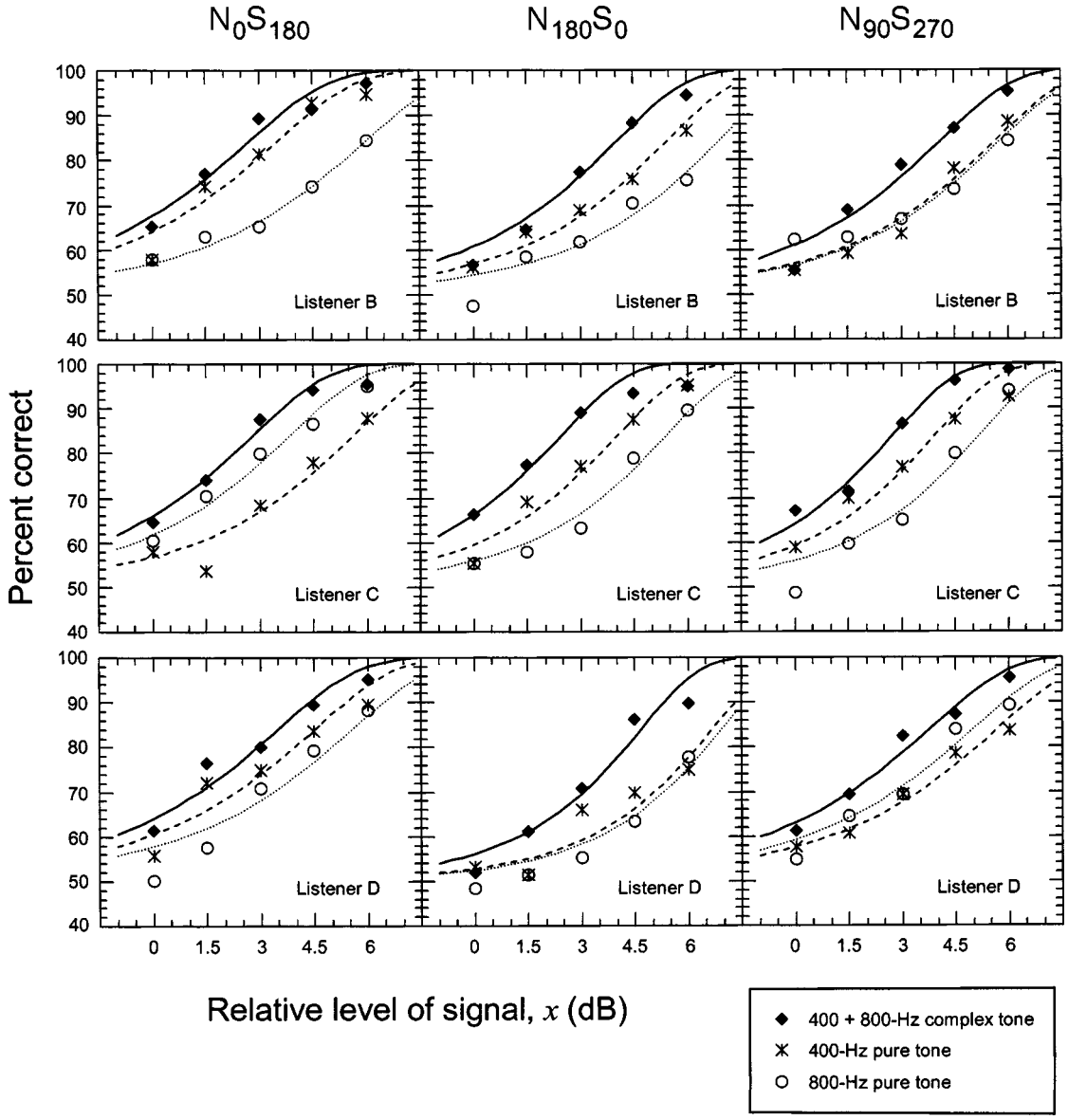

FIG. 6. Results from experiment 3. Each row of panels is for a separate listener and each column of panels is for a separate configuration. Within each panel, the symbols plot the thresholds from the 400-Hz pure tones (asterisks), 800-Hz pure tones (circles), and 400+800-Hz complex tones (solid diamonds). The smooth curves mark the fitted psychometric functions [see Eq. (1)]. The abscissa is *x*, in decibels, from Eq. (1), which corresponds to the level of the signal relative to the SPL values reported in Table III.

ment were higher than expected. The actual level of the signal at threshold, in dB SPL, can be found by adding the threshold value from Fig. 6 to the SPL values in Table III. It was found that the present thresholds were, on average, 4.9 dB higher than the corresponding thresholds measured earlier in experiment 2 (Fig. 2). The two experiments differ in method—experiment 2 measured adaptively tracked thresholds while experiment 3 measured psychometric functions—yet thresholds measured using adaptive methods have been shown to be within ± 1 dB of corresponding thresholds measured using psychometric functions (e.g., Hicks and Buus, 2000).

Approximately 1 dB of the across-experiment differences can be assigned to the differences between the definition of threshold in the two experiments: 70.7% for experiment 2 versus 76% ($d' = 1$) for experiment 3. A portion of the difference can also be ascribed to differences in experimental method, such as that in each trial of the adaptive tests of experiment 2 the target frequency was the same, yet across each trial of the blocks of experiment 3 the target frequency was randomly chosen from 400, 800, or 400+800 Hz. That is, in experiment 2, listeners could have come to expect the same frequency on every trial, but in experiment 3 they must be uncertain which frequency could occur on any trial. Such frequency uncertainty has been shown to raise detection thresholds (e.g., Creelman, 1960; Buus *et al.*, 1986). The effect size is quite small, however; for instance, Buus *et al.* (1986) observed an average of 2.3 dB for monaural detection of pure tones at 220, 1100, and 3850 Hz. Summed, these two effects could account for maybe 3 dB of the across-experiment difference observed here. The remainder of the difference remains unaccounted for.

The frequency-uncertainty hypothesis is of further interest as it can predict a larger reduction in threshold for a

complex tone over its components than otherwise, and so may offer an account of the threshold changes in this experiment being larger than expected for a k of 1.4. For instance, consider the situation where the 400- and 800-Hz pure tones are each detected through their own, independent, auditory filters whereas the 400+800-Hz complex tone is detected through a combination of both filters. As there will be twice as much masking noise for the complex-tone signal as for the pure-tone signals, the threshold of the complex tone (for $k=1.4$) will be 1.1 dB lower than the thresholds of either pure tone. Next, compare this to the situation where *all* three signals are detected by listening through a combination of the 400- and 800-Hz filters, as though the listener is uncertain which frequency could occur on any experimental trial and therefore monitors both together. Now, the amount of masking noise will be the same for the three signals, but as the complex-tone signal has two components to the one component of either pure-tone signal, its threshold will be (for $k=1.4$) 2.2 dB lower than the thresholds of each pure tone. Thus, the same value of k can give a predicted change in threshold of -1.1 dB (independent filters) or -2.2 dB (combined filters). As the analytic model assumes all the components are independent of each other, it is possible that the larger-than-expected changes in threshold observed in this experiment—as mentioned above, -1.8 dB (N_0S_{180}), -2.1 dB ($N_{180}S_0$), and -1.7 dB ($N_{90}S_{270}$)—are also an effect of frequency uncertainty.

V. GENERAL DISCUSSION

The present experiments were conducted in order to study whether the equalization stage of Durlach's (1972) ''equalization-cancellation'' model of binaural unmasking is ''free'' (in that it can use the *optimum* internal time delay at all frequencies) or is ''restricted'' (in that it is limited to the *same* delay across all frequencies). This question is of relevance to the understanding of the dichotic pitches, as Culling *et al.* have shown that a free-equalization model can predict pitch-matches to the majority of the types of dichotic pitches (Culling *et al.*, 1998a, b; Culling, 1999, 2000). If equalization was free, then the binaural detection threshold for a complex-tone signal in a broadband-noise masker would be equal in the N_0S_{180}, $N_{90}S_{270}$, and $N_{180}S_0$ configurations, but if equalization was restricted, then the binaural detection threshold would be greater in the $N_{90}S_{270}$ and $N_{180}S_0$ configurations than in the N_0S_{180} configuration. The experiments failed to find reliable differences in binaural detection thresholds across these three configurations, and therefore were consistent with free equalization.

An analytic model of the binaural detection threshold of a complex tone was also developed. It gave predictions of the threshold differences between free-equalization and restricted-equalization that were not only small but also depended upon the shape of the psychometric function that was assumed for binaural signal detection. Indeed, the *largest* predicted difference between free-equalization and restricted-equalization was only 2 dB (Table II). Accurate psychophysical procedures are needed to measure such small effects. While the issue of free versus restricted equalization is a theoretical question of some interest, its implications for actual human performance—especially in the domain of signal detection—might therefore be limited.

For example, consider the case where a listener is attempting to detect a signal located directly ahead and masked by a noise offset by 45° horizontally. The signal will be detected most readily if the masker is equalized and then cancelled. The ITD of the masker varies with frequency, being almost 600 μs at 300 Hz yet about 400 μs at 1500 Hz (Kuhn, 1977). An equalization restricted to just one delay could not follow this variation in natural ITD, but a free equalization would be able to follow it accurately and so maximize the detectability of the signal (a hybrid scheme could also be considered, in which equalization was restricted to following natural variations in ITD instead of restricted to following *fixed* ITDs, although, for naturally occuring sounds, that will give the same results as a free-equalization model). Nonetheless, the analytic model predicts that the resulting difference in detectability will be small. Consider a specific instance of this example, where the signal is a 100-Hz F_0 complex tone, from 200 to 1000 Hz inclusive and with equal-level components, and where the masker is a white noise. The signal ITD is fixed at 0-ms ITD, corresponding to 0°, while the masker ITD is varied in accordance with Kuhn's (1977, Fig. 1.3) 45° data (Fig. 7, top panel). The monaural threshold T_{M*} [Eq. (A10)] of each component will depend on frequency, as wider auditory filters at higher frequencies will pass more of the noise; to keep the present example simple, it is assumed that the effect can be characterized by allowing the monaural threshold to depend on $10\log_{10}(\mathrm{ERB})$, where ERB is the equivalent-rectangular bandwidth defined by Glasberg and Moore (1990). These values are shown as the squares in the bottom panel of Fig. 7. The internal noise R [Eqs. (A5) and (A14)] will also depend on frequency; the values were found using Eq. (A15) for the N_0S_{180} masking-level-difference. The expected binaural threshold T_{C*} for each component was then found using Eq. (A9), for each equalization delay between -1000 and $+1000$ μs, with the lowest values across the delay lines chosen. These values are shown by the asterisks in Fig. 7. The predicted thresholds for free or restricted equalization were then calculated by combining, respectively, across the optimal delay in each channel or across each delay over channel [cf. Eq. (A18)]. That for free equalization is shown in Fig. 7 as a solid line, and that for restricted equalization is shown by the dotted line. Either choice of equalization offers a reasonable gain in detecting the complex tone compared to the best individual component, but the difference between the two is only 0.4 dB. That is, for the task of detecting a flat-spectrum complex tone presented at 0° against a white-noise masker presented at 45°, restricted equalization will predict a threshold just 0.4 dB greater than free equalization. The difference is almost negligable.

One reason for the small magnitude of the effect is that the additional components will only make a sizeable change to the detectability of the complex if they themselves offer useful amounts of detectability. For instance, if two components each give a d' of 1.0, the combined d' will be 1.41,

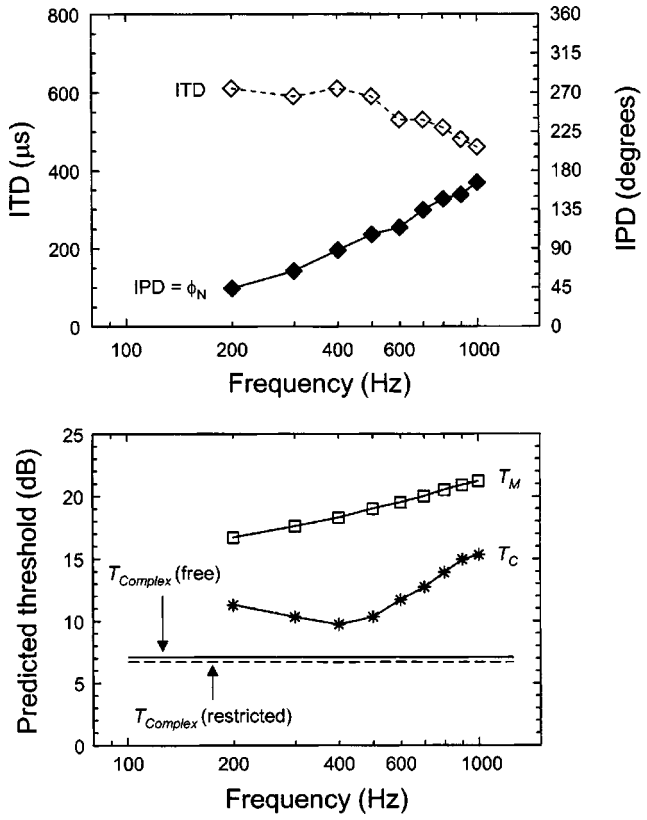

FIG. 7. Companion figures to the illustrative example in Sec. V, considering the detectability of a flat-spectrum complex tone in a white noise. Top panel: the ITD (left axis) and IPD (right axis) of the noise. The ITD was chosen to follow the 45°-data from Kuhn (1977, Fig. 1.3). Bottom panel: the monaural thresholds T_{M*} (squares) of each component of the complex tone, the binaural thresholds T_{C*} (asterisks) of each component of the complex tone, and the expected detection threshold $T_{Complex}$ of the complex given free equalization (dashed line) or restricted equalization (solid line). Note that the latter two differ by only 0.4 dB.

corresponding to a change in threshold of 1.5 dB (if $k = 1.0$). But if the second component is 5 dB less intense than the first, then it will offer a d' of only 0.1. The combined d' will be 1.05, corresponding to a change of threshold, relative to the first component, of just 0.2 dB. Similarly, a 10-dB difference will give a change of 0.02 dB. This situation, of a small number (or even just one) of components being considerably more detectable than others, would be expected to occur in most ecologically valid listening environments, as it would be surprising that sounds whose components were equally detectable *binaurally* were that common.[7] The question of free versus restricted equalization will make little difference to the binaural detectability of most sounds. It may affect domains outside signal detection, such as signal identification or pitch perception; one laboratory example is the case of the ''Fourcin'' dichotic pitch (Fourcin, 1970), which is generated by the addition of two independent broadband noises of differing ITDs, and for which Culling *et al.* (1998b) showed that accurate predictions of the perceived pitch required free equalization. Nevertheless, in light of the small differences predicted by the analytic model, it is likely that future experimental studies of free versus restricted equalization will be worth pursing only if the question becomes a key conceptual issue from a theoretical or a physiological viewpoint.

ACKNOWLEDGMENTS

This research was supported by an MRC Career Development Award. I wish to thank Chris Darwin and Stuart Gatehouse for many useful discussions and their comments on earlier drafts; Louise White for statistical advice; and the two reviewers and the two Associate Editors (Les Bernstein and Armin Kohlrausch) for their valuable criticisms. Some of the experimental results were presented at the 2002 HEARNET conference in Delmenhorst, the 2002 Binaural Bash, and the 2002 British Society of Audiology Short Papers Meeting on Experimental Studies of Hearing and Deafness [M. A. Akeroyd, Int. J. Audiol. **42**, 380–381 (2003)].

APPENDIX: A SIMPLE ANALYTIC MODEL OF THE BINAURAL DETECTION THRESHOLD OF A COMPLEX TONE

This appendix describes a method for predicting the binaural detection threshold of a complex tone using free or restricted equalization. It is based on the cancellation-by-subtraction model of N_0S_t detection described by van der Heijden and Trahiotis (1999, Appendix, Part 2). The present model extends that in allowing the noise to have any IPD and also in allowing cancellation to occur at any equalization delay. It assumes (1) that the masking noise can be represented by a sinusoidal function of the same frequency as each pure tone signal, (2) that there are no interaural intensity differences, and (3) that the internal noise which limits ultimate performance is introduced by the cancellation process.

The psychometric function for binaural signal detection is assumed to be of the form

$$d' = m\left(\frac{E}{N_0}\right)^k, \tag{A1}$$

where d' is the detectability of the signal, E is the signal energy, N_0 is the noise spectrum level, and m and k are free parameters [e.g., Egan, 1965; McFadden, 1966; Egan *et al.* 1966; cf. Eq. (1) in the main text]. In Secs. 1 and 2 below it is assumed that the detectability of the signal is proportional to its energy; that is, k equals 1.0. Section 3 below outlines the effects of choosing a different k.

1. Cancellation-by-subtraction model for a pure-tone signal

The first stage is to obtain an expression for the signal-to-noise ratio after cancellation-by-subtraction. The starting point is to follow van der Heijden and Trahiotis [1999, Eqs. (A7a) and (A7b)] in representing the target signals at the left and right ear as

$$x_L(t) = A_S \cos(2\pi ft + \phi_S/2), \tag{A2a}$$

$$x_R(t) = A_S \cos(2\pi ft - \phi_S/2), \tag{A2b}$$

where t is time, f is the signal frequency, A_S is the signal amplitude, and ϕ_S is the signal IPD. The masking noise is assumed to be represented in a similar manner:

$$n_L(t) = A_N \cos(2\pi ft + \phi_N/2), \tag{A3a}$$

$$n_R(t) = A_N \cos(2\pi ft - \phi_N/2), \tag{A3b}$$

where t is time, f is the noise frequency (as noted, the same as the signal frequency), A_N is the noise amplitude, and ϕ_N is the noise IPD. The monaural signal-to-noise ratio at either ear is given by the ratio of the signal power to the noise power and so, assuming the averaging period is considerably longer than 1 period, is equal to

$$\mathrm{SNR}(m) = \frac{A_S^2/2}{A_N^2/2}. \tag{A4}$$

The cancellation process is assumed to subtract the signal +noise at the right ear from the signal+noise at the left ear (for the moment, equalization will be excluded). The cancellation is assumed to be imperfect, however, and an internal noise is introduced whose power is R times that of the external noise (see van der Heijden and Trahiotis, 1999):

$$n_I(t) = \sqrt{R} A_N \cos(2\pi ft). \tag{A5}$$

The output of the cancellation process is therefore given by

$$d(t) = -2\sin(\phi_S/2)A_S \sin(2\pi ft) - 2\sin(\phi_N/2)A_N \sin(2\pi ft) + \sqrt{R}A_N \cos(2\pi ft). \tag{A6}$$

and so the binaural SNR at the output of the cancellation process will be (again assuming that the averaging period is considerably longer than 1 period)

$$\mathrm{SNR}(b) = \frac{4\sin^2(\phi_S/2)}{(R + 4\sin^2(\phi_N/2))} \frac{A_S^2/2}{A_N^2/2}. \tag{A7}$$

The second stage is to incorporate equalization. The application of an equalization delay of ϕ_E will delay one waveform by ϕ_E relative to the other one, with the result that the $\phi_S/2$ and $\phi_N/2$ terms in Eqs. (A6) and (A7) become $(\phi_S - \phi_E)/2$ and $(\phi_N - \phi_E)/2$. The binaural SNR will then be

$$\mathrm{SNR}(b) = \frac{4\sin^2((\phi_S - \phi_E)/2)}{(R + 4\sin^2((\phi_N - \phi_E)/2))} \frac{A_S^2/2}{A_N^2/2}, \tag{A8}$$

which gives a *gain* in SNR, G, from equalization-and-cancelation of [compare to van der Heijden and Trahiotis, 1999, Eq. (A9)]:

$$G = \frac{\mathrm{SNR}(b)}{\mathrm{SNR}(m)} = \frac{4\sin^2((\phi_S - \phi_E)/2)}{(R + 4\sin^2((\phi_N - \phi_E)/2))}. \tag{A9}$$

The third stage is to obtain predictions of the detection thresholds. If the experimentally observed monaural threshold is T_{M*} (the asterisk marks ''observed''), then the threshold from the binaural information alone T_B will be lower by G [see van der Heijden and Trahiotis, 1999, Eq. (A10)].

$$T_B = \frac{T_{M*}}{G}. \tag{A10}$$

The threshold T_B is only a ''hypothetical'' threshold, however, as it can never be observed; instead, it is assumed that the *experimental* threshold T_{C*} for the pure tone will (1) be based on cancellation at the optimal equalization delay and (2) be an optimal combination of the binaural information and the monaural information [see van der Heijden and Trahiotis, 1999, Eq. (A10)]. The first assumption requires that $\phi_E = \phi_n$ and therefore an optimally large gain in SNR of

$$G_{\mathrm{optimal}} = \frac{4\sin^2((\phi_S - \phi_E)/2)}{R}. \tag{A11}$$

Provided that the detectability d' of the signal is proportional to its energy, the second assumption leads to

$$T_{C*} = \frac{T_{M*}}{\sqrt{1 + G_{\mathrm{optimal}}^2}}. \tag{A12}$$

The experimentally observed masking level difference (in decibels) for the pure tone, $re\ T_{M*}$, will therefore be

$$10\log(T_{M*}) - 10\log(T_{C*}) = -5\log_{10}(1 + G_{\mathrm{optimal}}^2), \tag{A13}$$

$$\therefore \quad 10\log(T_{M*}) - 10\log(T_{C*}) = -5\log_{10}(1 + 16/R^2), \tag{A14}$$

because, in the present experiments, the signal and noise IPDs always differed by π radians, and so $G_{\mathrm{optimal}} = 4R$.

2. Obtaining the predicted thresholds for the complex-tone signals

The predictions of the thresholds differences for the complex tones were made thus:

(1) As the present interest was in the *change* in threshold between a pure tone and a complex tone, and in experiment 2 all the pure tones were set to be equally detectable, the values of T_{C*} for all the individual pure tones was set to 0 dB.

(2) The values of T_{M*} at each pure-tone frequency was found from these three equations and then R was found from Eq. (A14):

$$T_{M*}(\mathrm{N_0S_{180}}) = 0.000\,000\,026f^3 - 0.000\,046f^2 + 0.0148f + 11.2, \tag{A15}$$

$$T_{M*}(\mathrm{N_{180}S_0}) = T_{M*}(\mathrm{N_0S_{180}}) - (7.92(\log_{10} f)^2 - 51.11(\log_{10} f) + 82.41), \tag{A16}$$

$$T_{M*}(\mathrm{N_{90}S_{270}}) = T_{M*}(\mathrm{N_0S_{180}}) - 0.5(7.92(\log_{10} f)^2 - 51.11(\log_{10} f) + 82.41), \tag{A17}$$

where f is the frequency, in Hz. The $\mathrm{N_0S_{180}}$ function in Eq. (A15) was a polynomial fit to Durlach and Colburn's (1978, Fig. 50) summary of a wide set of $\mathrm{N_0S_{180}}$ data. The $\mathrm{N_{180}S_0}$ function in Eq. (A19) was based on Eq. (A16) offset by a polynomial function fitted to Colburn's (1977, PACS supplement, Fig. 6A) prediction of the differences between $\mathrm{N_0S_{180}}$ and $\mathrm{N_{180}S_0}$. The $\mathrm{N_{90}S_{270}}$ function in Eq. (A17) was assumed to be midway between the $\mathrm{N_0S_{180}}$ and $\mathrm{N_{180}S_0}$ values.

(3) For each value of equalization delay between -5000 and $+5000$ μs (in 1-μs steps), a value for the gain in binaural SNR G was found for each pure tone contributing to the complex tone, using Eq. (A9). These values were con-

verted to thresholds T_C using Eqs. (A10) and (A12) (with G_{optimal} replaced by the G at each delay). Note that the resulting values of T_C are also ''hypothetical'' thresholds, in that they represent the detection threshold at each frequency *if* cancellation had actually used that value of equalization delay. The dashed lines in each panel of Figs. 4 and 5 show T_C for each of the components used in the experiments.

(4) For the restricted-equalization model, the values of T_C were combined across each of the N frequencies of the complex tone at each of the set of equalization delays τ using the optimal-combination method of van der Heijden and Trahiotis (1998), again assuming that the detectability d' of the signal is proportional to its energy:

$$\frac{1}{T_{\text{complex}}(\tau)^2} = \sum_{n=1}^{N} \frac{1}{T_C(\tau,n)^2}. \tag{A18}$$

The solid lines in each panel of Figs. 4 and 5 show the values of T_{complex} for the stimuli used in experiments 2 and 3. The predicted *observed* threshold for the complex tone, $T_{\text{complex}*}$, is given by the *lowest* value of T_{complex} across the set of equalization delays.

(5) For the free-equalization model, cancellation occurs at the optimal equalization delay, and so the lowest values of T_C in each frequency-channel were optimally combined. The lowest value of T_C is, by definition, the experimental threshold for a pure tone, and as that was assumed to be 0 dB (see step 1), the predicted *observed* threshold for the complex tone using free equalization is

$$\frac{1}{T^2_{\text{Complex}*}} = N, \tag{A19}$$

which, in decibels, gives

$$10\log_{10}(T_{\text{Complex}*}) = 10\log_{10}\sqrt{N}. \tag{A20}$$

3. If *k* is not 1.0

The above analyses assume that the binaural detectability d' of a signal is proportional to its energy E. Egan and others (e.g., Egan, 1965; McFadden, 1966; Egan *et al.*, 1966) showed that the psychometric function for a signal in a noise of spectrum level N_0 could be described by Eq. (A1). They found that the value of m varied across interaural configuration but the value of k changed little, and was generally between 1 and 2. The value of k is important because the predictions of thresholds are based on an optimal combination of information from binaural or monaural sources (or from one or more component frequencies), and therefore incorporate the relationship between signal energy and detectability. With a nonunity k, the optimal combination of monaural and binaural thresholds is [see van der Heijden and Trahiotis, 1998, Eq. (A4)]:

$$\frac{1}{T_C^{2k}} = \frac{1}{T_B^{2k}} + \frac{1}{T_M^{2k}}. \tag{A21}$$

The result is that Eq. (A12) becomes

$$T_{C*} = \frac{T_{M*}}{(1+G^2_{\text{optimal}})^{1/(2k)}} \tag{A22}$$

and Eqs. (A18) and (A20) become, respectively,

$$\frac{1}{T_{\text{Complex}}(\tau)^{2k}} = \sum_{n=1}^{N} \frac{1}{T_C(\tau,n)^{2k}}, \tag{A23}$$

$$10\log_{10}(T_{\text{Complex}*}) = \frac{10}{k}\log_{10}\sqrt{N}. \tag{A24}$$

[1]The question of free or restricted equalization only applies to multi-channel EC models and does not arise in single-channel models, such as Durlach's (1972) or Green's (1966).

[2]A similar scheme of parallel cancellation across delay was described earlier by Schneider and Zurek (1989)

[3]''N'' stands for noise, ''S'' for signal, and the numbers refer to the IPD of each, in degrees, not the commonly used radians. Note that, for each component in all the stimuli, the phase difference between the signal and the noise is 180°, so maximizing the masking-level difference for each individually.

[4]This rationale assumes that the functions linking signal detectability to signal level are all of the same shape, no matter what the signal frequency or if the signal is a pure tone or a complex tone.

[5]This ANOVA also found a significant main-effect of adaptive test [$F(4,12)=4.18$, $p=0.02$], suggesting some long-term learning. The size of the effect was 1.6 dB. That further ANOVAS showed that learning was not observed for the either of the 5- or 17-component complex tones of experiment 2 [respectively, $F(4,12)=0.31$, $p>0.05$; $F(4,12)=1.49$, $p>0.05$], or for the corresponding 600-Hz pure-tones of experiment 1 [$F(4,12)=0.59$,$p>0.05$], indicates that the effect may be neglected.

[6]As part of their study of the ''binaural'' critical bandwidth, Langhans and Kohlrausch (1992) measured detection thresholds for complex tones with as many as 41 components at a 10-Hz frequency spacing. They did not observe any differential effect across binaural configurations of N_0S_{180} and $N_{180}S_0$. Although they did not consider directly the question of free versus restricted equalization, their lack of an effect of configuration is consistent with a free EC process.

[7]To illustrate this argument, synthetic stimuli were created for each of the vowels reported by Hillenbrand *et al.* (1995, Table V) using a MATLAB implementation of Klatt's cascade synthesizer (Klatt, 1980), and then the magnitudes were measured of the most-intense components nearest the first-formant and second-formant frequencies. Even the individual components that were *closest* in intensity were 6 dB apart (/ɔ/). The most-disparate components were 16 dB apart (/i/ and /u/).

Akeroyd, M. A., Moore, B. C. J., and Moore, G. A. (**2001**). ''Melody recognition using three types on dichotic-pitch stimulus,'' J. Acoust. Soc. Am. **110**, 1498–1504.

Bernstein, L. R., and Trahiotis, C. (**1982**). ''Detection of interaural delay in high-frequency noise,'' J. Acoust. Soc. Am. **71**, 147–152.

Bilsen, F. A., and Goldstein, J. L. (**1974**). ''Pitch of dichotically delayed noise and its possible spectral basis,'' J. Acoust. Soc. Am. **55**, 292–296.

Blauert, J. (**1997**). *Spatial Hearing: The Psychophysics of Human Sound Localization* (MIT, Cambridge).

Breebaart, J., van de Par, S., and Kohlrausch, A. (**2001**). ''Binaural processing model based on contralateral inhibition. II. Dependence on spectral parameters,'' J. Acoust. Soc. Am. **110**, 1089–1104.

Buus, S., Schorer, E., Florentine, M., and Zwicker, E. (**1986**). ''Decision rules in detection of simple and complex tones,'' J. Acoust. Soc. Am. **80**, 1646–1657.

Colburn, S. H. (**1977**). ''Theory of binaural interaction based on auditory-nerve data. II. Detection of tones in noise,'' J. Acoust. Soc. Am. **61**, 525–533.

Cramer, E. M., and Huggins, W. H. (**1958**). ''Creation of pitch through binaural interaction,'' J. Acoust. Soc. Am. **30**, 413–417.

Creelman, C. D. (**1960**). ''Detection of signals of uncertain frequency,'' J. Acoust. Soc. Am. **32**, 805–810.

Culling, J. F. (**1999**). ''The existence region of Huggins' pitch,'' Hear. Res. **127**, 143–148.

Culling, J. F. (**2000**). ''Dichotic pitches as illusions of binaural unmasking III: the existence regions of the Fourcin pitch,'' J. Acoust. Soc. Am. **107**, 2201–2208.
Culling, J. F., and Summerfield, Q. (**1995**). ''Perceptual separation of concurrent speech sounds: Absence of across-frequency grouping by common interaural delay,'' J. Acoust. Soc. Am. **98**, 785–797.
Culling, J. F., Summerfield, A. Q., and Marshall, D. H. (**1998a**). ''Dichotic pitches as illusions of binaural unmasking. I. Huggins pitch and the binaural edge pitch,'' J. Acoust. Soc. Am. **103**, 3509–3526.
Culling, J. F., Marshall, D. H., and Summerfield, A. Q. (**1998b**). ''Dichotic pitches as illusions of binaural unmasking. I. The Fourcin pitch and the dichotic repetition pitch,'' J. Acoust. Soc. Am. **103**, 3527–3539.
Durlach, N. I. (**1972**). ''Binaural signal detection: equalization and cancellation theory,'' in *Foundations of Modern Auditory Theory, Vol. II*, edited by J. V. Tobias (Academic, New York).
Durlach, N. I., and Colburn, H. S. (**1978**). ''Binaural phenomena,'' in *Handbook of Perception, Vol. IV*, edited by E. C. Carterette and M. P. Freidman (Academic, New York).
Egan, J. P. (**1965**). ''Masking level differences as a function of interaural disparities in intensity of signal and noise,'' J. Acoust. Soc. Am. **38**, 1043–1049.
Egan, J. P., Lindner, W. A., and McFadden, D. (**1966**). ''Masking level differences and the form of the psychometric function,'' Percept. Psychophys. **6**, 209–215.
Fourcin, A. J. (**1970**). ''Central pitch and auditory lateralization,'' in *Frequency Analysis and Periodicity Detection in Hearing*, edited by R. Plomp and G. F. Smoorenburg (Sijthoff, Leiden).
Frijns, J. H. M., Raatgever, J., and Bilsen, F. A. (**1986**). ''A central spectrum theory of binaural processing. The binaural edge pitch revisited,'' J. Acoust. Soc. Am. **80**, 442–451.
Glasberg, B. R., and Moore, B. C. J. (**1990**). ''Derivation of auditory filter shapes from notched-noise data,'' Hear. Res. **47**, 103–138.
Green, D. M. (**1966**). ''Signal-detection analysis of the equalization and cancellation model,'' J. Acoust. Soc. Am. **40**, 833–838.
Green, D. M., and Swets, J. A. (**1966**). *Signal Detection Theory and Psychophysics* (Krieger, New York).
Hartmann, W. M., and McMillon, C. D. (**2001**). ''Binaural coherence edge pitch,'' J. Acoust. Soc. Am. **109**, 294–305.
Hicks, M. L., and Buus, S. (**2000**). ''Efficient across-frequency integration: Evidence from psychometric functions,'' J. Acoust. Soc. Am. **107**, 3333–3342.
Hillenbrand, J., Getty, L. A., Clark, M. J., and Wheeler, K. (**1995**). ''Acoustic characteristics of American English vowels,'' J. Acoust. Soc. Am. **97**, 3099–3111.
Hirsh, I. J. (**1948**). ''The influences of interaural phase on interaural summation and inhibition,'' J. Acoust. Soc. Am. **20**, 536–544.
ISO (**1998**). ISO 389-1. ''Acoustics—Reference zero for the calibration of audiometric equipment, Part 1'' (International Standards Organization).
Klatt, D. H. (**1980**). ''Software for a cascade/parallel formant synthesizer,'' J. Acoust. Soc. Am. **67**, 971–995.
Klein, M. A., and Hartmann, W. M. (**1980**). ''Binaural edge pitch,'' J. Acoust. Soc. Am. **70**, 51–61.
Kohlrausch, A. (**1988**). ''Auditory filter shape derived from binaural masking experiments,'' J. Acoust. Soc. Am. **84**, 573–583.
Kuhn, G. F. (**1977**). ''Model for the interaural time differences in the azimuthal plane,'' J. Acoust. Soc. Am. **62**, 157–167.
Langhans, A., and Kohlrausch, A. (**1992**). ''Spectral integration of broadband signals in diotic and dichotic masking experiments,'' J. Acoust. Soc. Am. **91**, 317–326.
Levitt, H. (**1971**). ''Transformed up-down methods in psychoacoustics,'' J. Acoust. Soc. Am. **49**, 467–477.
Licklider, J. C. R. (**1948**). ''The influence of interaural phase relations upon the masking of speech by white noise,'' J. Acoust. Soc. Am. **20**, 150–159.
McFadden, D. (**1966**). ''Masking level differences with continuous and with burst masking noise,'' J. Acoust. Soc. Am. **40**, 1414–1419.
McFadden, D., (**1968**). ''Masking level differneces determined with and without interaural disparities in masker intensity,'' J. Acoust. Soc. Am. **44**, 212–223.
Schneider, B. A., and Zurek, P. M. (**1989**). ''Lateralization of coherent and incoherent targets added to a diotic background,'' J. Acoust. Soc. Am. **86**, 1756–1763.
van der Heijden, M., and Trahiotis, C. (**1998**). ''Binaural detection as a function of interaural correlation and bandwidth of masking noise: Implications for estimates of spectral resolution,'' J. Acoust. Soc. Am. **103**, 1609–1614.
van der Heijden, M., and Trahiotis, C. (**1999**). ''Masking with inteaurally delayed stimuli: The use of ''internal'' delays in binaural detection'' J. Acoust. Soc. Am. **105**, 388–399.

Monaural and interaural intensity discrimination: Level effects and the "binaural advantage"[a)]

Mark A. Stellmack, Neal F. Viemeister, and Andrew J. Byrne
Department of Psychology, University of Minnesota, Minneapolis, Minnesota 55455

(Received 28 August 2003; revised 30 April 2004; accepted 3 May 2004)

This study examined whether the level effects seen in monaural intensity discrimination (Weber's law and the ''near miss'') in a two-interval task are also observed in discrimination of interaural intensity differences (IIDs) in a single-interval task. Both tasks were performed for various standard levels of 4-kHz pure tones and broadband noise. The Weber functions ($10\log\Delta I/I$ versus I in dB) in the monaural and binaural conditions were parallel. For noise, the Weber functions had slopes close to zero (Weber's law) while the Weber functions for the tones had a mean slope of -0.089 (near miss). The near miss for the monaural and binaural tasks with tones was eliminated when a high-pass masker was gated with the listening intervals. The near-miss was also observed for 250- and 1000-Hz tones in the binaural task despite overall decreased sensitivity to changes in IID at 1000 Hz. The binaural thresholds showed a small (about 2-dB) advantage over monaural thresholds only in the broadband noise conditions. More important, however, is the fact that the level effects seen monaurally are also seen binaurally. This suggests that the basic mechanisms responsible for Weber's law and the near miss are common to monaural and binaural processing. [DOI: 10.1121/1.1763971]

PACS numbers: 43.66.Pn, 43.66.Fe [AK] Pages: 1149–1159

I. INTRODUCTION

The focus of the present paper is on monaural and binaural comparisons of intensity: Are effects of overall level that are observed in monaural intensity discrimination (Weber's law and the near miss) also exhibited in binaural comparisons of intensity? Below, it is argued that the most appropriate method for comparing monaural and binaural thresholds in this context is through the use of a two-interval monaural intensity-discrimination task and a single-interval interaural intensity-discrimination task. The monaural task is treated as a comparison of two samples of intensity across time while the binaural task is a comparison of two simultaneous samples of intensity across ears and, as a result, the two tasks have identical decision statistics from a signal-detection perspective. Approaching the examination of level effects in this way also provides a direct assessment of the extent of a ''binaural advantage'' in comparisons of intensity when all other factors are equal.

Note that monaural thresholds are often reported as the Weber fraction $10\log\Delta I/I$ although other units such as the decibel difference $10\log(\Delta I+I)/I$ sometimes are used, while interaural intensity difference-discrimination (IID-discrimination) thresholds are usually reported in the latter units. As previous results are discussed, the units of measurement will be specified as necessary.

A. Weber's law and the ''near miss''

Weber's law, one of the classic laws of perception, states that the just-noticeable difference (JND) in the intensity of a stimulus is proportional to the intensity of the stimulus to which that difference is added (the standard or pedestal). For suprathreshold auditory stimuli, Weber's law holds for the detection of increments in broadband stimuli such as noise (Miller, 1947; Raab and Goldberg, 1975). In contrast, intensity discrimination with pure tones often yields the so-called near miss to Weber's law, which describes a less-than-proportional increase in JNDs with increasing standard intensity (McGill and Goldberg, 1968). This means that the Weber fraction ($10\log\Delta I/I$) is constant as a function of standard intensity for broadband stimuli while for tones it decreases slightly with increasing standard intensity. In accounting for these observations, it is generally accepted that Weber's law characterizes intensity discrimination for a limited spectral region and the near-miss results from an increase in the extent and/or rate of growth of excitation with increasing intensity in the response of the peripheral auditory system to narrow-band stimuli (e.g. Florentine and Buus, 1981; see Viemeister, 1988 for a review). Consistent with this explanation, it has been shown that the near miss for narrow-band stimuli can be eliminated if the stimuli are presented in notched or high-pass maskers designed to restrict off-frequency listening (e.g. Viemeister, 1972; Moore and Raab, 1974; Viemeister, 1974). Because the presumed physiological basis for the difference in intensity discrimination performance across level for broadband stimuli and pure tones (i.e., Weber's law versus the near miss) resides at levels of processing that precede binaural interaction, it might be expected that similar effects would be exhibited in binaural processing.

Breebaart *et al.* (2001b) analyzed data of McFadden (1968) and Hall and Harvey (1984) consisting of detection thresholds for a 500-Hz interaurally out-of-phase pure-tone signal ($S\pi$) in the presence of a diotic (No) broadband masker and, separately, a diotic narrowband masker (50-Hz

[a)]A portion of these data were presented at the 145th Meeting of the Acoustical Society of America [M. A. Stellmack, N. F. Viemeister, and A. J. Byrne, J. Acoust. Soc. Am. **113**, 2269 (2003)].

wide). It was observed that these NoSπ detection thresholds increased at the rate of 1 dB/dB-increase in masker level for broadband noise maskers (Weber's law) while the slope is less than 1 for narrow-band maskers (the near miss). Breebaart *et al.* (2001a,b) were able to account for the previous results with a multichannel model, similar to those put forth to account for the near miss in monaural intensity discrimination, which shows near-miss effects for narrow-band maskers. In the model, the behavior of individual auditory filters or channels is characterized by Weber's law. For the situation in which a tonal Sπ signal is detected in a No masker, spread of excitation with increasing signal level for narrowband maskers produces activity in an increasing number of off-frequency auditory filters and leads to the near miss. For a broadband masker, off-frequency channels are masked and cannot contribute to detection of the signal and thresholds follow Weber's law.

Given the evidence suggesting that the effects of spread of excitation with increasing intensity are present in binaural processing, one would expect these effects to be exhibited in interaural comparisons of intensity. In order to test whether level effects in interaural intensity discrimination are similar to those observed in monaural intensity discrimination, in the present experiments thresholds in both listening tasks were measured for broadband noise and for 250, 1000, and 4000 Hz pure tones in the same set of listeners.

B. Comparing monaural intensity discrimination and interaural intensity difference discrimination

Hartmann and Constan (2002) presented a level-meter model to account for processing of IIDs of broadband and narrow-band noise. The fundamental assumption of their model is that the auditory system computes estimates of the power in the left- and right-ear signals, compares those estimates, and uses the difference to localize or lateralize the stimulus. Hartmann and Constan (2002) used the level-meter model to predict performance in lateralization tasks involving correlated or uncorrelated noise signals at the two ears. Because the level-meter model integrates level across the entire duration of a signal, it is insensitive to instantaneous intensity differences at the two ears that would be present for interaurally uncorrelated noise signals. As a result, lateralization performance should be similar for correlated and uncorrelated noise carriers as it would be dependent only upon the total power in the signals presented at the two ears. Hartmann and Constan (2002) found that thresholds were, indeed, very similar for correlated and uncorrelated noise signals although there was a slight advantage for correlated signals. The authors showed that this advantage could be accounted for by replacing the level-meter model with a loudness-meter model that incorporates temporal integration and thus is sensitive to some extent to short-term differences in the fine structures of the signals at the two ears. In the experiments described in this paper, the signals presented in the IID-discrimination conditions were identical in fine structure (correlated) at the two ears, so the distinction between the level-meter and loudness-meter models is unimportant in the present context. Of more relevance to the experiments described in this paper, Hartmann and Constan (2002) found that IID-discrimination thresholds were slightly better than monaural intensity-discrimination thresholds, although these thresholds were within a fraction of a dB of one another in units of $10\log(\Delta I+I)/I$. They attributed this small threshold difference to the different memory requirements of the two tasks. In the IID-discrimination task, intensity can be compared simultaneously across the ears, while in the monaural task the listener must compute and store an estimate of intensity in the two intervals for subsequent comparison. Therefore, Hartmann and Constan (2002) concluded that intensity information undergoes similar processing prior to (monaural) comparison across time or (binaural) comparison across ears. Hartmann and Constan (2002) did not undertake an examination of level effects.

Hartmann and Constan (2002) used a typical method for measuring IID-discrimination thresholds: A two-interval, two-alternative, forced-choice procedure in which one interval contains a stimulus with one value of IID while the stimulus in the other interval carries a slightly different IID (e.g., Hershkowitz and Durlach, 1969; Hafter *et al.*, 1977; Grantham, 1984; Yost and Dye, 1988). In such cases, the IID often is varied adaptively to yield an estimate of the JND. Changing the IID between intervals necessarily means that the monaural intensity in one or both ears also changes across intervals which leads to the concern that the discrimination task might be performed monaurally rather than on the basis of a comparison of the intensities at the two ears. In some cases, the fact that binaural thresholds are smaller than monaural thresholds is taken as indirect evidence that the binaural task was not performed based on monaural cues (e.g., Hafter *et al.*, 1977). In other cases, in order to "force" listeners to perform a binaural comparison within each interval, the overall levels of the signals at the two ears often are roved in tandem between intervals such that the change in intensity across intervals within either ear is no longer a reliable cue for solving the task but the change in IID across intervals remains unaffected (e.g., Grantham, 1984; Yost and Dye, 1988). The use of such a random rove in intensity makes it difficult to assess the effects of overall intensity on IID processing.

Hershkowitz and Durlach (1969) measured IID-discrimination thresholds as a function of overall level in a two-interval task with no rove for a 500-Hz pure tone. In their data, thresholds decreased slightly with increasing overall level, consistent with the near miss. However, the fact that they did not include a level rove leaves open the possibility that listeners performed the task on the basis of monaural cues. In addition, the two-interval IID-discrimination task that they used may not provide results that are most directly comparable to those of a two-interval monaural intensity-discrimination task, as suggested below.

Consideration of the presumed decision statistics used by listeners in the two-interval monaural intensity-discrimination task and the two-interval IID-discrimination task makes it clear that the two tasks are not analogous. By adopting an approach similar to that of Hartmann and Constan (2002), one can assume that in either task the listener extracts an estimate of the intensity of the signal in either ear

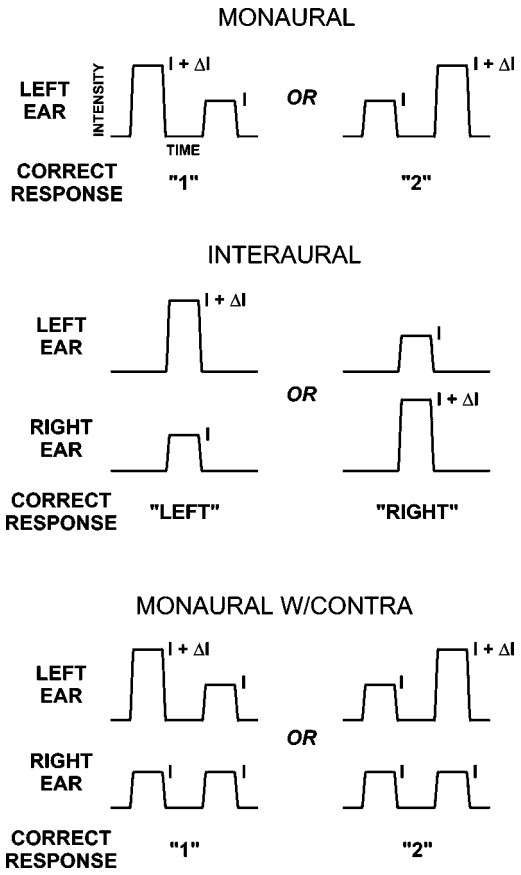

FIG. 1. A schematic representation of the stimulus envelopes for the three conditions used in the present experiment. Each section of the figure depicts the two possible trial types and the response that would be considered correct for each trial type. Stimuli are not drawn to scale.

in each listening interval. In the two-interval monaural intensity-discrimination task (depicted in the upper portion of Fig. 1), the listener presumably, compares the estimates of intensity in the two intervals to produce a decision statistic D_M (denoting the decision statistic in the monaural task), such that

$$D_M = I_1 - I_2, \tag{1}$$

where I_1 and I_2 are the estimates of intensity in the first and second intervals, respectively. If the listener is instructed to choose the interval with the higher intensity, this amounts to choosing interval 1 when D_M is positive and interval 2 when D_M is negative. In contrast, in the two-interval IID-discrimination task, the listener receives four ''samples'' of intensity, one in each ear in each listening interval. Assuming that no overall level rove is present, a listener might solve the task by basing responses upon the decision statistic D_{B2} (indicating the two-interval binaural task):

$$D_{B2} = (I_{R1} - I_{L1}) - (I_{R2} - I_{L2}), \tag{2}$$

where each I is the estimate of intensity in each ear and interval as indicated by the subscripts. In Eq. (2), the terms in parentheses represent a computation of the IID in each interval. When the term in parentheses is positive, this represents an IID favoring the right ear while negative totals are produced by IIDs favoring the left ear. The two IIDs are then compared across intervals to yield the decision statistic D_{B2}. If the listener's task is, for example, to choose which IID favors the right ear to a greater extent, this amounts to choosing interval 1 when D_{B2} is positive and interval 2 when D_{B2} is negative. When an equal overall level rove is added to the left- and right-ear signals in each interval, those additional terms will cancel out and the decision statistic reduces to Eq. (2).

Clearly, the decision statistics for the monaural and binaural tasks shown in Eqs. (1) and (2) differ in complexity. In the binaural task, the listener is presented with more information in each trial (in the form of additional samples of intensity) than in the monaural task. In order to produce a binaural listening task that involves a decision statistic that is analogous to that in the monaural task, it is necessary to reduce the amount of information presented in each trial. This can be accomplished through the use of a single-interval IID-discrimination task (depicted in the middle row of Fig. 1) in which the standard is presented to one ear and the standard plus increment is presented to the opposite ear in each trial. If the listener is instructed to indicate which ear contains the more intense signal, one form of the optimal decision variable, D_{B1}, for this single-interval task is

$$D_{B1} = I_R - I_L, \tag{3}$$

where the I's are the estimates of the signal intensities at the right and left ears (indicated by the subscripts). Consistent with the task at hand, the listener then responds ''right'' when D_{B1} is positive and ''left'' when the decision statistic is negative.

While the present analysis presumes that listeners base responses upon the difference between the samples of intensity received at the two ears in the single-interval binaural task, one legitimately could claim that the listener can still perform the binaural task monaurally by responding to the absolute intensity in one ear across trials (as a unilaterally hearing-impaired listener might). By the same token, one also could claim that the listener can perform the monaural task by listening to only one interval of each trial and making decisions on the basis of its absolute intensity (although no known naturally occurring hearing deficit produces such an effect). Presumably, neither of these strategies is the most sensible one from the normal-hearing listener's perspective in that he or she is discarding potentially useful information on each trial. In any case, in the approach taken here, no assumptions are made about the way in which the listener might use the information that is presented in each trial. Equivalent amounts of information simply are made available to the listener in the monaural and binaural tasks. That said, as will be seen in the data, binaural performance in the single-interval binaural task was usually slightly better than that in the two-interval monaural task which, to paraphrase Hafter *et al.* (1977), should help to dispel any fear that the binaural task was performed on the basis of the monaural cue. In addition, in Experiment 3 below, a single-interval monaural task was included to confirm that the single-interval binaural task most likely was not performed by attending to the stimuli in only one ear.

In the present experiments, an additional set of conditions was included to assess the advantage to be gained by

making comparisons across ears. In these conditions, the monaural intensity-discrimination task was repeated in the left ear with a fixed-level pedestal (at the level of the pedestal in the left ear) presented to the right ear in every listening interval. This condition is depicted at the bottom of Fig. 1. The stimuli in the two ears differed in intensity only when the stimulus in the left (ipsilateral) ear was incremented. Although it provided an opportunity for listeners to make a binaural comparison in each interval, the fixed-level pedestal presented to the right (contralateral) ear itself provided no information useful for performing the task and the decision statistic is the same as for the pure monaural condition [Eq. (1)]. Thus, these conditions will be referred to as ''monaural with contralateral pedestal'' or ''monaural with contra.''

The difference between the likely percepts in the monaural and binaural tasks may be a source of concern for some readers. For example, given the temporal parameters of the stimuli used here, it might be expected that the sequential monaural signals are perceived as discrete perceptual events. In contrast, when partially or fully correlated signals are simultaneously presented over headphones at the two ears, as in the binaural conditions, it would be expected that the percept is that of a single auditory event occupying some intracranial position. However, that intracranial position is presumably the result of a comparison of intensity at the two ears. In the present experiments, no assumptions are made about the manner in which the stimuli might be perceived. If the difference between the perceptions of the monaural and binaural stimuli is relevant, it contributes to the difference between monaural and binaural performance that is under investigation.

To summarize, the novel aspects of the experiments described below are: (1) An examination of level effects in IID discrimination and comparison of them to level effects in monaural intensity discrimination for the same set of listeners, and (2) the use of a single-interval IID-discrimination task to allow direct comparison to monaural intensity-discrimination thresholds measured in a two-interval task. Thresholds were measured with a pure-tone pedestal and with broadband noise pedestals for a range of pedestal levels in order to assess the effects of overall level. The results of Experiment 1 show that Weber's law holds for noise, and the near miss is obtained for a 4-kHz tone in both the monaural and binaural listening tasks. In Experiment 2, it will be seen that the near miss to Weber's law for a 4-kHz tone can be eliminated in both the monaural and binaural tasks when high-pass noise is used to limit off-frequency listening. In Experiment 3, the near miss is obtained across frequency in the binaural task even though binaural thresholds vary nonmonotonically as a function of frequency. Overall, while level effects were similar for the monaural and binaural tasks, the Weber fractions measured in the single-interval IID-discrimination task were lower than those measured in the monaural task by about 2 dB on average for noise and for low- and high-frequency pure tones (but not for a 1-kHz pure tone) indicating a very small binaural advantage in the comparison of intensity in certain stimulus conditions.

II. EXPERIMENT 1: LEVEL EFFECTS IN MONAURAL AND INTERAURAL INTENSITY DISCRIMINATION FOR 4-kHz TONES AND NOISE

A. Methods

Monaural intensity-discrimination thresholds and IID-discrimination thresholds were measured for 4-kHz pure-tone pedestals ranging from 30–90 dB SPL in 10-dB steps and for noise pedestals (Gaussian noise with a 10-kHz upper cutoff frequency) with spectrum levels ranging from 0–40 dB (measured at 1 kHz) in 10-dB steps. A frequency of 4 kHz was chosen for the pure-tone pedestal so that the dominant binaural cue would be interaural intensity. In the noise conditions, an independent sample of noise was generated for every trial and the sample of noise was identical across intervals and/or ears of each trial. In the pure-tone conditions, the 4 kHz pedestal was fixed in sine phase in all intervals.

Figure 1 shows a schematic representation of the three basic listening conditions of the present experiment as discussed in the Introduction. In the monaural condition, all stimuli were presented only to the left ear. In the binaural and monaural with contra conditions, the fine structures of the stimuli in the two ears were identical.

For all conditions, each interval was 200 ms in duration with 20-ms raised-cosine on and off ramps. In both monaural conditions, the two intervals of each trial were separated by 350 ms of silence.

The pedestal was fixed in intensity for an entire block of trials and the increment was varied adaptively using a three-down-one-up tracking rule that tracks to the 79.4% correct point on the psychometric function (Levitt, 1971). The initial step size was set to 4 dB (in units of $10 \log \Delta I/I$) and was reduced to 2 dB after four reversals. A block of trials was terminated after a total of 12 reversals, and the intensity increments at which the final eight reversals occurred (in dB) were averaged to produce a threshold estimate. All thresholds measured here are reported in units of $10 \log \Delta I/I$.

Two adaptive runs were completed for each pedestal level within a condition (monaural, monaural with contra, or interaural) and then two additional runs later were completed at each pedestal level, with the different pedestal levels presented in a pseudorandom order. Thus, the threshold estimates (in dB) of four blocks of trials were averaged to obtain the final threshold estimate for that condition. Listeners either ran the ''monaural'' conditions followed by the ''interaural'' conditions or vice versa. The conditions were grouped in this way to minimize confusion between any task-specific strategies that listeners might adopt. All listeners ran the monaural with contra conditions last. Upon completion of the experiment, a handful of monaural and interaural conditions were repeated to ensure that no obvious order-related effects were present. None were evident in that these latter thresholds were within the range of the thresholds measured initially. Only the initial thresholds are reported below.

Stimuli were generated and presented via MATLAB (Math Works) on a personal computer equipped with a high-quality, 24-bit sound card (Echo Audio Gina) at a sampling rate of 44.1 kHz. Stimuli were presented over Sony MDR-V6 stereo

headphones to listeners seated in an IAC sound-attenuating chamber. Each block of trials was initiated by the listener. On each trial, a ''ready'' light flashed on the computer screen for 250 ms followed by a 300-ms pause after which a trial was presented. Listeners entered their responses on the computer keyboard at which time the correct response was indicated on the screen and the next trial was initiated. Listeners were run in 2-h sessions, during which approximately 12–14 blocks of trials were run, until all stimulus conditions were completed.

In case performance in the single-interval binaural task could be facilitated by allowing each listener to establish an estimate of the perceptual midline, before each block of binaural trials, each listener was allowed to play a diotic tone or noise burst (depending upon which type of stimulus would be presented in the subsequent block of trials) and he or she was instructed to adjust the headphones so that the signal produced an intracranial image at the center of his or her head. Listeners were allowed to listen to the diotic signal as many times as necessary until they were satisfied that the headphones were positioned properly at which time a block of binaural trials was initiated.

The stimuli were described as completely as possible to all listeners in terms of the level changes that would occur in each interval and at each ear. The likely percepts that the listener would experience in each condition were described (e.g., a change in loudness in the monaural conditions; an intracranial image lateralized to one side in the monaural with contra and binaural conditions). Above all, the listeners were instructed to attend to the feedback and to make as many correct responses as possible.

The five listeners consisted of the first and third authors (S2 and S1, respectively) and three undergraduate students (two female, S3 and S4, and one male, S5) from the University of Minnesota who were paid to participate in the study. All listeners had pure-tone thresholds of 15 dB HL or better at octave frequencies from 250–8000 Hz. Listeners were allowed to practice in a variety of the monaural and binaural conditions until their thresholds stabilized. Very little practice was required for this set of listeners to reach asymptotic performance.

B. Results

The individual data for the pure-tone signal are shown in Fig. 2 while the data for the noise signal are shown in Fig. 3. The mean data for both stimulus types averaged across listeners are shown in Fig. 4. Thresholds are plotted as the just-detectable increment in units of $10 \log \Delta I/I$. The right-hand ordinates of Fig. 4 scale these values as the dB difference between the pedestal and increment $[10 \log(\Delta I+I)/I]$.

As a comparison to previous published data, the lowest monaural intensity-discrimination thresholds measured for any individual listener shown in Figs. 2 and 3 are approximately equal to mean thresholds reported elsewhere for 4-kHz tones (about -7 dB in units of $10 \log \Delta I/I$ for a pedestal level of 60 dB SPL; Jesteadt *et al.*, 1997) and broadband noise (about -7.1 dB in units of $10 \log \Delta I/I$ for a pedestal at about 20-dB spectrum level; Hartmann and Constan, 2002) while the thresholds averaged across all listeners in Fig. 4 are

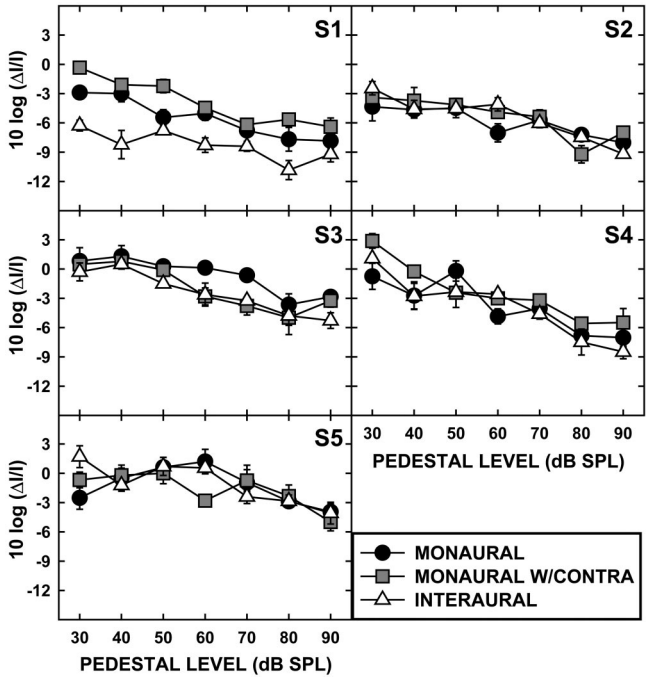

FIG. 2. Monaural and interaural intensity-discrimination thresholds for a 4-kHz pure tone as a function of pedestal level for five listeners. The different symbol types represent different listening conditions as shown in the legend. Error bars represent standard errors of the mean across the four threshold estimates measured in each condition.

higher. The slightly higher thresholds in the present experiment might be accounted for by the fact that the adaptive procedure of Jesteadt *et al.* (1977) tracked to a lower level of performance than the present procedure (70.7% versus 79.4% correct), while Hartmann and Constan (2002) presented diotic stimuli as opposed to the truly monaural stimuli of the present experiment.

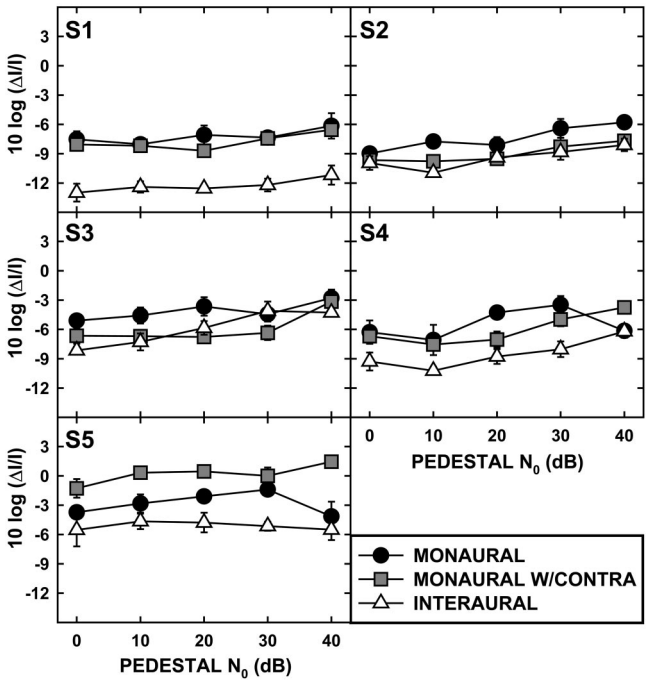

FIG. 3. Monaural and interaural intensity-discrimination thresholds for broadband noise in the same format and for the same five listeners as Fig. 2.

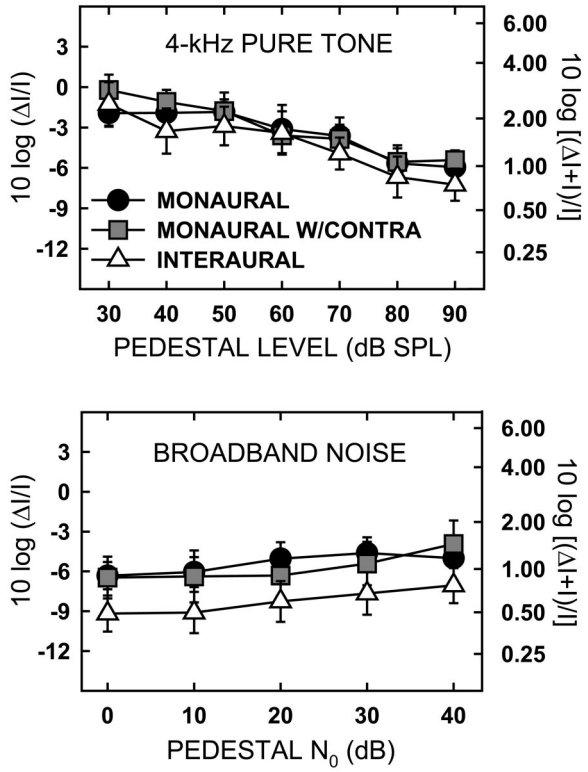

FIG. 4. Thresholds from Figs. 2 and 3 averaged across the five listeners for a 4-kHz pure tone and broadband noise. Error bars are standard errors of the mean across the five listeners.

The interaural thresholds shown in Fig. 4 are higher than thresholds reported elsewhere. For example, for a 5-kHz tone at 60-dB SPL mean level, Yost and Dye (1988) measured a threshold of about −11 dB ($10\log\Delta I/I$) while Hartmann and Constan (2002) measured a threshold of about −9.6 dB ($10\log\Delta I/I$) for broadband noise. [Both of these previous threshold values represent the IID within one interval of a two-interval task, converted from units of $10\log(\Delta I+I)/I$.] Because of the difference between number of intervals, it might be expected that the interaural thresholds measured in the present single-interval task would be higher than those measured in two-interval tasks. Furthermore, it is possible that the two-interval binaural task introduces a movement cue across intervals that is not present in the single-interval task and that produces an additional advantage beyond that afforded by the mere increase in number of intervals (Yost *et al.* 1974; Yost and Dye 1988) The specific methods used in the two-interval tasks (e.g., whether IID was varied symmetrically about some value or whether threshold IID was measured relative to a fixed standard; adaptive versus fixed-level procedures) as well as differences between threshold criteria further complicate the comparison to the single-interval thresholds.

The basic trends in the data are represented well in the mean data of Fig. 4. Thresholds in the interaural conditions (open symbols) are generally a few dB better (lower) in units of $10\log\Delta I/I$ than the corresponding monaural thresholds (filled circles), consistent with the observations of Hartmann and Constan (2002). The thresholds measured in the monaural with contralateral pedestal (monaural with contra) condition (filled squares) are nearly equal to those in the pure monaural condition. For the noise stimuli, thresholds are fairly constant across standard level with a slight increase at the highest levels, particularly in the monaural with contra and binaural (interaural) conditions. For the tonal stimuli, thresholds decrease with increasing standard level in the monaural and binaural conditions. In a task that was most like the monaural with contralateral standard condition of the present experiment, Elfner and Perrott (1967) similarly observed that discrimination thresholds decreased with increasing level for a 1-kHz tone.

Two-way repeated-measures ANOVAS performed on the two sets of data (noise and tone) confirm these basic observations. (For results reported below that were not statistically significant, $p>0.05$.) For the tonal stimuli, there was a significant effect of standard level, $F(6,24)=30.88$, $p<0.001$, but the differences between the three monaural/interaural conditions and the interaction were not statistically significant. When averaged across all three monaural and interaural conditions, the mean tonal data could be fit with a straight line with a slope of −0.089 that accounted for about 96% of the variability in the data.

For noise, there was a significant effect of standard level, $F(4,16)=10.03$, $p<0.001$, and monaural/interaural condition, $F(2,8)=6.64$, $p<0.02$, while the interaction was not significant. Because the effect of level for the noise pedestal was unexpected, post hoc repeated-measures one-way ANOVAS were run on the individual monaural, monaural with contra, and binaural conditions. The effect of level was not significant for the monaural condition while it was significant for the monaural with contra ($F(4,16)=13.44$, $p<0.0005$) and interaural conditions ($F(4,16)=5.47$, $p<0.05$). (These post hoc tests included a Bonferroni correction for multiple comparisons.) In Fig. 4, the mean thresholds for broadband noise in the monaural with contra and interaural conditions increase slightly with increasing pedestal level. The reason for the significant effect of level in these two conditions is not clear. As noted above, the interaction between pedestal level and monaural/binaural condition was not statistically significant which complicates the interpretation of this effect and underscores its small magnitude. As a result, we conclude that Weber's law approximately holds for all the broadband noise conditions.

Averaged across all subjects, levels, and the tone and noise conditions, the mean threshold in the monaural conditions was nearly 2 dB [$10\log(\Delta I/I)$] higher than the mean threshold for the interaural conditions although, as indicated above, the differences between the monaural and interaural conditions were not statistically significant for the 4-kHz tone. Based on psychometric functions for monaural intensity discrimination (Buus and Florentine, 1991), for ΔI that produces $d'=1$ (76% correct) in the monaural intensity-discrimination task, a change in $10\log(\Delta I/I)$ of 2 dB corresponds to a change in percent correct of less than 7%. Consistent with the results of Hartmann and Constan (2002), this suggests that any binaural advantage that exists is quite small.

The most noteworthy result is that there was no significant interaction between the effect of level and the effect of

monaural or binaural presentation of the stimuli. This indicates that for noise and, separately, for a 4-kHz tone, the monaural and interaural functions generally are similar in form across levels of the standard. Thresholds may increase slightly with level in the monaural with contra and interaural conditions with broadband noise. This effect, if real, is inconsistent with both Weber's law and the near miss and may be the result of processing that is peculiar to the binaural system.

C. Discussion

The results of Experiment 1 are consistent with the notion that the near miss to Weber's law that is observed with tones but not with broadband noise is attributable to effects associated with the spread of excitation that occurs with increasing level in the cochlea for band-limited signals, and that these effects similarly influence monaural and interaural comparisons of intensity. If this is the case, high-pass noise that limits off-frequency listening should eliminate the near miss in the interaural task as has been shown previously in monaural intensity discrimination. This is examined in Experiment 2.

III. EXPERIMENT 2: EFFECTS OF HIGH-PASS NOISE ON MONAURAL AND INTERAURAL INTENSITY DISCRIMINATION FOR A 4-kHz TONE

A. Methods

In this experiment, the two-interval monaural and single-interval binaural conditions (but not the monaural with contra condition) for the 4-kHz tone were repeated in the presence of a high-pass noise masker to determine whether the masker would eliminate the near miss to Weber's law. As such, the stimuli were identical to those described earlier except for the addition of high-frequency noise that was gated on and off simultaneously with each listening interval. The noise masker was Gaussian noise that was limited from 6–15 kHz in the frequency domain (by generating normally distributed amplitudes and rectangularly distributed phases in the passband, giving the masker essentially infinitely steep roll-offs) and converted to the time domain via inverse fast Fourier transform. The spectrum level of the noise was 25 dB below the SPL of the tonal pedestal in each condition (as in Viemeister, 1972).

It was felt that the interaural configuration of the masker potentially could affect performance in the interaural intensity discrimination task. As such, two separate masker conditions were run in the binaural listening task. In the diotic masker condition, identical samples of high-pass noise were presented to the two ears on each trial. In the dichotic masker condition, independent samples of noise were presented to the two ears on each trial. In all cases, new samples of noise were generated in each trial.

Consistent with the idea that the two-interval monaural intensity-discrimination task presents two samples of intensity across time while the single-interval interaural task presents two samples of intensity simultaneously to the two ears, two masker conditions were also run for the monaural task. In one condition, the same masker was presented in both intervals, making this condition analogous to the interaural condition with a diotic masker. In a second condition, independent samples of noise were presented in the two intervals of the monaural task, producing the monaural analog of the interaural dichotic masker condition. No difference was expected between the two masked monaural conditions, but they were included for completeness and to permit a strict comparison with the binaural conditions.

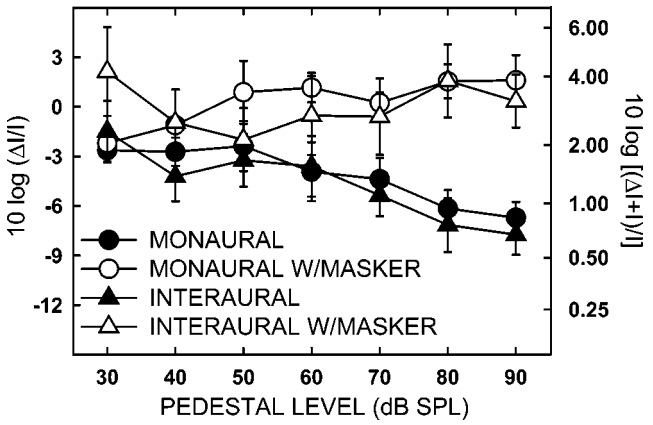

FIG. 5. Monaural and interaural intensity-discrimination thresholds measured for a 4-kHz pure tone with and without high-pass noise. The data are means across four listeners. Error bars are standard errors of the mean.

Data were gathered in Experiment 2 from only four of the five listeners from Experiment 1 (all but S3). As in Experiment 1, thresholds are based on the mean threshold of four adaptive runs in each condition, with those conditions run in a pseudorandom order.

B. Results and discussion

There were no apparent differences between thresholds measured in the two different masker conditions, so data were averaged across masker type for the monaural and interaural conditions. Because the general trends were similar across listeners, only mean thresholds are shown in Fig. 5. The data gathered with no masker (filled symbols) are means computed across the data from Experiment 1 of the four listeners who participated in Experiment 2 (while the data of Fig. 4 were averaged across five listeners). The thresholds measured in the presence of high-pass noise (open symbols) clearly show an elimination of the near miss. The monaural and interaural functions measured with high-pass noise have a nearly flat or slightly increasing slope in contrast to the decreasing slopes of the no-masker functions. Furthermore, the monaural and interaural thresholds measured in the presence of high-pass noise are nearly equal to one another, as they were in the no-masker conditions. These data provide additional support for the notion that the near miss to Weber's law for pure tones is due to auditory processes that similarly affect both monaural and interaural comparisons of intensity.

IV. EXPERIMENT 3: FREQUENCY EFFECTS IN MONAURAL AND INTERAURAL INTENSITY DISCRIMINATION

Experiments 1 and 2 showed that monaural and interaural intensity discrimination both exhibit similar effects of level (in terms of Weber's law and the near-miss). However, IID discrimination has been shown to exhibit frequency effects such that thresholds are elevated for pure tones around 1 kHz (Grantham, 1984; Yost and Dye, 1988). These effects appear to occur at the level of binaural interaction in that they are not observed in monaural intensity discrimination (e.g., Jesteadt *et al.*, 1977). If the mechanisms responsible for the near miss occur independently from binaural interaction, it would be expected that the near miss would be observed in spite of this elevation in thresholds at 1 kHz. In order to test this hypothesis, in the experiment described below, monaural and interaural intensity discrimination thresholds were measured for pure tones at 250 and 1000 Hz at several different pedestal levels.

A. Methods

In the first stage of this experiment, monaural, monaural with contra, and interaural thresholds were measured as in Experiment 1 for pure tones of 250 and 1000 Hz and a pedestal of 70 dB SPL. Because it was expected that interaural thresholds would be elevated for the 1000-Hz tone and to confirm that listeners were responding on the basis of an interaural comparison, an additional monaural condition was added in which only the left channel of the single-interval interaural condition was presented to listeners, producing a single-interval monaural intensity-discrimination condition. This mimics the situation that would exist if listeners were performing the interaural task on the basis of only the stimulus arriving at one ear. In the single-interval monaural condition, the listeners were told that they would hear one of two sounds: One at a fixed, standard loudness or one that would be at a higher loudness that would vary across trials, the assumption being that the signal and nonsignal trials would differ perceptually in terms of loudness. The listeners were told that they would have to learn the standard and louder stimuli on the basis of their experience and by using the feedback after each trial. Listeners were instructed to press one of two response keys on a computer keyboard to indicate whether the trial contained the quieter or louder stimulus. Listeners seemed to understand the instructions and none indicated that the task was unclear after they performed it. Only listeners S1, S2, S4, and S5 contributed data in this stage of the experiment.

In the second stage of the experiment, interaural intensity-discrimination thresholds were measured for 250- and 1000 Hz pure tones for pedestal levels of 30, 60, and 90 dB SPL. Only listeners S1 and S2 were available for this stage of the experiment.

No high-pass masker was present in any condition. All other methodological details are the same as in the previous experiments.

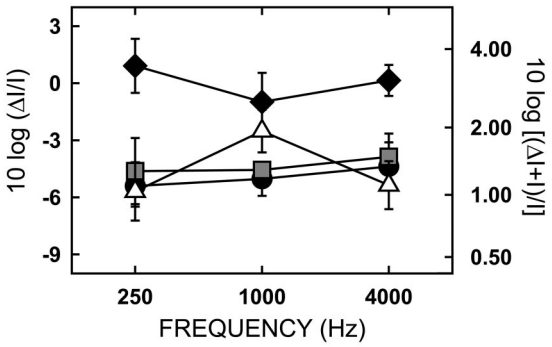

FIG. 6. Intensity-discrimination thresholds as a function of pure-tone frequency averaged across four listeners. The standard intensity was 70 dB SPL. Conditions represented by the different symbols are: Filled circles, monaural; shaded squares, monaural with contra; filled diamonds, single-interval monaural; open triangles, interaural. Error bars are standard errors of the mean across listeners.

B. Results and discussion

Figure 6 shows thresholds as a function of frequency averaged across all four listeners. Different symbols represent different conditions: Filled circles, monaural; shaded squares, monaural with contra; filled diamonds, single-interval monaural; open triangles, interaural. (Thresholds measured for a 4-kHz, 70-dB SPL tone were taken from Experiment 1 for comparison.) The expected frequency effect can be seen in the interaural thresholds (open triangles), where the mean threshold is largest at 1 kHz, but not in any of the monaural conditions. As was seen previously for a 4-kHz pure tone, there appears to be no ''binaural advantage'' at 250 Hz in these data. Because of the elevation in interaural thresholds at 1 kHz, the mean interaural threshold is actually higher than the two-interval monaural thresholds at that frequency and it approaches the single-interval monaural threshold indicating that any interaural cue that might be available at 1 kHz is very weak. The fact that thresholds in the monaural with contra data (shaded squares) show no frequency effect and are most similar to the monaural data (filled circles) across frequency suggests that listeners may not have made use of the fixed-level pedestal in the contralateral ear in these conditions. This is addressed further in Sec. IV B below.

Figure 7 shows thresholds averaged across listeners as a

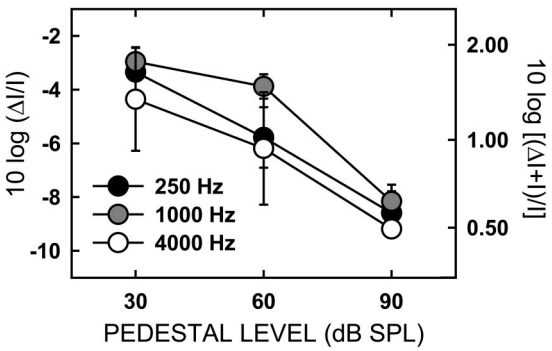

FIG. 7. Interaural intensity-discrimination thresholds as a function of pedestal level averaged across two listeners. Pure-tone frequency is represented by the different symbol types. Error bars are standard errors of the mean across listeners.

function of pedestal level for 250-, 1000-, and 4000-Hz pure tones. (The 4-kHz data were taken from Experiment 1 for these two listeners.) While the IID threshold for 1 kHz is highest by a small amount at each pedestal level, the near miss is observed for each individual frequency. As indicated earlier, this is to be expected if the mechanisms responsible for the near miss operate essentially independently of, while still influencing, the binaural mechanisms that produce the frequency effect.

V. GENERAL DISCUSSION

A. Weber's law and the near miss in monaural and interaural intensity discrimination

In the present experiments, comparable effects of overall level were seen in monaural intensity discrimination and IID discrimination. This is consistent with the belief that Weber's law holds for discrimination of intensity within localized spectral regions or ''channels'' for broadband stimuli and the near-miss results from effects associated with spread of excitation with increasing level for narrow-band stimuli, effects which presumably occur at the earliest stages of peripheral processing, that is, prior to comparison of monaural stimuli over time and binaural interaction (although, presumably, the advantage to be gained by increasing the number of active channels is realized at more central, decision-making levels of auditory processing which probably reside beyond the level of binaural comparison, as modeled by Breebaart *et al.*, 2001a). Accordingly, the near miss for tonal stimuli was eliminated in both the monaural and interaural tasks when high-pass noise was presented to limit off-frequency listening.

While the preceding explanation relies only on the increase in the number of channels of available information with increasing spread of excitation, a role for noncompressive growth cannot be ruled out based on the present data. At the lower levels, the higher thresholds for the tone shown in Fig. 4 presumably reflect its limited effective bandwidth relative to that for the noise. As level increases the threshold for the tone may decrease due to an increase in the effective bandwidth and/or the expanded growth of response in channels whose characteristic frequencies (CFs) are above the frequency of the tone. At the highest level of the tone, the effective bandwidth of the tone approaches that of the noise. If the effective bandwidths were the same then the threshold for the tone should be lower than that for the noise, reflecting the effects of expanded growth in off-frequency fibers. Expanded growth would not occur for the noise since there presumably are no ''off-frequency'' fibers. This is not seen in the data. An explanation is that the highest level used for the tone was not sufficient to show the predicted lower thresholds, i.e., had higher levels been examined, the Weber function for the tone may have crossed and gone below that for the noise. An alternative, rather unappealing explanation is that for some reason the listener cannot use the expanded growth even though the mechanical data (Ruggero *et al.*, 1997) indicate that it occurs at very high levels for below-CF tones.

Do the present data have any implications for the interpretation of previous IID-discrimination data? As described earlier, IID discrimination often is measured in a two-interval task in which the overall level is roved between intervals to reduce monaural intensity cues. The present results indicate that sensitivity to changes in IID vary with changes in overall level for pure tones. In the present tonal data, the JND changes by a fairly small amount (about 4 dB in $10 \log \Delta I/I$) over a wide range of pedestal levels (60 dB). This range of pedestal levels is much larger than that over which level is typically roved in a two-interval IID-discrimination task (e.g., Yost and Dye, 1988, roved level over a range of only 8 dB). Therefore, the rove would not be expected to have a large effect on JND estimates obtained in the typical roving-level procedure. However, as noted earlier, it remains the case that the two-interval IID-discrimination procedure introduces a potential cue of movement across intervals that might produce an advantage over single-interval IID discrimination.

B. Binaural advantage in intensity discrimination

When the same amount of information (in terms of number of samples of intensity) are presented to listeners monaurally and binaurally resulting in optimal decision statistics that are similar in form as shown in the Introduction, is there a binaural advantage in intensity discrimination? Thresholds measured in the single-interval IID-discrimination task showed a trend toward being slightly lower than those measured in the two-interval monaural intensity-discrimination task, although the difference was statistically significant only for noise. Binaural thresholds were actually higher than monaural thresholds for a 1-kHz tone, a frequency region of relative insensitivity to changes in IID. As noted by Hartmann and Constan (2002), who did find statistically significant differences between conditions, it appears that there is a small advantage to be had from making simultaneous interaural comparisons of level over comparisons of level across sequentially-presented monaural stimuli perhaps as a result of the additional memory requirement imposed by the monaural task. Clearly, this advantage is dependent upon the frequency content of the stimulus (see Fig. 6).

If there is, in fact, a small binaural advantage in intensity discrimination for certain stimuli as described above, this leads to the prediction that a fixed-level contralateral standard presented concurrently with the stimuli of the monaural intensity-discrimination task should provide a slight advantage over the purely monaural condition. However, thresholds in the monaural with contralateral standard conditions were not as low as those in the interaural conditions although both allowed for simultaneous interaural comparisons. Considering that for a given IID, the difference between the two possible IIDs (+IID and −IID) in the interaural task was twice that between the diotic and dichotic stimuli of the monaural with contra task, it would be expected that thresholds in the latter condition would be slightly higher than those in the former.

An alternative that is raised by the data of Experiment 3 is that the contralateral, fixed-level pedestal essentially was ignored in the monaural with contra condition and no binaural comparison was made. In other words, listeners' re-

sponses in this condition were based only on the stimuli presented to the left ear. This interpretation is supported by the fact that the monaural with contra thresholds showed no frequency effect in Experiment 3 like that which occurs in conditions where an interaural comparison must be made. If this interpretation is correct, then the monaural with contra thresholds of Experiment 1 are more similar to the monaural thresholds than to the binaural thresholds because the fixed-level pedestal in the right ear was ignored, effectively reducing the monaural with contra task to a purely monaural intensity-discrimination task.

Consistent with the present results, Shub and Colburn (2004) recently showed that thresholds in a monaural intensity-discrimination task for a 600-Hz pure tone were relatively unaffected when a fixed-level 600-Hz distractor tone was added to the contralateral ear. They also showed that thresholds increased dramatically when the level of the contralateral tone was roved between intervals of their two-interval task. Rather than concluding that listeners ignored the contralateral distractor, they interpreted their results as indicating that the contralateral distractor fuses with the ipsilateral stimulus and listeners respond to the overall loudness of the stimulus. As a result, when the level of the contralateral distractor is roved, the binaural loudness of the stimulus is an unreliable cue for discriminating intensity in the ipsilateral ear and thresholds are elevated. Another possibility is that listeners ignored the contralateral distractor when it was fixed but the roving contralateral distractor produced informational masking, an increase in thresholds attributed to variability or uncertainty in the parameters of a masker (e.g., Lutfi, 1990; Durlach, *et al.* 2003). The present monaural with contra data do not allow one to rule out any of the possible interpretations discussed here.

C. Monaural comparison to the two-interval IID-discrimination task

If, as argued in the Introduction, the two-interval IID-discrimination task is not strictly comparable to the two-interval monaural intensity-discrimination task, to what type of monaural task can the two-interval binaural task be compared? Examination of the decision rule for the two-interval binaural task shown in Eq. (2) reveals that the analogous monaural task would be one in which four samples of intensity are presented in each trial and the listener compares the first two samples and last two samples, then compares those results to one another. The task being described here is a monaural increment-discrimination task in which each of two intervals in a trial contains two signals of different intensity (a total of four temporally distinct monaural signals in a trial) and the listener is asked, for example, to determine which of two intervals contains a larger change in intensity. Data comparing the monaural increment-discrimination task to a two-interval IID-discrimination task are currently being gathered.

VI. CONCLUSIONS

(1) Monaural intensity-discrimination thresholds measured in a two-interval task and (binaural) IID-discrimination thresholds measured in a single-interval task generally appear to follow Weber's law for broadband noise stimuli. This means that the just-detectable increment in intensity is proportional to the standard intensity ($10 \log \Delta I/I$ is constant across I).

(2) Monaural and binaural thresholds similarly measured for a 4-kHz tone exhibit the near miss to Weber's law, such that $10 \log \Delta I/I$ decreases with increasing I. The near miss is eliminated in both the monaural and binaural tasks when high-pass noise is used to restrict off-frequency listening.

(3) IID-discrimination thresholds may be slightly better for broadband noise and low- and high-frequency pure tones than corresponding monaural thresholds, although this difference reached statistical significance only for noise. IID-discrimination thresholds were worse than monaural thresholds for a 1-kHz pure tone. Presenting the fixed-level standard to the contralateral ear in the monaural intensity-discrimination task provided little or no advantage over purely monaural intensity-discrimination thresholds. These results indicate that any binaural advantage is very small (a few dB at most in terms of $10 \log \Delta I/I$).

(4) Overall, the results suggest that the basic auditory processes that produce differences between level effects for noise and tones (i.e., Weber's law versus the near miss) similarly influence monaural and interaural comparisons of intensity. This result would be expected if these differences are attributable to processing that is common to both monaural and binaural comparisons of intensity.

ACKNOWLEDGMENTS

The authors thank Dr. Armin Kohlrausch and two anonymous reviewers as well as Dr. Les Bernstein and two anonymous reviewers of an earlier version of this manuscript for their helpful comments. This work was supported by Research Grant No. R01 DC 00683 and Research Grant No. R03 DC 05343-01, both from the National Institute on Deafness and Communication Disorders, National Institutes of Health.

Breebaart, J., van de Par, S., and Kohlrausch, A. (**2001a**). "Binaural processing model based on contralateral inhibition. I. Model structure," J. Acoust. Soc. Am. **110**, 1074–1088.

Breebaart, J., van de Par, S., and Kohlrausch, A. (**2001b**). "Binaural processing model based on contralateral inhibition. II. Dependence on spectral parameters," J. Acoust. Soc. Am. **110**, 1089–1104.

Buus, S., and Florentine, M. (**1991**). "Psychometric functions for level discrimination," J. Acoust. Soc. Am. **90**, 1371–1380.

Durlach, N. I., Mason, C. R., Kidd, Jr., G., Arbogast, T. L., Colburn, H. S., and Shinn-Cunningham, B. G. (**2003**). "Note on informational masking," J. Acoust. Soc. Am. **113**, 2984–2987.

Elfner, L. F., and Perrott, D. R. (**1967**). "Lateralization and intensity discrimination," J. Acoust. Soc. Am. **42**, 441–445.

Florentine, M., and Buus, S. (**1981**). "An excitation-pattern model for intensity discrimination," J. Acoust. Soc. Am. **70**, 1646–1654.

Grantham, D. W. (**1984**). "Interaural intensity discrimination: Insensitivity at 1000 Hz," J. Acoust. Soc. Am. **75**, 1191–1194.

Hall, J. W., and Harvey, A. D. G. (**1984**). "NoSo and NoSπ thresholds as a function of masker level for narrow-band and wideband masking noise," J. Acoust. Soc. Am. **76**, 1699–1703.

Hafter, E. R., Dye, R. H., Nuetzel, J. M., and Aronow, H. (**1977**). "Difference thresholds for interaural intensity," J. Acoust. Soc. Am. **61**, 829–834.

Hartmann, W. M., and Constan, Z. A. (**2002**). ''Interaural level differences and the level-meter model,'' J. Acoust. Soc. Am. **112**, 1037–1045.
Hershkowitz, R. M., and Durlach, N. I. (**1969**). ''Interaural time and amplitude JND's for a 500 Hz tone,'' J. Acoust. Soc. Am. **46**, 1464–1467.
Jesteadt, W., Wier, C. C., and Green, D. M. (**1977**). ''Intensity discrimination as a function of frequency and sensation level,'' J. Acoust. Soc. Am. **61**, 169–177.
Lutfi, R. A. (**1990**). ''How much masking is informational masking?'' J. Acoust. Soc. Am. **88**, 2607–2610.
McFadden, D. (**1968**). ''Masking-level differences determined with and without interaural disparities in masker intensity,'' J. Acoust. Soc. Am. **44**, 212–223.
McGill, W. J., and Goldberg, J. P. (**1968**). ''Pure-tone intensity discrimination and energy detection,'' J. Acoust. Soc. Am. **44**, 576–581.
Miller, G. A. (**1947**). ''Sensitivity to changes in the intensity of white noise and its relation to masking and loudness,'' J. Acoust. Soc. Am. **19**, 609–619.
Moore, B. C. J., and Raab, D. H. (**1974**). ''Pure-tone intensity discrimination: Some experiments relating to the 'near-miss' to Weber's law,'' J. Acoust. Soc. Am. **55**, 1049–1054.
Raab, D. H., and Goldberg, I. A. (**1975**). ''Auditory intensity discrimination with bursts of reproducible noise,'' J. Acoust. Soc. Am. **57**, 437–447.
Ruggero, M. A., Rich, N. C., Recio, A., Narayan, S. S., and Robles, L. (**1997**). ''Basilar-membrane responses to tones at the base of the chinchilla cochlea,'' J. Acoust. Soc. Am. **101**, 2151–2163.
Shub, D. E., and Colburn, H. S. (**2004**). ''Monaural intensity discrimination under dichotic conditions,'' Abstracts of the Twenty-Seventh Annual Midwinter Research Meeting of the Association for Research in Otolaryngology, **44**, Daytona Beach, FL.
Viemeister, N. F. (**1972**). ''Intensity discrimination of pulsed sinusoids: The effects of filtered noise,'' J. Acoust. Soc. Am. **51**, 1265–1269.
Viemeister, N. F. (**1974**). ''Intensity discrimination of noise in the presence of band-reject noise,'' J. Acoust. Soc. Am. **56**, 1594–1600.
Viemeister, N. F. (**1988**). ''Psychophysical aspects of auditory intensity coding,'' in *Auditory Function: Neurobiological Bases of Hearing*, edited by G. M. Edelman, W. E. Gall, and W. M. Cowan, Wiley, New York, 213–241.
Yost, W. A., and Dye, Jr., R. H. (**1988**). ''Discrimination of interaural differences of level as a function of frequency,'' J. Acoust. Soc. Am. **83**, 1846–1851.
Yost, W. A., Turner, R., and Bergert, B. (**1974**). ''Comparison among four psychophysical procedures used in lateralization,'' Percept. Psychophys. **15**, 483–487.
Levitt (**1971**). ''Transformed up-down methods in psychophysics,'' J. Acoust. Soc. Am. **49**, 467–477.

The effects of window delay, delinearization, and frequency on tone-burst otoacoustic emission input/output measurements

Michael Epstein[a] and Søren Buus
Institute of Hearing, Speech & Language and Communications & Digital Signal Processing Center, Electrical & Computer Engineering Department (440 DA), Northeastern University, Boston, Massachusetts 02115

Mary Florentine
Institute of Hearing, Speech & Language and Department of Speech-Language Pathology & Audiology (106/A FR), Northeastern University, Boston, Massachusetts 02115

(Received 17 December 2003; revised 8 May 2004; accepted 13 May 2004)

Tone-burst otoacoustic emissions (TBOAEs) are a potential tool for objectively examining cochlear activity in humans. However, their use requires knowledge of how the TBOAE input/output depends on measurement and analysis paradigms. The present experiment examined the effect of variations in response-window timing, response delinearization, and local changes in stimulus frequency on TBOAE input/output measurement. None of these experimental manipulations had a profound effect on TBOAE measurements as long as reasonable parameter choices were made. Nonetheless, judicial choice of the experimental parameters can optimize the assessment of BM I/O functions. It is concluded that the consistency of TBOAE I/O across the parameters tested makes it a viable tool to consider for examining human cochlear activity. © *2004 Acoustical Society of America.* [DOI: 10.1121/1.1768254]

PACS numbers: 43.66.Yw, 43.64.Jb [BLM] Pages: 1160–1167

I. INTRODUCTION

Otoacoustic emissions have been used to examine a variety of phenomena such as cochlear tuning (Shera *et al.*, 2002), critical bandwidth (Neumann *et al.*, 1997), and noise-hazard responses (Mansfield *et al.*, 1999). Otoacoustic emissions may also provide a noninvasive means for assessing some of the finer details of cochlear processing. The present experiment seeks to determine how stimulus and measurement parameters affect tone-burst otoacoustic emission measurements. This will provide some insight into whether or not they are consistent enough across measurement parameters to act as a potential tool for the assessment of cochlear activity.

Withnell and Yates (1998) first suggested the use of otoacoustic emissions to examine basilar-membrane nonlinearity. They were especially interested in identifying the level at which compression of the function begins, i.e., the compression threshold. Their work primarily used distortion-product otoacoustic emissions (DPOAEs) in guinea pigs. Buus *et al.* (2001) used DPOAEs to determine basilar-membrane I/O functions in humans, but they found that complexities associated with DPOAEs made it difficult to achieve their goal. For example, it is not possible to determine BM I/O functions using DPOAE measurements at high levels where the presence of multiple components is likely to lead to suppression. Suppression is likely to obscure the relationship between basilar-membrane vibration amplitude and otoacoustic emissions. In addition, low-frequency measurements cannot be performed because of noise-floor considerations. Due to such difficulties with DPOAEs, it seemed that TBOAEs might be a better choice for basilar-membrane I/O assessment in humans. Preferably, measures of TBOAEs should be made in a strong OAE-producing frequency region where the signal-to-noise ratio is high.

Previous studies using transient-evoked otoacoustic emissions (TEOAEs) hint at the potential for the use of TBOAEs for studying level-dependent amplification within the auditory system and for comparing results with psychoacoustic measures (Norton and Neely 1987; Neumann *et al.*, 1997). Although these studies do not specifically examine basilar-membrane mechanics, the data show input-output relations that resemble basilar-membrane I/O functions measured in animals. Thus, a quantitative understanding of TEOAE generation may provide a simple and direct method for assessing basilar-membrane I/O functions and their dependence on stimulus frequency.

Before any examination of tone-burst otoacoustic emissions as a potential means of determining basilar-membrane input-output functions or any other cochlear function can be performed, it is necessary to devise an effective technique for measuring the tone-burst otoacoustic emissions and to show that estimates of the I/O function are largely independent of specific choices of measurement parameters. To this end, a frequency at which the tone-burst otoacoustic emissions can easily be measured must be determined. Tone-burst OAEs might be useful in the assessment of cochlear function only if (1) the measurements can be obtained for a large range of input levels, (2) the outcome is largely independent of specific choices of stimulus and measurement parameters, and (3) they are reproducible.

Accordingly, this paper examines the effect of frequency and windowing on the measurement of TBOAE I/O functions. These measurements have two aims: to allow param-

[a]Electronic mail: mepstein@ece.neu.edu

 0001-4966/2004/116(2)/1160/8/$20.00

eters to be chosen that provide reliable estimates of the I/O function and to determine the extent to which the form of the I/O function is dependent on measurement parameters. In addition, the effect of response delinearization on TBOAE I/O functions was examined to determine whether it would help isolate the nonlinear cochlear reflections.

II. METHOD

A. Procedure

In order to identify a frequency region near 1 kHz that produces strong otoacoustic emissions, the entire basilar membrane was stimulated by clicks. Frequencies near 1 kHz were selected because TBOAEs tend to be strong in this frequency region.

The OAEs were determined from the real, positive part of the cross spectrum (determined using MATLAB) of two independent averages of the time- windowed responses measured in the ear canal in order to help eliminate as much noise as possible. This method is based on the assumption that the OAE is phase locked to the stimulus and has highly repeatable components with identical phases in the two buffers in the time domain, and with zero phase in the cross spectrum. Thus, the emissions will be real and positive. As the phase of the measured responses becomes more variable, the phase in the cross spectrum is increasingly likely to differ from zero. Averaging and using only the real, positive part of the cross spectrum reduces the level of the recording that is not phase locked to the signal. The two averages used to get the cross spectrum were obtained by alternatingly entering the results of recordings into two different buffers. Subjects were presented with 200 clicks and responses were recorded at a sample rate of 50 kHz for 81.92 ms (4096 samples), including the time of the click itself. These recordings were windowed using a 21.48-ms (1024 samples) Hanning window covering the first portion of the recorded signal. Because the stimulus was a click, the direct stimulus was effectively eliminated by the very small value of the windowing function during the signal. The cross spectrum of the two sets of recordings was examined visually. The strongest peak around 1 kHz was chosen for further examination. To ensure that the peak was stable, this measurement was performed three times and peaks were used only if they appeared clearly in all three measurements. Once chosen, detailed measurements of tone-burst otoacoustic emissions at and around this frequency were performed.

Tone-burst evoked emissions were measured by presenting a series of brief tone bursts and recording the sound in the ear canal for 81.92 ms at a sample rate of 50 kHz. To allow calculation of the cross spectrum, the recordings were stored for further analysis in two interleaved sets over 360 trials. The stored responses were Hanning windowed using a 1024-sample window (21.48 ms). The window started after a delay between 13 and 20 ms in the first part of the experiment. A fixed value was chosen on the basis of those results and used thereafter. The spectrum of the windowed ear-canal response was band-pass filtered between 400 and 1400 Hz.

To reduce the effect of external noise, a response to a tone burst would be included in the average only if the noise floor was estimated to be less than 10 dB SPL. The noise floor for the rejection decision was calculated using a 21.48-ms Hanning windowing (with a window delay of 13 ms) of the difference between two samples. The noise intensity was then calculated as the sum of the squared magnitudes of the real FFT components between 32 and 819 Hz. This measure is highly conservative and guarantees that any data points above the noise are presented with a high level of confidence. Some of the measurements below the noise floor are also likely to be reliable, but the level of confidence is lower. Measurements were made for levels ranging in 5-dB steps from approximately 10 dB below the minimum level (typically 15–30 dB SPL) that produced an emission whose level exceeded the background noise to the maximum obtainable level. These measurements were repeated three times for each condition and averaged. Tests were performed at five frequencies to examine the extent to which the OAE measurements depend on local variations in response.

One final procedural variable to be examined is delinearization. Delinearization eliminates any response that is linearly related to the stimulus such as reflections from areas outside the cochlea (e.g., ear canal and ossicles). Their elimination would enhance the targeted TBOAE. The responses to the delinearized trials were recorded in two separate interleaved sets for 120 measurements per level (60 per set). If the system were completely linear, the two sets of responses would cancel out and nothing would remain except random noise. Delinearization was performed by subtracting the response to tone bursts with three times the normal amplitude from that obtained from the sum of three times as many presentations of tone bursts at the normal amplitude.

B. Stimuli

The clicks were 70-dB SPL 0.1-ms stimuli that contained energy between 450 Hz and 8 kHz. For each subject, a dominant peak in the click-evoked otoacoustic emissions (COAE) spectra between 850 and 1150 Hz was identified. This frequency and four additional test frequencies around this peak (-0.5, -0.25, $+0.25$, and $+0.5$ Barks$+$COAE peak) were selected. At each frequency, the tone burst presented had an equivalent rectangular duration of $6/\text{frequency}$. These tone bursts had a Gaussian envelope to help contain the spectral spread of the signal due to onset and offset. The duration was chosen to obtain a useful compromise between frequency specificity and the ease of separating the stimulus from the emission that results from its presence. Using a long-duration signal makes the OAE difficult to measure because the signal would overlap the emission. Using a short-duration signal decreases frequency specificity because as the duration of the signal decreases, the bandwidth of the signal increases. Finally, during the delinearization trials, a tone with tripled amplitude was presented as every fourth stimulus.

C. Apparatus

Each subject was tested in a sound-attenuating booth. A PC-compatible computer with a signal processor (TDT AP2) generated the stimuli, and recorded responses. A TDT DA1

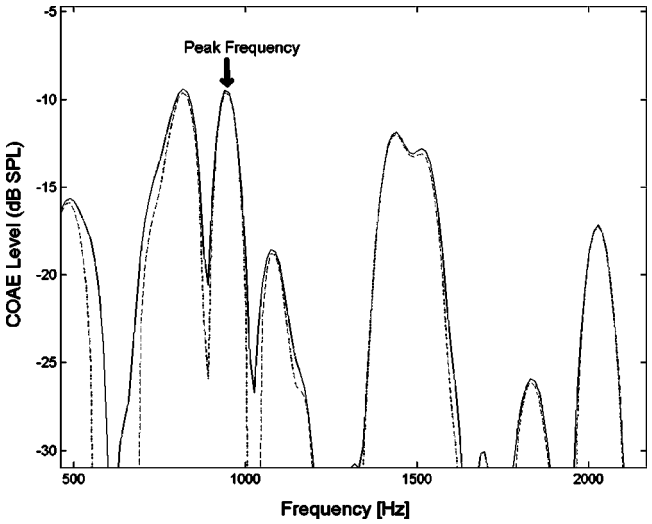

FIG. 1. Response to click stimuli for S1. The frequency in Hz is shown on the abscissa and the level of the resulting otoacoustic emission is on the ordinate. The peak frequency here that is closest to 1 kHz is 935 Hz. The solid lines show a single average measurement. The dotted lines show the positive, real part of the cross spectrum of two measurements.

converted the waveform calculated by the AP2 to an analog signal. The level of the stimuli was adjusted using a TDT PA4 attenuator and the signal was anti-alias filtered using a TDT FT5. The resulting signal was sent to a TDT HB6 headphone buffer and presented to the subject using an Etymotic Research ER-10C system, which also contained a microphone to record OAEs. The recordings from the ER-10C were anti-alias filtered, amplified, and converted to a digital signal using a TDT AD1. The digital signal was sent back to the AP2, which averaged the responses to the stimuli as explained previously and wrote the averaged signals to disk for further analysis.

D. Subjects

Six subjects (two male and four female) were tested monaurally. No subjects had a history of hearing difficulties or middle-ear pathology. Their audiometric thresholds did not exceed 10 dB HL for octave frequencies from 250 Hz to 4 kHz or 20 dB HL at 8 kHz (ANSI, 1989). Their ages ranged from 18 to 28 years.

III. RESULTS AND PRELIMINARY DISCUSSION

A. COAE measurement

Figure 1 is an example of the spectra obtained with the click stimuli for subject S1. The dotted line shows the cross spectrum between two different measurement sets. The solid line shows a single measurement set. Any real OAE should reveal a close correspondence between the two spectra. For this subject, the peak selected was at 935 Hz, and this frequency was used for further exploration with tone-burst stimuli. Similar analyses were made for the other five subjects to determine each one's dominant peak around 1 kHz.

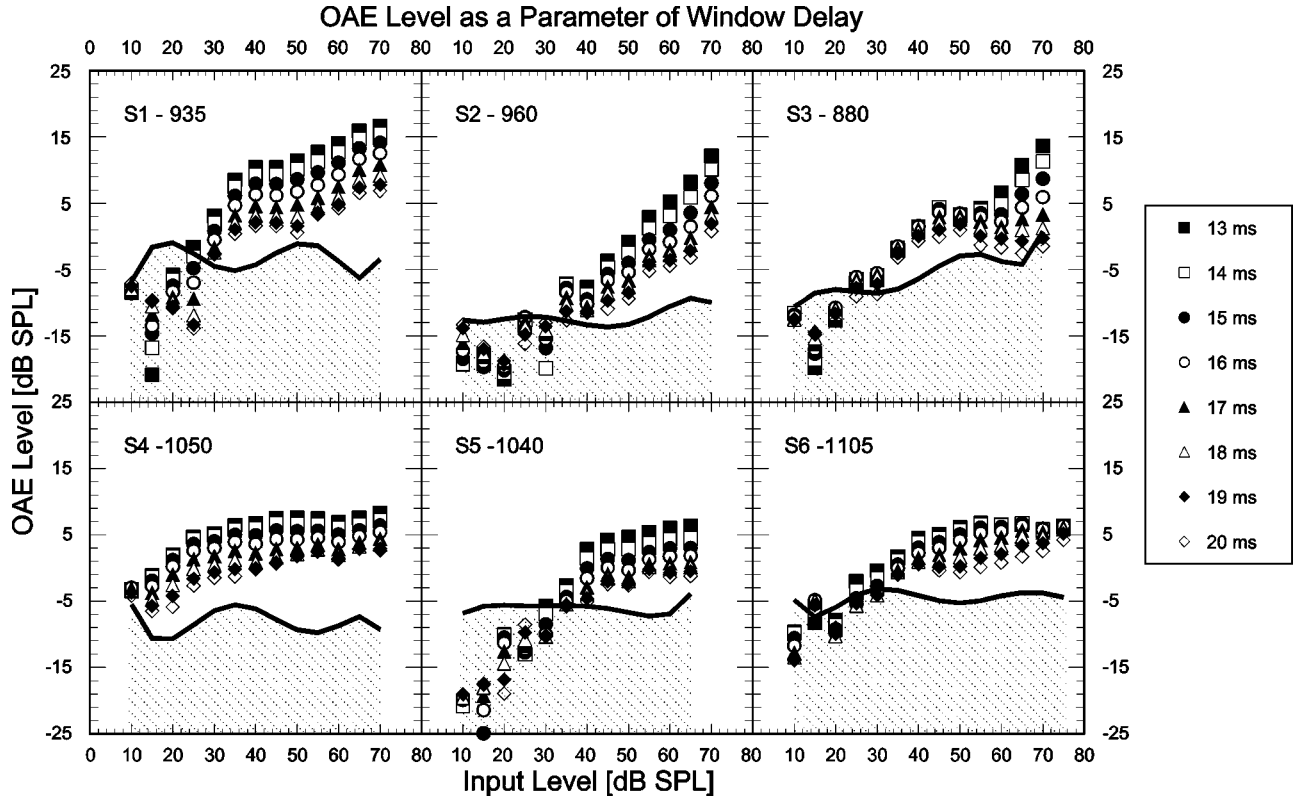

FIG. 2. The OAE level as a function of input level. Each panel is for a different subject. The OAEs were evoked by tone bursts and measured within a 21.48-ms window beginning 13 to 20 ms after the onset of the tone burst. Window delay is the parameter. Each delay is shown by a different symbol as indicated in the legend. The solid line is a polynomial fit to the background noise level.

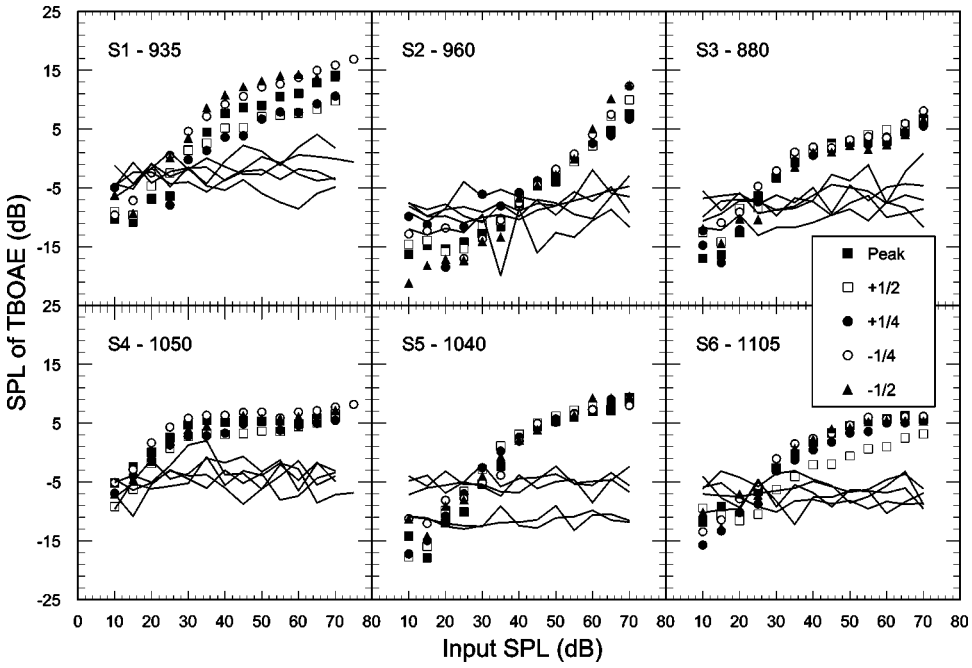

FIG. 3. The OAE level as a function of input level. The parameter is frequency offset in Barks. The noise floors are shown for comparison with Fig. 4. The average standard error of the mean emissions level above the noise floor is 0.77 dB with a range of levels from 0.15 to 1.47 dB. Peak frequency for each subject is given next to the subject label.

B. Effect of window delay

Figure 2 shows the results of varying the delay of the analysis window. Individual functions are shown for each window delay and the average noise floor is shown as a solid line.

Data that fall under the noise floor (i.e., within the shaded region) are considered questionable in terms of measurement accuracy and reliability. The curves all show a steeply increasing region followed by a flatter, compressive region. The TBOAE level decreases systematically as the delay increases, but the shape of the function hardly changes. The low-level slope is nearly linear for the delays examined. At moderate levels, a highly compressive I/O function is exhibited. There is also a slight increase in slope at higher levels. Similar results were obtained for most subjects, but some did exhibit a change in slope across the range of delays. Subject S3 showed an increase in slope above 55 dB SPL for delays of up to 16 ms, but the high-level slope decreased for 17- to 20-ms delays. The high-level function for subject S6 also changed shape across different window delays. The differences increased around 55–60 dB SPL. At 75 dB SPL, the highest level tested, the window delay seemed to have virtually no effect on the OAE level. This is likely to be due to the rapid decay of an OAE. For these two subjects, pushing the window too far back in time would cause a change in the resulting measurements. Therefore, it is important for the window to have a short or moderate delay. The location of the knee point of the function appears relatively invariant across all window delays for all subjects.

If the shape of the function depended markedly on the window delay, it would be difficult to decide which delay, if any, would show the ''true'' TBOAE I/O function. Overall, it was important to carefully select a time window that would not miss rapidly decaying OAEs, but would still avoid confusing the trivial reflections from the stimulus with an OAE. Therefore, a 15-ms window delay was used for all remaining measurements. A 15-ms delay seems to work well for all subjects, even those who exhibit rapidly decaying OAEs.

C. Effects of measurement frequency and delinearization

Figures 3 and 4 show six subjects' TBOAE responses at five frequencies at and around the spectral peak in the COAE response, with and without delinearization, respectively. All subjects' functions, except those of S2, exhibit a kneepoint close to 35 dB SPL. The functions exhibit similar slopes and compression, averaging about 0.23 above the kneepoint. Below the kneepoint, the functions are far less compressive. However, the delinearized functions in Fig. 4 are much closer to the noise floor than those in Fig. 3, surpassing the noise floor only when the input level reaches 35 or 40 dB SPL. In large part, this result may reflect that the I/O function is closer to being linear below the kneepoint, and that delinearization tends to cancel out any linear components of the response.

All subjects, except possibly S2, show some compressive portion of the I/O function. The compressiveness and the kneepoint varied from subject to subject, but were largely consistent across measurement frequency and delinearization conditions.

D. Summary of results

Generally, the delinearization produced poorer results with reduced magnitude of OAEs and a noise floor that was close to the OAE level. However, the delinearized functions tended to show compression slopes like those obtained without delinearization and virtually identical kneepoints as long as the relatively elevated noise floor in the delinearized responses did not obscure the kneepoint. The average delinearized slope was nearly equal to the slope obtained without delinearization in all cases.

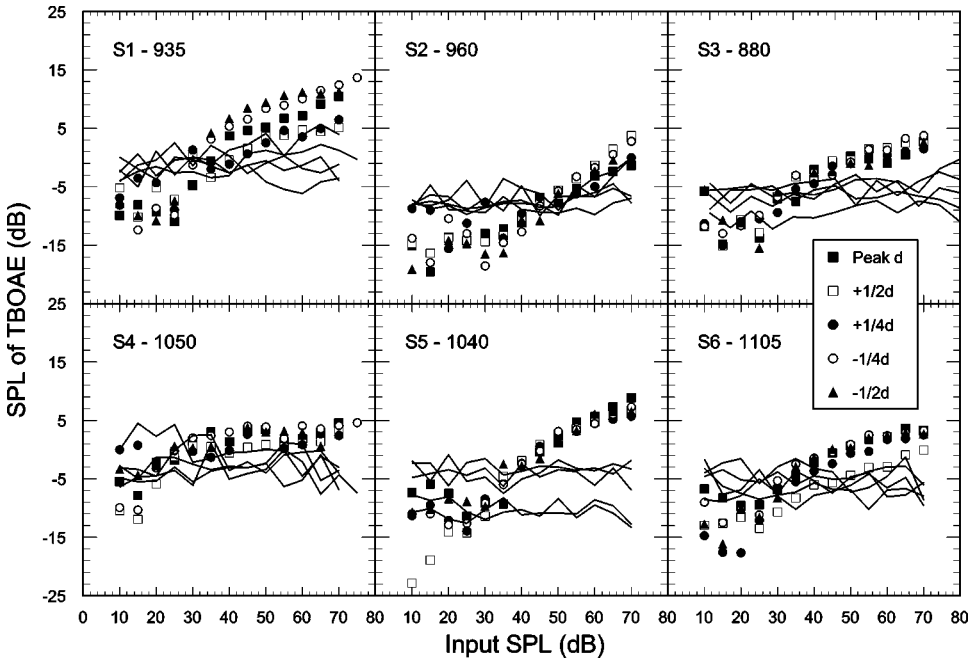

FIG. 4. The OAE level as a function of input level with delinearization. The parameter is frequency offset in Barks. The noise floors are also shown in order to illustrate the difference between the delinearized and normal functions (see Fig. 3). The standard error of the mean emission levels is 0.92 dB; they range from 0.02 to 3.08 dB. Peak frequency for each subject is given next to the subject label.

Table I shows the slope of the compressive upper part of the TBOAE I/O function and the kneepoint of the function for 13- to 20-ms window delays at the COAE peak frequency. Table Ia shows the correlation coeffecient r^2 for the fits to the functions fit to the windowing data. Tables II and III shows a summary of the slopes and kneepoints at the five selected frequencies with and without delinearization, respectively. Tables IIa and IIIa show the correlation coefficient r^2 for the fits to the functions for which the slopes are displayed in Tables II and III. Functions were fit using a simultaneous square-error minimization of two line fits, one above and one below the variable kneepoint. The fits were done using the data from 20 to 65 dB SPL to help avoid points very far below the noise floor and points at the upper end of the function where the slope might be changing rapidly. With a few exceptions, most notably subject S2, the

TABLE I. (a) Line-fit slopes of upper parts of the OAE functions (beyond the kneepoint) at peak frequency for window delays of 13 to 20 ms. (b) r^2 correlation coefficients for line-fit slopes of OAE functions from 20 to 65 dB SPL at peak frequency for window delays of 13 to 20 ms.

(a)

Window Delay	13	14	15	16	17	18	19	20	Mean
S1 Slope	0.23	0.23	0.23	0.23	0.23	0.22	0.21	0.20	0.22
S2 Slope	0.75	0.57	0.49	0.44	0.42	0.38	0.40	0.45	0.49
S3 Slope	0.39	0.28	0.18	0.08	0.00	−0.07	−0.09	−0.13	0.08
S4 Slope	0.05	0.03	0.03	0.05	0.06	0.08	0.10	0.12	0.06
S5 Slope	0.12	0.11	0.12	0.13	0.13	0.13	0.12	0.09	0.12
S6 Slope	0.16	0.15	0.15	0.17	0.17	0.14	0.14	0.11	0.15
Mean Slope	**0.28**	**0.23**	**0.20**	**0.18**	**0.17**	**0.15**	**0.14**	**0.14**	**0.19**
S1 Kneepoint	35.41	35.37	35.24	35.01	35.00	35.00	35.00	35.00	35.13
S2 Kneepoint	30.00	35.00	35.00	34.93	29.86	41.87	43.86	47.67	37.28
S3 Kneepoint	38.08	39.84	40.79	41.19	41.85	42.36	41.91	41.35	40.92
S4 Kneepoint	27.12	31.98	31.21	22.46	22.20	22.37	22.83	24.02	25.52
S5 Kneepoint	41.49	41.13	40.72	40.48	40.88	41.78	42.01	41.77	41.28
S6 Kneepoint	37.72	38.59	38.99	38.36	37.13	36.16	34.25	35.00	37.03
Mean Kneepoint	**34.97**	**36.99**	**36.99**	**35.40**	**34.49**	**36.59**	**36.64**	**37.47**	**36.19**

(b)

r^2 Window delay	13	14	15	16	17	18	19	20	Mean
S1	0.996	0.994	0.989	0.978	0.958	0.928	0.907	0.892	0.955
S2	0.858	0.907	0.923	0.927	0.965	0.978	0.986	0.976	0.940
S3	0.963	0.962	0.964	0.982	0.991	0.996	0.991	0.982	0.979
S4	0.934	0.931	0.923	0.930	0.945	0.956	0.960	0.951	0.941
S5	0.998	0.999	0.999	0.996	0.992	0.988	0.951	0.889	0.976
S6	0.978	0.988	0.993	0.995	0.994	0.990	0.974	0.954	0.983
Mean	**0.955**	**0.963**	**0.965**	**0.968**	**0.974**	**0.973**	**0.961**	**0.941**	**0.962**

TABLE II. (a) Line-fit slopes to the upper part of the function for an average of three TBOAE measurements for five frequencies without delinearization. The frequencies are expressed in the chart by their distance from the peak frequency in Barks. (b) r^2 correlation coefficients for line-fit slopes of an average of three TBOAE measurements for five frequencies *without* delinearization from 20 to 65 dB SPL.

(a)

	Frequency (Barks)					
	Peak	$+\frac{1}{2}$	$+\frac{1}{4}$	$-\frac{1}{4}$	$-\frac{1}{2}$	Mean
S1 Slope	0.22	0.18	0.23	0.24	0.10	0.19
S2 Slope	0.52	0.55	0.37	0.65	0.71	0.56
S3 Slope	0.14	0.18	0.16	0.17	0.17	0.16
S4 Slope	0.02	0.07	0.03	0.04	0.04	0.04
S5 Slope	0.25	0.21	0.20	0.27	0.29	0.24
S6 Slope	0.14	0.19	0.18	0.14	0.11	0.15
Mean Slope	**0.21**	**0.23**	**0.20**	**0.25**	**0.24**	**0.23**
S1 Kneepoint	37.86	33.73	37.58	34.77	37.63	36.32
S2 Kneepoint	35.35	35.47	34.99	35.82	34.14	35.15
S3 Kneepoint	36.28	34.96	35.35	33.49	35.77	35.17
S4 Kneepoint	26.52	27.29	29.06	25.06	28.68	27.32
S5 Kneepoint	38.36	36.87	36.88	37.74	36.35	37.24
S6 Kneepoint	37.11	30.42	35.44	33.39	36.08	34.49
Mean Kneepoint	**35.25**	**33.12**	**34.88**	**33.38**	**34.78**	**34.28**

(b)

	Frequency (Barks) r^2					
	Peak	$+\frac{1}{2}$	$+\frac{1}{4}$	$-\frac{1}{4}$	$-\frac{1}{2}$	Mean
S1	0.978	0.983	0.954	0.996	0.989	0.980
S2	0.991	0.985	0.931	0.956	0.982	0.969
S3	0.977	0.976	0.992	0.980	0.949	0.975
S4	0.918	0.923	0.748	0.877	0.932	0.880
S5	0.980	0.995	0.995	0.942	0.984	0.979
S6	0.990	0.987	0.983	0.984	0.958	0.980
Mean	**0.972**	**0.975**	**0.934**	**0.956**	**0.966**	**0.960**

slopes are quite similar across frequency and delinearization conditions.

If window delay has no effect, then all the values in a single row in Table I should be identical. Although some variations were present for some subjects at the lowest and highest window delays, only S3 showed large changes in slope for moderate values of window delay. An ANOVA on the effect of window delay indicated that there was a significant effect (P value <0.0001). However, Scheffe *post-hoc* analysis shows significant differences only exist between the longer and shorter windows (13/17, 13/18, 13/19, 13/20, 14/18, 14/19, 15/19, 15/20, and 16/20).

If frequency shifting and delinearization both have no effect, then all the values in a single row of Tables II and III should be identical. Again, some minor variation was seen in some subjects, but there was generally only a very small change in the slope resulting from small shifts in stimulus frequency and virtually no change was apparent when looking at average results. An ANOVA on the effect of frequency yielded a P value of 0.06, just greater than a result showing significance. Scheffe *post-hoc* analysis, however, showed that all frequency interactions yielded P values >0.3 except the interaction between $-\frac{1}{4}$ Bark and $+\frac{1}{2}$ Bark, which had a P value of 0.095, thereby reinforcing the assertion that there is no significant effect of small frequency changes on the amplitude of TBOAEs.

The slopes for subjects S5 and S6 appear to be larger with delinearization than without, but the mean slopes with and without delinearization were identical, indicating that delinearization does not have an effect on the shape of the upper portion of the TBOAE I/O function.

IV. GENERAL DISCUSSION

Although the change in slope caused by delinearization was small for most subjects, there was a general tendency for delinearization to reduce the levels of the OAEs near the kneepoint more than those at high levels. A small increase in slope occurred because of this low-level reduction. However, at the higher levels (approximately 65–80 dB SPL), the slope with and without delinearization was nearly identical in all cases. Overall, there was no benefit to using delinearization. In fact, it reduced the level of the signal both in absolute terms and, more importantly, relative to the noise floor. Thus, it made measurements more time consuming and more uncertain for low stimulus levels. To the extent that it is important to characterize the nearly linear low-level part of the function, delinearization is likely to be undesirable because it eliminates any linear part of the response. Accordingly, delinearization is counterproductive for the present purpose because merely using a window delay sufficiently eliminates the trivial echo.

TABLE III. (a) Line-fit slopes to the upper part of the function for an average of three TBOAE measurements for five frequencies with delinearization. The frequencies are expressed in the chart by their distance from the peak frequency in Barks. (b) r^2 correlation coefficients for line-fit slopes of an average of three TBOAE measurements for five frequencies *with* delinearization from 20 to 65 dB SPL.

(a)

	Frequency (Barks) (with delinearization)					
	Peak	$+\frac{1}{2}$	$+\frac{1}{4}$	$-\frac{1}{4}$	$-\frac{1}{2}$	Mean
S1/Slope	0.23	0.20	0.21	0.23	0.11	0.20
S2/Slope	0.30	0.47	0.26	0.51	0.45	0.40
S3/Slope	0.18	0.20	0.20	0.22	0.18	0.19
S4/Slope	0.03	0.04	0.03	0.02	−0.01	0.02
S5/Slope	0.46	0.35	0.32	0.37	0.34	0.37
S6/Slope	0.21	0.23	0.25	0.18	0.14	0.20
Mean Slope	**0.24**	**0.25**	**0.21**	**0.25**	**0.20**	**0.23**
S1/Kneepoint	40.20	30.02	29.94	38.07	41.77	36.00
S2/Kneepoint	35.03	35.54	34.47	35.77	35.33	35.23
S3/Kneepoint	37.46	35.65	35.84	34.63	36.25	35.97
S4/Kneepoint	28.18	27.89	30.03	29.82	31.10	29.41
S5/Kneepoint	36.01	37.16	37.11	36.58	34.50	36.27
S6/Kneepoint	35.77	38.75	30.44	38.07	44.60	37.52
Mean Kneepoint	**35.44**	**34.17**	**32.97**	**35.49**	**37.26**	**35.07**

(b)

	Frequency (Barks) r^2 delinearized					
	Peak	$+\frac{1}{2}$	$+\frac{1}{4}$	$-\frac{1}{4}$	$-\frac{1}{2}$	Mean
S1	0.965	0.835	0.748	0.966	0.982	0.899
S2	0.949	0.981	0.753	0.880	0.941	0.901
S3	0.885	0.931	0.947	0.981	0.854	0.920
S4	0.647	0.923	−0.069	0.846	−0.074	0.455
S5	0.903	0.959	0.956	0.973	0.919	0.942
S6	0.967	0.947	0.996	0.960	0.950	0.964
Mean	**0.886**	**0.929**	**0.722**	**0.934**	**0.762**	**0.847**

In considering using TBOAEs to characterize cochlear function, it is important that the measurement be robust, at least across a reasonable range of levels. If the form of the I/O function varied significantly with frequency, it would be impossible to know which measured function, if any, was the ''correct'' I/O function. Interestingly, the frequency at the peak of the COAE spectrum did not always produce the strongest TBOAE. For a given subject, the frequency that evoked the greatest response tended to be the same across all levels, but the relation of this frequency to the subject's COAE peak was not consistent across subjects. This may be a result of multiple, strong OAE-producing locations present near each other on the basilar membrane, which apparently cause the ''best'' frequency to depend on whether the evolving stimulus has a broad or narrow spectrum. Regardless of the cause, the functions did not tend to cross one another. Although no particular distance from the COAE peak seemed better than any other (on average), the frequency at the peak of the COAE spectrum generally produced a moderate to large response within the group of five frequencies. The measurements at various frequencies around the peak of the COAE spectrum showed that the form of the TBOAE I/O function was not dependent on frequency, at least in the range examined. In other words, there was little or no interaction between the test frequency and TBOAE I/O shape and it is sufficient to test at one frequency.

V. SUMMARY

Through an examination of measurement paradigms and parameters, an effective technique for measuring tone-burst otoacoustic emissions with minimal noise has been developed. These measures are largely independent of specific choices of measurement parameters and make a good starting point for considering the use of TBOAEs to examine cochlear function. The effect of frequency and windowing on the measurement of TBOAE I/O functions was examined and, under the conditions used, tone-burst OAEs can be measured without concern for these potential confounds as long as a moderate, sensible time-window delay is used. In practice, time windowing is a simple and effective way of eliminating almost all of the response to the signal itself, obviating the need for delinearization techniques, which tend to add noise and complexity to the measurements without providing any clear beneficial change to the results. In fact, delinearization tended to diminish the quality of the data, especially at low levels. In addition, small changes in frequency did not affect the shape, kneepoint, or slope of the I/O function, indicating that the exact test frequency selected for an individual is not critical. Thus, it is likely that any TBOAE measurements may be a useful tool for examining cochlear function and procedural choices can be made on the bases of simple criteria, such as the OAE-to-noise-floor level difference and the lowest level at which TBOAE can be observed.

ACKNOWLEDGMENTS

The author wish to thank Bertram Scharf and the reviewers for helpful comments. This research was supported by NIH/NIDCD Grant Nos. R01DC02241 and R01DC00187.

ANSI (**1989**). ''ANSI S3.6-1989: Specifications for audiometers,'' (American National Standards Institute, New York).

Buus, S., Obeling, L., and Florentine, M. (**2001**). ''Can basilar-membrane compression characteristics be determined from distortion-product otoacoustic-emission input-output functions in humans?'' in *Physiological and Psychophysical Bases of Auditory Function*, edited by D. J. Breebaart, A. J. M. Houtsma, A. Kohlrausch, V. F. Prijs, and R. Schoonhoven (Shaker, Maastricht, Netherlands), p. 373.

Mansfield, J. D., Baghurst P. A., and Newton V. E. (**1999**). ''Otoacoustic emissions in 28 young adults exposed to amplified music,'' Br. J. Audiol. **33**, 211–222.

Neumann, J., Uppenkamp, S., and Kollmeier, B. (**1997**). ''Relations between notched-noise suppressed TEOAE and the psychoacoustical critical bandwidth,'' J. Acoust. Soc. Am. **101**, 2778–2788.

Norton, S. J. and Neely, S. T. (**1987**). ''Tone-burst-evoked otoacoustic emissions from normal-hearing subjects,'' J. Acoust. Soc. Am. **81**, 1860–1872.

Shera, C. A., Guinan, Jr., J. J., and Oxenham, A. J. (**2002**). ''Revised estimates of human cochlear tuning from otoacoustic and behavioral measurements,'' Proc. Natl. Acad. Sci. U.S.A. **99**(5), 3318–3323.

Withnell, R. H., and Yates, G. K. (**1998**). ''Onset of basilar membrane nonlinearity reflected in cubic distortion tone input-output functions,'' Hear. Res. **123**, 87–96.

Compensation for pitch-shifted auditory feedback during the production of Mandarin tone sequences

Yi Xu[a)]
Haskins Laboratories, 270 Crown Street, New Haven, Connecticut 06511

Charles R. Larson and Jay J. Bauer
Department of Communication Sciences and Disorders, Northwestern University, 2240 Campus Drive, Evanston, Illinois 60208

Timothy C. Hain
Departments of Neurology, Otolaryngology, and Physical Therapy/Human Movement Sciences, Northwestern University, 645 N. Michigan, Suite 1100, Chicago, Illinois 60611

(Received 7 November 2003; revised 28 April 2004; accepted 30 April 2004)

Recent research has found that while speaking, subjects react to perturbations in pitch of voice auditory feedback by changing their voice fundamental frequency (F_0) to compensate for the perceived pitch-shift. The long response latencies (150–200 ms) suggest they may be too slow to assist in on-line control of the local pitch contour patterns associated with lexical tones on a syllable-to-syllable basis. In the present study, we introduced pitch-shifted auditory feedback to native speakers of Mandarin Chinese while they produced disyllabic sequences /ma ma/ with different tonal combinations at a natural speaking rate. Voice F_0 response latencies (100–150 ms) to the pitch perturbations were shorter than syllable durations reported elsewhere. Response magnitudes increased from 50 cents during static tone to 85 cents during dynamic tone productions. Response latencies and peak times decreased in phrases involving a dynamic change in F_0. The larger response magnitudes and shorter latency and peak times in tasks requiring accurate, dynamic control of F_0, indicate this automatic system for regulation of voice F_0 may be task-dependent. These findings suggest that auditory feedback may be used to help regulate voice F_0 during production of bi-tonal Mandarin phrases. © *2004 Acoustical Society of America.*
[DOI: 10.1121/1.1763952]

PACS numbers: 43.70.Aj, 43.75.Bc [AL] Pages: 1168–1178

I. INTRODUCTION

The demands of normal speech production require syllable rates of 5–7/sec, each usually consisting of a consonant and a vowel. Additionally, for speakers of a tone language like Mandarin Chinese, characteristic pitch contours over the voiced portion of the syllables (i.e., lexical tones) have to be produced to distinguish words that are otherwise phonologically identical. For example, the syllable /ma/ in Mandarin can mean ''mother,'' ''hemp,'' ''horse,'' or ''to scold'' if it is said with either a High (H), Rising (R), Low (L), or Falling (F) tone, as shown in Fig. 1(a). Understanding speech motor control requires knowledge of the mechanisms controlling production of strings of consonants, vowels and tones. Figure 1(b) displays mean fundamental frequency (F_0) tracings across four, 5-syllable Mandarin sentences produced by a male native speaker in Xu (1999). Each 5-syllable sentence carries a tone sequence of H*x*RHH, where *x* varies across H, R, L, and F. The local variations in pitch (indicated by standard deviation bars) are small in comparison to the F_0 changes for the different tones and reveal consistent productions within each tone sequence.

These consistent patterns suggest that in addition to a need for a control process to direct the implementation of the sequential lexical pitch targets (Xu and Wang, 2001), there may also be one or more processes that ensure that the production is executed reliably and precisely. In the present paper we address a candidate second process in the form of the reliance on auditory feedback to stabilize voice F_0 around a pitch trajectory or target. The role of kinesthetic feedback in the rapid control of speech movements has been demonstrated by previous research (Abbs and Gracco, 1984; Kelso *et al.*, 1984). The role of auditory feedback in the online control of natural speech, however, has not been clearly demonstrated before. Experiments using pitch-shifted auditory feedback presented during the nonsense words ''ta:tatas'' (Donath *et al.*, 2002; Natke *et al.*, 2003; Natke and Kalveram, 2001) demonstrated that if the first syllable was stressed, there was a response to the pitch-shift stimulus that persisted into the next syllable. Jones and Munhall (2002) presented pitch-shifted feedback during unnaturally prolonged vowels during Mandarin speech and also showed an effect on F_0. In both of these experiments the speech was not normal, and so the question remains whether auditory feedback is used on-line for control of F_0 during normal speech. Moreover, previous pitch-shifting studies suggest that auditory feedback contributes to long-term parametric adaptation rather than to online control of voice F_0 (Jones and Munhall, 2000; Jones and Munhall, 2002). That is, com-

a)Corresponding author: Yi Xu, Haskins Laboratories, 270 Crown Street, New Haven, Connecticut 06511. Telephone: (203) 865-6163, ext. 210; fax: (203) 865-8963; electronic mail: xu@haskins.yale.edu

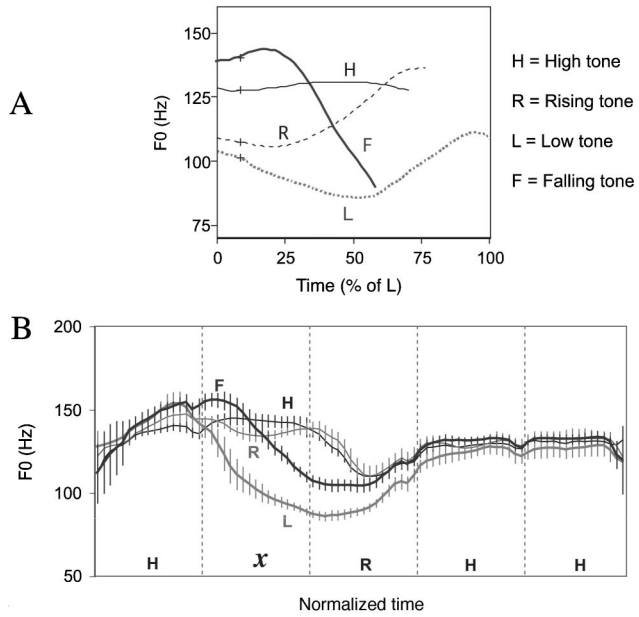

FIG. 1. (a) Mean F_0 contours of Mandarin syllable /ma/ spoken with four lexical tones: High (H), Rising (R), Low (L), and Falling (F). The syllables mean "mother," "hemp," "horse," or "to scold," respectively. Data averaged over 48 repetitions by eight male speakers (Xu, 1997). (b) Mean F_0 curves of the Mandarin tone sequences H*x*RHH where *x* varies across H, R, L, and F (which changes the meaning of the first word from "catty" to "cat-fan," "cat-rice," or "cat-honey." The vertical grids mark the syllable boundaries. The short vertical bars depict $+/-$ one standard deviation about the mean. Data averaged across five repetitions produced by one speaker from Xu (1999).

pensatory reactions to shifted auditory feedback tend to occur *after*, rather than during articulation of a linguistic unit such as a consonant or a vowel. A possible reason for not using auditory feedback for online control of articulation is that it is slow and may exceed the temporal domain of the targeted linguistic unit. In the case of lexical tones in Mandarin, the time interval available for each tone is the duration of the syllable (Xu and Wang, 2001). As found in Xu (1997), the mean duration of a simple CV syllable in Mandarin (where C is a nasal consonant like /m/, and V is a simple vowel or diphthong like /a/, /i/, /ao/ or /ai/) is about 180 ms. This means that for auditory feedback to be effective for the online control of voice F_0 in Mandarin speech, the system must respond significantly sooner than 180 ms.

Recent research suggests that this time constraint can be met in some situations. It has been demonstrated that German speakers compensate for the mismatch between intended F_0 and feedback pitch during production of nonsense syllables (Donath *et al.*, 2002; Natke *et al.*, 2003; Natke and Kalveram, 2001). The observed response latencies were about 150 ms, which is 30 ms shorter than the syllable durations reported by Xu (1997, 1999), and therefore may be quick enough for the correction to take effect within a single syllable. However, the authors of the study were convinced that these latencies were still too slow for the system to be effective in controlling F_0 within single syllables. Thus, they concluded that "the purpose of the auditory-vocal system is not to control voice F_0 precisely within single syllables, but rather on a supra-segmental level in the context of prosody (Donath *et al.*, 2002)." Furthermore, in a study that investigated the role of auditory feedback on Mandarin, Jones and Munhall (2002) found that Mandarin speakers responded to pitch-shifted auditory feedback with compensatory changes in voice F_0 with a response latency around 200 ms. This is longer than the mean syllable duration in Mandarin reported before (Xu, 1997, 1999), although slightly shorter than the 215 ms reported by Duanmu (1994). Previous research thus suggests that neither Mandarin nor German speakers respond to pitch-shifted feedback quick enough for auditory feedback to modulate F_0 within syllables.

In studies of voice F_0 compensation using nonspeech tasks, however, response latencies shorter than those reported by the aforementioned German and Mandarin studies have been found. In a study in which trained singers received pitch-shifted feedback during glissandos, response latencies were as short as 76 ms (Burnett and Larson, 2002). In studies where non-trained singers produced sustained vowels at constant F_0, latencies of 114 ms (Hain *et al.*, 2000) and 130 ms (Larson *et al.*, 2001) have been reported. If it can be shown that the system can also respond to perturbed auditory feedback with latencies shorter than syllable duration during normal speech, it would suggest that auditory feedback may be used to control voice F_0 online during a syllable, not just for suprasegmental features of longer duration. It therefore becomes necessary to explore possible explanations for the discrepancies in reported latencies between speech and nonspeech tasks.

One possibility is that the discrepancies in response latency across these studies are due to methodological differences. In studies on sustained vowels (Burnett *et al.*, 1998; Hain *et al.*, 2000; Larson *et al.*, 2001) or prolonged vowels during Mandarin speech (Jones and Munhall, 2002), latency was defined as an F_0 trajectory that exceeded $+/-2$ S.D.'s of the prestimulus mean F_0. As has been pointed out, this technique likely overestimates the actual time when the voice F_0 begins to respond to the pitch-shifted feedback (Donath *et al.*, 2002). Moreover, the technique requires a steady F_0 level prior to the stimulus, which is not appropriate for speech because the prestimulus F_0 trajectory varies. In addition, the latency reported by Jones and Munhall may also have been skewed since the speakers produced long sustained vowels during the experiment, which is not typical of normal Mandarin speech. Because of the discrepancies in latencies from previous studies (Burnett *et al.*, 1998; Burnett and Larson, 2002; Donath *et al.*, 2002; Hain *et al.*, 2000; Jones and Munhall, 2002; Larson *et al.*, 2001; Natke *et al.*, 2003; Natke and Kalveram, 2001) and the critical role this plays in defining functions of auditory feedback during speech, we adopted a technique similar to that developed by Donath and Natke (Donath *et al.*, 2002; Natke *et al.*, 2003) for measuring latency. We used a statistical test to determine whether the F_0 trajectories following the stimulus differ significantly from control (nonstimulated) trajectories during the production of disyllabic phrases in normal Mandarin speech.

Another issue, especially relevant to studies of speech in nontone languages such as German, is that the latency and magnitude of the compensatory responses of the audio-vocal system to pitch-shifted feedback vary depending on the

strength of the demand of the vocal task. In a study in which subjects were instructed to modulate their voice F_0 when they perceived pitch-shifted feedback, the response latencies were reduced (Hain *et al.*, 2000). Also, Natke *et al.* (2003) showed that the pitch-shift response is larger in magnitude in singing compared to previous studies of sustained vowels in nonsingers. These findings suggest that the response latencies and magnitudes reported in previous studies observed with sustained vowels may be slower and smaller than those involving dynamic pitch movement in natural speech.

The present study was therefore designed to test the following hypotheses using Mandarin speech. First, compensatory responses to pitch-shifted feedback occur during the natural production of tonal sequences in the language. Second, the compensatory responses are fast enough to serve as part of the online sensory-motor control mechanisms for tone production in speech. Third, the latency and magnitude of the compensatory responses vary with the demand of the tonal production, and are generally faster and larger for speech in which accurate F_0 control is necessary. To test these hypotheses, we devised a technique that introduces pitch-shifted stimuli at specific times during a disyllabic speech production.

The primary goal of the experiment was to see whether and how speakers react to the pitch-shifted auditory feedback during three bi-tone sequences representative of Mandarin speech: High-High (H-H), High-Rising (H-R), and High-Falling (H-F). The pitch-shift stimuli were timed so that they would occur either during the first syllable or during the transition between the first and second syllables. The object of testing these two timing variables was to test the effects of pitch-shifted feedback during relatively steady state F_0 contours and during dynamic F_0 contours. Both upward and downward pitch-shift stimuli were presented to assess whether stimulus direction interacted with the direction in the change in the tone associated with each bi-tonal sequence. For all three independent variables, we predicted that response magnitudes would be larger and response latencies and peak times would be shorter than those previously observed in a static vowel condition. These effects would suggest the need for a rapid response of sufficient magnitude to correct for production errors within the syllable.

II. METHODS

A. Subjects

Subjects consisted of six speakers whose first language was the Beijing dialect of Mandarin Chinese (four females and two males; ages 20–40). Subjects reported no history of hearing loss, neurological deficits and/or speech-language disorders.

B. Apparatus and stimuli

Subjects were seated comfortably in a small acoustically shielded chamber and asked to read aloud the experimental stimuli at approximately 70 dB SPL (self-monitored visually with a Dorrough Loudness Monitor model 40-A). Voice output was transduced through an AKG boom-set microphone (model HSC 200) at a microphone-mouth-distance of 3 cm. The microphone signal was amplified by a Mackie mixer (model 1202) and then processed for pitch-shifting through an Eventide Ultraharmonizer (H3000 SE). The microphone signal was then mixed with 70 dB SPL pink masking noise (Goldline Audio Noise Source, model PN2, spectral frequencies 1 to 5000 Hz) using a Mackie mixer (model 1202-VZL), routed through HP 350 dB attenuators, and presented to the subject over AKG headphones (model HSC 200) at 80 dB SPL after amplification by a Crown D75-A amplifier. Acoustical equipment was calibrated with a Brüel & Kjær 2203 sound level meter (A weighting). During each utterance a MIDI software program (Max v. 4.1 by Cycling '74) directed the Ultraharmonizer to randomly pitch-shift the voice feedback upwards or downwards by 200 cents for a duration of 200 ms, or to leave the feedback unchanged (control). The Ultraharmonizer automatically shifts pitch in units of cents because this scale is logarithmically related to F_0 and is constant relative to the absolute F_0 of a given subject. The subject's voice onset automatically activated the MIDI program using a locally fabricated Schmitt trigger circuit that detected a positive voltage ($\sim$100 mv) on the leading edge of the amplified vocal waveform and produced a TTL pulse with less than 1 ms delay. The output of this circuit then was fed to a modified Macintosh mouse to simulate a ''mouse click.'' The pointer of the mouse was kept stationary during an experiment over a ''button'' on the MIDI software program, and when a vocalization began, the trigger circuit activated the mouse to initiate the MIDI program. The MIDI program then presented a randomized signal to the Harmonizer. The variability in the timing of the MIDI output from the onset of the pulse from the vocal detection circuit was about 25 ms. The MIDI signal to the harmonizer was either a command to produce no shift in pitch feedback, an increase or a decrease in pitch feedback to the subject. The variability in the delay time for the harmonizer to present a pitch-shift stimulus was about 15 ms. Thus, the total variability in the delay time between onset of vocalization and the presentation of the pitch-shift stimulus to the subject was about 40 ms.

Subjects read a randomized list of disyllabic nonsense Mandarin phrases (/ma ma/) printed in Chinese characters, produced without a carrier frame, consisting of 3 bi-tonal patterns at a comfortable rate of about 0.5 s per phrase. Similar syllable sequences were used before in an acoustic study (Xu, 1997). The tonal patterns, High-High (H-H), High-Rising (H-R), and High–Falling (H-F), were chosen to place different linguistic demands on speech production seen in Mandarin (see Fig. 1). In the H-H phrase, the variation in F_0 is rather minimal as compared to both the H-R and H-F phrases. For the H-R phrase, the speaker must maintain a relatively high F_0 followed by a rapid F_0 drop with a subsequent rise. Thus to be perceived as H-R, there must be a distinct drop in F_0 to enable the subsequent rise, and both of these changes must differ from the F_0 of the ''High'' tone. The H-F phrase should require greater precision than the H-H phrase because the ''Falling'' tone must be clearly differentiated from the ''High'' tone. However, accuracy at the end of the ''Falling'' tone is inconsequential because glottal-

ization frequently occurs with the drop in F_0 when it is at the end of an utterance.

The second procedural variable we manipulated was the timing of the stimulus. Stimuli were either presented relatively early in the first syllable ($\sim$100 ms after vocalization onset) or near the beginning of the second syllable ($\sim$250 ms after vocal onset). The actual timing of the stimuli varied from 75–115 ms for the ''100 ms'' condition and 250–290 ms for the ''250 ms'' condition. The early timing condition was designed to disrupt the first (High) tone and possibly the transition into the second tone (High, Rising or Falling), while the later timing would primarily disrupt dynamic transitions into the second tone. The timing of the stimulus with respect to the syllable boundaries varied as a function of the speed of speaking but was generally within $+/-50$ ms of the syllable transition.

The final stimulus parameter we manipulated was the direction of the pitch-shift stimulus. Pitch-shift stimuli were either upward (increase in pitch of voice feedback) or downward (decrease in pitch of voice feedback). In keeping with previous studies, we anticipated that most responses would be opposite in direction to the stimulus (compensatory) and would occur in both stimulus directions. In addition, we anticipated that larger responses would be observed in the H-R and H-F phrases when the direction of the stimulus was opposite to the ongoing F_0 modulation at the time of the stimulus presentation. We predicted that for the H-R phrase, a downward stimulus in the 250 ms timing condition would elicit a smaller response than an upward stimulus because the latter would be perceived as a failure to reach the desired low F_0 trajectory, and subjects would respond with a greater response magnitude. We also predicted that downward stimuli occurring during the elevation prior to the tone drop in the H-F phrase would elicit a larger response than an upward stimulus.

For each phrase and timing condition, the subject produced about 20 repetitions as control trials, 20 with an increase in voice pitch feedback, and 20 with a decrease in pitch feedback. Prior to actual data collection, subjects produced several practice phrases, and their temporal patterns were measured for consistency. Consistency was evaluated in two ways. Our Mandarin speaking experimenter (YX) listened to the speech to be certain that the words were spoken with correct pronunciation. Second, we measured the temporal patterns of the waveforms on a computer screen to make sure the durations of each syllable were consistent across trials. We allowed for variations in timing of individual syllables of approximately 50 ms. If the productions lacked a consistent temporal pattern, subjects were instructed again on how to produce the phrases consistently. Consistent patterns were necessary to adjust the MIDI software to deliver the stimuli at the same relative time in the phrase for each subject. Between sets of trials, subjects rested and hydrated themselves.

C. Analysis

The subject's voice output and auditory feedback was low pass filtered at 5 kHz and digitized on-line onto a laboratory computer at 10 kHz (12-bit sampling). A control signal representing the onset and direction of the pitch-shift stimulus was digitized as well. In off-line analysis, voice and auditory feedback signals were low pass filtered (digital filter, 5th order) at the mean F_0 level for each subject, differentiated so as to equalize the waveform amplitude, and then smoothed with a five-point binomial, sliding window. A voice F_0 analog wave was then extracted using a software algorithm (Igor Pro v. 4.06 by Wavemetrics) that detected positive-going threshold-voltage crossings, interpolated the time fraction between each pair of sample points that constituted a crossing, and calculated the reciprocal of the period defined by the center points. The resulting F_0 analog (Hz) was further transformed into cents, using the following equation: $\text{cents} = 100\ (39.86 \log_{10}(\text{f2/f1}))$, where f1 is an arbitrary value of 196 Hz and f2 is the voice signal in Hertz. The conversion of all F_0 analog signals to cents allowed for a comparison of F_0 across different pitch levels and subjects. An interactive program was then used to generate event-related averages for each experimental condition. Each syllable phrase was time-aligned to the start of each vocalization to reduce the dispersion of temporal variations in the F_0 trajectory, marked as to the type of bi-tonal pattern (H-H, H-R, or H-F), and sorted based on the pitch-shift stimulus condition (up, down, or control). An average waveform of the F_0 analog was then generated for each bi-tonal pattern and stimulus condition per subject. Measures of the average response to the pitch-shift stimuli were made by a comparison with the average of the control wave for the specific condition for that subject.

An additional analysis was performed to estimate the response latency by determining if the averaged test waves differed significantly from the averaged control waves. For this procedure, F_0 analog waves were first decimated to 100 Hz. Then a t-test (equal variance; two tailed) was performed comparing all test trials of the F_0 analog wave for each condition with the corresponding set of control trials on a point-by-point basis. That is, t-tests were performed between test and control trials in 10 ms intervals. The result of this operation produced a wave comprised of a probability value (p) between a set of test and control waves for each 10 ms epoch of the ensemble average. Figure 2 illustrates the relation between the average waves (A), ''p'' values (B), and the difference wave (C) for one subject. Responses in which p values failed to reach a significance level of at least 0.02 and remain significant for at least 50 ms were defined as nonresponses. Latency was defined as the first p value that occurred at a significance level of 0.05 [the circled value in Fig. 2(b)]. Although a Bonferroni correction would normally be warranted for multiple t-tests, we believe that rejecting responses that do not last at least 50 ms is a more conservative approach to control for type I errors. The logic for this argument is that the twitch contraction times for most laryngeal muscles are less than 30 ms (Alipour-Haghighi *et al.*, 1987; Kempster *et al.*, 1988; Larson *et al.*, 1987), and a response that lasts at least 50 ms is more likely to represent a neuromuscular event than non-muscular signal transients. The response magnitude and the time of the peak response magnitude were measured from the maximal point on the difference wave, if these values occurred within a time frame

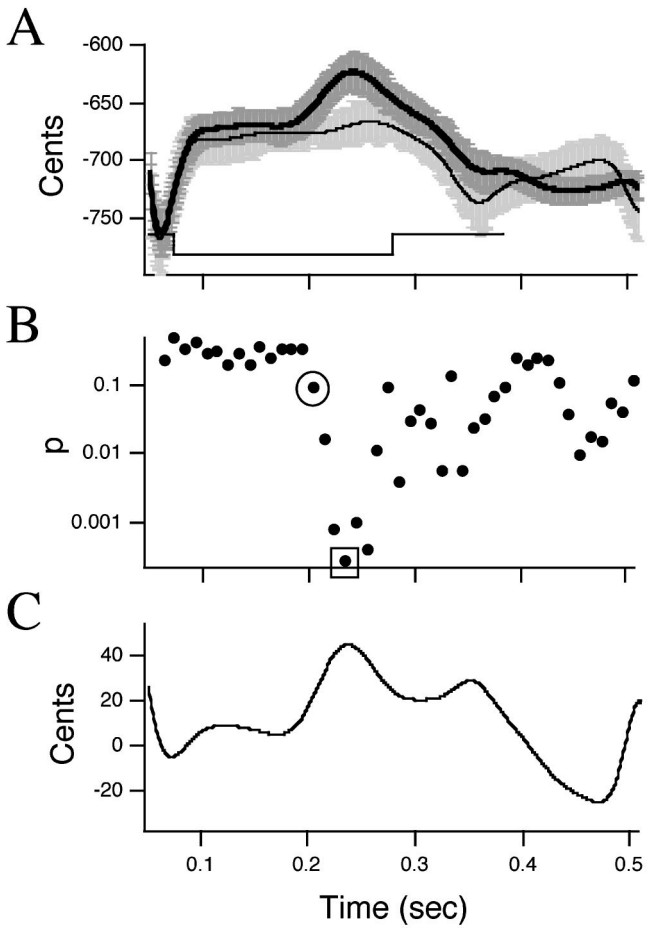

FIG. 2. (a) Averaged test wave (heavy black line) superimposed on standard error of the mean (SE) (dark gray wide line) in response to a downward pitch-shift stimulus. Control average wave (thin black line) superimposed on SE (light gray wide line). The square wave at the bottom indicates time and direction of stimulus (vertical dimension not to scale). (b) Probability (p) values resulting from a t-test comparison of test and control waves (see the text for details). The circled point is defined as response latency and the boxed point is the time of peak response magnitude. (c) The difference wave calculated by subtracting control from the test average wave.

defined by significant p values. However, in some cases, the difference wave was continuously changing throughout the period defined by significant p values and a peak in the difference wave could not be defined. In these instances, the peak time and peak magnitude were measured from the difference wave at the time indicated by the most significant p value [the boxed value in Fig. 2(b)]. The response direction with respect to the stimulus direction was also noted for each average wave and classified as compensatory or ''following.'' A response was considered to be compensatory if the response's direction was opposite to that of the stimulus direction, and conversely, a response was classified as ''following'' if the response was in the same direction as the pitch-shift stimulus.

TABLE I. Total number of ''following'' (FOL) and compensating (COMP) responses and nonresponses (NR) across three bi-tonal patterns (H-F, H-H, and H-R).

	H-F	H-H	H-R	TOTAL
FOL	3	0	4	7
COMP	15	18	15	48
NR	6	6	5	17
TOTAL	24	24	24	72

TABLE II. Total number of ''following'' (FOL) and compensating (COMP) responses and nonresponses (NR) across two timing conditions (100 and 250 ms).

	100	250	TOTAL
FOL	6	1	7
COMP	20	28	48
NR	10	7	17
TOTAL	36	36	72

For two of the disyllabic sequences there was a large, rapid drop in the F_0 trajectory (H-R, H-F). In most cases it was possible to measure a response just before or after the drop. However, in some cases, the response to the pitch-shift stimulus appeared to be a timing difference where the experimental average occurred either earlier or later than the control average (phase-shifted). In these cases, it was not possible to measure a change in magnitude and these were classified as ''nonresponses'' as a result of a phase-shift.

The statistical analysis of response magnitudes and latencies was done with repeated-measures ANOVAs. In cases where the averaged signals failed to differ significantly from control waves, neither latencies nor magnitudes were measured. These cases resulted in missing data for a subject for a condition. In order to meet the assumptions of a repeated-measures ANOVA, the missing data points were replaced with mean values calculated from the measured data from other subjects for that condition.

III. RESULTS

Out of a possible 72 averaged responses across subjects (12 averages per subject across 3 syllable conditions, 2 stimulus directions, and 2 onset conditions), there were 17 nonresponses, seven ''following'' responses, and 48 compensating responses. Tables I, II, and III provide a breakdown of response types across experimental conditions. It is noteworthy that no ''following'' responses were observed for the H-H productions and only one for the 250 ms timing condition. Compensating and nonresponses were rather evenly dispersed across bi-tonal patterns, stimulus timing, and stimulus direction. Eight nonresponses were due to an apparent phase shift in the observable response. Nine of the nonresponses were those in which the averaged waveform failed to differ significantly from the control waveform for a duration of at least 50 ms. The individual responses comprising the average ($\sim$20 responses per average) may have been a

TABLE III. Total number of ''following'' (FOL) and compensating (COMP) responses and nonresponses (NR) across stimulus direction (DOWN and UP).

	DOWN	UP	TOTAL
FOL	2	5	7
COMP	27	21	48
NR	7	10	17
TOTAL	36	36	72

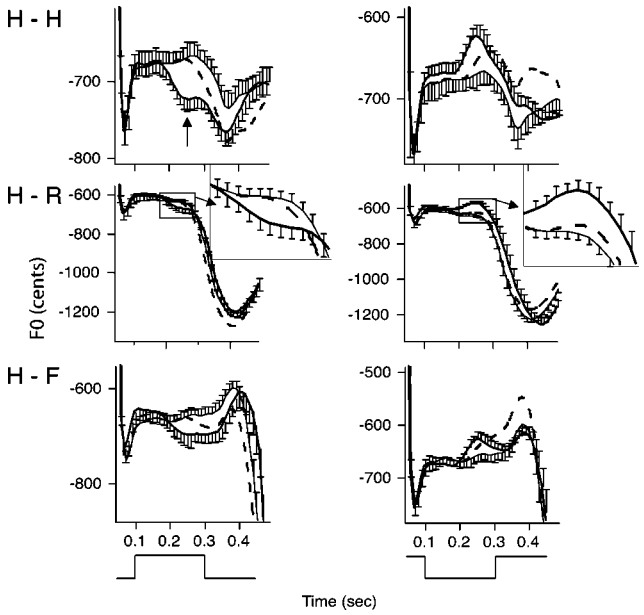

FIG. 3. Control (thin black line) and test average waves (thick black line) during H-H, H-R, and H-F sequences at the 100 ms stimulus timing condition. Heavy dashed lines are simulations produced by the model (see the text). The vertical arrow indicates time where the response magnitude was measured for this trace (see the text). Error bars represent the standard error of the mean for a single direction. The inset shows an expanded portion of average waves. Curves at the bottom indicate the time and direction of the stimulus. For all panels, the stimulus onset occurred approximately at 0.1 s. The *x*-axis (time) starts at 0.05 s, which is 0.05 s after vocalization onset. Note that the *y*-axis differs for each plot.

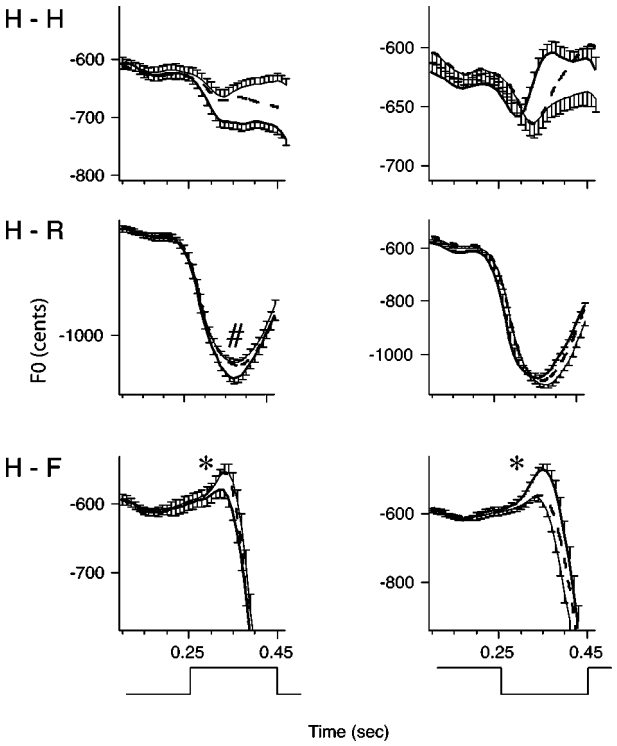

FIG. 4. Control (thin black line) and test average waves (thick black line) during H-H, H-R, and H-F sequences at the 250 ms stimulus timing condition. Error bars represent standard error of the mean for a single direction. H-R, ''#'' marks large difference between control and test waves mentioned in text. H-F, ''*s'' indicate rise in F_0 prior to major drop (see the text). Heavy dashed lines are simulations produced by model (see the text). Stimulus onset began at 0.25 s following vocal onset. In all illustrated examples, differences between control and test averages were statistically significant. The *x*-axis (time) starts at 0.1 s, which is 0.1 s after vocalization onset. Note that the *y*-axis differs for each plot. See the legend of Fig. 3 for further details. All traces for Fig. 3 and 4 were taken from the same subject.

mix of compensatory and ''following'' in direction. This may have resulted in the average being classified as a nonresponse due to cancelling of individual compensatory and following responses. However, it is difficult to make such determinations because of waveform variability. This is the reason for relying on the criteria of significant differences in *average* responses for determining whether responses occurred or did not.

There were a variety of responses types across subjects with the different phrases. For the H-H phrase, all responses occurred, by default, during steady F_0 productions. For the H-R phrase, some subjects produced a response prior to the drop in the F_0 trajectory, some during the drop, and some at the bottom of the trajectory. Most of the latter responses were observed with the 250 ms timing condition, however, a few were noted for the 100 ms timing condition as well. For the H-F phrase, most responses occurred prior to the drop in the F_0 trajectory, while a few occurred during the drop.

Figures 3 and 4 illustrate characteristic average responses to pitch-shifted stimuli (thick black lines with error bars) superimposed on average control curves (thin lines with error bars). Also shown are mathematical simulations (dashed lines with no error bars), which will be discussed subsequently. Figure 3 (H-H) displays representative data from one subject for the bi-tonal pattern (H-H) for increasing and decreasing pitch feedback under the 100 ms timing condition. The beginning of the traces on the left is 50 ms after vocal onset; vocal onset is not shown because of the large change in the cent magnitude with the onset of voicing. On the left side, an upward shift in pitch feedback shortly after vocal onset (indicated by the bottom trace representing the direction and timing of the stimulus) led to a decrease in the average response when compared with the control average. The response average drops below the control average at approximately 106 ms following the stimulus onset (latency) and reaches a peak depression (maximal separation between the control and response averages) of -59 cents at 165 ms (arrow). Following the peak response, the traces of the response and control averages converge following the stimulus offset. The traces on the right in Fig. 3 (H-H) represent the average response to a downward pitch-shift stimulus. The response latency occurs closer to 117 ms, and the response peak (38 cents) occurs at about 151 ms.

In Fig. 3 (H-R), the stimulus again begins 100 ms after onset of the ''High'' tone and ends at about the time the F_0 trajectory starts its descent toward the ''Rising'' tone. For both the increasing and decreasing stimuli, the response (thick lines with error bars) peaks prior to the beginning of the downward trajectory. The response to the downward stimulus approaches the trajectory of the control waves (thin lines with error bars), but never reaches it due to the time lag

TABLE IV. Mean latency (sd) in ms, magnitude (sd) in cents, and peak time (sd) in ms across three bi-tonal patterns.

PHRASE	LAT (sd)	MAG (sd)	PT (sd)
H-F	174 (79)	83 (50)	251 (73)
H-H	147 (41)	49 (20)	228 (45)
H-R	171 (70)	84 (45)	235 (70)

TABLE V. Mean latency (sd) in ms, magnitude (sd) in cents, and peak time (sd) in ms across timing conditions.

TIMING	LAT (sd)	MAG (sd)	PT (sd)
100	184 (77)	69 (42)	254 (76)
250	148 (50)	74 (44)	225 (49)

in the response trace. Such time lags were common in most subjects. The response to the upward stimulus peaks and then crosses the trajectory of the control wave as it seems to overshoot the control wave slightly. This behavior again could be interpreted as a time lag in the perturbed response. In both cases, responses occur prior to the end of the stimulus and are incorporated into the overall F_0 trajectory associated with the bi-tonal F_0 configuration.

For H-F phrases (Fig. 3), the F_0 remained at a higher level for a longer duration of time than was seen for the H-R phrases. Thus, the responses were seen during the steady phase of the F_0 prior to the ''Falling'' tone. The absolute response magnitude (59 cents) to the upward shift (left) is larger than that (41 cents) to the downward shift (right), as predicted for the rising F_0 trajectory prior to the drop in F_0. Following the early response, an apparent phase lag was seen during the ''Falling'' tone (Fig. 3 (H-F) left), and is similar to the phase-lag observed for the H-R phrases.

Figure 4 illustrates examples of responses to pitch-shift stimuli delivered 250 ms following vocal onset for the same subject as in Fig. 3. In these cases, the stimulus began during the first tone and terminated during the second tone. In the case of the H-H phrase (Fig. 4), responses are very similar to those seen in the 100 ms condition. That is, the overall F_0 trajectory was relatively flat through the entire phrase, and the responses compensated for the pitch-shifted auditory feedback. For both the H-R and H-F conditions, the stimulus was present during the time when there was a major reduction in F_0. There are three major observations for the responses in these conditions. First, sometimes a response appeared before the major drop in F_0 for the H-F phrases, as seen in Fig. 4 (H-F, left and right, indicated by ''*''s). Because the high tone of the H-R phrase was shorter in duration than that in the H-F phrase, this early response prior to the drop in F_0 was typically not seen in the H-R phrase. Second, the onset of the response during the high tone of the phrase also was accompanied by a phase-shift, which became apparent by the end of the phrase in Fig. 4 (H-F, both left and right). Both phase leads and phase lags of response with respect to the control were observed. Third, there was frequently a large difference between the control and response waveforms that occurred near the bottom of the contour associated with the beginning of the final F_0 rise [''#,'' Fig. 4 (H-R)]. Since the H-F phrase did not have a transition and since vocalization frequently ceased at or near the low point of the ''Falling'' tone, it was not possible to measure a response at the bottom of the trajectory.

Quantitative measures in Tables IV, V, and VI provide means and S.D.'s of response latency, magnitude, and peak time across subjects and conditions. The latency values shown in these tables vary from 147 to 184 ms. However, when values are broken down by specific conditions (Table VII), latencies for two of the H-H and one H-F condition were less than 130 ms. Latency values in other conditions were close to 200 ms. The overall median latency was 143 ms. For a statistical analysis of latency measures, a square root transformation was done to achieve a normal distribution. A three-factor repeated-measures ANOVA was performed on latency with phrase type, direction, and stimulus timing as independent variables. No main effects were found. However, there was a significant interaction between phrase type and stimulus direction [$F(2,10)=5.09$, $p=0.03$]. The latencies for both the H-H and H-F phrases increased for the downward stimuli compared to the upward stimuli, whereas for the H-R phrase, latencies decreased for the downward stimuli. The shorter latency for the H-R phrases with downward stimuli may indicate that when a planned drop in F_0 coincides with the approximate time of a downward response, the response latency is reduced (for the H-R phrase, the drop in the F_0 trajectory occurs sooner than in the H-F phrase). Although there appeared to have been a dramatic decrease in latency comparing the 100 ms and 250 ms timing conditions for the H-F condition as a function of stimulus direction, there was no overall effect on latency. Nevertheless, this change is in the same direction as changes in the peak time measures (see below). A similar finding was reported previously by Hain *et al.* (2000) for sustained vowels.

A three-factor repeated measures ANOVA was performed on magnitude with phrase type, stimulus timing, and stimulus direction as independent variables. Significant main effects on response magnitude were found for phrase type [$F(2,10)=9.36$, $p=0.005$] and stimulus direction [$F(1,5)=12.7$, $p=0.016$] (Table VIII). Post hoc testing revealed that responses for the H-R and H-F phrases were significantly larger than those for the H-H phrase ($p=0.008$ and $p=0.020$; *post hoc* Sheffé). Response magnitudes were generally greater for downward than upward stimuli. A significant interaction was observed between phrase type and stimulus timing [$F(2,10)=5.19$, $p=0.028$], which was due to the much greater increase in response magnitude for the H-R and H-F phrases compared to the H-H phrase. A significant interaction was also observed between stimulus timing and stimulus direction [$F(1,5)=17.43$, $p=0.009$]. This effect may be due to the much greater increase in response magnitude between the upward and downward stimuli for

TABLE VI. Mean latency (sd) in ms, magnitude (sd) in cents, and peak time (sd) in ms by stimulus direction.

DIRECTION	LAT (sd)	MAG (sd)	PT (sd)
DOWN	165 (67)	85 (49)	237 (68)
UP	164 (65)	58 (29)	240 (60)

TABLE VII. Mean latency (sd) in ms across three phrase types, two timing conditions, and two stimulus directions.

PHRASE		H-H		H-R		H-F	
TIMING		100	250	100	250	100	250
DIR	UP	127 (38)	124 (25)	192 (46)	192 (74)	210 (91)	121 (21)
	DOWN	174 (55)	159 (36)	162 (93)	138 (51)	243 (100)	146 (55)

the 250 ms timing condition compared with the 100 ms timing condition, most apparent for the H-R and H-F phrases. When examined across both timing and direction conditions, response magnitudes for both H-R and H-F phrases were greatest for downward stimuli with the 250 ms timing condition. This observation does not seem to confirm our hypothesis that response magnitudes should be larger for upward directed stimuli when the F_0 trajectory is downwards. We note, however, that the exact timing of the stimulus with respect to the F_0 trajectories varied with changes of speaking rate, both within and across subjects. As a result, for both H-R and H-F, the 250 ms stimuli coincided sometimes with the downward movement of the F_0 trajectory, sometimes with the upward movement, and sometimes with both of them. This variability in timing may have precluded the identification of systematic changes in response magnitude according to our hypotheses. Nevertheless, the H-F response measures made at the time of the slight rise in F_0 preceding the large drop in F_0 [Figs. 3 (H-F) and 4 (H-F)], produced, as predicted, larger responses for downward stimuli compared with upward stimuli [$F(1,16)=9.06$, $p=0.008$].

A three-factor repeated measures ANOVA was performed also on peak time with phrase type, stimulus timing, and stimulus direction as independent variables (Table IX). There were no significant main effects. However, there was a significant interaction between phrase type and stimulus timing [$F(2,10)=5.05$, $p=0.03$]. For the H-R and H-F phrases, peak times decreased for the 250 ms timing condition compared with the 100 ms timing, while for the H-H phrase, peak times increased between these two timing conditions. Overall, mean peak times were 238 ms. Thus, there was a reduction in latency and peak time measures when the pitch-shift stimuli occurred closer in time to the drop in the F_0 trajectory.

IV. MODELING OF RESPONSES

We simulated our data using a previously published model of responses to pitch-shift stimuli for sustained vowel phonations (Hain *et al.*, 2000). Our purpose was to not to reproduce experimental data, but rather to compare timing and magnitude of responses for the present speech task to responses expected for non-speech tasks. Figure 5 shows the main features of the model and Figs. 3 and 4 contain simulations to be compared with experimental data. The model of pitch stabilization uses negative feedback and delays to simulate compensatory responses to perturbations in the pitch of auditory feedback. The purpose of this approach was to be able to compare timing and magnitude of responses here to those predicted by this model, which was previously optimized for simulation of a nonspeech task.

In producing the output shown in Figs. 3 and 4 the control F_0 was used as the desired F_0 signal. There were several differences between simulation and experimental responses that can be seen from an inspection of Figs. 3 and 4. Experimental responses frequently began earlier than the simulation and were often larger. This is consistent with the finding of earlier and larger magnitude responses for the present data than for previous studies of less behaviorally relevant productions. Experimental responses also tended to lag control and simulation traces for the 100 ms delay condition (Fig. 3), which was not consistent for the 250 ms delay (Fig. 4). This observation suggests that given enough time, perturbations may slightly slow down production of the next syllable.

V. DISCUSSION

We conducted the present experiment with three main questions in mind. First, would native speakers of Mandarin respond to pitch-shifted auditory feedback during natural production of bi-tonal sequences by changing their vocal pitch to compensate for the pitch-shift? The answer to this question is ''yes''—most subjects responded to pitch-shift stimuli with a compensatory change in voice F_0 during the production of bi-tonal sequences, which consisted of various F_0 rises and falls. These results are compatible with those of previous studies (Donath *et al.*, 2002; Jones and Munhall, 2002; Natke *et al.*, 2003). Several ''following'' responses were also observed, which have been previously reported for sustained vowel productions.

Our second experimental question was as follows: Would the responses be fast enough to make a difference before the production of a tone is completed? The answer to this question seems to be ''sometimes.'' The median response latency (143 ms) was shorter than the 200 ms latency found by Jones and Munhall (2002), which may relate to differences in methods. Many responses had latencies less than 130 ms, and some were close to 100 ms. These latencies

TABLE VIII. Mean response magnitude (sd) in cents across three phrase types, two timing conditions, and two stimulus directions.

PHRASE		H-H		H-R		H-F	
TIMING		100	250	100	250	100	250
DIR	UP	42 (15)	51 (30)	85 (43)	58 (27)	56 (26)	51 (24)
	DOWN	50 (14)	48 (20)	91 (65)	105 (20)	78 (43)	129 (51)

TABLE IX. Mean response peak time (sd) in ms across three phrase types, two timing conditions, and two stimulus directions.

PHRASE		H-H		H-R		H-F	
TIMING		100	250	100	250	100	250
DIR	UP	217 (63)	249 (30)	224 (56)	240 (88)	284 (63)	204 (46)
	DOWN	216 (67)	224 (38)	261 (79)	202 (51)	312 (130)	223 (33)

are shorter than those reported by previous studies on pitch-shift experiments with nonsense syllables in German and prolonged vowels in Mandarin (Donath *et al.*, 2002; Jones and Munhall, 2002; Natke *et al.*, 2003), but are comparable to the latencies previously reported with sustained vowels (Hain *et al.*, 2000; Larson *et al.*, 2001). However, several responses had longer latencies, similar to those reported by Jones and Munhall (2002), and are also similar to secondary responses previously reported during sustained vowels (Burnett *et al.*, 1998; Hain *et al.*, 2000). Yet, the median latency of ~143 ms is shorter than the syllable duration of the Mandarin syllables for similar CV structures found in Xu (1997): 186 ms for /ma/ with many tonal combinations (duration values unpublished before), or Xu (1999): 180 ms for /mao/, /mi/, /mo/, /na/, /mai/ and /tao/, also with many tonal combinations. That is, with a delay less than a syllable (143 ms), the compensation can begin. Nevertheless, the mean response latency (~164 ms) was comparable to average syllable length. Moreover, response peak times (~238 ms) also occur after the average syllable has completed. Thus, due to variability in response latency, some responses are fast enough to make a difference within a phrase, but on average the responses are quite late compared to the syllable duration.

Our third question was whether the latency and magnitude of the compensatory responses would be generally faster and larger than those observed in conditions involving only nonspeech. There were four observations that supported this hypothesis. First, the response magnitudes during the production of natural tone sequences found in the present study are indeed significantly larger than those reported for sustained vowels (Burnett *et al.*, 1998) and are slightly larger than those reported during German nonsense speech (Donath *et al.*, 2002) or in a previous investigation of Mandarin tones produced with prolonged vowels (Jones and Munhall, 2002). Second, responses during the dynamic H-R and H-F phrases were generally larger than in the static H-H phrase. This indicates that auditory feedback may be more important for dynamic control of F_0 than static control. Third, during the slight rise in F_0 prior to the drop in the H-F phrase, response magnitudes were larger for downward stimuli compared to upwards stimuli. Finally, response latency decreased with downward stimuli in the H-R phrase, indicating that the system can alter timing of responses in addition to the magnitude depending on the need for auditory feedback to help control voice F_0. Moreover, in a recent study, Natke *et al.* (2003) reported that responses were larger during singing than during speech, and presumably singing requires greater F_0 accuracy than speech. It is noteworthy that the response magnitudes reported in the present study are approximately the same as those reported during singing (Natke *et al.*, 2003), and suggest F_0 control in Mandarin is as sensitive to auditory feedback as is in singing. Task-dependent modulation of reflexes, or other types of stereotypic responses to stimulation has been observed in many systems and is generally interpreted to reflect dependence of accurate motor execution on sensory monitoring (Gracco and Abbs, 1989; Gracco and Abbs, 1985; Saltzman *et al.*, 1998; Shaiman, 1989; Shaiman and Gracco, 2002).

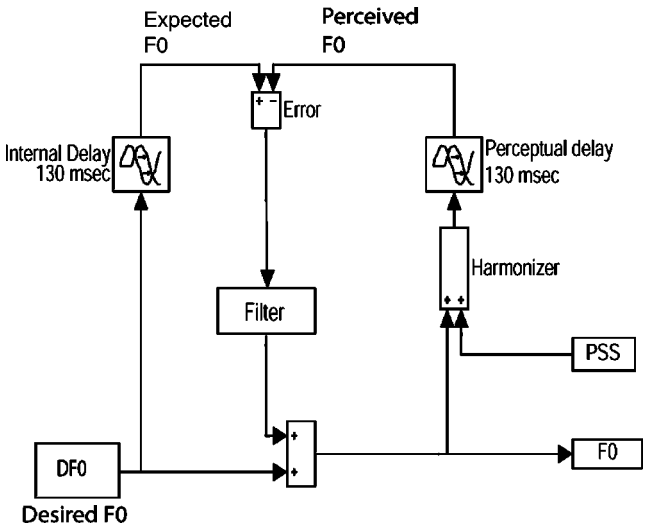

FIG. 5. Mathematical model of pitch stabilization. On the left side, *Desired* F_0 is input. Corrections are added at the summing junction at the center, bottom to produce F_0. Corrections are computed by comparing perceived F_0 (the upper right hand part of the diagram) with *Expected* F_0. *Perceived* F_0 is delayed by 130 ms with respect to F_0 reflecting delays in registration and production of sound. *Expected* F_0 is also delayed by 130 ms so that both signals are in the same time frame. The difference between *Expected* F_0 and *Perceived* F_0, *Error*, is filtered and used to adjust the F_0 signal.

An important experimental design feature of this study was the accurate timing of the stimuli with respect to the speech tokens. Care was taken to make sure stimuli were presented at the same approximate time in each of the phrases for all speakers by careful coaching of subjects, monitoring of signals produced by the subjects, and the use of a voice activated trigger circuit. However, we were unable to precisely control the timing of the MIDI program or the processing by the harmonizer, which together produced about 40 ms variability in timing. Because the primary goal, ascertaining whether production of F_0 contours during normal speech would be affected by perturbed auditory feedback, was supported by responses to pitch-shifted voice feedback within single or disyllabic phrases, the variability in stimulus timing does not appear to be a serious concern. However, stimulus timing variability may have contributed to the variability in the responses, and if future studies are able to deliver stimuli with greater control than was done in

the present study, results may more accurately reflect the degree to which auditory feedback is normally used to help regulate voice F_0 during speech.

With respect to our mathematical modeling, the model of Fig. 5, which serves well to simulate feedback driven modulation of sustained vowel phonations, accounts for general features of the responses during speech such as direction and approximate timing. A comparison between the simulations and experimental data in Figs. 3–4 illustrate that this model of vowel phonation fails to reproduce three aspects of speech. While it would be possible to adjust parameters of the model to fit the experimental data, we feel that it is more important to point out that these differences indicate that the auditory feedback stabilization system for speech is either separate from that used for vowel phonation, or that a common system can be rapidly reconfigured according to the demands of the task.

The first difference is that the model of vowel phonation fails to simulate the larger size of responses found under some speech conditions. In the context of the model, this would suggest that the gain of the feedback loop (incorporated in the ''Filter'' element in Fig. 5) is not fixed but rather can be varied, to account for this task-dependence. Response modulation has been found to occur in other systems as a function of motor activities such as walking, arm movements, cycling and grasping (Brooke *et al.*, 1991; De Serres *et al.*, 1995; Doemges and Rack, 1992; Dufresne *et al.*, 1980; Stein and Capaday, 1988; Zehr *et al.*, 2001).

The model also does not produce responses with latencies less than 130 ms, while experimentally such responses were noted. In the context of the model, reduced latencies could be obtained by reducing the matched delay elements. This again suggests that the auditory feedback stabilization mechanism can be modified substantially and rapidly depending on the specific task at hand.

Finally, the model does not produce enduring lags (delay) of perturbed vocalizations compared to control vocalizations, such as is seen in some traces of Fig. 3. Such lags presumably reflect intervention of other processes outside of the mechanisms that stabilize F_0. A possible explanation of these lags is that the rate of speech is slowed by mismatches between intended and perceived F_0. A speaker may simply be slowed down when a dissonance is detected. Another possibility is that the triggering of syllables is, to some extent, delayed by dissonance between intended and perceived F_0. This mechanism would predict an enduring lag between perturbed and control F_0 trajectories and would also account for the response durations that exceed a single syllable, as has been reported in nonsense syllables (Donath *et al.*, 2002). The observation that response magnitudes and timing varied as a function of the bi-tonal sequences supports the theory that this mechanism helps the speaker control voice F_0 across adjacent syllables. In tone languages this feature would be lexically relevant and in nontonal languages it would be important for the intonational aspects of speech production.

VI. CONCLUSION

We introduced pitch-shifted auditory feedback to native speakers of Mandarin while they were saying disyllabic sequences with different tonal combinations at a natural speaking rate. They reacted to the auditory feedback with compensatory pitch changes in most trials. The majority of the compensatory pitch changes occurred significantly sooner (143 ms) than the durations of typical Mandarin syllables (180 ms). In some conditions, latencies were short enough ($<$130 ms) for the response to correct for perturbations within the syllable, while in other cases latencies were too long. These findings, along with the observation that response magnitudes during tonal sequences involving dynamic F_0 trajectories were larger than sequences with a static F_0 trajectory, suggest the system may modulate the responses depending on the demand for auditory feedback to facilitate accurate and timely adjustments in F_0 control. Although the responses were both faster and larger than those during the production of sustained vowels (Burnett *et al.*, 1998; Hain *et al.*, 2000; Larson *et al.*, 2001), they are similar to those during singing (Natke *et al.*, 2003), suggesting that the production of tones requires a close control of voice F_0 similar to that used in singing. A simple mathematical model incorporating negative feedback was able to simulate the general features of the response patterns. This suggests that a control mechanism based on similar principles may be behind the observed compensatory responses. The modeling simulation also shows that both the timing and the magnitude of this control mechanism can be modified substantially and rapidly depending on the specific task at hand.

ACKNOWLEDGMENTS

This research was supported by NIH Grant No. DC006243-01A1 and NIH Grant No. DC03902. We gratefully acknowledge the helpful comments from two anonymous reviewers of a previous draft of the manuscript.

Abbs, J. H., and Gracco, V. L. (**1984**). ''Control of complex motor gestures: Orofacial muscle responses to load perturbations of lip during speech,'' J. Neurophysiol. **51**, 705–723.

Alipour-Haghighi, F., Titze, I. R., and Durham, P. (**1987**). ''Twitch response in the canine vocalis muscle,'' J. Speech Hear. Res. **30**, 290–294.

Brooke, J. D., Collins, D. F., Boucher, S., and McIlroy, W. E. (**1991**). ''Modulation of human short latency reflexes between standing and walking,'' Brain Res. **548**, 172–178.

Burnett, T. A., Freedland, M. B., Larson, C. R., and Hain, T. C. (**1998**). ''Voice f0 responses to manipulations in pitch feedback,'' J. Acoust. Soc. Am. **103**, 3153–3161.

Burnett, T. A., and Larson, C. R. (**2002**). ''Early pitch shift response is active in both steady and dynamic voice pitch control,'' J. Acoust. Soc. Am. **112**, 1058–1063.

De Serres, S. J., Yang, J. F., and Patrick, S. K. (**1995**). ''Mechanism for reflex reversal during walking in human tibialis anterior muscle revealed by single motor unit recording,'' J. Physiol. (London) **488**, 249–258.

Doemges, F., and Rack, P. M. H. (**1992**). ''Task-dependent changes in the response of human wrist joints to mechanical disturbance,'' J. Physiol. (London) **447**, 575–585.

Donath, T. M., Natke, U., and Kalveram, K. T. (**2002**). ''Effects of frequency-shifted auditory feedback on voice f_0 contours in syllables,'' J. Acoust. Soc. Am. **111**, 357–366.

Duanmu, S. (**1994**). ''Syllabic weight and syllable durations: A correlation between phonology and phonetics,'' Phonology **11**, 1–24.

Dufresne, J. R., Soechting, J. F., and Terzuolo, C. A. (**1980**). ''Modulation of the myotatic reflex gain in man during intentional movements,'' Brain Res. **193**, 67–84.
Gracco, V. L., and Abbs, H. H. (**1989**). ''Sensorimotor characteristics of speech motor sequences,'' Exp. Brain Res. **75**, 586–598.
Gracco, V. L., and Abbs, J. H. (**1985**). ''Dynamic control of the perioral system during speech: Kinematic analyses of autogenic and nonautogenic sensorimotor processes,'' J. Neurophysiol. **54**, 418–432.
Hain, T. C., Burnett, T. A., Kiran, S., Larson, C. R., Singh, S., and Kenney, M. K. (**2000**). ''Instructing subjects to make a voluntary response reveals the presence of two components to the audio-vocal reflex,'' Exp. Brain Res. **130**, 133–141.
Jones, J. A., and Munhall, K. G. (**2000**). ''Perceptual calibration of f0 production: Evidence from feedback perturbation,'' J. Acoust. Soc. Am. **108**, 1246–1251.
Jones, J. A., and Munhall, K. G. (**2002**). ''The role of auditory feedback during phonation: Studies of Mandarin tone production,'' J. Phonetics **30**, 303–320.
Kelso, J. A. S., Tuller, B., Vatikiotis-Bateson, E., and Fowler, C. A. (**1984**). ''Functionally specific articulatory cooperation following jaw perturbations during speech: Evidence for coordinative structures,'' J. Exp. Psychol. Hum. Percept. Perform. **10**, 812–832.
Kempster, G. B., Larson, C. R., and Kistler, M. K. (**1988**). ''Effects of electrical stimulation of cricothyroid and thyroarytenoid muscles on voice fundamental frequency,'' J. Voice **2**, 221–229.
Larson, C. R., Burnett, T. A., Bauer, J. J., Kiran, S., and Hain, T. C. (**2001**). ''Comparisons of voice f_0 responses to pitch-shift onset and offset conditions,'' J. Acoust. Soc. Am. **110**, 2845–2848.
Larson, C. R., Kempster, G. B., and Kistler, M. K. (**1987**). ''Changes in voice fundamental frequency following discharge of single motor units in cricothyroid and thyroarytenoid muscles,'' J. Speech Hear. Res. **30**, 552–558.
Natke, U., Donath, T. M., and Kalveram, K. T. (**2003**). ''Control of voice fundamental frequency in speaking versus singing,'' J. Acoust. Soc. Am. **113**, 1587–1593.
Natke, U., and Kalveram, K. T. (**2001**). ''Effects of frequency-shifted auditory feedback on fundamental frequency of long stressed and unstressed syllables,'' J. Speech Lang. Hear. Res. **44**, 577–584.
Saltzman, E., Löfqvist, A., Kay, B., Kinsella-Shaw, J., and Rubin, P. (**1998**). ''Dynamics of intergestural timing: A perturbation study of lip-larynx coordination,'' Exp. Brain Res. **123**, 412–424.
Shaiman, S. (**1989**). ''Kinematic and electromyographic responses to perturbation of the jaw,'' J. Acoust. Soc. Am. **86**, 78–88.
Shaiman, S., and Gracco, V. L. (**2002**). ''Task-specific sensorimotor interactions in speech production,'' Exp. Brain Res. **146**, 411–418.
Stein, R. B., and Capaday, C. (**1988**). ''The modulation of human reflexes during functional motor tasks,'' Trends Neurosci. **11**, 328–332.
Xu, Y. (**1997**). ''Contextual tonal variations in mandarin,'' J. Phonetics **25**, 61–83.
Xu, Y. (**1999**). ''Effects of tone and focus on the formation and alignment of f0 contours,'' J. Phonetics **27**, 55–105.
Xu, Y., and Wang, Q. E. (**2001**). ''Pitch targets and their realization: Evidence from Mandarin Chinese,'' Speech Commun. **33**, 319–337.
Zehr, E. P., Hesketh, K. L., and Chua, R. (**2001**). ''Differential regulation of cutaneous and *h*-reflexes during leg cycling in humans,'' J. Neurophysiol. **85**, 1178–1184.

Sex differences in voice onset time: A developmental study of phonetic context effects in British English

Sandra P. Whiteside,[a] Luisa Henry,[b] and Rachel Dobbin[b]
Department of Human Communication Sciences, University of Sheffield, Sheffield S10 2TA, United Kingdom

(Received 17 November 2003; revised 27 April 2004; accepted 12 May 2004)

Voice onset time (VOT) data for the plosives /p b t d k g/ in two vowel contexts (/i ɑ/) for 5 groups of 46 boys and girls aged 5; 8 (5 years, 8 months) to 13;2 years were investigated to examine patterns of sex differences. Results indicated that there was some evidence of females displaying longer VOT values than the males. In addition, these were found to be most marked for the data of the 13;2-year olds. Furthermore, the sex differences in the VOT values displayed phonetic context effects. For example, the greatest sex differences were observed for the voiceless plosives, and within the context of the vowel /i/. © *2004 Acoustical Society of America.*
[DOI: 10.1121/1.1768256]

PACS numbers: 43.70.Ep, 43.70.Gr [AL] Pages: 1179–1183

I. INTRODUCTION

There are relatively few studies documenting sex differences in VOT, and some report sex differences in VOT for both adults and children (Koenig, 2000; Ryalls *et al.*, 1997; Swartz, 1992; Whiteside and Marshall, 2001). Furthermore, the general pattern suggests that women produce longer VOT values than men (e.g., Koenig, 2000; Ryalls *et al.*, 1997; Swartz, 1992). The factors which contribute to these sex differences have not been fully established but suggestions have included aerodynamic, physiological and anatomical factors (e.g., Koenig, 2000; Swartz, 1992). It has also been suggested that sociophonetic factors could go some way in explaining sex differences in VOT in one particular accent of British English (e.g., in Sheffield, South Yorkshire) [see, Whiteside and Marshall (2001) for a discussion].

Given the evidence for emerging sex differences during preadolescence, adolescence and postadolescence in the frequency components of speech (e.g., Lee *et al.*, 1999), it is conceivable that VOT patterns may also continue to develop during adolescence. Therefore, sex differences in spectral components that may be emerging by this time may also be present in temporal components of speech such as VOT. There is some evidence to support the emergence of sex differences in VOT in the plosives /p b t d/ within a single vowel context (/i/) of a group of 30 preadolescent children between the ages of 6;9 (6 years, 9 months) and 10;7 (10 years, 7 months) (Whiteside and Marshall, 2001). The sex differences which emerged were characterized by the girls having longer VOT values for the voiceless plosives /p t/ compared to the boys at age 10;7. Furthermore, the net effect of these sex differences resulted in the girls' VOT patterns displaying a more marked ''voiced''/''voiceless'' contrast at age 10;7 for the cognate pairs /p b/ and /t d/.

One aim of the current study was to supplement the results of the aforementioned study in a number of different ways. First, new participants representing a wider age range were recruited to the study. In addition, speech data representing a richer phonetic inventory were gathered to explore sex and age differences in VOT patterns further. The VOT data of the full set of English plosives (/p b t d k g/) were examined in two peripheral vowel contexts (/i ɑ/) to gather additional data on the extent to which age and sex differences in VOT patterns may be influenced by phonetic context. Age and sex differences, and their interaction with different phonetic contexts, are more well established in the frequency domain of speech parameters such as vowel formant frequencies (Traunmüller, 1988). However, there is a lack of published data on how the interaction of factors such as age, sex and phonetic context affect the development of temporal speech parameters such as VOT. By investigating the effects of sex, age and phonetic context on VOT patterns, this study aims to add to the body of published data on individual differences in VOT (e.g., Koenig, 2000, 2001; Whiteside and Marshall, 2001), and how this temporal parameter develops in children between the ages of 5;8 and 13;2 years.

II. METHODOLOGY

A. Participants

Five groups of participants from two schools in Sheffield were recruited to the study: (*i*) mean age 5;8 years; $n=6$; (*ii*) mean age 7;10 years; $n=10$; (*iii*) mean age 9;10 years; $n=10$; (*iv*) mean age 11;10 years; $n=10$; and (*v*) mean age 13;2 years; $n=10$. Equal numbers of boy and girls participated in each age group. All subjects: (*i*) spoke with a similar regional accent; (*ii*) had lived in Sheffield all their lives and within 3–5 miles of the school; (*iii*) had age-appropriate intelligence levels as judged by the class teacher; (*iv*) were monolingual speakers of English; (*v*) had no speech, language or hearing problems; and (*vi*) volunteered to participate in the study with parental consent.

B. Speech stimuli

All subjects produced five repetitions of each of the plosives /p b t d k g/ in a syllable initial position within the

[a]Electronic mail: s.whiteside@sheffield.ac.uk.
[b]Present address: Speech and Language Therapy Department, Hull and East Riding Community NHS Trust, Victoria House, Park St, Hull HU2 8TD.

phrase frame of ''Say /pi, bi, ti, di, ki, gi, pat, bat, tat, dat, kad, gad/again.'' The phrases and target plosives were elicited from the children in a randomized order using a repetition task via live presentation. A repetition task was chosen in preference to either a reading task, or a picture naming task for a number of reasons. First, because the study included very young children with a range of reading abilities, this would have more than likely had an effect on the children's VOT values. Second, it would not have been possible to elicit correct renditions of the word ''ghee'' (/gi/) in a reading paradigm, as the lexical item in question is both borrowed (Hindi) and occurs infrequently in both spoken and written English. Third, it was not possible to represent all the target syllables pictorially to the children.

C. Recording and analysis

The speech data were recorded in a quiet room. Data was recorded directly onto a DAT (digital audio tape) recorder (Sony, model TCD-D3). Subsequently, speech samples from each subject were digitized onto a Kay Elemetrics Computerized Lab (CSL) model 4300 using a sampling rate of 16 kHz. From this digital information, sound pressure waveforms and wideband (146 Hz) FFT spectrograms were generated and displayed. A bandwidth of 146 Hz provided adequate temporal resolution to take VOT measurements which were made directly from the spectrograms by measuring the distance between the release of the plosive to the onset of voicing (marked by the first visible sign of low frequency periodic acoustic activity in the spectrograms). The point of the plosive's release was taken at the first transient burst for all samples, including those which displayed multiple bursts. In the cases where measures of VOT needed validation, sound pressure waveforms were used. In the cases where both the speech waveform and the spectrogram were referred to for validation, the VOT measurement was taken from the same data source. In the cases where VOT was unclear, e.g., plosives being released with affrication or the presence of background noise, the speech sample was discarded.

To ensure consistency in the VOT measurements, a test of interrater reliability was carried out. The interreliability measures were conducted by randomly selecting one subject from each of the five age groups for reanalysis by a second rater. A Pearson's product-moment correlation was used to calculate the level of interrater reliability. A significant correlation coefficient ($r=0.978$, $p<0.0001$) demonstrated a high level of interrater reliability.

III. RESULTS

The median, mean and standard deviation values for VOT measurements are given in Table I by plosive (/p, b, t, d, k, g/), vowel context (/i/ and /ɑ/) and sex for the five age groups (*i*) 5;8 years, (*ii*) 7;10 years, (*iii*) 9;10 years, (*iv*) 11;10 years, and (*v*) 13;2 years. Table I illustrates the comparability between the median and mean values. In addition, the mean values for the VOT measurements are depicted in Fig. 1. The VOT values across all age groups and subjects displayed expected patterns by place of articulation, and ''voiced''/''voiceless'' status; ''voiced'' plosives displayed shorter values than their ''voiceless'' cognates, and bilabial plosives displayed the shortest values, and velar plosives the longest. The order of magnitude of mean VOT values by plosive for all subjects was as follows: b (18 ms)<d (25 ms)<g (38 ms)<p (60 ms)<t (81 ms)<k (82 ms). In addition, the VOT values across all subjects and age groups displayed longer values within the context of the vowel /i/ (see Fig. 2).

With respect to developmental trends, the VOT data for the 5;8-year olds displayed a tendency for longer VOT values compared to the older age groups (see Table I and Fig. 1). In addition, the data for the 5;8-year olds displayed inconsistent trends in mean and median values with respect to sex differences. For example, longer values were observed for the females for some plosive and contexts (e.g., /tɑ/, /di/ and /kɑ/), but not for others (e.g., /dɑ/ and /gɑ/) (see Table I and Fig. 1). There were consistent trends of longer VOT values for the females in the data of some of the older age groups (e.g., the data for the 7;10-, 9:10-, and 13;2-year olds). (See Table I and Fig. 1.) Therefore, in order to examine the effects of sex on VOT values, Mann-Whitney U tests were carried out for four of the five age groups. Tests were not carried out for the 5;8-year olds due to the very small number of participants in this age group. Separate tests were run for each of four age groups (7;10 to 13;2 years), and for each plosive and vowel context. Mean VOT values for each subject were used in these nonparametric tests (for each age group: $n=5$ for M, and $n=5$ for F). Results indicated the following significant sex differences ($p<0.05$, two tailed): (*i*) age 7;10 years—/dɑ/ ($Z-2.611$)—here females displayed longer VOT values; (*ii*) age 9;10 years—/pi/ ($Z-1.984$), /pɑ/ ($Z-2.193$), /dɑ/ ($Z-1.984$)—females displayed longer VOT values for all three phonetic contexts; (*iii*) age 11;10 years—/bi/ ($Z-1.984$)—here males displayed longer VOT values compared to the females; and (iv) age 13;2 years—/pi/ ($Z-2.402$), /ki/ ($Z-2.193$), /kɑ/ ($Z-1.984$)—females displayed longer VOT values for all three phonetic contexts. In addition, the following data displayed trends towards significant differences ($p<0.1$): (*i*) age 7;10 years—/gi/ ($Z-1.776$)—here females displayed longer VOT values; (*ii*) age 9;10 years—/ti/ ($Z-1.776$)—females displayed longer VOT values; (*iii*) age 13;2 years—/ti/ ($Z-1.776$), /di/ ($Z-1.776$)—females displayed longer VOT values for both phonetic contexts.

IV. DISCUSSION

The VOT data for the plosives by place of articulation, and within the two different vowel contexts, replicate findings that are widely documented in the literature (e.g., Lisker and Abramson, 1964; Nearey and Rochet, 1994; Port and Rotunno, 1979; Ryalls *et al.*, 1997). However, given the differences in the syllabic structures representing the two vowel contexts, it is difficult to ascertain the true extent of the vowel context effects on the VOT values. This requires further investigation, but controlling for all aspects of phonetic context (i.e., syllable structure, place of articulation, vowel context) could only be achieved if real and nonwords were used as speech stimuli.

TABLE I. Median, mean and standard deviation voice onset time values (in ms) for /p b t d k g/ by vowel context, sex and age group.

		Age 5;8 years		Age 7;10 years		Age 9;10 years		Age 11;10 years		Age 13;2 years	
Plosive	Vowel	M	F	M	F	M	F	M	F	M	F
/p/											
Median		66.9	65.5	46.7	66.5	49.7	66.3	57.9	57.1	46.6	85.2
Mean	/i/	72.5	69.1	53.8	68.4	52.6	71.0	55.1	56.6	50.5	85.6
SD		21.3	26.0	22.1	28.0	15.0	21.8	10.4	10.7	13.3	17.6
Median		69.3	63.1	43.7	65.0	53.3	64.6	48.4	44.7	50.5	55.4
Mean	/ɑ/	71.1	70.4	47.9	63.1	52.0	65.7	48.1	47.2	51.0	58.0
SD		17.0	22.6	18.4	26.2	12.4	16.6	13.6	12.2	12.2	13.8
/b/											
Median		18.1	13.8	15.9	11.2	18.3	21.6	18.7	13.3	15.2	21.7
Mean	/i/	20.8	18.2	16.5	13.8	20.7	23.6	19.0	14.7	19.8	22.5
SD		9.2	10.5	5.4	7.0	8.7	8.1	5.4	4.2	11.0	7.5
Median		19.6	12.9	14.3	13.6	14.5	17.6	14.8	13.9	14.9	17.1
Mean	/ɑ/	21.8	17.2	15.6	14.8	16.2	18.5	15.4	14.4	15.7	18.4
SD		11.8	9.5	7.4	7.7	6.0	8.5	4.4	4.5	5.0	4.7
/t/											
Median		94.3	95.5	76.2	105.4	77.3	95.1	81.6	81.2	81.9	98.4
Mean	/i/	102.0	106.5	79.5	104.7	80.0	95.7	80.1	79.5	82.1	99.8
SD		26.4	26.2	23.6	26.9	16.6	20.4	9.7	16.3	12.3	21.5
Median	/ɑ/	79.3	114.6	60.9	73.5	67.4	74.4	68.3	63.9	69.0	74.0
Mean		87.9	109.5	63.7	76.4	67.3	75.0	69.3	65.6	67.2	77.2
SD		30.8	23.6	18.7	22.8	18.3	12.4	12.0	15.5	11.5	19.0
/d/											
Median		34.6	38.1	18.4	32.1	22.3	32.6	19.6	22.7	22.1	30.4
Mean	/i/	35.1	39.8	24.9	29.5	25.1	35.2	20.9	25.1	24.3	31.4
SD		13.6	16.7	17.7	14.2	11.5	11.6	8.9	6.9	8.0	9.0
Median		26.5	19.9	13.1	23.0	17.1	24.7	17.9	20.4	19.7	23.3
Mean	/ɑ/	28.0	21.0	14.8	22.8	19.2	28.0	18.9	21.2	20.9	25.6
SD		9.0	8.6	6.2	7.1	6.5	10.8	6.0	4.0	8.0	7.4
/k/											
Median		111.2	94.6	76.9	90.8	74.3	94.1	80.7	74.8	67.2	96.0
Mean	/i/	104.3	94.2	78.4	89.7	78.8	93.9	82.0	74.3	71.1	99.6
SD		23.4	21.4	19.7	22.1	22.0	17.0	11.8	10.3	15.7	22.0
Median		88.8	115.8	76.2	87.8	68.8	78.9	70.1	65.9	70.4	88.4
Mean	/ɑ/	96.1	106.8	74.4	87.2	70.1	80.5	72.1	67.3	71.8	90.0
SD		29.2	27.7	23.7	25.9	12.7	18.0	12.8	9.7	12.7	16.9
/g/											
Mean		44.8	42.3	36.8	49.0	42.1	45.4	32.8	31.7	36.1	39.4
SD	/i/	46.7	44.3	35.3	50.9	39.4	49.5	33.8	33.1	38.1	43.1
		15.8	14.0	14.3	17.0	11.4	13.8	8.9	6.5	11.0	12.5
Mean		41.0	22.6	36.0	31.3	38.9	40.7	25.5	29.4	33.8	34.1
SD	/ɑ/	46.7	25.4	36.8	31.0	37.8	42.1	27.5	29.7	33.9	40.6
		16.0	9.7	16.1	8.5	10.9	11.4	7.6	8.5	8.6	12.9

When the VOT data were examined for age-specific trends, it was found that the 5;8-year olds displayed a tendency for longer VOT values compared to the older age groups, a finding which corroborates earlier evidence (Kent and Forner, 1980). When the data were examined for sex differences, significant effects were found to be inconsistent, and varied with age and phonetic context. Where significant effects were found, all but one of these (age 11;10 years—/bi/) indicated that the females had significantly longer VOT values than the males. These trends corroborate the findings of an earlier developmental study (e.g., Whiteside and Marshall, 2001).

Upon closer inspection of the data it is possible to see that the 9;10- and 13;2-year olds displayed the largest number of significant sex differences across the different phonetic contexts. However, although the 9;10- and 13;2-year olds displayed the same number of significant differences across the full range of phonetic contexts, the magnitude of these sex differences appeared to be greater for the 13;2-year olds (see Table I and Fig. 1). Furthermore, when the trends towards significance ($p<0.1$) were examined, a greater number of trends were observed for the 13;2-year olds. These developmental trends suggest that sex differences in VOT may be developmental in nature, and that sex differences in VOT may emerge during adolescence. The more apparent lack of sex differences, and the inconsistencies in the data for the 5;8- and 11;10-year olds, deserves some explanation before the developmental emergence of the sex dif-

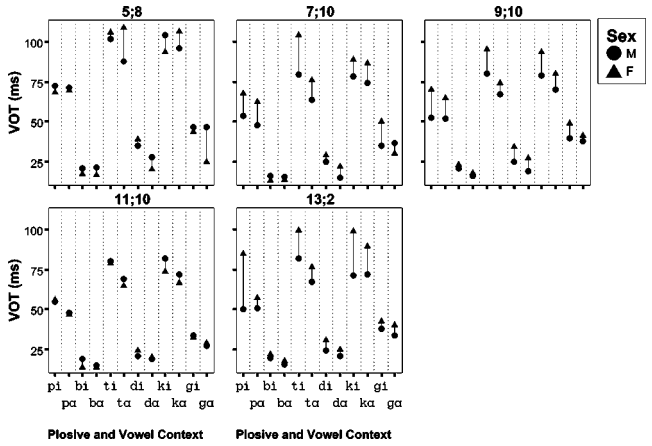

FIG. 1. Mean voice onset time values (in ms) for /p b t d k g/ by vowel context, sex and age group (5;8 years, 7;10 years, 9;10 years, 11;10 years and 13;2 years).

ferences in VOT is discussed. The inconsistent patterns of sex differences for the 5;8-year olds would not be totally unexpected, and could be explained in light of evidence which suggests that the anatomical and physiological variables which affect voicing and phonatory function show minimal sex differences around this age (e.g., Hirano *et al.*, 1983; Stathopoulos and Sapienza, 1997). However, due to the very small number of subjects who participated in this age group, it would be necessary to gather additional samples in order to substantiate this suggestion. The lack of sex differences for the 11;10-year olds is more difficult to explain in developmental terms as the data for this age group appear to be out of line with those for the 7;10-, 9;10- and 13;2-year olds (see Fig. 1). A possible explanation is the contribution of individual developmental differences to the findings reported here for such a small sample. Individual developmental differences in the developmental patterns of speech are widely documented, and have been found in both temporal and spectral components of speech (e.g., Hollien

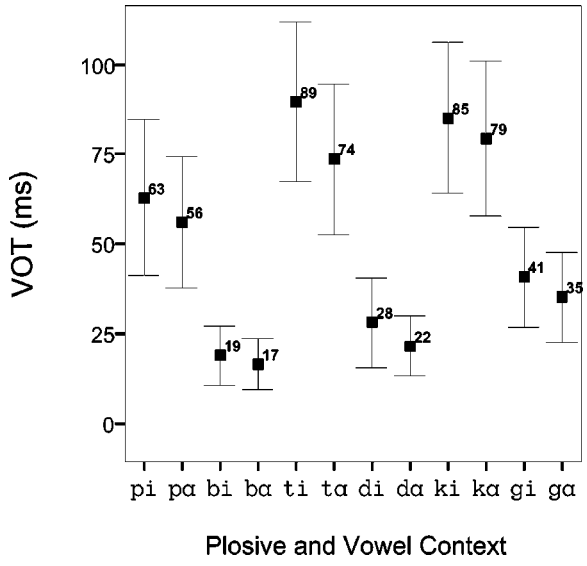

FIG. 2. Mean voice onset time values (in ms) for /p b t d k g/ for all speakers by vowel context. Error bars display ±1 SD of the mean, and mean VOT values are also indicated.

et al., 1994; Smith and Kenney, 1998). However, further data would be necessary from this age group in order to determine the extent of sex differences in VOT as a function of development.

The significant sex differences and the trends for sex differences in the VOT values of the 7;10- and 9;10-year olds are not totally unexpected in light of other acoustic phonetic evidence for sex differences in preadolescent children (e.g., Busby and Plant, 1995). In addition, the more apparent sex differences which are present in the VOT values of the 13;2-year olds could be explained in terms of the sexual dimorphism of the larynx (e.g., Hirano *et al.*, 1983) and the vocal tract (e.g., Fitch and Giedd, 1999) which emerge during adolescence. It is likely that during this period the female larynx will have relatively higher levels of tissue stiffness compared to the male larynx which is going through significant developmental change during this developmental phase of the human lifespan. These higher levels of tissue stiffness in the female larynx may give rise to increased levels of glottal resistance (e.g., Netsell *et al.*, 1991; Stathopoulos and Sapienza, 1997), which could in turn be contributing to the longer VOT values observed for the 13;2-year-old females compared to their male peers (Table I). The intrinsic pitch differences that have been observed for a close and elevated front vowel such as /i/ compared to an open and lowered back vowel such as /ɑ/ [Peterson and Barney, 1952; see, Netsell *et al.* (1991) for a discussion] serve to further illustrate the possible contribution of tissue stiffness to longer VOT values which are observed in the context of the vowel /i/ across all speakers (see Fig. 2), effects which may also be contributing to the larger sex differences observed for the VOT values of the voiceless plosives within this vowel context (see Table I and Fig. 1). It is also possible that sex differences in supralaryngeal dimensions, configurations and constrictions may also be contributing to the longer VOT values for the 13;2-year-old females. For example, the longer VOT values for the plosives, and in particular the voiceless plosives, within the vowel context /i/ (see Table I and Fig. 1) could be explained in terms of greater levels of airway resistance which cause a delay in the onset of voicing (e.g., Higgins *et al.*, 1998; Nearey and Rochet, 1994; Port and Rotunno, 1979). The smaller dimensions of the female supralaryngeal vocal tract and relatively smaller vocal tract constrictions, which will have greater levels of airway resistance compared to their male peers, may also explain why the 13;2-year-old females have longer VOT values, particularly for the voiceless plosives. Furthermore, the sex differences for the voiceless plosives, which are more marked in the context of the vowel /i/, suggests that the constrictions associated with the vowel /i/ relative to the vowel /ɑ/ may also have underlying sex differences which are contributing to an interaction between sex differences in VOT and vowel context. In addition to vowel context, the sex differences in the VOT values of the voiceless plosives of the 13;2-year olds also appeared to vary by place of articulation. Not only did the VOT values in the context of /i/ display the most marked sex differences, but these sex differences were also greatest for the plosives /p/ and /t/ within this vowel context (see Table I and Fig. 1). However, syllable structure may

have also been a contributory factor. Further data are therefore required to explore these suggestions further.

In summary, vowel context and place of articulation may be among the factors which have contributed to the sex differences in the VOT values of the voiceless plosives for the 13;2-year olds in the current study. In addition, the sexual dimorphism of the larynx (e.g., Hirano *et al.*, 1983) and the vocal tract (Fitch and Giedd, 1999) may also be contributory factors. However, the interaction between these factors, and how they impact upon age, sex and individual differences in voicing, voicing function and VOT patterns, deserve further investigation.

ACKNOWLEDGMENTS

Our thanks go to the participants, their parents and teachers for making this study possible.

Busby, P. A., and Plant, G. L. (**1995**). ''Formant frequency values of vowels produced by preadolescent boys and girls,'' J. Acoust. Soc. Am. **97**, 2603–2606.

Fitch, W. T., and Giedd, J. (**1999**). ''Morphology and development of the human vocal tract: A study using magnetic resonance imaging,'' J. Acoust. Soc. Am. **106**, 1511–1522.

Higgins, M. B., Netsell, R., and Schulte, L. (**1998**). ''Vowel-related differences in laryngeal articulatory and phonatory function,'' J. Speech Lang. Hear. Res. **41**, 712–724.

Hirano, M., Kurita, S., and Nakashima, T. (**1983**). ''Growth, development and aging of human vocal folds,'' in: *Vocal Fold Physiology: Contemporary Research and Clinical Issues*, edited by D. M. Bless and J. H. Abbs (College-Hill, San Diego).

Hollien, H., Green, R., and Massey, K. (**1994**). ''Longitudinal research on adolescent voice change in males,'' J. Acoust. Soc. Am. **96**, 2646–2654.

Kent, R. D., and Forner, L. L. (**1980**). ''Speech segment durations in sentence recitations by children and adults,'' J. Phonetics **8**, 157–168.

Koenig, L. L. (**2000**). ''Laryngeal factors in voiceless consonant production in men, women, and 5-year-olds,'' J. Speech Lang. Hear. Res. **43**, 1211–1228.

Koenig, L. L. (**2001**). ''Distributional characteristics of VOT in children's voiceless aspirated stops and interpretation of developmental trends,'' J. Speech Lang. Hear. Res. **44**, 1058–1068.

Lee, S., Potamianos, A., and Narayanan, S. (**1999**). ''Acoustics of children's speech: Developmental changes of temporal and spectral parameters,'' J. Acoust. Soc. Am. **105**, 1455–1468.

Lisker, L., and Abramson, A. S. (**1964**). ''A cross-language study of voicing in initial stops: acoustical measurements,'' Word **20**, 384–422.

Nearey, T. M., and Rochet, B. L. (**1994**). ''Effects of place of articulation and vowel context on VOT production and perception for French and English stops,'' J. Int. Phonetic Assoc. **24**, 1–19.

Netsell, R., Lotz, W. K., DuChane, A. S., and Barlow, S. M. (**1991**). ''Vocal tract aerodynamics during syllable productions: normative data and theoretical implications,'' J. Voice **5**, 1–9.

Peterson, G. E., and Barney, H. L. (**1952**). ''Control methods used in a study of vowels,'' J. Acoust. Soc. Am. **24**, 175–184.

Port, R. F., and Rotunno, R. (**1979**). ''Relation between voice-onset time and vowel duration,'' J. Acoust. Soc. Am. **66**, 654–662.

Ryalls, J., Zipprer, A., and Baldauff, P. (**1997**). ''A preliminary investigation of the effects of gender and race on voice onset time,'' J. Speech Lang. Hear. Res. **40**, 642–645.

Smith, B. L., and Kenney, M. K. (**1998**). ''An assessment of several acoustic parameters in children's speech production development: longitudinal data,'' J. Phonetics **26**, 95–108.

Stathopoulos, E. T., and Sapienza, C. M. (**1997**). ''Developmental changes in laryngeal and respiratory function with variations in sound pressure level,'' J. Speech Lang. Hear. Res. **40**, 595–614.

Swartz, B. L. (**1992**). ''Gender difference in voice onset time,'' Percept. Mot. Skills **75**, 983–992.

Traunmüller, H. (**1988**). ''Paralinguistic variation and invariance in the characteristic frequencies of vowels,'' Phonetica **45**, 1–29.

Whiteside, S. P., and Marshall, J. (**2001**). ''Developmental trends in voice onset time: some evidence for sex differences,'' Phonetica **58**, 196–210.

Perceptuomotor bias in the imitation of steady-state vowels[a)]

Gautam K. Vallabha[b)] and Betty Tuller
Center for Complex Systems and Brain Sciences, Florida Atlantic University, 777 Glades Road, Boca Raton, Florida 33431

(Received 11 July 2003; revised 20 April 2004; accepted 3 May 2004)

Previous studies suggest that speakers are systematically inaccurate, or biased, when imitating self-produced vowels. The direction of these biases in formant space and their variation may offer clues about the organization of the vowel perceptual space. To examine these patterns, three male speakers were asked to imitate 45 self-produced vowels that were systematically distributed in F1/F2 space. All three speakers showed imitation bias, and the bias magnitudes were significantly larger than those predicted by a model of articulatory noise. Each speaker showed a different pattern of bias directions, but the pattern was unrelated to the locations of prototypical vowels produced by that speaker. However, there were substantial quantitative regularities: (1) The distribution of imitation variability and bias magnitudes were similar for all speakers, (2) the imitation variability was independent of the bias magnitudes, and (3) the imitation variability (a production measure) was commensurate with the formant discrimination limen (a perceptual measure). These results indicate that there is additive Gaussian noise in the imitation process that independently affects each formant and that there are speaker-dependent and potentially nonlinguistic biases in vowel perception and production. © *2004 Acoustical Society of America.* [DOI: 10.1121/1.1764832]

PACS numbers: 43.71.Es, 43.71.An [RD] Pages: 1184–1197

I. INTRODUCTION

A persistent debate in speech research is over the nature of vowel representation and memory and over which methodologies constitute appropriate measures of the vowel percept. Vowel perception has several phenomena in common with nonspeech perception, most prominently context-sensitivity and noncategoricality (Pisoni, 1973). Consequently, auditory processes are thought to influence vowels more than consonants. On the other hand, vowel discrimination is partly mediated by phonetic labels (Repp *et al.*, 1979) and is worse among more prototypical exemplars of a category (Iverson and Kuhl, 1995; Shigeno, 1991). There is also a significant stimulus order effect in vowel discrimination that seems to depend on the phonetic range and location of the tokens (Repp and Crowder, 1990). Thus the perception of a vowel is influenced by its auditory quality, its phonetic status, and its location in the vowel space, and the tension among these three aspects has not been experimentally resolved.

One source of the experimental tension is that the standard methods of evaluating the vowel percept—categorization, identification, AX or ABX discrimination, multidimensional scaling and goodness ratings—share many of the same limitations. First, they quantize what is essentially a continuous and graded percept. Second, discrimination and multidimensional scaling methods are very time-consuming. The tradeoff between stimulus resolution and the number of stimuli restricts a discrimination experiment to only a small part of the vowel space (a surprisingly large number of results are based upon the one-dimensional [i-ɪ-ɛ-æ] continuum). Consequently, large areas of the vowel space are as yet unexplored. Finally, a discrimination experiment can only examine changes in phonetic quality that are projected onto the stimulus continuum; for instance, the only context effects observable with one-dimensional continua are contrast and assimilation. One way to avoid these problems is to exploit the fact that listeners are also speakers and use vowel imitation as a measure of vowel perception, and the F1/F2 patterns of the imitations as clues to vowel organization. Vowel production is intrinsically continuous and multidimensional, so in principle a subject's imitation can convey subcategorical qualities of the vowel percept.

There is substantial evidence that imitation is deeply linked to speech perception and production. Infants only a few weeks old attempt to mimic the vocalizations of adults around them and 20-week old infants can imitate the point vowels [i], [a], and [u] (Kuhl and Meltzoff, 1996). Such imitations, along with spontaneous babbling, are thought to forge the perception–production link that allows more advanced articulations (Kuhl, 2000). Moreover, when adult subjects are asked to listen to a syllable sequence and repeat it with as little delay as possible, they perform with remarkable accuracy at latencies as short as 150 ms (Porter and Lubker, 1980; also see Fowler *et al.*, 2003). In fact, the response latency for shadowing is smaller than the latency for a simple response (i.e., detecting the vowel and uttering a standard response). These results suggest a fast subcognitive link between speech perception and production. This link may be covertly active even in regular speech: Pardo and Fowler (2000) report that the productions of two speakers are more similar to each other after they had conversed than

[a)]This work was part of the first author's Ph.D. dissertation at the Center for Complex Systems and Brain Sciences, Florida Atlantic University. Portions of this work were also presented at the 142nd meeting of the Acoustical Society of America [J. Acoust. Soc. Am. **110**, 2657(A) (2001)].

[b)]Author to whom correspondence should be addressed. Currently affiliated with the Center for the Neural Basis of Cognition, Carnegie Mellon University, Pittsburgh, PA. Electronic mail: vallabha@cnbc.cmu.edu

before (without any instructions to imitate). Imitation has also been posited to be the driving force behind sound change in language (de Boer, 2000). For these reasons, imitation seems a particularly apt method for studying speech in general and the vowel space in particular.

The utility of imitation to speech perception research has been recognized since the 1960s. In one of the first imitation studies, Chistovich *et al.* (1966) synthesized 12 vowels along an [a-ɛ-i] trajectory in F1/F2 space and asked a phonetically trained female subject to imitate them. When the mean F2 of the imitations was plotted against the ordinal of the stimulus (1–12), the resulting curve showed four well-defined plateaus. In addition, the F2 histogram showed four peaks near the category centers and the standard deviation of F2 showed peaks near the boundaries of the putative categories. Chistovich *et al.* interpreted these results to indicate that the subject had between four and six categories across the [a-ɛ-i] continuum. Since the subject's native language (Russian) has only 3 vowel phonemes across the continuum, they posited that vowel representation is fundamentally discrete but at a finer granularity than the native phonemic categories. Kent (1973) failed to replicate the sub-phonemic granularity with American English speakers. Repp and Williams (1985) had a little more success: They asked two phonetically trained male speakers to imitate 150 ms synthetic vowels along the [æ-i] and [u-i] continua. There were clear peaks in the resulting formant histograms, indicating that the speakers had distinct response preferences. However, the formant frequency curves did not exhibit the plateaus observed by Chistovich *et al.* and the standard deviations did not show any consistent pattern across the two speakers.

It should be noted that both Kent (1973) and Repp and Williams (1985) found large intersubject differences in formant patterns. In retrospect, these differences are to be expected, since the vowels produced by a speaker are influenced by the physiology of the speaker and idiosyncrasies in the manner of production (Johnson *et al.*, 1993). These differences can in turn interact with how vowels are perceived by that speaker (Fox, 1982). Thus, each speaker has a different vowel space and, potentially, a different pattern of imitation responses. The intersubject differences also imply that (a) it is methodologically risky to average formant data across subjects and (b) response preferences in a speaker's imitations of synthetic vowels may simply be due to a mismatch between the synthetic targets and the production capabilities of the speakers.

Repp and Williams (1987) tested the ''stimulus mismatch'' explanation by asking speakers to imitate self-produced rather than synthetic vowels. They used as subjects the same two speakers from their earlier experiment. For each speaker, they chose 12 self-produced targets that were approximately equidistant along the [u-i] and [æ-i] continua. In addition, they also recorded the speakers' [hVd] utterances, and were thus able to map the speaker's ''prototypical'' vowels. Three of the results are striking: (1) The variability of the self-imitations was remarkably similar to the imitations of synthetic vowels; (2) the self-imitations were consistently inaccurate, regardless of the latency of the imitation; (3) the imitations seemed to be pulled towards regions with more prototypes, but seemed to end up *between* prototypes rather than *at* the prototypes. These results indicate that the imitation inaccuracies are not due simply to a mismatch between the stimulus and the speaker's production capabilities. Moreover, the similarity between the imitations of synthetic and self-produced vowels suggests that the inaccuracies are shaped by the phonetics of the targets and not just their auditory qualities.

In summary, the line of research initiated by Chistovich *et al.* (1966) has shown that speakers prefer certain formant frequency regions. There are also clear nonlinearities in vowel imitation that hint at the existence of representational categories but none of the studies have been able to identify the putative categories or relate them to phonemes or allophones.

One other inspiration for the study reported here comes from the imitation of visual stimuli. Stadler *et al.* (1991) created a grid of dots on a rectangular sheet of paper and presented them one at a time to each subject, who then had to reproduce the location of the dot from memory. The reproductions of the dots' locations were systematically biased toward the corners of the sheet, which Stadler *et al.* interpreted as evidence for a Gestalt structure in the visual field, i.e., that the visual system organized itself with respect to the boundary of the paper and distorted the perception of the homogenous stimulus array. Wildgen (1991) proposed that vowel systems may be organized in an analogous manner, with the corner vowels [i], [a], and [u] functioning as the attractors. This proposal is plausible since there is abundant evidence that the perceptual space of vowels is warped even with respect to an ''auditory'' space of bark or mel units, and that the warping is influenced by native vowel categories (e.g., Kewley-Port and Atal, 1989; Iverson and Kuhl, 1995).

In the present experiment, we reexamine the issue of vowel organization using a self-imitation paradigm. Our motivations are twofold. The first is to test whether the complex imitation patterns seen with one-dimensional continua such as [u-i] and [æ-i] would become more coherent with two-dimensional (2D) stimulus grid (and if they do, whether they are influenced by the natural vowels of the speaker). The second motivation is to test the null hypothesis that inaccuracies in imitation are caused by random articulatory or perceptual fluctuations and do not reflect any deeper phonetic organization. To evaluate this claim, we compare the speakers' patterns of imitation inaccuracies with those from an articulatory model (Rubin *et al.*, 1981) and a perceptual model based on formant difference limens.

II. METHOD

The experiment was conducted over two days. On Day 1, subjects were asked to imitate a set of 100 synthetic vowel-like stimuli; the purpose of this step was to encourage the subject to produce vowel-like sounds that were likely to be well distributed in formant space. They were also asked to read [hVd] words in citation and sentence contexts. For each subject, 45 vowels were chosen from the 100 self-produced vowels to serve as the targets. On Day 2, the 45 self-produced targets were presented for imitation. The steps are described in more detail below.

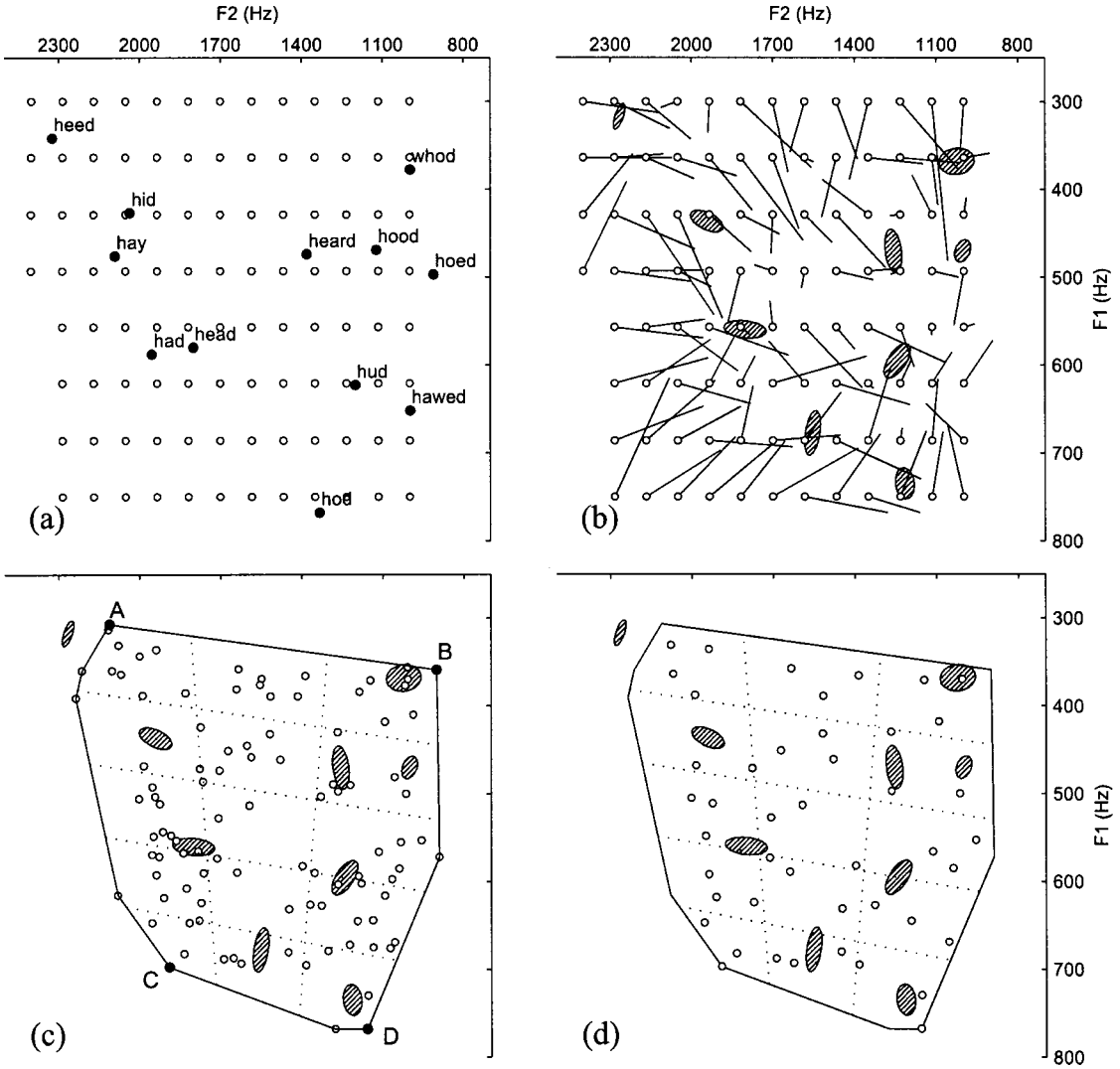

FIG. 1. Selection of the self-produced targets for subject CD. (a) The synthetic sounds (empty circles) and the mean locations of American English vowels from Hillenbrand *et al.* (1995). (b) The imitations of the synthetic sounds (tips of the lines) and the 1-sd ellipses for the prototypical vowels of the subject (hatched ellipses). (c) The subject's imitations (empty circles), their convex hull with its four corner points (solid line; see text), and the 5×3 vowel grid (dotted lines). (d) The 45 imitations chosen to be the targets.

A. Subjects

The subjects (CD,DR,FC) were three male native speakers of American English who volunteered to participate in the experiment. CD (39 years old) grew up near New York City; DR (40) grew up in North Carolina until the age of 14 years and in New York City after that; FC (31) grew up in New Hampshire. The subjects did not have any phonetic training, were not fluent in a second language, and did not have any hearing problems. FC and CD had participated in previous imitation experiments.

B. Stimuli

One hundred steady-state vowel-like stimuli were synthesized using the 1988 version of the Klatt synthesizer (KLSYN88a, Sensimetrics Corporation, Cambridge, MA). Each stimulus had three formants, with F1 taking on one of 8 values (300–750 Hz in steps of ~65 Hz), F2 taking on one of 13 values (998–2400 Hz in steps of ~115 Hz), and F3 constant at 2500 Hz [Fig. 1(a)]. For all stimuli, F0 was 120 Hz and the duration was 200 ms. F0 and the amplitude of voicing were linearly ramped at the beginning and end of each stimulus for 30 ms. The bandwidths of the formants were 60 Hz (F1), 90 Hz (F2) and 150 Hz (F3). Finally, the stimuli were sampled at 10 kHz.

C. Procedure

The subject was seated in a sound-insulated booth, and the vowel stimuli were presented binaurally over headphones (Telephonics TDH-39P) at a comfortable loudness. The subject's productions were recorded using a microphone (Sony electret condenser, ECM-23F) and digitized at a sampling rate of 10 kHz. The microphone was mounted on a table in front of the subject, and its position was adjusted so that it was about 10 inches from the subject's mouth when the subject was comfortably seated. Both the stimulus presentation and recording were computer-controlled using the Desklab system (Model 216; Gradient Technology, Inc., now defunct).

1. Prototypical vowels

Each subject was asked to read *heed*, *hid*, *head*, *had*, *hud*, *hod*, *hoed*, *hood*, and *who'd* five times in a list context and another five times in a sentence context.[1] These readings provided 10 tokens of the subject's natural productions of each of the 9 monophthongal vowels in American English.

2. Imitation of the synthetic stimuli [Fig. 1(b)]

The 100 stimuli were randomized and divided into 2 blocks of 50 stimuli each. The same randomized block and presentation order was used for all subjects. Because of the difficulty of imitating the synthetic stimuli, each stimulus was presented and imitated twice consecutively. This allowed subjects two chances to imitate each synthetic stimulus; only the second imitation was used subsequently. After each stimulus presentation, the subject had 4 s to initiate his imitation. The recording program registered the end of an imitation using an amplitude threshold, waited one second, and then presented the target for the next trial. Subjects were encouraged to produce all their imitations at the same level of subjective loudness; if an error occurred during the recording, the affected targets were presented again at the end of the block. Prior to the imitation session, the subjects were familiarized with the synthetic stimuli and the procedure in a brief training session in which they imitated 15 randomly chosen synthetic stimuli.[2]

3. Selection of the self-produced targets

The F1/F2 ''vowel quadrilateral'' of each speaker was approximated by the convex hull of the 100 imitations. Four points on the hull perimeter closest to the speaker's *heed*, *who'd*, *had*, and *hod* ellipses were chosen as the four ''corners'' of the quadrilateral. The top and bottom lines of the quadrilateral were each divided into three equal segments and the front and back lines were divided into five equal segments, resulting in 15 cells arranged in a 5×3 grid [Fig. 1(c); cells are denoted by row#-col#]. The utility of this division is that the 5×3 grid is qualitatively ''normalized'' to the vowel space of each subject. For example, all the speakers have [ə]-like tokens in cell 3-2 and [ʌ]-like tokens in cell 4-3.

For each subject, three productions were selected from each cell of the vowel grid, for a total of 45 targets [Fig. 1(d)]. The targets were chosen so that they covered a wide range of phonetic qualities. In addition, care was taken to exclude productions that were breathy or creaky, or had sharp variations in pitch and loudness (however, the durations of the targets were not controlled). If a cell did not have at least three productions [e.g., cell 2-1 in Fig. 1(d)], then the closest productions from adjacent cells were assigned to it. Finally, the targets were numbered from 1 to 45, with the three targets assigned to each cell ordered by decreasing F2. For example, the targets belonging to cells 1-1 and 2-1 were numbered [1,2,3] and [10,11,12], respectively.

4. Imitations of the self-produced targets

The presentation list for the imitations of the self-produced targets contained 10 instances of each of the 45 unique targets. The sequence of 450 stimuli was randomized and divided into 9 blocks of 50 each. The protocol for each imitation trial was same as for the synthetic stimuli, and the same randomized block and presentation order was used for all subjects. The use of the same presentation order for all subjects was an approximate control for vowel context effects. Targets with the same number have grossly similar phonetic quality for all speakers, e.g., the target sequence [3,26,43] denotes a [high-front, mid-back, low-back] vowel sequence. This control is not very strict, of course, but it was judged better than allowing subjects to have arbitrarily different vowel contexts. Prior to the imitation session, there was a training session with 15 randomly chosen self-produced targets.

D. Formant analysis

The formants for each imitation were estimated using a customized LPC analysis tool. A 256-point (25.6 ms) analysis frame was slid along the signal in steps of 64 points (6.4 ms). The analysis frame was Hamming-windowed, preemphasized at 100%, and submitted to LPC analysis. The optimal filter order was determined separately for each subject (Vallabha and Tuller, 2002). Next, the spectrum of the LPC filter was computed with a 512-point FFT and the locations of its peaks were estimated using three-point parabolic interpolation. The formant tracks were overlaid on a spectrogram to ensure that the LPC peaks accurately captured the spectral structure of the signal; if there were discrepancies, the filter order was adjusted. Finally, a segment containing at least five pitch pulses was selected from the least-varying portion of the production (i.e., with relatively flat F1 and F2 trajectories), and the formant estimates were averaged over the corresponding analysis frames. If the imitations were diphthongized, then the selection was made from the portion of the diphthong that most closely matched the quality of the target. Fortunately, most of the imitations were monophthongs with unambiguous steady states.

III. MODELS

The results from Repp and Williams (1987) suggest that we can expect systematic bias and noise in the imitations. In order to draw interesting conclusions about the underlying mechanisms, it is necessary to formulate plausible null hypotheses. The two models below are a first attempt at such a formulation, and they predict that any patterns observed in vowel imitation are due to noise in tongue positioning during vowel production and/or vowel perception.

A. Articulatory model

We simulated the effect of random articulatory perturbations using the ASY articulatory synthesizer (Rubin *et al.*, 1981). The vocal tract (VT) configurations for six American English vowels [i ɛ æ ɑ ə u] were obtained,[3] and the AUTO command in ASY was used to compute their formants. In order to increase coverage of the formant space, a raised version of [ɑ] was created and the VT configuration for [ə] was made more backed (these two vowels are denoted [ɑ′]

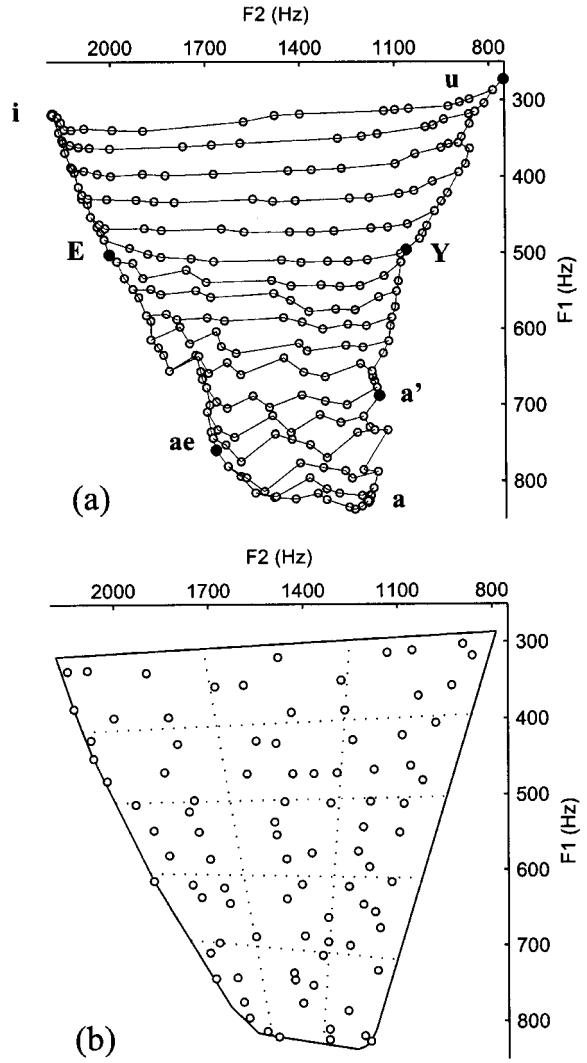

FIG. 2. Selection of targets for the articulatory model. (a) Locations of the 7 key vowels (solid circles; E=[ɛ], ae=[æ], Y=[ɣ], a=[ɑ]) and the interpolated vocal tract configurations (empty circles). Solid lines show the paths of the interpolations. (b) The convex hull of the 196 interpolated sounds (solid line), the corresponding vowel grid (dotted lines), and the 90 selected targets (empty circles).

and [ɣ], respectively; the latter symbol represents the close-mid back unrounded vowel). The vowels [i ɛ æ ɑ ɑ′ ɣ u] approximately mark the perimeter of the ''vowel space'' of the artificial vocal tract. The 10 ASY parameters which make up a VT configuration were linearly interpolated between the seven key vowels [Fig. 2(a)], resulting in 196 vocalic sounds. A vowel grid was constructed with these sounds using the same method as with the speakers' productions. Finally, six vowels were chosen from each of the 15 cells to serve as ''targets,'' yielding a total of 90 targets [Fig. 2(b)].

Each target was ''imitated'' (perturbed) 10 times. For each perturbation, zero-mean Gaussian noise was independently added to the *x* and *y* coordinates of the tongue body center.[4] The sd of the noise was 1 mm for both coordinates, which is a conservative estimate based on an x-ray microbeam study of the production of American English vowels (see Table IV of Beckman *et al.*, 1995). The use of the same noise sd for both coordinates is admittedly unrealistic. However, unequal radii are not meaningful unless the noise ellipse is correctly oriented, and there is no agreement in the literature about how the orientation interacts with the location and degree of constriction. In order to prevent unreasonably large perturbations, the noise was restricted to 2.5 mm or less. None of the other VT parameters, such as the tongue tip location, jaw angle, or lip aperture, were modified.

B. Perceptual model

It is clear from examining the results from Repp and Williams (1987) and Chistovich *et al.* (1966) that imitation frequently involves changes of vowel quality but not always of vowel category. However, most models of vowel perception (e.g., Syrdal and Gopal, 1986; Hillenbrand and Gayvert, 1993) emphasize categorization behavior without a systematic account of gradations in vowel goodness. We therefore formulated a very simple model of perception based on discrimination limens (DL), as follows. Each vowel percept is treated as a point in Bark formant space (Traunmüller, 1990). There is intrinsic noise in the perceptual process which independently perturbs the F1 and F2 values; this noise is Gaussian and its sd is given by the formant DL (assumed to be 0.28 barks for both F1 and F2; see below). Vowel production is assumed to be flawless, reproducing exactly the formants in the noisy vowel percept.

There is some experimental justification for treating the above model as a good first approximation: (1) Perceptual distances between vowels are well-matched by the Euclidean distances between the vowels in Bark space (Kewley-Port and Atal, 1989). Moreover, models of vowel categorization frequently operate in Bark space (Syrdal and Gopal, 1986; Iivonen, 1995). (2) The notion of a percept as a point in multidimensional space with intrinsic Gaussian noise is borrowed from signal detection-theoretic (SDT) approaches (Macmillan *et al.*, 1988; van Hessen and Schouten, 1998). (3) The use of formant DL as a measure of intrinsic variability is also borrowed from SDT. For example, Macmillan *et al.* (1988) used fixed discrimination to establish the ''sensory variance'' in vowel perception. We used the DL estimates from Kewley-Port and Zheng (1998), who found that the DL for single-formant change in isolated multiple-formant vowels, under ordinary listening conditions, is ~0.28 barks. This estimate holds for both F1 and F2 and for different regions of the vowel space.[5] Moreover, synthetic vowels spaced ~0.25 barks from each other result in fixed-discrimination d' values near 1.0 (Macmillan *et al.*, 1988). These results suggest that 0.28 barks corresponds to approximately 1 sd of perceptual variability across the entire vowel space. This assumption of uniform sensitivity is a useful first approximation, but it should be kept in mind that phonetic categories can induce local variations in the sensitivity (Iverson and Kuhl, 1995).

To allow the ASY and perceptual models to be meaningfully compared, the 90 ASY targets were also used for the perceptual perturbation. Each ASY target was converted to Bark space and perturbed 10 times. In each perturbation, zero-mean Gaussian noise with 0.28-bark sd was independently added to F1 and F2.

It is important to mark the scope of these models. Because of nonlinearities in the mapping from a vocal tract

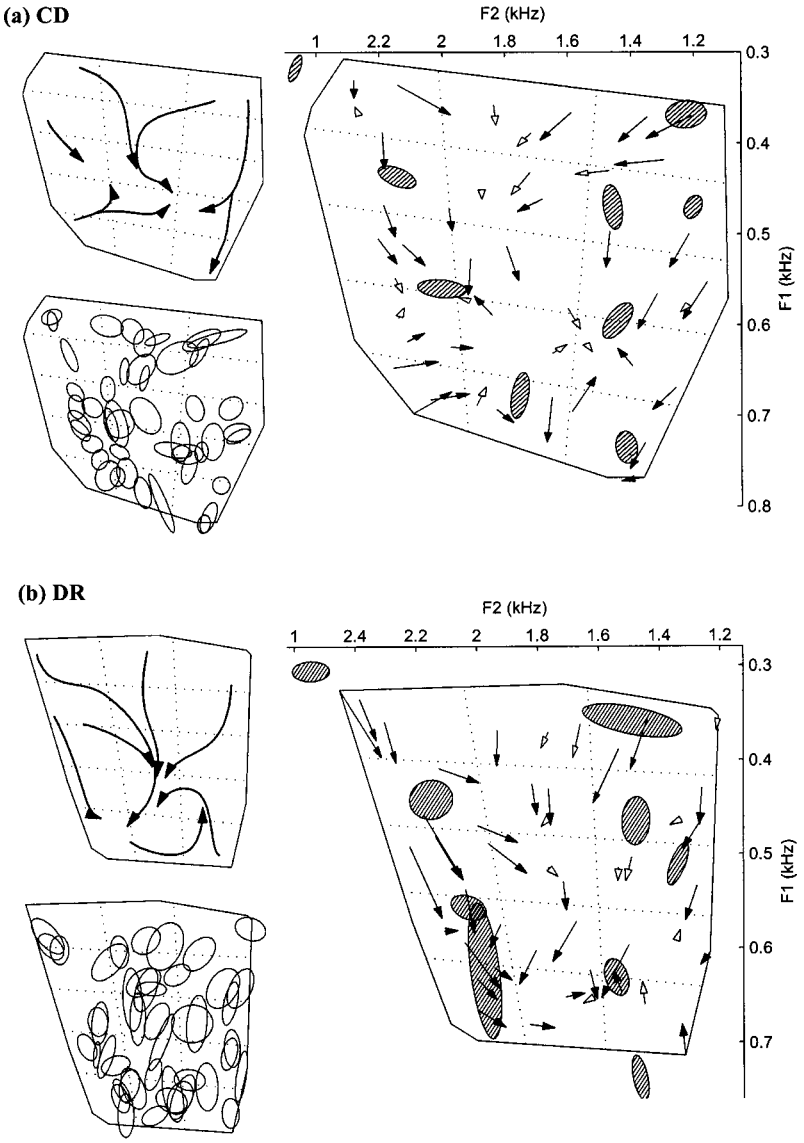

FIG. 3. (a) The imitation behavior of subject CD. Right subplot: The base of each arrow is a target and the tip is the mean of the 10 imitations of that target. Hatched regions are the 1-sd principal components for the [hVd] vowels. Solid arrowheads indicate statistically significant bias vectors (Hotelling's T^2 test, $p<0.05$). Top left: A sketch of the overall movement tendencies. Bottom left: The 1-sd principal components for each set of imitations; the center of the ellipse is the mean imitation. (b) The imitation behavior of subject DR.

configuration to a speech waveform, random perturbations of the tongue can potentially lead to systematic biases in the formants. Hence, the articulatory model can be taken as a nontrivial hypothesis about imitation bias patterns and imitation variability. The perceptual model incorporates assumptions about the Bark transformation and formant discrimination limen, so it too can be taken as a nontrivial hypothesis about imitation variability. However, it is incapable of generating any pattern of bias. This incapacity is inherent in the definition of the model and is not a ''prediction,'' so bias simply does not come with the scope of the model.[6]

IV. RESULTS

A. Qualitative results

In presenting the results, we concentrate on F1 and F2 patterns since only the F1 and F2 locations of the targets were controlled. When examining the results, it is important to keep in mind that we do not know whether the subjects perceived any differences between the targets and their imitations *as* they were producing them. One workaround would be to have the subject evaluate the targets and imitations in a post-experiment discrimination task, but this is also problematic since natural productions vary along dimensions other than phonetic quality.

Figures 3 and 4 summarize the imitation behavior of the subjects. Each arrow will henceforth be referred to as a ''bias vector.'' The principal component ellipses[7] show the variation around the corresponding means, and are shown separately in order to make the overall bias pattern more salient (all formants were converted to barks before the bias vectors and ellipses were calculated; the Hertz scale of the figure is for presentation only). There are five points to note in the figures:

(1) All three subjects exhibit a prominent and systematic bias over their entire vowel space. Even when a bias vector is not significant, its direction is usually consistent with adjacent bias vectors;
(2) The bias vectors do not seem to be influenced by the nearest prototypes. For example, CD's imitations of high-back targets (cells 1-3 and 2-3) ignore the [ʊ], [u]

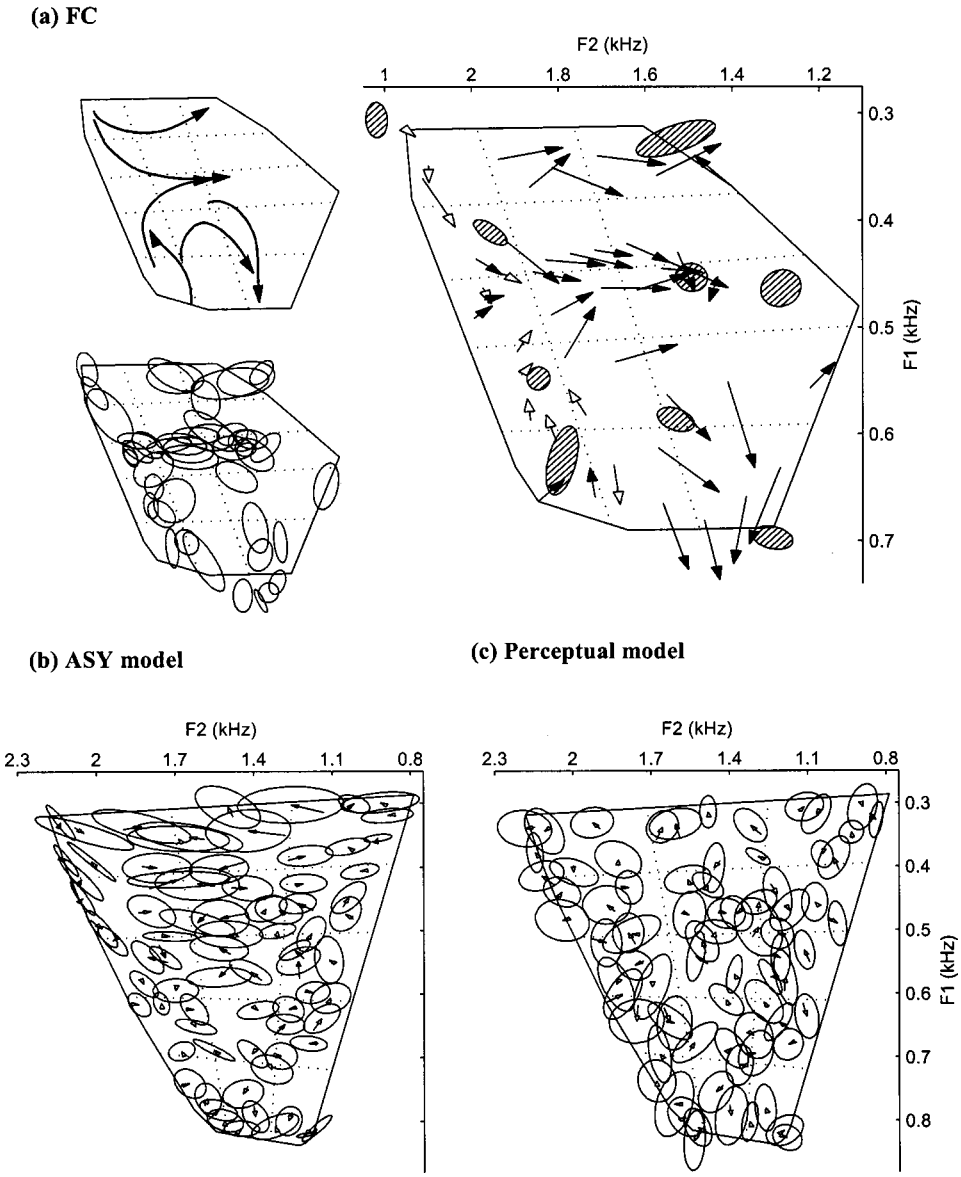

FIG. 4. (a) The imitation behavior of subject FC. The notation is the same as in Fig. 3. (b) and (c) The mean ''imitations'' and 1-sd ellipses for the articulatory (ASY) and perceptual models.

and [o] prototypes, while DR's imitations of high front targets (cell 2-1) ignore the [I] prototype;

(3) the biases sometimes appear to centralize (e.g., the high vowels for CD and DC), but in several cases they are directed away from the center (e.g., the bias patterns in CD's cell 4-3, DR's cell 4-2, and FC's cell 3-3 and 5-3). Morever, the ''Day 3'' bias pattern for CD (Fig. 7) clearly shows a general lowering rather than a neutralization;

(4) some patterns are interesting by their absence: Low-back vowels are lowered or raised but rarely move directly to the center, and in no case does a mid-back vowel move towards the high-back region (mid-vowels are almost never raised, in general);

(5) the imitations are very noisy. Note especially that the ellipses are 1-sd wide and, therefore, cover only ~40% of the distribution. Moreover, a nonsignificant bias vector does not imply accurate imitation—it usually indicates a lot of variability without any systematic component. Consequently, areas with nonsignificant vectors (e.g., high-central region for CD, low-front for FC) are not necessarily stable;

Figures 4(b) and (c) shows the ''imitation'' plots of the articulatory and perceptual models overlaid with each subject's 1-sd principal component ellipses (in order to make the plots less crowded, ellipses are shown for only 76 of the 90 targets). The key point to observe is that the articulatory model's bias patterns do not match the subjects' The model's bias vectors are smaller than the subjects' and are much less consistent, that is, adjacent targets do not usually move in the same direction. In fact, the ASY model's bias vectors seem as irregular as the perceptual model's (recall that by construction, the perceptual model does not exhibit any bias pattern). In addition, the ASY ellipses have a pronounced horizontal orientation, unlike either the perceptual model or the subjects' productions. The perceptual model's ellipses are slightly larger for front vowels, but this is only because their sd is defined to be 0.28 barks and the ellipses are being shown in a linear Hertz space.

TABLE I. Statistics of the bias vectors, calculated over the 45 bias vectors (for the subjects) and 90 (for the models). ASY=Articulatory model. PER =Perceptual model.

	Change in Hertz (mean±sd)		Change in Barks (mean±sd)		# significant[a] $p<0.05$, $p<0.01$
	F1	F2	F1	F2	
ASY	3±9	3±40	−0.02±0.07	0.01±0.18	16, 4
PER	−2±11	6±23	−0.02±0.09	0.02±0.10	5, 2
CD	13±21	4±73	0.12±0.18	0.05±0.33	31, 22
DR	26±25	−18±64	0.23±0.22	−0.05±0.26	34, 26
FC	9±31	−64±66	0.07±0.26	−0.29±0.31	34, 25

[a]Number of significant bias vectors, using the Hotelling T^2 test.

B. Quantitative results

1. Formant bias

Table I shows the F1 and F2 biases averaged over the bias vectors of all the targets. The subjects show significant ensemble effects; specifically, CD and DR tend to lower their imitations while FC tends to retract. This ensemble bias does not, by itself, account for the patterns in Figs. 3 and 4. Subtracting the ensemble bias from all the imitations still leaves a substantial number of significant bias vectors: 22, 18, and 28 for CD, DR and FC, respectively ($p<0.01$). Gross bias patterns such as the preference for the low-front region are still present after the subtraction (albeit less prominently than before).

In spite of the differences in ensemble bias, there is an underlying similarity among the subjects. This is shown by the bias magnitude, viz. the Euclidean distance from the target to the mean imitation measured in Bark units. Figure 5(a) shows the distribution of the bias magnitude for the models and subjects. Both model distributions are significantly different from the three subject distributions ($p<0.001$, Bonferroni-corrected Kolmogorov–Smirnov test). None of the other comparisons are significant (with the exception of CD-FC, significant only at $p<0.05$). Figure 5(b) shows that the subjects' bias magnitudes are larger than the models' even if the imitation variability is taken into account (the Hotelling T statistic is essentially the bias magnitude in sd units). The pairwise Kolmogorov–Smirnov tests confirm that the only significant differences are between the model and subject distributions ($p<0.001$).

One concern with the bias vector is that it can misrepresent the overall directionality of the imitations. Since it weights the directions of the individual vectors by their magnitudes, it cannot determine whether the imitations occur in one preferred direction, or in all directions with those in one direction being much larger. This concern is addressed by the circular variance, which only uses the unit vectors and ranges from 0 (the ten unit vectors all have the same direction) to 1 (the vectors are maximally dispersed).[8] Figure 5(c) shows the distribution of this measure, and illustrates that the subjects' imitations usually have a preferred direction with respect to the target whereas the models do not. Again, the only significant differences are between the model and subject distributions.

Finally, there is an intriguing negative correlation between the circular variance and the mean magnitude of the individual vectors ($r=-0.43$, -0.52, and -0.53 for CD, DR, and FC, all statistically significant at $p<0.05$). The models' correlations, on the other hand, are much smaller ($r=-0.13$ and -0.17) and neither approached significance. Since circular variance ignores the magnitude and the mean magnitude ignores the directions, there is no a priori relation between these two measures. Hence, these correlations are not artifactual, and reliably indicate that large deviations have a more consistent direction than small deviations.

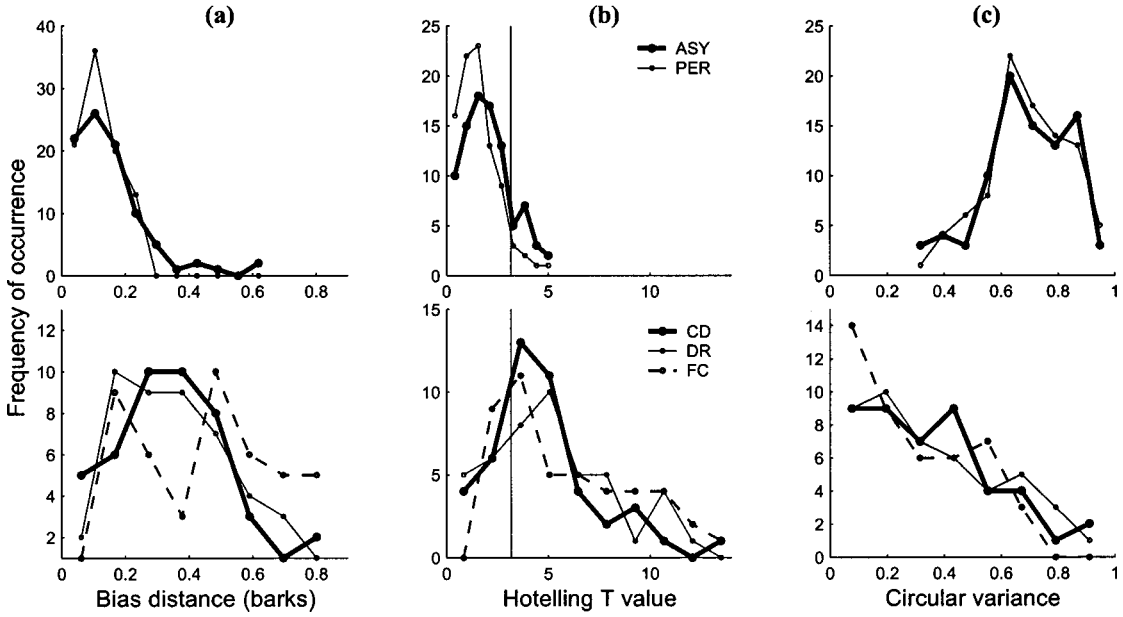

FIG. 5. Frequency polygons of the (a) Bark magnitudes of the bias vectors, and (b) the corresponding Hotelling T values. The vertical line indicates the 95% critical value. (c) Frequency polygon of the circular variances. ASY=articulatory model, PER=perceptual model. N=90 for ASY and PER, N=45 for the subjects.

TABLE II. Variability of the imitations. The statistics (such as F1 sd) were computed for 10 imitations of each target, and averaged across all the targets (90 for the models, 45 for the subjects). ASY=Articulatory model, PER =Perceptual model.

	Average standard deviation				Average F1×F2 correlation (# sig)[a]
	Hertz		Barks		
	F1	F2	F1	F2	
ASY	20	85	0.17	0.39	0.40 (21)
PER	31	63	0.26	0.28	0.29 (5)
CD	26	63	0.22	0.28	0.34 (4)
DR	30	65	0.26	0.29	0.33 (4)
FC	26	67	0.23	0.31	0.33 (6)

[a]Number of correlations significant at $p<0.05$, using the *t*-test.

2. Formant variability

There are two straightforward measures of variability—the standard deviation with respect to the mean imitation, and the Euclidean distance of the imitations from the corresponding mean imitations. As we show below, both measures point to the same conclusion.

Table II summarizes the F1 and F2 variability, averaged over all the targets. For almost all of the subjects' targets, the correlation between F1 and F2 is not significant, nor is the variance explained by the first principal component. Furthermore, the bark F1 and F2 sds are quite similar across the subjects, suggesting that the variability of each formant is uncorrelated with the others but of approximately the same magnitude. Figure 6 shows the distributions of the distance from the mean imitation, along with the best-fit Rayleigh distribution; the Rayleigh distribution is the one expected if F1 and F2 are independent zero-mean Gaussians with identical standard deviations (the Rayleigh parameter, *b*). As can be seen, the subjects' distributions match the theoretical distribution very closely, with parameters near 0.28 barks.[9] The only mismatch is for FC and the articulatory model, most likely due to the pronounced horizontal orientation of the ellipses for high vowels (for the model) and the mid vowels (for FC), which causes the F2 sd to be greater than the F1 sd.

There is one other piece of evidence for the independence of F1 and F2. The relation between the direction of the bias vector and the orientation of the major axis of the ellipse is extremely weak for the subjects and models ($p>0.2$, using a directional correlation coefficient, Jupp and Mardia, 1980). There are locations where the ellipse axis and bias direction are strongly related (e.g., high-back region for CD, mid-central region for FC), but this behavior is not characteristic of imitations over the entire vowel space. In brief, the variability of the subjects is more similar to the formant DL-based perceptual model than to the articulatory model.

3. Other acoustic measures

It is possible that the biases in F1 and F2 were perceptually counteracted by other systematic changes in the acoustics. To evaluate this possibility the durations, fundamental frequencies, and higher formants of the targets and imitations were compared to each other. Briefly, the subjects' imitations of the (150 ms) synthetic vowels were almost always of greater duration than the target (see Pisoni, 1980, for a similar lengthening effect). In imitating the self-produced targets, CD, DR, and FC showed mean duration changes of 17, 42, and −13 ms, respectively, but neither these changes nor the absolute durations were correlated with F1 or F2 changes. Likewise, the F0 of the imitations closely matched the F0 of the self-produced target (CD, DR, and FC had mean F0 differences of 6, 0, and −1 Hz), and the F0 differences were not related to F1 or F2.

The higher formants are more interesting. The F3 and F4 of the self-imitations were significantly different from the target, and the bias and variability are similar to that for F1 and F2. For example, the average sd was 0.21, 0.22, and 0.28 barks for F3 (CD, DR, and FC), and 0.23, 0.28, and 0.27 barks for F4. These F3 and F4 changes were not correlated with F1 and F2 changes, reinforcing the conclusion that formants are independently affected by noise at the magnitude of the formant DL. Also, the presence of bias for F3 and F4 suggests that the imitation subtly affects the entire spectrum of the vowel.

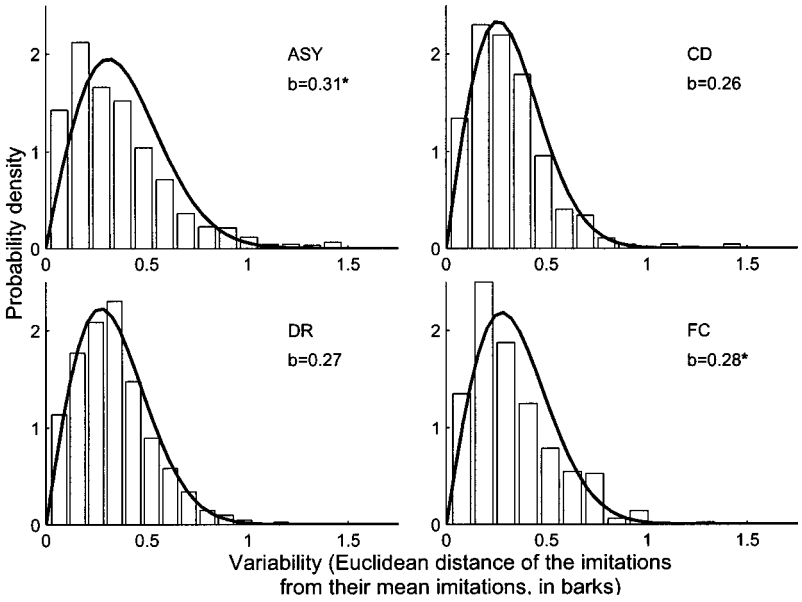

FIG. 6. Histograms and the corresponding best-fit Rayleigh distributions (solid lines) for the (Euclidean) bark distance of the imitations from the mean imitation. The b-value is the best-fit Rayleigh parameter, and an adjacent asterisk indicates that the Rayleigh fit is statistically different from the data ($p<0.05$, two-sample K-S test). ASY=Articulatory model.

V. LONG-TERM EFFECTS

From the data reported above, it is clear that subjects are biased in imitating themselves. However, is the particular pattern of bias exhibited by a subject a transient phenomenon, or is it a relatively durable aspect of their perception and production? An answer to this question would help to pin down the functional basis (if any) of the biases. As a first attempt towards an answer, two of the speakers (CD and FC) were asked to participate in a replication of ''Day 2'' of the imitation task 14 months after their original participation (this will henceforth be called ''Day 3;'' DR was not able to participate as he had moved out of state). The experimental protocol, stimulus sequence, and recording and playback apparatus were exactly the same as before.

Figure 7 shows the resulting bias vector patterns. There is a marked difference in CD's overall pattern (especially in cells 1-3, 3-1, and 5-1) with lowering being much more prominent. The median bias magnitude is also larger (0.44 barks, up from 0.33 barks before). FC also shows changes in the bias directions (e.g., in cells 1-1, 1-2, and 5-4) but the overall pattern is very similar to the original one and there is little change in the median bias magnitude. In contrast, the formant variabilities for Day 3 are quite similar to Day 2 for both subjects (the average F1 and F2 sds for Day 3 are 0.24 and 0.31 barks for CD, and 0.20 and 0.32 barks for FC; cf. Table II). Moreover, the distributions of distance from the mean imitations have Rayleigh parameters of 0.28 for both CD and FC, and they are not significantly different from the original distributions ($p>0.05$, two-sample K-S test).

These results do not provide a clear answer to the question of bias pattern durability. The durability seems to be subject-specific, possibly depending on the particular imitation strategy adopted by the subject. One interesting consistency between Figs. 3(a), 4(a), and 7 is the significance of the bias vectors—the original and replicated vectors of a target are usually both significant or both insignificant. Note, for example, CD's low-front and high-central regions and FC's mid-front region. Even more remarkable are the cases where consistently significant and insignificant targets occur next to each other (e.g., CD cell 3-3, FC cell 3-1). These results suggest that regions of the vowel space have characteristic levels of bias significance and are separated by fairly sharp boundaries, although it is unclear how these are related to phonemes.

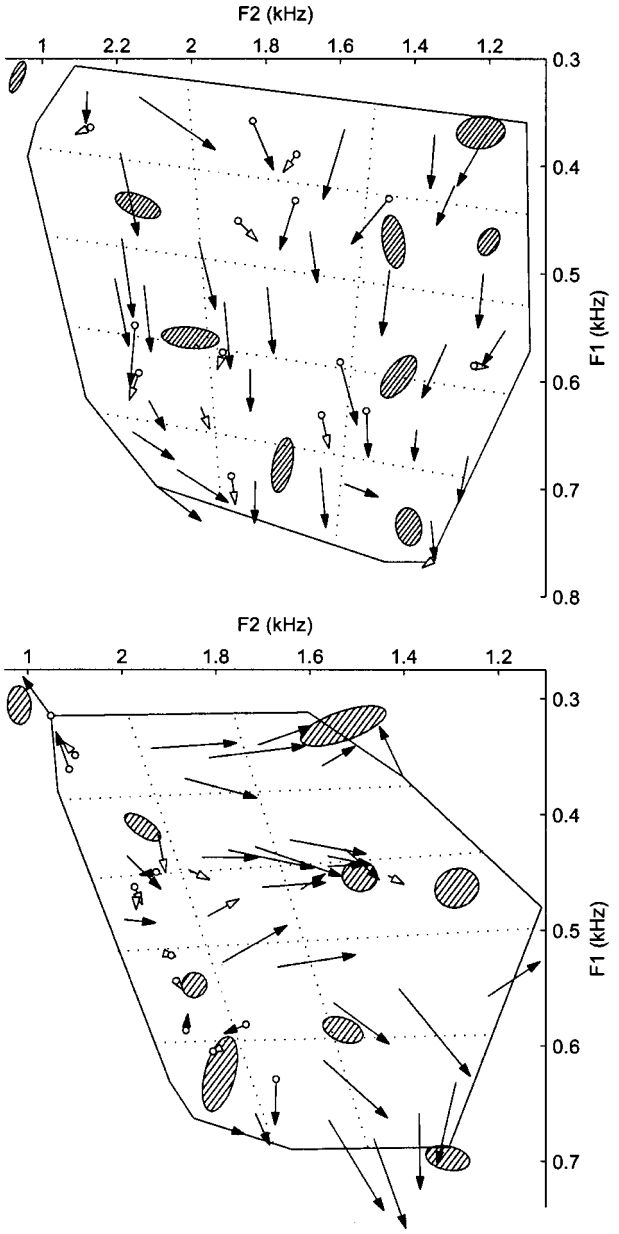

FIG. 7. Imitation behavior of CD and FC in the replicated experiment (''Day 3''). Empty arrowheads indicate statistically insignificant bias vectors (Hotelling's T2 test, $p>0.05$). An empty circle at the base of the arrow indicates that the original (''Day 2'') bias vector for that target was statistically insignificant.

VI. DISCUSSION

The main results of the experiments reported here can be summarized as follows:

(1) The subjects' imitations of self-produced vowels exhibit biases similar to those observed by Repp and Williams (1987). The bias magnitudes are significantly larger than those predicted by a model of articulatory noise;
(2) the biases do not seem to be influenced by proximal vowel prototypes;
(3) the imitations seem to be randomly distributed around the mean imitation, with F1 and F2 having independent Gaussian distributions with sds similar to the vowel formant DL of 0.28 barks. These results closely match the assumptions underlying the perceptual model (moreover, additive Gaussian noise in the formant space seems more plausible as a perceptual than an articulatory phenomenon);
(4) the directions and magnitudes of the bias are independent of the formant variability;
(5) the subjects vary markedly in their bias pattern and may even change them over time, but the magnitudes of the bias and the variability of the imitations (e.g., F1 and F2 sds) are both remarkably consistent within and across subjects.

These results imply that whatever the origin of the bias, its magnitude seems to be (a) instantiated or ''worked out'' in a similar manner across different subjects, and (b) overlaid

by noise that is independent of both the bias and the sound being imitated. The results related to the imitation bias are novel, robust, and unanticipated by existing theories of speech perception and production The results related to formant variability, on the other hand, fit nicely into existing theories and are conceptually straightforward. We discuss each set of results separately.

A. Formant variability

The distribution of F1 and F2 around the mean imitation indicates that the same vowel stimulus evokes different mimics. Some of these differences may be attributed to vowel context effects (Repp *et al.*, 1979), but it is likely that a large part of the variance stems from noise in the imitation process, and that this noise fluctuates across the vowel space and across different sessions. Pisoni (1980) observed a similar phenomenon—when his subjects imitated the same target in different sessions, the mean imitations were highly correlated across the sessions but the sds were not. Moreover, the noise level in the current experiment seems to be characteristic of imitation—the Hertz sds in Table II are of the same magnitude as those reported by Repp and Williams (1985, 1987) and Pisoni (1980). These similarities are even more remarkable in light of the differences among the experiments in recording and playback setups, analysis methods, experimental protocols, and linguistic backgrounds of the subjects.

In fact, the notion of noisy production and perception is rather uncontroversial. Noise is endemic in vowel production studies (e.g., Beckman *et al.*, 1995) and there is substantial evidence that the same stimulus can generate different percepts. This perceptual variability is clear in vowel experiments that use ratings rather than categorization (e.g., Sawusch and Nusbaum, 1979) and affects even phonetically trained listeners (Laver, 1965). Moreover, the assumption of normally distributed percepts is central to several theories of vowel perception (Macmillan *et al.*, 1988; Chistovich *et al.*, 1966; Maddox *et al.*, 2001; Uchanski and Braida, 1998). What is surprising, however, is that the F1 and F2 of the imitations are uncorrelated with each other (surprising because formants are naturally coupled in production). However, the correlation coefficient only measures linear dependence, so it is still possible that F1 and F2 are nonlinearly related (in particular, a nonmonotonic relation between F1 and F2 would result in a weak correlation). Such relations are difficult to evaluate with small samples such as ours, but characterizing them would be an interesting research issue in its own right.

There are two other surprising results regarding the formant variability. First, the formant variability of the articulatory model is similar to that of the perceptual models, even though the parameters of the two models were independently motivated—the 1 mm perturbation radius of the articulatory model was based on the variability of tongue movement, while the 0.28 bark sd of the perceptual model was based on vowel discrimination. Second, the F1 and F2 standard deviations are commensurate with the formant DL. This confirms speculations made by Kent and Forner (1979), but it also raises an interesting problem. If articulatory precision (σ) is matched to perceptual sensitivity and noise is assumed to be additive Gaussian, then a ''round trip'' through the system should be subject to noise of at least sqrt($\sigma^2+\sigma^2$). The current experiment suggests that the overall noise is still σ ($\approx$0.28 barks), which is only possible if perceptual and production noise ''balance'' each other in some way, or if there are nonlinearities (e.g., phonetic categorization) in the system. In either case, these results suggest an attunement between the production and perceptual systems (cf. Fox, 1982), though it is unclear whether the attunement is due to codevelopment (speakers tacitly learn the precision with which vowels may be produced or perceived) or coevolution (the intrinsic noise levels of the production and perception systems have become matched/balanced over time).

We note in passing that the formant variability of the articulatory model [Fig. 4(b)] shows that high-central vowels are much more variable than vowels in other locations, especially along F2. This result is consistent with predictions from quantal theory (Stevens, 1989) and with experiments in which subjects imitated tokens along the [i-u] continuum (Kent, 1973; Repp and Williams, 1985, 1987).

B. Formant bias

There are three theoretical issues underlying the bias: (1) Why is there bias at all? (2) what is the principle underlying the pattern of directions? and (3) what is the cause of the intersubject differences?

Some putative explanations can be dismissed at the outset. One is that the deviations are introduced into the waveform during recording or playback. Another is that during imitation, a speaker's self-perception of his production is distorted by bone conduction (Maurer and Landis, 1990), so that he is not really producing what he thinks he is producing. Both these explanations predict a unidirectional bias across the formant space, which conflicts with the diversity of bias directions both within and across subjects. The change in CD's bias directions between Day 2 and Day 3 also argues against a low-level or artifactual origin of the bias. There is a third strawman explanation, viz. that the movements are simply due to subjects' mishearing the target (by not paying attention, for example) or misarticulating their imitation. There is some plausibility to this argument, since our subjects reported that they were occasionally aware of a difference between the target and their mimic. However, note that Repp and Williams (1987) reported similar levels of inaccuracy even though their subjects had extensive phonetic training (we also obtained similar results in pilot studies with experienced subjects). Thus, the biases cannot be simply ascribed to a lack of skill.

Another concern is the robustness of the bias and the extent to which one can generalize from the limited number of subjects. In this regard, it should be noted that the key claim of the paper is the statistical significance of the bias and not its precise magnitude or the patterns of bias directions. There is additional evidence for the generality of the bias. First, the subjects in our pilot experiments also showed the bias. In fact, we had a fourth subject (a female speaker) in our experiment who showed bias to a larger degree than the three male subjects. We omitted her data since she had phonetic training and was also acquainted with the purpose

of the experiment, so we felt this might have affected her imitation behavior. Second, results from prior experiments bear out the fact of the bias (see Vallabha, 2003, Chapters 3 and 4); in these experiments, subjects imitated themselves in a ''chained'' manner, i.e., the imitation was played back to the subject as the target for the next imitation, and these imitation chains showed systematic drifts. It is a valid concern whether the *pattern* of bias directions generalizes across subjects; we make no such claims in this paper except to point out some regularities (e.g., it is extremely rare to see a mid-vowel quality shifting to a high-back quality).

A related concern is about the role of dialect differences among the subjects. We had originally assumed that the vowel space would be structured by the gross characteristics of the native language (e.g., the /i-I/ contrast is present in American English but absent in Spanish), and that subtle dialectal variations would be less of an issue. The results of the experiment do not support this view, and leave open the possibility that the intersubject differences in the bias patterns are due to dialectal differences (though the difference between CD's ''Day 2'' and ''Day 3'' does not support this possibility). In general, however, the dialect confound does not affect the larger point that it is surprising to find bias at all.

Below, we consider two different classes of explanation for the bias—production-based and perception-based. This distinction is made only to organize the exposition, and should not be taken as a claim that perceptual and production influences can be cleanly separated (for example, an explanation couched in terms of articulatory synergies can be reworded to refer instead to the perception of the acoustic consequences of the synergies). This caveat is especially pertinent because of the integrated nature of imitation.

1. Production-based explanations

The ASY model of noise only examined the consequences of random noise around each articulatory configuration and showed that such noise does not explain the directionality of the subjects' imitations. However, ASY models only the gross anatomy and kinematics of the vocal tract and does not (usually) take into account muscles that actually move the articulators or the functional synergies that exist between them. Thus, it is still possible that articulatory noise, shaped by physiological or functional constraints that are omitted from the ASY model, can lead to the kinds of movements seen in the current data.

The issue of physiological noise was addressed by Mooshammer *et al.* (1999), using a two-dimensional (2D) biomechanical tongue model that included the major tongue muscles and elastic properties of the tissues. In the context of the equilibrium-point motor hypothesis, they added independent signal-related Gaussian noise to the muscle commands and found that the noise does not account for the token-to-token articulatory variability observed with real speakers. Moreover, the acoustic variability (i.e., F1/F2 dispersion ellipses) of the Mooshammer *et al.* model is qualitatively similar to that seen with ASY [Fig. 4(b)]. Thus, physiological noise fails to account for the directionality of the imitations.

Another kind of noise is that shaped by functional constraints. This view posits that vocal tract muscles are controlled in a correlated manner, with the underlying principle being thought of as an abstract ''functional variable'' (Kelso and Tuller, 1983). Noise in the functional variables would lead to correlated noise among the components, which could cause much more directed variation than observed with uncorrelated noise. For vowels, two commonly used functional variables are the location and degree of the vocal tract constriction (cf. Stevens, 1989; Browman and Goldstein, 1990). If increases and decreases in constriction degree and location are equally likely, we would expect imitations to be distributed around the target, which is not the case with the current data. It is more plausible that increases and decreases are not equally likely (''functional noise''). If speakers prefer alveolar constrictions and less constricted vocal tracts, for example, we would expect front vowels to centralize and low and back vowels to advance and become slightly more open (Gay *et al.*, 1992; Perkell and Nelson, 1985). This notion is plausible and intriguing, but it is hampered by a lack of evidence. In addition, we would need to fit a different set of biases for each subject in order to explain the data. These objections are pragmatic and not conceptual, however, so the functional noise explanation cannot be ruled out completely.

Finally, observe that quantal theory (QT; Stevens, 1989) is also an unlikely explanation of the observed formant movements. QT tries to explain how point vowels such as [i] and [u] are stable and therefore prevalent in vowel systems, but the current data show subjects moving away from the [i] and [u] regions. Further, QT predicts that the vowel space is acoustically more stable near the point vowels [i], [a], and [u], but the subjects' variability ellipses do not show any such contrast between point and nonpoint vowel regions (Pisoni, 1980; but see Diehl, 1989).

2. Perception-based explanations

Imitation directionality has traditionally been explained as assimilation caused by a categorical phonemic code. Similarly, the perceptual magnet effect (Iverson and Kuhl, 1995) predicts perceptual assimilation towards the phonemic prototypes. Alternatively, if perception and production are seen as sharing a common control space (e.g., motor theory), then key locations of this space may function as attractors. Yet all these explanations fall short because in the two-dimensional space it is clear that movements are not always influenced by the nearest phoneme (and in any case, the bias direction patterns are too different across the subjects).

It is intriguing to consider the converse situation, namely, that the imitations are moving away from the prototypes and towards ''perceptual anchors'' located at the category boundaries (Macmillan *et al.*, 1988). Figure 3 shows some evidence of such movement—for example, the ''attractors'' in CD's low-back region and DR's low-front region seem to be at the edges of the [ʌ] and [æ] categories, respectively. It is also striking that the regions between the prototypes are so well-populated (the data from Repp and Williams, 1987, show a similar pattern). This proposal of ''boundary attraction'' is related to a theory advanced by Cowan and Morse (1986) to explain stimulus order effects. They proposed that a percept is initially a tightly bounded

region in the perceptual space and that as it decays, it expands and stretches towards the ''neutral point'' [ə]. Repp and Crowder (1990) tested this hypothesis and found that multiple neutral points were needed to explain their results. Intriguingly, they observed that ''vowels held in memory were assimilated toward some standard(s) located between prototypes'' (p. 2088). This suggests that the neutral (or stable) points may arise from an interaction between perceptual representations and category boundaries, and that the imitation biases are shaped by the locations of these points. While this theory is plausible, it should be kept in mind that imitations are unaffected by response latency (Repp and Williams, 1987). Representational decay may explain the bias directions, but some other factor is needed to explain the bias magnitudes.

There is one other potential explanation for the bias. In a recent study, Dissard and Darwin (2000) played synthetic one and two-formant sounds to subjects, and asked them to match the target by adjusting the formant frequency of a comparison sound. Interestingly, the matched sound deviated systematically from the target when the two sounds had different F0s. Dissard and Darwin suggested that this occurs because listeners' estimate of the formant location is biased towards the closest F0 harmonic. However, this explanation predicts that because there are fewer harmonics in the range of F1 frequencies, the biases should be more prominent across F1 than F2. This is not the case with the data (see Table I). Moreover, the F0 differences between the targets and imitations are quite small (less than 5 Hz).

VII. CONCLUSIONS

The current experiment has shown several robust effects in vowel imitation, three of which are particularly significant—formant standard deviations commensurate with formant difference limens, systematic inaccuracy of the imitations, and independence of variability and accuracy of the imitations. These effects confirm patterns found in previous studies and demonstrate the utility of using a grid of stimuli rather than a single continuum.

The subjects and the models have very similar degrees of variability (~0.28 bark Euclidean distance), indicating a convergence shaped by physiology, development and/or linguistic environment. The analyses also demonstrate that it is not sufficient to report statistics (such as standard deviations or histograms) for single formants, as was the procedure in prior vowel imitation studies; some of the statistical patterns are evident only by treating the percepts as two-dimensional points. The results also reinforce the view that bark distance is an approximate measure of perceptual distance.

The biases of the imitations are also instructive. They cannot be explained by random articulatory noise, nor are they consistent with theories of categorical phonemic codes. There are two explanations (functional noise and perceptual anchors) that cannot be rejected on the current evidence, but they are both are quite tentative and require further elaboration. In this context, two limitations of the current work must be noted. The first is the confound between individual differences and dialect differences. Controlling for dialect background is necessary to clarify the linguistic relevance of the bias patterns. The second limitation concerns the role of isolated steady-state vowels. Such sounds are unusual in any language, and the imitation bias may partly be the result of the speakers' perception–production system contorting itself to an unusual task. More natural target stimuli, such as vowels embedded in a syllabic context, may yield more consistent results both within and across subjects.

ACKNOWLEDGMENT

This research was supported by NIMH Predoctoral Training Grant No. MH19116 and NIMH Grant No. MH42900.

[1]Subjects read two sets of sentences, one repeated thrice, the other twice. The thrice-repeated sentences were: ''I had hoed my field and did not heed the hood. I hid from Hod, who'd been the Head at Hud.'' The twice-repeated sentences were: ''Who'd hoed the field? I had the hood on my head. Hod hid in the hood, and did not heed Hud.''

[2]CD and FC's imitations of the synthetic stimuli were available from previous pilot experiments and were reused (these were collected using the same protocol described here). The interval between ''Day 1'' and ''Day 2'' was 20 months (CD), 26 months (FC) and 2 days (DR). A point of concern is whether CD and FC's imitations were affected by the delay. Two points mitigate this concern. (1) we conducted several pilots where the delay between Day 1 and Day 2 was quite short, and all the pilot subjects exhibited bias and variability patterns that were qualitatively similar to CD and FC. (2) CD and FC's performance in the pilots, recorded shortly after their ''Day 1,'' is also similar to their performance reported here.

[3]The parameters were obtained from the ASY web site: http://www.haskins.yale.edu/Haskins/MISC/ASY/DYNAMIC/samples.html

[4]In ASY, the location of the tongue body center (TBC) is defined with respect to an arbitrary origin near the temporomandibular joint (the parameters are CL and CA, for length and angle, respectively). The tongue body rides on the jaw, so the true angle of the TBC is the sum of the jaw angle (JA) and CA. Hence, $x = \mathrm{CL}\cdot\cos(\mathrm{JA}+\mathrm{CA})$ and $y = \mathrm{CL}\cdot\sin(\mathrm{JA}+\mathrm{CA})$. CL is units of mermels (1 mermel≡1/112 cm≈0.09 mm). Once the noise was added, x and y were converted back to polar coordinates: $(\mathrm{JA}+\mathrm{CA})_{\mathrm{new}} = \arctan(y/x)$, and $\mathrm{CL}_{\mathrm{new}} = \mathrm{sqrt}(x^2+y^2)$. We wanted to perturb only the TBC and not the jaw, so $\mathrm{CA}_{\mathrm{new}} = (\mathrm{JA}+\mathrm{CA})_{\mathrm{new}} - \mathrm{JA}$. For a related approach, see Goldstein (1983).

[5]It would have been preferable to use DLs based on correlated patterns of formant changes rather than single-formant change. In one of the few such studies (Hawks, 1994), the results were established using trained listeners under minimal uncertainty, so the DLs were extremely small (~0.15 barks). We used the larger DL (0.28 barks) since it was based on more realistic methods (''ordinary listening conditions'').

[6]Ideally, the perceptual model should have incorporated the warping of the perceptual space due to the native vowel categories (e.g., Kewley-Port and Atal, 1989). Such a warping may produce imitation bias, and therefore increase the scope of the perceptual model. However, we are not aware of any models that attempt to link acoustics to subcategorical vowel qualities over the entire vowel space, and developing and validating such a model is beyond the scope of this paper.

[7]If we assume that the ten F1×F2 points come from a bivariate Gaussian distribution, then the principal components are the axes of the distribution, and the ellipses denote a radius of one standard deviation along the principal components. Equivalently, the ellipses are the equal-likelihood contours of the Gaussian distribution (likelihood=0.0925).

[8]The circular variance is computed as follows (Fisher, 1993). Each set of 10 imitations yields 10 unit vectors with respect to the target. The magnitude of their vector sum divided by the number of vectors gives the mean resultant length R. The circular variance is defined as $1-R$ and ranges from 0 (all vectors have the same direction) to 1 (the directions of the vectors cancel out each other). If there were no bias, then we would expect the different unit vectors to have inconsistent directions, and therefore the circular variance would be close to 1.

[9]Figure 6 does not show the distribution for the perceptual model since it is Rayleigh-distributed by definition. In general, $X_1, X_2, \ldots, X_K \sim N(0,\sigma) \Rightarrow X_i - \overline{X} \sim N(0,\sigma\sqrt{(K-1)/K})$. For the perceptual model, K

$=10$ and $\sigma=0.28$, so the Euclidean distance is distributed as Rayleigh (0.265).

Beckman, M. E., Jung, T., Lee, S., de Jong, K., Krishnamurthy, A. K., Ahalt, S. C., Cohen, K. B., and Collins, M. J. (**1995**), ''Variability in the production of quantal vowels revisited,'' J. Acoust. Soc. Am. **97**, 471–490.

Browman, C. P., and Goldstein, L. (**1990**), ''Gestural specification using dynamically defined articulatory structures,'' J. Phonetics **18**, 299–320.

Chistovich, L., Fant, G., de Serpa-Leitao, A., and Tjernlund, P. (**1966**), ''Mimicking of synthetic vowels,'' Royal Institute of Technology Speech Transmission Lab (Sweden), Quarterly Progress and Status Report **2**, 1–18.

Cowan, N., and Morse, P. A. (**1986**), ''The use of auditory and phonetic memory in vowel discrimination,'' J. Acoust. Soc. Am. **79**, 500–507.

de Boer, B. (**2000**), ''Self-organization in vowel systems,'' J. Phonetics **28**, 441–465.

Diehl, R. L. (**1989**), ''Remarks on Stevens' quantal theory of speech,'' J. Phonetics **17**, 71–78.

Dissard, P., and Darwin, C. J. (**2000**), ''Extracting spectral envelopes: Formant frequency matching between sounds on different and modulated fundamental frequencies,'' J. Acoust. Soc. Am. **107**, 960–969.

Fisher, N. I. (**1993**), *Statistical analysis of circular data* (Cambridge University Press, Cambridge).

Fowler, C. A., Brown, J., Sabadini, L., and Weihing, J. (**2003**), ''Rapid access to speech gestures in perception: Evidence from choice and simple response time tasks,'' J. Mem. Lang. **49**, 296–314.

Fox, R. A. (**1982**), ''Individual variation in the perception of vowels: implications for a perception–production link,'' Phonetica **39**, 1–22.

Gay, T., Boe, L. J., and Perrier, P. (**1992**), ''Acoustic and perceptual effects of changes in vocal tract constrictions for vowels,'' J. Acoust. Soc. Am. **92**, 1301–1309.

Goldstein, L. (**1983**), ''Vowel shifts and articulatory-acoustic relations,'' in Proceedings 10th International Congress of Phonetic Sciences, Dordrecht, The Netherlands, pp. 267–273.

Hawks, J. W. (**1994**), ''Difference limens for formant patterns of vowel sounds,'' J. Acoust. Soc. Am. **95**, 1074–1084.

Hillenbrand, J., and Gayvert, R. T. (**1993**), ''Vowel classification based on fundamental frequency and formant frequencies,'' J. Speech Hear. Res. **36**, 694–700.

Hillenbrand, J., Getty, L. A., Clark, M. J., and Wheeler, K. (**1995**), ''Acoustic characteristics of American English vowels,'' J. Acoust. Soc. Am. **97**, 3099–3111.

Iivonen, A. (**1995**), ''Explaining the dispersion of the single-vowel occurrences in an F1/F2 space,'' Phonetica **52**, 221–227.

Iverson, P., and Kuhl, P. K. (**1995**), ''Mapping the perceptual magnet effect for speech using signal-detection-theory and multidimensional-scaling,'' J. Acoust. Soc. Am. **97**, 553–562.

Johnson, K., Ladefoged, P., and Lindau, M. (**1993**), ''Individual differences in vowel production,'' J. Acoust. Soc. Am. **94**, 701–14.

Jupp, P. E., and Mardia, K. V. (**1980**), ''A general correlation coefficient for directional data and related regression problems,'' Biometrika **67**, 163–173.

Kelso, J. A. S., and Tuller, B. (**1983**), '''Compensatory articulation' under conditions of reduced afferent information: A dynamic formulation,'' J. Speech Hear. Res. **26**, 217–224.

Kent, R. D. (**1973**), ''The imitation of synthesized vowels and some implications for speech memory,'' Phonetica **28**, 1–25.

Kent, R. D., and Forner, L. L. (**1979**), ''Developmental study of vowel formant frequencies in an imitation task,'' J. Acoust. Soc. Am. **65**, 208–217.

Kewley-Port, D., and Atal, B. (**1989**), ''Perceptual differences between vowels located in a limited phonetic space,'' J. Acoust. Soc. Am. **85**, 1726–1740.

Kewley-Port, D., and Zheng, Y. (**1998**), ''Vowel formant discrimination: Towards more ordinary listening conditions,'' J. Acoust. Soc. Am. **106**, 2945–2958.

Kuhl, P. K., and Meltzoff, A. N. (**1996**), ''Infant vocalizations in reponse to speech: Vocal imitation and formant change,'' J. Acoust. Soc. Am. **100**, 2425–2438.

Kuhl, P. K. (**2000**), ''A new view of language acquisition,'' Proc. Natl. Acad. Sci. U.S.A. **97**, 11850–11857.

Laver, J. D. M. H. (**1965**), ''Variability in vowel perception,'' Lang Speech **8**, 95–121.

Macmillan, N. A., Goldberg, R. F., and Braida, L. D. (**1988**), ''Resolution for speech sounds: Basic sensitivity and context memory on vowel and consonant continua,'' J. Acoust. Soc. Am. **84**, 1262–1280.

Maddox, W. T., Molis, M. R., and Diehl, R. L. (**2001**), ''Generalizing a neuropsychological model of visual categorization to auditory categorization of vowels,'' Percept. Psychophys. **64**, 584–597.

Maurer, D., and Landis, T. (**1990**), ''Role of bone conduction in the self-perception of speech,'' Folia Phoniatr. **42**, 226–229.

Mooshammer, C. R., Perrier, P., and Payan, Y. (**1999**), ''Simulation of token-to-token variability in vowel production,'' J. Acoust. Soc. Am. **105**, 1356.

Pardo, J. S., and Fowler, C. A. (**2000**), ''Imitation of phrases in conversational speech,'' J. Acoust. Soc. Am. **107**, 2856.

Perkell, J. S., and Nelson, W. L. (**1985**), ''Variability in production of the vowels /i/ and /a/,'' J. Acoust. Soc. Am. **77**, 1889–1895.

Pisoni, D. B. (**1973**), ''Auditory and phonetic memory codes in the discrimination of consonants and vowels,'' Percept. Psychophys. **13**, 253–260.

Pisoni, D. B. (**1980**), ''Variability of vowel formant frequencies and the quantal theory of speech: a first report,'' Phonetica **37**, 285–305.

Porter, R. J., and Lubker, J. F. (**1980**), ''Rapid reproduction of vowel-vowel sequences—Evidence for a fast and direct acoustic-motoric linkage in speech,'' J. Speech Hear. Res. **23**, 593–602.

Repp, B. H., Healy, A. F., and Crowder, R. G. (**1979**), ''Categories and context in the perception of isolated steady-state vowels,'' J. Exp. Psychol. Hum. Percept. Perform. **5**, 129–145.

Repp, B. H., and Williams, D. R. (**1985**), ''Categorical trends in vowel imitation: Preliminary observations from a replication experiment,'' Speech Commun. **4**, 105–120.

Repp, B. H., and Williams, D. R. (**1987**), ''Categorical tendencies in imitating self-produced isolated vowels,'' Speech Commun. **6**, 1–14.

Repp, B. H., and Crowder, R. G. (**1990**), ''Stimulus order effects in vowel discrimination,'' J. Acoust. Soc. Am. **88**, 2080–2090.

Rubin, P., Baer, T., and Mermelstein, P. (**1981**), ''An articulatory synthesizer for perceptual research,'' J. Acoust. Soc. Am. **70**, 321–328.

Sawusch, J. R., and Nusbaum, H. C. (**1979**), ''Contextual effects in vowel perception I: Anchor-induced contrast effects,'' Percept. Psychophys. **25**, 292–302.

Shigeno, S. (**1991**), ''Assimilation and contrast in the phonetic perception of vowels,'' J. Acoust. Soc. Am. **90**, 103–111.

Stadler, M., Richter, P. H., Pfaff, S., and Kruse, P. (**1991**), ''Attractors and perceptual field dynamics of homogenous stimulus areas,'' Psychol. Res. **53**, 102–112.

Stevens, K. N. (**1989**), ''On the quantal nature of speech,'' J. Phonetics **17**, 3–45.

Syrdal, A. K., and Gopal, H. S. (**1986**), ''A perceptual model of vowel recognition based on auditory representation of American–English vowels,'' J. Acoust. Soc. Am. **79**, 1086–1100.

Traunmüller, H. (**1990**), ''Analytical expressions for the tonotopic sensory scale,'' J. Acoust. Soc. Am. **88**, 97–100.

Uchanski, R. M., and Braida, L. D. (**1998**), ''Effects of token variability on our ability to distinguish between vowels,'' Percept. Psychophys. **60**, 533–543.

Vallabha, G. K. (**2003**), *Perceptuomotor biases in vowel imitation*, Unpublished Ph.D. Dissertation (Florida Atlantic University, Boca Raton, FL).

Vallabha, G. K., and Tuller, B. (**2002**), ''Systematic errors in the formant analysis of steady-state vowels,'' Speech Commun. **38**, 141–160.

van Hessen, A., and Schouten, M. E. H. (**1998**), ''Response distributions in intensity resolution and speech discrimination,'' J. Acoust. Soc. Am. **104**, 2980–2990.

Wildgen, W. (**1990**), ''Basic principles of self-organization in language,'' in *Synergetics of Cognition*, edited by H. Haken and M. Stadler (Springer-Verlag, Berlin), pp. 429–452.

Categorization and discrimination of nonspeech sounds: Differences between steady-state and rapidly-changing acoustic cues[a)]

Daniel Mirman,[b)] Lori L. Holt, and James L. McClelland
Department of Psychology and Center for the Neural Basis of Cognition, Carnegie Mellon University, Pittsburgh, Pennsylvania 15213

(Received 13 February 2003; revised 9 April 2004; accepted 6 May 2004)

Different patterns of performance across vowels and consonants in tests of categorization and discrimination indicate that vowels tend to be perceived more continuously, or less categorically, than consonants. The present experiments examined whether analogous differences in perception would arise in nonspeech sounds that share critical transient acoustic cues of consonants and steady-state spectral cues of simplified synthetic vowels. Listeners were trained to categorize novel nonspeech sounds varying along a continuum defined by a steady-state cue, a rapidly-changing cue, or both cues. Listeners' categorization of stimuli varying on the rapidly changing cue showed a sharp category boundary and posttraining discrimination was well predicted from the assumption of categorical perception. Listeners more accurately discriminated but less accurately categorized steady-state nonspeech stimuli. When listeners categorized stimuli defined by both rapidly-changing and steady-state cues, discrimination performance was accurate and the categorization function exhibited a sharp boundary. These data are similar to those found in experiments with dynamic vowels, which are defined by both steady-state and rapidly-changing acoustic cues. A general account for the speech and nonspeech patterns is proposed based on the supposition that the perceptual trace of rapidly-changing sounds decays faster than the trace of steady-state sounds.
 [DOI: 10.1121/1.1766020]

PACS numbers: 43.71.Es, 43.71.Pc, 43.66.Ba [PFA] Pages: 1198–1207

I. INTRODUCTION

Patterns of performance in categorization and discrimination tasks differ across classes of speech sounds. Discrimination of stop consonants is closely predicted by categorization (Liberman *et al.*, 1957), but discrimination of vowels and fricatives exceeds categorization-based predictions (Eimas, 1963; Pisoni, 1973; Healy and Repp, 1982). We hypothesize that the differences in categorization and discrimination patterns arise as a result of differences in the way the auditory system processes the differing acoustic cues that distinguish vowels and consonants. Specifically, we suggest that the rapid transients characteristic of many consonants are processed quite differently than the relatively steady-state frequency information that characterizes steady-state vowel and fricative stimuli. From this hypothesis, we predict that nonspeech sounds that are defined by acoustic cues that reflect these differences will elicit the same patterns of categorization and discrimination performance as stop consonants and synthetic steady-state vowels. The experiments described in this report test this prediction by training listeners to categorize nonspeech sounds that vary along a rapidly-changing cue, a steady-state cue, or both types of cues and then examining categorization and discrimination of the sounds. Before turning to the experiments, we discuss in more detail the evidence for the points motivating our experiments.

A. Categorization and discrimination of different classes of speech sounds

Differences in categorization and discrimination of different classes of speech sounds can be analyzed by comparing observed discrimination performance to discrimination performance predicted from categorization. To predict discrimination from categorization, a discrimination curve is calculated based on the assumption that the listener makes discrimination judgments based entirely on whether the two stimuli are categorized as the same sound or different sounds. Stop consonants elicit sharp categorization functions and discrimination performance is accurately predicted by categorization, a pattern known as categorical perception (Liberman *et al.*, 1957; Wood, 1976; Repp, 1984). The categorization functions elicited by steady-state vowels and fricatives are less sharp and discrimination performance is much more accurate than predicted from categorization (Eimas, 1963; Pisoni, 1973; Healy and Repp, 1982). This result indicates that, at least with steady-state vowels, listeners are not merely using category labels to perform discrimination (e.g., Pisoni, 1971).

Some investigators (Ades, 1977; Healy and Repp, 1982) have attempted to explain differences in patterns of categorization and discrimination performance between steady-state speech sounds (vowels and fricatives) and rapidly-changing speech sounds (stop consonants) in terms of differences in auditory distinctiveness. Distinctiveness is considered a function of perceptual range, which is measured by the sum of the d' between adjacent stimuli (Ades, 1977).

[a)]A preliminary report on this work was presented at the 143rd Meeting of the Acoustical Society of America, June 2002.
[b)]Electronic mail: dmirman@andrew.cmu.edu

This account predicts a direct trade-off between discrimination performance (i.e., auditory distinctiveness) and categorization performance. However, Macmillan *et al.* (1988) controlled for perceptual range and found that differences between vowels and consonants remained. Thus, factors other than perceptual range must contribute to the differences in categorization and discrimination of consonants and vowels.

Steady-state vowels are a simplified approximation of natural vowels, which are additionally specified by dynamic acoustic information (Gottfried and Strange, 1980; Strange *et al.*, 1976). Direct comparisons for 12 vowels of American English indicate that steady-state formants are sufficient for approximately 75% correct vowel identification, but when synthetic formants follow natural formant contours, correct identification is improved to nearly 90% (Hillenbrand and Nearey, 1999). Experiments using stimuli based on natural vowels, which vary along both steady-state and rapidly-changing acoustic cues (Schouten and van Hessen, 1992), have shown a pattern that is not consistent with the predictions of the distinctiveness account of Ades (1977) and Healy and Repp (1982). In these experiments, categorization of dynamic vowels exhibited steep category boundaries (like stop consonants) but discrimination was high and exceeded categorization-based predictions (like steady-state vowels).

The cues that distinguish stop consonants are different from the cues that distinguish steady-state vowels; furthermore, natural, dynamic vowels are defined by a combination of cues (the importance of rapidly-changing cues to vowel identity may vary by vowel; e.g., Hillenbrand and Nearey, 1999). The acoustic patterns of stop consonants can be broadly defined by rapidly-changing acoustic cues. Stop consonants are primarily distinguished by rapid formant transitions and fine temporal distinctions such as voice onset time. In contrast, the acoustic patterns of vowels and fricatives can be broadly defined by steady-state acoustic cues. In particular, the synthetic steady-state vowels that are often used in studies of speech perception are distinguished only by formant center frequencies that remain constant for the duration of the sound. Fricatives, too, are primarily defined by relatively slow-varying acoustic properties (e.g., Jongman *et al.*, 2000). Thus, one possibility is that differences in patterns of categorization and discrimination between stop consonants and steady-state vowels and fricatives arise from general differences between processing rapidly-changing and steady-state acoustic cues.

B. Processing differences between rapidly-changing and steady-state sounds

There is considerable support for the broad distinction between steady-state and rapidly-changing sounds and the supposition that the auditory system processes such sounds differently. Specifically, processing of rapidly-changing sounds is more left-lateralized than processing of steady-state sounds. This result has been found in comparisons of human perception across classes of speech sounds (Cutting, 1974; Allard and Scott, 1975) and in nonhuman primate perception of conspecific calls (Heffner and Heffner, 1984; Hauser and Andersson, 1994). Further, it has been found that processing is more left-lateralized in humans when the formant transition durations are extended in speech sounds (Schwartz and Tallal, 1980) and in nonspeech sounds (Belin *et al.*, 1998). The same result has been demonstrated for nonhuman primates (Hauser *et al.*, 1998). In addition, recent evidence from patterns of correlation in learning to categorize based on different kinds of cues (Golestani *et al.*, 2002) suggests that steady-state and rapidly-changing cues rely on distinct processing mechanisms. The close similarity of lateralization results for speech and nonspeech sounds and for humans and nonhuman primates, as well as the correlations in learning rates, suggest that the auditory system processes rapidly-changing and steady-state sounds differently.

Poeppel (2003; see also Zatorre *et al.*, 2002) has proposed that different temporal integration windows in the left and right nonprimary auditory cortices account for these findings. In particular, Poeppel contends that left nonprimary auditory cortical processing depends on a short temporal integration window (20–40 ms) but right nonprimary auditory cortical processing depends on a longer temporal integration window (150–300 ms). Thus, processing rapidly-changing cues, requiring a shorter temporal integration window, is performed primarily by the left hemisphere. By contrast, analysis of slower-changing cues is performed by the right hemisphere with a longer temporal integration window, thus allowing greater spectral resolution. A similar proposal has been made by Shamma (2000), who argues that acoustic signals are represented at multiple time scales. In particular, rapidly changing sounds, such as plucked instruments and stop consonants, are represented on a fast time scale, but steady-state sounds, such as bowed instruments and vowels, are represented on a slow time scale.

In sum, there is considerable evidence indicating that rapidly-changing and steady-state acoustic cues are processed differently by the auditory system. Furthermore, patterns indicating this difference appear to be quite general, occurring in perception of speech and nonspeech sounds. The left hemisphere advantage emerges for both speech and nonspeech sounds that are defined by rapidly-changing cues, but not for sounds defined by steady-state cues. Similarly, the canonical categorical perception pattern of categorization and discrimination performance (specifically the accurate prediction of discrimination performance from categorization, as discussed above) emerges for stop consonants that are defined by rapidly-changing acoustic cues but not for vowels that are defined by steady-state cues. In the present experiments, we test whether novel nonspeech sounds that are defined by rapidly-changing cues will exhibit a categorical perceptionlike pattern. By comparison, we test whether nonspeech sounds defined by steady-state spectral cues will exhibit the pattern typically observed for synthetic steady-state voweis and fricatives.

II. EXPERIMENTS

The following experiments were designed to test categorization and discrimination of novel nonspeech stimuli. Each of the experiments employed a similar training and testing procedure. The key analyses were posttraining categorization and discrimination performance. Categorization posttest re-

sults were used to generate a ''predicted'' discrimination curve following signal detection theory (Macmillan and Creelman, 1991; Macmillan, 1987). The predicted discrimination curve was computed for each participant based on the hypothesis that participants make same-different discrimination judgments by considering whether the sounds belong to the same category or different categories. Thus, predicted discrimination d' for each pair of stimuli was the difference in (z-transformed) likelihood that the participant would respond that each pair member belongs to the same category. Sharp categorization functions mean that sounds are grouped into discrete categories. Thus, sharp categorization functions predict poor within-category discrimination (since all stimuli within a category consistently receive the same label) and good discrimination across the category boundary (since stimuli across the boundary consistently receive different labels). In contrast, less sharp categorization functions predict moderate discrimination across the entire stimulus series (since all stimuli are partly ambiguous and thus any pair will sometimes receive the same label, and sometimes receive different labels).

The specific research prediction was that rapidly-changing nonspeech sounds would elicit sharp categorization functions and poor within-category discrimination performance compared to discrimination across category boundary. That is, for rapidly-changing sounds categorization performance would accurately predict discrimination performance. In contrast, steady-state nonspeech sounds would elicit less sharp categorization functions, but good discrimination performance at every point on the series. That is, for steady-state sounds discrimination performance would exceed categorization-based predictions.

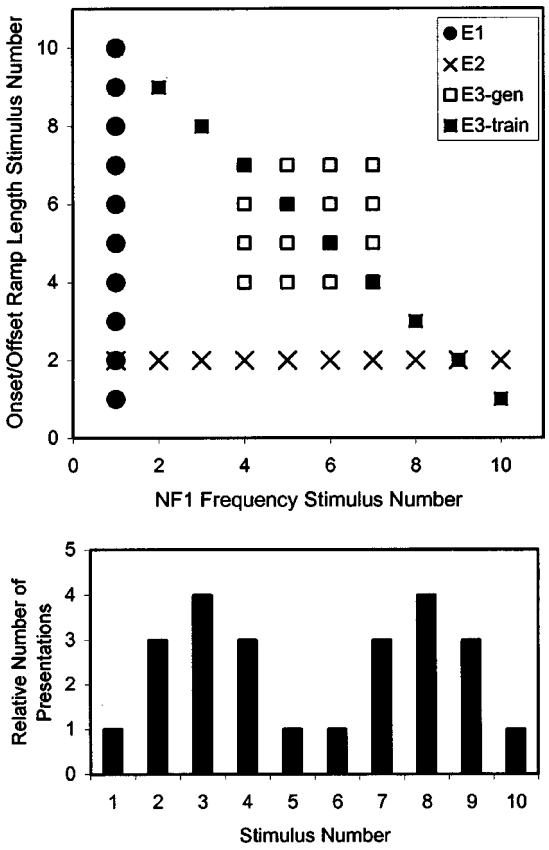

FIG. 1. Top panel: schematic representation of the sampling of the stimulus. The circles are stimuli that vary in ramp length (experiment 1), the crosses are stimuli that vary in NF1 frequency (experiment 2), and the squares are stimuli that vary in both ramp length and frequency (experiment 3; filled squares are standard training and testing stimuli, open squares are generalization testing stimuli). Bottom panel: Relative frequency of presentation of stimuli during categorization training.

A. Stimulus space

The stimuli forming categories learned by listeners were drawn from a novel two-dimensional acoustic space. The acoustic space was defined in one dimension by a rapidly-changing amplitude envelope cue and in the other dimension by a steady-state spectral cue to allow independent manipulation of the cues. The non-speech cues were chosen to be generally similar to cues that are manipulated in studies of speech perception. The steady-state spectral cue was held constant throughout the stimulus, analogous to steady-state vowels (e.g., Pisoni, 1973). The rapidly-changing cue was analogous to amplitude rise time, which plays a role in distinctions between classes of consonants (Van Tasell *et al.*, 1987), for example, the stop-glide contrast (e.g., /b/-/w/; Mack and Blumstein, 1983; Walsh and Diehl, 1991). This cue also has been investigated in the context of the nonspeech pluck-bow distinction (Cutting, 1982; Kewley-Port and Pisoni, 1984).

Each stimulus was composed of a 300-ms burst of white noise (10-kHz sample rate) with two 200-Hz bands of energy removed by 50-dB elliptic bandstop filters. This filtering process created two spectral notches characterized by their center frequencies. The center frequencies of the filters used to create the spectral notches remained constant across the entire stimulus duration, but differed from stimulus to stimulus to create a series that varied along a steady-state spectral dimension. In the experiments presented here, the first notch center frequency (NF1) started at 500 Hz and increased in equal steps (see experiment procedure below). The second notch center frequency (NF2) was fixed for all stimuli at 2500 Hz. This procedure is similar to the typical procedure for manipulating formant frequency to create a steady-state vowel series (e.g., Miller 1953; Hoemeke and Diehl, 1994). Finally, a symmetric linear onset and offset ramp was applied (as in the pluck-bow experiments, e.g., Kewley-Port and Pisoni, 1984). The duration of this ramp was manipulated to create a series distinguished by a rapidly-changing cue. Although the cues that distinguish these stimuli are abstractly similar to cues that distinguish speech sounds, these stimuli were perceived as bursts of noise and not as speech.

Figure 1 (top panel) is a schematic depiction of the sampling of this stimulus space in the following experiments. The axis labels represent generic steps along the series because step size was adjusted based on individual participants' sensitivity to make the steps approximately equally discriminable across listeners (see procedure for details). The horizontal axis represents steps along the NF1 series. The vertical axis represents steps along the ramp length series. Each stimulus series consisted of ten stimuli divided into two equal categories, with the category boundary (defined by ex-

plicit feedback during training) between stimulus 5 and stimulus 6 in the series.

B. Experiment 1

In the first experiment, the ramp length cue was manipulated to create a single-dimension stimulus series varying along a rapidly-changing cue. Following a sensitivity assessment and pretest, the participants were trained to categorize the stimuli and then were tested on categorization and discrimination.

1. Method

a. Participants. Participants were 16 Carnegie Mellon University undergraduates who had not participated in a previous experiment using stimuli based on these cues. Participants received course credit and/or a small payment. All participants reported normal hearing.

b. Stimuli. The stimuli were synthesized as described above using the MATLAB signal processing toolbox. NF1 and NF2 were fixed at 500 and 2500 Hz, respectively. The duration of the linear onset/offset ramp varied in equal steps starting at 5 ms. For example, with a step size of 15 ms, the first stimulus had symmetric onset and offset ramps of 5 ms, the second stimulus had 20 ms ramps, the third had 35 ms ramps, and so on. The size of the steps was determined by sensitivity assessment for each participant (as described below) so that the experimental stimuli would be approximately equally discriminable to each participant.

c. Procedure. Participants completed the experiment while sitting in sound attenuating booths, using labeled electronic button boxes to make responses. Sensitivity of each participant to the ramp length cue was assessed using a same-different discrimination task. An adaptive staircase procedure, in which the step size was increased if discrimination was not accurate enough and decreased if discrimination was too accurate, was used to identify an appropriate ramp step size. Discrimination performance was assessed on the difference between percent hits and percent false alarms[1] with a target range of 30% to 50%. The 32 ''different'' trials (4 repetitions of 8 pairs) consisted of stimulus pairs two steps apart. In addition, there were ten ''same'' trials for which stimulus pair members were identical. The staircase procedure was constrained to seven possible step sizes: 1, 3, 5, 7, 9, 12, and 15 ms. Stimulus pairs were presented with an interstimulus silent interval of 500 ms. After a block of discrimination trials, the participant's performance was assessed. If the participant was not sensitive enough ([%hits −%false alarms]$<$30), then a more discriminable stimulus set with a larger step size was selected. If the participant was too sensitive ([%hits−%false alarms]$>$50), then a less discriminable stimulus set with a smaller step size was selected. This test and step-size adjustment was repeated three times. The starting step size was 7 ms and all participants reached threshold discrimination at 12 or 15 ms steps. At the final step size, listeners participated in the pretest discrimination task consisting of 110 discrimination trials (80 different trials, 30 same trials).

Next, the participants heard 480 categorization training trials in each trial, one of the stimuli (drawn from the set of 10 separated by a step size determined by sensitivity assessment) was presented and the participants categorized it as belonging to one of two categories by pressing one of two buttons on a response box, labeled with arbitrary symbols. After the categorization response, the participants were shown the correct answer by a light above the correct button. Stimuli presented during training followed a bimodal distribution to reflect exposure to two natural categories (e.g., phonetic categories, Lisker and Abramson, 1964) and encourage category formation (Maye *et al.*, 2002; Rosenthal *et al.*, 2001). Feedback was consistent with the distribution-defined categories (category A: stimuli 1–5, category B: stimuli 6–10). Figure 1 (bottom panel) illustrates the relative frequency with which stimuli were presented during training. Categorization training was divided into two equal units (240 trials each) and separated by a discrimination test identical to the pretest.

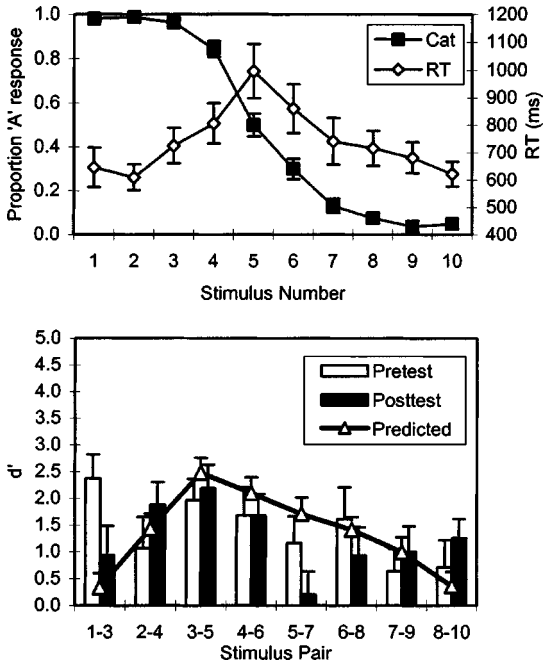

FIG. 2. Experiment 1 results: stimuli varying in ramp length. The top panel shows categorization responses (filled symbols) and reaction times (open symbols). The bottom panel shows discrimination results. Empty bars indicate pretest performance, filled bars indicate posttest performance, and the solid line is performance predicted from categorization according to the signal detection theory model.

After training, the participants completed a discrimination posttest identical to the pretest. Finally, each listener participated in a categorization test consisting of 100 categorization trials (10 trials$\times$10 stimuli) without feedback. Participants completed the experiment during a single 1.5-h session.

2. Results

Figure 2 (top panel) illustrates the average of participants' posttest category responses and corresponding reaction times as a function of stimulus step. Following just 480 training trials, participants learned to assign category labels with high accuracy (87% correct with respect to feedback-defined category labels). Furthermore, reaction times exhib-

ited a pronounced peak at the category boundary confirming that the participants treated the stimuli as belonging to different categories (Pisoni and Tash, 1974; Maddox *et al.*, 1998). Figure 2 (bottom panel) shows the results of the discrimination pretest (empty bars) and posttest (filled bars) as well as the posttest performance predicted from categorization (solid line). There was no change from pretest to posttest and a close correspondence between observed and predicted performance. A repeated measures ANOVA confirmed that there was no overall change from pretest to posttest ($F<1$), a trend towards more accurate discrimination near the center of the series [$F(7,105)=2.029, p=0.058$], and no interaction between location in series and change from pretest to posttest [$F(7,105)=1.492, p=0.178$]. The same test comparing observed and predicted discrimination performance indicated no overall difference between observed and predicted performance ($F<1$), a peak in discrimination accuracy near the center of the series [$F(7,105)=5.169, p<0.001$], and small series-member-specific differences between observed and predicted performance [$F(7,105)=2.114, p=0.048$]. Posthoc pairwise comparisons confirmed that this interaction was produced by deviations between observed and predicted performance at stimulus pairs 5–7 and 8–10.

3. Discussion

The relatively short training procedure used in this experiment was sufficient for participants to learn to categorize stimuli according to onset/offset ramp length. The high categorization accuracy and reaction time peak support this conclusion. In addition, although there was no evidence for a consistent learning-based change in discrimination performance, the posttest performance did fall very close to performance predicted from categorization. That is, for stimuli varying in length of onset/offset ramp, a rapidly-changing acoustic cue, it appears that discrimination and categorization performance are closely matched.

C. Experiment 2

In the second experiment the training and testing procedure of experiment 1 was replicated, but ramp length was held constant and NF1 was manipulated to create a stimulus series varying along a steady-state cue.

1. Method

a. Participants. Participants were 16 Carnegie Mellon University undergraduates who had not participated in a previous experiment using stimuli based on these cues. Participants received course credit and/or a small payment. All participants reported normal hearing.

b. Stimuli. The stimuli for this experiment were synthesized according to the procedure outlined above. However, in this case, the onset/offset ramps were fixed at 10 ms and NF1 was used as the category membership cue. All stimuli had a notch with center frequency of 2500 Hz (NF2) and another spectral notch (NF1) with a lower center frequency. Stimuli were distinguished by NF1, which started at 500 Hz and increased in center frequency in equal steps, the size of which was determined by sensitivity assessment. For example, with a step size of 50 Hz, the first stimulus in the set would have an NF1 center of 500 Hz, the second stimulus would have 550 Hz, the third 600 Hz, etc. The staircase procedure was constrained to 11 possible step sizes: 3, 5, 10, 15, 20, 25, 30, 40, 50, 60, and 75 Hz.

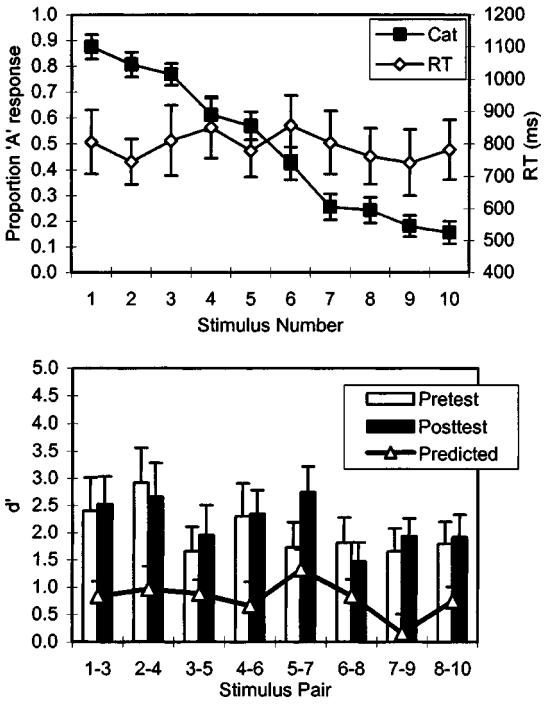

FIG. 3. Experiment 2 results: stimuli varying in NF1. The top panel shows categorization responses (filled symbols) and reaction times (open symbols). The bottom panel shows discrimination results. Empty bars indicate pretest performance, filled bars indicate posttest performance, and the solid line is performance predicted from categorization according to the signal detection theory model.

c. Procedure. The procedure was nearly identical to that of experiment 1. There were two differences in the sensitivity assessment stage. First, pilot studies indicated that sensitivity to this cue was quite variable across participants, thus the number of possible NF1 step sizes was increased to 11 (there were 7 possible ramp step sizes in experiment 1). To accommodate this increase the sensitivity assessment was extended to five blocks (three were used in experiment 1). The initial step size was 25 Hz and listeners' assessed sensitivities included all possible step sizes (3–75 Hz). Second, d' was used as a measure during sensitivity assessment with the target range of 1.5 to 2.5.

2. Results

Figure 3 (top panel) shows the categorization data, which indicate that participants learned to assign category labels with moderate accuracy (73.7% correct) although they did not exhibit a sharp category boundary, nor did they show a reaction time peak at the boundary. Furthermore, the pattern of discrimination results in Fig. 3 (bottom panel) shows that discrimination performance was higher than would be predicted from categorization performance, a pattern that is quite different from the results of experiment 1 (Fig. 2). Repeated measures ANOVA results indicated no change from pretest to posttest ($F<1$), a trend suggesting minor differ-

ences in discriminability across the series [$F(7,105) = 2.019, p = 0.059$], and no series member-specific change from pretest to posttest ($F < 1$). The same test comparing observed and predicted discrimination performance showed an overall difference between observed and predicted performance [$F(1,15) = 17.324, p < 0.001$], no significant differences in performance across the stimulus series [$F(7,105) = 1.845, p = 0.086$], and no stimulus pair-specific differences between observed and predicted performance ($F < 1$).

3. Discussion

Participants learning categories defined by NF1 (experiment 2) did not achieve the same level of accuracy in categorization as the participants learning categories cued by ramp length (experiment 1), despite the categorization training procedures being identical across experiments 1 and 2. By contrast, discrimination performance on stimuli defined by NF1 was quite high. In fact, participants' discrimination performance far exceeded the level that would be predicted from their categorization performance.

One possible explanation for this difference is that varying ramp length allows stimuli to be described as ''gradual'' and ''abrupt,'' but varying NF1 does not lend itself to verbal labels derived from experience outside the experiment. That is, it was easier to label the ramp length stimuli because they were consistent with labels that participants already know, but the NF1 stimuli require learning new labels. However, during postexperiment debriefing participants did not use ''gradual'' and ''abrupt'' to describe the variation in ramp length-based stimuli (there was no consistent response, participants provided such disparate descriptions as masculine/feminine and ''coming towards''/''going away''). Conversely, most participants described the NF1 variation as being ''pitch-like.'' Thus, if participants were using labels other than those specified by the experiment, categorization in experiment 2 should be more accurate (because NF1 variation was consistently heard as variation of a familiar cue, i.e., pitch), but the opposite pattern was observed.

The differences between experiments 1 and 2 could also be explained if the experiment 2 categorization task were more difficult than the experiment 1 task. If this were the case, 480 learning trials may not have been sufficient for listeners to learn categories in experiment 2. Sharper categorization functions and more accurate discrimination predictions may have emerged with more training. To test this possibility, an extended version of experiment 2 was conducted. This experiment used the same basic paradigm, but greatly extended categorization training. Listeners completed seven 1-h sessions (session 1: pretests and initial categorization training, sessions 2–6: categorization training, session 7: final categorization training and posttests). After 6720 categorization training trials (14 times more than experiment 2) listeners ($N = 10$) exhibited identical results: less sharp categorization (71% correct), no reaction time peak, and high discrimination performance exceeding categorization-based prediction. This replication indicates that the differences between results of experiments 1 and 2 are not due to a simple difficulty of learning category labels for the steady-state stimuli.

The pattern of data in experiment 2 is quite different from the sharp categorization and close correspondence between categorization and discrimination performance observed in experiment 1. The main difference between experiments 1 and 2 was that in the latter experiment, the cue that differentiated stimuli and defined their category membership was NF1, a steady-state spectral cue, but in experiment 1 the cue was onset/offset ramp length, a rapidly-changing cue. This pattern is similar to the reported differences in categorization and discrimination of stop consonants compared to steady-state vowels and fricatives and corresponds with studies indicating that the auditory system may process rapidly-changing and steady-state acoustic cues differently. Cue differences may interact with the cognitive processes that underlie categorization and discrimination.

As discussed in the Introduction, direct comparisons of categorization of dynamic and steady-state synthetic vowels have shown that rapidly-changing cues improve vowel identification (Hillenbrand *et al.*, 2001; Hillenbrand and Nearey, 1999). Importantly, this improvement in identification comes without a decrease in discrimination performance (Kewley-Port and Watson, 1994; Kewley-Port, 1995; Kewley-Port and Zheng, 1999). That is, speech sounds that are defined by both steady-state and rapidly-changing cues are categorized according to a sharp boundary and discriminated at levels that exceed categorization-based predictions (Schouten and van Hessen, 1992). In the preceding experiments, we have demonstrated that for nonspeech sounds that are distinguished by a rapidly-changing cue, categorization is sharp and accurately predicts discrimination, but for nonspeech sounds distinguished by a steady-state cue, categorization is less sharp and discrimination exceeds categorization-based prediction. If these results are driven, at leat in part, by differences in the way steady-state and rapidly-changing cues interact with the cognitive processes of categorization and discrimination, then the same sharpening of the categorization function and better-than-predicted discrimination performance should be observed when the nonspeech steady-state and rapidly-changing cues used in the previous experiments are combined. To test this prediction, the procedure used in experiments 1 and 2 was repeated, but the ramp length and NF1 cues were combined such that both the rapidly-changing cue and the steady-state spectral cue were available to participants performing the categorization and discrimination tasks.

D. Experiment 3

1. Method

a. Participants. Participants were 17 Carnegie Mellon University undergraduates who had not participated in a previous experiment using stimuli based on these cues. Participants received course credit and/or a small payment. All participants reported normal hearing.

b. Stimuli. The stimuli for this experiment were generated by combining NF1 and ramp cues. Stimuli differed along both cues such that either cue was sufficient for categorization. Filled square symbols in Fig. 1 (top panel) show an abstract representation of the stimulus space sampling. The ramp step size was fixed at 15 ms, but the NF1 step size

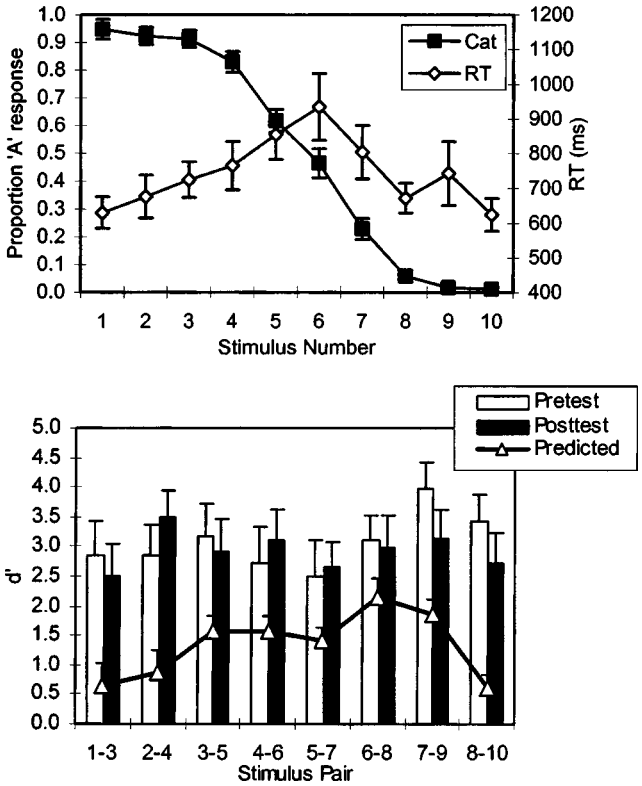

FIG. 4. Experiment 3 results: stimuli varying in both ramp length and NF1. The top panel shows categorization responses (filled symbols) and reaction times (open symbols). The bottom panel shows discrimination results. Empty bars indicate pretest performance, filled bars indicate posttest performance, and the solid line is performance predicted from categorization according to the signal detection theory model.

was determined by sensitivity assessment similar to experiment 2. The sensitivity assessment in experiment 1 and pilot studies resulted in nearly all participants having a 15-ms step size (with a few participants having a 12-ms step size). Therefore, it was assumed that sensitivity to ramp length was sufficiently constant across listeners to make independent sensitivity assessment for each cue unnecessary. In addition to the 10 training stimuli, 12 generalization stimuli from the region near the category boundary were synthesized in order to examine the shape of each participant's category boundary.

c. Procedure. The procedure was nearly identical to that of experiment 1. There were two changes made to the procedure to accommodate the change in stimuli. First, sensitivity assessment consisted of five blocks as in experiment 2 (although the performance criterion was based on the difference between percent hits and percent false alarms, as in experiment 1). Second, a generalization test was added to the end of the experiment. During the generalization test, the 16 stimuli (12 novel stimuli plus the 4 stimuli from the training set that are closest to the boundary) surrounding the boundary area (see Fig. 1, top panel, empty squares) were presented 20 times each without feedback (as in the categorization posttest).

2. Results

Figure 4 (top panel) shows that categorization posttest results were similar to those observed in experiment 1. The categorization function was sharp with high accuracy (84.5% correct) and reaction time exhibited a moderate peak at the category boundary. Regression analysis of the generalization responses with respect to each of the cues revealed significant effects of both cues [NF1: $t(14)=11.943, p<0.001$; ramp: $t(14)=14.011, p<0.001$]. That is, during generalization participants used both cues to make category assignments. The discrimination results shown in Fig. 4 (bottom panel) followed qualitatively the same pattern as observed in experiment 2. Comparison of pretest and posttest discrimination showed no significant differences (all F's <1). As in experiment 2, a comparison of predicted and observed discrimination posttest data showed an overall difference between observed and categorization-predicted performance [$F(1,16)=19.074, p<0.001$], some differences in discriminability across the stimulus series [$F(7,112)=2.178, p=0.041$], and no series member-specific differences between observed and predicted performance [$F(7,112)=1.268, p=0.272$]. Thus, for stimuli defined by both the ramp cue and the NF1 cue, categorization performance was similar to categorization of stimuli defined by just the ramp cue but discrimination performance was similar to discrimination of stimuli defined by just the NF1 cue.

3. Discussion

The sharp categorization function and above-predicted discrimination performance observed in this experiment reflected a "best of both worlds" of the patterns observed in experiments 1 and 2. That is, the combination of both acoustic cues elicited a maximally accurate combination of categorization and discrimination performance. The sharp categorization function and reaction time peak at the boundary were qualitatively similar to the result from experiment 1, in which the ramp length cue was the category-distinguishing cue. The high discrimination performance relative to the prediction from categorization was similar to the results of experiment 2, in which the steady-state NF1 cue was the category-distinguishing cue. These results are similar to the findings of researchers studying vowels with rapidly-changing cues (Schouten and van Hessen, 1992). In both speech and nonspeech contexts, when both steady-state and rapidly-changing cues are available, categorization is sharp (as with just the rapidly-changing cue) and discrimination exceeds categorization-based predictions (as with just the steady-state cue). Figure 5 summarizes the observed and categorization-based predicted discrimination performance for the three experiments and makes clear the difference in the patterns of performance. For stimuli that have a steady-state cue (experiments 2 and 3) to stimulus identity, discrimination performance is higher than predicted from categorization performance. But for stimuli that are defined only by a rapidly-changing cue (experiment 1), discrimination performance is accurately predicted by categorization performance.

III. GENERAL DISCUSSION

The present research examined differences in categorization and discrimination of sounds varying in rapidly-changing and steady-state acoustic cues. A novel stimulus

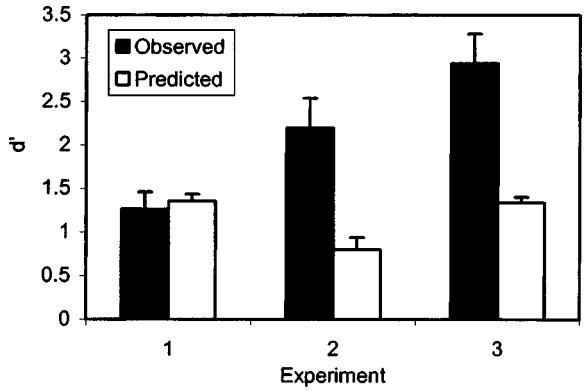

FIG. 5. Overall observed and predicted posttest discrimination performance by experiment. When a steady-state cue is available (experiments 2 and 3), discrimination performance exceeds categorization-based predictions.

space was created by applying bandstop filters and onset/offset ramps to bursts of white noise. Participants were taught to categorize stimuli varying along one of the dimensions of this space in blocks of categorization trials with feedback. Following training, participants were tested on categorization and discrimination of the stimuli. Results indicated that participants could categorize stimuli that varied along the rapidly-changing ramp length cue very effectively, with discrimination performance approximately at the level predicted by categorization performance (experiment 1). However, the same training procedure resulted in much less sharp categorization of stimuli that varied along the steady-state NF1 cue and produced discrimination that exceeded the level predicted from categorization responses (experiment 2). A study of categorization and discrimination along the NF1 cue following extensive categorization training (14 times more than experiment 2) found the same result. Thus, the difference in results between experiments 1 and 2 is not caused by a difference in rate of learning categories defined by these cues. When both cues were available (experiment 3), performance was ''the best of both worlds,'' combining the sharp categorization observed in the ramp cue experiment with discrimination performance that exceeded predictions from categorization, as observed in experiments using the steady-state NF1 cue.

The findings of these experiments mirror findings in speech perception. The pattern of categorization and discrimination of stop consonants is similar to the pattern of categorization and discrimination of the ramp-cued stimuli, whereas the pattern for steady-state vowels and fricatives is similar to the pattern for NF1-cued stimuli (Eimas, 1963; Pisoni, 1973; Healy and Repp, 1982; Repp, 1984). The pattern of categorization and discrimination of nonspeech sounds defined by both the ramp and NF1 cues is similar to the pattern for vowels defined by both steady-state spectral cues and rapidly-changing cues (Schouten and van Hessen, 1992). These data suggest that differences in patterns of categorization and discrimination performance reflect differences in processing of acoustic properties that speech and nonspeech sounds share. As reviewed in the Introduction, converging evidence from lateralization studies, individual difference studies, and studies in nonhuman animals all support the hypothesis that the auditory systems process rapidly-changing and steady-state cues differently and that these differences give rise to performance differences between vowels and consonants and between classes of nonspeech sounds.

To account for the cue-task interaction described in this report, it is useful to consider the demands of the discrimination task. Evidence suggests that decay of the perceptual trace is one factor limiting discrimination performance (e.g., Pisoni, 1973; Cowan and Morse, 1986). The perceptual trace decays relatively quickly, but if a category label has been assigned, the label may be available after the perceptual trace has decayed. In support of these hypotheses, researchers have demonstrated that discrimination performance falls closer to categorization-based predictions when the interstimulus-interval (ISI) between the sounds to be discriminated is extended (e.g., Pisoni, 1973; Cowan and Morse, 1986). Some researchers have suggested that the perceptual trace of stop consonants is less available for discrimination than the perceptual trace of steady-state vowels (Macmillan *et al.*, 1988). If so, this difference may explain differences in discrimination performance between the two types of speech sounds. Generalizing this idea to encompass nonspeech sounds, suppose that the perceptual trace of rapidly-changing sounds decays faster than that of steady-state sounds. Rapid decay of the perceptual trace would encourage reliance on category labels because they can be maintained in memory for a longer time. On the other hand, suppose steady-state sounds leave a longer-lasting perceptual trace. If the perceptual trace decays slowly, discrimination performance can exceed category label-based performance. In the context of the present experiments, this account claims that the perceptual trace of stimuli defined by the ramp cue decays more quickly than the perceptual trace of the stimuli defined by the NF1 cue. As the perceptual trace decays, listeners are forced to rely more on assigning category labels (learned during the categorization training phase), therefore discrimination performance is more closely predicted by categorization performance for the ramp stimuli (experiment 1) than for the NF1 stimuli (experiment 2). Thus, if one assumes that transient cues leave more transient perceptual traces, the memory demands of the discrimination task explain improved discrimination performance when steady-state cues are available. This account predicts that discrimination of nonspeech sounds defined by steady-state cues will fall closer to categorization-based predictions if longer interstimulus-intervals are used.

In summary, in the present experiments, listeners categorized and discriminated novel nonspeech sounds defined by a rapidly-changing acoustic cue, a steady-state cue, or both types of cues. The results showed three things. First, nonspeech sounds defined by a rapidly-changing acoustic cue elicited sharp categorization performance and discrimination performance that was accurately predicted by the assumption that the discrimination is performed solely on the basis of category labels. This pattern of results has been reported for stop consonants, which are distinguished by rapidly-changing acoustic cues such as formant transitions. Second, nonspeech sounds defined by a steady-state acoustic cue elicited less sharp categorization performance and discrimina-

tion performance exceeded predictions based on categorization performance. This pattern of results has been reported for synthetic steady-state vowels and fricatives, which are distinguished by steady-state acoustic cues such as formant frequency. Third, nonspeech sounds defined by both a rapidly-changing cue and a steady-state cue elicited both sharp categorization functions and discrimination performance that exceeded predictions based on categorization performance. This pattern of results has been reported for natural vowels that are distinguished by both steady-state and rapidly-changing acoustic cues. These similarities in data patterns for speech and nonspeech sounds suggest that categorization and discrimination performance are influenced by differences between auditory processing of rapidly-changing and steady-state acoustic cues for both types of sounds.

ACKNOWLEDGMENTS

This work was supported by a National Science Foundation grant (NSF BCS-0078768), by a James S. McDonnell Foundation award for Bridging Mind, Brain, and Behavior to LLH and Andrew Lotto, and by the Center for the Neural Basis of Cognition. DM was supported by NIH Training Grant No. T32N507433-03. JLM was supported by Grant No. MH64445 from the National Institute of Mental Health. The authors thank Andrew Lotto for stimulating discussion and Christi Adams, Siobhan Cooney, Seth Liber, Camilla Kydland, and Monica Datta for their help in conducting the experiments. The authors also thank Michael Owren and John Kingston for their helpful comments on an early draft.

[1]The relatively small number of trials during each block of sensitivity assessment causes traditional d' measurements to be somewhat unstable. This measure was used to keep this segment of the experiment relatively short.

Ades, A. E. (**1977**). ''Vowels, consonants, speech, and nonspeech,'' Psychol. Rev. **84**, 524–530.

Allard, F., and Scott, B. L. (**1975**). ''Burst cues, transition cues, and hemispheric specialization with real speech sounds,'' Q. J. Exp. Psychol. **27**, 487–497.

Belin, P., Zilbovicius, M., Crozier, S., Thivard, L., Fontaine, A., Masure, M.-C., and Samson, Y. (**1998**). ''Lateralization of speech and auditory temporal processing,'' J. Cogn Neurosci. **10**, 536–540.

Cowan, N., and Morse, P. A. (**1986**). ''The use of auditory and phonetic memory in vowel discrimination,'' J. Acoust. Soc. Am. **79**, 500–507.

Cutting, J. E. (**1974**). ''Two left-hemisphere mechanisms in speech perception,'' Percept. Psychophys. **16**, 601–612.

Cutting, J. E. (**1982**). ''Plucks and bows are categorically perceived, sometimes,'' Percept. Psychophys. **31**, 462–476.

Eimas, P. D. (**1963**). ''The relation between identification and discrimination along speech and nonspeech continua,'' Lang Speech **6**, 206–217.

Golestani, N., Paus, T., and Zatorre, R. J. (**2002**). ''Anatomical correlates of learning novel speech sounds,'' Neuron **35**, 997–1010.

Gottfried, T. L., and Strange, W. (**1980**). ''Identification of coarticulated vowels,'' J. Acoust. Soc. Am. **68**, 1626–1635.

Hauser, M. D., and Andersson, K. (**1994**). ''Left hemisphere dominance for processing vocalizations in adult, but not infant, rhesus monkeys: Field experiments,'' Proc. Natl. Acad. Sci. U.S.A. **91**, 3946–3948.

Hauser, M. D., Agnetta, B., and Perez, C. (**1998**). ''Orienting asymmetries in rhesus monkeys: The effect of time-domain changes on acoustic perception,'' Anim. Behav. **56**, 41–47.

Healy, A. F., and Repp, B. H. (**1982**). ''Context independence and phonetic mediation in categorical perception,'' J. Exp. Psychol. Hum. Percept. Perform. **8**, 68–80.

Heffner, H. E., and Heffner, R. S. (**1984**). ''Temporal lobe lesions and perception of species-specific vocalizations by macaques,'' Science **226**, 75–76.

Hillenbrand, J. M., and Nearey, T. M. (**1999**). ''Identification of resynthesized hVd/utterances: Effects of formant contour,'' J. Acoust. Soc. Am. **105**, 3509–3523.

Hillenbrand, J. M., Clark, M. J., and Nearey, T. M. (**2001**). ''Effect of consonant environment on vowel formant patterns,'' J. Acoust. Soc. Am. **109**, 748–763.

Hoemeke, K. A., and Diehl, R. L. (**1994**). ''Perception of vowel height: The role of F_1-F_0 distance,'' J. Acoust. Soc. Am. **96**, 661–674.

Jongman, A., Wayland, R., and Wong, S. (**2000**). ''Acoustic characteristics of English fricatives,'' J. Acoust. Soc. Am. **108**, 1252–1263.

Kewley-Port, D. (**1995**). ''Thresholds for formant-frequency discrimination of vowels in consonantal context,'' J. Acoust. Soc. Am. **97**, 3139–3146.

Kewley-Port, D., and Pisoni, D. B. (**1984**). ''Identification and discrimination of rise time: Is it categorical or noncategorical?'' J. Acoust. Soc. Am. **75**, 1168–1176.

Kewley-Port, D., and Watson, C. S. (**1994**). ''Formant-frequency discrimination for isolated English vowels,'' J. Acoust. Soc. Am. **95**, 485–496.

Kewley-Port, D., and Zheng, Y. (**1999**). ''Vowel formant discrimination: Towards more ordinary listening conditions,'' J. Acoust. Soc. Am. **106**, 2945–2958.

Liberman, A. M., Harris, K. S., Hoffman, H. S., and Griffith, B. C. (**1957**). ''The discrimination of speech sounds within and across phoneme boundaries,'' J. Exp. Psychol. **54**, 358–368.

Lisker, L., and Abramson, A. S. (**1964**). ''A cross-language study of voicing in initial stops: Acoustical measurements,'' Word **20**, 384–422.

Mack, M., and Blumstein, S. E. (**1983**). ''Further evidence of acoustic invariance in speech production: The stop-glide contrast,'' J. Acoust. Soc. Am. **73**, 1739–1750.

Macmillan, N. A. (**1987**). ''Beyond the categorical/continuous distinction: A psychophysical approach to processing modes,'' in *Categorical Perception: The Groundwork of Cognition*, edited by S. Harnad (Cambridge U.P., New York), pp. 53–85.

Macmillan, N. A., and Creelman, C. D. (**1991**). *Detection Theory: A User's Guide* (Cambridge U.P., New York).

Macmillan, N. A., Goldberg, R. F., and Braida, L. D. (**1988**). ''Resolution of speech sounds. Basic sensitivity and context memory on vowel and consonant continua,'' J. Acoust. Soc. Am. **84**, 1262–1280.

Maddox, W. T., Ashby, F. G., and Gottlob, L. R. (**1998**). ''Response time distributions in multidimensional perceptual categorization,'' Percept. Psychophys. **60**, 620–637.

Maye, J., Werker, J. F., and Gerken, L. (**2002**). ''Infant sensitivity to distributional information can affect phonetic discrimination,'' Cognition **82**, B101–B111.

Miller, R. L. (**1953**). ''Auditory tests with synthetic vowels,'' J. Acoust. Soc. Am. **25**, 114–121.

Pisoni, D. (**1971**). ''On the nature of categorical perception of speech sounds,'' Ph.D. thesis, University of Michigan, Ann Arbor.

Pisoni, D. B. (**1973**). ''Auditory and phonetic memory codes in the discrimination of consonants and vowels,'' Percept. Psychophys. **13**, 253–260.

Pisoni, D. B., and Tash, J. (**1974**). ''Reaction times to comparisons within and across phonetic categories,'' Percept. Psychophys. **15**, 285–290.

Poeppel, D. (**2003**). ''The analysis of speech in different temporal integration windows: Cerebral lateralization as 'asymmetric sampling in time,' '' Speech Commun. **41**, 245–255.

Repp, B. H. (**1984**). ''Categorical perception: Issues, methods, findings,'' Speech Lang. **10**, 243–335.

Rosenthal, O., Fusi, S., and Hochstein, S. (**2001**). ''Forming classes by stimulus frequency: Behavior and theory,'' Proc. Natl. Acad. Sci. U.S.A. **98**, 4265–4270.

Schouten, M. E., and Van Hessen, A. J. (**1992**). ''Modeling phoneme perception: I Categorical perception,'' J. Acoust. Soc. Am. **92**, 1841–1855.

Schwartz, J., and Tallal, P. (**1980**). ''Rate of acoustic change may underlie hemispheric specialization for speech perception,'' Science **207**, 1380–1381.

Shamma, S. A. (**2000**). ''Physiological basis of timbre perception,'' in *The New Cognitive Neurosciences, 2nd Edition*, edited by M. S. Gazzaniga. (MIT, Cambridge, MA), pp. 411–423.

Strange, W., Verbrugge, R. R., Shankweiler, D. P., and Edman, T. R. (**1976**). ''Consonant environment specifies vowel identity,'' J. Acoust. Soc. Am. **60**, 213–224.

Van Tasell, D. J., Soli, S. D., Kirby, V. M., and Widin, G. P. (**1987**). ''Speech

waveform envelope cues for consonant recognition,'' J. Acoust. Soc. Am. **82**, 1152–1161.
Walsh, M. A., and Diehl, R. L. (**1991**). ''Formant transition duration and amplitude rise time as cues to the stop/glide distinction,'' Q. J. Exp. Psychol. A **43A**, 603–620.
Wood, C. C. (**1976**). ''Discriminability, response bias, and phoneme categories in discrimination of voice onset time,'' J. Acoust. Soc. Am. **60**, 1381–1389.
Zatorre, R. J., Belin, P., and Penhune, V. B. (**2002**). ''Structure and function of auditory cortex: Music and speech,'' Trends Cogn. Sci. **6**, 37–46.

Coding of vowellike signals in cochlear implant listeners[a)]

Bernhard Laback[b)] and Werner A. Deutsch
Acoustics Research Institute, Austrian Academy of Sciences, Reichsratsstr. 17. A-1010 Wien, Austria

Wolf-Dieter Baumgartner
ENT-Department, Vienna University Hospital, Währinger Gürtel 18-20, A-1097 Wien, Austria

(Received 22 November 2002; accepted for publication 21 May 2004)

Neural-population interactions resulting from excitation overlap in multi-channel cochlear implants (CI) may cause blurring of the ''internal'' auditory representation of complex sounds such as vowels. In experiment I, confusion matrices for eight German steady-state vowellike signals were obtained from seven CI listeners. Identification performance ranged between 42% and 74% correct. On the basis of an information transmission analysis across all vowels, pairs of most and least frequently confused vowels were selected for each subject. In experiment II, vowel masking patterns (VMPs) were obtained using the previously selected vowels as maskers. The VMPs were found to resemble the ''electrical'' vowel spectra to a large extent, indicating a relatively weak effect of neural-population interactions. Correlation between vowel identification data and VMP spectral similarity, measured by means of several spectral distance metrics, showed that the CI listeners identified the vowels based on differences in the between-peak spectral information as well as the location of spectral peaks. The effect of nonlinear amplitude mapping of acoustic into ''electrical'' vowels, as performed in the implant processors, was evaluated separately and compared to the effect of neural-population interactions. Amplitude mapping was found to cause more blurring than neural-population interactions. Subjects exhibiting strong blurring effects yielded lower overall vowel identification scores. [DOI: 10.1121/1.1772398]

PACS numbers: 43.71.Ky, 43.71.Es, 43.66.Ts [PFA] Pages: 1208–1223

I. INTRODUCTION

Cochlear implant (CI) systems can in theory provide up to 22 independent frequency channels, which are allocated to tonotopically arranged stimulation electrodes. Although this arrangement achieves an extremely small number of excitation points compared to the number of auditory-nerve fibers in normal hearing, several studies have shown that increasing the number of channels beyond six to eight produces no further improvement of speech intelligibility in quiet (e.g., Fishman *et al.*, 1997; Dorman and Loizou, 1997a; Brill *et al.*, 1997). In noise, the number of channels beyond which asymptotic performance is reached can be higher, depending on the speech material used (e.g., Fu *et al.*, 1998; Garnham *et al.*, 2002). Moreover, listening experiments with normal-hearing (NH) listeners have indicated that the number of channels necessary to understand speech accurately in quiet is comparable to CI listeners (Shannon *et al.*, 1995; Dorman and Loizou, 1997a,b, 1993). Nevertheless, CI listeners exhibit considerable across-subject variability in speech recognition (Friesen *et al.*, 2001; Dorman, 1993, p. 181), whereas NH subjects show more uniform performance under comparable conditions (Friesen *et al.*, 2001). One possible reason for the large differences among CI listeners is individual differences in the degree of interactions between stimulation channels. Those can arise from variable extents of excitation overlap of ganglion cells from stimulating electrodes, e.g., as a result of variable distances between the electrode contacts and the stimulated cells or variable properties of the implanted cochlear structures with respect to current flow. It is well known from the literature on cochlear hearing impairment (acoustic hearing) that broadening of peripheral auditory filters causes blurring of the internal auditory representation of the speech spectrum. In electrical stimulation, excessive current spread from stimulating electrodes may cause a similar effect as described above for acoustic hearing. The higher the degree of spread of excitation, the more the tonotopic places that would normally correspond to low excitation amplitude (spectral valleys) are boosted relative to the amplitudes at the spectral peaks. Thus, the raising of levels at the spectral valleys of a speech signal in electrical hearing could be described as spectral blurring. ''Channel interactions'' is used here as a general term for the effects resulting from excitation overlap between stimulating electrodes (defined in more detail later in this section). Studies of channel interactions have found that they explain only a small percentage of the variance in speech recognition scores. As far as the authors are aware, no previous study has examined channel interactions when the entire array of electrodes was activated, as is the case of speech processed by implant processors. The current study investigates this condition in order to better understand the ''internal'' auditory representation of the speech spectrum. The primary goal was to determine how channel interactions caused by excitation overlap affect the transmission of spectral information in speech signals. An additional objective was to evaluate the effect of spectral alteration introduced by the process of nonlinear amplitude mapping imposed on each channel in the CI speech processor in order to fit the electrical dynamic range.

[a)]Parts of the work presented in this article have been presented at the 2001 Conference on Implantable Auditory Prostheses Asilomar.
[b)]Electronic mail: bernhard.laback@oeaw.ac.at

Vowellike signals were chosen to study the effects described above. The advantage of using vowel stimuli as compared to stimuli with arbitrary spectra is that listeners are already familiar with the underlying phonetic categories and no special training in labeling is necessary before performing an identification task. To measure the ''internal'' auditory representation of vowellike signals (hereafter referred to simply as ''vowels''), the method of vowel masking patterns (VMPs) was applied. Synthetic vowels were used as maskers, and masked thresholds of sinusoidal probes were obtained across the masker spectrum. The masked threshold at each probe frequency indicates the probe level at which the neural excitation evoked by the combination of vowel masker and probe just differs from the excitation caused by the masker alone at each probe frequency. Vowel masking patterns have been successfully applied for studying the ''internal'' representations of vowels in normal-hearing subjects (Moore and Glasberg, 1982; Sidwell and Summerfield, 1985) and hearing-impaired subjects (Sidwell and Summerfield, 1985; van Tasell *et al.*, 1987). Those VMP studies measured spectral masking induced by acoustic stimulation by determining the spread of excitation along the tonotopically organized structures in the auditory pathways. In this study, applying electrical stimulation, spectral masking refers to the spread of neural activation resulting from the dispersion of electrical current from stimulation electrodes.

Channel interactions can be the result of summation and cancellation effects in electrical fields generated by neighboring stimulation electrodes (Shannon, 1983). ''Electrical-field interactions'' occur when different electrodes are activated simultaneously in order to stimulate auditory fibers along the cochlea. Sequential stimulation strategies like CIS (''continuous interleaved sampling;'' Wilson *et al.*, 1991), that present trains of pulses nonoverlapping across the stimulation electrodes, limit this kind of interaction. However, ''neural-population interactions'' (NPIs) (Shannon, 1993) occur even in the case of nonsimultaneous stimulation if different electrodes alternately stimulate the same neural-population. Due to current spread in the cochlea, the pertaining neurons may effectively receive a pulse train of 200 pulses per second (pps) when two adjacent electrodes, each delivering 100 pps, are activated in interleaved fashion. Another aspect of this phenomenon is related to the refractoriness of the underlying neural population. Considering one of two electrodes exciting the same neural population as the masker and the other one as the probe, the neural response to the probe may be decreased by prior stimulation from the masker electrode. This effect could be denoted as forward masking across frequency channels.

In order to measure the effect of NPIs at specific electrode positions, Shannon (1983) proposed the method of forward masking patterns (FMPs). FMPs of a single-electrode masker are obtained by measuring the threshold shifts in detecting a probe electrode signal (electrical pulse train) across the electrode array at a fixed temporal interval following the masker offset. Since masker and probe are presented nonsimultaneously, ''electrical-field interactions'' should have no influence on FMP measurements.

Considerable across-subject differences in the magnitude of NPIs have been reported by several investigators who measured forward masking patterns using single-electrode maskers (Tong and Clark, 1986; Lim *et al.*, 1989; Cazals *et al.*, 1990; Cohen and Clark, 1996; Chatterjee and Shannon, 1998; Throckmorton and Collins, 1999). These studies are based on the hypothesis that the amount of masking effect induced by a single masker electrode on (nonsimultaneous) probes across the array is negatively correlated with speech recognition performance due to the mutual interference between stimulating electrodes, which blur the ''internal'' auditory representation of the speech spectrum. In some of these studies, FMPs were compared with speech recognition scores (Cazals *et al.*, 1990; Chatterjee and Shannon, 1998; Throckmorton and Collins, 1999). Cazals *et al.* (1990) found no relation between a forward-masking task and open-set speech recognition, applying monopolar stimulation with the six-electrode Ineraid implant by Symbion (4 mm electrode distance). Chatterjee and Shannon (1998) observed stronger dependence of FMPs on masker level and probe delay in a CI listener with low sentence recognition scores compared to other subjects with higher scores (Nucleus 22, bipolar stimulation mode). Throckmorton and Collins (1999) tested seven Nucleus 22 patients (bipolar stimulation mode) and reported a significant correlation between the average masking effect caused by the central electrode and consonant as well as sentence recognition. However, there was no significant correlation with vowel recognition scores. According to Throckmorton and Collins (1999), the correlation with consonant and sentence recognition could reflect the relevance of temporal aspects of forward masking, i.e., masking of consonants by preceding vowels with higher energy. The lack of a significant correlation between the average masking effect of the central electrode and vowel recognition performance appeared to indicate that across-channel (spectral) aspects of forward masking, as described earlier, were not important. However, the significant correlation between the average masking effect of the central electrode and an electrode discrimination task performed in the same study, which is a measure of the amount of excitation overlap, indicated that both temporal and spectral interactions may have been involved. More recently, Throckmorton and Collins (2002) measured speech recognition of NH subjects listening to stimuli simulating forward masking effects in cochlear implant listeners. The contribution of spectral interactions to the observed degradation in speech recognition was more pronounced than that of temporal interactions. In summary, only a few of the conditions tested in the above-mentioned studies showed a correlation between speech recognition performance and measures of forward masking.

Measuring neural-population interactions by means of FMP involves using only two electrodes, the masker and the probe. Complex signals like speech, however, require stimulation by more than two electrodes, which is likely to result in complex stimulation patterns and, as a result, a relatively high degree of NPIs. This assumption is based on the observation that maskers tend to elevate probe thresholds across the entire electrode array, rather than merely at neighboring electrodes (e.g., Throckmorton and Collins, 1999). In the present study, it is assumed that the measurement of ''inter-

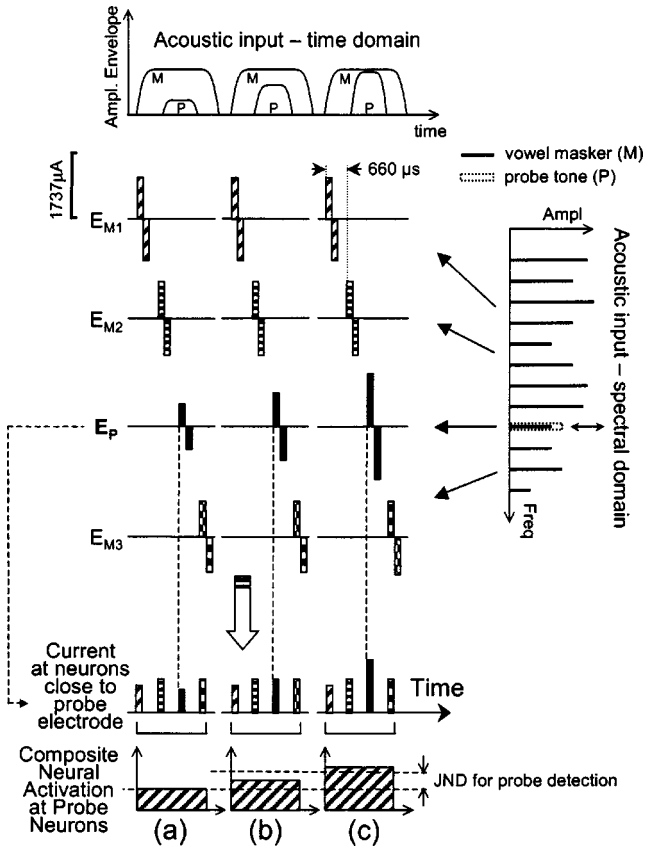

FIG. 1. Schematic illustration of neural-population interactions (NPIs) in a sequential stimulation strategy. The upper and the rightmost parts of the figure show the temporal and the spectral representation, respectively, of the acoustical input to the CI processor [masker (*M*) and probe (*P*)]. The corresponding electrode signals at three masker electrodes E_{M1}–E_{M3} and the probe electrode E_P are given below. The electrical current patterns occurring at the neurons most close to the probe electrode are shown beneath. The assumed composite neural activation at the pertaining neurons depicted at the bottom of the graph indicates that with an increasing amplitude of the probe pulses (E_p) from (a)–(c), the probe becomes audible. The distance between the upper and the lower dashed horizontal lines symbolizes the threshold criterion, i.e., the minimum detectable change introduced by the probe into the composite activation produced by the masker in relation to the variance in the composite activation produced by the masker alone. Note that although the acoustical masker and probe are presented simultaneously, the electrical pulses associated with masker and probe occur nonsimultaneously except for the frequency range of the probe, where masker and probe fall into the same filterband of the CI processor and therefore contribute to the same electrical pulses (black pulses).

nal'' auditory representations of a set of steady-state vowels can give insight into the transmission of spectral information associated with NPIs.

By applying a sequential stimulation strategy like CIS (as was done in the present study), the neural representation of each electrode signal can be affected by NPIs from other electrodes. Figure 1 illustrates schematically the process assumed to underly the masked threshold in a sequential stimulation strategy that is dependent on the probe level in three stimulation cycles (a–c). The upper and the rightmost parts of the figure show the temporal and the spectral representation, respectively, of the acoustical input to the CI processor [masker (*M*) and probe (*P*)]. *Ep* refers to a single electrode signal, the probe, and E_{M1}–E_{M3} represent several surrounding electrode signals, the maskers. Below the electrode signals, the corresponding electrical current patterns at the neurons closest to the probe electrode, the ''effective'' signals, are shown. The bottom part of the figure depicts the assumed composite neural activation at the pertaining neurons during each of the three stimulation cycles (a–c).

At the pulse rates of 1515 pps per channel applied in this study (due to excitation overlap the ''effective'' rate per channel could be much higher), the origins for the generation of the masked threshold may be different from those present when measuring masking at much lower pulse rates (e.g., Shannon, 1990; Chatterjee and Shannon, 1998). It is conceivable that neural firing is determined by the total energy of the pulses within a temporal sliding window. According to this assumption, the probe only becomes audible when it introduces a detectable change into the composite activation produced by the masker in relation to the variance in the composite activation produced by the masker alone. At low probe amplitudes (a) the spiking pattern at the neurons close to the probe electrode is dominated by signals from both adjacent (E_{M2} and E_{M3}) and distant (E_{M1}) masker electrodes, depending on their relative amplitudes and spread of excitation. In this case the probe is likely to be inaudible. Increasing the probe amplitude produces a current increase primarily at the pertaining neurons. In cycle (b), the contribution of the probe pulse to the composite activation is still weak. Therefore, the neurons may generate a spiking pattern which is not significantly different from that in condition (a). A further increase in probe amplitude (c) causes the composite activation to exceed the threshold criterion, as symbolized by the distance between the lower and the upper dashed line, and the probe signal may become audible.

So far, we have described the potential mechanisms of NPIs and how they might affect the masked thresholds of electrode signals. In order to extract the specific effect of NPIs for complex signals like vowels, one can compare the spectra at the level of the implant electrodes (referred to as ''electrical activation patterns'') with the corresponding VMPs. For the stimuli presented via the ''clinical'' CI processor (the wearable speech processor used by the subjects in everyday life) an additional source of spectral alteration results from the nonlinear dynamic range allocation performed in the stimulation channels. This effect can arise from applying a nonlinear amplitude compression function on channels with different threshold and most comfortable current levels as well as growth-of-loudness functions, and is subsequently referred to as CI compression. Potential consequences are reduced spectral contrast and spectral shifts of peaks and valleys in the spectrum. The specific effect of CI compression can be extracted by comparing the acoustic vowel spectra with the electrical activation patterns.

The current study describes two experiments pertaining to (1) the identification of synthetic vowels by CI listeners and (2) the effects of channel interactions for the vowel stimuli using VMPs. Stimuli for CI listeners were derived from eight synthetic vowels differing in spectral envelope only, which had been verified to be identifiable by NH listeners with a score of 99% to 100% correct in an vowel identification pretest. For CI listeners, the confusion among vowels was analyzed by calculating the information transfer

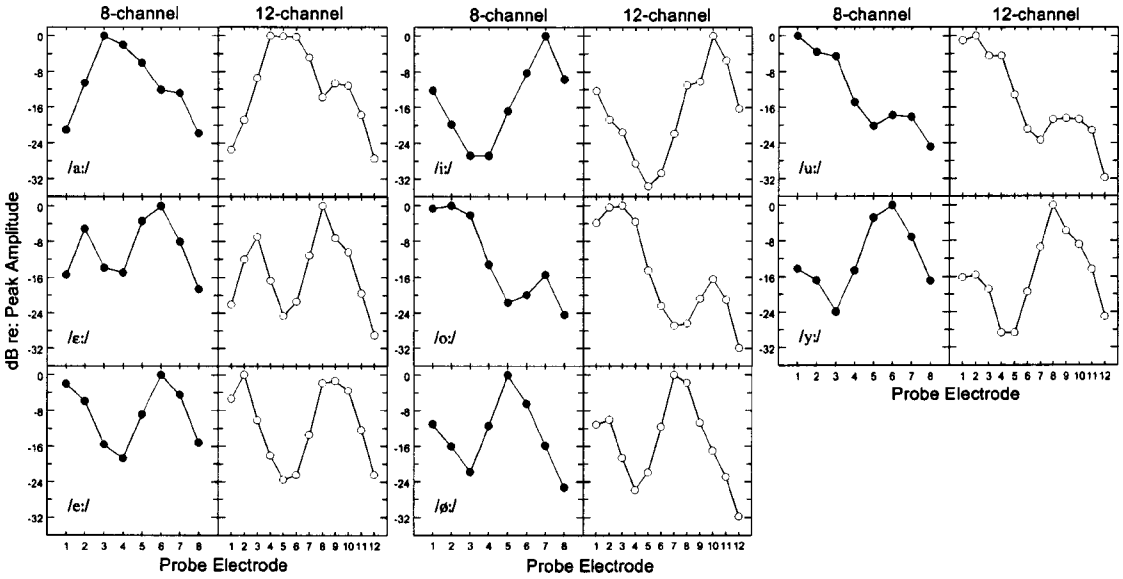

FIG. 2. Amplitude spectra of the vowels (CI Vowels) used in experiments I and II for 8-channel implantees (left) and 12-channel-implantees (right).

for all vowel pairs. Pairs with either low or high information transfer were selected for the second experiment. In experiment 2, VMPs were measured for each of the selected vowels. Since it is generally not known which spectral features CI listeners rely on, five different metrics of spectral similarity were applied to all VMP pairs and correlated with the vowel identification data. Three of the metrics, representing the ''whole-spectrum approach'' of the two viewpoints in vowel perception [''whole-spectrum'' versus ''formant-based'' approach (Bladon and Lindblom, 1981, p. 1421)], evaluate differences in spectral amplitudes with equal weight to all components. The other two metrics, representing the ''formant-based'' approach, emphasize differences in either formant positions or the spectral centroid. It was hypothesized that CI listeners rely more on ''whole-spectrum'' aspects in vowel identification than NH listeners because of the smaller number of frequency channels available. Furthermore, it was hypothesized that CI listeners exhibiting stronger spectral blurring resulting from NPIs and compression would show lower mean identification scores for all eight vowels.

In summary, the main questions addressed in this study are the following: (1) How well do cochlear implant users identify synthetic steady-state vowels using only spectral envelope cues? (2) Do VMPs reflect the patterns of confusion between vowels derived from the identification data? (3) What characteristics of VMPs are used by cochlear implant listeners to differentiate among the vowels, assuming that VMPs represent all of the relevant information available to CI listeners? (4) How do NPIs and CI compression affect the ''internal'' representations of the signals, and could the amount of blurring observed be used as a predictor of vowel identification performance?

II. EXPERIMENT I: VOWEL IDENTIFICATION

A. Stimuli

Steady-state vowels were used instead of natural spoken vowels because we wanted to force subjects to use only spectral shape cues. Natural vowels can provide identification cues apart from spectral shape, such as differences in fundamental frequency, duration, or small changes of spectral shape over time. Eight German vowels /a:, ɛ:, e:, i:, o:, ø:, u:, y:/ were generated by additive synthesis of 40 sinusoids (sine phase), spaced at 100-Hz intervals from 100 to 4000 Hz. The amplitudes of the sinusoids were determined as follows: Steady-state vowel segments were extracted from natural recordings of consonant–vowel–consonant tokens (German-spoken clinical vowel test) read by a male speaker at approximately 100-Hz fundamental frequency, and sampled at 44.1 kHz. One speech signal period, selected from the stationary part of the segment, was extracted and recopied several times. A 5000-point DFT spectrum was calculated from the resulting signal, and the amplitudes of the spectral components were determined by a peak-picking algorithm using quadratic interpolation to sharpen the peak estimation. Each of the 40 sinusoids was weighted with the amplitude of the closest spectral peak derived from the interpolated DFT spectrum. This process was used to compute stationary vowels (NH vowels), which served as stimuli in the normal hearing identification pretest.

The synthesis procedure for the stimuli used with the CI listeners was different. In order to avoid identification cues derived from differences in modulation depth in the electrical output as a result of varying amplitude relations of the harmonics within a filterband of the CI processor, sinusoids were placed only at the center frequencies (F_i) in each CI filterbank. The corresponding amplitudes were taken from the rms measurements of the CI processor's filterbank outputs (A_i) using the NH vowels as input. Finally, sinusoids were added in sine phase with frequencies F_i and amplitudes A_i. The resulting vowel stimuli (CI vowels) were used to test the CI listeners. Figure 2 shows amplitude spectra of the CI vowels. The total duration of each stimulus (including 70-ms raised-cosine ramps) was 0.9 s. It is worth noting that this duration is very much longer than the usual duration of

TABLE I. Demographic data for the cochlear implantees.

Subject	Sex	Age (years)	Age at onset of profound deafness (years)	Age at implantation (years)	Device	Mean/standard deviation of dynamic range across all active electrodes (μA)	Constant for amplitude compression (c-value)
S1	M	50	17	37	C40	800/104.3	1024
S2	F	57	28	51	C40	614/14.8	500
S3	F	70	50	65	C40	396/112.7	1024
S4	M	62	50	61	C40+	703/86	1024
S5	M	56	38.5	54	C40+	263/48	500
S6	F	68	37	67	C40+	325/34.5	500
S7	F	65	32	58	C40+	994/327	500

vowels in natural speech. All vowels were equated for A-weighted rms amplitudes.

It is important to note that the CI vowels, although perceived as highly inharmonic by normal ears, produced ''electrical'' spectral shapes very similar to those produced if the harmonic NH vowels were fed into the CI processor. The only difference between these two types of stimuli, from the viewpoint of the CI listener, is that in the case of the CI vowels the filterbank processing is applied two times (during synthesis, as well as during presentation), whereas in the case of the NH vowels the filterbank processing would have been performed only during presentation. A comparison of the ''electrical'' processor outputs between the NH vowels and the CI vowels revealed no differences in spectral peak positions and only marginal differences in between the spectral peaks (for both the 8 and 12 channel versions). Therefore, the CI vowels provided spectral shape cues to the CI listeners comparable to those provided by natural vowels.

To minimize loudness differences among vowels providing identification cues all vowels were loudness balanced before presentation. One of the vowels served as the reference stimulus (78 dB SPL in case of NH listeners and at a comfortable level in the case of CI listeners) and the listeners matched the other vowels in loudness to the reference. Then, the stimuli were presented in groups of four (1-2-3-4, 2-3-4-5, 3-4-5-6, 4-5-6-7, 5-6-7-8) and the subjects were instructed to identify vowels still deviating in loudness within each group. Whenever a different loudness occurred, the amplitude of the corresponding vowel was adjusted by the experimenter until the subject reported uniformity within the group. The whole sequence of vowels was presented in order to check the loudness balance. Care was taken that none of the vowels approached the saturation level in any of the processor channels. In such a case, the level of all vowels was reduced appropriately.

An even more efficient method to remove loudness as a cue to vowel identity would be to rove the amplitude of the stimuli across items. However, this procedure would have complicated the analysis of the relationship between the vowel identification data and the corresponding VMPs: the channel-specific nonlinear amplitude compression performed in the CI processor would produce spectral shape variations as a function of level, whereas the VMP measurement is obtained only at a single level.

The preprocessed stimuli were digitally stored and output at 44.1-kHz sampling rate using a 16-bit D/A converter (ADDA 2402 by Digital Audio Denmark), connected to a headphone amplifier (HB6, TDT) and an attenuator (PA4, TDT). When testing the normal-hearing control subjects the stimuli were presented via a circumaural headphone (HDA 200, Sennheiser) connected to the attenuator. For CI listeners, the output of the attenuator was connected to the auxiliary input of the CIS PRO+ processor (Med-El Corp). The experiments were controlled by custom-made software routines within the ST^X-system.[1]

B. Subjects and equipment

Three male and four female subjects implanted with multi-channel cochlear implants at the Vienna University Hospital participated in all experiments described in this study. Table I contains the demographic data for the subjects. All of them had at least 9 months experience with their device. Three of the subjects were supplied with the 8-channel (*Combi*-40) and the other four subjects with the 12-channel (*Combi*-40+) implant system from Med-El Corp (Zierhofer *et al.*, 1995, 1997). Both the *Combi*-40 and the *Combi*-40+ stimulate in monopolar configuration with an extracochlear reference electrode. The distance between the electrode contacts is 2.8 and 2.4 mm for the *Combi*-40 and *Combi*-40+, respectively. In every subject, except S7, all electrodes were active. In S7, electrodes 11 and 12 were deactivated due to excitation of the facial nerve.

The stimuli were delivered electrically to the auxiliary inputs of the patients' CIS PRO+ processor programmed using the CIS-strategy. The automatic gain control was deactivated during the experiments. Figure 3 provides a flowchart of the signal-processing steps performed in the CIS PRO+ processor. A software simulation of the processing steps was performed in order to provide a numerical calculation of the electrical current levels corresponding to the acoustic input signals and the threshold levels obtained in the experiments. The analog part of the processor contains an antialiasing filter and a preemphasis stage which attenuates low-frequency energy. This stage provides 8 dB of preemphasis between 1.5 and 3 kHz. It is followed by a 12-bit A/D-converter (Fs=15 kHz) and either an 8- or 12-channel filterbank (*Combi*-40/40+) with sixth-order digital IIR-filters. Envelope extraction is performed by means of full-wave rectification and subsequent low-pass filtering (second order IIR-design; cutoff frequency: 400 Hz). The extracted envelope is compressed according to the function

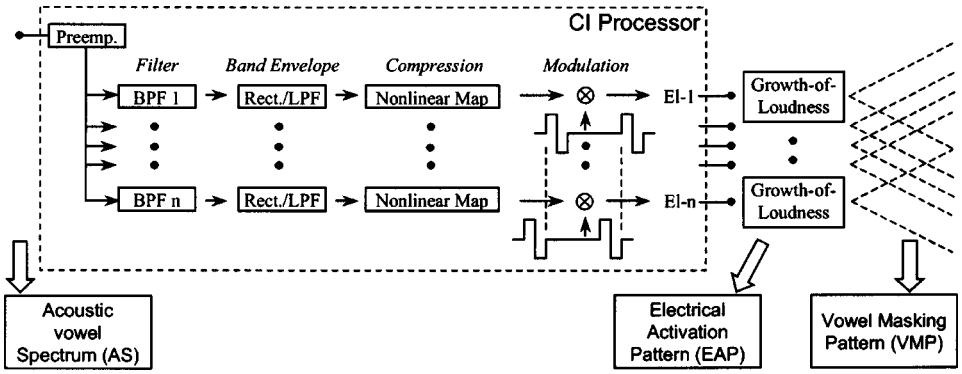

FIG. 3. Signal processing scheme of the CIS PRO+ processor. The levels of the three spectral representations as referenced in the study are indicated by arrows: acoustic vowel spectrum (AS), electrical activation pattern (EAP), and vowel masking pattern (VMP).

$$y = A\frac{\log 10(1+cx)}{\log 10(1+c)} + B, \quad (1)$$

where x and y are the linear amplitudes of the input and output signals in the range of 0 to 1, respectively. The constant c, which has a common value for all electrodes, determines the degree of amplitude compression. The constants A and B are set to map the acoustic amplitudes into the subject's electrical dynamic range. Finally, the compressed envelope is mapped to the channel-specific electrical dynamic range.

The current steps are linearly distributed across the dynamic range of electrical stimulation. The actual step size depends on the dynamic range of the patient, varying between 3.3 and 15.6 current units (cu) for the Combi-40 and between 2.4 and 13.6 cu for the Combi-40+. The CIS strategy was programmed to generate biphasic rectangular pulses (cathodic phase first) with phase durations of 40 and 26.7 μs for the Combi-40 and Combi40+, respectively, and a stimulation rate of 1515 pps per electrode. Throughout this paper the electrodes in the array are labeled with ascending numbers from apex (1) to base (8/12). The standard stimulation order 1-5-2-6-3-7-4-8 (Combi-40) and 1-7-2-8-3-9-4-10-5-11-6-12 (Combi-40+) was used, which is designed to minimize interactions between adjacent channels.

Three normal-hearing listeners served as control subjects in the vowel identification experiment. One was the first author and the other two were colleagues from the same lab. Their audiometric thresholds were all better than 10 dB HL between 125 and 8000 Hz. There was no indication of any present or past hearing disorder in these listeners.

C. Processor fitting, measure of loudness growth, and calibration

Threshold and maximum comfort levels were determined at the beginning of the first session, with each implantee using clinical fitting software (Table II). We applied a standard compression coefficient for all subjects.[2] The filterbank settings were the same as those applied in each subject's clinical fitting. The center frequencies of the filter bands were 360, 518, 745, 1071, 1541, 2216, 3188, and 4586 Hz (8-channel implant) and 339, 432, 550, 701, 893, 1138,

TABLE II. The threshold (THR) and most comfortable electrical currents (MCL) in decibels and the measure of loudness-growth (LG) for each electrode. The mean and standard deviation values across the electrodes are given at the right side.

		Electrode												
Measure	Subject	1	2	3	4	5	6	7	8	9	10	11	Mean	Standard deviation
THR		42.1	41.4	40.7	42.1	42.7	43.2	42.7	40.7	⋯	⋯	⋯	42.0	0.9
MLC	S1	60.8	59.1	59.9	59.9	59.9	58.9	57.9	57.7	⋯	⋯	⋯	59.3	1.1
LG		3.0	2.7	1.2	1.0	1.2	1.2	1.7	0.9	⋯	⋯	⋯	1.6	0.8
THR		40.0	38.9	40.9	39.1	40.7	40.0	41.4	41.4	⋯	⋯	⋯	40.3	1.0
MLC	S2	57.1	56.9	56.9	57.1	57.3	57.3	57.1	57.3	⋯	⋯	⋯	57.1	0.2
LG		1.4	3.2	3.0	1.0	0.4	0.4	0.4	0.2	⋯	⋯	⋯	1.3	1.2
THR		41.3	44.1	44.1	44.1	44.1	44.0	44.0	45.2	⋯	⋯	⋯	43.9	1.1
MLC	S3	56.6	55.4	56.3	56.1	52.6	52.3	52.3	55.8	⋯	⋯	⋯	54.7	1.9
LG		2.7	2.2	1.8	1.0	0.6	0.5	0.4	0.7	⋯	⋯	⋯	1.2	0.9
THR		29.8	29.8	29.8	29.8	27.2	27.2	29.8	29.8	31.8	31.8	31.8	29.2	1.2
MLC	S4	58.0	57.9	57.5	56.9	56.6	56.6	57.7	58.5	58.3	55.2	55.5	57.5	0.7
LG		0.7	0.6	1.0	0.7	1.0	0.8	1.1	0.6	0.4	0.3	0.4	0.8	0.2
THR		37.2	38.1	37.2	36.6	37.7	38.1	37.7	35.5	35.8	37.0	39.5	37.2	0.9
MLC	S5	51.9	51.3	51.3	51.6	51.6	51.3	51.0	49.4	48.8	47.9	48.8	51.2	0.8
LG		2.0	2.7	3.0	2.1	0.9	1.0	0.6	0.8	0.4	0.4	0.3	1.6	0.9
THR		35.5	36.1	38.6	39.0	37.2	36.6	36.6	39.0	37.2	39.0	42.3	37.3	1.4
MLC	S6	52.2	51.3	51.6	52.5	53.0	53.2	52.2	51.9	51.9	51.9	51.9	52.2	0.6
LG		1.1	0.8	0.5	0.2	1.0	0.3	0.5	0.2	0.2	0.2	0.4	0.6	0.4
THR		49.5	50.6	55.3	52.5	51.3	49.3	50.8	47.6	46.7	49.6	⋯	50.9	2.3
MLC	S7	64.8	63.8	64.8	64.8	64.8	59.2	59.5	59.2	61.4	59.2	⋯	62.6	2.8
LG		6.2	2.9	12.7	1.9	8.0	1.0	0.5	1.2	1.5	1.0	⋯	4.3	4.3

1450, 1848, 2355, 3000, 3823, and 4872 Hz (12-channel implant). The filters overlapped at the −3-dB points.

To obtain a measure of the exponent of the assumed power law function of loudness growth at individual electrodes, a loudness balancing task was performed (see Lim *et al.*, 1989; Throckmorton and Collins, 1999). First, the pulse amplitude producing comfortable loudness was determined for one electrode at the middle of the electrode array. Then, the pulse amplitudes at the remaining electrodes were matched in loudness to the reference electrode (A-B comparison). Both of these adjustments were performed by means of a manual up/down procedure. A measure of loudness growth at the individual electrodes (Table II) was defined from the ratio of the loudness-balanced levels and the absolute threshold levels in order to normalize the electrical activation patterns and the VMPs obtained in experiment II.

To determine the current levels at the electrodes corresponding to the stimulus amplitudes and the thresholds for the input signals to the CI processor, the transmission properties of the cochlear implant system had to be simulated by a software program meeting the specifications of the CI manufacturer and taking into account the patient-specific fitting parameters. Calibration and verification of the software parameters was performed using an ''artificial cochlea'' with a standard impedance of 6.8 kΩ (*Detectorbox* 40/40+ by Med-El). This real (but un-implanted) electrode array allows measurement of the electrical current levels delivered by the CI system, so that they can be compared with the current levels predicted by the software simulation. The loudness control of the CI processor was generally set at the maximum position.

D. Procedure

All subjects, both NH and CI listeners, were seated in front of a computer monitor that displayed large response buttons containing orthographic symbols for the eight vowels, a start button, and a repetition button. Subjects could initiate presentation of the stimuli and either indicate their identification response by clicking on one of the vowel buttons or repeat the last vowel presentation by clicking on the repetition button. No feedback was provided. Each block of trials consisted of 12 randomly ordered presentations of the eight vowels, for a total of 96 trials. After an initial training block, each of the subjects completed at least 2 blocks, for a total of 24 observations per vowel and subject. The collected data was cast into eight-by-eight confusion matrices and the percent-correct vowel identification was calculated.

TABLE III. Example of an vowel confusion matrix and overall percent-correct vowel recognition score (CI listener S3).

	Response								
Stimulus	a	ε	e	i	o	ø	u	y	
a	24	0	0	0	0	0	0	0	
ε	0	3	3	1	0	8	2	7	
e	0	2	1	0	4	4	12	1	
i	0	7	7	10	0	0	0	0	
o	0	0	0	0	13	0	11	0	
ø	0	0	0	0	0	12	0	12	
u	0	0	0	0	11	0	13	0	
y	0	6	7	3	0	4	0	4	
									41.7%
	24	18	18	14	28	28	38	24	

E. Results

1. NH listeners

Three normal-hearing listeners performed the vowel identification task as a pretest to verify that the NH vowels were fully identifiable. The average vowel identification performance ranged from 99% to 100% correct, indicating that all NH vowels were perfectly identifiable by untrained normal-hearing subjects.

2. CI listeners

The overall percent of correct vowel identification for the CI listeners was 74% (S1), 71% (S2), 42% (S3), 61% (S4), 61% (S5), 45% (S6), and 60% (S7). Most of the confusion patterns were systematic and confined to between two and five vowels. In other words, the subjects rarely responded randomly. Table III provides an example from subject S3 of a confusion matrix.

The confusion among these vowels was analyzed by calculating the information transfer for all vowel pairs. The confusion data for each subject was transformed into 28 2-by-2 submatrices and the relative transmitted information (RTI) was calculated for each pair according to the following formula (Miller and Nicely, 1955):

$$\mathrm{RTI}(x;y)=\left(-\sum_{i,j} p_{ij}\log_2\frac{p_i p_j}{p_{ij}}\right)\Big/ H(x), \tag{2}$$

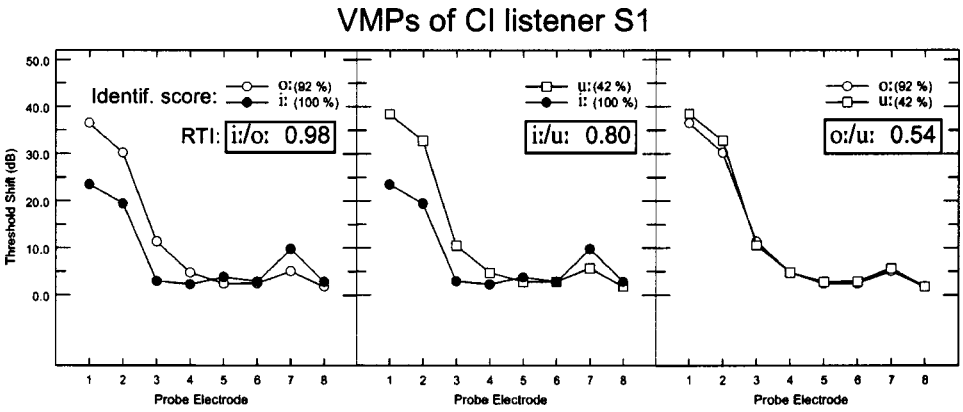

FIG. 4. Pair-wise comparison of VMPs for CI listener S1 for illustrative purposes: highly discriminated vowels /i:/ and /o:/ (left panel), less well discriminated vowels /i:/ and /u:/ (middle panel), and poorly discriminated vowels /o:/ and /u:/ (right panel). Correct identification scores (in percent) for each vowel and pair-wise relative transmitted information (RTI) are denoted at the top of each graph.

where p_i is the probability of the stimulus, p_j is the probability of the response, p_{ij} is the probability of joint occurrence of stimulus i and response j, and $H(x)$ is the entropy in the stimulus set. The rationale for using information transfer rather than relying on absolute identification rates was that this measure allows determination of mutual confusion for each vowel pair, taking into account the probability of chance identification, and it compensates for response bias. RTI was used as a criterion to determine the most similar and most dissimilar vowel pairs for each subject to use as maskers in the VMP measurement.

III. EXPERIMENT II: VOWEL MASKING PATTERNS

A. Stimuli

1. Vowel maskers

Three or four vowels with low or high RTIs were selected as vowel maskers for each subject to derive a stimulus set for the VMPs (three-stimulus sets in subjects S1 and S4 and four-stimulus sets in subjects S2, S3, S5, S6, and S7). Each of the three-stimulus sets was constructed to build one pair combination of low RTI values and two pair combinations of high RTI values. In the case of four-stimulus sets, the additional vowel either had low (subject S3) or high (subjects S2, S5, S6, and S7) mutual RTIs with the other members of the set. Figures 5 and 6 show which vowels were used for each subject. This stimulus configuration enabled measurement of differences in spectral similarity of VMPs corresponding to vowels exhibiting maximum and minimum RTIs.

2. Probe tones

Probe tones were sinusoids generated digitally at the center frequencies of the CI processor's filterbands. The overall duration was 240 ms, including 70-ms raised-cosine rise-fall times. The decision to use relatively long probe tones was based on pilot tests. When using shorter probe durations, two implantees reported difficulties in performing the task. The probes were presented at the temporal midpoint of the masker with the exact temporal position jittered randomly within a period of ± 220 ms. Jittering of the probe tone position was used, since pilot tests with NH subjects showed that probe tone jitter results in increased reproducibility of the obtained thresholds.[3] It is important to note that although the masker and probe were presented simultaneously, the electrical pulses associated with masker and probe were presented nonsimultaneously (due to the sequential stimulation inherent to the CIS strategy). Only in the frequency region of the probe did the masker and probe fall into the same filterband of the CI processor and would therefore be associated with the same electrical pulses (the pulses shown in black in Fig. 1). At a given probe signal duration of 240 ms and a stimulation cycle of 660 μs, 364 stimulation cycles occurred during presentation of the probe signal. For the 12-channel implantees the most basal channel (12) was omitted because its center frequency was outside the masker range.

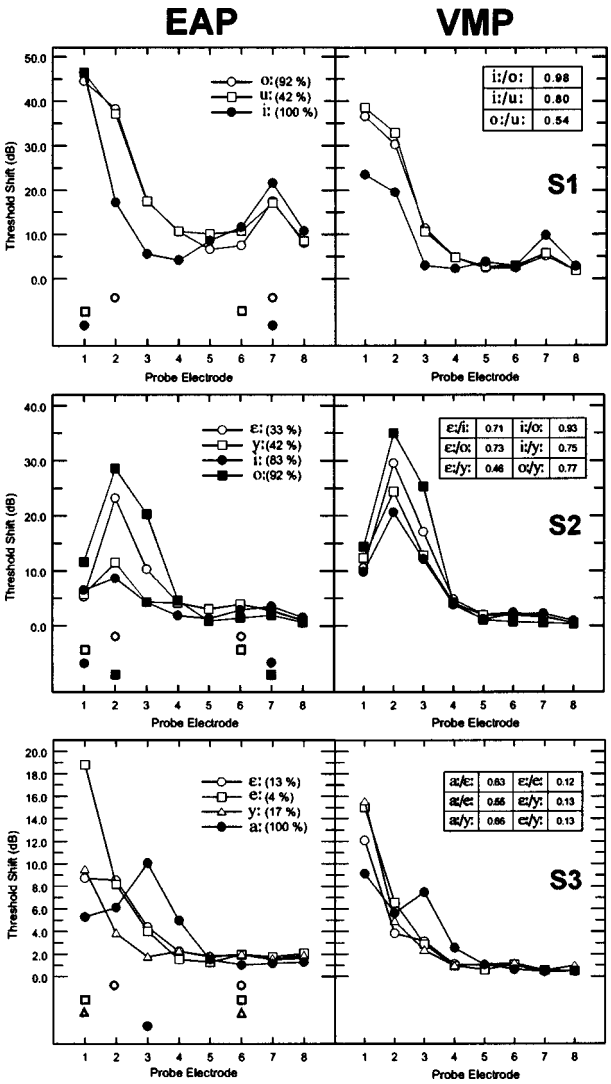

FIG. 5. Vowel masking patterns (right side) and electrical activation patterns (left side) for the 8-channel implantees S1, S2, and S3. The VMPs tested in each subject are plotted together in one graph. Open symbols correspond to the most often confused vowels (exhibiting the lowest RTI value) and filled symbols represent the vowels rarely if ever confused with the remaining vowels, thus having high mutual RTIs. The percent correct scores for each vowel are given at the top of the left-hand panels and the RTI values for all pair combinations are shown in the tables at the top of the right-hand panels. The symbols at the bottom of the electrical activation patterns indicate the peak frequencies in the corresponding vowel spectra (derived from the vowellike stimuli presented to the CI listeners, referred to as CI vowels).

B. Procedure

Masked thresholds of the probes were measured using a modified Békésy-tracking procedure. The probes were presented initially at a sufficiently high level above the expected masked thresholds, estimated in pilot tests. The step size was 6 dB at the beginning, 4 dB after the second reversal, 2 dB after the third reversal, and 1 dB from the fourth reversal on until the end of the run. After a total of nine reversals, the procedure was terminated as soon as the standard deviation over the last six reversals was below 3.5 dB (acoustically). The final threshold was taken from the arithmetic mean of the last six reversals. In order to obtain an estimate of test–retest reliability, about half of the threshold measurements were performed twice. In such cases the final threshold was defined as the mean of the two measurements.

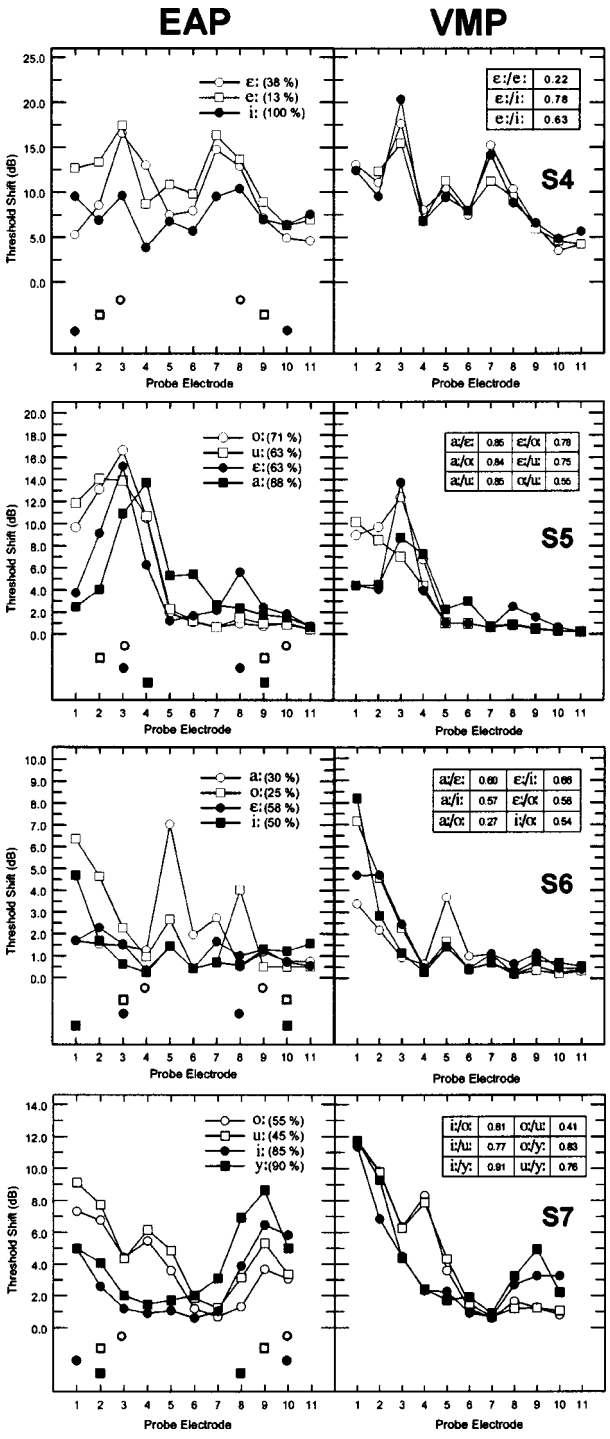

FIG. 6. As in Fig. 5, for 12-channel implantees S4, S5, S6, and S7.

Subjects were seated in front of a computer screen showing a symbol indicating the stimulus interval. By pressing a start button, the listener started an adaptive run consisting of a sequence of pulsating masker+probe stimuli with interstimulus pauses of 0.6 s. Each time the masker stimulus was switched on, the visual sign was displayed on the computer screen. The listeners were instructed to press and hold a ''tone'' button as long as they could hear the probe above the masker. The probe level was decreased with each presentation by the step size described. The button had to be released by the subject as soon as she/he could no longer hear the probe. From this moment on, the probe level was raised until the signal could be heard again. The procedure was repeated until the termination criterion was reached.

This modified Békésy-tracking method was used instead of a detection task in order to reduce the time required to obtain the VMPs. A potential problem with this method concerns the subject's detection criterion for probe tone detection. This criterion is not directly knowable by the experimenter. However, relying on the assumption that the individual subject's detection criterion does not change over time (or at least over the time course of one VMP measurement), no significant impact on either the shape of the VMPs or the similarity metrics applied to the VMP pairs is likely to occur. Changes in the subject's detection criterion would affect the overall VMP level, which was ignored by the similarity metrics (described in Sec. III C 1).

C. Results

1. Vowel masking patterns

The mean absolute difference of the masked threshold values between test and retest, averaged across thresholds and subjects, was 1.9 dB (acoustically). The obtained masked thresholds in the acoustical domain were converted to electrical current levels using the CI processor software simulation described in Sec. II B. The resulting VMPs show the degree of masking (defined as the difference between the masked thresholds and the thresholds in quiet for each electrode). In order to take into account the growth-of-loudness at different electrode positions, the difference between masked and unmasked thresholds was normalized using a measure of loudness growth obtained from the procedure described in Sec. II C. The normalization was performed using the ratio of loudness-balanced levels to threshold levels obtained. Thus, the VMP value for probe electrode i, VMP_i, was calculated as follows:

$$\mathrm{VMP}_i = (T_i^{msk} - T_i^{qu}) \frac{LB^{ref} - T^{ref}}{LB_i - T_i^{qu}}. \tag{3}$$

T^{ref} and T_i^{qu} are the unmasked thresholds of the reference electrode (used for loudness balancing) and probe electrode, LB^{ref} and LB_i are the loudness-balanced levels of the reference and probe, and T_i^{msk} is the masked threshold of the probe. All levels are specified in dB. A masking level of 0 dB indicates that no masking occurred.

Figure 4 shows, for illustrative purposes, VMPs resulting from this method of CI listener S1 in three separate graphs for each vowel pair combination. The left panel compares VMPs corresponding to the accurately discriminated vowels /i:/ and /o:/, the middle panel shows less well discriminated vowels /i:/ and /u:/ and the right panel the poorly discriminated vowels /o:/ and /u:/. The percent-correct identification scores for each vowel and the pair-wise RTI values are denoted at the top of each panel. The right-hand panels of Figs. 5 and 6 show VMPs for the three 8-channel and the four 12-channel implantees, respectively (the left-hand panels of these graphs contain electrical activation patterns, which are described in Sec. III C 3). The VMPs tested in each subject are plotted together on one graph. For easier identification of poorly and highly discriminated vowel pairs, the

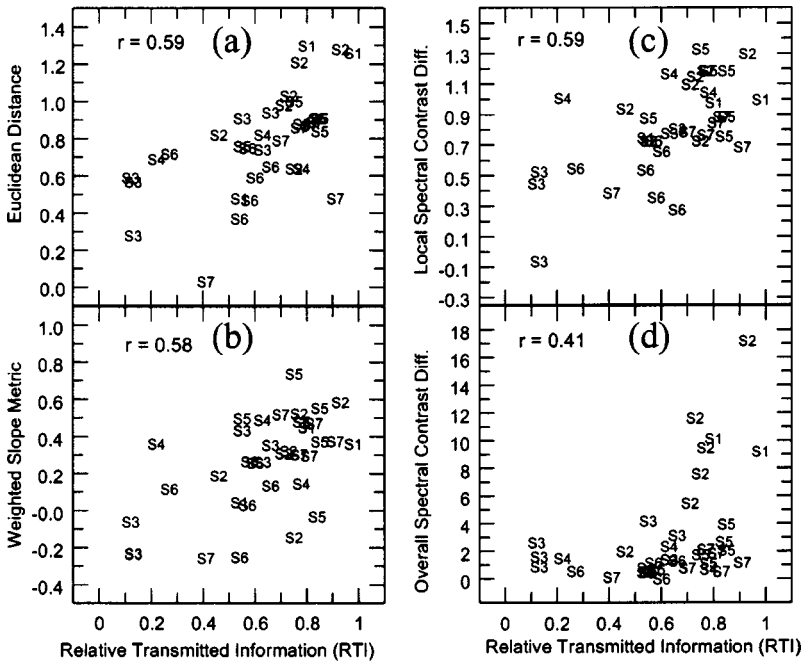

FIG. 7. Computed metric distances plotted as a function of the relative transmitted information (RTI) for each vowel pair, using the following metrics: Euclidean distance (top left), weighted slope metric (bottom left), local spectral contrast difference (top right), and overall spectral contrast difference (bottom right). The corresponding correlation coefficients are shown in each diagram.

open symbols correspond to the most often confused vowels (exhibiting the lowest RTI value) and the filled symbols represent the vowels rarely if ever confused with the remaining vowels, thus having high mutual RTIs. The percent-correct scores for each vowel are given at the top of the left-hand panels and the RTI values for all pair combinations are shown in the tables at the top of the right-hand panels.

In general, the VMPs were characterized by one to two pronounced spectral peaks and occasionally one additional smaller peak. The overall spectral patterns of most VMPs resembled those of the input vowels (CI vowels), as shown in Fig. 2.

2. The relation between vowel identification and vowel masking patterns

Visual inspection of the VMPs generally agreed well with the results of experiment I: vowel pairs with relatively low (mutual) RTIs had similar VMPs, whereas vowel pairs with high RTIs exhibited differences in the shapes of the corresponding VMPs. Three of the seven CI listeners tested (S1, S2, and S7) exhibited modest RTIs for vowel pairs showing high similarity in their VMPs. This could indicate that these listeners used one or more cues besides spectral differences to discriminate these vowels (e.g., differences in loudness still present after loudness balancing). In order to find the VMP features used by the CI listeners to identify the vowels, several metrics of similarity, applied to all VMP pairs, were compared with the corresponding RTI values.

a. Euclidean distance (ED). The Euclidean distance represents the summed ''distance'' between two spectra. It has been used in previous work analyzing acoustic spectra of vowels and other complex stimuli (Plomp, 1970, 1975), ''auditory'' vowel spectra (Bladon and Lindblom, 1981; Turner and Henn, 1989) and VMPs (van Tasell *et al.*, 1987). The ED gives equal weight to all spectral points. The ED between members of VMP pairs was computed as follows:

$$\mathrm{ED}=\log\left(\sqrt{\sum_{i=1}^{N}[X_i-Y_i]^2}\right), \tag{4}$$

where N is the number of tested electrodes and X_i and Y_i are the values of the VMPs (in dB) at electrode i. The logarithm of the ED was used because it provided a better fit to the identification data than linear values. In order to minimize the effect of differences in overall level between VMPs on the ED, the rms difference was minimized by shifting in level one VMP of each pair before calculating the ED. Figure 7(a) shows the relation between the RTI (on the abscissa) and the ED (on the ordinate) for all vowel pairs in all CI listeners. The Pearson product-moment correlation coefficient is $r=0.59$ ($p<0.0001$, $n=36$).

b. Weighted slope metric (WSM). Klatt (1982) argued that a metric giving equal weight to intensity differences at all frequencies (like the ED) is appropriate for predicting the subjective psychophysical distance of two sounds, but not for predicting their phonetic distance. He developed a metric called the ''weighted slope metric'' which emphasizes the peak locations of the spectra and is not sensitive to the relative peak heights, the between-peak information, and the spectral tilt. In his experiments, this metric correlated highly with vowel recognition data ($r=0.93$); its suitability was further confirmed in the work of Nocerino *et al.* (1985), van Tasell *et al.* (1987), Assmann and Summerfield (1989), and Turner and Henn (1989). Our version of the WSM is given by

$$\mathrm{WSM}=\log\left(\sum_{i=1}^{N} W_i[SLX_i-SLY_i]^2\right), \tag{5}$$

where N is the number of electrodes tested while SLX_i and SLY_i are the slopes of the spectra at electrode i. The slope at point i is defined as the dB difference between the levels at points $i+1$ and i. Since slope estimation at $i=N$ would require the hypothetical point $i=N+1$, the slope at $i=N$ was

taken from the value at point $i=N-1$. The weighting function W_i is averaged across the two spectra according to

$$W_i=\frac{WX_i+WY_i}{2}, \tag{6}$$

where

$$WX_i \ \ or \ \ WY_i=\frac{k_{L\,\max}}{k_{L\,\max}+D_{L\,\max\,i}}\times\frac{k_{G\,\max}}{k_{G\,\max}+D_{G\,\max\,i}}. \tag{7}$$

$D_{L\,\max(i)}$ is the dB difference between the ith electrode and the nearest local maximum of the spectrum *and* $D_{G\,\max(i)}$ is the dB difference between the level of the ith electrode and the global maximum of the spectrum. The weighting parameters $k_{G\,\max}$ and $k_{L\,\max}$ allow definition of the emphasis given on the slope differences close to local spectral peaks and close to the global spectral maximum, respectively. After experimentation with the weighting parameters we found that the values $k_{G\,\max}=20$ and $k_{L\,\max}=1$, as proposed by Klatt (1982), were among those providing the highest correlation coefficients with the identification data. These values, also applied to the calculations presented here, give a small weight to slope differences close to the global maximum and a high weight to those near local peaks. More emphasis on the global maximum consistently resulted in lower correlations. Increasing the weight on local peaks (up to the value proposed by Klatt) led to increasing correlations. We used the logarithm of Klatt's metric, since it better fitted our data. In summary, the WSM sums the differences in slopes between two spectra and gives greater weight to regions around local spectral peaks. Figure 7(b) shows the relation between RTI and WSM values. The correlation coefficient between these two measures is $r=0.58$ ($p<0.0001$, $n=36$).

c. Local spectral contrast difference (LSCD). The members of some VMP pairs corresponding to well-discriminated vowels had identical peak locations and differed in their between-peak spectral details (S1: /i:/-/o:/, /i:/-/u:/; S2: /i:/-/o:/; S5: /a:/-/ɛ:/, /a:/-/o:/, /ɛ:/-/o:/; S6: /a:/-/i:/; S7: /i:/-/y:/). To test the hypothesis that differences in the between-peak spectral details can account for the identification data, we developed a metric that is primarily sensitive to differences in local spectral contrasts. We defined the spectral contrast of a spectrum X at a specific spectral point i as the absolute value of the second difference at i, $XD_i=|X_{i-1}-2X_i+X_{i+1}|$. To obtain a measure of the difference in the local details between two spectra X and Y, we calculated the Euclidean distance over XD_i and YD_i. Consequently, our metric, called the local-spectral-contrast difference, is given by

$$\mathrm{LSCD}=\log\left(\sqrt{\sum_{i=2}^{N-1}[XD_i-YD_i]^2}\right), \tag{8}$$

where N is the number of tested electrodes and XD_i and YD_i are the second differences of the values of the VMPs at electrode i (in dB). In contrast to the ED, this metric is not sensitive to differences in global spectral aspects such as ''vertical'' shifts of broader frequency regions and spectral tilt. Moreover, the LSCD ignores the sign of spectral contrast values. Thus, the LSCD value is large if one spectrum contains narrow, but high-level, peaks (or valleys) and the other spectrum is flat. Figure 7(c) shows the relation between the RTI and the LSCD, whose correlation coefficient is $r=0.59$ ($p<0.0001$, $n=36$).

d. Overall spectral contrast difference (OSCD). It was observed that the members of some VMP pairs corresponding to well-discriminated vowels had identical peak positions and differed in their overall contrasts (S1: /i:/-/o:/, /i:/-/u:/; S2: /ɛ:/-/i:/, /i:/-/o:/, /o:/-/y:/; S3: /a:/-/ɛ:/, /a:/-/e:/, /a:/-/y:/; S4: /e:/-/i:/; S5: /a:/-/ɛ:/, /ɛ:/-/o:/; S7: /i:/-/y:/). This motivated us to include a metric which quantifies the difference in the overall spectral contrast between two spectra. We determined the overall spectral contrast of a VMP by calculating the rms of the level difference between consecutive peaks and valleys (or maxima and minima) across the VMP. Thus, the overall spectral contrast difference between two VMPs is given by

$$\mathrm{OSCD}=\left|\sqrt{\sum_{i=1}^{N-1}[LX_{i+1}-LX_i]^2}-\sqrt{\sum_{i=1}^{M-1}[LY_{i+1}-LY_i]^2}\right|, \tag{9}$$

where LX_i, LY_i are the consecutive extreme points (in dB) and N, M are the numbers of extreme points in LX and LY, respectively. Extreme points are defined as peaks or valleys in the spectrum and—as special cases—the lowest and highest frequency points. The relation between the RTI and this metric can be seen in Fig. 7(d). The calculated correlation coefficient amounts to $r=0.41$ ($p<0.01$, $n=36$).

e. Center of gravity difference (CGD). Since the tested vowels contained only two spectral peaks, we speculated that the center of gravity (Chistovich, 1985) might contain important information for discriminating between certain vowels. The center of gravity difference was defined as the first moment of the spectrum,

$$\mathrm{CGD}=\frac{\Sigma_{i=1}^{N}g(Z_i)Z_i}{\Sigma_{i=1}^{N}g(Z_i)}, \tag{10}$$

where Z_i are the frequencies in Bark corresponding to the filter center frequencies associated with electrodes i, $g(Z_i)$ are the values of the VMPs (in dB) at electrode i, and N is the number of tested electrodes. The correlation coefficient between the RTI and this metric is just significant ($r=0.37$, $p<0.03$, $n=36$).

The RTI values correlate with the two ''whole-spectrum'' metrics ED and LSCD about as well as with the ''formant-based'' metric WSM. This is in contrast to results obtained from NH and hearing-impaired listeners, showing higher correlations for the WSM than for the ED (Klatt, 1982; Turner and Henn, 1989; van Tasell *et al.*, 1987). The result indicates a higher importance of ''whole-spectrum'' aspects in CI listeners compared to ''acoustic'' listeners. Equal correlation between LSCD and RTI, as well as between ED and RTI, suggests that although the LSCD extracts one spectral feature only, it seems to capture the relevant information properly. The fact that LSCD does not differentiate between positive and negative spectral contrast values

indicates that CI users were sensitive to discontinuities in the ''internal'' spectral representation, regardless of whether they were spectral peaks or valleys. The lower correlations coefficients for OSCD (''whole-spectrum'') and CGD (''formant-based'') appear to indicate that these metrics explain a smaller portion of the variance in the identification data. An analysis of the statistical significance of the differences between the individual correlations according to the test described by Meng *et al.* (1992), however, indicated that the difference was statistically significant only between ED and CGD; $z=2.06$, $p<0.05$, $n=36$.

In summary, the CI listeners appeared to rely as much on ''whole-spectrum'' as on ''formant-based'' aspects of the ''internal'' stimulus representation in identifying loudness-balanced steady-state vowels. Concerning the ''whole-spectrum'' aspects, differences in local spectral details as captured by the metrics ED and LSCD appear to be more important than differences in the overall spectral contrasts (OSCD), although the difference between the correlation coefficients for LSCD and OSCD failed to reach statistical significance ($z=1.21$, $p>0.05$, $n=36$). The similar performance of the ''whole-spectrum'' and ''formant-based'' spectral similarity metrics may indicate that the CI listeners combined information from different spectral cues to identify the vowels. In fact, a metric comprising the linear sum of the metric distances for the three equally performing metrics ED, WSM, and LSCD, referred to as SD (summed distance), correlated stronger with the RTI ($r=0.65$; $p<0.0001$, $n=36$) than any of these three metrics. While the differences between these correlations failed to reach statistical significance ($z=1.0$, 1.10 and 1.23, respectively, $p>0.05$, $n=36$), the differences between the correlations for SD and both of the metrics OSC and CGD were significant ($z=1.84$ and $z=1.97$, respectively, $p<0.05$, $n=36$).

3. Comparison between acoustical vowel spectra, electrical activation patterns, and VMPs

The ''internal'' auditory representations of the vowellike stimuli processed through the CIS processors, as measured in the VMP experiment, may have been affected by two potential sources of spectral interference: CI compression and NPIs. To separate and quantify the specific effects caused by CI compression and NPIs, electrical activation patterns (referred to as EAPs) of the stimuli were computed. The comparison between the acoustic vowel spectra (referred to as ASs) and the EAPs is supposed to show the effect of CI compression, and comparison between the EAPs and the VMPs should show the effect of NPIs. The ASs were derived from the CI vowels (as shown in Fig. 2), because we wanted to determine the combined effect of nonlinear amplitude mapping and channel-specific growth-of-loudness functions rather than the effect of filterbank processing. Nonlinear amplitude mapping consisted of logarithmic compression combined with dynamic range mapping according to the threshold and maximum comfort currents. Effects of across-channel differences in growth-of-loudness functions were intended to be separated from effects caused by NPIs. Consequently, the EAPs were normalized for channel-specific growth-of-loudness functions as was done for the VMPs. Comparison of ASs and EAPs therefore captures the combined effect of nonlinear dynamic range allocation and across-channel differences in growth-of-loudness.

EAPs were obtained as follows: First, the electrical pulse amplitude patterns, S_i (i refers to the electrode number), associated with the CI vowels were calculated by means of the software simulation which enables the calculation of the electrical current-levels corresponding to acoustic input (see Sec. II B), including the subject-specific fitting parameters and the amplitude compression function. EAPs were then calculated by subtracting the threshold levels T_i^{qu} from the electrode levels S_i and normalizing them for the channel-specific growth-of-loudness functions, as was done for the VMPs [Eq. (3)]. The EAP level at electrode i is given by

$$\mathrm{EAP}_i=(S_i-T_i^{qu})\frac{LB^{ref}-T^{ref}}{LB_i-T_i^{qu}}. \tag{11}$$

The left-hand panels in Figs. 5 and 6 show the EAPs of the vowels corresponding to the previously described VMPs plotted on the right side. The spectral peak positions in the ASs corresponding to each EAP are indicated by the designated symbols at the bottom of the EAP graphs. Visual inspection of EAPs and VMPs suggests a close similarity in the majority of cases, while comparison of ASs and EAPs reveals a larger blurring effect. These data indicate that differences between the VMPs and the vowel spectra (spectral alterations due to signal transmission) are primarily caused by CI compression, and, secondarily, by neural-population interactions.

For the following quantitative comparisons between the three spectral representations (AS, EAP, and VMP), the three combinations of the representations are referred to as AS-EAP, EAP-VMP, and AS-VMP.

The three spectral representations AS, EAP, and VMP were compared by means of the average pair-wise calculated spectral similarity distances. Figure 8 plots, for each of the distance metrics ED, WSM, and LSCD, the subject-specific mean distances for the three representations, AS, EAP, and VMP, normalized to yield a value of one for the ASs. The data points correspond to the mean metric distance for the vowels tested with each CI listener. For the purpose of comparison, the overall vowel identification scores of the CI listeners, scaled to the rightmost axis, are shown at the right side of the graph.

For all three metrics, ASs yielded the highest metric distances, whereas the VMPs tended to exhibit the smallest distances. On average, the difference between ASs and EAPs was larger and more uniform across the listeners than between EAPs and VMPs. In other words, CI compression caused a higher degree of blurring of the across-vowel differences than NPIs.

It was hypothesized that the difference in the mean metric distances between the conditions AS, EAP, and VMP can be used as a predictor for overall vowel recognition performance, i.e., the mean vowel identification score for all eight vowels. Testing of this hypothesis was motivated by the finding of a correlation ($r=0.82$, $p<0.012$, $n=7$) between the mean identification scores for the vowels selected for the

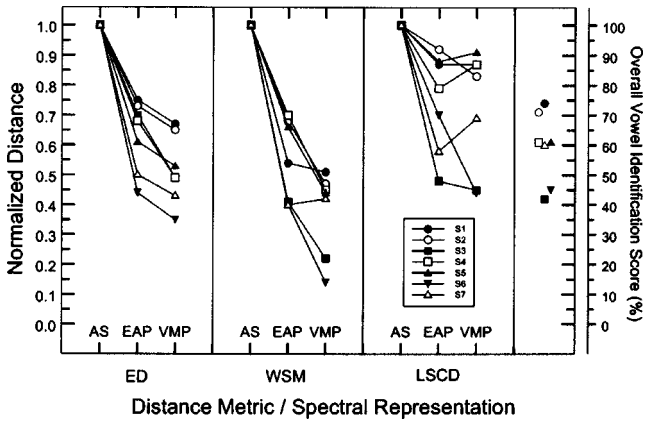

FIG. 8. Metric distances of the acoustical vowel spectra (ASs), the electrical activation patterns (EAPs), and the vowel masking patterns (VMPs), corresponding to each of the distance metrics ED, WSM, and LSCD (normalized to yield a value of 1 for the ASs). The data point represents the mean metric distances for the vowels tested for each CI listener. The overall vowel recognition scores are plotted at the right side, scaled to the rightmost axis.

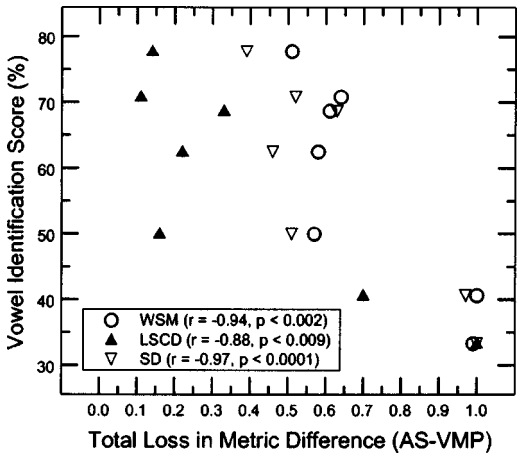

FIG. 9. Overall vowel identification scores of the CI listeners plotted as a function of the total burring effect, as given by the difference in metric distances between acoustic spectra and vowel masking patterns (AS-VMP). Higher values along the abscissa indicate a larger spectral blurring effect. Results for the metrics WSM, LSCD, and SD are denoted with circles, upward pointing triangles, and downward pointing triangles, respectively.

VMP measurements and for the entire set of vowels used in the identification experiment. A negative correlation between the metric difference AS-EAP and the overall vowel identification score would indicate the detrimental effect of CI compression. A negative correlation between the difference EAP-VMP and vowel identification would reflect a detrimental effect due to NPIs. Finally, the strength of the negative correlation between the metric difference AS-VMP and vowel identification would show to what degree the effects of CI compression and NPIs add up. For testing these assumptions, the metrics WSM, LSCD, and SD (the sum of ED, WSM, and LSCD) were used, which had been shown to best explain the confusion between the vowels used in the VMP experiment (see Sec. III C 2).

As expected, all correlations between overall vowel identification scores and the degree of spectral blurring, measured in terms of the differences AS-EAP, EAP-VMP, and AS-VMP, had negative signs. Regarding AS-EAP, both LSCD and SD correlated significantly ($r=-0.82$, $p<0.02$ and $r=-0.84$, $p<0.02$, respectively), while WSM correlated slightly below the level of significance ($r=-0.7$, $p<0.08$). Concerning EAP-VMP, both WSM and LSCD correlated below the significance level ($r=-0.61$, $p<0.14$ and $r=-0.68$, $p<0.09$, respectively) whereas SD correlated significantly ($r=-0.76$, $p<0.05$). For AS-VMP, WSM, LSCD, and SD correlated significantly ($r=-0.94$, $p<0.002$, $r=-0.88$, $p<0.009$, and $r=-0.97$, $p<0.0001$, respectively). Figure 9 plots, for each CI listener and the metrics WSM, LSCD, and SD, the overall vowel-identification scores as a function of the numerical difference AS-VMP, giving the total blurring effect (CI compression+NPIs).

The higher correlation between accuracy of vowel identification and the difference AS-VMP than AS-EAP or EAP-VMP indicates a summation of the blurring effects caused by CI compression and NPIs. On the whole, CI listeners exhibiting a stronger blurring effect (due to both CI compression and NPIs) have lower vowel identification scores.

IV. DISCUSSION

Using a vowel identification task to select vowel pairs with maximum and minimum RTI has been successfully applied to discriminate between the corresponding vowel masking patterns, as well as for evaluating the underlying spectral cues. CI users were able to identify steady-state vowellike signals—providing spectral cues only—with an average performance of 60%, ranging between 42% and 74%. The measurement of VMPs was straightforward; distinct VMP peaks coincided to a large extent with the peaks of the electrical activation patterns and showed a high spectral contrast. Several VMPs corresponding to vowel pairs with high RTI had identical spectral peak positions, differing only in local spectral details. The significant correlation ($r=0.6$, $p<0.0001$) between vowel identification and the spectral distance metric LSCD, which captures the underlying VMP feature, supports these conclusions.

The finding that VMP differences in the local spectral contrasts explain the vowel identification data about as well as spectral peak positions (WSM) differs from studies with either normal-hearing or hearing-impaired (non-implanted) listeners. While these studies support the ''formant-based approach'' rather than the ''whole-spectrum approach'' in vowel perception (Bladon and Lindblom, 1981, p. 1421), our results with CI listeners may be better described by a combination of these two approaches. A metric comprising the linear sum of the three equally performing metrics ED, WSM, and LSCD showed a higher correlation with the RTI than any of these three metrics. This may suggest that CI listeners combined different spectral cues to optimize vowel identification performance.

The relatively high importance of ''whole-spectrum'' aspects and, at the same time, relatively low importance of ''formant-based'' aspects in the CI listeners (as compared to literature data on normal hearing listeners) may result from the small number of frequency channels relative to that found in normal hearing. Filtering a signal into a small number of predefined frequency bands (compared to the large

number of auditory filters found in normal hearing) may be regarded as a transformation of ''formant-based'' spectral cues into ''whole-spectrum'' cues. As a consequence, the effect of the transformation increases when the number of filterbands is reduced (resulting in increased bandwidth for each filter). Lowering the number of channels raises the importance of level relations between different filters to estimate the frequency of spectral peaks. Therefore, one reason for the similar performance of the ''formant-based'' metric WSM and the ''whole-spectrum'' metrics ED and LSCD might be the small number of frequency channels available for CI users.

A factor possibly contributing to the relatively high importance of ''whole-spectrum'' aspects might be the amplitude compression function applied in the CI processor, which effectively expands changes in the input at low levels. This could increase the between-vowel differences at spectral valleys, where the components are lower in amplitude.

It is important to mention that the relatively high importance of whole-spectrum aspects could be specific to the closed-set of ''vowellike'' stimuli used in this study, where the available response categories were specified for the subjects. In everyday life, a vowel identification strategy focusing on the spectral peaks would be more efficient than a strategy giving equal weight to all components, since the information in-between the peaks would be masked in the presence of noise. On the other hand, the higher susceptibility to noise interference (i.e., the shallower psychometric function for speech recognition in noise) of CI listeners compared to NH listeners (e.g., Friesen *et al.*, 2001) might be an argument in favor of the higher importance of whole-spectrum aspects for vowel identification of CI listeners in general. This argument is based on the assumption that the shallower psychometric function of CI listeners is primarily due to the reduced availability of ''formant-based'' cues as a result of the smaller number of channels.

If our results are indeed generalizable to natural vowels (where additional identification cues such as duration, fundamental frequency and formant transitions are available), we may assume that peak-picking strategies [like *n-of-m* (Ziese *et al.*, 2000) or *SPEAK* (Skinner *et al.*, 1996)] might be counter-productive for patients receiving cochlear implants with a comparable number of channels and neural populations comparable to those of the implantees tested in this study. The omission of information in the spectral valleys might make it more difficult for the CI listeners to estimate the frequency of a spectral peak on the basis of comparison between the current levels at the electrodes in the vicinity of the peak. A counter-argument to this statement is that the omission of spectral valley information could improve vowel identification by the virtue of improved spectral contrast (peak-to-though ratio). Further research would be necessary to determine the contribution of each of these two opposed effects to the vowel recognition performance of CI users. One way to separate the two effects would be to test recognition performance with all combinations of the conditions with/without useful between-peak information and low/high degree of spectral contrast.

The overall effect of NPIs on the transmission of spectral information, quantified by comparing between-vowel differences of the electrical activation patterns and the vowel masking patterns, has been found to be relatively small for the tested CI listeners. A larger effect was found to arise from nonlinear dynamic range allocation in combination with across-channel differences in growth-of-loudness, referred to as CI compression. Obviously, the combined effect of logarithmic amplitude compression and across-channel differences in threshold and maximum comfort levels as well as growth-of-loudness functions introduces alterations of the spectral patterns, resulting in reduced between-vowel differences in the auditory representations. The alterations in spectral shape, as quantified by the between-vowel differences in spectral distance metrics (Fig. 8), appear to be primarily due to across-channel differences in the growth-of-loudness functions, which were more pronounced than the across-channel differences in the threshold and maximum comfort levels (Table II). Future studies may want to investigate whether this effect could be reduced by appropriate adjustment of amplitude compression functions as well as threshold and maximum comfort levels at each electrode, aiming to elicit homogeneous growth-of-loudness sensations across the electrode array.

It was observed that CI listeners, exhibiting a stronger spectral blurring effect due to CI processing and/or NPIs, show lower overall vowel identification scores. The highest correlation with vowel identification was found when the effects of both CI processing and NPIs were summed. This result underlines the potential usefulness of VMPs and the applied distance metrics to predict the transmission of spectral information in electrical stimulation.

The relatively small effect of neural-population interactions in the tested CI listeners, who all received implant electrodes in monopolar configuration, is a promising result given that some studies observed greater spread of excitation in monopolar compared to bipolar stimulation (Merzenich and White, 1977; van den Honert and Stypulkowski, 1987; Hartmann and Klinke, 1990). It would be of interest to obtain VMPs in bipolar configuration and to compare them with the VMPs measured in our study.

A. Summary

(1) CI listeners, supplied with the CIS strategy and monopolar electrode configuration, identified a closed set of eight loudness-balanced steady-state vowellike signals with a mean recognition score of 60% (SD: 12%).
(2) The vowel masking patterns reflected the confusion patterns among the vowels.
(3) The vowel masking patterns indicated equal relevance of ''whole-spectrum'' aspects and ''formant-based'' aspects in vowel identification in CI users.
(4) Both neural-population interactions and nonlinear amplitude mapping combined with across-channel differences in growth-of-loudness were shown to cause blurring of the characteristic spectral differences between the vowels. Nonlinear amplitude mapping combined with across-channel differences in growth-of-loudness had the larger effect.

(5) CI listeners exhibiting a stronger blurring effect, due to neural-population interactions and CI Compression, showed significantly lower overall vowel identification scores.

ACKNOWLEDGMENTS

We express our thanks and appreciation to the patients who gave us their time, effort, and patience. We would like to thank Dr. Steve Greenberg, the Associate Editor Dr. Peter Assmann, Dr. Quentin Summerfield, and an anonymous reviewer for their valuable contributions for improving the contents of the original manuscript. This research was funded by the Austrian Academy of Sciences.

ABBREVIATIONS

AS acoustical vowel spectrum
CGD center of gravity difference
CI cochlear implant
CI compression
nonlinear amplitude mapping in CI processor combined with channel-specific growth of loudness
CI processor
cochlear implant processor
CI vowel
vowellike signal used for cochlear implant listeners
CIS "continuous interleaved sampling" (-stimulation strategy)
EAP electrical activation pattern
ED Euclidean distance
FMP forward masking pattern
LSCD local spectral contrast difference
NH normal-hearing
NH vowel
vowellike signal used for normal hearing listeners
NPI neural-population interaction
OSCD overall spectral contrast difference
SD summed distance; sum of metrics ED, WSM, and LSCD
VMP vowel masking pattern
WSM weighted slope metric

[1]ST^X is a windows-based software system for acoustics, speech and signal processing, developed at the Acoustics Research Institute of the Austrian Academy of Sciences.

[2]The value c=500 was chosen on an empirical basis, representing a trade-off between making audible as many spectral components of the vowels as possible and preserving as much spectral contrast as possible. We decided to apply one common compression coefficient for all implantees, in order to be able to directly compare the experimental results across the individuals. The last column of Table I shows that the chosen compression constant of $c=500$ corresponded to the "clinical" fittings of CI listeners S2, S5, S6, and S7. In a pilot test with CI listener S1, we found that lowering the compression constant from 1024 to 500 produced a slight increase of 3% in the overall vowel identification score. It was assumed that lowering the compression constant had a similar effect in CI listeners S1, S3, and S4.

[3]A possible explanation for the increased reproducibility with probe tone jitter could be that in the condition without jitter, listeners might have difficulties, in particular in movements with decreasing amplitude, in distinguishing between actually hearing the probe and perceiving some kind of internal "persistence" of the probe (the listener expects to hear the probe at a certain temporal position and therefore believes to hear it although it is below the threshold). In case of temporal jitter, however, such a "persistence" effect may be less likely to occur since the temporal position of the probe is unpredictable and thus the listener cannot expect to hear the probe at a specific temporal position.

Assmann, P. F., and Summerfield, Q. (**1989**). "Modeling the perception of concurrent vowels: vowels with the same fundamental frequency," J. Acoust. Soc. Am. **85**, 327–338.

Bladon, R. A., and Lindblom, B. (**1981**). "Modeling the judgment of vowel quality differences," J. Acoust. Soc. Am. **69**, 1414–1422.

Brill, S. M., Gstoettner, W., Helms, J., von Ilberg, C., Baumgartner, W., Mueller, J., and Kiefer, J. (**1997**). "Optimization of channel number and stimulation rate for the fast continuous interleaved sampling strategy in the COMBI 40+," Am. J. Otol. **18**, 104–106.

Cazals, Y., Pelizzone, M., Kasper, A., and Montandon, P. (**1990**). "Multichannel cochlear implant patients with different open speech understanding show some similar basic psychophysical results," Acta Oto-Laryngol., Suppl. **469**, 150–155.

Chatterjee, M., and Shannon, R. V. (**1998**). "Forward masked excitation patterns in multielectrode electrical stimulation," J. Acoust. Soc. Am. **103**, 2565–2572.

Chistovich, L. A. (**1985**). "Central auditory processing of peripheral vowel spectra," J. Acoust. Soc. Am. **77**, 789–805.

Cohen, L. T., and Clark, G. M. (**1996**). "Cochlear implant place psychophysics. 2. Comparison of forward masking and pitch estimation data," Audiol. Neuro-Otol. **1**, 278–292.

Dorman, M. F. (**1993**). "Psychophysics," in *Cochlear Implants: Audiological Foundations*, edited by R. S. Tyler (Singular, San Diego).

Dorman, M. F., and Loizou, P. C. (**1997a**). "Speech intelligibility as a function of the number of channels of stimulation for normal-hearing listeners and patients with cochlear implants," Am. J. Otol. **18**, 113–114.

Dorman, M. F., and Loizou, P. C. (**1997b**). "Speech intelligibility as a function of the number of channels of stimulation for signal processors using sine-wave and noise-band outputs," J. Acoust. Soc. Am. **102**, 2403–2411.

Fishman, K. E., Shannon, R. V., and Slattery, W. H. (**1997**). "Speech recognition as a function of the number of electrodes used in the SPEAK cochlear implant speech processor," J. Speech Lang. Hear. Res. **40**, 1201–1215.

Friesen, L. M., Shannon, R. V., Baskent, D., and Wang, X. (**2001**). "Speech recognition in noise as a function of the number of spectral channels: comparison of acoustic hearing and cochlear implants," J. Acoust. Soc. Am. **110**, 1150–1163.

Fu, Q. J., Shannon, R. V., and Wang, X. (**1998**). "Effects of noise and spectral resolution on vowel and consonant recognition: acoustic and electric hearing," J. Acoust. Soc. Am. **104**, 3586–3596.

Garnham, C., O'Driscoll, M., Ramsden, R., and Saeed, S. (**2002**). "Speech understanding in noise with a Med-El COMBI 40+ cochlear implant using reduced channel sets," Ear Hear. **23**, 540–552.

Hartmann, R., and Klinke, R. (**1990**). "Impulse patterns of auditory nerve fibres to extra- and intracochlear electrical stimulation," Acta Oto-Laryngol., Suppl. **469**, 128–134.

Klatt, D. H. (**1982**). "Prediction of perceived phonetic distance from critical-band spectra: A first step," Proc. IEEE Int. Conf. Speech Acoust. Signal Process. **129**, 1278–1281.

Laback, B., Deutsch, W. A., Baumgartner, W. D., and Hamzavi, J. S. (**2001**). "Vowel identification and vowel masking patterns in multi-electrode electrical stimulation," presented at the Conference on Implantable Auditory Prostheses, Asilomar.

Lim, H. H., Tong, Y. C., and Clark, G. M. (**1989**). "Forward masking patterns produced by intracochlear electrical stimulation of one and two electrode pairs in the human cochlea," J. Acoust. Soc. Am. **86**, 971–980.

Merzenich, M., and White, M. (**1977**). "Cochlear implant—the interface problem," in *Functional Electrical Stimulation: Applications in Neural Prostheses*, edited by F. Hambrecht and J. Reswick (Marcel Dekker, New York), pp. 321–340.

Meng, X. L., Rosenthal, R., and Rubin, D. B. (**1992**). "Comparing correlated correlation coefficients," Psychol. Bull. **111**, 172–175.

Miller, G., and Nicely, P. (**1955**). "An analysis of perceptual confusions among some English consonants," J. Acoust. Soc. Am. **27**, 338–352.

Moore, B. C., and Glasberg, B. R. (**1982**). "Masking patterns for synthetic vowels in simultaneous and forward masking," J. Acoust. Soc. Am. **73**, 906–917.

Nocerino, N., Soong, F. K., Rabiner, L. R., and Klatt, D. H. (**1985**). "Comparative study of several distortion measures for speech recognition," Speech Commun. **4**, 317–331.

Plomp, R. (**1970**). ''Timbre as a multidimensional attribute of complex tones,'' in *Frequency Analysis and Periodicity Detection in Hearing*, edited by R. Plomp and G. F. Smoorenburg (Sijthoff, Leiden), pp. 397–410.
Plomp, R. (**1975**). ''Auditory analysis and timbre perception,'' in *Auditory Analysis and Perception of Speech*, edited by G. Fant and M. A. A. Tatham (Academic, London), pp. 7–12.
Shannon, R. V. (**1983**). ''Multichannel electrical stimulation of the auditory nerve in man. II. Channel interaction,'' Hear. Res. **12**, 1–16.
Shannon, R. V. (**1990**). ''Forward masking in patients with cochlear implants,'' J. Acoust. Soc. Am. **88**, 741–744.
Shannon, R. V. (**1993**). ''Psychophysics,'' in *Cochlear Implants: Audiological Foundations*, edited by R. S. Tyler (Singular, San Diego).
Shannon, R. V., Zeng, F. G., Kamath, V., Wygonski, J., and Ekelid, M. (**1995**). ''Speech recognition with primarily temporal cues,'' Science **270**, 303–304.
Sidwell, A., and Summerfield, Q. (**1985**). ''The effect of enhanced spectral contrast on the internal representation of vowel-shaped noise,'' J. Acoust. Soc. Am. **78**, 495–506.
Skinner, M. W., Fourakis, M. S., Holden, T. A., Holden, L. K., and Demorest, M. E. (**1996**). ''Identification of speech by cochlear implant recipients with the Multipeak (MPEAK) and Spectral Peak (SPEAK) speech coding strategies. I. Vowels,'' Ear Hear. **17**, 182–197.
Throckmorton, C. S., and Collins, L. M. (**1999**). ''Investigation of the effects of temporal and spatial interactions on speech-recognition skills in cochlear-implant subjects,'' J. Acoust. Soc. Am. **105**, 861–873.
Throckmorton, C. S., and Collins, L. M. (**2002**). ''The effect of channel interactions on speech recognition in cochlear implant subjects: predictions from an acoustic model,'' J. Acoust. Soc. Am. **112**, 285–296.
Tong, Y. C., and Clark, G. M. (**1986**). ''Loudness summation, masking, and temporal interaction for sensations produced by electric stimulation of two sites in the human cochlea,'' J. Acoust. Soc. Am. **79**, 1958–1966.
Turner, C. W., and Henn, C. C. (**1989**). ''The relation between vowel recognition and measures of frequency resolution,'' J. Speech Hear. Res. **32**, 49–58.
van den Honert, C., and Stypulkowski, P. H. (**1987**). ''Single fiber mapping of spatial excitation patterns in the electrically stimulated auditory nerve,'' Hear. Res. **29**, 195–206.
van Tasell, D. J., Fabry, D. A., and Thibodeau, L. M. (**1987**). ''Vowel identification and vowel masking patterns of hearing-impaired subjects,'' J. Acoust. Soc. Am. **81**, 1586–1597.
Wilson, B. S., Finley, C. C., Lawson, D. T., Wolford, R. D., Eddington, D. K., and Rabinowitz, W. M. (**1991**). ''Better speech recognition with cochlear implants,'' Nature (London) **352**, 236–238.
Zierhofer, C., Hochmair, I., and Hochmair, E. (**1995**). ''Electronic design of a cochlear implant for multichannel high-rate pulsatile stimulation strategies,'' IEEE Trans. Rehabil. Eng. **3**, 112–116.
Zierhofer, C., Hochmair, I. J., and Hochmair, E. S. (**1997**). ''The advanced COMBI 40+ Cochlear Implant,'' J. Speech Lang. Hear. Res. **18**, 537–538.
Ziese, M., Stutzel, A., von Specht, H., Begall, K., Freigang, B., Sroka, S., and Nopp, P. (**2000**). ''Speech understanding with the CIS and the n-of-m strategy in the MED-EL COMBI 40+ system,'' ORL J. Otorhinolaryngol. Relat. Spec. **62**, 321–329.

Vowel formant discrimination for high-fidelity speech[a)]

Chang Liu[b)] and Diane Kewley-Port[c)]
Department of Speech and Hearing Sciences, Indiana University, Bloomington, Indiana 47405

(Received 30 August 2002; accepted for publication 17 May 2004)

The goal of this study was to establish the ability of normal-hearing listeners to discriminate formant frequency in vowels in everyday speech. Vowel formant discrimination in syllables, phrases, and sentences was measured for high-fidelity (nearly natural) speech synthesized by STRAIGHT [Kawahara *et al.*, Speech Commun. **27**, 187–207 (1999)]. Thresholds were measured for changes in F1 and F2 for the vowels /ɪ, ɛ, æ, ʌ/ in /bVd/ syllables. Experimental factors manipulated included phonetic context (syllables, phrases, and sentences), sentence discrimination with the addition of an identification task, and word position. Results showed that neither longer phonetic context nor the addition of the identification task significantly affected thresholds, while thresholds for word final position showed significantly better performance than for either initial or middle position in sentences. Results suggest that an average of 0.37 barks is required for normal-hearing listeners to discriminate vowel formants in modest length sentences, elevated by 84% compared to isolated vowels. Vowel formant discrimination in several phonetic contexts was slightly elevated for STRAIGHT-synthesized speech compared to formant-synthesized speech stimuli reported in the study by Kewley-Port and Zheng [J. Acoust. Soc. Am. **106**, 2945–2958 (1999)]. These elevated thresholds appeared related to greater spectral-temporal variability for high-fidelity speech produced by STRAIGHT than for formant-synthesized speech.
[DOI: 10.1121/1.1768958]

PACS numbers: 43.72.Ja, 43.71.Es, 43.66.Fe [PFA] Pages: 1224–1233

I. INTRODUCTION

Vowel formant frequency discrimination for normal-hearing listeners has been established for synthetic speech under a variety of listening conditions in several recent studies (Hawks, 1994; Kewley-Port and Watson, 1994; Kewley-Port, 1996; Kewley-Port and Zheng, 1999). Thresholds for formant frequency discrimination, ΔF, are defined as the smallest change in formant frequency that can be detected. Kewley-Port and her colleagues have investigated formant discrimination for a decade, starting with the optimal listening conditions, in which highly trained subjects discriminated vowels with formant shifts from standard vowels in quiet with minimal stimulus uncertainty. Optimal listening conditions for vowel formant discrimination (Kewley-Port and Watson, 1994; Kewley-Port, 1996) provide an important baseline for isolated vowels. A piecewise-linear function of formant frequency provides a good fit to the thresholds for different talkers, revealing that ΔF is constant at 14 Hz in the F1 range, and then rises linearly such that formant discrimination conforms to Weber's law with $\Delta F/F$ at 1.5% in the F2 range.

Clearly, vowel discrimination tasks in more ordinary listening conditions, in which vowels are embedded in sentences and may be presented in noise, are much more complex than listening under optimal conditions. Under these conditions, in which participants listened to synthetic vowels in longer phonetic contexts such as syllables, phrases, and sentences, and under medium or high stimulus uncertainty, thresholds for formant frequency discrimination were elevated. Studies by Kewley-Port (1992; 1996; 2001) and Kewley-Port and Zheng (1999) have shown that there are at least two factors that significantly influence formant frequency resolution: level of stimulus uncertainty and length of phonetic context. Increasing the level of stimulus uncertainty and/or length of phonetic context degrades performance. Kewley-Port and Zheng (1999) found thresholds for ordinary listening conditions were 2.6 times higher than for optimal listening conditions. While thresholds were significantly poorer for syllables than for isolated vowels, thresholds for phrases did not significantly differ from thresholds for sentences. Effects of linguistic complexity on formant discrimination were investigated by measuring the thresholds using sentences with an additional identification task. Results suggested that there were no significant effects of identification task on formant discrimination for synthetic vowels.

Previous studies (Flanagan, 1955; Hawks, 1994; Kewley-Port and Watson, 1994; Sinnott and Kreiter, 1991) have investigated vowel formant frequency discrimination using formant synthesis (Klatt, 1980). In contrast, the present study, using the STRAIGHT resynthesis algorithms (Kawahara *et al.*, 1999), measured vowel discrimination for very natural sounding speech. A number of studies have shown that intelligibility and comprehension of synthetic speech is different from that of natural speech (Greene, 1986; Logan, Greene, and Pisoni, 1989; Pisoni, 1997; Pisoni, Manous, and Dedina, 1987; Ralston, *et al.*, 1991). Logan *et al.* (1989) examined the intelligibility of consonant–vowel–consonant (CVC)

[a)]Portions of the data were presented at the 140th meeting of the Acoustical Society of America [J. Acoust. Soc. Am. **108**, 2601].

[b)]Author to whom correspondence should be addressed at: Rm. 122, Cary Hall, Dept. of Communicative Disorders and Sciences, 3435 Main St., University at Buffalo, Buffalo, NY, 14214; electronic mail: cliu5@buffalo.edu
[c)]Electronic-mail: kewley@indiana.edu

monosyllabic English words in the modified rhyme test (MRT) for natural and synthetic speech and found that intelligibility was higher for natural speech (better than 99%) than for any of the 10 text-to-speech synthesis systems (ranging from 63% to 96%), including MITALK-79, DECTALK 1.8, and PROSE 2000 that used the formant synthesizer designed by Klatt (1980). Better intelligibility for natural speech than for synthetic speech was also observed for non-native speakers of English with isolated words, sentences, and short prose passages (Greene, 1986). A sentence-verification study by Pisoni *et al.* (1987) indicated that listeners responded consistently more quickly to natural speech than to synthetic speech, showing that synthetic speech was not perceived in the same way as natural speech, even though the sentences were highly intelligible. Ralston *et al.* (1991) investigated comprehension of synthetic and natural speech using a word-monitoring task. For both fourth-grade and college student subjects, word-monitoring response latencies were shorter for natural speech. Hillenbrand and Nearey (1999) examined the identification scores of natural and two types of resynthesized /hVd/ utterances (original formant and flat formant) using twelve American English vowels. Identification scores were higher for natural tokens (95.4%) than for resynthesized tokens with formant contours matched closely to the original (88.5%), suggesting that, even with essential acoustic information (formant frequencies and transitions) preserved, the resynthesized signal was less identifiable than natural speech. Overall, these studies indicate that subjects performed better when listening to natural speech than to synthetic speech. The difficulty in processing synthetic speech may be due to the lack of the additional redundancy and acoustic-phonetic variability found in natural speech (Pisoni, 1997).

The speech stimuli in the present study were produced by a new method for speech resynthesis, STRAIGHT (Kawahara *et al.*, 1999). Syllables, phrases, and sentences resynthesized from a female talker were essentially indistinguishable from the original in informal listening tasks. These natural-sounding speech tokens, termed high-fidelity speech in this paper, are perceived as more natural than our previous formant-synthesized speech, traditionally termed synthetic speech, albeit carefully crafted, using the KLTSYN synthesizer (Klatt, 1980).

In part, this study is a replication and extension of the study of Kewley-Port and Zheng (1999), who examined the effects of longer phonetic context and linguistic complexity on vowel formant discrimination using formant-synthesized speech. The primary stimuli in the present study were four vowels resynthesized by STRAIGHT (Kawahara *et al.*, 1999), with or without a formant shift, in syllables and a variety of phrases and sentences. In order to compare results from high-fidelity and synthetic speech, this experiment was designed to be similar to that of Kewley-Port and Zheng (1999) in the following ways: (1) the test vowels were embedded in a /bVd/ syllable; (2) performance was measured using adaptive tracking of formant thresholds for well-trained listeners in quiet; (3) phonetic context was manipulated from syllables to sentences; and (4) linguistic complexity was manipulated using different sentence materials and with the addition of an identification task. The present study extends the study of Kewley-Port and Zheng (1999) in several important ways to more closely reflect vowel processing in natural sentences. In Kewley-Port and Zheng (1999), the carrier sentences had low linguistic complexity with only one target position in the sentence. The level of linguistic complexity was increased in this experiment by creating more carrier sentences that were unique but with similar meanings (see Table I), and by presenting the target word at different positions such that the sentence identification task became more challenging.

TABLE I. Phrases and sentences used in the experiment of vowel formant discrimination.

Three phrases used for phonetic context of phrases:
/*bVd*/ is here.
Use /*bVd*/ again.
We used /*bVd*/.
Three sentences used for phonetic context of sentences:
The /*bVd*/ word is first on the page now.
The first word is /*bVd*/ on the page again.
The first word on the book is /*bVd*/ now.

Models of vowel formant discrimination need to take into account both peripheral and central factors. In our studies with formant-synthesized speech (Kewley-Port and Zheng, 1998), vowel formant discrimination was based on differences in the internal representations between the standard and the altered vowel, e.g., the differences between excitation patterns on the basilar membrane. On the other hand, Kewley-Port and Zheng (1999) demonstrated that formant discrimination was influenced by more central processes associated with longer phonetic context or higher levels of stimulus uncertainty, which requires more cognitive loading. The addition of an identification task did not have significant effects on formant discrimination, suggesting that formant discrimination was independent of word and sentence identification (Kewley-Port and Zheng, 1999). However, as mentioned earlier, the linguistic complexity was low in that study. Therefore this study was designed to extend those findings to high-fidelity speech in sentences with higher linguistic complexity by using more carrier sentences.

An added condition was to embed the test syllable in either the initial, middle, or final portion of the text. Many studies have shown that there are significant effects of the target stimulus position in sequences on auditory discrimination and identification tasks. Specifically, a target in the final position is the easiest, while targets in the middle positions are the hardest, to identify and discriminate (Watson *et al.*, 1975; McFarland and Cacace, 1992; Neath and Knoedler, 1994; Surprenant, 2001). These serial position effects in discrimination and identification are described as primacy and recency effect, observed in the complex tonal pattern recognition (Watson *et al.*, 1975; Surprenant, 2001) as well as in the sentence processing (Neath and Knoedler, 1994). The secondary goal of this study, therefore, was to investigate whether there would be serial position effects on vowel formant discrimination in phrases and sentences.

Previous research on sound discrimination suggested that a higher level of stimulus uncertainty, referring to the

level of the unpredictability of the target stimulus and stimulus position, significantly degraded discrimination of complex tonal patterns (Watson, 1987) and analogous vowel sequences (Kewley-Port *et al.*, 1986). In the present study, the level of stimulus uncertainty was selected to correspond to the level of word uncertainty occurring in modest-length sentences in normal conversation. Following the terminology in Watson's research (Watson, 1987), Kewley-Port (2001) categorized the level of stimulus uncertainty into four groups: low, medium, high, and very high, and suggested that thresholds were not significantly different for medium levels of stimulus uncertainty ranging from 8 to 22 stimuli per block. A medium level of stimulus uncertainty with eight to twelve stimuli per block was used in this study.

Summarizing, the goal of this study was to measure formant discrimination in high-fidelity speech stimuli in a laboratory task that simulated some of the factors associated with ordinary discourse, including different lengths of phonetic context, different sentence positions, and the addition of word/sentence identification to the formant discrimination task.

II. METHOD

A. Stimuli

Four American English vowels /ɪ, ɛ, æ, ʌ/ were used. These covered a wide range of formant frequencies from the lowest F1 to the highest F2 over the English vowel space. Forty nine-word sentences and nine three-word phrases with each of the four vowels at each of three positions (positions two, five, and eight in sentences) were recorded from a female talker to digital tape (DAT). Recordings were then digitized with a sampling frequency of 11 025 Hz and low-pass filter of 5500 Hz to sound files in a computer. The experimenters listened to the recordings, and three phrases and three sentences (Table I) with similar prosodic patterns were selected. Although each of the four syllables (/bVd/) occurred in the initial, middle, and final positions of the recorded sentences, only one syllable per vowel with a statement prosody from the same carrier sentence was selected as an original stimulus for future resynthesis of vowels. These original syllables (/bVd/) were selected from the eighth position of the nine-word sentence.

STRAIGHT, a method for speech resynthesis developed in MATLAB by Kawahara *et al.* (1999), was used to resynthesize syllables, phrases, and sentences from the recorded talker. In order to study formant discrimination, the STRAIGHT algorithms were modified to alter a selected formant by a percent increase in its formant frequency. The resynthesized /bVd/ syllables without any formant shift sounded the same as the original /bVd/ and these were selected as the standard stimuli in discrimination trials. All test stimuli with formant shifts were resynthesized from these standard stimuli. Formants were manipulated in our modified STRAIGHT algorithm as follows: a matrix, representing the two-dimensional spectrogram (amplitude×time ×frequency) of the standard (natural) /bVd/ stimulus, was obtained by the analysis in STRAIGHT. This spectrogram usually had multiple smooth peaks and troughs within each formant frequency range as shown in Fig. 1 for one time frame of the /ɛ/ vowel, with and without a shift in F2. This is different from typical LPC analysis, in which each peak corresponds to one formant. To shift a formant peak, the temporal location of the formant in the syllable, including transitions, was visually identified. Then the frequency ranges of the first three formants, F1, F2, and F3, were determined visually. Subsequently the highest peak in each formant frequency range and the lowest trough between the adjacent formants were determined by algorithm as the frequency values of the formant and valley, respectively. In each time frame (i.e., one spectrum), the portion between the valleys on either side of the formant peak was selected for formant shift.[1] In order to shift the selected formant frequency without any change in other formants, amplitude in the low-frequency valley was adjusted to be a constant across the frequency range corresponding to the frequency shift, while the high-frequency valley was collapsed by replacing the original amplitude values with the shifted peak, as shown in Fig. 1. This procedure preserves details in the formant peaks, leaving the valleys only somewhat changed. This modified two-dimensional matrix was reloaded into STRAIGHT and used with other unchanged acoustic parameters such as F0 and amplitude contours for resynthesis. Thus, the test vowels for formant discrimination were resynthesized in sets of 14 using modified STRAIGHT. F1 and F2 for each standard syllable was shifted systematically by 14 steps using a linear scale. The range of formant frequency shifts was from 0.9% to 10% for all the formants except the F1 of /bɪd/, which ranged from 2% to 15%. Because formant thresholds in Kewley-Port and Watson (1994) for F1 of /bɪd/ approached the upper limit of formant shift, which was 10% in their study, the maximum formant shift was extended to 15% for F1 for /bɪd/ in the present study. The step size for each formant shift was 0.7% for all the formants except 1% for F1 of /bɪd/.

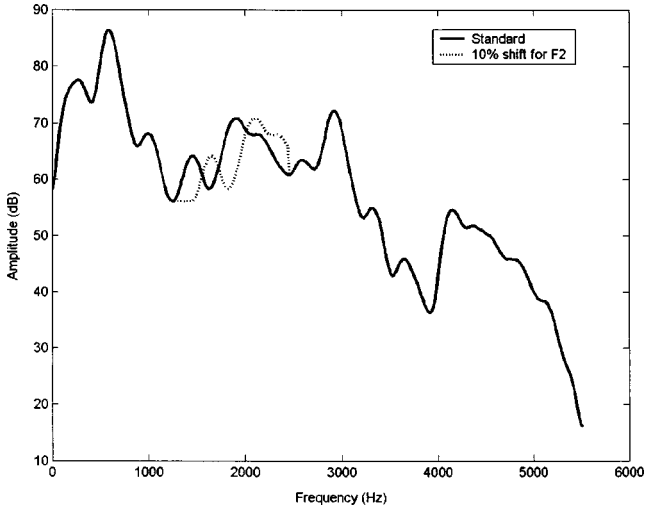

FIG. 1. Spectra using STRAIGHT analysis from the middle analysis frame for standard /ɛ/ vowel and /ɛ/ vowel with 10% shift for F2. Note that the spectra using STRAIGHT do not provide the harmonic fine structure and properties of the source, which are stored in other parameters in STRAIGHT.

To validate whether formants manipulated in STRAIGHT would yield similar perceptual thresholds to formants ma-

TABLE II. Formant frequencies, thresholds, and standard deviation of ΔF (Hz) for eight formants in three phonetic contexts: syllable, phrase and sentence, and sentence discrimination with identification.

	ɪ-F1		ɛ-F1		æ-F1		ʌ-F1		ʌ-F2		ɛ-F2		æ-F2		ɪ-F2	
Formant frequency	430		581		678		700		1454		1960		2078		2132	
	M	s.d.	M	s.d.	M	s.d.	M	s.d.	M	s.d.	M	s.d.	M	s.d.	M	s.d.
Syllable	49.2	5.9	34.7	6.3	36.3	20.0	34.4	15.6	56.8	48.8	74.2	21.3	88.3	51.5	115.1	55.9
Phrase	36.0	18.8	37.2	15.5	43.6	11.8	39.5	10.6	86.8	35.4	116.5	55.5	96.4	58.9	123.0	48.5
Sentence	48.2	12.5	36.3	16.6	47.1	10.0	48.6	12.0	103.4	38.5	83.5	59.6	106.2	57.3	120.0	58.6
Sentence+ID	41.9	11.6	37.6	16.7	50.1	11.1	47.4	8.9	97.5	43.0	104.0	61.9	110.5	60.9	123.0	60.0

nipulated more directly controlled by formant resonance synthesis, thresholds for formant discrimination were compared for the vowel /ɛ/ using STRAIGHT synthesis and KLTSYN formant synthesis (Klatt, 1980) in an earlier study (Liu and Kewley-Port, 2004). Results showed no significant difference between thresholds for the two synthesized vowels. The two synthesis methods also showed similar ranges and variability for thresholds across subjects, e.g., the lowest threshold was 8.5 Hz and highest was 36.5 Hz for F1 of the STRAIGHT-synthesized /ɛ/ vowel with a standard deviation of 12.3 Hz for four listeners (Liu and Kewley-Port, 2004), while thresholds for five listeners in Kewley-Port (2001) ranged from 8.5 to 30.8 Hz with a standard deviation of 9.1 Hz. Thus, our modified STRAIGHT method appears to provide a reliable way to manipulate vowel formant shifts in high-fidelity speech.

The standard and test syllables were inserted into the phrases and sentences using a digital wave form editor. Essentially, the original syllable was replaced by the resynthesized syllable. In some cases, small duration adjustments in the closures of the /b/ or /d/ consonants were necessary to make the phrase or sentence prosody sound natural. The resynthesized three-word phrases and nine-word sentences, with no parameters changed in STRAIGHT, sounded very natural and indistinguishable to the original natural ones, indicating that high fidelity was achieved in the resynthesized speech.

B. Listeners

Four young adult listeners between 23 and 34 years old were paid for their participation in the present study. They had pure-tone thresholds of 15 dB HL or better at octave intervals from 250 through 8000 Hz.

C. Procedure

Stimuli were presented to the right ears of listeners, who were seated in a sound-treated IAC booth, via TDH-39 earphones. Stimulus presentation was controlled by TDT modules including a 16 bit D/A converter, a programmable filter, and a headphone buffer. A low-pass filter with a cutoff frequency of 5000 Hz and a slope of 80 dB/octave, and an attenuation level set by the calibration procedure, was configured in the programmable filter. The standard vowel /ɛ/ with a duration of 3 s was used for calibration. The sound-pressure level measured in an NBS-9A 6-c^3 coupler by a Larson-Davis sound-level meter (model 2800) using the linear setting was adjusted to be 70 dB SPL. The sound-pressure level of the other standard syllables was also set to 70 dB SPL.

Formant discrimination for the two formants (F1 and F2) of each vowel was measured under medium stimulus uncertainty. For syllables, there were eight possibilities in each block, i.e., two formants from each of four vowels. A two-down, one-up tracking algorithm was used to estimate the 71% correct point on the psychometric function, ΔF (Levitt, 1971). For phrases and sentences, twenty-four possibilities, i.e., two formants for the four vowels in three positions, were randomly assigned to two groups, resulting in twelve possibilities for each block. For phrases and sentences, following presentation of the standard syllable alone in the first interval, the carrier phrases or sentences were played twice in the next two intervals, one with the standard syllable and one with the test syllable. The listener's task was to indicate which interval contained the test syllable, different from the standard. When the identification task was added to the discrimination task, the procedure was somewhat altered. Subjects first needed to respond on paper to indicate which of the four syllables they heard as well as which of the three sentence types they heard. After the identification response, subjects completed the discrimination response.

Each daily session lasted 1.5–2 h (depending on a listener's response latency) with 96 trials in each block and included the syllable, phrase, and sentence tasks, and the sentence task with the addition of the identification task. Two blocks of each task were presented in a sequence randomized daily for each listener. After extensive training (approximately 5000 trials), ΔF for each listener was averaged from the mean reversals over the last four blocks in which performance was judged as stable by visual inspection.

III. RESULTS

A. Formant frequency, length of phonetic contexts, and sentence position

Averages and standard deviations of the ΔF values across subjects are shown in Table II and Fig. 2. The formant frequency and thresholds expressed as ΔF in Hz were transformed to an auditory scale, i.e., barks and delta barks (ΔZ) (Traunmuller, 1990). The bark scale (Zwicker, 1961) was selected on the basis of analyses reported in Kewley-Port and Zheng (1999). They suggested that a transformation of ΔF to ΔZ, showing a roughly constant value to represent the perceptual shift across all the formant frequencies, provided the

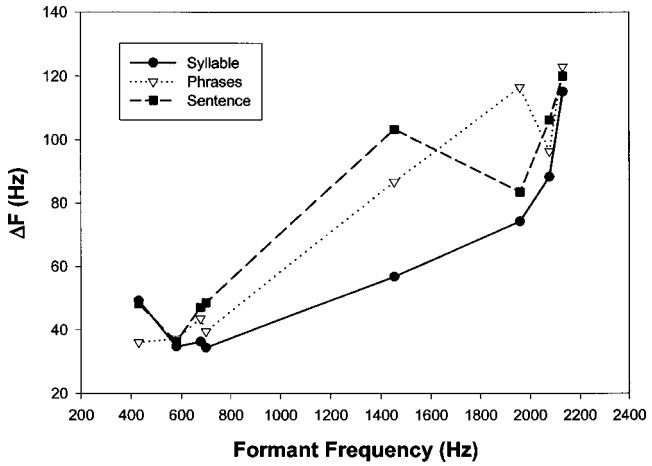

FIG. 2. Thresholds for discrimination of F1 and F2 in Hz as a function of formant frequency for three phonetic contexts: syllable (solid line), phrase (dotted line), and sentence (dashed line).

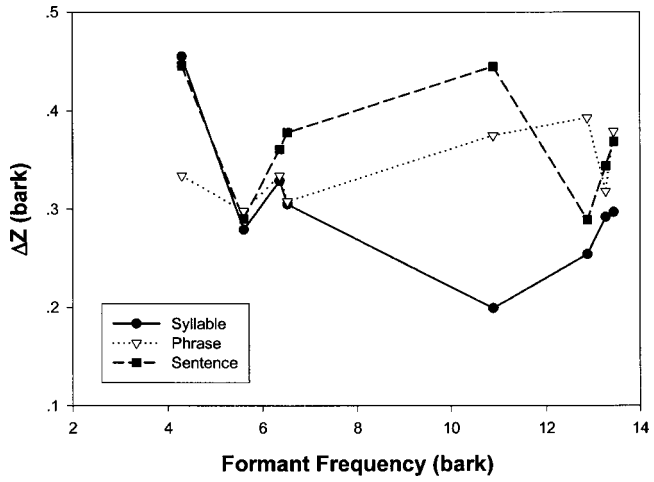

FIG. 4. Thresholds for discrimination of F1 and F2 in barks as a function of formant frequency for three phonetic contexts: syllable (solid line), phrase (dotted line), and sentence (dashed line).

best match to loudness pattern modeling of formant discrimination data.[2] Statistical analyses were done on both ΔF and ΔZ.

Overall, ΔF thresholds increased with increasing formant frequency and increasing complexity of phonetic context (Fig. 2). A two-factor (formant frequency $\times$phonetic context) repeated-measure analysis of variance (ANOVA) with ΔF as the dependent variable showed that formant frequency had a significant effect on ΔF ($F(7,21) = 8.023, p < 0.001$). Phonetic context did not have a significant effect on ΔF ($F(2,6) = 1.578, p = 0.281$) as shown more clearly in Fig. 3. This nonsignificant result was unexpected based on the results of Kewley-Port and Zheng (1999) and appears to be due to higher listener variability with this high-fidelity speech task. To make specific comparisons between the thresholds at different levels of phonetic context, planned comparison were calculated. There were no significant differences between thresholds for any two phonetic contexts ($p = 0.217$ between syllables and sentences; $p = 0.153$ between syllables and sentences; $p = 0.843$ between phrases and sentences).

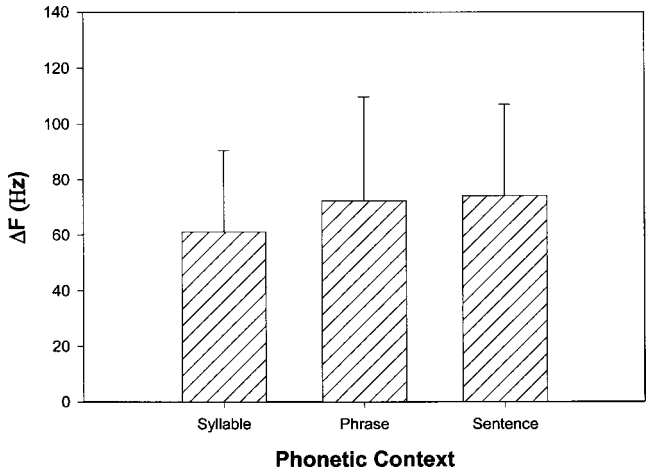

FIG. 3. Thresholds for discrimination of F1 and F2 in Hz as a function of the phonetic context: syllable, phrase, and sentence, averaged across formants. Error bars show standard deviations for each condition.

The planned comparisons of thresholds between F1 and F2 showed that ΔF for F2 was significantly higher than ΔF for F1 ($F(1,3) = 9.667, p = 0.05$) averaged over the three phonetic contexts. Thresholds for the four vowels as a function of formant frequency suggested different patterns between F1 and F2. For all three phonetic contexts, ΔF thresholds were rather similar over the F1 range with ΔF averaging about 40.1 Hz. However ΔF increased over the F2 range, corresponding to Weber's law with $\Delta F/F$ about 5.2% (averaged over phonetic context). These data can be compared to those of Kewley-Port and Watson (1994), who reported that formant thresholds for isolated vowels under optimal listening conditions were best fitted by a piecewise-linear function. The average of the three data sets in Fig. 2 for vowels in longer phonetic context were fitted separately for F1 and F2 with linear functions. Similar to the isolated vowels, the best fitting function had a slope of zero in the F1 range. However the average ΔF for F1 was almost 300% higher than for formant-synthesized isolated vowels, presumably due to a higher level of stimulus uncertainty, the longer phonetic context, and stimulus factors related to variability in these more natural speech stimuli. The slope of the F2 linear function, about 52 Hz per 1000 Hz change in F2, was higher than that for synthetic isolated vowels, 10 Hz per 1000 Hz, also showing degraded formant discrimination in this more complex task.

A two-factor (formant frequency$\times$phonetic context) repeated-measure analysis of variance (ANOVA) on ΔZ showed that formant frequency was not significant ($F(7,21) = 1.089, p = 0.405$), and that phonetic context was also not significant ($F(2,6) = 1.916, p = 0.227$). ΔZ, shown in Fig. 4, was a relatively flat function of formant frequency across the eight formant frequencies, although two high values of ΔZ threshold for F1 of /bɪd/ did not follow this pattern. The planned comparison of thresholds in ΔZ between F1 and F2 showed that there was no significant difference ($F(1,3) = 0.003, p = 0.959$), supporting the flattening effects of the *z*-scale transform for these stimuli.

The effect of word position in phrases and sentences on ΔZ, averaged across formants, is shown in Fig. 5. The

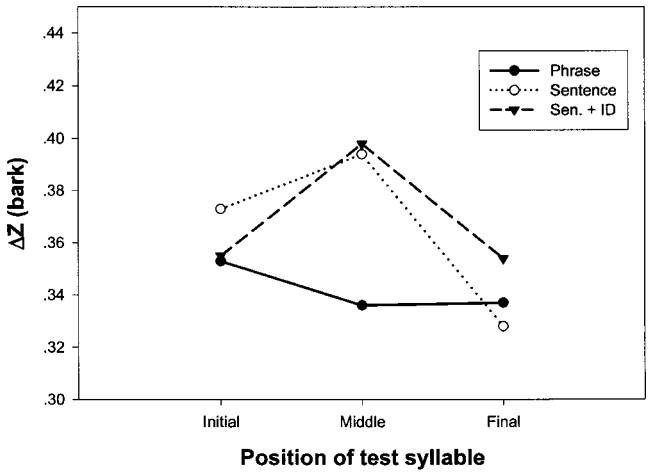

FIG. 5. Thresholds for discrimination of F1 and F2 in barks as a function of the word position (initial, middle, and final) for two phonetic contexts: phrase (solid line) and sentence (dotted line), and sentence task with identification (dashed line).

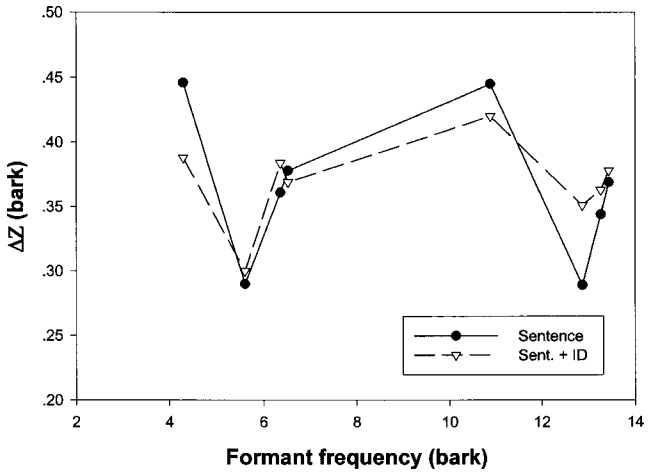

FIG. 6. Thresholds for discrimination of F1 and F2 in barks as a function of formant frequency for sentence task with (dashed line) and without identification (solid line).

terms ''initial, middle, and final'' are used here to describe actual positions in the three-word phrases, while in the nine-word sentences the terms denote word positions two, five, and eight. Generally, performance was best for the test syllable at the final position in sentences, and performance was worst for the middle position. However, performance was constant across word positions in the three-word phrases. A three-way repeated-measure ANOVA (formant frequency $\times$phonetic context$\times$position) was calculated for ΔZ. Results showed no significant effect of formant frequency ($F(7,21)=0.964, p=0.482$), phonetic context ($F(1,3)=0.676, p=0.471$), or word position ($F(2,6)=3.025, p=0.123$). However, a significant two-way interaction of formant and position ($F(14,42)=3.532, p<0.01$), and three-way interaction of formant, context, and position ($F(28,84)=1.964, p<0.05$) suggested that there were different patterns of position effects for different formants and phonetic contexts.

B. Sentence identification

The sentence identification task consisted of the discrimination task for sentences with the addition of an identification task using twelve possible target sentences. The discrimination functions for the sentence tasks with and without identification, shown in Fig. 6, are remarkably similar. A three-way ANOVA on ΔZ (formant frequency $\times$with and without ID$\times$position) showed that neither formant frequency ($F(7,21)=1.16, p=0.366$) nor the identification task ($F(1,3)=0.963, p=0.399$) had significant effects on formant thresholds. However, word position had a significant effect ($F(2,6)=5.18, p<0.05$), suggesting that position effects had a similar pattern with and without identification. Overall, subjects had no difficulty in identifying the sentences while maintaining good vowel discrimination, even though subjects commented that the addition of the identification task made the task more challenging.

IV. DISCUSSION

A. Factors influencing formant discrimination of high-fidelity speech

1. Formant frequency

As shown in Figs. 2 and 4, ΔF and ΔZ showed different patterns for the effect of increases in formant frequency. Formant thresholds in ΔF averaged over three phonetic contexts (syllables, phrases, and sentences) were well fitted by a piecewise-linear function, suggesting that ΔF is constant in the F1 range and increases linearly in the F2 range. ΔF for all three phonetic contexts showed similar patterns, although thresholds increased slightly for the longer phonetic contexts. Of the various auditory scales examined by Kewley-Port and Zheng (1999), the *z* scale in barks was the most effective at removing the variability produced by center formant frequency and fundamental frequency in thresholds for isolated synthetic vowels. The present study showed that ΔZ was nearly flat across formant frequency for all three phonetic contexts, indicating that this transformation is successful for high-fidelity speech as well as for formant-synthesized speech. Of course the spectral-temporal processing used in discrimination of the low F1 formants compared to the high F2 formants is probably different (noting the mid-frequency overlap of the first and second formants for males and females is about 25%). For example, thresholds for the lowest formant (/ɪ/, F1 = 399 Hz) exhibited highest ΔZ thresholds for the syllable and sentences contexts. A similar effect, showing a high threshold for the /ɪ/ vowel, was observed by Kewley-Port (2001) for formant-synthesized vowels and syllables at a higher level of stimulus uncertainty (her Fig. 3) and also by Liu (2002) for isolated high-fidelity vowels. These systematic threshold differences may indicate processing differences for the low-frequency vowel formants. Nonetheless, when formant discrimination functions are transformed using the bark scale, the function are roughly flat across the F1 and F2 range, suggesting that normal-hearing listeners may need roughly the same amount of formant frequency shift on the auditory scale to detect the vowel difference produced by formant shifts. This appears to

be generally true for high-fidelity speech even though there is more variability in ΔZ across the formants.

2. Length of phonetic context

As shown in Figs. 2 and 3, there was no significant effect of phonetic context even though average thresholds increased with increasing phonetic context. These results are in partial agreement with those for formant-synthesized vowels in the study of Kewley-Port and Zheng (1999). They reported no difference in thresholds in phrases and sentences for formant-synthesized speech, although syllable thresholds were significantly lower.

Comparison of thresholds for formants in isolated vowels in optimal listening conditions (Kewley-Port and Watson, 1994) and thresholds for formants in syllables, phrases, and sentences suggests a large increase in threshold with more complex phonetic context. The average threshold for formants in isolated vowels in optimal listening conditions was 0.109 barks for formant-synthesized speech (Kewley-Port and Watson, 1994) and 0.201 barks for high-fidelity speech (Liu, 2002). Thresholds for formants in high-fidelity syllables, phrases, and sentences were 0.301, 0.342, and 0.365 barks, respectively. This analysis shows quantitatively the asymptotic effect of longer phonetic context on formant thresholds.

3. Sentence identification

There was no significant difference between formant thresholds for sentences with and without the identification task. Transformed from hertz to barks, thresholds showed similar flat functions of formant frequency (Fig. 6) with average thresholds for sentences with and without identification that were equivalent, at 0.365 and 0.369 barks, respectively. The result that the sentence identification task had no significant effect on vowel formant discrimination for high-fidelity speech is consistent with the analogous study for formant-synthesized speech (Kewley-Port and Zheng, 1999). This consistency across studies suggests that formant resolution for vowels is independent of the word and sentence identification.

Formant frequency discrimination is initially based on neural impulses produced in the cochlea. The spectral shape of the speech stimuli is represented in the temporal and spectral information that is sent to the central auditory system via the auditory nerve. Models incorporating the difference in excitation or loudness patterns between a standard vowel and a vowel with a shifted formant (Kewley-Port and Zheng, 1998; Liu, 2002) indicate that listeners based their judgments on difference in spectral patterns, in particular the difference for the one to three harmonics adjacent to the formant peak (Sommers and Kewley-Port, 1996). As the discrimination task becomes more complex with longer phonetic context or higher level of stimulus uncertainty, the cognitive load at more central levels increases such that thresholds are elevated, here by a factor of 1.8 for sentences. Clearly the extraction of linguistic meaning and speech understanding take place at a high cognitive level. A question is whether the processing mechanisms required to do well in the combined discrimination and identification tasks are independent from one another. Because discrimination thresholds in our studies were generally elevated by higher cognitive load, but not affected by an additional identification task, we conclude that processes involved in word and sentence identification do not additionally affect the processes involved in encoding the spectro-temporal information in acoustic signals. This is consistent with theories of Fowler (1996) and others that the spectro-temporal information needed to extract linguistic meaning is directly perceived without intervening analytical processes.

4. Word position

Formant frequency discrimination of vowels embedded in sentences (Fig. 5) was best with the target word at final position, and worst at the middle. Other studies of auditory stimulus sequences (Watson *et al.*, 1975; McFarland and Cacace, 1992; Neath and Knoedler, 1994; Surprenant, 2001) also suggested that performance in identification and discrimination tasks was best when the target stimulus is in the final position, and worst in middle positions. In contrast, for three-word phrases word position had no effect, with performance essentially constant across position. This different pattern for phrases is probably due to the short length of the phrases.

McFarland and Cacace (1992) showed that performance in a tone recognition task improved toward constant, near-perfect performance as tone sequences were shortened from 13 to 7 items. They stated that limitations in short-term acoustic memory were responsible for reduced performance as length increased. The present data suggest that information for vowel discrimination in three-word phrases can be stored entirely within short-term acoustic memory, whereas nine-word sentences exceed memory limitations. In addition, primacy and recency effects appeared in the threshold functions for sentences in the present study, consistent with results of McFarland and Cacace's study (1992), which also showed primacy effects for the second item and recency effects for the second-to-last item when the length of items exceeded eight items. Usually, however, primacy and recency effects are obtained for the first and last item, respectively, in the sequence, not for the second and second-to-last item as seen in our study (Morton *et al.*, 1981; Neath and Knoedler, 1994; Surprenant, 2001). The differences in serial position effects across these studies might be due to the different stimuli (speech and nonspeech), different retention intervals, different inter-stimulus intervals (ISI),[3] and different methodologies (Yes-or-No and forced-choice adaptive procedure). Given the small but significant effects of utterance length versus word position on formant thresholds observed here, more extensive study of their relation to vowel processing in normal discourse should be undertaken.

B. Comparison of formant resolution between STRAIGHT-synthesized and formant-synthesized speech

STRAIGHT uses algorithms for speech analysis and synthesis that preserve most of the acoustic variability in natural speech and produce high-fidelity speech quality. In contrast,

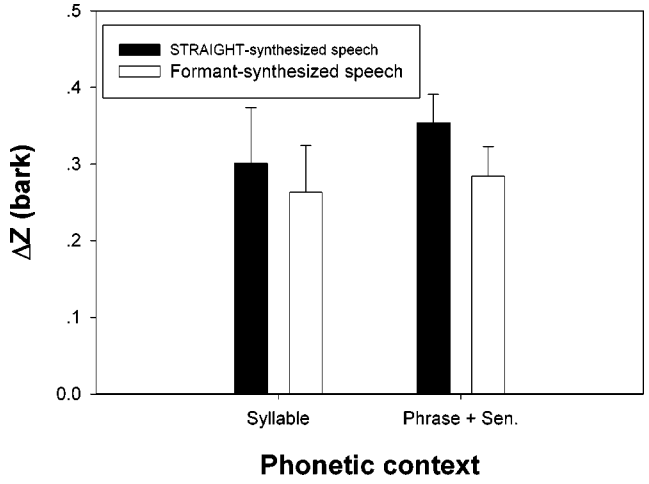

FIG. 7. Comparison of ΔZ between formant-synthesized speech and STRAIGHT-synthesized speech for syllable and more complex phonetic contexts (average of phrase and sentence). Error bars show standard deviations for each condition.

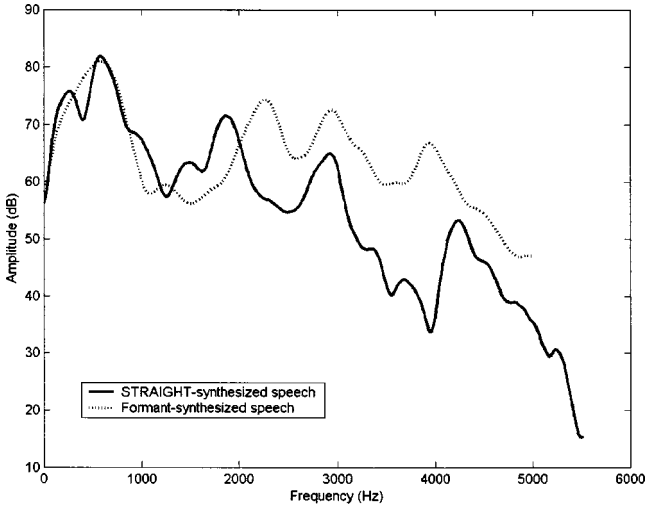

FIG. 8. Spectra using STRAIGHT analysis from the middle analysis frame for two versions of the /ɛ/ vowel generated by different synthesizer, STRAIGHT (Kawahara *et al.*, 1999) and Klatt (1980). Note that the spectra using STRAIGHT do not represent the harmonic fine structure and properties of the source, which are stored in other parameters in STRAIGHT.

typical formant synthesizers produce an unnatural, robotic speech quality. Thresholds for formant discrimination for STRAIGHT-synthesized speech were compared to those for formant-synthesized (Klatt, 1980) speech (Kewley-Port and Zheng, 1999) for syllables, phrases, and sentences. For syllables (see Fig. 7), results of two-tailed t-tests found no significant difference of formant discrimination for syllables between STRAIGHT-synthesized and formant-synthesized speech ($t(14)=1.137, p=0.274$). In both studies, thresholds for formants in phrases and sentences were similar and were therefore averaged to give one threshold estimate for longer phonetic context. A comparison of these averages between STRAIGHT-synthesized and formant-synthesized speech showed that there was a significant difference for longer phonetic context ($t(14)=3.211, p=0.007$), even though the magnitude of the difference was small (0.08 barks). The result that performance for formant discrimination is better for formant-synthesized speech than for STRAIGHT-synthesized speech contrasts with performance in speech recognition tasks in which formant-synthesized speech is less intelligible and listeners respond more slowly than to natural speech (Greene, 1986; Logan *et al.*, 1989; Ralston *et al.* 1991). However, both results may be related to acoustic-phonetic variability. The acoustic-phonetic variability and additional redundancy in high-fidelity/natural speech may help subjects to process natural speech more efficiently at higher cognitive levels (Pisoni, 1997). Speech recognition requires, first, the encoding of speech signals, and then searching a previously stored lexicon in long-term memory, integration of a variety of sources of knowledge, and the labeling of speech signals. Although formant synthesis can generate synthetic speech with quality close to that of natural speech (Allen, Hunnicutt, and Klatt, 1979; Klatt, 1980), typically synthetic speech lacks the acoustic-phonetic variability of natural speech required for good speech recognition. Formant discrimination primarily involves more direct comparison of acoustic information in short-term auditory memory. The acoustic-phonetic variability in high-fidelity STRAIGHT speech may make formant discrimination comparisons in short-term auditory memory more challenging than in the less variable, but unnatural, formant-synthesized speech. Preliminary acoustic analyses suggested that STRAIGHT-synthesized vowels were similar to formant-synthesized vowels in duration and F0 contour. However, STRAIGHT-synthesized vowels showed much more variability in the spectrum than formant-synthesized vowels. The spectra for STRAIGHT-synthesized and formant-synthesized /ɛ/ vowels using STRAIGHT analysis are shown in Fig. 8. There are several extra peaks near formant peaks in the spectrum of the STRAIGHT-synthesized /ɛ/ vowel, while the spectrum of the formant-synthesized /ɛ/ vowel shows a smooth function without extra peaks near formant peaks. The increased spectral variability for STRAIGHT-synthesized vowels may result in interactions between the formant peak and other extra peaks, and could account for higher thresholds for formant discrimination for STRAIGHT-synthesized vowels. Further studies of the acoustic differences between STRAIGHT-synthesized and formant-synthesized speech need to be completed.

C. A norm for formant frequency discrimination in high-fidelity speech

Several experimental factors were manipulated systematically in this study to investigate formant discrimination under laboratory listening conditions approximating those found in everyday communication. Discrimination tasks varied from easiest, for isolated vowels, to hardest, for vowels in sentences with addition of an identification task. Kewley-Port and Zheng (1999) reported that a norm for formant frequency discrimination in more ordinary listening conditions may be usefully estimated from an average over sentences with and without identification. This norm represents a typical value for discriminating differences in vowel formants in modest-length sentences based on our manipulation of a few of the host of factors that influence speech recognition. In formant-synthesized speech the estimated norm was 0.28

barks, whereas averaging thresholds over sentence conditions in high-fidelity speech synthesized by STRAIGHT yields a norm that is higher at 0.37 barks.

The concept of a norm for discriminating formants in normal discourse has relevance to understanding the communication process. Several studies have measured the distance between vowel formants from many talkers at the steady-state part of a /CVC/ syllable (Bradlow, 1993; Hillenbrand *et al.*, 1995). Kewley-Port and Zheng (1999) reported that 0.56 barks was the average of formant distances for F1 and F2 between the closest vowel pairs from 16 speakers with different dialects. Since the norm for thresholds is 0.37 barks for high-fidelity sentences, it appears that typical American English talkers produce vowels with formant distance far enough apart for normal-hearing listeners to discriminate vowels without any difficulty. In Fig. 6, there is a wide range of thresholds (0.16 barks) for vowel discrimination in high-fidelity sentences. But even the highest thresholds shown in Fig. 6 (0.46 barks for the threshold of the /I/ vowel in sentences) are still within the production margins for closely spaced vowels of 0.56 barks. These comparisons provide evidence for a good match between English vowel production and perception.

V. SUMMARY

The goal of this study was to investigate vowel formant frequency discrimination for high-fidelity speech. Several experimental factors were systematically manipulated. Results suggest that formant frequency discrimination represented on an auditory scale (ΔZ in barks) is roughly constant across formant frequencies. Similar patterns for formant discrimination in sentences with and without an identification task imply that formant resolution for vowels is independent of the word and sentence identification. In addition, length of phonetic context influences formant discrimination asymptotically such that a norm can be established for normal-hearing listeners' ability to discriminate vowel formants in modest-length, high-fidelity sentences. This norm is 0.37 barks (1/3 critical band) for discriminating vowel formants in high-fidelity, meaningful speech, higher than the norm (0.28 barks) for formant-synthesized speech, apparently because the high-fidelity speech synthesized by STRAIGHT has higher acoustic variability.

ACKNOWLEDGMENTS

This research was supported by the National Institutes of Health Grant No. DC-02229 to Indiana University. Discussion with Dr. Charles S. Watson was very helpful in designing the experiment. The authors are very appreciative of comments made by Brian C. J. Moore, Peter Assmann, and an anonymous reviewer on earlier versions of the manuscript.

[1]Our procedure for formant shifts was to shift the frequency of the selected formant peak only, with no change in any other formants or remote valleys (see Fig. 1). This is different from formant synthesizers, in which a shift of the selected formant peak produces changes in the amplitude of adjacent formants and valleys in order to simulate the spectral variation in natural speech. This effect becomes stronger when other formants are close to the selected formant in frequency (see examples in Klatt, 1980). The lack of these effects in the present STRAIGHT shifting procedure may be seen as a limitation of this method.

[2]Zwicker's (1961) critical-band scale, the *z* scale in barks, was chosen based on a comparison of the transformation of ΔF using log-frequency, barks, and two versions of the ERB-rate scale (e.g., Glasberg and Moore, 1990). Our earlier modeling work on formant frequency discrimination (Kewley-Port and Zheng, 1998; Liu, 2002) suggested that the difference of loudness patterns between the standard vowel and vowels at threshold was roughly constant regardless of the formant frequencies and listening conditions. Therefore, we hypothesized that formant frequency discrimination may be based on a constant perceptual difference between vowels. The bark scale gave rise to the most successful transformation of ΔF that yielded roughly constant frequency functions, better than ERB-rate and log-frequency scales.

[3]ISI was constant at 400 ms in the present study, although the signal (vowel) onset-to-onset interval varied from 400 ms to 2.2 s depending on the phonetic context. Several studies have suggested that performance for auditory discrimination of intensity, frequency, and duration improved when ISI increased and reached a constant level when ISI was beyond a certain value (Allan and Kristofferson, 1974; Taylor and Smith, 1975; Biswas *et al.*, 1997). These asymptotic values for ISI were different across studies, 500 ms for Allan and Kristofferson (1974) and Taylor and Smith (1975), and 1.0–3.0 s for Biswas *et al.* (1997). Because our range of vowel onset-to-onset interval was close or above the asymptotic value (500 ms) for ISI, there should not be significant effects of different vowel onset-to-onset intervals due to phonetic context on formant discrimination in this study.

Allan, L. G., and Kristofferson, A. B. (**1974**). ''Psychophysical theories of duration discrimination,'' Percept. Psychophys. **16**, 26–34.

Allen, J., Hunnicutt, S., and Klatt, D. (**1979**). *Conversion of Unrestricted Text to Speech* (Notes for MIT course).

Biswas, A., Watson, C., Barlow, S., Gygi, B., and Drennan, W. (**1997**). ''Optimal interstimulus interval for auditory discrimination of intensity, duration, and frequency for normal adults,'' J. Acoust. Soc. Am. **101**, 3150.

Bradlow, A. R. (**1993**). ''Language-specific and universal aspects of vowel production and perception: A cross-linguistic study of vowel inventories,'' Ph.D. dissertation, Cornell University, Ithaca, NY (unpublished).

Flanagan, J. (**1955**). ''A difference limen for vowel formant frequency,'' J. Acoust. Soc. Am. **27**, 288–291.

Fowler, C. A. (**1996**). ''Listeners do hear sounds, not tongues,'' J. Acoust. Soc. Am. **99**, 1730–1741.

Glasberg, B., and Moore, B. C. J. (**1990**). ''Deviation of auditory filter shapes from notched-noise data,'' Hear. Res. **47**, 103–138.

Greene, B. G. (**1986**). ''Perception of synthetic speech by nonnative speakers of English,'' Proceedings of the Human Factors Society, Vol. **2**, pp. 1340–1343.

Hawks, J. W. (**1994**). ''Difference limens for formant patterns of vowel sounds,'' J. Acoust. Soc. Am. **95**, 1074–1084.

Hillenbrand, J., Getty, L. J., Clark, M. J., and Weeler, K. (**1995**). ''Acoustic characteristics of American English vowels,'' J. Acoust. Soc. Am. **97**, 3099–3111.

Hillenbrand, J. and Neary, T. (**1999**). ''Identification of resynthesized /hVd/ utterances: Effects of formant contour,'' J. Acoust. Soc. Am. **105**, 3509–3523.

Kawahara, H., Masuda-Kastuse, I., and Cheveigne, A. (**1999**). ''Restructuring speech representations using a pitch-adaptive time-frequency smoothing and an instantaneous-frequency-based F0 extraction: Possible role of a repetitive structure in sounds,'' Speech Commun. **27**, 187–207.

Kewley-Port, D. (**1992**). ''Effect of levels of stimulus uncertainty and consonantal context on formant frequency discrimination,'' J. Acoust. Soc. Am. **91**, 2338.

Kewley-Port, D. (**1996**). ''Thresholds for formant-frequency discrimination of vowels in consonantal context,'' J. Acoust. Soc. Am. **97**, 3139–3146.

Kewley-Port, D. (**2001**). ''Vowel formant discrimination: Effects of stimulus uncertainty, consonantal context and training,'' J. Acoust. Soc. Am. **110**, 2141–2155.

Kewley-Port, D., and Watson, C. S. (**1994**). ''Formant-frequency discrimination for isolated English vowels,'' J. Acoust. Soc. Am. **95**, 485–496.

Kewley-Port, D., Watson, C. S., and Czerwinski, M. (**1986**). ''Informational masking in vowel sequences,'' J. Acoust. Soc. Am. Suppl. 1 **79**, S66.

Kewley-Port, D., and Zheng, Y. (**1998**). ''Auditory models of formant fre-

quency discrimination for isolated vowels,'' J. Acoust. Soc. Am. **103**, 1654–1666.
Kewley-Port, D., and Zheng, Y. (**1999**). ''Vowel formant discrimination: Towards more ordinary listening conditions,'' J. Acoust. Soc. Am. **106**, 2945–2958.
Klatt, D. H. (**1980**). ''Software for cascade/parallel formant synthesizer,'' J. Acoust. Soc. Am. **67**, 971–995.
Levitt, H. (**1971**). ''Transformed up-down method in psychoacoustics,'' J. Acoust. Soc. Am. **49**, 467–477.
Liu, C. (**2002**). ''Modeling vowel formant discrimination in quiet and noise for natural speech,'' Ph.D. dissertation, Indiana University, Bloomington, IN (unpublished).
Liu, C., and Kewley-Port, D. (**2004**). ''STRAIGHT: a new speech resynthesizer for vowel formant discrimination,'' Acoustic Research Online Letter **5**, 31–36.
Logan, J. S., Greene, B. G., and Pisoni, D. B. (**1989**). ''Segmental intelligibility of synthetic speech produced by rule,'' J. Acoust. Soc. Am. **86**, 566–581.
McFarland, D. J., and Cacace, A. T. (**1992**). ''Aspects of short-term acoustic recognition memory: Modality and serial position effects,'' Audiology **31**, 342–352.
Morton, J., Marcus, S. M., and Ottley, P. (**1981**). ''The acoustic correlates of 'speechlike:' A use of the suffix effect,'' J. Exp. Psychol. **110**, 568–593.
Neath, I., and Knoedler, A. J. (**1994**). ''Distinctiveness and serial position effects in recognition and sentence processing,'' J. Memory **33**, 776–795.
Pisoni, D. B. (**1997**). ''Perception of synthetic speech,'' *Progress in Speech Synthesis*, edited by J. P. H. van Santen, R. W. Sproat, J. P. Olive, and J. Hirschberg (Springer, New York), pp. 541–560.
Pisoni, D. B., Manous, L. M., and Dedina, M. J. (**1987**). ''Comprehension of natural and synthetic speech: Effects of predictability on the verification of sentences controlled for intelligibility,'' Comput. Speech Lang. **2**, 303–330.
Ralston, J. V., Pisoni, D. B., Lively, S. E., Greene, B. G., and Mullennix, J. W. (**1991**). ''Comprehension of synthetic speech produced by rule: Word monitoring and sentence-by-sentence listening times,'' Hum. Factors **33**, 471–491.
Sinnott, J. H., and Kreiter, N. A. (**1991**). ''Differential sensitivity to vowel continua in Old World monkeys (Macaca) and humans,'' J. Acoust. Soc. Am. **89**, 2421–2429.
Sommers, M., and Kewley-Port, D. (**1996**). ''Modeling formant frequency discrimination of female vowels,'' J. Acoust. Soc. Am. **99**, 3770–3781.
Surprenant, A. M. (**2001**). ''Distinctiveness and serial position effects in tonal sequences,'' Percept. Psychophys. **63**, 737–745.
Taylor, M. M., and Smith, S. M. (**1975**). ''Monaural detection with contralateral cue. V. Interstimulus interval in MDCC and amplitude discrimination,'' J. Acoust. Soc. Am. **57**, 1500–1511.
Traunmuller, H. (**1990**). ''Analytical expressions for the tonotopic sensory scale,'' J. Acoust. Soc. Am. **88**, 97–100.
Watson, C. S. (**1987**). ''Uncertainty, informational masking and the capacity of immediate auditory memory,'' *Auditory Processing of Complex Sounds*, edited by W. Yost and C. S. Watson (Erlbaum, Hillsdale, NJ), pp. 267–277.
Watson, C. S., Wroton, H. W., Kelly, W. J., and Benbassat, C. A. (**1975**). ''Factors in the discrimination of auditory patterns, I. Component frequency, temporal position, and silent intervals,'' J. Acoust. Soc. Am. **57**, 1175–1185.
Zwicker, E. (**1961**). ''Subdivision of the audible frequency range into critical band (*Frequenzgruppen*),'' J. Acoust. Soc. Am. **33**, 248.

Frequent word section extraction in a presentation speech by an effective dynamic programming algorithm[a)]

Yoshiaki Itoh[b)]
Iwate Prefectural University, Sugo, Takizawa-mura, Iwate 020-0193, Japan

Kazuyo Tanaka
University of Tsukuba 1-2 Kasuga, Tsukuba, 305-8550, Japan

(Received 10 January 2003; accepted for publication 3 May 2004)

Word frequency in a document has often been utilized in text searching and summarization. Similarly, identifying frequent words or phrases in a speech data set for searching and summarization would also be meaningful. However, obtaining word frequency in a speech data set is difficult, because frequent words are often special terms in the speech and cannot be recognized by a general speech recognizer. This paper proposes another approach that is effective for automatic extraction of such frequent word sections in a speech data set. The proposed method is applicable to any domain of monologue speech, because no language models or specific terms are required in advance. The extracted sections can be regarded as speech labels of some kind or a digest of the speech presentation. The frequent word sections are determined by detecting similar sections, which are sections of audio data that represent the same word or phrase. The similar sections are detected by an efficient algorithm, called Shift Continuous Dynamic Programming (Shift CDP), which realizes fast matching between arbitrary sections in the reference speech pattern and those in the input speech, and enables frame-synchronous extraction of similar sections. In experiments, the algorithm is applied to extract the repeated sections in oral presentation speeches recorded in academic conferences in Japan. The results show that Shift CDP successfully detects similar sections and identifies the frequent word sections in individual presentation speeches, without prior domain knowledge, such as language models and terms.
[DOI: 10.1121/1.1764834]

PACS numbers: 43.72.Kb, 43.72.Lc [DOS] Pages: 1234–1243

I. INTRODUCTION

Information retrieval for speech or motion images is a difficult problem, because in most cases no precise indexes or labels are assigned to such time sequence data. However, given the increase in real-world multi-media data in today's social environment, these kinds of information retrieval will be needed more and more. Consequently, several approaches have been proposed for information retrieval for speech or motion images by processing time sequence data. One of the representative approaches is model-based recognition. In model-based recognition, indexes or labels are assigned to the time sequence data by recognizing all the data by use of reference models prepared in advance. For example, a speech recognizer converts all the speech data to text data. The recognized text data are then subjected to information retrieval and other processes.[1–5] Therefore, performance depends on the speech recognizer, and obtaining correct speech labels is difficult, in view of the difficulty in correctly recognizing real-world nonsegmented and nonlabeled speech data. The word error rates for lectures or conversational speech fall around thirty percent,[6–8] for example. Thus, in this paper we propose a new approach for handling such real-world data.

Generally speaking, the most important words or phrases in a spontaneous speech tend to be repeated, such as in a presentation or lecture speech, because human speech stream involves redundancy. Extracting such repeated speech sections between two speech data sets requires nonlinear matching between two arbitrary sections of arbitrary length, one section from each data set. However, when ordinary algorithms are used, this matching requires an unfeasible amount of computation.

In the present paper, a new algorithm for resolving this problem is proposed. The method is called Shift Continuous Dynamic Programming (Shift CDP),[9,10] which performs fast nonlinear matching at a feature vector level between arbitrary sections of two time sequence data sets and detects similar sections, where the individual section length exceeds a certain fixed value. The algorithm allows endless input and enables real-time response to queries. The method can be utilized in many types of applications, such as speech and motion images.[11] The present paper also proposes a methodology for extracting acoustically similar sections in a single speech stream and identifying the frequent words sections by summing the extracted similar sections in the whole presentation speech, because the similar sections are supposed to

[a)]Portions of this work were presented in "A matching algorithm between arbitrary sections of two speech data for speech retrieval by speech," Proceeding of International Conference on Acoustics, Speech and Signal Processing, May 2001, "Automatic Labeling and Digesting for Lecture Speech Utilizing Repeated Speech by Shift CDP," Proceeding of EUROSPEECH2001, Sept. 2001 and "Speech labeling and the most frequent phrase extraction using same section in a presentation speech," Proceeding of International Conference on Acoustics, Speech and Signal Processing, May 2002.

[b)]Electronic-mail: y-itoh@iwate-pu.ac.jp

 0001-4966/2004/116(2)/1234/10/$20.00

express the same word or the same phrase. The matching is conducted at just the acoustic phonetic level; therefore, this approach does not require any prior domain knowledge, such as language models or terms. Speech recognizers cannot work well without such domain knowledge, because frequent words are often special terms that tend to fall outside the system vocabulary. For the same reason, usual word spotting methods cannot be composed. Related approaches can be considered to include phone sequence[12] or phonetic lattice based search,[13,14] which also does not require pre-built vocabulary. The proposed method can be applied to these approaches by merely adjusting matching distances,[15] and computation requirements are lower. For speaker-dependent or single-speaker applications, however, the proposed approach can be expected to yield the better performance, because quantization for phonetic codes includes quantization distortion that causes inevitable conversion errors in the phonetic code level.

When the proposed method is used, a certain specific label can be assigned to these extracted sections, providing a kind of digest that consists of important words and phrases that are repeated numerous times in the speech.

In the next chapter, Sec. II, the concept and the algorithm of Shift CDP are described in detail. Experiments are performed to evaluate the performance of the Shift CDP algorithm in detecting similar sections on the Otago English speech corpus.[16] Section III describes the methodologies of applying Shift CDP to extracting repeated speech sections in a presentation speech and summing up those same sections. Experiments for extracting repeated phrases and for identifying frequent words sections in a presentation speech are conducted. Conclusions are presented in Sec. IV.

II. SHIFT CONTINUOUS DP ALGORITHM

A. Definition and requirements

To extract similar speech sections between two speech data sets, sections of arbitrary length must be subjected to nonlinear matching. The authors previously proposed an algorithm for detecting similar sections between two time sequence data sets, called Reference Interval Free Continuous DP(RIFCDP).[17,18] The computational requirement is so heavy that the algorithm can handle only speech data of less than one minute, although the algorithm approximates the optimal path. The Shift Continuous DP (Shift CDP) is an improved and fast algorithm having the same detection performance as RIFCDP.

First, the definition of the problem is described here. Let the two time sequence data sets be the reference pattern R and the input pattern X, expressed by Eq. (1) below, where $R\tau$ and X_t both indicate a member of a feature parameter series, at the frame τ in R and time t in X, respectively.

$$R=\{R_1,\ldots,R\tau,\ldots,R_N\},$$
$$X=\{X_1,\ldots,X_t,\ldots,X_\infty\}. \tag{1}$$

Here, we assume that a similar section pair $(R^{(s)},X^{(s)})$ lies between the two coordinate points (τ_1,t_1) and (τ_2,t_2), shown in the next equation.

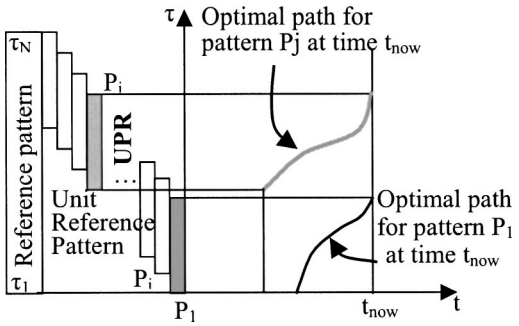

FIG. 1. The concept of the Shift CDP algorithm. A unit reference pattern that has a constant frame length is taken from the reference pattern. For each URP, a spotting algorithm by the CDP is performed, and similar sections of arbitrary length can be obtained by integrating individual URP spotting results.

$$R^{(s)}=\{R\tau_1,\ldots,R\tau_2\},$$
$$X^{(s)}=\{X\mathrm{t}_1,\ldots,X\mathrm{t}_2\}. \tag{2}$$

Here, the existence of a plurality of similar sections between R and X is assumed, and their order of appearance is assumed to be arbitrary. Similar section extraction consists of identifying the coordinates points for all the correct similar section pairs. The minimum length among the correct sections is given here, as it is often determined by the requirements of the application. For example, if speech sections of the same phoneme sequence are to be extracted, the minimum length should be dozens of milliseconds, and if speech sections of the same sentence are to be extracted, it should be a few seconds. The algorithm should be synchronous with input frames, in order to realize real-time processing.

The concept and a detailed algorithm of Shift CDP are described in the next section.

B. The algorithm of shift continuous DP (shift CDP)

In the algorithm for solving the above problem, all the matching should be done between (τ_1,t_1) and $(\tau_2,t_{\mathrm{now}})$ at each input, where $1\leqslant\tau_1\leqslant\tau_2\leqslant N$, $1\leqslant t_1\leqslant t_{\mathrm{now}}$, as shown in Fig. 1. Let the minimum and maximum length for $R^{(s)}$ be $N_{\min}$ and $N_{\max}$, respectively, such that $N_{\min}\leqslant\tau_2-\tau_1\leqslant N_{\max}$. These constraints specify the desirable length to be detected. Optimal matching is performed for the length from $N_{\min}$ to $N_{\max}$ at frame τ_2, which is assumed to be the end frame of the CDP. The CDP is performed for the $N_{\max}-N_{\min}$ patterns whose mean length is $(N_{\min}+N_{\max})/2$. Thus, the CDP has to be performed approximately $(N_{\max}-N_{\min})\times N$ times for the reference pattern, and the computational requirements are expected to be heavy, despite such constraints for matching length.

Shift CDP is able to reduce the computational requirements described above. The concept behind this algorithm is shown in Fig. 1. First, unit reference patterns are taken from reference pattern R. A unit reference pattern, (URP), has a constant frame length of N_{CDP}. The first URP is composed of frames from the first frame to the N_{CDP}-th frame in R. The starting frame of the second URP is shifted by N_{shift} frames, and the second URP is composed of the same number of N_{CDP} frames, from the $(N_{\mathrm{shift}}+1)$-th frame. In the same way,

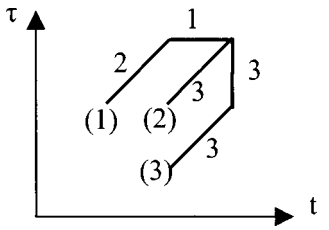

FIG. 2. Asymmetry local restrictions and slope weights for DP paths.

the kth URP is composed of N_{CDP} frames from the $(k \times N_{\mathrm{shift}}+1)$-th frame. The last URP is composed of N_{CDP} frames from the last frame of R toward the head of R. The number of URPs becomes $N_{\mathrm{CDP}}=[N/N_{\mathrm{Shift}}]+1$, where [ ] indicates an integer that does not exceed the value in brackets.

For each URP, CDP is performed. CDP applies DP to a URP at every time interval and searches for the optimal path of the URP at every time interval. Therefore, CDP is a spotting algorithm. Shift CDP is able to find similar sections by unifying the spotting results of each URP.

The cumulative distances at the end frame of a URP do not have to be normalized, because all the URPs are of the same length. As described above, Shift CDP is a very simple and flat algorithm that merely performs CDP for each URP and integrates the results.

C. Formalization of shift CDP

This section formalizes the Shift CDP algorithm. Let the vertical axis represent the reference pattern frame τ $(1 \leqslant \tau \leqslant N)$, and the horizontal axis represent input time t. The local distance between the input t and frame τ is denoted $D_t(\tau)$. Here, as shown in Fig. 2, asymmetric local restrictions are used as the DP path. The following formulas until Eq. (13) basically constitute the CDP algorithm that finds the optimal path for the ith URP and computes $A(t,i)$, which is the cumulative distance between the ith URP and the input pattern until the current time. $S_t(i,N_{\mathrm{CDP}})$, the starting time of the ith URP, is also obtained in this process.

Let $G_t(i,j)$, $G_{t-1}(i,j)$, and $G_{t-2}(i,j)$ denote the cumulative distance up to frame j in the ith URP at input times t, $t-1$, and $t-2$, respectively. Input time t is the current time, and $t-1$ is the previous time interval. In the same way, $S_t(i,j)$, $S_{t-1}(i,j)$, and $S_{t-2}(i,j)$ denote the starting time. Let $\tau_S(i)$ and $\tau_E(i)$ be the frames of R that correspond to the start and end frames of the ith URP. These locations should be computed before input. For the reduction of total computation, as shown in Fig. 2, $D3_t(\tau)$ and $D2_{t-1}(\tau)$ are computed and saved separately from $D_t(\tau)$ according to DP path restrictions. $D3_t(\tau)$ and $D2_{t-1}(\tau)$ denote three times of $D_t(\tau)$ and two times of $D_{t-1}(\tau)$, respectively, shown in Eqs. (5) and (13). Initial conditions are given as:

$$\begin{cases} G_t(i,j)=G_{t-1}(i,j)=G_{t-2}(i,j)=\infty \\ S_t(i,j)=S_{t-1}(i,j)=S_{t-2}(i,j)=-1 \end{cases} \quad (1 \leqslant i \leqslant N_{\mathrm{PAT}}, 1 \leqslant j \leqslant N_{\mathrm{CDP}}), \tag{3}$$

$$D2_{t-1}(\tau)=\infty \quad (1 \leqslant \tau \leqslant N). \tag{4}$$

The following are recurrence formulas that can be computed synchronously with input. To begin with, the local distances between each frame of R and current input t are computed beforehand. These prior computations suppress multiplications.

$$\begin{cases} D_t(\tau)=d(\tau,t) \\ D3_t(\tau)=3\times D_t(\tau) \end{cases} \quad (1 \leqslant \tau \leqslant N). \tag{5}$$

LOOP i $(1 \leqslant i \leqslant N_{\mathrm{PAT}})$: for each URP i,

LOOP j $(1 \leqslant j \leqslant N_{\mathrm{CDP}})$: for each frame j of URP i,

at $j=1$

$$\begin{aligned} &G_t(i,1)=D3_t(\tau_S(i)), \\ &S_t(i,1)=t, \end{aligned} \tag{6}$$

at $j \geqslant 2$

$$\begin{aligned} P(1)&=G_{t-2}(i,j-1)+D2_{t-1}(\tau_S(i)+j-1) \\ &\quad +D_t(\tau_S(i)+j-1), \\ P(2)&=G_{t-1}(i,j-1)+D3_{t-1}(\tau_S(i)+j-1), \end{aligned} \tag{7}$$

$$\begin{aligned} P(3)&=G_{t-1}(i,j-2)+D3_t(\tau_S(i)+j-2) \\ &\quad +D3_t(\tau_S(i)+j-1), \end{aligned}$$

but at $j=2$,

$$P(2)=D3_t(\tau_S(i))+D3_t(\tau_S(i)+1)$$

$$\alpha^*=\arg\min_{(\alpha=1,2,3)} P(\alpha), \tag{8}$$

$$Gt(i,j)=P(\alpha^*), \tag{9}$$

$$S_t(i,j)=\begin{cases} S_{t-2}(i,j-1) & (\alpha^*=1) \\ S_t(i,j-1) & (\alpha^*=2), \\ S_{t-1}(i,j-2) & (\alpha^*=3) \end{cases} \tag{10}$$

but at $j=2$ *and* $\alpha^*=3$, $S_t(i,2)=t$

End LOOP j, if $j=N_{\mathrm{CDP}}$: Finish the CDP for the ith URP.

End LOOP i, if $i=N_{\mathrm{PAT}}$: Finish the process of current frame t.

The three terms of P in Eq. (7) represent the three start points [(1)–(3)] of the path restrictions shown in Fig. 2. An optimal path is determined according to Eq. (8). The cumulative distance and the starting point are updated by Eq. (9) using $P(\alpha^*)$. These three equations are based on the standard DP algorithm.[19]

The adjustment degree $A(t,i)$ of the ith URP at time t is given by the cumulative distance at the last frame without normalization by the length of reference patterns, because all the URPs are of equal length.

$$A(t,i)=G_t(i,N_{\mathrm{CDP}}). \tag{11}$$

After similar sections are determined at time t, the cumulative distances, starting points, and local distances are updated, as shown below. This procedure merely renews the index of arrangements in the actual program and imposes no computational requirements.

$$\begin{cases} G_{t-2}(i,j)=G_{t-1}(i,j) & \\ G_{t-1}(i,j)=G_t(i,j) & (1\leqslant i\leqslant N_{\mathrm{PAT}}) \\ S_{t-2}(i,j)=S_{t-1}(i,j) & (1\leqslant j\leqslant N_{\mathrm{CDP}}), \\ S_{t-2}(i,j)=S_{t-1}(i,j) & \end{cases} \tag{12}$$

$$D2_{t-1}(\tau)=2\times D_t(\tau) \quad (1\leqslant\tau\leqslant N). \tag{13}$$

Here, the optimal path, the cumulative distance, and the starting time for each URP are obtained. Similar sections must be determined from these matching results. Similar sections can be determined in various ways, according to the application. For example,

(1) Detect the most similar section in the given input;
(2) detect any similar sections in the reference and the given input.

In this paper, a threshold value is set and all the sections are detected when the adjustment degree exceeds the threshold value, because the reference for input might contain a plurality of similar sections.

D. Evaluation experiments

1. Evaluation data and conditions

Experiments were performed in order to evaluate the performance of the Shift CDP algorithm in detecting similar sections. The object data in these experiments were isolated word speech data taken from the Otago speech corpus.[16] The data are from a total of 13 speakers (7 males and 6 females), each uttering 128 words twice. For each speaker, the 128-word speech samples of the first utterance are concatenated for the reference pattern, and the speech samples of the second utterance are concatenated in a different order for the input pattern. Here the precise boundaries of each word and the same word location between the reference pattern and the input pattern are obtained. The sampling frequency was 16 kHz, and the frame interval was 8 ms. A 36-dimensional graduated spectrum field[20] was used for feature parameters whose Euclidean distances determined the local distances. The graduated spectrum field is the feature representing the 18-dimentional gradient of a spectrum for a frequency axis and a time axis after a 20-filter-bank analysis and it showed better performance for speaker-independent isolated word recognition.[20] The distribution of the word length for 128 words by 13 speakers was similar to the normal distribution, where word length varied from 220 ms to 1.85 s and the mean word length was about 600 ms. Total length of the reference and input data varied from 65 to 93 s, and the average was 78 s.

E. Results and discussion

First, in order to evaluate detection performance when varying the threshold value for $A(t,i)$, an experiment was performed at various lengths of a URP ($N_{\mathrm{CDP}}=5$, 10, 20, 25, 30, 40, 50, 60, 70, 75, 90, 100, 125, 150, and 200 frames) where the number of shifts is one frame ($N_{\mathrm{Shift}}=1$). For measurement of the detection performance, ''Recall rate'' and ''Precision rate'' are introduced as shown in Eqs. (14) and (15). When both the detected sections are located in the same word section between the reference pattern and input pattern, the sections are considered to be correct.

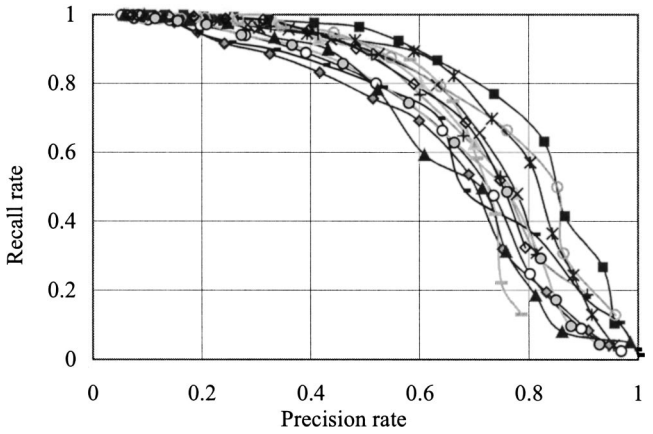

FIG. 3. Detection performance among 13 speakers. When the URP length is 480 ms (60 frames), the Shift CDP algorithm is able to detect about 70% of similar sections with a Precision rate of about 70%.

$$\textit{Recall rate}=\frac{(\textit{similar sections}\cap\textit{detected sections})}{(\textit{detected sections})}, \tag{14}$$

$$\textit{Precision rate}=\frac{(\textit{similar sections}\cap\textit{detected sections})}{(\textit{similar sections})}. \tag{15}$$

The results are shown in Figs. 3–6, with Precision rate indicated on the horizontal axis and Recall rate on the vertical axis. The graph of Fig. 3 shows the results for each of the 13 speakers. The graph shows that when URP length is 480 ms long (60 frames) the Shift CDP algorithm can detect about 70% of similar sections, with a Precision rate of about 70%. The graph of Fig. 4 compares performance for URP lengths of 480(■), 200(○), and 80(▲). The detection performance clearly declines with decreasing URP length. Two main factors are thought to be responsible for this. The first reason is that correct detection occurred for units shorter than words, such as phonemes. The second reason is that the short URP resulted in mis-detections, with shorter keywords causing many false alarms (FA) in word spotting. In this way, performance deteriorates when the length of URPs is set too short.

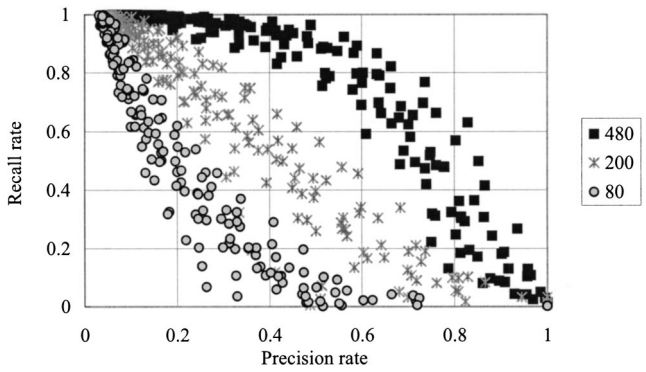

FIG. 4. Detection performance according to the length of a unit reference pattern (URP) in Shift CDP (case of shorter URP length). The detection performance deteriorates as URP length decreases from 480 ms.

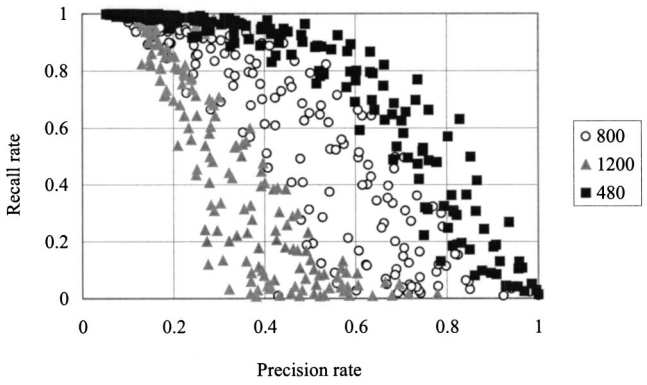

FIG. 5. Detection performance according to the length of a unit reference pattern (URP) in Shift CDP (case of longer URP length). The performance deteriorates when the length of a URP exceeds 600 frames. The best detection performance is obtained for a URP length of about 480 ms (60 frames).

The performance for URP length 480 ms is slightly better than that for 400 ms.

Figure 5 shows the case of longer URPs. The graph indicates the performance for URP lengths of 480(■), 800(○), and 1200 ms(▲). The performance deteriorates when the length of a URP exceeds 600 ms. This is due to the difficulty in extracting similar sections that are shorter than the URP length. The best detection performance is obtained at a URP around 480 ms (60 frames). This is thought to be related to the length of the average similar section, and suggests that URP length should be set to the average length or to a length slightly shorter than that of the target words to be detected.

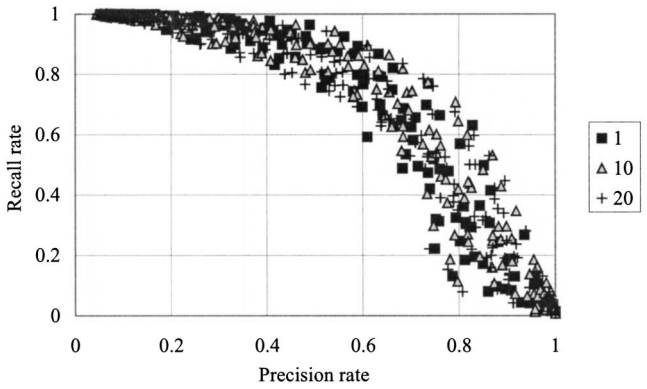

Performance comparison between frame shift numbers 1, 10, and 20.

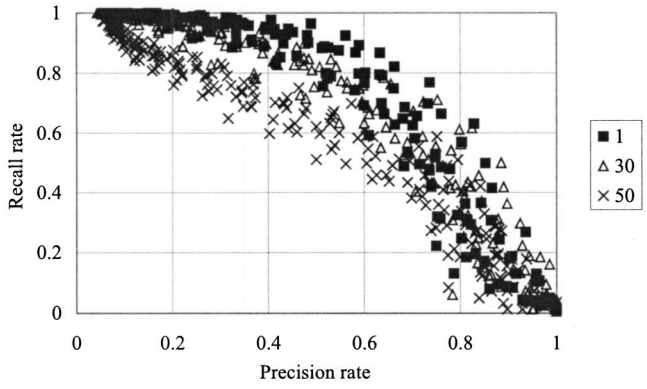

Performance comparison between frame shift numbers 1, 30, and 50.

FIG. 6. Detection performance according to the frame shift number in Shift CDP. Frame shifting is introduced in order to reduce the computation requirements. The smaller the shift number, the better the detection performance at shifting of 30 and 50 frames, which cause a serious deterioration in performance, but the deterioration at 20 frame shifts is small.

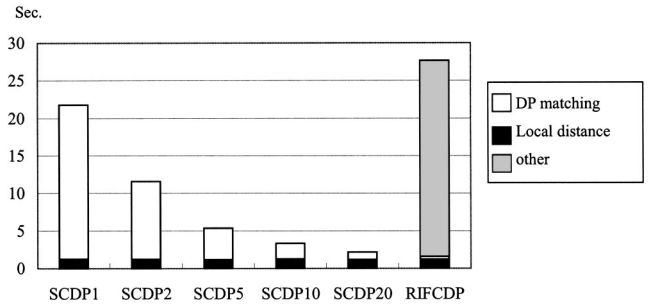

FIG. 7. Comparison of processing time for Shift CDP of frame shift numbers 1, 2, 5, 10, 20, and RIFCDP by use of a workstation (Sun Ultra5, 360 MHz). The lengths of a reference and an input pattern are set to 5 and 20 seconds, respectively. The line graph of the theoretical processing time is plotted. Shift CDP is faster than RIFCDP, even at shifting of one frame. The actual processing time fits the line graph, which plots theoretical data.

Another experiment was performed at various shifting frames ($N_{\mathrm{Shift}}=1$, 2, 5, 10, 15, 20, 25, 30, 40, 50 frames) where the length of the URP was set to 60 frames ($N_{\mathrm{CDP}}=60$). The main results are shown in Fig. 6. Frame shifting was introduced in order to reduce the computation requirements. The smaller the shift number, the better the detection performance, because time resolution is improved. Shifts of 30 and 50 frames cause a serious deterioration in performance, but shifts of 5 frames cause no deterioration in performance at all and shifts of 25 frames cause only very slight deterioration. Meanwhile, setting the shift number higher reduces computation requirements considerably. For example, when shift number is set to 25 frames, computation requirements are reduced to 1/25. In that case, two URPs cover each frame in the reference pattern R, and such redundancy is thought to work well for detection.

Lastly, Shift CDP is compared with the authors' former method, called RIFCDP, in terms of detection performance. Shift CDP yields performance no worse than that of RIFCDP.

F. Computational requirements

The order of time and space complexity is $O(N_R \times N_I)$, where N_R and N_I are the length of the reference and the input pattern, respectively. The main computations are local distance and DP path computations. Let all the computations $(+-/\times)$ be the same and be set to 1. The local distance computation requires $4D\times N_R\times N_I$ (D denotes the dimension of a feature vector) and the DP path computation requires $(4+20\times N_{\mathrm{CDP}}/N_{\mathrm{Shift}})N_R\times N_I$. Under the employed conditions, DP path computation is less than local distance computation when $N_{\mathrm{CDP}}=60$, $N_{\mathrm{Shift}}=10$, and $D=36$.

Actual processing time is measured by use of a workstation (Sun Ultra5, 360 MHz). Figure 7 shows the results of the actual processing time when the lengths of a reference and an input pattern are set to 5 and 20 seconds, respectively. For reference, the line graph of theoretical processing time is

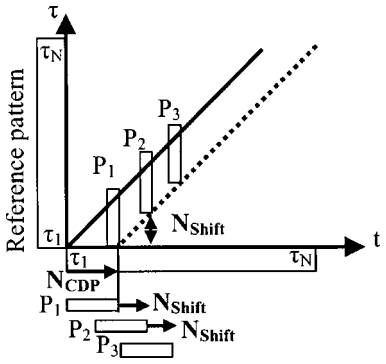

FIG. 8. Image for extracting similar sections from a presentation speech. URPs are constructed according to the progress of input.

plotted when the processing time of one-frame shifting is taken as 1.0. Shift CDP is faster than RIFCDP, even at one-frame shifting. The actual processing time approximates the line graph plotting the theoretical values as mentioned above. The processing time for Shift CDP decreases linearly in proportion to the frame shift number. At shifting of 20-frames, Shift CDP(SCDP25) requires 1/10 the processing time and 1/16 the memory usage required by SCDP1. Under these conditions, the main computational parts of Shift CDP become the computation of local distance; that is, the Euclidean distance of feature parameters.

III. FREQUENT WORD SECTION EXTRACTION FROM A PRESENTATION SPEECH

A. Similar speech extraction from a presentation speech by shift CDP

This section describes a method for extending Shift CDP to extract similar sections from a presentation speech frame-synchronously. A diagram of this appears in Fig. 8. URPs are constructed according to the progress of input. With the progress on N_{shift} frames, the next URP is composed of the same number of N_{CDP} frames, from the $N_{\text{shift}}+1$th frame. As soon as a URP is composed, the CDP is performed for the URP, as shown in the left figure of Fig. 9, and the search area becomes the bottom triangle that is shaded gray in the right figure of Fig. 9. The detailed algorithm for extracting similar sections from a long speech by use of Shift CDP is shown in the Appendix.

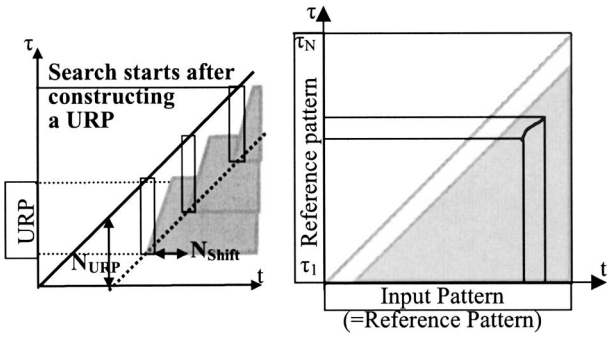

FIG. 9. Search Area, which becomes the bottom triangle that is shaded gray in the right figure. The reference pattern corresponds to a whole presentation. As soon as a URP is composed, Continuous DP is performed for the URP.

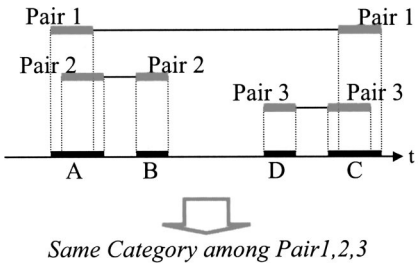

FIG. 10. Image for summing up similar section pairs. If the pair, 1 and 2, is already in the same category, this category has sections A, B, and C. If the right section of pair 3 overlaps with the section in the category, the right section is merged to section C and the left section is added as a new section of the category.

B. Summing repeated phrases

Shift CDP can determine where and how often repeated phrases appear in a presentation. Such information can be utilized to characterize the presentation. For example, the sequence of repeated phrases can be a kind of digest of the presentation, in view that such repeated phrases are thought to be important in the talk. This section describes one of the ways to sum the similar extracted sections.

Figure 10 shows a diagram for summing the similar section pairs. If the number of similar section pairs detected is P, these sections are classified into categories, which indicate the same phrase. Let Q be the number of categories, which increases according to the progress of classifying processing. The process for classifying the similar sections is shown below, where Pi and Cj denote the ith similar section pair and the jth category, respectively. Each pair has two elements (similar sections), and each category has a corresponding elements list (Cj has some similar sections).

(1) Classify each pair Pi into a category:

Extract one of the similar section pairs, Pi($1 \leqslant i \leqslant P$), and check for an overlap between Pi and all the elements of $Cj(1 \leqslant j \leqslant Q)$.

Overlap: If an overlap exists, add or merge the Pi elements to the Cj list (The overlap is determined by the overlapping section rate).

Nonoverlap: Create a new category C_{Q+1}, add 1 to the category number and its list composed of the two elements of Pi.

Continue until all the pairs are processed.

(2) Check for duplication between categories and unify each element into a single category.

One of the categories, $Cj(1 \leqslant j \leqslant Q)$, is extracted and checked for element duplication between Cj and the other categories $Ck(j \neq k)$.

Duplication: unify Cj and Ck into a new category

Continue until all the categories are processed;

(3) Output the frequency of each category:

Output the number of elements (category frequency) and the representative section for each category.

If some overlap exists between a section of Pi and a section of Cj at (1), these two sections are merged to the section of Cj. For example, when the pair, 1 and 2, is already in the similar category in Fig. 10, this category has sections A, B, and C. If the pair 3 is tested at (1), the right

section of the pair 3 is merged to section C and the left section is added as a new section of the category. The left section might be merged if it has an overlap with another section in Cj. Processes (3) and (4) are necessary, because the one category is divided into two or more different categories in processes (1) and (2).

C. Evaluation experiments

1. Evaluation data and Experimental conditions

Some experiments were conducted in order to evaluate the methodology described above. First, the method was applied to English speech data, and a sample result for a news speech is shown in order to confirm that the similar sections can be output and that the method works for English speech. Then, the method was applied to a Japanese presentation speech corpus[21] to evaluate the performance of extracting the most frequent word sections. The experimental conditions are the same for English and Japanese speech data, described in Sec. II C 1. The lengths of URP and frame shifting were set to 480 ms (60 frames) and 160 ms (20 frames), respectively. These are determined according to the results in Sec. II. The length of 480 ms corresponds to that of the shortest similar sections to be extracted and the duration time of three or more moras. N_{shift} was set so as to reduce the processing time, in view that the performance did not deteriorate when N_{shift} was set to less than 25 frames. The threshold processing of matching distance G, described in Sec. III A, was employed in order to judge similar sections. The threshold value was controlled so that similar sections for ten percent of all the speech data are output. An overlap was considered to exist if more than sixty percent overlap was found between two sections.

2. Results and discussion

a. Preliminary experiment for English news. Some preliminary experiments were conducted for English news. The Shift CDP algorithm was applied to a news speech in order to confirm that repeated phrases in the speech could be extracted. When the pairs that the system judged to be similar were listened to, all the pairs showed almost the same phoneme sequence, and no pairs showed distinctly different phoneme sequences.

When the two sections are extracted as the same speech, these sections are affixed with a label. Some labels are shared by many sections where existence of important speech is highly probable. These repeated phrases can be summed up in the way described in section 2.4, and in this case the result becomes the repeated phrases sequence, as follows.

''high school the,'' ''students in the senior class,'' ''presented Mrs. Amburgey,'' ''hundred dollars.''

The title of the speech is ''Student's surprise present moves teacher to tears,'' and the above repeated phrases sequence is thought to express the content of the story well.

b. Frequent word sections extraction in a presentation speech Some experiments were conducted to extract the frequent repeated word sections in a speech presentation. The Spontaneous Speech Corpus of Japanese[21] was used for these experiments. This corpus includes more than one hundred speech presentation data sets. One hundred speech presentation data sets were used, and the performance was evaluated in terms of whether the most frequently repeated word sections are identified in a ten-minute speech from the beginning of a presentation.

Correct frequent words are defined as those words that have more than two moras and whose meaning can be understood upon listening. The parts of speech for correct frequent words are listed in Table I. To determine the correct frequent words, morphological analysis is first performed for the transcription by use of a morphological analyzer, called ChaSen 2.02,[22] and then the number of appearances of each word is counted. Lastly, the five most frequent words are identified.

The system outputs frequent word sections according to their frequency in the presentation. Output sections are not always word sections. A frequent word is considered a correct extraction if and only if the word can be recognized by listening to the output section. When the output section includes two or more words, such as ''speech recognition,'' where both ''speech'' and ''recognition'' are among the most frequent words, both words are considered to be correctly extracted. When the same word might be in some output sections, only the first output is considered correct.

The actual processing time was measured by use of a conventional personal computer (Pentium III, 1 GHz), and was 73 minutes for a ten-minute speech data. One-third of the computation is the computation of the local distance between two feature vectors. Real-time processing is possible for one-minute speech data, and parallel processing is possible for the Shift CDP algorithm without surplus processing. When the extracted pairs were listened to, the tendency described in the previous section was observed.

TABLE I. Parts of speech of correct frequent words.

Nouns (common nouns, proper nouns, not including pronouns)
Verbs (including verb stems)
Adjectives
Adverbs
Conjunctions
Interjections
Abbreviations (such as HMM, MLLR)

TABLE II. Results of experiments for extraction of the most frequent word in a data set and extraction of the five most frequent words, for one hundred sets of presentation speech data. Two cases are shown, one for each number of candidates.

Target words	Candidates	Correct rate
The most frequent word (among 100 speeches)	Only one	56%
	Top three	73%
Five most frequent words (among 500 words)	Top five	52%
	Top ten	68%

TABLE III. Performance comparison with speech recognizers. The first row indicates the performance of our system (the same as in Table III) and the second and third rows indicate the performance when speech recognizers with two types of language models are used. One recognizer is for general purpose and has a vocabulary of 60 K words, and the other is a specific recognizer that is well trained by similar transcriptions and has a vocabulary of 20 K words.

	The most frequent word		Five most frequent words	
Candidates	Only one	Top three	Top five	Top ten
Proposed method	60	79	50.3	66.7
SR 60 K	3	3	17.3	25.5
SR 19 K	74	93	69.6	85.4

Table II shows the results of the experiment. The evaluation is performed for extraction of the most frequent word in each data set and for extraction of the five most frequent words in each data set. Thus, one hundred most frequent words and five hundred most frequent words are listed. In each case, two cases for the number of candidates are shown.

The most frequent word could be correctly identified 56% with only the top candidate. When the three sections were listened to for each data set, 73 percent of the most frequent words could be understood. In 83 percent of the cases, the most frequent word was an interjection, such as ''e:'' or ''ano:'' (where '':'' denotes a long vowel; these words are used in the manner of ''well'' or ''you know''), except for a few simulated presentation speeches. The evaluation, therefore, was also done for the five most frequent words. About seventy percent of those words are content words that exclude interjections and conjunctions from the list in Table I. When an attempt was made to identify the five most frequent words in the presentation, about 70% of such frequent words could be correctly identified with the top ten candidates. Half of such content words can be obtained when those ten candidate sections were listened to.

Phrases that are incorrectly identified are mainly functional words, such as ''with the'' and ''against,'' which are often repeated in the presentation.

Next, a speech recognizer was used to compare the performance with the result. Julius 3.12, which is a free Japanese Dictation Toolkit,[23] was employed. Two types of language models were exploited. The first language model is the standard one for general purpose, attached to this speech recognizer. The vocabulary size is about 60 000 words. The second one was well trained by similar transcriptions made from other speech presentations in the same conference. The vocabulary size is about 20 000 words. Three thousand gender-dependent triphone models were used for acoustic models.

The first row indicates the performance of the proposed method, which is the same as in Table III. The second and third rows indicate the performance with use of the speech recognizer with vocabulary sizes of 60 and 20 K, respectively.

The speech recognizer for general purpose with a vocabulary size of 60 K could extract neither the most frequent word nor the five most frequent words. Two reasons are thought to be responsible for this. The first is that the recognizer was not well trained and modeled for interjections, and the second is that many specific terms do not appear in the dictionary of the speech recognizer and these terms are often the most frequent words; for example, HMM or MLLR. Such a general speech recognizer is not ideally suited for this purpose.

TABLE IV. Output examples of the system using the similar sections, where Japanese utterances are translated to English. The left column corresponds to the five most frequent words, and the next column corresponds to the words included in the ten extracted sections.

Example 1		Example 2	
Five most frequent words	Extracted words	Five most frequent words	Extracted words
1. Well	1. Well	1. Well	1. utterance speed ratio
2. search	2. searchtime	2. utterance	2. well
3. time	3. interupted	3. speaker	3. function
4. stimulus	4. in this case	4. speed	4. double
5. sound	5. because	5. local	5. DP matching
	6. (silence)		6. pure speech
	7. search time		7. almost
	8. [k]		8. speaker
	9. noise		9. that is
	10. sound		10. what is

Use of the speech recognizer well trained for this purpose yielded results, shown in the third row, better than those of the system using similar sections. However, all the specific terms and language models including such words must be prepared beforehand. Thus, much prior knowledge about the presentation is required, such as what kinds of domains and what kinds of topics and keywords are spoken in the presentation. Apparently, such sufficient information can be given only in limited cases. Preparing special terms and language models is difficult. The approach using similar sections does not require such prior knowledge of the presentations and is applicable to any kind of domain.

Table IV shows the output examples of the system using the similar sections (the results are translated to English). The left column corresponds to the five most frequent words, and the next column corresponds to the words included in the ten extracted sections. Figure 11 shows the output image of the system. The system provides the user with information on where and how many times the frequent word is spoken in the presentation, by playing the extracted sections and showing the repeated number with their location information at the same time, in the manner shown in this figure. The topics and keywords in the presentation can be understood when just ten sections (less than ten seconds) are listened to, as shown in Fig. 11.

The same label can be affixed to these similar sections, and can be considered a speech label. Because these repeated phrases are thought to be important in the talk, the sequence of repeated phrases can serve as a kind of digest of the presentation.

IV. CONCLUSION

This paper proposes a new approach for identifying the frequent word sections in nonsegmented and nonrecognized

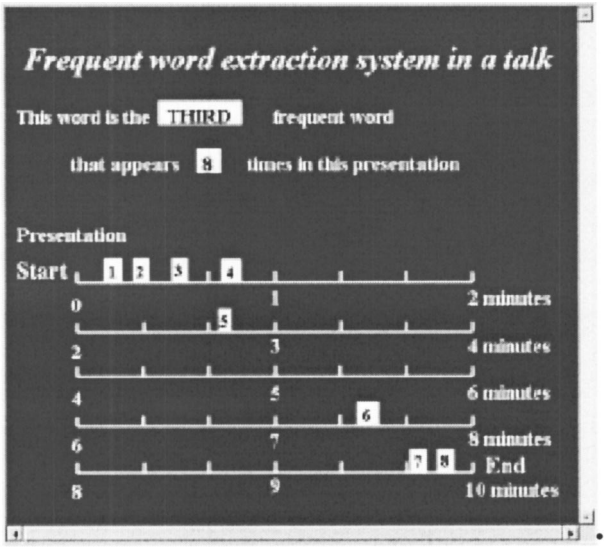

FIG. 11. Sample of the display for a user. The system provides the user with information on where and how many times the frequent word is spoken in the presentation, by playing the extracted sections and showing the number of repetitions, along with location information. Listening to ten sections (less than ten seconds) enables the user to understand the keywords.

speech presentations. The key technique for this approach is Shift CDP, which was developed for efficient extraction of similar sections between two time sequence data sets and extended to extract repeated words or phrases in a speech presentation. The experimental results show that Shift CDP could extract the acoustically similar speech sections, and by summing such sections, the frequent word sections can be identified without prior domain knowledge of the presentation. When a certain label is affixed to each of those extracted sections, the labeled sections can be considered those that characterize the speech presentation.

Currently, application of the method is limited to a speech delivered by a single speaker, such as an oral presentation. Topics for future study include extending the method to a speaker- and language-independent method that can be applied to oral discussions, by utilizing acoustic models of a language-independent phonetic code.[15] The extracted speech sections still involve nonsense speech sections. Therefore, developing a method for selecting adequate frequent phrase sections that characterize the whole speech is also an important task for the future. When the method is applied to information retrieval for a large speech data set, it still takes more time than the text search or phonetic lattice search. Speed for information retrieval remains to be improved.

ACKNOWLEDGMENTS

The authors used Spontaneous Speech Corpus of Japanese, and would like to express their sincere gratitude to Dr. Tetsuya Kawahara for helping them with processing this speech corpus.

APPENDIX: ALGORITHM FOR EXTRACTING SIMILAR SECTIONS IN A PRESENTATION SPEECH USING SHIFT CDP

LOOP1: for each Input $X_k(1 \leqslant k \leqslant N_I)$
$R_k = X_k$
If(URP Creating condition: N_{Shift} frames after prior URP)
URP_NUM++
LOOP2: for each $\text{URP}_i(1 \leqslant i \leqslant \text{URP\_NUM})$
Perform the CDP and get $G(i,k)$: Distance of URP_i at input k
If (URP_i detects a similar section)
Output the distance of URP_i: $G(i,k)$
Similar sections: $[S(i,k),k]$ and (S_i,E_i)
Integrates the result until input $k-1$
LOOP2 End
LOOP1 End

In LOOP2, a judgment is made as to whether URP_i detects a similar section at input time k. When URP_i detects a similar section, the two corresponding sections are output. S_i and E_i in the algorithm indicate the start frame and the end frame of URP_i, and these newly detected sections are integrated with the similar sections that had been detected up to the previous input time interval.

[1] M. Bacchiani, "Automatic transcription of voicemail at AT&T," Proceedings of International Conference on Acoustics, Speech, and Signal Processing, vol. I, 25–28 (2001).
[2] G. Zweig, J. Huang, and M. Padmanabhan, "Extracting caller information from voicemail," Proceedings of EUROSPEECH, vol. 1, 291–294 (2002).
[3] C. Hori, S. Furui, R. Malkin, H. Yu, and A. Waibel, "Automatic speech summarization applied to English broadcast news speech," Proceedings of International Conference on Acoustics, Speech, and Signal Processing, vol. I, 9–12 (2002).
[4] B. Peskin, S. Connolly, L. Gillick, S. Lowe, D. McAllaster, V. Nagesha, P. van Mulbregt, and S. Wegmann, "Improvements in Switchboard recognition and topic identification," Proceedings of International Conference on Acoustics, Speech, and Signal Processing, vol. I, pp. 303–306 (1996).
[5] O. Kimball, R. Iyer, H. Gish, S. Miller, and F. Richardson, "Extracting descriptive noun phrases from conversational speech," Proceedings of International Conference on Acoustics, Speech, and Signal Processing, vol. I, 33–36 (2002).
[6] J. Huang, V. Goel, R. Gopinath, B. Kingsbury, P. Olsen, and K. Visweswariah, "Large vocabulary conversational speech recognition with the extended maximum likelihood linear transformation (EMLLT) model," Proceedings of International Conference on Spoken Language Processing (2002).
[7] S. Matsoukas, T. Colthurst, O. Kimball, A. Solomonoff, F. Richardson, C. Quillen, H. Gish, and P. Dognin, "The 2001 BYBLOS English large vocabulary conversational speech recognition system," Proceedings of International Conference on Acoustics, Speech, and Signal Processing, vol. I 741–744 (2002).
[8] Hiroaki Nanjo, Kazuomi Kato, and Tatsuya Kawahara, "Speaking rate dependent acoustic modeling for spontaneous lecture speech recognition," Proceedings of EUROSPEECH, vol. 4, 2531–2534 (2002).
[9] Y. Itoh, "A matching algorithm between arbitrary sections of two speech data for speech retrieval by speech," Proceedings of International Conference on Acoustics, Speech, and Signal Processing, vol. 1, 593–596 (2001).
[10] Y. Itoh and K. Tanaka, "Automatic Labeling and Digesting for Lecture Speech Utilizing Repeated Speech by Shift CDP," Proceedings of EUROSPEECH2001, vol. 3, 1805–1807 (2001).
[11] H. Kojima, Y. Itoh, and R. Oka, "Location identification of a mobile robot by applying reference interval-free continuous dynamic programming to time-varying images," Proceedings of Third International Symposium on Intelligent Robotics Systems (1995).
[12] K. Ng and V. W. Zue, "Subword unit representations for spoken document

retrieval,'' Proceedings of EUROSPEECH1997, 1607–1610 (1997).
[13] K. M. Knill and S. J. Young, ''Fast implementation methods for Viterbi based word spotting,'' Proceedings of International Conference on Acoustics, Speech, and Signal Processing, vol. 1, 522–525 (1996).
[14] D. A. James and S. J. Young, ''A fast lattice-based approach to vocabulary independent wordspotting,'' Proceedings of International Conference on Acoustics, Speech, and Signal Processing, vol. 1, 377–380 (1994).
[15] K. Tanaka and H. Kojima, ''Speech recognition method with a language-independent intermediate phonetic code,'' Proceedings of International Conference on Spoken Language Processing, vol. IV, 191–194 (2000).
[16] S. Sinclair and C. Watson, ''The development of the Otago speech database,'' Proceedings of ANNES '95, edited by N. Kasabov and G. Cogill, Los Alamitos, CA: IEEE Press (1995).
[17] Y. Itoh, J. Kiyama, and R. Oka, ''A proposal for a new algorithm of reference interval-free Continuous DP for real-time speech or text retrieval,'' Proceedings of International Conference on Acoustics, Speech, and Signal Processing, vol. 1, 486–489 (1996).
[18] J. Kiyama, Y. Itoh, and R. Oka, ''Automatic detection of topic boundaries and keywords in arbitrary speech using Incremental Reference Interval-free Continuous DP,'' Proceedings of International Conference on Spoken Language Processing, vol. 1, 1946–1949 (1996).
[19] H. Sakoe and S. Chiba, ''Dynamic Programming algorithm optimization for spoken word recognition,'' IEEE Trans. Acoust., Speech, Signal Process. **ASSP-26**, 43–49 (1978).
[20] R. Oka and H. Matsumura, ''Speaker independent word speech recognition using the blurred orientation pattern obtained from the vector field of spectrum,'' Proceedings of International Conference on Pattern Recognition, 17–20 (1988).
[21] K. Maekawa, H. Koiso, S. Furui, and H. Isahara, ''Spontaneous speech corpus of Japanese,'' Proceedings of LREC2000, vol. 2, 947–952 (2000).
[22] M. Asahara and Y. Matsumoto, ''Extended models and tools for high-performance part-of-speech tagger,'' Proceedings of International Conference on Computational Linguistics, 21–27 (2000).
[23] T. Kawahara, T. Kobayashi, K. Takeda, N. Minematsu, K. Itou, M. Yamamoto, A. Yamada, T. Utsuro, and K. Shikano, ''Japanese dictation toolkit-plug-and-play framework for speech recognition R&D,'' IEEE workshop on Automatic Speech Recognition and Understanding (1999).
[24] G. A. Smith, H. Murase, and K. Kashino, ''Quick audio retrieval using active search,'' Proceedings of International Conference on Acoustics, Speech, and Signal Processing, vol. 6, 3777–3780 (1998).
[25] F. Chen, ''The use of emphasis to automatically summarize a spoken discourse,'' Proceedings of International Conference on Acoustics, Speech, and Signal Processing, vol. I, 229–232 (1992).

Theoretical study in applications of doublet mechanics to detect tissue pathological changes in elastic properties using high frequency ultrasound

Christopher Layman and Junru Wu[a)]
Department of Physics, University of Vermont, Burlington, Vermont 05405

(Received 19 January 2004; revised 7 May 2004; accepted 8 May 2004)

The mathematical framework of a new elastic theory—doublet mechanics (DM)—was reviewed. The fundamental difference between DM and classical continuum mechanics (CCM) is that the former has taken the discrete nature of tissue on the cellular level into account and the latter assumes tissue is uniform and continuous. Theoretical calculations based on DM were performed for reflection coefficients of a substrate–tissue layer–substrate assembly. Results of computer simulations have shown that ultrasound reflection coefficients in the range of 15–30 MHz are sensitive to changes in cell size and elastic moduli of tissue according to DM but not to CCM. Potential experimental applications of this technique to tissue characterization are discussed. [DOI: 10.1121/1.1768252]

PACS numbers: 43.80.Cs, 43.35.Cg [FD] Pages: 1244–1253

I. INTRODUCTION

The wave equation that has been used to describe ultrasound propagation is based on classical continuum mechanics (CCM); it assumes that materials are continuous (Kinsler *et al.*, 1982). Many bio-materials, such as soft tissue, however, have discrete structures at the cellular scale. At a relatively low frequency, for example 1–10 MHz, since the wavelength, λ, is of an order of millimeter or submillimeter, much greater than the size of cells (approximately of the order of micrometer), the wave equation derived from CCM is a legitimate approximation. When ultrasound frequencies used in medicine become higher and higher *in vivo* and *in vitro*, the wavelength gets smaller, and the discrete structure of tissue can no longer be ignored. Doublet mechanics (DM) or nanomechanics, a new elastic theory, was developed (Granik, 1997; Wu *et al.*, 2004) to address the granular feature of a medium.

The fundamental unit of a material in DM can be represented by a bundle of spheres or nodes separated by a finite distance. The strain of a bundle due to distortion can be expressed as a multi-scale *M*th-order Taylor expansion of the internodal distances at its equilibrium configuration (Ferrari, 2000). It was pointed out by our previous publication (Wu *et al.*, 2004) that readers should not relate the order (M) of the Taylor expansion to the degree of accuracy of this presentation in a common mathematic sense. In fact, the order of M represents the degree of the discreteness of a system; the higher the M order a Taylor expansion includes, the more discrete nature of the system DM represents (Ferrari *et al.*, 1997). For example, when $M=1$, i.e., only the first order of the Taylor expansion is used, it reduces to the CCM case, i.e., the system described by DM becomes a system that does not have a discrete nature at all. In this case, the results obtained from DM completely agree with those predicted by CCM. When $M=\infty$, on the other hand, DM describes a crystal which has a regular and periodic lattice structure. When $\infty > M > 1$, the discreteness of systems represented by DM is between continuous (nongranular) and periodically discrete.

In our recent paper (Wu *et al.*, 2004), a fundamental mathematical framework for applications of DM to ultrasound propagation in a discrete or granular material was introduced, in addition a multi-scale wave equation (MSWE) and the dispersion relations for longitudinal waves and shear waves were also derived. It was found that for $M=2$ of MSWE, the dispersion relation most closely resembles the experimental data of soft tissue, i.e., the phase velocity increases as frequency increases (Kremkau *et al.*, 1981; Bamber, 1981; Wu *et al.*, 2004).

A recent study (Liu and Ferrari, 2002) demonstrated that a mathematical model based on DM was able to distinguish the difference in cell size and elastic moduli of malignant breast tissue from normal breast tissue; it was, however, not possible by using continuum mechanics. They used DM ($M=2$) to calculate the ultrasound reflection coefficients of a thin tissue film embedded between two glass slides for a shear wave. By measuring the reflection coefficient of a glass–tissue–glass assembly, they found that elastic parameters of the malignant tissue were significantly different from the normal tissue according to DM. Classical continuum mechanics, however, predicted the elastic parameters were statistically undistinguishable between those two tissues. Therefore, they concluded that this technology may be useful to distinguish malignant tissue from normal tissue. In their modeling, the shear wave generated through the mode conversion (Liu, 2003) was considered nondispersive. Since they were interested mainly in low frequencies (1–10 MHz), neglecting dispersion did not introduce a significant error. If high frequency ultrasound (≈30 MHz) is used, it becomes essential to consider the dispersion (Wu *et al.*, 2004).

In this paper, we expand the technology developed by Liu and Ferrari to much higher frequencies. We first review the fundamental framework of DM, the derivation of wave

[a)]Author to whom correspondence should be sent. Electronic mail: junru.wu@uvm.edu

equations and dispersion relations for $M=2$. For a plastic (or glass) slide–tissue–plastic (or glass) slide assembly, results of computer simulations for longitudinal and shear wave reflection coefficients to satisfy specific boundary conditions are presented after considering the dispersion relation. Our computational results show that the sensitivity of this technique is greatly enhanced when high frequency ultrasound is used.

II. THEORY

The fundamental microstructure in DM is called a doublet bundle that contains a reference node and its n neighboring nodes separated by their equilibrium internode distance of η_α. In our application, η_α is chosen approximately to be equal to the tissue cell size. A detailed derivation of a multiscale wave equation, dispersion relation for longitudinal and shear waves was given in our earlier publication (Wu *et al.*, 2004). During the derivation, the loss was not included and the dispersion was caused by wave propagation through a micro discrete or partially discrete structure. Results obtained from our early paper indicate that the discreteness of a system may introduce dispersion. When the wavelength of ultrasound becomes close to η_α, dispersion associated with the discrete nature of a system may become important and dominant. In this paper, the final results of wave equations for $M=1$ and $M=2$ obtained in the early publication are given by Eqs. (1) and (3) as follows (definitions of symbols are given in the List of Symbols and our early publication):

$$\mathbf{C_{ijkl}}\frac{\partial^2 \mathbf{u_j}}{\partial \mathbf{x_k}\partial \mathbf{x_l}}=\rho\frac{\partial^2 \mathbf{u_i}}{\partial \mathbf{t}^2}, \tag{1}$$

where

$$\mathbf{C_{ijkl}}=\sum_{\alpha=1}^{\mathbf{n}}\sum_{\beta=1}^{\mathbf{n}}\mathbf{A}_{\alpha\beta}\tau^0_{\alpha\mathbf{i}}\tau^0_{\alpha\mathbf{j}}\tau^0_{\beta\mathbf{k}}\tau^0_{\beta\mathbf{l}}, \tag{2}$$

and

$$\mathbf{C_{ijkl}}\frac{\partial^2 \mathbf{u_j}}{\partial \mathbf{x_k}\partial \mathbf{x_l}}-\mathbf{C_{ijklmn}}\frac{\partial^4 \mathbf{u_j}}{\partial \mathbf{x_k}\partial \mathbf{x_l}\partial \mathbf{x_m}\partial \mathbf{x_n}}=\rho\frac{\partial^2 \mathbf{u_i}}{\partial \mathbf{t}^2}, \tag{3}$$

where

$$\mathbf{C_{ijklmn}}=\sum_{\alpha=1}^{n}\sum_{\beta=1}^{n}\mathbf{A}_{\alpha\beta}\frac{\eta_\alpha^2}{4}\tau^0_{\alpha\mathbf{i}}\tau^0_{\alpha\mathbf{j}}\tau^0_{\alpha\mathbf{k}}\tau^0_{\beta\mathbf{l}}\tau^0_{\beta\mathbf{m}}\tau^0_{\beta\mathbf{n}}. \tag{4}$$

A. Dispersion of longitudinal waves

The phase velocities $\mathbf{C^L_{p,1}}$ and $\mathbf{C^L_{p,2}}$ respectively for $M=1$ and $M=2$ longitudinal waves are

$$\mathbf{C^L_{p,1}}=\sqrt{\frac{\mathbf{A}_{11}-\mathbf{A}_{44}/2}{\rho}}=\sqrt{\frac{\lambda+2\mu}{\rho}}, \tag{5}$$

$$\mathbf{C^L_{p,2}}=\sqrt{\frac{\mathbf{A}_{11}-\mathbf{A}_{44}/2}{\rho}+\frac{1}{4\rho}\left(\frac{\eta_\alpha}{\lambda}\right)^2\left(\mathbf{A}_{11}-\frac{\mathbf{A}_{44}}{\sqrt{2}}+\frac{\mathbf{A}_{44}}{4}\right)(2\pi)^2}. \tag{6}$$

The longitudinal phase velocity for $M=1$ is dispersionless and agrees with that predicted by CCM. The longitudinal phase velocity for $M=2$, $\mathbf{C^L_{p,2}}$, is a function of η_α/λ, and increases when the wavelength decreases.

B. Dispersion of share waves

The shear waves phase velocities $\mathbf{C^S_{p,1}}$ and $\mathbf{C^S_{p,2}}$ respectively for $M=1$ and $M=2$ are

$$\mathbf{C^S_{p,1}}=\sqrt{\frac{\mathbf{A}_{44}/4}{\rho}}=\sqrt{\frac{\mu}{\rho}}. \tag{7}$$

$$\mathbf{C^S_{p,2}}=\sqrt{\frac{\mathbf{A}_{44}/4}{\rho}+\frac{1}{\rho}\left(\frac{\eta_\alpha}{\lambda}\right)^2\frac{\mathbf{A}_{44}}{32}(2\pi)^2}. \tag{8}$$

Notice that the phase velocity of $M=1$ for shear waves [Eq. (7)] is constant and agrees with that derived from CCM. Just like its longitudinal wave counterpart, there is no dispersion. For $M=2$, the phase velocity of shear waves is η_α/λ dependent.

C. Derivation of reflection coefficients

The system considered here consists of a thin tissue layer embedded between two plastic (or glass) slides [Fig. 1(a)]. The tissue layer is considered as a discrete material that is treated by DM. Plastic (or glass) slides are much thicker than the wavelength and are considered to be isotropic, uniform, and continuous for mathematical simplicity; they are treated by CCM. A plane-harmonic wave (0) is normally incident upon the interface between slide 1 and the tissue layer [Fig. 1(b)]. The first reflected plane-wave (1) bounces back from the first interface. The refracted wave (2) travels into the tissue layer. When it reaches the tissue-slide 2 interface, the second reflected wave (3) propagates vertically upward and the second refracted wave (4) propagates into slide 2. Since the incidence angle is 0 degrees (normal incidence), there is no mode conversion; i.e., the four waves (1) to (4) are either all longitudinal if the incident wave (0) is a longitudinal wave or all shear waves if the incident wave is a shear wave. Neglecting the common time-dependent term, $\mathrm{Exp}[-i\omega t]$ (ω is the angular frequency), plane waves of (0)–(4) in Fig. 1(b) can be respectively represented by Eqs.

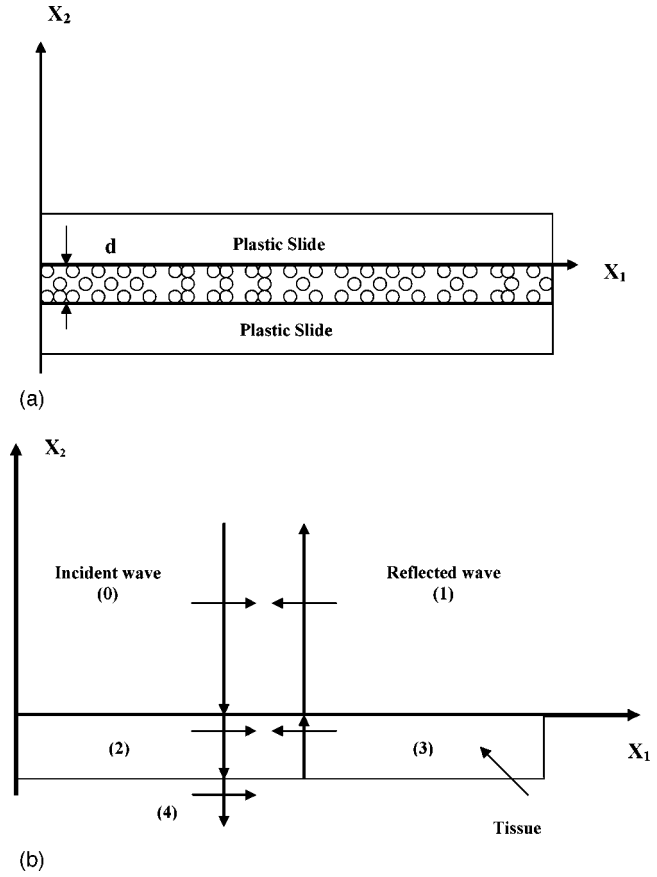

FIG. 1. (a) Illustration of a substrate–tissue layer–substrate assembly and its Cartesian coordinates. (b) Illustration of waves propagating in a substrate–tissue layer–substrate assembly. Vertical arrows represent wave propagation directions. Horizontal arrows show the polarization directions of shear waves.

(9)–(13) for longitudinal and Eqs. (14)–(18) for shear waves:

$$\mathbf{u}_2^{(0)} = \mathbf{A}_{0\mathbf{L}} \operatorname{Exp}[-\mathbf{i}\mathbf{k}_{1\mathbf{L}}\mathbf{x}_2], \tag{9}$$

$$\mathbf{u}_2^{(1)} = \mathbf{A}_{1\mathbf{L}} \operatorname{Exp}[\mathbf{i}\mathbf{k}_{1\mathbf{L}}\mathbf{x}_2], \tag{10}$$

$$\mathbf{u}_2^{(2)} = \mathbf{A}_{2\mathbf{L}} \operatorname{Exp}[-\mathbf{i}\mathbf{k}_{2\mathbf{L}}\mathbf{x}_2], \tag{11}$$

$$\mathbf{u}_2^{(3)} = \mathbf{A}_{3\mathbf{L}} \operatorname{Exp}[\mathbf{i}\mathbf{k}_{2\mathbf{L}}\mathbf{x}_2], \tag{12}$$

$$\mathbf{u}_2^{(4)} = \mathbf{A}_{4\mathbf{L}} \operatorname{Exp}[-\mathbf{i}\mathbf{k}_{1\mathbf{L}}\mathbf{x}_2], \tag{13}$$

$$\mathbf{u}_1^{(0)} = \mathbf{A}_{0\mathbf{S}} \operatorname{Exp}[-\mathbf{i}\mathbf{k}_{1\mathbf{S}}\mathbf{x}_2], \tag{14}$$

$$\mathbf{u}_1^{(1)} = -\mathbf{A}_{1\mathbf{S}} \operatorname{Exp}[\mathbf{i}\mathbf{k}_{1\mathbf{S}}\mathbf{x}_2], \tag{15}$$

$$\mathbf{u}_1^{(2)} = \mathbf{A}_{2\mathbf{S}} \operatorname{Exp}[-\mathbf{i}\mathbf{k}_{2\mathbf{S}}\mathbf{x}_2], \tag{16}$$

$$\mathbf{u}_1^{(3)} = -\mathbf{A}_{3\mathbf{S}} \operatorname{Exp}[\mathbf{i}\mathbf{k}_{2\mathbf{S}}\mathbf{x}_2], \tag{17}$$

$$\mathbf{u}_1^{(4)} = \mathbf{A}_{4\mathbf{S}} \operatorname{Exp}[-\mathbf{i}\mathbf{k}_{1\mathbf{S}}\mathbf{x}_2], \tag{18}$$

where $\mathbf{k}_{1\mathbf{L}} = \omega/\mathbf{c}_{1\mathbf{L}}$, $\mathbf{k}_{2\mathbf{L}} = \omega/\mathbf{c}_{2\mathbf{L}}$, $\mathbf{k}_{1\mathbf{S}} = \omega/\mathbf{c}_{1\mathbf{S}}$, and $\mathbf{k}_{2\mathbf{S}} = \omega/\mathbf{c}_{2\mathbf{S}}$. Here $\mathbf{c}_{1\mathbf{L}}$ and $\mathbf{c}_{2\mathbf{L}}$ are longitudinal wave phase velocities for the slide and tissue, and $\mathbf{c}_{1\mathbf{S}}$ and $\mathbf{c}_{2\mathbf{S}}$ shear wave phase velocities for the slide and tissue, respectively. The longitudinal and shear phase velocities for the slides are nondispersive and are described by results obtained for $M=1$, i.e., Eqs. (5) and (7), respectively (using the parameters of the slides) and the longitudinal and shear phase velocities for tissues are given by Eqs. (6) and (8), respectively; they are dispersive and obtained for $M=2$ cases. The reflection coefficients for longitudinal waves, $\mathbf{R}_\mathbf{L}$, and shear waves, $\mathbf{R}_\mathbf{S}$, are defined as

$$\mathbf{R}_\mathbf{L} = \frac{|\mathbf{A}_{1\mathbf{L}}|}{|\mathbf{A}_{0\mathbf{L}}|} \tag{19}$$

and

$$\mathbf{R}_\mathbf{S} = \frac{|\mathbf{A}_{1\mathbf{S}}|}{|\mathbf{A}_{0\mathbf{S}}|}. \tag{20}$$

The reflection coefficients, $\mathbf{R}_\mathbf{L}$, may be solved by satisfying the following continuity equations at the two interfaces $x_2=0$ and $x_2=-d$:

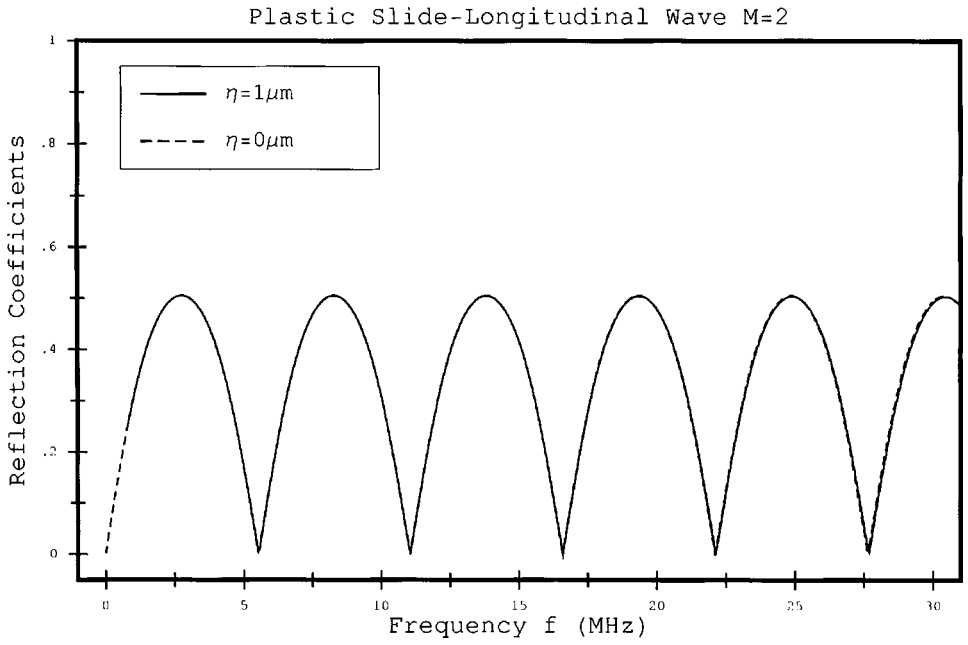

FIG. 2. Reflection coefficient of longitudinal waves for a plastic–tissue–plastic slide assembly versus frequency for $M=2$. $\eta=0$ and 1 μm.

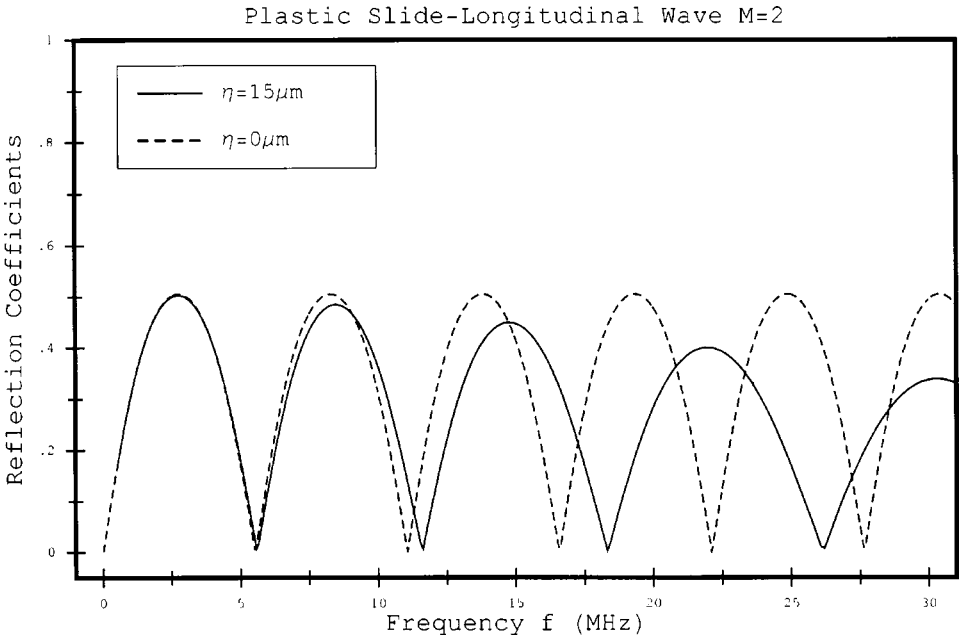

FIG. 3. Reflection coefficient of longitudinal waves for a plastic–tissue–plastic slide assembly versus frequency for $M=2$. $\eta=0$, and 15 μm.

(1) continuity of normal displacement at $x_2=0$:

$$\mathbf{u}_2^{(0)}+\mathbf{u}_2^{(1)}=\mathbf{u}_2^{(2)}+\mathbf{u}_2^{(3)}, \tag{21}$$

(2) continuity of normal stress at $x_2=0$:

$$\sigma_{22}^{(0)}+\sigma_{22}^{(1)}=\sigma_{22}^{(2)}+\sigma_{22}^{(3)}, \tag{22}$$

(3) continuity of normal displacement at $x_2=-d$:

$$\mathbf{u}_2^{(2)}+\mathbf{u}_2^{(3)}=\mathbf{u}_2^{(4)}, \tag{23}$$

(4) continuity of normal stress at $x_2=-d$:

$$\sigma_{22}^{(2)}+\sigma_{22}^{(3)}=\sigma_{22}^{(4)}. \tag{24}$$

The reflection coefficients, $\mathbf{R_S}$, may be solved by satisfying the following continuity equations at two interfaces $x_2=0$ and $x_2=-d$:

(1) continuity of transverse displacement at $x_2=0$:

$$\mathbf{u}_1^{(0)}+\mathbf{u}_1^{(1)}=\mathbf{u}_1^{(2)}+\mathbf{u}_1^{(3)}, \tag{25}$$

(2) continuity of shear stress at $x_2=0$:

$$\sigma_{21}^{(0)}+\sigma_{21}^{(1)}=\sigma_{21}^{(2)}+\sigma_{21}^{(3)}, \tag{26}$$

(3) continuity of transverse displacement at $x_2=-d$:

$$\mathbf{u}_1^{(2)}+\mathbf{u}_1^{(3)}=\mathbf{u}_1^{(4)}, \tag{27}$$

(4) continuity of shear stress at $x_2=-d$:

$$\sigma_{21}^{(2)}+\sigma_{21}^{(3)}=\sigma_{21}^{(4)}. \tag{28}$$

The expression for longitudinal and shear stress for $M=2$ was given by (Wu *et al.*, 2004)

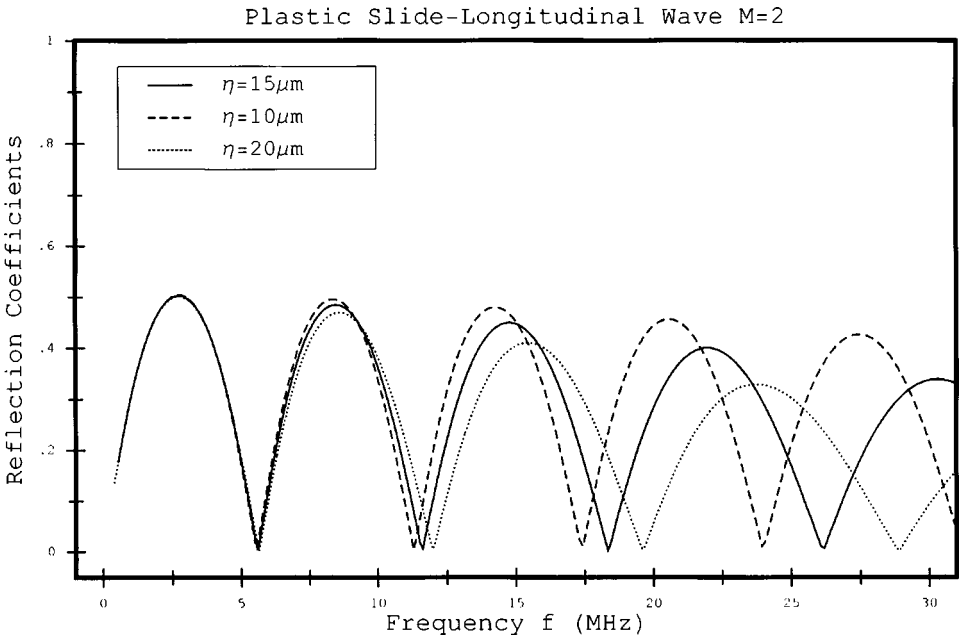

FIG. 4. Reflection coefficient of longitudinal waves for a plastic–tissue–plastic slide assembly versus frequency for $M=2$. $\eta=10$, 15, and 20 μm.

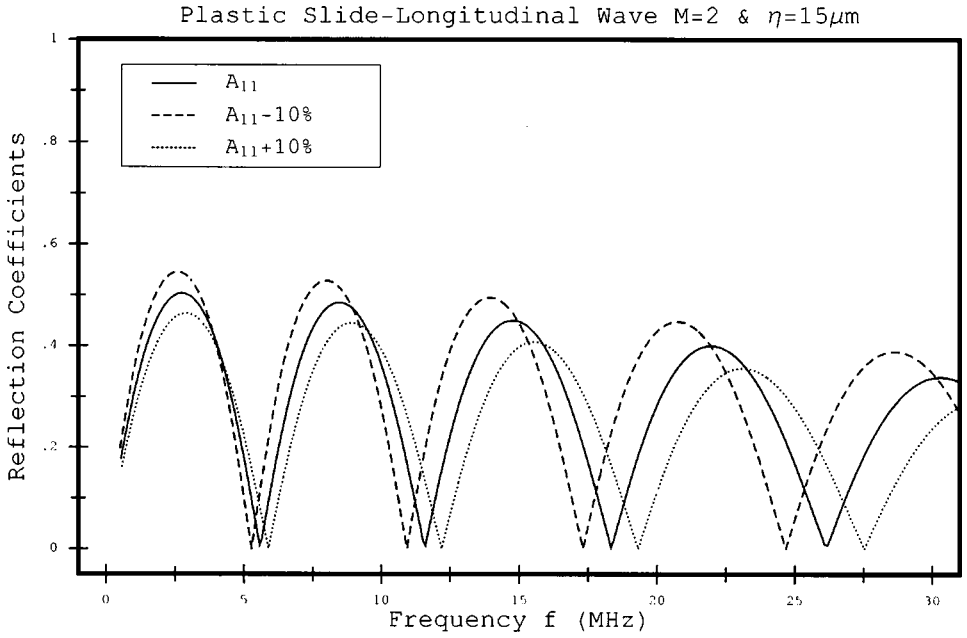

FIG. 5. Reflection coefficient of longitudinal waves for a plastic–tissue–plastic slide assembly versus frequency for $M=2$. $\eta=15$ μm and $\mathbf{A}_{11}$ changes $\pm 10\%$.

$$\sigma_{\mathbf{ij}}=\sum_{\alpha=1}^{\mathbf{n}} \tau^0_{\alpha\mathbf{i}}\left(\tau^0_{\alpha\mathbf{j}}\mathbf{p}_\alpha-\frac{1}{2}\eta_\alpha\tau^0_{\alpha\mathbf{j}}\tau^0_{\alpha\mathbf{k}}\frac{\partial \mathbf{p}_\alpha}{\partial \mathbf{x_k}}\right), \tag{29}$$

where

$$\mathbf{p}_\alpha=\sum_{\beta=1}^{\mathbf{n}} \mathbf{A}_{\alpha\beta}\varepsilon_\beta . \tag{30}$$

III. RESULTS OF COMPUTER SIMULATION

For a tissue layer, we assumed η_α ($\alpha=1,...,6)=\eta$, density $\rho=1000$ kg/m^3, and λ and μ were assigned to the averaged values in the literature for soft tissue; i.e., $\lambda=3.0$ GPa and $\mu=0.5$ GPa. The thickness of the tissue layer was 150 μm. For glass slides (Lide, 1993), density$=2.5\times10^3$ kg/m^3, $\lambda=26.4$ GPa, and $\mu=29.0$ GPa. For plastic (Polycarbonate, commercial name Lexan®) slides, density $=1.3\times10^3$ kg/m^3, $\lambda=3.2$ GPa, and $\mu=1.5$ Gpa; these were measured using an ultrasound spectroscopy technique (Wu, 1996).

Figure 2 consists of two curves for longitudinal waves: The solid and dotted lines represent the reflection coefficient of $M=2$ respectively for $\eta=1$ μm and $\eta=0$ for a plastic slide–tissue–plastic slide assembly, respectively. In this case, the difference of these two curves was negligible when $f<15$ MHz. Above 15 MHz, the difference was also small since $\eta=1$ μm, which is rather small relative to $\lambda=100$ μm. The oscillatory feature of both curves reflected the wave interference nature between the two reflected waves at the front and back interfaces of the tissue layer. Figure 3 includes two similar plots: one for $\eta=0$ and the other for $\eta=15$ μm (a size that is close to many cell sizes). Here the difference between DM ($M=2$, $\eta=15$ μm) and continuum

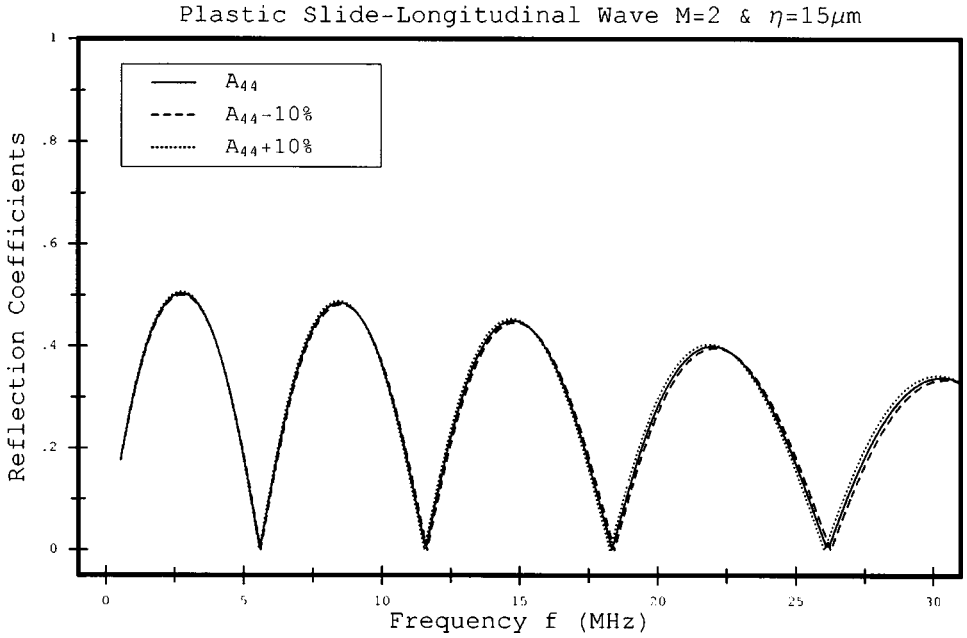

FIG. 6. Reflection coefficient of longitudinal waves for a plastic–tissue–plastic slide assembly versus frequency for $M=2$. $\eta=15$ μm and $\mathbf{A}_{44}$ changes $\pm 10\%$.

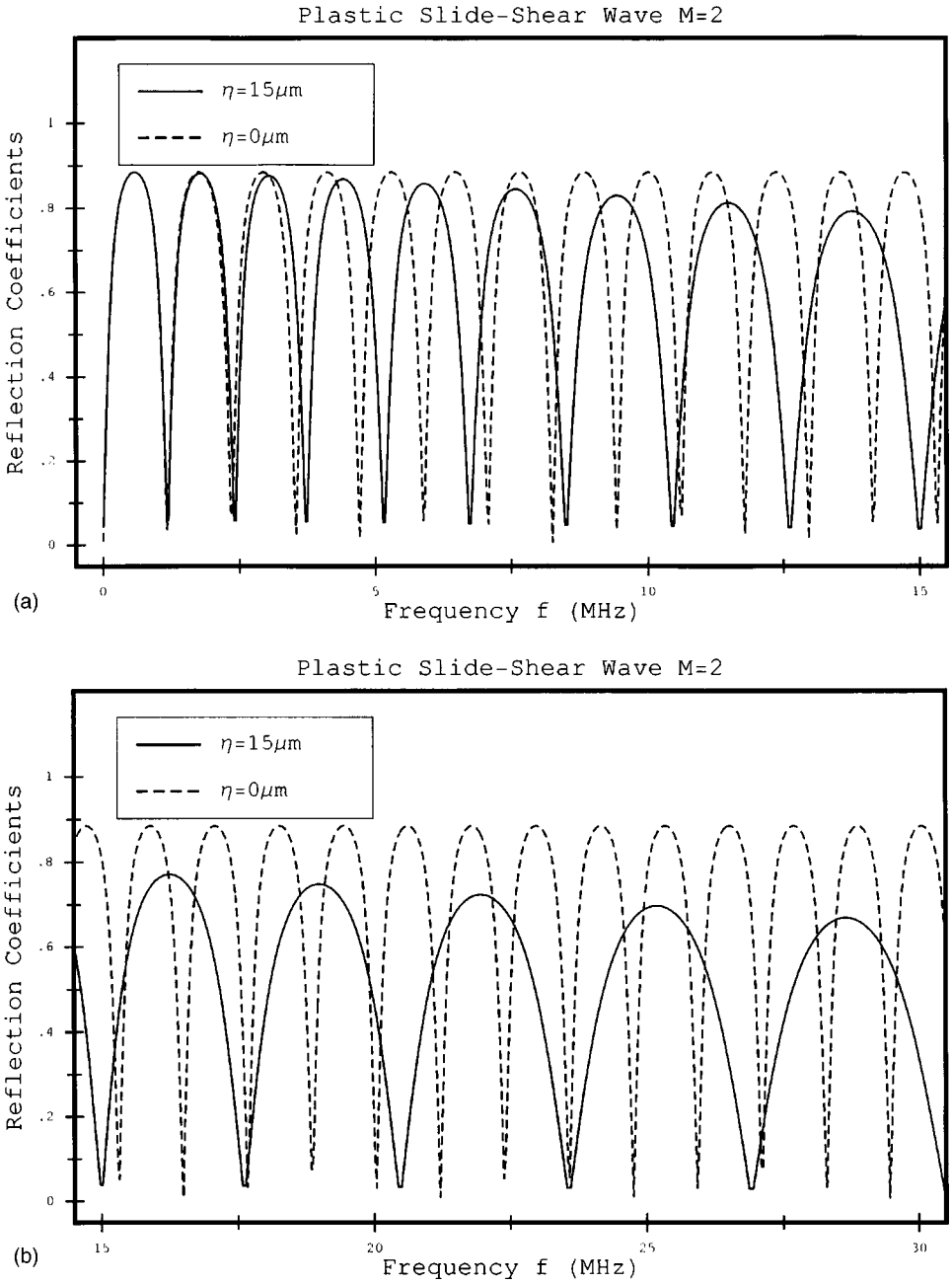

FIG. 7. (a) Reflection coefficient of shear waves for a plastic–tissue–plastic slide assembly versus frequency for $M=2$. $\eta=0$ and 15 μm, $0<f<15$ MHz. (b) Reflection coefficient of shear waves for a plastic–tissue–plastic slide assembly versus frequency for $M=2$. $\eta=0$ and 15 μm, $15<f<30$ MHz.

mechanics ($\eta=0$) became more evident, especially when $f>10$ MHz. Obviously, the reflection coefficient is η dependent. A comparison of reflection coefficients of various η, at frequencies between 0 and 30 MHz, is shown in Fig. 4. One may observe that at low frequencies ($f<5$ MHz), the reflection coefficient is nearly independent of η; it approaches the value predicted by CCM. Another observation is that when η is decreased from 20 to 10 μm, the peak reflection coefficients became greater, and the frequency at which the minimum reflection coefficients occur became smaller. For example, when η changed from 15 to 10 μm, the location of the fourth minimum shifted by 2.2 MHz (from 26.2 to 24 MHz). Meanwhile, the reflection coefficient maximum for the fourth peak increased by 0.05 (from 0.41 to 0.46).

Figures 5 and 6 demonstrate reflection coefficients of longitudinal waves as a function of frequency as parameters $\mathbf{A}_{11}$ and $\mathbf{A}_{44}$, respectively, change by $\pm 10\%$. Since $\mathbf{A}_{44}=4\mu$, and μ is related to a shear modulus in CCM and the value of the shear modulus has little influence on the properties of longitudinal waves, the reflection coefficient was much more sensitive to the change of $\mathbf{A}_{11}$ than that of $\mathbf{A}_{44}$. When $\mathbf{A}_{11}$ increased by 10%, the location of the fourth reflection minimum increased by 1.4 MHz and the reflection maximum of the fourth peak decreased by 0.6. Figure 6 shows that essentially no change occurs when $\mathbf{A}_{44}$ changes by 10%.

Figures 7(a) and (b) illustrate reflection coefficient ($M=2$) of shear waves as a function of frequency in a frequency range 0–15 MHz and 15–30 MHz, respectively. The dotted and solid lines represented cases of $\eta=0$ (corresponding to

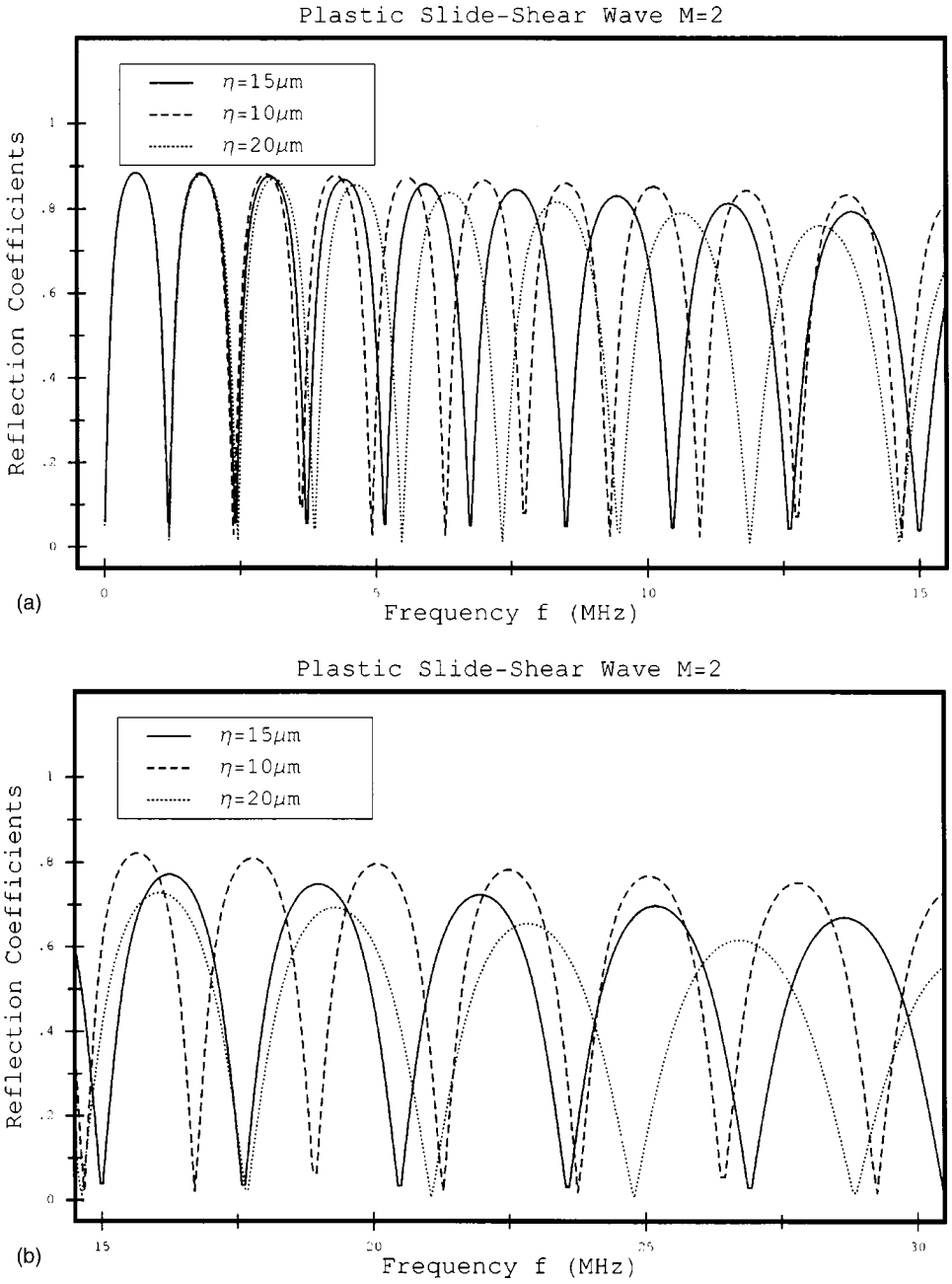

FIG. 8. (a) Reflection coefficient of shear waves for a plastic–tissue–plastic slide assembly versus frequency for $M=2$. η=10, 15 and 20 μm, $0<f<15$ MHz. (b) Reflection coefficient of shear waves for a plastic–tissue–plastic slide assembly versus frequency for $M=2$. η=10, 15, and 20 μm, $15<f<30$ MHz.

the CCM case) and η=15 μm, respectively. Like the longitudinal wave, for η=0, the peak value of the reflection coefficient was independent of frequency and for η=15 μm, it decreased as frequency increased. Another observation is for η=0; the frequency spacing between two nearest minima (or maxima) was independent of frequency and, for η=15 μm, it increased as frequency increased. Similar plots were shown in Figs. 8(a) and (b), when η was equal to 10, 15, and 20 μm. The general trend was very similar to the longitudinal case shown in Fig. 3. For example, when η changes from 15 to 10 μm, the location of the 13th minimum shifted downward about 5.6 MHz. Meanwhile, the reflection coefficient maximum for the 13th peak increased by 0.1.

In Figs. 9(a) and (b), $\mathbf{A}_{44}$ of tissue was treated as a parameter and changed by $\pm$10%; the shear reflection coefficient was sensitive to the change of $\mathbf{A}_{44}$. The 13th peak reflection coefficient decreased by 0.03 and the location of the 13th minimum increased by 1.4 MHz when $\mathbf{A}_{44}$ increases by 10%. Similar calculations were done in which the value of $\mathbf{A}_{11}$ for tissue was varied; the reflection coefficient stayed the same when $\mathbf{A}_{11}$ was varied $\pm$10% (not shown here).

The results of the reflection coefficients were compared between glass slides and plastic slides in Fig. 10. Figures 10(a) and (b) are for η=0 and η=15 μm, respectively. It is evident that the reflection coefficients were smaller if plastic slides were used.

IV. DISCUSSION

Our computer simulation results suggest that the reflection coefficients in DM are sensitive to changes in the inter-

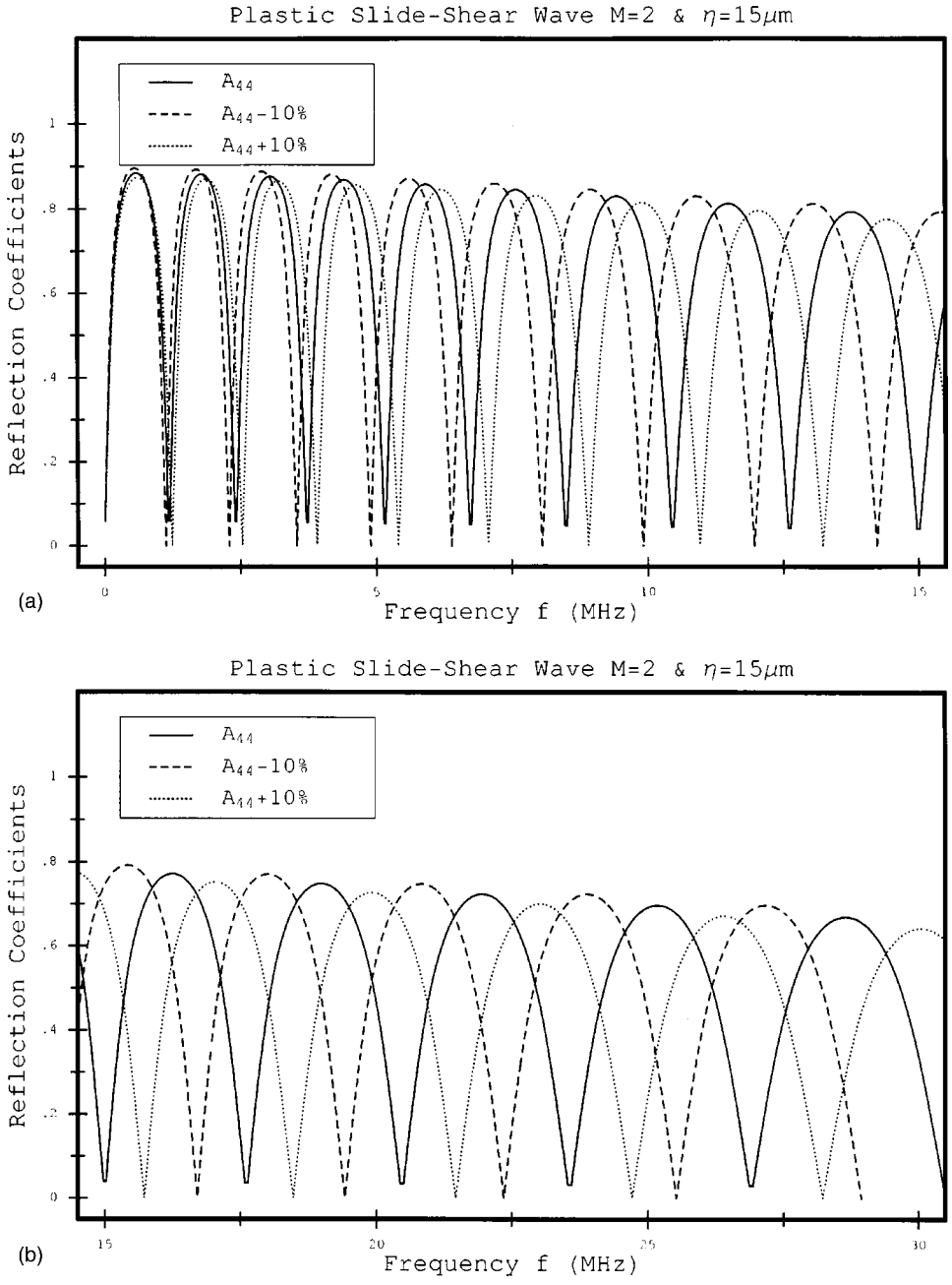

FIG. 9. (a) Reflection coefficient of shear waves for a plastic–tissue–plastic slide assembly versus frequency for $M=2$. $\eta=20$ μm, $\mathbf{A}_{44}$ changes $\pm 10\%$, $0<f<15$ MHz. (b) Reflection coefficient of shear waves for a plastic–tissue–plastic slide assembly versus frequency for $M=2$. $\eta=15$ μm, $\mathbf{A}_{44}$ changes $\pm 10\%$, $15<f<30$ MHz.

node equilibrium distance η_α and the elastic coefficients $\mathbf{A}_{11}$ or $\mathbf{A}_{44}$, depending on if it is longitudinal or shear waves that are used. By measuring the reflection coefficient as a function of frequency, η_α, $\mathbf{A}_{11}$, and $\mathbf{A}_{44}$ may be determined by a best fitting algorism (Liu and Ferrari, 2002). Lame's constants λ and μ of tissue can be calculated from Eqs. (5) and (7) once $\mathbf{A}_{11}$ and $\mathbf{A}_{44}$ are known. This property can be used to our advantage in detecting pathological changes of tissue samples associated with certain diseases. This concept was proved by a recent experiment (Liu and Ferrari, 2002). In the experiment, a broadband shear wave pulse of bandwidth between 5 and 13 MHz was used in a glass slide–tissue–glass slide assembly to detect the elastic property change from normal breast tissue to malignant breast tissue; statistically significant differences in η_α, $\mathbf{A}_{11}$, and $\mathbf{A}_{44}$ were detected. According to the above-presented theoretical results, working in the frequency range between 15 and 30 MHz will provide us much higher sensitivity than in low frequency range (5–13 MHz).

Attenuation is an issue we need to consider experimentally. The ultrasound round-trip attenuation of 150-μm tissue layer at the high end of frequencies—30 MHz—can be estimated to be 0.90 dB assuming the attenuation coefficient is 1 dB/(MHz cm); this is relatively small, but not negligible. If the attenuation is considered, the peak reflection coefficients should be smaller in all those figures. Considering the ultrasound signal entering the tissue layer, the main signal reduction is due to the impedance mismatch between slides and tissue. Since the acoustic impedance of the plastic is much closer to that of tissue than glass, it is advantageous to use

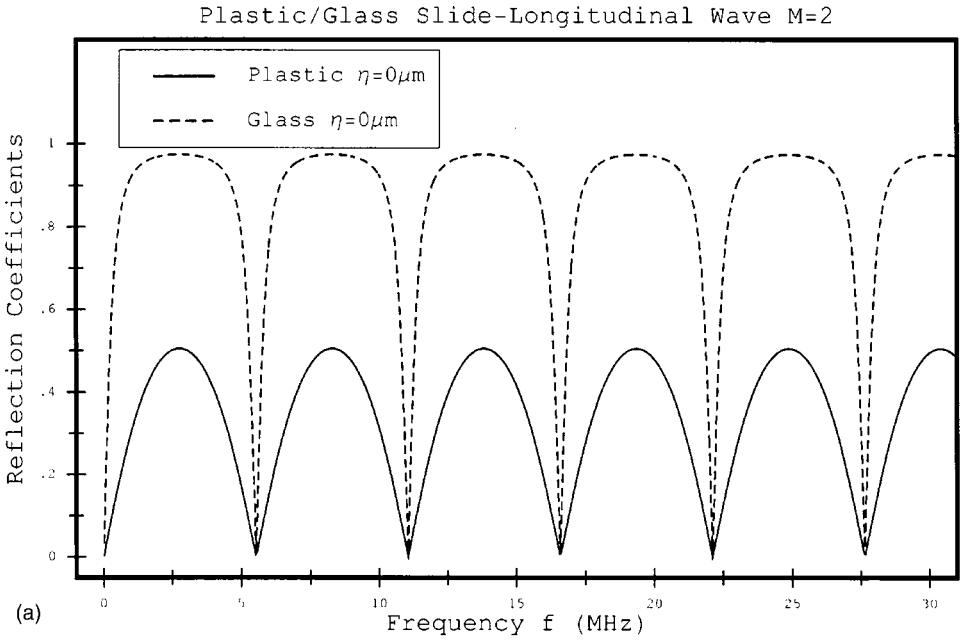

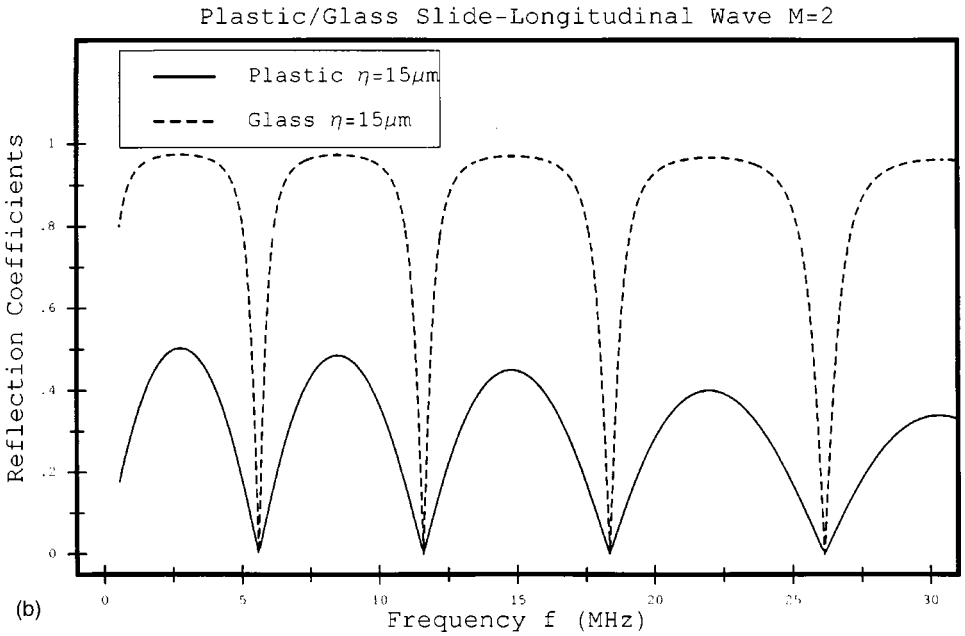

FIG. 10. (a) Comparison of reflection coefficient for $M=2$ of longitudinal waves for a plastic–tissue–plastic slide assembly versus frequency and that for a glass slide–tissue–glass slide assembly. $\eta=0$. (b) Comparison of reflection coefficient for $M=2$ of longitudinal waves for a plastic–tissue–plastic slide assembly versus frequency and that for a glass slide–tissue–glass slide assembly. $\eta=15$ μm.

the plastic slides. The sensitivity in detecting changes in η_α (between $\eta_\alpha=0$ and 15 μm) in tissue is higher for the plastic–tissue–plastic assembly than that for the glass–tissue–glass assembly as shown in Figs. 10; for glass slides the fourth peak reduced from 0.96 to 0.95 and for plastic slides the fourth peak decreased from 0.5 to 0.4. An experiment using high frequencies (15–30 MHz) has been planned.

LIST OF SYMBOLS

λ	Lame's constant
$\mathbf{A}_{\alpha\beta}$	micro-level elastic moduli matrix
$\mathbf{A}_{12}$	$\lambda+\mu$
$\mathbf{A}_{44}$	4μ
$\mathbf{p}_\alpha$	microstress
α, β	indices for nodes
τ_α	directional cosine unit vector
ζ_α	inter-nodal distance after elongation
$\mathbf{C_{ijkl}}$	$\Sigma_{\alpha=1}^{\mathbf{n}}\Sigma_{\beta=1}^{\mathbf{n}}\mathbf{A}_{\alpha\beta}\tau_{\alpha\mathbf{i}}^0\tau_{\alpha\mathbf{j}}^0\tau_{\beta\mathbf{k}}^0\tau_{\beta\mathbf{l}}^0$
$\mathbf{C}_{\mathbf{p,M}}^{\mathbf{s}}$	Mth-order shear phase velocity
$\mathbf{k_{iS}}$	wave-number for shear waves subscript $i=1$, 2 for slide and tissue respectively
ω	angular frequency
$\mathbf{f}$	frequency
μ	Lame's constant
$\mathbf{A}_{11}$	$\lambda+4\mu$
$\mathbf{A}_{15}$	-2μ
$\sigma_{\mathbf{ij}}$	macrostress
ρ	mass density
M	order of Taylor's expansion
η_α	internodal equilibrium distance

ε_α elongation (fractional change of internodal distance)
$\mathbf{C}^{\mathbf{L}}_{\mathbf{p,M}}$ *M*th-order longitudinal phase velocity
$\mathbf{k}_{\mathbf{iL}}$ wave-number for longitudinal waves subscript $i=1$, 2 for slide and tissue respectively
λ_0 wavelength
$\mathbf{u}$ displacement of a node

Auld, B. A. (**1990**). *Acoustic Fields and Waves in Solids*, 2nd ed. (Krieger, Malabar, FL), pp. 251–253.

Bamber, J. C. (**1981**). ''Speed of Sound,'' in *Physical Principles of Medical Ultrasonics*, edited by C. R. Hill (Ellis Horwood, Chichester, West Sussex, England), pp. 200–224.

Ferrari, M. (**2000**). ''Nanomechanics, and biomedical nanomechanics: Eshelby's inclusion and inhomogeneity problems at the discrete/continuum interface,'' Biomed. Microdevices **2**, 273–281.

Ferrari, M., Granik, V. T., and Imam, A. (**1997**). ''Introduction to Doublet Mechanics,'' in *Advances in Doublet Mechanics*, edited by M. Ferrari, V. T. Granik, and A. Imam (Springer, Berlin), pp. 1–26.

Granik, V. T. (**1997**). ''Comparison with other theories,'' in *Advances in Doublet Mechanics*, edited by M. Ferrari, V. T. Granik, and A. Imam (Springer, Berlin), pp. 51–82.

Kinsler, L. E., Frey, A. R., Coppens, A. B., and Sanders, J. V. (**1982**). *Fundamentals of Acoustics*, 3rd edition (Wiley, New York), pp. 98–105.

Kremkau, F. W., Barnes, R. W., and McGraw, C. P. (**1981**). ''Ultrasonic attenuation and propagation speed in normal human brain,'' J. Acoust. Soc. Am. **70**, 29–38.

Lide, D. R. (Ed.) (**1993**). *CRC Handbook of Chemistry and Physics*, 74th edition (CRC, Boca Raton).

Liu, J. (**2003**). Private communication. Shear waves instead of longitudinal waves were used in their work. It was not stated clearly in their previous publication (Liu and Ferrari, 2002).

Liu, J., and Ferrari, M. (**2002**). ''Mechanical spectral signatures of malignant disease? A small-sample, comparative study of continuum vs. nano-biomechanical data analyses,'' Dis. Markers **18**, 175–183.

Wu, J. (**1996**). ''Determination of velocity and attenuation of shear waves using ultrasonic spectroscopy,'' J. Acoust. Soc. Am. **99**, 2871–2875.

Wu, J., Layman, C., and Liu, J. (**2004**). ''Wave equations, dispersion relations and van Hove singularities for applications of doublet mechanics to ultrasound propagations in bio- and nano-materials,'' J. Acoust. Soc. Am. **115**, 893–900.

Amplification and spectral shifts of vocalizations inside burrows of the frog *Eupsophus calcaratus* (Leptodactylidae)

Mario Penna[a)]
Program of Physiology and Biophysics, Faculty of Medicine, University of Chile, Casilla 70005, Correo 7, Santiago, Chile

(Received 17 December 2003; revised 10 May 2004; accepted 12 May 2004)

A variety of animals that communicate by sound emit signals from sites favoring their propagation, thereby increasing the range over which these sounds convey information. A different significance of calling sites has been reported for burrowing frogs *Eupsophus emiliopugini* from southern Chile: the cavities from which these frogs vocalize amplify conspecific vocalizations generated externally, thus providing a means to enhance the reception of neighbor's vocalizations in chorusing aggregations. In the current study the amplification of vocalizations of a related species, *E. calcaratus*, is investigated, to explore the extent of sound enhancement reported previously. Advertisement calls broadcast through a loudspeaker placed in the vicinity of a burrow, monitored with small microphones, are amplified by up to 18 dB inside cavities relative to outside. The fundamental resonant frequency of burrows, measured with broadcast noise and pure tones, ranges from 842 to 1836 Hz and is significantly correlated with the burrow's length. Burrows change the spectral envelope of incoming calls by increasing the amplitude of lower relative to higher harmonics. The call amplification effect inside burrows of *E. calcaratus* parallels the effect reported previously for *E. emiliopugini*, and indicates that the acoustic properties of calling sites may affect signal reception by burrowing animals. © *2004 Acoustical Society of America.*
[DOI: 10.1121/1.1768257]

PACS numbers: 43.80.Gx, 43.80.Ka, 43.80.Ev [WA] Pages: 1254–1260

I. INTRODUCTION

Animals inhabiting burrows have been shown to make an efficient use of their shelters for sound broadcasting. Crickets (Bennet-Clark, 1970, 1987; Daws *et al.*, 1996) and frogs (Bailey and Roberts, 1981; Lardner and bin Lakin, 2002) calling from inside cavities amplify their vocalizations so that these sounds reach potential receivers at longer distances. Burrows from which male frogs *Eupsophus emiliopugini* vocalize in southern Chile have another acoustic effect. The cavities occupied by this leptodactylid amplify conspecific calls generated externally (Penna and Solís, 1996, 1999), an effect that would enhance the reception of neighbors' sounds by burrow occupants.

E. calcaratus is closely related to *E. emiliopugini*. Both species breed and call inside burrows in the same areas, but their activity peaks do not overlap in time; *E. calcaratus* calls and breeds during September and October, while *E. emiliopugini* is most active during November and December. The advertisement calls of both species consist of a single note of about 250-ms duration, but differ in their spectral structure. The call of *E. calcaratus* consists of a single note having a dominant frequency of about 1700 Hz, well above the average of 1100 Hz of *E. emiliopugini* (Formas, 1985; Penna and Solís, 1998, 1999).

In the present study, the amplitude and spectral changes of broadcast calls of *E. calcaratus* inside burrows occupied by males of this species are analyzed. The aim of this study is to explore the extent to which the amplification of external sounds occurs inside frog burrows, provided that the vocalizations of *E. calcaratus* have a spectral structure different from the congenic species. These measurements indicate that the amplification effect may affect signal reception by fossorial animals.

II. METHODS

A. Study site

Recordings of advertisement calls of *E. calcaratus* were conducted in La Picada (41°03′S, 72°30′W, 820 m), in the Vicente Pérez Rosales National Park, during the peak of the breeding period of this species, in late September and early October 1996–1997. Males of *E. calcaratus* usually call from inside burrows that are partially flooded and excavated among mosses (*Rhacomytrium*), grasses (*Scyrpus* and *Myrteola*) and ferns (*Gleichenia*). Frogs usually call standing in the water at the bottom of the burrow, positioned 2–10 cm from the burrow opening, with the vocal sacs distended.

Experiments of burrow resonance were conducted at a time when the vocal activity of *E. calcaratus* fades away, in late November and early December, time at which the breeding activity of *E. emiliopugini* reaches its peak. However, the weather conditions, topography and vegetation do not experience significant changes in the study site between the September–October and November–December periods. The burrows' dimensions (diameter, total length and length of the segment free from water) and shape did not show alterations between the two periods and were measured with a steel tape to the nearest cm. The inclination of the burrow was deter-

a)Electronic mail: mpenna@machi.med.uchile.cl

mined by measuring the angle between the steel tape inserted in the burrow and the horizontal.

B. Experimental procedures

Advertisement calls of 21 males of *E. calcaratus* were recorded with a directional microphone (AKG CK8, frequency response: ±2 dB in the 30–18 000-Hz range), positioned 25 cm in front of the opening of a burrow occupied by a calling frog. These recordings were conducted during 1996 (10 individuals) and 1997 (11 individuals). The microphone was connected to a cassette tape recorder (Sony TCD-5M, frequency response: ±3 dB in the 30–15 000-Hz range) and the signals recorded onto chromium dioxide tape (TDK SA 90). Air and substrate temperature measured with a telethermometer (Digi-Sense 8528-20) to the nearest 0.1°C after each recording, averaged 5.3°C (range 2.5–8.6°C) and 7.0°C (range 6.3–8.6°C), respectively. Thirteen males captured after their calls were recorded had an average snout-vent length—measured to the nearest 0.1 mm with a Vernier caliper—of 35 mm (range 33–49 mm) and an average body mass—measured to the nearest 0.1 g with a portable weighting scale—of 4.8 g (range 3.8–5.7 g).

The experimental setup and protocol of stimuli delivery were similar to those used in a previous study (Penna and Solís, 1999). Six calls of each of the 21 individuals chosen at random from recordings of ongoing vocal activity were re-recorded onto metal tape (TDK MA 60) with a second cassette tape recorder (Sony TCD-5M) and broadcast via a 6.5 in. loudspeaker (Polk MM10a) positioned 80 cm in front of the burrows. In addition, synthetic white noise and pure tones in the 200–6000-Hz range were presented.

Six advertisement calls of each of 10 individuals were presented in front of five burrows in 1996. This series of signals, plus six advertisement calls of each of 11 individuals recorded in 1997 (i.e., calls of 21 individuals) were presented in front of other five burrows during this year (i.e., a total of 155 six-advertisement call presentations). Call SPLs were measured with a portable sound level meter (Brüel & Kjær 2230). The SPLs of the playback calls of the 155 six-call presentations, measured with the microphone of the sound level meter positioned close to the burrow opening, pointing towards the loudspeaker, averaged 90.2 dB peak SPL (range 78.2–98.3 dB peak SPL).

The sounds delivered with the loudspeaker were recorded with two omni-directional tie-pin microphones (Realistic 33-3033; 8 mm diameter, 16 mm length, 2 mm cable gauge). The microphones were pinned with a wire holder 2–4 cm and 2–9 cm outside and inside the burrow opening, respectively. Each microphone was connected to a different channel of a cassette tape recorder (Sony TCD-5M) and the signals recorded onto chromium dioxide tape (TDK SA 90). The microphones were calibrated before and after recording from each burrow with a sound calibrator (Brüel and Kjær 4230). This was done by fitting the microphones into the calibrator with a plastic bearing that adapted the 8-mm microphone diameter to the 12.5-mm opening of the sound calibrator. The 1-kHz tone produced by this device, with a peak SPL of 96.8 dB, was recorded sequentially on each channel of the tape recorder. The tones, white noise and playback calls were subsequently delivered and recorded via the tie-pin microphones using the same recording level as for the calibration tone. The peak SPLs of the sounds recorded were calculated from the relationship of the amplitudes of the signals relative to the amplitude of the 1-kHz calibration tone.

The frequency response of the loudspeaker was measured in the open at an elevation of 1.5 m above ground level and with the microphone of the sound level meter suspended at the same height at a distance of 1 m. The output of the loudspeaker was flat within ±5 dB for the full range of the pure tones used (200–5500 Hz) and within ±2 dB for the 800–2500-Hz range, which encompasses the limits of burrow resonance and the main spectral peaks of the advertisement calls of *E. calcaratus*.

The two Realistic microphones were tested for differences in frequency response in a semi-anechoic booth in the laboratory. Differences between the output amplitudes of the two microphones for pure tones in the 200–5500-Hz range produced with our sound-generating system averaged −0.6 dB (range −1.10–0.43 dB).

C. Signal analysis

Recordings were digitized with a Macintosh computer (Power PC 7100), using the Sound Edit 16 software, at a sampling rate of 22 050 Hz. Sound files were imported to the Signalyze 3.12 software, for analysis of signal amplitudes and power spectra. The frequency range of the power spectra was 20–5500 Hz, and the frequency resolution 20 Hz.

Six advertisement calls of each of 21 individuals recorded at 25 cm from their burrow openings and subsequently used for playbacks were analyzed. Call duration, fundamental frequency, the two harmonics having the highest amplitudes and the dominant frequency were measured.

Amplitudes and power spectra of broadcast pure tones, white noise and playback calls recorded with the tie-pin microphones from inside and outside ten burrows were compared. Amplitude gains for tones and calls were obtained from the ratio between the maximum amplitude of a signal inside and outside a burrow. Averages of amplitude gains for the six playback calls of an individual and from all the individuals tested in a burrow were converted to dB. Spectra of playback calls inside and outside the burrows obtained at the time of the maximum amplitude of the signal were compared to explore relationships between the amplitude gains and the spectral changes of the calls inside burrows. The amplitude ratios between two adjacent harmonics having the highest amplitudes outside a burrow were measured. This procedure was adopted, instead of analyzing harmonics having a preset order, since in different individuals the dominant frequency corresponded to different harmonics, ranging from the first to fifth (see Sec. III). The method chosen intends to explore changes affecting the main call spectral components of each frog.

The amplitude of the harmonic having the higher frequency outside a burrow (referred to as the higher harmonic) was substracted from the amplitude of the harmonic having the lower frequency (referred to as the lower harmonic). Amplitude ratios in dB between the higher and lower harmonic inside a burrow were also computed and the corresponding

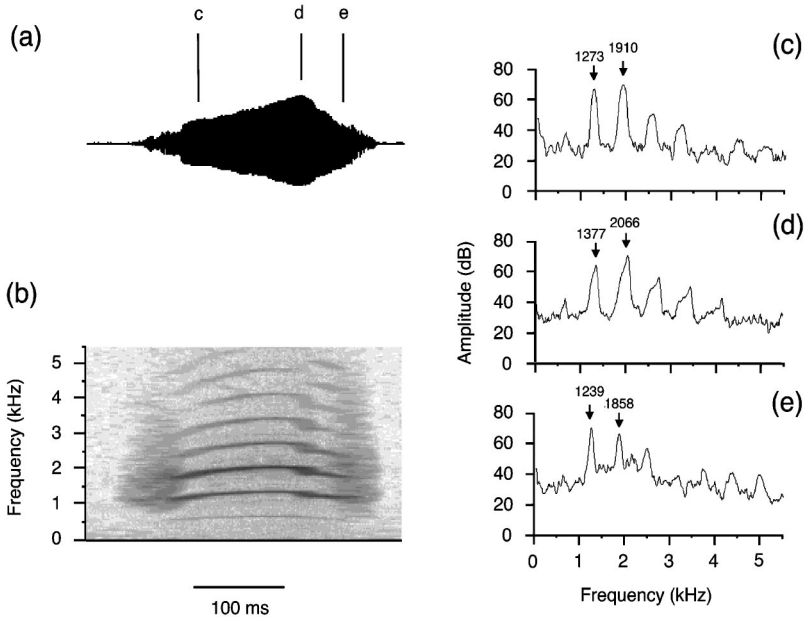

FIG. 1. Oscillogram (a), sonagram (b), and power spectra (c, d and e) of an advertisement call of *E. calcaratus*. Power spectra are taken at times (c, d and e) indicated in the oscillogram. Values of the two harmonics having the highest amplitudes are indicated on the power spectra. The dominant frequency corresponds to the second harmonic in (c) and (d) and to the first harmonic in (e).

amplitude ratio outside the burrow was subtracted from this value, to calculate amplitude ratio shifts of the lower and higher harmonic inside burrows. Averages for these shifts were calculated for the six playback calls of an individual tested in a burrow (see Sec. III).

D. Statistical analysis

The Spearman nonparametric correlation ($P<0.05$) was used to test for statistical significance of covariances between burrow length and resonant frequencies (see Sec. III) and spectral parameters (dominant frequency, lower harmonic and higher harmonic) of the calls of resident frogs. Variation between burrows and between individuals for amplitude gains and harmonic ratio shifts of playback calls recorded from inside and outside burrows was analyzed with the Friedman ANOVA ($P<0.05$). The dominant frequency of the calls of *E. calcaratus* used as stimuli, burrow dimensions and resonant frequencies were compared to those reported previously for *E. emiliopugini* with the Mann-Whitney U test (two tailed, $P<0.05$).

III. RESULTS

A. Call structure

The advertisement calls of 21 male frogs, recorded in the study area from 25 cm in front of the burrow openings, consisted of single notes with an average duration of 265 ms (range 173–388 ms), having slow rise and fall times, typically comprising about two-thirds and one-third of the call duration, respectively (Fig. 1). Calls had a harmonic structure and ascending, descending or ascending-descending pattern of frequency modulation in different individuals. The fundamental frequency was small in amplitude relative to higher harmonics and averaged 597 Hz (range 308–733 Hz). The dominant frequency in most of the individuals corresponded to the first or second harmonic (7 and 8 out of 21 individuals, respectively). The dominant frequency corresponded to the third, fourth and fifth harmonic in three, two and one individuals, respectively. The position of the dominant frequency in some cases shifted between adjacent harmonics within a call (Fig. 1). The dominant frequency measured at the time of the maximum call amplitude averaged 1689 Hz (range 1202–2192 Hz). However, because the dominant frequency can correspond to different harmonics in different individuals or at various times within a call, a more appropriate description of the spectral characteristics of the vocalizations is drawn from the two harmonics having the highest amplitudes, i.e., the lower and the higher harmonic. These spectral peaks averaged 1363 Hz (range 1136–1780) and 1951 Hz (range 1616–2216 Hz), respectively. Spectra of the six calls from individual males used for playbacks were relatively similar. Differences between the six calls of a given individual were on average 155 Hz (range 11–518 Hz) and 158 Hz (22–529 Hz), for the lower and higher harmonic, respectively. The fundamental frequency, lower harmonic, higher harmonic and call duration were not significantly related to air or substrate temperature, body size or mass (Spearman correlation, $P>0.1$). The call parameters analyzed were similar between the individuals recorded during 1996 and 1997 (Mann-Whitney U test, $P>0.1$).

B. Burrow measurements

1. Resonances

The ranges for dimensions of the burrows studied were total length: 6–34 cm, length of segment free from water: 4–13 cm, and opening diameter: 3–9 cm. The initial segments of the ten burrows had different inclinations relative to the horizontal: three burrows were vertical, two horizontal, and five had inclinations between 30° and 45°.

The resonance characteristics of ten burrows were determined by measuring the relative amplitudes of pure tones and amplitude spectrum of white noise. Resonant frequencies were evident as peaks of amplitude gains. The values of resonant frequencies determined with white noise were used for analysis, due to the better frequency resolution of mea-

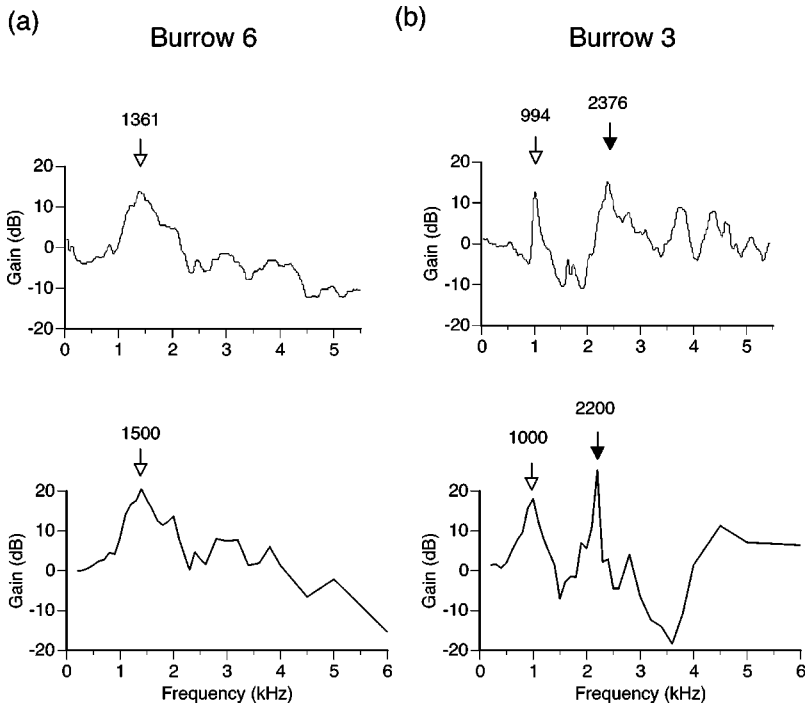

FIG. 2. Amplitude gains measured with white noise (upper) and pure continuous tones (lower) between inside and outside two burrows occupied by *E. calcaratus* calling males. The value of the fundamental resonant frequency (FRFs) and best resonant frequency (BRF) are indicated with open and filled arrows, respectively.

surements of amplitude gains in a continuous spectrum, relative to those based on discrete tone frequencies.

The lowest frequency at which a peak of amplitude gain occurred in a burrow is termed the fundamental resonant frequency (FRF). In seven out of ten burrows, the FRF corresponded to the highest gain in the spectrum [Fig. 2(a)], however, in three burrows the maximum gain occurred at a higher frequency [Fig. 2(b)]. This value is referred to as the best resonant frequency (BRF) of the burrow. The FRFs measured with white noise for the ten burrows ranged from 842 to 1836 Hz, with amplitude gains at FRF ranging from 4.6 to 16.7 dB. In the three burrows having a BRF different from the FRF, the BRF was between 1274 and 2527 Hz and the corresponding amplitude gain between 5.4 and 7.2 dB. Determinations of FRF with white noise and pure tones yielded similar results for most of the burrows. Differences between values measured with both methods were on average 37 Hz (range 4–104 Hz). Measurements of BRFs with white noise and pure tones differed on average by 142 Hz (range 4–588 Hz). For this measure, large differences occurred because in some burrows peaks of amplitude gain at similar frequencies present in both measurements differed in their relative amplitudes. Amplitude losses were evident at about 2000 Hz in eight burrows (see Fig. 2).

The values measured for FRF could be approximated by the fundamental frequencies calculated for one-end open cylinders of length equal to the segments of burrows free from water and to the total length of the burrows [fundamental frequencies of one-end open cylinders are equal to speed of sound in air/(cylinder length$\times$4), Kinsler *et al.*, 1982]. The FRFs measured covaried significantly with the fundamental frequencies calculated for the segment free from water and for the total length (Spearman correlation, $Z=1.97$; $P<0.05$ and $Z=2.09$; $P<0.05$, respectively). The BRF did not covary with these calculated values (Spearman correlation, $P>0.05$).

There was a tendency for the FRF and BRF to decrease with the total length of the burrow and with the length of the segment of the burrow free from water. However, significant relationships occurred only between FRF and total burrow length and length of the segment free from water (Spearman correlation, $Z=-2.09$; $P<0.05$ and $Z=-1.97$; $P<0.05$, respectively).

2. Playback calls

The spectral parameters analyzed (dominant frequency, lower harmonic and higher harmonic) of the calls of nine frogs recorded from 25 cm in front of the burrow openings, measured at the time of the maximum amplitude of the signals, did not covary with either the total burrow length, length of segment free from water, FRF or BRF of the burrows occupied by these individuals (Spearman correlation, $P>0.1$).

The amplitude gains of the six calls of a given individual inside a particular burrow were rather similar. For the 155 six-call presentations (of 10 individuals in five burrows and of 21 individuals in five burrows), differences between the amplitude gains of the six calls of an individual were on average 1.9 dB (range 0.24–6.50 dB). Average call amplitude gains between inside and outside a burrow were calculated for the six playback calls of an individual. Inside most of the burrows, calls were considerably amplified, but in certain burrows the call amplitude of some individuals was attenuated. For 142 and 13 out of 155 six-call presentations, the average call gains were positive (range 0.1–18.2 dB) and negative (i.e., amplitude losses; range -4.5–0.1 dB), respectively. A recording from a burrow in which a call was markedly amplified is shown in Fig. 3. The average call amplitude gains for individuals in the ten burrows tested are shown in Fig. 4. As seen in this figure, a maximum gain of about 18 dB was attained in burrow 6. However, some calls

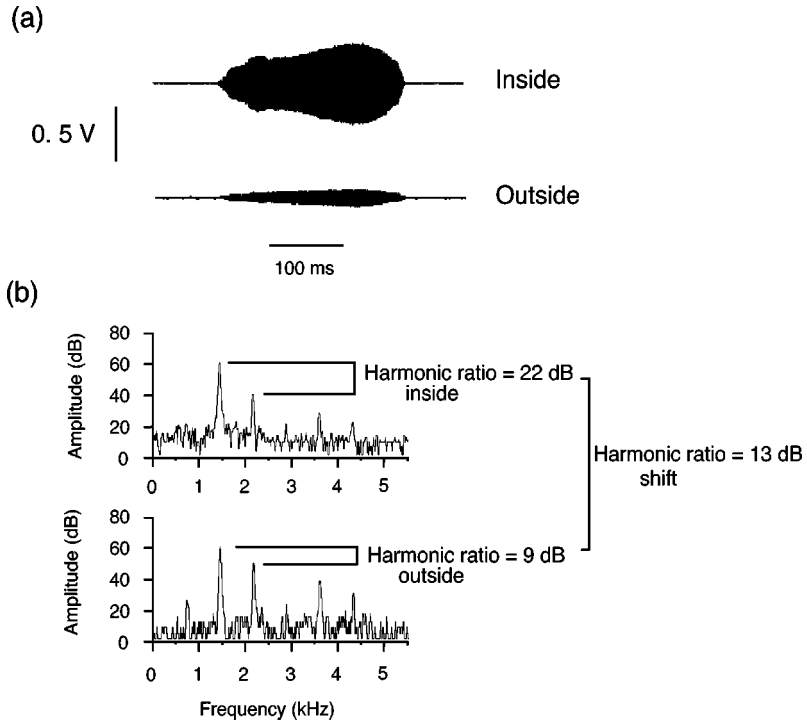

FIG. 3. Oscillograms (a) and power spectra (b) of a call recorded from inside and outside burrow 6. This call was amplified by 15 dB inside the burrow. An increase in the amplitude of the first harmonic relative to the second harmonic (i.e., a positive harmonic ratio shift; see text) is observed inside the burrow. The absolute amplitudes of the calls are not represented in the power spectra.

experienced losses reaching a minimum of about -5 dB in burrow 4.

The spectral changes of the calls inside burrows were explored by measuring the amplitudes of the lower and higher harmonic inside burrows, relative to values measured outside. The dB ratio between the amplitudes of these two harmonics (lower–higher) for a call outside a burrow was subtracted from the ratio between the same harmonics measured inside the burrow. This measure, referred to as harmonic ratio shift, is explained in Fig. 3. Average harmonic ratio shifts were calculated for the six playback calls of an individual in a burrow. The average harmonic ratio shifts for six-call presentations of individual frogs were positive in 132 and negative in 23 out of 155 presentations. The average harmonic ratio shifts calculated for each burrow from the averages of individual frogs were positive for nine out of ten burrows (Table I), indicating that inside the burrows the amplitude of the lower harmonic increased relative to the higher harmonic.

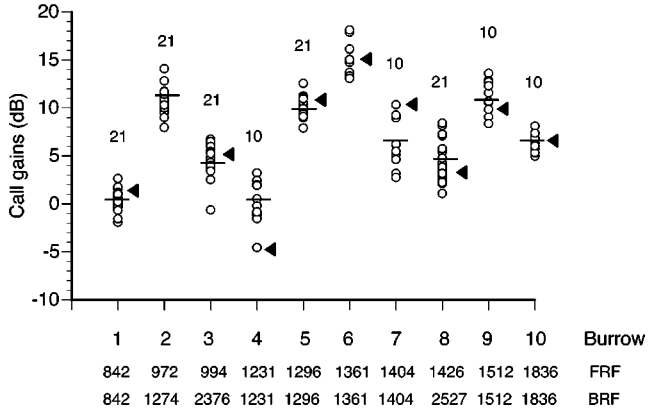

FIG. 4. Amplitude gains for playback calls recorded from inside and outside ten burrows. Circles represent averages of amplitude ratios (inside/outside) for six calls of an individual. Horizontal lines indicate averages of call gains for the individuals recorded from a burrow. Arrows indicate average amplitude gains for the calls of resident frogs in nine burrows. On the horizontal axis, burrows are displayed following an order of increasing fundamental resonant frequency. Numbers above symbols indicate individuals for which calls were played back in each burrow. Abbreviations: FRF: fundamental resonant frequency; BRF: best resonant frequency.

Differences in call gains and harmonic ratio shifts between burrows and between individuals were analyzed with the Friedman ANOVA ($P<0.05$). This analysis was performed on the ten six-call presentations that were tested in all ten burrows. Significant differences occurred between burrows for call gains (chi square$=82.21$, $P<0.0001$, df $=9$) and harmonic ratio shifts (chi square$=39.32$, $P<0.0001$, df$=9$). Between individuals, significant differences, but of a lower magnitude, occurred for call gains (chi square$=18.64$, $P<0.05$, df$=9$) and no differences occurred for harmonic ratio shifts (chi square$=12.87$, $P>0.1$, df $=9$).

Comparisons of the dominant frequencies of the calls used as stimuli and lengths and resonant frequencies of burrows occupied by *E. calcaratus* with those reported for *E. emiliopugini* (Penna and Solís, 1999) show that the dominant frequencies of the calls of the species in the present study were above those of *E. emiliopugini* (Mann-Whitney U test $Z=-3.76$, $P=<0.001$). The burrows from which males of both species call had similar total lengths and lengths free from water (Mann-Whitney U test, $P>0.1$), however, the FRF was significantly higher in *E. calcaratus* relative to *E. emiliopugini* (Mann-Whitney U test $Z=-3.04$, $P<0.01$). The BRFs did not differ significantly (Mann-Whitney U test, $P>0.1$), but the burrows of *E. calcaratus* had a tendency to have higher frequencies, since only one burrow of this species had a BRF below 1 kHz, whereas 6 out of 12 burrows of *E. emiliopugini* had BRFs below this value. Call gains inside

TABLE I. Amplitude gains and spectral changes of playback calls inside burrows of *Eupsophus calcaratus*. Harmonic ratio shifts were calculated by subtracting the amplitude ratio between the harmonics having the higher energy levels in a call recorded outside from that recorded inside a burrow (see text and Fig. 3). Burrows are listed following an order of increasing fundamental resonant frequency (FRF). Data correspond to averages, with ranges in parentheses (BRF: best resonant frequency).

Burrow	Total length (cm)	Segment free from water (cm)	Inclination (°)	FRF (Hz)	BRF (Hz)	No. of frogs tested	Call gain (dB)	Harmonic ratio shift (dB)
1	20	10	45	842	842	21	0.4 (−1.9–2.7)	8.6 (−2.1–25.6)
2	28	9	30	972	1274	21	10.8 (8.0–14.1)	10.2 (5.5–14.4)
3	32	10	90	994	2376	21	4.8 (−0.6–6.8)	0.5 (−27.1–19.9)
4	17	13	0	1231	1231	10	0.2 (−4.5–3.3)	6.4 (−7.1–9.8)
5	34	13	45	1296	1296	21	10.5 (7.9–12.6)	3.2 (0.1–4.7)
6	10	5	90	1361	1361	10	15.3 (13.1–18.2)	9.0 (0.9–14.8)
7	11	9	45	1404	1404	10	6.6 (2.8–10.4)	17.0 (−4.4–24.5)
8	14	8	0	1426	2527	21	4.7 (1.1–8.4)	12.0 (3.3–19.5)
9	6	4	90	1512	1512	10	11.3 (8.4–13.6)	−3.4 (−9.9–4.2)
10	8	8	45	1836	1836	10	6.4 (5.0–8.1)	9.0 (0.8–14.9)

burrows were similar between both species (Mann-Whitney U test, $P > 0.1$).

IV. DISCUSSION

Our measurements of the resonance of burrows of *E. calcaratus* with white noise and pure tones show relationships with the burrow dimensions; the FRF of the burrows covaried significantly with the total burrow length and with the length of the segment free from water. The similar covariation of FRF with both measures of burrow length may be accounted for by the difficulty to obtain precise measurements of the segment free from water, due to the inclination and the irregular shapes of the burrows, deviating from perfect cylinders. Furthermore, the FRF is significantly correlated with the fundamental resonant frequency calculated for pipes having the length of the burrows.

The amplification of calls of *E. calcaratus* inside burrows occupied by male frogs indicates that the acoustic properties of these shelters may affect sound reception by individuals engaged in vocal interactions. Maximum call amplifications of about 18 dB are measured in the present study, which are comparable to those measured previously for the congenic species, *E. emiliopugini* (Penna and Solís, 1999). The gains attained by advertisement calls of *E. calcaratus* inside burrows are not related to the resonant frequencies of these ducts (as seen in Fig. 4). The resonant frequencies of the burrows occupied by males of the two species are different and congruent with the spectral characteristics of their corresponding advertisement calls, suggesting that frogs choose or build burrows that amplify preferentially the conspecific calls. The Malaysian treefrog *Metaphrynella sundana* actively tracks changes in burrow resonant frequencies by shifting the dominant frequency of its call (Lardner and bin Lakim, 2002). Frogs inhabiting burrows may use auditory feedback of their own and/or neighbors' vocalizations for improving amplification while holding these calling posts.

The importance of burrow acoustics for sound reception relative to its possible function for broadcasting resident's vocalizations is emphasized by the lack of significant correlation between the spectral peaks of the advertisement calls and the resonant frequencies of the burrows occupied by calling frogs. Furthermore, the calls of residents played back from a loudspeaker positioned in front of burrows do not attain the highest gains relative to the calls of other individuals inside the burrows they occupy (see Fig. 4). Also, burrows having a vertical orientation are not appropriate to beam the sound towards possible receivers. However, further studies need to be carried out to establish the relevance of burrow amplification for call reception relative to a potential effect for call broadcast.

As shown by the Friedman ANOVA, the acoustic properties of burrows have greater effect than individuals on sound amplification and spectral changes of the calls inside burrows. This pattern of variation emphasizes the importance of burrows as a resource for acoustic communication, as reported for *E. emiliopugini* (Penna and Solís, 1999). The important variation of burrow resonant frequencies, spanning for more than one octave, together with the broad spectral characteristics of calls, having at least three frequency-modulated harmonics with high energy content, points to a broad correspondence between burrow resonance and vocalizations in this frog. A more precise matching between call DF and burrow resonance would be expected to occur in

species producing calls with narrow spectra. The importance of burrows for biological roles other than sound communication contributes to explain the wide variation of resonant frequencies. In *E. calcaratus*, oviposition takes place inside burrows and males apparently attend the eggs while calling.

The bogs from southern Chile are habitats in which the propagation of sounds having frequencies above about 1 kHz are substantially impaired (Penna and Solís, 1998), and, consequently, the advertisement calls of *E. calcaratus* are attenuated to an important extent. In addition, the auditory thresholds of this species for its advertisement calls are relatively high, averaging about 65 dB SPL, as measured by multiunit recordings in the torus semicircularis—the audiograms have a dip of better sensitivity between about 1200 and 2000 Hz (Penna and Plaza, unpublished data). The intensities of the vocalizations of *E. calcaratus* at the burrow openings are about 100 dB SPL peak, but drop to about 65 dB SPL at 2 m from the calling males (Penna, unpublished data).

The amplification and the spectral shift towards lower frequencies affecting the vocalizations inside burrows may counteract in part the constraints on the propagation range of advertisement calls of *E. calcaratus*, by boosting the amplitude of signals produced by callers positioned at distances longer than about 2 m above auditory thresholds and by shifting the spectral energy towards the range of better auditory sensitivity. This effect on the spectral contents of incoming sounds is not likely to increase interference from external noises on call reception. *E. calcaratus* breeds in a sound environment having low levels of noises of biotic origin. No other anuran species calls during the peak of the breeding period of *E. calcaratus* and no insects or birds call persistently at night in the study area. The noise sources in the temperate austral forest are predominantly abiotic (wind, rain and creeks) containing frequencies below1000 Hz and noise levels during calm atmospheric conditions are below 50 dB RMS SPL (fast-weighting scale) in the study site (Penna and Solís, 1998).

Amplification of incoming calls at the receiver location may contribute to the persistence of the antiphonal activity that frogs display with neighbors or when presented with natural and synthetic advertisement calls (e.g., Gerhardt and Huber, 2002). The ongoing antiphonal calling would in turn facilitate the orientation of females to the breeding areas. Female frogs have been shown to respond phonotactically to recordings of distant conspecific choruses (Gerhardt and Klump, 1988). However, further testing of the amplification effect of burrows on the calling behavior of *E. calcaratus* is needed in order to settle the communicative significance of this physical phenomenon. Playback experiments using stimulus of different intensities, from subthreshold levels onwards, would contribute an evaluation of this effect.

The data reported here extend the amplification effect of burrows for sounds of biological significance originally described for *E. emiliopugini* (Penna and Solís, 1999), to another species, suggesting that sites occupied by acoustically interacting animals have a general importance for signal reception. The acoustic properties of calling sites for sound reception may be especially valuable for anurans, for which no optimal relationships have been shown to occur between signal structure and sound transmission properties of the environments in which different species communicate (Penna and Solís, 1998; Kime *et al.*, 2000; Penna, 2002).

ACKNOWLEDGMENTS

This study was supported by FONDECYT Grant Nos. 1960859 and 1010569. CONAF provided authorization to work in the Vicente Pérez Rosales National Park. Juan Panza collaborated in the field experiments. Aníbal Martínez collaborated in the signal analysis. The experimental procedures used in this study comply with the regulations for animal care and protection of native species in Chile. Anonymous referees contributed comments that strengthened the manuscript.

Bailey, W. J., and Roberts, J. D. (**1981**). ''The bioacoustics of the burrowing frog *Heleioporus* (Leptodactylidae),'' J. Nat. Hist. **15**, 693–702.

Bennet-Clark, H. C. (**1970**). ''The mechanism and efficiency of sound production in mole crickets,'' J. Exp. Biol. **52**, 619–652.

Bennet-Clark, H. C. (**1987**). ''The tuned singing burrow of mole crickets,'' J. Exp. Biol. **128**, 383–409.

Daws, A. G., Bennet-Clark, H. C., and Fletcher, N. H. (**1996**). ''The mechanism of tuning of the molecricket singing burrow,'' Bioacoustics **7**, 81–117.

Formas, R. (**1985**). ''The voices and relationships of the chilean frogs *Eupsophus migueli* and *E. calcaratus* (Amphibia: Anura: Leptodactylidae),'' Proc. Biol. Soc. Wash. **98**, 411–415.

Gerhardt, H. C., and Huber, F. (**2002**). *Acoustic Communication in Insects and Anurans* (Univ. of Chicago, Chicago).

Gerhardt, H. C., and Klump, G. M. (**1988**). ''Phonotactic responses and selectivity of barking frogs (*Hyla gratiosa*) to chorus sounds,'' J. Comp. Physiol., A **163**, 795–802.

Kime, N. M., Rand, A. S., and Ryan, M. J. (**2000**). ''The transmission of advertisement calls in Central American frogs,'' Behav. Ecol. **11**, 71–83.

Kinsler, L. E., Frey, A. R., Coppens, A. B., and Sanders, J. V. (**1982**). *Fundamentals of Acoustics* (Wiley, New York).

Lardner, B., and bin Lakim, M. (**2002**). ''Tree-hole frogs exploit resonance effects,'' Nature (London) **420**, 475.

Penna, M. (**2002**). ''Environmental influences on anuran sound communication,'' J. Acoust. Soc. Am. **112**, 2257–2258.

Penna, M., and Solís, R. (**1996**). ''Influence of burrow acoustics on sound reception by frogs *Eupsophus* (Leptodactylidae),'' Anim. Behav. **51**, 255–263.

Penna, M., and Solís, R. (**1998**). ''Frog call intensities and sound propagation in the South American temperate forest region,'' Behav. Ecol. Sociobiol. **42**, 371–381.

Penna, M., and Solís, R. (**1999**). ''Extent and variation of sound enhancement inside burrows of the frog *Eupsophus emiliopugini* (Leptodactylidae),'' Behav. Ecol. Sociobiol. **47**, 94–103.

Repetition patterns in Weddell seal (*Leptonychotes weddellii*) underwater multiple element calls

Hilary B. Moors and John M. Terhune[a)]
Department of Biology, University of New Brunswick, P.O. Box 5050, Saint John, New Brunswick, E2L 4L5, Canada

(Received 5 November 2003; revised 10 April 2004; accepted 29 April 2004)

Many vocalizations produced by Weddell seals (*Leptonychotes weddellii*) are made up of repeated individual distinct sounds (elements). Patterning of multiple element calls was examined during the breeding season at Casey and Davis, Antarctica. Element and interval durations were measured from 405 calls all >3 elements in length. The duration of the calls (22 ± 16.6 s) did not seem to vary with an increasing number of elements ($F_{4,404}=1.83, p=0.122$) because element and interval durations decreased as the number of elements within a call increased. Underwater vocalizations showed seven distinct timing patterns of increasing, decreasing, or constant element and interval durations throughout the calls. One call type occurred with six rhythm patterns, although the majority exhibited only two rhythms. Some call types also displayed steady frequency changes as they progressed. Weddell seal multiple element calls are rhythmically repeated and thus the durations of the elements and intervals within a call occur in a regular manner. Rhythmical repetition used during vocal communication likely enhances the probability of a call being detected and has important implications for the extent to which the seals can successfully transmit information over long distances and during times of high level background noise.
[DOI: 10.1121/1.1763956]

PACS numbers: 43.80.Ka, 43.80.Ef [WWA] Pages: 1261–1270

I. INTRODUCTION

A. Weddell seal vocalizations

Weddell seals (*Leptonychotes weddellii*) have a circumpolar distribution around Antarctica and surrounding islands (Bertram, 1940). The females gather in small breeding groups on land-fast ice in early October, and pups are born from mid-October to mid-November (Kooyman, 1981). Mating occurs shortly after the pups are weaned (Kooyman, 1981; Thomas and Kuechle, 1982). Male Weddell seals establish territories below the ice near the pupping colonies and spend most of their time defending territorial boundaries until mating occurs (Kooyman, 1981).

Weddell seals have an extensive vocal repertoire (Thomas and Kuechle, 1982; Thomas *et al.*, 1988; Pahl *et al.*, 1997; Abgrall *et al.*, 2003). Many call types have been described and the repertoire exhibits geographic variation between different areas along the coastline (Thomas *et al.*, 1988, Abgrall *et al.*, 2003). These vocalizations play an important role in social communication (Thomas *et al.*, 1988). The seals appear to use sound in connection with their breeding behavior (Ray, 1967), and underwater vocalizations are frequently emitted near colonies (Kooyman, 1981). Territorial males are vocal underwater prior to and during the mating period (Thomas *et al.*, 1988), and some calls types, such as trills, are thought to be made only by males (Thomas and Kuechle, 1982; Oetelaar *et al.*, 2003). All vocalizations decrease sharply after the breeding season (Thomas *et al.*, 1987; Green and Burton, 1988).

B. Masking and anti-masking strategies

Seals are able to hear under water with a maximum sensitivity between 2 kHz and 32 kHz, although the overall hearing range is from 0.1 to 64 kHz. Vocalizations that seals emit span this range (Richardson, 1995). Although Weddell seal hearing abilities have never been examined, they are not expected to be substantially different from the hearing abilities of seals tested so far (Terhune and Turnbull, 1995).

Masking occurs when noise interferes with the ability of an animal (seal) to detect a sound even when the signal is above the animal's absolute hearing threshold (Richardson, 1995). Masking of seal calls will occur when a high level of background noise, abiotic or biotic, is encountered (Hawkins and Myrberg, 1983; Terhune and Ronald, 1986; Richardson, 1995). When vocalizing at large breeding sites, Weddell seals face the problem of masking due to overlapping calls of conspecifics (Thomas and Kuechle, 1982). At low calling rates, individual seal calls are typically distinct, but at high calling rates, calls tend to overlap each other almost continuously. At high calling rates, background noise produced by conspecifics limits the detection range of individual seal calls (Terhune and Ronald, 1986). Certain characteristics of seal calls, such as frequency separation (Terhune, 1999; Serrano and Terhune, 2002), abrupt onset and offset of calls (Watkins and Schevill, 1979; Serrano and Terhune, 2002), and increasing repetition of call elements (Watkins and Schevill, 1979; Terhune *et al.*, 1994; Serrano and Terhune, 2001), likely decrease the effect of masking and enhance the detection of individual calls.

a)Electronic mail: terhune@unbsj.ca

C. Repetition in vocalizations

An element is defined as a single distinct sound having a beginning and end that are clearly distinguishable from background noise. Thus, multiple element calls consist of more than one discrete sound. The repetition of call elements in underwater vocalizations would allow calls to stand out from background noise and avoid being masked (Watkins and Schevill, 1979). A regular sequence of brief sounds is more detectable against background noise than a single brief sound (Richardson, 1995). Multiple element Weddell seal calls that were overlapped by the call of another seal were found to be longer (due to the addition of elements) than were similar calls emitted without overlap (Terhune *et al.*, 1994). Similarly, harp seals (*Pagophilus groenlandicus*) increase the number of elements within multiple element calls when the number of calls per minute increases (Serrano and Terhune, 2001). Regular pulse repetition enhances acoustical detection thresholds for harbor seals (*Phoca vitulina*), demonstrating that seals who repeat short duration calls at regular rates enhance the probability of communicating with distant conspecifics in both masked and unmasked situations (Turnbull and Terhune, 1993).

Three distinct timing patterns (rhythms) in which elements of the calls occur at regular intervals have been described for harp seal multiple element calls (Moors and Terhune, 2003). Repetition patterns within calls have also been described in arthropods, frogs, birds, and other mammals (Alexander, 1968; Sebok, 1968; Lengagne *et al.*, 1999; Pavan *et al.*, 2000; Pollack, 2000; Schwartz , 2002; Wollerman and Wiley, 2002).

D. Objectives

In situations when background noise levels are high and/or variable, multiple element calls will be discernable if they fit a regular pattern that distinguishes them from random sounds or other seal calls having a different rhythm pattern. Some Weddell seal multiple element calls appear to have constant element and interval durations while others appear to have consistently increasing or decreasing element and interval durations throughout the calls (Thomas and Kuechle, 1982; Thomas *et al.*, 1988). This apparent stability of the timing in calls has not yet been measured. If constant timing was found within calls, as well as between calls, it would suggest that the seals produce rhythmically repeated vocalization patterns that could potentially increase the probability of call detection by distant conspecifics.

Our purpose in this study was to investigate the apparent stability of rhythms that occur in Weddell seal multiple element underwater calls and to determine if the element and interval durations, and frequencies within a call, follow consistent and regular patterns throughout the call.

II. MATERIALS AND METHODS

A. Recordings

Digital audio tape (DAT) recordings of Weddell seal underwater vocalizations were obtained near Weddell seal breeding groups during the 1997 breeding season. These recordings were made off the Eastern Antarctic coastline near two Australian Antarctic stations. Eight recordings (three from the same location) were made near Casey during 21 October–30 November and seven recordings (each at a different location) were made near Davis during 8 November–1 December, for a total of 15 recordings made at 12 locations.

The recordings were made during a period of 24 h light, near groups of females with pups on the ice. The number, sex and age of the vocalizing seals could not be determined, nor was it possible to determine the proximity of the seals to the hydrophone. Each recording lasted 1–2 h.

At each recording site, one hole was drilled through the sea-ice and the hydrophone was lowered approximately 2 m below the ice. Sony TCD-D3 DAT recorders (frequency response 0.02–20 kHz ± 1 dB) were used to make the recordings. At Casey, an ITC 6050C hydrophone (frequency response 0.002–30 kHz ± 1 dB), with a built in preamplifier was connected to the Sony DAT recorder. At Davis, a Brüel and Kjær 8100 hydrophone equipped with a Brüel and Kjær 2635 charge preamplifier (frequency response 0.002–30 kHz ± 1 dB) was used.

B. Data analysis

Gram (Version 6.0.9) was used to analyze the calls. A preliminary examination determined that six call type categories were the most commonly occurring multiple element call types on the recordings. These were Chugs (C), Knocks (K), Grunts (G), Whistle-Ascending (WA), Whistle-Ascending-Grunts (WAG) and Whistle-Descending (WD) calls (Thomas and Kuechle, 1982; Thomas *et al.*, 1988; Pahl *et al.*, 1997). Only calls of these types were analyzed. The call type categories were highly variable and so were further classified into subtypes that described the calls in greater detail and allowed calls most similar to each other to be grouped together. Call types were separated into distinct subtypes based on relative differences in waveform, spectral shape, timing and frequency of the calls within any one call type. It is important to note that the criteria used to classify the calls into subtypes in this study were arbitrary, and the classification scheme was based on differences that were distinct to the observer. The subtypes chosen were based on small sample sizes and the calls were not necessarily sorted into subtypes based on the same classification scheme as reported by other authors (Thomas and Kuechle, 1982; Thomas *et al.*, 1988; Pahl *et al.*, 1997; Abgrall *et al.*, 2003).

To restrict the possibility of analyzing a large number of calls from a single seal, an upper limit of 20 samples from each call type category (with the exception of the highly variable WD calls) were analyzed from any one recording. Up to 40 WD calls were analyzed from a recording; however these calls included several WD subtypes. Many of the WD calls also overlapped each other in time (though not usually in frequency). Therefore it is highly unlikely that any one seal made all of the WD calls at a single site. Only clear calls from which accurate measurements could be made repeatedly were chosen for analysis.

For each multiple element call type examined, the following features were noted:

(1) Call type category and subtype.
(2) Total number of elements in the call.
(3) Total length of the call.
(4) Element duration (ms) of each element in the call, up to the first 30 elements of the call. Measures from only the first 30 elements of the call were made due to practical reasons (time limitations), and because the majority of the calls analyzed (84%) were less than 30 elements long. For the calls analyzed, the signal to noise ratios were high enough (>5 dB) to permit consistent measures of element length.
(5) Interval (inter-element) duration (ms) of each interval in the call, up to the first 29 intervals of the call.
(6) Frequency (Hz) of elements in the call. The start and end frequencies (± 43 Hz) of each element in a call were measured. Frequency measures were made at the midpoint of broad bandwidth calls.

Data obtained for the element and interval durations and frequency were transformed into proportional data. Each value of a measurement (element or interval duration, or frequency) was transformed to a proportion of the previous measure. Transformed data for element durations was indicated as ''proele,'' for interval duration data as ''proint,'' and as ''prost'' or ''proend'' (the start and end frequencies) for frequency data. Transformed data were used because some of the calls appeared to consistently increase or decrease in frequency and timing throughout the call. Such patterns would be expected to show a significant difference between means for the absolute (raw) data. These same calls would be expected to show no or only slight difference between means for the transformed data if the increase or decrease in timing and frequency were regular (a constant proportion of the previous measure). Both the absolute and transformed data were examined to determine consistency within the calls.

For the absolute and transformed data the mean, standard deviation (SD), and coefficient of variance (CV) values were calculated for the element and interval durations of all calls. These basic statistics were also calculated for groups of calls of a particular number of elements (NOE; 3–5, 6–10, 11–20, 21–30, and >30 elements), from a particular site (Casey or Davis), or occurring with an apparent rhythm pattern. Using both absolute and transformed data, ANOVA's were used to determine the consistency of element and interval durations within calls. The consistency of element and interval durations was also tested for calls with a specified NOE, from a particular site, or occurring with a particular rhythm pattern.

Calls were then analyzed according to call type category and subtype. Mean, SD, and CV values of the absolute and transformed data for element durations, interval durations, and start and end frequencies of each element [$\log_2$(Hz)], were calculated for calls of each type and subtype. These values were also calculated for calls with a specified NOE, from a particular site, or occurring with a particular rhythm pattern within each type or subtype. ANOVA tests were then used to determine the similarity of measurements within each call type category and subtype.

The total duration of the calls was also examined. The mean total duration and SD values of calls consisting of a specific NOE were calculated. ANOVA's were then used to compare mean call durations.

III. RESULTS

A. All calls—NOE, site and pattern effects

A total of 405 Weddell seal multiple element calls were examined. WD calls were the most common call type category, compromising 292 (72%) of the calls analyzed. Up to 40 WD calls were analyzed from 3 of the 15 recordings. These three recordings were made at one location near Casey. There was a high incidence of WD calls on these recordings, however fewer than 20 WD calls were analyzed from each of the other 12 recordings due to lower calling rates and fewer calls overall on the tapes. For most call type categories, the calls analyzed from each tape were separated in time along the recording because many were uncommon or had low signal to noise ratios, which prohibited obtaining accurate measurements.

When all calls were examined together, the mean element durations (mean duration of Element 1, mean duration of Element 2, mean duration of Element 3, etc.) were not significantly different from each other ($F_{29,6667}=1.12, p=0.299$). Mean interval durations were significantly different from each other ($F_{28,6262}=7.61, p<0.0001$), due to large durations of the first few intervals. When the transformed data for interval durations were analyzed (interval duration as a proportion of the previous interval duration), the mean interval durations were no longer significantly different ($F_{27,5857}=0.79, p=0.770$). When all calls were analyzed together, the SD and CV values for element and interval durations were large. Mean element durations had an average CV value of 1.19 ± 0.36, and mean interval durations had an average CV value of 1.60 ± 0.29. The SD values of the transformed data were smaller than those for the absolute data with the average CV value for the proele data being 0.38 ± 0.11, and the average CV value for point data being 0.52 ± 0.41.

1. Trends related to the number of elements in a call

When calls were analyzed by NOE, calls with fewer elements tended to have longer element and interval durations than did calls with many elements (Figs. 1, 2). Calls with many elements also appeared to be more stable, with fewer fluctuations in mean duration values (Fig. 1). There was a tendency for longer calls with many elements to have slightly increasing element and interval durations throughout the calls (Fig. 1). ANOVA results indicated significant differences in element and interval durations of calls with 21–30 elements (elements: $F_{29,1966}=4.22, p<0.0001$, intervals: $F_{28,1889}=14.90, p<0.0001$), or >30 elements (elements: $F_{29,1949}=4.86, p<0.0001$, intervals: $F_{28,1884}=9.94, p<0.0001$) due to increasing mean duration values. When analyzing calls by NOE, for all but two of the cases in which significant differences were found in element and interval durations, the mean durations of the transformed data were not significantly different (all p-values >0.102). For the cases in which the transformed data showed significant differences (proele values of calls with 11–20 elements and

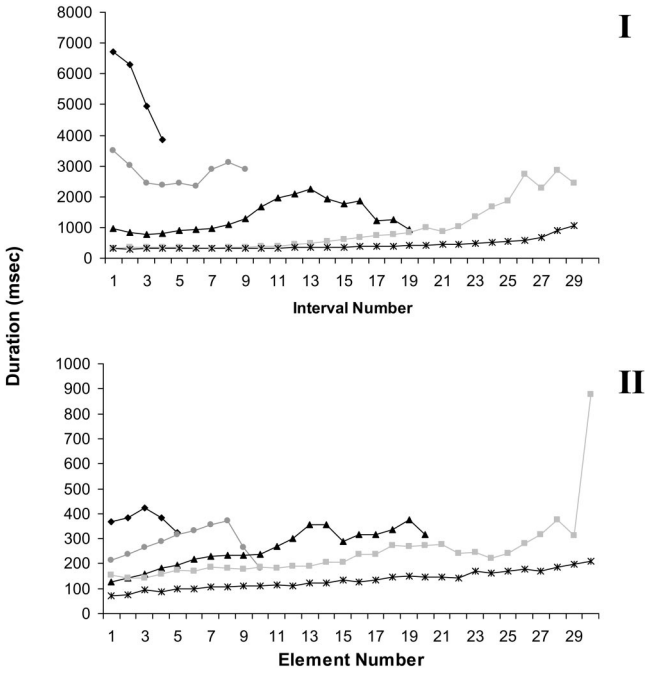

FIG. 1. Trends in mean duration values (ms) of intervals (I) and elements (II) of Weddell seal multiple element underwater calls, analyzed by a specific number of elements (NOE) per call: 3–5 elements (◆), 6–10 elements (•), 11–20 elements (▲), 21–30 elements (■), and 30+ elements (*). See text for details on variance associated with analyzing calls by NOE.

point values of calls with 21–30 elements), there appeared to be a high degree of variance near the beginning and end of the calls and when first and last few values were excluded from the tests, the mean durations were no longer significantly different. SD and CV values remained high for both element and interval durations, even when calls were analyzed by NOE. For example, the average CV value of calls 3–5 elements long was 0.87 ± 0.11 (element durations) and 0.98 ± 0.16 (interval durations). For the transformed data, the SD values were reduced and the average CV values were 0.25 ± 0.08 (proele) and 0.23 ± 0.05 (proint).

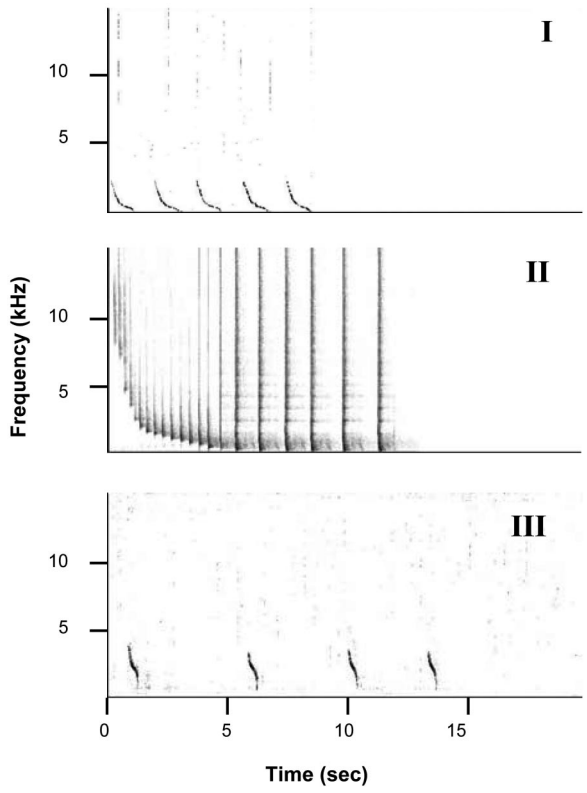

FIG. 2. Examples of timing patterns in Weddell seal multiple element underwater calls; I = Pattern cC (subtype WD10 call displayed), II = Pattern iI (subtype WD1 call displayed), III = Pattern cD (subtype WD8 call displayed); see the text for an explanation of terms. Analyzing bandwidth = 86 Hz.

2. Differences in calls analyzed at each site

Of the 405 multiple element calls analyzed, 290 were recorded at Casey and 115 were recorded at Davis. Mean element durations showed no significant differences at either site (Casey: $F_{29,5073} = 1.05$, $p = 0.392$, Davis: $F_{29,1593} = 1.01$, $p = 0.451$). Significant differences were found when analyzing mean interval durations (Casey: $F_{28,4783} = 8.06$, $p < 0.0001$, Davis: $F_{28,1478} = 3.38$, $p < 0.0001$). For both sites, when transformed data for interval duration were analyzed, means were not significantly different (Casey: $F_{27,4493} = 0.51$, $p = 0.983$, Davis: $F_{27,1363} = 1.03$, $p = 0.422$). The average CV values for element durations for calls analyzed by site were 1.23 ± 0.50 (Casey), and 0.80 ± 0.10 (Davis). The average CV values for interval durations were 0.62 ± 0.33 (Casey) and 1.07 ± 0.34 (Davis). When the transformed data were considered, the SD and CV values were greatly reduced, with average CV values of 0.34 ± 0.11 and 0.50 ± 0.47 (Casey) and of 0.44 ± 0.20 and 0.46 ± 0.30 (Davis) for element and interval durations, respectively. Differences between sites may be attributed to differences in sample size of each of the call types and subtypes at each site (Table I).

3. Rhythm patterns in Weddell seal calls

Timing of the element durations (indicated in lowercase letters), as well as the interval durations (indicated in capital letters), were considered when categorizing calls into rhythm patterns. Patterns of duration timing were either constant (indicated by the letters "c" or "C"), increasing ("i" or "I") or decreasing ("d" or "D"). Therefore, Pattern cI calls had constant element durations (indicated by "c") and increasing interval durations (indicated by "I") throughout the call. Seven rhythm patterns with respect to the timing of elements and intervals of the calls were identified in the Weddell seal vocalizations (Patterns cC, iC, cI, iI, dI, cD, and iD; Table II; Figs. 2, 3).

The most common rhythm for element durations was constant timing, while increasing interval durations was the most common rhythm for the interval timing. Decreasing timing was the most uncommon rhythm pattern for both element and interval durations (Table I). The most common rhythms were Pattern iI and Pattern cC. Patterns cI and cD were also frequently emitted, while only a small fraction of calls were produced with the remaining three rhythm patterns (Table I). None of the multiple element calls examined occurred without some form of patterning of the element and interval durations.

TABLE I. The number of Weddell seal multiple element underwater calls of each of the seven patterns occurring within each of the call subtypes (see the text). Patterns of duration timing were either constant (indicated by "c" or "C"), increasing ("i" or "I") or decreasing ("d" or "D"). Whether a particular pattern occurs within the call subtype at just Casey (Cas), at just Davis (Dav), or at both sites (Both) is indicated (in brackets). The total sample size for each call pattern is also given (Total).

Call Subtype	Pattern						
	cC	**iC**	**cI**	**iI**	**dI**	**cD**	**iD**
WD1	2 (Both)	3 (Cas)	23 (Both)	97 (Cas)	5 (Cas)	1 (Cas)	
WD2			1 (Cas)	27 (Cas)			
WD3	8 (Cas)		3 (Dav)				
WD4			9 (Dav)				
WD5				13 (Cas)			
WD6							2 (Cas)
WD7				3 (Cas)			
WD8						24 (Both)	11 (Dav)
WD9			10 (Dav)			27 (Cas)	1 (Cas)
WD10	13 (Cas)	2 (Cas)	5 (Cas)				2 (Dav)
G1	26 (Dav)	1 (Dav)	1 (Dav)			2 (Dav)	
G2	6 (Both)						
G3	1 (Dav)						
G4	2 (Dav)						
C1	18 (Both)		4 (Dav)				
C2	8 (Both)						
C3	4 (Both)						
K1			10 (Cas)				
K2	3 (Cas)						
K3	5 (Cas)						
WAG	8 (Dav)		8 (Dav)				
WA1	3 (Dav)						
WA2			2 (Dav)				
WA3	1 (Dav)						
Total	**108**	**6**	**76**	**140**	**5**	**54**	**16**

The rhythm patterns of the calls became evident by listening to the calls and by analyzing the absolute and transformed data. With constant duration patterns the mean element or interval durations (of the transformed data) tended to be close to 1.0 (Table II). This indicates that adjacent durations were approximately equal. When calls with increasing duration patterns were analyzed, mean durations tended to be greater than 1.0, usually above 1.1 (Table II) showing that durations were increasing as the calls progressed. This rhythm was easily identified when listening to the calls or looking at spectrograms. When decreasing patterns were analyzed, the transformed data produced mean durations of slightly less than 1.0 indicating that durations were decreasing. Decreasing rhythm was not easily identified by just listening to the vocalizations, but became apparent on spectrograms and by examining the time data. For example, the averages of all the mean proint values for calls with Pattern cD or iD timing were actually slightly greater than 1.0 because these calls tended to have longer interval durations near the beginning of the calls before the interval pattern of decreasing timing became established. When the mean durations of the first two interval values were excluded, the values for the Pattern cD and iD calls dropped below 1.0 (Table II). Patterns of both element and interval durations tended to show fluctuations, particularly at the beginning and end of calls (Fig. 3), however, the interval durations clearly demonstrated the constant, increasing or decreasing rhythm patterns, while the element rhythm patterns were not as evident.

TABLE II. Average values of the mean element and interval durations (standard deviation indicated in brackets) calculated for the transformed data (duration as a proportion of the previous measure) for each of the seven timing patterns of Weddell seal multiple element underwater calls. Timing of the element durations (ProEle; indicated by the lowercase letters), and interval durations (ProInt; indicated by uppercase letters) were both considered when categorizing calls into patterns.

Pattern	N	Average duration value	
		ProEle	**ProInt**
cC	108	1.04 (0.042)	1.09 (0.204)
iC	6	1.09 (0.124)	1.05 (0.215)
cI	76	1.08 (0.124)	1.18 (0.090)
iI	140	1.12 (0.091)	1.19 (0.154)
dI	5	0.99 (0.106)	1.10 (0.182)
cD	54	1.03 (0.142)	0.99 (0.103)[a]
iD	16	1.13 (0.268)	0.99 (0.166)[a]

[a]The first interval durations are not included in calculations due to the fluctuation of values at the beginning of the calls. When the first two interval durations were included the mean duration in both cases (for cD and iD calls) became 1.02 due to the presence of very high interval values within the first two intervals (see the text).

For the majority of cases when the absolute mean durations of elements and intervals were analyzed for the different rhythms, call attributes with constant timing showed no significant differences in mean duration values, while calls with increasing or decreasing timing did show significant differences (due to apparent increasing or decreasing mean durations). There were some exceptions to this. In the case of the Pattern cC calls, both element and interval durations showed significant differences between means (elements: $F_{29,1556}=5.23$, $p<0.0001$, intervals: $F_{28,1448}=6.18$, p

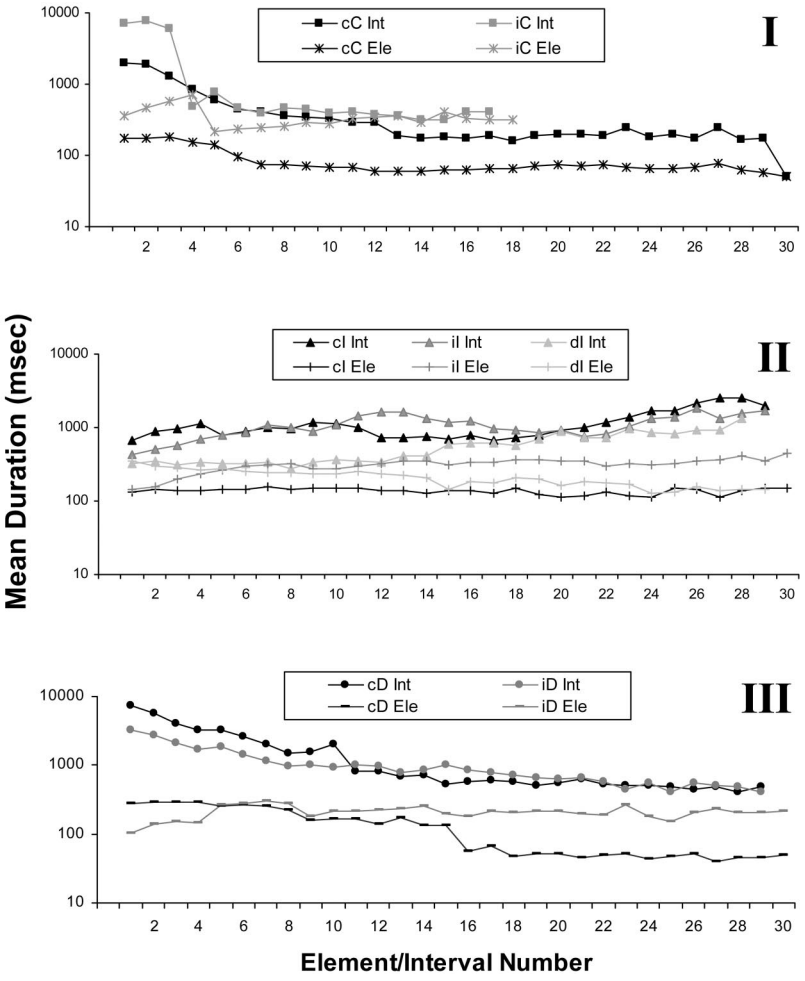

FIG. 3. Trends in mean element and interval durations of Weddell seal multiple element underwater calls occurring with each timing pattern: I = calls with constant interval durations (Patterns cC, iC), II = calls with increasing interval durations (Patterns cI, iI, dI), III = calls with decreasing interval durations (Patterns cD, iD). See the text for details on variance in calls analyzed by a rhythm pattern.

<0.0001). The initial element and interval durations were much longer than the remaining durations (which may be attributed to the trend of shorter calls having longer element and interval durations). This may also account for the significant difference observed among mean element durations of Pattern cD calls ($F_{29,434}=4.50, p<0.0001$). Of the 14 ANOVA tests performed using the transformed data for calls of each rhythm; the values were not found to be significantly different from each other in 12 cases (11 p-values >0.092; 1 p-value $=0.054$). The two cases where significant differences were found were for proint values of Pattern cC calls and proele values of Pattern iI calls. The proele values for Pattern iI calls showed significant differences due to variation near the beginning of the calls. When all but the first few values were included in the test, the means were not significantly different. For the Pattern cC calls, one of the mean proint values was larger than the rest due to a long interval duration measured from a single call. When this outlier value was excluded from the analysis, the mean proint values were no longer significantly different.

The SD and CV values of calls analyzed by pattern were smaller than when all calls were analyzed together. For example, the average CV values for element and interval durations of Pattern cC (absolute data) were 0.81 ± 0.29 and 1.10 ± 0.49, respectively. The average CV values for the transformed data were reduced to 0.29 ± 0.16 (proele), and 0.49 ± 0.43 (proint).

B. Call type categories and subtypes

The calls classified under the six broad call type categories were arbitrarily separated into 24 subtypes. While there was only one type of WAG call, the rest of the call types were classified into several subtypes. The WD calls showed the highest amount of variability and were classified into 10 different subtypes (Table I).

The calls of any one subtype were most commonly emitted with only one or two rhythm patterns (Table I). In the case of the WD1 calls, however, the calls occurred in six different timing patterns (although 92% of the WD1 calls occurred as Pattern cI or iI calls; Table I). In some cases, call subtypes were found to occur at both sites but with different rhythm patterns at each site. Many call subtypes also occurred with the same rhythm, while other rhythms were specific to only a few subtypes (Table I). Some subtypes demonstrating a specific rhythm had low sample sizes (Table I).

When calls were analyzed by call type category, SD and CV values of mean element and interval durations were gen-

TABLE III. The mean, standard deviation (in brackets) and coefficient of variance (CV) of the frequencies [$\log_2$(Hz)] measured at the beginning (Start Frequency) and end (End Frequency) of each element of all subtype WD1 Weddell seal multiple element underwater calls analyzed together. The number of the element from which the measures were taken is given (Element Number), as well as the number of calls analyzed (N).

		Start frequency		End frequency	
Element #	**N**	**Mean**	**CV**	**Mean**	**CV**
1	131	12.96 (0.789)	0.06	12.09 (1.040)	0.09
2	131	12.83 (0.798)	0.06	11.86 (0.901)	0.08
3	131	12.76 (0.746)	0.06	11.60 (0.885)	0.08
4	130	12.73 (0.721)	0.06	11.42 (0.876)	0.08
5	130	12.68 (0.728)	0.06	11.19 (0.911)	0.08
10	119	12.55 (0.754)	0.06	10.59 (0.950)	0.09
15	86	12.29 (0.865)	0.07	9.83 (1.085)	0.11
20	54	12.06 (0.884)	0.07	9.33 (1.122)	0.12
25	36	11.60 (0.872)	0.08	9.29 (1.219)	0.13
30	19	11.53 (1.031)	0.09	9.15 (0.911)	0.10

erally smaller than when all calls were analyzed together, or when all calls were analyzed by site or NOE. The average CV values for the element and interval durations of WD calls, the most variable call type, were 1.05 ± 0.34 (element durations) and 1.45 ± 0.37 (interval durations). The average CV values for the transformed data of the WD calls were 0.36 ± 0.11 (proele) and 0.48 ± 0.42 (proint). The SD and CV values obtained for calls analyzed by subtype were smaller than those of calls analyzed by call type categories. For example, the average CV values for WD1 calls were 0.89 ± 0.35 (element durations) and 1.27 ± 0.43 (interval durations). For the transformed data, average CV values were reduced to 0.33 ± 0.13 (proele durations) and 0.39 ± 0.22 (proint durations). When analyzing call type categories or subtypes from a particular site, having a specific NOE or occurring with a particular rhythm, SD and CV values were further reduced.

The frequency (kHz) of each call subtype was very consistent and had low SD and CV values (Table III). Frequency of the calls followed three patterns: rising start frequencies throughout the calls (displayed by subtypes G1 and WD3), falling start frequencies throughout the calls (subtypes C1, WD1, WD2, WD5, and WD8) or constant frequencies (subtypes C2, C3, G2, G3, G4, WD4, WD6, WD7, WD9, WD10, and all K, WAG and WA calls). For the majority of calls, the frequency tended to drop within individual elements; therefore start frequencies were typically higher than end frequencies (with the exception of the WA calls).

C. Trends in total call length

The total length of the calls averaged 22 ± 16.6 s. When the total lengths of the calls were analyzed by NOE, the mean total duration values ranged from 20 to 27 s. The SD values obtained for these means were high, however, the means were not significantly different from one another ($F_{4,404} = 1.83$; $p = 0.122$; Fig. 4). The calls with 31+ elements had the longest mean total duration (Fig. 4). These calls included calls >100 elements in length and therefore a greater mean duration value would be expected. However, the longest call (114.4 s) was a 4-element call, while the shortest call (1.9 s) was a 31-element call.

IV. DISCUSSION

A. Patterns in Weddell seal multiple element underwater calls

Element and interval durations were found to either increase, decrease or remain constant throughout any one call. In total, seven patterns of timing were identified. Both element and interval durations were used to determine the rhythm patterns within calls, however, interval rhythms were easier to identify than element rhythms (Table II; Fig. 3). The stability of the patterns was demonstrated by examining the transformed data for calls occurring with each rhythm. For the majority of cases within the seven patterns, the mean durations of the transformed data were not significantly different from each other, indicating that the increasing, decreasing or constant element and interval durations were regular. The variation in mean values of element and interval durations (absolute data) was high for calls of each rhythm. The variance may have been caused by differences between call type categories emitted with each rhythm, as most of the rhythm patterns were observed in several call types (Table I). When patterns within each call type category or call subtype were analyzed separately, SD and CV values were reduced for absolute and transformed data. Variance may also be attributed to differences between individual seals. The beginning and ending elements and intervals of a call were the

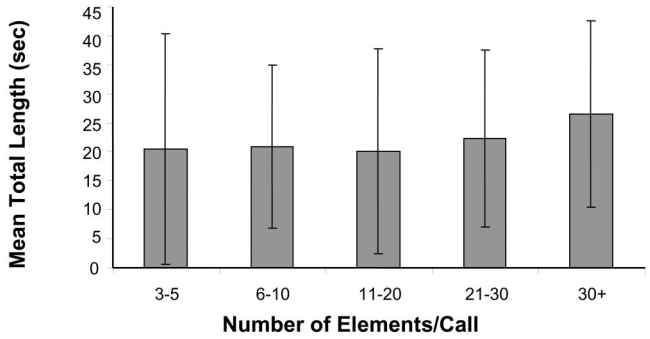

FIG. 4. Mean total length ± 1 SD of Weddell seal underwater multiple element calls analyzed in groups according to the number of elements present in the call.

most variable. The rhythm often became more clearly established after the first few elements were emitted and persisted throughout the main body of the call.

There were also stable frequency patterns found within the calls. The start frequencies of elements throughout any one multiple element call may either remain constant throughout the entire call, increase as the call progresses, or decrease as the call progresses. The subtypes of the calls were determined mainly by the spectrum shape of the calls, therefore the frequencies were very consistent for call subtypes regardless of pattern in which the calls were emitted (Table III).

The mean total duration of the calls analyzed (22 s) did not vary with an increasing number of elements (Fig. 4). This can be attributed to the fact that the element and interval durations tended to decrease as the number of elements within a call increased (Fig. 1). Terhune *et al.* (1994) suggested that when multiple element calls were overlapped, Weddell seals lengthen the duration of their calls by adding elements to the end of calls. The additional elements likely enhance detection of the calls by distant conspecifics. Contradictorily, the results of this study indicate that the seals do not just add elements to a call after the call has already begun, but predetermine the length of their calls prior to calling. A possible explanation is that the seals assess the level of background noise before calling and then plan their call with a predetermined NOE accordingly in order to maximize call detectability. Emitting calls with many elements would be the most beneficial during periods of high level background noise. This could be an example of an anti-masking strategy used by the seals. The relatively stable total duration of the calls may also be due to a physiological restriction on the seals such as limits imposed by the physical size of their air chambers. However, multiple element calls of 65.3 s or 540 elements have been recorded in Weddell seals (B. Pahl, unpublished data).

The total number of seals that produced the 405 calls analyzed is unknown. The Weddell seal recordings analyzed included many calls overlapping in time (but not in frequency), therefore it is likely that the calls were recorded from a number of seals at each site. It is possible that uncommon call subtypes were made by a single seal.

The results in this study are biased towards loud source level calls, presumably from nearby seals that were not masked by other calls or noises. The call subtypes were determined subjectively, however, the broader call type classification system followed that reported in previous studies (Thomas *et al.*, 1988; Pahl *et al.*, 1997).

B. Anti-masking properties of patterned calls

Acoustic communication requires not only detection, but also recognition of signals by a receiver (Klump, 1996). Wiley and Richards (1978) described two common tactics used by animals to combat degradation and masking of signals during transmission, and enhance the recognition of calls; (1) coding and (2) redundancy of information (in this case, repetition of call elements). Patterning and repetition of signals helps the receiver to differentiate between signals and noise (Bateson, 1968), and ensures accurate transmission of signals (Wiley and Richards, 1978).

The presence of rhythmical repetition in seal communications has important implications for the extent to which seals can successfully communicate over long distances and during high levels of background noise. Having stereotyped rhythmic patterns in their underwater vocalizations likely confers a number of advantages that would facilitate Weddell seal communication. In quiet surroundings, the repetition of the call elements likely enhances their detection relative to a single element call. This could potentially increase the detection range of a call by up to 80% (Turnbull and Terhune 1993). Most ice noises occur as single events and the regular repetition would distinguish multiple element calls from abiotic sources (Watkins and Schevill, 1979). When other seals are calling or the abiotic noise levels are high, the calls are more likely to be detected when the elements are repeated in a regular manner. Such calls will be longer and thus it is less likely that the entire call would be completely masked by other sounds. Once the first few elements of the multiple element call are emitted (thereby establishing the call pattern), listening conspecifics would theoretically be able to predict when successive elements should occur. If a listener was uncertain about the presence of a faint call, the regular repetition would enable them to confirm its presence by knowing when to expect subsequent elements. Chickadee (*Poecili carolinensis*) calls were found to contain a form of repetition, where properties of single notes provided cues about the syntactical structure of the entire call. A listener would only have to detect a portion of the call in order to receive the entire message (Freeburg *et al.*, 2003). By increasing call length through the addition of elements (Serrano and Terhune 2001), and by producing these elements at regular intervals, Weddell seals may be able to enhance the probability of call detection by a listener. Similarly, king penguins increase the number of elements in their calls when increasing wind speeds raise the level of background noise. By increasing the repetition of information during times of high levels of background noise, the birds could increase the probability of communicating during short time windows when the noise level drops (Lengagne *et al.*, 1999).

C. Possible functions of call patterning

Various animal species use patterns in timing of call elements in order to recognize signals produced by conspecifics. Grasshopper and cricket stridulations, and flash patterns produced by fireflies are often species specific (Alexander, 1968; Helverson and Helverson, 1998; Ronacher *et al.*, 2000). Studies of tree-frog mating calls have shown that timing structure of the calls encodes information about the species and sex of the frog making the calls (Schwartz *et al.*, 2002; Wollerman and Wiley, 2002). Bird songs may be unique to a species or an individual. Studies of rhythm in bird vocalizations have shown characteristic patterns emerging in songs of different bird species, regardless of whether the songs were developed through independent learning of an individual or through interactions of the individual with other birds. Rhythms present in songs of different species of

doves, pigeons, sparrows and shore birds have been statistically demonstrated (Baptista, 1996; Miller, 1996). Generally, variation in the duration of individual notes (elements) and the intervals between the notes in complex vocalizations are found to provide rhythms characteristic of a species (Baptista, 1996). Within the distinctive calls of the Carolina chickadee, the ordering of the elements within the call were not only species specific, but single elements within the calls were predictive of the bird's local capture site as well (Freeburg *et al.*, 2003). It is also possible that the patterns with which Weddell seals emit calls may serve species or individual recognition functions.

Improved species detection should occur if the receiver has only a few patterns to listen for. The seven rhythm patterns used by Weddell seals (which consist of only three timing trends; constant, increasing and decreasing) do not likely match those of other seal species in the area. The groan-like call of crabeater seals (*Lobodon carcinophagus*) is a low frequency, single-element long duration call (Stirling and Siniff, 1979). Leopard seals (*Hydrurga leptonyx*) typically produce single or double-element calls, the majority of which are trills that have frequency and duration patterns very different from Weddell seals (Stirling and Siniff, 1979; Rogers *et al.*, 1995; Thomas and Golladay, 1995). Ross seals (*Ommatophoca rossi*) produce pulsed sounds interspaced with long frequency modulated tones. Spectrograms of these calls showed different patterning than that of calls produced by Weddell seals (Watkins and Ray, 1985).

Sperm whales studied in the Mediterranean Sea produced click sequences consisting of four clicks (elements). The durations of these elements were found to be highly variable, while inter-click (interval) durations occurred in a 2:1:1 rhythmic pattern. It was suggested that the timing of the highly stable intervals, rather than the variable-length clicks of click sequences contained the information in the calls (Pavan *et al.*, 2000). It was also found that the patterning within harp seal calls occurred in the interval rather than the element timing (Moors and Terhune, 2003). Unlike the sperm whale and harp seal calls, both the element and interval durations of the Weddell seal calls occurred in specific patterns. This suggests that both the elements and the intervals of the call may contain information. It is important to note, however, that the patterns of interval duration in the calls are more stable and easier to identify than the element timing patterns (Table II; Fig. 3).

The call patterns identified in harp and Weddell seals are similar in many ways but they do exhibit fundamental differences. While the timing and frequency within harp seal multiple element call patterns is constant, the Weddell seal calls display timing and frequency shifts throughout the calls. Weddell seal element and interval durations also tend to be influenced by the number of elements within the call. This did not occur in the harp seal calls (Moors and Terhune, 2003).

For the Weddell seal calls, the waveform, bandwidth, and frequency range of individual call types exhibit considerable variation (Thomas and Kuechle, 1982; Pahl *et al.* 1997). If the species recognition for Weddell seals resides in the temporal patterns of the multiple element calls, perhaps the fine structure of the vocalizations is less important. Sounds given using the patterns would be distinct from random background noise and would match the familiar temporal model. Thus, the patterns of Weddell seal calls could serve to identify the species of the caller, independent of the frequency or waveform of the specific call type.

Rhythms within Weddell seal calls may also potentially encode information on the behavior or situation of the calling seal. The barking rate of an adult male California sea lion (*Zalophus californianus*) increased from 2.1 to 3.0 barks/s in air and from 1.0 to 1.4 barks/s underwater when the social context changed from nondirectional self advertisement, to chasing or confronting another sea lion (Schusterman, 1977). Diana monkeys (*Ceriopithecus diana diana*) emit long distance vocalizations which indicate the presence of very specific predators to conspecifics. These warning calls consist of a discrete number of syllables that varies depending on the type of predator present. Zuberbuhler *et al.* (1997) found a significant difference for the overall call length and the intersyllable (interval) durations between Diana monkey calls produced in the presence of leopards (*Panthera pardus*) and those produced in the presence of hawk eagles (*Stephanoaetus coronatus*). In the case of Weddell seal vocalizations, some of the variation within call rhythm patterns (for example, differences in rhythm between call types) may be related to the calls being emitted in different behavioral contexts. Before this can be determined the behavior of individual vocalizing seals has to be studied at the call rhythm level.

The consistency of timing within Weddell seal calls is demonstrated by the mean element and interval durations, which were relatively stable between each of the call subtypes (within the seven patterns) as well as within the patterns themselves. There was some variance in element and interval durations of the calls, although this may be due to the use of very precise time measures. The ability of seals to detect a difference of a few milliseconds is likely limited, although studies on this topic have not been conducted. There is some variation within the patterns, but the patterns themselves are very distinct, and thus listeners would be expected to have little confusion when trying to identify a specific call rhythm.

Further studies of seal call predictability are required in order to determine the extent to which rhythmically repeated calls aid in seal communication, if patterns emitted by seals serve a function for species identification, or if they carry information about the behavioral context in which the call is being made. The direct observation of individual calling seals will be required to determine the functional significance of the different vocalizations.

ACKNOWLEDGMENTS

We thank H. Burton of the Australian Antarctic Division and the Australian National Antarctic Research Expeditions (ANARE) for logistical support at Davis and Casey. D. Simon provided the recordings from Casey. H. Hunt, S. Turnbull and P. Rouget provided advice on an earlier draft of this manuscript. The National Science and Engineering Re-

search Council of Canada (NSERC) provided funding for this project with a USRA to H. B. M. and Discovery Grant to J. M. T.

Abgrall, P. A., Terhune, J. M., and Burton, H. R. (**2003**). ''Variation of Weddell seal (*Leptonychotes weddellii*) underwater vocalizations over mesogeographic ranges,'' Aquat. Mamm. **29**, 268–277.

Alexander, R. D. (**1968**). ''Arthropods,'' in *Animal Communication: Techniques of Study and Results of Research*, edited by A. Sebok (Indiana University Press, London), pp. 167–217.

Baptista, L. F. (**1996**). ''Nature and it's nurturing in avian development,'' in *Ecology and Evolution of Acoustic Communication in Birds*, edited by D. E. Kroodsma and E. H. Miller (Cornell University Press, Ithaca) pp. 39–60.

Bateson, G. (**1968**). ''Redundancy and coding,'' in *Animal Communication: Techniques of Study and Results of Research*, edited by A. Sebok (Indiana University Press, London), pp. 167–217.

Bertram, G. L. C. (**1940**). ''The biology of the Weddell and crabeater seals,'' Scientific Reports, British Graham Land Expedition 1934-1937, **1**, 1–139.

Freeburg, T. M., Lucas, J. R., and Lucas, B. (**2003**). ''Variation in chickadee calls of the Carolina chickadee population, *Poecile carolinensis*: identity and redundancy within notes,'' J. Acoust. Soc. Am. **113**, 2127–2136.

Green, K., and Burton, H. R. (**1988**). ''Annual and diurnal variations in underwater vocalizations of Weddell seals,'' Polar Biol. **8**, 161–164.

Hawkins, A. D., and Myrberg, A. A. (**1983**). ''Hearing and communication underwater,'' in *Bioacoustics: A Comparative Approach*, edited by B. Lewis (Academic, New York), pp. 347–405.

Von Helverson, D., and Von Helverson, O. (**1998**). ''Acoustic pattern recognition in a grasshopper: processing in the time or frequency domain?'' Biol. Cybern. **79**, 467–476.

Klump, G. M. (**1996**). ''Communication in the noisy world,'' in *Ecology and Evolution of Acoustic Communication in Birds*, edited by D. E. Kroodsma and E. H. Miller (Cornell University Press, Ithaca), pp. 321–338.

Kooyman, J. L. (**1981**). *Weddell Seal: Consummate Diver* (Cambridge University Press, New York).

Lengagne, T., Aubin, T., Lauga, J., and Jouventin, P. (**1999**). ''How do king penguins (*Aptenodytes patagonicus*) apply the mathematical theory of information to communicate in windy conditions?'' Proc. R. Soc. London, Ser. B **266**, 1623–1628.

Miller, E. H. (**1996**). ''Acoustic differentiation and speciation in shorebirds,'' in *Ecology and Evolution of Acoustic Communication in Birds*, edited by D. E. Kroodsma and E. H. Miller (Cornell University Press, Ithaca), pp. 39–60.

Moors, H. B., and Terhune, J. M. (**2003**). ''Repetition patterns in harp seal (*Pagophilus groenlandicus*) underwater multiple element calls,'' Aquat. Mamm. **29**, 278–288.

Oetelaar, M., Terhune, J. M., and Burton, H. R. (**2003**). ''Can the sex of a Weddell seal (*Leptonychotes weddellii*) be identified by its surface call?,'' Aquat. Mamm. **29**, 261–267.

Pahl, B. C., Terhune, J. M., and Burton, H. R. (**1997**). ''Repertoire and geographic variation in underwater vocalizations of Weddell seals (*Leptonychotes weddellii*, Pinnipedia: Phocidae) at the Vestfold Hills, Antarctica,'' Aust. J. Zool. **45**, 171–187.

Pavan, G., Hayward, T. J., Borasani, J. F., Priano, M., Fossati, C., and Gordon, J. (**2000**). ''Time patterns of sperm whale codas recorded in the Mediterranean Sea 1985–1996,'' J. Acoust. Soc. Am. **107**, 3487–3495.

Pollack, G. (**2000**). ''Who, what, where? Recognition and localization of acoustic signals by insects,'' Curr. Opin. Neurobiol. **10**, 763–767.

Ray, C. (**1967**). ''Social behavior and acoustics of the Weddell seal,'' Antarctic Journal of the United States **2**, 105–106.

Richardson, W. J. (**1995**). ''Marine mammal hearing,'' in *Marine Mammals and Noise*, edited by W. J. Richardson, C. R. Greene, C. I. Malme, and D. H. Thompson (Academic, Boston), pp. 205–240.

Rogers, T., Cato, D. H., and Bryden, M. M. (**1995**). ''Underwater vocal repertoire of the leopard seal (*Hydrurga leptonyx*),'' in *Sensory Systems of Aquatic Mammals*, edited by R. A. Kastelein, J. A. Thomas, and P. E. Nachtigall (De Spil, The Netherlands), pp. 223–236.

Ronacher, B., Krahe, R., and Hennig, R. M. (**2000**). ''Effects of signal duration on the recognition of masked communication signals by the grasshopper *Chorthippus biguttulus*,'' J. Comp. Physiol. [A] **186**, 1065–1072.

Schusterman, R. J. (**1977**). ''Temporal patterning in sea lion barking (*Zalophus californianus*),'' Behav. Biol. **20**, 404–408.

Schwartz, J. I., Buchanan, B. W., and Gerhardt, H. C. (**2002**). ''Acoustic interactions among male grey treefrogs, *Hyla versicolor*, in a chorus setting,'' Behav. Ecol. Sociobiol. **53**, 9–19.

Sebok, A. (**1968**). *Animal Communication: Techniques of Study and Results of Research.* (Indiana University Press, London).

Serrano, A., and Terhune, J. M. (**2001**). ''Within-call repetition may be an anti-masking strategy in underwater calls of harp seals (*Pagophilus groenlandicus*),'' Can. J. Zool. **79**, 1410–1413.

Serrano, A., and Terhune, J. M. (**2002**). ''Antimasking aspects of harp seal (*Pagophilus groenlandicus*) underwater vocalizations,'' J. Acoust. Soc. Am. **112**, 3083–3090.

Stirling, I., and Siniff, D. B. (**1979**). ''Underwater vocalizations of leopard seals (*Hydrurga leptonyx*) and crabeater seals (*Lobodon carcinophagus*) near the South Shetland Islands, Antarctica,'' Can. J. Zool. **57**, 1244–1248.

Terhune, J. M. (**1999**). ''Pitch separation as a possible jamming-avoidance mechanism in underwater calls of bearded seals (*Erignathus barbatus*),'' Can. J. Zool. **77**, 1025–1034.

Terhune, J. M., and Ronald, K. (**1986**). ''Distant and near-range function of harp seal underwater calls,'' Can. J. Zool. **64**, 1065–1070.

Terhune, J. M., Grandmaitre, N. C., Burton, H. R., and Green, K. (**1994**). ''Weddell seals lengthen many underwater calls in response to conspecific vocalizations,'' Bioacoustics **5**, 223–226.

Terhune, J., and Turnbull, S. (**1995**). ''Variation in the psychometric functions and hearing thresholds of a harbor seal,'' in *Sensory Systems of Aquatic Mammals*, edited by R. A. Kastelein, J. A. Thomas, and P. E. Nachtigall (De Spil, The Netherlands), pp. 81–93.

Thomas, J. A., and Kuechle, V. B. (**1982**). ''Quantitative analysis of Weddell seal (*Leptonychotes weddellii*) underwater vocalizations at McMurdo Sound, Antarctica,'' J. Acoust. Soc. Am. **72**, 1730–1738.

Thomas, J. A., and Golladay, C. L. (**1995**). ''Geographic variation in leopard seal (*Hydrurga leptonyx*) underwater vocalizations,' 223–236.

Thomas, J. A., Ferm, L. M., and Kuechle, V. B. (**1987**). ''Silence as an anti predation strategy by Weddell seals,'' Antarctic Journal of the United States **22**, 232–234.

Thomas, J. A., Puddicombe, R. A., George, M., and Lewis, D. (**1988**). ''Variations in underwater vocalizations of Weddell seals (*Leptonychotes weddellii*) at the Vestfold Hills as a measure of breeding population discreteness,'' Hydrobiologia **165**, 279–284.

Turnbull, S. D., and Terhune, J. M. (**1993**). ''Repetition enhances hearing detection thresholds in a harbour seal (*Phoca vitulina*),'' Can. J. Zool. **71**, 926–932.

Watkins, W. A., and Ray, C. G. (**1985**). ''In-air and underwater sounds of the Ross seal, *Ommatophoca rossi*,'' J. Acoust. Soc. Am. **77**, 1598–1600.

Watkins, W. A., and Schevill, W. E. (**1979**). ''Distinctive characteristics of underwater calls of the harp seal (*Phoca groenlandica*) during the breeding season,'' J. Acoust. Soc. Am. **66**, 983–988.

Wiley, R. H., and Richards, D. G. (**1978**). ''Physical constraints on acoustic communication in the atmoshpere: implications for the evolution of animal vocalizations,'' Behav. Ecol. Sociobiol. **3**, 69–94.

Wollerman, L., and Wiley, R. H. (**2002**). ''Possibilities for error during communication by neotropical frogs in a complex acoustic environment,'' Behav. Ecol. Sociobiol. **52**, 465–473.

Zuberbuhler, K., Noë, R., and Seyfarth, R. M. (**1997**). ''Diana monkeys long-distance calls: messages for conspecifics and predators,'' Anim. Behav. **53**, 584–604.

The effect of loading on disturbance sounds of the Atlantic croaker *Micropogonius undulatus*: Air versus water

Michael L. Fine[a] and Justin Schrinel
Department of Biology, Virginia Commonwealth University, Richmond, Virginia 23284-2012

Timothy M. Cameron
Department of Mechanical Engineering, Virginia Commonwealth University, Richmond, Virginia 23284-3015

(Received 4 December 2003; revised 3 March 2004; accepted 6 March 2004)

Physiological work on fish sound production may require exposure of the swimbladder to air, which will change its loading (radiation mass and resistance) and could affect parameters of emitted sounds. This issue was examined in Atlantic croaker *Micropogonius chromis* by recording sounds from the same individuals in air and water. Although sonograms appear relatively similar in both cases, pulse duration is longer because of decreased damping, and sharpness of tuning (Q factor) is higher in water. However, pulse repetition rate and dominant frequency are unaffected. With appropriate caution it is suggested that sounds recorded in air can provide a useful tool in understanding the function of various swimbladder adaptations and provide reasonable approximation of natural sounds. Further, they provide an avenue for experimentally manipulating the sonic system, which can reveal details of its function not available from intact fish underwater. © *2004 Acoustical Society of America.* [DOI: 10.1121/1.1736271]

PACS numbers: 43.80.Ka, 43.80.Lb [WA] Pages: 1271–1275

I. INTRODUCTION

The acoustics of swimbladders is of interest in diverse fields including acoustic communication (hearing and sound production) in fishes, sonar and deep scattering layers both in terms of fishery investigations and military applications. Classically, the swimbladder has been modeled as a pulsating underwater bubble (Bergeijk, 1964; Harris, 1964), an omnidirectional, resonant monopole that is vibrated by incident sound and then radiates near-field vibrations to the ears or scatters sound back to sonar receivers. Underwater studies have demonstrated that swimbladders have a lower Q, an index of sharpness of tuning, and are more rapidly damped than a free bubble (Batzler and Pickwell, 1970; McCartney and Stubbs, 1970; Sand and Hawkins, 1973; Weston, 1967), but this difference is typically explained as a consequence of damping by fish tissue rather than a property of the bladder. Weston (1967) demonstrated that a bladder's shape can alter its natural frequency, and more modern studies employing boundary element modeling have considered bladder shape as a variable (Francis and Foote, 2003). These models, however, do not consider the possibility that the bladder for other reasons may not act as a resonant bubble.

Recent work on toadfish and weakfish is not in agreement with the classical conceptions of swimbladder acoustics; their bladders appear to be low Q resonators (Bradbury and Vehrencamp, 1998) that gain little amplitude from resonance. Deflating the swimbladder does not affect hearing thresholds in the toadfish or in several other hearing generalist species (Fay and Popper, 1975; Lugli *et al.*, 2003; Yan *et al.*, 2000), and the directionality pattern of toadfish boatwhistles measured in the York River departs from omnidirectionality, in a pattern reflecting the heart shape of the swimbladder (Barimo and Fine, 1998). Physiological work comparing sound emission to bladder movement patterns measured with a laser vibrometer in air indicated motion resembling more a lateral quadrupole than a monopole (Fine *et al.*, 2001) although the bladder has a monopole component that dominates the radiation because of its small size compared to a wavelength of emitted sound (Barimo and Fine, 1998). Finally, the damping coefficient of the bladder in air is equivalent to that of an automobile shock absorber, not what would be expected of a resonant bubble (Fine *et al.*, 2001).

Similarly in weakfish, dominant frequency appears to be related to contraction parameters of the sonic muscle rather than the natural frequency of the bladder (Connaughton *et al.*, 2000, 2002). Different cycles of the pulse waveform vary in duration, and the inverse of the second cycle, the one with the greatest energy, closely predicts the dominant frequency of the call. Its duration increases in larger fish, which would take longer to complete a muscle twitch, resulting in a lower dominant frequency. Furthermore, in similarly sized fish its duration decreases at higher temperatures, which would permit a more rapid twitch, resulting in a higher dominant frequency. Neither of these findings is consistent with sound generation by the natural frequency of the bladder.

The weakfish were recorded in air to escape the difficulties inherent in small tanks including resonance and proximity to pressure release boundaries (Akamatsu *et al.*, 2002; Parvulescu, 1964), and the ventral surface of the toadfish swimbladder was exposed to air as the target in the laser vibrometer study. This exposure to air reduces the mass loading and radiation resistance on the bladder and indicates that body damping does not account for our failure to observe resonance effects. Reducing the mass and resistance loading decouples them from other loads and allows analysis of other

[a]Electronic mail: mlfine@vcu.edu

acoustic characteristics such as damping of the swimbladder wall. Because access to the bladder in air provides numerous advantages for acoustical and physiological investigations, it is important to experimentally determine the affect of changes in loading (air versus water) on fish swimbladder sounds. We examined this problem during an investigation of sounds in Atlantic croaker *Micropogonius chromis* by recording sounds from a series of fish in both air and water (each fish was compared against itself in both conditions).

II. METHODS

Croakers *Micropogonius undulatus* were caught in the Chesapeake Bay and maintained in running York River water in a tank at the Oyster Hatchery at the Virginia Institute of Marine Science. Individuals were netted and transported in a bucket with aeration to the adjacent boat harbor for recording. The harbor is enclosed except for a narrow passageway and is typically free of wave and boat engine noise. Each fish was recorded in air with a microphone while being hand held for several seconds. It was then quickly placed in a plastic mesh holder and immediately suspended to a depth of 0.75 m (water depth was 1.5 m) at a distance of 1 m from a Sippican calibrated omnidirectional hydrophone, also at 0.75-m depth. The hydrophone and fish were both positioned 1 m from a horizontal walkway, i.e., they were approximately 2 m from the wooden wall of the harbor. Some fish required gentle prodding with a dowel rod to induce sound production. Sounds were recorded on a Sony TCD model digital audio tape recorder (48 kHz bandwidth) and analyzed on a Kay Elemetrics 5500 Sonagraph. Typically five pulses per individual were analyzed although two of the fish in water produced fewer than five pulses in which case all pulses were measured (one fish produced three pulses and another four). The data for each fish were averaged and treated as an N of 1. We recorded sounds in both air and water for five fish and compared them by paired t-test. Because train duration and number of pulses were not normally distributed, they were compared with a Mann-Whitney U test.

III. RESULTS

Croaker disturbance call trains are longer in air than in water [$p=0.008$, Fig. 1(a)]. In fact some fish that call when being handled in air lapse into silence upon return to the water or produce fewer pulses [$p=0.03$, Fig. 1(b)], suggesting that being handled in air is perceived as a greater disturbance than being confined and prodded underwater.

Croaker calls appear generally similar on sonagrams whether recorded in air or water (Fig. 2) although expanded oscillograms indicate important differences (Fig. 3). Oscillograms of individual pulses start with a low amplitude half cycle that can be either positive or negative but is negative in these recordings. In water the next cycle has the greatest amplitude and contains most of the energy in the call followed by a rapid decay [Fig. 3(d)]. The major difference between waveforms in air and water is the decay pattern, which damps more rapidly in air. Coincident with greater damping, the power spectrum is broader and less peaked in air although central frequencies are similar in both spectra

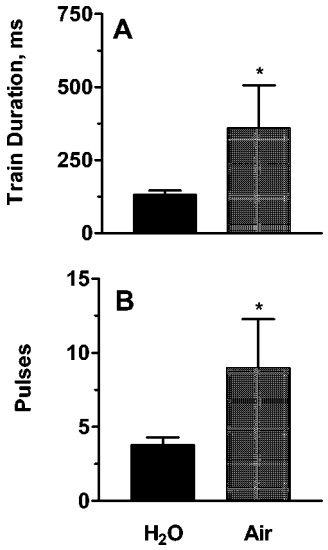

FIG. 1. Mean ± SE train duration (a) and number of pulses per train (b) for five croakers recorded in water and air.

(Fig. 3). Dominant frequencies and durations of the most intense cycle are also similar in air and water [Figs. 4(a) and (d)], and the duration of the most intense cycle largely determines the dominant frequency. Similarly, the pulse repetition rate was similar in both conditions [Fig. 4(f)]. Significant differences exist in the sharpness of tuning, and Q values approximately double from a mean of 1.3 to 2.9 [Fig. 4(b)], a factor of 2.2 sharper in water. Values for individuals range from 1.04 to 1.48 in air and from 2.08 to 3.09 in water. Again the increased sharpness is reflected in more rapid damping in air, with water sounds having a longer duration [Fig. 4(c)] and averaging an extra cycle [Fig. 4(e)].

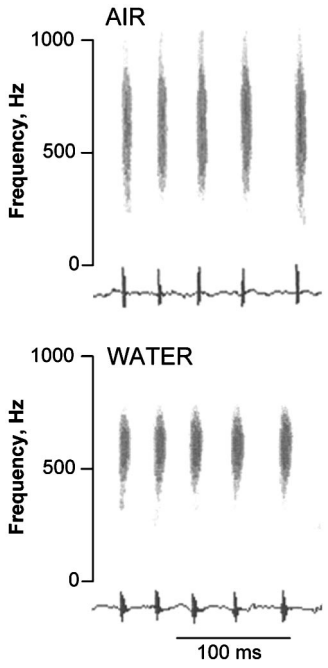

FIG. 2. Sonagram and oscillogram of a train of sounds recorded in air and under water from an individual croaker.

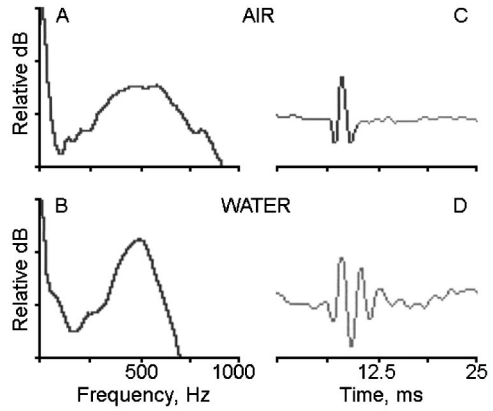

FIG. 3. Expanded oscillograms and power spectra of a sound pulse recorded in water and air from the individual in Fig. 2. Tick marks on the relative dB scale represent 7 dB.

IV. DISCUSSION

Examining the physiology and acoustics of sonic muscle-swimbladder mechanisms in sound production in air provides numerous advantages, particularly accessibility and simplified acoustics, compared to recording sounds in natural bodies of water, typically at unknown distances from the caller, or in tanks that are subject to various artifacts (Akamatsu *et al.*, 2002; Parvulescu, 1964). Further, some fish disturbance calls may actually be directed against aerial predators (Fine and Ladich, 2003), and sounds recorded in air and water generally appear qualitatively similar on sonagrams.

An important question is the effect of reflections from the harbor wall and the surface on the call waveforms. We discount wall reflections as important since pine has a similar acoustic impedance to sea water (1.57×10^6 to 1.54×10^6 Rayls, respectively) (Kinsler *et al.*, 2000), and saturation with water would diminish even this small difference. Wet soil grading to dry behind the sea wall will also not offer a sharp discontinuity. The air–water interface is a strong reflective barrier, but it will reflect a signal out of phase, making it unlikely that a longer signal, i.e., lower damping, is an artifact of reflection. Additionally the hydrophone and fish were positioned half way between the surface and the bottom, which will reflect a signal in phase. Opposite phases of reflections from the surface and bottom should ensure at least some measure of cancellation of these extraneous signals. In any event a true free acoustic field without reverberation from barriers and living organisms does not occur in the shallow waters in which croakers live. Our calculations (Table I) indicate that the mass loading of a 2-cm-radius bubble (approximate dimension of the croaker swimbladder) in water at 0.75 m depth is almost 1000 times greater than the mass loading in air, and the radiation resistance is 175 times greater in water. Reflections do not change the signal frequency, so loading effects are the only factor in considering the possibility of changes in resonant frequency. The large loading differences will have a much greater effect on the damping comparison than the artifacts of reflections.

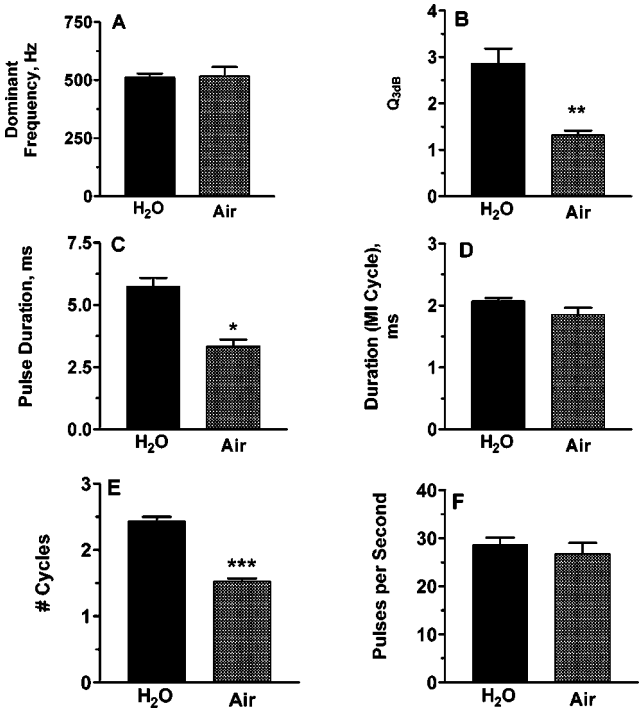

FIG. 4. Comparison of sound parameters (mean+SE) recorded in water and air for five croakers. Statistics are based on paired *t*-tests. $*p<0.05$, $**p<0.01$, $***p<0.001$.

TABLE I. Determination of $k\cdot a$; validation of low frequency approximation.

Parameter	Water @ 75 cm	Air
Static pressure, P (dynes/cm^2)	1.088×10^6	1.013×10^6
Density, ρ (g/cm^3)	1.025	1.21×10^{-3}
Speed of sound, c (cm/s)	1.5×10^5	3.4×10^4
Dominant oscillation frequency, f (Hz)	500	500
Wave number, $k=2\pi f/c$ (rad/cm)	0.0209	0.0924
Croaker swimbladder radius, a (cm)	2.0	2.048[a]
$k\cdot a$	0.042	0.189
Radiation mass[b] (g)	103	0.131
Radiation resistance[b] (dyne·s/cm)	1.36×10^4	77.7

[a]The swimbladder radius in air is calculated from the radius in water using Boyle's Law (for the same moles of gas at the same temperature: pressure×volume=constant).
[b]Kinsler *et al.* (2000), Eq. (8.10.24): $m_r=4\pi a^3\rho$ and $R_r=4\pi a^2\rho c(ka)^2$.

The current investigation makes it clear that there is a price incurred for the decreased mass and resistance loading in air, but we suggest that price may not be as great as it first appears. Pulse repetition rate for croaker sounds is similar between air and water. Since pulse repetition rate is determined by a central nervous system pattern generator, the basic neural control of sound production appears unchanged. Further, driving patterns of the swimbladder forced by sonic muscle contraction should be unchanged as indicated by the similarity in duration of the most intense cycle of the call, which has been shown to determine the dominant frequency of weakfish (Connaughton *et al.*, 2000, 2002) and croaker calls (Schrinel *et al.*, in progress). Muscle origin, insertion and action will not change in air, and the bladder will be vibrated in a similar pattern and frequency. The radiation pattern can be affected by changing "$k\cdot a$," where "k" is the wave number and "a" is the characteristic radius of the source, but in both air and water the low frequency limit approximation for $k\cdot a\ll1$ holds fairly well (Table I).

We suggest that the differences in these calls recorded in

air and water would not be particularly meaningful to the fish. Fishes primarily rely on the temporal structure of their calls for coding information (Fine *et al.*, 1977; Winn, 1964; Zelick *et al.*, 1999), and pulse rate does not change though pulse duration does. This difference in pulse duration would likely be at least partially masked by other fish signals and background noise in a chorus of calling fish. These signals were recorded under unusually quiet conditions, and measuring the duration of fish pulses recorded in natural bodies of water is notoriously difficult because it is almost impossible to determine precisely when a call disappears in the background noise. Therefore the final attenuated cycle in water is less likely to be heard unless the fish are close to each other. Although the frequency spectra are broader in air than in water, the dominant frequencies are similar. Since dominant frequency scales inversely with fish size in weakfish (Connaughton *et al.*, 2000, 2002) and croaker (Schrinel *et al.* in progress), it is reasonable to hypothesize that croakers could estimate relative size of the caller equally in aerial and underwater recordings. Frequency discrimination thresholds to tones measured in hearing generalist fishes are likely to be over 50 Hz for a 500-Hz tone and increase at higher frequencies (Fay and Megela Simmons, 1999). To our knowledge perception of differences in frequency spectra for pulsatile sounds has not been measured in fishes. The amplitude of the sound in the tails of the broader frequency spectrum is less than the amplitude surrounding the dominant frequency, and the more intense dominant frequency would tend to mask concurrent sound of lower amplitude (Fay and Megela Simmons, 1999). There is currently no basis to presume the fish would detect sound in the weaker tails of the distribution (the ability to discriminate frequencies degrades at higher frequencies, and lower frequencies are more likely to be masked by additional background noise).

Differences between air and water affect the related parameters of pulse duration, bladder damping and sharpness of tuning. The bladder experiences a forced rather than a resonant response from the sonic muscles since the dominant frequency is the same in both media. If the response were driven by a bladder resonance, the dramatic reduction in mass loading in air would increase the dominant frequency (Fine *et al.*, 2001; Kinsler *et al.*, 2000). However, the broader frequency peak in air suggests that the response of the bladder is not fully controlled by muscle contractions. The broader peak in air suggests that muscle contraction is a one-way actuator that drives the dominant frequency of the response, at least for the first quarter cycle, and perhaps longer, but that the swimbladder relaxes according to a free response controlled by its mechanical properties (mass, stiffness, damping) and the radiation mass and resistance loading.

A complete understanding of fish swimbladders as acoustic radiators must consider acoustic loading in their natural habitats. However, opening the inside of fishes to companion anatomical, physiological and acoustical study including measurements made in air will provide a deeper understanding of various bladder adaptations and their acoustic functions. Considering potential artifacts from tank recordings (Akamatsu *et al.*, 2002) and effects of background noise and environmental filtering in field recordings of unseen subjects (Fine and Lenhardt, 1983; Lugli and Fine, 2003; Mann and Lobel, 1997), aerial recordings provide a reasonable approximation of natural sounds. The duration of short sounds like weakfish and croaker pulses driven by a single muscle contraction represent the worst case, whereas effects on longer sounds such as a toadfish boatwhistle will be minimal in aerial recordings.

ACKNOWLEDGMENTS

We thank James McConnell of Acoustech Corporation for criticizing the mansuscript, Willy Reay of the Institute for Coastal and Estuarine Environmental Technology for help obtaining fish and logistical help, and Stan Allen for providing tank space at the oyster hatchery at the Virginia Institute of Marine Science. These experiments comply with the *Principles of animal care*, publication No. 86-23, revised 1985 of the National Institute of Health. Work was supported by a grant from the Virginia Marine Resources Commission. Contribution No. 2592 from the Virginia Institute of Marine Science.

Akamatsu, T., Okumura, T., Novarini, N., and Yan, H. Y. (**2002**). ''Empirical refinements applicable to the recording of fish sounds in small tanks,'' J. Acoust. Soc. Am. **112**, 3073–3082.

Barimo, J. F., and Fine, M. L. (**1998**). ''Relationship of swim-bladder shape to the directionality pattern of underwater sound in the oyster toadfish,'' Can. J. Zool. **76**, 134–143.

Batzler, W. E., and Pickwell, G. V. (**1970**). ''Resonant acoustic scattering from gas-bladder fishes,'' in *Proceedings of an International Symposium on Biological Sound Scattering in the Ocean*, edited by G. B. Farquhar (U.S. Government Printing Office, Washington, DC), pp. 168–179.

Bergeijk, W. A. v. (**1964**). ''Directional and nondirectional hearing in fish,'' in *Marine Bioacoustics*, edited by W. N. Tavolga (Pergamon, New York), pp. 281–299.

Bradbury, J. W., and Vehrencamp, S. L. (**1998**). *Principles of Animal Communication* (Sinauer, Massachusetts).

Connaughton, M. A., Fine, M. L., and Taylor, M. H. (**2002**). ''Weakfish sonic muscle: influence of size, temperature and season,'' J. Exp. Biol. **205**, 2183–2188.

Connaughton, M. A., Taylor, M. H., and Fine, M. L. (**2000**). ''Effects of fish size and temperature on weakfish disturbance calls: implications for the mechanism of sound generation,'' J. Exp. Biol. **203**, 1503–1512.

Fay, R. R., and Megela Simmons, A. (**1999**). ''The sense of hearing in fishes and amphibians,'' in *Comparative Hearing: Fish and Amphibians*, edited by R. R. Fay and A. N. Popper (Springer, New York), pp. 269–318.

Fay, R. R., and Popper, A. N. (**1975**). ''Modes of stimulation of the teleost ear,'' J. Exp. Biol. **62**, 379–387.

Fine, M. L., and Ladich, F. (**2003**). ''Sound production, spine locking and related adaptations,'' in *Catfishes*, edited by B. G. Kapoor, G. Arratia, M. Chardon, and M. Diogo (Oxford and IBH, New Delhi), pp. 249–290.

Fine, M. L., and Lenhardt, M. L. (**1983**). ''Shallow-water propagation of the toadfish mating call,'' Comp. Biochem. Physiol. **76A**, 225–231.

Fine, M. L., Winn, H. E., and Olla, B. L. (**1977**). ''Communication in fishes,'' in *How Animals Communicate*, edited by T. A. Sebeok (Indiana U.P., Bloomington), pp. 472–518.

Fine, M. L., Malloy, K. L., King, C. B., Mitchell, S. L., and Cameron, T. M. (**2001**). ''Movement and sound generation by the toadfish swimbladder,'' J. Comp. Physiol., A **187**, 371–379.

Francis, D. T., and Foote, K. G. (**2003**). ''Depth dependent target strengths of gadoids by the boundary-element method,'' J. Acoust. Soc. Am. **114**, 3136–3146.

Harris, G. G. (**1964**). ''Considerations on the physics of sound production by fishes,'' in *Marine Bio-acoustics*, edited by W. N. Tavolga (Pergamon, New York), pp. 233–247.

Kinsler, L. E., Frey, A. R., Coppens, A. B., and Sanders J. V. (**2000**). *Fundamentals of Acoustics*, 4th ed. (Wiley, New York).

Lugli, M., and Fine, M. L. (**2003**). ''Acoustic communication in two freshwater gobies: Ambient noise and short-range propagation in shallow streams,'' J. Acoust. Soc. Am. **114**, 512–521.

Lugli, M., Yan, H. Y., and Fine, M. L. (**2003**). ''Acoustic communication in two freshwater gobies: the relationship between ambient noise, hearing and sound spectrum,'' J. Comp. Physiol., A **189**, 309–320.

Mann, D. A., and Lobel, P. S. (**1997**). ''Propagation of damselfish (Pomacentridae) courtship sounds,'' J. Acoust. Soc. Am. **101**, 3783–3791.

McCartney, B. S., and Stubbs, A. R. (**1970**). ''Measurement of the target strength of fish in dorsal aspect, including swimbladder reonance,'' in *Proceedings of an International Symposium on Biological Sound Scattering in the Ocean*, edited by G. B. Farquhar (U.S. Government Printing Office, Washington, DC), pp. 180–211.

Parvulescu, A. (**1964**). ''Problems of propagation and processing,'' in *Marine Bio-acoustics*, edited by W. N. Tavolga (Pergamon, New York), pp. 87–100.

Sand, O., and Hawkins, A. D. (**1973**). ''Acoustic properties of the cod swimbladder,'' J. Exp. Biol. **58**, 797–820.

Weston, D. E. (**1967**). ''Sound propagation in the presence of bladder fish,'' in *Underwater Acoustics, vol 2*, edited by V. M. Albers (Plenum, New York), pp. 55–88.

Winn, H. E. (**1964**). ''The biological significance of fish sounds,'' in *Marine Bioacoustics*, edited by W. N. Tavolga (Pergamon, New York), pp. 213–231.

Yan, H. Y., Fine, M. L., Horn, N. S., and Colon, W. E. (**2000**). ''Variability in the role of the gasbladder in fish audition,'' J. Comp. Physiol., A **187**, 371–379.

Zelick, R., Mann, D. A., and Popper, A. N. (**1999**). ''Acoustic communication in fishes and frogs,'' in *Comparative Hearing: Fish and Amphibians*, edited by R. R. Fay and A. N. Popper (Springer, New York), pp. 363–411.

Adapting the Lagrangian speckle model estimator for endovascular elastography: Theory and validation with simulated radio-frequency data

Roch L. Maurice
Laboratory of Biorheology and Medical Ultrasonics, Research Center, University of Montreal Hospital, Montreal, Canada

Jacques Ohayon
Laboratory TIMC-IMAG, UMR CNRS 5525, Institut A. Bonniot, 38706 La Tronche, France

Gérard Finet
Department of Hemodynamics, Cardiovascular Hospital, Claude Bernard University, Lyon, France

Guy Cloutier[a)]
Laboratory of Biorheology and Medical Ultrasonics, Research Center, University of Montreal Hospital, Montreal, Canada

(Received 3 October 2003; revised 17 May 2004; accepted 17 May 2004)

Intravascular ultrasound (IVUS) is known to be the reference tool for preoperative vessel lesion assessments and for endovascular therapy planning. Nevertheless, IVUS echograms only provide subjective information about vessel wall lesions. Since changes in the vascular tissue stiffness are characteristic of vessel pathologies, catheter-based endovascular ultrasound elastography (EVE) has been proposed in the literature as a method for outlining the elastic properties of vessel walls. In this paper, the Lagrangian Speckle Model Estimator (LSME) is formulated for investigations in EVE, i.e., using a polar coordinate system. The method was implemented through an adapted version of the Levenberg-Marquardt minimization algorithm, using the optical flow equations to compute the Jacobbian matrix. The theoretical framework was validated with simulated ultrasound rf data of mechanically complex vessel wall pathologies. The results, corroborated with Ansys finite element software, demonstrated the potential of EVE to provide useful information about the heterogeneous nature of atherosclerotic plaques. © *2004 Acoustical Society of America.*
[DOI: 10.1121/1.1771615]

PACS numbers: 43.80.Vj [FD] Pages: 1276–1286

I. INTRODUCTION

Intravascular elastography, or equivalently endovascular elastography (EVE), was introduced in the late nineties as a new imaging modality that aims to outline the elastic properties of vessel walls. In EVE, the vascular tissue is compressed by applying a force from within the lumen. Indeed, the compression can be induced by the normal cardiac pulsation or by using a compliant intravascular angioplasty balloon. The feasibility of EVE was investigated *in vitro* with phantom studies (de Korte *et al.*, 1997) and with excised vessels (de Korte *et al.*, 1998 and 2000a; Brusseau *et al.*, 2001; Wan *et al.*, 2001), and *in vivo* on human coronary arteries (de Korte *et al.*, 2000b). Interestingly, it was demonstrated that EVE could provide information that is occlusive to intravascular ultrasound (IVUS) images.

However, *in vivo*, the position of the catheter in the lumen is generally off center and may move in response to the flow pulsatility. Moreover, the lumen geometry is often not perfectly circular. In such conditions, the ultrasound beam does not run parallel with tissue displacements, and appropriate coordinate systems are required to model both the ultrasound propagation and the tissue motion. Owing to that, (one-dimensional) 1-D-motion estimators may not be optimal for EVE applications. Ryan and Foster (1997) then proposed to use a 2-D correlation-based speckle tracking method to compute vascular elastograms. Additionally to a 2-D correlation-based estimator, Shapo *et al.* (1996a, 1996b) proposed the use of an angioplasty balloon to stabilize the catheter in the vessel lumen. Those phantom investigations tended to demonstrate the feasibility of EVE in the presence of motion artifacts, and its potential to provide new diagnosis information that may help in the functional assessment of atherosclerosis.

Another strategy was proposed by de Korte *et al.* (2000b) to minimize artifacts due to catheter motion. It consisted in using pre- and post-motion images near end-diastole for a pressure differential of approximately 5 mm Hg. The computed *in vivo* elastograms could detect an area composed of hardened material, which was corroborated with IVUS B-scans that revealed a large calcified area. This last method may become a standard procedure if one considers EVE without the use of an angioplasty balloon.

So far, EVE appears a very attractive and promising tool to characterize the mechanical properties of vessel walls. However, in return, it is potentially limited by motion arti-

[a)]Director of the Laboratory of Biorheology and Mecidal Ultrasonics, Electronic mail: guy.cloutier@umontreal.ca

 0001-4966/2004/116(2)/1276/11/$20.00

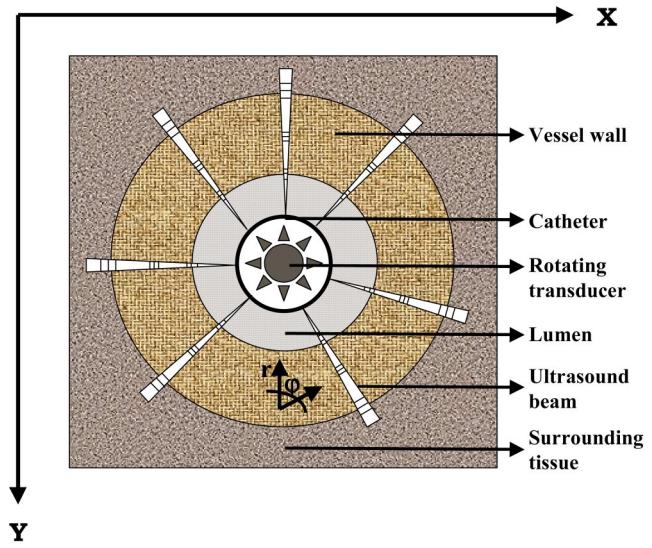

FIG. 1. A schematic illustration of the image acquisition process in IVUS and EVE. The transducer is placed at the tip of the catheter and cross-sectional imaging of the vessel is generated by sequentially sweeping the ultrasound beam over an angle of 360°. In this ideal situation, the ultrasound beam runs parallel with the vascular tissue motion, i.e., in the (r,φ) coordinate system.

facts. Furthermore, it is also limited by the heterogeneous nature of the vascular tissue and of the plaque itself that may induce very complex tissue deformations (nonrigid rotation, scaling, shear, etc.). Most of the current *elastographic* methods use correlation techniques to assess tissue motion and may not be optimal to investigate such complex strain patterns. In this paper we propose an adaptation of the Lagrangian Speckle Model Estimator (LSME) for strain computation in EVE, i.e., for a formulation in a polar coordinate system. The method was implemented through an adapted version of the Levenberg-Marquardt minimization algorithm, using the optical flow equations to compute the Jacobbian matrix. While the full 2-D polar strain tensor was assessed, only the radial strain parameter is displayed in this paper. The theoretical framework was validated with simulated ultrasound rf data of mechanically complex vessel wall pathologies. Namely, one *idealized* and one *realistic* plaque were investigated. Whereas the former allowed validating the potential of the method to differentiate between hard and soft vascular tissues, the latter showed its potential to characterize the heterogeneous nature of atherosclerosis. Interestingly, it is worth noting that a polar image-formation model that simulates the spatial variation of the ultrasound beam with depth was also introduced.

This paper is organized as follows. In Sec. II A, the forward problem in EVE is addressed; it is followed by the derivation of the tissue motion estimator in Sec. II B, and by the biomechanical simulations of the vessel walls in Sec. II C. Results are presented in Sec. III, while in Secs. IV and V we discuss the results and draw conclusions and perspectives to this work.

II. METHODOLOGY

Endovascular elastography (EVE) is a catheter-based modality, which gives insights about mechanical properties of the vessel wall. Following the example of IVUS, and as schematically illustrated in Fig. 1, the transducer is placed at the tip of the catheter and cross-sectional imaging of a vessel is generated by sequentially sweeping the ultrasound beam over a 360° angle. Mechanical parameters (radial strain, in this case) are estimated from analyzing the kinematics of the vascular tissue during the cardiac cycle (or in response to an angioplasty-balloon push).

A. The forward problem in EVE

1. The polar static-image-formation model

The image-formation model is for a rotating beam (single element or an array transducer system) and is thus expressed in polar coordinates. It is based on previous works by Bamber and Dickinson (1980). Such a model was used by Meunier and Bertrand (1995) to study speckle dynamics; it was also considered to investigate speckle motion artifacts (Kallel and Bertrand, 1994; Maurice and Bertrand, 1999b). Under assumptions such as space-invariance of the imaging system, and plane strain conditions for the motion (that is no transverse motion is involved), the following simple 2-D model was used (Maurice and Bertrand, 1999b):

$$I'(x,y)=h'(x,y)\otimes z'(x,y), \tag{1}$$

where $I'(x,y)$ is the radio-frequency (rf) image, $h'(x,y)$ is the point-spread function (PSF) of the ultrasound system, $\otimes$ is the 2-D convolution operator, and $z'(x,y)$ is a function representing the acoustic impedance variations, which was modeled as a white Gaussian noise (random distribution of uncorrelated scatterers within the region of interest). As it will be seen further in this section, the notation "′" is only for convenience and it does not refer to any mathematical operator.

Because the speckle dimension varies with depth for polar scan systems such as the one described in Fig. 1, Eq. (1) is valid only for small regions of interest (ROI). Accordingly, the linear image-formation model is formulated using the superposition integral, given by

$$I(r,\varphi)=\int\int h(r,\varphi,r',\varphi')z(r',\varphi')r'\,dr'\,d\varphi', \tag{2}$$

where r and φ are the radial (depth) and angular coordinates, respectively; $I(r,\varphi)$, $h(r,\varphi)$, and $z(r,\varphi)$ are the polar rf image, polar PSF, and the acoustic impedance function mapped in polar coordinates, respectively; (r',φ') is the position of the "point object" used to define the polar PSF. Furthermore, for a polar scan system, $h(r,\varphi)$ can be considered angular-position invariant; therefore, Eq. (2) becomes

$$I(r,\varphi)=\int\int h(r,r',\varphi-\varphi')z(r',\varphi')r'\,dr'\,d\varphi'. \tag{3}$$

It is convenient to model the PSF as a 1-D cosine modulated by a 2-D Gaussian envelope; that is a simple approximation of the far field PSF. The mathematical formulation can be expressed as

$$h(r,r',\varphi-\varphi') = e^{-((r-r')^2/2\sigma_r^2+(\varphi-\varphi')^2/2\sigma_\varphi^2)} \times \cos\left(2\pi\frac{f_{\text{tr}}}{c/2}(r-r')\right), \quad (4)$$

where σ_r is a pulse length parameter; $\sigma_\varphi \equiv \sigma_\varphi(r)$ is a beam-width parameter;[b] f_{tr} and c are the transducer frequency and the sound velocity in soft tissue, respectively. For simplicity, it is assumed that $\sigma_\varphi(r)$ is a linear function of r; it is expressed as

$$\sigma_\varphi(r) = \frac{r}{R_L}\sigma_0, \quad r \geqslant R_L, \quad (5)$$

with R_L being the lumen radius and σ_0 the beam width at $r = R_L$. In such a situation, the beam forms a sector that linearly increases with depth through the vessel wall. It is important to notice that Eqs. (4) and (5) define a very simple approximation of the PSF in the far-field. In practice, the near field beam profile is more complex. However, it can be assumed that the transducer is positioned near the middle of the lumen, so that the vessel wall is not in the near field.[c] Additionally to the divergence of the ultrasound beam profile, the nonplanar nature of the wavefronts also raises the complexity of the polar scan model; this aspect was not modeled in the current study.

In theory, $\sigma_\varphi(r)$ is a continuous function of r. However, for simplification it will be considered as a piecewise constant function, the n partitioning regions being defined by the boundaries $0 = r_0 < r_1 < r_2 < \cdots \leqslant r_n$. For convenience, each partition will be denoted as P_i, that is,

$$P_i =]r_{i-1}, r_i], \quad i = 1,...,n. \quad (6)$$

Equation (6) defines an interval; the reversed left bracket means that r_0 (the first element of the interval) is excluded. A discrete approximation of $\sigma_\varphi(r)$ is then defined as follows:

$$\sigma_\varphi(r)\big|_{r\in P_i} \cong \sigma_\varphi(P_i) = \frac{\overline{P_i}}{R_L}\sigma_0, \quad (7)$$

where $\overline{P_i}$ is the mean radial distance of the interval P_i. Now, assuming that the PSF is locally depth-invariant, i.e., on each P_i, the linear model of Eq. (3) can be approximated by the following convolution form:

$$I(r,\varphi) \cong \sum_{i=1}^{n} I(P_i,\varphi) = \sum_{i=1}^{n} [h(P_i,\varphi) \otimes z(P_i,\varphi)], \quad (8)$$

with

$$h(P_i,\varphi) = h(r,\varphi)\big|_{r\in P_i} = e^{-(r^2/2\sigma_r^2+\varphi^2/2\sigma_\varphi(r)^2)} \cos\left(2\pi\frac{f_{\text{tr}}}{c/2}r\right).$$

While the continuity of $I(r,\varphi)$ at the boundaries of the partitions can be questioned, Eq. (8) presents a simple approximation model of a polar scan system. Figure 2 illustrates the implementation of such a model for a 20 MHz transducer with a 60% bandwidth at -3 dB and a beam width (width at half maximum $= 2.35 \times \sigma_0$) of 0.1 mm. $z(r,\varphi)$ is assumed to be a continuum. For the purpose of the simulations presented below, $z(r,\varphi)$ was simply obtained by generating a 2-D normally distributed random field. The lumen and the tissue surrounding the vessel were assumed to be, respectively, 2.5 and 1.67 times less echoic than the wall.

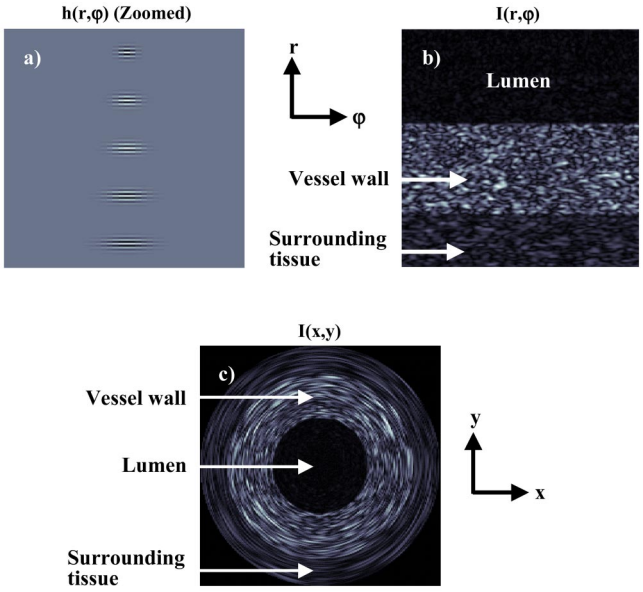

FIG. 2. Image-formation model for a 20 MHz polar scan system; (a) shows the beam profile as a function of depth; (b) presents the simulated polar B-mode image for an homogenous vessel section; (c) is the IVUS simulated image.

Figure 2(a) shows the beam profile as a function of depth. The beam width increases linearly, being minimal in the lumen and maximal in the surrounding tissue; the partition number n was set at 5. Figure 2(b) presents a simulated polar *B*-mode image for an homogenous vessel section, whereas Fig. 2(c) gives the equivalent IVUS image (in Cartesian coordinates).

2. The tissue-motion model

For a small ROI, tissue motion can be approximated by an affine transformation; this can be expressed in Cartesian coordinates as

$$\begin{bmatrix} p(x,y,t) \\ q(x,y,t) \end{bmatrix} = \underbrace{\begin{bmatrix} \theta_1 \\ \theta_4 \end{bmatrix}}_{\text{Tr}} + \underbrace{\begin{bmatrix} \theta_2 & \theta_3 \\ \theta_5 & \theta_6 \end{bmatrix}}_{\text{LT}} \begin{bmatrix} x \\ y \end{bmatrix}, \quad (9)$$

where θ_j is a function of time t ($\theta_j(t)$). Equation 9 expresses a translation of the center of the ROI (vector $[T_r]$) and a linear geometrical transformation of coordinates (matrix $[LT]$).[d] It can also be seen as trajectories that describe a tissue motion in a region of constant strain (Maurice and Bertrand, 1999a). Strain is usually defined in terms of the gradient of a displacement field; since $p(x,y,t)$ and $q(x,y,t)$ represent the new position of a point (x,y), the (u_x,u_y) components of the displacement vector in the (x,y) coordinate system are given by

$$\begin{bmatrix} u_x \\ u_y \end{bmatrix} = \begin{bmatrix} p(x,y,t)-x \\ q(x,y,t)-y \end{bmatrix} = \begin{bmatrix} \theta_1 \\ \theta_4 \end{bmatrix} + \Delta \begin{bmatrix} x \\ y \end{bmatrix}, \quad (10)$$

with

$$\Delta=\begin{bmatrix}\theta_2-1 & \theta_3\\ \theta_5 & \theta_6-1\end{bmatrix}.$$

In the above equation, Δ can be defined as the Cartesian deformation matrix. The ϵ_{ij}, which are the components of the strain tensor ϵ, are expressed in terms of the Δ_{ij} components as

$$\epsilon_{ij}(t)=\tfrac{1}{2}[\Delta_{ij}(t)+\Delta_{ji}(t)]. \tag{11}$$

Furthermore, the radial and tangential components of the displacement vector (u_r,u_φ) in the (r,φ) coordinate system are, respectively, given as

$$u_r=\sqrt{u_x^2+u_y^2},$$

$$u_\varphi=\arctan\left(\frac{u_y}{u_x}\right),$$

with

$$u_x\equiv u_x(x(r,\varphi),y(r,\varphi)) \quad \text{and} \quad u_y\equiv u_y(x(r,\varphi),y(r,\varphi)). \tag{12}$$

The polar deformation matrix, labeled as $\xi(t)$, then can be derived from Eqs. (12) and (10); it is given as

$$\xi(t)=\begin{bmatrix}\frac{\partial u_\varphi}{\partial\varphi} & \frac{\partial u_\varphi}{\partial r}\\ \frac{\partial u_r}{\partial\varphi} & \frac{\partial u_r}{\partial r}\end{bmatrix}$$

$$=\begin{bmatrix}\frac{\partial u_\varphi}{\partial u_x} & \frac{\partial u_\varphi}{\partial u_y}\\ \frac{\partial u_r}{\partial u_x} & \frac{\partial u_r}{\partial u_y}\end{bmatrix}\begin{bmatrix}\frac{\partial u_x}{\partial x} & \frac{\partial u_x}{\partial y}\\ \frac{\partial u_y}{\partial x} & \frac{\partial u_y}{\partial y}\end{bmatrix}\begin{bmatrix}\frac{dx}{d\varphi} & \frac{dx}{dr}\\ \frac{dy}{d\varphi} & \frac{dy}{dr}\end{bmatrix}$$

$$=\begin{bmatrix}\frac{\partial u_\varphi}{\partial u_x} & \frac{\partial u_\varphi}{\partial u_y}\\ \frac{\partial u_r}{\partial u_x} & \frac{\partial u_r}{\partial u_y}\end{bmatrix}\Delta\begin{bmatrix}\frac{dx}{d\varphi} & \frac{dx}{dr}\\ \frac{dy}{d\varphi} & \frac{dy}{dr}\end{bmatrix}, \quad \text{with} \begin{cases}x=r\cos\varphi,\\ y=r\sin\varphi\end{cases}. \tag{13}$$

The LSME computes the full 2-D-strain tensor $\xi(t)$. However, for the purpose of this paper, only the map of the $\xi_{rr}(=\epsilon_{rr})$ component (the radial strain, labeled in EVE as the elastogram) is displayed. For small deformations, the elastogram is expected to provide cartography of relative tissue stiffness inside the vessel wall. This assumption holds, for example, when pre- and post-motion rf images are acquired for a small pressure gradient, i.e., at the end-diastole. ξ_{rr} can be expressed as a function of the Cartesian deformation matrix (Δ) as

$$\xi_{rr}(t)=\frac{\partial u_r}{\partial r}=\begin{bmatrix}\frac{\partial u_r}{\partial u_x} & \frac{\partial u_r}{\partial u_y}\end{bmatrix}\Delta\begin{bmatrix}\cos\varphi\\ \sin\varphi\end{bmatrix}. \tag{14}$$

3. The polar dynamic-image-formation model

The 2-D polar dynamic-image-formation model for an in-plane tissue motion is now derived. It is worth remembering that $z(r,\varphi)$ is a map of the acoustic impedance variations $z'(x,y)$ in polar coordinates, which can mathematically be expressed as

$$z(r,\varphi)=z'(x,y)\big|_{\substack{x=r\cos\varphi\\ y=r\sin\varphi}}. \tag{15}$$

The affine transformation on $z'(x,y)$ can be set by only changing the (x,y) coordinates. Without loss of generality, it is assumed that translation is absent, and $[T_r]$ in Eq. (9) can thus be neglected. It is also interesting to notice that impressing $[LT]$ on the tissue to simulate deformation requires the computation of the inverse transformation $[LT^{-1}]$ on the coordinates. Hence, for an (r,φ) in-plane motion, the 2-D rf polar dynamic-image-formation model at time t becomes

$$I(r,\varphi,t)\cong\sum_{i=1}^{n} I(P_i,\varphi,t)$$

$$=\sum_{i=1}^{n}[h(P_i,\varphi)\otimes z_{LT_p^{-1}}(P_i,\varphi)],$$

with

$$z_{LT_p^{-1}}(P_i,\varphi)=z_{LT_p^{-1}}(r,\varphi)\big|_{r\in P_i}=z'_{LT^{-1}}(x,y)\big|_{\substack{x=r\cos\varphi\\ y=r\sin\varphi}}. \tag{16}$$

In Eq. (16), $z'_{LT^{-1}}(x,y)$ indicates a change in coordinates for the function $z'(x,y)$; that change involves the 2×2 matrix $[LT^{-1}]$. Similarly, $z_{LT_p^{-1}}(P_i,\varphi)$ indicates a change in coordinates for the function $z(P_i,\varphi)$ where the 2×2 matrix $[LT_p^{-1}]$ is involved. Implicitly, this means that $[LT]$ (as well as $[LT_p]$) is invertible. This assumption is valid for an incompressible continuum.

B. Tissue motion estimation in EVE

1. Lagrangian speckle image (LSI)

Vascular tissue may rotate, shear, stretch, or compress in the measurement plane. Such kinematics set a fundamental limitation to correlation-based tissue motion estimators, if they are not appropriately compensated for. In conventional elastography, where an external compression is induced, Ophir *et al.* (1999) proposed to partially compensate for such decorrelation by using temporal stretching of the post-motion signals, whereas Chaturvedi *et al.* (1998a,b) proposed the 2-D-companding method. Interestingly, the Lagrangian speckle image (LSI) was introduced to describe ultrasound signals compensated for tissue motion (Maurice and Bertrand, 1999a). For instance, in the dynamic image-formation model of Eq. (16), tissue motion is modeled by applying the linear transformation matrix $[LT_p^{-1}]$ to $z(r,\varphi)$. Hence, the motion-compensated image, said the LSI, is obtained through applying $[LT_p]$ (the inverse of $[LT_p^{-1}]$) to a post-motion rf image at time t given by $I(r,\varphi,t)$. For the polar dynamic image-formation model given by Eq. (16), the LSI (noted as I_{Lag}) is then expressed as

$$I_{\text{Lag}}(r,\varphi,t)=[I(r,\varphi,t)]_{LT_p}$$

$$\cong\left[\sum_{i=1}^{n} h(P_i,\varphi)\otimes z_{LT_p^{-1}}(P_i,\varphi)\right]_{LT_p}$$

$$=\sum_{i=1}^{n}[h_{LT_p}(P_i,\varphi)\otimes z(P_i,\varphi)|LT_p|]. \tag{17}$$

In the above equation, $|LT_p|$ is the determinant of the matrix $[LT_p]$.

2. The Lagrangian speckle model and the minimization problem

As described in Maurice and Bertrand (1999a), the motion-compensated rf image (LSI) directly involves the Lagrangian description of motion. For instance, it is expressed in Eq. (17) that the LSI brings back material points to the positions where they originally stood. Accordingly, a convenient model to formulate the LSI can be given as

$$I(r,\varphi,0) = I_{\mathrm{Lag}}(r,\varphi,t) + \Re(r,\varphi,t) = [I(r,\varphi,t)]_{LT_p} + \Re(r,\varphi,t), \quad (18)$$

where $\Re(r,\varphi,t)$ can be seen as an error term. The mathematical model for a tissue motion estimator then can be formulated as

$$\begin{aligned} &\underset{LT_p}{\mathrm{MIN}} \|I(r,\varphi,0) - [I(r,\varphi,t)]_{LT_p}\|^2 \\ &= \underset{LT_p}{\mathrm{MIN}} \|I(r,\varphi,0) - I_{\mathrm{Lag}}(r,\varphi,t)\|^2 \\ &= \underset{LT_p}{\mathrm{MIN}} \|\Re(r,\varphi,t)\|^2. \end{aligned} \quad (19)$$

The minimum is obtained using the appropriate $[LT_p]$. It is worth remembering that $[LT_p]$ is a linear transformation matrix; it maps the Cartesian trajectories [Eq. (9)] in a polar coordinate system. However, for a small ROI $(\Delta r, \Delta\varphi)$ that is far from the vessel lumen center, motion equivalently can be investigated using either a polar or a Cartesian coordinate system. In other words, the following approximation can be done to compute the elastogram:

$$\xi \cong LT - I, \quad (20)$$

where I is the 2-D-identity matrix.

3. The Levenberg-Marquardt nonlinear minimization

Several gradient-based methods exist to numerically solve minimization problems as given by Eq. (19). Here, tissue motion was assessed by using the Levenberg-Marquardt method (L&M) (Levenberg, 1963; Marquardt, 1944). As presented in Appendix A, at the kth iteration, the L&M regularized inversion was implemented as

$$\vec{\Delta\theta}^k = [J_{k-1}^T J_{k-1} + \lambda_k I]^{-1} J_{k-1}^T (\vec{I}_0 - \vec{I}_{\mathrm{Lag}}(\vec{\theta}^{k-1})), \quad (21)$$

where $\vec{\Delta\theta}^k$ is a vector of increments used to update the Lagrangian images ($\vec{\Delta\theta}^k$ is also known in the literature as the step size); $[J_{k-1}]$ is the Jacobian matrix; T designates the transpose operator; λ_k is a non-negative scalar, I is the identity matrix; $I_0(r,\varphi,0)$ and $I_{\mathrm{Lag}}(r,\varphi,t)$ are rewritten as I_0 and $I_{\mathrm{Lag}}(\vec{\theta})$, respectively; and $\vec{\theta}$ is the vectorization of $[LT_p]$.

4. The optical flow equations and the Jacobian matrix

The optical flow equations, or material derivatives, give a relationship between measures in Eulerian and Lagrangian coordinate systems, respectively (Horn, 1986). For instance, $I_{\mathrm{Lag}}(\vec{\theta}^{k-1})$ can be seen as a function that describes a material property. Under such an assumption, as presented in Appendix B, the full expression for the 6 components of the Jacobian matrix $[J_{k-1}]$ [Eq. (21)] is given as

$$\frac{\partial I_{\mathrm{Lag}}(\vec{\theta}^{k-1})}{\partial\vec{\theta}} \cong \frac{\partial I(\vec{\theta}^{k-1})}{\partial\vec{\theta}} = -\left\{\frac{\partial I}{\partial x}, \frac{\partial I}{\partial x}x, \frac{\partial I}{\partial x}y, \frac{\partial I}{\partial y}, \frac{\partial I}{\partial y}x, \frac{\partial I}{\partial y}y\right\}. \quad (22)$$

Equation (22) was implemented to compute the Jacobian matrix required to solve the minimization problem of Eq. (19).

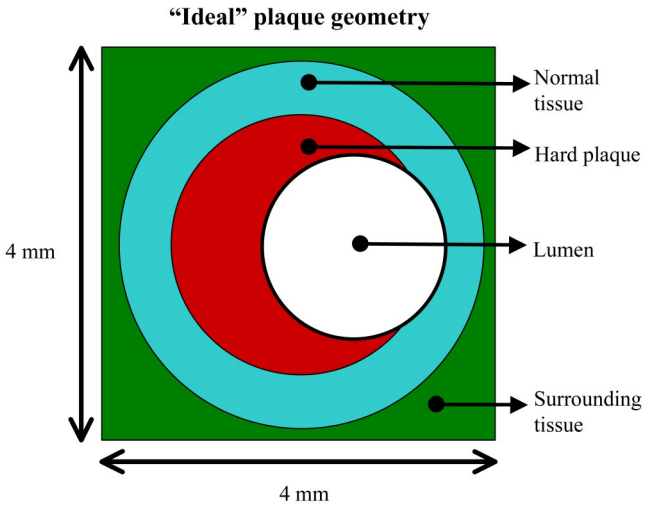

FIG. 3. Schematic representation of an "ideal" plaque. The Young's modulus for the normal vascular tissue was 80 kPa, while the plaque (three times stiffer) was set at 240 kPa. To emulate boundary conditions as provided by the surrounding environment, the Young's modulus for the surrounding tissue was set at 1000 kPa.

C. Biomechanical simulations of vessel wall kinematics

1. Model design and image analysis

The computational structural analysis was performed on one simulated idealized coronary plaque (Fig. 3), and on a model created from measurements made of a typical composite plaque identified from an *in vivo* IVUS image [Fig.

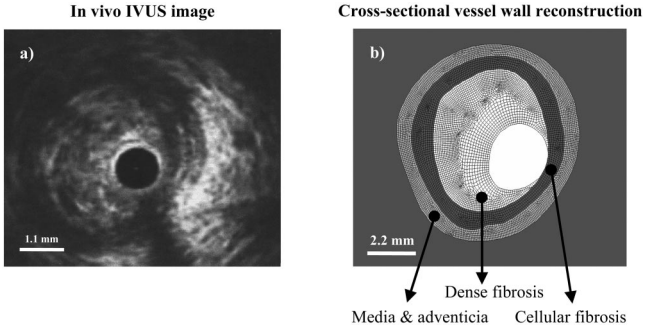

FIG. 4. (a) *In vivo* IVUS cross-sectional image of a coronary plaque; (b) 2-D finite element mesh of the unloaded real geometry with spatial distribution of the plaque constituents. The Young's modulus for the healthy vascular tissue (or adventicia and media) was 80 kPa, while the dense fibrosis (three times stiffer) was set at 240 kPa, and the cellular fibrosis at 24 kPa (ten times softer than the dense fibrosis).

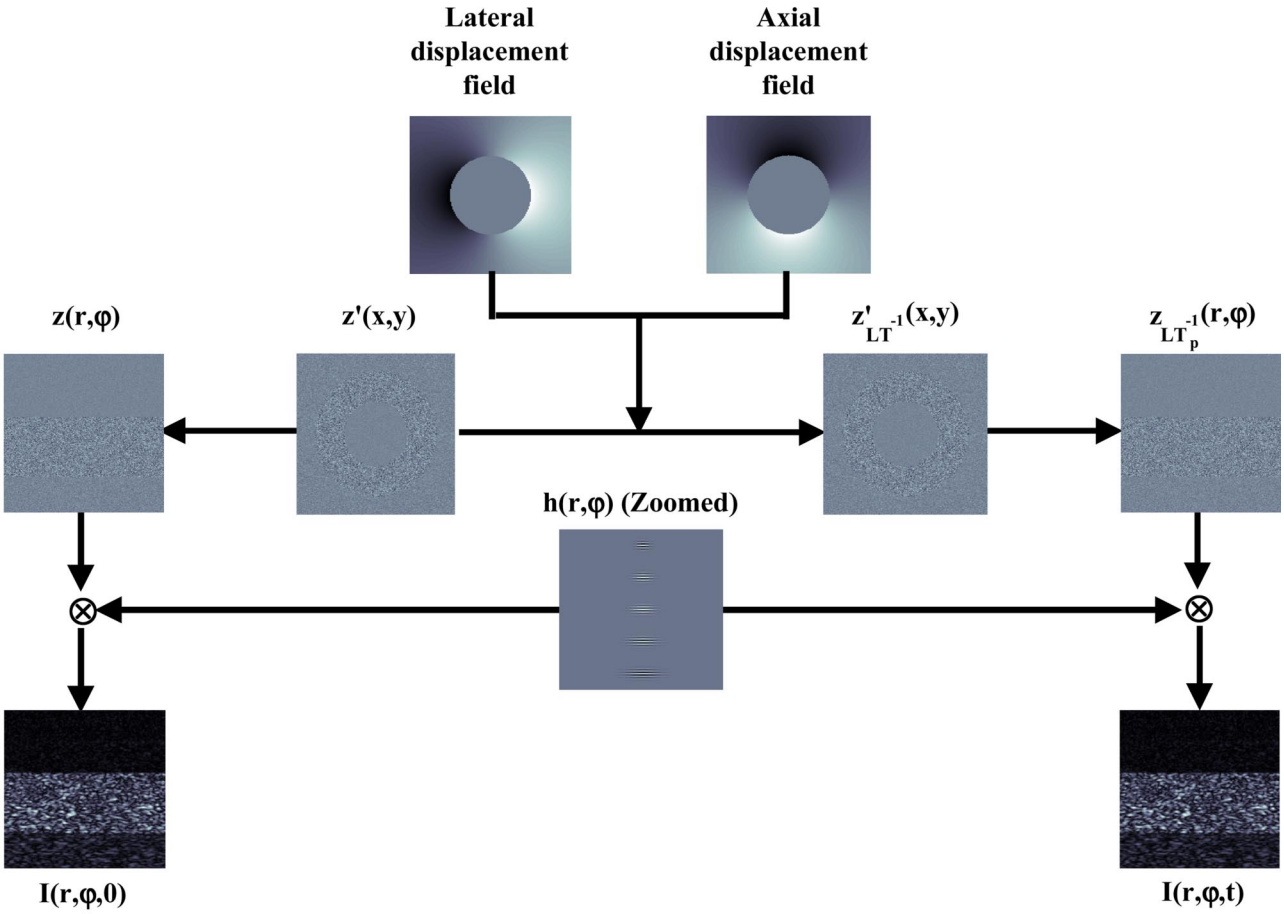

FIG. 5. Schematic implementation of the polar dynamic image-formation model.

4(a)]. Whereas the former allowed validating the potential of the method to differentiate between hard and soft vascular tissues, the latter investigated its potential to characterize the heterogeneous nature of atherosclerotic plaques, which is linked to the risk of rupture and thrombosis. The major difficulty in computational structural analysis based on *in vivo* imaging is to determine the unloaded physiological configuration of the artery, i.e., the configuration when the artery is subjected to no external load. This configuration has to be known for finite element (FE) simulations. To obtain this unloaded state, adenosine triphosphate (ATP) (Striadyne®, Wyeth France Laboratories) was injected to the patient,[e] as previously described by Ohayon *et al.* (2001). All contours in the IVUS image were manually traced [Fig. 4(b)]. These contours are those of the lumen border, media, adventicia, and plaque components (dense fibrosis and cellular fibrosis). The adventicia contour was added in the simulation and it had a mean thickness of 350 μm (Rioufol *et al.*, 1999), so as to take account of its protective role against any radial overstretching of the artery (Rachev, 1997). The various contours were digitized using the Un-Scan-It® software (Silk Scientific, Inc., Orem, UT).

2. Material properties

For the two models, the materials were considered as quasi-incompressible (Poisson ratios $\nu=0.49$) and isotropic with linear elastic properties. The Young's modulus for the healthy vascular tissue (or adventitia and media) was 80 kPa (Williamson *et al.*, 2003), while the dense fibrosis (much stiffer) was set at 240 kPa, and the cellular fibrosis (softer than the dense fibrosis) was chosen at 24 kPa (Ohayon *et al.*, 2001; Treyve *et al.*, 2003). Whereas the surrounding tissue was not investigated, the bulk boundary conditions, as it may eventually be provided by surrounding organs, were simulated by imbedding the vessel in a stiffer environment of 1000 kPa Young's modulus.[f]

3. Structural analysis

Finite element (FE) computations were performed using the ANSYS 5.7® software (Ansys, Inc., Cannonsburg, PA). Static simulations of coronary plaque under loading blood pressure were performed on the geometrical models previously described [Figs. 3 and 4(b)]. Nodal displacements were set to zero on the external boundaries of the surrounding tissue.

The various regions of the plaque components were then automatically meshed with triangular (6 nodes) and quadrangular (8 nodes) elements. The FE models were solved under the assumption of plane and of finite strains. The assumption of plane strain was made because axial stenosis dimensions were of at least the same order of magnitude as the radial dimensions of the vessel. Moreover, the assumption of finite deformation was required as the strain maps showed values up to 30% for physiological pressures (Loree *et al.*, 1992;

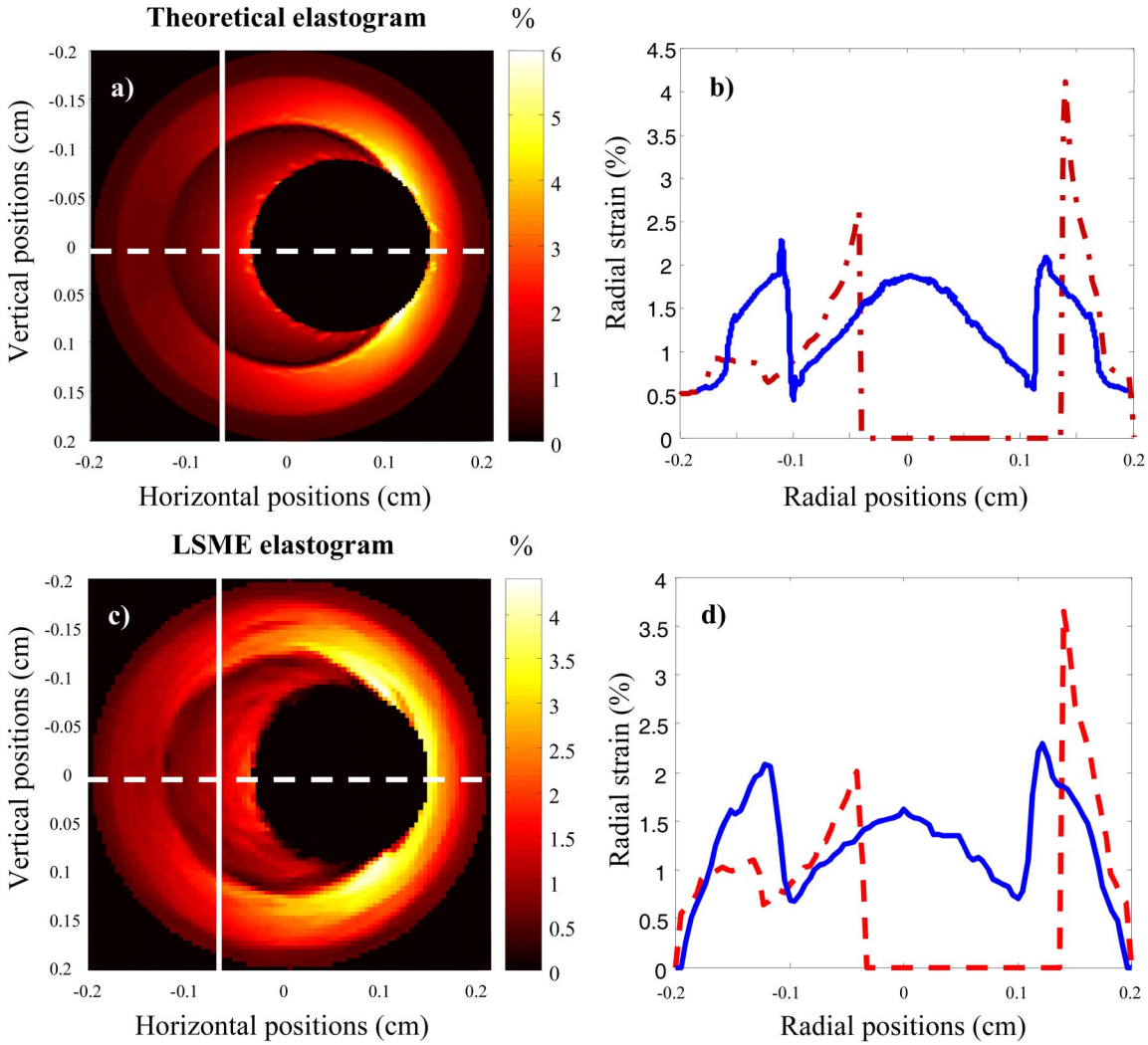

FIG. 6. (a) Theoretical radial strain elastogram, computed with Ansys FE software, for the idealized plaque; (b) theoretical radial strain distributions along the vertical and horizontal lines specified on (a); (c) radial strain elastogram as computed with the LSME; (d) LSME radial strain distributions along the vertical and horizontal lines specified in (c). The color bars express the strain in percent.

Cheng *et al.*, 1993; Lee *et al.*, 1993; Ohayon *et al.*, 2001; Williamson *et al.*, 2003). However, the kinetics reported here were achieved with small pressure gradients (around 15 mm Hg) such that the radial strain remained below 10%. The Newton–Raphson iterative method with a residual nodal tolerance of 4×10^{-4} N was used to solve the FE models. The calculations were performed with a number of elements close to 7200.

This computational structural FE analysis was used to perform the kinematics of the vascular tissue. The dynamic image-formation model [Eq. (16)] was implemented using the Matlab software (The MathWorks Inc, MA, USA, ver.

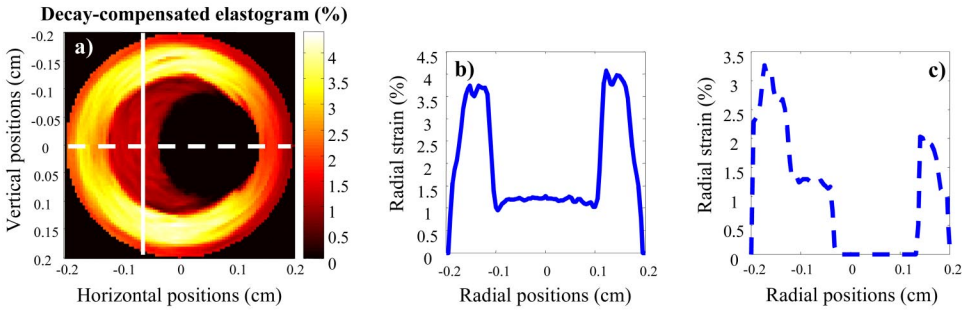

FIG. 7. (a) Strain-decay-compensated LSME elastogram, showing substantial contrast improvement between hard and soft materials; (b) vertical 1-D plot from the elastogram showing a contrast ratio close to 3 between the plaque and the normal vascular tissue, as can be expected; (c) horizontal 1-D plot from the elastogram, showing effective strain decay compensation, and thus a substantial improvement of the contrast ratio. The color bar expresses the strain in percent.

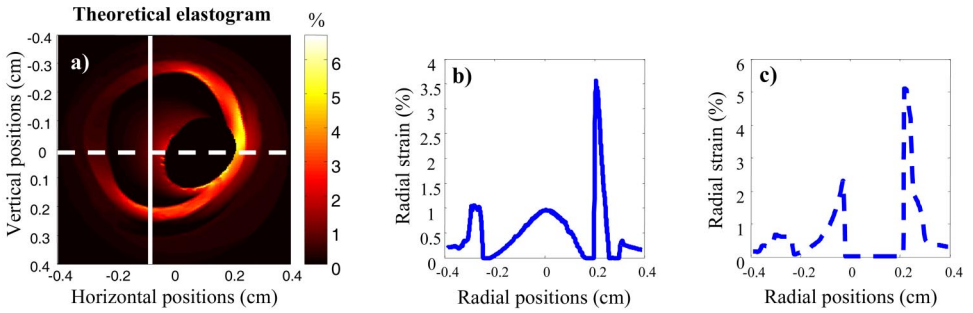

FIG. 8. (a) Theoretical radial strain elastogram for the real plaque, showing very complex strain patterns; (b) and (c) show vertical and horizontal 1-D plots from the elastogram, respectively. Strain decay is specifically observed at the inner portion of the vessel wall. The color bar expresses the strain in percent.

6.0). The process to simulate polar radio-frequency (rf) images is schematically presented in Fig. 5, for a homogeneous (pathology-free) vessel wall. It can be summarized as follows. It started by generating in Matlab a scattering function that simulated the acoustical characteristics of a transverse vascular section in Cartesian coordinates, $z'(x,y)$. The axial and lateral displacement fields were computed with Ansys and were applied upon $z'(x,y)$ to perform motion and then to provide $z'_{LT^{-1}}(x,y)$.[g]

The next step consisted in mapping $z'(x,y)$ and $z'_{LT^{-1}}(x,y)$ in a polar coordinate system (r,φ) to provide $z(r,\varphi)$ and $z_{LT_p^{-1}}(r,\varphi)$ [Eqs. (15) and (16)]. Both polar-mapped acoustic impedance functions were then convolved with the polar PSF $h(r,\varphi)$ to provide polar pre- and post-tissue-motion rf images [$I(r,\varphi,0)$ and $I(r,\varphi,t)$, given by Eq. (16)]. Those images were used as inputs to the LSME [Eq. (19)].

In summary, the static and the dynamic image-formation models associated with a polar scan were derived in Sec. II A, whereas the LSME was adapted for EVE in Sec. II B. In Sec. III, this new approach is validated using the biomechanical simulations of the vessel wall kinematics (for the ''ideal'' and the ''realistic'' plaque geometries) presented in Sec. II C. Indeed, radial elastograms (ϵ_{rr}), computed from simulated rf data with the LSME, are compared with ''theoretical'' ϵ_{rr} obtained with Ansys FE software. For the purpose of that study, a noise term was added to the rf data to simulate electronic noise. The signal-to-noise ratio was 20 dB.

III. RESULTS

The *idealized* vessel of Fig. 3 measured about 3.8 mm in the outer diameter, whereas the rf images extended to 4 mm×4 mm. The *real case* vessel of Fig. 4(b) measured about 7 mm in the outer diameter, whereas the rf images extended to 8 mm×8 mm. For the purpose of simulations, the intraluminal pressure gradients were set at 15.79 mm Hg and 11.73 mm Hg for the *idealized* and the *realistic* vessels, respectively. According to that, the dilation at the inner wall was around 7%[h] in both cases. The PSF characterized a 20 MHz central frequency transducer, as described in the forward problem (Sec. II A). The LSME (described in Sec. II B) was implemented to assess tissue motion. Measurement-windows of 0.38 mm×0.40 mm and 0.77 mm×0.80 mm, with 90% axial and lateral overlaps, were used for the idealized and the realistic cases, respectively. For more details concerning the definition of the measurement-window required with the LSME, the reader is referred to Fig. 1 of Maurice *et al.* (2004).

A. Investigation of the "ideal" plaque pathology

Figure 6(a) presents the theoretical radial strain elastogram, computed for the ''ideal'' pathology case, using Ansys FE software. The plaque can slightly be differentiated from the normal vascular tissue, whereas a region of higher strain values is observed at the right portion of the inner vessel wall. This ''mechanical artifact'' is a direct consequence of the well known strain decay phenomenon[i] (Shapo *et al.*, 1996a). For a more quantitative illustration, plots from the theoretical elastogram for two orthogonal orientations along x and y are presented in Fig. 6(b). Indeed, the vertical plot (—) shows low contrast between the plaque and the normal vascular tissue, whereas the horizontal plot (---) clearly points out the presence of strain decay.

Figure 6(c) presents the radial strain elastogram as computed with the LSME, using simulated rf images. As for the theoretical elastogram in Fig. 6(a), the plaque is slightly distinguishable from the normal vascular tissue. The plots of Fig. 6(d) confirm such an observation. Note that lower strain values were computed in the LSME elastogram than in theory, specifically at the inner wall. That strain underestimation in the regions close to the lumen is due to the windowing process required to assess tissue motion with the LSME.

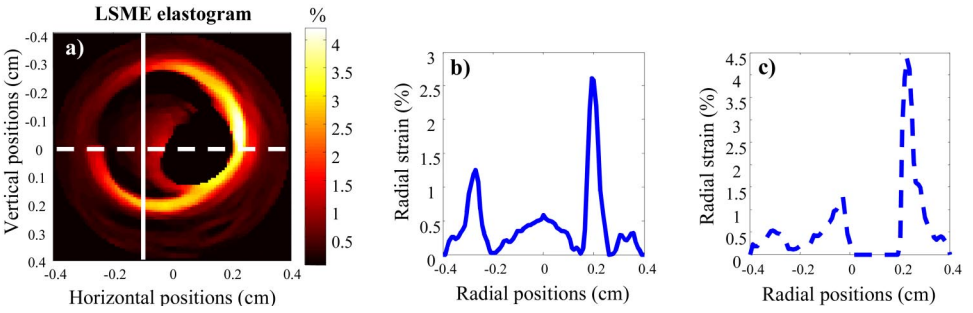

FIG. 9. (a) Radial strain elastogram as computed with the LSME for the real plaque; (b) and (c) vertical and horizontal 1-D plots from the elastogram, respectively. Because of strain decay, there is not a clear demarcation between cellular and dense fibroses, specifically in (c). The color bar expresses the strain in percent.

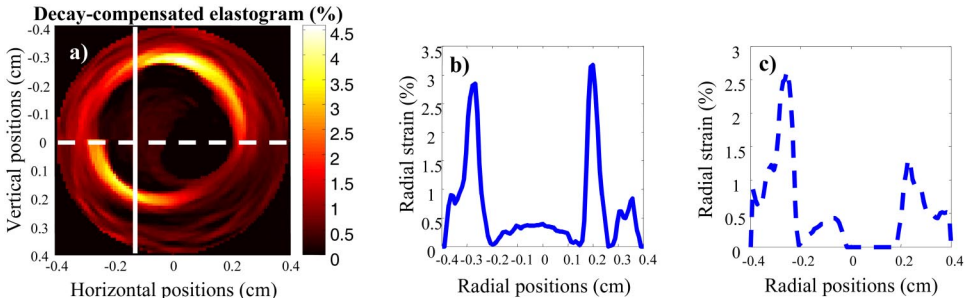

FIG. 10. (a) Strain-decay-compensated LSME elastogram for the real plaque, showing a substantial contrast improvement; (b) and (c) vertical and horizontal 1-D plots from the elastogram showing more effective contrast ratio between dense and cellular fibroses, after strain decay compensation. The color bar expresses the strain in percent.

Moreover, the maximum strain can be observed at the inner boundary around 1 and 5 o'clock. Such a softening artifact is a consequence of stress concentration at the interface between hard (plaque) and softer (normal) materials.

For the purpose of compensating for strain decay, the LSME radial strain elastogram was post-processed. Indeed, ϵ_{rr} was modulated with a function proportional to the square of the vessel radius.[j] In Fig. 7(a) is presented the strain-decay-compensated LSME elastogram, showing substantial contrast improvement. For instance, the axial plot of Fig. 7(b) shows an effective contrast ratio close to 3 between the plaque and the normal vascular tissue, as it can be expected. Equivalently, Fig. 7(c) also shows some valuable contrast ratio improvement.

B. Investigation of a "realistic" vessel wall pathology

Figure 8(a) presents the theoretical radial strain elastogram, computed for the "realistic" pathology case. Interestingly, complex strain patterns are observed; nevertheless, different regions can be identified. For instance, since the ratio of Young's moduli between the dense and the cellular fibroses was set to 10, both of those materials can be distinguished. Less contrast is seen between the cellular fibrosis and the healthy vascular tissue because their Young's modulus contrast was set to 3. As illustrated with vertical and horizontal 1-D plots from the elastogram [Figs. 8(b) and 8(c), respectively], strong strain decay is observed specifically at the inner portion of the vessel wall.

Figure 9(a) presents the radial strain elastogram as computed with the LSME, using simulated rf images. As for the theoretical elastogram in Fig. 8(a), very complex strain patterns are observed. Moreover, the dense and the cellular fibrosis tissues can be identified. However, while less prominent than in the "ideal" case study, strain decay remains a significant factor to compensate for improved image interpretation. This is illustrated in Figs. 9(b) and 9(c), where vertical and horizontal 1-D plots from the elastogram are presented. Whereas low strain values clearly indicate the presence of stiff materials in Fig. 9(b), this is not the case in Fig. 9(c).

In Fig. 10(a) is presented the strain-decay-compensated LSME elastogram, showing substantial contrast improvement. Now, the vertical plot [Fig. 10(b)] as well as the horizontal one [Fig. 10(c)] show a more effective contrast ratio between dense and cellular fibroses, and between cellular fibrosis and the normal vascular tissue. Moreover, it is interesting to notice the presence of moderate strain values (around 0.6 to 0.8%) at the extremities of the plots; this characterizes regions of healthy vascular tissue, namely the media and adventicia.

IV. DISCUSSION

Pathological conditions of vascular tissues often induce changes in the vessel wall elasticity. For instance, plaque deposit stiffens the vascular wall and then counteracts its dilation under systolic blood pressure. Hence, investigating mechanical and elastic properties of the arteries seems to be a suitable method to appreciate the dynamics of the arterial wall and its pathologies. In this paper, a model-based approach devoted to outline the elastic properties of the vessel wall with endovascular elastography (EVE) was presented. Results obtained from numerical simulations establish the potential of such a method to reliably assess strain patterns from very complex arterial and plaque structures.

A. About the forward problem

Regarding the forward problem in EVE, a polar static image-formation model was introduced. Taking into account the ultrasound beam divergence associated with high-frequency sector scans, this image-formation model was formulated using the superposition integral. The radial variation was conveyed with the beam width, which increases as a linear function of depth. This is actually a relatively simplistic approximation. In practice, the transducer point-spread function (PSF) is expected to be more complex. For example, the acoustic wavefronts may be nonplanar, and Eq. (4) (an approximation of the far field PSF) does not hold anymore. Since it was demonstrated that such complex wavefronts can induce speckle motion artifacts (Kallel and Bertrand, 1994; Maurice and Bertrand, 1999b), it would be worthwhile, in the future, to address the polar dynamic image-formation model with a more complex ("realistic") PSF geometry.

B. About the tissue motion estimation

To assess tissue motion, the Lagrangian speckle model estimator (LSME) was used. The LSME is a 2-D model-based estimator that allows computing the full 2-D deformation matrix Δ of Eq. (10) (Δ is directly assessed; no derivative of the displacement fields is required with this method). In this paper, it was adapted for EVE investigations. While the full 2-D polar deformation matrix $\xi(t)$ of Eq. (13) was assessed, only the radial strain component $\xi_{rr}(=\epsilon_{rr})$ was displayed. This was motivated by the fact that tissue motion,

in EVE, is expected to run parallel with the ultrasound beam. Interestingly, the method was implemented through an adapted version of the Levenberg-Marquardt minimization algorithm, using the optical flow equations to compute the Jacobbian matrix. The theoretical framework was validated using the biomechanical simulations of the vessel wall kinematics for an ''ideal'' and a ''realistic'' plaque geometries, respectively. Elastograms, computed from simulated rf data with the LSME, were supported by ''theoretical'' ones provided by Ansys FE software.

V. CONCLUSION

A new method to characterize mechanically complex vascular pathologies in endovascular elastography (EVE) was presented. First, a polar static image-formation model was introduced. The radial variation of the PSF, associated with the high-frequency IVUS instrument, was conveyed with the beam width, which increases as a linear function of depth. Second, the Lagrangian speckle model estimator (LSME) was adapted for EVE investigations. The LSME was formulated as a nonlinear minimization problem, for which an analytical formulation of the Jacobian matrix was derived. The hypothesis behind that model-based approach was that speckle can be seen as a material property. While the full 2-D polar strain tensor was assessed, only the radial elastograms were presented. Elastograms, computed with the method from simulated rf data of pathological vessel walls, were supported by theoretical ones provided by Ansys FE software. The results help to provide confidence in the potential of EVE to provide very useful information about the heterogeneous nature of atherosclerotic plaques.

ACKNOWLEDGMENTS

The authors gratefully acknowledge Dr. David Savéry for reviewing the manuscript, Mr. François Treyve for helping in numerical simulations with Ansys, and Ms. Isabelle Fontaine and Dr. Michel Bertrand for very helpful discussions. This work was supported by grants from the Natural Sciences and Engineering Research Council of Canada (#138570-01) and Valorisation-Recherche Québec (structuring group program). The salary of Dr. Cloutier is partially supported by a National Scientist award from the Fonds de la Recherche en Santé du Québec.

APPENDIX A: THE LEVENBERG-MARQUARDT NONLINEAR MINIMIZATION

$I_{\mathrm{Lag}}(r,\varphi,t)$ and $\Re(r,\varphi,t)$ [Eq. (19)] are implicit functions of θ_i [Eq. (9)]. For clarity and without loss of generality, let us rewrite $I_{\mathrm{Lag}}(r,\varphi,t)$ as $I_{\mathrm{Lag}}(\vec{\theta})$ and $\Re(r,\varphi,t)$ as $\Re(\vec{\theta})$, respectively; $\vec{\theta}$ is the vectorization of $[LT_p]$. At the kth iteration, one will have

$$\begin{aligned}\Re(\vec{\theta}^k) &= \Re(\vec{\theta}^{k-1}+\Delta\vec{\theta}^k)\\ &= I_0 - I_{\mathrm{Lag}}(\vec{\theta}^{k-1}) - \sum_j^n \frac{\partial I_{\mathrm{Lag}}}{\partial\theta_j}\Delta\theta_j^k|_{\theta_j^{k-1}},\end{aligned} \tag{A1}$$

with $I_0 = I(r,\varphi,0)$.

In Eq. (A1), $\vec{\theta}^{k-1}$ is computed at iteration $k-1$, $\Delta\theta_j^k$ is the increment of the jth component of $\vec{\theta}$, $I_{\mathrm{Lag}}(\vec{\theta}^{k-1})$ is the Lagrangian image at iteration $k-1$, and $\partial I_{\mathrm{Lag}}/\partial\theta_j$ are partial derivatives of I_{Lag} with respect to each component of $\vec{\theta}$. A more compact formulation of Eq. (A1) is given as

$$\vec{I}_0 - \vec{I}_{\mathrm{Lag}}(\vec{\theta}^{k-1}) = [J_{k-1}]\overrightarrow{\Delta\theta}^k + \vec{\Re},$$

with

$$J_{k-1} = \begin{bmatrix} \frac{\partial I_{\mathrm{Lag}}}{\partial\theta_1} & \frac{\partial I_{\mathrm{Lag}}}{\partial\theta_2} & \cdots & \frac{\partial I_{\mathrm{Lag}}}{\partial\theta_n} \\ \vdots & \vdots & & \vdots \\ \frac{\partial I_{\mathrm{Lag}}}{\partial\theta_1} & \frac{\partial I_{\mathrm{Lag}}}{\partial\theta_2} & \cdots & \frac{\partial I_{\mathrm{Lag}}}{\partial\theta_n} \end{bmatrix}, \tag{A2}$$

where $\vec{I}_0$, $\vec{I}_{\mathrm{Lag}}(\vec{\theta}^{k-1})$, and $\vec{\Re}$ are vectorizations of I_0, I_{Lag}, and $\Re$, respectively; $[J_{k-1}]$ is the Jacobian matrix; and $\overrightarrow{\Delta\theta}^k$ is a vector of increments used to update the Lagrangian images ($\overrightarrow{\Delta\theta}^k$ is also known in the literature as the step size). For such a model, the least-square error solution is given as

$$\Delta\theta^k = [J_{k-1}^T J_{k-1}]^{-1} J_{k-1}^T (\vec{I}_0 - \vec{I}_{\mathrm{Lag}}(\vec{\theta}^{k-1})), \tag{A3}$$

where the subscript T designates the transpose operator. When $J_{k-1}^T J_{k-1}$ is not invertible, a regularized version of Eq. (A3) may be required to ensure the convergence of the solution. The Levenberg-Marquardt method (L&M) converges to a potential solution for such a problem (Levenberg, 1963; Marquardt, 1944). The L&M regularized inversion was implemented as

$$\overrightarrow{\Delta\theta}^k = [J_{k-1}^T J_{k-1} + \lambda_k I]^{-1} J_{k-1}^T (\vec{I}_0 - \vec{I}_{\mathrm{Lag}}(\vec{\theta}^{k-1})), \tag{A4}$$

where λ_k is a non-negative scalar, and I is the identity matrix.

APPENDIX B: THE OPTICAL FLOW EQUATIONS AND THE JACOBIAN MATRIX

$I_{\mathrm{Lag}}(\vec{\theta}^{k-1})$ can be seen as a function that describes a material property. Assuming that such a material property is preserved with motion, the total derivative of $I_{\mathrm{Lag}}(\vec{\theta}^{k-1})$ can be expressed as

$$\begin{aligned}\frac{dI_{\mathrm{Lag}}(\vec{\theta}^{k-1})}{d\theta_i} &= \frac{\partial I_{\mathrm{Lag}}(\vec{\theta}^{k-1})}{\partial r}\frac{dr}{d\theta_i} + \frac{\partial I_{\mathrm{Lag}}(\vec{\theta}^{k-1})}{\partial\varphi}\frac{d\varphi}{d\theta_i}\\ &\quad + \frac{\partial I_{\mathrm{Lag}}(\vec{\theta}^{k-1})}{\partial\theta_i} = 0\\ \therefore\ \frac{\partial I_{\mathrm{Lag}}(\vec{\theta}^{k-1})}{\partial\theta_i} &= -\frac{\partial I_{\mathrm{Lag}}(\vec{\theta}^{k-1})}{\partial r}\frac{dr}{d\theta_i}\\ &\quad - \frac{\partial I_{\mathrm{Lag}}(\vec{\theta}^{k-1})}{\partial\varphi}\frac{d\varphi}{d\theta_i},\end{aligned} \tag{B1}$$

with

$$\frac{\partial I_{\mathrm{Lag}}(\vec{\theta}^{k-1})}{\partial\vec{\theta}} = I_{\mathrm{Lag}}(\vec{\theta}^{k-1}+\overrightarrow{\Delta\theta}^k) - I_{\mathrm{Lag}}(\vec{\theta}^{k-1}).$$

As introduced in the paper (section II B2), under the assumption of a small ROI $(\Delta r,\Delta\varphi)$ that is far from the vessel lumen center, tissue motion equivalently can be inves-

tigated using either the Cartesian or polar coordinates. Additionally, for small motion, the gradient of $I_{\mathrm{Lag}}(\vec{\theta}^{k-1})$ should not be significantly different from the gradient $I(r,\varphi,0)$. These hypotheses, in conjunction with Eq. (9), lead to

$$\frac{\partial I_{\mathrm{Lag}}(\vec{\theta}^{k-1})}{\partial \vec{\theta}} \cong \frac{\partial I(\vec{\theta}^{k-1})}{\partial \vec{\theta}} = -\left\{ \frac{\partial I}{\partial x}, \frac{\partial I}{\partial x}x, \frac{\partial I}{\partial x}y, \frac{\partial I}{\partial y}, \frac{\partial I}{\partial y}x, \frac{\partial I}{\partial y}y \right\}. \quad \text{(B2)}$$

Eq. (B2) gives the full expression for the 6 components of the Jacobian matrix $[J_{k-1}]$ [Eq. (21)].

[b)]The radial position-dependence of the PSF is associated with the divergence and the attenuation of the high-frequency IVUS instrument with depth. The attenuation was not taken into account in this study.

[c)]Whereas the lumen is in practice in the near field, it is here simulated as being in the far field [with a beam width $\sigma_{\varphi}(r)=\sigma_0$]. This simplifying hypothesis does not alter the generality of the model, since motion assessment is not relevant for the lumen.

[d)]$[LT]$ is used to define rotation as well as nonrigid motion due to compression, expansion, or shearing.

[e)]Adenosine triphosphate (ATP) temporarily (<3 sec) stops cardiac pulsations. During that period, the blood pressure decreases at approximately 20 mm Hg, allowing the acquisition of data at an optimum unload state of the arterial wall.

[f)]An alternative could have been the simulation of a softer surrounding tissue (about 100 kPa). Since the objective of those simulations was to obtain strain values in the range of 0–10% approximately, this would have required decreasing the nominal intraluminal pressure gradient such that the dilation at the inner wall remained below 10% to prevent signal decorrelation.

[g)]It is to note that $z'(x,y)$ was low-pass filtered with a 2-D-circular Gaussian filter having a 1-pixel standard deviation. Such a step was required in order to reduce the interpolation noise introduced when resampling $z'(x,y)$ to provide $z'_{LT^{-1}}(x,y)$.

[h)]Referring to ϵ_{rr} computed with Ansys FE software (Figs. 6 and 8), the maximum radial strain for both cases was close to 6%. Such a small amount of strain was required to prevent signal decorrelation. In practice, this can be achieved by acquiring pre- and post-motion rf images near end-diastole (de Korte *et al.*, 2000b).

[i)]Radial strain ϵ_{rr} is proportional to $1/r^2$. This decreasing of ϵ_{rr} with depth is usually defined as strain decay.

[j)]Since radial strain ϵ_{rr} decreases proportionally to $1/r^2$, the compensation for strain decay consists in multiplying ϵ_{rr} by a function proportional to r^2, with respect to the vessel lumen center.

Bamber, J. C., and Dickinson, R. J. (**1980**). ''Ultrasonic B-scanning: A computer simulation,'' Phys. Med. Biol. **25**, 463–479.

Brusseau, E., Fromageau, J., Finet, G., Delachartre, P., and Vray, D. (**2001**). ''Axial strain imaging of intravascular data: Results on polyvinyl alcohol cryogel phantoms and carotid artery,'' Ultrasound Med. Biol. **27**, 1631–1642.

Chaturvedi, P., Insana, M. F., and Hall, T. J. (**1998a**). ''2-D companding for noise reduction in strain imaging,'' IEEE Trans. Ultrason. Ferroelectr. Freq. Control **45**, 179–191.

Chaturvedi, P., Insana, M. F., and Hall, T. J. (**1998b**). ''Testing the limitations of 2-D companding for strain imaging using phantoms,'' IEEE Trans. Ultrason. Ferroelectr. Freq. Control **45**, 1022–1031.

Cheng, G. C., Loree, H. M., Kamm, R. D., Fishbein, M. C., and Lee, R. T. (**1993**). ''Distribution of circumferential stress in ruptured and stable atherosclerotic lesions: a structural analysis with histopathological correlation,'' Circulation **87**, 1179–1187.

de Korte, C. L., Pasterkamp, G., Van der Steen, A. F. W., Woutman, H. A., and Bom, N. (**2000a**). ''Characterization of plaque components with intravascular ultrasound elastography in human femoral and coronary arteries in vitro,'' Circulation **102**, 617–623.

de Korte, C. L., Van der Steen, A. F. W., Céspedes, E. I., Pasterkamp, G., Carlier, S. G., Mastik, F., Schoneveld, A. H., Serruys, P. W., and Bom, N. (**2000b**). ''Characterization of plaque components and vulnerability with intravascular ultrasound elastography,'' Phys. Med. Biol. **45**, 1465–1475.

de Korte, C. L., Van der Steen, A. F. W., Céspedes, E. I., and Pasterkamp, G. (**1998**). ''Intravascular ultrasound elastography in human arteries: Initial experience in vitro,'' Ultrasound Med. Biol. **24**, 401–408.

de Korte, C. L., Céspedes, E. I., Van der Steen, A. F. W., and Lancée, C. T. (**1997**). ''Intravascular elasticity imaging using ultrasound—Feasibility studies in phantoms,'' Ultrasound Med. Biol. **23**, 735–746.

Horn, B. K. P. (**1986**). Robot Vision (*McGraw-Hill*, New York), pp. 278–298.

Kallel, F., and Bertrand, M. (**1994**). ''Speckle motion artifact under tissue rotation,'' IEEE Trans. Ultrason. Ferroelectr. Freq. Control **41**, 105–122.

Lee, R. T., Loree, H. M., Cheng, G. C., Lieberman, E. H., Jaramillo, N., and Schoen, F. J. (**1993**). ''Computational structural analysis based on intravascular ultrasound imaging before in vitro angioplasty: prediction of plaque fracture locations,'' J. Am. Coll. Cardiol. **21**, 777–782.

Levenberg, K. (**1963**). ''A method for the solution of certain non-linear problems in least-squares,'' Q. Appl. Math **2**, 164–168.

Loree, H. M., Kamm, R. D., Stringfellow, R. G., and Lee, R. T. (**1992**). ''Effects of fibrous cap thickness on peak circumferential stress in model atherosclerotic vessels,'' Circ. Res. **71**, 850–858.

Marquardt, D. W. (**1944**). ''An algorithm for least-squares estimation of non-linear parameters,'' J. Soc. Ind. Appl. Math. **11**, 431–441.

Maurice, R. L., Ohayon, J., Frétigny, Y., Bertrand, M., Soulez, G., and Cloutier, G. (**2004**). ''Non-invasive vascular elastography: Theoretical framework,'' IEEE Trans. Med. Imaging **23**, 164–180.

Maurice, R. L., and Bertrand, M. (**1999a**). ''Lagrangian speckle model and tissue-motion estimation—Theory,'' IEEE Trans. Med. Imaging **18**, 593–603.

Maurice, R. L., and Bertrand, M. (**1999b**). ''Speckle-motion artifact under tissue shearing,'' IEEE Trans. Ultrason. Ferroelectr. Freq. Control **46**, 584–594.

Meunier, J., and Bertrand, M. (**1995**). ''Ultrasonic texture motion analysis: Theory and simulation,'' IEEE Trans. Med. Imaging **14**, 293–300.

Ohayon, J., Teppaz, P., Finet, G., and Rioufol, G. (**2001**). ''In vivo prediction of human coronary plaque rupture location using intravascular ultrasound and finite element method,'' Coron. Artery Dis. **12**, 655–663.

Ophir, J., Alam, S. K., Garra, B., Kallel, F., Konofagou, E., Krouskop, T., and Varghese, T. (**1999**). ''Elastography: ultrasonic estimation and imaging of the elastic properties of tissues,'' Proc. Inst. Mech. Eng. **213**, 203–233.

Rachev, A. (**1997**). ''Theoretical study of the stress-dependent remodeling on arterial geometry under hypertensive conditions,'' J. Biomech. **30**, 819–827.

Rioufol, G., Finet, G., Tabib, A. *et al.* (**1999**). ''The (often) four-layer apparence of coronary arteries by intravascular ultrasound: the tunica adventitia,'' J. Am. Coll. Cardiol. **16**, 77A (abstract).

Ryan, L. K., and Foster, F. S. (**1997**). ''Ultrasonic measurement of differential displacement strain in a vascular model,'' Ultrason. Imaging **19**, 19–38.

Shapo, B. M., Crowe, J. R., Skovoroda, A. R., Eberle, M. J., Cohn, N. A., and O'Donnell, M. (**1996a**). ''Displacement and strain imaging of coronary arteries with intraluminal ultrasound,'' IEEE Trans. Ultrason. Ferroelectr. Freq. Control **43**, 234–246.

Shapo, B. M., Crowe, J. R., Erkamp, R., Emelianov, S. Y., Eberle, M. J., and O'Donnell, M. (**1996b**). ''Strain imaging of coronary arteries with intraluminal ultrasound: Experiments on an inhomogeneous phantom,'' Ultrason. Imaging **18**, 173–191.

Treyve, F., Ohayon, J., Finet, G., and Rioufol, G. (**2003**). ''Modelling of the stress distribution in an atherosclerotic plaque in man using a finite element analysis,'' Comptes Rendus Mécanique **331**, 449–454.

Wan, M., Li, Y., Li, J., Cui, Y., and Zhou, X. (**2001**). ''Strain imaging and elasticity reconstruction of arteries based on intravascular ultrasound video images,'' IEEE Trans. Biomed. Eng. **48**, 116–120.

Williamson, S. D., Lam, Y., Younis, H. F., Huang, H., Patel, S., Kaazempur-Mofrad, M. R., and Kamm, R. D. (**2003**). ''On the sensitivity of wall stresses in diseased arteries to variable material properties,'' J. Biomech. Eng. **125**, 147–155.